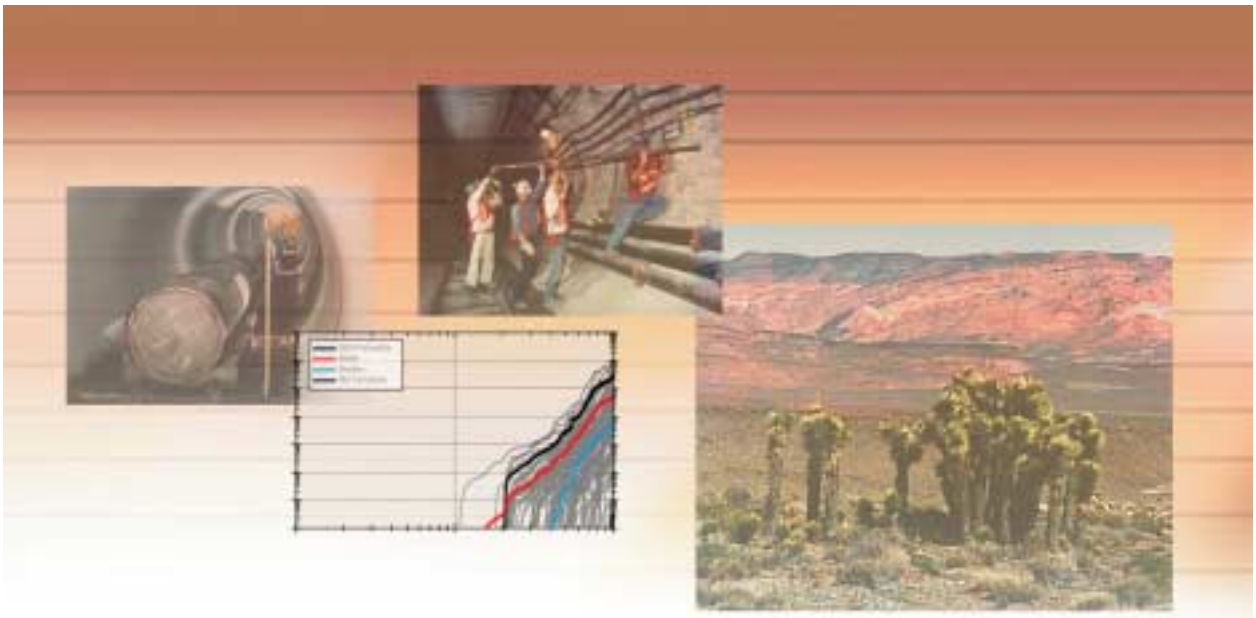

FY01 Supplemental Science and Performance Analyses,

Volume 1: Scientific Bases and Analyses

Part 1 of 2

U.S. Department of Energy
Office of Civilian Radioactive Waste Management

June 2001

QA: QA

TDR-MGR-MD-000007 REV 00 ICN 01

July 2001

FY 01 Supplemental Science and Performance Analyses

Volume 1:
Scientific Bases and Analyses

By
BSC

Prepared for:
U.S. Department of Energy
Yucca Mountain Site Characterization Office
P.O. Box 30307
North Las Vegas, Nevada 89036-0307

Prepared by:
Bechtel SAIC Company, LLC
1180 Town Center Drive
Las Vegas, Nevada 89144

Under Contract Number
DE-AC08-01RW12101

DISCLAIMER

This report was prepared as an account of work sponsored by an agency of the United States Government. Neither the United States Government nor any agency thereof, nor any of their employees, nor any of their contractors, subcontractors or their employees, makes any warranty, express or implied, or assumes any legal liability or responsibility for the accuracy, completeness, or any third party's use or the results of such use of any information, apparatus, product, or process disclosed, or represents that its use would not infringe privately owned rights. Reference herein to any specific commercial product, process, or service by trade name, trademark, manufacturer, or otherwise, does not necessarily constitute or imply its endorsement, recommendation, or favoring by the United States Government or any agency thereof or its contractors or subcontractors. The views and opinions of authors expressed herein do not necessarily state or reflect those of the United States Government or any agency thereof.

Prepared by:

David Dobson et al.
Lead Author

7/24/01
Date

Checked by:

Norma Rupert, for David Mohr

David Mohr et al.
Lead Checker

7/24/01
Date

Approved by:

Robert L. Howard
Integration Manager, Science and Analysis Project

24 July 01
Date

CHANGE HISTORY

Revision Number	Interim Change No.	Effective Date	Description of Change
00	00	06/2001	Initial issue
00	01	07/2001	Interim Change Notice to incorporate changes to figures and text in Sections 5.3.1.4.11, 5.3.2.4.2, 5.3.2.4.3, 5.4.2, 5.4.3, and 15 due to corrections made in the radiation heat transfer process between the drip shield and the drift wall in the two-dimensional, line-heat source, drift-scale, thermal-hydrologic submodel for the lower-temperature operating mode. Changes were also made to reference citations within Section 5, to correct Document Input Reference System (DIRS) numbers, and the name of an author. All changes are indicated by vertical bars in the page margins. Two DIRS database entries were changed: DIRS 155243 was replaced with DIRS 155449, and DIRS 154996 was replaced with DIRS 155457.

INTENTIONALLY LEFT BLANK

ACKNOWLEDGMENTS

The following individuals have contributed to the technical content and preparation of this document: Rob L. Howard, David Dobson, Ahmed M. Monib, Robert W. Andrews, Gudmundur S. Bodvarsson, Karen E. Jenni, Kevin Coppersmith, James A. Blink, Robert MacKinnon, James Nowak, Tammy Summers, Christine Stockman, Mike Gross, Aziz A. Eddebbarh, Anthony J. Smith, Kathy Gaither, Marco W. Lee, David Mohr, James L. Boone, Ardyth Simmons, Gerald Nieder-Westermann, Joe Wang, Andre Unger, MaryAnn Villavert, Stefan Finsterle, Yvonne Tsang, Eric L. Sonnenthal , Dale G. Wilder, Randolph L. Schreiner, Carol J. Passos, Thomas A. Buscheck, James Schreiber, Junghun Leem, Nicholas Francis, Steven Carlson, Alfred Reed, Chin-Fu Tsang, Donna Francis, Hang Yang, Amy R. Loch, Richard C. Metcalf, Darren M. Jolley, Dwayne Kicker, Joon H. Lee, Greg Gdowski, Kevin G. Mon, Bryan B. Bullard, Pasu Pasupathi, Gerald Gordon, John Case, Guy Ragan, Patrick V. Brady, Yueting Chen, Hui-Hai Liu, Patricia VanDillen, Ernest L. Hardin, Bruce Robinson, Stephanie Kuzio, Wesley Wu, Maryla Wasiolek, Jeffery J. Tappen, John F. Schmitt, Richard C. Quittmeyer, Robert Richards, John McCord, William Statham, Richard Aguilar, Greg Valentine, Randy Hedegaard, Jose Archuleta, Robert Youngs, James E. Houseworth, Nicolas Spycher, Paul Reimus, Stephen Blair, Thomas Corbett, Larry Saraka, Kurt R. Rautenstrauch, Bruce E. Kirstein, Thomas W. Doering, Stephen Alcorn, Bill Arnold, Melissa L. Hamner, Alycia N. Kahanaoi, Cecelia Sales, William R. Hunt, Norma E. Biggar, Robert Zimmerman, Amir S. Mobasheran, Terry Steinborn, Holly Miller, Daniel McGregor, Paul Kaplan, Denise R. Myers, Gordon Evans, Janette E. Lloyd, James T. Kam, David Stahl, Ming Zhu, Peter Persoff, Haywood Anderson, Steven H. Swenning, Patrick Rowe, Edward Kwicklis, Claudia Faunt, William Dudley, Pat Tucci, Rick Spengler, Zell Peterman, John Stuckless, Andy Wolfsberg, Arend Meijer, George Zyvoloski, Carl Axness, Leigh Lechel, Diane Hyer, Roger Eckhardt, Kayce Prince, Roseanne Perman, Rick Hyman, Ronda Hyman, Catherine A. Stewart, Sarah Fisher, Penny Meyer, Edna McKlveen, Jacqueline Krogh, Katie Miller, Crissy Cisneros, Linda Grisham, Vicky Obrad, Shelley Royall, Ann Merey, Nick Connerley, Daniel Brenton, Judy Gibes, Richard Danat, Cindy Dodson, Maria Therien, Valerie Kelly, Michelle Prater, Keenan K.N. Fong, Shirley Crawford, and Sandra Martin.

This work was supported by the Yucca Mountain Site Characterization Office as part of the Civilian Radioactive Waste Management Program, which is managed by the U.S. Department of Energy, Yucca Mountain Site Characterization Project.

INTENTIONALLY LEFT BLANK

CONTENTS

Page

CONTENTS (Continued)

Page

CONTENTS (Continued)

Page

CONTENTS (Continued)

Page

CONTENTS (Continued)

Page

CONTENTS (Continued)

Page

CONTENTS (Continued)

Page

CONTENTS (Continued)

Page

FIGURES

Page

FIGURES (Continued)

Page

FIGURES (Continued)

Page

FIGURES (Continued)

Page

FIGURES (Continued)

Page

FIGURES (Continued)

Page

FIGURES (Continued)

Page

FIGURES (Continued)

Page

FIGURES (Continued)

Page

FIGURES (Continued)

Page

FIGURES (Continued)

Page

FIGURES (Continued)

Page

FIGURES (Continued)

Page

FIGURES (Continued)

Page

FIGURES (Continued)

Page

FIGURES (Continued)

Page

FIGURES (Continued)

Page

FIGURES (Continued)

Page

TABLES

Page

TABLES (Continued)

Page

TABLES (Continued)

Page

TABLES (Continued)

Page

TABLES (Continued)

Page

TABLES (Continued)

Page

TABLES (Continued)

Page

TABLES (Continued)

Page

TABLES (Continued)

Page

INTENTIONALLY LEFT BLANK

ACRONYMS

AFC	active fracture concept
AECL	Atomic Energy of Canada Limited
AFM	active fracture model
AML	areal mass loading
AMR	analysis model report
ANC	acid neutralizing capacity
ANL	Argonne National Laboratory
ASTM	American Society for Testing and Materials
ATC	Alluvial Testing Complex
BDCF	biosphere dose conversion factor
BWR	boiling water reactor
CADI	contingent average daily intakes
CCT	critical crevice temperature
CDF	cumulative distribution function
CEDE	committed effective dose equivalent
CFD	computational fluid dynamics
CNWRA	Center for Nuclear Waste Regulatory Analysis
CSNF	commercial spent nuclear fuel
DCF	dose conversion factor
DDT	discrete-heat-source, drift-scale, thermal-conduction
DFM	discrete fracture model
DHLW	DOE high-level radioactive waste
DKM	dual permeability model
DMTH	discrete-source, mountain-scale, thermal-hydrologic
DOE	U.S. Department of Energy
DST	drift-scale test
EBS	engineered barrier system
ECRB	Enhanced Characterization of the Repository Block
EDA	Enhanced Design Alternative
EPRI	Electrical Power Research Institute
ESF	Exploratory Studies Facility
FCC	face-centered cubic
FEPs	features, events, and processes
FHH	Frankel-Halsey-Hill
FU	fractional uncertainty
GCM	generalized corrosion model
HIC	hydrogen induced cracking
HLW	high-level waste
HTOM	higher-temperature operating mode

ACRONYMS (Continued)

IAEA	International Atomic Energy Agency
ICPP	Idaho Chemical Processing Plant
ICRP	International Commission on Radiological Protection
INEEL	Idaho National Engineering and Environmental Laboratory
IHSI	Induction Heating Stress Improvement
LADS	License Application Design Selection
LDTH	line-averaged-heat-source, drift-scale, thermal-hydrologic
LMTH	line-source, mountain-scale thermal-hydrologic
LRO	long-range order
LTCTF	Long-Term Corrosion Test Facility
LTOM	lower-temperature operating mode
MIC	microbiologically influenced corrosion
MINC	multiple interacting continua
MPM	mixed potential model
MSTH	multiscale thermal-hydrologic
MTC	mass transfer coefficient
MTHM	metric tons of heavy metal
MTI	Materials Technology Institute
MTU	metric tons of uranium
NC-EWDP	Nye County Early Warning Drilling Program
NFE	near-field environment
NRC	U.S. Nuclear Regulatory Commission
NTS	Nevada Test Site
OIS	oxygen isotope stage
PDM	point defect model
PSHA	probabilistic seismic hazard analysis
PVHA	probabilistic volcanic hazard analysis
PWR	pressurized water reactor
RH	relative humidity
REE	rare earth element
RMEI	reasonably maximally exposed individual

ACRONYMS (Continued)

S&ER	Yucca Mountain Science and Engineering Report
SCC	stress corrosion cracking
SCE	saturated calomel electrode
SDT	smeared-heat-source, drift-scale, thermal-conduction
SHE	standard hydrogen electrode
SMT	smeared-heat-source, mountain-scale, thermal-conduction
SNF	spent nuclear fuel
SRP	Snake River Plain
SZ	saturated zone
TC	thermal-chemical
TCP	tetrahedrally close-packed
TEDE	total effective dose equivalent
TH	thermal-hydrologic
THC	thermal-hydrologic-chemical
THM	thermal-hydrologic-mechanical
TM	thermal-mechanical
TSP	total suspended particles
TSPA	total system performance assessment
TSPA-SR	total system performance assessment for the site recommendation
TSPA-VA	total system performance assessment for the viability assessment
TTT	time-temperature-transformation
UMTRA	Uranium Mill Tailings Remedial Action
USGS	U.S. Geological Survey
UTM	Universal Transverse Mercator
UZ	unsaturated zone
VA	viability assessment
YMP	Yucca Mountain Site Characterization Project

INTENTIONALLY LEFT BLANK

1 Introduction

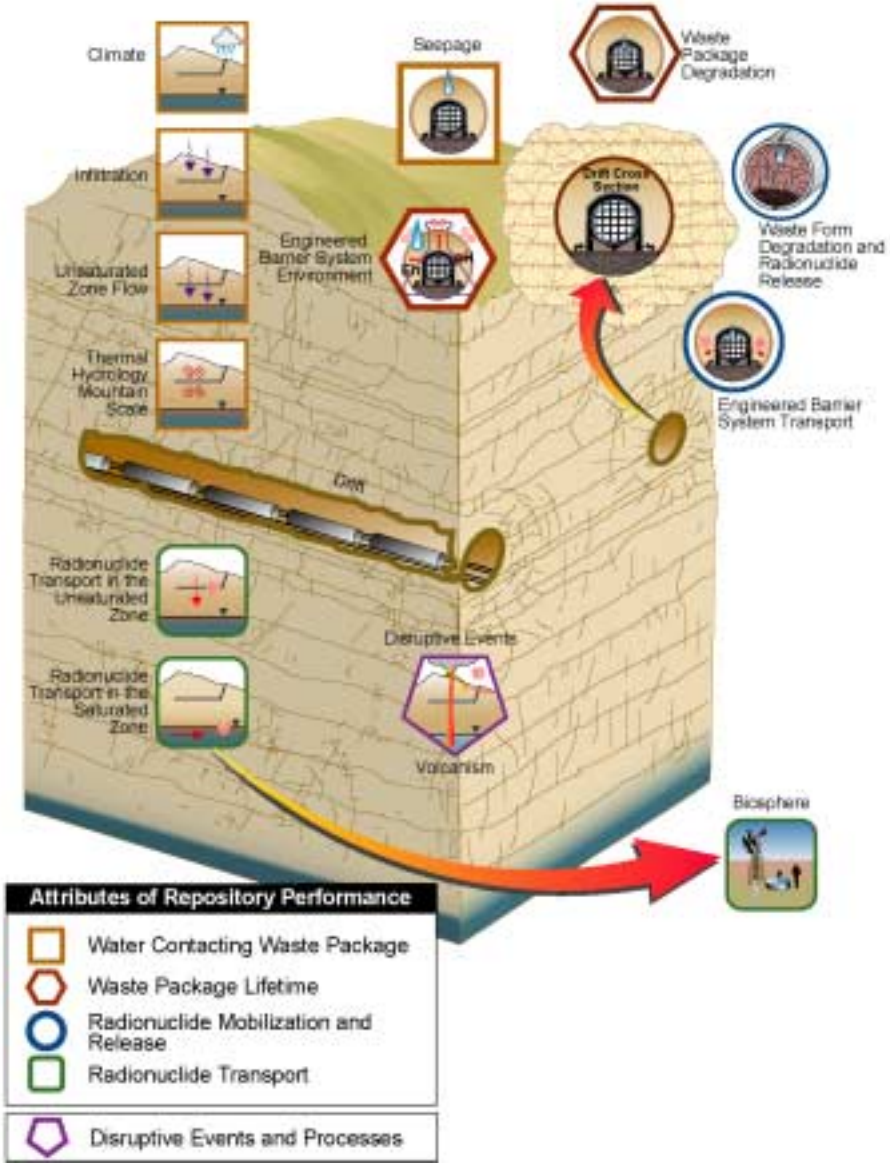

1. INTRODUCTION

The U.S. Department of Energy (DOE) is considering the possible recommendation of a site at Yucca Mountain, Nevada, for development as a geologic repository for the disposal of high-level radioactive waste and spent nuclear fuel. To facilitate public review and comment, in May 2001 the DOE released the *Yucca Mountain Science and Engineering Report* (S&ER) (DOE 2001 [DIRS 153849]), which presents technical information supporting the consideration of the possible site recommendation. The report summarizes the results of more than 20 years of scientific and engineering studies. A decision to recommend the site has not been made: the DOE has provided the S&ER and its supporting documents as an aid to the public in formulating comments on the possible recommendation.

When the S&ER (DOE 2001 [DIRS 153849]) was released, the DOE acknowledged that technical and scientific analyses of the site were ongoing. Therefore, the DOE noted in the Federal Register Notice accompanying the report (66 FR 23013 [DIRS 155009], p. 2) that additional technical information would be released before the dates, locations, and times for public hearings on the possible recommendation were announced. This information includes: (1) the results of additional technical studies of a potential repository at Yucca Mountain, contained in this *FY01 Supplemental Science and Performance Analyses: Vol. 1, Scientific Bases and Analyses*; and *FY01 Supplemental Science and Performance Analyses: Vol. 2, Performance Analyses* (McNeish 2001 [DIRS 155023]) (collectively referred to as the SSPA) and (2) a preliminary evaluation of the Yucca Mountain site's preclosure and postclosure performance against the DOE's proposed site suitability guidelines (10 CFR Part 963 [64 FR 67054 [DIRS 124754]).

By making the large amount of information developed on Yucca Mountain available in stages, the DOE intends to provide the public and interested parties with time to review the available materials and to formulate and submit comments. Before determining whether to recommend the Yucca Mountain site, the Secretary will consider public and stakeholder comments, as well as the available technical information.

1.1 BACKGROUND

The *FY01 Supplemental Science and Performance Analyses* is intended to supplement information contained in analysis and model reports supporting the S&ER (DOE 2001 [DIRS 153849]), which summarizes the extensive scientific and engineering analyses the DOE has conducted to assess how a potential repository might perform in the future. The S&ER describes the data collected during site characterization and the preliminary design of the repository facilities and waste packages that would contribute to the safe disposal of waste. Section 4 of the report explains the processes that could affect the ability of the site to isolate waste. These include both natural processes and processes caused or affected by human activities, such as the construction of the potential repository. Natural processes include the flow of water through the unsaturated zone of rock above the water table, water flow in the saturated zone of rock below the water table, and geochemical processes (such as dissolution or mineral precipitation) that could result in the transport of radionuclides.

Near the waste emplacement drifts, the natural system would be perturbed by the mechanical excavation of the drifts and by the heat generated by radioactive decay in the emplaced waste. The heat and the mechanical stresses could affect the natural processes in complex ways. The coupling of these natural and man-made processes may introduce additional complexity into models of repository performance. Therefore, the S&ER (DOE 2001 [DIRS 153849]) also explains how these coupled thermal-hydrologic-geochemical-mechanical processes would be likely to affect the long-term performance of the repository. These processes affect both the natural and the engineered barriers, including the drip shields, the waste forms, the waste packages, and the invert below the waste packages. In addition to the hydrologic and geochemical processes that would act in and around the potential repository, disruptive events, such as the possibility of volcanic eruptions, could affect the integrity of the repository. The S&ER describes the likelihood and consequences of disruptive events at Yucca Mountain.

The S&ER (DOE 2001 [DIRS 153849], Section 4.4) summarizes the results of a comprehensive quantitative analysis of the possible future behavior of a Yucca Mountain repository. This analysis, known as the *Total System Performance Assessment for the Site Recommendation* (TSPA-SR) (CRWMS M&O 2000 [DIRS 153246]), combines the results of detailed conceptual and numerical models of each of the individual and coupled processes in a single probabilistic model that can be used to assess how a repository might perform over long periods of time.

Despite the extensive scientific studies described in the S&ER (DOE 2001 [DIRS 153849]), the DOE has always recognized that significant uncertainties will remain in any assessment of the performance of a repository over thousands of years, as discussed in the S&ER (DOE 2001 [DIRS 153849], Sections 1.5, 4.1, and 4.4). These uncertainties are attributable to a variety of causes, ranging from uncertainty regarding the fundamental processes that may affect radionuclide migration to uncertainty related to the design and operation of the potential repository. For this reason, one part of the DOE approach to dealing with uncertainty relies on multiple lines of evidence that may contribute to the understanding of the performance of the potential repository. Another part of the DOE approach is a commitment to continued testing, monitoring, and analysis beyond the possible recommendation of the site.

This report has been prepared to address several specific aspects of the existing uncertainties related to the performance of a potential Yucca Mountain repository. It describes new information developed since the completion of the S&ER (DOE 2001 [DIRS 153849]) and its key supporting references, the TSPA-SR (CRWMS M&O 2000 [DIRS 153246]) and the analysis model reports and process model reports cited therein.

1.2 GOALS AND SCOPE

Based on internal reviews of the S&ER (DOE 2001 [DIRS 153849]) and other documents, the DOE has identified and performed several types of analyses to supplement the treatment of uncertainty in support of the consideration of a possible site recommendation. The information in this report is intended to supplement, not supplant, that contained in the analysis and model reports and process model reports supporting the S&ER. In general, the studies and analyses described in this document provide additional information of three types:

Unquantified Uncertainties Analysis–Specific uncertainties that were not treated explicitly in the S&ER and the TSPA-SR (CRWMS M&O 2000 [DIRS 153246]) are quantified. Unquantified uncertainties include parameter bounds, conceptual models, assumptions and, in some cases, input parameters consisting of statistically biased or skewed distributions. The primary goals of this effort were to provide insights into the significance of the unquantified uncertainties and the degree of conservatism in the overall assessment of repository performance in the TSPA-SR.

Updates in Scientific Information–New information has been developed for some of the process models that are important to performance. This work includes new experimental results, new conceptual models, and new analytical approaches, as well as the results of continued research. It also includes the identification and discussion of multiple lines of evidence that have been used directly, to support modeling, or indirectly, to develop confidence in modeling results. The primary goals of this effort were to provide insights into the impacts of the new scientific results and improved models (i.e., those updated since completion of the S&ER) and to develop additional confidence in the models and parameters used for total system performance assessment (TSPA).

Lower-Temperature Operating Mode Analysis–Because some of the processes that can affect performance are a function of the environment in the repository (e.g., temperature and humidity), the uncertainties associated with models of these processes also depend on environmental variables. In particular, operating the repository at temperatures above 96°C would result in water boiling and condensing, which requires models of flow and transport that are more complex—and possibly more uncertain—than models at lower temperatures. Therefore, the effects of a range of thermal operating modes on projected system performance, including lower operating temperatures in the potential repository (e.g., below 96°C at the drift wall or below 85°C at the waste package surface), have been evaluated. The uncertainties associated with various process models have been analyzed over a range of temperatures. The primary goals of evaluating a range of thermal operating modes were to provide insights into the effect of thermal parameters on predicted repository performance, including the uncertainty of those predictions, and to increase confidence in the predicted repository performance over a range of thermal conditions.

1.2.1 Outline of Report

This report describes the supplemental analyses that have been performed and the results of incorporating those analyses into a supplemental TSPA. It consists of two volumes: *FY01 Supplemental Science and Performance Analyses: Vol. 1, Scientific Bases and Analyses* and

FY01 Supplemental Science and Performance Analyses: Vol. 2, Performance Analyses (McNeish 2001 [DIRS 155023]). Volume 1 focuses on the technical work conducted within each process model area, encompassing uncertainty quantification, updated science and models, and lower-temperature operating mode analyses. Volume 2 describes the performance assessment analyses conducted using the updated information documented in Volume 1.

Table 1-1 shows the supplemental analyses that have been produced, the rationale for obtaining that supplemental information (i.e., unquantified uncertainties, updated scientific information, or lower-temperature operating mode analyses), and the section in this report where the work is documented. The last two columns of the table indicate how the supplemental information described in this volume is evaluated in the performance assessment analyses described in Volume 2 (McNeish 2001 [DIRS 155023]).

Section 2 of this volume describes the methodology used to define and conduct the updated analyses described in this report. The remaining sections are organized around the major processes that are expected to occur in Yucca Mountain and the proposed repository system. The structure of this document generally follows that of the S&ER (DOE 2001 [DIRS 153849]). Figure 1-1 illustrates the processes and their relationships.

Each of Sections 3 through 14 begins with a brief description of the conceptual basis for the process model supporting the S&ER (DOE 2001 [DIRS 153849]) and the TSPA-SR (CRWMS M&O 2000 [DIRS 153246]). Each section includes a description of new information and analyses that have been conducted and the results obtained using that new information. The specific content and the level of detail in Sections 3 through 14 vary, depending on the extent of the analyses that have been performed. The discussion may range from a summary level to detailed descriptions and analyses of the supplemental information. Depending on what specific information has been collected, the discussions may include the quantification of uncertainties, updated scientific information and models, and thermal sensitivity analyses. Where relevant, each section includes a discussion of other lines of evidence that provide additional evidence for and/or confidence in the process models. Finally, each section describes how the results of the new information at the process level were carried through to the abstracted models used for the supplemental TSPA analyses, which are documented in Volume 2 (McNeish 2001 [DIRS 155023]).

1.3 RATIONALE

1.3.1 Quantification of Uncertainties

As described in the S&ER (DOE 2001 [DIRS 153849]), many uncertainties associated with long-term repository performance were addressed quantitatively and probabilistically in the process models and performance assessment analyses. However, some uncertainties in processes and parameters were addressed through the use of bounding or conservative assumptions that were intended to simplify the analysis and ensure that the results were technically defensible. In a few cases, assumptions may have led to non-conservatisms when implemented in the model. The use of bounding values and conservative assumptions generally yields model simulations that predict poorer performance (i.e., higher projected doses) than analysts expect. However, because the degree of conservatism for each process or parameter has not been quantified, it is

difficult to assess the extent to which the total system results may also be conservative. This report describes the quantification of some of the uncertainties that were unquantified in the TSPA-SR (CRWMS M&O 2000 [DIRS 153246]). Unquantified uncertainties include parameter bounds, conceptual models, assumptions, point estimates, or input parameters that use statistically biased or skewed distributions.

1.3.1.1 Types of Uncertainties

Accounting for, classifying, and understanding the implications of uncertainties is a critical part of modeling any complex system. Managing those uncertainties is a critical part of designing and operating any complex system. Uncertainties may arise from such aspects as incomplete understanding, limited information, or lack of data, in addition to the uncertainties inherent in developing any model of a natural or engineered system. The DOE considers uncertainties of several different types, and incorporates them in several different ways, in evaluations and estimates of repository performance.

Scenario Uncertainty–Scenario uncertainty refers to uncertainty about how future states of the world will evolve. It includes the uncertainty associated with the features, events, and processes that may impact various components of the repository system. Scenarios of plausible future states of the repository system, as well as their likelihood of occurrence, must be inferred from direct and indirect field evidence; those scenarios that meet the criteria for likelihood of occurrence and impact to annual dose should be incorporated into assessments of repository performance.

Model Uncertainty–All models are simplifications of the real system being modeled, and simplifications necessarily introduce uncertainties. Model uncertainty encompasses several types: uncertainty in conceptual models, uncertainty in the mathematical descriptions of conceptual models, and uncertainty in the numerical implementation of models in computer codes.

Parameter Uncertainty and Variability–The parameters of the mathematical models used to predict the performance of the repository system are subject to both uncertainty and variability. Uncertainty in model parameters may arise from imperfect knowledge or limited data. Variability may arise from the randomness or heterogeneity of physical characteristics in the engineered system, natural system, or biosphere. In some cases, variability is modeled by including it as uncertainty in model parameters.

Spatial and Temporal Variability–For large-scale (e.g., igneous activity) and small-scale (e.g., rock porosity) processes and properties, variability over time and over the area of the repository may have an important impact on performance. Because variability is an intrinsic property of a system, it cannot be reduced with additional information. Because it has an important impact on performance, variability is included explicitly in some process and TSPA models.

1.3.1.2 Quantified and Unquantified Uncertainties

In the process models and the TSPA-SR model supporting the S&ER (DOE 2001 [DIRS 153849]), some uncertainties are quantified and others are unquantified. Quantified

uncertainties are those for which a detailed, unbiased, quantitative description of uncertainty (e.g., a probability distribution) has been developed from available data. An unbiased estimate is one that is neither deliberately conservative nor deliberately optimistic, that neither underestimates nor overestimates performance. In some cases, unbiased quantitative estimates of uncertainty were not feasible, for example, because of the limited availability of data or process complexity. Some uncertainties were not quantified because the range of possible scenarios, processes, models, hypotheses, and parameter values made little or no difference to the overall model results, so computational efficiency was gained by choosing a single representation of the uncertainty. Unquantified uncertainties in the TSPA-SR and supporting models include alternative models, alternative hypotheses, particular assumptions, and single point estimates used to represent an uncertain property value. Unquantified uncertainty may also exist when model inputs are treated probabilistically if the range of inputs is chosen to be a conservative bound on the range of all possible values.

1.3.1.3 Rationale for Quantifying Previously Unquantified Uncertainties

The DOE deliberately chose a mix of quantified, best estimate (realistic), and unquantified (typically conservative) models and parameter values to develop a defensible, compliance-based evaluation of the potential performance of the repository system. This evaluation is included in the analysis and model reports supporting the S&ER (DOE 2001 [DIRS 153849]). However, both the DOE and external reviewers of the Yucca Mountain Site Characterization Project (YMP) (e.g., the Nuclear Waste Technical Review Board and Advisory Committee on Nuclear Waste) recognize that additional insights into repository performance can be gained from analyzing the assumptions underlying the process models. Also, further examination of the sensitivity of the total system model to these assumptions and other uncertainties may provide relevant information about the significance of the uncertainties (i.e., the importance of a specific uncertainty to repository performance).

The mix of conservative, potentially nonconservative, and realistic inputs makes it difficult to interpret the uncertainty in annual dose estimates over time produced by the TSPA-SR model. Because some inputs are clearly conservative, the annual dose estimates do not represent a best or most realistic estimate of actual performance. However, since some inputs may not be conservative, it is not clear that the annual dose estimates are entirely conservative.

It is difficult to quantify the degree of conservatism among the different process models that compose the TSPA-SR (CRWMS M&O 2000 [DIRS 153246]). In coupled models, conservatisms and assumptions in one model can mask the importance of another. It is not possible to quantify the relative conservatism in a model or its parameters without evaluating the impact of the model or parameter on the output of the fully coupled model. It is also not possible to say how conservative a specific process model is without looking at how that input affects the annual dose estimates from the TSPA-SR model.

Finally, even if each model and input were conservative, the degree to which those conservative inputs would result in a conservative annual dose estimate is not clear. The mixture of inputs makes it difficult to ascertain the degree of conservatism in the overall TSPA-SR. The quantification of uncertainties discussed in this report represents an effort to develop an understanding of the degree of conservatism in the annual dose estimates from the TSPA-SR.

1.3.2 Updated Scientific Bases and Analyses

In addition to quantifying specific uncertainties previously unquantified, the DOE has continued to improve its scientific understanding of and the technical bases for the process and performance assessment models. This document describes updates to the process models that have occurred since the models supporting the S&ER (DOE 2001 [DIRS 153849]) were developed and documented. These updates appear as discussions of new or more extensive data, revised process models, and updated abstractions for the supplemental TSPA model. The updates are an expected result of the ongoing scientific and engineering analyses supporting the DOE, and they represent the progress that has been made over the period since the documents supporting the S&ER (DOE 2001 [DIRS 153849]) were finalized. The SSPA report provides a vehicle for documenting that additional information and evaluating its significance in performance analyses.

1.3.3 Thermal Sensitivity Analyses

The third element of the new information and technical improvements since the analyses and model reports supporting S&ER (DOE 2001 [DIRS 153849]) were completed is a set of analyses designed to increase understanding of the effects of a range of operating modes and temperatures on potential repository performance.

1.3.3.1 Thermally Driven Uncertainties

Two uncertainties related to thermal effects on potential repository performance are: (1) the way Yucca Mountain will respond to the heat generated by emplaced waste, and (2) the long-term performance of the materials used to package the waste when subjected to the expected repository environment.

Coupled Processes–As the temperature of the host rock rises, the extent, magnitude, duration, and significance of thermally induced coupled processes may also increase. These coupled processes include such effects as:

- Thermal hydrology (heat influencing water movement)
- Changes in rock matrix and fracture flow properties
- Dissolution, movement, and precipitation of salts and minerals.

Materials Corrosion–A key component of the flexible design summarized in the S&ER (DOE 2001 [DIRS 153849]) is the waste package, which is designed to isolate waste from the environment for an extended period of time. The outer shell of the waste package consists of a thick layer of corrosion-resistant Alloy 22, which forms a primary barrier to water contacting the waste. As Summarized in the S&ER, process model results indicate that the outer barrier has an extremely long lifetime, with a median time to first failure of 80,000 years (DOE 2001 [DIRS 153849], Section 4.2.4.4). Because of the key role the waste package plays in performance assessments, it is important to understand the potential failure modes of Alloy 22, particularly its susceptibility to localized corrosion.

Findings about localized corrosion of Alloy 22 in highly aggressive environments suggest a range of conditions under which the material may be more susceptible to localized corrosion. These specifically include aggressive environments where the temperatures are high and the relative humidity is such that an aqueous film containing salts can form on the surface of the material. Analyses summarized in the S&ER (DOE 2001 [DIRS 153849], Section 2.1.5) indicate that the susceptibility of Alloy 22 to corrosion can be significantly reduced by maintaining waste package surface temperatures below about 85°C or relative humidity below about 50 percent.

1.3.3.2 Rationale for Evaluating a Range of Thermal Operating Modes

The overall DOE strategy for handling uncertainties is to recognize and incorporate them to the extent possible, and to take steps to reduce or mitigate those uncertainties that may have a major impact on estimates of potential repository performance. Uncertainties can be *reduced* through additional scientific and technical studies; the effect of uncertainties can be *mitigated* by engineering design choices. Uncertainties that do not appear to have the potential to significantly impact performance assessments, or uncertainties for which reduction and/or mitigation measures are not available or effective, are typically accepted and incorporated into the process models and total system analyses. For example, in the analyses and models supporting the S&ER (DOE 2001 [DIRS 153849]), uncertainties related to the effect on process models caused by different thermal operating modes (e.g., operating the repository at lower temperatures) have been tested through sensitivity studies, but have otherwise not been incorporated in the TSPA-SR model. The process models have been examined to assess the possible impact of the uncertainties, but no additional measures have been taken to reduce or mitigate the effects of those uncertainties. The DOE is currently considering options for reducing or mitigating those uncertainties in the future.

This report presents several analyses performed to gain additional insight into the effect that repository temperatures may have on the uncertainty associated with specific process models. The goal of these analyses is to assess the extent to which the DOE's and the public's confidence in performance assessments might be improved if thermal uncertainties were mitigated by lowering the temperatures in the emplacement drifts and on the surface of the waste package. As stated previously, maintaining the host rock temperature below the boiling point of water may reduce uncertainties associated with coupled processes (Anderson et al. 1998 [DIRS 101656]; Cohon 1999 [DIRS 147531]). Similarly, uncertainties about localized corrosion rates may be mitigated by avoiding operating temperatures and humidity levels that could lead to an increased susceptibility of Alloy 22 to corrosion.

Refining the design and operating mode of the potential repository has been an ongoing, iterative process involving scientists, engineers, and decision-makers. The design and mode of operations of a potential repository have evolved as the DOE has learned more about the site and the performance contribution of various design and operating attributes. Engineering and design analyses demonstrate that there are a number of potential operational practices the DOE could employ to manage the repository environment S&ER (DOE 2001 [DIRS 153849], Section 2.1.4) and achieve lower operating temperatures. Because the physical processes judged to be most sensitive to thermal effects (i.e., coupled processes and materials corrosion) are relatively unaffected by the parameters that could be used to control operating temperatures, the DOE has

chosen in this report to evaluate thermal effects through focused evaluations of specific process models and system-level sensitivity analyses. Supplemental analyses look at a range of thermal operating modes including total system level analyses for a higher-temperature operating mode and lower-temperature operating mode and analyze their impact on specific processes and performance, including uncertainty in performance. If a decision is ultimately made to operate the repository to meet different thermal goals, a fully specified design and operating mode that can be demonstrated to meet those goals will be developed.

1.4 OVERVIEW OF ANALYSIS PROCESS

For this evaluation, the DOE has identified, considered, and evaluated the most recent and relevant information about Yucca Mountain and the potential repository system that is available from all sources, inside and outside the YMP. This information has been used to quantify uncertainties, update conceptual and numerical models, and provide additional lines of evidence about the possible future behavior of a repository. To the extent possible, the information has been incorporated in an updated supplemental TSPA model and evaluated for two thermal operating modes: for a repository operated as described in the S&ER (DOE 2001 [DIRS 153849]) and for a repository operated at temperatures that do not exceed 85°C. The sections below summarize the overall processes by which the new information discussed in this document was generated, evaluated, and analyzed.

1.4.1 Quantifying Uncertainties

The process for evaluating unquantified uncertainties involved: (1) identifying unquantified uncertainties to be evaluated; (2) developing more representative, quantified descriptions of those uncertainties; and (3) evaluating the implications of those newly quantified uncertainties for repository performance.

1.4.1.1 Identifying Unquantified Uncertainties

The first step in the process of quantifying uncertainties was to identify a set of process models and parameter inputs to the TSPA model for which significant uncertainty has not been quantified (i.e., where a conservative or nonconservative representation exists in the present performance assessment). Recent studies have focused on identifying potentially important unquantified uncertainties (CRWMS M&O 2000 [DIRS 153246], Appendix F; Cline 2000 [DIRS 153193]). From this set of models and parameters, a subset was identified that is expected to include those most important to annual dose estimates—either annual dose during the 10,000-year period covered by the proposed regulations or longer-term annual dose, out to hundreds of thousands of years (see Section 2.1.1). The longer time period was considered because annual doses over long time periods may produce insights about uncertainty in annual dose that are relevant to all time periods. In selecting uncertainties to address in these supplemental analyses, the DOE considered both the potential impact on TSPA results and the feasibility of modifications to the model and parameter inputs to the TSPA.

1.4.1.2 Quantifying Previously Unquantified Uncertainties

To quantify the uncertainties associated with the identified models and parameters, technical investigators developed unbiased representations of the specified uncertainties. To assist them, an iterative series of interviews were held with representatives from each of the main process model areas affecting performance. The interviews were followed by supplemental calculations and analyses. The emphasis in the discussions was on the physical realism of the models and parameter estimates. The technical investigators used their knowledge of project-specific data, literature data, analogue systems or processes, and the technical judgment of the broader scientific and engineering community to develop these unbiased representations. Specific implementation of the unbiased representations took a variety of forms, as described in Sections 3 through 14. Those forms range from new or updated parameter distributions to new or updated conceptual and mathematical models.

1.4.1.3 Evaluating Alternative Representations

The impacts of the new representations for previously unquantified uncertainties were evaluated through updated process models, sensitivity analyses, and supplemental TSPA analyses using the updated uncertainty treatment. The representations were implemented and the form and rationale for them documented. The implications of these new representations for process-level model results are discussed in Sections 3 through 14 of this document.

For many of these newly quantified uncertainties, supplemental TSPA sensitivity analyses were also conducted, as described in Volume 2 (McNeish 2001 [DIRS 155023]). These included subsystem performance analyses, TSPAs, and analyses similar to those documented and discussed in the TSPA-SR (CRWMS M&O 2000 [DIRS 153246]). The calculated annual doses from the revised representations have been compared to the estimates from the TSPA-SR.

1.4.2 Updating Scientific Bases and Analyses

In addition to the newly quantified uncertainties, additional scientific data have been collected, models have been revised, and analyses have been conducted since the TSPA-SR (CRWMS M&O 2000 [DIRS 153246]). In many cases, technical investigators have summarized new experimental data, updated process models to reflect an improved understanding, or abstracted models that more completely propagate process knowledge into the performance analyses. The incremental update to the scientific bases supporting the S&ER (DOE 2001 [DIRS 153849]) is documented in Sections 3 through 14.

1.4.3 Evaluating a Range of Thermal Operating Modes

The repository design and operating mode described in the S&ER (DOE 2001 [DIRS 153849]) are flexible enough to meet a range of potential thermal conditions or goals. A series of analyses has been conducted to determine feasible thermal ranges and the engineering and operating changes that would allow the potential repository to achieve specified operating temperature limits. For process models where thermal load potentially has an impact on the modeling and model results, technical investigators evaluated repository performance under different thermal loads. In some cases, this required updates to the technical models, which are indicated in Table 1-1 and discussed in Sections 3 through 14.

1.4.3.1 Selecting a Thermal Range

The first step in defining and conducting a thermal sensitivity analysis is to determine the thermal range that should be considered. A number of different thermal goals and constraints have been proposed, specifically focused on lower temperatures in the drift and on the surface of the waste package. A range of operating temperatures was selected for these thermal sensitivity analyses. The high end of the range corresponds to the flexible design and higher-temperature operating mode described in the S&ER (DOE 2001 [DIRS 153849]). The low end corresponds to an operating mode where the average maximum temperatures on the surface of the waste package do not exceed 85°C following closure of the potential repository (Table 2-1).

1.4.3.2 Identifying Operational Changes to Achieve Thermal Goals

The DOE identified a variety of operational changes that would result in lower temperatures in the potential repository. For a variety of thermal environments, the operating parameters that could affect potential repository temperatures were specified, along with the types of changes to those parameters that would be necessary to achieve various operating temperatures. This step also identified other key performance parameters that could be affected by the changes necessary to achieve lower operating temperatures, and is described more fully in Section 2.3 of this report.

1.4.3.3 Evaluating Performance

To evaluate performance over the thermal range being considered, the DOE conducted full supplemental TSPAs for both ends of the thermal range (Table 2-1). The results of the supplemental TSPA evaluations are documented in Volume 2 (McNeish 2001 [DIRS 155023]). In the process model analyses described in this volume, other parts of the thermal range were also evaluated.

1.5 QUALITY ASSURANCE

An activity evaluation was performed for this work activity in accordance with AP-2.21Q, *Quality Determinations and Planning for Scientific, Engineering, and Regulatory Compliance Activities* [DIRS 154534], and it was determined that activities supporting the development of this work and activities documented in this technical product are quality-affecting activities. This technical product and associated activities have been prepared subject to the requirements of the *Quality Assurance Requirements and Description* (DOE 2000 [DIRS 149540]) and implementing procedures. This document was prepared in accordance with the *Technical Work Plan for FY01 Supplemental Science and Performance Analyses: Volume 1-Scientific Bases and Analyses, Volume 2-Performance Analyses* (BSC 2001 [DIRS 155055]). There are no deviations from the technical work plan in this technical product.

The activity evaluation and a Process Control Evaluation for Supplement V, prepared in accordance with AP-SV.1Q, *Control of the Electronic Management of Information* [DIRS 153202]), are attached to the technical work plan. Section 10 of the technical work plan describes the controls that will be used in the electronic management of information for this work activity. The technical work plan provides important planning details and should be consulted if questions or issues arise related to this document and the work activities it describes.

As described in Section 1.2, the goal of the additional analyses presented in this technical report is to provide insights into the effects of uncertainty and both conservatisms and optimisms that were not evaluated in the family of analysis model reports that supported the S&ER (DOE 2001 [DIRS 153849]) and the TSPA-SR (CRWMS M&O 2000 [DIRS 153246]). Additional analyses are presented to examine the potential performance-related effects associated with operating the repository over a range of thermal operating modes. To provide these insights, the baselined models and analyses used as the technical basis for the TSPA-SR and the S&ER have been modified or extended beyond the bounds utilized in the TSPA-SR (CRWMS M&O 2000 [DIRS 153246]). These alternative representations are provided to evaluate the sensitivity of model performance to these unquantified uncertainties and to incorporate appropriate thermal dependencies into the conceptual representations used in the performance assessment. These alternative representations do not replace those documented in the supporting references to the TSPA-SR or the S&ER. While it may be necessary to modify a parameter distribution or model to examine the effects of these alternative representations, the models used as a basis for the TSPA-SR are not changed; these examinations are simply exploratory sensitivity analyses to provide the necessary insights into system behavior. In many respects, these analyses are no different than the types of sensitivity analyses, barrier importance analyses, and neutralization analyses presented in the TSPA-SR and the *Repository Safety Strategy: Plan to Prepare the Safety Case to Support Yucca Mountain Site Recommendation and Licensing Considerations* (CRWMS M&O 2001 [DIRS 154951]). If any of the revised models or analyses documented in this technical report are deemed to be more appropriate for the intended use of evaluating repository performance, they will be validated and documented in accordance with the quality assurance requirements for models and analyses in AP-3.10Q, *Analyses and Models* [DIRS 154517]. Until such time, they are considered scoping in nature to provide insights into the significance of uncertainty that was not explicitly evaluated in the TSPA-SR.

As a result of the special quality assurance controls applied as described in the Technical Work Plan (BSC 2001 [DIRS 155055]), not all of the models, analyses, and data used in this study are fully qualified. It has not yet been determined which, if any, of the models, analyses, and data need to be fully qualified. Because of quality assurance requirements, the models, analyses, and data used in this study are not intended to be used, as is, in a license application if the Yucca Mountain site is found to be suitable for the development of a repository.

1.6 COMPUTER SOFTWARE USAGE

A number of software codes were used or discussed in this study (Table 1-2). All qualified codes were appropriate for the intended use, and they were used only within the range of validation. All qualified codes were obtained from Software Configuration Management in accordance with AP-SI.1Q, *Software Management* [DIRS 154886].

The software name and version, software tracking number, qualification status reference information, location used, and computer type used are identified in Table 1-2. Reference to software codes within the text will indicate the software name and version, and the reader can use that information and this table to obtain other pertinent information.

Some references within the text may be to families of codes (e.g., the FEHM codes or the ASHPLUME codes). These references are generic in nature and are not intended to identify specific software or versions.

For each unqualified code, a software activity plan for use of unqualified software and a software user request have been submitted to Software Configuration Management. Several commercial software codes (e.g., THERMO-CALC, DICTRA, and FIDAP) were not submitted to Software Configuration Management due to software licensing issues. As only one copy of each of these codes exists on the Yucca Mountain Project, there is no technical issue regarding whether or not the correct version of the code was used. These codes are documented as part of Deficiency Report BSC-01-D-088 or Corrective Action Report BSC-01-C-002.

Commercial off-the-shelf software Tecplot V7.0, GMT V3.3.6, mView V2.20, EarthVision 5.1, SigmaPlot 4.0, and Microsoft Excel SR-1 were used to plot data documented within this report and the references specified. This report and the references document the technical decisions made by the analyst to arrive at the conclusions in this report. Where these plotting software were used, the analyst used professional judgment to determine the best display of the data. All of the technical decisions made regarding the use of the data displayed on the charts and plots in this report are documented in the body of the report, in the references specified for each figure, or both.

INTENTIONALLY LEFT BLANK

Table 1-1. Summary of Supplemental Models and Analyses

Key Attributes of System	Process Model (Section of S&ER)	Topic of Supplemental Scientific Model or Analysis	Reason For Supplemental Scientific Model or Analysis			Section of Volume 1	Performance Assessment Treatment of Supplemental Scientific Model or Analysis (Discussed In Volume 2)	
			Unquantified Uncertainty Analysis	Update in Scientific Information	Lower-Temperature Operating Mode Analysis		TSPA Sensitivity Analysis	Included in Supplemental TSPA Model
Limited Water Entering Emplacement Drifts	Climate (4.2.1)	Post-10,000-year Climate Model		X		3.3.1	X	X
	Net Infiltration (4.2.1)	Infiltration for post-10,000-year Climate Model		X		3.3.2	X	X
	Unsaturated Zone Flow (4.2.1)	Flow in PTn		X		3.3.3		
		3-D flow fields for cooler design; flow fields for post-10,000 yr climate, lateral flow; variable thickness of PTn; fault property uncertainty		X	X	3.3.4		
		Effects of lithophysal properties on thermal properties		X		3.3.5		X
	Coupled Effects on UZ Flow (4.2.2)	Mountain-scale Thermal-Hydrologic effects		X	X	3.3.5		
		Mountain-scale Thermal-Hydrologic-Chemical effects		X	X	3.3.6		
		Mountain-scale Thermal-Hydrologic-Mechanical effects		X	X	3.3.7		
	Seepage into Emplacement Drifts (4.2.1)	Flow-focussing within heterogeneous permeability field; episodic seepage	X		X	4.3.1, 4.3.2, 4.3.5	X	X
		Effects rock bolts and drift degradation on seepage	X			4.3.3, 4.3.4		
	Coupled Effects on Seepage (4.2.2)	Thermal effects on seepage	X		X	4.3.5	X	X
		Thermal-Hydrologic-Chemical effects on seepage	X		X	4.3.6		
		Thermal-Hydrologic-Mechanical effects on seepage		X	X	4.3.7		

Table 1-1. Summary of Supplemental Models and Analyses (Continued)

Key Attributes of System	Process Model (Section of S&ER	Topic of Supplemental Scientific Model or Analysis	Reason For Supplemental Scientific Model or Analysis			Section of Volume 1	Performance Assessment Treatment of Supplemental Scientific Model or Analysis (Discussed In Volume 2)	
			Unquantified Uncertainty Analysis	Update in Scientific Information	Lower-Temperature Operating Mode Analysis		TSPA Sensitivity Analysis	Included in Supplemental TSPA Model
Long-Lived Waste Package and Drip Shield	Water Diversion Performance of EBS (4.2.3)	Multiscale thermal-hydrologic model, including effects of rock dryout	X		X	5.3.1		X
		Thermal property sets	X	X		5.3.1		X
		Effect of in-drift convection on temperatures, humidities, invert saturations, and evaporation rates	X		X	5.3.2		
		Composition of liquid and gas entering drift	X		X	6.3.1	X	X
		Evolution of in-drift chemical environment	X		X	6.3.3	X	X
		Thermo-Hydro-Chemical model comparison to plug-flow reactor and fracture plugging experiment		X		6.3.1		
		Rockfall		X		6.3.4		
	In-Drift Moisture Distribution (4.2.5)	Environment on surface of drip shields and waste packages	X			5.3.2, 7.3.1		
		Condensation under drip shields	X			8.3.2	X	
		Evaporation of seepage	X		X	8.3.1 5.3.2	X	X
		Effect of breached drip shields or waste package on seepage	X		X	8.3.3	X	X
		Waste package release flow geometry (flow-through, bathtub)	X			8.3.4	X	
	Drip Shield Degradation and Performance (4.2.4)	Local chemical environment on surface of drip shields (including Mg, Pb) and potential for initiating localized corrosion	X			7.3.1		

Table 1-1. Summary of Supplemental Models and Analyses (Continued)

Key Attributes of System	Process Model (Section of S&ER	Topic of Supplemental Scientific Model or Analysis	Reason For Supplemental Scientific Model or Analysis			Section of Volume 1	Performance Assessment Treatment of Supplemental Scientific Model or Analysis (Discussed In Volume 2)	
			Unquantified Uncertainty Analysis	Update in Scientific Information	Lower-Temperature Operating Mode Analysis		TSPA Sensitivity Analysis	Included in Supplemental TSPA Model
Long-Lived Waste Package and Drip Shield	Waste Package Degradation and Performance (4.2.4)	Local chemical environment on surface of waste packages (including Mg, Pb) and potential for initiating localized corrosion	X			7.3.1		
		Aging and phase stability effects on A-22	X	X		7.3.2	X	
		Uncertainty in weld stress state following mitigation	X			7.3.3	X	X
		Weld defects	X			7.3.3	X	X
		Early failure due to improper heat treatment	X		X	7.3.6	X	X
		General corrosion rate of A-22: Temperature dependency	X		X	7.3.5	X	X
		General corrosion rate of A-22: Uncertainty/variability partition	X			7.3.5	X	X
		Long-term stability of passive films on A-22	X			7.3.4		
		Stress threshold for initiation of stress corrosion cracking	X	X		7.3.3	X	X
		Probability of non-detection of manufacturing defects		X		7.3.3	X	X
		Number of defects		X		7.3.5	X	X
		Distribution of crack growth exponent (repassivation slope)	X	X		7.3.7	X	X
Limited Release of Radionuclides from the Engineered Barriers	In-Package Environments (4.2.6)	Effect of HLW glass degradation rate and steel degradation rate on in-package chemistry	X		X	9.3.1	X	X
	Cladding Degradation and Performance (4.2.6)	Effect of initial perforations, creep rupture, stress corrosion cracking, localized corrosion, seismic failure, rock overburden failure, and unzipping velocity on cladding degradation	X		X	9.3.3	X	X

Table 1-1. Summary of Supplemental Models and Analyses (Continued)

Key Attributes of System	Process Model (Section of S&ER	Topic Of Supplemental Scientific Model or Analysis	Reason For Supplemental Scientific Model or Analysis			Section of Volume 1	Performance Assessment Treatment of Supplemental Scientific Model or Analysis (Discussed In Volume 2)	
			Unquantified Uncertainty Analysis	Update in Scientific Information	Lower-Temperature Operating Mode Analysis		TSPA Sensitivity Analysis	Included in Supplemental TSPA Model
Limited Release of Radionuclides from the Engineered Barriers	DHLW Degradation and Performance (4.2.6)	HLW glass degradation rates	X	X	X	9.3.1		
	Dissolved Radionuclide Concentrations (4.2.6)	Solubility of neptunium, thorium, plutonium, and technetium	X	X	X	9.3.2	X	X
	Colloid-Associated Radionuclide Concentrations (4.2.6)	Colloid mass concentrations	X			9.3.4	X	
	EBS (Invert) Degradation and Transport (4.2.6, 4.2.7)	Diffusion inside waste package	X	X		10.3.1	X	X
		Transport pathway from inside waste package to invert	X	X		10.3.2		
		Sorption inside waste package	X	X		10.3.4	X	X
		Sorption in invert	X	X		10.3.4	X	X
		Diffusion through invert	X			10.3.3	X	X
		Colloid stability in the invert	X			10.3.5		
		Microbial transport of colloids	X	X		10.3.6		

Table 1-1. Summary of Supplemental Models and Analyses (Continued)

Key Attributes of System	Process Model (Section of S&ER	Topic of Supplemental Scientific Model or Analysis	Reason For Supplemental Scientific Model or Analysis			Section of Volume 1	Performance Assessment Treatment of Supplemental Scientific Model or Analysis (Discussed In Volume 2)	
			Unquantified Uncertainty Analysis	Update in Scientific Information	Lower-Temperature Operating Mode Analysis		TSPA Sensitivity Analysis	Included in Supplemental TSPA Model
Delay and Dilution of Radionuclide Concentrations by the Natural Barriers	Unsaturated Zone Radionuclide Transport (Advective Pathways; Retardation; Dispersion; Dilution) (4.2.8)	Effect of drift shadow zone - advection/diffusion splitting	X		X	11.3.1	X	X
		Effect of drift shadow zone – concentration boundary condition on EBS release rates	X			11.3.1		
		Effect of matrix diffusion	X			11.3.2, 11.3.3		
		3-D transport			X	11.3.2		
		Effect of coupled Thermo-Hydrologic, Thermo-Hydro-Chemical, and Thermo-Hydro-Mechanical processes on transport		X	X	11.3.5		
	Saturated Zone Radionuclide Flow and Transport (4.2.9)	Groundwater specific discharge	X	X		12.3.1	X	
		Effective diffusion coefficient in volcanic tuffs	X			12.3.2	X	
		Flowing interval spacing				12.3.2	X	
		Flowing interval (fracture) porosity	X			12.3.2	X	
		Effective porosity in the alluvium	X			12.3.2	X	
		Correlation of the effective diffusion coefficient with matrix porosity	X			12.3.2	X	
		Bulk density of the alluvium	X	X		12.3.2	X	X

Table 1-1. Summary of Supplemental Models and Analyses (Continued)

Key Attributes of System	Process Model (Section of S&ER	Topic of Supplemental Scientific Model or Analysis	Reason For Supplemental Scientific Model or Analysis			Section of Volume 1	Performance Assessment Treatment of Supplemental Scientific Model or Analysis (Discussed In Volume 2)	
			Unquantified Uncertainty Analysis	Update in Scientific Information	Lower-Temperature Operating Mode Analysis		TSPA Sensitivity Analysis	Included in Supplemental TSPA Model
Delay and Dilution of Radionuclide Concentrations by the Natural Barriers	Saturated Zone Radionuclide Transport (4.2.9)	Retardation for radionuclides irreversibly sorbed on colloids in the alluvium	X	X		12.3.2	X	
		No matrix diffusion in volcanic tuffs case				12.5.2	X	
		Presence or absence of alluvium				12.5.2	X	
		Sorption coefficient in alluvium for I, Tc	X	X		12.3.2	X	X
		Sorption coefficient in alluvium for Np, U	X	X		12.3.2	X	
		Sorption coefficient for Np in volcanic tuffs	X			12.3.2	X	
		Kc model for groundwater colloid concentrations Pu, Am		X		12.5.2	X	
		Enhanced matrix diffusion in volcanic tuffs				12.5.2	X	
		Effective longitudinal dispersivity	X	X		12.3.2	X	
		New dispersion tensor		X		12.3.2		
		Flexible design			X	12.3.2		
		Different conceptual models of the large hydraulic gradient and their effects on the flow path and specific discharge		X		12.3.1		
		Hydraulic head and map of potentiometric surface		X		12.3.1		
	Biosphere (4.2.10)	Receptor of interest	X			13.3.1		
		Comparison of dose assessment methods	X			13.3.2		
		Radionuclide removal from soil by leaching	X			13.3.3		
		Uncertainties not captured by GENII-S	X			13.3.4		
		Influence of climate change on groundwater usage and BDCFs	X			13.3.5, 13.3.7		
		BDCFs for groundwater and igneous releases		X		13.3.6, 13.3.8 13.4	X	X

Table 1-1. Summary of Supplemental Models and Analyses (Continued)

Key Attributes of System	Process Model (Section of S&ER	Topic of Supplemental Scientific Model or Analysis	Reason For Supplemental Scientific Model or Analysis			Section of Volume 1	Performance Assessment Treatment of Supplemental Scientific Model or Analysis (Discussed In Volume 2)	
			Unquantified Uncertainty Analysis	Update in Scientific Information	Lower-Temperature Operating Mode Analysis		TSPA Sensitivity Analysis	Included in Supplemental TSPA Model
Low Mean Annual Dose Considering Potentially Disruptive Events	Volcanism/Igneous Activity (4.3.2)	Probability of dike intersection of repository for the operating mode described in S&ER		X		14.3.3.1		X
		Scaling factors to evaluate impacts of repository design changes			X	14.3.3.2		
		Contribution to release of Zones 1 and 2		X		14.3.3.3	X	
		Sensitivity to waste particle size distribution		X		14.3.3.4	X	
		New wind speed data		X		14.3.3.5	X	X
		Explanation of method for handling ash/waste particle size and density		X		14.3.3.6		
		Volcanism inputs for Supplemental TSPA Model		X		14.3.3.7		X
		New aeromagnetic data		X		14.3.3.8		

NOTE: S&ER = *Yucca Mountain Science and Engineering Report* [DOE 2001 [DIRS *153849*]).

[a] Performance assessment treatment of supplemental scientific model or analysis discussed in SSPA Volume 2 (McNeish 2001 [DIRS 155023]).

Table 1-2. Computer Software

Software Name	Software Version	Software Tracking Number (STN)	Qualified	DIRS Reference Number	Location Used	Computer Type Used
2kgrid8.for	1.0	10503-1.0-00	No	154787	LBNL	3
3DEC	2.0	10025-3.0-00	Yes	150512	LV, LLNL	3
add_repo_nodes.f	1.0	10548-1.0-00	No	155081	LANL	1
AddBound	1.0	10357-1.0-00	Yes	152823	LBNL	1
ANSYS	5.2SGI	30013-5.2SGI	Yes	152788	LV	4
ANSYS	5.6.2	10145-5.6.2-00	Yes	154671	LV	2
ASHPLUME	1.4LV-dll	10022-1.4LV-dll	Yes	154748	LV	3
AssignRock	1.0	10465-1.0-00	Yes	154321	LBNL	1
bot_sum.f	1.0	10349-1.0-00	Yes	153471	LBNL	2
CalBT.for	1.0	10504-1.0-00	No	154788	LBNL	3
CORPSCON	5.11.08	10547-5.11.08-00	No	155082	LANL	3
CutDrift	1.0	10375-1.0-00	Yes	152816	LBNL	1
CutNiche	1.3	10402-1.3-00	Yes	152828	LBNL	1
CWD	1.00	10363-1.0-00	Yes	152624	LV	3
DCPT	1.0	10078-1.0-00	Yes	132448	LBNL	3
DCPT	2.0	10078-2.0-00	No	154342	LBNL	3
Delb.dat	1.0	10507-1.0-00	No	154791	LBNL	3
DICTRA	2.0	10391-2.0-00	No	155083	LLNL	1
DRKBA	3.3	10071-3.3-00	Yes	149991	LV	3
EARTHVISION	5.1	10174-5.1-00	Yes	152614	LBNL	4
EQ3/6	7.2b	UCRL-MA-110662	Yes	153964	SNL	3
EQ6	7.2bLV	10075-7.2bLV-00	Yes	127275	SNL	3
EXT	1.0	10047-1.0-00	Yes	134141	LBNL	1
FEHM	2.11	10086-2.11-00	No	155084	SNL	1 and 3
FEHM	2.10	10086-2.10-00	Yes	132447	SNL	1 and 3
FEHM	2.00	10031-2.00-00	Yes	146971	SNL	1
FIDAP	8.0	10549-8.0-00	No	155189	LLNL	3
FLAC3D	2.0	10502-2.0-00	No	154783	LBNL	3
FLAC3D	2.0	10502-2.0-00	Yes	154783	LV	3

Table 1-2. Computer Software (Continued)

Software Name	Software Version	Software Tracking Number (STN)	Qualified	DIRS Reference Number	Location Used	Computer Type Used
FLUENT	5.5	10550-5.5-00	No	155190	LLNL	1
GENII-S	1.4.8.5	30034 V1.4.8.5	Yes	117076	LV	3
get_a_layer_v0.f	1.0	10221-1.0-00	Yes	147025	LBNL	1
GoldSim	6.04.007	10344-6.04.007-00	Yes	151202	LV	3
Gpzones.dat	1.0	10509-1.0-00	No	154792	LBNL	3
GSLIB	1.0 Module SISIM V1.203	10001-1.0MSISIMV1.203-00	Yes	134136	LBNL	1
GSLIB	2.0 Module SISIM V2.0	10098-2.0MSISIMV2.0-00	Yes	146609	LBNL	1
GVP	1.02	10341-SRR-1.02-00	Yes	152496	LV	3
hsource_v0.f	1.0	10225-1.0-00	Yes	147031	LBNL	1
Image Pro Plus	4.1	10422-4.1-00	No	155085	LLNL	1
INFIL	2.0	10307-2.0-00	No	139422	USGS	3
infil2grid	1.7	10077-1.7-00	No	154793	LBNL	3
ITOUGH2	3.2	10054-3.2-00	Yes	154337	LBNL	1
ITOUGH2	3.2_drift	10055-3.2_DRIFT-00	Yes	112757	LBNL	1
iTOUGH2	4.0	10003-4.0-00	Yes	139918	LBNL	1 and 2
iTOUGH2	4.4	10003-4.4-00	No	154784	LBNL	1
mddf.f	2.0	10456-2.0-00	Yes	154347	LBNL	1
Meshbd.f	1.0	10467-1.0-00	Yes	152871	LBNL	1
MINCgridv1.f	1.0	10469-1.0-00	Yes	154343	LBNL	2
MING	1.0	30018 V1.0	Yes	145225	SNL	3
mininipresf.f	1.0	10470-1.0-00	Yes	152872	LBNL	1
minrefine3df.f	1.0	10472-1.0-00	Yes	152880	LBNL	1
mk_generGL.f	1.0	10476-1.0-00	Yes	154349	LBNL	1
MkTable	1.00	10505-1.00-00	Yes	154921	LV	3
MoveMesh	1.0	10358-1.0-00	Yes	152824	LBNL	1
MSTHAC	6.4.2	10419-6.4.2-00	No	155324	LLNL	1
MULTIFLUX	1.0	10485-1.0-00	No	155087	SNL	1
MVIEW	2.20	10072-2.20-00	Yes	155201	LV	1, 2, and 4
NUFT	3.0s	10088-3.0s-00	Yes	127906	SNL, LLNL, LV	1
parallelf.java	1.0	10457-1.0-00	Yes	154346	LBNL	3

Table 1-2. Computer Software (Continued)

Software Name	Software Version	Software Tracking Number (STN)	Qualified	DIRS Reference Number	Location Used	Computer Type Used
Perm2Mesh	1.0	10359-1.0-00	Yes	152826	LBNL	1
RADPRO	3.22	10204-322-00	Yes	148637	LLNL	1
Routine Rick1	1.0	10474-1.0-00	Yes	154344	LBNL	1
SCCD	2.01	10343-SRR-2.01-00	Yes	152499	LV, SRR	3
SOLVEQ/CHILLER	1.0	10057-1.0-00	Yes	153217	LBNL	3
T2R3D	1.4	10006-1.4-00	Yes	113942	LBNL	1 and 2
THERMO-CALC	VM	10170-M-00	No	155088	LLNL	1
tin.dat	1.0	10512-1.0-00	No	154794	LBNL	3
TOUGH2	1.11MEOS9nTV1.0	10065-1.11MEOS9NTV1.0-00	Yes	113943	LBNL	1
TOUGH2	1.4	10007-1.4-01	Yes	146496	LBNL	1 and 2
TOUGH2	1.5	10007-1.5-00	No	154322	LBNL	1 and 2
TOUGHREACT	2.3	10396-2.3-00	No	153101	LBNL	1 and 2
TOUGHREACT	2.2	10154-2.2-00	Yes	153219	LBNL	1 and 2
vf_con.for	1.0	10466-1.0-00	Yes	154345	LBNL	3
WAPDEG	4.0	10000-4.0-2.0	Yes	155166	LV	3
Wingridder	2.0	10024-2.0-00	No	154785	LBNL	3
Wingridder	1.1	10024-1.1-00	Yes	154341	LBNL	3
XTOOL	10.1	10208-10.1-00	Yes	148638	SNL, LLNL, LV	1
YMESH	1.53	10172-1.53-00	Yes	147574	LLNL	1

NOTE: Computer type: (1) SUN UltraSparc, (2) DEC-Alpha, (3) PC, (4) SGI INDIGO.

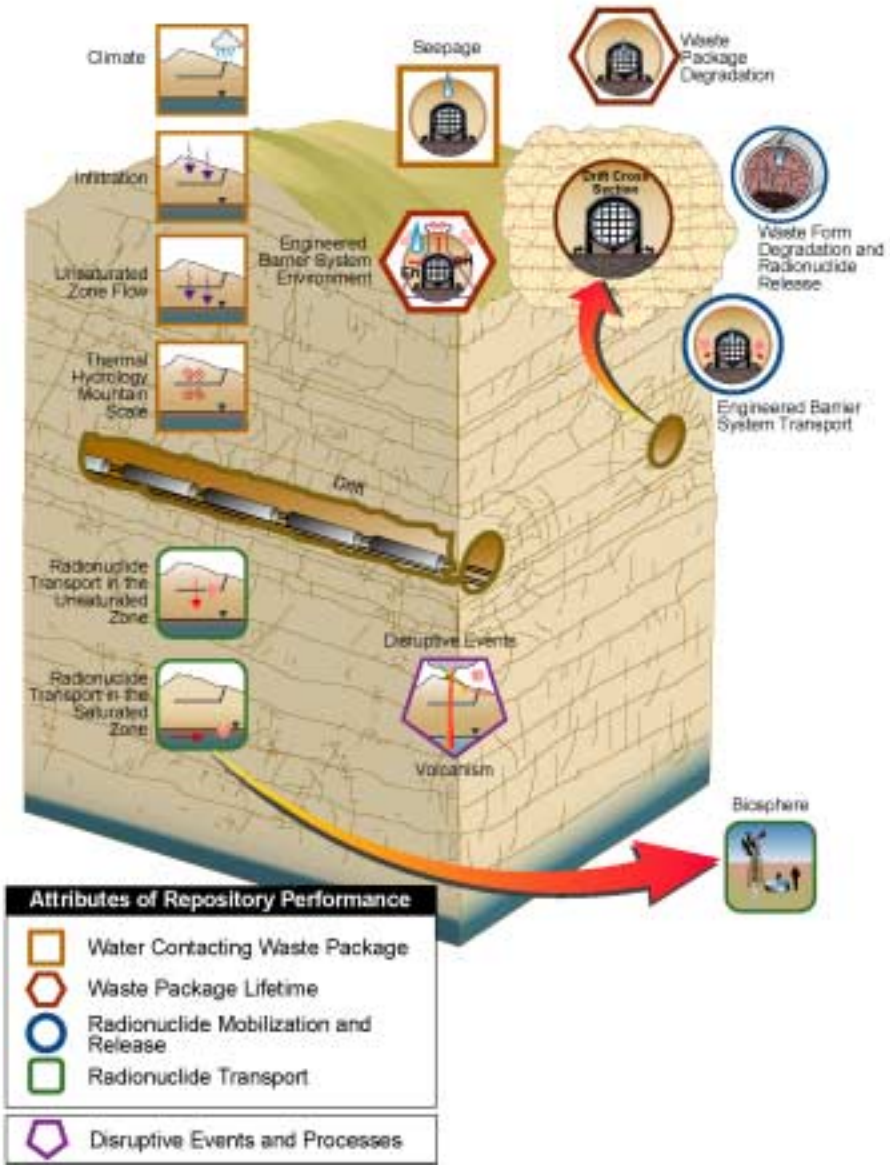

Figure 1-1. Components of the SSPA Analyses, showing the Relationship of Major Processes Expected to Occur in the Mountain and the Potential Repository System

INTENTIONALLY LEFT BLANK

2 Methods and Approach

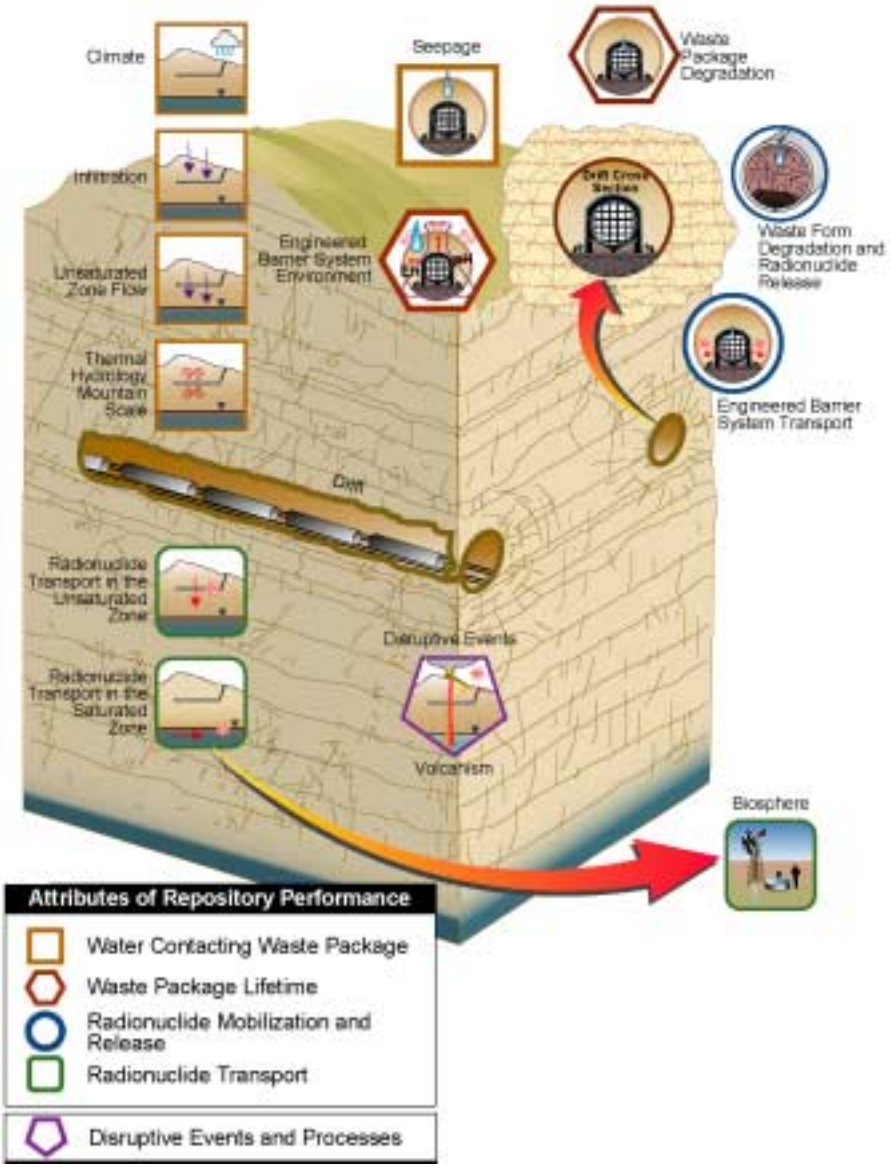

2. METHODS AND APPROACH

2.1 QUANTIFICATION OF UNCERTAINTIES

The U.S. Department of Energy (DOE) identified a variety of uncertainties, arising from different sources, during its assessment of the performance of a potential repository at the Yucca Mountain site. In general, the number and detail of process models developed for the Yucca Mountain site, and the complex coupling among those models, make the direct incorporation of all uncertainties difficult. The DOE has addressed these issues in a number of ways using an uncertainty strategy that is focused on producing a defensible, compliance-based evaluation of the performance of a potential repository. As part of that evaluation, many uncertainties have been treated in a defensible (typically conservative) manner in the analyses and model reports supporting the *Yucca Mountain Science and Engineering Report* (S&ER) (DOE 2001 [DIRS 153849]). Conservative assumptions and parameter bounds have been used to increase defensibility or decrease modeling complexity.

The result is that the DOE has used a mix of probabilistic representations and single-valued estimates to characterize parameters. There are also cases where more than one conceptual model may be consistent with available data and observations. In the absence of definitive data or compelling technical arguments for a specific conceptual, process, or abstracted model, a conservative representation was chosen. This approach has been used in other projects to demonstrate compliance with a regulatory standard (Goodwin et al. 1994 [DIRS 124152]), but it does not permit quantification of the degree of conservatism associated with projected performance relative to the regulatory standard. Mixing various degrees of conservatism in models and parameter representations reduces the transparency of the analysis and makes the development of coherent and consistent probability statements about projected repository performance difficult.

Accompanying the recognition of inherent uncertainties and a need for transparency is the responsibility to identify and communicate the uncertainties as clearly and meaningfully as possible. The DOE initiated the assessment of the treatment of uncertainties described in this volume to improve this identification and communication. Work has been done to quantify some previously unquantified uncertainties and evaluate their implications for overall repository performance. The approach used to evaluate these uncertainties is described below.

2.1.1 Identification of Unquantified Uncertainties

2.1.1.1 Preliminary Identification of Conservatisms

The evaluation began with the identification and definition of models and parameter inputs to total system performance assessment (TSPA) for which uncertainty has not been quantified (i.e., a conservative or nonconservative representation exists in the present performance assessment). Several recent studies focused on identifying potentially important unquantified uncertainties (CRWMS M&O 2000 [DIRS 153246], Appendix F; Cline 2000 [DIRS 153193]).

The *Total System Performance Assessment for the Site Recommendation* (TSPA-SR) (CRWMS M&O 2000 [DIRS 153246], Appendix F) identifies approximately 25 process model and TSPA-SR components in which key system attributes were modeled in a conservative manner.

The report also describes the rationale for these conservatisms. In a separate activity, other project technical reviewers conducted a preliminary evaluation of how realistic the process models are based on an assessment of model parameters and assumptions (Cline 2000 [DIRS 153193]). The reviewers selected 87 model components and evaluated them for representativeness, importance to the process model, and importance to repository performance. These evaluations were based on the professional judgment of the reviewers. The results of this preliminary evaluation suggest that levels of conservatism are found throughout the models and that the conservatisms were used as a way to address uncertainty. Many of these model components can be modified, or alternative representations can be developed to more realistically or fully capture uncertainties, and the impacts of those changes evaluated through supplemental analyses.

The TSPA-SR (CRWMS M&O 2000 [DIRS 153246]) and Cline (2000 [DIRS 153193]) provided a starting point for identifying the unquantified uncertainties to be addressed in the analyses documented in this report.

2.1.1.2 Selection of Uncertainties to be Quantified

TSPA analyses and associated sensitivity analyses have been conducted to identify those inputs to which the calculated annual dose estimates are most sensitive (e.g., CRWMS M&O 2000 [DIRS 153246]). However, sensitivity and uncertainty analyses can identify as contributors to uncertainty only those inputs that have been treated as variable (e.g., those quantities represented by a range of values). Uncertainties that were not represented in the models as uncertain inputs (e.g., single-valued estimates) cannot be identified as important contributors in uncertainty analyses. Therefore, the identification of unquantified uncertainties was extended beyond those identified by the activities described in Section 2.1.1.1. The results of those activities provided a starting point for discussions and consultations with Yucca Mountain Site Characterization Project technical investigators to gain insights into which unquantified uncertainties are most important to performance. Insights and suggestions from independent review groups (e.g., the Nuclear Waste Technical Review Board) on important uncertainties were also considered as part of the identification of unquantified uncertainties in the performance assessment modeling. Technical experts directly involved in the TSPA-SR modeling (CRWMS M&O 2000 [DIRS 153246]) have the most comprehensive understanding of which inputs have the greatest potential to affect the dose estimates. The project technical investigators have the most comprehensive understanding of how uncertainties in their area of technical expertise were treated and where conservatisms, nonconservatisms, and single-valued assessments may exist. In selecting unquantified uncertainties to address in the near-term, technical experts considered both the potential impact on TSPA results and the feasibility of modifications to the model and parameter inputs to the TSPA. Based on these objectives, the uncertainties listed in Table 1-1 were selected for these supplemental evaluations.

2.1.2 Quantification of Unquantified Uncertainties

To quantify the uncertainties associated with the various models and parameters identified in Table 1-1, technical investigators were asked to develop unbiased representations of the identified uncertainties. Unbiased estimates are neither deliberately conservative nor deliberately optimistic. To assist in this effort, an iterative series of discussions, followed by

supplemental calculations and analyses, were held with representatives from each of the process model areas shown in Table 1-1. The emphasis in the discussions was on the physical realism of the models and parameter estimates. The technical investigators used their knowledge of project-specific data, literature data, analogue systems or processes, and the technical judgment of the broader scientific and engineering community to develop these unbiased distributions.

In these discussions, a facilitator worked with the technical experts to develop complete expressions of uncertainties. Each discussion included the technical investigators who initially developed the process models abstracted for use in the TSPA and the performance assessment modelers familiar with the TSPA model and the specific input parameters. At the beginning of each discussion, facilitators provided an introduction to the use of expert judgment in quantifying uncertainties. This introduction included a discussion of the motivational and cognitive biases that can affect uncertainty assessments, as well as the responsibility of the technical investigators to consider and evaluate alternative interpretations and represent the uncertainty that would be expressed by the larger technical community.

During each discussion, the current treatment of each component in the TSPA-SR (CRWMS M&O 2000 [DIRS 153246]) was described, including the technical bases for the assessment and the manner in which the model has been abstracted for use in the performance assessment. This was followed by a consideration and discussion of alternative, more representative modeling approaches and parameter distributions. In some cases, the parameter/model uncertainty identified was broken down into several parts for more efficient uncertainty quantification. For example, for the waste form degradation topic, in-package chemistry (principally pH and the partial pressure of carbon dioxide) is primarily related to the rate of degradation of the internal components of the waste package. The components for which uncertainties were not quantified in the TSPA-SR included the high-level waste glass and steel support structures. These components include the high-level waste glass and steel internal support structures, so representative degradation rates and their uncertainties were developed for these components, as described in Section 9.3. The technical investigators were also asked to consider the implications of a lower-temperature operating mode (LTOM) for the uncertainties being evaluated. In this LTOM, waste package surface temperature does not exceed 85ºC during the postclosure period (see Section 2.3).

2.1.2.1 Development of New Information

The discussions were followed by a period of time during which the investigators could further develop their models and consider how uncertainties could best be represented. In updating their models and uncertainty treatment, the investigators considered the applicability of more representative (e.g., less conservative) models, the probability distributions for input parameters, and modeling uncertainties. Investigators compiled applicable data, conducted necessary calculations, and developed updated uncertainty distributions. Often the original conservative models and parameter assumptions were made because large uncertainties existed. Thus, the revised estimates were expected to indicate a broad range for the uncertain quantity. The objective was to quantify the uncertainties with probability distributions to the greatest extent possible, based on the judgment of the investigators. In addition to parameter distributions, in some cases alternative conceptual models were identified to provide a more representative assessment of the processes that may affect repository performance. After each period of

evaluation, the investigators met again and reviewed the models and parameters as a group until a consensus was reached that the uncertainties have been properly characterized. The technical bases (e.g., available data, modeling results, analogues, and professional judgment) and results of the assessments are documented in Sections 3 through 14 of this volume.

2.1.2.2 Evaluation of Newly-Quantified Uncertainties

The new information related to the uncertainty quantification was abstracted for the TSPA models, so the updated process model inputs and TSPA parameters capture the full range of newly quantified uncertainties. The method, approach, and analyses of overall system performance are described in Volume 2 (McNeish 2001 [DIRS 155023]).

2.2 UPDATED SCIENTIFIC BASES AND ANALYSES

The scientific analyses and models that provide the bases for the TSPA-SR (CRWMS M&O 2000 [DIRS 153246]) process models are provided in the analysis model reports supporting the S&ER (DOE 2001 [DIRS 153849]). These reports describe the key attributes of the system and the process models at the time of their development. That understanding is represented by observational and experimental data analyses, models of relevant processes, and representations of conceptual model and parameter uncertainties. Abstractions of this technical understanding are made to represent the essential elements of each process in the performance analyses. Sections 3 through 14 describe supplemental analyses based on updates to these scientific bases.

Modifications to the work presented in the S&ER (DOE 2001 [DIRS 153849]) include updates based on the newly-quantified uncertainties, new or updated models and analyses, and analyses to evaluate the effects of thermal operating modes. These assessments are summarized in Table 1-1 and described in detail in subsequent sections of this volume. In many cases, an assessment conducted to evaluate previously unquantified uncertainties is not easily distinguishable from an updated model. For example, neptunium solubility is identified in Table 1-1 as an unquantified uncertainty for which a bounding solubility was used (as a function of pH). To quantify the uncertainty, applicable solubility data were compiled and a new conceptual model was developed that draws on analogies to the dissolution of schoepite. Application of this conceptual model and consideration of available experimental data resulted in a revised solubility relationship that quantifies the associated uncertainties (see Section 9.3.4). Clearly, this assessment would fall in the updated-model category, but it is also in the unquantified uncertainty category.

In other cases, updates have focused on incorporating new data, using better model calibration, or building more physically representative models, without an explicit focus on uncertainty quantification. Finally, for some of the updates shown in Table 1-1, sensitivity analyses have been conducted to determine the potential importance of a parameter or a model without a concerted attempt to quantify the uncertainties in those parameters or models.

2.3 THERMAL SENSITIVITY ANALYSES

During development of the S&ER (DOE 2001 [DIRS 153849]), a systematic evaluation was performed to determine design features and operational practices that could be used to manage

the thermal environment in the repository, and particularly to produce a LTOM. This evaluation was updated in a design analysis (BSC 2001 [DIRS 154554]). Volume 2 (McNeish 2001 [DIRS 155023]) describes the results of a TSPA conducted for one LTOM within the range of potential options. This option, described in Section 2.3.4, was selected in part because it could be analyzed with the same models used to analyze the higher-temperature operating mode. Sensitivity studies at the process model level are used to explore the behavior of the system at other points in the range of thermal operating modes considered. The evaluation of the options identified in the S&ER (DOE 2001 [DIRS 153849]) and *Low Temperature Subsurface Layout and Ventilation Concepts* (BSC 2001 [DIRS 154554]) will be considered during the selection of the design and operating modes for the potential repository.

2.3.1 Design and Operating Mode Evolution

As discussed in Section 1.3.3 of this report, refining the design for the potential repository and the mode in which the design is operated has been an ongoing, iterative process involving scientists, engineers, and decision-makers. The repository design under consideration is flexible in that it can be operated over a range of thermal conditions. The iterative design process has focused on improving the understanding of the contribution of design features to the performance of a potential repository and to uncertainty in that performance. The approach used to evaluate performance over a thermal range examines the relationship of design features and operational practices to the range of operating temperatures and environmental conditions and evaluates the performance and uncertainties associated with the temperature variation. If an operational parameter is shown to have a significant effect on the performance of the repository, it is evaluated further to assess its impact.

Evaluations considering the performance of a design over a range of thermal operating modes provide information to guide the future development of the repository design and operations. The evolution of the design and operating mode will take advantage of insights gained through performance analyses. The flexible design, which will continue to evolve for license application if the Yucca Mountain site is recommended, will include a set of operational parameters that can be managed to accommodate a waste stream with potentially evolving thermal characteristics. Adjustments will continue during the emplacement period based on updated information pertaining to the waste stream and other repository variables.

The evaluation of the performance characteristics of the potential repository design over a range of operating conditions is an important step in the evolution of the design of a repository at Yucca Mountain. While certain details of design have been defined to understand the environmental conditions as input to the performance analyses, the focus of the evaluations presented in this document is on quantification of uncertainty in performance, rather than on verification of the functionality of specific design features or operational concepts. Thus, the evaluations are based on the thermal performance implications of the design and accompanying range of operating modes, rather than on the specific details of how the operating mode might be implemented as an optimized design.

2.3.2 Range of Thermal Operating Modes and Bases

The S&ER (DOE 2001 [DIRS 153849]) describes a flexible design that could be operated over a range of temperatures. These alternative thermal operating modes would each have advantages and disadvantages in analyses of potential repository performance.

Three possible operating strategies are discussed below. Total system performance assessments for the first and third examples are presented in Volume 2 (McNeish 2001 [DIRS 155023]). Other sensitivity studies are described in Sections 3 through 14 of this report to gain insights into the effect that managing the thermal environment in the repository might have on repository performance.

Manage Boiling Fronts within the Rock Pillars and Peak Cladding Temperatures–The higher end of the thermal operating mode under consideration provides a moderate temperature repository environment compared to the design described in the, *Viability Assessment of a Repository at Yucca Mountain* (DOE 1998 [DIRS 101779]). This mode, which is the basis for the evaluations in the S&ER (DOE 2001 [DIRS 153849]), is intended to keep the boiling fronts from coalescing in the rock pillars between the emplacement drifts, preserving the capability of the rock mass to drain percolation flux through the repository horizon at all times. The close spacing of waste packages with thermally blended inventories in this higher-temperature operating mode achieves a relatively uniform distribution of rock temperatures along the drift, limiting potentially complex thermal-mechanical effects resulting from a varying thermal gradient along the drift axis. This operating mode would also meet a design requirement established to maintain the integrity of the cladding by not exceeding a spent nuclear fuel (SNF) cladding temperature of 350ºC. The higher-temperature operating mode described in Table 2-1 addresses this strategy.

Keeping Drift Wall Temperatures Below Boiling–In the operating mode described in the S&ER (DOE 2001 [DIRS 153849]), the rock temperatures within the first several meters outside the emplacement drifts exceed the boiling point of water for about a thousand years. One possible lower-temperature objective is to keep all the rock in the repository below the boiling point of water to reduce uncertainties associated with coupled thermal-hydrologic-chemical-mechanical processes driven by the boiling of water. The lower-temperature operating mode in Table 2-1 addresses this operating strategy.

Manage Waste Package Surface Temperatures to Reduce Uncertainty in Corrosion Rates–The lower-temperature end of the range of thermal operating modes was defined by considering the potential for reducing uncertainty in the rate of corrosion for Alloy 22. Evidence described in the S&ER (DOE 2001 [DIRS 153849], Section 2.1.5) indicates that corrosion rates are dependent on both temperature and humidity, and that at temperatures below about 85°C and relative humidity (RH) below 50 percent, the susceptibility of Alloy 22 to crevice corrosion is very low. Operating the repository so that the temperature and relative humidity are below this window of crevice corrosion susceptibility may increase confidence that corrosion will not significantly reduce waste package service life. Measurements to date in repository-relevant water chemistries have shown very low general corrosion rates and no crevice corrosion of Alloy 22 (DOE 2001 [DIRS 153849], Sections 4.2.4.1 and 4.2.4.2). However, extrapolating measurements taken over short times (years) to the periods mandated in regulatory requirements

(e.g., 10,000 years) introduces uncertainties. The lower-temperature operating mode described in Table 2-1 addresses this strategy.

2.3.3 Operating Flexibility to Achieve a Range of Thermal Operating Modes

There are many ways of combining operational parameters to limit repository temperatures. Some of the possible combinations are discussed in the S&ER (DOE 2001 [DIRS 153849], Section 2.1.5) and several preliminary engineering evaluations, most notably *Low Temperature Subsurface Layout and Ventilation Concepts* (BSC 2001 [DIRS 154554]), *Operating a Below-Boiling Repository: Demonstration of Concept* (CRWMS M&O 2000 [DIRS 152146]), and *Natural Ventilation Study: Demonstration of Concept* (CRWMS M&O 2000 [DIRS 152269]). Figure 2.3.4-1 illustrates the variables affecting the thermal performance of the repository, from waste forms to emplacement drifts. Within the constraints imposed by the physical system, the repository can be operated in lower-temperature modes while also meeting other technical operational objectives. Drift wall and waste package temperatures and in-drift relative humidity can be managed by altering three operational features of any specified underground layout (CRWMS M&O 2000 [DIRS 152146], Section 3.2):

- Varying the thermal load to the repository by managing the thermal output of the waste packages
- Managing the period and rate of drift ventilation prior to repository closure
- Varying the distance between waste packages in emplacement drifts.

These factors are described below. Other operational parameters, such as long-term post-emplacement natural ventilation, could also be used to reduce peak repository temperatures (CRWMS M&O 2000 [DIRS 152269]). In addition, altering design features, such as emplacement drift spacing, could be used in conjunction with variations in operational parameters to achieve a lower-temperature repository environment.

Thermal Output of the Waste Packages–The major source of heat in the repository is commercial SNF, which will likely have a wide range of thermal outputs. The thermal load of the repository is directly related to the amount of thermal energy generated by radioactive decay in the fuel emplaced in it. The thermal energy contained in the fuel, in turn, is directly related to its age (time after removal from the reactor) and burnup (time and power level at which the fuel was irradiated in the reactor). The age and burnup of SNF received for emplacement in a repository will vary considerably, so the current operational plan for the repository specifies that the DOE will manage the fuel inventory by one or more of the following approaches:

- Fuel blending (placing low heat output fuel with high heat output fuel within a waste package)
- De-rating (limiting the number of SNF assemblies to less than the waste package design capacity)

- Placing high heat output fuel in smaller waste packages

- Aging (delaying emplacement of high heat output fuel until radioactive decay has reduced its heat level).

Managing the average thermal output of waste packages through any of these means can reduce peak temperatures in the repository (CRWMS M&O 2000 [DIRS 152146], Section 3.2).

Duration and Rate of Forced Ventilation–During active repository operations, some of the heat generated by the emplaced waste and the moisture in the surrounding rock can be removed from the repository by forced ventilation of the loaded emplacement drifts. The peak repository temperatures can be reduced by increasing the duration and rate of emplacement drift ventilation (CRWMS M&O 2000 [DIRS 152146], Section 3.2.3).

Distance Between Waste Packages–The distance between waste packages in emplacement drifts is another operational feature that can be modified to manage repository temperature. As waste packages are spaced farther apart, the average linear thermal density in the drift (measured in kilowatts of heat output per meter of drift length) decreases, delivering less heat per unit volume of the host rock when the drift-to-drift spacing remains fixed (CRWMS M&O 2000 [DIRS 152146], Section 3.2.2).

Natural Ventilation–Post-emplacement natural ventilation removes heat and water vapor without the use of fans, using the natural buoyancy of air heated by the waste. The subsurface ventilation system, described in the S&ER (DOE 2001 [DIRS 153849], Section 2.3), could support both forced and natural ventilation. To facilitate natural ventilation, the ventilation system would be enhanced through a combination of air balancing techniques, which involves managing features such as size of ventilation shaft diameters, location and number of intake/exhaust openings, and flow controls (CRWMS M&O 2000 [DIRS 152269]).

2.3.4 Assessing the Performance of a Range of Operating Modes

For the purpose of the *FY01 Supplemental Science and Performance Analyses*, a configuration was selected that allowed focusing of resources on analyses of uncertainties in parameters and on subsystem and total system performance. Should the Yucca Mountain site be determined suitable and be recommended for development by the DOE and the President, engineering and scientific analyses in support of the development of a license application may use other configurations and operations concepts, considering other criteria in addition to performance and uncertainty criteria.

The nominal case analyses for the evaluation of the high and low ends of the thermal operating modes each use the same repository configuration. The footprint of the repository on three sides was determined from proximity to faults, the water table, and the surface. The southern boundary could be extended somewhat to emplace the waste in a larger area to achieve lower temperatures (Figure 2.3.4-2). The waste packages, with a capacity of up to 21 pressurized water reactor fuel assemblies and a peak output at emplacement not to exceed 11.8 kW, would be placed on long-lived pallets within emplacement drifts with a 5.5-m diameter. The drifts would be spaced 81 m apart, and temperatures would be limited during the preclosure period by forced

ventilation. The higher-temperature operating mode would require about 50 years of ventilation with a heat-removal efficiency of 70 percent. The LTOM is modeled as requiring about 300 years of ventilation with an efficiency of 80 percent. Analyses of each thermal operating mode include uncertainty ranges for a number of important parameters, including infiltration rates of water into the mountain. Table 2-1 compares the two cases evaluated in the SSPA with the case used in the TSPA-SR (CRWMS M&O 2000 [DIRS 153246]).

In addition to the higher-temperature operating mode and lower-temperature operating mode analyses, a number of sensitivity analyses were performed to investigate the sensitivity of component, subsystem, and total system performance to conceptual model uncertainties, intrinsic parameter uncertainties, and design operation concept parameters. Some of these sensitivity analyses were performed at the process model level to explore the performance of the potential repository. Process-level analyses and sensitivity studies provide an alternative line of evidence to regression analyses of the (abstracted) total system performance analysis. Other independent lines of evidence used to increase confidence in projections of repository performance include laboratory and field measurements, natural and engineering analogues, and corroborating information from the technical literature.

All of the base case and sensitivity analyses include some common elements. In addition to the repository footprint, the common elements of these evaluations include the following.

Waste Package–The performance evaluations of thermal operating modes evaluated in this report use a corrosion-resistant Alloy 22 outer shell and a structurally strong stainless steel inner shell. In addition to the enhanced shell design, the waste package has a three lid design. A three lid design is used to accommodate stress mitigation techniques in the closure weld area. The additional length of this modified lid has been included in the supplemental analyses, which accounts for the difference in linear thermal loading difference between the S&ER higher-temperature operating mode and the SSPA higher-temperature operating mode.

Inventory–Ability to emplace at least 70,000 metric tons of heavy metal SNF and high-level radioactive waste.

Emplacement Drift Diameter–Emplacement drifts have a 5.5-m diameter.

Drip Shields–Continuous drip shields of corrosion-resistant titanium are assumed to cover the waste packages to divert seepage and limit advective transport of radionuclides from waste packages that may fail earlier than their intended service lifetime.

INTENTIONALLY LEFT BLANK

Table 2-1. Comparison of Higher-Temperature and Lower-Temperature Operating Modes Evaluated in the Fiscal Year 2001 Supplemental Science and Performance Analyses with the Design Analyzed in the Yucca Mountain Science and Engineering Report

Parameters	Science and Engineering Report Flexible Design Higher-Temperature Operating Mode[a]	SSPA Higher-Temperature Operating Mode	SSPA Lower-Temperature Operating Mode
Waste package spacing	0.1 m	0.1 m	Variable, with 1.2 m (average)
Maximum waste package thermal loading	11.8 kW	11.8 kW	11.8 kW
Linear thermal loading objective at emplacement	1.45 kW/m	1.35 kW/m	1.13 kW/m
Years of forced ventilation after start of the emplacement	50	50	300
Years of natural ventilation after forced ventilation period	0	0	0
Number of waste packages	~11,000	~11,000	~11,000
Size of pressurized water reactor waste packages	21 PWR	21 PWR	21 PWR
Required emplacement area	~1150 acres	~1,150 acres	~1,464 acres
Average waste package maximum temperature	>96°C	~160°C	<85°C

Source: DOE 2001 [DIRS 153849].

NOTE: [a]CRWMS M&O 2000 [DIRS 153849].

INTENTIONALLY LEFT BLANK

Table 2-1. Comparison of Higher-Temperature and Lower-Temperature Operating Modes Evaluated in the Fiscal Year 2001 Supplemental Science and Performance Analyses with the Design Analyzed in the Yucca Mountain Science and Engineering Report

Parameters	Science and Engineering Report Flexible Design Higher-Temperature Operating Mode[a]	SSPA Higher-Temperature Operating Mode	SSPA Lower-Temperature Operating Mode
Waste package spacing	0.1 m	0.1 m	Variable, with 1.2 m (average)
Maximum waste package thermal loading	11.8 kW	11.8 kW	11.8 kW
Linear thermal loading objective at emplacement	1.45 kW/m	1.35 kW/m	1.13 kW/m
Years of forced ventilation after start of the emplacement	50	50	300
Years of natural ventilation after forced ventilation period	0	0	0
Number of waste packages	~11,000	~11,000	~11,000
Size of pressurized water reactor waste packages	21 PWR	21 PWR	21 PWR
Required emplacement area	~1150 acres	~1,150 acres	~1,464 acres
Average waste package maximum temperature	>96°C	~160°C	<85°C

Source: DOE 2001 [DIRS 153849].

NOTE: [a]CRWMS M&O 2000 [DIRS 153849].

INTENTIONALLY LEFT BLANK

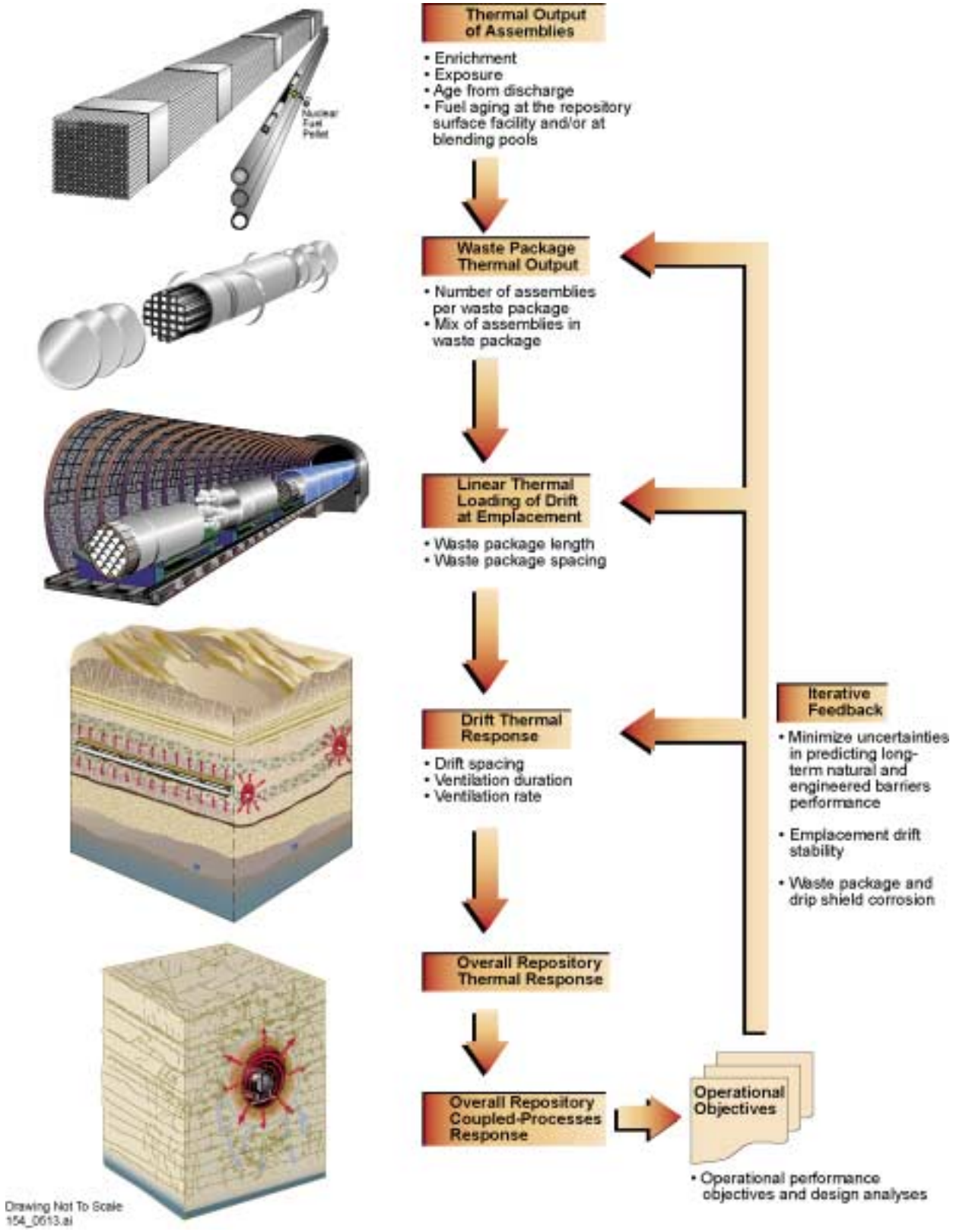

154_0513.ai

Source: DOE 2001 [DIRS 153849], Figure 2-8.

Figure 2.3.4-1. Variables Affecting the Thermal Performance of the Potential Repository

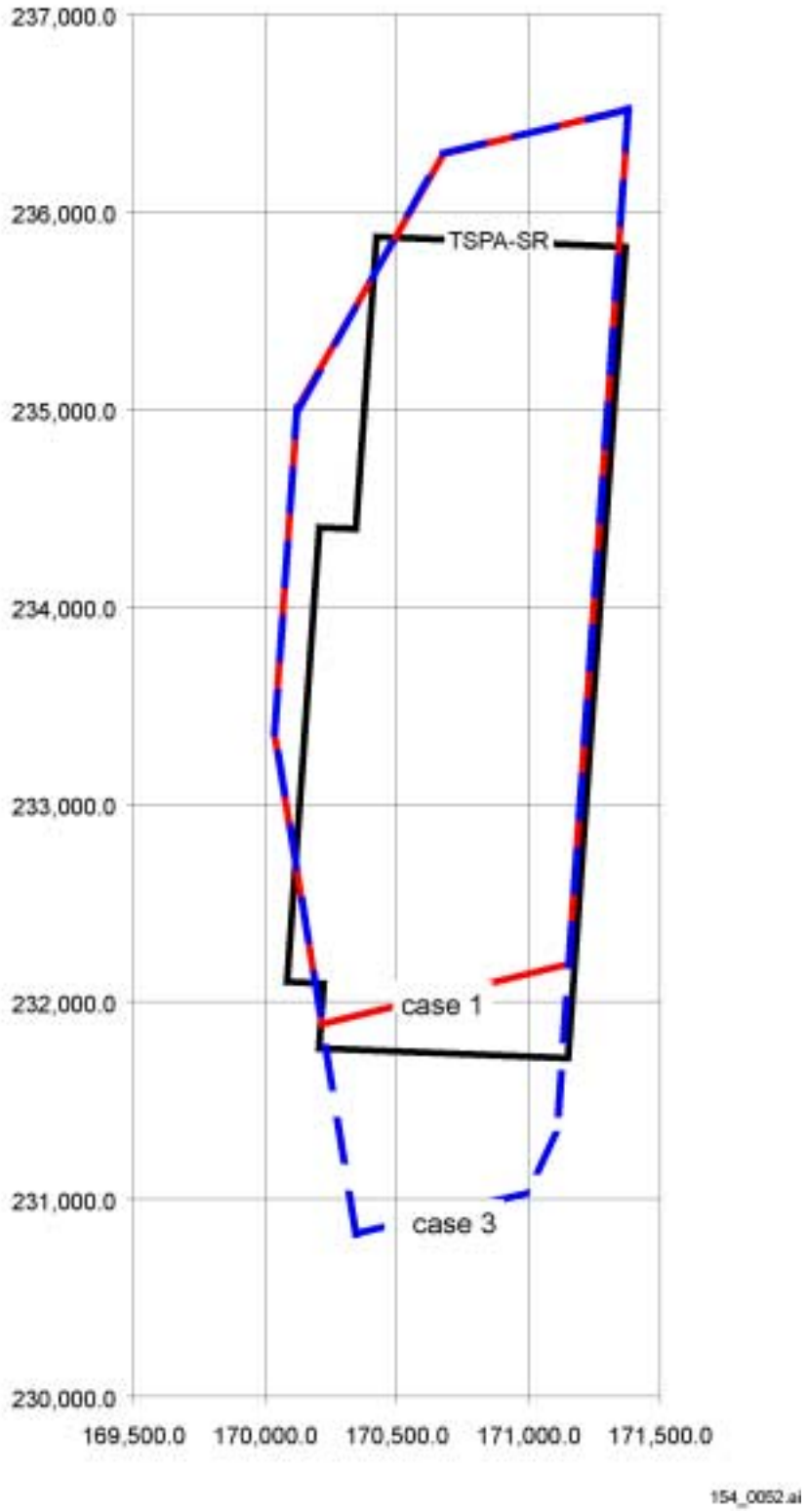

154_0052.ai

NOTE: Higher-temperature (case 1) and lower-temperature (case 3) operating modes. For comparison, the footprint used in the TSPA-SR (CRWMS M&O 2000 [DIRS 153246]) is shown.

Figure 2.3.4-2. Footprints Used in the Thermal Hydrology Analyses

3 Unsaturated Zone Flow

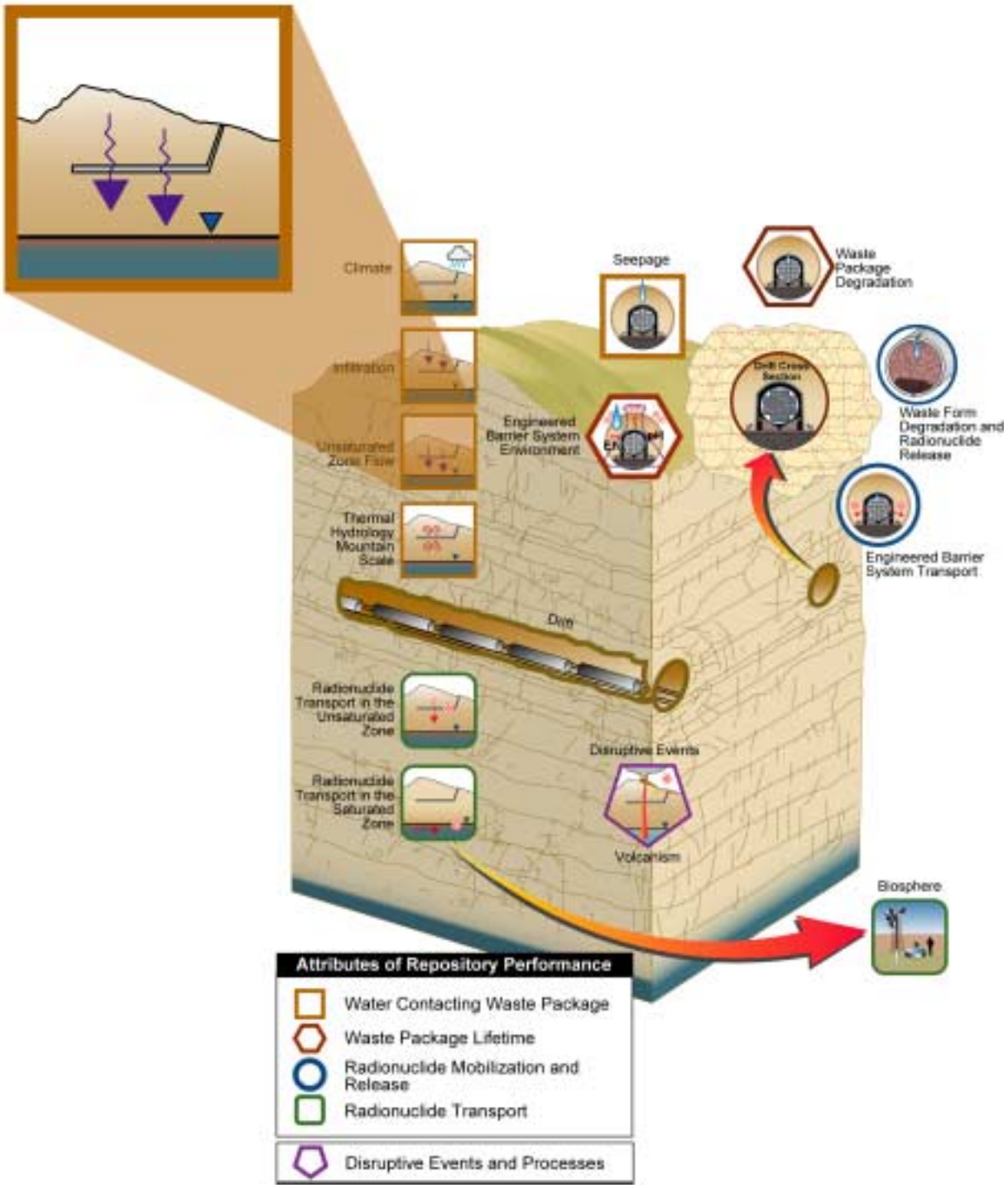

3. UNSATURATED ZONE FLOW

3.1 INTRODUCTION AND CONCEPTUAL BASIS

This section summarizes process modeling and uncertainty studies performed to refine our current understanding of water movement through the unsaturated zone (UZ) under ambient and thermal conditions, including the base-case thermal-loading scenario and the lower-temperature design. The understanding of the unsaturated flow is evolved from decades of site characterization and model calibration, with the bases described at length in the *Unsaturated Zone Flow and Transport Model Process Model Report* (CRWMS M&O 2000 [DIRS 151940]), which is supported by 24 detailed analysis and model reports. Figure 3.1-1 shows the relationships between the main UZ processes, with those that have undergone substantial revisions highlighted. The revisions extend previous evaluations to longer time frames, larger areal extents, and more coupled processes, in the direction of more realistic representations of the Yucca Mountain site to accommodate alternative thermal operating modes for a potential repository.

The ambient and predicted three-dimensional UZ flow fields are based on different climate states and infiltration scenarios, over large areas and alternative thermal-loading schemes needed to satisfy the performance criteria for the potential repository. The UZ mountain-scale models supply direct inputs to the drift-scale seepage models described in Section 4 and the UZ transport models described in Section 11. All other models for engineered barriers and for saturated zone and biosphere are also closely related to the unsaturated flow field. Modeling a realistic flow field and quantification of its uncertainties improves our understanding of the performance of the potential repository system.

The UZ models are representations of water movement affected by climate above the UZ, rock hydrologic properties of tuff matrix, fractures, and faults above the water table, and thermal impacts controllable by design of the potential repository. A dry climate and a deep water table characterize the ambient condition at Yucca Mountain. The current dry climate is likely to be replaced in the future by a wetter climate. Porous and fractured, welded and nonwelded, fault-bounded tuff layers may be modified by prolonged thermal influences. However, the conceptual basis developed over decades of investigations remains the same. The site representation of alternating tuff layers bounded by faults is consistent with the known geology of the site. Rock properties based on measurements in surface-based boreholes and cores are confirmed and modified by additional testing and observations along underground drifts. Long-term thermal tests continue to refine understanding of coupled processes.

3.2 TREATMENT OF UNSATURATED FLOW-RELATED ISSUES IN ANALYSIS AND MODEL REPORTS

The schematic in Figure 3.1-1 illustrates some of the UZ flow-relevant models. The following is a discussion of the key factors affecting unsaturated flow, how they were addressed in the Analysis Model Reports, and more recent analyses and model developments. These sections represent new work and extensions of existing work. Table 3-1 identifies the primary reason for the development of each section and indicates which of these analyses have been included in Total System Performance Assessment (TSPA) calculations.

Table 3-1. Summary of Supplemental Models and Analyses

Key Attributes of System	Process Model (Section of S&ER)	Topic of Supplemental Scientific Model or Analysis	Reason For Supplemental Scientific Model or Analysis			Section of Volume 1	Performance Assessment Treatment of Supplemental Scientific Model or Analysis[a]	
			Unquantified Uncertainty Analysis	Update in Scientific Information	Lower-Temperature Operating Mode Analysis		TSPA Sensitivity Analysis	Included in Supplemental TSPA Model
Limited Water Entering Emplacement Drifts	Climate (4.2.1)	Post-10,000-year Climate Model		X		3.3.1	X	X
	Net Infiltration (4.2.1)	Infiltration for post-10,000-year Climate Model		X		3.3.2	X	X
	Unsaturated Zone Flow (4.2.1)	Flow in PTn		X		3.3.3		
		3-D flow fields for cooler design; flow fields for post-10,000 yr climate, lateral flow; variable thickness of PTn; fault property uncertainty		X	X	3.3.4		
		Effects of lithophysal properties on thermal properties		X		3.3.5		
	Coupled Effects on UZ Flow (4.2.2)	Mountain-scale Thermal-Hydrologic effects		X	X	3.3.5		
		Mountain-scale Thermal-Hydrologic-Chemical effects		X	X	3.3.6		
		Mountain-scale Thermal-Hydrologic-Mechanical effects		X	X	3.3.7		

NOTE: S&ER = *Yucca Mountain Science and Engineering Report* (DOE 2001 [DIRS 153849]).

[a] Performance assessment treatment of supplemental scientific model or analysis discussed in SSPA Volume 2 (McNeish 2001 [DIRS 155023]).

3.2.1 Climate

Process Description–Potential future climate conditions at Yucca Mountain were analyzed in two analysis model reports (AMRs): *Future Climate Analysis* (USGS 2000 [DIRS 136368]) and *Documentation of Million-Year TSPA* (CRWMS M&O 2000 [DIRS 153038]). The future climate at Yucca Mountain for the next 10,000 years is treated as a sequence of three climate states: modern (interglacial) climate for 400 to 600 years, monsoon climate for 900 to 1,400 years, and glacial-transition (intermediate) climate for the balance of the 10,000-year period. The glacial-transition climate occurs either preceding or following the colder or wetter full glacial climate states. Three additional full-glacial climate states are specified within the longer period of 1,000,000 years, with different climate stages timed with the earth orbital clock. Full-glacial stages encompass about 21 percent over the next 1,000,000 years. The intermediate climate is the dominant climate for the next 1,000,000 years, as described in Section 3.3.1.5.

Current Modeling Approach and Uncertainties–The interpretation of past climates is the basis for potential future climate predictions. Both future climate reports used paleoenvironmental and paleoclimate reconstructions based on microfossil evaluations in Owens Lake cores and calcite isotope records from Devils Hole. The sequence and duration of past climate periods are identified from the records and applied to the Yucca Mountain site with similar climate setting. The precipitation and temperature records of present-day meteorological stations at colder and wetter sites are selected to represent future climate states. Each of the future climate states is identified with analogue sites that represent upper-bound, mean, and lower-bounded precipitation scenarios.

The use of paleoecological and paleoclimatic records and analogue site data is the basis of future climate predictions and for evaluation of associated data uncertainties. The climate is assumed to be cyclical with 400,000-year periods and the climate changes are assumed to relate to earth orbital precession and eccentricity parameters. Uncertainties are associated with these and other issues for the timing, duration, and nature of climate changes over the next 1,000,000 years. Tectonic changes and other climate forcing functions have remained relatively constant during the past 1 million years and are expected to remain relatively constant for the next 500,000 years, but may impact future climate at the 1-million-year time scale. Unanticipated, unknown, and unmeasurable future events and human-induced (anthropogenic) changes can be considered, but cannot be predicted. The modeling approach and uncertainties for climate in both AMR revisions and recent evaluations are discussed in detail in Section 3.3.1.

3.2.2 Net Infiltration

Process Description–Net infiltration is the fraction of precipitation (including snowmelt and surface water run-on) that moves through the ground surface and to a depth where the liquid water can no longer be removed by evaporation or transpiration by plants. The approach to simulate net infiltration is documented in *Simulation of Net Infiltration for Modern and Potential Future Climates* (USGS 2001 [DIRS 154674]), for three climate states in the next 10,000 years with associated upper-bound, mean, and lower-bound rates. The estimates of net infiltration are based on the precipitation rates and temperatures predicted for the future climates, for different locations and for each climate state. The net infiltration distributions are used as direct inputs at the upper boundary of the UZ Flow and Transport Model. Relatively high net infiltration rates

occur generally in the northern portion of the site at high elevations and along the ridge where fractured bedrock is exposed. Additional predictions for 10,000 years to 1,000,000 years after present are documented in *Documentation of Million-Year TSPA* (CRWMS M&O 2000 [DIRS 153038]).

Current Modeling Approach and Uncertainties–The infiltration model uses a distributed parameter, water-balance approach for simulating net infiltration processes through the root zone and run-off processes along the washes. The net infiltration model was calibrated with moisture profiles along a network of neutron-logged boreholes, soil and bedrock hydrologic properties, meteorological data, and flow measurements along washes. Vertical one-dimensional flow of infiltrating water through the root zone is assumed and is supported by field data indicating the absence of ponding of water, which would hydraulically facilitate lateral flow. The root-zone parameters were adjusted to extrapolate from present day conditions at Yucca Mountain to those anticipated to occur under future climate conditions.

Uncertainties from the future climate analysis contribute to the uncertainties in the net infiltration model. The uncertainty in net infiltration from imperfect knowledge of input parameters has been quantified for the intermediate (glacial-transition) climate, the dominant climate in the next 1,000,000 years. Extensive time series data of borehole water-contents, water-potential at soil/bedrock contacts, and stream flow measurements caused by transient precipitation events were collected to calibrate the modern (present day) models. Other uncertainties include the use of a water balance approach, the parameter adjustments for future climate states, and the onset of lateral flows at interfaces under episodic infiltration events and during wetter climates. The modeling approach and uncertainties for infiltration in both the AMR revision and recent evaluations are discussed in detail in Section 3.3.2.

3.2.3 Lateral Flow in Paintbrush Nonwelded Hydrogeologic Unit

Process Description–Net infiltration through the fractured bedrocks in the Tiva Canyon welded tuff unit is dominated by significant fracture flow before entering the Paintbrush nonwelded hydrogeological unit (PTn), as discussed in *Conceptual and Numerical Models for UZ Flow and Transport* (CRWMS M&O 2000 [DIRS 141187], p. 21), *Calibrated Properties Model* (CRWMS M&O 2000 [DIRS 144426], p. 28), and *UZ Flow Models and Submodels* (CRWMS M&O 2000 [DIRS 122797], p. 159 and Attachment II). With its characteristics of high matrix porosity and low fracture frequency and the existence of tilted layers of nonwelded vitric and bedded tuff units, PTn can effectively damp out episodic infiltration pulses and divert percolating water to the intercepting faults and fault zones. The difference between infiltration distribution above the PTn and percolation distribution below the PTn is substantiated by geochemical data collected in the field. More significant lateral flow in PTn is shown in more recent development, based on geochemical data.

Current Modeling Approach and Uncertainties–Current modeling approach uses: pneumatic data from sampling points above, within, and below the PTn to calibrate the effective vertical permeability through the PTn and faults; saturation and water potential data to calibrate the unsaturated characteristic parameters; and geochemical data to differentiate alternative conceptual models. The PTn can be represented by fine grids determined by geological data or by coarse grids with anisotropic permeability for the effects induced by multiple tuff layers. It is

also feasible to match the observed chloride spatial distribution in the potential repository horizon by adjusting the infiltration distribution.

The development of alternative conceptual models is used to address uncertainties associated with: lateral flows at PTn interfaces and within the PTn, the role of PTn in damping spatial and temporal variabilities, and the sustainability of fast flow paths (fractures and faults) through heterogeneous PTn units. The PTn tuffs have strong capillary and imbibition potentials. Systematic collections of hydrologic and geochemical data, together with conduction of controlled flow tests, are the bases to iteratively calibrate and validate the models and determine the effective parameters. The chloride data, together with other geochemical and age data, will continue to play an important role in determining the percolation distributions below the PTn to the potential repository horizon in the fractured Topopah Spring welded tuff unit (TSw). Significant lateral flow in the PTn leads to relatively uniform percolation distribution below PTn, in comparison with infiltration distribution above the PTn near the ground surface. Relatively uniform percolation could reduce the variability and associated uncertainties in assessment of UZ waste-isolation capacities. The modeling approach and uncertainties for lateral flow in the PTn in AMR revisions and recent evaluations are discussed in detail in Section 3.3.3.

3.2.4 Three-Dimensional Unsaturated Zone Flow Field

Process Description–The development of the three-dimensional flow field throughout the UZ, from the ground surface to the water table, has evolved over a decade, as documented in *UZ Flow Models and Submodels* (CRWMS M&O 2000 [DIRS 122797]) and in *Unsaturated Zone Flow and Transport Model Process Model Report* (CRWMS M&O 2000 [DIRS 151940]). The comprehensive UZ Flow and Transport Model and its submodels continue to evolve by calibration and validation against all relevant hydrologic, geothermal, and geochemical data. Net infiltration from the ground surface is redistributed by layers of welded and nonwelded tuff units, by interactions between fracture and matrix flow, and by lateral flows along layer interfaces to faults. Below the potential repository, significant lateral diversions are associated with perched water bodies, especially in the northern part of the potential repository block, as a result of zeolites immediately above and within the Calico Hills nonwelded tuff unit (CHn).

Current Modeling Approach and Uncertainties–The current basic model uses a steady-state moisture flow assumption, a volume-averaged modeling approach with dual-permeability model representation of fractures and tuff matrix, and a multilayer three-dimensional gridblock approximation, with each hydrogeologic unit characterized by averaged and calibrated rock properties. The calibrated property sets are developed for upper-bound, mean, and lower-bound infiltration rates of the modern (present-day) climate, to match observed ambient conditions of matrix liquid saturation, water potential and temperature data, perched water data, pneumatic data, and geochemical data. Multiple three-dimensional flow fields were generated to evaluate sensitivities to climate scenarios (including new simulations for the full-glacial stages), variable infiltration maps, and different perched water conceptual models (flow-through and by-passing the zeolitic CHn). The three-dimensional flow fields are direct inputs to TSPA calculations and to other process models. Thermal effects from potential repository heating were evaluated with the UZ Flow and Transport Model, taking the coupled processes into account.

Uncertainties in boundary conditions (especially the infiltration rates and distributions) and in rock properties contribute to uncertainties in the three-dimensional flow fields. Sensitivity and bounding studies were used to identify and quantify uncertainties. Confidence in the current understanding of the UZ system is built by comparing model and submodel results with sufficient data and evaluations to qualify/quantify sensitivity to processes, parameters, conceptual models, and numerical approaches. In the complex UZ system at Yucca Mountain, many aspects of flow and transport processes are not completely understood. These include infiltration boundary conditions, spatial variability of rock properties (especially in CHn and in faults), and the appropriateness of conceptual model assumptions (e.g., steady-state, fracture flow characteristics, fracture-matrix interaction, gridblock averaging, and scaling). Uncertainties are addressed by bounding and sensitivity studies as discussed in DOE 2001 ([DIRS 153849], Sections 4.1.1.2 and 4.1.1.3).

The focus of the site characterization and the UZ flow model study in the past several years has been on the primary potential repository block for the baseline (Enhanced Design Alternative [EDA] II, higher-temperature) design (DTN: SN9907T0872799.001 [DIRS 111485]). The primary block is accessible by surface-based boreholes and by two drifts of the Exploratory Studies Facility (ESF). The most recent UZ flow analyses address the impact of a new siting area for the potential repository, developed with the intent of creating cooler temperatures in the drift environment, by emplacing nuclear wastes at a lower density over a larger area than the primary area. Issues and uncertainties associated with the expanded potential repository include high infiltration and high water table in the north, absence of PTn along some washes and faults, and insufficiency of subsurface data, especially in the new southern block. The modeling approach and uncertainties for three-dimensional UZ flow field in both the AMR and process model report revisions and recent evaluations are discussed in detail in Section 3.3.4.

3.2.5 Thermal-Hydrologic Effects on Unsaturated Mountain-Scale Flow

Process Description–The mountain-scale thermal-hydrologic (TH) models provide analyses of temporal and spatial variability in the UZ conditions under thermal loads. The basic approach to modeling the mountain-scale effects of heat released by the nuclear wastes in emplacement drifts is documented in *Mountain-Scale Coupled Processes (TH) Models* (CRWMS M&O 2000 [DIRS 144454]). The original study used the EDA II design with an initial thermal load of 72.7 kW/acre (1.45 kW/m of drift) and a forced ventilation period of 50 years, during which 70 percent of the decay heat was specified to be removed. When the waste package dimensions that account for the three lid design are considered, the loading works out to be approximately 1.35 kW/m of drift. To reduce the drift wall temperature below the boiling point, lower areal thermal load (67.7 kW/acre, or approximately 1.13 kW/m of drift accounting for the additional length of a third lid on the waste packages), longer forced-ventilation period (300 years), and higher heat-removal efficiency (80 percent) are evaluated. Thermal conductivity and heat capacity of the rock mass are modified to account for the lithophysal porosity in the tuff matrix properties. This lower-temperature operating mode results in a maximum temperature of 85ºC at the drift wall, and therefore no boiling within the rock mass or fractures.

Current Modeling Approach and Uncertainties–Three- and two-dimensional simulations were conducted to address large-scale TH issues relating to climate and infiltration, interface of the potential repository unit (TSw) with the upper PTn and lower CHn units, perched water

bodies, faults, and water table. The two-dimensional models contained local refinements to explicitly represent the 5-m diameter emplacement drifts and in the pillars between drifts spaced 81 m apart. Induced temperature changes have effects at drift walls, within the pillars, at perched water bodies, at the water table, and throughout the UZ system. The coupled TH processes can change the extent of two-phase and dryout zones around the drifts, induce large liquid and gas flux in the near- and far-field environments, redistribute the moisture, and affect the drainage potential through the pillars.

Uncertainties in the UZ flow system model contribute to uncertainties in the mountain-scale TH processes. Additional uncertainties are associated with in-drift processes, including ventilation effects and heat-transfer mechanisms, removal of moisture and heat, and uneven distributions of heat loading. In the TH models, rock properties and boundary conditions are fixed. Some of the coupled effects are further evaluated in mechanical and chemical coupled process models (Sections 3.3.6 and 3.3.7). The uncertainties associated with spatial heterogeneity and scales are also evaluated in the Sections 4 and 11 on TH effects on seepage and on transport. Small-scale heater tests provide data near the drifts and enhance understanding of the coupled processes. For the mountain scale, confidence in the TH models can be built by application of the same modeling techniques for geothermal analogues, with extensive data on exploration and production data history over wide ranges of multi-phase conditions, geologic settings, and calibration experiences. The modeling approach and uncertainties for TH effects on mountain-scale flow in the AMR revision and recent evaluations are discussed in detail in Section 3.3.5.

3.2.6 Thermal-Hydrologic-Chemical Effects on Mountain-Scale Flow and Geochemistry

Process Description–The mountain-scale thermal-hydrologic-chemical (THC) model provides analyses of thermal loading effects on flow and geochemistry in the UZ. This is a new model developed from the models and data documented in two AMRs: the *Mountain-Scale Coupled Processes (TH) Models* (CRWMS M&O 2000 [DIRS 144454]), and the *Drift-Scale Coupled Processes (DST and THC Seepage) Models* (CRWMS M&O 2001 [DIRS 154426]). The mountain-scale models focus on coupled THC processes related to variations in infiltration rate, structure, lithology, rock properties, mineral dissolution and deposition, and flow processes at the mountain or potential repository scale. Small scale effects such as mineral precipitation in the boiling zone are captured in other sections of the drift-scale THC model.

Current Modeling Approach and Uncertainties–A two-dimensional grid was derived from the mountain-scale TH model with the same geologic layering, hydrologic and thermal properties, and thermal loading scenarios. The grid includes an extension of several hundred meters below the water table to provide a far-field constant-temperature boundary. Thermodynamic and kinetic parameters, calibrated against drift-scale heater tests, are used in the mountain-scale evaluations. The initial and infiltrating water chemistry was taken from matrix pore water collected near the ongoing drift-scale test (DST). Condensation and dryout/boiling can affect concentration through dilution and evaporation. Elevated temperature can enhance reaction rates and shift thermodynamic stabilities of coexisting minerals. Release of carbon dioxide out of water and transport in the gas phase via advection and diffusion can have a large effect on pH, mineral-water reactions, and reaction rates.

Uncertainties in mountain-scale flow (including gas convection, liquid flow focusing, and diversion) contribute to uncertainties in mountain-scale THC processes. Other uncertainties include thermodynamic and kinetic data of vitric and zeolitic tuffs, precipitating mineral assemblages, effective mineral-water reactive areas in heterogeneous unsaturated fracture rocks, fracture and lithophysal hydrologic properties, and distributions of water and gas chemistry in the UZ and in the infiltrating water. Sensitivity studies were conducted to understand the impact of THC processes on the mineral changes during thermal periods in the zeolitic CHn, on matrix porosity reduction in the TSw, on enhanced precipitation at the edges of the potential repository block with gas convection, and on many other THC effects. The modeling approach and uncertainties for THC effects on mountain-scale flow and geochemistry in both AMR revisions and recent evaluations are discussed in detail in Section 3.3.6.

3.2.7 Thermal-Hydrologic-Mechanical Effects on Mountain-Scale Flow

Process Description–A new coupled thermal-hydrologic-mechanical (THM) model is developed to calculate the impact of THM processes on flow at the mountain scale. Two well-established codes, TOUGH2 V1.5 for TH processes and FLAC 3D V2.0 for mechanical processes, are coupled together through carefully designed linkage routines. Four types of conservation equations are solved, including two mass-balance equations for the two fluid (liquid and gas) components, one energy (heat) balance equation, and one momentum conservation equation for the rock deformation forces. The mechanical behavior of porous and fractured media responds to changes in temperature, in effective stress, and in strain, resulting in permeability, porosity, and flow-field changes.

Current Modeling Approach and Uncertainties–A two-dimensional model is constructed with vertical layering extended from the ground surface to the water table. Laterally, the model extends from the centerline of the potential repository to a far-field outer boundary located at distance of 5,000 m to the east, over twice the radius of waste emplacement area (2,160 m). The thermal loading, ventilation period, and heat removal efficiency are the same as the values used by the mountain-scale TH model.

Uncertainties in the TH model contribute to uncertainties in THM model. Similar to any newly developed model, uncertainties are relatively large and require substantial input data to conduct the calibration, validation, and thereby build confidence in the models. Calculated changes of permeability depend on such factors as rock stiffness parameters and residual permeability values, heterogeneity of hydrologic and mechanical properties, boundary conditions, dimensionality of the model, and realistic geometries. Geotechnical engineering field and laboratory studies are needed to quantify the uncertainties of THM impact. The modeling approach and uncertainties for THM effects on mountain-scale flow in recent evaluations are discussed in detail in Section 3.3.7.

3.3 UNCERTAINTY ANALYSIS

3.3.1 Climate Model

3.3.1.1 Introduction

This section summarizes climate model developments since the *Total System Performance Assessment for the Site Recommendation* (TSPA-SR) (CRWMS M&O 2000 [DIRS 153246]). The initial release of the climate model, described in *Future Climate Analysis* (USGS 2000 [DIRS 136368]) and summarized in Section 3.3.1.3, addressed climate change for the next 10,000 years. The revision to the climate model focused on predicted precipitation rate and temperature values for glacial climate states that may occur in the next 1 million years, as discussed in *Documentation of Million-Year TSPA* (CRWMS M&O 2000 [DIRS 153038]) and summarized in Section 3.3.1.4. These preliminary climate predictions beyond 10,000 years were included in the TSPA-SR (CRWMS M&O 2000 [DIRS 153246], Section 3.2.5) to support transport sensitivity analyses. Associated uncertainties related to estimating the timing, duration, and nature of climate change are discussed in Section 3.3.1.8. The climate analyses for the next 1 million years are used as input to the updated infiltration model (Section 3.3.2). The new net infiltration results from the infiltration model, in turn, are used in the recent simulations of the flow and transport model (Section 3.3.4) for predicting the flow and transport subject to future climate states over the next 10,000 or 1 million years.

Uncertainties associated with the conceptual model, reliance on interpretation of past climatic conditions as input, and bounding assumptions are inherent to any estimates derived from predictions of future climates. Although the Environmental Protection Agency and U.S. Nuclear Regulatory Commission regulations 40 CFR Part 197 (64 FR 46976 [DIRS 105065]) set a period of 10,000 years for which the U.S. Department of Energy must demonstrate compliance with the radiological protection standard, the U.S. Environmental Protection Agency regulations contemplate post-10,000 year analysis of peak dose in the Environmental Impact Statement, and the National Academy of Sciences has discussed estimating climate beyond 10,000 years as a possible indicator of future repository performance (64 FR 46976 [DIRS 105065], pp. 46993 to 46995). The intent of examining disposal system performance beyond 10,000 years is to estimate its long-term performance to see if dramatic changes can be anticipated. To address uncertainties in system performance, it is necessary to derive estimates of mean annual temperature and precipitation rate. The two analyses of potential future climate conditions for Yucca Mountain, *Future Climate Analysis* (USGS 2000 [DIRS 136368]) and *Documentation of Million-Year TSPA* (CRWMS M&O 2000 [DIRS 153038]), used paleoenvironmental and paleoclimate reconstructions based on evaluations of geological evidence from the Owens Lake Basin, located on the eastern side of the Sierra Nevada mountain range approximately 160 km west of Yucca Mountain, and Devils Hole, located approximately 50 km south of Yucca Mountain. These evaluations are used to estimate future climate conditions. The approach used in both analyses:

- Identifies the sequence, duration, and impact of past climate states (glacial, interglacial, monsoon, and intermediate) suggested by the Owens Lake and Devils Hole paleoenvironmental records

- Selects present-day meteorological stations (analogue stations) to represent these past climate states and uses the record of daily temperature and precipitation from these stations to represent future climate and precipitation

- Compares the relations of delta oxygen-18 Devils Hole reconstructed climate interval (approximately 400,000 to 60,000 years before present) to orbital parameters from celestial mechanics theory to identify a pattern of past climates

- Projects this pattern into the future to establish the nature and timing of future climate change.

Microfossil records of diatoms and ostracodes from cores drilled at Owens Lake have been used to interpret regional climate history from their implied paleoenvironments, provide insight into glacial and interglacial climate change, and provide a means of comparing past climates with each other. Devils Hole is an active extensional fracture in the Paleozoic limestone that composes the regional Paleozoic aquifer. Calcite has precipitated on the walls of the fracture during the last 500,000 or more years, leaving a delta oxygen-18 record of precipitation-derived infiltrating water flowing through the fracture (CRWMS M&O 2000 [DIRS 153038], Section 6.4.1).

3.3.1.2 Goal of Climate Model

The goal of the climate model is to provide precipitation and temperature input data, as well as uncertainty in these data, for the infiltration model (USGS 2001 [DIRS 154674]) under future climate states predicted to occur within the next 1 million years, as discussed in Section 3.3.2. Therefore, predictions of climate and its influence on net infiltration are independent of uncertainties in the thermal load within the repository.

3.3.1.3 Summary of Revision 00 Future Climate Analysis

The climate at Yucca Mountain over the next 10,000 years is treated as a sequence of three climate states (interglacial, monsoon, and intermediate), the timing and characteristics of which are described in *Future Climate Analysis* (USGS 2000 [DIRS 136368]). The present climate state is interglacial. In *Future Climate Analysis* (USGS 2000 [DIRS 136368]), the interglacial and intermediate are referred to as modern and glacial transition, respectively; however to maintain consistency throughout this section, those names are not used. The intermediate climate is a climate state either preceding or following a glacial climate state and is, therefore, neither as cool nor as wet as a glacial climate state. Each climate state is defined by identifying an analogue station, that is, a site whose modern climate approximates the predicted future climate state for Yucca Mountain. The monsoon and intermediate climates are bounded by a range of climate values that have wetter-than-modern upper-bound values and modern or wetter-than-modern lower-bound values relative to the current climate at Yucca Mountain. Tables 3.3.1-1 and 3.3.1-2 list the mean annual precipitation and temperature inferred from the lower- and upper-bound analogue data, which are used as input to the infiltration model to calculate infiltration over the area of the UZ flow and transport model domain. Note that lower and upper bounds refer to precipitation in mm/yr, not temperature.

The precipitation values for the monsoon and intermediate climates exceed those of the present-day climate, indicating that the future climate will be wetter than the modern climate. Temperature, however, also defines an important difference between the modern climate and other climate states. The intermediate climate is cooler than the modern climate, so evaporation is substantially lower than during modern times. A lower level of evaporation means that precipitation can be more readily stored, and hence available for infiltration, than in the current climate. These results are summarized in the *Unsaturated Zone Flow and Transport Model Process Model Report* (CRWMS M&O 2000 [DIRS 151940], Section 3.5).

Uncertainty in climate impact for use in the TSPA is addressed by simulating flow and transport for upper- and lower-bound precipitation and temperature values. The other uncertainty of interest is in the timing of the climate change; durations of 400 to 600 years are expected for the present interglacial climate and 900 to 1,400 years for the monsoon climate, with the intermediate climate extending for the balance of the 10,000-year period in each case (CRWMS M&O 2000 [DIRS 151940], Section 3.5.1.5).

3.3.1.4 Model Development Since Revision 00

Documentation of Million-Year TSPA (CRWMS M&O 2000 [DIRS 153038]) uses the methodology established by and the assumptions set forth in *Future Climate Analysis* (USGS 2000 [DIRS 136368], Sections 6 and 5, respectively) to provide quantified estimates of temperature and precipitation and to estimate the timing of climate states in the Yucca Mountain, Nevada, area for the period from 10,000 to 1 million years beyond the present. This report identifies six potential future climates that alternate during the next 1 million years and proposes minor changes in climate durations predicted for the first 10,000 years from those described in *Future Climate Analysis* (USGS 2000 [DIRS 136368]). In addition to the three climate states mentioned previously, three full glacial climate states are predicted to occur during the next 1 million years.

Based on the paleoclimate record of the full glacial periods recorded in the last 800,000 years, these three full glacial scenarios were selected as representative of the range of severity of full glacial climate stages that may be expected in the next 1 million years. Eight modern meteorological stations were chosen as representative of the upper and lower temperature and precipitation bounds of these three glacial scenarios, as shown in *Documentation of Million-Year TSPA* (CRWMS M&O 2000 [DIRS 153038], Table 6-3). The temperature and precipitation values for the intermediate, monsoon, and interglacial climate states predicted to occur during the next 1 million years are identical to those shown in Tables 3.3.1-1 and 3.3.1-2.

3.3.1.5 Results of Analysis

Past and present climate states were identified based upon geological data (delta oxygen-18 and ostracode fossil data), and the timing of these states was determined by comparison with climate changes calculated from earth orbital parameters using the precession methodology. This methodology assumes that a relationship exists between the timing of long-term past climates and the timing of earth orbital parameters. Orbital parameters can be calculated from basic celestial mechanics, which can be used to estimate the timing of future climates once established (USGS 2000 [DIRS 136368], Section 6.4). Oxygen isotope stages (OISs), established from

studies of marine carbonate delta oxygen-18 records, reflect changes in delta oxygen-18 value of ocean water as continental ice sheets expanded and contracted. The timing and duration of these stages were correlated to the Devils Hole delta oxygen-18 chronology from OIS 11 (the oldest in the available Devils Hole record) through OIS 4 and into OIS 3 (the youngest in the available Devils Hole record). This represents a time interval extending from approximately 400,000 to 60,000 years before the present. Data reported by Petit et al. (1999 [DIRS 109450], Figure 1, p. 430) for Vostok Ice Core delta-deuterium samples were correlated to OIS 3 to 1, representing a time interval of the last 60,000 years. The precession methodology used to time future climate states was based on the past/present point of 399,000 years ago established in *Future Climate Analysis* (USGS 2000 [DIRS 136368], pp. 62 to 63) using the Owens Lake ostracode taxa record, which covers the last 800,000 years (CRWMS M&O 2000 [DIRS 151945], Section 6.3.4.1.2). The past/present point is the point in the past climate series representing the equivalent to the present-day climate. Chronological correlation between the Owens Lake sedimentary record and the Devils Hole delta oxygen-18 record is based on a sediment mass-accumulation curve that is a function of climate and is discussed in *Future Climate Analysis* (USGS 2000 [DIRS 136368], Section 6.5.1).

Ostracode occurrences from the Owens Lake record were used to determine the sequence and nature of past glacial climates in the last 400,000-year climate cycle because the hydrology of Owens Lake is closely linked to climate. Based on the ostracode occurrences, three full glacial climate states of different magnitudes were correlated to specific OISs: OIS 4, OIS 6, and OIS 8/10 (OIS 8 and 10 are grouped together in this analysis because they are similar). The OIS 6 glacial stage had the greatest effective moisture and coldest temperatures contained within the Owens Lake record. However, OIS 16 (centered about 600,000 years before present and outside the Owens Lake record) appears to have had greater effective moisture than OIS 6, based on paleolake records (Reheis 1999 [DIRS 109454], pp. 196 to 205). Therefore, Stage 6/16 is suggested to provide the most conservative effective-moisture estimates, yielding the greatest net infiltration over the Yucca Mountain site. Glacial Stage 8/10 was warmer and wetter relative to OIS 6/16, while glacial Stage 4 was drier and colder than OIS 8/10, but not as cold as OIS 6/16 (CRWMS M&O 2000 [DIRS 153038], Section 6.2).

The durations of each of the different climate states were estimated based on the timing of orbital parameters. The earth-orbital precession methodology was used to time future climate states from 10,000 to 1 million years based on the past/present match point of 399,000 years ago. Future climate is predicted to occur in repeating subcycles of intermediate, interglacial, alternating intermediate and monsoon, and one of three glacial stages. Eleven such four-stage subcycles, ranging from 71,000 to 115,000 years, are predicted to occur during the period between 10,000 and 1 million years, with intermediate, interglacial, monsoon, and glacial accounting for 64, 12, 3, and 21 percent, respectively, of the time as shown on Table 3.3.1-3.

As described in Section 3.3.1.3, the nature of future climate is forecast in terms of upper-, mean, and lower-bound precipitation rates and temperatures based upon meteorological stations at locations that currently have climate conditions similar to past climates observed in the Owens Lake chronological record. Meteorological stations for the interglacial, intermediate (referred to as glacial transition in Section 3.3.1.3), and monsoon climate states are identical to those used in *Future Climate Analysis* (USGS 2000 [DIRS 136368]). Additional meteorological stations were chosen to represent the upper and lower bounds of the glacial climate scenario under Stages 8/10,

6/16, and 4. These glacial stages (OISs) are discussed below: each is briefly described and the analog stations representing their upper and lower bounds are identified (CRWMS M&O 2000 [DIRS 153038], Table 6-3).

Glacial Stage 8/10–Glacial Stage (OIS) 8/10 represents the warmest and wettest of the glacial stages identified in the Owens Lake record, as indicated by the presence of *Candona caudata* and *Limnocythere ceriotuberosa* and the absence of *Cytherissa lacustris*. This combination of ostracodes indicates that the climate was dominated by the mean seasonal or annual latitude of the polar front, with winter-dominated precipitation but without periods of extended dominance by high-pressure, anti-cyclonic circulation.

The area east of the Cascade mountain range in Washington was chosen as a lower bound of the Stage 8/10 analogue (as well as the intermediate climate stage upper-bound analogue) because the region (1) is east of a high mountain range in a rain shadow similar to the Yucca Mountain region; (2) is winter-precipitation dominated; (3) is under the influence of the polar front during the winter; (4) is situated near the average position of the polar front throughout the year; and (5) does not experience extended dominance by cold Arctic high-pressure air. Additionally, ostracodes recovered from glacial stages 8 and 10 in the Owens Lake core occur presently in eastern Washington, supporting the link between distribution and climate. Because the Stage 8/10 upper bound needed to be wetter and slightly cooler than the lower bound, Chewelah, Washington, was selected based on geographic criteria and the fact that it has a mean annual precipitation of approximately 538 mm and a mean annual temperature of approximately 8°C.

Glacial Stage 6/16–Glacial Stage (OIS) 6 appears to have had the greatest effective moisture and the coolest glacial temperatures in the last 400,000-year cycle contained within the Owens Lake fossil record. The presence of the ostracode *Cytherissa lacustris*, which was recovered during much of the OIS 6 time, implies that the climate was dominated by polar and Arctic air masses; the modern distribution of this species is in the Canadian boreal forest and above the Arctic Circle.

Meteorological stations chosen to represent the upper and lower bounds were constrained by the limited distribution of *Cytherissa lacustris* within the United States. It has been collected at Lake Yellowstone, Wyoming, which is a fresh and cold lake. Because this region is dominated by polar air masses, Lake Yellowstone was chosen as the upper bound for the full glacial 6/16 climate state. The annual temperature at this station is cold (0.8°C) because of its high elevation and latitude. Therefore, it may be a conservative analogue. The lower-bound stations (Browning and Simpson, Montana) are in closer agreement with estimated OIS 6 temperatures (5.5ºC), even though *Cytherissa lacustris* has not been reported in this locality (CRWMS M&O 2000 [DIRS 153038], Section 6.3.2).

Glacial Stage 4–Glacial Stage (OIS) 4 was drier and colder than Stage 8/10, but not as cold as Stage 6/16; this is inferred from the combined presence of *Cytherissa lacustris*, *Candona caudata,* and *Limnocythere ceriotuberosa* in the Owens Lake record (CRWMS M&O 2000 [DIRS 153038], Section 6.2). Furthermore, analysis of flora in packrat middens suggests a mean annual precipitation between 266 mm and 321 mm and a mean annual temperature between 7.9°C and 8.5°C (Thompson et al. 1999 [DIRS 109464], Table 4, p. 24).

Meteorological stations chosen to represent the upper bound for the Stage 4 climate were identical to those used to represent the lower bound of the Stage 6/16 climate (CRWMS M&O 2000 [DIRS 153038], Table 6-3). The lower bound for Stage 4 is represented by Elko, Nevada, because it experiences cold, wet, snowy winters influenced by either polar lows or Arctic highs and cold, dry summers resulting from both the presence of cool, westerly flows and the absence of subtropical highs in the region. In addition, *Candona caudata* inhabit locations in the Ruby Mountains in northwest Nevada, representative of similar climate conditions measured at the Elko station.

3.3.1.6 Abstraction for Total System Performance Assessment

The 10,000-year proposed regulatory period has been divided into three climate regimes for TSPA calculations: interglacial (present-day), monsoon, and intermediate. In the TSPA-SR (CRWMS M&O 2000 [DIRS 153246], Section 3.2.1) the interglacial and intermediate are referred to as modern and glacial transition, respectively. The ranges of time periods for each climate are 0 to 600 years for the modern climate, 600 to 2,000 years for the monsoon climate, and 2,000 to 10,000 years for the glacial-transition climate. The climate change times are the only climate information used directly by the TSPA model. The other information is used indirectly, through its effects on infiltration. Additional climate effects are imposed by climate-induced changes in the water table and in saturated-zone recharge (Section 12).

For time periods greater than 10,000 years, it is appropriate to use a climate model that includes full-glacial and future interglacial climates in addition to the present-day interglacial, monsoon, and intermediate climates. For this reason, the previous climate model was extended for times up to 1 million years (Section 3.3.1.4). It is based on paleoclimate data in the same way as the 10,000-year climate model. Details of the climate sequence and analogues for the million-year climate are presented in the TSPA-SR (CRWMS M&O 2000 [DIRS 153246], Section 3.2.5) and *Documentation of Million-Year TSPA* (CRWMS M&O 2000 [DIRS 153038], Tables 6-3 and 6-6). A summary of this discussion is provided below.

Six climate states are specified for the post-10,000-year climate sequence: interglacial, monsoon, intermediate, and three different full-glacial climates. The present-day climate is an interglacial climate, used as an analogue for future interglacials as well. The intermediate climate is the same as the glacial-transition climate. Preceding each glacial state in the climate sequence is a period called intermediate/monsoon, when the climate is alternating between those two states. For TSPA simulations, the climate sequence was simplified by combining the alternating intermediate and monsoon climates into a single intermediate climate state. This approximation is acceptable for TSPA because monsoon climate is estimated to occur for less than 7 percent of the intermediate/monsoon climate state.

Temperature and precipitation data from the analogue stations were used in the infiltration model described in Section 3.3.2 to predict infiltration maps. These infiltration maps were then used as input for flow and transport simulations. Mountain-scale UZ flow fields were generated for four new cases for this extended climate analysis: Glacial Stage 6/16 low-infiltration case; Glacial Stage 6/16 medium-infiltration case; Glacial Stage 6/16 high-infiltration case; and Glacial Stage 4 low-infiltration case. All other cases are represented either by these or by a glacial-transition case that was already available. For calculation of UZ transport within the

TSPA simulation, UZ flow is approximated as a sequence of steady-state flow fields controlled by net infiltration rates calculated for each climate state. The UZ flow fields are used sequentially according to the predicted timing (starting time, ending time, duration) of each climate state.

3.3.1.7 Multiple Lines of Evidence

This analysis is based on meteorological data collected at natural analogue sites (the meteorological stations listed in CRWMS M&O 2000 [DIRS 153038], Table 6.3) for the climates expected to occur at Yucca Mountain over the next 10,000 and 1 million years. The prediction of future climates involves multiple lines of evidence: delta oxygen-18 data, fossil ostracode data, and earth-orbital data. The earth-orbital data are determined by celestial mechanics and have a high degree of certainty; they control the timing of climate states. However, the response of climate to the orbital parameters is not known with a high degree of certainty. The other data sets provide corroborative evidence of temperature and salinity changes, from which precipitation is estimated. Analogue stations that presently experience climate similar to that predicted for the future at Yucca Mountain are chosen to have either the indicator ostracode species or conditions favorable for their survival. Precipitation and temperature records for these analogue stations can be used to estimate future year-to-year variability.

3.3.1.8 Summary of Uncertainties and Their Treatment

Uncertainties in estimated future climate states consist of conceptual, data, and parameter uncertainties, which are tabulated below. These uncertainties affect the goal of the report, which is to provide temperature and precipitation values for different climate states. There is no simple or objective way of assessing the nature of uncertainty as it may apply to future climate change over the next 1 million years. If these uncertainties are not accepted, then the future climate bounding estimates would depend on a conservative estimate of climate based on the extreme temperature (cold) and precipitation (wet) values from the previous 400,000-year cycle instead of values estimated herein within the extremes. In general, these uncertainties were considered acceptable, given the intended purpose of the report and the use of its results in the downstream model.

Table 3.3.1-4 summarizes the key conceptual and parametric uncertainties regarding the development of the future climate analysis. Uncertainties are grouped according to category (i.e., conceptual, data, or parameter). Next, the primary uncertainty issue associated with each category is described, followed by possible methods for treating or addressing the uncertainty. Finally, the affected modeling goals are presented.

3.3.1.9 Summary and Conclusions

The future climate over the next 1 million years at Yucca Mountain is treated as a sequence of stages whose timing and characteristics are described in detail in *Documentation of Million-Year TSPA* (CRWMS M&O 2000 [DIRS 153038]). The alternating climate stages include intermediate, monsoon, interglacial, and three glacial stages (OIS 6/16, OIS 8/10, and OIS 4). Each stage is defined by mean annual precipitation rates and temperatures. Tables 3.3.1-5

and 3.3.1-6 list mean annual precipitation and temperature values used as input to the infiltration model discussed in Section 3.3.2 to calculate net infiltration for possible future glacial climate states over the next 1 million years. Precipitation and temperature data for the analog stations (CRWMS M&O 2000 [DIRS 153038], Table 6-3), are presented in DTN: GS000100001221.001 [DIRS 146816]. However, the values in Tables 3.3.1-5 and 3.3.1-6 do not necessarily represent the same analog stations, because the net infiltration model makes adjustments to account for the topography of the UZ flow and transport model area, as described in USGS (2001 [DIRS 154674], Section 6.4.2).

Because of the uncertainties identified in Table 3.3.1-4, only the Glacial Stage 6/16 climate (which would result in the most net infiltration) was used to estimate mean annual precipitation and mean annual temperature for the purposes of calculating net infiltration (BSC 2001 [DIRS 154873]). Selection of this stage is therefore the most conservative approach. To reduce the number of infiltration model simulations required in Section 3.3.2, specific combinations of mean annual temperature and mean annual precipitation from Stage 6/16 meteorological stations were used to infer upper-, mean, and lower-bound values for Stages 8/10 and 4, with the exception that the lower-bound Stage 8/10 is given by the upper-bound intermediate climate shown in Tables 3.3.1-1 and 3.3.1-2. An alternate Stage 6/16 meteorological station is used in Section 3.3.4.4 to represent the lower-bound Stage 8/10 and is provided in parentheses in Tables 3.3.1-5 and 3.3.1-6. Note that lower- and upper-bound refer to precipitation or net infiltration (see lower-bound glacial stage 8/10 in Table 3.3.2-3) in mm/yr, not temperature.

The upper-bound precipitation values for the full glacial climate exceed the upper bound of the present-day interglacial (modern) climate for the region by at least 160 mm/yr, while the lower bound of the Glacial Stage 4 climate is almost identical in value to the interglacial (modern) upper bound. Therefore, all glacial climate stages are wetter than the modern interglacial climate. Temperatures during the glacial climates are cooler than the modern interglacial climate, leading to substantially lower evaporation than presently occurs at Yucca Mountain. A lower level of evaporation means that precipitation will be more readily stored in the root zone (shallow subsurface soil and rocks), and hence available for infiltration, than in the current climate.

3.3.2 Net Infiltration Model

3.3.2.1 Introduction

New predictions of precipitation and temperature for future climates extending to the next 1 million years, described in Section 3.3.1, have resulted in extension of the initial release of the net infiltration model documented in *Simulation of Net Infiltration for Modern and Potential Future Climate* (USGS 2001 [DIRS 154674]) and summarized in Section 3.3.2.3. Preliminary infiltration scenarios for the extended climate regime were conducted for the TSPA-SR (CRWMS M&O 2000 [DIRS 153246]) to conduct transport sensitivity analyses. The new modeling discussed in Sections 3.3.2.4 and 3.3.2.5 encompasses a larger area, reflecting the UZ flow and transport model documented in *UZ Flow Models and Submodels* (CRWMS M&O 2000 [DIRS 122797]). The uncertainty of the infiltration scenario for the glacial-transition climate was assessed using the Monte Carlo method, as reported in the TSPA-SR (CRWMS M&O 2000 [DIRS 153246], Section 3.2.2.3) and summarized in Section 3.3.2.6.

Net infiltration is the fraction of precipitation, snowmelt, or surface water run-on that infiltrates and percolates below the zone of evapotranspiration. Predicted net infiltration varying with location constitutes the upper-boundary condition for flow-field simulations. Estimates of net infiltration presented here are based on the precipitation rates and temperatures for the interglacial/modern, monsoon, intermediate/glacial-transition, and full glacial climates predicted to occur over the next 1 million years, as presented in *Future Climate Analysis* (USGS 2000 [DIRS 136368]) and in *Documentation of Million-Year TSPA* (CRWMS M&O 2000 [DIRS 153038]). Each of these climate states has been identified with three analogue sites that represent upper-bound, mean, and lower-bound precipitation scenarios. These future climate scenarios, in turn, are based on past climates inferred from microfossil and oxygen-isotope data and on earth-orbital parameters, as described in Section 3.3.1 (USGS 2000 [DIRS 136368]; CRWMS M&O 2000 [DIRS 153038]). The approach used to simulate net infiltration using the net infiltration model is documented in *Simulation of Net Infiltration for Modern and Potential Future Climates* (USGS 2001 [DIRS 154674]). The net infiltration model is a quasi three-dimensional numerical model used to simulate surface flow and subsequent percolation of water through the root zone due to the effects of precipitation and temperature at the Yucca Mountain site. The resulting net infiltration estimates are spatially distributed and time-averaged. Uncertainty in net infiltration has been quantified for the intermediate climate, which is the dominant climate for the next 1 million years (as described in Section 3.3.1.5). Unquantified uncertainties in the net infiltration model broadly consist of conceptualization of the processes significant to the hydrologic cycle, numerical representation of the processes, and calibration and validation of the model, as described in detail in Section 3.3.2.8.

3.3.2.2 Goal of the Net Infiltration Model

The goal of the net infiltration model is to use precipitation and temperature data from analogue sites that represent future climate states (USGS 2000 [DIRS 136368]; CRWMS M&O 2000 [DIRS 153038]) to predict net infiltration rates for use as direct input to the UZ flow and transport model. Net infiltration, as calculated by the net infiltration model, is assumed to depend only upon surface processes. Therefore, it is assumed to be independent of the repository thermal regime even though surface temperatures (in the root zone) may become slightly elevated, as shown in Figure 3.3.5-2 or Figure 3.3.5-3. Therefore, the scope of the net infiltration model is limited to surficial hydrologic processes occurring only to the depth of the root zone. In the context of the UZ flow model, the surface (bottom of the root zone) is considered to be a perfectly insulated thermal boundary preventing heat loss to the atmosphere with a constant net infiltration rate as prescribed by the net infiltration model.

3.3.2.3 Discussion of Analysis Model Report Revision 00 Results

The predictions of future climate and precipitation, and the resulting infiltration rates, are documented in *Future Climate Analysis* (USGS 2000 [DIRS 136368]) and *Simulation of Net Infiltration for Modern and Potential Future Climates* (USGS 2001 [DIRS 154674]), respectively. These predictions show that as the climate changes from interglacial to monsoon to intermediate, the mean precipitation and site-average infiltration rates also increase, as shown in Tables 3.3.1-1 and 3.3.2-1, respectively. The highest net infiltration rates occur on the steep north-northeast facing slope of the Prow, the upper channel locations of Solitario Canyon, Drill Hole Wash, Pagany Wash, and Abandoned Wash, and generally in the northern portion of the

site. These results are summarized in *Unsaturated Zone Flow and Transport Model Process Model Report* (CRWMS M&O 2000 [DIRS 151940], Section 3.5.2).

3.3.2.4 Model Development Since Revision 00 of Analysis Model Reports

Additional climate prediction for 10,000 years to 1 million years after present have been documented in *Documentation of Million-Year TSPA* (CRWMS M&O 2000 [DIRS 153038]) and were used to calculate net infiltration rates for full glacial climates expected to occur within the next 1 million years (BSC 2001 [DIRS 154873]). Although the net infiltration model was not initially developed in Revision 00 for a full glacial state, no change has been made to the net infiltration model for its application to the full glacial state in the work described here. In summary, the net infiltration model was used to predict net infiltration at Yucca Mountain for six potential future climates: intermediate, monsoon, interglacial, and three different full-glacial states.

3.3.2.5 Results of Analysis

The net infiltration estimates presented in this section are for the 38.7 km^2 area used as the modeling domain for the UZ flow and transport model (CRWMS M&O 2000 [DIRS 122797]). Net infiltration rates estimated by the net infiltration model for the UZ flow and transport model domain differ slightly from those actually implemented in the model. This difference results from plan-view discretization effects in the model and the need to spatially average net infiltration rates over each node in the model domain (Bodvarsson 2001 [DIRS 154669], Attachment 12, pp. 203 to 211). Model results from the net infiltration model for the three different full-glacial climates are discussed below and summarized in Table 3.3.2-3.

Glacial Stage 6/16–Figure 3.3.2-1 illustrates net infiltration for the lower, mean, and upper bound for the glacial-climate scenario. Analogue-site data for the mean Glacial Stage 6/16 climate include an average precipitation rate of 429 mm/yr, which for the area of the UZ flow and transport model domain results in an average net infiltration of 87.9 mm/yr. For the lower- and upper-bound Stage 6/16 scenarios, the average net infiltration rate is estimated to be 24.4 mm/yr and 151.0 mm/yr, respectively.

The lower-bound net infiltration rate for this Stage 6/16 climate is therefore 9 mm/yr less than the upper-bound intermediate infiltration rate, while the upper-bound Stage 6/16-infiltration rate is 118.0 mm/yr greater. Therefore, net infiltration rates are significantly higher for the Stage 6/16 climate than for the intermediate, monsoon, or interglacial climates because of the combined influence of high mean annual precipitation rates and lower mean annual temperatures.

Glacial Stage 8/10–To simplify the net infiltration analysis, mean annual precipitation rates and temperatures used to represent the upper, mean, and lower bounds of the Stage 8/10 climate were chosen from meteorological stations, as described in Section 3.3.1.5. These stations are listed in Tables 3.3.1-5 and 3.3.1-6. Given this approximation, the mean and upper-bound net infiltration rates for the Stage 8/10 climate are identical to those for the Stage 6/16 climate. The lower-bound mean annual net infiltration rate for Stage 8/10 is identical to the upper-bound intermediate climate described in Section 3.3.1.3 (Table 3.3.2-1): 33.0 mm/yr, which is

8.6 mm/yr higher than the lower-bound Stage 6/16 rate. Therefore, the Stage 8/10 climate generates the most conservative estimate of net infiltration over the area of the UZ flow and transport model, as indicated by the choice of upper-, mean, and lower-bound mean annual precipitation rates and temperatures from analogue meteorological stations.

Glacial Stage 4–The mean and upper-bound net infiltration rates for Stage 4 are identical to the lower-bound and mean values of the Stage 6/16 climate, respectively. The lower-bound mean annual net infiltration rate for Stage 4 is estimated to be 12.9 mm/yr, which is slightly higher than the upper-bound interglacial (modern, Table 3.3.2-1), mean monsoon, and average of the lower-bound and mean intermediate (glacial transition, Table 3.3.2-1). Therefore, despite the fact that Stage 4 caused the least net infiltration of the three glacial climate stages and hence is least conservative, the Stage 4 climate does on average result in greater net infiltration than the intermediate, interglacial, and monsoon climate scenarios.

3.3.2.6 Abstraction for Total System Performance Assessment

A detailed analysis of infiltration uncertainty was conducted for the intermediate climate (glacial-transition climate in Section 3.3.2.3) using the Monte Carlo method, as documented in the TSPA-SR (CRWMS M&O 2000 [DIRS 153246], Section 3.2.2). The uncertainty in net infiltration (as considered in the TSPA analysis) is considered to result from imperfect knowledge of input parameters used by the net infiltration model. The uncertainty analysis with the intermediate climate focused on twelve key input parameters (Table 3.3.2-2, last entry) for which uncertainty distributions were developed. These distributions were then sampled stochastically for 100 Monte Carlo realizations, yielding 100 estimates of net infiltration rates. The result of the Monte Carlo analysis was an approximately lognormal histogram of net infiltration rates (CRWMS M&O 2000 [DIRS 143244], p. 23 to 27). Specifically, for the intermediate (glacial-transition) climate state, the mean ±1 standard deviation of the logarithm of net infiltration, in $\log_{10}$ (mm/yr), is 1.25 ±0.42. Converted, this means that annual net infiltration will be less than 7 mm in 16 percent of years, less than 17 mm in 50 percent of years, and less than 47 mm in 84 percent of years (numbers approximate). This analysis shows that the lower-bound and upper-bound infiltration rates derived using only analogue meteorological station temperature and precipitation data as shown in Table 3.3.2-1 are not truly bounds when all uncertainties in net infiltration model input parameters for the future climate states are taken into account (see last entry in Table 3.3.2-2). Also, the mean infiltration rate given in Table 3.3.2-1 (derived using only analogue meteorological station temperature and precipitation data) is not the statistical mean when the appropriate probabilistic weighting factors are applied to the net infiltration distribution generated by the Monte Carlo analysis.

The Monte Carlo analysis was constructed to quantify uncertainty in net infiltration rates for the intermediate (glacial transition) climate because that climate is dominant within the 10,000-year regulatory period. The intermediate climate is also the dominant climate state over the next 1 million years in the extended climate model (CRWMS M&O 2000 [DIRS 153038], Section 6.5.3). The uncertainty for the other climate states, and in particular for the full-glacial climates, has not yet been analyzed. Therefore, uncertainty in net infiltration over the next 1 million years is taken to be identical to that of the intermediate (glacial-transition) climate.

3.3.2.7 Multiple Lines of Evidence

Analogue studies that estimated groundwater recharge rates from hydrologic modeling studies provide an indication of infiltration under future glacial climate conditions. The analogue studies were conducted for two small basins in central Nevada (Lichty and McKinley 1995 [DIRS 100589], p. 3). Their purpose was to aid in estimating recharge to the paleohydrologic regime associated with Yucca Mountain under wetter climate conditions. Thus, the two selected sites, 3-Springs and East Stewart basins, are located north of and at a higher elevation than Yucca Mountain, where prevailing climatic conditions are thought to be representative of the range of paleoclimatic conditions near Yucca Mountain during the Quaternary. Both study sites are characterized by high relief and rough terrain, with elevations ranging from about 2,150 to 2,900 m above sea level for 3-Springs Basin and 2,950 to 3,320 m for East Stewart Basin (Lichty and McKinley 1995 [DIRS 100589], p. 3). The climate at 3-Springs Basin is semiarid, with annual precipitation generally in the range of 250 to 350 mm, most of which occurs as snow during winter months. The East Stewart Creek site is a subalpine drainage basin where annual precipitation ranges from 500 to 700 mm, again occurring predominantly as snow.

Two independent modeling approaches were conducted for each site, using observed hydrologic data for a six-year study period (October 1986 through September 1992). One approach used a traditional watershed hydrology method through a precipitation-runoff system that accounts for spatial variability of data. The other approach was based on the conservative nature of the chloride ion in certain geologic environments, using it as a natural tracer to compute a coupled water and chloride-ion mass-balance system of equations to estimate available water for net infiltration.

Results of the modeling approaches support the conclusion that reasonable estimates of average annual recharge to groundwater range from about 10 to 30 mm per year for 3-Springs Basin and from about 300 to 320 mm per year for East Stewart Basin (Lichty and McKinley 1995 [DIRS 100589], p. 26). The semiarid 3-Springs Basin provides net infiltration rates that are in the range between the upper-bound modern and upper-bound glacial-transition climates. The subalpine East Stewart Creek site provides net infiltration rates that are twice as large as the upper-bound Glacial Stage 6/16 climate. Therefore, the 3-Springs site provides a conservative estimate of net infiltration that is expected to occur over the next 10,000 years, while the East Stewart Creek site provides a conservative estimate of net infiltration that is expected to occur over the next 1 million years, as predicted by the net infiltration model.

Multiple lines of evidence for net infiltration under modern climate conditions are reviewed in the *Unsaturated Zone Flow and Transport Model Process Model Report* (CRWMS M&O 2000 [DIRS 151940], Section 3.5.2.8).

3.3.2.8 Summary of Remaining Uncertainties

Uncertainties in the net infiltration model broadly consist of conceptualization of the processes significant to the hydrologic cycle, numerical representation of the processes, and calibration of the model. Table 3.3.2-2 summarizes the key conceptual and parametric uncertainties regarding the development of the net infiltration model. Uncertainties are grouped according to category (i.e., conceptual, data, or parameter). Next, the primary uncertainty issue associated with each

category is described, followed by methods used for treating or addressing the uncertainty. Finally, the affected modeling goals are presented.

3.3.2.9 Summary and Conclusions

The predictions of future climate, precipitation, and resulting infiltration rates show that as climate changes from interglacial (modern) to monsoon to intermediate (glacial-transition) to glacial, the mean precipitation and infiltration rates also increase, as shown in Tables 3.3.1-1, 3.3.1-5, 3.3.2-1, and 3.3.2-3. The glacial climate scenario was subdivided into three stages (6/16, 8/10, and 4) with upper-, mean, and lower-bound mean annual precipitation and temperature data derived primarily from Stage 6/16 meteorological stations. This simplification was made to reduce the number of net infiltration model simulations required to calculate the impact of the glacial climate scenarios and because Stage 6/16 was anticipated to result in the greatest effective moisture and coolest glacial temperatures, and therefore the most conservative net infiltration scenario. Using the meteorological data presented in Tables 3.3.1-5 and 3.3.1-6, the Stage 8/10 glacial climate generated the most conservative estimate for net infiltration over the UZ flow and transport model area (Table 3.3.2-3). These values represent infiltration rates averaged over the model area, and are up to 37 percent higher than those in the TSPA-SR (CRWMS M&O 2000 [DIRS 153246], Table 3.2-6), which are rates averaged over the footprint of the potential repository.

3.3.3 Percolation Redistribution and Flow in the Paintbrush Nonwelded Hydrogeologic Units

3.3.3.1 Introduction

This section summarizes the modeling and uncertainty studies performed to evaluate percolation flux distribution and flow in the Paintbrush nonwelded (PTn) hydrogeologic units. Since the TSPA-SR (CRWMS M&O 2000 [DIRS 153246]), new field geochemical data have been used to calibrate the spatial distribution of net infiltration (see Section 3.3.3.4.1) and the anisotropy of permeability of the PTn (see Section 3.3.3.4.3) in UZ flow model simulations. Detailed PTn flow models have been constructed to evaluate lateral flow within the PTn caused by capillary barrier effects (see Section 3.3.3.4.2).

Flow in the PTn is important because the new flow simulation results from this study suggest that water flow within and through the PTn likely will be matrix dominated except, possibly, in the vicinity of major through-going fault zones that may create fracture-dominated preferential flow pathways through the unit. The PTn acted as a buffer, damping out variations in the transient net infiltration, so that flow beneath the PTn was essentially steady-state. The PTn redistributed percolation flux in space as well as in time Lateral flow diverted net infiltration above the potential repository area eastward to the Ghost Dance and Drill Hole Wash faults. Flow thus diverted bypassed the potential repository block.

3.3.3.2 Modeling Goals

The goals of the models used to study percolation distribution and flow in the PTn are:

- Evaluate the effects of the spatial distribution of net infiltration on percolation distribution and flow in the PTn
- Assess bounds on net infiltration rates, spatial distribution patterns, net infiltration rate variability, and associated uncertainties
- Evaluate the effects of lateral flow within the PTn on percolation and chloride redistribution
- Provide a methodological and conceptual basis for modeling percolation flux and lateral flow within the PTn
- Develop calibration procedures using natural and anthropogenic environmental tracers
- Identify conceptual uncertainties and estimate the uncertainty and variability of model-relevant parameters.

3.3.3.3 Discussion of Analysis Model Report Revision 00 Results

The PTn consists of nonwelded and vitric horizons and bedded tuffs intersected by faults and fault zones. The percolation distribution in the potential repository level below the PTn determines the degree of seepage into drifts, which in turn affects the performance of waste packages and engineered barrier systems. Uncertainties in the conceptual model, the data used for calibration, and flow and transport parameters in the current model were discussed in detail in *Calibrated Properties Model* (CRWMS M&O 2000 [DIRS 144426]) and *UZ Flow Models and Submodels* (CRWMS M&O 2000 [DIRS 122797]).

In addition to geologic and hydrologic information, geochemical data provide information on flow patterns within the UZ, including the PTn. Distribution of chemical constituents depends on the hydrologic and geochemical processes associated with surface precipitation, evapotranspiration, fracture-matrix interactions of flow and transport, large-scale mixing via lateral transport, and the history of climate changes and recharge. Natural and anthropogenic environmental tracers provide useful data for evaluating the processes over various time and space scales. By synthesizing geochemical, geologic, and hydrologic data, the model results enhance the understanding of flow and transport processes and the development of hydrologic parameter sets and conceptual models.

The initial issue of *UZ Flow Models and Submodels* (CRWMS M&O 2000 [DIRS 122797]) focused on the formulation of methodologies and the conceptual bases of using matrix pore-water geochemical data for flow model calibration. Analysis and modeling of pore-water geochemical data are documented in that AMR. Pore-water chemical concentration data were analyzed and modeled using three-dimensional chemical transport simulations and analytical methods. Water net infiltration-rate calibrations were performed using the pore-water chloride concentrations. Model results of chloride distributions match the observed data better using the

calibrated present-day-mean net infiltration rates than using the present day mean net infiltration rates without calibration (CRWMS M&O 2000 [DIRS 122797], Section 6.4). In addition, an analytical method was developed to analyze the transient transport of chemicals. This method was compared against the results of three-dimensional simulations under the same flow conditions and was able to capture major chloride and chlorine-36 transient behavior and trends predicted by the simulations (CRWMS M&O 2000 [DIRS 122797], Section 6.4.3.2).

3.3.3.4 Model Development Since Total System Performance Assessment for Site Recommendation

The following sections describe three developments in the evaluation of three-dimensional flow within the PTn since the TSPA-SR (CRWMS M&O 2000 [DIRS 153246]). These studies were done to test simulation models by comparing their results to all available qualified data, and revising where appropriate. Such revision, termed model calibration, increases confidence in the model and reduces associated uncertainties. Section 3.3.3.4.1 describes the use of chloride data to evaluate distribution of net infiltration with isotropic permeability within the PTn. Section 3.3.3.4.2 describes the use of a detailed two-dimensional model of the PTn to evaluate the importance of lateral flow due to capillary barrier diversion within the unit. Finally, in Section 3.3.3.4.3, the present-day mean net infiltration map developed by the infiltration model (Figure 3.3.3-1) was left unchanged, but the chloride data were matched by adjusting the anisotropy of the PTn. Thus, both of these conceptual models match the chloride data better than the initial models. A three-dimensional dual-permeability model and the T2R3D V1.4 and TOUGH2 V1.4 codes were employed for the simulations.

3.3.3.4.1 Chloride-Based Net Infiltration Rate

Net infiltration is defined as the penetration of surface water below the root zone to a depth from which it can no longer be removed by evapotranspiration. The infiltration model (USGS 2001 [DIRS 154674]) described in Section 3.3.2 provides net infiltration flux values (mm/yr), which are applied (as a boundary condition) to top-layer gridblock cells (Figure 3.3.3-1). By water balance, net infiltration flux is the sum of precipitation and run-on minus the sum of runoff and evapotranspiration, all of which vary spatially. As precipitation falls, it acquires chloride by uptake of aerosols from the atmosphere. As a result, precipitation, run-on, and runoff contain a known concentration of chloride. Infiltrating water has a higher chloride concentration than precipitation because some water, but no chloride, is lost to evapotranspiration. The net infiltration maps that are output by the infiltration model can therefore be used to calculate the chloride concentration of infiltrating water. The net infiltration flux and associated chloride concentration vary spatially over the site (Figure 3.3.3-1). When these are used as boundary conditions, the flow and transport model simulates chloride concentration everywhere in the UZ. Essentially no chloride is contributed by dissolution of UZ minerals. These simulated chloride concentrations can be compared with measurements on pore water samples to calibrate the model.

A systematic study incorporating new data from borehole SD-6 (DTN: GS981008312272.004 [DIRS 153677]) and calibration procedures has been conducted since the initial release of the infiltration model (USGS 2000 [DIRS 123650]). This study is documented in Bodvarsson (2001 [DIRS 154669], Attachment 11, pp. 72 to 83). As in that report, the available chloride data were

used to calibrate the net infiltration distribution without changing the hydrologic properties of the PTn. Measurements of pore water chloride concentrations offer a spatially distributed data set for assessing UZ flow and transport processes and for testing conceptual models. Calibration was done by dividing the surface infiltration area into nine regions (Figure 3.3.3-2) according to the availability and range of chloride data, the range of present-day mean net infiltration data (shown in Figure 3.3.3-1), and hydrogeologic and hydrostructural features. The chloride field data were assigned to corresponding simulation cells based on pore water sample locations. The revised water net infiltration flux for each simulation cell was computed using the chloride net infiltration flux and the assigned chloride concentration data from the cell. For cells where chloride data were not available, the net infiltration flux was interpolated based on the calculated net infiltration flux in nearby cells within the same region and the surface area of the cell. The map of chloride-based calibrated net infiltration is shown in Figure 3.3.3-2. Averaged present-day mean net infiltration was applied to regions where regional chloride data is unavailable (Regions I, II, and VIII). The overall and regional net infiltration volume and rates for the net infiltration schemes before and after the calibration are given in Table 3.3.3-1. In this table, before-calibration flow rates and fluxes (Figure 3.3.3-1) are the output from the infiltration model (DTN: GS000399991221.002 [DIRS 147022]), and after-calibration flow rates and fluxes (shown also in Figure 3.3.3-2) are the values after calibrating against chloride data. The result of calibrating the net infiltration map against chloride data was to increase the overall net infiltration by 9 percent but to decrease it in Region III, so net infiltration over the potential repository footprint is decreased. Three-dimensional flow and chloride transport simulations were conducted using both the present-day mean net infiltration from the infiltration model (Figure 3.3.3-1) and the chloride-based calibrated present-day mean net infiltration (Figure 3.3.3-2) to assess the two net infiltration schemes.

3.3.3.4.2 Lateral Flows Induced by Capillary Barriers within the Paintbrush Nonwelded Hydrogeologic Units

In unsaturated flow, water movement is generally, but not always, downward. One cause of lateral flow is the capillary barrier effect. This is caused by differences in moisture tension across an interface between adjacent hydrologic units. If moisture tension is greater in the upper unit (negative capillary pressure gradient), water will tend to flow laterally along the interface rather than downward. The PTn unit primarily consists of non- to partially welded tuffs and extends from the base of the densely to moderately welded, crystal-poor vitric subzones of the Tiva Canyon Tuff to the top of the densely welded, crystal-rich vitric subzone of the Topopah Spring welded tuff (TSw) (Buesch et al. 1995 [DIRS 145631], Table 4). Thus, the PTn encompasses the nonwelded, crystal-poor vitric subzone of the lower Tiva Canyon Tuff (Tpcpv), the pre-Tiva Canyon Tuff bedded tuff (Tpbt4), the Yucca Mountain Tuff (Tpy), the pre-Yucca Mountain Tuff bedded tuff (Tpbt3), the Pah Canyon Tuff (Tpp), the pre-Pah Canyon Tuff bedded tuff (Tpbt2), and the non- to partially and moderately welded, crystal-rich vitric subzones of the upper Topopah Spring Tuff (Tptrv). The dip of these layers is generally to the east at about ten degrees or lower. Within the PTn, several layers (Tpcpv1, Tpbt4, Tpbt2, Tptrv3, and Tptrv2) are less than 10 m thick within the potential repository footprint while other layers (Tpy, Tpbt3, and Tpp) show considerable variation in thickness across the potential repository area, with each showing a thinning trend to the south.

In the site-scale UZ flow model, the PTn unit is represented by six model layers (PTn21 through PTn26) (CRWMS M&O 2000 [DIRS 122797]). In the PTn lateral-flow modeling study, refined grids of these layers are used within the PTn to capture detailed flow behavior associated with capillary barriers. Six x-z grids in three vertical cross sections, with discretization as fine as $\Delta x = \Delta z = 1$ m, are used to evaluate the sensitivities to boundary conditions, net infiltration distributions, fracture/matrix properties, and fault properties.

Typical of the model results is the plot of vertical capillary gradients at Easting 171200, Northing 235119 (Figure 3.3.3-3). This figure shows that the simulated capillary-barrier effect is especially strong in layers PTn21 and PTn23 (Wu et al. 2001 [DIRS 154918], pp. 23 to 27). In the figure, negative capillary pressure gradients are defined for upward flow and positive for downward flow. The upward matrix capillary gradients within layers PTn21 and PTn23 are about 0.1 (bar/m), equal to the gravity gradient ($\rho_w \times g \approx 0.1$ bar/m), thus allowing lateral flow of water to occur. Negative matrix capillary pressure gradients also occur below 1,260 m above sea level, but these are too weak to offset gravity except at an elevation of 1,240 m, where they are opposed by an opposite gradient in the fracture network. Another negative matrix capillary pressure gradient occurs at an elevation of about 1,400 m, in the Tiva Canyon welded hydrogeologic unit where TCw11 overlies TCw12, but this interface is interrupted by topography and is not present everywhere. Matrix flow can therefore occur only in the horizontal direction within these layers. Fracture capillary barriers develop within layer PTn23, but not within layer PTn21. Figure 3.3.3-3 shows that near the bottom of layer PTn21, fracture capillary gradients are downward. The strong spikes shown in the figure signify the permeability and capillary contrast between layers.

The significant lateral (i.e., near-horizontal) flow implied by the model results within the PTn diverts a large amount of the percolation flux to a very narrow zone near the down-slope fault boundaries. Lateral flow modeled within the PTn is so strong that net infiltration patterns on the ground surface have little effect on flow within the PTn. In two-dimensional flow simulations of a 100-m long east-west cross section at Northing 235119 m, the percolation flux at the PTn-TSw interface was found to be very similar for three top-boundary conditions: net infiltration uniformly distributed, net infiltration concentrated at the west end (up-dip) of the model, and net infiltration concentrated at the east end (down-dip) of the model (Wu et al. 2001 [DIRS 154918], Section 4.1).

The simulation results with refined grids indicate that net infiltration values have more overall impact on capillary barriers or lateral flow than detailed spatial distributions of net infiltration along the model's top boundary. Figure 3.3.3-4 compares the impact of net infiltration rates on percentage of flow through faults and fault zones. In the figure, faults include the Solitario Canyon, Drill Hole Wash, Pagany Wash, and Toe (eastern boundary) faults. Fault properties are defined in *Calibrated Properties Model* (CRWMS M&O 2000 [DIRS 144426], p. 60 to 63). The figure shows that at the present-day mean net infiltration rate of 5 mm/yr (USGS 2001 [DIRS 154674]), about 25 percent of the percolation flux is laterally diverted into faults within the PTn. The fault zone is defined as the fault column with an additional 20-m wide zone west (up-slope) of each fault; as shown in Figure 3.3.3-4, the fault zone carries about 40 percent of the total flow at this net infiltration rate. As net infiltration increases, the percentage of fault flow decreases. This happens because, under the simulated conditions, both fractures and rock matrix in areas between faults become wetter with increased net infiltration, leading to generally weaker

capillary barriers between rock layers and, consequently, less lateral diversion of water to fault zones.

3.3.3.4.3 Percolation Redistribution by Anisotropic Paintbrush Nonwelded Hydrogeologic Unit Representations

This third set of model studies was performed to resolve the difference between the net infiltration distribution above the PTn and the calibrated net infiltration distribution (developed to match the chloride data below the PTn, as described in Section 3.3.3.4.1) below the PTn. With net infiltration distribution, the present-day mean net infiltration (DTN: GS000399991221.002 [DIRS 147022]), and the TSPA-SR (CRWMS M&O 2000 [DIRS 153246]) site-scale flow model parameters (DTN: LB991121233129.002 [DIRS 147334]), the simulated chloride concentrations are higher at the ESF north ramp, ESF south ramp, northeast Enhanced Characterization of the Repository Block (ECRB), and borehole UZ#16, and lower at the southwest ECRB, than the corresponding sample data (DTN: LA0002JF12213U.001 [DIRS 154760]; DTN: GS961108312261.006 [DIRS 107293]; DTN: LA9909JF831222.004 [DIRS 145598]; DTN: LA9909JF831222.010 [DIRS 122733]; DTN: LA9909JF831222.012 [DIRS 122736]). Low net infiltration rates lead to the higher simulated chloride concentrations at the northeast ECRB, while extreme higher net infiltration rates lead to the lower simulated chloride concentrations at the southwest ECRB. The chloride concentrations in infiltrated water (calculated from water net infiltration flux and chloride infiltration flux at the surface) along the ECRB vary significantly compared to the rather smooth measured concentration data at depth. This difference between surface and deep water chemistry is not expected for a system dominated by vertical flow.

The chloride data (which were matched in Section 3.3.3.4.1 by adjusting the net infiltration map) can also be matched by adjusting the horizontal permeability values, while not changing either present-day net infiltration map input or the vertical permeability values (which were determined by calibration against pneumatic damping and responses over the PTn (CRWMS M&O 2000 [DIRS 144426]). That is, either of these two conceptual models, calibrating the net infiltration map or introducing anisotropy, can be used.

In Section 3.3.3.4.1, chloride data were reconciled with the net infiltration map by adjusting the net infiltration map, while leaving rock properties unchanged. This resulted in less net infiltration over the potential repository footprint. In this Section, the chloride data are reconciled with the net infiltration map by adjusting the rock properties, leaving the net infiltration map unchanged. This has the effect of increasing lateral diversion. Both the new alternatives result in less transport than the original uncalibrated model.

To study the effect of PTn lateral flow on the degree of damping and the chloride distribution, three-dimensional simulations were conducted with increased PTn horizontal permeability (i.e., ratios of horizontal permeability to vertical permeability 10 and 100, respectively).

Figures 3.3.3-5 through 3.3.3-7 compare field data with the model results of chloride concentrations in the ESF and the ECRB, and in borehole UZ#16. The “kh/kv=1” case shown in the figures is the one without changing the PTn permeability field as in the original model. The damping effects vary in different locations and are visible in the figures. As horizontal

permeability is increased, the simulated chloride concentrations in borehole UZ#16 below the PTn hydrogeologic units are decreased and closer to the measured chloride data from pore-water samples. Decreased simulated chloride concentrations were also observed at boreholes NRG-6, NRG-7A, SD-7, SD-12, and UZ#4 as the PTn permeability was increased. Few changes were found, however, at boreholes SD-9 and UZ-14. The increased PTn lateral flow does have effects on the percolation and chemical distributions but the degree of the effects varies. In general the cases with increased PTn lateral flow match the chloride data better than the case with the original PTn permeability field. In order to achieve a more realistic and physically meaningful model, however, further studies are needed to conduct detailed calibrations to the PTn permeability field based on the available chemical distribution data.

3.3.3.5 Abstraction for Total System Performance Assessment

The work reported in this section is devoted to evaluating process model sensitivities and uncertainties. Consequently, simulation results from this study are not used to support any abstraction model that directly supports TSPA. The results found here indicate that the process modeling and associated model abstractions used to represent this component in the total system performance assessment baseline are conservative in that no credit is taken for the effects of this lateral flow component on total system performance. Therefore, any future changes in model abstractions for this component will not diminish the performance as represented in the total system performance baseline.

3.3.3.6 Multiple Lines of Evidence

The average percolation flux rate within the Topopah Spring Tuff of 4.5 mm/yr used in the UZ flow and transport model is based on surface infiltration data and hydrologic properties of the tuff. This rate can be checked against alternative lines of evidence to verify its reasonableness. Furthermore, Montazer and Wilson (1984 [DIRS 100161], pp. 47, 50, and 51) hypothesized that the PTn could cause significant lateral flow such that the flux within the TSw would be smaller than that in the PTn; this hypothesis also can be checked.

The carbon-14 content of UZ gas (after equilibration with pore water), together with water content data, can be used to calculate long-term average percolation fluxes in the TSw. This method is based on residence time of pore waters (Yang et al. 1996 [DIRS 100194], pp. 49 to 55; Yang et al. 1998 [DIRS 101441], p. 16) and water content measured for drill core in the laboratory (Rautman and Engstrom 1996 [DIRS 100642], pp. 26 to 32, and Appendix G; Rautman and Engstrom 1996 [DIRS 101008], pp. 27 to 32, and Appendix G; Engstrom and Rautman 1996 [DIRS 100670], pp. 23 to 28, and Appendix G). The flux is calculated from the total amount of water in the UZ between two elevations and the difference in apparent carbon-14 ages at the top and bottom of the zone in question.

The percolation flux calculated using carbon-14 data from borehole USW UZ-1 and water content data from USW UZ-14 (3 meters away) is 2.5 mm/yr (Yang 2001 [DIRS 154613], Table 2), based on carbon-14 values at the top and bottom of the TSw and total water content for the full thickness. This implies a transport velocity of 2.9 cm/yr. Carbon-14 data are not available from other boreholes, but the carbon-14 data from borehole USW UZ-1 can be regressed against depth to obtain values for percent modern carbon as a function of depth. This

relationship can then be used with water content data for borehole USW UZ-14, UE-25 UZ#16, USW SD-7, USW SD-9, and USW SD-12 to calculate average percolation fluxes of 2.4, 2.7, 1.8, 2.0, and 1.9 mm/yr, respectively, in the TSw (Yang 2001 [DIRS 154613], Table 3). All of these values are smaller than that used in the UZ flow and transport model, and thus, relative to this data set, the model provides a conservative estimate for repository performance.

The carbon-14 method described above was also used by Yang (2001 [DIRS 154613]) to calculate fluxes in the PTn in six boreholes for comparison with fluxes in the TSw. For boreholes USW UZ-14, UE-25 UZ#16, USW NRG-7a, USW SD-7, USW SD-9, and USW SD-12, the calculated average fluxes are 2.8, 2.1, 1.4, 1.1, 1.9, and 1.7 mm/yr (Yang 2001 [DIRS 154613], Table 3). The values for the PTn and TSw are subject to large uncertainties because of error in the analysis for carbon-14 and error propagation in the calculations. For example, the average percolation flux for six boreholes in the PTn by this method is 1.8 + 2.2/ -0.9 mm/yr (Yang 2001 [DIRS 154613], p. 12). As a result, the carbon-14 method is not sensitive enough to detect a lateral diversion of approximately 30 percent of the percolation flux as predicted in simulations discussed in Section 3.3.3.4.2.

3.3.3.7 Summary of Uncertainties and Their Treatment

Table 3.3.3-2 summarizes the key conceptual and parametric uncertainties in the modeling of percolation distribution and flow in PTn.

3.3.3.8 Summary and Conclusions

In previous simulations (CRWMS M&O 2000 [DIRS 122797]), the mean net infiltration value had a large impact on the percolation flux and chloride distributions in the potential repository horizon. The results of the refined models suggest that lateral flow within the PTn hydrogeologic unit may cause significant difference between the net infiltration distribution above the PTn and to the predicted percolation distribution below the PTn. The resulting detailed percolation distribution is fairly uniform, with the damping and lateral flow mechanisms in PTn greatly reducing the spatial heterogeneity of percolation flux compared to the net infiltration predicted by the infiltration model (USGS 2001 [DIRS 154674]). The percolation distribution is more important than the net infiltration distribution to assess the impact of the ambient flow field on the overall system behavior.

Percolation flux affects both waste-canister performance and solute travel times to the accessible environment. The present-day mean net infiltration was calibrated and the percolation distribution was analyzed using pore-water chloride concentration data. Modeled chloride results from three-dimensional simulation using the chloride-based net infiltration map are more uniform and match the chloride data better than the original net infiltration map developed for use in the Revision 00 study. PTn lateral-flow effects on percolation and chloride distribution were also studied by three-dimensional simulation with increased horizontal permeability. The degree of the effect varies by location. As expected, a more uniform chloride distribution under the PTn was observed in most places when lateral-flow effects increased. The combined results provide the means to test the appropriateness of the conceptual model, reduce uncertainties, and quantify parametric uncertainties. Unquantified conceptual uncertainties were assessed in analogue studies and other corroborating observations.

The spatial distribution of chloride concentration suggests a relatively uniform percolation flux beneath the PTn. A uniform percolation flux at the repository horizon could potentially reduce seepage into waste emplacement drifts. In previous interpretations, chloride data was matched by invoking a more uniform distribution of net infiltration at the surface (CRWMS M&O 2000 [DIRS 122797], Figure 6-24). In those simulations lateral flow within the PTn was less significant than vertical flow, resulting in a predominately one-dimensional downward flow pattern. The present interpretation for the uniform percolation flux is that the PTn is more anisotropic than has been described and acts to damp extreme episodic infiltration pulses. Another possible interpretation is the smaller degree of spatial variability for net infiltration at the surface and the smaller lateral movement of percolation between the surface and the potential repository horizon, with a nearly one-dimensional flow pattern.

3.3.4 Three Dimensional Flow Fields

This section summarizes the three-dimensional, steady-state, UZ flow fields generated using TOUGH2 V1.4 and the flow model of Yucca Mountain. These flow fields are used in various analyses, including TSPA calculations. Results must be considered in light of the uncertainty associated with input parameters, conceptual models, and the numerical modeling approach; consequently, the information in this section is presented in the context of uncertainties associated with UZ flow.

Following a brief introduction (see Section 3.3.4.1) and a list of model goals (see Section 3.3.4.2), this section presents the flow field results in three parts: the flow fields for TSPA-SR calculations (see Section 3.3.4.3), the new three-dimensional flow fields for performance assessment calculations to assess post-10,000 year climates using the four new infiltration maps corresponding to the full glacial climate (see Section 3.3.4.4), and the new flow fields related to an extended UZ model domain that would result from a new design for a cooler repository (see Section 3.3.4.5). Modeling abstractions performed for the TSPA were evaluated using the newly developed flow fields (see Section 3.3.4.6), and multiple lines of evidence, such as natural analogues, were examined in support of UZ flow studies at Yucca Mountain (see Section 3.3.4.7). The section on flow fields concludes with a tabulation and discussion of remaining uncertainties (see Section 3.3.4.8), followed by a brief synopsis (see Section 3.3.4.9).

3.3.4.1 Introduction

The UZ flow model, as described in *UZ Flow Models and Submodels* (CRWMS M&O 2000 [DIRS 122797]), simulated ambient conditions and performed predictive studies of changes in the mountain. These changes were caused by climate-related, thermal, and geochemical perturbations. More specifically, the flow model generated three-dimensional flow fields for TSPA calculations and provided input for other process models.

Data collected at Yucca Mountain over the last decade have been used to develop conceptual and numerical models of the hydrologic, geothermal, and geochemical behavior of the site. These data are used to calibrate and validate the flow model and its submodels, building confidence in the flow model description of ambient and future conditions in the UZ system. The comprehensive model calibration and validation studies have been carried out using borehole or tunnel measured saturation, water potential and temperature data, perched water data, pneumatic

data, and geochemical data (CRWMS M&O 2000 [DIRS 122797], Section 6.2; CRWMS M&O 2000 [DIRS 144426], Section 4). In addition, the flow model has been further calibrated and validated using the results of the water infiltration test at Alcove 1 in the ESF (CRWMS M&O 2000 [DIRS 122797], Section 6.8.1). All the three-dimensional flow fields documented in this section have been calibrated against observed field data, including matrix liquid saturations, water potentials, and perched water data.

The flow model and its submodels are relied on for characterizing flow and transport processes at Yucca Mountain. Such a comprehensive goal, which includes all relevant data, makes the models complex. Limitations and uncertainties associated with these models should be recognized to ensure successful application. The accuracy and reliability of the flow model predictions are critically dependent on the accuracy of hydrogeological conceptual models, estimated model properties, other types of input data (e.g., output from the infiltration model), and applied numerical modeling techniques. These models are limited mainly by the current characterization of the mountain system, including the geological and conceptual models (e.g., steady-state moisture flow assumption), the volume-average modeling approach, and available field and laboratory data.

Site investigations have shown that large variability exists in flow and transport properties over the spatial and temporal scales of the mountain. Despite the considerable progress made toward quantifying variability over spatial and temporal scales, the major remaining uncertainties of model parameters are: accuracy of estimated past, present, and future net infiltration rates over the mountain; quantitative descriptions of welded and nonwelded tuff heterogeneity, flow properties, and detailed spatial distributions of the properties within the mountain, especially below the potential repository; sufficiency of field studies, especially for fracture properties of zeolitic units and faults; alternative conceptual models of major fault water-flow transmission; and evidence of lateral diversion as a result of layer heterogeneity within the PTn unit and, as a result of zeolites, immediately above and within the CHn unit. These uncertainties affect the distribution of percolation flux and groundwater travel times in the UZ, as discussed in detail in Section 3.3.4.8.

3.3.4.2 Goals of the Flow Model

The fundamental goal of the flow model is to conceptually represent the UZ system of Yucca Mountain using a numerical model. Yucca Mountain is a complex, heterogeneous hydrogeologic system that is subject to many physical and geochemical processes. The flow model and its submodels are designed to capture these processes. The development of the flow model and its submodels has the following primary objectives:

- To integrate the available data from the UZ system into a single, comprehensive, calibrated three-dimensional model that simulates the ambient hydrologic, thermal, and geochemical conditions and predicts system response to future climate conditions

- To develop a number of submodels with representative boundary and initial conditions specifically for detailed studies of perched water, percolation through the PTn, flow through zeolitic CHn layers, and thermal effects from potential repository heating after waste emplacement

- To quantify the flow of moisture, heat, and gas through the UZ under the present-day and estimated future climate scenarios

- To predict groundwater flow patterns from the potential repository to the water table

- To contribute model parameters and model conditions for other specific studies, such as seepage into drifts

- To provide a defensible and credible model that accounts for relevant UZ flow processes for performance assessment and repository design.

More specifically, the flow model and its submodels provide estimates of important processes relevant to UZ flow regarding the performance of the potential repository, including:

- Spatially variable and temporally averaged values for percolation flux at the potential repository horizon

- The components of fracture and matrix flow and their interaction within and below the potential repository horizon

- The effects of observed perched water zones, associated flow barriers, and lateral flow diversion

- Probable flow paths from the potential repository to the water table

- The effects of faults on flow and transport processes

- The role played by the PTn unit in percolation redistribution, lateral flow diversion, and damping infiltration pulses

- Groundwater flow paths from the land surface to the repository horizon, groundwater and potential radionuclide migration paths from the potential repository to the water table, and breakthrough curves and collection areas at the water table.

3.3.4.3 Discussion of Three Dimensional Flow Fields Used in Initial Reports

As documented in *UZ Flow Models and Submodels* (CRWMS M&O 2000 [DIRS 122797]), 28 three-dimensional steady-state UZ flow fields were generated using the flow model. The purpose of developing multiple flow fields is to help constrain uncertainties, such as those surrounding the distribution and magnitude of net infiltration and the conceptualization of fracture flow in zeolitic rocks (i.e., perched water conceptual models) below the potential repository horizon. Eighteen of the flow fields have been submitted to the TSPA-SR for performance analyses. These 18 simulations were performed using the TSPA numerical grid; 2 perched water conceptual models (flow-through and by-passing); 9 infiltration maps representing 3 climate scenarios; and 3 calibrated fluid and rock parameter sets (CRWMS M&O 2000 [DIRS 122797], Section 7.5).

In the flow model (CRWMS M&O 2000 [DIRS 122797]), the UZ system is represented by a multilayer sequence of hydrogeologic units, approximated by layers of three-dimensional gridblocks. For each hydrogeologic layer within the model, a set of averaged (calibrated) rock properties is developed, as documented in the *Calibrated Properties Model* (CRWMS M&O 2000 [DIRS 144426]). The UZ model domain and the present-day, mean infiltration map with the TSPA grid are shown in Figure 3.3.4-1; the model domain covers a total area of approximately 40 km^2. Net surface infiltration of water from precipitation that penetrates the evapotranspiration zone is considered one of the most important factors affecting overall hydrologic behavior (as well as radionuclide transport) within the UZ system. The nine infiltration scenarios used for the flow simulations consist of present-day, monsoonal, and glacial-transition climates, each of which has lower-, mean, and upper-bound maps. The statistics of the nine infiltration rates are summarized in Table 3.3.2-1 for average values over the model domain.

Figure 3.3.4-2 illustrates percolation flux at the potential repository horizon, simulated using the present-day mean infiltration scenario with the flow-through perched water conceptual model (CRWMS M&O 2000 [DIRS 122797], Section 6.2.2). The figure shows that the simulated total (matrix plus fracture) percolation flux at the repository level has a nonuniform distribution, which was expected given the nonuniform distribution of net infiltration.

Figure 3.3.4-3 shows the simulated percolation flux at the water table with the same infiltration and perched water model scenarios. Compared to the distributed percolation flux at the potential repository horizon (Figure 3.3.4-2), the water table plot (Figure 3.3.4-3) indicates that significant lateral diversion occurs in the northern part of the model domain where thick zeolitic layers are located, leading to flow focusing along faults. In the southern part of the model domain, where the upper part of the CHn is vitric, flow appears to remain predominantly vertical between the potential repository horizon and the water table. In addition, the statistics of the three-dimensional, steady-state flow fields show that fracture flow makes up more than 80 percent of the total flow at the potential repository horizon and 70 to 90 percent of the total flow at the water table.

3.3.4.4 Three-Dimensional Flow Field Development with Post-10,000 Year Climate Scenarios

To assess post-10,000 year climates and their effects on repository performance, four new three-dimensional steady-state flow fields have been generated since the initial issue of *UZ Flow Models and Submodels* (CRWMS M&O 2000 [DIRS 122797]). These new flow fields have been used in the TSPA-SR. Table 3.3.4-1 lists the information for estimating average percolation fluxes simulated within the potential repository footprint for 13 infiltration scenarios, including four new infiltration maps, which correspond to the full glacial climate, used for simulation of the four new flow fields (see Section 3.3.2.5 and Table 3.3.2-3). These new infiltration scenarios are: (1) "full-glacial, lower bound #1," corresponding to the lower-bound average of Glacial Stage 4, the driest of the three glacial states described in Section 3.3.1; (2) "full-glacial, lower bound #2," corresponding to the "alternate" lower-bound average of net infiltration for Glacial Stage 8/10 (see Section 3.3.1.9); (3) "full-glacial, upper bound #1," corresponding to the upper-bound average of net infiltration for Glacial Stages 8/10 and 6/16, the wettest glacial stages; and (4) "full-glacial, mean #2," corresponding to the mean net infiltration

for Glacial Stages 8/10 and 6/16, as well as the upper bound for Glacial Stage 4. Precipitation, temperature, and net-infiltration for these new infiltration scenarios are summarized in Tables 3.3.1-5, 3.3.1-6, and 3.3.2-3. These new infiltration maps have, on average, much higher net infiltration rates within the UZ model domain than the nine rates listed in Table 3.3.2-1 for the modern, monsoonal, and glacial-transition climate states. Figure 3.3.4-4 shows the "full-glacial, mean #2" infiltration scenario.

The simulations using the four new infiltration maps and TOUGH2 Version 1.4 were conducted using the TSPA grid, the flow-through perched water conceptual model, and three sets of calibrated parameters corresponding to the lower-, mean, and upper-bound present-day infiltration maps. The simulated three-dimensional steady-state flow fields with the higher infiltration rates show larger percolation fluxes through the entire model, with dominant vertical flow in the southern part of the model domain and more focusing of flow into faults in the northern part.

Figures 3.3.4-5 and 3.3.4-6 show examples of the simulated percolation flux at the potential repository horizon and at the water table, respectively, for the "full-glacial, mean #2" infiltration scenario. The percolation pattern at the potential repository horizon (Figure 3.3.4-5) is similar to the surface infiltration map (Figure 3.3.4-4), which indicates little lateral flow within the PTn for this high-infiltration case. However, Figure 3.3.4-6 suggests that large-scale lateral flow to vertical faults occurs within the CHn unit, particularly in the northern part of the model domain, where the unit is extensively altered due to zeolites.

3.3.4.5 Conceptual and Numerical Evaluation of a Lower-Temperature Operating Mode

The most recent UZ flow analyses addressed the impact of an extended repository footprint (BSC 2001 [DIRS 154548]). This potential repository, developed with the intent of creating cooler temperatures in the drift environment, encompasses a larger area than earlier designs (Figure 3.3.4-7). The domain of the flow model as described above does not capture the southern extension of this potential repository; therefore, a new flow model has been developed to evaluate the ambient hydrologic conditions within this larger siting volume. This section describes the general hydrogeologic implications for repository design and presents the modeling setup and the preliminary results calculated using the extended model grid.

3.3.4.5.1 Hydrogeologic Implications for Repository Design

Characterization of the volume of rock at Yucca Mountain within which a potential repository could be constructed has been the focus of numerous geologic, hydrogeologic, and thermal studies. Lithologic layers comprising the potential repository horizon include the following Topopah Spring Tuff subunits: the lower part of the upper lithophysal zone (Tptpul), the middle nonlithophysal zone (Tptpmn), the lower lithophysal zone (Tptpll), and the lower nonlithophysal zone (Tptpln). This geologic volume, considered for hosting a repository, is identified in the *Subsurface Facility System Description Document* (CRWMS M&O 2000 [DIRS 151467], Section 1.2.2.1.8, p. 16).

A number of potential repository design strategies have been proposed over the past several years. Investigative studies to determine the hydrologic, transport, and thermal processes occurring within the repository horizon have often been closely tied to the prevailing draft repository design at the time of the study. The goal of this section is to decouple the details of design from a general understanding of the hydrogeologic implications of waste emplacement within the host rock. However, one principal factor that cannot be completely decoupled from design is seepage of water into waste emplacement drifts. Estimates of seepage depend upon predicted percolation. Additionally, the hydrologic characteristics within a lithologic layer will determine the flux rate at which seepage will occur in an emplacement drift. Since hydrologic characteristics are different within each of the host rock subunits, percentage estimates of seepage for each layer are also expected to differ. Modeling studies described in *Seepage Model for PA Including Drift Collapse* (CRWMS M&O 2000 [DIRS 153314], Section 6.6 and Attachment III, Figures AIII-1 and AIII-2) have shown that the percent of predicted seepage for the Tptpll is much lower than that for the Tptpmn (i.e., much higher percolation rates are needed in the Tptpll to cause seepage). Consequently, information about repository design (e.g., the number of drifts located in each lithologic unit) is essential for estimating the overall potential for seepage.

Data Characterizing the Potential Repository Host Horizon–An understanding of the relationship between repository design and hydrogeologic implications requires an assessment of available data. Types of data collected pertaining to the repository host rock include geologic, rock properties, mineralogic, and geochemical data. Figure 3.3.4-8 shows the location of data collection points used to characterize the potential repository horizon. Characterization data are relatively dense in the vicinity of the ESF (which includes the ECRB Cross Drift); however, north of N 235,100 m, south of N 229,000 m, and west of Solitario Canyon fault lie fewer well-characterized areas. In particular, boreholes from which qualified rock hydrogeologic properties have been obtained (indicated by triangular symbols) are not present in the northern, southern, and western areas of the potential repository horizon, with the exception of borehole USW WT-24. This paucity of data contributes to uncertainty to the understanding of geologic conditions and hydrogeologic flow and transport characteristics in areas surrounding central Yucca Mountain. Furthermore, even at borehole and ESF locations, data are biased vertically, or stratigraphically, to the near-surface rocks. Of the more than 70 surface-based vertical boreholes used in the development of the *Geologic Framework Model (GFM3.1)* (CRWMS M&O 2000 [DIRS 138860]), fewer than half penetrate the rocks below the TSw. Only ten boreholes provide data below the TSw (CRWMS M&O 2000 [DIRS 145771], Section 6.2), necessary for assessment of rock hydrologic properties of the potential repository host horizon.

Data available to characterize the spatial extent and volume of the potential repository horizon include a bedrock geologic map, borehole lithologic contacts, measured stratigraphic sections, and geologic data from the ESF. These data sources are identified in the *Geologic Framework Model (GFM3.1)* (CRWMS M&O 2000 [DIRS 138860], Section 4, p. 19). Each of the lithologic layers of the horizon is continuous beneath Yucca Mountain, except where displaced by large offset faults (e.g., the Solitario Canyon, Bow Ridge, and Dune Wash faults). The total thickness of the repository horizon ranges from about 50 to 230 m. Figure 3.3.4-9 shows a three-dimensional representation and cross-sectional view of the spatial distribution and thickness of the site lithology. The upper surface of the horizon has been clipped to maintain an overburden thickness of 200 m, while the lower surface has been clipped to maintain a water

table standoff distance of 160 m. The overburden and standoff requirements are prescribed in the *Subsurface Facility System Description Document* (CRWMS M&O 2000 [DIRS 151467], Sections 1.2.2.1.9 and 1.2.2.1.4, respectively). Note that in the north-south cross section, the elevation of the host rock units is higher in the south than in the north. This establishes a greater distance between the repository horizon and the water table, which may result in longer groundwater travel times in the UZ beneath southern Yucca Mountain. Figure 3.3.4-10 shows a plan view of the repository siting area for the lower-temperature operating mode (BSC 2001 [DIRS 154548]).

Significance of the PTn and CHn Units–Additional geologic information relevant to the assessment of potential repository performance includes the thickness and continuity of units lying above and below the repository horizon. The PTn and CHn major hydrogeologic units are believed to play an important role in UZ flow and transport (Section 3.3.3). The high matrix porosity and large storage capacity of the PTn may enable this unit to damp and distribute infiltration pulses above the horizon (CRWMS M&O 2000 [DIRS 151940], Section 3.3.3.2), while the occurrence of alteration minerals within the CHn below the potential repository may significantly retard radionuclide migration (CRWMS M&O 2000 [DIRS 138960], Section 6.3.2). Geologic data (BSC 2001 [DIRS 154622], Figure 19) indicate that the PTn ranges in thickness from greater than 165 m beneath northern Yucca Mountain to about 15 m in the south, with breaks in areal coverage along the Solitario Canyon, Iron Ridge, and Dune Wash fault systems (Figure 3.3.4-11). Where the PTn is thin or absent as the result of fault displacement, episodic infiltration/percolation events may perpetuate into the TSw rather than be attenuated and more evenly redistributed within the matrix of the PTn. The assumption that the PTn buffers episodic percolation flux may not always be true, because the role of faults and fractures and the potential for lateral diversion in these thin or absent areas of the PTn are uncertain.

The CHn, defined here as the combination of the Topopah Spring Tuff crystal-poor vitric nonwelded subzone (Tptpv1), the pre-Topopah Spring bedded tuff (Tpbt1), the Calico Hills Formation (Tac), and the pre-Calico Hills Formation bedded tuff (Tacbt), ranges in thickness from greater than 300 m in the northeast to less than 50 m in the southwest (Figure 3.3.4-12). Rock properties and mineralogy data suggest that much of the CHn is altered (primarily to sorptive zeolites) beneath Yucca Mountain, except for an area below the southern part of the mountain that remains predominantly vitric (CRWMS M&O 2000 [DIRS 154863], Section 6.5.3; CRWMS M&O 2000 [DIRS 138960], Section 6.3.2). The presence of low-permeability zeolites within the CHn will reduce percolation flux through the rock matrix and divert water to a more permeable pathway (e.g., fracture, fault, unaltered rock), thus limiting sorption and decreasing radionuclide travel times to the water table. The unaltered (vitric), nonwelded portion of the CHn accounts for only a small volume of the entire CHn, and its areal extent diminishes with depth (CRWMS M&O 2000 [DIRS 154863], Section 6.5.3). Although matrix permeabilities are much higher for the vitric CHn than for the zeolitic CHn, the presence of nonwelded vitric material may damp and distribute percolation flux, much like the matrix of the PTn. In light of these characteristics, the existence of the vitric CHn beneath the potential repository horizon is favorable to repository performance.

The presence of fractures within the CHn and their potential to serve as pathways for flow and transport is not well understood, and thus adds significant uncertainty to the modeling studies. Fracture networks occurring within the zeolitic CHn may enable groundwater carrying

radionuclides to bypass the sorptive zeolitic matrix, resulting in decreased travel times to the water table (CRWMS M&O 2000 [DIRS 144331], Section 6.1.1). Currently, this uncertainty is unconstrained, given that the only fracture hydrogeologic data available for the zeolitic CHn are from a single tested interval of borehole UE-25 UZ#16 (CRWMS M&O 2000 [DIRS 145771], Section 6.1.1). Liquid-release testing at Busted Butte, as described in *Unsaturated Zone and Saturated Zone Transport Properties (U0100)* (CRWMS M&O 2000 [DIRS 154024], Section 7), suggests that fractures within the vitric CHn may not play a significant role in flow and transport.

Faults–Faults are another aspect of the site that may have important hydrogeological implications. At the land surface, the infiltration focus may occur along fault zones lying beneath drainages. At depth, permeable faults may serve as conduits for flow where they intersect layers that laterally divert significant amounts of percolation. Faults with low permeability, those that juxtapose permeable rocks against low-permeability rocks, or those with high permeability and low capillary suction may form barriers to lateral flow. Though many different conceptualizations exist, several of which are summarized in *Unsaturated Zone Flow and Transport Model Process Model Report* (CRWMS M&O 2000 [DIRS 151940], Section 3.3.5), sparse data have been collected to surmise the hydrogeologic significance of faults, thus creating uncertainty in modeling studies. Nonetheless, it is reasonable to expect that fault properties vary both with depth and horizontally along an individual fault, as well as from fault to fault. A pattern of predominantly north-trending normal faults has been observed at Yucca Mountain (Figure 3.3.4-8) (BSC 2001 [DIRS 154622], Section 6.4.2). Major faults crosscutting the volume of repository host rock include the Solitario Canyon, Bow Ridge, Iron Ridge, and Dune Wash fault systems. As portrayed in the *Geologic Framework Model (GFM3.1)* (CRWMS M&O 2000 [DIRS 138860]), these faults show large (greater than 100 m) down-to-the-west displacement. The largest of these faults is the Solitario Canyon fault, which exhibits more than 400 m of displacement. Several northwest-trending faults have been observed in the northern part of the site. These faults have small vertical displacements, but coincide with prominent drainages (e.g., Drill Hole Wash, Pagany Wash, Sever Wash). According to the *Geologic Framework Model (GFM3.1)* (CRWMS M&O 2000 [DIRS 138860]), smaller mapped normal faults within the host rock volume include the Ghost Dance, Sundance, "Imbricate," "SolWest," Boomerang, and "SolJFat" faults. These faults typically show much less than 100 m of vertical displacement. Although repository design criteria may impose a standoff distance between faults and emplacement drifts, faults may still remain significant features of the flow domain as a result of lateral flow, particularly within the CHn, where zeolites are known to create water perching conditions. If faults are permeable features below the potential repository and transect rock layers with low permeability, then the fully saturated conditions associated with water perched above a low permeability layer may focus water into fault zones in that layer, resulting in reduced travel times to the water table.

Infiltration and Water Table Configuration–Additional uncertainties pertaining to the hydrogeologic implications of repository design are associated with infiltration and water table configuration. The spatial and temporal distribution of net infiltration provides an important upper boundary condition in the UZ flow and transport models. Regardless of design layout, the potential repository would most likely be located below areas of high infiltration as well as areas of low infiltration. The expected consequence of siting a repository below a high-infiltration source is greater percolation flux, compared with siting a repository below low-infiltration areas. Based on current infiltration maps (CRWMS M&O 2000 [DIRS 151940], Section 3.5.2), higher

infiltration rates correlate with higher elevations, such as in the northern part of Yucca Mountain and along the crest of the mountain. Higher infiltration rates are also modeled in Solitario Canyon and in the upper reaches of drainages east of Yucca Crest as a result of surface run-on. Infiltration rates are typically lower in the southern part of Yucca Mountain and beneath thick alluvium to the east. Percolation flux at the repository horizon may therefore be lower, in general, beneath the southern part of Yucca Mountain. This may promote longer groundwater travel times between the potential repository and the water table, and thus enhance repository performance. Uncertainties in percolation flux at the repository horizon arise, in part, out of uncertainties in the distribution of net infiltration.

Because groundwater travel times in the UZ are largely dependent on the distance between the potential repository and the saturated zone, it is important to establish the position of the water table. In general, water table elevations measured in the vicinity of the ESF and below southern Yucca Mountain, east of the Solitario Canyon fault, are consistent with a flat potentiometric surface at an elevation of about 730 m above mean sea level (Tucci et al. 1996 [DIRS 101303], p. 3). West of the Solitario Canyon fault, water levels show consistency at approximately 776 m above mean sea level. It is uncertain whether the 46-m water level transition across the Solitario Canyon fault is abrupt or gradual. Nevertheless, the effect of a gradual versus an abrupt transition, by itself, is not likely to be significant to modeling studies of flow and transport. It is more important to understand the water table configuration beneath northern Yucca Mountain. There has been much debate whether the high water levels observed in boreholes USW WT-24 and USW G-2 represent the regional potentiometric surface or indicate the presence of perched water. If the former hypothesis is true, it would suggest the presence of a large hydraulic gradient beneath northern Yucca Mountain, with water elevations in the north being approximately 300 m higher than those below central and southern Yucca Mountain. The existence of a large hydraulic gradient means a shorter distance exists between the repository horizon and the water table beneath northern Yucca Mountain. This limits the available siting volume for the potential repository, since a standoff distance of 160 m must be maintained between emplacement drifts and the current water table (CRWMS M&O 2000 [DIRS 151467], Section 1.2.2.1.4, p. 15).

Another important aspect of the elevation of the potentiometric surface is the potential for climate induced rises in the water table in the future. The *Yucca Mountain Science and Engineering Report* (DOE 2001 [DIRS 153849], Section 4.3.3.1) describes evidence of past fluctuations in the elevation of the water table near Yucca Mountain. Multiple lines of evidence suggest that a 120-m rise in water table elevation is the maximum potential increase due to a wetter future climate (CRWMS M&O 2000 [DIRS 151940], Section 3.7.5.2). Based on evidence obtained from recent boreholes in the Nye County Early Warning Drilling Program, Paces and Whelan (2001 [DIRS 154724]) concluded that water table fluctuations during the Pleistocene (the past 2 million years) at the sites examined may be limited to 17 to 30 m, rather than the 80 to 120 m range previously suggested. This new data is not consistent with large Pleistocene water table fluctuations at the sites examined, or by inference, beneath Yucca Mountain. Zeolitization of the tuffs, attributed to prolonged contact with water, is interpreted as an indicator of past elevations of the water table (DOE 2001 [DIRS 153849], p. 4-405). At Yucca Mountain, evidence of zeolitization indicates that the water table must have remained about 100 m higher than at present over the thousands of years required for zeolitization of the glassy tuffs. However, the upper boundary of the zeolitic zone is not parallel to the water table,

suggesting that it formed (at least in part) before the tectonic tilting of the tuffs, which occurred more than 12 million years ago, rather than during Pleistocene glacial stages.

In the event of a future climate-induced rise in the water table of 120 m, the northernmost emplacement drifts of the repository layout presented in the *Yucca Mountain Science and Engineering Report* would remain more than about 90 m above the higher water table level (DOE 2001 [DIRS 153849], Figure 1-13; see also Figure 3.3.4-13a). A smaller climate induced water table rise, consistent with recent data (Paces and Whelan 2001 [DIRS 154724]), would result in a minimum distance of about 180 m between the northernmost (closest) emplacement drifts and the water table.

In the TSPA-SR, the effects of a water table rise were incorporated conservatively by including a uniform maximum rise of approximately 120 m of the nearly level potentiometric surface below most of the potential repository (from 730 to 850 m). In the model, the rise in the water table is included for all climate states that are wetter than the modern climate; therefore, the water table rise occurs after 600 yrs (at the transition from modern to monsoonal climate) and persists beyond 10,000 yrs. The effects of the water table rise on the hydraulic gradient beneath the northernmost emplacement drifts were not explicitly included. Therefore, the performance implications of a water table rise on the gradient have not been examined directly. However, conclusions about the performance implications can be drawn from other information related to the Yucca Mountain site. For example, the values of total percolation flux at the water table are generally among the lowest in the area of the northernmost emplacement drifts because extensive zeolitization of the Calico Hills Formation in this area serves to laterally divert flow above the water table (CRWMS M&O 2000 [DIRS 153246], Figure 3.2-8). Similarly, the fraction of the total number of radionuclide particles released from the repository that reached the water table under the medium infiltration case and the glacial transition climate case is generally lowest in the area of the northernmost emplacement drifts (CRWMS M&O 2000 [DIRS 153246], Figure 3.7-11). This information suggests that any errors introduced by the simplified model of a uniform climate induced water table rise in the performance assessments are likely to be small. Furthermore, incorporating the higher water table elevations in the TSPA analyses conducted over longer time frames allows DOE to evaluate the robustness of repository performance beyond the regulatory time period.

The flexible design approach adopted by the DOE includes the ability to continue to enhance the design to best achieve performance-related benefits identified through ongoing analyses (DOE 2001 [DIRS 153849], Executive Summary, p. xxxv). The evolution of the design will be based on a process that includes enhancing components of the design to best achieve the performance-related benefits (DOE 2001 [DIRS 153849], Executive Summary, p. l). As the design evolves to that to be used to support a license application, should the site designation become effective, the performance related implications of water table rise on the northernmost drifts of the layout will be considered as appropriate. Specifically, the eventual layout will reflect performance considerations.

3.3.4.5.2 Three-Dimensional Flow Field Development with an Extended Model Domain

Model Domain and Numerical Grid–To consider a potential lower-temperature operating mode, a new model domain has been established and a new three-dimensional numerical grid

developed. Figure 3.3.4-7 shows the expanded model domain with the extended repository design, and Figure 3.3.4-13 shows a plan view of the numerical grid created for this model domain. This three-dimensional grid adds refinement in the footprint of the potential repository; as before, gridblocks are aligned along potential emplacement drifts. Note that drift alignment has changed; compare Figures 3.3.4-1 and 3.3.4-13 for the change. The new grid has 1,708 columns of gridblocks and, on average, 47 layers per column. Both the fracture and matrix continua are represented in a dual-permeability grid, which has 164,100 gridblocks and 671,958 connections. As presented below, modeling studies performed with the expanded numerical grid investigate the effects of the present-day mean infiltration scenario on moisture flow at and below the potential repository horizon.

Infiltration Map and Model Parameters–The present-day mean infiltration map used for flow simulations has an average value of 4.4 mm/yr, which is slightly less than the average value in Table 3.3.2-1. The reason for this difference is the consideration of a larger model domain with the extended grid, which captures a southern area with relatively low infiltration. The spatial distribution of the present-day mean infiltration is shown in Figure 3.3.4-14. Higher surface recharge rates occur principally in the northern part of the model domain and along Yucca Crest, east of the Solitario Canyon fault.

Additional modeling input used in the following flow simulations includes the calibrated base case rock hydrologic parameters described in *UZ Flow Models and Submodels* (CRWMS M&O 2000 [DIRS 122797], Table II-1).

Percolation Flux–The total (matrix plus fracture) percolation flux distribution at the repository horizon and at the water table, simulated using the present-day mean infiltration scenario, is shown in Figures 3.3.4-15 and 3.3.4-16, respectively. Compared with the surface infiltration pattern used for the top boundary condition (Figure 3.3.4-14), Figure 3.3.4-15 shows that lateral diversion of flow occurs between the land surface and the repository level. This effect is particularly pronounced in the northern part of the model domain, but is evidenced elsewhere by the increase in flux along fault zones. The lateral flow observed in the simulation results is attributed to the PTn, whose thickness beneath Yucca Mountain increases to the north. Vertical variations in the modeled hydrologic properties of the nonwelded PTn layers, better captured with the refined vertical grid resolution applied within the PTn, create sufficient contrast under the present-day mean infiltration rates to divert flow laterally down-dip. Faults are treated as structural pathways for flow, intercepting the lateral flow and focusing it downward. Previous modeling studies using the same infiltration conditions and base case hydrologic parameters with the TSPA grid, which has coarser vertical resolution within the PTn (Figure 3.3.4-2), show considerably less lateral flow associated with the PTn unit in the northern part of the model domain. Thus, the increased lateral flow seen in the extended model is a reflection of the numerical resolution applied. Greater resolution of intra-layer capillary gradients allows for better resolution of the potential for capillary barrier-driven lateral flow.

Figure 3.3.4-16 presents the simulated percolation flux at the water table. Compared with the surface infiltration map and the distributed percolation flux at the repository horizon (Figures 3.3.4-14 and 3.3.4-15, respectively), Figure 3.3.4-16 shows a much different flow pattern. As a result of extensive zeolitization in the upper CHn, large lateral flow occurs in the northern half of the northern repository block (north of N 234,000 m). This lateral flow is

mainly intercepted by the Drill Hole Wash, Pagany Wash, and Sever Wash faults. Lateral flow also occurs in the southern half of the potential repository domain, where it becomes intercepted by the Sundance and Ghost Dance faults. A relatively high simulated percolation flux not associated with fault zones in the central part of the potential repository footprint reflects the presence of vitric CHn, which does not divert flow laterally to the faults, but funnels it to the bottom of the vitric zone. The distribution of percolation flux simulated with the extended model grid is similar to the distribution of percolation flux simulated with the TSPA grid (Figure 3.3.4-3) for the same infiltration scenario and hydrologic parameter set.

3.3.4.6 Abstraction for Total System Performance Assessment

The work reported in this section is devoted to evaluating process-model sensitivities and uncertainties beyond those associated with the flow fields originally abstracted for the TSPA, which are documented in *Abstraction of Flow Fields for TSPA* (CRWMS M&O 2000 [DIRS 153104], Section 6). Simulation results from the study with the extended repository footprint model are not used to support any abstraction model that directly supports the TSPA. The results found here indicate that the process modeling and associated model abstractions used to represent this component (i.e., three-dimensional flow fields) in the TSPA baseline are representative (or conservative) with respect to the effects of this component on total system performance. Therefore, any future changes in model abstractions for this component will not diminish the potential repository's performance as represented in the total system performance baseline.

3.3.4.7 Multiple Lines of Evidence

Natural analogue studies of fluid flow processes for similar geologic and hydrologic settings provide multiple lines of evidence that support the three-dimensional flow models constructed for Yucca Mountain. These studies help constrain estimates of groundwater flow paths and percolation fluxes, and provide insights into processes controlling fracture and matrix flow under unsaturated conditions. Studies at Yucca Mountain and nearby Rainier Mesa provide the best insights into past and present flow conditions, and they can be used to help constrain models to predict future flow behavior.

Groundwater Travel Times and Fast Flow Regimes–Rainier Mesa, approximately 20 miles northeast of Yucca Mountain, has been the site of extensive underground observations of fluid flow (Wang 1991 [DIRS 109736]). About eight percent of the measured mean precipitation was observed to be infiltrating into one of the tunnels constructed in zeolitic tuffs at Rainier Mesa. This seepage was associated with a small number of faults and fractures (Wang 1991 [DIRS 109736], p. 79). These structural features are thought to be a pathway for flow from perched water above the zeolitic horizon (Wang 1991 [DIRS 109736], p. 82). The seepage is geochemically similar to meteoric water (Wang et al. 1993 [DIRS 108839], p. 677). Tracer tests and tritium samples indicate that the likely rate of fast pathway flow is from one to six years to travel from the surface to the water table, at a depth of 1,000 m. This travel time is orders of magnitude less than the matrix travel time calculated using measured matrix conductivities, but is supported by measurements of bomb-pulse chlorine-36 in several samples from one of the tunnels (Wang et al. 1993 [DIRS 108839], p. 677).

Bomb-pulse chlorine-36 isotope ratios have been found in several locations in the vicinity of some fault zones in the ESF, and indicate fast flow from the ground surface to the depth of the ESF that results in fluid travel times of less than 50 years. Elevated chlorine-36 signatures are confined to the immediate vicinity of faults and other features, suggesting that fast flow zones are localized, and large areas of the potential repository appear to be unaffected by fast path flow (CRWMS M&O 2000 [DIRS 141187]).

Percolation Flux Studies–Several dating methods have been used to constrain percolation fluxes at Yucca Mountain. The ages of calcites in the UZ have been used as a tool for estimating percolation fluxes (Marshall and Whelan 2000 [DIRS 154415]). Chloride content of pore waters and carbon-14 content of UZ gas, together with water content data, can be used to calculate long-term average percolation fluxes in the TSw. The carbon-14 method is based on residence time of pore waters (Yang et al. 1996 [DIRS 100194]; Yang et al. 1998 [DIRS 101441], p. 16) and water content measured for drill core in the laboratory (Engstrom and Rautman 1996 [DIRS 100670], pp. 23 to 28, and Appendix G; Rautman and Engstrom 1996 [DIRS 100642], pp. 26 to 32, and Appendix G; Rautman and Engstrom 1996 [DIRS 101008], pp. 27 to 32, and Appendix G). The flux is calculated from the total amount of water in the UZ between two points and the difference in apparent carbon-14 ages at the top and bottom of the zone in question. The use of relative ages eliminates the effect of any inherited carbon-14 ages that the groundwater may have acquired from surficial materials or soil gases.

The percolation flux calculated using the carbon-14 data from borehole USW UZ-1 and the water content data from borehole USW UZ-14 (3 m away) is 2.5 mm/yr (Yang 2001 [DIRS 154613], Table 2, and pp. 7 and 11), based on carbon-14 values at the top and bottom of the TSw and total water content for the full thickness of the unit. This equates to a transport velocity of only 2.9 cm/yr. Similar data sets are not available from other boreholes, but the carbon-14 data from borehole USW UZ-1 can be regressed against depth to obtain values for percent modern carbon as a function of depth. This relationship can then be used with water content data for boreholes USW UZ-14, UE-25 UZ#16, USW SD-7, USW SD-9, and USW SD-12 to calculate average percolation fluxes of 2.4, 2.7, 1.8, 2.0, and 1.9 mm/yr, respectively (Yang 2001 [DIRS 154613], Table 3). All of these values are significantly smaller than those used in the UZ flow and transport model (4.5 mm/yr) (CRWMS M&O 2000 [DIRS 151940], Table 3.7-4); thus, relative to this data set, the model provides a conservative estimate of repository performance.

3.3.4.8 Summary of Uncertainties Related to Three-Dimensional Unsaturated Zone Flow Fields

Establishing confidence in model simulations of the three-dimensional flow processes occurring at Yucca Mountain requires sufficient input data regarding model boundary conditions and spatial variability of the hydrologic characteristics of the system, in addition to appropriately defined conceptual models and numerical modeling techniques. Given the complexity of the UZ system at Yucca Mountain, none of these aspects can be completely understood. However, through sensitivity and bounding studies, a model can be used to identify and quantify uncertainty. Major uncertainties in the calculated UZ flow fields are discussed in this section and summarized in Table 3.3.4-2.

3.3.4.8.1 Conceptual Uncertainties

Steady-State Ambient Moisture Flow Assumption–Use of steady-state conditions for flow field development is a simplifying assumption supported by pneumatic and isotopic data that suggest the PTn unit, where present, effectively damps episodic infiltration pulses such that water flow below the PTn is approximately steady. If, alternatively, significant transient flow persists below the PTn, it may affect the simulation of percolation flux and estimated groundwater travel times in the UZ.

Applicability of van Genuchten Model to Unsaturated Fracture Flow–Because better alternatives are lacking, it is assumed that the van Genuchten relationships (van Genuchten 1980 [DIRS 100610], pp. 892 to 893), originally developed for porous media, can be used for liquid flow in the active fracture continuum. However, the physics of water flow in fracture networks is not exactly the same as in porous media. Uncertainties arising from the use of the van Genuchten approach include the predicted moisture conditions within fractures and the rock matrix. This affects capillary strength or, more specifically, capillary-barrier effects, which in turn affect predictions of seepage. Modeling studies using alternative methods, such as discrete fracture networks, or alternative moisture functions, such as Brooks-Corey relations (Brooks and Corey 1966 [DIRS 119392]), may prove useful in treating this uncertainty. However, these alternatives may have greater uncertainty than the methods currently used. More laboratory testing and field data collection could reduce uncertainty.

Model Used to Calculate Fracture/Matrix Flow Components–As discussed in *Conceptual and Numerical Models for UZ Flow and Transport* (CRWMS M&O 2000 [DIRS 141187], Section 6.4), a dual-permeability model (DKM) has been used in the UZ flow and transport model as the baseline approach for calculating flow and transport between fractures and the matrix. Capillary pressure and concentration gradients between fractures and the matrix are presented using a single-matrix-node approximation that cannot accurately describe the steep fronts near fracture-matrix interfaces because the matrix is treated as a single continuum in the DKM. This issue is especially important for modeling matrix diffusion and radionuclide transport in the UZ. Therefore, using the DKM may introduce some uncertainties into simulations of UZ flow and transport, which can be reduced by using more accurate matrix discretization schemes. A more detailed discussion of these schemes is provided in Section 11.3.2.

Effect of Large Gridblock Averaging and Vertical Resolution on Flow Fields–The distribution of simulated percolation flux and flow focusing is affected by the averaging of relatively detailed net infiltration data (available at 30 m spacing) onto large gridblocks of the flow model. Within the flow model, local peaks in the net infiltration map are typically averaged with nearby values that are much lower in magnitude. Though the total mass flux is conserved, loss of detail with regard to spatial variability can limit the ability of the flow model to capture areas of focused or fast path flow. Adding detailed numerical resolution to the repository footprint and along fault zones helps to reduce these averaging effects in critical areas. In addition to lateral resolution, model results are influenced by vertical grid resolution. Studies from the flow model have shown that enhanced vertical grid resolution within the PTn unit leads to more lateral flow. The representativeness of these results is uncertain given the assumed lateral continuity of rock properties. Comparing the modeling results against the observed data

helps determine optimal gridblock size. Moreover, this indicates the importance of maintaining consistent discretization throughout model development (i.e., calibration and flow field prediction).

Layer-Averaged Rock Properties–Because lateral variability in rock characteristics exists at Yucca Mountain, the use of spatially uniform parameters assigned within each model layer is a simplifying assumption that creates uncertainty in the model results. Sensitivity analyses with laterally heterogeneous rock properties could identify and quantify uncertainty associated with the layered approach. A model incorporating lateral heterogeneity is expected to show less lateral flow and more flow focusing.

Conceptual Model of Flow Within and Below Perched Water Zones–Zeolitically altered layers at the base of the TSw and within the CHn are believed to reduce percolation flux, lead to the development of perched water, and create lateral diversion. The extent to which these flow phenomena are affected by fractures and faults within zeolitic rocks is largely unknown, creating uncertainty in model results. Different perched water conceptual models have been developed in an attempt to bound uncertainty associated with the role of fractures in zeolitic rocks below the potential repository horizon. One conceptual model for perched water (the flow-through model) assumes that there are no large-scale, vertically connected fractures within the zeolitic rocks. However, fractures within zeolites are theorized to have greater permeability than the altered matrix; therefore, in this model some of the percolation flux passes vertically through the zeolitic CHn, while the rest is laterally diverted within perched water zones toward faults. Another conceptual model for perched water (the by-passing or unfractured zeolite model) assumes that fractures contribute no secondary permeability to the zeolitic rocks, which means the water perching mechanism is controlled only by the low-permeability matrix. This conceptual model creates more lateral flow diversion. As with fractures, alternative fault parameters have been used in simulations to evaluate model sensitivity.

3.3.4.8.2 Data and Parameter Uncertainties

Upstream Models–Net surface infiltration of water from precipitation that penetrates the evapotranspiration zone of the mountain is considered the most important factor affecting overall hydrologic behavior, in addition to radionuclide transport, within the UZ system. Uncertainties surrounding the distribution and magnitude of net infiltration are constrained by the development of upper-, mean, and lower-bound models for the present-day, monsoonal, glacial-transition, and full glacial climates. Flow fields are simulated for each of these scenarios. In addition, the location and nature of the vitric–zeolitic transition within the CHn is uncertain as modeled in the rock properties model of Yucca Mountain, which has implications for simulated percolation flux distributions, preferential flow paths, and radionuclide transport.

Rock Hydrologic Parameters Used for Model Calibration and Validation–The lack of data with which to characterize the hydrologic properties of fractures and major faults within and below the CHn makes estimation of fracture and fault flow components highly uncertain. A reevaluation of fracture parameters of the CHn using the Busted Butte test data and additional sensitivity analyses are needed to reduce this uncertainty.

3.3.4.9 Summary and Conclusions

A number of three-dimensional steady-state flow fields have been developed, as documented in *UZ Flow Models and Submodels* (CRWMS M&O 2000 [DIRS 122797]). Since the preparation of initial reports, additional flow fields have been generated to investigate the effects of a post-10,000 year climate (i.e., full glacial) and an expanded repository footprint.

Using different climate scenarios and conceptual models for flow, the simulated flow fields predict percolation distribution within the UZ system, components of fracture and matrix flow, probable flow paths below the potential repository, and groundwater travel times in the UZ. The flow model used to generate the three-dimensional steady-state flow fields provides parameters and bounding conditions for subsequent modeling studies and analyses, such as seepage into drifts and the TSPA.

Uncertainties associated with the three-dimensional flow fields are largely attributable to the limited data available to characterize the spatial and temporal distribution of net infiltration and the spatial variability of rock hydrologic properties. This also imparts uncertainty in conceptual models used to describe flow behavior, since these models are developed primarily from site data. The assumption of steady-state flow and the use of layer-averaged rock parameters are among these conceptual uncertainties. An additional source of uncertainty stems from the numerical techniques employed to simulate flow conditions, such as grid resolution, and the applicability of the van Genuchten relationships and the DKM approach. However, the impact of uncertainties associated with available data on model results for performance analysis is different depending on the type of data. For example, the net infiltration rate at Yucca Mountain has perhaps the most significant effect on repository performance (CRWMS M&O 2000 [DIRS 122797], Figure 6-57). For the current climate, this model boundary condition is believed to be well constrained as a result of decades of field and model calibration studies using measured data. Uncertainties associated with other data inputs will have a lesser impact on modeling results used for performance assessment because they affect only fluid distribution and flow paths, rather than net flow rates.

Through bounding and sensitivity studies, uncertainties in the three-dimensional flow fields can be identified, constrained, and perhaps quantified. Numerical simulations with the flow model have used 13 different infiltration maps to examine the effects of different climate scenarios on UZ flow. This helps bound model predictions of system response during potential future conditions. Different conceptual models, in particular those related to perched water below the potential repository horizon, have been developed and modeled to assess the sensitivity of model results to changes in fracture parameters (which are poorly constrained by site data) within the CHn.

Overall, the simulated flow-field results show the greatest sensitivity to the magnitude of net infiltration. Model results are also sensitive to grid resolution, seen particularly within the PTn unit (i.e., finer vertical resolution leads to greater lateral flow). Assumptions regarding the conceptualization and parameterization of fractures within the CHn unit and fault zones have large uncertainties as a result of limited or no data, yet these UZ features appear to have a significant impact on flow behavior below the repository. Additional sensitivity studies, using different conceptual models and a range of hydrologic parameters for fractures and faults, are

needed to assess the potential range of variability in flow behavior between the repository horizon and the water table. Furthermore, continual data collection from the existing underground tunnels and boreholes, and incorporation of these data into the modeling studies will significantly reduce the uncertainties associated with the model predictions.

3.3.5 Thermal-Hydrologic Effects on Unsaturated Zone Mountain-Scale Flow

3.3.5.1 Introduction

UZ flow (Sections 3.3.4 and 4.3) and transport (Section 11.0) will be affected by heat released from the decay of radioactive waste within emplacement drifts in the potential repository at Yucca Mountain. The effects of heat on UZ flow can be analyzed on different spatial and temporal scales. Mountain-scale TH response requires a model that includes the spatial variability of thermal and flow properties, infiltration, and physical features (such as faults) that may promote heterogeneous behavior.

This section summarizes the modeling and uncertainty studies performed to determine the effects of heat on mountain-scale UZ flow, liquid saturation, and temperature. Specifically this section summarizes work conducted since TSPA-SR to examine TH effects over a range of thermal loading by addressing both higher and lower-temperature operating modes for the repository. Section 4.3.5 will present an investigation of the evolution of near-drift TH conditions, on a much smaller scale, than the mountain-scale TH model, to more accurately determine the likelihood of seepage into an individual drift for a given set of thermal-loading conditions. The mountain-scale TH model presented in this section provides an analysis of temporal and spatial variability in UZ conditions under thermal load. Such variability may result from the temporal and spatial distribution of UZ thermal and flow properties, variation in infiltration, changes in lithology, and the presence of faults. In this analysis, the focus is on how the thermal-hydrologic coupled processes affect the magnitude and spatial distribution of mountain-scale liquid saturation, temperature, and the liquid flux at the repository horizon and the rest of the UZ.

Like any model, mountain-scale TH models are subject to uncertainties associated with the conceptual model, parameter selections, and data. These will be addressed in the following subsections and summarized in Section 3.3.5.8. Modeling studies discussed here include alternative thermal operating modes for below-boiling and above-boiling temperatures within the rock mass adjacent to the repository drift.

3.3.5.2 Goal of the Mountain-Scale Thermal Hydrologic Models

The mountain-scale TH simulations provide predictions for thermally affected liquid saturation, gas- and liquid-phase flux (together referred to as flow fields), and the distribution of temperature and saturation in the UZ. Of particular interest is the impact of thermal loading imposed by waste emplacement on water percolation at and near the repository host rock (e.g., drainage between pillars), and the potential flow barrier effects in the basal vitrophyre of the Topopah Spring Tuff and zeolites of the Calico Hills Formation underlying the repository horizon. These rock units impede the transportation of radionuclides from the repository to the water table because of their low permeability and/or high sorptivity.

The TH model therefore provides for qualitative and quantitative evaluation of repository-heat impact on the UZ and includes prediction of the following:

- Extent of the two-phase zone
- Liquid and gas flux in near and far field
- Moisture redistribution in the UZ
- Temperature near drifts and within pillars
- Drainage potential of the pillars
- Potential for flow and transport property changes in the PTn and CHn hydrogeologic units
- TH effects on the water table and perched water bodies
- Influence of climate and forced ventilation.

3.3.5.3 Discussion of Analysis Model Report Revision 00 Results

The *Mountain-Scale Coupled Processes (TH) Models* report (CRWMS M&O 2000 [DIRS 144454]) documents the development of the mountain-scale TH model used to support the TSPA-SR (CRWMS M&O 2000 [DIRS 153246]). The study reported in the above documents used the EDA II operating mode with an initial thermal load of 72.7 kW/acre (1.45 kW/m of drift) and a forced ventilation period of 50 years, during which 70 percent of the decay heat was assumed to be removed. The model evaluates the effects of heat on UZ flow and the distribution of liquid and temperature over a period of 100,000 years, and provides the necessary framework to test conceptual hypotheses of coupled heat and fluid flow in the UZ. The simulations were conducted using TOUGH2 V1.4.

The mountain-scale TH model (CRWMS M&O 2000 [DIRS 144454]) was developed from the UZ flow model and therefore retains geological and hydrologic properties of that model. The thermal and flow parameters used as input to the model were based on the calibrated property set (CRWMS M&O 2000 [DIRS 144426]) developed for the UZ flow model. The simulations were performed using a spatially varying mean-infiltration rate, which was altered according to the infiltration model climatic variation over the thermal-loading period.

Two-dimensional and three-dimensional simulations were conducted in the TH model (CRWMS M&O 2000 [DIRS 144454]). The two-dimensional simulations were based on two cross sections, NS#1 and NS#2, which contained local refinements to explicitly represent the 5-m diameter emplacement drifts. Figure 3.3.5-1 shows a plot of the two-dimensional cross section NS#2 with the location of the repository and the UZ hydrogeologic model units.

Sensitivity studies were performed to assess the model and parameter uncertainties. For the thermal input, two operation modes were defined: forced ventilation for the first 50 years (during which 70 percent of the decay heat generated by the emplaced waste was removed) and

no forced ventilation. To assess the effect of climate, simulations were also carried out with the present-day infiltration in effect for the entire 100,000 years and, alternatively, with present-day infiltration applied only for the first 600 years. This period was followed by monsoon infiltration from 600 to 2,000 years, after which glacial-transition infiltration was applied.

The primary objective of *Mountain-Scale Coupled Processes (TH) Models* (CRWMS M&O 2000 [DIRS 144454]) was to evaluate the effects of heat on mountain-scale flow. The simulations were therefore designed specifically to address large-scale flow issues such as the effects of faults, perched water bodies, the interface of the repository unit (TSw) with the overlying PTn and the underlying CHn hydrogeologic units. Because discretization for both the three-dimensional model and the NS#1 cross sections are coarse, the sensitivity studies were conducted only on the two-dimensional NS#2 cross section. In the local refinement of the two-dimensional NS#2 cross section, there are five lateral gridblocks between drifts spaced 81 m apart. This north-south section includes potential emplacement drifts located in the middle nonlithophysal and the lower lithophysal units of the Topopah Spring welded tuff.

As expected, simulation results predicted that at the repository horizon maximum temperatures occurred in the drift walls, and less elevated temperatures occurred in the pillars between adjacent drifts. For the operation mode with 50 years of forced ventilation, the temperatures in the pillars were predicted to rise to an average of 80° to 85°C. In the immediate vicinity of the drifts, the predicted temperature rose above boiling and reached 110°C at drifts with locally low ambient percolation flux (caused by spatially variable infiltration). The dryout in the fracture and matrix around the drifts was maintained for hundreds of years. Zones of increased liquid saturation appeared above the dryout zone, and liquid flow rates one to two orders of magnitude higher than the ambient flux, primarily through the fractures, were predicted for the first 100 years of emplacement. The liquid fluxes toward the emplacement drift are driven by capillary pressure gradients resulting from the drying around the drifts. However, the decay heat from the potential emplacement drifts easily vaporizes this enhanced liquid flux, so that in fact no liquid flux was predicted to reach the emplacement drift wall. That is, the coupled process models predict no flux crossing the drift during the thermal period when the rock mass temperatures are at or above boiling. As for the drainage of thermally induced liquid flux away from the emplacement drift, the simulations predicted that liquid flow through the pillars between the emplacement drifts mostly continued at a rate close to the ambient percolation flux for most of the thermal period.

For the operating mode with no provision for forced ventilation, simulated results pertaining to flux changes were qualitatively similar to those discussed above. Quantitatively, this case gave rise to higher temperatures, a larger degree of drying in the rock mass surrounding the drifts, and larger dryout zones that also persisted longer. For example, in the absence of forced ventilation for the first 50 years of waste emplacement, temperatures in the completely dry rock mass at the drifts were predicted to rise to 250°C, and temperatures within the pillars may rise to boiling (about 96°C) after 1,000 years of heating.

In the absence of ventilation, the two-phase boiling zone was predicted to extend 200 m above the drift, to the base of the PTn (about 1,270 masl at the center of the cross-section) (Figure 3.3.5-1). At the top of the CHn unit (about 910 masl), the predicted maximum temperature rose to 75° to 80°C. With ventilation, the models predicted a boiling zone that

extends to about 50 m above the drifts. Both models predicted little influence of perched water on UZ TH conditions at or above the drifts, because most perched water bodies are located 100 to 150 m below the potential repository, where temperatures did not rise to boiling conditions.

3.3.5.4 Model Development since Revision 00 of the Analysis Model Reports

Model development since the initial issue of *Mountain-Scale Coupled Processes (TH) Models* (CRWMS M&O 2000 [DIRS 144454]), which was based on the EDA II repository operating mode, involves studies of coupled processes for a range of operating modes (Section 2.3.2). The models use both the three-dimensional numerical model and the NS#2 cross-section model documented in the initial TH model. The models also use boundary and ambient conditions, and infiltration rates documented in the initial TH model. Even with forced ventilation, the initial TH models with the EDA II thermal load predicted above-boiling temperatures in the rock near the emplacement drifts for hundreds of years. TH simulations described in this study therefore focus on the lower-temperature options in which the rock temperatures are not expected to rise above boiling anywhere in the repository. To arrive at the lower-temperature case, a lower initial thermal load of 67.7 kW/acre (1.35 kW/m of drift, Section 2.3.2) is used with a forced-ventilation period of 300 years (during which 80 percent of the heat is removed). This areal thermal load is obtained by scaling the EDA II thermal-load of 72.7 kW/acre, with a drift lineal thermal-load of 1.45 kW/m, to the proposed drift loading of 1.35 kW/m. In this new TH analysis the 50-year, 70 percent forced ventilation operating mode is referred to as the higher-temperature case and the 300-year, 80 percent forced ventilation operating mode is referred to as the lower-temperature case. The initial study documented in *Mountain-Scale Coupled Processes (TH) Models* (CRWMS M&O 2000 [DIRS 144454]) is hereafter referred to as the EDA II Case.

These model developments focus on assessing uncertainties pertaining to thermally induced flux caused by a range of thermal load conditions. In this section, studies carried out to investigate TH conditions in both the higher-temperature (above boiling) and the lower-temperature (below boiling) repository are described using the new initial thermal load. Specifically, these model developments include:

- TH models for the higher-temperature (above boiling) case, in which 70 percent of the heat is removed for 50 years, using an effective drift thermal load of 1.35 kW/m. The equivalent three-dimensional areal load for this drift thermal load is then 67.7 kW/acre.

- TH models for lower-temperature (below boiling) operating mode, in which the effective drift thermal load is 1.35 kW/m and forced ventilation removes 80 percent of the heat for a 300-year period.

- TH models using a modified thermal conductivity and heat capacity of the rock mass, to account for the lithophysal porosity of the upper and lower lithophysal units in the matrix properties for both the lower-temperature and higher-temperature operating modes. Lithophysal cavities reduce the effective thermal conductivity and the thermal capacity of the matrix continuum in the upper-lithophysal (tsw33) and lower-lithophysal (tsw35) units. The justification and approach for incorporating the effect of lithophysal cavities in the TH models is presented in Section 4.3.5.4.

- Assessment of the impact of increased infiltration (resulting from uncertainty in the climate scenario) on seepage, particularly for the lower-temperature case.

Except for the modified thermal properties described above, the simulations presented in this study use the thermal and flow properties of the initial TH model. The revised PTn flow properties described in Section 3.3.3 are not used.

3.3.5.5 Mountain-Scale Thermal Hydrologic Results and Analysis

Table 3.3.5-1 summarizes the numerical model cases (cases 1 through 7) simulated to characterize the mountain-scale TH processes under thermal loading. All these simulations subsequent to the EDA II Case use a thermal load of 1.35 kW/m (67.7 kW/acre) as the initial thermal load. These simulations were conducted to evaluate the extent of the thermally disturbed zone and the mountain-scale predicted changes in temperature, saturation, and percolation flux. In particular, the TH model results that bound the uncertainty in performance issues are of interest. Therefore, several simulation cases are conducted to ascertain the effect of grid resolution, the emplaced thermal load, the period of forced ventilation, thermal properties, and the effect of uncertainty in effective net-infiltration rates. All the simulations use numerical grids, boundary and ambient conditions, and infiltration rates documented in *Mountain-Scale Coupled Processes (TH) Models* (CRWMS M&O 2000 [DIRS 144454]) and briefly discussed in Section 3.3.5.3.

Cases 1 and 2 in Table 3.3.5-1 provide the base-case UZ three-dimensional TH conditions for the lower-temperature repository operating mode, using the thermal properties for the EDA II Case and a set of the thermal properties modified to include lithophysal cavities associated with the upper-lithophysal (tsw33) and lower-lithophysal (tsw35) units (Figure 3.3.5-1). The three-dimensional model provides direct assessment of the application of UZ three-dimensional grid to model TH processes, so that changes in temperature and flux can be directly compared to the ambient-condition UZ flow-fields used in TSPA transport abstractions. However, the coarse grid and the planar (continuous heat-source) model used in the three-dimensional models prevent near-drift processes from being adequately resolved because temperature, saturation, and liquid flux are averaged over the large gridblocks that represent the repository. The coarse grids give rise to smaller changes in temperature, saturation, and flux than those given by the refined grid models. Cases 1 and 2 show no boiling and little change in liquid flux and liquid saturation, even near drifts. The predicted maximum temperature at the repository horizon is about 72ºC for these coarse grids (Bodvarsson 2001 [DIRS 154669], Attachment 6, pp. 69 to 70). This was expected, because even the EDA II Case thermal load with ventilation showed no substantial changes in flux and liquid saturation (CRWMS M&O 2000 [DIRS 144454]).

Several two-dimensional refined grid (NS#2) TH simulations were conducted to give a more realistic estimation of expected mountain-scale and near-drift changes in temperature, saturation, and flux. Cases 3 and 4 provide predictions of two-dimensional TH conditions for the higher-temperature repository (including the effects of lithophysal cavities). Cases 5 and 6 provide similar predictions for the lower-temperature (below boiling) repository thermal load, in which forced ventilation removes 80 percent of the heat for 300 years. Case 7 provides an upper-bound scenario of the effect of a higher net infiltration on the lower-temperature operating mode. The results of TH simulations were evaluated using temperature and liquid saturation

contours for entire cross-section at selected times during thermal period. The results were also evaluated using temperature and liquid flux profiles at location #1 (Figure 3.3.5-1) at the center of the cross-section and by using temperature and flux distribution above the drifts (Bodvarsson 2001 [DIRS 154669], Attachment 6, pp. 83 to 103).

Temperature–Figures 3.3.5-2 and 3.3.5-3 show the distribution of temperature along the refined cross section NS#2 after 1,000 years. The results are for the higher-temperature case (Case #3, 70 percent forced ventilation for 50 years, Figure 3.3.5-2), and the lower-temperature case (Case #5, 80 percent forced ventilation first 300 years, Figure 3.3.5-3). The figures show that at lateral distances of 100 m or more from the potential repository, no substantial increases in temperature are predicted. This response suggests that the ambient percolation flux (predominantly vertical) controls the temperature changes outside the potential repository boundaries. In the lower-temperature case, modification of thermal properties to include lithophysal cavities (Case #6) has little effect on the mountain-scale TH conditions because boiling does not occur. In the higher-temperature case (Case #4), lithophysal cavities may lead to higher temperatures in the drift and in the UZ above the drift (Bodvarsson 2001 [DIRS 154669], Attachment 6, pp. 71 to 76, 99 to 101).

Figures 3.3.5-4 and 3.3.5-5 show the temperature profiles at location #1 at the center of the repository for the higher-temperature refined grid NS#2 case, without and with lithophysal cavities (Case #3 and Case #4 respectively). In these figures, the initial inclination of the temperature profile indicates the ambient temperature gradient with present day infiltration. The drift is at an elevation of about 1,070 meters above sea level where ambient temperature is about 24ºC and the water table is at 730 masl where ambient temperature is about 32ºC.

In both cases, the TH model predicts completely dry drifts with temperatures rising above-boiling to about 115°C for Case #3 and 118ºC for Case #4 after 500 years. With lithophysal cavities (Figure 3.3.5-5, Case #4), a 50-m heat-pipe zone develops above the drift at 500 years. The heat pipe condition is represented by a near vertical temperature profile above the drift at this time. Vapor convection flow from the heat pipe raises temperatures 4°C to 5°C up to 150 m above the drift compared to the model with thermal properties of the initial TH model (Figure 3.3.5-4, Case #3). In both cases, the water table temperature rises from ambient (32ºC) to 67º to 68ºC after 10,000 years of thermal loading; the temperature at the top of the CHn (910 masl), on the other hand, rises to about 73º to 74ºC after 5,000 years, and then declines to about 65ºC by 10,000 years. Lithophysal cavities have little effect on temperature conditions below the repository. Units with lithophysal cavities predominantly occur at or above the elevation of the potential repository. Without lithophysal cavities, maximum temperature at the base of the PTn (Figure 3.3.5-4) is about 57°C after 1,000 years. With lithophysal cavities (Figure 3.3.5-5), the predicted maximum temperature at the base of the PTn rises to 70ºC, due to increased vapor convection above the drifts. Similar to the model results documented for the EDA II case in *Mountain-Scale Coupled Processes (TH) Models* (CRWMS M&O 2000 [DIRS 144454]), the maximum temperature in the drift pillars is about 85° to 90°C in these higher-temperature cases (Bodvarsson 2001 [DIRS 154669], Attachment 6).

Figure 3.3.5-6 shows the predicted temperature profiles at the same location for the lower-temperature case without lithophysal cavities (Case #5). The predicted maximum drift temperature is about 90°C after 500 years. Lithophysal cavities raise maximum drift-wall

temperature to 95°C, with little impact on the rest of the profiles (Bodvarsson 2001 [DIRS 154669], Attachment 6, p. 74, Case #6). In both cases, the temperatures at the base of the PTn are predicted to rise by a maximum of about 24° to 27ºC, to 44° to 47ºC after 2,000 years. At the water table the predicted maximum temperature is 60º to 63ºC after 10,000 years and at the top of the CHn, the maximum temperature is 65° to 67ºC after 5,000 years. For these lower temperature cases, the maximum temperature in the drift pillars is about 70° to 75°C. The higher predicted temperatures above are for the TH model with lithophysal cavities. Much lower temperatures are predicted when five times the ambient infiltration rate is considered (Bodvarsson 2001 [DIRS 154669], Attachment 6, pp. 75 to 76, 102 to 103, Case #7).

Liquid Saturation and Flux–Figure 3.3.5-7 shows a contour plot of fracture liquid saturation at 1,000 years for the higher-temperature case using the nonlithophysal thermal properties (Case #3). After 100 years (Bodvarsson 2001 [DIRS 154669], Attachment 6), completely dry fracture conditions are predicted near the drifts and in a few isolated locations with low ambient percolation flux, and the fractures remain dry for nearly 1,000 years. At 2,000 years, the fracture saturation in most drifts recovers to above 90 percent of ambient saturation. After 5,000 years, the liquid saturation is primarily controlled by the prevailing climate, with little influence from repository heat. Saturation within the pillars remains at or above ambient levels throughout the simulated period. In the lateral direction, the liquid saturation more than 50 m away from the repository stays at near-ambient conditions.

Figures 3.3.5-8 and 3.3.5-9 show the predicted fracture liquid flux profiles at location #1 for the models without and with lithophysal cavities, respectively, for the higher-temperature operating mode (Table 3.3.5-1, Cases 3 and 4). The analysis presents only fracture flux, because for the UZ flow properties used in the TH models, more than 95 percent of the flow within the TSw units is through the fractures. Under ambient conditions fracture flux at drift elevation is about 4.5 mm/yr.

Qualitatively, the predicted flux is similar to the results presented for the EDA II Case (i.e., high flux above the drift), but zero or small below the drift. Most or all of the predicted enhanced liquid flux above the drift is vaporized by the repository heat and does not cross the drift boundary for up to 2,000 years. Without lithophysal cavities (Figure 3.3.5-8, Case #3), the predicted maximum liquid flux above the drift rises to about 120 mm/yr after 100 years, but drops to 40 mm/yr after 500 years. At 1,000 years, the liquid flux above the drift is 25 to 40 mm/yr (enhanced by climate), but again declines to less than 1 mm/yr below the drift. At 2,000 years, the flux above the drift is about 20 mm/yr, but drops to about 10 mm/yr below the drift. With lithophysal cavities (Case #4, Figure 3.3.5-9), the flux above the drift at 1,000 years is about 35 mm/yr, but declines to 0 mm/yr below the drift. In this case, at 2,000 years, the flux above the drift is about 15 mm/yr, but declines to about 8 mm/yr below the drift.

For the lower-temperature cases, the heat perturbation is not large enough, to completely dry up the fractures near the drifts. As a consequence, the model predicts reduced (but nonzero) fracture liquid flux through the drift at all times. Figures 3.3.5-10 and 3.3.5-11 show the predicted fracture liquid flux in the models without and with lithophysal cavities (Cases 5 and 6, respectively). Up to 500 years, average liquid flux above the drift is about 5 mm/yr, but rises to about 15 mm/yr immediately above the drift and declines to less than 2 mm/yr below the drift for Case #6 and to about 2-3 mm/yr for Case #5. In both cases, at 1,000 years, average liquid flux

above the drift is 20 mm/yr, declines to 7 mm/yr at the drift horizon and rises to 20 mm/yr below the drift. From 1,000 to 2,000 years, the flux above and below the drift is primarily controlled by the climate because the fracture network above and below the drift is almost completely resaturated. Results using the refined drift-scale TH model (see Section 4.3.5) show a complete drying up more than 5 m below the drift during this period. Thus, although the refined-grid mountain-scale model does not predict complete drying of the fracture network below the drift (because the grid is still too coarse), it is expected that the near-field drift environment will be dry, and little or no liquid will seep below the drift for 1,000 to 2,000 years.

Figure 3.3.5-12 shows the flux profiles for the upper-bound infiltration case (Case #7, that is, five times the mean of present-day ambient, monsoon, and glacial-infiltration flux), for the lower-temperature operating mode without lithophysal cavities. In this case, the model shows (as expected) that the impact of heat on flow is minimal under conditions of high-infiltration flux, except in the immediate vicinity of the drift where minor drying is predicted. The flux in this case is primarily controlled by the prevailing climate used in the model (0 to 600 years, 5 times present-day mean infiltration; 600 to 2,000 years, 5 times mean monsoon infiltration; and 2,000 to 10,000 years, 5 times mean glacial transition infiltration).

3.3.5.6 Abstraction for Total System Performance Assessment

Previous subsections describe the two-dimensional and three-dimensional TH process models that explore the effects of heat on mountain-scale temperature, liquid saturation, and percolation flux for the higher- and lower-temperature repository operating mode over 100,000 years of thermal loading. The three-dimensional model provides mountain-scale TH conditions that could be abstracted by the TSPA-SR (CRWMS M&O 2000 [DIRS 153246]) for direct comparison with UZ ambient flow-field data. However, because the 5-m diameter drifts are much smaller than the 81-m wide gridblocks used in the three-dimensional ambient and TH model, the results of the mountain-scale TH models based on the three-dimensional grid are averaged out (smeared) and show little change in flux due to heat, as similarly predicted in the TH models developed to support the TSPA-SR. The two-dimensional refined grid model, which traverses all 53 drifts, gives a more realistic prediction of temperature, saturation, and fluxes on the mountain scale, as well as near the drifts and within the drift pillars at the repository horizon. The ambient and thermally affected two-dimensional model will therefore give a more realistic indication of the effect of heat flux at the mountain-scale. A more detailed investigation of the near-drift changes in flux, temperature, and saturation is discussed in the drift-scale TH model (see Section 4.3.5). The drift-scale model predicted increased saturation and flux due to condensation above the drift. The models also predict reduced liquid saturation and flux in the drift shadow below each drift lasting 1,000 to 2,000 years, during which most of the drainage occurs within the pillars. TSPA-SR models that assume the enhanced liquid flux above drifts represents expected percolation flux through the drifts during the thermal period use a very conservative approach, because flux out of the drifts, as predicted in Section 3.3.5.5, is much smaller than flux above the drifts. A less conservative approach would use flux below the drifts to predict the effects of heat on transport. Although not used for TSPA-SR, this less conservative approach will be used in TSPA-LA analysis for license application.

3.3.5.7 Multiple Lines of Evidence

Numerical modeling of mountain-scale thermal hydrology provides insight into the performance of the potential repository under thermal loading. Approaches for development of the numerical model and the simulation of thermal-hydrologic processes are generally based on geothermal- and petroleum-reservoir simulation methods. Nonisothermal heat and fluid flow in unsaturated fractured geological media such as Yucca Mountain can be modeled in a similar manner. The justification for model approaches employed here, and the validity of the results, depends on the successful modeling of fluid and heat transport in large geothermal systems, for which an extensive volume of field data is available to provide model validation. A detailed literature survey of the application of the TOUGH2 family of codes to model coupled heat and fluid transport in geological media is presented in initial *Mountain-Scale Coupled Processes (TH) Models* report (CRWMS M&O 2000 [DIRS 144454]). This document discusses the similarity between these natural-analogue applications and the TH processes modeled here. Table 3.3.5-2 documents recent applications of TOUGH2 in modeling geothermal systems. These systems are supported by extensive data collected during exploration and production, which allow for development of a calibrated natural-state model. The natural-state model is then used for prediction of future performance based on production history. A similar approach is used to develop the UZ natural-state (ambient) model (CRWMS M&O 2000 [DIRS 144454]), which is then used to predict TH conditions discussed in this Section.

In modeling the impact of heat on the UZ, the only available validation data are from small-scale heating experiments that mostly provide near-field response (within a few meters of the drift wall) over a couple of months to a few years. These experiments include, for example, the Single Heater Test (a 9-month heating period) and the larger Drift Scale Test (a 4-year heating period). These tests give temporal and spatial variation in temperature and liquid saturation in the UZ near the drift when heat is applied. The small spatial and temporal scales of these tests limit their use for validation of the mountain-scale TH processes that are expected to last thousands of years and provide UZ response to heat over hundreds of meters.

Therefore, numerical modeling of mountain-scale TH will play a crucial role in understanding the impact of heat on the performance of the UZ. The validity of the mathematical and numerical approaches in modeling UZ isothermal (ambient) and nonisothermal processes has been demonstrated by field data and natural-analogue models and is extensively discussed in *Unsaturated Zone Flow and Transport Model Process Model Report* (CRWMS M&O 2000 [DIRS 151940]). Although the TH model incorporates the results of the small-scale heating experiments, it relies mainly on the conceptual and mathematical validity of the modeling approach for flow, selection of thermal properties, and construction of the numerical grids. Performance assessment TH models, based on numerical simulation of fluid and heat flow, include important physical processes affecting repository and host rock behavior.

3.3.5.8 Summary of Uncertainties and Their Treatment

The uncertainties in model parameters associated with the mountain-scale TH model development were considered and the impact on mountain-scale UZ flow evaluated. A key uncertainty results from using limited data to perform mountain-scale predictions in a fractured

heterogeneous system where the impacts of heterogeneity on the mountain-scale processes are uncertain.

Table 3.3.5-3 summarizes uncertainties by category (i.e., conceptual, data, or parameter). The primary uncertainty issue associated with each category is described, followed by possible methods for treating or addressing that uncertainty. Each of the uncertainties is representative of decisions that may impact the model goals.

3.3.5.9 Summary and Conclusions

This TH modeling study investigates the effects of higher- and lower-temperature thermal loads on the UZ of Yucca Mountain. This study uses two-dimensional and three-dimensional dual-permeability submodels of the three-dimensional UZ flow model and incorporates the calibrated model properties of the UZ flow model. The study also investigates the effect of UZ lithophysal cavities on TH response. Detailed investigation of the UZ response to thermal loading, using both the higher-temperature operating mode (thermal load 1.35 kW/m, ventilation 70 percent for 50 years) and the lower-temperature operating mode (thermal load 1.35 kW/m, ventilation 80 percent for 300 years) is conducted using refined two-dimensional cross-sectional models that include explicit representation of the drifts of the repository. The models include expected future climatic changes in infiltration rate. The numerical grids are sufficiently refined to depict mountain-scale, long-term TH behavior resulting from thermal load within the drifts, but do not explicitly include detailed heat-transfer processes within the drifts.

This study indicates that the heat source and its distribution, the thermal and flow properties of the rock, and the infiltration rates control boiling and rewetting TH processes at the repository. In the higher-temperature cases (1.35 kW/m 70 percent ventilation for 50 years), temperatures are predicted to rise to boiling conditions only within the immediate area of the drifts. The temperatures may rise above 110°C at some drifts. Temperatures in the pillars are predicted to rise to an average of 85° to 90°C. The higher temperature is likely when the effects of lithophysal cavities on thermal properties are modeled. For the lower-temperature cases, (1.35 kW/m 80 percent ventilation for 300 years) predicted maximum temperature at the drifts is 90°C without lithophysal cavities and 95°C with lithophysal cavities. Therefore, no boiling is predicted even when the effects of lithophysal cavities on thermal properties are included. The lower-temperature operating mode also predicts little potential for temperature-induced property changes in the PTn (1270 masl), CHn (910 masl), and the water table (730 masl) where predicted maximum temperatures are 44° to 47ºC, 65° to 67ºC, and 60° to 63ºC, respectively.

For the higher-temperature cases, thermal loading at the repository results in significant changes in temperature, moisture distribution, and flux at the repository and in zones directly above and below the repository. The increase in liquid flow occurs only at early times (less than 100 years). This liquid does not enter the drifts because the heat within the potential repository drifts easily vaporizes this liquid flux. The model predicts that vertical liquid flow in the pillars between the drifts continues at a rate close to the ambient percolation flux for most of the thermal-loading period. In some locations, the flow may be enhanced by condensate drainage lasting for several hundred years. For these higher-temperature cases, localized dryout of the fracture and matrix continua at the repository is predicted, particularly below areas with low infiltration. This dryout zone may extend tens of meters into the drift shadow below each

potential repository drift. The temperature of the repository drifts rises to above boiling conditions. The temperature of the pillars rises to a maximum of 85° to 90°C. With lithophysal cavities, temperatures are predicted to rise to 70°C at the base of the PTn, and to 73°C at the top of the CHn and 67ºC at the water table, again showing little potential for temperature-induced property changes. Without lithophysal cavities predicted maximum temperature is 57ºC at base of the PTn, 73ºC at the top of the CHn and 67ºC at the water table. Lithophysal cavities therefore, primarily influence temperatures at or above the drifts.

For the lower-temperature cases, the TH models predict little change in UZ liquid flux except in the immediate vicinity of the potential repository drift (Section 3.3.5.5). Because boiling conditions do not occur, and the fractures are not completely dry, the mountain-scale TH model predicts reduced (but nonzero) flow crossing the repository horizon throughout the thermal-loading period. Within the first 2,000 years, average liquid flow crossing the drifts is less than 25 percent of the prevailing ambient flux, because repository heat is not large enough to vaporize all the percolation flux. In the lower-temperature case, the TH model still predicts substantial drying of the fractures in the drift shadow below the drifts, drying that lasts up to 2,000 years. The low fracture saturation in the drift shadow implies reduced potential for flow and transport below the drift for up to 2,000 years. The drying of the fractures below the drift is better resolved by TH simulations using a refined (about 1-m grid spacing) drift-scale grid (Section 4.3.5).

Lithophysal cavities reduce the effective thermal conductivity and the thermal capacity of the matrix continuum in the upper-lithophysal (tsw33) and lower-lithophysal (tsw35) units. For the same thermal load, explicitly accounting for the effects of lithophysal cavities leads to an increase in temperature caused by heat released over the same period. The three-dimensional model predicts a maximum increase of 1° to 2°C. In the refined model, the maximum temperature at the drift increases from 115° to 118°C for the higher-temperature cases. The models predict that at 1,000 years, temperatures up to 150 m above the drift are 1° to 5°C higher when thermal effects of lithophysal cavities are included. For the lower-temperature operating mode, the model still predicts a below-boiling-temperature scenario, even when the effects of lithophysal cavities are included. In this case, the predicted maximum temperature increases from about 90ºC to about 95°C at the drift after 500 years. This increased temperature results in more drying of fractures near the drifts and the development of drier fractures in the drift shadow below. Therefore, lithophysal cavities, although not contributing to boiling at the drifts for this lower-temperature operating mode, may lead to further lowering of liquid flux below the drift and enhanced drainage flux through the drift pillars.

When a higher infiltration flux (5 times mean) is applied, the TH model for the lower-temperature case predicts little or no drying of the fracture network, even near drifts. Therefore, heating in the lower-temperature case may have a minimal effect on percolation flux throughout the thermal cycle.

The mountain-scale TH model is designed to predict the scale of thermal disturbance to the hydrologic setting of the emplacement drifts outside the near-field, which is considered in Section 4.3.7. The initial TH model is based on the EDA II design with a thermal loading of 72.7 k/W acre and a 70 percent heat removal by ventilation for 50 years. Subsequent modeling considers seven cases, using the same thermal load (67.7 kW/acre) in all cases. The temperature

profile is varied in the latter modeling by changing the rate of heat removal and the duration of ventilation (two sets of rates). In addition, rock thermal properties are varied (lithophysal/non-lithophysal). Percolation flux is varied spatially and temporally. The results of modeling are predictions of change of temperature at key locations such as the top of the CHn and at the water table, the extent and process of two-phase flow due to boiling and the impact of drying on fracture flow around the drift. Liquid and gas flux and local temperature histories are important intermediate steps. In the higher-temperature case of the initial TH modeling, completely dry drift wall temperatures reach 250ºC, and pillar temperatures may locally rise to 97ºC. In the lower temperature case the drift wall temperatures may exceed 110ºC with maximum temperatures in the pillars averaging 85° to 90ºC. Percolation flux is found to be the primary control, at the mountain scale, of the boundary of the two-phase flow region, boiling front position, and the rate of recovery of flow to ambient flow conditions. Heat flow above the repository is by heat pipes, which do not significantly alter the ambient flow around the repository and little effect is expected on cooling and post cooling percolation flux.

The more recent modeling was not strictly based on the EDA II repository design. Thermal loading has been adjusted, rock properties and ventilation rates varied so that none of the drift rock temperatures are expected to rise above boiling for the lower temperature cases (Table 3.3.5-1). Infiltration rates and resulting percolation fluxes are varied in accord with predicted climatic variation from the Climate Model (Section 3.3.1). None of the cases predicts temperatures in the CHn high enough to alter the hydrologic or sorptive properties of this unit.

None of the expected effects of waste heat predicted by the mountain-scale TH model permanently change the hydrologic character of the site. The predicted short-term changes are over (in 1,000-2,000 years) before any releases are expected from the emplacement drifts and all of the short-term hydrologic changes at the mountain scale are conservative in their influence on UZ flow and transport. At higher percolation fluxes associated with wetter climates modeling implies there may be no significant TH effects. The consideration of seven cases with varying heat input (two thermal loads, two ventilation scenarios), variation of rock properties and changes in recharge/percolation flux, is more than adequate to identify any heat driven anomalies in the site and repository hydrologic behavior over a very wide range of temperatures. However even with the coarse grids, predicted drift wall temperatures may rise up 10ºC above the desired goal of 85ºC for “waste-package” surface at some locations. Additional ventilation may be required to meet “waste-package” surface temperature goals.

3.3.6 Thermal-Hydrologic-Chemical Effects on Unsaturated Zone Flow and Geochemistry

3.3.6.1 Introduction

This section summarizes the modeling and uncertainty studies performed for the evaluation of THC effects on flow and geochemistry in the UZ at the mountain scale. The major THC processes important for the UZ are (1) mineral precipitation/dissolution affecting flow and transport to and from the potential repository and (2) effects on the compositions of gas and liquid that may seep or flow into drifts. THC processes at the mountain scale affect the flow and sorption properties of rock units within the UZ. Modification of these properties through hydrothermal alteration of zeolitic and vitric tuffs and mineralization of fractures may influence

the amount of lateral flow that may divert water, thus reducing the percolation flux to the potential repository and the transport time to the saturated zone. Alteration may also affect the transport of radionuclides from the repository to the saturated zone. Uncertainties in the TSPA-SR (CRWMS M&O 2000 [DIRS 153246]) that the work in this section addresses are: (1) mountain-scale effects of THC processes on flow and transport, (2) mountain-scale THC effects on the variability of water chemistry entering drifts under thermal loading conditions. Natural analogue studies can be utilized to constrain the potential impact of THC processes on total repository performance and validate predictive models for Yucca Mountain.

The mountain-scale THC model is a new two-dimensional model developed after the TSPA-SR (CRWMS M&O 2000 [DIRS 153246]) that is based on the mountain-scale TH model documented in *Mountain-Scale Coupled Processes (TH) Models* (CRWMS M&O 2000 [DIRS 144454]), and the conceptual models and data for THC processes documented in *Drift-Scale Coupled Processes (DST and THC Seepage) Models* (BSC 2001 [DIRS 154677]). Many of the uncertainties in the conceptual models and data used for input and model validation are identical to those discussed in the latter AMRs. However, the drift-scale THC models are focused primarily on processes that affect seepage (and the chemistry of potential seepage) into drifts. Therefore, the effect of THC processes on flow in the Paintbrush hydrogeologic unit (PTn), the basal vitrophyre of the Topopah Spring Tuff, and the vitric and zeolitic zones in the Calico Hills hydrogeologic unit below the potential repository are not of particular concern for the drift-scale THC models.

The purpose of the mountain-scale THC model is to reduce the uncertainties associated with coupled THC processes that are caused by variations in geology (structure and lithology), infiltration rate, and temperature at a mountain or repository scale. Because these variations are larger than that of mineralogical variations in the welded units they are the most important to capture. These are processes that affect the percolation flux at the potential repository horizon (relevant to seepage) and flow below the potential repository (relevant to radionuclide transport in the UZ). Small-scale and localized processes, such as mineral precipitation in the boiling zone, can only be captured in finely gridded drift-scale models. Thus, the mountain-scale THC model is focused on larger-scale changes in chemistry and flow that are not localized to very small regions adjacent to the drift. Large-scale gas-phase convection and lateral flow are not represented in the THC Seepage models, and therefore, the mountain-scale THC model can address uncertainties in phenomena that may not arise in the drift-scale "chimney" models. However, these effects are prominent on the edges of the repository and do not invalidate the results of the THC Seepage models because they do consider local gas convection effects. The Mountain-Scale THC model provides a more heterogeneous set of results for a given time but is essentially is modeling the same processes as the THC Seepage models.

Three main types of uncertainty are discussed in the section: data uncertainties, uncertainties arising out of features, events, and processes, and conceptual uncertainties. Because the results in this section are from a new model, with limited analyses performed, the results should be considered as preliminary. In addition, long-term impacts have not yet been assessed.

The methods used to evaluate THC effects on flow and geochemistry include the estimation of thermodynamic and kinetic parameters, model development, testing and model validation using large-scale thermal test and laboratory experiments, and predictive process modeling. This

approach was chosen because it provides the means to test the appropriateness of the conceptual model, to evaluate uncertainties in different conceptual models, and to provide predictions of potential effects on water and gas chemistry, as well as changes in hydrologic properties that result in changes in flow. Uncertainties in some thermodynamic and kinetic parameters were evaluated using sensitivity studies and comparisons to data from the Drift Scale Test and laboratory experiments, which are discussed in Section 4.3.6. Remaining unquantified uncertainties were addressed in *Features, Events, and Processes in UZ Flow and Transport* (BSC 2001 [DIRS 154826]). Unquantified conceptual uncertainties were assessed in analogue studies and other corroborating observations (CRWMS M&O 2000 [DIRS 141407]).

The conceptual model for THC processes provides a framework for modeling the pertinent mineral-water-gas reactions in the host rock, under thermal loading conditions, as they influence the chemistry of water and gas in the mountain and associated changes in mineralogy. The data incorporated in the model include hydrologic and thermal properties from the calibrated property sets, geologic layering from the UZ three-dimensional flow and transport model, geochemical data (fracture and matrix mineralogy, aqueous geochemistry, and gas chemistry) derived from various sources, thermodynamic data (minerals, gases, and aqueous species), data for mineral-water reaction kinetics, and transport data. Simulations of THC processes included coupling among heat, water, and vapor flow; aqueous and gaseous species transport; kinetic and equilibrium mineral-water reactions; and feedback of mineral precipitation/dissolution on porosity, permeability, and capillary pressure for a dual-permeability (fracture-matrix) system.

The effect of coupled THC processes on the evolution of flow fields and water and gas chemistry in the UZ is evaluated in this section for a higher-temperature thermal operating mode based on the thermal loading and properties used in *Mountain-Scale Coupled Processes (TH) Models* (CRWMS M&O 2000 [DIRS 144454]). Because this is a new model, a higher-temperature baseline analysis was performed first, which may bound the upper limit of THC effects on mountain-scale flow and chemistry that may be expected under above-boiling conditions. Effects of THC processes at the drift scale under the lower-temperature operating mode are evaluated in Sections 4.3.6 and 6.3.1.5.

3.3.6.2 Goal of the Mountain-Scale Thermal-Hydrologic-Chemical Model

The goals of the model used for prediction of mountain-scale THC processes are:

- Provide a conceptual basis and methodology for developing a mountain-scale THC model to assess uncertainties in the modeling results. Use the results to assess uncertainties in the drift-scale THC models (as well as other UZ flow and transport models)

- Predict large-scale changes in hydrologic properties resulting from mineral precipitation/dissolution and associated THC effects on UZ flow

- Predict large-scale mineralogic changes that could impact UZ transport (i.e., effects on glassy and zeolitic units below the potential repository) (see Section 11.3.5)

- Predict large-scale changes in water and gas chemistry that can be used to extend the variability predicted by drift-scale models.

The important mountain-scale coupled THC processes are illustrated schematically in Figure 3.3.6-1. Some UZ processes, such as the distribution of net infiltration, may strongly affect THC processes by modifying the fluxes and concentrations of components in waters that migrate to the repository horizon. The effect of THC processes on UZ flow may include modification of the percolation flux beneath the nonwelded tuffs in the Paintbrush hydrogeologic unit (PTn) and alteration of flow paths (lateral flow) below the potential repository in the vitric and zeolitic layers of the Calico Hills hydrogeologic unit (CHn) and on the basal vitrophyre of the Topopah Spring Tuff. In addition, small-scale hydrologic processes, such as fracture-matrix interaction, have a strong effect on the chemical evolution of the system and the distribution of mineral precipitation in fractures and the matrix.

3.3.6.3 Basis of Mountain-Scale Thermal-Hydrologic-Chemical Model and Simulation Results

3.3.6.3.1 Description of the Mountain-Scale Thermal-Hydrologic-Chemical Model

A cross section was chosen from the UZ three-dimensional flow and transport model grid that follows a roughly north-south trend through the potential repository and runs perpendicular to the trend of the potential waste emplacement drifts (Figure 3.3.6-2). This orientation allows for the effects of THC processes on flow between drifts to be evaluated. The two-dimensional grid, geological layering, infiltration rates, and hydrologic and thermal properties were derived from *Mountain-Scale Coupled Processes (TH) Models* (CRWMS M&O 2000 [DIRS 144454]). Each drift is represented as an individual grid block. The purpose of the model is to evaluate processes in the UZ; however, the grid includes an extension of several hundred meters below the water table to provide a far-field constant-temperature boundary, but without any flow into or within this saturated region.

Mineral abundances were assigned to each hydrogeologic unit based on data from the three-dimensional mineralogical model V3.0 (DTN: LA9908JC831321.001 [DIRS 113495]) (for a single column taken near the center of the potential repository footprint) and from fracture data as described in *Drift-Scale Coupled Processes (DST and THC Seepage) Models* (BSC 2001 [DIRS 154677], p. 32, Section 4.1.2.1). Therefore, each model layer is characterized by uniform mineralogical abundances, although some layers may change from zeolitic to vitric along strike. Fault mineralogy was approximated by the average of the mineral abundances for each major hydrogeologic unit. The minerals, aqueous and gaseous species in the model geochemical system are listed in Table 3.3.6-1, and are the same as those in the extended-case geochemical system described in *Drift-Scale Coupled Processes (DST and THC Seepage) Models* (BSC 2001 [DIRS 154677], pp. 67 to 69, Section 6.1.7). Although the base case geochemical system captured more closely the pH and gaseous carbon dioxide concentrations in samples collected from the DST, silica concentrations were better in the extended case system simulations and therefore effects on flow owing to mineral precipitation may be more realistic. The initial and infiltrating water chemistry was set to that from the matrix pore water collected from the Topopah Spring middle nonlithophysal unit (Tptpmn) in Alcove 5, near the ongoing Drift Scale Test, as documented in *Drift-Scale Coupled Processes (DST and THC Seepage) Models* (BSC

2001 [DIRS 154677], Table 3). All other geochemical input data are derived from the latter report. Although this water may not be characteristic of all pore waters in the UZ, it has been used successfully in validation studies with the Drift Scale Test, as described in the AMR and also summarized in Section 4.3.6. Side boundaries taken far from the repository edges (see Figure 3.3.6-2) were set to be no-flux for flow, heat, and chemical transport. Details of the model simulations and parameters are described in Bodvarsson (2001 [DIRS 154669], Attachment 10, pp. 8 to 20)

Simulations were run under the higher-temperature design option using the mean infiltration rate for the modern climate. TOUGHREACT V2.3 was used for the simulations. Although the effects of other climate states imposed at later times have not been evaluated, the range in infiltration rates in this cross section is from nearly 0 to almost 50 mm/year. The simulations investigated the main thermal period up to the early post-thermal period (about 7,000 years). In addition to investigating the effects of above-boiling temperatures on THC processes, the higher-temperature option was chosen for consistency with the majority of the THC Seepage simulations, as discussed in *Drift-Scale Coupled Processes (DST and THC Seepage) Models* (BSC 2001 [DIRS 154677]). Climate effects were evaluated in this AMR and showed qualitatively the same behavior, with somewhat greater amounts of mineral precipitation under higher infiltration rates.

To assess uncertainties associated with mineral reaction rates, some of which were shown to have a strong effect on water and gas chemistry in the drift-scale THC simulations (BSC 2001 [DIRS 154677], p. 97), two simulations were performed that used alternative values for the reaction rate of anorthite. Anorthite (an endmember in the plagioclase feldspar solid solution series) has a strong effect on pH through its dissolution to form calcic zeolites. The lower rate (by three orders of magnitude) resulted in a smaller deviation in the chemical evolution of the initial water under ambient temperatures (corroborating evidence for effective reaction rates), with the model infiltration rate and initial and boundary gas-phase carbon dioxide concentrations. This simulation will be referred to as "Extended Case 1" and that with the higher rate for anorthite as "Extended Case 2." Some additional parameters were modified that have a less substantive effect on the simulation results, such as the initial precipitation rate of new secondary phases.

3.3.6.3.2 Effects of Thermal-Hydrologic-Chemical Processes on Hydrologic Properties and Mineralogy

Some of the more important indicators for the effect of THC processes on hydrologic properties and mineralogy are shown in Figure 3.3.6-3 after about 1,400 years of heating (Extended Case 1) and in Figure 3.3.6-4 after 5,000 years (Extended Case 2). The main difference in the results for the two cases was in the gas-phase carbon dioxide concentrations and pH. The differences were not great enough to markedly change the mineral abundances and distributions. Longer time periods were not considered in these simulations; however, two-dimensional drift-scale THC simulations have shown that amorphous silica precipitation during the boiling period occurs in the first few thousand years (BSC 2001 [DIRS 154677], p. 168). Later changes occurred slowly over the next several tens of thousands of years as a result of calcite precipitation. For reference, Figure 3.3.6-3a shows the distribution of net infiltration imposed along the top model boundary.

After 1,400 years, the temperatures around the repository are below boiling everywhere (Figure 3.3.6-3b), and the isotherms show some slight localized depression owing to focusing of the percolation flux near the center of the region having higher infiltration. These zones of focused flow are also the areas where there is a small fracture porosity reduction, in contrast to the majority of the area above the potential repository (where porosity increased in the large condensation zone). TH effects on the percolation fluxes at the mountain scale are discussed in Section 3.3.5. The porosity reductions are generally much less than 1 percent, similar to that seen in areas where the temperatures are still at their ambient value. Porosity reductions in the Tiva Canyon Tuff (TCw) are elevated relative to the ambient system as a result of increased calcite precipitation (Figure 3.3.6-3c). As can be seen in the latter figure, areas of calcite dissolution above and below the plane of the drifts is responsible for much of the porosity increase observed in Figure 3.3.6-3b. The distribution of amorphous silica is generally confined to boiling areas very close to the drifts, but larger regions are evident below the edges of the potential repository (Figure 3.3.6-3d). These areas are characterized by very low fracture saturation that developed in part from gas convection at the edges. At the northern edge, there is also a fault acting as a conduit for gas flow out of the heated zone.

Effects of THC processes below the repository are strongest in the zeolitic Calico Hills unit, where the zeolite minerals clinoptilolite, heulandite, and mordenite are initially stable and precipitating in the ambient system. They are also dissolving as the heat pulse migrates into the zeolitic units (Figure 3.3.6-3e). In this model simulation, the zeolites are being replaced by feldspars in the heated region, whereas the reverse reaction is taking place slowly in the unheated parts of the zeolitic zones. The effect on glassy units is notably small (Figure 3.3.6-3f), with very slow dissolution in the Paintbrush nonwelded unit (PTn) occurring equally in heated and unheated regions.

After 5,000 years, most of the region above and directly below the repository (in the TSw) shows a small net reduction in fracture porosity of less than 1 percent (Figure 3.3.6-4a). Above the northern edge, there persists a region of small porosity increase related to enhanced convection and condensation. Temperatures become more irregular as a result of diversion of water into the approximate center of the potential repository, combined with topographic effects (the deepest part of the potential repository that is also away from edges is warmest). Precipitation of fracture calcite is ubiquitous, with increases in both heated and unheated areas (Figure 3.3.6-4b). The areas that show the most effect as a result of heating are in the TCw and below in the zeolitic units, where calcic zeolites (clinoptilolite, heulandite, and mordenite predominantly) are dissolving to produce Na- and K- feldspars and increasing the calcium in the associated waters. A small increase in amorphous silica is evident below the northern edge of the potential repository (Figure 3.3.6-4c), where gas convection has kept this area very dry. However, amorphous silica has generally stopped precipitating and is slowly dissolving into the percolating cooler waters.

The distribution of precipitation and dissolution of clinoptilolite (Figure 3.3.6-4d) shows dissolution in the heated region of the Calico Hills Unit, with dissolution also progressing into zeolitized regions of the TCw, above the PTn. In general, the ambient temperature zeolitic units show precipitation, driven by the dissolution of remaining feldspars in these rocks. It is not known how rapidly such reactions are currently taking place in the mountain under the present conditions, but it is likely that changes on the order of 1 percent (volume of the rock) over

5,000 years are too large because the minerals are still present after several million years. Thus, it can be expected that the reverse reactions in the heated zone are also taking place more rapidly in the simulation than would occur in the actual system. The causes of the increased reaction rates can be due to several model parameters and processes, such as the effective reactive surface area, kinetic rate laws and parameters, inhibition caused by mineral coatings, thermodynamic stabilities of aluminosilicates, local initial water and gas chemistry, and rates of transport via diffusion and fracture-matrix interaction (matrix imbibition). Because the major precipitating zeolite is clinoptilolite, which is the major zeolite mineral seen in these rocks, the thermodynamic relations for the minerals appear to give the observed mineral paragenesis. Therefore the effective surface areas of the feldspars in the altered rocks may be much lower due to the alteration that has already taken place. Some of these uncertainties are discussed further in Sections 3.3.6.6, 4.3.6.8, and 6.1.3.8.

Changes in UZ flow due solely to mineral precipitation/dissolution above the potential repository are small, but qualitatively show diminishing fracture porosity over time with slight but increased flow diversion and focusing. Below the potential repository, the increased porosity in the zeolitic units could lead to somewhat higher percolation fluxes through these units and the interbedded vitric units. The result of this would be reduced lateral flow, and it could lead to increased travel times for radionuclide transport because of sorption in the zeolitic units and matrix diffusion in the vitric units. However, there are uncertainties regarding alteration rates of the basal vitrophyre so that if the rates were higher, the result could be increased lateral diversion below the potential repository.

The higher-temperature operating mode simulations cover a range of thermal conditions that bracket the expected response for a lower-temperature operating mode. For example, in mountain-scale simulations, temperatures are at a maximum near the center of the potential repository, with cooler regions at the margins due to enhanced heat loss, and grading into regions at the ambient geothermal gradient. Temperature-dependent reactions such as the breakdown of clinoptilolite are greatest where maximum temperatures persist for the longest period of time near the center of the potential repository and decline toward the margins. Simulations employing a lower-temperature design option would exhibit maximum changes in zeolite alteration similar to those at equivalent temperatures near the repository edges. A lack of boiling temperatures and reduced gas convection also would result in less precipitation of amorphous silica around the potential repository.

3.3.6.3.3 Effects of Thermal-Hydrologic-Chemical Processes on Water and Gas Chemistry

Effects on water chemistry are most pronounced during the early thermal period, when condensation and dryout/boiling are driving dilution and evaporative concentration. Also, at this time, elevated temperatures result in greatly enhanced reaction rates and shifts in the thermodynamic stabilities of coexisting minerals. Another important process is the exsolution of carbon dioxide out of the water and transport in the gas via diffusion and advection. The latter process, in turn, has a large effect on pH, and therefore on mineral-water reactions and reaction rates. The effect of these varied coupled processes on pH after 1,400 years of heating is shown in Figure 3.3.6-5a. The initial ambient pH in the model is about 8.3 at the repository horizon and 7.8 in the surface infiltrating water. The area in the center of the potential repository shows a

distribution similar to that observed in the drift-scale THC models (CRWMS M&O 2001 [DIRS 154677]), with somewhat higher pH waters (up to about 8.8) forming above and around the drifts owing to carbon dioxide loss and reactions with aluminosilicates. However, at the edges of the repository, the strong gas convection effects and the migration of carbon dioxide from the central region outward (Figure 3.3.6-5b) have resulted in lower near-neutral pH waters (down to about 7). Areas of enhanced dilution as a result of condensation and subsequent drainage in fractures are evident in the distribution of chloride shown in Figure 3.3.6-5c. Areas of very high chloride below the potential repository edges and in a fault at the northern edge are the result of strong convection of gas drying out these areas and condensing in areas above. The fracture liquid saturations in these high concentration areas are nearly zero.

Under a lower-temperature operating mode, the edge effects seen in higher-temperature operating mode simulations would be reduced because of smaller temperature gradients and the absence of boiling, thus leading to smaller spatial differences in gas and water chemistry. A lack of boiling temperatures and reduced gas convection also would result in less precipitation of amorphous silica around the repository.

3.3.6.4 Abstraction for Total System Performance Assessment

Although the results are based on a very limited analysis of possible scenarios (e.g., climate, geochemical conceptual models, thermodynamic data, and kinetic data), the small changes in porosity are a basis for not performing TSPA abstraction of the THC effects on flow. Therefore, results described in this section reduce uncertainties associated with assumptions made for model abstractions supporting the TSPA, since the effects of mountain-scale THC processes on flow were assumed to be negligible in the TSPA-SR. However, as discussed in Section 3.3.6.6, there are many unquantified uncertainties associated with mountain-scale THC processes. Therefore, conditions, parameter ranges, or both, may exist such that there are significant effects of THC processes on flow and transport that may make TSPA assumptions non-conservative.

3.3.6.5 Multiple Lines of Evidence

3.3.6.5.1 Yucca Mountain Self-Analogue

A good analogue for understanding future THC reactions at the mountain scale is the fossil hydrothermal system at Yucca Mountain itself (Bish and Aronson 1993 [DIRS 100006]). Detailed mineralogical examination of Yucca Mountain Tuffs showed that most zeolitic alteration occurred from 13 to 11.6 Ma, shortly after tuff emplacement. After formation of the major zeolitic horizons, deep-seated hydrothermal activity persisted until about 10 Ma. The preservation of low-temperature zeolites (clinoptilolite and mordenite) suggests that this activity was limited to temperatures of up to 90 to 100°C.

Conceptual models for mineral evolution at Yucca Mountain (Carey et al. 1997 [DIRS 101323]) suggest that the most likely mineralogical reactions caused by repository heating would include dissolution of volcanic glass and precipitation of clinoptilolite, clay, and opal-CT (i.e., opal with cristobalite- and tridymite-type stacking); dissolution and precipitation of silica polymorphs (cristobalite, opal-CT, tridymite, and quartz); alteration of feldspars to clays; and reactions involving calcite and zeolites. Present-day temperatures in drill hole G-3 compare closely to

paleotemperatures inferred from mineralogical data. In contrast, an increasing abundance of clays and zeolites, along with a decreased abundance of glass, indicate higher paleotemperatures for drill holes G-1 and G-2, which are closer to the center of the Timber Mountain caldera source of eruption (G-2 being the farthest north).

In addition to temperature, the water saturation also has a strong impact on water-rock reactions, as kinetically controlled reactions proceed much more rapidly under saturated conditions. Zeolite reactions are likely to proceed more slowly in the Yucca Mountain UZ (excluding perched water zones) than below the water table (Carey et al. 1997 [DIRS 101323]). The persistence of opal-CT below the water table indicates that kinetically controlled silica reactions at Yucca Mountain are slower than suggested by laboratory studies.

Thin coatings of calcite and silica polymorphs found on fractures and lithophysal cavities in the ESF record chemical and isotopic changes in the UZ over the past 10 million years (Marshall and Whelan 2000 [DIRS 154415]). In the Topopah Spring Tuff, uranium-lead ages of opal and chalcedony coatings can be used to constrain the ages of associated calcite. Strontium isotope ratios in calcite increase from the base to the outermost surface of the coatings, recording a systematic change in pore water isotopic composition due to water-rock interaction (Marshall and Whelan 2000 [DIRS 154415]). Marshall and Whelan (2000 [DIRS 154415]) constructed a one-dimensional advection-reaction model to predict the evolution of strontium isotope ratios in the water, which can be used to estimate approximate ages for precipitated calcite. The $\delta^{18}O$ values of the calcite samples gradually increase with decreasing model strontium age, suggesting a cooling trend with time, with elevated temperatures restricted to prior to 6 Ma.

3.3.6.5.2 Geothermal Systems

Many processes that are expected to take place under repository conditions are the same as those that occur in geothermal fields. These include evaporation, boiling, condensation, single- and two-phase fluid flow, mineral reaction, precipitation and dissolution, and consequent potential changes in fracture-matrix interaction. Coupled processes related to geothermal systems have been observed, measured, and simulated for more than two decades in the geothermal industry. Geothermal analogues are one of the major ways of building confidence in understanding the thermal-hydrologic behavior of the repository system as it is coupled to chemical processes over long time periods. Data from geothermal fields can be used to test coupled process modeling codes used by the project to match observations (e.g., chemical reactions and occurrence of heat pipes) in geothermal fields with those predicted by the code.

The versatility of geothermal reservoir simulators has made possible their application to a wide range of fluid and heat flow problems. To produce an adequate model, numerical codes must be able to handle processes of heat transfer; two-phase flow under nonisothermal conditions in one, two, and three dimensions with varying degrees of non-linearity; coupling of fluid and heat flows; and complex boundary conditions. Modeling of geothermal systems has provided major advances toward this goal, which adds confidence in numerical models for Yucca Mountain. For a detailed discussion of geothermal analogues and modeling, see Section 4.3.6.7. A brief discussion follows.

Bruton et al. (1995 [DIRS 117033]) reviewed literature and data for many geothermal fields as a means of selecting a field-analogue site for THC studies. Some of these fields were considered unsuitable because they occurred in rock types dissimilar to Yucca Mountain, a few lacked sufficient data or had access problems, and others were entirely liquid- or vapor-dominated fields. The geothermal system at Wairakei was selected as the site most amenable to study of THC processes because it possessed the greatest number of features similar to Yucca Mountain (Bruton et al. 1995 [DIRS 117033], p. 8).

Mineral-fluid relations in Wairakei and other New Zealand geothermal fields were simulated (Glassley and Christenson 1992 [DIRS 109923]; Bruton et al. 1993 [DIRS 109901]). The goal of these simulations was to validate the thermodynamic database used for Yucca Mountain THC models through comparisons between observed mineral assemblages and model simulations of equilibria for the Wairakei system. The Wairakei geothermal system provided the opportunity to demonstrate that the Yucca Mountain Project EQ3/6 thermodynamic database and associated model could simulate observed mineral-water compositions for a specific example within the possible range of temperatures and water conditions anticipated in a Yucca Mountain repository system. The results of these modeling studies were generally consistent with observed vein and matrix mineral equilibria at Wairakei for fluids at temperatures greater than 240°C. Field data and model results indicated that stable mineral assemblages could be significantly impacted by small differences in fluid chemistry, temperature, or pressure. Comparison of laboratory data with field data from natural hydrothermal waters at Wairakei for amorphous silica precipitation showed that significant discrepancies exist between results obtained with different test conditions (Carroll et al. 1998 [DIRS 124275]). Silica precipitation rates measured in the field were 400 times faster than those obtained in laboratory measurements. Silica precipitation under repository conditions at Yucca Mountain could exhibit rate behavior somewhere in the range between the laboratory and field experiments.

3.3.6.6 Summary of Uncertainties and Their Treatment

As is the case for all coupled process models, there are many uncertainties in the results of the Mountain-Scale THC model. However, the model results address the goals outlined (see Section 3.3.6.2) and are therefore considered acceptable, given the intended purpose of the model and the use of its results for downstream users. It is important to note that the primary conceptual models and data for coupled THC processes are derived from the drift-scale THC models (BSC 2001 [DIRS 154677]), which have undergone extensive validation to measured data from the DST and from laboratory experiments. To further reduce the uncertainty in the predictions of large-scale THC effects on mountain-scale flow and transport (if such a reduction were required by downstream users of the THC model results), the following sources of uncertainty could be examined:

- Uncertainties in three-dimensional TH processes at a mountain scale and their effect on THC processes (i.e., gas convection, focused flow)

- Uncertainties in thermodynamic data (i.e., relative stabilities of feldspars, clays, and zeolites) that relate specifically to vitric and zeolitic horizons

- Uncertainties in kinetic data (i.e., aluminosilicate rate laws and parameters and rates of nucleation) also related specifically to vitric and zeolitic horizons

- Uncertainties in geochemical conceptual models (e.g., mineral solid solutions, precipitating mineral assemblages, reactive surface area estimation)

- Uncertainties in the effective mineral-water reactive surface areas in heterogeneous unsaturated fractured rock, which is being addressed through continuing and new laboratory studies, the planned Cross-Drift Thermal Test, and sensitivity studies

- Uncertainties in fracture and lithophysal hydrologic parameters (i.e., fracture and lithophysal porosity and unsaturated hydrologic properties)

- Uncertainties in the distribution of water and gas chemistry in the UZ and in infiltrating water.

Table 3.3.6-2 summarizes the key conceptual and parametric uncertainties that are specific to the prediction of mountain-scale THC processes. Many general THC issues, and those related to seepage chemistry or localized mineral precipitation adjacent to drifts, are discussed in Sections 4.3.6 and 6.3.1.5.

3.3.6.7 Summary and Conclusions

The uncertainties associated with the effects of THC processes on flow and chemistry in the UZ at the mountain scale were outlined in this section. This new work involved two-dimensional simulations to address uncertainties that relate to the modification of UZ flow paths and fluxes, water and gas chemistry in the UZ, and the transport of radionuclides in the UZ. The results of these simulations, based on a limited range of input parameters, indicate that mineral precipitation/dissolution will not significantly affect the hydrologic properties and, therefore, the percolation flux compared to TH changes above the potential repository in the thermal and early post-thermal period. For comparison, TH effects on the percolation flux at the mountain scale are discussed in Section 3.3.5. Edge effects owing to gas convection produce mineral precipitation below the drifts (as a result of enhanced dryout) at the potential repository edge that is not observed in drift-scale THC simulations, as presented in *Drift-Scale Coupled Processes (DST and THC Seepage) Models* (BSC 2001 [DIRS 154677]). The ranges in water and gas compositions are wider than those predicted by the drift-scale THC models at a given time as a direct result of the edge effects. Whereas the range may be greater at a given time, the overall range in chemistry is comparable to that observed in the different drift-scale THC simulations over a longer time period. The range in pH of about 7 to 9 is strongly linked to changes in gas-phase carbon dioxide concentrations (relative to the ambient system away from the repository) that are much smaller in the higher-temperature potential repository center (and pH is higher) compared to the edges (which have somewhat elevated values and pH values down to approximately 7).

The important issues associated with the prediction of mountain-scale coupled THC processes have been summarized and their status assessed in this section; however, many uncertainties at the mountain-scale over extended time periods have yet to be addressed in a systematic fashion.

THC model validation, discussed in Section 4.3.6, encompasses some of the uncertainty issues, but large-scale issues related to conceptual model and data uncertainties (i.e., climate, infiltration, saturated zone effects, fault properties and conceptual models, and mineralogical and water chemistry variations) must be treated by simulating a range of possible conditions and by analysis and validation through study of natural analogues. THC processes at the drift-scale and at the laboratory-scale have been validated as discussed in Section 4.3.6. This work validates many aspects of the Mountain-Scale THC Model, but does not address the latter-mentioned parameters and processes. Uncertainties that arise out of ranges in parameters that have not been assessed can be further reduced through additional field thermal testing, laboratory experiments, and modeling. It should also be noted that the incorporation of new features or processes, such as heterogeneity, carry additional uncertainty to the simulations, even if they reduce other aspects of the uncertainty.

3.3.7 Thermal-Hydrologic-Mechanical Effects on Mountain-Scale Permeability

3.3.7.1 Introduction

This section presents a scoping simulation of the impact of THM processes on permeability at the mountain scale. This scoping work is documented in Bodvarsson (2001 [DIRS 154669], Attachment 9, pp. 1 to 78). The THM effect around the potential repository has largely been ignored in simulations of mountain-scale flow and was not included in the TSPA-SR (CRWMS M&O 2000 [DIRS 153246]). The uncertainty introduced by the assumption that THM processes have little impact on mountain-scale flow is addressed in this section.

3.3.7.2 Goal of Thermal-Hydrologic-Mechanical Model for Flow on the Mountain Scale

THM model studies are being conducted to provide insight into how mechanical stresses arising from the decay heat of the repository will affect rock mass permeability. These studies are intended to allow an assessment of how the permeability changes caused by THM coupled processes will affect the flow on the mountain scale from the land surface to the water table.

3.3.7.3 Model Development

The coupled THM study was performed using a joining of two codes: TOUGH2 V1.5 and FLAC 3D V2.0. This joint code is referred to as the "TOUGH-FLAC" code (Bodvarsson 2001 [DIRS 154669], Attachment 9, pp. 1 to 43). The two well-established codes were joined through three carefully designed linkage routines (Delb.dat V1.0, Gpzones.dat V1.0, and tin.dat V1.0). The first code is TOUGH2 V1.5, which incorporates the dual-permeability (fracture and matrix continua) approach. It has been proven successful in predicting the temperature and moisture distribution of field experiments at Yucca Mountain, including the Single Heater Test (CRWMS M&O 1999 [DIRS 129261], Section 12) and the Drift Scale Test (CRWMS M&O 2000 [DIRS 151964], Section 7). The second code is the industry-standard FLAC3D V2.0, which calculates fractured rock and soil mechanical processes in a continuum model.

The general conceptual model for THM processes may be described as a multiphase, non-isothermal and deformable medium where voids of the rock skeleton are filled partially with liquid water and partially with gas. Thus, it is a three-phase system (gas, liquid, and solid) where each of the fluid phases has two components (water and air). The gas phase is modeled as an

ideal gas mixture composed of dry air and water vapor, and the liquid phase consists of water and dissolved air. The mechanical behavior of the porous and fractured media responses to changes in temperature, skeletal effective stress, and strain is modeled with accompanying porosity and permeability changes. Coexisting fluid and solid components are assumed to be in local thermal equilibrium (i.e., locally they are at the same temperature). While a few main fractures may be discretely defined within a rock matrix, the main part of the fractured porous rock is treated as a single continuum or dual continuum (fracture system and matrix blocks). In a dual-continuum model, the temperature and pressure may be different in the matrix and fractures, while the total stress (as opposed to the effective stress) is assumed to be same in both continua. Four types of conservation equations are needed to fully describe such systems, including two mass-balance equations for the two fluid components, one energy-balance equation, and one momentum-conservation equation of rock deformation forces.

The fluid mass-balance equation of a coupled hydraulic and mechanical system can be rigorously derived by combining the fluid mass-conservation equation with the solid mass-conservation equation, considering the relative motion of the fluid to the moving solid, according to Rutqvist et al. (2001 [DIRS 154587]). In such a case, the volumetric strain in the mass-balance equation is coupled to the force-balance equation through Biot's storage and effective stress parameters (Biot 1941 [DIRS 121082]), and the final equations are solved simultaneously in a fully coupled model. In general, a reservoir engineering approach can be used by accounting for rock deformation changing the porosity. However, in the current application, a simpler approach of estimating change in porosity, and hence permeability, from a change in stress is used by adopting an empirical nonlinear relationship. Such an approach implies that the TOUGH2 V1.5 and FLAC3D V2.0 codes can be used in their standard versions, but linked together through numerically calculated porosity, permeability, and effective stress changes. The codes are executed iteratively, with transfer of data through external linking modules. Through various iterative schemes, either explicit or implicit sequentially coupled solutions can be achieved.

The model has been calibrated and partly validated against hydromechanical and thermomechanical data from the niche tests, and the Drift Scale Test. The thermomechanical responses (displacements caused by thermal expansion of rock) in the early time of the drift scale models simulation are within the range of measurements at the drift scale heater test (Bodvarsson 2001 [DIRS 154669], Attachment 9, p. 64). A calibration of the relationship between stress and permeability for the drift scale calibrated hydrogeological properties is described in Section 4.3.7.4.3. A similar calibration of the stress-permeability relation was conducted for this mountain scale model as described in the next section.

3.3.7.4 Application and Results on Mountain-Scale Flow

The model domain is designed by first taking a multiple-layered column extending vertically from the ground surface down to the water table. The vertical layering for the model is chosen to correspond to the vertical contacts at the Nevada State Plane Coordinates 170572.39 m (Easting) and 233194.536 m (Northing) used in *Development of Numerical Grids for UZ Flow and Transport Modeling* (CRWMS M&O 2000 [DIRS 114277], Attachment VI; DTN: LB990701233129.001 [DIRS 106785]). These coordinates represent an interior point near the center of the potential repository location. The layers are extended horizontally to form a two-dimensional section that runs along the northwest direction exactly normal to the

emplacement drifts in the TSPA-SR UZ site-scale model (CRWMS M&O 2000 [DIRS 114277]). The cross-sectional length of the repository along this section is approximately 4.2 km, and the section contains 53 emplacement drifts. The left boundary of the two-dimensional model domain is at the center of the repository, which has a half-symmetric length of 2,106 m (26.5 canisters spaced 81 m apart). This left boundary is closed to heat and fluid flow by symmetry and is allowed zero normal displacement mechanically (i.e., on rollers). The right boundary is set at a distance of 3,000 m from the right edge of the repository. At this boundary, a constant stress is maintained with a gradient according to Table 3.3.7-1, and no heat or fluid flow can cross it. The top boundary is the land surface at constant temperature and free to move mechanically, while the bottom boundary is at the water table, which is at constant temperature and on rollers mechanically.

The input hydraulic and thermal parameters for the layers are based on the mountain-scale calibrated property set presented in *Calibrated Properties Model* (CRWMS M&O 2000 [DIRS 144426], Section 6.1.4). The model input thermal parameters are modified to include effects of lithophysal cavities in the tsw33 and tsw35 hydrogeologic units, as shown in Table 4.3.5-1. Mechanical and thermal-mechanical (TM) parameters for TM rock mass units are extracted from *TBV-332/TBD-325 Resolution Analysis: Geotechnical Rock Properties* (CRWMS M&O 1999 [DIRS 126475], Section 7.2.3). In the present simulation, the below-boiling thermal operation mode is studied (Bodvarsson 2001 [DIRS 154669], Attachment 9, pp. 1 to 78). This is effected by imposing an initial thermal load of 67.7 kW/acre (1.35 kW/m of drift) with a forced ventilation period of 300 years, during which 80 percent of the heat is assumed to be removed. The thermal load is imposed on 26.5 drift elements located 81 m apart along the 2,106-m long repository at level 1080.3 m in the tsw35 hydrogeologic unit (the lower lithophysal unit of the Topopah Spring welded tuff). The half drift is located at the mid-symmetry line on the left side of the model.

THM-related parameter data used and their sources are shown in Table 3.3.7-1. These parameters are the same as those used for the drift scale model in Section 4.3.7, except that the parameters b_{max} and α have been re-calibrated for a higher mountain scale rock mass permeability. In this simulation conservative values of b_{max} and α were assumed corresponding to the strongest permeability increases observed at the niche experiment and to the strongest permeability decreases observed at the Drift Scale Test (Bodvarsson 2001 [DIRS 154669], Attachment 9, pp. 45 to 49). Thus, this model simulation does not cover the entire uncertainty range of hydromechanical properties, but is a conservative one.

Results of this simulation show that temperatures peak at about 800 to 1,600 years after emplacement, depending on locations and input conditions. The temperature distribution at 1,000 years is shown in Figure 3.3.7-1. As expected, temperature contours center around the repository. Figure 3.3.7-2 shows the horizontal stress distribution at 1,000 years. In this figure, a contour line marked by an arrow, separates a region of thermal compression (negative values) near the repository and a region of tension (positive values) near the land surface. The result is caused by the interaction between the horizontal stress imposed on the right boundary at 5,000 m and the mechanically free boundary at the land surface. Vertical stress distribution, which is not shown, has horizontal contours indicating stress variation due to the thickness of overburden.

Corresponding to the calculated stress distributions, Figures 3.3.7-3 and 3.3.7-4 show the changes in vertical and horizontal permeabilities caused by the THM effects. There is a decrease in permeability near the repository by a factor of about four and an increase in permeability in the layers near the land surface. Table 3.3.7-2 shows the changes in permeability for the various hydrostratigraphic layers. They are different for the different layers because the permeability change is a function of the initial permeability of each layer. The percentage change is larger for a layer with lower initial permeability. A calibration study related to this behavior using ESF niche test data is discussed in Section 4.3.7.4.3.

Overall, the permeability changes (Table 3.3.7-2) are moderate, ranging from a factor of 0.28 to 2.75 except for part of the most shallow layer near the land surface, where a factor of 38 was found. This latter value may be highly uncertain due to the vicinity of the free land surface. However, layers near the land surface do not play a critical role in the flow pattern at the mountain scale.

The modeled changes in permeability in the far field are due to elastic deformation and therefore are reversible upon cooling. Inelastic deformation and permanent changes in permeability may occur near the drifts as discussed in Section 4.3.7.5. Permeability changes due to rockfall are discussed in Section 4.3.7.4.

3.3.7.5 Abstraction of Total System Performance Assessment

The work reported in this section is devoted to evaluating process model simulations and uncertainties. Simulation results for this study are not yet used to support any abstraction models for the TSPA. The results obtained so far show changes of permeability resulting from THM processes below one order of magnitude, and are different for different hydrostratigraphic layers.

3.3.7.6 Multiple Lines of Evidence

The impact of THM processes on the performance of a potential high-level radioactive waste repository has been assessed through field studies at a variety of underground sites. At the Nevada Test Site, a series of TM/THM experiments were conducted in the G-tunnel in Rainer Mesa. Results show a direct relationship between thermal input and fracture permeability changes. Thus, increasing temperature on a rock block under triaxial confinement lowered the apparent permeability of a single fracture from 234 to 89 microdarcies (Hardin and Chesnut 1997 [DIRS 100534], pp. 4 to 6). Further, THM effects were also observed in experiments at the Stripa mines in Sweden. Fracture closure and reduction in permeability were confirmed by observation of diminished water inflow to heater and instrument boreholes (Nelson et al. 1981 [DIRS 150092]).

In addition to these experiments, corroborative results on coupled THM effects may be found in the geothermal literature. A survey of geothermal reservoir properties worldwide (Björnsson and Bodvarsson 1990 [DIRS 154606]) showed a correlation between permeability and temperature for various geothermal systems (Figure 3.3.7-5). The values are scattered, but they indicate a trend of decreasing permeability with increasing temperature. The low permeability at temperatures around 300°C and above is more likely caused by geochemical effects. The THM effects may be present at lower temperature. The straight-line fit through the points has a

regression coefficient of 0.5 (Bodvarsson 2001 [DIRS 154669], Attachment 4, p. 36) and shows a half-an-order decrease of permeability with a 100°C rise in temperature.

3.3.7.7 Summary of Uncertainties and Their Treatment

Table 3.3.7-3 provides a summary of the uncertainty issues related to THM effects on mountain-scale flow and their treatment.

3.3.7.8 Summary and Conclusions

A coupled THM continua code, which is a linkage of the TOUGH2 V1.5 and FLAC3D V2.0 codes through carefully designed interface routines, has been applied to the simulation of permeability changes in a region around a potential repository from the ground surface to the water table. Prior to this set of calculations, no fully coupled THM modeling had been done for the conditions at Yucca Mountain (i.e., unsaturated, highly fractured rock with heat input). Therefore, the uncertainty is unbounded. The results of the present study indicate compression near the repository and expansion from the land surface above the repository down to an elevation of 1,290 m. These cause corresponding changes in permeability. Table 3.3.7-2 shows the calculated changes in vertical and horizontal permeability values for the lower-temperature operating mode. The calculation was conducted with hydromechanical properties, conservatively calibrated against the geologic layers near the land surface that do not play a critical role in the flow pattern at the mountain scale. These changes are moderate, probably without significant impact on the TSPA for the potential repository. However, uncertainties remain for the higher-temperature operation mode and for more realistic geometries, as indicated in Table 3.3.7-3. The uncertainties will be further bounded as new heater test data become available and the model is updated.

INTENTIONALLY LEFT BLANK

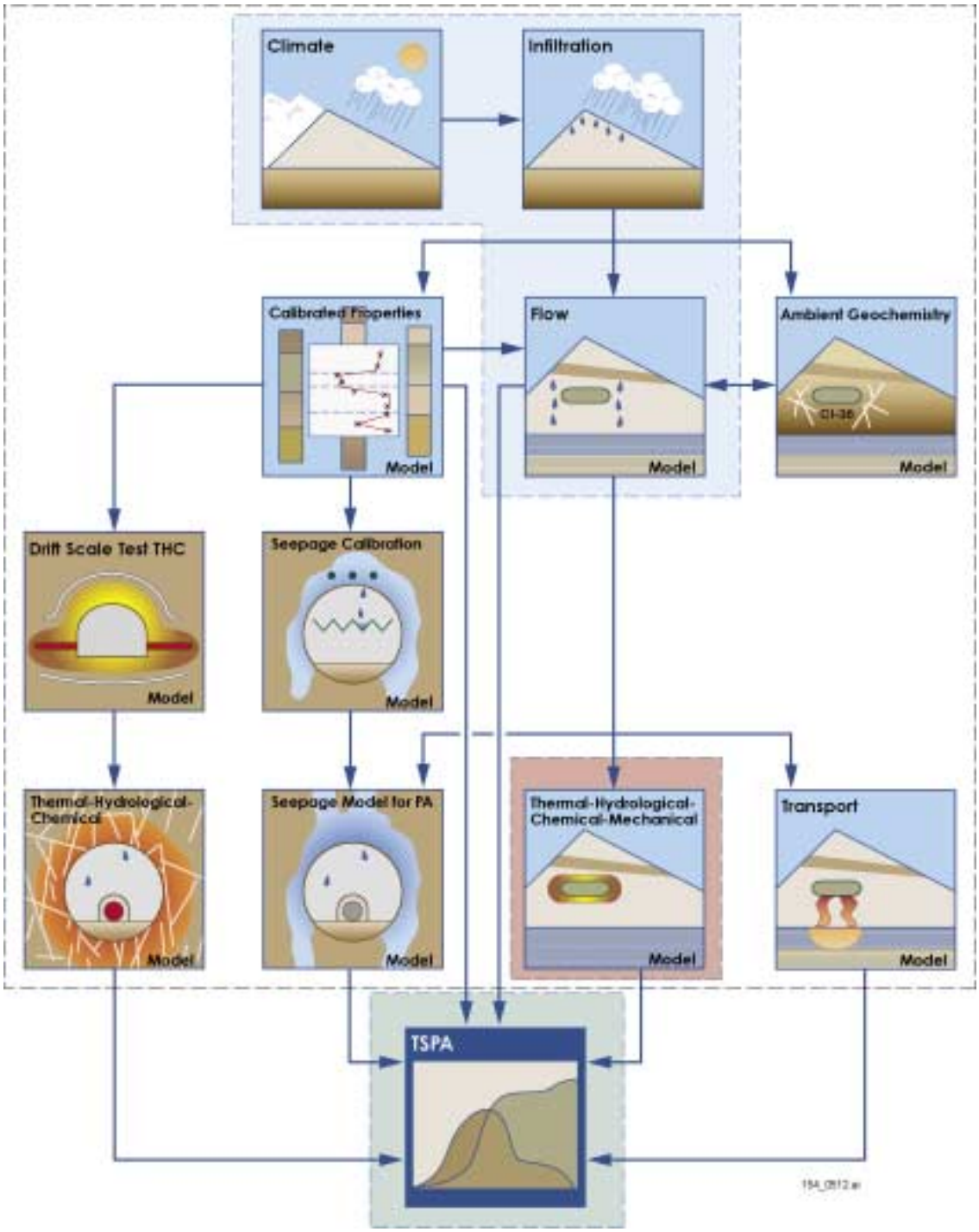

154_0512.ai

Source: Modified from CRWMS M&O 2000 [DIRS 151940], Figure 1-2.

NOTE: Most models relevant to this section are highlighted with color backgrounds.

Figure 3.1-1. Main Models Included in the Unsaturated Zone Process Model Report, Interrelations among them, and Connections to Total System Performance Assessment

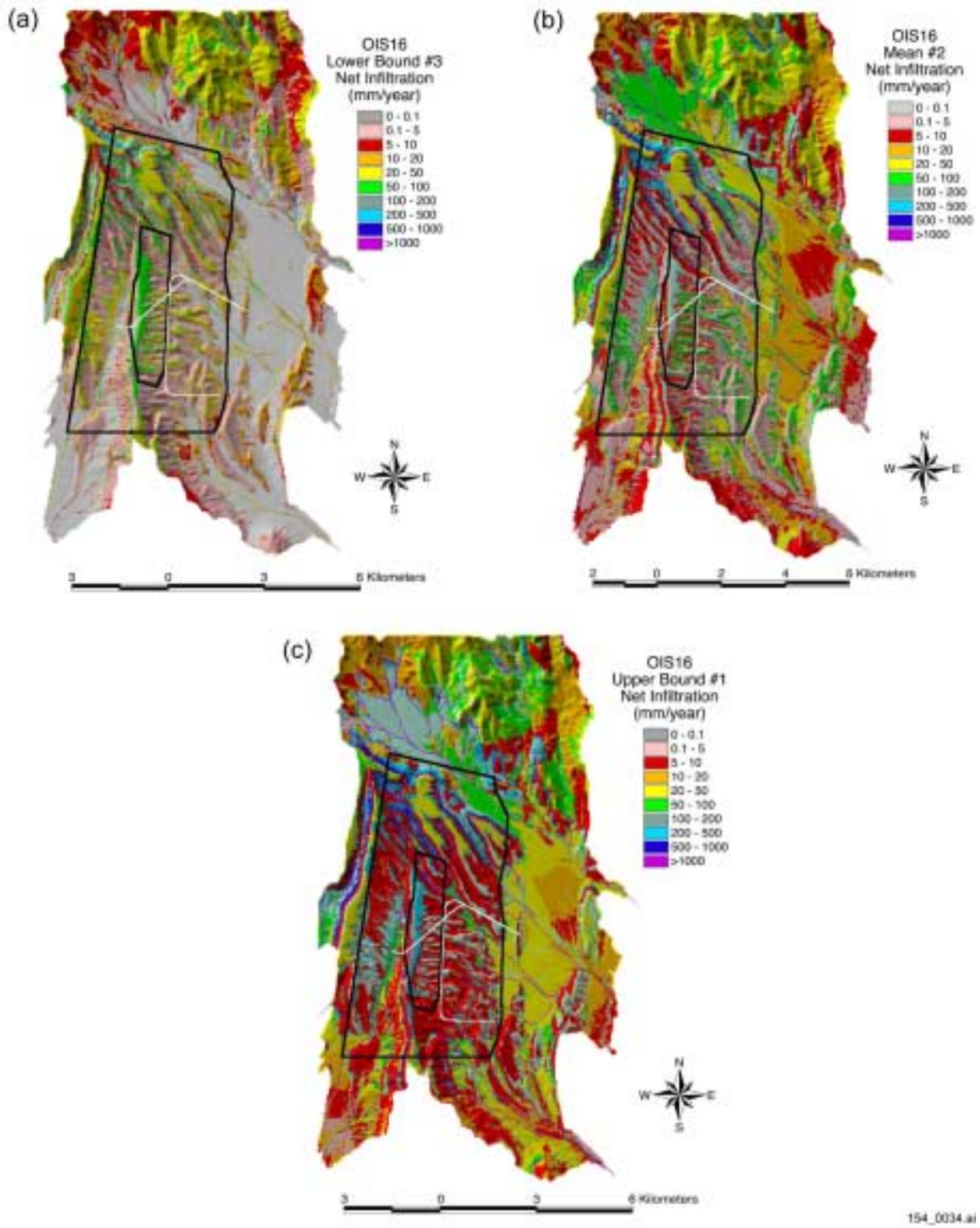

154_0034.ai
Source: BSC 2001 [DIRS 154873].

NOTE: Infiltration for lower (a), mean (b), and upper (c) bounds.

Figure 3.3.2-1. Net Infiltration for the Glacial Stage 6/16-Climate Scenario

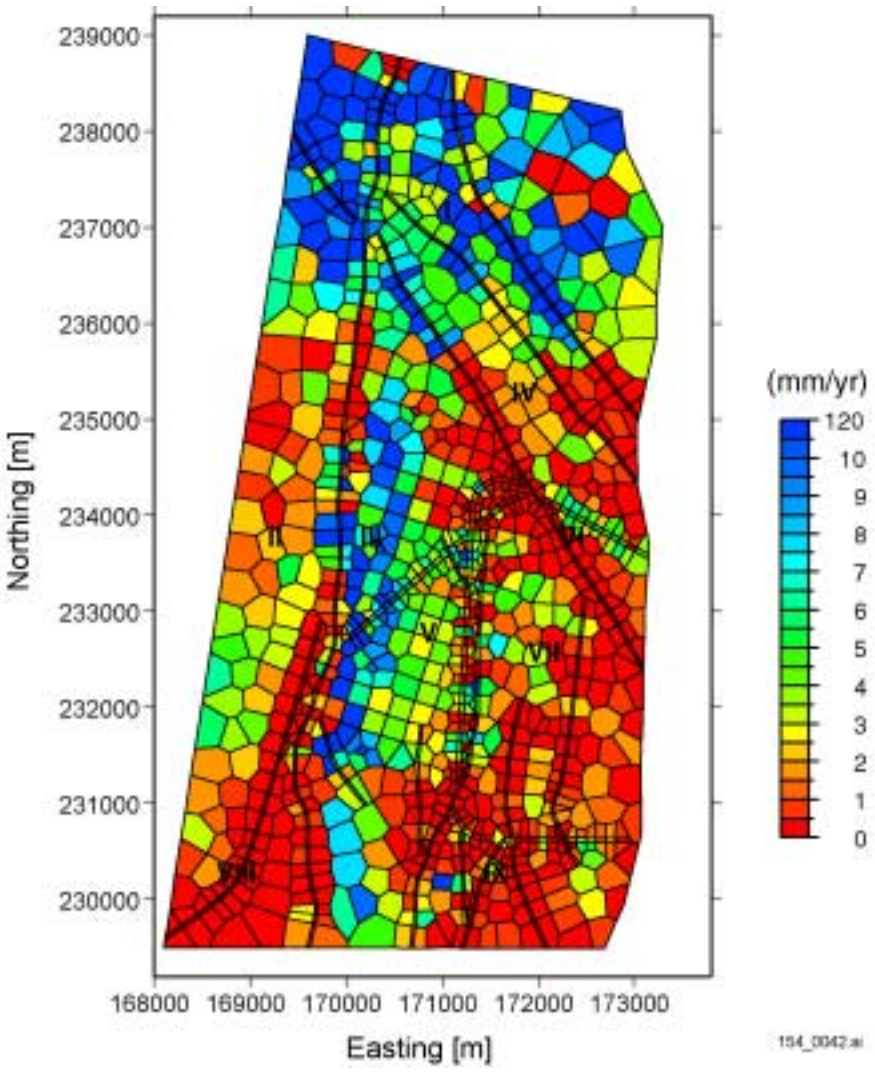

154_0042.ai

Source: DTN: GS000399991221.002 [DIRS 147022].

NOTE: Nevada coordinates in meters.

Figure 3.3.3-1. Present-Day Mean Net Infiltration

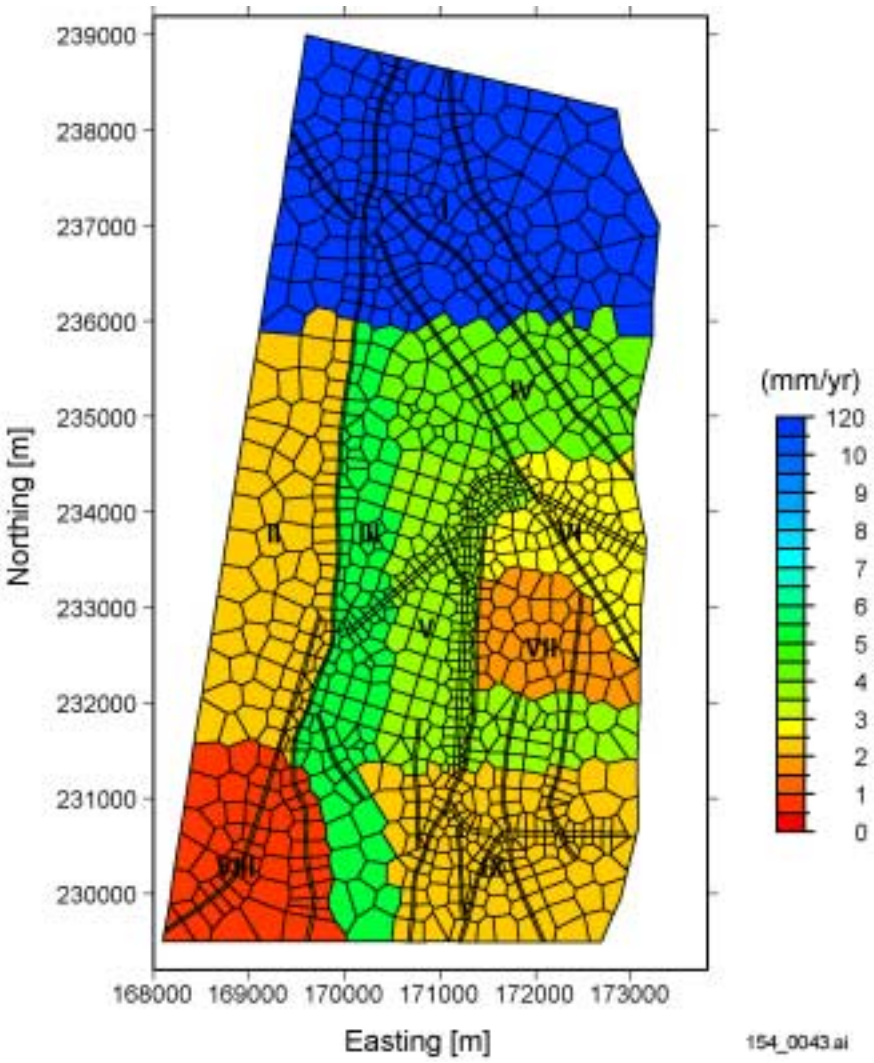

154_0043.ai

Source: Bodvarsson 2001 [DIRS 154669], Attachment 11, listed on p. 80.

NOTE: Uniform net infiltration in each region. Nevada coordinates in meters.

Figure 3.3.3-2. Chloride-Based, Present-Day Mean Net Infiltration

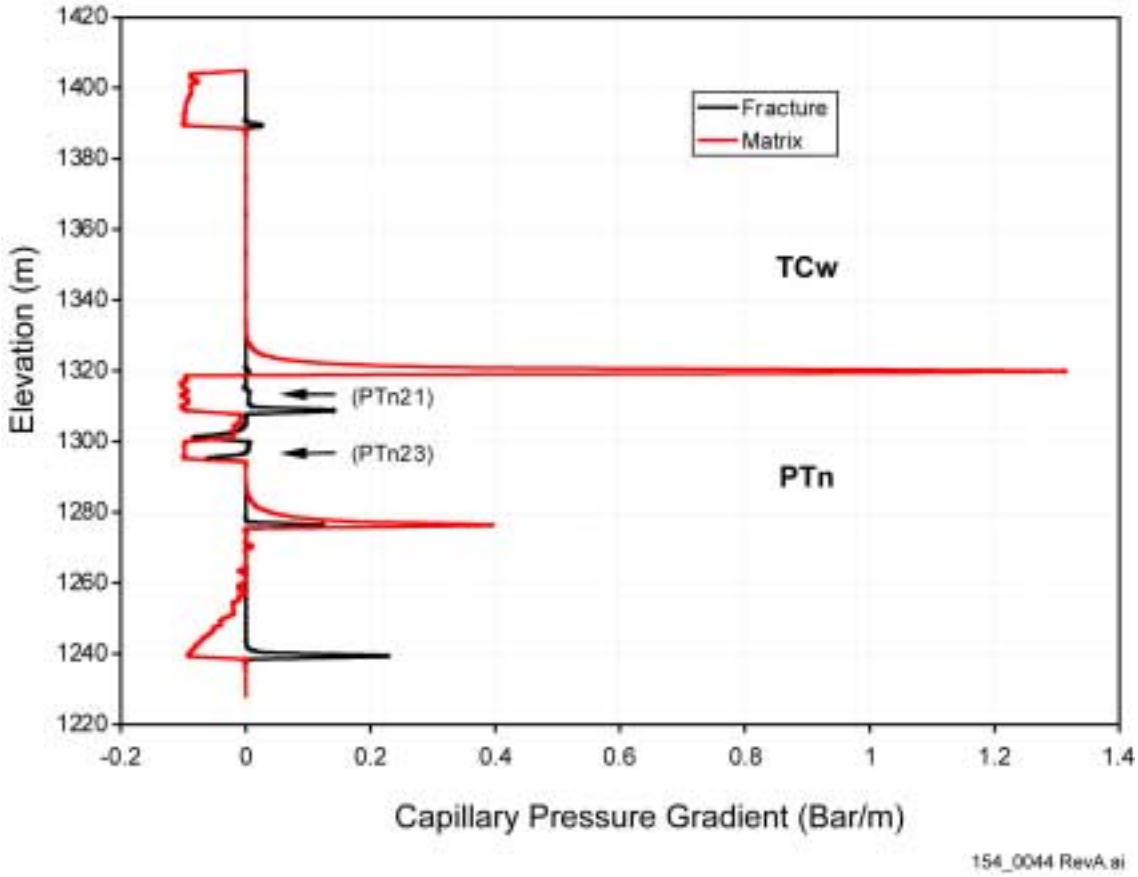

154_0044 RevA.ai

Source: Wu et al. 2001 [DIRS 154918], Figure 4.1-5.

NOTE: Capillary pressure measured in bar/m at coordinates 171200E, 235119N (coordinates using refined grid).

Figure 3.3.3-3. Vertical Capillary Pressure Gradients

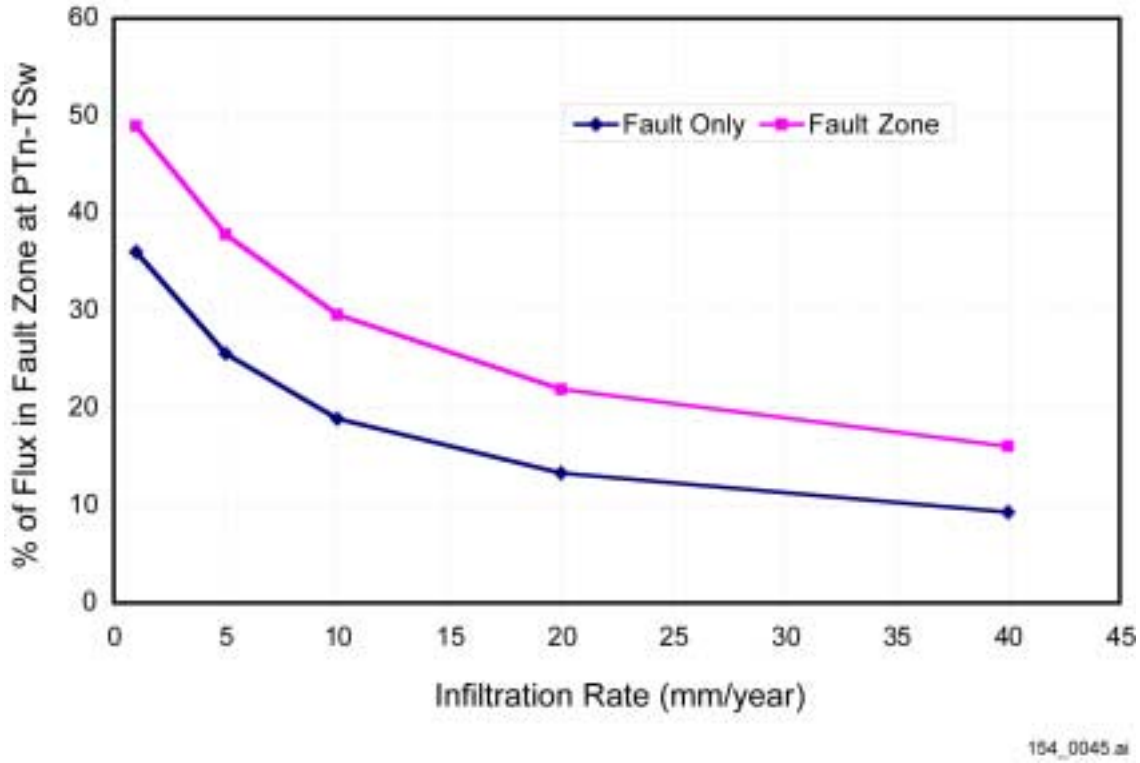

154_0045.ai

Source: Wu et al. 2001 [DIRS 154918].

NOTE: Effects of net infiltration values on percentage of flow through faults and fault zones, reflecting the amount of lateral water flow within the PTn unit along a vertical cross section, using the refined grid and uniform surface net infiltration pattern.

Figure 3.3.3-4. Effect of Net Infiltration on Percentage of Flow-Through Faults and Fault Zones

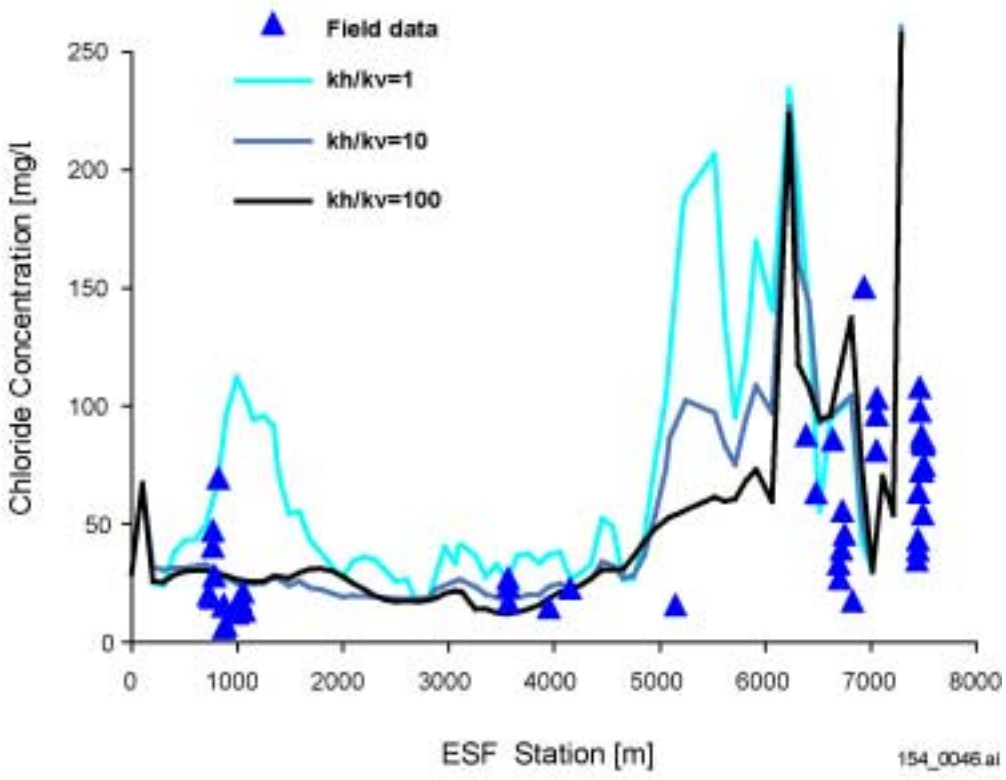

154_0046.ai

Source: Bodvarsson 2001 [DIRS 154669], Attachment 11, listed on p. 79.

NOTE: ESF = Exploratory Studies Facility; kh = horizontal permeability; kv = vertical permeability.

Figure 3.3.3-5. Effect of Horizontal Permeability on the Modeled Concentrations of Chloride in the Exploratory Studies Facility

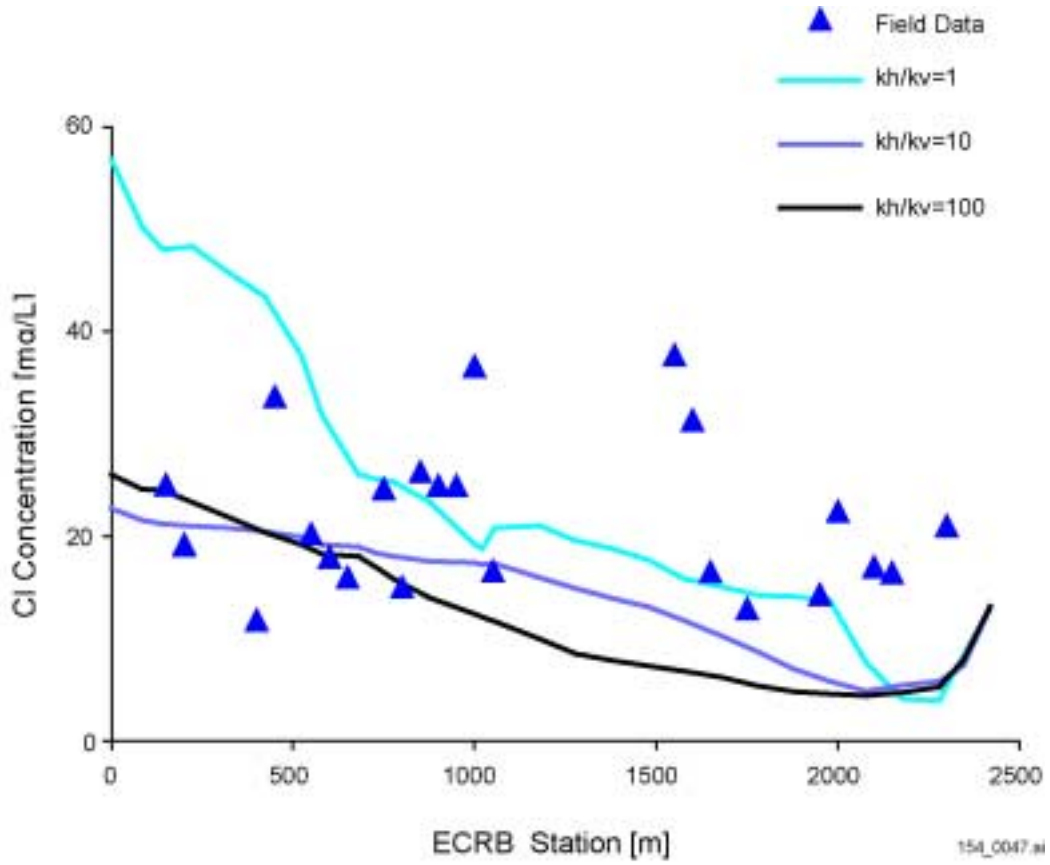

154_0047.ai

Source: Bodvarsson 2001 [DIRS 154669], Attachment 11, listed on p. 79.

NOTE: Model assumes infiltration at present-day mean rates. Cl = chloride; ECRB = Enhanced Characterization Repository Block.

Figure 3.3.3-6. Effect of Horizontal Permeability on the Modeled Concentrations of Chloride in the Enhanced Characterization Repository Block

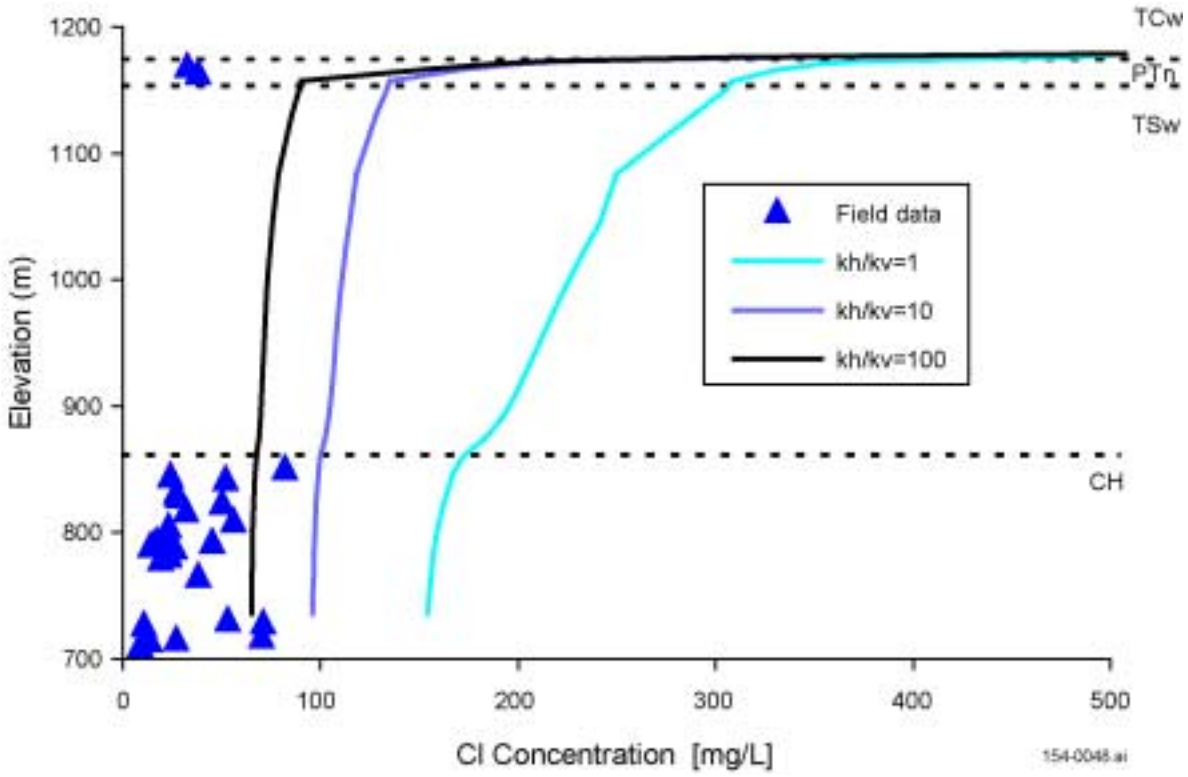

154_0048.ai

Source: Bodvarsson 2001 [DIRS 154669], Attachment 11, listed on p. 79.

Figure 3.3.3-7. Effect of Horizontal Permeability on the Modeled Concentrations of Chloride in Borehole UZ#16.

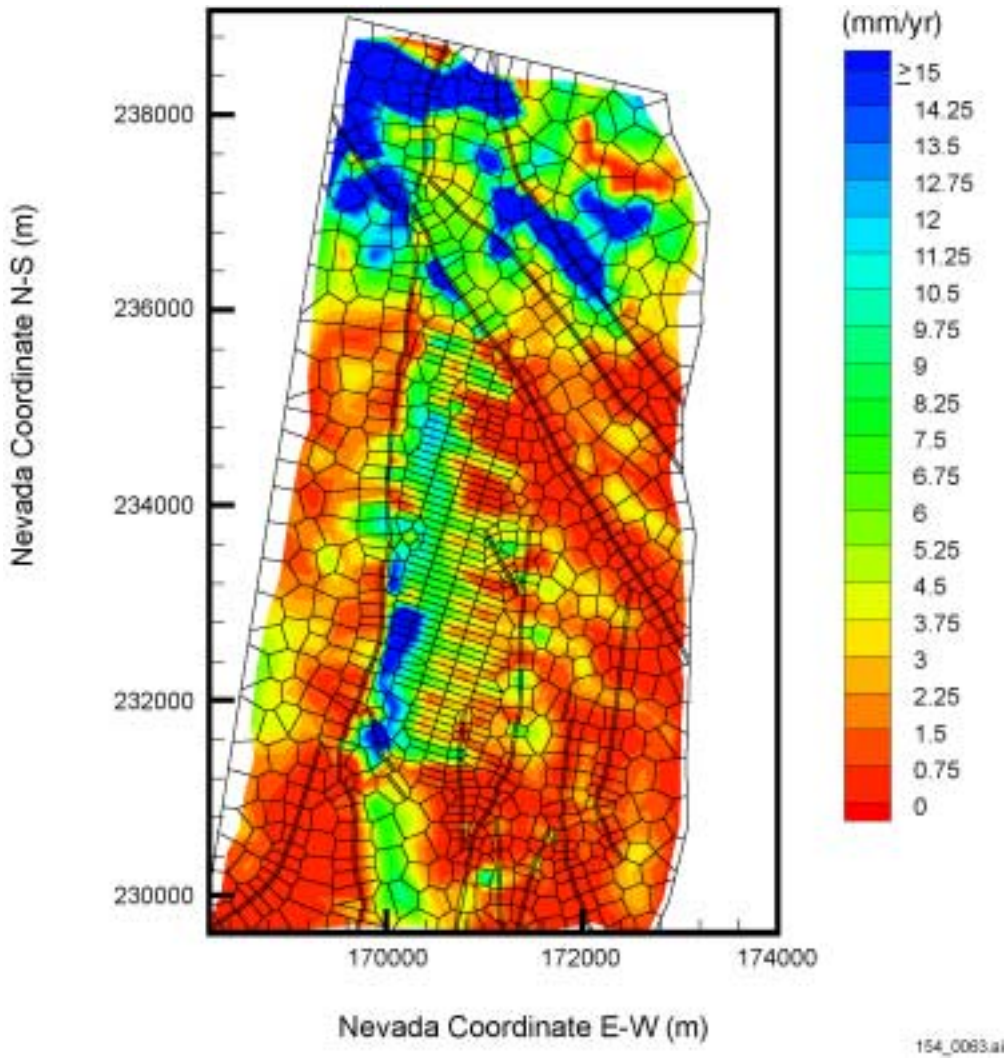

154_0063.ai

Sources: CRWMS M&O 2000 [DIRS 122797], Figure 6-3; DTN: GS000399991221.002 [DIRS 147022]; DTN: LB990801233129.003 [DIRS 122757].

NOTE: Simulation uses present-day, base-case, mean infiltration.

Figure 3.3.4-1. Plan View of Total System Performance Assessment Grid and Net Infiltration Distributed Over the Domain of the Unsaturated Zone Model

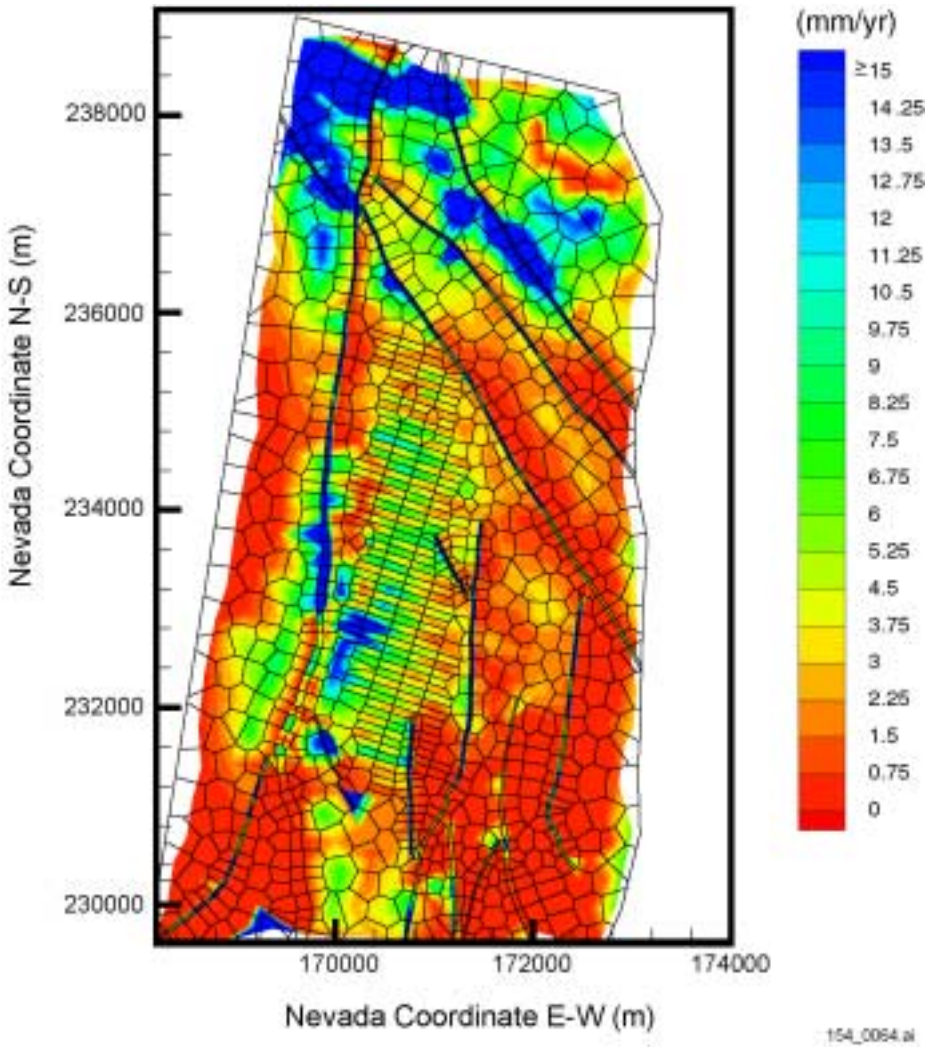

154_0064.ai

Source: CRWMS M&O 2000 [DIRS 122797], Figure 6-42.

NOTE: Simulation uses present-day, mean infiltration.

Figure 3.3.4-2. Simulated Percolation Flux at the Repository Horizon for the Flow-Through Perched Water Conceptual Model

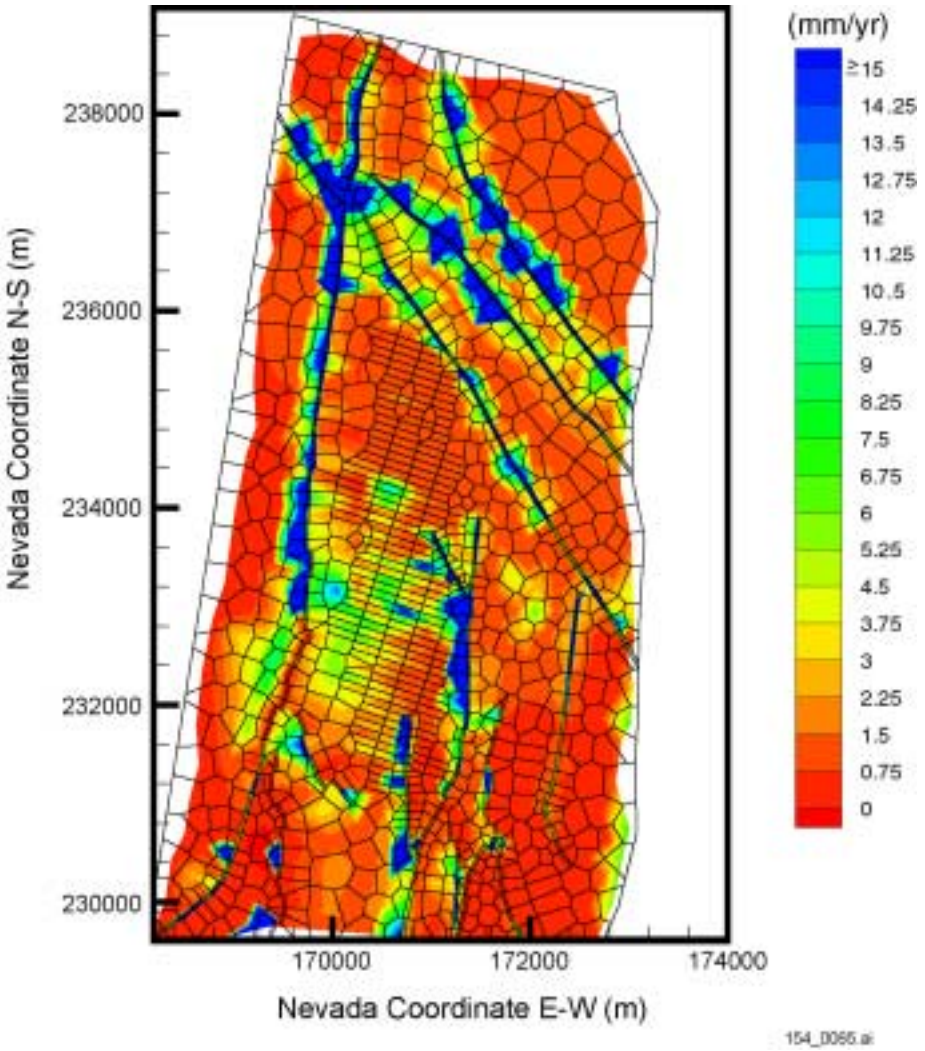

154_0065.ai

Source: CRWMS M&O 2000 [DIRS 122797], Figure 6-45; DTN: LB990801233129.003 [DIRS 122757].

NOTE: Simulation uses present-day, mean infiltration.

Figure 3.3.4-3. Simulated Percolation Flux at the Water Table for the Flow-Through Perched Water Conceptual Model

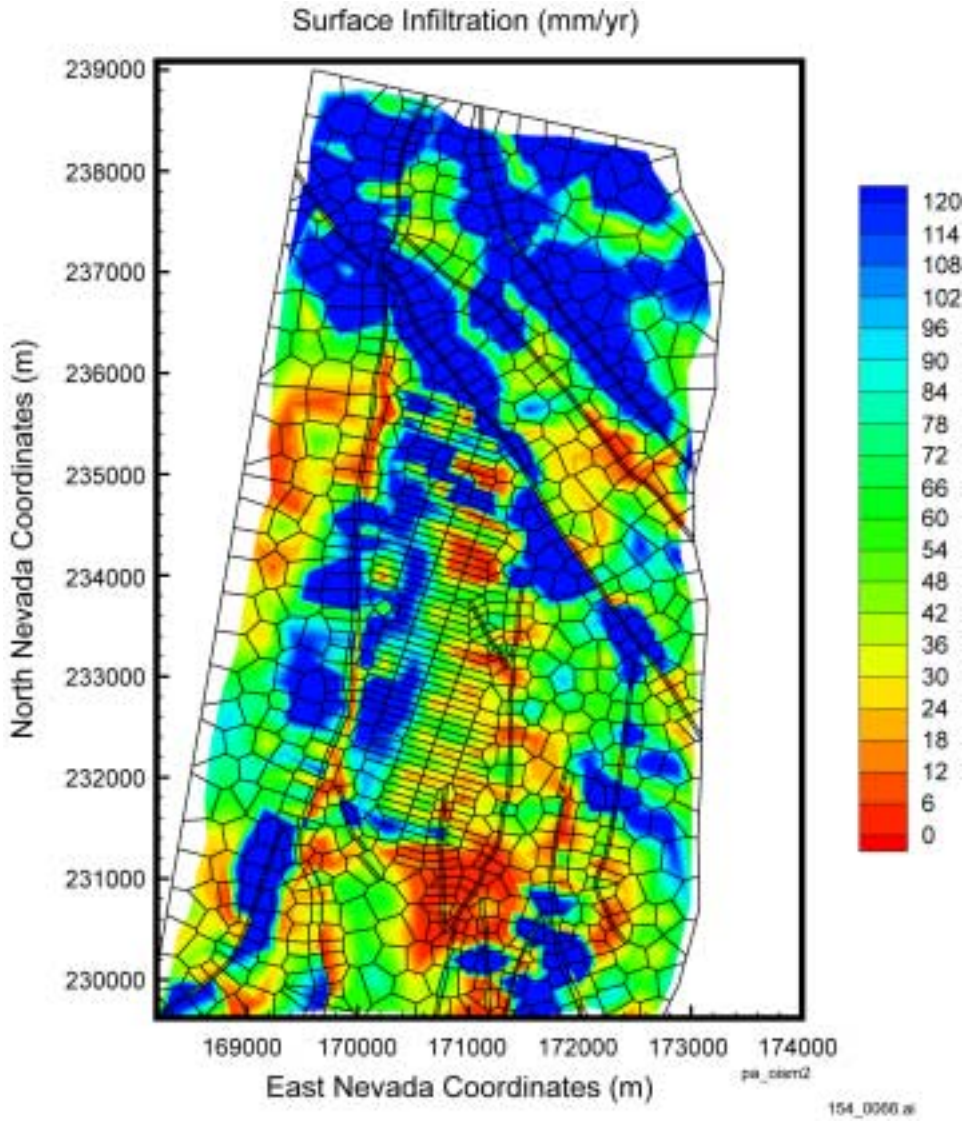

154_0066.ai

Source: Preliminary work described by Bodvarsson 2001 [DIRS 154669], Attachment 12, pp. 208 to 209; also based on data associated with BSC 2001 [DIRS 154564].

NOTE: Model assumes the full-glacial, mean #2 infiltration scenario.

Figure 3.3.4-4. Plan View of Net Infiltration Distributed Over the Domain of the Three-Dimensional Unsaturated Zone Total System Performance Assessment Model

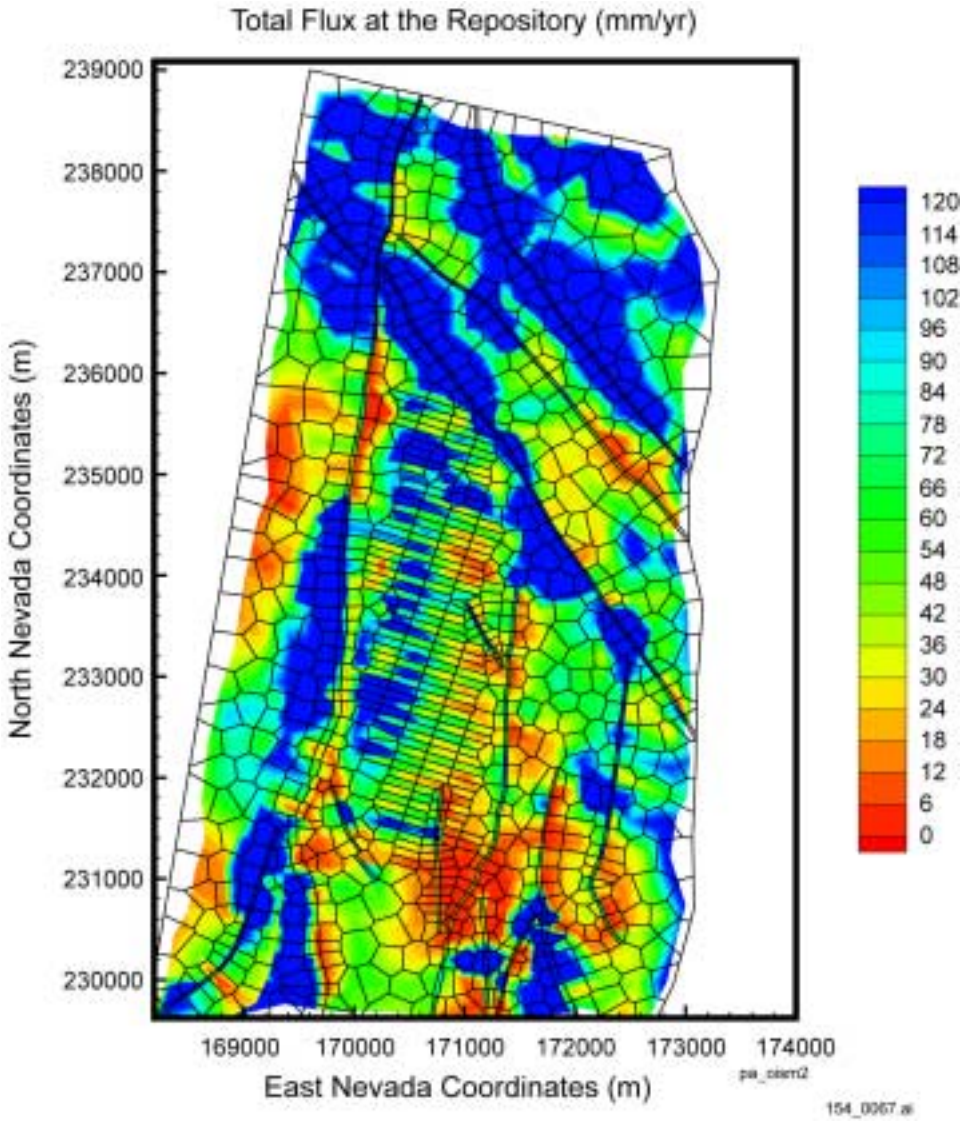

154_0067.ai

Source: Preliminary work described by Bodvarsson 2001 [DIRS 154669], Attachment 12, file listed on p. 209.

NOTE: Simulation uses the flow-through perched water conceptual model.

Figure 3.3.4-5. Simulated Percolation Flux at the Potential Repository Horizon under the Full-Glacial, Mean #2 Infiltration Scenario

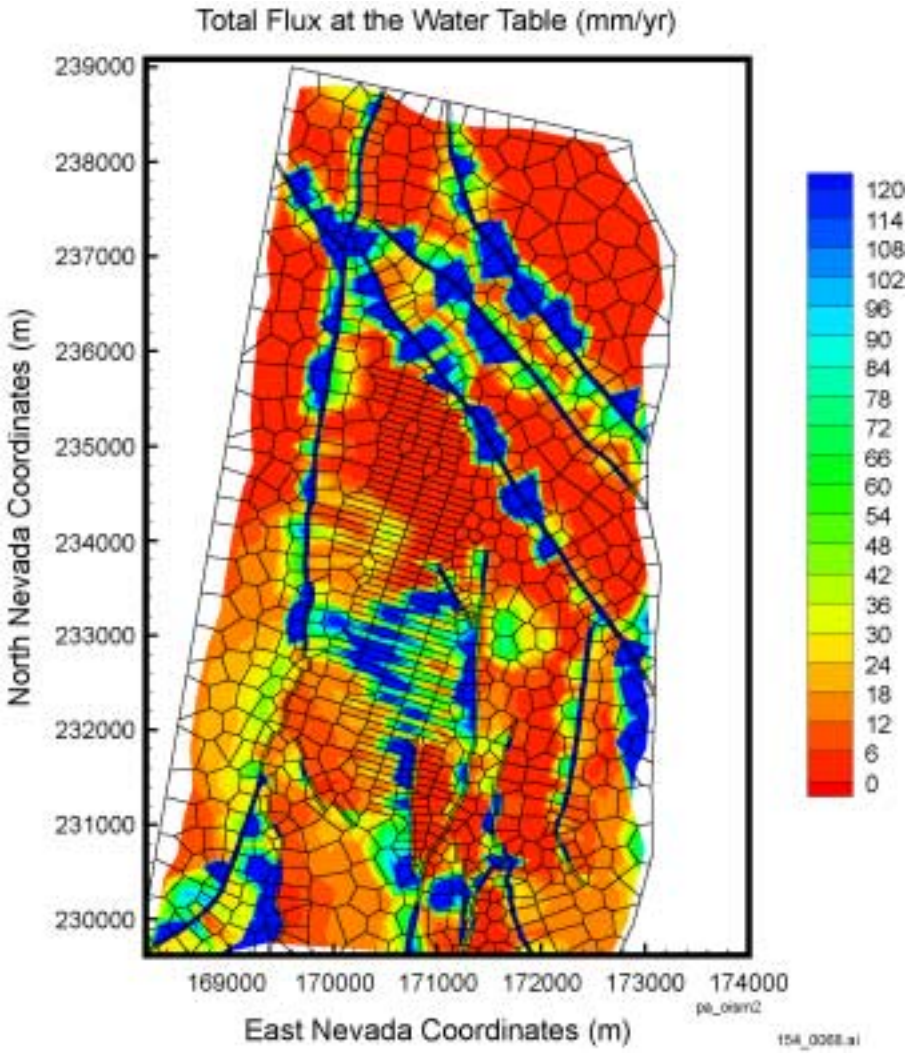

154_0068.ai

Source: Preliminary work described by Bodvarsson 2001 [DIRS 154669], Attachment 12, file listed on p. 209.

NOTE: Simulation uses the Flow-Through Perched Water Conceptual Model.

Figure 3.3.4-6. Simulated Percolation Flux at the Water Table under the Full-Glacial, Mean #2 Infiltration Scenario

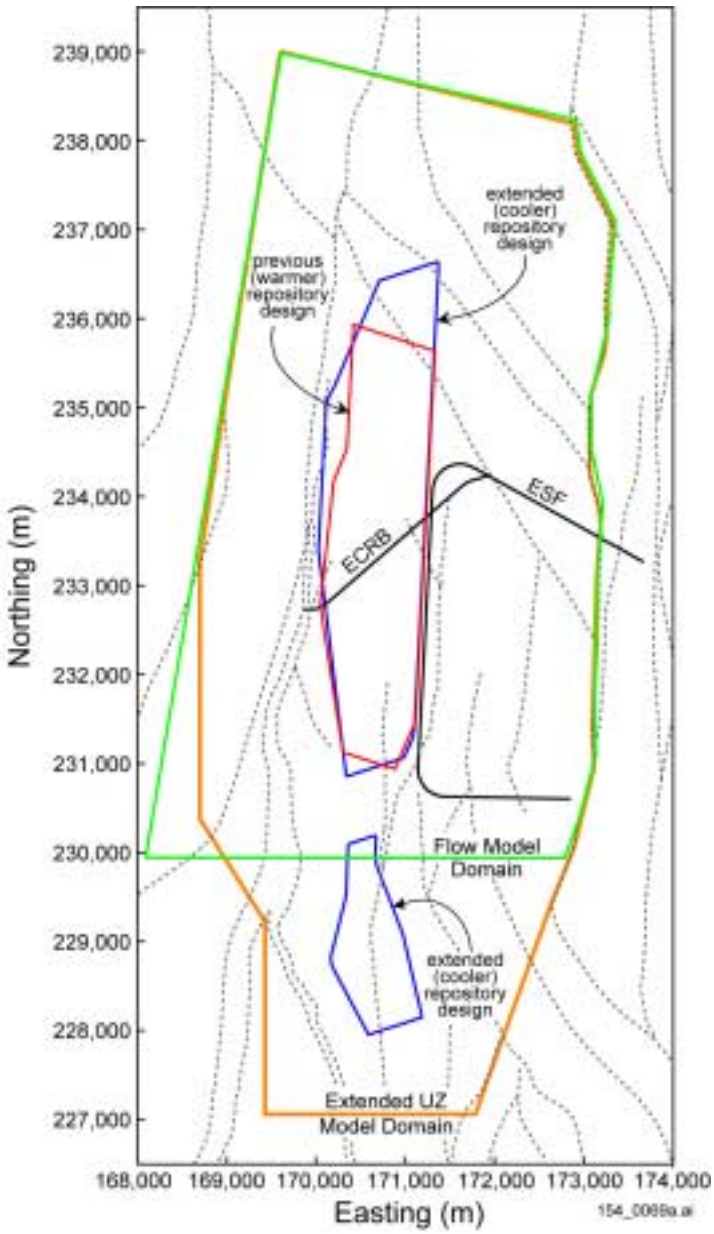

154_0069a.ai

Sources: DTN: MO9901MWDGFM31.000 [DIRS 103769]. References for repository layouts: Extended BSC 2001 [DIRS 154548]; Previous CRWMS M&O 1997 [DIRS 100245].

NOTE: Dotted lines represent faults as mapped in the Geologic Framework Model version 3.1. Nevada coordinates in meters. ECRB = Enhanced Characterization of the Repository Block; ESF = Exploratory Studies Facility; UZ = unsaturated zone.

Figure 3.3.4-7. Plan View of Unsaturated Zone Model Domains and Potential Repository Layouts

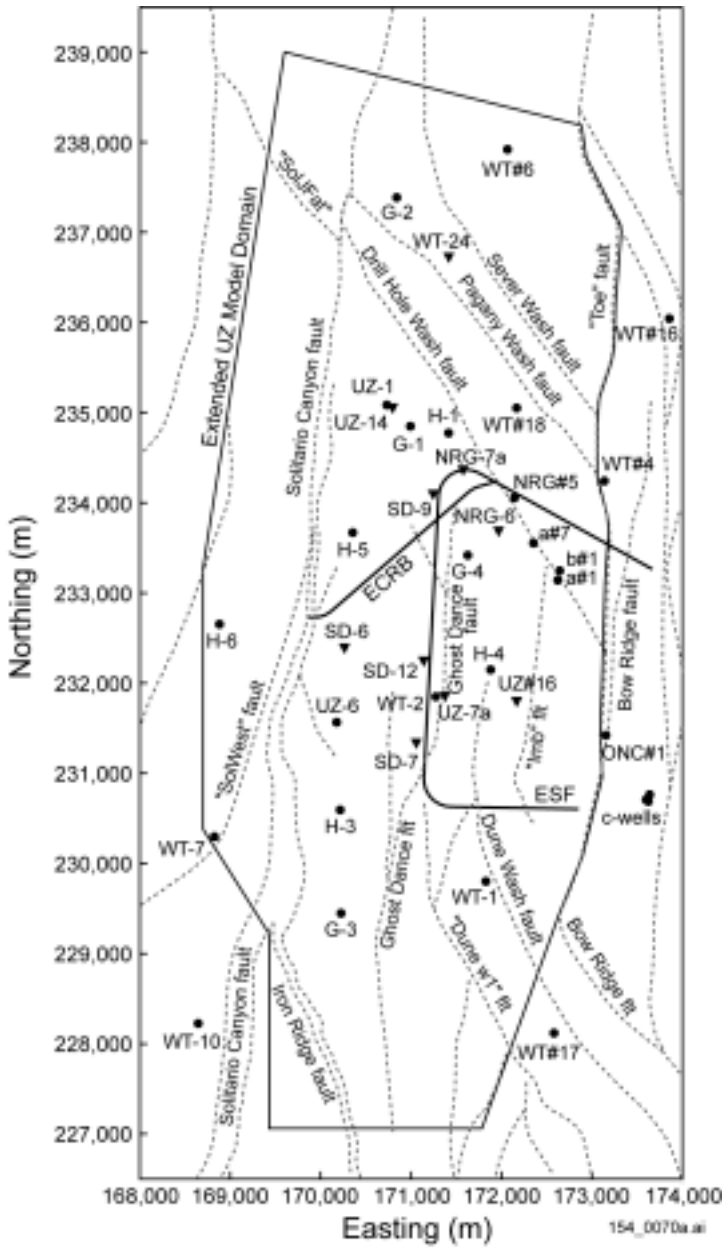

154_0070a.ai

Source: CRWMS M&O 2000 [DIRS 138860].

NOTE: Triangles represent wells from which qualified hydrogeologic rock property data were collected. Circles and triangles represent wells used to develop the geologic framework model. Dotted lines indicate fault traces per Geologic Framework Model version 3.1. Nevada coordinates in meters. ECRB = Enhanced Characterization of the Repository Block; ESF = Exploratory Studies Facility; UZ = unsaturated zone.

Figure 3.3.4-8. Data Locations Characterizing Repository Host Horizon Layers

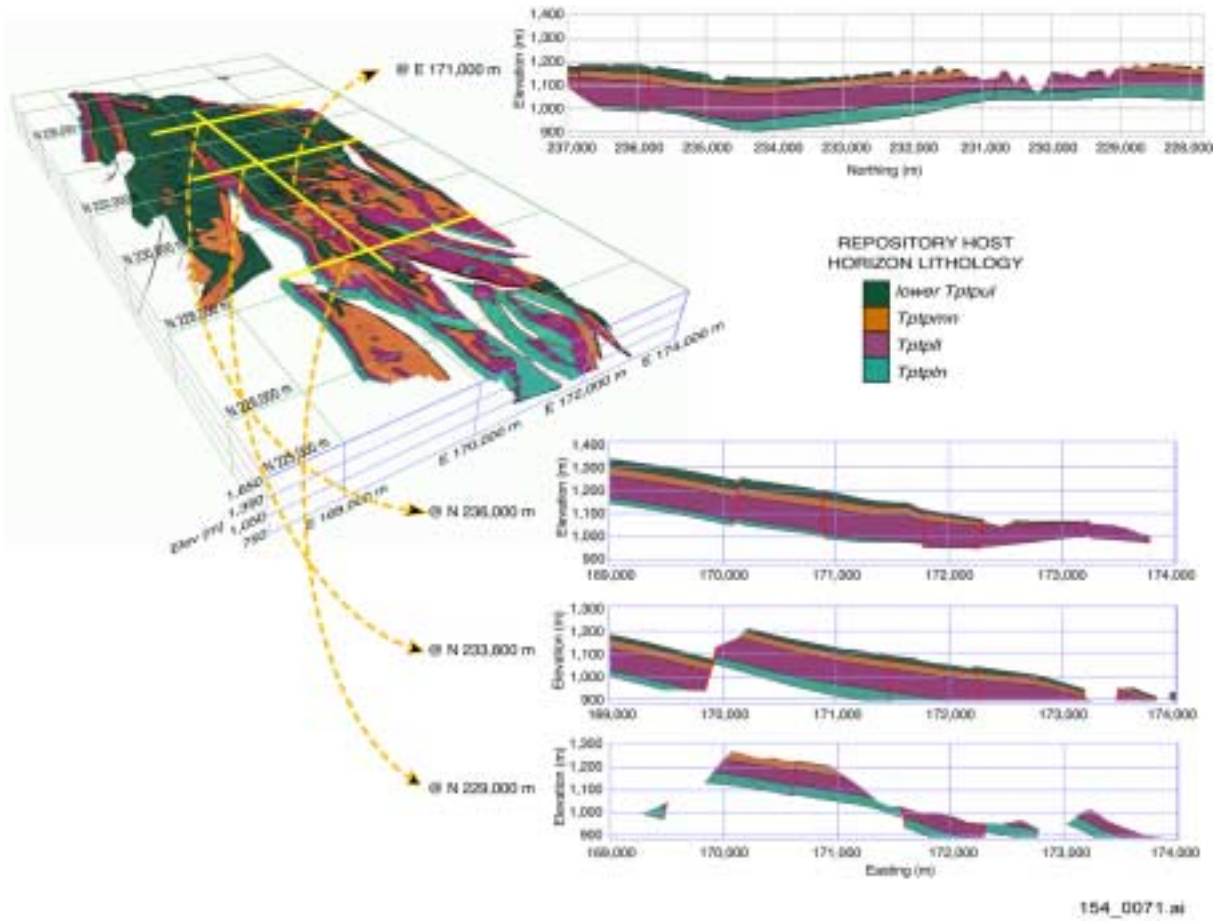

154_0071.ai

Source: Developed from DTN: MO9901MWDGFM31.000 [DIRS 103769].

NOTE: Upper and lower repository host horizon surfaces have been clipped to maintain an overburden thickness of 200 m and a water table standoff distance of 160 m. Nevada coordinates in meters.

Figure 3.3.4-9. Spatial Distribution of Lithostratigraphic Layers Constituting the Potential Repository Host Horizon

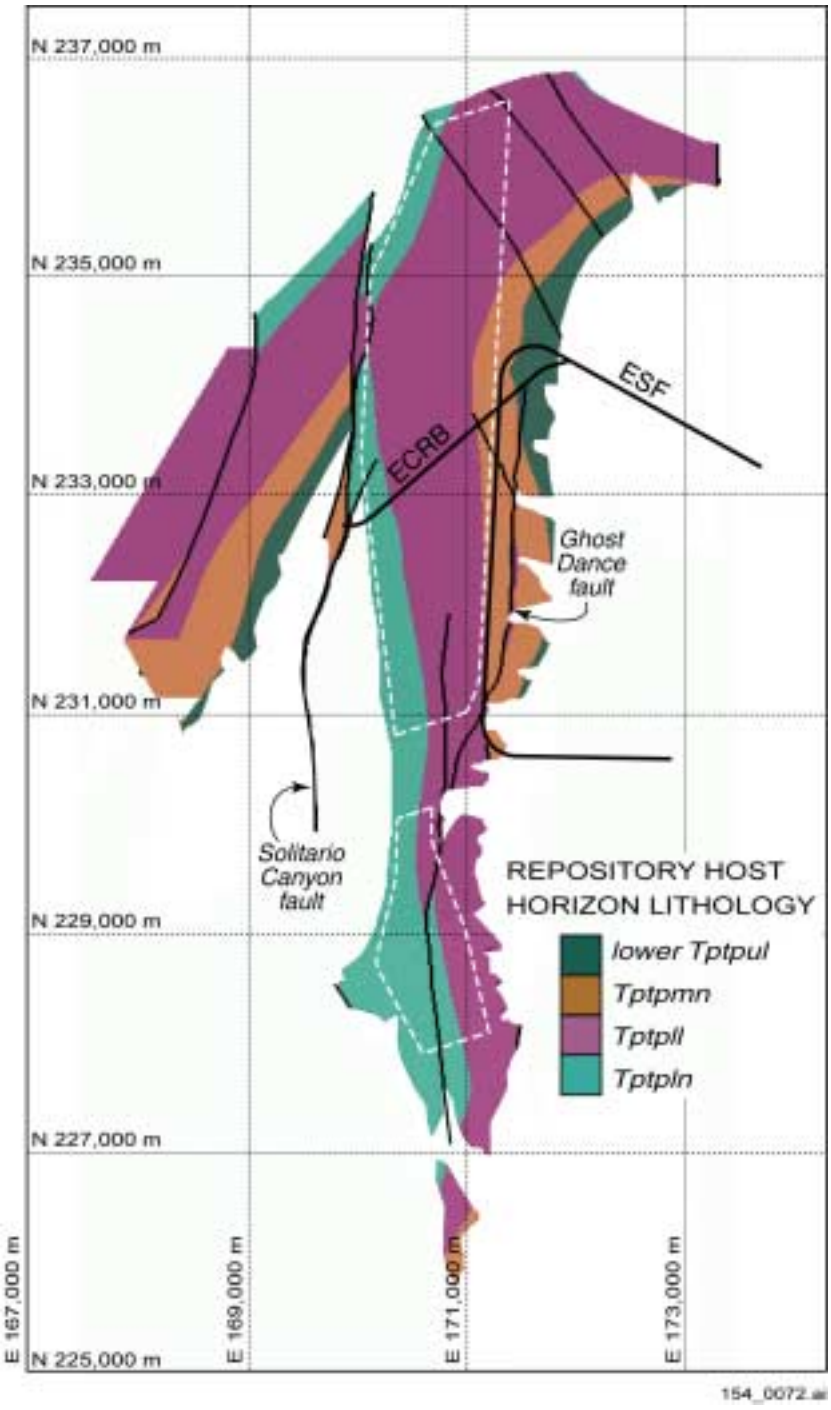

154_0072.ai

Source: Distribution of lithology from DTN: MO9901MWDGFM31.000 [DIRS 103769]. Design from BSC 2001 [DIRS 154548].

NOTE: The white dashed line identifies the plane of the current draft repository design. Nevada coordinates in meters. ECRB = Enhanced Characterization of the Repository Block; ESF = Exploratory Studies Facility; UZ = unsaturated zone.

Figure 3.3.4-10. Section Cut through the Potential Repository Siting Volume

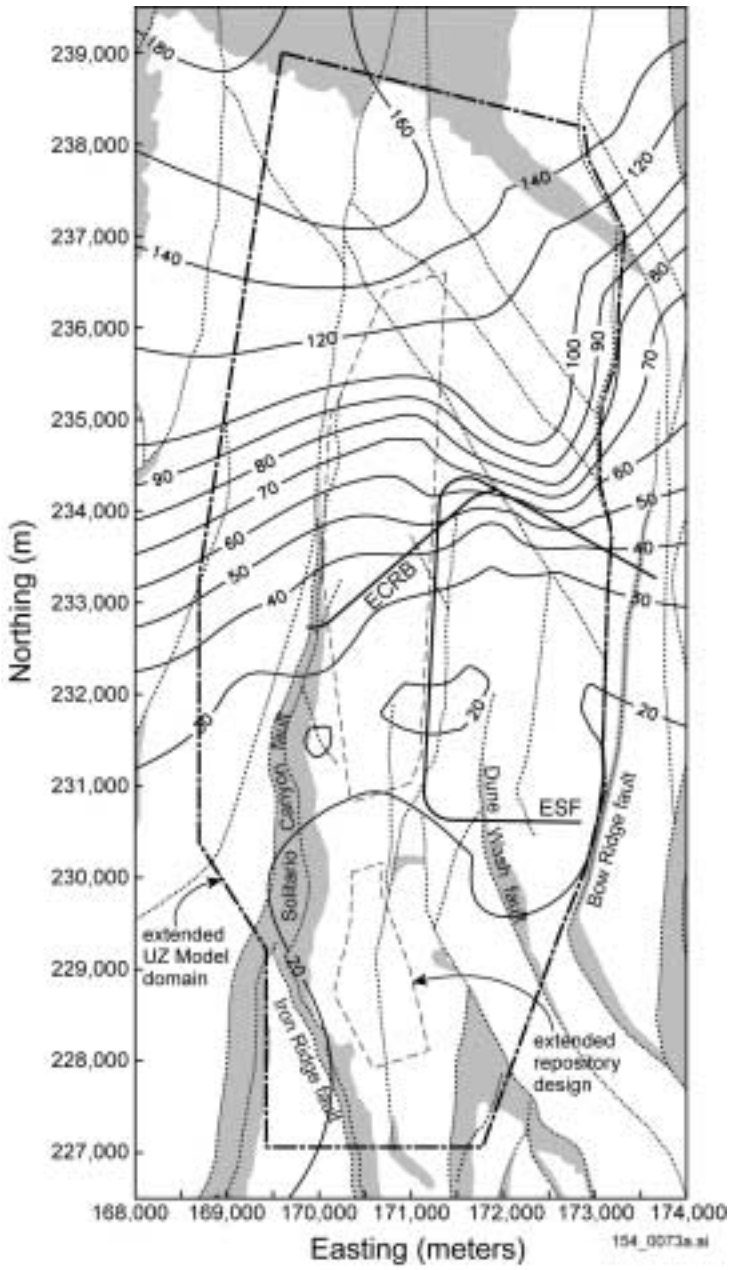

154_0073a.ai

Source: DTN: MO9901MWDGFM31.000 [DIRS 103769].

NOTE: Figure developed using Geologic Framework Model version 3.1 data. Contours indicate pre-faulted, pre-eroded PTn thickness in meters. Shaded areas are where the PTn has zero thickness as a result of faulting, erosion, or both. Nevada coordinates in meters. ECRB = Enhanced Characterization of the Repository Block; ESF = Exploratory Studies Facility; UZ = unsaturated zone.

Figure 3.3.4-11. PTn Occurrence and Thickness

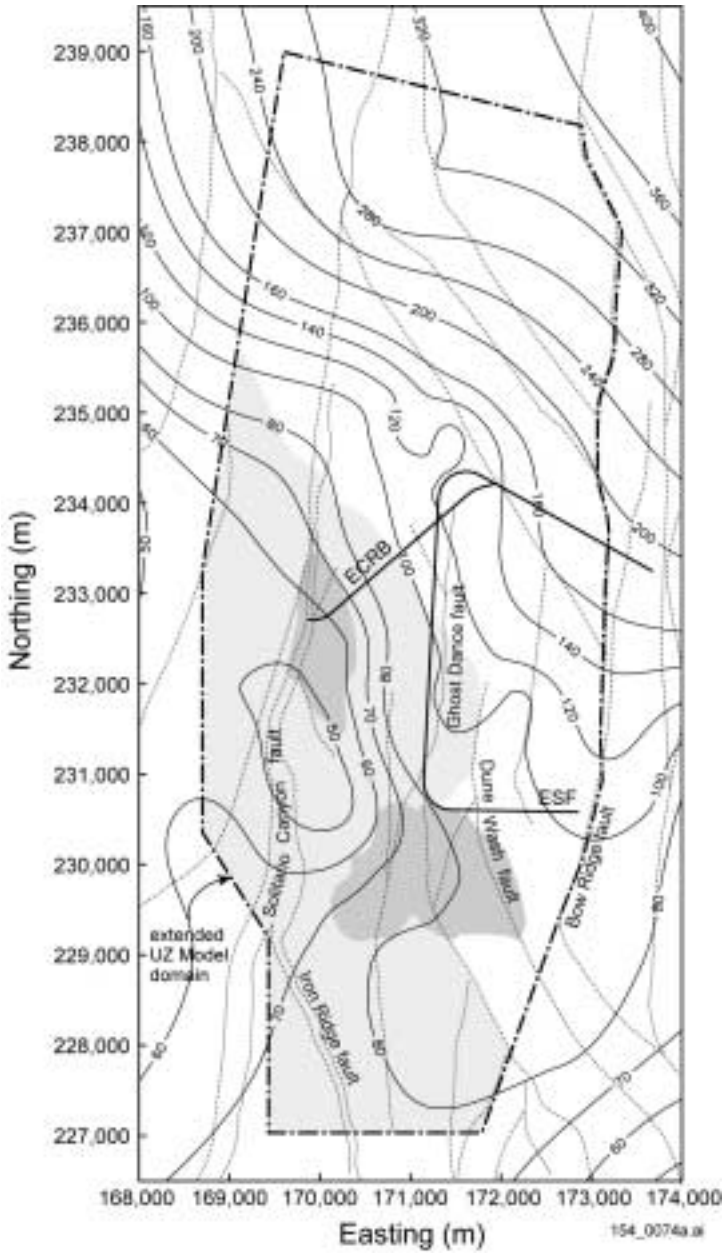

154_0074a.ai

Source: Thickness contours DTN: MO9901MWDGFM31.000 [DIRS 103769]. Vitric extent estimated using preliminary RPM3.2 data Bodvarsson 2001 [DIRS 154669], Attachment 15, pp. 148 to 151.

NOTE: Thickness contours developed using Geologic Framework Model version 3.1 data. Units are meters. Shaded areas represent estimated extent of vitric region within the extended Unsaturated Zone model domain near the top of the CHn (light shading) and near the base of the CHn (dark shading). Nevada coordinates in meters. ECRB = Enhanced Characterization of the Repository Block; ESF = Exploratory Studies Facility; UZ = unsaturated zone.

Figure 3.3.4-12. Pre-faulted, Pre-eroded Thickness Map of CHn (Tptpv1–Tacbt)

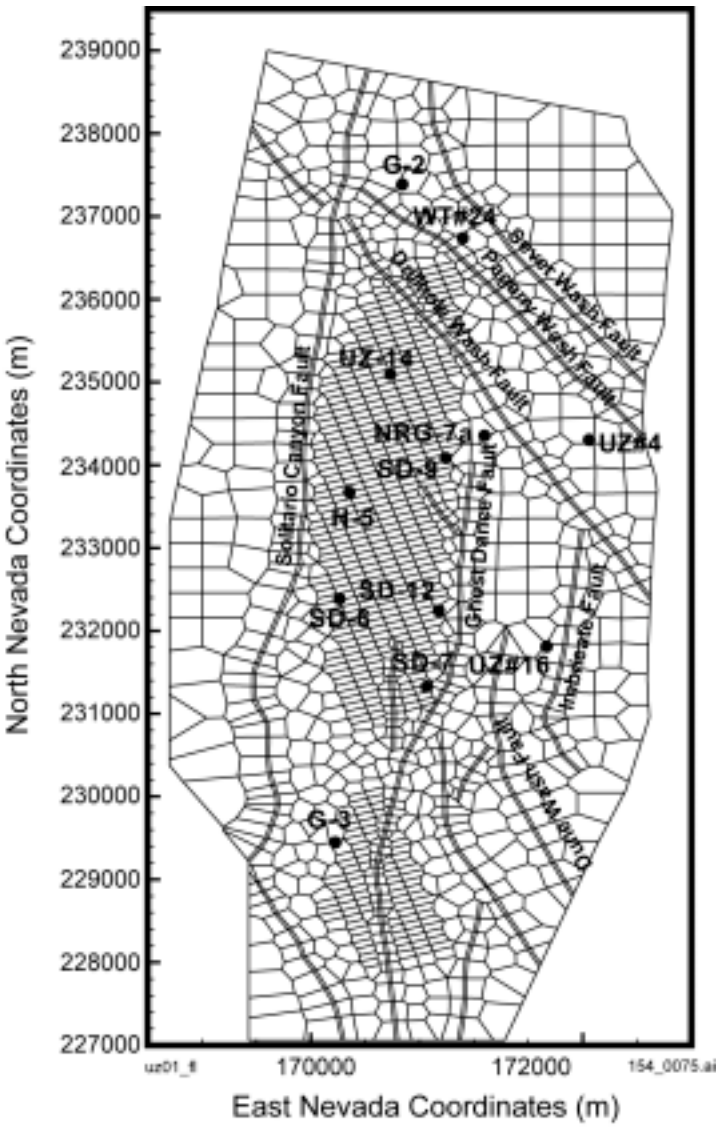

154_0075.ai

Source: BSC 2001 [DIRS 154548].

NOTE: Shown are modeled faults, several borehole locations, and refinements in the potential repository area (using the extended design for a cooler repository).

Figure 3.3.4-13. Plan View of the Extended Model Grid

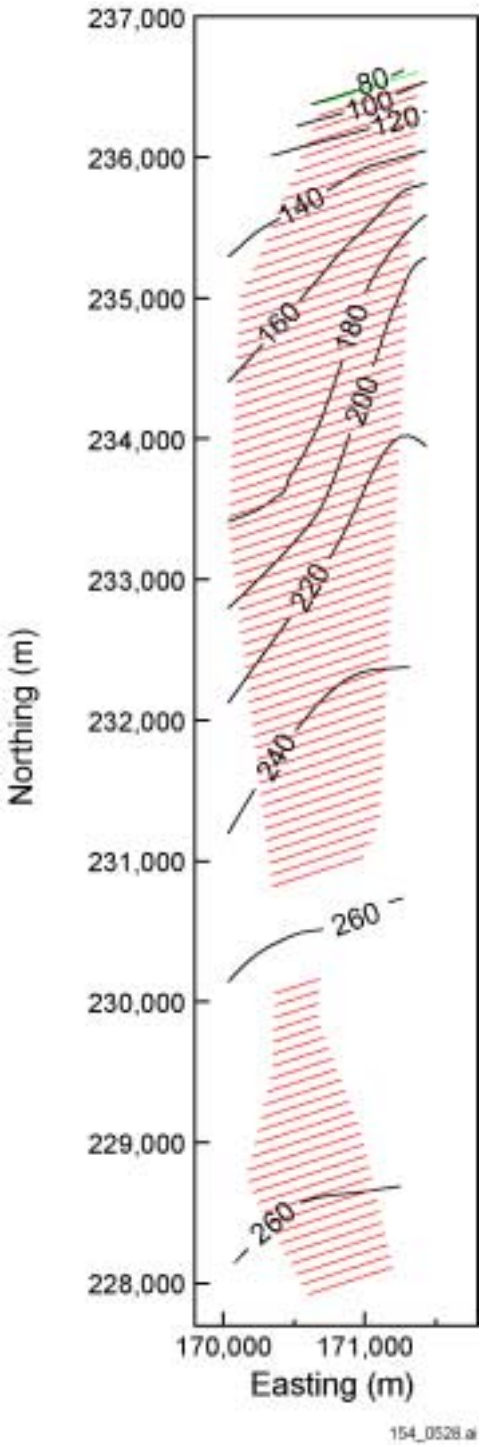

154_0528.ai

Source: Layout of the potential repository emplacement drifts from BSC (2001 [DIRS 154548], Item 1 of Figure 1 and Table 1).

NOTE: Contours in meters. Red lines indicate emplacement drifts. The northernmost drift (green) is a post-closure test drift.

Figure 3.3.4-13a. Approximate Vertical Distance Between Emplacement Drifts and a Water Table 120 m Above the Current Elevation

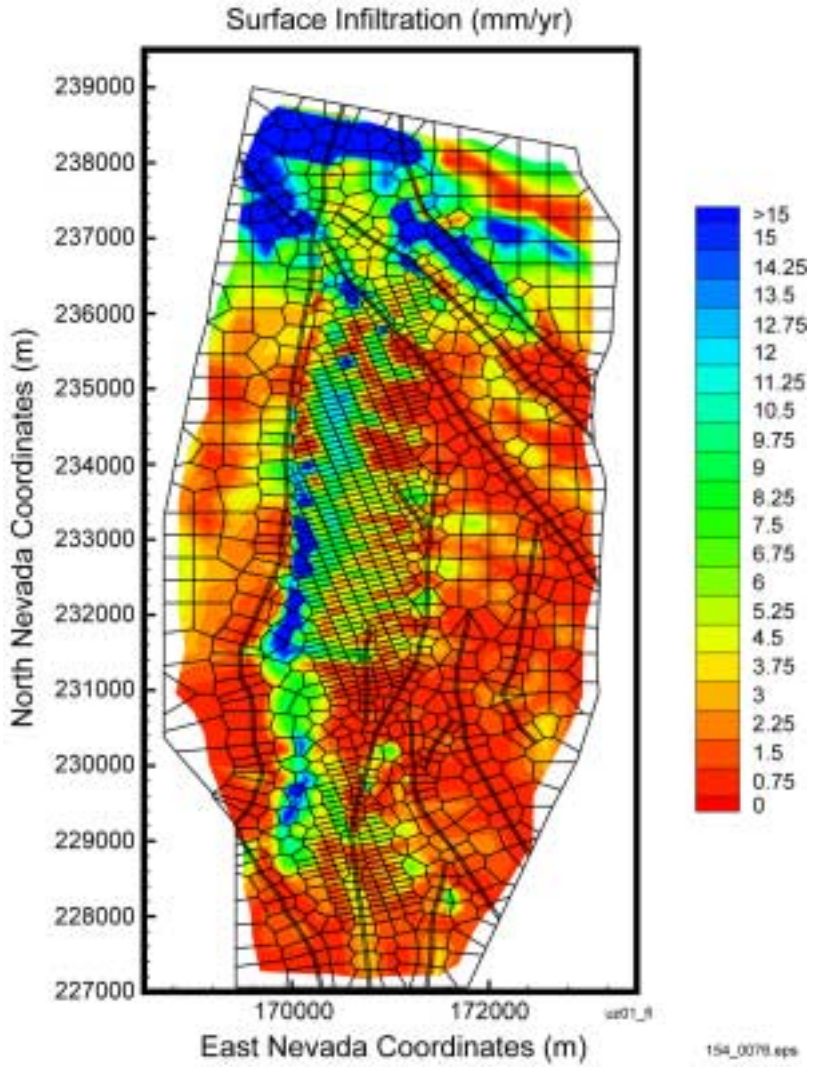

154_0076.eps

Source: Preliminary work described by Bodvarsson 2001 [DIRS 154669], Attachment 13, p. 13.

NOTE: Simulation uses present-day, mean infiltration (mm/yr).

Figure 3.3.4-14. Spatial Distribution of Infiltration in the Domain of the Extended Model

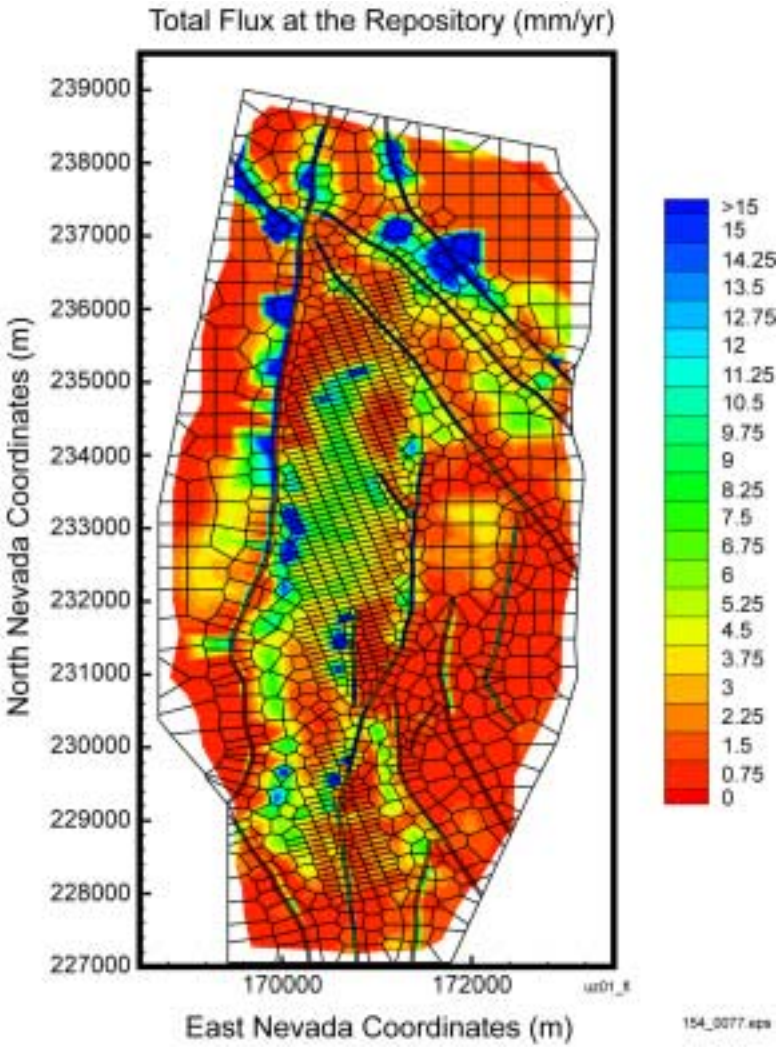

154_0077.eps

Source: Preliminary work described by Bodvarsson 2001 [DIRS 154669], Attachment 13, p. 15.

NOTE: Simulation uses present-day, mean infiltration (mm/yr).

Figure 3.3.4-15. Simulated Percolation Flux at the Potential Repository Horizon Using the Extended Model Grid

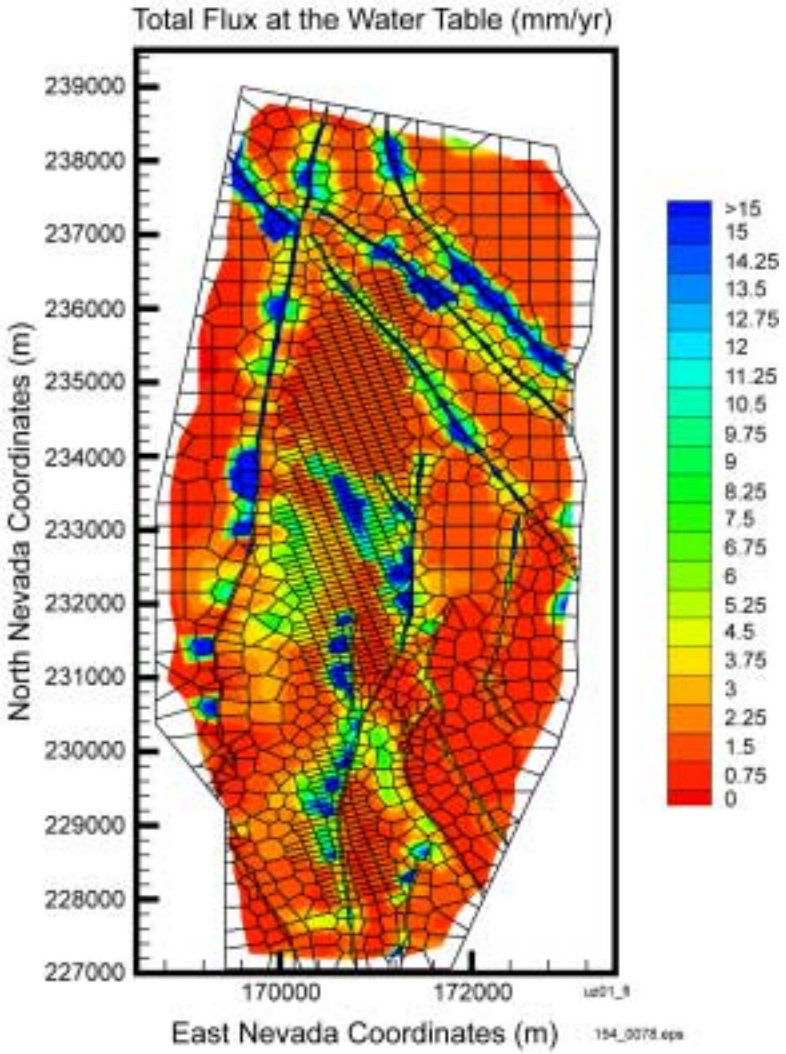

154_0078.eps

Source: Preliminary work described by Bodvarsson 2001 [DIRS 154669], Attachment 13, p. 16.

NOTE: Simulation uses present-day, mean infiltration (mm/yr).

Figure 3.3.4-16. Simulated Percolation Flux at the Water Table Using the Extended Model Grid

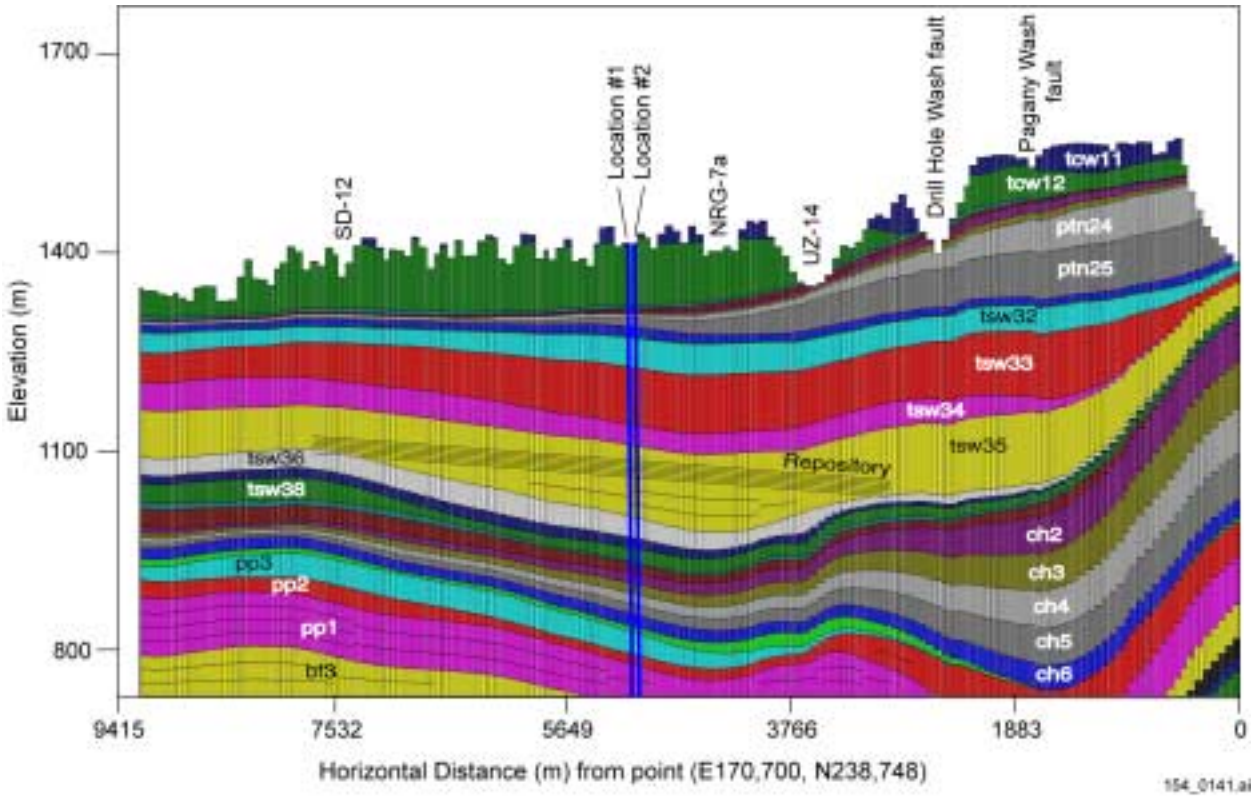

154_0141.ai

Source: CRWMS M&O 2000 [DIRS 144454], Figure 3.

NOTE: Lateral and vertical discretization, two-dimensional NS#2 cross section based on the refined numerical grid.

Figure 3.3.5-1. Location of the Potential Repository and Layering of the Hydrogeologic Units

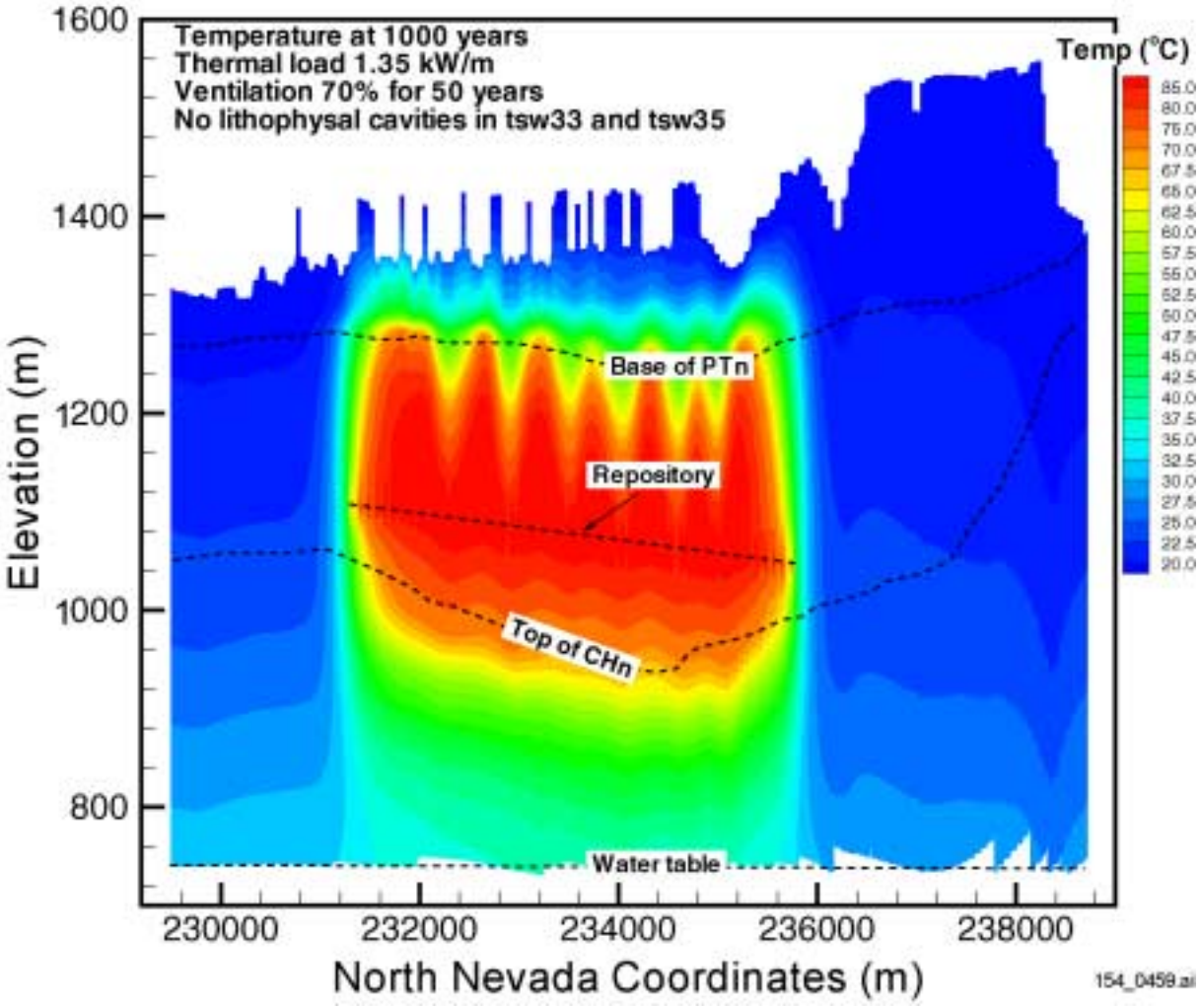

154_0459.ai

Source: Bodvarsson 2001 [DIRS 154669], Attachment 10, p. 11.

NOTE: Case #3: thermal load = 1.35 kW/m; ventilation = 70 percent for 50 years; no lithophysal cavities. Two-dimensional cross section.

Figure 3.3.5-2. Temperature Distribution for the Potential Higher-Temperature Repository at 1,000 Years

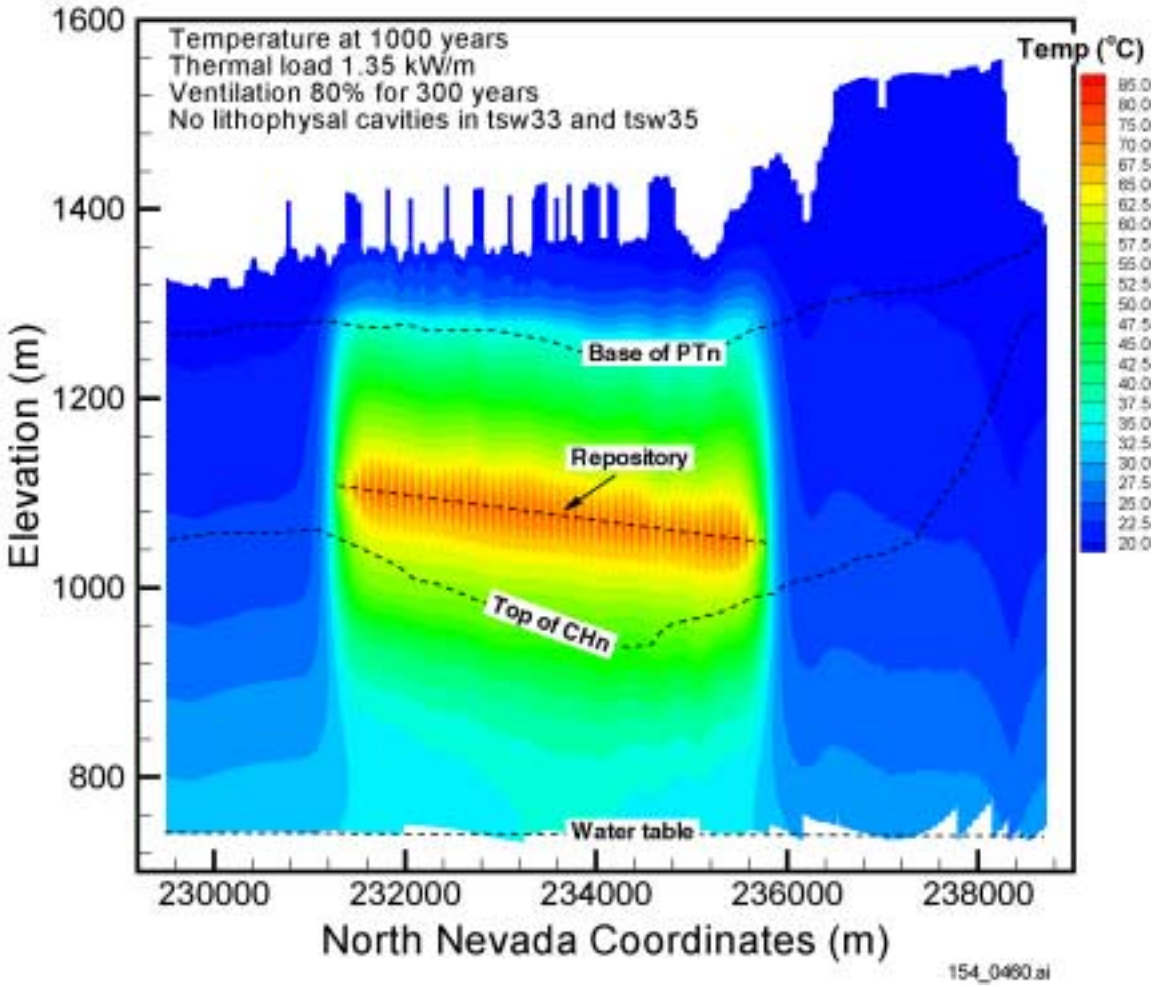

154_0460.ai

Source: Bodvarsson 2001 [DIRS 154669], Attachment 6, p. 101.

NOTE: Case #5: thermal load = 1.35 kW/m; ventilation = 80 percent for 300 years; no lithophysal cavities. Two-dimensional cross section.

Figure 3.3.5-3. Temperature Distribution for the Potential Lower-Temperature Repository at 1,000 Years

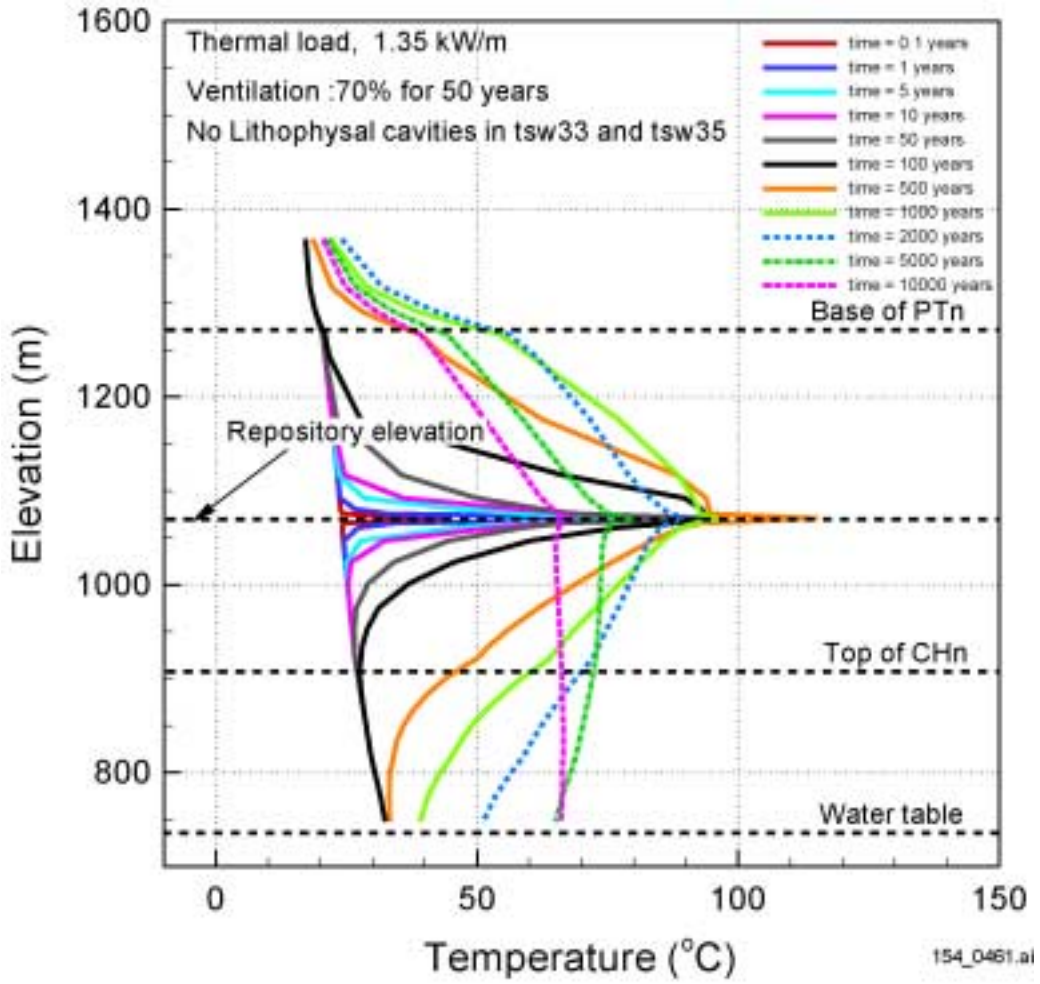

154_0461.ai

Source: Bodvarsson 2001 [DIRS 154669], Attachment 6, p. 83.

NOTE: Case #3: thermal load = 1.35 kW/m; ventilation = 70 percent for 50 years; no lithophysal cavities in tsw33 and tsw35. Two-dimensional cross section.

Figure 3.3.5-4. Temperature Profiles at the Center of the Potential Higher-Temperature Repository, No Lithophysal Cavities

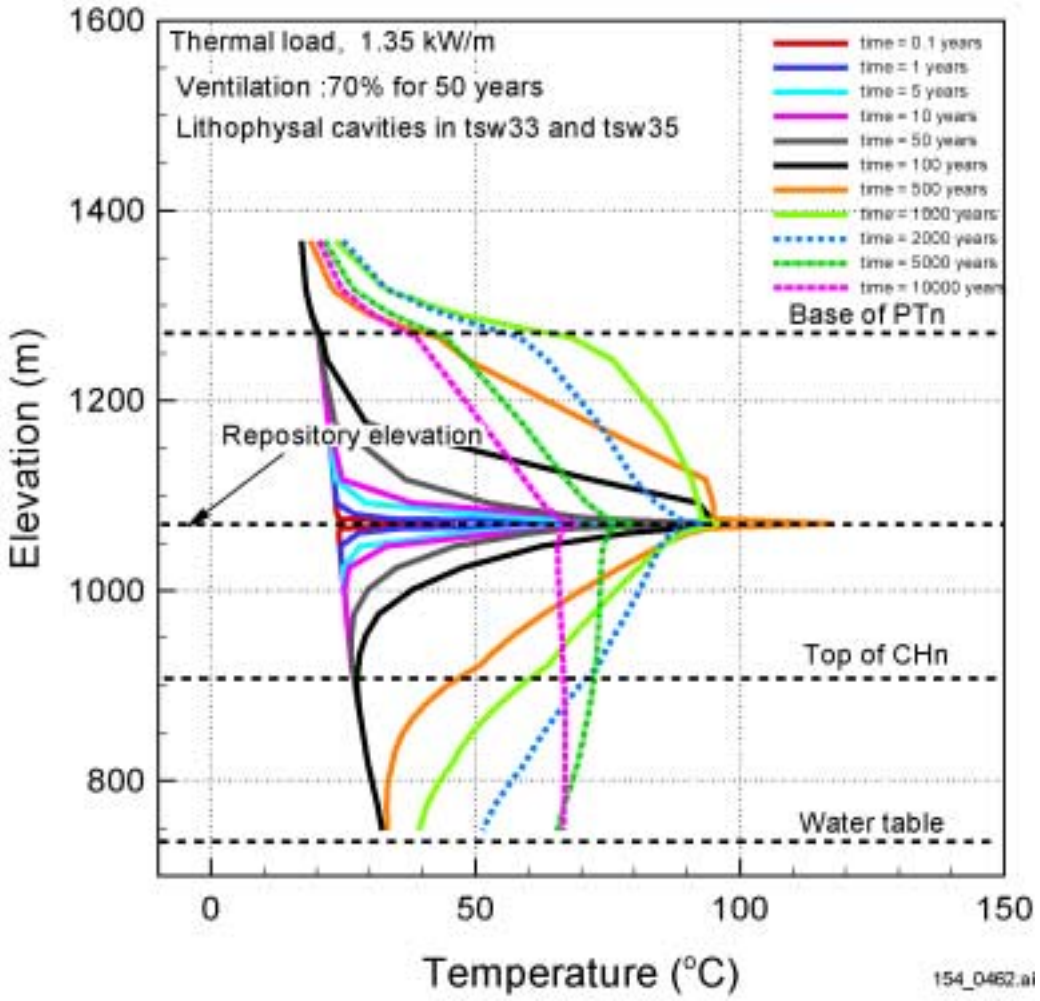

154_0462.ai

Source: Bodvarsson 2001 [DIRS 154669], Attachment 6, p. 84.

NOTE: Case #4: thermal load = 1.35 kW/m; ventilation = 70 percent for 50 years; with lithophysal cavities in tsw33 and tsw35. Two-dimensional cross section.

Figure 3.3.5-5. Temperature Profiles at the Center of the Potential Higher-Temperature Repository, with Lithophysal Cavities

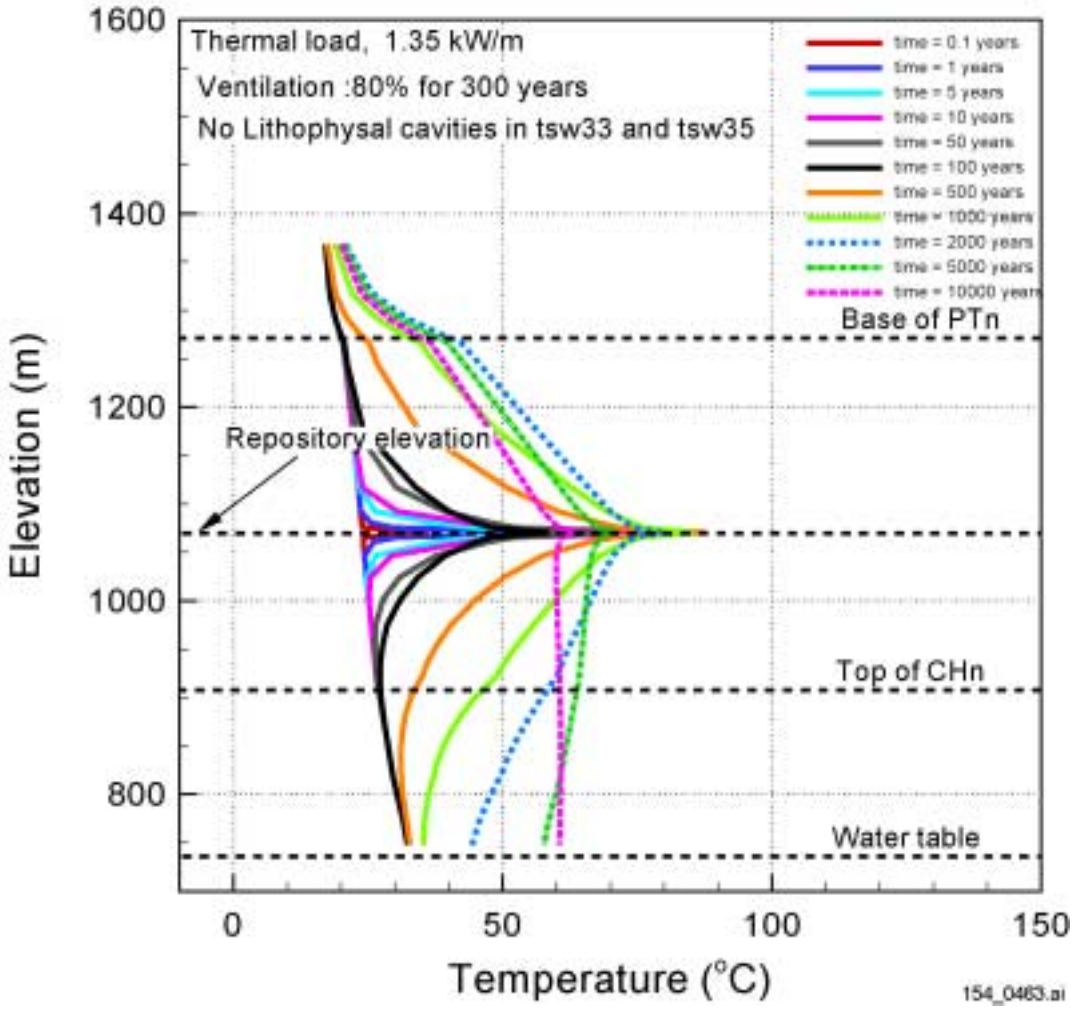

154_0463.ai

Source: Bodvarsson 2001 [DIRS 154669], Attachment 6, p. 85.

NOTE: Case #5: thermal load = 1.35 kW/m; ventilation = 80 percent for 300 years; no lithophysal cavities in tsw33 and tsw35. Two-dimensional cross section.

Figure 3.3.5-6. Temperature Profiles at the Center of the Potential Lower-Temperature Repository, No Lithophysal Cavities

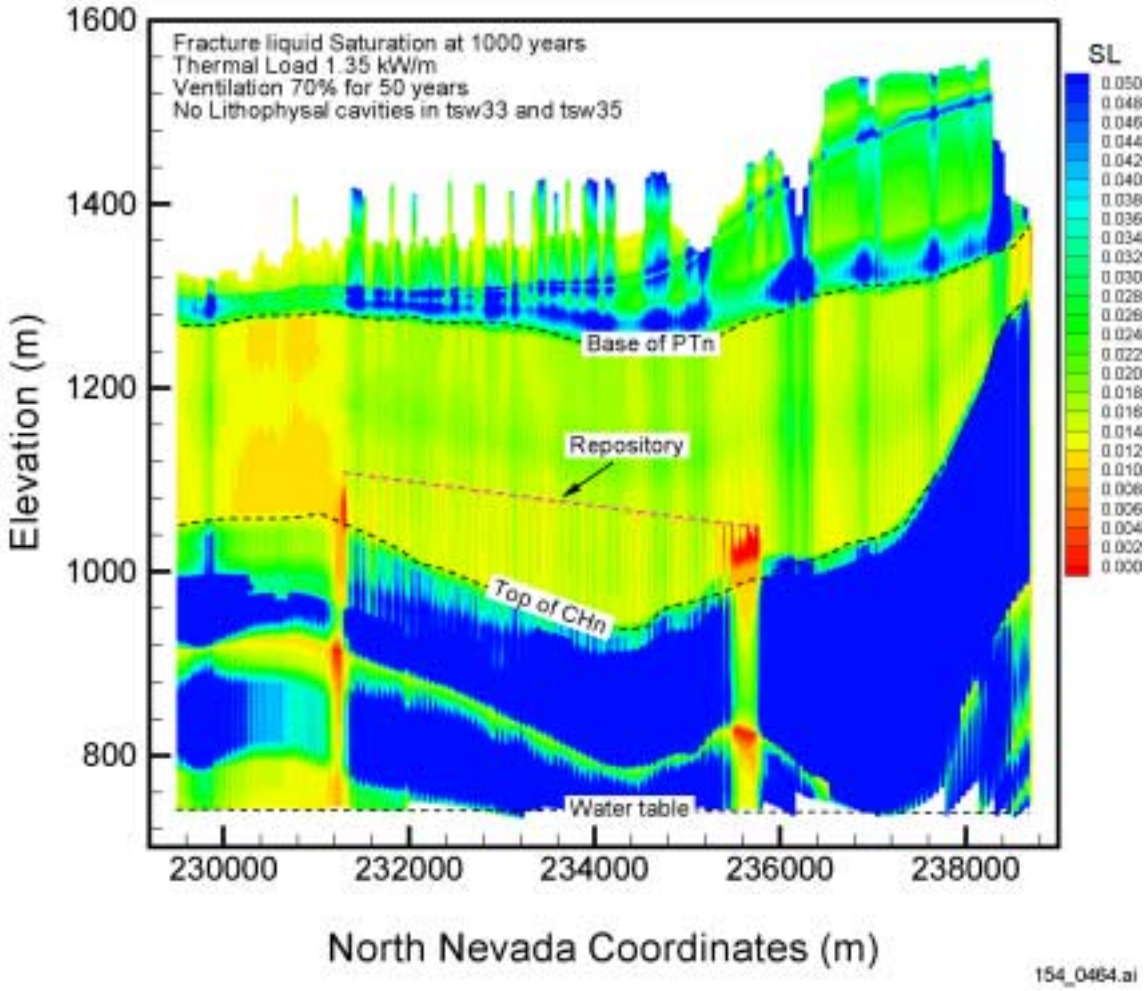

154_0464.ai

Source: Bodvarsson 2001 [DIRS 154669], Attachment 6, p. 100.

NOTE: Case #3: thermal load = 1.35 kW/m; ventilation = 70 percent for 50 years; no lithophysal cavities. Two-dimensional cross section.

Figure 3.3.5-7. Fracture Liquid Saturation for the Potential Higher-Temperature Repository at 1,000 Years

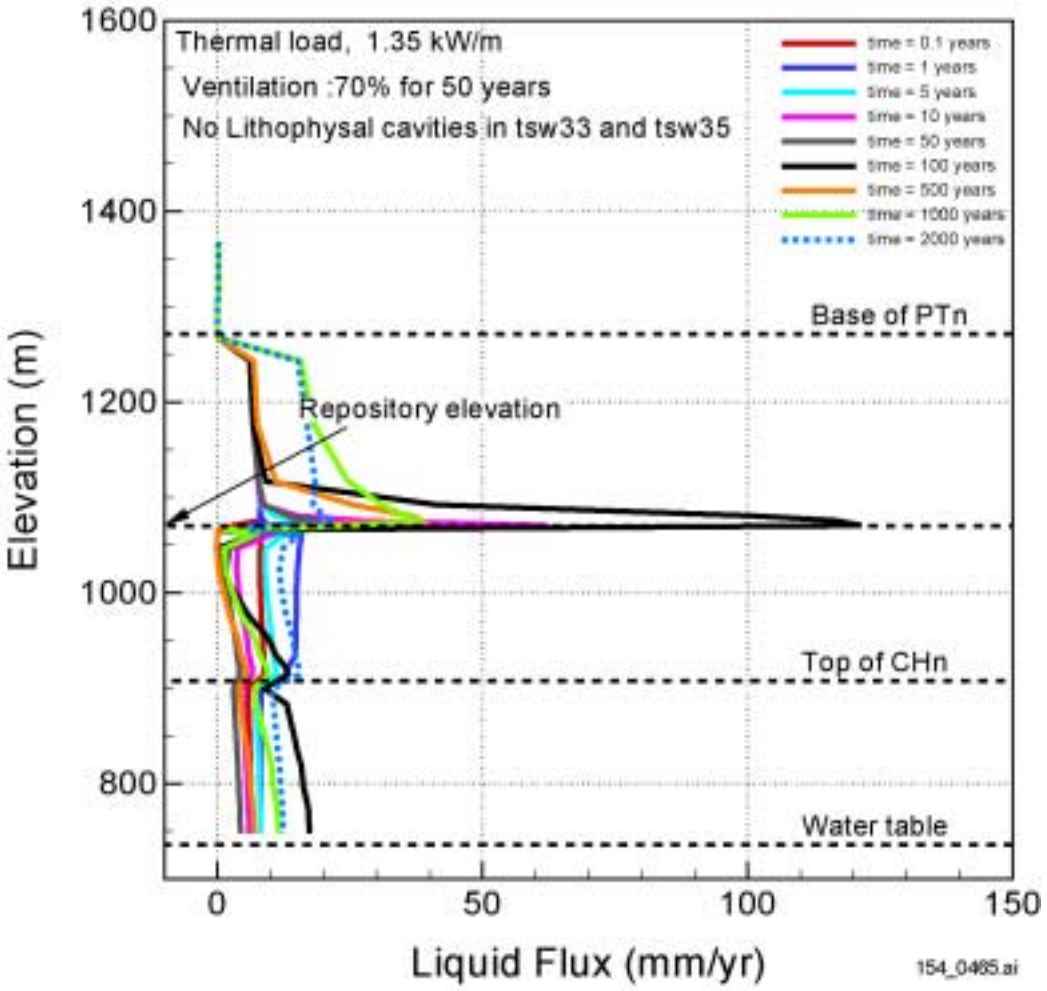

154_0465.ai

Source: Bodvarsson 2001 [DIRS 154669], Attachment 6, p. 91.

NOTE: Case #3: thermal load = 1.35 kW/m; ventilation = 70 percent for 50 years; no lithophysal cavities in tsw33 and tsw35. Two-dimensional cross section.

Figure 3.3.5-8. Fracture Liquid-Flux Profiles at Center of the Potential Repository for the Higher-Temperature Repository, No Lithophysal Cavities

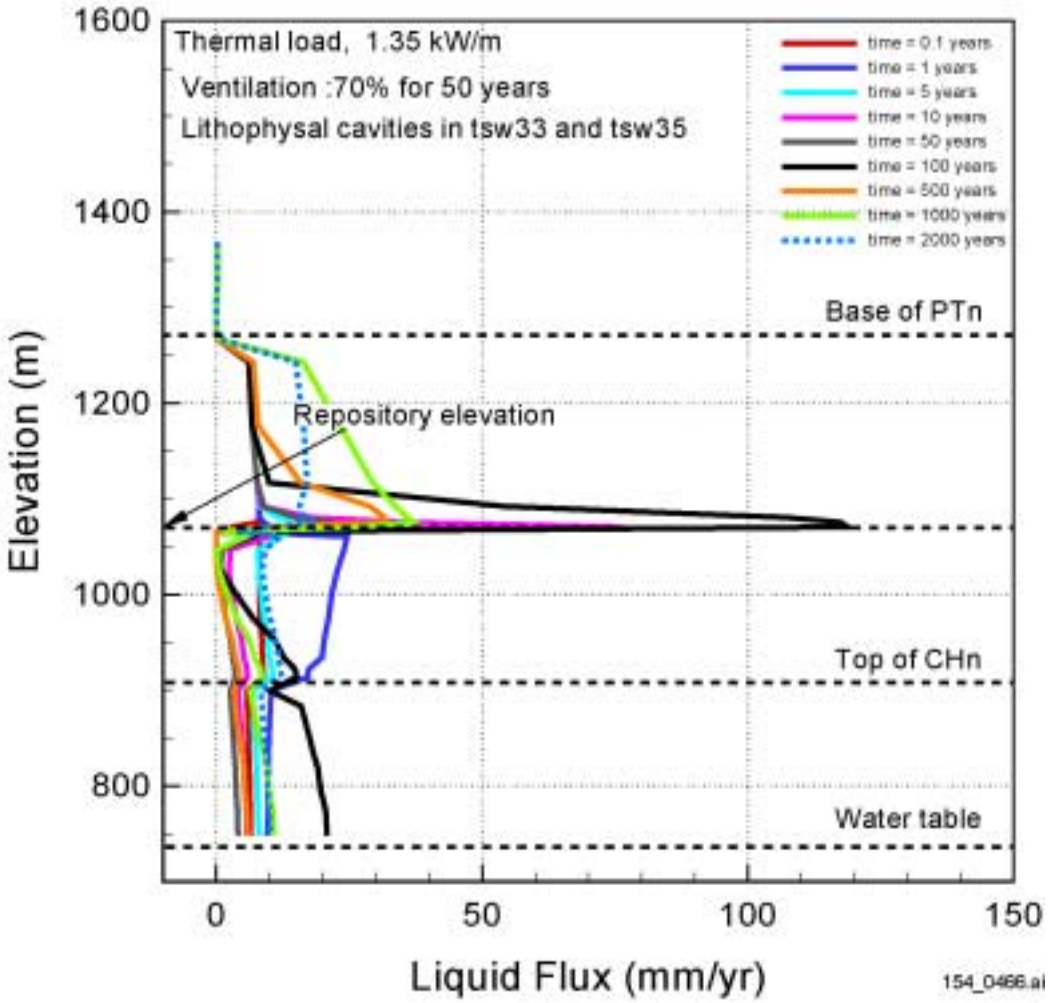

154_0466.ai

Source: Bodvarsson 2001 [DIRS 154669], Attachment 6, p. 92.

NOTE: Case #4: thermal load = 1.35 kW/m; ventilation = 70 percent for 50 years; with lithophysal cavities in tsw33 and tsw35. Two-dimensional cross section.

Figure 3.3.5-9. Fracture Liquid Flux Profiles at the Center of the Potential Higher-Temperature Repository, With Lithophysal Cavities

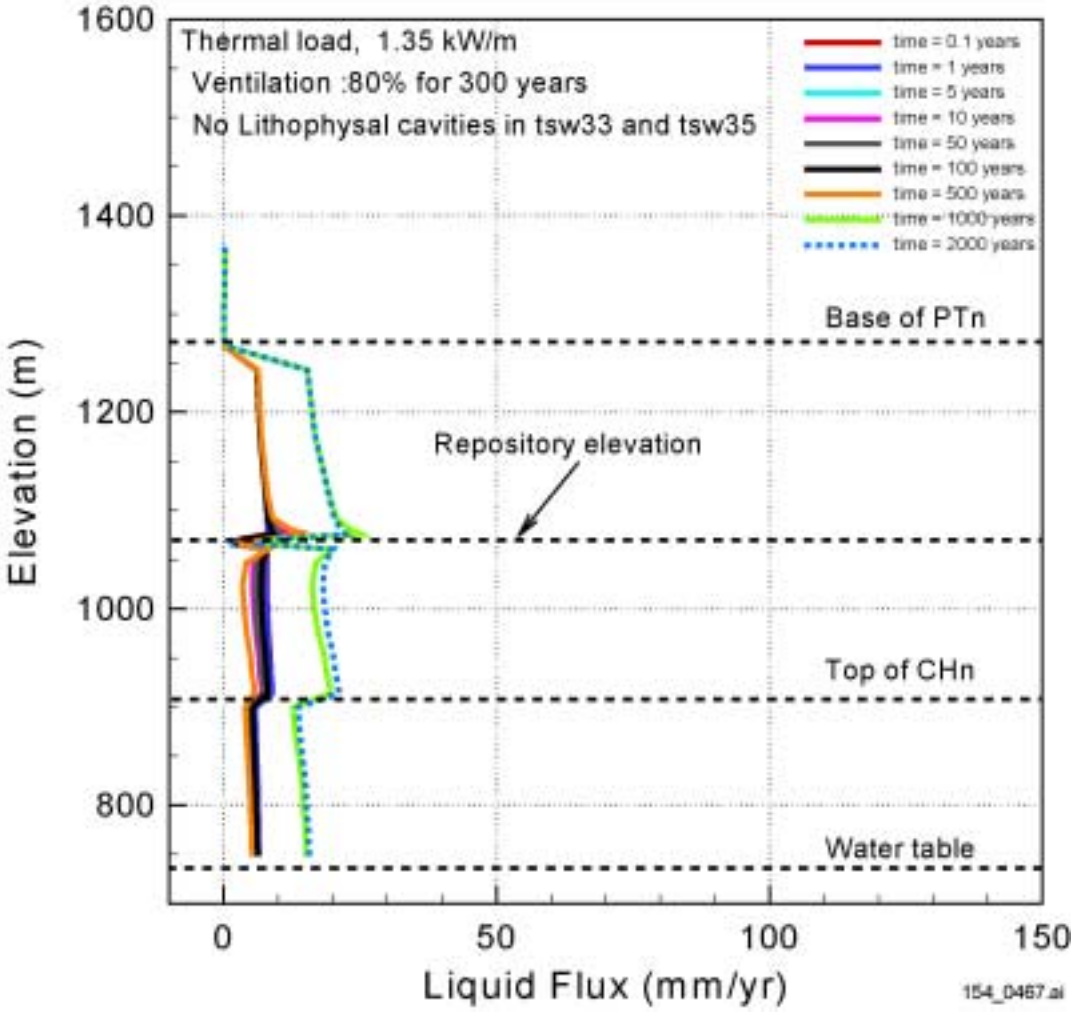

154_0467.ai

Source: Bodvarsson 2001 [DIRS 154669], Attachment 6, p. 93.

NOTE: Case #5: thermal load = 1.35 kW/m; ventilation = 80 percent for 300 years; no lithophysal cavities in tsw33 and tsw35. Two-dimensional cross section.

Figure 3.3.5-10. Fracture Liquid Flux Profiles at the Center of the Potential Lower-Temperature Repository, No Lithophysal Cavities

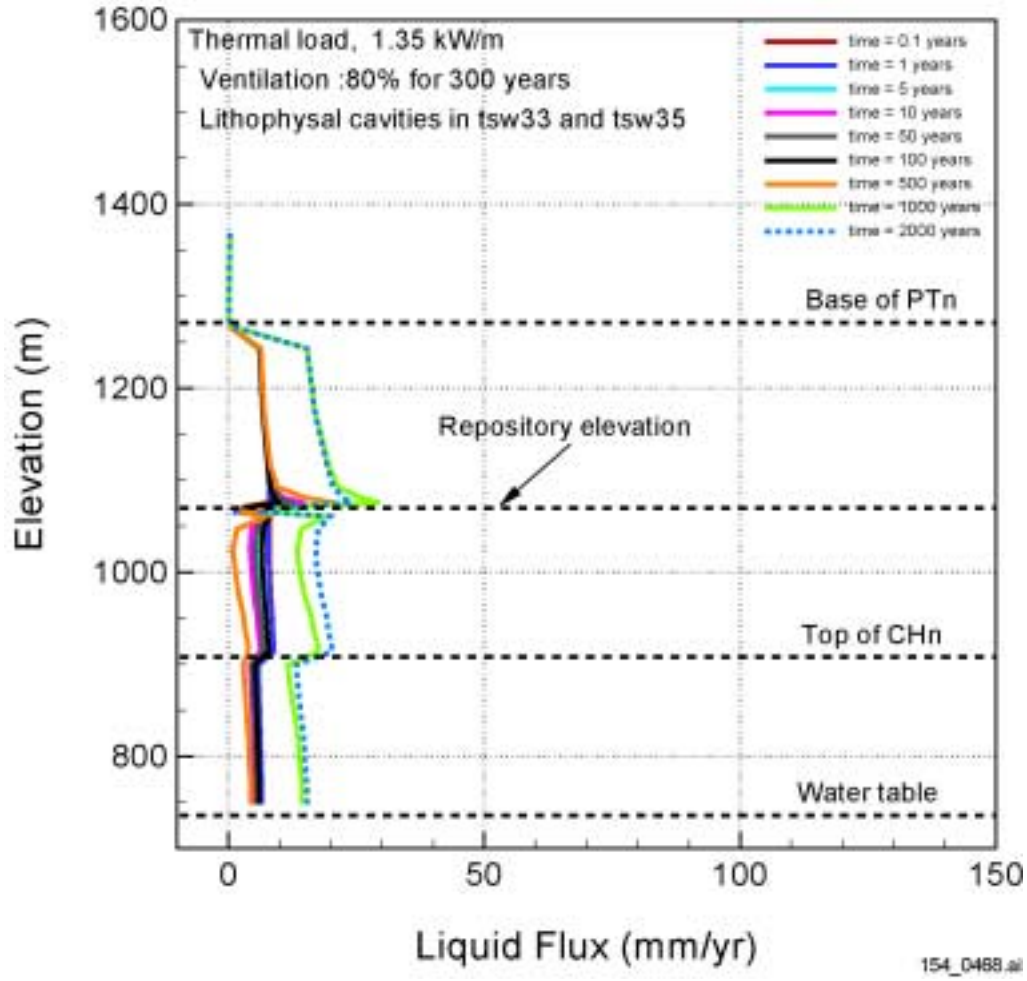

154_0468.ai

Source: Bodvarsson 2001 [DIRS 154669], Attachment 6, p. 94.

NOTE: Case #6: thermal load = 1.35 kW/m; ventilation = 80 percent for 300 years; with lithophysal cavities in tsw33 and tsw35. Two-dimensional cross section.

Figure 3.3.5-11. Fracture Liquid-Flux Profiles at the Center of the Potential Lower-Temperature Repository, With Lithophysal Cavities

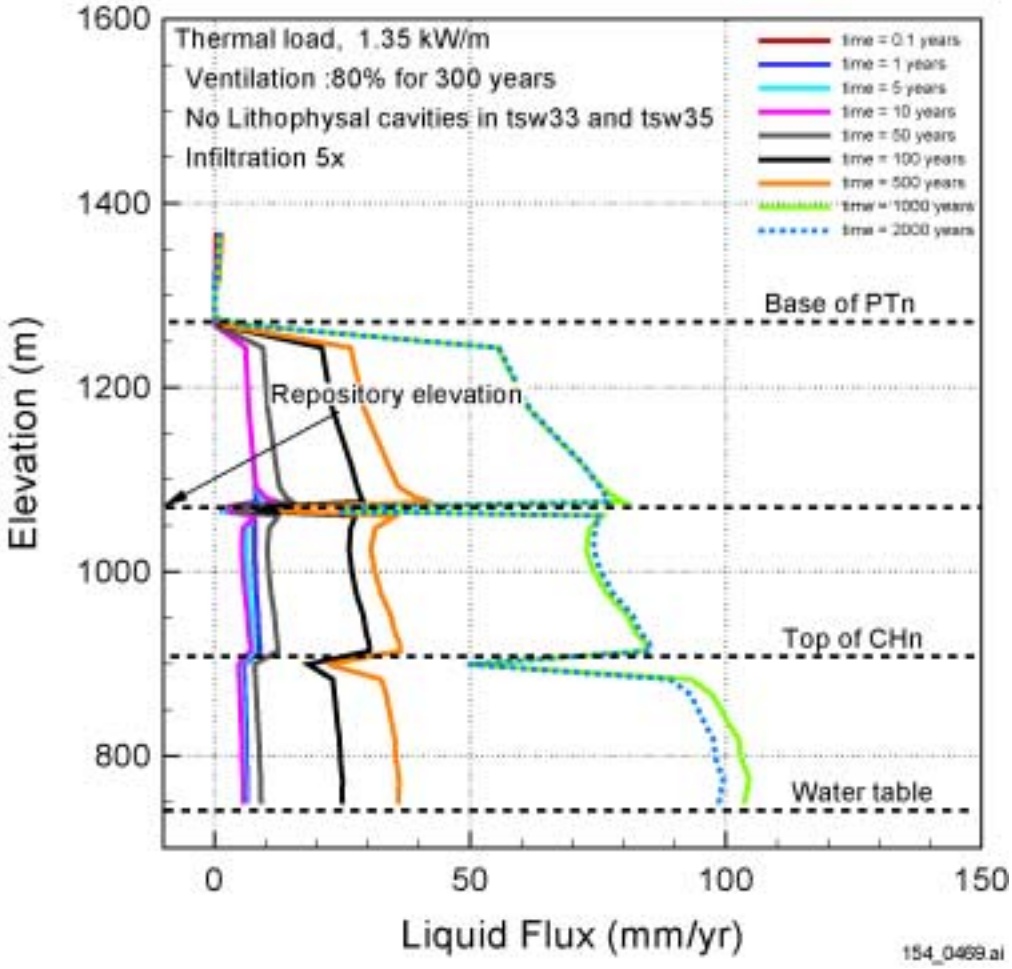

154_0469.ai

Source: Bodvarsson 2001 [DIRS 154669], Attachment 6, p. 103.

NOTE: Case #7: thermal load = 1.35 kW/m; ventilation = 80 percent for 300 years; no lithophysal cavities in tsw33 and tsw35. Two-dimensional cross section.

Figure 3.3.5-12. Fracture Liquid Flux Profiles at the Center of the Potential Lower-Temperature Repository, No Lithophysal Cavities and Increased Infiltration

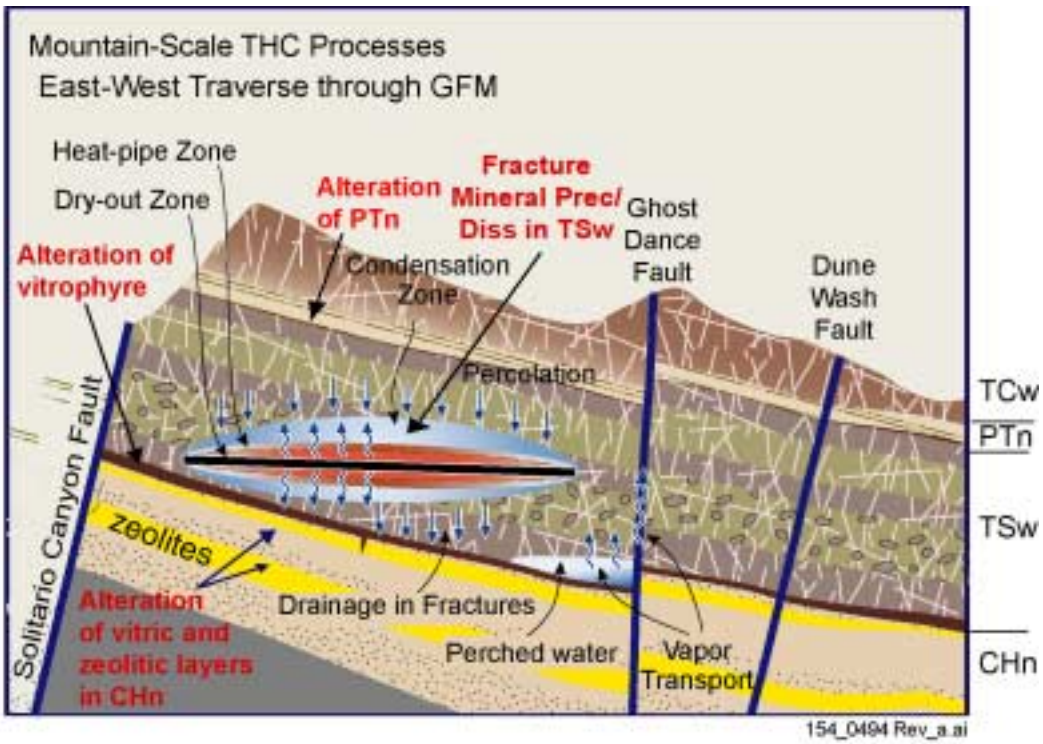

154_0494 Rev_a.ai

NOTE: Definitions: GFM = Geologic Frame Model; TCw = Tiva Canyon welded hydrogeologic unit; PTn = Paintbrush Tuff nonwelded hydrogeologic unit; TSw = Topopah Spring welded hydrogeologic unit; CHn = Calico Hills nonwelded hydrogeologic unit.

Figure 3.3.6-1. Schematic of Potential Mountain-Scale Thermal-Hydrologic-Chemical Processes and Initial Conditions

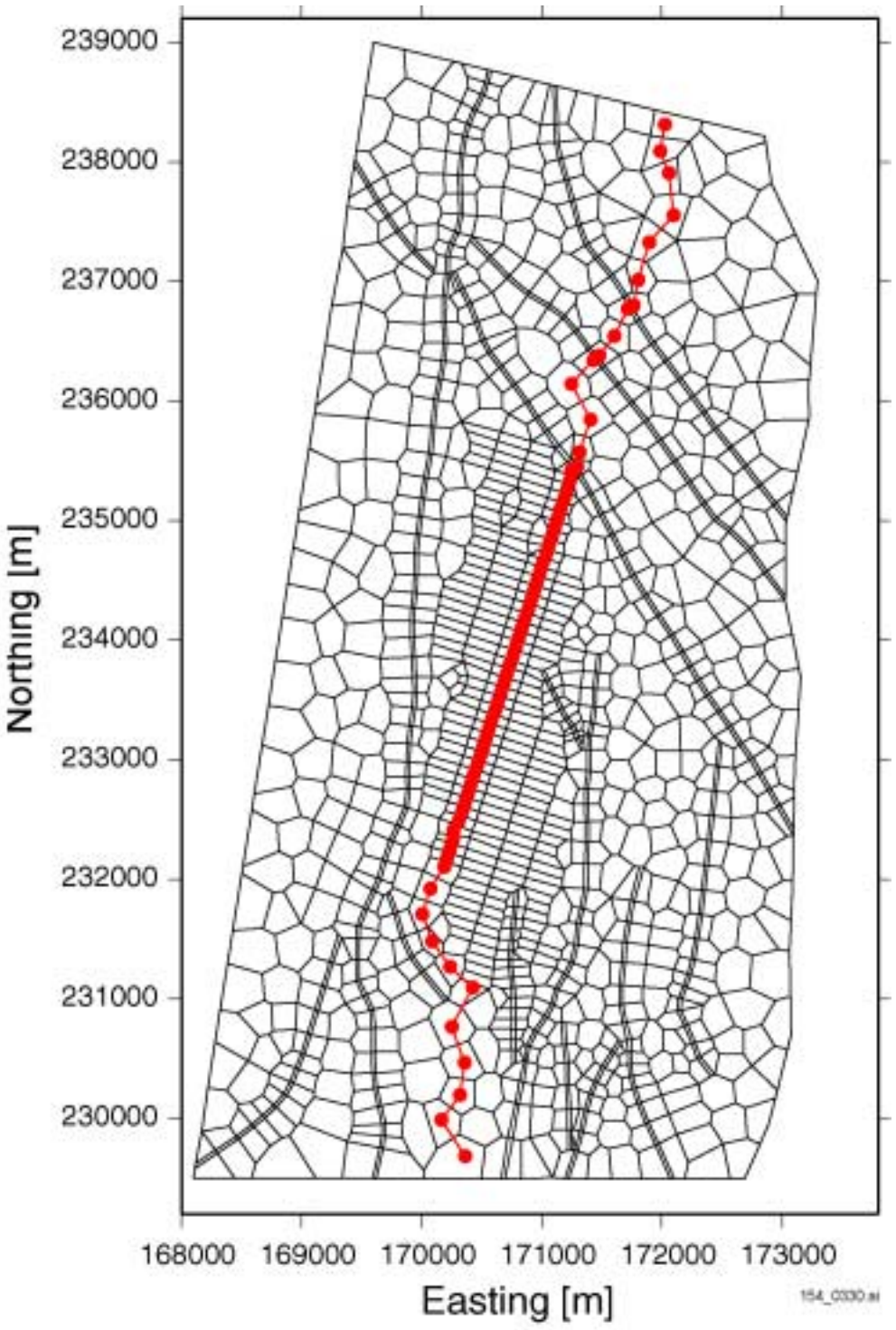

154_0330.ai

Source: Bodvarsson 2001 [DIRS 154669], Attachment 10, p. 11.

NOTE: Nevada Coordinates in meters.

Figure 3.3.6-2. Location of 2-D North-South Cross Section Superimposed on Diagram Showing the 3-D UZ Flow and Transport Model TSPA-SR Grid

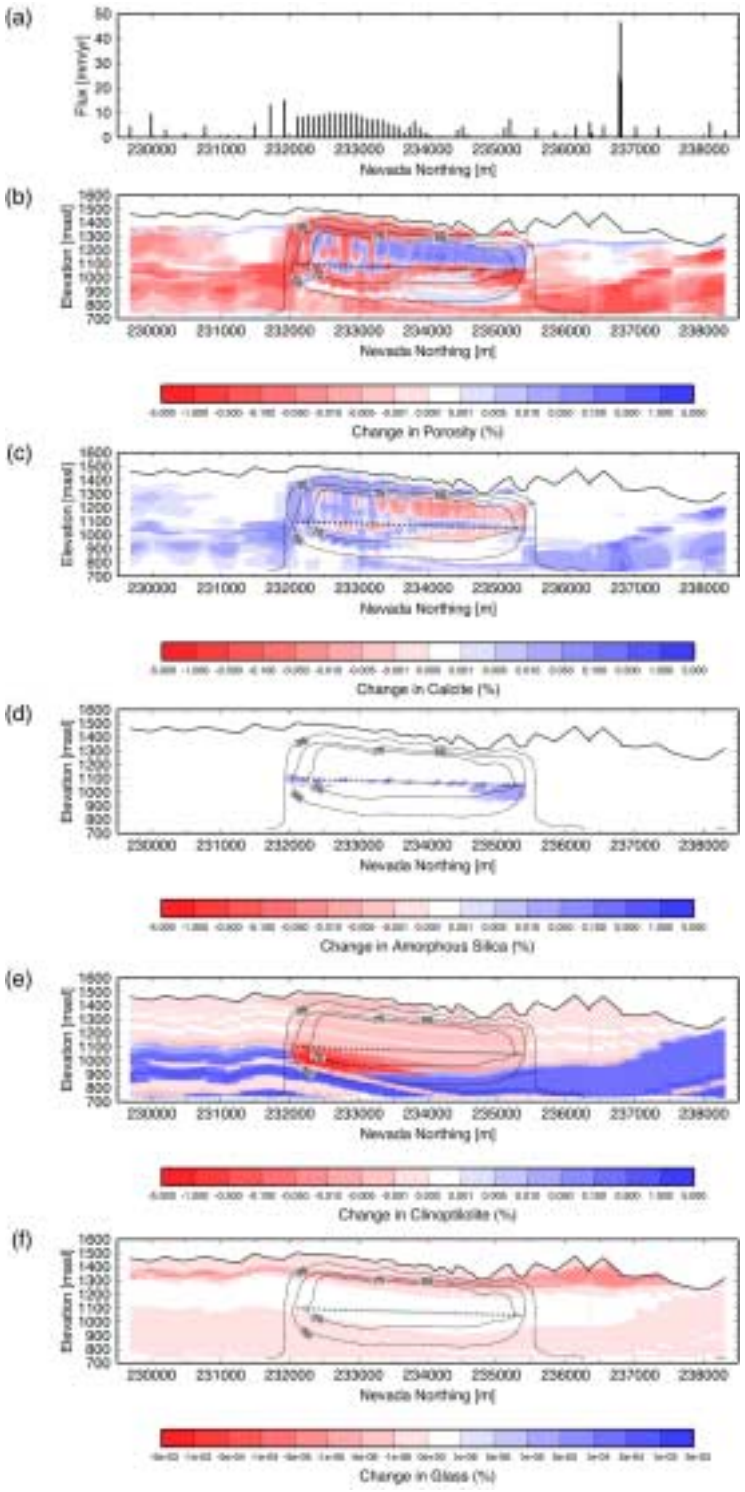

154_0254

Source: Bodvarsson 2001 [DIRS 154669], Attachment 10, pp. 12 to 14.

NOTE: Extended Case 1. Crosses denote model repository drift locations: (a) infiltration rate; (b) fracture porosity change with temperature contours; (c) fracture calcite change with temperature contours; (d) fracture amorphous silica precipitation with temperature contours; (e) matrix clinoptilolite change with temperature contours; and (f) matrix glass dissolution with temperature contours. masl = meters above sea level.

Figure 3.3.6-3. Infiltration Rate Distribution and Simulated Changes in Fracture Porosity, Mineralogy, and Temperature after about 1,400 Years of Heating

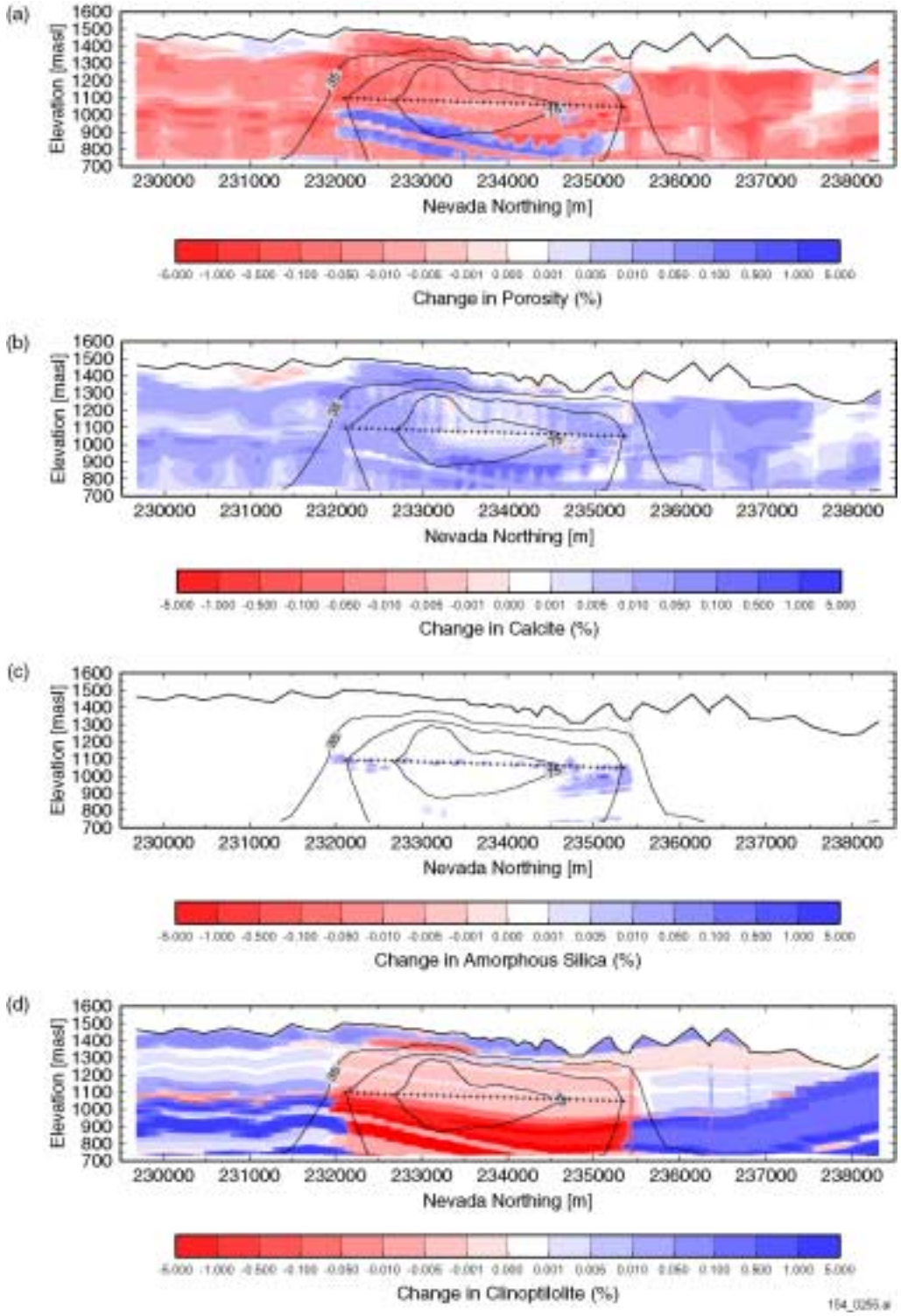

154_0255.ai

Source: Bodvarsson 2001 [DIRS 154669], Attachment 10, pp. 15 to 16.

NOTE: Extended Case 2. Crosses denote model repository drift locations: (a) fracture porosity change with temperature contours; (b) fracture calcite change with temperature contours; (c) fracture amorphous silica precipitation with temperature contours; and (d) matrix clinoptilolite change with temperature contours. masl = meters above sea level.

Figure 3.3.6-4. Simulated Changes in Fracture Porosity and Mineralogy after 5,000 Years of Heating

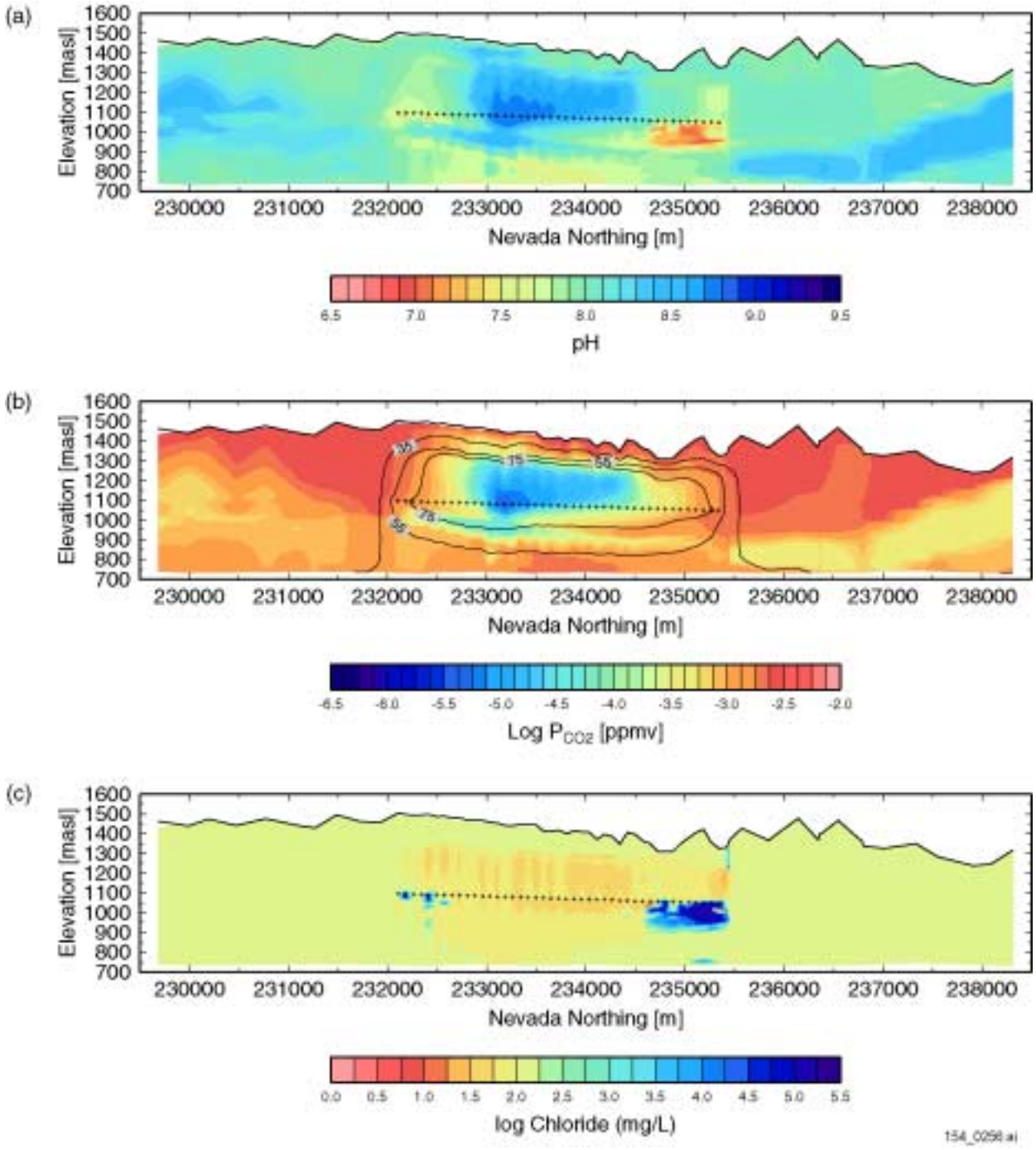

154_0256.ai

Source: Bodvarsson 2001 [DIRS 154669], Attachment 10, pp. 17 to 18.

NOTE: Extended Case 1. Crosses denote model repository drift locations: (a) pH of fracture water; (b) carbon dioxide concentration in gas in fractures with temperature contours; and (c) chloride concentration in fractures. masl = meters above sea level.

Figure 3.3.6-5. Simulated Water and Gas Chemistry after about 1,400 Years of Heating

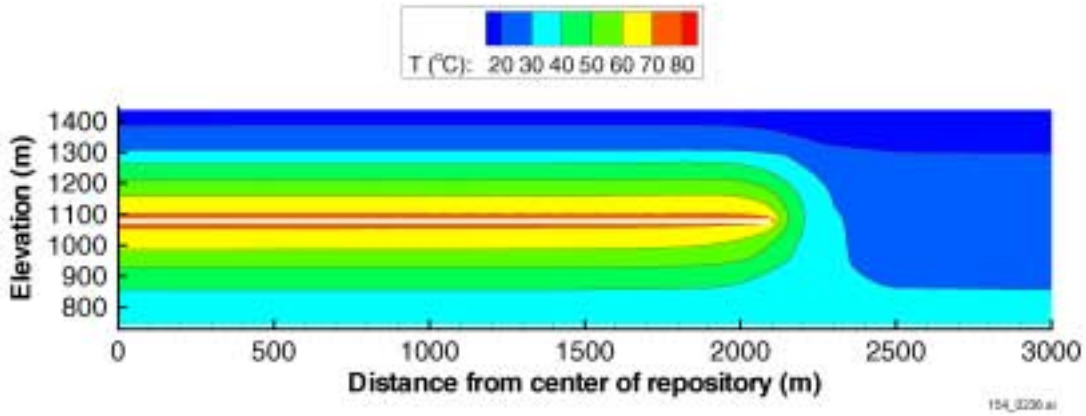

154_0236.ai

Source: Derived from Bodvarsson 2001 [DIRS 154669], Attachment 9, pp. 75 to 78.

Figure 3.3.7-1. Temperature Distribution at 1,000 Years

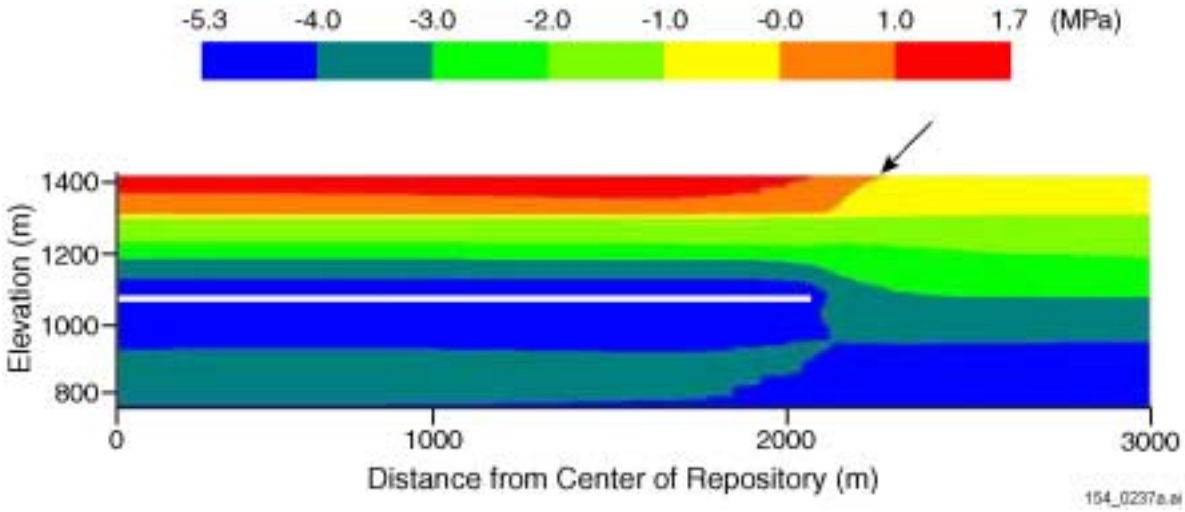

154_0237a.ai

Source: Derived from Bodvarsson 2001 [DIRS 154669], Attachment 9, pp. 75 to 78.

NOTE: Arrow points to contour that separates positive and negative stress values.

Figure 3.3.7-2. Contour of Horizontal Stress Distribution at 1,000 Years

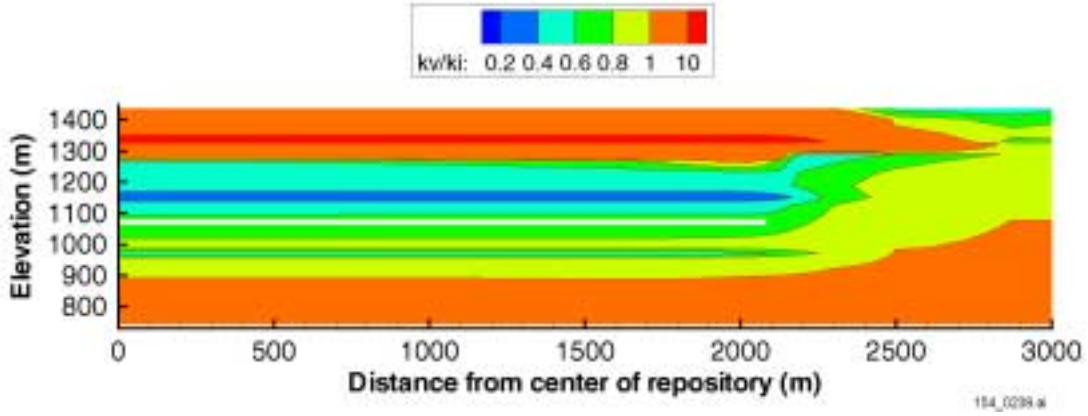

154_0239.ai

Source: Derived from Bodvarsson 2001 [DIRS 154669], Attachment 9, pp. 75 to 78.

Figure 3.3.7-3. Vertical Permeability Changes due to the Thermal-Hydrologic-Mechanical Effect at 1,000 Years

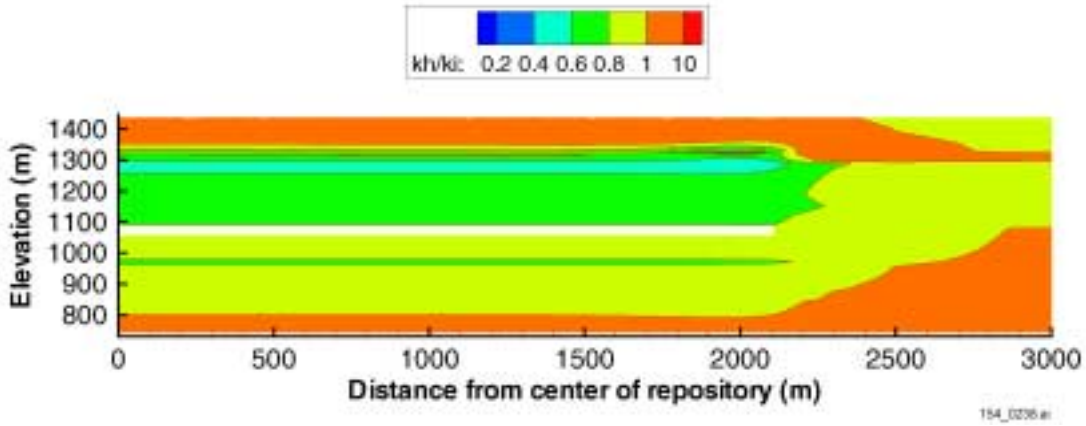

154_0238.ai

Source: Derived from Bodvarsson 2001 [DIRS 154669], Attachment 9, pp. 75 to 78.

Figure 3.3.7-4. Change in Horizontal Permeability Due to the Thermal-Hydrologic-Mechanical Effect at 1,000 Years

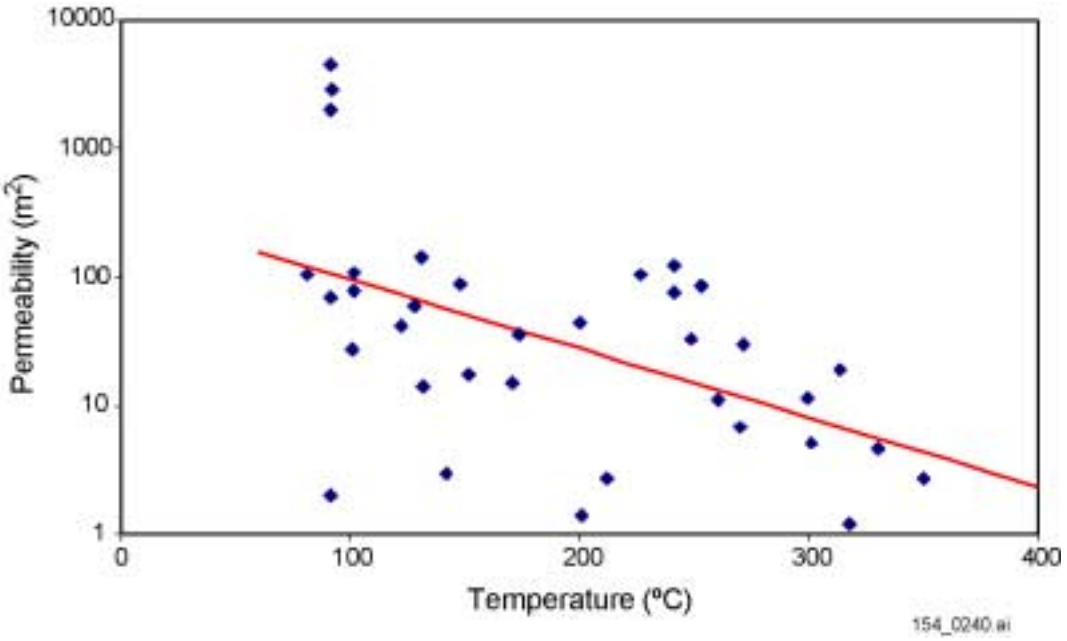

154_0240.ai

NOTE: Based on Figure 1 of Björnsson and Bodvarsson 1990 [DIRS 154606].

Figure 3.3.7-5. Correlation Between Permeability and Temperature of Geothermal Reservoirs Worldwide

Table 3.3.1-1. Mean Annual Precipitation for Analogues for the Lower and Upper Bound of the Three Climate Scenarios Adjusted for the Topography of the UZ Flow and Transport Model Area

Climate	Lower Bound (mm/yr)	Mean (mm/yr)	Upper Bound (mm/yr)
Interglacial[a]	186.8	190.6	268.6
Monsoon[b]	190.6	302.7	414.8
Intermediate[c]	202.2	317.8	433.5

Sources: [a] Adapted from USGS 2001 [DIRS 154674], Table 6-9.
[b] Adapted from USGS 2001 [DIRS 154674], Table 6-13.
[c] Adapted from USGS 2001 [DIRS 154674], Table 6-18.

NOTE: In *Simulation of Net Infiltration for Modern and Potential Future Climates* (USGS 2001 [DIRS 154674]), the interglacial and intermediate climates are referred to as modern and glacial transition, respectively.

Table 3.3.1-2. Mean Annual Temperature for Analogues for the Lower and Upper Bound of the Three Climate Scenarios Adjusted for the Topography of the UZ Flow and Transport Model Area

Climate	Lower Bound (°C)	Mean (°C)	Upper Bound (°C)
Interglacial[a]	19.3	19.3	19.3
Monsoon[b]	17.3	17.2	17.0
Intermediate[c]	10.2	9.8	9.4

Sources: [a] DTN: GS010508311221.001 [DIRS 154998].
[b] Adapted from USGS 2001 [DIRS 154674], Table 6-12.
[c] Adapted from USGS 2001 [DIRS 154674], Table 6-17.

NOTE: Lower and upper refer to precipitation (Table 3.3.1-1), not temperature. In *Simulation of Net Infiltration for Modern and Potential Future Climates* (USGS 2001 [DIRS 154674]), the interglacial and intermediate climates are referred to as modern and glacial transition, respectively.

Table 3.3.1-3. Climate Sequence from 10,000 to 1 Million Years

Climate State	Begin Time (years)	End Time (years)
Intermediate/Monsoon	10,000	38,000
Glacial, Stage 8/10	38,000	49,000
Intermediate	49,000	65,000
Interglacial	65,000	77,000
Intermediate/Monsoon	77,000	106,000
Glacial, Stage 8/10	106,000	120,000
Intermediate	120,000	137,000
Interglacial	137,000	148,000
Intermediate/Monsoon	148,000	200,000
Glacial, Stage 6/16	200,000	213,000
Intermediate	213,000	229,000
Interglacial	229,000	241,000
Intermediate/Monsoon	241,000	291,000
Glacial, Stage 4	291,000	329,000
Intermediate	329,000	345,000
Interglacial	345,000	355,000
Intermediate/Monsoon	355,000	401,000

Table 3.3.1-3. Climate Sequence from 10,000 to 1 Million Years (Continued)

Climate State	Begin Time (years)	End Time (years)
Glacial, Stage 8/10	401,000	409,000
Intermediate	409,000	422,000
Interglacial	422,000	432,000
Intermediate/Monsoon	432,000	471,000
Glacial, Stage 8/10	471,000	482,000
Intermediate	482,000	497,000
Interglacial	497,000	507,000
Intermediate/Monsoon	507,000	555,000
Glacial, Stage 6/16	555,000	595,000
Intermediate	595,000	611,000
Interglacial	611,000	622,000
Intermediate/Monsoon	622,000	672,000
Glacial, Stage 4	672,000	688,000
Intermediate	688,000	704,000
Interglacial	704,000	715,000
Intermediate/Monsoon	715,000	761,000
Glacial, Stage 8/10	761,000	788,000
Intermediate	788,000	801,000
Interglacial	801,000	811,000
Intermediate/Monsoon	811,000	854,000
Glacial, Stage 8/10	854,000	864,000
Intermediate	864,000	877,000
Interglacial	877,000	887,000
Intermediate/Monsoon	887,000	934,000
Glacial, Stage 6/16	934,000	957,000
Intermediate	957,000	970,000
Interglacial	970,000	981,000
Intermediate/Monsoon	981,000	1,000,000

Source: CRWMS M&O 2000 [DIRS 153038], Table 6-6.

Table 3.3.1-4. Summary of Uncertainty Issues Related to the Development of the Climate Model

Category	Uncertainty Issue	Treatment of Uncertainty Issue	Affected Goals
Conceptual Uncertainties	Timing and severity of climate changes during 400,000 year cycle. Past glacial and interglacial climate couplets differ from each other and past climates are repeated in a predetermined order.	Comparison of past records suggests climate cyclicity and the Devils Hole record records a series of glacial/interglacial couplets (CRWMS M&O 2000 [DIRS 153038], Section 6.3). The Owens Lake record is used to describe the climate conditions of the interval selected as the climate analogue. Climate change can be timed with an earth-orbital clock of precession and eccentricity, so the timing of future climate change can be estimated from the orbital clock. Orbital parameters for the earth can be readily calculated and the paleoclimatic record compared to the orbital parameters. Depends on the available record and the interpretation of paleoenvironments from the last 400,000 years. Temperature and precipitation characteristics of past glacial and interglacial couplets can differ from each other in a systematic way through a 400,000 year cycle, and if the sequence of an adjacent cycle is similar, then this relation can provide a criterion for the selection of particular past climates to project into the future.	Infiltration boundary condition for flow and transport models. Estimates of the sequence, magnitude, and timing of future climate states.
	Long-term earth-based climate-forcing functions, such as tectonic change, have remained relatively constant over the past 500,000 years.	Climate should not be greatly affected for the next 500,000 years (first half of the future climate analysis), but Tectonic activities may impact future climate at the 1 million-year time scale. The impact of potential future Tectonic activity was not estimated because it is not present in the Devils Hole and Owens Lake records.	
Data Uncertainties	The paleoecological and paleoclimatic records representative of Yucca Mountain.	Proxy data from the Yucca Mountain regional area are used to estimate past climates at Yucca Mountain.	Estimates of the timing, nature, and sequence of future climate states.
	Secular variation in the tidal dissipation and dynamical ellipticity of the earth.	Uncertainties are within the level of confidence of this methodology.	Estimates on the timing of future climate states.

Table 3.3.1-4. Summary of Uncertainty Issues Related to the Development of the Climate Model (Continued)

Category	Uncertainty Issue	Treatment of Uncertainty issue	Affected Goals
Parameter Uncertainties	Climate impact	Upper and lower bounds for each climate state estimated from what analogue meteorological stations Provide a range to capture the variability of climate	Temperature and precipitation estimates for different climate states
	Timing of future climates	Timing errors estimated are well within the level of confidence appropriate for their intended use	Timing of future climate states
	Methodological uncertainty	This methodology (forecasting) was selected over modeling because modeling requires the input of future boundary conditions which are unknown	Timing and sequence of climate states
	Unanticipated, unknown, and unmeasurable future events such as anthropogenic change, volcanic eruptions, tectonic change, change in solar output, and meteor showers	The most probable effect of anthropogenic change on future climate would be global warming, which would prolong the current interglacial period and delay the onset of future intermediate and glacial climates. This makes the climate modeling less certain, but because those climates are colder and wetter than the present climate, the present TSPA model is conservative for its intended use. Other climate-affecting events are unpredictable.	Estimates of the sequence, magnitude, and timing of future climate states

Table 3.3.1-5. Mean Annual Precipitation for the Lower and Upper Bound of the Three Glacial Climate Scenarios Adjusted for the Topography of the UZ Flow and Transport Model Area

Climate	Lower Bound (mm/yr)	Mean (mm/yr)	Upper Bound (mm/yr)
Glacial, Stage 8/10	433.5[a] (391.0[f])	429.0[c]	529.0[d]
Glacial, Stage 6/16	330.0[b]	429.0[c]	529.0[d]
Glacial, Stage 4	269.0[e]	330.0[b]	429.0[c]

Source: Adapted from BSC 2001 [DIRS 154873].

NOTES: [a] Rosalia, WA; Spokane, WA; St. John, WA (upper-bound intermediate climate meteorological stations).
[b] Browning, MT; Simpson 6NW, MT.
[c] Lake Yellowstone, WY; Browning, MT; Simpson 6NW, MT.
[d] Lake Yellowstone, WY.
[e] Simpson 6NW, MT.
[f] Browning, MT (alternate Stage 6/16 meteorological station).

Table 3.3.1-6. Mean Annual Temperature for the Lower and Upper Bound of the Three Glacial Climate Scenarios Adjusted for the Topography of the UZ Flow and Transport Model Area

Climate	Lower Bound (°C)	Mean (°C)	Upper Bound (°C)
Glacial, Stage 8/10	9.4[a] (5.3[f])	3.1[c]	0.78[d]
Glacial, Stage 6/16	5.5[b]	3.1[c]	0.78[d]
Glacial, Stage 4	5.7[e]	5.5[b]	3.1[c]

Source: Adapted from BSC 2001 [DIRS 154873].

NOTES: [a] Rosalia, WA; Spokane, WA; St. John, WA (upper-bound intermediate climate meteorological stations).
[b] Browning, MT; Simpson 6NW, MT.
[c] Lake Yellowstone, WY; Browning, MT; Simpson 6NW, MT.
[d] Lake Yellowstone, WY.
[e] Simpson 6NW, MT.
[f] Browning, MT (alternate Stage 6/16 meteorological station).

Lower and upper refer to precipitation (Table 3.3.1-5) or net infiltration (Table 3.3.2-3), not temperature.

Table 3.3.2-1. Average Net Infiltration Rates over the Unsaturated Zone Flow and Transport Model Domain for the Modern, Monsoon, and Glacial Transition Climate States

Climate	Lower Bound (mm/yr)	Mean (mm/yr)	Upper Bound (mm/yr)
Interglacial[a]	1.3	4.6	11.1
Monsoon[b]	4.6	12.2	19.8
Intermediate[c]	2.5	17.8	33.0

Sources: [a] Adapted from USGS 2001 [DIRS 154674], Table 6-9.
[b] Adapted from USGS 2001 [DIRS 154674], Table 6-13.
[c] Adapted from USGS 2001 [DIRS 154674], Table 6-18.

NOTE: In *Simulation of Net Infiltration for Modern and Potential Future Climates* (USGS 2001 [DIRS 154674]), the interglacial and intermediate climates are referred to as modern and glacial transition, respectively.

Table 3.3.2-2. Summary of Uncertainty Issues Related to the Development of the Net Infiltration Model

Category	Uncertainty Issue	Treatment of Uncertainty Issue	Affected Goals
Conceptual Uncertainties	The net infiltration model (USGS 2000 [DIRS 139422]) uses a distributed parameter, quasi-three-dimensional water-balance approach for simulating runoff and net infiltration processes without necessarily representing the physics of infiltration in soils and stream flow	The net infiltration model was compared successfully to several independent approaches to estimating net infiltration and recharge (USGS 2001 [DIRS 154674], Section 6.8) The net infiltration model was calibrated using moisture profile, soil and bedrock hydrologic properties, meteorological data and stream flow measurements at Yucca Mountain	Estimates of net infiltration rate resulting from the various different climate states
	The scope of the net infiltration model is limited to surficial hydrologic processes, with estimates of net infiltration limited to vertical flow though the depth of the root zone only	Vertical one-dimensional flow of infiltrating water through the root zone is supported by data (USGS 2001 [DIRS 154674], Section 6.8). Data indicating ponding of water within the root zone or on the soil/bedrock interface from the episodic infiltration events resulting in lateral flow has not been found	Estimates of net infiltration rate resulting from the various different climate states
Data Uncertainties	Precipitation rates and temperatures resulting from future climates	Data obtained from meteorological stations used in the Climate Model are believed to be representative of future climates at Yucca Mountain based upon ostracode populations and geographic similarity, location and proximity to Yucca Mountain	Estimates of net infiltration rate resulting from the various different climate states
	Accuracy of field data used to calibrate the net infiltration model for the modern (present-day) climate state	Extensive data regarding the time series of water-content profiles in boreholes by neutron logging, water potential at the soil/bedrock contact, and stream-flow measurements caused by transient precipitation events were collected	Parameters in the net infiltration model for the modern climate state
Parameter Uncertainties	Root-zone weighting parameters, vegetation density, changes in vegetation type and root zone thickness are a function of the climate state	These parameters were adjusted by a constant factor to extrapolate from present day conditions at Yucca Mountain to those anticipated to occur under future climate states (USGS 2001 [DIRS 154674], Section 6.9)	Estimates of net infiltration rate resulting from the various different climate states
	Uncertainty in net infiltration results from imperfect knowledge of input parameters used by the net infiltration model	A TSPA uncertainty analysis (Section 3.3.2.6) was conducted, focusing on twelve key input parameters for which uncertainty distributions were developed (USGS 2001 [DIRS 154674], Section 6.10.2). The key parameters were: bedrock porosity, bedrock root zone thickness, soil depth, precipitation, potential evapotranspiration, bedrock saturated hydraulic conductivity, soil saturated hydraulic conductivity, two bare-soil evaporation parameters, effective surface-water flow area, and parameters associated with sublimation and melting of snow cover	Estimates of net infiltration rate resulting from the various different climate states

Table 3.3.2-3. Average Net Infiltration Rates over the Unsaturated Zone Flow and Transport Model Domain for Full Glacial Climate States

Climate	Lower Bound (mm/yr)	Mean (mm/yr)	Upper Bound (mm/yr)
Glacial, Stage 8/10	33.0[a] (36.0[b])	87.9	151.0
Glacial, Stage 6/16	24.4	87.9	151.0
Glacial, Stage 4	12.9	24.4	87.9

Source: Adapted from BSC 2001 [DIRS 154919].

NOTES: [a] Derived using upper-bound intermediate climate meteorological station data (Tables 3.3.1-5, 3.3.1-6).
[b] Derived using alternate Stage 6/16 meteorological station data (Tables 3.3.1-5, 3.3.1-6).

Table 3.3.3-1. Net Infiltration Data by Region

Region	Area		Net Infiltration Volume				Net Infiltration Rate	
			Before Calibration		After Calibration		Before Calibration	After Calibration
	km^2	%	m^3/yr	%	m^3/yr	%	mm/yr	mm/yr
I	9.9	25.5	104435	58.9	104436	54.2	10.57	10.57
II	5.3	13.8	12317	6.9	12317	6.4	2.31	2.31
III	3.7	9.6	26266	14.8	20194	10.6	7.10	5.46
IV	3.6	9.4	8819	5.0	16267	8.4	2.43	4.48
V	4.6	11.9	12510	7.1	17534	9.1	2.71	3.80
VI	2.2	5.6	2479	1.4	5447	2.8	1.14	2.51
VII	1.8	4.6	3345	1.9	3345	1.7	1.88	1.88
VIII	3.0	7.7	2156	1.2	2156	1.1	0.73	0.73
IX	4.7	12.0	4996	2.8	11022	5.7	1.07	2.36
Overall	38.7	100.0	177323	100.0	192718	100.0	4.58	4.98

Source: Before calibration DTN: GS000399991221.002 [DIRS 147022]; after calibration Bodvarsson 2001 [DIRS 154669], Attachment 11.

Table 3.3.3-2. Summary of Uncertainty Issues Related to Percolation Redistribution and Flow in PTn

Category	Uncertainty Issue	Treatment of Uncertainty Issue	Affected Goals
Conceptual Uncertainties	Lateral flow at PTn interfaces and in PTn.	Sensitivity simulations to evaluate the impacts of fine tuff layers, lateral discontinuities, upper and side (fault) boundary conditions, fracture, matrix, and fault properties. Multi-scale evaluations for the conceptual basis of heterogeneity representation, multicontinuum approaches, and discrete flow path approaches.	Development of conceptual models is consistent with the geologic, hydrologic, and geochemical observations.
	Role of PTn in damping spatial and temporal variabilities.	Quantify the effectiveness of damping by sensitivity simulations, field data collection, environmental tracer distributions, and controlled field tests.	
	Fast flow through PTn.	Quantify the sustainability of fast flow through heterogeneous units, with strong capillary forces and imbibition potentials by sensitivity simulations, field data collection, water and rock age sampling, and controlled field tests.	
	Transition from porous medium to fracture flow at PTn interfaces.	Quantify transition from porous flow in porous layers to fracture flow in fractured layers by sensitivity simulations, field data collection, and controlled flow tests.	
Data Uncertainties	Uncertainties of data used for calibration and validation of PTn property model.	Systematic collection of water potential, water saturation, saturation characteristic curves, relative permeability curves, chemical contents, isotopic ages, and relevant geologic, hydrologic, and geochemical data.	Development of data bases from all available geologic, hydrologic, and geochemical data.
Parameter Uncertainties	Uncertainties in PTn parameters.	Conduct iterative calibration and validation studies to determine the effective parameters for process models, taking into account of all relevant data and observations.	Development of model parameter sets in agreement with all available geologic, hydrologic, and geochemical data.

Table 3.3.4-1. Average Percolation Fluxes (mm/yr) Simulated Within the Potential Repository Footprint for Thirteen Infiltration Scenarios

Infiltration Scenario	Average Surface Infiltration Rate[a]	Lower Bound			Mean			Upper Bound		
		Fracture	Matrix	Total	Fracture	Matrix	Total	Fracture	Matrix	Total
Interglacial[b]	--	0.20	0.06	0.26	4.02	0.52	4.54	11.59	0.26	11.85
Monsoon[b]	--	3.96	0.21	4.17	12.11	0.79	12.90	20.95	0.35	21.30
Intermediate[b]	--	1.59	0.15	1.74	19.51	0.94	20.45	38.50	0.49	38.99
OIS16 lower bound #1[c]	12.9	15.98	0.35	16.33	--	--	--	--	--	--
OIS16 lower bound #3[c]	36.0	27.72	0.44	28.16	--	--	--	--	--	--
OIS16 upper bound #1[c]	151.0	--	--	--	--	--	--	114.81	1.12	115.93
OIS16 mean #2[c]	87.9	--	--	--	70.57	1.74	72.31	--	--	--

Sources: [a] Preliminary work described in Bodvarsson 2001 [DIRS 154669], Attachment 12. Based on data associated with BSC 2001 [DIRS 154564].
[b] Lower bound, mean, and upper bound: CRWMS M&O 2000 [DIRS 122797], Section 6.6.
[c] Bodvarsson 2001 [DIRS 154669], Attachment 12.

Table 3.3.4-2. Summary of Uncertainty Issues Related to Three-Dimensional Flow Fields

Category	Uncertainty Issue	Treatment of Uncertainty Issue	Affected Goals
Conceptual Uncertainties	Effect of large gridblock averaging on flow field and grid resolution	Sensitivity analyses using different size gridblock models Examining modeling results against various types of observation data	Detailed distribution of percolation flux Smearing fronts in simulated tracer transport plumes or early breakthrough at water table
	Steady-state ambient moisture flow assumption	Sensitivity analyses with transient infiltration maps in PTn absent areas Investigate PTn dampening effects using modeling with pneumatic and isotopic data	Simulated percolation flux Estimated groundwater travel times in the UZ
	Ability of model to induce flow focusing	Stochastic modeling studies of fracture networks and permeability distributions Corroborated with seepage test data Alternative conceptual models for faults	Estimated fast flow pathways/weeps Input data to drift seepage models
	Model used to calculate fracture and matrix flow components and to handle fracture/matrix interactions	Sensitivity modeling studies using alternative dual-continuum conceptual models, such as MINC Use of hybrid model grids for different units, including discrete fracture and single porous media models	Estimated fracture/matrix flow components Radionuclide transport times in the UZ
	Layer-averaged rock properties	Proposed sensitivity analyses with laterally heterogeneous rock properties	Simulated flow focusing Input data to drift seepage models
	Transition of flow between porous-medium and fractured units	Corroborate with isotopic data and seepage tests in these areas, such as interface between PTn/TSw and CHv/CHz	Estimated fracture/matrix flow components in TSw and CHn
	Flow within/below perched water zones	Sensitivity analyses using different conceptualizations of CHn zeolitic fracture properties	Distribution of percolation flux below the repository horizon Estimated groundwater travel and radionuclide transport times in the UZ
	Applicability of van Genuchten's model to unsaturated fracture flow	Proposed tests with alternative moisture functions, such as Brook-Corey relations	Predicted moisture condition within fracture and matrix systems

Table 3.3.4-2. Summary of Uncertainty Issues Related to Three-Dimensional Flow Fields (Continued)

Category	Uncertainty Issue	Treatment of Uncertainty Issue	Affected Goals
Data Uncertainties	Uncertainties in upstream models (climate/infiltration, integrated site model)	Sensitivity and bounding modeling studies using various climate/infiltration scenarios Proposed sensitivity analyses using different geostatistical realizations of the distribution of mineral alteration with CHn	Predicted groundwater travel and radionuclide transport times in the UZ
	Uncertainties in data used to calibrate and validate UZ flow fields (e.g., fracture and fault parameters)	Proposed re-evaluation of air-permeability ≅ liquid permeability assumption for fractures Proposed sensitivity analyses and re-estimation of model parameters using refined grid resolution Proposed sensitivity analyses using heterogeneous distributions of key hydrologic parameters	Predicted moisture condition and percolation flux within fracture and matrix systems
Parameter Uncertainties	Uncertainties in UZ flow parameters, specifically fracture properties in CHn and fault properties	Reestimate fracture parameters using Busted Butte data Sensitivity studies with different fracture and fault properties	Predicted flow paths and groundwater travel times in the UZ
	Average percolation flux	Sensitivity modeling analyses with bounding-scenario infiltration rates	Groundwater water travel and tracer transport times in the UZ

Table 3.3.5-1. Summary of Numerical Model Cases for Mountain-Scale Thermal Hydrologic

Case No.	Numerical Grid	Thermal Load	Thermal Properties
1	3-D submodel, no drifts	67.7 kW/acre (1.35 kW/m); 80% forced ventilation for 300 years	Base 3-D case, no lithophysal cavities
2	3-D submodel, no drifts	67.7 kW/acre (1.35 kW/m); 80% forced ventilation for 300 years	3-D case, with lithophysal cavities
3	2-D cross section (NS#2) with locally defined drifts	67.7 kW/acre (1.35 kW/m); with 70% forced ventilation for 50 years	2-D, no lithophysal cavities
4	2-D cross section (NS#2) with locally defined drifts	67.7 kW/acre (1.35 kW/m); with 70% forced ventilation for 50 years	2-D, with lithophysal cavities
5	2-D cross section (NS#2) with locally defined drifts	67.7 kW/acre (1.35 kW/m); with 80% forced ventilation for 300 years	2-D, no lithophysal cavities
6	2-D cross section (NS#2) with locally defined drifts	67.7 kW/acre (1.35 kW/m); with 80% forced ventilation for 300 years	2-D, with lithophysal cavities
7	2-D cross section (NS#2) with locally defined drifts	67.7 kW/acre (1.35 kW/m); with 80% forced ventilation for 300 years	2-D, no lithophysal cavities, high infiltration, 5x mean

Source: Bodvarsson 2001 [DIRS 154669], Attachment 6.

NOTE: 2-D = two-dimensional; 3-D = three-dimensional.

Table 3.3.5-2. Recent Applications of TOUGH2 in Modeling Geothermal Systems

Site	Conditions, Phases	Physical Volume Modeled	Number of Model Elements	Calibration Method [a]	Length of Prediction Period	Calibration Inferences	Reference
Wairakei-Tauhara, New Zealand	2 phase	12 layers 3-D	1,417	NS, HM, P, T, w/ inverse modeling		More layers required	Bullivant and O'Sullivan 1998 [DIRS 144410]; O'Sullivan et al. 1998 [DIRS 154567]
Cerro Prieto, Mexico	1, 2 phase		347	NS, HM, P, T, many wells	2 Scenarios, 30 years	Location of upflow	Antunez et al. 1991 [DIRS 154568]
Nesjavellir, Iceland	2 phase	288 km^3 3-D	300	NS (100k years), HM (4 years)	30 years	Location of upflow zone	Bodvarsson et al. 1988 [DIRS 138603]; Bodvarsson et al. 1990 [DIRS 154574]; Bodvarsson et al. 1991 [DIRS 154575]; Bodvarsson et al. 1993 [DIRS 138618]
Kamojang, Indonesia	Vapor dominated	3-D	a) 456 b) 570	NS, P (20,000,000 years) HM, P (7 years)	30 years		O'Sullivan et al. 1990 [DIRS 137409]
East Olkaria, Kenya	2 phase	3 layers 3-D	150	HM, flow rate and enthalpy data (6.5 years)		High permeability region	Bodvarsson et al. 1987 [DIRS 136393]; Bodvarsson et al. 1987 [DIRS 136391]; Bodvarsson et al. 1990 [DIRS 136384]; Pham et al. 1996 [DIRS 154569]
		8 x 12 km, 3 layers 3-D	252		Many scenarios, 30 years		Bodvarsson et al. 1987 [DIRS 136393]; Bodvarsson et al. 1987 [DIRS 136391]; Bodvarsson et al. 1990 [DIRS 136384]
Krafla, Iceland	2 phase	100 blocks each 1 - $8x10^4$ m^3 1-D, 2-D, 3-D	100	Well test data, NS, T, P (20,000 years), HM	8 - 30 years with caution		Bodvarsson et al. 1984 [DIRS 144397]; Bodvarsson et al. 1984 [DIRS 137136]; Bodvarsson et al. 1984 [DIRS 137139]
Krafla-Hvitholar, Iceland	1, 2 Phase	2-D	85	NS, 3 Wells, T, P	3 Scenarios, 10 years	Importance of fault	Tulinius and Sigurdsson 1989 [DIRS 154571]
Amatitlan, Guatemala	2 Phase	140 km^3, 5 layers 3-D	1,220	NS T, P, HM (well flow testing ~30 days)	30 years with caution		Pham et al. 1996 [DIRS 154569]
Zunil, Guatemala	Vapor dominated	16 km^3 3-D	459	NS, T, P, well test data, interference test		Secondary upflow zone	Menzies et al. 1991 [DIRS 137923]

NOTE: [a] NS = Natural State; HM = History Matching; T = Temperature; P = Pressure; 2-D = two-dimensional; 3-D = three-dimensional.

Table 3.3.5-3. Summary of Uncertainty Issues Related to Thermal Hydrologic Effects on Mountain-Scale Flow

Category	Uncertainty Issue	Treatment of Uncertainty Issue	Affected Goals
Conceptual Uncertainties	Ventilation effect and heat transfer mechanism: Heat is evenly distributed within the drifts and all the waste is emplaced at time zero Ventilation removes only heat and not vapor Top and bottom boundaries are represented by fixed temperature, pressure, and saturation boundary Perched water does not affect TH processes at repository	Effects of thermal load variability not important beyond 100 years. All waste emplaced at time zero is a conservative approach When drift walls are dry then ventilation removes primarily heat Boundaries are far from repository Most Perched water up to 150 m below repository (CRWMS M&O 2000 [DIRS 144454], Section 5)	Maximum temperature Predicted liquid and gas flux UZ PTn, CHn, and water table temperature. Surface temperature (top of model) When close to drift impact on liquid flux and temperature
Data Uncertainties	Uncertainties in data used to calibrate and validate mountain-scale TH model	Data used in TH model are best available for mean UZ thermal and flow properties (CRWMS M&O 2000 [DIRS 144454], Section 4) Addressed by stochastic model used in Section 4.3.5	All
Parameter Uncertainties	Uncertainties in mountain-scale thermal properties: Drifts are assigned matrix and fractures properties of hydrogeological units in which they are located Thermal and flow properties not affected by temperature. Assumption supported by THM and THC analysis No hysteresis in flow properties	Effects of excavation and backfill are not important for the time scale considered (Section 4.3.4) Effects of TM-THC coupling are not significant especially in the lower temperature operating mode (Sections 3.3.6, 4.3.6, 4.3.7) Hysteresis effects are small (CRWMS M&O 2000 [DIRS 144454], Section 5)	Liquid flux and temperature (<100 yrs after emplacement) TM- and THC-process effects only long-term seepage

Table 3.3.6-1. Minerals, Aqueous Species, and Gaseous Species in the Mountain-Scale Thermal-Hydrologic-Chemical Model

Aqueous Species (primary)	**Gaseous Species (primary)**	**Minerals**
H_2O	CO_2	Calcite
H^+	H_2O	Tridymite
Na^+	Air	α–Cristobalite
K^+		Quartz
Ca^{+2}		Amorphous Silica
Mg^{+2}		Hematite
SiO_2		Fluorite
AlO_2^-		Gypsum
$HFeO_2^{-2}$		Goethite
HCO_3^-		Albite
Cl^-		K-Feldspar
SO_4^{-2}		Anorthite
F^-		Ca-Smectite
		Mg-Smectite
		Na-Smectite
		Opal
		Illite
		Kaolinite
		Glass
		Stellerite
		Heulandite
		Mordenite
		Clinoptilolite

Source: BSC 2001 [DIRS 154677], Table 8.

Table 3.3.6-2. Summary of Uncertainty Issues Related to the Prediction of Thermal Hydrologic-Chemical Effects on Mountain-Scale Unsaturated Zone Flow and Geochemistry

Category	Uncertainty Issue	Treatment of Uncertainty Issue	Affected Goals
Conceptual uncertainties	Effect of 3-D TH processes on mountain-scale geochemistry	Treated indirectly by evaluation of 2-D TH processes on geochemistry (this work)	Limits range of possible water compositions and amounts of mineral alteration owing to focused gas and liquid flow
	Impact of heating SZ on gas chemistry in UZ	Not treated	CO_2 degassing of SZ water could affect post-thermal water chemistry
	Surface temperature assumed constant instead of variable	Not treated	Variable surface temperature could result in more near-surface focusing of heat and vapor, and enhanced percolation flux around these areas
	Changes in infiltrating water chemistry associated with climate changes	Assessed indirectly through drift-scale-THC simulations using alternate water compositions	Results in more uncertainty of range in potential chemical compositions during post-thermal period
	Uncertainty in flow below potential repository and conceptual models for perched water	Not treated	Reaction rates in CHn zeolitic and vitric units are related to fluid fluxes as well as heat and therefore the different conceptual models for perched water may lead to a larger range in uncertainty for mineral alteration and effects on flow and transport
	Uncertainty in spatial distribution of net infiltration	Treated indirectly in drift-scale THC models through evaluation of different infiltration rates Larger-scale effects of different spatial distributions on flow focusing and THC processes not treated	Limits range of possible water compositions and distribution of mineral precipitation and dissolution
Data uncertainties	Uncertainties in mineralogy in repository unit	Treated indirectly by evaluation of mineralogy from two different geologic columns in drift-scale THC models Little data from Calico Hills unit under the potential repository footprint to constrain mineralogical abundances and variability	Limits prediction of potential effects on flow and transport in the Calico Hills unit, where glass, zeolite, and clay abundances are highly variable
	Thermodynamic and kinetic data specifically for zeolites, clays and glass	Treated through sensitivity studies on long-term behavior of ambient system water and gas chemistry and mineralogy assuming a fixed infiltration rate (BSC 2001 [DIRS 154677]) Many uncertainties unknown and should be treated through laboratory experiments under thermal conditions relevant to alteration of Calico Hills unit	Adds uncertainty to ranges of predicted water compositions, mineral assemblages, and changes in hydrologic properties

Table 3.3.6-2. Summary of Uncertainty Issues Related to the Prediction of Thermal Hydrologic-Chemical Effects on Mountain-Scale Unsaturated Zone Flow and Geochemistry (Continued)

Category	Uncertainty Issue	Treatment of Uncertainty Issue	Affected Goals
Parameter uncertainties	Uncertainties in fault parameters	Not treated	Faults may amplify THC processes because of their role as potential conduits for vapor and liquid flow and as a capillary barrier and therefore the range of potential effects have more uncertainty
	Large scale heterogeneity	Large-scale heterogeneity in mineralogical properties treated in part through variation in zeolitic or vitric attributes for layers and their changes in thickness	Heterogeneity in mineralogical properties could amplify local effects on hydrologic properties
	Uncertainty propagation	Treated preliminarily through alternate mineral reaction rates	Limits assessment of THC effects on flow, transport, and geochemistry in the UZ, and of uncertainty for TSPA

Table 3.3.7-1. Thermal-Hydrologic-Mechanical Parameter Data Used in Current Simulation

Parameter	Tptpmn	Tptpll	Source
Young's modulus	14.77 GPa	14.77 GPa	Extracted directly from CRWMS M&O 1999 [DIRS 126475], Table 10 to 15, and Table 24.
Poisson's ratio	0.21	0.21	
Thermal expansion coefficient	4.14 E-6 /°C	4.14 E-6 /°C	
Tensile strength	1.54 MPa	1.54 MPa	
Initial hydraulic aperture for Equation (4.3.7-2), b_i	286.9 μm	440.8 μm	The value of b_i is calculated from mean fracture spacing, *s*, and isotropic permeability, *k*, (CRWMS M&O 2000 [DIRS 144426], Section 6.1.4), assuming an ideal cubic block model, leading to the following formula: $b_i = \sqrt[3]{k \times 6 \times s}$.
Maximum joint closure for Equation (4.3.7-2), b_{max}	1486.0 μm	1486.0 μm	Model calibration against air-permeability experiments at Niches and DST (see Section 4.3.7.4.3), adjusted to a case of larger initial aperture. b_{max} is increased for the mountain scale properties compared to the calibrated value for the drift scale properties (Table 4.3.7-4) to match the maximum permeability increase observed at a initial permeability range of 1.7 to 4.5 $\times 10^{-11}$ m^2 (Figure 4.3.7-7), and to limit the possible permeability reduction less than 0.1 as observed in the DST.
Exponent for Equation (4.3.7-2), α	1.1 E-6	1.1 E-6	
Vertical stress gradient, σ_v	0.022 MPa/m	0.022 MPa/m	Within range of field measurements by Stock et al. 1985 [DIRS 101027] and Lee and Haimson 1999 [DIRS 129667].
Horizontal stress, σ_h	0.35 × σ_v MPa	0.35 × σ_v MPa	

Table 3.3.7-2. Changes In Permeability for Hydrostratigraphic Layers at the Mid-Repository Symmetry Boundary on the Left Side of the Model

Units	Elevation (m)	K_v/K_i	K_H/K_i
TCw	1447–1326	1.0 to 38	1.0 to 38
PTn	1326–1291	1.24 to 2.55	1.28 to 2.75
TSw31	1291–1289	1.80	2.27
TSw32	1289–1250	0.58	0.98
TSw33	1250–1167	0.40	0.72
TSw34 (Tptpmn)	1167–1134	0.28	0.66
TSw35 (Tptpll)	1134–1030	0.47 to 0.77	0.75 to 0.89
TSw36–37	1030–981	0.83 to 0.85	0.92 to 0.93
TSw38–39	981–960	0.53 to 0.72	0.80 to 0.88
CHn-pp4	960–869	0.9 to 1.0	1.0 to 1.1
Pp3_bf3	869–730	1.1 to 1.2	1.1 to 1.2

Source: Derived from Bodvarsson 2001 [DIRS 154669], Attachment 9, pp. 1 to 78.

NOTE: K_v = vertical permeability; K_H = horizontal permeability; K_i = initial permeability.

Table 3.3.7-3. Summary of Uncertainty Issues Related to Thermal-Hydrologic-Mechanical Effects on Mountain-Scale Flow

Category	Uncertainty Issue	Treatment of Uncertainty Issue	Affected Goals
Conceptual Model Uncertainties	Effects of THM processes versus TH only.	Implement a coupled THM code, joining TOUGH2 V1.5 and FLAC3D V2.0 codes, to study the impact of THM processes (Section 3.3.7.3).	Flux above and around the potential repository.
	3-D versus 2-D flow patterns.	2-D calculations have been done (Section 3.3.7.4); 3-D calculations to be conducted.	Flux above and around the potential repository.
Model Geometry Uncertainties	Horizontally uniform layers versus realistic inclined layers.	Calculation with layers assumed to be horizontal have been done (Section 3.3.7.4). Realistic-geometry simulations could reduce uncertainty.	Flux above and around the potential repository.
	Boundary conditions used.	Sensitivity study with range of conditions could reduce uncertainty.	Flux above and around the potential repository.
	Layering structure at the potential repository site.	The vertical stratigraphy at one location has been simulated (Section 3.3.7.4). Variation of layering structure to be considered.	Flux above and around the potential repository.
Parameter Uncertainties	Rock fracture stiffness in the layers. Residue permeability values.	A simulation with conservative values of fracture stiffness and residual aperture have been done (Section 3.3.7.4). A complete THM analysis of the Drift Scale Heater test with supplementary measurements could reduce uncertainty.	Flux above and around the potential repository.
	Heterogeneity in permeability spatial distribution.	Additional simulations needed on heterogeneous field representing the hydrogeologic units. Studies with multiple realizations to be conducted.	Flux above and around the potential repository.
	Property parameter values.	Hydraulic and thermal property parameters to be confirmed for the different layers.	Flux above and around the potential repository.

INTENTIONALLY LEFT BLANK

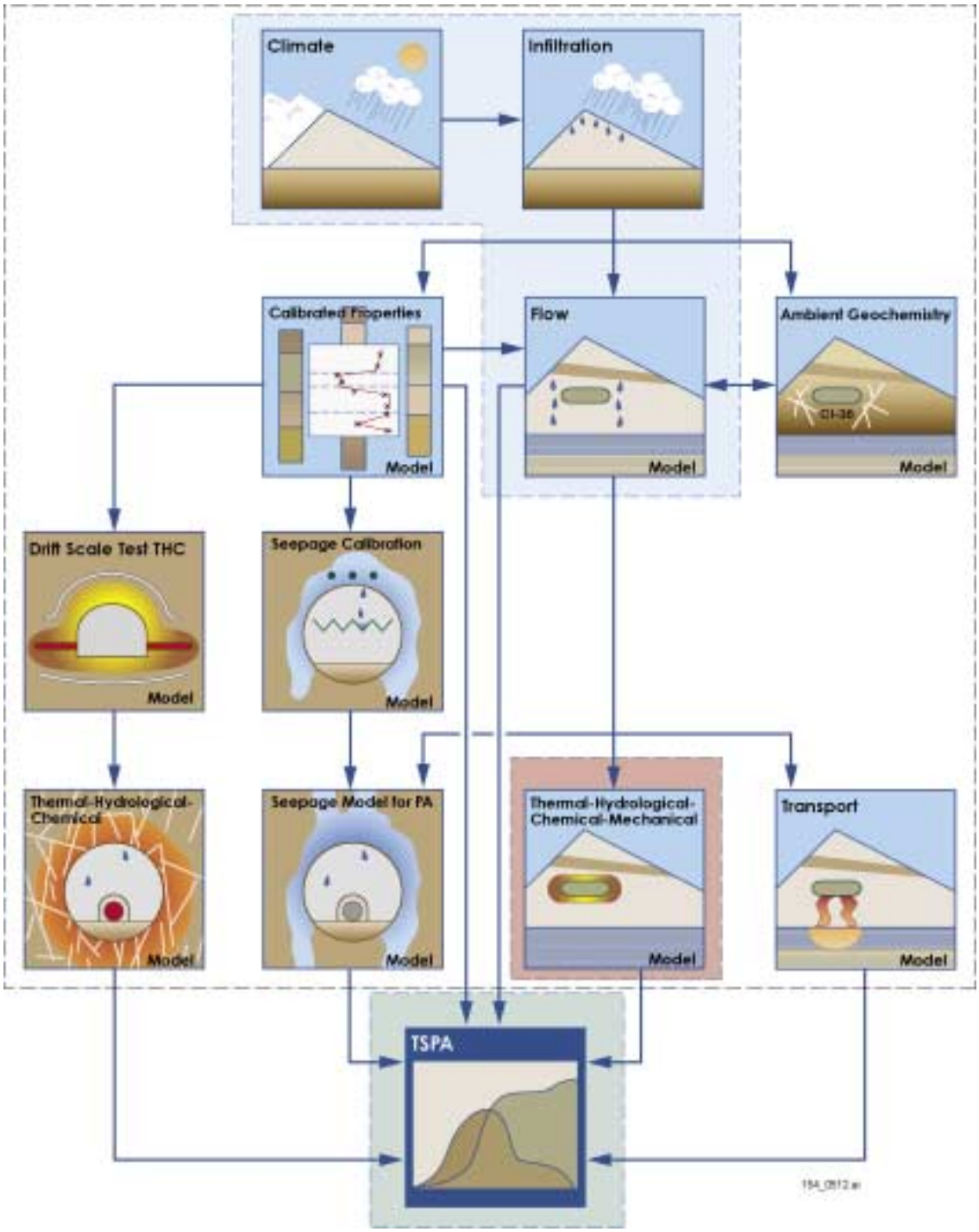

154_0512.ai

Source: Modified from CRWMS M&O 2000 [DIRS 151940], Figure 1-2.

NOTE: Most models relevant to this section are highlighted with color backgrounds.

Figure 3.1-1. Main Models Included in the Unsaturated Zone Process Model Report, Interrelations among them, and Connections to Total System Performance Assessment

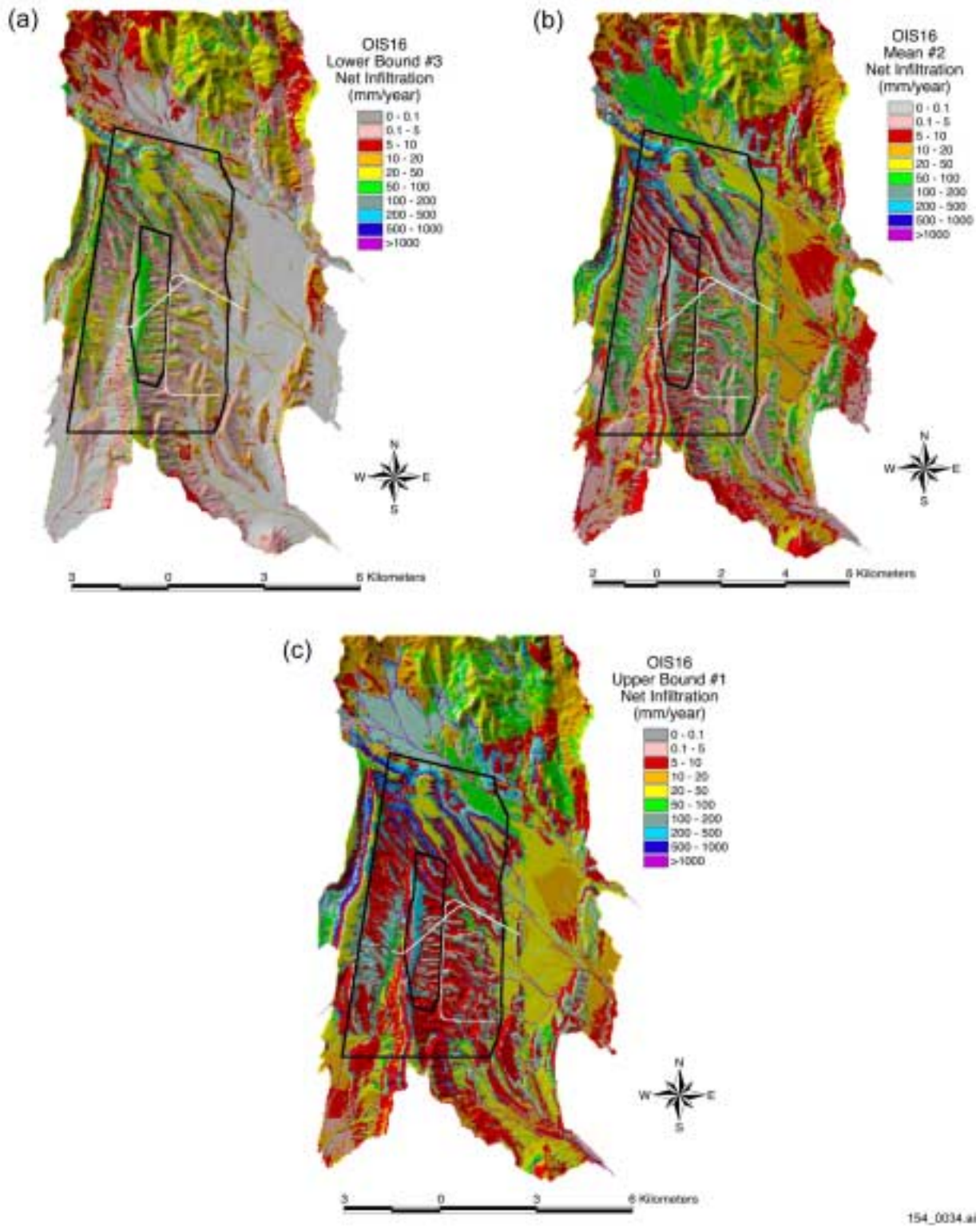

154_0034.ai
Source: BSC 2001 [DIRS 154873].

NOTE: Infiltration for lower (a), mean (b), and upper (c) bounds.

Figure 3.3.2-1. Net Infiltration for the Glacial Stage 6/16-Climate Scenario

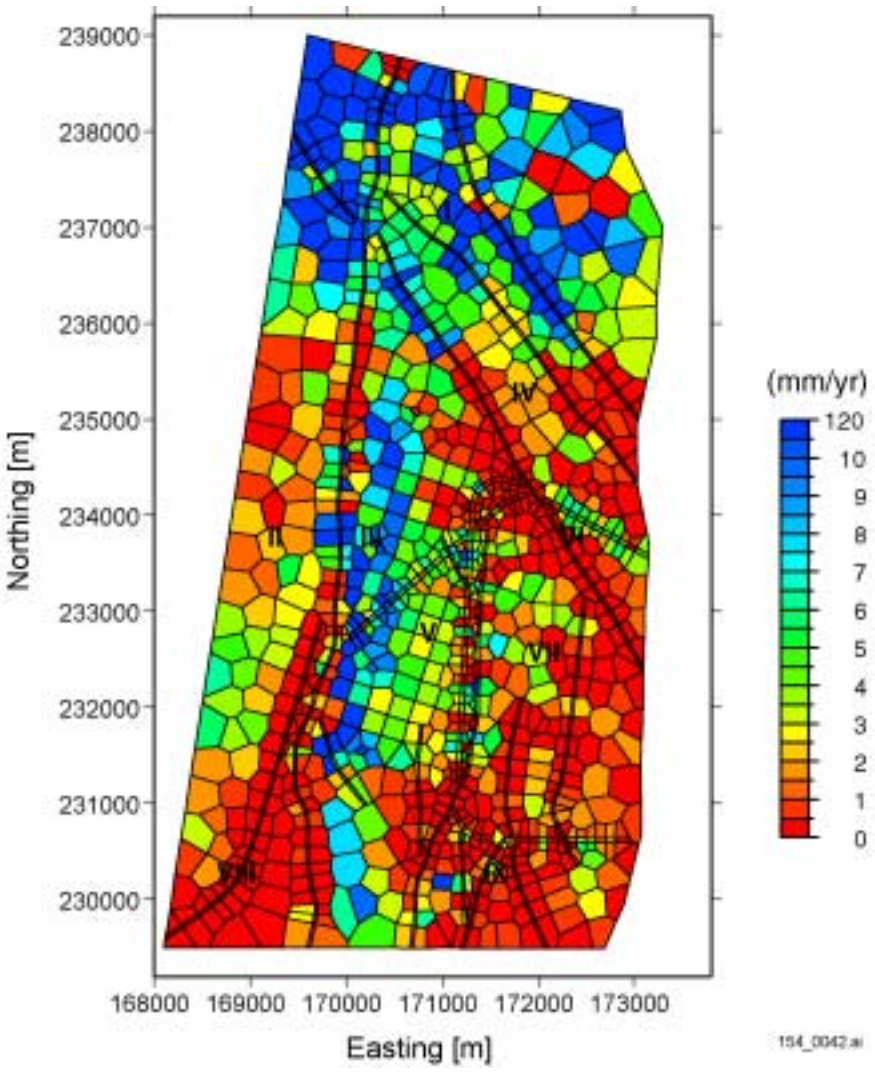

154_0042.ai

Source: DTN: GS000399991221.002 [DIRS 147022].

NOTE: Nevada coordinates in meters.

Figure 3.3.3-1. Present-Day Mean Net Infiltration

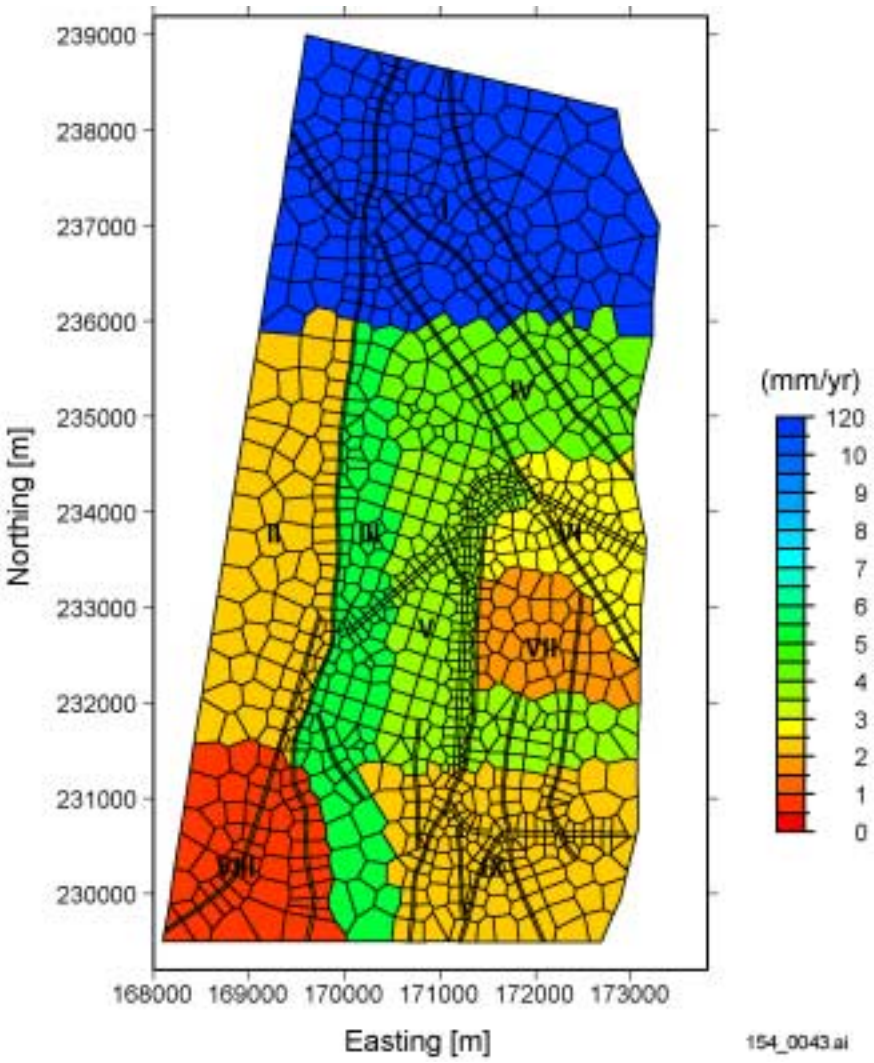

154_0043.ai

Source: Bodvarsson 2001 [DIRS 154669], Attachment 11, listed on p. 80.

NOTE: Uniform net infiltration in each region. Nevada coordinates in meters.

Figure 3.3.3-2. Chloride-Based, Present-Day Mean Net Infiltration

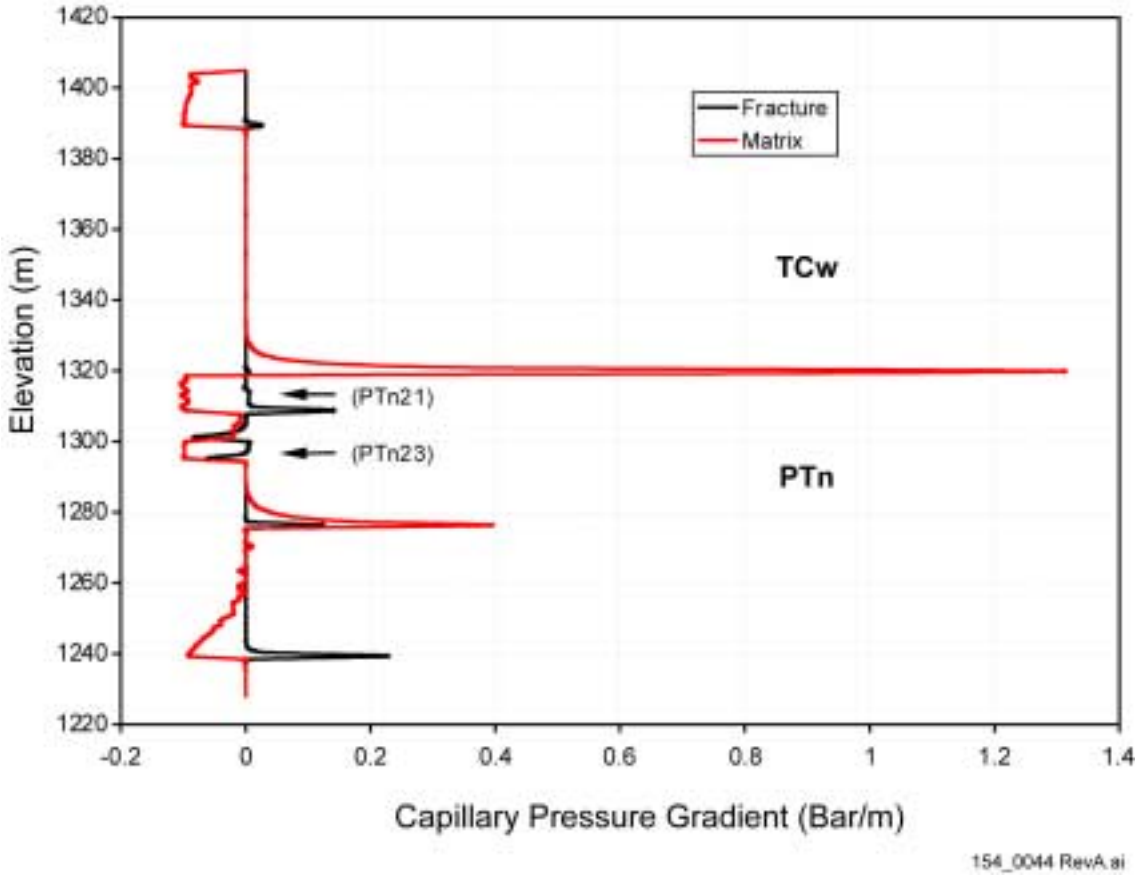

154_0044 RevA.ai

Source: Wu et al. 2001 [DIRS 154918], Figure 4.1-5.

NOTE: Capillary pressure measured in bar/m at coordinates 171200E, 235119N (coordinates using refined grid).

Figure 3.3.3-3. Vertical Capillary Pressure Gradients

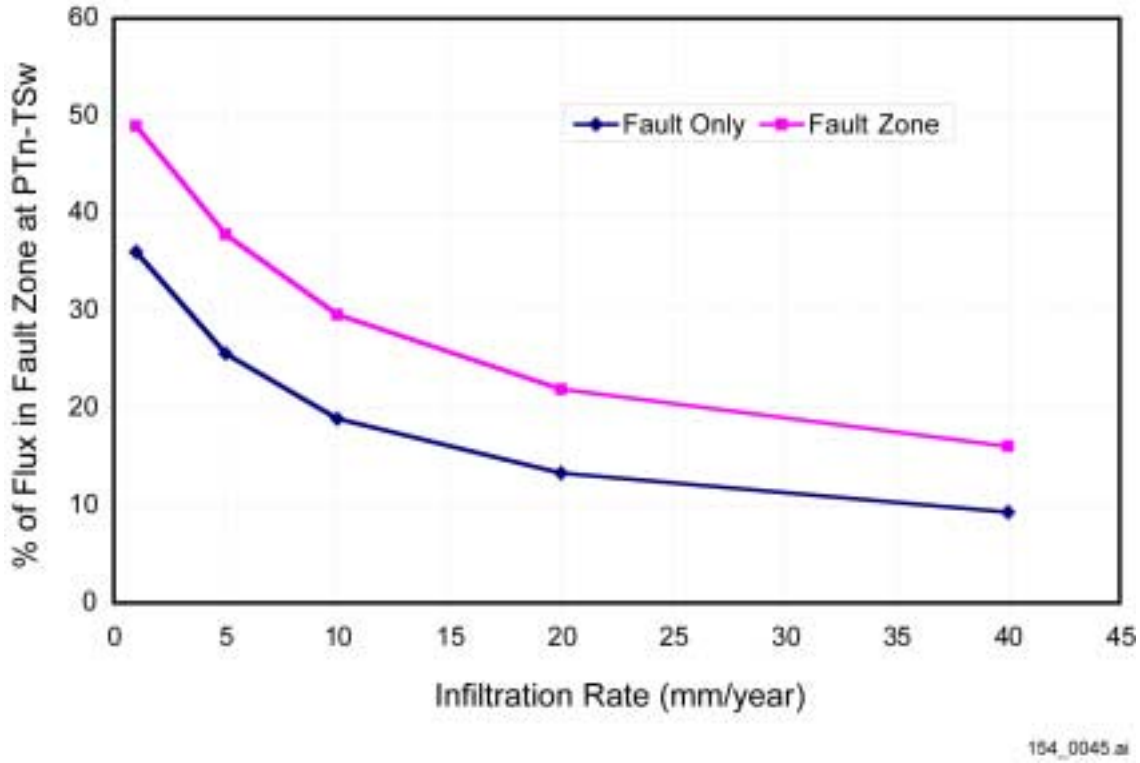

154_0045.ai

Source: Wu et al. 2001 [DIRS 154918].

NOTE: Effects of net infiltration values on percentage of flow through faults and fault zones, reflecting the amount of lateral water flow within the PTn unit along a vertical cross section, using the refined grid and uniform surface net infiltration pattern.

Figure 3.3.3-4. Effect of Net Infiltration on Percentage of Flow-Through Faults and Fault Zones

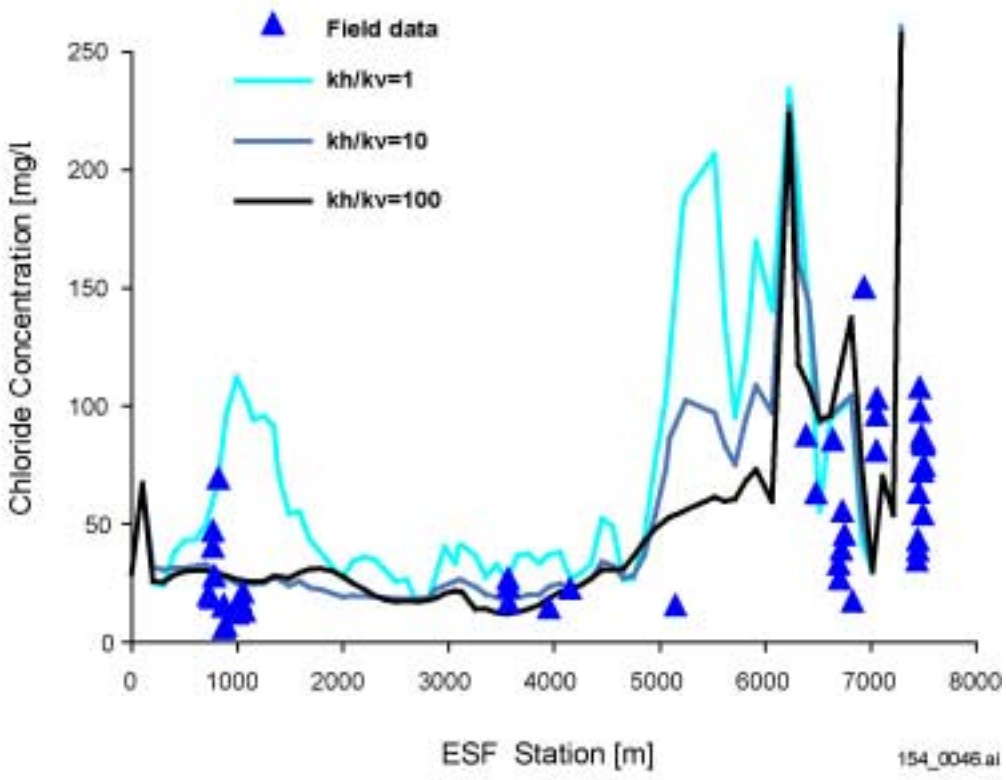

154_0046.ai

Source: Bodvarsson 2001 [DIRS 154669], Attachment 11, listed on p. 79.

NOTE: ESF = Exploratory Studies Facility; kh = horizontal permeability; kv = vertical permeability.

Figure 3.3.3-5. Effect of Horizontal Permeability on the Modeled Concentrations of Chloride in the Exploratory Studies Facility

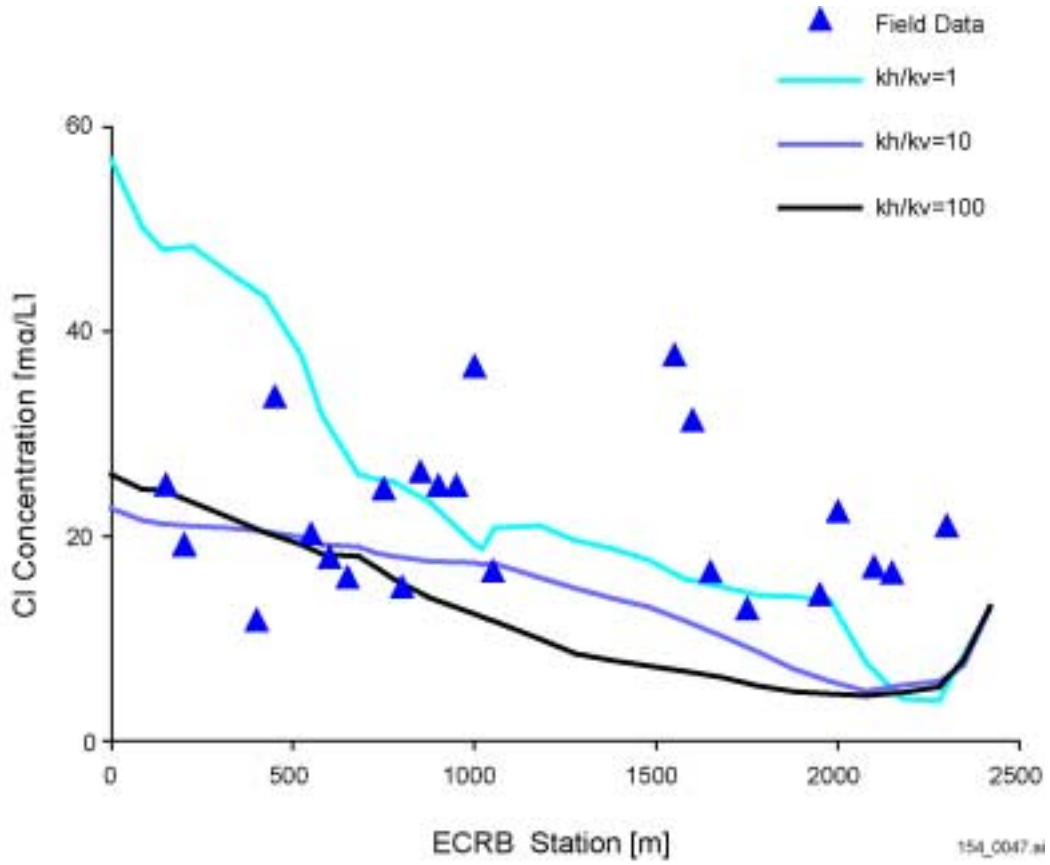

154_0047.ai

Source: Bodvarsson 2001 [DIRS 154669], Attachment 11, listed on p. 79.

NOTE: Model assumes infiltration at present-day mean rates. Cl = chloride; ECRB = Enhanced Characterization Repository Block.

Figure 3.3.3-6. Effect of Horizontal Permeability on the Modeled Concentrations of Chloride in the Enhanced Characterization Repository Block

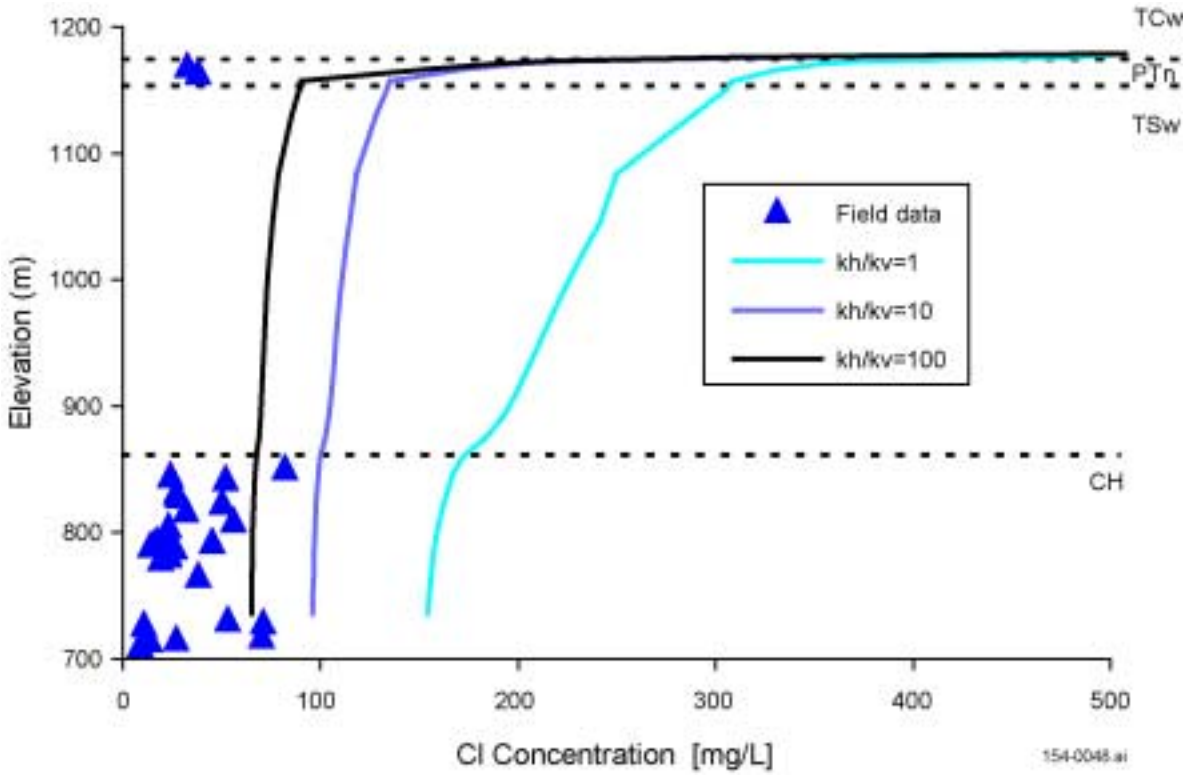

154_0048.ai

Source: Bodvarsson 2001 [DIRS 154669], Attachment 11, listed on p. 79.

Figure 3.3.3-7. Effect of Horizontal Permeability on the Modeled Concentrations of Chloride in Borehole UZ#16.

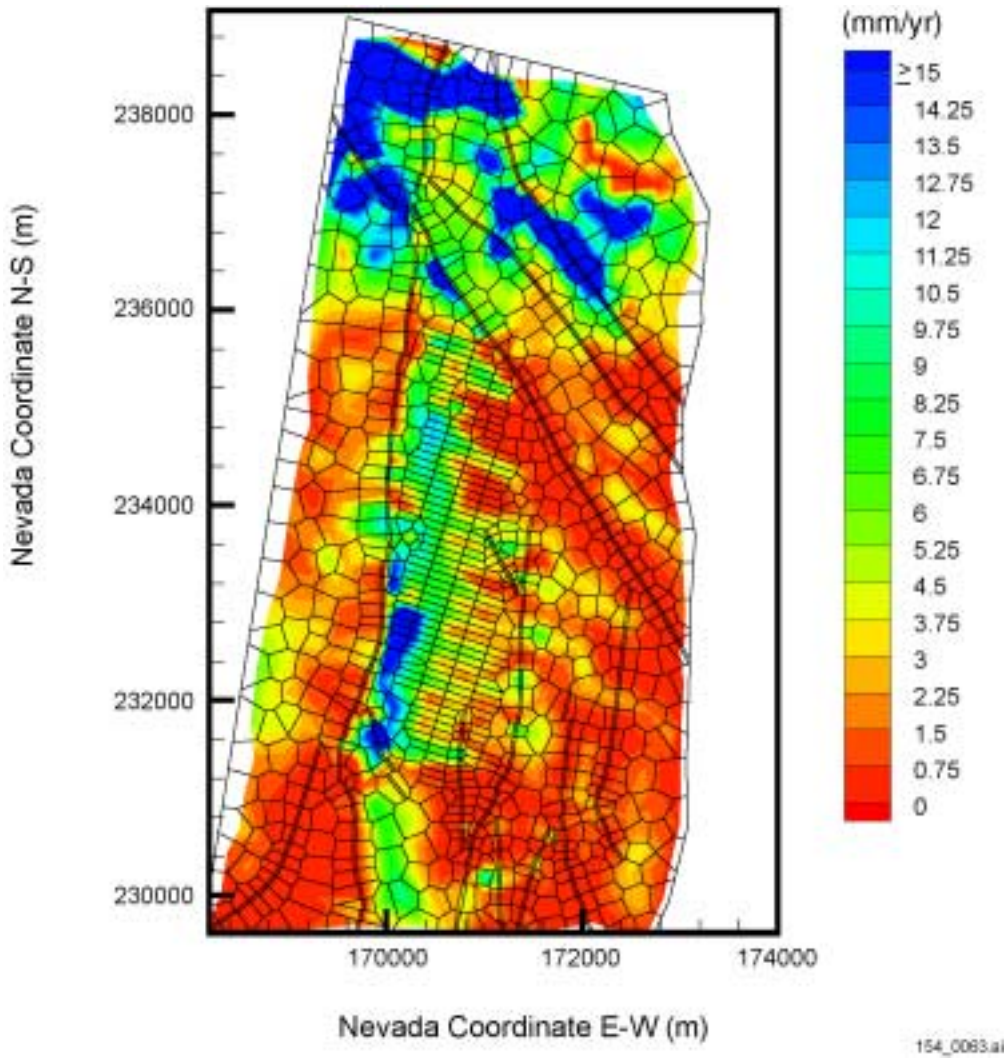

154_0063.ai

Sources: CRWMS M&O 2000 [DIRS 122797], Figure 6-3; DTN: GS000399991221.002 [DIRS 147022]; DTN: LB990801233129.003 [DIRS 122757].

NOTE: Simulation uses present-day, base-case, mean infiltration.

Figure 3.3.4-1. Plan View of Total System Performance Assessment Grid and Net Infiltration Distributed Over the Domain of the Unsaturated Zone Model

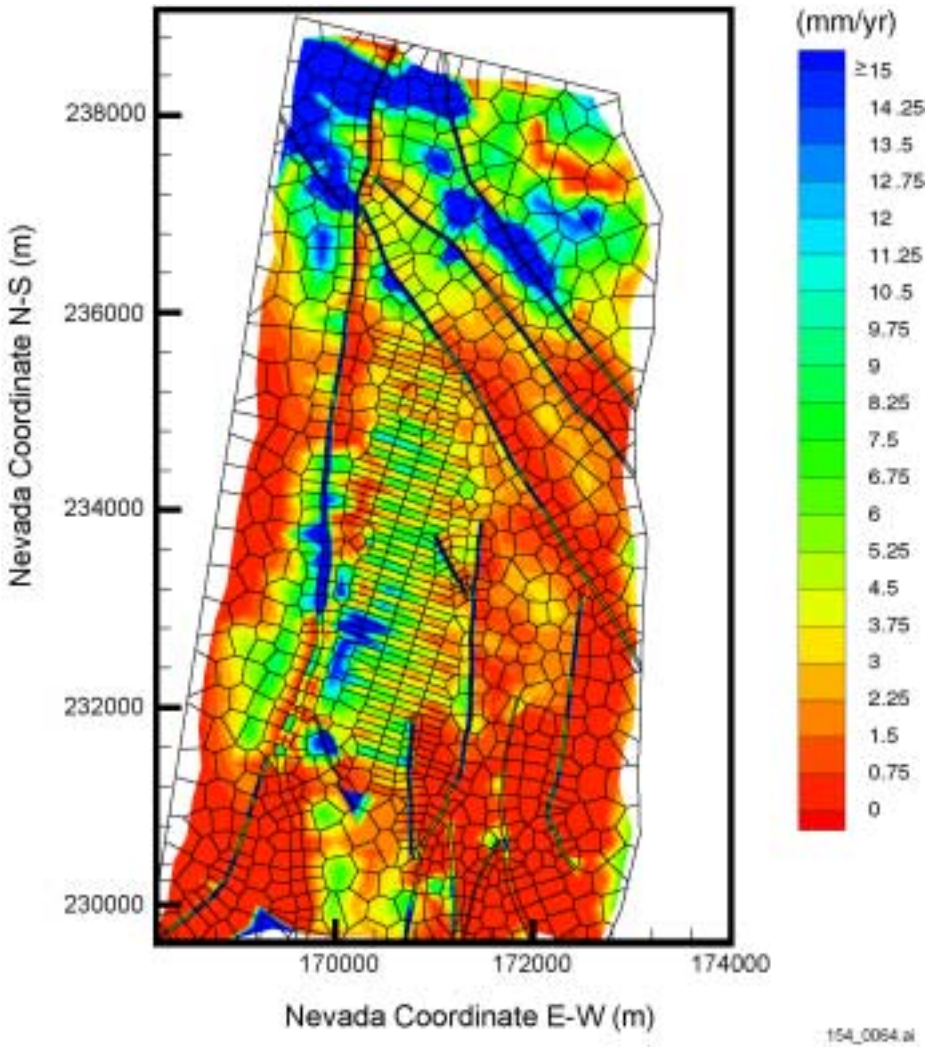

154_0064.ai

Source: CRWMS M&O 2000 [DIRS 122797], Figure 6-42.

NOTE: Simulation uses present-day, mean infiltration.

Figure 3.3.4-2. Simulated Percolation Flux at the Repository Horizon for the Flow-Through Perched Water Conceptual Model

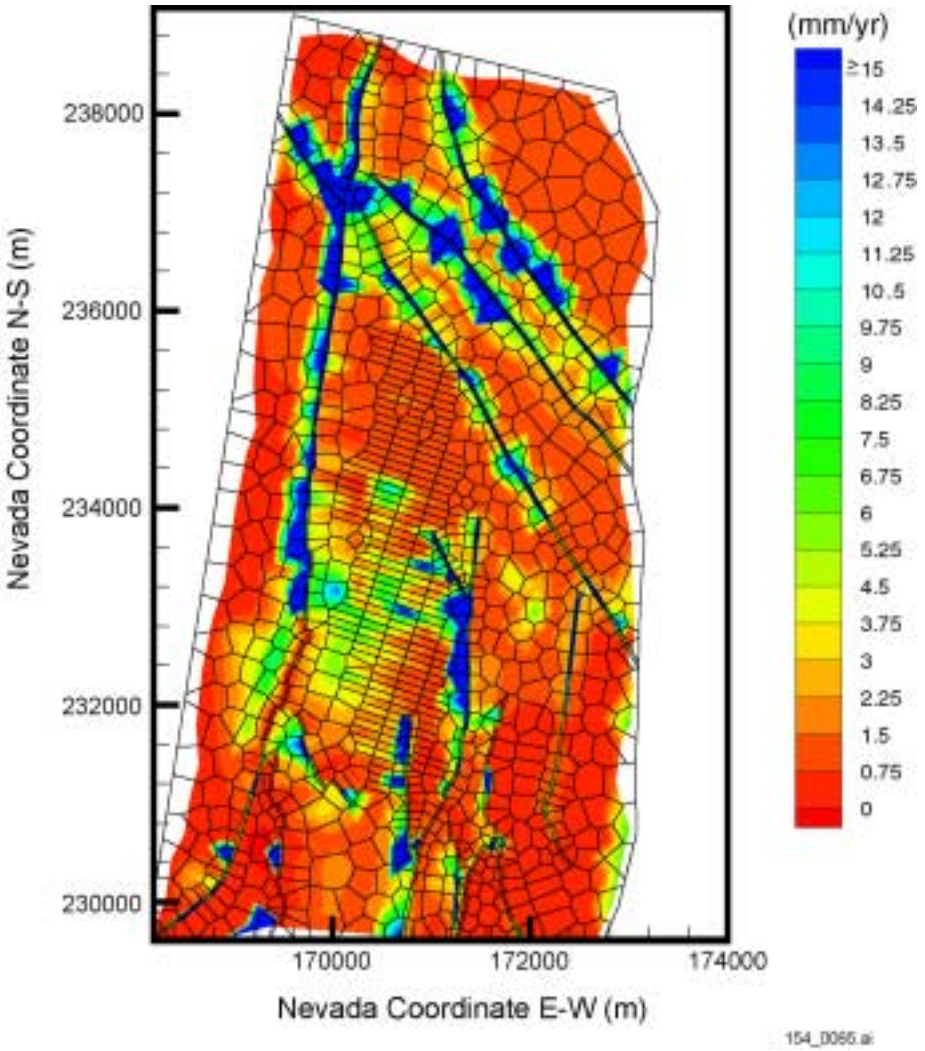

154_0065.ai

Source: CRWMS M&O 2000 [DIRS 122797], Figure 6-45; DTN: LB990801233129.003 [DIRS 122757].

NOTE: Simulation uses present-day, mean infiltration.

Figure 3.3.4-3. Simulated Percolation Flux at the Water Table for the Flow-Through Perched Water Conceptual Model

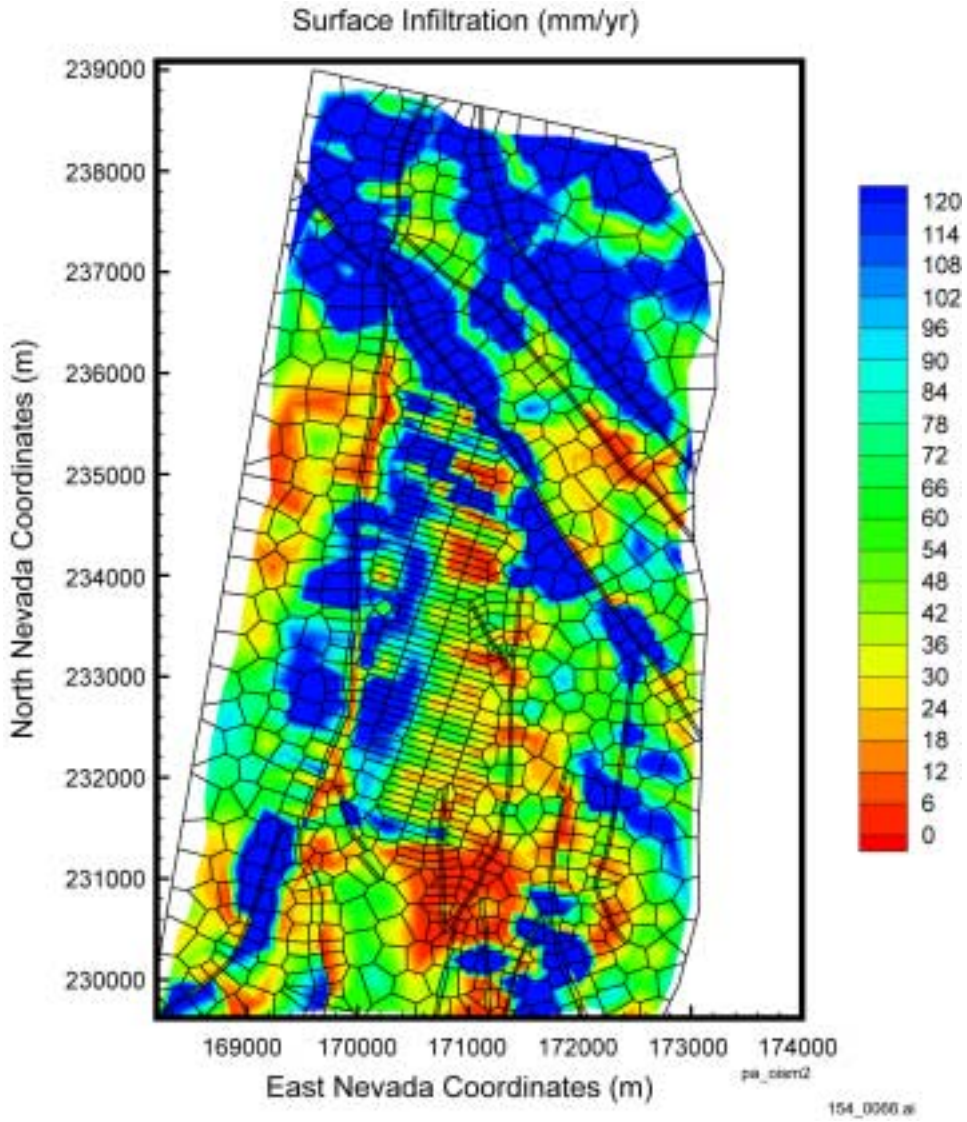

154_0066.ai

Source: Preliminary work described by Bodvarsson 2001 [DIRS 154669], Attachment 12, pp. 208 to 209; also based on data associated with BSC 2001 [DIRS 154564].

NOTE: Model assumes the full-glacial, mean #2 infiltration scenario.

Figure 3.3.4-4. Plan View of Net Infiltration Distributed Over the Domain of the Three-Dimensional Unsaturated Zone Total System Performance Assessment Model

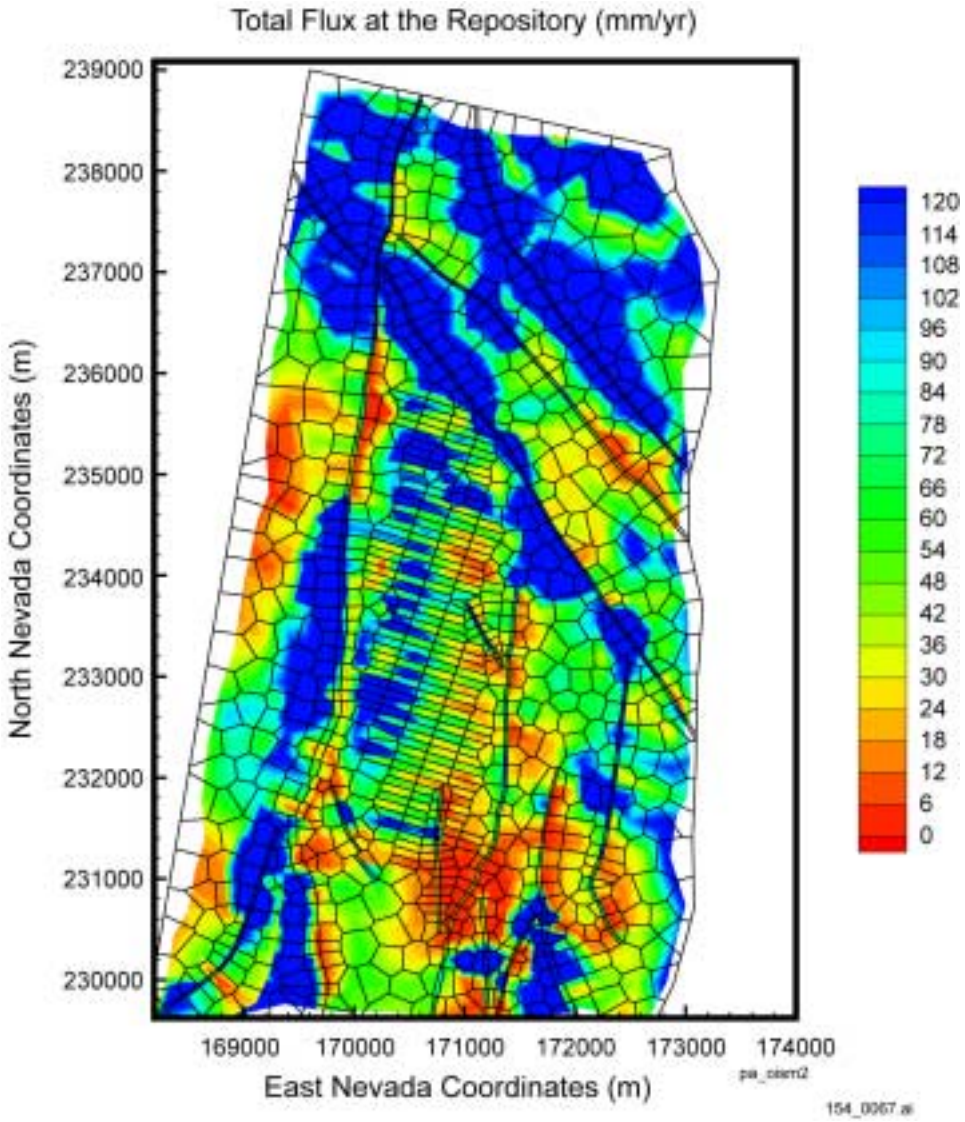

154_0067.ai

Source: Preliminary work described by Bodvarsson 2001 [DIRS 154669], Attachment 12, file listed on p. 209.

NOTE: Simulation uses the flow-through perched water conceptual model.

Figure 3.3.4-5. Simulated Percolation Flux at the Potential Repository Horizon under the Full-Glacial, Mean #2 Infiltration Scenario

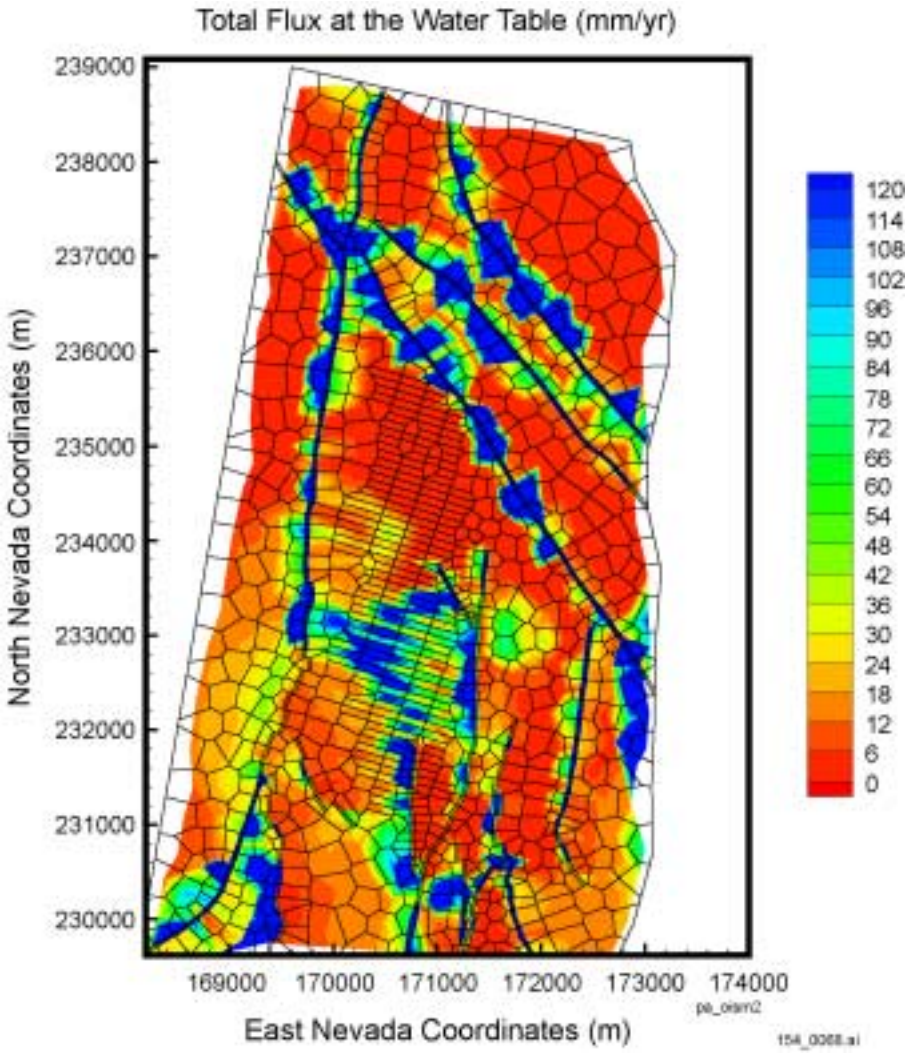

154_0068.ai

Source: Preliminary work described by Bodvarsson 2001 [DIRS 154669], Attachment 12, file listed on p. 209.

NOTE: Simulation uses the Flow-Through Perched Water Conceptual Model.

Figure 3.3.4-6. Simulated Percolation Flux at the Water Table under the Full-Glacial, Mean #2 Infiltration Scenario

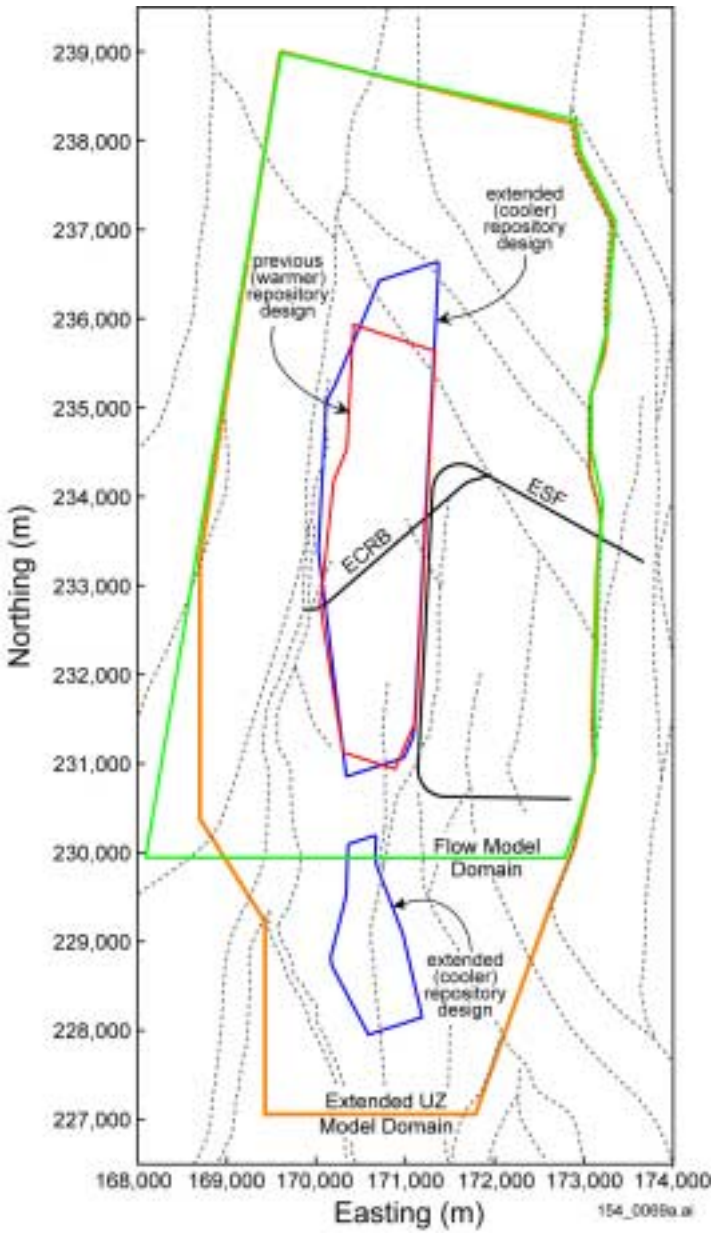

154_0069a.ai

Sources: DTN: MO9901MWDGFM31.000 [DIRS 103769]. References for repository layouts: Extended BSC 2001 [DIRS 154548]; Previous CRWMS M&O 1997 [DIRS 100245].

NOTE: Dotted lines represent faults as mapped in the Geologic Framework Model version 3.1. Nevada coordinates in meters. ECRB = Enhanced Characterization of the Repository Block; ESF = Exploratory Studies Facility; UZ = unsaturated zone.

Figure 3.3.4-7. Plan View of Unsaturated Zone Model Domains and Potential Repository Layouts

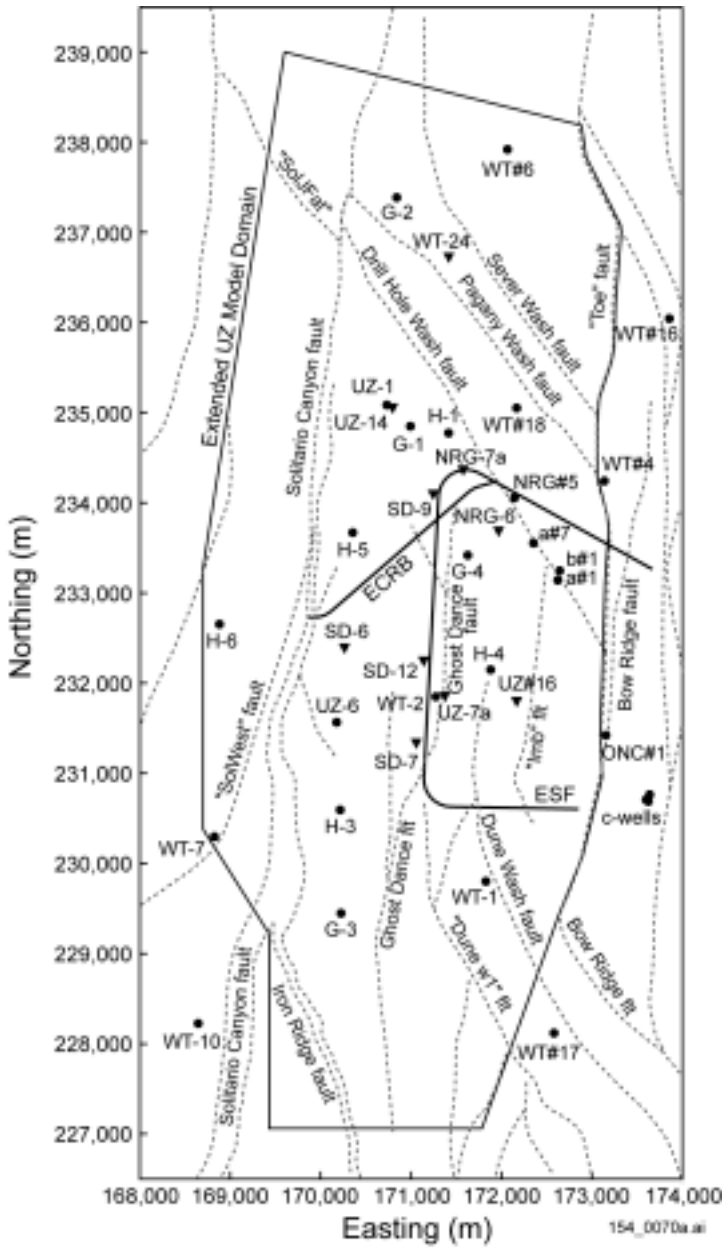

154_0070a.ai

Source: CRWMS M&O 2000 [DIRS 138860].

NOTE: Triangles represent wells from which qualified hydrogeologic rock property data were collected. Circles and triangles represent wells used to develop the geologic framework model. Dotted lines indicate fault traces per Geologic Framework Model version 3.1. Nevada coordinates in meters. ECRB = Enhanced Characterization of the Repository Block; ESF = Exploratory Studies Facility; UZ = unsaturated zone.

Figure 3.3.4-8. Data Locations Characterizing Repository Host Horizon Layers

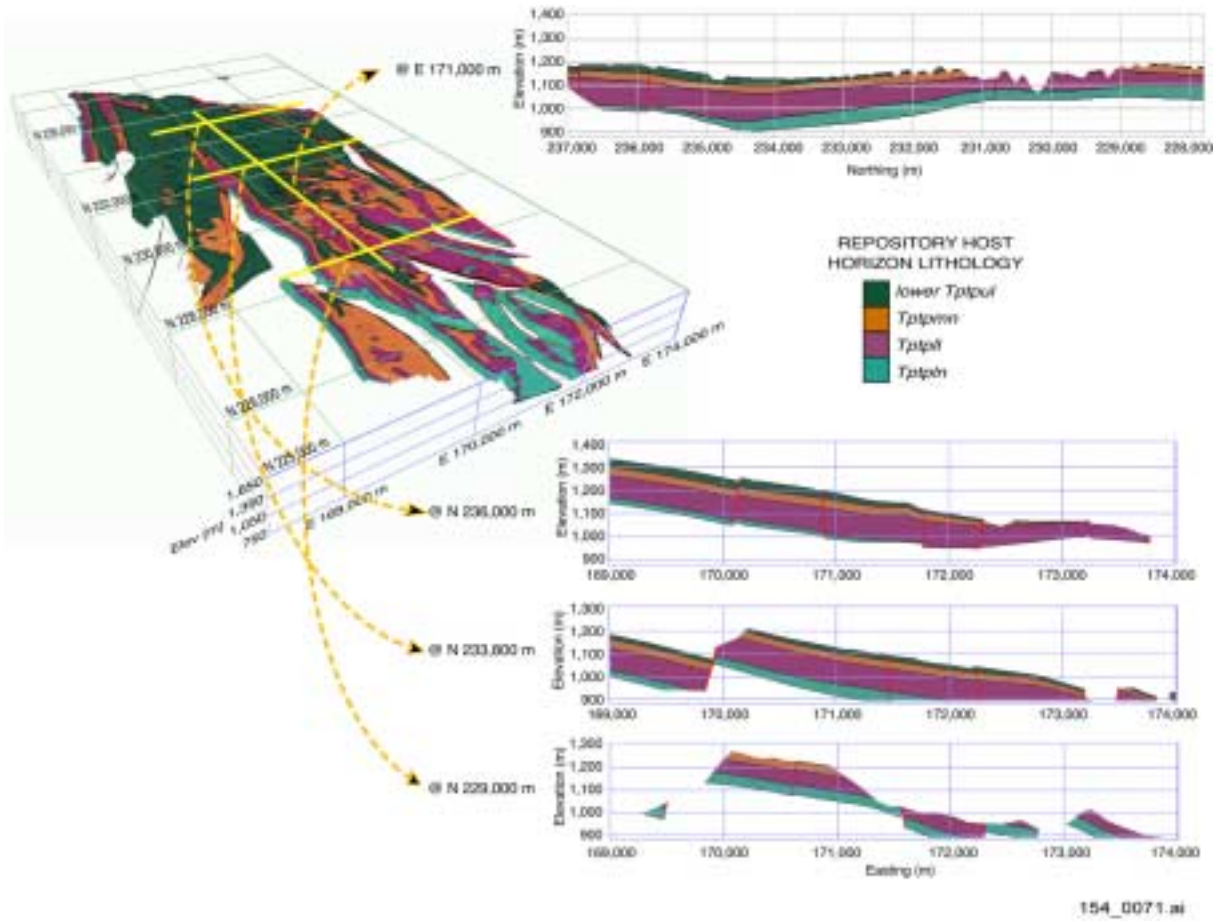

154_0071.ai

Source: Developed from DTN: MO9901MWDGFM31.000 [DIRS 103769].

NOTE: Upper and lower repository host horizon surfaces have been clipped to maintain an overburden thickness of 200 m and a water table standoff distance of 160 m. Nevada coordinates in meters.

Figure 3.3.4-9. Spatial Distribution of Lithostratigraphic Layers Constituting the Potential Repository Host Horizon

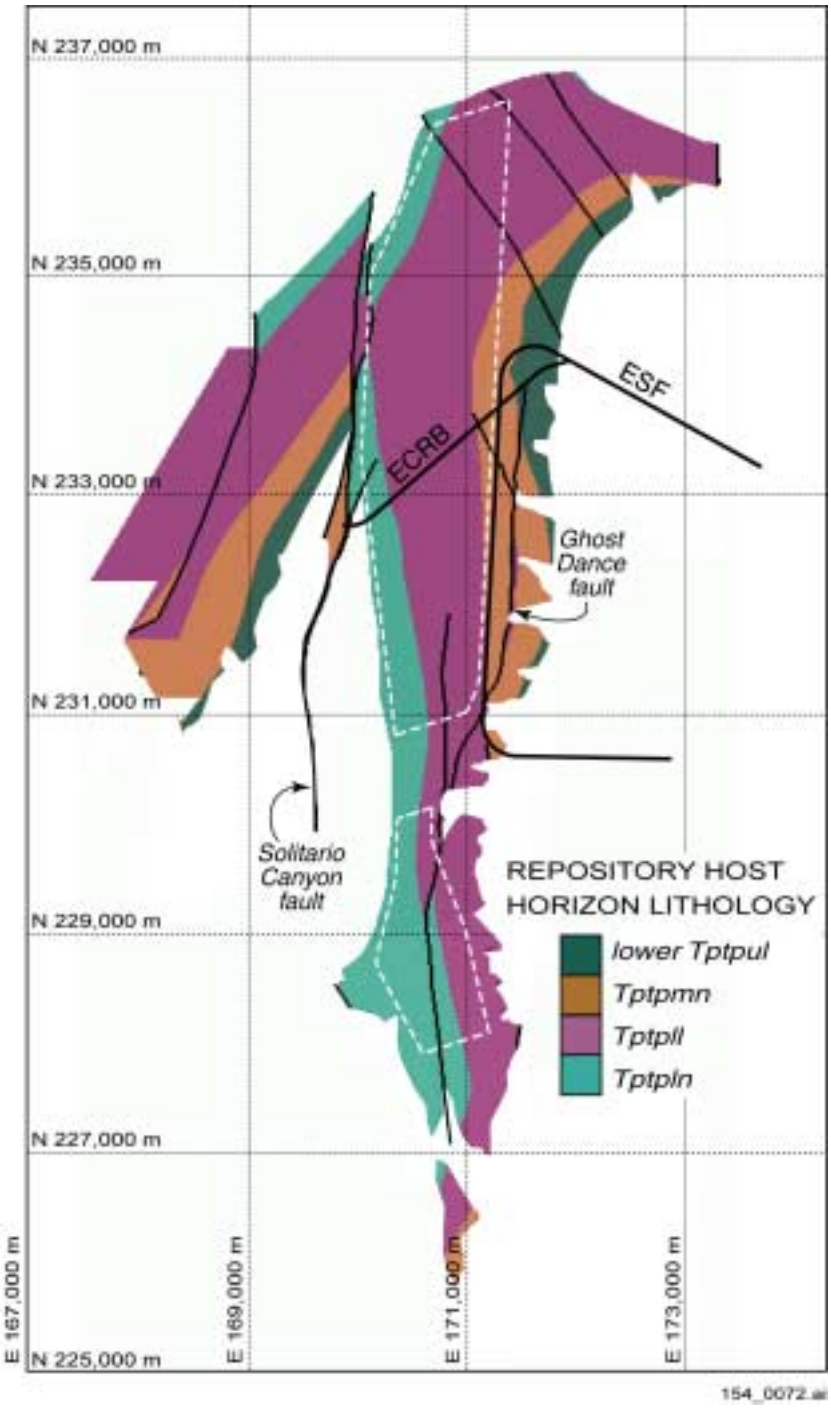

154_0072.ai

Source: Distribution of lithology from DTN: MO9901MWDGFM31.000 [DIRS 103769]. Design from BSC 2001 [DIRS 154548].

NOTE: The white dashed line identifies the plane of the current draft repository design. Nevada coordinates in meters. ECRB = Enhanced Characterization of the Repository Block; ESF = Exploratory Studies Facility; UZ = unsaturated zone.

Figure 3.3.4-10. Section Cut through the Potential Repository Siting Volume

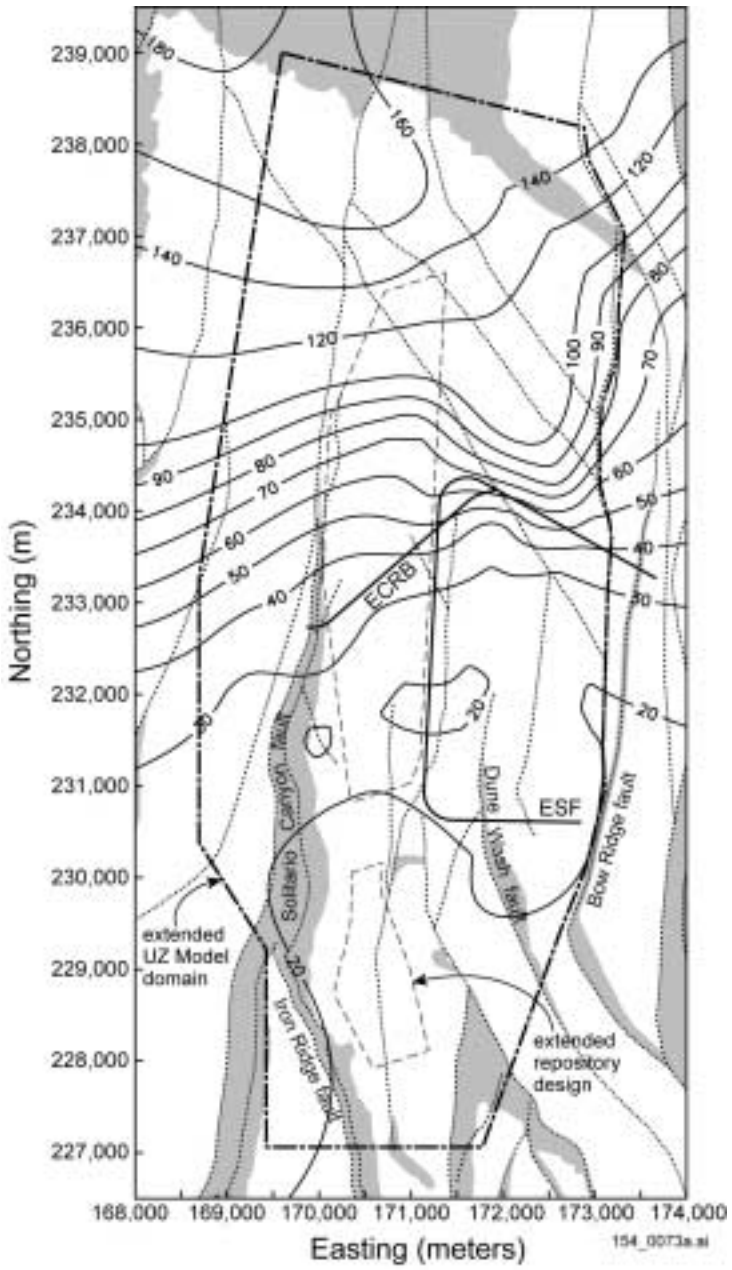

154_0073a.ai

Source: DTN: MO9901MWDGFM31.000 [DIRS 103769].

NOTE: Figure developed using Geologic Framework Model version 3.1 data. Contours indicate pre-faulted, pre-eroded PTn thickness in meters. Shaded areas are where the PTn has zero thickness as a result of faulting, erosion, or both. Nevada coordinates in meters. ECRB = Enhanced Characterization of the Repository Block; ESF = Exploratory Studies Facility; UZ = unsaturated zone.

Figure 3.3.4-11. PTn Occurrence and Thickness

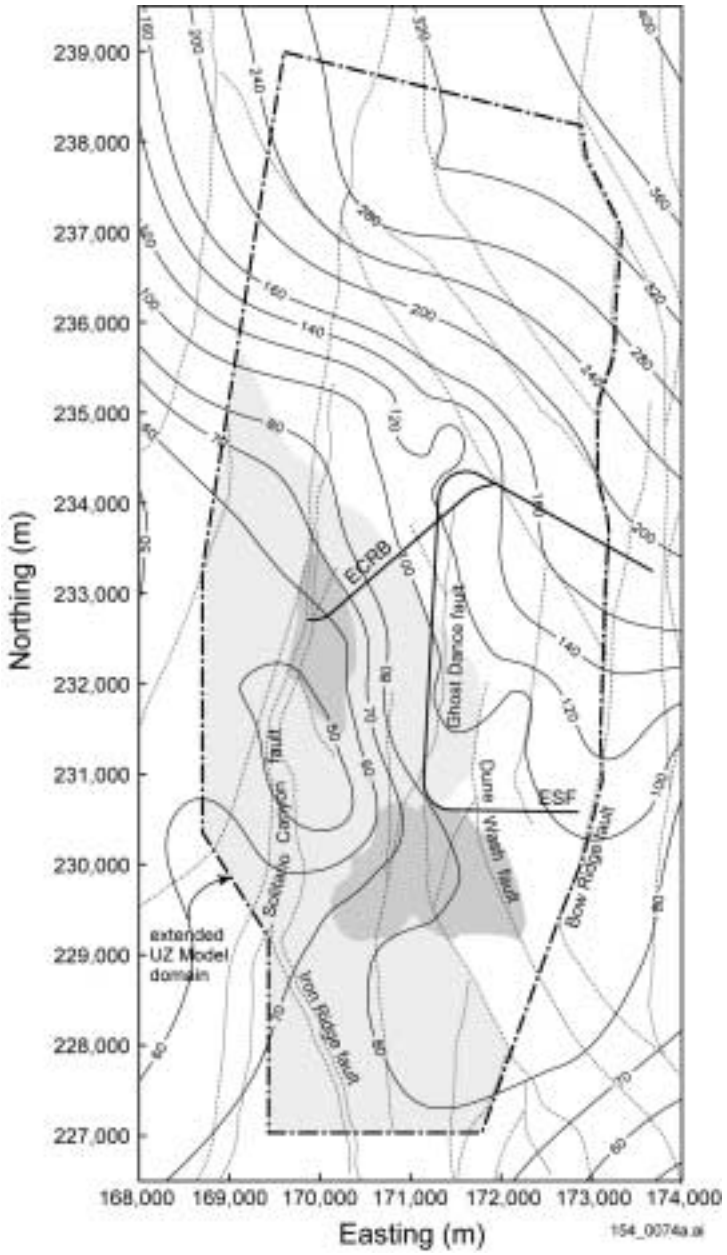

154_0074a.ai

Source: Thickness contours DTN: MO9901MWDGFM31.000 [DIRS 103769]. Vitric extent estimated using preliminary RPM3.2 data Bodvarsson 2001 [DIRS 154669], Attachment 15, pp. 148 to 151.

NOTE: Thickness contours developed using Geologic Framework Model version 3.1 data. Units are meters. Shaded areas represent estimated extent of vitric region within the extended Unsaturated Zone model domain near the top of the CHn (light shading) and near the base of the CHn (dark shading). Nevada coordinates in meters. ECRB = Enhanced Characterization of the Repository Block; ESF = Exploratory Studies Facility; UZ = unsaturated zone.

Figure 3.3.4-12. Pre-faulted, Pre-eroded Thickness Map of CHn (Tptpv1–Tacbt)

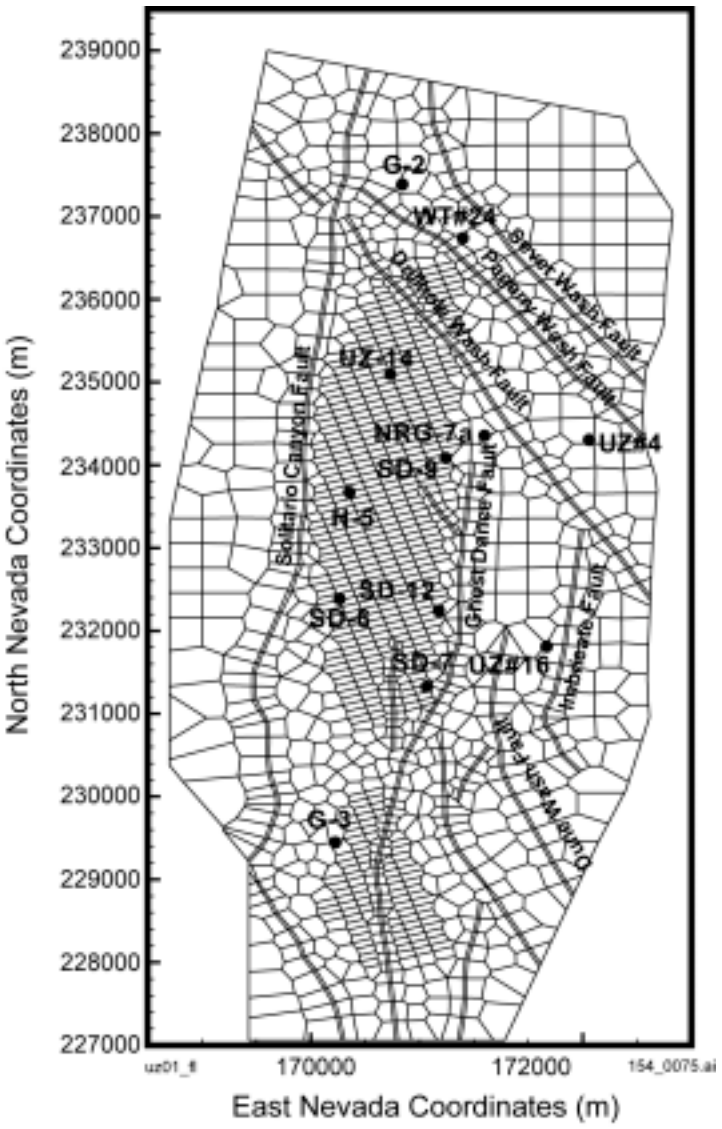

154_0075.ai

Source: BSC 2001 [DIRS 154548].

NOTE: Shown are modeled faults, several borehole locations, and refinements in the potential repository area (using the extended design for a cooler repository).

Figure 3.3.4-13. Plan View of the Extended Model Grid

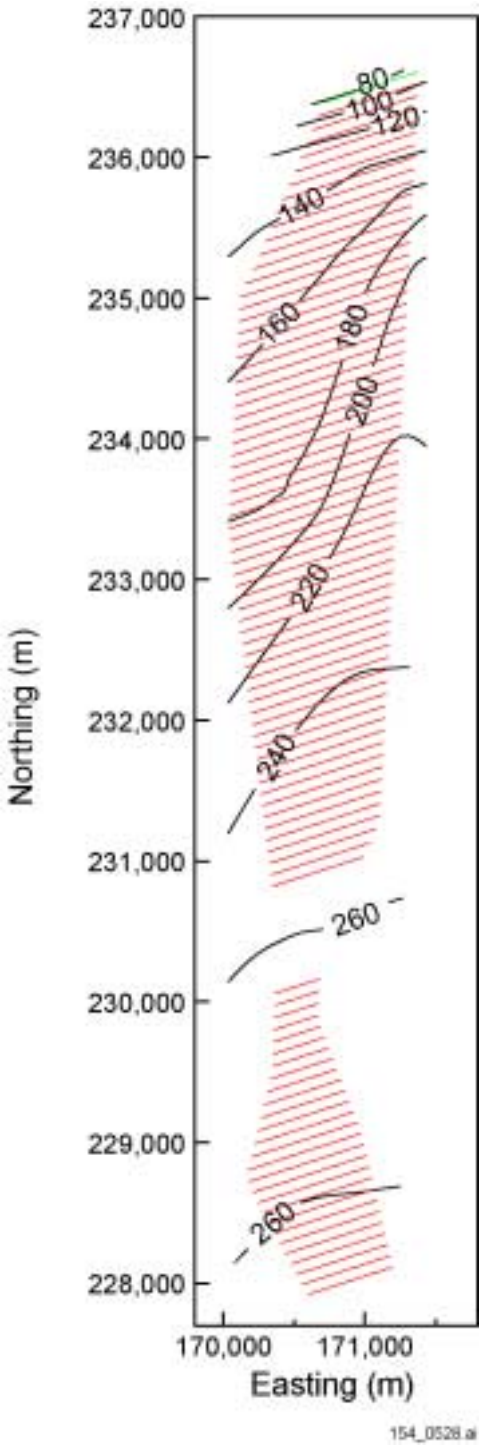

154_0528.ai

Source: Layout of the potential repository emplacement drifts from BSC (2001 [DIRS 154548], Item 1 of Figure 1 and Table 1).

NOTE: Contours in meters. Red lines indicate emplacement drifts. The northernmost drift (green) is a post-closure test drift.

Figure 3.3.4-13a. Approximate Vertical Distance Between Emplacement Drifts and a Water Table 120 m Above the Current Elevation

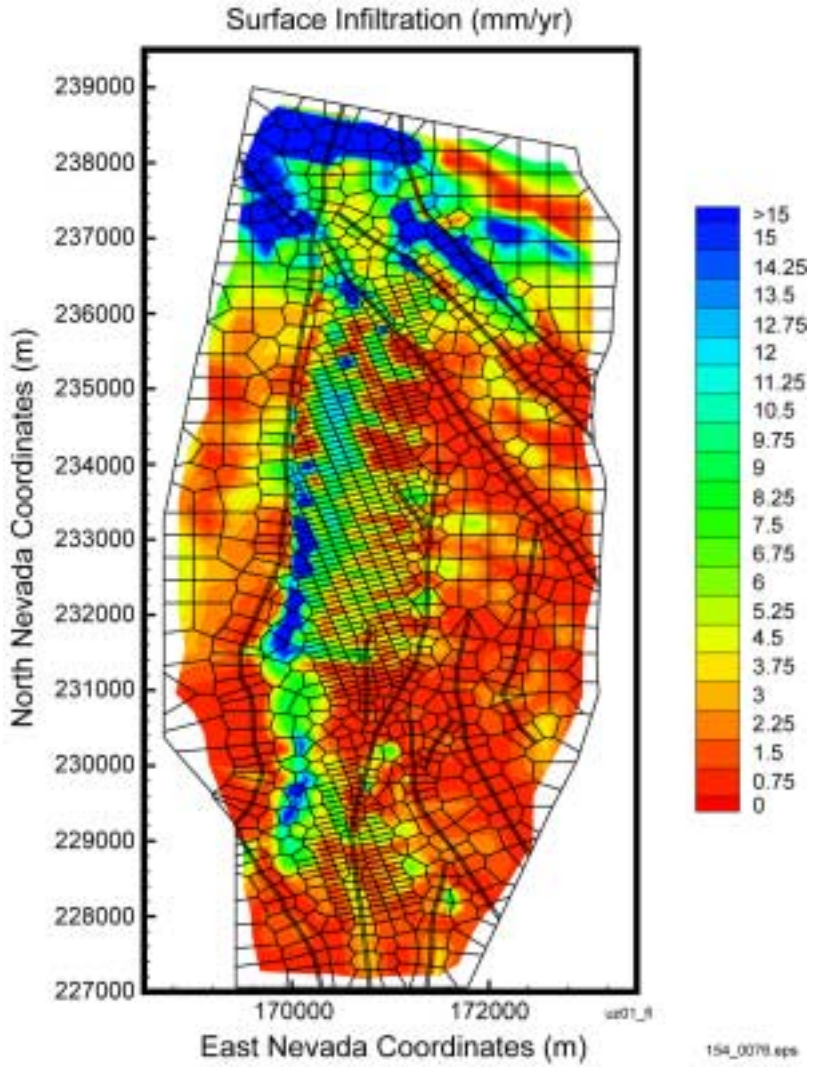

154_0076.eps

Source: Preliminary work described by Bodvarsson 2001 [DIRS 154669], Attachment 13, p. 13.

NOTE: Simulation uses present-day, mean infiltration (mm/yr).

Figure 3.3.4-14. Spatial Distribution of Infiltration in the Domain of the Extended Model

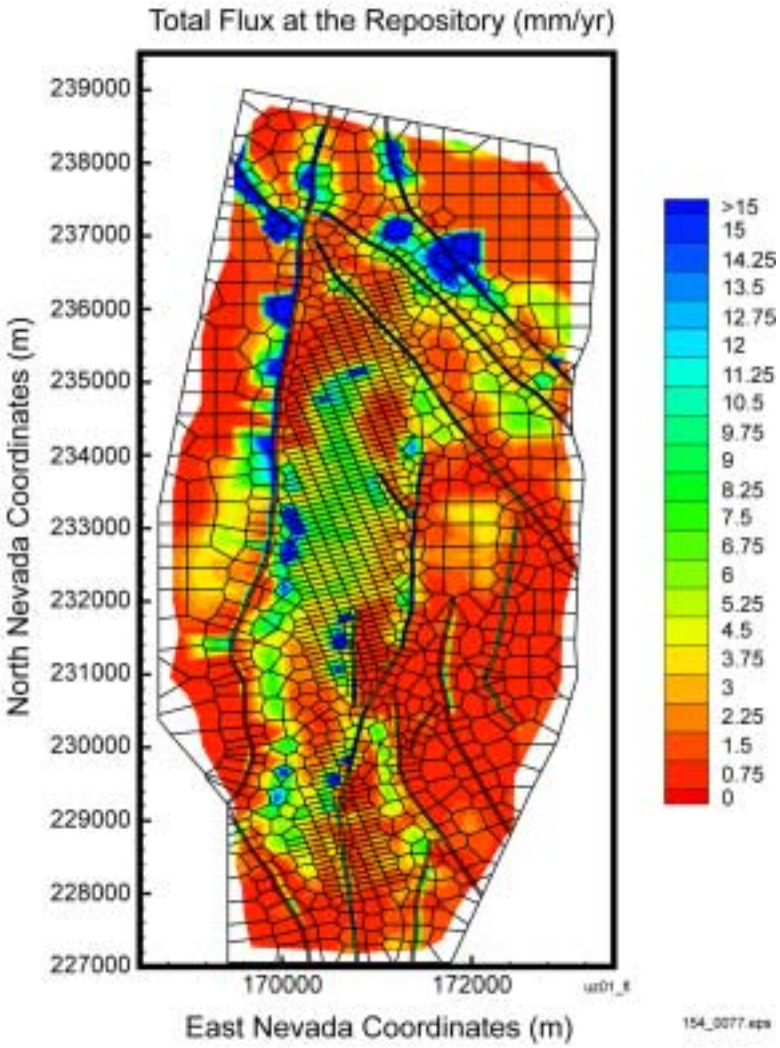

154_0077.eps

Source: Preliminary work described by Bodvarsson 2001 [DIRS 154669], Attachment 13, p. 15.

NOTE: Simulation uses present-day, mean infiltration (mm/yr).

Figure 3.3.4-15. Simulated Percolation Flux at the Potential Repository Horizon Using the Extended Model Grid

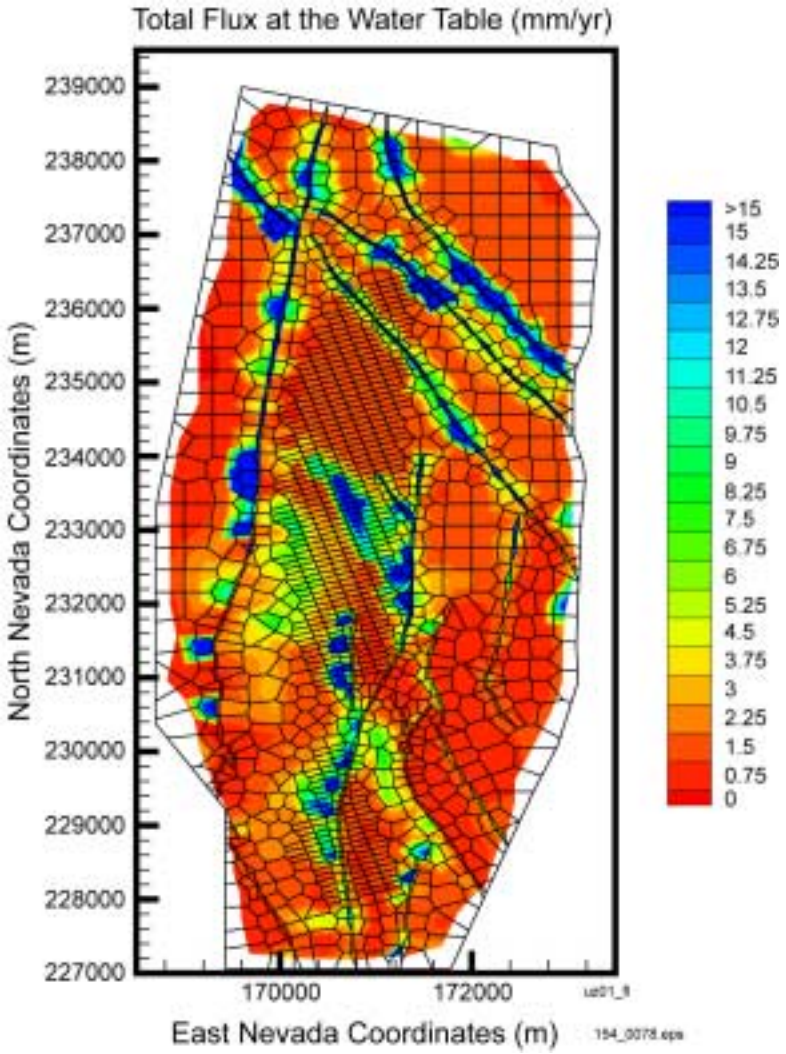

154_0078.eps

Source: Preliminary work described by Bodvarsson 2001 [DIRS 154669], Attachment 13, p. 16.

NOTE: Simulation uses present-day, mean infiltration (mm/yr).

Figure 3.3.4-16. Simulated Percolation Flux at the Water Table Using the Extended Model Grid

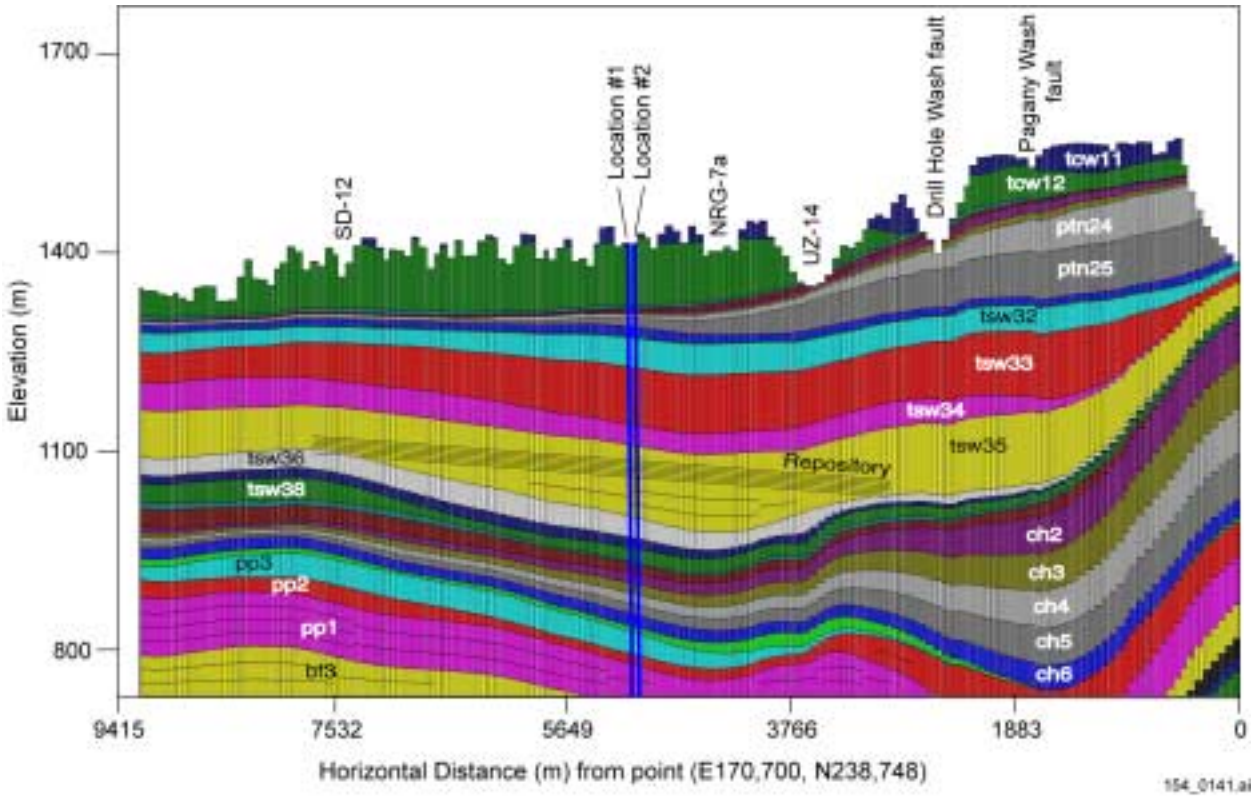

154_0141.ai

Source: CRWMS M&O 2000 [DIRS 144454], Figure 3.

NOTE: Lateral and vertical discretization, two-dimensional NS#2 cross section based on the refined numerical grid.

Figure 3.3.5-1. Location of the Potential Repository and Layering of the Hydrogeologic Units

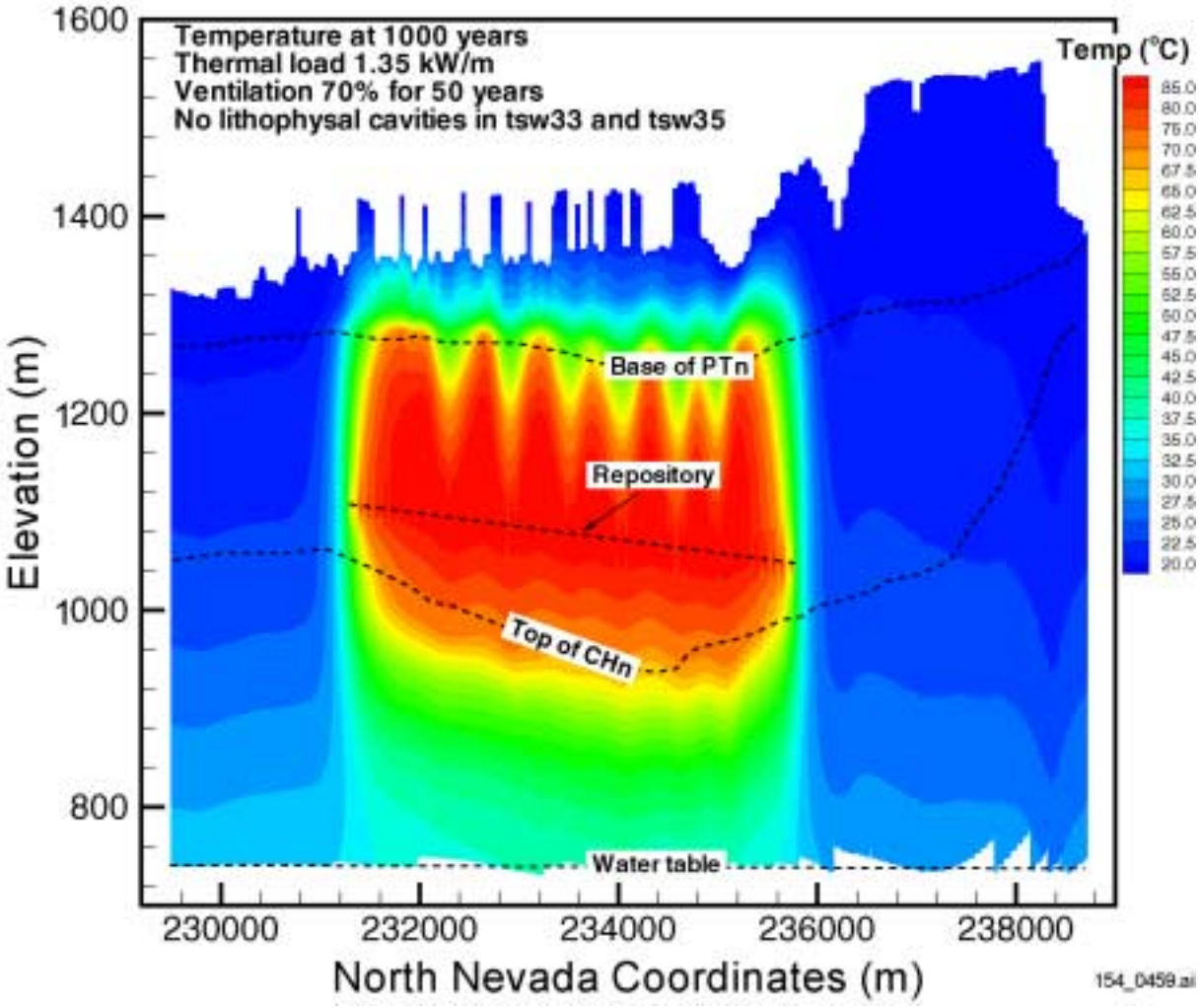

154_0459.ai

Source: Bodvarsson 2001 [DIRS 154669], Attachment 10, p. 11.

NOTE: Case #3: thermal load = 1.35 kW/m; ventilation = 70 percent for 50 years; no lithophysal cavities. Two-dimensional cross section.

Figure 3.3.5-2. Temperature Distribution for the Potential Higher-Temperature Repository at 1,000 Years

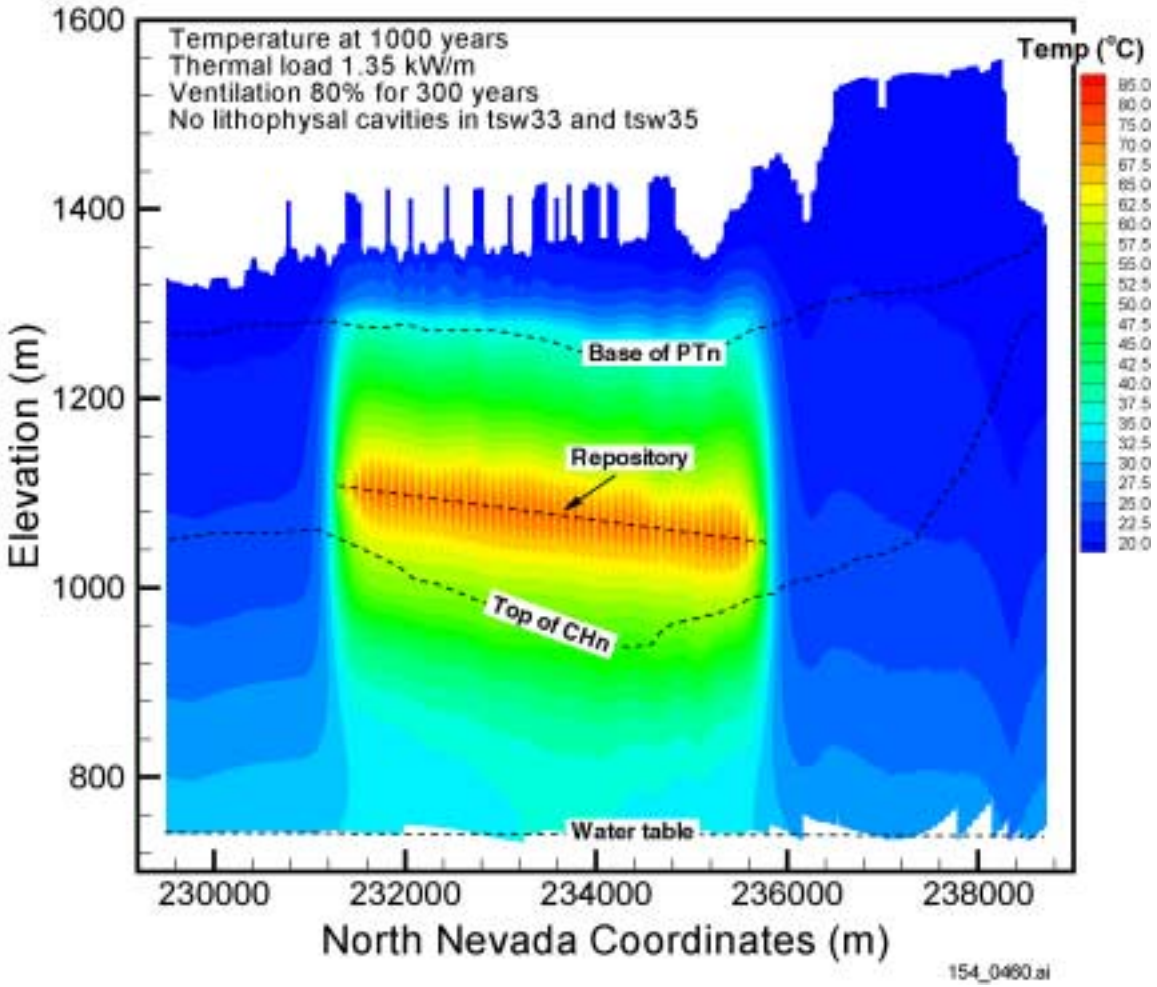

154_0460.ai

Source: Bodvarsson 2001 [DIRS 154669], Attachment 6, p. 101.

NOTE: Case #5: thermal load = 1.35 kW/m; ventilation = 80 percent for 300 years; no lithophysal cavities. Two-dimensional cross section.

Figure 3.3.5-3. Temperature Distribution for the Potential Lower-Temperature Repository at 1,000 Years

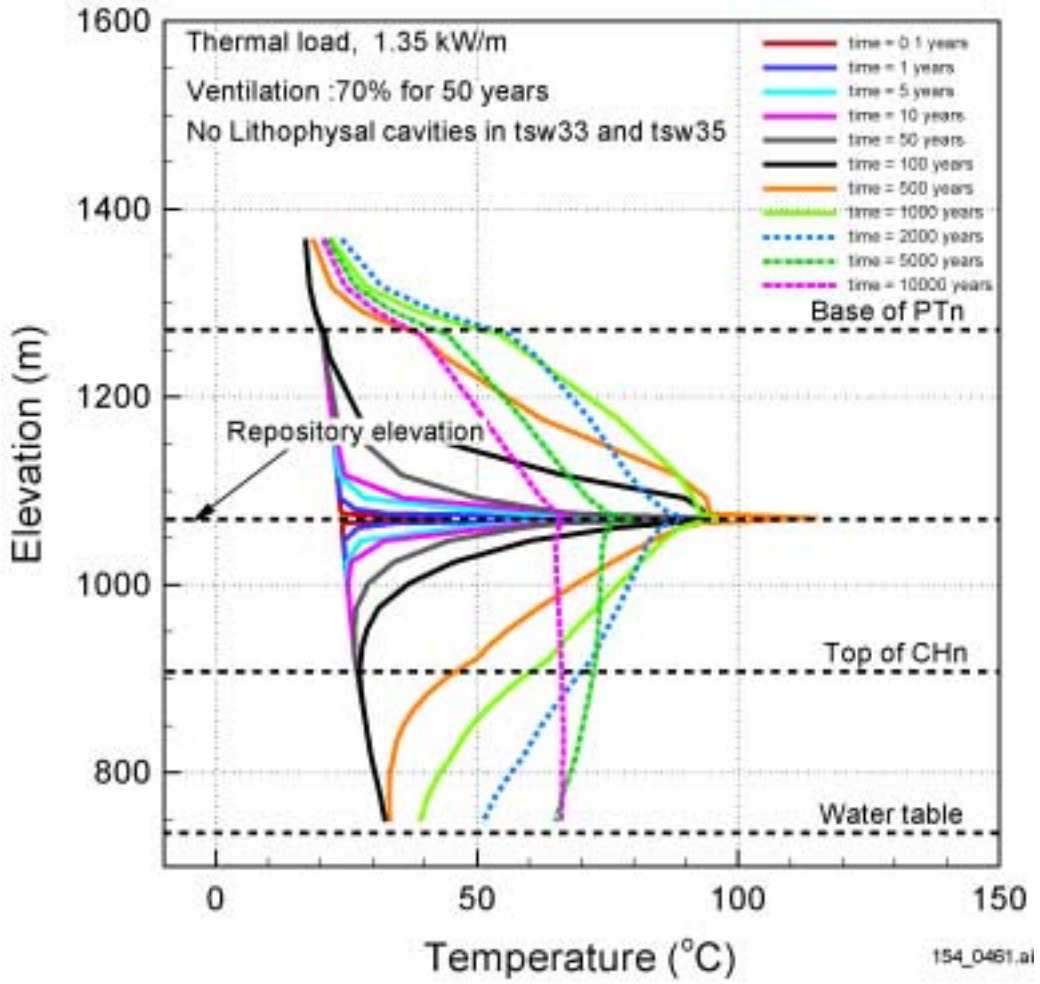

154_0461.ai

Source: Bodvarsson 2001 [DIRS 154669], Attachment 6, p. 83.

NOTE: Case #3: thermal load = 1.35 kW/m; ventilation = 70 percent for 50 years; no lithophysal cavities in tsw33 and tsw35. Two-dimensional cross section.

Figure 3.3.5-4. Temperature Profiles at the Center of the Potential Higher-Temperature Repository, No Lithophysal Cavities

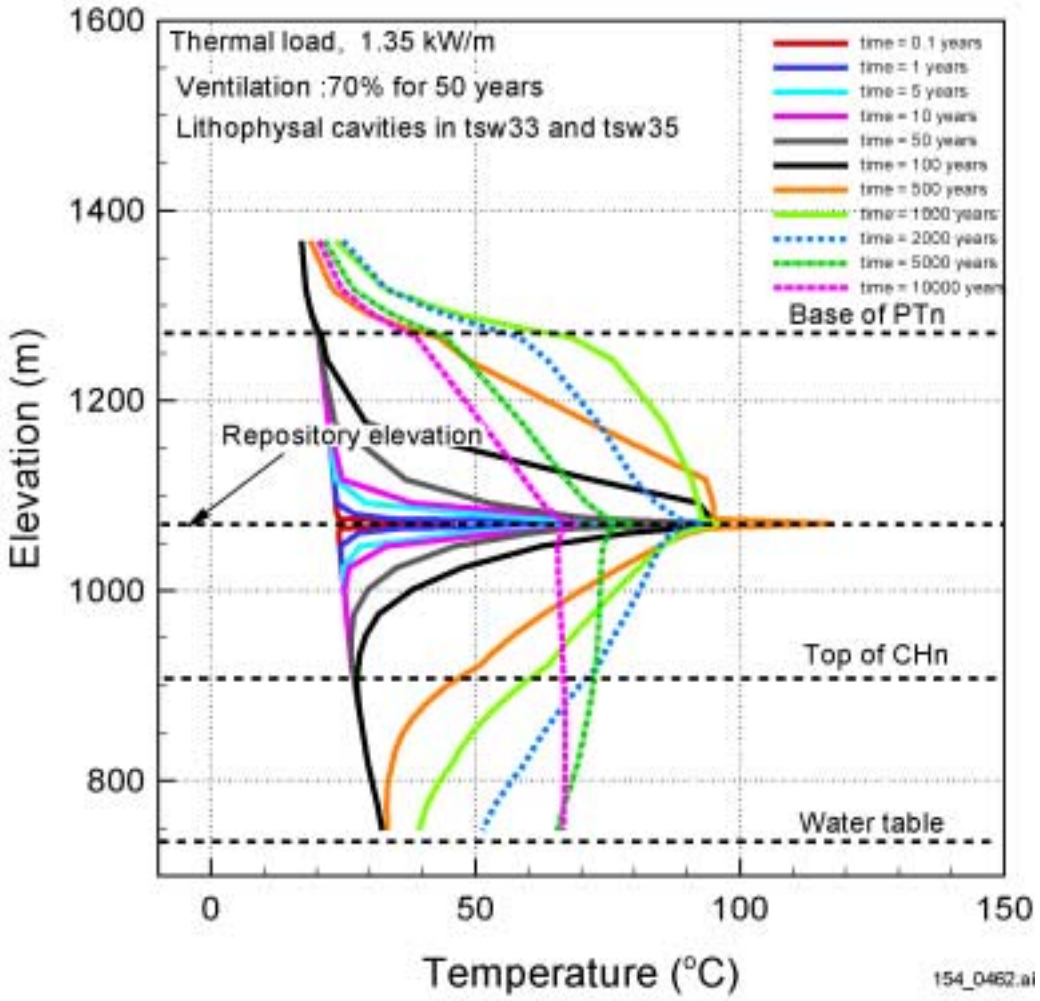

154_0462.ai

Source: Bodvarsson 2001 [DIRS 154669], Attachment 6, p. 84.

NOTE: Case #4: thermal load = 1.35 kW/m; ventilation = 70 percent for 50 years; with lithophysal cavities in tsw33 and tsw35. Two-dimensional cross section.

Figure 3.3.5-5. Temperature Profiles at the Center of the Potential Higher-Temperature Repository, with Lithophysal Cavities

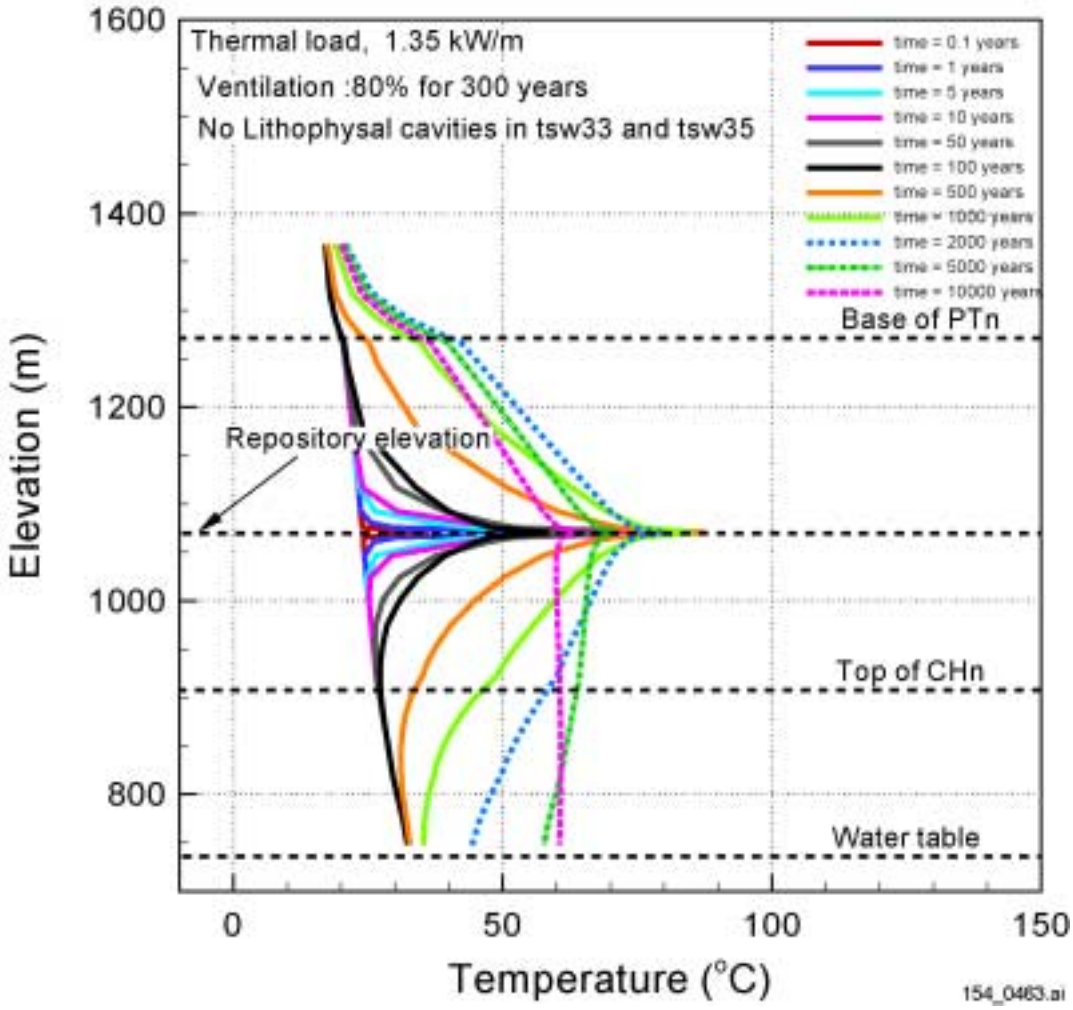

154_0463.ai

Source: Bodvarsson 2001 [DIRS 154669], Attachment 6, p. 85.

NOTE: Case #5: thermal load = 1.35 kW/m; ventilation = 80 percent for 300 years; no lithophysal cavities in tsw33 and tsw35. Two-dimensional cross section.

Figure 3.3.5-6. Temperature Profiles at the Center of the Potential Lower-Temperature Repository, No Lithophysal Cavities

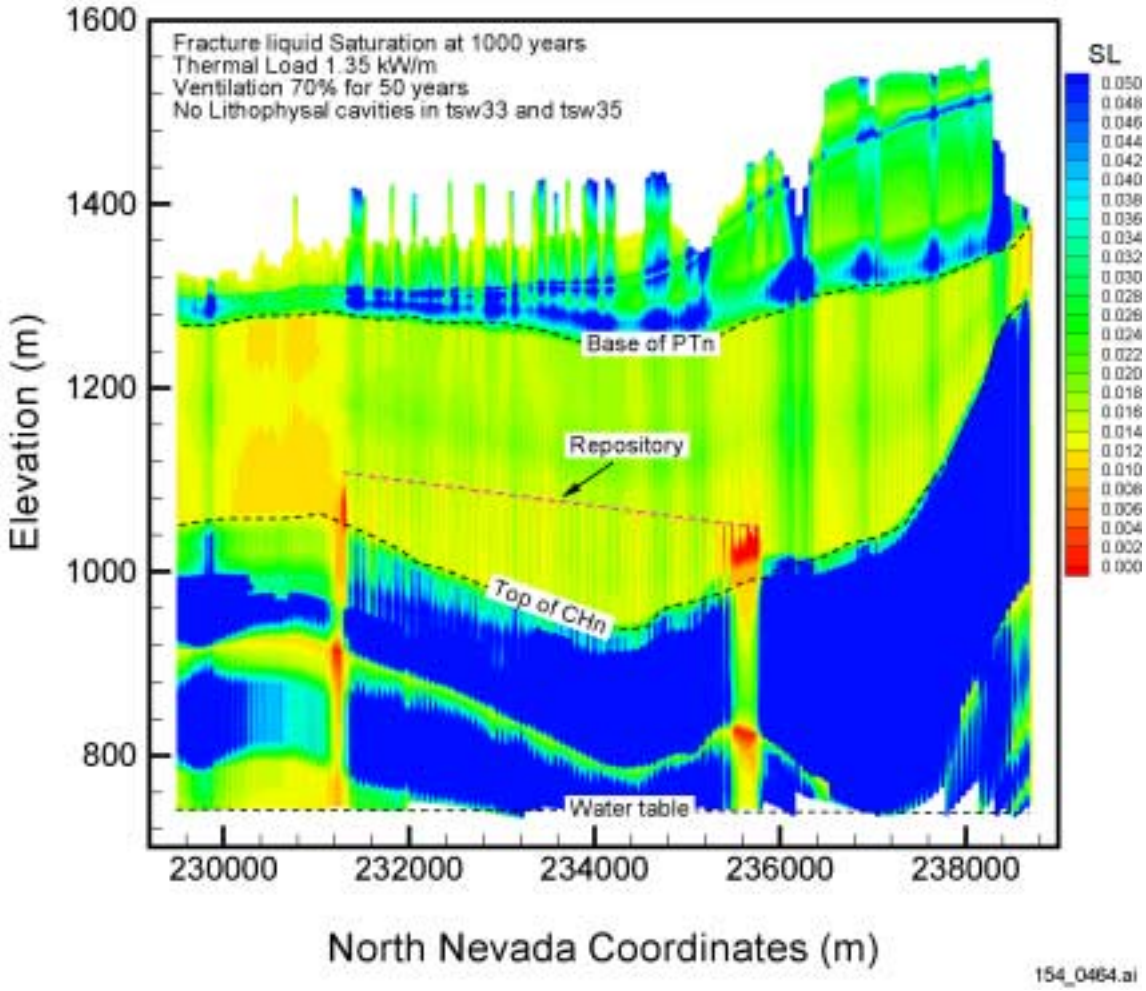

154_0464.ai

Source: Bodvarsson 2001 [DIRS 154669], Attachment 6, p. 100.

NOTE: Case #3: thermal load = 1.35 kW/m; ventilation = 70 percent for 50 years; no lithophysal cavities. Two-dimensional cross section.

Figure 3.3.5-7. Fracture Liquid Saturation for the Potential Higher-Temperature Repository at 1,000 Years

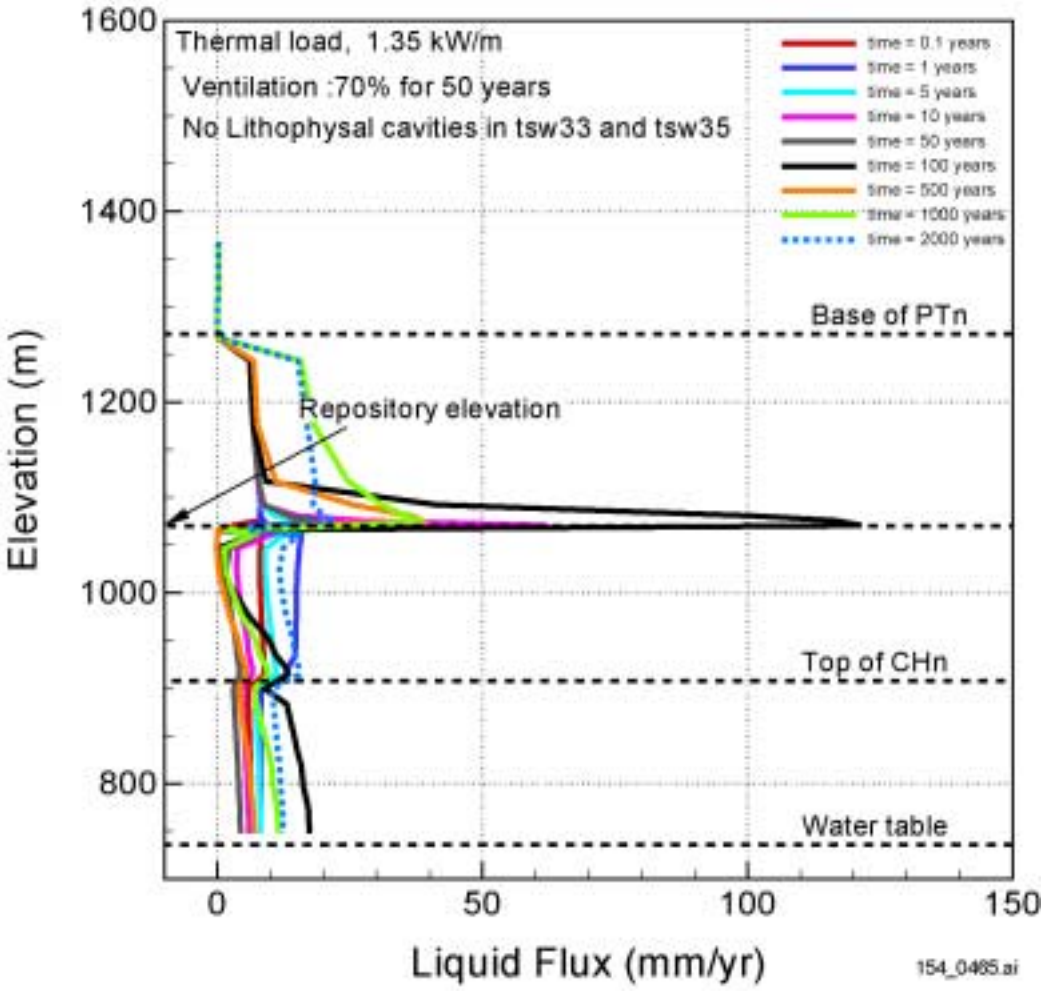

154_0465.ai

Source: Bodvarsson 2001 [DIRS 154669], Attachment 6, p. 91.

NOTE: Case #3: thermal load = 1.35 kW/m; ventilation = 70 percent for 50 years; no lithophysal cavities in tsw33 and tsw35. Two-dimensional cross section.

Figure 3.3.5-8. Fracture Liquid-Flux Profiles at Center of the Potential Repository for the Higher-Temperature Repository, No Lithophysal Cavities

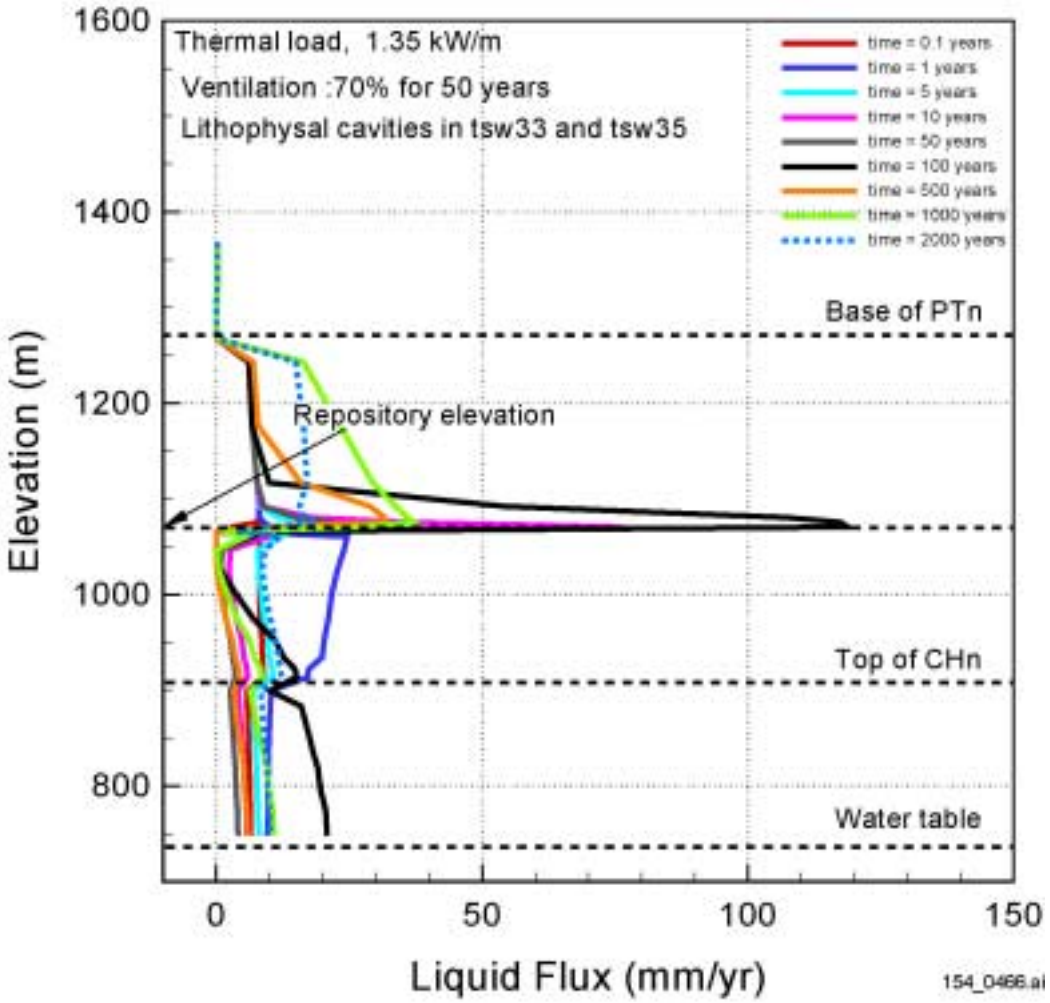

154_0466.ai

Source: Bodvarsson 2001 [DIRS 154669], Attachment 6, p. 92.

NOTE: Case #4: thermal load = 1.35 kW/m; ventilation = 70 percent for 50 years; with lithophysal cavities in tsw33 and tsw35. Two-dimensional cross section.

Figure 3.3.5-9. Fracture Liquid Flux Profiles at the Center of the Potential Higher-Temperature Repository, With Lithophysal Cavities

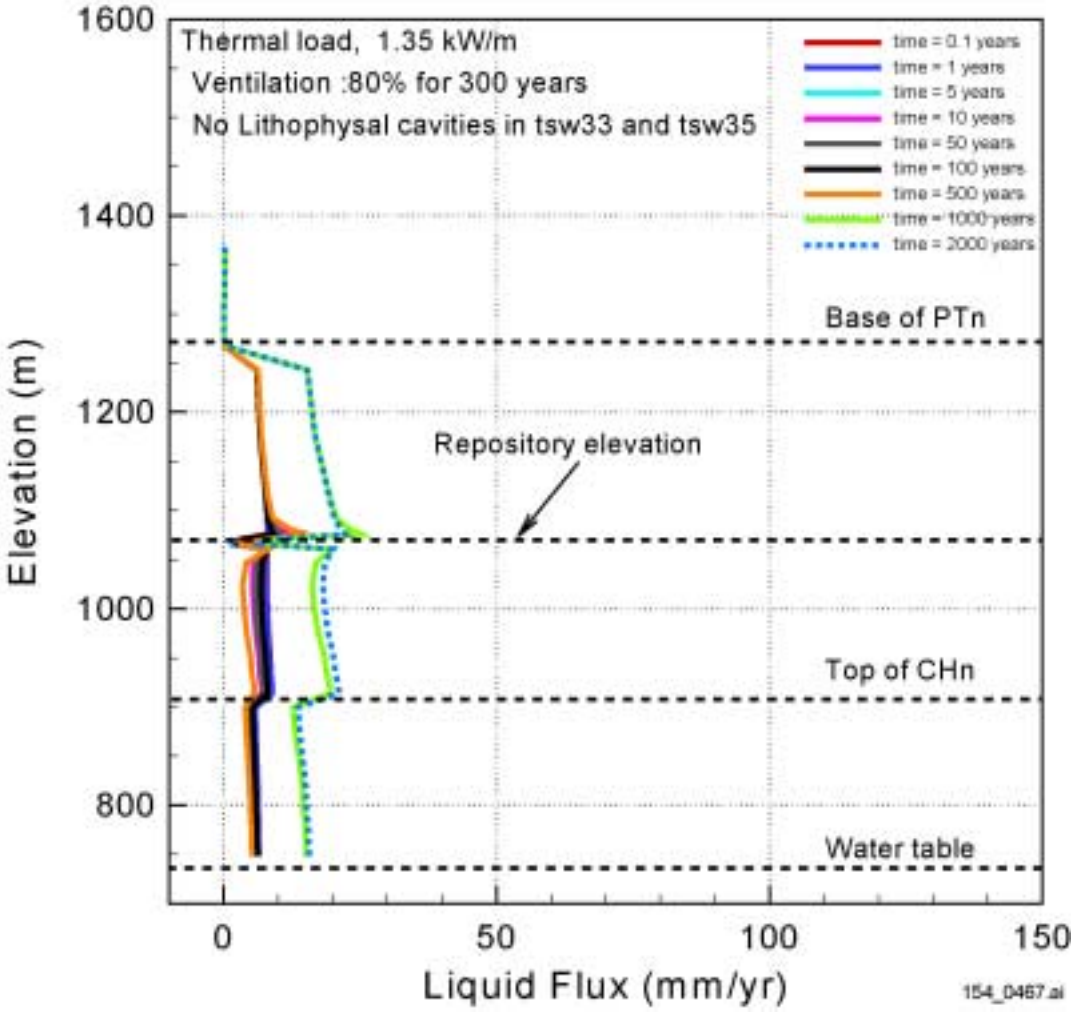

154_0467.ai

Source: Bodvarsson 2001 [DIRS 154669], Attachment 6, p. 93.

NOTE: Case #5: thermal load = 1.35 kW/m; ventilation = 80 percent for 300 years; no lithophysal cavities in tsw33 and tsw35. Two-dimensional cross section.

Figure 3.3.5-10. Fracture Liquid Flux Profiles at the Center of the Potential Lower-Temperature Repository, No Lithophysal Cavities

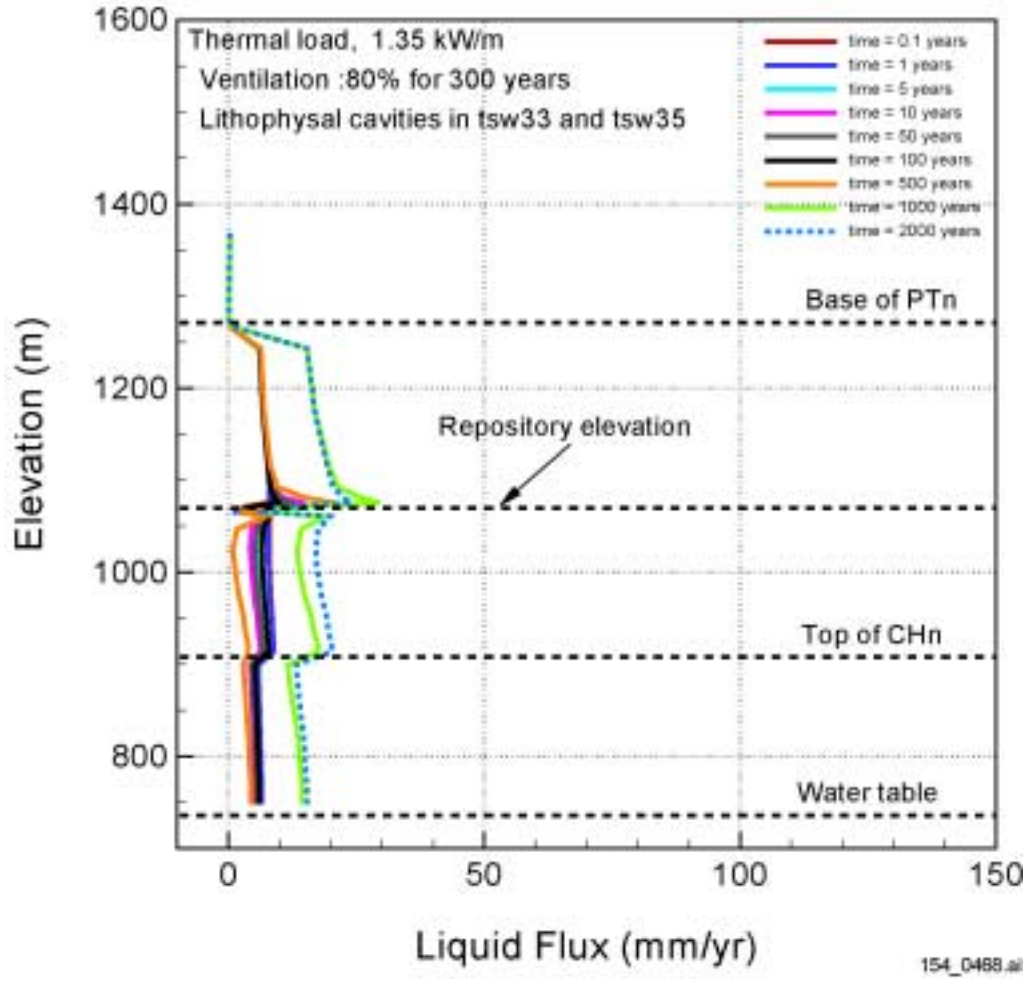

154_0468.ai

Source: Bodvarsson 2001 [DIRS 154669], Attachment 6, p. 94.

NOTE: Case #6: thermal load = 1.35 kW/m; ventilation = 80 percent for 300 years; with lithophysal cavities in tsw33 and tsw35. Two-dimensional cross section.

Figure 3.3.5-11. Fracture Liquid-Flux Profiles at the Center of the Potential Lower-Temperature Repository, With Lithophysal Cavities

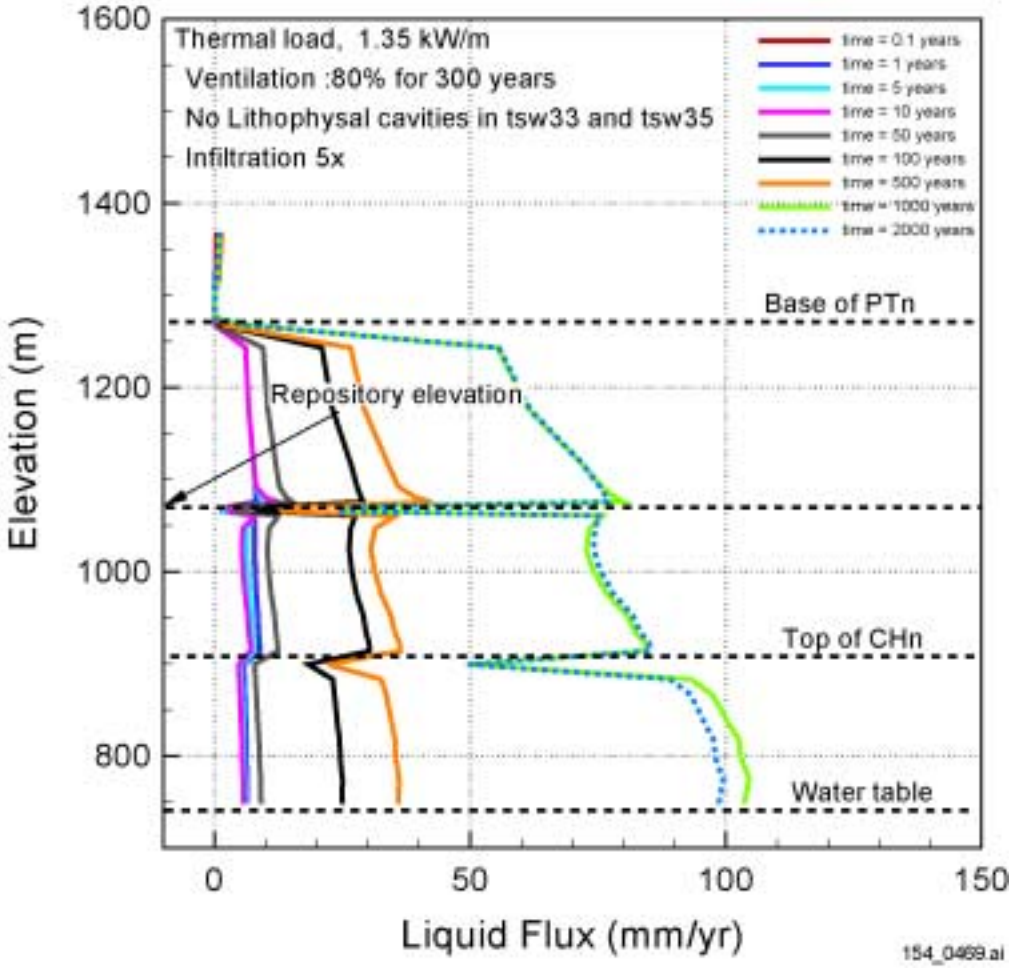

154_0469.ai

Source: Bodvarsson 2001 [DIRS 154669], Attachment 6, p. 103.

NOTE: Case #7: thermal load = 1.35 kW/m; ventilation = 80 percent for 300 years; no lithophysal cavities in tsw33 and tsw35. Two-dimensional cross section.

Figure 3.3.5-12. Fracture Liquid Flux Profiles at the Center of the Potential Lower-Temperature Repository, No Lithophysal Cavities and Increased Infiltration

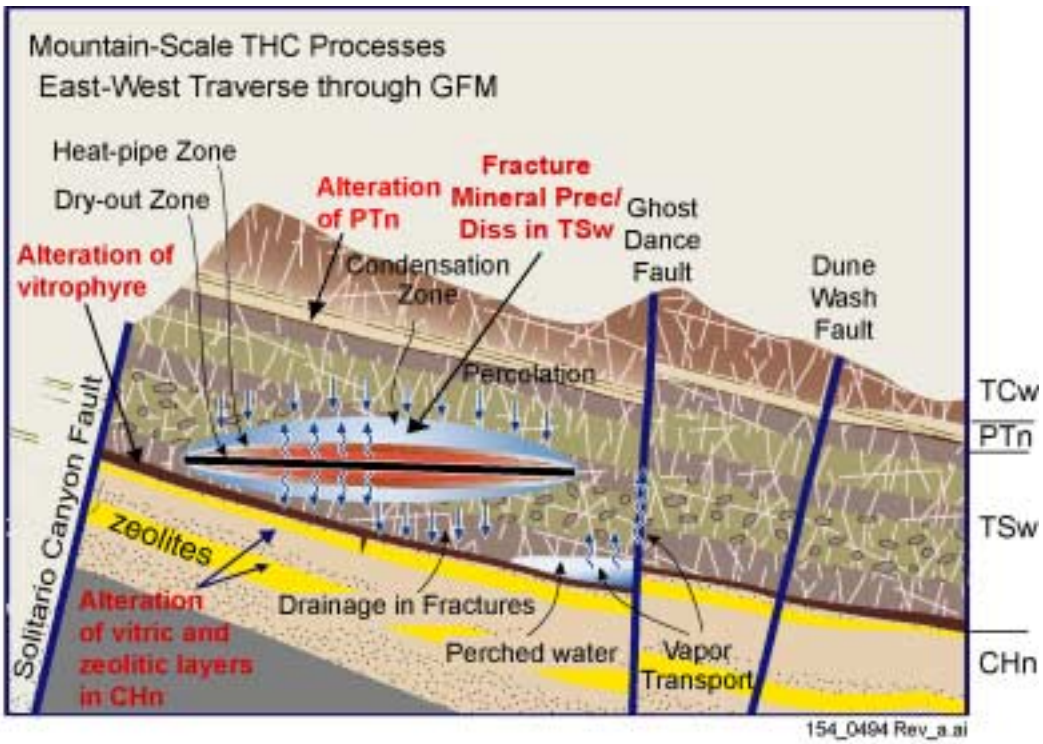

154_0494 Rev_a.ai

NOTE: Definitions: GFM = Geologic Frame Model; TCw = Tiva Canyon welded hydrogeologic unit; PTn = Paintbrush Tuff nonwelded hydrogeologic unit; TSw = Topopah Spring welded hydrogeologic unit; CHn = Calico Hills nonwelded hydrogeologic unit.

Figure 3.3.6-1. Schematic of Potential Mountain-Scale Thermal-Hydrologic-Chemical Processes and Initial Conditions

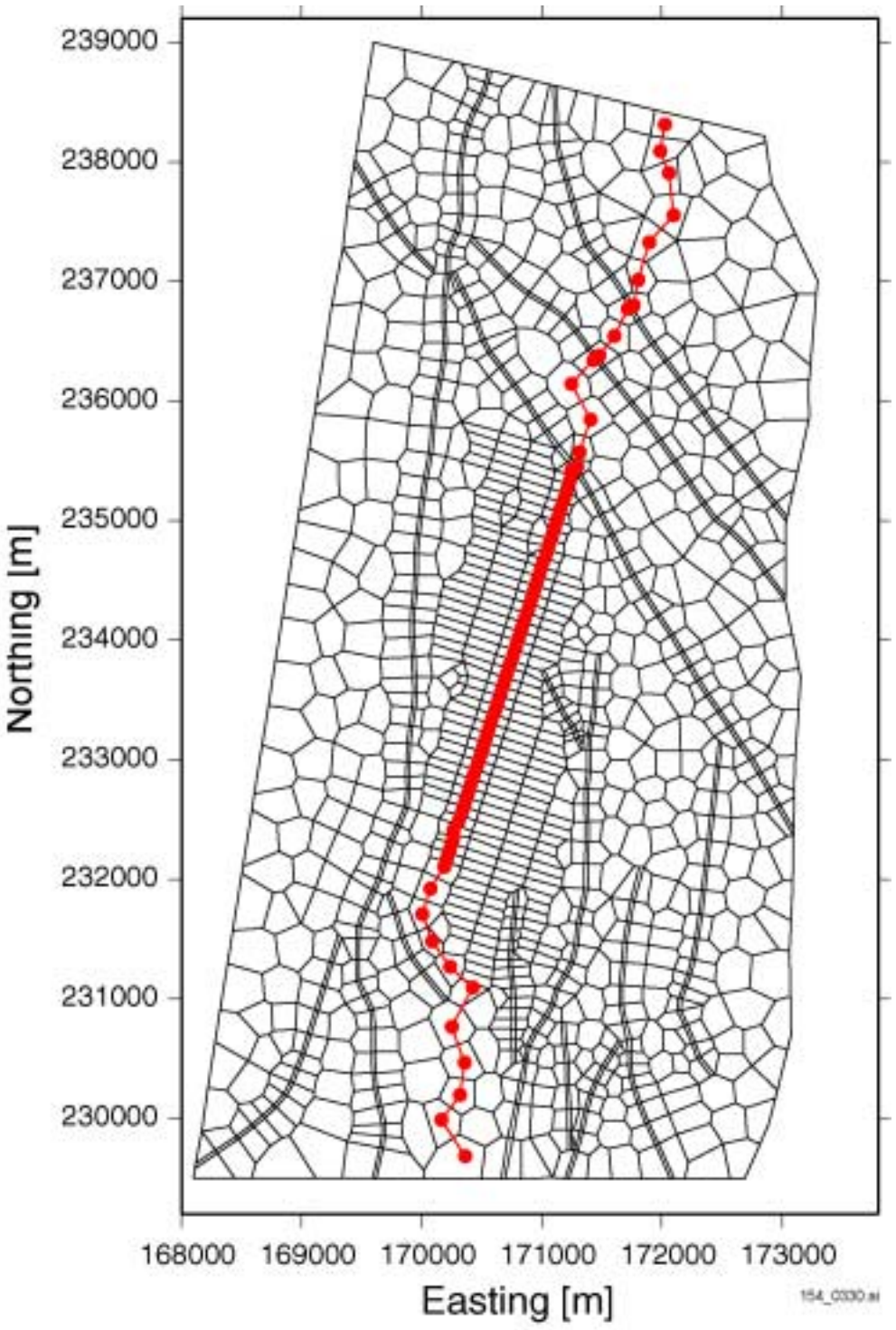

154_0330.ai

Source: Bodvarsson 2001 [DIRS 154669], Attachment 10, p. 11.

NOTE: Nevada Coordinates in meters.

Figure 3.3.6-2. Location of 2-D North-South Cross Section Superimposed on Diagram Showing the 3-D UZ Flow and Transport Model TSPA-SR Grid

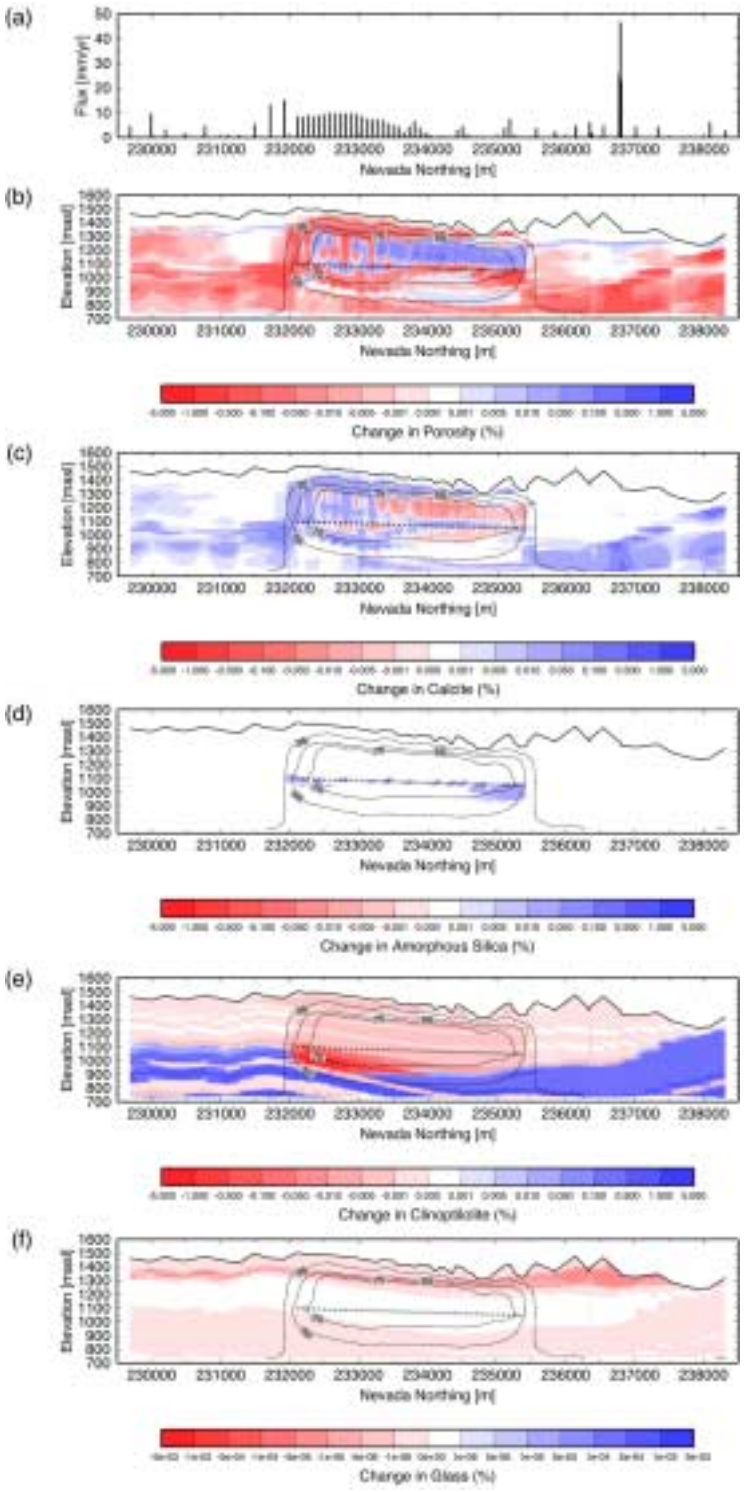

154_0254

Source: Bodvarsson 2001 [DIRS 154669], Attachment 10, pp. 12 to 14.

NOTE: Extended Case 1. Crosses denote model repository drift locations: (a) infiltration rate; (b) fracture porosity change with temperature contours; (c) fracture calcite change with temperature contours; (d) fracture amorphous silica precipitation with temperature contours; (e) matrix clinoptilolite change with temperature contours; and (f) matrix glass dissolution with temperature contours. masl = meters above sea level.

Figure 3.3.6-3. Infiltration Rate Distribution and Simulated Changes in Fracture Porosity, Mineralogy, and Temperature after about 1,400 Years of Heating

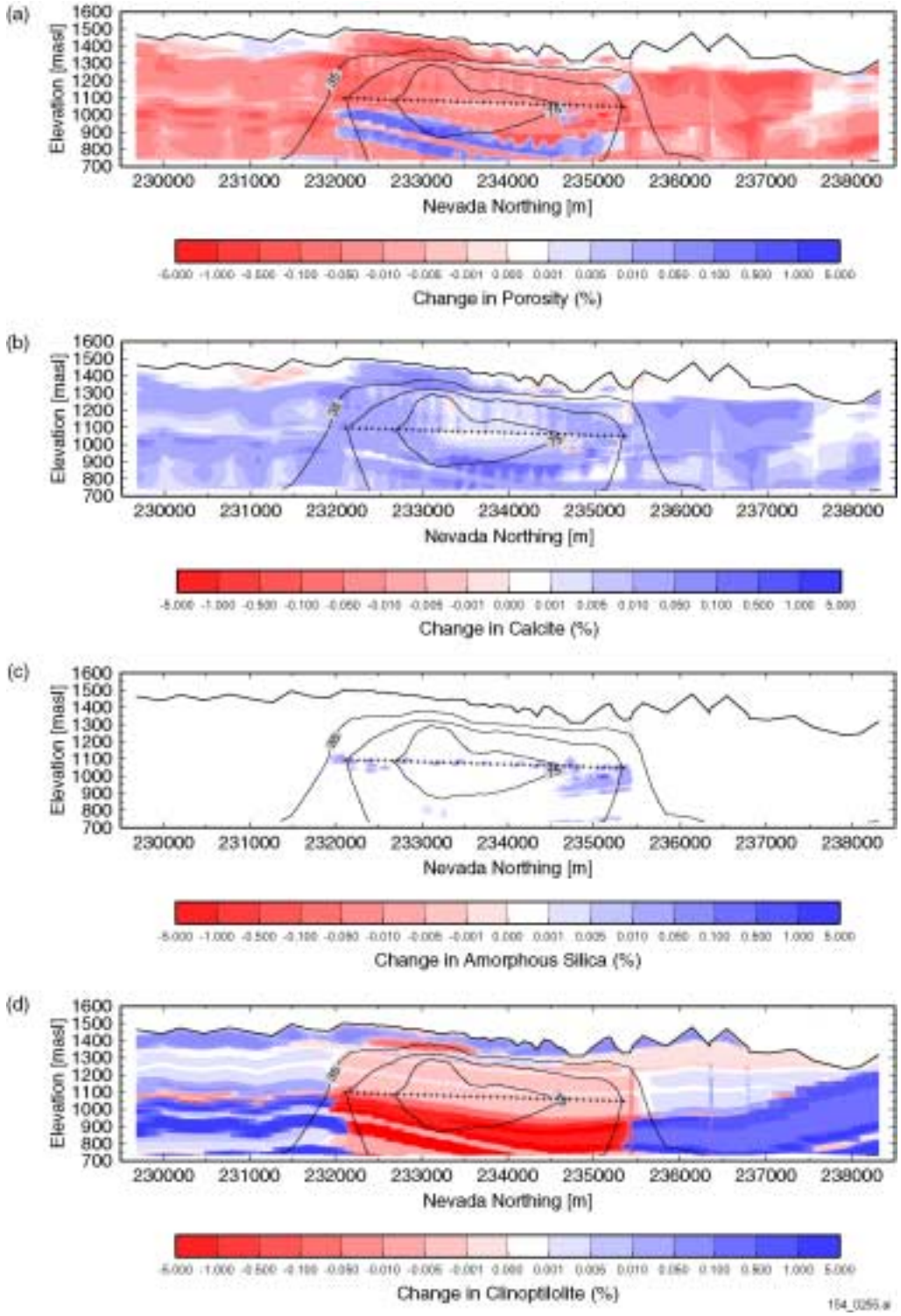

154_0255.ai

Source: Bodvarsson 2001 [DIRS 154669], Attachment 10, pp. 15 to 16.

NOTE: Extended Case 2. Crosses denote model repository drift locations: (a) fracture porosity change with temperature contours; (b) fracture calcite change with temperature contours; (c) fracture amorphous silica precipitation with temperature contours; and (d) matrix clinoptilolite change with temperature contours. masl = meters above sea level.

Figure 3.3.6-4. Simulated Changes in Fracture Porosity and Mineralogy after 5,000 Years of Heating

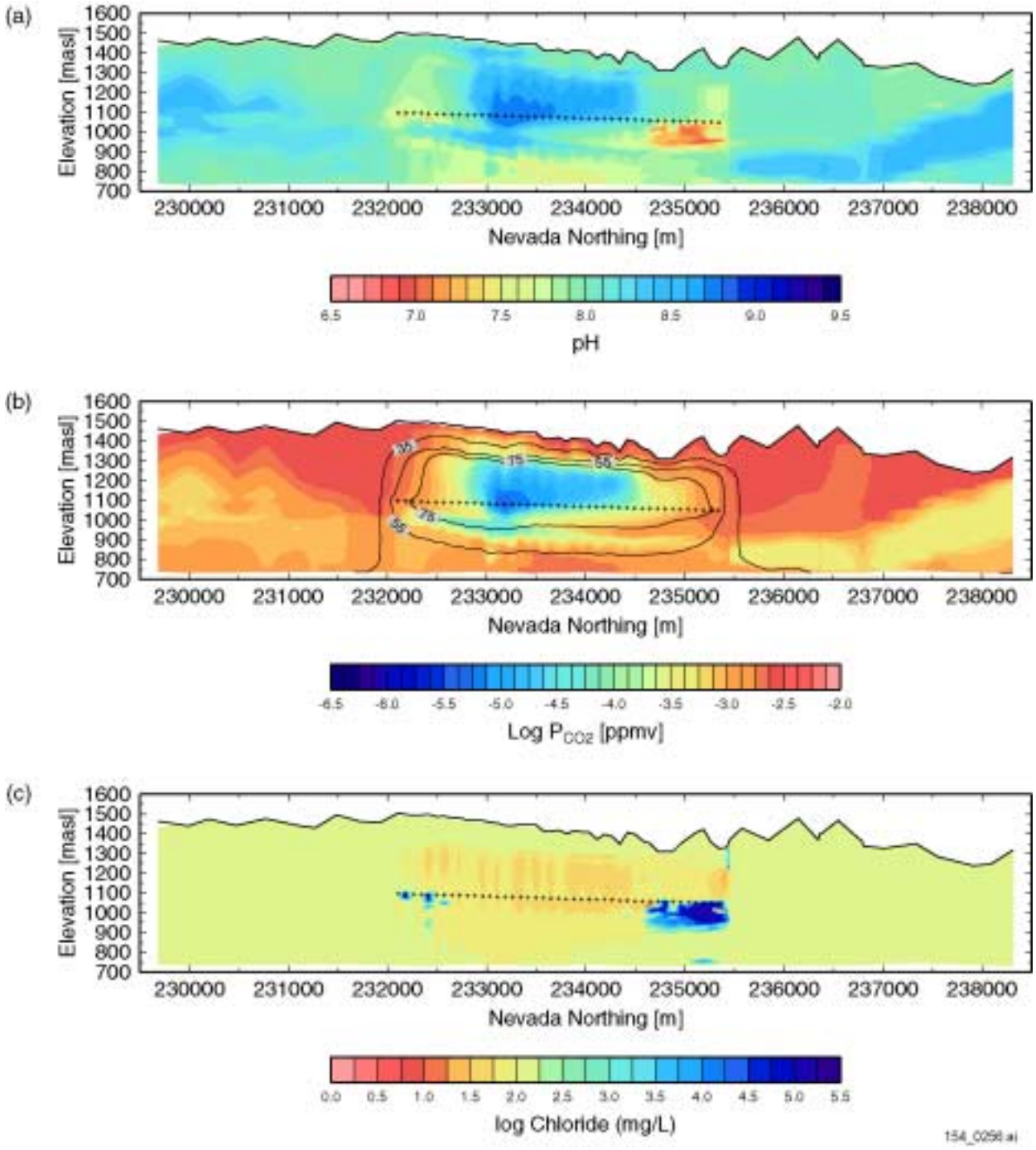

154_0256.ai

Source: Bodvarsson 2001 [DIRS 154669], Attachment 10, pp. 17 to 18.

NOTE: Extended Case 1. Crosses denote model repository drift locations: (a) pH of fracture water; (b) carbon dioxide concentration in gas in fractures with temperature contours; and (c) chloride concentration in fractures. masl = meters above sea level.

Figure 3.3.6-5. Simulated Water and Gas Chemistry after about 1,400 Years of Heating

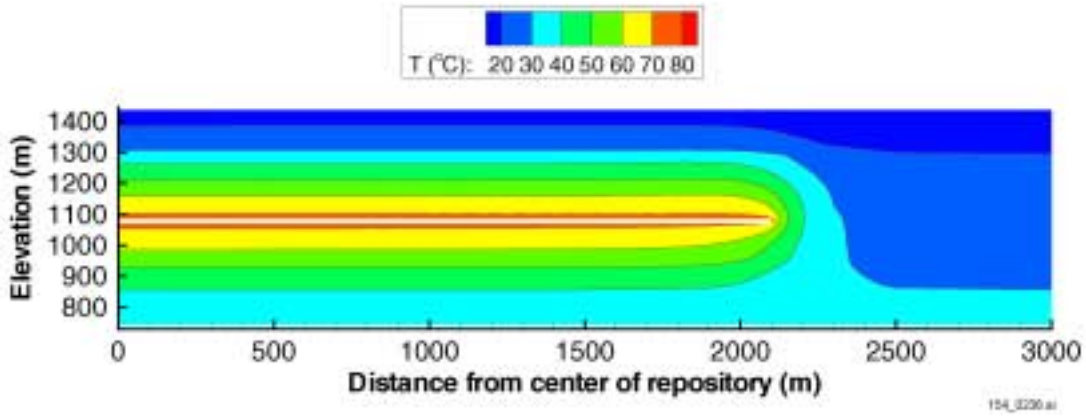

154_0236.ai

Source: Derived from Bodvarsson 2001 [DIRS 154669], Attachment 9, pp. 75 to 78.

Figure 3.3.7-1. Temperature Distribution at 1,000 Years

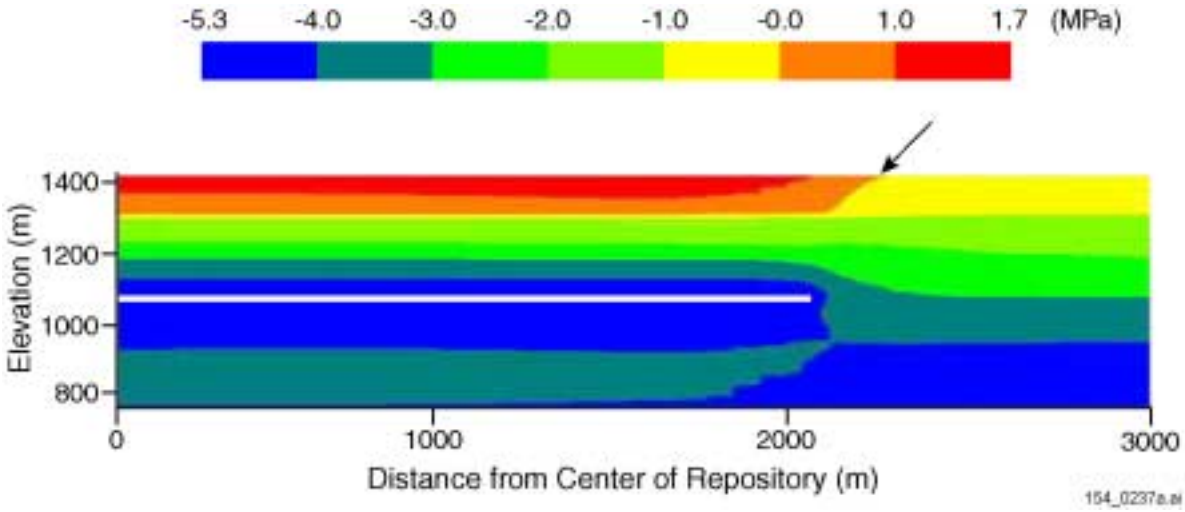

154_0237a.ai

Source: Derived from Bodvarsson 2001 [DIRS 154669], Attachment 9, pp. 75 to 78.

NOTE: Arrow points to contour that separates positive and negative stress values.

Figure 3.3.7-2. Contour of Horizontal Stress Distribution at 1,000 Years

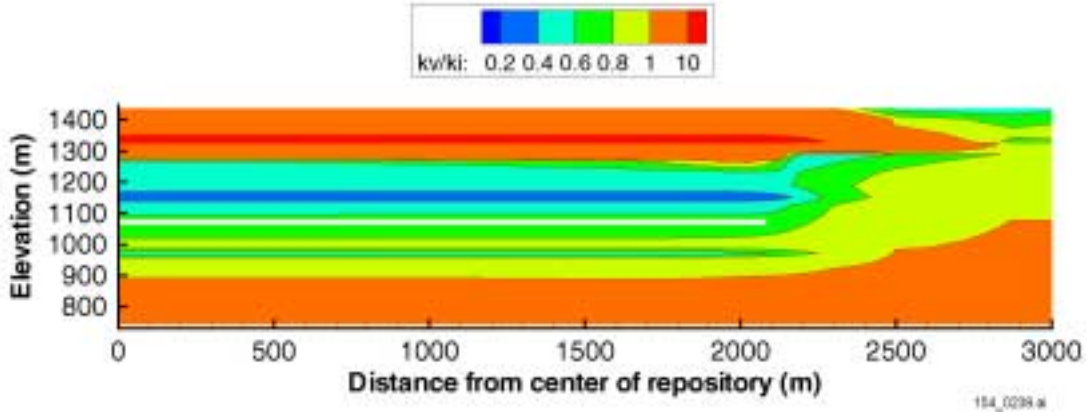

154_0239.ai

Source: Derived from Bodvarsson 2001 [DIRS 154669], Attachment 9, pp. 75 to 78.

Figure 3.3.7-3. Vertical Permeability Changes due to the Thermal-Hydrologic-Mechanical Effect at 1,000 Years

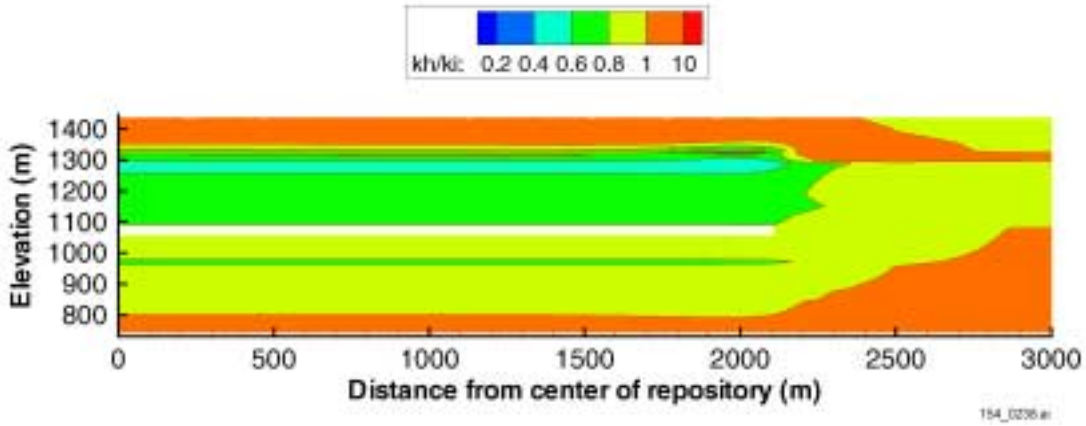

154_0238.ai

Source: Derived from Bodvarsson 2001 [DIRS 154669], Attachment 9, pp. 75 to 78.

Figure 3.3.7-4. Change in Horizontal Permeability Due to the Thermal-Hydrologic-Mechanical Effect at 1,000 Years

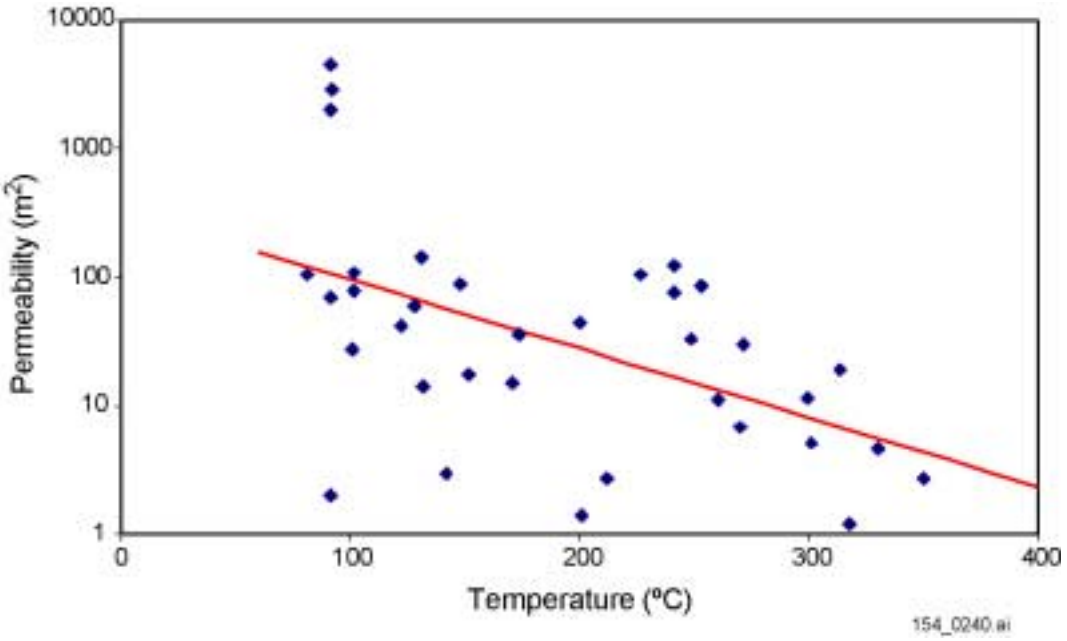

154_0240.ai

NOTE: Based on Figure 1 of Björnsson and Bodvarsson 1990 [DIRS 154606].

Figure 3.3.7-5. Correlation Between Permeability and Temperature of Geothermal Reservoirs Worldwide

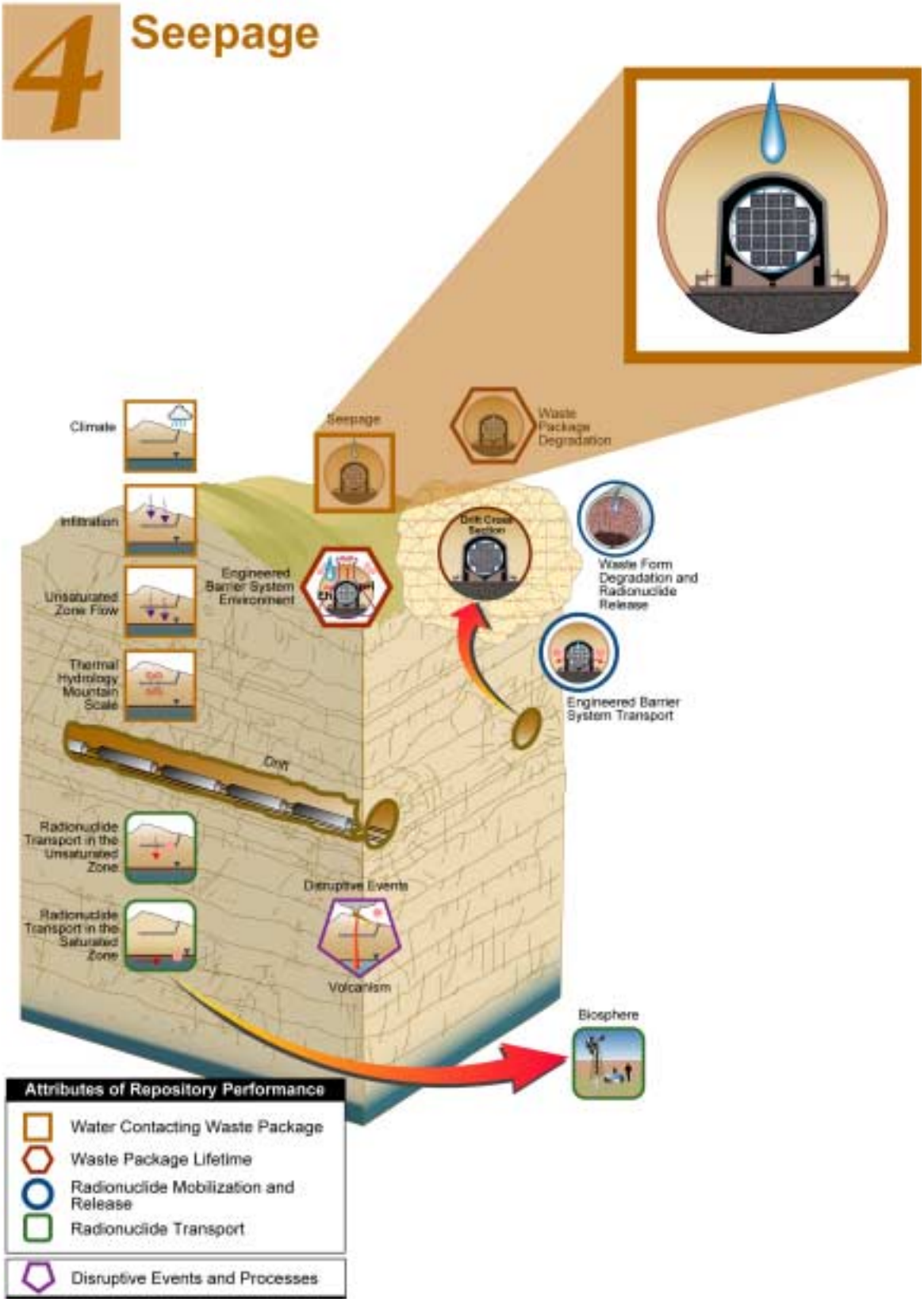
4
Seepage
Climate
Infiltration
Unsaturated Zone Flow
Thermal Hydrology Mountain Scale
Seepage
Waste Package Degradation
Engineered Barrier System Environment
Drift Cross Section
Waste Form Degradation and Radionuclide Release
Engineered Barrier System Transport
Drift
Radionuclide Transport in the Unsaturated Zone
Radionuclide Transport in the Saturated Zone
Disruptive Events
Volcanism
Biosphere
Attributes of Repository Performance
Water Contacting Waste Package
Waste Package Lifetime
Radionuclide Mobilization and Release
Radionuclide Transport
Disruptive Events and Processes

4. SEEPAGE

4.1 INTRODUCTION AND CONCEPTUAL BASIS

Seepage of water into waste emplacement drifts is considered one of the principal factors having the greatest impact on the long-term safety of the repository system (CRWMS M&O 2000 [DIRS 148713], Volume II, Table 4-1). The number of waste packages contacted by water, the corrosion rate of engineered barriers and waste packages, the dissolution and mobilization of radionuclides, and the release and migration of radionuclides to the accessible environment all depend on the rate, chemical composition, and spatial and temporal distribution of water seeping into the emplacement drifts.

This section summarizes process modeling and uncertainty studies performed to estimate seepage of liquid water into emplacement drifts as shown in Table 4-1. The initial issues of the seepage-related analysis model reports (AMRs) supported the *Total System Performance Assessment for the Site Recommendation* (TSPA-SR) (CRWMS M&O 2000 [DIRS 153246]). Additional studies and sensitivity analyses were conducted to address the following specific uncertainty issues:

- Data from long-term liquid-release experiments were analyzed to reduce the estimation uncertainty of seepage–relevant parameters and obtain estimates for the previously untested lower lithophysal zone of the Topopah Spring Tuff unit. The related modeling activity is fully documented in the *Seepage Calibration Model and Seepage Testing Data* (CRWMS M&O 2001 [DIRS 153045]). As a consequence of the new calibration results, the seepage model for *Total System Performance Assessment* (TSPA) was also updated, as documented in *Seepage Model for PA Including Drift Collapse* (CRWMS M&O 2000 [DIRS 153314]). Finally, the seepage abstraction was revised to reflect the reduced uncertainties (CRWMS M&O 2001 [DIRS 154291]). All these studies are concerned with seepage under ambient temperature conditions. The results of these activities were not included in the TSPA-SR; they are summarized in Section 4.3.1.

- Distributions of flow focusing factors were developed as part of the seepage abstraction process to account for potentially increased local flow rates as a result of intermediate-scale flow channeling. A conservative flow focusing model was applied in *Abstraction of Drift Seepage* (CRWMS M&O 2001 [DIRS 154291], Section 6.4.3). To better quantify flow focusing and to address the uncertainty associated with the estimation of flow focusing factors, a detailed process model was developed to simulate water flow through a stochastically generated, heterogeneous fracture continuum. The results of this study, which did not support the TSPA-SR (CRWMS M&O 2000 [DIRS 153246]) and which do not consider elevated temperature conditions, are reported in Section 4.3.2.

- Seep flow rates were increased by a safety factor to account for the potential impact of rock bolts on seepage (CRWMS M&O 2001 [DIRS 154291], Section 6.4.1). A detailed modeling study was performed to address the potential for seepage enhancement due to ground support measures, and thus the necessity of this safety factor. This study, the

Table 4-1. Summary of Supplemental Models and Analyses

Key Attributes of System	Process Model (Section of S&ER)	Topic of Supplemental Scientific Model or Analysis	Reason For Supplemental Scientific Model or Analysis			Section of Volume 1	Performance Assessment Treatment of Supplemental Scientific Model or Analysis[a]	
			Unquantified Uncertainty Analysis	Update in Scientific Information	Lower-Temperature Operating Mode Analysis		TSPA Sensitivity Analysis	Included in Supplemental TSPA Model
Limited Water Entering Emplacement Drifts	Seepage into Emplacement Drifts (4.2.1)	Flow-focussing within heterogeneous permeability field; episodic seepage	X		X	4.3.1 4.3.2 4.3.5	X	X
		Effects rock bolts and drift degradation on seepage	X			4.3.3 4.3.4		
	Coupled Effects on Seepage (4.2.2)	Thermal effects on seepage	X		X	4.3.5	X	X
		Thermal-Hydrologic-Chemical effects on seepage	X		X	4.3.6		
		Thermal-Hydrologic-Mechanical effects on seepage		X	X	4.3.7		

NOTE: S&ER = *Yucca Mountain Science and Engineering Report* (DOE 2001 [DIRS 153849]).

[a] Performance assessment treatment of supplemental scientific model or analysis discussed in SSPA Volume 2 (McNeish 2001 [DIRS 155023]).

results of which were not included in the TSPA-SR (CRWMS M&O 2000 [DIRS 153246]), is described in Section 4.3.3.

- Seepage is also potentially increased by a change in the drift geometry due to rockfall and drift degradation. A simplified, two-dimensional drift-degradation model supported the seepage calculations that were used for the TSPA-SR (CRWMS M&O 2000 [DIRS 153246]). A new seepage prediction model based on three-dimensional degradation profiles was developed to further study the impact of heterogeneity and degradation effects on seepage. This study, documented in Section 4.3.4, did not include thermal loading scenarios and was not used to support the TSPA-SR.

- In the studies supporting the TSPA-SR (CRWMS M&O 2000 [DIRS 153246]), effects of repository heat on seepage were deduced indirectly from results presented in *Mountain-Scale Coupled Processes (TH) Models* (CRWMS M&O 2000 [DIRS 144454]). A refined modeling study was performed to reduce conceptual uncertainties regarding grid resolution and heterogeneity. The study also examined the impact of lithophysal cavities on thermal properties; the potential for liquid water to penetrate a superheated region, causing episodic seepage events; and the development of a vaporization barrier. Moreover, percolation flux was calculated for a range of thermal operating modes. The new simulation work is presented in Section 4.3.5; it was not considered in the TSPA-SR.

- Thermal-hydrologic-chemical (THC) processes may impact seepage through thermally induced changes in unsaturated hydrogeologic properties. The TSPA-SR (CRWMS M&O 2000 [DIRS 153246]) was based on an abstraction of the data documented in *Drift-Scale Coupled Processes (DST and THC Seepage) Models* (CRWMS M&O 2000 [DIRS 142022]). Additional validation studies were performed, enhancing the confidence in the THC modeling approach. Sensitivity analyses were performed to examine different in-drift designs, different heterogeneous host rock units, different systems of components and minerals, different kinetic models for mineral-water interactions, different permeability-porosity relations during precipitation and dissolution, and changed thermodynamic data and initial conditions. All these studies, which are fully documented in *Drift-Scale Coupled Processes (DST and THC Seepage) Models* (BSC 2001 [DIRS 154677]), helped reduce conceptual uncertainties in the THC models. Additional studies of coupled processes were performed for an extended range of temperatures covering various thermal operating modes. All these studies are summarized in Section 4.3.6.

- A distinct-element analysis was performed to examine thermal-mechanical (TM) effects of drift excavation and repository heat on hydrogeological properties (CRWMS M&O 2000 [DIRS 149040]). This analysis has been revised and extended to provide a more robust estimate of TM effects in fracture permeability. In addition, a fully coupled thermal-hydrologic-mechanical (THM) continuum model was developed and calibrated against air-permeability data from three niches and the Drift Scale Test area. The successful calibration increased confidence in the conceptual model and reduced uncertainties in the subsequent prediction runs, which included two thermal operating modes. This study is presented in Section 4.3.7.

All the following sections discuss calculations done before the TSPA-SR (CRWMS M&O 2000 [DIRS 153246]), as documented in AMRs, and the calculations done after the TSPA-SR, as documented in updates to the AMRs and this report. Each section contains a discussion of independent evidence from analogue sites. In addition, the remaining unquantified uncertainties are identified and summarized.

Like any other model, seepage models are simplifications and abstractions of recognized processes and features. These processes and features were included in a specific seepage model based on their expected significance, which can be evaluated through sensitivity analyses. Experiments were designed and conducted to identify, understand, and characterize significant processes and parameters. Remaining uncertainties and property variabilities were considered either by stochastic simulations and uncertainty propagation analyses or by modeling appropriately increased parameter uncertainties in the TSPA calculations. Conservative approaches were used for effects that could not be explicitly accounted for because the amount, type, or quality of characterization data was insufficient.

Any remaining uncertainty is only of concern if it affects the goal of the respective study. Conversely, even a small, well-understood, and accurately quantified uncertainty may be unacceptable if the outcome of an analysis is very sensitive to a change in the corresponding conceptual model, its data, or parameter values. The following discussion therefore includes both quantified and unquantified uncertainties.

4.2 TREATMENT OF SEEPAGE-RELATED ISSUES

Figure 4.2-1 illustrates some seepage-relevant phenomena and processes. The following paragraphs discuss the key factors affecting drift seepage and how they were addressed in the reports listed in Section 4.1. As mentioned above, some of these reports were revised and finalized after the TSPA-SR (CRWMS M&O 2000 [DIRS 153246]). Note, however, that the general modeling approach outlined here is identical to the one used for the AMRs that support the TSPA-SR. These sections represent new work and extensions of existing work. Table 4-1 identifies the primary reason for the development of each section and indicates which of these analyses have been included in TSPA calculations.

4.2.1 Spatial and Temporal Flow Focusing

Process Description–Flux and spatial distribution of downward percolating water is one of the most important factors affecting seepage rates and seep locations. Water movement is controlled by net infiltration at the surface and subsequent multiscale moisture redistribution. Hydrostratigraphic units (such as the PTn) and features (such as faults) govern large-scale flow patterns, and thus lead to a redistribution of infiltration and percolation fluxes. On an intermediate scale, flow through the fracture network may be focused (funneling effect) or dispersed (bifurcation). This leads to zones of locally higher percolation fluxes and areas of reduced water flow between them. Water within such a high-flux zone may be further channeled by variabilities in the fracture network. Finally, heterogeneity and flow instabilities within individual fractures lead to small-scale flow channels (rivulets or fingers). In addition to spatial flow focusing, episodic events may lead to temporally increased percolation fluxes, followed by

periods of reduced percolation. This phenomenon can be referred to as temporal flow focusing (analogous to spatial flow focusing).

Current Modeling Approach and Uncertainties–Uncertainties in the spatial and temporal distribution of percolation flux encountering the emplacement drifts were addressed on the different scales (i.e., mountain scale, intermediate scale, drift scale, sub-drift scale) and were propagated through the downstream models using deterministic sensitivity analyses (CRWMS M&O 2000 [DIRS 122797], Section 6.6), probabilistic flow focusing factors (CRWMS M&O 2001 [DIRS 154291], Section 6.3.3), and an estimation of effective seepage-relevant parameters (CRWMS M&O 2001 [DIRS 153045], Section 6.3.3 and 6.4.3).

4.2.2 Capillary Barrier Effect

Process Description–Under unsaturated conditions, the rate of water dripping into the opening is expected to be less than the downward percolation rate because the cavity acts as a capillary barrier (Philip et al. 1989 [DIRS 105743], pp. 16 to 28). If percolating water encounters the cavity, the relatively strong capillary forces in the geologic formation retain the water, preventing it from seeping into the drift. Water accumulates at the drift ceiling, where the increase in saturation leads to capillary pressures that are locally less negative than in the surrounding rock, allowing water to be diverted around the drift. If the lateral hydraulic conductivity is insufficient to divert all the water, seepage is initiated; the corresponding flux is referred to as the "seepage threshold." The effectiveness of the capillary barrier is determined by the capillarity, as well as the permeability and connectivity of the fractures.

Current Modeling Approach and Uncertainties–The capillary barrier effect was incorporated through use of a physically based numerical model that included saturation-dependent capillary pressures and relative permeabilities. Conceptual uncertainties in fractured rock (with regard to the capillary barrier effect) were addressed by theoretical analyses (Finsterle 2000 [DIRS 151875], pp. 2055 to 2066); direct observations during the seepage field tests (CRWMS M&O 2000 [DIRS 141400], Section 6.2); calibration of the model against seepage-relevant data, followed by model validation exercises (CRWMS M&O 2001 [DIRS 153045], Section 6.3.4 and 6.4.4); and analogue studies (see Section 4.3.1.7). Remaining uncertainties regarding the location-specific effectiveness of the capillary barrier are being addressed by performing additional seepage tests under controlled humidity conditions (see Section 4.3.1.5).

4.2.3 Excavation-Disturbed Zone

Process Description–The properties of the fractured rock in the immediate vicinity of the drift wall control the capillary barrier effect, which occurs within a relatively small region around the opening. The thickness of this boundary layer is approximately given by the height to which water rises on account of capillarity, and it is likely to be smaller than the extent of the zone affected by excavation-induced stress redistribution and related rock deformations (e.g., opening and closing of existing fractures, generation of new microfractures and cracks) (Wang and Elsworth 1999 [DIRS 104366], pp. 751 to 757).

Current Modeling Approach and Uncertainties–The seepage-relevant properties of the region affected by the capillary barrier were determined by calibration against liquid release test data.

As a result of the calibration approach used, the potential impact of the excavation-disturbed zone on seepage was automatically considered, effectively eliminating potential conceptual and parametric errors in a modeling approach that requires the development of a hydromechanical model. Additional effects and uncertainties are discussed in Section 4.3.7.

4.2.4 Drift Geometry and Drift Surface Effects

Process Description–The geometry (i.e., the shape and size) of the emplacement drift determines the likelihood of encountering seeps and the ease with which water can be diverted around the opening. The geometry of drift wall roughness and the characteristics of the drift surface (e.g., wettability, micro-roughness, dust, coating) partially control local water accumulation, droplet formation, the potential for film flow along the drift wall, and, eventually, dripping locations. The frequency, location, size, and geometry of breakouts and partial drift collapse affect the integrity of the capillary barrier. Breakouts may lead to distinct topographic lows, which increase seepage, or a more cone-shaped drift, which would promote flow diversion and decrease seepage.

Current Modeling Approach and Uncertainties–Simulations of seepage into drifts with cavities extending from the drift surface were conducted to examine the impact of rockfall on seepage rates (CRWMS M&O 2000 [DIRS 153314], Section 6.4). Rock bolts were treated in a conservative manner by forcing water flowing in the vicinity of a rock bolt to seep (CRWMS M&O 2000 [DIRS 153314], Section 6.7). Detailed submodels on the significance of the presence of rock bolts for ground support and drift degradation are presented in Sections 4.3.3 and 4.3.4, respectively.

4.2.5 Ventilation and Evaporation-Condensation Effects

Process Description–The drift temperature, drift humidity, and regulation of temperature and humidity in the drift by ventilation determine evaporation and condensation effects. Evaporation at the drift wall generally reduces drop formation and dripping, and creates a dryout zone around the drift. If relative humidity in the drift is kept below 100 percent by ventilation, then seepage of liquid water is reduced or completely suppressed. However, local differences or temporal changes in drift temperature may lead to condensation of vapor, causing droplet formation at the drift wall and other surfaces within the drift. Accumulation of condensate can lead to dripping.

Current Modeling Approach and Uncertainties–Ventilation effects were not explicitly modeled. Neglecting ventilation effects in a seepage prediction model is a conservative approach: such calculations lead to increased seepage because water that potentially evaporates is considered to be dripping into the opening, enhancing the seepage rate. However, if significant evaporation occurred during the seepage experiments, then the parameter estimates obtained by calibration would be nonconservative (see Section 4.3.1.8). Uncertainties regarding evaporation effects were addressed by selecting conservative parameter sets in the seepage abstraction (CRWMS M&O 2001 [DIRS 154291], Section 6.3 and 6.4). In-drift moisture migration and condensation are separate issues (see Section 5).

4.2.6 Thermal Effects and Coupled Processes

Process Description–Repository heat may impact seepage through coupled thermal-hydrologic-chemical-mechanical effects on rock properties or through the redistribution of water around the drifts and the development of a vaporization barrier. Thermal expansion, as well as dissolution and precipitation of minerals, leads to changes in fracture aperture and fracture coatings, potentially affecting unsaturated zone (UZ) hydrogeologic properties and fracture-matrix interaction. Vaporization and recondensation leads to pressure changes and redistribution of water and heat. A vaporization barrier may prevent percolation water from reaching the drifts. The chemistry of the seepage water may be affected by thermally induced changes in the thermodynamic and geochemical environment.

Current Modeling Approach and Uncertainties–The thermal effects on the hydrologic, mechanical, and chemical processes are examined through coupled process models, as described in Sections 4.3.5 through 4.3.7. Uncertainties in these models stem mainly from uncertainties in the coupling terms and additional parameters that have to be specified. These conceptual and parametric uncertainties are examined through extensive sensitivity analyses. In general, however, these coupled models are used to support the simplifying or conservative approaches used during seepage abstraction.

4.3 DISCUSSION OF KEY PROCESSES, MODELS, AND RELATED UNCERTAINTIES

4.3.1 General Seepage Evaluation and Estimation of Seepage-Relevant Parameters

4.3.1.1 Introduction

This section summarizes the modeling and uncertainty studies performed to determine the seepage-relevant hydrogeologic parameters of the geologic formation in which the potential repository will be sited. Air-permeability and short-term seepage data from liquid-release tests conducted in Exploratory Studies Facility (ESF) Niche 2 (Station 36+50) were used to develop and calibrate a model (the seepage calibration model) for the estimation of seepage-related parameters. This model, along with the related seepage model for performance assessment and the corresponding seepage abstraction, was documented in *Seepage Calibration Model and Seepage Testing Data* (CRWMS M&O 2000 [DIRS 119412]), *Seepage Model for PA Including Drift Collapse* (CRWMS M&O 2000 [DIRS 122894]), and *Abstraction of Drift Seepage* (CRWMS M&O 2000 [DIRS 142004]). The results from these three reports (which are briefly summarized in Section 4.3.1.3) support the TSPA-SR evaluation of seepage fraction and seep flow rate (CRWMS M&O 2000 [DIRS 153246], Section 3.2.4).

New air-permeability and long-term, near-steady seepage data from liquid-release tests conducted in ESF Niches 3 (Station 31+07) and 4 (Station 47+88), as well as borehole SYBT-ECRB-LA#2, were used to extend the model and reduce the uncertainty in the estimated parameters (CRWMS M&O 2001 [DIRS 153045], Section 6). The seepage model for performance assessment and related seepage abstraction have been updated accordingly, as documented in *Seepage Model for PA Including Drift Collapse* (CRWMS M&O 2000 [DIRS 153314]) and *Abstraction of Drift Seepage* (CRWMS M&O 2001 [DIRS 154291]),

respectively. These three AMRs are summarized in Sections 4.3.1.4 and 4.3.1.6. The new results were not available in time to be used for the TSPA-SR (CRWMS M&O 2000 [DIRS 153246]). However, they are consistent with and therefore support the previous findings that were used for TSPA-SR (CRWMS M&O 2000 [DIRS 153426]). A short description of this additional seepage testing is provided in Section 4.3.1.5.

Uncertainties with respect to specific seepage-related issues (such as flow focusing, rock bolts, drift degradation, and the impact of thermal, chemical, and mechanical effects on seepage) are presented in Sections 4.3.2 to 4.3.7. The method used to determine seepage-relevant properties consists of a combination of field testing, process modeling, and effective parameter estimating. This approach was chosen because it provides the means to test the appropriateness of the conceptual model, to reduce and quantify parametric uncertainties, and to obtain seepage-relevant, model-related parameters suitable for use in drift-scale seepage prediction models. Random errors in the field data used for model calibration were accounted for in the calculation of the parameter estimation uncertainties, which in turn were propagated through the seepage model for performance assessment (CRWMS M&O 2000 [DIRS 153314]) to arrive at uncertainty ranges for use in the subsequent seepage abstraction (CRWMS M&O 2001 [DIRS 154291]). Remaining unquantified uncertainties (specifically regarding spatial variability of seepage-relevant rock properties, local percolation flux distribution, and the impact of design decisions regarding ventilation, thermal loading, repository extent, and drift orientation) were addressed through appropriately broadened uncertainty distributions and conservative modeling in the abstraction (CRWMS M&O 2001 [DIRS 154291], Sections 5, 6.3, and 6.4; see also Sections 4.3.2 to 4.3.7). Unquantified conceptual uncertainties were assessed in analogue studies and other corroborating observations.

4.3.1.2 Goal of Models

The goals of the models used to derive seepage-relevant parameters and examine seepage behavior—the seepage calibration model (CRWMS M&O 2001 [DIRS 153045]), the seepage model for performance assessment (CRWMS M&O 2000 [DIRS 153314]), and the abstraction of drift seepage (CRWMS M&O 2001 [DIRS 154291])—are:

- Provide a methodological and conceptual basis for the development of seepage prediction models
- Derive seepage-relevant parameters
- Identify conceptual uncertainties and estimate uncertainty and variability of seepage-relevant parameters
- Determine the seepage rate, its variability, and its uncertainty.

The seepage models were intended to provide estimates of the seepage flux averaged over a 5-m drift segment (the approximate length of a waste package) as a function of the percolation flux on the drift scale. Consequently, the seepage models were not expected to accurately predict individual seepage events or the precise spatial distribution along the emplacement drift axis or

the drift ceiling. Instead, average seepage rates were calculated for a drift segment, which is the scale of interest.

Once seepage rates were evaluated deterministically for a wide range of conditions (which was the purpose of the seepage model for performance assessment), a probabilistic analysis was performed to include uncertainty and spatial variability in TSPA calculations.

4.3.1.3 Discussion of Results

The development of a conceptual seepage model was guided by the recognition that the seepage process in a fractured porous medium is too complex to warrant the construction of a detailed process model. Such a model would consist of a deterministic calculation of unsaturated water flow through a fracture network, which would have to include multiscale variabilities in hydraulic properties. The necessary characterization data are not available, and it is not feasible to obtain them in full. A key element of the chosen approach was therefore the reliance on inverse modeling and the estimation of seepage-relevant, model-related parameters. This approach was considered appropriate because:

- A detailed simulation of individual seeps is not necessary for the intended use of the model: estimating average seepage rates into emplacement drifts.
- Certain factors affecting seepage can be combined into effective parameters; estimating effective parameters partly compensates for processes and features not explicitly considered in the model.
- Calibrating a model against data from seepage experiments ensures the model captures the relevant processes.
- The estimated parameters can be considered optimal and used directly in the prediction model.
- The relative simplicity of a calibrated continuum model leads to less uncertainty in subsequent seepage predictions.

The development of the seepage calibration model is documented in *Seepage Calibration Model and Seepage Testing Data* (CRWMS M&O 2000 [DIRS 119412]). A geostatistical analysis of post-excavation air-permeability data provided the basis for generating a heterogeneous property field, which was mapped onto the model grid. Short-term liquid-release tests from ESF Niche 2 (Station 36+50, located in the middle nonlithophysal zone of the Topopah Spring welded unit [Tptpmn]) were simulated, and the model was calibrated against a relatively small set of cumulative seepage data. The calibrated model was then tested using data from additional liquid-release experiments from Niche 2. Based on the same conceptual model, an extensive sensitivity analysis was performed, using the seepage model for performance assessment (CRWMS M&O 2000 [DIRS 122894]) to derive a database of seepage rates to be used in the subsequent seepage abstraction (CRWMS M&O 2000 [DIRS 142004]), in which probability density functions for seepage rate and seepage fraction were developed.

These results were considered in the TSPA-SR (CRWMS M&O 2000 [DIRS 153246], Section 3.2.4). However, the sensitivity and error analyses revealed strong correlations and relatively large uncertainties in the estimated parameters, mainly because the amount of water used in the short-term liquid-release tests was insufficient (CRWMS M&O 2000 [DIRS 119412], Section 6.4). Additional, longer-term liquid-release tests were needed to reduce the estimation uncertainty, to better evaluate the spatial variability of seepage, and to obtain seepage data from the lower lithophysal zone of the Topopah Spring unit (Tptpll). New seepage tests were conducted, and the affected documents were revised (see Section 4.3.1.4).

4.3.1.4 Discussion of Revision 01 Results

The revised seepage studies were based on the general modeling approach outlined in *Seepage Calibration Model and Seepage Testing Data* (CRWMS M&O 2000 [DIRS 119412]). However, they incorporated the new data that became available for model calibration. The analyzed data included more than 200 air permeabilities, as well as seepage rates from approximately 60 liquid-release tests conducted at three niche sites along the ESF (Niches 3 [Station 31+07], 2 [Station 36+50], and 4 [Station 47+88]) and in Enhanced Characterization of the Repository Block (ECRB) Cross Drift borehole SYBT-ECRB-LA#2, located in the Tptpll unit (CRWMS M&O 2001 [DIRS 153045]).

Figure 4.3.1-1 shows an example of a three-dimensional, heterogeneous model used to determine seepage-relevant, model-related parameters through calibration against seepage rate data obtained on the drift scale. Details about the calibration process can be found in *Seepage Calibration Model and Seepage Testing Data* (CRWMS M&O 2001 [DIRS 153045], Sections 6.3.3 and 6.4.3). The calibrated model was able to predict seepage rate data from other long-term liquid-release tests reasonably well, especially when considering the prediction uncertainty (CRWMS M&O 2001 [DIRS 153045], Sections 6.3.4 and 6.4.4; see also Figure 4.3.1-2). The resulting estimates for permeabilities and the van Genuchten capillary strength parameter, $1/\alpha$, were used in the seepage model for performance assessment to calculate seepage thresholds and seepage rates as a function of percolation flux, as described in *Seepage Model for PA Including Drift Collapse* (CRWMS M&O 2000 [DIRS 153314], Section 6.6). That document also describes additional sensitivity analyses regarding parameters of secondary importance (such as the van Genuchten parameter n, the standard deviation and correlation length of the permeability field), certain conceptual model features (such as the correlation between permeability and the van Genuchten capillary strength parameter, $1/\alpha$, the stochastic realization of the permeability field), and the impact of rock bolts and drift degradation on seepage.

The calibration and validation studies presented in *Seepage Calibration Model and Seepage Testing Data* (CRWMS M&O 2001 [DIRS 153045], Section 6) were not reflected in the TSPA-SR (CRWMS M&O 2000 [DIRS 153246]). However, they are consistent with and support the AMRs used for the TSPA-SR. In addition, they addressed some of the uncertainty issues related to seepage, specifically:

- The conceptual model and its numerical implementation proved adequate for the simulation and reproduction of average drift-scale seepage behavior in a fractured rock.

- Parameters were derived (specifically the van Genuchten capillary strength parameter, $1/\alpha$) that are relevant for seepage on the scale of interest. Parameters determined through calibration are suitable for use in the numerical seepage prediction model and its submodels, which were developed for sensitivity analyses.

- Estimation uncertainties were determined using conventional linear error analysis, which accounts for the goodness-of-fit and the sensitivity of the simulated data to the parameter of interest. Parameter values from individual borehole intervals, test locations, and hydrogeologic units were averaged, and measures of variability were calculated.

- Seepage rates were predicted over appropriate parameter ranges for subsequent use in seepage abstraction and probabilistic TSPA calculations.

The additional studies documented in the revised AMRs confirmed the appropriateness of the approach developed in the original AMRs. Moreover, the extended data set used for calibration and model validation reduced estimation uncertainty and increased confidence in the models. The long-term seepage experiments provided more reliable data on a larger, more relevant scale, enabling the calculation of suitable averages. Because near-steady seepage data were available, the correlation between the estimated parameters was lowered, which again reduced estimation uncertainties and the impact of potential systematic errors. Seepage data from the lower lithophysal unit were analyzed for the first time, providing unit-specific estimates. These new estimates replaced the previous conservative modeling that had been made in the seepage abstraction regarding this unit.

4.3.1.5 Developments Since Revision 01

While seepage tests in multiple locations in the Tptpmn unit are available, only a few tests were performed at a single location in the Tptpll from a borehole drilled into the ceiling of the ECRB Cross Drift. Additional seepage tests in that unit are currently being conducted as part of the Systematic Borehole Testing Program in the ECRB Cross Drift. Moreover, seepage testing in ESF Niche 5 (also located in the Tptpll) has been initiated. The results from these additional seepage tests will help develop more reliable distribution functions for seepage parameters used in TSPA calculations.

As outlined in *Seepage Calibration Model and Seepage Testing Data* (CRWMS M&O 2001 [DIRS 153045], Sections 7.4 and 7.5), evaporation losses during the liquid-release tests have been identified as a potential systematic error in the measured seepage rates, and thus in the parameters derived from these data. To address this issue, current seepage tests include measures to control relative humidity or monitor the evaporation potential. Laboratory experiments were designed to increase the understanding and quantify evaporation potentials from a fractured porous geologic formation. Modeling approaches are being explored that would account for evaporation losses. Quantifying evaporation will help diminish the potential bias in the seepage data and seepage-relevant parameters, reducing uncertainty in seepage predictions.

Additional studies and model refinement are discussed in Sections 4.3.4 to 4.3.7.

4.3.1.6 Abstraction for Total System Performance Assessment

The complex physical processes affecting drift seepage cannot be addressed comprehensively in an analytical or numerical model, mainly because it is impossible to obtain sufficient characterization data over many scales to describe all the relevant geometric features and hydrologic properties. The characterization and modeling approach focused on obtaining effective parameters based on seepage-relevant hydraulic data. The seepage model for performance assessment provided seepage estimates over a wide range of hydrologic conditions (CRWMS M&O 2001 [DIRS 153314], Section 6.6).

Finally, seepage abstraction was performed to obtain probability distributions for the fraction of waste packages encountering seepage and the seep flow rate, accounting for parameter uncertainty, spatial variability, and other effects, such as focusing (see Section 4.3.2), rock bolts (see Section 4.3.3), drift degradation (see Section 4.3.4) and coupled processes (see Sections 4.3.5 through 4.3.7).

As discussed in *Abstraction of Drift Seepage* (CRWMS M&O 2001 [DIRS 154291], Section 6.3.3), seepage is mainly a function of the geometric-mean fracture permeability and the fracture capillary-strength parameter $1/\alpha$. The effects of uncertainties in these parameters are evaluated by calculating seepage for three cases: a base case, a high-seepage case, and a low-seepage case. A triangular shape is chosen for the seepage uncertainty distributions. Table 4.3.1-1 summarizes the seepage fraction, the seepage rate, and its standard deviation at the three points defining the triangular distribution as a function of percolation flux.

Table 4.3.1-1 and the distributions for the flow-focusing factor (CRWMS M&O 2001 [DIRS 154291], Figures 5 and 6) are the final products of the seepage abstraction, which are used in TSPA simulations to estimate seepage. More details about the development of these distribution functions can be found in *Abstraction of Drift Seepage* (CRWMS M&O 2001 [DIRS 154291], Section 6).

4.3.1.7 Multiple Lines of Evidence

The conceptual understanding of drifts acting as capillary barriers, which reduce seepage in comparison to the prevalent percolation flux, is supported by direct and indirect observations in underground openings, as discussed below.

The flow model for the UZ predicts that much of the groundwater will be diverted around the emplacement drifts such that the seepage flux will be much smaller than the percolation flux. A large number of different types of analogues exist that can be used to test this conclusion. These include both natural and man-made underground openings. This section provides some examples from a variety of rock types and for a variety of climatic settings.

4.3.1.7.1 Caves

Caves provide some of the best-known and longest-term examples of seepage flux in the UZ. Most caves are located in limestone, though a few are located in lava tubes. Both rock types

provide a reasonable hydrologic analogue for emplacement drifts in welded tuffs at Yucca Mountain because in all three cases (limestones, lava tubes, and welded tuffs), porosity is small and fracturing that can provide pathways for water flow is common.

Some caves are located in zones of such low percolation flux that they have little, if any, measurable seepage flux. These relatively dry caves are common throughout the southwestern United States; because of their dryness, pollen and other delicate plant and animal materials have been preserved for tens of thousands to hundreds of thousands of years (Davis 1990 [DIRS 144461]; Rogers et al. 2000 [DIRS 154320]). In fact, Davis (1990 [DIRS 144461]) notes that dryness in caves is critical to preservation of biotic remains (Davis 1990 [DIRS 144461], p. 338). That such preservation is common is supported by the fact that more than 1,000 packrat middens have been collected from caves (i.e., rock alcoves, rock crevices, and caverns) throughout arid North America (Davis 1990 [DIRS 144461], p. 341), and some of these are more than 40,000 yrs old.

Other well-known examples of preservation within caves in the UZ include hundreds of caves that contain archaeological artifacts and paintings. These are common in Europe, Africa, and India, and are reported from Asia, North America, and South America (Stuckless 2000 [DIRS 151957]). In both Europe and Africa, paintings have been dated at about 30,000 yrs. Charcoal used in paintings in the Chauvet cave in France has been dated at 32,410 to 32,340 B.C. by Chauvet et al. (1996 [DIRS 152249]). Some of the paintings in this cave show an important feature of seepage flux: some of the water that enters the cave runs down the walls rather than dripping, as modeled in the TSPA model. This evidence from analogue sites suggests that film flow along the walls is a process that may also occur in emplacement drifts, reducing the amount of water that potentially drips onto the waste packages. This effect was conservatively neglected in TSPA-SR calculations.

The caves near Altamira, Spain, are located in the UZ of a fractured limestone formation that contains clay-rich layers. These caves contain paintings that are about 14,000 yrs old. Precipitation at this site is approximately 10 times greater than at Yucca Mountain. Nevertheless, seepage rates into the caves are estimated to be less than 1 percent of the expected percolation flux (Stuckless 2000 [DIRS 151957]). Moreover, there are essentially no fluctuations in the observed seepage rates, even though the precipitation rate is not constant and the UZ is only about 7 m thick (Villar et al. 1985 [DIRS 145806]).

A similar study has been reported for Kartchner Caverns in southern Arizona. Precipitation there is approximately three times that at Yucca Mountain (Buecher 1999 [DIRS 154295]), but the climate is monsoonal and most of the precipitation occurs in just two months. The caverns are located in a limestone block with an area of approximately 350 by 550 m and are covered by approximately 10 to 65 m of limestone, cherty limestone, and cherty dolomite (Jagnow 1999 [DIRS 154296]). The caverns are cut by more than 60 faults, so fracture permeability should be large. Nonetheless, less than 2 percent of the annual precipitation reaches the caves, and nearly half of that is lost to evaporation (Buecher 1999 [DIRS 154295]).

4.3.1.7.2 Excavated Openings

Man-made underground openings include the tombs of Egypt. A total of ten tombs were visited by a project scientist in October 2000. Most of these were excavated in limestone approximately 3,500 to 3,000 yrs ago, and although the climate there is somewhat drier than at Yucca Mountain, precipitation events have been strong enough to cause mud flows within the Valley of the Kings (Weeks 1998 [DIRS 154297]). Small areas of spallation of plaster from walls and ceilings can be seen in many tombs, but evidence of dripping seems to be lacking. As with Chauvet Cave, there is occasional evidence for water flow down the wall (Figure 4.3.1-3).

Buddhist monks carved several temples into basalt flows at Ajanta, India, between the second century B.C. and the sixth century A.D. and decorated them with paintings on plastered surfaces. The climate in the area is monsoonal and the precipitation, which is more than five times that at Yucca Mountain, falls in four months (Stuckless 2000 [DIRS 151957]). Nonetheless, most of the paintings are well preserved except for small areas of spallation.

The Christians of Cappadocia, Turkey, excavated underground cities and churches during the second through eleventh centuries A.D. The geology is similar to that of southern Nevada in that the bedrock is a thick sequence of silicic volcanic rocks. Visits to the underground cities and churches produced no evidence of dripping from the ceiling, but evidence for flow down a wall was found where a fracture intersected the wall (Stuckless 2000 [DIRS 151957]). As with the Egyptian tombs and Buddhist temples, some of the church paintings showed evidence of spallation.

4.3.1.7.3 Mineral Depositions in Lithophysal Cavities

Lithophysal cavities within the Topopah Spring Tuff provide a direct record of long-term seepage within the UZ at Yucca Mountain. These originated as gas pockets within the ash-flow sheet and range in diameter from a few centimeters to a meter. Locally, between 1 and 40 percent of these cavities contain secondary minerals that record a history of water ingress. Careful dating shows that the secondary minerals developed at a fairly uniform rate during at least the last 10 million years (Neymark and Paces 2000 [DIRS 127012]). The thickness of the secondary minerals, together with the chemistry of pore waters and ages of deposition, allow calculation of a seepage rate (Marshall et al. 2000 [DIRS 151018]). The results indicate only 1 L of water per 5-m length of tunnel per year, which is significantly less than rates predicted with the seepage model for performance assessment, on the order of 10 to 1,000 L per waste package per year (CRWMS M&O 2001 [DIRS 154291], Section 6.5). Marshall et al. (2000 [DIRS 151018]) also note that no lithophysal cavities have been found that show any evidence of dripping into the cavities, such as stalactitic deposits. These findings support the concept of a capillary barrier reducing seepage below percolation flux.

4.3.1.7.4 Rainier Mesa

Rainier Mesa, located approximately 30 km northeast of Yucca Mountain, is underlain by a sequence of welded and nonwelded tuffs similar to those that underlie Yucca Mountain. Precipitation is about double the mean at Yucca Mountain, and percolation is estimated to be about eight percent of precipitation (Wang et al. 1993 [DIRS 108839], p. 676). Tunnels

excavated on the Nevada Test Site at Rainier Mesa were generally located in zeolitic tuffs, which are believed to be near full saturation. Faults and joints are abundant in these zeolitic-bedded tuffs. When intersected by tunnels, some of these joints (and especially through-going faults) have yielded significant amounts of water. The seeping features are thought to be pathways for flow from a perched water zone above the zeolitic horizon. Seepage water is geochemically similar to meteoric water and is associated with fast flow paths. Seepage at Rainier Mesa occurs only in tunnels constructed in the zeolites; no seepage has been observed in the tunnel intersecting vitric tuff units. These observations suggest that seepage into tunnels may be localized and restricted to certain flow paths and units. This corroborates the modeling results, which indicate that the seepage fractions are less than one (i.e., that not all waste packages are expected to encounter seepage). More details can be found in *Natural Analogs for the Unsaturated Zone* (CRWMS M&O 2000 [DIRS 141407], Section 6.5.1.2) and Wang et al. (1993 [DIRS 108839], pp. 675 to 681).

4.3.1.7.5 Absence of Seepage into Sealed Exploratory Studies Facility and Enhanced Characterization of the Repository Block Cross Drift Segments

Currently, no natural seepage into the ESF has been observed. Furthermore, no construction water was observed to seep into the ESF main drift as the tunnel boring machine passed the crossover point during the excavation of the ECRB Cross Drift. However, evaporation and moisture removal through ventilation of the ESF are likely to be larger than potential seepage rates, preventing the direct observation of liquid water dripping into the drift.

To study seepage under ambient conditions, sections of the ECRB were sealed by bulkheads in an attempt to reduce unwanted ventilation effects. Two bulkheads were installed in June 1999. During a first entry into the closed-off drift sections in January 2000, moisture was found on the vent line, cables, and pipes. The observed moisture was speculated to be condensate induced by heat sources, such as the tunnel lighting and the tunnel boring machine at the end of the tunnel. A third bulkhead was installed to reduce heat flow from the tunnel boring machine. Drip detection sheets, wind speed sensors, and surface thermocouples were installed. The lights were turned off in July 2000, and the ECRB sections behind the bulkheads were again sealed. The bulkheads were re-opened in January 2001. While parts of the drift were dry, the canvas sheets showed drip marks or were wet, especially in the zone near the Solitario Canyon fault, where there is no overlying PTn. Preliminary evaluations of the drip detection sheets, the chemistry of water samples taken from buckets, and the wind and temperature data suggest that the observed moisture conditions are likely a result of condensation. Although seepage has not been detected, its presence would be consistent with the predictions of the seepage model for the high percolation region near the Solitario Canyon fault.

4.3.1.8 Summary of Uncertainties and Their Treatment

The uncertainty of the parameters estimated with the seepage calibration model (CRWMS M&O 2001 [DIRS 153045]) were considered acceptable given the intended purpose of the model and the use of its results by the seepage model for performance assessment and the seepage abstraction.

Further evaluation of the following sources of uncertainty would reduce the prediction uncertainty of the seepage studies if further reduction were required by users of the seepage model results:

- Uncertainties in the liquid-release test data, specifically those caused by unquantified evaporation losses, should be evaluated. Current and proposed studies (e.g., laboratory, field, theoretical, numerical) may address this issue.

- Because seepage experiments were performed at only a few sites, specific conditions prevailing at other locations and medium- and large-scale spatial variability in hydrogeologic properties may increase the range of potential seepage behavior. Current and planned seepage experiments at additional sites may address this issue.

- For predictions of future seepage into emplacement drifts, extrapolations beyond the conditions encountered during model development, calibration, and validation are performed, which inherently increases the potential for systematic errors. These conceptual uncertainties are addressed through analogue studies, which establish multiple lines of evidence (see Section 4.3.1.7), and through conservative approaches to modeling in the seepage abstraction and TSPA calculations.

Table 4.3.1-2 summarizes the key conceptual and parametric uncertainties, as well as potential data errors affecting the development of seepage-relevant parameters through calibration of a process model against data from liquid-release tests. It should be noted that each conceptual decision, data point, and parameter value remains uncertain, and thus affects the goals outlined in Section 4.3.1.2 to a certain degree. The results of downstream models (specifically the TSPA calculations), as well as the findings of decision and policymakers, will determine whether the remaining uncertainty can be considered acceptable or not.

4.3.1.9 Summary and Conclusions

Seepage into emplacement drifts is considered a key factor affecting the performance of a potential repository at Yucca Mountain. Theoretical analyses, numerical modeling studies, field testing, and observations at analogue sites suggest that seepage into underground openings excavated in unsaturated geologic formations is smaller than the local percolation flux. This is mainly a result of capillary pressure holding water in the formation, diverting it around the excavated opening, and preventing it from entering the drift. The effectiveness of this capillary barrier depends on percolation flux, hydrogeologic properties, and the geometry of the drift.

A sequence of models was used to predict the fraction of waste packages affected by seepage, seepage threshold, and seep flow rates. Seepage process models were calibrated against seepage-relevant data from liquid-release tests. Seepage rates were then calculated over a wide range of parameter values and compiled in an abstraction process. Finally, probability distributions of the key parameters were introduced and conservative approaches were used to arrive at probabilities for seepage into emplacement drifts.

These analyses indicate that seepage fluxes are lower than percolation fluxes, even under conservative modeling, and that only a fraction of the waste packages will encounter seepage.

Naturally, seepage predictions remain uncertain. Some of the identified uncertainties can be further reduced through additional testing and modeling studies.

The overall approach of estimating drift seepage by developing a physically based process model and calibrating it against data from liquid-release tests to obtain site-specific, model-related, and seepage-relevant parameters on the scale of interest was documented in *Seepage Calibration Model and Seepage Testing Data* (CRWMS M&O 2000 [DIRS 119412]). The conceptual model and estimated parameters were then used to develop a database for the subsequent seepage abstraction, as documented in *Seepage Model for PA Including Drift Collapse* (CRWMS M&O 2000 [DIRS 122894]) and *Abstraction of Drift Seepage* (CRWMS M&O 2000 [DIRS 142004]). The abstracted probability functions for seepage rate and seepage fraction supported the TSPA-SR (CRWMS M&O 2000 [DIRS 153246], Section 3.2.4). Additional seepage tests were conducted, providing estimates of reduced uncertainty for both the Tptpmn and Tptpll units. These new results, which are not reflected in the TSPA-SR (CRWMS M&O 2000 [DIRS 153246]), confirmed the previous findings and will help reduce prediction uncertainties in future TSPA calculations.

4.3.2 Flow Focusing and Discrete Flow Paths in the Topopah Spring Welded Hydrogeologic Units

4.3.2.1 Introduction

Water percolating downward in the UZ may be focused into discrete flow paths along high-mobility channels. This process tends to concentrate flow, potentially increasing seepage in certain locations, but at the same time reduces the number of waste packages encountering seepage. This section summarizes the modeling studies performed to investigate flow focusing and the characteristics of discrete flow paths that may develop within the UZ fracture network in the TSw. It describes new work that has been conducted since the TSPA-SR (CRWMS M&O 2000 [DIRS 153246]), in the form of sensitivity studies and a scoping analysis, to further assess flow focusing and discrete flow patterns.

Flow focusing and the development of flow channels cannot be directly observed in the field. Therefore, flow-focusing phenomena are mainly addressed through indirect field evidence and the use of models based on physical processes. Related uncertainties stem from uncertainties and ambiguities in conceptual models, characterization data used in these models, and interpretations of modeling results. Unquantified conceptual uncertainties are assessed through analogue studies and other corroborating observations.

Analyses and models supporting the TSPA-SR (CRWMS M&O 2000 [DIRS 153246]) used a coarse site-scale grid (100 m or more in horizontal directions) and layer-averaged fracture properties, ignoring the variability in fracture permeability fields within a geologic layer. Detailed flow patterns on a smaller scale, such as fracture spacing, cannot be derived from such a model; therefore, smaller-scale models, such as the drift seepage model, use a higher resolution. This means a gap exists between the site-scale and drift-scale models in modeling flow focusing phenomena. During the seepage abstraction that supported TSPA-SR, flow focusing factors were sampled from probability density functions, which were derived using simplified methods from the weeps model and active fracture model (AFM) (CRWMS M&O 2000 [DIRS 142004],

Section 6.4). This approach yielded flow focusing up to a factor of 47 (CRWMS M&O 2000 [DIRS 142004], Section 6.4). This section describes an intermediate-scale model that bridges that gap specifically to address the issue of spatial flow focusing. The effects of faults on flow focusing are not included because of the scale used in the modeling studies.

To quantify flow focusing and address the uncertainty associated with the estimation of flow focusing factors, a stochastic fracture continuum model was developed that honors fracture data from welded tuffs by using measured fracture permeability data. This model was used to study flux allocation mechanisms and flow patterns. It was also used to assess the frequency and flux distributions of major water-bearing flow paths and transport pathways from the bottom of the PTn to the potential repository horizon.

The flow focusing factor (the ratio of local flux to average percolation flux) evaluated in this section is used to determine the upper (spatially variable) boundary flux of the drift-scale model by sampling from the frequency distribution of the flow focusing factor. The modeling results in this section indicate that the flow focusing factors currently used in the TSPA models are very conservative.

4.3.2.2 Goal of the Heterogeneous Flow Model for Site-Scale Domains

Flow focusing along preferential paths, such as well-connected fracture networks, may control patterns of percolation through the highly fractured TSw and directly affect seepage into emplacement drifts. The detailed mechanisms that control unsaturated flow and transport in fractured rocks are site-specific and difficult to characterize. Accurate description of flow focusing processes in unsaturated fractures may be important for the detailed prediction of flow patterns or water seepage into the potential emplacement drifts. However, knowing uncertainty ranges and the average behavior of flow focusing and discrete paths may be more important to the TSPA calculations. This section addresses uncertainties from earlier studies that did not provide sufficient detail on fracture flow at the necessary scale. In addition, drift-scale modeling studies on seepage into drifts show that the amount of water that bypasses or breaks through a capillary barrier of a drift wall depends not only on the capillarity and permeability of the surrounding fracture system, but also on the heterogeneity of the water flux and flow paths (CRWMS M&O 2001 [DIRS 153045], Section 6.1.5).

Various conceptual models have been proposed for describing water flow through the thick, fractured UZ at Yucca Mountain. These models range from continuous flow through a well-connected fracture network (e.g., CRWMS M&O 2000 [DIRS 122797]) to sparse, discrete flow through a small fraction of the fracture network (Pruess et al. 1999 [DIRS 117112]). Modeling approaches used to characterize fracture flow include:

- Continuum modeling (e.g., the effective continuum model) and dual-permeability modeling (Wu et al. 1999 [DIRS 117161]).
- Stochastic modeling representing discrete fractures as currently applied to drift-scale processes (Finsterle 2000 [DIRS 151875]).

The objective of this modeling effort is to understand flow focusing mechanisms and quantify the sensitivity of flow focusing to permeability distributions, correlation structures, and boundary conditions over site-scale domains for the TSw units, from the base of the PTn to the potential repository horizon.

4.3.2.3 Discussion of Initial Results

Initial analyses of flow patterns were conducted for several reports in support of the TSPA-SR: *UZ Flow Models and Submodels* (CRWMS M&O 2000 [DIRS 122797]), *Seepage Calibration Model and Seepage Testing Data* (CRWMS M&O 2000 [DIRS 119412], and *Seepage Model for PA Including Drift Collapse* (CRWMS M&O 2000 [DIRS 122894]. The baseline three-dimensional site-scale model was based on the geologic framework model; it consists of alternating layers of welded and nonwelded tuff units. Hydrologic properties were modeled as uniform within each layer. Fault displacements within the model domain were explicitly taken into account. The hydrologic parameters of the layers were determined by calibrations against all known data, including borehole data regarding saturation and water potentials, temperature profiles, perched water and geochemical information, pneumatic pressure signals, and laboratory core data collected in vertical boreholes and horizontal tunnels.

In *Abstraction of Drift Seepage* (CRWMS M&O 2001 [DIRS 154291], Section 6.4.3), the flow focusing factor was estimated using the AFM. The flow focusing factor was used to conservatively estimate the local enhancement of percolation flux applied to the upper boundary of the drift-scale seepage models. In the drift-scale models, the model domains were populated with stochastically generated permeability values. These fields were conditioned on air-permeability data collected in many boreholes drilled above the crown of the niche excavations in the Tptpmn and Tptpll units. The seepage calibration model was then calibrated against available seepage test results for these units. Previous TSPA-SR estimates of the flow focusing factor were based on interpretations of an AFM parameter (CRWMS M&O 2000 [DIRS 153246]). This parameter did not take into consideration the spatial variability of fracture permeabilities within the welded tuff units, and it was chosen to be conservative (using a flow focusing factor of 50 times the local percolation flux). Details about the drift-scale seepage modeling effort are provided in Section 4.3.1.

4.3.2.4 Flow Focusing Study Developments Since the Initial Results

The three-dimensional flow model in *UZ Flow Models and Submodels* (CRWMS M&O 2000 [DIRS 122797]) used a relatively coarse grid that was unable to resolve potential flow focusing on smaller scales representative of the observed fracture spacings. As a result, the TSPA-SR used the conservative flow focusing factor (CRWMS M&O 2000 [DIRS 153246], Section 3.2.4).

The current effort uses a two-dimensional modeling approach for which a finer grid has been developed. This approach attempts to address uncertainties associated with percolation patterns on the scale of fracture spacing. Fracture permeabilities are assigned to the gridblocks based on the mean value, the standard deviation, and the correlation length of the measured permeability distributions. Using gridblock sizes smaller than fracture spacings and a correlation length longer than the gridblock size results in zones of high permeability channels, representing the behavior of discrete fractures and allowing flow to be focused.

The two-dimensional vertical cross section that forms the basis for the modeling studies summarized in this section has an upper boundary at the bottom of the PTn and a lower boundary at the potential repository horizon. The cross section is 100 m wide and 150 m high. The horizontal dimension of the model is considered sufficient because the correlation length for variability in fracture permeability and spacing is on the order of 1 m. The 150-m vertical extent of the model corresponds to the average distance from the top of the TSw to the top of the potential repository horizon over the potential repository area (CRWMS M&O 2000 [DIRS 114277], Attachment II). The top of the TSw (i.e., the bottom of the PTn) is selected as the upper boundary because the PTn behaves as a porous medium with limited fracture flow, resulting in a more uniform percolation flux (CRWMS M&O 2000 [DIRS 144426], p. 28). Uniform percolation flux (5 mm/yr) boundary conditions are prescribed at this upper boundary as the base case, while nonuniform, spatially distributed percolation flux is used for the supporting sensitivity analyses (see Section 4.3.2.5.2). The two side boundaries are treated as no-flow boundaries; the bottom boundary allows gravitational drainage out of the model.

Only the fracture continuum was modeled in this study because prior modeling studies have shown that at high infiltration rates, the rock matrix in the highly fractured TSw units carries little water under steady-state conditions (CRWMS M&O 2000 [DIRS 122797], Tables 6-22, 6-23, and 6-24). Moreover, modeling indicates that the matrix is not expected to have a major impact on the development of preferential flow paths (i.e., weeps) within the model boundaries because matrix permeability is orders of magnitude lower than the permeability of the fracture network (CRWMS M&O 2000 [DIRS 144426], Table 13). The properties of the fracture system are based on those reported in the *Calibrated Properties Model* (CRWMS M&O 2000 [DIRS 144426], Section 6). There are five different hydrogeologic layers (tsw31 through tsw35) within the two-dimensional model, each of which is represented by different fracture properties (e.g., porosity, fracture spacing, capillary pressure, relative permeability functions).

Fracture permeability is prescribed stochastically, based on measured air-permeability data (Bodvarsson 2001 [DIRS 154669], Attachment 6, pp. 24 to 25). The empirical log-permeability data are represented using a spherical semivariogram model (Deutsch and Journel 1992 [DIRS 100567], p. 23). Details of the methodology for generating stochastic fracture permeabilities are discussed in *Seepage Calibration Model and Seepage Testing Data* (CRWMS M&O 2001 [DIRS 153045], Section 6.3.2 and 6.4.2), which concludes that the fracture permeability near the potential repository is essentially random, with no significant spatial correlation.

Fracture permeability distributions are generated by multiplying the mean fracture permeability of each hydrogeologic unit (CRWMS M&O 2000 [DIRS 144426], Section 6.1.2) by randomly generated multipliers. The software code SISIM (Version 1.203) is used to generate the two-dimensional, spatially correlated permeability field multipliers for each gridblock ($0.25\ m \times 0.5\ m$), using a sequential indicator simulation (Deutsch and Journel 1992 [DIRS 100567], p. 151). Two correlation lengths of 1 m (for the base case, Realization #1) and 3 m (for the sensitivity analysis described in Section 4.3.2.5.2) are used to represent weak spatial correlations. The mean and standard deviations of the random permeability field are based on measured air-permeability data (Bodvarsson 2001 [DIRS 154669], Attachment 6, pp. 24 to 25). The fracture permeability, which was generated from field measurements, varies nearly three orders of magnitude, from below 100 millidarcy to over 100 darcy. The upper hydrogeologic

units (tsw31, tsw32, and tsw33) have relatively high permeabilities, while the layer immediately above the potential repository horizon (tsw34) has a lower permeability. All fracture properties other than permeability are modeled as constant over each hydrogeologic unit within the entire model domain.

4.3.2.5 Model Results and Analyses

This section summarizes modeling results obtained and analyses conducted since the TSPA-SR (CRWMS M&O 2000 [DIRS 153246]), including base case results, sensitivity analyses, and tracer transport simulations.

4.3.2.5.1 Base Case Results

Figure 4.3.2-1 shows the distribution of simulated liquid mass flux within the two-dimensional model domain using the base case scenario. The figure clearly shows that a number of nearly vertical, high-flux, discrete flow paths develop for this scenario. It also indicates that about five to ten major pathways (or weeps) are present in the upper hydrogeologic layer (above the elevation of -110 m). More pathways are present in the lower layer.

Figure 4.3.2-2 shows the vertical liquid flux at two different elevations: (a) 25 m below the top of the model, and (b) at the bottom of the model (i.e., –150 m). At both elevations, the figure shows a significant spatial variability in the flux, with values ranging from about 0 to almost 30 mm/yr. Statistically, little difference exists between the flow patterns in Figures 4.3.2-2a and 4.3.2-2b, suggesting that flow path characteristics develop within tens of meters from the top of the model and remain statistically similar over the remaining vertical extent of the model (i.e., 100 m). This similarity is illustrated in Figure 4.3.2-3, where the normalized flux (with respect to the mean infiltration rate at the top) is given on the horizontal axis and the flux frequency distribution on the vertical axis. The frequencies are generated by grouping the vertical flux results along an elevation, counting the total found in each group, and calculating the percent contribution relative to the total horizontal distance (or area) in each category. Frequency distributions at four depths are compared: 25, 50, 100, and 150 m. The figure shows similar flux frequency distributions at each elevation, with flow focusing increasing downward.

With percolation normalized to average infiltration, as shown in Figure 4.3.2-3, the flux frequency and distribution at all elevations are statistically similar. The majority of normalized fluxes range from zero to two, with infrequent weeps at high fluxes. The maximum flux that occurs in the system is generally about five to six times more than the prescribed infiltration rates at the upper boundary. This flow focusing factor is considerably lower than what is currently used in the TSPA-SR models, in which local fluxes were increased by up to a factor of 47 over prevailing percolation flux (CRWMS M&O 2000 [DIRS 142004], Section 6.4.3.2). The wide spread of flow focusing factors used in TSPA-SR yields a wider, albeit conservative, distribution of drift seepage.

4.3.2.5.2 Sensitivity Studies in Support of the Main Conclusion

Several sensitivity analyses were performed; the scenarios described in the following text are summarized in Table 4.3.2-1. These sensitivity studies used:

- Different infiltration rates
- A second realization for fracture permeability (Realization #2)
- A different correlation length of 3 m to generate the permeability (Realization #3)
- Different infiltration patterns (uniform versus pulse).

Figure 4.3.2-4 shows that the flux frequency and distribution for all the infiltration rates (with infiltration rates on the top boundary varying from 1 to 500 mm/yr) in terms of normalized percolation flux are statistically similar. This indicates that discrete flow paths are insensitive to net infiltration rates.

The second realization of fracture permeability (Realization #2) (Bodvarsson 2001 [DIRS 154669], Attachment 14, pp. 25 to 32) is created by initiating the random number generator with a different seed number (Deutsch and Journel 1992 [DIRS 100567]). This realization yields a percolation distribution statistically similar to the first realization. Simulations performed using the 3-m correlation length for the permeability field (Realization #3) result in fewer but slightly larger weeps. The distribution pattern for this realization is similar to the pattern shown in Figure 4.3.2-3 for the 1-m correlation length case. The sensitivity study with the nonuniform infiltration boundary condition (Realization #4) shows that if a spatially variable infiltration is used, the flow patterns behave as if the flux condition at the upper boundary were uniform.

As discussed above, frequency plots for all the sensitivity studies are similar, suggesting that a general frequency plot for the flow-focusing factor can be developed for use in TSPA abstraction. The conclusions of these sensitivity studies support those of the base case. The flow focusing factor is likely to be considerably lower than what is currently used in the TSPA-SR models (CRWMS M&O 2000 [DIRS 153246], Section 3.2.4.3).

4.3.2.5.3 Results with Tracer Transport

Tracer transport analyses are used with the two-dimensional model to provide additional insight into flow focusing and discrete pathways. The results of some of the transport modeling using the base case flow model are presented in this section (i.e., uniform top infiltration flux and 1 m correlation length for fracture permeability). A conservative, nonsorbing tracer with a molecular diffusion coefficient of $D_m = 3.2 \times 10^{-11}$ m^2/s at constant concentration is prescribed at the top model boundary. Under steady-state flow, the tracer is transported into the model domain from the top by advection and diffusion. Figure 4.3.2-5 shows the concentration contours in the model domain after one year of tracer release at the top boundary. Note that all matrix blocks are omitted in these simulations, so retardation (caused by matrix diffusion and sorption) is implicitly neglected. The results show areas of high tracer concentrations (Figure 4.3.2-5), indicating the existence of nonuniform, complex transport pathways (i.e., the development of several fast-flow channels, or fingering). A comparison of Figures 4.3.2-1 and 4.3.2-5 indicates

that faster transport pathways generally follow faster flow pathways. Therefore, concentration distributions within the model domain serve as indicators of preferential flow.

4.3.2.6 Abstraction for Total System Performance Assessment

As Figure 4.3.2-4 demonstrates, the results of the analyses can be used to estimate the flow focusing factor for the seepage abstraction. The normalized flux distributions are similar, and it is reasonable to define a single distribution that applies to all expected percolation rates. A regression curve with confidence bands, summarizing the results of all the simulations, is shown in Figure 4.3.2-6.

The distribution shown in Figure 4.3.2-6 cannot be used directly to define the flow focusing factor for seepage abstraction because the factor is defined in such a way that it is always greater than 1. The part of the normalized flux distribution that is below 1 is accounted for implicitly in the abstraction model (CRWMS M&O 2001 [DIRS 154291], Section 6.4.3.2). However, two important observations must be made: (1) the flow enhancement indicated by these simulations is usually less than three and always less than about six, and (2) there is little spread in the results from different simulations.

In contrast, the uncertainty distributions for the flow focusing factors defined for the TSPA-SR seepage abstraction (CRWMS M&O 2000 [DIRS 153246]) were quite broad, ranging as high as 47 (CRWMS M&O 2001 [DIRS 154291], Section 6.4.3.2). The distributions were derived using a method developed to estimate the spacing of actively flowing fractures on scales below the resolution of the UZ site-scale model. In fact, two methods were used to estimate the flowing-fracture spacing; one implied relatively small spacings averaging 1 to 2 m, while the other implied larger spacings averaging 20 to 30 m (CRWMS M&O 2001 [DIRS 154291], Table 15). The lower values (from the unsaturated active fractures method) are more consistent with the results presented here. For the seepage abstraction, an uncertainty distribution was defined that spanned both methods. The inclusion of the larger focusing factors was considered to be conservative, and it has been shown that larger flow focusing factors tend to produce higher radionuclide doses because of increased total seepage (CRWMS M&O 2000 [DIRS 153246], Section 5.2.1.2).

The average flow enhancement in the results shown in Figures 4.3.2-4 and 4.3.2-6, considering only the part of the normalized-flux distribution above 1, is slightly less than a factor of 2. These results are bounded by an exponential distribution with a mean of 2 (truncated at 1). Thus, the results indicate that it would be more realistic to use a flow focusing factor of about 2 in TSPA simulations, rather than the distributions of focusing flux that were defined for the seepage abstraction.

The results presented here are used to define the flow focusing factor for the TSPA sensitivity analyses presented in Volume 2 (McNeish 2001 [DIRS 155023], Sections 3.2.2.3, 3.2.2.7, and 4). The distributions shown in Figures 4.3.2-4 and 4.3.2-6 represent spatial variability in the amount of flow focusing. However, the current seepage abstraction does not allow for spatial variability of the flow focusing factor (CRWMS M&O 2000 [DIRS 148384], Section 6.3.1.2), and there may be additional sources of uncertainty that have not been addressed in these analyses. It is preferable to use an uncertainty distribution set to the bounding exponential

distribution with a mean of 2. This adjustment would acknowledge that uncertainty exists in the amount of flow focusing, rather than using a single deterministic value of approximately 2 for the sensitivity analysis. In this way, the higher flow focusing factors would be accounted for in at least some of the TSPA realizations.

4.3.2.7 Multiple Lines of Evidence

Evidence of flow focusing occurring at Yucca Mountain can be inferred from observations of calcite and opal occurring in some cavities in the Yucca Mountain UZ. These secondary minerals formed as deposits precipitated by percolating water (Paces et al. 2000 [DIRS 154412]). The mineralization indicates that seeps are not regularly spaced in the underground excavations and that not all fractures sustain flow. Furthermore, many cavities represent sites of seepage that have remained stable for millions of years (Marshall et al. 2000 [DIRS 151018]).

In the excavation of Niche 1 in the vicinity of the Sundance fault, a damp feature was observed (DOE 2001 [DIRS 153849], Figure 4-18). The Sundance fault is one of several faults and features with bomb-pulse signals detected from chlorine-36 measurements (Fabryka-Martin et al. 1997 [DIRS 100145]). The feature was nearly vertical, and it was approximately 0.3 m wide and 3 m long. It dried out before a bulkhead could be installed to prevent contact with ventilation air and has not fully rewetted after two years of observation with the bulkhead closed.

Another damp feature was observed during the excavation of ESF Niche 1 (Station 35+66), the first niche excavated for the seepage studies. This feature, at the end of the niche, was wet to the touch and had a darker color until ventilation dried it up (Wang et al. 1999 [DIRS 106146]).

Nearly uniform distributions of water potential in the Topopah Springs welded tuff (Rousseau et al. 1997 [DIRS 100178], p. 45, 1999 [DIRS 102097], p. 123) and areally near-uniform perched water chloride concentrations indicate that the effective flow focusing factor is small, or generally less than two. This indicates that there are many small flow paths instead of a few large ones, and that the small flow paths are separated by large regions with reduced percolation.

4.3.2.8 Summary of Remaining Uncertainties

Uncertainties associated with the flow focusing studies have been discussed in the preceding text. The main uncertainties associated with these studies can be summarized as: (1) accuracy in describing the fracture permeability fields in the units between the PTn and the potential repository, (2) use of a fracture continuum model, and (3) the effects of matrix heterogeneity. A more complete list of the uncertainty issues particular to flow focusing and their treatment is given in Table 4.3.2-2.

4.3.2.9 Summary and Conclusions

Modeling studies using a stochastic fracture continuum model have been conducted to evaluate flow focusing through fractures from the bottom of the PTn to the potential repository horizon. These studies were carried out using a 100-m wide and 150-m deep two-dimensional cross section covering the upper five TSw hydrogeological units at Yucca Mountain. Mean fracture parameters used in the simulations were obtained from the *Calibrated Properties Model* (CRWMS M&O 2000 [DIRS 144426], Section 6). Heterogeneous fracture permeability

distributions were generated using a stochastic approach conditioned on field-measured air-permeability data. The studies considered various percolation fluxes, correlation lengths, and uniform and nonuniform percolation-flux boundary conditions. The results provide a quantitative analysis of flow focusing. All simulation results indicate that the flow focusing factor is likely to be much smaller than the value used in previous TSPA calculations; therefore, the TSPA calculations are conservative with respect to flow focusing issues, since they use a flow focusing factor that may be an order of magnitude higher than that suggested by the scoping studies presented in this section. This means that the current conservative TSPA approach may overestimate the seepage flux. In addition, the sensitivity analyses indicate that frequency distributions of normalized flux are insensitive to the magnitudes or spatial distributions of percolation fluxes specified on the upper boundary. The frequency distributions are also insensitive to the spatial correlation structure of the permeability fields within the UZ. The flux frequency distribution function may be incorporated into the TSPA for a more realistic representation of the UZ flow and transport field.

4.3.3 The Effect of Rock Bolts on Seepage

This section summarizes the modeling and uncertainty studies performed to evaluate the potential for rock bolts to enhance seepage above that predicted by the models summarized in Section 4.3.1. Model results abstracted for the TSPA-SR (CRWMS M&O 2000 [DIRS 153246], Section 3.2.4) suggested that the presence of rock bolts would enhance seepage; however, more detailed models, recently developed and summarized here, show that rock bolts do not enhance seepage.

4.3.3.1 Introduction

The use of grouted rock bolts is one proposed method of providing ground support for emplacement drifts. Grouted rock bolts might be used in the Tptpmn, but not in the Tptpll, the other rock unit in which emplacement drifts would be located. Rock bolts are steel rods grouted into a borehole normal (i.e., perpendicular) to the drift wall. They accomplish two purposes: they bind the mass of rock above the drift to prevent large rockfalls, and they provide an anchor point for the steel mesh that is placed against the drift wall to prevent raveling (i.e., small rockfalls). Rock bolts present a concern with respect to seepage because they may provide a direct flow conduit to the drift wall. If so, they increase the likelihood that a flowing fracture will be intersected and flow will be diverted to the drift wall to become seepage.

Uncertainties specific to modeling the effect of rock bolts on seepage (in addition to the general uncertainties for seepage models; see Section 4.3.1) are summarized below.

Properties of the Grout Material–How the properties of the grout material, modeled as the conduit for flow diversion toward the drift wall, will change over time is unknown. Because seepage is a process relevant to long-term performance, knowledge of the changing properties as the grout degrades over time are necessary to evaluate the effects of rock bolts on seepage. This uncertainty is addressed by evaluating seepage enhancement over a large range of grout properties. The steel rod portion of the rock bolt system is modeled as impermeable or completely absent. Any contribution to seepage enhancement due to corrosion of the steel rod,

either at the steel-grout interface or within the rod itself, is adequately addressed by varying the properties of the grout surrounding the rod.

Properties of the Formation Surrounding the Rock Bolt–The properties of the formation surrounding the rock bolt are heterogeneous on scales larger than the rock bolt, as evidenced by the distinct permeabilities measured at ESF Niche 3 (located at Station 31+07), Niche 2 (Station 36+50), and Niche 4 (Station 47+88) (CRWMS M&O 2001 [DIRS 153045], Section 6.2.2), and they are uncertain because evaporation is considered to have a negligible effect in the testing and calibration process (CRWMS M&O 2001 [DIRS 153045], Section 5.6). This uncertainty is addressed by evaluating seepage enhancement for several values of the formation capillary strength parameter, $1/\alpha$, which is potentially the most uncertain parameter.

Use of a Homogeneous Model–The use of a homogeneous model, which neglects the heterogeneities on scales smaller than the rock bolt, may affect the results. This uncertainty is addressed by comparing base case seepage results from this model to those from a heterogeneous model.

4.3.3.2 Goal of the Rock Bolt Model

The goal of the rock bolt model is to evaluate the potential for rock bolts to enhance seepage above the levels predicted by the base case seepage model (Section 4.3.1). The rock bolt model is presented in *Seepage Model for PA Including Drift Collapse* (CRWMS M&O 2000 [DIRS 153314], Section 6.7) and *Abstraction of Drift Seepage* (CRWMS M&O 2001 [DIRS 154291], Section 6.4.1).

4.3.3.3 Discussion of Initial Results

In the initial version of *Seepage Model for PA Including Drift Collapse* (CRWMS M&O 2000 [DIRS 122894], Section 6.7), the treatment of rock bolts as a seepage-enhancing factor considered an extremely simple model for rock bolts. Rock bolts were modeled as "needles" extending from the drift wall (the last grid node before the drift wall) vertically downward into the drift, unlike bolt holes, which extend upward away from the drift. Because the "needle" is a single connection, there is no opportunity for lateral flow away from it near the drift wall. The size and properties of this node were unmodified with respect to the surrounding grid. This is in contrast to an actual rock bolt hole, which would have a smaller horizontal cross section and, depending on the properties of the material in the hole (or lack thereof), might create a permeability or capillary barrier and divert flow. These simplifications are likely to significantly impact the results. Seepage enhancement was found to stabilize for needle lengths of 0.15 to 0.25 m. The seepage enhancement for one needle was found to be 3 percent.

4.3.3.4 Discussion of Updated Results

No new analysis or model of the effect of rock bolts on seepage was presented in the update to *Seepage Model for PA Including Drift Collapse* (CRWMS M&O 2000 [DIRS 153314], Section 6.7).

4.3.3.5 Discussion of Current Results

A more complete model of the effect of rock bolts, presented in this section, considers several factors, including:

- The properties of degraded grout and rock bolt material, including the case in which the rock bolt and grout are completely removed from the hole such that the rock bolt hole is a capillary barrier
- The dimensions of the rock bolt and grout
- Uncertainty in the hydraulic properties of the formation
- A range of percolation rates
- The possibility for lateral diversion away from the rock bolt at or near the drift wall
- Rock-bolt density and orientation.

A sketch of the conceptual model for how a rock bolt hole and percolation may interact to enhance seepage (Figure 4.3.3-1) shows that flow along a fracture may encounter a rock bolt hole and either be diverted around the hole or enter the hole. How much flow enters the hole and how much is diverted around it depends on the dimensions of the hole, the angle of the fracture with respect to the hole, the rate of flow, the channeling of flow in the fracture, the hydraulic properties of the grout filling the hole (or the absence of grout, if it has completely degraded), and the local saturation of the grout. Flow that enters the hole will not necessarily result in seepage. The head (or reduction in capillary pressure) at the collar of the hole (i.e., where the hole intersects the drift wall) may not be sufficient to induce seepage, especially if there are pathways for the water to flow back into the formation and be diverted around the drift. Similarly, if seepage is already occurring without the presence of rock bolts, enough diversion capacity may exist such that the rock bolts will not increase seepage.

The proposed use of ground support is documented in *Ground Control for Emplacement Drifts for SR* (CRWMS M&O 2000 [DIRS 146022], Section 6.2). The proposed rock bolt and grout dimensions are 3 m long (CRWMS M&O 2000 [DIRS 146022], Section 6.5.2.2), with a rock bolt diameter of 0.0254 m and a grout annulus thickness of 0.00635 m (CRWMS M&O 2000 [DIRS 146022], Table 4-10). The rock bolts would be emplaced with a lateral spacing of 1.5 m (CRWMS M&O 2000 [DIRS 146022], Section 6.5.2.2). The properties and expected longevity of the rock bolt and grout system are documented in *Longevity of Emplacement Drift Ground Support Materials* (CRWMS M&O 2000 [DIRS 150202], Section 6.4). The design permeability of newly emplaced grout is less than 10^{-18} m^2 (10^{-12} m/s) (CRWMS M&O 2000 [DIRS 150202], Sections 6.4.1 and 6.4.3.1), and its expected life at that permeability is 300 yrs (CRWMS M&O 2000 [DIRS 150202], Section 6.4.3.1).

A refined model that includes a range of properties for the grout and the formation and a range of percolation rates has been prepared. The model uses a two-dimensional, radially symmetric grid with a vertical symmetry axis generated using the software iTOUGH2 V4.0. The grid size is

0.1 m, with finer discretization (down to 0.001 m) at the interface between the grout and the surrounding rock. Because this is a radially symmetric grid, the drift opening, which is created using the software routines MoveMesh V1.0 and CutNiche V1.3, is spherical instead of cylindrical. Knight et al. (1989 [DIRS 154293], p. 37) find that seepage exclusion from a cylindrical cavity is similar to that from a spherical cavity of twice the radius. This is explained by relating the seepage exclusion potential of an opening to the total curvature of the boundary of the opening. The total curvature of a cylindrical cavity can be described by two radii, one finite and one infinite (perpendicular and parallel to the axis of the cylinder, respectively), while that of a spherical cavity can be described by two radii that are equal and finite. In the model, the equivalent radius used for the spherical "drift" is twice that of the design drift radius.

For the base case, seepage into the opening without any rock bolts is modeled. Percolation rates of 5, 14.6, 73.2, 213, and 500 mm/yr are applied uniformly to the upper model boundary, as used in *Seepage Model for PA Including Drift Collapse* (CRWMS M&O 2000 [DIRS 153314], Section 6.3.7). Parameter Set A from that report, as well as the alternative $1/\alpha$ values of 400 and 200 Pa (CRWMS M&O 2000 [DIRS 153314], Section 6.3.5), are used for the excavation-disturbed zone in the Tptpmn rock unit surrounding the drift. A constant zero capillary pressure is specified at the drift wall boundary, a gravity drainage condition at the lower boundary (assigned in the grid using the software routine AddBound v 1.0, and a no-flow condition at the lateral boundary, all of which are consistent with the current models of seepage at Yucca Mountain (CRWMS M&O 2001 [DIRS 153045], Section 6.3.2.4; CRWMS M&O 2000 [DIRS 153314], Section 6.3).

To investigate the impact of a rock bolt on seepage, only the case of a rock bolt hole extending vertically upward from the crown of the drift is modeled. This case is sufficient to investigate the impact of the presence of the rock bolt hole on seepage (see Section 4.3.3.8). Three slightly different grids (Cases 1 to 3) are prepared to explore diversion capacity away from the rock bolt hole. Case 1 allows flow between the rock bolt hole and the surrounding rock along the entire length of the bolt hole. Case 2 restricts flow between the rock bolt hole and the surrounding rock for 0.1 m above the crown of the drift. Case 3 restricts flow between the rock bolt hole and the surrounding rock for 0.5 m above the crown of the drift. Cases 2 and 3 represent scenarios in which the first feature capable of carrying flow away from the rock bolt hole is found 0.1 m or 0.5 m, respectively, into the hole. A 0.0254-m radius bolt hole with a 0.0127-m radius rock bolt and a 0.0127-m grout annular thickness is modeled. These features are added to the grid using the software routine AssignRock V1.0. The difference between the design grout annular thickness and that modeled is conservative. The modeled rock bolt hole has less potential as a capillary barrier to exclude in-flow, a larger surface area to intercept flow, and more potential to conduct flow to the drift wall. Thus, results from this model will overestimate the seepage enhancement due to rock bolts; however, results show that this conservatism is not a concern with respect to accuracy.

Because the greatest impact of the rock bolts on seepage may come many thousands of years into the future (after cooldown and rewetting of the potential repository horizon and during wetter future climates), the grout is not likely to retain its design hydraulic properties. It may even disintegrate completely, leaving an open hole. A range of properties is used for the grout to address this uncertainty. Figure 4.3.3-2 shows the 13 parameter combinations evaluated. The lower-left combination (permeability = 10^{-18} m^2; $1/\alpha = 10^7$ Pa) corresponds to the design

grout, while the upper right combination (permeability = 10^{-10} m^2; $1/\alpha = 10$ Pa) corresponds to an open rock bolt hole. The other parameter combinations are selected to be equally spaced between the end points.

To summarize, a sensitivity study was performed in which several model parameters and the grid were varied to adequately address uncertainties in the conceptual model and input parameters. The varied parameters were:

- The permeability and capillarity of the grout
- The capillarity of the formation
- The percolation rate
- The length over which flow is restricted from the rock bolt into the formation adjacent to the drift wall.

Details of the model and sensitivity study are presented in Bodvarsson (2001 [DIRS 154669], Attachment 3, pp. 62, 63, and 68 to 70). The sensitivity study uses the software TOUGH2 V1.5 to simulate unsaturated flow.

No seepage enhancement is predicted for any of the combinations of percolation rate, formation parameter, grout parameter, and numerical grid. This result is different from the previous "needle" calculation, where 3 percent seepage enhancement was shown for one rock bolt. However, the current result is understandable, especially considering two key points about the previous simulation. First, the area onto which flow may be incident, if the lateral surfaces are considered, is 1.25 m^2 in the previous model, as opposed to 0.24 m^2 in the current model (a ratio of 5 to 1). If only the horizontal surfaces are considered, the ratio increases to more than 100 to 1. Second, the parameters from the seepage calibration model, which are used in the seepage model for TSPA (CRWMS M&O 2000 [DIRS 153314]), are predicated on the use of 0.05 m connection distances between the drift wall and the first node adjacent to the drift wall (CRWMS M&O 2001 [DIRS 153045], Sections 1, 6.3.2.2, and 6.4.2.2). The previous calculation found significant seepage enhancement only when that connection was 3 to 5 times the recommended length, restricting the lateral flow away from the rock bolt.

4.3.3.6 Abstraction for Total System Performance Assessment

As discussed above, *Seepage Model for PA Including Drift Collapse* presents a simple estimate of the possible effects of degraded rock bolts on seepage (CRWMS M&O 2000 [DIRS 122894], Section 6.7). Based on that estimate, seep flow rates were conservatively increased by 50 percent to account for the effect of rock bolts and drift degradation in the seepage abstraction for the TSPA-SR (CRWMS M&O 2000 [DIRS 142004], Section 6.3.1). Additional work that had not been included in the TSPA-SR (CRWMS M&O 2000 [DIRS 153246]), did not address new models of the effects of rock bolts on seepage (CRWMS M&O 2000 [DIRS 153314], Section 6.7; CRWMS M&O 2001 [DIRS 154291], Section 6.4.1). The more detailed study of rock bolt effects presented here found no significant increase in seepage because of either intact

or degraded rock bolts. Thus, it would be appropriate to eliminate the increase in seepage due to rock bolts. A possible revision that includes this change is discussed in Section 4.3.4.6.

4.3.3.7 Multiple Lines of Evidence

Because of the specificity of this investigation (i.e., seepage enhancement resulting from rock bolts), multiple lines of evidence to support the conclusions are rare, if they exist at all. The lack of seepage enhancement due to rock bolts also complicates the use of corroborating evidence. The lack of observations of seepage enhancement due to rock bolts in similar situations is not necessarily proof that seepage cannot be enhanced by rock bolts in similar situations. Though the use of multiple lines of evidence may be complicated by these factors, it may be useful to discuss evidence that contradicts the conclusions reached in this section.

The results of this analysis appear to run counter to observations of occasional dripping at rock bolts in the ESF and associated tunnels. There are several factors associated with these rock bolts that suggest this dripping is not an enhancement of background-percolation seepage. The type of rock bolt used in the ESF and associated tunnels is not the same one that will be used in the emplacement drifts; in the current tunnels, hollow steel bolts are used. These bolts are expanded against the sides of the hole using water pressure (the end of the bolt is capped), possibly leaving water inside the bolt (which may drip out). In addition, temperature, humidity, and pressure variations in the tunnels could lead to condensation inside the hollow bolts that would lead to dripping. This water would not come from the rock formation because the bolt is impermeable. Lastly, water that was used in the mining of these tunnels and for drilling of the rock bolt holes may be condensing and creating saturated conditions on the outside of the bolts because the bolts are better thermal conductors than the surrounding rock.

The analysis results also appear to run counter to observations of seepage enhancement caused by rock bolts in saturated zone tunnels. However, in the saturated zone, the concept of the tunnel as a capillary barrier does not apply. By definition, the potential at all points around the drift is zero, so the seepage percentage is 100 percent. Rock bolts then add to the surface area of the drift or to the likelihood that the drift will intersect a flowing feature, and thus must enhance seepage. As demonstrated above, the ability of the drift to act as a capillary barrier in the UZ is essential to its being able to divert flow away from the rock bolt and around the drift.

4.3.3.8 Summary of Uncertainties and Their Treatment

Table 4.3.3-1 presents a summary of uncertainty issues related to rock bolts. Additional issues may be classified as conceptual uncertainties. These are discussed below, and justifications are given for why they do not impact the model.

1. The use of a homogeneous permeability field in this model may bias it toward lower seepage. This concern is unjustified because comparison of the seepage percentage predicted by this model with that predicted by the seepage model for performance assessment (Figure 4.3.3-3) indicates that, for the formation parameters used, no significant difference exists. There is more difference in the seepage percentage between the different formation parameters than there is between the models. Further, because the result of concern is seepage enhancement rather than seepage percentage,

the use of a consistent model (i.e., a homogeneous one) for both the base case and the rock bolt simulations is the important issue. The impact of homogeneity or heterogeneity on seepage enhancement is considered a second-order effect.

2. The use of a vertical rock bolt rather than an inclined rock bolt minimizes the area onto which percolation is incident. Current simulations show that, for certain grout parameter combinations, flow enters even a vertical rock bolt hole from the sides, enhancing percolation through the grout with respect to the percolation around the hole. The key to the lack of seepage enhancement is the potential for sufficient lateral diversion at or near the drift wall to direct flow in the hole away from the hole. There will be even more diversion potential for an inclined hole because the height of any "disconnected" length of the hole will be less, and the diversion potential along the angled portion of the drift wall is much greater than at the crown of the drift.

Alternative models for the investigation of seepage enhancement because of rock bolts include:

- Continuum models employing multiple realizations of heterogeneous permeability fields
- Discrete fracture models
- Models that include inclined rock bolt holes.

The discussion above suggests that the first and third alternative models are unlikely to give significantly different results. The key element of the discrete fracture model (i.e., discrete features for flow into or out of the bolt hole) is adequately captured by the two current models, in which the bolt hole is disconnected from the formation near the drift wall.

4.3.3.9 Summary and Conclusions

The potential for seepage enhancement into emplacement drifts in the Tptpmn due to rock bolts has been evaluated, and no evidence of seepage enhancement was found. Parameter uncertainties for the grout and the formation are addressed through sensitivity studies using multiple parameter combinations. Grout permeability varied from 10^{-18} to 10^{-10} m^2, and capillarity varied from 10^7 to 10^1 Pa. Tptpmn formation capillarity varied between 200 and 589 Pa. Sensitivity studies were used to address conceptual uncertainties about the appropriate modeling of flow restrictions away from the rock bolt adjacent to the drift wall because of a lack of fractures to conduct flow. Three numerical grids were used: the first has a full-connection between the rock bolt and the formation adjacent to the drift wall, the second restricts flow between the rock bolt and the formation for 0.1 m above the drift wall, and the third restricts flow between the rock bolt and the formation for 0.5 m above the drift wall. A range of percolation rates, from 5 to 500 mm/yr, was used to adequately cover the rates expected at the potential repository horizon.

Evidence of seepage enhancement due to rock bolts in the UZ and the saturated zone was found not to be relevant as evidence against the conclusions reached. Processes that will not be found in the emplacement drifts (e.g., short-term release of mining water, use of hollow rock bolts, saturated conditions surrounding the drift) are concluded to be responsible for the observed seepage enhancement in the ESF and associated tunnels.

The conclusion of this investigation of the potential for enhancement of seepage into emplacement drifts in the Tptpmn caused by intact or degraded rock bolts is that there is no significant enhancement of seepage, and that rock bolts may be neglected as a seepage-enhancement factor for performance assessment.

4.3.4 Drift Degradation

4.3.4.1 Introduction

Analyses and models supporting the TSPA-SR (CRWMS M&O 2000 [DIRS 153246]) used a three-dimensional model to examine simple drift degradation scenarios, which are summarized in Section 4.3.4.3. Studies conducted after the TSPA-SR, which are discussed in Section 4.3.4.4, utilize significantly more detailed drift degradation profiles based on a discrete region key-block analysis (CRWMS M&O 2000 [DIRS 151635]; DTN: MO0010RDDAAMRR.002 [DIRS 154048]). By using the discrete region key-block approach, more realistic representations of drift degradation are achieved, resulting in an improved understanding of the impact of heterogeneity on flow fields.

Drifts in which waste packages will be emplaced are subject to degradation in the form of permeability changes in the rock around the drift and rockfall from the drift ceiling. The former results from the excavation process (i.e., the stress release caused by the excavated cavity); the latter results from the multiple fractures present in the rock, which in turn could cause the blocks created by intersecting fracture sets to become loose and fall into the drift. Either type of drift degradation will create uncertainty if seepage estimations are based on a drift without degradation. This uncertainty is addressed by: (1) defining a heterogeneous permeability model at the drift scale that is consistent with field data, (2) selecting the best-calibrated parameters associated with the Tptpmn and the Tptpll lithostratigraphic units in which the potential repository will be situated, (3) considering the possible ways that the drift can degrade, (4) selecting scenarios of degradation, (5) implementing these scenarios as model inputs, and (6) calculating the change in seepage for each of these scenarios.

The effects of drift degradation on potential seepage into drifts at Yucca Mountain as used in the TSPA-SR (CRWMS M&O 2000 [DIRS 153246]) are documented in *Seepage Model for PA Including Drift Collapse* (CRWMS M&O 2000 [DIRS 122894], Sections 6.3, 6.4, and 6.6.4). The major change to this AMR (CRWMS M&O 2000 [DIRS 153314], Section 6.1) was the modification of the drift boundary condition, as discussed in Section 4.3.4.3. New studies used modified drift degradation scenarios, which are presented in Sections 4.3.4.4 and 4.3.4.5.

4.3.4.2 Goals of Drift Degradation Submodel

The goals of the drift degradation submodel are as follows:

1. To use a heterogeneous model, with the best available calibrated parameters, to study the impact of drift seepage due to heterogeneity of flow fields and degradation effects

2. To identify possible cases for drift seepage and propose scenarios or cases for study

3. To perform simulation studies on these cases and estimate the impact of drift degradation on seepage.

4.3.4.3 Discussions of Revision 00 and Revision 01 Results

In *Seepage Model for PA Including Drift Collapse* (CRWMS M&O 2000 [DIRS 122894], Section 6.6), simulations were performed to calculate seepage values for a range of values of percolation flux at the drift to study the effects from various processes, such as excavation-induced drift degradation, and to provide results as input to the TSPA-SR (CRWMS M&O 2000 [DIRS 153246]).

The results in a revision to *Seepage Model for PA Including Drift Collapse* (CRWMS M&O 2000 [DIRS 153314], Section 6.6) are different. Changes make the revised AMR consistent with the *Seepage Calibration Model and Seepage Testing Data* (CRWMS M&O 2001 [DIRS 153045], Sections 5 and 6). Additionally, the seepage calibration model provided results for the Tptpll lithostratigraphic unit, which were not available at the time the initial report was issued.

A heterogeneous permeability field of the fracture continuum is the basis for the conceptual model used to examine the heterogeneity of flow fields. The numeric representation was generated using parameter sets (described below) in conjunction with the SISIM module of GSLIB V2.0. The three-dimensional block defined by the generated heterogeneous field is 20 m tall, 15 m wide, and 5.23 m along the drift axis. It contains a drift that is 5.5 m in diameter and positioned to have an overlying thickness of 9.75 m, an underlying thickness of 4.75 m, and a distance to either side of 4.75 m. The vertical cross-sectional dimensions of the block were chosen to be wide enough to capture flow diversion around the drift (Philip et al. 1989 [DIRS 105743], p. 21, Figure 1). The heterogeneous field was chosen so that flow focusing or channeling within the scale of the model is accounted for in the simulation.

Flow calculations were performed using the numerical simulator ITOUGH2 V3.2_drift. A number of routines were also used for preprocessing of inputs for this simulator, as listed in Table 1 of *Seepage Model for PA Including Drift Collapse* (CRWMS M&O 2000 [DIRS 153314]).

Three parameter sets for repository placement, obtained by calibration against field data from relevant formations, are used in this study. The first set, Set A ($k_{FC} = 1.38 \times 10^{-12} m^2$; $1/\alpha = 589$ Pa; $n = 2.55$; $\sigma = 1.93$), is the set of calibrated mean parameters for the Tptpmn unit given by the seepage calibration model (CRWMS M&O 2001 [DIRS 153045]; DTN: LB0010SCMREV01.002 [DIRS 153393]). Note that k_{FC} is the calibrated mean permeability, α and n are the van Genuchten parameters, and σ is the standard deviation of $\ln k_{FC}$.

The second parameter set, Set B ($k_{FC} = 1.38 \times 10^{-11} m^2$; $1/\alpha = 871$ Pa; $n = 2.57$; $\sigma = 1.93$), is the set of calibrated mean parameters chosen for the Tptpll unit (DTN: LB0010SCMREV01.002 [DIRS 153393]). Note that $\sigma = 1.93$ is used for both sets as a more conservative value (details are included in *Seepage Model for PA Including Drift Collapse* [CRWMS M&O 2000 (DIRS 153314)], Section 6.3.3).

An additional parameter set, Set B′, is also considered for the Tptpll unit. It is identical to Set B except that it uses a $1/\alpha$ value of 537 Pa. Set B′ is intended to compensate for the effect of lithophysal cavities, which tend to increase seepage (CRWMS M&O 2001 [DIRS 153045], Section 6.3.3.3).

Drift degradation may occur in three ways:

1. Rockfall from the ceiling of the drift
2. Loosening of rock blocks that increases fracture apertures (fracture dilation)
3. Extended rock failure in the drift ceiling.

Based on these possibilities, a drift degradation submodel was designed to evaluate the impact of drift degradation on seepage. The submodel is shown in Figure 4.3.4-1 as four alternative scenarios, discussed in the following paragraphs.

Rockfall from Drift Ceiling–*Drift Degradation Analysis* used the key-block theory to calculate rockfall probability in the drifts under various scenarios, based on fracture maps in the ESF (CRWMS M&O 2000 [DIRS 151554], Tables 20 to 21, 26 to 27, 35 to 36, 41 to 42). Based on the probabilities developed for the Tptpmn unit, the number of key blocks per kilometer of the drift was calculated to be fewer than 44 over these scenarios, and the volume of total rockfall per kilometer to be less than 36 m^3. This implies that rockfall occurs on the average of one block every 23 m and that the mean size of the block is about 0.8 m^3. This is confirmed by the finding that 80 percent of the blocks are smaller than 1 m^3 (CRWMS M&O 2000 [DIRS 151554], Figures 19 to 20, 27 to 28, 32 to 33, 36 to 37). Hart (Brekke et al. 1999 [DIRS 119404], p. E-12) used a two-dimensional discrete-element method and found rockfall to occur at the springline of the drift, with the size of the block depending on the modeled fracture spacing. To study the effect of rockfall on seepage, two calculations were made, one in which a 1.0 m^3 block was taken out from the crown of the drift and one in which the 1.0 m^3 block was taken out at the springline (Figure 4.3.4-1, top right and left).

Fracture Dilation–Stress is relieved at the drift because of excavation, and fractures are expected to dilate at certain areas around the drift (Figure 4.3.4-1, lower left). Such fracture dilation depends on the orientation of the fracture set and generally occurs within one drift radius (Brekke et al. 1999 [DIRS 119404], Figures E-5, E-11, and E-13). An increase in fracture aperture generally causes an increase in fracture permeability and a decrease in $1/\alpha$ value. The measured increase in permeability from the pre-excavation to the post-excavation values (Wang et al. 1999 [DIRS 106146], p. 328; DTN: LB0011AIRKTEST.001 [DIRS 153155]) is a result of this effect. Both Set A and Set B, which are based on in situ post-excavation calibration results, already have taken this increase into account. This means that the rock properties used already represent the total effect of the near-field disturbed zone and the far field, as shown in the lower left of Figure 4.3.4-1. Results are given in *Seepage Calibration Model for PA Including Drift Collapse* (CRWMS M&O 2000 [DIRS 153314], Tables 4 to 8).

Extended Rock Failure at the Drift Roof–Over time, extended rock failure may also occur at the roof of the drift. Kaiser (Brekke et al. 1999 [DIRS 119404], pp. D-11, D-12) estimated the failure at the roof to be 0.1 to 1 m in depth, or 0.4 to 1.2 m in depth if seismic effects were included. Generally, Kaiser expected that stress-induced failure at the drift crown would occur

to a depth of half the drift radius (i.e., about 1.375 m). *Drift Degradation Analysis* (CRWMS M&O 2000 [DIRS 151554], Figures 39 to 40) used a discrete region key-block analysis that shows a more extended failure region, up to one drift radius above the drift ceiling. In the seepage study, a case is designed in which an extended cavity is found in the drift roof with a step shape of 0.5 m at the crown, 1 m depth at 0.5 m to one side, and so on, reaching 3 m depth at 2 m laterally from the drift crown (Figure 4.3.4-1, lower right). This shape is similar to that shown as a worst-case profile in *Drift Degradation Analysis* (CRWMS M&O 2000 [DIRS 151554], Figure 40). The step-shaped failure is 1 m thick.

Table 4.3.4-1 presents the calculated seepage percentages for Set A for three stochastic realizations (R1, R2, and R3) with drift degradation modes as defined in Figure 4.3.4-1, and compares them with the no-degradation case. (Seepage percentage is defined as the ratio of liquid that seeped into the drift to the total liquid arriving on a cross-sectional area corresponding to the footprint of the drift.) Only the cases where the percolation flux (Qp) is 500 mm/yr are shown in the table. This is the greatest value for which seepage percentages were calculated; it is four times as great as the simulated percolation under a glacial climate (CRWMS M&O 2000 [DIRS 153314], Section 6.3.7). The results show that the effect of a single rockfall is not significant for seepage. A deeper rock failure in the drift roof increases seepage. Calculations were also made with Set B, resulting in zero seepage for all cases, with or without drift degradation.

Additional simulations were done for other Q_p values to explore the effect of drift degradation on seepage threshold. The seepage threshold is a specific percolation flux at which seepage occurs. Figure 4.3.4-2 shows the calculated seepage percentage as a function of percolation flux Q_p for realization R3. It is seen in this figure that the effect of drift degradation for the three scenarios as defined above decreases with decreasing Q_p, so its impact on seepage threshold is relatively small. This can perhaps be explained by the fact that, under vertical percolation flux in a heterogeneous medium, the seepage threshold depends significantly on the horizontal cross section (footprint) of the drift. If the cross-sectional area does not change much, the seepage threshold will also not change much.

4.3.4.4 Developments Since Revision 01 of the Analysis Model Report

The previous studies, as described in Section 4.3.4.3 above, show that the extended rock failure case causes the largest impact on seepage. A more quantitative evaluation is presented in this section. Instead of the schematic rock failure profile shown in Figure 4.3.4-1, detailed degraded drift profiles calculated using a discrete region key-block analysis (DTN: MO0010RDDAAMRR.002 [DIRS 154048]) were used. The key-block analysis provides the following detailed three-dimensional drift profiles for seepage simulations, using a 0.305-m grid size.

For the Tptpmn unit:

1. Worst degradation (largest rockfall volume) profile
2. Profile at 75th percentile
3. No degradation (91.9 percent).

For the Tptpll unit, Set B′:

1. Worst degradation (largest rockfall volume) profile
2. Profile at 75th percentile
3. No degradation (99.6 percent).

For the Tptpmn, 91.9 percent of the drift length exhibits no drift degradation. Of the 8.1 percent that does exhibit degradation, the 75th percentile means that 75 percent of the 8.1 percent has a rockfall volume less than that shown in the 75th percentile drift profile. Similarly for Tptpll, 0.4 percent (100 percent to 99.6 percent) of the drift length exhibits drift degradation, with the 75th percentile profile indicating that 75 percent of 0.4 percent of the drift length has a rockfall volume that is less than that shown.

A typical example of the detailed degraded drift profile is shown in Figure 4.3.4-3 for the worst degradation profile in the Tptpnm unit.

4.3.4.5 Results of Analysis

Table 4.3.4-2 presents the seepage percentages for Set A of the Tptpmn unit with drift degradation modes (worst degradation case and degradation at 75th percentile) and compares them with the no-degradation case. Three realizations of the heterogeneous fields were used in these calculations (R1, R2, and R3). Figure 4.3.4-4 shows the results for Realization R1 graphically.

A series of percolation flux values (up to 500 mm/yr) was used to explore the effect of drift degradation on seepage threshold. Figure 4.3.4-4 shows that the effect of drift degradation for the scenarios decreases with decreasing Q_p, so its impact on seepage threshold is relatively small.

The results also indicate that seepage enhancement due to rockfall ranges from 0 to 5 percentage points for Q_p up to 500 mm/yr, owing to drift degradation for the worst case and 75th percentile case. The enhancement does not seem to depend on whether it is the worst case (i.e., the largest rockfall) or 75th percentile. These results suggest that the shape of the cavity in the ceiling may be more important for seepage enhancement than the volume. Confirming calculations were performed by using a homogeneous medium, and they also show more seepage for the 75th percentile case (Bodvarsson 2001 [DIRS 154669], Attachment 2, pp. 51 and 52).

Table 4.3.4-3 presents the seepage percentages for Set B′, representing the lower lithophysal unit, with drift degradation modes (worst degradation case and degradation at 75th percentile) and compares them with the no-degradation case. Here, because of the low seepage, values of Q_p up to 2,500 mm/yr were used. Three realizations of the heterogeneous fields were used in these calculations (R1, R2, and R3). Figure 4.3.4-5 shows the results for Realization R1 graphically. The results show that the seepage threshold is not significantly affected by drift degradation in the Tptpll unit; the enhancement is two percentage points or less.

Calculations with Set B parameter values resulted in zero seepage for all cases with percolation flux up to 2,500 mm/yr, with or without drift degradation (Bodvarsson 2001 [DIRS 154669], Attachment 2, p. 51).

4.3.4.6 Abstraction for Total System Performance Assessment

Seepage Model for PA Including Drift Collapse (CRWMS M&O 2000 [DIRS 153314], Section 6.6.4) showed that drift degradation tends to increase seepage. Seepage was consequently modeled for a few schematic degraded drift profiles. In the TSPA seepage abstraction, the worst of those modeled cases (Figure 4.3.4-1, lower right) was used for a conservative estimate of the possible effect of drift degradation on seepage. Compared with results presented in *Seepage Model for PA Including Drift Collapse* (CRWMS M&O 2000 [DIRS 153314], Sections 6.6.1, 6.6.2, and 6.6.3), the final estimate in the TSPA seepage abstraction included a 50 percent increase in seep flow rate to account for the potential effects of both drift degradation and degraded rock bolts (CRWMS M&O 2001 [DIRS 154291], Section 6.4.1). Rock bolt effects are examined in Section 4.3.3, in which it is concluded that rock bolts do not significantly increase seepage into emplacement drifts. Also, it will be shown here that the previous treatment of drift degradation effects in *Seepage Model for PA Including Drift Collapse* (CRWMS M&O 2000 [DIRS 153314], Section 6.6.4) was conservative.

Since the reporting of the abstractions used in the TSPA-SR (CRWMS M&O 2000 [DIRS 153246]), additional simulations of seepage for degraded drift profiles have been performed for drifts in the Tptpmn and Tptpll units and for a range of percolation fluxes (Bodvarsson 2001 [DIRS 154669], Attachment 2, pp. 51 to 54). The discussion in Sections 4.3.4.4 and 4.3.4.5 includes these new results, along with the simulations presented in the *Drift Degradation Analysis* (CRWMS M&O 2000 [DIRS 151635], Section 6) and included in the TSPA-SR (CRWMS M&O 2000 [DIRS 153246], Figure 3.2-15). Note that the earlier work (CRWMS M&O 2000 [DIRS 153314], Section 6.6.4) used schematic degradation profiles with a uniform third dimension (parallel to drift axis) (i.e., a constant thickness in this direction). This is a simplification, from which no uncertainty range was calculated, and hence TSPA seepage abstraction used a 50 percent increase to account for potential effects of both drift degradation and degraded rock bolts (CRWMS M&O 2001 [DIRS 154291], Section 6.4.1). In the additional simulations presented here, this simplification was removed by using three-dimensional degradation profiles from *Drift Degradation Analysis* (CRWMS M&O 2000 [DIRS 151635]). This is a major step in reducing conceptual uncertainty. The new results show that compared to the no-degradation case, average seepage over the realizations in the Tptpmn unit (Set A) increased by 29 percent for the worst-case drift degradation and by 63 percent for the 75th percentile drift degradation at 500 mm/yr percolation flux (see Table 4.3.4-2). At 213.4 mm/yr percolation flux, the worst-case drift degradation increased average seepage by 17 percent, while the 75th percentile drift degradation increased seepage by a factor of about 6. For the lower lithophysal unit (Set B´), the seepage increase was greater for the worst-case drift degradation, with seepage increasing by or a factor of 2 to 3 for percolation flux ranging from 1,500 to 2,500 mm/yr. In addition, the seepage threshold decreased slightly: the worst-case degradation simulation showed a small amount of seepage at 1,000 mm/yr, whereas the base case had no seepage at that percolation flux.

These results must be put in perspective. As indicated in Section 4.3.4.4, no drift degradation occurred in 91.9 percent of the Tptpmn total drift length and in 99.6 percent of the Tptpll total drift length. Furthermore, most locations experiencing drift degradation had much less than the cases modeled here (75 percent of the locations with degradation had less degradation than the

75th percentile case). Thus, according to this analysis, a significant increase in seepage resulting from drift degradation would be relatively rare.

This increase in seepage at so few locations would not likely affect the overall average seepage. For example, take the largest increase mentioned above, an increase in seepage by a factor of 6 at 213.4 mm/yr for the Tptpmn unit. This increase applies to less than 8.1 percent at most, and probably less than 4 percent, of the locations (considering the 50th percentile drift degradation to have a much smaller effect on seepage). Thus, the increase in mean seep flow rate would be less than $0.04 \times 6 = 0.24$, or 24 percent. Since all the other calculated seepage increases were much less than a factor of 6, the increase in mean seep flow rate from drift degradation is likely much less than 24 percent. Furthermore, the effects would be even smaller for the lower lithophysal unit because the drift degradation analysis indicates less degradation in that unit and the seepage analysis indicates less seepage increase in that unit.

The results show that the impact on seepage calculated with this three-dimensional degradation profiles at different probability percentiles is similar to the result of the schematic profile, and the range is within the range used in the TSPA-SR (CRWMS M&O 2000 [DIRS 153246], Section 3.2.4). In addition, the calculated seepage increases are small enough that they are well within the ranges of variability and uncertainty in seepage, as determined in the seepage abstraction for the TSPA-SR (CRWMS M&O 2000 [DIRS 153246]). Thus, it appears that it is not necessary to increase the estimated seepage to account for drift degradation effects. Coupled with the finding in Section 4.3.3 that it is not necessary to increase the estimated seepage to account for rock bolt effects, it can be concluded that the seepage abstraction could be used for the TSPA model without the increase that was applied to account for drift degradation and rock bolts. That is, Table 13 of *Abstraction of Drift Seepage* (CRWMS M&O 2001 [DIRS 154291]) could be adapted for use rather than Table 16 of the same report. However, the TSPA analysis for this report is not adjusted for the new information discussed above, because further simulations are underway to account for heterogeneity by using multiple realization evaluations to provide results for seepage abstraction. Nevertheless, the new analysis has removed certain conceptual uncertainties as related to drift degradation and also to rock bolt effects (see Section 4.3.3) and make the TSPA abstraction on these issues more defensible.

4.3.4.7 Multiple Lines of Evidence

Underground tunnels or cavities are subject to potential degradation conditions, such as permeability changes in the rock surrounding the opening. Rockfalls are also frequently observed. No significant enhancement in seepage resulting from such degradation has been reported, and in general, seepage into underground cavities in unsaturated rocks, if any, is found to be a very small fraction of percolation flux. As discussed in Section 4.3.1.7, examples include tunnels in Rainier Mesa 30 km northeast of Yucca Mountain (Wang et al. 1993 [DIRS 108839]), caves in the UZ of a fractured limestone bedrock near Altamira, Spain, and observations of seepage into sealed segments of the ESF and the ECRB Cross Drift at Yucca Mountain. The model is consistent with the information from these sources. Further discussion on multiple lines of evidence related to seepage is presented in Section 4.3.1.7.

4.3.4.8 Summary of Uncertainty and Its Treatment

The uncertainty about seepage enhancement resulting from drift degradation has been addressed by starting with a detailed conceptual model that accounts for capillary-barrier diversion (due to the drift) and channelized or focused flow (due to fracture continuum heterogeneity). The parameter values needed for the simulations are based on those derived in the seepage calibration model using field data from the Tptpmn and Tptpll units. Finally, detailed drift degradation shapes obtained in the regional key-block analysis of field fracture data in the two units were used. For each of the two units, three cases were taken: (1) a no-degradation case, (2) a 75th percentile case, and (3) a worst case (i.e., largest rockfall volume). Simulations of seepage were performed for a series of percolation fluxes. For each case, three realizations of the heterogeneous field were used to account for geostatistical variations. Results indicate that seepage threshold is not affected by drift degradation and that seepage enhancement over a percolation flux up to 200 mm/yr for Tptpmn and 2,500 mm/yr for Tptpll units are about 5 percentage points or less. Table 4.3.4-4 summarizes uncertainty issues related to drift degradation and how they are addressed.

4.3.4.9 Summary and Conclusions

Four scenarios of detailed degraded drift profiles in the Tptpmn and Tptpll units, calculated using a discrete region key-block analysis (CRWMS M&O 2000 [DIRS 151635]), were selected for seepage calculations. Two types of drift degradation with implications for seepage enhancement have been examined: dilation and rockfall, with dilation effects having been previously considered.

Both rockfall and extended rock failure effects have been analyzed. The model has been refined over previous studies by use of a three-dimensional key-block analysis (replacing prior schematic two-dimensional rock failure profiling) and by incorporation of a revised set of calibrated mean parameters for the Tptpll.

Results in this section are based on seepage calibration model results (CRWMS M&O 2001 [DIRS 153045], Section 6.3.3 and 6.4.3). As more data from these units are obtained, parameter values with their uncertainties and probability weightings can be developed, allowing the seepage percentages presented in Section 4.3.4.6 to be used in performance assessment to obtain the best estimates (with uncertainty ranges) for use at Yucca Mountain. Uncertainty associated with geostatistics is evaluated through calculations of three realizations. Results for each case are shown in Tables 4.3.4-2 and 4.3.4-3. The spread of results from the three realizations gives an indication of geostatistical variation.

In summary, this section demonstrates that the impact of drift degradation and heterogeneity of the flow field can be evaluated. Generally, for both the Tptpmn and Tptpll units, simulated seepage enhancement due to drift degradation is calculated to be relatively small, with larger effects for larger percolation flux (Q_p) values. Seepage enhancement is between 0 and 5 percentage points in all three realizations, and less than 2 percentage points for the Tptpll. The enhancement does not seem to depend on whether it is worst case (i.e., largest rockfall) or 75th percentile. Seepage threshold was unaffected in almost all cases. The shape of a drift cavity created by rockfall may be more important to drift seepage than the volume of rockfall.

The current analysis has removed the conceptual uncertainty of schematic drift degradation profile by using calculated three-dimensional degradation profiles from the drift degradation analysis at different probability percentiles. This has made the TSPA uncertainty ranges used more defensible.

4.3.5 Thermal Effects on Seepage

4.3.5.1 Introduction

This section summarizes the modeling and uncertainty studies performed to determine the effects of heat on seepage of liquid water into emplacement drifts. The preceding sections discuss how, at ambient preemplacement conditions, the emplacement drift acts as a capillary barrier to divert water around the drift opening, and how seepage fluxes are lower than percolation fluxes. Analysis of seepage under ambient conditions emphasizes factors that determine whether water reaching the drift wall will actually seep into the drift. In this section, the focus is on how the thermo-hydrologic (TH) coupled processes affect the magnitude and spatial distribution of the percolation flux in the vicinity of the drift, since the percolation flux is the controlling factor for determination of seepage potential.

Modeling studies discussed in this section include alternative thermal operating modes for below-boiling and above-boiling temperatures within the rock mass as well as fracture heterogeneity, which has been shown to promote seepage (Tsang et al. 1997 [DIRS 100186]; Nitao 1997 [DIRS 100641]). As a result of these modeling and uncertainty studies, a more realistic abstraction for the TSPA is recommended. Thermal seepage models, as with any other models, are subject to uncertainties because of various factors, such as data, parameters, conceptualization, and numerical model implementation. A key issue for thermal seepage is the parameter uncertainty of different thermal operating modes and the effect of lithophysal cavities on thermal conductivity and heat capacity. Model implementation of the drift and discretization around the drift contribute to numerical model uncertainty. Perhaps the most important conceptual model uncertainty issue pertaining to thermal seepage is heterogeneity in important fracture parameters. Because of the limitation of data for coupled processes, the treatment of uncertainties must primarily be addressed by sensitivity studies. The uncertainty issues and their treatment are summarized in Section 4.3.5.8.

4.3.5.2 Goal of Thermal-Hydrologic Model for Seepage

The TH models presented in this section are intended to provide insight into how decay heat from emplaced waste will affect the magnitude and spatial distribution of percolation flux reaching the emplacement drifts and affect the potential for seepage into the drifts. The effect of TH processes on seepage is considered for the higher-temperature operating mode (HTOM) and the lower-temperature operating mode (LTOM). The results from these models will be used in a TSPA abstraction.

4.3.5.3 Mountain-Scale Coupled Process Model

4.3.5.3.1 Discussion of Revision 00 Results

Effects of repository heat on seepage into the drift were deduced indirectly from results presented in *Mountain-Scale Coupled Processes (TH) Models* (CRWMS M&O 2000 [DIRS 144454]). This model evaluates the effects of heat on UZ flow and distribution of liquid and temperature over a period of 100,000 yrs. The effect of climate was accounted for by applying the present-day infiltration rate for the first 600 yrs, followed by monsoon infiltration from 600 to 2,000 yrs and by glacial-transition infiltration thereafter. By necessity, numerical gridblocks used in three-dimensional flow modeling at the mountain scale are relatively large. To resolve the flow in the vicinity of the potential emplacement drifts, additional TH simulations were carried out for two-dimensional cross sections NS#1 and NS#2 (CRWMS M&O 2000 [DIRS 144454], Figure 1), with locally refined numerical grids to explicitly represent each 5-m diameter emplacement drift. The two-dimensional cross sections run approximately from the north to the south of the repository footprint, with the numerical discretization such that there are two or four lateral gridblocks (for NS#1 and NS#2 cross sections, respectively) between two adjacent emplacement drifts spaced at 81 m.

Because the primary objective of *Mountain-Scale Coupled Processes (TH) Models* (CRWMS M&O 2000 [DIRS 144454]) was to evaluate the effects of heat on mountain-scale flow, simulations were designed specifically to address large-scale flow issues relating to faults, perched water bodies, stratigraphic interface of the repository Topopah Spring unit with the upper Paintbrush and the lower Calico Hills units, etc. Therefore, the discussion about the effect of heat on potential seepage into the drifts is brief. Conclusions on thermal seepage were derived mainly from the simulated results from NS#2. This north-south section encompasses potential emplacement drifts located in different subunits of the Topopah Spring welded tuff, including the middle nonlithophysal and the lower lithophysal unit. The applied thermal load of 72.7 kW/acre for the three-dimensional mountain-scale numerical simulations translates to a line load of 1.45 kW/m in the two-dimensional simulations where the emplacement drifts are explicitly modeled. Forced ventilation for the first 50 yrs effectively removes 70 percent of the decay heat generated by the emplaced waste (Wilkins and Heath 1999 [DIRS 104247]).

Simulation results show that maximum temperatures occur in the drifts and minimum temperatures occur in the pillars between adjacent drifts. The temperatures in the pillars are predicted to rise to an average of 80° to 85°C. Temperatures rise to boiling in the immediate vicinity of the drifts, but may reach 110°C in drifts where ambient percolation flux is lower than average because of spatially variable infiltration. The dryout in both the fracture and matrix around the drifts is maintained for hundreds of years. Above the dryout zone are zones of increased liquid saturation, and large liquid flow rates (one to two orders of magnitude higher than the ambient flux) are predicted for the first one hundred years of emplacement, primarily through the fractures. The liquid fluxes toward the emplacement drift are driven by capillary pressure gradients resulting from the drying around the drifts. However, the ample decay heat from the potential emplacement drifts easily vaporizes this enhanced liquid flux, so in fact no liquid flux ever reaches the emplacement drift wall. That is, the coupled-process models predict no possibility for seepage when the temperatures in the rock mass around the drift are above boiling. This exclusion of liquid water is termed the “vaporization barrier.” Vapor generated

from the heat is driven away from the emplacement drift by pressure gradient, and subsequently condenses in cooler rocks and can drain down in fractures. Simulations predict that the drainage of thermally induced liquid flux through the pillars between the emplacement drifts mostly continues at a rate close to the ambient percolation flux for the thermal period, when temperatures in the rock mass remain above ambient.

4.3.5.3.2 Development since Revision 00

The work in *Mountain-Scale Coupled Processes (TH) Models* (CRWMS M&O 2000 [DIRS 144454]) was based on the Enhanced Design Alternative (EDA) II repository design, which specifies an initial thermal load of 72.7 kW/acre (1.45 kW/m of drift) and a forced ventilation period of 50 yrs, during which 70 percent of the decay heat is removed (Wilkins and Heath 1999 [DIRS 104247]). The thermal load of EDA II (Wilkins and Heath 1999 [DIRS 104247]) gave rise to above-boiling temperatures in the rocks in the vicinity of the emplacement drifts for hundreds of years. The EDA II thermal impact is referred to as the higher-temperature case. Model development since the higher-temperature case documented in the TSPA-SR (CRWMS M&O 2000 [DIRS 153246]) involves studies of coupled processes for a range of temperatures.

In the lower-temperature options, the rock temperature does not go above boiling anywhere in the repository. In the LTOM, an initial thermal load of 67.7 kW/acre (1.35 kW/m of drift) and a forced ventilation period of 300 yrs (during which 80 percent of the heat is removed) are applied.

Model development since *Mountain-Scale Coupled Processes (TH) Models* (CRWMS M&O 2000 [DIRS 144454]) also focuses on assessing uncertainties pertaining to thermal seepage, particularly for potential emplacement drifts in the lower lithophysal unit (where more than 70 percent of the potential repository would be located). As heterogeneity is known to promote flow channeling and fast flow that can enhance seepage, small-scale heterogeneity in the fracture properties is incorporated. The approach of Monte Carlo simulations is taken in order to investigate whether the general conclusions continue to hold—that no liquid flux can penetrate the vaporization barrier of the higher-temperature repository and reach any drift. Also, studies are being carried out to determine whether a vaporization barrier to prevent downward-percolating liquid flux from seeping into the emplacement drift would also exist for a lower-temperature repository operating mode.

All model developments since *Mountain-Scale Coupled Processes (TH) Models* (CRWMS M&O 2000 [DIRS 144454]) are documented in Bodvarsson (2001 [DIRS 154669], Attachment 6, pp. 24 to 51, and Attachment 17, pp. 39 to 75).

Specifically, these developments include:

1. Refinement of numerical model grids in all subunits of the Topopah Spring welded tuff. Instead of studying flow effects on all potential emplacement drifts in NS#2, this model concentrates on only one emplacement drift in NS#2, located in the lower lithophysal unit. The lateral boundary of the model extends to the midpoint between two adjacent drifts at 40.5 m from the center of the emplacement drift. The refined grids allow for better resolution of the distribution of percolation flux in the vicinity of

an emplacement drift than the Rev 00 AMR results, which are based on coarse grids (two or four lateral gridblocks between two potential adjacent drifts).

2. Incorporation of small-scale heterogeneity in the fracture permeability, with values ranging over four orders of magnitude (based on air-permeability measurements in boreholes in the ESF and the ECRB Cross Drift) (DTN: LB0011AIRKTEST.001 [DIRS 153155], DTN: LB0012AIRKTEST.001 [DIRS 154586], DTN: LB002181233124.001 [DIRS 146878], DTN: LB980901233124.004 [DIRS 105855], DTN: LB980901233124.001 [DIRS 105821], DTN: LB980912332245.001 [DIRS 110828]). The random heterogeneous fields are superposed on the $1\,\mathrm{m} \times 1\,\mathrm{m}$ gridblocks around the drift (measurements do not show any spatial correlation larger than the size of the gridblock).

3. Inclusion of a discrete high-permeability feature that intersects the emplacement drift, in addition to the heterogeneous fracture permeability field in the repository unit. This is intended for studying the competing processes of fast drainage in a preferential path to the drift and the vaporization potential of that liquid drainage flux due to the waste heat.

4. Exercising of models with items (1) through (3) above using the same hydrological and thermal properties for the lithophysal units as in the AMR for the above-boiling operation mode.

5. Exercising of models with items (1) and (2) above using the thermal conductivity and heat capacity of the rock mass, which accounts for the lithophysal porosity of the upper and lower lithophysal units in the matrix properties for the HTOM and LTOM.

In *Mountain-Scale Coupled Processes (TH) Models* (CRWMS M&O 2000 [DIRS 144454]), the thermal-conductivity and heat-capacity parameters used were based on laboratory core measurements. Mapping data along the ECRB drift walls (Mongano et al. 1999 [DIRS 149850], Figures 2 and 3) indicate that the mean lithophysal porosity, ϕ_L, of the upper and lower lithophysal units is 0.216 and 0.125, respectively. Since the thermal conductivity (λ) of air is almost 2 orders of magnitude smaller than that of rock and 20 times smaller than that of water, the bulk thermal conductivity of the lithophysal units would be lower if the lithophysal porosity were explicitly accounted for. Applying a parallel model to incorporate the lithophysal porosity, the bulk rock thermal conductivity becomes the weighted average:

$$\lambda_{\text{with lithophysae}} = \lambda_{\text{matrix}} (1 - \phi_L) + \lambda_{\text{air}} \phi_L \qquad \text{(Eq. 4.3.5-1)}$$

Implicit in Equation 4.3.5-1 is that the lithophysal cavity is always air-filled, regardless of whether the thermal-conductivity measurements were made on "wet" matrix cores (where the matrix porosity is 100 percent water-filled) or on "dry" matrix cores (where the matrix porosity is air-filled). This is reasonable because the capillary barrier effect noted earlier also acts to exclude water from the lithophysae, even if the matrix is saturated.

The rock grain heat capacity C_R was similarly modified to account for the effect of lithophysal porosity on heat conduction in the matrix continuum, according to:

$$C_R^* = C_R (1- \phi_m - \phi_L)/ (1- \phi_m) \quad \text{(Eq. 4.3.5-2)}$$

where ϕ_m is the matrix porosity.

A comparison of parameter values for the thermal properties used in *Mountain-Scale Coupled Processes (TH) Models* (CRWMS M&O 2000 [DIRS 144454]) to the developments since issuance of the AMR, which included lithophysae effects on thermal properties, is presented in Table 4.3.5-1.

4.3.5.3.3 Results of Analysis since Revision 00

All model developments since *Mountain-Scale Coupled Processes (TH) Models* are documented in Bodvarsson (2001 [DIRS 154669], Attachment 6, pp. 24 to 51, and Attachment 17, pp. 39 to 75). As discussed in Section 4.3.5.3.2, simulations of flow in the vicinity of one emplacement drift in the lower lithophysal unit were carried out for different realizations of fracture heterogeneity. Presence of lithophysal cavities gives rise to uncertainty pertaining to TH effects on seepage. These gas-filled cavities modify the thermal properties of the rock matrix from those in the AMR, as outlined in Table 4.3.5-1. To resolve the uncertainty due to lithophysal properties on the TH processes, simulations using the lithophysae thermal property (Table 4.3.5-1) are compared with those using the property set (with no effect of lithophysae) in *Mountain-Scale Coupled Processes (TH) Models* (CRWMS M&O 2000 [DIRS 144454]). To illustrate, the time evolution of temperature at the drift wall using both the nonlithophysae and lithophysae property sets are shown in Figures 4.3.5-1a and 4.3.5-1b for the HTOM and LTOM, respectively. Note the sharp increase of temperature following cessation of forced ventilation at 50 and 300 yrs, respectively, in Figures 4.3.5-1a and 4.3.5-1b. In Figure 4.3.5-1a, another temperature increase occurs at dryout at about 80 yrs, when no more water is available to absorb the heat of vaporization. In both operating modes, the drift wall temperatures from the property set incorporating the effects of lithophysal cavities are at most 6 C° higher than the ones from the AMR property set. This indicates that lithophysal cavities do not significantly impact the temperatures. However, the possible impact of these gas-filled lithophysal cavities on thermally induced fluid flow in the fractures and the matrix, and the subsequent moisture redistribution, has not yet been investigated rigorously. This is a remaining uncertainty that could be resolved by new conceptual models and field measurements in the lithophysal unit.

A primary objective of the current studies is to determine whether fast-flow liquid flux promoted by fracture heterogeneity can penetrate the vaporization zone around a potential emplacement drift. Monte Carlo studies (Bodvarsson 2001 [DIRS 154669], Attachment 6 and 17) show that even with the incorporation of fracture heterogeneity (based on field measurements), results similar to those in the AMR for homogeneous fracture property are obtained. That is, even though substantial enhancement in the fracture fluxes does occur at several meters above the drift, these enhanced liquid fluxes do not reach the drift crown during the thermal period. In Figure 4.3.5-2, fracture liquid fluxes as a function of lateral distance from the center of the drift are plotted for two horizontal lines at different times since waste emplacement. In Figure 4.3.5-2a, the fracture liquid fluxes are shown at an elevation of 5 m above the top of

the drift. It is clear that fluxes exceed the ambient infiltration rate (about 4.8 mm/yr for present day until 600 yrs after waste emplacement), especially 100 yrs after waste emplacement. The enhanced fluxes result from the increased fracture saturation in the condensation zone and capillary suction toward the dryout zone. In Figure 4.3.5-2b, the fluxes are shown for the elevation of the drift horizon. Here, it is evident that none of the enhanced fluxes can cross the drift horizon within the drift. On the other hand, Figure 4.3.5-2b shows drainage fluxes in the pillars beyond the drift wall, which is at 2.5 m from the drift center. The drainage flux moves out laterally with time because of the drying around the drift.

Figure 4.3.5-2 is typical of simulations with different realizations of the heterogeneous permeability field for the higher-temperature case. Results from different realizations confirmed this phenomenon of enhancement of fracture fluxes several meters above the drift from the condensation, and reduction (often to zero) of fracture fluxes below the condensation zone, both above and below the drift. Maximum thermally enhanced liquid fluxes occur about 100 yrs after emplacement. However, the evaporative energy of decay heat for the above-boiling operating mode appears to be effective in keeping liquid water from reaching the emplacement drift. Thus, for the HTOM, where above-boiling temperatures occur around the emplacement drift, simulated results show that fracture fluxes would not likely seep into the drift.

Contour plots of liquid saturation show the moisture redistribution and give insight to thermally induced distribution of liquid flow. Zones of increased liquid saturation usually lead to higher liquid fluxes, and vice versa. Figures 4.3.5-3a and 4.3.5-3b show contours of liquid saturation in the fractures around an emplacement drift at 50 and 100 yrs after emplacement of radioactive wastes for the higher-temperature case. The thermal property set that incorporates the effects of lithophysal cavities, as described in Table 4.3.5-1, is used in these simulations. Figure 4.3.5-3a shows that at 50 yrs, a dryout has formed below the emplacement drift; however, there is no perceptible dryout zone above or lateral to the drift. Figure 4.3.5-3b shows that at 100 yrs after waste emplacement, the extent of the dryout zone has increased considerably. A pattern of considerably larger drying below the drift (rather than above or to the side of the drift) persists. This phenomenon of a “dry shadow” below the drift can significantly impact transport, as discussed in Section 11.3.5. Because of the underlying small-scale heterogeneities in the permeability field, localized zones of condensate accumulation appear. This is in contrast to the continuous condensate zone in simulations with a uniform permeability distribution. The liquid saturation in the condensate-zone fractures can increase to 5 percent from the ambient values of 1 to 1.5 percent. This increased saturation beyond the dryout zone laterally results in drainage through the cooler region between two adjacent emplacement drifts. These phenomena of drying and wetting continue past 1,000 yrs after waste emplacement. Throughout this period, the extent of the dryout zone does not exceed 10 m above the drift or 15 m laterally. Below the drift, however, the dryout zone extends down to a maximum of 60 m. Simulated results for different realizations of permeability fields produce similar patterns, with only minimal variations in the extent of dryout zones and the amount of condensate build-up.

The drying around the emplacement drift resulting from vaporization in a HTOM is also illustrated in a contour plot of liquid saturation in the matrix. Figure 4.3.5-4 shows the liquid saturation distribution in the matrix at 1,000 yrs after emplacement (Bodvarsson 2001 [DIRS 154669], Attachment 6, p. 37). Note the large decrease of the liquid saturation from ambient (about 0.9) to less than 0.01 and the extent of the drying.

Since none of the simulations with stochastic permeability fields led to seepage during the thermal period for the higher-temperature case, one stochastically generated permeability field was modified: the permeability of a column of fracture elements intercepting the drift crown was artificially increased by a factor of 100 to investigate the impact of a high-permeability discrete feature, such as a fault, on thermal seepage. The simulated results are shown in Figure 4.3.5-5. Again, fracture liquid fluxes are plotted as a function of lateral distance from the center of the drift for a horizontal line at the drift elevation and at different times since waste emplacement. Figure 4.3.5-5 shows that no liquid flux can cross the drift horizon within the drift up to 1,000 yrs after emplacement, and that there is enhancement of drainage flux beyond the drift. The small "ambient" flux shown within the drift at 0.01 yrs is an artifact of the numerical model: in this particular simulation, the drift has not been modeled as a capillary barrier, but has nonzero capillary suction that can draw water at the initial drying. However, the thermal effect quickly overcomes this artifact: Figure 4.3.5-5 shows no seepage into the drift throughout the thermal period of 1,000 yrs, even for this case of an artificial high-permeability discrete feature intersecting the drift at the center line.

Similar Monte Carlo simulations were carried out for the lower-temperature case (Bodvarsson 2001 [DIRS 154669], Attachment 6 and 17). As expected, the simulated results show smaller thermal perturbation around the emplacement drift compared to the higher-temperature case. Figure 4.3.5-6 shows the temperatures at the emplacement drift wall as a function of time (logarithmic scale) for both operating modes. The figure also includes a third lower-temperature scenario with 300 yrs of forced ventilation and an initial thermal load of 1.45 kW/m. The higher-temperature case predicts a maximum drift wall temperature of approximately 120°C, whereas the maximum drift wall temperature for the LTOM is about 84°C with a heat load of 1.35 kW/m, or 88°C with a heat load of 1.45 kW/m. All these results were obtained through simulations using the lithophysae thermal property set listed in Table 4.3.5-1. Note that, because temperatures are gridblock averages, simulated drift-wall temperatures will increase with refinement of the numerical grid.

The higher-temperature case predicts a maximum drift wall temperature of approximately 120°C, whereas the maximum drift wall temperature for the LTOM is about 84°C with a heat load of 1.35 kW/m, or 88°C with a heat load of 1.45 kW/m. All these results were obtained through simulations using the lithophysae thermal property set listed in Table 4.3.5-1. Note that, because temperatures are gridblock averages, simulated drift-wall temperatures will increase with refinement of the numerical grids.

Since the smaller thermal perturbation from the lower-temperature case produces no boiling anywhere in the rock, there is minimal redistribution of moisture. If the contours of matrix liquid saturation were plotted on the same scale as that in Figure 4.3.5-4 for the higher-temperature case, little reduction of liquid saturation from the ambient value would be observed anywhere at any time after emplacement.

A far smaller amount of water resides in the fractures (the pore volume of the fracture continuum is at least an order of magnitude smaller than that of the matrix, and the ambient liquid saturation in the fractures is about two orders of magnitude smaller than in the matrix). Hence, contours of liquid saturation in the fractures will be more sensitive to the small heat perturbation of the lower-temperature case. The thermal perturbation of the lower-temperature case can produce

some drying below the emplacement drift in the fractures. Even below boiling, vapor pressure increases with increased temperature, reducing the amount of water in the liquid phase. Figures 4.3.5-7a and 4.3.5-7b show the fracture liquid saturations from the lower-temperature case at 50 and 500 yrs after emplacement. Note that Figure 4.3.5-7a shows a slight increase in saturation immediately above the square drift. This results from ponding of downward flux on the drift top, since the drift is modeled as a capillary barrier with zero capillary suction. Decay heat to the rock increases when forced ventilation ceases at 300 yrs, so at 500 yrs the drying in the fracture extends downward to about 40 m. The drying is absent above and to the side of the drift because the effect of downward percolation flux and shedding to the side of the drift (which acts as a capillary barrier) more than compensates for the small amount of drying in the fractures due to vaporization. For the same reason, Figure 4.3.5-7 shows no localized zones of condensate build-up, as seen in Figure 4.3.5-3 for the higher-temperature case.

Because the temperatures are below boiling for the lower-temperature case, a great enhancement of percolation flux from ambient values would not be expected above the drift. This is confirmed by Figure 4.3.5-8a, where the fracture liquid fluxes at 5 m above the top of the drift are plotted as a function of lateral distance from the center of the drift at different times since emplacement (compare with Figure 4.3.5-2a). In Figure 4.3.5-8b, the fracture liquid fluxes are plotted at the drift center horizon. The drift acts as an effective capillary barrier so that no liquid flux enters the drift. Rather, it sheds around the drift, giving rise to an increased liquid flux immediately outside the drift wall at 2.5 m.

The results described above indicate that on one hand the TH coupled processes of boiling and condensation in the HTOM increase uncertainties associated with the movement of water; on the other hand, the presence of the vaporization barrier when temperature is above boiling quite certainly prevents percolation flux from reaching the drift wall, reducing the uncertainties associated with seepage into the drift compared to the LTOM.

4.3.5.4 Multiscale Thermal-Hydrologic Model

4.3.5.4.1 Discussion of Revision 00 Results

The *Multiscale Thermohydrologic Model* (CRWMS M&O 2000 [DIRS 149862]) is used primarily to develop time-varying estimates of key engineered barrier system performance measures (e.g., drift wall temperature, waste package temperature, relative humidity in the drift). These performance measures depend on TH behavior within a few meters of the emplacement drifts, and also on the scale of the repository (because of differences in local stratigraphy and local percolation flux). Thus, the multiscale thermal-hydrologic (MSTH) model takes a multiscale approach that combines one-dimensional, two-dimensional, and three-dimensional drift-scale thermal and TH models with a conduction-only three-dimensional mountain-scale model. Results of this show that over the entire range of the infiltration flux conditions considered, seepage is not predicted to occur during the boiling stage of the HTOM. After the cessation of boiling in the host rock (but not necessarily in the drift), seepage is predicted to occur only at a limited set of locations under high infiltration conditions. Under low to moderate infiltration conditions, no seepage into the drift is predicted to occur by the MSTH model. During the period in which boiling has ceased in the host rock but continues in the drift, seepage may occur under high infiltration conditions, but water entering the drift quickly evaporates.

Similar to the findings reported in Section 4.3.5.3.3, the MSTH model results show that at several meters above the drift crown, thermally induced percolation fluxes are greatly enhanced from their ambient values. However, these enhanced percolation fluxes are not able to penetrate the vaporization barrier to reach the drift wall.

Although the TH simulations in the MSTH model show no evidence of seepage during the boiling period (i.e., when temperatures are above boiling) for the HTOM (and little evidence of seepage during the below-boiling stage except under high infiltration conditions), the TSPA-SR (CRWMS M&O 2000 [DIRS 153246], Section 3.2.4) adopted a conservative approach, in which the increased percolation fluxes at 5 m above the drift crown calculated with the MSTH model were chosen as the seepage fluxes in the abstracted seepage model presented in *Abstraction of NFE Drift Thermodynamic Environment and Percolation Flux* (CRWMS M&O 2001 [DIRS 154594]). This conservative approach gives rise to an artificial peak in the abstracted seepage flow rates for all 610 locations within the heated repository footprint immediately after the forced ventilation period of 50 yrs. The justification for the conservative approach is partly based on the observation that the MSTH model uses a homogeneous fracture continuum within any given hydrostratigraphic unit (i.e., drift-scale heterogeneity is neglected), while drift-scale heterogeneity is known to promote focusing and channeling of flow.

4.3.5.4.2 Model Development since Total System Performance Assessment-Site Recommendation Investigating Heterogeneity

Drift-scale heterogeneity of fracture properties was incorporated into the three-dimensional heterogeneous line-averaged-heat-source, drift-scale thermal-hydrologic (LDTH) submodel of the MSTH model (BSC 2001 [DIRS 154985]). While REV 00 of the MSTH model demonstrates that seepage into the drift rarely occurs, it is possible that the very low occurrence of predicted drift seepage results partly from the modeling of a homogeneous fracture continuum within the host rock units. Since the issue of whether heterogeneity can increase the occurrence of liquid flux penetrating through a vaporization barrier is specific to above-boiling temperatures, the lower-temperature case is discussed in this subsection.

The three-dimensional heterogeneous LDTH models used are all based on the two-dimensional LDTH submodel at a location close to the geographic center of the repository. This location has infiltration fluxes that are higher than the repository averages for the present-day, monsoon, and glacial climates. A mean infiltration flux of 10.14 mm/yr for the first 600 yrs, 24.09 mm/yr from 600 to 2,000 yrs, and 38.66 mm/yr after that is modeled. The host rock unit at this location is the Tptpll. The three-dimensional LDTH model has a longitudinal dimension of 5 m (approximately the length of one waste package). Gridblock spacing in the longitudinal direction is 1.0 m. Capillary pressure and relative permeability are described by van Genuchten's function, with the capillary strength parameter $1/\alpha$ correlated to the heterogeneous fracture permeability field according to Leverett's scaling rule (Leverett 1941 [DIRS 100588], p. 159). The fracture porosity is correlated to the heterogeneous fracture permeability field according to the cubic law (Bear 1988 [DIRS 101379], p. 166). Random fields for heterogeneous fracture properties were generated by the Fourier spectral method in three dimensions (Nitao 1997 [DIRS 100641]) for the key fracture properties: permeability, porosity, and the van Genuchten "alpha" parameter. In the heterogeneous fracture field, fracture permeability values are isotropic, which is realistic. All stochastic realizations use a lognormal distribution with values of $\log_{10}$ standard deviation and

correlation lengths in the principal directions (BSC 2001 [DIRS 154985], Table 6-8). Some of the stochastic realizations used a $\log_{10}$ standard deviation that is considerably greater than the value of 0.72 determined from air-permeability data gathered at ESF Niche 2 (Station 36+50) (CRWMS M&O 2000 [DIRS 141400], Table 5).

Eight separate stochastic realizations were considered (Table 4.3.5-2): four pertain to a center location in the repository (Cases A-56 to D-56) and four pertain to an edge location (Cases A-34 to D-34). Six of these realizations use a standard deviation larger than that derived from air-permeability measurements made in Niche 2 (Station 36+50) (CRWMS M&O 2000 [DIRS 141400], Figures 11 and 12). The larger values of $\log_{10}$ standard deviation were chosen to increase the focusing of liquid-phase flow, and thereby increase the likelihood of seepage into the drift. Case A is intended to examine the influence of a large correlation length in the vertical direction, as compared to the horizontal direction. This has the effect of focusing flow along vertically oriented heterogeneities, which increases the tendency for seepage. Case B was intended to investigate whether capillarity is correlated with permeability. Case C is considered to be a more realistic case in that there is no vertical biasing to the shape of heterogeneities, which is more consistent with gas-permeability measurements made in Niche 2 (Station 36+50), and the standard deviation for permeability used in the realization (1.0) is close to that derived from those measurements (0.72). Case D examines the influence of a large standard deviation in the permeabilities while using a moderate ratio of vertical to horizontal correlation length.

4.3.5.4.3 Results of the Analysis Investigating Heterogeneity

TH simulations with the three-dimensional LDTH model applied to heterogeneous fields show no seepage entering the emplacement drift during the boiling stage of the HTOM, even when using stochastic hydrologic parameters favoring seepage that are well outside of currently available distributions measured at the site. Hence, the conclusion that no seepage occurs during the boiling stage appears to be robust and is not altered by the incorporation of small-scale heterogeneity. These results are consistent with those presented in Section 4.3.5.3.3.

Figure 4.3.5-9 shows the influence of drift-scale heterogeneity of permeability on the distribution of percolation flux in the host rock for Realization C-56. The influence of three different climate states is readily apparent as three distinct steps in the percolation histories. Close to the drift wall, the influence of decay heat on local percolation flux is seen to occur in three stages: (1) an initial stage of thermally enhanced percolation flux, which is seen as a distinct spike just after 50 yrs; (2) a period in which rock dryout reduces percolation flux; and (3) a post-boiling period. During the early portions of the post-boiling period, percolation flux is enhanced (seen as a second spike at approximately 700 yrs) as a result of a residual condensate zone that developed earlier, during the boiling stage. Note that 700 yrs corresponds to the time when the boiling zone has receded past the location 3 m above the drift (Figure 4.3.5-9b). This relatively short-lived phenomenon (on the order of hundreds of years) is followed by a period where percolation flux is no longer influenced by decay heat. Figure 4.3.5-10 shows that although the distribution of percolation flux is heterogeneous, there is a negligible influence on the distribution of temperature and relative humidity in the host rock.

Because such extreme examples of heterogeneity were considered and a large number of realizations were not considered, it is not possible to use these calculations to determine the

probability of seepage during the post-boiling period. However, these calculations are useful for making the following observations:

1. During the boiling period, seepage is extremely unlikely.

2. During the post-boiling period, the likelihood and magnitude of seepage increase with the $\log_{10}$ of the standard deviation of the fracture permeability.

3. During the post-boiling period, the likelihood and magnitude of seepage increase with the ratio of vertical to horizontal correlation length.

4. During the post-boiling period, correlating the capillary strength parameter ($1/\alpha$) of the fractures with the fracture permeability according to Leverett's scaling rule resulted in a greater seepage magnitude than cases for which $1/\alpha$ was constant.

5. The duration of the boiling period is never reduced as a result of fracture heterogeneity. In fact, the duration of boiling is slightly greater for the heterogeneous cases than for the homogeneous cases. The greater duration of boiling for the heterogeneous cases results from the influence of buoyant gas-phase convection being reduced by the heterogeneous fracture-permeability distribution, with the low-*k* features obstructing buoyant gas-phase convection. Thus, buoyant gas-phase convection plays a less significant role in the rate of cooldown in the drift for a heterogeneous case than for a corresponding homogeneous case.

6. During both the boiling and post-boiling periods, temperatures at the drift wall are insensitive to heterogeneity. Figures 4.3.5-9 and 4.3.5-10 show simulation results for the most realistic stochastic realizations considered (BSC 2001 [DIRS 154985], Cases C-56 and C-34, Table 6-8). These figures illustrate the effect of the vaporization barrier discussed in Section 4.3.5.6.1. In the simulation results shown in Figure 4.3.5-9, liquid water percolated downward 5 m above the drift crown, but 3 m above the drift crown, there was no percolation flux between approximately 60 and 340 yrs. Percolation flux was also zero in the interval between the drift crown and 3 m above the drift crown. The upper drift-wall temperature, shown in Figure 4.3.5-10, was above 100°C during this time. After the boiling period, these simulations produced no seepage due to diversion by capillary forces (BSC 2001 [DIRS 154985], Table 6-10).

4.3.5.5 Analytical Solution to Assess Liquid Fingering through a Superheated Regime

The possibility of large, randomly fluctuating infiltration rates caused by asperity-induced episodic flow through the fractures was considered. The analytical solution of Phillips (1996 [DIRS 152005]) was used to determine the penetration distance of the infiltration into the superheated fractured rock. Cumulative distribution functions for the episodicity and a critical penetration distance were developed to provide estimates for the probability of liquid water penetrating through the superheated region to a prescribed location.

The conceptual model governing asperity-induced episodic infiltration models fractures as consisting of randomly distributed "pinch-point" and "storage" apertures within the fractures. The pinch-point apertures act as capillary barriers to the infiltration of water, which accumulates in a volume above the pinch-point dictated by the storage aperture. The water continues to accumulate in the storage aperture until the head above the pinch-point aperture exceeds the associated capillary rise height. Once this happens, the water flows downward under the forces of gravity and at a rate dictated by the permeability of the aperture. The water continues to flow through the aperture until the accumulated water is completely drained. This behavior leads to an asperity-induced episodic infiltration of water through fractured rock that occurs randomly in space and time.

A region of superheated rock is modeled as existing below the source of asperity-induced episodic infiltration. The water percolates downward into the superheated rock and begins to boil. The rate of evaporation is dictated by the conductive heat transfer from the adjacent rock to the flowing water. The analytical solution of Philips (1996 [DIRS 152005]) is used to determine the penetration distance of the water into the superheated rock based on the flow rate, volume of water available for drainage, and heat transfer from the adjacent rock. Although the size of the liquid fingers (or "weeps") flowing down the fractures will be considered in three dimensions, the flow process is modeled as occurring in one dimension to facilitate an analytical solution.

The conceptual model described above consists of two primary processes: (1) the accumulation and drainage of water in fractures and (2) the penetration of that water into superheated rock. The sections below describe the mathematical models for each of these processes.

4.3.5.5.1 Accumulation and Drainage of Water in Fractures

The capillary rise height, h [m], in a fracture plane above the pinch-point aperture can be calculated using the Young-Laplace equation (Bear 1988 [DIRS 101379], p. 445):

$$h = \frac{2\sigma}{\rho g b_2} \qquad \text{(Eq. 4.3.5-3)}$$

where

- σ = the surface tension of water [N/m]
- ρ = the liquid density [kg/m^3]
- g = the gravitational constant [9.81 m/s^2]
- b_2 = the pinch-point aperture [m]

The maximum volume of water, V [m^3], that can be stored above the pinch-point aperture is expressed as a function of the capillary rise height:

$$V = h b_1 w \qquad \text{(Eq. 4.3.5-4)}$$

where

b_1 is the storage aperture ($b_1 > b_2$) and w is the width [m] of the ribbon or "finger" of water flowing along the fracture plane (the width, w, is measured in a direction perpendicular to the aperture).

When the accumulation of water in the storage aperture produces a head that exceeds the capillary rise height given by Equation 4.3.5-3, the water will flow through the pinch-point aperture. The mass flow rate, $\dot{m}_o$ [kg/s], can be determined by treating it as steady laminar flow between parallel plates separated by the pinch-point aperture (Bear 1988 [DIRS 101379], p. 166):

$$\dot{m}_o = \left[\frac{b_2^{\,2}}{12\mu}\rho g\right]\rho b_2 w \qquad \text{(Eq. 4.3.5-5)}$$

where

μ = the dynamic viscosity of water [kg/m-s]
kg/m-s = the flow velocity [m/s].

The time, t_d [s], required to drain the water through the pinch-point aperture can be calculated by dividing the total mass of accumulated water by the mass flow rate through the pinch-point aperture:

$$t_d = \frac{\rho V}{\dot{m}_o} \qquad \text{(Eq. 4.3.5-6)}$$

The mass flow rate (Equation 4.3.5-5) and the time required to drain the water (Equation 4.3.5-6) are used in subsequent calculations to determine the water-penetration distance into superheated rock. In addition, the episodicity of the water flowing through the fracture can be determined based on the duration of the accumulation and drainage processes. The episodicity factor, e, is defined as the ratio of the drainage time, t_d [s], to the accumulation time, t_a [s]. It represents the fraction of time that breakthrough flow occurs in a fracture experiencing asperity-induced accumulation and drainage. The accumulation time, t_a, can be expressed by dividing the maximum mass of accumulated water (as derived from Equation 4.3.5-4) by the mass flow rate of infiltrating water coming into the storage aperture:

$$t_a = \frac{\rho V}{\rho u A} \qquad \text{(Eq. 4.3.5-7)}$$

where

u = a Darcy infiltration flux rate [m/s] that can be specified by surface infiltration

A = a cross-sectional area representing a catchment region that collects and focuses water into the fracture.

The catchment area represents the bulk cross-sectional area associated with the Darcy velocity for each fracture that has flowing water. If the fingers of water flowing down the fractures are separated by a uniform "weep" distance, a, the cross-sectional area, A, can be expressed as a^2 (Ho and Wilson 1998 [DIRS 123261]). The episodicity factor, e, can then be expressed as follows:

$$e = \frac{t_d}{t_a} = \frac{\rho u A}{\dot{m}_o} \qquad \text{(Eq. 4.3.5-8)}$$

The episodicity factor is bounded by 0 (no flow) and 1 (always flowing). The drainage time may, in some cases, exceed the accumulation time, which yields a constant flow condition. In these cases, the maximum value of the episodicity factor is set equal to one. As an example, if the episodicity factor is equal to 0.1, flow drains through the fracture only one-tenth of the time. Over one year, percolation draining through this fracture would only occur approximately five weeks.

4.3.5.5.2 Water Penetration into Superheated Rock

Phillips (1996 [DIRS 152005]) developed an analytical model of infiltration into superheated fractured rock. A ribbon of liquid water is modeled as flowing down a fracture in an unsaturated rock matrix and boiling as it passes the boiling-point isotherm. The temperature in the superheated rock beyond the boiling-point isotherm is greater than the boiling temperature, but the temperature of the penetrating liquid remains at the boiling temperature. The penetration distance into the superheated rock is a function of the mass flow rate of liquid across the boiling-point isotherm, the heat conduction available from the surrounding rock, and the properties of the fluid and rock. The solution models the flow as one-dimensional and the heat flux and initial mass flow rate as constant. The penetration distance, l [m], derived by Phillips (1996 [DIRS 152005]) is given as:

$$l = \left(\frac{2}{\pi}\right)^{0.25} L_3 \left(\frac{\alpha t}{w^2}\right)^{0.25} \quad \text{for } t < w^2/\alpha \qquad \text{(Eq. 4.3.5-9)}$$

where

α = the effective thermal diffusivity of the rock matrix [m^2/s]
t = the duration of the infiltration event [s]
L_3 = a characteristic length.

The characteristic length is defined as follows:

$$L_3 = \left(\frac{\dot{m}_o h_{fg}}{q}\right)^{0.5} \qquad \text{(Eq. 4.3.5-10)}$$

where

q = the heat flux available to boil the water penetrating into the superheated rock [W/m^2]

h_{fg} = the latent heat of vaporization [J/kg]

Phillips (1996 [DIRS 152005]) expresses this heat flux in terms of Fourier's Law (i.e., thermal conductivity multiplied by temperature gradient). The duration of the infiltration event, t, in Equation 4.3.5-9 is equal to the drainage time, t_d, which specifies a period of constant mass flow rate supplied to the superheated region, as required by the Phillips (1996 [DIRS 152005]) solution.

An energy balance on the evaporating ribbon of water specifies that the heat flux, q, is proportional to the rate of water evaporation. Therefore, Equation 4.3.5-10 can be interpreted as the ratio of the mass flow rate of water entering the superheated region to the mass rate of water being evaporated. If this ratio is large, then the penetration distance can be large because the mass flow rate is able to overcome the rate of evaporation. The characteristic length, L_3, in Equation 4.3.5-10 is also an approximate solution for the penetration distance when $t \geq w^2/\alpha$ (Phillips 1996 [DIRS 152005], pp. 1669 to 1670).

The downward flow rate at a location, z, in the superheated region can be derived from a mass balance between the downward flow rate and the mass rate of evaporation. The mass balance is given in Phillips (1996 [DIRS 152005], Equation 10) as follows:

$$\frac{\partial}{\partial z}[\dot{m}(z)] = -\left(\frac{8}{\pi}\right)^{0.5} \frac{q}{h_{fg}} \frac{z}{\left[\alpha w^{-2}(t - t_z)\right]^{0.5}} \quad \text{for } t_z < t < w^2/\alpha \qquad \text{(Eq. 4.3.5-11)}$$

where

z = the distance below the boiling-point isotherm [m]
$\dot{m}(z)$ = the mass-flow rate of water [kg/s] at location z
h_{fg} = the latent heat of vaporization [J/kg]
α = thermal diffusivity [m^2/s]
t = the total time elapsed since the water entered the superheated region (s)
t_z = the time required for the water to penetrate to a distance z.

Equation 4.3.5-11 can be integrated between 0 and z ($0 < z < l$) with the boundary condition $\dot{m}(z=0) = \dot{m}_o$ (defined in Equation 4.3.5-5) to yield the following expression for the mass flow rate of water at location z:

$$\dot{m}(z) = \dot{m}_o - \left(\frac{2}{\pi}\right)^{0.5} \frac{q}{h_{fg}} \frac{z^2}{\left[\alpha w^{-2}(t - t_z)\right]^{0.5}} \quad \text{for } t_z < t < w^2/\alpha \qquad \text{(Eq. 4.3.5-12)}$$

In this episodic analysis, the total time available for water to penetrate into the superheated zone is limited by the time it takes for the water to drain from the pinch-point aperture (t_d). After this time, the source term for water infiltration, $\dot{m}_o$, goes to zero. Therefore, in Equation 4.3.5-12 the total time elapsed, t, can be approximated as the total drainage time, t_d. In addition, t_z is solved using Equation 4.3.5-9 with $l = z$:

$$t_z = \frac{\pi}{2}\left(\frac{z}{L_3}\right)^4 \frac{w^2}{\alpha} \qquad \text{(Eq. 4.3.5-13)}$$

Equation 4.3.5-12 can then be used to estimate the mass flow rate of water at a particular location in the superheated region during asperity-induced episodic infiltration events. This will be of particular interest in the application discussed below to determine the amount of water that can penetrate a superheated region surrounding a tunnel containing heat-generating waste packages.

4.3.5.5.3 Assumptions

Although the asperity-induced episodic infiltration model provides convenient analytical expressions for the episodicity and water-penetration distances, it also includes a number of important assumptions:

- Although the configuration of the infiltrating weeps is three-dimensional, the flow of water through the fractures is modeled as one-dimensional in the downward direction. Water accumulation and drainage is governed by a weep width that constrains the physical boundaries of accumulation and drainage in the lateral direction.

- All fluid and material properties are modeled as constant over time. In the application presented here, properties were averaged over temperature ranges from ambient (20ºC) to boiling (96ºC for Yucca Mountain). Distributions were obtained from previous Yucca Mountain reports, as summarized in Table 4.3.5-3.

- Fracture-matrix interaction (e.g., imbibition) is ignored in this analysis. If a significant amount of matrix imbibition exists, the water-penetration distance into the superheated distance will be less.

4.3.5.5.4 Application and Results

The asperity-induced episodic infiltration model is applied to the thermal seepage problem using the input parameters tabulated in Table 4.3.5-3.

Figure 4.3.5-11 shows a cumulative probability plot of the episodicity factor (Equation 4.3.5-8) for two weep widths (0.01 and 1 m) and different flow focusing conditions. The amount of flow focusing depends on weep spacing. Figure 4.3.5-11 shows that the smaller the weep width, the larger the episodicity factor; the episodicity factor is much lower when there is no flow focusing.

Figure 4.3.5-12 shows a plot of the cumulative probabilities for 300 realizations of the water-penetration distance (Equation 4.3.5-9) divided by the superheated distance (Table 4.3.5-3,

9th row) for different widths of the infiltrating water. Approximately 30 percent of the 300 realizations show water penetration to the drift wall when the weep width is equal to 1 m. Only about 15 percent of the realizations show penetration to the drift wall when the weep width was equal to 0.001 m. Figure 4.3.5-12 also shows that the results begin to converge as the weep width approaches a value of 1 m. In the three-dimensional solution presented by Phillips (1996 [DIRS 152005]), a weep width of 1 m yields a solution that is identical to an analogous two-dimensional solution that uses an infinite weep width along the direction of the fracture plane. Therefore, a weep width of 1 m can be viewed as a limiting condition that allows the greatest water-penetration distance for the three-dimensional solution. This value has been used in TSPA calculations of episodicity and flow of water at the drift wall, as described in the next section.

Figure 4.3.5-12 shows a cumulative distribution function of the ratio of the mass flow rates at the drift wall to the initial mass flow rates, $\dot{m}_o$, for 300 realizations with a weep width of 1 m, using Equations 4.3.5-12 and 4.3.5-13. The desired location, z, is set equal to the superheated distance to the drift wall, d. If the time available for infiltration, t (which is set equal to the drainage time, t_d), is less than the time required for the water to reach the drift wall, t_z, then the mass flow rate is set to zero. The majority of the values are near zero because, as shown in Figure 4.3.5-12, the majority of the realizations do not result in water penetration to the drift wall. This distribution can be useful for determining the impact of asperity-induced episodic flow and penetration to the drift wall on performance assessment seepage analyses that evaluate the amount of water that can contact the waste packages.

4.3.5.6 Abstraction for Total System Performance Assessment

The results presented above show that it is very difficult for water flow to reach the emplacement drifts when the drift walls are above the boiling temperature. Under these conditions, seepage into the drifts is greatly reduced and possibly eliminated entirely. The analyses conducted with the mountain-scale coupled-process model (Section 4.3.5.3) and the MSTH model (Section 4.3.5.4) found no seepage into the drift during the thermal period for the HTOM, even with heterogeneity included. The analysis of penetration of episodic pulses through superheated rock (Section 4.3.5.5) showed that it is possible for seepage to occur, but it also found that water did not reach the drift wall under most parameter combinations.

4.3.5.6.1 Reduction of Seepage by the Vaporization Barrier

In the base case TSPA model, the dry superheated zone around the drifts was neglected and seepage was conservatively allowed to occur throughout the thermal period (CRWMS M&O 2000 [DIRS 153246], Section 3.3.3.2.3). This has no effect on the results of the base case nominal scenario because the waste packages and drip shields are still intact during the thermal period, so no radionuclide releases can occur (CRWMS M&O 2000 [DIRS 153246], Section 4.1.2). However, results of other scenarios could be affected (e.g., if there were an unexpected early failure of both drip shield and waste package at the same location).

An extension of the TSPA model to make it more realistic would be to calculate seepage differently (or modify the base case calculation) when the drift wall temperature is above boiling. Seepage could be reduced even when temperatures are subboiling, as they are for the LTOM, but

the reduction is more uncertain and more analysis would be required to quantify a sufficient range of conditions to be able to include it in the TSPA model. Another issue, especially for the LTOM, is the effect of forced ventilation. The dryout zone around the drifts caused by removal of moisture by the ventilation system would tend to reduce seepage into the drifts, but that effect is not currently included in the TH or seepage models.

In the following paragraphs, a relatively simple abstraction is described for the reduction in seepage when the drift walls are above boiling (i.e., for the HTOM).

Two types of results are available. The simulations using the mountain-scale coupled-process model and the MSTH model indicate no seepage when the drift wall temperature is above boiling. More extreme conditions were considered using the analytical model of penetration of episodic pulses through superheated rock, and some of those conditions resulted in water reaching the drift. The distribution of reductions in flux calculated with the analytical model is shown in Figure 4.3.5-12. That figure shows that almost three-fourths of the realizations that were modeled resulted in no water reaching the drift. The rest had varying amounts of flow reduction, ranging all the way up to almost no reduction. Average reduction ratio for the 300 realizations is approximately 0.2. The distribution represents a possible range of spatial variation; that is, some locations would be expected to have little reduction in seepage, but most locations would be expected to have seepage reduced to zero, with an average reduction of approximately 80 percent.

The abstraction recommended for TSPA simulations is to sample a random number that varies from 0 to 0.2 and multiply the seepage calculated by the seepage abstraction model by that factor whenever the drift wall is above the boiling temperature. When the drift wall is below boiling, the seepage calculated by the seepage abstraction model should be used without change. This abstraction is easy to implement and covers the range of results given by the TH models. The sensitivity of TSPA results to this random parameter will be an indication of whether the TH seepage reduction is important to the results.

4.3.5.6.2 Effects of Episodicity on Seepage

The mechanism suggested in Section 4.3.5.5 for producing episodic pulses of flow down fractures is not limited to the thermal period, but could occur at any time. It is not clear whether this process actually occurs in Yucca Mountain. It requires that water be trapped in a storage aperture until enough pressure builds up to break through the capillary resistance of a pinch-point aperture. This type of episodic flow has not been observed in Yucca Mountain, and it might not be possible under ambient conditions to trap water for long enough because of possible dissipation by imbibition into the matrix or evaporation. However, because episodic flow pulses could lead to greater seepage into drifts (e.g., CRWMS M&O 2000 [DIRS 153314], Section 6.6.6; CRWMS M&O 2001 [DIRS 154291], Section 6.4.4), it is important to consider the possible impact of this mechanism on TSPA results.

A method for including episodic flow in the seepage abstraction was presented in *Abstraction of Drift Seepage* (CRWMS M&O 2001 [DIRS 154291], Section 6.4.4), though it was not included in the final abstraction because episodic flow was thought to be unlikely. However, that method can now be used to evaluate the effects of asperity-induced episodic flow. In the abstraction

method, episodic flow is parameterized by an episodicity factor, which is the fraction of time that flow occurs. Distributions of episodicity factors calculated for asperity-induced episodic flow are presented in Figure 4.3.5-11. As discussed in Section 4.3.5.5.4, the middle curve (w = 1 m, $A = a^2$) is considered to be appropriate for use in TSPA simulations. That curve is reasonably well represented as a log-uniform distribution between 10^{-4} and 10^{0}.

The individual distributions shown in Figure 4.3.5-11 represent spatial variability in the episodicity factor (i.e., they represent a range of episodicity values that could occur at different spatial locations). The three different curves represent uncertainty—the most representative values for the weep width, w, and cross-sectional area, A, are uncertain. The abstraction method (CRWMS M&O 2001 [DIRS 154291], Section 6.4.4) does not allow for spatial variability of the episodicity factor; episodicity effects are represented by a single factor in each TSPA realization. However, the importance of episodicity to TSPA results can be determined by sampling the episodicity factor from an uncertainty range and examining its effect on the results. The log-uniform distribution between 10^{-4} and 10^{0} that was suggested above is a reasonable choice for the uncertainty distribution because it encompasses the average values of all three episodicity distributions in Figure 4.3.5-11.

4.3.5.7 Multiple Lines of Evidence

Simulations in the above section show that there is an increase of liquid flux in the condensation zones outside of drying that can account for the phenomenon of water being moved away from the drift and draining in the cooler region of the pillar between two adjacent emplacement drifts. This phenomenon of drainage of water outside an above-boiling region of rock mass is corroborated by observations in the Drift Scale Test being conducted in the ESF. The temperatures in boreholes parallel to the wing heaters in the Drift Scale Test consistently show a heat pipe signature beyond the drying zone of the wing heaters (Birkholzer and Tsang 2000 [DIRS 154608]). The heat pipe signature of a temperature maintained at boiling is an indication of potential water movement in the fractures, as all water collection in the Drift Scale Test has been possible only in those borehole sections when the temperature is at boiling.

In the analysis above, the effect of moisture removal by forced ventilation has not been accounted for. Forced ventilation has the effect of reducing water seeping into the drift. Evaporation of seeped water has been observed in seepage tests being carried out in the ESF and the ECRB Cross Drift. The challenge there is to assess quantitatively the impact on seepage of drying from ventilation.

4.3.5.8 Summary of Uncertainties and Their Treatment

Thermal seepage models, like any other models, are subject to uncertainties due to various factors, such as data, parameters, conceptualization, and numerical model implementation. Of all the uncertainty issues, the ones that contribute the greatest uncertainty to the thermal effects on seepage are different thermal operating modes, the effects of lithophysal cavities on thermal properties, and the heterogeneity of fracture permeability. Studies pertaining to these uncertainty issues are highlighted in the analyses presented above. A more complete list of the uncertainty issues particular to thermal seepage and their treatment is given in Table 4.3.5-4.

4.3.5.9 Summary and Conclusions

Modeling and uncertainty studies have been performed to predict how decay heat from emplaced waste would affect the magnitude and spatial distribution of percolation flux reaching the emplacement drifts, and, in turn, the potential of seepage into the drifts. The effect of TH processes on seepage has been considered for the HTOM and LTOM.

The studies discussed above are based on two separate numerical models (Sections 4.3.5.3 and 4.3.5.4) and an analytical model (Section 4.3.5.5). The results show that it is very difficult for water flow to reach the emplacement drifts when the drift walls are above the boiling temperature. That is, for the higher-temperature repository, the dry superheated zone around the drift possibly eliminates seepage into the drift. The analyses conducted with the mountain-scale coupled-process model (Section 4.3.5.3) and the MSTH model (Section 4.3.5.4) found no seepage into the drift during the thermal period for the HTOM, even with heterogeneity and extreme conditions included. The analysis of penetration of episodic pulses through superheated rock (Section 4.3.5.5) shows that it is possible for seepage to occur, but it also found that water did not reach the drift wall under most parameter combinations.

For the lower-temperature case, the studies in Section 4.3.4.3 show that other than some drying in the fractures below the drift, the decay heat causes little redistribution of moisture or enhancement of fracture liquid fluxes. Therefore, the thermal effect on seepage is insignificant when the temperature is below boiling.

Based on the results of the process models, the TSPA-SR (CRWMS M&O 2000 [DIRS 153246]) model during the thermal period has been modified to make it more realistic. The modification was to remove the very conservative assumption of taking the typical percolation flux to be that at 5 m above the drift, and to remove the assumption to neglect the dry superheated zone around the drifts as a vaporization barrier for seepage. However, the recommended extension to the TSPA-SR model still is conservative. Instead of adopting the results of no seepage during the thermal period from the numerical models under expected repository conditions, the TSPA model will use the results of the analytical model of penetration of episodic pulses through superheated rock, where seepage can occur under more extreme conditions than those expected.

4.3.6 Thermal-Hydrologic-Chemical Effects on Seepage and Potential Seepage Chemistry

This section summarizes modeling and uncertainty studies performed for the evaluation of THC effects on seepage and on the chemistry of water and gas in the near-field environment (NFE) that may enter drifts as seepage or through gas flow.

4.3.6.1 Introduction

THC processes may impact seepage through changes in fracture porosity and permeability, fracture unsaturated hydrologic properties (e.g., capillarity), and fracture-matrix interaction. Changes in the chemistry of water that may enter drifts through seepage take place via numerous processes, including water-rock interaction, evaporation or boiling and condensation, interactions with the gas phase, transport processes, and climate changes. Uncertainties in the conceptual models, data used for input and model validation, and predictions of THC effects as they

influence seepage and seepage chemistry are discussed in *Drift-Scale Coupled Processes (DST and THC Seepage) Models* (CRWMS M&O 2000 [DIRS 142022]) and its revisions (CRWMS M&O 2001 [DIRS 154426]; BSC 2001 [DIRS 154677]). The TSPA-SR (CRWMS M&O 2000 [DIRS 153246]) was based on an abstraction (CRWMS M&O 2000 [DIRS 123916]) of the data documented in the initial version of *Drift-Scale Coupled Processes (DST and THC Seepage) Models* (CRWMS M&O 2000 [DIRS 142022]). This work is summarized in Section 4.3.6.3. Since the TSPA-SR, several new analyses, models, sensitivity studies, assessments of unquantified uncertainties, and validation studies have been performed; these are documented in the latest revision of *Drift-Scale Coupled Processes (DST and THC Seepage) Models* (BSC 2001 [DIRS 154677]) and in this report (see Sections 4.3.6.4, 4.3.6.5, and 6.1.3.5).

The methods used to evaluate THC effects on seepage and seepage chemistry include the development of conceptual and numerical models, estimation of geochemical parameters such as thermodynamic and kinetic data, model validation using large-scale thermal tests and laboratory experiments, and predictive (process) modeling. This approach was chosen because it provides the means to test the appropriateness of the conceptual model, evaluate uncertainties in different conceptual models, and predict effects on seepage rate and seepage chemistry over time. Uncertainties in some thermodynamic and kinetic parameters were treated using sensitivity studies and comparisons to data from the Drift Scale Test and laboratory experiments. Remaining unquantified uncertainties regarding spatial variability of seepage-relevant formation properties; the distribution of local percolation flux; variability in initial and infiltration water chemistry; and the impact of design decisions regarding ventilation, thermal loading, potential repository area, and drift orientation were addressed through appropriately broadened uncertainty distributions and conservative considerations in the abstraction (CRWMS M&O 2000 [DIRS 123916]). Unquantified conceptual uncertainties were assessed in analogue studies, laboratory experiments, and other corroborating observations.

The conceptual model for THC processes provides a comprehensive basis for modeling the pertinent mineral-water-gas reactions in the host rock under thermal loading conditions as they influence the chemistry of water and gas that may enter drifts during 100,000 yrs. Data are incorporated from the drift-scale calibrated property sets, the UZ flow and transport model, geochemical data (fracture and matrix mineralogy, aqueous geochemistry, and gas chemistry), thermodynamic data (minerals, gases, and aqueous species), data for mineral-water reaction kinetics, and transport data (BSC 2001 [DIRS 154677]). Simulations of THC processes include coupling between heat, water, and vapor flow; aqueous and gaseous species transport; kinetic and equilibrium mineral-water reactions; and feedback of mineral precipitation or dissolution on porosity, permeability, and capillary pressure (hydrologic properties) for a dual-permeability (fracture-matrix) system.

The effect of coupled THC processes on the evolution of flow fields and potential seepage chemistry in the UZ around drifts has been investigated for different potential future climate change scenarios, calibrated property sets, initial mineralogy, and heterogeneous permeability fields.

4.3.6.2 Goal of Drift-Scale Thermal-Hydrologic-Chemical Models

The goals of the models used for prediction of drift-scale THC processes and their abstraction are:

- Provide a conceptual basis and methodology for developing drift-scale THC models
- Validate the THC model by comparing its results to results from field and laboratory experiments
- Identify conceptual uncertainties and address uncertainty through sensitivity studies that vary key parameters
- Predict changes in hydrologic properties resulting from mineral precipitation/dissolution and associated THC effects on flow and seepage
- Predict changes in water and gas chemistry around drifts, which are the potential elements that could enter drifts through seepage or gas flow.

The coupled THC processes important for evaluation of changes in the chemistry of the NFE and effects on flow are illustrated schematically in Figure 4.3.6-1. In particular, the influence of certain UZ hydrologic processes (such as fracture-matrix interaction) and thermal-hydrologic processes (such as the development of a heat pipe) have a strong effect on the chemical evolution of the system.

4.3.6.3 Discussion of Initial Results

The work summarized in this section was performed to support the TSPA-SR (CRWMS M&O 2000 [DIRS 153246]). In addition to providing the basis for the development of the drift-scale THC models, the analyses presented in the initial version of *Drift-Scale Coupled Processes (DST and THC Seepage) Models* (CRWMS M&O 2000 [DIRS 142022]) supply the following:

- Validation of drift-scale THC process model by simulation of the Drift Scale Test and comparison to measured gas and water chemistry collected through August 1999
- Prediction of THC effects around drifts for a higher-temperature backfill design with drift emplacement in the Tptpmn unit (two-dimensional column model at the USW SD-9 borehole)
- Evaluation of different modeled geochemical systems (base case and extended case)
- Evaluation of the effects of changing climate states on THC processes, along with upper- and lower-bound infiltration rates and corresponding drift-scale calibrated property sets.

The base case and extended case geochemical systems were developed to address uncertainties in the geochemical conceptual models and allow for predictions that are less affected by

reactions that have larger uncertainties, such as those involving zeolites and clays. The base case geochemical system consisted of calcite, silica polymorphs (i.e., tridymite, cristobalite, quartz, and amorphous silica), gypsum, appropriate aqueous species, and carbon dioxide gas. The extended case system included additional zeolite and clay minerals, ferric iron oxide/hydroxide minerals, and fluorite.

4.3.6.3.1 Validation of the Drift-Scale Thermal-Hydrologic-Chemical Process Model with the Drift Scale Test

Results of the validation analysis showed that modeled carbon dioxide concentrations in the gas phase captured the general trends seen in measured compositions. The base case geochemical system provided a much closer match to measured gas-phase carbon dioxide concentrations and the pH of waters that were collected from boreholes near the boiling zones. Apparent discrepancies between modeled and measured carbon dioxide concentrations were observed for samples collected at boiling temperatures because the sampled gas was mostly steam, with little air, and most of the steam was removed by condensation before analysis. However, when the carbon dioxide concentrations were adjusted for water removed, the trends were qualitatively similar in the boiling intervals (BSC 2001 [DIRS 154677], Section 6.2.7.2). The ranges of modeled and measured pH for waters collected in boreholes near the boiling interval were also shown to be similar. Because the comparisons of the water and gas chemistry from the extended system results were not as good as those from the base case system, the uncertainties associated with model validation were greater for the associated aqueous species (i.e., Al, Fe, K, and pH). These uncertainties are likewise also associated with predictions done with the THC Backfill Seepage Model, described in the following section. However, because the initial water and gas compositions are only known approximately, and their spatial distributions unknown, a quantitative evaluation of the uncertainties associated with the predictions is not feasible. Yet the range of predicted and measured compositions in the drift-scale test for waters that may potentially seep into drifts are not extremely great and the model results generally capture this range.

4.3.6.3.2 Initial Report of Thermal-Hydrologic-Chemical Effects on Flow and Potential Seepage

The effect of coupled THC processes on the time evolution of flow fields in the UZ around drifts was investigated for different climate change scenarios, calibrated property sets, initial mineralogy, and heterogeneous permeability fields. Predictions of the changes in flow around drifts as they could influence seepage were based on simulations of 100,000 yrs, which included a preclosure period of 50 yrs with 70 percent of the heat removed by ventilation. The EDA II design, including backfill (Wilkins and Heath 1999 [DIRS 104247]), was considered as the base case design. This design was used for the TSPA-SR and included a higher-temperature thermal operating mode with 50 yrs of forced ventilation. The predicted extent of the dryout zone and the time of rewetting were different for each modeled climate history and calibrated rock property set, with the upper-bound infiltration showing the smallest dryout zone and earliest time of rewetting of the drift crown. Predicted porosity reductions in the Tptpmn in the NFE were small (less than 1 percent), with minor effects on permeability and thermal-hydrologic processes. The simulation using the upper-bound climate showed the most porosity loss, resulting primarily from continued buildup of calcite (owing to its smaller solubility with increasing temperature)

over long time periods. The conclusions drawn from this work, using an initial fracture porosity of 1 percent and homogeneous rock properties within each unit, were that THC processes would have a negligible effect on seepage.

4.3.6.3.3 Initial Report of Thermal-Hydrologic-Chemical Effects on Potential Seepage Water and Gas Chemistry

Predictions of the chemistry of the water and gas that may enter emplacement drifts showed that general trends of carbon dioxide gas and aqueous species concentrations around the drifts did not differ significantly for the different climate states and property sets. Water and gas composition trends predicted around emplacement drifts by the THC seepage models during the early phase of heating and the dryout period were generally similar to trends observed in the Drift Scale Test and predicted with its THC simulations. Rewetting has not yet been observed in the Drift Scale Test, so no field data can be used to evaluate water and gas compositions at the time of rewetting. The THC simulations indicate that concentrations of carbon dioxide gas may increase around the drifts during rewetting (relative to ambient values) and concomitant small reductions in pH may occur.

4.3.6.4 Discussion of Updated Results

The update to *Drift-Scale Coupled Processes (DST and THC Seepage) Models* (BSC 2001 [DIRS 154677]) included several additional models, analyses, validations, and sensitivity analyses that were done after the TSPA-SR. Additional validation of the Drift Scale Test THC model included comparisons to another year of water and gas data, along with evaluation of the effect of different reaction rates and geochemical systems. Some aspects of the THC model data and approach were validated by simulating a plug-flow reactor experiment performed under subboiling (about 94°C) conditions and at an elevated carbon dioxide partial pressure (see Section 4.3.6.7).

Three new drift-scale models were added in the updated report: a no-backfill model in the Tptpmn unit, a Tptpmn model with heterogeneous fracture permeability distributions, and a drift-scale THC model in the Tptpll geologic unit (with no backfill). The update also incorporated better-constrained thermodynamic and kinetic data, an improved consideration of initial mineral precipitation, increased reactive surface areas in fractures, and a stronger coupling of permeability to porosity changes. The base case geochemical system was modified to include fluorite, and the extended case system was changed with the addition of opal-ct and the removal of sepiolite and potassium-smectite. Numerous sensitivity studies were performed, including:

- Different in-drift designs (backfill versus no-backfill)
- Potential repository host rock units (Tptpmn versus Tptpll)
- Alternative conceptual models of pertinent geochemical systems (base case versus extended case)
- Effects of uncertainty in thermodynamic data (free energies and activity coefficient models)

- Treatment of certain mineral-water reactions for specific minerals (kinetic rate constants, reactive surface areas, and equilibrium versus kinetic conceptual models)

- Fracture permeability-porosity relations during mineral precipitation/dissolution

- Stochastic realizations of strong initial spatial heterogeneity in fracture permeability with accompanying effects on THC processes around drifts.

4.3.6.4.1 Thermal-Hydrologic-Chemical Model Validation

The model was validated by comparing measured gas and water chemistry from the Drift Scale Test to the results of simulations using the Drift Scale Test THC model. In particular, simulation results were compared to measured gas-phase carbon dioxide concentrations and the chemistry of waters collected from hydrology boreholes during the test. Comparisons of model results to measured changes in carbon dioxide concentrations over nearly three years (Figure 4.3.6-2) show that the model captures the initial rise in concentration in all of the borehole intervals where comparisons were made, areas that have very different thermal histories.

Figure 4.3.6-3 shows variations in pH, calcium, and chloride for two borehole intervals from the Drift Scale Test between the initial measured matrix pore water composition and the simulated concentrations for the base case and extended case geochemical systems, as well as for additional sensitivity studies on selected geochemical models and parameters. Comparisons between observed and modeled water chemistry (pH, chloride, sulfate, and calcium) and carbon dioxide concentrations in the gas phase from the Drift Scale Test indicate that a limited set (base case) of aqueous species, minerals (calcite, silica phases, gypsum), and gases (water, air, and carbon dioxide) can describe the general evolution of Drift Scale Test waters with respect to pH, carbon dioxide, and conservative anions. A more complete geochemical system (extended case), including a wide range of aluminosilicates (such as feldspars, clays and zeolites), yields modeled aqueous silica concentrations closer to those observed, as well as providing information on the concentrations of additional species (potassium, aluminum, iron, and fluorine). The initial extended geochemical system shifted the pH to values higher than those observed and to correspondingly lower gas-phase carbon dioxide concentrations. After the initial model results were documented, revision of less well-constrained thermodynamic data for smectites and zeolites, reduction in the reaction rate of anorthite, and minor changes in the mineral assemblage in the extended case geochemical system resulted in simulated compositions that were more consistent with measured water and gas compositions from the Drift Scale Test. However, gas phase carbon dioxide concentrations and pH still compare to measured values somewhat better with the base case geochemical system.

The lower chloride concentrations in the water samples collected from boreholes, compared to the initial pore water (Figures 4.3.6-3e and 4.3.6-3f), indicate that these waters have experienced little interaction with the matrix pore water. The modeled matrix pore water, however, shows a decrease in the concentration of chloride of about 15 percent as a result of the imbibition of dilute condensate draining through fractures. The minimal fracture-matrix interaction under thermal-hydrologic conditions supports the basic model of a limited area for liquid imbibition resulting from low liquid saturations in fractures and the equations embedded in the modified AFM (BSC 2001 [DIRS 154677]).

Model validation was also performed through simulations of the plug-flow reactor laboratory experiment (Kneafsey et al. 2001 [DIRS 154460]; BSC 2001 [DIRS 154677], Section 6.7). These results are discussed in Section 4.3.6.7.

4.3.6.4.2 Thermal-Hydrologic-Chemical Effects on Flow and Potential Seepage

Simulations of a no-backfill design predict a smaller dryout zone (particularly below the drift) and a somewhat earlier time of rewetting than simulations of a design that includes backfill. This is primarily the result of a slightly lower thermal load imposed in the simulations performed for the updated report, although the removal of backfill caused the crown to become somewhat hotter and the base cooler. In all simulations, the dryout zone continued to expand until about 600 yrs, when a wetter climate with a greater infiltration flux was imposed. Depending on the modeled scenario, the maximum extent of the dryout zone is predicted to be between 6 and 10 m above the drift center, and the predicted time of rewetting at the drift crown varies between 800 and 1,200 yrs.

The predicted reduction in porosity in the NFE over 100,000 yrs for the Tptpmn THC no-backfill model (homogeneous permeability) is less than 3 percent of the initial fracture porosity, which reduces the permeability by less than one order of magnitude. This is somewhat greater than the reduction predicted for the Tptpmn THC backfill model (a less than 1 percent change in fracture porosity), but it is still relatively minor. The permeability calculation is based on uniform areas of precipitation in plane parallel fractures; the actual effects on permeability and flow in heterogeneous fractures with rough surfaces and nonuniform mineral precipitation could be greater. Comparison of the purely thermal-hydrologic simulation results to those including coupled THC processes show only small differences in predicted water and gas fluxes, liquid saturation, and permeability around the drift. The porosity reduction after rewetting of the drift wall results almost entirely from precipitation of calcite and amorphous silica. Amorphous silica contributes to most of the initial mineral precipitation up until the early rewetting stage, with maximum deposition spreading above the drift in a zone roughly coincident with the maximum extent of the dryout zone (8 to 10 m from the drift center). The silica dissolves slowly after rewetting. Calcite precipitates throughout the boiling and later cooling stages, becoming most of the mineral precipitated at 100,000 yrs.

Heterogeneity in fracture permeability can have varied effects on thermal-hydrologic processes, including flow focusing and irregularity in isotherms and liquid saturation. TH and THC simulations were performed for three heterogeneous fracture permeability realizations (with a range in permeability of four orders of magnitude) under the mean infiltration rate climate change scenario (6 mm/yr to 600 yrs, 16 mm/yr to 2,000 yrs, and 25 mm/yr to 100,000 yrs) for the Tptpmn unit (DTN: LL000114004242.090 [DIRS 142884]). The range in permeability is consistent with that used in the ambient seepage analyses discussed in Section 4.3.1. Although some regions at the outer edge of the dryout zone have high fracture saturation, the water does not reach the drift wall when the dryout zone is well developed (Figure 4.3.6-4). Areas of highest initial liquid saturation also having lower permeability and generally located above the drift tend to show the greatest reduction in fracture permeability, down to about 25 percent of the initial value after 20,000 yrs in some regions (Figure 4.3.6-5). This localized permeability reduction tends to cause some additional flow focusing, but the changes are considerably less than the initial range in permeability. The corresponding maximum fracture porosity reductions

are approximately 5 percent of the initial value, resulting in permeability reductions of less than one order of magnitude (about 75 percent). Porosity reductions for the extended geochemical system were slightly greater than those for the base case system, as a result of additional minerals precipitating and somewhat higher silica concentrations in the extended case simulated waters. The maximum amount of amorphous silica precipitated was about 2 percent (volume percent of fracture) in the extended case and somewhat less in the base case, with maximum amounts in the high-saturation (and low-permeability) zones near the drift.

4.3.6.4.3 Thermal-Hydrologic-Chemical Effects on Potential Seepage Water and Gas Chemistry

THC simulations in the *Drift-Scale Coupled Processes (DST and THC Seepage) Models* report (BSC 2001 [DIRS 154677]) predicted notable differences in pH and carbon dioxide concentrations, depending on the geochemical system considered (base case or extended case). This resulted in large part from the dissolution of anorthite (one component in a plagioclase feldspar solid-solution phase) to form clays and zeolites, which occurred under ambient conditions and increased under thermal loading. Thermodynamic and kinetic data were revised for the updated report so that the initial water composition was closer to a steady-state composition under ambient conditions, resulting in better-constrained water compositions, pH, and carbon dioxide concentrations predicted under thermal loading. This significantly reduced the differences between predictions using the base case and extended case geochemical systems. In general, pH values were lower and carbon dioxide concentrations higher in the base case than in the extended case. The extended case geochemical system may overestimate the effect of mineral-water reactions on the geochemistry of waters and gases, and may therefore provide an upper limit on the extent of changes in chemical and hydrologic properties around emplacement drifts. In both cases, fairly dilute and near-neutral to moderately alkaline water compositions are predicted around drifts, with pH values in the range of 7 to 9 and gas phase carbon dioxide concentrations generally below 10,000 ppmv. As the last water evaporates, what remains behind becomes highly concentrated but nearly immobile (Figure 4.3.6-6). Calculated water and gas compositional trends in the Tptpmn and Tptpll units were similar because the models share the same mineralogy and water chemistry.

Spatial variations in water chemistry around the drift were not strongly affected by permeability heterogeneities. The highest concentrations of conservative species were in the low-permeability, high-liquid saturation areas that underwent boiling at the base of the heat pipe zone. Variations in pH and chloride around the drift for the heterogeneous and initially homogeneous Tptpmn THC models during the peak dryout time of 600 yrs are shown in Figures 4.3.6-6 and 4.3.6-7. Areas of higher pH developed at the base of the boiling zone (i.e., the edge of the dryout zone, shown as white in the figures), primarily because of carbon dioxide loss, but also as a result of hydrolysis reactions in the extended case. Percolation of water from the surface eventually pushes this higher-pH water below the drift (the model domain actually extends to the surface and to the water table). The areas of higher pH are generally below and to the side of the dryout zone in the extended case simulations, whereas in the base case the higher pH waters are in a narrower region mostly above and to the side because this is the area of greatest carbon dioxide depletion. Chloride concentrations show the large increases expected in the boiling zone and the dilution effect in the condensation zone. Strong fracture

drainage of the more dilute condensate water results in a well-developed plume extending over 100 m below the drift.

An uncertainty that was not considered was the effect of lithophysal porosity on THC processes. Obvious effects of lithophysae would be to provide a larger volume for the vapor phase and to force a greater flux of water into the matrix and fractures if the lithophysae act as capillary barriers. This could result in changes in gas-phase carbon dioxide transport and increased fracture-matrix interaction. Increased fracture-matrix interaction and condensation in lithophysal cavities (and subsequent drainage into connected fractures) could result in less-dilute seepage water chemistry and increased mineral precipitation in fractures.

4.3.6.5 Model Development Since the Issuance of the Updated Report

Recent model development has involved studies of coupled processes for an expanded range of temperatures. This work was based on the EDA II repository design (Wilkins and Heath 1999 [DIRS 104247]), which specified an initial thermal load of 72.7 kW/acre (1.45 kW/m in the drift) and a ventilation period of 50 yrs, during which 70 percent of the decay heat would be removed. The thermal load of the EDA II design gives rise to above-boiling temperatures in the rocks near the emplacement drifts for hundreds of years. Model development conducted since the update of *Drift-Scale Coupled Processes (DST and THC Seepage) Models* (BSC 2001 [DIRS 154677]) has focused on lower-temperature options in which the rock temperature does not exceed the boiling point of water anywhere in the potential repository. The LTOM considered a linear thermal load of 1.13 kW/m and removal of 80 percent of decay heat by ventilation for 300 yrs. The two operating modes, the HTOM and the LTOM, are referred to as the higher-temperature case and the lower-temperature case, respectively.

Several simulations were performed for the lower-temperature case and for uncertainty analyses on the higher-temperature case. These sensitivity simulations included different top boundary (i.e., soil zone) gas phase carbon dioxide concentrations and different initial and boundary water compositions (pore water and perched water). Different initial and infiltrating water chemistry have a greater effect on the chemistry of potential seepage than the changes in boundary carbon dioxide concentrations. The major difference in the simulations for the lower-temperature case is the absence of a dryout zone. Because of evaporation, the waters tend to have relatively high concentrations of conservative anions (e.g., chloride) at a given liquid saturation, but the fracture liquid saturations are near the residual saturation of one percent, well below what would cause seepage. Details regarding the effects on potential seepage chemistry are provided in Section 6.3.1.5. The effects of THC processes on porosity and permeability in the LTOM were slight (less than 1 percent over 20,000 yrs) because amorphous silica, the primary phase that results in porosity loss during boiling, is generally undersaturated except in areas adjacent to the drift wall where substantial evaporation has taken place.

4.3.6.6 Abstraction for Total System Performance Assessment

Abstraction of drift-scale THC processes is described in Section 6.3.1.6. This includes the composition and fluxes of potential seepage water at specific locations at the drift wall and the associated gas phase compositions.

4.3.6.7 Multiple Lines of Evidence

The emplacement of heat-generating nuclear waste in a potential geologic repository at Yucca Mountain will result in enhanced water-rock interaction around the emplacement drifts compared to the rates of reaction occurring under ambient conditions. As the waste package heats the surrounding environment, water present in the matrix and fractures of the nearby rock may vaporize and migrate through fractures to cooler regions where condensation would occur. The condensate would dissolve gases and minerals, and mineralized water flowing under gravity back towards the heat source would evaporate, depositing the dissolved minerals. Such mineral deposition would reduce porosity and permeability above the potential repository, thus altering the flow paths of percolating water (Nitao and Glassley 1999 [DIRS 154486]). Natural analogue studies of water-rock interaction in geothermal systems and along igneous contacts, as well as hydrothermal field and laboratory experiments, provide multiple lines of evidence for THC effects on permeability and porosity that would change seepage (Apps 1995 [DIRS 154615]). A number of natural analogue examples and field and laboratory studies are summarized below, followed by a more detailed examination of the Yellowstone geothermal system and a tuff dissolution-precipitation experiment. The processes demonstrated by these examples are then related to Yucca Mountain, with an emphasis on how differences in scale could influence the impact that these processes may have on the performance of the potential repository.

4.3.6.7.1 Effects of Water-Rock Interaction on Fluid Flow: Natural Analogues

The effects of water-rock interaction on important hydrogeological properties, such as permeability and porosity, have been widely documented for a number of geologic settings. Geothermal systems and igneous contacts, such as those discussed below, illustrate how heat and water can cause mineral dissolution and precipitation, resulting in changes in formational fluid flow properties. Water-rock interaction tends to be more extensive in long-lived, water-saturated geothermal systems than along shallow intrusive and extrusive contacts occurring above the water table, where short-lived thermal perturbations provoke minimal mineralogic changes. These geologic systems encompass the time scales and heterogeneities necessary to evaluate models for the potential Yucca Mountain repository and provide important information needed to build, calibrate, and evaluate numerical models for the Yucca Mountain system. Three geothermal systems and three magmatic contact areas are summarized in the following paragraphs.

Imperial Valley Geothermal Fields, California–The effects of water-rock interaction have been studied at a number of geothermal fields (Salton Sea, East Mesa, Heber, Brawley, Cerro Prieto, and the Dunes) within the Imperial Valley (e.g., Schiffman et al. 1985 [DIRS 154644]; Cho et al. 1988 [DIRS 154599]). Elders (1987 [DIRS 154632]) examined the Salton Sea geothermal field as a potential natural analogue for evaluating processes related to radioactive waste storage. Low-permeability carbonate-cemented sandstones form the primary caprock, and represent the first of four distinct hydrothermal alteration zones. Fractures provide fluid flow pathways that cut across low-permeability shale interbeds. Complex sequences of fracture mineralization observed at the Salton Sea indicate that fractures episodically opened and sealed throughout the life of the geothermal system (Elders 1982 [DIRS 154602]). Silica sealing has been documented at the Dunes geothermal system (Bird and Elders 1976 [DIRS 154601]). Seven distinct zones of sandstones and conglomerates located in what originally were the most

permeable strata within the sedimentary section underwent intensive silicification, resulting in a significant reduction in porosity and permeability. The formation of these silicified zones was interpreted to be due to the lateral migration of hot brine to a cooler environment.

Wairakei Geothermal Field, New Zealand–The Wairakei geothermal field illustrates the influence of fractures and alteration on fluid flow. Grindley (1965 [DIRS 154663]) noted that wells intersecting normal faults have high permeabilities, whereas nonproductive wells usually intersect hydrothermally cemented rocks with intrinsically low (less than 1 millidarcy) permeabilities. Bruton (1995 [DIRS 100105]) observed that vein mineral assemblages typically contain fewer phases than those found associated with the matrix and interpreted that fracture, vein, and vug minerals are the products of a fluid-dominated system, whereas the more complex matrix alteration mineralogy results from high rock-water ratios. The intensely altered, impermeable rocks overlying the main reservoir at Wairakei serve to protect the producing zone from cold water encroachment.

Medicine Lake Geothermal System, California–The Quaternary Medicine Lake volcano in northern California is host to a higher-temperature geothermal system. Exploratory drilling has revealed that the geothermal reservoir is capped by hydrothermally-altered rock that is rich in smectite-group swelling clays that form a barrier to fluid flow (Hulen and Lutz 1999 [DIRS 154600]). Glassy dacitic to rhyolitic tuffs and pumiceous lavas have been strongly altered to smectitic clays, calcite, zeolites, quartz, potassium feldspar, hematite, and pyrite. This argillic alteration mineral assemblage forms a hydrologic barrier between a shallow, cool groundwater zone and a deeper, hot geothermal reservoir.

Banco Bonito Obsidian Flow, New Mexico–The effects of elevated temperatures on tuff mineralogy can be examined along the contact between the Banco Bonito obsidian flow and the Battleship Rock Tuff, located on the southwest rim of the Valles Caldera in northern New Mexico (Stockman et al. 1994 [DIRS 117820]). Upon eruption, the Banco Bonito flow (with an estimated eruptive temperature of 850°C) came into contact against the porous tuff, resulting in some baking and deformation of the immediate tuff contact zone. Stockman et al. (1994 [DIRS 117820]) conducted detailed geochemical transects in the tuff outward from the obsidian contact but observed relatively small changes in chemical composition and only minor hydrothermal alteration, and suggested that the studied contact area was located above the local water table, resulting in little water-rock interaction.

Paiute Ridge Intrusive Complex, Nevada–The Paiute Ridge intrusive complex (Matyskiela 1997 [DIRS 100058]; Lichtner et al. 1999 [DIRS 121006]), located about 40 km northeast of the potential repository, consists of a series of dikes and domed lopoliths emplaced between the Paintbrush and Timber Mountain tuffs, above the local water table. Thermal modeling of the intrusions suggest that they are large enough (at least 30 m) to have sustained boiling around the intrusive margins for thousands of years. Lichtner et al. (1999 [DIRS 121006]) noted several physical changes in the tuffaceous host rock resulting from the intrusions, including the presence of a gray to black vitrophyre within 0.5 to 1 m of the contact, with abundant anastamosing joints that are parallel to the contact. The degree of contact welding decreases within 1 to 3 m from the contact, and devitrification and partial alteration of volcanic glass to clay extends from the outer margin of the vitrophyre up to 15 m from the contact.

Determining the nature and intensity of the alteration of the tuff caused by intrusive activity is complicated by variable amounts of hydrothermal alteration of the tuff host rock that occurred prior to intrusion of the basaltic dikes and sills. Matyskiela (1997 [DIRS 100058]) studied the Papoose Lake basalt sill in the Paiute Ridge complex and suggested that all tuffs within 50 m of the sill contact have been altered to some extent. Matyskiela observed that the most intense alteration was focused along the margins of widespread (1 to 15 m) near-vertical fractures that parallel extensional faults in the area. The tuff matrix glass and pores within 1 cm of the fractures have been completely replaced by an impermeable and nonporous zone of clinoptilolite and cristobalite, and later-formed chalcedony and rare calcite fill most fractures. Matyskiela interpreted that the reduced matrix permeability and the sealing of fracture margins caused by this alteration event would result in enhanced fluid flow through the fractures. Lichtner et al. (1999 [DIRS 121006]) question several of these interpretations, such as whether alteration is most intense closest to the intrusive contact and the fracture margin mineralization is related to the Paiute Ridge intrusive event.

Grants Ridge Intrusion, New Mexico–The Grants Ridge intrusion consists of a shallow basaltic plug that intruded into nonwelded, pumice-rich rhyolitic tuff and volcaniclastic sediments (WoldeGabriel et al. 1999 [DIRS 110071]). A 10-m wide aureole developed around the 150-m wide plug, characterized by partial melting, changes in color, brecciation, and stoping. Despite initial temperatures greater than 1,000°C at the contact zone, only minor devitrification of the surrounding tuff was observed. WoldeGabriel et al. (1999 [DIRS 110071]) interpreted the lack of hydrothermal alteration in the contact zone to indicate that the plug was intruded into an unsaturated environment.

4.3.6.7.2 Effects of Water-Rock Interaction on Fluid Flow: Observations from Field and Laboratory Experiments

Field and laboratory experiments provide important information regarding water-rock interaction under controlled conditions. Many of these experiments have been used to address issues of permeability reduction and self-sealing in geothermal fields and enhanced oil-recovery operations. Key factors influencing mineral dissolution and precipitation include fluid chemistry, rock mineralogy, ratio of reactive surface area to solution mass, reaction temperature, and occurrence of condensation and boiling processes. Two of the main mechanisms for silica sealing are cooling of silica-saturated waters and boiling. Operators of geothermal fields often experience silica scaling problems with geothermal brines as they are flashed and cool (Mroczek 1994 [DIRS 154621]). The precipitation of silica polymorphs (such as amorphous silica) is enhanced when fluids that are supersaturated with respect to silica flow slowly through rocks with large surface areas (Wells and Ghiorso 1991 [DIRS 154645]). Boiling can result in even greater amounts of silica precipitation because all dissolved silica will be precipitated as a fluid boils to dryness. The following section summarizes a series of experiments that describe the effects of water-rock interaction on permeability and porosity for a number of rock types. While the experiments encompass a range of temperatures (50° to 250°C) similar to those predicted for the potential Yucca Mountain repository, one important difference is that most of the experiments were conducted under saturated conditions, which would tend to promote increased water-rock interaction. In spite of this difference, the experimental results can still be used to constrain and validate coupled process THC models for the Yucca Mountain system.

Permeability Changes in Hydrothermal Flow-Through Experiments–A series of experiments were performed to observe silica dissolution and precipitation in intact granite and Yucca Mountain ash-flow tuff samples (Morrow et al. 1981 [DIRS 142169]; Moore et al. 1983 [DIRS 154631]; Moore et al. 1986 [DIRS 142166]; Moore et al. 1994 [DIRS 154630]; Daily et al. 1987 [DIRS 131816]). In these experiments, water was flowed through rock samples with an applied temperature gradient and changes in rock permeability and fluid chemistry were monitored. For the granite, permeability decreased one to two orders of magnitude over the 1- to 3-week duration of the experimental run. Changes in effluent fluid chemistry indicated initial silica supersaturation, which declined with time until reaching quartz solubility concentrations after about 6 days. Scanning electron microscopy and petrographic analyses showed regions with precipitated fibrous silica and patchy masses of silica, quartz, and calcium-rich zeolites within the granite. In one experiment, almost all the cracks near the cooler edge were filled with silica, whereas half the cracks near the heated side were open. The large change in permeability relative to the small amount of mineralization suggests that the precipitates formed "bridges" that clogged cracks, having a great effect on permeability.

In contrast to the granite experiments, little change in permeability was observed for the flow-through experiments conducted by Moore et al. (1986 [DIRS 142166]) involving Topopah Spring and Bullfrog ash-flow tuff samples over the time and spatial scale of the experiments. The much smaller reduction in permeability was attributed to the tuffs having much higher porosities and larger aperture flow paths that would be less easily clogged by mineralization. Changes in water chemistry over time suggest that the rate of silica dissolution in the tuff was significantly greater than silica reprecipitation. While the temperatures of these experiments ranged from 90° to 250°C, with higher temperature conditions resulting in increased dissolved silica concentrations, elevated pore pressures of 1 to 10 mPa indicate that boiling did not occur, in part accounting for the minimal amounts of mineralization. Daily et al. (1987 [DIRS 131816]) flowed water through a reopened healed natural fracture in Topopah Spring welded tuff and observed significant permeability reduction for flow through the fracture occurring at temperatures greater than 89°C.

Chigira and Watanabe (1992 [DIRS 154641]) also investigated the effect of hydrothermal reactions on fracture permeability. In their experiments, water saturated with silica was injected into polished granite fracture segments with apertures ranging from 0.05 to 0.1 mm. Negative temperature gradients (from hot to cold) of 50° and 100°C/m were employed for the two runs. In one experiment, system permeability decreased by more than four orders of magnitude because of fracture plugging. Scanning electron microscopy and optical microscopic observation of the fracture surfaces indicate that amorphous silica particles precipitated evenly over the various mineral phases of the granite, with increased mineralization occurring along the cooler fracture segments.

An experimental investigation of silica self-sealing incorporating boiling was performed by Rimstidt et al. (1989 [DIRS 142190]). A heat pipe reactor containing chips of ash-flow tuff from Yucca Mountain was operated for 30 days. Within the experimental apparatus, three distinct zones were observed. In the condensation zone, etching and dissolution features evidenced dissolution of the tuff. In the center zone, few indications of dissolution or precipitation were observed. In the bottom region, extensive precipitation of amorphous silica, iron oxyhydroxides,

stilbite, and possibly clays was observed, resulting in a tightly cemented region along the face of the heater. Such mineralization would lead to significant permeability reductions.

Evidence of Water-Rock Interaction from Enhanced Oil Recovery Operations–Water-rock interaction has been evaluated in a variety of diagenetic studies associated with thermal recovery of heavy oils. Field studies have used two approaches to document water-rock interaction associated with steam flooding: looking at changes in pre- and post-flood rock mineralogy and monitoring changes in produced fluid chemistry. Laboratory experiments have examined both fluid and rock chemistry to identify the primary reactions controlling water-rock interaction occurring in sandstone reservoirs under steam-flood conditions.

A detailed study of heavy oil-bearing lithic-rich sandstone was conducted on core samples collected from the Clearwater Formation at the Cold Lake Oil Sands pilot site in eastern Alberta (Sedimentology Research Group 1981 [DIRS 154634]; Hutcheon 1984 [DIRS 154633]). High pH steam was continuously injected into the field for two years. Temperatures reached 230° to 260°C in the stratigraphic section of interest during the course of the steam flood.

The steamed core was more indurated than the pre-steam core, with increases in smectite and corresponding decreases in kaolinite and porosity within and immediately below the steam flood interval. The effective porosity and permeability of the altered sandstones were reduced by post-steam smectite grains, which formed thick rims on framework crystals. Kaolinite replacement by smectite resulted in a volume increase, also serving to reduce porosity and permeability.

Steam flooding of the Aberfeldy heavy oil field (Saskatchewan) resulted in only minor mineralogic changes, consisting of the formation of small amounts of illite and chlorite (Lefebvre and Hutcheon 1986 [DIRS 154637]). The absence of authigenic smectite in the post-steam flood core samples likely results from the lack of sodium-bearing minerals in the quartzose sandstones. This study demonstrates the importance of lithology in determining which secondary minerals will form as a result of water-rock interactions.

In another study that shows the importance of mineralogy in water-rock interaction, Hutcheon and Abercrombie (1990 [DIRS 154638]) monitored the composition of produced waters from three thermal recovery oil wells at Tucker Lake, Alberta. Steam was injected in each well for up to 90 days, followed by 7 months of pumping. Reservoir temperatures during the post-steam injection production phase ranged from 95° to 186°C, with temperatures progressively decreasing over time. Early recovered waters were dilute as a result of condensed steam. However, as production proceeded, fluid compositions became more saline as formation waters mixed with the condensate. While sodium and chloride contents for all produced waters increased with time, potassium contents stabilized after 50 days of production, suggesting that its concentration was controlled by mineral reactions. Geochemical modeling of produced fluids (Hutcheon and Abercrombie 1990 [DIRS 154638]) suggests that the activity of potassium is controlled by reactions involving potassium-feldspar and illite, while the $Ca^{2+}/(H^{+})^{2}$ activity ratio is controlled by the calcite-carbon dioxide reaction.

Autoclave and flow-through laboratory experiments using natural and synthetic oil field sands document the formation of significant quantities of smectite in the pore spaces, resulting in

permeability decreases. Experiments conducted by Boon (1978 [DIRS 154643]) using Athabasca shales show that considerable quantities of montmorillonite formed as a result of water-rock reactions. Experiments conducted using Cold Lake oil sands (Boon et al. 1983 [DIRS 154640]) resulted in the formation of analcime, chlorite, smectite, and calcite at the expense of quartz, kaolinite, and dolomite. In a similar series of experiments, Kirk et al. (1987 [DIRS 154639]) also observed decreases in kaolinite and dolomite, increases in smectite and calcite, and a pronounced decrease in the overall permeability (50 percent to 98 percent overall reduction) of the steam-flood cores. Similar decreases in permeability (65 percent to 78 percent reduction), primarily caused by the formation of smectite (iron-saponite), were observed in a series of coreflood experiments conducted by Zhou et al. (1999 [DIRS 154635]).

Boon (1978 [DIRS 154643]) observed that silica-rich solutions were produced by heating deionized water together with oil sands, and that the amount (and rate) of silica dissolution is positively correlated with temperature and pH. The change in dissolved silica concentrations correlates with temperature, and the measured concentrations obtained from a number of experiments lie between those predicted by the quartz and chalcedony geothermometers (Gunter et al. 1992 [DIRS 154642]). This dissolution process is analogous to the condensation end of a heat pipe, where the dilute fluid would rapidly dissolve silica. The condensate could either flow into cooler rock, becoming supersaturated with respect to silica, or flow back into the boiling zone, where the silica concentration of the solution would increase as boiling progresses. Both scenarios would lead to silica precipitation and reduced permeability for certain portions of the formation.

4.3.6.7.3 Self-Sealing at the Yellowstone Geothermal System

Mineral dissolution and precipitation and associated changes in permeability resulting from water-rock interaction have been observed in a number of geothermal systems (Grindley and Browne 1976 [DIRS 154531]; Fournier 1983 [DIRS 154614]). One of the best examples of self-sealing has been documented at the Yellowstone geothermal system through detailed studies of continuously cored research boreholes (White et al. 1975 [DIRS 154530]; Keith et al. 1978 [DIRS 106316]; Keith and Muffler 1978 [DIRS 152663]). Water-rock interaction at Yellowstone has resulted in extensive hydrothermal alteration, especially along veins and fractures, where most fluid flow occurs. Matrix permeability measurements, lithologic and alteration descriptions, and fracture and vein characterization were conducted on core samples from two of these boreholes (Y-5 and Y-8) to evaluate the effects of lithology and hydrothermal alteration on permeability and porosity (Dobson et al. 2001 [DIRS 154547]; Dobson et al. 2001 [DIRS 154503]). Hydrothermal self-sealing appears to have generated the existing permeability barrier that delineates the top of the convecting geothermal system at Yellowstone. Changes in pressure and temperature in the Y-8 borehole associated with the transition between conductive and convective flow correspond to a zone of silicification with large porosity and permeability reductions. The presence of bladed calcite near this interval and elevated delta oxygen-18 values of hydrothermal quartz suggest that the silica seal may have formed in response to transient boiling events associated with depressurization (Sturchio et al. 1990 [DIRS 154524]).

While the Yellowstone system and the potential Yucca Mountain repository share many of the same THC processes, the effects of the processes are expected to differ significantly because of large differences in scale between the two systems. The Yellowstone geothermal system is a

liquid-dominated, convecting geothermal system with much higher fluxes of heat and fluid than those predicted for the Yucca Mountain system. The dissolution, transport, and precipitation of silica are highly dependent on system temperature, mineralogy, and fluid flux rate, as well as whether boiling occurs. Rates of silica dissolution and equilibrium silica concentrations in geothermal fluids at Yellowstone are significantly higher than those predicted for Yucca Mountain because of the higher temperatures (170° to 240°C) encountered in the Yellowstone system (White et al. 1975 [DIRS 154530]). Downhole water samples from the Y-7 and Y-8 wells have silica concentrations of 364 and 290 mg/L, respectively (Sturchio et al. 1989 [DIRS 154529], p. 11028), more than three times greater than those predicted for the Yucca Mountain system (Kneafsey et al. 2001 [DIRS 154460]) and twice that observed in the waters collected from higher-temperature intervals in the Drift Scale Test (BSC 2001 [DIRS 154677], Figure 24). The outflow of silica-enriched waters from geysers and hot springs at Yellowstone resulted in the formation of extensive silica sinter deposits. While rates for fluid flow within the Yellowstone system are difficult to quantify, Sturchio et al. (1987 [DIRS 154525], p. 12029) estimate a conservative formational velocity of 1,500 m/yr (4.8×10^{-5} m/s) at Yellowstone, about four to five orders of magnitude higher than those predicted for Yucca Mountain. Even higher rates would be expected for focused flow along fractures. It is also difficult to accurately estimate the rate of silica precipitation and concomitant permeability reduction for the Yellowstone system. Most of the wells drilled at Yellowstone from 1967 to 1968 experienced significant plugging or complete sealing by 1992 (Fournier et al. 1993 [DIRS 154527], p. 33), suggesting that silica sealing accompanying boiling occurs fairly rapidly. All these factors have to be scaled properly before using the Yellowstone example to semi-quantitatively validate the Yucca Mountain THC simulations.

4.3.6.7.4 Tuff Dissolution and Precipitation in a Boiling, Unsaturated Fracture: Laboratory Experiments and Numerical Simulations

As part of an ongoing effort to evaluate multiple lines of evidence for THC effects on flow in fractured media, a laboratory experiment (Kneafsey et al. 2001 [DIRS 154460]) and related numerical simulations (BSC 2001 [DIRS 154677], Section 6.7; Bodvarsson 2001 [DIRS 154669], Attachment 4, pp. 7 to 38; Dobson 2001 [DIRS 154922]) were performed to investigate plugging of fractures caused by mineral dissolution and precipitation. The laboratory experiment consisted of two stages: dissolution of crushed Topopah Spring ash-flow tuff in a plug-flow apparatus and mineralization resulting from fluid flow and boiling within a vertical fracture. For the accompanying simulations, TOUGHREACT V2.2 and V2.3 was used to model the tuff dissolution and precipitation processes. The experiment and simulations can be used to evaluate the processes and time scales of tuff dissolution and secondary mineral precipitation, and serve to validate use of the TOUGHREACT codes. The experiment and simulations indicate that boiling and concomitant mineralization could cause significant reductions in fracture porosity and permeability on a local scale.

Experiment Description and Results–A two-part experiment was conducted to evaluate tuff dissolution and fracture sealing (Kneafsey et al. 2001 [DIRS 154460]). To replicate mineral dissolution by condensate water in fractured tuff (Figure 4.3.6-8), deionized water equilibrated with 50,200 ppm carbon dioxide was flowed for 1,500 hours through crushed Yucca Mountain Tuff (75 to 150 micron size) at 94°C and a rate of 25 ml/hr (DTN: LB0011THCDISSX.001 [DIRS 153380]). The reacted water exiting the tuff column was collected and regularly sampled

for major dissolved species, total alkalinity, electrical conductivity, and pH. The resulting steady-state fluid composition (achieved after 230 hours) had a total dissolved solids content of about 140 mg/L; silica was the dominant dissolved constituent.

A portion of the steady-state reacted water was flowed at 10.8 ml/hr into a 31.7-cm tall, 16.2-cm wide vertically oriented planar (saw-cut) fracture in welded Topopah Spring Tuff that was maintained at 80°C at the top and 130°C at the bottom (DTN: LB0101THCPRCPX.001 [DIRS 154577]). The two blocks were separated with 17.7-micron gold shims; however, the hydraulic aperture calculated using the initial air permeability was about 31 microns. The dimensions of the fracture, the magnitude of the temperature gradient, and the flow rate were based on the relations derived by Phillips (1994 [DIRS 154459]; Phillips 1996 [DIRS 152005]). The fracture began to seal within five days, as indicated by a declining outflow rate and leaks in the inlet side of the fracture. Increased pressure was required to maintain the flow of water at 10.8 ml/hr following the leak sealing. After several unsuccessful attempts to plug leaks and the near-zero rate of effluent collection, it was concluded that the aperture was effectively sealed.

The fracture was opened at the conclusion of the experiment to examine the precipitate location, mineralogy, and morphology (Figure 4.3.6-9). Aperture sealing to fluid flow occurred with only 3 to 20 percent of the total fracture volume filled with solid precipitate, primarily composed of amorphous silica (Kneafsey et al. 2001 [DIRS 154460]). The precipitate was deposited almost exclusively at fracture locations where adjacent matrix temperatures exceeded the boiling point. The precipitate morphology appeared to vary as a function of temperature. Porous, veiny, honeycomb-like bridging structures formed in the hottest regions (about 120°C), similar to morphologies noted for Single Heater Test samples (CRWMS M&O 1999 [DIRS 129261], pp. 6-40 to 6-43). Wall-coating precipitate with vitric luster and bridging structures was deposited at locations that had temperatures near 110°C. Solid, well-formed bridging structures with minor amounts of wall coating occurred at locations that had temperatures near 100°C, and fine-grained precipitate was observed in a few locations in the subboiling region.

4.3.6.7.4.1 Simulation Description and Results

Numerical simulation of the laboratory experiment was conducted using TOUGHREACT V2.3 in two different phases: tuff dissolution and fracture sealing. The descriptions and results of these simulations are described in this section.

Tuff Dissolution Plug-Flow Simulations–A series of isothermal TOUGHREACT V2.3 simulations were performed to model tuff dissolution using a 149-element one-dimensional mesh with dimensions and interface areas identical to those of the plug-flow experiment, plus one additional boundary element to obtain the appropriate outlet conditions (BSC 2001 [DIRS 154677], Section 6.7). Initial mineralogy used for plug-flow simulations was obtained from the Tptpmn (tsw34) matrix composition. An initial fluid composition was calculated using SOLVEQ/CHILLER V1.0 and the measured pH and carbon dioxide concentration of the experimental inlet water. Trace amounts of other dissolved constituents were used in the simulation to reduce computational problems caused by zero values. The plug-flow column was liquid-saturated with no separate gas phase present. The flow rate (25 ml/hr) and temperature (94°C) of the dissolution simulation were set to the values used in the experiment.

Simulation runs were conducted using TOUGHREACT V2.2 and V2.3. Most of the TOUGHREACT V2.3 concentration profiles have steady-state compositions that are slightly higher than the corresponding values obtained from the TOUGHREACT V2.2 runs because the change in water density was incorporated into the mineral surface area calculations in the new version of the code.

Two grain-size models were tested to evaluate the sensitivity of surface area values on kinetic mineral reactions. The first model employed mineral surface areas calculated using spherical grains with a diameter of 60 μm, with clay minerals represented by rectangular plates with dimensions $60 \times 60 \times 1.2$ μm. The second model used spherical grains with diameters of 120 μm and clay minerals with dimensions $120 \times 120 \times 2.4$ μm. Large (up to 100 percent) differences observed for sodium, silica, and calcium concentrations between simulations using the two models result from the twofold difference in calculated initial surface areas (DTN: LB0011THCDISSM.002 [DIRS 154578]).

The calculated concentrations of sodium and silica for the 60-μm grain size (i.e., larger surface area per unit volume) plug-flow simulations closely match the fluid compositions observed in the experimental study (BSC 2001 [DIRS 154677], Section 6.7). The predicted concentrations for the major (greater than 1 mg/L) dissolved species (with the exception of bicarbonate) are within a factor of two of the measured average steady-state concentrations. Differences between the modeled and measured values in pH and alkalinity result from cooling and degassing of the experimental samples after exiting the tuff dissolution column. The outflow compositions match the simulated results closely after they have been corrected for these processes using SOLVEQ/CHILLER V1.0.

Fracture Plugging Simulations–A series of two-dimensional simulations were performed to model fracture sealing using a variety of mesh designs, each with dimensions identical to those in the tuff fracture experiment. The injected fluid composition was taken from measured values obtained from the experiment, and the rock mineralogy was considered to be similar to that used for the plug-flow experiment. The initial fracture permeability was set to the observed experimental conditions, while the flow rate and fracture width were reduced by half (5.4 ml/hr and 15.5 μm, respectively) to account for the half-symmetry model used. To simplify the simulation, the rock matrix blocks were assigned a zero permeability to force the injected water to flow through and interact only with the fracture elements. Amorphous silica was allowed to precipitate under equilibrium conditions to remove uncertainties associated with kinetically controlled nucleation and growth. Because the formation of colloidal silica results in an extremely high surface area, making kinetic precipitation of silica extremely rapid at boiling, equilibrium precipitation conditions are a reasonable proxy for the fracture plugging simulation.

Two mesh designs were employed to resolve the sharp chemical and liquid saturation gradients present in the fracture. Both designs contain two columns of rock blocks and one column of fracture blocks. The outermost rock column consists of elements with fixed temperatures to approximate the experimental temperature gradient (80° to 130°C). One of the mesh designs has 317 elements per column, each 1 mm in height. The other is a variably discretized mesh, with 177 elements per column that range in height from 0.25 to 5 mm; the finer gridding is present in the transition area between vapor-phase and two-phase conditions. Maximum time steps for the simulations are restricted by the minimum gridblock size, with maximum times of

0.3333 seconds for the 1-mm spacing and 0.0833 seconds for the variable spacing. Fluid is injected in the uppermost fracture element, and the lowermost fracture element is assigned a very large volume (greater than 10^{50} m^3) to act as a constant pressure boundary.

The initial results of these simulations indicate the generation of a nearly isothermal region, with an overlying water column above and a vapor zone below (Figure 4.3.6-10). The precipitation of amorphous silica at the base of the two-phase zone accounts for all of the porosity (and thus permeability) reduction in the fracture system. The zone of mineralization (Figure 4.3.6-10) appears to be more restricted in vertical extent in the simulations than was observed in the fracture-sealing experiment (Figure 4.3.6-9). A gradual buildup in pressure occurs in the top of the fracture system with time, resulting in a corresponding downward shift of the base of the boiling zone. Silica precipitation for a given fracture element near the base of the boiling zone results in local porosity reductions of about 60 percent. Additional precipitation in a given element block is retarded by the downward shift in the boiling front resulting from the increase in pressure, which in turn results from the throttling of the fracture (Figure 4.3.6-11). Silica precipitation and porosity reduction continue to follow the boiling front downward, spreading the effects of boiling and concomitant mineralization. Some of the differences between the experiment and the simulations may result from variability in the two-dimensional fracture surface, as well as from fluctuations resulting from fluid leaks and a short-term power outage that occurred during the experiment.

The experiment has a steep temperature gradient, resulting in a narrow boiling zone. Although the grid resolution was as low as 0.25 mm, the transition to dryout was too sharp to obtain full mass conservation given the current implementation in TOUGHREACT V2.3. Therefore, the rate of sealing is underestimated in the simulations by about 25 percent. Significant permeability reduction occurred within 1 to 10 days after the initiation of fluid flow for both the experiment and the simulations.

4.3.6.7.4.2 Applicability to Yucca Mountain Processes: Scaling Effects

It is important to consider differences in scale between the laboratory experiment and associated simulations, along with predicted conditions for the potential Yucca Mountain repository. A number of factors (e.g., thermal gradient, fluid flux, fracture aperture) serve to enhance the amount of silica dissolution, transport, and precipitation and the corresponding fracture permeability reduction in the experiment described above. Table 4.3.6-1 gives a comparison of these factors.

One key issue to address is the rate of potential fracture sealing for the Yucca Mountain system. Fracture sealing occurred rapidly (about 5 days) in the laboratory experiment. A number of factors must be considered in evaluating these data and scaling them to the NFE:

- Water flow rate in fractures (reflux of water via heat pipe effect)
- Fracture apertures and geometry
- Thermal gradient and thickness of boiling front and condensation zone
- Mobility of boiling front with time
- Fracture-matrix interaction
- Effective mineral surface area in condensation zone.

The fracture aperture used for the tuff experiment falls within the range observed at Yucca Mountain, so the key differences between the Yucca Mountain system and the experiment are fracture flow rates (fluid flux) and the width of the boiling zone (gradient). The ratios of fluid flux rates to thermal gradients in the experiment and the potential Yucca Mountain system can be used for approximate scaling calculations to predict how long it would take to plug fractures at the potential repository (Bodvarsson 2001 [DIRS 154669], Attachment 4, pp. 37 to 38). If the width of the boiling front over which silica precipitation occurs can be scaled approximately by the thermal gradient, then the rate of fracture sealing (plugging) can be estimated as:

$$Plugging_{YM} = (Plugging_{EXP}) \times (\frac{FluidFlux_{EXP}}{FluidFlux_{YM}}) \times (\frac{Gradient_{EXP}}{Gradient_{YM}}) \qquad \text{(Eq. 4.3.6-1)}$$

Where YM indicates Yucca Mountain and EXP indicates the experiment. For Yucca Mountain plugging, this is $5 \text{ days} \times 20{,}000 \times 210$, or approximately 60,000 yrs. This estimated rate of fracture sealing is slower than the rate obtained by Nitao and Glassley (1999 [DIRS 154486]), whose THC simulations for the potential Yucca Mountain repository predict that a porosity reduction of greater than 90 percent for the area 6 m above the drifts will occur 1,500 to 4,000 yrs after waste emplacement if boiling conditions last that long. In comparison, the current higher-temperature design drops below boiling at the drift wall approximately 1,200 yrs after waste emplacement.

The processes controlling the rate of fracture plugging are more complex than this simple scaling calculation suggests. The mineralogy, effective mineral surface area, and temperature control the amount of silica that can dissolve in the condensate. The rate of downward fluid flow from the condensation zone to the boiling zone serves as the limiting factor to the amount of silica transport and resulting mineralization that can occur in the fractures. As noted above, the rate of fracture fluid flux at Yucca Mountain is predicted to be about 20,000 times lower than the rate used for the laboratory experiment. Water flow at Yucca Mountain is controlled by several factors, such as surface infiltration rates (which vary on regional and climatic scales), focused flow along high permeability faults and fractures, and reflux of fluids associated with condensation above the drift zones. Localized zones with elevated flux rates within the boiling front would be most susceptible to silica self-sealing. The geometry and apertures of fractures are important aspects of fracture sealing. As the results of the experiment and simulations indicate, small amounts of total porosity reduction (via mineralization) are required along sharp, stationary boiling fronts and within narrow apertures to seal a fluid conduit. As individual pathways seal, water will flow into larger aperture regions where there is less capillary control buffering the flow. During the evolution of sealing, this may cause fluids in later-generation flow paths to flow faster.

4.3.6.7.5 Summary of Multiple Lines of Evidence for Thermal-Hydrologic-Chemical Processes

The effects of water-rock interaction on permeability and porosity can be observed in geothermal systems and along igneous contacts, as well as in hydrothermal experiments. Liquid-dominated geothermal systems, such as Wairakei and Yellowstone, exhibit extensive hydrothermal alteration resulting from water-rock interaction at elevated temperatures. Parameters such as

fluid chemistry, initial rock mineralogy and permeability, the degree of fracturing, fluid flux, and the duration and intensity of heating all influence the degree and nature of mineral dissolution and precipitation that takes place over time. Much less extensive changes are observed along igneous contacts in the UZ (e.g., at Banco Bonito and Paiute Ridge), where the amount of fluid available for water-rock interaction is greatly reduced and the thermal perturbation tends to be much shorter in duration. Field and laboratory experiments confirm these general observations and highlight the importance of processes such as boiling and condensation in controlling mineral precipitation and dissolution. When applying the results of these experiments and associated models to the Yucca Mountain system, proper scaling of the magnitude of THC processes must be applied to assess the potential impact of these processes on potential repository system performance.

4.3.6.8 Summary of Uncertainties and their Treatment

The uncertainties associated with the results of simulations in *Drift-Scale Coupled Processes (DST and THC Seepage) Models* (BSC 2001 [DIRS 154677]) were considered acceptable given the intended purpose of the model, the results of validation studies, and the use of the results by other models (e.g., the TSPA-SR [CRWMS M&O 2000 (DIRS 153246)]). To further reduce the uncertainty in the predictions of THC effects on flow around drifts, seepage, and seepage chemistry, the following sources of uncertainty should be examined in a more systematic fashion:

- Uncertainties in the effective mineral-water reactive surface areas in heterogeneous unsaturated fractured rock (this issue is being addressed through continuing and new laboratory studies, the planned ECRB Cross Drift thermal test, and sensitivity studies)
- Uncertainties in thermodynamic data
- Uncertainties in kinetic data
- Uncertainties in geochemical conceptual models (e.g., mineral solid solutions and precipitating mineral assemblages)
- Uncertainties in fracture hydrologic parameters (i.e., fracture porosity and unsaturated hydrologic properties)
- Uncertainties in thermal-hydrologic conceptual models (e.g., vapor-pressure lowering, enhanced vapor diffusion) and their effects on THC processes
- Uncertainties introduced by code implementations and numerical errors (e.g., grid-induced errors such as orientation and refinement).

Key conceptual and parametric uncertainties regarding the prediction of THC processes related to seepage and their validation by thermal testing and laboratory experiments are summarized in Table 4.3.6-2. Other issues that specifically relate to uncertainties in the geochemical aspects of the THC models, and to predicting the water and gas composition directly at the drift wall, are listed in Table 6.3.1.8-1.

4.3.6.9 Summary and Conclusions

The treatment of coupled THC processes in the UZ is an analysis of a natural barrier that is an important item for waste isolation (YMP 2000 [DIRS 149733]). The work summarized in this section contributes to the analyses and modeling data used to support performance assessment. The analysis of coupled THC processes in the UZ does not directly support any of the principal factors of the postclosure safety case addressed in the repository safety strategy (CRWMS M&O 2001 [DIRS 154951], Volume II, Section 4.1). However, the other factor for site recommendation consideration, effects of heat on flow, is addressed by the analysis of coupled THC processes, which simulate the effect of mineral dissolution and precipitation on the permeability of the fracture continuum.

The effects of THC processes on seepage and on the chemistry of potential seepage water and gas have been evaluated through drift-scale THC model simulations for a range of operating temperatures and designs (see Section 4.3.6.5), validation using the ongoing Drift Scale Test (see Section 4.3.6.3.1), and laboratory experiments (see Section 4.3.6.7.2). The results of these simulations and analyses, which are based on a limited range of input parameters, indicate that mineral precipitation will not affect flow around the drifts to a degree greater than that already produced by the natural variability in hydrologic properties. Simulations have reproduced the results of a laboratory experiment showing fracture sealing within several days. With appropriate time and spatial scaling of percolation fluxes and thermal gradients, the results are consistent with long-term models that predict relatively small changes in fracture permeability. Predictions of ranges in water and gas compositions, also based on a limited set of input parameters, indicate a fairly restricted range in the chemistry of potential seepage water. In zones where the fracture liquid saturation is above the residual saturation of one percent, the waters are fairly dilute and neutral to mildly alkaline (i.e., pH in the range of about 7 to 9). Model validation with the waters collected from near-boiling to below-boiling zones in the Drift Scale Test have captured the overall trends in water chemistry of reactive and nonreactive solute species and pH. Changes in pH are strongly linked to changes in gas-phase carbon dioxide concentrations, the trends of which have also been reproduced by model simulations of the Drift Scale Test.

Many uncertainties associated with the prediction of coupled THC processes as they affect seepage are difficult to assess or have not yet been addressed systematically. The more important issues have been summarized and their status briefly assessed. THC model validation encompasses many of the uncertainty issues and has generally been successful with experiments of short duration for which the initial conditions are known. Uncertainties arising out of ranges in parameters that have not been assessed could be further reduced through additional field thermal testing, laboratory experiments, and modeling.

4.3.7 Thermal-Hydrologic-Mechanical Effects on Seepage

4.3.7.1 Introduction

Section 4.3.7 summarizes the modeling and uncertainty studies performed to determine the effects of coupled THM processes on seepage of liquid water into emplacement drifts. Sections 4.3.1 through 4.3.4 discuss how, at ambient preemplacement conditions, the

emplacement drift acts as a capillary barrier to divert water around the drift opening so seepage fluxes will be lower than percolation fluxes. Analysis of seepage under ambient conditions puts emphasis on factors that determine whether water reaching the drift wall will, in fact, seep into the drift. This section focuses on how the THM coupled processes change the near-field permeability and affect the magnitude and spatial distribution of the percolation flux in the vicinity of the drift. These, in turn, affect seepage threshold and seepage potential.

Like all such models, THM seepage models are subject to uncertainties resulting from conceptualization, parameters, and data. In particular, the degree of complexity in THM coupling incorporated into the numerical model to assess its impact on seepage represents a significant uncertainty. Until now, no transient fully three-way coupled THM computer simulator was available to study the potential Yucca Mountain site. For the TSPA-SR (CRWMS M&O 2000 [DIRS 153246]), two-way coupled TH, TM, and hydromechanical processes have been calculated separately or in a sequential snapshot approach. In this approach, TH responses are calculated first, followed by a separate TM analysis to calculate thermal stresses, which is used in a third analysis to calculate fracture permeability changes. In most of these analyses, the rock mass is treated as a continuum (implicitly modeling fractures), while a few attempts have been made to model the rock mass with discretely defined fractures. Since the TSPA-SR, the two-way coupled analysis with discretely defined fractures has been revised and extended. In addition, a new numerical model for transient, fully coupled THM continuum analysis of a fractured media has been developed and applied. Since the TSPA-SR, this model has been used to assess uncertainties in a transient, fully coupled analysis where the significance of THM processes on the percolation flux are examined.

A further uncertainty is associated with what property parameters are assigned for the mechanically induced permeability changes in the fractured rock. Such parameters may include fracture normal stiffness and residual fracture apertures. These need to be tested or calibrated against field measurements at an appropriate scale.

A number of these uncertainties are addressed in the following sections. Modeling studies discussed include the use of alternative modeling approaches and consideration of two different thermal operating modes for below-boiling and above-boiling temperatures within the rock mass.

4.3.7.2 Goal of Thermal-Hydrologic-Mechanical Models for Seepage

These studies are intended to provide insight into how drift excavation and the decay heat from emplaced waste would affect near-field rock permeability and the magnitude and spatial distribution of percolation flux around a potential emplacement drift (and, consequently, the potential of seepage into the drifts) for two different thermal operating modes. Two alternative conceptual and numerical models will be used: the distinct-element model and the fully coupled THM continua model.

4.3.7.3 Distinct Element Analysis

4.3.7.3.1 Discussion of Initial Results

In support of the TSPA-SR (CRWMS M&O 2000 [DIRS 153246]), a calculation to provide an estimate of TM effects on fracture permeability was conducted, as documented in *Calculation of*

Permeability Change Due to Coupled Thermal-Hydrological-Mechanical Effects (CRWMS M&O 2000 [DIRS 149040]). The method used in this calculation was to simulate the TM behavior of a region of fractured rock that surrounds a section of a long horizontal emplacement drift in the Topopah Spring Tuff at Yucca Mountain. The stress field in the rock mass surrounding emplacement drifts in a potential repository at Yucca Mountain will be altered by excavation of drifts and by the heating and cooling cycle associated with emplacement of radioactive waste. The directions and magnitudes of the principal stresses will change significantly as a result of thermal loading, then will revert during cooldown. Compressive stress will build up rapidly in the host rock, especially after the end of the forced ventilation period. The stress field will gradually decay as the temperature in the rock decreases.

Rock mass permeability is an important TH property for assessment of potential drift seepage. The potential repository host rock is a fractured, densely welded ash-flow tuff. Because the rock has low matrix permeability, the rock mass permeability can be conceptualized as mainly associated with fractures, and fracture permeability is highly dependent on fracture deformation. These fractures will deform as stress conditions evolve. Two types of fracture deformation will contribute to THM coupling: normal displacement perpendicular to the fracture plane and shear displacement parallel to a fracture plane. It is widely accepted that the hydrologic behavior of a fractured rock mass is controlled by a relatively few well-connected fractures. Thus, a model that incorporates discrete fractures was used. Fracture deformation during various phases of the heating-cooling cycle is used to predict changes in rock mass permeability.

The rock mass surrounding an emplacement drift was simulated in three dimensions as a rectangular prism 50 m wide, 60 m high, and 30 m thick. A cylindrical (5.5-m diameter) horizontal drift was excavated through the region. The simulated region was intersected by three sets of fractures: one vertical set oriented parallel to the drift, one vertical set oriented perpendicular to the drift, and one horizontal fracture set. Two fracture densities were used for each set of fractures: a low fracture density (0.1/m) for regions more than 15 m from the drift and a high fracture density (0.5/m) for regions within 15 m of the drift. These fracture densities are lower than those observed in situ and used in TH modeling (CRWMS M&O 2000 [DIRS 151964]). However, the lower fracture density is appropriate because not all fractures are geomechanically active (i.e., free to deform or slide) or hydrologically conductive. The fracture densities calculated by Albin et al. (1997 [DIRS 101367], Drawings OA-46-296, OA-46-297, OA-46-298, OA-46-299) for the Tptmn include a large number of sealed and partially sealed fractures that are expected to have relatively little effect on mechanical and hydrologic properties. Descriptive fracture statistics provided by Albin et al. (1997 [DIRS 101367], p. 82) suggest that approximately four out of five fractures contain at least some secondary mineral in-filling. In sections of the ESF main drift, mapping studies also included fractures with trace lengths as short as 30 cm (Albin et al. 1997 [DIRS 101367], p. 10). The shorter fractures are expected to have a relatively small impact on mechanical and hydrologic properties.

Moreover, in practice, a trade-off exists between fracture density and the permissible volume of the inner (fractured) model, given the available memory resources and the computational requirements of the numerical code used for the calculations. Use of a higher fracture density would have mandated a smaller inner model given available computational resources.

Stresses equivalent to the in situ stresses were imposed on the sides and top of the prism. Since this calculation was primarily concerned with fracture deformation, the stress boundary conditions were chosen for the vertical sides of the model to provide a lower limit on normal stress across vertical fractures, thus making it easier for them to open and/or slip. This boundary condition is most appropriate for the regions near the edge of a repository. The base of the prism was fixed in the vertical direction, but allowed to move in the horizontal directions. Fracture deformation values estimated at a series of times were then used to compute permeability change in a cross section perpendicular to the emplacement drift. These values for permeability change were then contoured for different times.

The methodology for estimating TM effects on permeability incorporated a distinct element model that can capture the mechanical behavior of discrete fractures. In the distinct-element method, the rock mass is composed of an assembly of deformable blocks that are interfaced by discontinuities. Fractures in the rock mass are entered individually into a distinct-element code (3DEC V2.0), and both normal and shear deformation are predicted for the individual fractures. The example calculation discussed in this section uses fracture spacings appropriate for the middle nonlithophysal region of the repository.

The thermal field imposed by the emplacement of nuclear waste containers was simulated within the 3DEC V2.0 distinct element code using a conduction-only thermal model that calculates temperatures, thermally induced stresses, and displacements in a half-space. The thermal model is weakly coupled to the discrete element mechanical simulator in 3DEC V2.0, in that thermal stresses and displacements were incorporated into the predicted stress and displacement fields. The thermal load of the model was based on the EDA II design (Wilkins and Heath 1999 [DIRS 104247]), in which ventilation is used to remove heat from the emplacement drift for the first 50 yrs after emplacement. The EDA II design shows a "spike" in the pillar temperature starting at 50 yrs, when ventilation ceases, followed by a cooling between 50 and 100 yrs. A simple step function was used for the thermal power input. Power was supplied at a constant level of 460 watts for 50 yrs to simulate the ventilation phase, then raised to 615 watts and held constant for 100 yrs, then reduced. Overall, at locations more than a few meters away from the drift, the temperatures matched those predicted using by TH models well enough for use in this calculation. This heating schedule produced temperatures similar to the maximum pillar temperature but over a longer time, followed by a rapid cooldown.

The numerical model was then used to estimate stress and deformation values in the block at a series of times after emplacement. Normal and shear deformation were predicted for multiple locations on each fracture face. The results included two-dimensional images of permeability multipliers calculated from predicted values of normal and shear displacement of fractures, and indicate that the major TM effect on fracture permeability occurs during cooldown for both shear and normal deformation.

Results indicate that shear deformation of fractures during the cooldown of a potential geological repository may cause the fracture permeability in a region within two drift diameters of a drift wall to increase by as much as an order of magnitude. Specifically, shear deformation on vertical fractures during cooldown produces the maximum amount of permeability change, and increases in permeability of a factor of five may occur on vertical fractures at distances beyond two drift diameters from the drift wall.

Results also indicate that normal deformation of fractures may cause permeability to increase as well, but to a lesser extent than shear deformation. Normal deformation during heating may cause permeability to decrease significantly within one drift diameter of the drift wall. During cooling, vertical fractures above the drift may open and the permeability can increase by a factor of two.

4.3.7.3.2 Updated Model Developments

The distinct-element analysis has been revised and extended to provide a more robust estimate of the TM effects on fracture permeability in the rock mass around an emplacement drift. This work is new since the TSPA-SR (CRWMS M&O 2000 [DIRS 153246]), and is documented in Blair (2001 [DIRS 155005]). In the new analyses, the higher-temperature and lower-temperature cases were simulated. The higher-temperature case simulates a heat input of 1.45 kW/m of drift applied with a forced ventilation period of 50 yrs, during which 70 percent of the decay heat is removed. Details of this input scenario and updated thermal parameters are discussed in Section 4.3.5. In addition, fixed displacement boundary conditions were used on the sides of the model. This analysis also used the cubic law to relate changes in fracture aperture to changes in rock mass permeability. The analysis incorporated the effect of shear slip along fractures by computing both stress reduction and fracture dilation as a function of shear displacement. Three fracture sets were used, including two subvertical sets and one subhorizontal set that were mapped in the middle nonlithophysal unit of the Topopah Spring Tuff. An emplacement drift orientation of 72° was used. Temperatures used in the simulations were predicted using the NUFT V3.0s code and the line-averaged-heat-source, drift-scale, thermal-hydrologic (LDTH) model L4L4 (CRWMS M&O 2000 [DIRS 151825]), which is appropriate for determining the evolving stress and deformation fields in the TM model. The use of L4C4 is consistent with process models used in TSPA features, events, and processes and is expected to bound the thermal driving forces for the TM model. This LDTH model is one of 31 LDTH submodels used in the TH process-level model that generates repository-wide thermodynamic conditions for the TSPA-SR. The L4C4 LDTH model is located just east of the center of the repository (Easting 170501 m, Northing 233807 m). This model is two-dimensional; the emplacement drift is located in the tsw35 hydrologic unit. Because this is a two-dimensional model, no heat loss from repository edge effects is included. This ensures that the highest temperatures and the greatest thermal gradients drive TM processes in the simulation.

Input parameters used for the simulations were derived primarily from *TBV-332/TBD-325 Resolution Analysis: Geotechnical Rock Properties* (CRWMS M&O 1999 [DIRS 126475]), and are listed in Table 4.3.7-1.

Permeability changes were determined at eight time increments: 10, 50, 55, 100, 200, 400, 1,000, and 100,000 yrs after waste emplacement. Data developed for the higher-temperature case have been entered into the Technical Data Management System (DTN: LL010109723123.011 [DIRS 154664]). The data were developed using EARTHVISION V5.1 and 3DEC V2.0.

The model inputs for the LTOM analyses were identical to the high temperature case, except that temperatures from the LTOM thermal-hydrology analyses were used.

4.3.7.3.3 Results from Updated Distinct Element Analysis

Results from this analysis indicate that the principal stress direction will rotate from primarily vertical to primarily horizontal, oriented perpendicular to the emplacement drift axes as temperatures in the rock near the emplacement drifts increase. Compressive stresses as high as 60 MPa are predicted in narrow zones in the floor and roof of the drift. The rotation of the principal stress direction is due primarily to the boundary condition imposed at the center of the pillars. In this analysis, the rock at pillar center was not allowed to move in the horizontal direction perpendicular to the drift. This caused horizontal compressive stress to increase as the rock tried to expand during heating. This analysis also indicates that fracture permeability further into the rock will be substantially reduced for vertical and subvertical fracture sets, while the permeability of horizontal fracture sets will remain relatively unchanged.

The changes in predicted fracture permeability field develop soon after the end of the forced ventilation period in association with temperature increases in the near-field rock at that time and persist throughout the 1,000-yr simulation interval. Figure 4.3.7-1 shows the distribution of calculated permeability ratios at 55 yrs, and Figures 4.3.7-2 to 4.3.7-4 show histograms of the calculated permeability ratios in different fracture sets at 55, 1,000 and 100,000 yrs. Figure 4.3.7-1 shows fracture permeability in the first 2 m of rock forming the emplacement drift wall increasing substantially. Fracture permeability may also increase in the region above the drift, extending to one drift diameter above the drift crown. However, increases in permeability greater than one order of magnitude are not predicted beyond 0.5 m from the drift except in the region above the drift and away from the drift wall; a substantial decrease in permeability is predicted throughout the rock mass.

Figures 4.3.7-2 and 4.3.7-3 show that at 55 and 1,000 yrs, permeability may be substantially reduced for vertical and subvertical fractures, while the permeability of horizontal fractures remains relatively unchanged. This change in the predicted fracture permeability field develops soon after the end of the ventilation period (in association with a temperature increase at that time) and persists throughout the 1,000-yr simulation interval.

Upon cooldown, fracture permeability may increase above initial values for horizontal and vertical fractures. Figure 4.3.7-4 shows that the increase in fracture permeability upon cooldown is in the range of one to two orders of magnitude.

The permeability ratio distributions for horizontal and vertical fracture sets are summarized in Tables 4.3.7-2 and 4.3.7-3, respectively. The results for the two vertical fracture sets, which are very similar, have been combined and the bins representing decreased permeability ratio broadened to encompass two orders of magnitude. The results show that permeability ratios for the majority of the horizontal fractures at all times predicted in this study have remained about the same, to within one order of magnitude. The permeability ratios for most vertical fractures decreased by several orders of magnitude during the period between 50 and 1,000 yrs. At 100,000 yrs, the permeability ratio for both horizontal and vertical shows values well in excess of one, indicating that these fractures reopen upon cooling.

This recent analysis predicted higher stresses and larger changes in fracture permeability than were predicted in the calculation presented in Section 4.3.7.3.1. These changes are due to the

use of a different set of boundary conditions and a revised relationship between fracture deformation and permeability change.

The THM distinct-element model has also been used to simulate rock mass behavior and estimate changes in fracture permeability for the LTOM case. This case is designed to keep the drift wall temperature well below boiling throughout the lifetime of the repository. The inputs for the LTOM predictions were identical to those for the HTOM case, with the exception that LTOM temperatures were used. Results for the LTOM case show that, as expected, the stress levels in the rock mass are lower than for the HTOM case and that the highest stresses occur after the end of ventilation at 300 yrs after emplacement. In addition, the results show that the fracture permeability remains basically unchanged for the first 300 yrs of storage while ventilation is maintained. A typical histogram of permeability ratio values for times during ventilation period (Figure 4.3.7-4a) shows results for 100 yrs after emplacement.

Results also show that after the end of the ventilation period (300 yr), a decrease in fracture permeability of one to two orders of magnitude is predicted for approximately 50 percent of the vertical fractures. This reduction of fracture permeability is predicted to persist until 400 yrs after emplacement (Figure 4.3.7-4b), and gradually changes over time, with fracture permeability decreasing by 3 orders of magnitude in approximately 20 percent of the vertical fractures by 1,000 yrs after heating.

While the predicted decreases in fracture permeability due to TM effects after the end of the ventilation period may be significant for the LTOM case, they are smaller in magnitude, and affect fewer fractures, than the changes in fracture permeability predicted for the HTOM case. The HTOM case predicted a decrease of 6 orders of magnitude in permeability for most vertical fractures during the period from 55 yrs to more than 1,000 yrs after emplacement.

The following conclusions concerning the pre-cooldown period result from the distinct element analysis:

- The primary effect of the TM processes will be to rotate the principal stress direction from primarily vertical to primarily horizontal, oriented perpendicular to the emplacement drift axes. Compressive stresses as high as 60 MPa are predicted in narrow zones in the floor and roof of the drift.

- Permeability will be substantially reduced for vertical and subvertical, while the permeability of horizontal fracture sets will remain relatively unchanged.

- The change in the predicted fracture permeability field develops soon after the end of the ventilation period (in association with a temperature increase at that time) and persists throughout the 1,000-yr simulation interval.

- Heating associated with waste emplacement is predicted to cause the drift walls to displace inward as horizontal stress levels increase. This movement will cause fracture permeability to increase substantially in the first two meters of rock around the emplacement drift. Fracture permeability may also increase in the region above the drift, extending to one drift diameter above the drift crown. Increases in permeability

greater than one order of magnitude are not predicted beyond 0.5 m from the drift, except in the region above the drift.

4.3.7.3.4 Model Validation for Distinct Element Model

The distinct-element model has been used to simulate deformation observed in the Drift Scale Test conducted in the middle nonlithophysal unit. Deformation measurements using multiple-point borehole extensometer systems have been made in several boreholes in the Drift Scale Test. Moreover, deformation measurements were made in three boreholes during excavation of the heated drift section of the Drift Scale Test drifts.

The distinct-element model was used to simulate deformation in several of the boreholes during excavation of the drift and the first 545 days of heating of the Drift Scale Test. Rock property inputs used for these simulations were the same as those used for the emplacement drift simulations discussed above and listed in Table 4.3.7-1 and temperatures were taken from TH simulations of the Drift Scale Test presented in the *Thermal Tests Thermal-Hydrological Analyses/Model Report* (CRWMS M&O 2000 [DIRS 151964]).

Results of the validation show that the overall response of the distinct element model correctly predicts both the magnitude and trends of the deformation observed in the Drift Scale Test. Details of the validation are presented in Blair (2001 [DIRS 155005]).

4.3.7.4 Coupled Thermal-Hydrologic-Mechanical Continua Model

One of the major advances since the initial work presented in *Calculation of Permeability Change Due to Coupled Thermal-Hydrological-Mechanical Effects* (CRWMS M&O 2000 [DIRS 149040]) is the implementation of a coupled THM continua code and its application to the study of drift-scale THM effects on flow and seepage. This work consisted of a distinct element analysis used to calculate permeability changes caused by mechanical and TM responses. The new coupled continuum model provides an opportunity to study THM effects using an alternative conceptual and numerical model. In addition to changes in permeability, changes in percolation flux can be directly assessed.

4.3.7.4.1 Description of a Fully Coupled Thermal-Hydrologic-Mechanical Continua Model

Since the initial work, and in parallel with the continued TM analysis using the distinct-element method, a fully coupled THM code has been implemented. It is a joining together of two well-established codes through carefully designed linkage routines. The first is the TOUGH2 V1.5 code, which uses the dual-permeability continuum (fracture and matrix continua) approach. It has been proven successful in predicting the temperature and moisture distribution of field experiments at Yucca Mountain, including the Single Heater Test (CRWMS M&O 1999 [DIRS 129261]) and the Drift Scale Test (CRWMS M&O 2000 [DIRS 151964]). The second is the industry-standard FLAC3D V2.0 code, which can calculate fracture rock and soil mechanical processes in a continuum model.

The general conceptual model for THM processes may be described as a multiphase, non-isothermal, and deformable medium where voids of the rock skeleton are filled partially

with liquid water and partially with gas. Thus, it is a three-phase system (gas, liquid, and solid) in which each of the fluid phases has two components (water and air). The gas phase is modeled as an ideal gas mixture composed of dry air and water vapor; the liquid phase consists of water and dissolved air. The mechanical behavior of the porous and fractured media responses to changes in temperature, skeletal effective stress, and strain, with accompanying porosity and permeability changes. Coexisting fluid and solid components are modeled as in local thermal equilibrium (i.e., locally they are at the same temperature). While a few main fractures may be discretely defined within a rock matrix, the main part of the fractured and porous rock is treated as a single continuum or multicontinuum (fracture system and matrix blocks). In a multicontinuum model, the temperature and pressure may be different in the matrix and fractures, while the total stress (as opposed to the effective stress) is modeled as the same in both continua. Four types of conservation equations are needed to fully describe such a system, including two mass balance equations for the two fluid components, one energy balance equation, and one momentum conservation equation of rock deformation forces.

The fluid mass balance equation of a coupled hydraulic and mechanical system can be rigorously derived by combining the fluid mass conservation equation with the solid mass conservation equation, considering the relative motion of the fluid to the moving solid according to Rutqvist et al. (2001 [DIRS 154587]). In such a case, the volumetric strain in the mass-balance equation is coupled to the force-balance equation through Biot's storage and effective stress parameters (Biot 1941 [DIRS 121082]), and the final equations are solved simultaneously in a fully coupled model. In general, a reservoir engineering approach can be used by accounting for rock deformation changing the porosity. However, in the current application, an alternative approach of estimating change in porosity, and hence permeability, from a change in stress is used by adopting an empirical nonlinear relationship. For a fractured rock, the second approach is more direct because a relationship between fracture normal stress and fracture permeability can be used directly. Such normal stress versus fracture permeability relationships is frequently determined from laboratory tests, or can preferably be back-calculated from field tests at a relevant scale. By using this approach, the TOUGH2 V1.5 and FLAC3D V2.0 codes can be used in their standard versions, but linked together through numerically calculated porosity, permeability, and effective stress changes. The codes are executed iteratively with transfer of data through external linking modules. Through various iterative schemes, either explicit or implicit sequentially coupled solutions can be achieved.

Figure 4.3.7-5 presents the principal linkage of TOUGH2 V1.5 and FLAC3D V2.0. The two codes should be run with a mutually compatible mesh, according to Figure 4.3.7-5b. A TOUGH2 V1.5 mesh has one grid point within each grid element where temperature, fluid pressures, and saturation is defined, whereas FLAC3D V2.0 nodes are located in element corners. Thus, when transferring temperature and pressure from TOUGH2 V1.5 to FLAC3D V2.0, the data have to be interpolated from mid-element to corner nodes. No interpolation is required for the reverse data transfer from FLAC3D V2.0 to TOUGH2 V1.5 because stress and strain are defined in FLAC3D V2.0 elements, which are identical to TOUGH2 V1.5 elements.

The two codes are linked through material-specific functions (or modules) that are consistent with the continuum concepts used in both codes. In TOUGH2 V1.5, the fracture and matrix flow and interaction are modeled using a dual-permeability (overlapping continuum) concept or,

alternatively, an equivalent continuum concept. In FLAC3D V2.0, an orthotropic elastic or isotropic elasto-plastic equivalent continuum model is used.

4.3.7.4.2 Application of Coupled Thermal-Hydrologic-Mechanical Continua Model to the Current Study

In this study, the joined "TOUGH-FLAC" code was applied to study the effects of the THM coupling on the flow and temperature evolution in the vicinity of a potential repository drift. The effect of the THM coupling on the fluid flow and temperature field around a drift was investigated by comparing the THM results to a pure TH simulation (i.e., using the TOUGH2 V1.5 code only). A continuum approach was used for both the TOUGH2 V1.5 part and the FLAC3D V2.0 part of the coupled code in a consistent way.

Figure 4.3.7-6a presents a schematic picture of the fractured rock system with one emplacement drift being modeled. At Yucca Mountain, the two stratigraphic units in which the emplacement drifts may be located (Tptpmn and Tptpll) are highly fractured, and the fractures are well-connected (CRWMS M&O 2000 [DIRS 153314], Section 6.7 and Figure 8). There are three dominant sets of fractures that are oriented almost orthogonal to each other, two subvertical and one subhorizontal (CRWMS M&O 2000 [DIRS 151635], Figure 5). From a TM point of view, the extensive fracturing implies that the rock is considerably softer and has a lower thermal expansion coefficient than the corresponding intact rock. However, previous simulations of TM induced displacements at the Single Heater Test and the Drift Scale Test indicate that the mechanical deformations in the rock mass can be reasonably well captured with a linear elastic or nonlinear elastic mechanical model (CRWMS M&O 1999 [DIRS 154585], Section 4.2). This is true provided that the rock mass deformation modulus and thermal expansion coefficient are reduced by about 50 percent of the value for intact rock. This implies that the bulk rock mass behavior should be essentially elastic, although locally a small slip may occur on fracture planes. Near the drift wall, on the other hand, inelastic shear slip or tensile fracturing may occur because of the strong stress redistribution and a lack of confinement in that region. The extent of this particular zone is difficult to predict because it depends on the strength parameters of the rock mass, which can only be roughly estimated.

As discussed above, because of the high density and connectivity of the fracture network, the conceptual model used is the dual-permeability model. This model is also used for the TOUGH2 V1.5 part of the coupled THM simulations described below. For the hydromechanical changes, the dominant part is the fracture continuum, where changes in the stress field will cause significant changes in fracture apertures and, hence, fracture permeability. To couple the changes in the three-dimensional stress field to the rock mass permeability, a simplified cubic block conceptual model is utilized (Figure 4.3.7-6b). In this model, the current hydraulic fracture aperture b depends on the current fracture normal stress σ_n according to the following exponential function (Bodvarsson 2001 [DIRS 154669], Attachment 9, pp. 9 and 21 to 25):

$$b = b_i + \Delta b = b_i + b_{\max}\left[\exp(\alpha\sigma_n) - \exp(\alpha\sigma_{ni})\right] \qquad \text{(Eq. 4.3.7-1)}$$

where

b_i = the initial aperture

b_{max} = the maximum aperture (at zero normal stress)

α = a parameter to be calibrated

σ_{ni} = the initial stress normal to the fractures.

Equation 4.3.7-1 and the conceptual cubic block model give the following relations for stress versus fracture permeability in three orthogonal (2 horizontal and 1 vertical) directions. In these equations, the initial fracture permeability is isotropic:

$$\frac{k_x^f}{k_i^f} = \frac{1}{2}\left[1 + \frac{b_{\max}}{b_i}\left(\exp(\alpha\sigma_y) - \exp(\alpha\sigma_{yi})\right)\right]^3 + \frac{1}{2}\left[1 + \frac{b_{\max}}{b_i}\left(\exp(\alpha\sigma_z) - \exp(\alpha\sigma_{zi})\right)\right]^3 \quad \text{(Eq. 4.3.7-2a)}$$

$$\frac{k_y^f}{k_i^f} = \frac{1}{2}\left[1 + \frac{b_{\max}}{b_i}\left(\exp(\alpha\sigma_x) - \exp(\alpha\sigma_{xi})\right)\right]^3 + \frac{1}{2}\left[1 + \frac{b_{\max}}{b_i}\left(\exp(\alpha\sigma_z) - \exp(\alpha\sigma_{zi})\right)\right]^3 \quad \text{(Eq. 4.3.7-2b)}$$

$$\frac{k_z^f}{k_i^f} = \frac{1}{2}\left[1 + \frac{b_{\max}}{b_i}\left(\exp(\alpha\sigma_x) - \exp(\alpha\sigma_{xi})\right)\right]^3 + \frac{1}{2}\left[1 + \frac{b_{\max}}{b_i}\left(\exp(\alpha\sigma_y) - \exp(\alpha\sigma_{yi})\right)\right]^3 \quad \text{(Eq. 4.3.7-2c)}$$

The parameters in Equation 4.3.7-2 are determined as described in the next section by model calibration against a number of Yucca Mountain ESF field experiments at the scale of a drift. In addition to changes in fracture permeability, the fracture porosity is corrected for the aperture changes in Equation 4.3.7-1, and the capillary pressure varies as permeability changes according to the Leverett (1941 [DIRS 100588]) function.

For the linkage function from TOUGH2 V1.5 to FLAC3D V2.0, only the effect of thermally induced strain and stresses are considered. The changes in effective stress and bulk density caused by the multiphase fluid pressure and saturation changes are neglected. This is defensible considering that the fracture system is unsaturated, with a capillary pressure of less than 0.01 MPa. This is a very small pressure for a system that has in situ stresses and thermal stresses with magnitudes on the order of several to tens of MPa.

4.3.7.4.3 Calibration against Niche and Drift Scale Heater Tests

The parameters in the stress-permeability function (Equation 4.3.7-2) are estimated through model calibration against air-permeability measurements conducted at three excavated niches located in the Tptmn unit and one excavated niche in the Tptpll unit. The air-permeability tests measure the permeability of the fracture continuum, which is the main component controlling flux and seepage. In the Tptpmn unit, the air-permeability was measured before and after excavation in three boreholes located about 0.65 meters above the niches (DTN: LB0011AIRKTEST.001 [DIRS 153155]). The permeability was measured along each

borehole in sections about 0.3 meters long, and in almost every section the permeability changed during the excavation of the niche. The ratio of post-excavation to pre-excavation permeability varies between 1.0 (no change) and approximately 1,000 (three orders of magnitude increase); on average, the permeability increased by more than one order of magnitude. Figure 4.3.7-7 presents the pre-excavation to post-excavation permeability as a function of the initial permeability in each measurement point along borehole UM, located above Niche 2 (Station 36+50) in the Tptpmn. The results indicate a general trend that permeability changes are larger in initially lower-permeability sections than in the higher-permeability sections.

Preliminary results are also available from a similar test conducted at a niche in the Tptpll unit (DTN: LB002181233124.001 [DIRS 146878]; DTN: LB0012AIRKTEST.001 [DIRS 154586]). At this niche, the air permeability was measured in boreholes above the niche and in a borehole on the side of the niche. In general, the results show that the average permeability in each borehole changed by a factor of approximately 2 to 9 above the crown of the drift (2 m from the crown) and by a factor of less than 2 on the side of the drift (1.5 to 2 m from the edge of the drift).

The stress permeability changes induced by the excavation of a niche are simulated using the FLAC3D V2.0 part of the coupled code and the stress permeability relationship in Equation 4.3.7-2. There are two parameters to be fitted in the equation, α and b_{max}. For the increase of permeability as evidenced in the niche tests, the key parameter is α. In Figure 4.3.7-7, a point noted by **x** is used as the fitting point, relating the post- and pre-excavation ion ratio (-) (i.e., k_f^f / k_i^f) with the pre-excavation permeability (m^2) (i.e., k_i^f), where k_f^f is the geometric mean of the three permeability values in the x, y, and z directions computed from Equation 4.3.7-2.

Next, a calibration of the fracture residual aperture residual aperture (i.e., the limiting aperture remaining after compressive stresses induced by excavation and heating have closed the fracture as far as possible), which is related to b_{max} in Equation 4.3.7-2, was conducted against air-permeability measurements in the Drift Scale Test. Those measurements (CRWMS M&O 2000 [DIRS 151964]) showed that the air permeability near the drift decreased at most by a factor of 0.1 during heating. This permeability decrease may be caused partly by an increase in liquid fracture saturation and partly by mechanical fracture closure from TM effects. A conservative approach for the THM calculation is to take the measured reduction in permeability as caused entirely by TM effects, probably overestimating the TM effects. Therefore, the residual aperture was calibrated to limit the permeability changes during closure to 0.1. This is an important parameter in the simulations.

For confirmation, Figure 4.3.7-8 (left) presents the distribution of permeability changes calculated from a calibrated model in the Tptpmn unit. In this figure, the permeability before and after excavation has been calculated from the geometric mean of the anisotropic permeability values in three directions. The calculated permeability values at borehole UM are calibrated to a permeability change of 20, which is in the middle range for pre-excavation to post-excavation changes for the corresponding initial permeability (3.7×10^{-13} m^2) in Figure 4.3.7-7. Figure 4.3.7-8 (right) shows the simulated excavation induced permeability changes in the Tptpll unit. In this case, the same parameters for the hydromechanical function are used, with the exception of the initial permeability. Because the initial permeability is higher

in the Tptpll rock unit (2.4×10^{-12} m^2), the change in permeability is smaller than the changes in the Tptpmn unit. The simulation results in these figures are consistent with the observed data in both the Tptpmn and Tptpll units.

4.3.7.4.4 Application and Results of the Coupled Thermal-Hydrologic-Mechanical Model

A fully coupled THM simulation using the explicit solution scheme was conducted on a one-half symmetric drift located at Yucca Mountain (Figure 4.3.7-9). The model domain is a multiple-layered column extending vertically from the ground surface down to the water table. The vertical layering for the model was chosen to correspond to the vertical contacts at Nevada State Plane Coordinates 170572.39 m (Easting) and 233194.536 m (Northing), with corresponding geologic contacts for the three-dimensional UZ site-scale model 1999 TSPA grid (DTN: LB990701233129.001 [DIRS 106785]; CRWMS M&O 2000 [DIRS 114277], Attachment VI). The hydrologic and thermal properties of the layers are taken from the drift scale calibrated property sets (DTN: LB0011DSTFRAC1.001 [DIRS 153470]; DTN: LB990861233129.001 [DIRS 110226]). The ground surface boundary was set at constant temperature and mechanically free, and the water table boundary at constant temperature and mechanically fixed. By symmetry, only half of the distance between two drifts (40.5 m) was modeled because the drift spacing is 81 m. A drift of 5.5-m diameter was simulated as being excavated in the Tptpll unit. The drift was treated as a single element with a porosity near one and a mechanically free boundary. The waste emplacement was designed such that two thermal operating modes were simulated. The first is referred to as the higher-temperature or above-boiling case, in which a heat input of 1.45 kW/m of drift is applied with a forced ventilation period of 50 yrs, during which 70 percent of the decay heat is removed. The second is referred to as the lower-temperature or below-boiling case, in which a heat input of 1.35 kW/m of drift is applied with a forced ventilation period of 300 yrs, during which 80 percent of the decay heat is removed. Details of these input scenarios and updated thermal parameters are discussed in Section 4.3.5. The THM parameters are shown in Table 4.3.7-4, including the calibrated parameters α and b_{max}.

Results of the fully coupled THM continua model analysis are shown in the next series of figures (Bodvarsson 2001 [DIRS 154669], Attachment 9, pp. 32 to 76).

Figure 4.3.7-10 shows the changes in vertical and horizontal permeability around the drift because of excavation. There is a significant increase by a factor up to 10 in rock permeability above the crown of the drift. Near the springline of the drift, vertical permeability is increased but horizontal permeability is decreased, resulting in much smaller changes in mean permeability. Note that the complex pattern of changes is obtained by calculating permeability in a given direction by combining two permeability values in the two fracture directions parallel to it (see Equation 4.3.7-2).

Figure 4.3.7-11 shows the temperature distribution at 10 yrs for the HTOM and LTOM. As expected, the temperature increase centers around the drift, and the disturbance is more pronounced in the higher-temperature case. Figures 4.3.7-12 and 4.3.7-13 present changes in the horizontal and vertical permeabilities (respectively) after 10 yrs. On the whole, there is a decrease in permeability around the drift caused by thermal stress induced by the decay heat.

This decrease is able to overcome the initial excavation-induced permeability increases, except possibly in areas very close to the crown of the drift. Changes in both cases are similar.

Figure 4.3.7-14 shows the temperature distributions at 1,000 yrs for the higher-temperature and lower-temperature cases. The differences are apparent. In the former, temperatures near the drift are still above boiling, and temperatures at about 80 m above the drift are over 80°C. In the latter, temperatures are 20° to 40C° lower, and at 80 m above the drift the temperature is about 60°C. Figures 4.3.7-15 and 4.3.7-16 show the changes in horizontal and vertical permeabilities at 1,000 yrs. There is a trend of little or no change in permeability in the lower lithophysal layer near the drift, to a larger change 10 to 60 m above the drift, to the largest change (k_h/ki is about 0.5 and k_v/h_i is about 0.1) in the layer about 65 to 85 m above the drift (1,145 to 1,165 m section in the figure), to less change in the layer above.

The largest change, at the 1,145- to 1,165-m level, is due first to the initially lower permeability of the Tptpmn, which will experience a larger change factor due to stress changes. This is consistent with the niche calibration data discussed in Section 4.3.7.4.3. In that case, the stress change results from excavation, while in this case the stress change results from temperature rise. Secondly, the shallower layers above the drift, which have less overburden, will respond to stress changes more readily (i.e., the effective rock stiffness is relatively less).

An interesting observation is that these changes are almost the same regardless of the operating mode. The change of k_v/ki = 0.1 indicates that the thermal stress has caused a reduction of fracture permeability to the residual value. This is true even in the LTOM, so a higher-temperature cannot induce additional changes. The residual permeability was estimated by calibration against the Drift Scale Test (see Section 4.3.7.4.3), where a reduction of air-permeability values to 0.1 of their initial values was observed. As discussed in Section 4.3.7.4.3, this reduction could be due to a combination of TM effects and relative permeability change with saturation. Attributing it all to the TM effect is a conservative limit for THM evaluation. If the TM part of the change had been chosen not at this full value, the results in these figures would show less permeability reduction. Thus, the residual permeability value of the formation and the stiffness of the formation at Yucca Mountain are important parameters for the evaluation of THM processes. A reevaluation of field observations at Yucca Mountain and, in particular, the on-going Drift Scale Test will be of paramount importance.

The saturation and percolation flux distributions at 1,000 yrs with and without THM coupling are shown in Figures 4.3.7-17 and 4.3.7-18 for the higher- and lower-temperature cases, respectively. The main difference in saturation profiles between TH and THM results is the higher saturation in the Tptpmn unit at the 1,145- to 1,165-m level. This corresponds to the THM induced reduction in permeability, with a corresponding increase of capillarity in this layer. The liquid flow patterns, on the other hand, are quite similar between the TH and THM cases. The reduced permeability in the 1,145- to 1,165-m zone is accompanied by a higher relative permeability from the increased liquid saturation, which may have compensated for part of its impact. Another reason for similarity in liquid flux patterns may be that permeability reduction is constant horizontally across the flow domain; the vertical downward flux cannot flow around regions of reduced permeability, and is thus forced to take the same flow pattern. Therefore, the percolation fluxes immediately above the drift appear to be very similar for both the TH and THM results.

The following conclusions may be drawn from the coupled THM continua analysis:

- The fully coupled THM model has been calibrated against ESF niche and Drift Scale Test data. During drift excavation, permeability above and below the drift is expected to increase by one order of magnitude or more, while permeability to the side of the drift is expected to have much smaller changes.

- With waste emplacement and thermal input, thermal stress will reduce permeability all around the drift. Although this reduction is relative to the initial excavation-induced permeability increase, there is a net permeability decrease after about one year of heating.

- In the longer term, after around 1,000 yrs, thermal effects will cause permeability changes far from the drift (up to 100 m). Except in the region very close to the drift walls, there is permeability reduction caused by thermal stress, with most changes in the vertical permeability. The reduction is a function of initial local permeability values, being larger for initially low values. The reduction is large enough so that the permeability at 1,000 yrs in the Tptpmn unit about 60 m above the drift will reduce to its residual value (i.e., permeability at residual aperture).

- Rock stiffness parameters and residual permeabilities are important parameters for the THM analysis, which suggests additional testing and further analysis of Drift Scale Test data may be needed.

4.3.7.4.5 A Discussion of Permanent Permeability Changes Due to Thermal-Hydrologic-Mechanical Processes

Part of the permeability changes induced by the excavation and heating of the rock could remain after the repository has cooled to the ambient temperature. Such permanent changes are important for a performance assessment of a repository. In the simulations presented in this section, permanent changes are induced as results of drift excavation. These changes are as much as an order of magnitude in a zone near the drift that extends from the drift wall into the rock for about one drift radius. The subsequent heating and cooling of the rock mass did not induce any significant permanent changes in the permeability field in these simulations. The permeability change during the heating of the rock was induced by a predominant elastic closure of rock fracture, but after cooling these changes would be diminished by an elastic, fully reversible recovery of fracture apertures. Thus, a permanent permeability change would not result unless the rock mass behaved inelastically. The most significant inelastic behavior is likely to occur in the form of shear slip and tensile failure along preexisting fracture planes and in the inelastic zone near the drift. Such inelastic behavior would tend to increase the permeability in this zone; at the same time, a general non-recoverable redistribution of the stress field around the drift would cause small changes in the permeability field outside the inelastic region. Furthermore, even if the rock mass behavior away from the drift wall is essentially elastic as a whole, local inelastic behavior may occur, for example, in the form of fracture slip and crushing of asperities during fracture compression. Such small-scale inelastic behavior may not be significant for the general deformation of the rock mass as measured by extensometers, but may still be significant for the local fracture aperture and thus the local fracture permeability.

In the Single Heater Test, a small stick-slip displacement behavior was observed by extensometers during the cooling phase, which could be interpreted as fracture slip phenomenon. Permanent displacements of up to 1 mm occurred in the rock near the heat source and at the drift walls. Furthermore, a permanent general increase in the permeability field by a factor of up to 3.5 was observed in the Single Heater Test area. These permanent permeability changes occurred during the heating and cooling of the rock mass and may be caused by permanent mechanical opening of fractures. Further information on permanent changes will be available after the completion of the Drift Scale Test. A careful analysis of test data will be very important to shed light on this issue.

4.3.7.5 Abstraction for Total System Performance Assessment

The work reported in this section is devoted to evaluating process model sensitivities and uncertainties. Simulation results from this study are not yet used to support any abstraction model that directly supports a TSPA. The results found so far indicate that percolation flux values and distribution immediately above the drift are not significantly affected by the THM processes. Further, permeability changes caused by THM effects, apart from the immediate neighborhood of the drift that is part of the drift degradation analysis (see Section 4.3.4), are about one order of magnitude, which is within the range of the ambient seepage model (see Section 4.3.4). Thus, results to date do not indicate a significant THM induced impact on the performance as represented in the total system performance baseline.

4.3.7.6 Multiple Lines of Evidence

The impact of THM processes (such as excavation and heating) on the performance of the potential repository at Yucca Mountain have been assessed through field studies at a variety of underground sites. These studies indicate that the effects of excavation on rock stability tend to be highly site-specific, depending on rock physical properties, the presence and orientation of faults and fractures, and the local stress regime. Excavation often leads to localized increases in permeability. Heating generally results in an increase in stress and a reduction in permeability due to thermal expansion. The results of THM experiments conducted at the Nevada Test Site and the Stripa underground laboratory in Sweden are summarized below.

4.3.7.6.1 Nevada Test Site Thermal-Hydrologic-Mechanical Experiments

Four TM/THM experiments relating to high-level nuclear waste research were conducted at the G-tunnel in Rainier Mesa. These tests included a single borehole heater test, a small-diameter heater test, a heated block test, and a prototype engineered barrier system field test. One objective of the heated block test was to measure rock mass mechanical and TM properties of ash-flow tuff under controlled thermal and stress loading conditions. The block was subjected to maximum temperatures ranging from 76° to 130°C and equal biaxial stresses with magnitudes up to 10.6 MPa (Zimmerman et al. 1986 [DIRS 145625]). The effective modulus of deformation ranged from 0.4 to 0.83 times the intact rock measurements, depending on the number of joints included and their apertures. A slight dependence of modulus on stress was indicated, but no significant temperature effects on modulus were identified.

A second objective of the heated block test was to determine the effects of excavation, stress, and temperature changes on the permeability of a single joint. The permeability of a single near-vertical fracture was measured using three vertical boreholes in a linear array. The largest changes in permeability were associated with excavation of the block, when the apparent permeability increased from 76×10^{-12} m^2 to $758\times10^{-12}m^2$. Subsequent compressive loading decreased the permeability but did not completely reverse the unloading conditions, and the apparent permeability ranged from 252×10^{-12} m^2 to 332×10^{-12} m^2 microdarcies over a stress range of 3.1 to 10.6 MPa (Zimmerman et al. 1986 [DIRS 138273], p. ix and Section 11). Increased temperature under biaxial confinement decreased the fracture aperture, lowering the apparent permeability from 234 to 89 microdarcies during heating caused by thermal expansion of the rock. These observations are consistent (of the same order of magnitude) with the Yucca Mountain THM modeling and field studies described earlier.

4.3.7.6.2 Underground Testing at Stripa

A time-scaled heater test was performed at Stripa to investigate the long-term TM response to thermal loading (Chen et al. 1980 [DIRS 154672]). Analysis showed that, in the full-scale and time-scale heater tests, heat flow conformed to linear conduction theory and was not affected by fractures or other discontinuities. Thermoelastic deformation of the rock mass was nonlinear and less than expected. Early in the tests, measured displacements were much less than predicted by linear thermoelasticity. Later, the displacements increased uniformly, but in fixed proportions to predicted levels. This was likely a result of the closing of fractures in response to thermal expansion. Fracture closure was confirmed by observation of diminished water inflow to the heater and instrument boreholes (Nelson et al. 1981 [DIRS 150092]) and by increased compressional wave velocity during heating (Paulsson et al. 1980 [DIRS 154570]). The closing of fractures (and resulting changes in fracture permeability due to thermal input) is consistent with the results of the Yucca Mountain studies described in this section.

4.3.7.6.3 Geothermal Reservoir Temperature-Permeability Correlation

In addition to field studies of coupled THM processes that provide direct evidence of how a potential repository at Yucca Mountain would perform, corroborative results on coupled THM effects may be found in the geothermal literature. A survey of geothermal reservoir properties worldwide (Björnsson and Bodvarsson 1990 [DIRS 154606]) showed a correlation between permeability and temperature for various geothermal systems (Figure 4.3.7-19). The values are scattered, but they indicate a trend toward decreasing permeability with increasing temperatures. The low permeability at temperatures around 300°C and above is more likely caused by geochemical effects. The THM effects may be present at lower temperatures. The straight-line fit through the points has a regression coefficient of 0.5 and shows a half-order decrease in permeability with a 100C° increase in temperature (Bodvarsson 2001 [DIRS 154669], Attachment 4, p. 36).

4.3.7.7 Summary of Uncertainties and Their Treatment

Table 4.3.7-5 provides a summary of the uncertainty issues related to THM effects on seepage and their treatment.

4.3.7.8 Summary and Conclusions

Two alternative conceptual and numerical models have been used to study the impact of coupled THM processes on potential seepage into drifts: the distinct-element model and the fully coupled THM continua model. Two thermal operation modes were also considered, one with above-boiling temperatures near the repository and the other with below-boiling temperatures. Detailed results on stresses, deformations, and changes in permeability at a series of times after waste emplacement have been calculated. While significant changes may be found very close to the drift walls (covered by drift degradation scenarios), permeability changes may be about one order of magnitude; a comparison of percolation fluxes and saturation about 20 m directly above a drift in the Tptpll unit do not show much difference between the fully coupled THM and purely TH cases. Thus, the results so far do not require adjustments in seepage estimates already in the TSPA baseline (CRWMS M&O 2000 [DIRS 153246]).

Two models are presented to evaluate uncertainties and the effect of different thermal operating modes. A distinct element analysis representing a two-way TM coupled analysis is presented in Section 4.3.7.3. Using temperatures imported from a multiscale thermal model at discrete time intervals, the results of the distinct element analysis concludes heating associated with waste emplacement will cause drift walls to displace inward as horizontal stress levels increases. Model results predict fracture permeability will increase substantially in the first 2 m of rock around the emplacement drift. The distinct element model also predicts fracture permeability will increase in the region above the drift, extending to one drift diameter above the drift wall (see Section 4.3.7.3.3). Increases in permeability greater than one order of magnitude are not predicted beyond 0.5 m from the drift, except in the region above the drift (see Section 4.3.7.3.3). Beyond the immediate zone of increased permeability, permeability is substantially reduced in vertical fractures, leading to an overall reduction in permeability (see Section 4.3.7.3.3, Bullet 2).

A coupled THM continua model calibrated against ESF niche data and the Drift Scale Test is consistent with available data (see Section 4.3.7.4.1). With waste emplacement and thermal input, the coupled model predicts thermal stress will reduce permeability all around the drift (see Section 4.3.7.4.4, Bullet 2). Although this reduction is relative to the initial excavation-induced permeability increase, there is a net permeability decrease after about one year of heating. In the longer term, thermal effects will cause permeability to change far from the drift (up to 100 m), with most change occurring in the vertical permeability. Permeability reduction is a function of initial local permeability values, being larger for initially low values.

While the results of these two approaches predict permeability reductions in the elastic regions away from the drift wall, there are apparent contradictory results at the drift wall: there is an increase in permeability in the distinct element analysis, but there is a decrease in permeability in the continuum analysis. These contradictions are caused by different model conceptualizations and are affected by local fracture and rock mass strength parameters. Because this region is near a free surface, a distinct element model provides more freedom of block movements along fracture planes, while such movements are prevented in the continuum model. This difference in simulation results may have an effect on the immediate neighborhood of the drift that is part of the drift degradation analysis (see Section 4.3.4).

Permanent changes in permeability are the results of inelastic rock behavior (see Section 4.3.7.4.5). The only inelastic strain to be expected is from shear displacement along preexisting fractures. This transitional behavior between elastic and inelastic behavior may occur during heating and cooling. The continuum THM model predicts no significant inelastic behavior, while the distinct element model predicts significant inelastic behavior and permanent changes near the drift wall. Outside the potentially inelastic region near the drift wall (which is part of the drift degradation analysis; see Section 4.3.4), the nonlinear inelastic behavior of the rock may be insignificant, as results from the Single Heater Test and Drift Scale Test indicate (see Section 4.3.7.4.2). However, the distinct element modeling (see Section 4.3.7.3.3) indicates a permanent permeability increased in regions away from the drift wall in the case of a high heat load. Further information on potential permanent changes in permeability will be available after the completion of the Drift Scale Test.

The permeability decreases caused by THM effects, apart from the immediate neighborhood of the drift that is part of the drift degradation analysis, are about one order of magnitude, which is within the range of the ambient seepage model (see Sections 4.3.4 and Section 4.3.7.5). Permeability increases predicted by the distinct element model are also within the range of the ambient seepage model. Consequently, the results so far indicate that percolation flux values and distribution above the drift are not significantly affected by THM processes not already captured by drift-scale degradation. The results do not indicate a significant TM or THM induced impact on repository performance that would change the results of the uncoupled TH analysis supporting the TSPA-SR (CRWMS M&O 2000 [DIRS 153246]; see also Section 4.3.7.5). In terms of performance, the evaluation of thermal operating modes suggests they have little effect on the THM responses on the rock beyond what has been captured in the TSPA-SR.

A number of uncertainties have been addressed in this section; however, many still remain, some of which are indicated in Table 4.3.7-5. A comprehensive comparison between the distinct-element model results and results from the fully coupled THM continua model has not yet been done. Though the coupled THM continua model has been calibrated against available data from the niche excavation tests and the Drift Scale Test, more comprehensive calibration studies are still needed. In particular, rock stiffness with respect to thermal stresses and the residual permeability values of the geological layers above the drift are important parameters for modeling THM impact. Finally, how heterogeneity in the initial permeability field around a drift interfaces with coupled THM processes in affecting the potential for drift seepage also needs to be addressed.

Table 4.3.1-1. Triangular Distributions of Seepage Fraction, Seep Flow Rate, and Standard Deviation of Seep Flow Rate as a Function of Percolation Flux

	Minimum of Triangle (Low-Seepage Case)			Peak of Triangle (Base Case)			Maximum of Triangle (High-Seepage Case)		
q (mm/yr)	f_s	Mean Q_s (m^3/yr)	Std. Dev. Q_s (m^3/yr)	f_s	Mean Q_s (m^3/yr)	Std. Dev. Q_s (m^3/yr)	f_s	Mean Q_s (m^3/yr)	Std. Dev. Q_s (m^3/yr)
2.4	0	0	0	0	0	0	0	0	0
5	0	0	0	0	0	0	8.31×10^{-2}	8.57×10^{-2}	3.95×10^{-2}
14.6	0	0	0	0	0	0	8.31×10^{-2}	0.401	9.55×10^{-2}
60.0	0	0	0	0	0	0	0.310	0.701	0.815
73.2	6.60×10^{-3}	0.365	7.99×10^{-2}	5.41×10^{-2}	0.365	7.99×10^{-2}	0.376	0.788	1.02
213	6.60×10^{-3}	3.99	0.210	5.41×10^{-2}	4.24	0.210	0.452	4.24	2.34
500	7.65×10^{-2}	1.56	3.94	0.129	6.20	5.39	0.512	12.1	6.89
1000	0.261	27.1	16.1	0.303	30.9	17.3	0.609	35.6	18.5
3000	1	129	64.7	1	129	64.7	1	129	64.7

Source: Based on CRWMS M&O 2001 [DIRS 154291], Table 16.

Table 4.3.1-2. Summary of Uncertainty Issues Related to the Determination of Seepage-Relevant Parameters

Category	Uncertainty Issue	Treatment of Uncertainty Issue	Affected Goals
Conceptual uncertainties	Drift acting as capillary barrier	Based on unsaturated flow theory (Philip et al. 1989 [DIRS 105743]) Implemented through choice of unsaturated flow process model (Section 4.2.2; CRWMS M&O 2001 [DIRS 153045], Section 5) Confirmed through reproducibility (calibration) and prediction (validation) of seepage test data (CRWMS M&O 2001 [DIRS 153045], Sections 6.3.4 and 6.4.4) Corroborated by direct observations and natural analog studies (Section 4.3.1.7) Alternative conceptual models examined (CRWMS M&O 2001 [DIRS 153045], Section 6.5)	Development of general understanding of seepage process and basis for seepage prediction models
	Ability of model to predict seepage under natural percolation conditions (validity of extrapolation assumption)	Demonstrated ability to predict seepage tests in validation exercise (CRWMS M&O 2001 [DIRS 153045], Sections 6.3.4 and 6.4.4) Examined extrapolation to natural conditions in theoretical study (Finsterle 2000 [DIRS 151875])	Seepage predictions for waste emplacement drifts using calibrated model
	Significance of microfractures, film flow, small-scale surface roughness	Accounted for through estimation of effective parameters in seepage experiment (Section 4.3.1.3; CRWMS M&O 2001 [DIRS 153045], Section 6.1.6)	Determination of seepage-relevant parameters

Table 4.3.1-2. Summary of Uncertainty Issues Related to the Determination of Seepage-Relevant Parameters (Continued)

Category	Uncertainty Issue	Treatment of Uncertainty Issue	Affected Goals
Conceptual uncertainties (Continued)	Role of excavation-disturbed zone (EDZ)	Seepage test conducted within EDZ to directly obtain EDZ-related parameters relevant for seepage (Section 4.2.3)	Determination of seepage-relevant parameters
Data uncertainties	Evaporation losses prior to and during liquid-release tests	Assumed to be insignificant (CRWMS M&O 2001 [DIRS 153045], Sections 5.6 and 7.4) Partly accounted for in calibration of Tptpll data (CRWMS M&O 2001 [DIRS 153045], Section 6.3.3.2) Addressed in future seepage tests through humidity control and monitoring	Determination of unbiased parameters
	Storage and memory effect	Accounted for through simulation of actual test sequence during inversion (CRWMS M&O 2000 [DIRS 119412], Section 6.4) Mitigated by conducting long-term seepage experiments (CRWMS M&O 2001 [DIRS 153045], Section 6.1.6)	Determination of unbiased parameters
	Random measurement errors	Accounted for in error analysis (CRWMS M&O 2001 [DIRS 153045], Table 11)	Determination of parameter uncertainty
Parameter uncertainties	Formation-specific parameters	Seepage tests performed in Tptpmn and Tptpll to obtain unit-specific, seepage-relevant parameters (CRWMS M&O 2001 [DIRS 153045], Sections 6.3 and 6.4) Determined average properties and measure of variability (CRWMS M&O 2001 [DIRS 153045], Table 11)	Determination of seepage-relevant parameters
	Heterogeneity	Use of heterogeneous seepage models (CRWMS M&O 2001 [DIRS 153045], Sections 6.3.2 and 6.4.2; CRWMS M&O 2000 [DIRS 153314], Section 6.3) Calibration and prediction partly based on multiple realizations of permeability field (CRWMS M&O 2001 [DIRS 153045], Sections 6.3.3.3; CRWMS M&O 2000 [DIRS 153314], Section 6.3) Standard deviation increased in seepage abstraction (CRWMS M&O 2001 [DIRS 154291], Section 6.2)	Distribution of seepage-relevant parameters
	Uncertainty propagation	Stochastic data uncertainty reflected in estimation uncertainty (CRWMS M&O 2001 [DIRS 153045], Table 11) Deterministic seepage predictions over entire range of potential parameter values as basis for probabilistic sampling (CRWMS M&O 2000 [DIRS 153314], Section 6.6) Parameter distributions developed based on estimation uncertainties and variability measures (CRWMS M&O 2001 [DIRS 154291], Section 6.2) Distribution of other input parameters (e.g., percolation flux) developed based on deterministic runs and sensitivity analyses (CRWMS M&O 2001 [DIRS 154291], Sections 6.2 and 6.3) Linear uncertainty propagation analyses and Monte Carlo simulations performed as part of model validation (CRWMS M&O 2001 [DIRS 153045], Sections 6.3.4 and 6.4.4)	Distribution of parameters in TSPA calculation

Table 4.3.2-1. Cases Considered in Flow Focusing Sensitivity Studies

Realization	Infiltration (mm/yr)	Infiltration Pattern	Correlation Length for Fracture Permeability (m)
Realization #1	1 to 500	Uniform	1
Realization #2	1 to 500	Uniform	1
Realization #3	1 to 500	Uniform	3
Realization #4	5	Spatial Pulse/5 m	1

Table 4.3.2-2. Summary of Uncertainty Issues Related to Flow Focusing and Discrete Flow Paths in the TSw Hydrogeologic Unit

Category	Uncertainty Issue	Treatment of Uncertainty Issue	Affected Goals
Conceptual uncertainties	Representation of multiscale flow focusing	Large-scale flow redistribution captured in mountain-scale model Intermediate-scale flow focusing addressed through flow focusing factors in abstraction Small-scale flow focusing explicitly accounted for in heterogeneous drift-scale model	Percolation distribution for seepage models
	Development of flow channels	Mountain-scale model assumes homogeneous hydrostratigraphic units Percolation calculation in high-resolution, stochastic permeability field	Simulating intermediate-scale channel development
	Validity of weeps model, active fracture model, and stochastic fracture continuum model	Weeps model used to obtain upper limit of weep spacing in seepage abstraction Active fracture model used to obtain lower limit of weep spacing in seepage abstraction Sensitivity analyses of effect of fracture/matrix interaction on flow focusing	Determination of flow focusing factors for seepage abstraction
	Role of lithophysal cavities	Lithophysal cavities included in seepage model Accounted for through estimation of effective parameters	Small-scale flow focusing
	Role of PTn	PTn assumed to dampen spatial and temporal flow focusing Transient simulations performed for locations without PTn	Assessment of steady-state assumption
Data uncertainties	Observing or testing preferential flow	Continue weep observations in Niche 5 and others Chlorine-36 observations and analyses in ESF Analyze observed saturation and water potential distributions to derive weep spacing Analogue studies from appropriate sites	Validating flow focusing model

Table 4.3.2-2. Summary of Uncertainty Issues Related to Flow Focusing and Discrete Flow Paths in the TSw Hydrogeologic Unit (Continued)

Category	Uncertainty Issue	Treatment of Uncertainty Issue	Affected Goals
Parameter uncertainties	Parameters for generating stochastic fracture permeabilities for the TSw hydrogeologic units above the potential repository horizon	Determined through calibration against pneumatic and air-permeability data	Determination of flow focusing and distribution of weep spacing
	Matrix effects	Must be evaluated through sensitivity studies	Fracture and matrix flow components of focused flow

Table 4.3.3-1. Summary of Uncertainty Issues Related to Rock Bolts

Category	Uncertainty Issue	Treatment of Uncertainty Issue	Affected Goals
Conceptual uncertainties	Rock bolt condition	Detailed simulations conducted for various rock bolt properties (intact, grouted, and empty hole)	Impact of rock bolts on seepage
	Flow into and out of rock bolt hole	Detailed simulations conducted Sensitivity analyses performed regarding potential of backflow from rock bolt into formation Conservative simulation performed with maximum inflow into and no outflow from rock bolt	Impact of rock bolts on seepage
Data uncertainties	Observation of dripping from rock bolts	Discussed alternative conceptual models explaining observed dripping from rock bolts	Validating rock bolt model
Parameter uncertainties	Parameters of rock bolts	Performed sensitivity analysis for large range of rock bolt properties	Determination of seepage increase due to rock bolts

Table 4.3.4-1. Seepage Percentage for Alternative Drift-Degradation Scenarios for Qp = 500 mm/yr and Set A

Condition	Seepage Percentage		
	R1	R2	R3
No-degradation case	7.1	7.1	13
1 m rockfall from crown of drift	7.2	7.3	12
1m rockfall from springline of drift	7.1	7.1	13
3 m rock failure in drift roof	9.0	11	15

Source: CRWMS M&O 2000 [DIRS 153314], Table 12.

Table 4.3.4-2. Seepage Percentage for Set A Drift Degradation Scenarios

Q_p (mm/yr)		14.6	73.2	213.4	500
Base Case	R1	0.0	0.0	0.46	5.69
	R2	0.0	0.0	0.82	11.04
	R3	0.0	0.0	0.15	10.71
	Average	0.0	0.0	0.48	9.15
Worst Case	R1	0.0	0.0	0.48	8.97
	R2	0.0	0.0	0.86	13.99
	R3	0.0	0.0	0.34	12.58
	Average	0.0	0.0	0.56	11.85
75% Case	R1	0.0	0.0	2.87	10.63
	R2	0.0	0.0	3.39	17.53
	R3	0.0	0.0	2.36	16.50
	Average	0.0	0.0	2.87	14.89

Source: TerBerg 2001 [DIRS 155032].

Table 4.3.4-3. Seepage Percentage for Set B´ Drift Degradation Scenarios

Q_p (mm/yr)		500	1000	1500	2000	2500
Base Case	R1	0.0	0.0	0.33	0.55	0.83
	R2	0.0	0.0	0.50	1.05	2.09
	R3	0.0	0.0	0.0012	1.03	2.86
	Average	0.0	0.0	0.28	0.88	1.93
Worst Case	R1	0.0	0.2	0.65	1.42	2.41
	R2	0.0	0.0	1.50	3.04	4.56
	R3	0.0	0.0	0.11	1.94	4.25
	Average	0.0	0.07	0.75	2.13	3.74
75% Case	R1	0.0	0.0	0.33	0.59	1.24
	R2	0.0	0.0	0.50	1.06	2.32
	R3	0.0	0.0	0.33	1.36	3.10
	Average	0.0	0.0	0.39	1.00	2.22

Source: TerBerg 2001 [DIRS 155032].

Table 4.3.4-4. Summary of Uncertainty Issues Related to Determining Seepage-Relevant Parameters

Category	Uncertaint Issue	Treatment of Uncertainty Issue	Affected Goals
Conceptual uncertainties	Frequency and geometry of rockfalls	Used 3-D drift geometry from detailed rockfall analyses based on a rock-mechanics code and in situ fracture geometric data	Impact of rockfall on seepage
Data uncertainties	Seepage data from degraded drift	Seepage-relevant parameters obtained by calibration include effects of roughness Calibrated model used to simulate seepage into degraded drift	Validating seepage model
	Rockfall data	Observation in ESF and other tunnels and cavities	Validating rockfall model
Parameter uncertainties	Seepage-relevant parameters	Simulations performed with best-estimate parameter set of Tptpmn and Tptpll Sensitivity analyses performed for various percolation fluxes	Determining seepage increase from drift degradation

Table 4.3.5-1. Analysis Model Report Revision 00 and Post-Analysis Model Report Lithophysae Thermal Property Values

Unit	AMR Thermal Property Values			Lithophysae Thermal Property Values		
	C_R J/(kg °K)	λ_{wet} W/m °K	λ_{dry} W/m °K	C_R^* J/(kg °K)	λ wet, with lithophysae W/m °K	λ dry, with lithophysae W/m °K
Tptpul (TSw33)	882.5	1.683	0.79	657.2	1.55	0.84
Tptpmn (TSw34)	948	2.33	1.56	948	2.33	1.56
Tptpll (TSw35)	900	2.02	1.2	770.5	1.87	1.27

Source: Bodvarsson 2001 [DIRS 154669], Attachment 17, pp. 46 to 48.

Table 4.3.5-2. Statistical Parameters Used in the Three-Dimensional Heterogeneous Line-Averaged-Heat-Source, Drift-Scale Thermohydrologic Model Realizations

Stochastic Realization	Standard Deviation of *k* (log_{10})	Correlation Length (m)			van Genuchten Alpha Value Correlated to *k*
		Lateral (x)	Longitudinal (y)	Vertical (z)	
A-56	1.5	0.5	0.5	4.0	yes
A-34	1.5	0.5	0.5	4.0	yes
B-56	1.5	0.5	0.5	4.0	no
B-34	1.5	0.5	0.5	4.0	no
C-56	1.0	1.0	1.0	1.0	yes
C-34	1.0	1.0	1.0	1.0	yes
D-56	2.3	1.0	1.0	2.0	yes
D-34	2.3	1.0	1.0	2.0	yes

Source: BSC 2001 [DIRS 154985], Table 6-8.

Table 4.3.5-3. Input Parameters for Application of Asperity-Induced Episodic Infiltration at Yucca Mountain

Input Parameter	Value/Distribution	Basis/Reference
Fracture storage aperture, b_1 [m]	Assumed log-normal distribution $\mu_{ln(b1)}$ = -6.3 $\sigma_{ln(b1)}$ = 0.48	Mean aperture for TSw34, TSw35, and TSw36 from CRWMS M&O 2000 [DIRS 141418], Table 3. Standard deviation from CRWMS M&O 2000 [DIRS 141418], Table 4, last row, 6th column; DTN: SN0005T0581699.005 [DIRS 151514]. Values, originally in log space, were converted to natural log space for use in Mathcad 7.
Fracture pinch-point aperture, b_2 [m]	Assumed log-normal distribution $\mu_{ln(b2)}$ = -9.2 $\sigma_{ln(b2)}$ = 0.48	Mean log aperture calculated using Equation 27 and values in CRWMS M&O 2000 [DIRS 141418], Table 4, 6th row, 1st - 4th columns. Standard deviation from CRWMS M&O 2000 [DIRS 141418], Table 4, last row, 6th column; DTN: SN0005T0581699.005 [DIRS 151514]. Values originally in log space were converted to natural log space for use in Mathcad 7.
Width of individual weep, *w* [m]	Varied from 0.001 to 1	These limits bound values of weep widths observed by Kneafsey and Pruess 1998 [DIRS 145636] and Nicholl et al. 1994 [DIRS 141580].
Spacing between weeps, *a* [m]	Uniform distribution between log values of -0.14 and 1.78 (log-uniform distribution in real space)	The limits of the distribution are calculated by taking one standard deviation below and above the lower- and upper-bound log of the means, respectively, as given in CRWMS M&O 2001 [DIRS 154291], Section 6.4.3, Table 15; DTN: SN0012T0511599.003 [DIRS 153688], which calculated flow focusing effects using results from three-dimensional UZ flow models.
Dynamic viscosity, μ [kg/m-s]	4.89×10^{-4}	Calculated at average temperature for subboiling conditions at (20+96)/2=58ºC (Incropera and DeWitt 1985 [DIRS 100623], Table A.6).
Surface tension, σ [N/m]	0.067	Calculated at average temperature for subboiling conditions at (20+96)/2=58ºC (Incropera and DeWitt 1985 [DIRS 100623], Table A.6).
Liquid density, ρ [kg/m^3]	984 (used for sub-boiling conditions) 961 (used for boiling conditions)	Subboiling value calculated at average temperature of (20+96)/2=58ºC. Boiling value calculated at 96ºC (Incropera and DeWitt 1985 [DIRS 100623], Table A.6).
Heat of vaporization, h_{fg} [J/kg]	2.27×10^6	Calculated at 96ºC (Incropera and DeWitt 1985 [DIRS 100623], Table A.6).
Extent of boiling front from drift center [m]	Assumed uniform distribution from 2.75 to 7.95	The lower value of the distribution is based on the drift radius; the upper value is the average maximum boiling extent calculated from 610 locations (DTN: LL000509112312.003 [DIRS 150798]). The superheated distance to the drift wall, *d*, is calculated by subtracting 2.75 m from the resulting distribution.
Thermal diffusivity, α [m/s^2]	5.25×10^{-7}	Value calculated by dividing thermal conductivity of dry rock (1.2 W/m-K) by rock-grain density (2540 kg/m^3) and rock-specific heat (900 J/kg-K) (DTN: SNT05071897001.012 [DIRS 106089]).
Heat load, *Q* [W/m]	148	The source data are from DTN: SN9907T0872799.001 [DIRS 111485] (see "DRFT-Scale 2-D models" worksheet in Excel file "heat TSPA-SR--9918.4-Ta.xls"). These data are multiplied by 0.94131 per CRWMS M&O 2000 [DIRS 149862], p. 83, and then an average heat generation [W/m] is calculated for 1000 years with 70% energy removal for 50 years. This is calculated by integrating the resulting heat generation curve for 1,000 years (Kaleidagraph v. 3.5.1) and then dividing the area by 1,000 years.

Table 4.3.5-3. Input Parameters for Application of Asperity-Induced Episodic Infiltration at Yucca Mountain (Continued)

Input Parameter	Value/Distribution	Basis/Reference
Infiltration rate, *u* [mm/year]	Uniform distribution from 1 to 45	In CRWMS M&O 2000 [DIRS 153246], Table 3.2-2, glacial-transition average infiltrations are given as 2.2 mm/yr for low (probability 17%), 20 mm/yr for medium (probability 48%), 37 mm/yr for high (probability 35%). The weighted average infiltration is then approximately 23 mm/yr (0.17x2.2 + 0.48x20 + 0.35x37). The limits of the uniform distribution are chosen to range from below the low-case mean to above the high-case mean, with the appropriate weighted mean of 23 mm/yr. A nice, simple choice is a uniform distribution from 1 to 45 mm/yr.

Table 4.3.5-4. Summary of Uncertainty Issues Related to Thermohydrologic Effects on Seepage

Category	Uncertainty Issue	Treatment of Uncertainty Issue	Affected Goals
Parameter uncertainties	Thermal operating modes	Sensitivity studies for both higher- and lower-temperature operating modes	Thermal effects on UZ flow and seepage
	Impact of lithophysal cavities on thermal properties	Incorporate effects of lithophysal cavities in thermal conductivity and heat capacity values Sensitivity studies using properties with and without effects of lithophysal cavities	Temperature distribution, thermal effects on seepage
	Temperature-dependent heat capacity of the rock mass	Needs to be incorporated for sensitivity studies	Temperature distribution, spatial and temporal
	Hydrologic properties	Not expected to be significant for higher-temperature operating mode Need sensitivity studies for lower-temperature operating mode	Seepage
Data uncertainty	Thermal conductivity (effects of lithophysal cavities)	Field measurements needed	Temperature distribution, spatial and temporal
	Effect of faults on thermally induced flow	Sensitivity studies Data limitation, need liquid phase field testing in faults, need characteristic curves in faults	Thermal seepage
Conceptual model uncertainty	Effects of lithophysal cavities on gas and liquid flow	Need new conceptual model and validation against measurements	Redistribution of moisture
	Applicability of “active fracture” option of the dual-permeability model for coupled processes	Need sensitivity studies and validation against planned Cross Drift Thermal Test	Thermal seepage
	Heterogeneity (small scale)	Monte Carlo and sensitivity studies in progress	Thermal seepage
	Ventilation	Only reduction of heat from ventilation has been addressed Need realistic model on moisture removal	Thermal seepage, temperature

Table 4.3.5-4. Summary of Uncertainty Issues Related to Thermohydrologic Effects on Seepage (Continued)

Category	Uncertainty Issue	Treatment of Uncertainty Issue	Affected Goals
Numerical model uncertainty	Assumed geometry of a square drift	Less diversion of water than actual drift geometry	Thermal seepage, shedding of water
	Implementation of capillary barrier within the drift	Different treatment used	Thermal seepage, shedding of water
	Discretization	Different refinement of grids have been implemented Further refinement needed	Temperature, thermal seepage

Table 4.3.6-1. Comparison of Experimental and Potential Yucca Mountain Repository Conditions

	Experimental Conditions	Potential Yucca Mountain System
Thermal gradient	158°C/m	0.75°C/m (BSC 2001 [DIRS 154677], Figure 37b, p. 1126)
Fracture fluid flux	6E-4 m/s	3 E-8 m/s (Bodvarsson 2001 [DIRS 154669], Attachment 4, pp. 37 to 38)
Fracture aperture	31 μm	About 10 to 1,000 μm (small-scale fracture aperture measurements to 200μm were observed as reported in DTN: GS990908314224.009 [DIRS 146877]; smaller scale apertures inferred from modeling results)

Source: Experimental conditions DTN: LB0101THCPRCPX.001 [DIRS 154577].

Table 4.3.6-2. Summary of Uncertainty Issues Related to the Prediction of Thermal-Hydrologic-Chemical Effects on Seepage and Potential Seepage Chemistry

Category	Uncertainty Issue	Treatment of Uncertainty Issue	Affected Goals
Conceptual Uncertainties	Uncertainty in the dual-permeability model and its extension for coupled THC processes	Has not been treated directly Treated indirectly through model validation with the Drift Scale Test	Cannot resolve changes in matrix hydrologic properties and geochemistry near the fracture wall and effects on imbibition
	Mineral precipitation and dissolution take place nonuniformly in the fracture medium and in the matrix	Not treated directly, but indirectly as follows: In initial report, implemented an active fracture model that limits the reactive surface area and the area for diffusive transport between fractures and matrix In update, implemented permeability relation to change in hydraulic aperture, which captures the effect of mineral precipitation in narrower apertures Treated indirectly through model validation	Leads to uncertainty in the range of predicted changes in hydrologic properties and flow

Table 4.3.6-2. Summary of Uncertainty Issues Related to the Prediction of Thermal-Hydrologic-Chemical Effects on Seepage and Potential Seepage Chemistry (Continued)

Category	Uncertainty Issue	Treatment of Uncertainty Issue	Affected Goals
Conceptual Uncertainties	Effect of lithophysae on THC processes	Effect on thermal properties treated in post-update analyses Effect on hydrologic properties and their effect on transport and coupled THC processes were not treated	Results in greater uncertainty in the width of boiling zone and associated zone of maximum mineral precipitation. Adds uncertainty to gas phase transport and timing of simulated gaseous carbon dioxide concentrations
	Changes in infiltrating water chemistry and associated climate changes	Assessed indirectly through simulations using alternate water compositions	Results in more uncertainty in the range of potential chemical compositions during post-thermal period
	Implementation of THC numerical approaches in transitions from boiling to dryout zones	Reduced minimum liquid saturation for treating chemical reactions and refined to capture saturation gradients Assessed effect in extreme case of steep thermal gradient and narrow zone of saturation decline to zero	Adds uncertainty to prediction of maximum changes in hydrologic properties and transient changes in water chemistry during dryout and rewetting at a subgrid scale
Data Uncertainties	Composition of fracture water	Post-update analysis used alternative perched water analysis for fracture, matrix, and infiltrating water composition	Not a significant factor during early thermal period, but adds to uncertainty during port-thermal period as percolating waters rewet the drift
	Matrix pore water compositions	Alternate pore water analyses used in post-update analyses	Limits the range of potential water compositions that are predicted
	Thermodynamic and kinetic data	Treated through sensitivity studies on long-term behavior of ambient system chemistry, assuming a fixed infiltration rate Many uncertainties unknown and treated through model validation (Drift Scale Test and laboratory experiments)	Adds uncertainty to ranges of predicted water compositions, mineral assemblages, and changes in hydrologic properties
Parameter Uncertainties	Range in fracture porosity	Not treated directly Effect on permeability treated indirectly through implementation of permeability relation to hydraulic aperture	Limits range of possible effects on hydrologic properties and transport
	Heterogeneity	Fracture permeability treated heterogeneity in updated report Heterogeneity in matrix properties not treated Local heterogeneity in mineralogical properties not treated Heterogeneity in initial water geochemistry not treated directly; treated indirectly through alternate compositions	Matrix properties not significant because of low permeability Heterogeneity in mineralogic properties could amplify local effects on hydrologic properties Heterogeneity in water chemistry could lead to local mixing effects, leading to a greater range in uncertainty in predicted chemistry

Table 4.3.6-2. Summary of Uncertainty Issues Related to the Prediction of Thermal-Hydrologic-Chemical Effects on Seepage and Potential Seepage Chemistry (Continued)

Category	Uncertainty Issue	Treatment of Uncertainty Issue	Affected Goals
Parameter Uncertainties	Uncertainty propagation	Deterministic seepage chemistry and effects on seepage (i.e., flow) predictions over limited range of potential parameter values Distribution of other input parameters (e.g., infiltration and heat loading) developed based on deterministic runs and sensitivity analyses.	Distribution of parameters in TSPA calculation

Table 4.3.7-1. Input Parameters and Data Tracking Numbers for Distinct Element Analysis

Description	Value	Units	Data Tracking Number
Matrix Properties			
Dry Bulk Density	2,270	kg/m^3	MO0003SEPDRDDA.000 [DIRS 147607]
Intact Rock Elasticity Modulus	33.03	GPa	MO9911SEPGRP34.000 [DIRS 148524]
Rock Mass Elasticity Modulus	24.71	GPa	MO9911SEPGRP34.000 [DIRS 148524]
Poisson's Ratio	0.21	none	MO9911SEPGRP34.000 [DIRS 148524]
Joint Properties			
Joint Friction	41	degree	MO0003SEPDRDDA.000 [DIRS 147607]
Joint Cohesion	0.09	MPa	MO9911SEPGRP34.000 [DIRS 148524]
Joint Dilation Angle	29	degree	MO9911SEPGRP34.000 [DIRS 148524]
Initial Joint Aperture	0.098	mm	LB990501233129.001 [DIRS 106787]
Thermal Properties			
Thermal Expansion Coefficient	9.73E-6	degree C^{-1}	MO0004RIB00035.001 [DIRS 153848]
Stress and Stress Gradient			
In Situ Stress	7.6	MPa	MO0007RIB00077.000 [DIRS 154087]
Vertical Stress Gradient	0.023	MPa/m	MO0007RIB00077.000 [DIRS 154087]
Input Temperatures			
Input Temperatures	various	degree C	LL000114004242.090 [DIRS 142884]

Source: Blair 2001 [DIRS 155005], Table 2.

Table 4.3.7-2. Permeability Ratio Distribution for Horizontal Fractures

Time (years)	Permeability Ratio (%)							
	1.00E-5	1.00E-3	0.01	1	10	100	1000	Total
10	3.6	0.8	16.8	59.9	12.0	3.3	3.7	100
50	1.1	0.3	2.6	67.0	21.6	3.5	3.9	100
55	4.4	0.6	16.0	59.2	12.2	2.9	4.8	100
100	2.2	0.3	3.4	62.4	23.6	3.1	5.0	100
200	1.5	0.1	0.9	43.3	44.3	4.2	5.7	100
400	1.4	0.1	0.8	50.9	36.7	4.4	5.7	100
1000	1.5	0.1	0.8	55.2	32.2	4.6	5.7	100
100,000	0	0	0	2.2	45.5	40.9	11.4	100

Source: Blair 2001 [DIRS 155005], Table 4.

Table 4.3.7-3. Permeability Ratio Distribution for Vertical Fractures

Time (years)	Permeability Ratio (%)							
	1.00E-5	1.00E-3	0.01	1	10	100	1000	Total
10	4.7	2.7	43.2	40.2	4.7	2.1	2.4	100
50	3.1	2.1	49.6	35.6	5.0	2.2	2.5	100
55	62.6	7.6	17.6	5.6	2.0	1.8	2.7	100
100	80.6	2.8	7.3	3.0	1.81	1.7	2.8	100
200	75.7	4.0	9.3	3.9	2.3	1.9	3.0	100
400	74.2	4.0	10.2	4.2	2.5	2.0	3.0	100
1000	69.9	5.1	12.3	4.9	2.7	2.0	3.1	100
100,000	0	0	0	3.9	18.6	61.8	15.7	100

Source: Blair 2001 [DIRS 155005], Table 5.

Table 4.3.7-4. Thermal-Hydrologic-Mechanical Property Parameters Used in Simulations

Parameter	Tptpmn	Tptpll	Source
Young's modulus	14.77 GPa	14.77 GPa	CRWMS M&O 1999 [DIRS 126475], Table 10 to 15 and Table 24
Poisson's ratio	0.21	0.21	
Cohesion	2.6 MPa	2.6 MPa	
Friction angle (degrees)	57	57	
Dilation angle (degrees)	29	29	
Thermal expansion coefficient	4.14 E-6 /°C	4.14 E-6 /°C	
Tensile strength	1.54 MPa	1.54 MPa	
Initial hydraulic aperture for Equation 4.3.7-2, b_i	80.0 μm	164.8 μm	The value of b_i is calculated from mean fracture spacing (s) and isotropic permeability assuming an ideal cubic block model, leading to the following formula: $b_i = \sqrt[3]{k \times 6 \times s}$ (Bodvarsson 2001 [DIRS 154669], Attachment 9, pp. 21 to 29)
Maximum joint closure for Equation 4.3.7-2, b_{max}	541.6 μm	541.6 μm	Determined by model calibration against air-permeability experiments at ESF niches and Drift Scale Test (Bodvarsson 2001 [DIRS 154669], Attachment 9, pp. 12 to 26)

Table 4.3.7-4. Thermal-Hydrologic-Mechanical Property Parameters Used in Simulations (Continued)

Parameter	Tptpmn	Tptpll	Source
Exponent for Equation 4.3.7-2, α (1/Pa)	1.1 E-6	1.1 E-6	Determined by model calibration against air-permeability experiments at ESF niches and Drift Scale Test (Bodvarsson 2001 [DIRS 154669], Attachment 9, pp. 12 to 26)
Gradient of vertical stress σ_v	0.022 MPa/m	0.022 MPa/m	Within range of field measurements by Stock et al. (1985 [DIRS 101027]) and Lee and Haimson (1999 [DIRS 129667])
Horizontal stress σ_h	$0.35 \times \sigma_v$ MPa	$0.35 \times \sigma_v$ MPa	

Table 4.3.7-5. Summary of Uncertainty Issues Related to Thermal-Hydrologic-Mechanical Effects on Seepage

Category	Uncertainty Issue	Treatment of Uncertainty Issue	Affected Goals
Conceptual Model Uncertainties	Use of two-way coupling versus fully coupled THM coupling	TM analysis and fully coupled THM analyses have been done (Section 4.3.7.4.4)	Flux around drift and seepage into drift
	Use of distinct element method versus continua method	Distinct element and continua methods have been used (Sections 4.3.7.3 and 4.3.7.4) Reconciliation of the outcomes of the two methods to be conducted	Flux around drift and seepage into drift
	Capillary-permeability relationship	Leverett's relationship was used (Section 4.3.7.4.2); sensitivity studies to be conducted	Flux around drift and seepage into drift
Model Geometry Uncertainties	Boundary conditions used	A reasonable choice of boundary conditions was made for the current studies. Sensitivity study with range of conditions to be conducted	Flux around the drift and seepage into drift
	Drift near edge of repository	Current study considers a drift away from the repository boundary. Simulation of a drift near edge of repository to be conducted	Flux around the drift and seepage into drift
Parameter Uncertainties	Rock fracture stiffness in the layers Residue permeability values	Current values used were obtained from a calibration study using the ESF niche and Drift Scale Test data (Section 4.3.7.4.3) A complete THM analysis of the Drift Scale Test with supplementary measurements to be conducted	Change in permeability around seepage into drift
	Heterogeneity in permeability spatial distribution	Current study uses multiple hydrostratigraphic layers vertically; however, it assumes homogeneous properties within each layer. Additional simulations needed on heterogeneous field representing the hydrogeologic units. Studies with multiple realizations to be conducted	Flux around the drift and seepage into drift

INTENTIONALLY LEFT BLANK

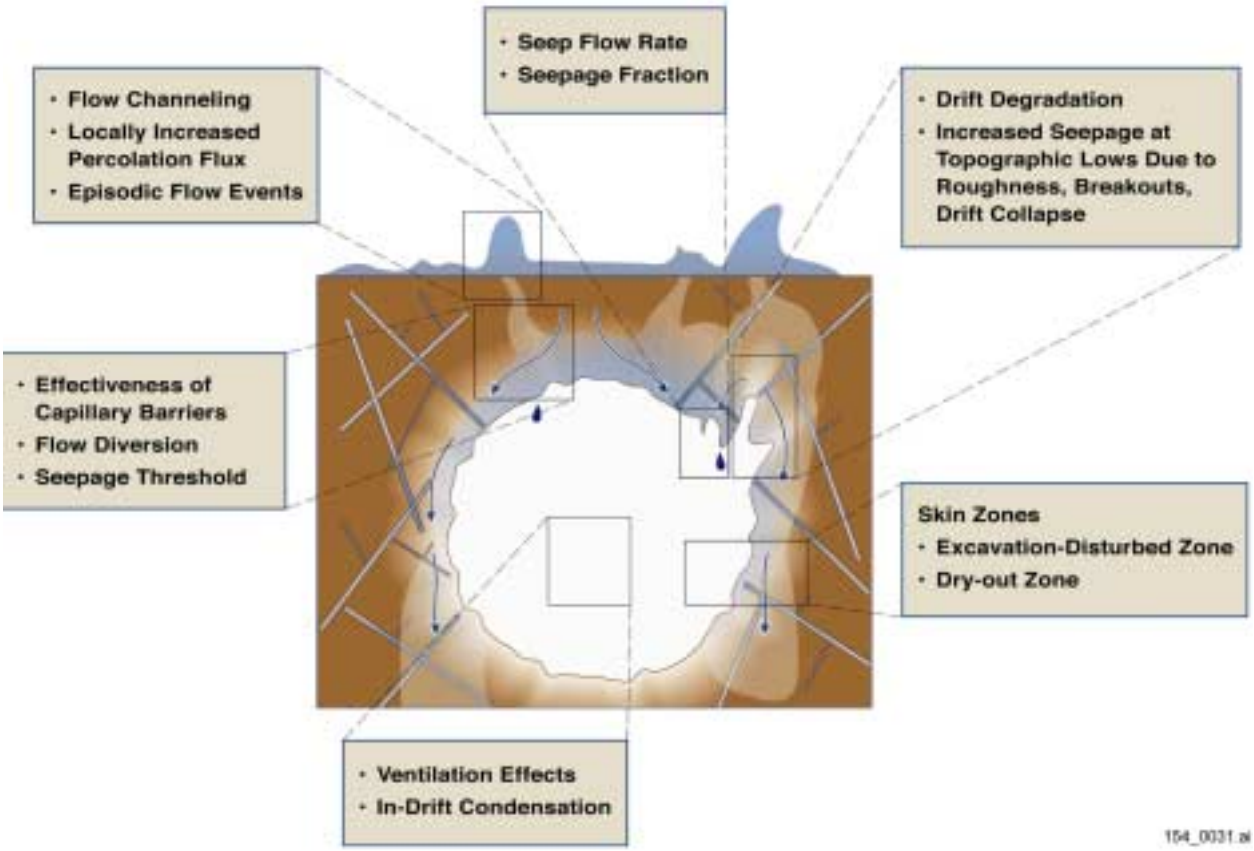

154_0031.ai

Figure 4.2-1. Seepage-Relevant Features and Processes

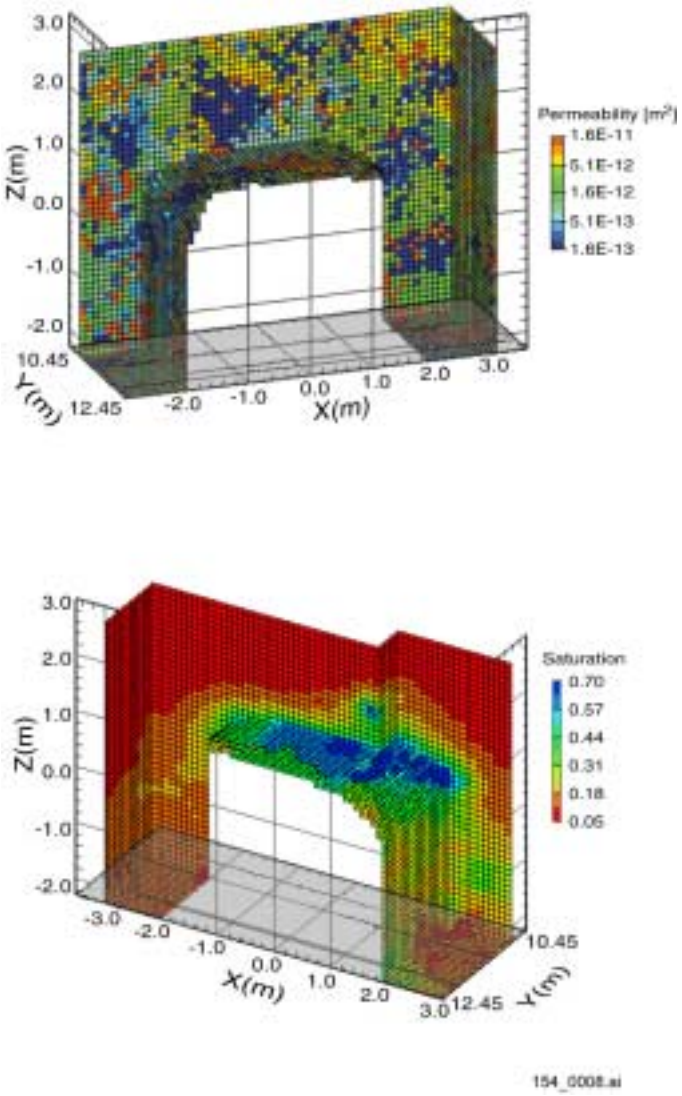

154_0008.ai

Source: CRWMS M&O 2001 [DIRS 153045], Figures 11 and 12c.

NOTE: Permeability field (upper) and late-time saturation distribution (lower) for a simulated liquid release test in Exploratory Studies Facility Niche 4 (located at stations 47 and 88).

Figure 4.3.1-1. Permeability and Saturation for a Simulated Liquid Release

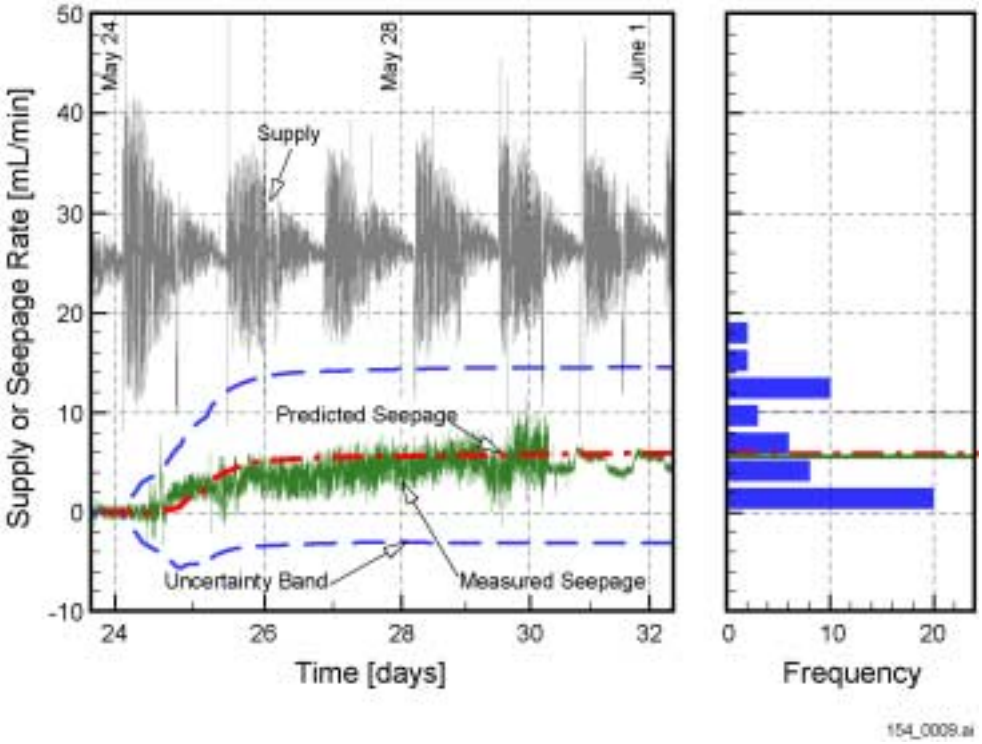

154_0009.ai

Source: CRWMS M&O 2001 [DIRS 153045], Figure 7c.

NOTE: Seepage experiments conducted in Zone 1 of borehole SYBT-ECRB-LA#2. The simulation uncertainty is calculated using first-order second-moment uncertainty propagation analysis. The right panel shows the histogram of the seepage rate at the end of the experiment as predicted by Monte Carlo simulations. Time is days since 00:00, April 30, 2000.

Figure 4.3.1-2. Water Supply, Measured Seepage Rates, and Predicted Seepage Rates

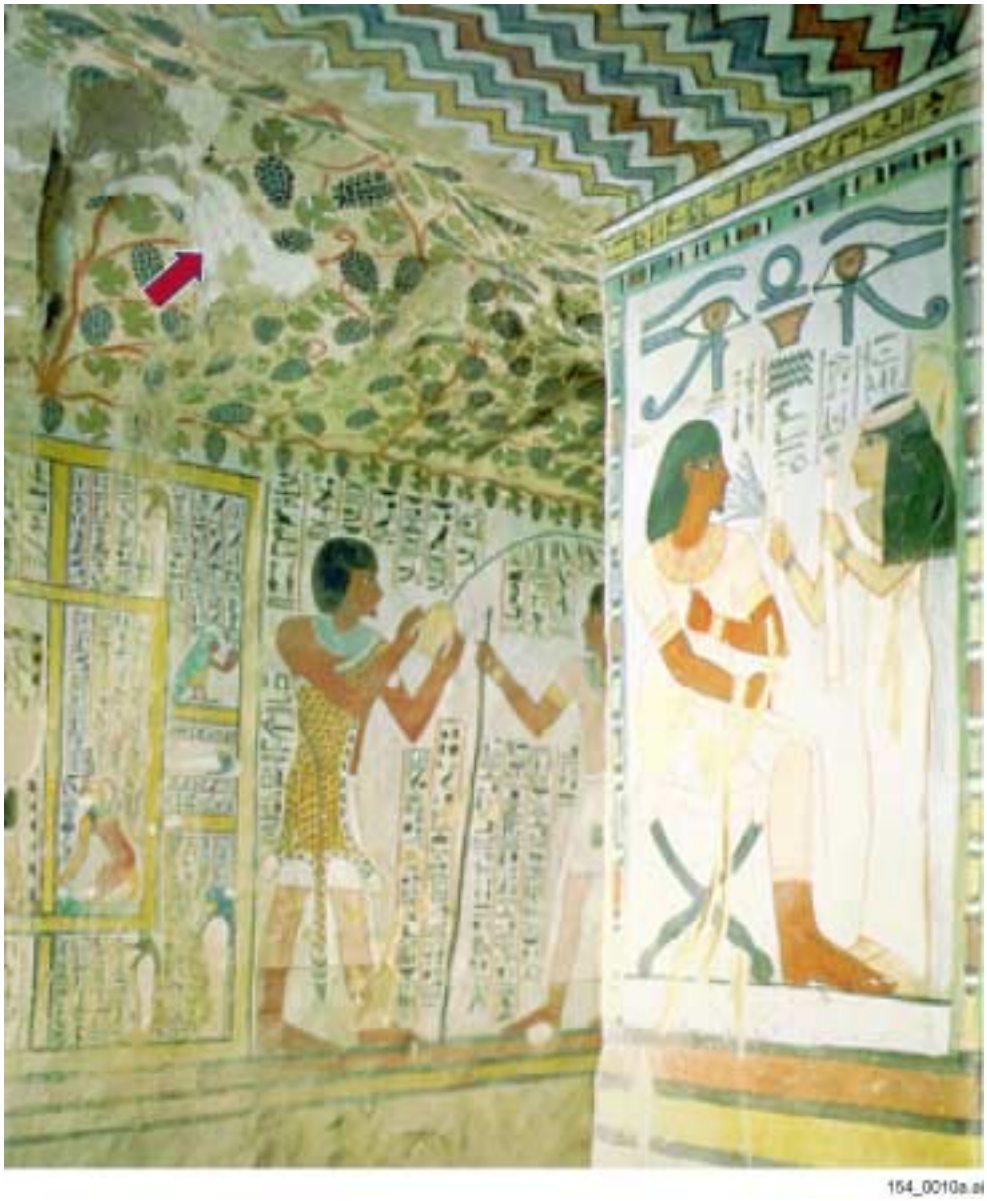

154_0010a.ai

NOTE: Photo shows spallation (see arrow) of vertical plaster wall, but no effect to plastered ceiling. The line between the zigzag pattern and the leaf pattern separates the ceiling from the wall.

Figure 4.3.1-3. Tomb of Sennefer in the Egyptian Valley of the Kings

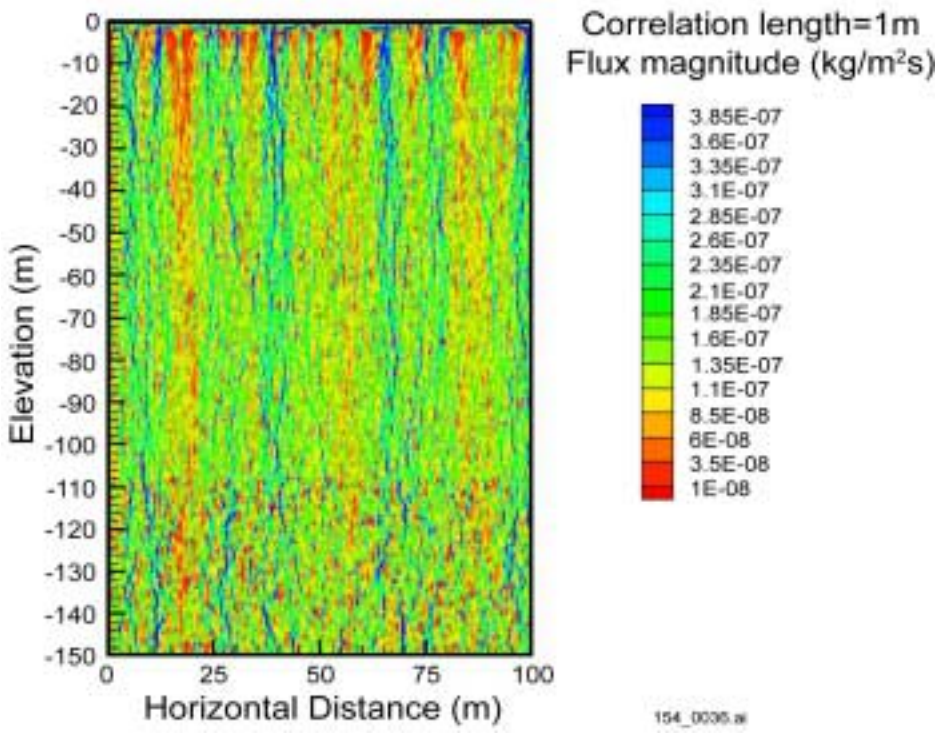

154_0036.ai

Source: Bodvarsson 2001 [DIRS 154669], Attachment 16, data file listed on p. 11.

NOTE: Simulation using the base case scenario with 1-m correlation length, forming several high-flux flow paths.

Figure 4.3.2-1. Distribution of Flux Magnitude within the Two-Dimensional Model Domain

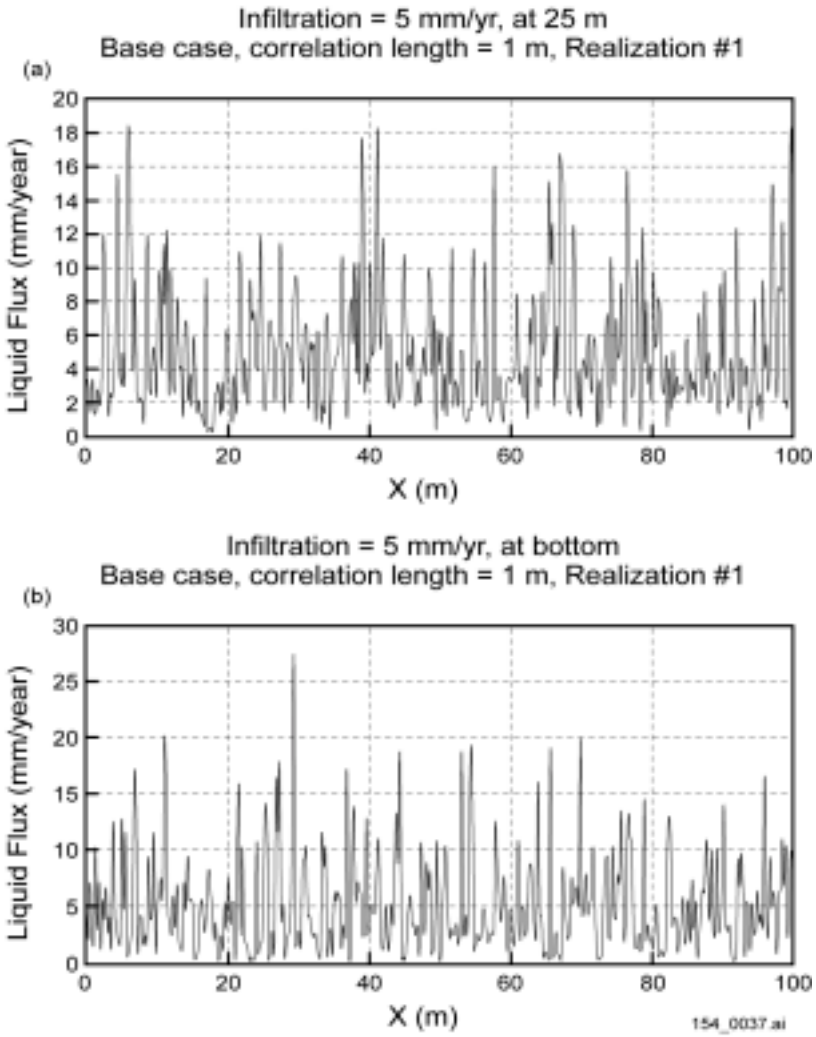

154_0037.ai

Source: Bodvarsson 2001 [DIRS 154669], Attachment 16, p. 12 and data files listed on p. 11.

NOTE: Simulated using the base case scenario, correlation length = 1 m, infiltration = 5 mm/yr, (a) at a depth of 25 m or (b) at the bottom.

Figure 4.3.2-2. Distribution of Vertical Fluxes within the Two-Dimensional Model Domain

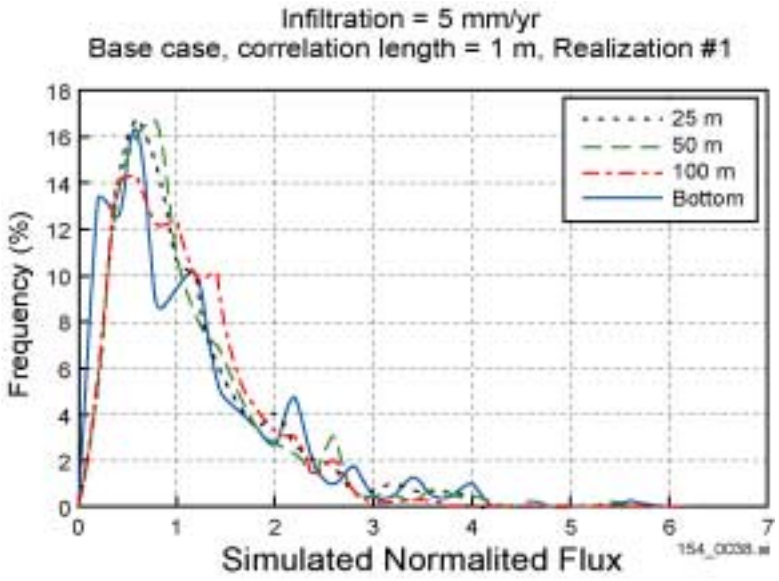

154_0038.ai

Source: Bodvarsson 2001 [DIRS 154669], Attachment 16, p. 13.

NOTE: Simulated using the base case scenario, correlation length = 1 m, infiltration = 5 mm/yr, and Realization #1.

Figure 4.3.2-3. Comparison of Frequency Distribution of Simulated Fluxes at Different Elevations within the Two-Dimensional Model Domain

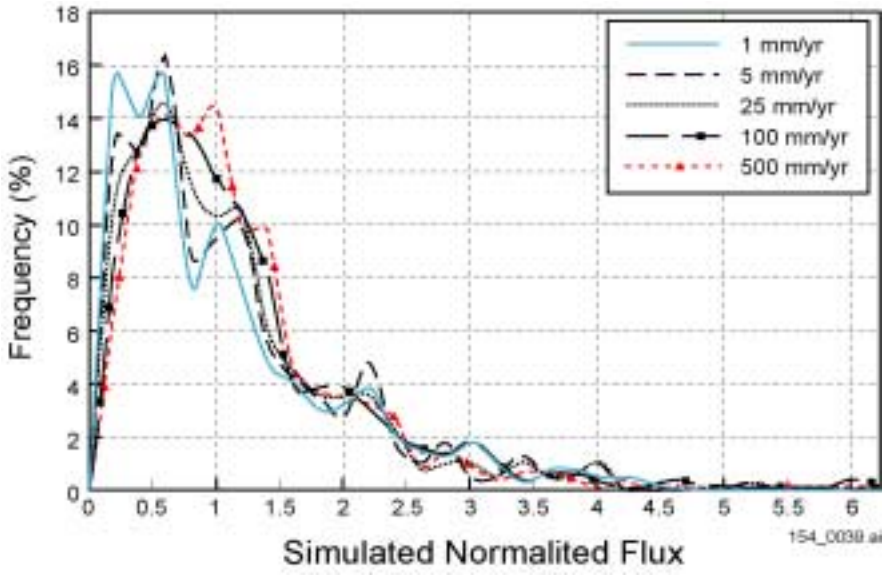

154_0039.ai

Source: Bodvarsson 2001 [DIRS 154669], Attachment 16, p. 14.

NOTE: Simulated with Realization #1, flux at potential repository horizon.

Figure 4.3.2-4. Frequency Distribution of Simulated Fluxes at Different Infiltration Rates within the Two-Dimensional Model Domain

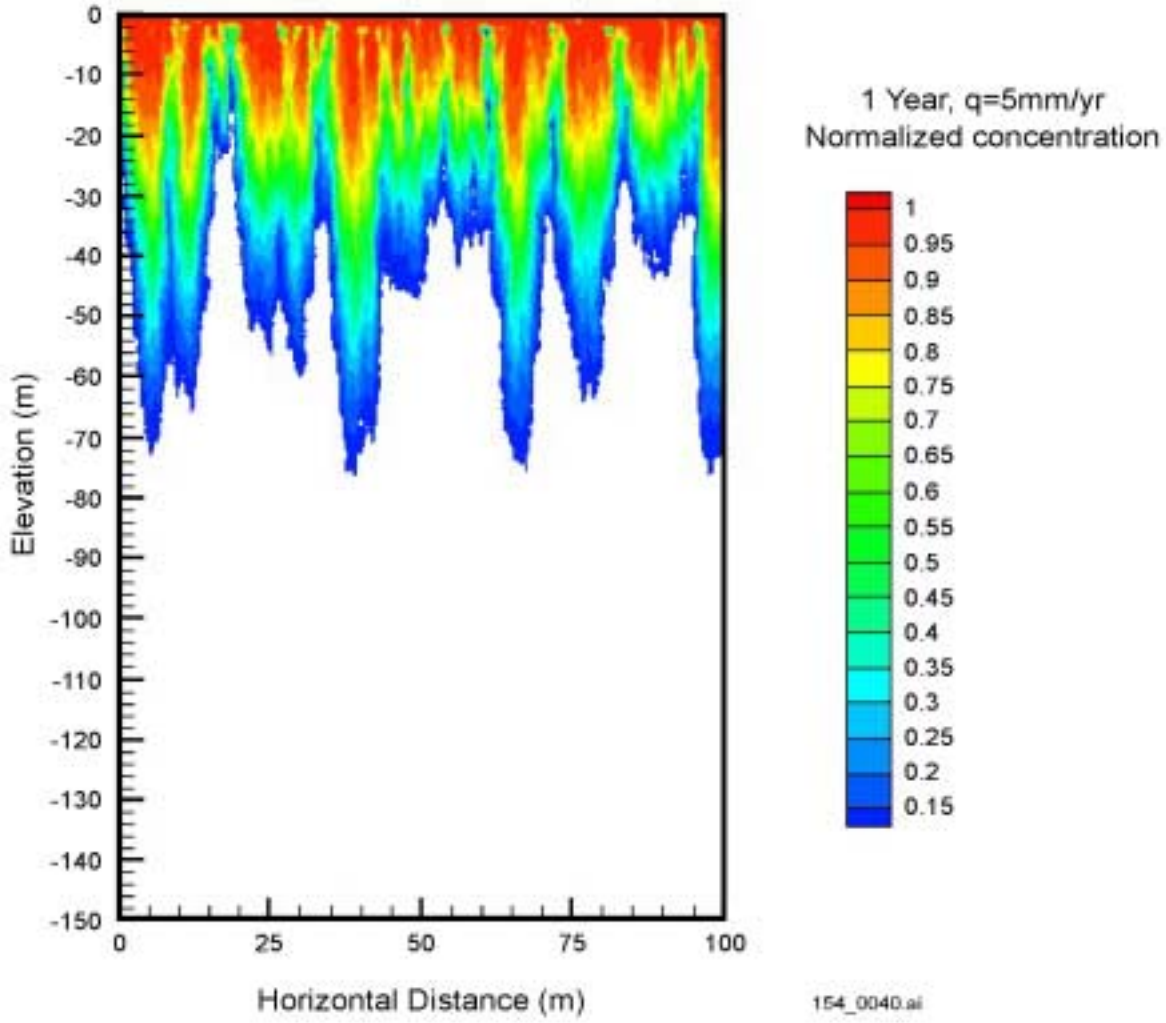

154_0040.ai

Source: Bodvarsson 2001 [DIRS 154669], Attachment 16, p. 20.

NOTE: Simulated distribution of tracer concentration within the model domain; simulation time = 1 yr, q = 5 mm/yr.

Figure 4.3.2-5. Simulated Preferential Flow Pathways

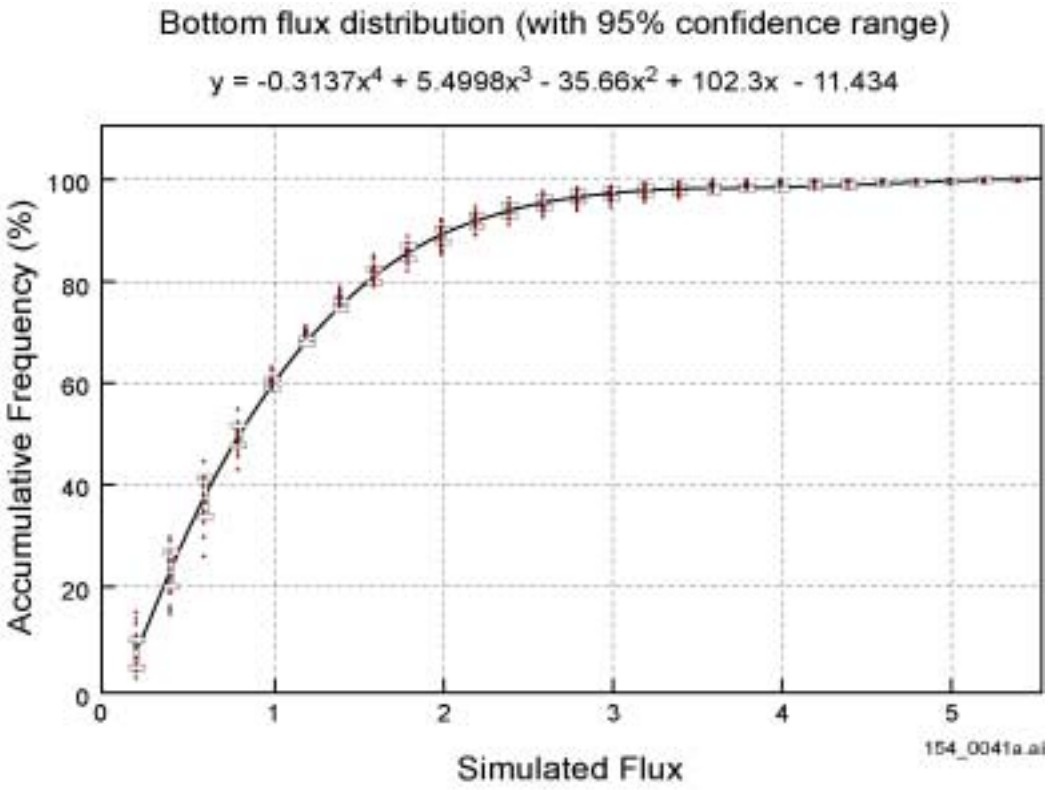

154_0041a.ai

Source: Bodvarsson 2001 [DIRS 154669], Attachment 16, p. 22.

NOTE: Results averaged over all simulations. Regression: $y = -0.3137x^4 + 5.4998x^3 + 35.66x^2 + 102.3x - 11.434$. Range is given as the 95-percent confidence interval.

Figure 4.3.2-6. Distribution and Range of Cumulative Flux as a Function of Percolation Flux for the Bottom of the Model Domain

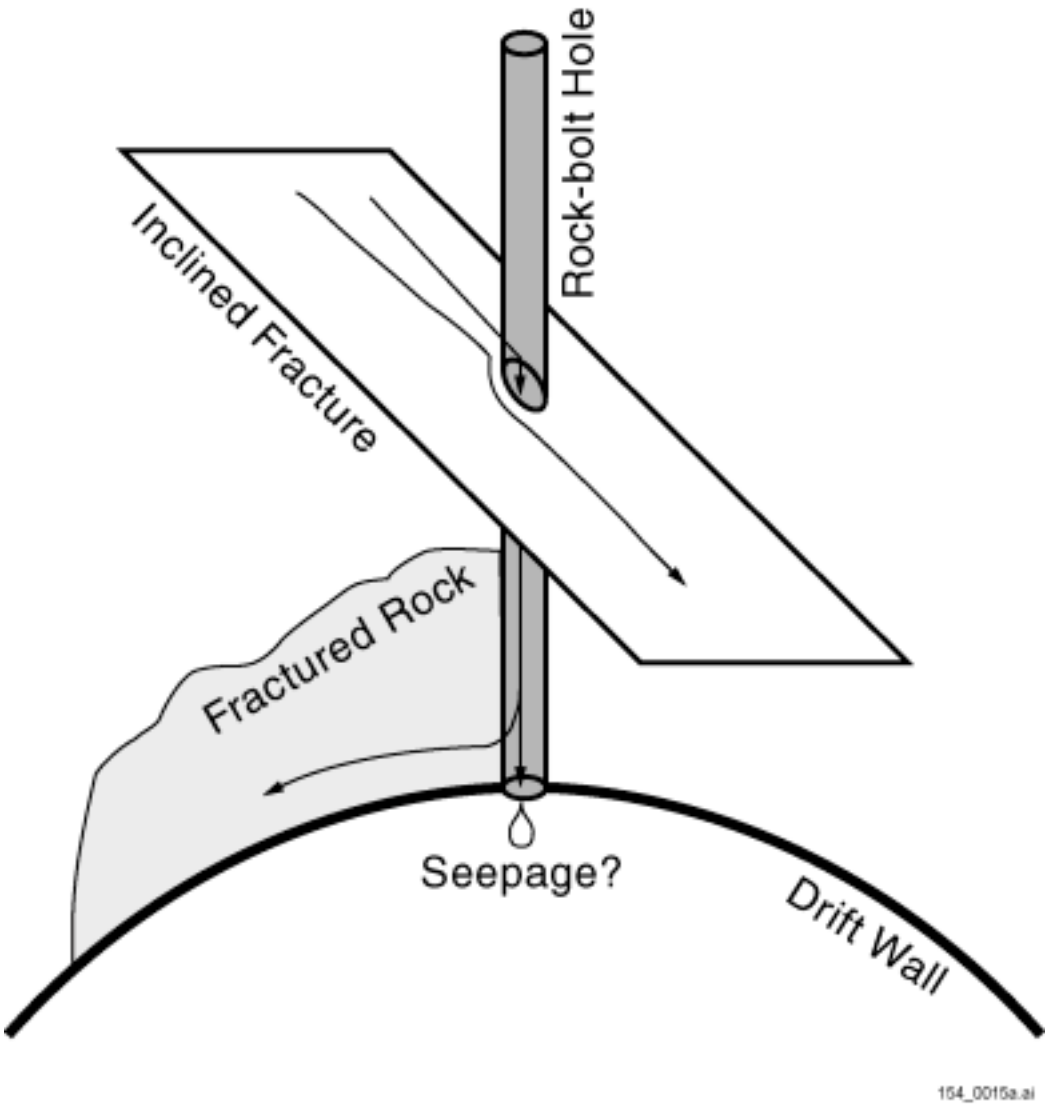

154_0015a.ai

NOTE: Arrows show possible flow paths, which may result in seepage directly attributable to the presence of a rock bolt hole.

Figure 4.3.3-1. Conceptual Model of How a Rock Bolt Hole Might Affect Seepage

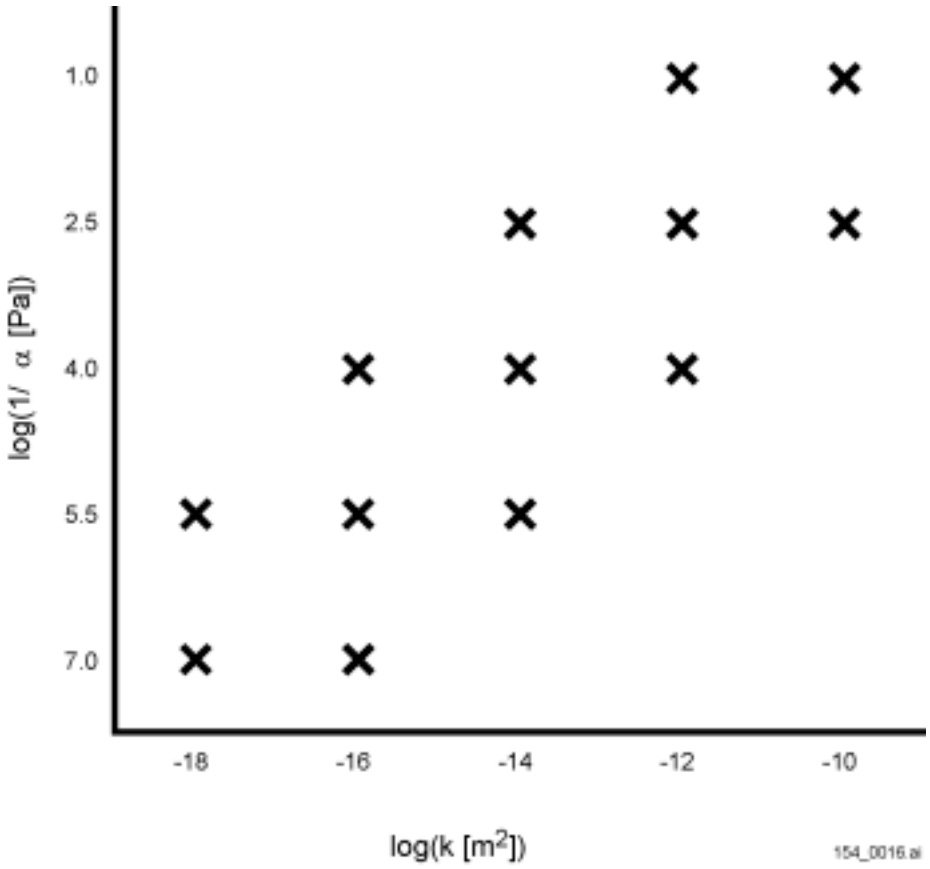

154_0016.ai

NOTE: Permeability is k and capillarity is 1/α.

Figure 4.3.3-2. Grout Parameter Combinations

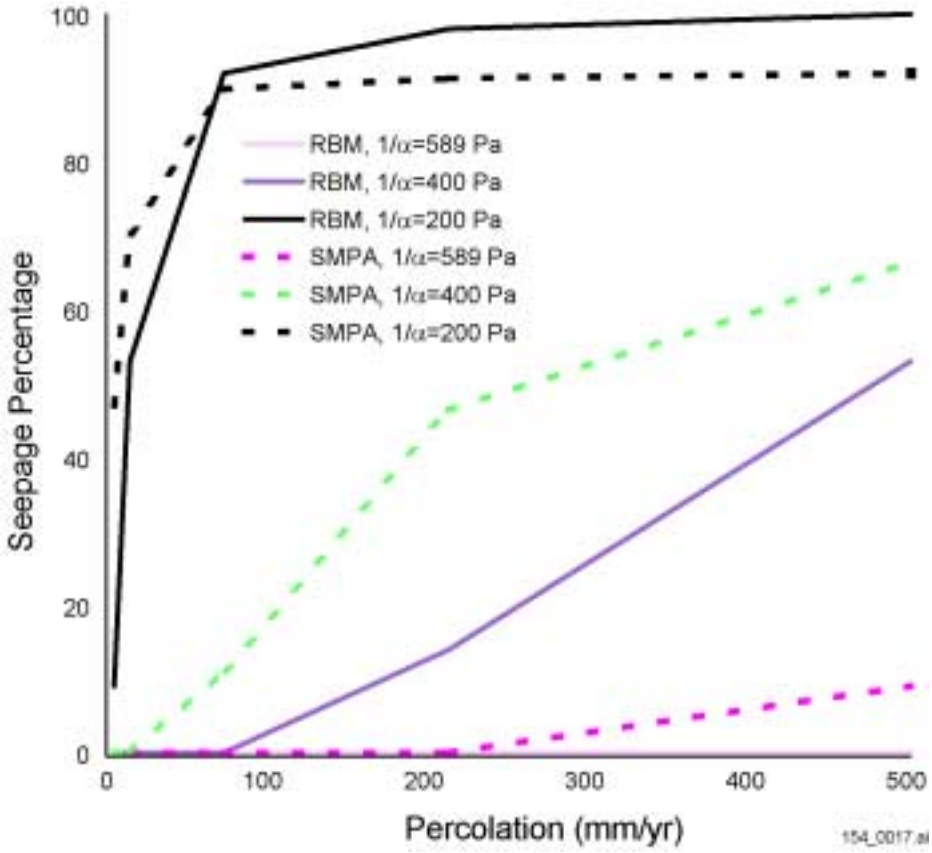

154_0017.ai

Source: DTN: LB0011SMDCREV1.002 [DIRS 153570]; TerBerg 2001 [DIRS 155102].

NOTE: Seepage percentage predicted by homogeneous rock bolt model (RBM) (without rock bolt) compared to that for the heterogeneous seepage model for performance assessment (SMPA) (CRWMS M&O 2000 [DIRS 148384], Section 6.3.1). For the cases with $1/\alpha$ equal to 200 and 400 Pa, the permeability is 0.9×10^{-12} m^2 rather than 1.4×10^{-12} m^2.

Figure 4.3.3-3. Comparison of Seepage Percentage

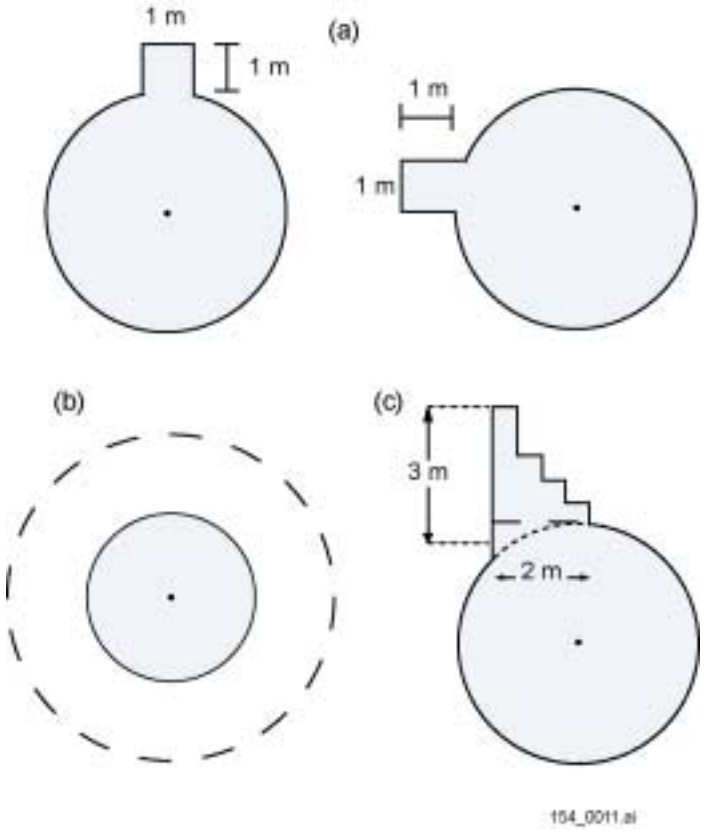

154_0011.ai

NOTE: Two cases of rockfall from the drift ceiling (upper panel), fracture dilation (lower left panel), and extended rock failure at the drift roof (lower right panel).

Figure 4.3.4-1. Drift Degradation Submodel Scenarios

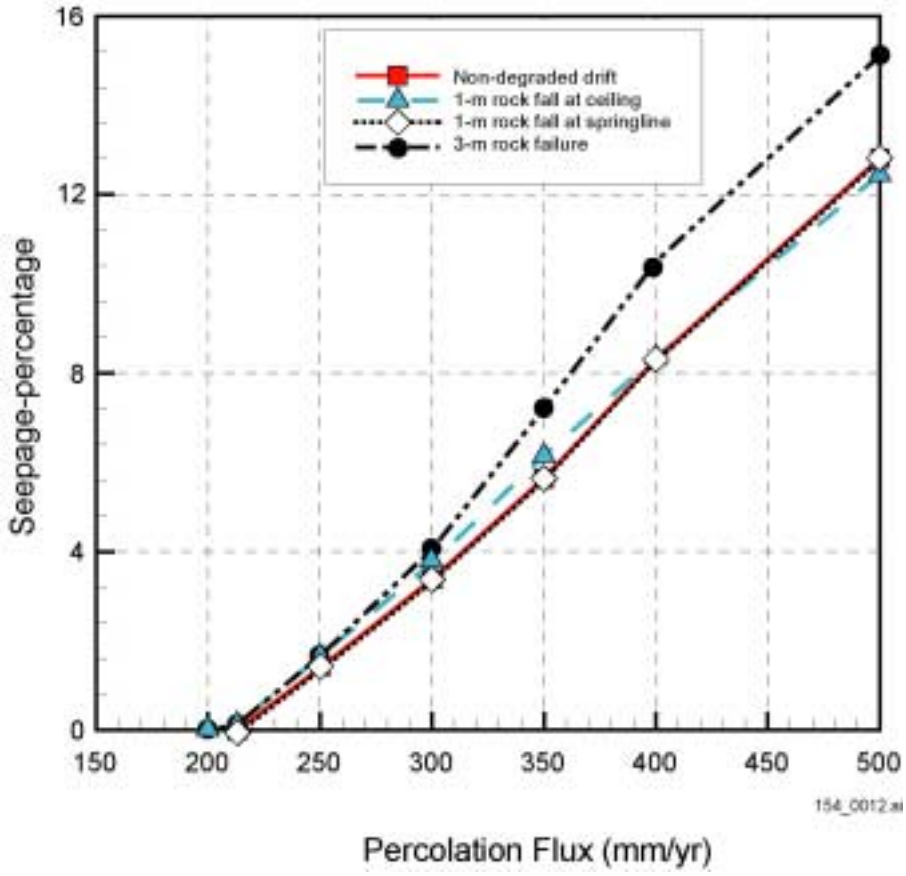

154_0012.ai

Source: DTN: LB0011SMDCREV1.002 [DIRS 153570], LB0011SMDCREV1.001 [DIRS 153574].

Figure 4.3.4-2. Seepage Percentage as a Function of Percolation Flux for the Three Set A Drift Degradation Scenarios

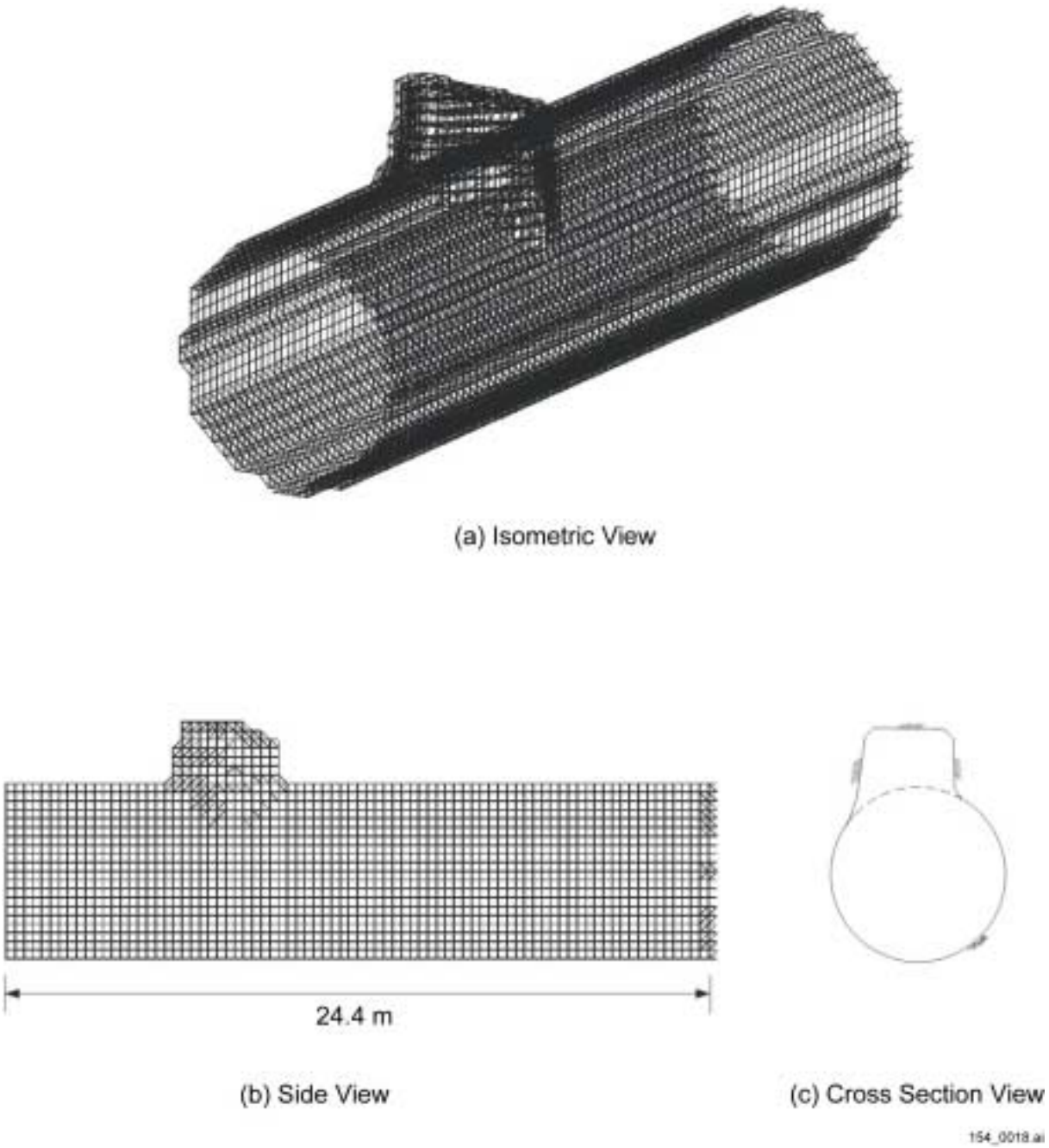

154_0018.ai

Source: DTN: MO0010RDDAAMRR.002 [DIRS 154048].

Figure 4.3.4-3. Emplacement Drift Profile for the Tptpmn Unit, Worst Case

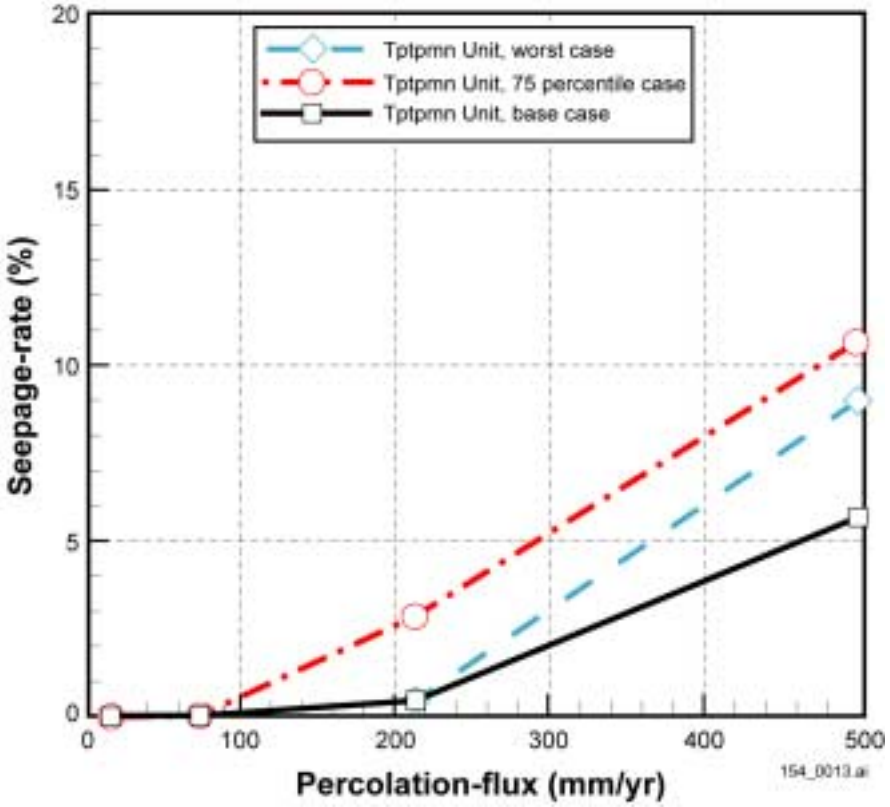

154_0013.ai

Source: TerBerg 2001 [DIRS 155032].

Figure 4.3.4-4. Seepage Percentage as a Function of Percolation Flux for Realization 1 of the Two Set A (Tptpmn) Degradation Scenarios and the Undegraded Base Case

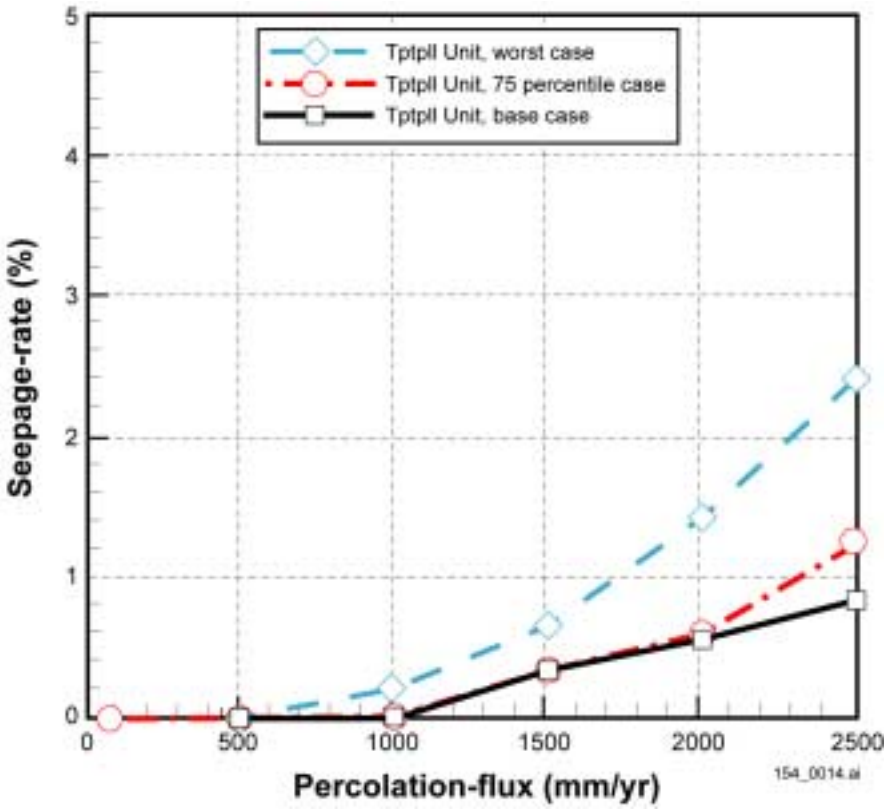

154_0014.ai

Source: TerBerg 2001 [DIRS 155032].

Figure 4.3.4-5. Seepage Percentage as a Function of Percolation Flux for Realization 1 of the Two Set B´ Degradation Scenarios and the Undegraded Base Case

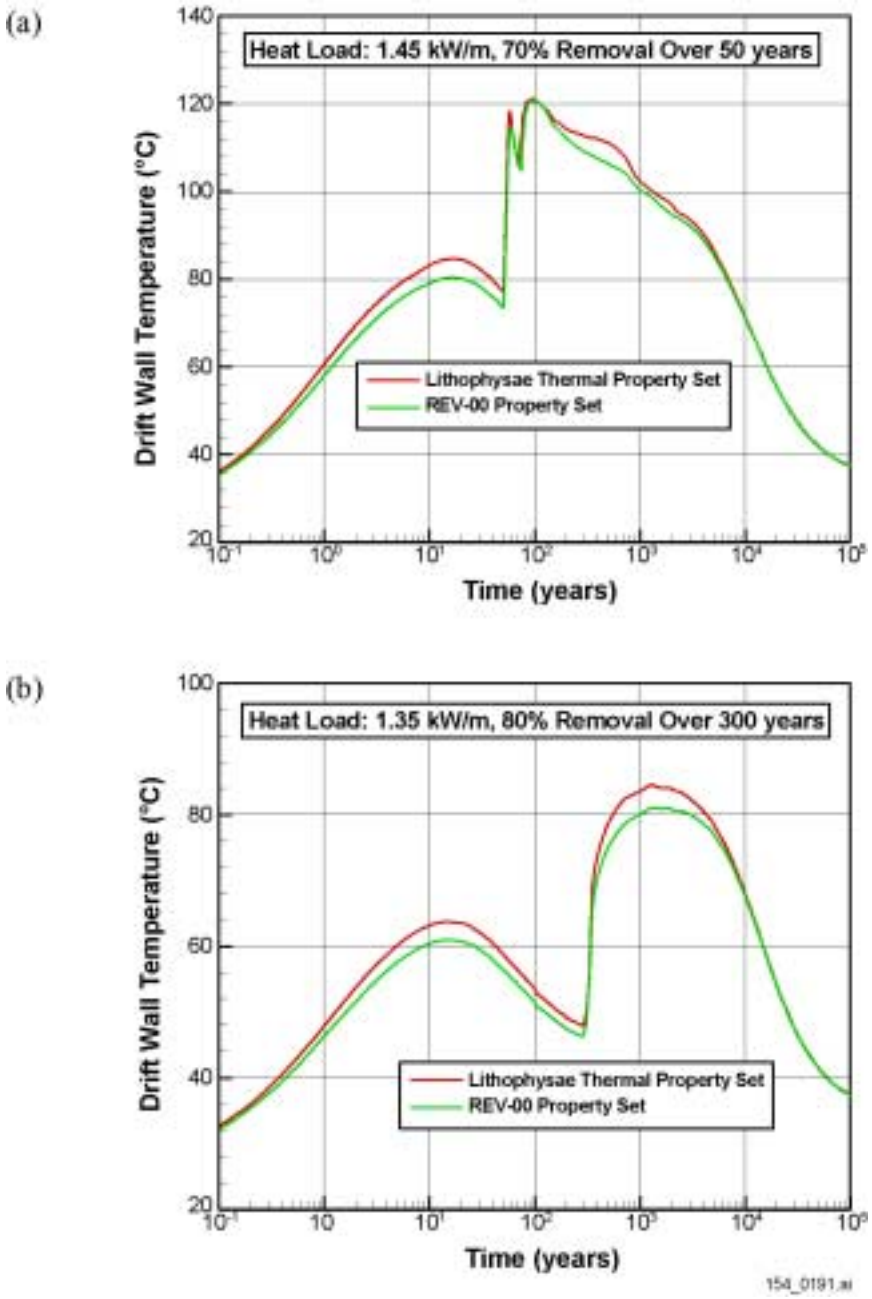

154_0191.ai

Source: Bodvarsson 2001 [DIRS 154669], Attachment 17, pp. 75 and 76. REV-00 refers to CRWMS M&O 2000 [DIRS 143665].

NOTE: Sensitivity of drift wall temperature to thermal properties (with and without the effects of lithophysal cavities) for (a) the higher-temperature case [heat load of 1.45 kW/m and ventilation of 70 percent over 50 years], and (b) the lower-temperature case [heat load of 1.35 kW/m and ventilation of 80 percent over 300 years].

Figure 4.3.5-1. Sensitivity of Drift Wall Temperature to Thermal Properties

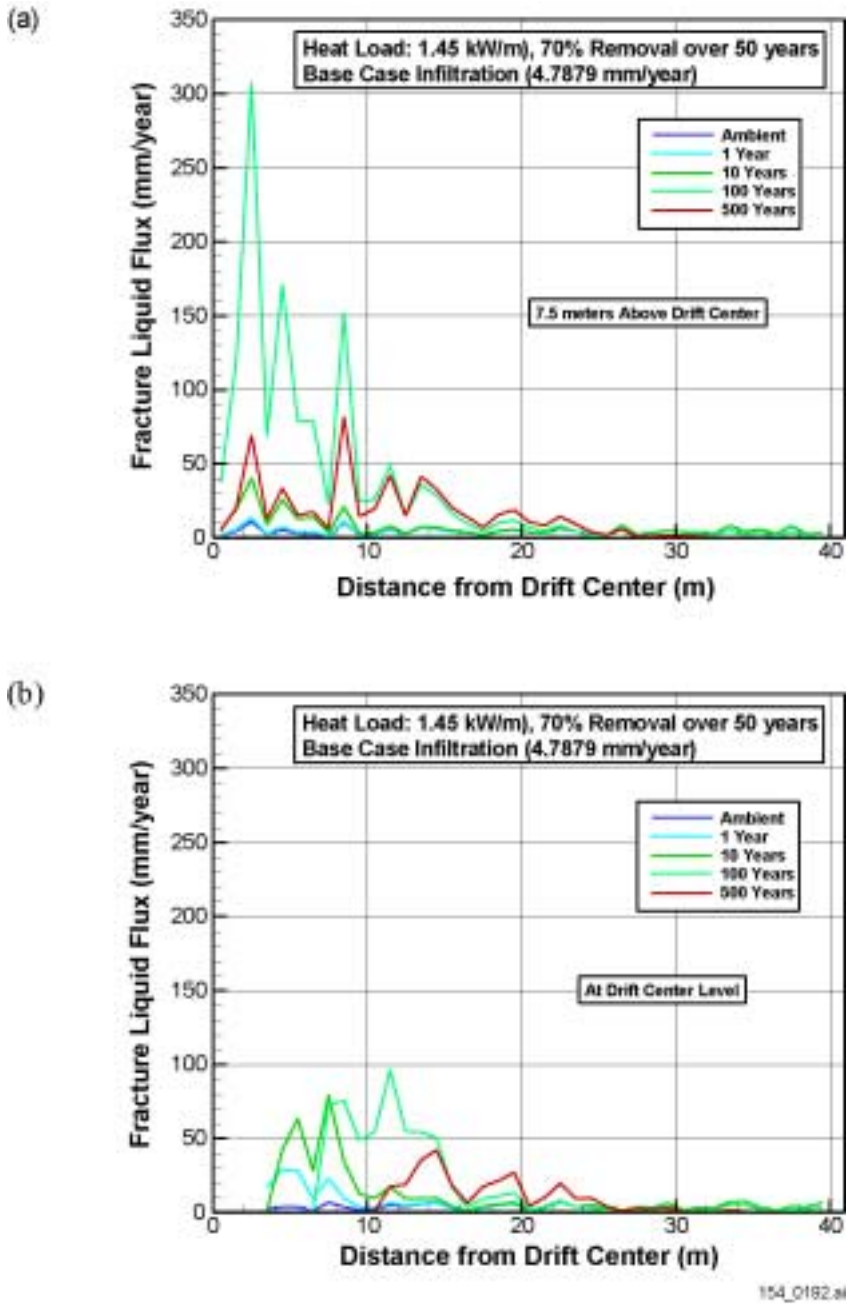

154_0192.ai

Source: Bodvarsson 2001 [DIRS 154669], Attachment 17, pp. 63 and 64.

NOTE: Fracture liquid fluxes for the higher-temperature case (heat load of 1.45 kW/m, ventilation of 70 percent over 50 yrs, and base case infiltration of 4.7879 mm/yr] at (a) a horizontal plane 7.5 m above drift center and (b) a horizontal plane along the drift center.

Figure 4.3.5-2. Fracture Liquid Fluxes as a Function of Lateral Distance from Drift Center

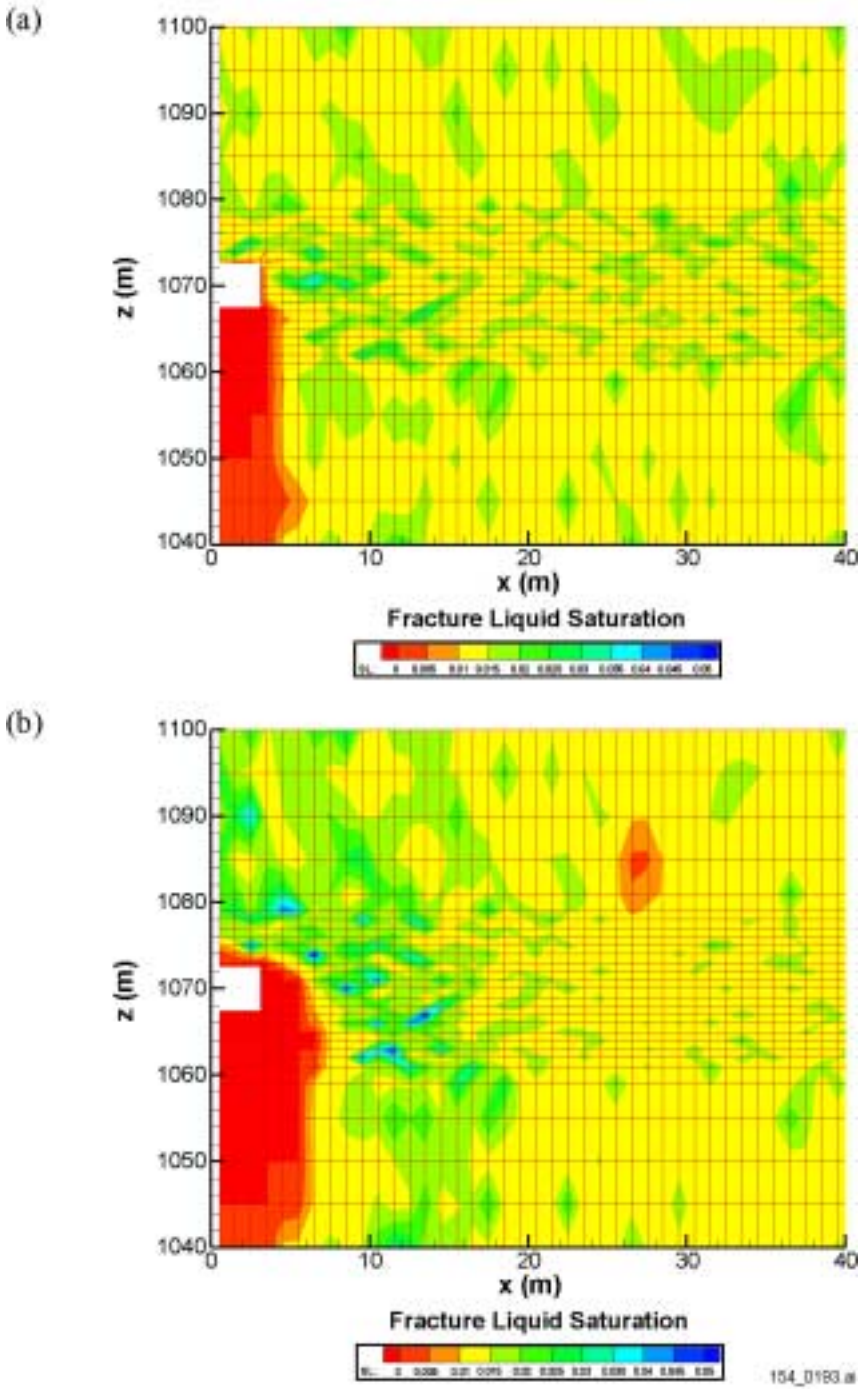

154_0193.ai

Source: Bodvarsson 2001 [DIRS 154669], Attachment 17, pp. 60 and 61.

NOTE: Higher-temperature operating mode at (a) 50 years after waste emplacement and (b) 100 years after waste emplacement.

Figure 4.3.5-3. Liquid Saturation Contours Around the Drift to Mid-Pillar

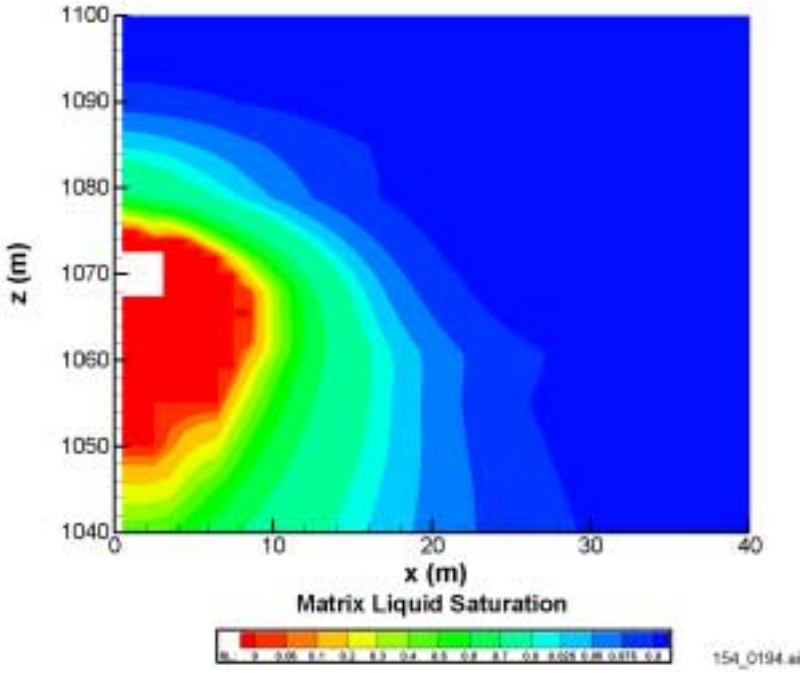

154_0194.ai

Source: Bodvarsson 2001 [DIRS 154669], Attachment 17, p. 62.

NOTE: Higher-temperature case; matrix permeability is homogeneous.

Figure 4.3.5-4. Matrix Liquid Saturations at 1,000 Years after Waste Emplacement

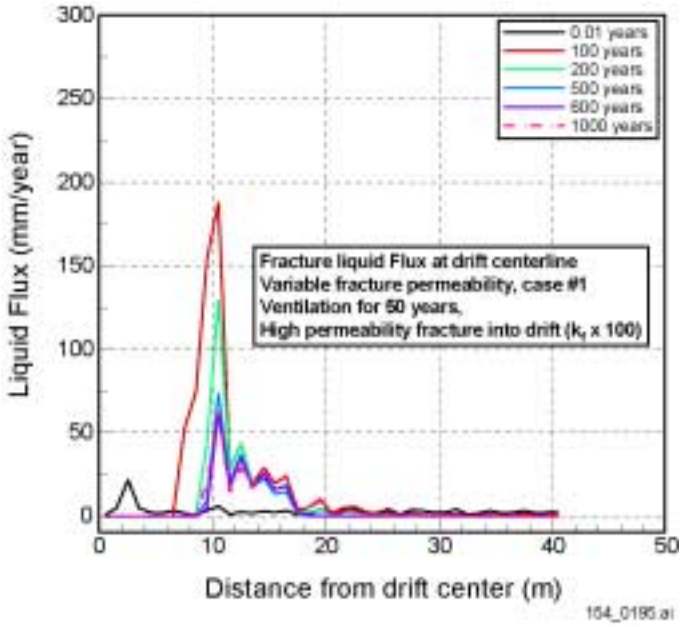

154_0195.ai

Source: Bodvarsson 2001 [DIRS 154669], Attachment 6, p. 46.

NOTE: Fracture liquid fluxes as a function of lateral distance from drift center, at a horizontal plane along the drift center for the higher-temperature case. These results are based on a heterogeneity field that has an artificially large permeability discrete feature intercepting the drift. Test conditions include fracture liquid flux at drift centerline, variable fracture permeability (Case 1), ventilation for 50 yrs, and high permeability fracture into drift ($k_1 \times 100$).

Figure 4.3.5-5. Fracture Liquid Fluxes as a Function of Lateral Distance from Drift Center

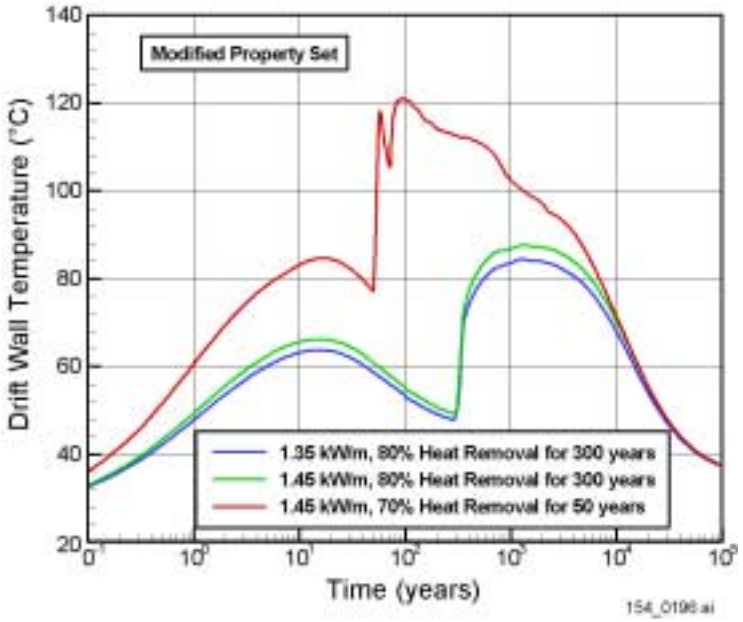

154_0196.ai

Source: Bodvarsson 2001 [DIRS 154669], Attachment 17, p. 74.

NOTE: Test conditions under the modified property set. Higher-temperature case = 1.45 kW/m, 70% heat removal for 50 years. Lower-temperature case = 1.35 kW/m, 80% heat removal for 300 years. Modified property set = high-permeability fracture into drift (as in Figure 4.3.5-5).

Figure 4.3.5-6. Comparison of Drift Wall Temperatures for the Higher-Temperature and Lower-Temperature Cases

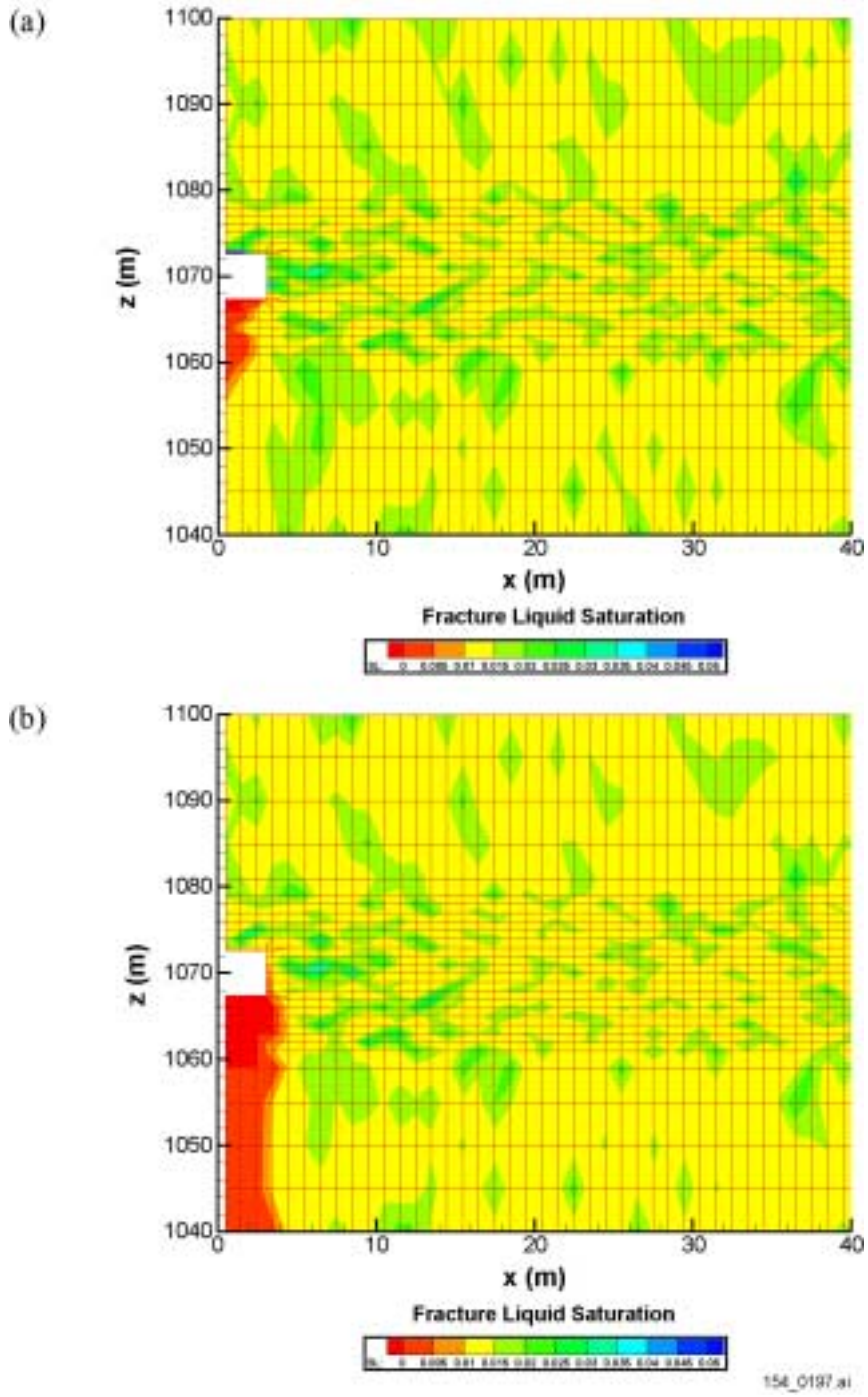

154_0197.ai

Source: Bodvarsson 2001 [DIRS 154669], Attachment 17, pp. 70 and 71.

NOTE: Fracture saturation contours at (a) 50 and (b) 500 years after waste emplacement.

Figure 4.3.5-7. Fracture Saturation Contours for the Lower-Temperature Case

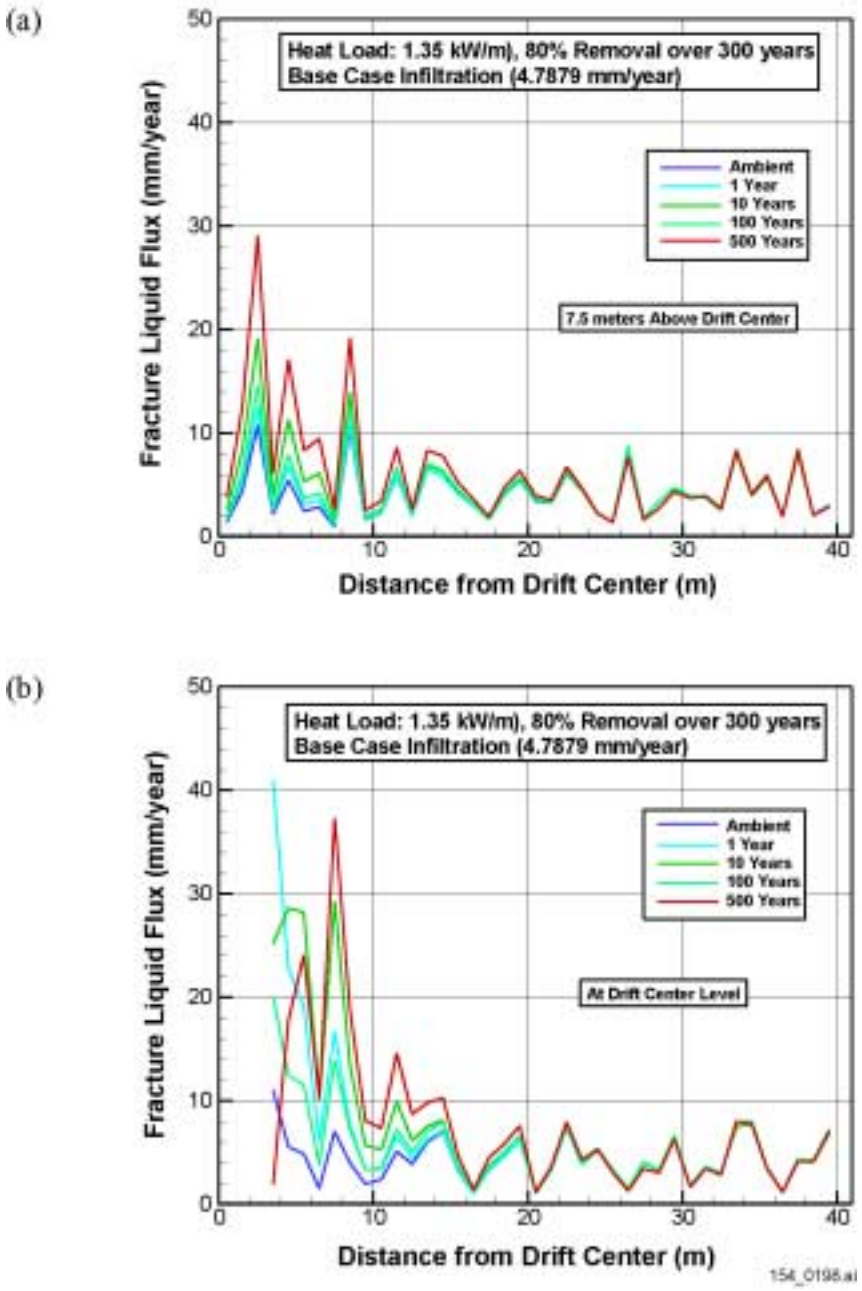

154_0198.ai

Source: Bodvarsson 2001 [DIRS 154669], Attachment 17, pp. 72 and 73.

NOTE: Fracture liquid fluxes (a) at a horizontal plane 5 m above the drift crown, and (b) at a horizontal plane along the drift center. Test conditions: heat load of 1.35 kW/m, ventilation of 80 percent removal over 300 years, and base case infiltration of 4.7879 mm/yr.

Figure 4.3.5-8. Fracture Liquid Fluxes as a Function of Lateral Distance from Drift Center for the Lower-Temperature Case

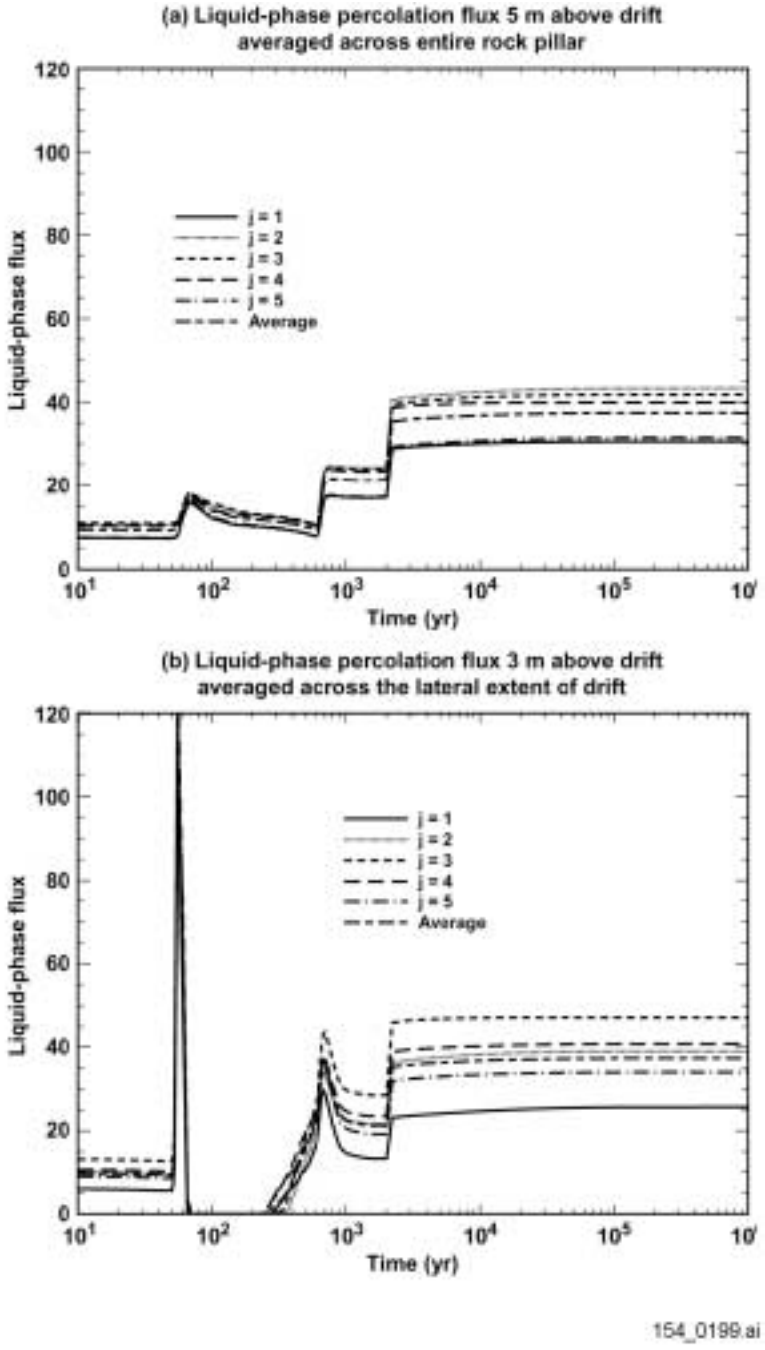

154_0199.ai

Source: BSC 2001 [DIRS 154985], Figure 6-96.

NOTE: Stochastic Realization C-56 and an areal mass loading of 56 MTU/acre. This realization assumes a $\log_{10}$ standard deviation of 1.0, which is reasonably close to the measured value of 0.72 in Niche 2 (Station 36 +. 50). Histories are given at five longitudinal locations (j = 1, 2, 3, 4, and 5) and for the equivalent two-dimensional homogeneous line-averaged-heat-source, drift-scale, thermal-hydrologic model. All liquid-phase fluxes at the drift wall and in the drift are zero for this case. Test conditions for (a): liquid-phase percolation flux 5 m above drift, averaged across the entire rock pillar. Test conditions for (b): liquid-phase percolation flux 3 m above drift, averaged across the lateral extent of the drift. Liquid-phase flux in mm/yr.

Figure 4.3.5-9. Liquid-Phase-Flux Histories at Various Locations in the Host Rock

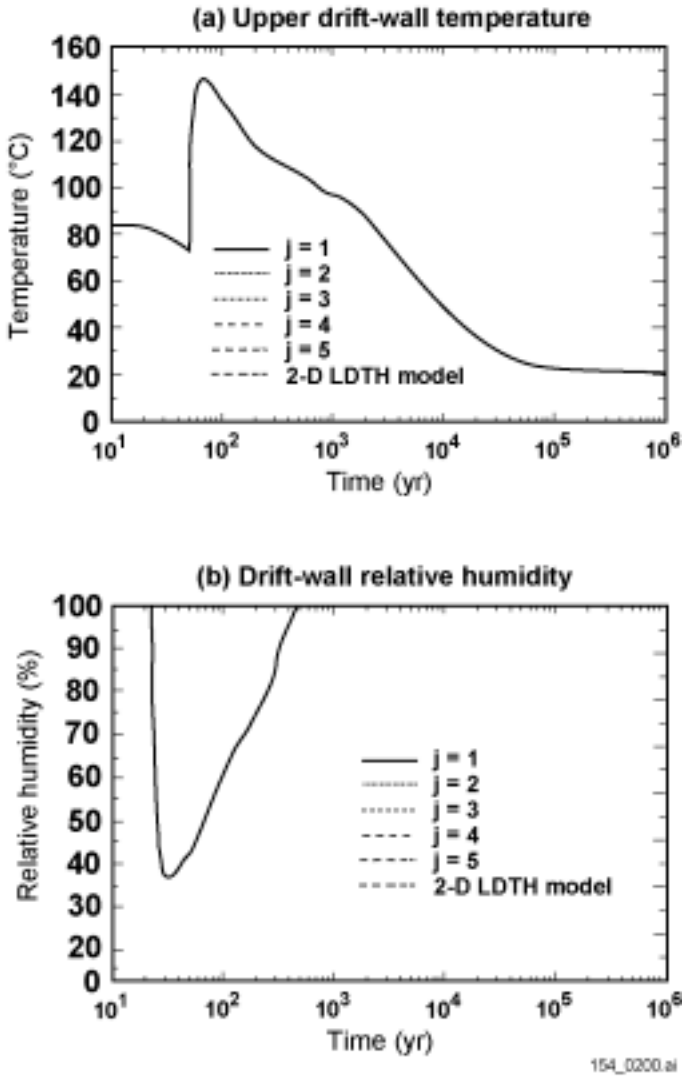

154_0200.ai

Source: BSC 2001 [DIRS 154985], Figure 6-95.

NOTE: Stochastic Realization C-56 and an areal mass loading of 56 MTU/acre (a) for upper drift wall temperature and (b) for drift wall relative humidity. This realization assumes a $\log_{10}$ standard deviation of 1.0, which is reasonably close to the measured value of 0.72 in Niche 2 (Station 36 + 50). Histories are given at five longitudinal locations (j = 1, 2, 3, 4, and 5) and for the equivalent two-dimensional homogeneous line-averaged-heat-source, drift-scale, thermal-hydrologic model. The curves for all five locations and the two-dimensional model coincide. The local temperatures and relative humidities in the host rock are insensitive to drift-scale heterogeneity of permeability.

Figure 4.3.5-10. Temperature and Relative Humidity History at the Drift Wall

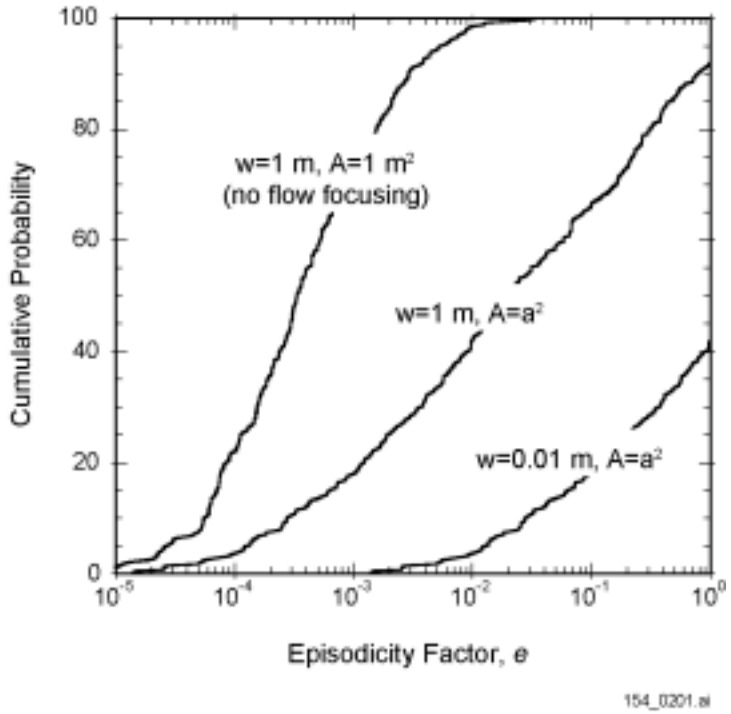

154_0201.ai

Source: DTN: SN0104T0511599.004 [DIRS 154713]

NOTE: $A = a^2$ indicates flow focusing; $A = 1\ m^2$ indicates no focusing.

Figure 4.3.5-11. Cumulative Distribution Function of the Episodicity Factor for Different Weep Widths and Flow Focusing Conditions

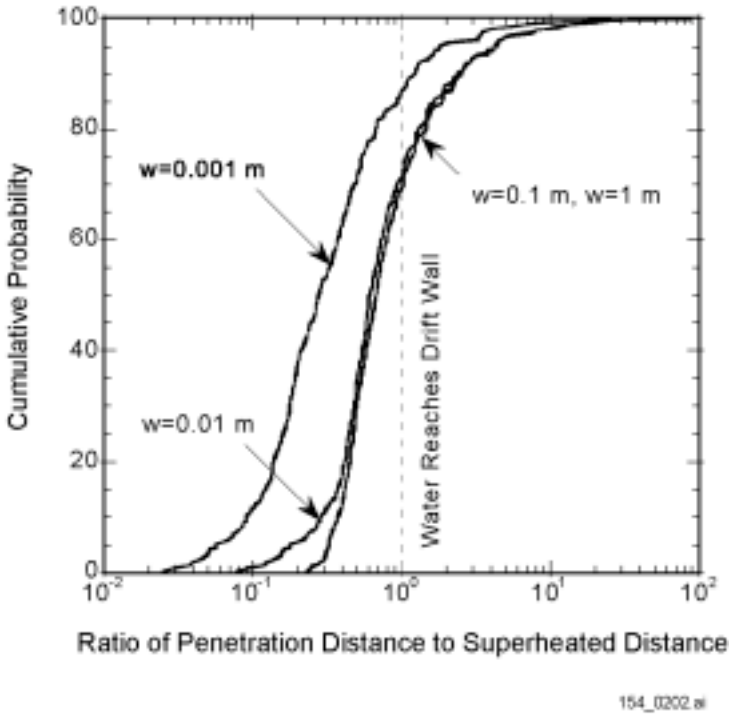

154_0202.ai

Source: DTN: SN0104T0511599.004 [DIRS 154713]

NOTE: Cumulative probability functions for the ratio of the penetration distance to superheated distance for infiltrating water using the three-dimensional solution in Phillips 1996 [DIRS 152005]; *w* = weep width.

Figure 4.3.5-12. Cumulative Probability for the Ratio of Penetration Distance to Superheated Distance

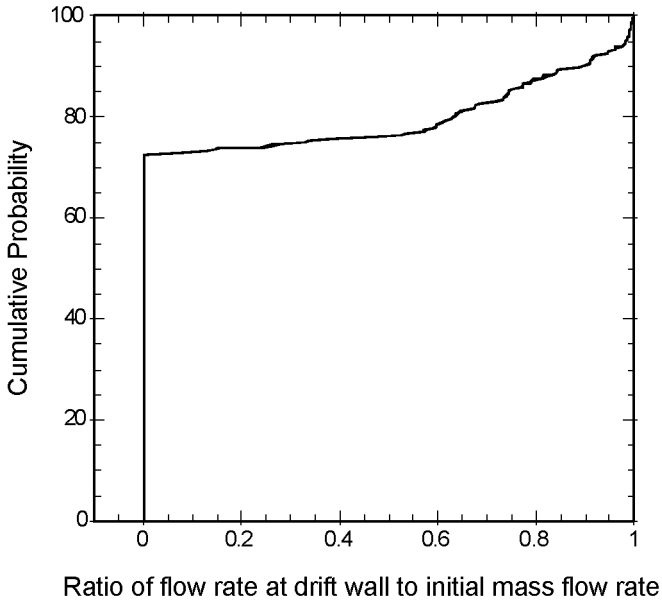

154_0203.ai

Source: DTN: SN0104T0511599.004 [DIRS 154713]

NOTE: Weep width = 1 m.

Figure 4.3.5-13. Cumulative Probability of the Ratio of the Mass Flow Rate at the Drift Wall to the Initial Mass Flow Rate

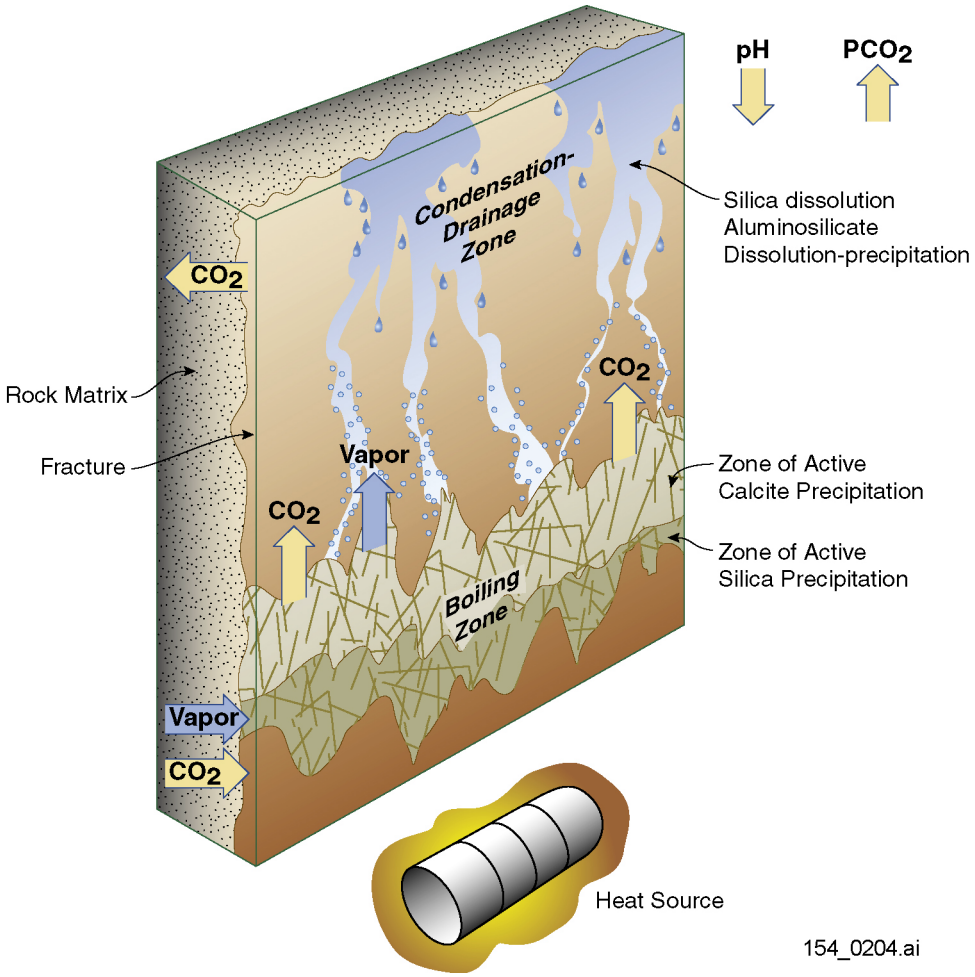

154_0204.ai

Figure 4.3.6-1. Schematic Diagram of the Relation between Thermal-Hydrologic Processes and Geochemical Processes

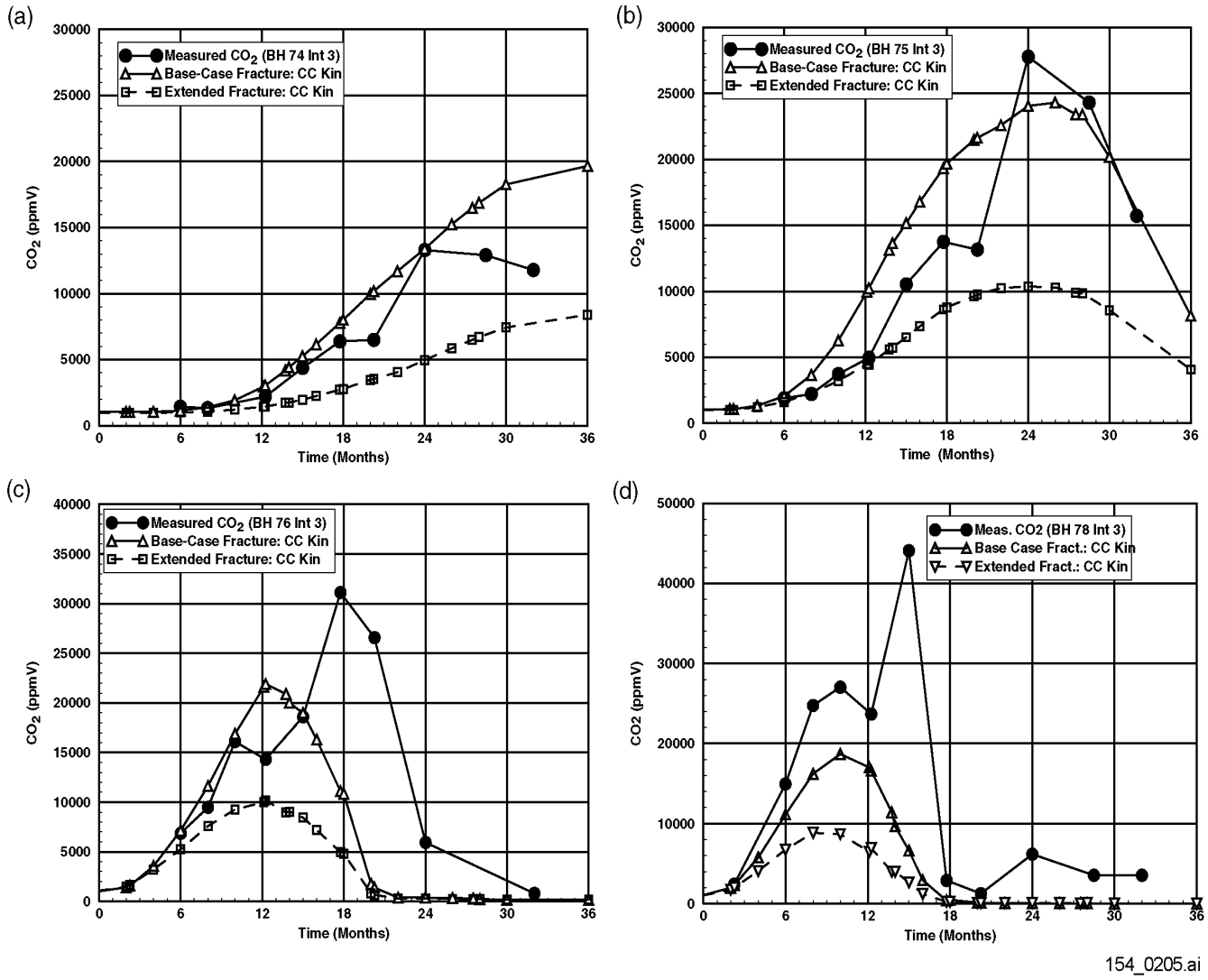

154_0205.ai

Source: BSC 2001 [DIRS 154667], Figure 18.

NOTE: CO_2 = gas-phase carbon dioxide, BH = borehole. Base case CC kin and extended-case CC kin in fractures to measured concentrations in boreholes: (a) borehole interval 74-3 at node above interval; (b) borehole interval 75-3; (c) borehole interval 76-3; (d) borehole interval 78-3 at node near end of interval.

Figure 4.3.6-2. Comparison of Modeled Carbon Dioxide Concentrations

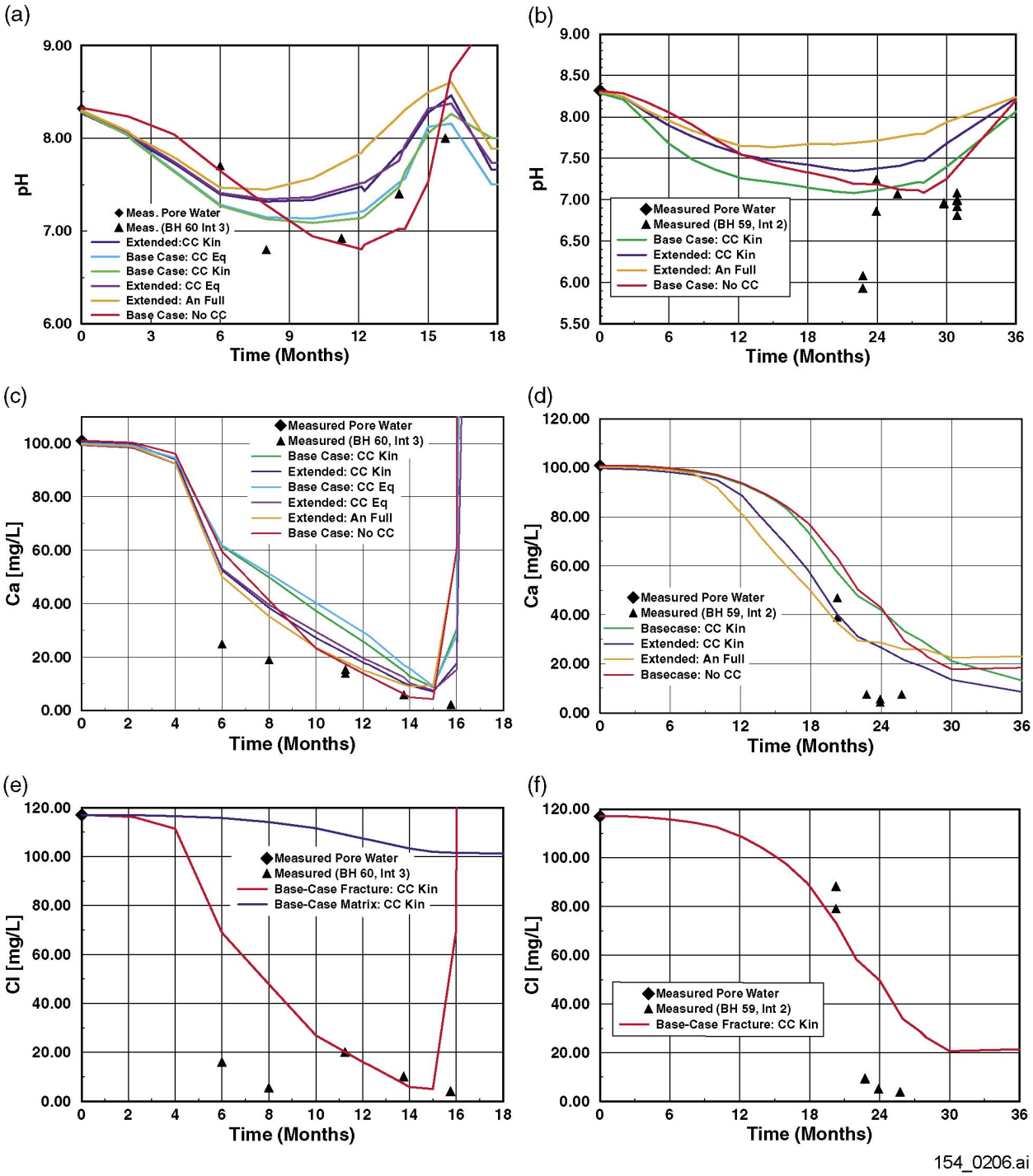

154_0206.ai

Source: BSC 2001 [DIRS 154667], Figures 19 (pH), 20 (chloride), and 23 (calcium).

NOTE: Changes in pH, total calcium, and total chloride in water samples collected from borehole intervals 60-3 and 59-2 compared to modeled fracture water compositions at nearby model grid nodes. The ambient pore water composition of each component is shown as a diamond at time zero on each plot.

Figure 4.3.6-3. Measured and Modeled Fracture Water Compositions

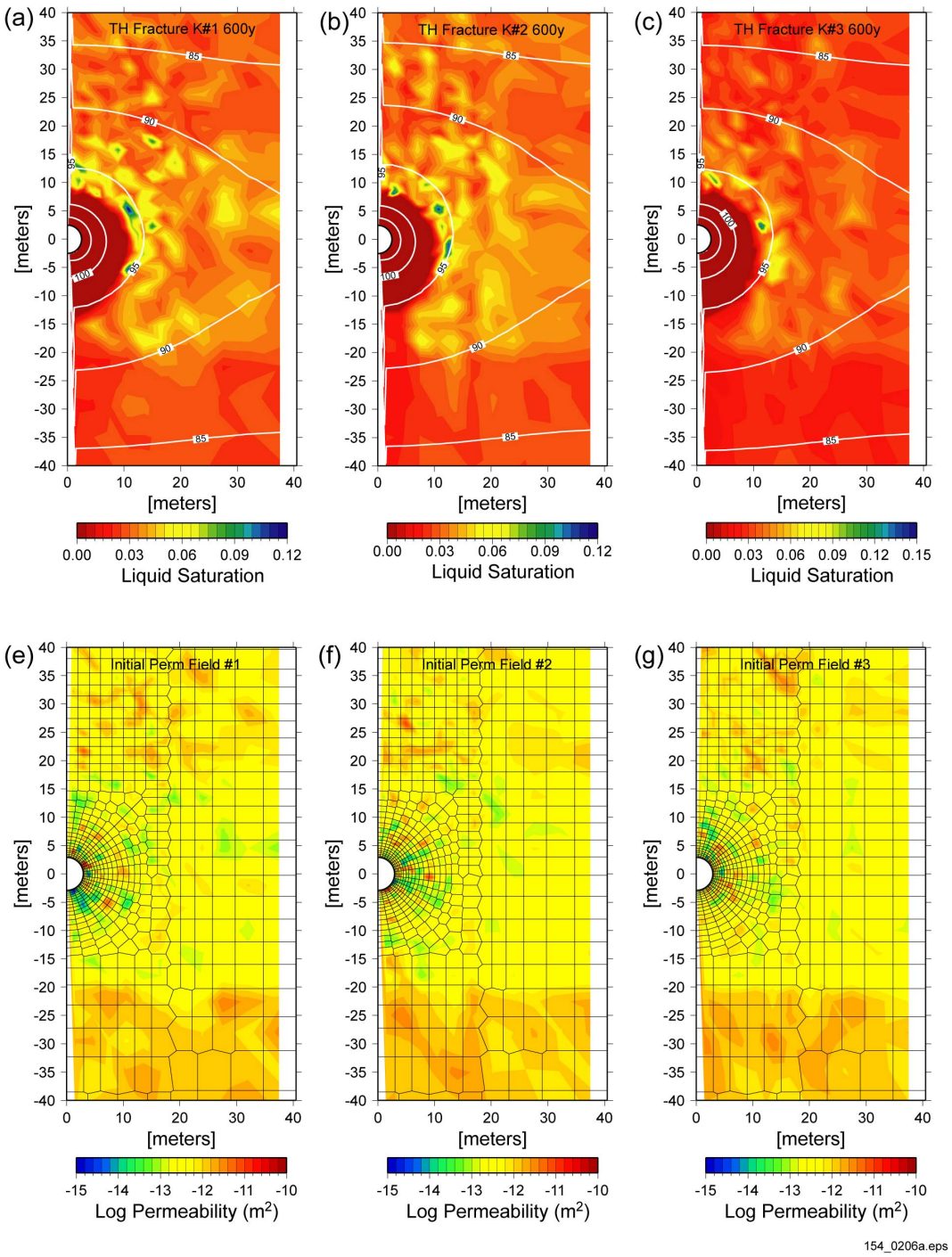

154_206a.eps

Source: BSC 2001 [DIRS 154667], Figure 74.

NOTE: Infiltration rate = 6 mm/yr; 600y = 600 Years; TH = thermal-hydrologic; k = permeability. Thermal-hydrologic simulations for (a) permeability realization #1, (b) realization #2, and (c) realization #3, (e) initial permeability realization #1, (f) initial permeability realization #2, (g) initial permeability realization #3. Model domain extends for a few hundred meters above and below area shown.

Figure 4.3.6-4. Fracture Liquid Saturations at 600 Years from Thermal-Hydrological Simulations for Three Permeability Realizations

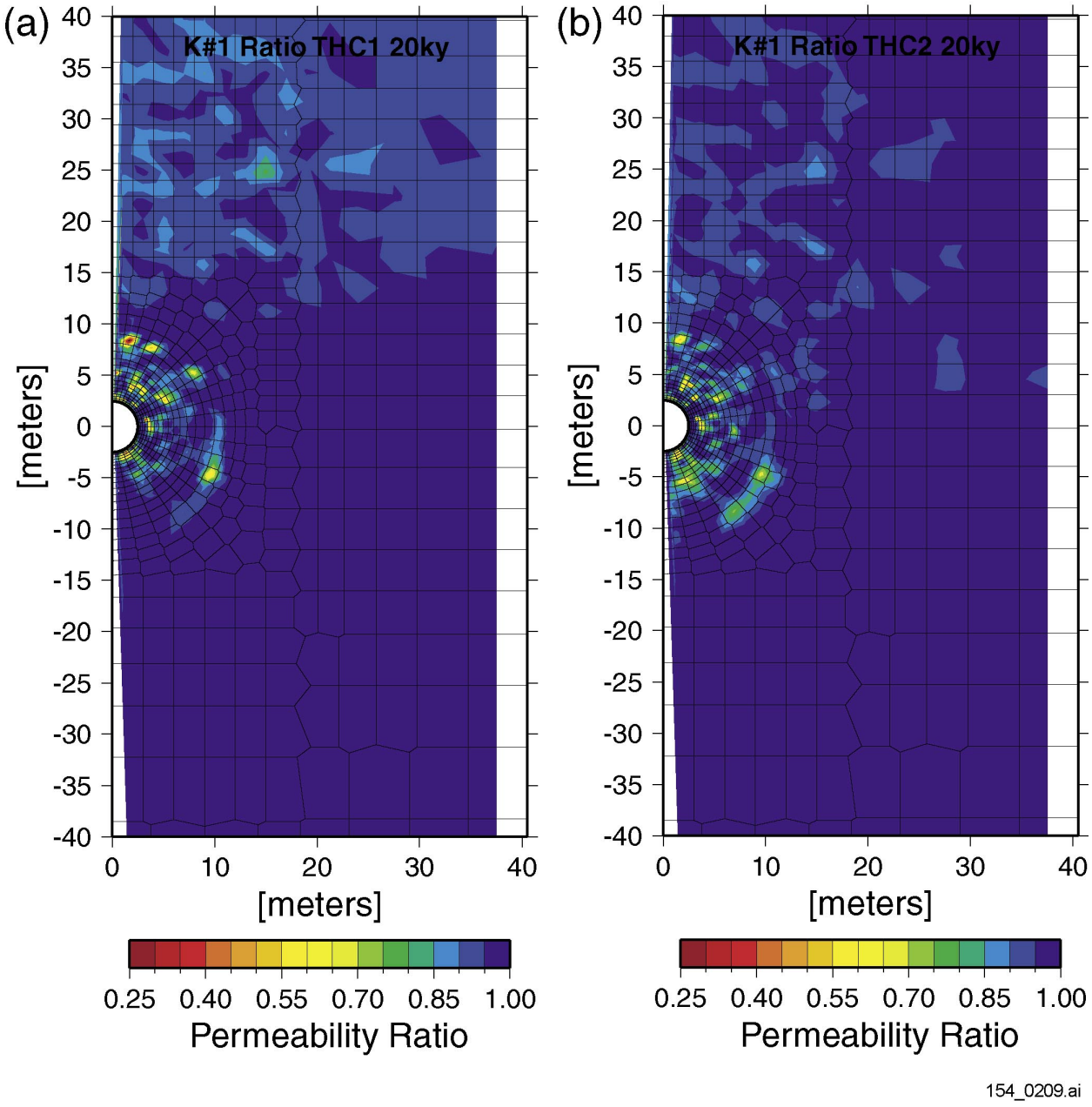

154_0209.ai

Source: BSC 2001 [DIRS 154667], Figure 75.

NOTE: 20ky = 20,000 years; THC = thermal-hydrologic-chemical; K = permeability. Results for (a) extended geochemical system, (b) base-case geochemical system. Model domain extends for a few hundred meters above and below area shown.

Figure 4.3.6-5. Fracture Permeability Ratio After 20,000 Years for Realization #1

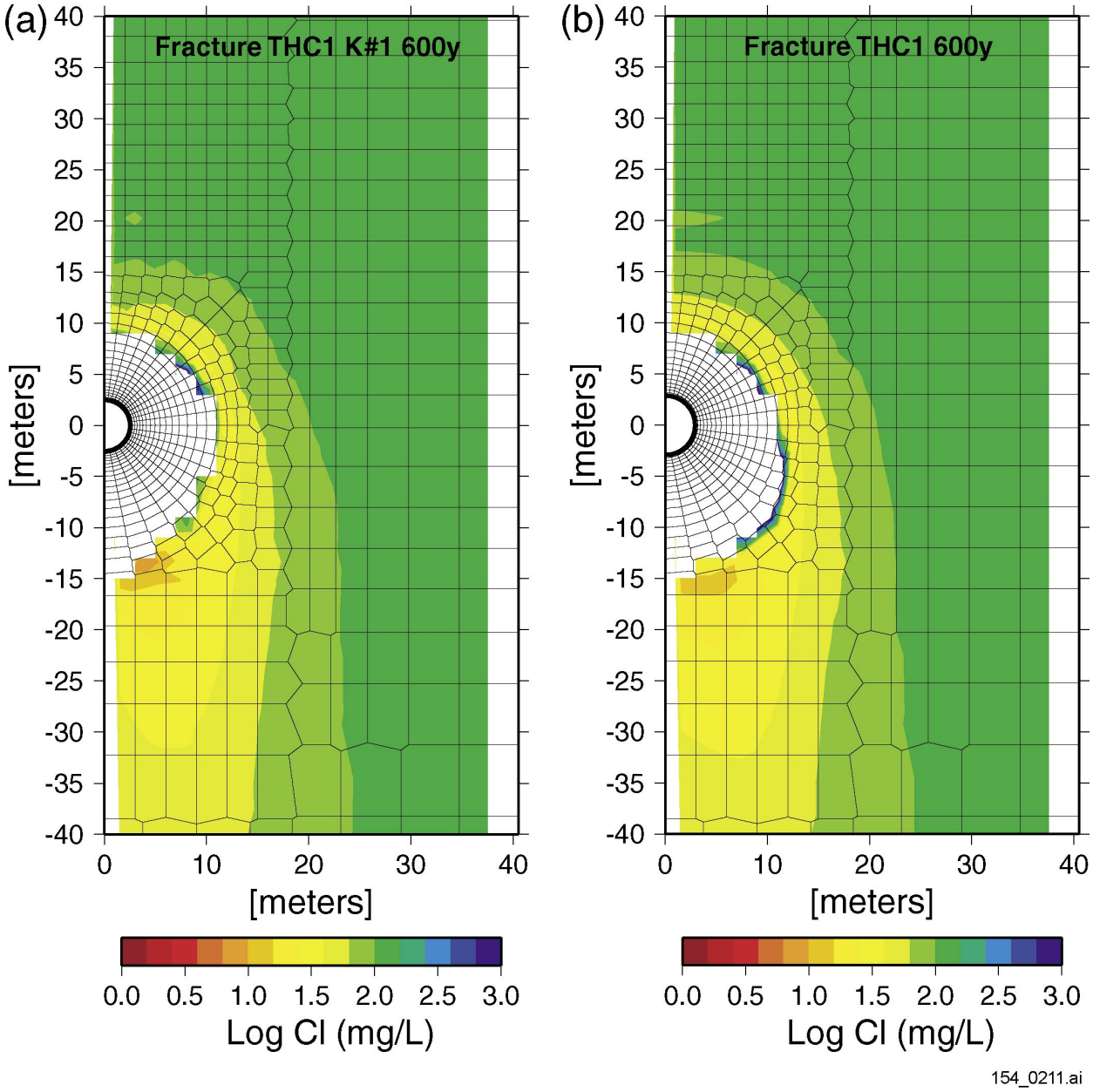

154_0211.ai

Source: BSC 2001 [DIRS 154667], Figure 82.

NOTE: THC = thermal-hydrologic-chemical; K = permeability; 600y = 600 Years. Results for (a) the extended geochemical system, permeability realization #1; (b) the extended geochemical system, initially homogeneous Tptpmn. Model domain extends a few hundred meters above and below area shown.

Figure 4.3.6-6. Chloride Concentrations in Fracture Water After 600 Years

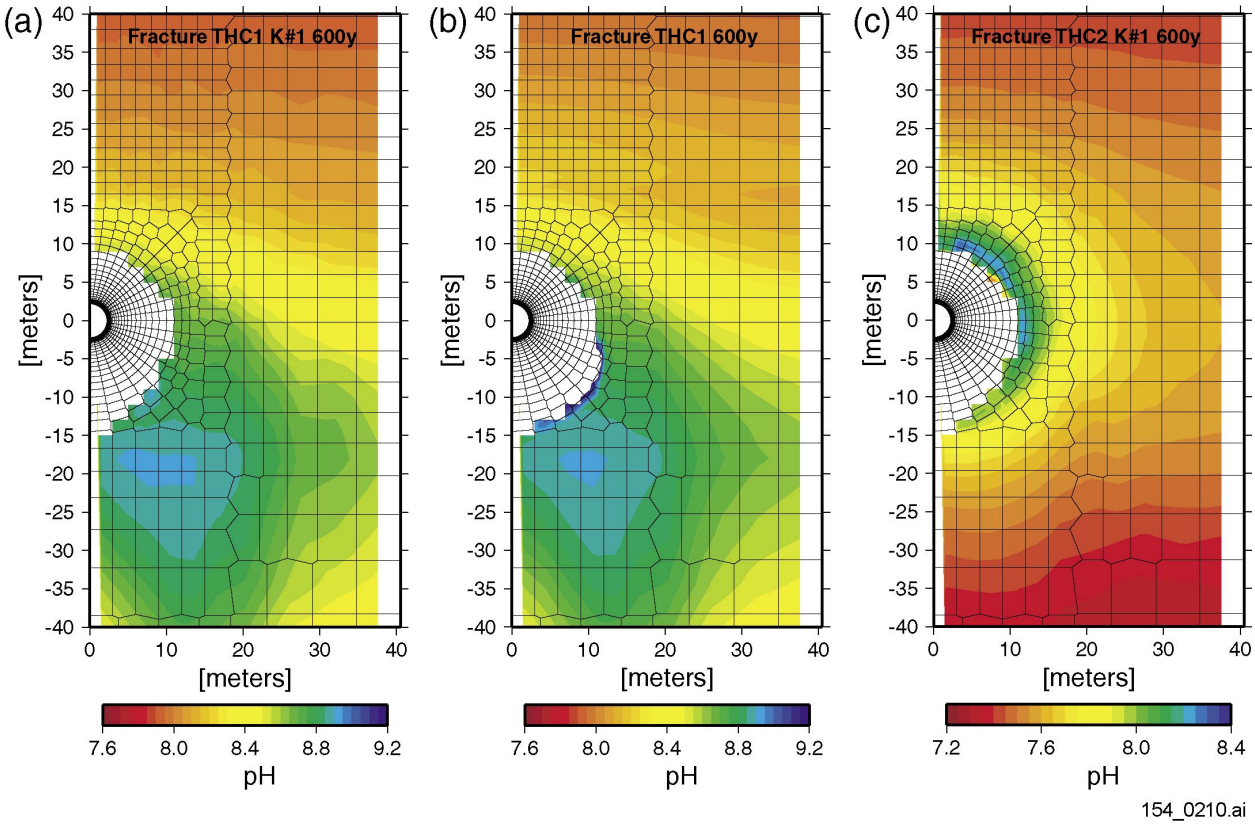

154_0210.ai

Source: BSC 2001 [DIRS 154667], Figure 80.

NOTE: THC = thermal-hydrologic-chemical; K = permeability; 600y = 600 Years. White area is dry. Results for (a) extended geochemical system, permeability realization #1; (b) extended geochemical system, initially homogeneous Tptpmn; (c) base-case geochemical system (heterogeneous permeability realization #1). Model domain extends a few hundred meters above and below area shown.

Figure 4.3.6-7. Fracture Water pH After 600 Years

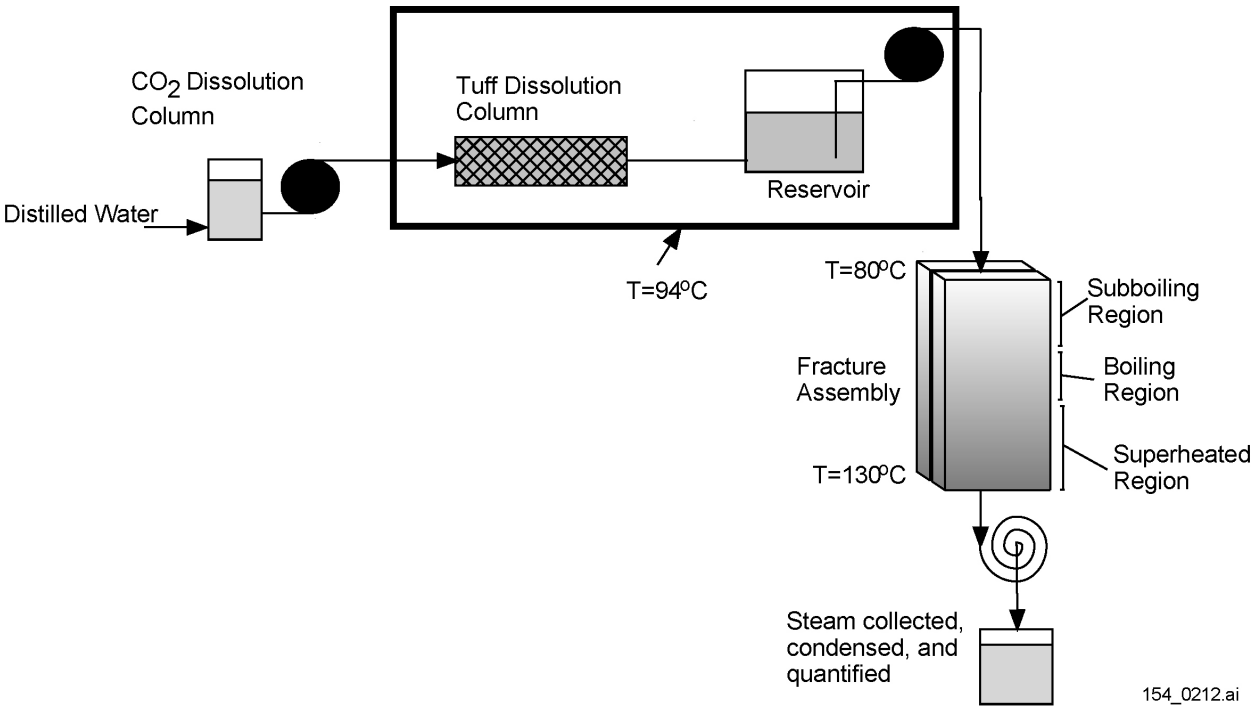

154_0212.ai

Source: Kneafsey et al. 2001 [DIRS 154460], Figure 1.

NOTE: CO_2 = carbon dioxide, T = temperature.

Figure 4.3.6-8. Schematic of Experiment to Replicate Mineral Dissolution and Precipitation by Condensate-Water in Fractured Tuff

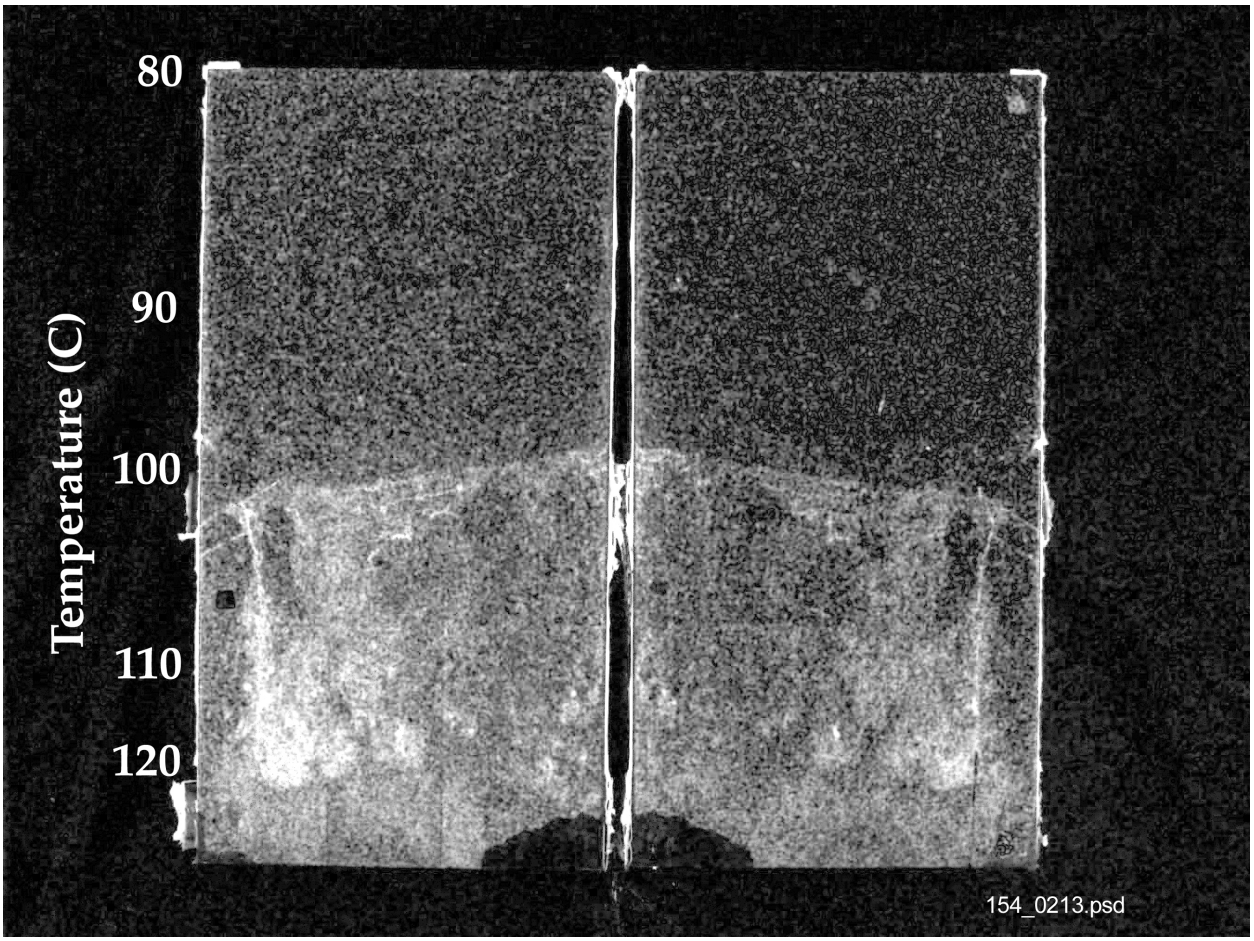

154_0213.psd

Source: Kneafsey et al. 2001 [DIRS 154460], Figure 2.

NOTE: Enhanced image showing fracture temperature profile and fluorescing precipitate (light shades) under ultraviolet illumination on both fracture faces. Vertical fracture dimension is 0.317 m.

Figure 4.3.6-9. Image of a Fracture Opened at the Conclusion of an Experiment to Examine Precipitate Location, Mineralogy, and Morphology

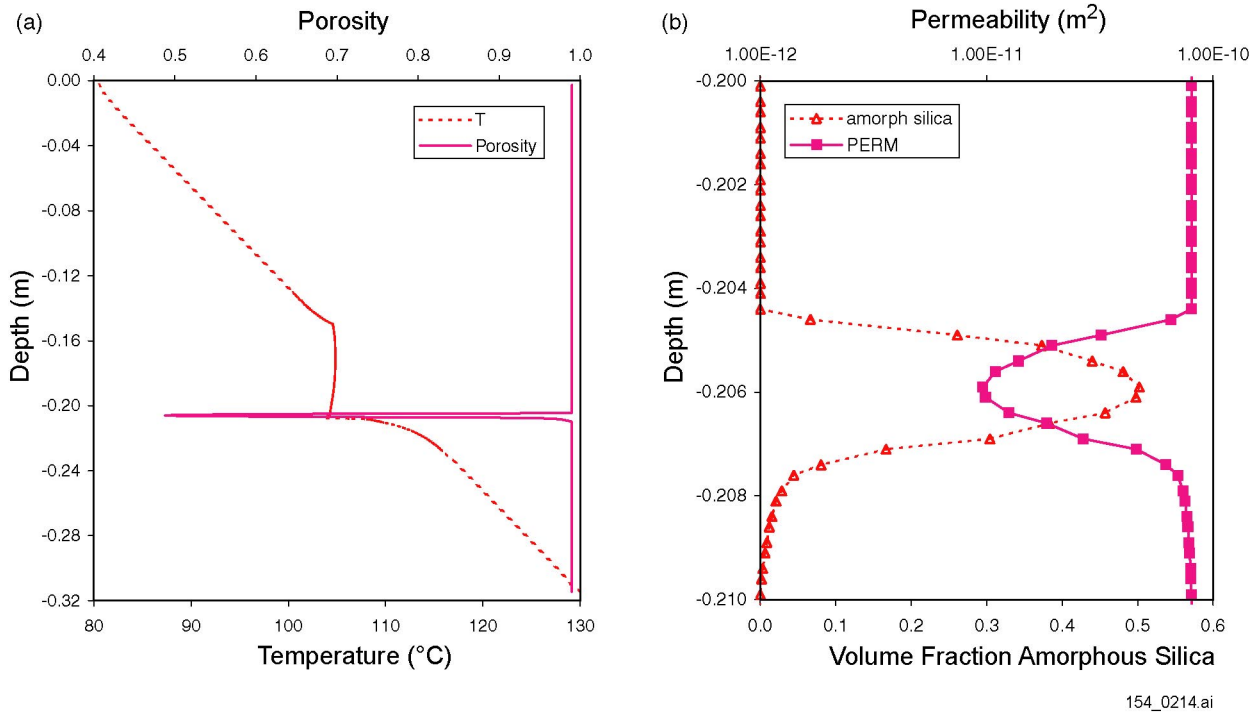

154_0214.ai

Source: Bodvarsson 2001 [DIRS 154669], Attachment 4, p. 35.

NOTE: T = time; amorph = amorphous; PERM = permeability. Depth profiles for (a) temperature and porosity, and (b) permeability and amorphous silica precipitation for a simulated fracture plugging experiment at 0.6 days. Depth interval for (b) is located at the base of the two-phase zone. The porosity and permeability reduction, caused by amorphous silica precipitation, occurs at the base of the boiling front.

Figure 4.3.6-10. Depth Profiles for a Simulated Fracture Plugging Experiment

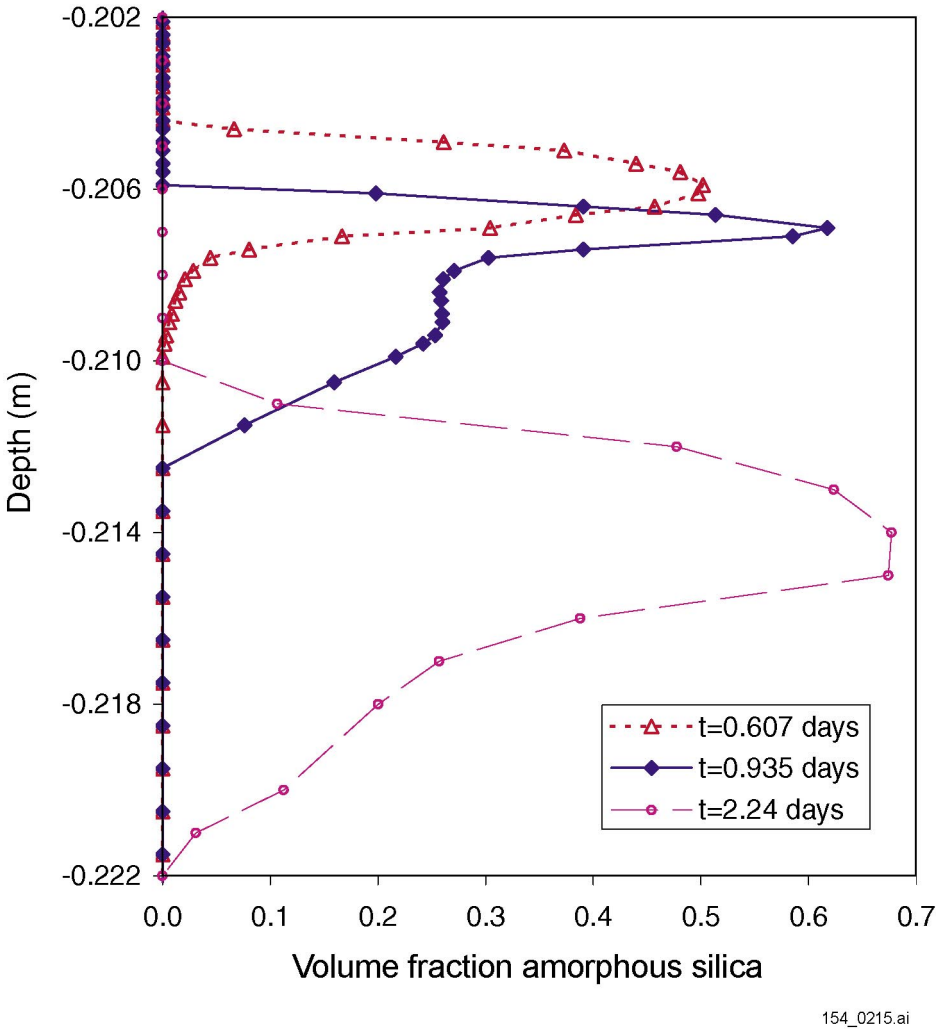

154_0215.ai

Source: Bodvarsson 2001 [DIRS 154669], Attachment 4, p. 29.

NOTE: t = time. Volume fraction of precipitated amorphous silica at 0.6, 0.9, and 2.2 days. The upper portion of precipitated silica is redissolved over time as precipitation follows the boiling front downward. Maximum porosity reduction approaches 70% over the time span of the simulation.

Figure 4.3.6-11. Precipitated Amorphous Silica for Simulated Fracture Plugging Experiment

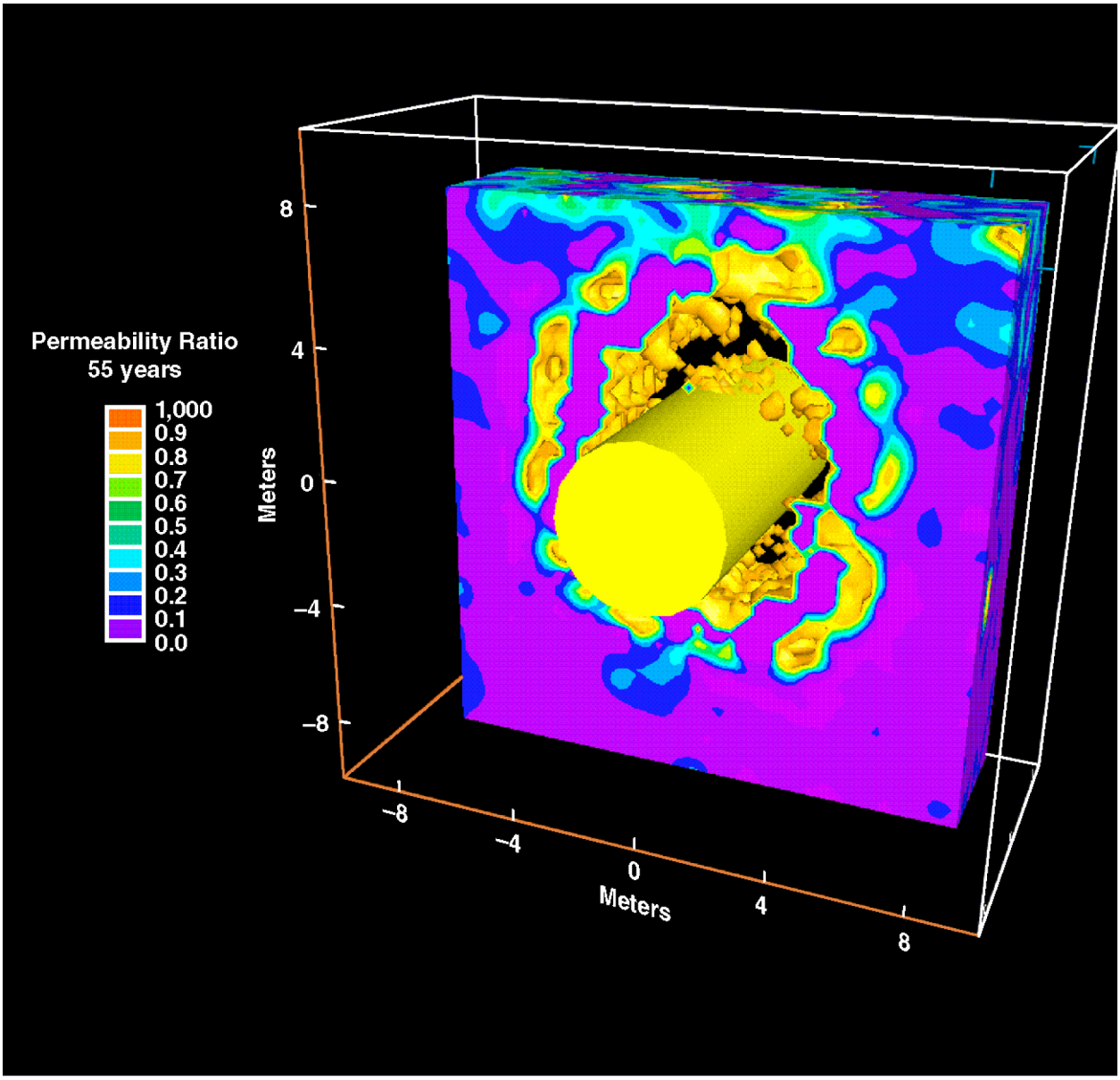

154_0478.ai

154_0478.ai

Source: Blair 2001 [DIRS 155005] p. 90.

NOTE: Zones of increased permeability removed.

Figure 4.3.7-1. Permeability Ratios at 55 Years for Higher-Temperature Case

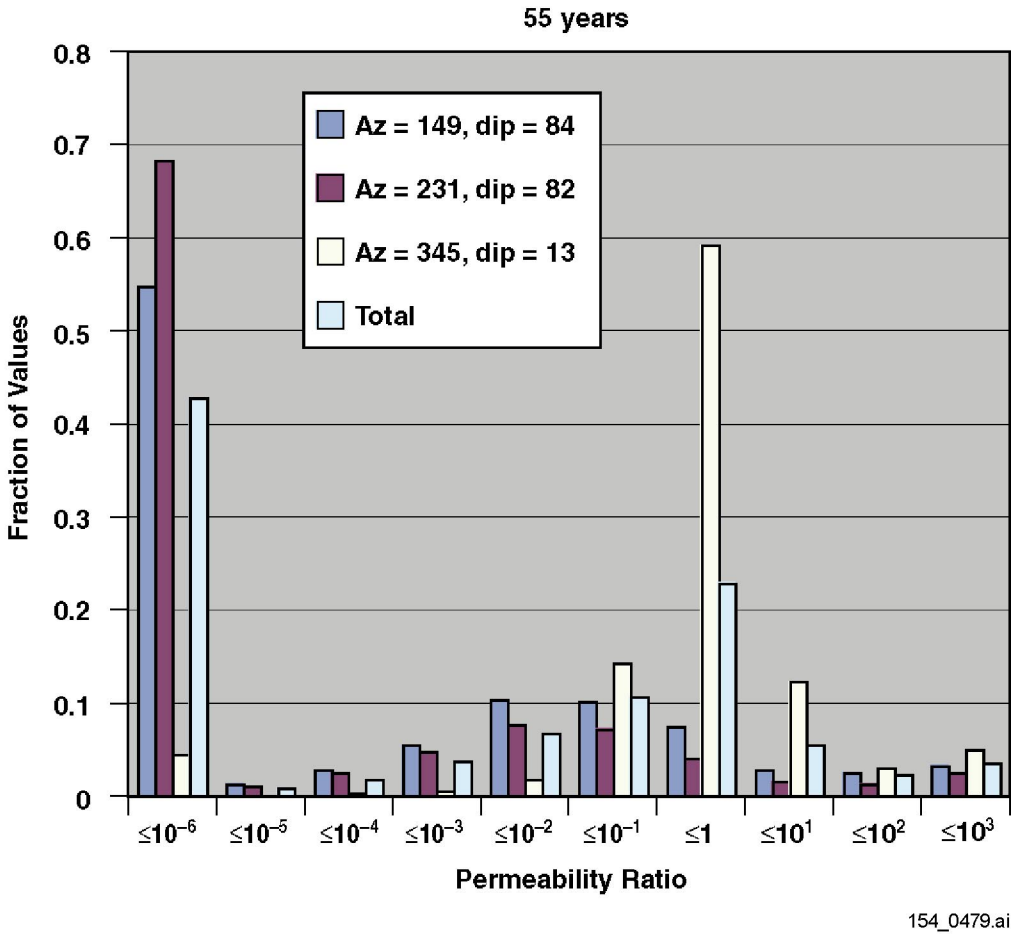

154_0479.ai

Source: Blair 2001 [DIRS 155005], p. 91.

NOTE: The histogram bins each span one order of magnitude, except for the lowest, which includes all permeability ratios below 10^{-6}.

Figure 4.3.7-2. Histogram of Permeability Ratios at 55 Years for Each Fracture Set for Higher-Temperature Case

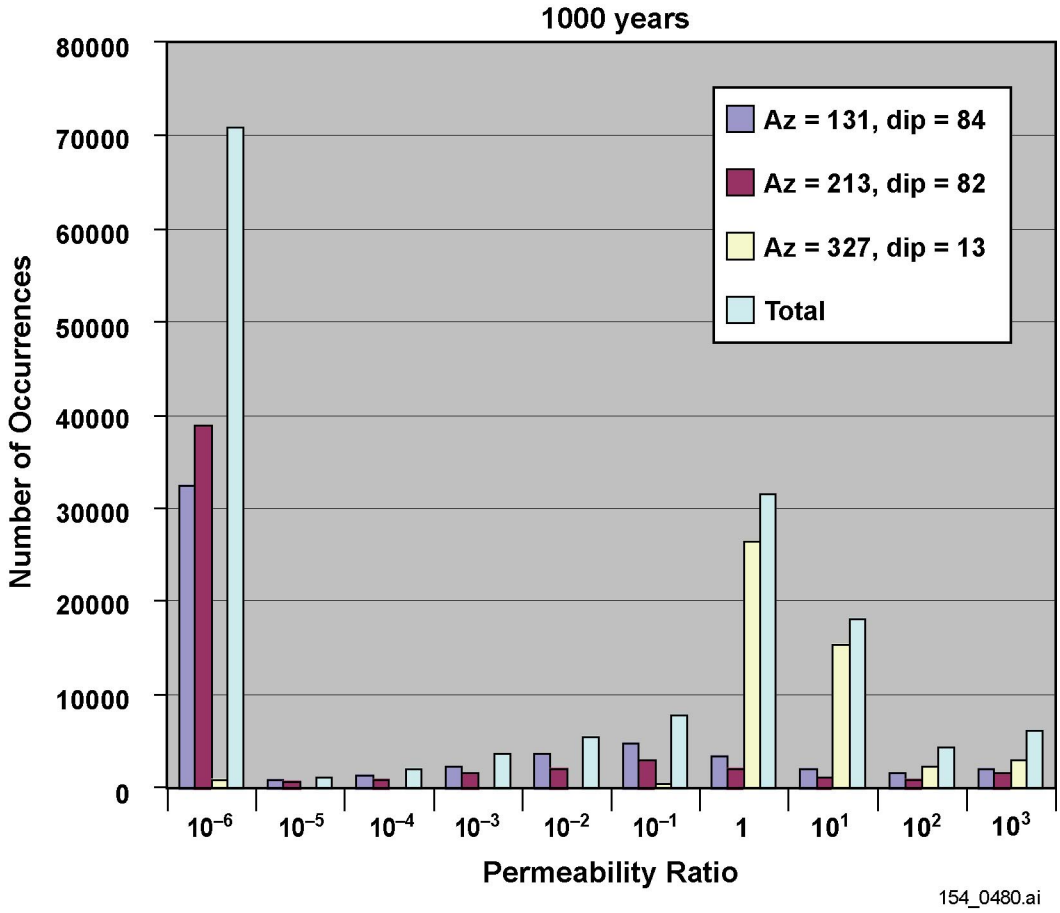

154_0480.ai

Source: Blair 2001 [DIRS 155005], p. 106.

Figure 4.3.7-3. Histograms of Permeability Ratios at 1,000 Years for Each Fracture Set for the Higher-Temperature Case

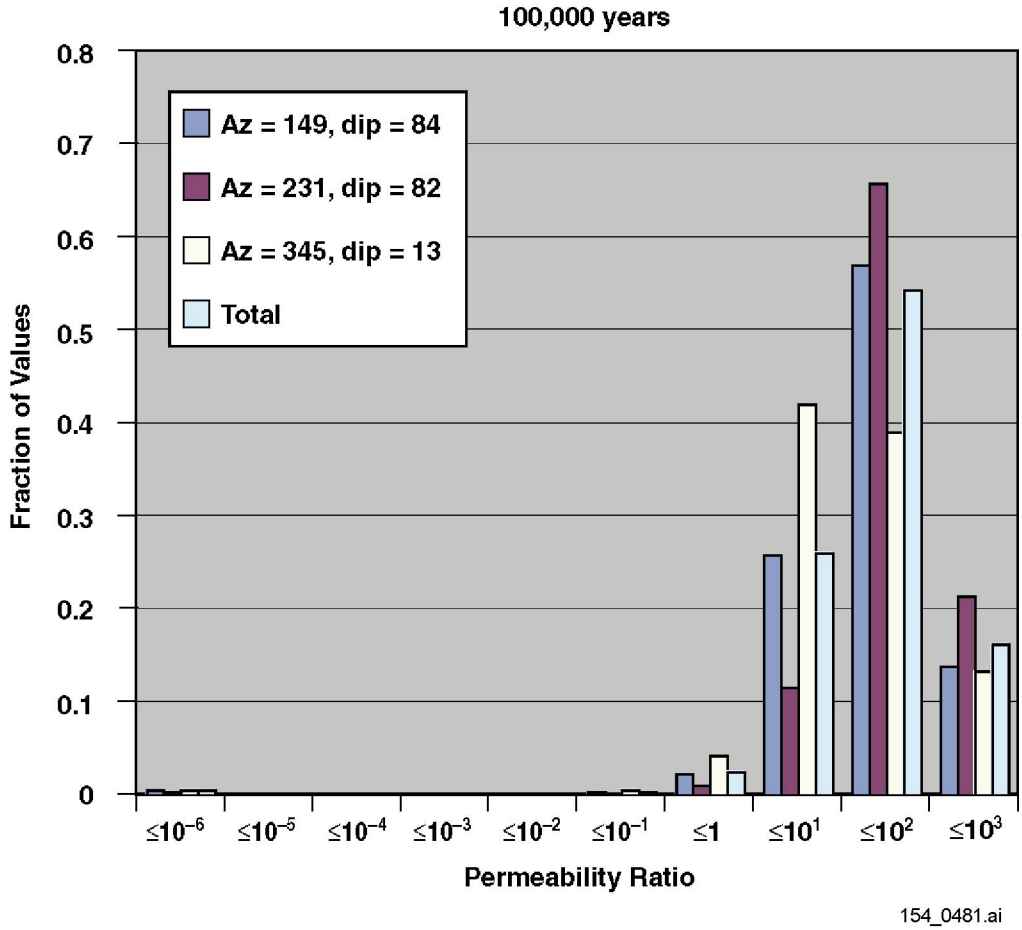

154_0481.ai

Source: Blair 2001 [DIRS 155005], p. 108.

NOTE: The histogram bins each span one order of magnitude, except for the lowest, which includes all permeability ratios below 10^{-6}.

Figure 4.3.7-4. Histogram of Permeability Ratios at 100,000 Years for Each Fracture Set for the Higher-Temperature Case

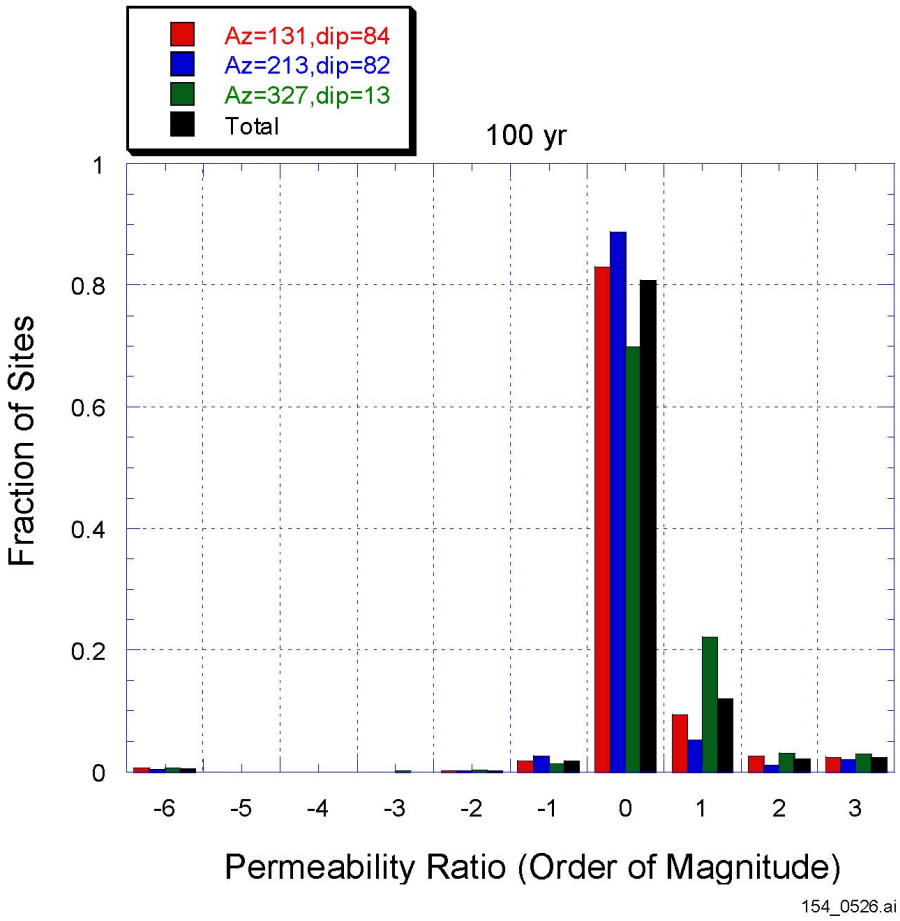

154_0526.ai

Source: Blair 2001 [DIRS 155005].

Figure 4.3.7-4a. Fracture Permeability Multipliers for the Lower-Temperature Operating Mode Case 100 Years after Emplacement

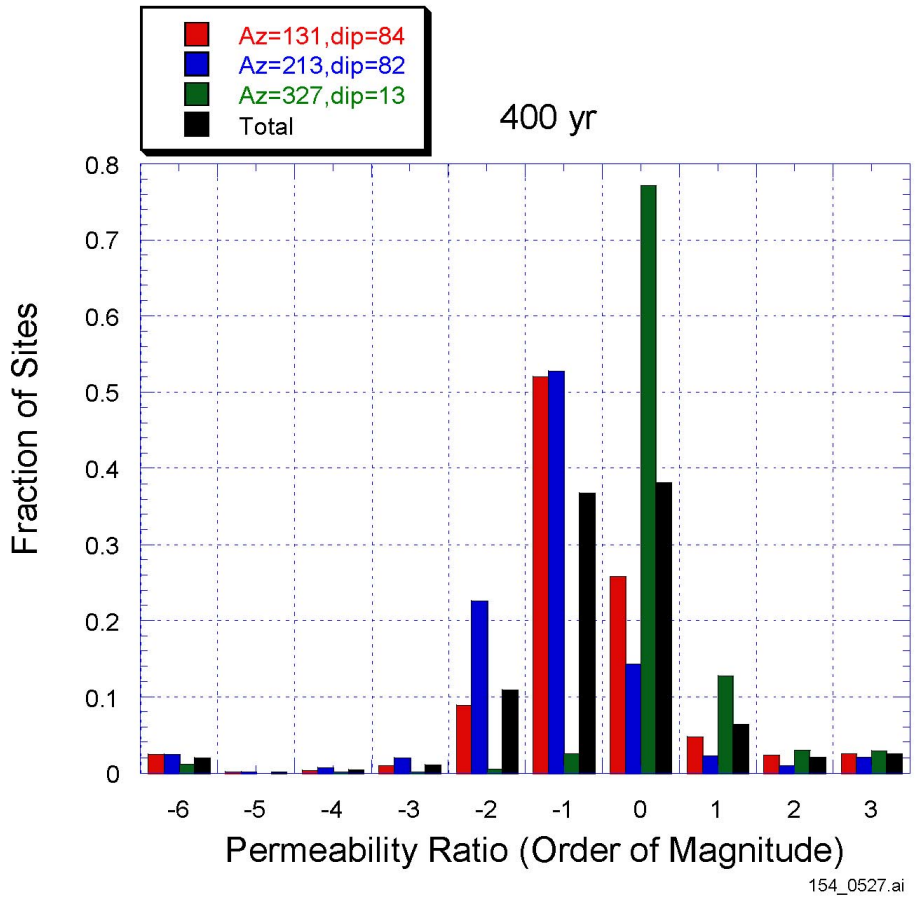

154_0527.ai

Source: Blair 2001 [DIRS 155005].

Figure 4.3.7-4b. Fracture Permeability Multipliers for the Lower-Temperature Operating Mode Case 400 Years after Emplacement

(a)

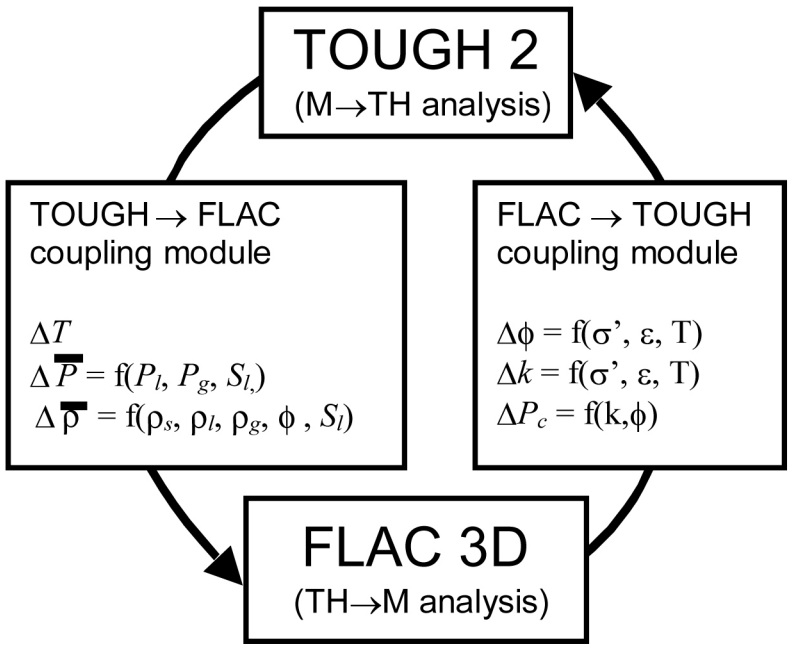

(b)

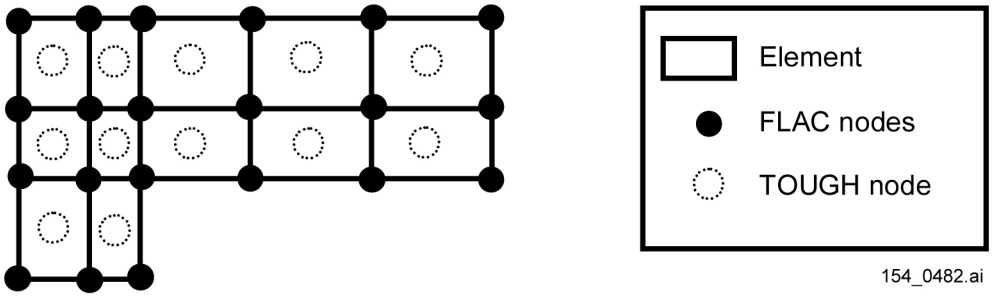

154_0482.ai

NOTE: TH = thermal-hydrologic, M = mechanical. Symbols: porosity (ϕ), permeability (k), effective stress (σ'), strain (ε), temperature (T), pressure (P), mean, solid, liquid, and gas densities respectively ($\overline{\rho}$, ρ_s, ρ_l, and ρ_g), liquid pressure (P_l), gas pressure (P_g), capillary pressure (P_c), liquid saturation (S_l).

Figure 4.3.7-5. Linking TOUGH2 and FLAC3D Codes

(a)

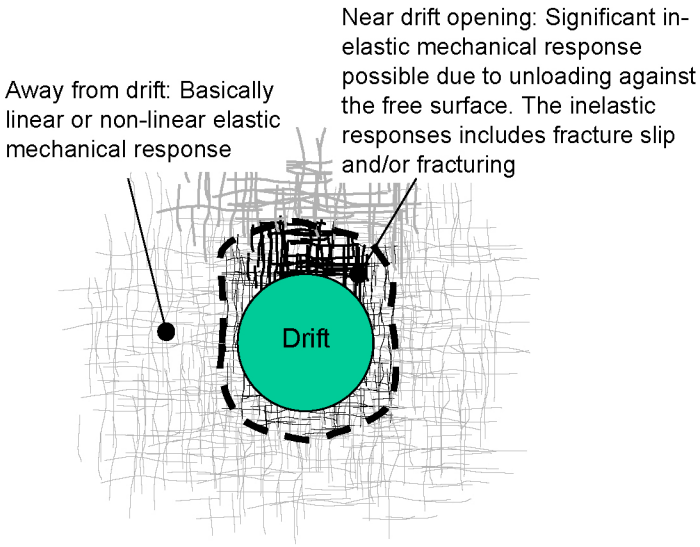

(b)

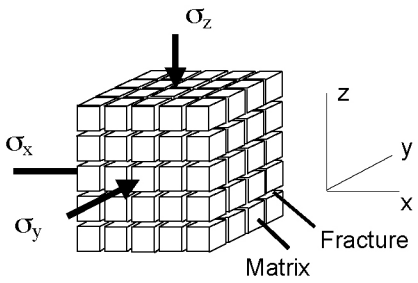

$$k_x = k_x(\sigma_y, \sigma_z)$$

$$k_y = k_y(\sigma_x, \sigma_z)$$

$$k_z = k_z(\sigma_x, \sigma_y)$$

154_0483.ai

154_0483.ai

Figure 4.3.7-6. Schematic Diagram of the Fracture Rock System Near a Drift and the Conceptual Stress Permeability Model Used

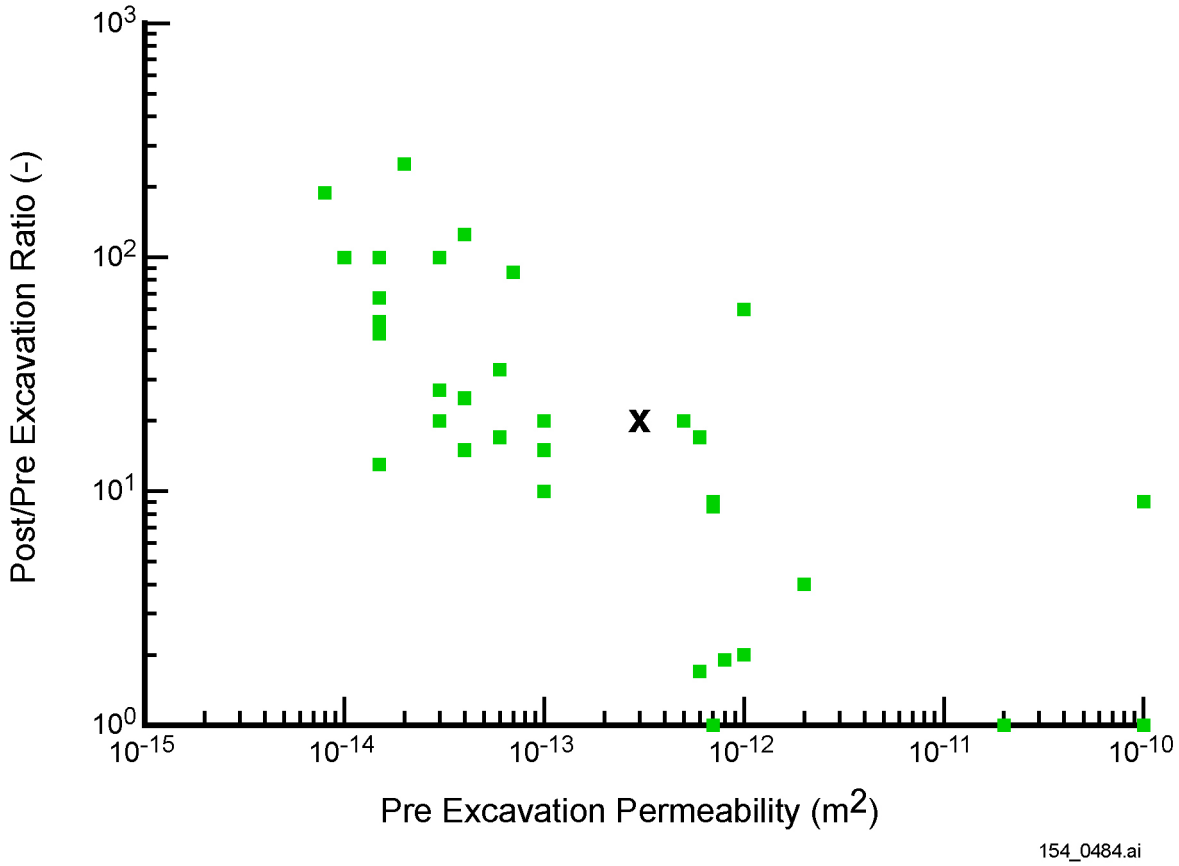

154_0484.ai

Source: Bodvarsson 2001 [DIRS 154669], Attachment 9, p.14.

NOTE: Data for Niche 2 (Station 36 + 50). The matching point for calibration is indicated by "**x**".

Figure 4.3.7-7. Changes in Post- to Pre-Excavation Permeability as a Function of Initial Permeability

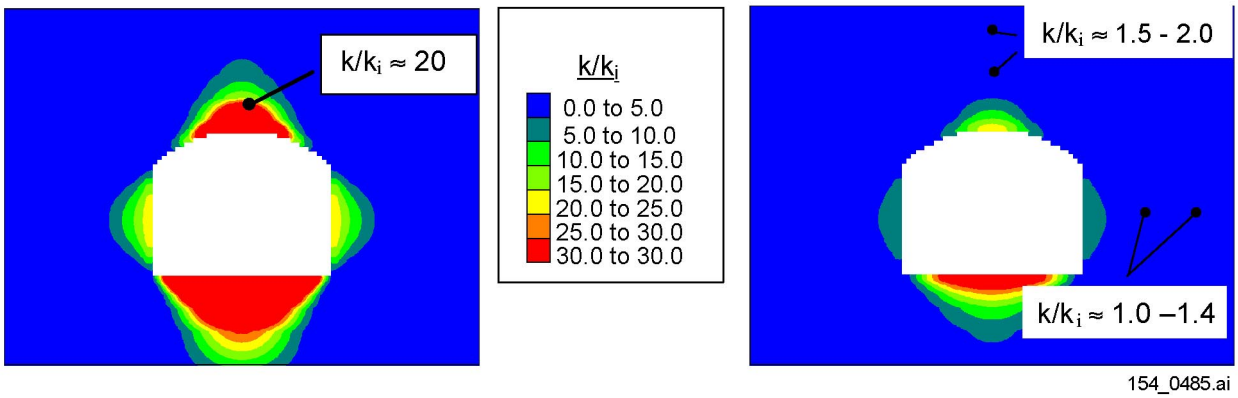

154_0485.ai

Source: Bodvarsson 2001 [DIRS 154669], Attachment 9, pp. 27 to 30.

NOTE: Data for niches in Tptpmn (left) and Tptpll (right).

Figure 4.3.7-8. Contour Plot of Pre- to Post-Excavation Permeability Ratio from the Calibrated Model

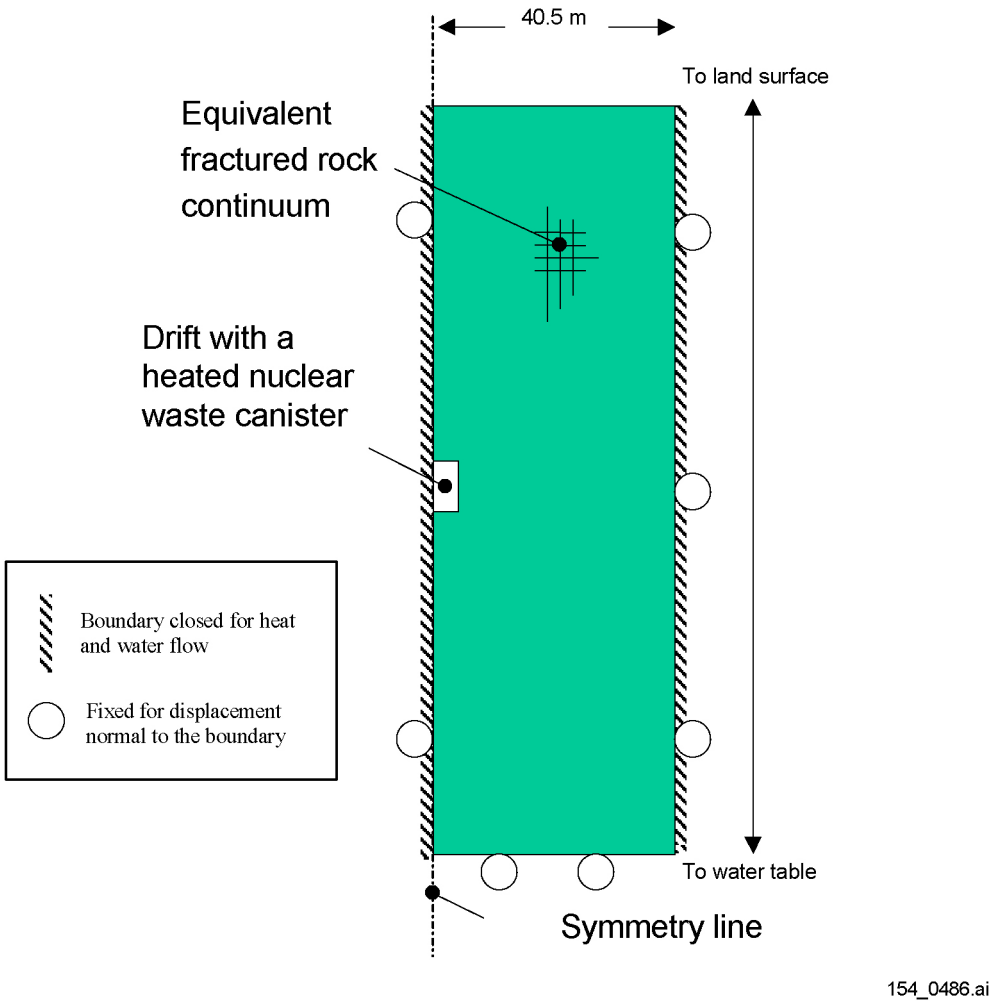

154_0486.ai

Source: Bodvarsson 2001 [DIRS 154669], Attachment 9, p. 34.

NOTE: Drift located in the Tptpll unit with 81-m drift spacing.

Figure 4.3.7-9. Model Geometry and Boundary Conditions for a Nuclear Waste Emplacement Drift

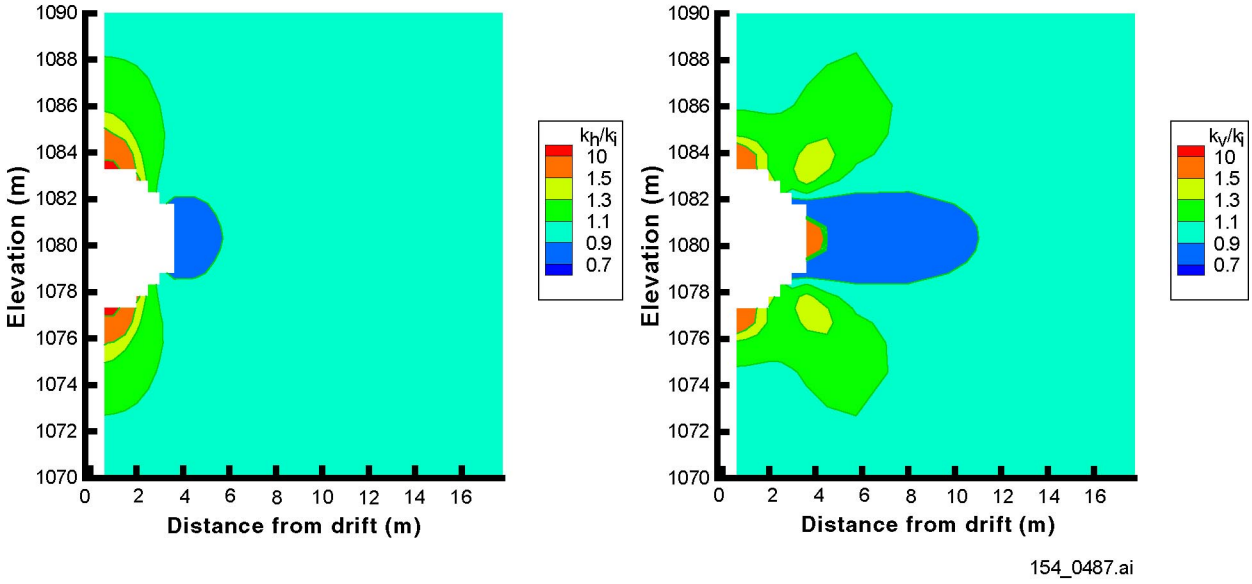

154_0487.ai

Source: Bodvarsson 2001 [DIRS 154669], Attachment 9, pp. 60 to 61.

NOTE: (a) horizontal, k_h, and (b) vertical, k_v, permeabilities.

Figure 4.3.7-10. Changes in Horizontal and Vertical Permeabilities Before and After Excavation

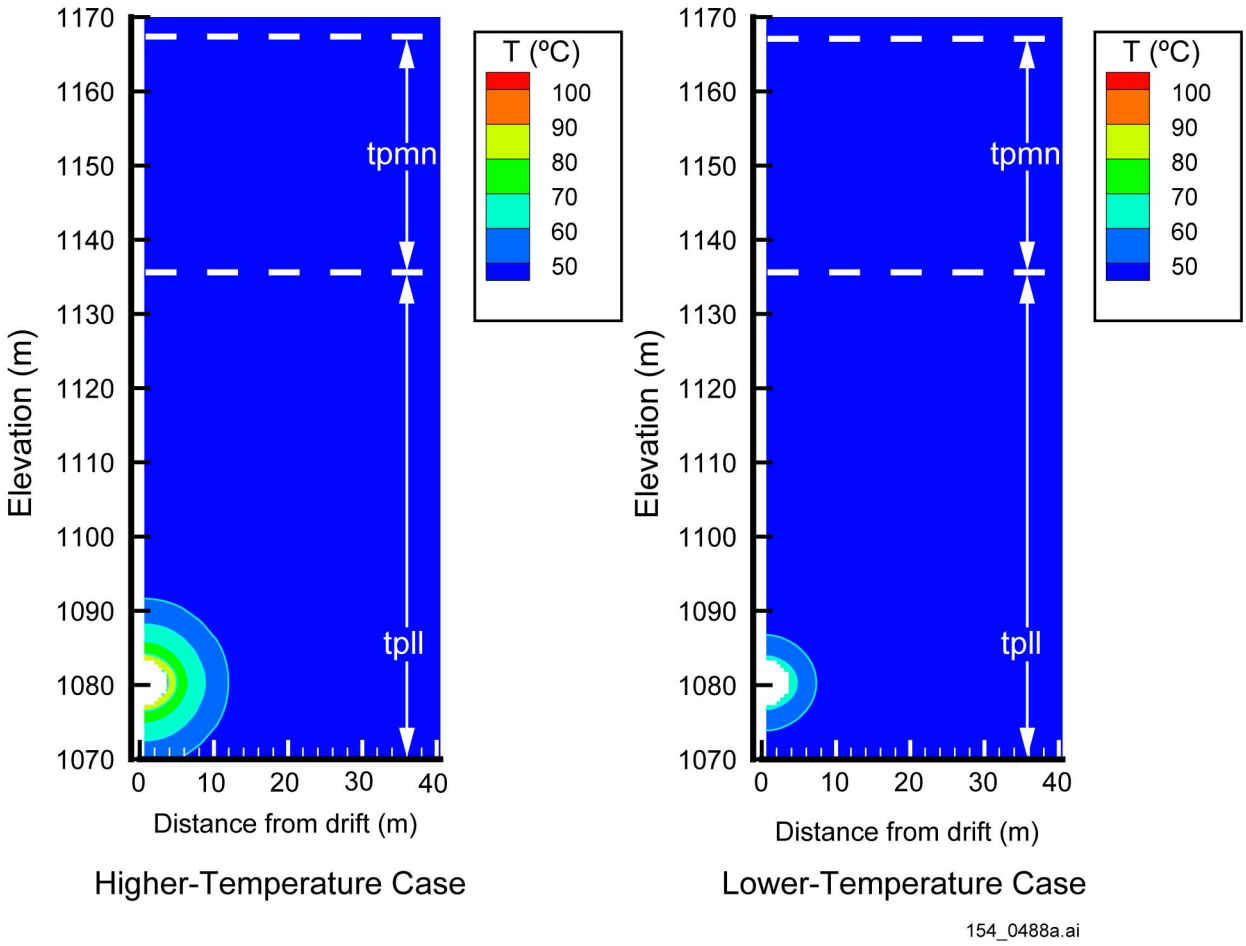

154_0488a.ai

Source: Bodvarsson 2001 [DIRS 154669], Attachment 9, p. 65.

Figure 4.3.7-11. Temperature Distribution at 10 Years

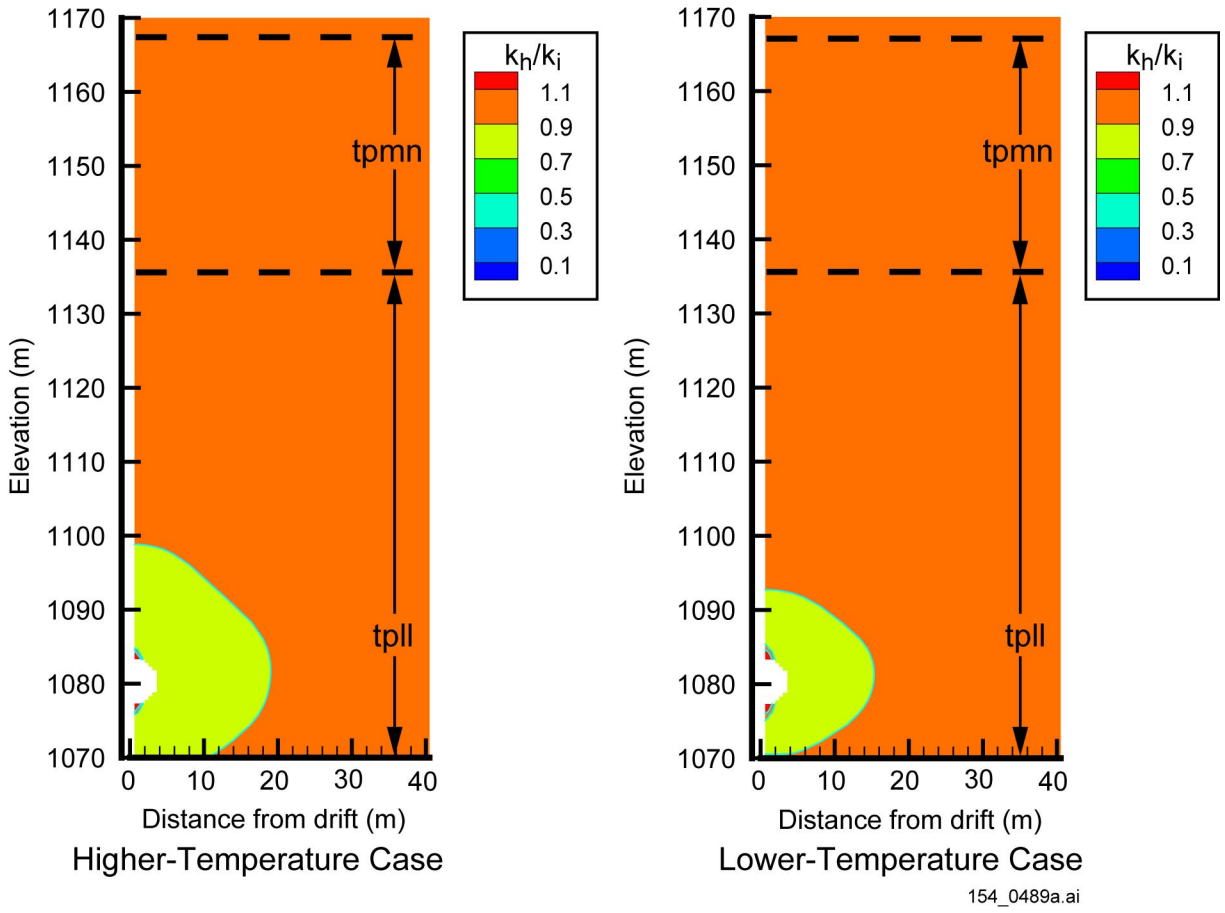

154_0489a.ai

Source: Bodvarsson 2001 [DIRS 154669], Attachment 9, pp. 57 to 74.

Figure 4.3.7-12. Horizontal Permeability Changes at 10 Years

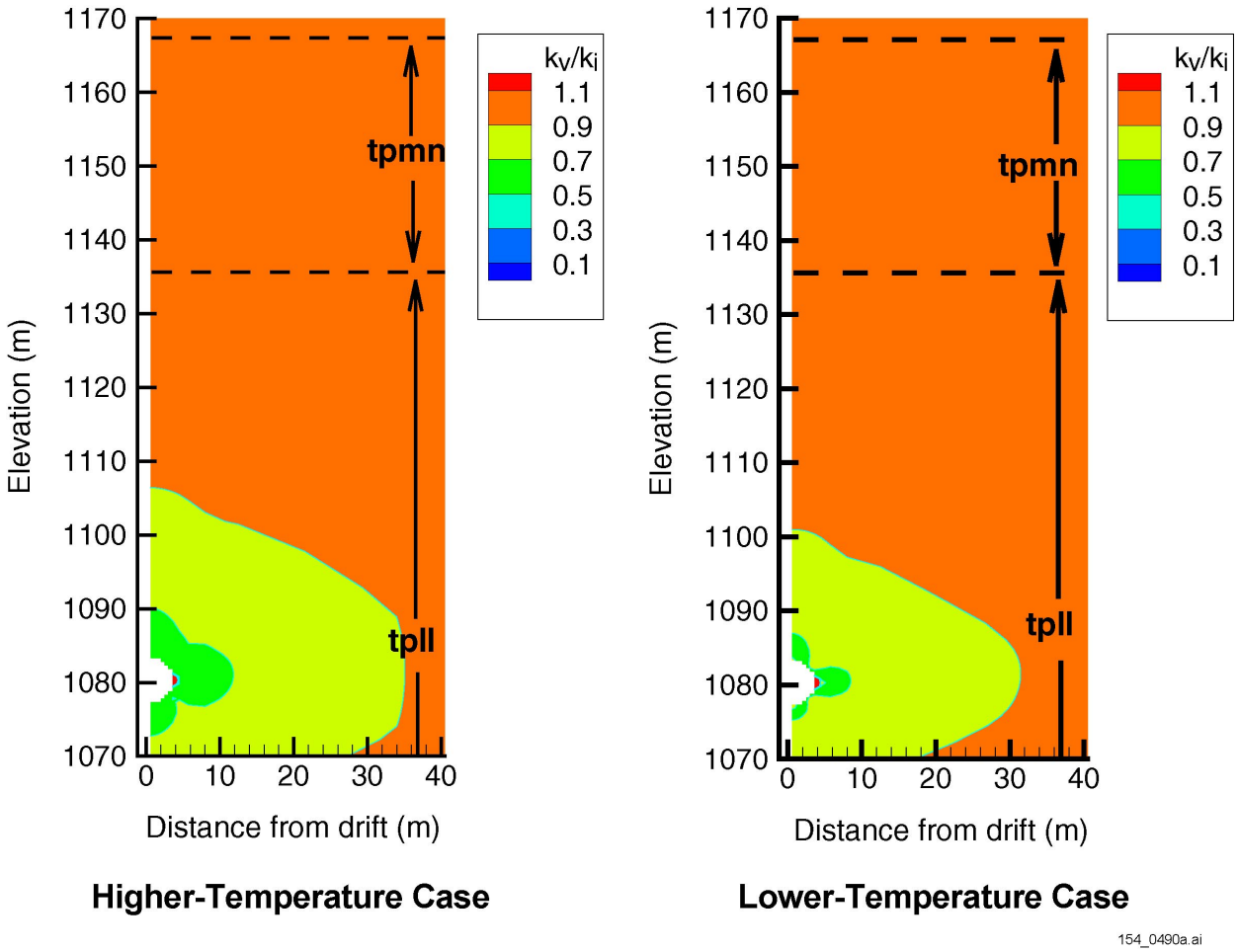

154_0490a.ai

Source: Bodvarsson 2001 [DIRS 154669], Attachment 9, pp. 57 to 74.

Figure 4.3.7-13. Vertical Permeability Changes at 10 Years

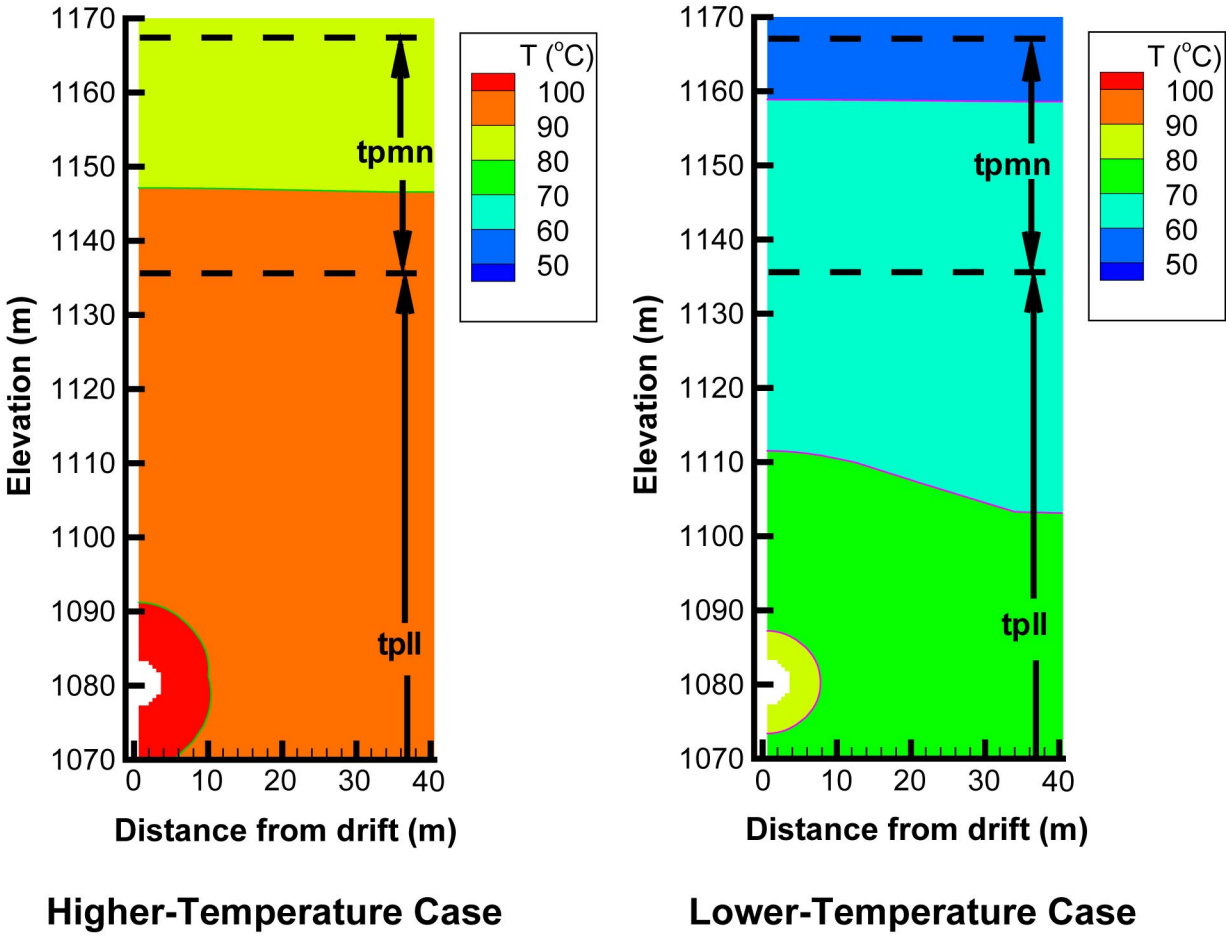

154_0491.ai

Source: Bodvarsson 2001 [DIRS 154669], Attachment 9, p. 69.

Figure 4.3.7-14. Temperature Distributions After 1,000 Years

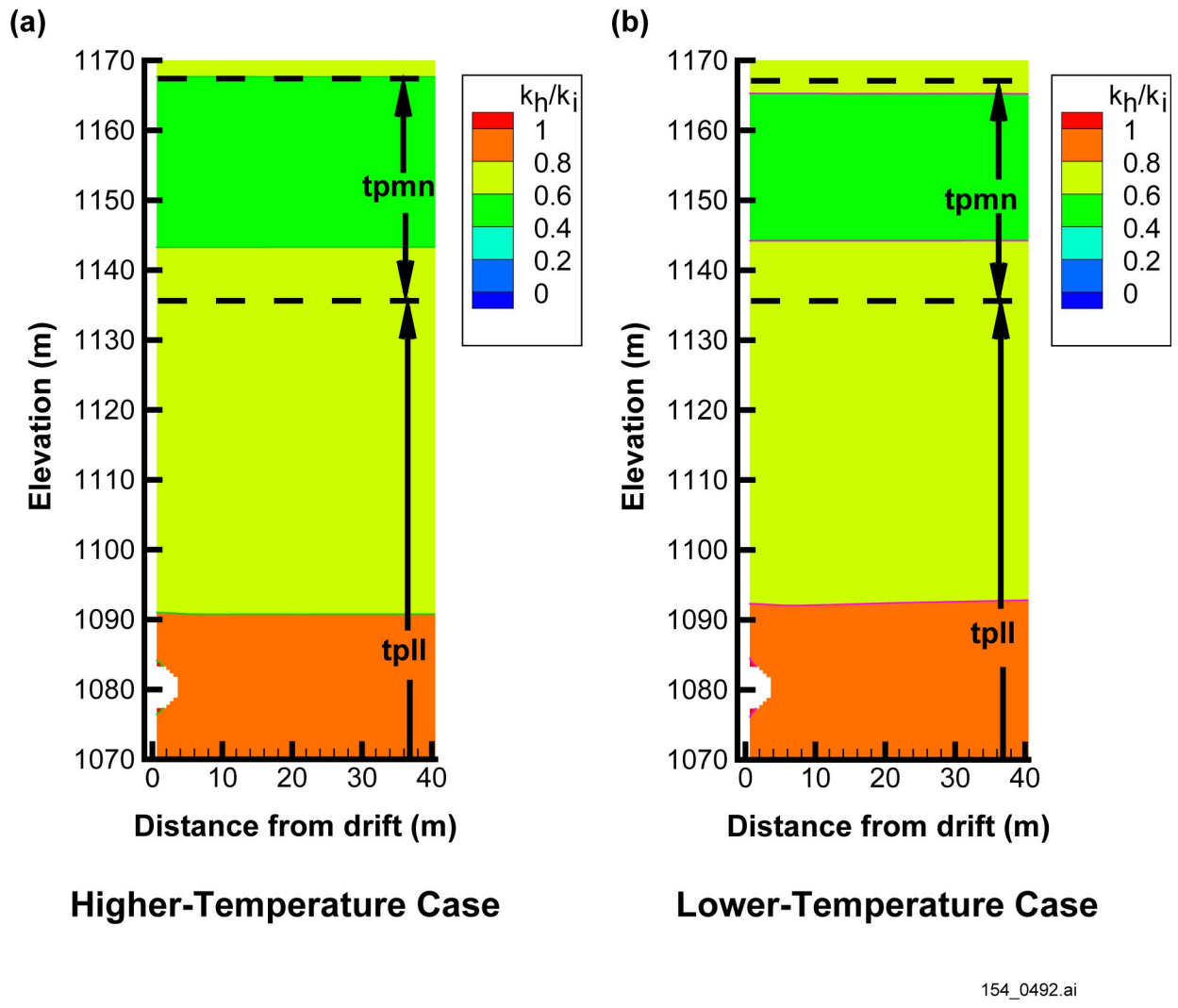

154_0492.ai

Source: Bodvarsson 2001 [DIRS 154669], Attachment 9, pp. 55 to 76.

Figure 4.3.7-15. Horizontal Permeability Changes at 1,000 Years

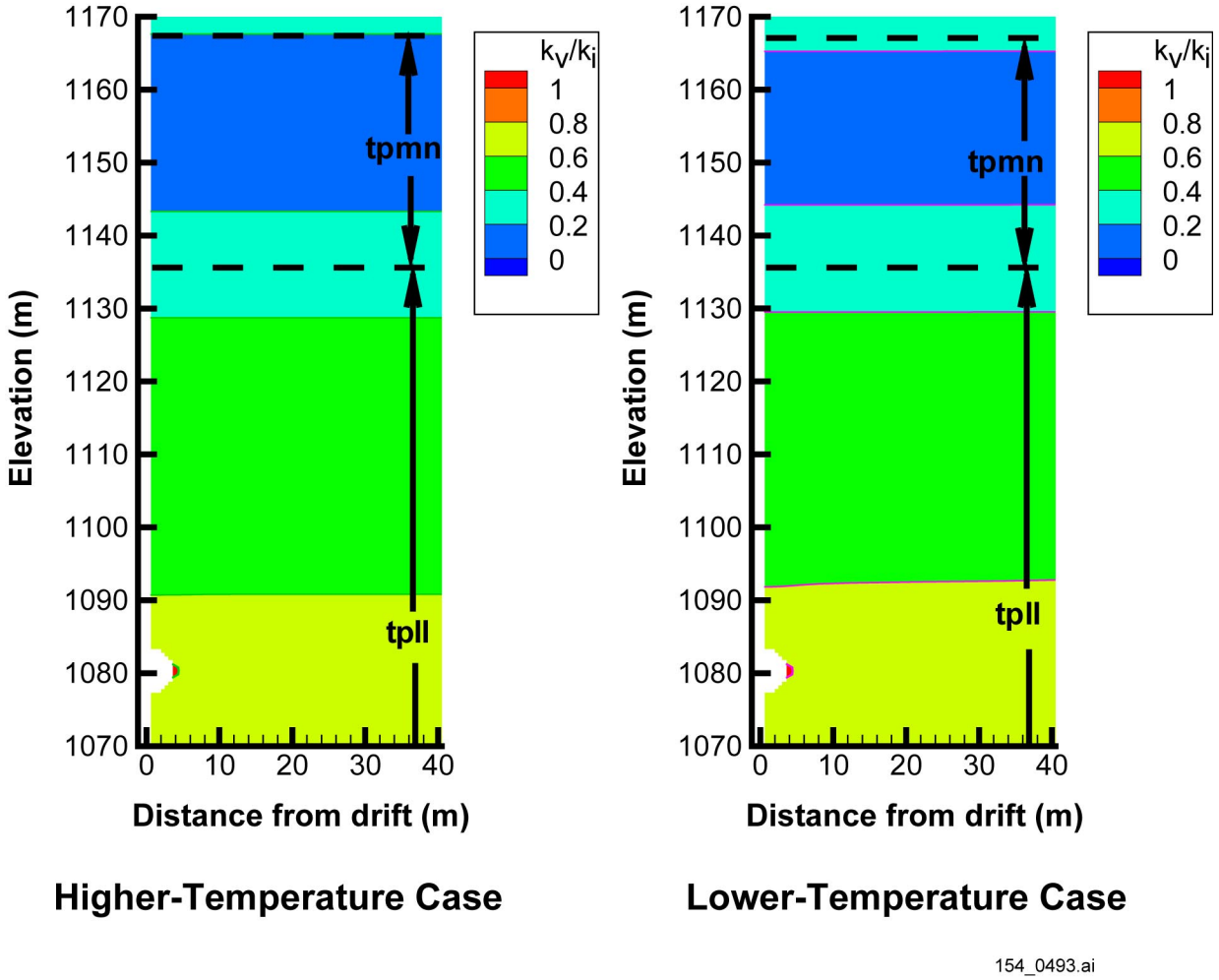

154_0493.ai

Source: Bodvarsson 2001 [DIRS 154669], Attachment 9, p. 70.

Figure 4.3.7-16. Vertical Permeability Changes at 1,000 Years

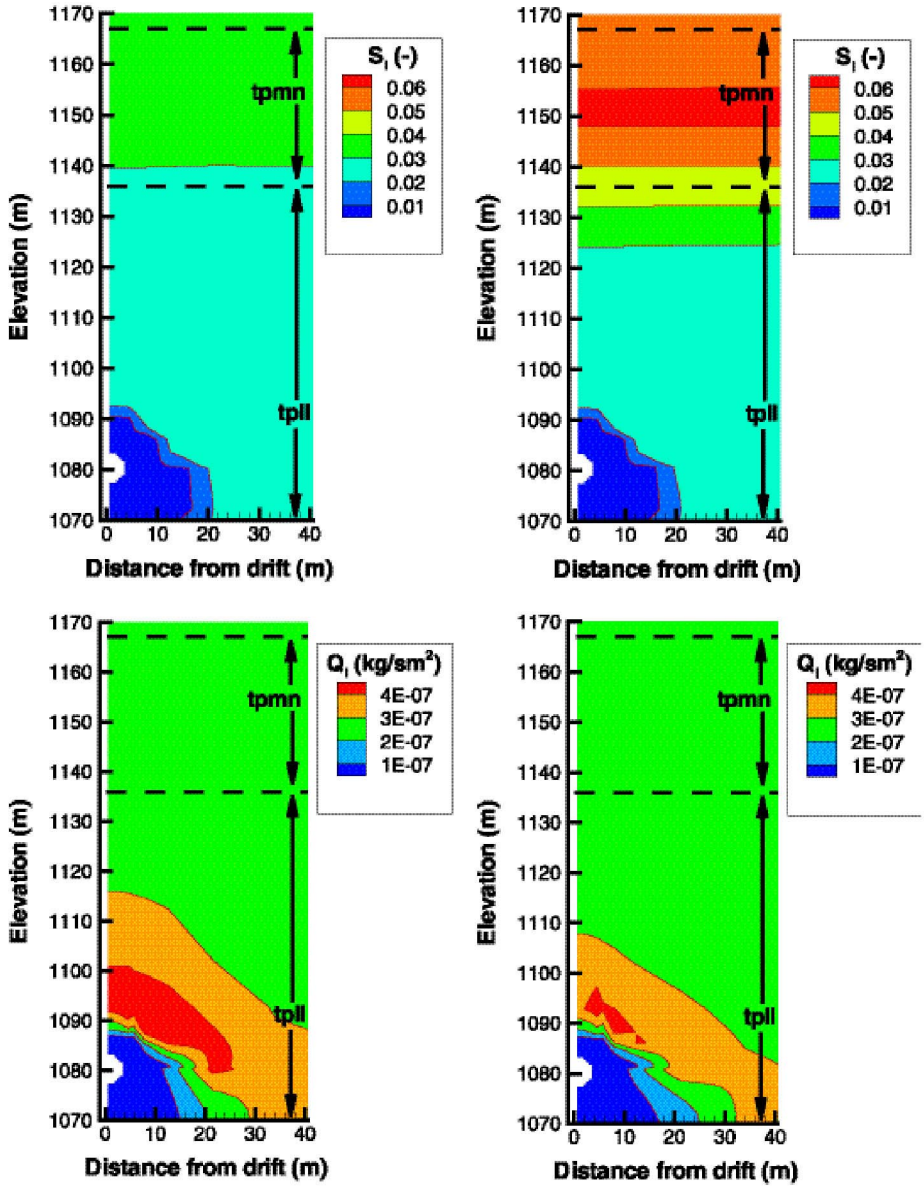

154_0188.ai

Source: Bodvarsson 2001 [DIRS 154669], Attachment 9, pp. 55 to 76.

NOTE: Comparison of results for saturation (upper panels) and percolation flux (lower panels) with thermal-hydrologic-mechanical processes (right) and purely thermal-hydrologic processes (left).

Figure 4.3.7-17. Distribution of Saturation and Percolation Flux for Thermal-Hydrologic-Mechanical and Thermal-Hydrologic Processes for the Higher-Temperature Case

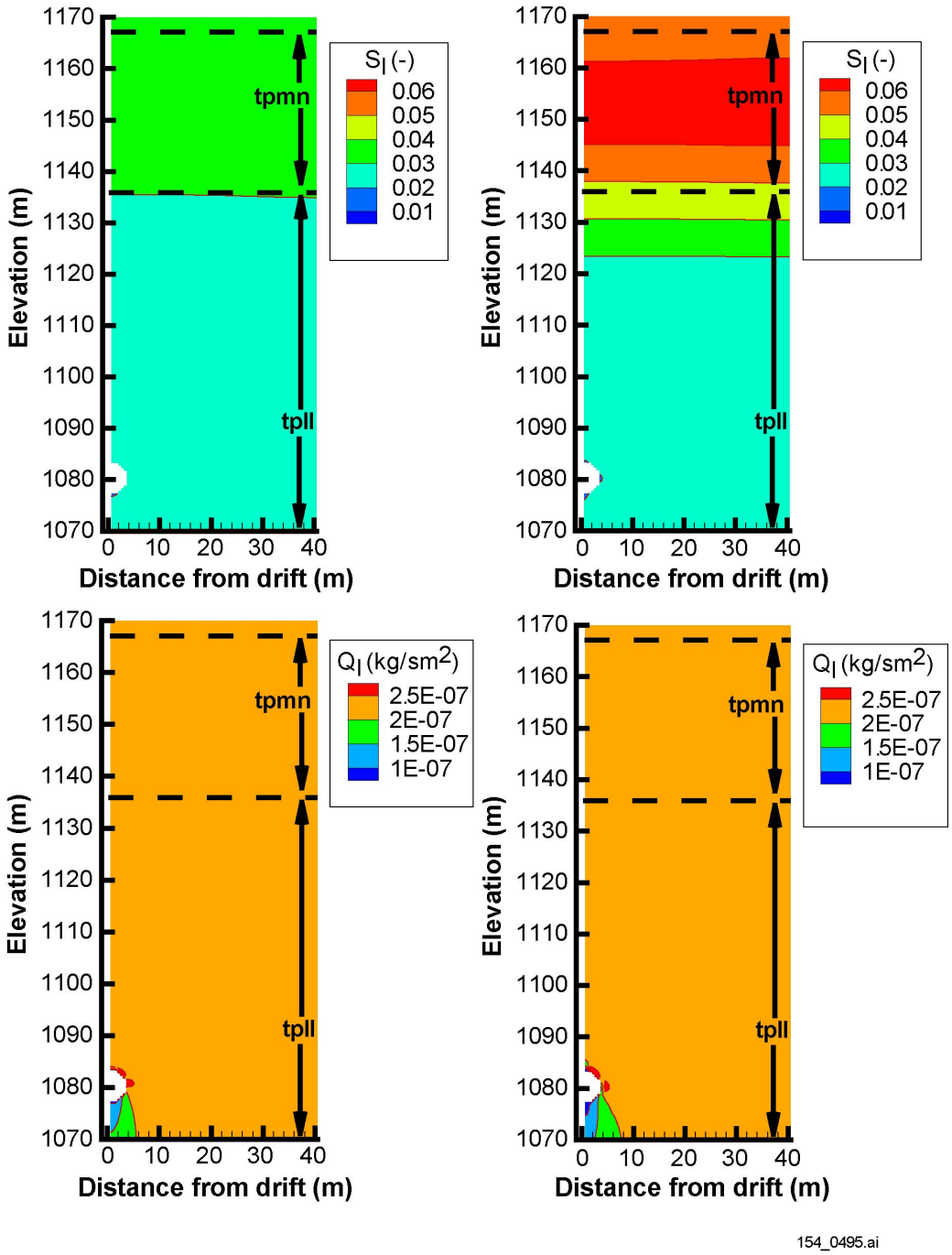

154_0495.ai

Source: Bodvarsson 2001 [DIRS 154669], Attachment 9, pp. 55 to 76.

NOTE: Results for the lower-temperature case. Comparison of results for saturation (upper panels) and percolation flux (lower panels) with thermal-hydrologic-mechanical processes (right) and purely thermal-hydrologic processes (left).

Figure 4.3.7-18. Distribution of Saturation (S_1) and Percolation Flux (Q_1) for Thermal-Hydrologic-Mechanical and Thermal-Hydrologic Processes for the Lower-Temperature Case

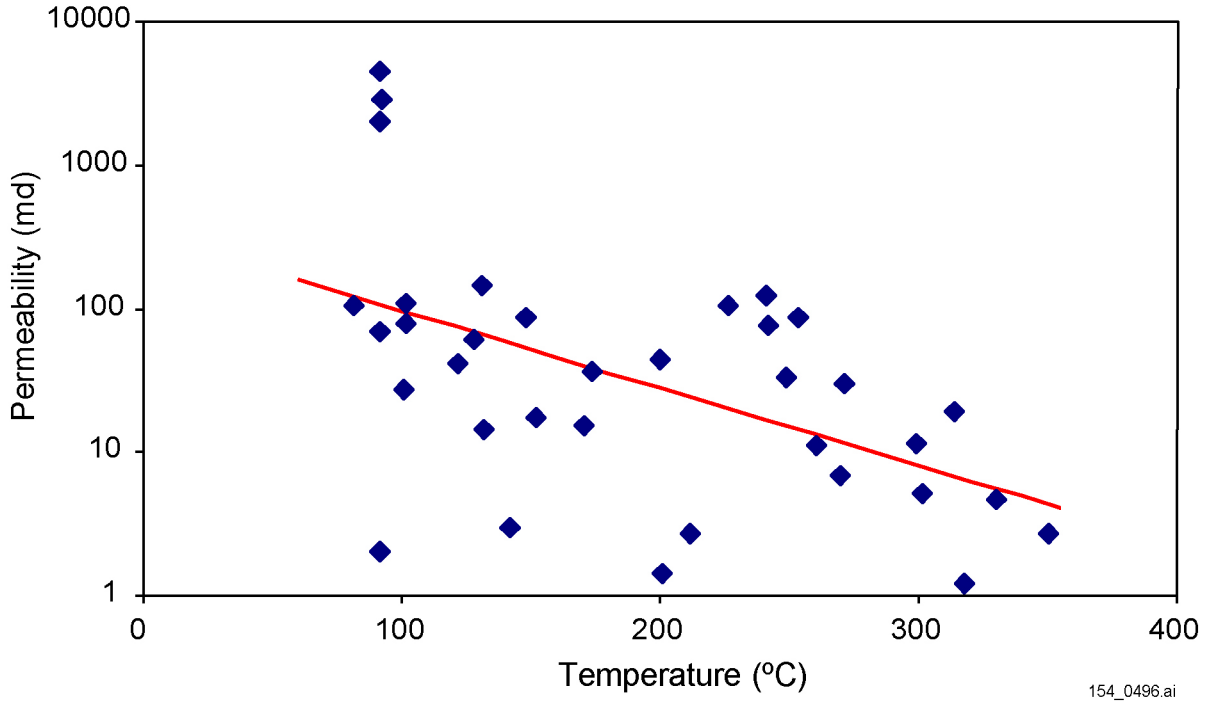

154_0496.ai

Source: Based upon a survey by Björnsson and Bodvarsson 1990 [DIRS 154606]. Fit of the line from Bodvarsson 2001 [DIRS 154669], Attachment 4, p. 36.

Figure 4.3.7-19. Correlation Between Permeability and Temperature for Worldwide Geothermal Reservoir

INTENTIONALLY LEFT BLANK

5 Effects of Decay Heat on In-Drift Thermal-Hydrologic Conditions

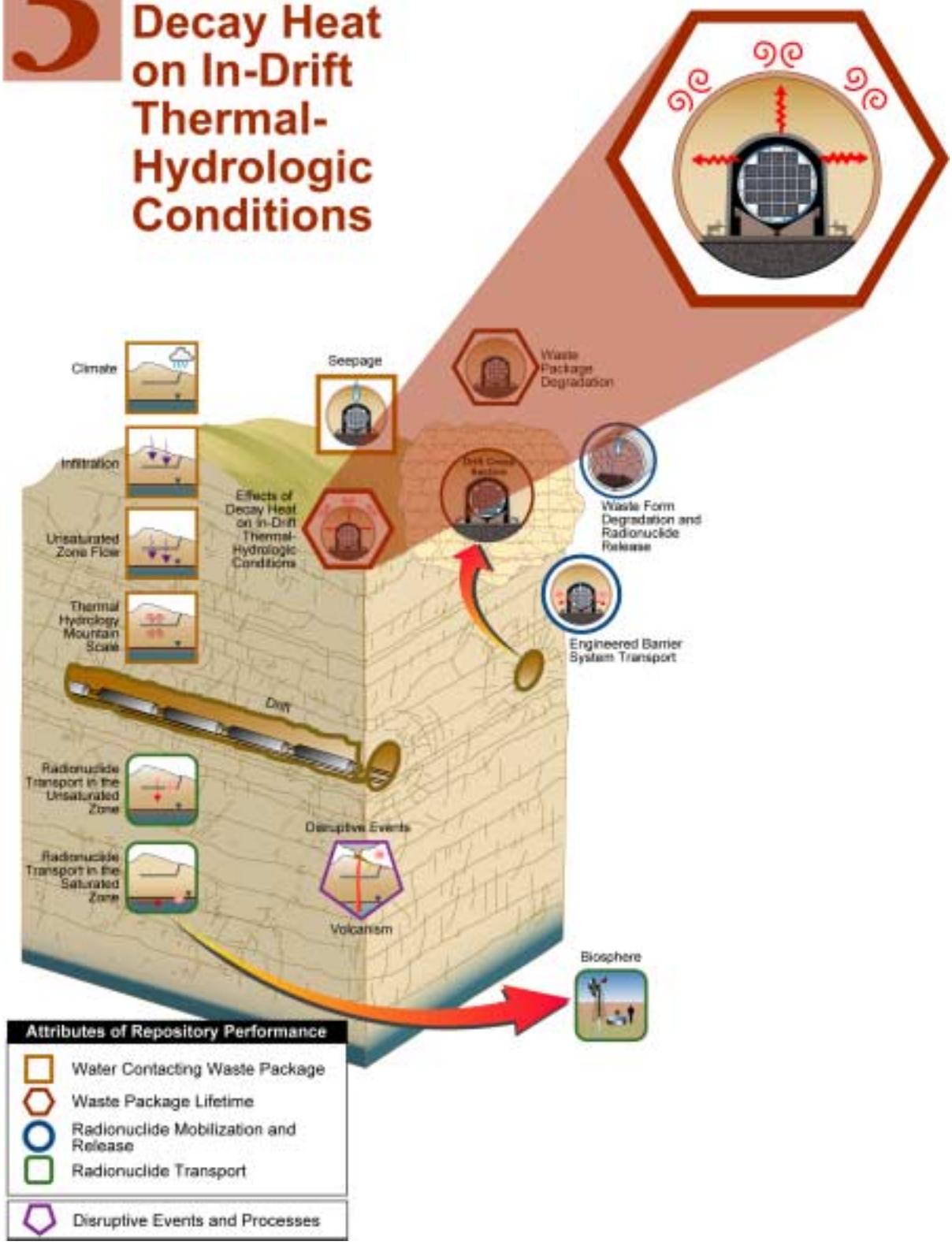

5. EFFECTS OF DECAY HEAT ON IN-DRIFT THERMAL-HYDROLOGIC CONDITIONS

This section discusses model development and analyses conducted since completion of the *Yucca Mountain Science and Engineering Report* (S&ER) (DOE 2001 [DIRS 153849]), in the area of thermal-hydrologic (TH) influences on in-drift conditions. The section begins with a short review of the conceptual basis for TH modeling of the in-drift environment. The review is followed by a summary of the treatment of thermal hydrology in *Total System Performance Assessment for the Site Recommendation* (TSPA-SR) (CRWMS M&O 2000 [DIRS 153246]), which is the model that supports the S&ER. The purpose of this section is to document the improvements that have been made to the TH process model and its abstraction for total-system modeling since completion of the TSPA-SR. The model revisions and analyses were conducted to improve the implementation of the scientific conceptual model, quantify previously unquantified uncertainties, and evaluate how a lower-temperature operating mode (LTOM) would affect the in-drift TH environment, as summarized in Table 5-1.

The improved model was exercised at the process-level and the total system-level for this report. Section 5.1 introduces the conceptual basis upon which the model is based. Section 5.2 reviews how the in-drift TH environment was modeled in support of the TSPA-SR and S&ER. Section 5.3 describes uncertainties in the models, improvements in the models to reduce those uncertainties, and analyses conducted to better understand them. This section (5.3) is split into two parallel subsections addressing the multiscale TH modeling of in-drift conditions and modeling of ventilation and convection. These sections are followed by another section (Section 5.3.3) summarizing the available natural and anthropogenic analogue information applicable to in-drift TH conditions. Each of the two parallel sections (Sections 5.3.1 and 5.3.2) includes a discussion of process model goals, representation in TSPA-SR (CRWMS M&O 2000 [DIRS 153246]), subsequent model improvements, and quantification of uncertainty using the improved model. The two parallel subsections include 17 discussions of individual aspects of uncertainty. For convenience, each of these discussions includes a short summary, and there is an overall summary of the 17 analyses in Section 5.4.3.

The final section (Section 5.4) of the chapter discusses the results of the exercise of the multiscale TH model in support of the SSPA Volume 2 (McNeish 2001 [DIRS 155023]) base case higher-temperature operating mode (HTOM) and LTOM. It also provides an overall summary of results of the process model-level results that quantified uncertainty.

5.1 INTRODUCTION AND CONCEPTUAL BASIS

The heat produced by radioactive decay of the nuclear waste in the potential repository will have an effect on the seepage water into the potential repository drifts, water movement through the potential repository, and the patterns of natural water flow in the unsaturated rock layers which set the boundary conditions for the in-drift environment. The nature and extent of these effects, however, will depend on thermal loading (or areal heat output), ventilation rates and durations, and consequent operating temperature mode (i.e., above-boiling or below-boiling). The goals of the process-level and total system performance modeling of the effects of decay heat on in-drift thermal-hydrologic conditions are to develop estimates for the evolution of key environmental conditions in the emplacement drifts. These models must consider the effects of heat on water

Table 5-1. Summary of Supplemental Models and Analyses

Key Attributes of System	Process Model (Section of S&ER)	Topic Of Supplemental Scientific Model or Analysis	Reason For Supplemental Scientific Model or Analysis			Performance Assessment Treatment of Supplemental Scientific Model or Analysis[a]		
			Unquantified Uncertainty Analysis	Update in Scientific Information	Lower-Temperature Operating Mode Analysis	Section of Volume 1	TSPA Sensitivity Analysis	Included in Supplemental TSPA Model
Long-Lived Waste Package and Drip Shield	Water Diversion Performance of EBS (4.2.3)	Multiscale thermal-hydrologic model, including effects of rock dryout	X		X	5.3.1		X
		Thermal property sets	X	X		5.3.1		X
		Effect of in-drift convection on temperatures, humidities, invert saturations, and evaporation rates	X		X	5.3.2		
	In-Drift Moisture Distribution (4.2.5)	Environment on surface of drip shields and waste packages	X			5.3.2		
		Evaporation of seepage	X		X	5.3.2	X	X

NOTE: S&ER = *Yucca Mountain Science and Engineering Report* (DOE 2001 [DIRS 153849]).

[a] Performance assessment treatment of supplemental scientific model or analysis discussed in SSPA Volume 2 (McNeish 2001 [DIRS 155023]).

movement in the host rock near emplacement drifts; however, this section reports only the results for TH conditions within the drift or at the drift wall. Key parameters contributing to the environmental conditions in the emplacement drifts include temperature, relative humidity, and evaporation rates that affect the performance of the engineered barriers and the transport of radionuclides that may eventually be released.

The major effects of decay heat on water movement that could impact the in-drift conditions would occur immediately after permanent closure (DOE 2001 [DIRS 153849], Section 4.2.2), at which time the ventilation system is shut down. Initially, heat will be transported outward away from the drifts by heat conduction through the rock and the movement of air through fractures. A portion of the heat will be transported by water that vaporizes near the heat sources and condenses in cooler rock farther away. If the heat flux (from the waste package resulting from decay of the waste) is high enough, rock near the drifts will be heated to the boiling point of water (nominally 96°C [205°F] at the elevation of the potential repository), and then to higher temperatures after most of the water in this region has evaporated. How the rock responds (dryout/rewetting) will impact the conditions within the drift. The time during which rock drying and wetting occurs, and thus impacts the in-drift conditions will depend on local thermal loading, percolation flux, and location in the potential repository layout (i.e., near the center or the edge). As the heat produced by radioactive heat declines with time, temperature within the emplacement drifts will return to pre-emplacement levels.

Thermally-driven processes are most intense within, and in the immediate vicinity of, the emplacement drifts. However, larger-scale processes (mountain scale) must be considered as well because they affect the drift environments. Thermal processes at the drift scale (a few meters to tens of meters, or several feet to several tens of feet) include conduction within the rock and the radiant heat transfer within the drifts. To these are added all the processes associated with liquid and gas flow including thermal effects due to evaporation and conduction. Additional important considerations at the mountain scale (hundreds of meters to thousands of meters, or several hundred feet to several thousand feet) include the surface topography, the stratigraphy of the unsaturated zone, and the spatial variations in infiltration. Surface topography refers to the thickness of the overburden above the emplacement drifts and is a factor in how quickly a location cools off. The stratigraphy of the unsaturated zone influences the thermal and hydrologic properties of this zone that can be quite different across stratigraphic units. The spatial variation of thermally-driven processes indicate that higher infiltration leads to lower temperature and higher relative humidity, and faster cooling of the potential repository edge as compared with its center.

Consistent with the *Unsaturated Zone Flow and Transport Model Process Model Report* (CRWMS M&O 2000 [DIRS 151940], Section 3.10.3.1), the engineered barrier system thermal hydrologic models use the dual-permeability conceptual flow model to characterize the flow of heat and moisture through the rock of the potential repository. The flow of heat and moisture are modeled as flowing through two interacting continua, with each continuum being assigned its own spatially variable hydrologic properties, such as permeability and porosity. Fracture-matrix interaction is represented with an active-fracture model, in which only a portion of the fractures are actively flowing under unsaturated conditions (CRWMS M&O 2000 [DIRS 151940], Section 3.3.4).

Drift-scale modeling must include coupling of drift-scale processes with mountain-scale processes to properly account for effects such as faster cooling of waste packages near the potential repository edge, as compared to waste packages near the potential repository center. Because of scale issues, directly modeling the evolution of in-drift thermal hydrology in detail and in three dimensions would require extreme levels of computational effort. To alleviate this problem, a multiscale model, called the *Multiscale Thermohydrologic Model* report (CRWMS M&O 2000 [DIRS 149862]) (MSTH model), was developed that combines submodels that consider the scale of interest for a particular portion of the problem. The validation of the MSTH model, as discussed in Section 5.3.1.2.1, relies on comparison between model results and field studies designed to test the validity of the model. This comparison is reported in the *Multiscale Thermohydrologic Model* report (CRWMS M&O 2000 [DIRS 149862], Section 6.13.2). That document reports good agreement between the model and the measurements made in the Drift Scale Test. The Drift Scale Test was designed to test the coupled process models, including the MSTH model, and is being conducted underground in the environment appropriate for testing these models.

The multiscale approach also breaks the problem into more tractable pieces by considering dimensionality requirements (one-, two- or three-dimensional) for the issue of concern. For example, considerations of mid-pillar temperatures may be appropriately modeled with two-dimensional calculations, but temperature distributions within a drift with varying package outputs requires a three-dimensional calculation because temperatures vary in three dimensions. The multiscale approach divides the problem into thermal and thermal-hydrologic submodels so that the effects of convective heat transfer and phase change of water in the rock, in addition to conduction can be addressed efficiently. By dividing the problem into a more efficient conduction submodel can be used to address detailed three-dimensional problems where that submodel is sufficient, such as when there is no moisture present or when there are no effective pathways for moisture movement. When conduction submodels are not sufficient, a convective heat transfer submodel can be applied, but without considering as much three-dimensional detail. By combining these in a MSTH model, both heat and mass transfer can be efficiently evaluated.

A major strength of the MSTH model is that it precisely represents the influence of many details of potential repository design on the predicted thermal-hydrologic responses throughout the potential repository volume. This means that the MSTH model results are design-specific and that the use of different design parameters would potentially yield different results. However, the results may be considered to be approximately applicable to alternative designs that share similar dependent-parameter attributes, such as peak temperatures and that share similar design attributes, such as waste package spacing. In the *Multiscale Thermohydrologic Model* report (CRWMS M&O 2000 [DIRS 149862]), thermal-hydrologic responses were analyzed for a case in which boiling temperatures extend a short distance (< 10 m for the mean infiltration-flux scenario) into the rock. This is the TSPA-SR (CRWMS M&O 2000 [DIRS 153246]) design case.

For the SSPA, two cases were analyzed using the MSTH model (BSC 2001 [DIRS 154864]). The first case analyzed, called the HTOM, is similar to the TSPA-SR design case, but analyzed with updated models. Operating the potential repository at lower temperatures would reduce the magnitude and duration of the effects of decay heat on water movement. In addition, lower temperatures would result in reduced chemical reaction rates so that the effects of the coupled

THC processes would also be reduced, as discussed in the *Drift-Scale Coupled Processes (DST and THC Seepage) Models* (BSC 2001 [DIRS 154677]). The second case analyzed, called the LTOM, is one where temperatures do not exceed approximately 85°C on the waste package surface. These potential repository conditions are achieved in the model analyses that were conducted using the specific operational-mode assumptions listed in Table 5.1-1. If corrosion testing and modeling for the SSPA and a potential license application conclude that localized corrosion in the 85°C to boiling temperature range is not likely for potential repository chemical conditions, then the intermediate case could be analyzed.

5.2 REVIEW OF TOTAL SYSTEM PERFORMANCE ASSESSMENT-SITE RECOMMENDATION TREATMENT

The in-drift TH environments for TSPA-SR (CRWMS M&O 2000 [DIRS 153246]) simulations were computed using the MSTH model (CRWMS M&O 2000 [DIRS 149862], Section 6.1). This AMR included modeling of the no-backfill scenario, providing temperature and relative humidity at several in-drift locations, and liquid evaporation rate and saturation values in the drift invert gravel. Because the processes couple beyond the drift wall, the MSTH model calculates conditions within the rock in order to accurately reflect the development of TH conditions within the drifts. Thus, in addition to in-drift uses of these results, the MSTH model provided information regarding near-field water flow rates to the thermal seepage model. Although the information provided by the analysis of the thermal hydrology to other TSPA-SR (CRWMS M&O 2000 [DIRS 153246]) model components, and inputs from other TSPA components to the analysis of thermal hydrology, are summarized in Figure 5.2-1, this section focuses on the in-drift processes. A multiscale modeling and abstraction method was developed to couple drift-scale processes with mountain-scale processes. This method uses a series of submodels, one mountain-scale and three drift-scale submodels, to abstract the thermal hydrologic quantities throughout the potential repository area (Figure 5.2-2). The four submodels are described briefly below. Additional details are included in the *Multiscale Thermohydrologic Model* (CRWMS M&O 2000 [DIRS 149862]).

Line-Averaged-Heat-Source, Drift-Scale, Thermal-Hydrologic Submodel–The line-averaged-heat-source, Drift-Scale, Thermal-Hydrologic (LDTH) submodel is a two-dimensional drift-scale (chimney) model that computes temperature and moisture-related quantities (relative humidity, liquid saturation, liquid flow rate or flux, and liquid evaporation rate) at several locations within and near the drift. This submodel effectively represents average thermal hydrologic behavior at any specific location within the potential repository, taking into account the location-specific thermal and hydrologic properties, boundary conditions, and percolation flux. The (LDTH) submodels use the dual-permeability method (DKM), modified with the active fracture concept (AFC) for fluid flow in the fractured porous rock. The DKM conceptualizes the fractured rock as having two interacting materials, one representing the matrix and one representing the fractures (CRWMS M&O 2000 [DIRS 149862], Section 6.3). The AFC accounts for the contact area between the fracture and the matrix, as well as the frequency of fractures. The AFC means that the fracture flow only occurs through some of the fractures. Within the drift, thermal radiative heat transfer is explicitly represented and natural-convective heat transfer is represented using an effective thermal conductivity of the air occupying the space between the drip shield and the drift wall (CRWMS M&O 2000 [DIRS 153246]).

Smeared-Heat-Source, Mountain-Scale, Thermal-Conduction Submodel–The smeared-heat-source, mountain-scale, thermal-conduction (SMT) submodel is a three-dimensional model that includes the stratigraphy, topography, and layout of the potential repository considering only thermal-conduction heat transfer. It is used to determine the repository-scale variations in host-rock temperature resulting from the total heat output and includes the influence of the potential repository edges, the topography, and the mountain-scale variability in stratigraphy and thermal properties of the geologic units.

Smeared-Heat-Source, Drift-Scale, Thermal-Conduction Submodel–The smeared-heat-source, drift-scale, thermal-conduction (SDT) submodel is a one-dimensional model that considers only thermal-conduction heat transfer. It is used to establish temperature relationships and to account for the influence of repository edges, topography, and mountain-scale variability in stratigraphy and thermal properties of the geologic units.

Discrete-Heat-Source, Drift-Scale, Thermal-Conduction Submodel–The discrete-heat-source, drift-scale, thermal-conduction (DDT) submodel includes conductive heat transfer, plus radiant heat transfer within open drifts. This submodel is a three-dimensional model of a drift segment containing representative waste package types and heat outputs representative of the overall potential repository. The scale of the submodel includes a drift segment of sufficient extent to include six waste packages plus two halves (the half-waste packages are on symmetry boundaries). This submodel provides information on the package-to-package heat-output variability along the drift. The model drift segment contains waste.

It is useful to think of the LDTH submodel as the core submodel. The LDTH submodel is run for multiple locations spaced throughout the potential repository area. The remaining three submodels, which are conduction-only submodels (SMT, SDT, DDT), are required to account for the influence of three-dimensional mountain and drift-scale heat flow on drift-scale TH behavior. The MSTH model addresses differences between the potential repository center and edge locations by coupling the SDT submodel with the SMT submodel. The coupling uses the average temperatures of the potential repository host rock obtained from the SMT submodel. The resulting temperatures inherently include the repository edge effects, because they originated from the SMT submodel. The abstracted average results were modified to reflect package-specific temperatures calculated by the DDT submodel.

The MSTH model relates the results from the submodels to capture the effects of key factors that can affect TH conditions in the emplacement drifts and surrounding rock (drift wall):

- Variability of the percolation flux on the scale of the potential repository footprint
- Temporal variability of percolation flux (as influenced by climate change)
- Uncertainty in percolation flux (as represented by the mean, high, and low infiltration flux conditions described in Section 3.3.2)
- Variability in hydrologic properties (e.g., those properties which control fracture-matrix interaction and capillary in fractures) on the scale of the potential repository footprint

- Edge-cooling effect (cooling increases with proximity to the edge of the potential repository)
- Dimensions and properties of the engineered barrier system components, such as the drip shield and invert
- Waste package-to-waste package variability in heat-generation rate
- Variability in overburden thickness on the scale of the potential repository footprint
- Variability in rock thermal conductivity (emphasizing the host-rock units) on the scale of the potential repository footprint.

The MSTH model involves drift-scale calculations at a number of potential repository locations to capture effects and variability of properties and flux. A set of calculations for a given case involved only one computer run using the SMT submodel and only one computer run using the DDT submodel. However, the LDTH submodel and the SDT submodel were run for 31 locations within the potential repository and for five areal mass loadings (to represent edge effects). The results of these 155 submodel runs were interpolated over the potential repository area as a function of local heating conditions to provide a continuous distribution of the thermal hydrologic variables throughout the potential repository area. To model the preclosure ventilation period, the number of model runs was doubled (one pertains to the pre-closure period and the other pertains to the post-closure period), but these additional runs were for a shorter time period (CRWMS M&O 2000 [DIRS 149862], Section 6.6.1). Ventilation was modeled using a waste package design criteria heat output of 70 percent, as stated in the *Ventilation Model* (CRWMS M&O 2000 [DIRS 120903], Section 6.1), for 50 years. Ventilation is expected to dry out the drifts and the surrounding rock because dry air from the surface would be circulated through the drifts. However, this drying was neglected in the TSPA-SR (CRWMS M&O 2000 [DIRS 153246]), which is conservative in the sense that more moisture is left in the model, thus lowering the overall heat removal results. The assessment of conservatism is at a high level. More detailed consideration of the effects of ventilation could change that conclusion. For example, ventilation-caused-drying (which is neglected in the base case, but quantified in sensitivity analyses in this section) decreases local thermal conductivity, and hence elevates in-drift temperatures. The preliminary judgement implied by the statement that neglect of drying is conservative is that the temperature increase due to neglect of latent heat removal in the waste stream is larger than the increase due to local depression of thermal conductivity, and that higher temperatures lead to higher dose rates or higher uncertainties in dose rate.

The abstracted temperature, relative humidity, and other quantities were developed for an array of 610 locations in the potential repository (by interpolation among the 31 LDTH and SDT locations) and the two waste package types, Commercial Spent Nuclear Fuel (CSNF) and DOE high-level radioactive waste (DHLW). The 610 locations are shown in Figure 5.2-3.

There were eight different waste packages considered at each of the 610 locations, which resulted in 4,880 individual environment histories. These histories were abstracted into 30 groups for waste package corrosion, radionuclide release, and EBS transport calculations. The same TH results were determined for all three infiltration-flux cases (mean, high, and low

flux scenarios) in the TSPA-SR model. Thus, the TH results were combined into ten distinct groups: five infiltration bins (bins are category groups based on varying infiltration rates) for each of the two waste types. However, because of the importance of the variability in waste package failure time, the full suite of 1,220 sets of results (610 locations times two waste types) were provided as input to the waste package and drip shield degradation models. The TH information provided as input to the various EBS models is summarized in Figure 5.2-1, and the parameters that were provided as bin averages are identified. Where bin averaging was not noted in TSPA-SR (CRWMS M&O 2000 [DIRS 153246], Figure 3.3-7), the full set of spatial locations were identified. A complete list of EBS and near-field environment (NFE) variables calculated with the MSTH model at 610 locations are provided in Table 5.2-1.

The procedures used for averaging the various thermal-hydrologic quantities over the infiltration bins are described in detail in *Abstraction of NFE Drift Thermodynamic Environment and Percolation Flux* (CRWMS M&O 2001 [DIRS 154594]). There is one case where the thermal hydrology abstraction does not simply average information from the MSTH model and that is in the determination of the evaporation rate of water at the top of the drip shield. As discussed in Section 7.3.1 of this document, one of the parameters used for the in-drift chemical environment abstraction is the ratio of water evaporation rate to water in flow rate. The MSTH model can calculate these quantities only in a porous medium, which is not the situation at the top of the drip shield. The seepage flow rate at the top of the drip shield is taken from the seepage abstraction (Section 4.3.1), and the evaporation rate is bounded by the amount of heat available to vaporize water on the upper portion of the drip shield. These bounding values are used to estimate how much water could be evaporated by the waste package heat output at any given time (CRWMS M&O 2001 [DIRS 154594], Section 6.3.10).

5.2.1 Overview of Total System Performance Assessment-Site Recommendation Thermal-Hydrologic Results

Calculations indicate that the heat generation rate from radioactive decay decreases rapidly with age of waste for a period of time followed by slowly decreasing levels for thousands of years. The initial heat output and its rate of decrease with time depend upon the type of nuclear waste. Calculations indicate that the potential repository characterized in the TSPA-SR (CRWMS M&O 2000 [DIRS 153246]) would initially produce approximately 80 MW of thermal power (BSC 2001 [DIRS 155107], Section 2). The thermal power output will decrease to approximately 25 percent in 100 years, 12 percent in 300 years, and 2 percent of its initial value in 10,000 years.

For the TSPA-SR (CRWMS M&O 2000 [DIRS 153246]) design, a requirement was imposed that continuous forced ventilation of emplacement drifts during operations would remove at least 70 percent of the total decay heat generated during a period of 50 years after the first waste is emplaced (CRWMS M&O 2000 [DIRS 120903], Section 6.5). A conservative model, accounting only for heat removed as sensible heat in the ventilation air (ignoring latent heat removed by evaporation of moisture), indicates that a ventilation air flow rate of up to 15 m^3/s in each emplacement drift will provide this level of heat removal (CRWMS M&O 2000 [DIRS 120903], Section 6.5). The remaining heat output during the preclosure period will be transferred to the host rock by radiation, conduction, and convection, increasing the host rock temperature.

5.2.2 Information Generated by the Multiscale Thermal-Hydrologic Model

Results of the MSTH model are discussed below. Additional plots of results are available in the *Multiscale Thermohydrologic Model* report (CRWMS M&O 2000 [DIRS 149862]) and *Abstraction of NFE Drift Thermodynamic Environment and Percolation Flux* (CRWMS M&O 2001 [DIRS 154594]).

Figure 5.2-4 shows the computed average CSNF waste package temperature for the five infiltration bins (CRWMS M&O 2001 [DIRS 154594], Section 6.1) in the mean-infiltration case. The infiltration fluxes are discussed in Section 3.3.2. A large temperature increase occurs shortly after closure of the potential repository (50 years after emplacement) when ventilation ceases. During cool down, waste packages near the potential repository edge cool faster than waste packages in the center of the potential repository. The waste packages in the 0- to 3-mm/yr and the greater than 60-mm/yr infiltration bins cool faster than the others because all locations in those bins are at the edges of the potential repository (Figure 5.2-3). The differences among the infiltration bins are greatest during the early cooling period. By 10,000 years, the temperature of all the bins has converged and temperatures return to approximately ambient temperature. The results from the MSTH model for codisposal waste packages (codisposal waste packages have slightly lower temperatures because of a lower heat output) are quite similar to those for CSNF packages (CRWMS M&O 2001 [DIRS 154594], Section 6.3.2).

Figure 5.2-5 shows the computed average CSNF waste package relative humidities for the five infiltration bins in the medium-infiltration case. The relative humidity decreases sharply when the temperature rises after ventilation ceases. However, the calculated preclosure relative humidity is artificially high in Figure 5.2-5, because removal of moisture by ventilation is not included in the model. As with the temperature results, the differences among the infiltration bins are greatest during the early cooling period. By 10,000 years, the bin-averaged relative humidity values are above 90 percent and all are within about 2 percent of each other; by 100,000 years the bin-averaged relative humidity values are essentially back to ambient (nearly 100 percent relative humidity). Corresponding to their lower temperatures, the codisposal waste package relative humidity values are somewhat higher than the CSNF waste package relative humidity values (CRWMS M&O 2001 [DIRS 154594], Section 6.3.3).

Figure 5.2-6 shows the computed average percolation flux 5 m above the emplacement drifts for the five infiltration bins in the medium-infiltration case. As expected, the percolation flux is higher for the higher-infiltration bins. Infiltration response to the climate changes is clearly visible at 600 years and 2,000 years. All five curves have a large spike at about 70 years due to the drainage of thermally mobilized water. The increased percolation flux could lead to a pulse of seepage into the drifts at that time. For most bins, the percolation flux in the figure does not decrease below the initial percolation flux, indicating that the boiling front usually does not extend out 5 m above the drifts.

5.3 UNCERTAINTY ANALYSES

The analyses of the evolution of the TH conditions are based on the predictive modeling of the MSTH model with associated uncertainties. Accommodating uncertainties in the assessment of performance requires recognizing that uncertainties exist, and explicitly identifying those that

may be important to performance. The DOE approach to dealing with uncertainties is described in the S&ER (DOE 2001 [DIRS 153849], Sections 4.1.1.2 and 4.4.1.2).

Three basic approaches are used to deal with uncertainties. The first is to identify the important parameters (DOE 2001 [DIRS 153849], Sections 4.2.2.3 and 4.2.3) and establish probability distributions for them. When probability distributions can be determined, the uncertainty can be quantified. Some distributions can be determined from collected data. These distributions are used to estimate the probability that a variable will assume different values over the spatial and temporal scales of an operating repository. The uncertainties that can be quantified are incorporated directly into performance assessment results.

The second approach to evaluate uncertainty is to develop alternative models for key processes. This approach seeks to reduce uncertainties that cannot be readily quantified (i.e., the possibility that the models used for compliance analyses do not include, or accurately simulate, processes that may be important to performance). The alternative model approach is most applicable to scenarios that have uncertainties associated with an approach, assumption, or conceptualization incorporated within a model that cannot be readily quantified.

A third approach to evaluating uncertainty is to establish bounding values of parameters or bounding approximations for processes or models. Establishing bounds that parameter values are unlikely to exceed, while not quantifying the uncertainty, places limits on the uncertainty. Likewise, limits are determined beyond which the results are insensitive to the further variation in the value. Sensitivity studies can assist in establishing these bounds by considering the range of parameter values that influence the results. Thus, establishing bounding values can provide an evaluation of uncertainty influences on results where actual quantification of the uncertainty is either unachievable or impractical.

The first method provides quantitative estimates of the effects of the uncertainty on potential repository performance. Using alternative models can also help quantify the uncertainty by comparing the results. However, unless all alternatives are exercised, the quantification of uncertainty is not complete. Therefore, where all possible alternatives cannot be defined, the quantification of uncertainty using the alternative model approach would not be as rigorous as the probability distribution method. In contrast, the third method, establishing bounds, does not provide absolute quantification of uncertainty, but it is useful when the effects are difficult to quantify or when specific conditions are expected to have minor effects on overall performance of the potential repository. Sensitivity studies give insight into the impacts of uncertainties, but they do not quantify the uncertainties directly.

Variability in parameters is sometimes classified as an uncertainty. However, variability, in and of itself, is not an uncertainty. If the variability in properties is well constrained and can be understood or characterized well enough (through existing data or observation) to be described deterministically, then it need not be considered uncertain and need not be described probabilistically. However, if the variability is not sufficiently constrained or well understood, then uncertainty is introduced and the approaches to evaluating that uncertainty, including quantification of it, must be applied. Although this difference seems subtle, the influence on uncertainty is quite different. In the case where the variability is well understood and accounted for, analyses can be deterministic without variability introducing uncertainty. Where this is not

the case, which is the more common occurrence, the variability introduces uncertainty that must be addressed.

As discussed in the *Near-Field/Altered-Zone Models Report* (Hardin 1998 [DIRS 100123], Section 1.4.2), heterogeneity is an intrinsic characteristic of geologic media, and the effect of heterogeneity on flow and transport cannot be removed by gathering more data on formation properties. However, the accuracy with which the effect of heterogeneity on flow and transport can be calculated may be improved. Uncertainty arises from imperfect knowledge of the variables and mathematical relations among them. Uncertainty can be reduced with additional data or better methods of interpolating between measured data.

Because variability usually is not sufficiently constrained or understood to allow the deterministic approach, in this section variability will be discussed within the context of parameter uncertainty. However, the general approach is the same: to quantify the variability, to establish appropriate bounds on the parameter, or to consider impacts through sensitivity studies.

5.3.1 Multiscale Model of In-Drift Thermal-Hydrologic Conditions

5.3.1.1 Goal of the Model

The overall goal of the MSTH model is to provide analyses of the temperature, relative humidity, and liquid saturation in the drift and surrounding rock to the TSPA. The MSTH model also supports models of seepage, engineered barrier system degradation, radionuclide transport, and flow and transport, and provides inputs to other coupled process model analyses. The MSTH model evaluates the effects of heat on vapor and liquid flow and the distribution of liquid and temperature within and external to the emplacement drifts. The areas addressed by the MSTH model include: (1) temperature and relative humidity conditions at various locations within the drift, (2) gas and liquid flow rates through the rock and into the drifts, (3) the extent of the two-phase zone induced by boiling or evaporation, (4) temperature and saturation changes in the unsaturated zone, and (5) removal of moisture and reduction of waste package temperatures through ventilation. However, only the aspects that relate to in-drift conditions are discussed in this section. The in-rock conditions are necessary to calculate the in-drift conditions, but are not reported here.

An important part of the model goal is to develop a mechanistic understanding of the impact of uncertainty sufficient to build confidence that the modeled results are applicable and can be relied on in assessing the potential health and safety impacts to the public. This section discusses the analyses that have been performed to identify and analyze those uncertainties. The process for identification and evaluation of the uncertainties that were performed for the TSPA-SR design (CRWMS M&O 2000 [DIRS 153246]) is presented first, followed by a discussion of the approaches that were used to address uncertainties not quantified by the TSPA analyses.

5.3.1.2 Representation in Total System Performance Assessment-Site Recommendation

Uncertainties associated with the MSTH model were evaluated to quantify their magnitudes or identify them as unquantified. Approaches were then developed to determine the significance of the unquantified uncertainties.

There are four types of thermal-hydrologic uncertainties, based on the source of the uncertainty. The first is the uncertainty associated with the thermal-hydrologic models and their assumptions, abstractions, numerical simplifications, or representations. The second includes uncertainties introduced by physical processes. The third type includes uncertainties introduced through model sensitivities to input data such as thermal conductivity, invert thermal properties, and invert hydrologic properties. The last type includes uncertainties associated with sensitivity to removal of heat and moisture through ventilation. The key uncertainties (grouped according to whether they are model, process, or input uncertainties) are summarized in Table 5.3.1.2-1, which also provides pointers to discussions of further analyses.

5.3.1.2.1 Model Uncertainty

The TH coupling of heat and mass transfer can be treated in a number of ways. For heat transfer, conduction models are the most straightforward; however, these fail to incorporate the coupling of heat transfer with moisture that can be dominant within the engineered barrier system and near-field environment. The MSTH model combines conduction with the effects of latent heat and advective heat transfer. The merging of conduction and convective submodels can introduce uncertainty. However, the model has been used effectively to analyze field tests. As noted in the *Multiscale Thermohydrologic Model* (CRWMS M&O 2000 [DIRS 149862], Section 6.13.2), there is good agreement between the model and the measurements made in the Drift Scale Test. The Drift Scale Test was designed to test the coupled process models, including the MSTH model, and is being conducted underground in the environment appropriate for testing these models. Based on the agreement between test measurements and the model, it is not expected that there are large uncertainties related to how the submodels are integrated. The agreement between the simulated and measured temperatures in the region close to the heated drift indicates that the representation of thermal radiation inside the heated drift is adequately represented in the Drift Scale Test implementation of the MSTH model.

Three different approaches have been used by the Yucca Mountain Site Characterization Project (YMP) to model the physical processes involving flow: the equivalent continuum model, the discrete fracture model (DFM), and the DKM approaches. Because they represent alternative models, the results can be compared to help determine the extent of uncertainties within the models. All three approaches are discussed for completeness; however, the MSTH model relies on the DKM approach. A more complete comparison of these methods, and the results of analyses using these methods, can be found in the *Near-Field/Altered-Zone Models Report* (Hardin 1998 [DIRS 100123], Section 3.3.3).

The equivalent continuum model treats flow of water and vapor as if it were occurring in a single continuum with properties that are representative of or equivalent to those of the separate rock matrix and fracture continua. The challenge for this approach is to determine the appropriate properties that are either equivalent to the combination of the properties in the separate continua or that yield results equivalent to those from assessing each continuum individually. Furthermore, this method does not recognize the potential for fundamentally different flow phenomena between fractures and pores within the rock matrix; rather, it treats the TH conditions as if complete equilibrium existed between the hydrologic conditions in the matrix and fractures. Because the equivalent continuum model does not treat fractures as discrete features, TH effects are averaged over the entire spatial domain. In effect, the equivalent

continuum model assumes instantaneous heat and mass transfer between the matrix and fracture continua. It does not adequately address transient effects, such as transient, episodic infiltration. The assumption of local equilibrium between fractures and matrix is appropriate if the liquid-phase flux in the fractures is sufficiently small (Buscheck and Nitao 1991 [DIRS 121169]; Nitao et al. 1993 [DIRS 147403]).

The DFM treats TH conditions in the fracture and matrix separately. In this method, the separate continua do not overlap each other. While this method may be physically more accurate, it requires a complete understanding of the fracture, the matrix continua, and their interactions. To apply this approach to repository- or mountain-scale problems would require extreme amounts of data and computational effort. Because of mathematical limitations on the numerical solution of the relevant equations, the DFM can be applied only for the simplest geometry of fracture networks. In addition, these fracture networks must have a high degree of spatial symmetry so the model domain can be spanned by a practical number of gridblocks.

The DKM treats the matrix and fractures as separate but overlapping continua. While it does not incorporate actual fracture spacing—the fractures are accounted for by permeability applied over the same intervals as the matrix blocks (i.e., overlapping continua)—the DKM does account for interaction between the TH conditions within the two continua. The DKM treats the matrix and the fractures as two distinct porous continua, with transfer terms to represent the mass and heat flux between them. The DKM does not assume capillary pressure equilibrium between fracture and matrix continua. Two sets of properties (one for fractures, one for matrix) are associated with each geometric gridblock.

The MSTH model relies on dual-permeability continuum models with an active fracture model (AFM) to account for interactions between fractures and matrix. Because these models do not directly analyze the actual flow and fracture systems, there is uncertainty in the model. However, comparisons of the models against field tests indicate that the models are appropriate and that large uncertainties are not expected. The agreement between the simulations and measurements in the Drift Scale Test indicates that the LDTH submodels in the MSTH model, together with the use of the drift-scale hydrologic property set, are validated for their intended use (CRWMS M&O 2000 [DIRS 149862], Section 6.13.2).

The major assumptions that apply to the TH models are: the dual-permeability flow model, the van Genuchten/Mualem saturation-desaturation relations, the matrix and fracture hydrologic properties determined by inverse modeling, the active-fracture coupling model between matrix and fracture continua, and the lack of incorporation of small-scale heterogeneity. These assumptions were addressed in a peer review, which found them to be able to represent a range of infiltration rates without producing unphysical hydrologic properties (CRWMS M&O 1999 [DIRS 148463], p. 47, paragraph 3). However, the peer review identified several concerns regarding the physical meaning or defensibility of these assumptions. It was determined that these uncertainties cannot be individually quantified; their resolution depends on field and laboratory tests or experiments to confirm the appropriateness of this group of assumptions.

The AFM reflects the observation that the contact area for interaction between water in fractures and the pores of the rock matrix is not the same as the fracture-surface contact area. Laboratory and field studies support the understanding that flow in fractures does not occupy the entire

fracture-system volume. Most of the studies, including laboratory studies, were conducted under isothermal conditions, and many laboratory studies relied largely on artificial (machined) fractures (Nicholl et al. 1994 [DIRS 141580]; Liu et al. 1998 [DIRS 105729]). Currently, the AFM uses a fracture-interaction factor that varies as a function of saturation within the fracture. Although the active-fracture concept is intuitive, it is based on inverse modeling to match saturation data from field tests, not on a detailed physical basis from laboratory studies (CRWMS M&O 2000 [DIRS 141187], p. 47). This introduces model uncertainty.

Modeling of ventilation effects by reducing waste package heat output by 70 percent, without considering dryout of the near-field rock, does not consider the processes of moisture and heat removal associated with the drying processes. Thus, air ventilation will more effectively remove heat and moisture, until the rock is dried, than the models would indicate if these processes are not included. Thus, neglecting the effects of moisture removal provides an upper bound on temperatures and drift wall saturations, and thus on uncertainty of the effects of ventilation on those thermal-hydrologic properties until such time as the moisture is removed so that the rock has dried out. At that time, the thermal conductivity would be that of the dry rock and if the models used the wet rock thermal conductivity they would underpredict the temperatures. However, the temperature peaks during early times when the ventilation would most likely still be removing moisture. Therefore, those later time temperatures should remain below the calculated peak temperatures and underpredicting later temperatures should not exceed the bounding temperatures calculated. The saturations will be less than calculated because of removal by moisture and therefore this thermal-hydrologic property will be conservatively bounded by the MSTH model calculations.

The MSTH model only calculates the ratio of water evaporation rate to water flow rate for a porous medium. The evaporation rate and flow rate at the top of the drip shield cannot be directly calculated by the model for an open drift. Thus, the liquid flow rate at the drip shield is taken from the seepage abstraction (CRWMS M&O 2000 [DIRS 153246], Section 3.2.4), and the evaporation rate provided is bounded by the amount of heat available to vaporize water on the upper portion of the drip shield. These bounding values estimate how much water could be evaporated by waste package heat output at any given time (CRWMS M&O 2001 [DIRS 154594], Section 6.3.10). Seepage estimates are conservatively bounded; therefore, the uncertainty introduced by the lack of direct calculation should also be bounded. The evaporation rate (more specifically, the amount of liquid water that potentially would not evaporate) may not be bounded as well, since this approach does not consider other processes that could impact evaporation rates. However, the approach provides an upper bound on evaporation if ventilation effects are ignored. It can be argued that liquid water on drip shields and waste packages is more adverse than humid air and, therefore, that the MSTH model approach bounds the issue of concern. However, the presence of deliquescent salts can result in water film on the waste packages. Therefore, an assessment needs to be made to determine whether it can justifiably be assumed that liquid water, not humid air, is more adverse, and that bounding the amount of water that can be evaporated is an acceptable approach.

Localized effects of seepage on TH response were not included in the TH models. If seepage was included, relative humidity would be higher and temperatures would be lower at locations where seepage occurs. However, as shown in the TSPA-SR (CRWMS M&O 2000 [DIRS 153246], Section 4.1.2), there is no seepage at about 87 percent of the waste package

locations evaluated in the TSPA model. For the small fraction of locations with seepage, the effect on relative humidity and temperature would be significant only during the first few hundred years.

The MSTH model provides an approximation of heat transfer for different time scales by coupling submodels that reflect the differing scales. The approach relies on estimates of equivalent AMLs in the calculations and the use of scanning curves. This introduces uncertainty with respect to whether the heat transfer assumptions and conceptualizations in the various submodels, and the combining of the submodel results, adequately reflect the physical reality. This uncertainty is not quantifiable and requires testing or comparison against other approaches.

Another uncertainty that may impact the results of TH modeling includes the arrangement and heat output of different types of waste packages. This engineering heterogeneity can influence the details of TH responses within the drifts. While the uncertainties are a function of the final design and cannot be entirely assessed at this time, agreement with field test data indicates that the model approaches are appropriate for determining this influence (CRWMS M&O 2001 [DIRS 149862], Section 6.13.2).

The stochastic representation of fracture heterogeneity in the seepage model is not incorporated in the MSTH model. Conversely, the seepage model for the TSPA-SR (CRWMS M&O 2000 [DIRS 153246]) did not include dryout and heating of the near-field rocks to couple these models. The MSTH model was used to predict percolation flux in the host rock 5 m above the drift wall, which was then used as input to the seepage model for calculating seepage during the thermal pulse. This introduces an uncertainty about the applicability of the model. However, the impacts of seepage are bounded because the thermal percolation flux at 5 m is modeled as flowing into ambient temperature and saturation rock. This is a conservative approach that ignores the temperature and seepage mitigation processes of evaporation and imbibition in the near-field rock during the thermal period. The effects of seepage during the thermal period on the temperature and relative humidity in the emplacement drifts were evaluated independently using the MSTH model, to determine the influence of seepage on in-drift thermal-hydrologic conditions. These effects were found to be negligible for the relatively small but bounding values of seepage that could occur (CRWMS M&O 2000 [DIRS 149862], Sections 6.11 and 6.12).

The multiscale estimation methodology does not include the effects of mountain-scale gas-phase convective circulation (at a scale larger than the lateral size of the LDTH columns, approximately 40 m) and the movement of water vapor along the axis of emplacement drifts from warmer to cooler regions. The multiscale modeling approach neglects heat transfer by these mechanisms, so the predicted temperatures and the duration of the thermal period are probably overpredicted. The principal effect on TSPA is probably a delay in calculated time of the return of moisture to the in-drift environment. However, differences in timing on the order of hundreds of years will have a minor impact on the estimated longevity for the drip shield and waste package (with expected lifetimes greater than 10,000 years).

5.3.1.2.2 Uncertainties in Physical Processes

There are potential changes to hydrologic properties in the surrounding rock caused by coupled thermal-hydrologic-chemical (THC) and thermal-hydrologic-mechanical (THM) processes. Based on prior evaluations of their significance, such changes were not addressed (CRWMS M&O 2000 [DIRS 153246], Section 3.3.3.1.2). Previous analyses (BSC 2001 [DIRS 154677]) concluded that chemical processes would not cause significant changes to hydrologic properties. These analyses considered the mass balance of mineral dissolution and deposition within the fractures. They also considered dissolution and deposition to be uniform within the entire fracture porosity represented in grid elements no smaller than a few tens of centimeters. There remains an unquantified uncertainty related to whether the uncertainty in fracture porosity, the heterogeneity in fracture porosity, or the localized deposition of minerals that could cause smaller than gridblock-sized plugging of fractures could change this conclusion. The report *Calculation of Permeability Change Due to Coupled Thermal-Hydrological-Mechanical Effects* (CRWMS M&O 2000 [DIRS 149040]) also concluded that fracture permeability could increase by an order of magnitude due to irreversible shear movement. However, this increase was determined to be within the range of fracture permeability variability. Therefore, the influence of THC and THM coupling was not incorporated into the MSTH model. The uncertainty to be evaluated is whether heterogeneity of fracture porosity, localized deposition, or design changes (such as orientation of drifts relative to the fracture patterns) could change the previous conclusions.

Boiling point temperatures are a function of pressure imposed on a liquid. The physics of this process is well understood and has been incorporated into the MSTH model. The MSTH model is comprised of four submodels that are discussed in Section 5.2. However, the models must calculate the increase in pressure based on the permeability of the rock matrix and the size of the matrix blocks. Fracture permeability is sufficiently high that pressures will not build up within the fractures, so this phenomenon is not applicable to the fracture continua. Therefore, although the process is understood, there is uncertainty regarding the characterization of the matrix block. These uncertainties are the same as those for unsaturated zone flow, and are discussed in Section 3.3. No assessment is made in the TH models of changes in capillary pressure based on potential changes in fracture porosity due to coupled processes. It is judged that this is of lesser importance than other processes. Small changes in capillary pressure would not have a significant impact because of the existing wide distribution of pore sizes, and thus capillary pressure, in the rock. Therefore, the uncertainties from this factor are expected to fall within the existing variability in capillary pressure and would not be significant.

However, testing wafers of welded tuff have indicated that the heating history may have some effect on moisture retention in the rock. Tests show that the suction potential decreases much more rapidly with increasing saturation during wetting than it does during drying (Wilder 1996 [DIRS 100792], Section 2.1.1). This hysteresis, where more moisture is retained in the samples during drying than during subsequent wetting, is not as pronounced at elevated temperatures, and at 93.6°C, the hysteresis was reversed. No process has been identified that can explain smaller hysteresis at 78°C than at other temperatures, or explain the hysteresis reversal at 94°C; in this test, the samples were heated from 25°C to 94°C, then cooled to 78°C. Thus, the heating history may have some effect on the moisture retention curves. Rewetting behavior at an elevated temperature was also summarized in the *Syntheses Report on Thermally Driven Coupled*

Processes (Hardin and Chesnut 1997 [DIRS 150043], Section 2.7.5), which reports similar decreases in hysteresis with temperature but not the reversal in hysteresis. The hysteresis effect is probably related to changes in surface tension and the rock-water-air contact angle at elevated temperatures (Hardin and Chesnut 1997 [DIRS 150043], Section 2.10). Hysteritic behavior is generally ignored, for computational expediency, in TH models. It has been judged that this appears to be defensible (DOE 2001 [DIRS 153849], Section 4.2.2.2.2). The effects would be to overpredict imbibition or rewetting. Therefore, ignoring this hysteresis would result in conservatively (upper) bounded values of rewetting. However, ignoring this factor may not result in conservative bounds on peak drift wall temperatures. If the dryout of rock is underpredicted (i.e., wetting is overpredicted), the result may be the use of wet rather than dry thermal conductivities in the model. Thermal conductivities for wet rock are higher than for dry rock, so the calculated temperatures would be lower.

5.3.1.2.3 Input Data Uncertainties

The unsaturated zone flow model (CRWMS M&O 2000 [DIRS 151940]) is the basis for the hydrologic properties used as inputs to the MSTH model. There are uncertainties associated with the use of inverse modeling to determine the physical properties that are used in the MSTH model. Therefore, uncertainties associated with the unsaturated zone flow model, such as uncertainties in the average infiltration rate as a function of climate (CRWMS M&O 2000 [DIRS 153246]), also apply to the MSTH model. The assessment of uncertainties in these properties is discussed within the context of the unsaturated zone (mountain-scale) model (Section 3.3.5) where property distributions are determined. However, the impact of propagating these uncertainties through the TH models has not been directly quantified. Sensitivity studies performed with the MSTH model have been compared to field tests and the appropriate property set determined (BSC 2001 [DIRS 154677]). As noted previously, there was good agreement between the MSTH model simulations of the Drift Scale Test and the measured parameters (CRWMS M&O 2000 [DIRS 149862]). This agreement indicates that the drift-scale hydrologic property set used as input to the modeled simulations is valid for its intended use.

The effects of percolation flux variability, beyond those accounted for in the detailed chimney models, have not been included (CRWMS M&O 2000 [DIRS 149862], Section 1.0 and Figure 1-1). Variability is described by a distribution of infiltration. Three infiltration cases (low, medium, and high) are considered in the MSTH model. The infiltration values included in the chimney models incorporate the distribution of measured values that reflect the impacts of topography, ground cover, and stratigraphy on the distributions. Because the distributions are quantified, this uncertainty is considered to be quantified. In addition to incorporating uncertainties in percolation flux by considering the low, mean, and high infiltration flux conditions, the MSTH model considers temporal variability (e.g., changes in climate) and spatial variability (e.g., repository cooling at the edges) in the models. To this extent, this is a quantified uncertainty.

The waste package thermal output depends on design and operating details that are not finalized. Thus, the output used in the MSTH model may not accurately reflect the output of actual waste as it would be emplaced. Likewise, the final potential repository layout, ventilation, and waste package arrangement may be different than the one analyzed in the current MSTH model calculations. This uncertainty does not add to the uncertainty of the analyzed conditions, which

use specific design parameters. What this uncertainty underscores is the ultimate need to perform MSTH model calculations for the final design and repository conditions that will be considered during any potential license application and decision to emplace waste.

Uncertainty is also introduced into the MSTH model from the uncertainties associated with lithophysal porosity (see Section 3.3.5). The uncertainty introduced into the MSTH model almost entirely relates to the impact on thermal conductivity and heat capacity used in the models for the lower lithophysal unit. Higher porosity results in lower the thermal conductivity and heat capacity of the rock. Thus, if the porosity is higher than the value used to determine these parameters, the transient temperature rise may actually be greater than that calculated by the models. This uncertainty would be of diminishing concern with time, although, as discussed in Section 5.3.1.4.8, effects of thermal conductivity can persist for 10,000 years for the HTOM. The effects of heat capacity uncertainty, as noted in Section 5.3.1.4.9, disappear within 1,000 years after emplacement. For the LTOM, the magnitude and duration of effects would be less than those indicated.

Lithophysal porosity can also affect the effective porosity for vapor storage. If the porosity is considerably larger than that used in the models, then there may be a lag in how quickly water vapor moves through the system compared to the models. During active boiling periods, this would create uncertainty in the temperatures that develop and in the amount of water mobilized. If the vapor is stored so that it does not move as rapidly or as far, then moisture will remain closer to the drifts and temperatures will not be as high. Therefore, this uncertainty would tend to result in conservative estimates of temperature, but possibly nonconservative estimates of saturation and moisture conditions in the rock adjacent to the drifts. Whether this uncertainty persists beyond the active boiling period will depend on how effectively the rock stores the water, thus adding to uncertainty. However, as noted in Section 5.3.1.4.1, the magnitude of this uncertainty is not expected to be large. Vapor storage would be less of an issue, if at all, for LTOM where temperatures in the rock would be below boiling.

Uncertainty in thermal conductivity is mainly related to the difference between wet and dry rock thermal conductivity. While thermal conductivity is a function of the porosity and mineralogy of the rock, there is not much variability in thermal conductivity as a result of these factors, and the values can be bounded. However, there is a significant difference between the thermal conductivities of wet and dry rock. Because the moisture conditions can vary both spatially and temporally, and because the moisture conditions are calculated by the TH models, this uncertainty is not as easily bounded. Thermal conductivity always influences the temperatures calculated. Because some processes are not incorporated into the models (e.g., rewetting hysteresis), it is possible that wet thermal conductivity will be used when a dry thermal conductivity would be more appropriate. This would result in underprediction of temperatures but overprediction of moisture conditions.

Finally, there is uncertainty in the value of heat capacity used in the models. As noted, porosity can influence the heat capacity. However, because heat capacity is only important to temperature calculations during the thermal transient phase (as noted in Section 5.3.1.4.9, the effects disappear within 1,000 years of emplacement), and because it becomes unimportant after that period, the uncertainty introduced is not judged to be significant.

5.3.1.3 Reduction in Total System Performance Assessment Uncertainty Due to Model Improvements

In Section 5.3.1.2, uncertainty was grouped into three major categories: model uncertainty, process uncertainty, and input data or parameter uncertainty. This section discusses work performed after the issuance of the TSPA-SR (CRWMS M&O 2000 [DIRS 153246]) that reduces the uncertainties discussed in Section 5.3.1.2. Improvements in the models used in the Volume 2 (McNeish 2001 [DIRS 155023]) TSPA include consideration of two of the three design cases outlined in Section 5.1: the above-boiling case and the low temperature (85ºC) on the surface of the waste package case. The third design case, limiting drift wall temperatures to sub-boiling, was not considered in the SSPA (Table 5.1-1). These model improvements allow for identification of parameters and conditions that are sensitive to design details, thus helping to reduce the uncertainties related to use of a single design case for analyses. In addition, after the TSPA-SR (CRWMS M&O 2000 [DIRS 153246]) analyses, sensitivity studies and other analyses were performed to consider the consequences of additional uncertainties.

Improvements were made to the multiscale TH models (MSTH model) (CRWMS M&O 2000 [DIRS 149862]) in the way the submodels are constructed and combined. The improved smeared-heat-source mountain-scale thermal (SMT) submodel includes a depiction of the Yucca Mountain potential repository layout that more accurately represents the locations of the potential repository edges and the emplacement drifts. The version of the MSTH model used in the TSPA-SR (CRWMS M&O 2000 [DIRS 153246]) accurately reflected the eastern repository boundary and depicted the western boundary with some approximations. The northern and southern boundaries, however, were not as well represented. Figures 5.4.1-1 and 5.4.2-1 show the SSPA model depictions of the potential repository layout.

The drift-scale submodels in the MSTH model used in the TSPA-SR (CRWMS M&O 2000 [DIRS 153246]) used a square representation of the drifts. The improved submodels incorporate a stair-step grid approximation of the circular emplacement drifts (Figure 5.3.2.3-1). Although an analysis (CRWMS M&O 2000 [DIRS 149862], Section 6.5.2) in support of the TSPA-SR determined that the impacts of the square approximation were not significant, the use of a near-circular shape reduces the associated uncertainty.

The DDT submodel has also been modified since the TSPA-SR (CRWMS M&O 2000 [DIRS 153246]) to directly incorporate thermal radiation connections both inside and outside the drip shield. This is a more rigorous approach that allows for direct calculation of radiative heat transfer. It removes the uncertainties associated with using different approaches and approximations for temperatures at locations below the drip shield (where radiation connections were used) and outside the drip shield (where effective thermal conduction approximations based on changing temperatures were used). This improved approach addresses some of the uncertainty identified in Table 5.3.1.2-1 as "coupling of submodels." As discussed in Section 5.3.2.4.5.2, using correlation-based effective thermal conductivity parameter for thermal radiation under predicts the early time temperatures at the drip shield (compared to using explicit thermal conductivity from radiation). As described in Section 5.3.1.4.2, from closure of the potential repository until about 1,000 years, the effective parameter for thermal radiation underpredicts the average surface temperature of the drip shield by as much as 10ºC at closure of the potential repository. The peak temperature on the drip shield is underpredicted by the

effective parameter by about 5ºC at closure of the potential repository. At 1,000 years, the temperature defect is about 1ºC.

The effective thermal conductivity used in the MSTH model for natural convection was revised (see Section 5.3.2.4.5) based on repository-wide average temperatures instead of a selected subset at the potential repository center, as was used in the MSTH AMR (CRWMS M&O 2000 [DIRS 149862], Section 5.3 in the TSPA-SR (CRWMS M&O 2000 [DIRS 153246]). An explicit representation of thermal radiation heat transfer from the heat source to the drift wall was used to generate the temperature time-histories applied to the development of a new time-dependent effective thermal conductivity for natural convection. The effective thermal conductivity governs the approximate rate at which heat is transferred from the heat source to the drift wall. By its very nature, the effective thermal conductivity is temperature-dependent. Therefore, a more representative temperature will decrease the uncertainties in the rate of heat transfer and, thus, in the calculated temperatures.

The setup of the spatial grids (for solution of the finite difference approximations to the differential equations) in the DDT submodel for the areas outside the drip shield has been made identical with the grids used in the LDTH submodel. This helps to address the model uncertainty identified in Table 5.3.1.2-1 as "coupling of submodels," and removes problems that could be created by mismatches in information passed across gridblocks.

The improved MSTH model more accurately reflects edge effects. Previously, the submodels used a fixed, effective, local areal mass loading (AML), selected based on the peak temperature for that location. The improved approach continues to use the nominal AML initially, but uses an evolution of the local effective AML to reflect the time-varying influence of edge cooling. This capability is incorporated into the LDTH and DDT submodels; therefore, all thermal interactions that reflect the evolving influence of edge effects are addressed in the improved models. The edge effects are illustrated in Figures 5.4.1-4 and 5.4.2-4, which show snapshots in time of the distribution of temperature across the potential repository footprint for the HTOM and LTOM, respectively.

The improved MSTH model also accounts for the presence of lithophysae, which can cause uncertainties in the models from multiple standpoints. First, uncertainty is generated from the effects of lithophysal porosity on the storage capacity of the rocks for vapor (the conceptualization is that the cavities will not fill with water), as discussed in Sections 4.3.5.3.2 and 5.3.1.4.1. Second, lithophysal porosity can influence thermal conductivity, as discussed in Sections 4.3.5.3.2 and 5.3.1.4.9. The TSPA-SR analyses (CRWMS M&O 2000 [DIRS 153246]) used thermal conductivity based on water-filled lithophysae.

The way that steel in the invert is incorporated into the models has also been improved since the TSPA-SR (CRWMS M&O 2000 [DIRS 153246]). Previous models based thermal conductivity measurements for the steel in the invert on intact, non-degraded steel. However, for most of the time of concern, the steel will have been significantly degraded by corrosion, so thermal conduction will not be as high as assumed. In the updated models, the thermal conductivity used for the steel components was the same as that of the crushed tuff. This value was selected based on an assessment that the steel would completely degrade and that the iron rust would have thermal conductivity similar to that of the rock. This will result in higher in-drift temperatures,

and thus will be more conservative relative to the peak temperatures within the drift. This approach addresses, partially, the uncertainties identified in Table 5.3.1.2-1 as "Invert Properties-Input Data Uncertainty."

5.3.1.4 Quantification of Uncertainty Using Process Models

In addition to reducing model uncertainties by incorporating improvements to the multiscale thermal hydrologic model (MSTH model), sensitivity analyses were performed to further evaluate the consequences (or quantification) of uncertainties in processes and model inputs. Before and after the TSPA-SR analyses were conducted (CRWMS M&O 2000 [DIRS 153246]), sensitivity studies or other analyses were performed to consider the consequences of the uncertainties in eleven areas. These analyses were conducted to improve confidence in the models supporting the TSPA, but they do not provide inputs directly to the Volume 2 SSPA (McNeish 2001 [DIRS 155023]). The results of these analyses are discussed in the subsequent Sections of 5.3.1.4. These sections address uncertainty elements introduced in Section 5.3.1.2 and Table 5.3.1.2-1.

The areas in which uncertainty consequences were analyzed are:

1. Sensitivity of TH results to neglecting the potential for vapor storage within the lithophysal cavities (porosity). Current models do not provide analyses of cavity storage separate from the overall fracture porosity in the DKM model (Section 5.3.1.4.1)

2. Sensitivity of in-drift temperature and relative humidity to the effects of heterogeneous fracture properties on seepage. Previous models did not incorporate the effects of heterogeneity on seepage or on MSTH model results. Seepage was determined based on average or representative fracture properties, considering both variability and anisotropy (Section 5.3.1.4.2)

3. The impacts of imbibition hysteresis noted for intact samples under wetting and drying conditions (Section 5.3.1.4.3)

4. Sensitivity studies of the impact of mountain-scale buoyant gas-phase convection on temperatures and their durations (Section 5.3.1.4.4)

5. Effects of THC coupled processes, especially those related to changes in hydrologic properties (Section 5.3.1.4.5)

6. Effects of THM coupled processes related to changes in hydrologic properties (Section 5.3.1.4.6)

7. Sensitivity of MSTH model results to uncertainties in the bulk permeability of the host rock. Bulk permeability is used as an input to the multiscale TH models, so uncertainty in this parameter might cause uncertainty in the results (Section 5.3.1.4.7)

8. Sensitivity of MSTH model results to uncertainties in the host rock thermal conductivities used in the models (Section 5.3.1.4.8)

9. Sensitivity of the TH models to the way lithophysal porosity impacts other input parameters, such as bulk or host rock thermal conductivity (Section 5.3.1.4.9)

10. Sensitivity of the TH models to uncertainties in the thermal conductivity of the invert materials and in how they are incorporated into the models (Section 5.3.1.4.10)

11. Sensitivity of the TH parameters to design and operational parameters (Section 5.3.1.4.11).

5.3.1.4.1 Effects of Lithophysal Porosity on Vapor Storage

The MSTH model and other hydrologic models use the DKM, in which the matrix and fracture continua consider two-phase flow (vapor and liquid). Previous analyses combined lithophysal porosity with fracture porosity, and assumed the combined porosity could be saturated under some circumstances. Although unanticipated processes (i.e., those that allow for localized saturation) could allow water to fill the lithophysal cavities, it is unlikely that this would occur in a freely draining unsaturated zone. Further, it is recognized that the physical processes that determine if seepage will occur into openings (drifts) also apply to the lithophysal cavities. Thus, it is likely that the lithophysal cavities will be unoccupied by water, except for film on cavity walls, and therefore will be entirely gas or vapor filled. This is consistent with observations that secondary mineral deposits are limited to the bottom of cavities and footwalls of fractures, and that they were deposited in unsaturated conditions (Whelan et al. 2001 [DIRS 154773], p. 6).

Gas-filled lithophysal cavities would provide a storage volume for water vapor from the boiling zone. Discussion of the uncertainty due to not separately incorporating this porosity into the thermal-hydrologic models is discussed in Section 4.3.5.3.2. The most important influence of lithophysal porosity will be on thermal conduction due to lower conductivity for air-filled voids than for rock matrix. The analyses of the effects of lithophysal porosity on thermal conductivity, and in turn, on in-drift temperatures, are discussed in Sections 5.3.1.4.8 and 5.3.1.4.9.

Neglecting vapor storage within lithophysal porosity is not expected to have a significant effect on the MSTH model results because of the magnitude of expansion of water as it goes from liquid to vapor phase. One pore-volume of water will result in 1000 pore-volumes of vapor (Ellenwood and Mackey 1962 [DIRS 154867], Plate 4C). The matrix and lithophysal pore volumes are similar, so the combined porosity is roughly double the pore-volume of the liquid that would be vaporized. Therefore, the error introduced by neglecting the vapor storage capacity of lithophysal porosity within the computational elements is the difference of accounting for one- instead of two pore-volumes of vapor (out of the 1,000 pore-volumes of vapor generated) that are not displaced to the next computational element. This results in a 0.1 percent overcalculation of the amount of vapor displaced to the next zone in the numerical model.

The uncertainty introduced by neglecting this 0.1 percent of the vapor displaced is less than would result from not accounting for the porosity heterogeneity among zones of the numerical model. The range of porosity for the potential repository units is from 10 to 60 percent (Mongano et al. 1999 [DIRS 149850], p. 17), a six-fold range of porosity. Thus, porosity

averaged over zones in the numerical model would have a greater impact on storage than would neglecting lithophysal porosity (one-fold versus six-fold effects).

5.3.1.4.2 Effects on In-Drift Temperature and Humidity of Fracture Heterogeneity Aspects of Seepage

Uncertainties in MSTH model results can be introduced by heterogeneous seepage resulting from fracture property heterogeneity. These uncertainties are listed as model uncertainty in Table 5.3.1.2-1, Items 6 and 7. Analyses of the influence of seepage heterogeneity were conducted, subsequent to the MSTH model analysis (CRWMS M&O 2000 [DIRS 149862]), to address the in-drift environment uncertainties associated with the limited evaluations of seepage in the MSTH model. The two-dimensional LDTH submodel was used in the original MSTH model analysis. Because the MSTH model incorporates LDTH submodels at 31 locations in the potential repository, it captures the influence of repository-scale variability of hydrologic properties and conditions (e.g., infiltration flux). However, as incorporated in the original MSTH model analysis, the two-dimensional LDTH submodels did not account for the influence of drift-scale heterogeneity such as the influence of drift-scale heterogeneity of fracture properties, including permeability, porosity, and the capillary properties (the most important being the van Genuchten α parameter).

Over nearly the entire range of infiltration-flux conditions considered in the MSTH model (CRWMS M&O 2000 [DIRS 149862]), seepage into the drift is not predicted to occur. Nonzero drift-seepage fluxes were only predicted to occur in regions of the potential repository having the highest infiltration (and percolation) flux for the "upper" infiltration-flux case. An important reason for the low occurrence of predicted drift seepage is the assumption (in the LDTH submodel) of a uniform fracture continuum within any given hydrostratigraphic unit (particularly the host-rock units). This is equivalent to assuming no drift-scale heterogeneity of fracture properties in the host rock. This assumption, together with the use of a two-dimensional LDTH model, reduces the tendency for the occurrence of drift seepage to be predicted.

Previous studies of both isothermal and nonisothermal seepage (Tsang et al. 1997 [DIRS 123761]; Nitao 1997 [DIRS 100640]; Hardin 1998 [DIRS 100123], Section 3.6) indicate that with heterogeneous fracture properties, average seepage rates increase and the threshold for seepage decreases. Therefore, a sensitivity study with a three-dimensional LDTH model using heterogeneous fracture properties was conducted to determine what thermal-hydrologic variables predicted by the MSTH model would change as a result of drift-scale fracture heterogeneity.

The sensitivity analyses of the effects of heterogeneous fracture properties on in-drift conditions were conducted by selecting eight sets of fracture properties, from the stochastic realizations of fracture properties (Table 5.3.1.4.2-1). These sets were chosen not to be representative, but rather to assure that seepage could occur under all of the climate infiltration-flux conditions considered for Yucca Mountain. The selection of these sets should not be interpreted as being an indication of whether such heterogeneous conditions are realistic. Rather, they should be regarded as extreme examples of fracture heterogeneity that were selected to substantially challenge the hypothesis that boiling conditions at the drift wall are capable of thwarting seepage. They will, thus, result in conservatively bounded analyses. Therefore, the objective of these analyses, which used the *Three-Dimensional Heterogeneous LDTH Model from the MSTH*,

REV 00/ICN 02A, model (BSC 2001 [DIRS 155007], Section 6.14), were to determine: whether fracture heterogeneity can result in liquid-phase flow penetrating through the boiling zone and result in a reduction in the duration of boiling, and to determine which in-drift thermal-hydrologic variables predicted by the MSTH model would be most significantly influenced by drift-scale fracture heterogeneity. In these sensitivity studies, the drift wall was an interface between materials (rock and porous-medium-air) that have different permeability. This approach allowed water to directly seep into the drift in the calculation.

The three-dimensional heterogeneous LDTH submodels used were based on the two-dimensional LDTH submodel at the L4C3 location (CRWMS M&O 2000 [DIRS 149862]), which is close to the geographic center of the potential repository. The host rock unit at this location is the tsw35 model unit (Tptpll unit), which is the predominant host rock unit in the potential repository. The mean infiltration-flux case was used. The L4C3 location has infiltration fluxes that are higher than the potential repository averages (BSC 2001 [DIRS 155007], Table 6-7).

The lateral gridding in the two-dimensional and three-dimensional LDTH models was slightly more refined outside the drift than was used in the original calculations (CRWMS M&O 2000 [DIRS 149862]. The finer gridding was used to assure that drift-scale heterogeneity would be represented with adequate resolution in the immediate vicinity of the drift. The three-dimensional LDTH model has an axial dimension of 5 m (approximately the length of one waste package), and it treats the upper 39.7 m of the host-rock unit (Tptpll) (17.4 m above and 16.8 m below the drift) from the drift to the mid-pillar location as having heterogeneous fracture properties.

As was noted, eight stochastic realizations were modeled (Table 5.3.1.4.2-1). All stochastic realizations used a log-normal distribution with values of $\log_{10}$ standard deviation and correlation lengths in the principal directions. In the heterogeneous fracture field, fracture permeability was assumed to be isotropic (as it is assumed in the hydrostratigraphic units that have homogeneous fracture permeability). Four of the realizations were for an AML of 56 MTU/acre, which is representative of heating conditions at the center of the potential repository. Four of the realizations were for an AML of 34 MTU/acre, which is representative of heating conditions close to the potential repository edge. The stochastic realizations were chosen in pairs (one for center and one for edge) to:

- Consider cases with greater potential for flow focusing, and thus seepage, by including greater heterogeneity than was noted in the field (Table 5.3.1.4.2-1, Cases A and B) and greater vertical correlation. These cases have a $\log_{10}$ standard deviation of 1.5, which is greater than the value of 0.72 determined from air-permeability data performed at Niche 3650 (CRWMS M&O 2000 [DIRS 153045], Table 4, p. 38) and also include a factor of 8 greater correlation length in the vertical direction.

- Evaluate the effects of excluding the relation between permeability and capillary strength (lower capillary strength associated with higher permeability) by assuming a constant value of capillary strength. Cases A and B (Table 5.3.1.4.2-1) were the same except that Case B used a constant value of capillary strength, whereas Case A used the capillary-strength parameter ($1/\alpha$) correlated to the heterogeneous fracture permeability field according to Leverett's scaling rule (Leverett 1941 [DIRS 100588], p. 159).

- Consider effects on seepage of slightly greater heterogeneity than measured in Niche 3650 ($\log_{10}$ standard deviation of 1 compared to 0.72), but without vertical biasing (Table 5.3.1.4.2-1, Case C), and to consider the effects of greater heterogeneity with a $\log_{10}$ standard deviation of 2.3 (Table 5.3.1.4.2-1, Case D) but with less focusing than Cases A and B (2x compared to 8x vertical correlation). More detailed discussion of these cases and their objectives is contained in the draft update to the MSTH model AMR (BSC 2001 [DIRS 155007], Section 6.14.4).

Detailed results follow:

- Seepage can vary from none to nearly the full amount of the percolation flux for fracture heterogeneity, as the permeability varies from slightly above that measured in underground tests (Case C) to very heterogeneous fracture properties. Table 5.3.1.4.2-2 summarizes seepage conditions in the drift after TH conditions return to near-ambient.

- The likelihood and magnitude of seepage increase with the $\log_{10}$ of the standard deviation of the fracture permeability (BSC 2001 [DIRS 155007], Section 6.14.5).

- The likelihood and magnitude of seepage increase with the ratio of vertical to horizontal correlation length. (BSC 2001 [DIRS 155007], Section 6.14.5).

- Correlating the capillary-strength parameter [$1/\alpha$] of the fractures with the fracture permeability according to Leverett's scaling rule resulted in a greater seepage magnitude than cases for which [$1/\alpha$] was constant (BSC 2001 [DIRS 155007], Section 6.14.5).

- The duration of boiling is never reduced as a result of fracture heterogeneity (BSC 2001 [DIRS 155007], Figures 6-83a, 6-83c, and 6-84), and the duration of boiling is slightly greater for the heterogeneous cases than for the homogeneous cases. The greater duration of boiling for the heterogeneous cases results from the influence of buoyant gas-phase convection being reduced by the heterogeneous fracture-permeability distribution (low-*k* features obstruct buoyant gas-phase convection). Thus, buoyant gas-phase convection plays a less significant role in the rate of cool down in the drift for the heterogeneous cases than for a corresponding homogeneous.

- Temperatures at the drift wall or on the drip shield are insensitive to heterogeneity during the boiling and post-boiling periods, with the exception that there is a slight increase in the duration of the boiling period for the heterogeneous cases (BSC 2001 [DIRS 155007], Section 6.14.5).

- Relative humidity in the drift is unaffected by fracture heterogeneity during the boiling period (BSC 2001 [DIRS 155007], Figures 6-83b and 6-83d).

- Relative humidity reduction in the drift is diminished during the post-period only for cases where seepage contacts the drip shield (BSC 2001 [DIRS 155007], Figures 6-83b and 6-83d). This effect decreases with decreasing seepage flux onto the drip shield (BSC 2001 [DIRS 155007], Figures 6-93d and 6-94d). For cases with no seepage flux

onto the drip shield, the relative humidity reduction is not diminished (BSC 2001 [DIRS 155007], Figures 6-95d and 6-97d).

- For heterogeneous cases with seepage flux contacting the drip shield, the evaporation rate on the drip shield is greater than the evaporation rate for the corresponding homogeneous case (BSC 2001 [DIRS 155007], Figure 6-85) or for the heterogeneous cases with no seepage contacting the drip shield. This observation only applies to the post-boiling period because there is no seepage during the boiling period for the heterogeneous cases or the corresponding homogeneous cases; consequently, there is virtually no evaporation on the drip shield for the heterogeneous or homogeneous cases during the boiling period.

Summary–The results of the seepage analyses indicate that no seepage will occur during the boiling period, regardless of the fracture property heterogeneity. This study indicated that the in-drift thermal-hydrologic conditions calculated (CRWMS M&O 2000 [DIRS 149862]) would not be changed during the boiling period by virtue of adding the influence of drift-scale fracture heterogeneity. Further, the study found that the duration of boiling was not reduced as a result of fracture heterogeneity. These results, which are consistent with those using a different model in Chapter 4, justify the neglect of seepage in calculating the in-drift TH conditions.

For the post-boiling period, heterogeneity influences the seepage potential (BSC 2001 [DIRS 155007], Section 6.14.5), and can do so significantly, with seepage varying from 0 to as much as 86 percent of percolation flux for heterogeneous fracture systems with strong vertical correlation. The likelihood and magnitude of seepage increase with the $\log_{10}$ of the standard deviation of the fracture permeability, and further with the ratio of vertical to horizontal correlation length.

Temperatures were insensitive to heterogeneity during both the boiling and post-boiling periods, with the exception that there is a slight increase in the duration of the boiling period for the heterogeneous cases. In-drift relative humidity was unaffected by fracture heterogeneity during the boiling period, and diminished during the post-boiling period only for cases where seepage contacts the drip shield. For cases with no seepage flux onto the drip shield, relative humidity reduction was unaffected by heterogeneity.

If seepage flux contacts the drip shield, the evaporation rate on the drip shield will be greater for heterogeneous cases than the corresponding homogeneous case or the heterogeneous cases with no seepage contacting the drip shield.

5.3.1.4.3 Effects of Imbibition Hysteresis

The primary issue for capillary (or imbibition) hysteresis concerns matrix flow. The capillary properties of the matrix (quantified by the van Genuchten α and m parameters) are developed for drainage (or drying) conditions. Laboratory samples of the rock matrix are fully wetted and placed in a centrifuge, wherein water is incrementally removed by applying increasing suction potential. A moisture retention curve is developed, which is capillary pressure as a function of liquid saturation. Moisture retention data collected in this fashion is representative of the drying phase of the potential repository host-rock evolution. However, in all thermal-hydrologic

modeling studies of the potential Yucca Mountain repository, these data are also assumed to be applicable to the rewetting of the host rock by capillary imbibition in the matrix. This assumption is equivalent to neglecting hysteresis between drying and imbibition behavior.

Imbibition hysteresis was discussed in Niemi and Bodvarsson (1988 [DIRS 155057]). The issue of imbibition diffusivity was addressed in the *Near-Field/Altered-Zone Models Report* (Hardin 1998 [DIRS 100123]). That report used the concept of the matrix imbibition diffusivity, which is a function of the van Genuchten α and m parameters, to compare the magnitude of matrix imbibition arising from various hydrologic property sets that had been used in thermal-hydrologic modeling studies of the potential Yucca Mountain repository. That report also determined the value of matrix imbibition diffusivity from the laboratory measurements of matrix imbibition of Flint et al. (1996 [DIRS 100676]). For all of the hydrologic property sets considered in Hardin (1998 [DIRS 100123] the values of matrix imbibition diffusivity were greater than that obtained from the laboratory measurements of matrix imbibition for the corresponding host rock unit. The differences in matrix imbibition diffusivity between the laboratory measurements and those determined from the property sets in Hardin (1998 [DIRS 100123], Table 3-3) probably are the result of capillary hysteresis; in other words, the imbibition diffusivity is less than the diffusivity for drainage conditions. For most of the potential repository host-rock units, the matrix properties for the base-case hydrologic property sets used in all TH calculations of the SSPA are similar to those of the 1997 TSPA-VA base-case hydrologic property set. Therefore, it is possible that the rate at which the dryout zone around emplacement drifts is rewetted by matrix imbibition is overpredicted by the TH model calculations in this report, including the MSTH model calculations.

Jury et al. (1991 [DIRS 102010], pp. 65 to 68) discuss the hysteresis in moisture content in the relationship of moisture potential versus volumetric moisture content. Moisture potential is not uniquely related to moisture content because the potential energy state is determined by conditions at the air-water interfaces and the nature of the surface films, rather than by the quantity of the water present in the pores. The welded tuff pores at Yucca Mountain are variable in size and shape and in the degree of interconnection. Jury et al. (1991 [DIRS 102010], p. 65) state that it is common for porous media to have bottleneck pores, in which there are large cavities but narrow points of connection to adjacent pores. Water is retained in small pores, which fill first when water is admitted to a system; however, they do not always empty again during drying in the same order as they were filled.

As the welded or nonwelded tuff is dried by evaporating water, pores will begin to empty from the state of near saturation in the tuff matrix. However, water may be trapped in the larger pore space in such a way that the pores will not empty in the order that they might be filled if water is introduced to dry welded tuff. The sudden release of a relatively large amount of water from a large pore floods surrounding pores and decreases the matrix potential in them temporarily. If matrix potential is measured in a small porous system having discrete differences in pore size, the relationship between moisture potential and moisture content for drying might be "saw toothed" (Jury et al. 1991 [DIRS 102010], Figure 2.14).

In welded tuff, the pore size distribution contains pores over a range of sizes, and the water and moisture potential distributions tend to average out so that a relatively smooth curve is obtained.

The moisture content for a given moisture potential is higher than for the wetting system, as shown by Jury et al. (1991 [DIRS 102010], Figure 2.14).

In addition, as discussed by Jury et al. (1991 [DIRS 102010]), surface wetting also introduces hysteresis. The grain surfaces will form a nonzero contact angle with water when wetted. This results in thicker films than would be present in the drying phase where water films are drawn tightly over the surface by adsorptive forces.

The conceptual model for water retention described above shows that the rates of imbibition generally would be overpredicted. The impacts of this overprediction would be an underprediction of temperature and an overprediction of relative humidity. Thus, the conceptual model suggests that liquid fluxes would be conservatively bounded, so determinations of the dryness of the waste package inner diameter will be conservative. However, waste package and drip shield temperatures would be nonconservatively bounded, which means that waste package and potential repository temperatures could exceed those calculated. As additional measurements characterize hysteresis properties in moisture retention in the matrix for welded and nonwelded tuffs, and in fractures for welded tuff, the uncertainty in temperatures will decrease.

5.3.1.4.4 Effects of Mountain-Scale Gas Phase Convection

Depending on its magnitude, the influence of mountain-scale and drift-scale buoyant gas-phase convection can influence MSTH model results in several ways. Buoyant gas-phase convection increases the rate of heat transfer away from the potential repository horizon and emplacement drifts. Therefore, if its magnitude is large enough, buoyant gas-phase convection will decrease temperatures in the host rock and in the emplacement drifts. For cases where boiling occurs, the decrease in temperatures can reduce the duration of boiling. Buoyant gas-phase convection can also increase the magnitude of heat-mobilized liquid-phase flux above the emplacement drifts.

To be significant to thermal-hydrologic conditions at the potential repository horizon, buoyant gas-phase convection requires thermally perturbed conditions arising from radioactive decay heat. The development of convection cells for layers heated from below depends on the critical Raleigh number. That dimensionless number is, in turn, proportional to the thermal expansion of the fluid, the temperature difference or gradient, and the intrinsic permeability (more specifically, the bulk permeability of the fracture continuum), and it is inversely proportional to thermal diffusivity and fluid viscosity (Phillips 1991 [DIRS 140641], pp. 144 to 145). Of these parameters, the several orders of magnitude range of variation of permeability has a more dominant effect on convection than thermal diffusivity which varies over a narrower range.

Sensitivity analyses were performed (Buscheck 2001 [DIRS 155012]) to consider a range of bulk permeability (k_b) values that incorporated plus or minus one (low-k_b and high-k_b) and two (very low-k_b and very high-k_b) standard deviations around the mean. For these analyses, the permeability distribution was isotropic. Since vertical anisotropy restricts buoyancy, the use of an isotropic permeability distribution provides an upper bound of the possible effects of buoyancy for any given value of permeability. Analyses by Phillips (1991 [DIRS 140641], p. 145) indicate that the critical Raleigh number is smaller when the ratio of permeability in the horizontal direction to the vertical direction is low, which may occur in some regions of the

welded fractured units. The influence of vertical anisotropy is not directly addressed by the sensitivity analyses discussed in this section.

Figure 5.3.1.4.4-1 shows liquid flux calculations for the HTOM at 5 m above the drift for a central drift location. This location was chosen to be consistent with locations where seepage had been evaluated in past analyses (CRWMS M&O 2000 [DIRS 153363], Section 3.2.3.1.5). In the low-k_b case, these flux values represent the case in which buoyant gas-phase convection has a negligible influence on thermal-hydrologic behavior. The high-k_b case is more conducive for buoyant gas-phase convection to be significant. The mean k_b case is one in which the influence of buoyant gas-phase convection is modest, but not negligible. After about 20,000 years, there is no significant difference between the flux for the three cases. This indicates that the model results are not sensitive to considerations of buoyant gas-phase convection at late times when temperatures approach ambient conditions.

During the boiling period, the high-k_b case resulted in peak values of heat-mobilized flux above the emplacement drift being nearly twice those of the mean and low-k_b cases. These peak values occur during the early portion of the boiling period. This indicates that heat-mobilized liquid flux is sensitive to buoyant gas-phase convection during the early portion of the boiling period. The peak liquid flux for the high-k_b was 220 mm/yr, compared with 115 mm/yr for the mean and low-k_b cases. This indicates that heat-mobilized liquid flux is very sensitive to buoyant gas-phase convection during the early portion of the boiling period. The peak liquid flux for the high-k_b case was 220 mm/yr, compared with 115 mm/yr for the mean- and low-k_b cases. For cases in which the influence of buoyant gas-phase convection is negligible, the flow of heat-mobilized water vapor is vertically symmetric with respect to the potential repository horizon: about half flows above the potential repository horizon and about half flows below the potential repository horizon. When the influence of buoyant gas-phase convection is strong, it results in very pronounced vertical asymmetry of the water-vapor flow field, causing nearly all of the heat-mobilized vapor flow to occur above the potential repository horizon. This asymmetry in the water-vapor flow field causes the condensate flux above the potential repository horizon to be nearly twice that of the case where buoyant gas-phase convection is negligible.

Figure 5.3.1.4.4-2 shows the results for the LTOM analyses under the same conditions used in the HTOM analyses. The stairstep responses indicate the impacts of different climates from 0 to 600 years and from 600 to 2,000 years. Results for the LTOM do not show the significant differences between the low, mean, and high-k_b cases in contrast to the HTOM analyses from 1,000 to 2,000 years. This is mainly because, without boiling, there is much less water mobilized by vaporization and condensation. These analyses indicate the same long-term flux responses as the HTOM calculations: about 22 mm/yr, with a difference of less than 1 mm/yr among the low, mean, and high-k_b cases.

Heat mobilized liquid flux 5 m above the drift is more sensitive to buoyant gas-phase convection than it is at 1 m above the drift (compare Figure 5.3.1.4.4-3 with Figure 5.3.1.4.4-1). Analyses discussed in Section 5.3.1.4.2 indicate that seepage does not occur into drifts during the active boiling period. This is consistent with Figure 5.3.1.4.4-3 which show that there is no liquid flux 1 m above the drift in the HTOM case until after 700 years for the very-high and mean-k_b cases. At that point, the sensitivity to buoyant gas-phase convection is again apparent.

Around 1,000 years, there is greater flux in the very high-k_b case (52 mm/yr) than in the mean-k_b case (32 mm/yr), indicating some sensitivity of liquid flux to buoyant gas-phase convection. However, this amount of flux is about the same magnitude as the ambient flux range and less than the long-term flux from the wetter climates (up to 100 mm/yr). There is no significant difference in liquid-phase flux at 1-m and 5-m above the drift in the LTOM, reflecting the minimal thermal mobilization of water.

The influence of mountain-scale buoyant gas-phase convection on temperatures within the host rock and on the duration of boiling conditions was addressed in previous analyses (Buscheck et al. 1994 [DIRS 105157]). These analyses considered the impact of mountain-scale buoyant gas-phase convection on TH results for a number of different potential repository AML scenarios. Among the AMLs considered in those analyses was a 55.3-MTU/acre case that is comparable to the HTOM case AML (Table 5.1-1). The LTOM AML of 45.7 MTU/acre is bracketed by the 55.3 and 35.9-MTU/acre cases considered by Buscheck et al. (1994 [DIRS 105157]). Therefore, the results of the earlier analyses are adequate for evaluating uncertainties in the MSTH model results due to the effects of mountain-scale buoyant gas-phase convection and are discussed in the following paragraphs.

Buscheck et al. (1994 [DIRS 105157]) evaluated the effects of convection by considering values of bulk fracture permeability (k_b). As shown in Buscheck et al. (1994 [DIRS 105157], Table I), permeability ranged from sufficiently low (0.28 darcy) to limit convection (satisfying the critical Raleigh number) to a range (1 to 10 darcy) that is representative of the permeability range (and of the buoyant gas-phase convection effects) expected for the potential repository, and then to values that would represent the upper bounds (40 to 84 darcy) of permeability (1 darcy is approximately 10^{-12} m^2). The values of permeability used by Buscheck et al. (1994 [DIRS 105157]) are consistent with, the uncertainty and sensitivity analyses for this report. Specifically, the mean permeability value used in the MSTH model analyses for the lower lithophysal unit is 2.4 darcy which falls between the two values evaluated (1 and 10 darcy). Analyses of the sensitivity of MSTH model results to variability in k_b considered two standard deviations of k_b (see Section 5.3.1.4.7) about the mean. The upper value that represents two standard deviations (log scale) is 38.1 darcy, similar to the value of 40 darcy used by Buscheck et al. (1994 [DIRS 105157]). Thus, the 84-darcy case represents an extreme bound on the uncertainty. The lower value, two standard deviations, is 0.15 darcy. This is somewhat lower than the 0.28 darcy used by Buscheck et al. (1994 [DIRS 105157]). However, the 0.28 darcy case has a permeability that is sufficiently low that it does not generate significant mountain-scale buoyant gas-phase convection. A lower value would simply give the same non-convection results. Those analyses found, as did earlier analyses (Buscheck and Nitao 1994 [DIRS 130561]; Buscheck and Nitao 1993 [DIRS 140907]), that the permeability threshold where mountain-scale convection begins to dominate moisture movement is about 1 darcy.

The analysis (Buscheck et al. 1994 [DIRS 105157], Table I) evaluated the effect on peak temperature of neglecting convection (using 0.28 darcy as a negligible convection case). For a potential 55.3 AML repository (similar to the higher temperature operating mode), the peak temperature was reduced by 1.2, 3.7, and 5.2°C at 1 darcy (the most representative of the values used in current analyses), 10 darcy and 40 darcy respectively. The difference interpolated between these results to 2.4 darcy (the value for the lower lithophysal unit, in which most of the potential emplacement drifts would be located) is about 2°C. The analyses further indicated that

there would be a difference of about 200 years in the duration of the temperature elevation above the boiling point for the lower lithophysal unit mean-k_b case and the 0.28-darcy case. This is based on differences in duration (from the 0.28 darcy case) of 60 years and 681 years for the 1 and 10 darcy cases, respectively. The same analyses indicate that for k_b of 40 darcy, about two standard deviations higher than the mean in the lower lithophysal unit, the peak temperature difference would be about 3°C lower than in the lower lithophysal unit mean-k_b case, and the difference in the duration of boiling would be reduced by more than a factor of two. Because these early analyses used no ventilation period, their duration of boiling is greater than expected in the potential repository.

The Buscheck et al. (1994 [DIRS 105157]) analyses performed for the 35.9 MTU/acre AML case are applicable, as a lower bound, to the LTOM case (45.7 MTU/acre) evaluated in this report. Those analyses found that for the 35.9 MTU/acre AML case, there was no difference in peak temperatures between the 0.28-darcy and 1-darcy cases, and only a 0.1°C difference between the 0.28-darcy and 10-darcy cases. If a linear interpolation to 2.4 darcy applies between the 35.9 and 55.3 MTU/acre AML cases, the temperature difference between the lower lithophysal unit mean-kb case and a permeability two standard deviations higher would be less than 1°C for an AML of 45 MTU/acre. If a linear interpolation of peak temperature is used between the 35.9 and 55.3 MTU/acre AML cases, the 45-MTU/acre case would peak at about 96°C, just at the boiling point of water at the potential repository elevation and there would be no duration above boiling.

Summary-The primary effect of neglecting mountain-scale gas-phase convection occurs on the potential repository temperatures and the duration of boiling. Based on the results of the studies described above, it can be concluded that neglecting mountain-scale buoyant gas-phase convection in the MSTH model analyses will conservatively bound temperatures on the high side. For the HTOM, the calculated temperatures would be less than 2°C too high for the mean-k_b case. A permeability two standard deviations higher than the mean would produce temperatures about 1° and 3°C higher than actual for the lower and higher-temperature operating modes, respectively.

5.3.1.4.5 Effects of Thermal-Hydrologic-Chemical Processes

Changes in porosity and permeability from mineral dissolution and precipitation have the potential to modify percolation fluxes and seepage fluxes at the drift wall. Porosity changes in matrix and fractures are directly tied to volume changes as a result of mineral precipitation and dissolution. Since the molar volumes of minerals created by hydrolysis reactions (i.e., anhydrous phases, such as feldspars, reacting with aqueous fluids to form hydrous minerals, such as zeolites or clays) are often larger than those of the primary reactant minerals, dissolution-precipitation reactions can lead to porosity reductions. This section summarizes an analysis (BSC 2001 [DIRS 154677]) of the effects of THC coupled processes.

As noted in Section 5.3.1.2.2, the TSPA-SR (CRWMS M&O 2000 [DIRS 153246] was supported by analyses that indicated that THC processes would not have a significant impact on hydrologic properties. These analyses are documented in *Drift-Scale Coupled Processes (DST and THC Seepage) Models* (BSC 2001 [DIRS 154677]; see also Sections 4.3.6.3.2 and 4.3.6.4.2 of this document). Fracture permeability changes can be approximated using the porosity change

and an assumption of plane parallel fractures of uniform aperture (Steefel and Lasaga 1994 [DIRS 101480], p. 556). However, this approximation yields a permeability of zero only for a zero fracture porosity. In many experimental and natural systems, permeability reductions to values near zero occur at porosity significantly greater than zero. This is usually the result of mineral precipitation or fracture closure of the narrower interconnecting apertures. The hydraulic aperture, as calculated from fracture spacing and permeability (determined through air-permeability measurements) assuming a cubic law relation, is a closer measure of the smaller apertures in the flow system. These analyses used the hydraulic aperture.

Analyses documented in *Drift-Scale Coupled Processes (DST and THC Seepage) Models* (BSC 2001 [DIRS 154677] Section 7) concluded that predicted porosity changes due to water-rock interaction around waste emplacement drifts are small and show a reduction mostly due to mineral precipitation, with essentially no effect on predicted thermal-hydrologic conditions around drifts. The Tptpmn THC backfill model predicted small fracture porosity changes due to mineral precipitation and a small effect of porosity changes on permeability. Depending on the infiltration rate, the largest fracture porosity reductions occurred approximately 15 to 18 m above and to the side of the drift (BSC 2001 [DIRS 154677] Section 6.3.4 and Figure 52). The predicted reduction in porosity and permeability in the NFE over 100,000 years for the Tptpmn (no backfill and homogeneous permeability) is less than 3 percent of the initial fracture porosity and less than one order of magnitude, respectively. This is somewhat greater than calculated for the Tptpmn THC backfill model (less than 1-percent change in fracture porosity), but still relatively minor.

These results (BSC 2001 [DIRS 154677], Section 7) are based on uniform areas of precipitation in plane parallel fractures; the actual effects in heterogeneous fractures with rough surfaces and nonuniform mineral precipitation may be greater. The analysis does not account for the effects of anisotropy in the fracture permeabilities. Comparison of the results of purely thermal-hydrologic simulations to those including coupled THC processes show only small differences in predicted water and gas fluxes, liquid saturation, and permeability around the drift. The porosity reduction that occurs well after rewetting of the drift wall is predicted to be almost entirely due to calcite and amorphous silica. The latter contributes to most of the initial precipitation during the initial cooling stage, with maximum deposition spreading above the drift in a zone roughly coinciding with the maximum extent of the dryout zone (8 to 10 m from the drift center). Dissolution of salts is expected to occur during this stage, but the effect on fracture porosity and permeability is negligible. Calcite is predicted to precipitate mostly during later cooling stages. During the cooling stages, amorphous silica dissolves slightly, as do some primary minerals, such as feldspars; however, this dissolution is not sufficient to reverse the porosity reduction that occurs due to precipitation (BSC 2001 [DIRS 154677]). Below the drift, little mineral alteration takes place during heating and cooling because of the drift shadow effect, resulting in a region sheltered from infiltrating water.

The analyses (BSC 2001 [DIRS 154677], Section 7) further concluded that heterogeneity in fracture permeability can have varied effects on thermal hydrology, including flow focusing and irregularity in isotherms and liquid saturations. TH simulations were performed for three heterogeneous fracture permeability realizations with a range in permeability of four orders of magnitude, under the mean infiltration climate change scenario, for the Tptpmn unit. Areas of highest initial liquid saturation, which have lower permeability and generally reside above the

drift, tend to show the greatest reduction in fracture permeability, down to about 25 percent of the initial value in some regions. This localized permeability reduction tends to cause some additional flow focusing, but the permeability changes are considerably less than the initial range in permeability. The corresponding maximum fracture porosity reductions are approximately 5 percent of the initial value.

Porosity reductions (BSC 2001 [DIRS 154677], Section 7) for the extended geochemical system are slightly greater than those for the base case system owing to more mineral species precipitating and somewhat higher silica concentrations in the former. The maximum amount of amorphous silica precipitated is about 2 percent (volume percent of fracture) in the extended case and somewhat less in the base case, with maximum amounts in the high saturation zones near the drift.

Because of the large amount of data needed and the complexity of natural systems, many uncertainties exist in modeling coupled THC processes (BSC 2001 [DIRS 154677], Section 7). The necessary data include the fundamental thermodynamic properties of minerals, aqueous species, and gases; the kinetic data for mineral-water reactions; and the representation of the unsaturated hydrologic system for fractured tuffs. In addition, site-specific thermal-hydrologic, geologic, and geochemical data are necessary to describe the initial and boundary conditions. For these reasons, it may not be possible to assign a model uncertainty based on the uncertainties of the data themselves; therefore, model validation gives a true test of whether the system can be described sufficiently well for the intended purposes of the model.

A comparison of simulated THC processes to those processes measured during the Drift Scale Test was conducted (BSC 2001 [DIRS 154677], Section 6.2). It was found that the simulations captured the important changes in pH, aqueous species concentrations, and gas-phase carbon dioxide concentrations at specific locations over time. This provides sufficient validation of the capability of the model to predict spatial and temporal variation in water and gas chemistry.

5.3.1.4.6 Effects of Thermal-Hydrologic-Mechanical Processes on Multiscale Thermal-Hydrologic Model Results

The influence of uncertainty on TSPA-SR results relates to whether ignoring THM effects, as the current models do, can significantly affect MSTH model results. The THM effects addressed in this section are those related to hydrologic effects, specifically changes in permeability. While fracture aperture changes due to THM effects may influence the water retention potential of fractures, no attempt has been made to address these processes other than the correlation between permeability and van Genuchten α discussed in Section 5.3.1.4.2. As noted in Sections 5.3.1.4.8 and 5.3.1.4.9, porosity influences thermal conductivity. However, the fracture porosity (about 1 percent; see Section 4.3.6.3.2) is less than 10 percent of the total porosity (see Section 5.3.1.4.9 for lithophysal porosity values). Changes in that 10 percent will not have as significant an effect on thermal conductivity as changes in the matrix and lithophysal porosity. THM may also influence convective heat transfer by causing changes in the permeability of the fractures. Section 5.3.1.4.4 addresses the sensitivity of the MSTH thermal model results to mountain-scale convection; this section focuses entirely on THM-induced changes in permeability that could be the cause of such convection.

Analyses of THM effects on hydrologic properties, specifically on fracture permeability, are reported in the *Near Field Environment Process Model Report* (CRWMS M&O 2000 [DIRS 153363], Section 3.5). The analyses used a distinct element model to represent fracture-bounded blocks. The analyses identified a potential for localized increases in permeability of up to a factor of six. The changes were based on predicted shear displacements and an empirical relationship between displacement and permeability change.

More recent work evaluated permeability changes due to both normal and shear deformations (Blair 2001 [DIRS 155005]). In this work, the model boundaries were extended horizontally to the mid-pillar region on either side of the drift and vertically to 100 m above and below the emplacement drift, but the fractured region remained relatively small at $20 \times 20 \times 10$ m due to computational limitations. A fixed stress boundary condition, equivalent to the weight of the overburden, was applied to the upper boundary, and fixed displacement boundary conditions were applied to the sides and lower boundary. Shear deformations were assumed to increase fracture apertures as mismatched fracture surfaces slide past each other so that the cubic law could be used to assess permeability changes resulting from shear as well as normal deformations. All fractures were assumed to have the same initial aperture. The predicted permeability changes are quite sensitive to aperture changes because of the cubic law, so that the initial fracture aperture used in the simulations is expected to affect the model results. Model input parameters are given in Table 5.3.1.4.6-1.

Heating was found to cause a rotation of the stress field at the level of the emplacement drift. The maximum principal stress rotated from vertical to horizontal during the heating period, then rotated back to vertical by 100,000 years as the rock cooled. The rotation of the local stress field closed subvertical fractures and opened subhorizontal fractures during the heating period. In the HTOM case, permeability decreased by five to six orders of magnitude in 80 percent of the subvertical fractures, and by lesser amounts in most of the other subvertical fractures, by 100 years into heating. The five order of magnitude reduction in permeability persisted until at least 1,000 years for 70 percent or more of the subvertical fractures. Over the same time interval, permeability increased by up to one order of magnitude in 20 to 45 percent of the subhorizontal fractures and remained little changed in most of the rest. Predicted permeabilities increased for all fractures during cool-down, generally by one or two orders of magnitude. The THM effects are concentrated at the emplacement drift level where the temperature perturbations are greatest. The rock a few drift diameters above and below the emplacement drift level will likely experience more modest THM-induced permeability changes because the temperature changes are smaller.

The LTOM case was analyzed and results show that as expected, the stress levels in the rock mass are much lower than for the HTOM case, and that the highest stresses occur after the end of ventilation at 300 years after emplacement. In addition, the results show that for the LTOM the fracture permeability remains basically unchanged for the first 300 years of storage while ventilation is maintained. Results also show that after the end of the ventilation period (300 yr) a decrease in fracture permeability of one to two orders of magnitude is predicted for approximately 50 percent of the vertical fractures. This reduction of fracture permeability is predicted to persist until 400 years after emplacement, and gradually changes over time, with fracture permeability decreasing by 3 orders of magnitude in approximately 20 percent of the vertical fractures at 1,000 years after heating.

While the predicted decreases in fracture permeability due to TM effects after the end of the ventilation period may be significant for the LTOM case, they are much smaller in magnitude and affect far fewer fractures than the changes in fracture permeability predicted for the HTOM case. THM modeling results for both the HTOM and LTOM cases are discussed in detail in Section 4.3.7.

The analyses of thermal-hydrologic sensitivity to bulk permeability (see Section 5.3.1.4.7) considered a range of permeabilities, as shown in the first three columns of Table 5.3.1.4.6-2. The seepage analyses described in Section 5.3.1.4.2 also considered a range of permeabilities and the effects of heterogeneity. Table 5.3.1.4.6-2 reports the ranges considered for heterogeneous fracture permeability without strong vertical focusing in the seepage sensitivity studies (Table 5.3.1.4.2-1, Case A) because this range is more constrained than the extreme cases. In Table 5.3.1.4.6-2, the ranges evaluated in Sections 5.3.1.4.2 and 5.3.1.4.7 are compared with potential changes in permeabilities due to shear displacement (increases) and normal displacements (decreases). These changes, shown in the last column of the table, were calculated by applying the order of magnitude increase and five orders of magnitude decrease to the mean permeability values listed in the first column of the table for units tsw34 and tsw35. Although the magnitude of THM changes only applies to regions near the drift (i.e., to the tsw34 and tsw35 units that constitute most of the potential repository horizon (BSC 2001 [DIRS 155010]). The upper bound is based on the one order of magnitude increase in permeability found for a substantial number of subhorizontal fractures during the heating phase of the THM model. The lower bound is based on the five order of magnitude drop in permeability during the heating phase for subvertical fractures. At later times, after a significant amount of cooling has occurred, a higher permeability bound of two or three orders of magnitude at the drift elevation is appropriate based on the THM results. Changes of these magnitudes only apply to the near-drift environment (i.e., to the TSw34 and TSw35 units that constitute the potential repository horizon). The thermal-mechanical effects depend on temperature changes that will be progressively less pronounced away from the drift level, but can be considered to form a loose upper bound on the potential THM influence on the permeability of the other units.

The range of possible changes in permeability due to THM processes (Table 5.3.1.4.6-2, column 5) was compared with permeability variability/uncertainty ranges used in the sensitivity analyses discussed in Sections 5.3.1.4.2 and 5.3.1.4.7 (Table 5.3.1.4.6-2, columns 3 and 4). The range of increased permeabilities due to THM was smaller than the range considered in the permeability sensitivity analyses. However, reductions in permeability along vertical fractures predicted by the THM analysis were greater than those considered in the sensitivity analyses. As noted in Section 5.3.1.4.7, there was no difference between the mean- and low-k_b analyses in temperatures or relative humidities on the drip shield or the drift wall. This would indicate that, although THM effects reduced the permeability below the low k_b values, the model results would not be affected. Normal deformations would diminish with decreased temperature changes. The maximum decreases in permeability due to normal displacement take place at 100 years, then gradually decrease with time (Blair 2001 [DIRS 155005], Section 6.3.3). For the HTOM, it appears that the sensitivity analyses of temperature and relative humidity effects are applicable to the ranges of possible permeability changes from THM processes. Therefore, neglecting changes in permeability due to THM effects will have a range of effects on MSTH model results those discussed in Sections 5.3.1.4.2 and 5.3.1.4.7.

Changes to the upper or lower, rather than the mean values of the permeability could be beyond the ranges evaluated in the seepage and bulk permeability analyses. If the lower values are decreased, the effect will be to hinder liquid as well as vapor flow. If the upper values are decreased, the changes will be closer to the ranges evaluated in Sections 5.3.1.4.2 and 5.3.1.4.7. If THM processes cause increases to the upper permeability values, large-scale buoyant gas-phase convection could be promoted and the effects will be beyond those evaluated in (Section 5.3.1.4.4). However, the THM model predicts contrasting changes in permeability during the heating phase, with vertical permeability generally declining by a greater margin than horizontal permeability increases, so that increased large-scale convection is doubtful. It can also be argued that higher permeability fractures do not impede vapor or water flow, so increases are not likely to result in major differences in MSTH model temperature results. This is supported by analyses of the influence of permeability range on the MSTH model. As noted in Section 5.3.1.4.7, after 1,000 years the temperatures on the drift wall and drip shield are insensitive to the range of permeability evaluated. At earlier times, the most significant difference was in the HTOM, for which the temperature was about 2° to 4°C lower in the high case during the first 50 years. The relative humidity results for the drip shield were insensitive to the permeabilities, and the results for the drift wall were nearly insensitive to permeabilities, with a difference of less than 1-percent between the high k_b results and the mean and low k_b results. Thus, it is concluded that THM induced increases to lower-bound permeability values will result in permeabilities and TH effects within the bounds addressed in previous sensitivity analyses. For THM changes to upper-bound permeabilities, the seepage analyses for Case-D fractures considered larger-than-normal heterogeneities (2.3 log k sigmas) (see Section 5.3.1.4.2). Although these analyses would be more applicable to the extreme cases, they would not cover THM changes of five orders of magnitude.

The most significant uncertainty regarding the THM results is probably due to model and process uncertainties rather than input data uncertainties. Because of the convolution of model and process uncertainty, the approach used to date to evaluate the impacts of uncertainty has been to compare model analyses with field tests. Although these comparisons do not provide quantification or direct evaluation of the uncertainties, they do allow for an assessment of whether the model results are realistic. The remainder of this section focuses on comparisons of model results with measurements at the Large Block Test (CRWMS M&O 2000 [DIRS 153363], Section 3.6.1.1).

Deformation of the large block during the test was monitored using multiple-point-borehole-extensometers, and a distinct element code (3DEC V2.0) was used to simulate TM behavior. The distinct element method was chosen because it allows discrete fractures to be incorporated into the simulation. The TM model attempts to predict fracture displacements, which are thought to control permeability changes in the tuff. Accurately modeling fracture displacements is a necessary (but not sufficient) condition for modeling THM processes in a realistic manner. Deformation of the large block was calculated at eighteen times of between the start of the test up to 450 days after the start of heating. The model temperatures were derived from the TH analysis performed using submodels of the MSTH model and documented in the *Thermal Tests Thermal-Hydrological Analyses/Model Report* (CRWMS M&O 2000 [DIRS 151964], Section 6.4.3).

A series of simulations (Blair 2001 [DIRS 155309]) was conducted to evaluate the effects of the number of fractures in the model and the coefficient of thermal expansion. These simulations are listed in Table 5.3.1.4.6-3, and the geometry of the model domain for the various simulations is shown in Figure 5.3.1.4.6-1.

The multiple-point-borehole-extensometers in borehole WM2 functioned well throughout the test, and data from anchor WM2-4 representing the entire WM2 baseline comprise the best available basis for comparing model displacements with field data (Figure 5.3.1.4.6-2). The model simulations differ only in the number of fractures or the thermal expansion coefficient. Model 1, the continuum model, incorporates no fractures. Model 2 includes the six largest fractures, and incorporates a higher thermal expansion coefficient than the other models. Models 3 and 4 incorporate only the six and seven largest fractures respectively, while Model 5 includes more than twenty additional, smaller fractures.

Models 3 and 4 did a good job of predicting the deformation at anchor WM2-4 over much of the test duration, including both the heating and cooling phases (Figure 5.3.1.4.6.2). Model 3 predicts slightly less displacement than Model 4. Models 3 and 4 underpredict the total displacement during cooldown by 0.4 mm, and they predict some contraction of the block at about 270 days that is not reflected by observations. Model 1 (continuum) and Model 5 (many fractures) both underpredict the maximum deformation by significant amounts (1.6 and 1 mm, respectively). Model 2 (high coefficient of thermal expansion) overpredicts the maximum deformation, but it shows the best fit to displacement during the first 20 days of heating. Model 5 (many fractures) does not show contraction with cooldown, and Model 1 (continuum) underpredicts the magnitude of the cooldown displacement. Model 2 (high coefficient of thermal expansion) correctly predicts the relative change in displacement during cooldown (1.8 mm), but the final displacement value of 2.6 mm is too high.

Results from the Large Block Test indicate that the distinct element model predicts deformation behavior more accurately than the continuum model. Moreover, not all fractures were active; the deformation was controlled by a subset of 6 to 10 major fractures. Modeling results also indicate that a coefficient of thermal expansion value of 5.27×10^{-6} per °C is appropriate for the Large Block Test. This is lower than the value measured on laboratory samples, but consistent with the value determined from deformation measurements in the Single Heater Test (CRWMS M&O 2000 [DIRS 153363], Section 3.6.1.2) conducted in the ESF. Although the Large Block Test model simulations were not used to predict changes in permeability or moisture retention, simulations that fail to account correctly for fracture displacements likely will fail to predict changes in permeability and other hydrologic properties related to fracture aperture.

Summary–The influence of THM processes on permeability is generally within the range of the seepage and bulk permeability effects reported in Sections 5.3.1.4.2 and 5.3.1.4.7, respectively, for the upper bounds of permeability. Increases in the upper permeability bounds may promote buoyant gas-phase convection (Section 5.3.1.4.4). The decreases in the lower permeability values by as much as five orders of magnitude are beyond the ranges investigated in the permeability sensitivity studies; however, it does not appear that these changes will significantly affect temperature or relative humidity. The decrease in vertical permeability should reduce seepage into the drifts, although this effect will be at least partially offset by the re-opening of vertical fractures during cooldown. Based on these assessments, it is concluded that the

uncertainties from neglecting THM within the MSTH models will not increase those addressed in the sensitivity studies for the HTOM.

5.3.1.4.7 Sensitivity to Host Rock Bulk Permeability

Sensitivity analyses were performed to consider the impacts of uncertainties in the values of fracture permeability used in the MSTH model. In the MSTH model, fracture and matrix are handled as the separate but overlapping continua (dual-permeability model) in which the permeability of the matrix and the fractures are expressed as different bulk permeabilities applied uniformly to the rock mass. Since the actual fracture permeability is heterogeneous, applying a bulk permeability to the heterogeneous system could introduce uncertainties in the results. Because the fracture permeability rather than the matrix permeability (which is significantly smaller) dominates the TH processes, the practice has been to refer to the bulk permeability (k_b) without distinguishing between the matrix and fracture permeability. Thus, the term "bulk permeability" actually refers to the bulk fracture permeability. This practice will be followed throughout this section.

Sensitivity analyses (Buscheck 2001 [DIRS 155012]) were designed to address the potential for impacts by comparing the results over a wide range of fracture properties. The first analysis considered the impacts that a range of k_b representing approximately one standard deviation above and below the mean values (identified as high, mean, and low k_b) had on both temperatures and relative humidity on the drift wall and drip shield in the center of the potential repository (CRWMS M&O 2000 [DIRS 149862)], Figure 5-2, location L5C3) for the HTOM with the mean infiltration flux. Analyses were also conducted for two standard deviations above and below the mean values (identified as very high, mean, and very low k_b). Although the analyses were for the L5C3 location, they are applicable to the portion of the potential repository in which the host rock is the Tptpll unit, which comprises more than three-quarters of the potential repository area. The actual values for k_b used in determining the very high, high, mean, low, and very low k_b values in the models are shown in Table 5.3.1.4.7-1. As can be observed in Figure 5.3.1.4.7-1, the temperatures beyond 1,000 years on the drift wall and the drip shield were insensitive to the k_b used in the models for the HTOM. A few decades after closure there was some sensitivity of drift wall and drip shield temperature to bulk permeability. The drift wall temperatures were consistent for the mean and low k_b cases, but slightly higher than the temperature for the high k_b case. The drip shield temperatures were not sensitive to differences between mean and low k_b, while the high k_b resulted in a slightly lower temperature. For the very high and high k_b cases, the peak temperature is 11°C and a few °C lower, respectively than in the mean k_b, low k_b, and very low k_b cases.

The relative humidity results for the drip shield (Figure 5.3.1.4.7-1) were insensitive to the k_b and nearly insensitive for the drift wall; there was less than a 1-percent difference among the five cases. The results suggest that for the mean infiltration case, the MSTH model relative humidity results for the drift wall and drip shield are relatively insensitive to repository-scale permeability variability. This indicates that repository-scale variability of k_b will not significantly modify MSTH model predictions of temperature and relative humidity in portions of the potential repository for which the Tptpll is the host rock unit. The weak dependence of temperature and relative humidity on k_b in the Tptpll unit indicates that temperature and relative humidity

predictions by the MSTH model would also be relatively insensitive to k_b in portions of the potential repository where the host-rock unit is other than the Tptpll.

Sensitivity of the MSTH model liquid saturation in the invert material was also evaluated. Figure 5.3.1.4.7-2 shows the predicted liquid saturation in the higher-temperature operating model for the same location within the potential repository footprint as the temperature and relative humidity assessments discussed above. The results are for the upper invert layer directly below the drip shield in the central portion of the drift (Figure 5.3.2.3-1 shows the computational cells in the invert). The index i in Figure 5.3.1.4.7-2 is 4 for the outermost invert cell and l for the innermost cell. These analyses were performed for the mean infiltration flux case.

Figure 5.3.1.4.7-2 shows that the liquid saturation in the upper invert is zero until about 2,000 years after emplacement for the mean and low k_b cases and about 3,000 years for the high k_b case (Figure 5.3.1.4.7-2). The very high k_b case has an onset of rewetting at about 4,000 years. The general trend from these five permeability cases is that the onset of rewetting increases with k_b and that the final "steady-state" value of liquid saturation increases with decreasing permeability. As the permeability decreases, liquid saturation in the fractures must increase to accommodate a given percolation flux; the increased liquid saturation results in lower capillary tension in the fractures and adjoining rock matrix. The lower capillary tension in the host rock promotes more wicking of moisture into the crushed-tuff invert. Because the capillary properties of the fractures were not varied along with the permeability and because a single continuum was used to represent the crushed-tuff invert, the trend between these permeability cases should be viewed qualitatively rather than quantitatively.

A similar set of analyses was performed for the LTOM. These analyses considered the same range of permeability and the same location within the potential repository footprint as can be observed in Figure 5.3.1.4.7-3; the temperatures on the drift wall and the drip shield are insensitive to the k_b bulk permeability used in the models. The relative humidity on the drip shield and drift wall is also insensitive to the permeability. This indicates that repository-scale variability of permeability will not significantly modify MSTH model predictions of temperature and relative humidity in portions of the potential repository for which the Tptpll is the host rock unit. The weak dependence of temperature and relative humidity on permeability also indicates that temperature and relative humidity predictions by the MSTH model would also be relatively insensitive to permeability in portions of the potential repository where the host-rock unit is other than the Tptpll.

The relative humidity of the drift wall for the LTOM is always nearly 100 percent (which is the relative humidity for ambient conditions), whereas for the HTOM, relative humidity drops to 20 percent about 10 years after closure and then gradually increases with time until it reaches nearly 100 percent around 1,000 years after emplacement; thus, relative humidity at the drift requires about 1,000 years to return to ambient conditions. For this reason, the results of the MSTH model are not only insensitive to variations in k_b of two standard deviations about the mean, but are also conservatively bounded in the maximum relative humidity for this lower temperature operating mode. If there are any effects on the results from permeability much different from the mean permeability value (e.g., due to capillary effects), the results could only reduce the relative humidity. Because relative humidity effects performance at higher values, the results of the MSTH model provide a conservative bound.

The sensitivity of the MSTH model liquid saturation in the invert material was also evaluated for the LTOM. Figure 5.3.1.4.7-4 shows the predicted liquid saturation at the same location in the potential repository footprint as the temperature and relative humidity assessments discussed above. The results are for the upper invert layer directly below the drip shield, in the central portion of the drift (Figure 5.3.2.3-1). These analyses were performed for the mean infiltration flux case. The onset of rewetting occurs earlier in the invert for the LTOM than for the HTOM (compare Figures 5.3.1.4.7-4 and 5.3.1.4.7-2). The same trends between the permeability cases are observed in the LTOM as in the HTOM. The general trend is that the onset of rewetting increases with permeability and that the final "steady-state" value of liquid saturation increases with decreasing permeability. Because the capillary properties of the fractures were not varied along with the permeability of the fractures and because a single continuum was used to represent the crushed-tuff invert, the trend between these k_b cases should be viewed qualitatively rather than quantitatively.

Comparison of Results of Higher- and Lower-Temperature Operating Modes-Peak temperatures on the drift wall in the central portion of the potential repository for the HTOM and the LTOM are about 144 and 74°C, respectively; under mean infiltration and mean permeability conditions for the MSTH submodel. The temperatures decrease to ambient (i.e., approximately 22.5°C for the glacial climate) around 100,000 years. The relative humidity on the drift wall for the HTOM drops to about 20 percent about 10 years after closure, then increases to nearly 100 percent at about 1,000 years. The temperatures at the time that the drift wall relative humidity approaches 100 percent are about 90°C, and decrease to 70°C around 4,000 years. Thus, there is a period of about 3,000 years when the relative humidity is nearly 100 percent and temperatures are higher than 70°C. For the LTOM, the relative humidity is always nearly 100 percent. The drift wall temperatures for the LTOM are between 70 and 74°C from about 400 to 1,500 years. Thus, there is a period of about 900 years when the temperatures are slightly above 70°C and the relative humidity is nearly 100 percent.

Summary-Uncertainty in the values of bulk permeability that were used as inputs to the MSTH model, as evaluated in the sensitivity studies of two standard deviations from the mean value, had very little effect on the temperature and relative humidity at the drift wall and drip shield for the HTOM and LTOM. Liquid saturation in the invert has the same weak dependence on bulk permeability for the HTOM and the LTOM. The general trend is that the onset of rewetting increases with permeability and that the final "steady-state" value of liquid saturation increases with decreasing permeability. Because the capillary properties of the fractures were not varied along with the k_b of the fractures and because a single continuum was used to represent the crushed-tuff invert, the trend between these k_b cases should be viewed qualitatively rather than quantitatively.

5.3.1.4.8 Sensitivity to Host Rock Thermal Conductivity

Sensitivity analyses were performed to consider the uncertainties in drift-wall and drip-shield temperature, and relative humidity, and invert liquid saturation that result from uncertainties in the values of host rock thermal conductivity used in the MSTH model. Section 5.3.1.4.11 discusses the Waste Package temperatures and relative humidities. The MSTH model uses values of bulk host rock thermal conductivity as input. In field and laboratory measurements of host-rock thermal conductivity used in these thermal-hydrologic calculations, there is not

discrimination between the relative contributions of the fractures and matrix to the bulk thermal conductivity. However, it is recognized that fractures and void spaces can have a significant impact on the thermal conductivity. It has been also recognized (CRWMS M&O 2000 [DIRS 149862], Sections 4.1.7 and 5.2.4) that there is a significant difference in thermal conductivity between wet (or saturated) rock and dry (or unsaturated) rock. The liquid saturation state of the rock mass must be determined by the MSTH model analyses for any given time. Therefore, there are uncertainties in the value of thermal conductivity to use, which could introduce uncertainties in the MSTH model results.

The calculation *Thermal Conductivity Properties for the Tptpll and Tptpul* (BSC 2001 [DIRS 155008]) was performed to estimate the range of matrix and rock mass thermal conductivity under various states of saturation in the lower lithophysal zone of the Topopah Spring unit (Tptpll), which accounts for variability in matrix properties, and in larger-scale features. For the lower lithophysal unit, the thermal conductivity data are limited to only several samples. Therefore, predictive relations were evaluated for application with matrix properties from several boreholes and rock mass properties from Enhanced Characterization of the Repository Block (ECRB) mapping and borehole geophysics measurements to provide a range of thermal conductivity based upon more abundant data on matrix properties.

The Kunii and Smith predictive relation (Kunii and Smith 1960 [DIRS 153166], p. 75) provides a method for predicting the stagnant thermal conductivity based upon matrix porosity, the thermal conductivity of the solids, and the thermal conductivity of the fluid (air or water) for porous rocks. Two bounding relationships were also considered for parallel flow and series flow (Hadley 1986 [DIRS 153165], p. 914). An evaluation of these relationships was made under the assumption of constant mineralogy and uniform thermal conductivity within these units. This assumption is reasonable given the small changes in grain density that are observed for these units (Rautman and Engstrom 1996 [DIRS 101008], p. 28).

The thermal conductivity of the rock mass for the Tptpll unit was estimated based upon an evaluation of the lithophysal porosity using two different methods. The first method used the information from mapping the ECRB drift (Mongano et al. 1999 [DIRS 149850]). The second method used information from core data and bulk density from geophysical measurements for borehole USW SD-7 at Yucca Mountain (BSC 2001 [DIRS 155008]). The porosity estimates from descriptive statistics of the ECRB mapping and the calculation of the lithophysal porosity from borehole USW SD-7 are comparable, and show that the mean values for lithophysal porosity are 0.125 and 0.120, respectively (see Section 4.3.5.3.2). The second method showed a low degree of correlation among the parameters of matrix saturation, matrix porosity, and air-filled lithophysal porosity.

The Monte Carlo simulation method (Hahn and Shapiro 1967 [DIRS 146529], pp. 237 to 241) was used to calculate expectation and variance of thermal conductivity for the Kunii and Smith (1960 [DIRS 153166], p. 75) predictive relation, the parallel predictive relation, and a composite predictive relation. The composite predictive relation uses the Kunii and Smith predictive relation for matrix properties and the parallel predictive relation (Hadley 1986 [DIRS 153165], p. 914) for the air-filled lithophysal porosity. The results of these calculations for the Tptpll unit (BSC 2001 [DIRS 155008], Section 6) are shown as the high and low cases in Table 5.3.1.4.8-1.

Sass et al. (1988 [DIRS 100644], p. 35) conducted a heat flow investigation for borehole USW G-4 located at Yucca Mountain, which was based upon a large number of measured thermal conductivities and a profile obtained in water-filled casing. This information can be used to determine if the predicted changes in thermal conductivity between the Tptpmn and the Tptpll units, based upon the composite model presented above, are reasonable. Sass et al. quotes a value for the average thermal conductivity of 2.02 W/(m●K) based upon 13 samples of densely welded tuff in USW G-4. Between depths of 150 and 400 m, Sass et al. found that the gradient averaged 17.8 ± 0.04ºC/km. The calculated heat flux rate was 36 ± 1 mW/m^2. A second calculation was performed below 400 m, where an abrupt increase in thermal gradient was observed. The thermal gradient increased to 30.1 ± 0.06ºC/km, which is nearly twice the observed gradient at this depth. Considering the thermal conductivity of the Calico Hills to be 1.07 ± 0.04 W/(m●K), substitution into Equation 1 (Sass et al. 1988 [DIRS 100644], p. 35) yields 32 mW/m^2. Sass et al. concluded that given the numerous sources of possible error, the agreement between these two independent heat flow determinations was excellent, and that heat flow in the UZ is primarily by heat conduction.

The same technical approach (BSC 2001 [DIRS 155008], Section 6, Figure 34) was adopted for evaluation of the thermal gradients between the Tptpmn and the Tptpll units for borehole USW G-4. The composite predictive relation presented above was found to be in better agreement with the geophysical measurements of temperature gradients in borehole USW G-4 (DTN: GS960708312132.002 [DIRS 113584]) than other models investigated.

Using the values of thermal conductivity determined in the analyses described above (BSC 2001 [DIRS 155008]), the MSTH model sensitivity analyses (Buscheck 2001 [DIRS 155012]) using the LDTH Submodel were designed to address the potential for impacts of uncertainty in thermal conductivity by comparing the results of analyses over the range of thermal conductivity values determined. Table 5.3.1.4.8-1 reports the values of thermal conductivity used in the models. The high and low values represent those determined by the Monte Carlo simulations and the mean determined from the ECRB measurements, geophysical measurements, and analyses of Sass et al. (1988 [DIRS 100644]).

The first set of sensitivity analyses considered the HTOM impacts. These analyses evaluated that the range of conductivity (the high, mean, and low conductivities shown in Table 5.3.1.4.8-1) had on temperature and relative humidity on the drift wall and the drip shield for a location in the center of the potential repository (CRWMS M&O 2000 [DIRS 149862], Figure 5-2, location L5C3) for the HTOM case with the mean infiltration flux. Although the analyses were for the L5C3 location, they are applicable to the portion of the potential repository in which the host rock is the Tptpll unit, which comprises more than three-quarters of the potential repository area.

Temperatures on the drift wall and drip shield are sensitive to the thermal conductivity (K_{th}) used in the models for as long as 100,000 years (Figures 5.3.1.4.8-1a and 5.3.1.4.8-1b). The MSTH model temperature results are more sensitive to variability in K_{th} values represented by values lower than the mean than they were to values above the mean. The drift wall peak temperatures for the low K_{th} values are nearly 220ºC, compared to almost 150ºC for the mean. The difference was around 70ºC, which was almost 50 percent higher than the mean value temperatures. The difference between the mean and high K_{th} temperatures was much less (about 12ºC): 136ºC for

the high K_{th} compared to 148ºC for the mean value, which is only 5 percent lower than the temperatures for the mean value. At 1,000 years after emplacement, the difference between the mean and high K_{th} results is negligible (2º to 3ºC), with the mean K_{th} temperatures around 96 to 97ºC, the boiling temperature of water. This is significant, since at 1,000 years the low K_{th} temperatures are 112ºC and rock at the drift wall would remain above the boiling point for approximately another 1,000 years.

Similar sensitivity to the K_{th} values used in the MSTH model analyses was observed in temperatures on the drip shield. The peak temperature for the low K_{th} was 234ºC, compared to 160ºC for the mean and 150ºC for the high K_{th} values. The differences between the mean calculation results and the low and high K_{th} calculation results are 46 percent and 6 percent, respectively. Again, the differences persist for up to 100,000 years, while the difference between the mean and high K_{th} results essentially become insignificant within about 1,000 years. The temperatures drop to the boiling point at about the same time as the drift wall temperatures (approximately 1,500 years and 2,000 years for the mean/high and low K_{th} values, respectively).

There are significant differences in calculated relative humidity on the drift wall for the low and mean K_{th} cases (Figure 5.3.1.4.8-1c). The low K_{th} results in very low relative humidity in the early postclosure times: it starts at 3 to 5 percent from 50 to 60 years and gradually increases, up to 60 percent at 1,000 years. Relative humidity calculated for the mean value of K_{th} is 20 percent in the 50- to 60-year time frame, increasing to 60 percent by 400 years. The comparable, time-wise, values for the high K_{th} are 28 percent and 70 percent, as shown on Table 5.3.1.4.8-2.

However, the impact on performance due to the differences in relative humidity is more significant during later times, when humidity exceeds 60 percent. As noted in Table 5.3.1.4.8-2 the humidity reaches 60 percent for the mean K_{th} within 400 years after emplacement and increases to 95 percent at 1,000 years after emplacement. The relative humidity calculated for the high K_{th} case is 70 percent at 400 years (17 percent higher than the mean value results) and nearly 100 percent at 1,000 years. For the high K_{th} case, those same relative humidity levels of the mean K_{th} case would occur at 280 and 700 years, respectively. The time required for the drift wall to attain ambient (near 100 percent) relative humidity is 900, 1,000, and 2,000 years for the high, mean, and low K_{th} cases, respectively. If the K_{th} values were actually lower than the mean used in the performance assessment, the results would be bounding; the relative humidity would be significantly lower for longer periods of time.

The relative humidity results for the drip shield (Figure 5.3.1.4.8-1d) are sensitive to K_{th} for values of K_{th} smaller than the mean; however, they are relatively insensitive for values of K_{th} larger than the mean value used in the MSTH model analyses. The most divergent case, low K_{th}, has a much lower relative humidity than either the mean or high K_{th} case for the first 2,000 years. Beyond 2,000 years, there are minor differences between these cases.

Sensitivity of the MSTH model liquid saturation in the invert material was also evaluated. Figure 5.3.1.4.8-2 shows the predicted liquid saturation for the same locations as the temperature and relative humidity assessments discussed above. The results are for the upper invert layer directly below the drip shield in the central portion of the drift (Figure 5.3.2.3-1). These analyses were performed for the mean infiltration flux case. The liquid saturation in the invert is zero until about 2,100 years after emplacement for the mean and high K_{th} cases and about 3,200 years

for the low K_{th} case. From the onset of rewetting (i.e., onset of nonzero liquid saturation values) until about 13,000 years after emplacement, the liquid saturation within the invert is somewhat sensitive to the K_{th} used in the model. The difference in liquid saturation at 4,000 years is only 2.6 percent between the high K_{th} case (2.8 percent saturation) and the low K_{th} case (0.2 percent saturation). There is approximately a 2,000-year difference in time for liquid saturation to reach 2 percent, which is nearly 3,000 years for the high K_{th} case and 5,000 years for the low K_{th} case. The high and mean K_{th} cases are quite similar. This leads to the conclusion that it is likely that only much lower K_{th} values would significantly change the liquid saturation conditions in the invert for K_{th} variations greater than those considered. In the long-term period of the HTOM, there is essentially no difference due to variation in K_{th}.

A set of analyses similar to those of the HTOM were performed for the LTOM. These analyses using the LDTH submodel considered the same range of thermal conductivity and the same location in the potential repository footprint as the HTOM analyses.

As can be observed in Figures 5.3.1.4.8-3a and 5.3.1.4.8-3b, temperatures on the drift wall and the drip shield were sensitive to the K_{th} used in the models for as long as 100,000 years. The MSTH model temperature results were more sensitive to variability in K_{th} values (represented by values lower than the mean) than they were to values above the mean. The drift wall peak temperatures for the low K_{th} values were approximately 88ºC, compared to 73ºC for the mean. The difference was 15ºC, which was about 21 percent higher than the mean value temperatures. The difference between the mean and high K_{th} temperatures was much less, around 3ºC, 70ºC for the high K_{th} compared to 73ºC for the mean value, which is only 4 percent lower than the temperatures for the mean value. At 10,000 years after emplacement, the difference between the mean and high K_{th} results is negligible, while there is a difference of 5ºC between the low and mean K_{th} cases. For the high and mean value cases, the drift wall temperatures drop below 70ºC at 1,400 years after emplacement, whereas the low K_{th} temperatures do not drop below 70ºC until 3,800 years after emplacement.

A similar sensitivity trend to the K_{th} values used in the MSTH model analyses was observed in the temperatures on the drip shield. The peak temperature for the low K_{th} was 93ºC, compared to 77ºC for the mean and 75ºC for the high K_{th} values. The differences between the mean calculation results and the low and high K_{th} calculation results are 21 percent and 3 percent, respectively. Again, the differences persist for up to 100,000 years, while the difference between the mean and high K_{th} results essentially become insignificant within about 10,000 years. The temperatures drop to below 70ºC at approximately 2,000 years and 4,000 years for the mean/high and low K_{th} values, respectively.

There are no differences in calculated relative humidity on the drift wall for the low, high, and mean K_{th} cases (Figure 5.3.1.4.8-3c). All cases result in nearly 100 percent relative humidity for all times. The lower temperatures do not result in rock dryout, and the MSTH model analyses do not account for moisture removal by ventilation. Therefore, the relative humidity remains close to 100 percent (ambient conditions) for all times. The impact of ventilation is discussed in Section 5.3.2.4. The relative humidity results for the drip shield (Figure 5.3.1.4.8-3d) are very insensitive to the K_{th} used in the MSTH model analyses.

Figure 5.3.1.4.8-4 shows the predicted liquid saturation for the same locations as the temperature and relative humidity assessments discussed above. The results are for the upper invert layer directly below the drip shield in the central portion of the drift (Figure 5.3.2.3-1). These analyses were performed for the mean infiltration flux case. The liquid saturation in the invert is zero for all thermal conductivity cases until about 1,100 to 1,200 years after emplacement for the mean and high K_{th} cases and about 2,000 years for the low K_{th} case. From the onset of rewetting until 20,000 years after emplacement, there is a degree of sensitivity of liquid saturation within the invert to the K_{th} used in the model. The difference in liquid saturation at 7,000 years is 1.8 to 1.9 percent liquid saturation between the high K_{th} case (5.1 percent saturation) and the low K_{th} case (3.2 to 3.3 percent saturation). There is a 2,000-year difference in time when the invert liquid saturation reaches 3 percent between the high and low K_{th} cases, which reach 3 percent liquid saturation at 3,000 and 5,000 years respectively. The time difference increases up to 3,000 years for 3.2 percent between the high and low K_{th} cases.

Comparison of Results of Higher- and Lower-Temperature Operating Modes-Peak temperatures on the drift wall in the central portion of the potential repository for the HTOM and the LTOM are about 148 and 73°C, respectively, under mean infiltration and permeability conditions. The temperatures decrease to ambient (i.e., approximately 22.5°C) around 100,000 years. The relative humidity on the drift wall for the HTOM drops to about 20 percent about 60 years after emplacement, then increases to 95 percent at about 1,000 years. The temperatures at the time that the drift wall relative humidity approaches 100 percent are about 90°C, and decrease to 70°C around 4,000 years. Thus, there is a period of about 3,000 years when the relative humidity is nearly 100 percent and temperatures are higher than 70°C. For the LTOM, the relative humidity is always nearly 100 percent. The drift wall temperatures for the LTOM are between 70 and 74°C from about 400 to 1,500 years. Thus, there is a period of about 900 years when the temperatures are slightly above 70°C and the relative humidity is nearly 100 percent. For the LTOM, the drip-shield relative humidity is very insensitive to K_{th}. For the HTOM, drip-shield relative humidity is sensitive to K_{th} for values less than the mean K_{th}; this sensitivity lasts for about 2,000 years. For values of K_{th} greater than the mean value, relative humidity is much less sensitive, with relative humidity being somewhat higher for the high K_{th} case during the first 1,100 years.

Summary–The MSTH model results for the drift wall and drip shield are sensitive to the variations in K_{th} used as input in the models for the mean infiltration case up to as long as 100,000 years after emplacement. The MSTH model temperature results were more sensitive to variability in K_{th} values represented by values lower than the mean than they were to values above the mean. For the HTOM, the drift wall peak temperatures for the low K_{th} values were 70ºC higher than for the mean case, nearly 220ºC compared to 148ºC for the mean, compared to a 8ºC difference between the mean and high K_{th} temperatures (136ºC). At 1,000 years after emplacement, the difference between the mean and high K_{th} results is negligible (2 to 3ºC), with the mean K_{th} temperatures about 96º to 97ºC, the boiling point of water. At 1,000 years after emplacement, the low K_{th} drift wall temperatures are 112ºC, and rock at the drift wall would remain above the boiling point for approximately another 1,000 years.

For the LTOM, the drift wall peak temperatures for the low K_{th} values were approximately 88ºC, compared to 73ºC for the mean case. The difference between the low and mean cases, 15ºC, is

about 21 percent higher than the mean-value temperatures. The difference between the mean and high K_{th} temperatures was only 3ºC, 70ºC for the high K_{th}, compared to 73ºC for the mean value, which is only 4 percent lower than the temperatures for the mean value. At 10,000 years after emplacement, the difference between the mean and high K_{th} results is negligible, but a 5ºC difference between the low and mean cases remains. For the high and mean K_{th} cases, the drift wall temperatures drop below 70ºC at 1,400 years after emplacement, whereas the low K_{th} temperatures do not drop below 70ºC until 3,800 years after emplacement.

Drip shield temperatures exhibited similar sensitivity to the K_{th} values used in the MSTH model analyses. These sensitivities persist for up to 100,000 years. For the HTOM, the peak drip shield temperature of the low K_{th} was 234ºC, compared to 160ºC for the mean and 150ºC for the high K_{th} values. The difference between the mean and high K_{th} results essentially becomes insignificant within about 1,000 years. The temperatures drop to the boiling point of water at about the same time as the drift wall temperatures, approximately 1,500 and 2,000 years for the mean/high and low K_{th} values, respectively. For the LTOM, the peak temperature for the low K_{th} was 93ºC, compared to 77ºC for the mean and 75ºC for the high K_{th} values. The differences between the mean calculation results and the low and high K_{th} calculation results are 21 percent and 3 percent, respectively. The difference between the mean and high K_{th} results essentially becomes insignificant within about 10,000 years. The temperatures drop to below 70ºC at approximately 2,000 and 4,000 years for the mean/high and low K_{th} values, respectively.

Only during the first 13,000 years after emplacement in the HTOM and 20,000 years after emplacement in the LTOM, respectively, is the saturation in the invert material somewhat sensitive to the values of K_{th} used in the MSTH model. For the HTOM, the liquid saturation in the invert is zero for all the thermal conductivity cases until about 2,100 years after emplacement for the mean and high K_{th} cases and about 3,200 years for the low K_{th} case. After the onset of saturation until about 13,000 years after emplacement, the saturation at 4,000 years is only 2.6 percent between the high K_{th} case (2.8 percent saturation) and the low K_{th} case (0.2 percent saturation). Thus, although there is sensitivity with saturation of less than 5 percent, the implications on performance are minimal. It is likely that only much lower K_{th} values would significantly change the saturation conditions in the invert for thermal conductivity variations greater than those considered. In the long-term period of the HTOM, there is essentially no difference due to variation in K_{th}. For the LTOM, the liquid saturation in the invert is zero for all the thermal conductivity cases until about 1,100 to 1,200 years after emplacement for the mean and high K_{th} cases and about 2,000 years for the low K_{th} case. There is a difference in saturation of 1.8 to 1.9 percent between the high K_{th} case (5.1 percent saturation) and the low K_{th} case (3.2 to 3.3 percent saturation) at 7,000 years. There is a 2,000-year difference in time between the high and low K_{th} cases, when the invert saturation reaches 3 percent, which reach 3 percent saturation at 3,000 and 5,000 years, respectively. The time difference increases up to 3,000 years for 3.2 percent between the high and low K_{th} cases.

5.3.1.4.9 Sensitivity of Multiscale Thermal-Hydrologic Model Results to Lithophysal Porosity

Sensitivity analyses of the impact of K_{th} uncertainties, largely due to lithophysal porosity impacts on thermal conductivity, were discussed in Section 5.3.1.4.8. In addition to the impacts on the thermal conductivity, the lithophysal porosity can also impact the heat capacity. Heat capacity is

a function of rock mass density, and therefore subsequently a function of porosity. The heat capacity, thus, will decrease with increased porosity. Mapping data along the ECRB drift walls (Mongano et al. 1999 [DIRS 149850]) indicate that the mean lithophysal porosity of the lower lithophysal unit is 0.125 (see Section 4.3.5.3.2). The matrix porosity of the lower lithophysal unit (tsw35) is 0.115 (DTN: MO9901RIB00044.000 [DIRS 109966]). Because the lithophysal porosity is roughly equal to the matrix porosity, uncertainty in the lithophysal porosity can significantly impact the porosity and the heat capacity used in the MSTH model analyses.

Sensitivity studies were performed using the LDTH submodel of the *Multiscale Thermohydrologic Model* (CRWMS M&O 2000 [DIRS 149862]) to consider the effects of uncertainties in the lithophysal porosity on both thermal conductivity and heat capacity (BSC 2001 [DIRS 155008]), which in turn affect temperature, relative humidity, and liquid saturation at the drift wall and drip shield (Buscheck 2001 [DIRS 155012]). These sensitivity studies were performed for the same potential repository location as sensitivity studies in Section 5.3.1.4.8, which considered the lithophysal porosity on thermal conductivity alone. By comparing the results of the mean, high, and low lithophysal porosity results with the K_{th} analyses (Section 5.3.1.4.8), an assessment can be made of the sensitivity of the results to the lithophysal porosity, or more specifically to the influence of lithophysal porosity on heat capacity. Figure 5.3.1.4.9-1 shows the first analysis, which considered the effects that the range of lithophysal porosity (Table 5.3.1.4.9-1) had on the temperature and relative humidity on the drift wall and drip shield for a location in the center of the potential repository (location L5C3 reference) for the HTOM with the mean infiltration flux. Although the analyses were for the L5C3 location, they are applicable to the portion of the potential repository in which the host rock is the Tptpll unit, which comprises more than three-quarters of the potential repository area.

As can be observed by comparing the results shown on Figure 5.3.1.4.8-1a with the results shown on Figure 5.3.1.4.9-1a, the peak temperatures on the drift wall were 2 to 3ºC cooler for the low lithophysal porosity case that included effects of the porosity on the heat capacity than that which did not. Likewise, peak temperatures were 16ºC higher for the high lithophysal porosity than for the comparable case from Section 5.3.1.4.8 that did not include these effects on the heat capacity. Similar, but of smaller magnitude, differences were noted for the temperatures on the drip shield (Figures 5.3.1.4.8-1b and 5.3.1.4.9-1b). The differences for the drift wall and drip shield disappeared within 1,000 years of emplacement. Relative humidity differences were noted for the drift wall only, and only for the low lithophysal porosity case where there was an approximately 3 percent relative humidity difference when the porosity impacts on the heat capacity were considered (Figures 5.3.1.4.9-1c and 5.3.1.4.8-1c). There was no impact on the drip shield relative humidity (Figures 5.3.1.4.9-1d and 5.3.1.4.8-1d). Invert saturation (Figure 5.3.1.4.9-2) was not affected by neglecting the influence of lithophysal porosity on heat capacity. These observations indicate that neglecting the influence of lithophysal porosity on heat capacity will not add to uncertainty in the results from the MSTH model.

Comparisons of results for the LTOM with and without consideration of the influence of lithophysal porosity on heat capacity reveal no difference. This is seen by comparing results of the analyses of temperatures on the drift wall and drip shield that included consideration of the effects of lithophysal porosity on heat capacity (Figures 5.3.1.4.9-3a and 5.3.1.4.9-3b) with the results of the analyses that did not include the influence of lithophysal porosity on heat capacity

(Figures 5.3.1.4.8-3a and 5.3.1.4.8-3b). There is no difference in any of the curves. This result is consistent with the conclusions for the HTOM.

Figure 5.3.1.4.9-4 shows the predicted liquid saturation for the same location as the temperature and relative humidity assessments discussed above. The results are for the upper invert layer that is directly below the drip shield in the central portion of the drift (Figure 5.3.2.3-1). These analyses were performed for the mean infiltration-flux case. Comparison of Figure 5.3.1.4.9-4, which shows the results of analyses that considered the influence of lithophysal porosity on heat capacity, with Figure 5.3.1.4.8-4, which does not include the consideration of the influence of lithophysal porosity on heat capacity, indicates that there is no impact on the MSTH model invert saturation results as a result of neglecting the influence of lithophysal porosity on heat capacity.

5.3.1.4.10 Sensitivity to Invert Thermal Conductivity

The current design for the invert consists of a set of carbon steel beams crossing the drift and anchored to the drift wall. The beams are stabilized by longitudinal connectors and crushed tuff gravel ballast. The steel contacts the lower drift wall at the edges of the invert, and the lower portion of the drift wall contacts only the ballast. The carbon steel (as-built) has a higher thermal conductivity than the crushed tuff ballast. However, the carbon steel corrodes in a few hundred to a few thousand years, and the conductivity of the resulting iron oxide fragments is more similar to the ballast than to steel. Therefore, during much of the thermal period, the conductivity of the invert will be lower than its initial value.

The uncertainty (and temporal variability) of the invert thermal conductivity is exacerbated by the geometry of the steel structure. In regions that include both ballast and portions of beams, the invert will have a higher lateral or axial thermal conductivity than vertical conductivity. The software used in the MSTH model currently does not have the capability to input anisotropic thermal conductivity for different regions. This capability could be added, or the effect could be mitigated by a careful choice of invert layer geometry. The effect of the beam structure has been evaluated in a conduction-dominated regime by using the ANSYS software, which does have anisotropic conductivity (CRWMS M&O 2000 [DIRS 142736]). In this section, the invert thermal conductivity is varied parametrically to determine its influence on in-drift temperature distribution.

The LDTH submodel (CRWMS M&O 2000 [DIRS 149862]) was used in the sensitivity analysis (Reed 2001 [DIRS 155076]). The submodel results are suitable for determining the sensitivity of TH parameters to invert thermal conductivity. However, these sensitivity results do not include edge effects, variability of infiltration across the potential repository footprint, or three-dimensional in-drift phenomena. The MSTH model results for the HTOM described in Section 5.4 should be used if values of TH parameters are needed, rather than the sensitivity of those parameters to uncertainty of invert thermal conductivity.

The two-dimensional LDTH submodel was implemented for the L5C3 location in the potential repository footprint (as in a number of other sensitivity evaluations). This location has a thick cover of lower lithophysal rock that is not near the interface with the middle non-lithophysal subunit above. The surface infiltration rates (based on the methodology and input data in CRWMS M&O (2000 [DIRS 149862]) at this location are 5.7 mm/yr for the present-day climate

(0 to 600 years), 15.1 mm/yr for the monsoonal climate (600 to 2,000 years), and 23.2 mm/yr for the glacial-transition climate (beyond 2,000 years). The submodel included explicit thermal radiation between the drip shield and drift wall, and it applied a correlation-based effective thermal conductivity approach for natural convection heat transfer. Mass transfer within the emplacement drift was computed using a bulk permeability of 10^{-8} m^2 for the in-drift air elements (Buscheck 2001 [DIRS 155012]), which was a compromise between adequate mass transfer and computer run time (see Section 5.3.2.4.5). The heat source in the model was volumetrically averaged within the volume enclosed by the drip shield. The calculations used the same initial linear heat loading, 1.3534 kW/m, as the HTOM, and they also used the same ventilation parameters: 50 years of forced ventilation at an assumed heat removal efficiency of 70 percent.

The invert geometry in the calculation includes two vertical layers (regions), with two gridblocks in the lower layer and four gridblocks in the upper area (Figure 5.3.2.3-1). The sensitivity study considered a range of material thermal conductivity for the upper invert layer. The lower invert material thermal conductivity was 0.15 W/m•K for all the sensitivity runs because it included only ballast without the steel beams.

Table 5.3.1.4.10-1 shows the range of invert thermal conductivity used in the study. The base case thermal conductivity was the lowest value considered; it was based on the decrease of the as-built value toward that of crushed tuff as the carbon steel corrodes. Additionally, low thermal conductivity in the invert was expected to increase the in-drift temperatures because overall heat transfer would be somewhat less effective. The as-built case assumed that the steel does not corrode. The additional-steel case assumed that the amount of steel in the invert design is increased at some future date. Two overlapping continua were used in the model, for compatibility with the dual continuum approach in the host rock. Because a realistic, dual-continuum, hydrologic property set for crushed tuff is not yet available, the continua had identical thermal and hydrologic properties for the base, as-built, and additional-steel cases, with the thermal conductivity equally split between the two continua. A fourth case, designated the intermediate case, used a steel-like conductivity in one continuum and a ballast-like conductivity in the other.

Five locations in the engineered barrier system (EBS) were used to evaluate the sensitivity to the invert thermal conductivity, using material-appropriate TH parameters. The five locations and associated parameters included:

- The top of the drip shield (temperature and relative humidity)
- The base of the drip shield (temperature and relative humidity)
- The crown of the drift wall (temperature and liquid saturation)
- The rib (i.e., the widest point, sometimes referred to as the springline) of the drift wall (temperature and liquid saturation)
- The center of the lower level of the invert (temperature and liquid saturation).

These five EBS locations were selected to illustrate the potential for vertical and horizontal variability with the drift to be influenced by the invert thermal conductivity.

Figures 5.3.1.4.10-1 and 5.3.1.4.10-2 illustrate the temperature-time histories at two of the five selected EBS locations. The temperature histories at the other three locations (drift wall rib, drip shield top, and drip shield base) were similar to the drift wall crown, both in terms of general shape and the tight spacing (insensitivity) of the four thermal conductivity cases. Table 5.3.1.4.10-2 shows the peak temperatures at all five locations. The calculated time of peak temperature for the HTOM was calculated to occur between 65 and 70 years after emplacement (15 to 20 years after closure). The largest temperature variation was in the lower invert, which can vary by about 9ºC over the range of conductivity investigated. The other four locations had peak temperature variation between conductivity cases of 9ºC or less. Figure 5.3.1.4.10-1 and Table 5.3.1.4.10-2 indicate that the drift wall and drip shield temperatures are slightly higher for the base (low) invert thermal conductivity case than for the higher thermal conductivity cases. For the lower conductivity case, the rate of conduction heat transfer downward through the invert was reduced, which elevated temperatures on the invert floor and at the base of the drip shield. The hotter floor surface exchanged energy with the top and side of the drift (crown and rib) by radiation, thus elevating temperatures there as well. In the lower half of the invert, Figure 5.3.1.4.10-2 illustrates that a reduction in the heat transfer rate through the upper portion of invert, as expected for the base (low) invert conductivity cases, caused somewhat lower temperatures in the lower region of the invert material. The lower invert temperature was also more sensitive to thermal conductivity than the other locations in the drift. The lowest upper invert thermal conductivity (0.15 W/m•K) caused the largest temperature drop across the invert.

The liquid saturation in the drift wall and lower portion of the invert are shown in Figures 5.3.1.4.10-3 and 5.3.1.4.10-4 (the drift wall rib saturation histories are similar to those shown for the crown). For all the invert conductivity cases, the host rock (drift wall) matrix saturation falls quickly and does not resaturate until about 1,000 years. At this time, rock temperature drops to the local saturation temperature and water quickly returns to the host rock. Figure 5.3.1.4.10-4 indicates that the invert liquid saturation history is more sensitive to the invert conductivity than is the host rock saturation. The base thermal conductivity case (0.15 W/m•K) shows the invert saturation becoming nonzero at about 1,300 years, increasing to a maximum value of about 0.1, then dropping to a long-term value of 0.057. A rapid transition through the boiling point (Figure 5.3.1.4.10-2) for this case results in rapid rewetting at this location. The other three cases show nonzero invert saturation at about 2,200 years, with maximum saturation of about 0.057. All the cases converge to the same long-term value (0.057), as expected, when the temperature returns to ambient. The period of high invert saturation for the low-conductivity case and the oscillations during rewetting for the lowest two conductivity cases have not been explained. The simple treatment of hydrologic properties in the invert (compared to the host rock) is a potential cause that is being evaluated in support of a potential license application.

Figure 5.3.1.4.10-5 shows the relative humidity at the drip shield top (the drip shield base is similar). The relative humidities are similar over the range of invert thermal conductivity investigated. The base-case thermal conductivity (0.15 W/m•K) resulted in slightly lower relative humidity at the drip shield due to slightly higher temperatures (Table 5.3.1.4.10-2).

Summary–The three higher invert thermal conductivity cases produce similar temperature, liquid saturation, and relative humidity at the five EBS locations considered. The base case (0.15 W/m•K) invert thermal conductivity case resulted in differences in all three TH parameters. The late time values for all cases are similar after about 100,000 years. The invert saturation for the base case invert conductivity has an earlier rewetting initiation and a lengthy (100,000 years) higher-saturation plateau prior to converging on the same long-term saturation as the other cases. The values of temperature for the intermediate case are within a few degrees of the base case, allowing other sensitivity calculations in Section 5 to use either of the invert conductivity values.

5.3.1.4.11 Sensitivity to Design and Operational Parameters

The analyses presented in this report focus on three goals: incorporating new science, quantifying uncertainties, and evaluating the performance and uncertainty associated with HTOM and LTOM. This section discusses the sensitivity of TH parameters to design and operating parameters that could be used to achieve a LTOM goal.

Figure 5.3.1.4.11-1 depicts the HTOM and LTOM in terms of values of peak waste package temperature resulting from different choices of design and operating parameters. The figure shows that the HTOM has waste package peak temperatures of about 175ºC, lower than the peak values presented in the *Viability Assessment of a Repository at Yucca Mountain, Total System Performance Assessment* (DOE 1998 [DIRS 100550], Volume 3, Figure 3-22), which shows a peak temperature of about 200ºC using bin-averaged, rather than hottest waste package, temperatures. Two LTOM options are shown, both resulting in peak waste package temperatures of about 85ºC based on two-dimensional calculations.

Three design parameters—drift diameter, drift spacing, and waste package capacity—are shown in the inner portion of Figure 5.3.1.4.11-1. These parameters were held constant for the purposes of this report, which focuses on determining performance and associated uncertainty for a range of thermal operating environments. If the site is recommended, design parameters can be varied during the preparation of a license application to optimize a combination of criteria, including worker safety, cost, and reduction in performance uncertainty.

The outer portion of Figure 5.3.1.4.11-1 shows operating parameters, including waste package spacing, forced and natural ventilation rates, and ventilation duration. These parameters can be changed even after a repository has been constructed. The two LTOM options use different values of operational parameters to approach the same TH conditions. The option analyzed in this document uses the first 64 drifts in the footprint (a contiguous, planar area), variable gaps between waste packages (1.1-m average), and 300 years of forced ventilation at a rate of 15 m^3/s. The resulting linear heat loading at emplacement of this option is 1.13 kW/m (Buscheck 2001 [DIRS 155449]).

Another lower-temperature option uses a larger footprint, has wider gaps between waste packages (2-m average), and shifts from forced to natural ventilation after 50 years (BSC 2001 [DIRS 155010]; BSC 2001 [DIRS 155011]). The natural ventilation rate used in the second reference is an average of 3 m^3/s for the 50- to 100-year period and 1.5 m^3/s for the 100- to 300-year period. The resulting linear heat loading at emplacement of this option is 1.0 kW/m.

The two options trade forced ventilation duration and waste package spacing (and potential repository footprint).

Natural ventilation and other methods to achieve lower potential repository temperatures have been the subject of study for several years (BSC 2001 [DIRS 154855]; CRWMS M&O 2000 [DIRS 152269]; CRWMS M&O 2000 [DIRS 152146]). The lower-temperature option shown in (Figure 5.3.1.4.11-1) is based on design and operational parameters developed from sensitivity calculations in these three references. Additional documentation is in BSC (2001 [DIRS 155010]) and BSC (2001 [DIRS 155011]).

The in-drift TH parameter histories, including variability across the potential repository footprint, are shown in Section 5.4.2 for the LTOM. The MSTH model calculations (Buscheck 2001 [DIRS 155449]) were repeated for the same AML and linear heat loading of 1.13 kW/m as the LTOM base case (see Table 5.1-1). The new calculation (Buscheck 2001 [DIRS 155449]) used a line loading arrangement with 10-cm gaps between all waste packages, rather than more widely spaced waste packages. The linear heat loading was maintained at the same level, since the waste packages were moved together by de-rating the hotter waste packages. The de-rating was done simplistically, by removing spent nuclear fuel assemblies from the hotter PWR waste packages until the target heat loading was achieved (at the 16 fuel assembly level). If a lower-capacity waste package option is developed during a potential license application, it could achieve goals of lower peak power by using smaller PWR waste packages or by blending BWR and PWR assemblies in the same waste package. Flexibility could be reserved for the blending of the two types of assemblies by developing an adapter-insert that would fit into the PWR basket slot and contain an opening the size of the smaller BWR assemblies.

Figure 5.3.1.4.11-2 compares the postclosure distribution of peak waste package temperature and relative humidity across the potential repository footprint for the LTOM option described in this report and the de-rated waste package capacity option for the medium infiltration history case, although the MSTH model results also include cases for lower and higher infiltration levels. The distributions are displayed as cumulative complementary distribution functions; the values on the y-axis are the fraction of waste packages hotter than the indicated value on the x-axis. The base case resulted in 98.3 percent of the waste packages not exceeding the goal of 85ºC, and a peak of 86.0ºC for the hottest waste package in the 7620 calculated waste package temperature-time histories. The abstracted temperature histories used in TSPA are somewhat lower because histories are grouped into bins, within which the average is used. The de-rated waste package case resulted in 100 percent of the waste packages not exceeding the goal of 85ºC, and a peak of 82.6ºC for the hottest waste package. The de-rated waste package option had slightly cooler results than the LTOM base case, for the same potential repository footprint. The cooler temperatures are due to the smaller range of thermal powers among the waste packages and the more effective radiation heat transfer between closely spaced waste packages.

For waste packages that exceed the 85ºC goal, a low humidity can prevent the formation of aqueous films that are required for corrosion initiation. Figure 5.3.1.4.11-2 also shows the postclosure relative humidity distribution (among the 1.7 percent of the ensemble of waste packages that exceed 85ºC for some period of time in the LTOM base case) when the temperature of each waste package falls below 85ºC. The initiation threshold for crevice

corrosion of 85ºC is based on more aggressive water chemistry than is expected on waste package surfaces (Section 6).

To compare other options, a simplified version of the MSTH model was used (Buscheck 2001 [DIRS 155449]). In the simpler model, the same four submodels were used, but only a single location (L5C3) was used for the smeared-heat-source drift-scale temperature (SDT) and line-source drift-scale thermal-hydrologic submodels. The L5C3 location is near the potential repository center and is within the lower-lithophysal stratigraphic unit.

Figure 5.3.1.4.11-3 shows postclosure temperature and relative humidity histories (Buscheck 2001 [DIRS 155449]) for the hottest waste package surface for three LTOM implementations that share the same areal mass loading of 45.7 MTU/acre: the LTOM base case, the de-rated waste package case, and a wider drift spacing case that uses the HTOM waste package arrangement, but with a drift spacing of 97 m instead of 81 m. As summarized in Table 5.3.1.4.11-1, the peak temperatures are 84.3ºC for the base case, 81.7ºC for the de-rated waste package case, and 88.8ºC for the wider drift spacing case. These results indicate that all three methods achieve similar temperatures for LTOM designs. Line loading with a limited range of waste package thermal powers (i.e., using de-rated waste packages) is most effective at limiting peak temperature, and wider spacing of waste packages within the drifts is more effective than wider spacing of drifts. The relative effectiveness of these design and operating parameters (waste package capacity, waste package spacing, and drift spacing) is consistent with the conceptual understanding of three-dimensional radiation heat transfer among the waste packages.

A comparison of Figures 5.3.1.4.11-2 (full MSTH model) and 5.3.1.4.11-3 (simplified MSTH model) shows that the simplified MSTH model calculates peak temperatures about 1 to 2ºC less than the full MSTH model. It was expected that the peak temperatures would be somewhat lower because it is not likely that the location chosen for the simplified MSTH model would be the location of peak power. The location was chosen, however, to be in a central region with low infiltration flux so that it would be near the overall peak temperature. The advantage of using the simplified MSTH model is that additional design variables can be investigated with a smaller suite of calculations, yet with results (at the chosen location) that are the same as the full MSTH model results.

The postclosure relative humidity histories at the hottest waste package surface are shown in Figure 5.3.1.4.11-3 for the three LTOM cases. Depending on the composition of the dust on the waste package surface, the threshold relative humidity for water film formation (deliquescence) varies. Figure 5.3.1.4.11-3 can be used to determine the time at which the threshold humidity is reached. This value can then be used with the temperature panel of the same figure to estimate the likelihood of crevice corrosion during the thermal pulse for the hottest waste packages in the potential repository. Figures 5.3.1.4.11-2a and 5.3.1.4.11-3a indicate that the LTOM base and the case with wider drift spacing have some waste package surfaces above the 85ºC temperature threshold. Figure 5.3.1.4.11-2a shows 1.7 percent of the LTOM-PA case waste package temperatures exceeding the threshold. For the case with the hottest waste packages, the wider drift spacing case, the surface of a typical waste package is above 85°C for about 500 years (shortly after closure at 300 years to about 800 years, Figure 5.3.1.3.11-3a). During that period, the humidity ranges between 48 and 69 percent (Figure 5.3.1.4.11-3b). Figure 5.3.1.4.11-2b

shows that for the waste packages that exceed 85ºC for the LTOM-PA case, the relative humidity ranges between 48 and 62 percent at the time that the waste-package surface temperature returns to 85ºC. (The curve ranges from 100 percent to 98.3 percent because only 1.7 percent of the waste packages exceed 85°.) Figure 5.3.1.4.11-2 (panels a and b) also shows that none of the waste packages exceed 85ºC for the de-rated waste-package case.

Summary–Design and operating parameters can be used to achieve LTOM goals. The initial calculations for three different lower-temperature options predicted temperatures within 4°C of the 85°C goal. The LTOM-PA case achieves the goal for nearly all of the waste packages. Use of operating parameters to maintain temperature flexibility offers the advantage of preserving some flexibility even after construction of a potential repository. A simplified MSTH model can be used to calculate local temperatures while maintaining the fidelity of the calculations to the potential repository footprint, the infiltration flux map, and waste package spacing and power distribution. The simplified model runs faster and produces temperatures within about 1 to 2ºC of the full MSTH model. For the 300-year forced ventilation option, waste package peak temperature can be limited to about 85ºC by adjusting waste package capacity, drift spacing, or waste package spacing. Adjusting waste package capacity was the most effective of the three methods because of the smaller range of waste package thermal powers. Adjusting drift spacing was the least effective because it results in the largest linear heat loading (1.35 kW/m). However, the differences in effectiveness only resulted in a peak waste package temperature variation of about 7ºC among the three cases investigated.

5.3.2 Ventilation and Convection Modeling of In-Drift Thermal-Hydrologic Conditions

This section discusses phenomena involving movement of gas and transfer of heat within emplacement drifts. There are four such phenomena, which are discussed conceptually below.

Two-Dimensional Convection–Air moves naturally within a plane perpendicular to the drift axis, driven by the temperature gradient between the warmer waste package and the intermediate-temperature drip shield, and also between the drip shield and cooler drift wall (Figure 5.3.2-1 illustrates the air flow pattern (Dunn 2001 [DIRS155308])). The figure shows the flow pattern in a quarter-scale test (Jurani 2001 [DIRS 155128]) in an insulated pipe without a drip shield. For the flow pattern beneath the drip shield in a potential repository following closure, the air rises above the waste package, turns outward and falls along the inner surface of the drip shield, transferring heat to the drip shield as it moves. The cooler air at the bottom of the drip shield rises along the waste package, picking up more heat. A similar flow pattern would be established between the drip shield and drift wall. These flow patterns augment the heat transfer due to thermal radiation between the components. Natural convection is more important during the postclosure period when high-flow-rate forced ventilation is absent.

Natural convection is driven by the temperature difference between the hot drip shield and cooler drift wall. Radiative heat transfer is driven by the difference between the fourth power of those

temperatures; therefore, thermal radiation is most important at higher temperatures. For the LTOM, thermal radiation is less effective than for the HTOM, and two-dimensional convection of air can be an important contributor to limiting the temperature of the waste package.

Three-Dimensional Convection–Air moves within segments of the emplacement drift. This convection is produced by the temperature gradient along the drift axis, and the flow patterns are three-dimensional, as illustrated conceptually in Figure 5.3.2-2. There is axial flow from hotter to cooler regions under the crown of the drip shield and under the crown of the emplacement drifts. Cooler air returns in the opposite direction near the invert. There are two scales of this convection. The smaller scale is between a group of waste packages that have different thermal powers due to their differing waste contents. The larger scale is between the sections of the emplacement drifts near and far from the edge of the potential repository. The edge regions are cooler because, in addition to the heat flow upward and downward from the potential repository horizon, the edge regions also have lateral heat transfer outward from the perimeter drifts. This

INTENTIONALLY LEFT BLANK

phenomenon is most important in the postclosure period when high-flow-rate forced ventilation is absent.

Natural Circulation Within the System of Drifts and Natural Ventilation to the Surface– After closure, when forced ventilation ceases, air continues to move within the system of underground drifts, although at reduced rates and possibly in different flow patterns than described above. When this flow includes a path to the surface (through fractures or intentionally open shafts), it is termed "natural ventilation." The difference in air density at the entrance and exit of the loop drives natural ventilation. Heat produced by the waste packages contributes to this natural ventilation.

When air flow is confined to a closed path within the natural fractures and the underground system of drifts, it is termed "natural circulation." Heat from the waste packages drives natural circulation. For natural circulation and natural ventilation, the transfer of heat from the emplacement drifts to the perimeter of the potential repository or the mountain surface, due to heating of the air in the emplacement drifts, is augmented by evaporation of water from near-field rock into the air. The movement of water and heat in this manner is important in that it can limit the temperature of the waste package and the seepage of liquid water into the emplacement drifts.

Forced Ventilation–During the preclosure period, fans will force air through the emplacement drifts, transporting heat and water. This ventilation will dominate the above three phenomena during the preclosure period and will remove a large fraction of the heat from the waste packages. Because the intensity of the heat source decreases with time as radionuclides decay, using a longer period of ventilation will reduce the peak temperatures that occur after ventilation ceases. Thus, extended ventilation is one option for attaining a LTOM.

The remainder of Section 5.3.2 discusses the goal of the in-drift gas movement models, the treatment in TSPA-SR (CRWMS M&O 2000 [DIRS 153246]), the improvements made to the TSPA modeling for the SSPA, and six sensitivity analyses at the process-model level. These sensitivity analyses are an independent line of work from the TSPA model because of the reduced extent of simplification and abstraction and because subsystem parameters are used (rather than dose rate) to develop insights.

5.3.2.1 Goal of the Models

Process models for in-drift convection and ventilation have improved significantly during the last few years. This subsection describes the goals for these models, in support of a potential license application. The following subsections describe the representation of convection and ventilation in the TSPA-SR (CRWMS M&O 2000 [DIRS 153246], Section 3.3; CRWMS M&O 2000 [DIRS 149862], Section 6.6.1), recent improvements in support of uncertainty quantification for the Supplemental Science and Performance Analyses (SSPA), and application of those improved models for HTOM and LTOM.

For two-dimensional convection, the goal of the process model is to include a realistic representation of heat transfer within the drift in the MSTH model described in Sections 5.2 and 5.3.1. The process model should include evaporation and condensation due to differences,

within the plane perpendicular to the drift axis, between the local air temperature and the temperatures of the waste package, drip shield, and drift wall. The fraction of the heat transferred to the rock by two-dimensional convection will increase with time, due to the less effective radiative heat transfer as temperature decreases. Similarly, accurate treatment of two-dimensional convection will be important for the LTOM.

For three-dimensional convection, the goal of the model is to include a realistic representation of heat transfer within the drift in the MSTH model described in Sections 5.2 and 5.3.1. The model should include local evaporation and condensation due to differences, along the drift axis, between the local air temperature and the temperatures of the waste package, drip shield, and drift wall. The significance of three-dimensional convection will vary with time. At times soon after closure, small-scale axial convection due to waste package power variability will be most important. Later, the cooling effect of the edge of the potential repository will drive larger-scale axial convection.

For natural circulation within the system of drifts and natural ventilation to the surface, the goal of the model is to include their influence on postclosure in-drift thermal-hydrologic conditions and to calculate the volume and paths of the post-closure air flow. These calculations should include the influence of evaporation and condensation of water on local air temperature and density. Results of the modeling can also be used by the design organization to determine if connecting drifts should be added to link the network of exhaust drifts with the perimeter drifts just prior to closure.

For forced ventilation, the goal of the model is to calculate the time-dependent efficiency of heat and water removal by ventilation, including the effects of evaporation and condensation of water. These results should be coupled to the MSTH model (Sections 5.2 and 5.3.1).

5.3.2.2 Representation in Total System Performance Assessment-Site Recommendation

For two-dimensional convection, the LDTH submodel of the MSTH model (CRWMS M&O 2000 [DIRS 149862], Section 4.1.10; see also Section 5.2), used time-dependent equivalent heat transfer coefficients for the in-drift regions under and outside the drip shield TSPA-SR (CRWMS M&O 2000 [DIRS 153246], Section 3.3). These coefficients, which change with time due to the temperature effects on natural convection and radiative heat transfer, are based on concentric cylinder representations of the waste package, drip shield (after closure), and the drift wall. The radiation portion of the heat transfer coefficient was based on an analytic solution published by Incropera and DeWitt (1985 [DIRS 100623], p. 609, Equation 13.25). The two-dimensional convection portion of the heat transfer coefficient was based on an empirical correlation for concentric cylinders described by Kuehn and Goldstein (1978 [DIRS 130084]). The calculation of the equivalent heat transfer coefficient that includes convection and radiation is described in *Effective Thermal Conductivity for Drift-Scale Models Used in TSPA-SR* (CRWMS M&O 2001 [DIRS 153410]). The two-dimensional convection calculation was approximate because spatially-uniform coefficients were used within each air region, which is not consistent with the below-drift-center location of the waste package, and also does not consider the local air flow patterns.

Although the MSTH calculation includes vaporization of water from the near field rock into the drift air, it only accounts for a small fraction of the water that evaporates into the drifts from the rock. This limitation is the result of not including movement of air axially along the drift, which continually provides a dry-air moisture sink in the drift, into which water can vaporize.

For three-dimensional convection, the MSTH model described in Sections 5.2 and 5.3.1 calculates the influence of the edge of the potential repository and the spatial distribution of water infiltration on the temperatures along the drift axis. The model did not include the influence of these axial temperature variations on three-dimensional convection (of heat and water vapor) within segments of the emplacement drifts.

Natural circulation within the system of drifts and natural ventilation to the surface after closure were not included in the initial model of the HTOM.

For forced ventilation, a dry air flow model was coupled to a conduction (in the rock) thermal model to develop an initial estimate of ventilation efficiency (the ratio of the heat removed in the air to the heat released from the waste) for the HTOM. The result of this calculation was an efficiency of 74 percent for 50 years of ventilation at 15 m^3/s, as described in *Ventilation Model* (CRWMS M&O 2000 [DIRS 120903], p. 39). Quarter-scale tests (Jurani 2001 [DIRS 155128]) verified that the ventilation efficiency is greater than the calculated value for the HTOM (see Section 5.3.2.4.1). The model and tests did not include the effects of water evaporating from the rock into the air, which would increase the efficiency. A slightly conservative value of preclosure ventilation efficiency, 70 percent, was used in the multiscale thermal-hydrologic model. This was implemented by using only 30 percent of the thermal power of the waste packages for calculation of combined radiative and natural convection heat transfer from the waste packages to the drift wall during the preclosure period.

5.3.2.3 Reduction in Total System Performance Assessment Uncertainty Due to Model Improvements

For modeling of heat and mass transfer across the air gap in the drift, two aspects of the MSTH model were improved in support of the Volume 2 (McNeish 2001 [DIRS 155023]) TSPA. Both of these improvements resulted in higher confidence in calculated temperature histories of the drip shield and waste package. The specific improvements are discussed below.

Explicit Calculation of Thermal Radiation between the Drip Shield and Drift Wall in the Line-Source Drift-Scale Thermal-Hydrologic Submodel–In the TSPA-SR (CRWMS M&O 2000 [DIRS 153246]), the heat transfer between the drip shield and drift wall was calculated using an equivalent heat transfer coefficient that accounted for thermal radiation and natural convection. Both the radiation and the natural convection correlations were based on concentric cylinders, and both correlations were evaluated using temperature time histories developed for prior designs.

The LDTH calculations in support of the HTOM and LTOM base-case TSPA calculations for the SSPA used explicit treatment of radiation between the drip shield and drift wall. Therefore, the use of an effective thermal conductivity (to decrease computational burden) was limited to the smaller heat transfer contribution of natural convection. This improvement removed part of the

uncertainty due to approximate treatment of thermal radiation in prior TSPA calculations. These uncertainties were due to the geometric simplification associated with the concentric cylinder (without invert) correlation that was used. These uncertainties were also due, in part, to the evaluation of the correlation at temperature time histories that were not calculated specifically for the most current design.

Mass Balance in the Invert for the Line-Source Drift-Scale Thermal-Hydrologic Submodel–In checking the initial MSTH calculations for the SSPA Volume 2 (McNeish 2001 [DIRS 155023]) base cases, it was determined that a numerical instability was causing unphysical results to occur at some invert locations, usually near the side of the invert, and at some times, usually many thousands of years after closure. These results include oscillation of invert saturation and also include high fluxes into invert regions without corresponding increases in saturation or fluxes leaving these regions.

Two potential causes were identified for the numerical instability. The first was the equivalent continuum treatment of the invert gravel. Although the model calculates the hydrologic processes in the invert using two continua, there is a lack of continuum-specific hydrologic properties for the gravel rocks and the spaces between the rocks. Thus, the model is usually run with both continua having identical properties. The hydrologic treatment of the invert is being improved in support of a potential license application.

The second potential cause for the numerical instability was a fairly coarse gridding (Figure 5.3.2.3-1) combined with a large mismatch in thermal conductivity across small distances, due to the presence of the high-conductivity steel beams in the upper regions of the invert. In considering this situation, it was recognized that the carbon steel beams would corrode after several centuries of exposure to high-relative, humid air. After corrosion, the conductivity of the oxidized steel would be more similar to the conductivity of tuff gravel than to the original steel. Thus, the thermal conductivity of the invert was set to 0.15 W/m•K for all invert zones for the SSPA Volume 2 (McNeish 2001 [DIRS 155023]) base-case calculations. The result of this change was a significant decrease in the numerical instabilities observed in the invert saturation (Section 5.3.1.4.10 shows specific results).

The uncertainties associated with invert thermal properties and invert hydrologic treatment are important to different results of the model and different times. Prior calculations used a high thermal conductivity in the upper part of the invert (as-built conditions) for the entire calculation period. After the steel degrades, this assumption would result in higher calculated heat flow through the invert and lower calculated in-drift temperatures, compared to the expected situation. The underprediction of in-drift temperatures would be manifested beginning a few decades to centuries after humidity increases in the drift. Thus, the underprediction of in-drift temperatures could affect peak temperature calculations for the LTOM. The current calculations use a degraded thermal conductivity for the invert steel for the entire calculation period. Until the steel degrades, this assumption would result in lower calculated heat flow through the invert and higher calculated in-drift temperatures, compared to the expected situation. For the HTOM, high humidity conditions are precluded in the drift for centuries to about 1,000 years after closure, depending on the location with respect to the potential repository edge and the value of humidity at which carbon steel begins to corrode. Since the HTOM peak in-drift temperatures occur within a few decades of closure, the treatment of invert conductivity in support of the SSPA

Volume 2 TSPA (McNeish 2001 [DIRS 155023]) will result in some conservatism (overprediction) in the in-drift peak temperatures.

The uncertainty of the invert saturation, due to the thermal conductivity treatment, is most important for sub-boiling temperatures (all times for the LTOM and after centuries to about 1,000 years for the HTOM). The relationship between the invert temperature and the drip shield temperature will determine if condensation will occur primarily on the invert or on the drip shield. Since such condensation is a potential driver of waste package corrosion and of radionuclide transport after waste package failure, the location of the source of the condensation can be significant. The time of most significance is after the waste packages fail, and the current treatment is most realistic at those times. Thus, for in-drift water movement, the treatment of invert beams as low-conductivity degraded steel removes some of the uncertainty that could propagate to radionuclide release rates from the engineered barrier system.

5.3.2.4 Quantification of Uncertainty Using Process Models

As discussed in Section 5.3.2.3, some reductions or quantification of thermal-hydrologic uncertainties were included in the HTOM and LTOM for the SSPA Volume 2 (McNeish 2001 [DIRS 155023]) base case analyses. Other reductions or quantification of uncertainties were addressed using process-level models, including sensitivity studies. Some of the process-level analyses were conducted directly in support of the SSPA, while others had been conducted earlier. The results of the base case TSPA analyses and the process-level analyses provide 1) additional understanding of recognized uncertainties associated with thermal-hydrologic modeling as implemented in the multi-scale thermal-hydrologic model; 2) increased confidence in predicted temperature, relative humidity, and other measures of the in-drift environment over a range of thermal conditions bounded by the lower and higher temperature operating modes assumed; and 3) increased confidence in the results of the TSPA-SR.

This section describes the new and prior process-level analyses pertaining to the:

- Effects of forced ventilation efficiency and duration on in-drift temperatures and relative humidity (Sections 5.3.2.4.1, 5.3.2.4.2, and 5.3.2.4.3)
- In-drift humidity changes due to postclosure seepage or to near-field rock dryout caused by forced ventilation (Section 5.3.2.4.4)
- Treatment of natural convection and thermal radiation across the drift air gaps between the drift wall, drip shield, and waste package (Section 5.3.2.4.5)
- In-drift condensation distribution due to axial and cross-sectional temperature distributions (Section 5.3.2.4.6).

These analyses were conducted to better understand uncertainties and build confidence in the models supporting the TSPA for the HTOM and LTOM. They do not provide inputs directly to the SSPA Volume 2 TSPA (McNeish 2001 [DIRS 155023]).

5.3.2.4.1 Ventilation Efficiency from ANSYS and MULTIFLUX Calculations and from Scaled Tests

The MSTH model calculations in support of the TSPA-SR base cases (CRWMS M&O 2000 [DIRS 153246]) are described in Sections 5.3.1.3, 5.3.2.3, and 5.4. For the HTOM and LTOM, the calculations assumed a ventilation efficiency (the rate of heat removed by ventilating air divided by the rate of heat produced by the radioactive waste) constant in time and space. The HTOM calculations used a 50-year ventilation period with a constant ventilation efficiency of 70 percent. Because the heat source decreases with time, the ventilation efficiency improves as ventilation duration increases. Thus, the LTOM used a 300-year ventilation period with a constant ventilation efficiency of 80 percent. These values are rounded down from the time average of the ANSYS results described below for conservatism.

This section summarizes the ANSYS and MULTIFLUX calculations that support these values of ventilation efficiency, and the preliminary results of quarter-scale tests conducted to validate the calculations. The calculated and measured ventilation efficiencies are somewhat higher than those used in the TSPA base case calculations; therefore, the uncertainty in the TSPA calculations includes some bias toward warmer calculated temperatures than actually expected. The influence of such uncertainty and bias are quantified in Section 5.3.2.4.2.

ANSYS Calculations and Scaled Tests–For the two ventilation flow rates (10 and 15 m^3/s) for 200 years after emplacement, drift wall rock and the exit air temperatures were calculated at various time increments. ANSYS (V5.2 SGI) was used (CRWMS M&O 2000 [DIRS 120903]) with inlet air at 25°C and 0 percent relative humidity, an initial drift wall temperature of 70°C, and an initial waste package temperature of 70°C. The calculated results for the drift wall temperatures are shown in Figures 5.3.2.4.1-1 and 5.3.2.4.1-2. Drift wall temperatures presented are averages of the crown, spring line, and invert temperatures. The resulting air temperatures are shown in Figures 5.3.2.4.1-3 and 5.3.2.4.1-4.

Wall temperature (perimeter average) peaks within the first few years at the air inlet end of the drift and within five to fifteen years at the air discharge end of the drift. Air temperature peaks slightly later than wall temperature at the inlet end of the drift, but in the same time frame as the walls at the outlet end. For ventilation at 10 m^3/s, the maximum temperatures calculated occur at year 10 and are 94°C for the perimeter-averaged wall temperature at the exit end, with a corresponding maximum air temperature of 79°C. For ventilation at 15 m^3/s, calculated maximums occurred at the same time but were lower, 76°C for the wall and 64°C for the air.

The time histories of the rate of heat generation and removal for the 10 m^3/s and 15 m^3/s ventilation rates are presented in Figures 5.3.2.4.1-5 and 5.3.2.4.1-6. The heat generated is the same for both ventilation rates; it is the heat produced by average waste packages placed to produce a linear heat load of 1.54 kW/m in the drift. Heat removal by convective transfer from the waste package and the drift wall surface is included. Heat is removed by dry air; additional heat removal that will occur if moisture evaporates into the air is not addressed in the ANSYS calculations.

Peak heat removal rates occur within the 5 to 15 year time frame, but efficiency continues to increase due to natural decay in the magnitude of the heat source. Heat removed by ventilation

at the rates of 10 and 15 m^3/s, respectively, was calculated by ANSYS to be 68 percent and 74 percent of the heat generated during the initial 50 years, 73 percent and 78 percent during the first 100 years, and 77 percent and 82 percent during a 200-year ventilation period.

A series of quarter-scale tests of ventilation efficiency was conducted in late 2000. A 1 m^3/s flow rate in a quarter-scale test is similar to a 15 m^3/s flow rate in a full-scale emplacement drift. Linear power loadings of 0.18 and 0.36 kW/m are similar to values of 0.72 and 1.44 kW/m in a full-scale drift. The calculated ventilation efficiencies (using ANSYS) of 74 percent for both of these tests (averaged over the 10-day test duration) are lower than the measured efficiencies of 86 percent and 83 percent for the two heating levels (Jurani 2001 [DIRS 155128]). The measured efficiencies of the test are based on measured temperature and flow rates (DTN: SN0106F3409100.003 [DIRS 155255]) and conversion to enthalpy change (Howard 2001 [DIRS 155132]). These tests are not yet complete, and several test condition and instrumentation issues are open. Nevertheless, the preliminary conclusion that the ANSYS calculations are conservative is reasonable, since some efficiency-enhancing effects were not included in the calculations.

MULTIFLUX Calculations–The MULTIFLUX model was developed by the University of Nevada, Reno under contract with the CRWMS M&O (Danko et al. 2001 [DIRS 154924]). The MULTIFLUX model couples a lumped parameter in-drift heat and mass transfer (airway) model to the NUFT code (V3.0), which models heat and mass transfer within the rock. NUFT is a TH computer code developed by Lawrence Livermore National Laboratory that is capable of analyzing mass transport coupled to energy transport by conduction, convection, and radiation in geologic media with multiple gas and liquid phases (including phase change). NUFT is also the software used in the MSTH model (see Section 5.2).

The MULTIFLUX model uses a number of initial NUFT runs to solve the heat and moisture mass transfer in the rock. These runs establish the relationship of rock temperature and partial vapor pressure to the heat and moisture flux at the drift wall surface. The MULTIFLUX software (V1.0) then uses the airway model to calculate heat and mass transfer within predefined drift segments. The airway model is based on computational fluid dynamics (CFD): it uses correlation-based heat transfer coefficients for natural and forced convection. At a given time step, the calculation using the airway model is repeated until the drift wall temperature, saturation, and humidity match the NUFT values at selected axial nodes. Then, the exit air temperature and humidity from a drift segment are used as the inlet conditions for the next segment. This process is repeated for successive drift segments until temperature, saturation, and humidity values have been calculated for the entire drift. The process is repeated for successive time steps.

Drift wall rock and exit air temperatures were calculated at various time increments for the two ventilation flow rates (10 and 15 m^3/s) at 200 years after emplacement. MULTIFLUX was used with inlet air at 25°C and 30 percent relative humidity, an initial drift wall temperature of approximately 24°C, and an initial waste package temperature of 25°C (BSC 2001 [DIRS 155025]). These two cases are similar to the ones simulated by the ANSYS model. The calculated drift wall temperatures (perimeter average) are shown in Figures 5.3.2.4.1-7 and 5.3.2.4.1-8. The resulting air temperatures are shown in Figures 5.3.2.4.1-9 and 5.3.2.4.1-10.

Drift wall temperature peaks within the first few years at the air discharge end of the drift. For a ventilation rate of 10 m^3/s, the maximum temperature calculated occurred at 2 to 5 years and was about 93°C. This result is very close to the ANSYS prediction of 94°C for the maximum wall temperature in 10 years. The corresponding maximum air temperature of 85°C calculated for the 10 m^3/s case is somewhat higher than the ANSYS result of 79°C. For 15 m^3/s, the maximum temperature calculated by MULTIFLUX occurred at 2 to 5 years and was approximately 71°C. This value is slightly lower than the ANSYS prediction of 76°C for the maximum wall temperature at 10 years. The corresponding maximum air temperature of 67°C calculated for the 15 m^3/s case using MULTIFLUX is somewhat higher than the ANSYS result of 64°C.

The rates of heat generated and removed with time for the 10 and 15 m^3/s ventilation rates are presented in Figures 5.3.2.4.1-11 and 5.3.2.4.1-12. Heat generated by the waste packages is the same for both ventilation rates; it is the heat produced by average waste packages that are placed to produce a linear heat load of 1.45 kW/m in the drift, an updated (smaller) value than used in the earlier ANSYS calculations. Heat removal by convection from the waste package and drift wall surfaces is included. Both sensible heat removal and latent heat removal from the emplacement drift by ventilation are included.

Heat removed by ventilation at the rates of 10 and 15 m^3/s, respectively, was calculated by MULTIFLUX to be 91 percent and 94 percent of the heat generated during the initial 50 years, 93 percent and 95 percent during the first 100 years, and 96 percent and 97 percent during a 200-year ventilation period. These rates of heat removal are significantly higher than predicted by the ANSYS calculations, which are 68 percent and 74 percent for 50 years, 73 percent and 78 percent for 100 years, and 77 percent and 82 percent for 200 years. The differences in predicted percentage of heat removal between the two models are 23 percent and 20 percent for 50 years, 20 percent and 17 percent for 100 years, and 19 percent and 15 percent for 200 years. The reasons for the higher heat removal prediction calculated by MULTIFLUX are partially due to the additional heat removal by natural convection and latent heat transfer, which were included in MULTIFLUX but not in ANSYS, due to the lower linear heat load (1.45 versus 1.54 kW/m) and due to a higher inlet pressure in the more recent MULTIFLUX calculations. The primary cause of the different ventilation efficiencies is likely to be the lumped parameter convection heat transfer coefficients used in the two models. The ANSYS calculations used 1.89 $W/m^2 \bullet k$ while the MULTIFLUX calculations used a value about three times larger. The correlation used in MULTIFLUX included roughness and entrance effects while the ANSYS calculation did not include these effects. The value of the ANSYS heat transfer coefficient was only about 20 percent larger than the natural convection heat transfer coefficient in an unventilated drift. The differences in heat removal need to be further studied and verified by the measurement data from the ventilation tests being conducted by the YMP.

The peak temperatures and efficiencies from the two models are summarized in Table 5.3.2.4.1-1. The inclusion of natural convection and latent heat in MULTIFLUX and the updated (lower) heat load result in higher efficiencies than for ANSYS. The smaller differences between drift wall and air temperatures in MULTIFLUX are consistent with a higher efficiency.

Relative humidity profiles calculated by MULTIFLUX at the 10 and 15 m^3/s ventilation rates are shown in Figures 5.3.2.4.1-13 and 5.3.2.4.1-14. As the air temperature increases along the

emplacement drift, the relative humidity of air decreases because of the increase in saturation pressure (the denominator of the fraction that defines relative humidity). The relative humidity increases with ventilation duration as the air cools the emplacement drift and some water evaporates from the rock into the drift air. The lowest values of relative humidity (3 to 5 percent) occur at the end of the emplacement drift during the early (high temperature) period of ventilation. The highest values of relative humidity (32 to 34 percent) occur near the emplacement drift entrance at the maximum ventilation time.

The latent heat removal rates modeled by MULTIFLUX (Figures 5.3.2.4.1-11 and 5.3.2.4.1-12) are shown as the area between the "heat removed by ventilation" and "sensible heat removal by ventilation" curves. The results of integrating the area between the curves are shown in Table 5.3.2.4.1-2. The values shown in the table indicate that latent heat removal is a very small portion of the total heat removed by ventilation. This conclusion is also consistent with the hand calculations shown in Section 5.3.2.4.4.

Summary–Ventilation at rates of 10 to 15 m^3/s is capable of removing a large fraction (over 70 percent) of preclosure heat from emplacement drifts and controlling peak postclosure emplacement drift temperatures. Most of the heat removal is due to sensible heating of air as it moves across the heated waste packages and drift wall; only a small percent of heat removal by ventilation is due to the latent heat of water vaporized from the near-field rock.

Preliminary quarter-scale tests measured higher ventilation efficiencies than the ones calculated with the ANSYS model. The quarter-scale tests have not yet been modeled with MULTIFLUX. Based on the repository-scale calculations summarized in Table 5.3.2.4.1-1, the MULTIFLUX efficiencies should be closer to the test results than the ANSYS calculations. The difference in the convective heat transfer coefficients used in the two models is the primary source of the differences in the calculated ventilation efficiency.

Peak postclosure drift wall temperatures below 75°C are achievable at ventilation flow rates of 15 m^3/s and heat loads of 1.45 kW/m. Relative humidity during preclosure is dominated by the air temperature, with a minor influence due to water evaporating from the rock into the air (additional calculations of in-drift humidity effects due to evaporating water are shown in Section 5.3.2.4.4). Humidity remains below 35 percent during the entire preclosure period. As the air temperature increases along the emplacement drift, the relative humidity decreases. The lowest values of relative humidity (3 to 5 percent) occur at the end of emplacement drift during the early stage of ventilation. The relative humidity increases with time as ventilation cools the emplacement drift.

5.3.2.4.2 The Effect of a 10 Percent Uncertainty in Ventilation Efficiency and Assuming Ventilation Efficiency Is Time-Invariant

Preclosure temperatures and the postclosure peak temperature can be limited by removing heat from the system using preclosure ventilation. In Section 5.3.2.4.1, calculations and measurements of ventilation efficiency are summarized. Ventilation efficiency is defined as the rate of heat removed from the potential repository in the ventilation air divided by the rate of heat added due to radioactive decay of the emplaced waste. This subsection evaluates the sensitivity of thermal-hydrologic performance parameters (such as peak postclosure temperature)

to the uncertainty in ventilation efficiency and to the assumption that ventilation efficiency is constant in time. The sensitivity was evaluated for both the HTOM and LTOM.

The LDTH submodel from the MSTH model (CRWMS M&O 2000 [DIRS 149862]) was used in the sensitivity analysis. The submodel results (Leem 2001 [DIRS 155457]) are suitable for determining the sensitivity of thermal-hydrologic parameters to the ventilation efficiency uncertainty. However, these sensitivity results do not include edge effects, variability of infiltration across the potential repository footprint, or three-dimensional in-drift phenomena. The MSTH results shown in Section 5.4, for the HTOM and LTOM base cases, should be used if values of thermal-hydrologic parameters are needed, rather than the sensitivity of those parameters to ventilation uncertainty.

The two-dimensional LDTH submodel was implemented (Leem 2001 [DIRS 155457]) for the L5C3 location in the potential repository footprint, as in a number of other sensitivity evaluations. This location has a thick cover of lower lithophysal rock (it is not near the interface with the middle non-lithophysal subunit above it). The surface infiltration rates (based on the methodology and input data in CRWMS M&O 2000 [DIRS 149862]) at this location are 5.7 mm/yr (present day climate, 0 to 600 years), 15.1 mm/yr (monsoonal climate, 600 to 2,000 years), and 23.2 mm/yr (glacial-transition climate beyond 2,000 yr). The submodel includes explicit thermal radiation between the drip shield and drift wall, and it applies a correlation-based effective thermal conductivity approach for natural convection heat transfer. The heat source in the model is volumetrically averaged within the volume enclosed by the drip shield. The invert in the model uses a thermal conductivity somewhat higher than the TSPA base cases described in Sections 5.3.1.3, 5.3.2.3, and 5.4. The sensitivity of the results to invert thermal conductivity were investigated in Section 5.3.1.4.10, which concluded that the results of sensitivity studies would not be significantly affected by the difference between the base case for the TSPA calculations and the base case for the two-dimensional submodel.

The HTOM calculations used the same initial linear heat loading, 1.35 kW/m, as the TSPA base case (Table 5.1-1). The two-dimensional base case used for the HTOM sensitivity calculations also used the same ventilation parameters as the TSPA base case, 50 years of forced ventilation at an assumed heat removal efficiency of 70 percent. Similarly, the sensitivity base case used for the LTOM sensitivity calculations used the same values as the TSPA base case: 1.13 kW/m initial linear heat loading and 300 years of forced ventilation at an assumed efficiency of 80 percent.

The thermal hydrology sensitivity calculations focused on the effect of the ventilation efficiency on in-drift thermal-hydrologic conditions. In addition to the base case for each operating mode, constant ventilation efficiency cases were run in which the ventilation efficiency was 10 percent higher or 10 percent lower than the base case. The base case ventilation efficiency used in the sensitivity calculation is an averaged value throughout the pre-closure period, and the +/-10 percent value could consider local and temporal changes in the ventilation efficiency. Because the ventilation efficiency was determined as a function of time using the ANSYS (V5.2) software, the time-dependent ventilation efficiency was also considered in the LDTH sensitivity analysis for each operating mode, HTOM and LTOM (Section 5.3.2.4.5). The time-dependent cases are denoted, f(t), in the results below. Finally, it was noted that the time-averaged efficiency for each of the time-dependent cases was actually somewhat higher than the base case;

therefore, one additional case was run for each operating mode. The additional case used a constant ventilation efficiency equal to the average of the time-dependent efficiency, to allow direct comparison of the effect of time-dependency on in-drift thermal-hydrologic parameters.

Figure 5.3.2.4.2-1 shows the time-dependent ventilation efficiency for the HTOM and LTOM. These curves were developed from the *Ventilation Model* (CRWMS M&O 2000 [DIRS 120903]). The time-dependent values for the LTOM after the first 50 years were calculated from the ratio between the HTOM and LTOM efficiencies, since the forced ventilation efficiency values provided for the LTOM linear heat loading were only for 0 to 50 years. The predicted ventilation efficiency values for the LTOM beyond 50 years are probably conservative (Section 5.3.2.4.1), since the efficiency of ventilation is increased in a low temperature condition, and temperatures for the LTOM decrease with time during the 50 to 300-year period.

Higher-Temperature Operating Mode Results–The use of a ventilation efficiency in the LDTH submodel reduces the heat available to be transported from the waste packages into the near-field rock. Figure 5.3.2.4.2-2 shows the time history of available waste package heat for the constant base case and time-dependent f(t) ventilation cases. The total heat (available for transport plus removed by ventilation) is also shown.

The drip shield top and drift wall crown peak postclosure temperatures of the HTOM are well above the boiling point, 96°C, for all the ventilation efficiency cases (Figures 5.3.2.4.2-3 and 5.3.2.4.2-4). Increasing the ventilation efficiency across the 20 percent range investigated (60 percent to 80 percent), decreases the peak postclosure temperatures of the drip shield and drift wall crown by about 14°C each. The postclosure temperature results for the time-dependent ventilation efficiency case are similar (within 1°C) to those for the corresponding constant ventilation efficiency (73 percent). As the drift wall and drip shield temperatures increase, the driving force for heat transfer to the ventilation air increases, causing the ventilation efficiency to increase and the rock and drip shield temperatures to decrease. During the preclosure period, high waste package temperature is less significant than during postclosure because of the short duration of high temperature and because of the low humidity during preclosure.

The relative humidity histories at the same locations as the temperature histories are shown in Figures 5.3.2.4.2-5 and 5.3.2.4.2-6. For constant (in time and space) ventilation efficiencies, the time for relative humidity to increase to 50 percent decreases by about 120 years and 80 years for the drip shield top and drift wall crown, respectively, as ventilation efficiency increases from 60 percent to 80 percent. The shorter time to return toward ambient humidity values is due to less heating of the near-field rock when ventilation is more effective. For the time-dependent ventilation efficiency case, there is a much lower humidity minimum, consistent with the higher preclosure temperature.

The saturation of the invert decreases from the initial condition of about 10 percent to a dry value within 10 years for all the ventilation efficiency cases (Figure 5.3.2.4.2-7). The dry conditions persist well beyond the closure of the potential repository. The increase of invert saturation back to ambient values, beyond 1,000 years, is shown in Section 5.4.1.

A summary of the thermal hydrology sensitivity modeling results is presented in Table 5.3.2.4.2-1.

Lower-Temperature Operating Mode Results–Figure 5.3.2.4.2-8 shows the time history of available waste package heat for the constant and time-dependent ventilation cases. The total heat (available for transport plus removed by ventilation) is also shown.

The drip shield top and drift wall crown peak postclosure temperatures of the LTOM are below 80°C (Figures 5.3.2.4.2-9 and 5.3.2.4.2-10). Increasing the ventilation efficiency across the 20 percent range investigated (60 percent to 80 percent), decreases the peak postclosure temperatures of the drip shield and drift wall crown by 7°C. The postclosure temperature results for the time-dependent ventilation efficiency case are similar (within 1°C) to those for the corresponding constant ventilation efficiency (83 percent). During the preclosure period, the relative humidity of the ventilation air will be less than 30 percent, so that corrosion of the drip shield and waste package is unlikely. Nevertheless, further study is warranted of the ventilation efficiency during the transient period of the first five to ten years when components reach quasi-steady temperatures. It is encouraging that the transient period in the initial quarter scale tests of ventilation efficiency (DTN: SN0106F3409100.003 [DIRS 155255]) was faster than the model calculations (CRWMS M&O 2001 [DIRS 155328]). Continued test results and more sophisticated calculations will be used, in support of a potential license application, to better define the preclosure temperature spike duration and magnitude.

Values of relative humidity for the drip shield top decrease to no less than about 75 percent during the preclosure period for the constant efficiency cases, and to about 40 percent for the time-dependent efficiency case (Figure 5.3.2.4.2-11). However, it should be noted that these values are based on two-dimensional equilibration of stagnant drift air with the near-field rock, which ignores the humidity influence of the ventilation air. During the preclosure period, the relative humidity will be set by the ventilation air inlet relative humidity (Section 5.3.2.4.4). The postclosure minimum for drip shield top humidity is about 80 percent. At the drift wall, there is essentially no reduction in humidity in the LTOM sensitivity calculations. The saturation of the lower, center region of the invert shows a similar pattern for the LTOM (Figure 5.3.2.4.2-12) and the HTOM (Figure 5.3.2.4.2-7). The initial saturation of about 10 percent decreases to a minimum that is totally dry for some of the ventilation efficiency cases, and partly dried for others. Beyond 50 years, however, the continuing ventilation of the LTOM removes sufficient heat that the invert begins to rewet, reaching saturation of 1.5 to 4.5 percent, depending on the ventilation efficiency. Then, when the potential repository is closed, there is a postclosure drying of the invert. The increase of invert saturation back to ambient values, beyond 1,000 years, is shown in Section 5.4.2.

A summary of the thermal hydrology sensitivity modeling results is presented in Table 5.3.2.4.2-2.

Summary–In-drift temperatures are sensitive to ventilation efficiency, with a 20 percent decrease in efficiency resulting in a drip shield peak postclosure temperature increase of 14°C for the HTOM and 7°C for the LTOM. The transient period during the first five to ten years is expected to receive further study in calculations and testing to support a potential license application considering the mass transfer by the pre-closure ventilation. Operational procedures,

including partial loading of drifts to spread out the transient period, are also being considered to mitigate the potential preclosure temperature spike.

5.3.2.4.3 The Effect of Calculating Temperatures Based on Simultaneous Emplacement of Appropriately Aged Waste Packages

The MSTH model (CRWMS M&O 2000 [DIRS 149862]) focuses on temperature, saturation, and humidity during the postclosure period. This emphasis allows a simplified approach for the waste emplacement period of the preclosure phase of a potential repository. The simplification is to emplace all waste simultaneously, but use thermal decay curves that are appropriate for the age of waste as it is sequentially emplaced in accordance with an assumed waste acceptance schedule. For the LTOM, the TSPA used a 300-year ventilation period. The TSPA scenario does not specify if this period is an average (with some waste packages receiving more and some receiving less ventilation duration), the duration for the initial waste packages emplaced, or the duration for the final waste packages emplaced. One scenario for waste emplacement assumes a 22-year emplacement period. In this section, the base case ventilation duration is varied by ±22 years to determine the effects of the uncertainty of ventilation duration on in-drift TH parameters in the TSPA-SR (CRWMS M&O 2000 [DIRS 153246]) scenario. This emplacement period is taken from the *Reference Design Description for a Geologic Repository* (CRWMS M&O 2000 [DIRS 151967], Table 2). The first two years of the scenario, which had low rates of waste emplacement, were not included. The waste emplacement rates implicit in this scenario represent assumptions used only for this analysis.

This sensitivity analysis (Leem 2001 [DIRS 155457]) employed the LDTH submodel using the same implementation methods described in Section 5.3.2.4.2.

The base case for the sensitivity analysis is the LTOM base case design, with a 1.13 kW/m initial linear heat loading and 300 years of forced ventilation at an assumed (constant) ventilation efficiency of 80 percent (Table 5.1-1).

Results–The peak postclosure temperatures at the top of the drip shield and the crown of the drift wall are below 80ºC for all three ventilation duration cases (Figures 5.3.2.4.3-1 and 5.3.2.4.3-2). The peak postclosure temperatures of the drip shield and drift wall decrease 2°C as the ventilation duration increases from 278 years to 322 years. An additional interpretation of these results is that aging of 20 to 40 years for a 300-year ventilation period would not produce a significant (greater than a few degrees centigrade) reduction in peak postclosure temperatures.

Values of relative humidity for the drip shield top never decrease below 75 percent in all three ventilation duration cases (Figure 5.3.2.4.3-3). At the drift wall, the humidity remains nearly 100 percent at all times.

In all three ventilation durations investigated, the saturation at the lower center of the invert dries within a few decades during the preclosure period, rewets to about 3 percent saturation by potential repository closure, then quickly dries again (Figure 5.3.2.4.3-4). Section 5.4 shows the subsequent rewetting of the invert beyond 1,000 years for the LTOM base case. The sensitivity

of the in-drift TH parameters to ventilation duration in the LTOM is summarized in Table 5.3.2.4.3-1.

Summary–In the LTOM, the duration of ventilation (300 years) is long enough that the TH results are insensitive (within a few degrees centigrade of peak in-drift temperatures) to variations of plus or minus a few decades of ventilation duration.

5.3.2.4.4 The Influence of Near-Field Rock Dryout Due to Forced Ventilation on In-Drift Relative Humidity

The moisture contained in the host rock, if evaporated into the ventilation air, can influence the temperature and humidity conditions in an emplacement drift. Determination of water movement in the surrounding rock mass during preclosure ventilation requires complex models (e.g., MULTIFLUX, described in Section 5.3.2.4.1) to simulate the coupled heat and mass transfer processes.

To illustrate the overall effect of water removal by ventilation on the psychrometric environment in the drift, a constant rate of water removal from the rock was assumed in two numerical examples. Both examples include the effects of vaporization of near-field water on in-drift relative humidity and heat removal efficiency. The first example considers the initial dryout of the rock by the ventilating air. MSTH model (CRWMS M&O 2000 [DIRS 149862]) results presented later in this subsection, and limited measurements in the Exploratory Studies Facility (ESF), support a dryout depth of several meters. The observation of ventilation-caused dryout in the ESF supports dryout times less than a few years. To obtain a high-side but realistic bounding value of dryout-caused influx of water into the ventilation air, a dryout depth of 3 meters during a time span of 6 months was used in the example calculation. The second example considers continuing evaporation of water into the ventilating air, with the water furnished by percolation flux moving downward through the unsaturated zone and being intercepted by the dryout zone (about two drift diameters wide, from the first example). Recognizing that the results of this steady-state influx of water will be less than the initial dryout-period influx, a typical flux value of 10 mm/yr was used; the insensitivity of the resulting humidity to the influx (reported below) supports selection of a typical, rather than lower bound, value. The LDTH submodel of the MSTH model was used to investigate the influence of preclosure rock dryout on in-drift temperature and humidity. The submodel was implemented using assumed in-drift gas pressure and composition to drive movement of water vapor from the rock into the drift.

Finally, the LDTH submodel was used to investigate the influence of postclosure seepage of liquid water on in-drift temperature and humidity. The submodel was implemented using assumed seepage of liquid water into in-drift locations.

Initial Dryout–Ventilation air will initially evaporate existing water from the rock. As the depth of evaporation increases, the evaporated water must move through larger and larger regions of previously dried rock. In this example calculation, it is assumed that the initial dryout period is about 6 months and that the dryout extends to a depth of 3 m beyond the drift wall. It is assumed that the air enters the drift at a rate of 15 m^3/s, a temperature of 25ºC, and a relative humidity of 30 percent. Finally, it is assumed that the air is heated by the waste packages and drift walls to a temperature of 45ºC as it travels through the first 500 m of the drift.

Based on the intake air parameters, the water vapor pressure at the drift inlet depends on the temperature and relative humidity of the inlet (Hartman 1982 [DIRS 128009], pp. 596 to 597)

$$p_{v1} = R_1\{0.6105\exp[17.27t_{ao1}/(t_{ao1}+237.3)]\}$$
$$= 30\%\{0.6105\exp[17.27\times 25/(25+237.3)]\} = 949.9\,Pa$$

where

p_{v1} = water vapor pressure at the emplacement drift inlet (Pa)
R_1 = relative humidity of intake air at emplacement drift inlet (percent)
t_{ao1} = air temperature at the emplacement drift inlet (ºC)

The specific humidity (water-air ratio) of the intake airflow is (Hartman 1982 [DIRS 128009], p. 597):

$$\omega_1 = 0.622\times p_{v1}/(p_b - p_{v1}) = 0.622\times 949.9/(88720-949.9)$$
$$= 0.00673\,(\text{kg water})/(\text{kg air})$$

where

ω_1 = specific humidity of intake air (kg water)/(kg air)
p_b = barometric pressure at potential repository level (88,720 Pa; CRWMS M&O 1999 [DIRS 106794], p. 6, Section 3.4).

The rate of water (or moisture) entering the emplacement drift with the intake airflow is:

$$W_1 = Q\times\rho_1\times\omega_1 = 15\times 1.0561\times 0.00673 = 0.10664\ \text{kg water/s}$$

where

W_1 = rate of moisture entering drift with intake airflow (kg water/s)
Q = airflow rate at emplacement inlet (m^3/s)
ρ_1 = density of air at potential repository level (1.0561 kg/m^3) (CRWMS M&O 1998 [DIRS 105230], p. II-2, 3530 ft altitude, 70°F).

For the first 500 m of an emplacement drift with a 5.5-m diameter, the volume of a 3-m annulus of rock is:

$$V_r = 500\times(\pi/4)\times[(5.5+6)^2 - (5.5)^2] = 40{,}055\ \text{m}^3$$

When the rock volume, V_r, is multiplied by an average matrix porosity of ϕ = 11.3 percent, an initial matrix saturation of about S = 90 percent, and ρ_w = 1,000 kg/m^3 density of water, the water content of the dryout zone is calculated to be 4,074,000 kg. To remove this amount of water in a period of 6 months, the average rate of water entering the ventilation airflow is:

$$W_2 = V_r \times \phi \times S \times \rho_w \left(365/2 \times 24 \times 3600\ s\right)$$
$$= 0.2583 \text{ kg water/s}$$

This water addition into the ventilation airflow will increase the specific humidity (water-air ratio) to:

$$\omega_2 = (W_1 + W_2)/(Q \times \rho_1)$$
$$= (0.10664 + 0.2583)/(15 \times 1.0561) = 0.02304\ kg\ water/kg\ air$$

Compared with ω_1 = 0.00673 kg water/kg air at intake, the water content of the airflow at 500 m more than tripled because of moisture removal by ventilation during dryout of the first 500 m of the wall rock.

For ω_2 = 0.02304 kg water/kg air, the water vapor pressure of airflow 500 m downstream of the drift inlet is (Hartman 1982 [DIRS 128009], p. 597):

$$p_{v2} = p_b/[(0.622/\omega_2) + 1]$$
$$= 88720/[(0.622/0.02304) + 1] = 3169\ Pa$$

The saturation pressure (p_{s2}) of air at the 500-m point, where the air temperature (t_{ao2}) = 45°C, is (Hartman 1982 [DIRS 128009], p. 596):

$$p_{s2} = 610.5 \exp[17.27 t_{ao2}/(t_{ao2} + 237.3)]$$
$$= 610.5 \exp[17.27 \times 45/(45 + 237.3)] = 9578\ Pa$$

The relative humidity (R_2) of the airflow at the 500-m point is (Hartman 1982 [DIRS 128009], p. 597):

$$R_2 = (p_{v2}/p_{s2}) \times 100\%$$
$$= (3169/9578) \times 100\% = 33\%$$

If no moisture was removed from the drift wall, the relative humidity at the 500-m point due to temperature change alone would be (p_{v1}/p_{s2}) = 9.9 percent.

The contribution to heat removal of the latent heat of water vaporization during the dryout period can also be calculated. First, the average rate of water removal from the wall rock of a 500-m drift segment is placed on a per-meter-of-drift basis:

$$W_2' = (0.2583\ kg\ water/s \div 500\ m = 0.0005167\ kg\ water/(m\ s)$$

During the dryout period, the water in the host rock, which has an initial temperature of 25°C, is heated and vaporized into the ventilation air stream. For an increase in air temperature to 45°C at the 500-m point, the lineal power (heat) removal due to sensible and latent heating is:

$$\begin{aligned} H_{water} &= W_2' \{c_{p1}(45°C - 25°C) + h_{vaporization}\} \\ &= 0.0005167\ kg/m \bullet s \times \{4.178\ kJ/kg \bullet C \times (45°C - 25°C) + 2418.42\ kJ/kg\} \\ &= 1.29\ kJ/m \bullet s \\ &= 1.29\ kW/m \end{aligned}$$

where c_{p1} is the specific heat of water (kJ/kg•C).

For an average temperature of ((45+25)/2) = 35°C, the value of c_{p1} is 4.178 kJ/kg•C and the value of $h_{vaporization}$ (heat of vaporization) is 2418.42 kJ/kg (linearly interpolated from Incropera and DeWitt 1985 [DIRS 114109], p. 774).

Compared with the initial linear heat loadings of 1.35 and 1.13 kW/m (see Table 5.1-1) for the HTOM and LTOM, the lineal latent heat removal during the dryout period is significant.

Evaporation of Percolation Flux–Following the initial dryout of the 3-m rock annulus, it is assumed that a percolation flux of 10 mm/yr will be intercepted over an 11.5 m-wide path (a 3-m dryout zone, a 5.5-m drift diameter, and a 3-m dryout zone combined). All percolation water entering this zone is assumed to be removed by the ventilation air in the drift. The rate of water removal is:

$$\begin{aligned} W_3 &= Q_p \times A \times \rho_w \\ &= (10\ \text{mm/yr} \times 0.001\ \text{m/mm} \div 31536000\ \text{s/yr}) \times (500\,m \times 11.5\,m) \times 1000\ kg/m^3 \\ &= 0.001823\ \text{kg water/s} \end{aligned}$$

where

W_3 is the rate of percolation water evaporation into the drift air
Q_p *is* the percolation flux
A is the area of percolation flux intercepted
ρ_w is the density of water

This is only about 1.7 percent of the water removal rate during the dryout period. Using the same methods as the preceding example, the water addition rate can be converted to an air relative humidity. Because the percolation water addition is small compared to the initial water content of the air, the resulting relative humidity of the airflow at the 500-m point will be 10.01 percent, similar to the 9.9 percent value if no water were added due to steady percolation.

The contribution to heat removal of the latent heat of water vaporization due to percolation after the near-field rock dryout period can be calculated in a manner similar to the dryout period example above. The water removal rate calculated above, 0.001823 kg water/s, corresponds to 0.000003646 kg water/(m•s). Using this rate, the latent plus sensible heat removal due to water

is calculated to be 9.1 W/m, only about one percent of the initial linear heat loadings of 1.35 and 1.13 kW/m for the HTOM and LTOM. This contribution of water latent plus sensible heating to ventilation heat transfer due to vaporization of percolation flux is similar to the MULTIFLUX results presented in Section 5.3.2.4.1.

Effect of Preclosure Dryout of Near-Field Rock on Postclosure In-Drift Temperature and Relative Humidity–The dryout of the host rock surrounding emplacement drifts due to ventilation with relatively dry air results in a reduction in the thermal conductivity in the dryout zone. As is shown in Table 5.3.1.4.8.1, thermal conductivity decreases with liquid saturation. The preclosure LDTH submodels used in the MSTH model do not account for preclosure dryout and the influence of that dryout on reducing thermal conductivity in the host rock around emplacement drifts. Thus, the postclosure LDTH submodels used in the MSTH model start with liquid saturation in the host rock being very close to ambient conditions. Note that for the thermal-hydrologic model calculations conducted for this section (Buscheck 2001 [DIRS 155012]), the ambient liquid saturation is 0.94 in the matrix continuum, Figure 5.3.2.4.4-1). This section investigates whether explicitly accounting for rock dryout during the preclosure period significantly influences predicted thermal-hydrologic conditions during the postclosure period. The LDTH submodel at the L5C3 location was used to investigate this sensitivity. The location and infiltration boundary conditions for the two-dimensional submodel were the same as those described in Section 5.3.2.4.2. Four different cases (called Cases 1, 2, 3, and 4) are considered for both the HTOM and LTOM, with each case having different assumptions about thermal-hydrologic conditions within the emplacement drifts during the preclosure ventilation period.

For each of the four cases and for both of the operating modes, the model was implemented in three steps. The first step was to run the model during the preclosure period to obtain the drift-wall temperature history, using the base-case ventilation efficiencies: 70 percent for 50 years for the higher-temperature operating mode and 80 percent for 300 years for the lower-temperature operating mode. Section 5.3.2.4.2 discusses the sensitivity of thermal-hydrologic behavior to uncertainty in the ventilation efficiency. The second step was to repeat the preclosure calculation for the rock portion of the model, using the Step-One drift-wall temperature history and an assigned gas boundary condition at the drift wall.

In Step Two, the gas boundary condition was assigned to have a gas-phase pressure of 99 percent of ambient pressure and a relative humidity of 30 percent during the preclosure ventilation period for Case 1. A relative humidity of 30 percent is close to the mean annual relative humidity at the ground surface at Yucca Mountain. The psychrometric properties of the intake air for the ventilation of the emplacement drifts are summarized in (BSC 2001 [DIRS 155246], Table XXVII-1). The emplacement drifts are ventilated by pulling (rather than pushing) air, which causes the gas-phase pressure in the ventilated drifts to be reduced by a maximum of about 1 percent relative to ambient conditions (CRWMS M&O 2000 [DIRS 154176], p. 22). Cases 2 and 3 assign different values of either gas-phase pressure or relative humidity, while Case 4 uses different ventilation efficiencies than in Cases 1, 2, and 3. Thus, the ventilated emplacement drift functions as a sink for the humid gas in the host rock due to the lower gas-phase pressure and lower water vapor content of the in-drift air compared to the air in the near-field rock. Note that under ambient conditions, relative humidity in the host rock is greater than 99 percent.

The final preclosure distributions of temperature, liquid saturation, gas-phase pressure, and relative humidity in the host rock from Step Two become the initial rock conditions for the Step-Three postclosure calculation. Thus, Step Three captures the influence of preclosure dryout of the host rock. Step Three is similar to Step One in that the line-averaged heat-generation rate of the waste packages is represented in the LDTH submodel, rather than representing the influence of this heat generation with a specified boundary temperature as was done in Step Two. During the postclosure period, 100 percent of the heat generated by waste packages is represented in the LDTH model. Figures 5.3.2.4.2-2 and 5.3.2.4.2-8 show the heat-generation histories for the higher- and lower-operating modes, respectively.

This three-step process was repeated for Cases 2, 3, and 4 for both the higher- and lower-temperature modes. Case 2 is the same as Case 1 except relative humidity in the drift is assigned to be 5 percent (instead of 30 percent) during the preclosure period. The value of 5 percent corresponds to the minimum relative humidity of the ventilation air (4.77 percent), which is calculated to occur at 10 years (BSC 2001 [DIRS 155246]). A relative humidity of 5 percent represents an extreme lower bound for the in-drift relative humidity conditions during the ventilation period. Case 3 is the same as Case 1 except gas-phase pressure in the drift is assigned to be 95 percent of ambient during the preclosure period. Case 4 is the same as Case 1 except the ventilation efficiencies are assigned to be 60 percent for 50 years for the HTOM and 70 percent for 300 years for the LTOM (10 percent less than the other cases for both operating modes).

Figure 5.3.2.4.4-1 shows the lateral extent of host-rock dryout at the end of the preclosure ventilation period for Case 1. At the time of closure, liquid saturation in the matrix is reduced to about 0.5 at distances of 3 m and 1 m laterally away from the drift wall, for the higher- and lower-temperature operating modes, respectively.

For the higher-temperature operating mode, Figure 5.3.2.4.4-2 compares the results of Case 1 to those of the base-case L5C3 LDTH submodel (the base case neglects the influence of rock dryout during the preclosure period). The results of the base-case L5C3 LDTH submodel, together with those of the LDTH submodels at the 32 other geographic locations in the potential repository, are included in the generation of the MSTH model results described in Section 5.4.1. Figure 5.3.2.4.4-2 shows that Case 1 and the base case result in almost identical postclosure temperature at the drift wall and drip shield, relative humidity at the drip shield, and liquid saturation in the invert and at the drift wall. The preclosure dryout predicted for Case 1 has a negligible effect on postclosure thermal-hydrologic conditions around the drift. The rapid increase in temperatures (above the boiling point of water) following the cessation of ventilation generates a much larger dryout zone than that generated during the preclosure ventilation period, thereby overwhelming the influence of the preclosure dryout calculated in Step Two of the three-step calculation.

For the lower-temperature-operating mode, Figure 5.3.2.4.4-3 compares the results of Case 1 to those of the base-case L5C3 LDTH submodel, (the base case neglects the influence of rock dryout during the preclosure period). The results of the base-case L5C3 LDTH submodel, together with those of the LDTH submodels at the 32 other geographic locations in the potential repository, are included in the generation of the MSTH model results described in Section 5.4.2. Figure 5.3.2.4.4-3 shows that Case 1 and the base case result in almost identical postclosure

temperature at the drift wall and drip shield, relative humidity at the drip shield, and liquid saturation in the invert and at the drift wall. The preclosure dryout predicted for Case 1 has a negligible effect on postclosure thermal-hydrologic conditions around the drift. Rewetting of the host rock (primarily by matrix imbibition) requires about one hundred years after closure. However, peak temperatures at the drift wall and drip shield occur even later, two to three hundred years after closure for the lower-temperature operating mode, and are not affected by the inclusion of preclosure dryout in the LDTH submodel calculation. Because the dryout zone (which corresponds to the region of reduced thermal conductivity in the host rock) has collapsed prior to the occurrence of peak temperatures for the LTOM, rock dryout has a negligible influence on peak temperatures, as well as on other thermal-hydrologic conditions in the emplacement drifts.

Figure 5.3.2.4.4-4 compares the lateral extent of host-rock dryout at the end of the preclosure ventilation period for the HTOM and LTOM for Cases 1, 2, 3, and 4. The lower input value of relative humidity in the drift for Case 2 (5 percent) compared to Case 1 (30 percent) causes the lateral extent of dryout to extend further into the rock. The lower input value of gas-phase pressure in the drift for Case 3 (95 percent of ambient) compared to Case 1 (99 percent of ambient) causes the lateral extent of dryout to extend further into the rock. Case 4, which uses a lower ventilation efficiency than Case 1, results in higher temperature at the drift wall during the preclosure ventilation period and causes the lateral extent of dryout to extend further into the rock. For all three cases (2-4), the influence of this effect is greater for the higher-temperature-operating mode than for the lower-temperature operating mode. Summarizing, the lateral extent of host-rock dryout increases with decreasing relative humidity and gas-phase pressure in the drift and it increases with increasing drift-wall temperature. Figure 5.3.2.4.4-5 compares Cases 1, 2, 3, and 4 for the HTOM. Although Cases 1, 2, and 3 produced slightly different lateral extents of preclosure dryout, they result in almost identical postclosure temperature at the drift wall and drip shield, relative humidity at the drip shield, and liquid saturation in the invert and at the drift wall. Recall that Case 1 has a virtually identical temperature, liquid saturation, and relative humidity conditions as in the base-case LDTH submodel that ignored the influence of preclosure dryout. Therefore, Cases 1, 2, and 3 result in the same temperature, liquid saturation, and relative humidity conditions as in the base-case LDTH submodel that neglects preclosure dryout. Case 4 results in slightly higher temperatures, and in slightly lower liquid saturation and relative humidity, than in Cases 1, 2, and 3. The primary cause of the higher temperature and lower liquid saturation and relative humidity in Case 4 is that it utilized a lower heat removal efficiency during the preclosure ventilation period, resulting in higher temperatures at the beginning of the postclosure period. The secondary cause of the higher temperatures is the large dryout zone that results in a larger region of reduced thermal conductivity, causing postclosure temperatures to be somewhat higher.

Figure 5.3.2.4.4-6 compares Cases 1, 2, 3, and 4 for the lower-temperature-operating mode. Cases 1, 2, and 3 produce essentially identical postclosure temperature at the drift wall and drip shield, relative humidity at the drip shield, and liquid saturation in the invert and at the drift wall. Recall that Case 1 has similar temperature, liquid saturation, and relative humidity conditions as in the base-case LDTH submodel that ignored the influence of preclosure dryout. Therefore, Cases 1, 2, and 3 result in the same temperature, liquid saturation, and relative humidity conditions as in the base-case LDTH submodel that neglects preclosure dryout. Case 4 also results in similar liquid saturation and relative humidity conditions; however, Case 4 results in

slightly higher temperatures than in the other cases. The cause of the higher temperature in Case 4 is that it utilized a lower heat removal efficiency during the preclosure ventilation period, resulting in higher temperatures at the beginning of the postclosure period.

Effect of Postclosure Seepage on In-Drift Temperature and Relative Humidity–Seepage into the drift was not predicted to occur for most of the range of infiltration flux conditions considered in the TH model calculations developed in the *Water Distribution and Removal Model* (CRWMS M&O 2001 [DIRS 152016]) and used in the TSPA-SR (CRWMS M&O 2000 [DIRS 153246]). One reason for the low prediction of drift seepage is the assumption of a uniform fracture continuum within each hydrostratigraphic unit. This assumption is equivalent to assuming no drift-scale heterogeneity of fracture properties in the host rock, reducing the tendency for drift seepage. The two-dimensional nature of the current LDTH submodel also contributes to the lack of heterogeneity in the horizontal direction.

To overcome the tendency of the LDTH models to predict little or no seepage, a sensitivity study was conducted during the preparation of the *Water Distribution and Removal Model* (CRWMS M&O 2001 [DIRS 152016]). The LDTH submodel was modified to impose seepage within the drift for a design and operating point similar to the HTOM. The model added the seepage uniformly over the upper drip shield surface and drift floor (i.e., the upper invert surface) between the base of the drip shield and the intersection of the drift floor and lower drift wall. Sources of liquid water were specified at each of the gridblocks overlying the drip shield or drift floor, including the gridblock overlying the column of gridblocks adjacent to the vertical side of the drip shield.

Three values of seepage percentage were considered: 0, 3, and 30 percent. For this sensitivity study, the seepage percentage was taken to be the percentage of the incident percolation flux in the host rock that directly overlies the invert on which the seepage was imposed. The invert lateral width of 3.2 m (CRWMS M&O 2000 [DIRS 149862], Figure 6-2) is less than the 5.5-m drift diameter. Because the LDTH submodels have boundary conditions that prevent lateral diversion of water, the percolation flux in the host rock (averaged across the model domain) is equivalent to the average infiltration flux specified at the top of that LDTH submodel location. The L4C4 location used for this sensitivity study was near the geographic center of the potential repository, and it experiences slightly higher than average infiltration (and percolation) flux conditions. The infiltration flux was calculated to be 10.13, 28.88, and 42.00 mm/yr for the present-day, monsoonal, and glacial climate states, respectively (CRWMS M&O 2001 [DIRS 152016], Table 5-4). For the 30 percent-seepage case, the resulting seepage fluxes were 3.04, 8.66, and 12.6 mm/yr, respectively, calculated over a footprint that is 3.2214 m wide.

To avoid artificial addition or subtraction of sensible heat from the drift due to seepage, an assumption was made that the water seeping into the drift had equilibrated with the host rock temperature at the crown of the drift. A maximum allowable temperature of 96°C was set to assure that the seepage flux entered the drift as liquid water. This assumption was implemented by extracting the temperature history for the host rock at the crown of the drift for the case with 0 percent seepage (i.e., no prescribed seepage into the drift). The temperature history was used to linearly interpolate an enthalpy history from the steam tables (Keenan et al. 1969 [DIRS 134666]).

Figure 5.3.2.4.4-7 shows the influence of drift seepage on temperature and relative humidity at the drip shield. Drift seepage flux is seen to have negligible influence on drip-shield temperature and relative humidity.

Summary–The volume of water that can enter the ventilation air during dryout of the near-field rock is sufficient to triple the relative humidity of the exiting ventilation air (from about 10 percent to 33 percent). During the dryout period (based on the assumed dryout rate), the latent heat of the vaporizing water can remove all of the heat flux from the waste packages. This is a higher value than the latent heat removed in ventilation air as calculated with MULTIFLUX in Section 5.3.2.4.1, indicating that much of the mobilized moisture may be removed as vapor may be through fractures in the mountain, rather than in the ventilation air.

After dryout of the near-field rock, the vaporization of percolating water into the ventilation air is slow enough that only small changes in ventilation air humidity and cooling rate are calculated. The MULTIFLUX results summarized in Section 5.3.2.4.1 corroborate the hand calculations.

After closure, most in-drift temperature and humidity histories are not significantly influenced by the low saturation of near-field rock dried during the ventilation period. In the LTOM, the saturation at the drift wall does not rewet for about a century after ventilation ceases; however, based on these two-dimensional calculations, the low saturation does not significantly affect in-drift temperatures or relative humidity at the drip shield.

Finally, if seepage water equilibrates thermally with the near-field rock prior to seeping, direct imposition of seepage water into in-drift zones does not significantly affect in-drift temperatures or humidity at the drip shield.

5.3.2.4.5 Use of an Effective In-Drift Heat Transfer Coefficient to Represent Radiation in the Line-Source Drift-Scale Thermal-Hydrologic and the Discrete-Source Drift-Scale Thermal Submodels

An effective thermal conductivity applied to the in-drift air elements in the drift-scale models of the potential repository can be used to approximate complex modes of heat transfer, including thermal radiation and natural convection, by using a standard Fourier law of heat conduction approach. The effective thermal conductivity parameter governs the calculated rate at which heat is transferred from the heat source (by all relevant modes of heat transfer) to the drift wall or from the drip shield to the drift wall after closure of the potential repository. There are two advantages to using an effective thermal conductivity in the models. First, complex modes of heat transfer can be approximated by models of the potential repository that are currently incapable of handling the necessary transport mechanisms required by a particular mode of heat transfer (i.e., highly turbulent natural convection in an open cavity). Second, applying this method greatly reduces model run times.

It is noted that the effective thermal conductivity is temperature dependent. As such, it is necessary to have an a priori knowledge about the temperatures so that an effective parameter can be developed. Since this is a potential limitation in the development of the effective parameter, the sensitivity of the process-level models to effective thermal conductivity developed with similar, but different, temperature-time histories is investigated in Figures 5.3.2.4.5-1

through 3. Additionally, since temperatures (used to develop the parameter) vary with potential repository location (e.g., center and edge), effective thermal conductivities are developed for a variety of different areal mass loadings. Subsequently, ranges of effective thermal conductivity based on areal mass loading are developed to approximate temperature driven variability associated with potential repository edge and center effects (e.g., refer to Figure 5.3.2.4.5-4).

The effective conductivity method of calculating multimode heat transfer is an approximation, and a series of analyses have evaluated its ability to mimic more complex modes of heat transfer. The results of these analyses (Francis 2001 [DIRS 155075]), which are summarized below, indicate that the temperatures calculated by MSTH drift-scale submodels had some sensitivity (up to 2.5ºC difference) to effective thermal conductivity at early times. However, beyond 1,000 years after emplacement, the models were insensitive to this parameter.

An effective thermal conductivity used to approximate either thermal radiation or natural convection heat transfer is strongly dependent on temperature. Because the temperature varies in time (Figure 5.3.2.4.5-1), the thermal radiation and natural convection components vary in time. Specifically, the maximum effective thermal conductivity for thermal radiation occurs at the maximum temperature of the heat-generating surface, rather than at the maximum temperature difference between the surfaces. It is a function of the fourth power of the absolute temperatures of the exchanging surfaces as well as surface and geometric radiative properties (e.g., the surface resistance is dependent on the surface emissivity, the geometric resistance is dependent on the view factor). However, the maximum effective thermal conductivity for natural convection occurs at the maximum temperature difference between the surfaces. The temperature of the in-drift components (and how they vary in time) provides the basis for development of effective conductivity.

This part of Section 5.3.2.4.5 focuses on the development of an approximate thermal conductivity to represent thermal radiation. Because some of the analyses studied both radiation and natural convection approximations, some aspects of the natural convection approximation were also discussed. The next part of this section addresses the development of an approximate thermal conductivity to represent natural convection.

5.3.2.4.5.1 Sensitivity of Effective Thermal Conductivity and Resulting Temperatures to Design Details

An illustration of the sensitivity of effective thermal conductivity to the specifics of the design is shown in *Effective Thermal Conductivity for Drift-Scale Models Used in TSPA-SR* (CRWMS M&O 2001 [DIRS 153410], Sections 5 and 6). Analyses conducted for that report compute the effective conductivity for thermal radiation and natural convection using engineered barrier system temperatures and geometry associated with the License Application Design Selection (LADS) Enhanced Design Alternative (EDA) II (CRWMS M&O 1999 [DIRS 107292], Section 5.1). Section 3 of CRWMS M&O (2001 [DIRS 153410]) provides the assumptions associated with the development of the LADS-based parameters. The following are the most important assumptions:

- Heat transfer occurs between concentric cylinders.

- The surfaces are isothermal (i.e., the temperature of a surface does not vary appreciably with respect to angular position).

- The correlation used for natural convection is for an average heat transfer coefficient (CRWMS M&O 2001 [DIRS 153410], Section 5.2) to obtain the correct overall heat flux; however, this method does not capture the variation of temperature due to natural convection air movement patterns.

- The same temperature difference (at any given time) between surfaces is used to generate each component of effective thermal conductivity.

The effective thermal conductivity for thermal radiation, natural convection, and the total (both modes) effective conductivity are shown in Figures 8 through 10 of CRWMS M&O (2001 [DIRS 153410]). These values were calculated using a selected subset (potential repository center) of LADS EDA II temperatures for the waste package, drip shield, and drift wall. In that design, the natural convection component represents about 11 percent of the total heat transfer at the time of peak waste package temperature. At later times, the natural convection component represents about 4 percent of the total. The combined-mode effective thermal conductivity parameter developed in CRWMS M&O (2001 [DIRS 153410], Figure 10) was used in the TH and THC analyses supporting the TSPA-SR (CRWMS M&O 2000 [DIRS 153246]).

Because the design operating temperatures and geometry were somewhat different in the TSPA-SR (CRWMS M&O 2000 [DIRS 153246]) than in the EDA II, an updated effective thermal conductivity was computed. The temperature (CRWMS M&O 2001 [DIRS 154594]) and geometry (CRWMS M&O 2000 [DIRS 151014]) were calculated for the TSPA-SR design. The differences in the results illustrate the sensitivity of the potential repository drift-scale models to this in-drift parameter. The in-drift temperatures used in the development of the updated parameters were repository-wide averaged values for the waste package, drip shield, and drift wall, using the mean infiltration flux thermal hydrology results obtained from the process model described in the *Multiscale Thermohydrologic Model* (CRWMS M&O 2000 [DIRS 149862]). This provides a better overall representation of the potential temperature variability than the potential repository-center temperatures used in the earlier EDA II analysis.

Figure 5.3.2.4.5-1 shows a comparison between the results for the TSPA-SR design (CRWMS M&O 2000 [DIRS 153246]) and the EDA II results. To about 10,000 years, the EDA II temperatures are greater than the TSPA-SR temperatures, resulting in a larger thermal radiation component and a larger combined-mode effective thermal conductivity parameter. However, the inner (between the waste package and the drip shield) effective thermal conductivity for the TSPA-SR design is larger than it is for the EDA II design, even though at early times the temperatures are lower (at late times the TSPA-SR design temperatures are greater). This is due to differences in drip shield geometry and radiative surface properties (CRWMS M&O 2001 [DIRS 153410], Equation 6). Additionally, the temperature difference between the waste package and drip shield is greater for the TSPA-SR design, resulting in a larger natural convection component.

The sensitivity of the potential repository drift-scale models to the effective thermal conductivity was investigated by applying each of the curves from Figure 5.3.2.4.5-1 to a single LDTH

submodel location and comparing the resulting temperature differences at a number of different locations within the EBS. The sensitivity study used a two-dimensional line-source drift-scale thermal-hydrologic submodel (location L4C4), as described in the *Multiscale Thermohydrologic Model* (CRWMS M&O 2000 [DIRS 149862], Section 6). This location was selected because it is near the geographic center of the potential repository footprint and therefore representative of the degree of edge effects for much of the footprint. The submodel applies the active fracture flow model between the fracture and matrix continua in the host rock, as do all the submodels used in this analysis. The submodel calculated the heat flow across the outer air gap (between the drip shield and the drift wall) using a monolithic heat source with the dimensions of the drip shield. The temperature evaluations were made at the upper and lower points of the drip shield and at the crown and springline of the drift wall. Temperature difference evaluations were made for both preclosure and postclosure, as shown in Figures 5.3.2.4.5-2 and 5.3.2.4.5-3, using information from the LADS EDA II design (CRWMS M&O 1999 [DIRS 107292]) and the TSPA-SR (CRWMS M&O 2000 [DIRS 153246]).

Figures 5.3.2.4.5-2 and 5.3.2.4.5-3 show that the heat source temperatures (top and lower drip shield) computed from the TSPA-SR design-based effective thermal conductivity are hotter than those computed using the LADS EDA II design-based conductivity. This is because the effective thermal conductivity outside the drip shield—and, thus, the total effective heat transfer rate across the air gap—is lower, according to Figure 5.3.2.4.5-1. The shift in heat transfer from the air gap to the invert for the TSPA-SR design-based effective thermal conductivity results in lower drift wall temperatures, as indicated in Figures 5.3.2.4.5-2 (preclosure) and 5.3.2.4.1-3 (postclosure). The figures show that a maximum temperature difference between the two cases of about 2.5°C occurs at the waste packages early after closure. After about 1,000 years, the temperature difference is a fraction of a degree at any location considered within the drift.

5.3.2.4.5.2 Comparison of Effective Thermal Conductivity Results to Explicit Radiation Results

Using a two-dimensional LDTH submodel (the L4C3 location, near the center of the potential repository) of the MSTH model (CRWMS M&O 2000 [DIRS 149862]), an explicit representation (using computed view factors) of thermal radiation heat transfer from the drip shield to the drift wall was used to generate temperature time-histories. These temperatures were then used to develop new effective thermal conductivity parameters, based on concentric cylinder correlations for thermal radiation and natural convection. The location of the submodel is in the lower lithophysal host rock unit (tsw35). At this location, the infiltration rate boundary conditions (based on the methodology and input data in CRWMS M&O 2000 [DIRS 149862]) of 6.7 mm/yr for the present-day climate (0 to 600 years), 18.6 mm/yr for the monsoonal climate (600 to 2,000 years), and 27.7 mm/yr for the glacial-transition climate (beyond 2,000 years) (Francis 2001 [DIRS 155075]) are approximately representative of the average infiltration rates over the heated potential repository footprint.

The submodel was exercised with explicit thermal radiation heat transfer and with separate effective thermal conductivities for natural convection and thermal radiation. The results were then used to establish the relative importance of each of the effective thermal conductivity components. Additionally, a determination was made of how well the effective thermal

conductivity for thermal radiation actually represents a geometrically complex mode of heat transfer.

Four AMLs were used to develop effective thermal conductivities for the HTOM and LTOM. Sections 5.2 and 5.4 provide a description of how multiple AMLs in drift-scale submodels of the MSTH model are used to evaluate the increasing influence of the potential repository edge as time progresses. The effective thermal conductivity parameters for the HTOM were tested using the base AML of 55 MTU/acre (Table 5.1-1).

As discussed in Section 5.2, the drift-scale submodels normally treat the drift air as a porous medium with a high permeability to capture some of the movement of air due to natural convection. For the effective thermal conductivity comparison, the bulk permeability of the in-drift air was set to zero to eliminate (duplicative) explicit calculation of natural convection. The four two-dimensional TH potential repository drift-scale submodels with explicit thermal radiation represented in the drift were then used to determine the EBS temperatures, and these temperatures were used to develop the effective thermal conductivities for thermal radiation and natural convection. At each given time, the same temperature difference between the drift wall and drip shield was used to develop both parameters. Figure 5.3.2.4.5-4 illustrates the total effective thermal conductivity developed from temperatures averaged from five locations on the heat-generating surface (the drip shield in some of the submodels) and eighteen locations on the drift wall. The total effective thermal conductivity contains a component for thermal radiation as well as natural convection. At early times, the higher AML curves are most appropriate at the central location of the potential repository for this implementation of the submodel. At later times, the most appropriate effective AML for the two-dimensional submodel decreases (based on consideration of three-dimensional mountain-scale effects). The AML-dependent postclosure effective thermal conductivities bound the values obtained from the TSPA-SR (CRWMS M&O 2000 [DIRS 153246]) effective conductivity calculation, which are based on temperatures averaged over the potential repository footprint.

To determine the effect of approximating thermal radiation in the emplacement drift using an effective (approximated) thermal conductivity, drip shield and drift wall temperatures were computed using the base AML (55 MTU/acre) for the HTOM and three in-drift heat transfer approaches. The approaches were explicit thermal radiation (with no approximated natural convection), approximated thermal radiation (with no approximated natural convection), and approximated thermal radiation and natural convection. For each approach, the model was run twice to investigate the influence of explicit natural convection in the porous medium used to represent the in-drift air. One run used zero bulk permeability in the air (to suppress explicit natural convection), and the other used a value of 10^{-8} m^2 for air-permeability (the recommended value based on the sensitivity analysis discussed in Section 5.3.2.4.5.3). Although this selected value for the in-drift air bulk permeability is somewhat arbitrary, the sensitivity study conducted for the in-drift air bulk permeability indicates the effective reasonableness of this value within a large range of potential values. However, the "actual" specification of this value will be dependent on a computational fluid dynamics flow solution of turbulent buoyant convection in an open cavity of appropriate geometric scale. Since this information is not presently available, use of the base value (10^{-8} m^2) along with the effective thermal conductivity to estimate the turbulent natural convection in the repository-scale models is recommended based on the results

of the sensitivity studies described in this section. Figure 5.3.2.4.5-5 shows the surface-averaged drip shield temperature histories for the six model implementations.

The average drip shield temperatures (Figure 5.3.2.4.5-5), which are based on an effective thermal conductivity parameter for thermal radiation, under-predict the early time temperatures (obtained from explicit thermal radiation) at the drip shield. At closure of the potential repository, the effective thermal conductivity for thermal radiation underpredicts the average surface temperature of the drip shield obtained using explicit thermal radiation by about 10ºC. At the time of peak drip shield temperature, the under-prediction is about 6ºC. At 1,000 years, the drip shield temperature under-prediction using a combined-mode effective thermal conductivity is about 1ºC. The differences between the cases with and without a bulk permeability are slight and occur at early times only. The lowest drip shield temperatures occur when using the combined-mode effective thermal conductivity with a bulk permeability specified. However, this curve is only lower by a fraction of a degree when compared to the temperature time-history curve generated by the combined-mode effective thermal conductivity without a bulk permeability specified for the in-drift elements. The differences between the model results are attributed to conceptual model geometric differences (concentric cylinders compared to eccentric, or off-center, cylinders with an invert).

The drift wall temperatures that correspond to the drip shield temperatures shown in Figure 5.3.2.4.5-5a are much less sensitive to the treatment of heat transfer across the air gap. The drift wall temperatures obtained from the effective thermal conductivity are slightly higher (i.e., have a higher heat transfer rate) than those obtained from explicit thermal radiation. The difference is typically less than a fraction of a degree. Therefore, when host rock temperatures are the driving forces for a process being studied (e.g., drift-scale THC water chemistry and gas-phase compositions at the emplacement drift wall), the choice of an effective thermal conductivity parameter used to represent the in-drift heat transfer processes is adequate. Conversely, when in-drift temperature levels and spatial distributions are the driving forces for a process being studied (e.g., condensation on the coolest surfaces within the drift), explicit representation of thermal radiation is desirable. This conclusion was implemented in the MSTH postclosure calculations in support of the SSPA, as described in Section 5.3.1.3. That is, explicit thermal radiation was used between the drip shield and drift wall in the line-source drift-scale TH submodel, and explicit thermal radiation was also used both under and over the drip shield in the discrete-source drift-scale thermal submodel.

Because the porous media flow codes such as NUFT (V3.0) and TOUGH2 (see Chapters 3 and 4 of this document) are currently incapable of modeling turbulent natural convection in an open-air cavity, the effective thermal conductivity for natural convection within the emplacement drift should be applied. However, since the specification of an in-drift bulk permeability had little influence on temperature predictions, the porous medium approximation in the drift air can be used to simultaneously transport mass across the air gap without introducing any significant error in the temperature distribution. It is reasonable to specify a bulk permeability to the in-drift air elements of at least a value equal to the fracture permeability in the host rock.

The applicable curves for effective thermal conductivity for natural convection are shown later in this section. A detailed analysis for the selection of a proper in-drift bulk permeability also follows.

5.3.2.4.5.3 The Effect of the Bulk Permeability of In-Drift Air on Temperature Distributions Calculated by the Line-Source Drift-Scale Thermal-Hydrologic Submodel

The LDTH submodel of the MSTH model (CRWMS M&O 2000 [DIRS 149862]) uses a porous medium to model the in-drift air and uses an approximated thermal conductivity that includes heat transferred by natural convection between concentric cylinders. The previous part of this section considered bulk permeabilities of either $0\ m^2$ or $10^{-8}\ m^2$ assigned to the in-drift air elements. In those simulations, it was found that for either an explicit thermal radiation or an effective thermal conductivity (representing thermal radiation and natural convection), the influence of the in-drift bulk permeability on the temperature at the drip shield or drift wall was negligible. In this part of the section, a more comprehensive range of bulk permeabilities is considered, along with hydrologic and temperature results.

The model selected for the sensitivity analysis of the HTOM is a two-dimensional LDTH submodel from the MSTH model. The submodel considered was at the base AML (55 MTU/acre). The submodel location (L5C3; see Section 5.3.1.2) was selected because it is near the L4C4 and L4C3 locations and because it is not near the top of the lower lithophysal subunit. The surface infiltration rates at this location (based on the methodology and input data in CRWMS M&O (2000 [DIRS 149862]) are 5.7 mm/yr for the present-day climate (0 to 600 years), 15.1 mm/yr for the monsoonal climate (600 to 2,000 years), and 23.2 mm/yr for the glacial-transition climate (beyond 2,000 years) (Francis 2001 [DIRS 155075]). It includes explicit thermal radiation for the in-drift elements, and it applies the effective thermal conductivity curve for natural convection heat transfer. Table 5.3.2.4.5-1 gives the range of bulk permeability for the air elements in the emplacement drift considered in this sensitivity study. The locations and TH parameters used to evaluate differences in the models are the:

- Drift wall crown (temperature and liquid saturation)
- Drift wall springline (temperature and liquid saturation)
- Top of the drip shield (temperature and relative humidity)
- Base of the drip shield (temperature and relative humidity)
- Bottom-center of the invert (temperature and liquid saturation).

These locations illustrate the potential for both vertical and horizontal variability associated with the in-drift bulk permeability specification.

Temperature Dependence on In-Drift Bulk Permeability–Figures 5.3.2.4.5-6 through 5.3.2.4.5-8 show the temperatures at the base of the drip shield, at the crown of the drift wall, and at the bottom-center of the invert for the range of in-drift bulk permeabilities described in Table 5.3.2.4.5-1.

Figure 5.3.2.4.5-6 shows the temperature histories at the base of the drip shield for the range of air permeabilities; the temperatures at the top of the drip shield showed even less sensitivity to air-permeability. It is evident from Figure 5.3.2.4.5-6 that the in-drift bulk permeability does not affect the drip shield temperature for most of the permeability values, and permeability has only a small effect (less than 4°C) for the largest value investigated ($2x10^{-5}\ m^2$). For the high bulk permeability case, the drip shield temperatures are somewhat lower from closure of the potential

repository until about 200 to 300 years. The reduction in temperature at the drip shield surface is reasonable, since the higher air-permeability results in a larger rate of heat transfer from the heat source to the drift wall. However, the computational burden of the high air-permeability was significant; this case could not be run to the full 10^6 years due to a continuous reduction in time step. The simulation reached about 3,000 years and was manually terminated because the time step had decreased to only a fraction of a second. Time step reductions occurred in the simulation due to the disparity in fluid velocities associated with the air elements inside the drift and the adjacent host rock elements.

Since the porous media flow codes describe physical processes, this apparent numerical "problem" is actually an indication of the importance of turbulent natural convection within the emplacement drift. That is, even though the temperature difference between the drip shield and the drift wall is small at late times, the length scales associated with these components (e.g., the drift wall) still ensures a highly turbulent flow condition (e.g., the fluid Rayleigh number is still very large at late times) around the interior (drip shield) and exterior (drift) walls. (Note: the fluid Rayleigh number is based on appropriate fluid properties, a length scale, and a temperature difference such that it provides an indication of turbulent or laminar flow within the drift.) An in-drift bulk permeability can be defined based on knowledge of the fluid Rayleigh number. As shown in Webb and Hickox (2001 [DIRS 154777]), a Rayleigh-number-based effective permeability for the in-drift air elements increases as the fluid Rayleigh number to the one-half power. Therefore, for large Rayleigh numbers, the required effective permeability for in-drift flow becomes very large. As indicated above, large values of air-permeability pose problems for the porous media flow codes. Indeed, this is the primary motivation for the development of an effective thermal conductivity for turbulent natural convection (heat transfer only) used in the porous media flow code coupled with a (nonzero) value for the in-drift air-permeability to ensure mass transfer within the drifts (see the next subsection).

Figure 5.3.2.4.5-7 shows that the temperature histories at the drift wall crown are also insensitive to the air-permeability range investigated. The temperatures at the springline of the drift wall are even less sensitive than at the crown. The highest value of air-permeability slightly shifts the distribution of heat flow, increasing the fraction toward the drift wall (and increasing the drift wall temperature), while decreasing the fraction through the invert (and decreasing the invert temperature). However, the magnitude of the shift in heat transfer results in a temperature change of only a few degrees at those locations.

Effect of In-Drift Bulk Permeability on Hydrologic Parameters–Figures 5.3.2.4.5-9 through 5.3.2.4.5-12 show the time histories of the relative humidity and air-mass fraction at the base of the drip shield and of the saturation in the near-field rock at the drift wall and in the invert. These hydrologic parameters were calculated for the range of in-drift bulk permeabilities described in Table 5.3.2.4.5-1.

The relative humidity histories illustrated in Figure 5.3.2.4.5-9 are directly related to the corresponding temperature histories in Figures 5.3.2.4.5-6. The relative humidity histories for the base case and "fracture k_b" air permeabilities are nearly identical due to the nearly identical temperature time-histories and approximately similar in-drift permeabilities. In contrast, the high air-permeability case produced a slightly higher relative humidity than the base case. This is due to a combination of slightly lower temperatures and higher in-drift permeability, allowing

more water vapor to enter the emplacement drift from the surrounding host rock. As more water vapor enters the drift, the air mass fraction in the drift elements decreases, increasing the numerator of the fraction that defines relative humidity (water-vapor pressure divided by water-vapor-saturation pressure at the local temperature). Figure 5.3.2.4.5-10 shows that the in-drift air mass fraction for the high bulk permeability case is generally lower than the base case for the first 1,600 years, which is the major cause of the slightly higher relative humidity for this case.

For the low air-permeability case, the prohibition of vapor flow from the near-field rock forces a constant air mass fraction. However, the saturation pressure, which is the denominator of the fraction that defines relative humidity, increases with temperature, resulting in a depressed relative humidity during the period of high temperature.

Figure 5.3.2.4.5-11 shows the negligible sensitivity of the saturation histories at the drift wall crown to the range of air permeabilities investigated. The histories at the drift wall springline show even less sensitivity to the air-permeability. Figure 5.3.2.4.5-12 shows that the sensitivity of the invert saturation to in-drift air-permeability is also weak. Slight differences occurred between the four air-permeability cases because of differences in mass transfer rates at the drift wall contacts, both at dryout and later at resaturation. The base case invert saturation also showed some numerical instability during rewetting; similar numerical artifacts were observed in the invert thermal conductivity sensitivity calculations described in Section 5.3.1.4.10.

Based on temperature and hydrologic parameter results, it is concluded that the potential repository drift-scale models are insensitive to the choice of bulk permeability specified for the in-drift air elements. A nonzero bulk permeability must be assigned to the in-drift elements to avoid artificial depression of relative humidity during the high temperature period (Figure 5.3.2.4.5-9), and all three of the nonzero values investigated produced similar temperature and hydrologic results. The higher end of the permeability range investigated results in more realistic movement of air; however, it also greatly increases computational run times. The intermediate values (base case and fracture bulk permeability) of air-permeability allow some movement of air and produce realistic values of relative humidity without the long computational times associated with a high air-permeability.

Thus, the development of an effective thermal conductivity for natural convection heat transfer has succeeded in that it produces realistic temperatures and hydrologic parameters without long computational time requirements. It reduces the complex mode of heat transfer to a faster, simpler computational model, with the only loss of information being the small variations of temperature on the drip shield surface and on the drift wall surface.

Sensitivity Studies of a High Bulk Permeability Inside the Drift Without the Effective Thermal Conductivity–The high air-permeability case from Table 5.3.2.4.5-1 was rerun without including the effective thermal conductivity for turbulent natural convection using the same LDTH submodel of MSTH model (CRWMS M&O 2000 [DIRS 149862]). The result was compared to the low air-permeability case described above; the low permeability case included an effective thermal conductivity for natural convection while specifying a bulk permeability of zero in the drift. This comparison provides an estimate of how well a porous medium model using a large in-drift air-permeability represents heat transfer driven by (turbulent) buoyancy

effects between the drip shield and the drift wall. The effective thermal conductivity (averaged over the hot and cold surfaces) for buoyant, turbulent natural convection is based on an empirical correlation for concentric cylinders. This correlation has been tested against experimental data and Navier-Stokes computational fluid dynamics (CFD) numerical models. For the purposes of the comparison described below, the effective thermal conductivity model with zero air-permeability is expected to give more physically reasonable temperature predictions than the porous medium code using a high permeability. Because of the zero air-permeability, relative humidity predictions would not be more physically realistic.

Figure 5.3.2.4.5-13 shows the temperature histories at the top of the drip shield for the two cases. The histories at the base of the drip shield are almost identical, but show slightly less sensitivity. The high air-permeability case without an effective thermal conductivity for natural convection underpredicts the heat transfer rate from the drip shield to the drift wall (i.e., the drip shield temperature is higher than the effective thermal conductivity case with zero air-permeability).

Figure 5.3.2.4.5-13 can be compared with Figure 5.3.2.4.5-6, which compares the drip shield temperature using the porous medium model with an additional effective thermal conductivity for natural convection. When a high air-permeability is combined with an effective thermal conductivity, as in the lowest temperature case from Figure 5.3.2.4.5-6, the calculation takes credit for natural convection in two ways, resulting in a somewhat low peak drip shield temperature. However, the use of a high air-permeability in a porous medium model, with no effective thermal conductivity for natural convection, does not adequately capture the extent of heat transfer from natural convection, resulting in a somewhat high peak drip shield temperature. It should be noted that the differences in peak drip shield temperature are relatively small ($\pm$4°C) compared to the total amount of heating of the drip shield (135°C) above ambient temperature.

Figure 5.3.2.4.5-14 shows the temperature at the crown of the emplacement drift. The early time temperatures are slightly lower (about 1°C) for the case of high air-permeability and no effective thermal conductivity for natural convection. This is due to a slight shift of heat flow to the invert to compensate for the underprediction of convective heat transfer.

The conclusion of this comparison is that, for reasonable computation times, in-drift air-permeability in a porous medium model cannot be made large enough to reproduce the temperature characteristics associated with the effective thermal conductivity for turbulent natural convection.

5.3.2.4.5.4 Comparison of Turbulent Natural Convection Air Flow in a Porous Medium Model and a Navier-Stokes Computational Fluid Dynamics Model

The correlation-based approach described above is based on concentric cylinder geometry. There are also some empirical correlations available for eccentric cylinders in which the center of the inner cylinder is offset (vertically downward in the current design). However, the noncircular nature of the drip shield and the presence of the invert limit the benefit of extending an approach based on published correlations to eccentric cylinders. An alternative approach is to calculate the velocities and temperature distributions for natural convection between the drip shield and drift wall (and between the waste package and drip shield) using Navier-Stokes CFD models. The advantage of such calculations is that the geometric details can be accurately

modeled. The results of the calculations can be used to develop design-specific correlations for the LDTH and (DDT) submodels.

Preliminary results of the CFD analyses can be used to assess the applicability of the porous medium model with supplemental concentric cylinder correlations for natural convection, which was employed to calculate temperatures and humidities for the SSPA Volume 2 (McNeish 2001 [DIRS 155023]) TSPA.

Webb and Hickox (2001 [DIRS 154777]) used a finite element CFD (FIDAP V8.0) code to analyze natural convection in an open space using the Navier-Stokes equations and in a porous medium using correlation-based Nusselt numbers for the heat transfer between the moving air and each cylinder. The resulting temperature, vertical velocity, and heat flux distributions for the two methods are shown in Figures 5.3.2.4.5-15 through 5.3.2.4.5-17. These figures represent the results using nondimensional numbers. The figures normalize distance by dividing by the inner cylinder radius. Thus, for the temperature and velocity figures, zero is at the inner cylinder and 2.6 is at the outer cylinder. The heat flux figure measures normalized distance around the outer cylinder perimeter, with zero at the bottom and 2.6 is at the top. Temperature was normalized by first subtracting the average of the two wall temperatures, then dividing by the difference between the wall temperatures. Thus, zero on the normalized temperature scale is the average temperature of the walls. Velocity was normalized by dividing by the square root of the product of the gravitational constant, thermal expansion coefficient of air, difference between the wall temperatures, and radial distance between the walls. Heat flux was normalized by dividing by the product of the diameter of the outer cylinder, the air thermal conductivity, and the difference between the local wall temperature and average air temperature.

Figures 5.3.2.4.5-15 through 5.3.2.4.5-17 show that the porous medium approach can produce reasonable average values, but that the details of the spatial distributions are not replicated by the porous medium model. The computational times for the CFD model were not excessive in this case (minutes) because the model was run in a steady-state mode. Transient calculations would use significantly more computational resources (days of computational time for convergence to steady-state for this short-transient problem) and would only be justifiable to develop correlations for use in more computationally efficient models, such as the MSTH model.

Natural convection has also been calculated using the Navier-Stokes CFD capability of ANSYS (BSC 2001 [DIRS 155024]). The initial results were a successful comparison of calculated temperatures and velocities for a concentric cylinder geometry to an empirical correlation from the literature. Initial calculations for a realistic geometry that includes both the invert and drip shield are shown in Figure 5.3.2.4.5-18. This calculation used a steady-state solver with a 1 kW waste package (about 0.2 kW/m) and a 40°C boundary condition 5 m into the near-field rock. This heat source is consistent with a pressurized water reactor waste package several centuries after the thermal peak. In the calculation, the drift wall temperature was about 55°C and the waste package temperature was about 62°C. Peak velocities in this calculation are in the range of 10 to 15 cm/s.

The quarter-scale ventilation test was also used to simulate natural convection by ceasing forced convection and allowing the thermal profile to stabilize, using a heat flux of 0.12 kW/m and an ambient temperature boundary condition at the edge of the insulation (Jurani 2001

[DIRS 155128]). The heat flux was equivalent to a full-scale heat load of about 0.5 kW/m, similar to a boiling water reactor waste package about a century after emplacement. However, the boundary temperature was lower than for a potential repository situation, resulting in lower-than-repository temperatures at the drift wall and waste package. The test was modeled with the Fluent V5.5 software package. The air velocity profile is shown in Figure 5.3.2-1 (Dunn 2001 [DIRS 155308]). The peak velocities of 10 to 16 cm/s are consistent with those in the waste package design initial calculation.

5.3.2.4.5.5 Summary

Based on the results described in this section, the MSTH model used for the SSPA Volume 2 (McNeish 2001 [DIRS 155023]) TSPA used explicit thermal radiation, an effective thermal conductivity for turbulent natural convection, and in-drift air bulk permeability of 10^{-8} m^2.

Figures 5.3.2.4.5-19 and 5.3.2.4.5-20 show the effective thermal conductivities for natural convection that were used, based on this section, in the base case evaluations of the HTOM and LTOM of the design evaluated for the SSPA. In developing these effective conductivities, the three-dimensional effect of the potential repository edge was represented by considering multiple AMLs within the centrally-located two-dimensional LDTH submodel. A lower AML in the two-dimensional submodel is implemented by using a larger effective drift spacing, which in turn reduces the drift wall temperature. At lower drift wall temperatures, radiation is less effective, and the drip shield (and waste package) temperatures must increase to transfer the heat. Thus, the temperature difference between the surfaces is greater for the lower AML and the effective thermal conductivity for natural convection is larger because buoyant convection is driven by the temperature difference.

The effective thermal conductivity for turbulent natural convection based on a correlation developed for concentric cylinders probably does not introduce significant uncertainty in EBS component temperatures (more than several degrees centigrade) based on the insensitivity of those temperatures (Figures 5.3.2.4.5-5, 5.3.2.4.5-6, and 5.3.2.4.5-13). The effective thermal conductivity for natural convection is more sensitive to the temperatures at which the correlation is evaluated (Figure 5.3.2.4.5-1). Efforts to update the effective conductivity for the current design values (rather than using an effective conductivity developed for an earlier design) have proved worthwhile.

In general, a nonzero bulk permeability in the emplacement drift should be specified to reasonably compute the moisture effects on the in-drift relative humidity. The base case in-drift bulk permeability (10^{-8} m^2), in conjunction with the effective thermal conductivity for natural convection, provides nearly the same EBS temperature results while allowing for an appropriate representation of the heat and mass transfer processes occurring within the emplacement drifts. However, if only near-field (rather than EBS) processes are required of a model, a value of zero for air-permeability in the drift is adequate.

5.3.2.4.6 The Influence of Axial and Cross-Sectional Variations in Temperature on In-Drift Condensation

The variations in geometry and thermal output of waste package will result in variation of temperature within a cross-section of an emplacement drift and along the drift axis. Because the in-drift air will be circulated due to natural convection, resulting in a spatially uniform composition, water will preferentially evaporate from warmer surfaces and condense on cooler surfaces due to the small difference in equilibrium of vapor pressure at the temperatures of the surfaces. Surface roughness and the presence of dust will influence the vapor pressure at the surfaces.

The MSTH model (CRWMS M&O 2000 [DIRS 149862]) includes evaporation and condensation on in-drift surfaces, based on thermodynamic properties of the gas and liquid phases. The water then moves along the drift surface under the influence of gravity and capillary forces in the highly permeable porous medium used to simulate the air (air properties are discussed in Section 5.3.2.4.5). This treatment captures much of the two-phase process; however, it does not calculate the details of the geometry of condensation (film thickness or growth of individual drops) on surfaces which can be affected by roughness and on dust which can dissolve into the condensing water.

The TSPA-SR (CRWMS M&O 2000 [DIRS 153246]) model includes humid-air corrosion of the waste packages and drip shields when in-drift air humidity is high enough to deliquesce onto salts in the dust. Therefore, condensation on the waste packages and drip shields is assumed in the current implementation of corrosion in TSPA. In TSPA-SR (CRWMS M&O 2000 [DIRS 153246]), radionuclide transport in the engineered barrier system was assumed to be diffusive until breach of the drip shields by corrosion or disruptive events; the basis of this assumption was that condensate film or drops could be too thin (or small) to flow, flow very slowly, or be hindered by corrosion products, detrital material, or mineral precipitates.

For one SSPA Volume 2 (McNeish 2001 [DIRS 155023]) unquantified uncertainty sensitivity study, the condensation model was improved (Section 8.3.2). Condensation on the underside of the drip shield can occur in the improved model if the vapor pressure at the invert is higher than the saturation pressure at the drip shield. This situation is implemented by assuming there is condensation when the drip shield temperature is less than the invert temperature; the implementation ignores chemical and capillary effects on the vapor pressure in the invert. Condensation is assumed to drip from the drip shield onto the waste package, analogous to the dripping of seepage from a drip shield breach. The volume of condensation is sampled from zero to 100 percent of the evaporation rate of water from the invert (an output of the MSTH model). This sampling qualitatively accounts for the competition for evaporated water by other cool surfaces such as the drift wall and for run-off of some of the condensate along the side of the drip shield.

Improvements in the three-dimensional DDT submodel of the MSTH model have increased the accuracy of in-drift temperature history calculations (Sections 5.3.1 and 5.3.2) that support the improved condensation model described in Section 8.3.2. Results of the base case calculations (Buscheck 2001 [DIRS 155449]) for the HTOM and LTOM are summarized in

Tables 5.3.2.4.6-1 and 5.3.2.4.6-2, respectively. Those results are the focus of the discussion following the tables.

In addition to being an input to the improved, but simple, condensation model in Section 8.3.2, the in-drift temperature histories could be used in detailed condensate geometry calculations in support of a potential license application. Section 10.3 includes a discussion of models to determine condensation film thickness as a function of substrate material, temperature, and relative humidity, to estimate the area for diffusion of radionuclides within the film. That analysis could be useful in developing a model to determine if condensation could form a source for slow flow that could support advection. Test results from the quarter-scale canister tests (Howard et al. 2001 [DIRS 153282]) and from the scope of work that is identified in the technical work plan for the sealed section of the ECRB cross-drift (BSC 2001 [DIRS 155051], Section 1, Items 27 to 33) are other inputs that can be used to support condensate formation and flow modeling.

Table 5.3.2.4.6-1 illustrates the temperatures in three cross-sections through the ten waste package computational cell for the HTOM. The cell includes eight full waste packages and two half waste packages, with the distribution of waste package types and thermal powers being representative of the full inventory of the potential repository. The three cross-sections are through the mid-lengths of the hottest waste package (pressurized water reactor, PWR), an average power waste package (boiling water reactor, BWR), and a cool waste package (defense high level waste DHLW). The times selected include the time of peak preclosure temperature, just after closure, peak postclosure temperature, three times during the slow cooling of the potential repository (as the waste decays), and a final time at which near-ambient temperatures have been reached. The DDT submodel represents radiation under and above the drip shield explicitly, but uses a perimeter-averaged correlation to represent natural convection. More accurate temperatures along the drift wall perimeter will be available when Navier-Stokes computational fluid dynamics models are applied to this system. Section 5.3.2.4.5 illustrates initial results of such models.

During the preclosure period, the low relative humidity of the ventilation air will limit the water content of the in-drift air enough that water films will be negligible. At the peak of the postclosure temperature for the HTOM, all temperatures are sufficiently high that water films would not form. However, under some conditions, highly deliquescent salts in dust on some components may cause condensate formation at low humidity or elevated temperature; these conditions are being studied in support of a potential license application.

Two thousand years after the waste emplacement, before temperatures have cooled to below-boiling values, the range of temperature differences on all surfaces within the three-dimensional cell is less than 4°C. Within a cross section, the range is as little as several tenths of a degree at the cool waste package to as much as almost 3°C at the design basis (hottest) waste package. Along the drift axis, the range is less than 1°C at the drift wall, and as much as about 3°C at the waste package. Thus, the axial range is similar to the range within a cross section.

As temperatures decrease through the boiling point, the coolest surfaces in the drift are at the drift wall. The invert zone under the drip shield is slightly warmer than the drip shield itself.

Since the invert temperature is an average through its half-depth, its surface is hotter than either its average or the drip shield surface. Thus, for the natural convection (perimeter-averaged) correlation and the low value of invert thermal conductivity used in the calculation, condensation would be favored on the drift wall near the coolest waste package. However, condensation depends on surface conditions as well as temperature; thus the temperature relationships are not enough to draw conclusions about condensate geometry on rock, titanium, and gravel.

Airflow patterns of natural convection are expected to shift the temperature of the drip shield (upper region) upward and the temperature of the invert surface under the drip shield downward. Therefore, natural convection could result in a cooler invert than the drip shield, reducing potential condensation on the underside of the drip shield. As corroboration of this logic, observations of the quarter-scale canister test were that the invert was cooler than the drip shield, with no dripping or rivulets observed under the drip shield (Howard et al. 2001 [DIRS 153282]).

Table 5.3.2.4.6-2 illustrates the temperatures in five cross-sections through the ten waste package computational cell for the LTOM. The cell includes the same sequence of waste packages as for the HTOM. However, there are variable length gaps between the waste packages with the goal of smoothing the local lineal heat loading. This geometric smoothing is an alternative to the axial radiation heat transfer between waste package ends that smoothes the local lineal heat loading in the HTOM. The five cross-sections are through the mid-lengths of the hottest waste package (PWR), an average power waste package (BWR), a cool waste package (DHLW), a warm gap, and a cool gap between waste packages. The times selected include the time of peak preclosure temperature, just after closure, three times representing the broad period of near-peak postclosure temperature, during the slow cooling of the potential repository (as the waste decays), and a final time at which near-ambient temperatures have been reached.

During the preclosure period, the low relative humidity of the ventilation air will limit the water content of the in-drift air enough that water films will be negligible. Under some conditions, highly deliquescent salts in dust on some components may be able to cause condensation at low humidity; these conditions are being studied in support of a potential license application. As soon as ventilation ceases for the LTOM, all temperatures are sufficiently low that condensate could form.

At the time of peak waste package temperature, the range of temperature differences on all surfaces within the three-dimensional cell is about 10°C. Within a cross section, the range is as little as 1°C at the cool waste package to as much as 8°C at the design basis (hottest) waste package. Along the drift axis, the range is about 2°C at the drift wall, and about 9°C at the waste package. Thus, the axial range is similar to the range within a cross section.

As temperatures cool, the coolest surfaces in the drift are at the drift wall. The invert zone under the drip shield is slightly warmer than the drip shield itself. Because the invert temperature is an average through its half-depth, the surface is hotter than either the average or the drip shield surface. As for the HTOM, shifts in temperature patterns around the perimeter of air flow loops could reverse the temperature relationship between the drip shield and invert surface, resulting in little condensation on the drip shield underside.

Summary–Temperatures and invert evaporation rates are used as inputs to the drip shield condensation model (see Section 8.3.2) for one SSPA Volume 2 (McNeish 2001 [DIRS 155023]) unquantified uncertainty sensitivity study. Current values of the three-dimensional temperature distribution from the MSTH model would produce condensation on the underside of the drip shields for that model.

The distribution of temperatures within the drift (and the surface properties of the drift wall, drip shield, and invert gravel) will determine the location and thickness of condensation films. Natural convection effects on the temperature distribution along the drip shield perimeter (not included in the MSTH model results) could result in a cooler invert than the drip shield, reducing condensation on the underside of the drip shield. This uncertainty (the absence or presence of condensation under the drip shield) will be addressed in more sophisticated models, the quarter-scale test, and the 44 percent-scale tests in support of a potential license application.

5.3.3 Quantification of Uncertainty Using Analogues

Analogues and multiple lines of evidence from several other sections of this document are pertinent to the in-drift thermal-hydrologic processes within the EBS. In Section 3.3.2, Infiltration Model, there is discussion on the infiltration analogues that have been done. These are pertinent to the in-drift thermal-hydrologic processes in that the analogue is corroborating the amount of infiltration that is being predicted and the resulting seepage that potentially make its way through the various geologic components to the potential repository level. Section 3.3.3, Flow in PTn, discusses the flow potential in the PTn and TSw units. These analogues are useful in understanding lateral flow in the units.

As stated in Section 3.3.4.7, natural analogue studies of fluid flow processes for similar geologic and hydrologic settings provide multiple lines of evidence. Studies have been ongoing at various locations on the Nevada Test Site. One area of similar geologic and hydrologic settings is Rainier Mesa (see Section 3.3.4.7). Another area under investigation is Yucca Mountain. Section 3.3.6.5 discusses some of the "self-analogues" that have been ongoing at Yucca Mountain. Of particular interest are the analogues of geothermal systems and how the coupled processes that are being modeled relate to them (see Sections 3.3.6.5 and 3.3.7.6).

In Section 4, Seepage, there are analogues identified that discuss other scientific work regarding the flow of water in underground openings. Of particular relevance are the discussions in Sections 4.3.1.7, 4.3.2.7, 4.3.5.7, 4.3.6.7, and 4.3.7.7.

Further discussions on natural analogues are contained in the S&ER (DOE 2001 [DIRS 153849], Section 4.2.2.2.3.3). The analogues identified in that report and the aforementioned discussion can be used to demonstrate that the effects of decay heat on waste movement can be evaluated. They also serve to aid in the development and understanding of the process models and abstractions, and predicting future conditions. There is a wide range of information available, from core-scale and outcrop evaluations of fossil thermal-hydrologic-chemical couple processes, understanding of efficient heat transfer mechanism, changes in operating geothermal fields, to dynamic processes with mechanical changes.

5.4 SUMMARY AND PARAMETERS PROVIDED TO TOTAL SYSTEM PERFORMANCE ASSESSMENT

This section summarizes the results of Section 5. Sections 5.3.1.3 and 5.3.2.3 describe changes made to the MSTH model to implement improvements developed since the TSPA-SR (CRWMS M&O 2000 [DIRS 153246]). Sections 5.4.1 and 5.4.2 present results using the improved MSTH model to calculate in-drift thermal-hydrologic conditions for the HTOM and the LTOM, respectively. Section 5.4.3 summarizes the results of applying the MSTH model, its submodels, or other models to investigate the sensitivity of in-drift thermal-hydrologic performance to uncertainties and parameters.

Section 5.2 describes the implementation of the MSTH model (CRWMS M&O 2000 [DIRS 149862]) in the TSPA-SR (CRWMS M&O 2000 [DIRS 153246]). The remainder of the section describes the current implementation of the MSTH model. The most straightforward way to calculate the in-drift thermal-hydrologic parameter histories would be to set up the entire mountain in the MSTH model, including heat and mass transfer at all locations, three-dimensional geometric aspects, and finer zone size in regions of highest gradients and regions important to performance. Unfortunately, such a model would run slowly, perhaps with the simulation time clock running slower than real time. To decrease computational time and memory demands, a common practice is to use nested grids. In this approach, the initial problem is set up with coarse gridding over the full domain. The problem is then rerun repeatedly with smaller and smaller domains and finer zone sizes. Thus, each iteration uses the results from the previous iteration as the input boundary conditions.

In the MSTH model, this idea is developed further. In addition to geometric nesting, the MSTH approach also includes dimensionality nesting (combining two- and three-dimensional results) and physics nesting (combining conduction-dominated results with heat and mass transfer results). Table 5.4-1 provides a roadmap of the submodels and the sequential steps used to combine their outputs. The result is a set of thermal-hydrologic parameter histories (subsystem performance measures) that incorporate the overall footprint of the potential repository, the stratigraphy and infiltration flux distribution, the location of potential individual repository drifts, and the arrangement of individual waste packages (with individual thermal power output histories) within the drifts. The model includes radiation, convection, and conduction heat transfer modes; the movement of liquid and gaseous fluids; and phase change effects.

The thirteen-step process is illustrated in Figure 5.2-2. The SMT, SDT, and LDTH submodels are combined (as described in Steps 1 to 7) to produce the LMTH combined temperatures. Then, the LMTH and DDT submodels are combined (as described in Steps 8-11) to produce the DMTH combined temperatures. Finally, the LDTH submodels are used with the DMTH temperatures to develop the values for all other parameters output by the model.

The thirteen-step process is one of a number of possible computationally efficient methods of combining submodels to address dimensionality, physical processes, and geometric complexity. The method has evolved with the TSPA system-level model. This evolution is based on assumptions or separate calculations that conclude neglect of some processes at some scales will not significantly affect the thermal-hydrologic performance measures. For example, three processes that could have been included in the MSTH model, but were not, are east-west

convective loops above the drifts, north-south convective loops wider than the half-drift spacing, and axial movement of air and water vapor within the drift. Each of these effects could be calculated with the submodels and implemented in the full MSTH model if found to be significant. Similarly, if results of thermal-hydrologic-chemical or thermal-hydrologic-mechanical calculations indicate changes in hydrologic parameters over time, these changes can be included in future implementations of the MSTH model. It is expected that the MSTH model implemented for a potential license application would include additional capabilities such as those listed in this paragraph.

5.4.1 Higher-Temperature Operating Mode Base Case Results

This section describes the MSTH model base-case calculations (Buscheck 2001 [DIRS 155449]) for the HTOM, which includes the mean, upper, and lower infiltration-flux scenarios. Figure 5.4.1-1 is a plan view of the MSTH model representation of the potential HTOM repository; also shown are the geographic locations for which TH conditions are shown in Figures 5.4.1-2 and 5.4.1-3. These locations were chosen to illustrate the manner in which TH behavior is influenced by proximity to the edges of the potential repository. Three of these locations are close to the center of the potential repository; two are located in the extreme northeast and southwest corners of the potential repository area, and two are at the extreme eastern and western edges of the potential repository, approximately midway between the northern and southern boundaries of the potential repository. The temperature and relative-humidity histories fall into three distinct clusters: one for the potential repository center, one for the potential repository corners, and one for the potential repository edge locations (Figure 5.4.1-2). In addition, the relative humidity reduction can be classified into three sequential periods (Figure 5.4.1-2).

During an early period which lasts from 200 to 1,000 yr (Figures 5.4.1-2c and 5.4.1-3a), the relative humidity reduction on waste packages depends on the magnitude and duration of rock dryout. The duration of rock-dryout increases with distance from the potential repository edges. The farther a given waste package is located from the potential repository edge, the longer the duration of boiling in the local host rock and the longer the duration of rock dryout (and relative humidity reduction). The surface of the waste packages always have a lower relative humidity than the adjacent host rock; consequently, during the early period, the reduction in relative humidity on waste packages increases with distance from the potential repository edges.

The depth of dryout varies with location within the footprint and with infiltration flux. The deepest horizontal extent of boiling temperatures was 13.l, 10.6, and 10.1 m from the drift center, for the lower, mean, and upper infiltration flux scenarios, respectively.

An intermediate period, which lasts from 1,000 yr to about 20,000 yr, during which time heat-transfer in the drift controls the magnitude of relative humidity reduction on waste packages. During this period, the reduction in relative humidity on waste packages decreases with distance from the potential repository edges, which is the reverse of the trend during the early period. During the intermediate period, the reduction in relative humidity is greater at the potential repository edges because the efficiency of thermal radiative heat transfer decreases with temperature. Consequently, for a given local heat generation rate there is a larger temperature difference $\Delta T_{\text{wp-dw}}$ between the waste package and drift wall at locations with lower temperature

(such as occurs close to the potential repository edges). Moreover, the reduction in relative humidity, which depends on the ratio of $P_{sat}(T_{dw})/P_{sat}(T_{wp})$, results in a larger relative humidity reduction for a given $\Delta T_{wp\text{-}dw}$, where P_{sat} is the saturation vapor pressure, T_{dw} is the drift wall temperature, and T_{wp} is the waste package temperature.

A late period, beginning around 20,000 yr, during which time the reduction in relative humidity on waste packages becomes decreasingly sensitive to proximity to the potential repository edges. For a given waste package type, the reduction in relative humidity becomes increasingly similar across the potential repository area.

Figure 5.4.1-4 shows the influence of the edge-cooling effect. Locations close to the potential repository edges cooling more quickly than those at the center. Figure 5.4.1-5 shows the development of the reduction in relative humidity on waste packages. At early times, the reduction in relative humidity increases with distance away from the potential repository edges, while at intermediate to later times, the reduction in relative humidity decreases with distance from the potential repository edges.

Figures 5.4.1-3b and 5.4.1-3c show the relationship between liquid saturation in the invert and evaporation rate. During early times, while the invert is dry, the evaporation rate is zero. The onset of rewetting in the invert corresponds to the end of the boiling/rock-dryout period. Consequently, the time of the onset of rewetting increases with distance from the potential repository edges. The two geographic locations that experience a larger eventual increase in liquid saturation in the invert correspond to the two locations wherein the local host rock is either the middle or the lower nonlithophysal Topopah Spring welded tuff unit (Tptpmn or Tptpln). Wherever the local host-rock unit is comprised of the lower lithophysal unit (Tptpll), the maximum liquid saturation in the invert is nearly the same (and lower than in locations where the local host-rock unit is either Tptpmn or Tptpln). Apparently, there is a difference in rewetting behavior in the invert that depends on the local host-rock unit. The second spike in the invert evaporation rate occurs shortly after 600 years when a substantial increase in infiltration flux occurs. The increase in infiltration rate is accompanied by an increase in liquid-phase flux into the invert, which makes more water available for evaporation in the invert.

Figure 5.4.1-6 shows the complementary cumulative distribution functions for temperature and relative humidity on the drift wall and on the waste package for the mean, lower, and upper infiltration-flux scenarios. For the mean-infiltration-flux scenario, the peak waste package temperature ranges from 126.1º to 184.9ºC. The peak waste package temperature is similar for the mean and lower infiltration-flux scenarios. The upper infiltration-flux scenarios result in lower peak waste package temperatures, particularly for the coolest waste packages; the range for this scenario is 105.4º to 183.1ºC. The time required for the drift-wall to cool down to 96ºC (which is the boiling point of water at the potential repository horizon) is more sensitive to infiltration flux than peak temperature (Figure 5.4.1-6b). The time required for the waste package to attain relative humidity equal to 80 percent is similar for the mean and upper-infiltration flux scenarios (Figure 5.4.1-6c). The lower-infiltration-flux scenario results in much more persistent relative humidity reduction on waste packages, particularly for the driest waste packages. The waste package temperature at the time when relative humidity equals 80 percent on the waste package is similar for the mean and upper infiltration-flux scenarios

(Figure 5.4.1-6d); the lower infiltration-flux scenario results in lower temperatures when relative humidity equals 80 percent is attained.

Figure 5.4.1-7 shows the waste package-to-waste package variability of temperature and relative humidity at a location in the potential repository relatively close to the geographic center for the mean infiltration-flux scenario. Peak waste package temperatures range from 152.3º to 180.1ºC. The use of line-load waste package spacing results in a relatively narrow range of peak temperatures (27.8ºC). The three coolest waste packages are all DHLW waste packages. The three hottest waste packages are all PWR waste packages. The old PWR waste package and BWR waste packages fall in the middle of the temperature range. The reduction in relative humidity on waste packages correlates directly with temperature on the waste package. Therefore the PWR waste packages always experience the greatest relative humidity reduction, while the DHLW waste packages experience the least relative humidity reduction. At late times there is a greater range of relative humidity reduction resulting from waste package-to-waste package variability than arising from the distance from the potential repository edges (compare Figures 5.4.1-7b and 5.4.1-2d).

The HTOM thermal-hydrologic results were abstracted and provided to TSPA (Francis and Itamura 2001 [DIRS 155321]) for use in SSPA Volume 2 (McNeish 2001 [DIRS 155023]).

5.4.2 Lower Temperature Operating Mode Base Case Results

This section describes the multiscale thermal-hydrologic (MSTH) model base-case calculations (Buscheck 2001 [DIRS 155449]) for the LTOM, which includes the mean, upper, and lower infiltration-flux scenarios. Figure 5.4.2-1 gives the plan view of the MSTH model representation of the potential LTOM repository; also shown are the geographic locations for which TH conditions are given in Figures 5.4.2-2 and 5.4.2-3. The potential LTOM repository area is 20 percent larger than the potential HTOM repository (Figure 5.4.1-1). These locations were chosen to illustrate the manner in which TH behavior is influenced by proximity to the edges of the potential repository. Four of these locations are close to the center of the potential repository; two are located in the extreme northeast and southwest corners of the potential repository area, and two are at the extreme eastern and western edges of the area, approximately midway between the northern and southern boundaries. The temperature and relative-humidity histories fall into three distinct clusters (one for the potential repository-center locations, one for the potential repository corners, and one for the potential repository-edge locations), and the reduction in relative humidity can be classified into two sequential periods (Figure 5.4.2-2).

An early-to-intermediate period lasts for about 20,000 years, during which time heat-transfer in the drift controls the magnitude of the reduction in relative humidity on waste packages. Because the temperatures for the LTOM are always below the boiling point of water, there is no rock dryout period, and no reduction in relative humidity in the host rock (Figure 5.4.2-2c); therefore, all reductions in relative humidity on waste packages arise as a result of the temperature differences, $\Delta T_{\text{wp-dw}}$, between waste packages and the drift wall. The early-to-intermediate period for the LTOM case has the same trends as observed for the intermediate period for the HTOM case (Section 5.4.1). During this period, the reduction in relative humidity on waste packages decreases with distance from the potential repository edges.

A late period, beginning around 20,000 years, occurs during which the reduction in relative humidity on waste packages becomes decreasingly sensitive to proximity to the potential repository edges. For a given waste-package type, the reduction in relative humidity becomes increasingly similar across the potential repository area.

Figure 5.4.2-4 shows the influence of the edge-cooling effect, with locations close to the potential repository edges cooling more quickly than those at the center. Figure 5.4.2-5 also shows the trend of the reduction in relative humidity on waste packages increasing with proximity to the potential repository edges.

Figures 5.4.2-3a and 5.4.2-3b show the relationship between liquid saturation in the invert and evaporation rate. At the end of the ventilation period, the invert is assumed to be dry in the model. Rewetting of the invert begins immediately after the end of the ventilation period, which occurs at 300 yr. Therefore, evaporation rates in the invert are always nonzero. Rewetting of the invert occurs more quickly at potential repository-edge locations than at potential repository-center locations because the edge-cooling effect reduces the amount of heating available to evaporate the incoming water. At 300 yr, a rapid increase is seen in the evaporation rate as the liquid-phase flux into the invert immediately increases following the end of the ventilation period. The two geographic locations that experience a larger eventual increase in liquid saturation in the invert correspond to the two locations wherein the local host rock is either the middle or lower non-lithophysal Topopah Spring welded tuff unit (Tptpmn or Tptpln). Wherever the local host-rock unit is comprised of the lower lithophysal unit (Tptpll), the maximum liquid saturation in the invert is nearly the same (and lower than in locations where the local host-rock unit is Tptpmn or Tptpln). Apparently, there is a difference in re-wetting behavior in the invert that depends on the local host-rock unit.

Figure 5.4.2-6 gives the complementary cumulative distribution functions for temperature and relative humidity on the waste package for the mean, lower, and upper infiltration-flux scenarios. For the mean-infiltration-flux scenario, the peak waste package temperatures range from 59.2º to 86.0ºC, with only 1.7 percent of the waste packages ever exceeding 85ºC. For the low-infiltration-flux scenario, the temperatures are higher than in the mean-infiltration-flux scenario, ranging from 60.5º to 87.6ºC, with 7.2 percent of the waste packages exceeding a peak temperature of 85ºC. The upper infiltration-flux scenario results in lower peak waste package temperature that ranges from 59.0º to 85.3ºC, with only 0.02 percent of the waste packages ever exceeding 85ºC.

Figure 5.4.2-6b, which gives the complementary cumulative distribution function of the time required for waste packages to attain a relative humidity of 80 percent show a distinct change in the slope of the curves at a complementary cumulative distribution function value of 0.7; this sharp break in the slope of the complementary cumulative distribution function curves indicates that there are two distinctively different groups of waste packages with respect to the duration of relatively dry relative humidity on the waste-package surfaces. In the MSTH model (Buscheck 2001 [DIRS 155449]), 30 percent of the waste packages are DHLW waste packages and 70 percent are CSNF waste packages. A detailed inspection of the underlying data that are plotted in Figure 5.4.2-6b show that the break in slope at a complementary cumulative distribution function value of 0.7 correspond with the fact that 30 percent of the waste-package inventory that attains an relative humidity of 80 percent first (i.e., having a complementary

cumulative distribution function value between 0.7 and 1.0) is entirely comprised of DHLW waste packages. Those waste packages that have a complementary cumulative distribution function value between 0.0 and 0.7 are nearly entirely comprised of CSNF waste packages. Thus, 99 percent of the DHLW waste packages have a relatively short duration of reduced relative humidity, requiring less than 877 years to attain a relative humidity of 80 percent; the remaining 1 percent of the DHLW waste packages require between 877 and 1020 years to attain a relative humidity of 30 percent. All CSNF (PWR and BWR) waste packages require at least 877 years to attain a relative humidity of 80 percent; the driest PWR requires 4864 years to attain a relative humidity of 80 percent.

The time required for the waste package to attain a relative humidity of 80 percent is similar for all three infiltration flux scenarios (Figure 5.4.2-6b). Because rock dryout does not occur, the reduction in relative humidity depends entirely on multi-scale heat flow occurring in the rock at the mountain scale and within the drift at the waste package scale. The waste package temperature at the time when the relative humidity reaches 80 percent on the waste package is highest for the lower-infiltration-flux scenario and lowest for the upper infiltration-flux scenario (Figure 5.4.2-6c).

The LTOM results in a more persistent relative humidity reduction on waste packages than does the HTOM (compare Figure 5.4.2-6b with Figure 5.4.1-6c). Moreover, the LTOM results in lower waste package temperatures at 80 percent relative humidity than does the HTOM (compare Figure 5.4.2-6c with Figure 5.4.1-6d). In general, the LTOM case results in lower waste package temperatures at any given value of relative humidity on the waste package than does the HTOM case.

Figure 5.4.2-7 shows the waste package-to-waste package variability in temperature and relative humidity at a location in the potential repository that is relatively close to the geographic center. Peak waste package temperatures range from 73.1 to 85.4ºC. The three coolest waste packages are all DHLW waste packages. The three hottest waste packages are all PWR waste packages. The old PWR waste package and BWR waste packages fall in the middle of the temperature range. The reduction in relative humidity on waste packages correlates directly with temperature on the waste package. Therefore the PWR waste packages always experience the greatest reduction in relative humidity, while the DHLW waste packages experience the smallest reduction in relative humidity. At late times, there is a greater range of relative humidity reduction resulting from waste package-to-waste package variability than arising from the distance from the potential repository edges (compare Figure 5.4.2-7b with Figure 5.4.2-2d).

Figure 5.4.2-8 compares the TH conditions on typical PWR waste package surfaces for the HTOM and LTOM cases. All geographic locations (edge, corner, and center) are included within the shaded regions for the two operating modes. The bands of the TH conditions represent the progression in time, ending at ambient conditions of about 25°C and 100 percent relative humidity. The LTOM results in lower relative humidity for any given temperature, or lower temperature for any given relative humidity for all locations except for the corner of the

potential repository where the HTOM results in lower relative humidity or temperature than the central LTOM locations. The LTOM thermal-hydrologic results were abstracted and provided to TSPA (Francis and Itamura 2001 [DIRS 155321]) for use in Volume 2 (McNeish 2001 [DIRS 155023]).

5.4.3 Process Model Results

Section 5.3.1 evaluated the multiscale model for in-drift hydrologic conditions, while Section 5.3.2 evaluated ventilation and convection modeling of in-drift thermal-hydrologic conditions. Quantification of uncertainties related to in-drift hydrologic conditions and to ventilation and convection evaluations are presented in Sections 5.3.1.4 and 5.3.2.4, respectively, based on the process models used to investigate the sensitivity of in-drift TH performance to a number of uncertainties and parameters. Each of those sections includes a short summary of the results of the sensitivity calculations.

In this section, the results of the sensitivity studies are compared to determine which parameters and uncertainties are most important for in-drift TH performance. Table 5.4.3-1 shows the results of the sensitivity studies. The table indicates which uncertainty is dealt with in each subsection and lists the parameter or uncertainty range considered in the sensitivity studies. When a sensitivity study evaluated the effects of considering or not considering the parameter in the analyses rather than considering a range of values, this is indicated as include or exclude. The table indicates the values used in the base case analyses (or whether the parameter was included or excluded), the performance measures considered, and what the results of the sensitivity studies indicated were the effects of the range of parameter values or uncertainty on the performance measure.

Analyses were conducted using the submodels of the multiscale thermal-hydrologic model, to consider the sensitivity to operational parameters, and the sensitivity to the uncertainty and variability of properties of the natural and engineered systems. These analyses considered both the HTOM and LTOM cases. The focus was on the effects of heat-driven coupled-processes on in-drift thermal-hydrologic conditions. The TH conditions considered include temperature and relative humidity at the waste packages and drip shield, and saturation at the drift wall and in the invert.

Peak temperatures at the drip shield and waste package were most sensitive to ventilation parameters and to thermal conductivity values used in the models. The uncertainty in host rock thermal conductivity had the most significant effect. The drift wall and drip shield peak temperatures had a range of 85 and 20°C (for the HTOM and LTOM) resulting from a thermal conductivity range of 1.13-2.01 W/m•K (saturated) and 0.54-1.54 W/m•K (dry). The key factor determining the spatial variability of thermal conductivity is the variability of lithophysal porosity. The range of drift wall and drip shield temperatures was about 100 and 25°C (for the HTOM and LTOM) when a range of 0 to 25 percent of lithophysal porosity was used. The increase in temperature was due to the additional effect of porosity on heat capacity, in addition to the effect on thermal conductivity.

The second most significant factors were those related to ventilation. There was a range of about 60°C (for both the HTOM and LTOM) in pre-closure peak drip shield temperatures resulting from using constant versus time-dependent ventilation efficiency. A 14 and 7°C postclosure drip shield temperature range (for the HTOM and LTOM) resulted from a 20 percent variation in ventilation efficiency (heat removal). For the LTOM, it was concluded that a 44-year variability in ventilation duration from one part of the potential repository to another would have only a minor effect on postclosure temperatures.

The significant uncertainties resulting from using 2D analyses were also quantified. The detailed 3D analyses of in-drift TH effects calculated 26 and 8°C ranges (for the HTOM and LTOM) in postclosure peak temperatures from the hottest to the coolest waste packages.

The ventilation efficiency was calculated using two independent models, and compared to the quarter-scale tests. The models, which used a wide range of convective heat transfer coefficients, bracketed the measured results. The influence of water entering the drift and evaporating into the dry ventilation air was not significant on overall ventilation efficiency, and had only a minor effect on ventilation air humidity.

A number of other parameters were investigated, including the effect of lithophysal porosity on gas storage, seepage effects on in-drift humidity, imbibition hysteresis, buoyant gas-phase convection in the rock, THC and THM processes, host rock permeability, invert conductivity, and treatment of thermal radiation and natural convection in the drift. These parameters had only small effects on the magnitude of in-drift temperatures. However, the invert conductivity and the sophistication of natural convection models were found to influence which part of the EBS are cooler than others, with potential influence on formation of condensate which could be the source for corrosion or transport.

Finally, multiple approaches to achieving LTOM temperatures were evaluated. Derating PWR waste packages was the most effective method of reducing peak temperatures, followed by waste package spacing, and finally, drift spacing (for line-loaded drifts). However, the range of temperatures among these methods was small (within 7°C); therefore, other factors such as worker safety or cost should be considered when selecting a license application design for lower-temperature operation.

Summary–In general the model results considered in Section 5 have provided: 1) additional understanding of recognized uncertainties associated with thermal-hydrologic modeling as implemented in the MSTH model and ventilation models; 2) increased confidence in predicted temperature, relative humidity, and other measures of the in-drift environment over a range of thermal conditions bounded by the assumed HTOM and LTOM, and 3) increased confidence in the results of the TSPA-SR. Those results that use the more detailed process models are an additional line of evidence from the TSPA (abstracted) model results.

INTENTIONALLY LEFT BLANK

Table 5.1-1. Design Parameters Used in Sensitivity Studies to Address Three Operational Modes

Design feature	Higher-Temperature Operation Mode (above boilin repository)	96°C Drift Wall (Not Analyzed)	Lower-Temperature Operating Mode (85°C Waste Package)
Drift spacing	81 m	81 m	81 m
Areal Mass Loading	54.5 MTU/acre	54.5 MTU/acre	45.7 MTU/acre
Repository footprint	4.65 km^2	4.65 km^2	5.58 km^2
Lineal Power density	1.35 kW/m	1.35 kW/m	1.13 kW/m
Length of Ventilation	50 yrs forced	300 yrs forced	300 yrs forced
Heat removal by Ventilation	70 %	80%	80%
Waste Package configuration/spacingation	Line load, 10 cm	Line load, 10 cm	Line/point load, gaps from 10 cm to 2.8 m

Source: BSC 2001 [DIRS 154864].

Table 5.2-1. Near Field Environment and Engineered Barrier System Thermal-Hydrologic Variables Calculated with the Multiscale Thermal-Hydrologic Model at 610 Repository Locations for No-Backfill Realizations

Thermal-Hydrologic Variable	Drift-Scale Location
Near Field Environment Parameters	
Temperature	Near Field Environment rock (5 m above drift and along the entire repository horizon)
	Maximum lateral extent of boiling
	Upper drift wall (crown of the drift)
	Lower drift wall (below invert)
	Drift wall (perimeter average)
Relative Humidity	Drift-wall (perimeter average)
Liquid-phase matrix saturation	Drift wall (perimeter average)
Liquid-phase flux	Near Field Environment host rock (5 m and 3 m above crown of drift)
	Drift-wall (upper surface perimeter average in matrix & fractures)
Gas-phase (water vapor) flux	Drift wall (perimeter average)
Gas-phase (air) flux	Drift wall (perimeter average)
Evaporation rate	Near Field Environment rock (5 m above drift)
Engineered Barrier System Parameters	
Temperature	Drift wall (perimeter average)
	Drip shield (perimeter average and upper surface)
	Waste Package (surface average)
	Invert (average)
Relative humidity	Drift-wall (perimeter average)
	Backfill (crown)
	Drip shield (perimeter average)
	Waste package
	Invert (average)

Table 5.2-1. Near Field Environment and Engineered Barrier System Thermal-Hydrologic Variables Calculated with the Multiscale Thermal-Hydrologic Model at 610 Repository Locations for No-Backfill Realizations (Continued)

Thermal-Hydrologic Variable	Drift-Scale Location
Engineered Barrier System Parameters	
Liquid-phase matrix saturation	Drift wall (perimeter average)
	Invert (average)
Liquid-phase flux	Drip shield (crown, upper surface average, and lower side at the base)
	Invert (average)
Gas-phase air-mass fraction	Drip shield (perimeter average)
Gas-phase pressure	Drip shield (perimeter average)
Capillary Pressure	Invert (average)
	Drift wall (crown, in matrix and in fractures)
Gas-phase (water vapor) flux	Drift wall (perimeter average)
Gas-phase (air) flux	Drift wall (perimeter average)
Evaporation Rate	Drip shield (perimeter total and crown) (calculated during the abstraction)
	Invert (total)

Source: Modified from CRWMS 2000 [DIRS 153363], Table 3-6.

Table 5.3.1.2-1. Key Thermal-Hydrologic Uncertainties

Model (Conceptual) Uncertainty (Section 5.3.1.2.1)	Process Uncertainty (Section 5.3.1.2.2)	Input Data Uncertainty (Section 5.3.1.2.3)
Use of effective thermal conductivity and thermal radiation approaches		
Porous media approximation of comprehensive fluid dynamics processes	Hysteresis of imbibition	Invert properties
Use of single continuum versus DKM approach for invert materials	THM and THC changes to hydrologic properties	Host rock bulk permeability
Neglecting dryout during ventilation		Host rock thermal conductivity
Coupling of submodels		Host rock heat capacity
Localized effects of seepage		Heat output of waste packages
Neglecting fracture heterogeneity impacts on seepage		Impacts of lithophysal porosity on thermal conductivity
Neglecting effects of mountain-scale gas-phase convection		Wet and dry thermal conductivity
Effects of lithophysal porosity on vapor storage		Duration of ventilation

Source: Developed for this document.

NOTE: DKM = dual permeability mode
THM = thermal-hydrologic-mechanical
THC = thermal-hydrologic-chemical.

Table 5.3.1.4.2-1. Statistical Parameters Used in the Three-Dimensional, Heterogeneous Line-Averaged-Heat-Source, Drift-Scale Thermal-Hydrologic Model Realizations

Stochastic Realization	Standard Deviation of *k* (log_{10})	Correlation Length (m)			van Genuchten Alpha Value Correlated to *k*
		Lateral (x)	Axial (y)	Vertical (z)	
A-56	1.5	0.5	0.5	4.0	yes
A-34	1.5	0.5	0.5	4.0	yes
B-56	1.5	0.5	0.5	4.0	no
B-34	1.5	0.5	0.5	4.0	no
C-56	1.0	1.0	1.0	1.0	yes
C-34	1.0	1.0	1.0	1.0	yes
D-56	2.3	1.0	1.0	2.0	yes
D-34	2.3	1.0	1.0	2.0	yes

Source: BSC 2001 [DIRS 155007], Table 6-8.

Table 5.3.1.4.2-2. Summary of Seepage Conditions When TH Conditions Have Returned to Near-Ambient (Glacial Climate)

Stochastic Realization	Seepage Percentage Entering Drift (%)	Seepage Percentage Contacting Drip Shield (%)
A-56	37.5	30.4
A-34	54.8	13.6
B-56	27.9	0.1
B-34	21.3	4.4
C-56	0.0	0.0
C-34	0.0	0.0
D-56	42.9	11.0
D-34	85.5	26.4

Source: BSC 2001 [DIRS 155007], Table 6-10.

NOTE: Seepage percentage is the fraction of the incident average percolation flux.

Table 5.3.1.4.6-1. Input Parameters and Data Tracking Numbers for Distinct Element Analysis

Description	Value	Units	Data Tracking Number (DTN)
Matrix properties			
Dry bulk density	2,270	kg/m^3	MO0010RDDAAMRR.002 [DIRS 154048]
Intact rock elasticity modulus	33.03	GPa	MO9911SEPGRP34.000 [DIRS 148524]
Rock mass elasticity modulus	24.71	GPa	MO9911SEPGRP34.000 [DIRS 148524]
Poisson's ratio	0.21	none	MO9911SEPGRP34.000 [DIRS 148524]
Joint properties			
Joint friction	41	degrees	MO0003SEPDRDDA.000 [DIRS 147607]
Joint cohesion	0.09	MPa	MO9911SEPGRP34.000 [DIRS 148524]
Joint dilation angle	29	degrees	MO9911SEPGRP34.000 [DIRS 148524]
Initial joint aperture	0.098	mm	LB990501233129.001 [DIRS 106787]
Thermal properties			
Thermal expansion coefficient	9.73E-6	degrees C^{-1}	MO0004RIB00035.001 [DIRS 153848]
Stress and stress gradient			
In situ stress (at 380m depth)	7.6	MPa	MO0007RIB00077.000 [DIRS 154087]
Vertical stress gradient	0.023	MPa/m	MO0007RIB00077.000 [DIRS 154087]
Input temperature			
Input temperatures	various	degrees C	LL000114004242.090 [DIRS 142884]

Source: Blair 2001 [DIRS 155005], Table 2.

Table 5.3.1.4.6-2 Comparison of Range of Bulk (Fracture) Permeability Values for Geologic Units Considered in Multiscale Thermal-Hydrologic Model Sensitivity Studies to Potential Range from THM Effects

Geologic Unit	Mean Value of Permeability (k), m^2 (As Reported in Table 5.3.1.4.7-1)	Variability of Permeability in Thermal-Hydrologic Sensitivity Studies		Potential Changes From Mean *k* Due to THM
		Permeability Range Considered in Effects of Bulk Permeability, m^2 (Section 5.3.1.4.7)*	Range of Permeability Considered in Seepage Analyses (Section 5.3.1.4.2)	
tsw32	2.51 E-12	1.58 E-13 3.98E-11		2.5 E-17 1.5 E-11
33	8.79 E-13	5.55 E-14 1.39 E-11		8.8 E-18 5.3 E-12
34	3.68E-13	2.32 E-14 5.83 E-12		3.7 E-18 2.2 E-12
35**	2.38 E-12	1.50 E-12 3.77 E-13	2.9 E-14 2.8 E-11	2.4E-17 1.4 E-11
36/37	1.38 E-12	8.71 E-13 2.19E-12		1.4 E-17 8.3 E-12

Source: The last column was produced by multiplying column two by six and dividing by 100,000, applying the results of Blair 2001 [DIRS 155005], Section 6.3.3.

NOTE: * = ± 2 standard deviations from mean
** = lower lithophysal subunit.

Table 5.3.1.4.6-3. Summary of Thermal-Hydrologic-Mechanical Simulations of the Large Block Test

Simulation #	Number of Fractures	CTE (per °C)	Description
1	0	5.27 E-06	Continuum model
2	6	9.73 E-06	High CTE with 6 major fractures
3	6	5.27 E-06	Low CTE with 6 major fractures
4	7	5.27 E-06	Same as 3 with one additional fracture
5	28	5.27 E-06	Additional fractures included in fracture analysis

Source: Produced using files from Blair 2001 [DIRS 155309].

NOTE: CTE = coefficient of thermal expansion.

Table 5.3.1.4.7-1. Bulk (Fracture) Permeability Values for Geologic Units used in the Multiscale Thermal-Hydrologic Model Analyses, Along with the Assumed Value of Sigma used in the Sensitivity Study of k_b

Unit	Permeability (k), m^2	log(k)	sigma (log k_b)	two sigma (log k_b)
tsw32	2.51e-12	-11.600	0.60	1.2
33	8.79e-13	-12.056	0.60	1.2
34	3.68e-13	-12.434	0.60	1.2
35	2.38e-12	-11.623	0.60	1.2
36/37	1.38e-12	-11.860	0.60	1.2

Source: Produced using files from Buscheck 2001 [DIRS 155012].

NOTE: No sigmas for tsw31 or 38/39. The high and low k_b cases assumed one sigma and that the very high and very low k_b cases assume two sigma deviation from the mean k_b value.

Table 5.3.1.4.8-1. Lithophysal Unit Thermal Conductivity Values Used in the MSTH Model Sensitivity Analyses

	Lithophysal Porosity		Saturated Thermal Conductivity (W/m•K)		Dry Thermal Conductivity (W/m•K)	
K_{th} Case	Lower Lithophysal Unit, Tptpll	Upper Lithophysal Unit, Tptpul	Lower Lithophysal Unit, Tptpll	Upper Lithophysal Unit, Tptpul	Lower Lithophysal Unit, Tptpll	Upper Lithophysal Unit, Tptpul
High K_{th}	0%	5%	2.02	2.13	1.54	1.43
Mean K_{th}	12.5%	21.6%	1.87	1.55	1.27	0.84
Low K_{th}	25%	38%	1.13	0.74	0.64	0.31

Source: Adapted from BSC 2001 [DIRS 155008].

Table 5.3.1.4.8-2. Comparison of Relative Humidity Conditions on Drift Wall as Function of K_{th} for the Higher-Thermal Operating Mode Case

K_{th}	RH at 50-60 years post-emplacement	RH at 400 years post-emplacement	RH at 1000 years post-emplacement	Time to reach 60% Relative Humidity	Time to reach 95% Relative Humidity
High K_{th}	28%	70%	100%	280 years	700 years
Mean K_{th}	20%	60%	95%	400 years	1000 years
Low K_{th}	3-5%	23%	60%	1000 years	2000 years

Source: Produced using files from Buscheck 2001 [DIRS 155012].

Table 5.3.1.4.9-1. Lithophysal Porosity Values used in MSTH Model Sensitivity Analyses

K_{th} Case	Lithophysal Porosity	
	Lower Lithophysal Unit, Tptpll	Upper Lithophysal Unit, Tptpul
High K_{th}	0%	5%
Mean K_{th}	12.5%	21.6%
Low K_{th}	25%	38%

Source: Produced using files from BSC 2001 [DIRS 155008], Table 24.

Table 5.3.1.4.10-1. Thermal Conductivity in the Upper Half of the Invert for the Sensitivity Calculation

Case	Nominal Thermal Conductivity (W/m•K)	First Continuum Thermal Conductivity (W/m•K)	Second Continuum Thermal Conductivity (W/m•K)
Base (no steel credit)	0.15	0.075	0.075
Intermediate	0.835	0.76	0.075
As-built	1.52	0.76	0.76
Additional steel	3.04	1.52	1.52

Source: Produced using files from Reed 2001 [DIRS 155076].

Table 5.3.1.4.10-2. Calculated Peak Temperatures for Each Invert Conductivity

EBS Locations	Temperature (°C) Resulting From The Invert Conductivity			
	Base	Intermediate	As-Built	Additional Steel
Drift wall crown	147	146	145	145
Drift wall rib	150	148	148	147
Invert lower-center	143	150	152	152
Drip shield top	161	159	159	158
Drip shield base	163	160	160	159

Source: Produced using files from Reed 2001 [DIRS 155076].

Table 5.3.1.4.11-1. Waste Package Peak Temperatures for the Three Lower-Temperature Operating Mode Sensitivity Cases

Case	Design Parameters	Operational Parameters	Fraction of Waste Packages with Peak Temperature >85°C (Full MSTH Results)	Peak Waste Package Temperature (Full MSTH Results)	Peak Waste Package Temperature (L5C3 MSTH Results)
LTOM-PA Base Case	5.5 m drift diameter 81 m drift spacing 21 PWR WPs	15 m^3/s ventilation for 300 yr, 1.1 m average WP spacing	1.7%	86.0°C	84.3°C
Wider Drift Spacing	5.5 m drift diameter 97 m drift spacing 21 PWR WPs	15 m^3/s ventilation for 300 yr, 0.1 m WP spacing	Not calculated	Not calculated	88.8°C
De-rated WP Capacity	5.5 m drift diameter 81 m drift spacing 16 PWR WPs	15 m^3/s ventilation for 300 yr, 0.1 m WP spacing	0%	82.6°C	81.7°C

Source: Produced using files from Buscheck 2001 [DIRS 155449].

NOTES: The three sensitivity cases use the full MSTH model and a simplified implementation of the MSTH model at a single location in the repository footprint.

PWR = pressurized water reactor; MSTH = multiscale thermal-hydrologic; WP = waste package.

Table 5.3.2.4.1-1. Preclosure Temperatures and Ventilation Efficiencies Calculated with Two Models

Parameter	10 m^3/s		15 m^3/s	
	ANSYS	MULTIFLUX	ANSYS	MULTIFLUX
Peak Drift Wall Temperature	94°C	93°C	76°C	71°C
Peak Air Temperature	79°C	85°C	64°C	67°C
Average Efficiency, 50-yr duration	68%	91%	74%	94%
Average Efficiency, 100-yr duration	73%	93%	78%	95%
Average Efficiency, 200-yr duration	77%	96%	82%	97%

Source: Produced from information in CRWMS M&O 2000 [DIRS 120903] and BSC 2001 [DIRS 155025].

Table 5.3.2.4.1-2. Fraction of Total Heat Removal via Ventilation Due to Latent Heat of Water Vaporized from the Near-Field Rock

Period From Start of Ventilation (year)	Average Latent Heat Removal During the Period (% of Total Heat Removal by Ventilation)	
	10 m^3/s	15 m^3/s
0.5	1.93%	0.99%
5	2.82%	1.38%
25	2.21%	1.35%
50	1.98%	1.30%
100	1.95%	1.31%
200	2.08%	1.43%
300	2.24%	1.55%

Source: Produced from information in BSC 2001 [DIRS 155025].

Table 5.3.2.4.2-1. Summary of HTOM Thermal-Hydrologic Parameter Sensitivity to Ventilation Efficiency

Case	Time-Averaged Ventilation Efficiency	Drip Shield Top Peak Preclosure Temperature (°C)	Drip Shield Top Peak Postclosure Temperature (°C)	Drift Wall Crown Peak Temperature (°C)	Time for Drip Shield To RH > 50 % (year)	Time for Drift Wall Crown RH > 50 % (year)
-10%	60%	117	166	153	460	320
Base case	70%	94	158	146	400	280
Averaged f(t)	73%	87	156	144	380	260
f(t)	73%	146	155	143	380	260
+10%	80%	70	152	139	340	240

Source: Produced using files from Leem 2001 [DIRS 155457].

Table 5.3.2.4.2-2. Summary of Lower-Temperature Operating Mode Thermal-Hydrologic Parameter Sensitivity to Ventilation Efficiency

Case	Time-Averaged Ventilation Efficiency	Drip Shield To Peak Preclosure Temperature (°C)	Drip Shield Top Peak Postclosure Temperature (°C)	Drift Wall Crown Peak Temperature (°C)
-10%	70%	82	79	76
Base case	80%	63	76	72
Averaged f(t)	83%	57	75	71
f(t)	83%	120	74	71
+10%	90%	43	72	69

Source: Produced using files from Leem 2001 [DIRS 155457].

Table 5.3.2.4.3-1. Summary of Lower-Temperature Operating Mode Thermal-Hydrologic Parameter Sensitivity to Ventilation Duration

Case	Ventilation Duration	Drip Shield To Preclosure Temperature (°C)	Drip Shield Top Peak Postclosure Temperature (°C)	Drift Wall Crown Peak Postclosure Temperature (°C)
Shorter Ventilation Duration	278 years	63	77	73
Base case	300 years	63	76	72
Longer Ventilation Duration	322 years	63	75	71

Source: Produced using files from Leem 2001 [DIRS 155457].

Table 5.3.2.4.5-1. Bulk Permeabilities for In-Drift Air

Case Study	Bulk Permeability (m^2)
Low value	0
Fracture-permeability-limited	4.76×10^{-12}
Base case	10^{-8}
High value	2×10^{-5}

Source: Produced using files from Francis 2001 [DIRS 155075].

Table 5.3.2.4.6-1. In-Drift Temperatures for the Higher-Temperature Operating Mode (Page 1 of 2)

Location	Temperature, °C						
	10 yr*	51 yr	65 yr**	200 yr	1000 yr	2000 yr	100,000 yr***
Design Basis PWR WP							
Waste Pkg Upper Half	119.9	166.2	184.5	154.8	134.2	114.2	26.9
Waste Pkg Lower Half	123.3	171.3	188.5	156.7	134.9	114.6	27.0
Drip Shield Top-Center	107.8	150.9	173.3	149.0	131.9	112.8	26.8
Drip Shield Top-Corner	105.2	147.5	170.7	147.7	131.5	112.6	26.8
Drip Shield Bottom-Corner	106.7	149.8	172.5	148.5	131.8	112.7	26.8
Drift Wall Crown	98.4	139.1	164.9	144.8	130.4	111.9	26.7
Drift Wall 1:30	98.8	139.8	165.4	145.0	130.4	111.9	26.7
Drift Wall Rib	99.2	140.3	165.8	145.2	130.5	112.0	26.7
Drift Wall 4:30	99.3	140.4	165.9	145.3	130.5	112.0	26.8
Invert Top-Center	119.6	166.7	185.1	154.9	134.2	114.2	26.9
Invert Top-Right	101.5	143.2	167.9	146.2	130.9	112.2	26.8
Average WP (BWR)							
Waste Pkg Upper Half	112.1	156.6	177.3	152.0	133.2	113.7	26.9
Waste Pkg Lower Half	114.6	160.3	180.2	153.3	133.7	114.0	26.9
Drip Shield Top-Center	103.3	145.9	169.7	148.3	131.8	112.7	26.8
Drip Shield Top-Corner	101.6	143.6	168.0	147.5	131.5	112.5	26.8
Drip Shield Bottom-Corner	102.5	145.1	169.1	148.0	131.6	112.6	26.8
Drift Wall Crown	96.1	137.0	163.5	145.3	130.6	112.0	26.7
Drift Wall 1:30	96.5	137.6	163.9	145.5	130.7	112.0	26.7
Drift Wall Rib	96.7	137.8	164.0	145.6	130.7	112.0	26.7
Drift Wall 4:30	96.4	137.5	163.8	145.4	130.7	112.0	26.8
Invert Top-Center	112.1	157.4	178.1	152.2	133.3	113.7	26.9
Invert Top-Right	98.4	139.9	165.5	146.3	131.0	112.2	26.8
Cool WP (DHLW)							
Waste Pkg Upper Half	92.8	130.8	158.5	142.3	129.5	111.4	26.7
Waste Pkg Lower Half	93.2	131.3	158.8	142.5	129.6	111.5	26.7
Drip Shield Top-Center	91.7	129.6	157.7	142.0	129.4	111.4	26.7
Drip Shield Top-Corner	91.4	129.2	157.4	141.9	129.4	111.3	26.7
Drip Shield Bottom-Corner	91.1	128.8	157.2	141.8	129.3	111.3	26.7
Drift Wall Crown	89.4	126.7	155.7	141.1	129.1	111.1	26.6
Drift Wall 1:30	89.5	126.9	155.9	141.2	129.1	111.2	26.6

Table 5.3.2.4.6-1. In-Drift Temperatures for the Higher-Temperature Operating Mode (Page 2 of 2)

Location	Temperature, °C						
	10 yr*	51 yr	65 yr**	200 yr	1000 yr	2000 yr	100,000 yr***
Cool WP (DHLW)							
Drift Wall Rib	89.2	126.5	155.6	141.1	129.1	111.1	26.7
Drift Wall 4:30	88.5	125.5	154.8	140.7	129.0	111.1	26.7
Invert Top-Center	93.0	131.1	158.8	142.5	129.6	111.5	26.7
Invert Top-Right	89.7	127.1	156.0	141.3	129.2	111.2	26.7

Source: Produced using files from Buscheck 2001 [DIRS 155449].

NOTE: * = Time of Preclosure Peak T
** = Time of Postclosure Peak T
*** = Near-Ambient T.

Table 5.3.2.4.6-2. In-Drift Temperatures for the Lower-Temperature Operating Mode (Page 1 of 2)

Location	Temperature, °C						
	10 yr*	301 yr	500 yr	780 yr**	1000	4000	100,000***
Design Basis PWR WP							
Waste Pkg Upper Half	84.6	76.2	97.4	98.4	97.0	73.8	26.5
Waste Pkg Lower Half	86.8	77.9	98.6	99.3	97.7	74.1	26.5
Drip Shield Top-Center	73.3	67.2	91.8	94.4	93.8	72.4	26.4
Drip Shield Top-Corner	70.6	65.0	90.5	93.5	93.0	72.0	26.3
Drip Shield Bottom-Corner	71.5	65.8	91.0	93.9	93.3	72.2	26.4
Drift Wall Crown	63.2	59.3	87.1	91.2	91.1	71.2	26.2
Drift Wall 1:30	63.5	59.5	87.3	91.3	91.2	71.2	26.3
Drift Wall Rib	64.1	60.0	87.5	91.5	91.4	71.3	26.3
Drift Wall 4:30	64.4	60.3	87.7	91.6	91.4	71.3	26.3
Invert Top-Center	83.1	74.9	96.7	98.0	96.6	73.6	26.5
Invert Top-Right	66.9	62.2	88.8	92.4	92.1	71.6	26.4
Average WP (BWR)							
Waste Pkg Upper Half	75.6	67.9	92.0	94.7	94.1	72.7	26.4
Waste Pkg Lower Half	77.3	69.1	92.8	95.3	94.6	73.0	26.4
Drip Shield Top-Center	68.2	62.6	88.8	92.4	92.2	71.8	26.3
Drip Shield Top-Corner	66.7	61.5	88.1	91.9	91.8	71.6	26.3
Drip Shield Bottom-Corner	67.4	62.0	88.4	92.2	92.0	71.7	26.3
Drift Wall Crown	62.6	58.5	86.4	90.7	90.8	71.2	26.2
Drift Wall 1:30	62.8	58.7	86.5	90.8	90.8	71.2	26.2
Drift Wall Rib	63.0	58.8	86.5	90.8	90.9	71.2	26.3
Drift Wall 4:30	62.9	58.7	86.5	90.8	90.9	71.2	26.3
Invert Top-Center	74.9	67.3	91.8	94.6	93.9	72.7	26.4
Invert Top-Right	64.3	59.8	87.1	91.2	91.2	71.4	26.3
Hot Gap							
Drip Shield Top-Center	67.8	61.9	88.0	91.8	91.7	71.6	26.3
Drip Shield Top-Corner	66.8	61.2	87.6	91.5	91.5	71.5	26.3
Drip Shield Bottom-Corner	67.2	61.5	87.8	91.7	91.6	71.5	26.3
Drift Wall Crown	64.0	59.0	86.3	90.6	90.7	71.2	26.2
Drift Wall 1:30	64.1	59.1	86.4	90.7	90.8	71.2	26.2
Drift Wall Rib	64.1	59.1	86.4	90.7	90.8	71.2	26.3
Drift Wall 4:30	63.8	58.9	86.2	90.6	90.7	71.2	26.3
Invert Top-Center	70.9	64.3	89.5	92.9	92.6	72.0	26.4
Invert Top-Right	64.9	59.8	86.8	91.0	91.0	71.3	26.3

Table 5.3.2.4.6-2. In-Drift Temperatures for the Lower-Temperature Operating Mode (Page 2 of 2)

Temperature, °C							
Location	**10 yr***	**301 yr**	**500 yr**	**780 yr****	**1000 yr**	**4000 y**	**100,000*****
Cool Gap							
Drip Shield Top-Center	66.1	59.2	86.1	90.5	90.6	71.2	26.3
Drip Shield Top-Corner	65.1	58.6	85.7	90.2	90.4	71.1	26.3
Drip Shield Bottom-Corner	65.3	58.6	85.7	90.2	90.4	71.1	26.3
Drift Wall Crown	62.5	57.0	84.8	89.6	89.9	70.9	26.2
Drift Wall 1:30	62.6	57.1	84.9	89.6	89.9	70.9	26.2
Drift Wall Rib	62.6	57.0	84.8	89.6	89.9	70.9	26.3
Drift Wall 4:30	62.3	56.8	84.6	89.5	89.8	70.8	26.3
Invert Top-Center	68.8	60.7	87.0	91.1	91.1	71.4	26.3
Invert Top-Right	63.3	57.5	85.1	89.8	90.0	70.9	26.3
Cool WP (DHLW)							
Waste Pkg Upper Half	62.9	57.9	85.3	90.0	90.2	71.0	26.3
Waste Pkg Lower Half	63.2	58.1	85.5	90.1	90.3	71.1	26.3
Drip Shield Top-Center	61.9	57.4	85.1	89.8	90.1	71.0	26.3
Drip Shield Top-Corner	61.7	57.3	85.0	89.7	90.0	70.9	26.3
Drip Shield Bottom-Corner	61.5	57.1	84.9	89.7	90.0	70.9	26.3
Drift Wall Crown	60.0	56.2	84.3	89.3	89.6	70.8	26.2
Drift Wall 1:30	60.1	56.2	84.4	89.3	89.7	70.8	26.2
Drift Wall Rib	59.9	56.1	84.3	89.2	89.6	70.8	26.2
Drift Wall 4:30	59.5	55.8	84.1	89.1	89.5	70.7	26.3
Invert Top-Center	63.1	58.1	85.5	90.1	90.3	71.1	26.3
Invert Top-Right	60.3	56.4	84.4	89.3	89.7	70.8	26.3

Source: Produced using files from Buscheck 2001 [DIRS 155449].

NOTE: * = Time of Preclosure Peak T
** = Time of Postclosure Peak T
*** = Near-Ambient T.

Table 5.4-1. Sequence of Steps to Combine Submodel Results in the Multiscale Thermal-Hydrologic Model (Page 1 of 2)

Step	Dimensionality	Physical Processes	Physical Domain	Heat Source	Boundary Conditions	Number of Submodel Runs
1. Smeared-heat-source mountain-scale thermal **(SMT) submodel**.						
	3D	Conduction only, vertical property variation	Repository footprint plus >0.7 km edges, surface to 1 km below water table	Smeared, 1-m thick, within footprint, reduced during ventilation	No heat flow at sides, constant temperature at bottom and surface	1
2. Smeared-heat-source drift-scale thermal **(SDT) submodel**. At 33 selected columns. Run at 4 AMLs bracketing the actual AML						
	1D	Conduction only in rock, vertical property variation, radiation in drift, approximated natural convection	Surface to water table	Smeared, 1-m thick, reduced during ventilation	Constant temperature at surface, constant temperature at water table	4x33=132
3. **Interpolate** results at each column and time step to additional locations within the footprint. HTOM: 671 locations, LTOM: 762 locations						
4. At each location and selected time steps, determine the interpolated AML in the SDT array to match the local SMT temperature. **Result**: At each location and time step there is an effective repository horizon AML that represents the effectiveness of the heat sink volume in removing heat from the drift. An ERHAML less than the true AML indicates 3D mountain-scale heat flow.						
5. Line-heat-source drift-scale thermal-hydrologic **(LDTH) submodel**. At the same columns as in the SDT submodels. Run at 4 drift spacings creating AMLs bracketing the actual AML						
	2D	Heat and mass transfer, vertical property variation, radiation in drift, approximated natural convection	Mid-drift to mid-pillar, surface to water table	Waste package volume-preclosure, volume under drip shield-postclosure, line-averaged, reduced during ventilation	No heat or mass flow at sides, constant temperature, pressure, and relative humidity at surface, imposed water flux map at surface, constant temperature, pressure, and saturation at water table	4x33=132

Table 5.4-1. Sequence of Steps to Combine Submodel Results in the Multiscale Thermal-Hydrologic Model (Page 2 of 2)

Step	Dimensionality	Physical Processes	Physical Domain	Heat Source	Boundary Conditions	Number of Submodel Runs
6. **Interpolate** temperatures at each zone and time step to additional locations within the footprint. HTOM: 671 locations, LTOM: 762 locations						
7. At each of the locations and selected time steps, use the effective ERHAML (from Step 4) to interpolate among the AMLs **Result**: Temperatures at 671 or 762 locations (higher- or lower-temperature operating mode), consistent with edge effects, infiltration map and drift layout, but not including three-dimensional WP-to-WP variations. These are termed line-source, mountain-scale thermal-hydrologic **(LMTH)** temperatures.						
8. Discrete-heat-source drift-scale thermal **(DDT) submodel** At one location. Run at same AMLs as SDT and LDTH submodels.						
	3D	Conduction only in rock, vertical property variation, radiation in drift, radiation under drip shield, no natural convection	Mid-drift to mid-pillar, surface to water table, No drip shield during preclosure	Eight full and two half WPs (of same diameter, but individual lengths and thermal powers), reduced during ventilation	No heat flow at sides, constant temperature at bottom, constant temperature at surface	4
9. For each AML, at selected positions in each cross-section (perpendicular to the drift axis), and at selected times, the temperatures are **averaged along the axial direction**. The HTOM has 28 axial positions (each WP mid-length and end). The lower-temperature operating mode has 36 positions, including two in each of the four non-minimum gaps						
10. For each AML, at each WP mid-length, and at the selected times and positions in each cross-section, **the WP-specific axial deviation** is calculated (local temperature minus average temperature from Step 9)						
11. The location-specific (in the footprint) ERHAML is used to **interpolate** among the four axial deviation histories (for the selected cross-sectional positions, selected times, and selected axial positions). These deviation histories are used to adjust the LMTH temperatures from Step 7, producing discrete-source, mountain-scale, thermal-hydrologic **(DMTH)** temperature histories at all locations and positions within locations **Result: Temperatures across the entire domain and time history**						
12. At each location, and at selected cross-sectional and axial positions, and at selected times, the WP-specific temperatures (DMTH) are compared to the four (AML-based) LDTH temperatures from Step 6 to develop a new set of Effective WP AMLs. These effective AMLs take into account axial in-drift geometry and WP power variability in addition to repository edge effects, the infiltration map, and the layout of drifts.						
13. At each location, and at selected cross-sectional and axial positions, and at selected times, the Effective WP AMLs are used to **interpolate** on the four (AML-based) LDTH sets of (non-temperature) parameters. **Result: All non-temperature variables across the entire domain and time history**						

Source: Produced from information in CRWMS M&O 2000 [DIRS 149862].

NOTES: Selected times and positions refer to positions and times used in downstream models.
AML = areal mass loading; WP = waste package.

Table 5.4.3-1. Sensitivity of In-Drift Thermal-Hydrologic Performance to Uncertainties and Parameters (Page 1 of 3)

Section	Parameter or Uncertainty	Range of Parameter or Uncertainty	Base Case	Performance Measure	Effect of Parameter or Uncertainty Range on Performance Measure
5.3.1.4.1	Gas storage in lithophysal cavities	Include or Exclude	Exclude	Fraction of vaporizing liquid included in model	0.1% over-estimate of volume of vaporized liquid displaced to adjacent zones
5.3.1.4.2 HTOM, LTOM	Fracture heterogeneity aspects of seepage	Include or Exclude	Exclude	Seepage flux-, DW T & RH; DS T & RH	Increases likelihood of seepage during the sub-boiling period
5.3.1.4.3	Imbibition hysteresis	Include or Exclude	Exclude	DW & DS T&RH	Non-conservatively bounded T (under predict) Conservatively bounded RH (over-predict)
5.3.1.4.4 HTOM, LTOM	Buoyant gas-phase convection (drift-)	$\pm$ 2 standard deviations k_b = 0.15 – 38 Darcy, Half-pillar scale	k_b = 2.4	Percolation flux, DW & DS T	HTOM boiling period: up to double the heat-mobilized liquid-phase flux; peak temperature range of 11°C; boiling period range of 50 years
5.3.1.4.5	THC processes	Include or Exclude	Exclude	change in bulk permeability (k_b)	Changes within natural variation of k_b
5.3.1.4.6 HTOM	THM processes	Include or Exclude	Exclude	change in bulk permeability (k_b)	>5 orders magnitude decrease k_b during thermal period, 6x permanent increase in k_b (within range of k_b variability)
5.3.1.4.7 HTOM, LTOM	Host rock permeability	k_b = 0.15 –- 38 Darcy	Mean k_b (unit dependent) K_b = 2.38	DW T & RH, DS T & RH, INV_U S	DW T 11°C
5.3.1.4.8 HTOM, LTOM	Host rock thermal conductivity	K_{th} = 1.13-2.02 wet K_{th} = 0.64-1.54 dry	Mean: 1.87 wet; 1.27 dry	DW T & RH, DS T & RH, INV_U S	DW & DS T ~85°C range, HTOM; DW & DS T ~20°C range, LTOM
5.3.1.4.9 HTOM, LTOM	Lithophysal porosity (combined influence on thermal conductivity and heat capacity)	0 to 25%	Mean porosity: 12.5%	DW T & RH, DS T & RH, INV_U S	DW & DS T ~100°C range, HTOM; DW & DS T ~25°C range, LTOM

Table 5.4.3-1. Sensitivity of In-Drift Thermal-Hydrologic Performance to Uncertainties and Parameters (Page 2 of 3)

Section	Parameter or Uncertainty	Range of Parameter or Uncertainty	Base Case	Performance Measure	Effect of Parameter or Uncertainty Range on Performance Measure
5.3.1.4.10 LTOM	Invert thermal conductivity	0.15 to 3.04	0.15	DW T & S, DS T & RH, INV_L T & S	DW & DS 2-4°C range, INV_L 9°C range, INV S 5-9% after rewetting
5.3.1.4.11 LTOM	WP capacity drift spacing WP spacing	16-21 PWR SNFAs 81-97 m drift spacing 0.1-2 m average WP spacing	21 SNFAs, 81 m drift spacing 0.1 m WP spacing	Peak WP T	7°C range
5.3.2.4.1 HTOM	Ventilation Efficiency, HTOM	ANSYS, MULTIFLUX, Quarter-Scale Test	ANSYS	15 m^3/s Average Efficiency, 50 yrs (or scaled values)	ANSYS 74%, MULTIFLUX 94%, Test 83%
5.3.2.4.2 HTOM, LTOM	Ventilation Efficiency	$\pm$10%	70% HTOM, 80% LTOM	DS T postclosure peak	HTOM 14°C range, LTOM 7°C range
5.3.2.4.2 HTOM, LTOM	Ventilation efficiency time dependence	Constant or time-dependent	Constant	DS T preclosure peak	HTOM 59°C range, LTOM 63°C range
5.3.2.4.3 LTOM	Ventilation Duration	$\pm$22 years	300 years	LTOM DS T postclosure peak	2°C range
5.3.2.4.4 HTOM, LTOM	Water entering drift	6 months to dryout 3 m rock, 10 mm/yr flux entering from 11.5 m wide region; Calculated dryout	No water entering drift	RH at 500 m in ventilation air, kW/m latent heat removal, DS T postclosure	9.9% no water entry, 33% during dry out, 10.1% after dry out; 1.29 kW/m during dry out, <0.01 kW/m after dryout; Negligible T effect
5.3.2.4.4 HTOM	In-drift seepage, and NF dry out due to ventilation	0-30% percolation flux seepage	0% seepage	DS T postclosure	Negligible effect
5.3.2.4.5 HTOM, LTOM	Treatment of thermal radiation	Correlation-based or explicit	Explicit	Peak DS T	6°C range (HTOM)

Table 5.4.3-1. Sensitivity of In-Drift Thermal-Hydrologic Performance to Uncertainties and Parameters (Page 3 of 3)

Section	Parameter or Uncertainty	Range of Parameter or Uncertainty	Base Case	Performance Measure	Effect of Parameter or Uncertainty Range on Performance Measure
5.3.2.4.5	Treatment of natural convection heat transfer	Correlation-based or Navier-Stokes CFD	Correlation-based	DS and WP T	Can match perimeter-average T, with CFD-based correlation; details along perimeter can affect condensation locations
5.3.2.4.5 HTOM	Treatment of natural convection mass transfer	0 to 2×10^{-5} m^2 in-drift bulk permeability	10^{-8} m^2	DW T & S, DS T & RH, INV_L T & S	INV_L/DW & DS 2-4°C range, INV_L S minor changes during re-wetting
5.3.2.4.6 HTOM, LTOM	3D in-drift effects	2D versus 3D	3D	WP T (DB, AVG, COOL) postclosure peak	HTOM 26°C range, LTOM 8°C range

Source: Produced from results in Sections 5.3.1.4 and 5.3.2.4 of this document.

NOTES: 2D = two-dimensional; 3D = three-dimensional; CFD = computational fluid dynamics; DS = drip shield; DW = drift wall; HTOM = higher-temperature operating mode; INV_L = lower-center of invert; INV_U = upper layer of invert just outboard of the drip shield; LTOM = lower-temperature operating mode; NF = near-field; PWR = pressurized water reactor; RH = relative humidity; S = saturation; SNFA = spent nuclear fuel assembly; T = temperature; WP = waste package.

DB, AVG, COOL (WP) = Design Basis (11.8 kW initial), Average (7.4 kW average BWR), Cool (DOE high-level waste glass), 0.3 kW waste packages.

INTENTIONALLY LEFT BLANK

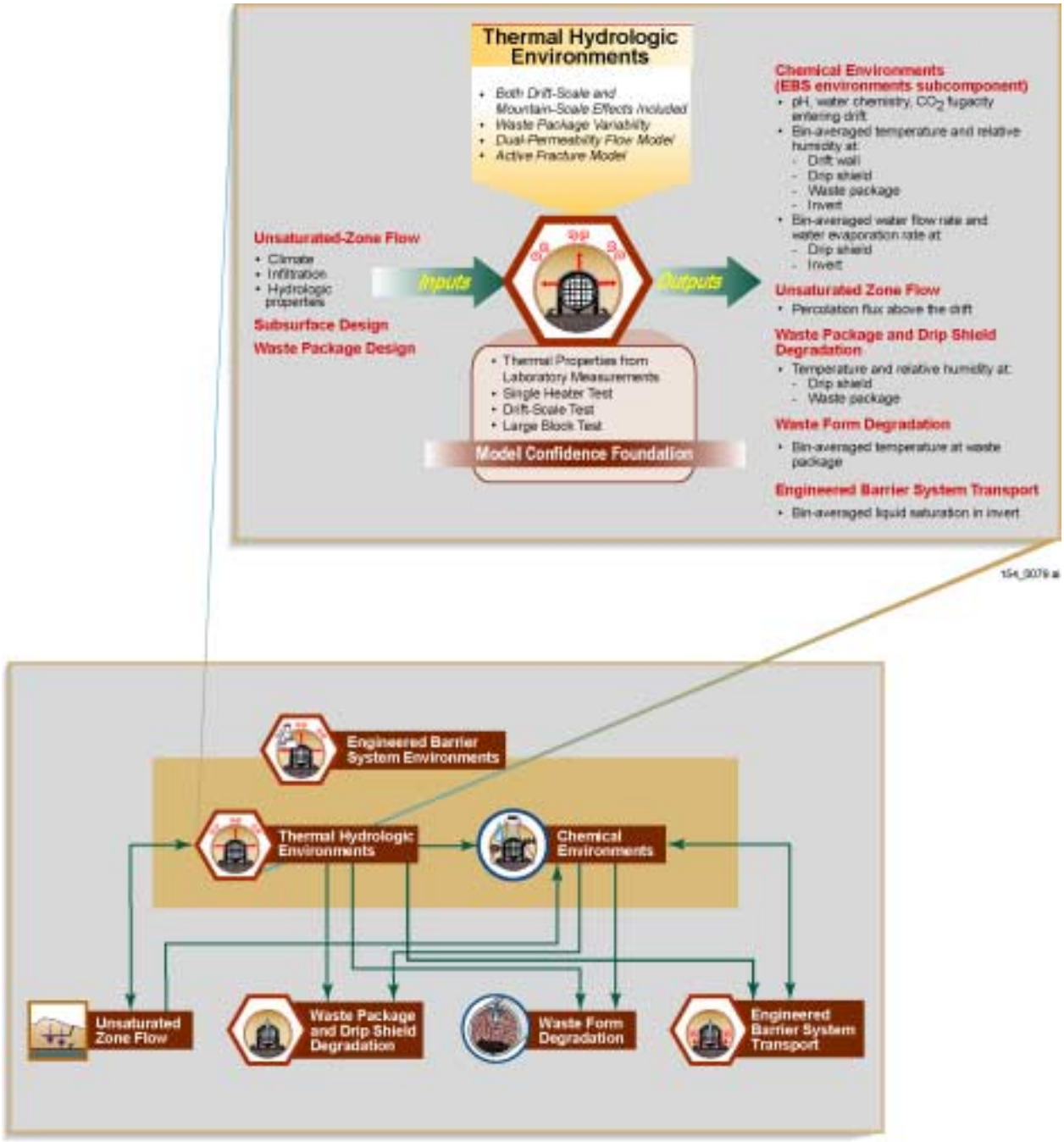

154_0079.ai

Source: CRWMS M&O 2000 [DIRS 153246], Figure 3.3-7.

Figure 5.2-1. Relationship of the Multiscale Thermal-Hydrologic Model to Other Models

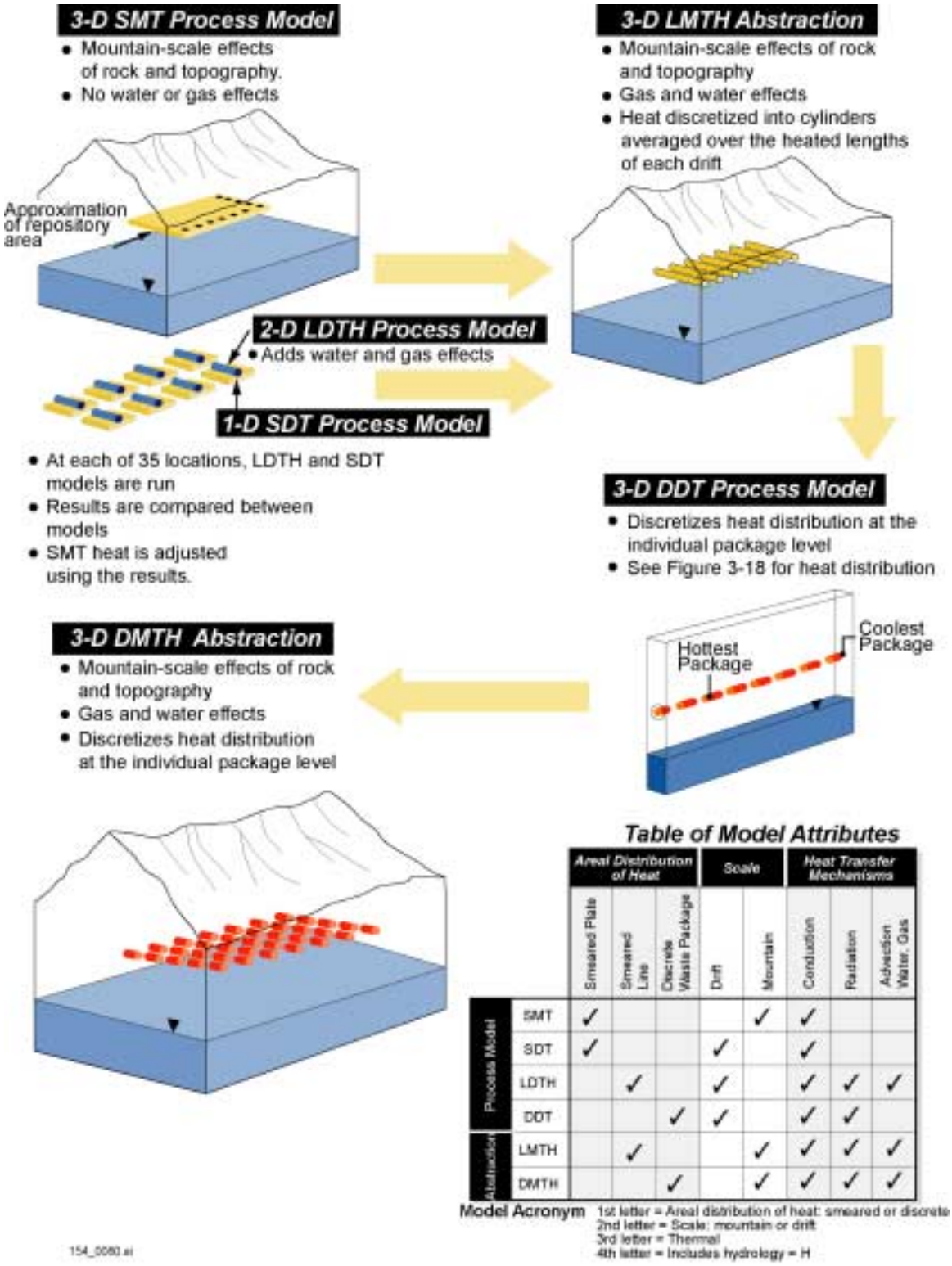

154_0080.ai

Source: Adapted from CRWMS M&O 2000 [DIRS 149862], Figure 1-1.

Figure 5.2-2. Illustration of the Multiscale Thermal-Hydrologic Model

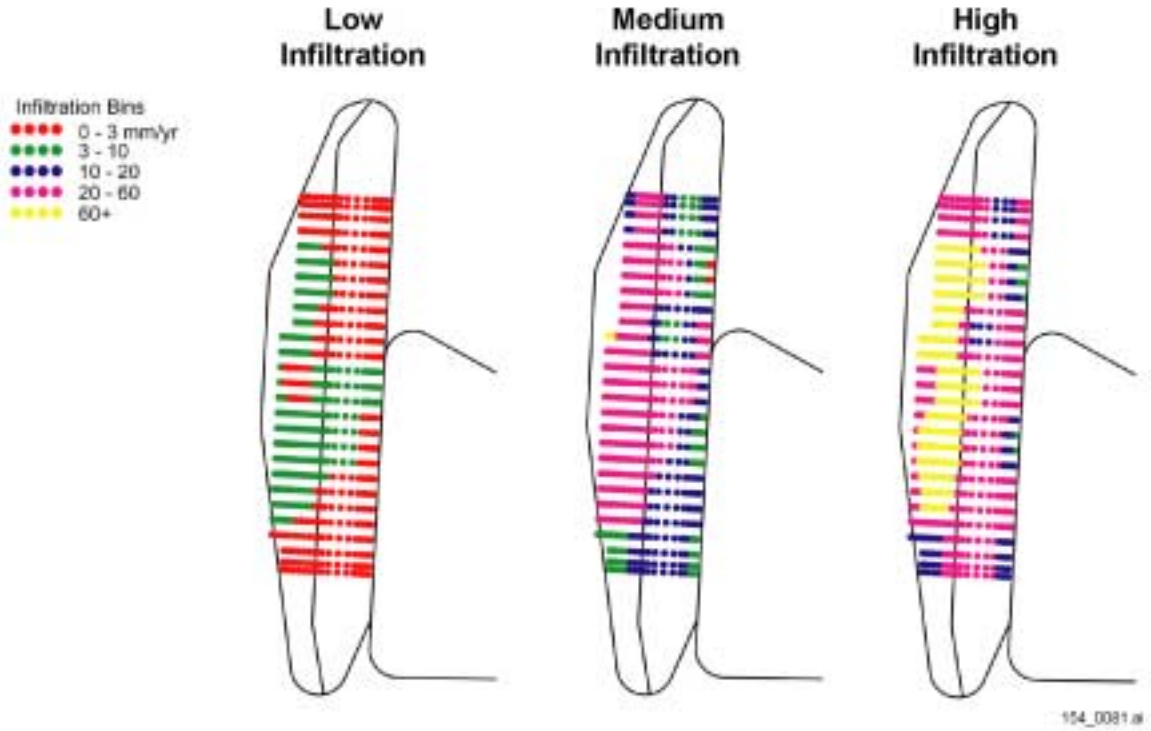

154_0081.ai

Source: CRWMS M&O 2000 [DIRS 153246], Figure 3.3-3.

Figure 5.2-3. Locations at Which Thermal-Hydrologic Parameters are Calculated by the Multiscale Thermal-Hydrologic Model

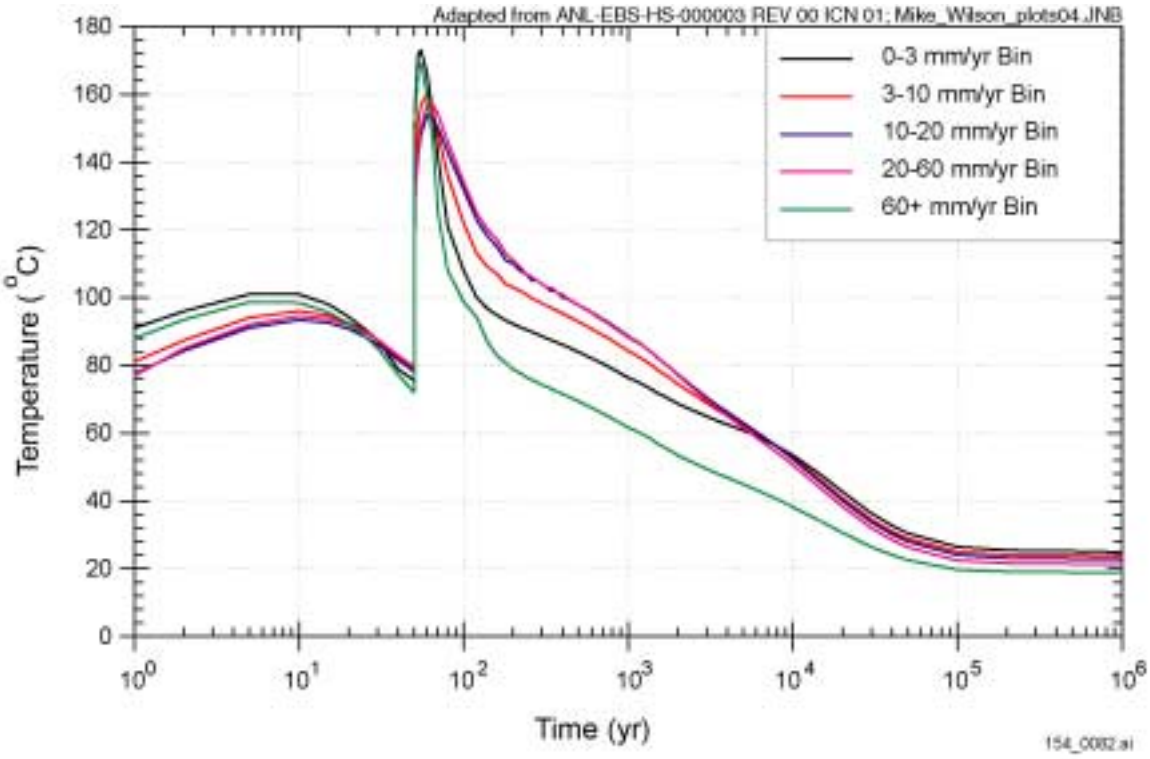

154_0082.ai

Source: CRWMS M&O 2000 [DIRS 153246], Figure 3.3-9.

NOTE: Commercial spent nuclear fuel temperature histories averaged into infiltration-level bins. Data for medium overall infiltration into the mountain.

Figure 5.2-4. Waste Package Temperature Histories

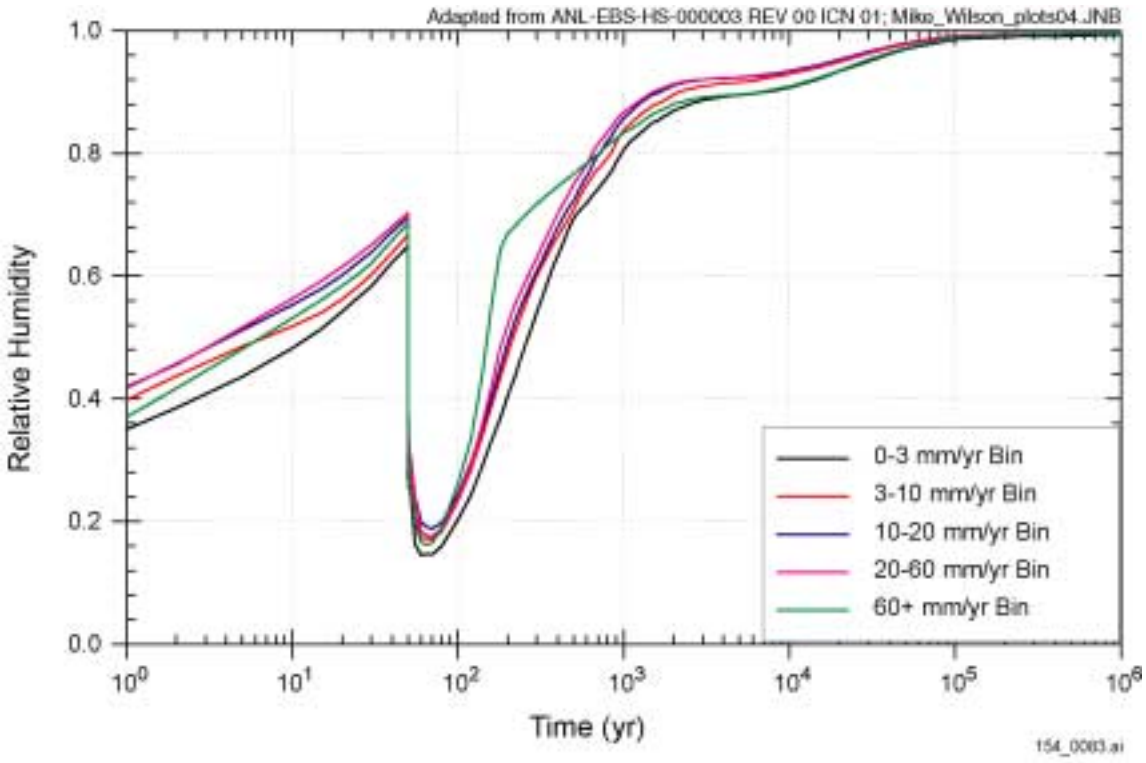

154_0083.ai

Source: CRWMS M&O 2000 [DIRS 153246], Figure 3.3-10.

NOTE: Relative humidity histories averaged into infiltration-level bins. Data for medium overall infiltration into the mountain.

Figure 5.2-5. Waste Package Relative Humidity Histories

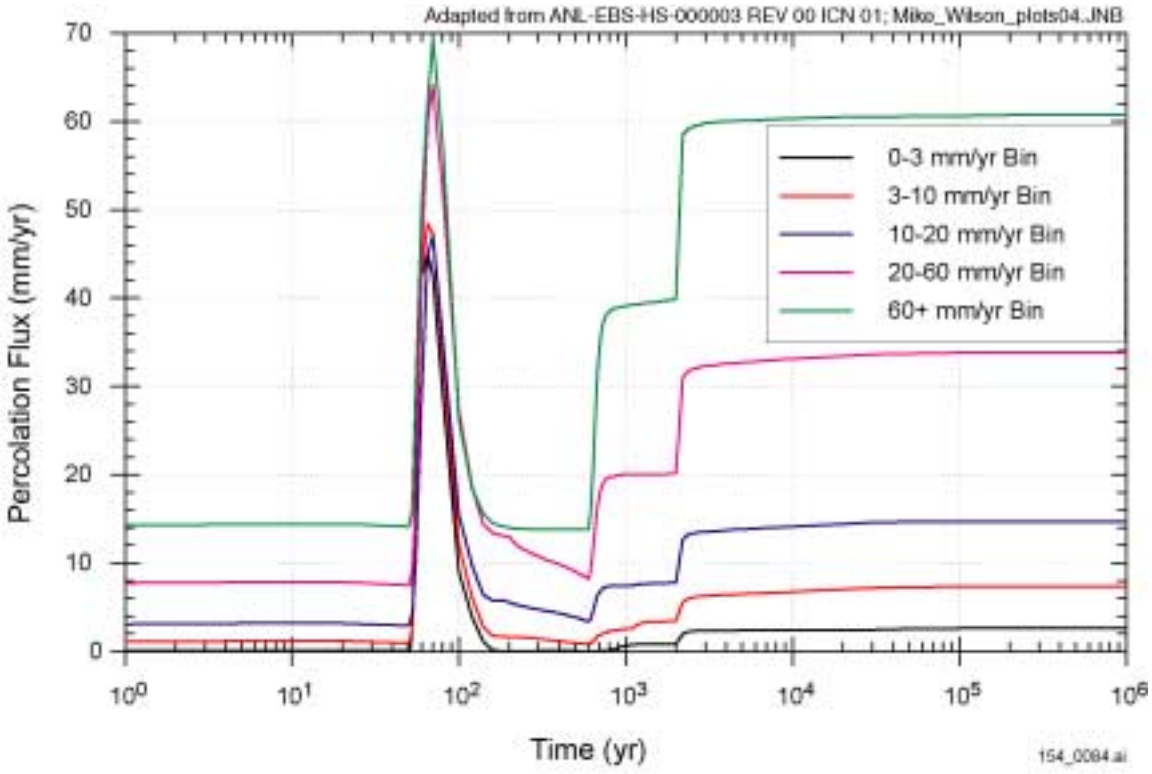

154_0084.ai

Source: CRWMS M&O 2000 [DIRS 153246], Figure 3.3-11.

NOTE: Percolation flux histories averaged into infiltration-level bins. Data for medium overall infiltration into the mountain.

Figure 5.2-6. Histories of Percolation Flux 5 m Above the Drift Crown

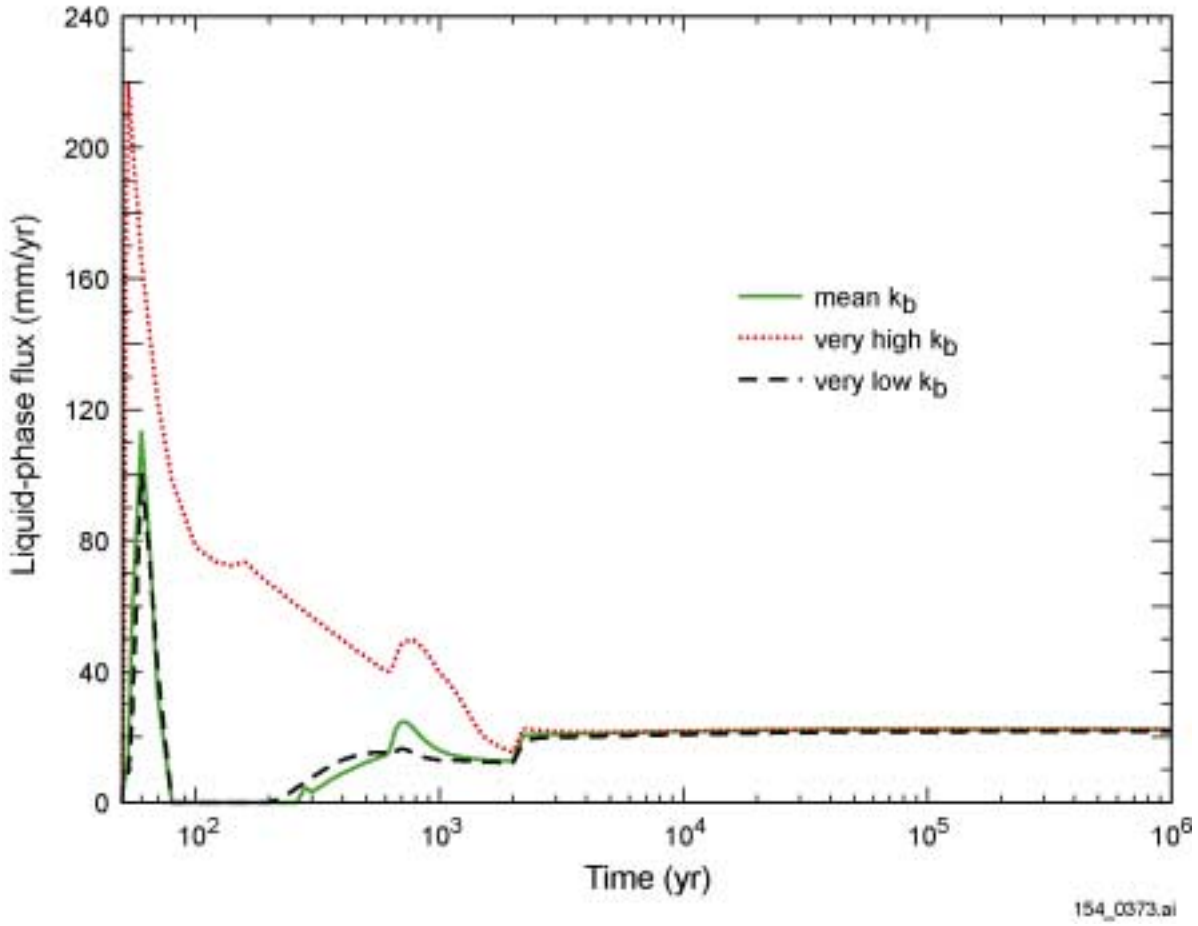

154_0373.ai

Source: Produced using files from Buscheck 2001 [DIRS 155012].

NOTE: Results for a central location in the potential repository. k_b = bulk permeability.

Figure 5.3.1.4.4-1. Liquid Phase Flux 5 m above Drift Wall as a Function of Permeability for the Higher-Temperature Operating Mode

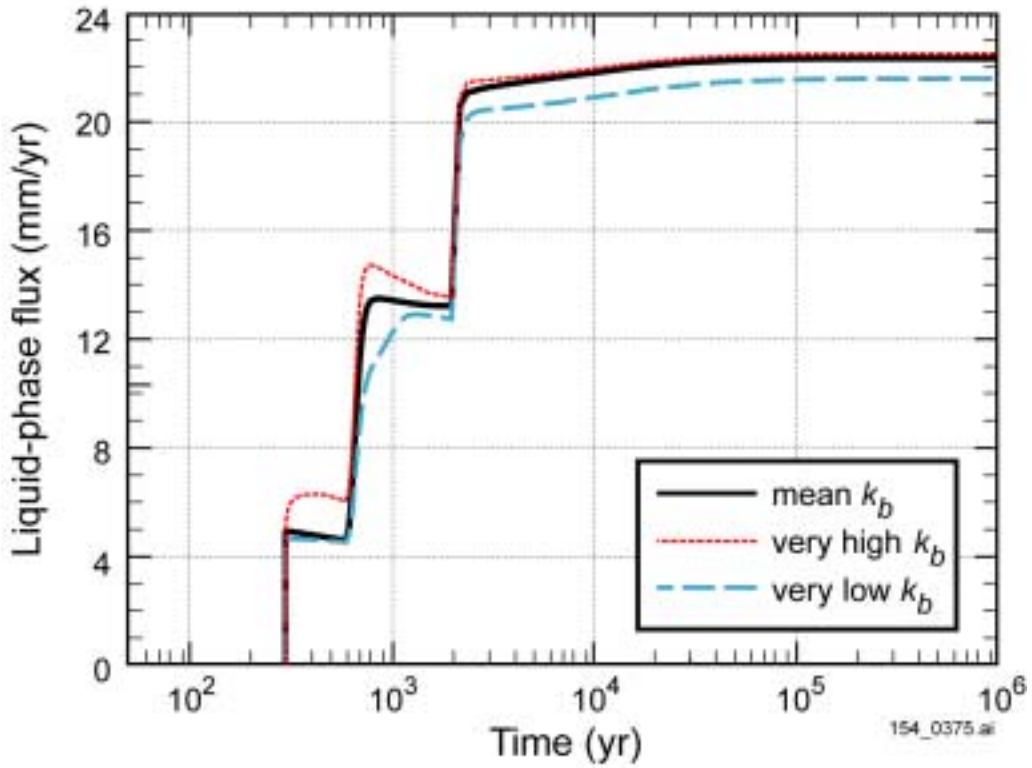

154_0375.ai

Source: Produced using files from Buscheck 2001 [DIRS 155012].

NOTE: Results for a central location in the potential repository. k_b = bulk permeability.

Figure 5.3.1.4.4-2. Postclosure Liquid Phase Flux 5 m above Drift Wall as a Function of Permeability for the Lower-Temperature Operating Mode

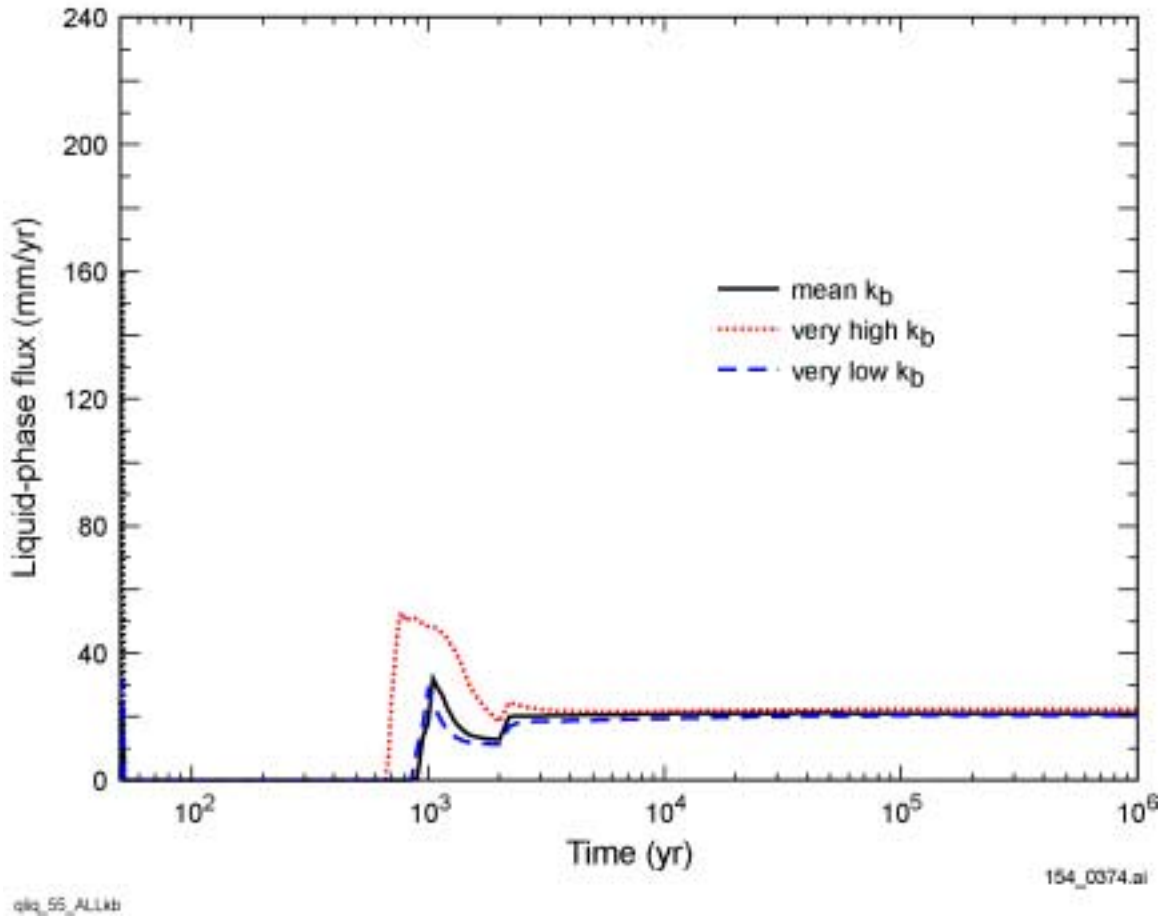

154_0374.ai

Source: Produced using files from Buscheck 2001 [DIRS 155012].

NOTE: Results for a central location in the potential repository. k_b = bulk permeability.

Figure 5.3.1.4.4-3. Liquid Phase Flux 1 m above Drift Wall as a Function of Permeability for the Higher-Temperature Operating Mode

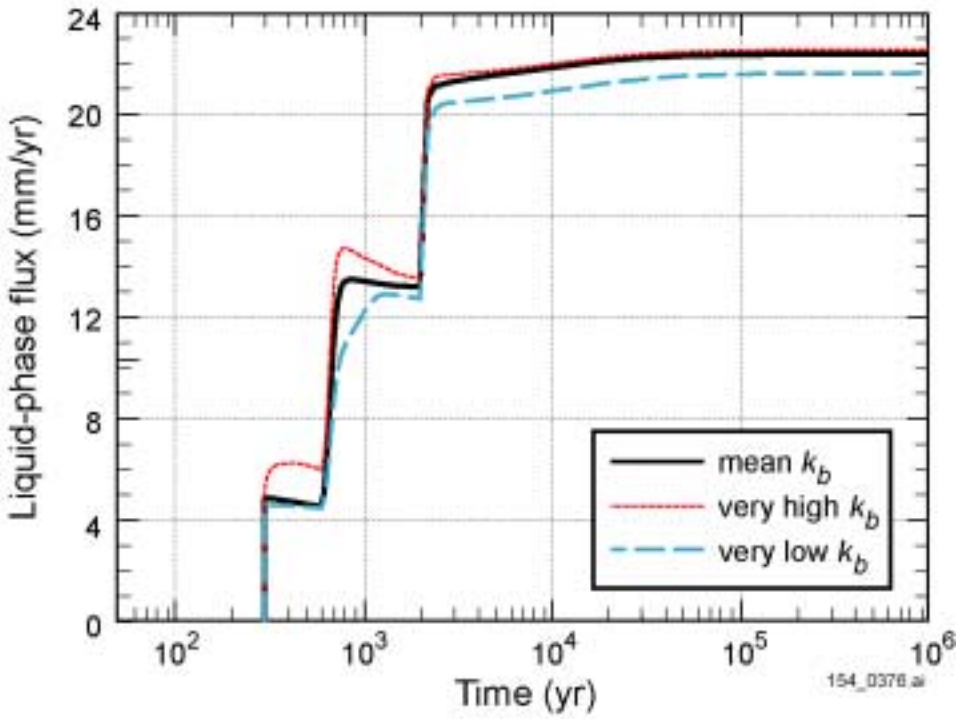

154_0376.ai

Source: Produced using files from Buscheck 2001 [DIRS 155012].

NOTE: Results for a central location in the potential repository. k_b = bulk permeability.

Figure 5.3.1.4.4-4. Postclosure Liquid Phase Flux 1 m above Drift Wall as a Function of Permeability for the Lower-Temperature Operating Mode

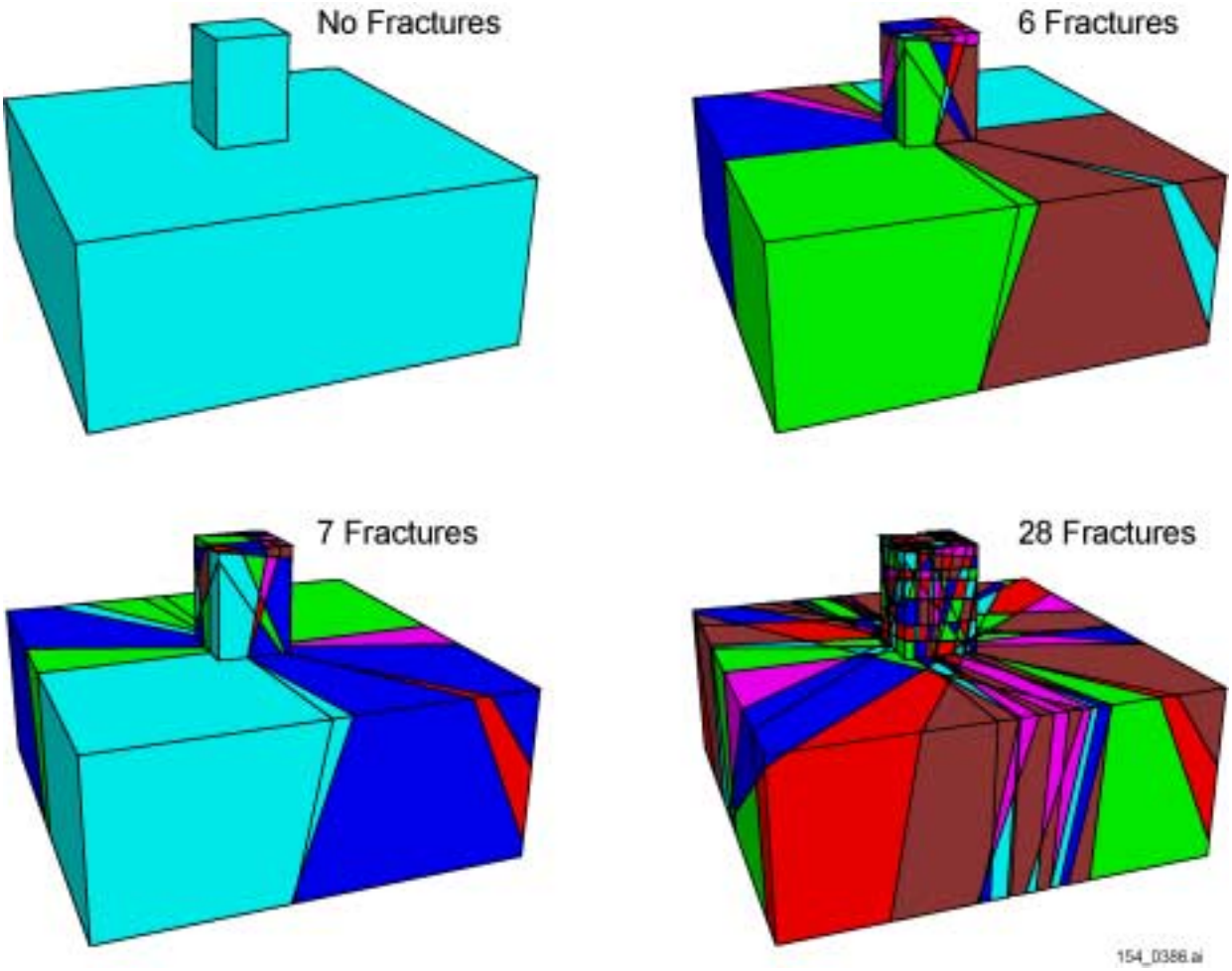

154_0386.ai

Source: Produced using files from Blair 2001 [DIRS 155309].

Figure 5.3.1.4.6-1. Simulations of the Large Block Test

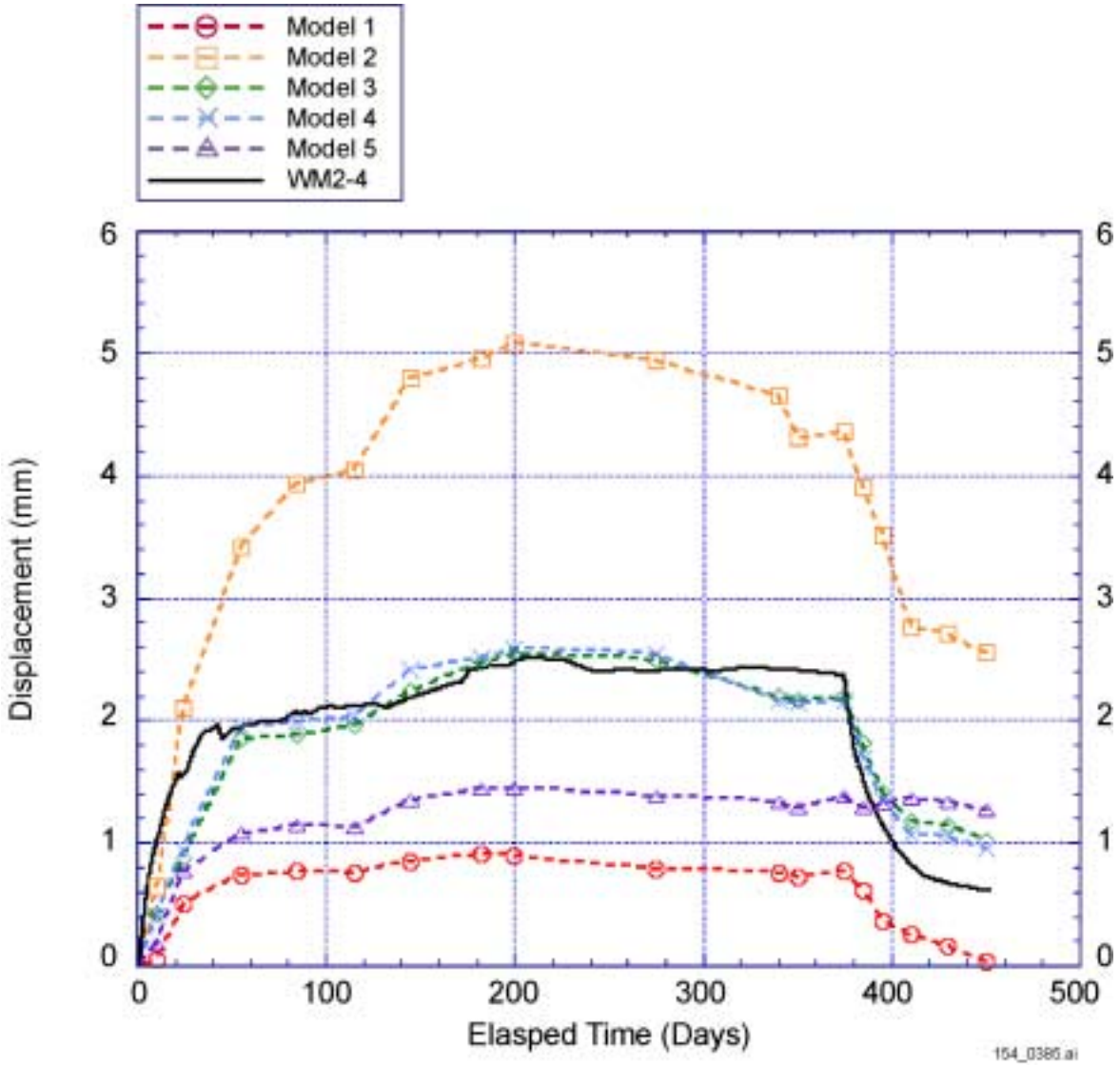

154_0385.ai

Source: Produced using files from Blair 2001 [DIRS 155309].

NOTE: Simulated (dashed lines) and observed (solid line) deformation data.

Figure 5.3.1.4.6-2. Comparison of Simulated and Observed Deformation for Borehole WM-2 in the Large Block Test

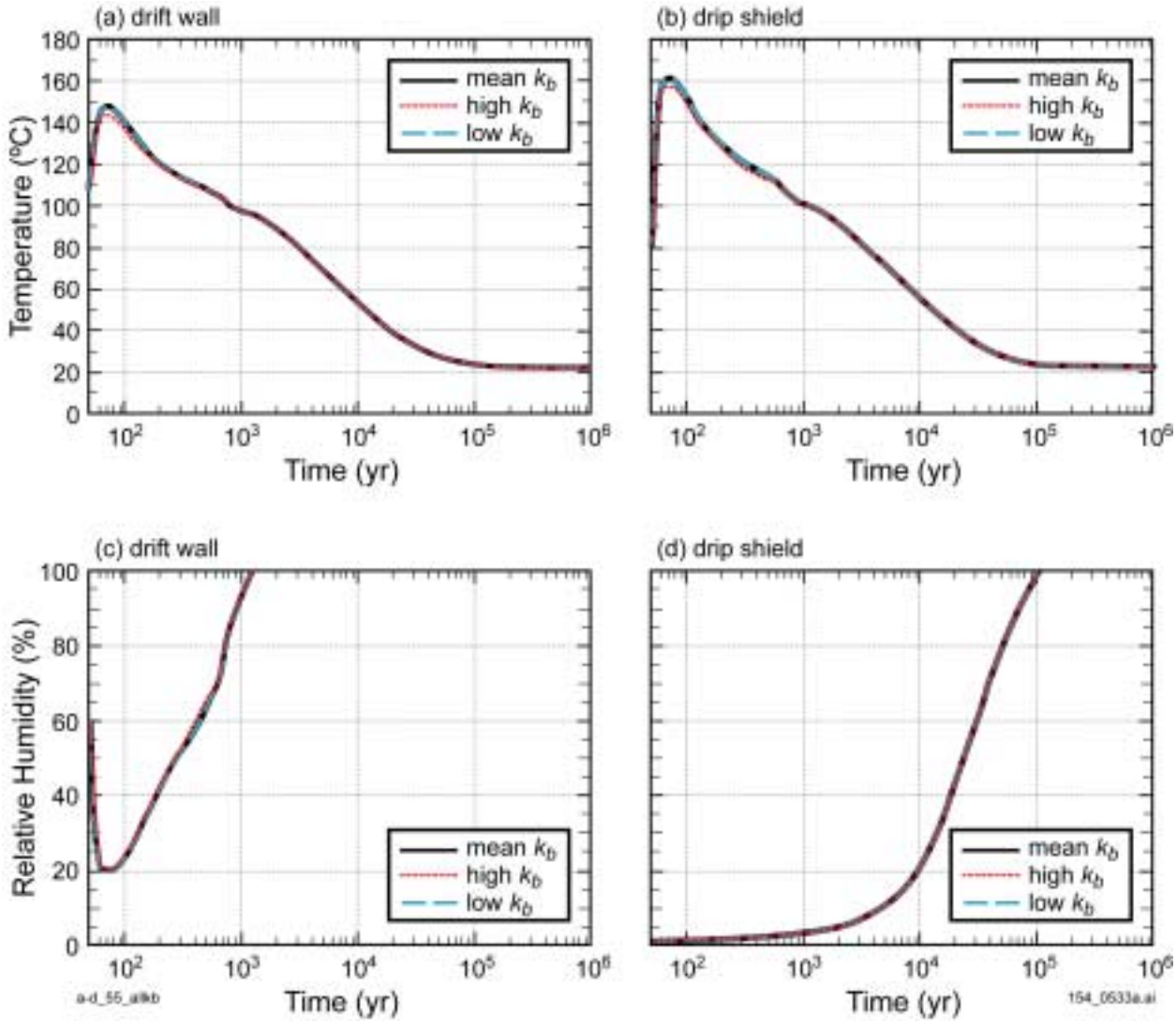

154_0533a.ai

Source: Produced using files from Buscheck 2001 [DIRS 155012].

NOTE: Higher-temperature operating mode drift wall and drip shield temperatures and relative humidities at the central repository location (Location L5C3) as a function of bulk permeability (k_b) for the mean infiltration-flux scenario.

Figure 5.3.1.4.7-1. Drift Wall and Drip Shield Temperatures and Relative Humidities as a Function of Bulk Permeability for the Higher-Temperature Operating Mode (Page 1 of 2)

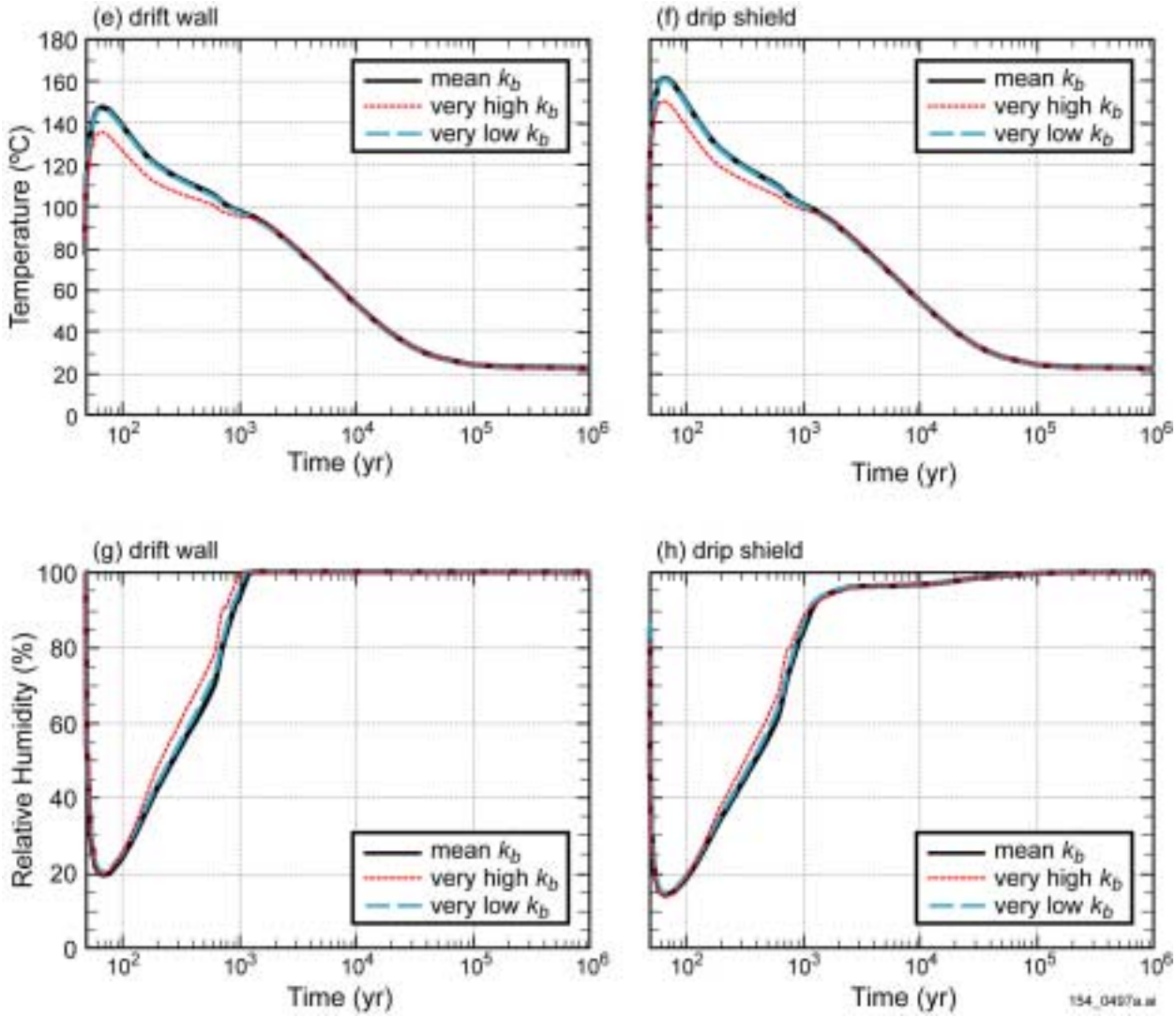

154_0497a.ai

Source: Produced using files from Buscheck 2001 [DIRS 155012].

NOTE: Higher-temperature operating mode drift wall and drip shield temperatures and relative humidities at the central repository location (Location L5C3) as a function of bulk permeability (k_b) for the mean infiltration-flux scenario.

Figure 5.3.1.4.7-1. Drift Wall and Drip Shield Temperatures and Relative Humidities as a Function of Bulk Permeability for the Higher-Temperature Operating Mode (Page 2 of 2)

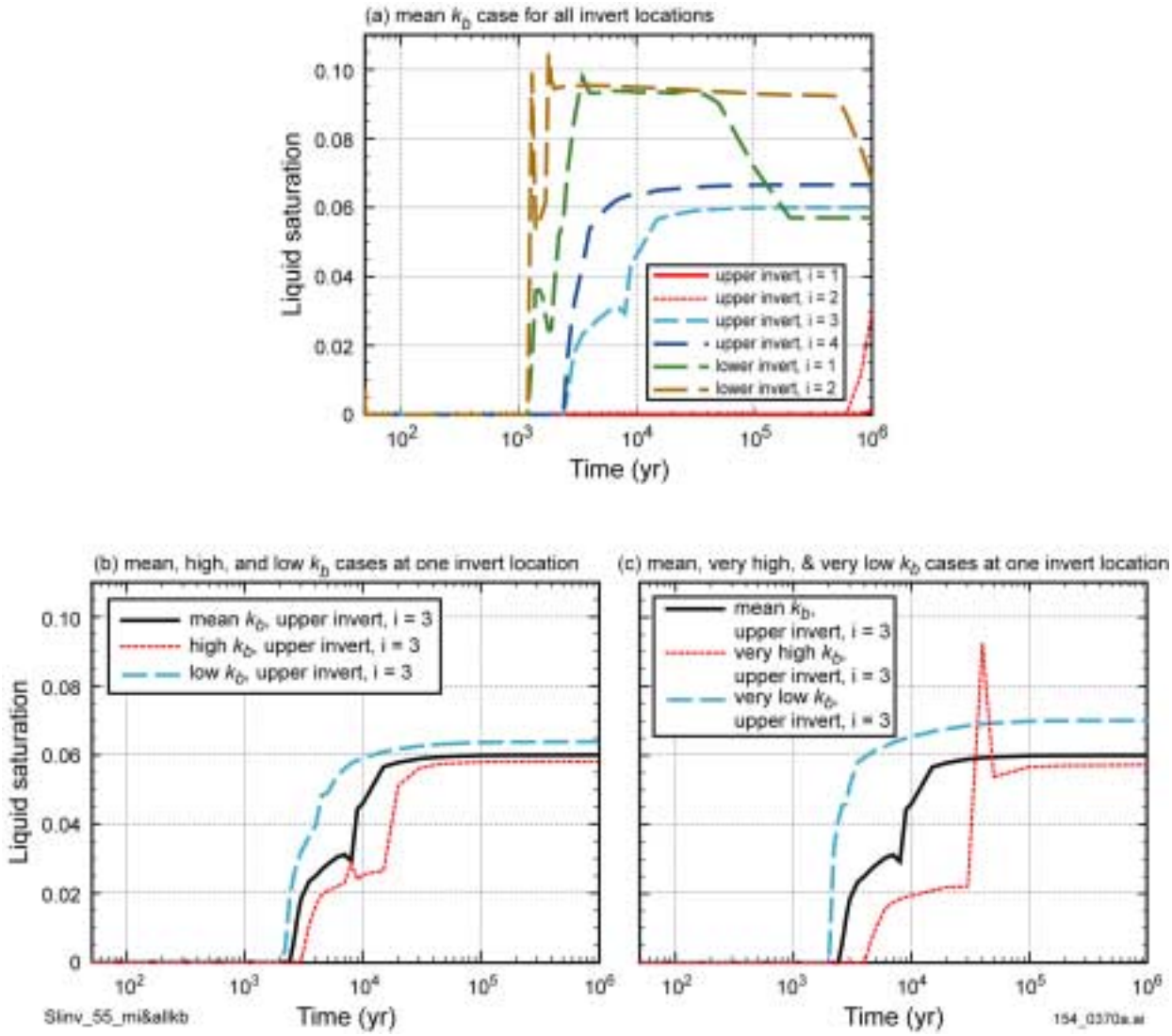

154_0370a.ai

Source: Produced using files from Buscheck 2001 [DIRS 155012].

NOTE: Higher-temperature operating mode invert liquid saturations at the central repository location (Location L5C3) as a function of bulk permeability (k_b) for the mean infiltration-flux scenario.

Figure 5.3.1.4.7-2. Invert Liquid Saturations as a Function of Bulk-Permeability for the Higher-Temperature Operating Mode

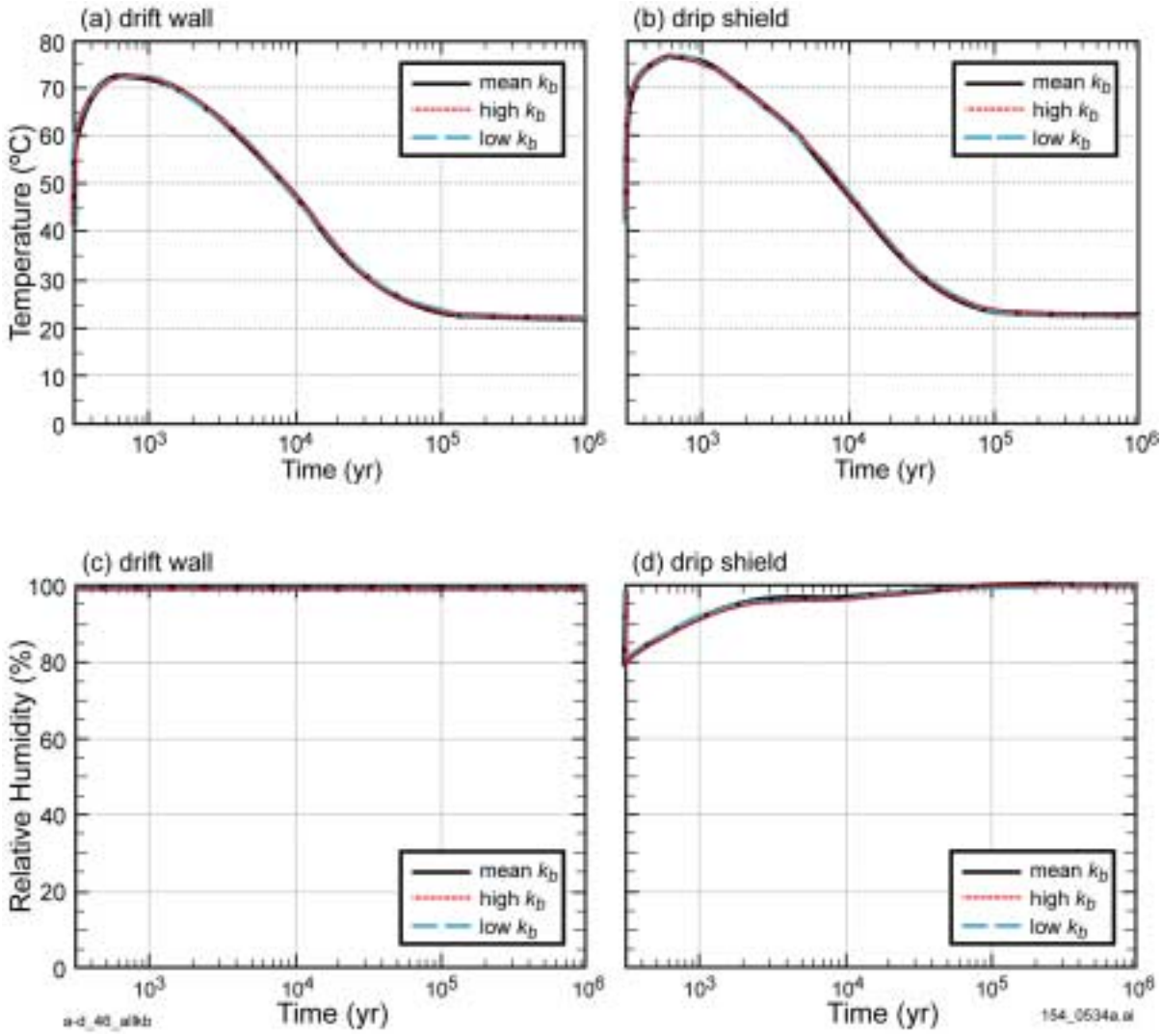

154_0534a.ai

Source: Produced using files from Buscheck 2001 [DIRS 155012].

Figure 5.3.1.4.7-3. Drift Wall and Drip Shield Temperatures and Relative Humidities as a Function of Bulk Permeability for the Lower-Temperature Operating Mode (Page 1 of 2)

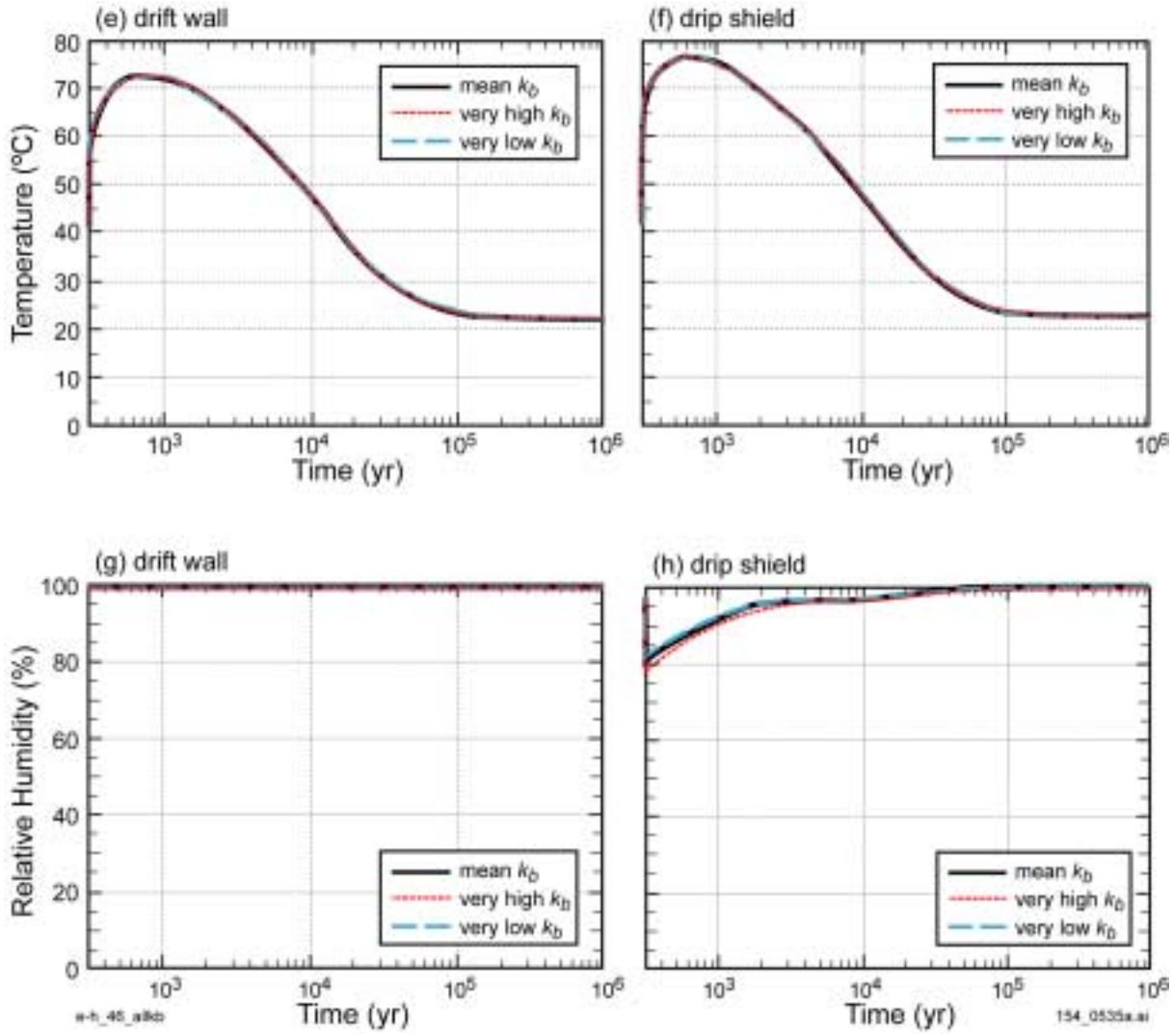

154_0535a.ai

Source: Produced using files from Buscheck 2001 [DIRS 155012].

NOTE: Lower-temperature operating mode drift wall and drip shield temperatures and relative humidities at the central repository location (Location L5C3) as a function of bulk permeability (k_b) for the mean infiltration-flux scenario.

Figure 5.3.1.4.7-3. Drift Wall and Drip Shield Temperatures and Relative Humidities as a Function of Bulk Permeability for the Lower-Temperature Operating Mode (Page 2 of 2)

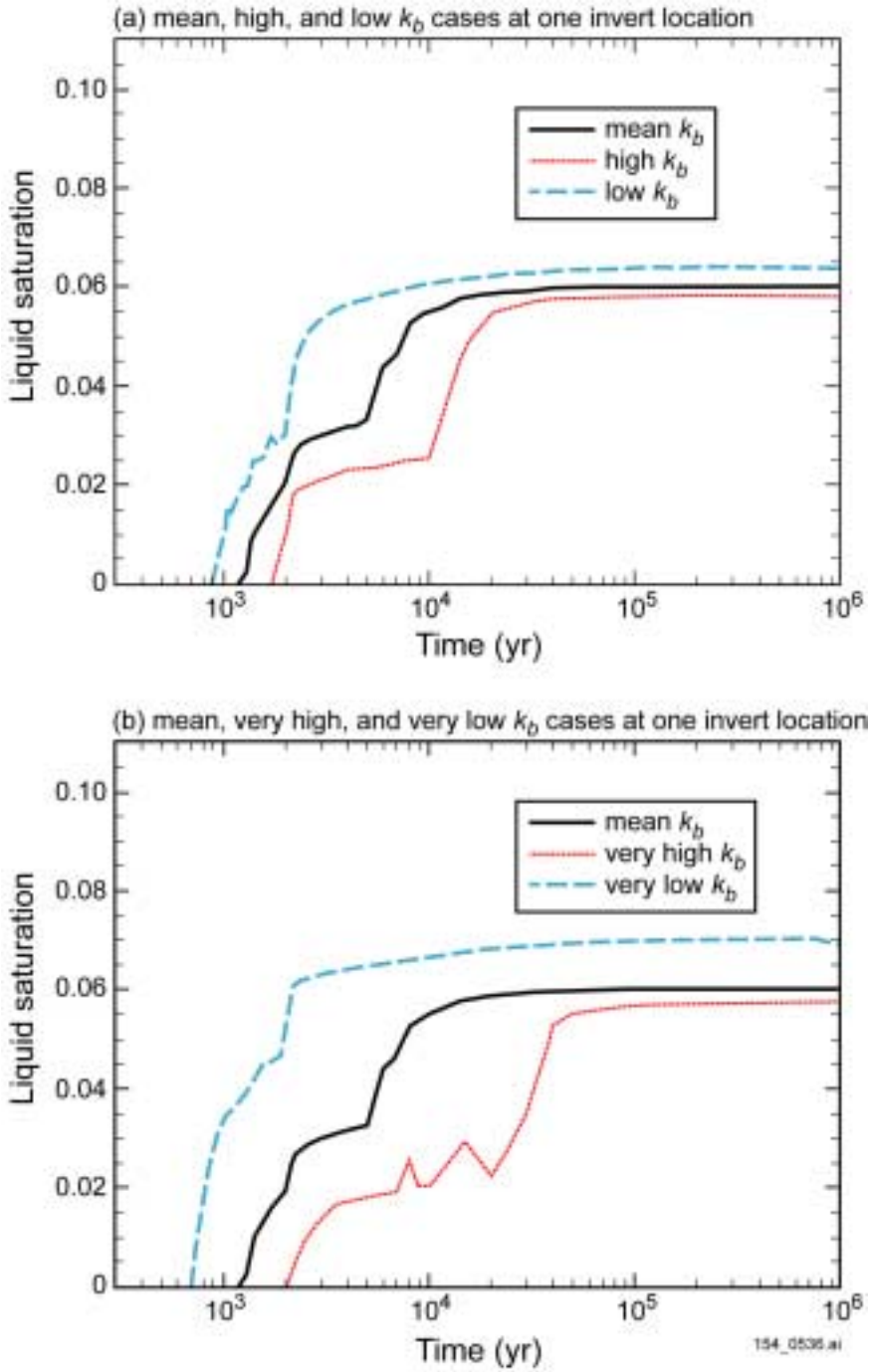

154_0536.ai

Source: Produced using files from Buscheck 2001 [DIRS 155012].

NOTE: Lower-temperature operating mode invert liquid saturations at the central repository location (Location L5C3) as a function of bulk permeability (k_b) for the mean infiltration-flux scenario.

Figure 5.3.1.4.7-4. Invert Liquid-Saturations as a Function of Bulk Permeability for the Lower-Temperature Operating Mode

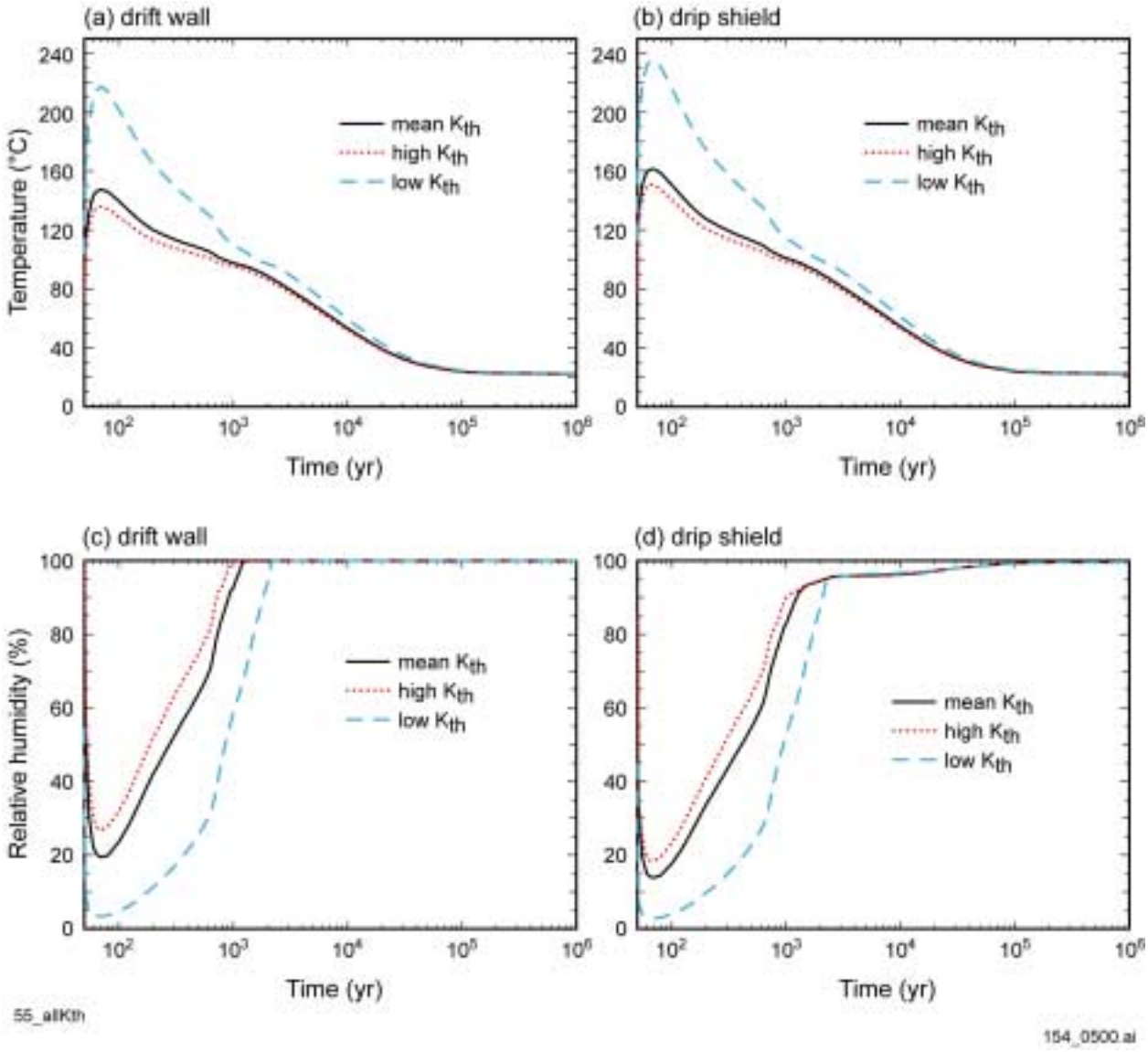

154_0500.ai

Source: Produced using files from Buscheck 2001 [DIRS 155012].

Figure 5.3.1.4.8-1. Temperature and Relative Humidity at the Drift Wall and Drip Shield as a Function of Host-Rock Thermal Conductivity for the Central Repository (L5C3) Location of the Higher-Temperature Operating Mode and the Mean Infiltration-Flux Scenario

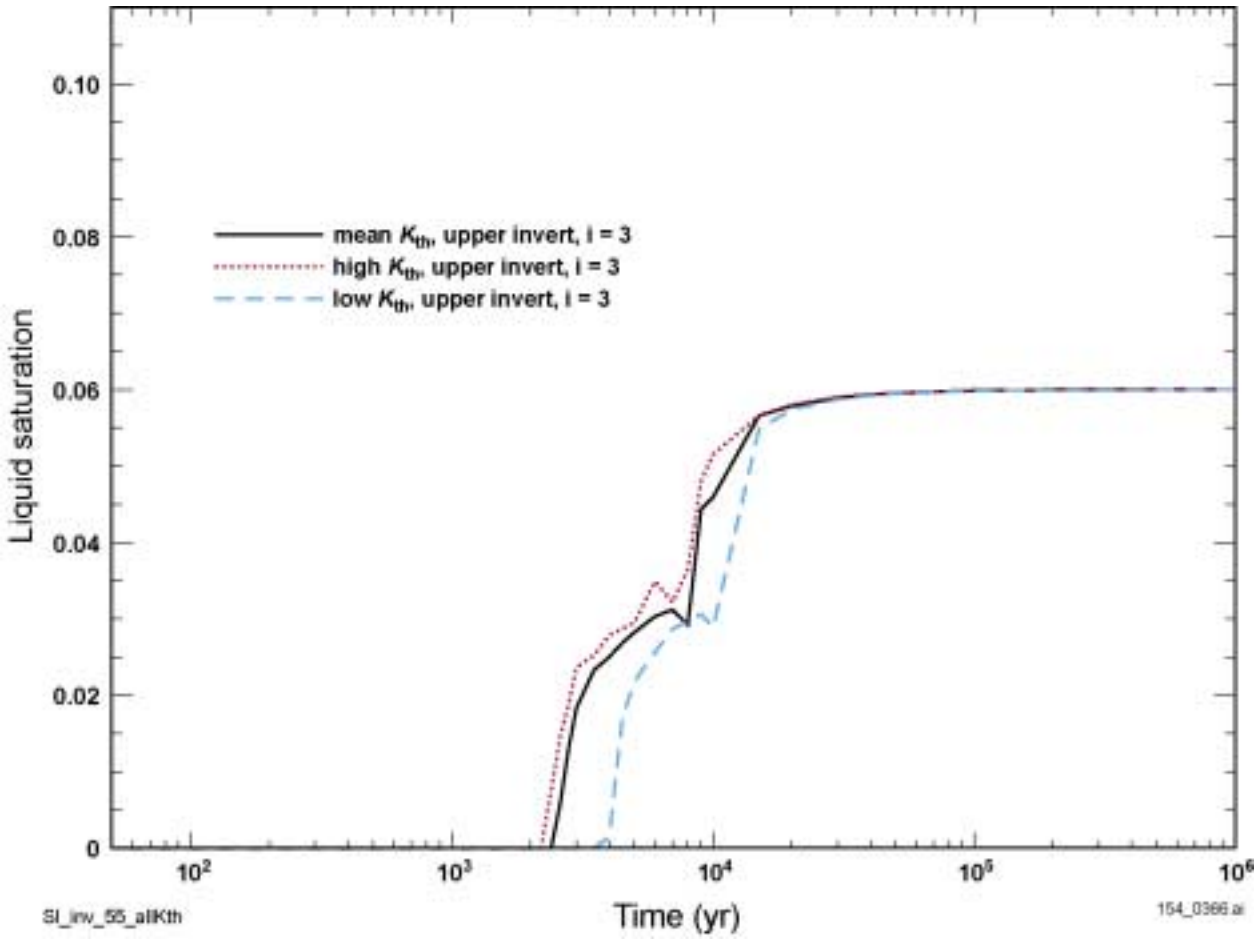

154_0366.ai

Source: Produced using files from Buscheck 2001 [DIRS 155012].

Figure 5.3.1.4.8-2. Liquid-Saturation in the Invert as a Function of Host-Rock Thermal Conductivity for the Central Repository (L5C3) Location of the Higher-Temperature Operating Mode and the Mean Infiltration-Flux Scenario

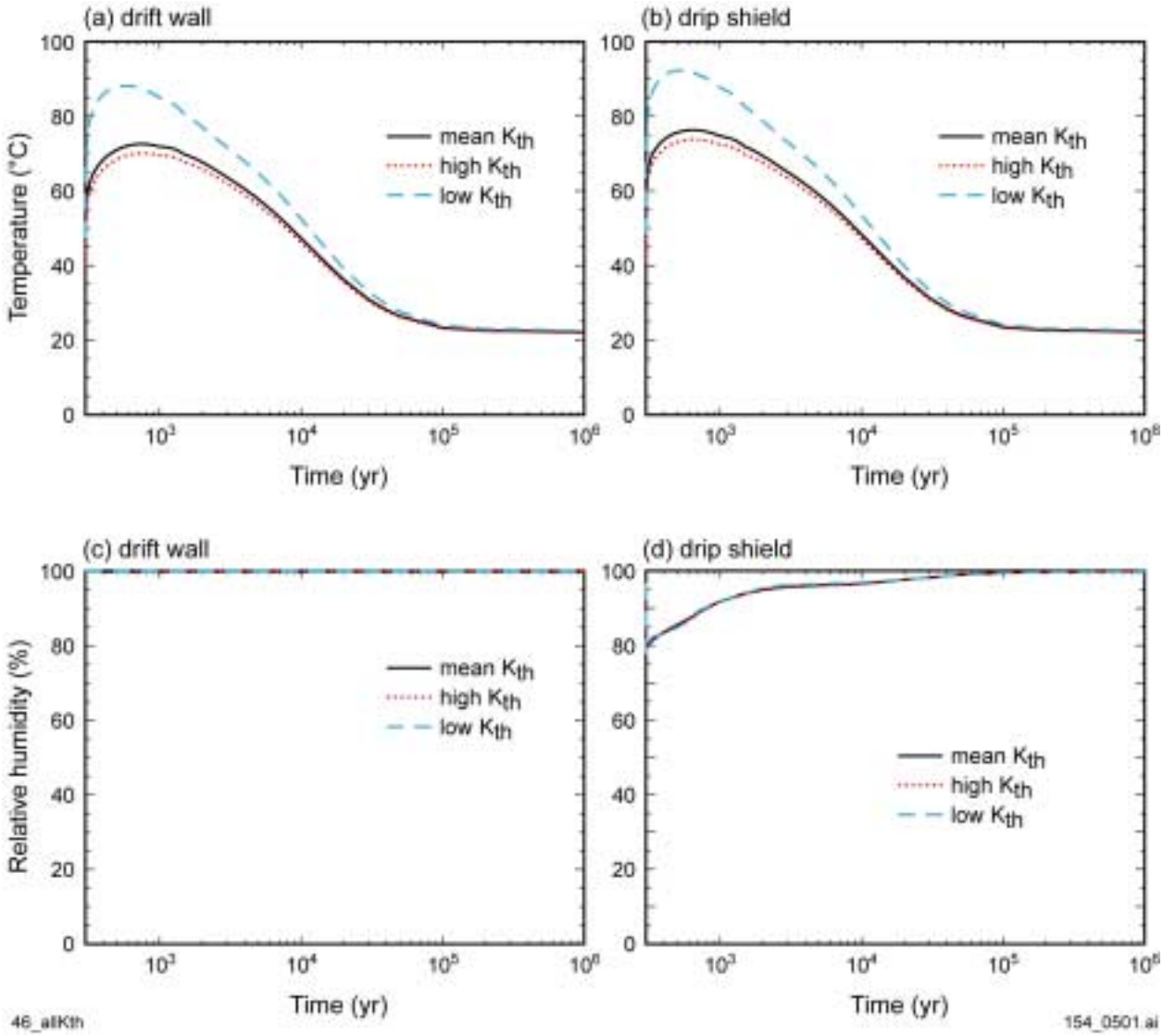

154_0501.ai

Source: Produced using files from Buscheck 2001 [DIRS 155012].

Figure 5.3.1.4.8-3. Temperature and Relative Humidity at the Drift Wall and Drip Shield as a Function of Host-Rock Thermal Conductivity for the Central Repository (L5C3) Location of the Lower-Temperature Operating Mode and the Mean Infiltration-Flux Scenario

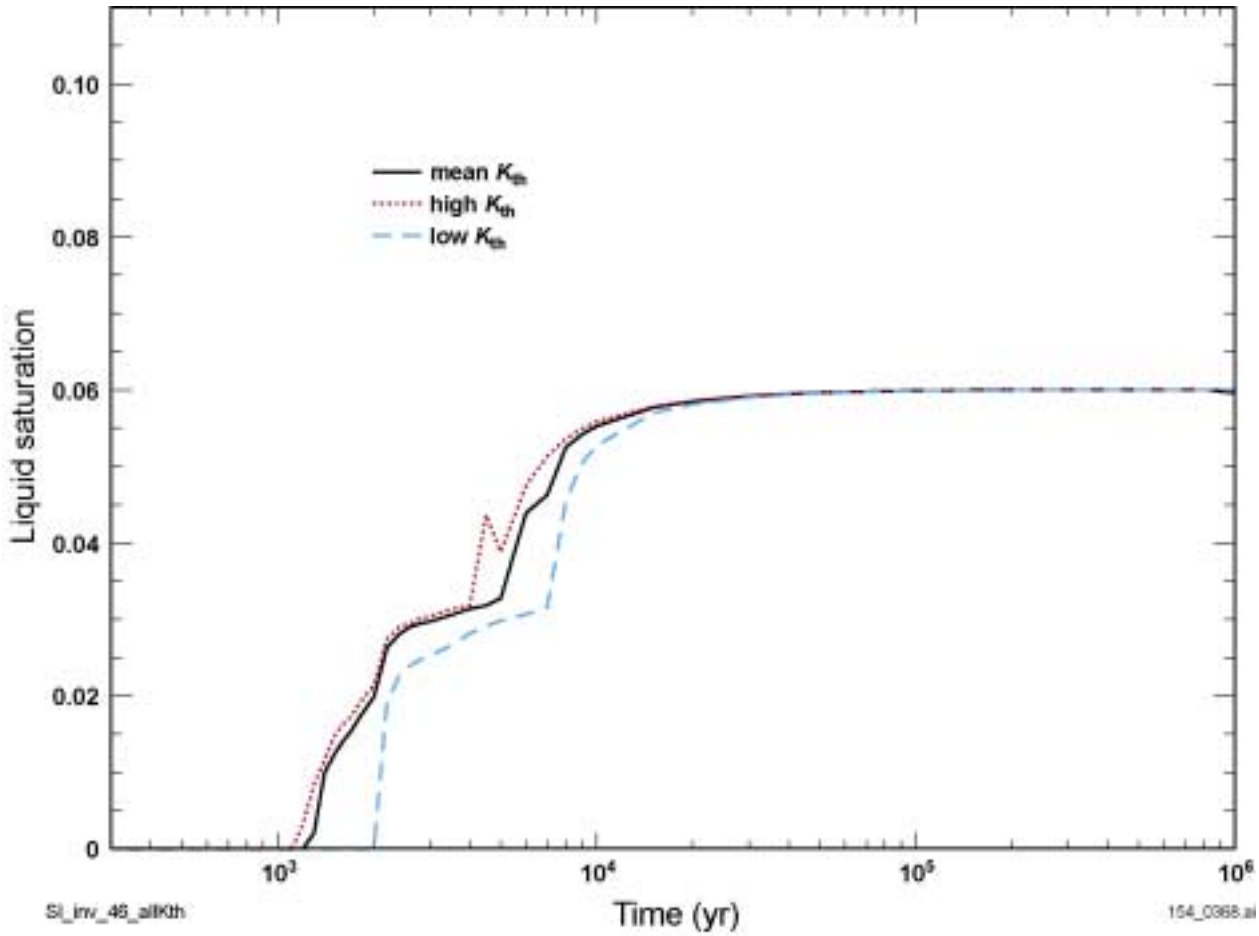

154_0368.ai

Source: Produced using files from Buscheck 2001 [DIRS 155012].

Figure 5.3.1.4.8-4. Liquid-saturation in the Invert as a Function of Host-Rock Thermal Conductivity for the Central Repository (L5C3) Location of the Lower-Temperature Operating Mode and the Mean Infiltration-Flux Scenario

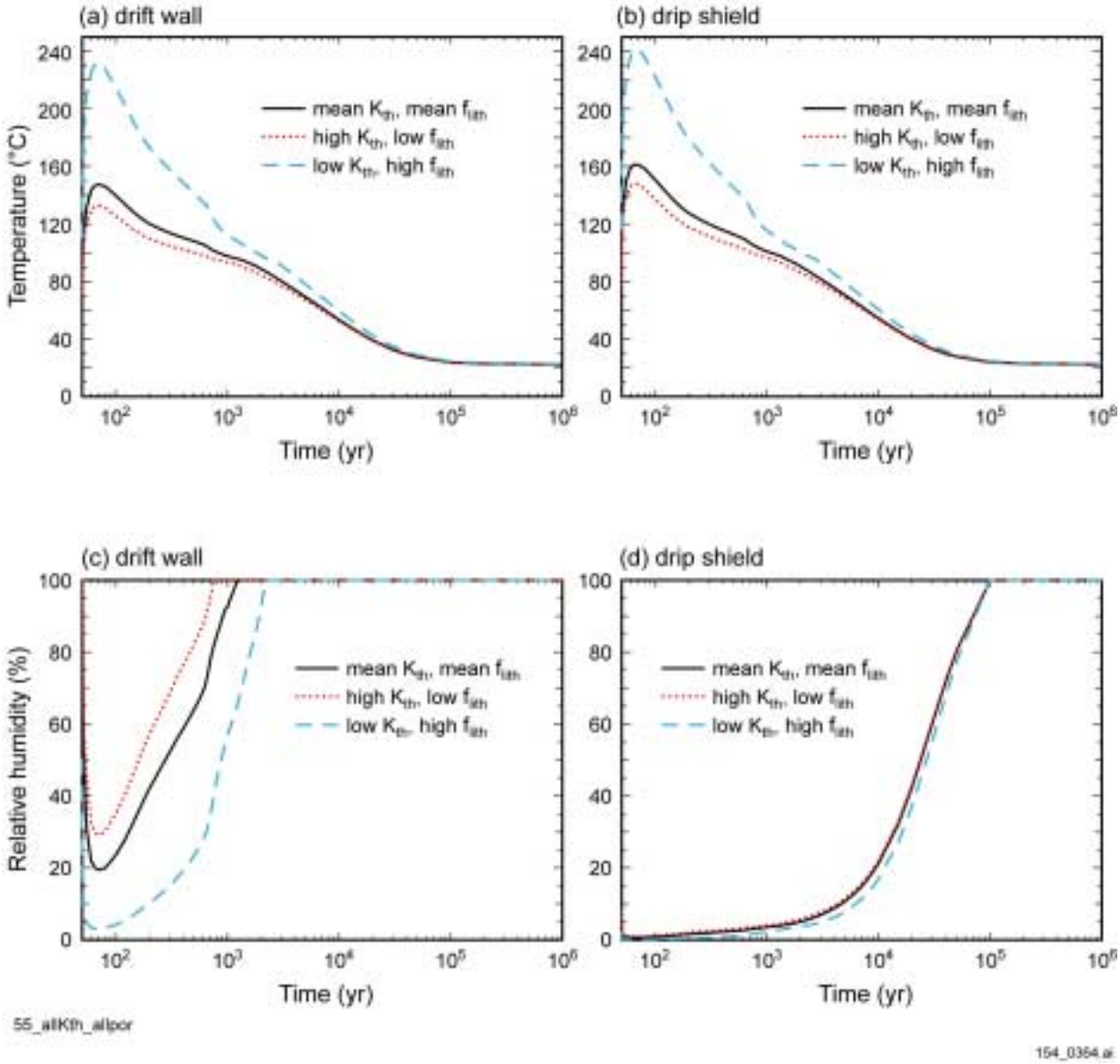

154_0364.ai

Source: Produced using files from Buscheck 2001 [DIRS 155012].

NOTE: Higher-temperature operating mode, drift wall and drip shield temperature and relative humidity at the central repository location (Location L5C3) as a function of mean, high, and low lithophysal porosity (f_{lith}) associated with appropriate thermal conductivity (K_{th}) for the mean infiltration-flux scenario.

Figure 5.3.1.4.9-1. Higher-Temperature Operating Mode as a Function of Mean, High, and Low Lithophysal Porosity (f_{lith}) for the Mean Infiltration-Flux Scenario

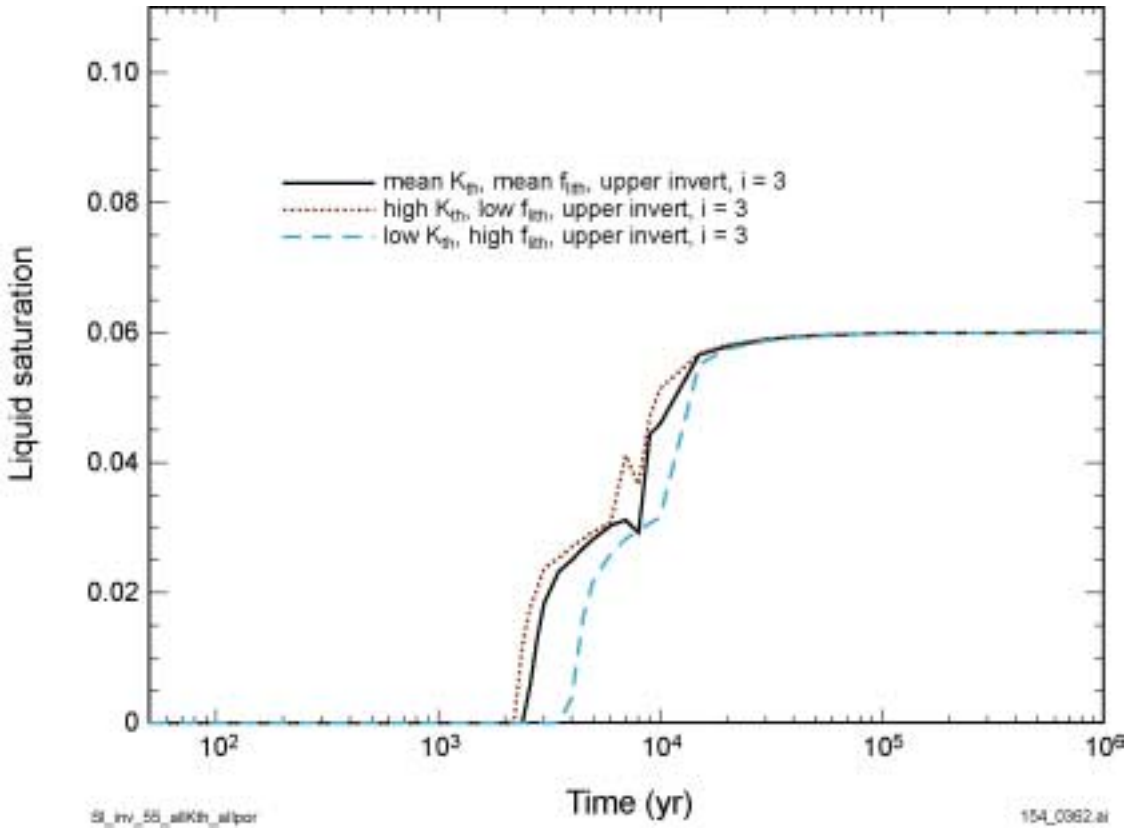

154_0362.ai

Source: Produced using files from Buscheck 2001 [DIRS 155012].

NOTE: Higher-temperature operating mode invert liquid saturations at the central repository location (Location L5C3) as a function of mean, high, and low lithophysal porosity (f_{lith}) associated with appropriate thermal conductivity (K_{th}) for the mean infiltration-flux scenario.

Figure 5.3.1.4.9-2. Higher-Temperature Operating Mode Invert Liquid-Saturations as a Function of Mean, High, and Low Lithophysal Porosity (f_{lith}) for the Mean Infiltration-Flux Scenario

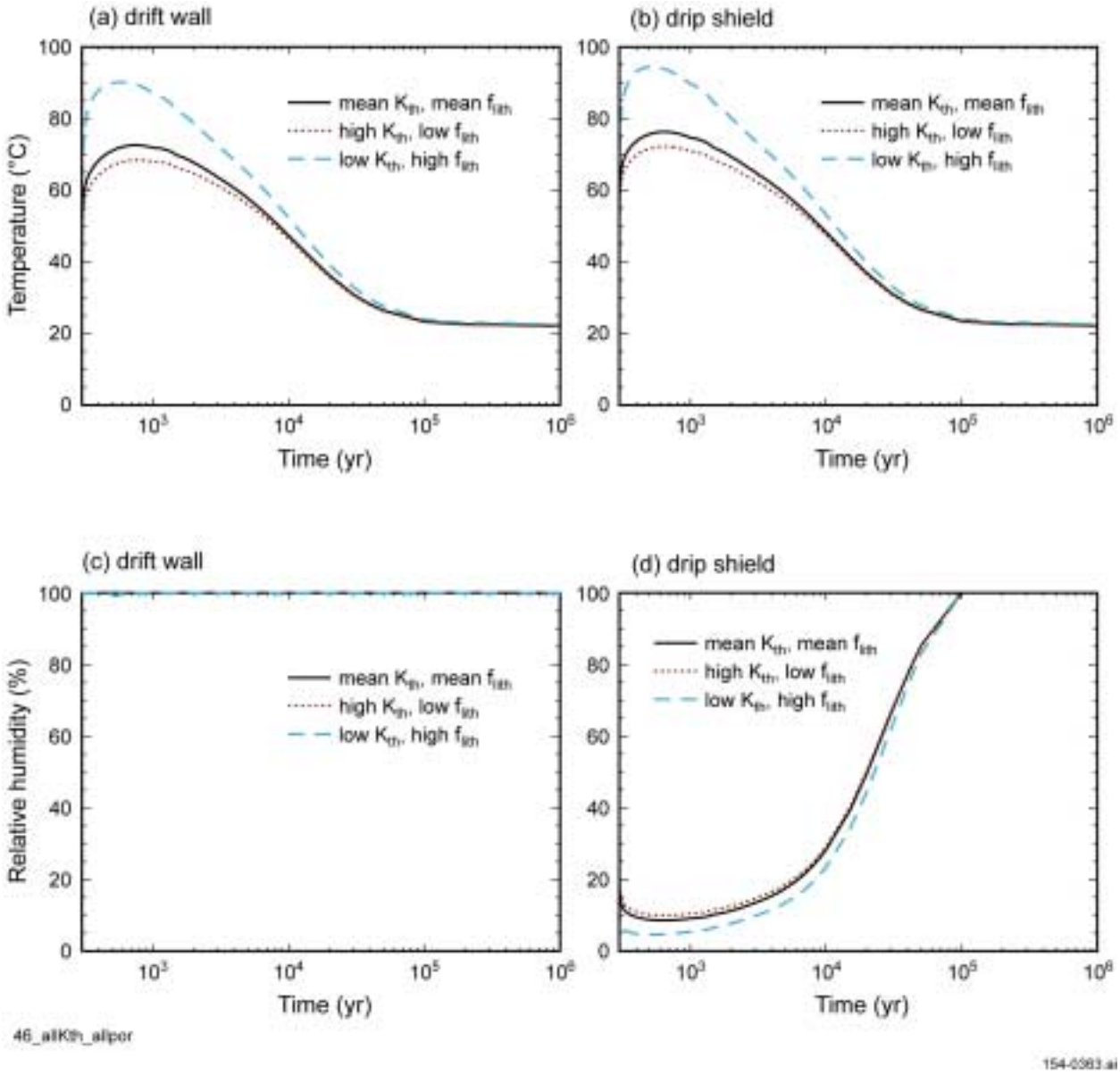

154_0363.ai

Source: Produced using files from Buscheck 2001 [DIRS 155012].

NOTE: Lower-temperature operating mode drift wall and drip shield temperatures and relative humidities at the central repository location (Location L5C3) as a function of mean, high, and low lithophysal porosity (f_{lith}) associated with appropriate thermal conductivity (K_{th}) for the mean infiltration-flux scenario.

Figure 5.3.1.4.9-3. Lower-Temperature Operating Mode Drift Wall and Drip Shield Temperatures and Relative Humidities as a Function of Mean, High, and Low Lithophysal Porosity (f_{lith}) for the Mean Infiltration-Flux Scenario

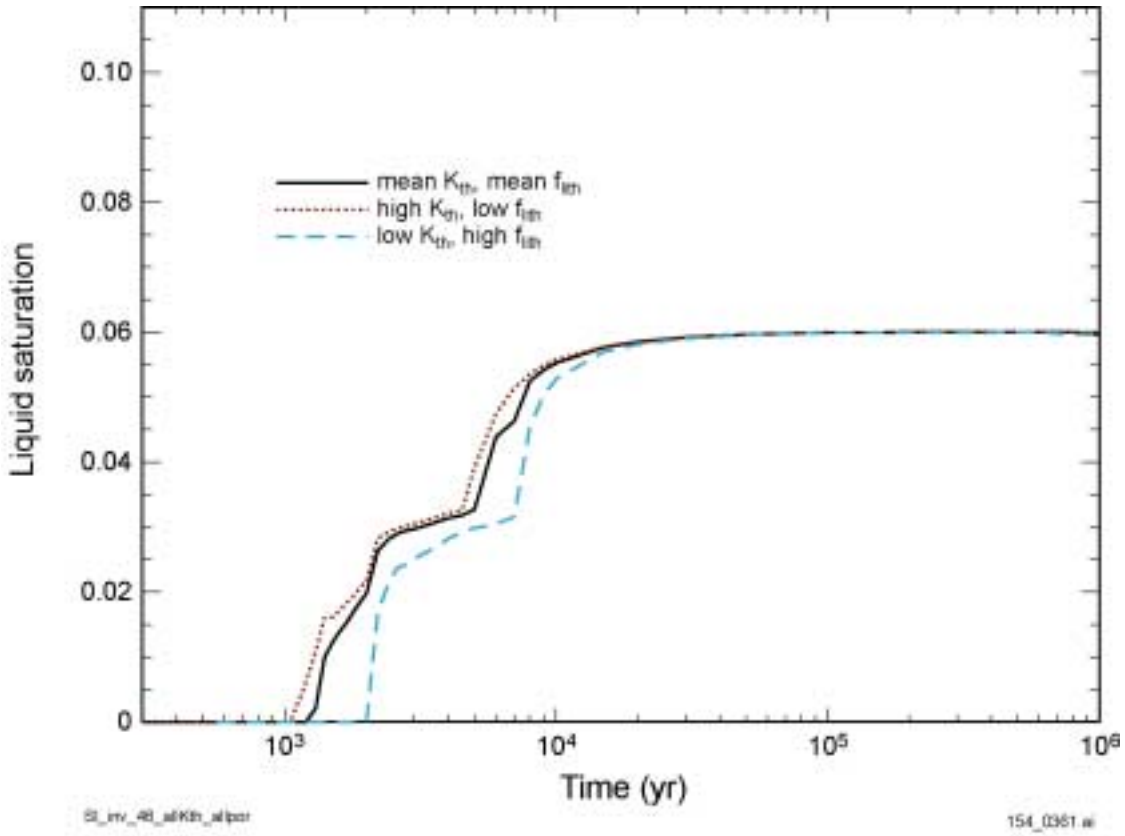

154_0361.ai

Source: Produced using files from Buscheck 2001 [DIRS 155012].

Figure 5.3.1.4.9-4. Lower-Temperature Operating Mode Invert Saturation for the Central Repository Location (Location L5C3) as a Function of Mean, High and Low Lithophysal Porosity (f_{lith}) Associated with Appropriate Thermal Conductivity (K_{th}) for the Mean Infiltration-Flux Scenario

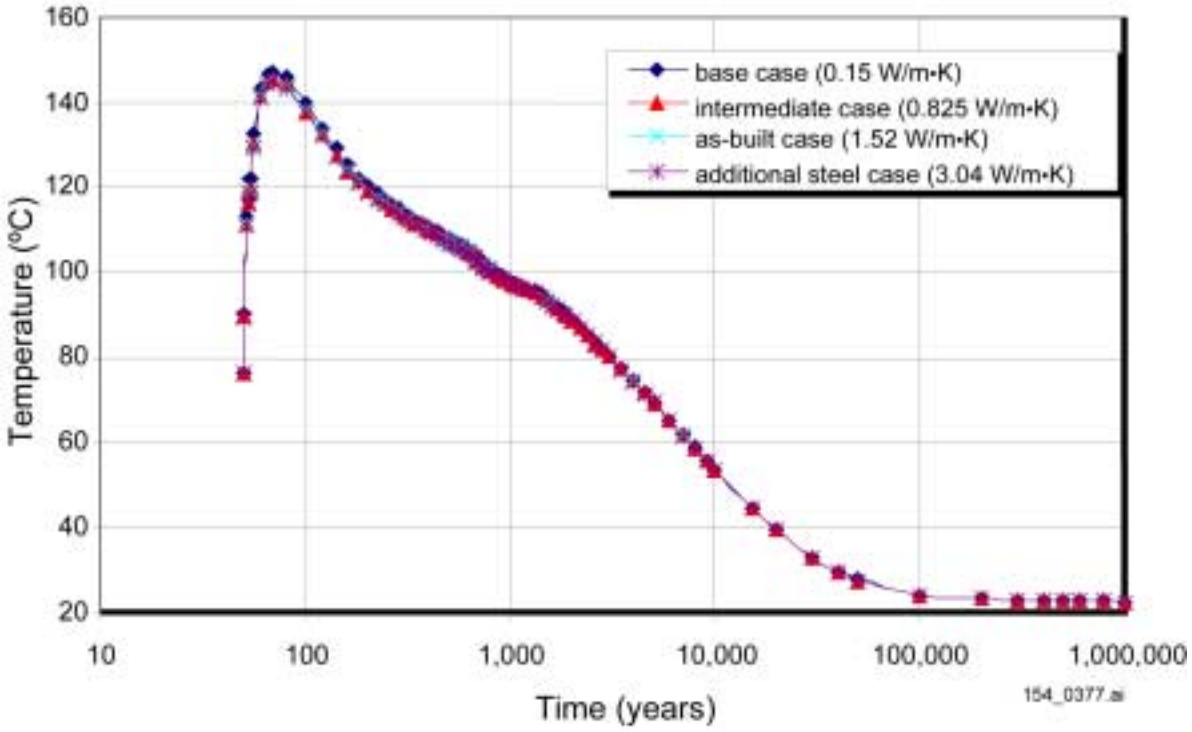

154_0377.ai

Source: Produced using files from Reed 2001 [DIRS 155076].

Figure 5.3.1.4.10-1. Drift Wall (Crown) Temperature Sensitivity to Invert Thermal Conductivity for the Higher-Temperature Operating Mode

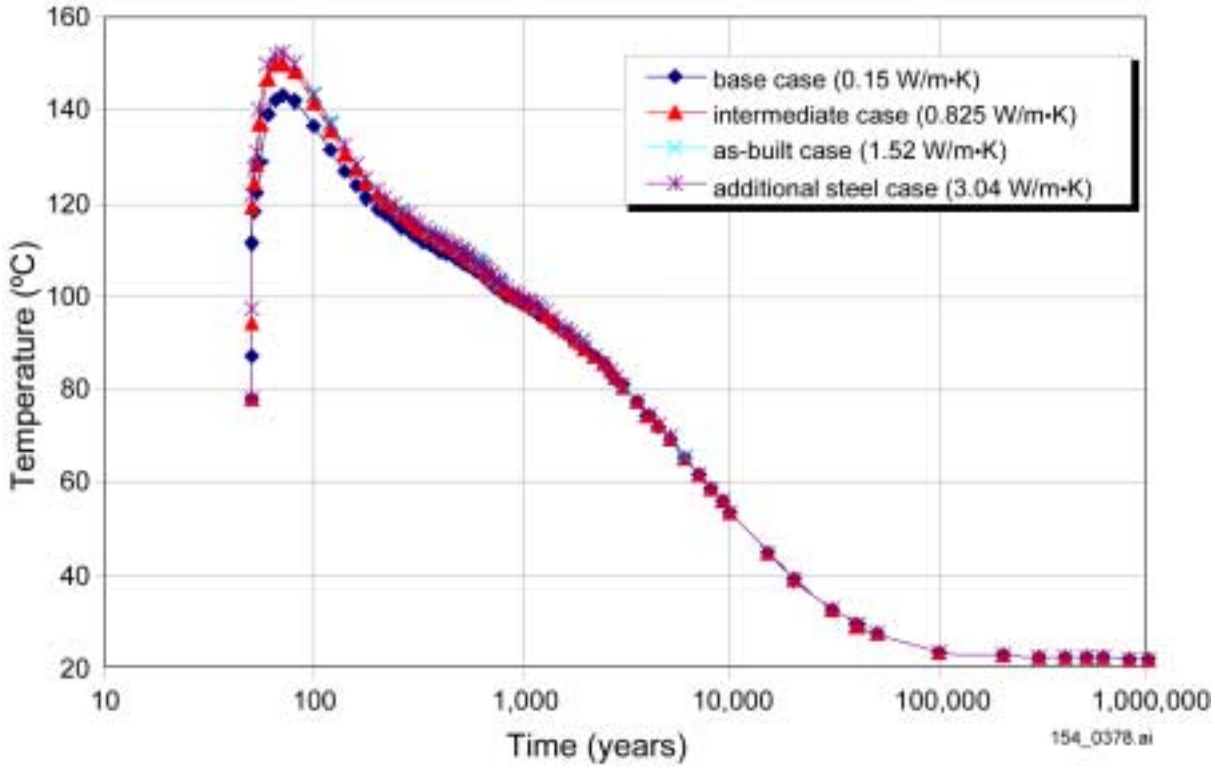

154_0378.ai

Source: Produced using files from Reed 2001 [DIRS 155076].

Figure 5.3.1.4.10-2. Invert (Lower-Center) Temperature Sensitivity to Invert Thermal Conductivity for the Higher-Temperature Operating Mode

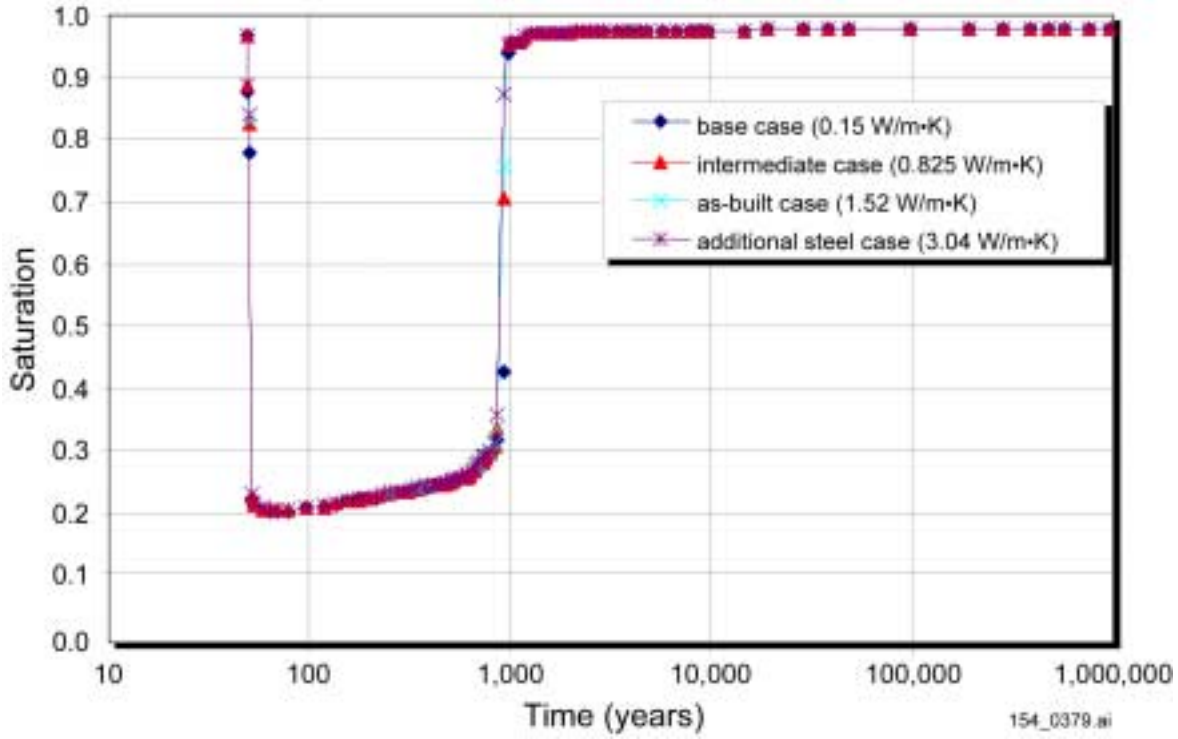

154_0379.ai

Source: Produced using files from Reed 2001 [DIRS 155076].

Figure 5.3.1.4.10-3. Drift Wall (Crown) Liquid Saturation Sensitivity to Invert Thermal Conductivity for the Higher-Temperature Operating Mode

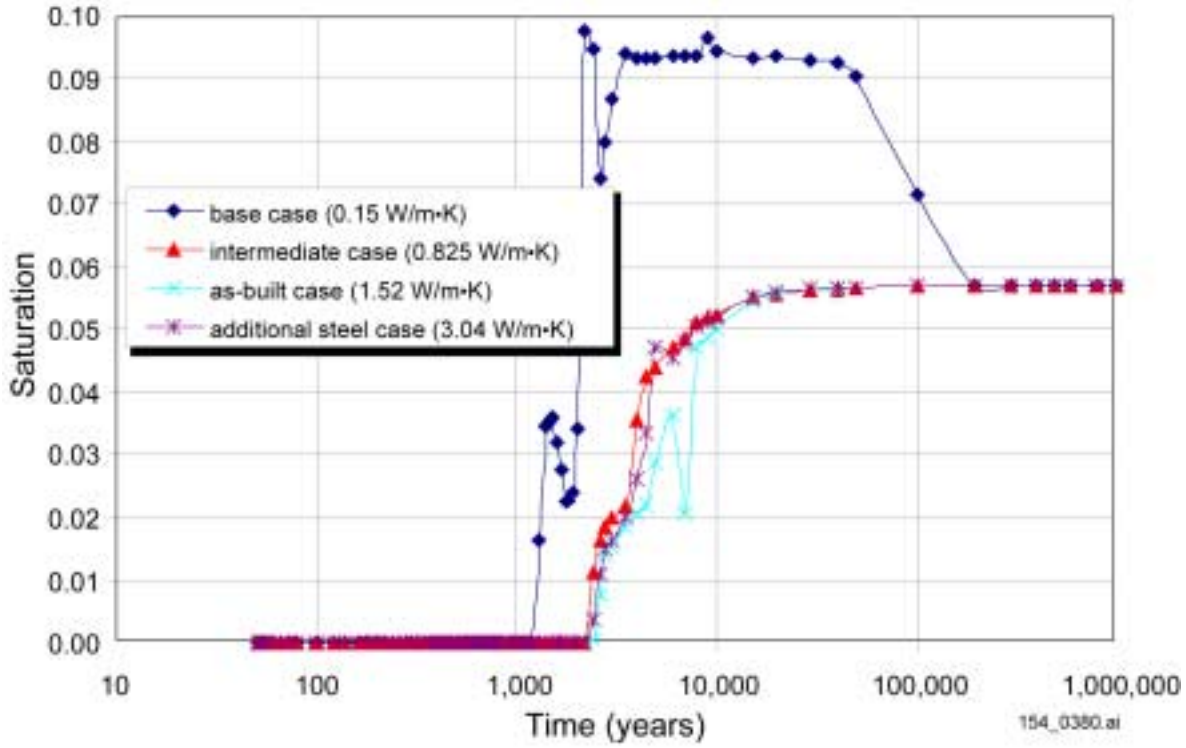

154_0380.ai

Source: Produced using files from Reed 2001 [DIRS 155076].

Figure 5.3.1.4.10-4. Invert (Lower-Center) Liquid Saturation Sensitivity to Invert Thermal Conductivity for the Higher-Temperature Operating Mode

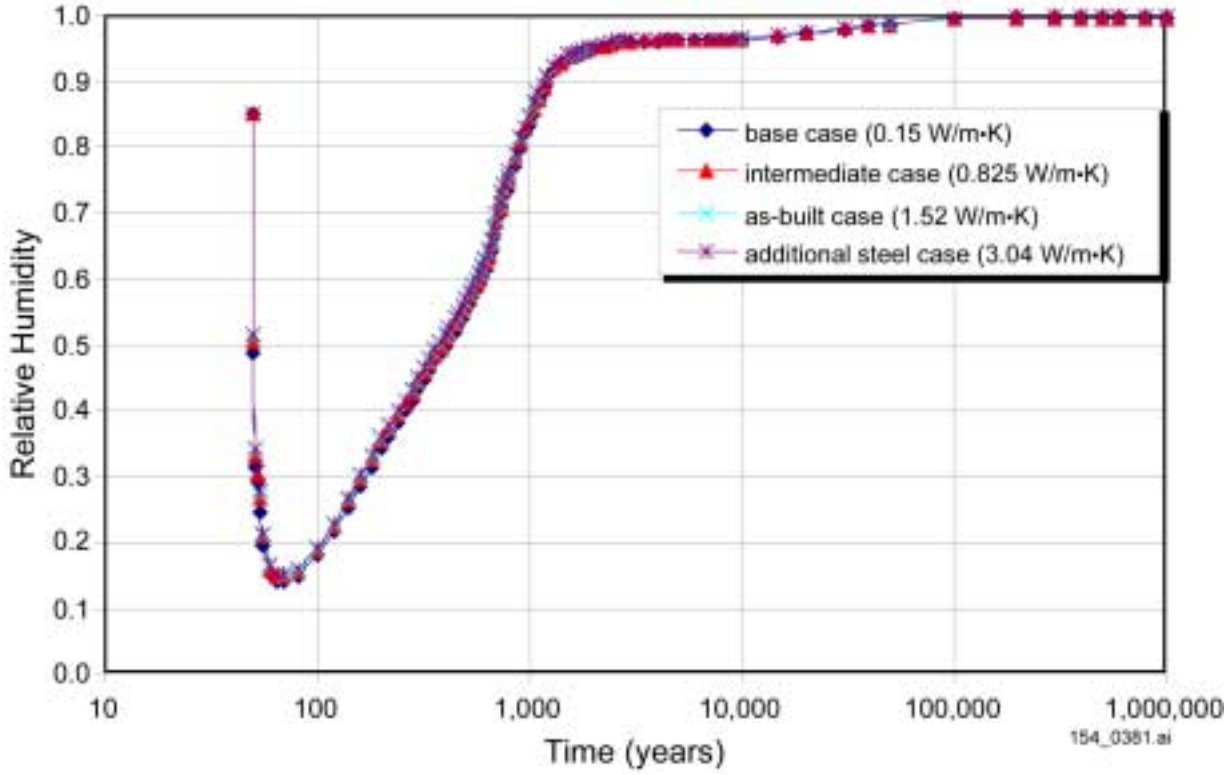

154_0381.ai

Source: Produced using files from Reed 2001 [DIRS 155076].

Figure 5.3.1.4.10-5. Drip Shield (Top) Relative Humidity Sensitivity to Invert Thermal Conductivity for the Higher-Temperature Operating Mode

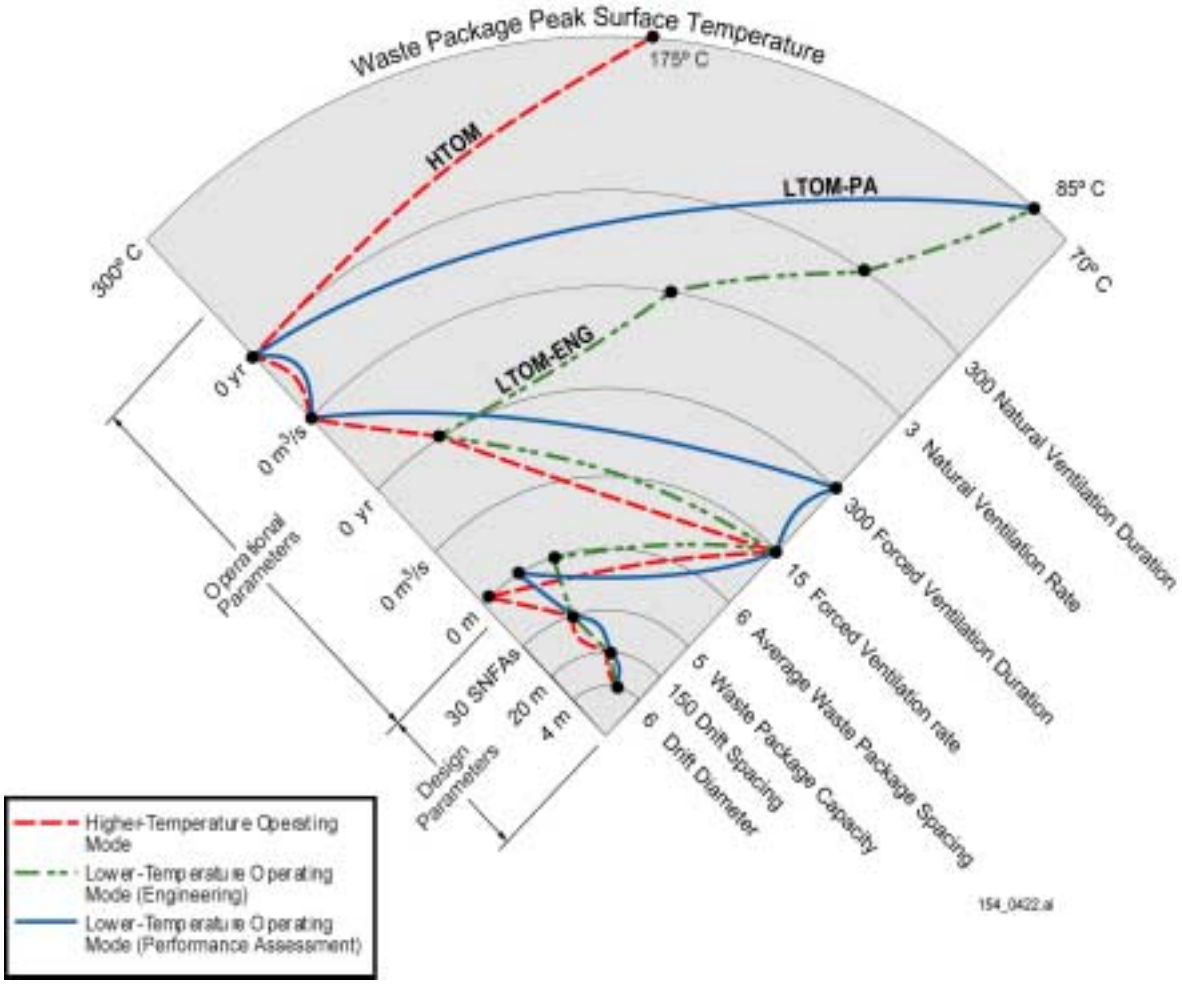

154_0422.ai

Source: Produced from information in BSC 2001 [DIRS 154864] and BSC 2001 [DIRS 155010].

NOTE: Two sets of parameters are shown that can meet the lower-temperature operating mode goal. Black dots represent values of design and operating parameters which, when combined, result in the peak waste package temperatures shown. Lines through the black dots represent three combinations of parameters being evaluated during the SR time period. HTOM = higher-temperature operating mode; PA = performance assessment base case; ENG = engineering evaluations.

Figure 5.3.1.4.11-1. Design and Operating Mode Parameters Used to Meet Peak Waste Package Temperature Goals

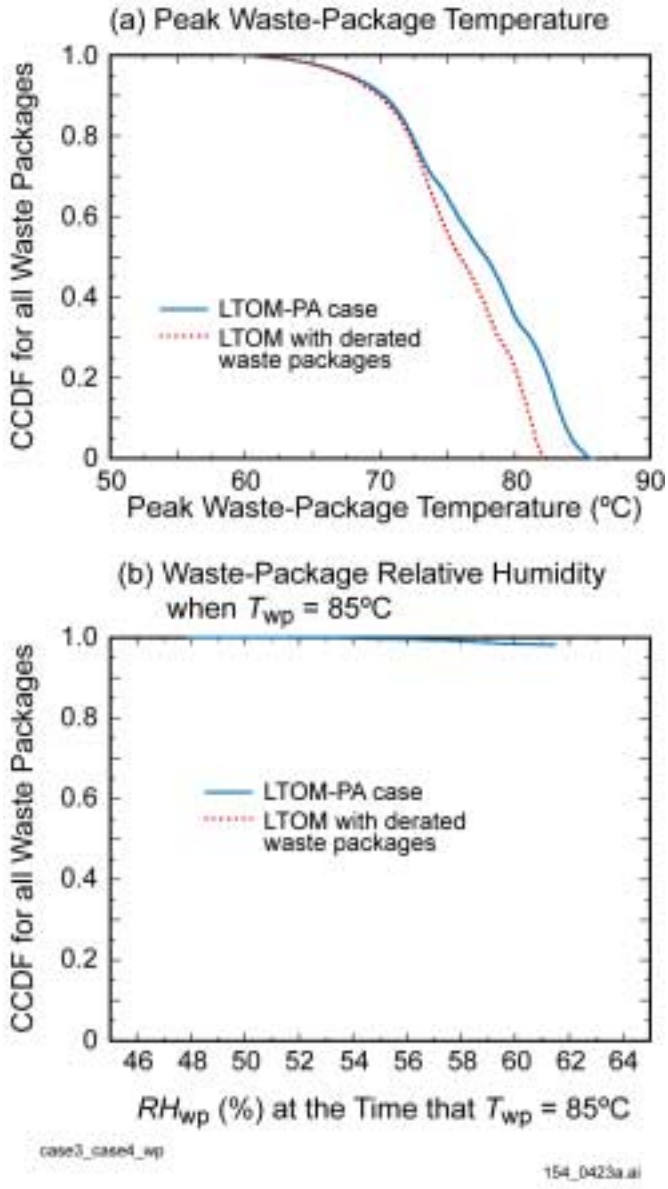

154_0423a.ai

Source: Produced using files from Buscheck 2001 [DIRS 155449].

NOTE: Temperature and relative humidity (*RH*) when the waste package temperature (T_{wp}) is 85ºC considering repository footprint, infiltration flux map, and variability among waste packages. LTOM-PA = lower-temperature operating mode used in the performance assessment base case. CCDF = complementary cumulative distribution function.

Figure 5.3.1.4.11-2. Waste Package Temperatures and Relative Humidity for Two Methods of Achieving the Lower-Temperature Operating Mode

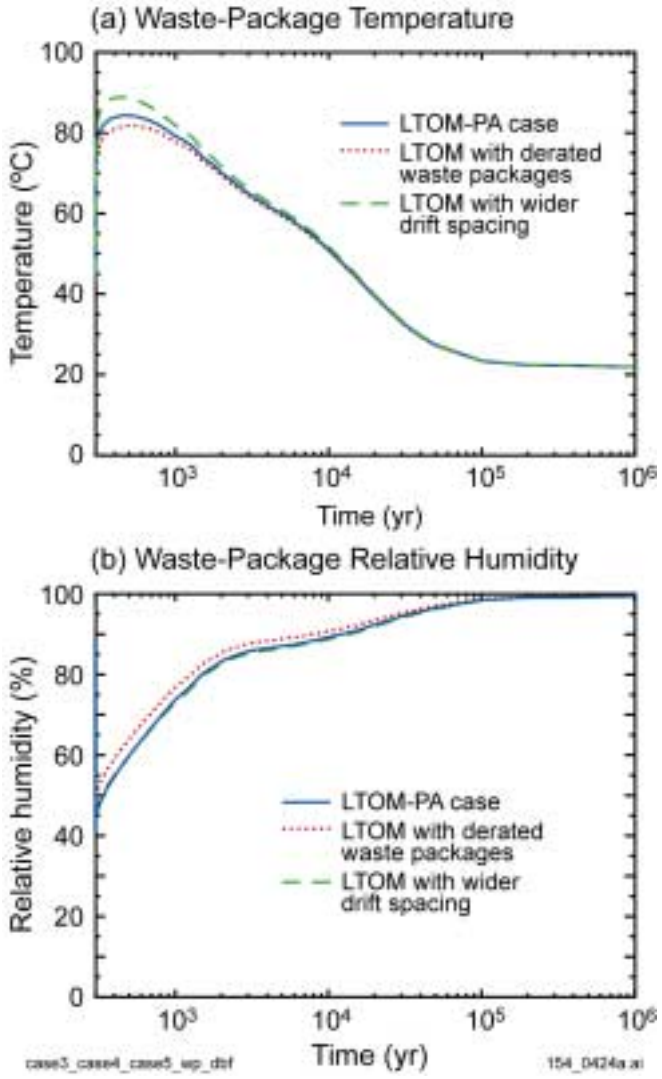

154_0424a.ai

Source: Produced using files from Buscheck 2001 [DIRS 155449].

NOTE: Figure depicts three lower-temperature operating mode cases using the multiscale thermal-hydrologic model at the L5C3 location in the footprint of the potential repository. LTOM = lower-temperature operating mode.

Figure 5.3.1.4.11-3. Temperature and Relative Humidity Histories at the Waste Package Surface for Three Lower-Temperature Operating Mode Designs

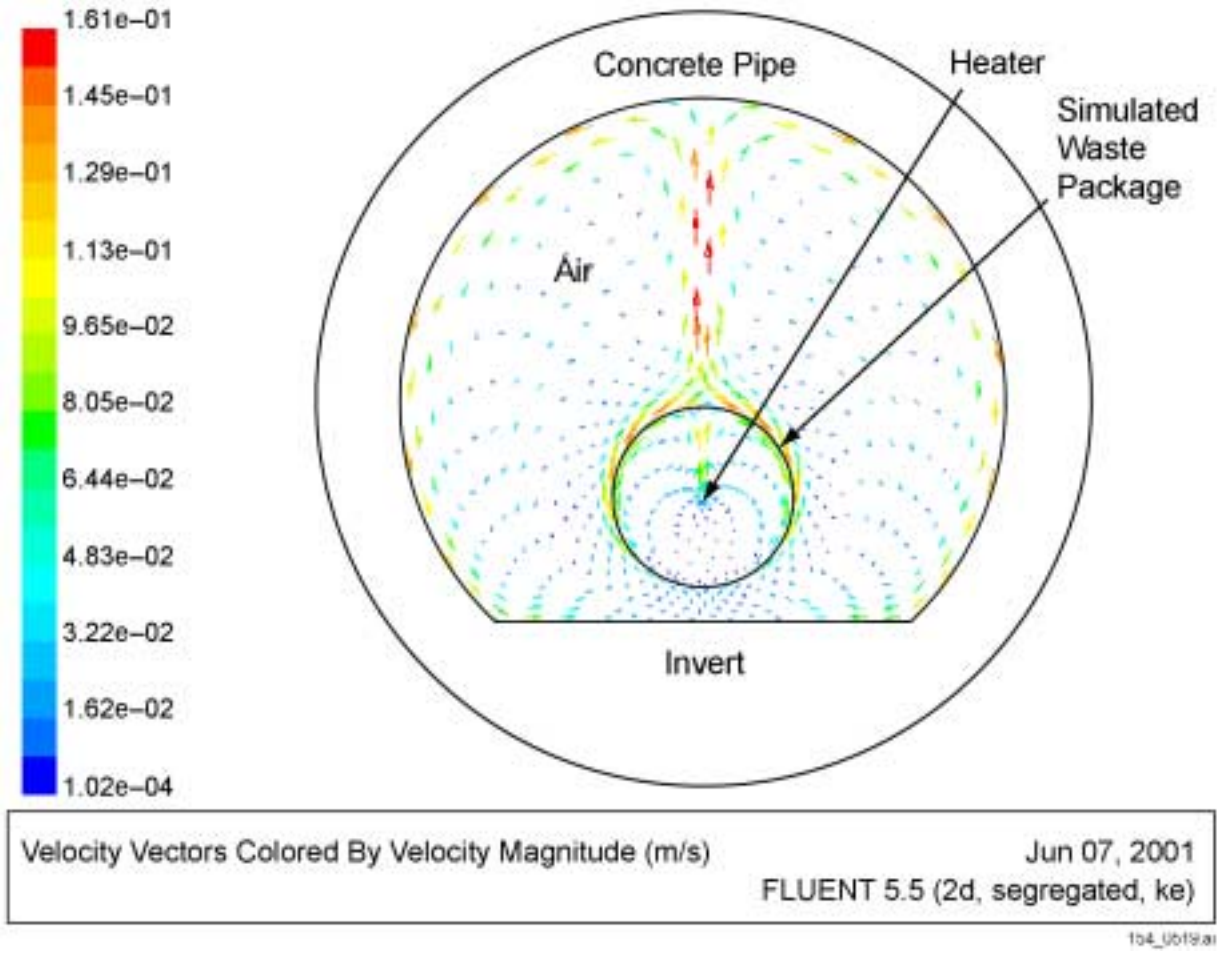

154_0519.ai

Source: Produced using files from Dunn 2001 [DIRS 155308].

NOTE: Similar patterns are expected to develop above and below the drip shield.

Figure 5.3.2-1. Air Flow Pattern in a Prediction of a Quarter-Scale Test of In-Drift Convection

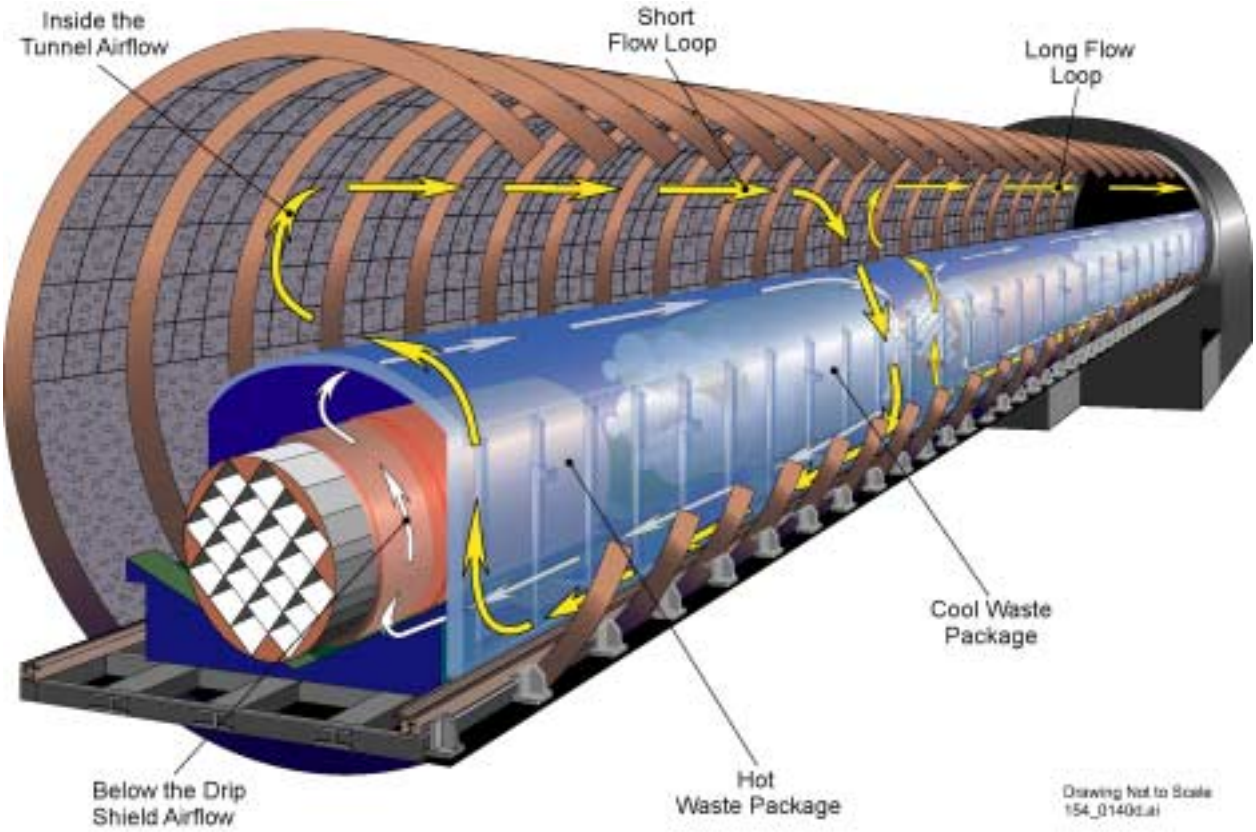

154_0140d.ai

Source: Adapted from CRWMS M&O 2001 [DIRS 154771], p.48.

Figure 5.3.2-2. Three-Dimensional Air Flow in a Closed Emplacement Drift

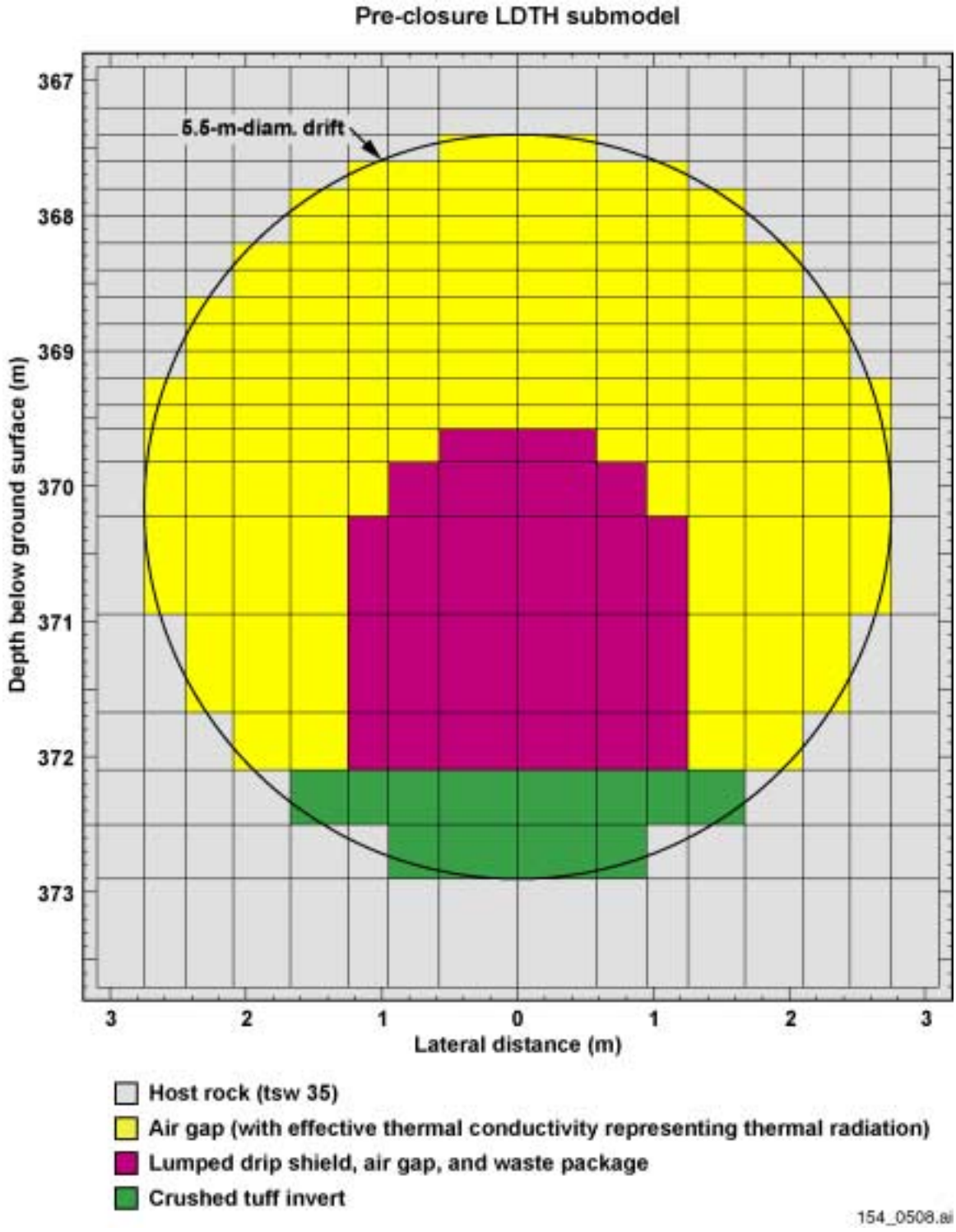

154_0508.ai

Source: Modified from CRWMS M&O 2000 [DIRS 149862], Figure 6-2, using updated invert dimensions and vertical location for one location in the repository.

NOTE: The values on the vertical axis shift with location within the potential repository footprint.

Figure 5.3.2.3-1. Numerical Mesh Used in the Line-Source Drift-Scale Thermal-Hydrologic Submodels

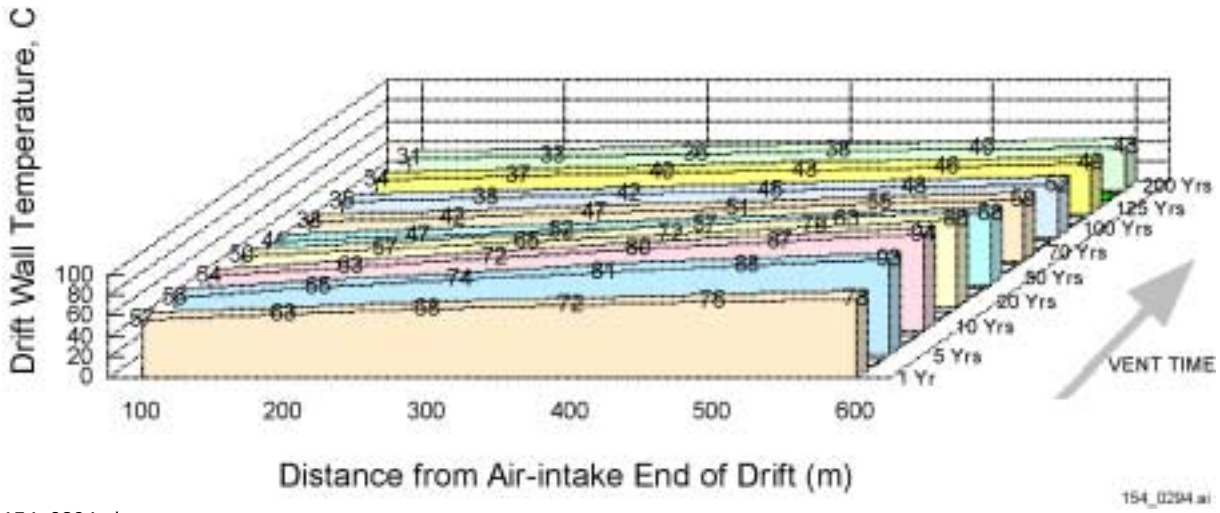

154_0294.ai

Source: CRWMS M&O 2000 [DIRS 120903], Figure 4.

Figure 5.3.2.4.1-1. Wall Temperature During Continuous Ventilation at 10 m^3/s

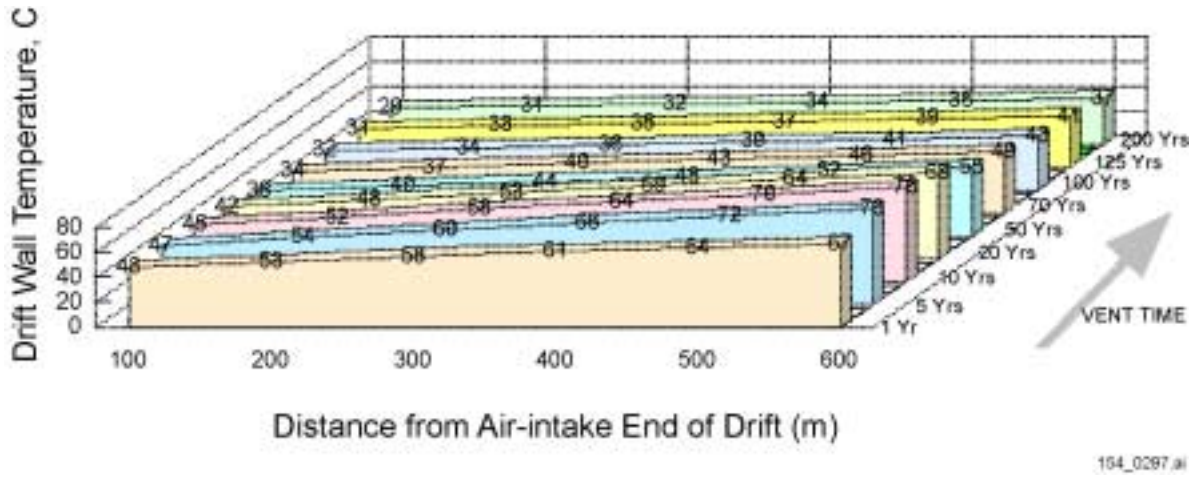

154_0297.ai

Source: CRWMS M&O 2000 [DIRS 120903], Figure 7.

Figure 5.3.2.4.1-2. Wall Temperature During Continuous Ventilation at 15 m^3/s

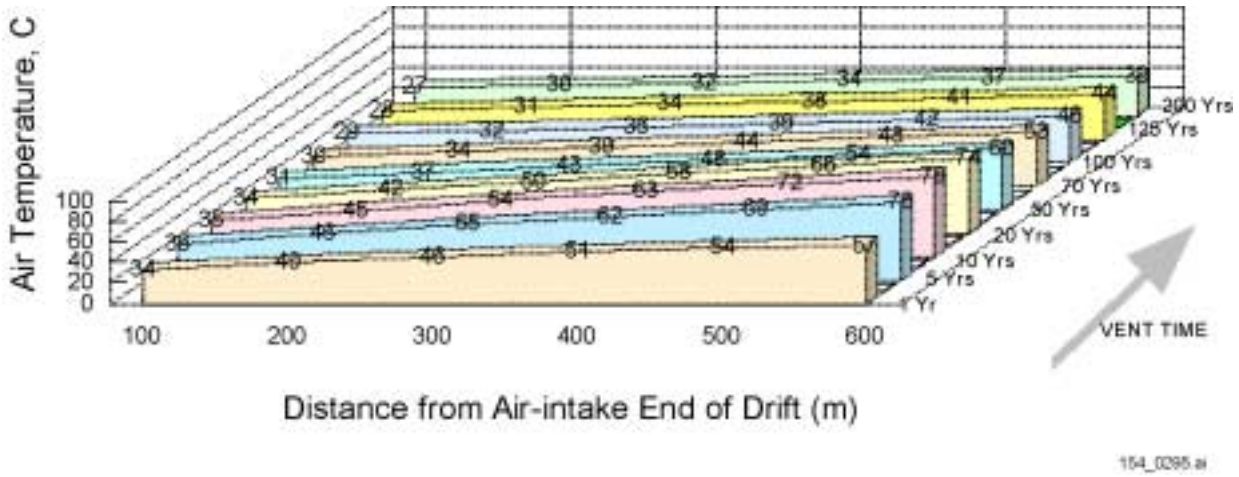

154_0295.ai

Source: CRWMS M&O 2000 [DIRS 120903], Figure 5.

Figure 5.3.2.4.1-3. Air Temperature During Continuous Ventilation at 10 m^3/s

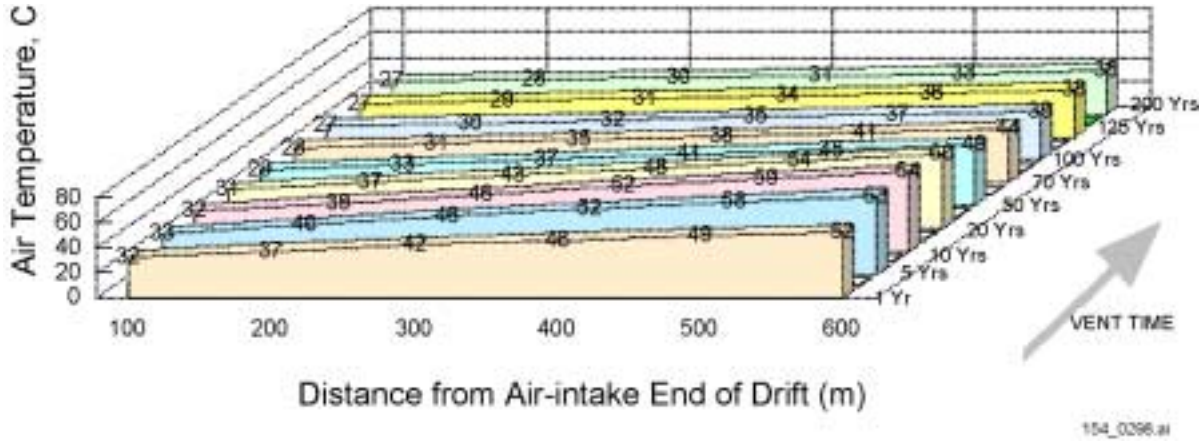

154_0298.ai

Source: CRWMS M&O 2000 [DIRS 120903], Figure 8.

Figure 5.3.2.4.1-4. Air Temperature During Continuous Ventilation at 15 m^3/s

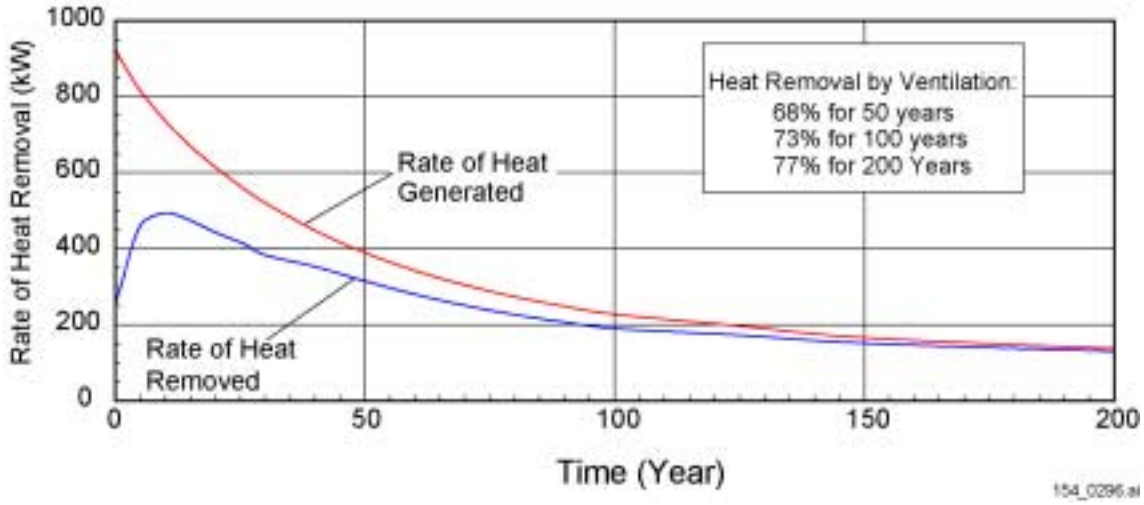

154_0296.ai

Source: CRWMS M&O 2000 [DIRS 120903], Figure 9.

Figure 5.3.2.4.1-5. Heat Removed During Continuous Ventilation at 10 m^3/s

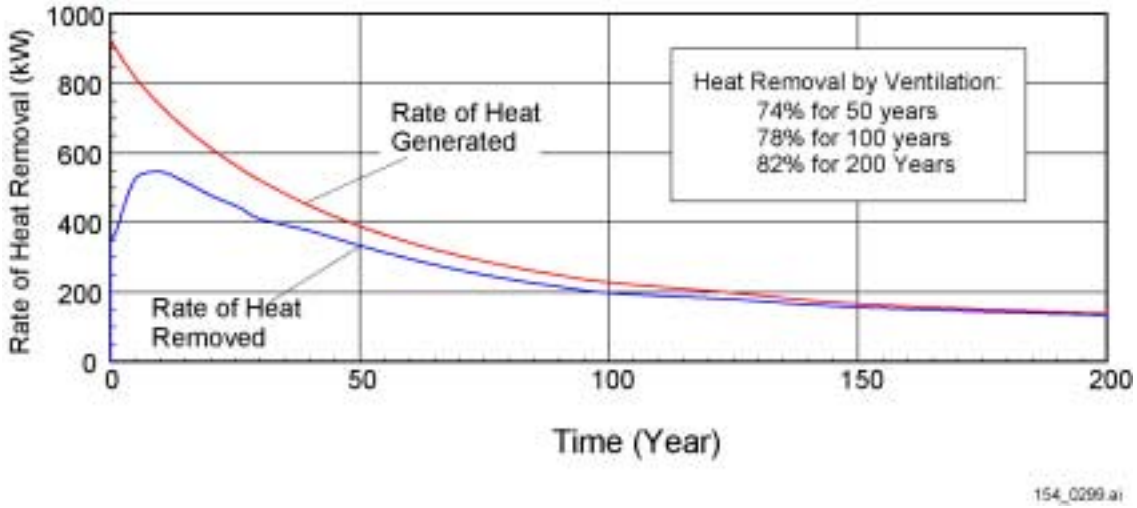

154_0299.ai

Source: CRWMS M&O 2000 [DIRS 120903], Figure 9.

Figure 5.3.2.4.1-6. Heat Removed During Continuous Ventilation at 15 m^3/s

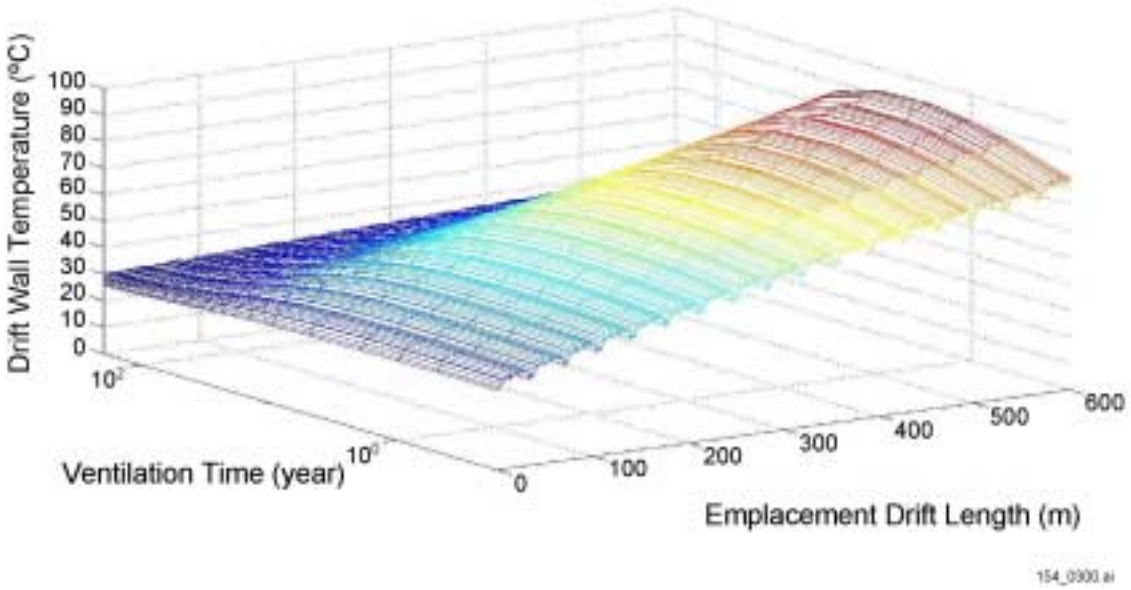

154_0300.ai

Source: BSC 2001 [DIRS 155025], Figure 10.

NOTE: MULTIFLUX Results.

Figure 5.3.2.4.1-7. Wall Temperature During Continuous Ventilation of 10 m^3/s

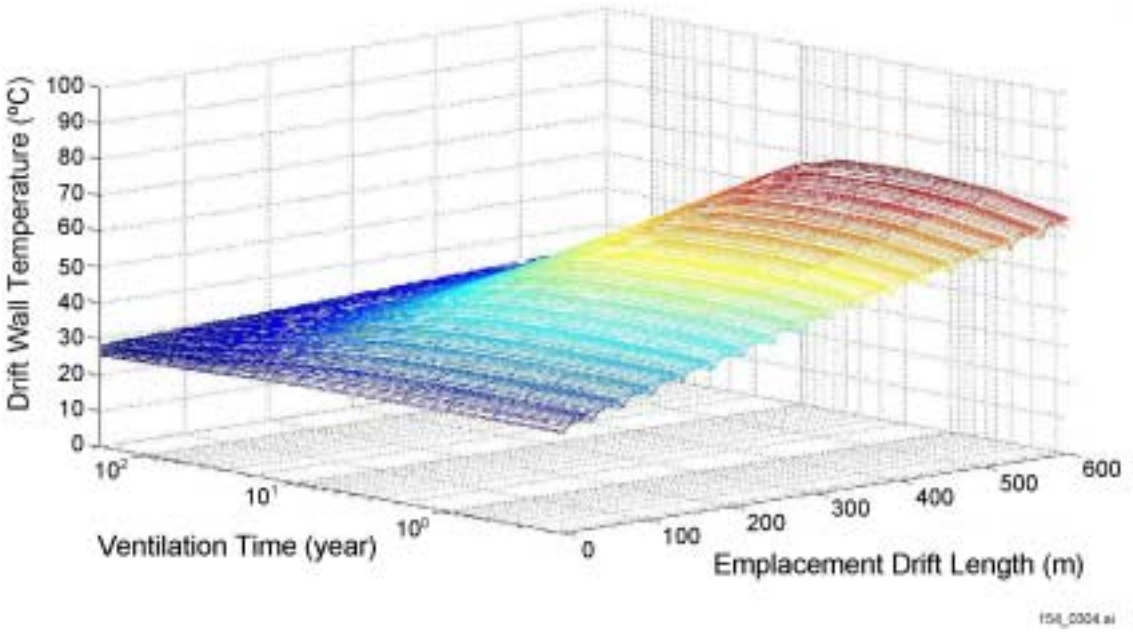

154_0304.ai

Source: BSC 2001 [DIRS 155025], Figure 14.

NOTE: MULTIFLUX Results.

Figure 5.3.2.4.1-8. Wall Temperature During Continuous Ventilation of 15 m^3/s

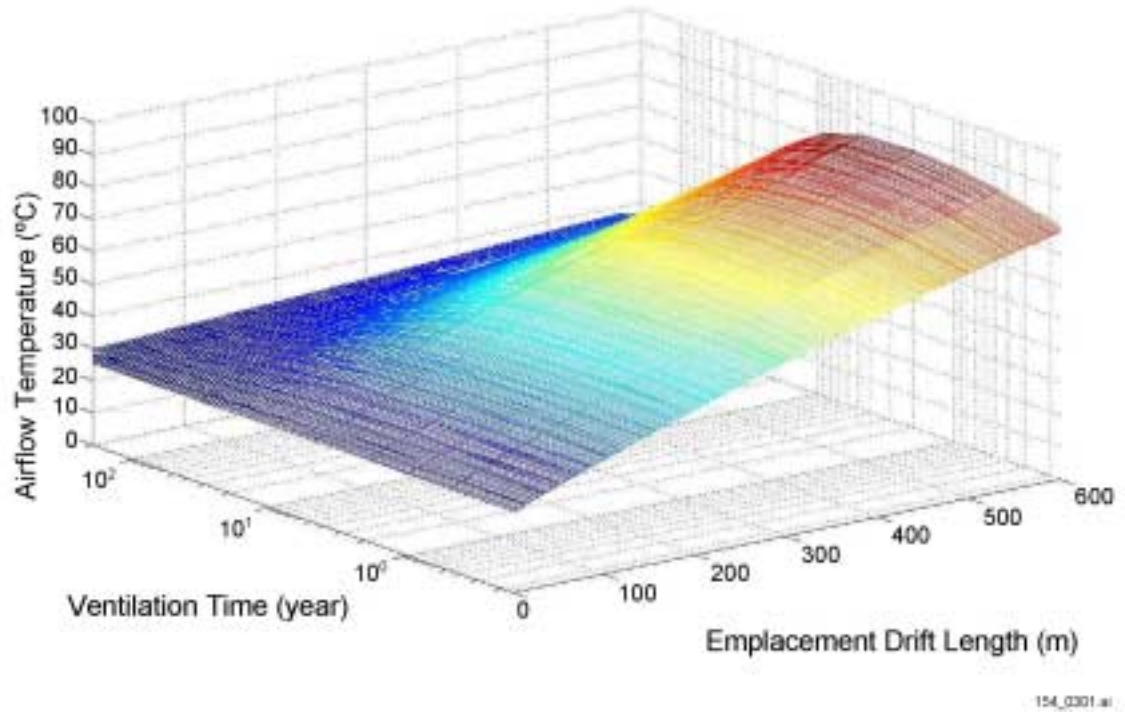

154_0301.ai

Source: BSC 2001 [DIRS 155025], Figure 11

NOTE: MULTIFLUX Results.

Figure 5.3.2.4.1-9. Airflow Temperature During Continuous Ventilation of 10 m^3/s

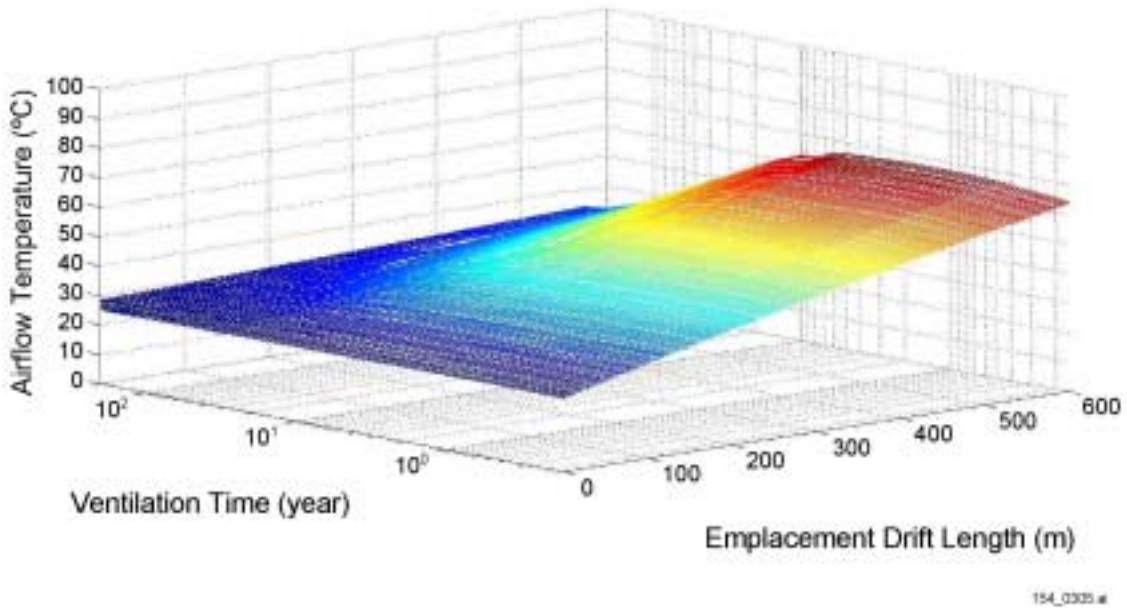

154_0305.ai

Source: BSC 2001 [DIRS 155025], Figure 15.

NOTE: MULTIFLUX Results.

Figure 5.3.2.4.1-10. Airflow Temperature During Continuous Ventilation of 15 m^3/s

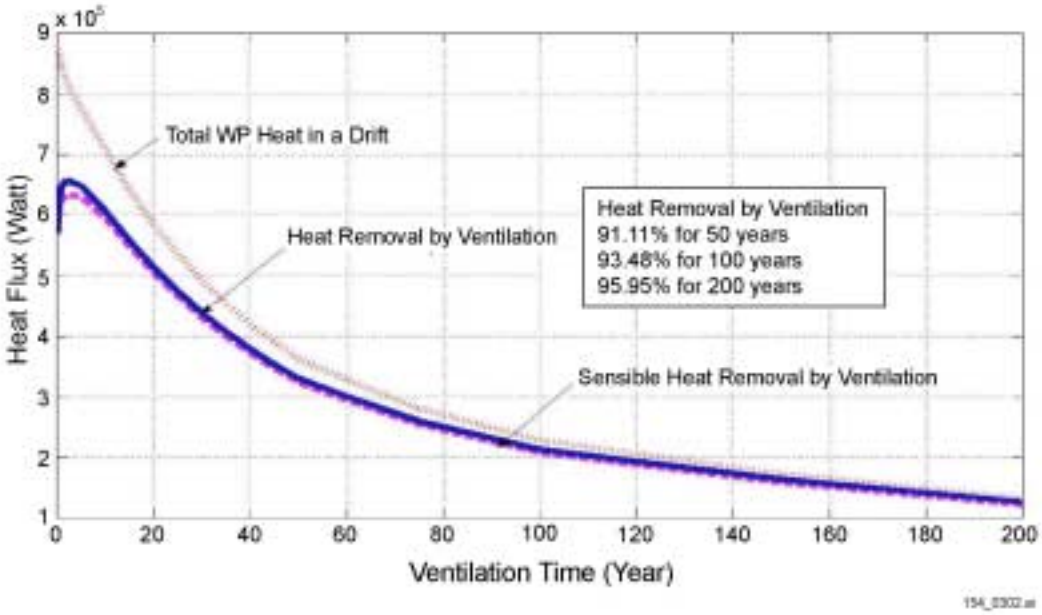

154_0302.ai

Source: BSC 2001 [DIRS 155025], Figure 12.

NOTE: MULTIFLUX Results.

Figure 5.3.2.4.1-11. Heat Removed During Continuous Ventilation of 10 m^3/s

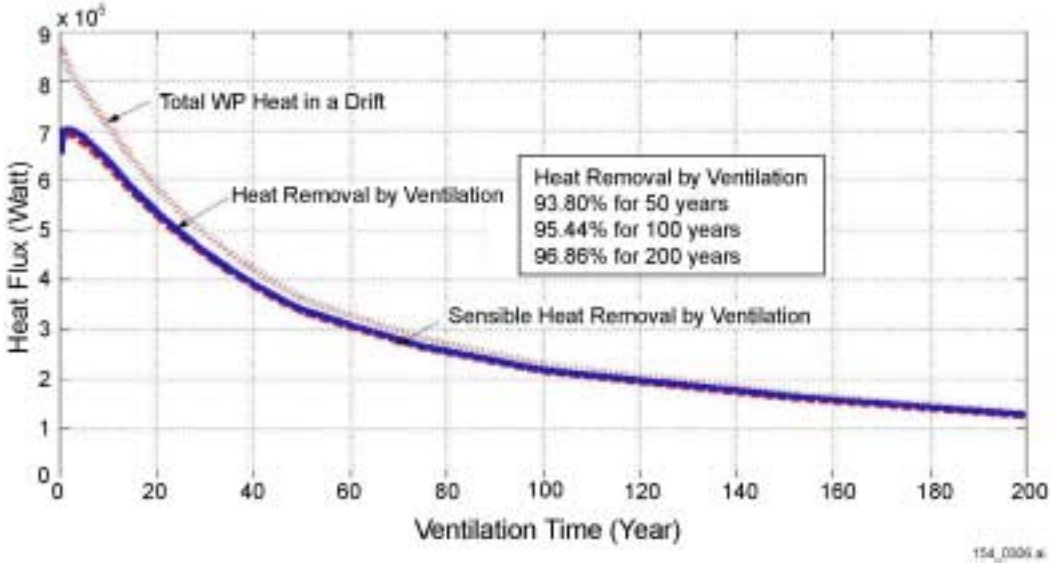

154_0306.ai

Source: BSC 2001 [DIRS 155025], Figure 16.

NOTE: MULTIFLUX Results.

Figure 5.3.2.4.1-12. Heat Removed During Continuous Ventilation of 15 m^3/s

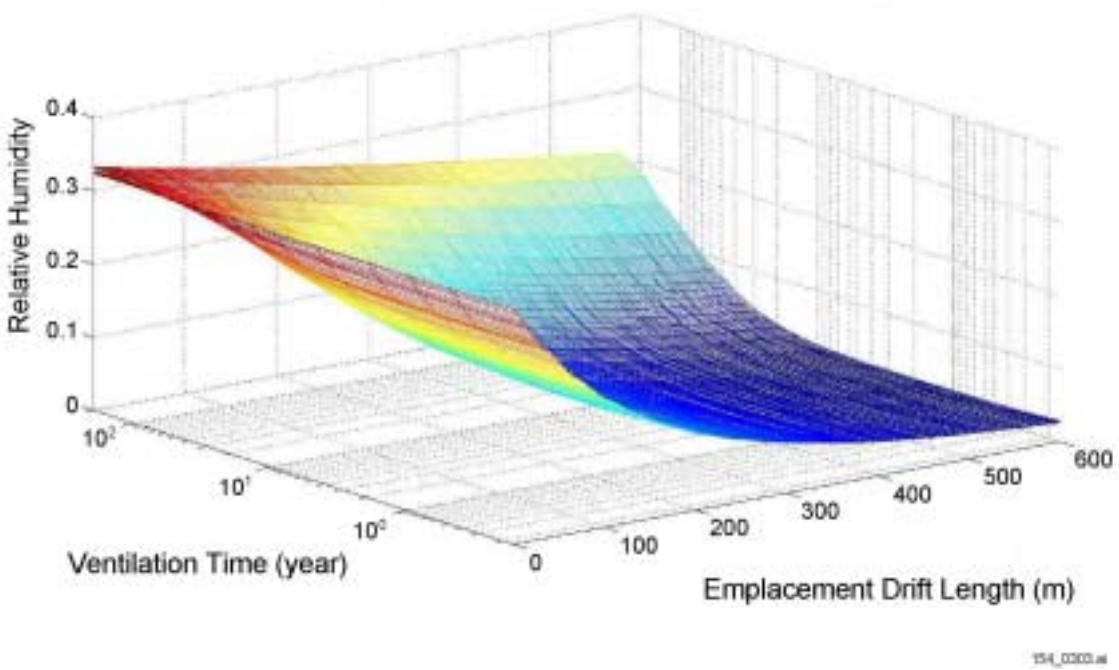

154_0303.ai

Source: BSC 2001 [DIRS 155025], Figure 13.

NOTE: MULTIFLUX Results.

Figure 5.3.2.4.1-13. Relative Humidity During Continuous Ventilation of 10 m^3/s

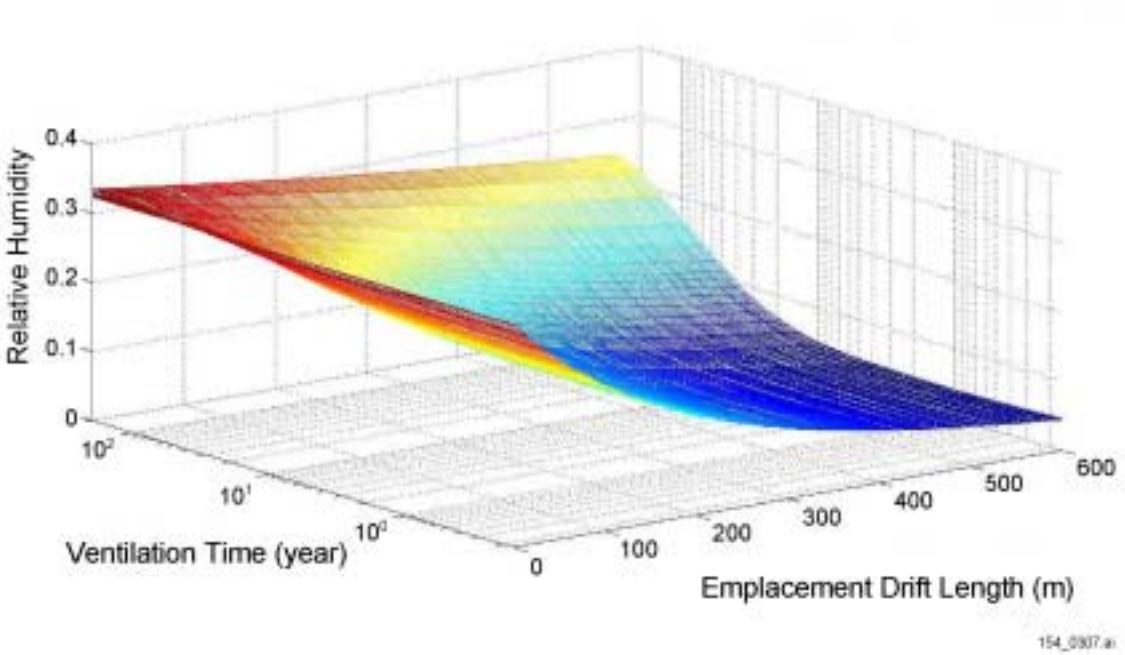

154_0307.ai

Source: BSC 2001 [DIRS 155025], Figure 17.

NOTE: MULTIFLUX Results.

Figure 5.3.2.4.1-14. Relative Humidity During Continuous Ventilation of 15 m^3/s

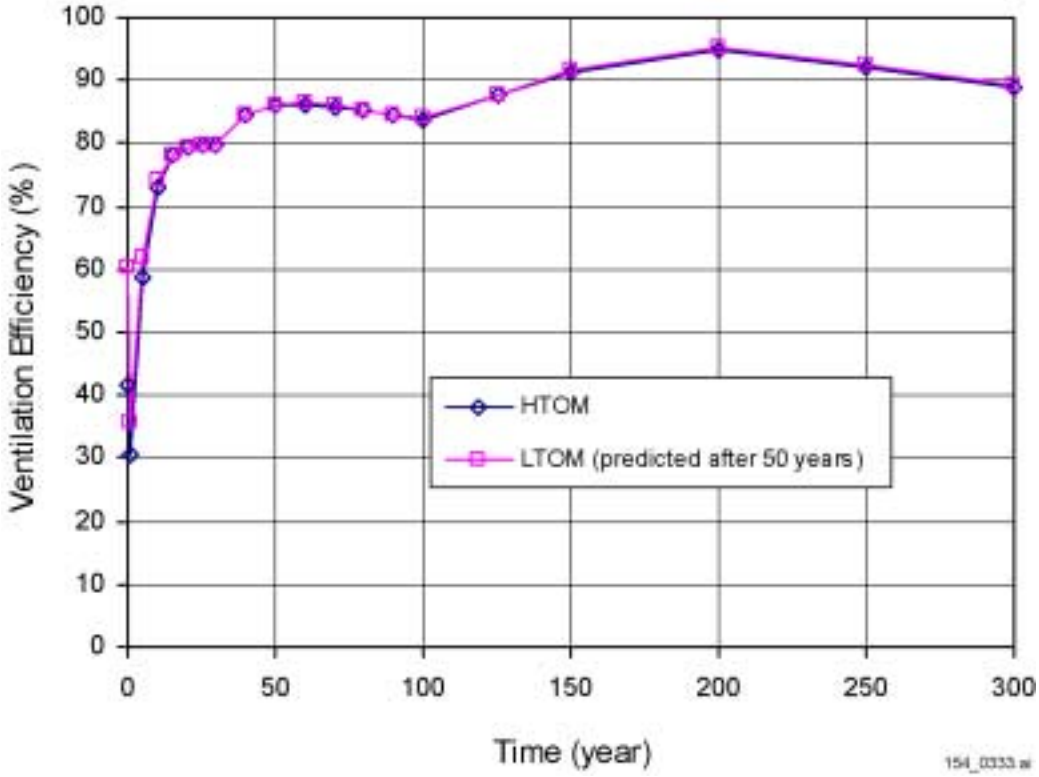

154_0333.ai

Source: Produced using files from Leem 2001 [DIRS 155457].

NOTE: HTOM = higher-temperature operating mode; LTOM = lower-temperature operating mode.

Figure 5.3.2.4.2-1. Time-Dependent Ventilation Efficiencies for the Higher- and Lower-Temperature Operating Modes

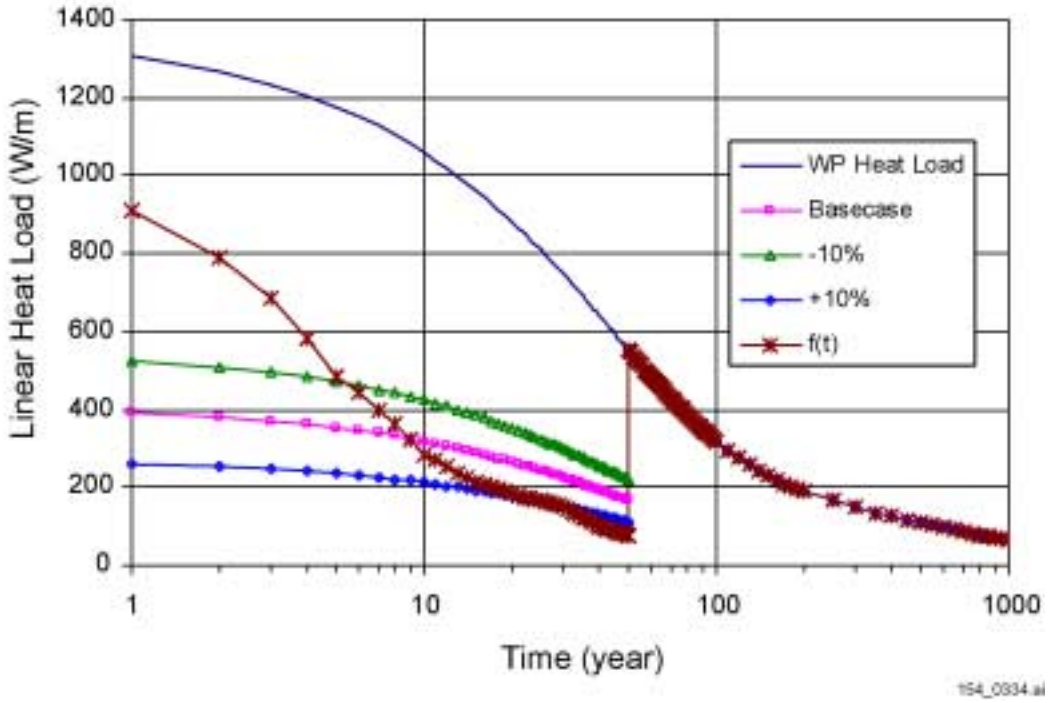

154_0334.ai

Source: Produced using files from Leem 2001 [DIRS 155457].

NOTE: WP = waste package.

Figure 5.3.2.4.2-2. Time History of Heat Available to Enter the Near-Field Rock for the Higher-Temperature Operating Mode Ventilation Cases

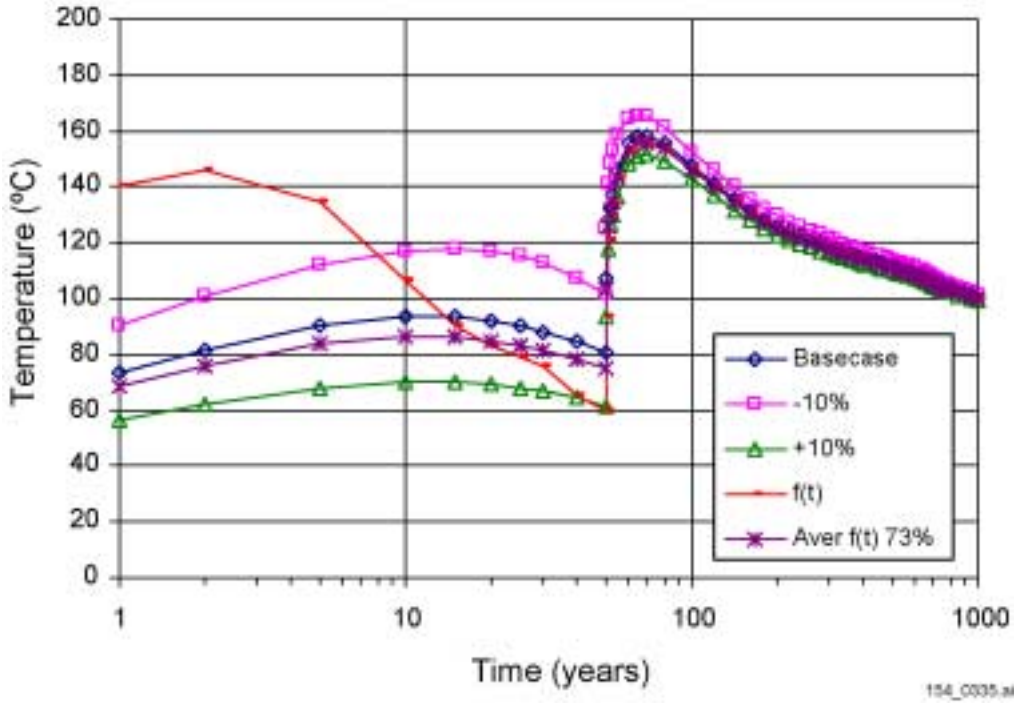

154_0335.ai

Source: Produced using files from Leem 2001 [DIRS 155457].

NOTE: Temperature histories presented as a function of ventilation efficiency.

Figure 5.3.2.4.2-3. Drip Shield Top Temperature Histories for the Higher-Temperature Operating Mode

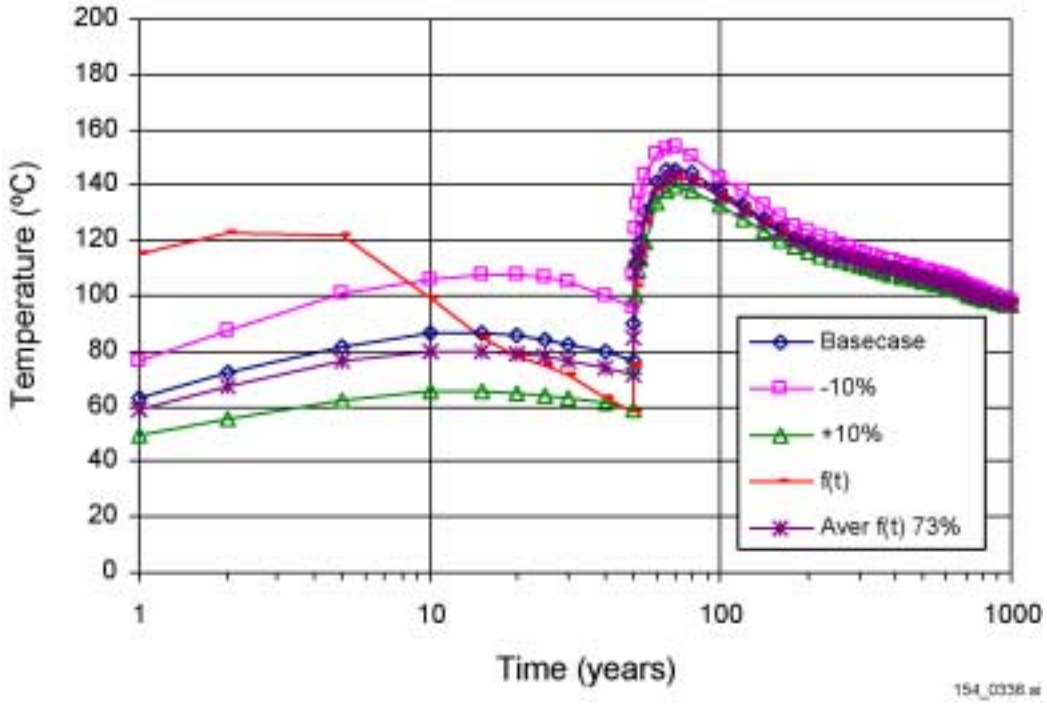

154_0336.ai

Source: Produced using files from Leem 2001 [DIRS 155457].

NOTE: Temperature histories presented as a function of ventilation efficiency.

Figure 5.3.2.4.2-4. Drift Wall Crown Temperature Histories for the Higher-Temperature Operating Mode

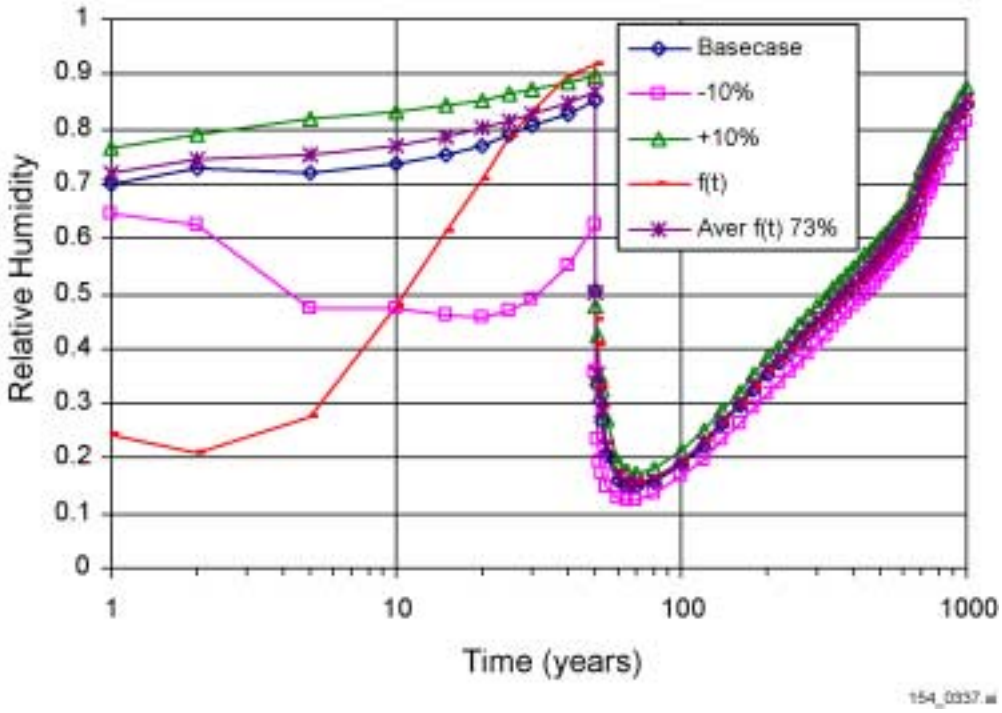

154_0337

Source: Produced using files from Leem 2001 [DIRS 155457].

NOTE: Relative humidity histories presented as a function of ventilation efficiency.

Figure 5.3.2.4.2-5. Drip Shield Top Relative Humidity Histories for the Higher-Temperature Operating Mode

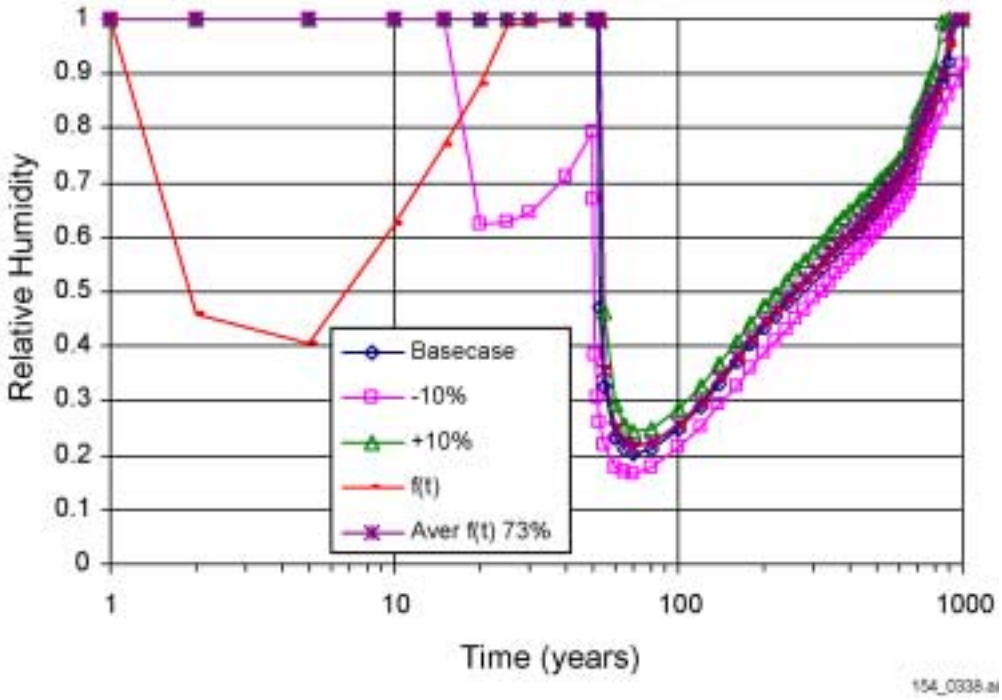

154_0338.ai

Source: Produced using files from Leem 2001 [DIRS 155457].

NOTE: Relative humidity histories presented as a function of ventilation efficiency.

Figure 5.3.2.4.2-6. Drift Wall Crown Relative Humidity Histories for the Higher-Temperature Operating Mode

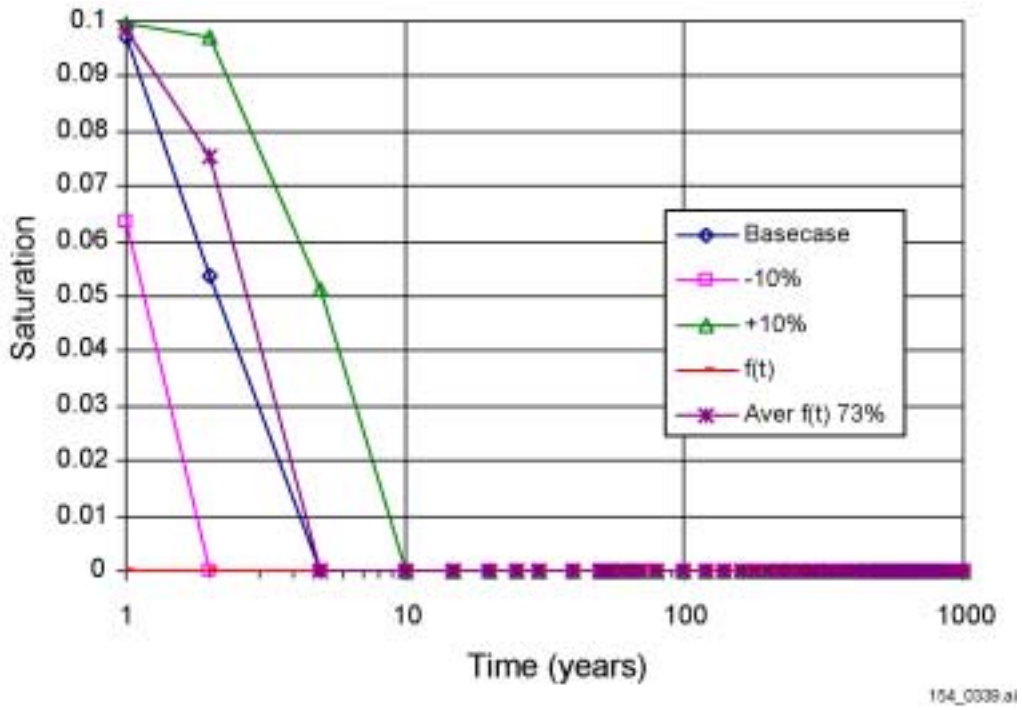

154_0339.ai

Source: Produced using files from Leem 2001 [DIRS 155457].

NOTE: Saturation histories presented as a function of ventilation efficiency.

Figure 5.3.2.4.2-7. Invert (Lower Center) Saturation Histories for the Higher-Temperature Operating Mode

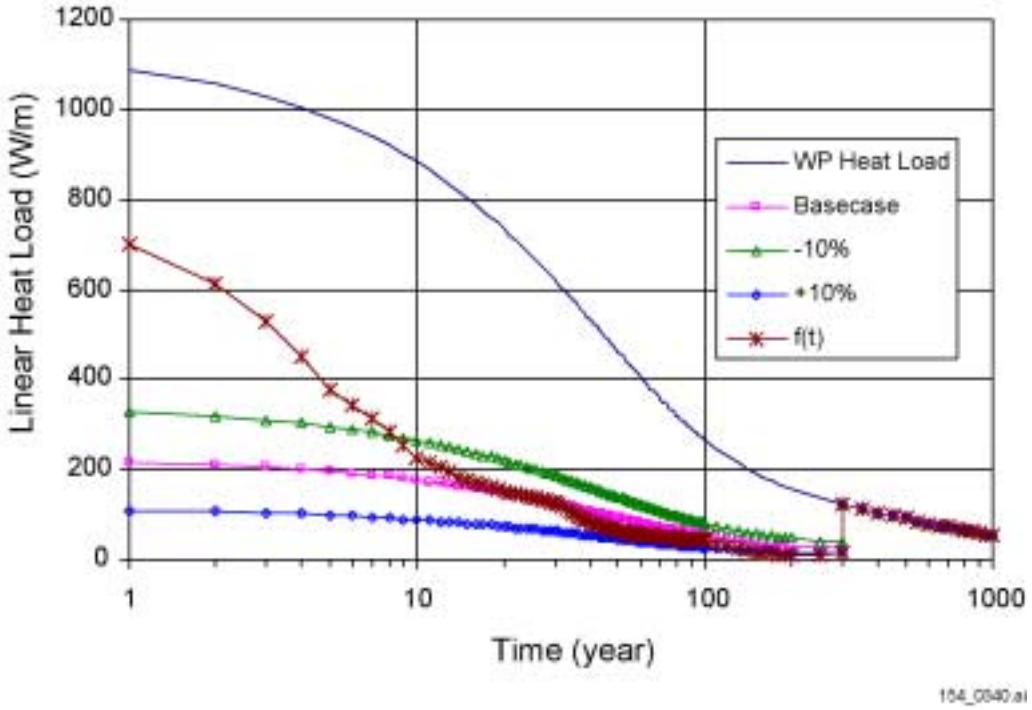

154_0340.ai

Source: Produced using files from Leem 2001 [DIRS 155457].

Figure 5.3.2.4.2-8. Time History of Heat Available to Enter the Near-Field Rock for the Lower-Temperature Operating Mode Ventilation Cases

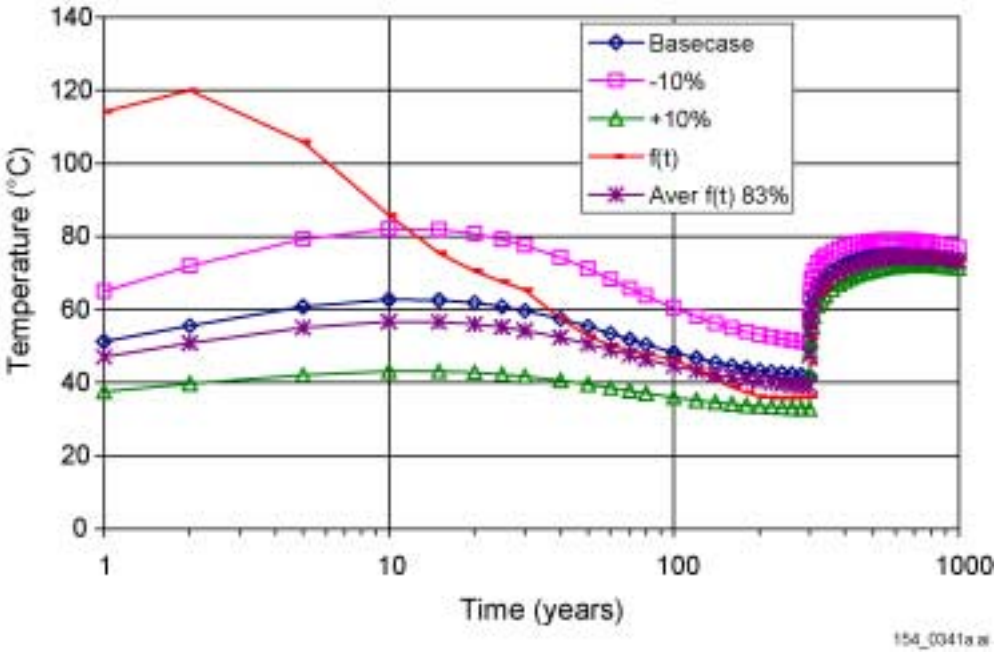

154_0341.ai

Source: Produced using files from Leem 2001 [DIRS 155457].

NOTE: Temperature histories presented as a function of ventilation efficiency.

Figure 5.3.2.4.2-9. Drip Shield Top Temperature Histories for the Lower-Temperature Operating Mode

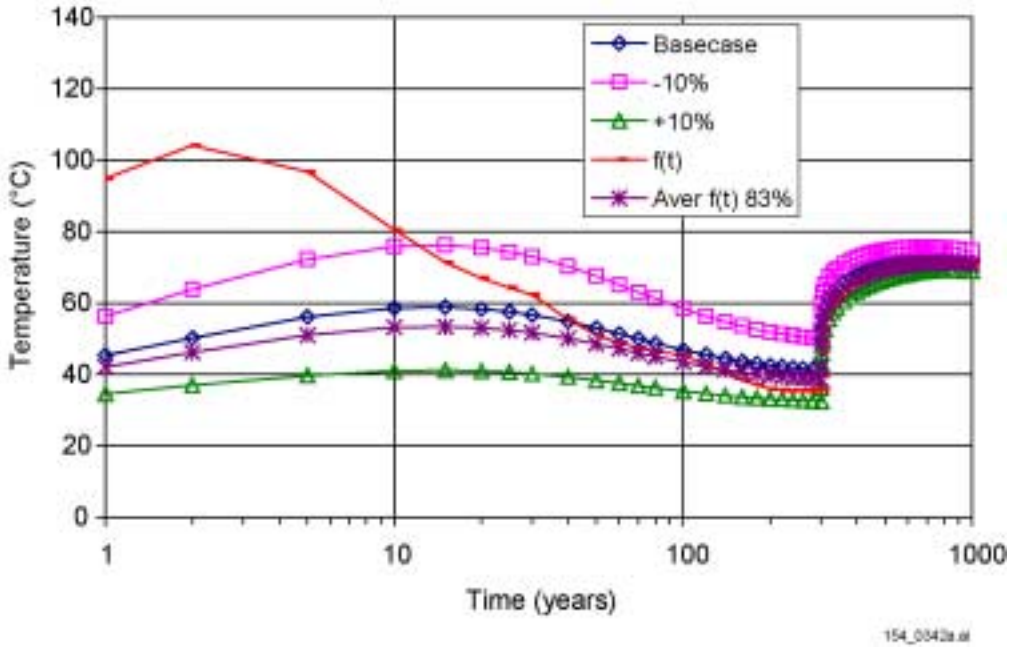

154_0342.ai

Source: Produced using files from Leem 2001 [DIRS 155457].

NOTE: Temperature histories presented as a function of ventilation efficiency.

Figure 5.3.2.4.2-10. Drift Wall Crown Temperature Histories for the Lower-Temperature Operating Mode

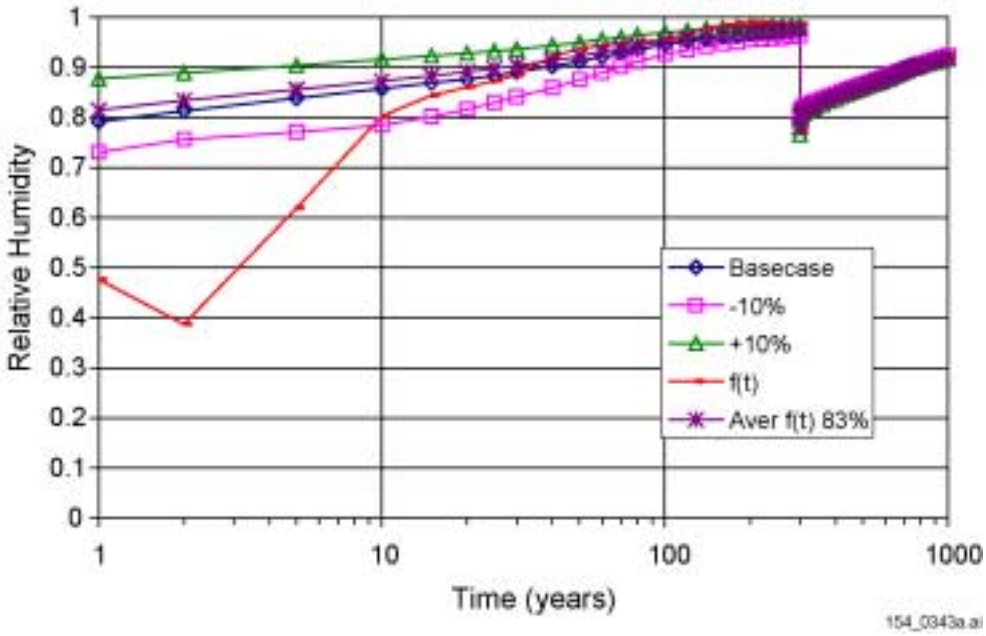

154_0343.ai

Source: Produced using files from Leem 2001 [DIRS 155457].

NOTE: Relative humidity histories presented as a function of ventilation efficiency.

Figure 5.3.2.4.2-11. Drip Shield Crown Relative Humidity Histories for the Lower-Temperature Operating Mode

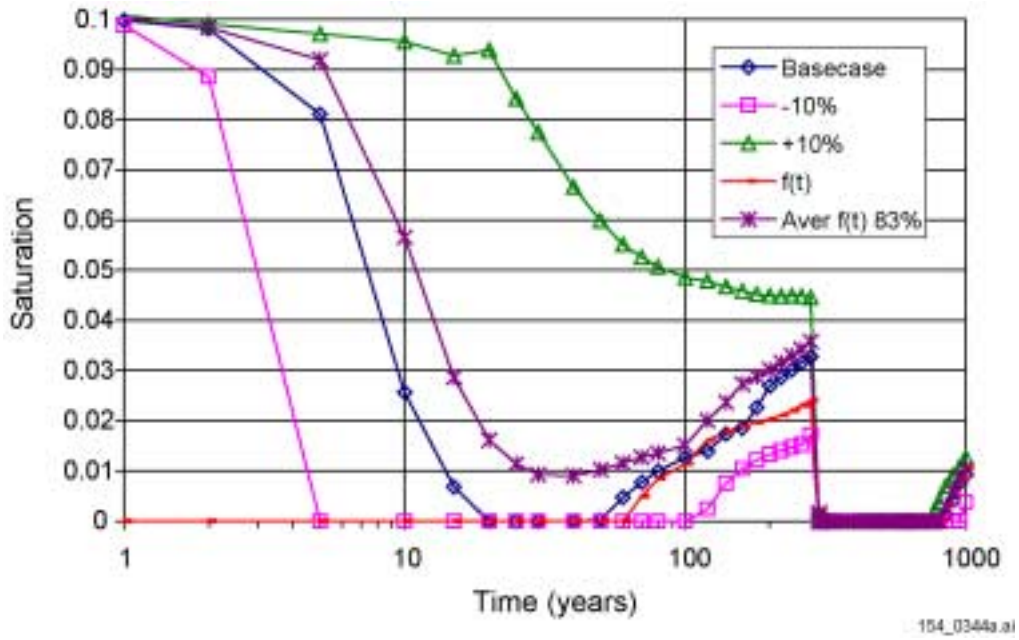

154_0344.ai

Source: Produced using files from Leem 2001 [DIRS 155457].

NOTE: Saturation histories presented as a function of ventilation efficiency.

Figure 5.3.2.4.2-12. Invert (Lower Center) Saturation Histories for the Lower-Temperature Operating Mode

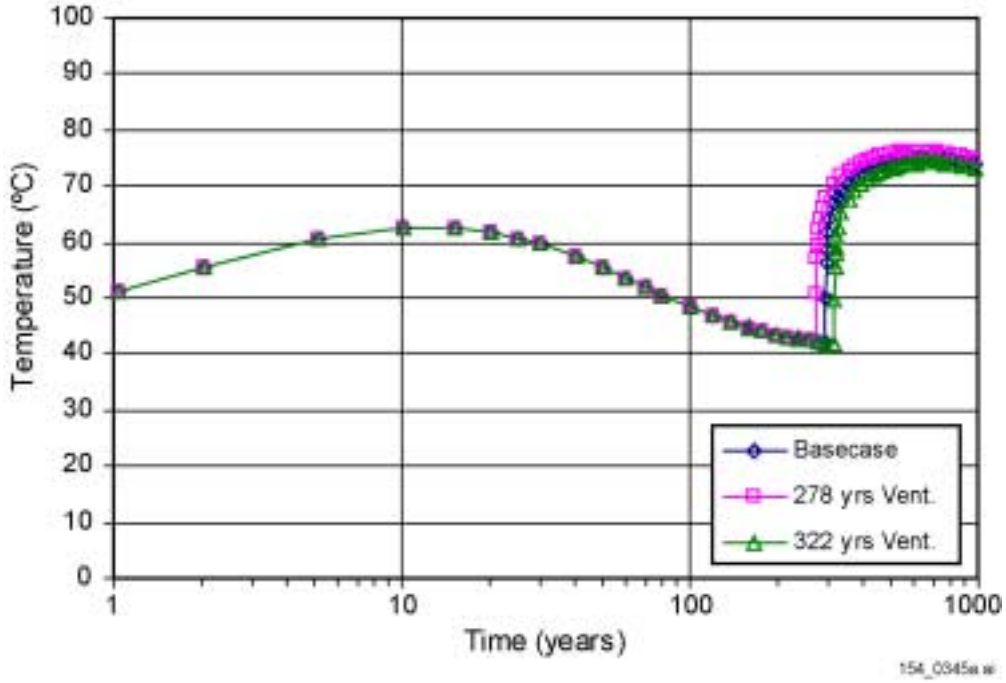

154_0345.ai

Source: Produced using files from Leem 2001 [DIRS 155457].

NOTE: Temperature histories presented as a function of ventilation duration.

Figure 5.3.2.4.3-1. Temperature Histories at the Top of the Drip Shield for the Lower-Temperature Operating Mode

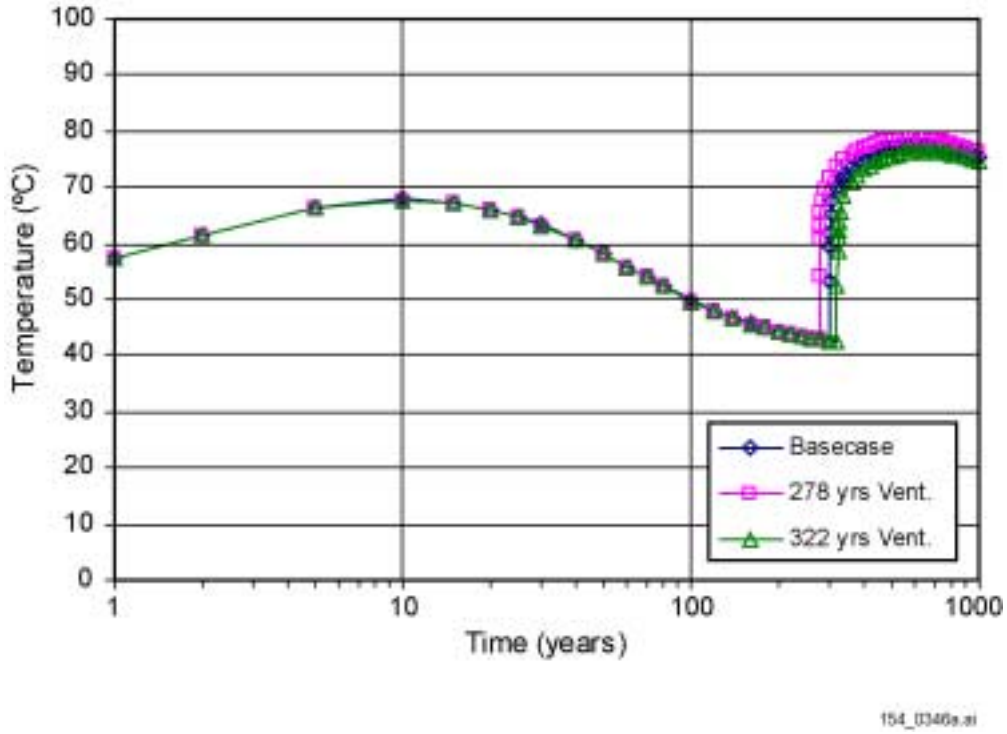

154_0346.ai

Source: Produced using files from Leem 2001 [DIRS 155457].

NOTE: Temperature histories presented as a function of ventilation duration.

Figure 5.3.2.4.3-2. Temperature Histories at the Drift Wall Crown for the Lower-Temperature Operating Mode

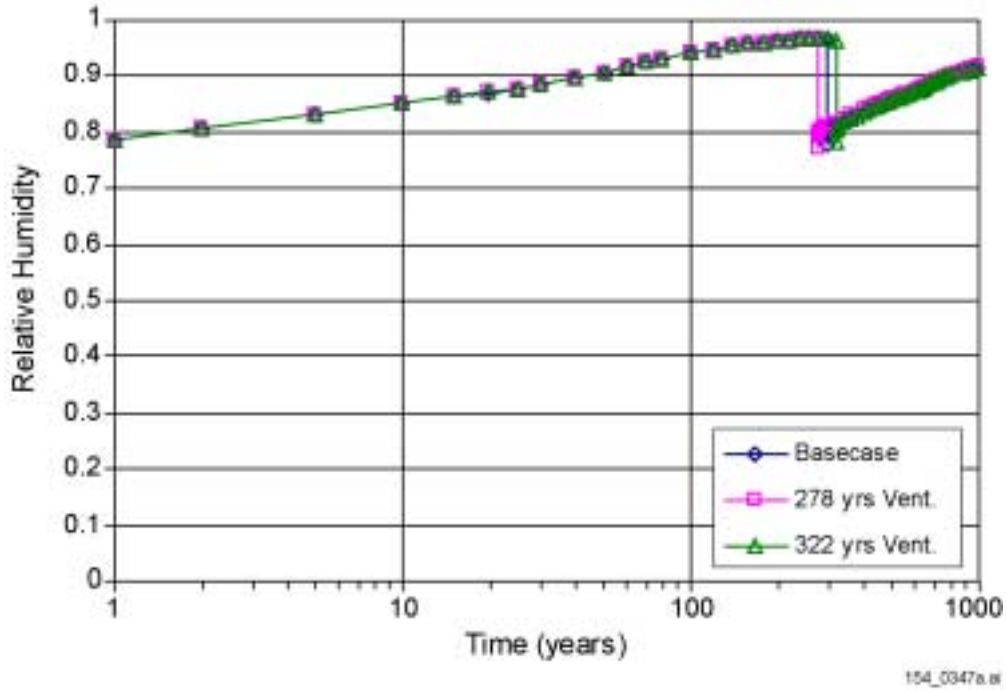

154_0347.ai

Source: Produced using files from Leem 2001 [DIRS 155457].

NOTE: Relative humidity histories presented as a function of ventilation duration.

Figure 5.3.2.4.3-3. Relative Humidity Histories at the Top of the Drip Shield for the Lower-Temperature Operating Mode

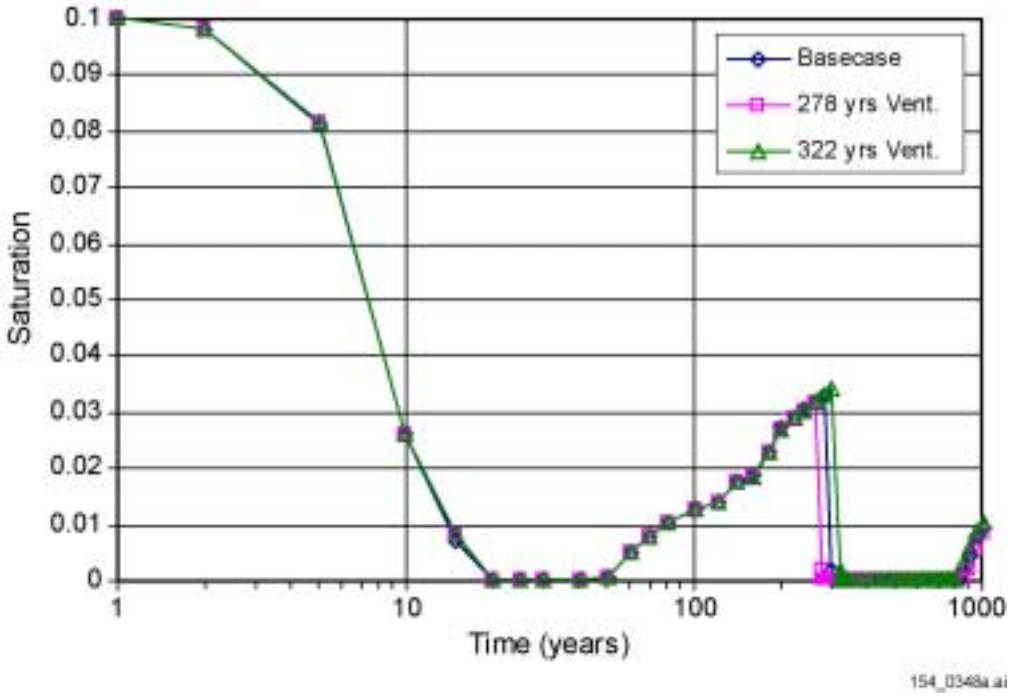

154_0348.ai

Source: Produced using files from Leem 2001 [DIRS 155457].

NOTE: Saturation histories presented as a function of ventilation duration.

Figure 5.3.2.4.3-4. Saturation Histories at the Lower-Center of the Invert for the Lower-Temperature Operating Mode

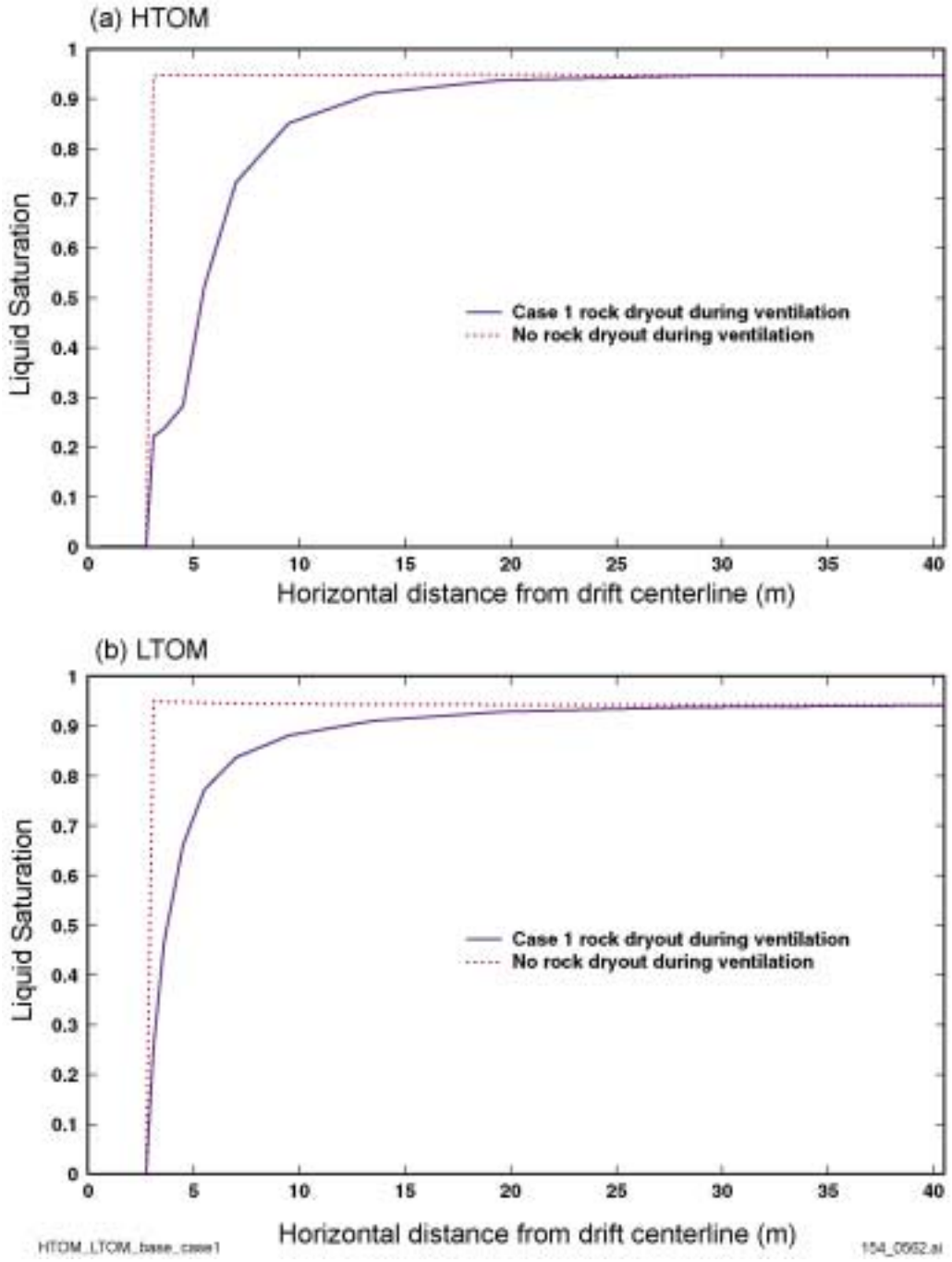

154_0562.ai

Source: Buscheck 2001 [DIRS 155012].

NOTE: The liquid saturations pertain to the matrix continuum.

Figure 5.3.2.4.4-1. Lateral Extent of Host-Rock Dryout Due to Ventilation for Case 1 for the Higher- and Lower-Temperature Operating Modes

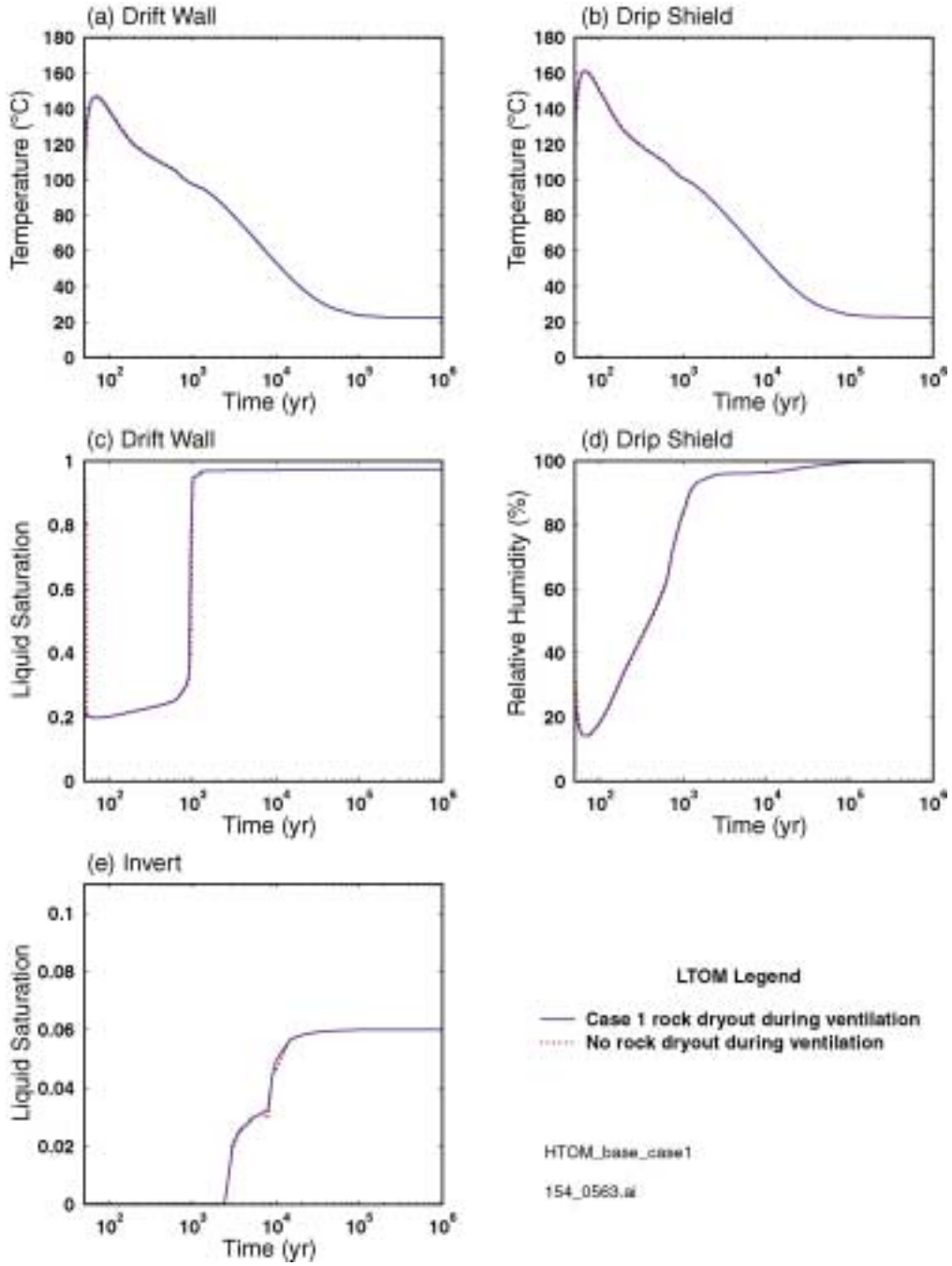

154_0563.ai

Source: Buscheck 2001 [DIRS 155012].

NOTE: The results for the base-case LDTH submodel that neglects the influence of preclosure dryout are also given. The drift wall liquid saturation pertains to the matrix continuum.

Figure 5.3.2.4.4-2. Temperature of the Drift Wall and the Drip Shield, Relative Humidity on the Drip Shield, and Liquid Saturation at the Drift Wall and in the Invert for Case 1 of the Higher-Temperature-Operating Mode

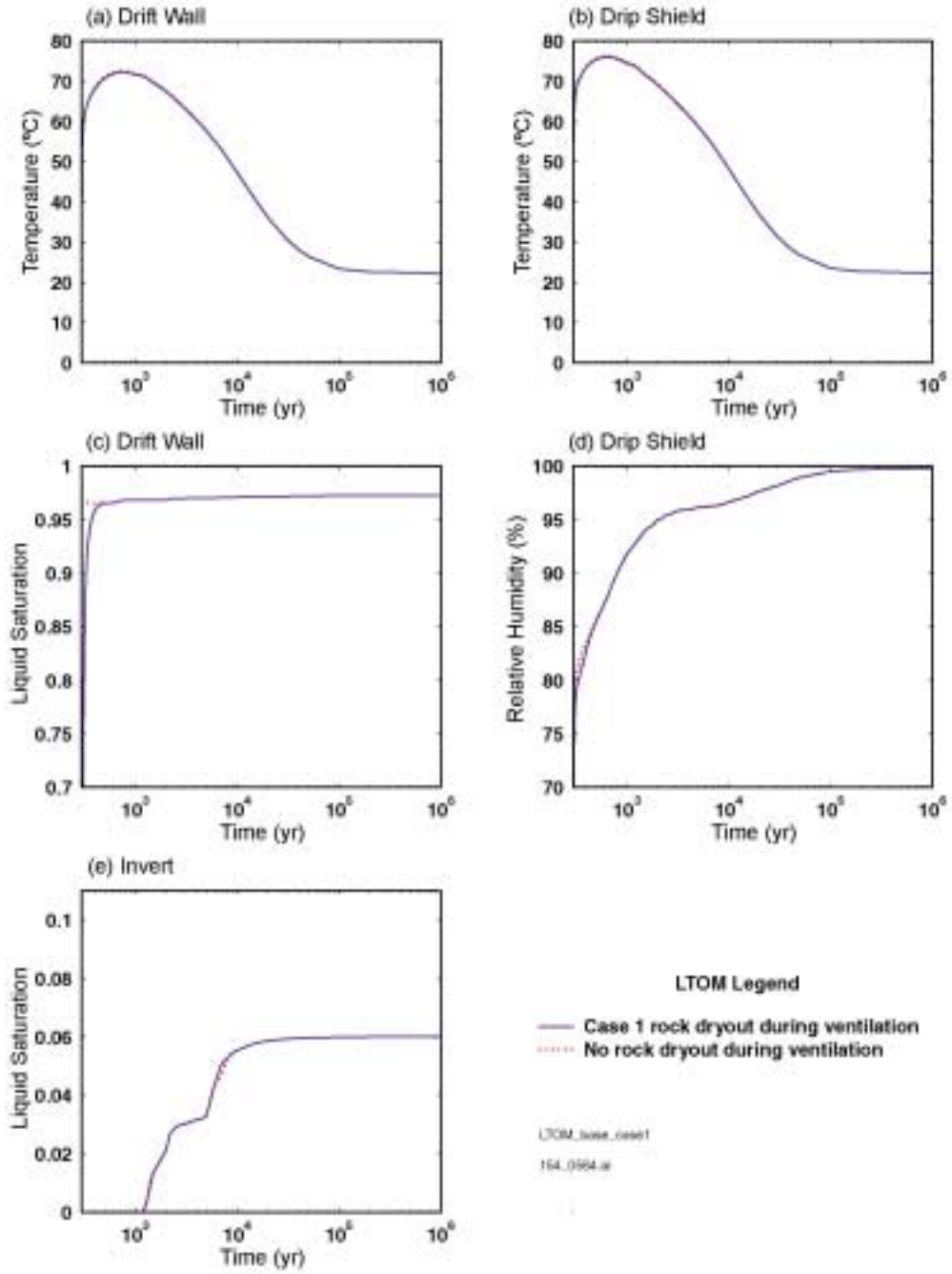

154_0564.ai

Source: Buscheck 2001 [DIRS 155012].

NOTE: The results for the base-case LDTH submodel that neglects the influence of preclosure dryout are also given. The drift wall liquid saturation pertains to the matrix continuum.

Figure 5.3.2.4.4-3. Temperature of the Drift Wall and the Drip Shield, Relative Humidity on the Drip Shield, and Liquid Saturation at the Drift Wall and in the Invert for Case 1 of the Lower-Temperature-Operating Mode

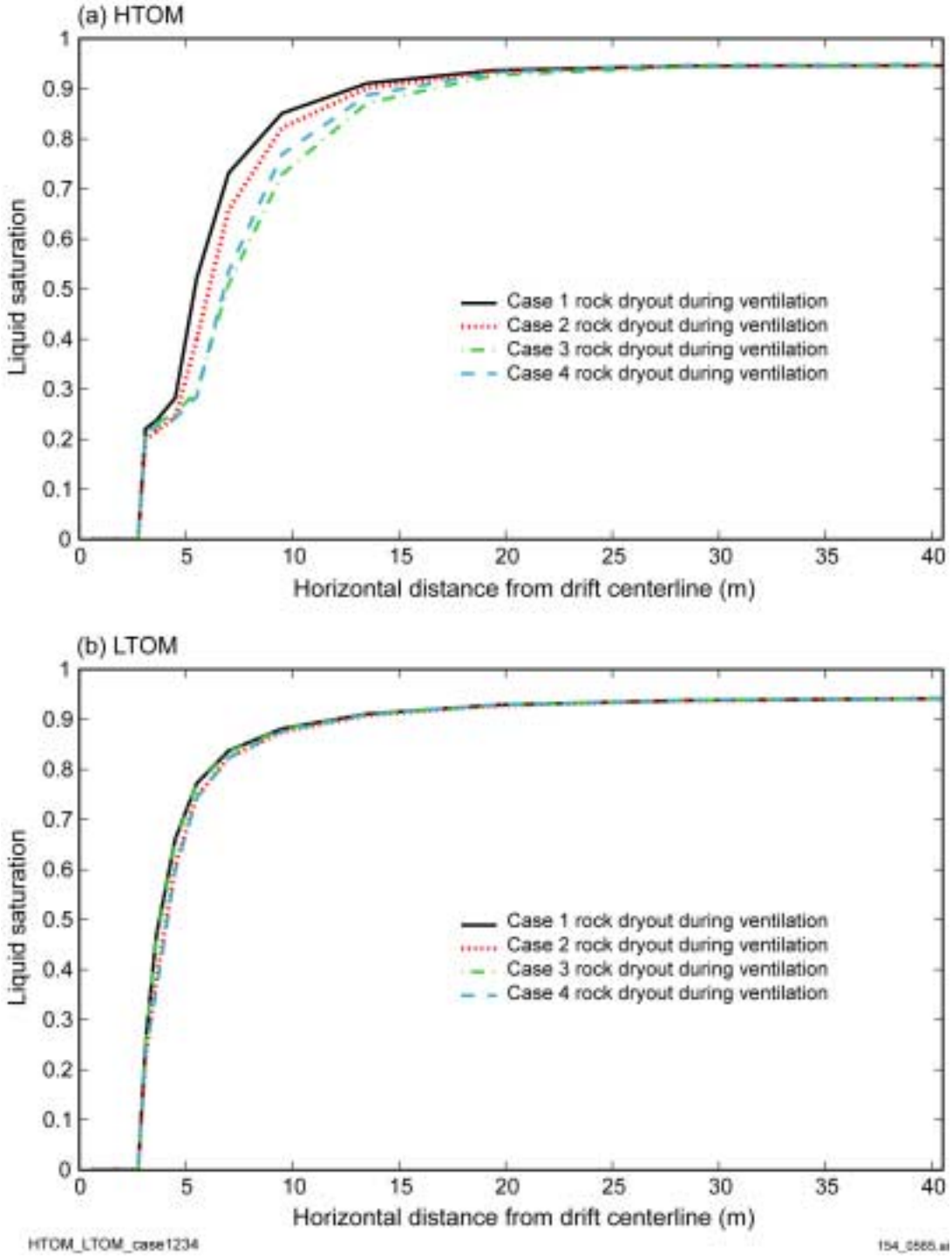

154_0565.ai

Source: Buscheck 2001 [DIRS 155012].

NOTE: The liquid saturations pertain to the matrix continuum.

Figure 5.3.2.4.4-4. Lateral Extent of Host-rock Dryout Due to Ventilation for Cases 1, 2, 3, and 4 for the Higher- and Lower-Temperature Operating Modes

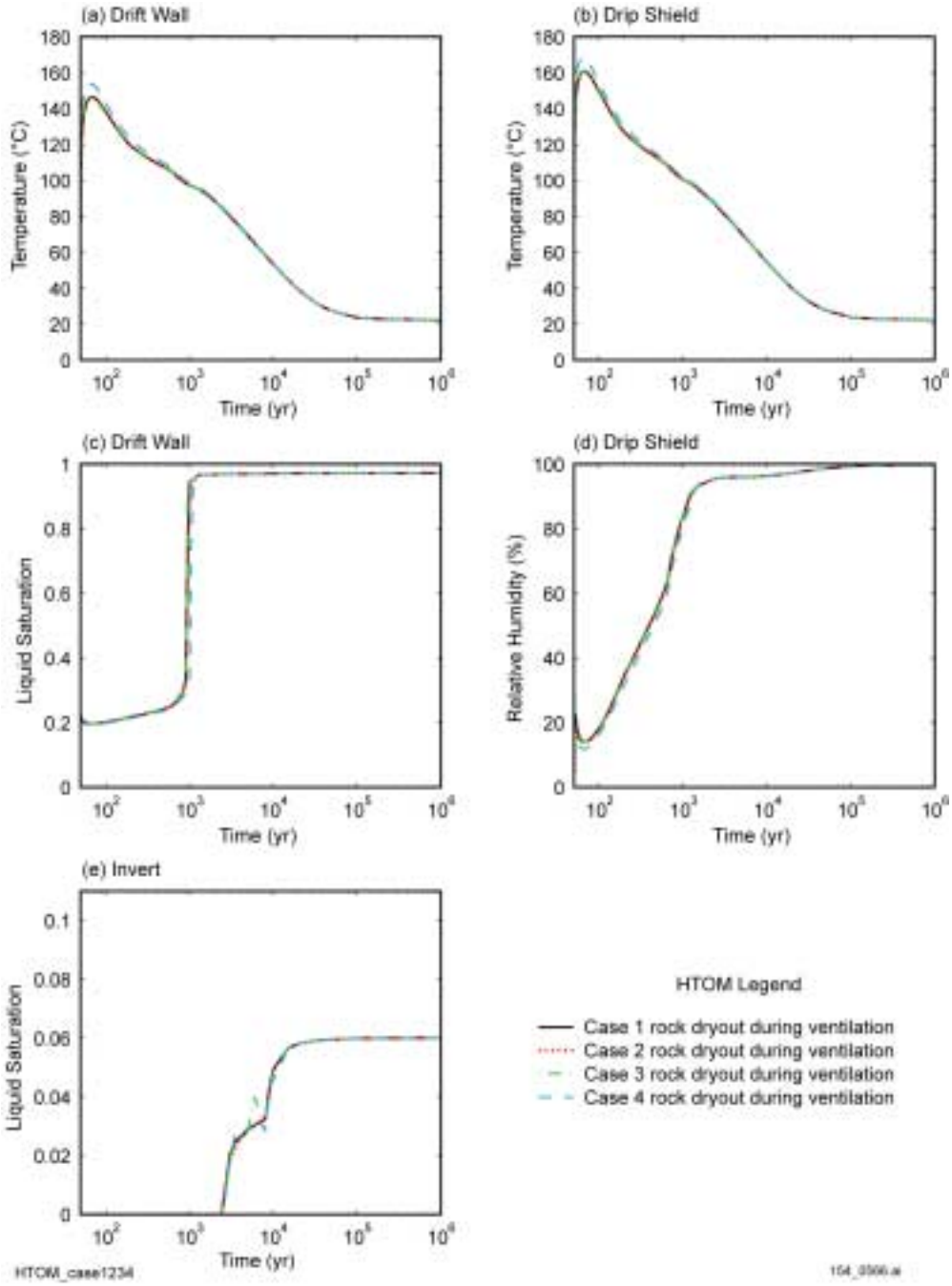

Source: Buscheck 2001 [DIRS 155012].

NOTE: The drift wall liquid saturation pertains to the matrix continuum.

Figure 5.3.2.4.4-5. Temperature of the Drift Wall and the Drip Shield, Relative Humidity on the Drip shield, and Liquid Saturation at the Drift Wall and in the Invert for Cases 1, 2, 3, and 4 of the Higher-Temperature Operating Mode

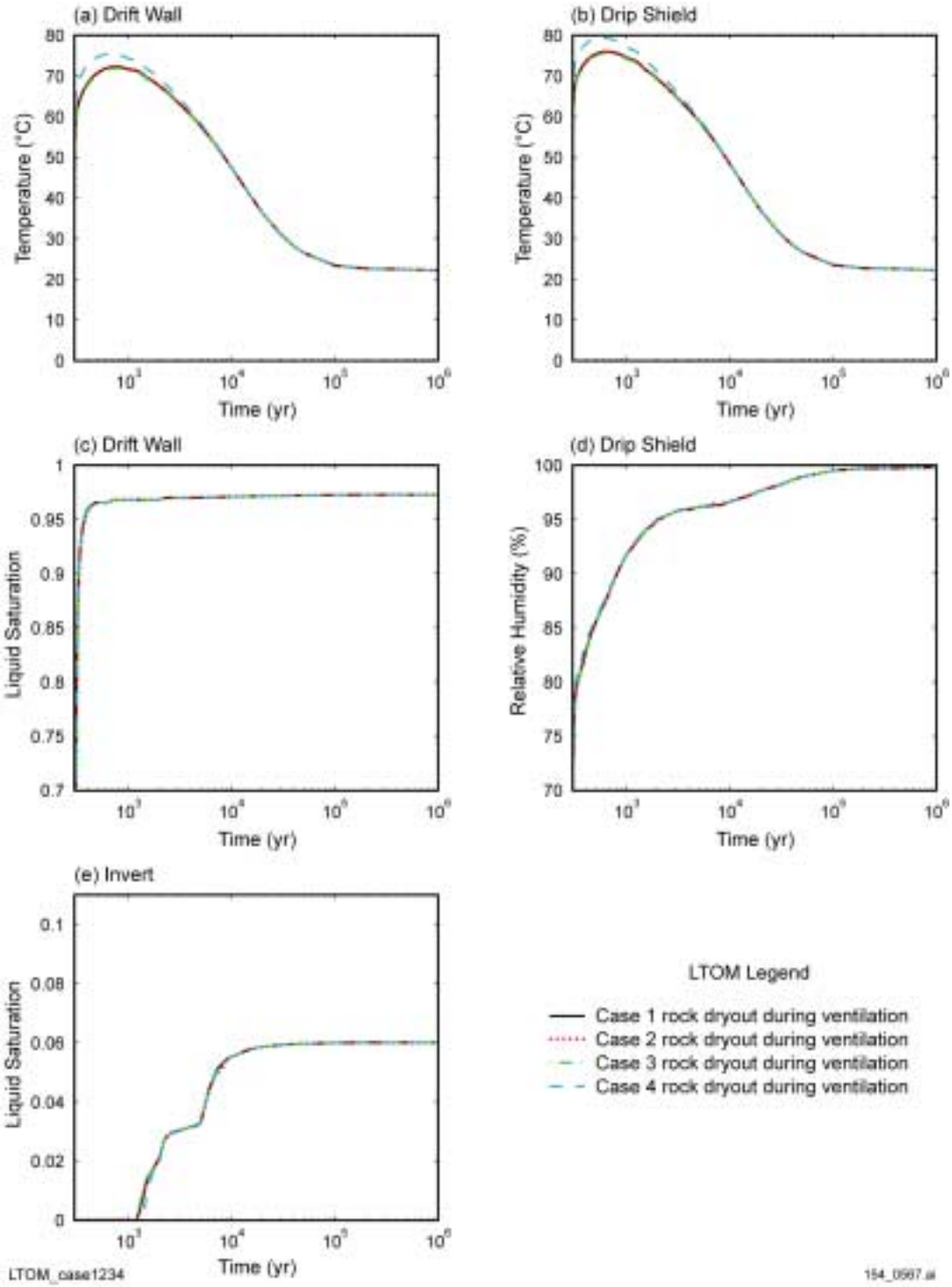

154_0567.ai

Source: Buscheck 2001 [DIRS 155012].

NOTE: The drift wall liquid saturation pertains to the matrix continuum.

Figure 5.3.2.4.4-6. Temperature of the Drift Wall and the Drip Shield, Relative Humidity on the Drip Shield, and Liquid Saturation at the Drift Wall and in the Invert for Cases 1, 2, 3, and 4 of the Lower-Temperature Operating Mode

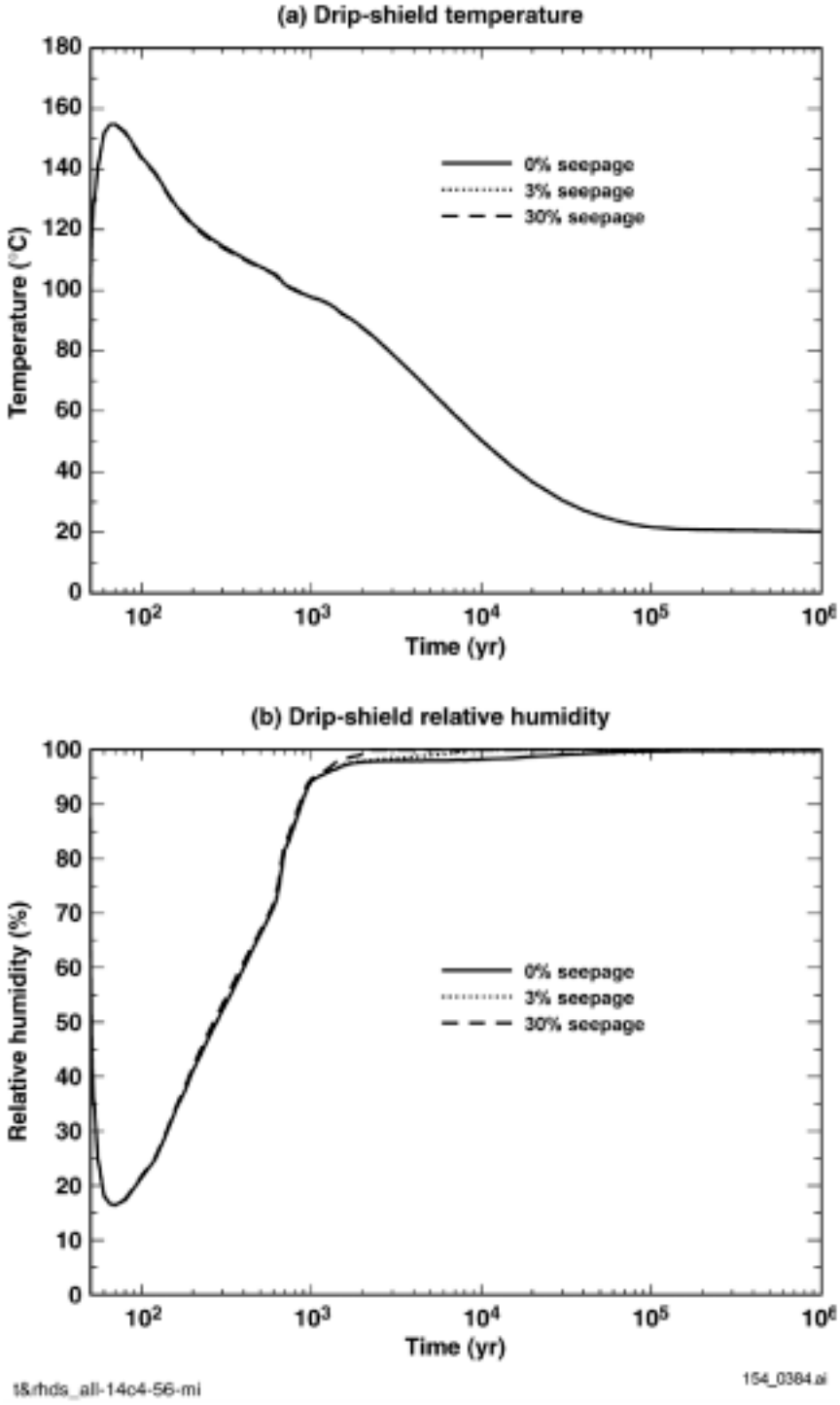

154_0384.ai

Source: Produced using files from CRWMS M&O 2001 [DIRS 152016], Figure 6-34.

Figure 5.3.2.4.4-7. Temperature (a) and Relative Humidity (b) Histories at the Drip Shield for 0 Percent, 3 Percent, and 30 Percent of the Percolation Flux Seeping into the Drift

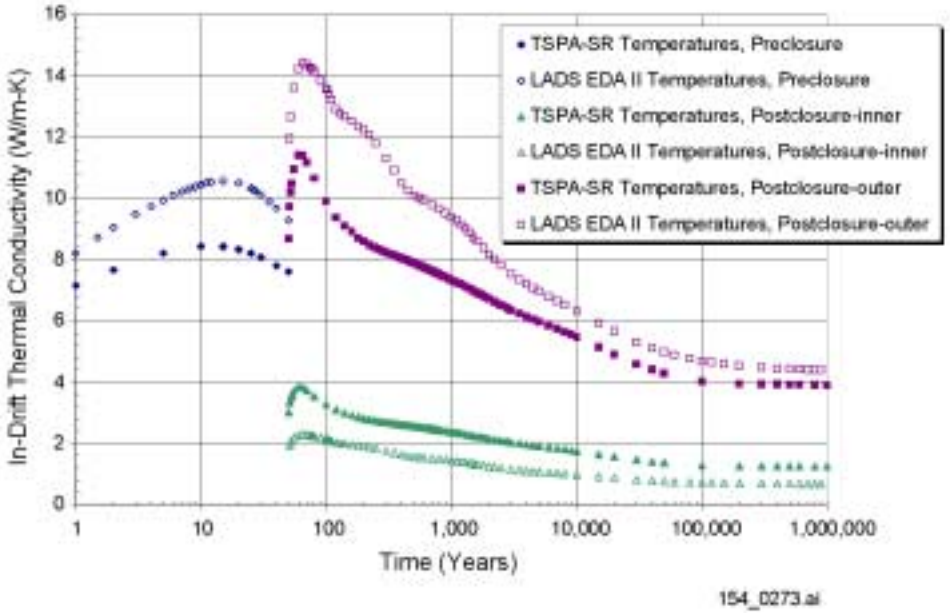

154_0273.ai

Source: Produced using files from Francis 2001 [DIRS 155075].

NOTE: Comparison of the license application design selection (LADS) design and TSPA-SR Rev 00 effective thermal conductivities (postclosure inner is between the waste package and drip shield, postclosure outer is between the drip shield and drift wall).

Figure 5.3.2.4.5-1. Comparison of Thermal Conductivities

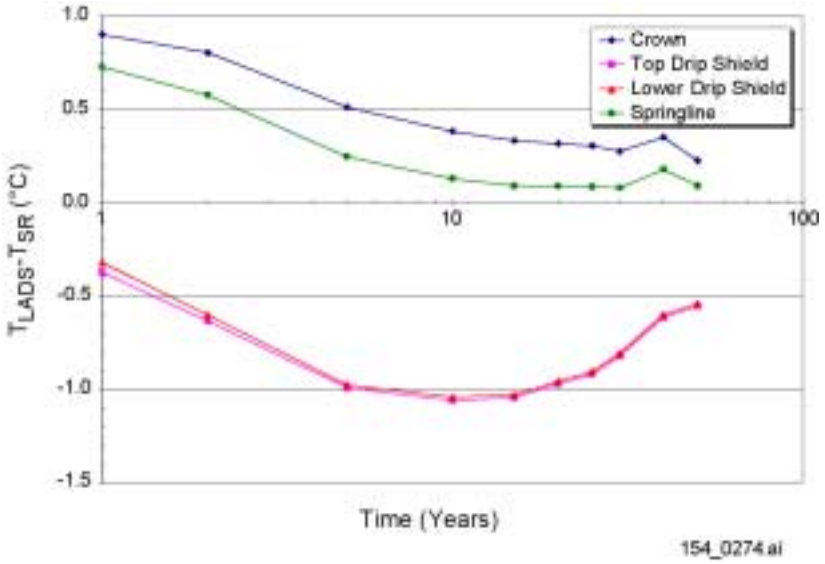

154_0274.ai

Source: Produced using files from Francis 2001 [DIRS 155075].

NOTE: Comparison of preclosure temperature differences at a number of in-drift locations due to effective thermal conductivities developed from two repository designs.

Figure 5.3.2.4.5-2. Comparison of Preclosure Temperature Differences at In-Drift Locations

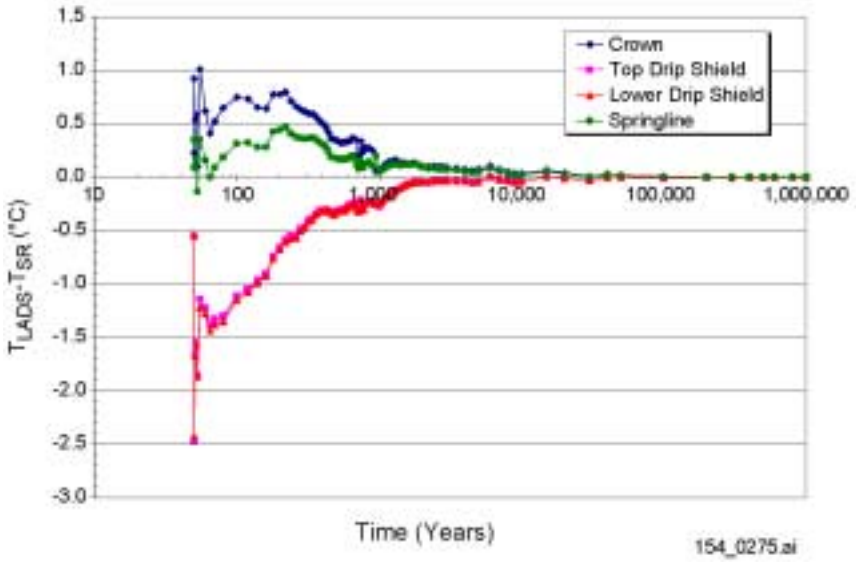

154_0275.ai

Source: Produced using files from Francis 2001 [DIRS 155075].

NOTE: Comparison of postclosure temperature differences at a number of in-drift locations due to effective thermal conductivities developed from two repository designs.

Figure 5.3.2.4.5-3. Comparison of Postclosure Temperature Differences at In-Drift Locations

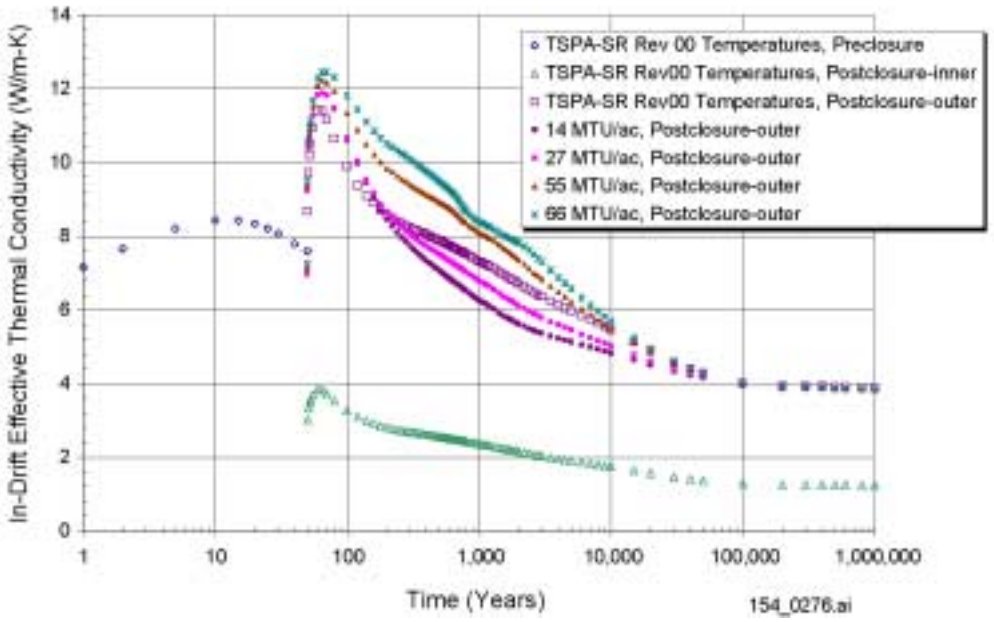

154_0276.ai

Source: Produced using files from Francis 2001 [DIRS 155075].

Figure 5.3.2.4.5-4. Comparison of the Effective Thermal Conductivities Developed Using the TSPA-SR Rev 00 Design and Using Four Areal Mass Loadings

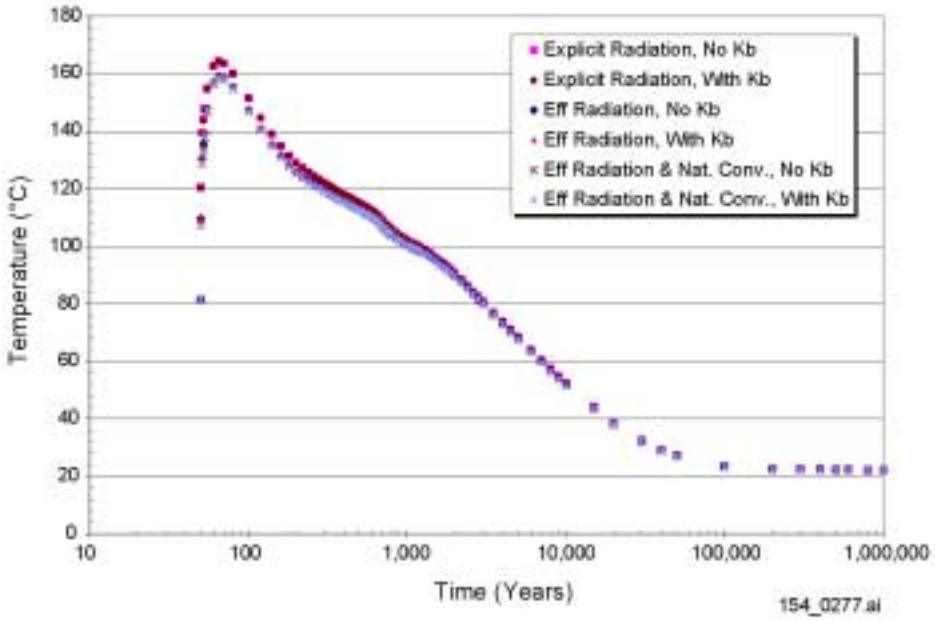

154_0277.ai

Source: Produced using files from Francis 2001 [DIRS 155075].

Figure 5.3.2.4.5-5. Temperature at the Drip Shield for Explicit and Approximated Thermal Radiation and Natural Convection

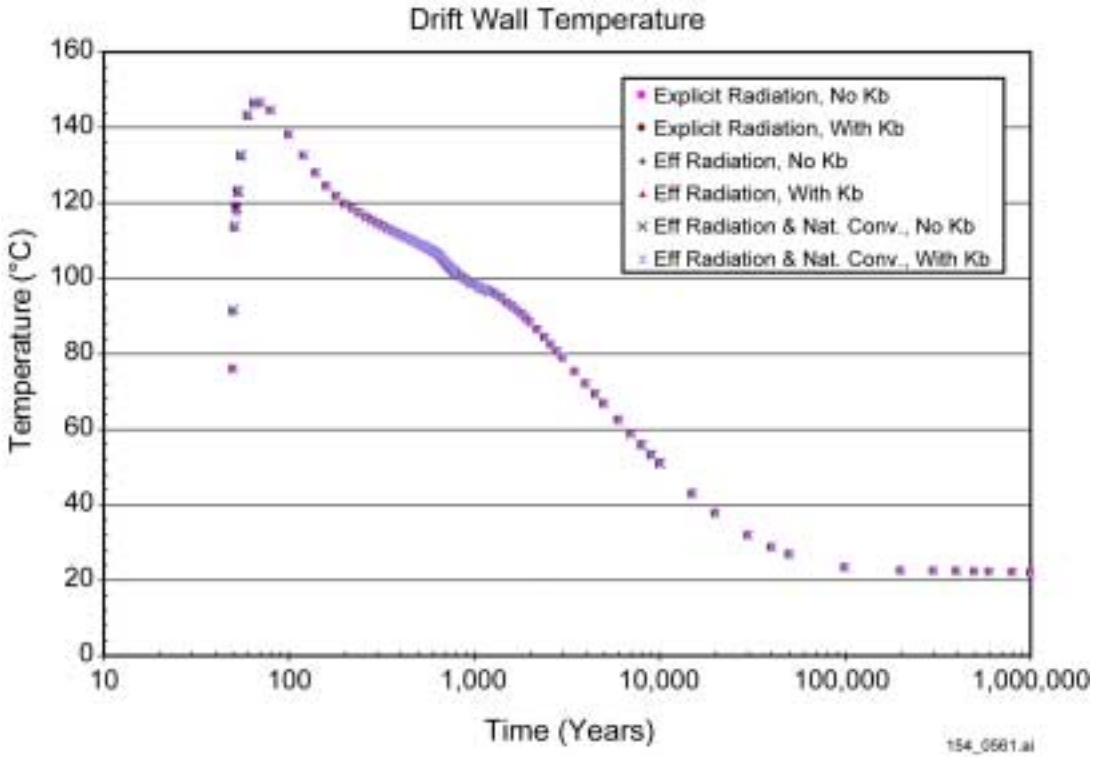

154_0561.ai

Source: Produced using files from Francis 2001 [DIRS 155075].

Figure 5.3.2.4.5-5a. Temperature Comparison at the Drift Wall for Explicit and Approximated Thermal Radiation and Natural Convection

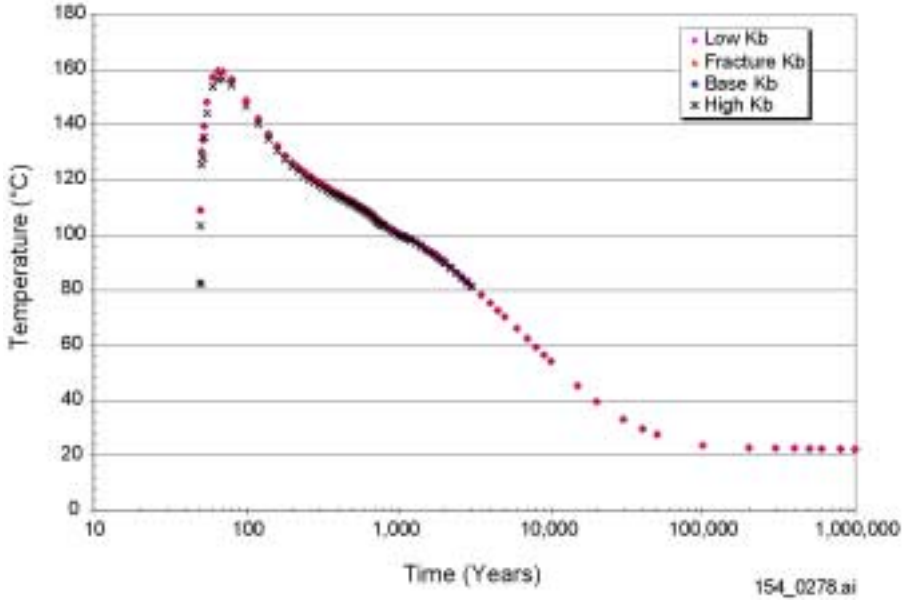

154_0278.ai

Source: Produced using files from Francis 2001 [DIRS 155075].

NOTE: Temperature histories at the base of the drip shield for a range of air permeabilities and the higher-temperature operating mode.

Figure 5.3.2.4.5-6. Temperature Histories at the Base of the Drip Shield

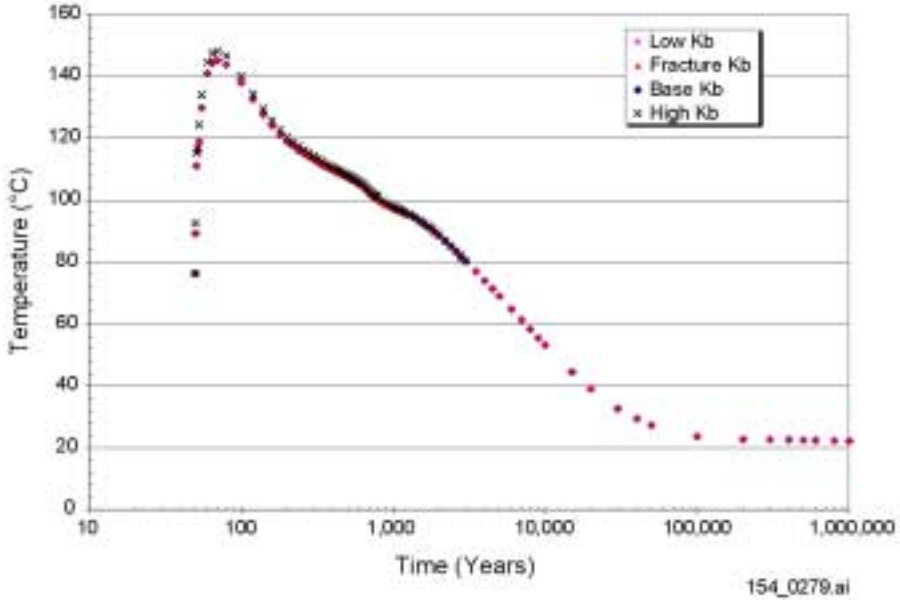

154_0279.ai

Source: Produced using files from Francis 2001 [DIRS 155075].

NOTE: Temperature histories at the crown of the drift wall for a range of air permeabilities, for the higher-temperature operating mode.

Figure 5.3.2.4.5-7. Temperature Histories at the Crown of the Drift Wall

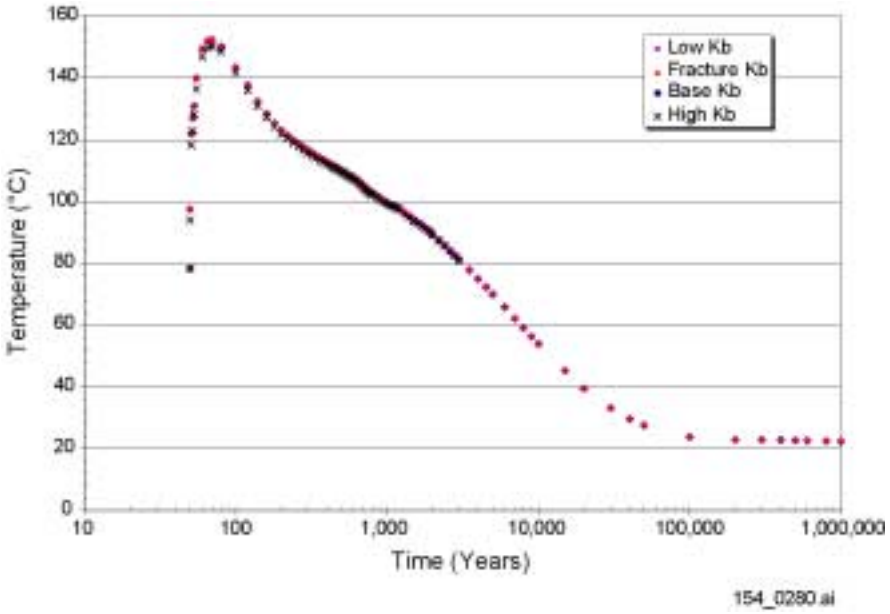

154_0280.ai

Source: Produced using files from Francis 2001 [DIRS 155075].

NOTE: Temperature histories at the bottom-center of the invert for a range of air permeabilities, for the higher-temperature operating mode.

Figure 5.3.2.4.5-8. Temperature Histories at the Bottom-Center of the Invert

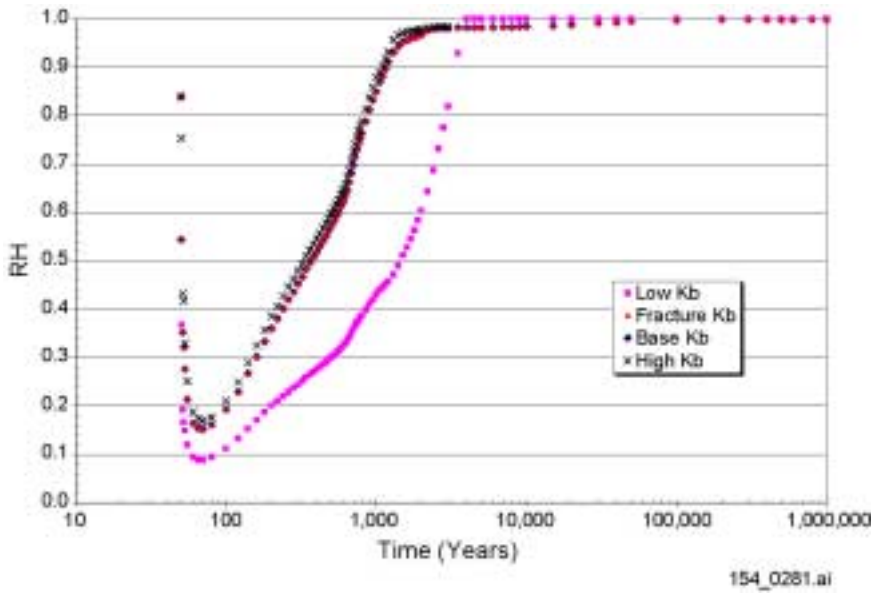

154_0281.ai

Source: Produced using files from Francis 2001 [DIRS 155075].

NOTE: Relative humidity (RH) histories at the base of the drip shield for a range of air permeabilities, for the higher-temperature operating mode.

Figure 5.3.2.4.5-9. Relative Humidity Histories at the Base of the Drip Shield

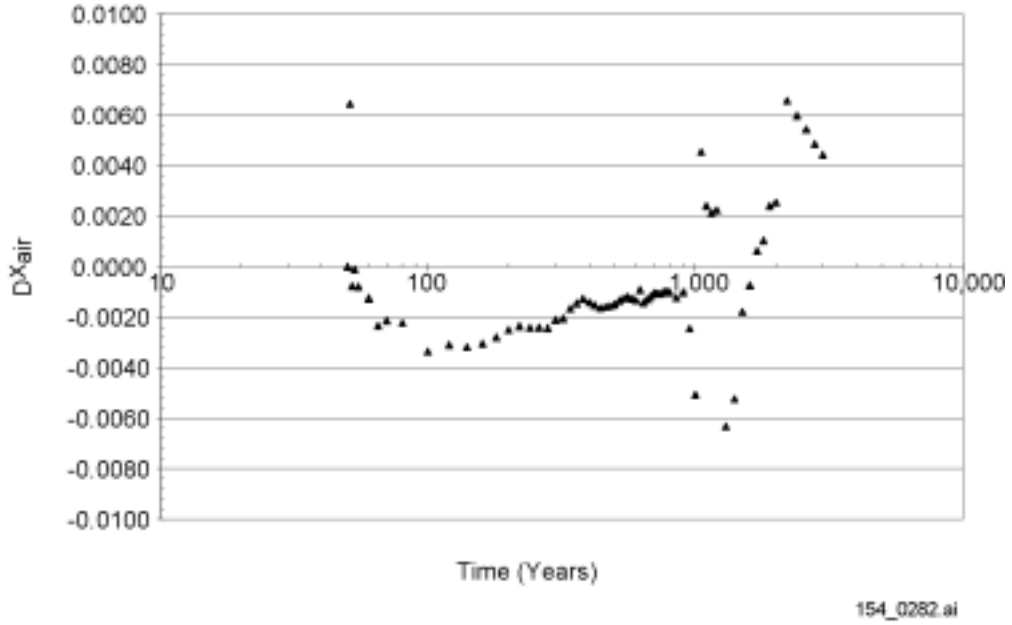

154_0282.ai

Source: Produced using files from Francis 2001 [DIRS 155075].

NOTE: Air mass fraction (D^Xair) differences between the high permeability case and the base case, at the base of the drip shield for the higher-temperature operating mode.

Figure 5.3.2.4.5-10. Air Mass Fraction Differences Between the High Permeability and Base Cases at the Base of the Drip Shield

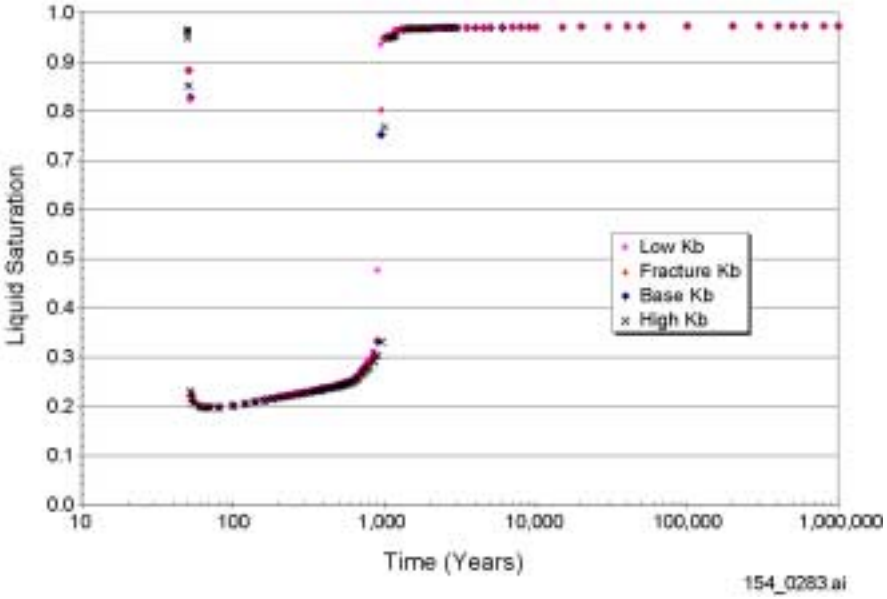

154_0283.ai

Source: Produced using files from Francis 2001 [DIRS 155075].

NOTE: Saturation history of near-field rock at the crown of the drift wall for a range of air permeabilities, for the higher-temperature operating mode.

Figure 5.3.2.4.5-11. Saturation History of Near-Field Rock at the Crown of the Drift Wall

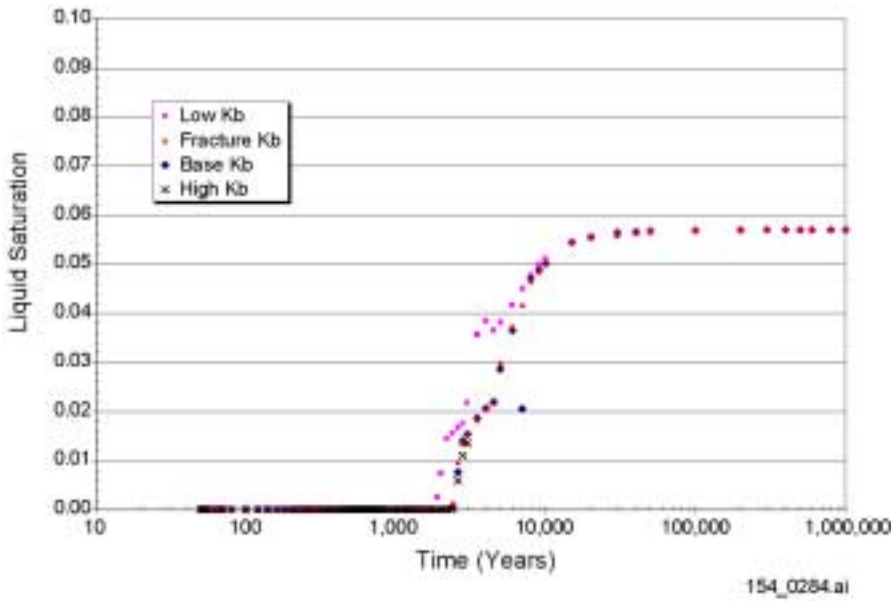

154_0284.ai

Source: Produced using files from Francis 2001 [DIRS 155075].

NOTE: Saturation history of the bottom-center of the invert for a range of air permeabilities, for the higher-temperature operating mode.

Figure 5.3.2.4.5-12. Saturation History of the Bottom-Center of the Invert

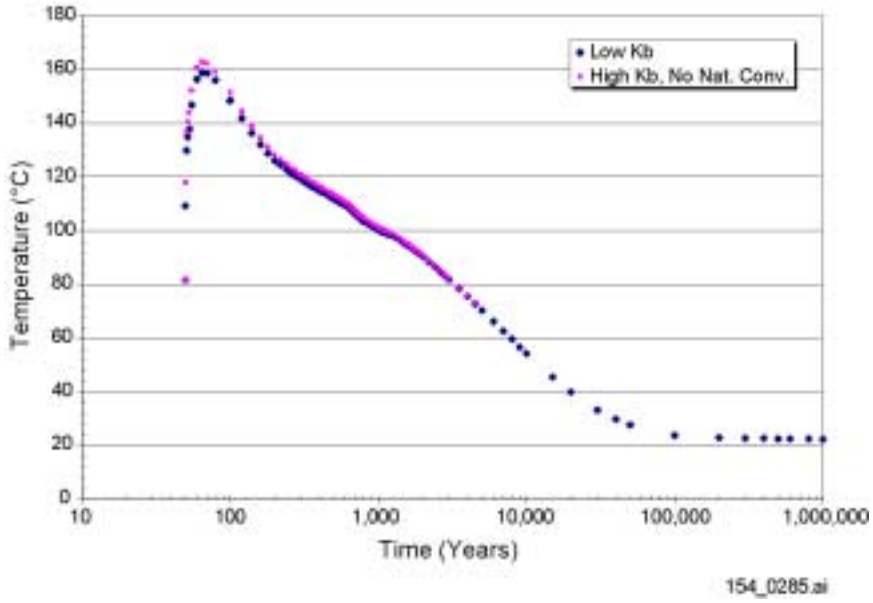

154_0285.ai

Source: Produced using files from Francis 2001 [DIRS 155075].

NOTE: Temperature histories at the top of the drip shield calculated with a porous medium model and with a correlation-based effective thermal conductivity model.

Figure 5.3.2.4.5-13. Temperature Histories at the Top of the Drip Shield

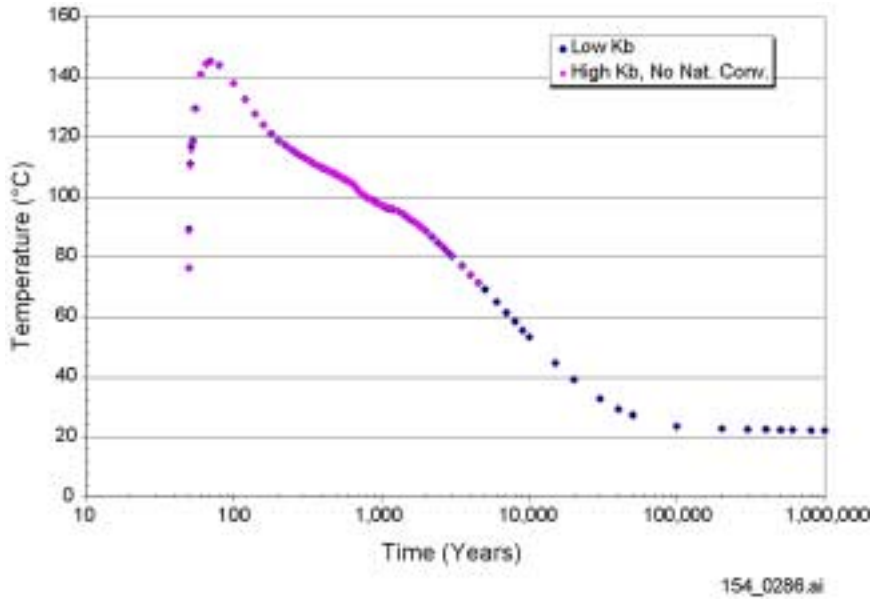

154_0286.ai

Source: Produced using files from Francis 2001 [DIRS 155075].

NOTE: Temperature histories at the crown of the drift wall calculated with a porous medium model and with a correlation-based effective thermal conductivity model.

Figure 5.3.2.4.5-14. Temperature Histories at the Crown of the Drift Wall

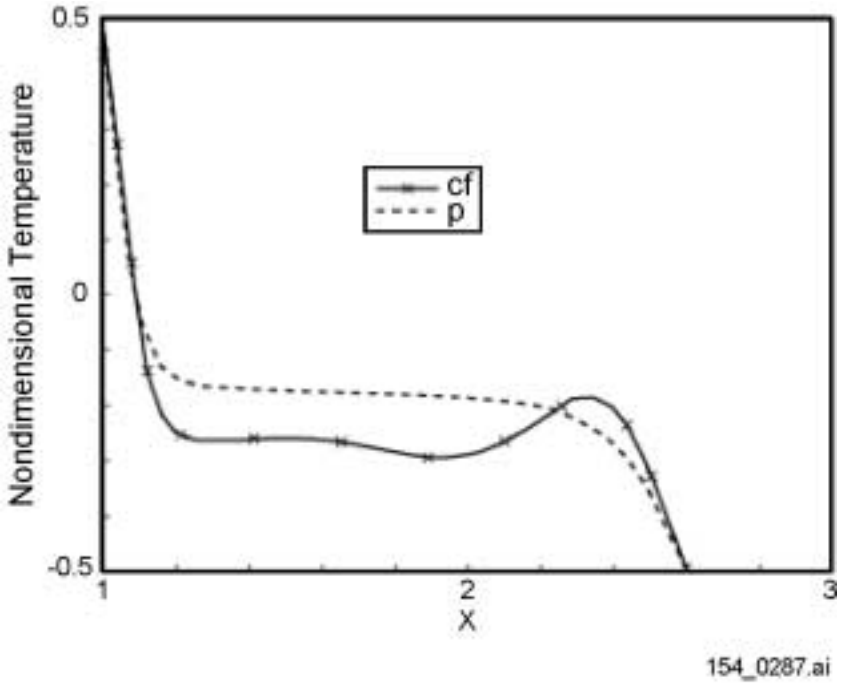

154_0287.ai

Source: Produced using files from Francis 2001 [DIRS 155075].

NOTE: X = horizontal distance; cf= Navier-Stokes CFD model; p= porous medium model.

Figure 5.3.2.4.5-15. Nondimensional Temperature Versus Nondimensional Horizontal Distance for the Horizontal Midplane Through the In-Drift Air

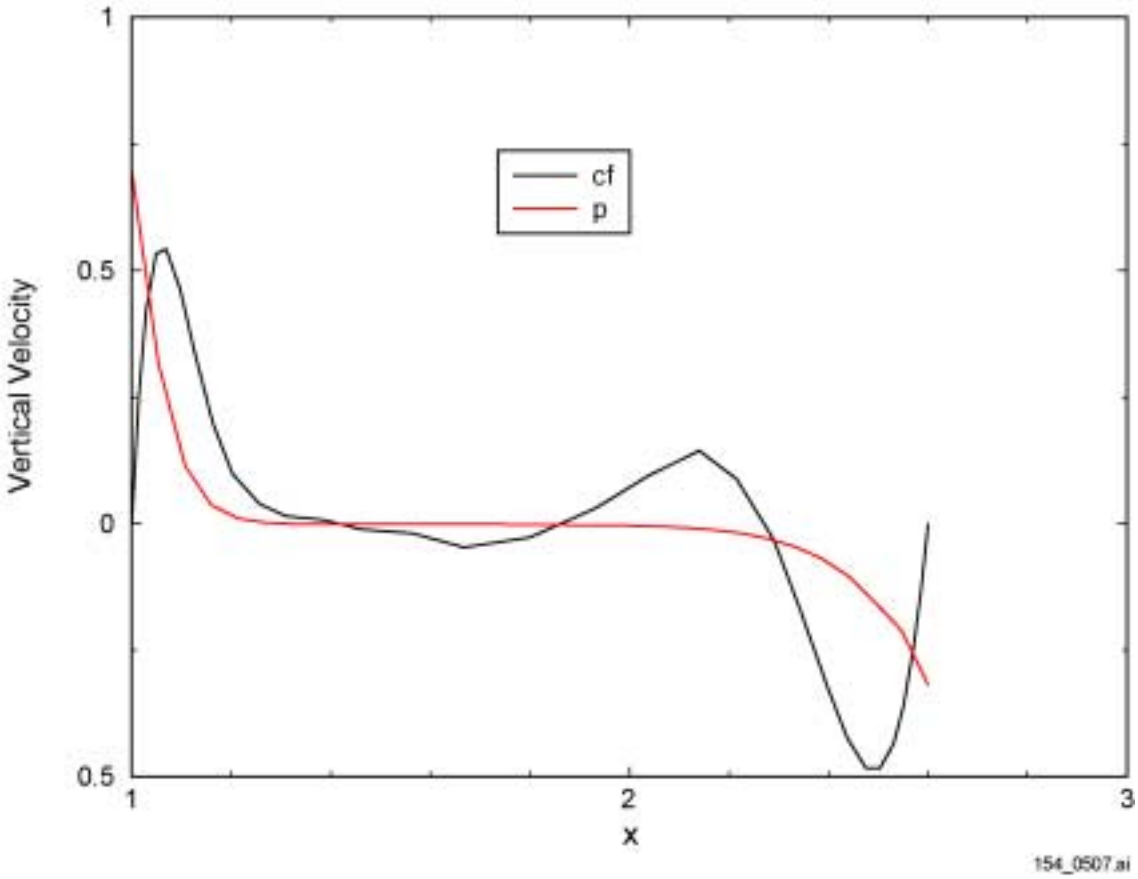

154_0507.ai

Source: Produced using files from Francis 2001 [DIRS 155075].

NOTE: X = horizontal distance. Figure corrected after publication of original source. cf = Navier-Stokes CFD model; p= porous medium model.

Figure 5.3.2.4.5-16. Nondimensional Vertical Velocity Versus Nondimensional Horizontal Distance for the Horizontal Midplane Through the In-Drift Air

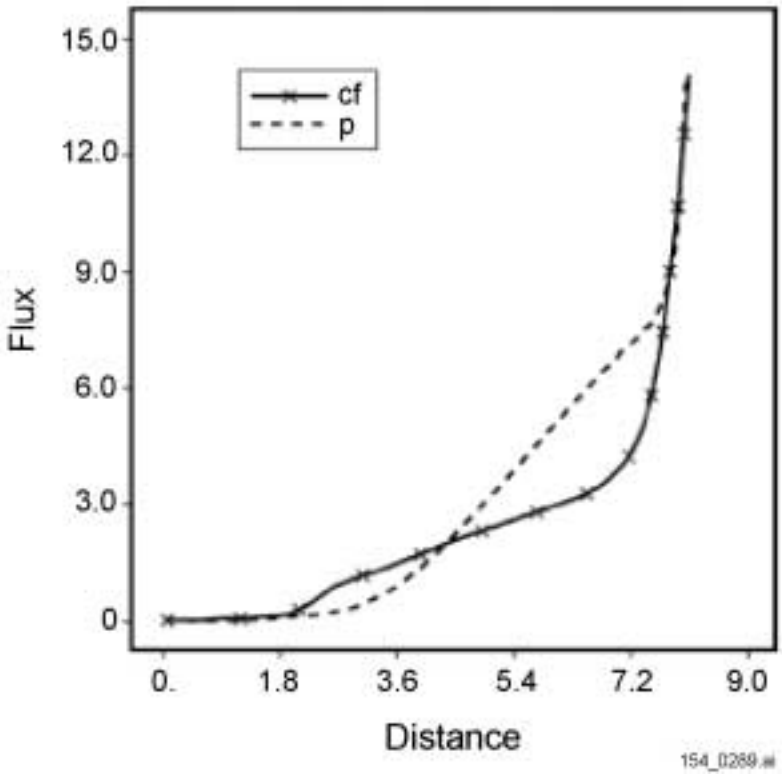

154_0289.ai

Source: Produced using files from Francis 2001 [DIRS 155075].

NOTE: cf= Navier-Stokes CFD model; p= porous medium model.

Figure 5.3.2.4.5-17. Nondimensional Heat Flux on the Cool (Outer) Cylinder Versus Non-Dimensional Distance Along the Cylinder Perimeter

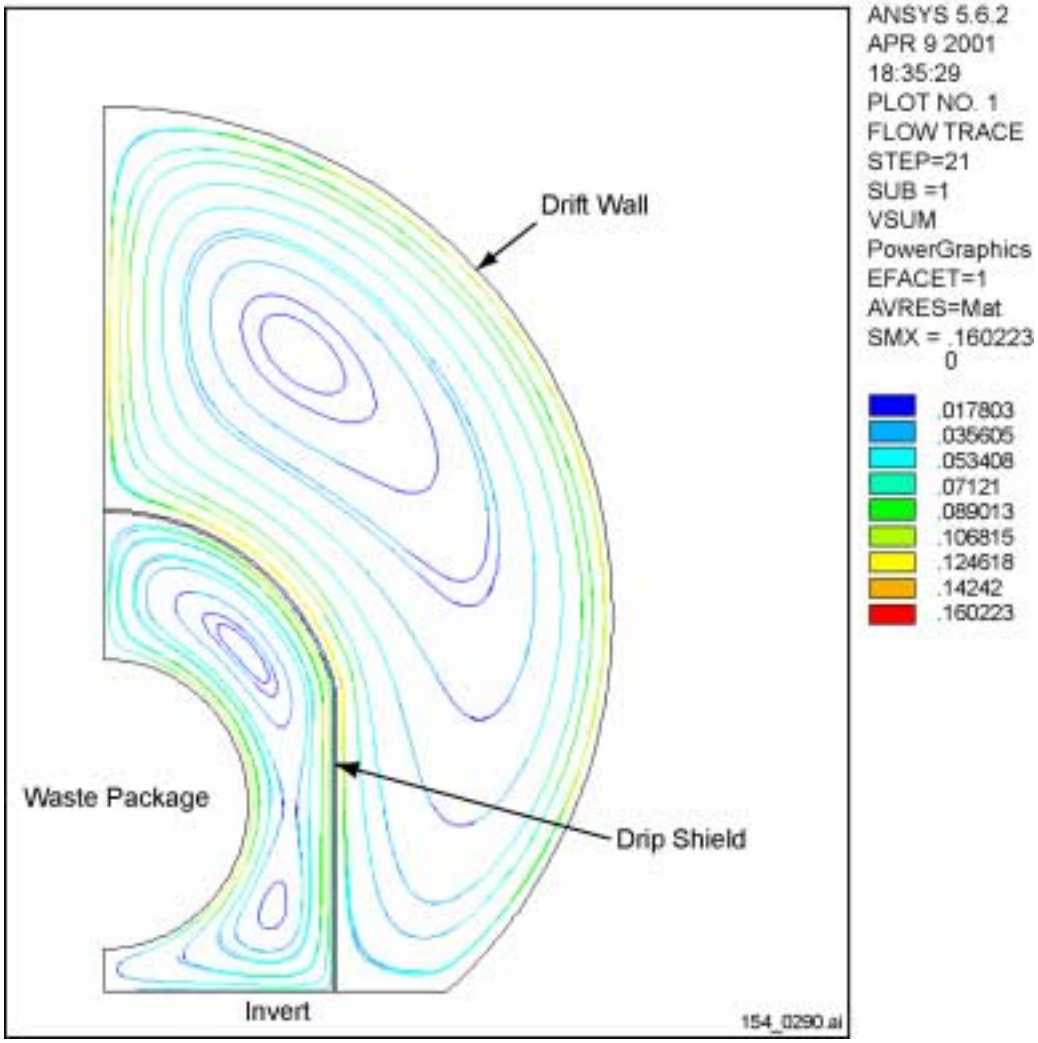

154_0290.ai

Source: Produced using files from Francis 2001 [DIRS 155075].

Figure 5.3.2.4.5-18. Natural Convection Flow Velocities Calculated Using ANSYS

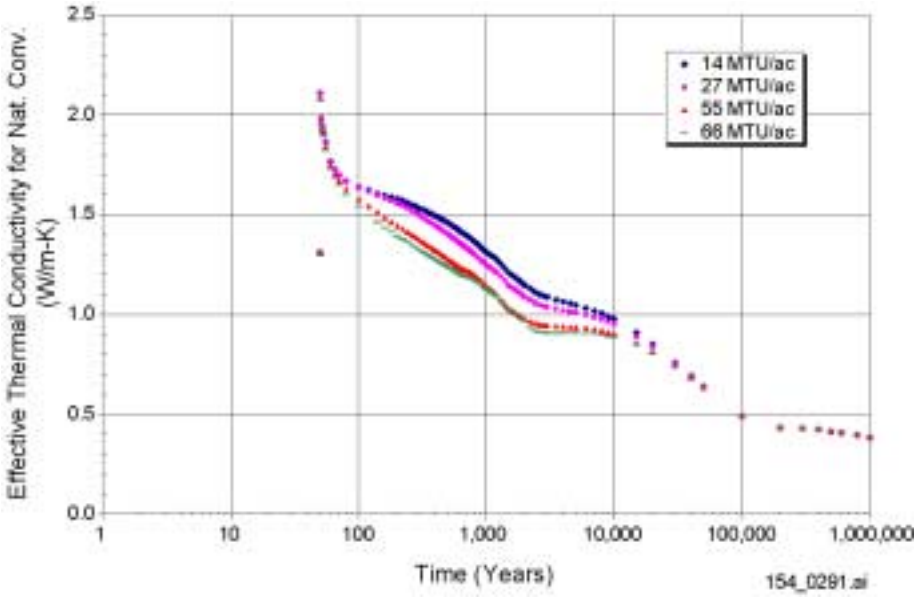

154_0291.ai

Source: Produced using files from Francis 2001 [DIRS 155075].

NOTE: Effective thermal conductivity for natural convection for the higher-temperature operating mode used in the SSPA Volume 2 supplemental analyses (McNeish 2001 [DIRS 155023]).

Figure 5.3.2.4.5-19. Effective Thermal Conductivity for Natural Convection for the Higher-Temperature Operating Mode

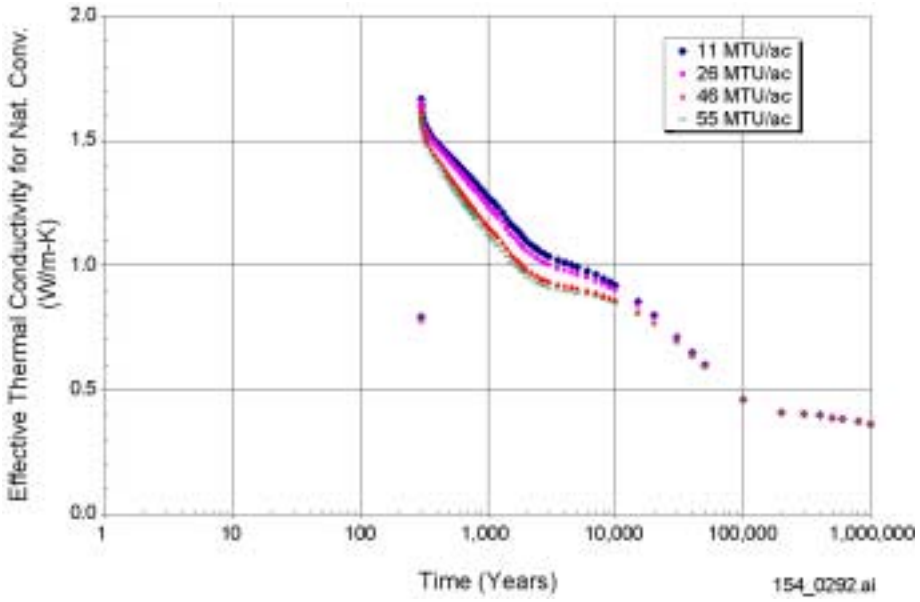

154_0292.ai

Source: Produced using files from Francis 2001 [DIRS 155075].

NOTE: Effective thermal conductivity for natural convection for the lower-temperature operating mode used in SSPA Volume 2 supplemental analyses (McNeish 2001 [DIRS 155023]).

Figure 5.3.2.4.5-20. Effective Thermal Conductivity for Natural Convection for the Lower-Temperature Operating Mode

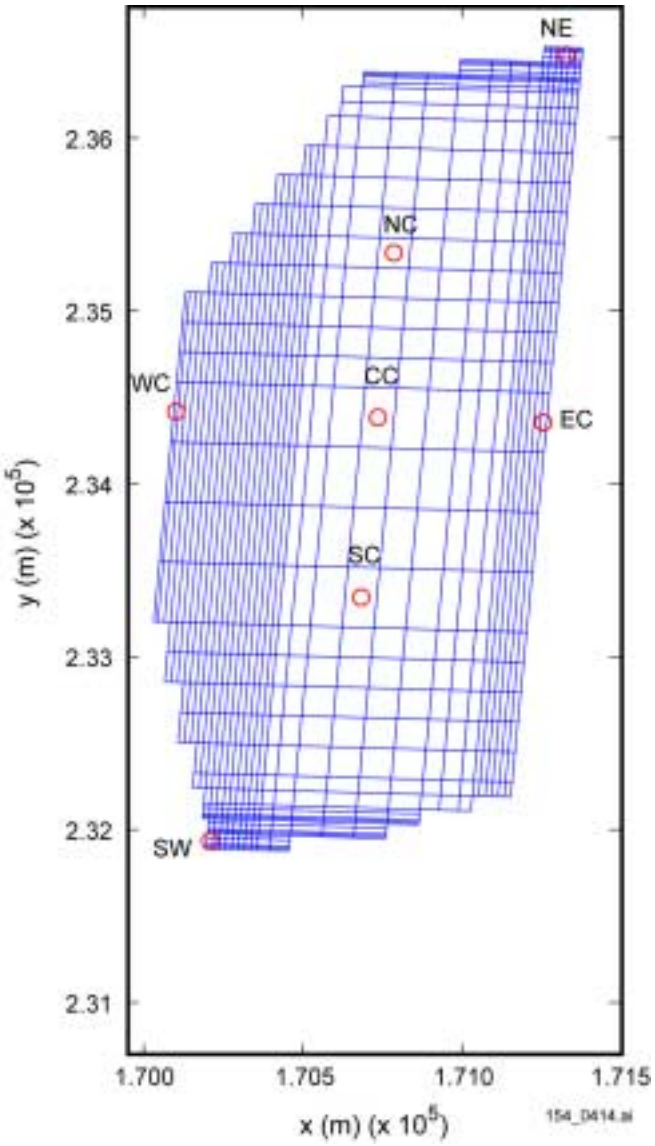

154_0414.ai

Source: Produced using files from Buscheck 2001 [DIRS 155449].

NOTE: Plan view of the potential Higher-Temperature Operating Mode repository showing the geographic locations considered in various analyses. X = east-west distances, Y = north-south distances.

Figure 5.4.1-1. Location of Seven Sites Used in Analyses of the Higher-Temperature Operating Mode Repository

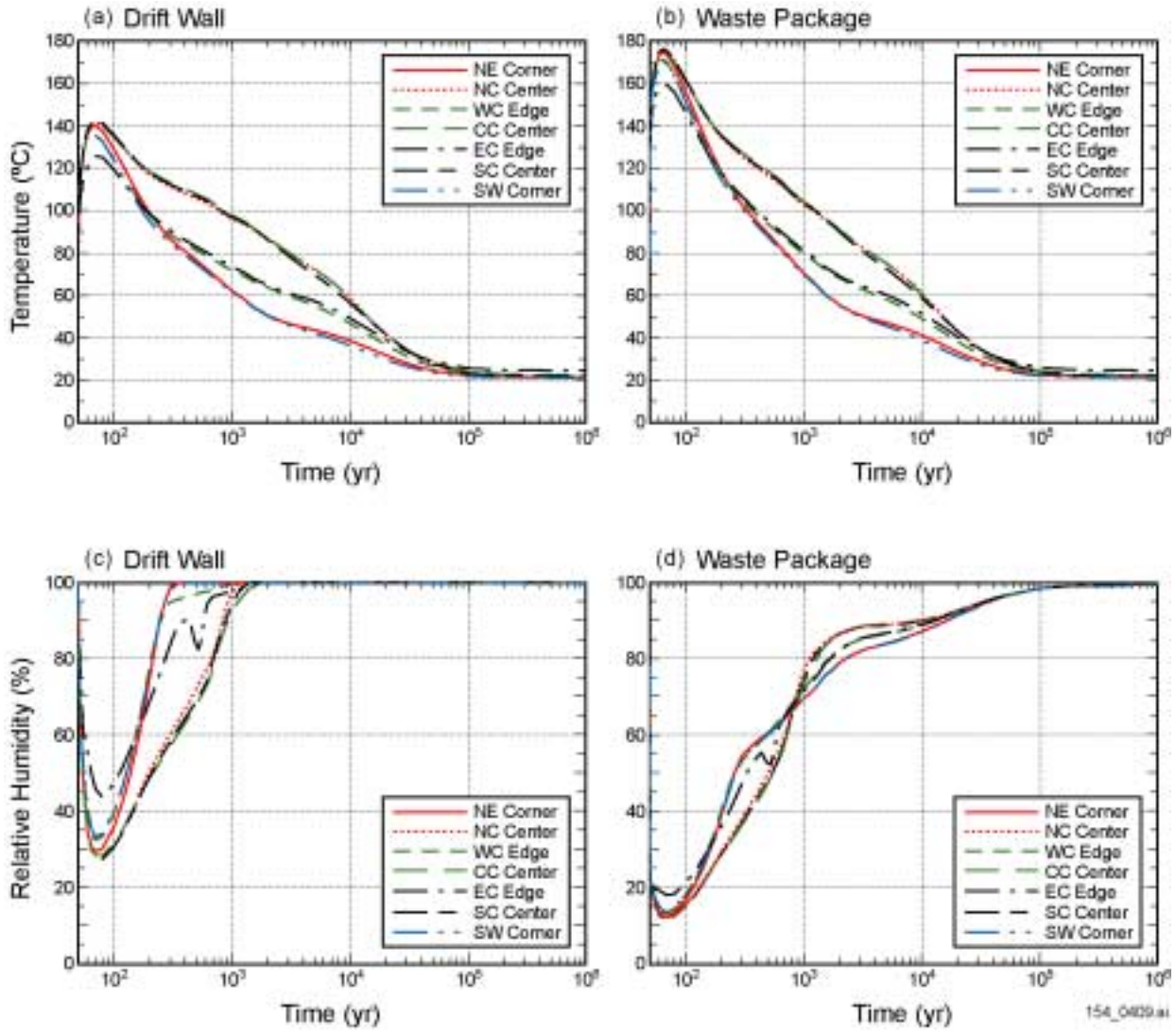

154_0409.ai

Source: Produced using files from Buscheck 2001 [DIRS 155449].

NOTE: Average 21-PWR commercial SNF waste package mean-infiltration flux scenario.

Figure 5.4.1-2. Temperature and Relative Humidity Histories on the Drift Wall and the Waste Package for Seven Locations in the Higher-Temperature Operating Mode Repository

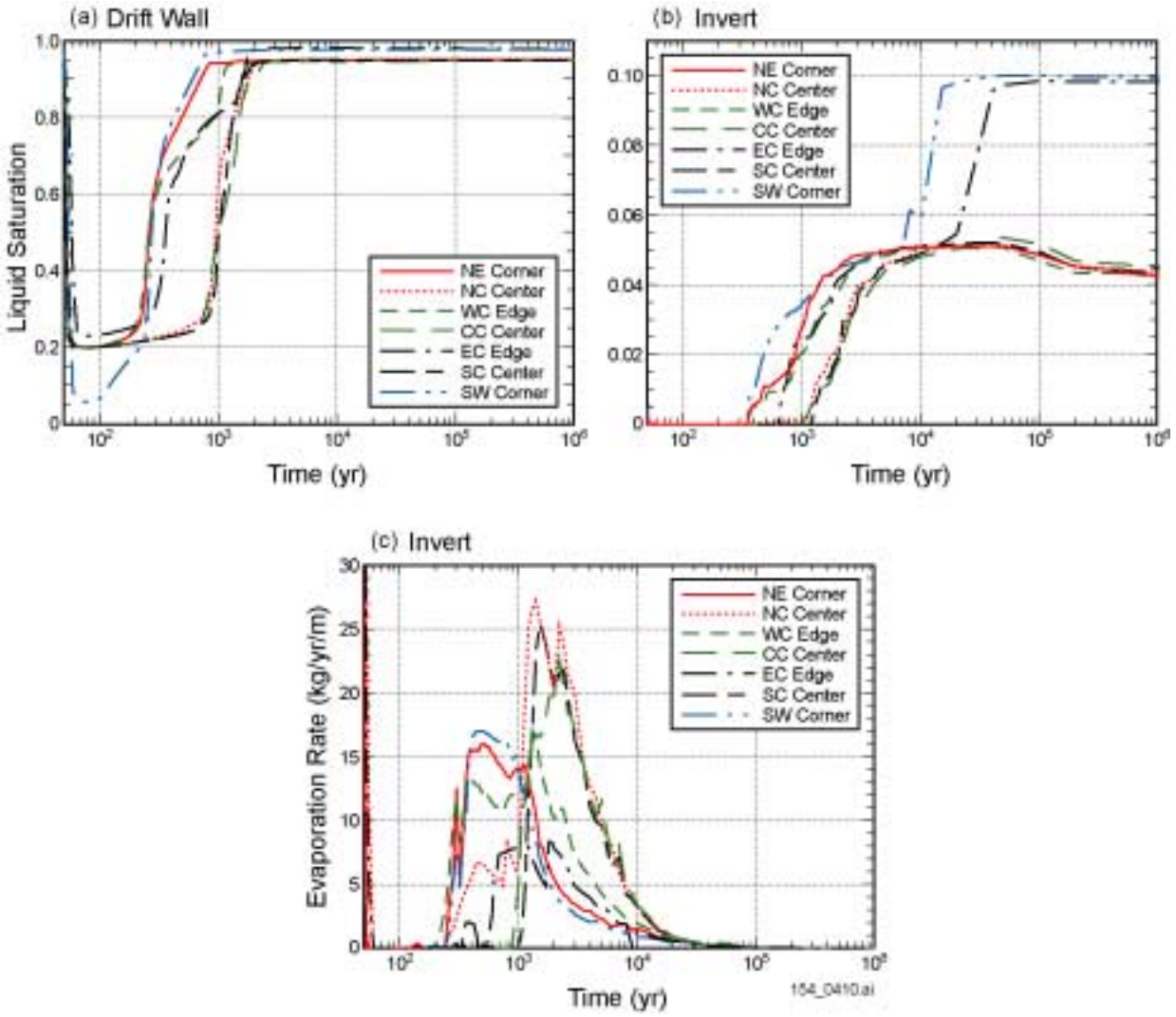

154_0410.ai

Source: Produced using files from Buscheck 2001 [DIRS 155449].

NOTE: Average 21-PWR CSNF waste package Mean-infiltration-flux scenario. Liquid-saturation curves are given for (a) the matrix at the drift wall and for (b) the invert. Evaporation-rate histories are given for the invert (c).

Figure 5.4.1-3. Liquid Saturation and Evaporation Rate Histories for Seven Locations in the Higher-Temperature Operating Mode Repository

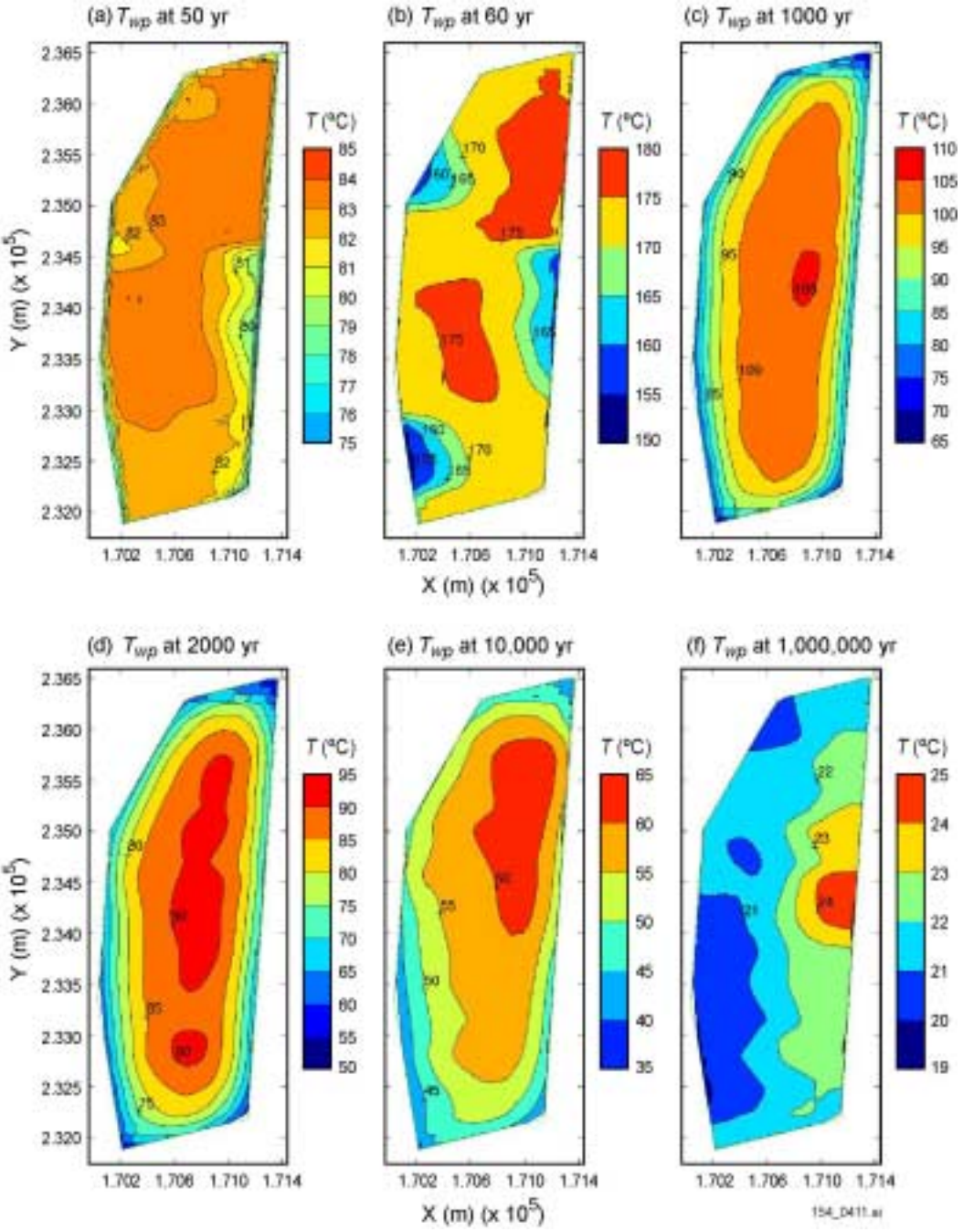

154_0411.ai

Source: Produced using files from Buscheck 2001 [DIRS 155449].

NOTE: Average 21-PWR waste package Mean-infiltration-flux scenario. T_{WP} = waste package temperature, X = east-west distances, Y = north-south distances.

Figure 5.4.1-4. Contour Plots of Waste-Package Temperature for Six Times in the Higher-Temperature Operating Mode Repository

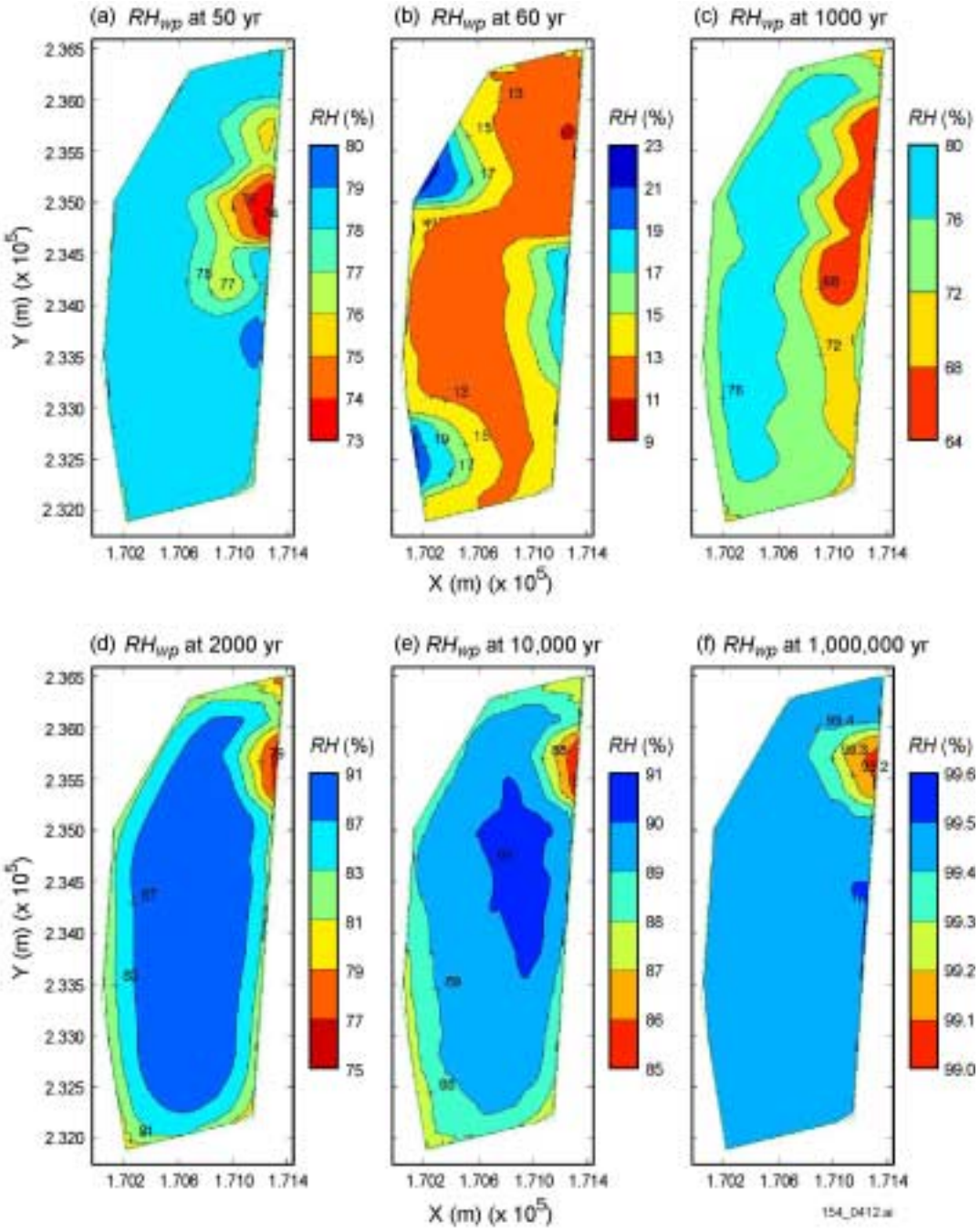

154_0412.ai

Source: Produced using files from Buscheck 2001 [DIRS 155449].

NOTE: Average 21-PWR waste package Mean-infiltration-flux scenario. RH_{WP} = waste package relative humidity, X = east-west distances, Y = north-south distances.

Figure 5.4.1-5. Contour Plots of Waste-Package Relative Humidity at Six Times for the Higher-Temperature Operating Mode Repository

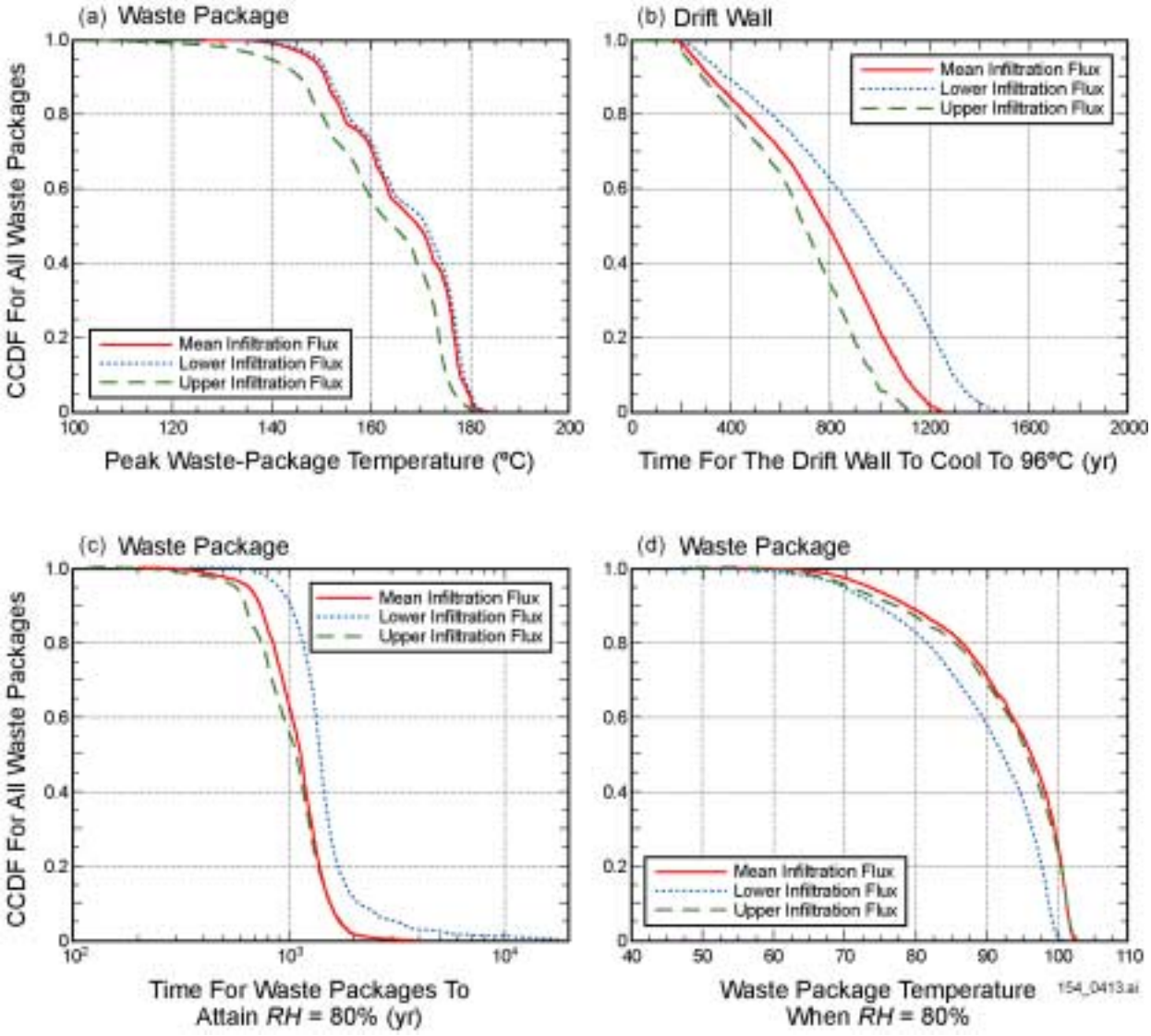

154_0413.ai

Source: Produced using files from Buscheck 2001 [DIRS 155449].

NOTE: CCDF = complementary cumulative distribution function.

Figure 5.4.1-6. Complementary Cumulative Distribution Function of Temperature and Relative Humidity Conditions on the Drift Wall and Waste Package for the Higher-Temperature Operating Mode Repository

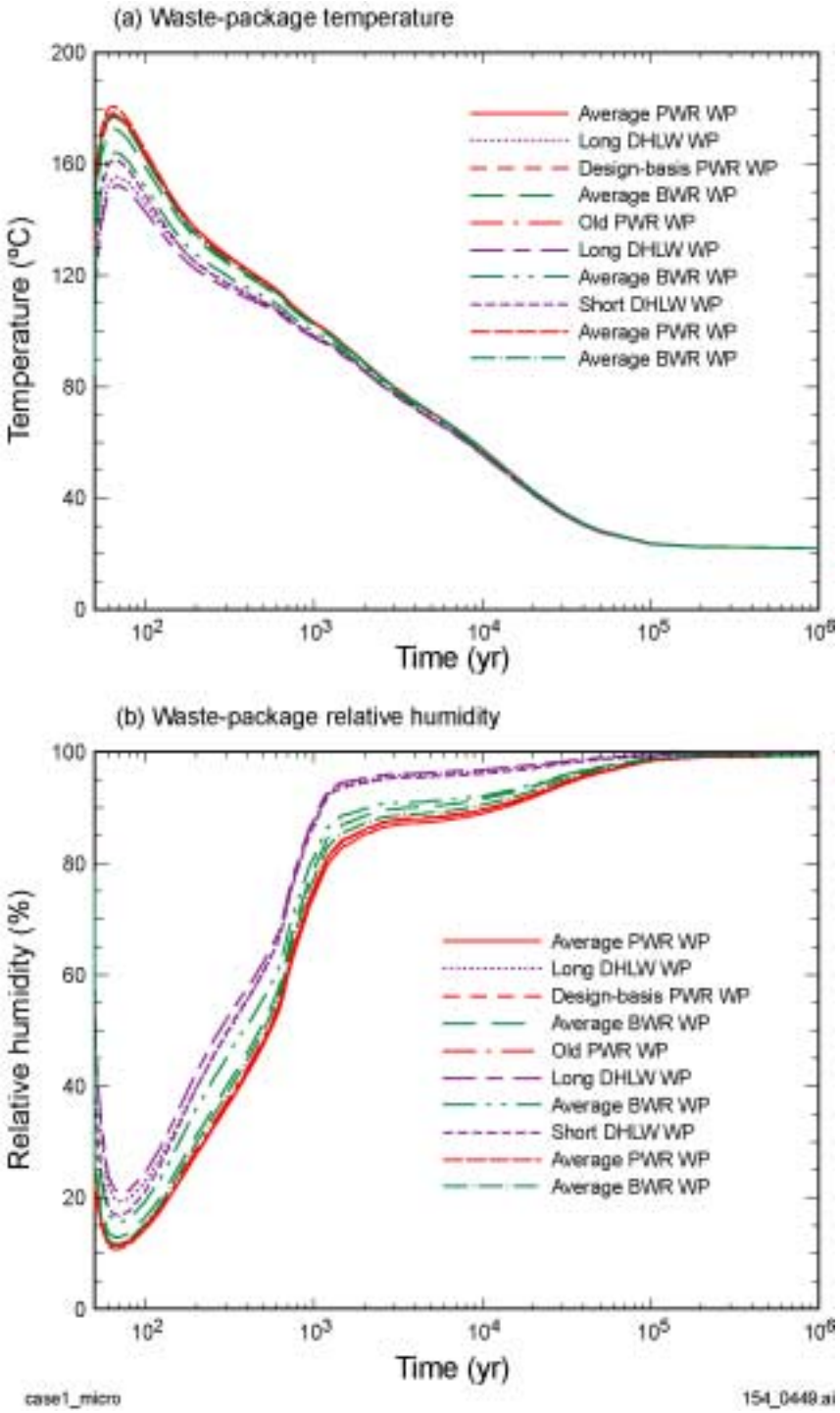

154_0449.ai

Source: Produced using files from Buscheck 2001 [DIRS 155449].

NOTE: Curves are for the 10 waste packages considered in MSTH model calculations at the L5C3 location and the mean-infiltration-flux scenario.

Figure 5.4.1-7. Temperature and Relative Humidity Histories for the Higher-Temperature Operating Mode Predicted by the Multiscale Thermal-Hydrologic Model

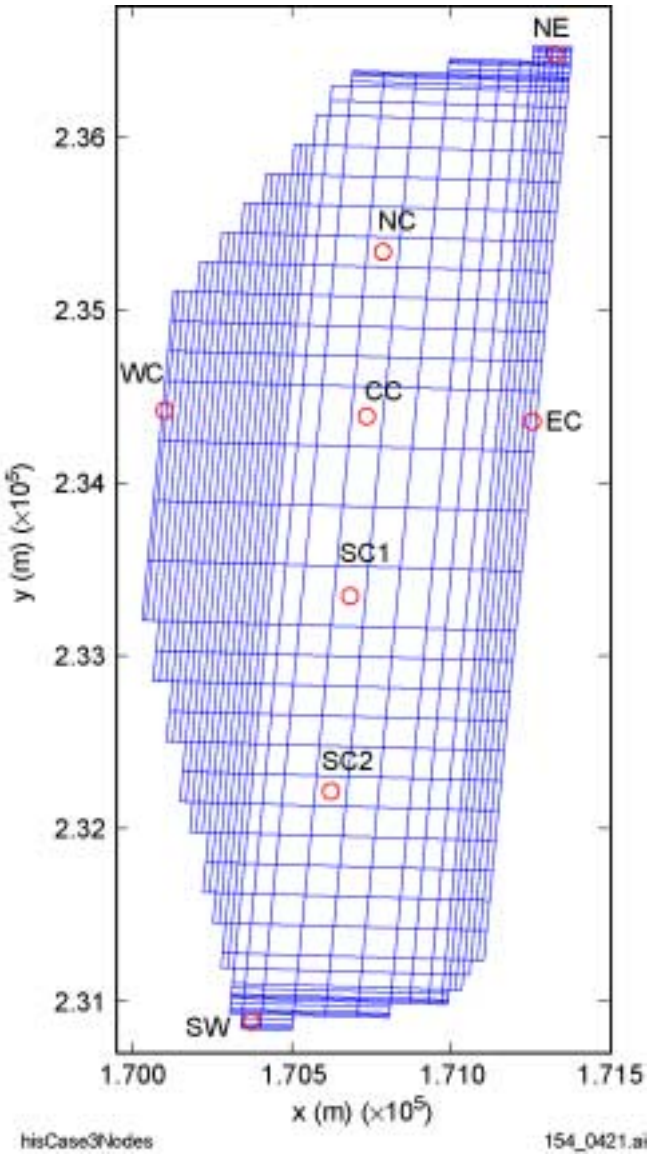

154_0421.ai

Source: Produced using files from Buscheck 2001 [DIRS 155449].

NOTE: Plan view of the potential lower-temperature operating mode repository showing the geographic locations considered in various analyses. X = east-west distances, Y = north-south distances.

Figure 5.4.2-1. Location of Eight Sites Used in Analyses of the Potential Lower-Temperature Operating Mode Repository

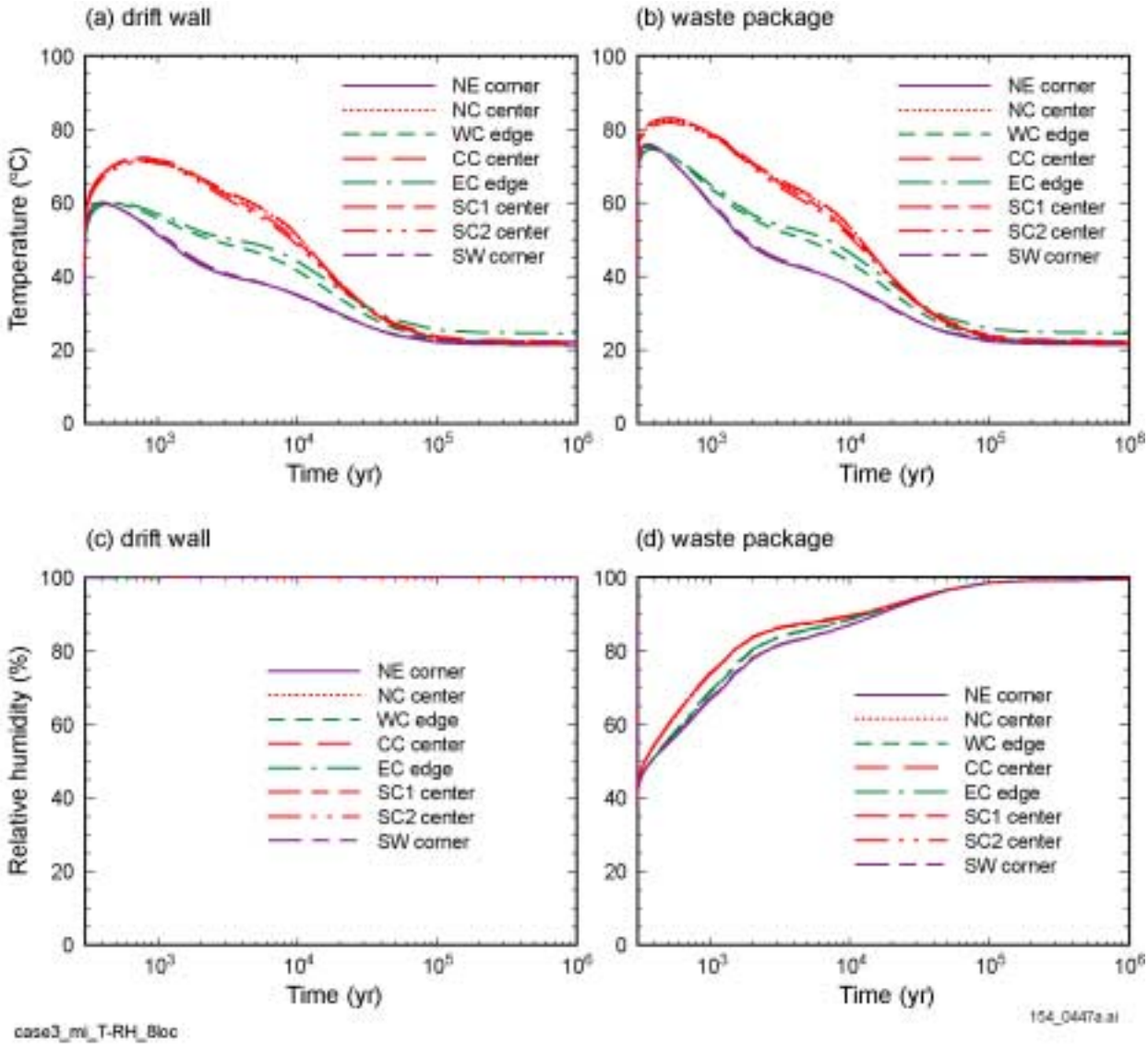

154_0447a.ai

Source: Produced using files from Buscheck 2001 [DIRS 155449].

NOTE: Average 21-PWR CSNF waste package Mean-infiltration-flux scenario.

Figure 5.4.2-2. Temperature and Relative Humidity Histories on the Drift Wall and on the Waste Package for Eight Locations in the Potential Lower-Temperature Operating Mode Repository

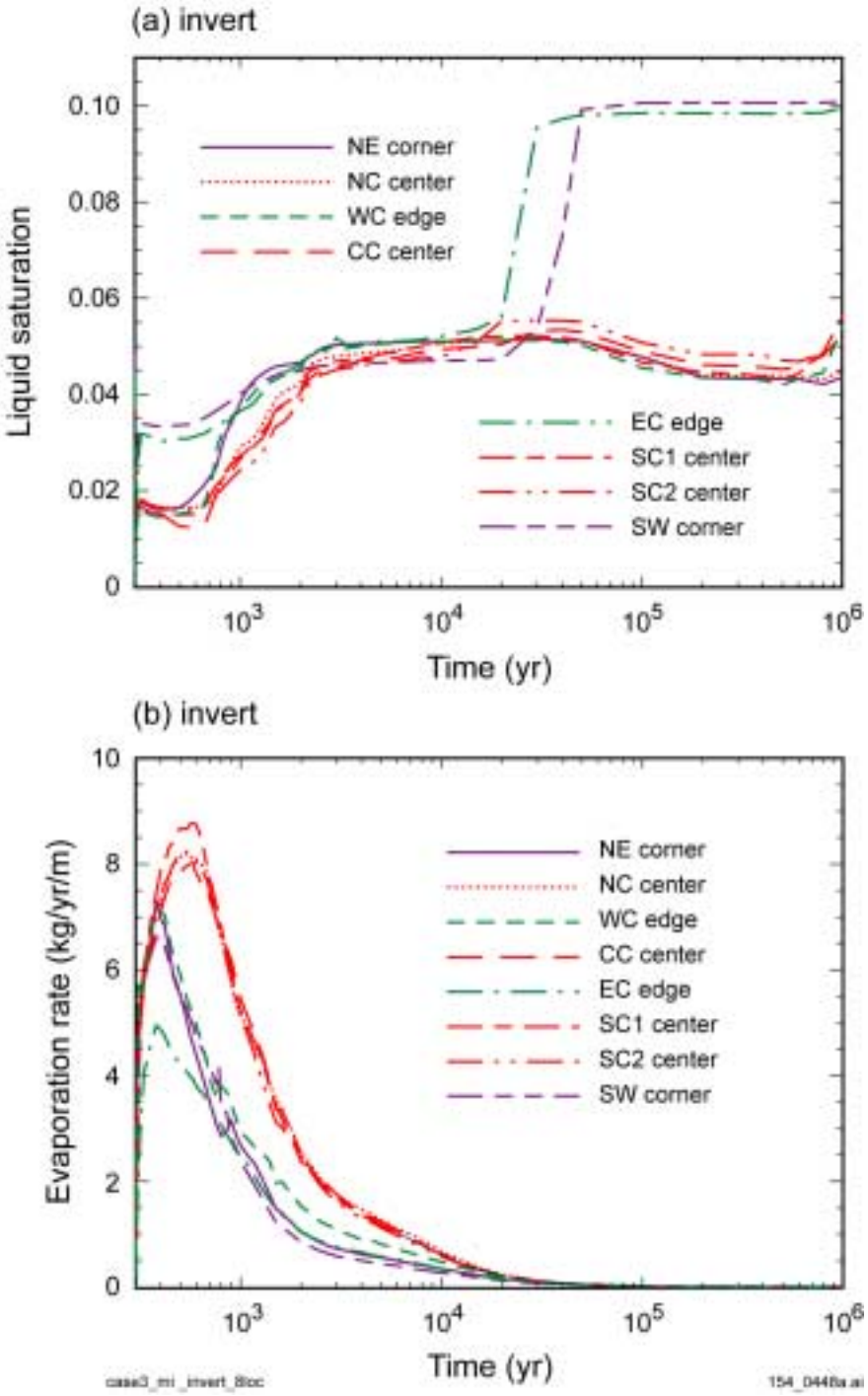

154_0448a.ai

Source: Produced using files from Buscheck 2001 [DIRS 155449].

NOTE: Average 21-PWR CSNF waste Mean-infiltration-flux scenario.

Figure 5.4.2-3. Liquid Saturation and Evaporation Rate Histories in the Invert for Eight Locations in the Potential Lower-Temperature Operating Mode Repository

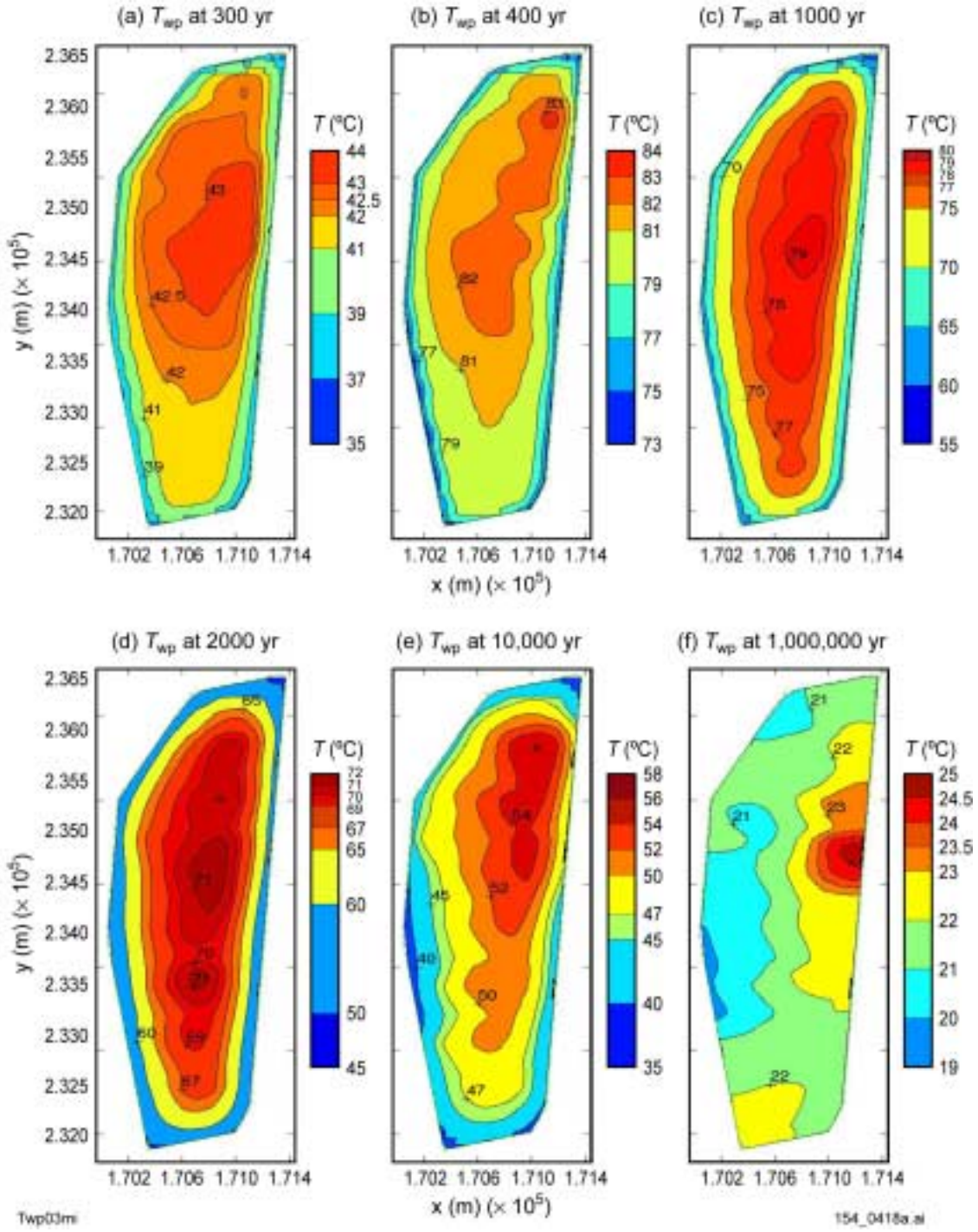

154_0418a.ai

Source: Produced using files from Buscheck 2001 [DIRS 155449].

NOTE: Average 21-PWR waste package Mean-infiltration-flux scenario. T_{WP} = waste package temperature, X = east-west distances, Y = north-south distances.

Figure 5.4.2-4. Contour Plots of Waste-Package Temperature for Six Times in the Lower-Temperature Operating Mode Repository

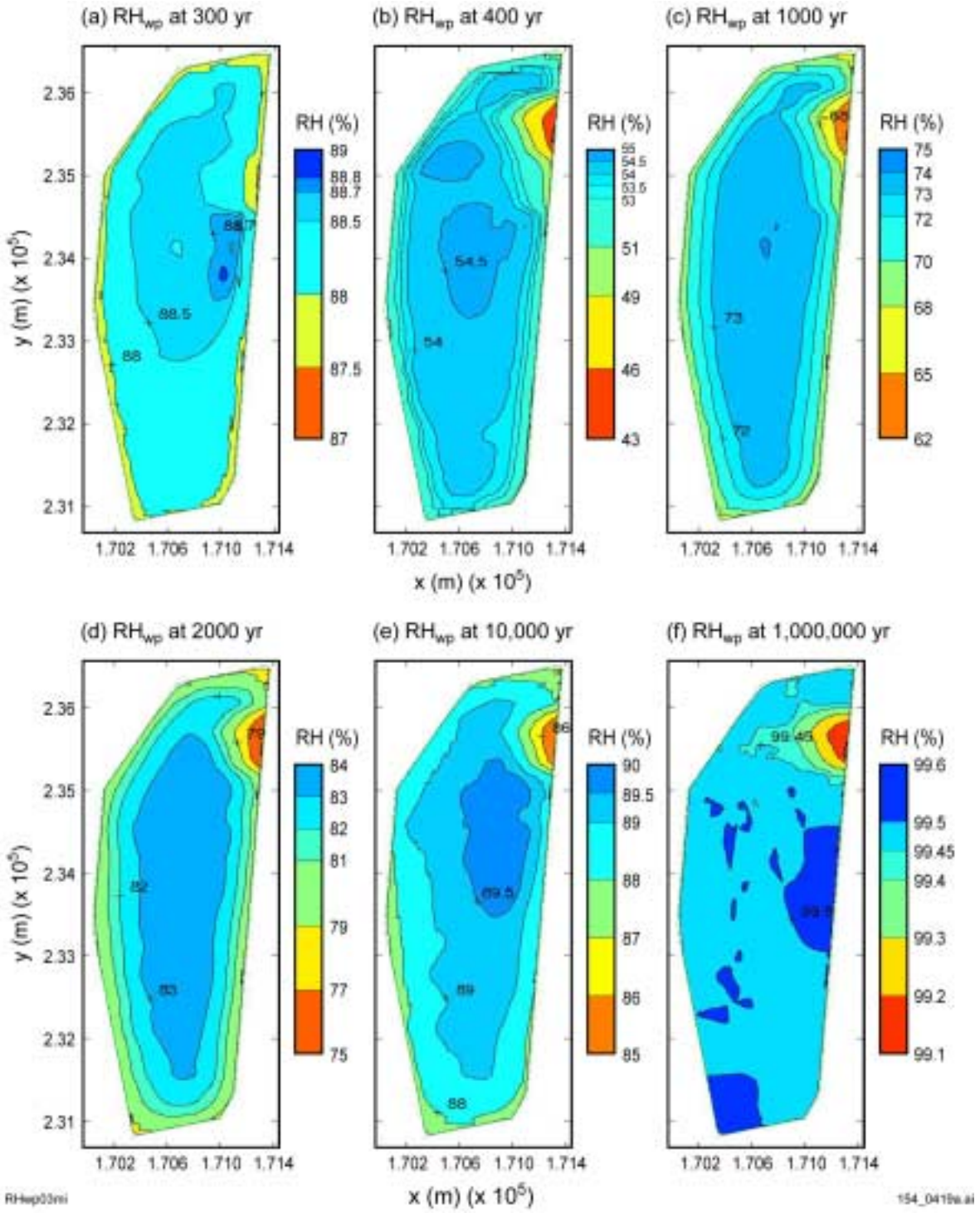

154_0419a.ai

Source: Produced using files from Buscheck 2001 [DIRS 155449].

NOTE: Average 21-PWR waste package Mean-infiltration-flux scenario. RH_{WP} = waste package relative humidity, X = east-west distances, Y = north-south distances.

Figure 5.4.2-5. Contour Plots of Waste-Package Relative Humidity at Six Times for the Lower-Temperature Operating Mode Repository

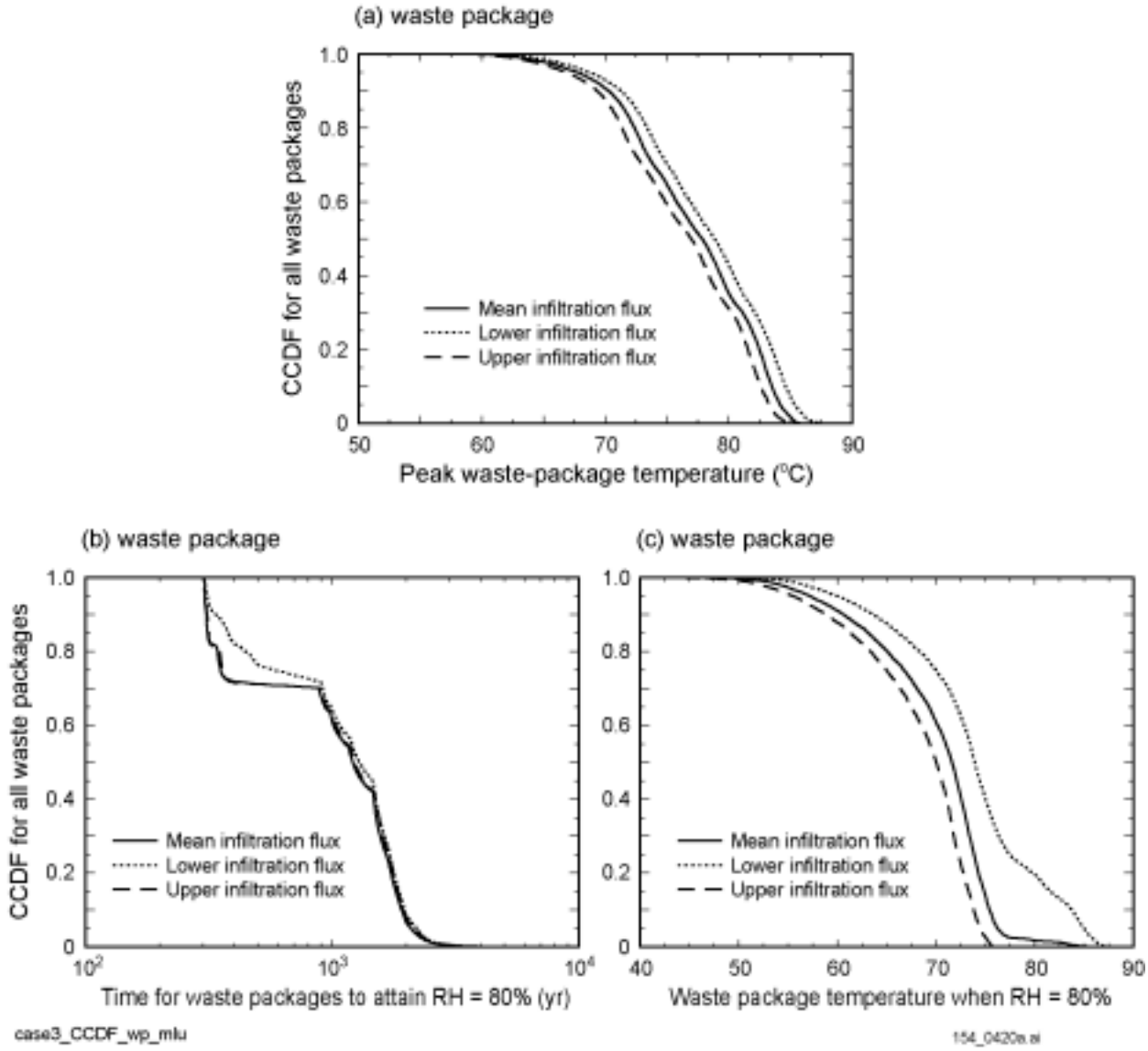

154_0420a.ai

Source: Produced using files from Buscheck 2001 [DIRS 155449].

NOTE: CCDF = complementary cumulative distribution function.

Figure 5.4.2-6. Complementary Cumulative Distribution Function of Temperature and Relative Humidity Conditions on the Waste Package for the Potential Lower-Temperature Operating Mode Repository

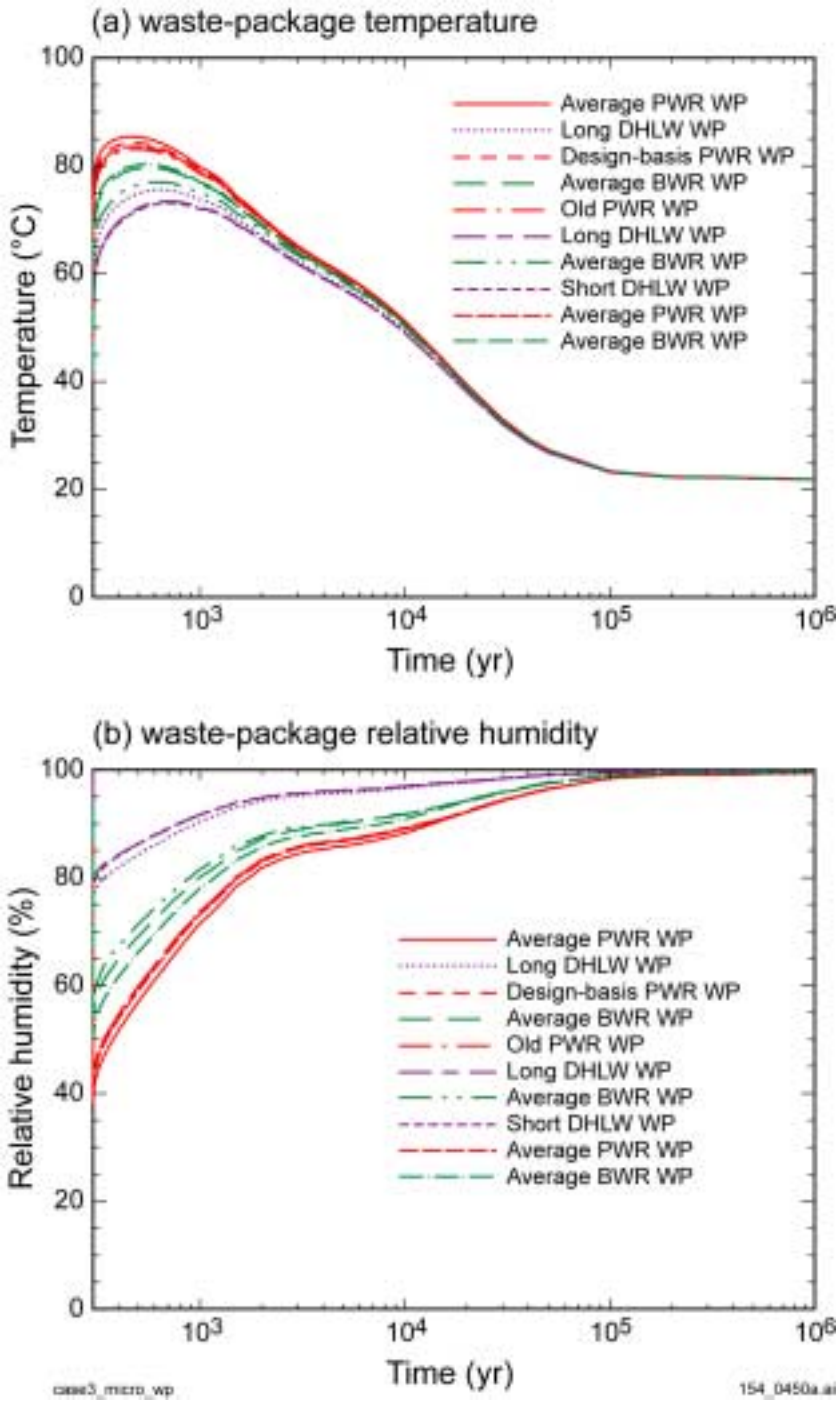

154_0450a.ai

Source: Produced using files from Buscheck 2001 [DIRS 155449].

NOTE: Curves are for the 10 waste packages considered in the MSTH model calculations at the L5C3 location for the Mean-infiltration-flux scenario.

Figure 5.4.2-7. Temperature and Relative Humidity for the Lower-Temperature Operating Mode, Histories Predicted by the Multiscale Thermal-Hydrologic Model

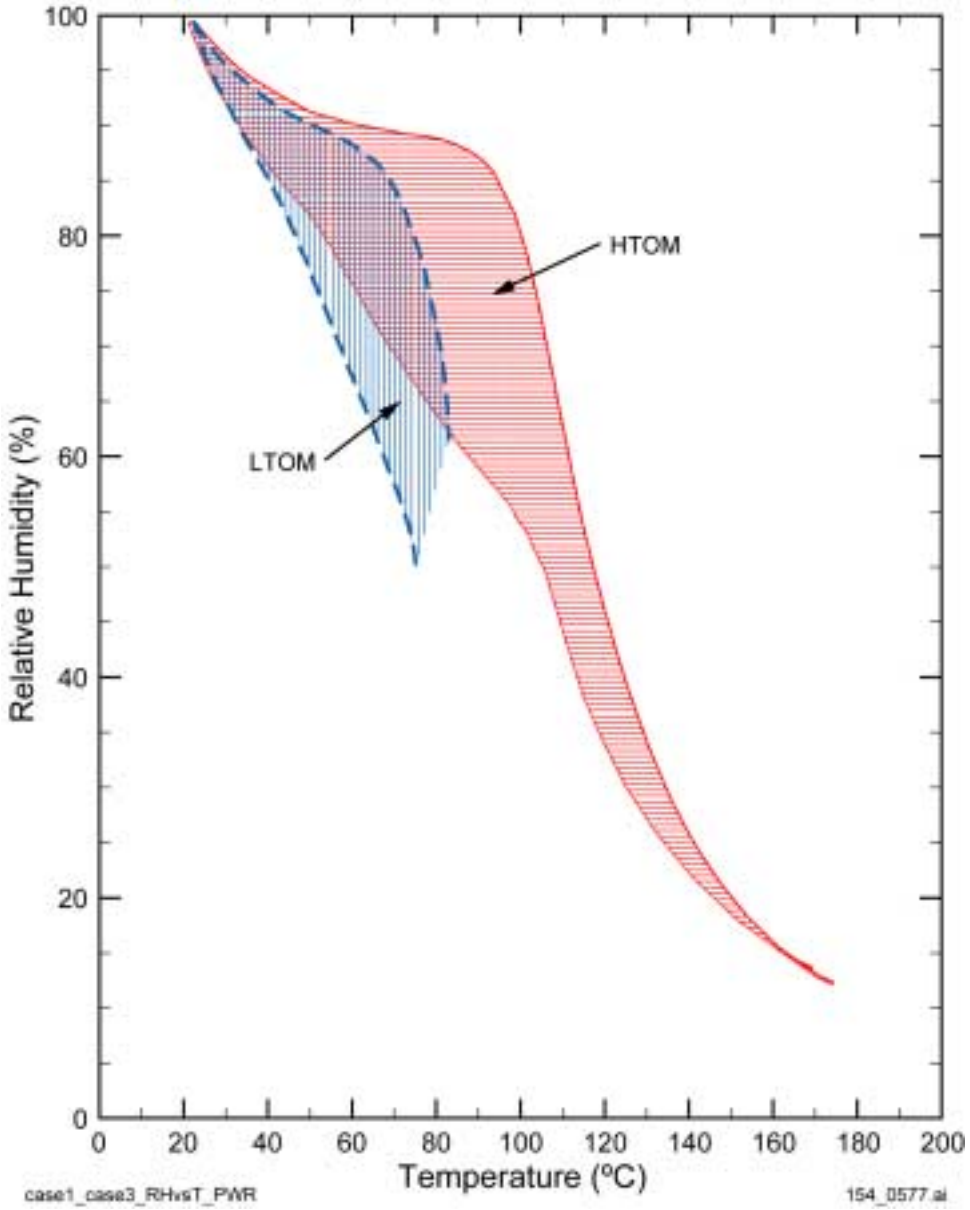

154_0577.ai

Source: Produced using files from Buscheck 2001 [DIRS 155449].

Figure 5.4.2-8. Thermal-Hydrologic Parameter Evolution for the Higher- and Lower-Temperature Operating Modes

6 In-Drift Physical and Chemical Environment

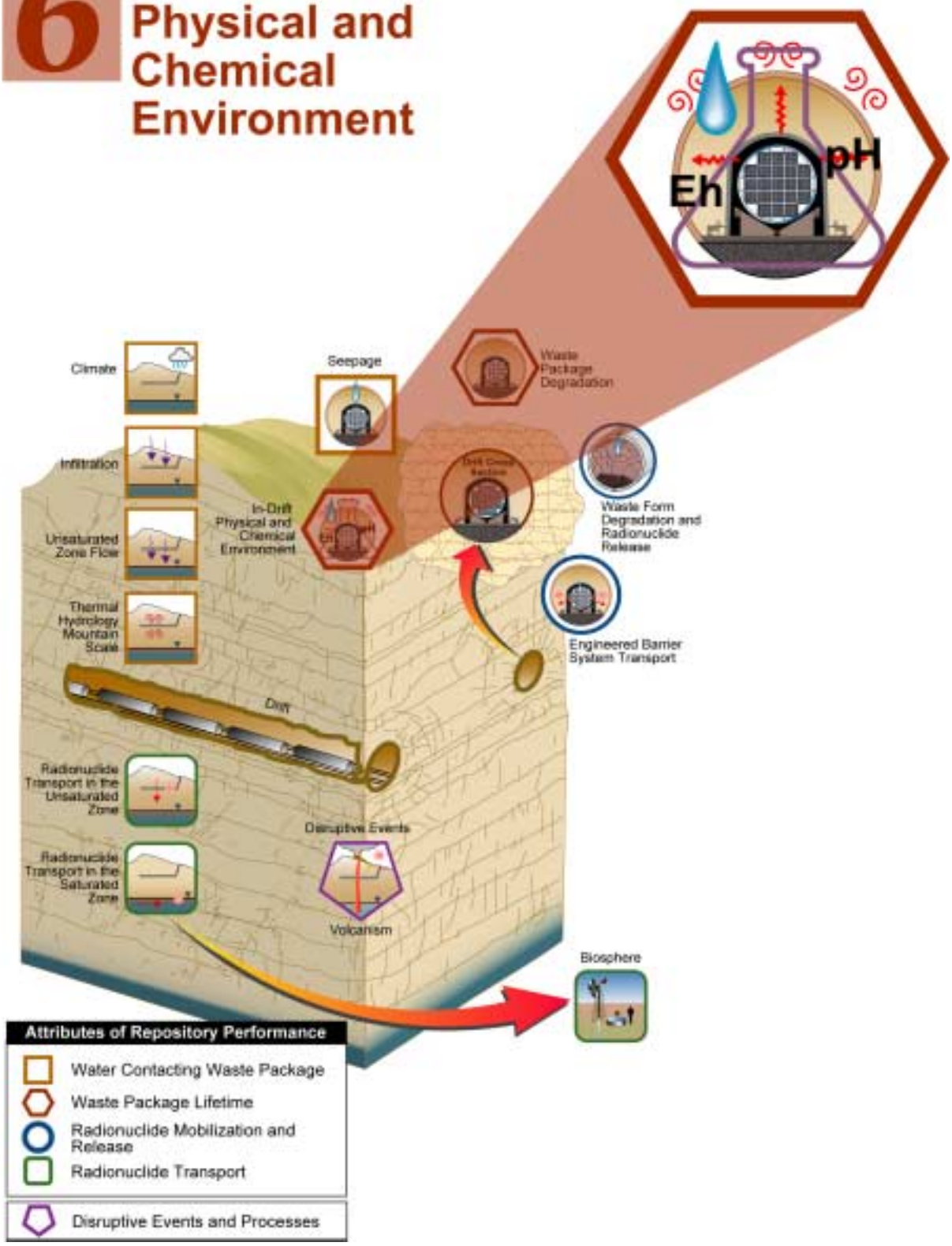

6. IN-DRIFT PHYSICAL AND CHEMICAL ENVIRONMENT

6.1 INTRODUCTION

Drip shield and waste package degradation (see Section 7) depends on the environmental conditions to which these components are exposed: the in-drift physical and chemical environment. Drift degradation and consequent rockfall have the potential to affect drip shield integrity and the thermal-hydrologic, chemical (THC) environment in drifts. After a waste package is breached, the transport of radionuclides released from the waste form (see Section 10) also depends on the environment in the emplacement drifts. A descriptive conceptualization of the in-drift processes and parameters that can affect the environment is given in *Physical and Chemical Environmental Abstraction Model* (CRWMS M&O 2000 [DIRS 151563]) and in the *Total System Performance Assessment for the Site Recommendation* (TSPA-SR) (CRWMS M&O 2000 [DIRS 153246], Sections 3.3 and 3.6). More recent models and analyses are summarized in Table 6-1.

Important in-drift processes that can affect the physical and chemical environment include evaporation and condensation of water, formation of salts by precipitation, dissolution of salts, microbial activity, reaction of gas phase constituents with aqueous solutions and solids, corrosion, and mass transport, including initiation and changes in transport paths such as those caused by drip shield and waste package degradation (see Section 10).

Principal in-drift parameters that can affect those processes are influx rates of seepage water (see Section 4) and advection or diffusion rates of incoming gas from the host rock, other advective and diffusive mass transport rates (see Section 10), evaporation rate (see Section 5), relative humidity (see Section 5), temperature (see Section 5), gas phase composition, aqueous solution composition, compositions of solid phases within and around the drift, and the effects of rockfall due to host rock degradation.

The treatment of these processes and parameters in the TSPA-SR (CRWMS M&O 2000 [DIRS 153246]), including uncertainties, is reviewed in Section 6.2.

Scientific bases for the total system performance uncertainty analyses in Volume 2 (McNeish 2001 [DIRS 155023]) and results of supplemental subsystem performance uncertainty analyses are introduced and presented in Section 6.3 under the following subheadings.

Composition of Liquid and Gas Entering Drift (Thermal-Hydrologic-Chemical) (Section 6.3.1)–Includes the composition of seepage water and gas and the rates at which water and gas enter the drift. An introduction to THC seepage models is provided in Section 6.3.1.1. Goals of modeling are provided in Section 6.3.1.2. Sections 6.3.1.3 and 6.3.1.4 describe the original model work and later updates. Results of new simulations that further evaluate the uncertainty of predicted water and gas compositions due to variations in thermal operating mode are presented in Section 6.3.1.5. The remainder of Section 6.3.1 abstracts the currently available data for use in the total system performance assessment (TSPA) effort and summarizes remaining model uncertainties and the implications for predicted compositions of fluids that could enter the drift.

Table 6-1. Summary of Supplemental Models and Analyses

Key Attributes of System	Process Model (Section of S&ER)	Topic of Supplemental Scientific Model or Analysis	Reason For Supplemental Scientific Model or Analysis			Section of Volume 1	Performance Assessment Treatment of Supplemental Scientific Model or Analysis[a]	
			Unquantified Uncertainty Analysis	Update in Scientific Information	Lower-Temperature Operating Mode Analysis		TSPA Sensitivity Analysis	Included in Supplemental TSPA Model
Long-Lived Waste Package and Drip Shield	Water Diversion Performance of EBS (4.2.3)	Composition of liquid and gas entering drift	X		X	6.3.1	X	X
		Evolution of in-drift chemical environment	X		X	6.3.3	X	X
		Thermo-Hydro-Chemical model comparison to plug-flow reactor and fracture plugging experiment		X		6.3.1		
		Rockfall		X		6.3.4		

NOTE: S&ER = *Yucca Mountain Science and Engineering Report* ([DOE 2001 [DIRS 153849]).

[a] Performance assessment treatment of supplemental scientific model or analysis discussed in SSPA Volume 2 (McNeish 2001 [DIRS 155023]).

Effects of Engineered Materials on the Chemical Environment (Section 6.3.2)–Includes engineered materials, such as steel and cement, but not the contents of the waste packages (see Section 9). A brief introduction and modeling goals are provided in Sections 6.3.2.1 and 6.3.2.2. Section 6.3.2.3 describes current work and previously unquantified uncertainties in the modeling of steel corrosion, alloy corrosion, and cement grout degradation. Section 6.3.2.6 summarizes remaining uncertainties.

Evolution of In-Drift Chemical Environment (Section 6.3.3)–Includes evaporation and condensation of water, formation of salts by precipitation, dissolution of salts, microbial activity, reaction of gas phase constituents with aqueous solutions, and resulting changes in aqueous solution composition. This section discusses three submodels within the engineered barrier system (EBS). Section 6.3.3.3 discusses initial results and previously unquantified uncertainties. Section 6.3.3.4 discusses developments since the initial release of the analysis model reports (AMRs). Section 6.3.3.5 contains analysis results, which are abstracted in Section 6.3.3.6. Remaining uncertainties are listed in Section 6.3.3.7, and a final summary of the information is provided in Section 6.3.3.8.

Rockfall (Section 6.3.4)–Includes sensitivity studies for model predictions of size ranges and quantities of rock that may fall into drifts. Section 6.3.4.1 introduces key processes and modeling software. A discussion of past efforts, unquantified uncertainties, and uncertainties selected for quantification is found in Section 6.3.4.3. Analysis results are detailed in Section 6.3.4.5. Multiple lines of evidence are provided in Section 6.3.4.7. Remaining uncertainties are listed in Section 6.3.4.8, and a summary and conclusion are provided in Section 6.3.4.9.

Section 6.4 presents, a summary and discussion of parameters and information provided to the TSPA for the uncertainty analyses in Volume 2 (McNeish 2001 [DIRS 155023]), including model uncertainties and input data uncertainties.

6.2 REVIEW OF TOTAL SYSTEM PERFORMANCE ASSESSMENT-SITE RECOMMENDATION TREATMENT

6.2.1 Composition of Liquid and Gas Entering the Drifts (Thermal-Hydrologic-Chemical)

The model for compositions of liquid and gas entering the drifts is the THC seepage model (CRWMS M&O 2000 [DIRS 142022]). This model predicts, at the drift scale, the composition of seepage and the associated gas-phase chemistry for 100,000 years, including the effects of heating. Uncertainties are discussed in more detail in Sections 6.3.1.1 and 6.3.1.3.

Work documented in *Drift-Scale Coupled Processes (DST and THC Seepage) Models* (CRWMS M&O 2000 [DIRS 142022]) included one THC seepage model with a drift located in the middle nonlithophysal unit of the Topopah Spring tuff (Tptpmn). The simulated design included backfill, an initial mean linear heat load of 1.54 kW/m, and a 50-year preclosure period with 70 percent heat removal. This thermal load was predicted to yield temperatures above the boiling point of water (near 96ºC at Yucca Mountain) in the rocks in the vicinity of the emplacement drifts for hundreds of years. THC seepage simulations were also performed for an

ambient temperature case (no heat load) to serve as a baseline for evaluations of model results under thermal loading conditions. Uncertainties in this THC seepage model were not explicitly quantified in the TSPA-SR (CRWMS M&O 2000 [DIRS 153246]) treatment.

The initial THC seepage model (CRWMS M&O 2000 [DIRS 142022]) is based on information obtained, in part, from thermal testing in the Tptpmn unit, which may exhibit somewhat different thermal-hydrologic (TH) behavior or mineralogy than the lower lithophysal unit (Tptpll), in which most of the repository emplacement drifts will be located. Although this could change the system response, the bulk chemistry is similar for all of the welded host rock units.

Two geochemical systems were considered in this model. The first was an extended case system that included aluminum silicates (e.g., clays, zeolites, feldspars, and sepiolite), silica phases (e.g., quartz, amorphous silica, tridymite, and glass), gypsum, calcite, fluorite and iron minerals (e.g., hematite, and goethite), and a suite of aqueous species, including calcium, magnesium, sodium, potassium, silica, chloride, aqueous carbonate species, sulfate, fluoride, aluminum, and iron. The second was a base case system that excluded aluminum silicate minerals and iron minerals, thus excluding such aqueous species as aluminum, magnesium, potassium, and iron, which are found in these minerals.

The inclusion or exclusion of aluminum silicate minerals in the system provided a first crude approach for evaluating the model sensitivity to the effective reaction rates of these minerals: either reacting at rates determined from published kinetic and thermodynamic data and estimated reactive surface areas, or reacting so slowly that the reactions could be neglected.

The initial THC seepage model (CRWMS M&O 2000 [DIRS 142022]) is useful to evaluate, in a semiquantitative sense, the model sensitivity to the reaction rates of aluminum silicate minerals and to a range of infiltration rates, including future climates wetter than the present day. However, under the high infiltration rate conditions most favorable to in-drift seepage, uncertainties in these parameters are likely to be overshadowed by the assumed composition of fluids infiltrating at the top model boundary. Therefore, while the initial THC seepage model (CRWMS M&O 2000 [DIRS 142022]) simulations provide some quantitative assessment of uncertainties related to mineral reaction rates and infiltration rates, the effect of infiltration composition remains to be quantified. None of the uncertainties discussed here were included in the TSPA-SR model (CRWMS M&O 2000 [DIRS 153246]). The complete data set for the abstraction detailed in Section 6.3.1.6 can be found in Jolley (2001 [DIRS 154762]).

6.2.2 Effects of Engineered Materials on the Chemical Environment

An evaluation of corrosion products on the aqueous concentrations of metal ions in solution in an oxidizing environment was conducted and found to have a minimal impact on the concentrations of major ions in solution, as reported in the *In Drift Corrosion Products* report (CRWMS M&O 1999 [DIRS 125130], Section 7.2). That conclusion was based on a generalized set of Eh-pH diagrams for the major elements in a three- or four-chemical component system and a general search of available scientific literature.

Uncertainties in the models about the effects of engineered materials on the chemical environment were not explicitly quantified in the TSPA-SR model (CRWMS M&O 2000

[DIRS 153246]). The uncertainties are in three general areas: corrosion of steel and alloys, cement grout reactions, and colloids. The first two areas are specifically discussed in Section 6.3.2.3; the third area is discussed in Section 10.3.5. An evaluation of the effects of corrosion products on the aqueous concentrations of metal ions in solution in an oxidizing environment was conducted. Two conclusions were that only minor impacts are expected to occur in the bulk in-drift chemical environment and that any impacts will occur during active corrosion of the metals and alloys in an oxidizing environment, as reported in the *In Drift Corrosion Products* report (CRWMS M&O 1999 [DIRS 125130], Section 7.2). It was also concluded that effects of cementitious materials would be negligible (CRWMS M&O 2000 [DIRS 153246], Section 3.3.4.5.4).

6.2.3 Evolution of In-Drift Chemistry

The model of the evolution of the in-drift chemical environment uses inputs from three models: the precipitates and salts model, the invert water mixing model, and the microbial communities model.

The precipitates and salts model is based on literature data that describe the minerals and salts produced by evaporative concentration and the relations between solution composition and relative humidity. This model was developed and validated in *In-Drift Precipitates/Salts Analysis* (CRWMS M&O 2001 [DIRS 153265]). It is composed of two submodels that predict pH, chloride concentration, and ionic strength as a function of relative humidity, carbon dioxide fugacity, temperature, seepage water composition, and relative rates of evaporation and seepage. When the relative humidity is above 85 percent, the EQ3/6 Pitzer submodel (often referred to as the high relative humidity salts submodel) is used. Below 85 percent relative humidity, the low relative humidity salts submodel is used. Lookup tables produced for the TSPA-SR (CRWMS M&O 2000 [DIRS 143665]) are documented in *Precipitates/Salts Model Results for THC Abstraction* (CRWMS M&O 2001 [DIRS 153995]). The complete data set for the inputs, outputs, and lookup tables detailed in Section 6.3.3.5.1 can be found in Jolley (2001 [DIRS 154762]).

Uncertainties about mixing in the invert of seepage waters, concentrated brines, waters containing corrosion products, and waters containing waste degradation products were not explicitly quantified in the TSPA-SR (CRWMS M&O 2000 [DIRS 153246]). Instead, ranges of solution compositions were evaluated for properties such as solubility under an in-drift carbon dioxide gas fugacity for a given time period. There was also no explicit unified water chemistry that was internally consistent for all areas of the drift.

The microbial communities model is not intended to quantify localized microbial activity or its consequences, but bounds overall microbial growth and activity in the EBS. The *In-Drift Microbial Communities* report (CRWMS M&O 2000 [DIRS 151561]) provides bounding estimates of the numbers of microbes that could grow in the repository drift as a function of time. This time-dependent set of calculations includes the evaluation of several sets of uncertain parameters, such as the effects of drift temperature and relative humidity, changes in water chemistry and gas entering the drift, and variability in percolation flux through time. The calculations also incorporate the material masses and compositions used in the repository and waste package designs and variable corrosion rates for those materials. Uncertainties directly

associated with the TSPA-SR model (CRWMS M&O 2000 [DIRS 153246]) include: the composition (including the key microbial nutrients nitrate and phosphate) and rate of flux for gas and water entering the drift, the composition of EBS components and their degradation products, and the chemical interactions of EBS components with one another. The in-drift microbial communities model has been validated by testing against laboratory data, natural system observations, and other modeling efforts. Uncertainties in the models of evolution of the in-drift chemical environment were not explicitly quantified in the TSPA-SR model (CRWMS M&O 2000 [DIRS 153246]).

6.2.4 Environment on the Surfaces of the Drip Shield and Waste Package

Uncertainties in corrosion rates due to uncertainties in the chemical environment on the surfaces of the drip shield and waste package were quantified in the TSPA-SR model (CRWMS M&O 2000 [DIRS 153246]) by sampling over a wide range of corrosion rates. The range also encompasses the range of corrosion rates expected because of the predicted range of chemical conditions on the drip shield and waste package. However, explicit uncertainties in the chemical environment on the drip shield and waste package were not quantified in this section. These issues are discussed in Section 7.

6.2.5 Rockfall

The deterioration of the rock mass surrounding the potential repository emplacement drifts was predicted using a probabilistic key-block analysis. Key blocks are formed in the rock mass surrounding an excavation by the intersection of three or more planes of structural discontinuities. *Drift Degradation Analysis* (CRWMS M&O 2000 [DIRS 151635]) provides an assessment of the possible formation of key blocks within the potential repository horizon based on the orientations of discontinuities in the Exploratory Studies Facility (ESF) main loop and in the Enhanced Characterization of the Repository Block (ECRB) Cross Drift. Block failure due to seismic and thermal effects has also been analyzed.

Uncertainty in the rockfall model is affected by how well the data inputs describe actual fracture conditions. The natural variability of fractures within a rock mass always represents uncertainty in the design of structures in rock. The extensive fracture data collected at Yucca Mountain provide a good representation of fracturing at the emplacement drift horizon. Fracture data have been represented in the discrete region key block analysis model by simulating joint radii, spacings, and positioning with beta distributions based on field mapping data (CRWMS M&O 2000 [DIRS 151635], Section 6.3.2). Individual joints within each joint set are represented as circular discs in three-dimensional space with radii drawn from a distribution estimated on the assumption that the radius is equal to twice the mapped trace length (CRWMS M&O 2000 [DIRS 151635], Section 5.1). All joint spacing data have been corrected for "true" spacing (i.e., the spacing measured normal to the plane of the joint sets) (CRWMS M&O 2000 [DIRS 152286], Section 6.4.2.1). This correction for true spacing is referred to as a Terzaghi correction. The range of fracture variability from tunnel mapping has been captured in the rockfall model through multiple Monte Carlo simulations of the rock mass. To account for uncertainties associated with seismic, thermal, and time-dependent effects on rockfall, a conservative reduction of joint strength parameters has been included in the approach.

It was concluded in the TSPA-SR (CRWMS M&O 2000 [DIRS 153246], Section 3.3.1.4) that the effect of rockfall on thermal hydrology and other in-drift conditions is likely to be negligible because the calculated volume of fallen rock is small (about 0.1 percent) compared with the unoccupied drift volume of 16,650 m^3/km in the emplacement drifts (i.e., drift volume outside the drip shield and above the invert).

Uncertainties in the model for rockfall were not explicitly quantified for TSPA activities.

6.3 UNCERTAINTY ANALYSES AND NEW MODELS

6.3.1 Composition of Liquid and Gas Entering the Drifts

This section discusses results and uncertainties of THC simulations (THC seepage models) that have been performed to predict the chemical evolution of pore water and gases that could enter emplacement drifts. Most of these simulations, as well as the validation of modeled processes and evaluations of model uncertainty, are presented in detail in *Drift-Scale Coupled Processes (DST and THC Seepage) Models* (CRWMS M&O 2000 [DIRS 142022]; BSC 2001 [DIRS 154677]). Work presented in the initial issue of that report (CRWMS M&O 2000 [DIRS 142022], Section 6.3) is reviewed in Section 6.3.1.3. This earlier work evaluated model uncertainties with respect to infiltration rates and mineral reaction rates, but was otherwise of limited scope in terms of addressing other model uncertainties. A substantial amount of new work was presented in a revision of that report (BSC 2001 [DIRS 154677], Sections 6.4 through 6.6), which examined model sensitivity to various factors such as thermodynamic and kinetic input data, repository host rock unit, and drift design parameters, with the goal of assessing (at least qualitatively) some of the important model uncertainties. This work is discussed in Section 6.3.1.4. New simulations were performed to further evaluate the uncertainty of predicted water and gas compositions around drifts with respect to design heat load (temperature), boundary carbon dioxide concentrations, and initial water compositions (Bodvarsson 2001 [DIRS 154669], Attachment 5, pp. 10 to 59). Results of these new simulations are presented in Section 6.3.1.5.

Results of the initial THC seepage simulations (CRWMS M&O 2000 [DIRS 142022]) were abstracted for the TSPA-SR (CRWMS M&O 2000 [DIRS 153246]), but model uncertainties were not explicitly quantified. Abstraction of recent THC seepage simulations and other work is discussed in Section 6.3.1.6. A summary of remaining model uncertainties and implications on the predicted composition of fluids that could enter drifts is presented in Sections 6.3.1.8 and 6.3.1.9.

6.3.1.1 Introduction

The THC seepage models provide an analysis of the effects of THC processes in the near-field host rock around the potential emplacement drifts on the seepage water chemistry and gas-phase composition. This analysis includes a comprehensive description of the pertinent mineral-water-gas interaction processes in the host rock and their effect on the near-field environment. The THC seepage models take into account the effects of mineral dissolution and precipitation, the effects of carbon dioxide exsolution and transport in the region surrounding emplacement drifts, and the resulting changes to porosity, permeability, seepage, and chemical

composition of seeping waters. As such, these models are subject to the uncertainty of a large number of input parameters, as well as to the uncertainties in the methods implemented to simulate these complex coupled processes and assumptions regarding the physical setup of the model. Uncertainties in model input data that could affect calculated water and gas compositions include:

- Thermodynamic data (equilibrium constants for mineral-water reactions and aqueous species dissociation)
- Kinetic data (rate constants, reactive surface areas, and activation energies)
- Initial compositions of pore water and gas (carbon dioxide)
- Initial composition of infiltration water and gas (carbon dioxide)
- Infiltration rates
- Transport parameters (diffusion coefficients of aqueous species and gases, tortuosity)
- Initial rock mineralogy (model location and stratigraphy)
- Number of geochemical constituents included in simulations
- Number and types of potential secondary mineral phases
- Rock thermal, physical, and hydrologic properties (including input data for water-saturated and unsaturated rock).

Process model uncertainties may also affect calculated water and gas compositions. These include:

- Formulation of models to simulate fluid flow in dual-permeability media (e.g., fracture-matrix interactions, relative permeability and saturation-capillary pressure models)
- Activity coefficient models
- Kinetic mineral precipitation and dissolution models
- Inclusion or exclusion of certain specific THC processes (e.g., active fracture model, vapor pressure lowering, mineral solid solutions, and redox reactions).

Uncertainties in the setup of the model could also affect the results of THC seepage models. These include:

- Physical model representation (stratigraphic/geologic extrapolations)
- Representation of the fracture and matrix continua in the model mesh

- Model discretization (in space and time)
- Boundary conditions (e.g., drift open versus closed to fluid flow).

These uncertainties illustrate that, given the large number of input parameters and the complexity of the modeled THC processes, a rigorous quantification of model uncertainty is not achievable. For this reason, the THC modeling work has concentrated on limiting and qualitatively assessing uncertainty, rather than attempting statistical quantification.

Generally, reducing the uncertainty of THC seepage models was achieved by validating simulated THC processes against field and experimental data. TH process models have been extensively tested against field data and experiments conducted in the ESF, as well as in the laboratory, providing a basis to assess and reduce the uncertainty in TH process models and their input parameters (see Sections 3.3.5, 3.3.6, 4.3.6, 4.3.7, and 5.3.1). Simulated THC processes have been validated against water and gas compositions measured during thermal tests (i.e., the Drift Scale Test and Single Heater Test) and a plug flow reactor laboratory experiment. Uncertainty was also reduced by calibrating some of the model input data against observed hydrologic and geochemical data, as well as performing various sensitivity studies on the effect of fracture permeability heterogeneity, mineral reaction rates, host rock mineralogy, and the geochemical systems considered. The validation of THC simulations against experimental data is ongoing (e.g., Section 4.3.6.7), and the possibility of further validation of THC seepage models against natural analogues is being pursued.

From these efforts it would appear that uncertainties related to parameters directly affecting water-rock-gas chemical reactions, besides TH conditions (e.g., equilibrium constants, reaction rates, and input rock, water, and gas compositions) have a large effect on computed water and gas compositions. Therefore, limiting the uncertainty of these parameters is critical for increasing the confidence in THC seepage models. Uncertainties in reaction-related parameters are compounded by uncertainties in hydrologic parameters. It may not always be clear whether uncertainties in chemical reaction parameters have a greater effect on computed water and gas compositions than uncertainties in hydrologic parameters. However, in cases studied here, it would appear that small variations in fundamental thermodynamic properties of reacting minerals and aqueous species, for example, can cause large changes in effective reaction rates, which may affect computed water and gas compositions more significantly than hydrologic property changes of similar proportions.

Temperature is also a critical parameter, because it directly affects equilibrium constants and reaction rates, the degree of water evaporation and boiling, and the amount of carbon dioxide volatilization from pore water, with direct implications on computed water and gas chemistries. In this case, however, uncertainties in rock properties affecting computed temperatures (i.e., rock conductivity and heat capacity) are overshadowed by the direct effect of design heat load (e.g., high temperature versus low temperature). For this reason, the effect of design heat load is also evaluated by simulating two different predetermined design heat load covering a range largely encompassing potential uncertainties affecting the heat load values themselves. Thermal and hydrologic effects at the edge of the repository can also affect temperature significantly, and therefore affect computed gas and water compositions at these locations. These edge effects are evaluated with mountain-scale THC simulations presented in Section 3.3.6.

6.3.1.2 Goal of Model

The THC seepage models consist of two-dimensional, half-drift (symmetric) chimney models extending vertically from near the ground surface down to the water table and horizontally from drift center to the midpoint between drifts (Figure 6.3.1.2-1). The goal of these models is to analyze the effect of THC processes in the rock around emplacement drifts, including predicting the composition of waters and gases that could enter the drift (addressed in this section) and evaluating the effect of THC processes on seepage (addressed in Section 4.3.6).

Given the large number of input data and their uncertainties, the THC seepage models cannot be expected to predict exact water and gas compositions, especially over the long simulated time periods required to evaluate repository performance. The THC seepage models are still useful in evaluating general chemical trends around the drift with time (over a 100,000-year time period) and the variations of these trends with variations in model input data, drift design parameters, heat loads, locations, and boundary conditions.

The goal of the THC seepage models is not to simulate actual seepage into the drift. The range of simulated infiltration rates (which includes rates for future climate conditions of high infiltration, up to 47 mm/yr) remains well below the theoretical seepage threshold for the rock properties assumed around the drift (see Section 4.3.1). Therefore, the models are used to compute the compositions of pore water and gas in rock fractures around the drifts, and these fluids are assumed to be representative of fluids that could enter the drift. Pore water compositions in the rock matrix are also computed by the THC seepage models, but are not discussed here because the rock permeability is many orders of magnitude smaller in the matrix than in fractures, so any water entering drifts would enter from fractures instead of the rock matrix.

Finally, the THC seepage models did not consider advective fluid movement across the drift wall. Because the seepage threshold is never exceeded, this has no direct effect on the percolation of water towards the drift crown. The THC seepage models were not intended to model water-rock interactions in the drift, such as in the invert (or in the backfill material that was considered in earlier repository designs). Therefore, the effect of pore water potentially reacting with the invert is neglected. Another consequence of closing the drift wall to advective fluid flow is the exclusion, from modeled processes, of the effects of any imposed pressure and relative humidity boundary conditions within the drift. These conditions are likely to differ from conditions within the rock during preclosure ventilation, and could remain so for some time after closure. One of the main consequences is that the effect of water removal (evaporation) at the drift wall due to ventilation is not considered in the THC seepage model simulations. The effects of water imbibition in the invert and of seepage evaporation in the drift are, however, evaluated by the acid neutralizing capacity/pH mixing model and the precipitates and salts model discussed in Section 6.3.3.

6.3.1.3 Discussion of Results and Identification of Previously Unquantified Uncertainties

The initial work documented in *Drift-Scale Coupled Processes (DST and THC Seepage) Models* (CRWMS M&O 2000 [DIRS 142022], Section 6.3) included one THC seepage model with a

drift located in the Tptpmn. The simulated design included backfill, an initial mean linear heat load of 1.54 kW/m, and a 50-year preclosure period with 70 percent heat removal. This thermal load was predicted to yield temperatures above the boiling point of water (near 96ºC at Yucca Mountain) in the rocks in the vicinity of the emplacement drifts for hundreds of years. THC seepage simulations were also performed for an ambient temperature case (no heat load) to serve as a baseline for evaluations of model results under thermal loading conditions. Uncertainties in this THC seepage model were not explicitly quantified in the TSPA-SR (CRWMS M&O 2000 [DIRS 153246]).

The initial THC seepage model (CRWMS M&O 2000 [DIRS 142022]) is based on information obtained, in part, from thermal testing in the Tptpmn unit, which may exhibit somewhat different TH behavior or mineralogy than lower lithophysal units, in which most of the repository emplacement drifts will be located. Although this could change the system response, the bulk chemistry is similar for all welded host rock units.

Two geochemical systems were considered in this model. The first was, an extended case system that included aluminum silicates (e.g., clays, zeolites, feldspars, and sepiolite), silica phases (e.g., quartz, amorphous silica, tridymite, and glass), gypsum, calcite, fluorite, iron minerals (e.g., hematite and goethite), and a suite of aqueous species (including calcium, magnesium, sodium, potassium, silica, chloride, aqueous carbonate species, sulfate, fluoride, aluminum, and iron). The second was, a base case system was considered that excluded aluminum silicate minerals and iron minerals, thus excluding aqueous species such as aluminum, magnesium, potassium, and iron, which are found in these minerals.

The inclusion or exclusion of aluminum silicate minerals in the system provided a first crude approach to evaluate the model sensitivity to the effective reaction rates of these minerals: either reacting at rates determined from published kinetic and thermodynamic data and estimated reactive surface areas, or reacting so slowly that the reactions could be neglected.

The initial THC seepage model (CRWMS M&O 2000 [DIRS 142022]) predicted large variations in carbon dioxide concentrations and water compositions at ambient temperatures (no heat load) around the drift when using the extended case geochemical system, and much less with the base case system. Predicted ambient trends showed fairly large pH increases, calcium depletion, and sodium enrichment resulting from the dissolution of feldspars to form calcium zeolites (stellerite) and clays (illite and smectites). Fairly steady ambient water compositions could not be achieved unless aluminosilicate minerals were excluded from the modeled geochemical system. This was observed even though rate constants and effective mineral surface areas were already significantly reduced to yield low effective reaction rates accounting for processes such as mineral armoring. The apparently overestimated dissolution of feldspars to form clays and zeolites was in large part attributed to poorly constrained thermodynamic data for these minerals. A revision of these data (see Section 6.3.1.4) yielded much steadier concentration trends under ambient conditions. In this respect, the initial THC seepage simulations (CRWMS M&O 2000 [DIRS 142022]), as compared to revised THC model results (BSC 2001 [DIRS 154677]), are useful to illustrate the large effect that thermodynamic and kinetic data impose on computed water and gas compositions. For example, small changes in the Gibbs free energies of zeolites and clay minerals (on the order of 0.5 percent) affected predicted concentrations of carbon

dioxide gas and reactive aqueous species such as calcium, magnesium, and sodium by several orders of magnitude (see Section 6.3.1.4).

The initial THC seepage model (CRWMS M&O 2000 [DIRS 142022]) was also useful to evaluate the effect of infiltration on computed water and gas compositions around drifts because a wider range of infiltration rates was considered than in subsequent work (BSC 2001 [DIRS 154677]). Three infiltration rate scenarios were considered, each with varying infiltration over time to simulate future wetter conditions: a mean case (rates between 6 and 25 mm/yr), an upper-bound case (rates between 15 and 47 mm/yr), and a lower-bound case (rates between 0.6 and 6 mm/yr). A fixed ambient mean infiltration rate near 1 mm/yr was also considered for ambient THC simulations.

The different infiltration cases did not significantly affect predicted trends of temperature at the wall of the modeled drift, with no more than an approximately 15 percent temperature variation (under thermal load) between the lower-bound and upper-bound infiltration cases. A similar conclusion was reached for the *Multiscale Thermohydrologic Model* (CRWMS M&O 2000 [DIRS 149862], Sections 6.11.1.4, 6.11.2, 6.11.3.2, and 6.11.4.2), and the *Water Distribution and Removal Model* (CRWMS M&O 2001 [DIRS 152016], Sections 6.3.3.1 and 6.3.3.2).

During the cooling phase, significant fluid composition differences were predicted around the drift between the lower-bound and the mean infiltration cases (up to 1.5 pH units and nearly two orders of magnitude carbon dioxide concentration). Such large differences were not observed between the mean and upper-bound infiltration cases (mostly within half an order of magnitude). As previously, these simulations were affected by overly reactive aluminosilicate minerals, which likely exacerbated the predicted concentration differences between the lower-bound and mean infiltration cases. As infiltration rates increase, advective rates (i.e., seepage velocity) increase relative to reaction rates, such that calculated concentrations become more dependent on advective rates than on reaction rates (and less sensitive to the latter).

The probability of seepage into drifts increases with increasing infiltration rates. However, as infiltration rates increase, the effect of mineral reactions on water composition decreases (at least for minerals with slow reaction rates such as aluminosilicate minerals), and the assumed composition of infiltration waters and gases becomes important in determining the composition of fluids that may enter drifts. Therefore, in this respect, uncertainties on the assumed composition of infiltrating water should largely dominate the effect of uncertain infiltration rates. In addition, if uncertainties in reaction rates can be minimized through a justifiable calibration of thermodynamic and kinetic data to the initial (measured) water composition, as was done for the revised THC simulations (BSC 2001 [DIRS 154677]) (see Section 6.3.1.4), the assumed composition of initial pore water and infiltration water input into the model (and associated carbon dioxide partial pressures) become among the main model uncertainties regarding predicted water compositions.

To summarize, the initial THC seepage model (CRWMS M&O 2000 [DIRS 142022]) is useful to semiquantitatively evaluate the model sensitivity to the reaction rates of aluminum silicate minerals and to a range of infiltration rates including future climates wetter than the present day. However, under high infiltration rate conditions most favorable to in-drift seepage, uncertainties in these parameters are likely to be overshadowed by the assumed composition of fluids

infiltrating at the top model boundary. Therefore, while the initial THC simulations provide some quantitative assessment of uncertainties related to mineral reaction rates and infiltration rates, the effect of infiltration composition remains to be quantified. None of these uncertainties were included in the TSPA-SR (CRWMS M&O 2000 [DIRS 153246]).

6.3.1.4 Revised Model Developments and Results

Unquantified uncertainties identified since the TSPA-SR (CRWMS M&O 2000 [DIRS 153246]) include those related to the rates of fast-reacting minerals (such as calcite and amorphous silica), differences in repository host rock geologic units (effects of mineralogy and rock TH properties), drift design parameters, drift wall boundary conditions, and initial pore-water compositions. Several of these uncertainties were addressed in the revised THC drift-scale modeling studies (BSC 2001 [DIRS 154677]), while others required additional work (see Section 6.3.1.5). Similar uncertainties apply to alternative thermal operating modes. However, some of these uncertainties (e.g., reaction rates) affect predicted fluid compositions more strongly at high temperatures than at low temperatures. The effect of a lower thermal load on model uncertainty is evaluated in Section 6.3.1.5.

The revised *Drift-Scale Coupled Processes (DST and THC Seepage) Models* (BSC 2001 [DIRS 154677]) included a THC seepage model with a drift located in the Tptpll, consideration of heterogeneous permeability distributions, more extensive validation of modeled THC processes, and an evaluation of the model sensitivity to various input parameters. The seepage models were simulated with a higher-temperature operating mode, with a slightly lower (but otherwise similar) thermal load compared to the initial THC simulations (CRWMS M&O 2000 [DIRS 142022]), and with a more recent drift design that excluded backfill.

6.3.1.4.1 Thermal-Hydrologic-Chemical Seepage Model Developments

Three new THC seepage models were presented in the revised *Drift-Scale Coupled Processes (DST and THC Seepage) Models* (BSC 2001 [DIRS 154677]).

Tptpmn Thermal-Hydrologic-Chemical No-Backfill Model–This model considers a heat load in the Tptpmn (BSC 2001 [DIRS 154677], Section 6.4). This model is essentially the same as the THC seepage model presented in the initial THC simulations (CRWMS M&O 2000 [DIRS 142022]) (see Section 6.3.1.3), but with the following important differences:

- No backfill is in the drift
- Slightly lower heat load (1.45 kW/m)
- Revised drift thermal conductivities (invert, inner, and outer zones)
- Stronger coupling of permeability to porosity changes
- A revised activity-coefficient model for aqueous species, revised thermodynamic and kinetic data, and treatment of clay minerals (smectites) as an ideal solid solution phase rather than individual phases

- Calcite reacts at equilibrium with an allowed supersaturation gap that results in effectively larger reaction rates

- Increased effective fracture mineral reactive surface areas (over 50 percent higher)

- Increased initial precipitation rate of secondary minerals under kinetic constraints (by at least one order of magnitude)

- Increased carbon dioxide diffusion coefficient (by a factor of approximately 30).

Tptpmn Thermal-Hydrologic-Chemical Heterogeneous Model–This model is identical to the Tptpmn no-backfill model, except that it considers initial heterogeneous fracture permeability variations of about four orders of magnitude (BSC 2001 [DIRS 154677], Section 6.5). The purpose of this model is to address the effects of fracture permeability heterogeneity at the drift scale on water and gas chemistry, hydrologic properties, and the potential for enhanced or reduced seepage owing to THC processes (see Section 4.3.6).

Tptpll Thermal-Hydrologic-Chemical Model–This model considers a heat load in the Tptpll without backfill (BSC 2001 [DIRS 154677], Section 6.6). The main differences between the Tptpll THC model and the Tptpmn seepage models described above are:

- Different repository host rock unit

- Increased invert thickness (from 0.6 to 0.8 m)

- Updated hydrologic properties calculations, including fracture permeabilities for most units of the Topopah Spring tuff, capillary properties of the Tptpll, and fracture porosities of all units (except Tptpmn)

- Updated rock mineralogy, volume fractions, and mineral surface areas calculations for all units, with the addition of an opal phase in the geochemical systems considered.

For these new THC seepage models, sensitivity studies involving systematically changing input parameters over a wide range of values were not conducted. Variations in input parameters were mostly related to model improvements and changes in drift design parameters and drift location, but nonetheless allowed some qualitative or semiquantitative assessment of the model sensitivity to various input data and design parameters.

These new models considered only the mean infiltration scenario modeled in the initial THC simulations (CRWMS M&O 2000 [DIRS 142022]): initial 6 mm/yr, changing to 16 mm/yr at 600 years, then 25 mm/yr after 2,000 years. For each model, two geochemical systems were considered (as in the previous study): a base case without feldspars, clays, zeolites, or iron minerals and an extended case including these minerals. Some minor changes were also made to the type of minerals considered compared to the initial THC simulations.

Compared to the initial THC simulations, the revised THC seepage models (BSC 2001 [DIRS 154677]) produced a fairly steady hydrochemical system under ambient conditions (no thermal load), yielding water compositions close to the initial (observed) water composition.

This was achieved primarily by calibrating the equilibrium constants of smectites (clays) and zeolites to the initial (measured) pore-water composition. This exercise corresponded to a change of 0.5 percent or less of the Gibbs free energies of these minerals, which is largely within the original error margin of these values. These small changes significantly affected reaction trends and rates, such that the large fluctuations in calculated ambient water compositions in the initial THC simulations were not observed (Figures 6.3.1.4-1 and 6.3.1.4-2).

The steadiness of water and gas concentrations calculated under ambient conditions over long periods of time was improved by allowing calcite to remain supersaturated (by the same amount as in the initial water) before precipitating, and by significantly decreasing the surface area of anorthite (three orders of magnitude). The mineral sepiolite was removed from the modeled system to improve calculated ambient magnesium concentrations. In addition, the revised THC seepage models (BSC 2001 [DIRS 154677]) included a top boundary water with a lower pH (pH = 7.75 versus 8.32) and higher partial pressure of carbon dioxide (approximately 3,700 versus 900 ppmv) than was considered in the initial THC simulations, as this seemed to improve the results of simulations under ambient conditions.

Changes in the revised THC simulations (BSC 2001 [DIRS 154677]) in thermodynamic and other input data described above can be regarded as a model calibration against the initial (ambient) water composition. These changes were necessary and justifiable (i.e., the model should be able to reproduce observed ambient conditions before an attempt is made to simulate thermal loading), as well as defensible (i.e., changes were carried out within the range of the uncertainty of the affected data). As a result, the revised THC simulations can be viewed as better constrained than the initial THC simulations. Another effect of these changes was that in the revised THC simulations, fewer differences were observed between water compositions calculated using the base case and extended case geochemical systems than were observed in the initial THC simulations.

6.3.1.4.2 Sensitivity to General Model Improvements (Tptpmn Models)

Most differences in computed water and gas chemistries (at the drift wall) between the initial (CRWMS M&O 2000 [DIRS 142022]) and revised THC seepage models (BSC 2001 [DIRS 154677]) are not related to differences in drift design (backfill versus no backfill), differences in host rock unit (Tptpmn versus Tptpll), or improvements in implemented process models. These differences, with exceptions discussed below, are primarily attributed to the changes, previously mentioned, made to thermodynamic and other input data to better reproduce ambient water compositions.

The general predicted trends of carbon dioxide concentrations around the drift are similar to those predicted in the initial THC simulations (CRWMS M&O 2000 [DIRS 142022]), with a large decrease during dryout followed by a steep increase during the initial cooling and rewetting stage (Figure 6.3.1.4-1). Predicted concentrations during dryout are below ambient values and are generally smaller in the initial THC simulations than in the revised THC simulations (by up to three orders of magnitude when using the base case geochemical system, not shown here) because the carbon dioxide diffusion coefficient in the initial THC simulations is smaller (by a factor of 30) than in revised THC simulations (diffusive fluxes into the drift are most significant

during this time period). During other simulated time periods, the increased diffusion coefficient does not appear to have a significant effect.

Modeled concentration trends of aqueous species in the revised THC simulations (BSC 2001 [DIRS 154677]) are less variable than in the initial THC simulations, with concentrations returning to ambient values within the simulated time period (Figures 6.3.1.4-1 and 6.3.1.4-2). At the drift wall, predicted pH values range from pH = 7.1 to 8.6, and the total aqueous carbonate concentrations remain less than 250 mg/L over the 100,000-year simulated time interval (range defined by the revised THC simulations using the extended case and base case geochemical systems). With time, calcium and sodium concentrations do not show marked decreases and increases, respectively, as was predicted in the initial THC simulations. Chloride and fluoride concentrations show trends similar to those previously modeled in the initial THC simulations for similar infiltration rates.

The only significant qualitative differences between the water compositions predicted in the revised Tptpmn THC model (BSC 2001 [DIRS 154677]) and the initial model results are that the large variations in pH and the concentrations of carbon dioxide, aqueous carbonate, calcium, magnesium, and sodium during the cooling stage are no longer predicted. In this respect, the predicted water composition in fractures around the drift in the revised THC simulations fall within a narrower range than in the initial THC seepage model (CRWMS M&O 2000 [DIRS 142022]). This is largely the result of the better-constrained thermodynamic data for clays and zeolites, also with other changes noted earlier. Comparison between the initial and revised results provides some qualitative analysis of the model sensitivity to the choice of minerals included in simulations, their stability, and reaction rates. Because ambient simulations in the revised THC simulations predict water compositions more consistent with the initial (measured) water composition, it is expected that the overall uncertainty of the revised THC seepage models (BSC 2001 [DIRS 154677]) has been reduced (at least to a range within the uncertainty of input pore water and infiltration water compositions).

6.3.1.4.3 Sensitivity to Host Rock Unit (Tptpll versus Tptpmn)

Differences in mineralogy and mineral surface areas between the Tptpmn and Tptpll hydrogeologic units are small and, therefore, have only a small effect on modeled water compositions around drifts within the 100,000-year time period investigated. The same can be said for differences in hydrologic properties between both units. Under ambient and thermal loading conditions, overall concentration trends predicted for fractures (at the drift wall) for the considered chemical species differ little between the Tptpmn and the Tptpll models. During the cooling phase, the difference in predicted concentrations around the modeled drift between both models remains mostly within 50 percent, except for fluoride, as discussed below.

Predicted fluoride concentrations in the Tptpll model under ambient and thermal loading conditions are higher (by up to an order of magnitude) than in the Tptpmn model because of CaF_2 dissolution (Figure 6.3.1.4-3). This mineral is observed in fractures and lithophysae of the TSw geologic units (Carlos et al. 1995 [DIRS 101326], Appendix I) and was included as a fracture mineral in the Tptpll model (TSw geologic units). However, it was not included as a primary mineral in the Tptpmn model (secondary mineral only). In the Tptpll model, predicted ambient fluoride concentrations tend toward equilibrium with fluorite (5 to 6 mg/L for the

modeled ambient geochemical conditions) because the reaction rate of this mineral is fast. However, less than 1 mg/L is reported in the initial pore water. Predicted fluoride concentrations are therefore sensitive to the presence of fluorite in the modeled rock units. Including this as a primary mineral is likely to provide an upper bound for predicted fluoride concentrations.

6.3.1.4.4 Sensitivity to Heterogeneous Permeability Distribution

Comparisons of predicted water chemistry data around the modeled drift between initially homogenous and heterogeneous models show little difference (Figures 4.3.6-6 and 4.3.6-7 in Section 4.3.6.4.3). Spatial differences in water chemistry are not affected significantly by permeability heterogeneities for these simulations, so it is expected that heterogeneities in fracture permeability (within the range observed in the Tptpmn unit) would not significantly affect the overall composition of fluids that could enter the drifts.

6.3.1.4.5 Increasing Confidence through Additional Model Validation and Sensitivity Studies

In addition to the new THC seepage models, the revised *Drift-Scale Coupled Processes (DST and THC Seepage) Models* (BSC 2001 [DIRS 154677]) presents a systematic evaluation of mineral reaction rate uncertainty using data collected during the Drift Scale Test. Although these sensitivity analyses cover a relatively short time (two to three years) compared to the simulated length of the THC seepage models (100,000 years), these relate to the same process models as those implemented in the THC seepage models. These analyses also use the same revised thermodynamic data for clays and zeolites and assumed calcite supersaturation gap as in the THC seepage models (BSC 2001 [DIRS 154677]), and, therefore, relate directly to the validity and uncertainty of these models.

These analyses were conducted by comparing the compositions of waters and gases collected during the Drift Scale Test with compositions predicted using THC simulations of this thermal test and assuming various reaction rates and sets of reacting minerals. The simulations conditions included a base case geochemical system without aluminum silicate minerals (see Section 6.3.1.3) or an extended case system that includes these minerals, included calcite reacting at equilibrium or under kinetic constraints (with a supersaturation gap), and included anorthite reacting with surface areas differing by three orders of magnitude.

Results are shown in Figures 4.3.6-2 and 4.3.6-3, with further details presented in Section 4.3.6.4.1, as well as in *Drift-Scale Coupled Processes (DST and THC Seepage) Models* (BSC 2001 [DIRS 154677], Section 6.2.8). These figures do not show large differences in predicted concentrations for the various cases investigated, and have generally similar predicted concentration trends and concentrations mostly remaining within the same order of magnitude as measured values.

The initial analyses also included THC simulations of a plug-flow reactor tuff dissolution experiment (BSC 2001 [DIRS 154677], Section 6.7). These simulations are discussed in Section 4.3.6.7. In general, using the same thermodynamic and kinetic data, as well as the same rock mineralogy and geochemical components as those used in the THC seepage models (BSC 2001 [DIRS 154677]), these simulations yield relatively good agreement between

measured and predicted water compositions. While these THC simulations were useful to demonstrate the validity of modeled processes, the length of the modeled experiment (two months) is likely too short to fully assess the uncertainty of the THC seepage model over thousands of years. Nevertheless, this work improved the confidence in the THC seepage models (BSC 2001 [DIRS 154677]) and their input thermodynamic and kinetic data.

6.3.1.5 Recent Work

Additional THC simulations were conducted to further evaluate the uncertainties associated with the THC seepage models (Bodvarsson 2001 [DIRS 154669], Attachment 5, pp. 10 to 59). The conditions for these simulations are summarized in Table 6.3.1.5-1. The goal of these simulations was to evaluate previously unquantified uncertainties that may significantly affect the predicted compositions of fluids that could enter drifts. From the list of potential uncertainties discussed in Section 6.3.1.1 and the uncertainty analyses presented in Sections 6.3.1.3 and 6.3.1.4, three uncertainties were selected for further analysis: the effects of operating temperature, the effects of different carbon dioxide partial pressures at the top model boundary, and the effects of different initial pore water (and infiltration) compositions.

For these analyses, a set of consistent (thus directly comparable) THC seepage model simulations were developed, with each model using identical model grid and setup parameters, including identical pressure and temperature boundaries, identical rock thermal and hydrologic properties, and identical drift design (no backfill). These simulations also made use of identical input thermodynamic and kinetic data, initial rock compositions, mineral surface areas, and geochemical systems. These simulations were performed using the updated Tptpll THC seepage model (BSC 2001 [DIRS 154677], Section 6.6). Slight changes were made in the drift configuration, thermal properties of in-drift systems, and thermal properties of the Tptpll unit to reflect more recent revisions. Also, smaller time steps were used for the first simulated 2,000 years. Two heat loads were considered.

The first case used an initial heat load of 1.45 kW/m and a 50-year forced ventilation period, during which 70 percent of the heat is assumed to be removed. These are the same conditions as in the revised THC models (BSC 2001 [DIRS 154677]), giving rise to above-boiling temperatures in rocks around the drift for hundreds of years (referred to the higher-temperature case). The second case used, an initial heat load of 1.13 kW/m and a 300-year forced ventilation period, during which 80 percent of the heat is assumed to be removed. These conditions give rise to temperatures staying below boiling in rocks around the drift, with temperatures at the surface of the waste package remaining below 85ºC (referred to as the lower-temperature case).

The results of the higher-temperature case are similar to those documented in the Tptpll THC seepage model (BSC 2001 [DIRS 154677]; (see also Section 6.3.1.4). This is because of the small differences between the simulation conditions. The update of the Tptpll thermal properties from values used in BSC (2001 [DIRS 154677]) caused less than a 10 percent change in calculated drift wall temperatures. Predicted carbon dioxide and aqueous concentrations at the drift crown, after rewetting, mostly remained within 10 percent as well (DTN: LB0011DSTTHCR1.001 [DIRS 154759], Table 6.3.1.5-1).

For both operating temperature modes, two conditions of carbon dioxide partial pressures at the top model boundary were considered:

- A partial pressure of $10^{-2.5}$ bars (approximately 3,700 ppmv at the top boundary atmospheric pressure). This is the same partial pressure as in the THC seepage models (BSC 2001 [DIRS 154677]) (referred to as the high-CO_2 case)

- A partial pressure corresponding to the saturation pressure of carbon dioxide in the initial pore water (at an approximate boundary temperature of 17ºC). This pressure is calculated to be $10^{-3.2}$ bars (near 750 ppmv at the top boundary atmospheric pressure) (referred to as the low-CO_2 case).

For all of these simulations, as in the initial THC simulations (BSC 2001 [DIRS 154677]), the carbon dioxide partial pressure in the drift was assumed to be unaffected by ventilation and dictated primarily by the pore water composition at the drift wall. Preliminary simulations for another lower-temperature, high-CO_2 case, using input data similar to (but revised since) those described above, also investigated the effect of fixing the carbon dioxide partial pressure at atmospheric pressure (near 400 ppmv) in the drift during 300 years of ventilation (DTN: LB0102DSTHLTD.001 [DIRS 154868]). The effect on water composition (pH) at the drift wall was small (less than 0.5 pH units) and short-lived, with little effect after 300 years and essentially no effect after 1,000 years. For this reason, this case was not pursued further.

There is a large degree of uncertainty regarding the pore water composition in the potential repository host units. No full characterization of pore waters from the Tptpll is available. At the time of the start of the initial work (BSC 2001 [DIRS 154677]), the only nearly complete pore water analyses for samples collected from a rock unit near the potential repository footprint were analyses of three samples ultra centrifuged from core obtained from the Tptpmn geologic unit in Alcove 5 near the Drift Scale Test. These analyses are shown in Table 6.3.1.5-2 (samples labeled HD-PERM-1, HD-PERM-2, HD-PERM-3), together with other water compositions discussed later. An average of the two Alcove 5 water analyses with the closest pH and concentrations (HD-PERM2 and HD-PERM3) was used as the initial pore water composition in the initial and revised THC seepage models, as described in *Drift-Scale Coupled Processes (DST and THC Seepage) Models* (BSC 2001 [DIRS 154677], Section 4.1). This water composition, computationally re-equilibrated at the temperature and carbon dioxide concentration at the top model boundary, was also used for infiltration water in the previous models. To evaluate the model sensitivity to the use of other initial waters, additional simulations were conducted using different water compositions (i.e., UZ-14 perched water and infiltration water).

UZ-14 perched water was used as the initial pore water (Table 6.3.1.5-2). This water is calculated to be at saturation with calcite at 25ºC, charge balanced, and is not subject to the uncertainties regarding extraction procedures of pore waters from welded tuffs. The pH of this water is lower (pH = 7.8) than that of the Alcoves Tptpmn pore water (pH = 8.3), and its calculated carbon dioxide partial pressure at 25ºC (corresponding to approximately 2,500 ppmv at the drift atmospheric pressure) is greater than in the water used previously (near 1,000 ppmv at the drift atmospheric pressure). This water is representative of sodium-bicarbonate waters (such as groundwater from Well J-13) that yield an alkaline brine upon evaporative concentration.

Infiltration water consisted of the same UZ-14 perched water as described above, but re-equilibrated with calcite at the approximate boundary temperature of 17ºC and the same carbon dioxide partial pressure as in the high-CO_2 case ($10^{-2.5}$ bars, for consistency of all high-CO_2 cases).

The higher- and lower-temperature cases were investigated using the UZ-14 perched-water composition. It is emphasized, however, that this water exhibits a carbon dioxide partial pressure that is not consistent with measurements in the ESF and borehole UZ-1, as discussed below. Therefore, the use of UZ-14 water as initial pore water in the THC seepage models should only be viewed as a sensitivity exercise. For this reason, as well as time constraints, analyses using the UZ-14 water were not abstracted for TSPA (see Section 6.3.1.6).

6.3.1.5.1 Higher-Temperature and Lower-Temperature Operating Mode Comparison (Alcove 5 Pore Water)

This section discusses differences between the two operating temperature modes, as simulated with the THC seepage models (BSC 2001 [DIRS 154677]), with respect to predicted water and gas compositions around drifts. Differences in TH behavior between the two operating temperature modes are also discussed in Sections 4.3.5, 5.4.1 and 5.4.2 for TH simulations considering input TH parameters and heat loads similar to those used in the THC seepage models.

The higher-temperature case causes temperatures above boiling in rocks around the drift. The drift wall is predicted to dry out for approximately 1,600 years, after which time the drift crown starts to rewet. The extent of predicted rock dryout around the drift varies depending on the infiltration rate and host rock thermal properties. The THC seepage models predict dryout from approximately 6 to 12 feet at the crown in fractures. However, these models may predict a larger dryout zone than other TH simulations (e.g., Sections 4.3.5, 5.4.1, 5.4.2) because lowering of the water vapor pressure, which is caused by the capillary pressure in the rock matrix, is not considered in THC simulations. This may affect the predicted composition of water around the drift. Neglecting vapor pressure lowering could result in overestimating concentrations of aqueous species, as a result of overestimated evaporative concentration. In this respect, the higher-temperature case may be viewed as providing an upper bound on the effect of evaporative concentration. In contrast, in the lower-temperature case, rocks around the drift are not predicted to dry out, significantly reducing the effect of evaporative concentration at the drift wall. This is one of the two main differences between the two operating temperature modes being investigated.

The second important difference between the higher- and lower-temperature cases, with respect to the composition of fluids that may enter drifts, results from the large temperature effect on mineral reaction rates and stability. Temperature also increases the partial pressure of gases (e.g., carbon dioxide) dissolved in the pore water. Most rock-forming minerals are less stable and dissolve faster at high temperatures. One exception is calcite, which has a decreasing solubility with increasing temperature.

Figures 6.3.1.5-1 through 6.3.1.5-3 compare predicted concentrations of carbon dioxide and aqueous species in fractures at the drift crown for the higher-temperature, lower-temperature, and

ambient (no heat load) cases, using Alcove 5 pore water as the initial and infiltrating water composition. In the higher-temperature case, the drift wall is dry from approximately 50 to 1,600 years, so no aqueous species concentrations are shown.

For the cases considered here, the most visible effect of increasing temperature on water chemistry is the volatilization of carbon dioxide from the pore water (there are a large number of naturally dissolved carbonate species in the pore water). This is a common phenomenon observed in many geothermal areas around the world. In the TSw geologic units, the porosity and liquid saturation are significantly larger in the rock matrix than in fractures (DTN: LB990861233129.001 [DIRS 110226]; DTN: GS980808312242.014 [DIRS 106748]). Therefore, the bulk of the water (moisture) present in the rock is contained in the matrix, not in fractures. When heated, carbon dioxide exsolved from matrix water is transported into fractures. This can cause the carbon dioxide partial pressure to rise above ambient values in fractures, and also cause a pH decrease in fracture water when steam condenses. However, during the dryout period in the higher-temperature case, carbon dioxide concentrations at the drift wall fall largely below ambient values (i.e., decrease up to four order of magnitude) as the result of boiling and displacement by steam. During early rewetting of fractures at the drift crown, the carbon dioxide partial pressure in the higher-temperature case is still depressed relative to the lower-temperature case, causing predicted pH values approximately 0.4 units higher than in the lower-temperature case. The volatilization of carbon dioxide causes total aqueous carbonate concentrations at the drift wall to decrease below ambient values in fractures (by a factor of approximately two in the lower-temperature case and approximately four in the higher-temperature case).

For most major cations and anions, except aqueous carbonate species, initial concentrations predicted in fractures at the drift crown at the time of rewetting (near 1,600 years) in the higher-temperature case are considerably larger (one or more orders of magnitude) than concentrations predicted in the lower-temperature case. This is primarily because of the larger evaporative concentration. Accordingly, the higher concentrations correspond to significantly smaller water saturation in fractures, which results in lower percolation fluxes. In this case, the predicted water saturation in fractures at the time of rewetting is too small for any significant water movement to occur. These effects of evaporative concentration, together with the depletion of aqueous carbonate species (Figures 6.3.1.5-1 to 6.3.1.5-3), appear to be more significant than the effect of mineral reactions (at least with respect to the composition of fluids at the drift wall), as very little mineral precipitation or dissolution is predicted to occur (see Section 4.3.6.4).

The general character of predicted water chemistry at the drift crown is examined later in terms of temperature and initial water composition. Predicted water compositions are more affected at high than at low temperatures, although in both cases water and gas compositions return to ambient values along with temperatures. This would indicate no long-lasting (greater than 100,000 years) effects from the thermal perturbations on predicted fluid compositions around the drift. In other words, the long-term composition of fluids around the drift seems to be largely dominated by the composition of infiltrating water (assumed, in the present case, to be similar to the initial pore water), regardless of the thermal operating mode of the repository.

6.3.1.5.2 High-CO_2 Compared with Low-CO_2 (Alcove 5 Pore Water)

The effect of the different carbon dioxide partial pressures at the top model boundary (reflected by the composition of infiltration water) is not seen until approximately 800 to 1,000 years. During this initial period of time, predicted fluid compositions at the drift wall are similar for the high-CO_2 and low-CO_2 cases in both operating modes. After that time, the effect is limited, resulting in an increased pH (by 0.2 to 0.4 units) for the low-CO_2 case compared to the high-CO_2 case in both operating modes and under ambient conditions (Figures 6.3.1.5-4 and 6.3.1.5-5). The carbon dioxide partial pressure differences affect predicted concentrations of reactive aqueous species to a negligible extent, with concentration reductions (at the drift wall) in the 10 percent range for calcium, sodium, and silica, and concentration increases of similar proportions for fluoride. For the water compositions used, the THC seepage model results were therefore not very sensitive to the range of investigated carbon dioxide partial pressures.

6.3.1.5.3 Uncertainty in Initial and Infiltration Water Compositions

The water analyses used to determine initial pore water and infiltration compositions in the THC seepage models were from the Tptpmn unit in Alcove 5 (HD-PERM samples in Table 6.3.1.5-2). As mentioned earlier, these were the only available nearly full suites of analyses from a repository host unit. The scarcity of such data is due to the fact that these units contain little water and the rock matrix has a low permeability, such that water extraction from the rock samples is difficult. Analyses are uncertain because the volumes of extracted samples are small and the impact of the extraction process (ultracentrifuge) on the water quality is largely unknown. For these reasons, these analyses were compared to water compositions of a few other samples (Table 6.3.1.5-2). These additional samples were selected because they could be good candidates for input into the THC seepage models. The source of each analysis in Table 6.3.1.5-2 is described below. Some of these analyses were incomplete and/or out of charge balance, and it was necessary to recalculate some of the analytical parameters.

Analyses labeled HD-PERM-1, HD-PERM-2, HD-PERM-3 are for three water samples ultracentrifuged from core obtained from the Tptpmn geologic unit in Alcove 5 (Table 6.3.1.5-2). Bicarbonate was not determined and it was recalculated from charge balance. The average of HD-PERM-2 and HD-PERM-3 (nearly identical analyses) was used as the initial pore water composition in the THC seepage models, as well as in the other THC seepage simulations discussed so far.

Sample DXD042 (Table 6.3.1.5-2) was ultracentrifuged from a core sample collected in the ECRB Cross Drift (CS2150), in the Tptpll unit. The pH and total aqueous carbonate content of this sample were not available, and were computed assuming calcite saturation. The resulting calculated carbon dioxide partial pressure of this sample was atmospheric (at 25ºC). The sample was therefore re-equilibrated with calcite at a carbon dioxide value (10^{-3} bars) consistent with measured values in the ESF. Another sample ultracentrifuged from core collected in Niche 2 in the Tptpmn unit approximately one kilometer away revealed an essentially identical composition. The potassium concentration was below the detection limit. A potassium concentration was calculated from the illite-microcline equilibrium boundary for this water.

The analysis labeled SD-6 (Table 6.3.1.5-2) is for water extracted from core collected in borehole SD-6, interval 443.5 to 443.8 ft, in the upper part of the PTn hydrogeologic unit above the potential repository. This borehole is located (in plan view) near the center of the potential repository footprint. The original water analysis was not in charge balance. The bicarbonate concentration was adjusted for charge balance and at the same time, the pH was recalculated assuming calcite saturation (at 25°C).

The TSw-Avg composition (Table 6.3.1.5-2) was used in some of the early THC modeling work related to the thermal tests at Yucca Mountain (Tsang et al. 1999 [DIRS 148905]). This composition was determined by averaging the analyses of waters extracted from core samples taken directly above and below the potential repository units (in drill holes UZ-16, SD-9, and SD-12) and reported in Yang et al. (1996 [DIRS 100194]), and by balancing charge on bicarbonate. The potassium concentration was an assumed value at the time.

The analysis labeled UZ-14-Pore (Table 6.3.1.5-2) is for water extracted from core collected in borehole UZ-14 at interval 1258.5 to 1258.8 (ft), at the same depth where perched water was collected. The pH of the sample was not reported. It was computed assuming calcite saturation (at 25ºC) and adjusting charge balance on bicarbonate. The potassium concentration was not determined, and the value shown was calculated from the illite-microcline equilibrium boundary for this water.

The analysis labeled UZ-14-Perch (Table 6.3.1.5-2) is for perched water collected from borehole UZ-14 in 1993. This analysis is charge balanced and yields almost exact calcite saturation (at 25°C). It has not been corrected.

The mean J-13 analysis (Table 6.3.1.5-2) is for groundwater samples collected in well J-13. Bicarbonate was adjusted for charge balance (from input alkalinity). The water from J-13 has been extensively studied and serves as a benchmark for many studies involving Yucca Mountain waters. This water also has been used extensively as a proxy for the pore water in the host rock when modeling chemical processes in the near-field environment.

These water compositions (using corrected concentrations) were plotted on a Piper diagram to evaluate the character and variability of these data (Figure 6.3.1.5-6). These compositions show significant scatter, with Alcove 5 samples at the calcium-sulfate-chloride end of the composition range and the J-13 sample at the sodium-bicarbonate end. These analyses are useful in illustrating the range of uncertainty regarding initial pore water and infiltration water compositions input into the THC seepage models. As noted earlier, the composition of infiltrating water is anticipated to dictate the long-term compositions of waters that could enter drifts.

One piece of available information that can be used to narrow the range of potential pore water compositions in the TSw units is the carbon dioxide concentrations measured in pore gas samples collected in the potential repository host rock. The gas analyses are not subject to the uncertainties regarding sample volume and extraction that affect pore water samples. Ambient carbon dioxide concentrations were measured in pore gas samples from potential repository units in drill hole UZ-1 over a 3-year period (DTN: GS930408312271.014 [DIRS 145533]) and in boreholes drilled in the ESF (DTN: LB991215123142.001 [DIRS 128157]). These

concentrations range from approximately atmospheric (400 ppmv) to 1,300 ppmv. These values are significantly lower than concentrations calculated for the UZ-14, SD-6, and J-13 water samples (between approximately 2,700 and 5,800 ppmv). Because of their comparatively elevated carbon dioxide partial pressures, the UZ-14, SD-6, and J-13 samples are uncertain representatives of pore waters from potential repository units, even though analyses of two of these samples are the most reliable because the samples did not need extraction.

Results of THC seepage simulations with UZ-14 perched water were plotted on Piper diagrams with results of the same simulations conducted with Alcove-5 water. These plots can be directly compared to the Piper plot of potential initial water compositions (Figure 6.3.1.5-6). The predicted evolution of the Alcove 5 and UZ-14 waters is shown for fractures at the drift crown: under ambient conditions (Figure 6.3.1.5-7), for the lower-temperature case (Figure 6.3.1.5-8), and for the higher-temperature case (Figure 6.3.1.5-9). Points are shown for given times and corresponding temperatures, and cover the 100,000-year simulated time period.

When heated, both waters generally exhibit a similar behavior, with a larger response (scatter) in the higher-temperature case than in the lower-temperature case, as would be expected. The effect of carbon dioxide volatilization due to the temperature increase, discussed earlier, is clearly shown by the progressive decarbonation of the waters as they undergo heating (lower right triangle on these plots), then return to ambient values as the temperature decreases. Under ambient conditions, both water compositions are predicted to evolve with time from a somewhat more calcium-dominant nature to a somewhat more sodium-dominant character. This trend is typically observed in natural systems over long periods of time. For the simulated UZ-14 water, this trend under ambient conditions is predicted to yield a composition of the same nature as J-13 water. After the thermal perturbation, the composition of both waters returns to ambient values within the simulated time period. Except for the large depletion of aqueous carbonates during the heating period, the scatter in predicted compositions for the two waters falls largely within the variability of potential initial water compositions (Figure 6.3.1.5-6).

The initial pH of the UZ-14 perched water is lower by approximately 0.5 units than the average (HD-PERM-2 and HD-PERM-3) Alcove 5 pore water used in previous simulations (Table 6.3.1.5-2). Under ambient conditions, the pH of UZ-14 perched water in fractures is predicted to increase, from an initial value of 7.8 to approximately 8.1 after 100,000 years. A smaller increase, from 8.3 to 8.4, is predicted with Alcove 5 fracture pore water for the same time period. Upon heating, at the crown of the drift, the pH in the UZ-14 case remains within the range defined by ambient conditions. However, at the base of the drift where evaporation is strongest, pH increases to a maximum near 9.4 for the higher-temperature case and 8.6 for the lower-temperature case. This is not observed with simulations using the Alcove 5 pore water, which predict pH to remain below the range of ambient pH values as long as temperatures exceed ambient values (Figure 6.3.1.5-5). This difference in pH trends is consistent with experimental data (Rosenberg et al. 2001 [DIRS 154862]).

6.3.1.6 Abstraction for Total System Performance Assessment

The abstraction of the above THC calculations follow arguments similar to those as reported in the *Abstraction of Drift-Scale Coupled Processes* (CRWMS M&O 2000 [DIRS 123916]). However, the abstraction includes more variability and an expanded set of time periods, uses

only the results from the extended case models, and includes an ambient period that uses the results from the extended mineral case ambient modeling runs. The decision to base the abstraction solely on the extended mineral case results was made to ensure conservation of charge balance and to ensure consistency between THC model results and abstraction results. The abstracted results presented below carry with them the assumptions, caveats, and limitations of the THC model calculations presented in the preceding sections.

6.3.1.6.1 Use of Abstraction

This abstraction is intended to simplify the THC results presented in Section 6.3.1.5 so that other modeling efforts, such as those found in Section 6.3.3 below and previously documented in the *In-Drift Precipitates/Salts Analysis* model (CRWMS M&O 2001 [DIRS 153265]), can produce a set of appropriate in-drift chemistry lookup tables for TSPA model calculations. The simplifications include a number of time histories of aqueous species (e.g., anion and cation concentrations) that are at or near charge balance and gas phase components (e.g., partial pressure of carbon dioxide, PCO_2) at a representative location in the near-field host rock adjacent to the emplacement drift wall. The abstraction will also produce lookup tables that set the initial results for other abstracted geochemical processes occurring within the repository drift (e.g., in drift gas values will be used to indicate which PCO_2 value to use for the waste form solubility abstractions).

There are three primary uses of the abstraction tables presented below (see Sections 6.3.1.6.3.1 and 6.3.1.6.3.2). First, the abstraction tables are used as input for initial water and gas chemistries, as used in the *In-Drift Precipitates/Salts Analysis* (CRWMS M&O 2001 [DIRS 153265]), to determine the compositions of the brine and precipitates that react with the surfaces of the drip shield, waste package, and invert (see Section 6.3.3). Second, the tables are used to set the PCO_2 in the drift for the given time period. This parameter is used as a governing parameter on several lookup tables that determine the pH and compositional information of fluids interacting with waste package materials and mixing of fluids in the invert (see Section 6.3.3). The PCO_2 values also determine one of the parameters necessary for selecting the solubility of the various radionuclides from their respective functions or lookup tables (see Section 6.4.1). Third, the tables are used as a source of variability and uncertainty in the chemical regime that is imposed on the in-drift environment. The chemistries reported in the tables below represent waters that have interacted with the Tptpll in the following ways: different spatial locations around the drift wall (crown and base of invert); different imposed PCO_2 starting conditions in the soil horizon (high PCO_2 and low PCO_2); different thermal operating modes (higher-temperature versus lower-temperature); and differences between waters primarily derived from fracture seepage (fracture water at crown of drift) and invert imbibition (matrix water at base of invert). These different conditions represent much of the uncertainty and/or variability that is presently incorporated into the chemical system being modeled above.

One specific uncertainty that has been evaluated in the THC calculations in Section 6.3.1.5, but for which results were not abstracted for incorporation into downstream calculations, is the use of a different starting water chemistry (perched water sampled in well UZ-14).

6.3.1.6.2 Conceptual Approach for Abstraction

Two specific criteria are inherent in this abstraction. The first is the need to simplify the THC results reported above for use in the TSPA model. The second is the need to generally reproduce the obvious changes in gas and ion concentrations entering the drift that occur through time as they have potential to influence performance of EBS materials, chemical conditions, and radionuclide transport characteristics.

Two sets of tables have been prepared for use in EBS calculations. The first represent the chemical composition of the seepage flux through the crown of the drift (see Section 6.3.1.6.3.1). The assumption applied to these tables is that any seepage coming into the drift from above would be water that would flow through fractures into the drift. This is a reasonable assumption based on *Abstraction of Drift-Scale Coupled Processes* (CRWMS M&O 2000 [DIRS 123916], Section 5.1.1). The results from *Thermal Hydrology EBS Design Sensitivity Analysis* (BSC 2001 [DIRS 154855]; DTN: MO0008SPATHS03.001 [DIRS 151812]) indicate that seepage into the invert is controlled by matrix flow over the regulatory period and that fracture flow into the invert dominates after the repository cools. As the abstracted water chemistries do not drastically differ between fractures and the matrix, it is assumed that the tables representing the waters being imbibed or wicked into the invert will be those associated with water found in the matrix at the base of the invert (see Section 6.3.1.6.3.2). This is a reasonable assumption based on the principles of matrix imbibition in unsaturated porous media (Jury et al. 1991 [DIRS 102010], pp. 87 to 110) and the similarities in water chemistries.

A discussion in *Abstraction of Drift-Scale Coupled Processes* (CRWMS M&O 2000 [DIRS 123916], pp. 18 to 19) explains the general difficulty of applying a specific statistical methodology to the abstraction. Therefore, the following approach was used to determine the number and duration of the periods. The same reason leads to the approach devised in selecting a specific THC result for that given period, as discussed below.

The establishment of the abstraction periods was based on determining a few appropriate inflection points, then using those points to visually inspect the given THC calculation files produced, as discussed in Section 6.3.1.5 (Table 6.3.1.5-1). After initial inspection of the results, several inflection points were selected: length of the preclosure period (50 or 300 years), length of the boiling period (for higher-temperature cases only), obvious pH changes (about 0.2 units) with a secondary discriminator of noticeable change (generally an order of magnitude) in PCO_2 concentrations, and the reimposition of ambient conditions (post-100,000 year results). These criteria were sufficient to limit the number of abstraction periods to six for the high-temperature abstraction and five for the lower-temperature abstraction (Table 6.3.1.6-1). The six time periods for the higher-temperature abstraction are a preclosure period from 0 to 50 years, a boiling period from 51 to 1500 years, a cooldown period from 1,501 to 4,000 years, an extended cooldown period ranging between 4,001 and 25,000 years, a transition to ambient period from 25,001 to 100,000 years, and an ambient period that goes from 100,001 to 1 million years. The five periods for the lower-temperature abstraction are a preclosure period from 0 to 300 years, a postclosure hot period from 301 to 10,000 years, a cooldown period ranging between 10,001 and 30,000 years, a transition to ambient period between 30,001 and 100,000 years, and an ambient period that goes from 100,001 to 1 million years.

The specific ion concentration, pH, and PCO_2 were determined in a somewhat different way or the ambient period (post-100,000 year) than the other periods discussed below. To determine the ambient period chemistry, the associated ambient temperature case THC calculation (e.g., Run ID thc6_ambL; Table 6.3.1.5-1) was abstracted by taking the results from year 2,000 to year 100,000 and averaging them. The basis for this is two-fold: first, the pH, PCO_2, and ion concentrations do not differ significantly over this period. Second, the infiltration rate is assumed to change at year 2,000 to a rate associated with that of a glacial climate and would be more representative of the boundary conditions for the post-100,000 year period.

For all other periods, the methodology for selecting the specific THC run time is as follows. The time-dependent sets of results (pH, PCO_2, and the reported ions) for the given period abstraction are averaged. The averaged values for pH, PCO_2, and the ions are compared to each individual time-dependent result value. The value nearest to the average is flagged (i.e., all pH values in each of the reported times are looked at and the pH value nearest the average is marked). After all the ions, the pH, and the PCO_2 are sequentially evaluated and flagged, the individual time-dependent chemistry that was most representative of the averaged values for pH, PCO_2, and the reported ions was selected for use during the abstracted period. If there was a tie (e.g., four flags each for time x and time y), the complete chemistries of those that tied were reevaluated for the next closest set of values nearest the average until a determination could be made.

This selection approach has the effect of maintaining consistency with the THC results, since the abstracted chemistry is actually a specific time-dependent result from the THC model and the abstracted chemistry is as close to an averaged chemistry over that period as can be obtained without actually using the averages for the period. This approach also maintains charge balance (sum of cations vs. sum of anions), an important factor in minimizing the potential error to some ions of importance (speciation calculations are often charge balanced by adjusting ions such as Na^+ or Cl^-), as discussed in Section 6.3.3 below, where adding Na^+ or Cl^- could change the ultimate compositional character of the brines interacting on the waste package. This abstraction can also be directly validated, since the values used are actual results from the THC model.

For the boiling period, a decision was made to use the results from the THC calculations for the higher-temperature operating mode directly rather than the compositions from the condensate zone above the drift as previously abstracted (CRWMS M&O 2000 [DIRS 123916], p. 19). This decision is intended to be a somewhat conservative assumption, as the cations and anions are more concentrated in these potential fluids than in those of the condensate water. The rationale for this assumption is that the higher concentrations would tend to form more concentrated brines on the surfaces of the waste package and drip shield. A conceptual basis for this assumption is that the composition of fluids that could flow into the drift would not be too unlike the compositions reported at the drift wall as the calculations in the THC model neared a saturation of 0.0001 because any salts deposited in the fractures from complete evaporation due to boiling and dryout would be rapidly redissolved by condensate water as it flowed down a fracture into the drift.

6.3.1.6.3 Abstracted Results

The results presented below have two main discriminators: the temperature (thermal operating mode) that the drift is allowed to obtain and the imposed soil gas PCO_2 conditions. For use in

TSPA calculations, the tie-in to different thermal operating modes is evident. However, implementing the imposed soil gas PCO_2 condition tables is not. Therefore, for each realization in the TSPA model, either the high soil gas PCO_2 condition or the low soil gas PCO_2 condition will be selected. Once a soil gas mode is selected, it must remain the same throughout the realization. This can be achieved by creating a stochastic switch where, at the beginning of each realization, a uniform distribution from 0 to 1 is sampled, with the low soil gas PCO_2 tables being used over the range of 0 to 0.49 and the high soil gas PCO_2 tables being used over the range from 0.50 to 1. There are separate sets of tables for seepage at the crown (or sides) of the drift and for water imbibed into the invert.

When setting the PCO_2 concentrations for in-drift gas in the TSPA model, the value of PCO_2 for the node at the crown of the drift differs from the value for the node at the base of the invert during any given period (compare Tables 6.3.1.6-1 and 6.3.1.6-5). However, within the drift the value of PCO_2 should be constant throughout. Therefore, when selecting the appropriate PCO_2 value for use within the drift for a given time period, values from the tables associated with the chemistries at the crown of the drift should be used because as advective flow into the drift from the fractures should dominate the fraction that might diffuse through the invert into the drift. Once a given PCO_2 is selected for a period, it should be the only concentration of CO_2 that is used in the drift, including conditions in the invert and breached waste packages. Therefore, this value should be the concentration of PCO_2 for any radionuclide solubility calculation or invert mixing calculation (see Section 6.3.3 for further discussion).

Also presented on each table below are the actual THC model run time for the selected chemistry and the temperature at the drift wall for that given run time. These values may not necessarily apply to TSPA modeling, as the TSPA model will use TH results from a different source. They are given here to maintain the traceability of the abstraction to the process model results. All electronic input and output files for this abstraction are documented in Jolley (2001 [DIRS 154762]).

6.3.1.6.3.1 Tables for the Chemical Composition of Seepage at Crown of Drift

Tables 6.3.1.6-1 through 6.3.1.6-4 list the chemical composition of seepage entering the crown and sides of the drift via advection through fractures. The tables also set the PCO_2 level within the drift. The PCO_2 values for water imbibing into the drift (Tables 6.3.1.6-5 through 6.3.1.6-8) should not be used to set the PCO_2 concentrations within the drift. Using two different PCO_2 values for the same volume of gas is physically incorrect. Based on the assumptions and boundary conditions of the process model (BSC 2001 [DIRS 154677]), gas compositions in the drift would be set by advection through the fractures, not diffusion through the rock matrix.

Higher-Temperature Operating Mode–Tables 6.3.1.6-1 and 6.3.1.6-2 show the composition of seepage entering the crown (or sides) of the drift via advection through fractures when evaluating the higher-temperature operating mode. Table 6.3.1.6-1 is for use during low soil gas PCO_2 realizations in TSPA modeling. Table 6.3.1.6-2 is for use during high soil gas PCO_2 realizations in the TSPA.

Lower-Temperature Operating Mode–Tables 6.3.1.6-3 and 6.3.1.6-4 show the composition of seepage entering the crown (or sides) of the drift via advection through fractures when evaluating the lower-temperature operating mode. Table 6.3.1.6-3 is for use during low soil gas PCO_2 realizations in TSPA modeling. Table 6.3.1.6-4 is for use during high soil gas PCO_2 realizations in the TSPA.

6.3.1.6.3.2 Tables for the Chemical Composition of Water Imbibed into the Invert

Tables 6.3.1.6-5 through 6.3.1.6-8 show the chemical composition of water entering the invert via matrix imbibition from the host rock. These four tables do not show the PCO_2 of the gas in the drift.

Higher-Temperature Operating Mode–Tables 6.3.1.6-5 and 6.3.1.6-6 show the composition of water entering the invert via matrix imbibition from the host rock when evaluating the higher-temperature operating mode. Table 6.3.1.6-5 is for use during low soil gas PCO_2 realizations in TSPA modeling. Table 6.3.1.6-6 is for use during high soil gas PCO_2 realizations in the TSPA.

Lower-Temperature Operating Mode–Tables 6.3.1.6-7 and 6.3.1.6-8 show the composition of water entering the invert via matrix imbibition from the host rock when evaluating the lower-temperature operating mode. Table 6.3.1.6-7 is for use during low soil gas PCO_2 realizations in TSPA modeling. Table 6.3.1.6-8 is for use during high soil gas PCO_2 realizations in the TSPA.

6.3.1.7 Multiple Lines of Evidence

See Section 3.3.6.5 for details of the physical and chemical processes that apply to these calculations.

6.3.1.8 Summary of Remaining Uncertainties

6.3.1.8.1 Thermal-Hydrologic-Chemical Seepage Models

Except for the analyses reported in Section 6.3.1.5, sensitivity studies of the THC seepage models did not involve systematically changing input parameters over a range of values. Variations in input data were mostly related to model improvements and changes in drift design parameters and drift location, which then enabled assessment of model sensitivity to various input parameters. Investigated ranges of input parameters were typically within the bounds of values reasonably applicable to the Yucca Mountain thermal, hydrologic, and geochemical environments.

Table 6.3.1.8-1 summarizes the uncertainties regarding the predicted composition of fluids that may enter emplacement drifts and lists how these uncertainties were treated and their potential effect on model results. This table complements uncertainties summarized in a similar fashion in Table 4.3.6-2, relating to seepage and general seepage chemistry. Although many uncertainties are listed on these tables, only a few appear to dominate the overall uncertainty of the predicted water compositions and thus the uncertainty of further analyses which rely on these results. These include, in order of importance:

- Kinetic and thermodynamic data
- Input initial and infiltration water compositions
- Secondary mineral phases included in simulations
- Trace primary mineral phases (and related aqueous species) included in simulations.

If calibration of the most uncertain kinetic and thermodynamic data can be achieved, such that the model reproduces observed water composition trends (as done in recent analyses), the current uncertainty in water composition input into the model (initial and infiltration) may become the dominant model uncertainty.

6.3.1.8.2 Abstraction

All the uncertainties discussed above regarding the THC seepage model results are propagated in the abstraction of these results (discussed in Section 6.3.1.6). Some of these uncertainties have been assessed by the THC seepage models, but have not been incorporated in the abstractions for the TSPA. These include the variability imposed by the location of the repository (since the majority of the repository is located in the Tptpll but some portions of it may be constructed in the Tptpmn or other units. THC seepage simulations using the Tptpmn lithology around the drift were not conducted because results indicated that the model is not very sensitive to changes in repository host rock unit. The only significant difference between results of the Tptpmn and Tptpll THC seepage models was that higher fluoride concentrations were predicted because small amounts of CaF^2 were included as primary minerals in the TSw units of the Tptpll model (see Section 6.3.1.4). The same mineralogy (including fluorite) was used in the Tptpll model (see Section 6.3.1.5). Therefore, water compositions abstracted from this model are more conservative, in terms of the fluoride concentrations, than in earlier abstractions (CRWMS M&O 2000 [DIRS 123916], p. 9). These earlier abstractions were for a Tptpmn host rock unit. However, the main differences between these earlier abstractions and those from the updated studies are not a result of host rock mineralogy (except for fluoride), but the result of apparently overestimated effective-reaction rates of aluminum silicate minerals in the initial abstraction, as discussed in Sections 6.3.1.3 and 6.3.1.4.

Climate change and increased water availability during glacial times were previously evaluated and found to impact the abstraction tables used in TSPA modeling by a factor of two to five (CRWMS M&O 2000 [DIRS 123916], p. 25). These effects have not been carried forward into this set of abstractions, are therefore an unqualified uncertainty in this work. Another climate-change issue concerns the possible variations through time of soil-zone carbon dioxide partial pressure caused by climate change, which might change the precipitation of calcite, the availability of bicarbonate ion, and the pH. This is demonstrated by Jolley (1997 [DIRS 154535]), who predicted soil-gas carbon dioxide partial-pressure fluctuations between

present-day 1,000 ppmv to 4,700 ppmv during wetter and cooler climates. The THC seepage modeling studies presented in Section 6.3.1.5 indicate that fixed carbon dioxide partial pressures (750 and 3,700 ppmv) at the top model boundary have little effect relative to other model uncertainties (notably those regarding input water compositions in the model).

The THC seepage models do not evaluate locations close to the edge of the repository, where increased infiltration and lower temperatures resulting from edge-effects may affect predicted concentrations of fluid around drifts.

An evaluation of the composition of the initial water used in the THC seepage models is presented in Section 6.3.1.5. A number of possible input water compositions exists for these models, with large uncertainties caused primarily by the difficulty of extracting and analyzing pore water from the low-permeability repository host units (e.g., Higgins et al. 1997 [DIRS 101246]). To address the issue of initial water uncertainty, THC seepage simulations have been initiated using perched water from well UZ-14 (see Section 6.3.1.5). The carbon dioxide partial pressure of this water (and therefore its pH) is not consistent with reliable analyses of carbon dioxide concentrations in pore gas samples from the potential repository host units (see Section 6.3.1.5). Therefore, this water was used only for sensitivity analyses. The results of these evaluations have not been incorporated into a TSPA.

Other specific issues related to the THC seepage model uncertainties discussed earlier that could have a direct bearing on results of the TSPA through the abstracted data include:

- $[Ca_5(PO_4)_3(OH, F, Cl)$ could be added as a primary mineral in the model. If phosphates are included in the simulations, this mineral may affect the predicted phosphate geochemistry. It could also provide a lower bound of predicted fluoride concentrations (under ambient conditions) in geologic units where CaF_2 is either absent or not fully reacting. For the results abstracted here, fluorite equilibrium sets an upper limit in predicted fluoride concentrations (under ambient conditions).

- Lithophysae in the rock properties of the Tptpll could be included, which can add calcite to the mineral inventory and change the porosity of portions of the Tptpll, affecting abstracted water compositions from the THC seepage model.

- An evaluation could be done to determine how the spatial distribution of modeling gas advection versus diffusion out in the host rock might control gas fugacities at localized portions of the drift wall (i.e., advection in highly fractured areas could mask the effect of diffusion in less fractured areas even after the repository is sealed). In conjunction, sensitivity studies on the THC model boundary condition imposed at the drift wall (no advection) could add more understanding of drift wall processes.

- The effect of unrepresentative chemical thermodynamic or kinetic data, or of an incompletely defined geochemical system, on predicted concentrations of key species such as calcium and magnesium could influence model uncertainty.

An example of this last effect is the differences between the predicted calcium, sodium, and magnesium concentrations between the initial (CRWMS M&O 2000 [DIRS 142022]) and

revised THC model simulations (BSC 2001 [DIRS 154677]) (see Section 6.3.1.4). Small changes in equilibrium constants for clays (calcium, sodium, and magnesium smectites) and zeolites, within the original uncertainty of these values, together with other changes discussed in Section 6.3.1.4, caused differences of several orders of magnitude in predicted concentrations for these species. Consequently, a comparison of the abstracted data for both cases (CRWMS M&O 2000 [DIRS 123916], Table 3 with Tables 6.3.1.6-1 and 6.3.1.6-2 show similar large differences. The small change in thermal-chemical (TC) data significantly affects the results of other models that rely on output data from the updated THC seepage models. This change also determines the likelihood of success for such models to predict the accumulation of magnesium and calcium chloride salts on waste packages during the boiling periods (see Section 6.3.3). However, the changes in kinetic and thermodynamic data between the initial (CRWMS M&O 2000 [DIRS 142022]) and updated THC seepage models (BSC 2001 [DIRS 154677]; see also Section 6.3.1.4) were made to calibrate these models such that ambient pore water compositions could be reproduced. Therefore, in this case, the uncertainty lies more strongly in the pore water composition than in the model adjustments that were necessary to reproduce these data. This further emphasizes the potential large effect of initial water composition uncertainty on TSPA results, as noted earlier.

6.3.1.9 Summary and Conclusions

6.3.1.9.1 Thermal-Hydrologic-Chemical Seepage Models

THC seepage models were used to predict the composition of fluids (water and gas) that could enter potential emplacement drifts. Because of the large number and variability of input parameters, as well as the complexity of modeled THC processes, a rigorous quantification (in a statistical sense) of the uncertainty of the THC seepage predictions is not achievable. For this reason, the uncertainty of THC seepage models can only be evaluated in a deterministic, semiquantitative or qualitative manner, with a focus on narrowing rather than quantifying uncertainty. Limiting the uncertainty of the THC seepage models relies strongly on model validation against field and experimental data. While most of these data cover a short time range compared to the long simulated periods of time (thousands of years) in the THC seepage models, successful validation efforts using the same model input data as for the THC seepage models boost confidence in the model results.

Uncertainties affecting the predicted composition of fluids that could enter drifts were identified (Section 6.3.1.1). Some of these uncertainties were evaluated in a semiquantitative manner from modeling work presented in *Drift-Scale Coupled Processes (DST and THC Seepage) Models* (BSC 2001 [DIRS 154677]; see also Sections 6.3.1.3 and 6.3.1.4). Others were addressed by more recent work see Section 6.3.1.5). These evaluations related primarily to infiltration rates, thermodynamic and kinetic data, pore water and infiltration water compositions, boundary carbon dioxide partial pressures, potential repository operating temperature modes, and potential repository host rock units. Other uncertainties more directly related to TH parameters and flow and transport process models were discussed in Section 4.3.6. These uncertainties, treatments, and potential effects on the predicted composition of fluids that may enter drifts are summarized in Tables 4.3.6-2 and 6.3.1.8-1.

The model input thermodynamic and kinetic data, are among the main uncertainties affecting predicted compositions of fluids at the drift wall directly affecting predicted mineral reaction rates. An attempt was made to improve the confidence in model results by adjusting the most uncertain kinetic and thermodynamic data (within their uncertainties) in such a way that observed ambient water compositions would be reproduced fairly well. Once such calibration was achieved, uncertainties in the model results appeared to become more a function of the uncertainty over input initial and infiltration water compositions. At high infiltration rates, predicted concentrations are more a function of transport than reaction. Thus, the model result uncertainty becomes more directly related to infiltration and initial water composition and less dependent on reaction or infiltration rates. At low infiltration rates, the effect of uncertainties in reaction and infiltration rates becomes large, but the likelihood of seepage into the drift is minimal. Therefore, with respect to predicting the composition of fluids that may enter drifts, the uncertainty in the composition of initial infiltration water input into the THC seepage models may largely overwhelm other uncertainties.

Among the various cases evaluated, THC simulations were performed using two significantly different input water chemistries (UZ-14 perched water and Alcove-5 pore water) with significant differences in initial pH and carbon dioxide partial pressures. Using both waters under a higher- and a lower-temperature operating mode, the scatter defined by the predicted water compositions at the drift crown over time fell largely (but not entirely) within the variability of water compositions that could be used for input into the model. For the cases considered, the largest effect of thermal loading on predicted water compositions, relative to ambient water compositions, was decarbonation through volatilization of carbon dioxide. This is a common heating effect observed in natural geothermal systems. Higher temperatures increase the variability of predicted concentrations at the drift wall relative to lower temperatures. However, this effect is predicted to be relatively short-lived. The general nature of predicted water compositions returns largely to within the range defined by observed ambient compositions within 10,000 years. As temperatures decrease and return to ambient values (within 100,000 years), the predicted water compositions at the drift crown return to ambient values for all temperature and water composition cases considered.

6.3.1.9.2 Abstraction

As discussed in Section 6.3.1.6.1, the abstraction tables provide input into downstream models (see Section 6.3.3) and to TSPA modeling. Look up tables, provided in Sections 6.3.1.6.3.1 and 6.3.1.6.3.2, are designed to represent the process model results reported in Section 6.3.1.5 above. They include evaluation or implementation of several uncertain parameters. Depending on the thermal operating mode, the chemistries have been abstracted into five or six periods that represent changes in temperature (122° to 23°C), pH (7.23 to 8.57), and PCO_2 (1.06×10^{-3} to 8.91×10^{-6}), along with the following ions: calcium, magnesium, sodium, chloride, SiO_2, HCO_3, SO_4K, AlO_2F, and FeOOH. These tables are representative of the chemistries that would enter the drift through time for the conditions specified in the process model reported in Section 6.3.1.5.

6.3.2 Effects of Engineered Materials on the Chemical Environment

6.3.2.1 Introduction

Corrosion of steel and other alloys, chemical reactions of cementitious grout in conjunction with rock bolts, and formation of colloids from engineered materials have the potential to affect the in-drift chemical environment as it relates to the performance of the potential repository system.

6.3.2.2 Goal of Model

The models for corrosion, reactions of cementitious materials, and colloid formation are intended to evaluate the significance of these processes and quantify their effects where necessary.

6.3.2.3 Discussion of Total System Performance Assessment-Site Recommendation Result, and Identification of Previously Unquantified Uncertainties

Uncertainties in the models of the effects of engineered materials on the chemical environment were not explicitly quantified in the TSPA-SR (CRWMS M&O 2000 [DIRS 153246]) in three general areas, each of which is specifically discussed below. Except for the effects of boiling, uncertainties associated with alternative thermal operating modes are generally the same as those for the higher-temperature mode in the TSPA-SR. For example, the ability to model the effects of temperature on in-drift aqueous geochemistry will still be necessary at temperatures below 96°C.

6.3.2.3.1 Corrosion of Steel and Alloys

An evaluation of corrosion products on aqueous concentrations of metal ions in solution in an oxidizing environment was conducted, and the corrosion products were found to have a minimal impact on the concentrations of major ions in solution (CRWMS M&O 1999 [DIRS 125130], Section 7.2). The discussion in the *In Drift Corrosion Products* report (CRWMS M&O 1999 [DIRS 125130]) was based on a generalized set of Eh-pH diagrams for the major elements in a three-or four-chemical component system (generally, oxygen, hydrogen, and sometimes carbon dioxide) and a search of available scientific literature. The conceptual evaluation predicts the composition of the corrosion product and gives some understanding of the remaining chemical species in solution. This general prediction indicates that as the steels corrode nearly all of the corrosion products from the steels and alloys will form oxides and oxyhydroxide minerals, and it indicates that the aqueous concentrations of any aqueous species formed during the corrosion of these materials will also be small.

However, two important uncertainties were identified. First, the composition of steels, alloys, and their associated corrosion products can have an impact on the aqueous concentrations of trace metals in solution that may interact with either the waste package surface or the waste form. The compositions of steels and alloys used in geochemical modeling are based on values reported in the American Society for Testing and Materials standard for the given steel or alloy design (BSC 2001 [DIRS 154441], Section 6), and they do not include concentrations of trace metals that could dissolve into fluids that come in contact with the materials or their associated corrosion products.

The second important uncertainty deals with the ability of iron hydroxides and oxyhydroxides (by far the largest mass of corrosion products resulting from engineered materials) to sorb radionuclides and trace metals. If sorption is included in the performance calculations, a significant reduction in any of the dissolved concentrations of trace metals can be achieved. In previous EBS and TSPA-SR (CRWMS M&O 2000 [DIRS 153246]) modeling efforts, the sorptive ability of the corrosion products was conceptually acknowledged but conservatively ignored. However, these unquantified effects are being looked at in some detail, as discussed in Section 10. Because the model in Section 10 is based on a K_d approach, it is not fully linked with the effects of the aqueous chemistry modeled in Section 6.3.3. In addition, a K_d model will not operate outside the bounds in which the K_d data were collected, whereas a surface complexation model will. However, before a surface complexation model for sorption onto corrosion products is developed, the evaluation of sorption by the simpler K_d approach is needed to assess the potential consequences on radionuclide release from the EBS (i.e., its significance to performance). The results from implementing the K_d model discussed in Section 10 will define the need to develop a more detailed surface complexation approach that will be valid for the range of aqueous chemistries that may be imposed on the corrosion products produced from the degradation of the engineered materials placed in a repository drift. With the implementation of a surface complexation model, the uncertainty of having competitive uptake of the various radionuclides and trace metals can be modeled in a coupled manner.

An analysis of in-drift gas flux and compositions (CRWMS M&O 2000 [DIRS 129278], Section 6.2.2) using a simple mass balance approach indicates that oxygen gas depletion in the drift from the corrosion of steels and alloys will be about 14 percent. When this depletion is integrated over the expected material lifetimes, it does not drive the repository into sub-oxic or anoxic conditions. However, this analysis is based on TH models developed for the TSPA for the viability assessment (VA) (CRWMS M&O 1998 [DIRS 100358], Section 4.4.2.1), and it is only a simplified mass balance analysis. Some uncertainties exist with this analysis, which could further limit the amount of O_2 available for reaction. These include differences in thermal design, exclusion of the waste form as a sink of O_2, uncertain corrosion rates, and differences in gas transport (diffusion dominated vs. advection dominated). These processes if adequately evaluated in process models could result in further depletion of oxygen that could cause a decrease in corrosion rates. Ideally, the process models would capture all of these unquantified effects. Fortunately, the impact of not having quantified these uncertainties is small. Quantifying these uncertainties gives the increased potential for reducing corrosion and solubility, which would have a beneficial impact on the lifetime of the engineered materials and the rate at which the radionuclides would be released into solution. The potential for sub-oxic conditions is at its greatest during the boiling period. In a cooler design, this effect would be minimized. Modeling documented in the *Engineered Barrier System: Physical and Chemical Environment Model* (CRWMS M&O 2000 [DIRS 151951]), tends to corroborate this; on a detailed scale, the opportunity to drive the oxygen levels down into a regime that may be sub-oxic only exists for short periods of time. These periods are associated with boiling periods, when gas and water fluxes into the drift will be limited. These same general results were also reported in the total system performance assessment for the viability assessment (TSPA-VA) (CRWMS M&O 1998 [DIRS 100358], Section 4.4.2.1). Overall, no impacts to TSPA-SR (CRWMS M&O 2000 [DIRS 153246] would occur because the effects of including these unquantified uncertainties have been conservatively bounded by the TSPA-SR and are thought to

reduce waste package corrosion and the potential solubility of radionuclides (CRWMS M&O 1999 [DIRS 125130], Section 6.5.3.1).

In addition to the uncertainties with oxygen gas, there are uncertainties in other gas components, such as carbon dioxide and nitrogen. Several uncertainties concerning carbon dioxide are addressed in other sections (e.g., Section 6.3.1). Nitrogen is generally so abundant (80 percent of air) that the uncertainties associated with it are not important to EBS models for the reasons discussed above (i.e., the boiling periods will reduce the gas flux, otherwise nitrogen will be sufficiently abundant).

6.3.2.3.2 Cement Grout

An evaluation of the role of carbonation of cement grout as a controlling factor on whether the grout used in rock bolt emplacement could produce alkaline waters (pH greater than 9) is found in *Seepage/Cement Interactions* (CRWMS M&O 2000 [DIRS 129281], Section 7). This analysis indicates that the pH of seepage water is impacted by cement grout longevity. The duration of the impact to EBS chemistry is currently bounded at 40 years. However, due to uncertain parameters, the effects could last on the order of 40,000 years, based on rapid diffusion of carbon dioxide gas in the host rock, or to about 300,000 years for aqueous-phase advection or diffusion reactions with emplaced grout. With this large uncertainty range, cement grout could influence chemistry in those portions of the repository where rock bolts are used for at least several thousand years. Some of the uncertainties associated with the carbonation of the cement grout are discussed in the *Seepage/Cement Interactions* report.

Carbonation is thought to be the major driver in the evolution of the composition of cement leachate. The unknown parameters are the uncertainties in diffusion coefficient and the mass of calcium available for reaction. The effects of these uncertainties will be minor if sensitivity analyses demonstrate that impacts to performance from cement leachate-influenced seepage water are minor.

A new cementitious materials model that predicts the composition of seepage water that interacts with cement has been provided in *Engineered Barrier System: Physical and Chemical Environment Model* (CRWMS M&O 2000 [DIRS 151951], Table 6.3-3). This model reports three potential leachate compositions available through time (CRWMS M&O 2000 [DIRS 123916]) that could be used as inputs to the *In-Drift Precipitates/Salts Analysis* model (CRWMS M&O 2001 [DIRS 153265], Section 4) to predict the effects of cement leachate on precipitation and subsequent chemistries. This model is adapted from simplifying assumptions and studies of concrete reported in the literature. These compositions provide a broader range of chemistries than previously available. The results of the cementitious materials model will allow, if appropriate, an investigation of water chemistries that have not been carried forward from current EBS and TSPA models into subsequent modeling for consequence. The sensitivity of the precipitates salts model to grout-influenced leachate on seepage is discussed in Section 6.3.3.5.1.1. The sensitivity study in Section 6.3.3.5.1.1 evaluates several different starting water compositions (including cement leachate) to determine whether a specific reaction pathway (or chemical divide) will occur during evaporation and cause an unexpected aqueous composition to develop. The results of the study indicate that after the cement leachate waters were evaporated, they reflected the chemical composition of the original input waters that were

used to model the leaching reaction with cement. Thus, the chemical divide did not develop a water composition different than the abstracted waters used in the TSPA-SR (CRWMS M&O 2000 [DIRS 153246]). However, this analysis did not include other water chemistries that may have the potential to leach the cement grout, such as those abstracted in Section 6.3.1.6.3.

The study of additional uncertainties in the cementitious materials model pertaining to confirmatory testing of rock bolt longevity, carbonation of the grout, microbial attack of organic superplasticizers, and other aspects of grouted rock bolt performance have not been performed. The final design of ground support in the emplacement drifts is under development, and the analysis of ground support function is preliminary. Accordingly, the longevity of grouted rock bolts in response to thermal loading and environmental conditions remains uncertain. Rock mass deformation could lead to failure of the rock bolts (not necessarily associated with failure of the drift openings). It should be noted that most of these uncertainties are of minor consequence to the TSPA-SR (CRWMS M&O 2000 [DIRS 153246]) because the sensitivity analyses demonstrate that the impact to performance from cement leachate-influenced seepage water is minor.

6.3.2.3.3 Colloids

The uncertainties related to the chemical effects of colloids generated from corrosion products are discussed in Section 10.3.5.

6.3.2.4 Model Development

With the exception of the development of the sorption and colloids models discussed in Section 10, the inclusion of cement leachate water as a sensitivity study is discussed in Section 6.3.3.5.1.1.

6.3.2.5 Multiple Lines of Evidence

It is generally known that steels and alloys corrode over time (see Section 6.3.2.3.1), that cement can carbonate and degrade over time (see Section 6.3.2.2), and that colloids can be generated from corrosion products (Section 10.3.5). Some additional evidence for these processes is discussed in Sections 7 and 10.

6.3.2.6 Summary of Remaining Uncertainties

One uncertainty not discussed directly above is the effect of variations in the amounts and compositions of materials introduced into the drift (e.g., Alloy 22 used in the waste package design) that might differ in the final design from those assumed at this stage of design. These types of uncertainty will not have any significant impact on TSPA-SR results (CRWMS M&O 2000 [DIRS 153246]). *Committed Materials in Repository Drifts* (BSC 2001 [DIRS 154441]) mitigated much of the previous design uncertainty by providing masses and material compositions for the in-drift ground support design. However, this type of information is not reported for access or perimeter drifts or any other lined access tunnels. In addition, only compositional information as provided in American Society for Testing Materials standards or other design assumptions is reported. This information is not sufficient to evaluate the impacts of trace elements that may be present. However, some issues concerning impacts due to trace

elements are discussed in Section 7.3.1. Additionally, many trace elements will behave the same way that radionuclides will in the EBS. Many, for example, would be expected to sorb and form solid solutions. Although there are uncertainties, impacts on TSPA-SR results should be minimal, as these types of physical processes (such as sorption) were conservatively ignored.

As an example, one item of particular importance pertaining to uncertainty with an unfinalized subsurface design is the potential effects to the chemical environment from using large quantities of cementitious materials in the construction of main drifts and ventilation shafts. Locally, these volumes of cement would be far larger than the reported quantities planned for use in grouting rock bolts. Perhaps on a local scale, this quantity could be on the order of magnitude of the cement use in the VA design (CRWMS M&O 1998 [DIRS 100358], Section 4.3), in which the emplacement drifts were lined with concrete. This uncertainty would have an effect on water chemistries if alkaline plumes generated from unsaturated zone (UZ) waters that are equilibrating with concrete used in lining ventilation shafts and access drifts (some shafts or drifts could potentially be located above the repository horizon) flow into an emplacement drift. Coupled with this uncertainty is a potential for an alkaline plume generated from the same type of source that might flow and react with a contaminant plume containing radionuclides that may have left the drift and could be moving in the UZ.

6.3.2.7 Conclusions

Most of the uncertainty not previously investigated in models is discussed or incorporated above. Table 6.3.2-1 summarizes the key uncertainties and model improvements discussed above. Additional work on these uncertainties is needed for a more comprehensive understanding of the processes being modeled. However, the uncertainties addressed above should not impact the validity of the TSPA-SR results (CRWMS M&O 2000 [DIRS 153246]). This is due to conservative TSPA modeling assumptions (e.g., no credit was taken for sorption onto corrosion products including it would only improve performance).

6.3.3 Evolution of the In-Drift Chemical Environment

6.3.3.1 Introduction

The model of the evolution of the in-drift chemical environment uses input from three submodels: the precipitates/salts model, the microbial communities model, and the seepage/invert interactions model.

6.3.3.2 Goal of Model

The submodels discussed below are used to determine in-drift geochemical conditions that may influence materials corrosion and to estimate the composition of waters and gas that can affect dissolution and transport of radionuclides from the EBS. These submodels are influenced by coupled thermal-hydrologic-chemical-mechanical processes that will occur over thousands to millions of years. Some of the main inputs considered are the effects of temperature, relative humidity, introduced material compositions, material lifetimes, and compositions of gas and water fluxing into the drift. These inputs influence the timing and duration of many of the chemical-dependent processes that could occur, and thus, have great ability to impact radionuclide release from the EBS. Therefore, these submodels are used to determine the

chemical conditions over time that are used for the calculation of radionuclide release from the EBS.

6.3.3.3 Discussion of Results and Identification of Previously Unquantified Uncertainties

6.3.3.3.1 Precipitates/Salts Model

The precipitates/salts model was developed and validated for the TSPA-SR (CRWMS M&O 2000 [DIRS 153246]) in the *In-Drift Precipitates/Salts Analysis* (CRWMS M&O 2001 [DIRS 153265]). This model is composed of two submodels that predict pH, chloride concentration, and ionic strength as a function of relative humidity, carbon dioxide fugacity, temperature, seepage water composition, and relative rates of evaporation and seepage. When the relative humidity is above 85 percent, the EQ3/6 Pitzer submodel (often referred to as the high relative humidity model) is used. Below 85 percent relative humidity, the low relative humidity salts submodel is used. Lookup tables produced for the TSPA-SR (which provide pH, chloride concentration, and ionic strength as a function of abstraction period, relative humidity, relative evaporation rate, and temperature) are documented in *Precipitates/Salts Model Results for THC Abstraction* (CRWMS M&O 2001 [DIRS 153995]). This modeling approach is based on literature data that describe the minerals and salts produced by evaporative concentration and the relations between solution composition and relative humidity.

Precipitates/Salts Model Unquantified Uncertainties–The accuracy of the high relative humidity salts model was tested using three sets of independently collected laboratory data for the evolution of solids and water composition during evaporation (CRWMS M&O 2001 [DIRS 153265], Section 6.5.1). Two sets of data were derived from evaporation of synthetic J-13 well water (one prepared at a concentration factor of approximately 100), and a third set was derived from evaporation of synthetic Topopah Spring tuff pore water. For each measurement, the pH changes were predicted within a pH unit or less, the chloride concentrations were predicted within 20 percent, and the ionic strength was predicted within a factor of 2. In addition, handbook solubilities for ten simple salts having solubilities greater than 1 molal were easily predicted within a factor of 10 and almost always within a factor of 2. Model results also compare favorably with the results obtained using the qualified project thermodynamic database (DTN: MO0009THRMODYN.001 [DIRS 152576]) over its validated ionic strength range.

Data are not available to directly evaluate the accuracy of the low relative humidity salts model. However, this model does produce reasonable trends for changes in chloride and ionic strength as relative humidity decreases for the waters modeled. It also produces results consistent with the high relative humidity model at 85 percent relative humidity.

A final method used to evaluate and account for uncertainty in the precipitates/salts analysis is the generation of a set of lookup tables intended to cover the range of possible combinations of input values (CRWMS M&O 2001 [DIRS 153995], Tables 2 through 4). The primary objective of the lookup tables is to summarize the effects of evaporation processes for a wide range of possible conditions so that evaporation effects and uncertainty can be easily incorporated into coupled analyses. These lookup tables are used in several ways. They are used to evaluate the

sensitivity of input variables on outputs; for example, the sensitivity of pH to the relative evaporation flux is evaluated by comparing the pH output for a range of values for the relative evaporation flux. Input variables that are not included in the tables are not sensitive inputs, except for the composition of the incoming seepage water, which was held constant in this analysis (the sensitivity of these outputs to water composition is evaluated in Section 6.3.3.5.). Similarly, an estimate of the approximate maximum range of possible values of a given output variable for a range of input conditions can be assessed from the lookup tables.

Model validation has demonstrated that, given accurate inputs for starting water and gas compositions, the precipitates/salts model will likely provide results that are within a factor of two for chloride concentrations and ionic strength and within a pH unit for pH predictions (CRWMS M&O 2001 [DIRS 153265], Section 6.5.1). These quantified ranges of uncertainty can be propagated into downstream models. These ranges reflect only the uncertainties involved in simple evaporation of a given starting water.

Application of the precipitates/salts model to the drift environment has additional uncertainties involving the conceptual model, model design, model implementation, and model assumptions (CRWMS M&O 2001 [DIRS 153265], Sections 6.2, 6.3, 6.4, and 6.5). These include:

- Physical model representation (a flow-through homogeneous mixing cell)
- Steady-state and equilibrium assumptions
- Chemical activity models
- Thermodynamic database constants
- Composition of seepage water for a given time period
- Temperature, relative humidity, and gas fugacity inputs
- Relative humidity threshold for dry conditions, and
- Mineral assemblage determination.

These uncertainties reflect each major type of uncertainty identified in Section 1.2.1.1. Given the complexity of the modeled processes and large number of input parameters for this model, a rigorous quantification of each of these uncertainties is not possible. Therefore, work in this area has concentrated on assessing uncertainties in the model introduced by conservatively chosen parameter values or assumptions, which is the primary motivation for the unquantified uncertainties analyses (Section 1.2.1.3), and on performing sensitivity analyses on input parameter uncertainties. The bounding assumption in the precipitates/salts model that may introduce the most important biased effect on TSPA calculations is the relative humidity threshold assumption, which is based on the properties of a nitrate brine. This assumption is investigated, as well as the sensitivity of the model to seepage water composition, carbon dioxide fugacity, and mineral suppressions.

Precipitates/Salts Model Assumptions–In some cases, simplifying assumptions were required to reduce the complexity of the precipitates/salts analysis and to avoid sophisticated approaches where data and preexisting models were lacking. The major assumption identified in the TSPA-SR (CRWMS M&O 2000 [DIRS 153246], Appendix F) and used in the precipitates/salts analysis is the threshold relative humidity of corrosion initiation. Currently, that threshold is assumed to be 50 percent. Below 50 percent, no brine is assumed to be stable within the drift; thus, no liquid water can occur that could cause corrosion. This threshold corresponds to the

approximate equilibrium relative humidity of a saturated aqueous solution of sodium nitrate at its boiling point of approximately 120°C (CRWMS M&O 2000 [DIRS 151568], Section 6.4.2). According to this assumption, sodium nitrate is the last salt to precipitate during evaporation of in-drift waters. This assumption is developed in *Environment on the Surfaces of the Drip Shield and Waste Package Outer Barrier* (CRWMS M&O 2000 [DIRS 151568], Section 6.4.2) and is based on the solubility of nitrate salts and experiments conducted on well J-13 water.

A relative humidity of 50 percent was assumed to be conservative for the TSPA-SR (CRWMS M&O 2000 [DIRS 153246] because a more soluble and hygroscopic salt, such as calcium chloride or magnesium chloride, was not likely to develop based on results and initial documentation of laboratory evaporation experiments. In addition, evaporation of the seepage provided by the THC model described in *Abstraction of Drift-Scale Coupled Processes* (CRWMS M&O 2000 [DIRS 123916]) and abstracted for in-drift calculations resulted in a sodium-dominated brine in which calcium and magnesium were depleted primarily by evaporative precipitation of anhydrite, calcite, and sepiolite (DTN: MO0001MWDEQ346.007 [DIRS 154636]). In these waters, the last salts expected to precipitate would be the nitrate salts.

To date, laboratory and field experiments (e.g., the Single Heater Test and Drift Scale Test) using waters based on observed Yucca Mountain waters have not documented production of a calcium or magnesium chloride brine. However, laboratory experiments are ongoing, and the possibility that a calcium/magnesium chloride brine could be produced from evaporation of waters similar to tuff matrix pore water has not been eliminated. It is possible that processes other than pure evaporation may give rise to a seepage composition that has a chloride:sodium molar ratio greater than one. In the THC calculations developed for preliminary performance analyses, mineral data were adjusted to enhance model calibration (Section 6.3.1.4). The results showed an increase in the chloride:sodium molar ratio from less than one to greater than one during the early cooldown period of the higher-temperature cases (Section 6.3.3.6). Simple evaporation of a chloride- sodium-calcium-magnesium water having a chloride:sodium molar ratio greater than one will cause depletion of sodium (due to halite precipitation) and production of a calcium and magnesium chloride brine (Section 6.3.3.5). At its elevated boiling temperature, such a brine would lower the relative humidity threshold below 30 percent (Weast and Astle 1981 [DIRS 100833], p. E-44; Dean 1992 [DIRS 100722], p. 11.6), further shortening the dry period. Because corrosion can occur in the presence of this type of brine, the possibility of such a brine forming is an important consideration. Further modeling efforts, lab experiments and field experiments could reduce the uncertainty in this area. For example, analysis of reflux water samples collected from the Drift Scale Test during cooldown to determine whether its evaporation would give rise to a calcium and magnesium chloride brine.

Studies of the alternative thermal operating modes indicate that higher temperatures give rise to higher chloride:sodium molar ratios. The lower-temperature results have a much smaller tendency to produce chloride:sodium ratios greater than one (Section 6.3.3.6), but the possibility of producing a calcium and magnesium chloride brine still exists in the lower-temperature mode.

6.3.3.3.2 Seepage/Invert Interactions Model

Seepage/Invert Interactions (CRWMS M&O 2000 [DIRS 129283]) contains no qualitative calculations or predictions. It was written to develop a logical conceptual model for physical and

chemical interactions between seepage and invert materials; to screen potential processes and reactions that may occur between seepage and the invert; and to outline how seepage/invert processes may be quantified. The conceptual model (CRWMS M&O 2000 [DIRS 129283], Figure 1) consists of three generalized inputs (sources of fluid flux) into the invert: the fluids that are diverted by the waste package and drip shield; the effluent leaving any failed waste package; and, any flux entering the invert from the host rock via wicking or imbibition. Also expected with these three sources are different volumes of water. These three volumetric sources of inputs to the invert will have traveled along different pathways, and therefore will be influenced chemically by the engineered materials along their individual pathways. Due to these differing pathways, predicting the bulk chemistry in the invert after mixing these fluids is the major uncertainty that needs to be quantified. Development of the quantitative model will increase the understanding of the physical processes involved during seepage/invert interactions. The processes that would need to be included include the effects of in-drift gas compositions and temperatures, precipitation and resultant fluid compositions that occur from mixing reactions, and changes to the physical properties of the invert (i.e., reduced porosity due to precipitation), among others.

Currently, sources exist for predicting the compositions and fluxes of the three conceptualized fluids. Compositions are generated in the precipitates/salts model, as discussed in Section 6.3.3.3.1, or in *In-Drift Precipitates/Salts Analysis* (CRWMS M&O 2001 [DIRS 153265], Section 7.2) and *In-Package Chemistry Abstraction* (CRWMS M&O 2000 [DIRS 129287], Section 6). However, in previous calculations, only the composition of waters evaporating in the invert from waters fluxing from the crown of the drift was used to set the chemical conditions within the invert (CRWMS M&O 2001 [DIRS 153265]). No mixing reactions were applied when fluids from other sources were thought to interact in the invert.

In summary, for *Seepage/Invert Interactions* (CRWMS M&O 2000 [DIRS 129283]), water chemistry and interactions in the invert fall in the area of EBS geochemical modeling, which has not been implemented past its conceptual framework. Therefore, the uncertainties are large. Since uncertainty has not been quantified, the appropriate chemistries that need to be applied to transport processes in the invert have not been determined. For cases such as those discussed in Sections 6.3.2 and 10.3.4, the invert chemistry will affect sorption. The chemistries will also affect the solubility and precipitation of radionuclides, and therefore could affect potential releases from the EBS.

6.3.3.3.3 Microbial Communities Model

The *In-Drift Microbial Communities* model (CRWMS M&O 2000 [DIRS 151561]) provides bounding estimates through time of the numbers of potential microbes that could grow in the repository drift. This time-dependent set of calculations includes the evaluation of several sets of uncertain parameters, including the affects of drift temperature and relative humidity, changes in water chemistry and gas entering the drift, and variability in percolation flux through time. The parameter that effects the modeling results the most is the material lifetimes (degradation rates) of the steels and alloys that are to be emplaced in the drift, because these rates affect the availability of nutrients and energy for biomass growth. Thus, the calculations also incorporate the material masses and compositions used in the repository and waste package designs and variable corrosion rates for those materials. Four unresolved issues (not all are classified as

uncertainties) directly associated with the *In-Drift Microbial Communities* model (CRWMS M&O 2000 [DIRS 151561]) include: the incorporation of gas fluxes and compositions associated with the TSPA-VA analysis (CRWMS M&O 1998 [DIRS 100358], Section 4.4.2.1), an unqualified thermodynamic database for the redox half reactions, an incomplete description of the design materials that might be used, and the use of an unqualified data source for augmenting the water chemistries (like those abstracted in Section 6.3.1.6 above) to add appropriate amounts of nitrate and phosphate (key nutrients required for microbial growth) to those chemistries, because they are not included in upstream modeling calculations. For these remaining issues, the uncertainty from the gas flux is small because the results are not very sensitive to this parameter. Any future changes in the thermodynamic database should not substantially change the results of the *In-Drift Microbial Comminutes* model (CRWMS M&O 2000 [DIRS 151561]) because the majority of the calculations are nutrient-limited instead of energy-limited. The other issues listed above are far less uncertain than the material degradation rates.

One uncertainty not yet incorporated into the model is the addition of uranium as a considered redox species. This has previously been ignored; however, results from the model show that the period of greatest microbial growth is after waste package failure, when the waste package internal components and the waste form are degrading (CRWMS M&O 2000 [DIRS 151561], Figures 11 and 14). Ignoring the uranium redox couple in this instance would mean that a substantial amount of potential redox energy is being neglected in the calculations, which could result in an even higher growth rate during the period when the waste form is degrading.

Included in the modeled results are bounding estimates for carbon dioxide gas production, colloid generation, and biofilm size and distribution (CRWMS M&O 2000 [DIRS 151561], Tables 73, 74, and 75). The impacts of these findings, along with other processes that were not addressed in the model, can have an impact throughout the EBS. Some of these impacts may affect waste package performance, transport of radionuclides, and dissolution of the waste form. Unmodeled processes that are discussed in the AMR include colloidal transport of radionuclides sorbed to microbes, impacts on dissolution of radionuclides due to increased carbon dioxide partial pressures in the drift, potential localized changes to aqueous geochemistry in and out of the waste packages due to the formation of siderophores and generation of polysaccharide based biofilms, and the impacts on waste package corrosion of biofilm processes.

Impacts from biofilms accumulating on surfaces such as the waste package could be substantial. This process is often termed microbially influenced corrosion (MIC). The same impacts could also affect waste form dissolution. Geochemical modeling in the EBS has not evaluated the impacts due to the addition of organic microbial exudates, such as siderophores and polysaccharides. Even the TC data set used for speciation and reaction path modeling does not include organic species (CRWMS M&O 2000 [DIRS 152575]). However, there is a brief discussion on how these byproducts of microbial growth and metabolism might affect radionuclide transport in *In-Drift Microbial Communities* (CRWMS M&O 2000 [DIRS 151561], Section 6.3.5).

Carbon dioxide gas generation from microbial respiration, especially during waste form degradation, could be significant, as shown by some of the bounding estimates for carbon dioxide concentrations from *In-Drift Microbial Communities* (CRWMS M&O 2000 [DIRS 151561], Table 75). These estimates would represent a substantial increase to the in-drift

P_{CO2} values used in initial models for waste package chemistry and waste form solubility. This substantial increase could significantly elevate reported radionuclide solubilities, alter the pH of in-drift waters due to the direct interaction of the elevated carbon dioxide with waters, resulting in carbonate buffering, and influence sorption properties of corrosion products due to carbonate complexation.

The *In-Drift Colloids and Concentration* model (CRWMS M&O 2000 [DIRS 129280], Table 2) did not evaluate microbes as a potential colloid, based on a bounding but unquantified modeling assumption that biological influences have been known to enhance colloid agglomeration. As an example of how abundant microbial colloids could become, the in-drift colloids model reports a range for U.S. Department of Energy high-level radioactive waste colloids between 6×10^{-8} and 1×10^{-11} mol/L (CRWMS M&O 2000 [DIRS 129280], Table 1). However, potential levels of colloid generation reported in CRWMS M&O (2000 [DIRS 151561], Table 73) and converted to mol/L is above the midpoint of that distribution (1.92×10^{-9}). This indicates that an equivalent number of microbes could exist as colloids within the EBS, and therefore, could become an additional source of colloids leaving the drift. The uncertainties associated with a new model for microbial transport are described in detail in Section 10.3.6. However, the numbers provided above are based on a bounding estimate (the largest biomass reported from the modeling run with the largest biomass produced) taken from a modeling case that rapidly corrodes the internals of a 44-BWR waste package. The levels of colloids released from the EBS produced over the time length of modeling runs reported in *In-Drift Microbial Communities* (CRWMS M&O 2000 [DIRS 151561]) will not be maintained at this bounding level. Refer to Section 10.3.6 for an expanded discussion of these topics.

6.3.3.4 Model Development since Revision 00 of the Analysis Model Reports

6.3.3.4.1 Precipitates/Salts Model

The precipitates/salts model has been modified in several ways since the revised *In-Drift Precipitates/Salts Analysis* report (CRWMS M&O 2001 [DIRS 153265]) was released. Each modification involved the high relative humidity submodel. The Pitzer database was improved by the addition of several minerals and thermodynamic data, and the amount of output data reported in lookup tables was increased. These changes are discussed in Mariner (2001 [DIRS 155041]).

To ensure that the Pitzer database modifications did not affect validation of the high relative humidity model, the J-13 and Topopah Spring tuff pore water evaporation experiments were resimulated. The predictions and experimental data are plotted in Figures 6.3.3-1, 6.3.3-2, and 6.3.3-3 for the qualified outputs prepared for the TSPA-SR (CRWMS M&O 2000 [DIRS 153246]) calculations. For the J-13 evaporation simulations, differences between the new and old predictions of pH, chloride concentration, and ionic strength are approximately 1 percent or less. In the tuff pore water evaporation simulation, pH predictions are lower but appear to improve by creating a smoother trend. The chloride concentration and ionic strength predictions were nearly unchanged. A more detailed account of the Pitzer database modifications and their implications is included in Mariner (2001 [DIRS 155041]).

Another modification since the initial calculations is that the lookup tables include additional outputs. Instead of providing only the predicted pH, chloride, and ionic strength approximation, concentrations of the full suite of elements and a select number of aqueous species potentially used to estimate alkalinity are provided (Section 6.3.3.6). Many of these outputs can be validated and therefore qualified by existing experimental data, but the rest may not. Those that can likely be validated are carbon, potassium, fluorine, nitrogen, sodium, sulfur, HCO_3^-, CO_3^{-2}, H^+, and OH^-. Those that may not be able to be validated are aluminum, calcium, iron, magnesium, silicon, $H_3SiO_4^-$, $H_2SiO_4^{-2}$, and $MgOH^+$.

An additional improvement to the lookup tables is that they now provide for the possibility of condensation. Previous TSPA analyses indicated that condensation instead of evaporation might occur at times. The precipitates/salts model was run to determine the outputs appropriate for seepage plus condensation. These results were added to the tables.

6.3.3.4.2 Seepage/Invert Interactions Model

6.3.3.4.2.1 Introduction to Acid Neutralizing Capacity/pH Mixing Model

Uncertainties in mixing of natural water and leaking radioactive waste-bearing solutions while in the in-drift environment were not explicitly quantified in the TSPA-SR (CRWMS M&O 2000 [DIRS 153246]) treatment. Instead, ranges of solution compositions were evaluated for properties, such as solubility, under an in-drift carbon dioxide gas fugacity for a given time period. There was also no explicit unified water chemistry that was internally consistent for all areas of the drift. The present in-drift mixing model attempts to establish a unified water chemistry model within the drift. This can be applied to prior TSPA model development by producing analogous output feeds of pH, ionic strength, and acid neutralizing capacity (ANC) for mixed solutions in the drift.

This section gives a theoretical approach to abstracting the various process models for calculating the following variables for in-drift mixed solutions: ionic strength, pH, and ANC (which is an indication of the resistance of a solution to pH changes). These in-drift solutions are mixtures of seepage fluxes from the crown above the drift, the water wicked through the rock and corroded metals in the invert, and the diffusion film or flux from a waste package after failure.

The new aspects of this ANC/pH in-drift mixing model integrate process model chemistry (CRWMS M&O 2001 [DIRS 153265]; CRWMS M&O 2000 [DIRS 129287]; CRWMS M&O 2000 [DIRS 129283]) to provide consistent solution chemistry for use in modeling radionuclide solubilities, colloidal properties and transport, radionuclide sorption, and carbon dioxide gas equilibria within and leaving the repository drift for the TSPA model. Additionally, ionic strength is evaluated as part of the combined water source mixtures in order to provide values to the TSPA model.

The integrated outputs of this model are designed to be the same TSPA model feeds as before: pH, ionic strength, plus ANC values in solutions which are mixed from three sources (crown seepage, invert wicking, and waste package leakage).

6.3.3.4.2.2 Acid Neutralizing Capacity Definitions–Theoretical and Operational

In this abstraction, the theoretical and operational definitions of ANC follow those suggested by Morel and Hering (1993 [DIRS 151052], pp. 166 to 167): the theoretical ANC "of a solution is the negative of the TOTH (Total Hydrogen Concentration in Solution) expression when the components are the principal components of the solution at the carbon dioxide equivalence point." The reason for defining the ANC in this way is that it is numerically equivalent to the operational laboratory measurement of ANC described below, and that it is possible to simulate the ANC of mixed waters theoretically using EQ3/6 V7.2b software or in simple laboratory ANC titration experiments. Another advantage is that this derivation follows directly the use of the Morel and Hering (1993 [DIRS 151052], pp. 9 to 31). Tableaux format of species and chemical components are the basis for setting up a chemical speciation calculation with EQ3/6 V7.2b software.

According to Morel and Hering (1993 [DIRS 151052], pp. 166 to 167), the ANC of a solution is its acid neutralizing capacity when the end point of the titration (with mineral acid) is the carbon dioxide equivalence point. The carbon dioxide equivalence point is the pH of a pure carbon dioxide solution, and is where the ANC goes to zero.

The geochemistry term "acid neutralizing capacity" to the carbon dioxide equivalence point is numerically equivalent to the analytical chemistry term "titration alkalinity" or the engineering term "alkalinity" as equivalent weight of $CaCO_3$ (Butler 1982 [DIRS 154647], p. 1-30; Stumm and Morgan 1981 [DIRS 100829], pp. 171 to 208.]). ANC is normally computed as equivalents per kg of water for high precision work (Stumm and Morgan 1981 [DIRS 100829], pp. 171 to 208). ANC is a conservative parameter when computed as equivalents per kg of water, which is invariant with changes in temperature, pressure, and carbon dioxide fugacity. This makes it ideally suited for chemical mixing models in systems like the drift, where carbon dioxide equilibria affect most chemical changes that can occur.

6.3.3.4.2.3 Theoretical Acid Neutralizing Capacity Abstraction Equations by Source Species Inputs

These abstraction equations were derived for each of the three sources of solution in the drift by consulting directly with geochemists who had been involved with the process. The three sources of in-drift ANC were the ANC_{WPL} (from waste package leaking), the ANC_{CS} (from crown seepage), and the ANC_{IW} (from invert wicking).

Crown Seepage

$$ANC_{CS} = [HCO_3^-] + 2[CO_3^{-2}] + [OH^-] - [H^+] + [MgOH^+] + [H_3SiO_4^-] + 2[H_2SiO_4^{-2}] \quad \text{(Eq. 6-1)}$$

Waste Package Leaking

$$ANC_{WPL} = [HCO_3^-] + 2[CO_3^{-2}] + 2[UO_2CO_3] + [OH^-] - [H^+] + [MoO_4^{-2}] \quad \text{(Eq. 6-2)}$$

Invert Wicking

$$ANC_{IW} = [HCO_3^-] + 2[CO_3^{-2}] + [OH^-] - [H^+] + [MgOH^+] + [H_3SiO_4^-] + 2[H_2SiO_4^{-2}] \quad \text{(Eq. 6-3)}$$

The criteria were to develop the top five or six contributing ANC species for each source, and then to abstract for the TSPA model the two or three species that provided at least 70 percent of the ANC for each source. The species that contributed to ANC were identified to isolate species from EQ3/6 runs (CRWMS M&O 2001 [DIRS 153265]; CRWMS M&O 2000 [DIRS 129287]) with a contribution to the total $[H^+]$ in the system, total hydrogen concentration in solution (Morel and Hering 1993 [DIRS 151052], pp. 161 to 191), at the carbon dioxide equivalence point.

The carbonate equilibria, with both aqueous species and carbon dioxide gas, are considered primary contributors for all three sources of ANC in the drift, as with most fresh waters and sea water (Stumm and Morgan 1981 [DIRS 100829], pp. 171 to 229). The silicate species are considered secondary ANC contributors for the crown seepage and invert wicking sources. One of the species in the molybdate equilibria, $[MoO_4^{-2}]$, is considered a secondary ANC contributor for the waste package leaking sources. Two species, $[MgOH^+]$ and $[UO_2CO_3^{-2}]$, are considered secondary or tertiary ANC contributors, but posed special problems in allowing an accurate abstraction for pH computations. For the current version of the ANC mixing model, $[MgOH^+]$ and $[UO_2CO_3]$ are considered negligible for calculations to second-order accuracy, but they will be added for completeness in later model revisions.

6.3.3.4.2.4 In-Drift Acid Neutralizing Capacity Mixing Model Equations

Waters from various sources are mixed in oceans, estuaries, lakes, the confluence of rivers, waste water disposal sites, and probably in potential repository drifts. As Morel and Hering (1993 [DIRS 151052], pp. 191 to 195) have shown, given detailed recipes for the waters and a description of the mixing process, one can predict the chemical characteristics of the mixture by mixing conservative properties of the waters, like the ANC. Although substantially more complicated in the details of the present case, this is the basic principle which guides the development of the in-drift ANC mixing model equations in this section. As Morel and Hering (1993 [DIRS 151052], pp. 191 to 195) explained, total concentrations can be divided by total masses to get an average concentration when solutions mix, but pH cannot be determined as a simple average of the pH values of the original 2 solutions. Like Morel and Hering (1993 [DIRS 151052], pp. 191 to 195), simple linear mixing models of ANC as weighted by the mass of solution for a given time step are used. However, the linear ANC mixing models are converted into the required non-linear pH mixing model in the following section.

$$ANC_{CS+IW} = \{(W_{CS} * ANC_{CS}) + (W_{IW} * ANC_{IW})\} / (W_{CS} + W_{IW}) \quad \text{(Eq. 6-4)}$$

where W_{CS}, W_{IW} are the masses of solution (kg) from the crown seepage and the invert wicking, respectively. This approach assumes complete mixing of the crown seepage and invert wicking solutions in every case. (There is an implied fractional mixing factor of 1.00 multiplied by both products in the numerator of Equation 6-4.)

For the case of solutions leaking from the waste package, it was assumed that this might often be through a diffusive film that would mix incompletely with waters in the drift. A representative mixing function was developed to abstract this behavior assuming one-half (from the tail at 1.1 percent mixing to the mean at 100 percent mixing) of a standard normal distribution (Evans et al. 1993 [DIRS 112115], pp. 114 to 118), with the relative frequencies scaled to 1.00 by dividing by a scaling factor ($F_{SCALING}$ = 0.398942). The mixing function assumes a symmetrical half of a normal distribution because it physically corresponds to a cross section of the symmetrical waste package in the symmetrical drift, consistent with the *Multiscale Thermohydrologic Model* (CRWMS M&O 2000 [DIRS 149862], pp. 89, 106, and 107). Operationally, slightly faster computations can be performed for one half of a symmetrical drift cross section. Although the possible mixing ranges from 1.1 percent at the tail to 100 percent mixing at the mean within the mixing function, there is a case that can provide 0 percent mixing of the waste package leaking. If the mass of solution coming from the waste package goes to zero, Equation 6-5 reduces to Equation 6-4, which shows 100 percent mixing of the crown and invert sources and no mixing from the waste package.

Two important characteristics of the envisioned diffusion and mixing process are abstracted with this function: some mixing always takes place if there is mass flux from the waste package (the minimum mixing is 1.1 percent), and the fractional mixing factor, F_{MIXING} (1.1 to 100 percent), is normally distributed. The *x* values from -3 through 0 may be pseudo-randomly generated in external stochastic algorithms (such as GoldSim in the TSPA model).

$$ANC_{MIXED} = ((F_{MIXING} * (ANC_{WPL} * W_{WPL})) + ((ANC_{CS+IW}) * (W_{CS} + W_{IW}))) / ((F_{MIXING} * W_{WPL}) + W_{CS} + W_{IW}) \quad \text{(Eq. 6-5)}$$

where

$$F_{MIXING} = (1/(\sigma *(2\pi)^{0.5}) \exp((-1/(2\sigma^2)) * (x - \mu)^2)) / F_{SCALING}$$

with *x* = -3 through 0, $F_{SCALING}$ = 0.398942, $\mu = 0$, and $\sigma = 1$.

6.3.3.4.2.5 In-Drift pH from In-Drift Acid Neutralizing Capacity Mixing Equations

The calculations to compute pH from ANC measurements have to be abstracted as a series of successively more detailed approximations expressed in terms of $[H^+]$, equilibrium constants, species concentrations, ionization fractions, and carbon dioxide partial pressures. The initial pH values, calculated only from the log K value of water, are used to estimate the ionization fractions and species of the carbonate equilibria in the ANC mixing equations. The initial pH values computed from the carbonate equilibria allow ionization fractions and species concentrations for the in-drift ANC equations to be calculated, which cannot be solved without prior estimates of the solution pH. This is why a succession of improved estimates of pH is necessary. Estimates of pH are necessary to solve the nonlinear, in-drift ANC equation accurately for pH. The ultimate answer being calculated is the pH of the mixed solutions in the drift for use in the TSPA model.

First Iteration Set: Carbonate Equilibria–Present versions of the in-drift pH mixing equations ignore activity coefficient variations (all activity coefficients are assumed equal to one),

variations of log K for the appropriate equilibria as a function of temperature (all log K values are only abstracted for the 25°C case at present), variations of log K for the appropriate equilibria as a function of ionic strength (all log K values are only abstracted for the infinite dilution case at present), and precipitation of solids during the mixing process. These simplifications will be changed to more complex formulations that are more representative in any future revisions of the in-drift pH mixing model.

To begin the iterative process of calculating the in-drift pH for the mixed solutions, an initial approximation uses the input pH value from the source with the largest mass flux term for a given time step. This is substituted in the simple ANC equation for a pure carbonate system (Equation 6-6) given by Stumm and Morgan (1981 [DIRS 100829], p. 188, Equation 17) after the carbonate species are replaced by terms containing $[H^+]$, P_{CO2}, and the various carbonate equilibria (Stumm and Morgan 1981 [DIRS 100829], pp. 204 to 206).

$$ANC = [HCO_3^-] + 2[CO_3^{-2}] + [OH^-] - [H^+] \quad \text{(Eq. 6-6)}$$

which rearranges after substitution of Equations 6-7 through 6-9 into Equation 6-10.

$$[H_2CO_3^*] = (K_H * P_{CO2}) \quad \text{(Eq. 6-7)}$$

$$K_1 = \{H^+\}\ \{HCO_3^-\}/\ \{\ H_2CO_3^*\} = [H^+]\ [HCO_3^-]\ /\ [H_2CO_3^*] \quad \text{(Eq. 6-8)}$$

Since all activity coefficients are assumed to be one in this version, then species activities {•} are equal to concentrations [•].

$$K_2 = \{H^+\}\ \{CO_3^{-2}\}/\ \{HCO_3^-\} = [H^+]\ [CO_3^{-2}]\ /\ [HCO_3^-] \quad \text{(Eq. 6-9)}$$

Since all activity coefficients are assumed to be one in this version, then species activities {•} are equal to concentrations [•].

$$ANC = ((K_1 * K_H * P_{CO2}) / [H^+]) + ((2 * K_1 * K_2 * K_H * P_{CO2}) /$$

$$[H^+]^2) + [OH^-] - [H^+] \quad \text{(Eq. 6-10)}$$

where $K_H = 10^{-1.47}$, $K_1 = 10^{-6.352}$, $K_2 = 10^{-10.329}$, and P_{CO2} is the variable input partial pressure of carbon dioxide at atmospheric pressure. Near these total pressures, it is numerically equal to the fugacity of carbon dioxide (Stumm and Morgan 1981 [DIRS 100829], pp. 42, and 204 to 206).

Rearranging terms in Equation 6-11 to substitute for $[OH^-]$ in Equation 6-10 and making it equal to Equation 6-6 yields Equation 6-12:

$$[H^+] * [OH^-] = 10^{-14.00} = K_W \quad \text{(Eq. 6-11)}$$

$$[HCO_3^-]_{INPUT} + 2[CO_3^{-2}]_{INPUT} + [OH^-]_{INPUT} - [H^+]_{INPUT} =$$

$$((K_1 * K_H * P_{CO2}) / [H^+]) + ((2 * K_1 * K_2 * K_H * P_{CO2}) / [H^+]^2) +$$

$$(K_W / [H^+]) - [H^+] \quad \text{(Eq. 6-12)}$$

First Iteration Set: Inputs and Principles of Computation–Equation 6-12 is the basis for the first set of iterations to determine the in-drift mixed solution pH values. Two sets of pH calculations are performed for each time step: the pH from two-source mixing (crown seepage and invert wicking) and the pH from all three sources mixing (crown seepage, invert wicking, and waste package leaking). For most calculations, the three source terms will have the largest impact on dose after the period when waste packages begin leaking. However, in the later stages of waste form and waste package deterioration, radionuclides may be found in the invert solutions derived from two-horizontal wicking of contaminated invert waters after they have earlier mixed from the waste package to the drift floor.

Each species on the left side of Equation 6-12 is calculated from source input weighted either by Equation 6-4 or Equation 6-5, depending on whether there is an ANC contribution from waste package leakage.

Technically, the various carbonate, silicate, and molybdate species cannot be linearly mixed if they are only used separately as individual species. However, the mixed individual specs concentrations are used on the left side of Equations 6-12, 6-29, and 6-49 to sum to ANC_{MIXED}, which may be linearly mixed. On the right side of Equations 6-12, 6-29, and 6-49, individual species are replaced with terms composed of equilibrium constants, carbon dioxide fugacity, and hydrogen ion concentration which is iterated to solve for $ANC_{MIXED.}$

First Iteration Set: Convergence Criteria–The last stage for the left side is summing all 4 terms to compute a value for the weighted ANC from the sources. This ANC sum is then used to control the pH iteration computation through the convergence criterion that the right side computation is complete when the right side ANC is greater than the left side ANC.

Each term on the right side of Equation 6-12 is solved by substituting the carbonate equilibrium constants and the assigned variable P_{CO2} in the drift. Then, the only unknown variable is the $[H^+]$, which is solved by computer to optimize the right side ANC estimate. In order to begin the iterative process of computing the in-drift pH for the mixed solutions, an initial estimate starts at pH = 0.0 and goes to pH = 15.0 by 0.1 pH unit steps. With this approximation, all of the right side terms of Equation 6-12 are evaluated and the ANC sum is compared to check if it is larger than the left side ANC. If it is within the convergence criterion, the computation is sent to a high precision subroutine that computes $[H^+]$ within 0.01 pH unit. If it is not within the convergence criterion, the initial input $[H^+]$ is increased by 0.1 pH units. After this final $[H^+]$ is determined by the iteration process, it is used as an input estimate to the next iterative process discussed below.

Second Iteration Set: Silicate Equilibria–A more detailed abstraction of the acid neutralizing capacity of mixed solutions in the drift includes silicates from the crown seepage and invert wicking in Equation 6-13:

$$ANC = [HCO_3^-] + 2[CO_3^{-2}] + [H_3SiO_4^-] + 2[H_2SiO_4^{-2}] + [OH^-] - [H^+] \qquad \text{(Eq. 6-13)}$$

which rearranges after substitution of Equations 6-12, and Equations 6-14 through 6-23 to Equation 6-24. Equations 6-16 through 6-23 are based on the diprotic acid dissociation equilibria and ionization fractions given by Stumm and Morgan (1981 [DIRS 100829], p. 174) for carbonate equilibria and are applied here for silicate equilibria.

$$K_{1Si} = \{H^+\}\ \{H_3SiO_4^-\}/\ \{H_4SiO_4\} = [H^+]\ [H_3SiO_4^-] / [H_4SiO_4] = 10^{-9.86} \quad \text{(Eq. 6-14)}$$

Because all activity coefficients are assumed to be one in this version, then species activities {•} are equal to concentrations [•] (Smith and Martell 1976 [DIRS 127382], p. 39)

$$K_{2Si} = \{H^+\}\ \{\ H_2SiO_4^{-2}\}/\ \{\ H_3SiO_4^-\} = [H^+]\ [H_2SiO_4^{-2}] / [H_3SiO_4^-] = 10^{-13.1} \quad \text{(Eq. 6-15)}$$

$$Si_{Total} = [H_4SiO_4] + [H_3SiO_4^-] + [H_2SiO_4^{-2}] \quad \text{(Eq. 6-16)}$$

$$[H_4SiO_4] = Si_{Total} * \alpha_{0Si} \quad \text{(Eq. 6-17)}$$

$$[H_3SiO_4^-] = Si_{Total} * \alpha_{1Si} \quad \text{(Eq. 6-18)}$$

$$[H_2SiO_4^{-2}] = Si_{Total} * \alpha_{2Si} \quad \text{(Eq. 6-19)}$$

$$\alpha_{0Si} = (1 + (K_{1Si} / [H^+]) + ((K_{1Si} * K_{2Si}) / [H^+]^2))^{-1} \quad \text{(Eq. 6-20)}$$

$$\alpha_{1Si} = (([H^+] / K_{1Si}) + 1 + (K_{2Si} / [H^+]))^{-1} \quad \text{(Eq. 6-21)}$$

$$\alpha_{2Si} = (([H^+]^2 / (K_{1Si} * K_{2Si})) + ([H^+] / K_{2Si}) + 1)^{-1} \quad \text{(Eq. 6-22)}$$

Substituting Equation 6-18 in Equation 6-16 yields Equation 6-23:

$$[H_4SiO_4] = ([H_3SiO_4^-]/ \alpha_{1Si}) - [H_3SiO_4^-] - [H_2SiO_4^{-2}] \quad \text{(Eq. 6-23)}$$

Substituting Equation 6-21 in Equation 6-23 gives Equation 6-24:

$$[H_4SiO_4] = ([H_3SiO_4^-]/ ((((([H^+] / K_{1Si}) + 1 + (K_{2Si} / [H^+]))^{-1}) -[H_3SiO_4^-]$$

$$- [H_2SiO_4^{-2}]) \quad \text{(Eq. 6-24)}$$

Rearranging Equation 6-14 yields Equation 6-25, and substitution of Equation 6-24 in Equation 6-25 yields Equation 6-26:

$$[H_3SiO_4^-] = K_{1Si} * [H_4SiO_4]) / [H^+] \quad \text{(Eq. 6-25)}$$

$$[H_3SiO_4^-] = K_{1Si} * ([H_3SiO_4^-]/ ((((([H^+] / K_{1Si}) + 1 + (K_{2Si} / [H^+]))^{-1})$$

$$- [H_3SiO_4^-] - [H_2SiO_4^{-2}]) / [H^+] \quad \text{(Eq. 6-26)}$$

Rearranging Equation 6-15 yields Equation 6-27:

$$[H_2SiO_4^{-2}] = (K_{2Si} * [H_3SiO_4^-]) / [H^+] \quad \text{(Eq. 6-27)}$$

Substituting Equations 6-6, 6-10, 6-11, 6-24, and 6-27 in Equation 6-13 gives Equation 6-28:

$$ANC = ((K_1 * K_H * P_{CO2}) / [H^+]) + ((2 * K_1 * K_2 * K_H * P_{CO2}) / [H^+]^2)$$

$$+ (K_{1Si} * \{[H_3SiO_4^-] / ((((([H^+] / K_{1Si}) + 1 + (K_{2Si} / [H^+]))^{-1}) - [H_3SiO_4^-] - [H_2SiO_4^{-2}])\} / [H^+])$$

$$+ (2 * K_{2Si} * [H_3SiO_4^-] / [H^+]) + (K_W / [H^+]) - [H^+] \quad \text{(Eq. 6-28)}$$

Equating Equations 6-28, and 6-13 yields Equation 6-29:

$$[HCO_3^-]_{INPUT} + 2[CO_3^{-2}]_{INPUT} + [H_3SiO_4^-]_{INPUT} + 2[H_2SiO_4^{-2}]$$

$$_{INPUT} + [OH^-]_{INPUT} - [H^+]_{INPUT} = ((K_1 * K_H * P_{CO2}) / [H^+]) + ((2 * K_1 * K_2 * K_H * P_{CO2})$$

$$/ [H^+]^2) + (K_{1Si} * \{[H_3SiO_4^-] / ((((([H^+] / K_{1Si}) + 1 + (K_{2Si} / [H^+]))^{-1}) - [H_3SiO_4^-]$$

$$- [H_2SiO_4^{-2}])\} / [H^+]) + (2 * K_{2Si} * [H_3SiO_4^-] / [H^+]) +$$

$$(K_W / [H^+]) - [H^+] \quad \text{(Eq. 6-29)}$$

Equation 6-29 is the basis for iterating $[H^+]$ to estimate $ANC_{Right\ Hand\ Side}$ for the combined carbonate and silicate systems, just like Equation 6-12 was for the carbonate system alone. The convergence criteria are the same, and the iteration process is the same for solving Equation 6-29 as it was for Equation 6-12, so those procedures are not repeated here.

Third Iteration Set: Molybdate Equilibria–A more detailed abstraction of the acid neutralizing capacity of mixed solutions in the drift includes $[MoO_4^{-2}]$ from the waste package added to Equation 6-13 to yield:

$$ANC = [HCO_3^-] + 2[CO_3^{-2}] + [H_3SiO_4^-] + 2[H_2SiO_4^{-2}] +$$

$$[MoO_4^{-2}] + [OH^-] - [H^+] \quad \text{(Eq. 6-30)}$$

Equations 6-31 to 6-40 are based on the diprotic acid dissociation equilibria and ionization fractions given by Stumm and Morgan (1981 [DIRS 100829], p. 174) for carbonate equilibria and are applied here for molybdate equilibria.

$$K_{1Mo} = \{H^+\}\{MoO_4^{-2}\} / \{HMoO_4^{-1}\} = [H^+][MoO_4^{-2}] / [HMoO_4^{-1}] = 10^{-4.24} \quad \text{(Eq. 6-31)}$$

Because all activity coefficients are assumed to be one in this version, then species activities $\{\bullet\}$ are equal to concentrations $[\bullet]$.(Smith and Martell 1976 [DIRS 127382], p. 18)

$$K_{2'} = \{H^+\}^2 \{MoO_4^{-2}\} / \{H_2MoO_4\} = [H^+]^2 [MoO_4^{-2}] / [H_2MoO_4] = 10^{-8.24} \quad \text{(Eq. 6-32)}$$

Subtracting Equation 6-31 from Equation 6-32 yields:

$$K_{2Mo} = \{H^+\} \{HMoO_4^{-1}\} / \{H_2MoO_4\} =$$

$$[H^+] [HMoO_4^{-1}] / [H_2MoO_4] = 10^{-4.00} \quad \text{(Eq.6-33)}$$

Because all activity coefficients are assumed to be one in this version, then species activities {•} are equal to concentrations [•].

$$Mo_{Total} = [H_2MoO_4] + [HMoO_4^{-1}] + [MoO_4^{-2}] \quad \text{(Eq. 6-34)}$$

$$[H_2MoO_4] = Mo_{Total} * \alpha_{0Mo} \quad \text{(Eq. 6-35)}$$

$$[HMoO_4^{-1}] = Mo_{Total} * \alpha_{1Mo} \quad \text{(Eq. 6-36)}$$

$$[MoO_4^{-2}] = Mo_{Total} * \alpha_{2Mo} \quad \text{(Eq. 6-37)}$$

$$\alpha_{0Mo} = (1 + (K_{1Mo} / [H^+]) + ((K_{1Mo} * K_{2Mo}) / [H^+]^2))^{-1} \quad \text{(Eq. 6-38)}$$

$$\alpha_{1Mo} = (([H^+] / K_{1Mo}) + 1 + (K_{2Mo} / [H^+]))^{-1} \quad \text{(Eq. 6-39)}$$

$$\alpha_{2Mo} = (([H^+]^2 / (K_{1Mo} * K_{2Mo})) + ([H^+] / K_{2Mo}) + 1)^{-1} \quad \text{(Eq. 6-40)}$$

Substituting Equation 6-36 in Equation 6-34 yields Equation 6-41:

$$[H_2MoO_4] = ([HMoO_4^{-1}]/ \alpha_{1Mo}) - [HMoO_4^{-1}] - [MoO_4^{-2}] \quad \text{(Eq. 6-41)}$$

Substituting Equation 6-39 in Equation 6-41 gives Equation 6-42:

$$[H_2MoO_4] = ([HMoO_4^{-1}]/(([H^+] / K_{1Mo}) + 1 + (K_{2Mo} / [H^+]))^{-1}) -$$

$$[HMoO_4^{-1}] - [MoO_4^{-2}]) \quad \text{(Eq. 6-42)}$$

Rearranging Equation 6-31 yields Equation 6-43, which then can be substituted in Equation 6-42, producing Equation 6-44, which allows the three molybdenum species to be described only in terms of equilibrium constants, $[MoO_4^{-2}]$, and $[H^+]$. Rearranging Equation 6-32 allows Equation 6-45 to be expressed in a form where Equations 6-43 and 6-45 do not have the same components. Then Equation 6-46 is computed by substituting Equation 6-44 in Equation 6-45. This allows an internal quality assurance check by using Equations 6-34 through 6-40 to check Equation 6-47.

$$[HMoO_4^{-1}] = ([H^+][MoO_4^{-2}]/ K_{1Mo}) \quad \text{(Eq. 6-43)}$$

$$[H_2MoO_4] = (([H^+][MoO_4^{-2}]/ K_{1Mo}) /(([H^+] / K_{1Mo}) + 1 + (K_{2Mo} / [H^+]))^{-1})$$

$$- ([H^+][MoO_4^{-2}]/ K_{1Mo}) - [MoO_4^{-2}]) \quad \text{(Eq. 6-44)}$$

$$[MoO_4^{-2}] = (K_{2'} * [H_2MoO_4]) / [H^+]^2 \quad \text{(Eq. 6-45)}$$

$$[MoO_4^{-2}] = (K_{2'} * \{(([H^+][MoO_4^{-2}]/ K_{1Mo}) /(([H^+] / K_{1Mo}) + 1 + (K_{2Mo} / [H^+]))^{-1})$$

$$- ([H^+][MoO_4^{-2}]/ K_{1Mo}) - [MoO_4^{-2}]\}) / [H^+]^2 \quad \text{(Eq. 6-46)}$$

$$\alpha_{0Mo} + \alpha_{1Mo} + \alpha_{2Mo} = 1 \quad \text{(Eq. 6-47)}$$

Substituting Equations 6-46 and 6-28 in Equation 6-30 gives:

$$ANC = ((K_1 * K_H * P_{CO2}) / [H^+]) + ((2 * K_1 * K_2 * K_H * P_{CO2}) / [H^+]^2)$$
$$+ (K_{1Si} * \{([H_3SiO_4^-]/ (([H^+] / K_{1Si}) + 1 + (K_{2Si} / [H^+]))^{-1}) - [H_3SiO_4^-] - [H_2SiO_4^{-2}]\} / [H^+])$$
$$+ \{(2 * K_{2Si} * [H_3SiO_4^-] / [H^+]) + (K_{2'} * \{(([H^+][MoO_4^{-2}]/ K_{1Mo}) /(([H^+] / K_{1Mo}) + 1$$
$$+ (K_{2Mo} / [H^+]))^{-1}) - ([H^+][MoO_4^{-2}]/ K_{1Mo}) - [MoO_4^{-2}]\}) / [H^+]^2\} +$$
$$(K_W / [H^+]) - [H^+] \qquad \text{(Eq. 6-48)}$$

Equating Equation 6-48 and Equation 6-30 yields Equation 6-49:

$$[HCO_3^-]_{INPUT} + 2[CO_3^{-2}]_{INPUT} + [H_3SiO_4^-]_{INPUT} + 2[H_2SiO_4^{-2}]_{INPUT}$$
$$+ [MoO_4^{-2}]_{INPUT} + [OH^-]_{INPUT} - [H^+]_{INPUT} = ((K_1 * K_H * P_{CO2}) / [H^+])$$
$$+ ((2 * K_1 * K_2 * K_H * P_{CO2}) / [H^+]^2) + (K_{1Si} * \{[H_3SiO_4^-]/ ((([H^+] / K_{1Si})$$
$$+ 1 + (K_{2Si} / [H^+]))^{-1}) - [H_3SiO_4^-] - [H_2SiO_4^{-2}]\} / [H^+]) + \{(2 * K_{2Si} *$$
$$[H_3SiO_4^-] / [H^+]) + (K_{2'} * \{(([H^+][MoO_4^{-2}]/ K_{1Mo}) /(([H^+] / K_{1Mo}) + 1$$
$$+ (K_{2Mo} / [H^+]))^{-1}) - ([H^+][MoO_4^{-2}]/ K_{1Mo}) - [MoO_4^{-2}]\}) / [H^+]^2\}$$
$$+ (K_W / [H^+]) - [H^+] \qquad \text{(Eq. 6-49)}$$

Equation 6-49 is the basis for iterating $[H^+]$ to estimate $ANC_{Right\ Hand\ Side}$ for the combined carbonate, silicate, and molybdate systems, just like Equation 6-29 was for the carbonate and silicate system. The convergence criteria are the same, and the iteration process is the same for solving Equation 6-49 as it was for Equations 6-29 and 6-12.

6.3.3.4.2.6 Ionic Strength Mixing Equations

Ionic strength is not a conservative parameter. Technically, it varies with temperature, pressure, and changing valence with changing species for a given element's total concentration in solution. In this computation, it is assumed to mix linearly within an order of magnitude of the true ionic strength, which is the same error criteria used for the ionic strengths that are fed to the model. These simplifications will be changed to more complex formulations that are more representative in future revisions of the in-drift ionic strength mixing model.

$$I_{CS+IW} = \{(W_{CS} * I_{CS}) + (W_{IW} * I_{IW})\} / (W_{CS} + W_{IW}) \qquad \text{(Eq. 6-50)}$$

where W_{CS} and W_{IW} are the masses of solution (kg) from the crown seepage and the invert wicking, respectively. This approach assumes complete mixing of the crown seepage and invert wicking solutions in every case. (There is an implied fractional mixing factor of 1.00 multiplied times both products in the numerator of Equation 6-50.)

For the case of solutions leaking from the waste package, it was assumed that this might often be through a diffusive film that would mix incompletely with all of the waters in the drift. A representative mixing function was developed to abstract this behavior assuming one half (from the tail at 1.1 percent mixing to the mean at 100 percent mixing) of a standard normal distribution (Evans et al. 1993 [DIRS 112115], pp. 114 to 118), with the relative frequencies scaled to 1.00 by dividing by a scaling factor, $F_{SCALING} = 0.398942$. The mixing function assumes a symmetrical half of a normal distribution because it physically corresponds to a cross section of the symmetrical waste package in the symmetrical drift, consistent with the *Multiscale Thermohydrologic Model* (CRWMS M&O 2000 [DIRS 149862], pp. 89, 106, and 107). Operationally, this allows slightly faster computations if they are performed for one half of a symmetrical drift cross section.

Two important characteristics of the envisioned diffusion and mixing process are abstracted with this function: some mixing always takes place if there is mass flux from the waste package (minimum mixing is 1.1 percent), and the fractional mixing factor, F_{MIXING} (1.1-100 percent), is normally distributed. The x values from -3 through 0 may be pseudo-randomly generated in external stochastic algorithms (such as GoldSim in the TSPA model):

$$I_{MIXED} = ((F_{MIXING} * (I_{WPL} * W_{WPL})) + ((I_{CS+IW}) * (W_{CS} + W_{IW}))) /$$

$$((F_{MIXING} * W_{WPL}) + W_{CS} + W_{IW}); \qquad \text{(Eq. 6-51)}$$

The ionic strength produced as output for each time slice in the TSPA model is I_{MIXED}, which is the mixture of solutions from all three sources (crown, invert, and waste package). In general, the I_{MIXED} value will be the output ionic strength used in sorption, solubility, and colloidal transport computations in the TSPA model because its solution will contain the majority (or all) of the radionuclide species at a given location in the drift.

6.3.3.4.2.7 Output Feeds to Other Subroutines of the Total System Performance Assessment Model

The approach taken by the in-drift ANC and pH model for consistency with other previously developed TSPA subroutines is to compute of the previous output parameters (pH and ionic strength) for the mixed solutions from all three sources (crown seepage, invert wicking, and waste package leaking) producing pH_{MIXED}, and I_{MIXED}.

For most other subroutines (like sorption, solubility, colloids) the appropriate feeds will be the three source variables pH_{MIXED}, and I_{MIXED} produced from Equations 6-49, and 6-51, respectively. The mixing ANC parameter is an important one that may help describe chemistry in other subroutines when it is available. ANC_{MIXED} (computed from Equation 6-5) will also be output for feeds to other geochemical subroutines in the model.

6.3.3.4.3 Microbial Communities Model

Improvements to the microbial communities model dealing with microbial sorption and transport as colloids are described in Section 10.3.6.

6.3.3.5 Results of Analysis

6.3.3.5.1 Precipitates/Salts Model

6.3.3.5.1.1 Sensitivity of Starting Water Composition on Evaporative Chemical Evolution

An important uncertainty in the TSPA-SR (CRWMS M&O 2000 [DIRS 153246]) calculations is the sensitivity of the starting water composition on the evaporative chemical evolution of water in the drift. The TSPA-SR model makes the assumption that nitrate salts will set the lower limit on the relative humidity at which liquid water is stable within the drift (the relative humidity threshold discussed in Section 6.3.3.3.1). To address this uncertainty, a sensitivity analysis was performed. The results, documented in detail in Mariner (2001 [DIRS 155041]), show that the chemical composition of the remaining unevaporated water can be highly sensitive to the starting water composition. Furthermore, they suggest that the relative humidity threshold assumption may not be conservative in some instances. These results, summarized below, illustrate the importance of chemical divides that are encountered when mineral phases precipitate (Mariner 2001 [DIRS 155041]).

Evaporation of water is the net transfer of water molecules from liquid to vapor. As water evaporates from an aqueous solution, each solute concentrates until it becomes supersaturated with respect to a mineral phase and precipitates. Continued evaporation and precipitation causes the composition and properties of the remaining aqueous solution to evolve into a solution that is markedly different from the starting composition.

A chemical divide is demonstrated in the following example. If halite (NaCl) reaches saturation and begins to precipitate, and the sodium:chloride molar ratio is greater than one, then chloride will become depleted in solution while excess sodium will continue to concentrate. Inversely, if the ratio is less than one, then sodium will become depleted while excess chloride will continue to concentrate. This mechanism implies that a small difference in the original sodium:chloride ratio can determine whether a sodium or a chloride brine develops beyond the halite chemical divide.

For the sensitivity analysis, evaporation calculations were performed for several waters observed at Yucca Mountain or predicted to potentially occur in the drift. These calculations are described in detail in Mariner (2001 [DIRS 155041]). The waters evaluated include the following:

- In situ J-13 ground water; that is, average J-13 well water from Harrar et al. (1990 [DIRS 100814]) corrected for carbon dioxide degassing (DTN: MO0006J13WTRCM.000 [DIRS 151029])

- Topopah Spring tuff pore water (CRWMS M&O 2001 [DIRS 154426], Table 3, p. 36; DTN: LB0101DSTTHCR1.001 [DIRS 154656])

- Water perched on top of the Calico Hills formation at the base of the Topopah Spring tuff (CRWMS M&O 2000 [DIRS 144986], Table 8)

- Water collected from the Single Heater Test (Borehole 16, collected 2/3/97, Suite 2) (CRWMS M&O 1997 [DIRS 101540], Table 5-19, p. 5-49)

- Water collected from the Drift Scale Test (Borehole 60-3, collected 1/26/99) (CRWMS M&O 2001 [DIRS 154426] Table 9, p. 89; DTN: LL990702804244.100 [DIRS 144922])

- Water predicted by the THC model (CRWMS M&O 2000 [DIRS 142022] to seep into the drift (DTN: MO9912SPAPAI29.002 [DIRS 148596])

- Water predicted to result from reaction with cement within the drift (CRWMS M&O 2000 [DIRS 151951], Table 6.3-3, pp. 79 to 80).

Evaporation of the first five waters was evaluated at three different fixed fugacities of carbon dioxide: 10^{-1}, 10^{-3}, and 10^{-6}. The last two waters were evaluated for periods 2, 3, and 4 of the THC abstraction, (CRWMS M&O 2000 [DIRS 123916]). Figures showing the evaporative evolution of these waters are presented in Mariner (2001 [DIRS 155041]). Only selected figures are provided here. The most recent evaporation calculations (see Section 6.3.3.6) are not directly included in this sensitivity analysis. However, in many ways these calculations are well represented by water #2, which was used to initialize the Topopah Spring tuff pore water composition in the THC model for the current TSPA calculations.

The calcite chemical divide generally occurs during the early stages of evaporation because calcite is not highly soluble in water and the starting waters are either saturated or nearly saturated with respect to calcite. Figure 6.3.3-4 shows the precipitates/salts model prediction of the evaporative evolution of in situ J-13 ground water (water #1 above) at a carbon dioxide fugacity of 10^{-3}. For this water, a carbonate-rich, calcium-poor water evolves similar to that observed in the laboratory for synthetic J-13 well water. Waters #3, #4, and #5 above give similar results. In each of these cases, regardless of the fixed fugacity of carbon dioxide, sodium becomes the dominant cation and carbonate (with one exception) becomes the dominant anion. For the Drift Scale Test water (#5), chloride either becomes or is always predicted to be the dominant anion, but carbonate still concentrates in the solution (at the expense of calcium) and achieves or maintains the position of second most abundant anion in solution. These waters are predicted to evolve in a manner consistent with the relative humidity threshold assumption of 50 percent established for a sodium nitrate brine.

For waters #2, #6, and #7, the calcite chemical divide causes depletion of carbonate and concentration of aqueous calcium with increased evaporation. Figure 6.3.3-5 shows the predicted evolution of an observed Topopah Spring tuff pore water. The reason carbonate is depleted instead of calcium is that these waters have excess calcium relative to carbonate alkalinity. Beyond the calcite divide, excess calcium concentrates until the solutions become supersaturated with respect to gypsum ($CaSO_4 \cdot 2H_2O$). At this point, either calcium or sulfate will deplete depending on their molar ratio in solution. The chemical divides of other calcium minerals, such as fluorite and calcium (hydroxy) silicates, may be encountered anywhere during the reaction progress, but they do not affect the calcium concentration appreciably unless the concentrations of the non-calcium reactants are within about a factor of 10 of calcium or are greater than calcium. In waters #2, #6, and #7, calcite and gypsum are by far the most important

divides within the range of the high relative humidity model. For #6 and #7, there is excess sulfate compared to calcium, so calcium becomes depleted. For #2, there is excess calcium, so calcium continues to concentrate in solution while sulfate becomes depleted.

After the calcite and gypsum chemical divides, the divides for halite (NaCl) and sylvite (KCl) are encountered. If there is more chloride than the sum of sodium and potassium when halite and sylvite reach saturation, then sodium and potassium will be depleted and a calcium chloride brine will likely develop instead of a sodium/potassium nitrate brine. A calcium chloride brine would lower the relative humidity threshold, as discussed in Section 6.3.3.3. This scenario would also allow for high concentrations of magnesium chloride.

Whether a calcium (or magnesium) chloride brine is likely to develop in the repository is uncertain. Of the seven waters in this sensitivity analysis, only evaporation of water #2 is likely to generate such a brine. However, this water was used to initialize the Topopah Spring tuff matrix and fracture water composition in the THC model for the current TSPA calculations (Section 6.3.1). The low relative humidity model of the current precipitates/salts model is based on the assumption that a nitrate brine will develop, as predicted in *Environment on the Surfaces of the Drip Shield and Waste Package Outer Barrier* (CRWMS M&O 2000 [DIRS 151568], Section 6.4.2). With the discovery that a chloride brine may develop, this assumption may no longer be appropriate in all cases. In fact, the latest THC model results predict that waters in the vicinity of the drift will have compositions during the thermal period conducive to generating a calcium chloride brine (Section 6.3.3.6). Future development of the low relative humidity model will focus on accommodating this possibility.

6.3.3.5.1.2 Sensitivity of Mineral Suppressions on Evaporative Chemical Evolution

In a complicated hydrogeochemical system such as pore water in tuff, it is difficult to predict each mineral that will or will not precipitate as a result of evaporation. Some minerals may be inhibited by a lack of nucleation sites or by slow kinetics. Often, however, data needed to determine what will likely happen for potential minerals are either unavailable or inconclusive. In this sensitivity analysis, the sensitivity of mineral suppressions to precipitates/salts model output was assessed by varying the set of minerals suppressed and evaluating the effects on the precipitates/salts model predictions for pH, ionic strength, and chloride concentration.

The first sensitivity analysis on mineral suppressions is documented in Section 5.4 of *In-Drift Precipitates/Salts Analysis* (CRWMS M&O 2001 [DIRS 153265]). Albite-low was suppressed in one set of calculations and then unsuppressed in an identical set of calculations. The results indicated that while the mineral assemblage changed (albite-low precipitated in one set but not in the other) and the aluminum concentration was affected, this mineral suppression had no effect on the output (pH, chloride, and ionic strength) to the TSPA. Aluminum was a minor constituent in the incoming seepage water, so albite-low was a minor constituent of the mineral assemblage. This analysis suggests that minerals that involve minor constituents will not markedly affect chloride and ionic strength predictions. However, it is theoretically possible that suppression of minor constituents may affect pH because the hydrogen ion activity may also be low (e.g., 10^{-8} at pH 8) and poorly buffered.

The addition of several minerals to the Pitzer database provided another opportunity to assess the sensitivity of mineral suppressions on output feeding the TSPA-SR calculations (CRWMS M&O 2000 [DIRS 153246]). The largest change in these calculations resulted from the precipitation of gyrolite, a calcium hydroxysilicate not present in the original Pitzer database. During the boiling period (period 2) of the THC abstraction (CRWMS M&O 2000 [DIRS 123916]), precipitation of gyrolite lowered the pH nearly a full unit, from around 9.3 to around 8.5. However, chloride and ionic strength were essentially unaffected. For periods 3 and 4, the pH was nearly unaffected by the different set of minerals because gyrolite was no longer favored to precipitate. In periods 2, 3, and 4, several new minerals precipitated, while several minerals originally predicted to precipitate did not. The corresponding negligible differences in pH, chloride, and ionic strength predictions suggest that these outputs are not highly sensitive to the set of mineral suppressions chosen. This analysis is presented in detail in Mariner (2001 [DIRS 155041]).

While the above analysis suggests that the uncertainty in mineral suppressions have only minor effects on the pH, chloride, and ionic strength outputs to the TSPA, more work is warranted to evaluate the uncertainty and sensitivity of mineral suppressions on TSPA calculations.

6.3.3.5.2 Seepage/Invert Interactions Model

6.3.3.5.2.1 Results of Analyses

Table 6.3.3-1 shows the results of an example simulation that could be run on the in-drift ANC/pH mixing model given the input data available from the TSPA model at the time of calculation. The approach was to examine a hypothetical case where pH differences might be expected between the three different water sources entering the drift at about the 50,000-year time frame.

The initial solution fluxes are W_{wpl} = 0.15 kg/yr (BSC 2001 [DIRS 153724], Attachment 1), W_{iw} = 0.54 kg/yr (DTN: SN0007T0872799.014 [DIRS 152545]), and W_{cs} = 100 kg/yr (CRWMS M&O 2000 [DIRS 153246], Figure 4.1-14). The actual mean value in bin is 140 kg/yr, and although the lower resolution Figure 4.1-14 looks like about 200 kg/yr, the final value is abstracted to 100 kg/yr. which is abstracted to 100 kg/yr. The pH values are 3.98, 7.90, and 7.89, respectively. Chemistry concentrations for model inputs were obtained from the 50,798 year input of file CSNF_20.6i for the waste package, which is at 25°C and the high carbon dioxide case (BSC 2001 [DIRS 153724], Attachment 1). The file supplying model input for the invert is HHi5.xls, which is the 25,000 to 100,000 year, higher-temperature, high-carbon dioxide case; the file for the crown is HHc5.xls, which is the 25,000 to 100,000 year, higher-temperature, high-carbon dioxide case (Jolley 2001 [DIRS 154762]). For the crown and the invert, it was assumed that relative humidity was greater than 85 percent and that there was no evaporation or condensation. Metcalf (2001 [DIRS 154842]) provides the documentation of the calculations.

One important result is that it takes large waste package leakage fluxes (1251 kg/yr) to decrease the mixed solution pH to below pH 7.0. Additional Monte Carlo runs may identify lower fluxes that could generate acidic pH values in the mixed solutions. However, it appears likely that any such fluxes will be tens to hundreds of times the given waste package leakage flux rate of 0.15 kg/yr.

Another important result is that the mixed solution becomes more acidic (lower pH) with the addition of the pH 4.0 waste package solution to the pH 7.9 invert wicking and crown seepage solutions. This is what would be expected, and is analogous to an ANC titration in the laboratory.

However, examination of Table 6.3.3.5.2-1 shows that there are some rows which have quite variable pH values for a constant W_{wpl} value (Table 6.3.3.5.2-1, range of pH). This is because the waste package leakage flux is multiplied by the percentage mixing factor (F_{mixing}) to give a variable waste package solution mass, which is mixed with the other two solutions during the Monte Carlo simulations. As the mixing factor gets closer to one (100 percent mixing of the waste package solutions), the resulting pH in this case will be more acidic.

In the bottom row of the table, pH values of 7.0, 7.8, 7.6, 7.7, 7.7, and 4.3 correspond to F_{mixing} values of 0.231, 0.079, 0.122, 0.102, 0.087, and 0.800, respectively. The highest pH value of 7.8 corresponds to the lowest mixing percentage from the waste package (7.9 percent), and the lowest pH value of 4.3 corresponds to the highest mixing percentage from the waste package (80.0 percent). One strength of the model is that it will provide pH distributions for various amounts of mixing and changing flux from the waste packages.

Two validation test cases were performed using the examples from Morel and Hering (1993 [DIRS 151052], pp. 194 to 195) and Stumm and Morgan (1996 [DIRS 125332], pp. 170 to 172), as shown in Table 6.3.3.5.2-2. Both test cases show reasonable agreement between calculated results and the mixing results in the literature.

The first case from Morel and Hering (1993 [DIRS 151052], pp. 194 to 195) is best suited to test the capability of the model because it has the needed species concentrations for the carbonate alkalinity, as required by Equation 6-49 in the in-drift ANC/pH model. Two volumes of River A, with a pH of 8.2 and ANC = 10^{-3} equivalents/liter (Eq/L), are mixed with three volumes of River B, with a pH of 5.7 and ANC = 10^{-5} Eq/L. The assumption is made that the solutions have a density of 1.00 gm/cm^3 in order to convert volume to mass needed in the model and that the waters are at 25°C. The pH is within 0.01 pH unit of the reference value and the mixed ANC value is within one percent of the reference value.

The second case, from Stumm and Morgan (1996 [DIRS 125332], pp. 170 to 172), shown in Table 6.3.3.5.2-2, mixes acid lake water with alkaline river water in a 1:1 mixing ratio. It does not, however, specify the exact bicarbonate and carbonate ion concentrations needed for the model, instead assuming all ANC is bicarbonate and there is negligible carbonate concentration. It was not stated with certainty which equilibrium constants had been used for the Stumm and Morgan (1996 [DIRS 125332]) calculation. Nevertheless, the pH agreed with the reference value (pH = 7.2 versus 7.20), and the mixed ANC value was equal to the reference value.

For the carbonate contribution to ANC, the model is reasonably accurate and precise, given quality input data. Efforts continue to find other validation cases for the silicate and molybdate contributions. Since the model is only an abstraction of all of the species contributing alkalinity and acidity to a solution, model pH values will only be given to 0.1 pH units. In some instances, this abstraction error will dominate calculation error for model applications in complicated chemical systems. One example may be seen in the first row of Table 6.3.3.5.2-1, where all

mixtures are a pH of 8.5, yet the highest source water pH is 7.9 and no carbon dioxide gas is considered lost from solution. This difference may be caused by having only seven species contributing to the abstracted model pH values in Table 6.3.3.5.2-1, as opposed to the tens or hundreds of species in the EQ3/6 V7.2b speciation calculations they were abstracted from.

6.3.3.5.3 Microbial Communities Model

Improvements to the microbial communities model, dealing with microbial sorption and transport as colloids, are described in Section 10.3.6.

6.3.3.6 Abstraction for the Total System Performance Assessment

6.3.3.6.1 Precipitates/Salts Model

Preliminary performance assessment calculations called for a new set of precipitates/salts model lookup tables. These lookup tables were prepared to represent the effects of relative humidity and fluxes of evaporation and seepage on invert water composition. The abstracted THC invert water compositions presented in Section 6.3.1 were used as input. As recommended in Section 6.3.1.6.3, the fugacity of carbon dioxide was not taken from the invert abstraction. Rather, it was taken from the fracture crown abstraction for the corresponding case and time period.

The precipitates/salts model calculations begin with the high relative humidity submodel. EQ3NR (EQ3/6 V7.2b) input files were prepared for each period and thermal/carbon dioxide mode. After adding the input data from the abstractions in Section 6.3.1, nitrate, which is not included in the THC model, was added at a NO_3:Cl molar ratio of 0.1. On a log scale, this order of magnitude appears to be representative of the NO_3:Cl ratio in Topopah Spring tuff pore water analyses (CRWMS M&O 2000 [DIRS 144986], Table 6). Nitrate is added because its occurrence in Yucca Mountain waters presents the possibility that a nitrate brine may develop by evaporative processes (CRWMS M&O 2000 [DIRS 151568], Section 6.4.2). Because nitrate, like chloride, is highly unreactive, it is assumed that the NO_3:Cl ratio would remain constant in the THC calculations had it been included. The input files were set up to require electrical balancing on sodium, except when electrical balancing on another component would have caused a smaller change in the concentration of a component. This only happened for the cooldown period of each higher-temperature case, when sulfate was the better choice for electrical balancing. Finally, K-feldspar, maximum microcline, dolomite, quartz, albite, tridymite, diaspore, enstatite, wollastonite, anorthite, and anhydrite were suppressed from precipitating. These minerals were suppressed because their formation is likely too slow at the temperatures and pressures modeled (CRWMS M&O 2001 [DIRS 153265], Table 16; Klein and Hurlbut 1999 [DIRS 124293]) or because their precipitation would be inconsistent with the minerals predicted by the THC model to precipitate. An example of the latter is that gypsum is used in the THC model instead of anhydrite. Several of the suppressed minerals likely never became supersaturated in the calculations; they were included as suppressed minerals in the input files simply to prevent rerunning calculations in the event an undesired mineral became supersaturated. Suppression of a mineral in the input files has no effect on the outcome unless the mineral becomes supersaturated.

The EQ3N/R (EQ3/6 V7.2b) runs produced pickup files that initialized sets of EQ6 runs designed to evaporate water (remove water) incrementally, precipitate supersaturated unsuppressed minerals, and equilibrate the solution with the fugacity of carbon dioxide of the crown for the corresponding time period and thermal/carbon dioxide mode. Reaction progress was limited to that required to produce an activity of water of 0.85, which corresponds to an aqueous solution equilibrated with air having a relative humidity of 85 percent. At this activity, ionic strength ranges between about 4 and 10 molal, depending on the dominant ions and pH. The pickup files from these runs were then used to initialize solid-centered flow-through EQ6 calculations in which both seepage and evaporation occur. The ratio of evaporation rate to seepage rate was varied from –9.0 to 0.999 to cover all realistic possibilities for this ratio. The value of –9.0 represents condensation (negative evaporation) at a rate that is 9 times that of seepage, while the value of 0.999 represents an evaporation rate that is 99.9 percent of the seepage rate. In some cases, the latter value resulted in water activity values less than 0.85, so the ratio was reduced to prevent the activity from exceeding 0.85. These runs generated steady-state water compositions that were independent of the starting solution (CRWMS M&O 2001 [DIRS 153265]). For each ratio of evaporation rate to seepage rate, steady-state results were added to the lookup tables. These results included pH, ionic strength, the molalities of each component, and the molalities of a set of aqueous species that potentially contribute to alkalinity. An example lookup table for the subset of output parameters is presented in Table 6.3.3-1.

For precipitates/salts model results at relative humidity values less than 85 percent, the low relative humidity model was used, following the same procedure outlined in *In-Drift Precipitates/Salts Analysis* (CRWMS M&O 2001 [DIRS 153265]). It was used to predict pH, ionic strength, and chloride concentration as a function of relative humidity. These predictions were also added to each lookup table and to the example in Table 6.3.3-1. The complete set of lookup tables and supporting model input and output files were transmitted to the TSPA implementation team (Jolley 2001 [DIRS 154762]).

The results show some new trends for pH compared to the trends observed in the calculations performed for the TSPA-SR (CRWMS M&O 2000 [DIRS 153246]). Unlike the previous boiling period predictions, where the pH increased above 9 (CRWMS M&O 2001 [DIRS 153995], Figure 2), the preliminary performance assessment pH calculations never increase much above 8. The pH instead generally remains in the range of 6.5 to 8, except during the thermal periods of the higher-temperature scenarios. Under these conditions, the pH falls to around 5 or slightly lower as evaporation produces ionic strengths above 1 molal. These lower pH predictions are caused by the differences in the abstracted seepage and gas compositions used as input. The changes in these abstracted input compositions are discussed at length in Section 6.3.1.

Predictions of the chloride and ionic strength do not show new trends. Their molalities increase in approximately the same proportions as previously observed when relative humidity decreases and ratios of the rates of evaporation and seepage increase (CRWMS M&O 2001 [DIRS 153995]). However, as discussed in Section 6.3.3.5.1.1, the results of the high relative humidity model show that during the thermal period, a calcium chloride brine could possibly develop due to predicted chemical divides and the excess of chloride in the seepage water during the thermal periods. This possibility is not captured in the low relative humidity model results for chloride concentration or in the relative humidity threshold assumption, which assumes dry

conditions below a relative humidity of 50 percent. Future development of the low relative humidity model and relative humidity threshold assumption will focus on predicting and incorporating the possibility of generating a chloride brine.

6.3.3.6.2 Seepage/Invert Interactions Model

Only the sections dealing with the precipitates/salts model have been incorporated into the TSPA model at this time.

6.3.3.6.3 Microbial Communities Model

See Section 10.3.6 for details on the TSPA abstraction for microbial transport and sorption.

6.3.3.6.4 Multiple Lines of Evidence

For the precipitates/salts model, a number of natural analogues and models for evaporation and chemical divides are discussed in *In-Drift Precipitates/Salts Analysis* (CRWMS M&O 2001 [DIRS 153265], Section 6.1) and *Environment on the Surfaces of the Drip Shield and Waste Package Outer Barrier* (CRWMS M&O 2000 [DIRS 151568], Section 6.5). They include laboratory evaporation studies and studies of the formation of natural brines and evaporites. These studies support the conceptual model and demonstrate the general trends predicted by the precipitates/salts model.

The most rigorously studied lines of evidence for the precipitates/salts model currently include three sets of laboratory evaporation experiments and handbook solubility values of highly soluble salts. The laboratory experiments, conducted on synthetic J-13 well water and Topopah Spring tuff pore water, provide measurements of how the aqueous composition changes upon evaporation. These data, which were not used to calibrate or develop the precipitates/salts model, are predicted within acceptable limits of accuracy by the model (CRWMS M&O 2001 [DIRS 153265], Section 6.5).

Additional evidence that may be applicable to some of the processes discussed in this section can be found in Sections 7.3.1, 8, and 10.

6.3.3.7 Summary of Remaining Uncertainties

6.3.3.7.1 Precipitates/Salts Model

The sensitivity analyses performed in support of the unquantified uncertainties analysis and documented in Mariner (2001 [DIRS 155041]) provide preliminary assessments of uncertainties associated with starting water composition, carbon dioxide fugacity, and mineral suppressions. While these assessments provide insight into some of the uncertainties of the current model, especially with regard to the relative humidity threshold assumption and the potential evolution of a calcium/magnesium chloride brine, more work is needed in these areas to quantify the uncertainties.

An initial low order approximation on the probability of the formation of magnesium and calcium chloride brines can be estimated. The probability is estimated from the combination of

the different modeling runs done on the seven different water compositions described in Section 6.3.3.5.1.1. Out of the seven starting waters tested there were three different model runs done for each water for a total of 21 different starting waters. The results in Section 6.3.3.5.1.1 indicate that only the three modeling runs associated with the Topopah Spring Tuff pore water could proceed through the chemical divide where calcium and magnesium chlorides would form. Assuming equal weighting to each of the modeled runs would indicate that there would be a 14 percent chance of the starting water composition going toward a calcium/magnesium chloride brine due to evaporative processes. Different weighting from additional analyses will affect the probability of producing high chloride brines.

To caveat the 14 percent probability, an exhaustive list of all possible starting water compositions is not included. Nor does it preclude that the Topopah Spring pore water is the most likely end member composition for water dripping on a waste package, and thus could be weighted to be the most representative. Evidence to perhaps negate selecting the Topopah Spring pore water as the most representative is the results from the cement-modified waters. The cement-modified waters use as the initial starting water composition Topopah Spring pore water yet the reactions with the cement grout prior to evaporation change the chemistry sufficiently to preclude the formation of the magnesium chloride brine. Other EBS materials or byproducts that could modify the composition of waters before they contact the waste package include corrosion products, dust, and biofilms.

Remaining unquantified uncertainties include uncertainties in the representation of processes that govern the evaporative evolution of seepage under repository conditions. These include the physical model representation (currently assumed to be a simple flow-through mixing cell), steady-state and equilibrium assumptions, chemical activity models, and thermodynamic database constants. For simple evaporation of synthesized J-13 well water and Topopah Spring tuff pore water in a beaker, uncertainties in thermodynamic constants, activity models, and equilibrium assumptions do not prevent reasonably accurate predictions of pH, chloride concentration, and ionic strength (Section 6.3.3.3.1). However, the question remains whether the uncertainties observed for these laboratory experiments are representative of the dominant evaporative processes in a repository.

6.3.3.7.2 Seepage/Invert Interactions Model

With only a conceptual model discussed and model development in its initial stages (see Section 6.3.3.4.2), any further discussion on uncertainties can only be speculation.

6.3.3.7.3 Microbial Communities Model

In addition to the uncertainty already discussed in Section 6.3.3.3.3, any future design changes will introduce some programmatic uncertainty (i.e., the potential for material masses, compositions, and locations to be changed is possible prior to finalization for the license applications of future designs). However, parameters such as degradation rates and the potential for spatial variability in microbial colonization are much more important sources of modeling uncertainty, since these can have a greater direct impact on waste package degradation and radionuclide transport. The potential impacts include things like increased corrosion of waste packages due to MIC or increased solubility of waste forms due to production of siderophores.

Calculations performed using this model may need to be revisited as the repository design matures and/or process modeling matures, particularly as these changes are effected by the materials committed to the repository after closure.

6.3.3.8 Summary and Conclusions

6.3.3.8.1 Precipitates/Salts Model

As demonstrated by model validation summarized in Section 6.3.3.3.1, the precipitates/salts model predicts the effects of simple evaporation in laboratory experiments within a factor of 2 or less for chloride concentrations and ionic strength and within a pH unit for pH predictions. In addition, handbook solubilities for a set of ten salts having solubilities greater than 1 molal are easily predicted within a factor of 10 and almost always within a factor of 2. While all three parameters (pH, chloride, and ionic strength) were provided to TSPA-SR (CRWMS M&O 2000 [DIRS 153246]), only pH and ionic strength predictions were used.

According to the precipitates/salts model results for the TSPA-SR calculations, the relative humidity threshold assumption of 50 percent, corresponding to a sodium nitrate brine, holds as a valid assumption. The starting water compositions used for these TSPA-SR calculations were provided by *Abstraction of Drift-Scale Coupled Processes* (CRWMS M&O 2000 [DIRS 123916]). Evaporation of these waters (identified as water #6 in Section 6.3.3.5 above) will not result in the development of a calcium (or magnesium) chloride brine because of an excess of sulfate, carbonate, and/or silica in these waters (Mariner 2001 [DIRS 155041]). Calcium is depleted by precipitation of gypsum (or anhydrite if not suppressed), calcite, and calcium (hydroxy)silicates (and magnesium is largely depleted by analogous mineral precipitation) due to this excess.

This assumption may not be valid for the calculations presented in Section 6.3.3.6. These results indicate that during the thermal periods, especially in the higher-temperature scenarios, the relative concentrations of the dominant ions (i.e., sodium, chloride, calcium, and magnesium) would likely give rise to a calcium/magnesium chloride brine (Section 6.3.3.5.1.1). The uncertainty associated with the evolution of such a brine is borne largely in the uncertainty of the starting water composition. Therefore, any future efforts to quantify the uncertainty of developing a calcium/magnesium chloride brine must include quantification of the uncertainty of the input starting water composition.

6.3.3.8.2 Seepage/Invert Interactions Model

Since the in-drift ANC/pH mixing model will not be implemented for uncertainty analysis in this version of the TSPA model, a calculation employing the waste package chemistry as the only fluid in the invert should be used to check the maximum effect possible (zero mixing of the waste package leaking with more dilute invert or crown waters) when the ANC/pH mixing model is implemented. Any future work should also consider that evaporation fluxes from the mixing invert and waste package solutions may concentrate solution chemistry values above present maximum values in the TSPA model.

6.3.3.8.3 Microbial Communities Model

The *In-Drift Microbial Communities* model (CRWMS M&O 2000 [DIRS 151561]) addresses a significant portion of the uncertainty discussed briefly in Section 6.3.3.3.3. However, the biggest source of uncertainty lies in further investigating issues that are discussed in 6.3.3.3.3. Although there are important uncertainties associated with organic complexation and production of siderophores, the models produced seem to address enough of the uncertainty that they would not significantly change the results of the TSPA-SR (CRWMS M&O 2000 [DIRS 153246]). As an example, the new microbial transport model reported in Section 10.3.6 would not affect the conclusions of the TSPA-SR because sorption was conservatively excluded from the calculations.

6.3.4 Rockfall

6.3.4.1 Introduction

The deterioration of the rock mass surrounding the potential repository emplacement drifts was predicted based on a probabilistic key-block analysis. Key blocks are formed at the surrounding rock mass of an excavation by the intersection of three or more planes of structural discontinuities. The *Drift Degradation Analysis* (CRWMS M&O 2000 [DIRS 151635]) provides an assessment of the possible formation of key blocks within the potential repository horizon that is based on the orientations of discontinuities present in the ESF main loop and in ECRB Cross Drift. Block failure due to seismic and thermal effects has also been analyzed.

The rockfall analyses provide data to the EBS postclosure performance assessment that may modify estimates of seepage into the emplacement drifts due to the mechanical effects of rockfall during the period of compliance (see Section 4.3.4). These data also support disruptive events analyses (see Section 14.4). Additionally, the rockfall analyses provide data and information to support repository design, including both waste package and subsurface design.

Technical literature was reviewed to determine the most appropriate approach to developing a key-block analysis (CRWMS M&O 2000 [DIRS 151635], Section 6.5). As a result of this review, the discrete region key block analysis (DRKBA V3.3) software was selected for the development of the rockfall model. The DRKBA V3.3 probabilistic approach is unique, and is distinguished from traditional key-block analyses in that it not only assesses the maximum size of key blocks, but it also predicts the number of potential key blocks that will be formed within a referenced length of tunnel. The approach also allows for a variety of tunnel and jointing configurations. DRKBA V3.3 simulates structural discontinuities as circular discs placed in the rock mass according to probabilistic distributions determined from tunnel-mapping data. Joint planes are simulated by a Monte Carlo technique from probability distributions representing the orientation, spacing, and trace length of the corresponding joint set. DRKBA V3.3 determines where joint planes intersect to form blocks, then analyzes these blocks to determine if they are geometrically feasible (i.e., if the shape of the block is such that it is physically possible to slide or fall into the tunnel opening). If the blocks are geometrically feasible, DRKBA V3.3 then determines if they are mechanically stable (i.e., if the gravitational forces that cause the block to move into the tunnel opening are less than the frictional forces on the sliding surfaces of the block).

6.3.4.2 Goal of Model

DRKBA rockfall model predicts size ranges and quantities of rock that may fall into drifts in order to assess the effects of fallen rocks on the in-drift physical and chemical environment.

6.3.4.3 Discussion of Total System Performance Assessment-Site Recommendation Results and Identification of Unquantified Uncertainties

Uncertainties in the model for rockfall were not quantified in the treatment in the TSPA-SR (CRWMS M&O 2000 [DIRS 153246]).

The usefulness of the rockfall model is affected by how well the data inputs describe the actual fracture conditions. The natural variability of fractures within a rock mass always represents uncertainty in the design of structures in rock. The extensive fracture data collected at Yucca Mountain provide a good representation of fracturing at the emplacement drift horizon. Fracture data have been represented in the DRKBA model by simulating joint radii, spacings, and positioning with beta distributions based on field mapping data (CRWMS M&O 2000 [DIRS 151635], Section 6.3.2). Individual joints within each joint set are represented as circular discs in three-dimensional space with radii drawn from a distribution estimated on the assumption that the radius is equal to twice the mapped trace length (CRWMS M&O 2000 [DIRS 151635], Section 5.1). All joint spacing data have been corrected for "true" spacing, that is, the spacing measured normal to the plane of the joint sets (CRWMS M&O 2000 [DIRS 152286], Section 6.4.2.1). This correction for true spacing is referred to as a Terzaghi correction. The range of fracture variability from tunnel mapping has been captured in the rockfall model through multiple Monte Carlo simulations of the rock mass. To account for uncertainties associated with seismic, thermal, and time-dependent effects on rockfall, a conservative reduction of joint strength parameters has been included in the approach.

Unquantified Uncertainties Selected for Quantification–Selected for quantification are uncertainties in values for *M*, a multiplier of fracture trace lengths to determine the radius of the joint plane, and a Terzaghi correction for subhorizontal fractures in the DRKBA model. Uncertainty in the range of fracture variability was also selected. Quantification was done at the subsystem level with sensitivity studies on *M*, the Terzaghi correction, and the number of Monte Carlo simulations.

The uncertainties described above are not affected by temperature variation. The *Drift Degradation Analysis* (CRWMS M&O 2000 [DIRS 151635], Section 7.1) showed that thermal effects have a minor impact on rockfall. Uncertainties associated with alternative thermal operating modes are qualitatively the same as those for the higher-temperature mode described in the TSPA-SR report (CRWMS M&O 2000 [DIRS 153246]).

6.3.4.4 Model Development

The DRKBA rockfall model was developed prior to the TSPA-SR (CRWMS M&O 2000 [DIRS 153246]). There has been no subsequent rockfall model development.

6.3.4.5 Results of the Analysis

Values of *M* and the Terzaghi correction were sampled over suitable ranges, and the resulting rockfall quantities and size ranges were determined. The number of Monte Carlo simulations was also varied to test the sensitivity of the model to the number of simulations. The results of the sensitivity analyses are described in this section. Details of the calculations associated with the sensitivity analyses are provided in the *Rockfall Sensitivity Calculations* (BSC 2001 [DIRS 154537]).

6.3.4.5.1 Sensitivity of Fracture Size in the Discrete Region Key Block Analysis Rockfall Model

The *Drift Degradation Analysis* (CRWMS M&O 2000 [DIRS 151635], Attachment XIV) presents the results of a sensitivity calculation for the extent of the modeled joint plane based on the mapped joint trace length. It is recognized that the actual extent of a joint plane cannot be fully known based on field mapping data; the mapped trace length of a joint represents some portion of the overall joint plane. Underrepresenting the extent of the joint plane would not be conservative in a key-block analysis. Since the underrepresented joint planes may not extend or connect to adjacent joint planes, underrepresentation would limit the number of blocks otherwise generated in the model. Conversely, overstating the extent of the joint plane would increase connectivity among joint planes, creating more blocks in the model and resulting in an increased, or conservative, estimate of block development. However, infinite joint planes would not be an accurate representation of the jointed rock mass. The basis to sufficiently model the extent of the joint plane based on the available field data is provided in the *Drift Degradation Analysis* (CRWMS M&O 2000 [DIRS 151635], Attachment XIV).

Joint planes are represented as circular discs in the DRKBA rockfall model with the assumption that the radius of the joint plane is equal to twice the mapped trace length (CRWMS M&O 2000 [DIRS 151635], Section 5.1). The multiplier *M* is used to obtain the radius of the circular fracture disc from the trace length:

$$R = M * TL \qquad \text{(Eq. 6.3.4-1)}$$

where *R* is the radius of the circular fracture disc and *TL* is the trace length of the mapped fracture.

The sensitivity calculation in the *Drift Degradation Analysis* (CRWMS M&O 2000 [DIRS 151635], Attachment XIV) showed that for a circular joint plane described using a radius equal to twice the mapped trace length (i.e., $M = 2$), there is an approximate 3 percent probability that the actual joint radius is greater than the modeled value. Based on these findings, it was concluded that the fracture size used in the DRKBA rockfall model is conservative.

To further document the sensitivity of the size of the joint plane in the DRKBA rockfall model, a series of rockfall analyses was developed for the Tptpmn and Tptpll units, with the joint radius multiplier (*M*) incrementally varied for each analysis. Values of *M* were set equal to 1.0, 1.5, 2.0, 2.5, and 3.0. With the exception of the joint radius, all inputs for these analyses were consistent with inputs for the static condition presented in the *Drift Degradation Analysis* (CRWMS M&O 2000 [DIRS 151635], Sections 6.3.1, 6.3.2, and 6.3.3).

Figures 6.3.4-1 and 6.3.4-2 present the key-block analysis results in the format of cumulative frequency of occurrence for the Tptpmn and Tptpll units. The DRKBA V3.3 input and output files and associated calculation files are provided in the *Rockfall Sensitivity Calculations* (BSC 2001 [DIRS 154537]). The cumulative frequencies of occurrence corresponding to the 50, 75, 90, 95, and 98 percentile block volume for each unit are listed in Tables 6.3.4-1 and 6.3.4-2. The maximum block sizes predicted from the analyses are also presented in these tables. The predicted numbers of key blocks per unit length of emplacement drift are listed in Table 6.3.4-3. For radius multipliers greater than 1.5, the cumulative block size distributions are relatively similar (Figures 6.3.4-1 and 6.3.4-2). The greatest sensitivity from the variation of the joint radius is in the frequency of blocks developed. As shown in Table 6.3.4-3, block development is limited when the radius of the joint plane is equal to the fracture trace length (i.e., $M = 1$). As the radius multiplier increases, the number of blocks increases, with a substantial increase in the number of blocks when the multiplier exceeds 2.0. This trend illustrates that as the extent of the joint plane increases, there is an increased connectivity among joint planes, creating a higher frequency of block development in the model.

6.3.4.5.2 Sensitivity of the Number of Monte Carlo Simulations in the Discrete Region Key Block Analysis Rockfall Model

In the DRKBA rockfall model, random joint patterns are generated with joint centers positioned in three-dimensional space, then each joint set is considered in sequence for each Monte Carlo simulation. The forming of key blocks is therefore different in each Monte Carlo simulation. To document the sensitivity of the model to the number of Monte Carlo simulations for the sensitivity analyses, a series of test runs was conducted. The test runs were intended to show sensitivity to the number of Monte Carlo simulations in the prediction of block size distribution, maximum block size, and the number of blocks. The DRKBA V3.3 input and output files, and associated calculation files, are provided in the *Rockfall Sensitivity Calculations* (BSC 2001 [DIRS 154537]).

Test runs were conducted for the Tptpmn unit with 100, 200, 400, 600, and 800 Monte Carlo simulations. Figure 6.3.4-3 shows the block size distribution curves in the form of cumulative frequency of occurrence. The prediction of block size distribution is similar for all simulations, as indicated in Figure 6.3.4-3. The predicted numbers of blocks per 10 simulations for the 5 Monte Carlo simulation cases are presented in Figure 6.3.4-4. The results are in good agreement for the 400, 600, and 800 simulation cases. The maximum block sizes predicted for each case are shown in Figure 6.3.4-5. The 98 percentile blocks are nearly identical for all Monte Carlo simulation cases. The maximum block size remains consistent after 400 simulations.

For the Tptpll unit, test runs with 100, 200, 400, 600, and 800 Monte Carlo simulations were conducted. Figure 6.3.4-6 shows the block size distribution curves for each case. The prediction of block size distribution is similar for all simulations. The predicted numbers of blocks per 10 simulations for each case are presented in Figure 6.3.4-7. The results show a relatively low number of blocks per 10 simulations for all cases, with the number of blocks remaining consistent after 400 simulations. The maximum block sizes predicted for each of the Monte Carlo simulation cases are shown in Figure 6.3.4-8. The maximum blocks predicted are similar for all simulations, with the maximum block size typically between 1 and 2 m^3.

6.3.4.5.3 Sensitivity of the Terzaghi Correction for Spacing of Subhorizontal Fractures in the Discrete Region Key Block Analysis Rockfall Model

The procedure for determining joint set spacing is documented in *Fracture Geometry Analysis for the Stratigraphic Units of the Repository Host Horizon* (CRWMS M&O 2000 [DIRS 152286], Section 6.4.2). A Terzaghi correction, which is a mathematical correction to determine the "true" spacing measured normal to the joint plane, was applied to the mapped joint spacing data. For vertical joints striking perpendicular to the axis of the tunnel, the Terzaghi correction factor would be 1, that is, the mapped spacing is equal to the true spacing, without a correction. Correction factors are most significant for subhorizontal fractures. For the subhorizontal fracture set from mapped fractures in the Tptpmn unit, the average Terzaghi correction factor is approximately 15, indicating that the true spacing of subhorizontal joints is 15 times less than the mapped spacing (BSC 2001 [DIRS 154537]). These Terzaghi correction factors with an average of approximately 15 were used in the *Drift Degradation Analysis* (CRWMS M&O 2000 [DIRS 151635]). For joints mapped along a horizontal scanline, a subhorizontal joint dipping 8 degrees or more will have a maximum Terzaghi correction factor of approximately 7 (i.e., 1/(sin 8) is approximately 7). For joints dipping less than 8 degrees, the Terzaghi correction factor ranges from 7 to infinity. Therefore, the uncertainty associated with the correction factor increases within this range.

To document the sensitivity of the DRKBA rockfall model to the Terzaghi correction factor, analyses were conducted with a maximum correction factor of 7. The joint spacing distributions for the original true joint spacing and the modified true spacing (i.e., with a Terzaghi correction factor less than or equal to 7) are shown in Figures 6.3.4-9 and 6.3.4-10, respectively. The beta distribution parameters for joint spacing, which are required input for the DRKBA V3.3 program (CRWMS M&O 2000 [DIRS 151635], Sections 6.3.1 and 6.3.2), are provided in Table 6.3.4-4. The details for the calculation of each beta parameter are provided in the *Rockfall Sensitivity Calculations* (BSC 2001 [DIRS 154537]). With the exception of the beta distribution parameters for the subhorizontal joint set of the Tptpmn unit, all inputs for these analyses were consistent with inputs for the static condition presented in the *Drift Degradation Analysis* (CRWMS M&O 2000 [DIRS 151635], Sections 6.3.1, 6.3.2, and 6.3.3).

Figure 6.3.4-11 presents the key-block analysis results in the format of cumulative frequency of occurrence for the Tptpmn unit. The DRKBA V3.3 input and output files and associated calculation files are provided in the *Rockfall Sensitivity Calculations* (BSC 2001 [DIRS 154537]). The cumulative frequencies of occurrence corresponding to the 50, 75, 90, 95, and 98 percentile block volume for the Tptpmn unit are listed in Table 6.3.4-5. The maximum block sizes predicted from the analysis are also presented in this table. The predicted numbers of key blocks per unit length of emplacement drift are, under static condition with modified Terzaghi correction in the Tptpmn, 50 and 33 km, respectively, for the original and modified cases (BSC 2001 [DIRS 154537]).

As shown in Figures 6.3.4-9 and 6.3.4-10, the frequency of widely spaced joints increases with the modified Terzaghi correction. The impact of this change in the DRKBA rockfall model is a reduction in the number of blocks per kilometer and a slight increase in the overall distribution of block sizes (Figure 6.3.4-11). The increased spacing of the subhorizontal joint set in the Tptpmn unit resulted in the development of fewer blocks with a slightly larger volume.

6.3.4.6 Abstraction for Total System Performance Assessment

The subsystem sensitivity analysis presented above quantifies the sensitivity of parameters in the DRKBA rockfall model. Since the sensitivity analysis does not change the results of the rockfall model presented in the *Drift Degradation Analysis* (CRWMS M&O 2000 [DIRS 151635], Section 6), an abstraction for TSPA is not applicable.

6.3.4.7 Multiple Lines of Evidence

The number of blocks predicted by the DRKBA static rockfall model for the various stratigraphic units within the potential repository horizon is consistent with field observations in the ESF (CRWMS M&O 2000 [DIRS 151635], Section 6.5). The DRKBA rockfall model predicts the highest frequency of blocks in the Tptpmn unit and the lowest frequency of blocks in the Tptpll unit. Field observations are consistent with this trend.

The size of key blocks observed in the ECRB Cross Drift is generally less than 0.5 m^3. The maximum size block observed in the ECRB Cross Drift is captured within the range of predicted block sizes from the DRKBA rockfall model (CRWMS M&O 2000 [DIRS 151635], Table 44).

The seismic component of the DRKBA rockfall model predicts that the seismic effect on both the size and number of blocks is minor. Natural analogues from mines, tunnels, and caves can be used to test this prediction. There have been several compilations of effects on underground openings in response to earthquakes (Stevens 1977 [DIRS 154501]; Pratt et al. 1978 [DIRS 151817]; Carpenter and Chung 1986 [DIRS 154504]; Sharma and Judd 1991 [DIRS 154505]).

The damage from earthquakes results from shear waves. These are generated when the energy from an earthquake passes through a density contrast; the largest one is between air and rock at the surface of the earth. If the dimensions of an underground opening are considerably less than the wavelength of a shear wave, the amplitude of motion will be about twice as large at the surface as at depth (Stevens 1977 [DIRS 154501], p. 20). In addition, the effects of surface waves decrease with increasing depth, much in the same way that the effects of ocean waves decrease with depth of water. A consequence of this is that the damage reported in shallow near-surface tunnels is greater than that reported in deep mines (Pratt et al. 1978 [DIRS 151817]). Data presented by Sharma and Judd (1991 [DIRS 154505], Figure 7) indicate that damage to underground facilities at the depth for the potential repository is rare, even at accelerations of 0.4 g.

Pratt et al. (1978 [DIRS 151817], p. 20) report that peak accelerations less than 0.2 g have caused no reported damage to tunnels. Sharma and Judd (1991 [DIRS 154505], p. 275) note that their database of 192 reports of underground observations contains 98 cases with no damage, and that there are probably hundreds of other undocumented cases of no damage. In fact, damage to underground openings is inevitable only when the underground facility is displaced by a fault (Carpenter and Chung 1986 [DIRS 154504]; Stevens 1977 [DIRS 154501]).

Stevens (1977 [DIRS 154501]) and Pratt et al. (1978 [DIRS 151817], p. 26) both suggest that the host material for an underground facility may be important in predicting the amount of damage caused by shaking. Competent rock is expected to outperform unconsolidated material.

Carpenter and Chung (1986 [DIRS 154504]) discuss potential problems for deep geologic disposal sites in response to earthquakes. They strongly recommend that faults with the potential for movement be avoided, which is consistent with design criteria for the potential repository at Yucca Mountain. They also note that modeling studies suggest potential problems for waste handling equipment in shafts. The potential facility at Yucca Mountain would avoid this problem by using inclines for the emplacement of waste.

As noted earlier, there are several examples of the performance of underground facilities during earthquakes. The following paragraphs contain a few specific, well-documented examples.

On July 28, 1976, a magnitude 7.8 earthquake occurred in Tang-Shan, China, a city with substantial mining and industrial facilities. Surface intensities at Tang-Shan were such that in the area where the strongest shaking occurred, 80 to 90 percent of the surface structures collapsed. However, there was generally no serious damage to important engineered structures immediately below the surface, regardless of their depth or size (Wang 1985 [DIRS 151821], p. 741).

The U.S. Geological Survey reported in the lessons and conclusions of the Alaskan earthquake on March 28, 1964, that no significant damage was reported to underground facilities, including mines and tunnels, as a result of the earthquake, although some rocks were shaken loose in places. Included in this analysis were studies of the coal mines in the Matanuska Valley (which were undamaged), the railroad tunnels near Whittier, the tunnel and penstocks at the Eklutna hydroelectric project, and the Chugach Electric Association tunnel between Cooper Lake and Kenai Lake. There were also no reports of damage to the oil and gas wells in and along Cook Inlet. These reports of no damage from the Alaskan earthquake are significant; it was one of the largest (magnitude 8.5) to occur in this country, and surface damage was extreme (Pratt et al. 1978 [DIRS 151817], p. 32).

Tunnels in the epicentral region of the Kobe, Japan, earthquake (January 16, 1995; magnitude 6.9) experienced no major damage (partial or total collapse) for peak ground accelerations measured at the surface of approximately 0.6 g (Savino et al. 1999 [DIRS 148612]).

On June 29, 1992, a magnitude 5.6 earthquake occurred at Little Skull Mountain, which is about 20 km from Yucca Mountain. Within days of the earthquake, a team of scientists examined the interior of the tunnel 125 m deep in the epicentral region of the earthquake. The team reported no evidence of damage in the tunnel that could be associated with the earthquake (Savino et al. 1999 [DIRS 148612]).

6.3.4.8 Summary of Remaining Uncertainties

The remaining uncertainties within the DRKBA rockfall analyses are associated with the assessment of seismic, thermal, and long-term degradation effects on block development. Currently, these uncertainties are accounted for by applying a conservative reduction in joint strength properties in the rockfall model (CRWMS M&O 2000 [DIRS 151635], Section 7.2). To provide a better understanding and quantification of these uncertainty sources, additional rockfall analyses are planned in support of the license application. The additional activities include:

- Appropriate boundary conditions for thermal and seismic loading
- Critical fracture patterns from the rockfall Monte Carlo simulations
- Appropriate thermal and mechanical properties of rock blocks and joints
- Long-term degradation of joint strength parameters
- Site-specific ground motion time histories appropriate for the postclosure period.

6.3.4.9 Summary and Conclusions

Previously unquantified uncertainties associated with the DRKBA rockfall model have been identified, including the extent of fracture planes, the Terzaghi correction for spacing of subhorizontal joints, and the number of Monte Carlo simulations. The quantification of these uncertainties and the multiple lines of evidence presented in Section 6.3.4.7 provide additional confidence that the DRKBA model for rockfall can adequately predict the size ranges and quantities of rock that may fall into emplacement drifts.

As described in Section 6.3.4.5.1, uncertainty about the extent of the fracture planes has been quantified by varying the radius of the fracture plane. The results indicate that increasing the joint radius has a marginal impact on the block size distribution, and the maximum block size increases only slightly. The number of blocks, however, increases significantly with increasing joint radius. An increase in fracture extent in the DRKBA model causes greater fracture connectivity, resulting in an increase in block development. The radius multiplier in the DRKBA rockfall model, *M*, acts as a calibrator of the actual extent of the joint plane. Based on the field occurrence of blocks presented in the *Drift Degradation Analysis* (CRWMS M&O 2000 [DIRS 151635], Section 6.5), a radius multiplier of 2, as originally used in the DRKBA rockfall model, provides a reasonable yet conservative estimate of the number of blocks. The sensitivity study presented in Section 6.3.4.5.1 indicates that the frequency of blocks substantially increases when the radius multiplier exceeds 2. Therefore, a radius multiplier of 2.5 or greater would result in an excessive, inappropriate number of blocks, based on field evidence of block development in the ESF.

As described in Section 6.3.4.5.2, uncertainty about the impact on block development of the number of Monte Carlo simulations used in the DRKBA rockfall model has been quantified. The results indicate that 400 Monte Carlo simulations are sufficient to capture the range of block development in the rockfall model.

As described in Section 6.3.4.5.3, uncertainty about the correction factor applied to the spacing of the subhorizontal joint set has been quantified. The results indicate that a reduction in the correction factor from a mean value of 15 to a maximum value of 7 causes a decrease in the

number of blocks simulated and a slight increase in the distribution of block sizes. Given the significant reduction in the Terzaghi correction factor, the resulting impact on block development is minor.

The sensitivity analyses for the DRKBA rockfall model presented in this section confirm the appropriateness of the analysis parameter selection in the *Drift Degradation Analysis* report (CRWMS M&O 2000 [DIRS 151635]). These sensitivity analysis results indicate no impact to the repository subsystems potentially affected by rockfall.

6.4 SUMMARY AND PARAMETERS PROVIDED TO TOTAL SYSTEM PERFORMANCE ASSESSMENT

6.4.1 Summary of the Total System Performance Assessment Implementation of the Precipitates/Salts Model Lookup Tables

The TSPA parameters provided by the precipitates/salts model are summarized in the set of lookup tables presented in Section 6.3.3.6.1. The important independent variables are the design operating mode, time period, relative humidity, and relative evaporation rate (Q^e/Q^s, also known as R^{es}). Given values for each of these inputs, the lookup tables can be used to estimate output values for pH, ionic strength, and molalities of selected dissolved components and individual aqueous species.

The lookup tables include results for each possible design operating mode and time period, but they do not include values for each possible value of relative humidity, and the relative evaporation rate (Q^e/Q^s). Relative humidity and Q^e/Q^s are allowed to vary within each time period; thus, only results for a subset of values for these inputs that cover the expected ranges of these parameters are included in the tables. When relative humidity is less than 85 percent, pH is interpolated as a linear function of relative humidity, while each molality output (e.g., ionic strength, Cl molality, etc.) is interpolated as a linear function of relative humidity and the logarithm of the output value (e.g., log [ionic strength]). When relative humidity is greater than or equal to 85 percent, pH is interpolated as a linear function of the logarithm of one minus Q^e/Q^s (i.e., log $(1 - Q^e/Q^s)$) while each molality output is interpolated as a linear function of the logarithm of $(1 - Q^e/Q^s)$ and the logarithm of the output (e.g., log [ionic strength]). Log-log plots of the non-pH outputs versus $(1 - Q^e/Q^s)$ show a high degree of linearity, which supports these linearizations.

6.4.2 Summary of the Total System Performance Assessment Implementation of the Acid Neutralizing Capacity/pH Mixing Model

The in-drift mixing model attempts to establish a unified water chemistry model within the drift, which fits seamlessly with prior TSPA model development by producing integrated output feeds of pH, ionic strength, and acid neutralizing capacity (ANC) for mixed solutions in the drift. These in-drift solutions are mixtures of seepage fluxes from the crown above the drift, the water wicked through the rock and corroded metals in the invert, and the diffusion film or flux from a waste package after failure.

The necessary variable inputs to the in-drift ANC/pH mixing model from other source components of the TSPA model are the incoming water fluxes from the crown seepage, invert

wicking, and waste package leakage, and the associated major species concentrations that comprise the ANC: $[HCO_3^-]$, $[CO_3^{-2}]$, $[OH^-]$, $[H^+]$, $[MgOH^+]$, $[H_3SiO_4^-]$, $[H_2SiO_4^{-2}]$, $[UO_2CO_3^{-2}]$, and $[MoO_4^{-2}]$.

The new aspects of this ANC/pH in-drift mixing model integrate process model chemistry (CRWMS M&O 2001 [DIRS 153265]; BSC 2001 [DIRS 154620]; CRWMS M&O 2000 [DIRS 129283]) to provide consistent solution chemistry for use in modeling radionuclide solubilities, colloidal properties and transport, radionuclide sorption, and carbon dioxide gas equilibria within and leaving the repository drift for the TSPA model. Additionally, ionic strength is evaluated as part of the combined water source mixtures to provide values to the TSPA model. The integrated outputs of this model are designed to be the same TSPA model feeds: pH, ionic strength, plus ANC values in solutions that are mixed from three sources (i.e., crown seepage, invert wicking, and waste package leakage).

For most of the TSPA submodels (e.g., sorption, solubility, and colloids), the appropriate output feeds will be the mixed solution variables from three sources: $pH_{3Source}$, and $I_{3Source}$, produced from Equations 6-55 and 6-57, respectively. The mixing ANC parameter, $ANC_{3Source}$ (computed from Equation 6-5), is an important variable that may help describe chemistry in future subroutines when it is available. Cl^- may be linearly mixed exactly like ANC if it is needed in other subroutines.

6.4.3 Incoming Liquid and Gas Abstraction Results

Tables of water chemistry and carbon dioxide gas abundance for use in TSPA calculations are found in Sections 6.3.1.6.3.1 and 6.3.1.6.3.2 (with the appropriate lookup tables). Implementation of the tables, and guidelines for their use, are discussed in Section 6.3.1.6.3. If ionic strengths are needed for TSPA calculations based on the chemistries presented in Sections 6.3.1.6.3.1 and 6.3.1.6.3.2, they can be calculated for each period using Equation 4 from the *In-Drift Precipitates/Salts Analysis* (CRWMS M&O 2001 [DIRS 153265], p. 45).

6.4.4 Integration of Water Chemistries in the Drift between Total System Performance Assessment Model Components

In the TSPA-SR model (CRWMS M&O 2000 [DIRS 153246]), carbon dioxide levels in the drift were not coordinated between EBS component models and no integration was attempted within the TSPA model. This led to different assumed carbon dioxide levels in the same place at the same time during TSPA model runs. The overall effect of these differences are uncertain, although in the cases where coordination of carbon dioxide levels between models did not occur, parameters were selected to maximize radionuclide solubility and create a bounding condition. However, many systems in the drift are influenced by the fugacity of carbon dioxide in the drift air. Radionuclide solubilities depend on carbon dioxide fugacities. Aqueous solutions in and near the drift will have a pH that depends on the carbon dioxide fugacity. While some integration can be obtained by alterations of the TSPA model, full integration will require the incorporation of ongoing development and analyses of the various models that make up the EBS.

6.4.5 In-Drift Salts and Precipitates Modeling

The in-drift precipitates/salts model was developed to predict solution chemistry in the drift and invert external to the waste package. The input parameters to this model are the concentration (or activity) of each incoming model component in the water entering at the crown of the drift, temperature, relative humidity, carbon dioxide fugacity, the seepage rate, and the relative evaporation rate (CRWMS M&O 2001 [DIRS 153265], Section 4.1.3). The outputs of the model are the pH and ionic strength of the solution and the chloride concentration (CRWMS M&O 2001 [DIRS 153265], Sections 6.6.3 and 6.6.4).

The original model utilized the average composition of well J-13 water as a source of incoming model component concentrations (or activities) (CRWMS M&O 2001 [DIRS 153265], Section 4.1.3). Later work (CRWMS M&O 2001 [DIRS 153995]) applied the salts/precipitates model to abstracted THC water compositions developed in the *Abstraction of Drift-Scale Coupled Processes* (CRWMS M&O 2000 [DIRS 123916], Section 6.1). These are the only waters that have been documented. Further study continues on different input waters, and these continuing efforts should further reduce uncertainty in this input.

The output water chemistry of this model should serve as an input to other models in the drift in some cases, including the chemistry inside the waste package and the models that determine waste form dissolution and radionuclide solubility. At present, these models use well J-13 water or other waters as input. In addition, other inputs to the precipitates/salts model are currently being analyzed. This will give a wider range of modeled data and reduce uncertainty. More information on these efforts can be found in Section 6.3.3.

6.4.6 In-Package Chemistry Models

The chemistry inside the waste package is modeled in the *In-Package Chemistry for Waste Forms* (BSC 2001 [DIRS 153724]) and abstracted in the *In-Package Chemistry Abstraction* (CRWMS M&O 2000 [DIRS 129287]). This pair of reports uses a set carbon dioxide fugacity and a standard well J-13 water composition to predict water chemistry inside the waste package. Comparisons are made in the modeling effort to two other water types to determine the influence of water chemistry variation (CRWMS M&O 2000 [DIRS 111880], Section 6.3.2). These predictions are standardized for different time periods (CRWMS M&O 2000 [DIRS 129287], Section 6) to facilitate incorporation in the TSPA. These compositions, which include pH, total carbonate, Eh, ionic strength, F, and Cl parameters, are then used to model the degradation rates of waste package contents.

While this model is relatively insensitive to predicted variations in input water chemistry (CRWMS M&O 2000 [DIRS 111880], Section 6.2.3), any future work should consider the results of the in-drift precipitates/salts model applied to various drift waters as input to the in-package chemistry model, at least in the cases where it is predicted that these high ionic strength waters will enter the waste package. This consideration will lead to a more internally consistent model. Variation of carbon dioxide as an input by coordinating time periods with the in-drift precipitates/salts analysis would also make the model more internally consistent. These waters, as they emerge from the waste package, should be mixed with other predicted waters in the drift to form a more complete model of the EBS chemistry.

As in the in-drift precipitates/salts model, work continues for various input waters and some variation in the fugacity of carbon dioxide in the drift. These efforts will improve understanding of in-package chemical environment and lead to better predictive modeling of the environment.

6.4.7 Integration of Model Inputs

For certain elements, radionuclide solubility depends on temperature and the fugacity of carbon dioxide (CRWMS M&O 2001 [DIRS 154286], Section 6), as does waste form dissolution rate (CRWMS M&O 2000 [DIRS 136060], Section 6). The chemical composition of water inside the waste package depends on flux through the waste package (CRWMS M&O 2000 [DIRS 111880], Section 6). Water composition in the waste package also depends on carbon dioxide concentrations, although this can be conservatively ignored (CRWMS M&O 2000 [DIRS 111880], Section 6.2). Even if the model output is not sensitive to a particular input, it is important that common input parameters be consistent across the different models for a particular space and time. If the inputs for a parameter such as carbon dioxide fugacity are different for the different models in the same space and time, it will call into question the validity of the total system model, even if the parameter has little or no effect on the final output of the component model. In addition, models that are sensitive to carbon dioxide fugacity cannot be varied to demonstrate this sensitivity because the input data does not exist for relevant waters.

Another problem occurs because there is no attempt to coordinate the chemistries of different waters in the TSPA model. Because there is no mixing of waters and no coordination of carbon dioxide chemistry within the drift between models, a complete picture of drift conditions is not formed in the model. While parameters were selected to be conservative or bounding, improvement in and integration between EBS submodels improves confidence in them. The integration of carbon dioxide will require more information from the component models, as will mixing of the waters in the EBS. However, some integration can be accomplished with available information. One potential method is the ANC model (Section 6.3.3.4.2.3), which would take available data and provide a more complete picture of EBS chemistry by mixing waters from the in-drift water chemistry analyses and the in-package chemistry analyses. A complete explanation of this model is found in Section 6.3.3.4.2.3.

INTENTIONALLY LEFT BLANK

Table 6.3.1.5-1. Thermal-Hydrologic-Chemical Seepage Simulations

Infiltration-Property Set	Geochemical System	Simulation Type	Temperature Case	CO_2 Case	Initial Water Composition	Run ID
Mean Infiltration	NA	TH	Higher	NA	NA	th6_ht1
			Lower	NA	NA	th6_lt3
Mean Infiltration	Extended	THC	Higher	High	Alcove 5 (Pore)	thc6_ht1
			Higher	Low	Alcove 5 (Pore)	thc6_ht1L
			Higher	High	UZ-14 (Perched)	thc6_ht1w3
			Lower	High	Alcove 5 (Pore)	thc6_lt3
			Lower	Low	Alcove 5 (Pore)	thc6_lt3L
			Lower	High	UZ-14 (Perched)	thc6_lt3w3
			Ambient	Low	Alcove 5 (Pore)	thc6_ambL
			Ambient	High	UZ-14 (Perched)	thc6_ambw3

Source: Bodvarsson 2001 [DIRS 154669], Attachment 5, pp. 10 to 59. Unless indicated otherwise in the text, the input data are identical to those for the Tptpll model (BSC 2001 [DIRS 154677], Section 6.6).

NOTE: NA = Not Applicable. See text for additional information.

Table 6.3.1.5-2. Composition of Selected Pore Water and Other Waters from Yucca Mountain

Parameter	Units	HD-PERM-1 Tptpmn	HD-PERM-2 Tptpmn	HD-PERM-3 Tptpmn	DXD042 Tptpll	SD-6 Ptn	TSw-Avg TSw	UZ-14-Pore Tptpln/ Tptpv	UZ-14-Perch Tptpln/ Tptpv	J-13 TSw/ CHn
pH	pH	7.79	8.32	8.31	8.10[a]	7.52[a] (7.2)	8.2	7.66[a]	7.8	7.41
Na^{+}	mg/L	61	61	62	47.3	51.6	91	67	35	45.8
K^{+}	mg/L	6	7	9	0.2[a] (<0.5)	1.8	4[c]	2[a]	4.1	5.04
Ca^{+2}	mg/L	98	106	97	15.5[a] (9.1)	62.4	27	43	31	13
Mg^{+2}	mg/L	25.7	16.6	17.4	0.98	12	5	3.7	2.5	2.01
SiO_2	mg/L	79	66	75	95.6	92.8	60	35	40.7	60.1
Cl^{-}	mg/L	123	110	123	16.4	33	41	88	7	7.14
SO_4^{-2}	mg/L	124	111	120	8.5	101	40	19	24.2	18.4
HCO_3^{-}	mg/L	211[a]	233[a]	178[a]	128[a]	154[a] (95)	219[a] (191)	144[a] (170)	146.4	138[a] (128.9)
NO_3^{-}	mg/L	22	3	10	10[c]	57	13	16	17.1	8.78
F^{-}	mg/L	0.36	0.96	0.76	N/A	N/A	N/A	N/A	N/A	2.18
$\log(P_{CO2})$[a]	bars	-2.51	-3.00	-3.1	-3.00[b]	-2.37	-2.88	-2.53	-2.65	-2.29
CO_2 (approx.)[a, e]	ppmv	3500	1100	900	1100	4800	1500	3400	2500	5800
Calcite S.I.[a, d]	log(Q/K)	0.56	1.16	1.00	0.00[b]	0.00[b]	0.50	0.00[b]	0.03	-0.75

Sources: HD-PERM-x (DTN: MO0005PORWATER.000 [DIRS 150930]); UZ-14D (Yang et al. 1996 [DIRS 100194], Table 6, Sample UZ-14D, 8/21/93); DXD042 (DTN: LA9909JF831222.004 [DIRS 145598]; LA9909JF831222.006 [DIRS 146231]); SD-6 (DTN: LA0002JF12213U.001 [DIRS 154760]); TSw-Avg (CRWMS M&O 1999 [DIRS 129261], Table 4.5.1); UZ-14-Pore (DTN: LA0002JF12213U.001 [DIRS 154760]); UZ-14-Perch (Yang et al. 1996 [DIRS 100194], Table 6, Sample UZ-14D]); mean J-13 (DTN: MO0006J13WTRCM.000 [DIRS 151029]).

NOTES: [a] Calculated (values in parenthesis, if any, are the original data) - See text and Bodvarsson 2001 [DIRS 154669], Attachment 5, pp. 38 to 43, 47 to 49, 55 to 58.
[b] Fixed condition in order to compute pH - See text.
[c] Assumed.
[d] Saturation index at 25°C.
[e] At the drift atmospheric pressure (near 0.88 bars).
N/A = Not Available.

Table 6.3.1.6-1. Abstraction Results for High Temperature and Low Carbon Dioxide Partial Pressure in the Tptpll Lithology for Seepage at the Crown of the Drift

	Preclosure	Boiling	Cool Down	Extended Cool Down	Transition to Ambient	Ambient
	(0-50 yr)	(51-1,500 yr)	(1,501-4,000 yr)	(4,001-25,000 yr)	(25,001-100,000 yr)	(100,001-1,000,000 yr)
Actual THC Model Run Time (yr)	49.97	300.00	1,800.01	10,000.00	50,001.50	Averaged
Temperature (°C)	79.30	122.87	95.80	54.02	27.37	23.60
PCO_2 (v.frac)	9.20E-04	8.91E-06	1.66E-05	1.62E-03	5.71E-04	4.39E-04
pH	7.90	7.23	8.42	7.92	8.45	8.55
Ca (mol/L)	1.17E-03	2.34E-02	4.51E-03	1.48E-03	1.88E-03	1.97E-03
Mg (mol/L	5.94E-04	4.75E-02	6.50E-04	9.69E-05	2.50E-04	2.57E-04
Na (mol/L)	5.24E-03	4.23E-01	4.48E-03	4.30E-03	4.52E-03	4.39E-03
Cl (mol/L)	4.36E-03	3.72E-01	6.62E-03	3.27E-03	3.29E-03	3.29E-03
SiO_2(aq) (mol/L)	3.66E-03	3.45E-01	1.02E-02	2.55E-03	1.45E-03	1.44E-03
HCO_3 (mol/L)	4.96E-04	3.08E-04	3.34E-05	1.36E-03	2.53E-03	2.58E-03
SO_4 (mol/L)	1.59E-03	9.28E-02	2.86E-03	1.20E-03	1.20E-03	1.21E-03
K (mol/L)	2.39E-04	3.96E-02	5.33E-04	1.95E-04	1.04E-04	9.23E-05
AlO_2 (mol/L)	3.75E-08	2.45E-13	1.06E-08	6.27E-09	1.12E-09	6.74E-10
F (mol/L)	5.64E-04	3.32E-03	3.96E-04	4.06E-04	3.28E-04	3.11E-04
$HFeO_2$ (mol/L)	4.01E-11	6.09E-10	1.55E-09	4.54E-11	4.58E-12	1.97E-12

Source: Data derived from THC simulations thc6_ht1L and thc6_ambL (Table 6.3.1.5-1) as archived in Jolley (2001 [DIRS 154762]).

Table 6.3.1.6-2. Abstraction Results for High Temperature and High Carbon Dioxide Partial Pressure in the Tptpll Lithology for Seepage at the Crown of the Drift

	Preclosure	Boiling	Cool Down	Extended Cool Down	Transition to Ambient	Ambient
	(0-50 yr)	(51-1,500 yr)	(1,501-4,000 yr)	(4,001-25,000 yr)	(25,001-100,000 yr)	(100,001-1,000,000 yr)
Actual THC Model Run Time (yr)	49.97	300.00	1,800.01	10,000.00	50,001.50	Averaged
Temperature (°C)	79.30	122.86	95.80	54.02	27.37	23.2
PCO_2 (v.frac)	9.20E-04	8.92E-06	2.26E-05	3.45E-03	1.06E-03	7.67E-04
pH	7.90	7.23	8.37	7.74	8.29	8.41
Ca (mol/L)	1.17E-03	2.34E-02	4.35E-03	1.61E-03	2.08E-03	2.18E-03
Mg (mol/L)	5.94E-04	4.75E-02	5.90E-04	5.38E-05	1.87E-04	1.98E-04
Na (mol/L)	5.24E-03	4.23E-01	4.71E-03	4.57E-03	4.83E-03	4.68E-03
Cl (mol/L)	4.36E-03	3.72E-01	6.65E-03	3.28E-03	3.31E-03	3.31E-03
SiO_2(aq) (mol/L)	3.66E-03	3.45E-01	1.05E-02	2.80E-03	1.57E-03	1.55E-03
HCO_3 (mol/L)	4.96E-04	3.08E-04	3.76E-05	1.92E-03	3.22E-03	3.25E-03
SO_4 (mol/L)	1.59E-03	9.28E-02	2.86E-03	1.20E-03	1.20E-03	1.21E-03
K (mol/L)	2.39E-04	3.96E-02	5.55E-04	2.09E-04	1.12E-04	9.74E-05
AlO_2 (mol/L)	3.75E-08	2.45E-13	8.85E-09	4.31E-09	7.86E-10	4.59E-10
F (mol/L)	5.64E-04	3.32E-03	4.08E-04	3.91E-04	3.14E-04	2.97E-04
$HFeO_2$ (mol/L)	4.01E-11	6.09E-10	1.41E-09	4.40E-11	4.47E-12	1.87E-12

Source: Data derived from THC simulations thc6_ht1 (Table 6.3.1.5-1) and thc6_16_25_g4_amb (DTN: LB0011DSTTHCR1.001 [DIRS 154759]) as archived in Jolley (2001 [DIRS 154762]).

Table 6.3.1.6-3. Abstraction Results for Low Temperature and Low Carbon Dioxide Partial Pressure in the Tptpll Lithology for Seepage at the Crown of the Drift

	Preclosure	Post Closure Hot	Cool Down	Transition to Ambient	Ambient
	(0-300 yr)	(301-10,000 yr)	(10,001-30,000 yr)	(30,001-100,000 yr)	(100,001-1,000,000 yr)
Actual THC Model Run Time (yr)	53.00	700.00	20,000.00	51,411.30	Averaged
Temperature (°C)	52.92	73.40	35.59	25.89	23.60
PCO_2 (v.frac)	1.19E-03	1.48E-03	8.75E-04	5.11E-04	4.39E-04
pH	8.02	7.84	8.26	8.50	8.55
Ca (mol/L)	1.33E-03	1.08E-03	1.66E-03	1.92E-03	1.97E-03
Mg (mol/L)	5.00E-04	1.60E-04	1.81E-04	2.60E-04	2.57E-04
Na (mol/L)	4.08E-03	4.66E-03	4.65E-03	4.48E-03	4.39E-03
Cl (mol/L)	3.43E-03	3.40E-03	3.28E-03	3.29E-03	3.29E-03
SiO_2(aq) (mol/L)	2.44E-03	3.24E-03	1.69E-03	1.43E-03	1.44E-03
HCO_3 (mol/L)	1.29E-03	7.60E-04	2.15E-03	2.59E-03	2.58E-03
SO_4 (mol/L)	1.26E-03	1.24E-03	1.20E-03	1.20E-03	1.21E-03
K (mol/L)	1.37E-04	2.66E-04	1.35E-04	9.83E-05	9.23E-05
AlO_2 (mol/L)	7.28E-09	2.88E-08	2.12E-09	9.51E-10	6.74E-10
F (mol/L)	3.91E-04	4.69E-04	3.60E-04	3.21E-04	3.11E-04
$HFeO_2$ (mol/L)	6.08E-12	4.91E-11	3.17E-12	2.03E-12	1.97E-12

Source: Data derived from THC simulations thc6_lt3L and thc6_ambL (Table 6.3.1.5-1) as archived in Jolley (2001 [DIRS 154762]).

Table 6.3.1.6-4. Abstraction Results for Low Temperature and High Carbon Dioxide Partial Pressure in the Tptpll Lithology for Seepage at the Crown of the Drift

	Preclosure	Post Closure Hot	Cool Down	Transition to Ambient	Ambient
	(0-300 yr)	(301-10,000 yr)	(10,001-30,000 yr)	(30,001-100,000 yr)	(100,001-1,000,000 yr)
Actual THC Model Run Time (yr)	53.00	700.00	20,000.00	51,411.30	Averaged
Temperature (°C)	52.92	73.40	35.59	25.89	23.2
PCO_2 (v.frac)	1.19E-03	1.48E-03	1.71E-03	9.38E-04	7.67E-04
pH	8.02	7.84	8.09	8.35	8.41
Ca (mol/L)	1.33E-03	1.08E-03	1.87E-03	2.14E-03	2.18E-03
Mg (mol/L)	5.00E-04	1.60E-04	1.19E-04	1.97E-04	1.98E-04
Na (mol/L)	4.08E-03	4.66E-03	4.95E-03	4.79E-03	4.68E-03
Cl (mol/L)	3.43E-03	3.40E-03	3.30E-03	3.31E-03	3.31E-03
SiO_2(aq) (mol/L)	2.44E-03	3.25E-03	1.84E-03	1.55E-03	1.55E-03
HCO_3 (mol/L)	1.29E-03	7.61E-04	2.84E-03	3.31E-03	3.25E-03
SO_4 (mol/L)	1.26E-03	1.24E-03	1.20E-03	1.20E-03	1.21E-03
K (mol/L)	1.37E-04	2.66E-04	1.44E-04	1.06E-04	9.74E-05
AlO_2 (mol/L)	7.28E-09	2.87E-08	1.47E-09	6.64E-10	4.59E-10
F (mol/L)	3.91E-04	4.69E-04	3.42E-04	3.06E-04	2.97E-04
$HFeO_2$ (mol/L)	6.08E-12	4.91E-11	3.10E-12	2.00E-12	1.87E-12

Source: Data derived from THC simulations thc6_lt3 (Table 6.3.1.5-1) and thc6_16_25_g4_amb (DTN: LB0011DSTTHCR1.001 [DIRS 154759]) as archived in Jolley (2001 [DIRS 154762]).

Table 6.3.1.6-5. Abstraction Results for High Temperature and Low Carbon Dioxide Partial Pressure in the Tptpll Lithology for Matrix Imbibition into the Invert

	Preclosure	Boiling	Cool Down	Extended Cool Down	Transition to Ambient	Ambient
	(0-50 yr)	(51-1,500 yr)	(1,501-4,000 yr)	(4,001-25,000 yr)	(25,001-100,000 yr)	(100,001-1,000,000 yr)
Actual THC Model Run Time (yr)	5.00	250.01	2,000.00	10,000.00	49,806.80	Averaged
Temperature (°C)	75.02	120.69	93.89	53.96	27.48	23.69
PCO_2 (v.frac)	1.56E-03	2.20E-05	1.08E-05	1.44E-03	5.06E-04	4.07E-04
pH	7.86	8.10	8.36	7.89	8.49	8.57
Ca (mol/L)	8.75E-04	1.29E-02	1.34E-02	1.85E-03	1.79E-03	1.92E-03
Mg (mol/L)	3.54E-04	7.66E-03	1.84E-03	2.69E-05	1.99E-04	2.07E-04
Na (mol/L)	4.40E-03	5.82E-02	2.44E-03	3.46E-03	4.71E-03	4.54E-03
Cl (mol/L)	3.26E-03	5.88E-02	1.33E-02	3.26E-03	3.29E-03	3.29E-03
SiO_2(aq) (mol/L)	3.78E-03	3.80E-02	6.49E-03	3.07E-03	1.41E-03	1.35E-03
HCO_3 (mol/L)	8.30E-04	2.90E-05	2.53E-05	1.15E-03	2.44E-03	2.52E-03
SO_4 (mol/L)	1.17E-03	2.06E-02	8.94E-03	1.19E-03	1.20E-03	1.21E-03
K (mol/L)	4.39E-04	1.10E-02	3.74E-04	1.98E-04	1.17E-04	9.83E-05
AlO_2 (mol/L)	1.24E-08	3.53E-11	5.11E-08	3.04E-09	1.01E-09	7.30E-10
F (mol/L)	5.53E-04	3.30E-04	2.12E-04	3.74E-04	3.41E-04	3.19E-04
$HFeO_2$ (mol/L)	5.47E-11	2.01E-09	1.25E-09	4.49E-11	4.66E-12	1.97E-12

Source: Data derived from THC simulations thc6_ht1L and thc6_ambL (Table 6.3.1.5-1) as archived in Jolley (2001 [DIRS 154762]).

Table 6.3.1.6-6. Abstraction Results for High Temperature and High Carbon Dioxide Partial Pressure in the Tptpll Lithology for Matrix Imbibition at the Base of the Invert

	Preclosure	Boiling	Cool Down	Extended Cool Down	Transition to Ambient	Ambient
	(0-50 yr)	(51-1,500 yr)	(1,501-4,000 yr)	(4,001-25,000 yr)	(25,001-100,000 yr)	(100,001-1,000,000 yr)
Actual THC Model Run Time (yr)	5.00	250.01	2,000.00	10,000.00	50,001.50	Averaged
Temperature (°C)	75.02	120.68	93.89	53.96	27.44	23.26
PCO_2 (v.frac)	1.56E-03	2.15E-05	4.60E-05	3.40E-03	9.44E-04	7.13E-04
pH	7.86	8.27	8.04	7.70	8.33	8.43
Ca (mol/L)	8.75E-04	2.30E-02	1.37E-02	1.97E-03	2.01E-03	2.13E-03
Mg (mol/L)	3.54E-04	2.87E-02	2.45E-03	1.50E-05	1.35E-04	1.53E-04
Na (mol/L)	4.40E-03	2.24E-01	3.96E-03	3.71E-03	5.02E-03	4.82E-03
Cl (mol/L)	3.26E-03	2.24E-01	1.60E-02	3.27E-03	3.31E-03	3.31E-03
SiO_2(aq) (mol/L)	3.78E-03	7.10E-02	6.32E-03	3.40E-03	1.52E-03	1.46E-03
HCO_3 (mol/L)	8.30E-04	2.35E-05	4.13E-05	1.73E-03	3.15E-03	3.19E-03
SO_4 (mol/L)	1.17E-03	5.35E-02	9.67E-03	1.19E-03	1.20E-03	1.21E-03
K (mol/L)	4.39E-04	4.20E-02	6.11E-04	2.12E-04	1.24E-04	1.03E-04
AlO_2 (mol/L)	1.24E-08	3.93E-12	2.59E-08	2.05E-09	7.25E-10	5.06E-10
F (mol/L)	5.53E-04	4.18E-04	2.15E-04	3.66E-04	3.24E-04	3.04E-04
$HFeO_2$ (mol/L)	5.47E-11	2.81E-09	8.49E-10	4.36E-11	4.53E-12	1.86E-12

Source: Data derived from THC simulations thc6_ht1 (Table 6.3.1.5-1) and thc6_16_25_g4_amb (DTN: LB0011DSTTHCR1.001 [DIRS 154759]) as archived in Jolley (2001 [DIRS 154762]).

Table 6.3.1.6-7. Abstraction Results for Low Temperature and Low Carbon Dioxide Partial Pressure in the Tptpll Lithology for Matrix Imbibition into the Invert

	Preclosure	Post Closure Hot	Cool Down	Transition to Ambient	Ambient
	(0-300 yr)	(301-10,000 yr)	(10,001-30,000 yr)	(30,001-100,000 yr)	(100,001-1,000,000 yr)
Actual THC Model Run Time (yr)	49.97	750.01	20,000.00	51,411.30	Averaged
Temperature (°C)	50.89	72.11	35.63	25.96	23.69
PCO_2 (v.frac)	1.05E-03	1.27E-03	8.17E-04	4.57E-04	4.07E-04
pH	8.06	7.79	8.28	8.53	8.57
Ca (mol/L)	1.22E-03	1.64E-03	1.60E-03	1.84E-03	1.92E-03
Mg (mol/L)	3.78E-04	9.72E-05	1.24E-04	2.07E-04	2.07E-04
Na (mol/L)	4.22E-03	3.47E-03	4.83E-03	4.67E-03	4.54E-03
Cl (mol/L)	3.25E-03	3.43E-03	3.28E-03	3.29E-03	3.29E-03
SiO_2(aq) (mol/L)	3.02E-03	4.52E-03	1.67E-03	1.36E-03	1.35E-03
HCO_3 (mol/L)	1.28E-03	6.02E-04	2.11E-03	2.50E-03	2.52E-03
SO_4 (mol/L)	1.19E-03	1.26E-03	1.20E-03	1.20E-03	1.21E-03
K (mol/L)	2.21E-04	3.22E-04	1.58E-04	1.10E-04	9.83E-05
AlO_2 (mol/L)	1.89E-09	6.68E-09	1.61E-09	9.37E-10	7.30E-10
F (mol/L)	4.57E-04	4.08E-04	3.78E-04	3.33E-04	3.19E-04
$HFeO_2$ (mol/L)	1.33E-11	4.45E-11	3.19E-12	2.03E-12	1.97E-12

Source: Data derived from THC simulations thc6_lt3L and thc6_ambL (Table 6.3.1.5-1) as archived in Jolley (2001 [DIRS 154762]).

Table 6.3.1.6-8. Abstraction Results for Low Temperature and High Carbon Dioxide Partial Pressure in the Tptpll Lithology for Matrix Imbibition at the Base of the Invert

	Preclosure	Post Closure Hot	Cool Down	Transition to Ambient	Ambient
	(0-300 yr)	(301-10,000 yr)	(10,001-30,000 yr)	(30,001-100,000 yr)	(100,001-1,000,000 yr)
Actual THC Model Run Time (yr)	30.00	750.01	20,000.00	51,411.30	Averaged
Temperature (°C)	53.52	72.11	35.63	25.96	23.26
PCO_2 (v.frac)	1.09E-03	1.28E-03	1.66E-03	8.53E-04	7.13E-04
pH	8.05	7.79	8.10	8.38	8.43
Ca (mol/L)	1.19E-03	1.64E-03	1.83E-03	2.06E-03	2.13E-03
Mg (mol/L)	3.89E-04	9.71E-05	6.70E-05	1.44E-04	1.53E-04
Na (mol/L)	4.25E-03	3.47E-03	5.11E-03	4.99E-03	4.82E-03
Cl (mol/L)	3.26E-03	3.43E-03	3.30E-03	3.31E-03	3.31E-03
SiO_2(aq) (mol/L)	3.08E-03	4.53E-03	1.82E-03	1.47E-03	1.46E-03
HCO_3 (mol/L)	1.26E-03	6.03E-04	2.82E-03	3.22E-03	3.19E-03
SO_4 (mol/L)	1.19E-03	1.26E-03	1.20E-03	1.20E-03	1.21E-03
K (mol/L)	2.40E-04	3.23E-04	1.67E-04	1.17E-04	1.03E-04
AlO_2 (mol/L)	2.41E-09	6.67E-09	1.14E-09	6.67E-10	5.06E-10
F (mol/L)	4.67E-04	4.08E-04	3.57E-04	3.17E-04	3.04E-04
$HFeO_2$ (mol/L)	1.37E-11	4.45E-11	3.11E-12	2.00E-12	1.86E-12

Source: Data derived from THC simulations thc6_lt3 (Table 6.3.1.5-1) and thc6_16_25_g4_amb (DTN: LB0011DSTTHCR1.001 [DIRS 154759]) as archived in Jolley (2001 [DIRS 154762]).

Table 6.3.1.8-1. Summary of Uncertainty Issues Related to Predicted Composition of Fluids Entering Drifts

Category	Uncertainty Issue	Treatment of Uncertainty Issue	Affected Goals
Conceptual Uncertainties	Geochemical system considered (minerals, gases, and aqueous species)	Treated by including major rock-forming minerals, major aqueous species, and major gases of interest (carbon dioxide, air, and steam) in the system Effects of secondary mineral phase precipitation is most uncertain at higher temperatures and may require further evaluation Uncertainty is limited under ambient conditions if ambient water concentrations can be reproduced Trace minerals and aqueous species are not considered (not in the current scope for the THC model)	Precipitation of secondary phases not currently included in simulations could significantly affect the predicted composition of waters around the drift at high temperature. Reactions between trace minerals and aqueous species could affect predicted concentrations of major species through pH change
	Drift wall is closed to advective fluid flow (but open to carbon dioxide diffusive fluxes)	Case of open drift wall is not addressed Infiltration rates (even at high rates indicative of future wet climates) are below seepage thresholds, so there is no effect on water percolation fluxes around the drift Effect of carbon dioxide diffusive transport across the wall is taken into account and may be more important than advective fluxes Evaporative concentration effects (due to ventilation) are indirectly taken into account by the salts and precipitates model (Section 6.3.3) Effects of atmospheric carbon dioxide in the drift during ventilation (through diffusive fluxes) were investigated and determined to be short-lived after ventilation ends	Boundary conditions of pressure and relative humidity in the drift could affect evaporative concentration effects at the drift wall, most particularly during ventilation. Such boundary conditions have not been determined Carbon dioxide advective fluxes into the drift are not calculated, which could affect the pH of pore water at the drift wall In-drift interactions are not considered (this was not a goal of the THC seepage models)
	Precipitation/ nucleation kinetics	Not treated This affects minerals such as silica and calcite, which have fast reaction rates. Reaction of calcite at equilibrium with a supersaturation gap may approximate nucleation processes Silica precipitation is modeled with a very fast reaction rate	In areas where rapid boiling occurs, predicted silica concentrations are overestimated and silica precipitation is underestimated. However, the water saturation in these areas is very small such that the actual amounts of silica are minute
	Water chemistry is not computed below a set water saturation (10^{-4}) or above a set ionic strength (4) (Activity coefficient model limitations)	Salts precipitation in the last remaining water, when boiling or evaporating is not considered The composition of the last aqueous phase for which geochemical speciation is computed (prior to dryout) is saved by the model. This composition is assumed to mix instantly with percolating water during rewetting	Some solid phases precipitated upon dryout may not dissolve instantly upon rewetting. In this case, assuming instant dissolution may overpredict dissolved salt concentrations when rewetting occurs

Table 6.3.1.8-1. Summary of Uncertainty Issues Related to Predicted Composition of Fluids Entering Drifts (Continued)

Category	Uncertainty Issue	Treatment of Uncertainty Issue	Affected Goals
Conceptual Uncertainties (Continued)	Vapor pressure lowering due to changes in water activity caused by dissolved salts	Not treated This effect would only become significant once most of the water has already evaporated (i.e., when ionic strength becomes large - for example, at 3m NaCl, the reduction in vapor pressure would only be approximately 10%)	By neglecting this effect, evaporative concentration is overestimated
	Vapor pressure lowering due to capillary pressure	Not treated The effect on evaporative concentration is mostly bounded by the higher- and lower-temperature cases (without vapor pressure lowering)	Neglecting vapor pressure lowering increases the effect of evaporative concentration around the drift (resulting in overestimated water salinities)
	Oxidation-reduction processes are neglected	Not treated (considers only oxidized conditions) Oxidizing conditions prevail in the unsaturated zone at Yucca Mountain such that the redox species considered in the THC seepage model (iron and sulfate) occur only in their oxidized state	Limited anticipated effect. Likely no effect for iron and sulfate in the current models. Redox reactions involving microbial processes and species not presently modeled (nitrates, phosphates) could have some effect on pH
	Mineral solid-solutions	Treated as ideal for clays; no treatment for other minerals Taken indirectly into account through calibration of thermodynamic data such that ambient water compositions can be reproduced Compositions of primary solid solution phases, when known, are indirectly taken into account in the amounts of individual end-members input into the model Individual mineral phases with fixed solid-solution compositions (determined by analysis) are included in simulations (e.g., zeolites)	Limited anticipated effect. In the current THC seepage models, this would primarily affect the composition of precipitating alkali feldspars (thus affecting predicted Na and K concentrations). However, these minerals typically form nearly pure secondary phases in nature (i.e., as modeled). Zeolites in the repository host units (mostly stellerite) are not abundant and not particularly variable in composition
	Ion-exchange and surface complexation	Not treated Dominant primary rock minerals in the rock wall around the drifts are not strong ion exchangers THC seepage simulations do not include trace elements that could be strongly affected by surface complexation	Limited effect for the current application range of the THC seepage models. Could shift somewhat the predicted concentrations of Na, K, Ca, and Mg
	Capillary pressure effect on chemical potentials of reacting species	Not treated It is taken indirectly into account through calibration of thermodynamic data such that ambient water compositions can be reproduced	Could potentially shift predicted concentrations of some species

Table 6.3.1.8-1. Summary of Uncertainty Issues Related to Predicted Composition of Fluids Entering Drifts (Continued)

Category	Uncertainty Issue	Treatment of Uncertainty Issue	Affected Goals
Data Uncertainties	Infiltration water and initial pore-water composition	Alternate water analyses are used in recent analyses Additional systematic evaluations may be needed with additional compositions Uncertainty can be assessed by comparing predictions of ambient water compositions with measured ambient pore-water compositions and pore-gas CO_2 concentrations	Currently one of the main uncertainties affecting predicted water compositions around the drift (and likely more so through infiltration/transport than through reaction)
	Carbon dioxide partial pressures at top model boundary	Treated in recent analyses Composition of infiltration-water input into the model essentially dictates the boundary carbon dioxide pressure; therefore the uncertainty in infiltrating water composition overcomes this uncertainty	Within the investigated range (750 and 3700 ppmv), no effect until 800-1000 years, then small pH effect (0.4 units) at the drift wall, and negligible effect on other predicted concentrations
	Thermodynamic and kinetic data	Treated partly through sensitivity studies on long-term behavior of ambient system chemistry, assuming a fixed infiltration rate When possible within the uncertainty of the original data, treated through calibration with observed water composition and mineralogical data Other uncertainties treated through model validation (Drift Scale Test and laboratory experiments)	One of the main uncertainties affecting predicted water compositions around the drift. However, it can be constrained by calibration and model validation against observed data, such that ambient simulations predict concentrations consistent with observed values
	Host rock mineralogy	Treated in updated model (Tptpmn versus Tptpll host rock unit) Bulk chemical composition of the potential repository host units do not differ significantly	No significant effect on the predicted compositions of major aqueous species. Small amounts of fast reacting minerals containing elements present in minor quantities in pore water (e.g., fluorite) can have a large effect on the predicted concentrations of these minor species (e.g., F^-)
	Infiltration rates	Alternate infiltration rate scenarios are used in original analysis. Stepwise increase in infiltration rates are used in all analyses At high infiltration rate conditions most conducive to in-drift seepage, water compositions are more function of transport than reaction such that the uncertainty regarding the composition of infiltration, rather than the rate, becomes more important	Affects predicted concentrations at the drift wall. However, the effect is stronger under low infiltration conditions least susceptible to cause in-drift seepage

Table 6.3.1.8-1. Summary of Uncertainty Issues Related to Predicted Composition of Fluids Entering Drifts (Continued)

Category	Uncertainty Issue	Treatment of Uncertainty Issue	Affected Goals
Parameter Uncertainties	Heterogeneity	Fracture permeability heterogeneity treated in updated model Heterogeneity in matrix properties not treated Local heterogeneity in mineralogical properties not treated Heterogeneity in initial water geochemistry not treated directly; treated indirectly through alternate compositions used	Possible local changes in predicted water compositions around the drift. However, the bulk composition of waters around the drift is not expected to be significantly affected
	Transport parameters (diffusion coefficients and tortuosity)	Carbon dioxide diffusion coefficient changed by a factor of 30 between initial and updated analyses Sensitivity to diffusion coefficient for aqueous species was not investigated; however, tortuosity factor was changed from 0.2 to 0.7 between initial and updated analyses	Affects predicted concentrations of carbon dioxide at the drift wall during dryout; otherwise, the effect appears limited

NOTE: See also Table 4.3.6-2.

Table 6.3.2-1. Summary of Uncertainties on the Effects of Engineered Materials in the In-Drift Chemical Environment and any Associated Model Improvements

Key Uncertainty Not Included in TSPA-SR Models	Model Improvements Discussed in SSPA Vol. 1
Trace elemental compositions and effects on chemistry	No
Radionuclide or metal sorption onto corrosion products	Yes (Section 10)
Oxygen gas depletion (generation of sub-oxic conditions)	No
Cement leachate effects on in-drift chemistry	Yes (Section 6.3.3.5.1.1)
Generation of colloids from corrosion products	Yes (Section 10)
Alkaline plumes interacting with EBS	No

Source: TSPA-SR refers to CRWMS M&O 2000 [DIRS 153246].

Table 6.3.3-1. Example Precipitates/Salts Model Lookup Table for Selected Outputs

Input Parameters		Precipitates/Salts Model Output for: Invert Low Temp, Low CO2 Preclosure Period (0-300 yr)											
RH (%)	Qe/Qs[a]	pH	Ionic Strength (molal)	Total Cl (molal)	Total F (molal)	Total N (molal)	HCO3- (molal)	CO32- (molal)	OH- (molal)	H+ (molal)	H2SiO42- (molal)	H3SiO4- (molal)	MgOH+ (molal)
< 50.3	na[b]	NA	NA	NA	NA	NA	NA	NA	NA	NA	NA	NA	NA
50.3	NA	7.30	2.61E+01	2.70E-02	NA	NA	NA	NA	NA	NA	NA	NA	NA
51.0	NA	7.30	2.38E+01	3.72E-01	NA	NA	NA	NA	NA	NA	NA	NA	NA
53.1	NA	7.30	1.49E+01	1.69E+00	NA	NA	NA	NA	NA	NA	NA	NA	NA
55.2	NA	7.30	1.15E+01	2.20E+00	NA	NA	NA	NA	NA	NA	NA	NA	NA
60.5	NA	7.30	6.26E+00	2.99E+00	NA	NA	NA	NA	NA	NA	NA	NA	NA
65.7	NA	7.30	4.68E+00	3.22E+00	NA	NA	NA	NA	NA	NA	NA	NA	NA
71.0	NA	7.30	4.32E+00	3.28E+00	NA	NA	NA	NA	NA	NA	NA	NA	NA
76.2	NA	7.30	4.24E+00	3.29E+00	NA	NA	NA	NA	NA	NA	NA	NA	NA
81.5	NA	7.30	4.33E+00	3.27E+00	NA	NA	NA	NA	NA	NA	NA	NA	NA
85.0	NA	7.30	4.29E+00	3.17E+00	3.87E-04	3.17E-01	5.88E-04	2.17E-05	2.84E-06	2.24E-08	1.85E-10	4.18E-06	7.38E-08
> 85	-9.00	6.75	9.62E-04	3.25E-04	4.54E-05	3.25E-05	6.99E-05	2.99E-08	3.28E-07	1.87E-07	1.85E-14	7.04E-08	1.74E-10
> 85	0.00	7.71	9.63E-03	3.25E-03	4.54E-04	3.25E-04	6.88E-04	3.38E-06	3.24E-06	2.18E-08	2.06E-11	6.84E-06	1.22E-08
> 85	0.90	7.53	7.46E-02	3.24E-02	3.18E-04	3.24E-03	5.23E-04	2.74E-06	2.51E-06	3.81E-08	1.64E-11	5.11E-06	2.20E-08
> 85	0.99	7.44	5.34E-01	3.18E-01	3.42E-04	3.18E-02	5.58E-04	5.33E-06	2.61E-06	5.40E-08	3.35E-11	4.87E-06	3.83E-08
> 85	0.999	7.38	3.92E+00	2.72E+00	4.47E-04	2.72E-01	7.10E-04	2.75E-05	3.24E-06	2.37E-08	2.25E-10	5.02E-06	6.37E-08
> 85	> 0.999	7.30	4.29E+00	3.17E+00	3.87E-04	3.17E-01	5.88E-04	2.17E-05	2.84E-06	2.24E-08	1.85E-10	4.18E-06	7.38E-08

Source: Jolley 2001 [DIRS 154762]. This reference also presents a complete set of lookup tables.

NOTES: [a] Q_e/Q_s is the evaporative flux divided by the seepage flux.

[b] Not applicable to model (dry conditions at relative humidity less than 50.3 percent).

Table 6.3.3.5.2-1. Sensitivity Analysis of the In-Drift ANC/pH Model

W_{wpl} (kg/yr)	Run 1 pH	Run 2 pH	Run 3 pH	Run 4 pH	Run 5 pH	Run 6 pH	Range of pH	Mean pH
1.15	8.5	8.5	8.5	8.5	8.5	8.5	8.5	8.5
251.15	8.5	8.5	7.9	8.4	8.3	8.2	7.9-8.5	8.3
501.15	7.9	8.5	7.6	8.2	7.6	8.0	7.6-8.5	8.0
751.15	7.4	8.4	7.2	7.9	8.1	8.0	7.2-8.4	7.8
1001.15	8.4	8.4	8.1	7.9	7.3	7.4	7.3-8.4	7.9
1251.15	8.4	7.4	7.9	6.3	7.2	8.4	6.3-8.4	7.6
1501.15	8.4	7.4	7.9	7.3	6.4	5.9	5.9-8.4	7.2
1751.15	6.0	7.2	4.7	4.7	8.4	8.4	4.7-8.4	6.6
2001.15	7.3	8.4	7.7	4.6	8.3	7.3	4.6-8.4	7.3
2251.15	7.6	8.2	7.6	4.6	8.1	8.2	4.6-8.2	7.4
2501.15	8.2	7.9	8.4	4.5	4.4	4.4	4.4-8.4	6.3
2751.15	8.2	4.3	7.8	4.4	4.6	4.3	4.3-8.2	5.6
3001.15	7.5	5.1	7.4	4.5	7.4	7.7	4.5-7.7	6.6
3251.15	4.3	4.6	4.3	7.9	7.9	8.1	4.3-8.1	6.2
3501.15	4.6	4.4	6.6	8.3	5.4	7.0	4.4-8.3	6.1
3751.15	6.0	4.6	4.2	6.4	8.2	4.5	4.2-8.2	5.7
4001.15	7.0	7.8	7.6	7.7	7.7	4.3	4.3-7.8	7.0

Source: Metcalf 2001 [DIRS 154842].

NOTE: Sensitivity analysis of in-drift ANC/pH model showing variation of mixed solution pH as a function of waste package leakage flux (W_{wpl}) and percentage waste package mixing (F_{mixing}) with other water sources by Monte Carlo simulation (seen as variation across a row of pH for a given W_{wpl}).

Table 6.3.3.5.2-2. Validation Analyses of In-Drift ANC/pH Model Showing Agreement Between Mixing Model Results and Literature Mixing Examples

Parameter	Morel and Hering[a]	Stumm and Morgan[b]	In-drift ANC/pH Mixing Model-1[c]	In-drift ANC/pH Mixing Model-2
Water pH (mixed)	7.91	7.2	7.90	7.20
ANC_{mixed} (Eq/L)	4.06 E-04	9.5 E-05	4.04 E-04	9.50 E-05

Sources: [a] Morel and Hering 1993 [DIRS 151052], pp. 194 to 195.
[b] Stumm and Morgan 1996 [DIRS 125332], pp. 170 to 172.
[c] Metcalf 2001 [DIRS 154842].

Table 6.3.4-1. Block Volume Corresponding to Various Levels of Predicted Cumulative Frequency of Occurrence, Emplacement Drift in Tptpmn Unit, Static Condition

Cumulative Frequency of Occurrence (%)	Joint Radius Multiplier (*M*)				
	1.0	1.5	2.0	2.5	3.0
50	0.16	0.01	0.04	0.01	0.01
75	0.30	0.16	0.21	0.16	0.16
90	0.61	0.44	0.55	0.52	0.50
95	1.35	0.67	1.06	0.98	0.98
98	1.35	1.18	1.86	1.86	2.17
Maximum	1.35	1.86	14.30	20.87	13.05

Source: BSC 2001 [DIRS 154537].

NOTE: Block volume measured in m^3.

Table 6.3.4-2. Block Volume Corresponding to Various Levels of Predicted Cumulative Frequency of Occurrence, Emplacement Drift in Tptpll Unit, Static Condition

Cumulative Frequency of Occurrence (%)	Joint Radius Multiplier (*M*)				
	1.0	1.5	2.0	2.5	3.0
50	0.24	0.04	0.01	0.01	0.01
75	0.24	0.16	0.07	0.16	0.10
90	0.24	0.38	0.24	0.38	0.24
95	0.24	1.49	0.86	0.86	0.47
98	0.24	1.49	1.29	3.36	0.86
Maximum	0.24	1.49	1.29	3.36	3.36

Source: BSC 2001 [DIRS 154537].

NOTE: Block volume measured in m^3.

Table 6.3.4-3. Predicted Number of Key Blocks per Unit Length along Emplacement Drift, Static Condition

Lithologic Unit	Joint Radius Multiplier (*M*)				
	1.0	1.5	2.0	2.5	3.0
Tptpmn	1	11	50	152	265
Tptpll	0	2	2	5	6

Source: BSC 2001 [DIRS 154537].

NOTE: Blocks per unit length measured in km.

Table 6.3.4-4. Beta Distribution Parameters for Spacing of the Subhorizontal Joint Set of the Tptpmn Unit

Beta Distribution Parameters	Original True Spacing[a]	Modified True Spacing[b]
a (m)	0.0018	0.0018
b (m)	15.2606	15.2606
p	0.2010	0.3834
q	5.2988	5.8050

NOTES: [a] CRWMS M&O 2000 [DIRS 151635], Table 7, Joint Set Number 3.
[b] BSC 2001 [DIRS 154537], file New-Beta-Tptpmn V1 - modified Terzaghi.xls.

Table 6.3.4-5. Block Volume Corresponding to Various Levels of Predicted Cumulative Frequency of Occurrence, Emplacement Drift in Tptpmn Unit, Static Condition with Modified Terzaghi Correction

Cumulative Frequency of Occurrence (%)	Terzaghi Correction Factor	
	Original	Modified
50	0.04	0.04
75	0.21	0.24
90	0.55	0.81
95	1.06	1.54
98	1.85	2.36
maximum	14.29	19.35

Source: BSC 2001 [DIRS 154537].

NOTE: Block volume measured in m^3.

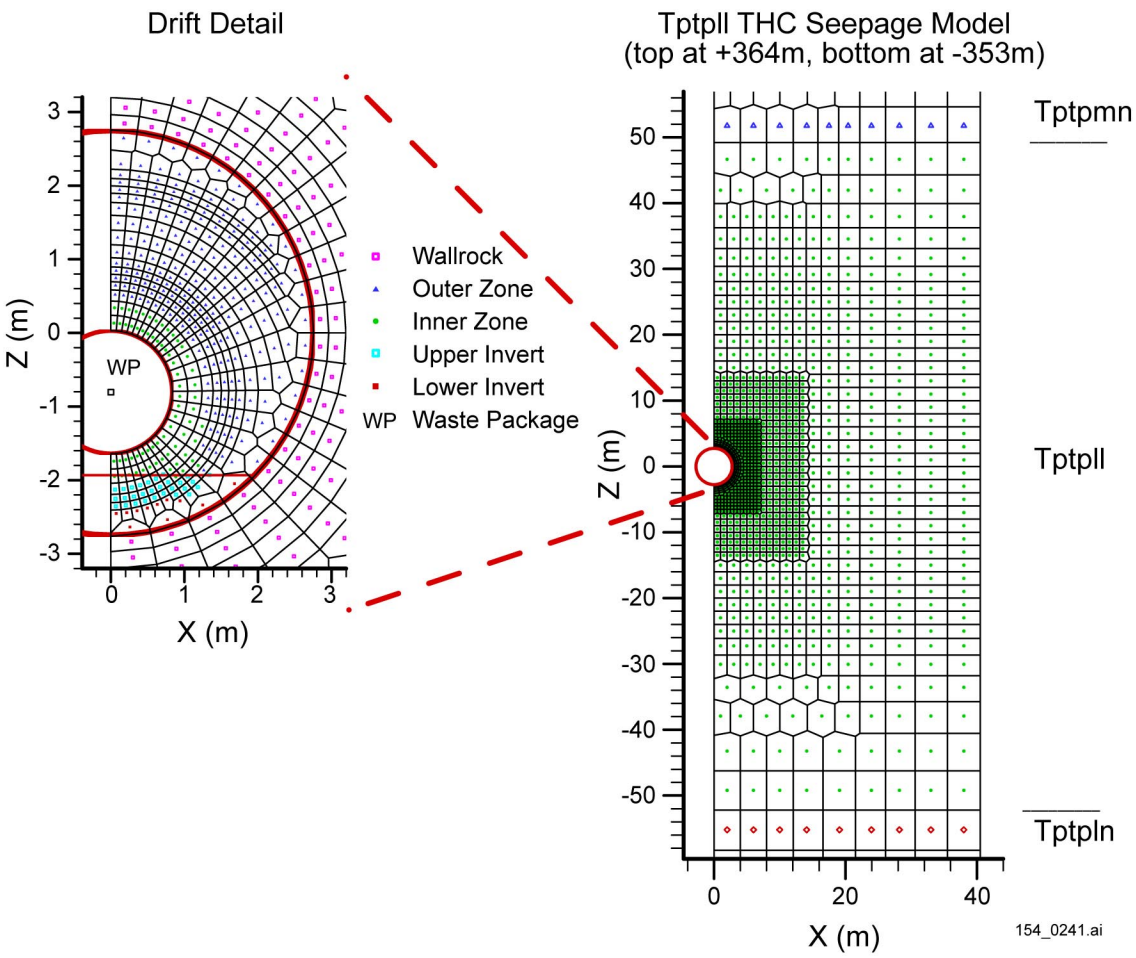

154_0241.ai

Source: Adapted from BSC 2001 [DIRS 154677], Figures 84 and 85.

NOTE: Laterally, the mesh covers half the distance between drift centers. Vertically, the mesh extends from near ground surface down to the regional water table. THC = thermal-hydrologic-chemical.

Figure 6.3.1.2-1. Example of Thermal-Hydrologic-Chemical Seepage Model Mesh with Drift in the Topopah Spring Tuff Lower Lithophysal Geologic Unit (Tptpll)

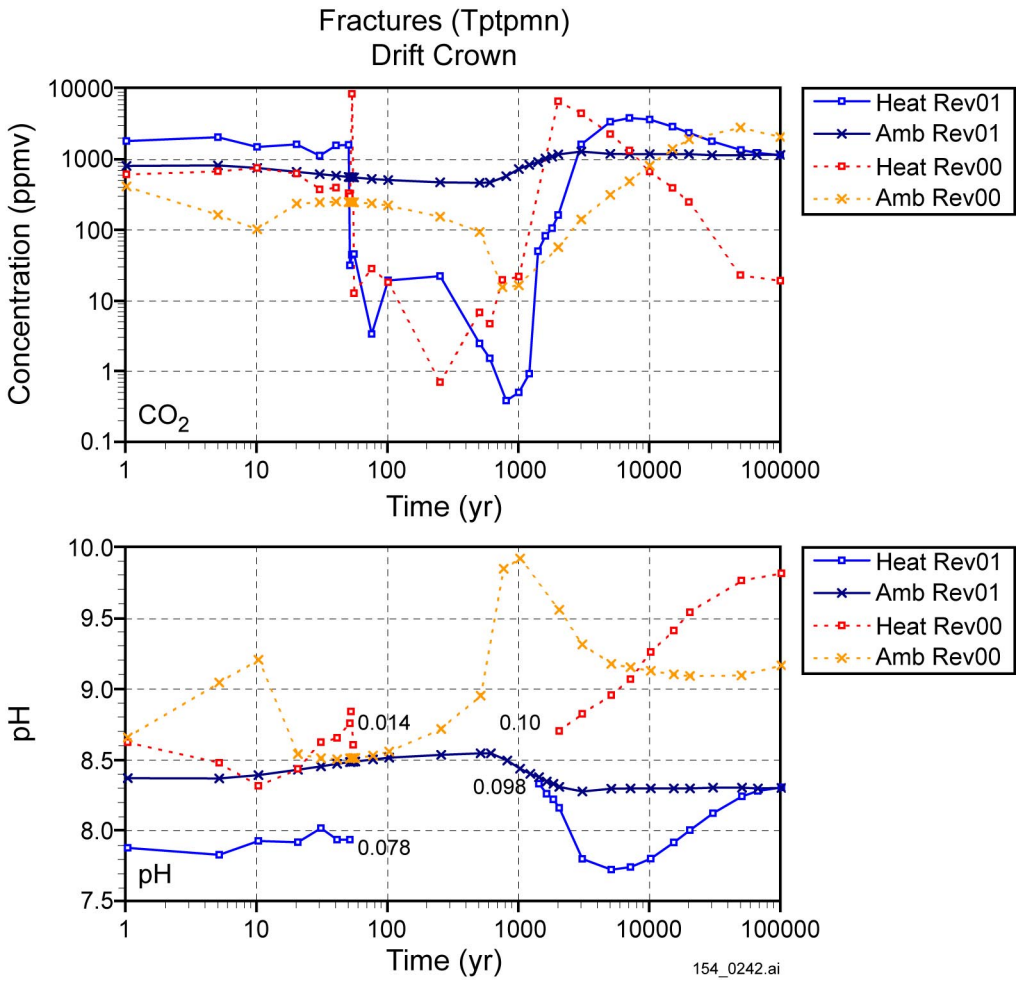

154_0242.ai

Source: CRWMS M&O 2000 [DIRS 142022]; BSC 2001 [DIRS 154677].

NOTE: Comparison of initial and updated simulation results. Results are for simulations under heat load (Heat) and ambient (Amb) conditions (extended-case geochemical system). The infiltration rate changes from 6 to 16 mm/yr at 600 years and from 16 to 25 mm/yr at 2,000 years, except for the ambient case (fixed rate of 1 mm/yr). For pH, the dryout period is left blank (no water); numbers by each curve indicate the last output liquid saturation before dryout and the first output liquid saturation during rewetting.

Figure 6.3.1.4-1. Time Profiles for Thermal-Hydrologic-Chemical Simulations of Carbon Dioxide (Pore Gas) Concentration and pH (Pore Water) in Fractures at the Drift Crown

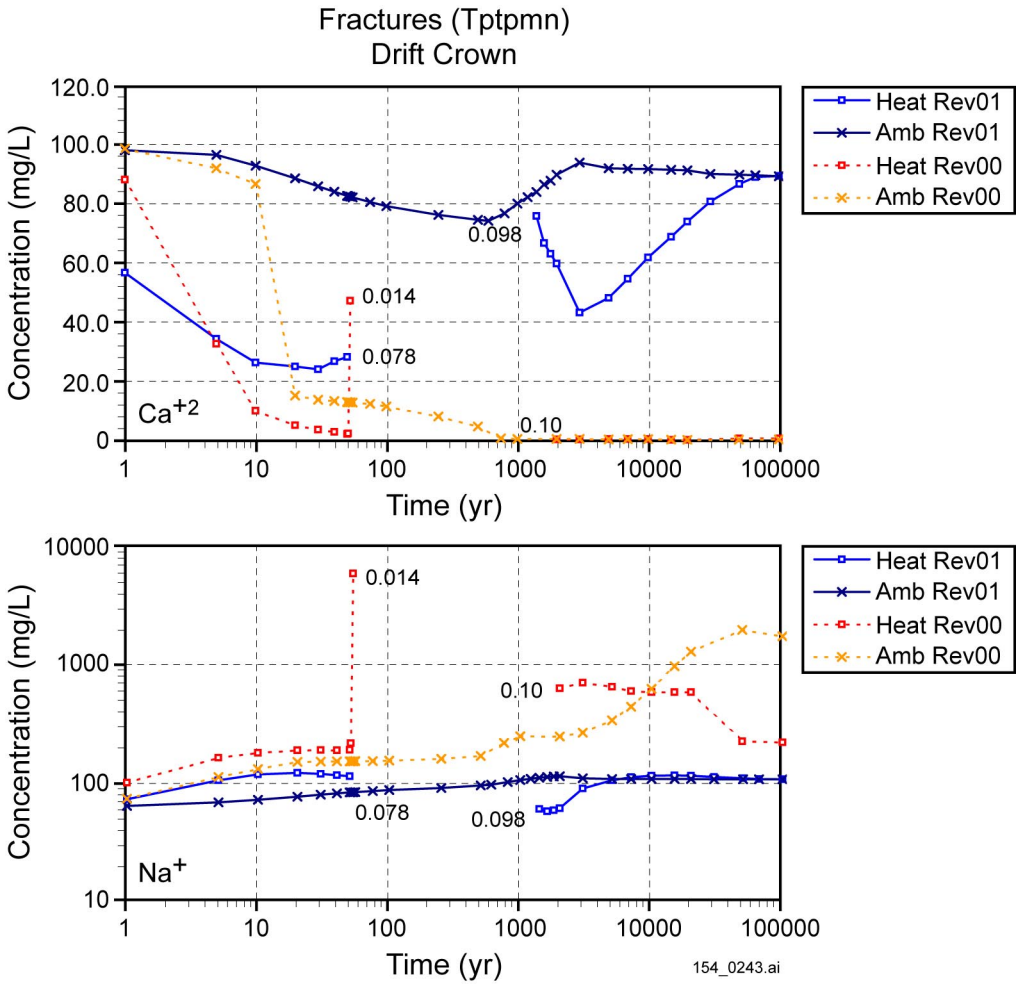

154_0243.ai

Source: CRWMS M&O 2000 [DIRS 142022]; BSC 2001 [DIRS 154677].

NOTE: Comparison of simulation results for Revision 00 and Revision 01. Results are for simulations under heat load (Heat) and ambient (Amb) conditions (extended-case geochemical system). The infiltration rate changes from 6 to 16 mm/yr at 600 years and from 16 to 25 mm/yr at 2,000 years, except for the REV 00 ambient case (fixed rate of 1 mm/yr). The dryout period is left blank (no water); numbers by each curve indicate the last output liquid saturation before dryout and the first output liquid saturation during rewetting.

Figure 6.3.1.4-2. Time Profiles for Thermal-Hydrologic-Chemical Simulations of Aqueous Calcium and Sodium Concentrations in Fractures at the Drift Crown

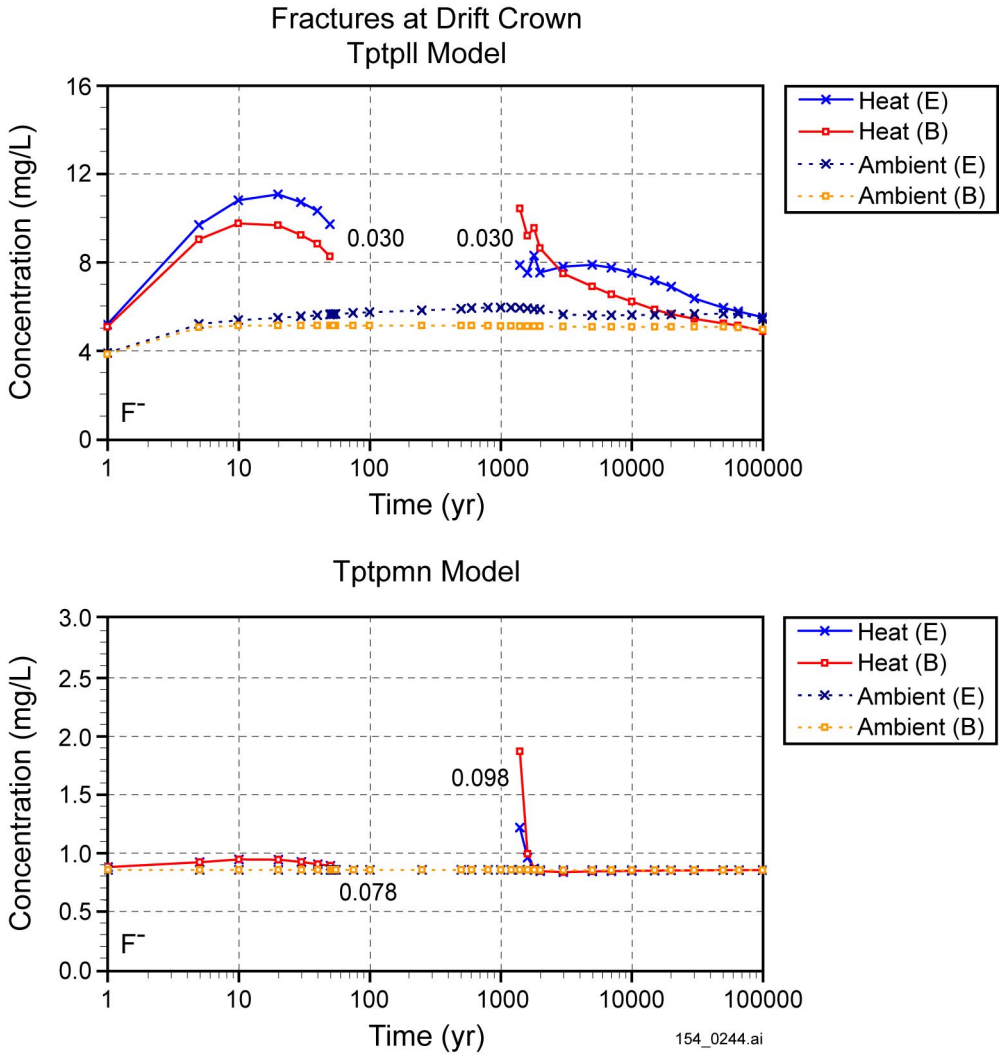

154_0244.ai

Source: BSC 2001 [DIRS 154677].

NOTE: Comparison of simulation results for Tptpll and Tptpmn in Revision 01. Results are for simulations under heat load (Heat) and ambient (Amb) conditions, for the extended-case (E) and base-case (B) geochemical systems. The infiltration rate changes from 6 to 16 mm/yr at 600 years and from 16 to 25 mm/yr at 2,000 years. The dryout period is left blank (no water); numbers by each curve indicate the last output liquid saturation before dryout and the first output liquid saturation during rewetting.

Figure 6.3.1.4-3. Time Profiles for Thermal-Hydrologic-Chemical Simulations of Total Aqueous Fluoride Concentrations in Fractures at the Drift Crown for the Tptpll and Tptpmn Hydrogeologic Units

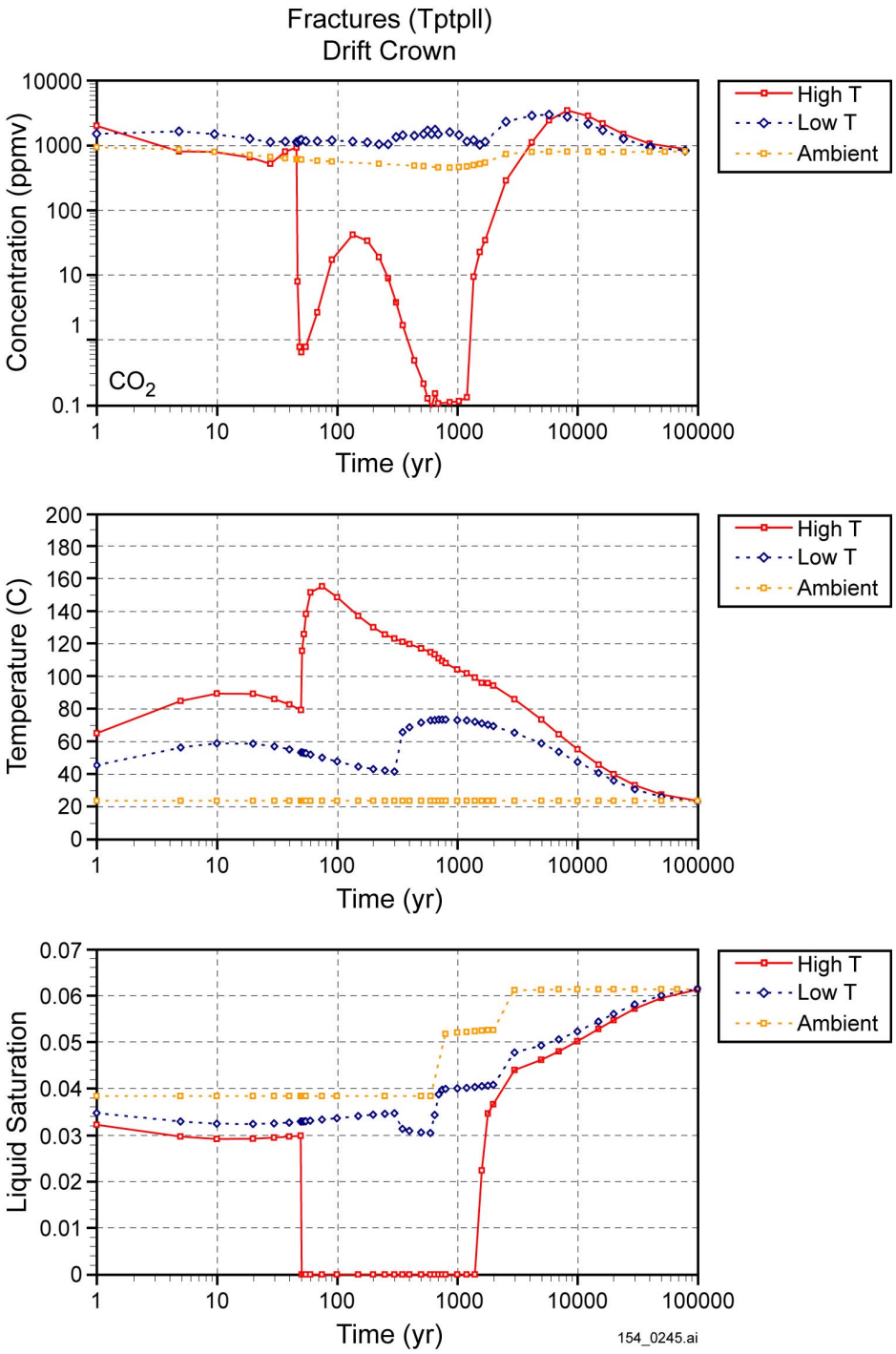

154_0245.ai

Source: Bodvarsson 2001 [DIRS 154669], Attachment 5, pp. 10 to 59).

NOTE: Comparison of simulation results for the higher-temperature versus lower-temperature case (post-Revision 01). The infiltration rate changes from 6 to 16 mm/yr at 600 years and from 16 to 25 mm/yr at 2,000 years.

Figure 6.3.1.5-1. Time Profiles of Thermal-Hydrologic-Chemical Simulations of Modeled Carbon Dioxide Concentrations (Pore Gas), Temperature, and Liquid Saturation in Fractures at the Drift Crown

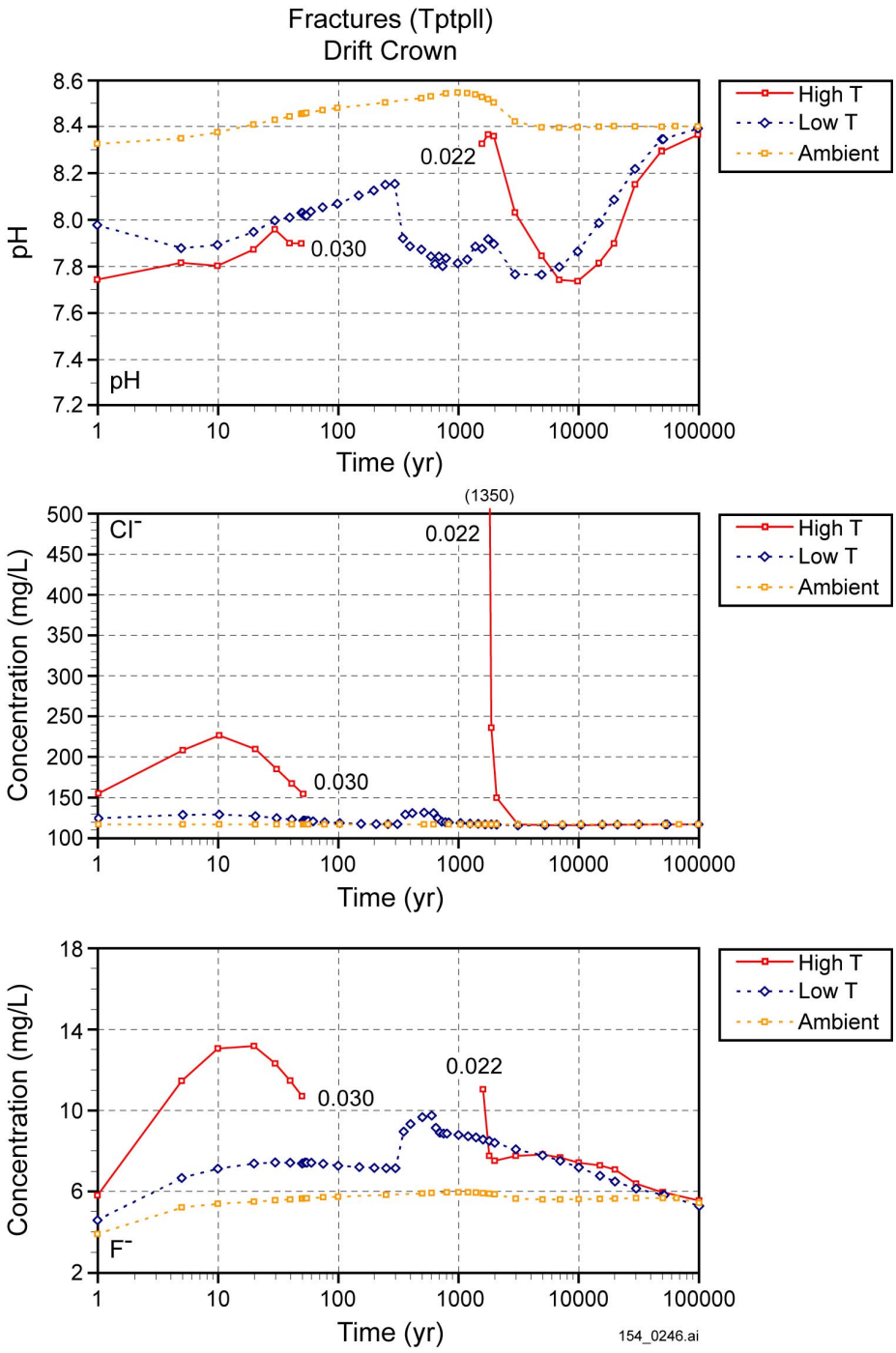

154_0246.ai

Source: Bodvarsson 2001 [DIRS 154669], Attachment 5, pp. 10 to 59).

NOTE: Comparison of simulation results for the higher-temperature versus lower-temperature case (post-Revision 01). The infiltration rate changes from 6 to 16 mm/yr at 600 years and from 16 to 25 mm/yr at 2,000 years. For the higher-temperature case, the dryout period is left blank (no water); numbers by each curve indicate the last output liquid saturation before dryout and the first output liquid saturation during rewetting.

Figure 6.3.1.5-2. Time Profiles for Thermal-Hydrologic-Chemical Simulations of Modeled pH, Total Aqueous Chloride, and Total Aqueous Fluoride Concentrations in Fractures at the Drift Crown

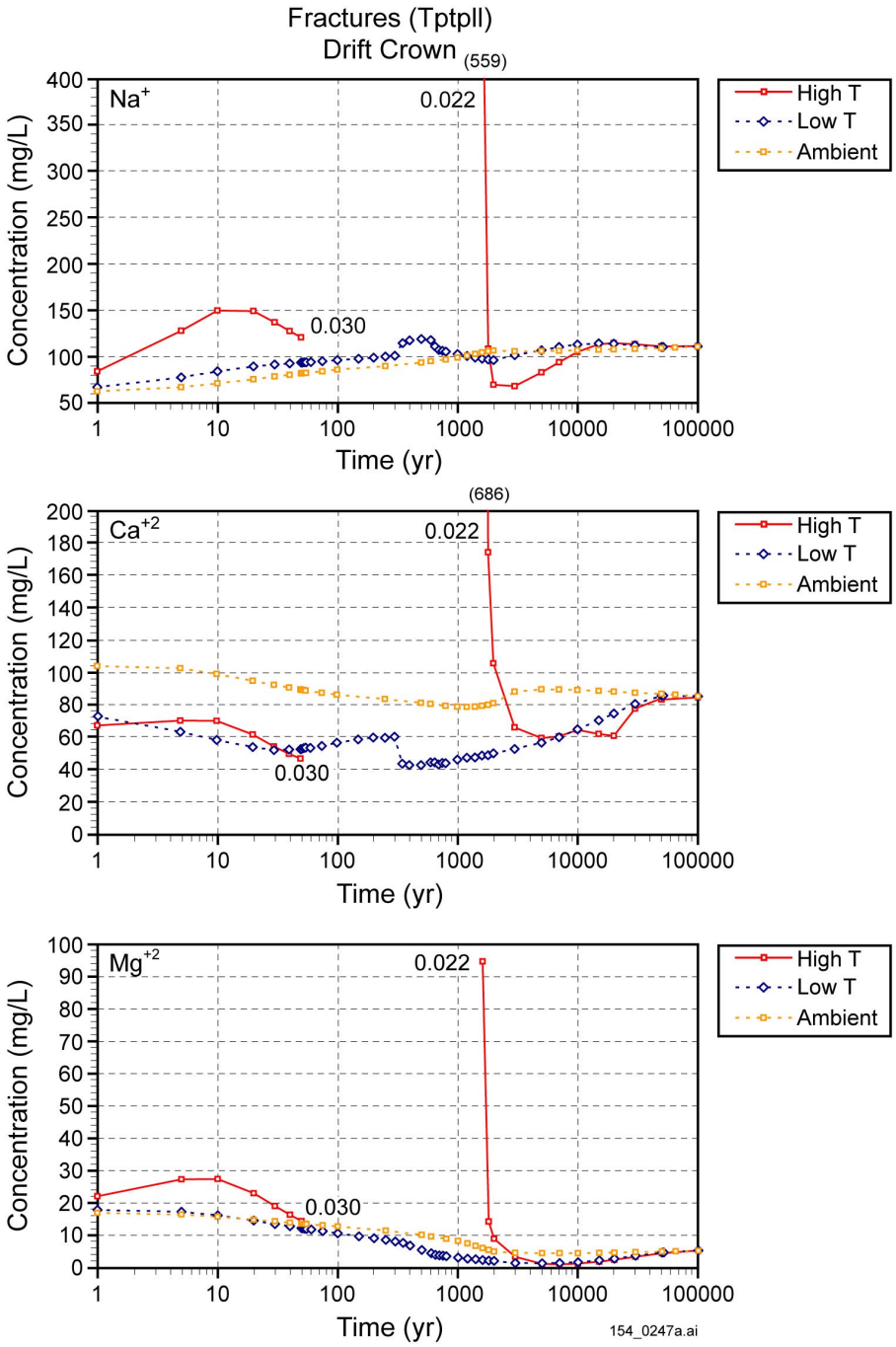

154_0247a.ai

Source: Bodvarsson 2001 [DIRS 154669], Attachment 5, pp. 10 to 59).

NOTE: Comparison of simulation results for the higher-temperature versus lower-temperature case (post-Revision 01). The infiltration rate changes from 6 to 16 mm/yr at 600 years and from 16 to 25 mm/yr at 2,000 years. For the higher-temperature case, the dryout period is left blank (no water); numbers by each curve indicate the last output liquid saturation before dryout and the first output liquid saturation during rewetting.

Figure 6.3.1.5-3. Time Profiles for Thermal-Hydrologic-Chemical Simulations for Modeled Total Aqueous Sodium, Calcium, and Magnesium Concentrations in Fractures at the Drift Crown

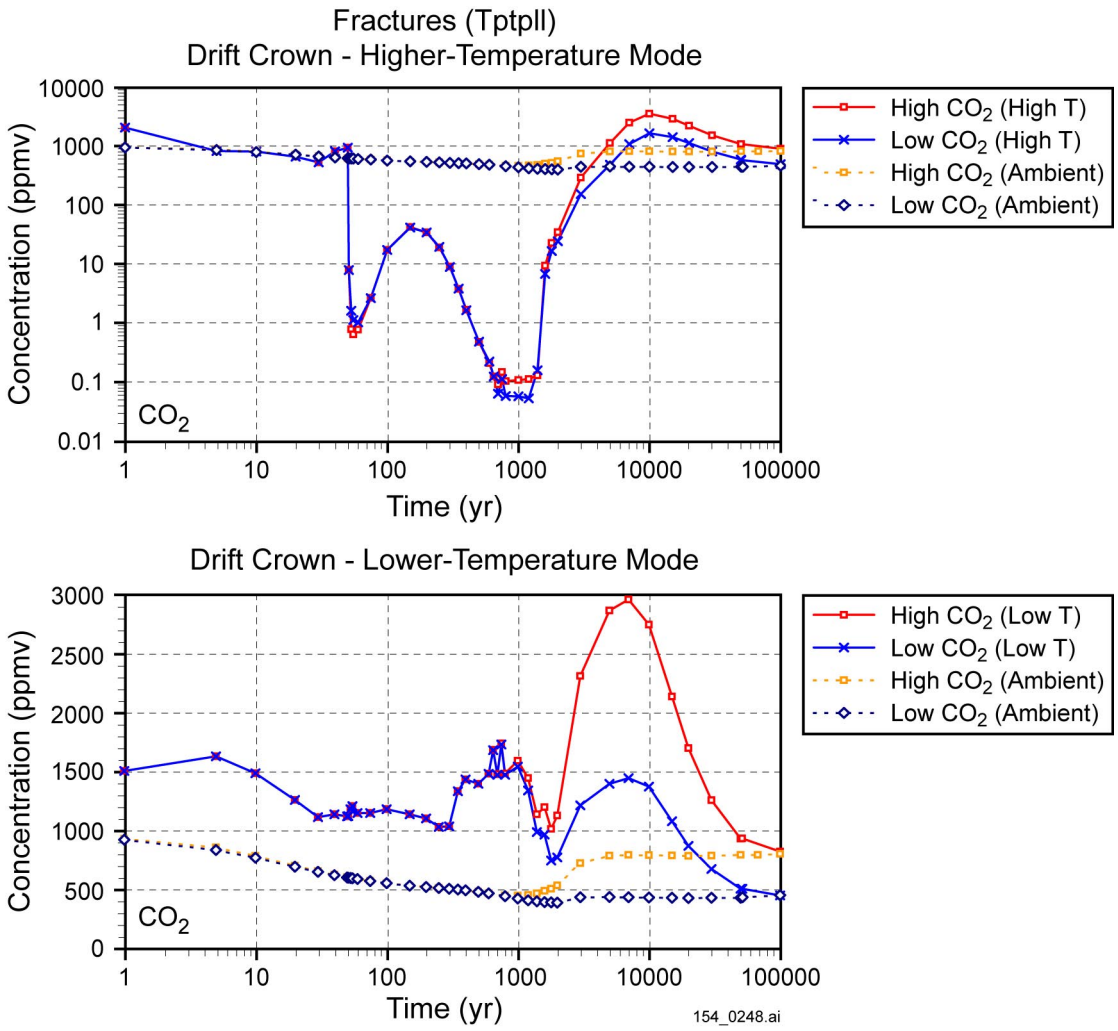

154_0248.ai

Source: Bodvarsson 2001 [DIRS 154669], Attachment 5, pp. 10 to 59).

NOTE: Comparison of simulation results for high carbon dioxide versus low carbon dioxide cases (post-Revision 01). Results are for the higher-temperature (High T) and lower-temperature (Low T) cases, and assuming approximately 3,700 ppmv (High CO_2) and 750 ppmv (Low CO_2) carbon dioxide concentrations at the top model boundary. The infiltration rate changes from 6 to 16 mm/yr at 600 years and from 16 to 25 mm/yr at 2,000 years.

Figure 6.3.1.5-4. Time Profiles for Thermal-Hydrologic-Chemical Simulations of Modeled Carbon Dioxide Concentrations (Pore Gas) in Fractures at the Drift Crown

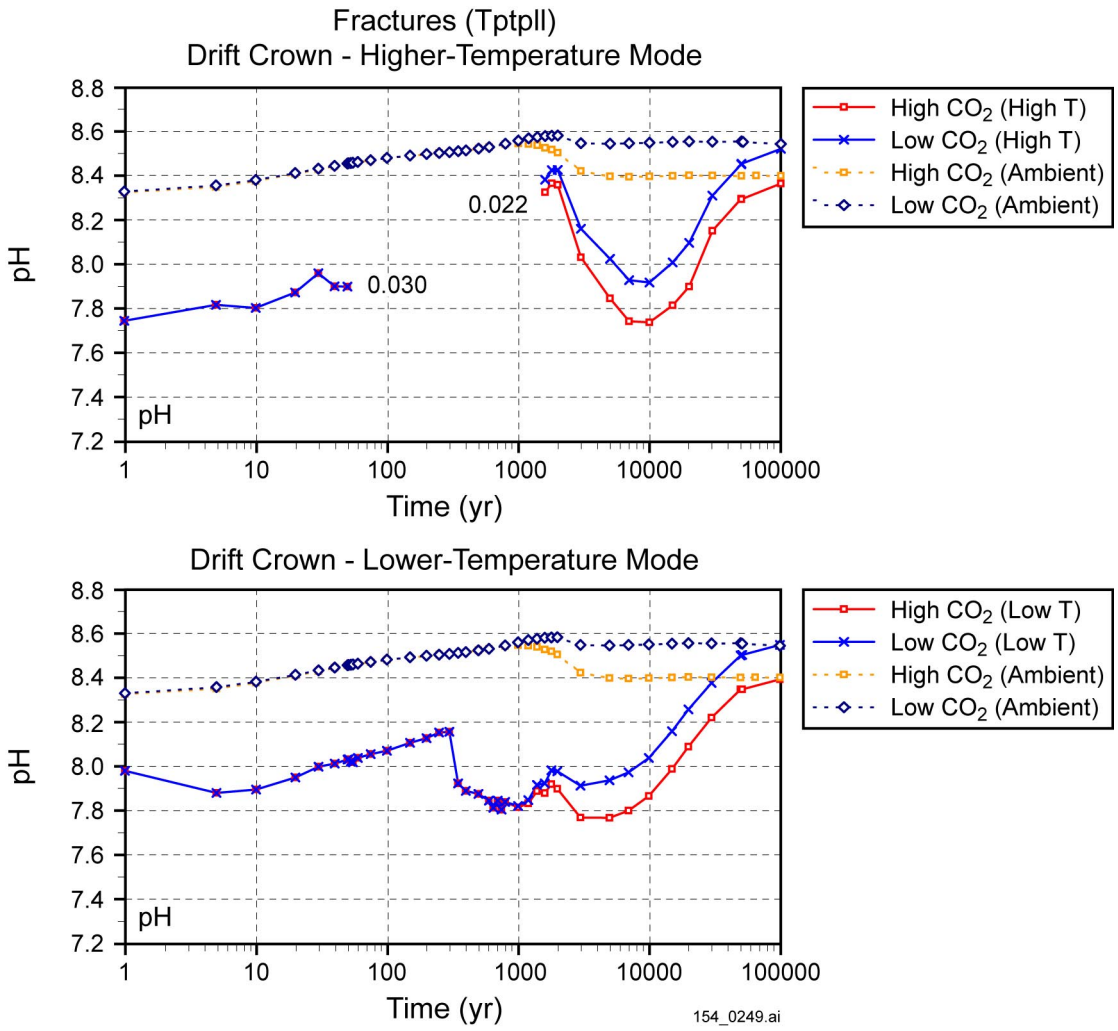

154_0249.ai

Source: Bodvarsson 2001 [DIRS 154669], Attachment 5, pp. 10 to 59).

NOTE: Comparison of simulation results for high carbon dioxide versus low carbon dioxide cases (post-Revision 01). Results are for the higher-temperature (High T) and lower-temperature (Low T) cases, and assuming approximately 3,700 ppmv (High CO_2) and 750 ppmv (Low CO_2) carbon dioxide concentrations at the top model boundary. The infiltration rate changes from 6 to 16 mm/yr at 600 years and from 16 to 25 mm/yr at 2,000 years.

Figure 6.3.1.5-5. Time Profiles for Thermal-Hydrologic-Chemical Simulations of Modeled pH in Fractures at the Drift Crown

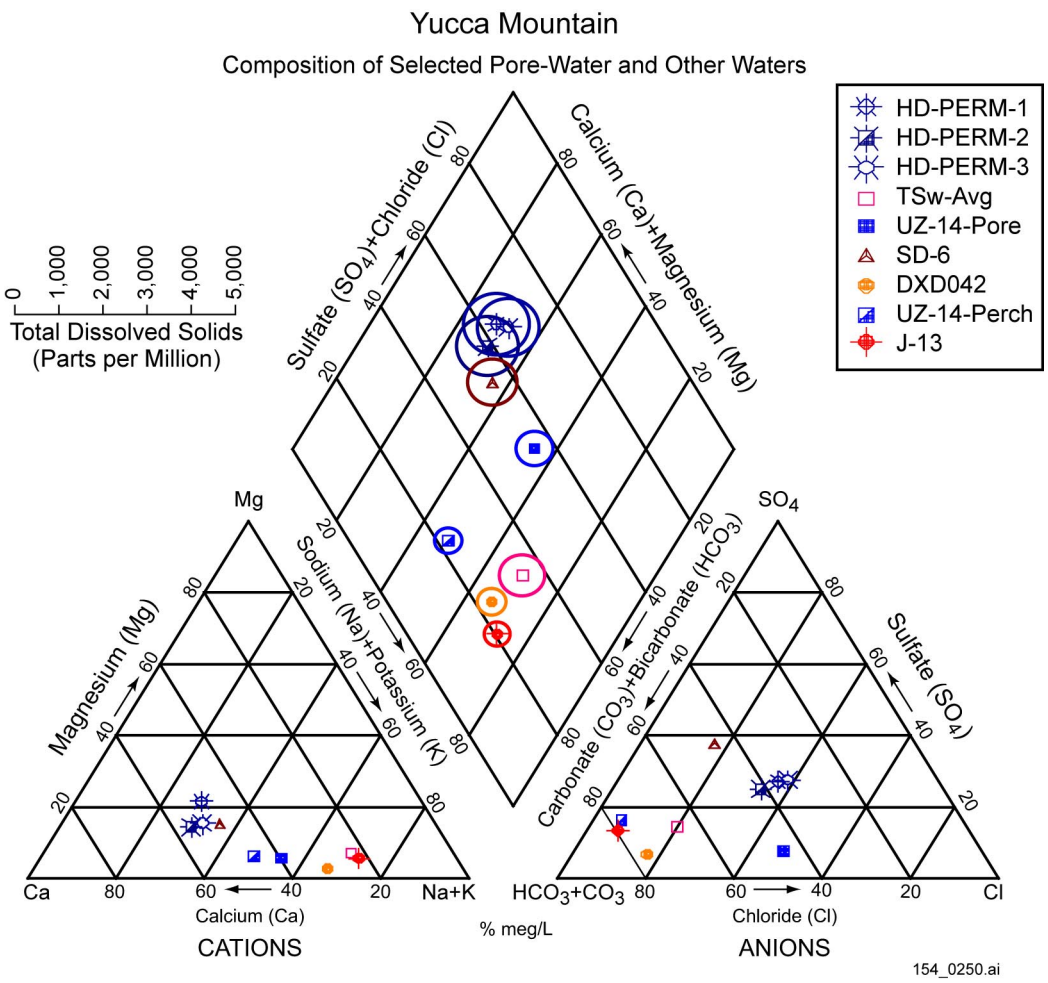

154_0250.ai

Source: MO0005PORWATER.000 [DIRS 150930]; LA9909JF831222.004 [DIRS 145598]; LA9909JF831222.006 [DIRS 146231]; LA0002JF12213U.001 [DIRS 154760]; CRWMS M&O 1999 [DIRS 129261], Table 4.5.1; Yang et al. 1996 [DIRS 100194], Table 6; MO0006J13WTRCM.000 [DIRS 151029]; Bodvarsson 2001 [DIRS 154669], Attachment 5, pp. 38 to 43, 47 to 49, 55 to 58 – (See text for additional details).

NOTE: The diameters of circles plotted around points on the diamond-shaped part of the diagram are proportional to the total salinity of the samples and drawn at the displayed scale. Samples listed in Table 6.3.1.5-2.

Figure 6.3.1.5-6. Piper Diagram for the Compositions of Selected Pore Water and Other Water

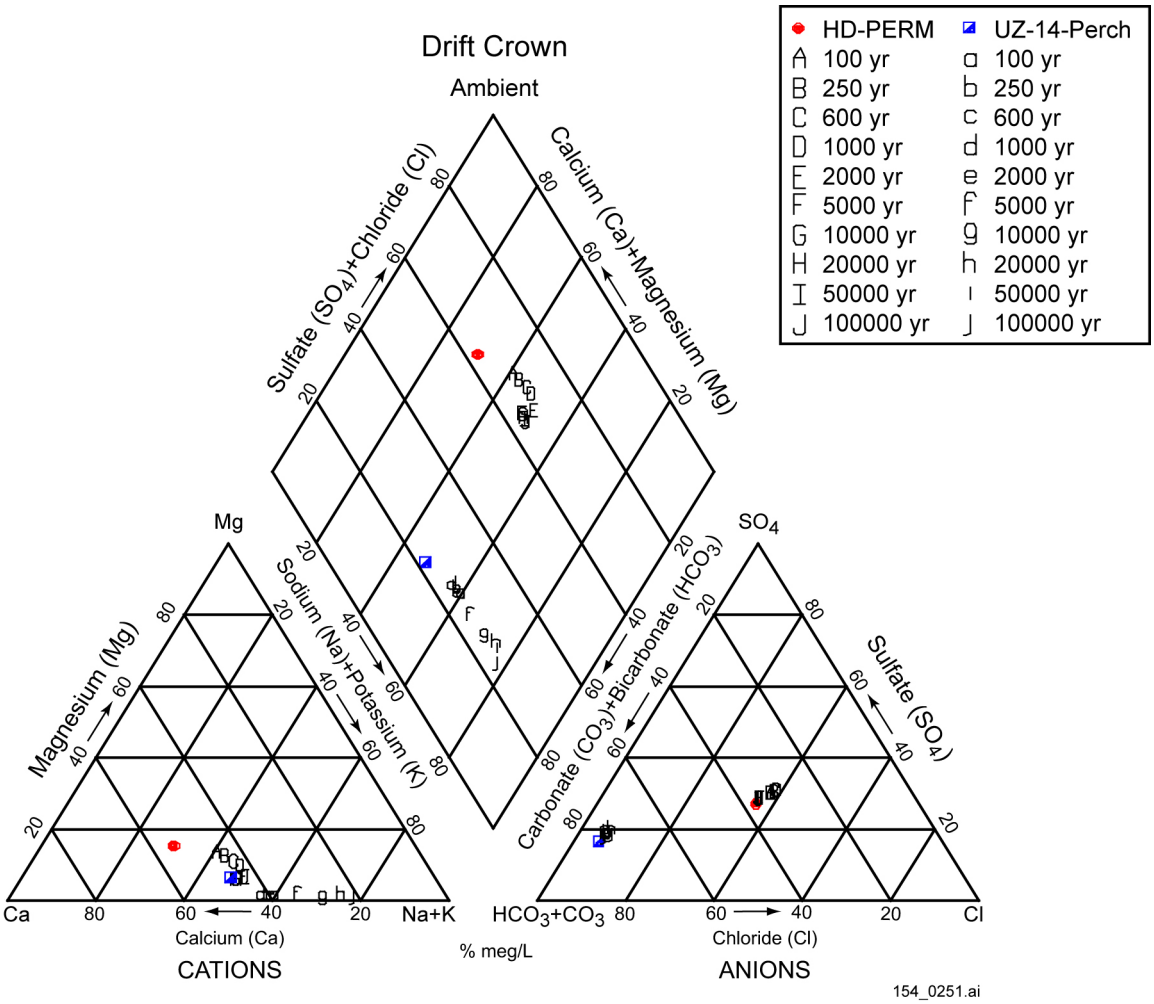

154_0251.ai

Source: Bodvarsson 2001 [DIRS 154669], Attachment 5, pp. 10 to 59).

NOTE: Thermal-hydrologic-chemical simulations for Alcove-5 pore water versus UZ-14 perched water in post-Revision 01 simulations. Evolution of water compositions modeled under ambient conditions (near 24ºC; no thermal perturbation). Points are plotted for selected time intervals as shown in the legend.

Figure 6.3.1.5-7. Piper Diagram of the Modeled Evolution of Water Compositions for Two Initial Water Compositions Under Ambient Conditions

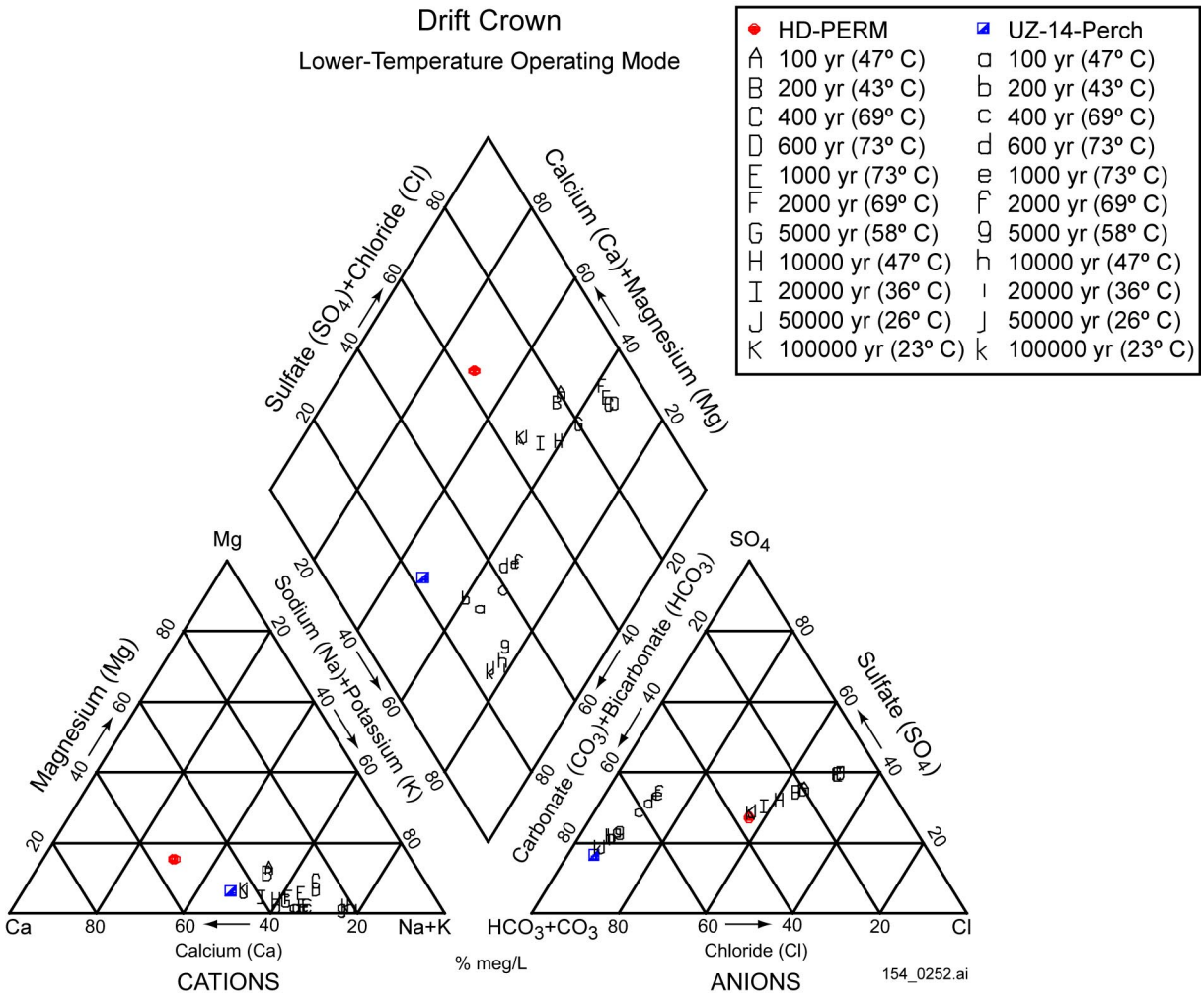

154_0252.ai

Source: Bodvarsson 2001 [DIRS 154669], Attachment 5, pp. 10 to 59.

NOTE: Thermal-hydrologic-chemical simulations for Alcove-5 pore water versus UZ-14 perched water. Results for post-Revision 01 simulations. Piper diagram showing the modeled evolution of water compositions for the lower-temperature case and two initial water compositions. Points are plotted for selected time intervals (and corresponding temperatures) as shown in the legend.

Figure 6.3.1.5-8. Piper Diagram of the Modeled Evolution of Water Compositions for the Lower-Temperature Case and Two Initial Water Compositions

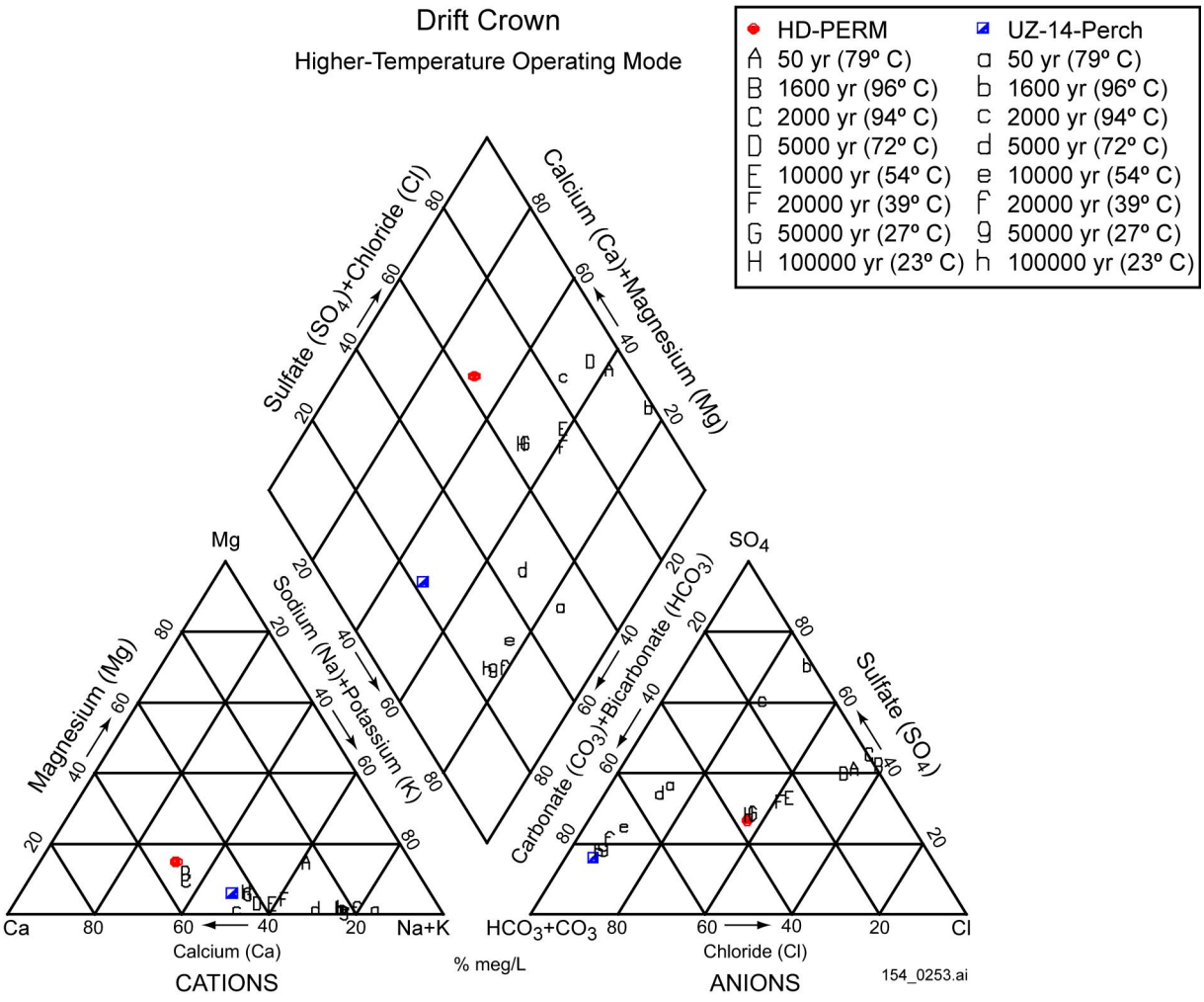

154_0253.ai

Source: Bodvarsson 2001 [DIRS 154669], Attachment 5, pp. 10 to 59).

NOTE: Thermal-hydrologic-chemical simulations for Alcove-5 pore water versus UZ-14 perched water. Results for post-Revision 01 simulations. Piper diagram showing the modeled evolution of water compositions for the higher-temperature case for two initial water compositions. Points are plotted for selected time intervals (and corresponding temperatures) as shown in the legend.

Figure 6.3.1.5-9. Piper Diagram of the Modeled Evolution of Water Compositions for the Higher-Temperature Case and Two Initial Water Compositions

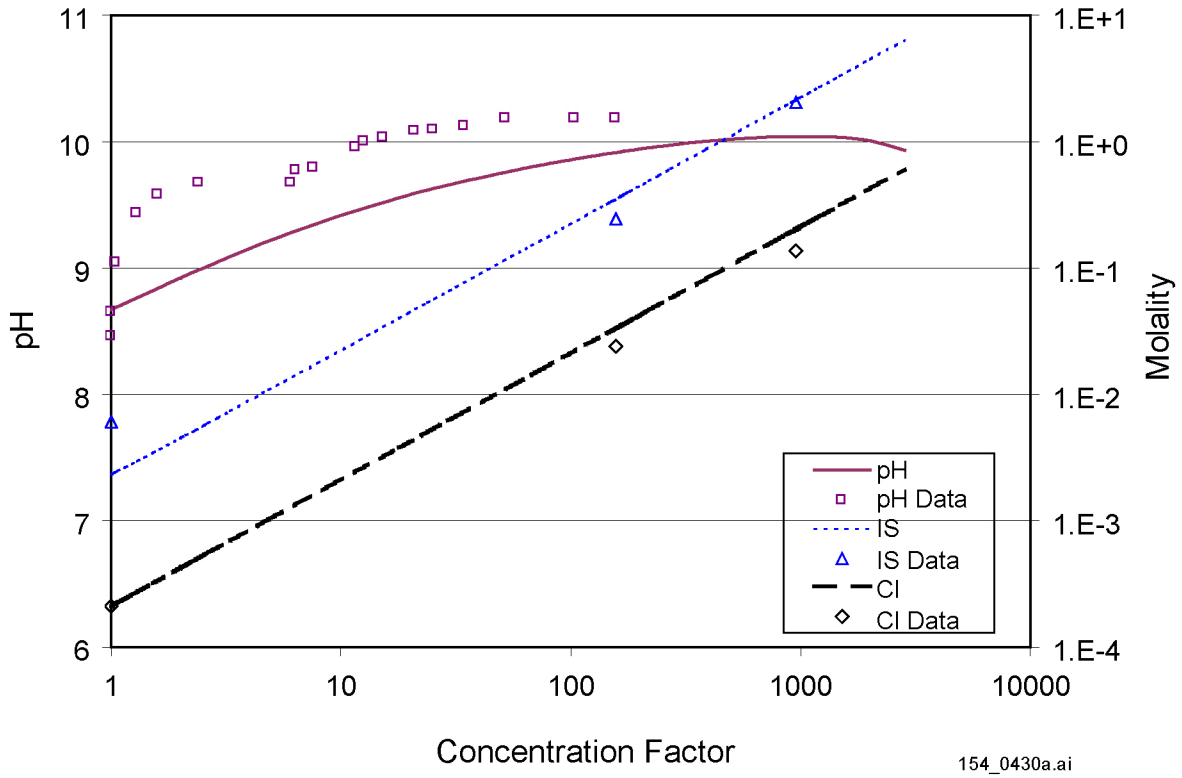

154_0430a.ai

Source: Data from Rosenberg et al. 1999 [DIRS 125338]. Model predictions from Jolley 2001 [DIRS 154762].

NOTE: IS = ionic strength; Cl = chloride.

Figure 6.3.3-1. Ionic Strength, pH, and Chloride Model Predictions versus Well J-13 Evaporation Data

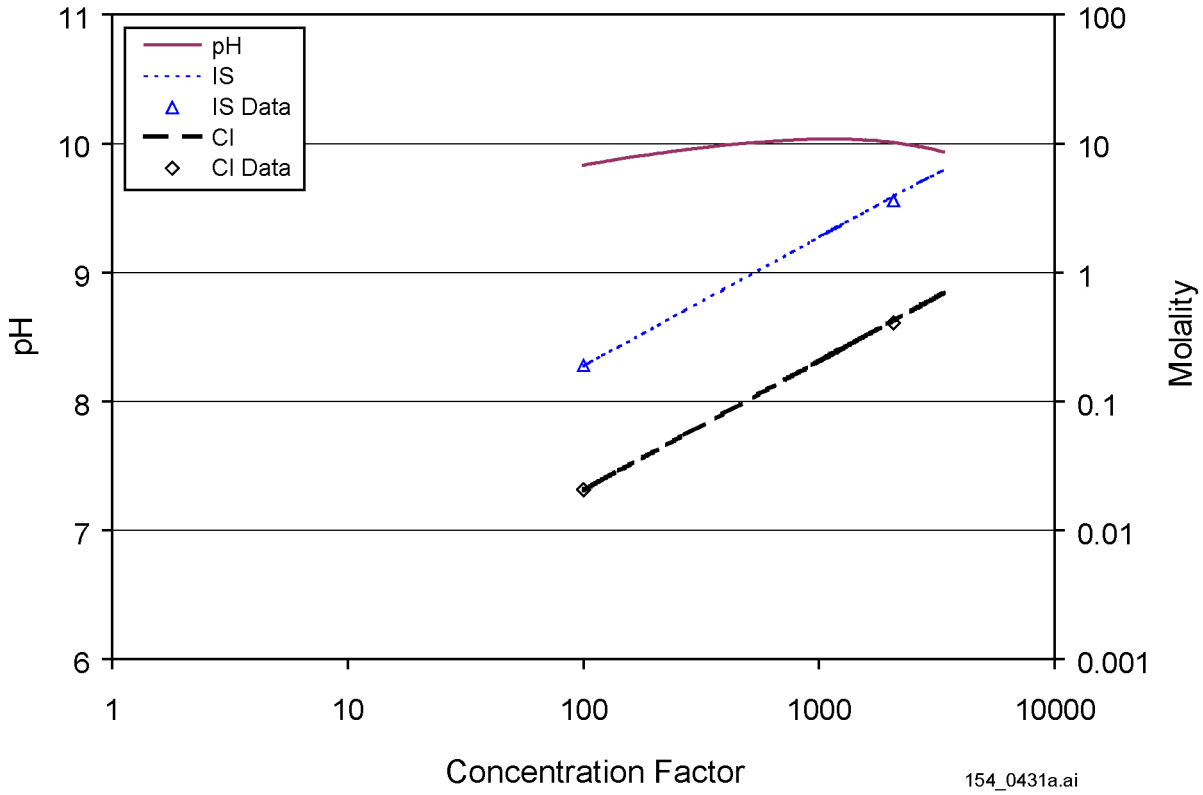

154_0431a.ai

Source: Data from CRWMS M&O 2000 [DIRS 151568]. Model predictions from Jolley 2001 [DIRS 154762].

NOTE: IS = ionic strength; Cl = chloride.

Figure 6.3.3-2. Ionic Strength, pH, and Chloride Model Predictions versus 100 x Well J-13 Evaporation Data

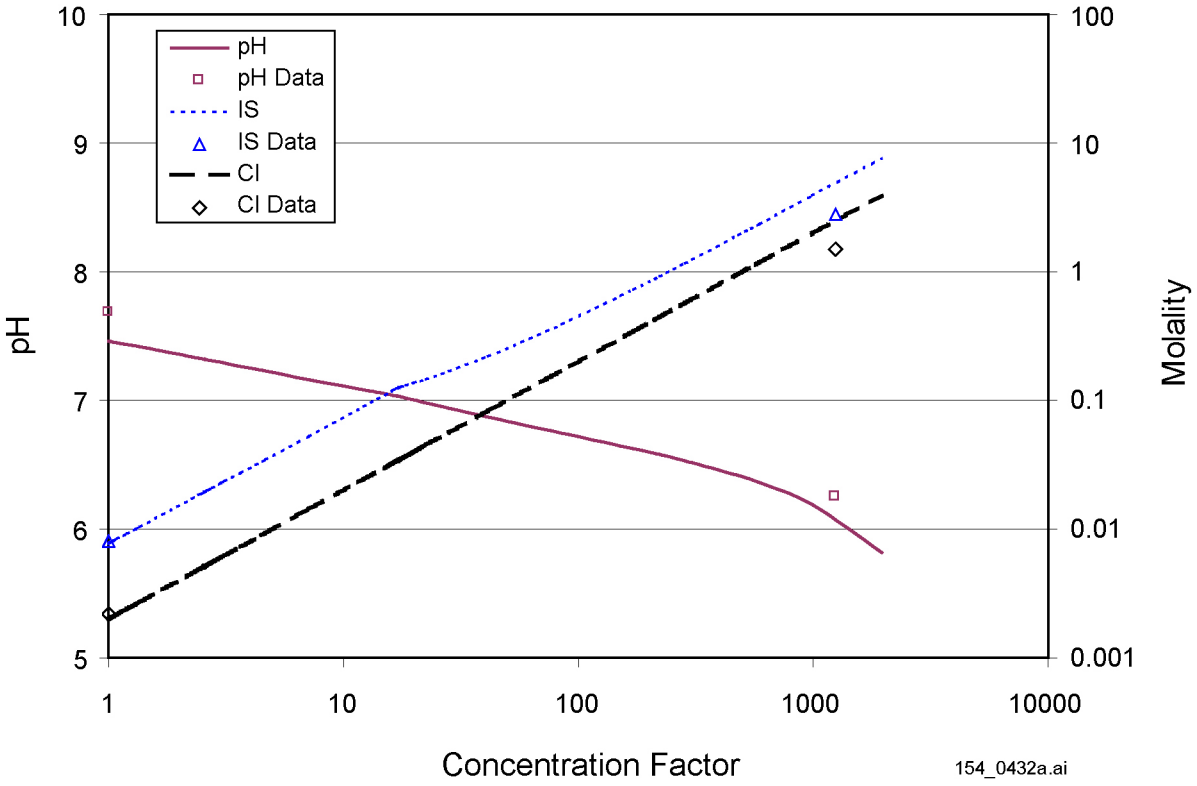

154_0432a.ai

Source: Data from Rosenberg et al. 1999 [DIRS 125339]. Model predictions from Jolley 2001 [DIRS 154762].

NOTE: IS = ionic strength; Cl = chloride.

Figure 6.3.3-3. Ionic Strength, pH, and Chloride Model Predictions versus Topopah Spring Tuff Pore Water Evaporation Data

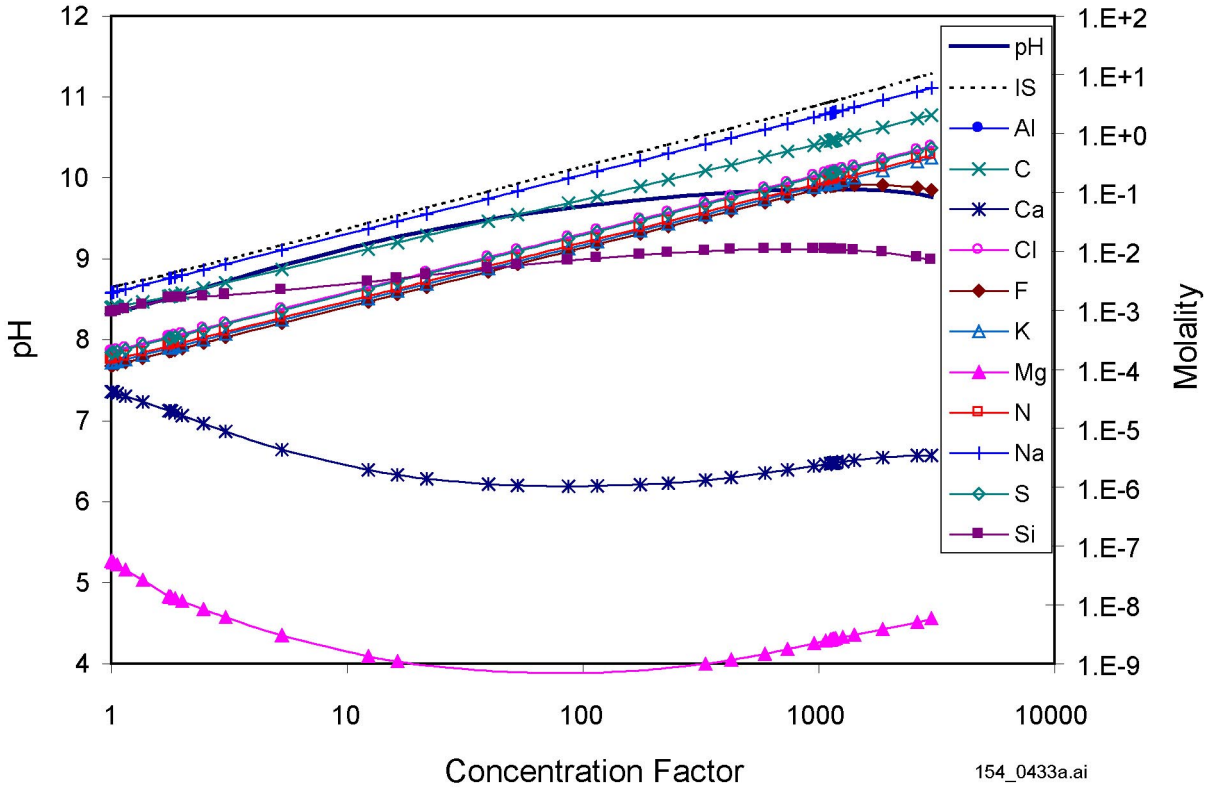

154_0433a.ai

Source: Jolley 2001 [DIRS 154762]; Mariner 2001 [DIRS 155041].

NOTE: IS = ionic strength.

Figure 6.3.3-4. Aqueous Evaporative Evolution of In Situ J-13 Well Water at f_{CO2} of 10^{-3}

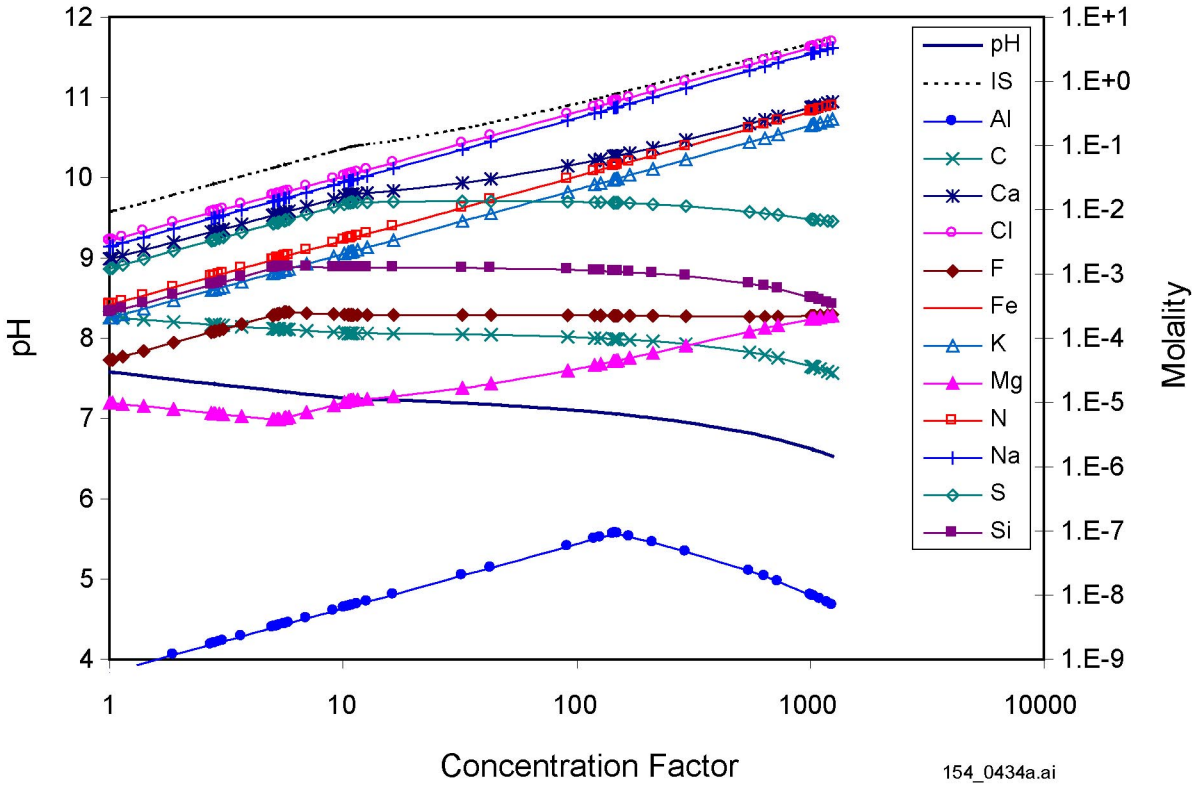

154_0434a.ai

Source: Jolley 2001 [DIRS 154762]; Mariner 2001 [DIRS 155041].

NOTE: IS = ionic strength.

Figure 6.3.3-5. Aqueous Evaporative Evolution of Topopah Spring Tuff Pore Water at f_{CO2} of 10^{-3}

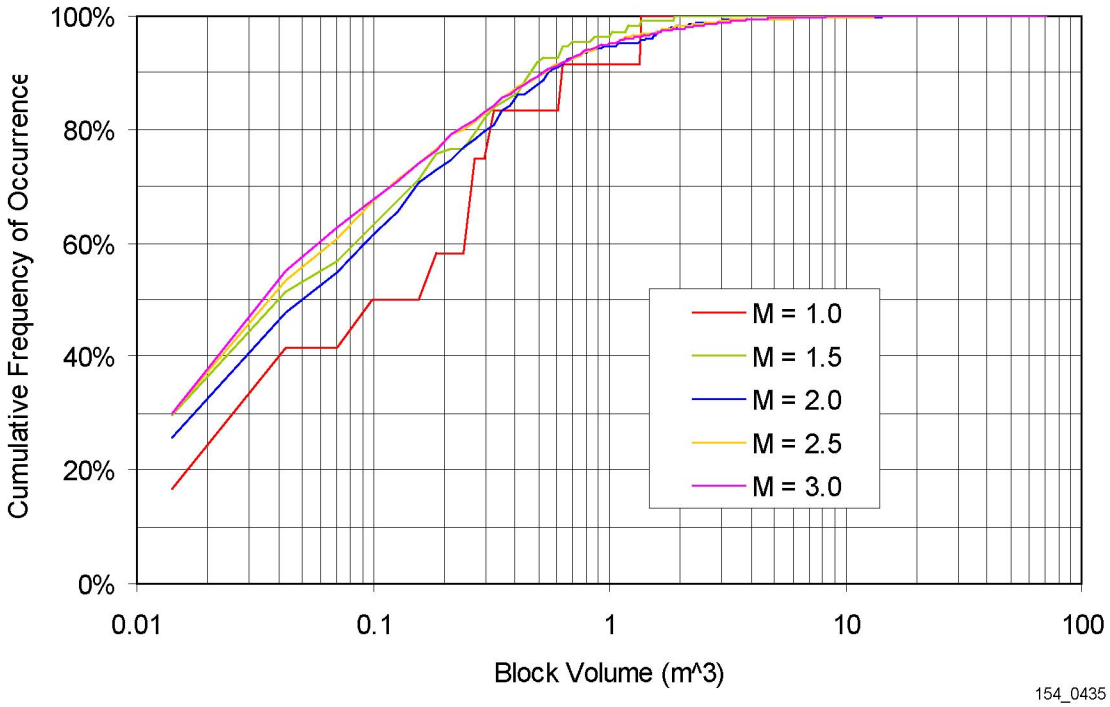

154_0435

Source: BSC 2001 [DIRS 154537].

NOTE: Data for the Tptpmn Unit, 75°-Azimuth.

Figure 6.3.4-1. Cumulative Key-Block Size Distribution for Various Sizes of Joint Planes in the Tptpmn Unit

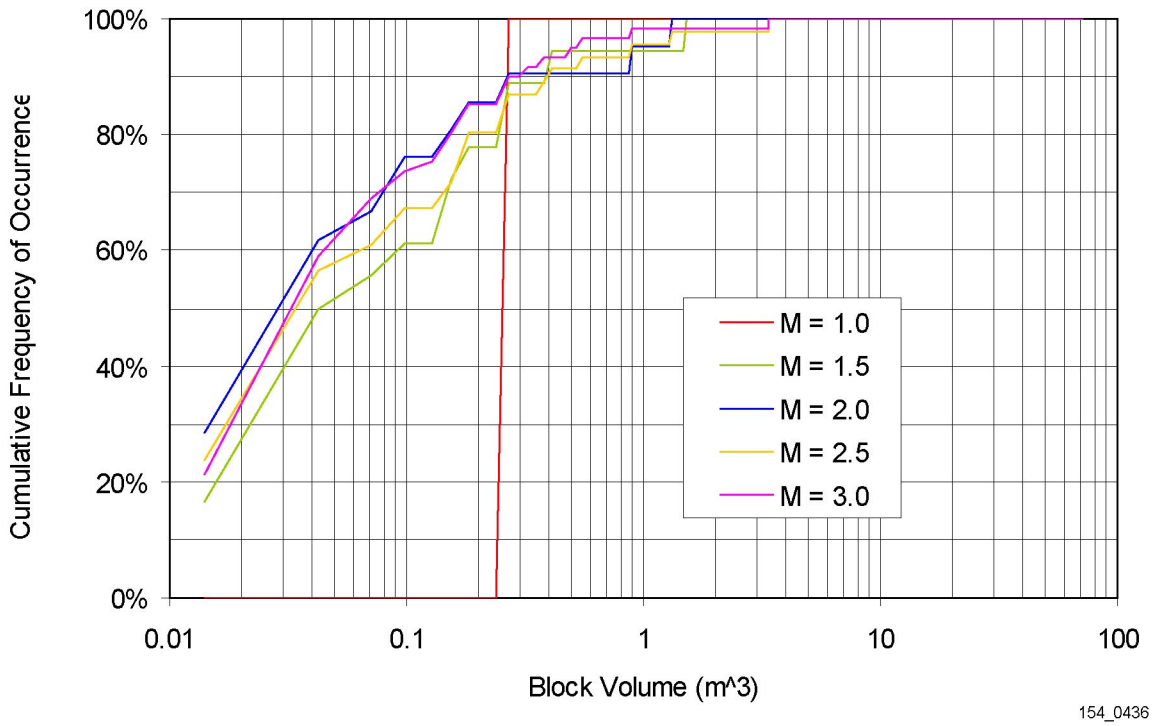

154_0436

Source: BSC 2001 [DIRS 154537].

NOTE: Data for the Tptpll Unit, 75°-Azimuth.

Figure 6.3.4-2. Cumulative Key-Block Size Distribution for Various Sizes of Joint Planes in the Tptpll Unit

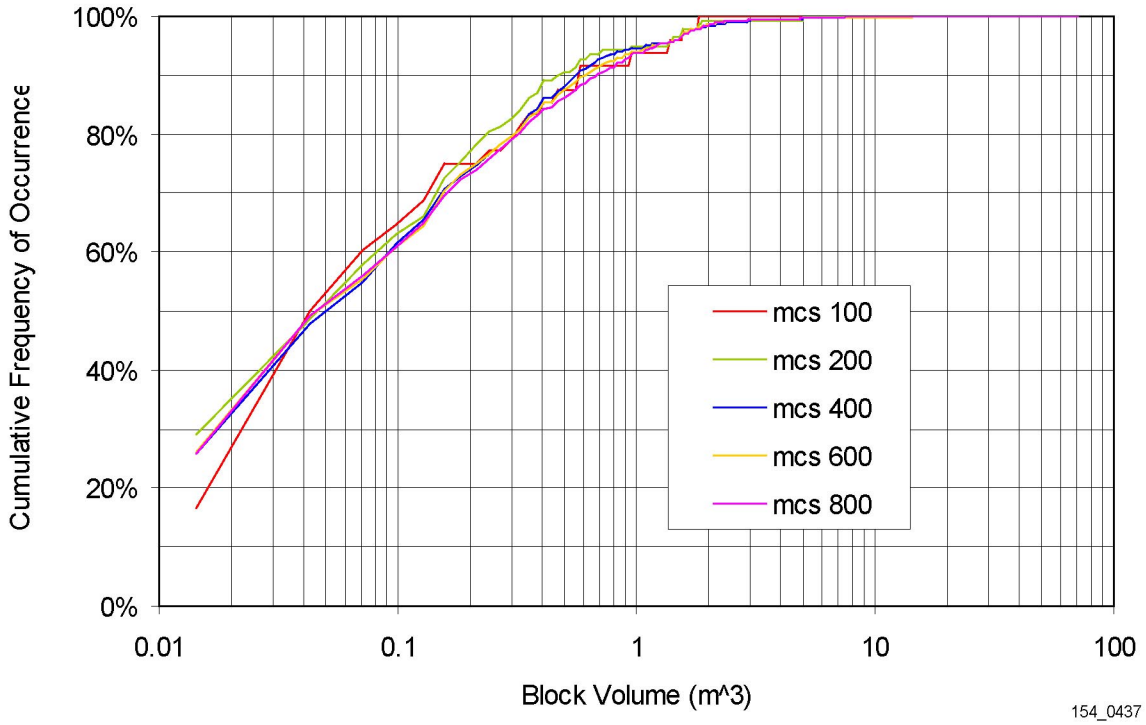

154_0437

Source: BSC 2001 [DIRS 154537].

Figure 6.3.4-3. Cumulative Block Size Distributions for Various Monte Carlo Simulations in the Tptpmn Unit

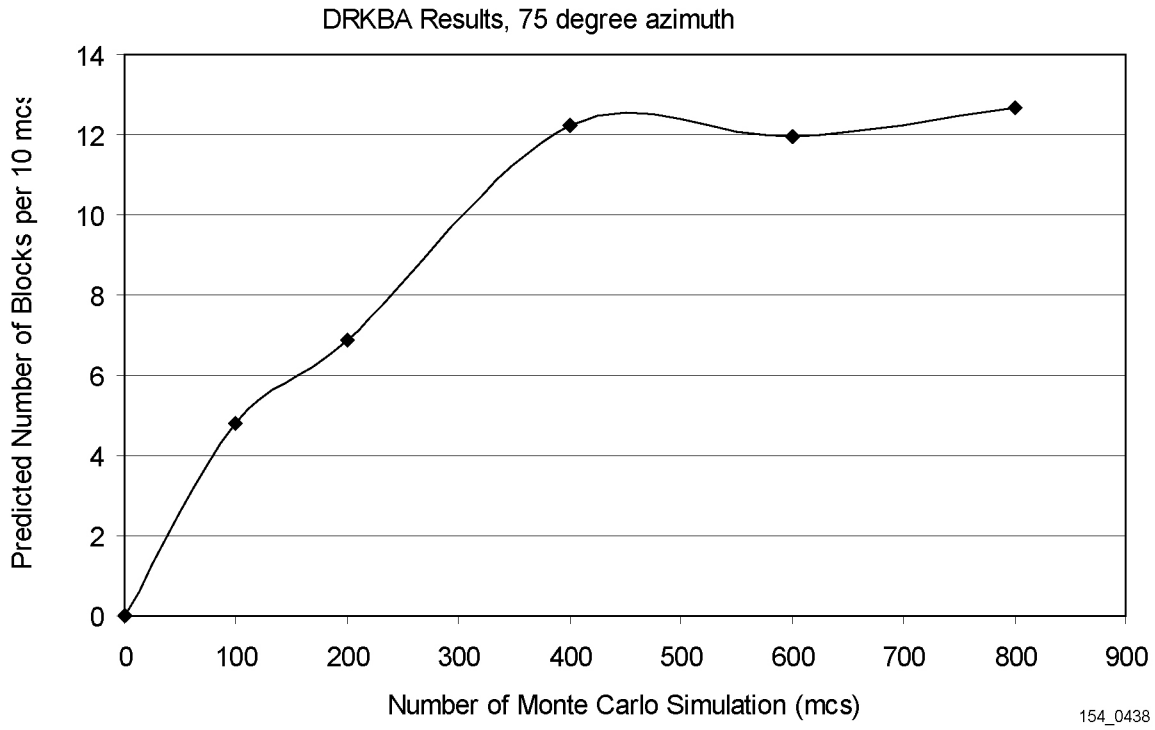

154_0438

Source: BSC 2001 [DIRS 154537].

NOTE: Data for the Tptpmn Unit, 75º azimuth, using the discrete region key-block analysis (DRKBA) software.

Figure 6.3.4-4. Predicted Number of Key-Blocks for Various Monte Carlo Simulations in the Tptpmn Unit

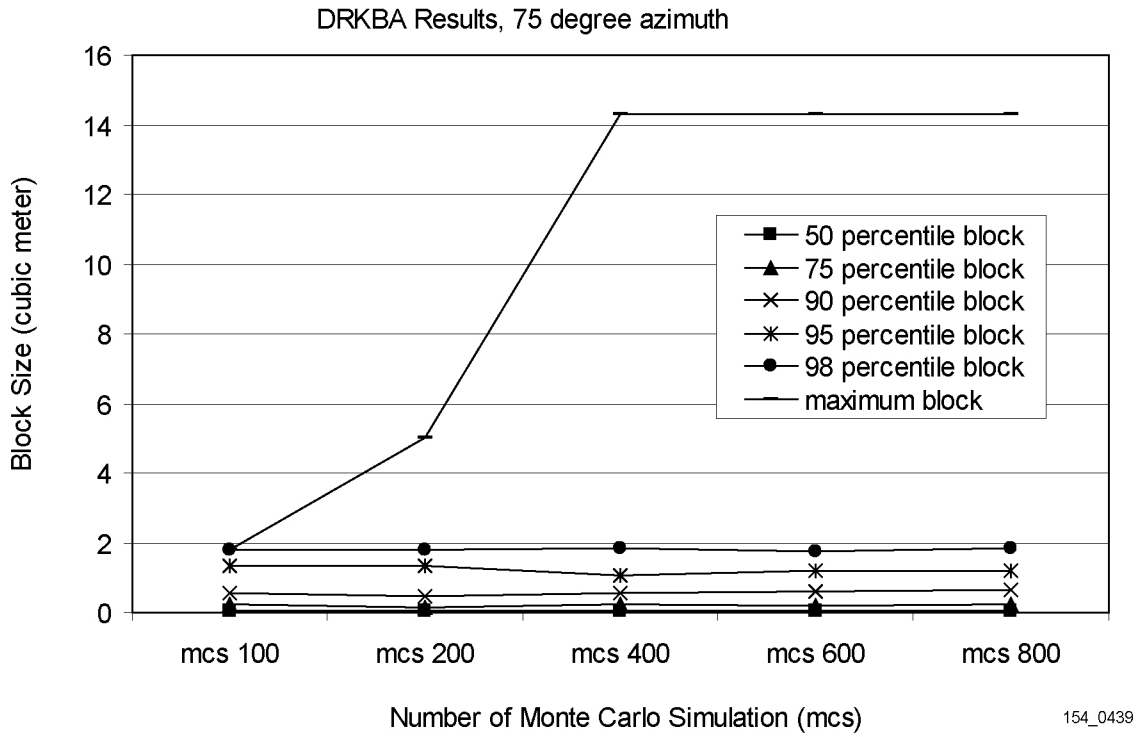

154_0439

Source: BSC 2001 [DIRS 154537].

NOTE: Data for the Tptpmn unit, 75º azimuth, using the discrete region key-block analysis (DRKBA) software.

Figure 6.3.4-5. Predicted Maximum Block Size for Various Monte Carlo Simulations in the Tptpmn Unit

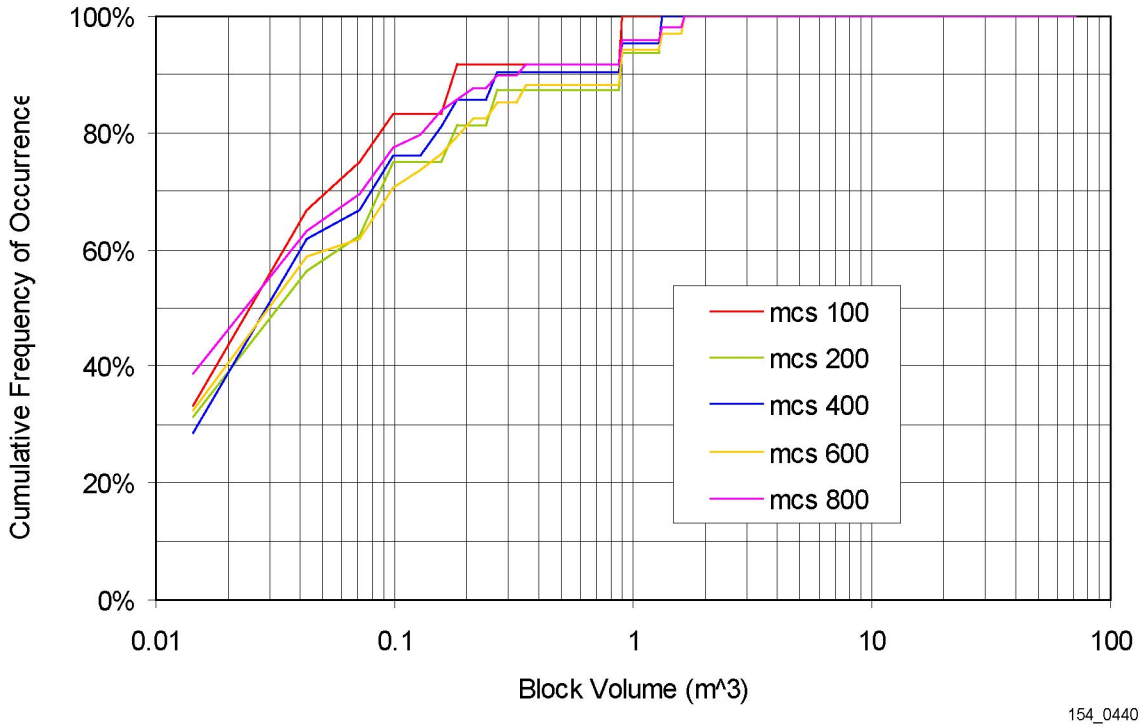

154_0440

Source: BSC 2001 [DIRS 154537].

Figure 6.3.4-6. Block Size Distributions for Various Monte Carlo Simulations in the Tptpll Unit

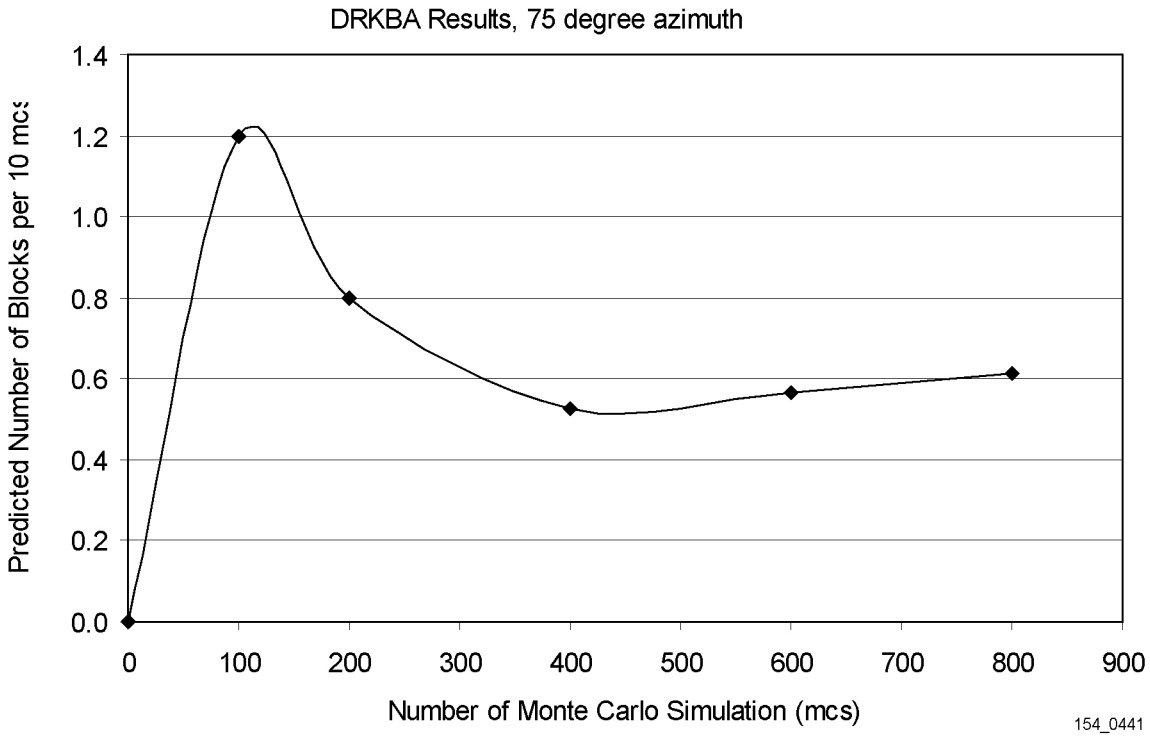

154_0441

Source: BSC 2001 [DIRS 154537].

NOTE: Data for the Tptpll unit, 75º azimuth, using the discrete region key-block analysis (DRKBA) software.

Figure 6.3.4-7. Predicted Number of Key Blocks for Various Monte Carlo Simulations in the Tptpll Unit

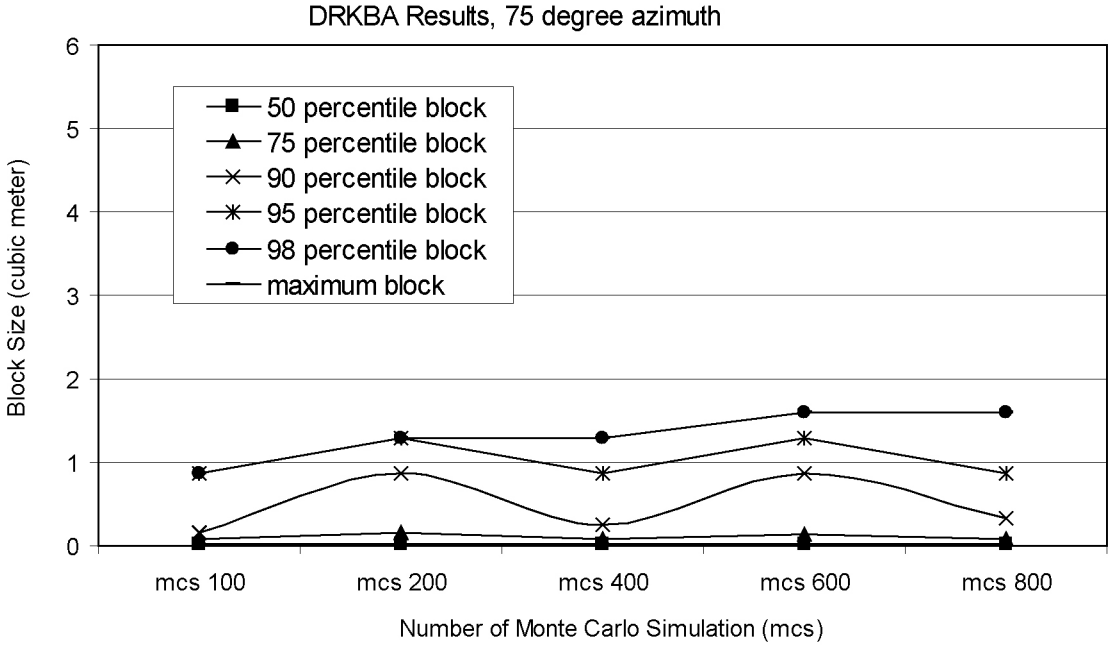

Note: The maximum block is the same as the 98 percentile block for each Monte Carlo simulation.

154_0442

154_0442

Source: BSC 2001 [DIRS 154537].

NOTE: Data for the Tptpll unit, 75º azimuth, using the discrete region key-block analysis (DRKBA) software.

Figure 6.3.4-8. Predicted Maximum Block Size for Various Monte Carlo Simulations in the Tptpll Unit

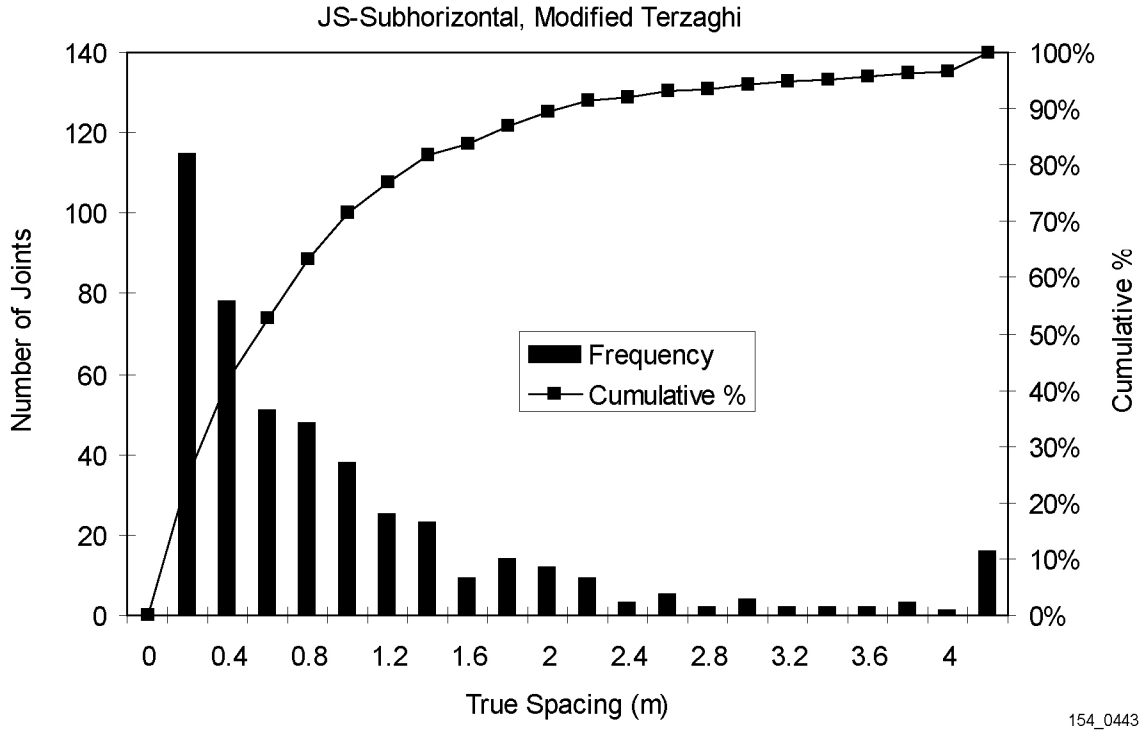

154_0443

Source: BSC 2001 [DIRS 154537].

NOTE: Data for the Tptpmn Unit Subhorizontal Joint Set, Original True Spacing.

Figure 6.3.4-9. Histogram and Cumulative Frequency Distribution of Fracture Spacing

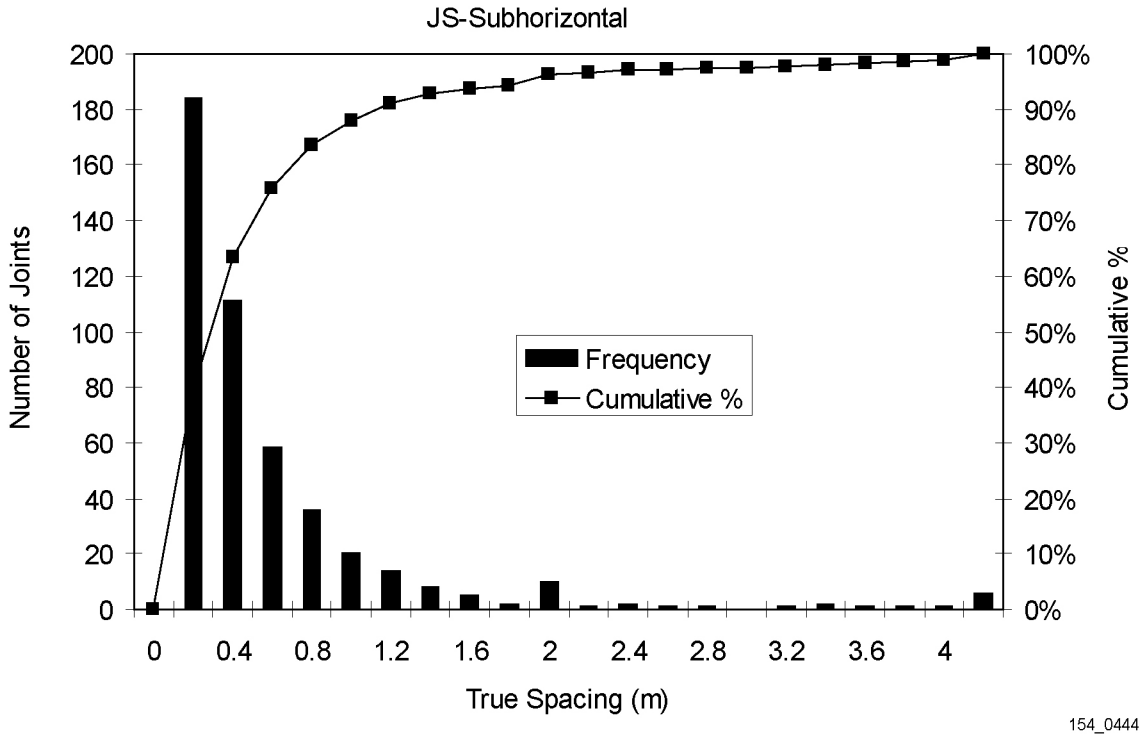

154_0444

Source: BSC 2001 [DIRS 154537].

NOTE: Data for the Tptpmn Unit Subhorizontal Joint Set, Modified True (Terzaghi) Spacing.

Figure 6.3.4-10. Histogram and Cumulative Frequency Distribution of Fracture Spacing

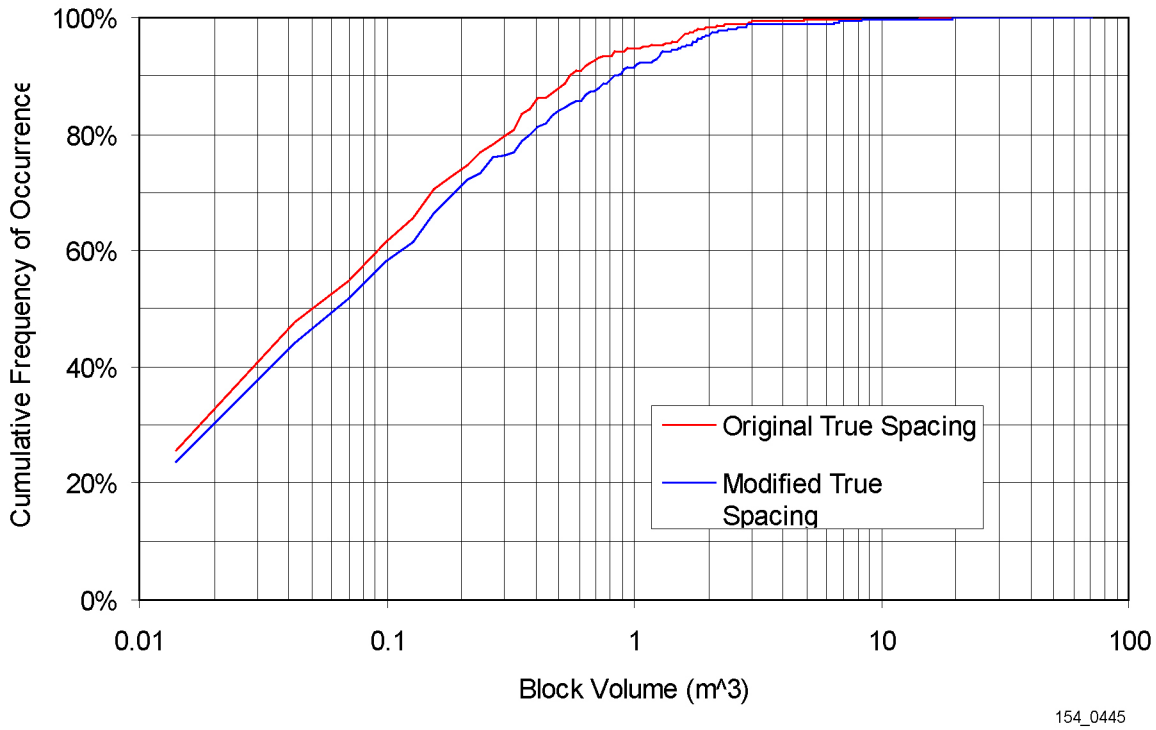

154_0445

Source: BSC 2001 [DIRS 154537].

NOTE: Data for the Tptpmn Unit, 75°-Azimuth, Subhorizontal Joint Set.

Figure 6.3.4-11. Cumulative Key-Block Size Distribution using Original and Modified Terzaghi Corrections

INTENTIONALLY LEFT BLANK

7 Waste Package Degradation

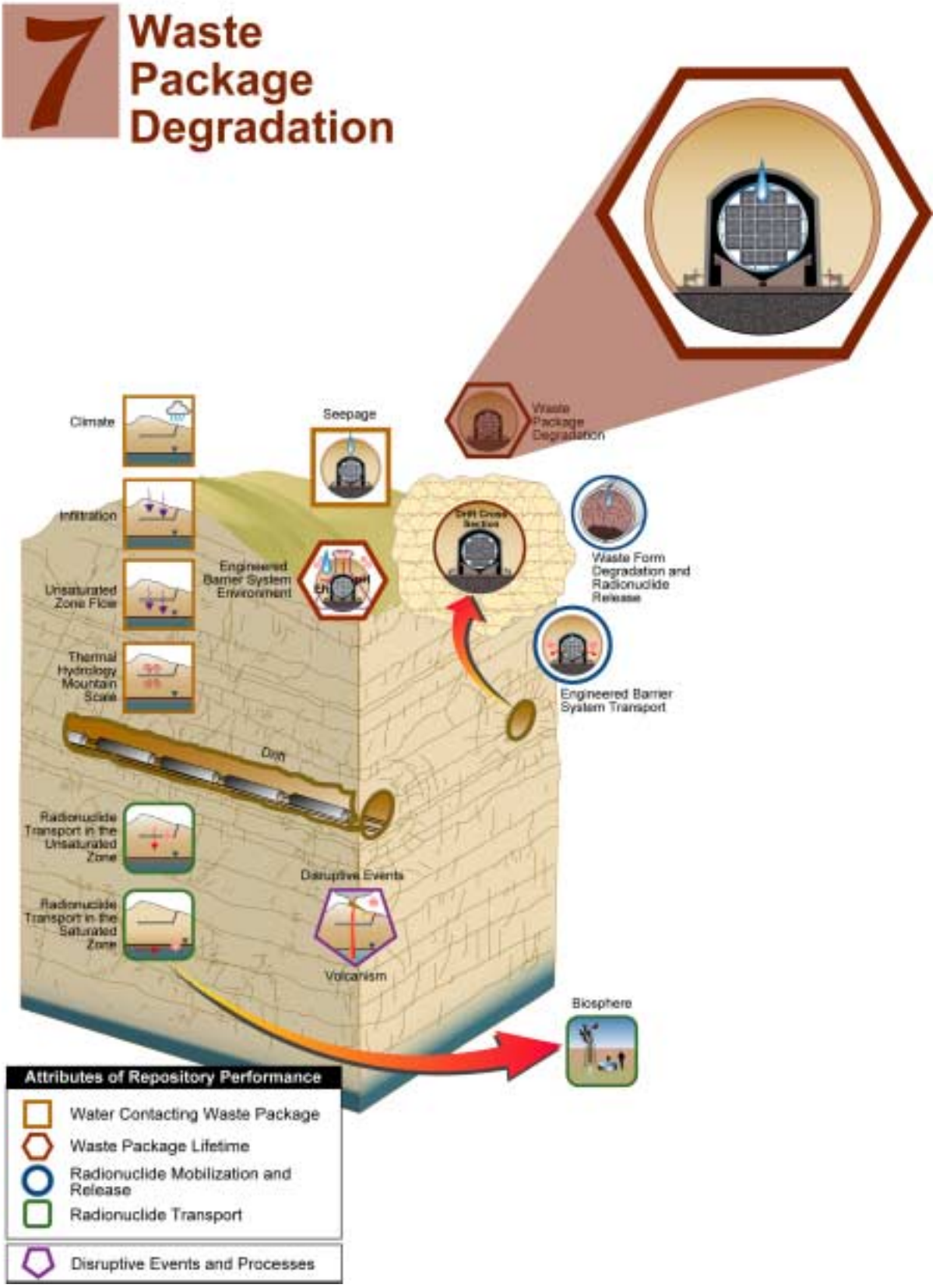

7. WASTE PACKAGE AND DRIP SHIELD DEGRADATION

This section documents analyses conducted to quantify conservatism and unquantified uncertainties in the corrosion models and parameters that were incorporated in the waste package and drip shield degradation analysis for the *Total System Performance Assessment for the Site Recommendation* (TSPA-SR) (CRWMS M&O 2000 [DIRS 153246]). This section also documents new data and analyses that were developed to model degradation of the waste package and drip shield materials since the completion of the TSPA-SR analysis. Most of the new analyses documented relate to the degradation of the Alloy 22 outer barrier of the waste package. Those updated corrosion models and parameters (with quantified uncertainties) and their abstracted models were input into the integrated waste package degradation model (i.e., the WAPDEG V4.0 model) (CRWMS M&O 2000 [DIRS 151566]) to evaluate the effects of the quantified uncertainties and conservatism on waste package (and, for a few cases in Section 7.4, drip shield) degradation. Where necessary, sensitivity analyses are also conducted for the evaluation. A waste disposal container becomes a waste package when it is loaded with waste (such as commercial spent nuclear fuel [CSNF], U.S. Department of Energy (DOE) spent nuclear fuel, and DOE high-level radioactive waste) and sealed (CRWMS M&O 2000 [DIRS 152104], Section 1.0).

7.1 INTRODUCTION

The lifetimes of the waste package and drip shield will depend on the environmental conditions to which they are exposed and the degradation processes that occur in those environments. Environmental conditions within the emplacement drifts that influence the degradation of the waste package and drip shield are closely coupled to the thermal-hydrologic and geochemical processes occurring within the emplacement drifts. These processes involve the evaporation and condensation of water under changing thermal conditions, the redistribution and precipitation of dissolved salts, and the effects of gaseous species on solution chemistry. Also included in the conceptualization are the contributions of construction material degradation processes (i.e., ground structural support materials) and the effects of microbial action.

Once the exposure environments have been established, the most important and relevant degradation processes can be identified, which can be used for confirming the selection of materials for the drip shield and the waste package. Corrosion has been judged the most relevant and important degradation process in the selection of the materials for the waste package and drip shield. A number of corrosion processes have been investigated in detail and the results used to support the selection of materials and the design of these components.

Waste Package and Drip Shield Materials–Degradation modes for the waste package and drip shield depend on the materials used to make these components and, as mentioned earlier, on the environment in which they perform. Figure 7.1-1 provides a visual perspective to illustrate the physical arrangement of the waste packages and drip shield in the drift and shows schematically the arrangement of different types of waste packages and the drip shield. Figure 7.1-2 shows a schematic sketch of a typical waste package designed for 21 pressurized water reactor fuel assemblies, along with the materials used for the various components. Titanium (Grade 7 was selected for construction of the drip shield because of its high resistance to corrosion (CRWMS M&O 2000 [DIRS 153802], Section 3.1.1.1). This corrosion resistance results from the

formation of a passive oxide film that is stable over a relatively wide range of exposure environments.

Alloy 22 was selected for construction of the waste package outer barrier (CRWMS M&O 2000 [DIRS 153802], Section 3.1.1.2). The main alloying elements in this material are nickel, chromium, molybdenum, iron, tungsten, and cobalt. Alloy 22 is less susceptible to localized corrosion in environments that contain chloride ions than Alloys 825 and 625, materials of choice in earlier waste package designs (CRWMS M&O 2000 [DIRS 153802], Section 3.1.1.2). Alloy 22 was developed for application in a wide variety of chemical environments with highly corrosive conditions (Gdowski 1991 [DIRS 100859], pp. 1 to 8). This material is one of the most corrosion-resistant nickel alloys for the expected range of repository environments (Gdowski 1991 [DIRS 100859], pp. 1 to 8). Alloy 22 and its predecessor alloys have been used for the past 50 years in a variety of environments and have performed extremely well. For example, test coupons made from Alloy C, which is a predecessor of Alloy 22, continue to maintain a mirror-like finish after almost 50 years of exposure to a marine environment (McCright 1998 [DIRS 100289], Figure ES-1). In comparison to Alloy C, Alloy 22 has greater corrosion resistance. This is based on the fact that Alloy C and Alloy C-276 have a comparable corrosion resistance (Gdowski 1991 [DIRS 100859], Section 1.2) and the resistance of Alloy 22 to crevice corrosion is greater than that of Alloy C-276 (Gdowski 1991 [DIRS 100859], Tables 22 and 25).

Stainless Steel Type 316NG will be used for construction of the structural support shell inside the waste package outer barrier to increase the overall strength of the waste package. Because the stainless steel inner shell is used primarily for structural support for the outer barrier, the potential performance credit of the shell as a corrosion barrier to the ingress of water into the waste package is not considered in waste package performance and total system performance assessment (TSPA) analysis. The key factor in placing the structural material on the inside is that its strength does not begin to degrade until the outer shell is breached by corrosion or other degradation modes.

As discussed in Section 7.2, degradation processes evaluated for the drip shield and waste package for the TSPA-SR (CRWMS M&O 2000 [DIRS 153246]) include general and localized corrosion under humid-air and aqueous conditions, stress corrosion cracking, and hydrogen induced cracking. Also considered in the TSPA-SR analysis were the effects of microbiologically influenced corrosion (MIC), aging of the waste package outer barrier, and manufacturing flaws on stress corrosion cracking of the waste package outer barrier. The WAPDEG model was used to evaluate the combined effects of the various degradation modes and to estimate the range of lifetimes of the drip shields and the waste packages, including an evaluation of uncertainties.

Since the completion of the TSPA-SR (CRWMS M&O 2000 [DIRS 153246]) analysis, the models and parameters of the degradation processes included in the waste package and drip shield degradation analysis were reevaluated to further quantify associated uncertainties and to reduce conservatism that was introduced to bound the degradation processes. The degradation processes, models, and parameters that were reevaluated are documented in Sections 7.3.1 through 7.3.7. The updated corrosion models and parameters, along with their quantified uncertainties and their abstracted models, were input to the WAPDEG model to evaluate the

effects of the quantified uncertainties and conservatism on the waste package and drip shield degradation, which is documented in Section 7.4.

Table 7-1 shows the correlation between the supplemental analyses that have been produced for waste package and drip shield degradation, the rationale for obtaining that supplemental information (i.e., unquantified uncertainties, new science, or lower-temperature operating mode analyses), and the subsection in this section where the work is documented. Details of the goals and scope are discussed in Section 1.2 of this volume.

7.2 OVERVIEW OF TOTAL SYSTEM PERFORMANCE ASSESSMENT-SITE RECOMMENDATION REV 00 TREATMENT

This section provides an overview of the treatment used to address and quantify the uncertainties in the various corrosion models and their parameters that have been incorporated into the waste package and drip shield degradation analysis for the TSPA-SR model (CRWMS M&O 2000 [DIRS 148384]). In general, the approach used in the TSPA-SR in dealing with the uncertainties in each of the process models (and the abstraction models used in the TSPA) is to employ conservative assumptions and bound the models. The conservatism and uncertainties in each of the process models discussed in this section were captured in their respective abstraction models and incorporated into the WAPDEG model, the integrated waste package degradation model (CRWMS M&O 2000 [DIRS 151560]).

Of the degradation processes (and their associated uncertainties) discussed in this section, the uncertainties of the models and parameters of key degradation processes are re-evaluated, updated and further quantified. Details of the analyses for the uncertainty update and quantification are discussed in Section 7.3. These key degradation processes are:

- Chemical environment on waste package and drip shield surfaces (Section 7.3.1)
- Thermal aging and phase stability of Alloy 22 outer barrier (Section 7.3.2)
- Stress corrosion cracking (Section 7.3.3)
- Passive film stability of Alloy 22 outer barrier (Section 7.3.4)
- Temperature-dependent general corrosion, especially temperature dependency, of Alloy 22 outer barrier (Section 7.3.5)
- Early waste package failure by improper heat treatment (Section 7.3.6).

Effects of these updated and quantified uncertainties on the waste package performance are discussed in Section 7.4. Testing and analyses of all the corrosion processes considered in the TSPA-SR analysis are being continued to address and quantify their effects and associated uncertainties on waste package and drip shield degradation under expected repository exposure conditions.

Table 7-1. Summary of Supplemental Models and Analyses

Key Attributes of System	Process Model (Section of S&ER)	Topic of Supplemental Scientific Model or Analysis	Reason For Supplemental Scientific Model or Analysis			Performance Assessment Treatment of Supplemental Scientific Model or Analysis[a]		
			Unquantified Uncertainty Analysis	Update in Scientific Information	Lower-Temperature Operating Mode Analysis	Section of Volume 1	TSPA Sensitivity Analysis	Included in Supplemental TSPA Model
Long-Lived Waste Package and Drip Shield	In-Drift Moisture Distribution (4.2.5)	Environment on surface of drip shields and waste packages	X			7.3.1		
	Drip Shield Degradation and Performance (4.2.4)	Local chemical environment on surface of drip shields (including Mg, Pb) and potential for initiating localized corrosion	X			7.3.1		
	Waste Package Degradation and Performance (4.2.4)	Local chemical environment on surface of waste packages (including Mg, Pb) and potential for initiating localized corrosion	X			7.3.1		
		Aging and phase stability effects on Alloy-22	X	X		7.3.2	X	
		Uncertainty in weld stress state following mitigation	X			7.3.3	X	X
		Weld flaws	X			7.3.3	X	X
		Early failure due to improper heat treatment	X		X	7.3.6	X	X
		General corrosion rate of Alloy-22: Temperature dependency	X		X	7.3.5	X	X
		General corrosion rate of Alloy-22: Uncertainty/variability partition	X			7.3.5	X	X
		Long-term stability of passive films on Alloy-22	X			7.3.4		
		Stress threshold for initiation of stress corrosion cracking	X	X		7.3.3	X	X
		Probability of non-detection of manufacturing flaws		X		7.4.3	X	X
		Distribution of crack growth exponent (repassivation slope)	X	X		7.3.3	X	X

NOTE: S&ER = *Yucca Mountain Science and Engineering Report* (DOE 2001 [DIRS 153849]).
[a] Performance assessment treatment of supplemental scientific model or analysis discussed in SSPA Volume 2 (McNeish 2001 [DIRS 155023]).

7.2.1 Thermal Aging

The long-term aging of Alloy 22 at elevated temperatures may cause the precipitation of intermetallic phases, affecting the corrosion resistance of the metal. Experiments to obtain the data needed to develop the model and analysis for the aging process are typically conducted at temperatures higher than those expected in the repository. This is necessary because the precipitation of intermetallic phases at expected repository temperatures would be extremely slow, and would be difficult to observe after reasonable test periods. This necessitates the extrapolation of parameters to temperatures expected in the repository environment.

The thermal aging model for Alloy 22 assumes Arrhenius-type kinetics (CRWMS M&O 2000 [DIRS 147639], Sections 6.2 and 6.5). Precipitation of intermetallic phases and long-range ordering can be accelerated by increasing the exposure temperature to levels well above those expected in the repository. The best estimate of the thermal aging model indicates that thermal aging of Alloy 22 base metal would not progress to a significant level in the first 10,000 years (CRWMS M&O 2000 [DIRS 147639], Section 6.2). However, the model estimate has large uncertainties.

The effects of intermetallic phase precipitation and long-range ordering on corrosion of Alloy 22 have been investigated with electrochemical techniques (CRWMS M&O 2000 [DIRS 144229], Section 6.7). From the corrosion tests conducted, it appears that aging of Alloy 22 results in anodic shifts in the observed corrosion potential. However, the shift is not significant enough to substantially alter passive film stability and result in significantly enhanced corrosion. The TSPA-SR (CRWMS M&O 2000 [DIRS 148384]) assumes the closure weld of the waste package outer barrier and heat-affected areas near the closure weld are subject to thermal aging, and the effect on corrosion is accounted for with a corrosion rate enhancement factor (CRWMS M&O 2000 [DIRS 151566], Sections 4.1.11 and 5.9). The enhancement factor is determined from the ratio of measured passive current densities for fully aged and unaged samples (CRWMS M&O 2000 [DIRS 144229], Section 6.7); it is based on a ratio of the nonequilibrium passive current densities for unaged metal and fully aged metal (CRWMS M&O 2000 [DIRS 144229], Section 6.7). The enhancement factor is represented with a range of values to account for uncertainty in the thermal aging process and the effects on corrosion. Based on measured data, the factor is assumed to be a uniform distribution with an upper bound of 2.5 and a lower bound of 1 (CRWMS M&O 2000 [DIRS 151566], Sections 4.1.11 and 5.9). The enhancement factor is applied only to the closure weld region of the waste package outer barrier and assumed to represent variability in the aging effect on the closure weld region. Additional data and analyses to quantify and reduce the present uncertainties are discussed in Section 7.3.2.

Thermal aging of Titanium Grade 7 under repository-relevant thermal conditions is expected to have little impact on the corrosion resistance of this material (CRWMS M&O 2000 [DIRS 144971], Section 5.9). Because no credit is claimed for the corrosion resistance of Stainless Steel Type 316NG, the TSPA calculation is insensitive to the uncertainty associated with its corrosion.

7.2.2 General Corrosion

General corrosion is the relatively uniform thinning of materials without significant localized corrosion. Conceptual models for general corrosion of the drip shield and waste package outer barrier are discussed in *General Corrosion and Localized Corrosion of the Drip Shield* (CRWMS M&O 2000 [DIRS 144971]) and *General Corrosion and Localized Corrosion of Waste Package Outer Barrier* (CRWMS M&O 2000 [DIRS 144229]), respectively. The mode of general corrosion differs depending on the local environment; the repository environment will result in three general corrosion modes (dry oxidation, humid-air corrosion, and aqueous-phase corrosion).

General Corrosion Initiation Threshold–Dry oxidation (dry-air corrosion) occurs at a relative humidity below the threshold for humid-air corrosion (CRWMS M&O 2000 [DIRS 144229], Sections 5.1 and 6.1). Humid-air corrosion is defined as a corrosion condition in the absence of dripping water. Aqueous-phase corrosion requires the presence of dripping water. In the TSPA-SR (CRWMS M&O 2000 [DIRS 153246]), a carbonate-base water (which has characteristics of J-13 well water) was considered the most likely to contact the drip shield and waste package (CRWMS M&O 2000 [DIRS 151568], Section 6.4.2). Sodium nitrate salt is the most soluble salt formed during the evaporative concentration testing of simulated J-13 well water and has the lowest deliquescence point among salts produced from the testing (CRWMS M&O 2000 [DIRS 151568], Section 6.4.2). The threshold relative humidity for humid-air and aqueous-phase corrosion is based on the deliquescence point of sodium nitrate salt (CRWMS M&O 2000 [DIRS 151568], Section 7.0; CRWMS M&O 2000 [DIRS 144229], Section 4.1.2). Because hygroscopic salts could form from the salts entrapped in the dusts settled on the waste package and drip shield surfaces, the deliquescence point of sodium nitrate salt is conservatively assumed also for the threshold of corrosion initiation for humid-air condition. However, for humid-air corrosion and aqueous-phase corrosion conditions, the deliquescence point of the assemblage of mixed salt phases resulting from evaporation of condensed water interacting with the dusts and/or dripping water onto the waste package and drip shield surfaces could be lower than “pure” sodium nitrate salt. Additional analyses for potential development of other more hygroscopic salts (e.g., magnesium and calcium chloride salts) from drift dust containing soluble salts and from non-carbonate dominated waters contacting the waste package are discussed in Section 7.3.1.

Dry Oxidation–Dry oxidation occurs at a relative humidity below the threshold for humid-air corrosion. This process results in the formation of an adherent, protective oxide film of uniform thickness. The rate of dry-air corrosion may be limited by the rate of mass transport through the growing metal oxide film. In such cases, the oxide thickness is expected to obey a parabolic growth law (film thickness proportional to the square root of time). This scenario has been adopted for Alloy 22 and Stainless Steel Type 316NG, mainly due to the availability of data at elevated temperatures to support such a model (CRWMS M&O 2000 [DIRS 144229], Section 6.1. There are sufficient data to support the application of a logarithmic law to the dry-air corrosion of titanium (CRWMS M&O 2000 [DIRS 144971], Section 6.1).

The rates of dry-air corrosion are small for Alloy 22 (CRWMS M&O 2000 [DIRS 144229], Section 6.1) and Titanium Grade 7 (CRWMS M&O 2000 [DIRS 144971], Section 6.1). Given

the extremely small magnitudes and uncertainties of these rates, dry-air corrosion is expected to have no significant impact on waste package and drip shield performance.

Humid-Air and Aqueous-Phase General Corrosion Rate–Humid-air corrosion is assumed to occur above the threshold relative humidity (provided that there are no impinging drips), and aqueous-phase corrosion is assumed to occur in the presence of dripping water (CRWMS M&O 2000 [DIRS 144229], Sections 6.2 and 6.3). The distributions of general corrosion rates for Alloy 22 and Titanium Grade 7 used in the TSPA-SR are based upon weight-loss data from the Long-Term Corrosion Test Facility (LTCTF) over a two-year period. The test program includes sample coupons exposed to a variety of test media (e.g., water chemistry, temperature) to cover a potential range of corrosion conditions in the repository. The test program is ongoing and designed to provide corrosion data for at least 60 months of exposure.

To date, corrosion data for Alloy 22 and Titanium Grade 7 indicate that the general corrosion rates for humid-air and aqueous-phase corrosion are about the same (i.e., water chemistry has no significant effect) (CRWMS M&O 2000 [DIRS 153802], Sections 3.1.5.4.2 and 3.1.5.4.3). The data also show little sensitivity to exposure temperature for the water chemistry and temperature ranges considered in the test program. Because the general corrosion rate is expected to decrease with exposure time, the current general corrosion rate models based on data from the Long-Term Corrosion Test Facility represent reasonably conservative corrosion behaviors of those highly corrosion-resistant materials under the expected repository conditions. Therefore, in the TSPA-SR, it was conservatively assumed that the rate of humid-air corrosion is represented by the same corrosion rate distribution used for aqueous-phase corrosion during the period where humid-air corrosion is operable (CRWMS M&O 2000 [DIRS 153802], Section 3.1.5.4.2). It was further assumed that the corrosion rate is constant and does not decrease with time at times greater than two years. Less conservative corrosion models assume that the rate decays with time. The calculated general corrosion rates were corrected for the effects of silica scale deposits on the sample coupons, which were estimated to increase the general corrosion rate from the weight-loss measurements by as much as 0.063 μm/yr (CRWMS M&O 2000 [DIRS 144229], Section 6.5.5). The corrections were made by sampling the silica scale correction factor from a uniform distribution between zero and 0.063 μm/yr and adding the sampled factor to the general corrosion rate from the weight-loss measurements (CRWMS M&O 2000 [DIRS 152542], Sections 2 and 3).

The general corrosion rate distributions for Alloy 22 and Titanium Grade 7 include substantial uncertainties. Most of the uncertainties result from insufficient resolution of the weight-loss measurements of the sample coupons due to the extremely low corrosion rates of the materials in the test media. The testing data and information are not sufficient to quantify the uncertainty fully, and the fraction of the corrosion rate distribution that is attributed to spatial variability (and conversely uncertainty) is not known. The conceptual approach in the waste package and drip shield degradation analysis in the TSPA-SR assumes that this fraction is unknown and varies uniformly, ranging from pure uncertainty to pure variability. The Gaussian variance partitioning technique was used to accomplish the separation of the uncertainty and variability from the original distribution (CRWMS M&O 2000 [DIRS 151566], Section 6.4.7). Long-term corrosion testing continues, and the results will be used to reduce uncertainties. Near-term activities that address the treatment of this uncertainty are described in Sections 7.3.4 and 7.3.5.

7.2.3 Localized Corrosion

The generic localized corrosion model for waste package materials assumes that localized attack occurs if the open circuit corrosion potential (E_{corr}) exceeds the threshold (critical) potential for breakdown of the passive film (E_{crit}). In some cases, the threshold potential is assumed to be the repassivation potential. The repassivation potential is the level at which a failed passive film repassivates, or heals, thereby protecting the surface. In other cases, the threshold potential is assumed to be the pit or crevice initiation potential. Therefore, initiation of localized corrosion processes can be expressed in terms of the threshold electrochemical potential. For the highly corrosion-resistant materials under consideration, the threshold potential approach is recommended because it is more solidly rooted in the theoretical concepts underlying passive film stability.

A correlation was developed to compare corrosion and threshold potentials as a function of exposure conditions and determine whether localized corrosion initiates for the waste package (Alloy 22) and drip shield (Titanium Grade 7) (CRWMS M&O 2000 [DIRS 144971], Section 6.4; CRWMS M&O 2000 [DIRS 144229], Section 6.4.3). The correlation is based upon standard cyclic polarization measurements in a variety of test solution media covering a broad range of temperatures. The uncertainty in the corrosion potential due to gamma radiolysis (i.e., a maximum positive shift of about 250 mV for Alloy 22) has been addressed (CRWMS M&O 2000 [DIRS 144971], Section 6.8; CRWMS M&O 2000 [DIRS 144229], Section 6.4.4). The current potential-based localized-corrosion initiation threshold model is considered to represent the realistic behavior of Alloy 22 and Titanium Grade 7 under the expected repository conditions. Estimates of uncertainty in the selection of corrosion and threshold potential have been made and are incorporated in WAPDEG analyses. Because the threshold potentials on the waste package and drip shield surfaces were not exceeded, both the waste package and drip shield are never subject to localized corrosion for the entire simulation period (CRWMS M&O 2000 [DIRS 151566], Sections 5.3 and 5.4).

When exposure conditions are such that the threshold potential is exceeded, localized corrosion rates are applied to simulate penetration of the waste package and drip shield by the rapid-penetrating localized corrosion. The rates of localized corrosion for Alloy 22 and Titanium Grade 7 have been bounded with the range of values found in the published literature (CRWMS M&O 2000 [DIRS 144229], Section 6.6.6; CRWMS M&O 2000 [DIRS 144971], Section 6.7). The localized corrosion rates for Alloy 22 are assumed to be log-uniformly distributed between the bounds of 0.0127 mm/yr and 1.27 mm/yr, and the distribution is assumed to represent uncertainty in the localized corrosion rate (CRWMS M&O 2000 [DIRS 144229], Section 6.6.6). The localized corrosion rates for Titanium Grade 7 are assumed to be uniformly distributed between the bounds of 0.49 mm/yr and 1.12 mm/yr, and the distribution is assumed to represent uncertainty in the localized corrosion rate (CRWMS M&O 2000 [DIRS 144971], Section 6.7).

7.2.4 Microbiologically Influenced Corrosion

It has been observed that Titanium Grade 7 and Alloy 22 are relatively resistant to MIC (CRWMS M&O 2000 [DIRS 144971], Section 6.9; CRWMS M&O 2000 [DIRS 144229], Section 6.8). Furthermore, microbial growth in the repository will be limited by the availability of nutrients. In general, the impact of MIC can be accounted for by adjusting E_{corr}, E_{crit}, pH, and

the sulfide concentration in the area affected by the microbial activity (CRWMS M&O 2000 [DIRS 144229], Section 6.8).

The TSPA-SR analysis assumes that when the relative humidity at the surface of the waste package and drip shield is greater than a threshold value (i.e., 90 percent relative humidity), microbial activity becomes important enough that MIC can occur on Alloy 22 (CRWMS M&O 2000 [DIRS 151566], Section 5.8). The analysis assumes conservatively that when the relative humidity condition is met, microbial activity is at such a level that the biofilm covers the entire surface of all the waste packages and drip shields (CRWMS M&O 2000 [DIRS 151566], Section 4.1.10).

The TSPA-SR assumes that Titanium Grade 7 is not subject to MIC (CRWMS M&O 2000 [DIRS 151566], Section 5.8). The effect of MIC of Alloy 22 is modeled with a corrosion rate enhancement factor. The enhancement factor is determined from the ratio of measured corrosion current densities for abiotic and inoculated samples. Based on measurement data, the enhancement factor is assumed to be a uniform distribution with an upper bound of 2 and a lower bound of 1 (CRWMS M&O 2000 [DIRS 144229], Section 6.8). As discussed, this enhancement factor is applied to the entire surface of the waste package outer barrier and assumed to represent variability in the MIC effects on corrosion (CRWMS M&O 2000 [DIRS 151566], Sections 4.1.10 and 6.4.14).

7.2.5 Stress Corrosion Cracking

Stress corrosion cracking (SCC) is a potential degradation mode that can result in penetration of the waste package outer barrier (Alloy 22). SCC of materials may occur when an appropriate combination of material susceptibility, tensile stress, and environment is present. SCC is assumed to occur only in the regions around the closure welds of the Alloy 22 outer barrier because the residual stress in this weld cannot be relieved completely. It is assumed that residual stress in all welds used in the fabrication of the waste package outer barrier and Titanium Grade 7 drip shield are fully annealed, and thus are not subject to SCC (CRWMS M&O 2000 [DIRS 151564], Section 5.0). The effect of rockfall on the waste package outer barrier is excluded because of protection provided by the drip shield (CRWMS M&O 2000 [DIRS 153802], Section 1.0). SCC of the drip shield is possible under the applied stresses resulting from rockfall; however, it is assumed that SCC is of low consequence to drip shield performance, so it is not modeled (CRWMS M&O 2000 [DIRS 151564], Section 6.5.5).

An effective approach to eliminate the threat of SCC and the resultant through-wall cracking in the closure weld is to implement a post-weld stress mitigation process to either remove residual tensile stresses in the weld region or reduce them below threshold values for SCC initiation and growth. The closure of the waste package outer barrier is designed to include two lids (inner and outer) with two separate post-weld stress mitigation processes: laser peening of the inner lid weld and induction annealing stress relief of the outer lid weld. This two-lid design and stress mitigation strategy forms part of the conceptual model for the SCC model. The SCC model includes two alternative models, one based on the slip-dissolution mechanism at the crack tip for crack initiation and propagation, and another based on the threshold stress intensity factor at the tip of preexisting flaws. The slip dissolution model is preferred because it is the more conservative model, the U.S. Nuclear Regulatory Commission (NRC) has accepted the method,

and the model has been used for predicting the performance of boiling water reactor piping (Carpenter and Lund 1999 [DIRS 154988]; ASM International 1987 [DIRS 103753], p. 930). Additional data and analyses to quantify and reduce the present uncertainties in associated model parameters as described below are discussed in Section 7.3.3.

Slip Dissolution Model–The slip dissolution model employs a threshold stress for crack initiation (CRWMS M&O 2000 [DIRS 151564], Section 6.5.2). SCC is initiated if the threshold stress is exceeded on a smooth surface. The SCC propagation rate is calculated as a function of local environment and stress intensity factor. The time-to-failure is determined by integrating the calculated propagation rate. Thus, the residual stress and corresponding stress intensity factor are the two most important parameters in SCC analysis with the slip dissolution model.

In the TSPA-SR (CRWMS M&O 2000 [DIRS 153246]), the slip dissolution model and its parameters are based primarily on published data. Limited data have been obtained under repository-relevant conditions. The parameters for the slip dissolution model are based on data for stainless steel in the boiling water reactor industry. Because stainless steels are much more prone to SCC than Alloy 22, these parameter estimates are conservative. The rate of repassivation is captured by the repassivation-slope parameter. A characteristic of the slip dissolution (or film rupture model) is that SCC susceptibility decreases with increasing values of repassivation slope (CRWMS M&O 2000 [DIRS 151564], Section 6.4.4). In the TSPA-SR (CRWMS M&O 2000 [DIRS 153246]), the model parameter for repassivation slope is represented by a uniform distribution with an upper bound of 0.84 and a lower bound of 0.75, and the variation of the parameter value is due to uncertainty (CRWMS M&O 2000 [DIRS 151564], Section 6.4.4).

Threshold Stress Model for Crack Initiation–Although the slip dissolution model assumes that crack growth can initiate at any surface defect that can generate a stress intensity factor, regardless of defect size and tensile stress, examination of the relevant SCC literature indicates that there is a threshold stress below which SCC will not initiate on a "smooth" surface (i.e., free of surface breaking flaws). The uncertainty in the threshold stress for initiation of stress corrosion cracking is conservatively estimated to be approximately 20 to 30 percent of the material yield strength (CRWMS M&O 2000 [DIRS 148375], Section 6.5.2). The threshold stress and its uncertainty range are conservative and based on the determination of such thresholds for more susceptible alloy systems (e.g., stainless steels) exposed to very aggressive environments, such as boiling magnesium chloride. Uniform distribution between the bounds indicated above is assumed for the threshold stress uncertainty.

Closure-Weld Residual Stress Uncertainty–The stress profile (stress vs. depth) and corresponding stress intensity factor profile in the closure lid welds, before and after stress mitigation, are determined from analyses of measured residual stresses in welds as well as finite element modeling (CRWMS M&O 2000 [DIRS 151564], Section 6.2.2.2). The residual stress analysis shows that the dominant stress in the closure lid welds after stress mitigation is the hoop stress, which drives radial cracks through the closure lid weld region. The radial stress state, which drives circumferential cracks, does not remain tensile throughout the thickness of the closure lid weld region; therefore, there will be no through-wall cracking caused by circumferential cracks (CRWMS M&O 2000 [DIRS 151564], Section 6.2.2 and Attachment I). This analysis indicates that only radial flaws are potential sites for through-wall SCC if it occurs.

The uncertainties in the residual stress profile (and corresponding stress intensity factor profile) were estimated from literature data (CRWMS M&O 2000 [DIRS 151564], Section 6.2.2.5). A separate uncertainty range was developed for each of three cases: optimum, realistic, and worst case. A stress uncertainty range of ±5 percent was used to represent the optimum case that is achievable through stringent control of such processes as welding, stress mitigation, material variability, and other fabrication steps. The stress uncertainty range of ±10 percent is used to represent the realistic case that is achievable through appropriate levels of process controls. The stress uncertainty range of ±30 percent is used to represent the worst case that might result from inadequate control of the processes (CRWMS M&O 2000 [DIRS 151564], Section 6.2.2.5). The TSPA-SR (CRWMS M&O 2000 [DIRS 153246]) considers an uncertainty range of the worst case (±30 percent of yield stress) as the base case and evaluates the ranges of ±10 percent and ±5 percent in sensitivity analyses (CRWMS M&O 2000 [DIRS 151566], Section 4.1.8). Triangular distributions around the mean are assumed for the residual stress uncertainty.

Manufacturing Flaws in Closure Weld–An input to the SCC modeling approach is information regarding defects, incipient cracks, and manufacturing defects. Preexisting manufacturing flaws in the closure lid welds are the most likely sites for SCC failure. The frequency and size distributions for manufacturing flaws in the closure welds are based on published data for stainless steel pipe welds in nuclear power plants. The published data used to develop the manufacturing defect model utilize relevant welding techniques and post-weld inspection methods.

In the TSPA-SR analysis (CRWMS M&O 2000 [DIRS 153246]), preexisting surface-breaking defects and defects embedded in the outer 25 percent of the weld thickness are considered as potential sites for SCC crack growth (CRWMS M&O 2000 [DIRS 151549], Section 5.2). There is uncertainty associated with this assumption because, as general corrosion propagates, some of the existing surface-breaking defect flaws may disappear and some of the embedded defects may become surface-breaking defects. Use of this assumption is conservative because the WAPDEG model does not allow existing surface-breaking defects to be removed due to general corrosion processes during the simulation, leading to a greater number of defects capable of propagation. In addition, weld flaws are assumed to be randomly distributed spatially, as represented by a Poisson process (CRWMS M&O 2000 [DIRS 151549], Section 5.2). This assumption is reasonable for the manufacturing process being considered.

As described above, the residual stress analysis shows that the dominant stress in the closure lid welds after stress mitigation is hoop stress, which drives radial cracks through the closure lid weld region. This analysis indicates that only radial flaws are potential sites for through-wall SCC if it occurs. The TSPA-SR (CRWMS M&O 2000 [DIRS 153246]) assumes that all manufacturing flaws are oriented in such a way that they could grow in the radial direction in the presence of hoop stresses. This is a highly conservative assumption. More realistically, most weld flaws, such as lack of fusion and slag inclusions, would be expected to be oriented within a few degrees of the weld centerline (CRWMS M&O 2000 [DIRS 151564], Section 6.5.1). Available published data and limited flaw measurements from the viability assessment design mockups also show that most weld flaws (about 99 percent) tend to be oriented in a circumferential direction (CRWMS M&O 2000 [DIRS 151564], Section 6.5.1). Analyses show it is extremely unlikely that cracks initiating from circumferential flaws grow in the radial direction (CRWMS M&O 2000 [DIRS 151564], Section 6.5.1).

7.2.6 Hydrogen-Induced Cracking

Evaluation of hydrogen-induced cracking (HIC) is based upon a threshold hydrogen concentration. The drip shield design avoids any galvanic couple that would lead to the possibility of HIC. In the TSPA-SR analysis (CRWMS M&O 2000 [DIRS 153246]), a simple and conservative model was developed to evaluate the effects of HIC on the drip shield. The basic premise of the model is that failure will occur after the hydrogen content exceeds a certain limit, or critical value. This model is very conservative because it assumes that, once the environmental and material conditions can support that particular corrosion process, failure will be effectively instantaneous. The threshold hydrogen concentration value of 400 μg/g was used initially for the HIC analysis of drip shield. Based on the threshold hydrogen concentration data for Titanium Grade 16, which is between 1,000 and 2,000 μg/g (CRWMS M&O 2000 [DIRS 151559], Section 6.1.3), the threshold value for Titanium Grade 7 was updated to be at least 1,000 μg/g. This assumption is used because the threshold hydrogen concentration data are not available for Titanium Grade 7, and Titanium Grade 7 and 16 are similar alloys because of their similar chemical compositions (CRWMS M&O 2000 [DIRS 151559], Section 6.1.3).

A quantitative evaluation indicates that a wide margin of safety exists for the drip shield against the effects of HIC. Hydrogen concentration in the drip shield due to a galvanic couple with steel ground supports likely will not exceed the threshold value. The estimated hydrogen concentrations are less than the critical hydrogen concentration of 1,000 μg/g (CRWMS M&O 2000 [DIRS 151559], Section 6.3.3). Analyses of a worst case scenario, which assumes local concentration of hydrogen from the galvanic coupling and impact of the contact area by a rockfall, conclude that hydrogen embrittlement is unlikely even though the hydrogen concentration may exceed the critical value. This is because the stress intensity factor induced by a rockfall is below the fracture toughness that may be degraded by hydrogen absorption (CRWMS M&O 2000 [DIRS 151559], Section 6.3.4). The analyses show that Titanium Grade 7 is an excellent choice of material for the drip shield with regard to degradation caused by HIC and that the drip shield is able to sustain the effects of HIC under expected conditions at the repository.

7.3 UNCERTAINTY ANALYSES

This section documents additional analyses conducted since the completion of the TSPA-SR (CRWMS M&O 2000 [DIRS 153246]) to quantify previously unquantified uncertainties in the waste package degradation model. The degradation processes for which uncertainties are quantified and/or reevaluated are:

- Chemical environment on the waste package and drip shield surfaces
- Aging and phase stability of Alloy 22 outer barrier
- Stress corrosion cracking of Alloy 22 outer barrier
- Passive film stability of Alloy 22 outer barrier
- General corrosion of Alloy 22 outer barrier

- Early waste package failure by improper heat treatment

- Other issues, including the threshold temperature for Alloy 22 localized corrosion and the effects of radiolysis on the Alloy 22 corrosion rate.

Natural analogues and industrial analogues, where available, are documented as multiple lines of evidence to support the degradation models and the uncertainty quantification. Where applicable, additional analyses are presented to address and quantify uncertainties in the waste package degradation processes that could be affected by alternative thermal operating modes.

7.3.1 Environments on Waste Package and Drip Shield Surfaces

7.3.1.1 Introduction

In order to understand waste package and drip shield performance in the potential repository, it is necessary to characterize the range of environments to which they might be exposed. These environments, combined with the material's properties, determine the potential degradation modes and the extent of the degradation.

The aqueous salt films that could form on these components will result either from hygroscopic salts that have been deposited on the surfaces or from evaporative concentration of dilute waters contacting these components. In order to determine the effect of aqueous films on the degradation of engineered barrier system (EBS) components, the brines that could form are characterized in terms of parameters that influence the corrosion processes. These parameters include pH, the hygroscopic characteristics of the salts, gas solubility (e.g., oxygen and carbon dioxide) in these waters, and the compositions of these waters.

Analysis of natural brines indicates that, in terms of pH, there are two types of brines: high pH sodium-carbonate-base brines, and near-neutral pH brines, which contain calcium and/or magnesium (Drever 1997 [DIRS 147480], Chapter 15). The high-pH brines do not contain significant calcium and magnesium because of the low solubility of magnesium-containing calcium carbonate and magnesium silicates under high pH conditions. These high pH brines may also contain a limited amount of soluble fluoride.

The near-neutral pH brines can contain soluble calcium and magnesium. Salt precipitates from these types of brines may contain chlorides of calcium and/or magnesium. These chloride salts are very hygroscopic (i.e., they form aqueous solutions at low relative humidities), and their saturated solutions have boiling points in excess of 160°C. Dissolution of pure chloride salts can result in very concentrated chloride solutions for low relative humidity conditions. This topic is discussed in Section 7.3.1.3.1.

The chemical composition of the waters also includes constituents that may only be present in small quantities due to solubility limitations. It is known, however, that some minor constituents, such as lead, arsenic, and mercury, may enhance the corrosion susceptibility of nickel alloys under specific conditions. A discussion of lead in the ambient system waters is presented in Section 7.3.1.3.3. Studies of arsenic and mercury in the ambient system waters are ongoing.

The contributions to aqueous solution formation by particulate matter and aerosols entrained in the ventilation air and by dust deposited with the drift are being actively investigated. Studies are underway to identify the soluble salt species contained in these sources, their contribution to the amount of salt deposited, and their projected contribution to the total amount of salt deposited. To supplement these studies, data obtained by the National Atmospheric Deposition Program/National Trends Network (NADP/NTN 2001 [DIRS 154843]) for ionic species deposition are considered. These data are discussed in Section 7.3.1.3.4.

7.3.1.2 Goal of the Analyses

The following sections discuss information that supplements the analyses contained in previous documentation on this subject (CRWMS M&O 2000 [DIRS 151568]). The goal is to specify the environmental conditions that affect waste package and drip shield degradation as a function of temperature and relative humidity, considering lower- and higher-temperature operating modes of the potential repository. These environmental conditions include water composition, pH, presence of minor constituents, deliquescence points of deposited salts, and compositions of the aqueous solution at the deliquescence points.

Other goals of the analyses include reducing uncertainties pertaining to minor constituents that may be contained in waters that contact the waste packages and drip shields and uncertainties pertaining to soluble salts that may be deposited on these EBS components due to ventilation and drift dust.

7.3.1.3 New Analyses Since Total System Performance Assessment-Site Recommendation

7.3.1.3.1 Range of Water Chemistries on the Waste Package and Drip Shield

As an indication of the types of seepage waters that may contact waste packages and drip shields in the emplacement drifts, the range of water chemistries of saline lakes was considered. An examination of these lake waters indicates a wide range of compositions exists in nature (Drever 1997 [DIRS 147480]; see also Table 7.3.1-1 for examples). Table 7.3.1-1 notes lakes where chloride is the dominant anion, with significant amounts of calcium cation (e.g., Bristol Dry Lake, California). There are other lakes where the anion content includes significant amounts of sulfate and carbonate in addition to chloride (e.g., Alkali Valley, Oregon). The calcium and magnesium content in these high-carbonate lakes is very small.

Numerous factors influence the compositions of these saline lakes (Drever 1997 [DIRS 147480]). These include the compositions of the initial dilute water, which undergoes evaporative concentration; the partial pressure of carbon dioxide; and the mineralogy through which the waters that contribute to the lakes transverse. These processes must also be considered to specify the range of compositions of waters that may contact the drip shields and waste packages.

Numerous dilute waters have been sampled at Yucca Mountain. The compositions of these waters are listed in Table 7.3.1-2. Water from well J-13 has been well-characterized and its composition bounds established from numerous samplings (Harrar et al. 1990 [DIRS 100814]).

Compositions of the other waters are based on fewer measurements. The uncertainty in the measurements of pore water compositions (PERM-2 and PERM-3) is discussed in Section 6.

Applying the principal of the chemical divide (See Section 6) to evaporative concentration, the dilute waters of the well J-13 and the UZ-14 perched water form high pH sodium-carbonate-base brines. In contrast, the pore waters (PERM-2 and PERM-3 in Table 7.3.1-2) form near neutral pH brines that contain soluble magnesium and/or calcium. Of particular interest for corrosion concerns is the type of chloride salt that would form from evaporation to dryness. Halite (NaCl) has been identified as an evaporite mineral from a simulated well J-13 water and tachyhydrite ($Mg_2CaCl_6 \bullet 12H_2O$) has been identified from a simulated pore water (Rosenberg et al. 2000 [DIRS 152766]). The same reasoning for formation of $MgCl_2$ and/or $CaCl_2$ aqueous solutions can be applied to the brines that result from hygroscopic salts deposited on the waste packages and drip shields from particulate matter and aerosols entrained in the ventilation air and from drift dust.

The presence of chloride-containing salts allows for the possibility of formation of chloride-dominated waters, such as those seen in nature. The chemical separation of relatively pure chloride salts can occur in the host rock surrounding the drifts or on the waste packages or drip shields; therefore, the waters in contact with these EBS components could be chloride-dominated for at least some time period. With time, as the relative humidities increases and more salts become soluble, the composition of the waters in contact with drip shields and waste packages will contain other ionic species. It is well documented in the corrosion literature that anions such as nitrate, carbonate, fluoride, and sulfate can mitigate against the aggressiveness of chloride-enhanced corrosion (e.g., Thomas 1994 [DIRS 120498]). The project data confirm that the presence of these ions in solution reduces the aggressiveness of chloride ions to Alloy 22 corrosion (CRWMS M&O 2000 [DIRS 144229], Section 6.4.2). A recent project data indicates that nitrate ions can mitigate against the aggressiveness of chloride ions to Alloy 22 corrosion even in nearly saturated calcium chloride solution at 120°C (Pasupathi 2001 [DIRS 155252]).

Previous analyses of the environment on the waste package outer barrier and drip shield focused on carbonate-base dilute waters contacting these EBS components (CRWMS M&O 2000 [DIRS 151568]), Section 6.4.2; see also Table 7.3.1-2 for composition of the dilute water). Experimental data and modeling indicate that these types of waters evolve into high-pH brines that do not contain significant amounts of soluble calcium or magnesium. Low to neutral pH variants of these waters were used in corrosion testing. The low pH variant is a sodium chloride-nitrate-sulfate solution at pH 2.7; the near-neutral pH solution was a high boiling point sodium-chloride-nitrate solution (CRWMS M&O 2000 [DIRS 151568], Section 6.4.2).

Present analyses also include non-carbonate base dilute waters contacting these EBS components. See Table 7.3.1-2 for composition of the dilute water. These waters will evolve into near-neutral pH brines that contain soluble calcium and magnesium, as has been confirmed experimentally (Rosenberg et al. 2001 [DIRS 152766]). The presence of these cations in the aqueous solutions could result in the formation of limited amounts of water that are stable at low relative humidities. However, the soluble amount of calcium and magnesium in these waters decreases during evaporative concentration due to the formation of insoluble precipitates, such as carbonates and silicates.

The quantity of highly concentrated water that may be in contact with the waste package and drip shield is limited by the amount of dilute water that must undergo evaporative concentration. As an example, a 1-L solution of 7.4 M $MgCl_2$, which will boil at 155°C (Casale 1967 [DIRS 155014]), requires the magnesium ion content from 5,400 L of PERM-2 water. In actuality, the availability of magnesium ions will be decreased significantly by the formation of insoluble precipitates; therefore, a larger quantity of dilute water would be necessary to supply the required amount of ions.

Modeling and experimental studies are ongoing to investigate the factors controlling the environments on the waste package and drip shield. In particular, the relationship between solution chemistry and partial pressure of CO_2 (P_{CO2}) is of interest, since P_{CO2} has a strong influence on the precipitation of insoluble magnesium and calcium species. An initial low-order approximation on the probability of the formation of magnesium and calcium chloride brines was attempted based on the combination of the different modeling runs done on the seven different water compositions (see Section 6.3.3.7.1). The initial approximation indicates that there would be a 14 percent chance of the starting water composition going toward a calcium/magnesium chloride brine due to evaporative concentration processes. However, the approximation is considered still qualitative and subjective, and cautions should be exercised in using the information in a quantitative analysis (see Section 6.3.3.7.1).

Modeling and experimental efforts are also focusing on minor constituents, such as lead, mercury, and arsenic, that may be present in the waters that contact the waste package and drip shield. These efforts focus on characterizing the availability of these species at Yucca Mountain, the solubility limits and the factors controlling solubility in natural waters, and the speciation of these components in solution. Corrosion studies of candidate materials in solutions based on these types of waters are ongoing. Some aspects of lead solubility in natural waters are discussed in Section 7.3.1.3.4.

7.3.1.3.2 Brine Formation Dependence on Relative Humidity

The formation of brines on EBS components and their characteristics are functions of incoming water chemistry, temperature, and relative humidity. It is assumed that the occurrence of brines on the components is controlled by the most hygroscopic salt contained in the deposited salts (CRWMS M&O 2000 [DIRS 151568], Sections 6.1 and 6.4.1; CRWMS M&O 2001 [DIRS 153265]). The composition of the brines may, however, include other ionic species that dissolve in the brines formed by the hygroscopic salts. Regardless of the deposited salts, the consequences for waste package degradation depend on the time, temperature, and relative humidity projections of any particular repository design.

For the deposited salts that evolve into high pH brines, aqueous solution formation is assumed to be controlled by the hygroscopic properties of sodium nitrate ($NaNO_3$) (Table 7.3.1-3). The deliquescence point of sodium nitrate varies from 50 percent relative humidity at the boiling point (120.6°C) (Kracek 1928 [DIRS 122125], pp. 351 to 373) of the saturated solution to 73 percent relative humidity at 30°C (Table 7.3.1-3). Hence, higher relative humidities are required for brine formation at lower temperatures. Other salts that may determine aqueous solution formation as a function of relative humidity include sodium chloride (NaCl). For

sodium chloride, the deliquescence point is nominally 75 percent relative humidity over a temperature range of 30° to 80°C (Table 7.3.1-3).

For the deposited salts that evolve into near-neutral pH brines, aqueous solution formation is assumed to be controlled by the hygroscopic properties of either calcium chloride ($CaCl_2$) or magnesium chloride ($MgCl_2$). Both of these salts are very hygroscopic (Table 7.3.1-3). The deliquescence point for magnesium chloride increases from 22 percent relative humidity at 100°C to 32 percent relative humidity at 30°C. No deliquescence point data for calcium chloride have been reported; however, the boiling point at sea level is 164.3°C (Kracek 1928 [DIRS 122125], pp. 351 to 373). The relative humidity at the boiling point (sea level) is about 15 percent.

7.3.1.3.3 Soluble Salts in the Ventilation Air

Particulate matter entrained in the ventilation air will introduce inorganic and organic material into the drifts that may affect the corrosion processes occurring on the waste package and drip shield. Hygroscopic salts, which are entrained in the ventilation air, may enhance the degradation of the EBS components by forming high ionic strength aqueous solutions at low relative humidities (CRWMS M&O 2000 [DIRS 151568], Section 6.1), facilitating electrochemical corrosion processes. The entrained organic matter could supply nutrients for microbiological activity. The Yucca Mountain Site Characterization Project (YMP) has an ongoing program to characterize the particulate matter in air in the vicinity of Yucca Mountain. Information from the National Atmospheric Deposition Program/National Trends Network (NADP/NTN 2001 [DIRS 154843]) on the annual deposition of ionic species supplements this data collection.

The National Atmospheric Deposition Program/National Trends Network has been monitoring the deposition of several ionic species throughout the United States. The ionic species include chloride, sulfate (SO_4), nitrate (NO_3), sodium, calcium, magnesium, and potassium. Included in this program is a monitoring station at Red Rock Canyon (Site NV00) in Clark County, Nevada, where monitoring has been ongoing since 1985. The deposition rates (kilogram/hectare) of these ions are listed in Table 7.3.1-4.

The deposition rates for nitrate and sulfate are well in excess of the corrosively aggressive chloride. The nitrate and sulfate contents of waters have a mitigating effect on the aggressiveness of the chloride (see Section 7.3.5.4). In addition, sulfate ion may remove calcium from solution during evaporative concentration to brines as relatively insoluble calcium sulfate minerals (e.g., gypsum and hemi-hydrate). The calcium and magnesium content reported is due to carbonate.

7.3.1.3.4 Minor Constituents in Yucca Mountain Waters

Minor constituents, which may be present in waters that contact the EBS components, may enhance the degradation of these components. Minor constituents such as lead, arsenic, and mercury are of concern. The following discussion addresses the issues of lead content in natural waters and those phenomena that may limit the aqueous lead content. Future work will address the industrial experience of lead-, mercury-, and arsenic-enhanced corrosion and the content of

these elements in natural waters. These studies and laboratory testing for trace constituent solubility in concentrated brines are expected to improve uncertainties associated with minor constituents in water contacting the waste packages and drip shields.

Ambient Lead Groundwater Geochemistry at Yucca Mountain–Lead concentrations measured in groundwater in the vicinity of Yucca Mountain occur at trace levels (Perfect et al. 1995 [DIRS 101053]). The median lead concentrations of groundwater samples (those which had reported Pb concentration) collected within a 100,000-km^2 area in the southern Great Basin, which includes Yucca Mountain and the Nevada Test Site, is 9 ppb (Perfect et al. 1995 [DIRS 101053]; Lee 2001 [DIRS 155241]). The median value for Pb concentration was obtained from the data by using only those entries for which there is a reported Pb concentration. Of the 3,733 entries, 399 have values for Pb. A median of 9 ppb is obtained when only Pb concentration entries greater than or equal to zero are considered. This corresponds to 256 entries (Lee 2001 [DIRS 155241]). Two samples collected from the Obsidian Butte Brine Pond Site have lead concentrations near 3 ppm. The possible sources of lead at Yucca Mountain include trace concentrations present in the volcanic rock and foreign sources, perhaps wind-blown sediments or aerosols.

Waters with a range of chemical compositions are expected to come in contact with EBS components at Yucca Mountain. As discussed in Section 7.3.1.3.1, two types of water have received the most attention based on their chemical composition. The first type is water similar in composition to water from well J-13, a water-supply well near Yucca Mountain (Harrar et al. 1990 [DIRS 100814]). J-13 well water was used as the basis for estimating the chemistry of drift seepage water in a recent performance assessment (CRWMS M&O 1998 [DIRS 108004]). Perfect et al. (1995 [DIRS 101053]) reported J-13 well water analyses. In one sample, 3 ppb lead was detected; in the other sample, no lead was detected.

Another assessment of the chemistry of seepage water at Yucca Mountain suggests using a pore water-type composition from rocks in the Paintbrush (PTn) hydrostratigraphic unit in the unsaturated zone (UZ) above the repository (Sonnenthal and Bodvarsson 1999 [DIRS 117127]). The Paintbrush unit is a nonfractured tuff unit directly above the repository horizon unit, the Topopah Springs tuff (TSw). Although lead analyses of the Paintbrush pore water could not be found, it is likely that dissolved lead concentrations are similar to the trace concentrations reported in the surrounding groundwater.

The trace lead levels measured near Yucca Mountain are similar to lead concentrations measured in other natural groundwater. For example, dissolved lead is less than 1 ppb in the Gorleben aquifer in Germany (Lieser and Ament 1993 [DIRS 154845]). Even in groundwaters that contact lead-contaminated sediments, the levels are not high. For example, pore water measured in lead-contaminated estuarine sediments are less than 5 ppb (Carroll et al. 1999 [DIRS 154744]).

Dissolved lead concentrations in groundwater are controlled by lead adsorption on mineral surfaces and organic matter, as well as by precipitation of lead minerals (e.g., carbonates, sulfides, and phosphates) (Drever 1997 [DIRS 147480], pp. 189 to 192).

Current geochemical models may not adequately predict the processes that control lead concentration (e.g., EQ3/6 V7.2b). Ion exchange and sorption, which may reduce lead concentration, are not included in the models. Also, aqueous complexes that may be important in controlling lead concentration (Rickard and Nriagu 1978 [DIRS 154847]; Ferri et al. 1987 [DIRS 154849]; Bilinski and Schindler 1982 [DIRS 144730]) are not considered in these models.

The lead uptake onto minerals at Yucca Mountain has not been experimentally determined but, based on literature studies of other waters containing minerals found at Yucca Mountain (e.g., smectite, illite, zeolites, amorphous silica, cristobalite), it is expected that sorption of lead to those mineral surfaces is important in limiting lead concentration in groundwater at Yucca Mountain. For example, pure mineral separates suspended in groundwater show that lead is concentrated on quartz, kaolinite, calcite, and smectite (bentonite) surfaces. The greatest sorption coefficient (i.e., the ratio of lead on mineral phase to lead in solution) was measured for smectite (Freedman et al. 1994 [DIRS 155016]). The enhanced lead uptake is due to lead exchange for calcium in smectite interlayers (Siantar and Fripiat 1995 [DIRS 154850]; Nagy and Konya 1998 [DIRS 154851]). Roy et al. (1993 [DIRS 154852]) also report lead sorption to kaolinite and illite in complex ash-water suspensions at pH 12. In the absence of these minerals, lead remained dissolved in the solution.

Evaporative Evolution of Yucca Mountain Groundwaters and Lead Chemistry–Rosenberg et al. (2000 [DIRS 152766]) recently examined the evaporative evolution of both simulated J-13 well water and simulated PTn pore water from the UZ in a series of subboiling laboratory experiments, with and without crushed tuff present. The study did not include lead analysis, but is relevant nonetheless in terms of expected pH and mineral precipitation.

J-13 Well Water–The J-13 well water experiments indicate loss of calcium, magnesium, and HCO_3 from solution as carbonates, with magnesium likely going into a slightly disordered $CaCO_3$ phase. Evaporation produced an alkaline Na-HCO_3-CO_3 brine. The pH stabilized at about 10 after an approximately 50-fold concentration. After 1000-fold concentration, amorphous silica, aragonite, and calcite had precipitated from solution. Some clays also formed after complete evaporation.

Unsaturated Zone Pore Waters–After approximately 1000-fold concentration, the solution lost calcium and SO_4, suggesting removal of these species as gypsum. Aqueous concentrations of magnesium, fluoride, HCO_3, and SiO_2 also decreased with evaporation, suggesting some carbonate precipitation as well. The pH stabilized at about 6. Evaporation of this water produced a Na-K-Ca-Mg-Cl-NO_3 brine. The minerals recovered after complete evaporation contain a magnesium-smectite.

These experiments show that minerals that precipitate during evaporation of Yucca Mountain waters produce phases known to sorb lead (Wang and Stumm 1987 [DIRS 154853]). Additional experiments are in progress to determine the partitioning of lead between the precipitated minerals, candidate surfaces, and brine solutions during evaporative concentration.

7.3.1.4 Temperature Effect on Aqueous Solution Occurrence

The controlling factors for occurrence of aqueous solutions are relative humidity, temperature, and the particular salt. As discussed previously, the deliquescence point for most salts is temperature-dependent. In general, deliquescence points increase with decreasing temperature. However, ionic strengths of the salt solutions formed at the deliquescence points are very high, independent of temperature (CRWMS M&O 2000 [DIRS 151568], Section 6.4.1).

The effect of the hygroscopic nature of $NaNO_3$ on controlling the occurrence of aqueous solutions on the waste package and drip shield was discussed previously (CRWMS M&O 2000 [DIRS 151568], Section 6.4.1). The hygroscopic nature of $MgCl_2$ and $CaCl_2$ allows the formation of aqueous solutions at temperatures in excess of 155°C at very low relative humidities. The accelerating effect of temperature on corrosion will make these solutions more aggressive. A lower-temperature operating mode may offer an advantage in that if these salts are present, this higher-temperature corrosion mode will not occur.

As discussed in Section 7.3.1.3.1, the quantity of these salts and their saturated solutions that could form on the waste package and drip shield surfaces is expected to be limited. In addition, over the entire temperature range, the solutions will be very concentrated at the deliquescence point. With increasing relative humidity, aqueous solutions become more dilute and other, less hygroscopic salts deliquesce. The formation of mixed-ion solutions then becomes more probable. Hence, the time period when these conditions are operative is necessary for understanding their corrosive effect. Anions such as nitrate, carbonate, fluoride, and sulfate are known to mitigate against the aggressiveness of chloride-enhanced corrosion (Thomas 1994 [DIRS 120498]). The project data confirm that the presence of these ions in solution reduces the aggressiveness of chloride ions to Alloy 22 corrosion (CRWMS M&O 2000 [DIRS 144229], Section 6.4). A recent project data indicates that nitrate ions can mitigate against the aggressiveness of chloride ions to Alloy 22 corrosion even in nearly saturated calcium chloride solutions at 120°C (Pasupathi 2001 [DIRS 155252]). An additional discussion on effects of environment on Alloy 22 corrosion is contained in Section 7.3.5.4.

7.3.1.5 Summary and Conclusions

Aqueous films will develop on the waste package and drip shield surfaces either by deliquescence of hygroscopic salts or evaporative concentration of the dilute waters contacting these EBS components. The chemical characteristics of these aqueous films will determine the extent of the electrochemical corrosion processes that occur on these components.

The range of water chemistries that contact the waste package and drip shield is constrained by the natural system. Dilute natural waters can evolve into high-pH, sodium-carbonate brine or into near-neutral-pH brine. The high-pH brine is primarily composed of sodium salts, while the near-neutral-pH brine may contain calcium and/or magnesium ions. Precipitated salts from the near-neutral-pH brine may contain chlorides salts of magnesium and/or calcium. These are very hygroscopic salts (i.e., they form aqueous solutions at very low relative humidities). However, because the soluble amounts of calcium and magnesium ions in the solution would decrease significantly during evaporation by the formation of insoluble precipitates, large quantities of seepage water would be necessary to provide significant quantities of these ions in concentrated

solutions. Other salts may also dissolve to a limited extent in these aqueous solutions. In addition, with rising relative humidities other precipitated salts will deliquesce, and hence mixed-ion solutions are more likely. Anions such as nitrate, carbonate, fluoride, and sulfate are known to mitigate against the aggressiveness of chloride-enhanced corrosion (Thomas 1994 [DIRS 120498]). The project data confirm that the presence of these ions in solution reduces the aggressiveness of chloride ions to Alloy 22 corrosion (CRWMS M&O 2000 [DIRS 144229], Section 6.4). A recent project data indicates that nitrate ions can mitigate against the aggressiveness of chloride ions to Alloy 22 corrosion even in nearly saturated calcium chloride solutions at 120°C (Pasupathi 2001 [DIRS 155252]).

The ventilation system could bring soluble salts into the drifts. The extent of this contribution to the chemical composition of aqueous films in contact with the waste packages and drip shields may be estimated from rain deposition data. Sulfate and nitrate concentrations are higher than the chloride concentration, and calcium and magnesium are in the form of carbonate salts. The sulfate ions would remove calcium from concentrated solutions as calcium sulfate. The contribution of the soluble salts entrained in the ventilation air would then be expected to diminish the amounts of magnesium and calcium chloride solutions that might form.

The concentration of lead in natural dilute waters is low, and lead is not expected to concentrate to a significant extent because of precipitation as an insoluble species. Acidic conditions, where the solubility is high, are not expected to occur.

7.3.2 Aging and Phase Stability

7.3.2.1 Overview

7.3.2.1.1 Goal of Model

In the mill annealed condition, Alloy 22 is primarily a single-phase, face-centered cubic (FCC) solid solution with excellent corrosion resistance in a wide range of environmental conditions. Over time, other phases can precipitate out and degrade both the mechanical properties and the corrosion resistance of the alloy. The goal of this model is to determine whether the single-phase solid solution is stable under repository conditions, and if not, how fast other phases might precipitate. Precipitation kinetics in the annealed base metal, as well as in the annealed and laser-peened welds, must be modeled. In the TSPA-SR (CRWMS M&O 2000 [DIRS 153246]), a corrosion enhancement factor ranging from 1.0 to 2.5 was applied to the closure welds to bound the effects of any phase instabilities. The new scientific data in this section are presented to increase confidence in the conservatism of this approach. The new data, however, do not yet indicate that the enhancement factor should be removed.

7.3.2.1.2 Background

The time it takes for these precipitation reactions to occur increases as the temperature decreases. At the expected repository temperatures, the kinetics of these precipitation reactions are too slow to measure experimentally. For this reason, the rates at which they occur are measured at temperatures that are high with respect to expected repository temperatures and then extrapolated to lower temperatures. Extrapolation from the relatively short laboratory time frame (tens of years) to the long repository time frame (tens of thousands of years) must be done over durations

spanning orders of magnitude. Because of the extended time period over which the extrapolation is done, small changes in the short-term data can have a large effect on the predicted results (CRWMS M&O 2000 [DIRS 147639], pp. 133, 134, 139, Figure 98). Theoretical calculations should be used to establish confidence in such extended extrapolations.

Several of the phases that form in Alloy 22 are Frank-Kasper, tetrahedrally close-packed (TCP) phases (Shoemaker and Shoemaker 1988 [DIRS 154989], pp. 19 to 45, Section 4): μ, P, and σ. These phases tend to be rich in molybdenum and/or chromium (Raghavan et al. 1984 [DIRS 154707], p. 789, Tables III and IV). Since these elements are largely responsible for the corrosion resistance of Alloy 22, precipitation of TCP phases can lead to degradation of the corrosion properties. The TCP phases are also very brittle and tend to precipitate (at least initially) on grain boundaries, leading to a reduction in the toughness and, to a lesser extent, the ductility of Alloy 22 (Summers et al. 1999 [DIRS 146915], pp. 922 to 923, Figures 2 and 3). As discussed below, the available data suggest that precipitation of these phases would be kinetically inhibited at expected repository temperatures. These data, however, were qualitative and had a large uncertainty associated with them; they were taken over a five-year time period and extrapolated to 10,000 years. A bounding argument was made in *Aging and Phase Stability of Waste Package Outer Barrier* (CRWMS 2000 [DIRS 147639], Section 6.2) to account for uncertainty in the short-term data. With the bounding structure, it was determined that the corrosion rate of Alloy 22 was enhanced by a factor of 2.5 (CRWMS M&O 2000 [DIRS 144229], Section 6.7.3). Theoretical calculations have since been done (see Section 7.3.2.2) to support the short-term experimental data. These calculations require more quantitative experimental support to reduce uncertainties. The amount of precipitation is currently being quantified as a function of time and temperature in order to do this.

At temperatures below approximately 600°C, long-range ordering (LRO) occurs in Alloy 22. This ordering has been linked to an increase in the susceptibility of similar nickel-chromium-molybdenum alloys to hydrogen embrittlement and stress corrosion cracking. It was tentatively concluded from very limited short-term data that LRO would not occur as long as the temperature was kept below about 260°C (CRWMS M&O 2000 [DIRS 147639], Section 6.5). New data, discussed below, indicate that this temperature limit is conservative. Again, theoretical calculations have been done to determine the rate at which ordering occurs, but conclusions from these calculations will remain uncertain until some experimental validation is done.

Welding produces a cast microstructure with chemical segregation regardless of the alloy used. In Alloy 22, segregation of primarily molybdenum causes TCP phases to precipitate during welding (Cieslak et al. 1986 [DIRS 104966], p. 2041). The chemical segregation of an as-welded structure, as well as these TCP phases, can result in degradation of the mechanical and corrosion properties of Alloy 22 welds when compared to the base metal. Although no enhanced corrosion rate was seen for welded Alloy 22 samples in long-term immersion tests involving chemical environments relevant to the potential repository at Yucca Mountain (CRWMS M&O 2000 [DIRS 144229], Section 6.5.2), no sensitive measurements have yet been made on Alloy 22 welds with a thickness that would be typical of the current waste package design in relevant environments. Data available from Alloy 22 immersion testing using the standard American Society for Testing and Materials (ASTM) G28A method (ASTM 3.02, *Standard Test Methods of Detecting Susceptibility to Intergranular Corrosion in Wrought, Nickel-Rich,*

Chromium-Bearing Alloys [DIRS 154712]) with a boiling solution of 50 percent H_2SO_4 and 42 g/l of $Fe_2(SO_4)_3$ indicate that the weld could have a corrosion rate that is approximately 2 to 2.5 times that of the annealed Alloy 22 base metal (Summers et al. 2000 [DIRS 154854], Figure 5; Heubner et al. 1989 [DIRS 107792], p. 256, Table 4). A similar enhancement of the corrosion rate of Alloy 22 welds was seen in boiling 2.5 percent HCl (Summers et al. 2000 [DIRS 154854], Figure 12). In 4M chloride solution at 95°C (pH = 8), the general corrosion rate of Alloy 22 welds was found to be comparable to the base metal (Dunn et al. 1999 [DIRS 154481], pp. 3 to 5). An enhancement factor of 2.5 for the general corrosion rate of unannealed Alloy 22 welds over that of annealed base metal is reasonable, and may even be conservative.

Growth of TCP phases in Alloy 22 welds due to thermal aging causes a further reduction of the corrosion resistance and mechanical properties of the weld. The kinetics of the reactions that occur in the weld may be different than those discussed above for the base metal because the precipitates are already nucleated in the weld and there is chemical segregation. New preliminary data (see Section 7.3.2.2) do not indicate that further nucleation and growth of TCP phases in Alloy 22 welds will occur at temperatures below approximately 200°C. Given the short-term nature of these data, conclusions will remain uncertain until theoretical calculations that take into consideration the numerous phases involved, their compositions, and segregation in the weld are performed and experimentally validated.

The planned solution and induction annealing of Alloy 22 welds will likely improve their corrosion resistance and mechanical properties. Growth of TCP phases in the welds will also occur at a rate somewhere between that seen for TCP phase nucleation and growth in annealed Alloy 22 base metal and that seen for unannealed weld metal. Heating outside the intended hot zone during induction annealing could nucleate TCP phases in the surrounding base metal, which may locally affect corrosion resistance and precipitation kinetics. The effect of such TCP phase nucleation is currently being investigated. Cold work due to laser peening may enhance both the corrosion rate of the weld and the TCP phase precipitation and LRO kinetics; these effects are also currently under investigation.

7.3.2.2 New Scientific Data Supporting the Model

This section discusses new scientific data and analyses conducted for thermal aging and phase stability of Alloy 22 since the completion of the TSPA-SR (CRWMS M&O 2000 [DIRS 153246]). As discussed previously, in the TSPA analysis, a corrosion enhancement factor with a range of 1.0 to 2.5 was applied to the closure welds to bound the effects of any phase instabilities. The new scientific data and analyses in this section support and enhance confidence in the conservatism of this approach. The new data, however, do not yet indicate that the enhancement factor should be removed.

7.3.2.2.1 Critical Temperature for Long-Range Ordering

The current model (CRWMS M&O 2000 [DIRS 147639], Section 6.5) for LRO in Alloy 22 was determined from the shortest times at which LRO was observed in Alloy 22 (annealed base metal). The model indicates that LRO is not likely to occur in 10,000 years as long as the temperature is kept below approximately 260°C for significant time periods (CRWMS

M&O 2000 [DIRS 147639], Section 6.5). This critical temperature is reached by solving Equation 5 in *Aging and Phase Stability of Waste Package Outer Barrier* (CRWMS M&O 2000 [DIRS 147639], Section 6.5) for a time of 8.8×10^7 hours (10,000 years), noting that T is temperature in Kelvin. New data (Figure 7.3.2-1) indicate that a critical temperature of 300°C is more realistic for the same time period.

A sample aged for 1,000 hours at 482°C was examined with transmission electron microscopy. No evidence of LRO was observed. This point falls very close to the line in Figure 7.3.2-1, suggesting that the new data are more realistic than the data used in the TSPA-SR (CRWMS M&O 2000 [DIRS 153246]). As an estimate for the uncertainty in the critical temperature, the data were extrapolated using the points at 538°C for 100 hours and 482°C for 1,000 hours in one case, and the points at 482°C for 1,000 hours and 427°C for 20,000 hours in another. The critical temperatures obtained for these cases were 289°C and 309°C, respectively. A realistic critical temperature for the occurrence of LRO in 10,000 years is thus 300 ± 11°C. This value may be conservative because the kinetics are calculated for an isothermal anneal (i.e., at a constant temperature). The waste package temperature in the repository peaks below 200°C and decreases over time (CRWMS M&O 2000 [DIRS 148384], Section 6.3.1). The extrapolation of short-term data over long time periods is being verified theoretically.

7.3.2.2.2 Theoretical Modeling of Precipitation of Tetrahedrally Close-Packed Phases and Long-Range Ordering in Alloy 22

Theoretical modeling was performed to determine phase diagrams and other thermodynamic properties of the phases that form in Alloy 22. It was also used to calculate the rate at which the relevant phase transformations occur (Turchi 2001 [DIRS 154934]).

The stability of the binary nickel-chromium, nickel-molybdenum, and molybdenum-chromium alloys and of the ternary nickel-chromium-molybdenum alloys was investigated. The study also focused on the role of additional solutes, such as silicon, carbon, cobalt, niobium, tantalum, and tungsten, on stability, ordering, and precipitation in Alloy 22. Figure 7.3.2-2 shows, as an example, the phase fraction versus temperature for Alloy 22 using a composition of 21.2Cr-13.5Mo-4Fe-3W-2Co-0.5Mn-0.3V-0.08Si-0.01C-bal. Ni (wt. percent). These results indicate that the TCP phases (P and probably μ) are stable at repository temperatures and will form if they are not kinetically inhibited. It is also apparent in Figure 7.3.2-2 that preparing samples for measurements of the corrosion and mechanical properties must be done considering the temperature range at which the relevant phases form. The phases that would be stable under potential repository conditions form at temperatures below approximately 800°C. Sigma phase forms at higher temperatures, but is not stable at the lower temperatures expected in the potential repository.

Kinetic and thermodynamic modeling were combined and applied to the study of diffusion-controlled transformations (Turchi 2001 [DIRS 154943]). These kinetic studies were focused on the time-dependent formation of complex TCP phases and LRO in terms of phase evolution from the FCC matrix for times up to 10,000 years. To date, a first series of calculations has been performed to predict the time-temperature-transformation (TTT) diagram for the case of the 10 percent transformation of an FCC-based nickel-chromium matrix in the ordered Ni_2Cr phase where experimental results were available (Karmazin 1982

[DIRS 154881]). A second series of simulations was done for the case of a ternary nickel-chromium-molybdenum alloy with a nominal composition of 55.7Ni-21.1Cr-13.5Mo (wt. percent). The transformation of P-phase from the FCC-based matrix ranging from 1 to 20 percent was considered as a function of time and temperature. These results are superimposed over the TTT diagrams reported in *Aging and Phase Stability of Waste Package Outer Barrier* (CRWMS M&O 2000 [DIRS 147639], Figure 96) in Figure 7.3.2-3. The results in Figure 7.3.2-3 are comparable to those in *Aging and Phase Stability of Waste Package Outer Barrier* (CRWMS M&O 2000 [DIRS 147639], Figure 96). A quantitative analysis of phase formation in samples annealed at various temperatures and for several aging times is being done to reduce uncertainties in this study's conclusions. In these simulations, grain boundary formation is not considered. Precipitation on grain boundaries, which is observed, occurs at a faster rate than bulk precipitation, which was treated here.

7.3.2.2.3 Weld Stability

Gas-tungsten-arc welds, which were made from 0.5-inch thick Alloy 22 base metal in a single V groove configuration using nine passes, were examined using optical microscopy at magnifications of 200 and 400 times. These welds were produced and aged at 593°, 649°, 704°, and 760°C for times up to 1,000 hours at Haynes International, Inc. in Kokomo, Indiana (Summers et al. 2000 [DIRS 154854]). Volume fraction measurements were also made. The measurements to date are preliminary. The amount and size of precipitates in the welds vary with position in the weld. For example, relatively few and smaller precipitates tend to be present near weld pass boundaries, while many larger precipitates tend to be present at the top of the last weld pass (CRWMS M&O 2000 [DIRS 147639], Figure 68). The measurements presented here represent averages over several positions in the weld. Future studies will correlate precipitate amount with location in the weld. These welds are also much thinner than those called out in the current waste package design. Welding conditions, such as heat input, that might affect the starting weld structure and the subsequent precipitation kinetics will be different for thicker welds. A study of precipitation kinetics in thicker welds is currently planned. Also, several phases are expected in Alloy 22 welds; σ, μ, and P have been observed (Cieslak et al. 1986 [DIRS 104966], p. 2041). The growth kinetics for each of these phases may be different. In the base metal, it is likely that the amount of σ-phase precipitating is small at temperatures below about 750°C and that μ- and P-phases are similar. In the weld, however, the amount of σ-phase may be quite high due to chemical segregation. More refined studies that take these factors into account are being done to reduce uncertainties associated with conclusions drawn about weld stability.

In the as-welded condition, the volume fraction of precipitates measured was 0.029 at 200-fold magnification and 0.025 at 400-fold magnification. The times required for this volume fraction to increase to 0.05 and 0.10 are listed as a function of temperature in Table 7.3.2-1. These times are plotted against reciprocal temperatures in Figure 7.3.2-4.

The data in Figure 7.3.2-4 are for isothermal conditions. The temperature of the repository is expected to peak below 200°C and decrease over thousands of years. Weld stability does not appear to be a problem for Alloy 22. Because the extrapolation is done over very long times from relatively short-term data, very small changes in the measured data can cause a shift in the extrapolated cutoff temperature to give a 10,000-year life of a hundred degrees or more.

Theoretical calculations similar to those being made for TCP phase precipitation will be done to account for any uncertainties associated with segregation in the welds, the different phases present, and the other experimental difficulties mentioned above.

7.3.2.3 Effect of Temperature on Precipitation Kinetics

The time to cause precipitation reactions in Alloy 22 is exponentially dependent on temperature. For example, a curve fit to the data in Figure 7.3.2-1 yields:

$$time = 3.0 \cdot 10^{-13} \exp\left(\frac{27098}{T}\right) \qquad \text{(Eq. 7.3.2-1)}$$

where T is temperature in Kelvin and *time* is in hours. This exponential temperature dependence is very strong. Solving Equation 7.3.2-1 for T = 673 K (400°C) yields a time of 90,000 hours (10 years). At 573 K (300°C), the time is 10^8 hours (10,000 years), an increase of four orders of magnitude. Further reductions in temperature have similar orders of magnitude increases in time.

The temperature dependence in Equation 7.3.2-1 assumes the temperature remains constant. The temperature of the waste package is not expected to be constant. It has been calculated to peak below about 200°C and decrease over time (CRWMS M&O 2000 [DIRS 153246], Section 3.3.3). Thus, estimates based on isothermal conditions are conservative. Because of the strong temperature dependence of the rate of these precipitation reactions, the margin in the conclusion that phase instabilities will not occur greatly increases as temperature decreases.

7.3.2.4 Alternative Lines of Evidence to Support Model

7.3.2.4.1 Critical Temperature for Precipitation of Tetrahedrally Close-Packed Phases

The data available for the phase stability of Alloy 22 base metal used in the TSPA-SR (CRWMS M&O 2000 [DIRS 153246]) did not indicate that precipitation of TCP phases is likely even at 300°C for 10,000 years (CRWMS M&O 2000 [DIRS 147639], Section 6.2). These data, however, had a large degree of uncertainty, so a bounding argument was made to account for this uncertainty. The mechanical and corrosion properties of aged Alloy 22 have been measured (Rebak et al. 2000 [DIRS 146910]). The times to give a degradation of the Charpy impact toughness from 264 to 150 ft-lb and the times to cause an increase in the corrosion rate, measured with the ASTM G28A procedure (ASTM 3.02 [DIRS 154712]), from 0.8 to 2.03 mm/year were extrapolated to 10,000 years. These data are reproduced with estimated error bars in Figure 7.3.2-5. The uncertainty associated with these data is much less than that associated with the data in *Aging and Phase Stability of Waste Package Outer Barrier* (CRWMS M&0 2000 [DIRS 147639], Section 6.2). Extrapolation of these data indicates that the phase instabilities that cause this property degradation will not occur in 10,000 years, even at temperatures much higher than 300°C.

According to Figure 7.3.2-5, the time at which the ASTM G28A (ASTM 3.02 [DIRS 154712]) corrosion rate reaches 80 mpy is approximately 7 hours at 704°C. The time at which the Charpy impact toughness decreases to 150 ft-lb is 60 hours at 704°C. The fully aged structure used as a

bounding case for the TSPA-SR model was created by aging Alloy 22 base metal for 173 hours at 700°C (CRWMS M&O 2000 [DIRS 153246]). These data indicate that the microstructural changes responsible for the degradation of the mechanical and corrosion properties at relatively high temperatures are not likely to occur under expected repository conditions.

7.3.2.4.2 Natural Analogues

Awaruite is a naturally occurring, ordered iron-nickel metallic mineral with an approximate stoichiometry of Ni_3Fe. It was first discovered in Awarua, New Zealand, but has been found at various locations around the world (Krishnarao 1964 [DIRS 154746], p. 443). Josephinite, a rock found in Josephine County, Oregon, contains grains of awaruite that are larger than other sources of awaruite. Josephinite also has, in some instances, a unique mixture of minerals that has been tied to changes in the local environment and higher temperatures associated with hornblende diorite dikes from igneous intrusions (Dick 1974 [DIRS 154749], p. 297; Göpel et al. 1990 [DIRS 154750], p. 26). The age of these dike intrusions has been measured, using potassium-argon dating, at approximately 150 to 155 million years (Dick 1974 [DIRS 154749], p. 292). Other nearby rocks also associated with the formation of josephinite have been dated, using lead isotopes, at 159 ± 8 million years (Göpel et al. 1990 [DIRS 154750], p. 24). Thus, the age of josephinite is on the order of 150 million years.

Some samples of josephinite contain taenite (the high-temperature, disordered, FCC Ni-Fe metallic phase) as well as awaruite. The composition and amount of each of these phases in the two-phase mixture have been fit to the Fe-Ni phase diagram, showing that these phases formed in the temperature range of 460° down to about 400°C (Botto and Morrison 1976 [DIRS 154716]). The fact that the composition and amount of these phases fits the phase diagram at the higher temperatures indicates that no changes have occurred at lower temperatures. Taenite is not stable below about 350°C; α-Fe and awaruite are the stable phases at ambient temperatures. The fact that taenite, not α-Fe, is present in josephinite also indicates that no changes have occurred in the 150 million years since these samples formed.

Out of necessity, phase stability is studied at temperatures greater than those expected in the repository so the rate at which phase changes occur can be measured. These rates are measured as a function of temperature, and the functional relationship is extrapolated to the lower repository temperatures. The stability of the metallic structures in josephinite over millions of years suggests no low-temperature mechanism with rates significantly greater than those predicted exists, thus providing confidence in the implicit assumption that the high-temperature mechanisms used to extrapolate kinetics are the same as the low-temperature mechanisms that will be active under repository conditions.

7.3.3 Stress Corrosion Cracking

Stress corrosion cracking is a potential degradation mode that can result in penetration of the waste package outer barrier material (Alloy 22). Stress corrosion cracking of materials may occur when an appropriate combination of material susceptibility, tensile stress, and environment is present. The current analysis assumes conservatively that, in the presence of tensile stress, Alloy 22 is susceptible to stress corrosion cracking in any environment that can have a stable water film form on the waste package surface, irrespective of the chemistry of the water film

(CRWMS M&O 2000 [DIRS 151566], Section 5.7). This is based on industrial experience with stress corrosion crack failures of recirculating coolant pipes in a boiling water reactor. The recirculating coolant is high-purity, neutral-pH water (ASM International 1987 [DIRS 103753], p. 930).

The closure of the waste package outer barrier is designed to include two lids with two separate post-weld stress mitigation processes: laser peening of the inner lid welds and induction annealing stress relief of the outer lid welds. This two-lid design and stress mitigation strategy form part of the basis for the stress corrosion crack model. In the TSPA-SR stress corrosion cracking is assumed to occur only in the regions around the closure welds of the waste package outer barrier because the residual stress in the closure welds cannot be relieved completely by stress mitigation techniques (CRWMS M&O 2000 [DIRS 151566], Section 5.6). It is assumed that all welds used in the fabrication of the waste package outer barrier (other than the closure welds) and the Titanium Grade 7 drip shield are fully annealed, and thus are not subject to stress corrosion cracking (CRWMS M&O 2000 [DIRS 151564], Section 5.0). The approach is also employed in the current analysis. Stress corrosion cracking of the drip shield is possible under the applied stresses resulting from rockfall; however, it is assumed to be of low consequence to drip shield performance, so it is not modeled in the analysis described in *Stress Corrosion Cracking of the Drip Shield, the Waste Package Outer Barrier, and the Stainless Steel Structural Material* (CRWMS M&O 2000 [DIRS 151564], Section 6.5.5).

7.3.3.1 Goal of the Analysis

The TSPA-SR analysis uses the slip dissolution model for stress corrosion crack analysis of the waste package (CRWMS M&O 2000 [DIRS 151566], Section 3.2.4). The slip dissolution model calculates the stress corrosion crack propagation rate, V, as a function of the local exposure environment (represented by parameter n for the repassivation rate [or repassivation slope] at the crack tip) and the stress intensity factor, K_I (CRWMS M&O 2000 [DIRS 151564], Section 6.4.4):

$$V = \overline{A}\left(K_I\right)^{\overline{n}} \qquad \text{(Eq. 7.3.3-1)}$$

where V is the crack growth rate in mm/s and K_I is the stress intensity factor in MPa $(\text{m})^{1/2}$. Parameters $\overline{A}$ and $\overline{n}$ in the above equation are expressed in terms of the repassivation rate, n, as follows:

$$\overline{A} = 7.8x10^{-2}\, n^{3.6}\left(4.1x10^{-14}\right)^{n} \qquad \text{(Eq. 7.3.3-2)}$$

$$\overline{n} = 4n \qquad \text{(Eq. 7.3.3-3)}$$

The slip dissolution model has been used in the boiling water reactor industry as a crack propagation prediction tool (ASM International 1987 [DIRS 103753], p. 930) and is accepted by the NRC (Carpenter and Lund 1999 [DIRS 154988]). The time-to-failure from stress corrosion cracking (i.e., the time to through-wall penetration by a stress corrosion crack) is determined by integrating the calculated propagation rate. Thus, the residual stress and corresponding stress intensity factor are important parameters in the stress corrosion cracking analysis for the slip

dissolution model (CRWMS M&O 2000 [DIRS 151549], Section 6.4). Another important parameter is the threshold stress for stress corrosion crack initiation. The current model assumes that stress corrosion cracking initiates only if the threshold stress is exceeded at the tip of an "intrinsic" flaw or a weld flaw (CRWMS M&O 2000 [DIRS 151564], Section 6.5.2). In addition, because stress corrosion cracks initiated from weld flaws are likely the ones that fail waste packages (CRWMS M&O 2000 [DIRS 151566], Section 6.5.2), the size, frequency, and orientation of weld flaws are also important to the stress corrosion cracking analysis of waste packages. The goal of the analyses discussed in this section is to reexamine the uncertainties and conservatism in the important stress corrosion cracking model parameters in the TSPA-SR analysis (CRWMS M&O 2000 [DIRS 153246]) and to quantify and update their uncertainties by incorporating the data and analyses that have become available since the completion of the TSPA-SR.

7.3.3.2 Identification of Unquantified Uncertainties in Total System Performance Assessment-Site Recommendation

As discussed above, this section reviews approaches to treating uncertainties associated with the stress corrosion cracking model parameters in the TSPA-SR model This section also identifies stress corrosion cracking model parameters for which uncertainties were not quantified or for which an excessive conservatism was employed in the analysis. In particular, the important stress corrosion model parameters reviewed in this section are:

- Parameter *n* in the slip dissolution model
- Residual stresses in the outer and inner closure lid welds of the Alloy 22 waste package outer barrier
- Threshold stress for stress corrosion crack initiation in the Alloy 22 outer barrier
- Orientation of weld flaws in the waste package outer barrier closure welds
- Plugging of stress corrosion cracks in the drip shield and waste package outer barrier by calcite precipitation.

Parameter *n* in the Slip Dissolution Model–In the slip dissolution model, the rate of repassivation at the crack tip is captured by the parameter *n*, referred to as the repassivation slope. A characteristic of the slip dissolution (or film rupture model) is that stress corrosion crack susceptibility decreases with increasing values of *n* (CRWMS M&O 2000 [DIRS 151564], Section 6.4.4). In the TSPA-SR (CRWMS M&O 2000 [DIRS 153246]), because limited data were available under repository conditions, the parameter was evaluated based on data for stainless steel in boiling water reactors (CRWMS M&O 2000 [DIRS 148375], Section 3.2.2). Because stainless steels are more prone to stress corrosion cracking than Alloy 22, the parameter estimates are considered conservative. In the *WAPDEG Analysis of Waste Package and Drip Shield Degradation* (CRWMS M&O 2000 [DIRS 151566], Section 4.1.9), *n* is represented by a uniform distribution with an upper bound of 0.84 and a lower bound of 0.75, and the variation of the parameter value is assumed to be due to uncertainty.

From recently obtained longer-term data for Alloy 22 under repository-relevant conditions, the model parameter *n* and its uncertainty have been reevaluated. The parameter is now represented by a uniform distribution with an upper bound of 0.920 and a lower bound of 0.843 (CRWMS M&O 2000 [DIRS 151564], Section 6.4.4). As for the TSPA-SR case (CRWMS M&O 2000 [DIRS 153246]), variation in the parameter value is assumed to be due to uncertainty. With the updated uncertainty distribution for *n*, the through-wall penetration time of a 20-mm thick Alloy 22 layer by stress corrosion cracking increases significantly relative to that obtained using the previous uncertainty distribution (CRWMS M&O 2000 [DIRS 151549], Section 6.4.5). The updated uncertainty distribution for *n* represents the current state of knowledge, and no further characterization and quantification of uncertainty in *n* is attempted in the current analysis.

Closure-Weld Residual Stress Uncertainty–The closure welds of the outer and inner lid of the waste package outer barrier will be treated by induction heating and laser peening, respectively, to mitigate stresses and generate compressive stress at the surface and down to a significant depth. The stress mitigation treatments will be limited to the closure weld area. In particular, the induction heating will be performed in such a way that other areas are not heated to undesirable temperatures. The resulting residual stress profiles in both of the closure lids were calculated, as a function of depth (CRWMS M&O 2000 [DIRS 151564], Section 6.2.2.2). As discussed in the *Abstraction of Models of Stress Corrosion Cracking of Drip Shield and Waste Package Outer Barrier and Hydrogen Induced Corrosion of Drip Shield* (CRWMS M&O 2000 [DIRS 151549], Section 6.3), hoop stress is the dominant stress to potentially drive radial cracks through the wall thickness. Therefore, the profile with the highest hoop stress was used as a mean stress profile for the outer and inner closure lid welds.

Because no measured data are available for the waste package design, the uncertainties in the residual stress were addressed in the TSPA-SR (CRWMS M&O 2000 [DIRS 153246]) by considering three scenarios (optimum, realistic and worst case) for welding and post-weld mitigation operations and assigning separate uncertainty ranges for each scenario (CRWMS M&O 2000 [DIRS 151564], Section 6.2.2.5). The uncertainty bounds for individual scenarios were based on literature data. The optimum case is the best case scenario that is achievable through stringent control of such processes as welding, stress mitigation, material variability, and other fabrication steps, and is represented by the stress uncertainty range of ±5 percent of the yield strength. The realistic case is assumed achievable through appropriate levels of process controls, and is represented with the stress uncertainty range of ±10 percent of the yield strength. The worst case is a case that might result from inadequate control of the processes, represented with the stress uncertainty range of ±30 percent of the yield strength (CRWMS M&O 2000 [DIRS 151564], Section 6.2.2.5). The TSPA-SR (CRWMS M&O 2000 [DIRS 153246]) considers the uncertainty range of the worst case (±30 percent of the yield strength) as the base case, and evaluates the ranges of ±10 percent and ±5 percent of the yield strength in sensitivity analyses (CRWMS M&O 2000 [DIRS 151566], Section 6.2.2.5). The triangular distributions around the mean and the bounds (i.e., ±5, ±10, and ±30 percent of the yield strength) are assumed for the residual stress uncertainty. The TSPA-SR (CRWMS M&O 2000 [DIRS 153246]) base case uncertainty bounds are highly conservative, based on information available in the literature and considering the strict process control and inspections that will be implemented during the waste package manufacturing process.

Additional analyses have been conducted since the completion of the TSPA-SR (CRWMS M&O 2000 [DIRS 153246] to further quantify the residual stress uncertainty and remove the conservatism in the base case. In the absence of measured data for the waste package design, those analyses focused on relevant literature data for similar stress mitigation techniques applied to similar materials (Offer 1983 [DIRS 154454]; Chrenko 1980 [DIRS 154451]; Shack and Ellingson 1980 [DIRS 154456]; Pasupathi 2000 [DIRS 149968]). The outer closure lid weld region of the waste package outer barrier will be induction annealed (CRWMS M&O 2000 [DIRS 144128], Section 6.4). Consideration of the literature data resulted in a revision of the symmetric upper and lower bounds on the stress and stress intensity factor profile uncertainty distribution from ±30 percent to ±21.4 percent. The inner closure lid weld region of the waste package outer barrier will be laser peened (CRWMS M&O 2000 [DIRS 144128], Section 6.4). Consideration of the literature data resulted in the development of a cumulative distribution function for the symmetric upper and lower bounds on the stress and stress intensity factor profile uncertainty distribution. Details of the analyses and uncertainty quantification approach are described in Sections 7.3.3.3.1 and 7.3.3.3.2 for the outer lid and inner lid welds, respectively.

Threshold Stress for Crack Initiation–Although the slip dissolution model assumes crack growth can initiate at any surface flaw that can generate a stress intensity factor, regardless of flaw size and tensile stress, examination of relevant literature (Erbing Falkland 2000 [DIRS 149956], p. 661, Figure 8; Haynes International 1998 [DIRS 154463]) indicates that there is a threshold stress below which stress corrosion cracking will not initiate on a "smooth" surface (i.e., free of surface breaking flaws). In the absence of relevant Alloy 22 test results, literature results on Stainless Steel Type 304 were used to assess the expected stress corrosion crack susceptibility of Alloy 22 in terms of initiation threshold stress. These results were obtained in very aggressive boiling magnesium chloride or in 0.1 M sodium chloride solutions dripped onto stressed specimens heated to 200°C. Under these very aggressive conditions, lower-bound initiation threshold stresses of 20 to 30 percent of the yield strength were observed, so this range was conservatively selected for waste package design applications. Accordingly, in the TSPA analysis, the uncertainty in the threshold stress for initiation of stress corrosion crack is conservatively estimated to be approximately 20 to 30 percent of the Alloy 22 yield strength (CRWMS M&O 2000 [DIRS 151564], Section 6.5.2). A uniform distribution between the bounds is assumed for the threshold stress uncertainty.

However, in these very aggressive environments, initiation stress threshold values for higher nickel-content stainless steels and nickel-base alloys may exceed 80 percent of the yield strength. In the case of Alloy 22 U-bends (10 to 15 percent strain) in boiling magnesium chloride, the initiation threshold may exceed approximately 200 percent of the yield strength (Erbing Falkland 2000 [DIRS 149956], p. 661, Figure 8; Haynes International 1998 [DIRS 154463]). The literature data and YMP measured data generated since completion of the TSPA-SR (CRWMS M&O 2000 [DIRS 153246]) were used to reevaluate the initiation threshold stress and quantify its associated uncertainty. In Section 7.3.3.3.3, it is concluded that the initiation threshold stress should be sampled from a uniform distribution between 80 and 90 percent of the yield strength. Details of the analysis and approach are described in Section 7.3.3.3.3.

Orientation of Manufacturing Flaws in Closure Weld-The waste package analysis considers both incipient cracks and manufacturing flaws. Preexisting manufacturing flaws in the closure

lid welds are the most likely sites for waste package failure by stress corrosion cracking. Therefore, characteristics of flaws in the waste package closure welds are important input to the waste package stress corrosion cracking analysis. In the TSPA-SR (CRWMS M&O 2000 [DIRS 153246]), the frequency and size distributions for manufacturing flaws in the closure welds were developed based on published data for stainless steel pipe welds in nuclear power plants (CRWMS M&O 2000 [DIRS 152097], Section 6.2.1.1). The published data used to develop the manufacturing defect model are those utilizing welding techniques and post-weld inspection methods that are relevant to waste package manufacturing (CRWMS M&O 2000 [DIRS 152097], Section 6.2.1.1).

As discussed previously, the hoop stress is the dominant stress in the closure lid welds, which drives radial cracks through the closure lid weld region. This analysis indicates that only radial flaws are potential sites for through-wall stress corrosion cracking, if it occurs. The TSPA-SR (CRWMS M&O 2000 [DIRS 153246]) assumes conservatively that all manufacturing flaws are oriented in such a way that they could grow in the radial direction in the presence of hoop stresses (CRWMS M&O 2000 [DIRS 151566], Section 5.5). This is a highly conservative assumption. Considering additional literature information and limited measured data from the mockups developed for the viability assessment analysis, analyses were conducted to quantify the uncertainty associated with the orientation of weld flaws in the waste package closure welds. It was determined in Section 7.3.3.3.4 that, based on weld flaw orientation, the fraction of weld flaws capable of propagation in the radial direction should be sampled from a lognormal distribution with a mean of one percent, an upper bound of 50 percent, and lower bound of 0.02 percent. Details of the analysis and approach, along with the quantified uncertainty, are described in Section 7.3.3.3.4.

Plugging of Stress Corrosion Cracks by Calcite Precipitation–Analyses have shown that stress corrosion cracking of the drip shield is possible under the applied stresses resulting from rockfall (CRWMS M&O 2000 [DIRS 149574]). However, the TSPA-SR (CRWMS M&O 2000 [DIRS 153246]) assumed that stress corrosion cracking failure of the drip shield is of low consequence to the intended performance of the drip shield; therefore, it was not modeled in the analysis (CRWMS M&O 2000 [DIRS 153802], Section 3.2.1). The basis of the assumption made in the TSPA-SR (CRWMS M&O 2000 [DIRS 153246]) was as follows. Cracks in passive alloys, such as Titanium Grade 7 or Alloy 22, tend to be very tight (i.e., small crack opening displacement) by nature (CRWMS M&O 2000 [DIRS 151564], Section 6.5.5). The opposing sides of through-wall cracks will continue to corrode at very low passive corrosion rates until the gap region of the tight crack opening is "plugged" by the corrosion product particles and mineral precipitates, such as carbonate, present in the water. Any water transport through this oxide/salt-filled crack area will occur mainly by diffusion-type transport processes (CRWMS M&O 2000 [DIRS 151564], Section 6.5.5). Thus, the effective water flow rate through cracks in the drip shield would be expected to be extremely low and should not contribute significantly to the overall radionuclide release rate from an underlying failed waste package. Therefore, because the primary role of the drip shield is to keep water from contacting the waste package, stress corrosion cracking of the drip shield is of low consequence to waste package performance.

Quantitative bounding analyses have been undertaken to determine whether calcite and other minerals can precipitate at a sufficiently high rate to plug cracks resulting from stress corrosion. In addition to corrosion products, mineral deposits and possibly particulates could increase the

volume of materials and plug the crack faster. The analyses will also determine the time frame at which calcite and other minerals can precipitate in the stress corrosion cracks. The calculation depends mainly on two parameters: the evaporation at the surface of the waste package or drip shield, in particular in the vicinity of cracks, and the precipitation rate of minerals (Nicot 2001 [DIRS 154452]). The analyses focus on the extended cooldown period (from 2,000 to 100,000 years) that occurs after the boiling period (50 to 1,000 years), when stress corrosion cracks still have an impact on the performance of the waste packages. The analyses consider calcite and amorphous silica as minerals that potentially precipitate within the stress corrosion cracks. The analyses consider two end-member scenarios for potential water flow characteristics in the cracks: film flow and water bridging across the crack opening (Nicot 2001 [DIRS 154452], Section 5.3.3). The water bridging scenario employs highly conservative assumptions, such as no corrosion of the crack wall, no mixing of the bridging water with the outside environment, no water transport along the crack wall, and no consideration of mineral precipitate in the presence of fine particulates of corrosion products along the crack wall.

The analysis results show that for the film flow scenario, cracks are plugged by mineral precipitates within a decade (Nicot 2001 [DIRS 154452], Tables 6-3 and 6-5). For the conservative scenario (i.e., water bridging scenario), plugging of stress corrosion cracks takes 600 to 1,000 years if the crack opening occurs prior to 20,000 years (Nicot 2001 [DIRS 154452], Tables 6-4 and 6-6). Considering the conservatism employed in the water-bridging scenario, the time to plugging the cracks would be sooner than the bounding estimates. Because the time periods required for the crack plugging by mineral precipitates are much shorter than the time steps used in the TSPA analysis (CRWMS M&O 2000 [DIRS 153246]), the assumption for the crack plugging is well justified. No further characterization and quantification of uncertainty in the time to plugging the stress corrosion cracks is attempted in the current analysis.

7.3.3.3 Quantification of Model Parameter Uncertainties

This section discusses additional analyses conducted to quantify uncertainties of the important stress corrosion cracking model parameters identified in Section 7.3.3.2. The analyses include new measured data from ongoing YMP testing programs and any new analyses developed. The analyses also incorporate additional literature data and information relevant to the current waste package design and repository exposure environments. As discussed in Section 7.3.3.2, the stress corrosion cracking model parameters to be considered further for uncertainty quantification are:

- Residual stresses in the outer and inner closure lid weld regions of the Alloy 22 waste package outer barrier
- Threshold stress for stress corrosion crack initiation in the Alloy 22 outer barrier
- Orientation of weld flaws in the waste package outer barrier closure welds.

No further uncertainty quantification beyond the discussion presented in Section 7.3.3.2 is undertaken for the parameter n in the slip dissolution model and plugging of stress corrosion cracks in the drip shield and waste package outer barrier by calcite precipitation.

7.3.3.3.1 Uncertainties in Residual Stress in Outer Lid Closure Welds

As discussed in Section 7.3.3, the closure welds of the outer lid of the waste package outer barrier will be treated by induction heating to mitigate stresses and generate compressive stress at the surface and down to a significant depth. The induction heating treatment will be limited to the closure weld area, and will be performed in such a way that other areas are not heated to undesirable temperatures. The resulting residual stress profiles as a function of depth in the outer closure lid welds were calculated (CRWMS M&O 2000 [DIRS 151564], Section 6.2). As discussed in the *Abstraction of Models of Stress Corrosion Cracking of Drip Shield and Waste Package Outer Barrier and Hydrogen Induced Corrosion of Drip Shield* (CRWMS M&O 2000 [DIRS 151549], Sections 5.3 and 6.3.1.1), the profile with the highest hoop stress from the calculated residual stress profiles was used as a mean stress profile for the outer closure lid weld region. This section provides the technical basis and an approach to quantifying the uncertainty in the calculated mean residual stress. It is assumed in this analysis that the stress measurement uncertainty is the primary contributor to the total uncertainty in the residual stress. Because no stress profile data are available for the waste package design, the uncertainty quantification is based on literature data generated for similar stress mitigation techniques, such as the induction heat treatment process referred to as Induction Heating Stress Improvement (IHSI) (Offer 1983 [DIRS 154454]).

The measurement of residual stresses in components may involve the use of one or more techniques to obtain the total stress state. The techniques used may require the destruction of the component to determine the residual stresses, or they may be performed in a totally nondestructive manner. Because the data generated for IHSI utilized the mechanical (strain gage stress relief) and x-ray residual stress techniques for measurement, these two techniques are therefore the focus of this analysis, and the errors and accuracy associated with those techniques are quantified. Those are two of the most popular residual stress measurement techniques. The x-ray residual stress technique is a nondestructive technique; the strain gage stress relief technique is a destructive technique (Offer 1983 [DIRS 154454]).

X-Ray Diffraction Residual Stress Measurements–The x-ray diffraction technique is the most routinely used nondestructive technique for determining surface residual stresses. It determines the stress by measuring the interplanar spacings in the material. If subsurface residual stresses must be measured, then material can be removed (making this method a destructive technique) and the measurement repeated.

The x-ray technique for measuring residual stress is based on the fact that the lattice spacings (d-spacings) of the atomic planes in a crystalline material are altered by stress. The lattice spacings can be measured by determining the angular position of the diffracted x-ray beam (Bragg's Law). This technique is strictly valid for measurements of stress in a material that is homogeneous, isotropic, and elastic. Wrought austenitic stainless steels and wrought nickel alloys generally meet these requirements.

One of the assumptions made in performing x-ray residual stress measurements is that the penetration depth of the x-ray beam is small, so in the volume being examined, the stress perpendicular to the surface is zero because of the lack of constraint at the surface. For steels and nickel alloys using chromium K-alpha radiation, as used in the evaluations reported for the

IHSI-treated welds (Offer 1983 [DIRS 154454]), this assumption is valid because most of the diffracted energy comes from a depth of less than 0.013 mm.

The approach used in making x-ray residual stress measurements on IHSI-treated welds used in the current analysis utilized a combination of strain gage and x-ray results to obtain the total surface residual stress. The error in the strain gage measurement results is within 1.0 ksi (Chrenko 1980 [DIRS 154451]). X-ray residual stress measurements were then performed on the full-thickness pieces of pipe. The total original inside surface residual stress present at a certain location was obtained by algebraically combining the x-ray residual stress with the stress relaxed at that location when the piece was cut out of the original pipe.

Chrenko (1980 [DIRS 154451]) reports that the accuracy of the x-ray residual stress measurements for the types of samples used in the IHSI study was ±34.5 to 48.3 MPa.

Strain Gage Stress Relief Residual Stress Measurements–The strain gages can also be used to obtain near-surface and through-thickness residual stress results by application initially to the outer diameter and inner diameter surfaces of the pipe. When the full thickness bar is parted out, both the outer diameter and inner diameter gages are read. The parting out stress is used for both x-ray and future strain gage residual stress information.

Detailed measurements of the residual stress distributions indicate that, except for the rapidly varying surface stresses, the distribution of residual stress through the thickness of the 101.6 mm weldments investigated is reasonably linear in most cases (Shack and Ellingson 1980 [DIRS 154456]). For a linear distribution, the bulk residual stress as measured by strain gages on the inner and outer surfaces of full wall-thickness specimens gives a good measure of the stress available to drive the crack (Shack and Ellingson 1980 [DIRS 154456]). For thicker pipes (19 mm thick and greater), the approach used—measuring the strain relieved on the inner diameter and outer diameter surfaces, slicing along the neutral plane, then strain gaging the newly created surfaces and repeating the process on thinner and thinner strips—allows investigators to continue the approximation process to the level of accuracy required for the specific application.

Based on the measured data reported in Offer (1983 [DIRS 154454]), the through-thickness strain gage data produced for the IHSI-treated welds was obtained at 3.18 to 6.35 mm increments of depth. For these final thicknesses, linear interpolation was performed to estimate the residual stress state.

Quantification of Uncertainty Due to Measurement Error–The sources of measurement error for the x-ray diffraction residual stress technique are: (1) local surface residual stresses due to cold work, (2) errors in parting out stresses associated with strain gages, and (3) inhomogeneous grain structure. Total error is estimated to be ± 34.5 to 48.3 MPa.

The sources of measurement error for the strain gage residual stress technique are: (1) parting out stresses due to removal of bar by machining, (2) additional machining on neutral surfaces to produce thin strips, and (3) interpolation of results in finite thickness strips.

In reviewing the strain gage residual stresses at various azimuthal locations in a given pipe (Offer 1983 [DIRS 154454]), it was noted that the results usually varied less than ±69 MPa. If it is assumed that this variation is the result of real variations in residual stress due to the welding process added with measurement error, then the measurement error must be less than ±69 MPa (10 ksi). The accuracy of the actual strain gage residual stress values is ±6.9 MPa (1 ksi) (Chrenko 1980 [DIRS 154451]).

Based on the analyses of the x-ray and strain gage measurement errors (Chrenko 1980 [DIRS 154451]) and the azimuthal variation of strain gage residual stresses (Offer 1983 [DIRS 154454]), it is concluded that the measurement error associated with strain gage measurement of surface and through-thickness residual stresses after the induction heating stress mitigation can be bounded by ±69 MPa. Assuming a yield strength of 322 MPa of Alloy 22 at 125°C, the residual stress uncertainty in the outer lid closure welds is bounded by ±21 percent of yield strength of Alloy 22. The same uncertainty bounds are also applied to the corresponding stress intensity factor profile. For comparison, the TSPA-SR base case (CRWMS M&O 2000 [DIRS 153246]) uses ±30 percent of yield strength for the bounds of residual stress uncertainty (CRWMS M&O 2000 [DIRS 151566], Section 4.1.8).

7.3.3.3.2 Uncertainties in Residual Stress in Inner Lid Closure Welds

As discussed in Section 7.3.3, laser peening has been proposed to mitigate stresses and generate compressive stresses at the surface and down to a significant depth in the closure weld region of the inner lid of the Alloy 22 waste package outer barrier. The resulting residual stress profiles, after laser-peening treatment, were calculated as a function of depth in the inner closure lid weld region (CRWMS M&O 2000 [DIRS 151564], Section 6.2). From the calculated residual stress profiles, the profile with the highest hoop stress was used as a mean stress profile for the entire inner closure lid weld region (CRWMS M&O 2000 [DIRS 151549], Section 6.3.1.1). This section provides the technical basis and approach to quantifying the uncertainty in the calculated mean residual stress. It is assumed in this analysis that the total uncertainty in the residual stress is due to the stress measurement uncertainty. Because there are no data available for residual stress of laser-peened closure lid welds of the waste package design, literature data available for similar stress mitigation techniques were used to quantify the uncertainty in the residual stress in the inner closure lid weld region.

The uncertainties in the residual stress and stress intensity factor profiles for the laser-peened closure welds of the Alloy 22 waste package inner lid are estimated from stress states measured on shot-peened Incoloy 908 samples (Pasupathi 2000 [DIRS 149968]). The use of data obtained for Incoloy 908 is appropriate for this application because Incoloy 908 is a nickel-based superalloy similar to Alloy 22 (Pasupathi 2000 [DIRS 149968]). Furthermore, the analyses in this section are meant to develop a material-independent scaling term, the fractional uncertainty, which can be multiplied by the yield strength of the material under study to obtain the stress and stress intensity factor uncertainty distributions. A total of 17 stress measurements, along with their estimated measurement error, were used to estimate the observed fractional uncertainty for the data. The residual surface stresses are centered on a value consistent with the reference value of the materials' yield strength. The uncertainty in the values is consistent with a normal distribution, as shown in the following discussions.

The 17 stress measurements used in the current analysis are from a report from the Plasma Fusion Center of the Massachusetts Institute of Technology (Pasupathi 2000 [DIRS 149968], Table VI). X-ray diffraction residual stress techniques were employed to measure the stress at the surface of a shot-peened Incoloy 908 sample. A measurement error was estimated for each measurement, which results from the random error in the determination of the diffraction peak angular position and the empirically determined value of the x-ray elastic constant. Those parameters are required for calculating stress from strain measurements. This measurement error is used to weight the values for estimating the mean and standard deviation of the stress values. The observed trend in the errors is that lower (more negative) stress values have more error associated with them. The consequence of this is that the weighted mean estimate is higher in value than the unweighted estimate.

Analysis of the data shows that they can be treated as a normal distribution. This is demonstrated graphically by the fractile and probability plots of the data values compared with the normal distribution values, as shown in Figures 7.3.3-1 and 7.3.3-2. The plots show that the data values follow the normal distribution values reasonably closely.

The descriptive statistics of the sample are listed in Table 7.3.3-1. The weighted mean is calculated to be -899.2 MPa. This is consistent in magnitude with the reference yield strength for this material, 896 MPa. The weighted standard deviation of the data is calculated to be 45 MPa. With these values, the fractional uncertainty, defined as the ratio of the standard deviation to the absolute value of the mean, is about five percent.

Confidence values may be estimated for the fractional uncertainty (FU*)* by assuming that the mean is fixed and known (i.e., contributes little to the uncertainty variation) and that the ratio of the sample variance to the variance follows a chi-square distribution with *(n-1)* degrees of freedom, $\chi^2(n-1)$, under the normal assumption (Bulmer 1979 [DIRS 111961], Chapter 8, pp. 129-132). The fractional uncertainty is sampled as follows:

$$FU \sim \sqrt{\frac{(n-1)\cdot s^2}{\chi^2(n-1)}} \cdot \frac{1}{\bar{x}} \qquad \text{(Eq. 7.3.3-4)}$$

Parameters in the equation are defined in Table 7.3.3-1. Using these assumptions, the median value for the fractional uncertainty is 0.051. A portion of the resulting cumulative distribution function is reproduced in Table 7.3.3-2.

In the TSPA-SR (CRWMS M&O 2000 [DIRS 153246]), the residual stress uncertainty model for the waste package closure welds used, as its upper bound, the yield strength scaling factor (*F*) (CRWMS M&O 2000 [DIRS 151549], Section 6.3.1). In the current residual stress uncertainty model, the upper bound is three times the fractional uncertainty (FU) value derived from Equation 7.3.3-4. For the mean case, the bounds of the residual stress uncertainty are ±15.3 percent of the yield strength, and those of the 95th percentile case are ±21.3 percent of the yield strength. For comparison, the TSPA-SR base case uses ±30 percent of the yield strength for the bounds of residual stress uncertainty.

For each realization of the WAPDEG analysis, the fractional uncertainty (FU) was sampled and multiplied by 3, and a value for *z* (representing the uncertainty variation away from the mean) was sampled from a triangular distribution with a lower bound of -1, an upper bound of 1, and a mode of 0 (CRWMS M&O 2000 [DIRS 151549], Attachments II and III). These values were then multiplied together, yielding a new *z* value, which was passed to the stress corrosion cracking model (CRWMS M&O 2000 [DIRS 151549], Attachments II and III). Note that the yield strength scaling factor (*F*) in the TSPA-SR stress corrosion cracking model (CRWMS M&O 2000 [DIRS 151549], Attachments II and III) is no longer necessary because it has been incorporated into the product and is therefore set to 1, thus having no effect on the model. The stress corrosion cracking model then evaluated the uncertainty scaling factor and calculated the stress and stress intensity factor profiles to be used for the current realization.

7.3.3.3.3 Threshold Stress for Initiation of Stress Corrosion Cracking in Alloy 22

Initially, in the absence of relevant Alloy 22 stress corrosion cracking test results, literature results on Stainless Steel Type 304 were used to assess the expected susceptibility of Alloy 22 in terms of initiation stress threshold. These results were obtained in either very aggressive boiling magnesium chloride or in 0.1 M sodium chloride solutions dripped onto stressed specimens heated to 200°C. Under these very aggressive conditions, lower-bound initiation stress threshold of 10 to 30 percent of yield strength was observed. This range was conservatively selected for waste package design applications. In these same very aggressive environments, initiation stress threshold values for higher nickel-content stainless steels and nickel base alloys may exceed 80 percent of the yield strength. In the case of Alloy 22 U-bends (10 to 15 percent strain) in boiling magnesium chloride, the initiation stress threshold may exceed approximately 200 percent of the yield strength (Erbing Falkland 2000 [DIRS 149956], p. 661, Figure 8; Haynes International 1998 [DIRS 154463]).

More recently, a series of constant load and slow strain rate stress corrosion initiation tests was performed in more relevant test environments to assess the expected stress corrosion susceptibility of Alloy 22 in terms of stress threshold for crack growth initiation. In addition, highly stressed U-bend specimens of Alloy 22 were examined after up to two years of exposure in a range of environments in the Long-Term Corrosion Test Facility. These crack initiation tests were performed on Alloy 22 specimens with machined surfaces typical of those expected on the waste package, and no evidence of stress corrosion crack initiation has been found to date. These tests included:

- Constant load tests at 105° to 125°C on approximately 100 specimens (Figures 7.3.3-3 and 7.3.3-4) with a range of stresses up to approximately 250 percent of yield strength in concentrated J-13 well water solutions (equivalent to being evaporatively concentrated to approximately 5500-fold, pH = 12.4). Details of the testing solution composition are given in *Environment on the Surfaces of the Drip Shield and Waste Package Outer Barrier* (CRWMS M&O 2000 [DIRS 151568], Section 6.12). These tests included a range of metallurgical conditions, including annealed, welded, thermally aged and cold-worked material. No stress corrosion crack initiation was observed on any Alloy 22 specimen in any of these tests out to approximately 2,500 hours of exposure.

- Alloy 22 U-bend tests (estimated stress at approximately 200 percent of yield strength) at 90°C, including annealed and as-welded materials exposed up to two years in the Long-Term Corrosion Test Facility over a range of expected and bounding waste package surface environmental conditions (simulated concentrated water [approximately 1000-fold J-13 well water, pH = 8], simulated acidic water [approximately 1000 to 3000-fold J-13 well water, pH = 2.7], and simulated dilute water [approximately 10-fold J-13 well water, pH = 9.9]). Details of the testing solution composition are given in *Environment on the Surfaces of the Drip Shield and Waste Package Outer Barrier* (CRWMS M&O 2000 [DIRS 151568], Section 6.12). The materials did not exhibit any cracking during the exposure period.

- Slow strain rate tests at 76° to 105°C covering a range of relevant and bounding environments (including trace element lead additions) and applied potentials (Table 7.3.3-3). Examination of these results indicates a high degree of stress corrosion crack resistance at open circuit potentials in relevant environments, even in the presence of dissolved lead at pH values as low as 3. If beneficial buffer ions are not present (e.g., in a chloride-rich 4 M NaCl solution), the potential for either stress corrosion crack or crevice corrosion exists at applied potentials greater than approximately 350 mV versus Ag/AgCl. However, it should be noted that the expected waste package surface environments will be buffered and less prone to stress corrosion cracking.

In addition to the various SCC initiation tests cited above, fracture mechanics type crack growth tests have been performed at 110°C in near-saturated (approximately 50,000 fold) J-13 well water at a pH of 13.43 (Andresen et al. 2000 [DIRS 154462], pp. 2 and 6). In these tests, a sharp flaw generated by fatigue pre-cracking the specimens is subjected to slow load cycling in the desired test environment at stress intensities of 30 or 45 $MPa \cdot m^{½}$ until an active stress corrosion (or corrosion fatigue) crack is initiated. The crack is then forced to continue growing by very slow load cycling. With time, the cycling frequency is reduced in steps, and eventually, the sample is held under constant load and the crack growth rate measured. For Alloy 22, this growth rate is extremely low and tends to arrest with time at constant load. The measured growth rate on 20 percent cold-worked Alloy 22 samples was approximately 4×10^{-10} mm/s, a rate that is near the lower limits of such measurements. For materials with such low growth rates, and under the constant loading conditions representative of the waste package closure welds (i.e., no load cycling occurs), there is a high probability that even if an actively growing stress corrosion crack were to initiate, it would subsequently arrest after a small amount of growth (Andresen et al. 2000 [DIRS 154462], p. 5).

Based on these recent tests, the stress threshold can be conservatively increased to a range of 80 to 90 percent of yield strength. A uniform distribution is assumed between the bounds, and the entire distribution represents uncertainty in the stress threshold. Although a still higher value could be justified based on the recently available Alloy 22-specific test results, it is prudent to limit the upper bound value to 90 percent of yield strength at this time to provide a safety margin, considering the relatively limited test exposure times compared to the waste package emplacement period under consideration.

7.3.3.3.4 Uncertainties in Orientation of Manufacturing Flaws in Closure Lid Welds

As discussed in Section 7.3.3.2, the residual stress analyses showed that the hoop stress is the dominant stress in the closure lid welds; thus, only radial flaws are potential sites for through-wall stress corrosion cracking, if it occurs, in the presence of hoop stress. The stress corrosion cracking analysis in the TSPA-SR (CRWMS M&O 2000 [DIRS 153246]) assumed conservatively that all manufacturing flaws are oriented in such a way that they could grow in the radial direction in the presence of hoop stresses (CRWMS M&O 2000 [DIRS 151566], Section 5.6).

Only two weld methods are being considered for the fabrication process, gas metal arc and tungsten inert gas methods. These welding processes are designed to eliminate slag inclusions, a common flaw in other welding techniques. The most common flaws for gas metal arc and tungsten inert gas are lack of fusion flaws due to missed side wall or lack of penetration in the side wall. These flaws are generally large and readily detected by ultrasonic and radiographic inspections. Because both ultrasonic and radiographic methods will be used for post-weld inspections, there should be no large undiscovered flaws. Furthermore, flaws from the lack of fusion are, by definition, oriented in the direction of the weld bead, and thus are not subject to the applied hoop stress profile (CRWMS M&O 2000 [DIRS 152753]).

The observations noted above are supported by the limited data available from the lid welds on a 4-inch thick carbon-steel cylinder mockup using multiple passes for the viability assessment waste package design. Overall, sixteen indications were detected by ultrasonic testing on the bottom lid weld. Thirteen of these were classified as potential lack of fusion flaws because of their location at the weld fusion zone and their orientation parallel to the weld groove orientation. The other three indications were due to laminations in the base metal. Similarly, on the top lid welds of the same cylinder, three indications were detected; all were classified as lack of fusion very near the base of the weld root. The orientation of all of these indications was planar with respect to welding direction (CRWMS M&O 1998 [DIRS 107722]).

Shcherbinskii and Myakishev (1970 [DIRS 149953]) describe a statistical treatment of weld flaw orientations based on analysis of a significant data set of flaw orientation measurement and conclude that planar-type weld flaws, detected ultrasonically, tend to be predominately oriented parallel to the direction of the weld center line. More than 98 percent of the flaws detected fall within ±16 degrees of the weld center line in the case of steam pipe welds (e.g., the tails of the distributions decrease to less than 2 percent probability as the azimuth angle approaches 90 degrees (Shcherbinskii and Myakishev 1970 [DIRS 149953], Figure 1)). A similar conclusion, drawn from the data for plate welds (Shcherbinskii and Myakishev 1970 [DIRS 149953], Figure 2), indicates that statistical distribution of the flaws with respect to the orientation angle can be approximated with a centered normal distribution with a maximum standard deviation of 5 degrees. This yields a probability of 99 percent that a flaw is oriented within about ±13 degrees of the weld centerline. This suggests that less than one percent of these flaws have a potential to undergo stress corrosion cracking (i.e., radial crack propagation) under the action of the applied hoop stresses. Visual inspection of both the figures suggests a maximum probability of less than 2 percent at an azimuth between 12 and 16 degrees.

In summary, most weld flaws, such as lack of fusion and slag inclusions, would be expected to be oriented within a few degrees of the weld centerline (CRWMS M&O 2000 [DIRS 151564], Section 6.5.1). Available published data and YMP limited flaw measurements from the viability assessment design mockups also show that most weld flaws (about 99 percent) tend to be oriented in the circumferential direction (CRWMS M&O 2000 [DIRS 151564], Section 6.5.1). Recent analyses showed it is extremely unlikely that cracks initiating from circumferential flaws grow in the radial direction (CRWMS M&O 2000 [DIRS 151564], Section 6.5.1). Based on the information presented above, the uncertainty in the fraction of weld flaws in the waste package closure welds, which are capable of growing in the radial direction in the presence of hoop stress, is represented as a lognormal distribution with a mean of one percent, upper bound of 50 percent, and lower bound of 0.02 percent. The entire range of the distribution is assumed to be due to uncertainty. Considering the data in Shcherbinskii and Myakishev (1970 [DIRS 149953]), the mean of one percent is reasonably conservative.

7.3.3.4 Uncertainties Associated with Lower-Temperature Operating Mode

This section discusses model and parameter uncertainties associated with a lower-temperature operating mode.

Temperature Threshold for Stress Corrosion Cracking of Alloy 22–The range of temperatures evaluated for the stress corrosion cracking susceptibility of Alloy 22 in repository-relevant environments, such as concentrated J-13 well-type waters, is limited to date. For the relevant environments studied, stress corrosion crack propagation has been observed on fatigue pre-cracked fracture mechanics-type specimens over the temperature range of 95° to 110°C in basic saturated water, simulated acidic water, and simulated concentrated water (Andresen et al. 2000 [DIRS 154462]). Previous double cantilever beam specimens tested at Lawrence Livermore National Laboratory in less relevant unbuffered solutions (5 wt.% NaCl, pH = 2.7) indicated crack growth at 90°C (Roy et al. 1998 [DIRS 119544]). No testing was conducted for other temperatures. In contrast to the observed stress corrosion crack initiation and growth observed on pre-cracked (defected) specimens, no stress corrosion crack initiation has been reported on a "smooth" surface. Initiation tests to date include U-bend specimens exposed up to two years in the LTCTF in simulated concentrated, acidic, and dilute water environments at 60° and 90°C and in 15 to 20 percent basic saturated water at 105° to 125°C for up to 2,500 hours of exposure (Andresen et al. 2000 [DIRS 154462]) at levels exceeding yield stress. In slow strain rate tests, stress corrosion cracking was not initiated in Alloy 22 tested at 90°C in 5 wt.% NaCl, pH = 2.7 solutions (Roy et al. 1999 [DIRS 154455]). However, the available literature indicates that stress corrosion crack initiation can occur at higher temperatures on stressed Alloy 22 C-bend samples at 200°C in acidified Salton Sea-type brines (Kolts 1986 [DIRS 154453], Table 2). Alloy 22 was also tested in 25 wt.% NaCl, pH = 2 solutions with 135 ppm $PbCl_2$ at 200°C, but no cracking was observed after one week of exposure (Kolts 1986 [DIRS 154453], Table 2). Under more aggressive conditions, stress corrosion crack initiation and growth was observed on an Alloy 22 U-bend specimen tested in pH = 0.53, 1000-fold J-13 water solutions containing about 1,300 ppm lead at 250°C (Barkatt and Gorman 2000 [DIRS 154496]). In contrast, slow strain rate tests performed recently at Lawrence Livermore National Laboratory at a more realistic temperature of 76°C, either in pure aerated water containing 1 wt.% $PbCl_2$ or simulated acidic water with 100 ppm Pb $(NO_3)_2$ added, showed no evidence of stress corrosion crack initiation.

Although test results for Alloy 22 below 90°C in potentially relevant environments are limited (the only reported results are the U-bends tested in the LTCTF at 60°C and slow strain rate test results at 76°C), insight can be gained on the likely temperature dependency and potential threshold temperature for initiation and growth of cracks by examining literature information for other austenitic corrosion-resistant alloys where lower temperature results are available. One extensive series of test results on temperature dependency was obtained on pre-cracked Stainless Steel Type 304 and 304L fracture mechanics specimens in aerated 22 wt.% NaCl solutions, as well as more limited data in 42 wt.% $MgCl_2$ solutions (Speidel 1981 [DIRS 154457], Figure 10). In this series of tests, stress corrosion crack initiation and growth was observed on non-sensitized specimens over the test range from 50° to 130°C and on sensitized specimens down to room temperature. Increasing the nickel content above about 32 wt.% and the molybdenum content above about 5 wt.% significantly increased stress corrosion cracking resistance by increasing the threshold stress intensity factor, although the effect of lower temperatures was not reported for these highly corrosion-resistant alloys. Other results from the literature showed no stress corrosion crack initiation on U-bends of Alloys 800, 825, and 600 exposed for five years to a marine environment at Kure Beach at ambient temperature (Sedriks 1996 [DIRS 105113], p. 286). However, other results on non-sensitized stainless steels indicate that stress corrosion cracking can occur at room temperature in marine environments (Sedriks 1996 [DIRS 105113], p. 287). In one reported case, cracking was observed after less than 11 months of ambient exposure under dust containing up to 3.5 wt.% of water-soluble chloride in a Swiss tunnel (Sedriks 1996 [DIRS 105113], p. 288).

In summary, based on available results, there is currently no basis for establishing a threshold temperature below which stress corrosion cracking will not occur in Alloy 22 in chloride-containing environments, although the high nickel and molybdenum content (about 56 wt.% nickel and 13 wt.% molybdenum) in the alloy would tend to indicate that stress corrosion cracking is very unlikely below about 50°C.

7.3.4 Long-Term Passive Film Stability of Alloy 22

Long-term stability of the passive film on the surface of the Alloy 22 waste package outer barrier is one of the key issues that determine the long-term performance of the waste packages in the potential repository. A comprehensive testing and analysis program has been initiated to understand and develop a predictive model for the long-term stability of the passive film under expected repository exposure conditions. This section provides a brief description of the conceptual understanding of the passivity and passive film formation and growth on highly corrosion-resistant alloys relevant to Alloy 22.

7.3.4.1 Introduction

The corrosion models in the waste package degradation analysis for the TSPA-SR (CRWMS M&O 2000 [DIRS 153246]) are based on relatively short-term testing data. As discussed in Section 7.3.4.2, corrosion performance of highly corrosion-resistant alloys like Alloy 22 depends on the integrity of the thin, compact, adherent passive film formed on the alloy surface in contact with the corrosive environment. Extrapolation of the measured short-term corrosion rates over a repository time frame assumes that the integrity of this passive film remains stable over very long times. In addition, the individual corrosion models incorporated in the WAPDEG model

are empirical in nature. Because of the long service life of waste packages (10,000 years), empirical methods and models inherit significant uncertainties in long-term projection of corrosion degradation.

This section discusses the approach to developing a mechanistic predictive model for long-term performance of the Alloy 22 waste package outer barrier under expected repository exposure conditions. The mechanistic model, referred to as the generalized corrosion model (GCM), is based on two models: the mixed potential model (MPM) (Macdonald 1992 [DIRS 154719]) for predicting the electrochemical corrosion potential (ECP) and the corrosion current density, and the point defect model (PDM) (Macdonald 1999 [DIRS 154721]), which describes the growth and breakdown of the passive film that exists on the alloy surface. The model is in an early stage of development and requires experimental data for Alloy 22 under repository exposure conditions to estimate the value of its parameters.

Also discussed in this section are the features and application of the GCM using example calculations performed with the current (early developmental stage) version of the model. The present example calculations are limited to general corrosion processes and employ simplifying assumptions and data on other material. This is necessary because of the limited data available for Alloy 22 under repository conditions. The example calculation results for general corrosion processes discussed in this section should be viewed as preliminary and qualitative in nature.

7.3.4.2 Conceptual Description of Passivity and Passive Film Stability

Passivity can be defined as a phenomenon concerned with the formation of a thin, compact, and adherent oxide or oxyhydroxide film that protects a metal and alloy from corrosive degradation. It has now been accepted that the passive film is not a single layer, but rather has a stratified structure (Macdonald 1992 [DIRS 154720]; Marcus and Maurice 2000 [DIRS 154738], pp. 145 to 150). According to this bilayer model, the passive film consists of an inner layer of oxide and an outer layer of hydroxide or oxyhydroxide. The inner oxide layer plays the role of a barrier layer against corrosion, and the outer layer plays the role of an exchange layer.

Passive Film Formed on Metals–In general, the chemical composition and thickness of passive films depend on the nature of the metal, the pH of the electrolyte in which the metal is passivated, and the electrochemical potential (Macdonald 1992 [DIRS 154720]; Macdonald 1999 [DIRS 154721]). For example, for nickel that can passivate in solutions over a wide range of pH, the passive film is generally composed of nickel(II) cations with an inner layer of NiO and an outer layer of $Ni(OH)_2$. More noble (positive) passivation potential can enhance the development of a continuous oxide layer in the inner part of the film (Marcus and Maurice 2000 [DIRS 154738], pp. 142 to 153).

The passive films formed on metal surfaces are generally not electronic conductors, but rather semiconductors or insulators. The electronic structures of passive films can be determined by photoelectrochemical measurements. However, the structural analyses are rather difficult, inherent to the nanometer thickness of passive films and the roughness of the surfaces because of dissolution. The passive film formed on nickel (in 0.05 M H_2SO_4) has shown crystallites, the size of which are reduced with increasing potential. The shape of crystallites also changes with potential (Marcus and Maurice 2000 [DIRS 154738], pp. 145 to 153). Another factor that should

be considered is active dissolution, which occurs as long as the surface is not completely passivated. The dissolution rate increases exponentially with increasing potential (Tafel's law); dissolution may create new sites for oxide nucleation and can, thus, favor a higher density of oxide nuclei (Marcus and Maurice 2000 [DIRS 154738], pp. 145 to 153). The passive film formed on nickel has revealed crystallinity, with the surface exhibiting terraces and steps. On the other hand, the passive oxide film formed on chromium can have a nanocrystalline structure. These oxide nanocrystals are cemented together by the chromium hydroxide outer layer, making the passive film extremely protective against corrosion-induced damage.

Passive Film Growth Mechanisms–As summarized in the literature (Macdonald 1992 [DIRS 154720]; Macdonald 1999 [DIRS 154721]), the barrier oxide layer (inner layer) forms by the generation of oxygen vacancies (and hence new film) at the metal/film interface, balanced in the steady state by dissolution of the barrier layer at the barrier layer/outer layer interface. The outer layer forms via the hydrolysis and precipitation of cations transmitted through the barrier layer or by hydrolytic restructuring of the barrier layer/outer layer interface. The distinctly different origins of the barrier and outer layers are amply demonstrated by the fact that both layers may incorporate alloying elements from the alloy substrate, but only the outer layer incorporates species from the solution. Furthermore, with respect to the laboratory frame of reference, the barrier layer grows into the substrate metal, whereas the outer layer grows outwards into the solution (Macdonald 1992 [DIRS 154719]; Macdonald 1999 [DIRS 154721]). Thus, while the growth of the barrier layer is exclusively due to the generation of oxygen vacancies at the metal/barrier layer interface, the growth of the outer layer is commonly (but not exclusively) due to the transmission of cations through the barrier layer, either through cation vacancies or as cation interstitials, and their eventual emission at the barrier layer/outer layer interface. The origin of the outer layer is not exclusively due to cation transmission, because it may also form via hydrolytic restructuring of the barrier layer at the barrier layer/outer layer interface (Macdonald 1992 [DIRS 154720]; Macdonald 1999 [DIRS 154721]).

Current is carried by all charged species in the barrier layer, including cation vacancies ($V_M^{\chi'}$), cation interstitials ($M_i^{\chi+}$), and oxygen vacancies ($V_O^{\bullet\bullet}$), which are generated and annihilated at the interfaces (Figure 7.3.4-1, Reactions 1 to 6), and by dissolution of the barrier layer (Figure 7.3.4-1, Reaction 7), depending on whether a change in oxidation state occurs (Macdonald 1992 [DIRS 154719]; Macdonald 1999 [DIRS 154721]). The principal mode of transport of the defects is migration under the influence of a strong electric field, the magnitude of which is postulated to be established by the potential differences across the film and interfaces and by buffering due to Esaki (band-to-band) tunneling within the barrier layer. Because a barrier layer exists on all passive metals, all barrier layers are oxygen vacancy conductors to an extent that, in the steady-state, is determined by the dissolution rate of the film. However, other defects may dominate the structural and electronic defect structures of the barrier layer. For example, the defect structure of the barrier layer on nickel is dominated by cation vacancies, while that on zinc is dominated by cation interstitials, even though oxygen vacancies exist in both cases.

Chromium Enrichment in Passivated Nickel-Base Alloys–Chromium concentration plays a significant role in the passivation of austenitic nickel-base alloys, such as Alloy 600 and Alloy 690. The passive films in these alloys can be described by the bilayer model

(Macdonald 1992 [DIRS 154720]; Macdonald 1999 [DIRS 154721]). The concentration of Cr^{+3} in the inner oxide layer is higher than the nominal chromium content of the alloy (Lorang et al. 1990 [DIRS 154718]; Marcus and Maurice 2000 [DIRS 154738], p. 153). The mechanism of surface enrichment of chromium in the barrier layer has been developed within the framework of the PDM (Zhang and Macdonald 1998 [DIRS 154743]; Zhang and Macdonald 1998 [DIRS 154742]) and is based on the selective oxidation of the elements at the alloy/barrier layer interface, differences in transport properties of the species in the barrier layer, and selective oxidation of the elements at the barrier layer/outer layer interface. In the specific case of the passive film on iron-chromium alloys, enrichment of the barrier layer in chromium appears to entail the dissolution of iron and the oxidative segregation of chromium (Marcus and Maurice 2000 [DIRS 154738], p. 153). Iron atoms are detached from the surface and go into solution as ions, whereas chromium atoms are rapidly oxidized and the passive film forms by the nucleation and growth of a Cr_2O_3-like phase (Marcus and Maurice 2000 [DIRS 154738], p. 153). However, the barrier layers on iron-chromium and nickel-chromium alloys are not pure chromium oxide (Cr_2O_3), and they still contain significant amounts of other metal species, such as nickel, ferrous, and ferric ions (Lorang et al. 1990 [DIRS 154718]). Finally, it is important to note that the accurate description of alloy segregation phenomena requires solving the "moving boundary" (i.e., Stefan's) problem, because the interfaces at which the segregation reactions occur and the phases bounded by these interfaces move differently with respect to the laboratory frame of reference. This is the approach adopted in the PDM (Zhang and Macdonald 1998 [DIRS 154743]; Zhang and Macdonald 1998 [DIRS 154742]).

Role of Molybdenum–The exact mechanism of the effect of molybdenum on the corrosion resistance of nickel-chromium-molybdenum alloys is not fully understood. However, there is a consensus that molybdenum reduces the rate of anodic dissolution in the active state (Marcus and Maurice 2000 [DIRS 154738], pp. 155 to 158), but it is not clear whether this observation is relevant to the corrosion of a passive alloy. In this model, molybdenum is postulated to be located preferentially at local defects on the surface, which normally act as dissolution sites. The slowing down of the dissolution rate could be due to the increased metal-metal bond strength where molybdenum is present (Marcus and Maurice 2000 [DIRS 154738], pp. 155 to 158). Further, the presence of molybdenum counteracts the deleterious effect of species such as sulfur in that it bonds to sulfur and then dissolves, thus eliminating the detrimental effect of sulfur (Marcus and Maurice 2000 [DIRS 154738], p. 158). With regard to dissolution in the passive state, no consistent relationship has emerged between the passive current density and the molybdenum content of the alloy (e.g., Bojinov et al. 2001 [DIRS 154715]).

An analytical prediction of the role played by molybdenum (or any alloying element) in inhibiting passivity breakdown on alloys is provided by the point defect model (Urquidi and Macdonald 1985 [DIRS 154741]), which is found to account quantitatively (within the accuracy of the experimental data) for the impact of molybdenum on the pitting resistance of 18 chromium-8 nickel stainless steels (e.g., AISI Type 304 versus Type 316). In this model, highly oxidized alloy elements that are present substitutionally in the barrier layer lattice form immobile, positively charged centers. For example, recognizing that the barrier layer on chromium containing stainless steels and nickel-base alloys is essentially Cr_2O_3, substitution of Mo^{6+} into a chromium cation vacancy would produce the immobile species $Mo_{Cr}^{3\bullet}$. This species may interact electrostatically with the mobile, negatively charged cation vacancies ($V_{Cr}^{3'}$) that are

responsible for passivity breakdown via condensation at the metal/film interface under supra breakdown conditions (Macdonald 1992 [DIRS 154720]; Macdonald 1999 [DIRS 154721]). Thus, the solute-vacancy interaction reduces the free cation vacancy concentration and diffusivity, which results in a positive shift in the breakdown voltage and a lengthening of the induction time (i.e., the alloy becomes more resistant to passivity breakdown). The electrostatic interaction is described rigorously in terms of ion-pairing theory that is commonly employed to describe ionic interaction in solutions. This solute-vacancy interaction model (Urquidi and Macdonald 1985 [DIRS 154741]) successfully accounts for the positive shift in the breakdown voltage upon adding molybdenum to the alloy without the need for arbitrary, adjustable parameters. Most importantly, the solute-vacancy interaction model accounts for why molybdenum must be present in the barrier layer at concentrations greater than about 2 percent for significant protection to be achieved.

Finally, complexing between $Mo_{Cr}^{3\bullet}$ and a defect will only occur if the defect is negatively charged (i.e., if the defect is a cation vacancy). However, the Cr_2O_3 passive film on chromium containing alloys is normally n-type in electronic character; hence, the dominant defect is either a cation interstitial or an oxygen vacancy, both of which are formally positively charged. Consequently, there should be little solute ($Mo_{Cr}^{3\bullet}$) – vacancy ($V_O^{\bullet\bullet}$ or $M_i^{\chi+}$) interaction and pairing, and molybdenum should have little consistent impact on the passive current density, as observed.

7.3.4.3 Approach to Mechanistic Modeling of Long-Term Passive Film Stability

This section describes an approach to developing a mechanistic predictive model for the long-term performance of waste packages (i.e., Alloy 22 outer barrier) under expected repository exposure conditions. Development of the mechanistic model, referred to as the GCM, is underway.

The individual corrosion models incorporated in the WAPDEG model are empirical. Because of the long service life of waste packages (10,000 years), such empirical methods and models inherit significant uncertainties in long-term projection of corrosion degradation. In particular, empirical models, which may be best expressed in statistical form (e.g., in the form of extreme value statistics) for such long-term projections, require a large database of "identical systems" with relationships that are governed by some underlying distribution function (e.g., a Poisson distribution function). However, in the case of geological isolation of the waste over extremely long time periods, no such systems or associated databases exist, so there are significant uncertainties in the application of empirical statistical methods to the prediction of damage.

An alternative strategy is a mechanistic approach, which is based on the philosophy that future events can be predicted on the basis of the natural laws that are invariant in space and time. These mechanistic/deterministic models require that the path over which the system will evolve in the future be specified in sufficient detail to provide a prediction of the desired accuracy. Furthermore, the process (or processes) by which degradation occurs must be described in terms of a physically realistic mechanism, the quality of which ultimately governs the accuracy and veracity of the prediction. Nevertheless, deterministic prediction of corrosion damage is now well established and has been applied in the prediction of general and localized corrosion

damage in a variety of systems, including condensing heat exchangers (Macdonald et al. 1994 [DIRS 154735]) and water-cooled nuclear reactors (Macdonald 1999 [DIRS 154721]).

All deterministic models comprise constitutive equations (which describe relationships between components and parameters in the mechanisms) and constraints (that constrain the solutions to those that satisfy the relevant natural laws). Because corrosion is an electrochemical process, the relevant natural laws are the conservation of charge, the conservation of (equivalent) mass, and Faraday's law, which specifies the equivalence of mass and charge (96,487 coulombs/equivalent). Because the natural laws are the summation of previous scientific experience, much of which is not directly related to the mechanism of interest, deterministic models are broadly based and extraordinarily resilient. Most importantly, they require little calibration, and then only to derive values for poorly known model parameters if these parameters cannot be determined by independent experiment.

The algorithm used in the GCM is based on two models: the MPM (Macdonald 1992 [DIRS 154719]) for predicting the electrochemical corrosion potential and the corrosion current density (I_{corr}), and the PDM (Macdonald 1999 [DIRS 154721]), which describes the growth and breakdown of a passive film on the alloy surface. Because the MPM and the PDM are deterministic, the resulting GCM is also deterministic.

The MPM is based on the physical condition that charge conservation must be obeyed in the system (Macdonald 1992 [DIRS 154719]); that is, because electrochemical reactions (corrosion reactions) transfer charge across a metal/solution interface at rates measured by the partial currents, the reactions are constrained by the charge conservation constraint. These partial currents depend on the potential drop across the metal/solution interface.

The PDM has been developed to provide a mechanism-based description of the growth and breakdown of the passive oxide films that form on metal surfaces when in contact with oxidizing environments (Macdonald 1992 [DIRS 154720]; Macdonald 1999 [DIRS 154721]). The PDM is based upon a number of postulates and assumptions:

- The passive film is a bilayer structure made up of a highly defective barrier (inner) layer that forms from the metal substrate and an outer layer that forms by the hydrolysis and subsequent precipitation of an oxide, oxyhydroxide, or hydroxide. The outer layer has a low inherent defect concentration and generally contains species that are co-precipitated from the solution (Section 7.3.4.1).

- The defects contained within the barrier (inner) layer include cation vacancies ($V_M^{\chi'}$), cation interstitials ($M_i^{\chi+}$), and oxygen vacancies ($V_O^{\bullet\bullet}$). These point defects are generated and annihilated at the metal/barrier layer and barrier layer/solution interfaces in a series of elementary reactions (Figure 7.3.4-1).

- The barrier (inner) layer is responsible for the phenomenon of passivity. However, the outer layer may contribute significantly to the total interfacial impedance, and hence may control the rate of charge transfer.

- A single metal oxidation state exists within the barrier layer. This assumption is too restrictive to accommodate all systems, including iron, where the barrier layer comprises magnetite containing both iron(II) and iron(III) species. A more general model that recognizes the presence of multiple oxidation states in the barrier layer is under development.

In general, it is expected that one defect will dominate the defect structure of the barrier layer. The physics governing the identity of the dominant defect is discussed by Macdonald (1999 [DIRS 154721]). The identity of the principal defect is determined by the relative energies of formation of the defects in the barrier layer. For a barrier layer with a high cation oxidation state (e.g., WO_3 on W), the energies of formation of cation vacancies and cation interstitials are much greater than the energy of formation of an oxygen vacancy, so that the passive film on tungsten, for example, is an oxygen vacancy conductor. For systems with low cation oxidation states (e.g., nickel and zinc), the energies of formation of cation vacancies and cation interstitials are lower than the energy of formation of the oxygen vacancy. Accordingly, the barrier layers on these metals are expected to be cation vacancy or cation interstitial conductors. Experiments show that the barrier layer on nickel is a cation conductor, while that on zinc is consistent with the dominant defect being a zinc interstitial (Macdonald 1999 [DIRS 154721]). The passive film on Alloy 22 is presumably defective Cr_2O_3, which occupies a position that is between the two extremes outlined above. Accordingly, it is not possible to predict, a priori, the dominant defect in the barrier layer. However, electrochemical studies suggest that the passive current is independent of voltage, which is consistent with the dominant defect being a cation interstitial or an oxygen vacancy. While this issue must be resolved by experiment, the dominant defect is assumed to be the cation interstitial in the current model development. In addition, the steady-state thickness of the barrier layer, including the dependence of the contacting solution on pH, is expressed in terms of the same parameters in the PDM.

7.3.4.4 Application of the General Corrosion Model

In this section, applications of the mechanistic GCM (currently under development) are discussed. Example calculations with the current version of the model are included in the discussion, though they are limited to general corrosion processes. Because the model is in an early stage of development and experimental data for Alloy 22 under repository exposure conditions is needed to estimate the model parameter values, simplifying assumptions and data for less corrosion-resistant materials (such as stainless steel) are employed in the example calculations.

7.3.4.4.1 Summary of the Current Version of the General Corrosion Model

The current version of the GCM (under development) modifies the older MPM (Macdonald 1992 [DIRS 154719]) by using the PDM (Macdonald 1999 [DIRS 154721]) to calculate the partial anodic current density, and by using a modified Butler-Volmer equation for the redox reactions to recognize that the corrosion processes occur on the surface under a thin electrolyte film. The current GCM used to simulate general corrosion processes differs in a number of important respects from the earlier MPM, used to model the electrochemical properties of nuclear reactors (e.g., corrosion processes in boiling water reactor primary coolant circuits) (Macdonald 1992 [DIRS 154719]). This section summarizes the most important of these differences.

The GCM incorporates the PDM (Macdonald 1999 [DIRS 154721]) to describe the anodic processes occurring at the metal surface. In the present version of the model, it is assumed that the barrier layer is a cation interstitial conductor, but other conduction mechanisms are readily assumed by changing parameter values. Recent work by Bojinov et al. (2001 [DIRS 154715]) using a modification of the PDM suggests that the barrier layer on iron-chromium-molybdenum alloys is an oxygen vacancy conductor, but it is not known whether this conclusion also applies to Alloy 22, which is a nickel-base alloy. Finally, in applying the PDM to the MPM, it is assumed that the temperature dependencies of the standard rate constants in the model can be described by Arrhenius factors of the type $\exp[-E_a(1/T - 1/T_o)/R]$, where E_a is the activation energy, T is temperature in Kelvin, and $T_o = 298.15$ K.

The current GCM considers corrosion beneath a thin liquid film that forms on the surface through evaporative concentration. In the current calculations, the thin electrolyte film is assumed to contain a single electrolyte, which for the present purposes is assumed to be sodium chloride plus the requisite H^+ and counter anion as determined from the pH. The solubility of oxygen and the mean molal activity coefficient are calculated from the sodium chloride concentration, the former by using Sechenov's coefficients for carbon dioxide (which are assumed to hold also for oxygen) for temperatures up to 200°C, as given by Naumov et al. (1974 [DIRS 154739]), and the latter from the extensive data of Liu and Lindsay (1972 [DIRS 154717]) on the thermodynamics of the NaCl-H_2O system.

No redox species other than hydrogen and oxygen are considered in the model. This assumption reflects the general opinion that the radiation dose rates at the surface are not sufficiently large to produce significant amounts of radiolysis products, such as H_2O_2. However, the radiolysis products are considered in the thin layer MPM that was developed a number of years ago to explore the impact of radiolysis on the electrochemical and corrosion properties of a high-level nuclear waste canister (Urquidi and Macdonald 1985 [DIRS 154741]). That study, which focused on copper alloys, suggested that there could be observable radiolysis effects, but that finding depends strongly on the dose rate that is assumed to exist at the canister surface.

The MPM was originally developed for describing electrochemical and corrosion processes in the heat transport circuits of boiling water reactors (Macdonald 1992 [DIRS 154719]); hence, it assumed that pH was not a variable. However, the pH is a system variable in the present application, so the expressions for the exchange current densities of the hydrogen-electrode reaction and the oxygen-electrode reaction have been modified by inclusion of the factor $(C_{H^+}/10^{-pK_w/2})^{exponent}$, where $pK_w = -log(K_w)$, K_w is the activity product of water at the prevailing temperature and C_{H^+} is the concentration of hydrogen ion, which is calculated from the known pH. The exponent is set equal to 0.5 for Alloy 22. A similar factor is introduced for the dependence of the exchange current density on the activity of water (a_W), in this case in the form of a_W^p, where p = 1.4 for the hydrogen-electrode reaction (Anderko et al. 2001 [DIRS 154714]) and p = 1.0 for the oxygen-electrode reaction. The latter value was assumed in lieu of experimental data for Alloy 22. Finally, it is assumed that the temperature dependencies of the exchange current densities for the hydrogen-electrode reaction and the oxygen-electrode reaction can be described by an Arrhenius factor of the form $\exp(-14244/RT)$, where T is temperature in Kelvin, as per the original MPM (Macdonald 1992 [DIRS 154719]).

The potential scale employed in this work is the standard hydrogen electrode (SHE) scale, but that scale is not particularly useful for comparison with experimental data, which commonly are reported on the saturated calomel electrode (SCE) scale or the saturated silver/silver chloride electrode scale. However, conversion factors from one scale to another are temperature-dependent. In the current version of the model, the potential is reported on the SCE and SHE scales.

7.3.4.4.2 Example Simulation for Application of the Current Generalized Corrosion Model for General Corrosion Process

The model developed for the present analysis has not been optimized because of the unavailability of parameter input data for Alloy 22 under thin electrolyte films in simulated repository environments. Accordingly, the parameter values employed in the calculations described below generally refer to stainless steels, as used in previous applications of the MPM (Macdonald 1992 [DIRS 154719]), or are best estimates. One of the principal reasons for developing the model in its present form is to focus attention on the parameters that need to be measured experimentally. Future work will prioritize these parameters, using the present model to perform extensive sensitivity analyses. Finally, this model is under development and still requires additional work before it can be considered reasonably complete. Nevertheless, the model is capable of yielding realistic parameter values, and optimization is expected to produce predictions that are in accord with experimental observations. This view is based on previous experience with this model in predicting corrosion potentials in the primary coolant circuits of water-cooled nuclear reactors.

By way of illustration, the current model was used to calculate the electrochemical corrosion potential and the corrosion current density as a function of oxygen partial pressure and temperature (Macdonald 2001 [DIRS 154736], pp. 18 to 22). The results are given in Figures 7.3.4-2 and 7.3.4-3. The thin electrolyte film on the metal surface is assumed to be saturated in sodium chloride. The electrochemical corrosion potential displays a typical sigmoid variation with the log of oxygen partial pressure, and the potential becomes more negative with increasing temperature (Figure 7.3.4-2). Furthermore, the actual values are typical of stainless steels in aerated brines.

Figure 7.3.4-3 shows the predicted corrosion current density as a function of the partial pressure of oxygen (Macdonald 2001 [DIRS 154736], pp. 18 to 22). No dependence of the corrosion current density (i_{corr}) on the oxygen partial pressure (p_{O2}) is noted. This is a consequence of assuming that the passive film is a cation interstitial conductor and that no change in oxidation state exists between the cation in the barrier layer and the metal species in the solution. Hence, the steady-state anodic partial current density is independent of potential. This relationship would hold if the oxygen vacancy was assumed to be the principal defect in the barrier oxide layer, provided that no change in oxidation state occurred upon film dissolution or ejection of a cation from the barrier layer at the barrier layer/solution interface. On the other hand, if the principal defect is the cation vacancy, or if the oxidation state of chromium changes upon barrier layer dissolution (Reaction 7, Figure 7.3.4-1) or upon cation ejection (Reactions 4 and 5, Figure 7.3.4-1), regardless of the identity of the principal defect, the corrosion current density will be potential-dependent. The current model incorporates all of these possible processes through the PDM.

Figure 7.3.4-4 shows the calculated electrochemical corrosion potential versus the thickness of the thin electrolyte film that is assumed to exist on the alloy surface (Macdonald 2001 [DIRS 154736], pp. 18 to 22). The data display two regions of interest: that at very low thickness values (corresponding to thin-film behavior) and that at large thickness values (corresponding to thick-film or bulk-electrolyte behavior). In both cases, the film is assumed to be quiescent, which is considered to be a good approximation for the thin-film scenario but not for the thick-film scenario. The assumption is inappropriate in the latter case because bulk systems are characterized by mass transport process other than diffusion (e.g., natural convection), so the model underestimates the limiting currents for the transport of oxygen and hydrogen ions to the metal surface. This has the effect of shifting the calculated electrochemical corrosion potential in the negative direction (Figure 7.3.4-4). The model needs to be improved to account for these processes.

Figures 7.3.4-5 and 7.3.4-6 show the calculated electrochemical corrosion potential and corrosion current density, respectively, as a function of pH for the assumed conditions of 100°C, 0.21-atm oxygen partial pressure, 0.01-cm electrolyte film thickness on the alloy surface, and saturated sodium chloride solution (Macdonald 2001 [DIRS 154736], pp. 18 to 22). The electrochemical corrosion potential is predicted to shift in the negative direction, and the corrosion current density is predicted to decrease exponentially with increasing pH. The origins of these shifts are complex and involve equilibrium and kinetic factors. Nevertheless, these relationships are observed commonly in experimental data.

7.3.4.5 Other Lines of Evidence to Support the Long-Term Passive Film Stability Model

Josephinite, a rock containing nickel-iron metallic minerals (Section 7.3.2.4), is about 150 million years old. It formed from the reduction of nickel- and iron-bearing minerals in the environment created by serpentinization of igneous rocks. Because the environment and temperature change with time during the formation of josephinite, its structure and mineral content changes from sample to sample, and even within individual samples (Botto and Morrison 1976 [DIRS 154716], p. 272).

The metallic mineral tends to be concentrated in the interior of josephinite samples (Figure 7.3.4-7). Because the environment in which josephinite forms becomes less and less reducing with time, there tends to be a relatively thick nonmetallic outer layer on these samples that protects the metal within. In some regions, however, the metallic nickel-iron apparently is at or near the surface. According to Botto and Morrison (1976 [DIRS 154716], p. 243), nickel-iron metal is sometimes seen at the surface of josephinite samples where the serpentine layer has been worn off during movement in streams. Whether metal is present on the surface of josephinite samples is currently being verified.

Current waste package corrosion modeling is based on relatively short-term testing. The corrosion rate in these tests is determined by a relatively thin passive film that controls the rate of oxide penetration into the bulk. Extrapolation of the measured corrosion rates over a repository time frame assumes that the integrity of this passive film remains stable over long times. Although the composition of the nickel-iron metallic mineral in josephinite differs from that of Alloy 22, if metal were found to be present on the surface of josephinite samples, that

would imply that a passive film can remain stable over long time periods, even in wet environments.

7.3.5 General Corrosion of Alloy 22

7.3.5.1 Goal of the Analysis

General corrosion is the relatively uniform thinning of materials without significant localized corrosion. The mode of general corrosion differs depending on the local environment. The repository environment will result in three different general corrosion modes: dry oxidation, humid-air corrosion, and aqueous-phase corrosion. The threshold relative humidity for both humid-air and aqueous-phase corrosion is based on the deliquescence point of sodium nitrate salt (CRWMS M&O 2000 [DIRS 151568], Section 7.0; CRWMS M&O 2000 [DIRS 144229], Section 4.1.2). Humid-air corrosion is defined as a corrosion condition in the absence of dripping water; aqueous-phase corrosion requires the presence of dripping water. Dry oxidation (dry-air corrosion) occurs at any relative humidity below the threshold for humid-air corrosion. Because the rates are extremely small under the expected repository thermal conditions, dry oxidation is expected to have no significant impact on waste package (CRWMS M&O 2000 [DIRS 144229], Section 6.1) or drip shield performance (CRWMS M&O 2000 [DIRS 144971], Section 7.0), so it is not considered in the current analysis.

The measured general corrosion rates of Alloy 22 from the immersion tests in the LTCTF have consistently indicated no discernible effect of temperature on the general corrosion rate, at least over the temperature range tested (60° to 90°C). The tests have also indicated no discernible effect of solution chemistry on measured general corrosion rates. Solutions considered in the testing include simulated dilute water, simulated concentrated water, simulated acidic water, and the saturated vapor environments above these waters (CRWMS M&O 2000 [DIRS 144229], Sections 6.5.2 and 6.9.1). Although no immersion tests have been conducted in simulated saturated water to date, cyclic polarization experiments have been conducted (CRWMS M&O 2000 [DIRS 144229], Section 6.4.2 and 6.4.3). Analyses have shown that the weight-loss method used in the LTCTF is not sensitive enough to quantify the effect of repository-relevant exposure conditions on the Alloy 22 general corrosion rate (CRWMS M&O 2000 [DIRS 144229], Section 6.5.3).

As discussed in Section 7.3.4, the passive dissolution (general corrosion) of highly corrosion-resistant alloys such as Alloy 22 is governed by the transport properties of reacting species (e.g., metal ions, oxygen ion, vacancies and interstitials) in the very thin (typically a few nanometers), compact, adherent passive film that forms on the alloy surface in contact with the corrosive environment and the dissolution rate of the passive film. These processes are influenced by the characteristics of the passive film, electrochemical potential across the film, and the chemistry of solution contacting the film. Chromium and nickel oxides, which are the major constituents of the passive film of nickel-chromium-molybdenum alloys like Alloy 22 (Lorang et al. 1990 [DIRS 154718]), are stable and exhibit extremely low dissolution rates over a wide range of solution chemistry (see Section 7.3.4.2). The transport properties of the reacting species and reaction rates in the passive film are considered thermally activated processes (see Section 7.3.4.4.1), so the general corrosion rate of the Alloy 22 waste package outer barrier is expected to have a certain level of temperature dependency. However, as discussed above, the

TSPA-SR (CRWMS M&O 2000 [DIRS 153246]) assumed temperature-independent constant rates for general corrosion of the Alloy 22 outer barrier. This lack of temperature dependency of the general corrosion rate has been identified as one of the unquantified uncertainties in the waste package degradation model (Table 7-1). Because waste package temperatures are variable from location to location in the repository and change with time (i.e., decrease with time after their peak shortly after waste emplacement), the general corrosion degradation rate of waste packages is expected to be variable over time and across the repository. In addition, different general corrosion degradation behaviors of waste packages may results from alternative thermal operating modes.

The goal of the current analysis is to construct a model for the temperature dependence of general corrosion of the Alloy 22 waste package outer barrier by analyzing the limited data developed since the TSPA-SR (CRWMS M&O 2000 [DIRS 153246]). Three alternative models are developed and discussed in Section 7.3.5.3. The temperature-dependent general corrosion models are incorporated into the waste package degradation analysis to study the effect of the previously unquantified uncertainty on waste package degradation. Also presented in this section is a qualitative analysis of the effects of the chemical environment on corrosion of the Alloy 22 waste package outer barrier.

7.3.5.2 Identification of Unquantified Uncertainties in Total System Performance Assessment-Site Recommendation

The distribution of general corrosion rates for Alloy 22 used in the TSPA-SR (CRWMS M&O 2000 [DIRS 153246]) is based on weight-loss data from the LTCTF over a two-year period (CRWMS M&O 2000 [DIRS 144229], Section 6.9.1). The test program includes sample coupons exposed to a variety of test media (e.g., water chemistry and temperature) to cover a range of exposure conditions relevant to the potential repository. The corrosion data for Alloy 22 gathered to date from the LTCTF indicate that the general corrosion rate for humid-air and aqueous-phase corrosion is about the same (i.e., water chemistry has no significant effect). The data also show little sensitivity to potential repository temperature for the water chemistry and temperature ranges considered in the test program. The general corrosion rates were corrected for the effects of potential formation of silica scale deposits on the sample surfaces. Silica deposition was estimated to potentially increase the corrosion rate determined from weight-loss measurements by as much as 0.063 μm/yr (CRWMS M&O 2000 [DIRS 144229], Section 6.5.5; CRWMS M&O 2000 [DIRS 153802], Section 3.1.5.4.2).

The TSPA-SR (CRWMS M&O 2000 [DIRS 153246], Section 3.4.1.2) conservatively assumed that the rate of humid-air corrosion is represented by the same corrosion rate distribution used for aqueous-phase corrosion. It was further assumed that the corrosion rate is constant and does not decrease with time at times greater than two years. Because the general corrosion rate is expected to decrease with exposure time (see Section 7.3.5.4.2), the current general corrosion models are reasonably conservative representations of the corrosion behavior of the highly corrosion-resistant materials used for the waste package outer barrier (and drip shield) under expected repository conditions.

The general corrosion rate distributions for Alloy 22 and Titanium Grade 7 include substantial uncertainties (CRWMS M&O 2000 [DIRS 144229], Sections 6.5.2 and 6.9.1; CRWMS

M&O 2000 [DIRS 144971], Section 6.5.2; CRWMS M&O 2000 [DIRS 152542], Section 6). Most of these uncertainties result from insufficient resolution of the weight-loss measurements of the sample coupons due to the extremely low corrosion rate of the materials in the test media. The uncertainty in the measured general corrosion rates is not fully quantifiable, and the fraction of the total variance in the corrosion rate distribution that is attributed to spatial variability (and, conversely, to uncertainty) is not known. The approach in the waste package and drip shield degradation analysis in the TSPA-SR (CRWMS M&O 2000 [DIRS 153246]) assumes that this fraction is uncertain and could range from pure uncertainty to pure variability (CRWMS M&O 2000 [DIRS 151566], Section 6.4.7).

As discussed previously, because the passive dissolution (general corrosion) rate of Alloy 22 depends on the transport properties of the reacting species (e.g., metal ions, oxygen ion, vacancies, and interstitials) and reaction rates in the thin, compact adherent passive film, which are considered thermally activated processes (see Section 7.4.4.4.1), a certain level of temperature dependency of the general corrosion rate of the Alloy 22 waste package outer barrier is expected. Therefore, among those uncertainties in the Alloy 22 general corrosion rate, the lack of temperature dependence of the general corrosion rate is the most likely source of unquantified uncertainty for the expected exposure conditions in the potential repository. Therefore, the current analysis attempts to quantify the temperature dependence of the general corrosion rate using the limited project and literature data available for Alloy 22 under repository-relevant exposure conditions. Additionally, the current analysis assumes that the entire variation of the current Alloy 22 general corrosion model (i.e., the general corrosion rate distribution resulting from the two-year weight-loss measurements from the LTCTF) is due to uncertainty. This is based on the error analysis results of the weight-loss measurement data of Alloy 22 samples (CRWMS M&O 2000 [DIRS 144229], Section 6.5.3).

7.3.5.3 Quantification of Temperature Dependence of Alloy 22 General Corrosion Rate

In this section, three alternative temperature-dependent general corrosion rate models for the Alloy 22 outer barrier are derived, assuming the temperature dependency follows an Arrhenius relationship (Scully et al. 2001 [DIRS 154513], p. 31). For all models, it is assumed that the current general corrosion rate distribution derived from the two-year weight-loss measurements (CRWMS M&O 2000 [DIRS 152542]) is representative for an exposure temperature of 60°C. The rate at any other temperature is determined by the Arrhenius equation, given a slope term (or activation energy term) is known. The Arrhenius equation for the general-corrosion rate is:

$$R = \exp\left[c_0 - \frac{c_1}{T}\right] \qquad \text{(Eq. 7.3.5-1)}$$

where

R = general-corrosion rate
T = temperature (Kelvin)
c_0 = intercept term
c_1 = slope term

Assuming the current general corrosion rate distribution from the LTCTF is at 60°C and given the slope term is known, the intercept term is determined by the equation:

$$c_0 = \ln(R_o) + \frac{c_1}{T_o} \qquad \text{(Eq. 7.3.5-2)}$$

where R_o is the rate sampled from the general corrosion rate distribution assumed to be at T_o and T_o is 333.15 K (60°C).

The temperature dependency in the first two models is determined from a set of passive current density data collected from potentiostatic polarization experiments (Scully et al. 2001 [DIRS 154513], Section 1.4; Lee 2001 [DIRS 154891]). The first model was developed using the entire data set. The second model was developed using the same data set, except for one apparent outlier point.

7.3.5.3.1 Temperature-Dependent Alloy 22 General Corrosion Model I

To determine the Arrhenius-equation slope (c_1) for the temperature dependency of the Alloy 22 general corrosion rate for repository-relevant conditions, passive current density data collected from potentiostatic polarization experiments were used (Scully et al. 2001 [DIRS 154513], Section 1.4; Lee 2001 [DIRS 154891]). Tests were performed on air-aged Alloy 22 crevice specimens at pH levels of 2.75 and 7.75 and temperatures of 80°, 85° and 95°C. All specimens were in a non-deaerated aqueous environment containing LiCl, Na_2SO_4, and $NaNO_3$, with $[Cl^-]$ versus $[SO_4^{2-}] + [NO_3^-]$ ratios of 10 to 1 and 100 to 1. The passive dissolution rates (i.e., general corrosion rates) were calculated from the measured passive current density using Faraday's law, as discussed in *General Corrosion and Localized Corrosion of Waste Package Outer Barrier* (CRWMS M&O 2000 [DIRS 144229], Section 6.5.1). A total of twelve passive current densities were determined, as seen in Table 7.3.5-1, for the various combinations of the exposure condition parameters (temperature, pH, and $[Cl^-]$ versus $[SO_4^{2-}] + [NO_3^-]$ ratio). Each current density is reported with an estimated median value and average value (with a reported standard error). The average values are used in the slope determination.

The Arrhenius equation slope for this data set was calculated by determining the correlation between the natural log rates and the reciprocal of the temperatures in Kelvin. The last two columns in Table 7.3.5-2 are the deviation from the average for each variable, multiplying the temperature deviations by the rate deviations (cross product) and itself (squared). Taking the ratio of the two column sums, as seen in Table 7.3.5-2, results in a value of 7,997 K for the value of c_1, the slope term. The model fit of the data is shown in Figure 7.3.5-1.

Dividing the slope term by the gas constant results in the more familiar activation energy term as 66 kJ/mole. Figure 7.3.5-2 shows the cumulative distribution functions (CDFs) for the Alloy 22 general corrosion rate that result from the model. The 60°C CDF represents the general corrosion rate used in the TSPA-SR (CRWMS M&O 2000 [DIRS 153246]). The 100^{th} percentile rate is approximately 0.14 µm/yr, and the 50^{th} percentile rate is approximately 0.045 µm/yr. At 125°C, which is close to the boiling point of a saturated $NaNO_3$ solution (i.e., the maximum temperature for having a stable aqueous solution for corrosion in the presence of $NaNO_3$ salt), the 100^{th} percentile rate is approximately 7 µm/yr (approximately a 60-fold

increase from the 60°C rate), and the 50th percentile rate is approximately 2.2 μm/yr (approximately a 50-fold increase from the 60°C rate). At ambient temperatures (25°C), the 100th percentile rate decreases to 0.008 μm/yr (8 nm/yr) and the 50th percentile rate to approximately 0.0025 μm/yr (2.5 nm/yr). In this updated model, the general corrosion rates decrease approximately three orders of magnitude for a temperature range from the maximum temperature for corrosion (125°C) to ambient temperature (25°C). The waste package temperatures are expected to be variable from location to location in the repository and to decrease with time after their peak shortly after waste emplacement. Because of spatial and temporal variability in the waste package temperature, this updated temperature-dependent model causes significant variability in the general corrosion degradation rate of waste packages.

7.3.5.3.2 Temperature-Dependent Alloy 22 General Corrosion Model II

Examining the residual values in model I, one data point (identified in bold in Table 7.3.5-1) was over twice as large in magnitude as all the other residuals. This large residual corresponds to the specimen from the test condition of 95°C, 2.75 pH, and 100:1 electrolyte ratio. Based on model I, a *t*-statistic of 2.264 was calculated. This value is the number of standard deviations by which the suspected value differs from the value predicted by the model. The p-value, or probability that a legitimate value will differ from the model by this number of standard deviations (for a value this extreme, both small and large), is 0.047. Comparing the relative error in the data set between the median values and the average values, the suspect value has a relative error of 11.39 compared to the next largest relative error value of 0.43. Examining the standard deviations associated with each average value, the suspected value's standard deviations ranges from 22 to 146 times larger than the others do. This indicates the error associated with this value is at least an order of magnitude larger than the other averages. The above discussion indicates that the data point in question is clearly an outlier. All of the evidence discussed above indicates either that a more robust estimation should be performed that is not as sensitive to outliers (e.g., median regression or weighted regression), or that the outlier should be removed from the data set and the analysis be redone to see how much the suspect value actually affects the results.

Removing the outlier and determining the Arrhenius equation slope from the remaining eleven current density averages results in a value of 4372.96 K for the value of *c1*, the slope term. Dividing the slope by the gas constant results in the more familiar activation energy term as 36 kJ/mole. The model fit of the data without the outlier is shown in Figure 7.3.5-3. Comparing Figure 7.3.5-3 with Figure 7.3.5-1 shows that removing the outlier from the model not only decreases the slope, but also reduces the predictor bounds.

Figure 7.3.5-4 shows the CDFs for the Alloy 22 general corrosion rate model, excluding the outlier point. The 60°C CDF represents the general corrosion rate used in the TSPA-SR (CRWMS M&O 2000 [DIRS 153246]). At 125°C, the 100th percentile rate is approximately 1.2 μm/yr (approximately a 25-fold increase from the 60°C rate) and the 50th percentile rate is approximately 0.4 μm/yr (approximately 9-fold increase from the 60°C rate). At ambient temperatures (25°C), the 100th percentile rate decreases to 0.03 μm/yr (30 nm/yr) and the 50th percentile rate to approximately 0.01 μm/yr (10 nm/yr). In this updated model, the general corrosion rates decrease approximately two orders of magnitude for a temperature range from the maximum temperature for corrosion (125°C) to ambient temperature (25°C). The corrosion rates and rate variation with temperature observed using this model are more realistic than those

obtained with the previous model (including the outlier point). Furthermore, as discussed above, exclusion of the outlier decreases the activation energy term by approximately 30 kJ/mole.

7.3.5.3.3 Temperature-Dependent Alloy 22 General Corrosion Model III

A recent experiment was conducted over a broader temperature range for which a passive current density was collected from a potentiostatic polarization experiment (Lloyd et al. 2001 [DIRS 155186]; Lee 2001 [DIRS 154871]). The potentiostatic experiment was performed at a potential of 350 mV (vs. Ag/AgCl) in a 1.0 M NaCl (pH = 1) solution. The temperature was raised in increments, starting at 25° and ending at 85°C. The passive current density was measured at five temperature levels: 25°, 45°, 65°, 75°, and 85°C. A steady-state current density measurement was determined at each temperature level. The passive dissolution rates (i.e., general corrosion rates) were calculated from the measured passive current density using Faraday's law, as discussed in *General Corrosion and Localized Corrosion of Waste Package Outer Barrier* (CRWMS M&O 2000 [DIRS 144229], Section 6.5.1). The passive current density data and the calculated passive dissolution rate (general corrosion rate) are given in Table 7.3.5-3.

Determining the Arrhenius slope from these five measurements results in a value of 3,852 K for the slope term, *c1*. Dividing the slope term by the gas constant results in the more familiar activation energy term as 32 kJ/mole. This slope was determined from these five passive dissolution rate values by applying the same analysis performed for the previous two models. Figure 7.3.5-5 shows the CDFs for the general corrosion rates at 25°, 60°, and 125°C calculated with Alloy 22 General Corrosion Model III. Comparing Figure 7.3.5-5 with Figure 7.3.5-4 shows that the third model (32 kJ/mole activation energy term) results in a temperature behavior similar to the second model (36 kJ/mole activation energy term). Since WAPDEG (Version 4.0) results from these two models would be similar, only the results with the second general corrosion model (36 kJ/mole activation energy term) are presented in Section 7.4.

7.3.5.4 Effects of Environment on the Corrosion of Alloy 22

As discussed previously, the corrosion data from the LTCTF show little dependence on the chemistry of the test solutions. These long-term tests (exposure times greater than two years) were supplemented with short-term cyclic polarization tests, which also showed no discernible dependence on chemistry (CRWMS M&O 2000 [DIRS 144229], Sections 6.4.2, 6.4.3, 6.5.1 and 6.5.2). This was expected for a corrosion-resistant material such as Alloy 22 and types of test environments containing ions such as nitrates and sulfates, which tend to buffer the effects of chlorides (Thomas 1994 [DIRS 120498]; CRWMS M&O 2000 [DIRS 144229], Section 6.4; Pasupathi 2001 [DIRS 155252]). However, it is necessary to understand the types of environments in which material corrosion would show dependence on chemistry and if there is a potential for the evolution of such environments at Yucca Mountain. Available data are limited, and a comprehensive testing and analysis program is underway to determine the bounds of environments beyond which accelerated corrosion is possible. However, the available information can be used to develop qualitative conclusions.

In the present design, which includes a drip shield, the expected environment on the waste package as long as the drip shield functions is largely determined by the temperature and relative

humidity history and the characteristics of dust particles present on the surface (see Section 7.3.1.3.3). The environment is also affected by the ionic species deposited from the soluble salts transported by the ventilation air. Preliminary data from the analysis of dust particles in the Exploratory Studies Facility show that the samples contain significant amounts of soluble chlorides, nitrates, and sulfates. Data from the atmospheric deposition monitoring program (see Section 7.3.1.3.3) also show that significant amounts of nitrates, chlorides, and sulfates are deposited from the atmosphere and available to interact with the materials in the emplacement drifts, including the waste package and drip shield. Based on this, the possibility of formation of a potentially more aggressive chloride-only solution on the waste package from deliquescence of the soluble salts in the dust particles or from the atmospheric deposition was considered. However, a review of the data shows that formation of "pure" chloride solutions on the surface of the waste package is highly unlikely because of the significantly greater amounts of nitrates and sulfates present (see Section 7.3.1.3.1). The buffering effect of these ions against the corrosive aggressiveness of chloride ions is well known (Thomas 1994 [DIRS 120498]; CRWMS M&O 2000 [DIRS 144229], Section 6.4; Pasupathi 2001 [DIRS 155252]).

When and if the drip shields fail to perform their intended function (i.e., divert dripping water from the surface of the waste package), the waste package may be susceptible to aggressive chemistries that could lead to accelerated general and localized corrosion. Previous analyses to determine the expected environment on the waste package surface used carbonate-based waters (J-13 well water-type), which resulted in high pH brines upon evaporative concentration (see Section 7.3.1). Alloy 22 corrosion rates due to the aqueous film formed from the deliquescence of the salt deposits from the solutions are very low because of the beneficial effects of the buffering nitrate and sulfate ions. Development of a chloride-only environment containing sodium chloride, while not likely, is not expected to have a significant effect on corrosion rates (Dunn et al. 2001 [DIRS 154511]).

More recent analyses (see Sections 7.3.1 and 6.3.3.7.1) have included the evolution of non-carbonate based dilute waters (such as pore water in the host rock) on the waste package and drip shield surfaces. These waters, in contrast to the J-13 well water-type, may evolve into brines containing chlorides of calcium and magnesium, since these cations are not completely removed by precipitation as carbonates and silicates. The presence of magnesium/calcium chlorides is significant because these could result in the formation of highly corrosive solutions at low relative humidities (20 to 30 percent) and have been shown to cause localized corrosion at elevated temperatures. An initial low-order approximation on the probability of the formation of magnesium and calcium chloride brines was attempted based on the combination of the different modeling runs done on the seven different water compositions (see Section 6.3.3.7.1). The initial approximation indicates that there would be a 14 percent chance of the starting water composition going toward a calcium/magnesium chloride brine due to evaporative concentration processes. However, the approximation is considered qualitative and subjective, and cautions should be exercised in using the information in a quantitative analysis (see Section 6.3.3.7.1).

However the possibility of development of saturated solutions of "pure" magnesium and calcium chloride salts is very unlikely for two reasons. First, the formation of an aqueous film containing these salts will also result in the dissolution of other soluble anions, such as nitrates and sulfates, thereby producing a more benign buffered solution (see Section 7.3.1.3.1). This will continue as the relative humidity increases in the repository. Anions such as nitrate, carbonate, fluoride, and

sulfate are known to mitigate against the aggressiveness of chloride-enhanced corrosion (Thomas 1994 [DIRS 120498]). The project data confirm that the presence of these ions in solution reduces the aggressiveness of chloride ions to Alloy 22 corrosion (CRWMS M&O 2000 [DIRS 144229], Section 6.4). Recent project data indicate that nitrate ions can mitigate against the aggressiveness of chloride ions to Alloy 22 corrosion even in nearly saturated calcium chloride solutions at 120°C (Pasupathi 2001 [DIRS 155252]). Second, the soluble amounts of calcium and magnesium in these waters are very limited, since many of the available cations are removed during evaporative concentration due to the formation of insoluble mineral precipitates (see Section 7.3.1.3.1).

Another potential environmental constituent that could affect the long-term corrosion behavior of Alloy 22 is the presence of lead salts. Presence of lead in test solutions (up to several thousand ppm) has been shown to cause localized corrosion and stress corrosion cracking in Alloy 22 (Barkatt and Gorman 2000 [DIRS 154496]). Development of such an environmental scenario is also highly unlikely because the amount of measured lead concentration in Yucca Mountain waters is very low (several ppb). In addition, preliminary tests conducted in lead containing buffered (mixed ionic) solutions have shown no deleterious effects (see Section 7.3.3.3.3).

Thus, a qualitative review of available information suggests that development of environments in which corrosion of Alloy 22 shows a measurable dependence on the chemistry of the environment is highly unlikely. It also suggests that the potential for the development of environments leading to localized corrosion of Alloy 22 is unlikely. As discussed below, a sensitivity analysis is conducted to study potential effects of magnesium and calcium chloride salts on general corrosion of the Alloy 22 outer barrier.

Sensitivity Analysis for Effects of Magnesium and Calcium Salts on Waste Package Degradation–As discussed above and in Section 7.3.1.3, development of magnesium and calcium chloride salts on the waste package and drip shield surfaces is possible under expected repository conditions. However, the formation of an aqueous film containing these salts will also result in the dissolution of other soluble anions, such as nitrates and sulfates, thereby producing a more benign buffered solution (see Section 7.3.1.3.1). This will continue as the relative humidity increases in the repository. A recent project data indicates that nitrate ions can mitigate against the aggressiveness of chloride ions to Alloy 22 corrosion even in nearly saturated calcium chloride solutions at 120°C (Pasupathi 2001 [DIRS 155252]). Therefore, the potential for the development of environments leading to localized corrosion of Alloy 22 is unlikely. However, because of low deliquescence points of these salts (see Table 7.3.1-2b), general corrosion of waste package and drip shield could initiate much earlier while the temperatures at the surfaces are still sufficiently high.

In order to investigate potential effects of the possible presence of magnesium and calcium chloride salts on the waste package and drip shield surfaces, a sensitivity analysis was conducted using a relative humidity threshold for the initiation of general corrosion based on the deliquescence points of magnesium chloride salt ($MgCl_2$) (see Table 7.3.1-2b). Use of this threshold will allow general corrosion to initiate at an earlier time. This allows for the potential of general corrosion at lower relative humidities and higher temperatures (around 14 percent RH at 164°C). The general corrosion rate used is temperature-dependent General Corrosion

Model II (Section 7.3.5.3.2) and considered to be 100 percent uncertainty. Figure 7.3.5-8 shows a graph of the general corrosion rate cumulative distribution functions at 25, 60, 120, and 165°C for General Corrosion Model II. The median general corrosion rate at 165°C is about 1.05 μm/yr and the upper bound rate is about 3.16 μm/yr.

The simulation parameters used are similar, with the exception of the relative humidity threshold, to those presented in Section 7.4.3.3. The temperature and relative humidity histories of the waste package and drip shield surfaces are sampled from the thermal hydrology time histories for the entire repository (see Section 7.4.3.2). Figure 7.3.5-9 shows the upper-bound, mean, and 95^{th}, 75^{th} and 25^{th} percentile confidence intervals of the failure profile for the waste packages with time, which result from the use of a relative humidity threshold for the initiation of general corrosion based on the deliquescence points of magnesium chloride salts. Lower-bound and 5^{th} percentile confidence interval are not shown in the figure. The upper-bound profile indicates that the earliest possible failure time for a waste package is approximately 20,000 years, 5,000 years later than in the Baseline Waste Package Degradation Model hereafter referred to as the nominal case (Section 7.4.1). The failure profiles in the figure are similar to the failure profiles of the case using the relative humidity threshold based on the deliquescence points of $NaNO_3$ salt (see Table 7.3.1-2b), as shown in Figure 7.4-22 (Section 7.4.3.3). As discussed below, all breaches before 55,500 years are due to crack penetrations. The median estimate of the first breach time of the upper-bound profile is approximately 118,000 years (30,500 years for the nominal case and approximately 2,000 years earlier than the simulation shown in Figure 7.4-22). For the mean profile, approximately 80 percent of the waste packages fail by the end of the simulation time (1 million years). This is the same fraction as in the simulation shown in Figure 7.4-22. The time to fail 10 percent of the waste packages for the upper-bound and mean profiles is approximately 66,000 and 194,000 years, respectively (23,000 and 56,000 years, respectively, for the nominal case). These times are 6,000 and 8,000 years earlier, respectively, than those for the simulation presented in Figure 7.4-22.

Figure 7.3.5-10 shows the first patch penetration profiles of the waste packages with time, which result from the use of a relative humidity threshold for the initiation of general corrosion based on the deliquescence points of magnesium chloride salts (see Table 7.3.1-2b). The first patch breach times of the upper-bound and 95^{th} percentile profiles are approximately 55,500 and 92,000 years, respectively. Comparison of the patch breach profiles with the failure (first breach) profiles (Figure 7.3.5-9) indicates that the initial breach (or failure) of the waste packages is mostly by SCC penetration in the closure lid welds of the Alloy 22 waste package outer barrier. For the 75^{th} percentile profile, the first patch penetration time is approximately 228,000 years. For the mean profile, approximately 71 percent of the waste packages have patch failures by the end of the simulation time (1 million years).

In summary, the effect of the use of a relative humidity threshold for the initiation of general corrosion based on the deliquescence points of magnesium chloride salt is insignificant. The failure times are a few thousand years earlier, and approximately one percent more patch failures result. As seen in Table 7.3.1-2b, the use of the deliquescence points of magnesium chloride salt, which is more hygroscopic than $NaNO_3$ salt, causes an earlier corrosion initiation and increased general corrosion rates at higher temperatures of the Alloy 22 outer barrier (see Figure 7.3.5-8). This insensitivity of waste package degradation to the more aggressive

corrosion initiation threshold is due mostly to the fact that the time period, during which the waste package temperature is above the boiling temperature of $NaNO_3$ salt (120.6°C, see Table 7.3.1-2b) and the waste packages are subject to higher general corrosion rates, is much shorter than the waste package lifetime.

7.3.5.5 Other Lines of Evidence to Support Alloy 22 General Corrosion Model

This section discusses alternative lines of evidence in support of the Alloy 22 general corrosion model used in the TSPA. Literature data and industrial analogues are presented as alternative lines of evidence for the time dependence of the general corrosion rate (i.e., the general corrosion rate decreases with exposure time).

Time-Dependent General Corrosion Behavior of Alloy 22-The general corrosion rates used for Alloy 22 in the waste package degradation analysis are based on the two-year weight-loss results from the LTCTF (CRWMS M&O 2000 [DIRS 144229], Section 6.9.1). These results were conservatively selected for extrapolation over repository time scales based on the observation that the measured corrosion rate is continuing to decrease with time (Figure 7.3.5-6).

The trend of decreasing general corrosion rate with time is consistent with the expected corrosion behavior of passive alloys such as Alloy 22 under repository-type aqueous conditions. Similar passive behavior has also been observed for nickel-, chromium-, and molybdenum-type corrosion-resistant alloys. For example, Alloy C is found to retain a very thin passive film, indicated by the retained mirror-like finish after 44 years of exposure at Kure Beach to a marine environment (i.e., salt air with alternate wetting and drying as well as the presence of surface deposits) (Baker 1988 [DIRS 154510], p. 134). More recent examination of specimens from this alloy after more than 50 years of exposure indicates that the samples continue to maintain a mirror-like finish and passive film behavior (McCright 1998 [DIRS 100289], Figure ES-1). Under these same conditions, the less corrosion-resistant Alloy 600 exhibited a corrosion rate of 0.008 μm/yr after 36 years of exposure. These long-term results provide corroborative support for the expected excellent long-term passive corrosion behavior of Alloy 22 under chloride-containing aqueous environments that are relevant to repository exposure conditions.

In addition, the time-dependent corrosion behavior can be inferred by the long-term monitored corrosion results (represented by loss in tensile strength measurements) on passive-type aluminum alloys exposed to a marine environment (ASM International 1987 [DIRS 103753], p. 911, Figure 42). The initial rate is relatively high at short times (less than one year), but the rates drop off rapidly with increasing exposure time. This is the expected behavior for alloys where the passive film grows by a parabolic diffusion-controlled process or by a logarithmic process.

7.3.6 Early Waste Package Failure: Improper Heat Treatment

An extensive literature review was conducted for the TSPA-SR (CRWMS M&O 2000 [DIRS 153246]) to collect information to develop scenarios and conditions that could lead to early failure of waste packages. From this literature review and analysis, a number of potential mechanisms were identified that could lead to early waste package failures under repository conditions (CRWMS M&O 2000 [DIRS 147359]). Those mechanisms were further evaluated to

develop the probability of their occurrence and the consequence of the mechanism to waste package failures under repository conditions (CRWMS M&O 2000 [DIRS 147359], Section 6.1 and 6.2). All the mechanisms except weld flaws in the waste package closure welds were screened out based on a low probability of occurrence (CRWMS M&O 2001 [DIRS 153937], Section 6.2.12). The analysis results for weld flaw frequency and size were used as inputs to the waste package SCC analysis (CRWMS M&O 2000 [DIRS 151549], Section 6.2.2; see also Section 7.2.5).

A recent reevaluation of the potential early failure mechanisms in *Analysis of Mechanisms for Early Waste Package Failure* (CRWMS M&O 2000 [DIRS 152097]) has concluded that improper heat treatment of waste packages needs to be considered in the waste package and TSPA analysis. This is necessary because the consequence of improper heat treatment could lead to a gross failure of affected waste packages, although the probability of this occurrence is very low. Accordingly, improper heat treatment of waste package is considered in the current waste package degradation analysis. As discussed below, the affected waste packages are assumed to fail with a non-mechanistic failure mode.

Estimation of the Number of Affected Waste Packages–The probability of improper heat treatment of a waste package is estimated in *Analysis of Mechanisms for Early Waste Package Failure* (CRWMS M&O 2000 [DIRS 152097], Section 6.2.3). The main probability component is the branch on the event tree (CRWMS M&O 2000 [DIRS 152097], Section 6.2.3.1, Figure 9, Branch 10) in which the furnace suffers a nondetectable failure and a subsequent independent test fails to detect the improper treatment (CRWMS M&O 2000 [DIRS 152097], Section 6.2.3). This event tree is assumed to apply both for the heat treatment of the waste package before the waste loading and for the induction annealing of the closure weld regions. The current analysis further assumes that the waste package undergoes a second independent inspection before waste loading with a failure probability of one in a hundred, which corresponds to an human error probability of failure to follow a written operating procedure (CRWMS M&O 2000 [DIRS 152097], Section 6.2.3.1). The given probability of an improper heat treatment is p, where $p = 2.21 \times 10^{-5}$ (CRWMS M&O 2000 [DIRS 152097], Figure 9). Combining the two failure modes, the total failure probability is $1.01 \times p = 2.23 \times 10^{-5}$.

A Poisson distribution is used to model the number of waste packages that suffer an improper heat treatment in the repository. The Poisson distribution assumes that the affected waste packages are independent. This assumption is reasonable considering that improper heat treatment is caused by non-detected equipment malfunctioning and non-reported operator errors. The appropriate parameter for the distribution is the expected number of improperly heat-treated waste packages. Assuming there are 11,770 waste packages (CRWMS M&O 2000 [DIRS 148384], Section 6.3.4, Table 6-31) and the probability of improper heat treatment is 2.23×10^{-5}, then the expected number of improperly heat-treated waste packages is the product of these two numbers (0.263). Given this value as the mean of the Poisson distribution, probabilities for the number of packages that are improperly heat-treated are calculated from the Poisson distribution function. The resulting probabilities for the number of waste packages improperly heat-treated per repository are given in Table 7.3.6-1. The results show that there is a 76.9 percent chance that no single waste package is improperly heat-treated. The probability of having at least one waste package improperly heat-treated is 20.2 percent, and the probability of having two waste packages affected is 2.6 percent. The probability of having three waste

packages with improper heat treatment is about 0.2 percent. Assuming a total of 100 realizations for the waste package degradation analysis using the WAPDEG model, those probabilities provide that 77 out of 100 realizations would have no waste packages affected by improper heat treatment. Out of 100 realizations, 20 realizations would have at least one waste package affected and 3 realizations would have two waste packages affected. Because improper heat treatment is a low probability event, it is modeled directly in the TSPA analysis presented in Volume 2 (McNeish 2001 [DIRS 155023]).

Consideration of Improper Heat Treatment in Waste Package Performance Analysis– Disposal containers will be subjected to heat treatment processes to relieve stresses as part of the manufacturing process. A disposal container becomes a waste package after being loaded with waste and sealed (CRWMS M&O 2000 [DIRS 152104], Section 1.0]). These processes include solution annealing of containers before being loaded and local induction annealing for stress mitigation of the outer lid welds of the waste package outer barrier.

Improper heat treatment would be caused by heating and subsequent cooling operations outside the specified operation ranges. The most likely causes would be operator error or equipment malfunctioning when out-of-range operations are not reported or detected. Operations that could damage waste package integrity include heating the container to undesirable temperatures for an extended period of time or improper cooling following the heating process. Any of these operations could result in extensive precipitation of undesirable secondary phases, both on grain boundaries and in the grain interiors (grain bulk) of the Alloy 22 waste package outer barrier. This could lead to severe aging and phase instability problems, which would result in significant degradation of the container's mechanical properties (CRWMS M&O 2000 [DIRS 147639], Section 6.3 and Section 7.3.2.1.2 of this volume) and an increased susceptibility to localized corrosion of the outer barrier (CRWMS M&O 2000 [DIRS 147639], Section 1.1; Dunn et al. 2001 [DIRS 154511], Figure 1; see also Section 7.3.2). Therefore, waste packages that are improperly heat-treated may be subject to SCC and enhanced general and localized corrosion.

As indicated, the improper heat treatment event is modeled directly in the current TSPA analysis. In evaluating the potential of early failures by improper heat treatment and its consequence, a non-mechanistic failure of the outer and inner closure lids of the waste package outer barrier is assumed as well as the failure of the closure lid of the stainless steel structural inner shell. Details of the TSPA implementation are discussed in Volume 2 (McNeish 2001 [DIRS 155023]). The following assumptions are employed:

- Those waste packages affected are assumed to fail immediately when they undergo corrosion.

- The area on the waste package affected by improper heat treatment is assumed to be equal to the closure weld patches because improper heat treatment is most likely to occur during the induction annealing of the outer closure lid welds of the waste package outer barrier (CRWMS M&O 2000 [DIRS 151564], Section 6.2.2.4).

- The materials of the entire affected area are assumed to be lost upon failure of the waste packages because the affected area will be subjected to SCC and highly enhanced localized and general corrosion.

- The weld region of the inner closure lid of the outer barrier and the closure lid of the stainless steel structural inner shell fail at the same time when the outer closure-lid weld region fails.

The above assumptions are conservative because only the weld region of the outer-lid of the outer barrier would be affected by potential improper heat treatment during the stress mitigation heat treatment (e.g., induction annealing), and the inner-lid of the outer barrier is not likely affected. The conservative assumptions were made to avoid detailed analyses for estimating "more realistic" open area of the affected waste package. In a more realistic scenario, the breached weld patches of the affected waste package would remain with the waste package until the weakened areas affected by a major mechanical impact or corroded away by general corrosion.

7.3.7 Other Issues

This section documents additional analyses and information that are not associated with those discussed in the previous subsections.

7.3.7.1 Margin for Localized Corrosion Susceptibility for the Range of Thermal Operating Modes

Two parameters commonly used for assessing thresholds below which localized corrosion will not occur in a given alloy/environment system are critical crevice temperature (CCT) and critical potential (e.g., repassivation potential). The current approach in the waste package performance analysis uses critical potential as the threshold parameter (CRWMS M&O 2000 [DIRS 147648], Sections 6.3.1 and 6.4.1; CRWMS M&O 2000 [DIRS 151566], Sections 4.1.5 and 4.1.6). The use of CCT is also discussed in *General Corrosion and Localized Corrosion of Waste Package Outer Barrier* analysis model report (CRWMS M&O 2000 [DIRS 144229], Section 6.4.3). In considering the advantages of lower-temperature operating modes, the use of a CCT parameter is more informative than a critical potential. There are industrial standards for evaluating CCT (e.g., ASTM G-48 and Materials Technology Institute (MTI) standard MTI-2). The CCT values for Alloy 22 evaluated in these tests could be as low as approximately 58°C (Table 7.3.7-1). Although useful in ranking a range of alloys, these standard tests utilize aggressive environments (in particular, a ferric chloride solution) that are not directly relevant to expected waste package surface environments because the potential for ferric chloride generation is very remote. Although not directly relevant, testing with ferric chloride solution may be used for a conservative lower bound for the expected CCT for magnesium and calcium chloride solutions. Although unlikely to develop, a limited quantity of such solutions could evolve from non-carbonate waters that might be present on the waste package surface from either dripping or deliquescence of the salts contained in deposits on the waste package surface (see Section 7.3.1).

Recent test results by the NRC (Dunn et al. 1999 [DIRS 154481], p. 3-10, Figure 3-10) and Lawrence Livermore National Laboratory for relatively pure concentrated sodium chloride

solutions (pH range of 2.5-8.0; see Table 7.3.7-1) are somewhat more germane than the results with ferric chloride solution, but they are still not directly relevant to potential waste package surface environments. These results with concentrated sodium chloride solutions yield CCT values as low as 85°C, which can be used as a conservative lower-bound CCT. Of more direct relevance are the CCT values that can be derived from specimens exposed to a range of relevant environments (simulated acidic water, simulated dilute water, and simulated concentrated water) at 90°C in the LTCTF. Other relevant data can be derived from the cyclic polarization tests that were conducted for a broader range of relevant environments (CRWMS M&O 2000 [DIRS 144229], Sections 6.4 and 6.5). These test environments all contain realistic concentrations of one or more beneficial buffer ions (nitrate, sulfate, carbonate, and silica ions), which are expected to be present along with chloride ions in the solutions contacting the waste package surface. The CCT values obtained in these tests, as summarized in Table 7.3.7-1, yield a CCT value of at least 90°C (the maximum temperature employed in the LTCTF). These values are greater than 120°C for all relevant test environments, as determined from extrapolation of the measured cyclic polarization corrosion potentials and critical potentials versus test temperature to the point of intersection, as discussed in *General Corrosion and Localized Corrosion of Waste Package Outer Barrier* (CRWMS M&O 2000 [DIRS 144229], Section 6.4.3).

Another basis for assessment of CCT can be derived from the Halar creviced (at each end of gage length) slow strain rate tests performed at Lawrence Livermore National Laboratory. The tests were conducted for conditions that included a range of temperatures from 76° to 105°C, applied potentials from open circuit potential to 400 mV vs. Ag/AgCl, and a range of relevant environments. This test yields a very conservative CCT because the passive film is continuously fractured and reformed throughout the test. Examination of the results previously discussed in Section 7.3.3.3.3 (Table 7.3.3-3) indicates that the normal range of fracture ductility without corrosion effects is about 50 to 60 percent for both the uncreviced and creviced cases. In near-neutral 4M NaCl solutions, a CCT of 98°C occurs between 350 and 400 mV vs. Ag/AgCl (Tests ARC22-123 and ARC22-117), whereas in basic saturated water (pH 13, Test ARC22-120), it lies above 105°C even at 400 mV vs. Ag/AgCl. However, if both nitrate and sulfate ions are removed, leaving primarily NaCl (approximately 3M) in solution, crevice corrosion occurs between 200 and 300 mV vs. Ag/AgCl (Test ARC22-122 vs. ARC22-126) at 98°C, indicating that the pH 13 NaCl solution is more aggressive for Alloy 22 than the near-neutral solution. At highly oxidizing conditions (400 mV vs. Ag/AgCl), simulated concentrated water (Test ARC22-112) appears to be a more aggressive environment than basic saturated water (Test ARC22-119), with a CCT value of 76°C or less. However, at a lower but still highly oxidizing condition (317 mV vs. Ag/AgCl), no crevice corrosion is observed at 76°C in the environment. Under the expected case of open circuit potential, no crevice corrosion is observed at 76°C in any of the environments tested, including those with lead additions (Tests ARC22-13 and ARC22-16 to 18), even under very aggressive, continuous straining conditions.

As discussed above, the CCT value for Alloy 22 in the range of relevant environments and expected corrosion potentials (approximately -200 mV vs. Ag/AgCl) (CRWMS M&O 2000 [DIRS 144229], Section 6.4.2) is greater than 90°C, and very likely greater than 120°C. Additional margin would be obtained from lower-temperature operating modes because of the difference in temperature dependencies between the corrosion and repassivation potentials. The corrosion potential rises only slightly with decreasing temperature (due to increasing oxygen solubility), as described by the Nernst equation, and the repassivation potential increases rapidly

with decreasing temperature, as observed over a broad range of sodium chloride concentrations (Cragnolino et al. 1999 [DIRS 152354], p. 2-33, Figure 2-11). This increasing difference in potentials with decreasing temperature would also provide margin for any upward drift of corrosion potential with time, as well as for any decrease in repassivation potential over long time periods. These potential changes with time may occur due to potentially decreasing protectiveness of the passive film on Alloy 22, which could be caused by some unexpected passive film degradation mechanism. It also provides margin for unexpected (but possible) environments that may lack beneficial buffering ions or contain higher than expected trace element concentrations, including dissolved lead.

7.3.7.2 Effects of Radiolysis on Alloy 22 Corrosion Rates

Section 7.3.1 discusses the highly unlikely potential for the development of an aqueous environment very early after waste package emplacement due to the presence of magnesium and calcium chloride salts in the deposited salts from the non-carbonate based pore water. Because of this, it is possible that the radiation levels at the outer surface of the waste packages may be high enough to result in the formation of more aggressive conditions due to radiolysis. To address this condition, a brief review of the available information was conducted.

Engineering calculations of the expected radiation levels at the surface of the waste package have been performed. For a bounding-case waste package containing 21-PWR fuel assemblies (75 GWd/MTU burnup and 5-year decay), the maximum surface radiation level in the fueled region was calculated to be 1,039 rem/hour (BSC 2001 [DIRS 153752]). This value is an upper bound at the time of emplacement. For an assumed ventilation period of 50 years, during which time no aqueous environment is expected, this value decays down to levels in the range of 85 to 90 rem/hour (BSC 2001 [DIRS 153752]). The calculated levels are further reduced to approximately 25 rem/hour at 100 years after emplacement.

The effects of radiation on waste package materials corrosion will differ depending on the environment (i.e., dry, humid, or wet). At relative humidities where a thin film of liquid can form from the deliquescence of the deposited salts, and if dissolved nitrogen from air is present in the water film, radiation could lead to formation of acidic conditions, and thus enhanced corrosion rates. However, there is little information available in the literature on the effects of radiation on Alloy 22. Limited data are available on the effects of radiation fields on the corrosion of nickel alloy C-4 in highly aggressive $MgCl_2$ brines. There was no observable influence from the radiation field below 1,000 rem/hour (Smailos et al. 1990 [DIRS 154820]; Shoesmith and King 1999 [DIRS 112178]). Above these levels, localized corrosion was observed. Based on these limited data, it is concluded that even in the presence of $MgCl_2$ brines, the radiation levels are not high enough to result in an enhancement of corrosion rates of the Alloy 22 outer barrier.

7.3.7.3 Additional Natural and Archaeological Analogues

Although corrosion data for Alloy 22 are available only for a two-year time period, there are abundant data from analogues that suggest that corrosion rates should be very low in an open space within an unsaturated environment. A vault excavated into limestone at the base of the great pyramid of Giza contained a disassembled cedar boat that was well-preserved in spite of its

4,500-year-old age. The tombs in the valley of the kings of Egypt were carved into limestone within an unsaturated zone. The tomb of Meketre contained 24 wooden boxes, each with painted figurines, which were all well preserved after nearly 4,000 years (Stuckless 2000 [DIRS 151957]). Several items that are more delicate than metals and alloys were recovered from the tomb of Tutankhamen, including reed baskets of fruit, bread, and dried cornflowers. Even an iron knife, which was free of rust when pulled from its scabbard, was preserved within the unsaturated zone for approximately 3,500 years (Stuckless 2000 [DIRS 151957]).

Some of the oldest examples of metal preserved within the unsaturated zone come from a cave in Israel. Bronze items have been nearly perfectly preserved for almost 6,000 years. Other items preserved in the cave and pictured in a recent issue of National Geographic (Ozment 1999 [DIRS 155058]) include ivory, wood, and fabric. Although the climate in this example is drier than that of southern Nevada, it shows how well the unsaturated zone can protect even nondurable materials.

The durability of the iron (99.7 percent) pillar of Asoka, India, is attributed to its location in a relatively dry environment and to its having minimal impurities. Johnson and Francis (1980 [DIRS 125291], p. 6.5) indicate that the pillar was constructed by forge-welding together many solid disks. They suggest that conditions during welding may have been favorable for formation of corrosion-resistant oxides.

Stuckless (2000 [DIRS 151957]) reviews examples of metal and other materials preserved in Europe, where the environments are wetter than those of Israel or southern Nevada. Examples from Roman mines excavated into the unsaturated zone include a copper plaque from Riotinto, Spain, that is nearly 2,000 years old. Other items from around the same period include iron and bronze tools, a bronze pump, leather ore buckets, hemp, and a wooden Archimedian screw.

7.3.7.3.1 Cask of Nails

An ancient hoard of buried nails has been used in a study of the corrosion of iron. These nails were found on the site of the most northerly fortress of the Roman Empire at Inchtuthil, Scotland. An estimated total of over a million nails were buried in a 5-m deep pit and covered with 3 m of compacted earth in a successful attempt to hide the nails from Pictish tribes when the fortress was abandoned in 87 A.D. (Miller et al. 1994 [DIRS 126089]). The fortress was excavated in the 1950s, when the surviving nails (850,000 or so) were unearthed. Although the nails were composed of iron, they were heterogeneous in composition, with regions of high and low carbon contents. The surfaces of all the nails exhibited some corrosion, but the degree of corrosion was greatly controlled by location within the hoard. The nails toward the inside of the hoard showed minimal corrosion, limited to formation of a thin corroded layer; those on the outside of the hoard, especially near the top, were corroded to the extent that they formed a solid crust. This example serves to illustrate the protective role of a corrosion-formed crust in reducing or preventing further corrosion.

7.3.7.3.2 Meteorites

Naturally occurring metal and metallic oxides also demonstrate low corrosion rates in the environment of the southwestern United States. Iron from the meteorite that created Meteor

Crater in Arizona has existed at the surface of the earth for thousands of years. At Yucca Mountain, ilmenite ($FeTiO_2$) and magnetite (Fe_3O_4) have existed within the unsaturated zone for the entire history of the mountain without visible alteration.

It has been suggested that iron meteorites may be good analogues of steel alloy waste packages. Iron meteorites are essentially nickel-iron alloys (nickel content usually ranges between 5 and 11 wt. percent, with a maximum of 60 wt. percent) with minor amounts of cobalt (0.3 to 1.0 wt. percent) and traces of chromium (5 to 2500 ppm), chlorine (1 to 10 ppm), and titanium and vanadium (0.5 to 5.0 ppm) (Johnson and Francis 1980 [DIRS 125291], p. 4.2). Although iron meteorites lack the high chromium concentration of Alloy 22, their validity as an analogue would be increased by the ability to monitor such present environmental parameters as pH, Eh, soil moisture, etc., and to estimate past environmental parameters in the setting where they fell to earth. This means that only meteorites that can be traced to their depositional sites would yield useful information for such a study.

The presence or absence of a fusion crust (i.e., a magnetite (Fe_3O_4)-wüstite ($Fe_{1-x}O$) rind formed by rapid oxidation during atmospheric descent) may be a factor in the range of weathering that occurs at sites where meteorites fragment both on descent and upon impact. At Canyon Diablo, Arizona, meteoritic material that developed a fusion crust during descent was, with the exception of silica-coated metal particles, more resistant to weathering than masses formed on impact, which developed a thin fusion crust (Johnson and Francis 1980 [DIRS 125291], p. 4.20).

The nickel content of a meteorite appears to affect its resistance to corrosion. Phases with 20 to 30 wt.% nickel (ataxites) have frequently shown superior resistance to terrestrial corrosion than phases with less nickel. By measuring potentials between selected phases, Buddhue (Johnson and Francis 1980 [DIRS 125291], p. 6.4) determined that corrosion over a period of centuries consumed kamacite (Fe-7.5 percent Ni) while preserving phases such as taenite (Fe-25 percent Ni), schreibersite $(Fe, Ni)_3P$ (Johnson and Francis 1980 [DIRS 125291], p. 6.4) as the meteorite mineral most resistant to corrosion), and draubreelite ($FeCr_2S_4$). The better-preserved phases are higher in chromium and nickel.

Johnson and Francis (1980 [DIRS 125291]) investigated general corrosion of more than 40 iron artifacts and a few meteorites, and obtained a rate of uniform corrosion of 0.1 to 10 μm/yr over a range of environmental conditions. Chapman et al. (1984 [DIRS 127768]) used a corrosion rate of 1μm/yr (in the middle of this range) to obtain a lifetime of 5×10^4 years for the mechanical stability of the Nagra (Switzerland) waste package container.

Johnson and Francis (1980 [DIRS 125291], p. 6.7) noted that dry and tomb-like environments were the most benign to all ancient materials because lack of moisture condensation suppressed corrosion. They further suggested that if temperatures are below the range where rapid oxidation occurs (varying by metal), elevated temperatures (above the dew point) are an advantage to preservation of metals.

7.4 EFFECT OF UPDATED UNCERTAINTIES ON WASTE PACKAGE PERFORMANCE

This section evaluates the effects of using updated data (i.e., updated and quantified uncertainties) in the corrosion models of waste package performance described in Section 7.3. The WAPDEG model is used in the analysis. The analysis is conducted by comparing the results of the baseline (or nominal case) WAPDEG analysis with the results of a new WAPDEG analysis conducted using updated corrosion models.

7.4.1 Baseline Waste Package Degradation Model

All simulations were conducted using Version 4.0 of the WAPDEG software and Version 6.04.007 of the GoldSim software. The baseline integrated WAPDEG model, the model used to produce the analyses presented in this section, differs slightly from the model used in the initial TSPA-SR (CRWMS M&O 2000 [DIRS 148384]). The baseline model is referred to as the updated WAPDEG model in the *WAPDEG Analysis of Waste Package and Drip Shield Degradation* (CRWMS M&O 2000 [DIRS 151566]), and the initial TSPA-SR WAPDEG model (CRWMS M&O 2000 [DIRS 153246]) is referred to as the current WAPDEG model. The baseline WAPDEG model incorporated some of the updated and quantified uncertainties in the corrosion models (see Section 7.3) completed after the TSPA-SR (CRWMS M&O 2000 [DIRS 153246]) was issued. Differences between the baseline WAPDEG model and the current WAPDEG model include:

- The radii of the Alloy 22 waste package outer barrier closure lid used in the baseline WAPDEG model are slightly larger than those used in the current WAPDEG model.

- The treatment of the weld flaw abstraction model has been updated. The input parameters and functional forms used in the baseline WAPDEG weld flaw model are based on analyses presented in the process level and abstraction analysis model reports (CRWMS M&O 2000 [DIRS 152097]; CRWMS M&O 2000 [DIRS 151549]).

- The lower bound on the distribution for the location parameter for the probability of nondetection of weld flaws is larger in the baseline WAPDEG model than the bound used in the current WAPDEG model.

- The baseline WAPDEG model uses one more input than the current WAPDEG model in its treatment of the weld flaw abstraction model (i.e., the fraction of surface-breaking flaws).

- The baseline WAPDEG model uses a revised threshold stress uncertainty for SCC initiation that is uniformly distributed between 10 percent and 40 percent of the yield strength. The current WAPDEG model uses a threshold stress uncertainty that is uniformly distributed between 20 percent and 30 percent of the yield strength.

- The baseline WAPDEG model has an updated uncertainty range for parameter n, the crack growth exponent (sometimes referred to as the repassivation slope) of the slip dissolution model. In the baseline WAPDEG model, n is given by a uniform

distribution between 0.843 and 0.920. In the current WAPDEG model, n is given a uniform distribution between 0.75 and 0.84.

Results of a WAPDEG analysis (i.e., waste package and drip shield failure time and number of crack, pit, and patch penetrations) are reported as a group of degradation profile curves that represent the potential range of the output parameters. The results are presented for the upper and lower bounds, mean, and 95^{th}, 75^{th}, 25^{th}, and 5^{th} percentiles as a function of time for the following output parameters:

- Waste package first breach (or failure)
- Drip shield first breach (or failure)
- Waste package first crack penetration
- Waste package first patch penetration
- Waste package crack penetration numbers per failed waste package
- Waste package patch penetration numbers per failed waste package
- Drip shield patch penetration numbers per failed drip shield.

Localized corrosion does not initiate for either the waste package (Alloy 22 outer barrier) or the drip shield because the exposure conditions on the drip shield and waste package surface are not severe enough to initiate localized corrosion. In the current conceptual model, the drip shields will be fully annealed before being placed in the emplacement drift, and rockfall-induced SCC is the only potential mechanism for a through-wall crack penetration of the drip shield. However, the SCC cracks will be short and tight and plugged with corrosion products and precipitates such as calcite (see Section 7.3.3.2). Therefore the rockfall-induced SCC cracks will not compromise the intended design function of the drip shield (i.e., diversion of dripping water). SCC of the drip shield is not considered further in the current analysis. Thus, for the drip shield, the first patch breach time profile is the same as the failure time profile.

The upper-bound, lower-bound, mean, and 95^{th}, 75^{th}, 25^{th}, and 5^{th} percentile curves do not correspond to individual realizations. They are summary statistics related to consideration of 100 realizations. In the bullets below, the origin of the upper-bound, lower-bound, mean, and 95^{th}, 75^{th}, 25^{th}, and 5^{th} percentile curves for first breach of the waste package are discussed. Similar wording could be applied to discussion of the origins of the drip shield first breach curves, waste package first crack penetration curves, etc.

- At each point in time, the upper-bound curve shows the realization with the greatest fraction of failed waste packages calculated in any one of the 100 realizations. This may not be the same realization at each point in time. The upper bound curve becomes non-zero at the time of failure of the first waste package in all 100 realizations. Note that the upper-bound curve represents a case with an extremely low probability, and the same is true for the lower-bound curve discussed below.

- At each point in time, the 95^{th} percentile curve shows the realization with the 95^{th} greatest fraction of waste packages failed (i.e., 95 realizations out of 100 have a smaller fraction of failed waste packages). This may not be the same realization at each point in time. The 95^{th} percentile curve becomes non-zero at the time when at least 5 realizations have at least 1 waste package failure.

- At each point in time, the 75th percentile curve shows the realization calculated in any one of the 100 realizations with the 75th greatest fraction of failed waste packages, (i.e., 75 realizations out of 100 have a smaller fraction of waste packages failed). This may not be the same realization at each point in time. The 75th percentile curve becomes non-zero at the time when at least 25 realizations have at least 1 waste package failure.

- At each point in time, the 25th percentile curve shows the realization calculated in any one of the 100 realizations with the 25th greatest fraction of failed waste packages (i.e., 25 realizations out of 100 have a smaller fraction of waste packages failed). This may not be the same realization at each point in time. The 25th percentile curve becomes non-zero at the time when at least 75 realizations have at least 1 waste package failure.

- At each point in time, the 5th percentile curve shows the realization calculated in any one of the 100 realizations with the 5th greatest fraction of failed waste packages (i.e., 5 realizations out of 100 have a smaller fraction of waste packages failed). This may not be the same realization at each point in time. The 5th percentile curve becomes non-zero at the time when at least 95 realizations have at least 1 waste package failure.

- At each point in time, the mean curve shows the mean of all the fractions of failed waste packages in the 100 realizations. The mean curve becomes non-zero at the time of failure of the first waste package in all 100 realizations.

The effect of the updated and quantified uncertainties in the corrosion models (see Section 7.3) on waste package performance is evaluated by comparing results of the WAPDEG analysis using the updated corrosion models with the results of the baseline WAPDEG analysis. The nominal case results are discussed first in this section. Details concerning the development of the nominal case WAPDEG analyses can be found in the *WAPDEG Analysis of Waste Package and Drip Shield Degradation* (CRWMS M&O 2000 [DIRS 151566]).

WAPDEG results for the following cases are presented and described in the following sections:

- Baseline WAPDEG model

- Updated weld residual stress profile uncertainty bounds for the Alloy 22 waste package outer and inner closure lid weld regions

- Updated stress threshold uncertainty for stress corrosion cracking (SCC) crack growth initiation

- Updated general corrosion models assuming 100% uncertainty in the general corrosion rates

- Updated general corrosion models incorporating the temperature-dependent general corrosion rate

- Integrated Models using the temperature-dependent general corrosion models discussed in Section 7.3.5.

The upper and lower bounds, mean, and 95th, 75th, 25th, and 5th percentile confidence intervals of the first breach (failure) profile for the waste packages with time for the baseline WAPDEG model were calculated (Figure 7.4-1). The upper-bound profile, which is the upper extreme of the probable range of the first breach time, indicates that the earliest possible first breach time for a waste package is approximately 15,000 years. Note that the estimated earliest possible first breach time has an extremely low probability. It can be shown by comparison with the upper-bound profile in Figure 7.4-4 (showing the first crack breach profiles of waste packages with time) that the first breach is by SCC crack penetration. The median estimate (50 percent of waste packages failed) of the first breach time of the upper bound profile is approximately 35,000 years. The median estimate of the first breach time of the mean profile is approximately 108,000 years. The time to fail 10 percent of the waste packages for the two profiles is approximately 23,000 and 56,000 years, respectively.

Figure 7.4-2 shows the first breach profiles of drip shields with time for the baseline WAPDEG model. As discussed earlier, the drip shields are not subject to localized corrosion, and SCC of the drip shield is not considered in the current analysis. Therefore, the first breach profiles shown in the figure are by general corrosion only. The upper and under sides of the drip shield are exposed to conditions in the emplacement drift and subject to corrosion. In addition, both sides experience the same exposure conditions regardless of whether the drip shields are dripped on or not. Thus, in the analysis, the general corrosion rate for the drip shields is sampled twice independently, once for the patches on the upper side and once for the patches on the under side. This results in reduced variability in the degradation profiles and a fast failure rate (i.e., many drip shields failing over a short time). This is shown in the upper-bound profile, in which the drip shield first breach starts at approximately 20,000 years and 50 percent of the drip shields fail within a couple of thousand years after the initial failure. Similar trends are also seen with the 95th, 75th, and median profiles. In terms of the number of patch penetration openings per failed drip shield with for the baseline WAPDEG model (Figure 7.4-3), the upper-bound profile shows that as the drip shields fail, a large number of patches are perforated over a relatively short time period (i.e., a few thousand years). There are kinks in the upper-bound curve in Figure 7.4-3 at early times (e.g., at 30,000 years) because the number of failed drip shields increases rapidly at these times (Figure 7.4-2). This causes the average number of patch penetrations per failed drip shield to decrease significantly at these times.

Figures 7.4-4 and 7.4-5 show, respectively, the first crack penetration and first patch penetration profiles of the waste packages with time for the baseline WAPDEG model. The first crack breach times of the upper-bound and 95th percentile profiles are approximately 15,000 and 20,000 years, respectively (Figure 7.4-4), and the first patch breach times of the upper-bound and 95th percentile profiles are approximately 33,000 and 43,000 years, respectively (Figure 7.4-5). Comparison of the first crack and patch breach profiles with the first breach profiles in Figure 7.4-1 indicates that the initial breach (or failure) of the waste packages is likely by SCC penetration in the Alloy 22 waste package outer barrier closure lid welds. For the 75th percentile profiles in the figures, the first crack and patch penetration times are approximately 32,500 and 58,000 years, respectively.

Figure 7.4-6 shows the profile for the average number of crack penetrations per failed waste package for the baseline WAPDEG model. As discussed for Figure 7.4-4, the upper-bound and 95th percentile profiles show the first crack penetration at approximately 15,000 and 20,000 years, respectively. The mean profile never develops more than 25 crack penetrations per waste package. SCC cracks in passive alloys such as Alloy 22 tend to be tight (i.e., have a small crack opening displacement) (CRWMS M&O 2000 [DIRS 151564], Section 6.5.5). The opposing sides of through-wall SCC cracks will continue to corrode at low passive corrosion rates until the gap region of the tight crack opening is "plugged" by the corrosion product particulates and precipitates such as calcite. Any water transport through this oxide/salt-filled crack area will be mainly by diffusion-type processes (CRWMS M&O 2000 [DIRS 153940], Section 6.4.3). Refer to Section 7.3.3.2 for a summary discussion on the recent analysis of plugging of SCC cracks by calcite precipitates. Thus, the effective water flow rate into the waste packages and the radionuclide release rate from the waste packages through the SCC cracks would be expected to be extremely low.

Figure 7.4-7 presents the profile for the average number of patch openings per failed waste package for the baseline WAPDEG model. For the upper-bound profile, which represents an extremely low probability case, the first patch breach occurs at approximately 33,000 years (also see Figure 7.4-5), and approximately 12 patches of the failed waste packages (approximately 1.2 percent of the waste package surface area) are breached by 100,000 years. For the mean profile, there will be approximately 2 patch openings in each of the failed waste packages by 100,000 years.

7.4.2 Effect of Updated and/or Quantified Uncertainties in the Stress Corrosion Cracking Model Parameters

7.4.2.1 Weld Flaw Orientation

Uncertainty in the fraction of weld flaws that are capable of growing in a radial direction in the presence of hoop stress is quantified in Section 7.3.3. As discussed in that section, hoop stress is the dominant stress that can grow through-wall radial cracks resulting in waste package failure. The WAPDEG model assumes that, if SCC occurs, only those flaws could grow in a radial direction in the presence of hoop stress. A sensitivity study was conducted using the WAPDEG model (CRWMS M&O 2000 [DIRS 151566]) in which the fraction of the weld flaws considered capable of propagation in the radial direction was sampled from a bounded lognormal distribution with a median value of 0.01 (1 percent) and ±3 standard deviations bounds (0.0002 and 0.50). This is obtained by multiplying the fraction of flaws (CRWMS M&O 2000 [DIRS 151566], Section 6.4.11) considered to be capable of propagation by the sampled value.

Figure 7.4-8 shows the upper-bound, lower-bound, mean, 95th, 75th, 25th, and 5th percentile confidence intervals of the first breach profile for the waste packages with time incorporating the updated uncertainty for weld flaw orientation. The upper-bound profile, which is the upper extreme of the probable range of the first breach time, indicates that the earliest possible first breach time for a waste package is approximately 20,000 years (15,000 years for the nominal case). The median estimate (50 percent of waste packages failed) of the first breach time of the upper-bound profile is approximately 55,000 years (30,500 years for the nominal case). The median estimate of the first breach time of the mean profile is approximately 120,000 years

(108,000 years in the nominal case). The time to fail 10 percent of the waste packages for the two profiles (the upper-bound and mean profiles) is approximately 34,500 and 70,000 years, respectively (23,000 and 56,000 years, respectively, for the nominal case).

7.4.2.2 Residual Stress Uncertainty Bounds

A second sensitivity study was conducted, based on the revised models, to determine the uncertainty in the stress and stress intensity factor profiles. In this analysis, the uncertainty bounds of residual stress of the Alloy 22 waste package outer closure lid welds (induction annealed) were set to ±21.4 percent of the yield strength (Section 7.3.3.3.1), and the residual stress uncertainty bounds of the Alloy 22 waste package inner closure lid welds (laser peened) were sampled from a cumulative distribution function (Table 7.3.3-2). In the WAPDEG model nominal case simulations, the residual stress uncertainty bounds for both of the Alloy 22 waste package outer barrier closure lids were set to ±30 percent (CRWMS M&O 2000 [DIRS 151566], Section 6.5.1). The residual stress uncertainty bounds used in this sensitivity study would increase the minimum depth at which SCC crack growth could initiate (Figures 7.4-11 and 7.4-12), delaying the waste package first breach times relative to the nominal case simulations. Details of the residual stress uncertainty model implementation are presented in *WAPDEG Analysis of Waste Package and Drip Shield Degradation* (CRWMS M&O 2000 [DIRS 151566], Section 6.4.12).

Figure 7.4-9 shows the upper-bound, lower-bound, mean, 95^{th}, 75^{th}, 25^{th}, and 5^{th} percentile confidence intervals of the first breach profile for the waste packages with time incorporating the updated stress uncertainty bounds for the outer and inner lids of the waste package outer barrier. The upper-bound profile, which is the upper extreme of the probable range of the first breach time, indicates that the earliest possible first breach time for a waste package is approximately 20,000 years (15,000 years for the nominal case). The median estimate (50 percent of waste packages failed) of the first breach time of the upper-bound profile is approximately 48,000 years (30,500 years for the nominal case). The median estimate of the first breach time of the mean profile is approximately 106,000 years (108,000 years for the nominal case). The time to fail 10 percent of the waste packages for the two profiles is approximately 33,000 and 57,000 years, respectively (23,000 and 56,000 years, respectively, for the nominal case).

7.4.2.3 Updated Threshold Stress Uncertainty for Stress Corrosion Crack Initiation

A third sensitivity study was conducted, based on the revised models, to determine the uncertainty in the stress threshold necessary for SCC crack initiation. In this analysis, the stress threshold was considered to vary uniformly between 80 and 90 percent of the Alloy 22 yield strength. Figure 7.4-10 shows the upper-bound, lower-bound, mean, 95^{th}, 75^{th}, 25^{th}, and 5^{th} percentile confidence intervals of the first breach profile for the waste packages with time incorporating the updated stress threshold uncertainty for SCC crack initiation. The upper-bound profile, which is the upper extreme of the probable range of the first breach time, indicates that the earliest possible first breach time for a waste package is approximately 30,000 years (15,000 years for the nominal case). The median estimate (50 percent of waste packages failed) of the first breach time of the upper-bound profile is approximately 82,500 years (30,500 years for the nominal case). The median estimate of the first breach time of the mean profile is

approximately 140,000 years (108,000 years in the nominal case). The time to fail 10 percent of the waste packages for the two profiles is approximately 62,000 and 90,000 years, respectively (23,000 and 56,000 years, respectively, for the nominal case). In this case, crack and patch beach times are comparable (i.e., neither failure mode can be considered to dominate the overall failure behavior of the waste packages).

Figures 7.4-11 and 7.4-12 (CRWMS M&O 2000 [DIRS 151549], Figures 11 and 13) show the median stress profiles in the Alloy 22 outer and inner closure lid weld regions, along with stress profiles with the uncertainty bounds of ±5, ±10, and ±30 percent of the yield strength. Also shown in the figures is the lower bound of the stress threshold distribution (80 percent of the yield strength). For the Alloy 22 waste package outer lid, the crack tip has to reach a depth of approximately 11 mm before crack growth can initiate (Figure 7.4-11). A greater level (near 30 percent) of uncertainty is necessary for any SCC cracks to begin propagation in the Alloy 22 inner lid. This would lead to few cracks penetrating the inner lid. However, because the WAPDEG model conservatively assumes that manufacturing flaws (which are treated in WAPDEG as preexisting cracks) maintain their depth relative to the general corrosion penetration front at all times (CRWMS M&O 2000 [DIRS 151566], Section 5.7), there can be a significant number of crack penetrations. The WAPDEG results for the upper-bound average number of cracks per failed waste package incorporating the updated stress threshold uncertainty for SCC crack initiation (Figure 7.4-13) indicate that cracks do not start penetrating the Alloy 22 inner lid until approximately 35,000 years (less than 5,000 years after the first patch penetration, but significantly delayed relative to the nominal case value of 15,000 years). The average number of cracks per failed waste package never exceeds approximately 15 cracks, whereas in the nominal case approximately 33 cracks per failed waste package are estimated.

7.4.3 Effect of Updated and Quantified Uncertainties in Alloy 22 General Corrosion

This section discusses the WAPDEG sensitivity analysis results using the updated uncertainty in the Alloy 22 general corrosion rate distribution (Section 7.4.3.1). Also presented in this section are the effects of the previously unquantified uncertainty in the temperature effect on the Alloy 22 general corrosion rate on the waste package degradation. As discussed in Section 7.3.5.3, three alternative temperature-dependent general corrosion rate models were developed for the Alloy 22 outer barrier assuming the temperature dependency follows an Arrhenius relationship. These models are: 1) temperature-dependent Alloy 22 general corrosion model I (Section 7.3.5.1); 2) temperature-dependent Alloy 22 general corrosion model II (Section 7.3.5.2); and 3) temperature-dependent Alloy 22 general corrosion model III (Section 7.3.5.3). Because the model II and III behave similarly, only the WAPDEG analysis results using the model I and II are documented in this section.

7.4.3.1 General Corrosion Rate Uncertainty

A sensitivity study was conducted in which all variance in the general corrosion rates for Titanium Grade 7 and Alloy 22 was considered to be solely due to uncertainty (i.e., 100 percent uncertainty). Details of the general corrosion rate uncertainty model implementation can be found in the *WAPDEG Analysis of Waste Package and Drip Shield Degradation* (CRWMS M&O 2000 [DIRS 151566], Section 6.4.7). Figure 7.4-14 shows the first breach profiles of drip shields with time assuming 100% uncertainty in the general corrosion rates for the Alloy 22

waste package outer barrier and the Titanium Grade 7 drip shield. Because the drip shields are subject to general corrosion only (i.e., not subject to localized corrosion and SCC not considered), the first breach profiles shown in the figure are from general corrosion only. In the upper-bound profile, the drip shield first breach starts at approximately 20,500 years, and all the drip shields fail within a few years after the initial failure. The slight variability in drip shield failure time is due solely to variability in general corrosion initiation time caused by variability in the temperature and relative humidity profiles used in the analysis. For the 95th percentile, all drip shields fail at 37,000 years. The 75th percentile curve shows the drip shield failures at 77,000 years.

Unlike the drip shield degradation model, the waste package degradation model has sources of variability other than the general corrosion rates. In each WAPDEG realization, the number of manufacturing flaws per waste package and their sizes are sampled from a cumulative distribution function (representing variability) derived from parameters (CRWMS M&O 2000 [DIRS 151566], Section 6.4.11). The general corrosion initiation time is variable; it depends on the time at which the critical relative humidity threshold for corrosion initiation is satisfied, which in turn depends on the thermal-hydrologic history files used for the given waste package (CRWMS M&O 2000 [DIRS 151566], Section 6.4.8). The effects of MIC, and aging and phase stability are modeled with enhancement factors, which are used as multipliers to the general corrosion rate, and are considered to be 100 percent variable (CRWMS M&O 2000 [DIRS 151566], Section 6.3.2 and 6.3.3). The MIC enhancement factor applies to the entire Alloy 22 waste package surface (CRWMS M&O 2000 [DIRS 151566], Section 4.1.10), while the aging and phase stability enhancement factor applies only to the Alloy 22 closure lid weld regions (CRWMS M&O 2000 [DIRS 151566], Section 4.1.11).

Figure 7.4-15 shows the upper-bound, lower-bound, mean, 95th, 75th, 25th, and 5th percentile confidence intervals of the first breach profile for the waste packages with time assuming 100 percent uncertainty in the general corrosion rates for the Alloy 22 waste package outer barrier and the Titanium Grade 7 drip shield. The upper-bound profile indicates that the earliest possible first breach time for a waste package is approximately 15,000 years, similar to the nominal case. The median estimate of the first breach time of the upper-bound profile is approximately 40,000 years (30,500 years for the nominal case). The median estimate of the first breach time of the mean profile is approximately 120,000 years (108,000 years for the nominal case). The time to fail 99 percent of the waste packages for the mean profile is approximately 700,000 years (approximately 300,000 years in the nominal case). The use of the 100 percent uncertainty assumption results in a broader (spread over a longer time) mean failure curve than the nominal case. This is because in the nominal case, even if a low median general corrosion rate is sampled for a waste package, variability around that median could allow for higher corrosion rates for the patches of the waste package. With the use of 100 percent uncertainty, no such variability exists.

7.4.3.2 Temperature-Dependent Alloy 22 General Corrosion Model I

This section documents the WAPDEG results using the Alloy 22 temperature-dependent general corrosion model I. The temperature dependence of this model is based on the passive current density data collected from potentiostatic polarization experiments by Scully et al. (2001 [DIRS 154513], Section 1.4; also see Section 7.3.5.3.1).

Figure 7.4-16 shows the upper-bound, lower-bound, mean, 95th, 75th, 25th, and 5th percentile confidence intervals of the first breach profile for the waste packages with time incorporating the temperature-dependent general corrosion model for the Alloy 22 outer barrier. The upper-bound profile, which is the upper extreme of the probable range of the first breach time, indicates that the earliest possible first breach time for a waste package is approximately 15,000 years, similar to the nominal case. The median estimate (50 percent of waste packages failed) of the first breach time of the upper-bound profile is approximately 204,000 years (30,500 years for the nominal case). For the mean profile, approximately 23 percent of the waste packages failed by the end of the simulation time (1 million years). The time to fail 10 percent of the waste packages for the two profiles is approximately 62,500 and 625,000 years, respectively (23,000 and 56,000 years, respectively, for the nominal case).

Figure 7.4-17 shows the first patch penetration profiles of the waste packages with time incorporating the temperature-dependent general corrosion model for the Alloy 22 outer barrier. The first patch breach times of the upper and 95th percentile profiles are approximately 272,000 and 592,000 years, respectively. Comparison of the first patch breach profiles with the first breach profiles (Figure 7.4-16) indicates that the initial breach (or failure) of the waste packages is all by SCC penetration in the closure lid welds of the Alloy 22 outer barrier. For the 75th percentile profile, the first patch penetration time is approximately 944,000 years. For the mean profile, approximately 6 percent of the waste packages have patch failures by the end of the simulation time (1 million years).

Thermal-Hydrologic History Sampling–If the general corrosion model is not temperature dependent, then the thermal-hydrologic history files used have little effect on the results of a WAPDEG simulation. The primary role of the thermal-hydrologic history file would be to determine the corrosion initiation time, since the critical relative humidity for corrosion initiation is a function of exposure temperature (CRWMS M&O 2000 [DIRS 151566], Section 6.4.8). Small variations in the corrosion initiation time would have little effect on the simulation results, particularly since the waste package lifetime exceeds significantly typical corrosion initiation times. For this reason, 14 thermal-hydrologic history files were used to represent the variability in thermal-hydrologic exposure conditions (CRWMS M&O 2000 [DIRS 151566], Section 6.4.1).

Development of a temperature-dependent general corrosion model for the Alloy 22 outer barrier necessitates considering all possible thermal-hydrologic history files in WAPDEG simulation. In the WAPDEG model developed for the TSPA-SR, three infiltration scenarios (low, medium, and high) were considered (CRWMS M&O 2000 [DIRS 148384], Section 6.3.1). The low infiltration scenario is considered to occur for 17 percent of the simulations, the medium infiltration scenario is considered to occur for 48 percent of the simulations, and the high infiltration scenario is considered to occur for 35 percent of the simulations. These values are in agreement with those found in the TSPA-SR model document (CRWMS M&O 2000

[DIRS 148384], Section 6.3.1). The repository is divided into about 600 spatial locations (CRWMS M&O 2000 [DIRS 148384], Section 6.3.1). At each location, thermal-hydrologic histories (e.g., waste package temperature and relative humidity, drip shield temperature, relative humidity, and other factors versus time) are developed for two waste package types (CSNF and codisposed waste forms), resulting in a total of approximately 1,200 different histories for each infiltration scenario. Each history is assigned a weight based on the fraction of repository area that the spatial location represents. The histories are binned (i.e., grouped) based on the percolation flux range into which they can be grouped (e.g., Bin 1 = 0 to 3 mm/yr, and Bin 2 = 3 to 10 mm/yr) (CRWMS M&O 2000 [DIRS 148384], Section 6.3.1). There are up to 5 bins for each infiltration scenario, although some bins do not have any time histories in them. In the potential repository design, 11,770 waste packages are modeled (3,910 codisposed and 7,860 CSNF) (CRWMS M&O 2000 [DIRS 148384], Section 6.3.4).

A thermal hydrology preprocessor (MkTable Version 1.00) was developed to prepare the temperature and relative humidity history input to the WAPDEG analysis. MkTable is executed before each realization of the WAPDEG code. It reads the total number of CSNF and codisposed waste packages (generally supplied by the TSPA-SR model (CRWMS M&O 2000 [DIRS 148384]) as discussed above and, based on the infiltration scenario under consideration (also supplied by the TSPA-SR model), randomly samples a set of 15 thermal-hydrologic histories to be used by the WAPDEG code in simulating waste package degradation for the given realization. The histories are chosen consistent with the fraction of codisposed and CSNF waste packages in the potential repository and with the weights assigned to each individual thermal-hydrologic history file.

Figure 7.4-18 shows the upper-bound, lower-bound, mean, 95^{th}, 75^{th}, 25^{th}, and 5^{th} percentile confidence intervals of the first breach profile for the waste packages with time incorporating the temperature-dependent general corrosion model for the Alloy 22 outer barrier with thermal-hydrologic history sampling. The upper-bound profile indicates that the earliest first breach time for a waste package is approximately 6,000 years, earlier than in the nominal case. As discussed below, all breaches before 24,000 years are due to crack penetrations. The median estimate of the first breach time of the upper-bound profile is approximately 190,000 years (30,500 years for the nominal case). For the mean profile, approximately 25 percent of the waste packages failed by the end of the simulation time (1 million years). The time to fail 10 percent of the waste packages for the two profiles is approximately 24,000 and 550,000 years, respectively (23,000 and 56,000 years, respectively, for the nominal case).

Figure 7.4-19 shows the first patch penetration profiles of the waste packages with time incorporating the temperature-dependent general corrosion model for the Alloy 22 outer barrier with thermal-hydrologic history sampling. The first patch breach times of the upper and 95^{th} percentile profiles are approximately 24,000 and 92,000 years, respectively. Comparison of the patch breach profiles with the first breach profiles (Figure 7.4-18) indicates that the initial breach (or failure) of the waste packages is mostly by SCC penetration in the closure lid welds of the Alloy 22 waste package outer barrier. For the 75^{th} percentile profile, the first patch penetration time is approximately 670,000 years. For the mean profile, approximately 7 percent of the waste packages have patch failures by the end of the simulation time (1 million years).

Integrated Model I Simulation-The integrated model I waste package degradation simulation using the temperature-dependent Alloy 22 general corrosion model I with thermal-hydrologic history sampling consists of a combination of the parameters studied in the individual one-off analyses documented in the preceding sections. These include:

- The temperature-dependent Alloy 22 general corrosion model I with thermal-hydrologic history sampling
- The fraction of weld flaws capable of propagation given by a ±3 standard deviation truncated lognormal distribution (mean = 0.01, +3 standard deviations = 0.5, -3 standard deviations = 0.0002) (Section 7.4.2)
- The stress threshold for the initiation of SCC given by a uniform distribution between 80 and 90 percent of the Alloy 22 yield strength (Section 7.4.2)
- The uncertainty bounds of residual stress for the Alloy 22 waste package outer closure lid welds (induction annealed) set to ±21.4 percent of the yield strength (Section 7.3.3.3.1)
- The residual stress uncertainty bounds of the Alloy 22 waste package inner closure lid welds (laser peened) sampled from a cumulative distribution function (Section 7.3.3.3.1, Table 7.3.3-2).

The results of using these simulation parameters are shown in Figures 7.4-20 and 7.4-21.

Figure 7.4-20 shows the upper-bound, lower-bound, mean, 95^{th}, 75^{th}, 25^{th}, and 5^{th} percentile confidence intervals of the first breach profile for the waste packages with time for the integrated model I. The upper-bound profile indicates that the earliest first breach time for a waste package is approximately 30,000 years, later than the 15,000 years for the previous nominal case. As discussed below, almost all breaches are due to patch penetrations. The median estimate of the first breach time of the upper-bound profile is approximately 876,000 years (30,500 years for the previous nominal case). For the mean profile, approximately 2.5 percent of the waste packages failed by the end of the simulation time (1 million years). The time to fail 10 percent of the waste packages for the upper-bound profile is approximately 392,000 years (23,000 years for the previous nominal case).

Figure 7.4-21 shows the first crack penetration profiles of the waste packages with time for the integrated model I. Due to the low fraction of manufacturing flaws capable of propagating and the high stress threshold for initiation of crack growth, little cracking is observed. The first crack breach time of the upper-bound and 95^{th} percentile profiles is approximately 68,000 and 552,000 years, respectively. Comparison of the first crack breach profiles with the first breach profiles (Figure 7.4-20) indicates that the initial breach (or failure) of the waste packages is generally by patch penetration. For the mean profile, approximately 0.2 percent of the waste packages have crack failures by the end of the simulation time (1 million years).

7.4.3.3 Temperature-Dependent Alloy 22 General Corrosion Model II

This section documents the WAPDEG analysis results using the Alloy 22 temperature-dependent general corrosion model II, which was developed using the same data for the model I except one outlier (see Section 7.3.5.3.2). The WAPDEG analysis was conducted with the thermal-hydrologic histories sampled randomly.

Figure 7.4-22 shows the upper-bound, lower-bound, mean, 95th, 75th, 25th, and 5th percentile confidence intervals of the first breach profile for the waste packages with time. The upper-bound profile indicates that the earliest first breach time for a waste package is approximately 20,000 years, 5,000 years later than in the nominal case. As discussed below, all breaches before 55,500 years are due to crack penetrations. The median estimate of the first breach time of the upper-bound profile is approximately 120,000 years (30,500 years for the nominal case). For the mean profile, approximately 80 percent of the waste packages failed by the end of the simulation time (1 million years). The time to fail 10 percent of the waste packages for the two profiles is approximately 72,000 and 202,000 years, respectively (23,000 and 56,000 years, respectively, for the nominal case).

Figure 7.4-23 shows the first patch penetration profiles of the waste packages with time. The first patch breach times of the upper and 95th percentile profiles are approximately 55,500 and 94,000 years, respectively. Comparison of the patch breach profiles with the first breach profiles (Figure 7.4-22) indicates that the initial breach (or failure) of the waste packages is generally by SCC penetration in the closure lid welds of the Alloy 22 waste package outer barrier. For the 75th percentile profile, the first patch penetration time is approximately 228,000 years. For the mean profile, approximately 70 percent of the waste packages have patch failures by the end of the simulation time (1 million years).

Integrated Model II Simulation-The integrated model II waste package degradation simulation using the temperature-dependent Alloy 22 general corrosion model II (excluding the outlier) with thermal-hydrologic history sampling consists of a combination of the individual one-off studies documented in the preceding sections. These include:

- The temperature-dependent Alloy 22 general corrosion model II (excluding the outlier) with thermal-hydrologic history sampling
- The fraction of weld flaws capable of propagation given by a ±3 standard deviation truncated lognormal distribution (mean = 0.01, +3 standard deviations = 0.5, -3 standard deviations = 0.0002) (Section 7.4.2)
- The stress threshold for the initiation of SCC given by a uniform distribution between 80 and 90 percent of the Alloy 22 yield strength (Section 7.4.2)
- The uncertainty bounds of residual stress for the Alloy 22 waste package outer closure lid welds (induction annealed) set to ±21.4 percent of the yield strength (Section 7.3.3.3.1)

- The residual stress uncertainty bounds of the Alloy 22 waste package inner closure lid welds (laser peened) sampled from a cumulative distribution function (Section 7.3.3.3.1, Table 7.3.3-2).

The results of using these simulation parameters are shown in Figures 7.4-24 and 7.4-25.

Figure 7.4-24 shows the upper-bound, lower-bound, mean, 95^{th}, 75^{th}, 25^{th}, and 5^{th} percentile confidence intervals of the first breach profile for the waste packages with time. The upper-bound profile indicates that the earliest first breach time for a waste package is approximately 120,000 years, later than the 15,000 years for the previous nominal case. As discussed below, almost all breaches are due to patch penetrations. The median estimate of the first breach time of the upper-bound profile is approximately 318,000 years (30,500 years for the previous nominal case). For the mean profile, approximately 63 percent of the waste packages failed by the end of the simulation time (1 million years). The time to fail 10 percent of the waste packages for the upper-bound profile is approximately 210,000 years (23,000 years for the previous nominal case). The time to fail 10 percent of the waste packages for the median profile is approximately 422,000 years (23,000 years for the previous nominal case).

Figure 7.4-25 shows the first crack penetration profiles of the waste packages with time. Due to the low fraction of manufacturing defects capable of propagating and the high stress threshold for initiation of crack growth, little cracking is observed. The first crack breach time of the upper-bound and 95^{th} percentile profiles is approximately 120,000 and 260,000 years, respectively. Comparison of the first crack breach profiles with the first breach profiles (Figure 7.4-24) indicates that the initial breach (or failure) of the waste packages is generally by patch penetration. For the mean profile, approximately 8 percent of the waste packages have crack failures by the end of the simulation time (1 million years).

The temperature-dependent Alloy 22 general corrosion model I (including the outlier) results in earlier first waste package failure times than the model II obtained by excluding the outlier however, fewer realizations have waste package failures and those that do have fewer failed waste packages. For the mean waste package failure curves for the two models, the temperature-dependent Alloy 22 general corrosion model II (excluding the outlier) results in 63 percent of the waste packages failed by the end of the simulation time (1 million years) while the temperature-dependent Alloy 22 general corrosion model I (including the outlier) results in only 2.5 percent of the waste packages (see Section 7.4.3.1) failed by the end of the simulation time.

7.4.4 Recommended Nominal Case for Volume 2

The recommended model for use in Supplemental Science and Performance Analysis Volume 2 (i.e., the model recommended to be used in the Total System Performance Assessment Model to analyze total system performance; McNeish 2001 [DIRS 155023]) is integrated model II using the temperature-dependent Alloy 22 general corrosion model II (excluding the outlier) with thermal-hydrologic history sampling. Analysis and discussion in Section 7.3.5.3 clearly indicate that there is an outlier in the Alloy 22 data set on which both models are based. The effect of including the outlier in the model development process increases the activation energy from 36 to 66 kJ/mol or approximately 83 percent. The use of the larger slope results in higher than

expected general corrosion rates (up to 7 μm/yr) at higher temperatures and lower than expected general corrosion rates at low temperatures (on the order of 3 nm/yr). This results from the effect of the outlier on the slope determined. The use of the lower slope produces more reasonable general corrosion rates (up to 1.2 μm/yr at higher temperatures and about 30 nm/yr at lower temperatures). The work of Smailos et al. (1990 [DIRS 154820], Table 5) shows that the corrosion rate of Alloy C-4 (a less corrosion resistant alloy than Alloy 22) in highly concentrated Q-Brine solutions (Smailos et al. 1990 [DIRS 154820], Table 2) for the composition of Q-Brine is less than 1 μm/yr at 150°C. For these reasons, the temperature-dependent Alloy 22 general corrosion model II (excluding the outlier) is more realistic and better suited to distinguishing between different thermal operating modes.

7.5 SUMMARY AND PARAMETERS PROVIDED TO TOTAL SYSTEM PERFORMANCE ASSESSMENT

The analyses conducted to quantify conservatism and uncertainties in the waste package degradation models and parameters were discussed in the previous sections. Also included in these discussions were data and information obtained subsequent to the development of analysis model reports for the various degradation mechanisms. Results of the integration of these models into the WAPDEG analyses were included in these discussions as well.

Previous analyses of the possible environments on the surfaces of the waste package and drip shield focused on carbonate-base dilute waters. These waters, when concentrated by evaporation, result in high pH brines. More recent analyses have included non-carbonate base dilute waters. These are similar to the pore waters in the host rock and, when evaporatively concentrated, evolve into near-neutral pH brines with dissolved calcium and magnesium ions. The presence of these cations in aqueous solution could result in the formation of limited amounts of calcium and magnesium chloride salt solutions that are stable at low relative humidities. However, because the available amounts of calcium and magnesium ions in the solution would decrease significantly during evaporation by the formation of insoluble precipitates, large quantities of seepage water would be necessary to provide concentrations sufficient to result in aggressive environments. However, the formation of an aqueous film containing these salts will also result in the dissolution of other soluble anions, such as nitrates and sulfates, thereby producing a more benign buffered solution. This will continue as the relative humidity increases in the repository. Nitrate ions can mitigate against the aggressiveness of chloride ions to Alloy 22 corrosion even in nearly saturated calcium chloride solutions at 120°C (Pasupathi 2001 [DIRS 155252]). Therefore, the potential for the development of environments leading to localized corrosion of Alloy 22 is unlikely. Because of low deliquescence points of these salts, general corrosion of waste package and drip shield could initiate much earlier while the temperatures at the surfaces are still sufficiently high.

A sensitivity analysis for potential effects of increased general corrosion rates of the waste package outer barrier due to the possible presence of magnesium and calcium chloride salts has shown that the effect is insignificant. This insensitivity of waste package degradation to the more aggressive corrosion initiation threshold is due mostly to the fact that the time period, during which the waste package temperature is above the boiling temperature of $NaNO_3$ salt (120.6°C, see Table 7.3.1-2b) and the waste packages are subject to higher general corrosion rates, is much shorter than the waste package lifetime.

New analyses to evaluate potential environments also included assessments of the presence of potentially deleterious minor constituents, such as lead. The measured concentrations of lead in the waters at Yucca Mountain are very low. In addition, a review of data in the literature shows that sorption of lead to the surface of minerals such as smectite and calcite will limit the amount of lead in solution. Evaporative concentration of Yucca Mountain waters has shown that lead is likely removed from the solution as lead-containing mineral precipitates, and, therefore, the amount of lead available in solution is expected to be insignificant.

Aging and phase stability of Alloy 22 was reevaluated using new data and analyses. These analyses confirm the prior conclusion that aging of the Alloy 22 waste package outer barrier will not pose a problem. Since this conclusion is based on limited data, alternative lines of evidence were evaluated, including mechanical property changes due to aging, natural analogues, and theoretical modeling. All of these corroborate the conclusion that for the estimated peak waste package temperatures of 200°C or lower, aging effects such as long-range ordering or grain boundary and bulk precipitation of secondary phases will not affect waste package performance.

In the case of stress corrosion cracking of the Alloy 22 barrier, new analyses were conducted to quantify the uncertain parameters and remove some of the conservatism in the previous analyses for the TSPA-SR (CRWMS M&O 2000 [DIRS 153246]). Models of the residual stress uncertainty, the threshold stress for stress corrosion cracking initiation, and the orientation of manufacturing flaws were revised based on new data, literature reviews, and analyses. In addition, the analyses included an evaluation of the effects of temperature on stress corrosion cracking, which showed that there is currently no basis for establishing a temperature threshold for stress corrosion cracking. Some of the new data evaluated included SCC test data on Alloy 22 in solutions containing lead. The data show that under very aggressive (unrealistic) conditions (pH of 0.53, 250°C, and 1,300 ppm lead), Alloy 22 may fail because of stress corrosion cracking. However, tests under acidic conditions with the anions that are present in the Yucca Mountain groundwater (1 wt percent lead in mixed-ion solutions at a pH of 2.7 and 76°C) show no stress corrosion cracking failures. Overall, the technical bases for the stress corrosion cracking model were improved significantly with the new data and analyses.

In the corrosion models used to predict the long-term corrosion behavior of Alloy 22 in the TSPA-SR (CRWMS M&O 2000 [DIRS 153246]), data from relatively short-term tests (two years of exposure) were used. Extrapolation of two-year data to predict performance over thousands of years was based on the assumption that the passive film on the surface would remain stable over a long period. To reduce the uncertainties associated with this assumption, a comprehensive testing and analysis program has been initiated. A mechanistic conceptual model for predicting the behavior of the passive film has been developed, and this conceptual model, along with associated model parameters, is being implemented into the passive film stability model. Preliminary calculations have been performed using values for model parameters that are based on stainless steels in nuclear power plant piping. A testing program is underway to provide data relevant to Alloy 22 for the conditions expected in the potential repository. When completed, the passive film stability model will be incorporated into the integrated WAPDEG model to analyze the effects of long-term passive film stability on waste package performance. The DOE's current position is that the passive film on Alloy 22 would remain stable under the exposure conditions expected in the potential repository. Data from ongoing testing programs

and detailed mechanistic modeling will provide useful information to determine the long-term stability of the passive film under repository-relevant exposure conditions.

Previous analyses of Alloy 22 general corrosion were based on data from weight-loss measurements on samples exposed for approximately two years. Because of the low corrosion rates in the material, the data showed significant uncertainties that are due mostly to measurement uncertainty (see Section 7.3.5.2). As a result, the data showed no discernible effects of temperature, environment, or exposure times on corrosion rates. New analyses based on new electrochemical data have been conducted to evaluate the effects of temperature. While the correlation developed is based on limited data over a small temperature range, the model provides a basis for evaluating waste package performance over ranges of time and location in the potential repository.

Potential early failures of waste packages by improper heat treatment are included in the waste package and TSPA analysis. Although the probability of the occurrence is very low, the consequence of improper heat treatment could lead to a gross failure of affected waste packages. The analysis results show that the probability of having at least one waste package improperly heat-treated is 20.2 percent, and the probability of having two waste packages affected is 2.6 percent. The probability of having three waste packages with improper heat treatment is about 0.2 percent. Assuming a total of 100 realizations for the waste package degradation analysis using the WAPDEG model, those probabilities provide that 77 out of 100 realizations would have no waste packages affected by improper heat treatment. Out of 100 realizations, 20 realizations would have at least one waste package affected and 3 realizations would have two waste packages affected.

Based on the additional analyses documented in this report, the following corrosion models and/or parameters are recommended for the waste package degradation analysis:

- Temperature-dependent Alloy 22 general corrosion model II (excluding one outlier from the passive current density data) with the total variance of the general corrosion rates from the weight-loss measurements due to uncertainty and the thermal-hydrologic histories sampled (see Section 7.3.5.3.2)

- The fraction of weld flaws capable of propagation in the radial direction given by a ±3 standard deviation truncated lognormal distribution with a mean of 0.01 and bounded between 0.5 (+3 standard deviations) and 0.0002 (-3 standard deviations) (see Section 7.3.3.3.4)

- The stress threshold for the initiation of stress corrosion cracking given by a uniform distribution between 80 and 90 percent of the Alloy 22 yield strength (see Section 7.3.3.3.3)

- The uncertainty bounds of residual stress of the Alloy 22 waste package outer closure lid welds (induction annealed) set to ±21.4 percent of the yield strength (see Section 7.3.3.3.1)

- The uncertainty bounds of residual stress of the Alloy 22 waste package inner closure lid welds (laser peened) sampled from a cumulative distribution function (see Section 7.3.3.3.2 and Table 7.3.3-2).

Because early waste package failure caused by improper heat treatment is a low probability event, it is modeled directly in the TSPA presented in Volume 2 (McNeish 2001 [DIRS 155023]) and not included in the waste package degradation analysis result summary that is discussed below. The new analyses, data, and models were incorporated into the integrated WAPDEG V4.0 model. The upper-bound profile, which is the upper extreme (very low probability) of the probable range of the first breach time, indicates that, not considering early waste package failures, the earliest first breach time for a waste package is approximately 120,000 years (Figure 7.4-24), much later than the 15,000 years for the previous baseline model (Figure 7.4-1) and the 10,000 years of the TSPA-SR base case (CRWMS M&O 2000 [DIRS 151566], Figure 18). Almost all breaches are due to patch penetrations by general corrosion. The median estimate (50 percent of waste packages failed) of the first breach time of the upper-bound profile is approximately 318,000 years (Figure 7.4-24), compared to 35,000 years for the previous baseline model (Figure 7.4-1). For the mean profile, approximately 63 percent of the waste packages failed by the end of the simulation time (1 million years). The time to fail 10 percent of waste packages for the upper-bound profile is approximately 250,000 years, compared to 23,000 years for the previous baseline model. These failure times are significantly longer than the TSPA-SR results (CRWMS M&O 2000 [DIRS 153246]).

Overall, new data and analyses have been developed to quantify the uncertainties in the waste package degradation models, and these have improved the technical bases for the assessment of waste package performance. The analysis results with the new baseline waste package degradation model having incorporated the quantified uncertainties of the key degradation models demonstrate that the waste package performance analysis results in the TSPA-SR base case (Figure 7.4-1 of this volume) are conservative and provide sufficient margins in the predictions of waste package performance.

INTENTIONALLY LEFT BLANK

Table 7.3.1-1. Compositions of Brines from Saline Lakes in Western North America

Species	Concentration (milligram/kilogram)				
	Alkali Valley, Oregon	**Carson Sink, Nevada**	**Mono Lake, California**	**Searles Lake, California**	**Bristol Dry Lake, California**
SiO_2	542	19	14	–	–
Ca	–	261	4.5	16	43,296
Mg	–	139	34	–	1,061
Na	117,000	56,800	21,500	110,000	57,365
K	8,850	3,240	1,170	26,000	33,294
HCO_3	2,510	322	5,410	–	–
CO_3	9,1400	–	10,300	27100	–
SO_4	46,300	786	7,380	46,000	223
Cl	45,700	88,900	13,500	121,000	172,933
Total	314,000	152,000	56,600	336,000	279,150
pH	10.1	7.8	9.6	Not reported	Not reported

Source: Eugster and Hardie 1978 [DIRS 100743].

Table 7.3.1-2. Compositions of Yucca Mountain Waters

Species	Concentration (mg/L)		
	Well J-13 water	**PERM-2**	**PERM-3**
	(carbonate base water)	**(non-carbonate base water)**	**(non-carbonate base water)**
K	5.04	7	9
Na	45.8	61	62
Ca	13.0	106	97
Mg	2.01	16.6	17.4
SiO2	61.0	66	75
HCO_3	128.9	Not reported	Not reported
Cl	7.14	110	123
F	2.18	Not reported	Not reported
SO_4	18.4	111	120
NO_3	8.78	3	10

Source: CRWMS M&O 2000 [DIRS 151568], Tables 14 and 15.

Table 7.3.1-2b. Deliquescence Point Data of Pure Salts of $MgCl_2$, NaCl, and $NaNO_3$

Temperature (°C)	Deliquescence Point (percent)		
	$MgCl_2$	NaCl	$NaNO_3$
0	33.66	75.51	--
5	33.60	75.65	78.57
10	33.47	75.67	77.53
15	33.30	75.61	76.46
20	33.07	75.47	75.36
25	32.78	75.29	74.25
30	32.44	75.09	73.14
35	32.05	74.87	72.06
40	31.60	74.68	71.00
45	31.10	74.52	69.99
50	30.54	74.43	69.04
55	29.93	74.41	68.15
60	29.26	74.50	67.35
65	28.54	74.71	66.64
70	27.77	75.06	66.04
75	26.94	75.58	65.56
80	26.05	76.29	65.22
85	25.11	--	65.03
90	24.12	--	65.00
95	23.07	--	--
100	21.97	--	--
108.67	--	--	--
120.6	--	73.90	50.10
164.27	14.80[a]	--	--

Source: Greenspan 1977 [DIRS 104945], Table 2.

NOTE: [a] Data for $CaCl_2$ salt.

Table 7.3.1-3. National Atmospheric Deposition Program/National Trends Network Deposition Data for Site NV00, Red Rock Canyon, Clark County, Nevada

Deposition Rate (kilogram/hectare)								
Year	**Ca**	**Mg**	**K**	**Na**	**NH_4**	**NO_3**	**Cl**	**SO_4**
1985	1.00	0.142	0.054	0.215	0.29	1.97	0.34	1.26
1986	0.53	0.083	0.025	0.148	0.29	1.84	0.21	1.10
1987	0.74	0.101	0.036	0.194	0.45	2.70	0.30	1.37
1988	0.80	0.119	0.092	0.203	0.23	1.77	0.26	1.08
1989	0.31	0.043	0.013	0.076	0.23	0.70	0.06	0.38
1990	1.75	0.251	0.040	0.170	0.90	2.69	0.31	1.39
1991	1.84	0.254	0.047	0.271	0.47	3.07	0.39	1.76
1992	0.91	0.108	0.036	0.241	0.61	3.23	0.35	2.20
1993	1.02	0.143	0.063	0.262	0.57	3.39	0.36	1.73
1994	1.25	0.147	0.026	0.102	0.36	1.57	0.15	0.77
1995	0.88	0.122	0.045	0.213	0.56	3.26	0.28	1.67
1996	1.45	0.122	0.047	0.148	0.21	1.57	0.16	0.65
1997	0.87	0.070	0.038	0.101	0.42	1.80	0.16	1.05
1998	1.47	0.198	0.055	0.206	0.74	4.41	0.36	1.97
1999	0.75	0.088	0.014	0.088	0.55	2.39	0.18	1.06

Source: NADP/NTN 2001 [DIRS 154843].

Table 7.3.2-1. Preliminary Measurements of Time to Give Precipitate Volume Fractions of 0.05 and 0.10 in Aged Alloy 22 Welds

Temperature (°C)	**Time to Give 5% Precipitates (Hours)**	**Time to Give 10% Precipitates (Hours)**
760	5.7	15
704	32	87
649	105	469
593	210	1065

Source: Summers 2001 [DIRS 155018].

Table 7.3.3-1. Descriptive Statistics of Surface Residual Stress Data of Shot-Peened Samples

Estimator	Unweighted	Weighted
Mean ($\bar{x}$) (MPa)	-902.3	-899.2
Standard error (MPa)	10.8	10.9
Median (MPa)	-896	–
Mode (MPa)	-891	–
Standard deviation (*s*) (MPa)	44.3	44.8
Sample variance (s^2)	1965.2	2006.7
Fractional uncertainty	0.049	0.050
Kurtosis	0.5	–
Skewness	0.3	–
Range (MPa)	179	–
Minimum (MPa)	-987	–
Maximum (MPa)	-808	–
Count (*n*)	17	–

Source: Bullard 2001 [DIRS 155035].

Table 7.3.3-2. Cumulative Density Function Values of Fractional Uncertainty

Probability	Fractional Uncertainty
0.50	0.051
0.90	0.065
0.95	0.071
0.99	0.083
0.999	0.100

Source: Bullard 2001 [DIRS 155035].

Table 7.3.3-3. Slow Strain Rate Test Results for Alloy 22

Specimen ID	Test Environment	Applied Potential (mV vs. Ag/AgCl)	Crevice	Temperature (°C)	Summary Results
ARC22-12	Air	N/A	N/A	Room Temp.	Full ductility (58% strain to failure nominal)
ARC22-123	4M NaCl	350	None	98	Full ductility (55% strain to failure nominal)
ARC22-117	4M NaCl	400	Halar	98	SCC at gage (6% strain to failure)
ARC22-120	BSW pH 13	400	None	105	Full ductility (52% strain to failure nominal)
ARC22-119	BSW pH13	400	Halar	105	Full ductility (61% strain to failure nominal)
ARC22-115	BSW pH 13, no NO_3	400	Halar	105	Full ductility (56% strain to failure nominal)
ARC22-129	BSW pH 13, no SO_4	400	Halar	105	Full ductility (60% strain to failure nominal)
ARC22-128	BSW pH 13, no NO_3 or SO_4	400	Halar	98	Severe crevice corrosion at gage 4% strain to failure
ARC22-126	BSW pH 13, no NO_3 or SO_4	300	Halar	98	Crevice corrosion at gage 22% strain to failure
ARC22-122	BSW pH 13, no NO_3 or SO_4	200	Halar	98	Full ductility (60% strain to failure nominal)
ARC22-124	BSW pH 13, no NO_3 or SO_4	100	Halar	98	Full ductility (60% strain to failure nominal)
ARC22-127	BSW pH 13, no NO_3 or SO_4	Open Circuit	Halar	98	Full ductility (60% strain to failure nominal)
ARC22-125	SSW pH 6.25	400	Halar	100	Full ductility (53% strain to failure nominal)
ARC22-112	SCW	400	Halar	76	Some impact on ductility (41% strain to failure)
ARC22-113	SCW	317	Halar	76	Full ductility (53% strain to failure nominal)
ARC22-15	SAW	Open circuit	Halar	76	Full ductility (60% strain to failure nominal)
ARC22-13	1% $PbCl_2$, pH 4, aerated water	Open circuit	N/A	95 to 76	Full ductility (57% strain to failure nominal)
ARC22-16	Pb in SAW pH 3	Open circuit	Halar	76	Full ductility (60% strain to failure nominal)
ARC22-17	Pb in SAW pH 3	Open circuit	Halar	76	Full ductility (60% strain to failure nominal)
ARC22-18	Pb in SAW pH 3	Open circuit	Halar	76	Full ductility (60% strain to failure nominal)

Source: Pasupathi 2001 [DIRS 154935].

NOTE: BSW = basic saturated water; SSW = simulated saturated water; SCW = simulated concentrated water; SAW = simulated acidified water; N/A = not applicable. Specimens were tested at a strain rate of 1.66×10^{-6} per second, which is a reasonably conservative strain rate. Halar is a polymeric coating material used to create crevice on the specimens.

Table 7.3.5-1. Passive Current Density Data from Potentiostatic Polarization Experiments for Alloy 22

				Passive Current Density (A/cm^2)		
Material	**pH**	**Electrolyte**	**Temperature**	**Median**	**Average**	**Std. Dev.**
C22	2.75	10:1	95	1.6518E-07	1.4792E-07	5.6918E-08
			85	1.2847E-07	1.3076E-07	2.0348E-08
			80	6.1482E-08	8.6809E-08	7.0242E-08
	2.75	100:1	95	1.4224E-07	8.1326E-07	**1.8234E-06**
			85	1.0094E-07	1.2480E-07	5.8973E-08
			80	7.1118E-08	7.3412E-08	1.2407E-08
	7.75	10:1	95	1.7435E-07	1.6255E-07	3.4218E-08
			85	1.0507E-07	9.6353E-08	5.6074E-08
			80	1.3765E-07	1.3508E-07	5.1741E-08
	7.75	100:1	95	1.8353E-07	2.0494E-07	8.0975E-08
			85	1.4224E-07	1.4224E-07	1.7168E-08
			80	1.2847E-07	1.2939E-07	3.4114E-08

Source: Lee 2001 [DIRS 154891].

NOTE: The entry in bold is identified as an outlier. Testing was conducted with crevice specimens in non-deaerated solutions.

Table 7.3.5-2. Calculations for the Temperature Dependence Term for the Alloy 22 General Corrosion Rate Model

Temp (°C)	**Passive Current Density (A/cm^2)**	**1/Temp (K^{-1})**	**Ln(Rate)**		**Cross-Product Deviations**	**Squared Deviations**
95	1.4792E-07	0.002716284	-15.72656244		-5.03878E-07	4.06261E-09
85	1.3076E-07	0.002792126	-15.84986627		-1.39672E-06	1.46493E-10
80	8.6809E-08	0.002831658	-16.25955079		-2.71128E-05	2.66619E-09
95	8.1326E-07	0.002716284	-14.02220919		-0.000109137	4.06261E-09
85	1.2480E-07	0.002792126	-15.89655338		-1.96179E-06	1.46493E-10
80	7.3412E-08	0.002831658	-16.42718163		-3.57684E-05	2.66619E-09
95	1.6255E-07	0.002716284	-15.63225176		-6.51511E-06	4.06261E-09
85	9.6353E-08	0.002792126	-16.15524792		-5.09289E-06	1.46493E-10
80	1.3508E-07	0.002831658	-15.81741606		-4.28305E-06	2.66619E-09
95	2.0494E-07	0.002716284	-15.40054284		-2.12839E-05	4.06261E-09
85	1.4224E-07	0.002792126	-15.76578315		-3.79024E-07	1.46493E-10
80	1.2939E-07	0.002831658	-15.86044838		-6.50503E-06	2.66619E-09
	Averages	0.002780023	-15.73446782	**Sum**	-0.00021994	2.75012E-08
					Ratio	7,997

Source: Bullard 2001 [DIRS 155034].

Table 7.3.5-3. Passive Current Density Data from Potentiostatic Polarization Experiments and Calculated Passive Dissolution Rate for Alloy 22

Material	E_{cont} (mV vs. Ag/AgCl)	Electrolyte	pH	Temperature	Passive Current Density (A/cm^2)	Passive Dissolution Rate (mm/yr)
Alloy 22	350	1 M NaCl	1.0	25	1.29E-08	1.238 E-04
Alloy 22	350	1 M NaCl	1.0	45	2.24E-08	2.147 E-04
Alloy 22	350	1 M NaCl	1.0	65	5.45E-08	5.232 E-04
Alloy 22	350	1 M NaCl	1.0	75	7.23E-08	6.944 E-04
Alloy 22	350	1 M NaCl	1.0	85	1.10E-07	1.052E-04

Source: Lee 2001 [DIRS 154871].

NOTE: E_{cont} is the controlled applied potential to polarize the specimens. Testing was conducted with cylindrically shaped specimens.

Table 7.3.6-1. Poisson Probabilities for Improper Heat Treatment of Waste Packages

Number of Packages	Probability	Cumulative Probability
0	0.76896	0.76896
1	0.20202	0.97098
2	0.02654	0.99752
3	2.32392E-3	0.99984
4	1.52634E-4	0.99999
5	8.01996E-6	1.00000

Source: Bullard 2001 [DIRS 155036].

Table 7.3.7-1 Critical Crevice Temperatures for Alloy 22

Test Environment	Concentration	pH	Estimated E_{rp}	Estimated E_{Corr}	Estimated Critical Crevice Temperature	Reference
			mV vs. SHE	mV vs. SHE	(°C)	
NaCl Solution	0.5M Cl^-	2.5 or 8	620		95	Dunn et al. 1999 [DIRS 154481]
NaCl Solution	1.0M Cl^-	2.5 or 8	550		85	Dunn et al. 1999 [DIRS 154481]
NaCl Solution	4.0M Cl^-	2.5 or 8	300		85	Dunn et al. 1999 [DIRS 154481]
NaCl Solution	4.0M Cl^-	~7	<350	-40	<100	Dunn et al. 1999 [DIRS 154481]
LTCTF Acidified 1000-fold well J-13 water (SAW)	0.8M Cl^-	2.7	780	~40	>90[a]	CRWMS M&O 2000 [DIRS 144229], Table 3
50,000-fold well J-13 water	~3 M Cl^-	13	~600	-40	>100	CRWMS M&O 2000 [DIRS 144229], Table 24
50,000-fold well J-13 water without sulfate and nitrte ions	~3 M Cl^-	13	<600	-40	<98	Table 7.3.3-3 of this volume
SCW, SAW, SDW exposed in LTCTF		2.7 to 8			>90	CRWMS M&O 2000 [DIRS 144229], Table 3
Cyclic Polarization results in full range of potential environments				~-40	>120	CRWMS M&O 2000 [DIRS 144229], Section 6.4.3
4% NaCl/0.1%$Fe_2(SO_4)_3$/0.01M HCl	as shown	2		~600	102	Haynes International 1997 [DIRS 100896]
6% FeCl3 + 1% HCl	as shown	<1.2[b]		>800	58	Agarwal and Herda 1997 [DIRS 107676], Table 5

Source: [b] ASM = ASM International 1987 [DIRS 133378], p. 304.

NOTES: E_{rp} = repassivation potential; E_{corr} = corrosion potential; LTCTF = Long-Term Corrosion Test Facility at Lawrence Livermore National Laboratory; SAW = simulated acidic water; SCW = simulated concentrated water; SDW = simulated dilute water.

[a] Maximum aqueous crevice corrosion rate less than 0.07 μm/yr after two years.

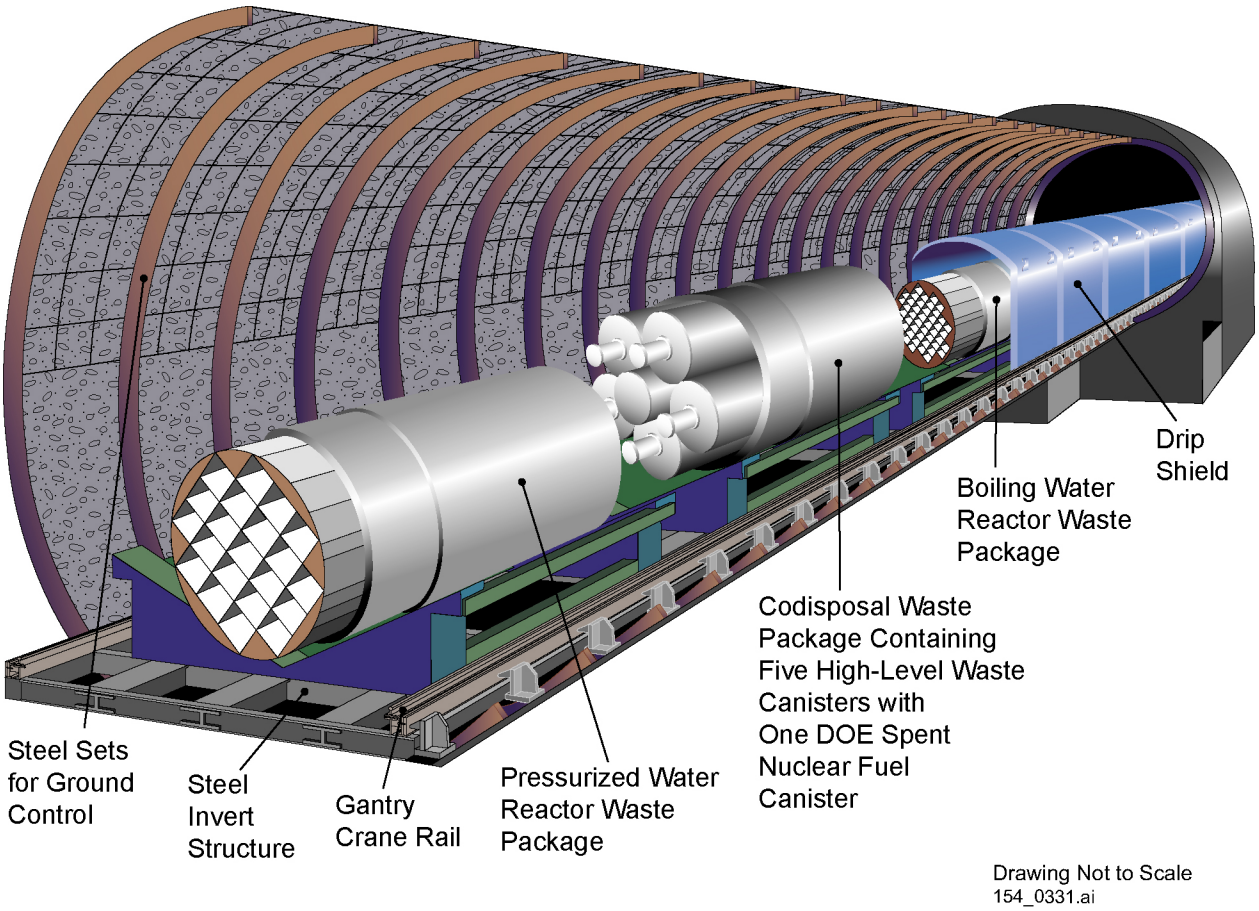

154_0331.ai

Source: CRWMS M&O 2000 [DIRS 153802], Figure 1-2.

Figure 7.1-1. Arrangements for Different Types of Waste Packages and the Drip Shield in an Emplacement Drift

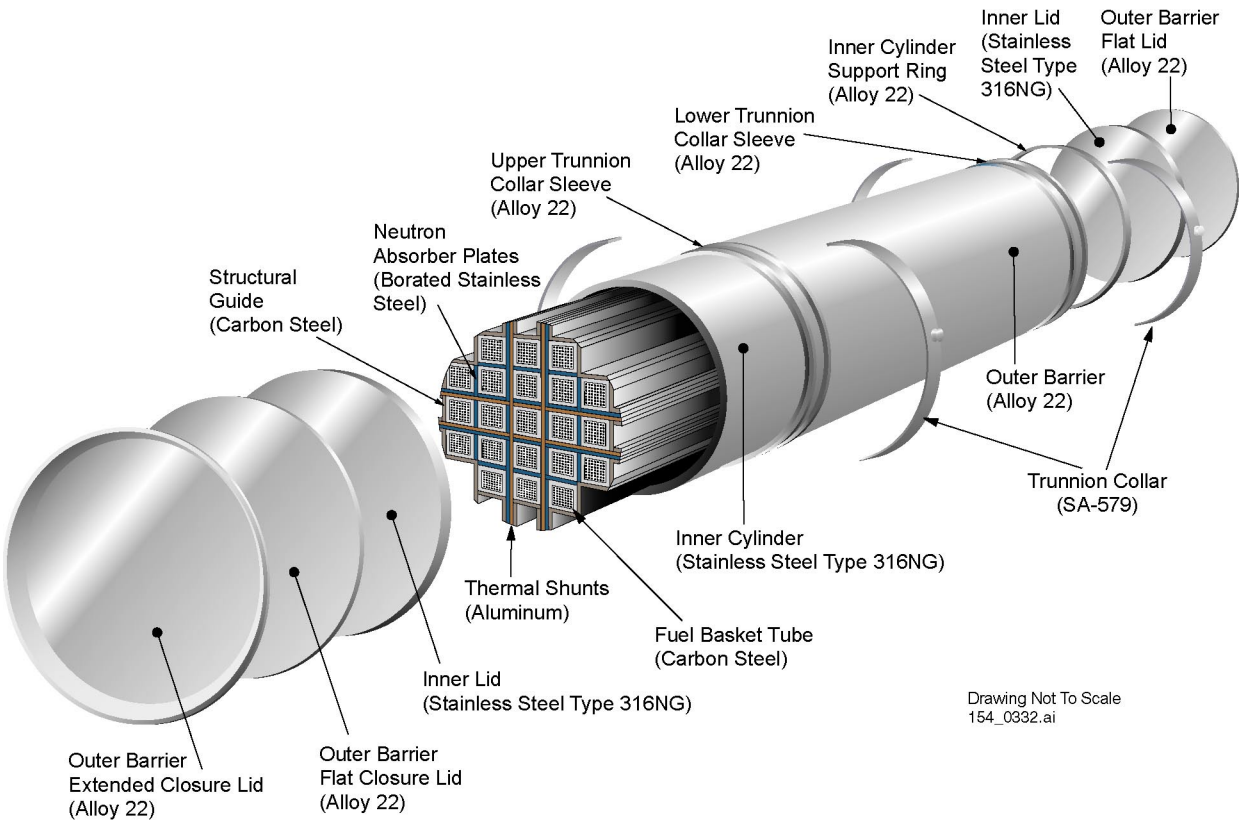

154_0332.ai

Source: CRWMS M&O 2000 [DIRS 153802], Figure 1-1.

Figure 7.1-2. Typical Waste Package Designed for 21-PWR Fuel Assemblies

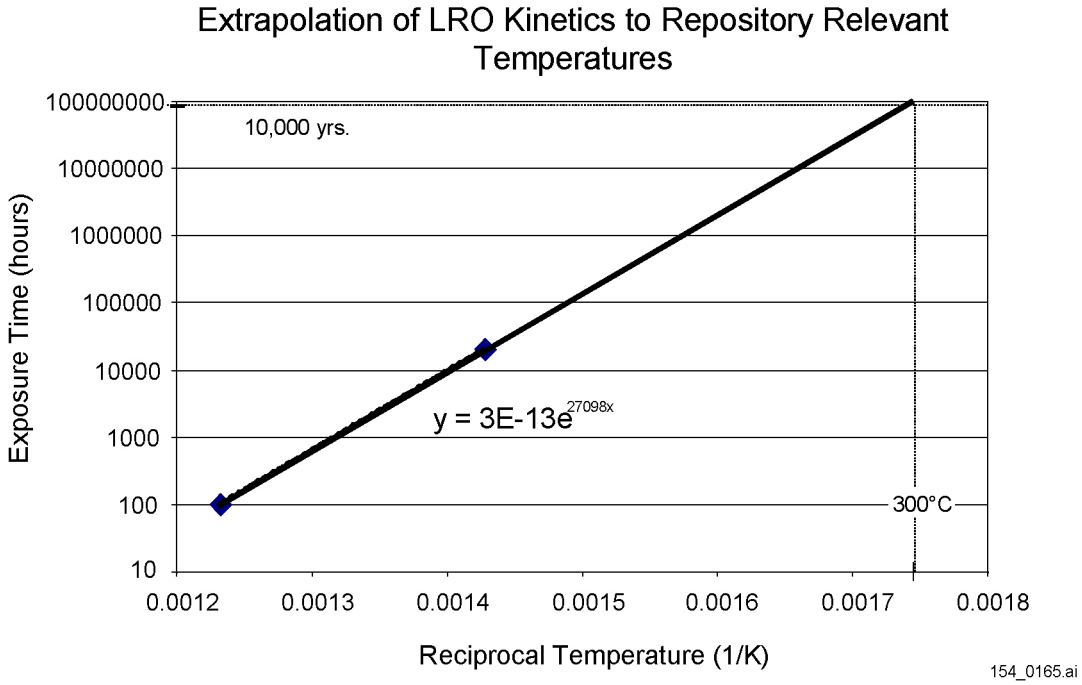

154_0165.ai

Source: Summers 2001 [DIRS 155019].

NOTE: The data in this graph correspond to aging at 538°C for 100 hours and 427°C for 20,000 hours.

Figure 7.3.2-1. Graphical Extrapolation of the Kinetic Data for Long-Range Ordering in Alloy 22 Base Metal

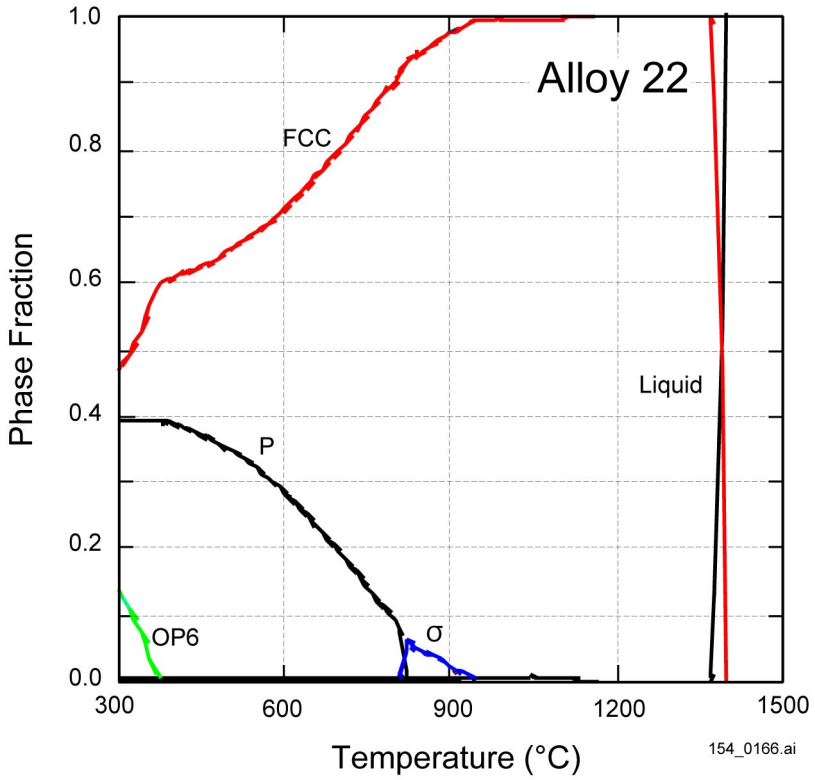

154_0166.ai

Source: Turchi 2001 [DIRS 154934].

NOTE: The calculation assumes a composition (weight percent) of 21.2 Cr-13.5 Mo-4 Fe-3 W-2 Co-0.5 Mn-0.3 V-0.08 Si-0.01 C-bal. Ni, which is typical for Alloy 22. At low temperatures, three phases are predicted to be thermodynamically stable: OP6 (which refers to the ordered phase), P, and the FCC solid solution phase. μ and P phases are similar and are not treated separately here. Sigma (σ) phase is only stable at higher temperatures.

Figure 7.3.2-2. Phase Fraction Predicted for Alloy 22 as a Function of Temperature

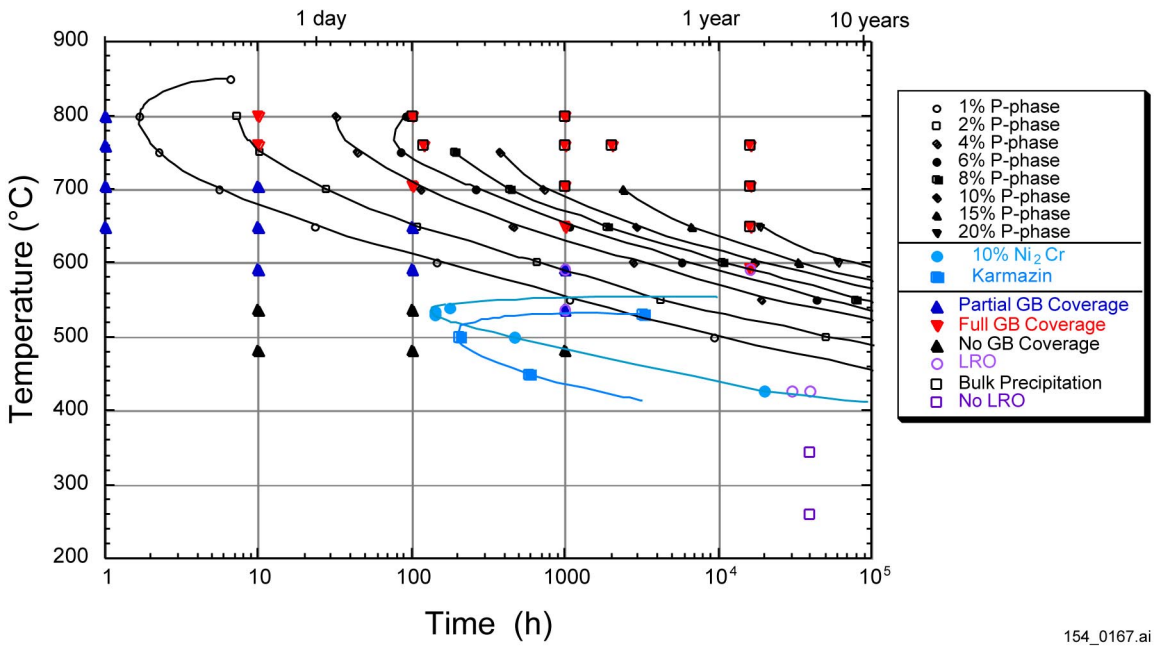

154_0167.ai

Source: Turchi 2001 [DIRS 154934].

NOTE: Lower curves describe the prediction and the results extracted from the work of Karmazin (1982). The binary alloy assumes that 10 percent of the matrix transforms into the ordered phase of Ni_2Cr-type. The ternary alloy (surrogate of Alloy 22 with 55.7 Ni-21.1 Cr-13.5 Mo in weight percent) assumes to transform into the P phase, with the transformation rate ranging from 1 to 20 percent. GB = grain boundary; LRO = long range ordering.

Figure 7.3.2-3. Isothermal Time-Temperature-Transformation Diagrams for an FCC-Based Matrix of a Binary Nickel-Chromium Alloy and a Ternary Nickel-Chromium-Molybdenum Alloy

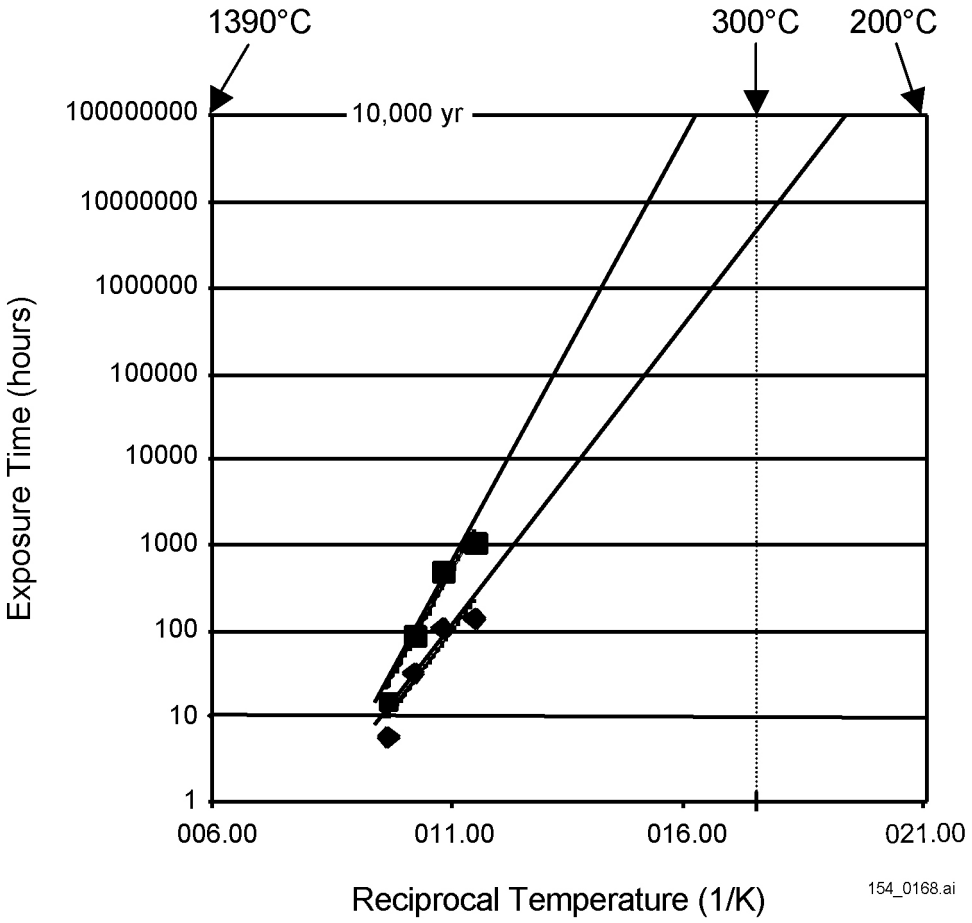

154_0168.ai

Source: Summers 2001 [DIRS 155018].

NOTE: Extrapolation of these data indicate that further nucleation and growth of the phases that form during welding of Alloy 22 is possible in 10,000 years at temperatures between 200 and 300°C and higher.

Figure 7.3.2-4. Extrapolation of Volume Fraction Data from Half-Inch Thick, Alloy 22, Double-V, Gas-Tungsten-Arc Welds

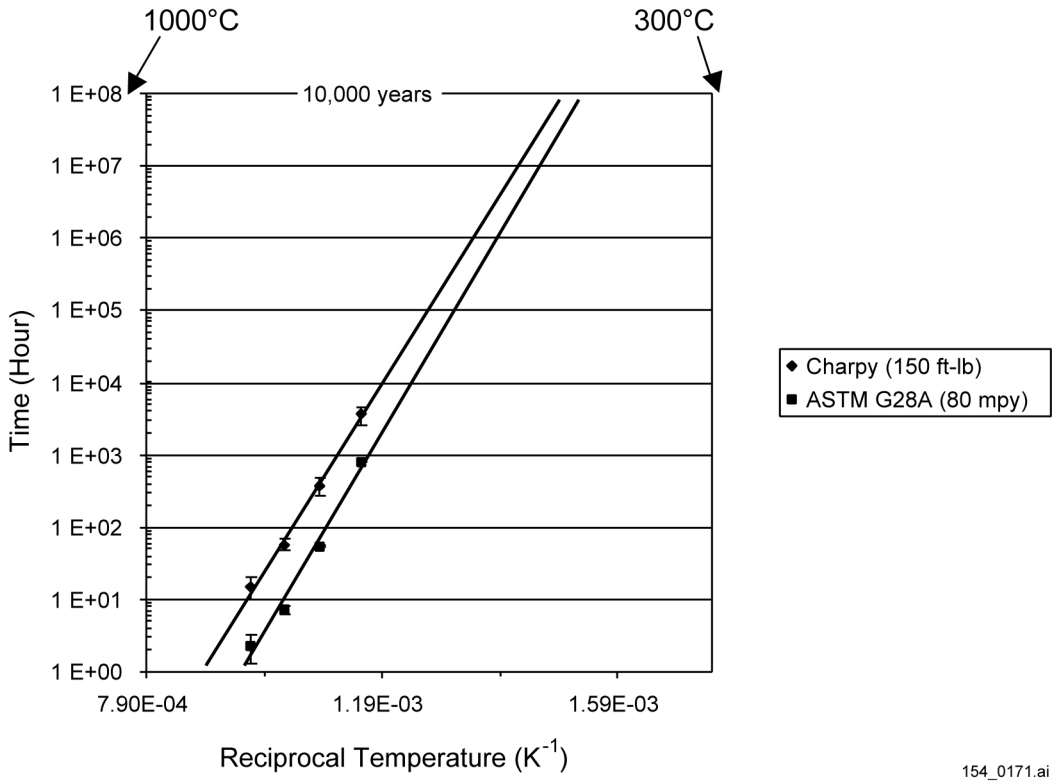

154_0171.ai

Source: Rebak et al. 2000 [DIRS 146910]; G 28-97 1997 [DIRS 154712].

Figure 7.3.2-5. Extrapolation of Mechanical (Charpy Impact Toughness) and Electrochemical (Corrosion Resistance) Behavior of Alloy 22

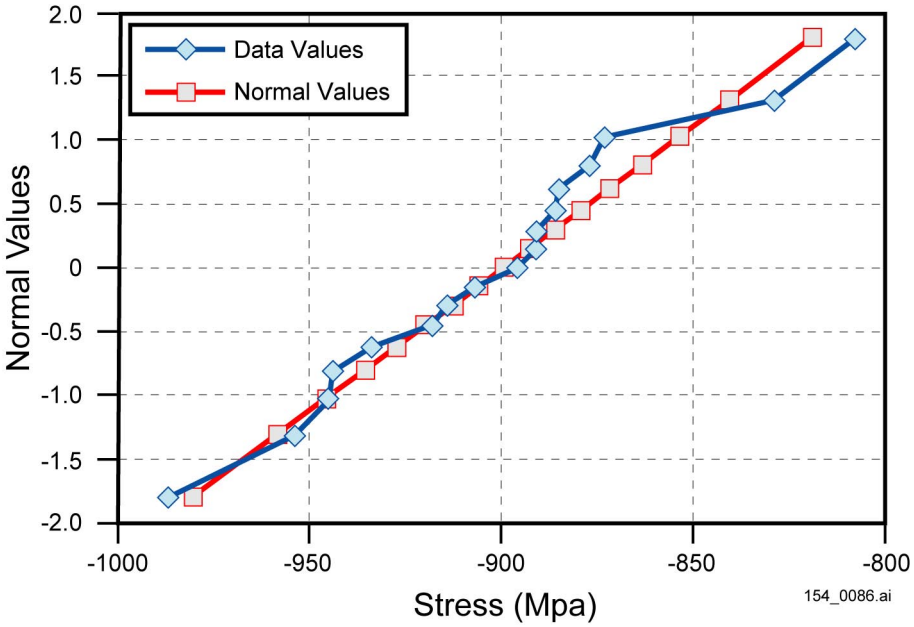

154_0086.ai

Source: Bullard 2001 [DIRS 155035].

Figure 7.3.3-1. Fractile Plot of Measured Surface Residual Stress Values for Shot Peened-Incoloy 908 Samples

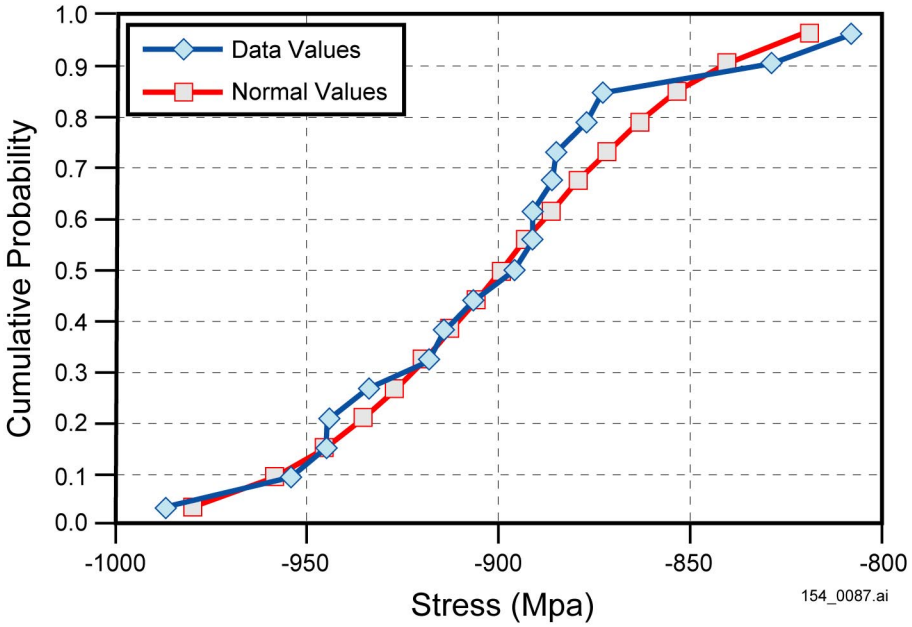

154_0087.ai

Source: Bullard 2001 [DIRS 155035].

Figure 7.3.3-2. Probability Plot of Measured Surface Residual Stress Values for Shot Peened Incoloy 908 Samples

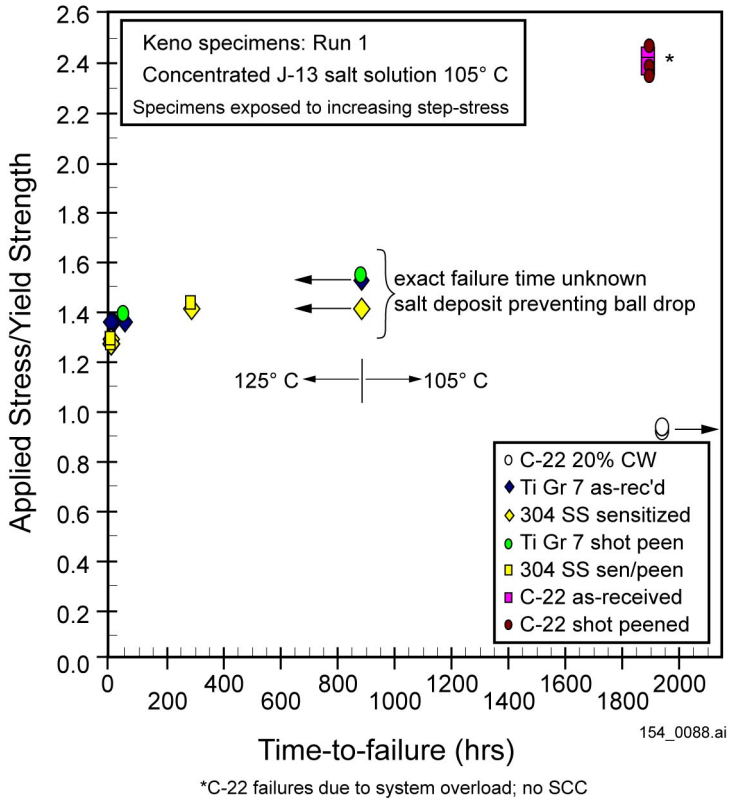

154_0088.ai

Source: Pasupathi 2001 [DIRS 154936].

NOTE: Test used basic saturated water (approximately 5500-fold well J-13 water, pH = 12.4).

Figure 7.3.3-3. Constant Load (Uniaxial Tension) Stress Corrosion Crack Initiation Test No. 1

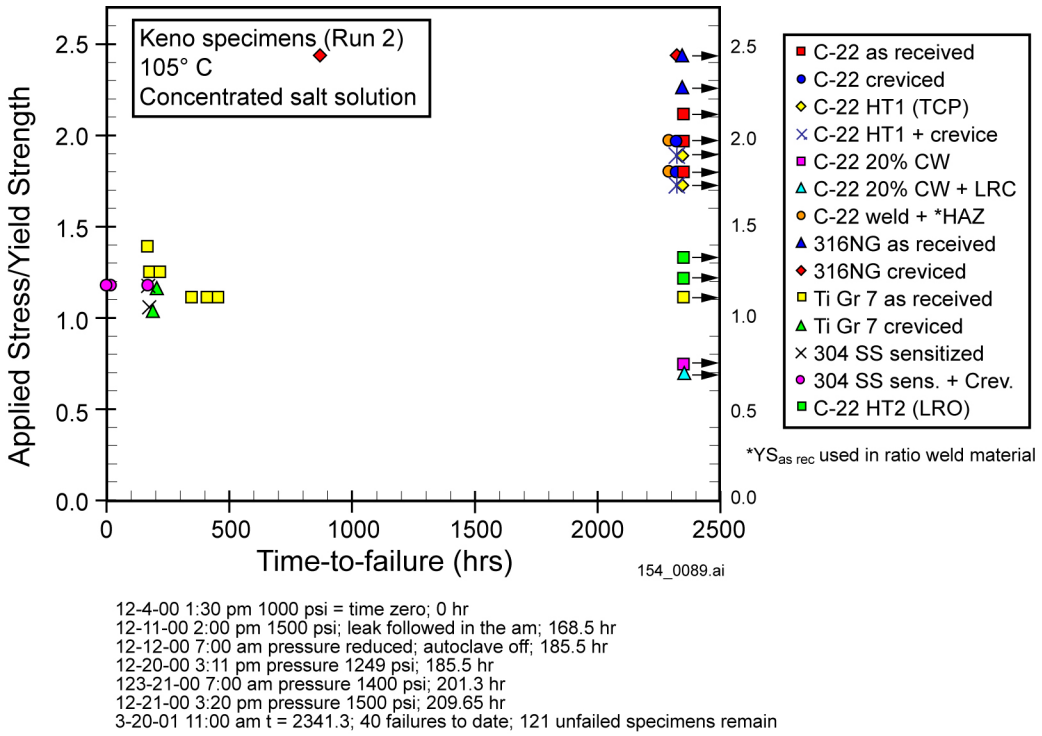

12-4-00 1:30 pm 1000 psi = time zero; 0 hr
12-11-00 2:00 pm 1500 psi; leak followed in the am; 168.5 hr
12-12-00 7:00 am pressure reduced; autoclave off; 185.5 hr
12-20-00 3:11 pm pressure 1249 psi; 185.5 hr
123-21-00 7:00 am pressure 1400 psi; 201.3 hr
12-21-00 3:20 pm pressure 1500 psi; 209.65 hr
3-20-01 11:00 am t = 2341.3; 40 failures to date; 121 unfailed specimens remain

154_0089.ai

Source: Pasupathi 2001 [DIRS 154936].

NOTE: Test used Basic Saturated Water (approximately 5500-fold well J-13 water, pH = 12.4).

Figure 7.3.3-4. Constant Load (Uniaxial Tension) Stress Corrosion Crack Initiation Test No. 2

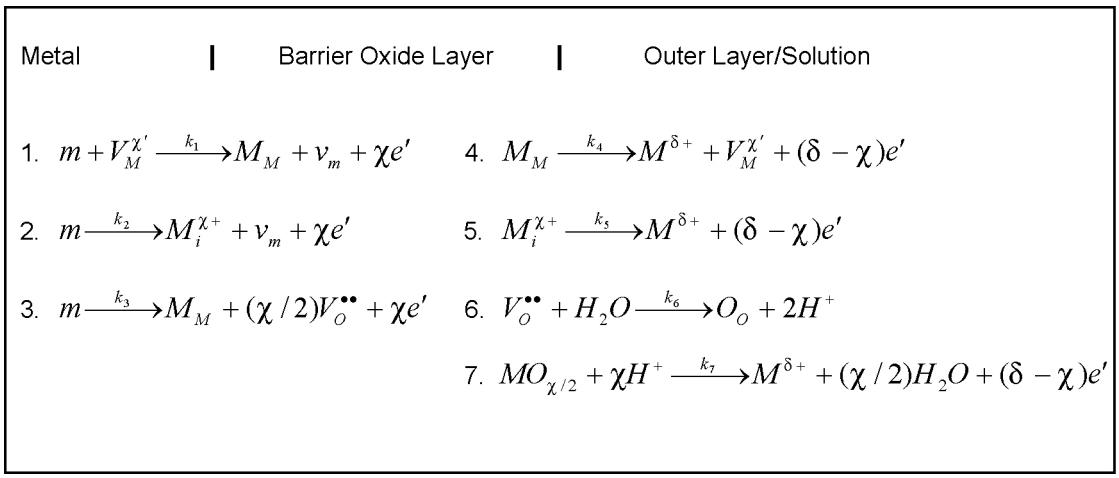

154_0132.ai

154_0132.ai

Source: Macdonald 2001 [DIRS 154736], pp. 18 to 22.

NOTE: m = metal atom, M_M = metal cation in cation site, O_O = oxygen ion in anion site, $M_i^{\chi+}$ = cation interstitial, $V_M^{\chi'}$ = cation vacancy, and $V_O^{\bullet\bullet}$ = oxygen vacancy, and v_m = vacancy in metal phase.

Figure 7.3.4-1. Elementary Interfacial Reactions Postulated in the Point Defect Model to Generate or Annihilate Point Defects in the Barrier Layer of a Passive Film

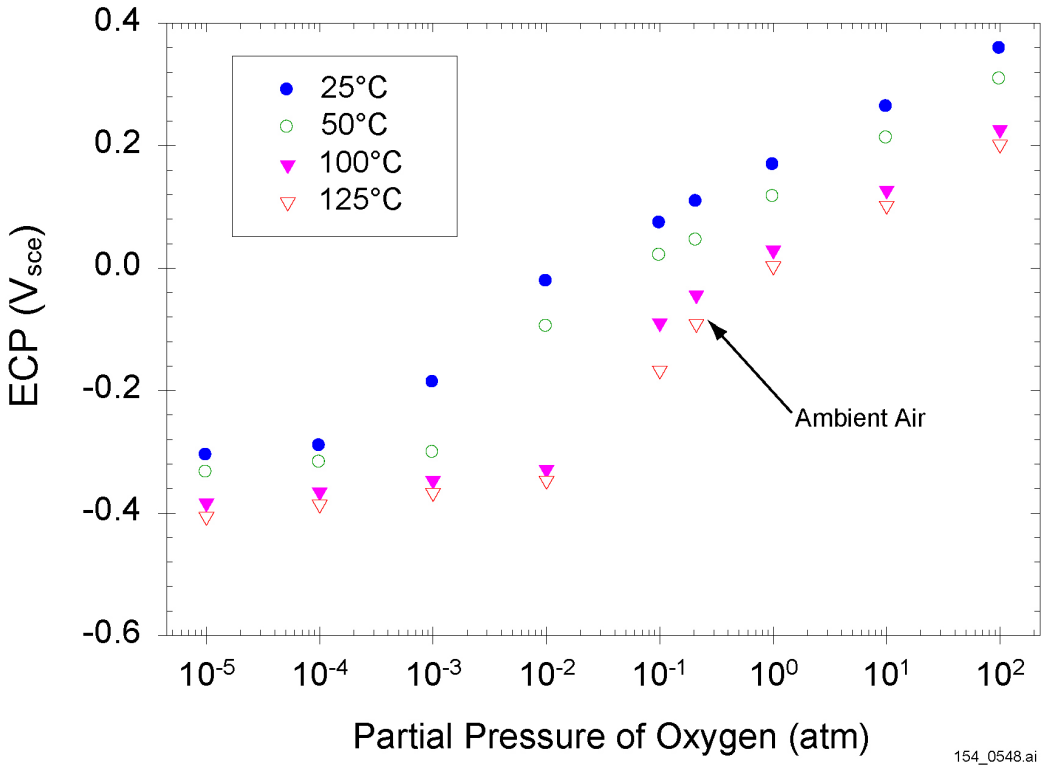

154_0548.ai

Source: Macdonald 2001 [DIRS 154736], pp. 18 to 22.

NOTE: Parameter values assumed in the analysis: pH = 3, saturated NaCl solution, electrolyte film thickness = 0.01 cm. SCE = saturated calomel electrode.

Figure 7.3.4-2. Dependence of Electrochemical Corrosion Potential on the Partial Pressure of Oxygen and on Temperature

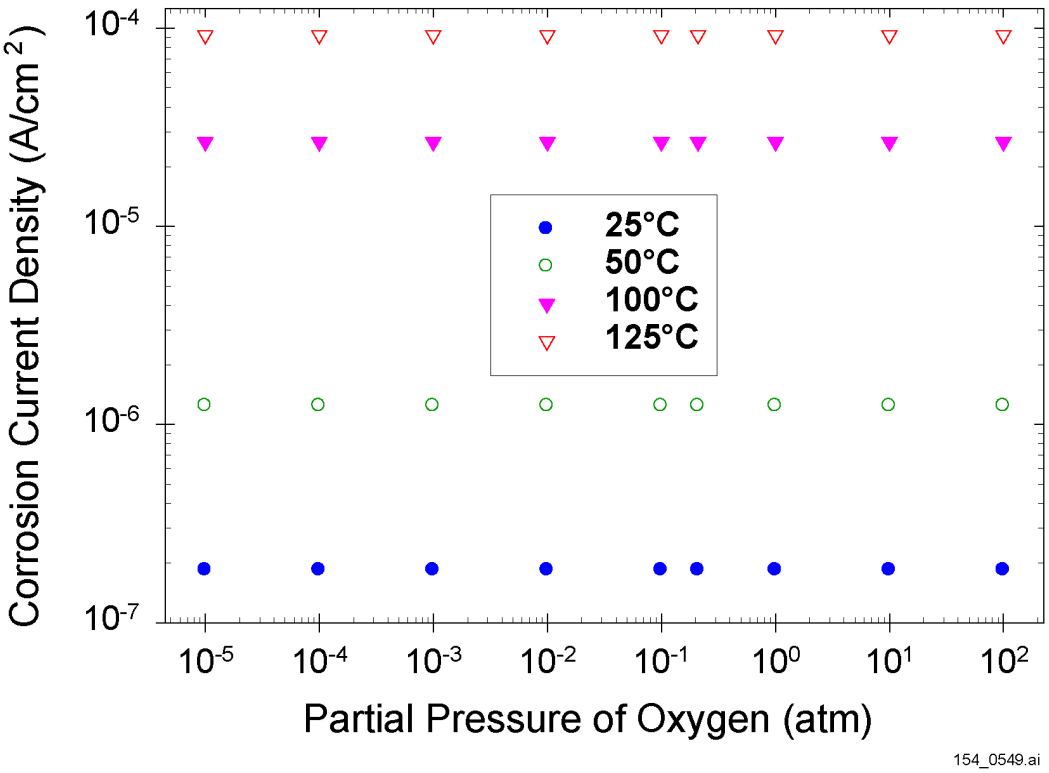

154_0549.ai

Source: Macdonald 2001 [DIRS 154736], pp. 18 to 22.

NOTE: Parameter values assumed in the analysis: pH = 3, saturated NaCl solution, electrolyte film thickness = 0.01 cm.

Figure 7.3.4-3. Corrosion Current Density as a Function of the Partial Pressure of Oxygen and Temperature

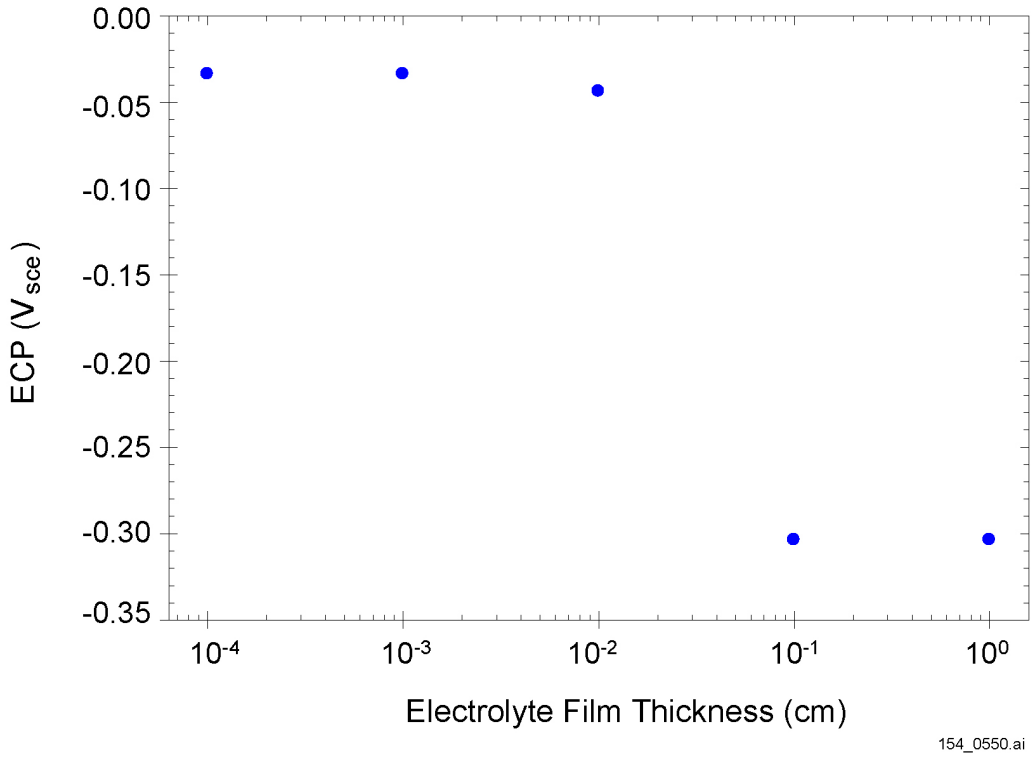

154_0550.ai

Source: Macdonald 2001 [DIRS 154736], pp. 18 to 22.

NOTE: Parameter values assumed in the analysis: T=100°C, pH = 3, oxygen partial pressure = 0.21 atm, saturated NaCl solution. SCE = saturated calomel electrode.

Figure 7.3.4-4. Calculated Electrochemical Corrosion Potential Versus Thickness of the Electrolyte Film on the Metal Surface

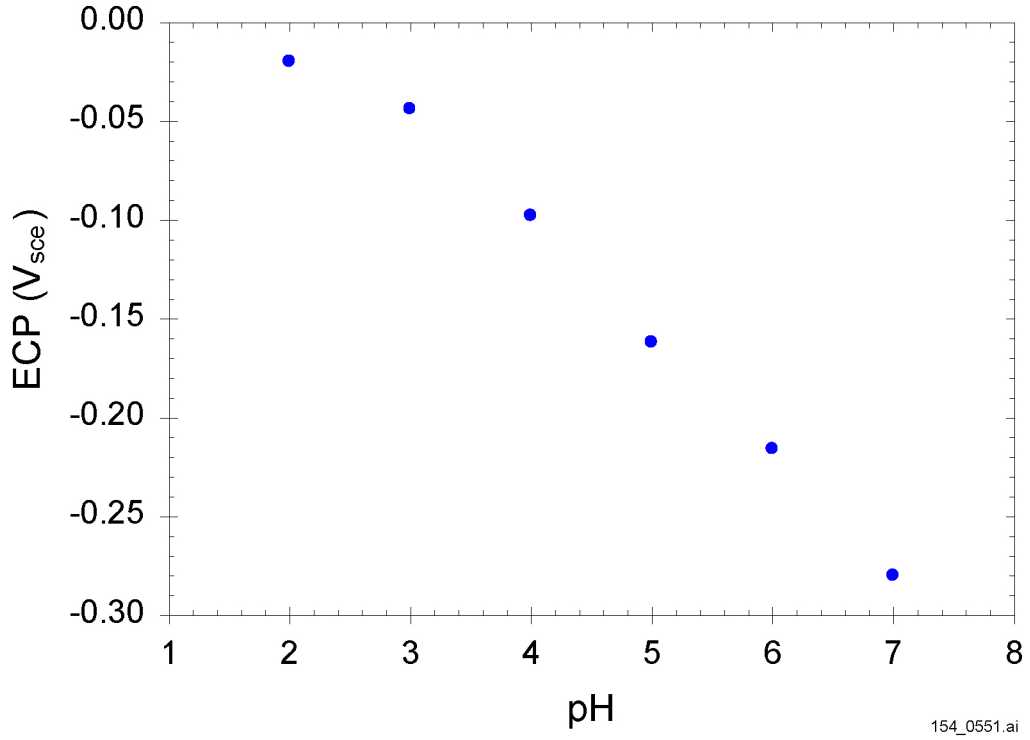

154_0551.ai

Source: Macdonald 2001 [DIRS 154736], pp. 18 to 22.

NOTE: Parameter values assumed in the analysis: T = 100°C, oxygen partial pressure = 0.21 atm, saturated NaCl solution, electrolyte film thickness = 0.01 cm. SCE = saturated calomel electrode.

Figure 7.3.4-5. Calculated Electrochemical Corrosion Potential Versus pH of the Thin Electrolyte Film on the Alloy Surface

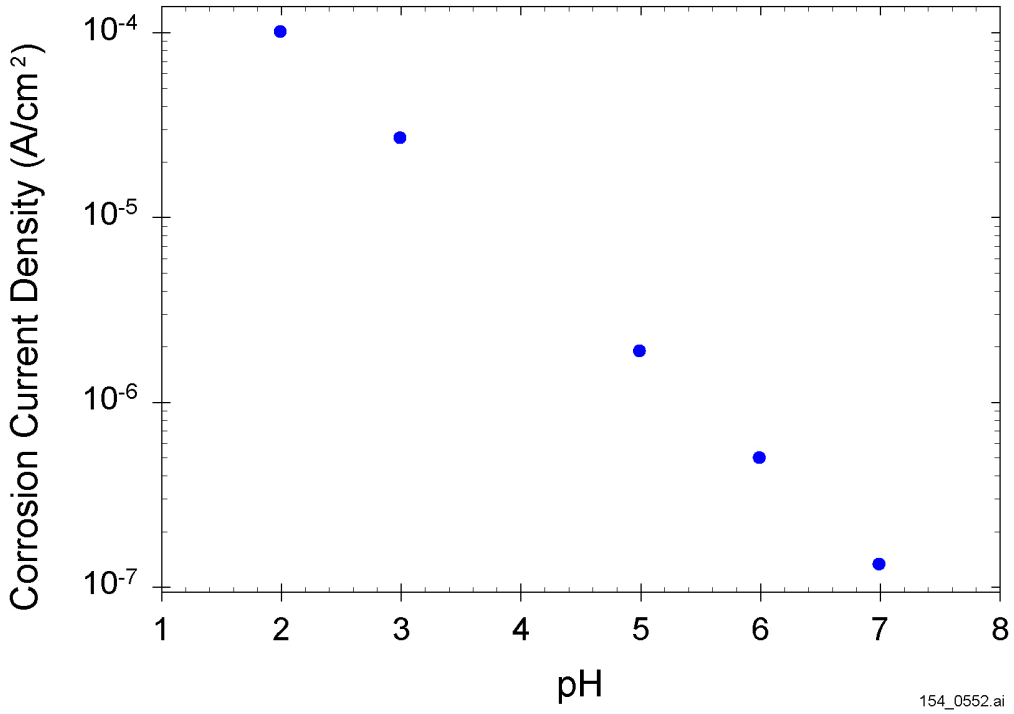

154_0552.ai

Source: Macdonald 2001 [DIRS 154736], pp. 18 to 22.

NOTE: Parameter values assumed in the analysis: T = 100°C, oxygen partial pressure = 0.21 atm, saturated NaCl solution, electrolyte film thickness = 0.01 cm.

Figure 7.3.4-6. Calculated Corrosion Current Density Versus pH of the Thin Electrolyte Film on the Alloy Surface

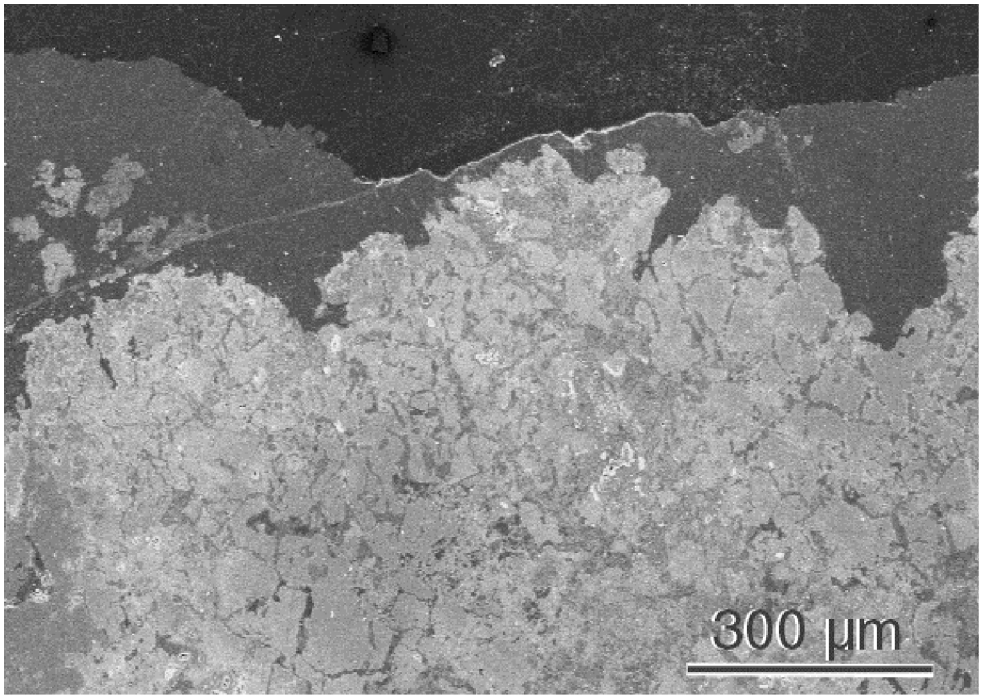

154_0138.ai

154_0138.ai

Source: Summers 2001 [DIRS 155017].

NOTE: The outer layers consist primarily of a magnesium silicate, presumably serpentine (darkest outer layer), and an iron oxide, presumably magnetite (darker gray regions). The interior of the sample is a mixture of many nonmetallic minerals and the Fe-Ni metal (brighter regions).

Figure 7.3.4-7. Mineral Variations Shown in a Scanning Electron Microscope Micrograph of a Cross Section of a Josephinite Sample

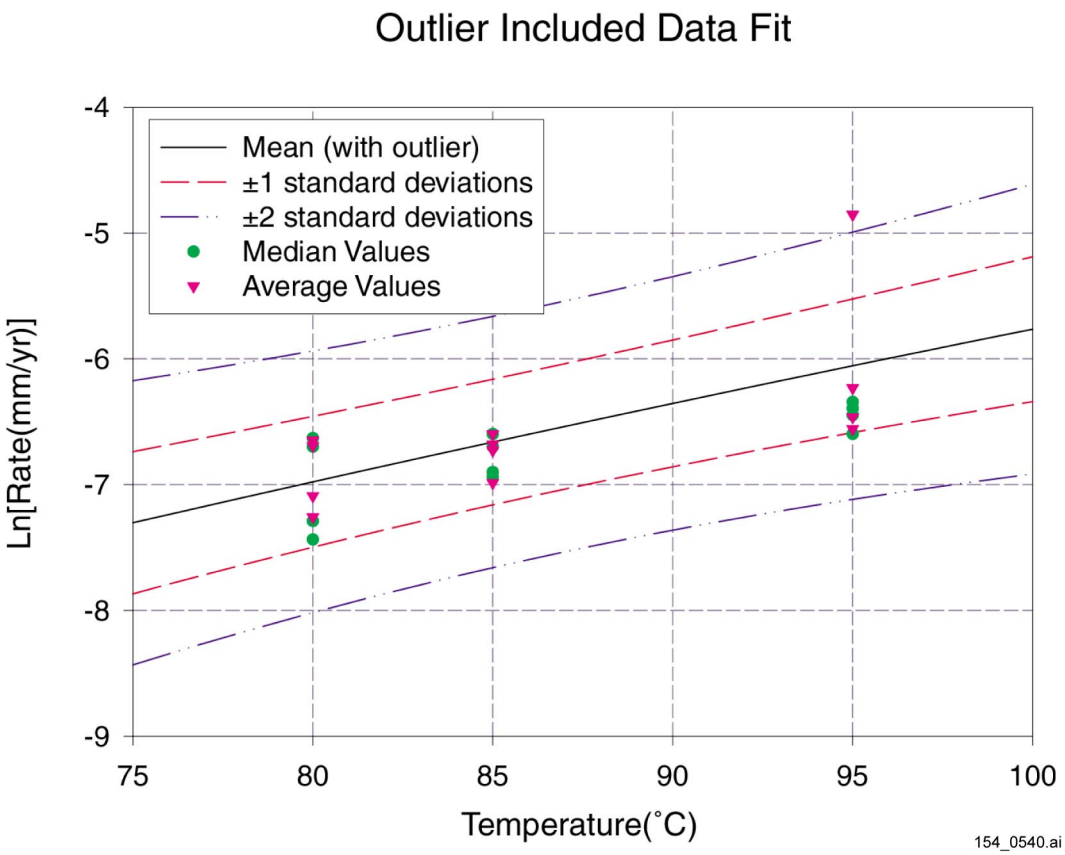

154_0540.ai

Source: Bullard 2001 [DIRS 155034].

NOTE: The data are used to evaluate the temperature dependence term only. The rate data are not used to determine the general corrosion rate values for the model.

Figure 7.3.5-1. Data Fit for Temperature Dependence of Alloy 22 General Corrosion Model I Using the Entire Data Set

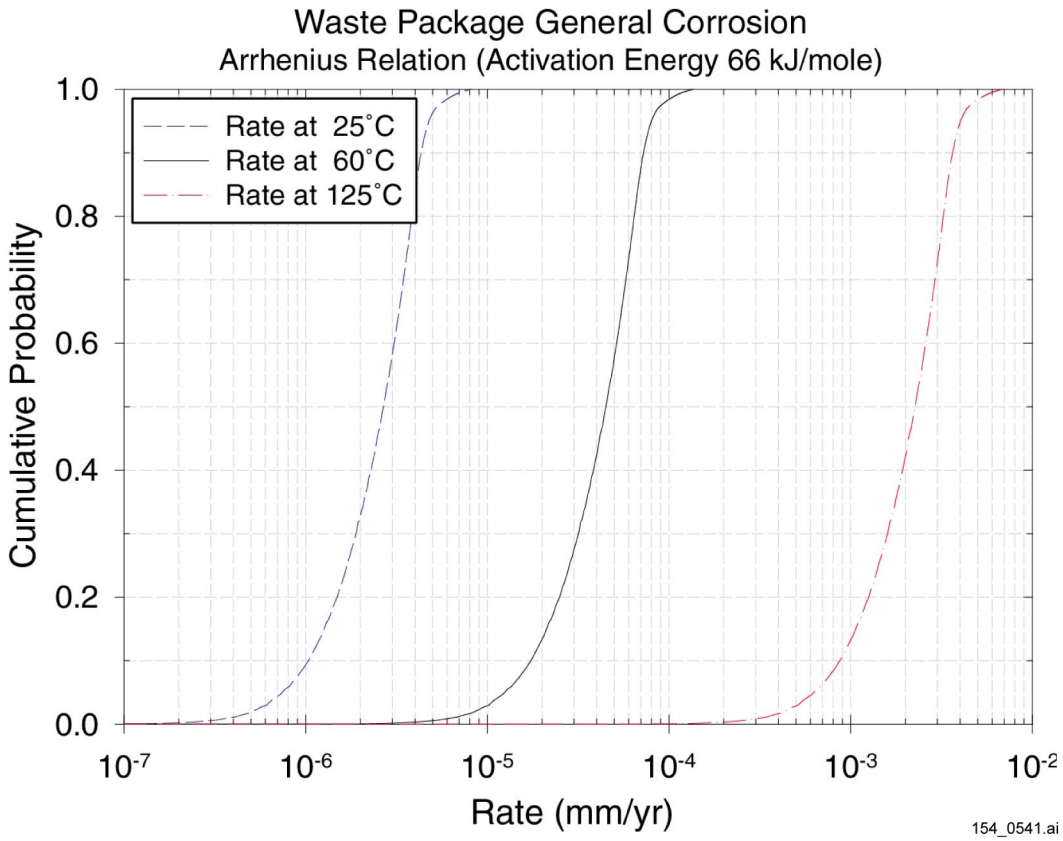

154_0541.ai

Source: Bullard 2001 [DIRS 155034].

Figure 7.3.5-2. Cumulative Distribution Functions of General Corrosion Rate of the Waste Package Outer Barrier at 25, 60, and 125°C Calculated with Temperature-Dependent Alloy 22 General Corrosion Model I

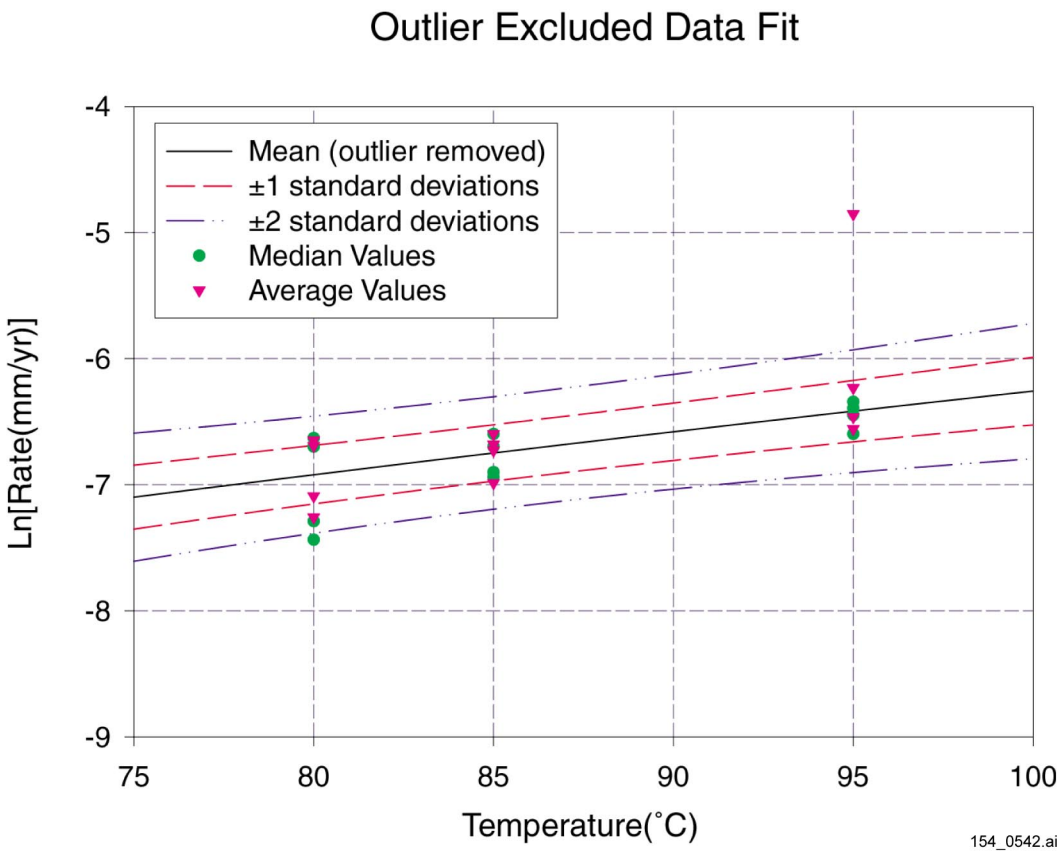

154_0542.ai

Source: Bullard 2001 [DIRS 155034].

NOTE: The data are used to evaluate the temperature-dependent term only. The rate data are not used to determine the general corrosion rate values for the model.

Figure 7.3.5-3. Data Fit for Temperature Dependence of Alloy 22 General Corrosion Model II with the Outer Excluded

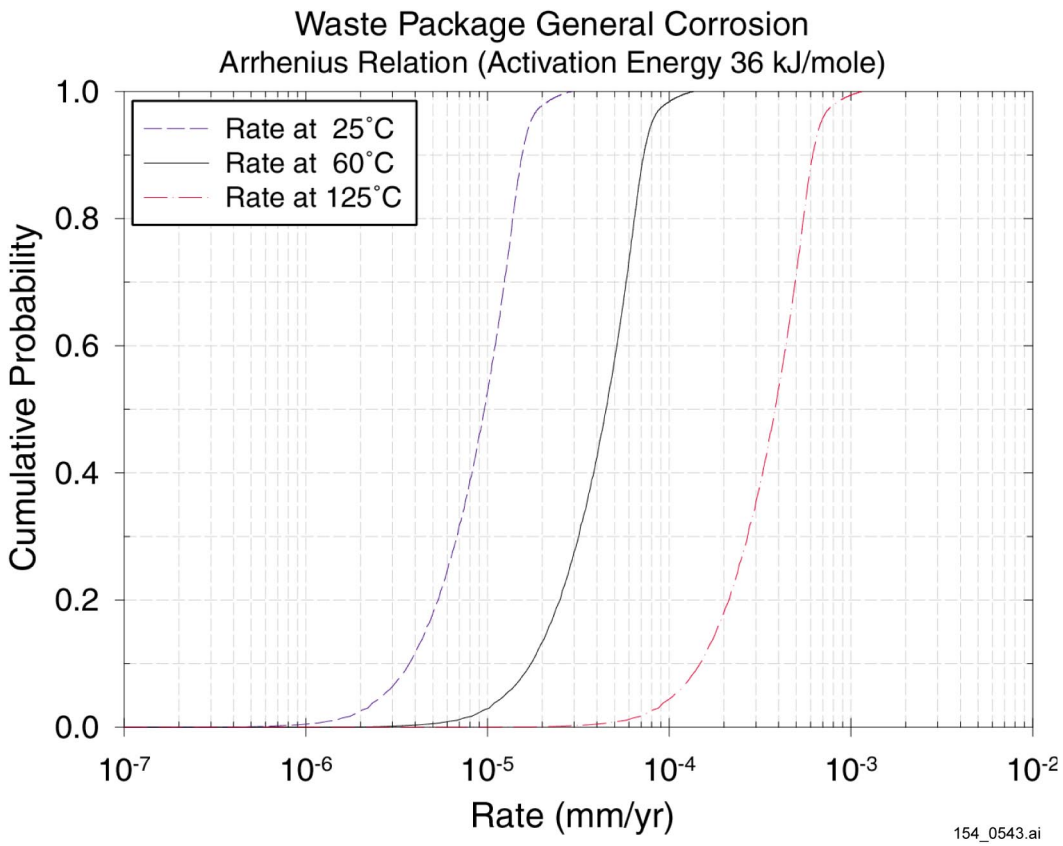

154_0543.ai

Source: Bullard 2001 [DIRS 155034].

Figure 7.3.5-4. Cumulative Distribution Functions of General Corrosion Rate of the Waste Package Outer Barrier at 25°, 60°, and 125°C Calculated with Temperature-Dependent Alloy 22 General Corrosion Model II

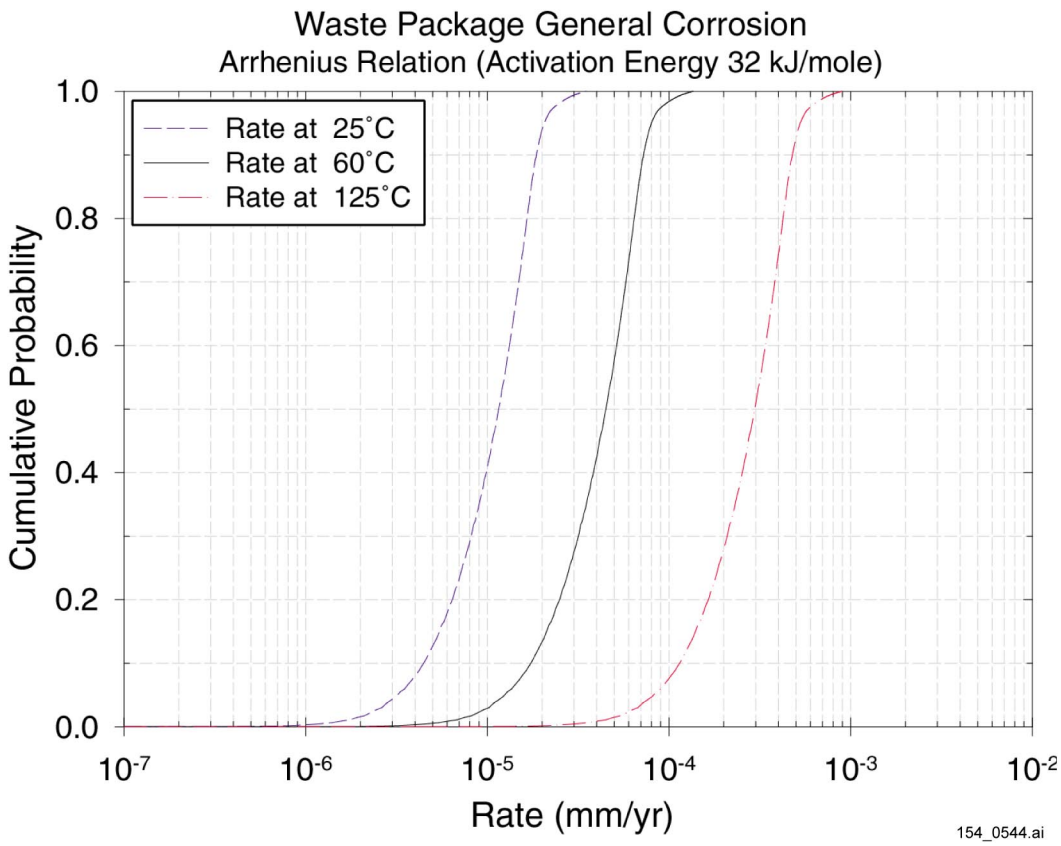

154_0544.ai

Source: Bullard 2001 [DIRS 155034].

Figure 7.3.5-5. Cumulative Distribution Functions of General Corrosion Rate of the Waste Package Outer Barrier at 25, 60, and 125°C Calculated with Temperature-Dependent Alloy 22 General Corrosion Model III

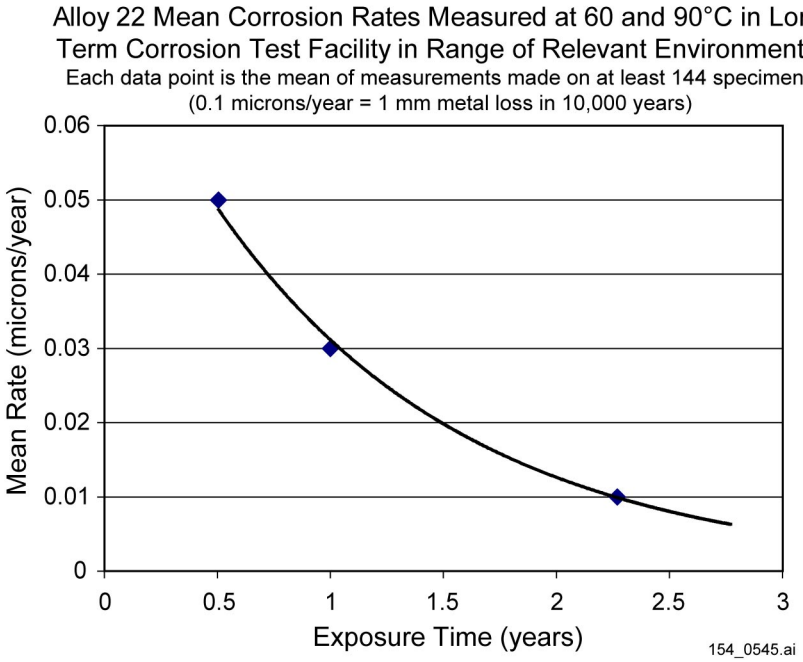

154_0545.ai

Source: Bullard 2001 [DIRS 155034].

Figure 7.3.5-6. Mean General Corrosion Rate of Alloy 22 Versus Exposure Time for Weight Loss Specimens from the Long-Term Corrosion Testing Facility

FIGURE REMOVED

Figure 7.3.5-7

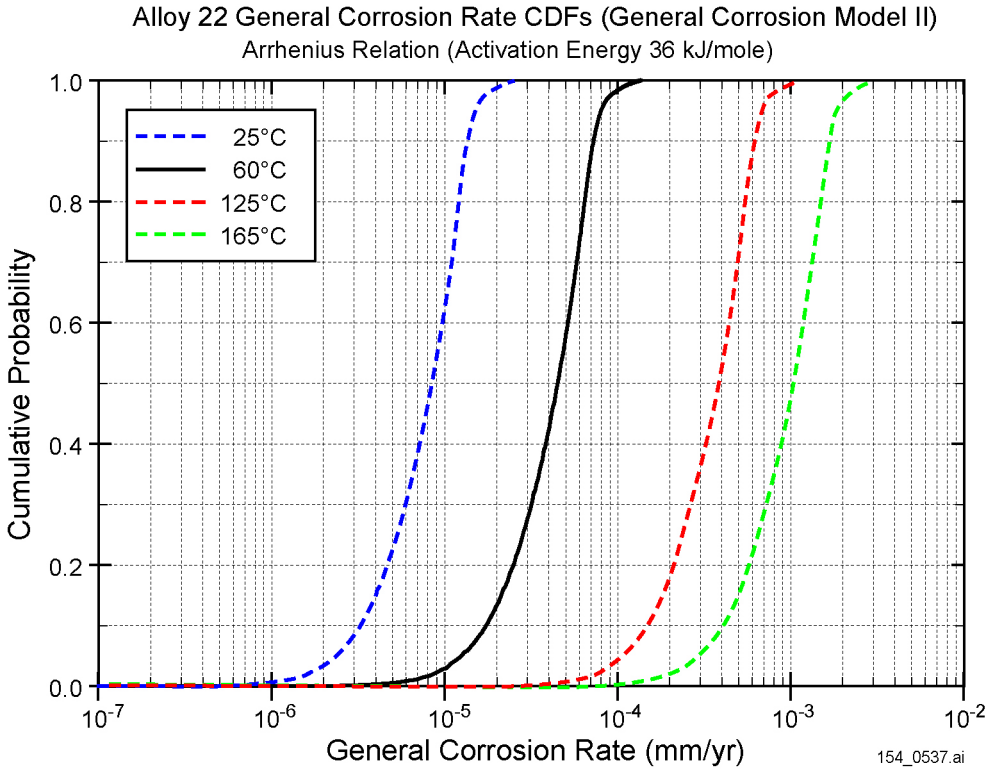

154_0537.ai

Source: Mon 2001 [DIRS 155202].

NOTE: Cumulative distribution functions of general corrosion rate of the Alloy 22 waste package outer barrier at 25, 60, 125, and 165°C with temperature-dependent Alloy 22 general corrosion model II.

Figure 7.3.5-8. Cumulative Distribution Functions of General Corrosion Rate of the Alloy 22 Waste Package Outer Barrier

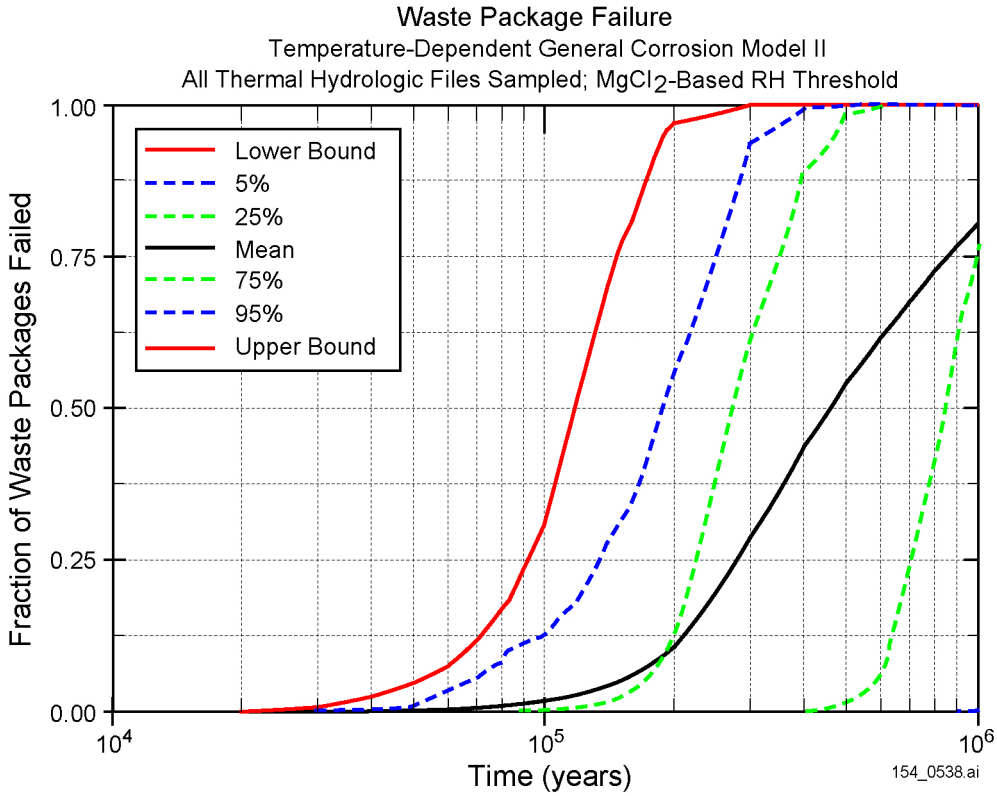

154_0538.ai

Source: Mon 2001 [DIRS 155202].

NOTE: Waste package failure profile with time incorporating the temperature-dependent Alloy 22 general corrosion model II and using a critical relative humidity function based on $MgCl_2$ deliquescence points. Shown are the upper bound, mean, and 95th, 75th and 25th percentile confidence intervals of the failure (first breach) profile of waste packages with time. The analysis assumes 100 percent uncertainty in the general corrosion rates for the Alloy 22 waste package outer barrier. The relative humidity and temperature histories of the waste packages and drip shields included in the analysis are sampled from the temperature and relative humidity histories for the entire repository.

Figure 7.3.5-9 Waste Package Failure Profile with Time Incorporating the Temperature-Dependent Alloy 22 General Corrosion Model II

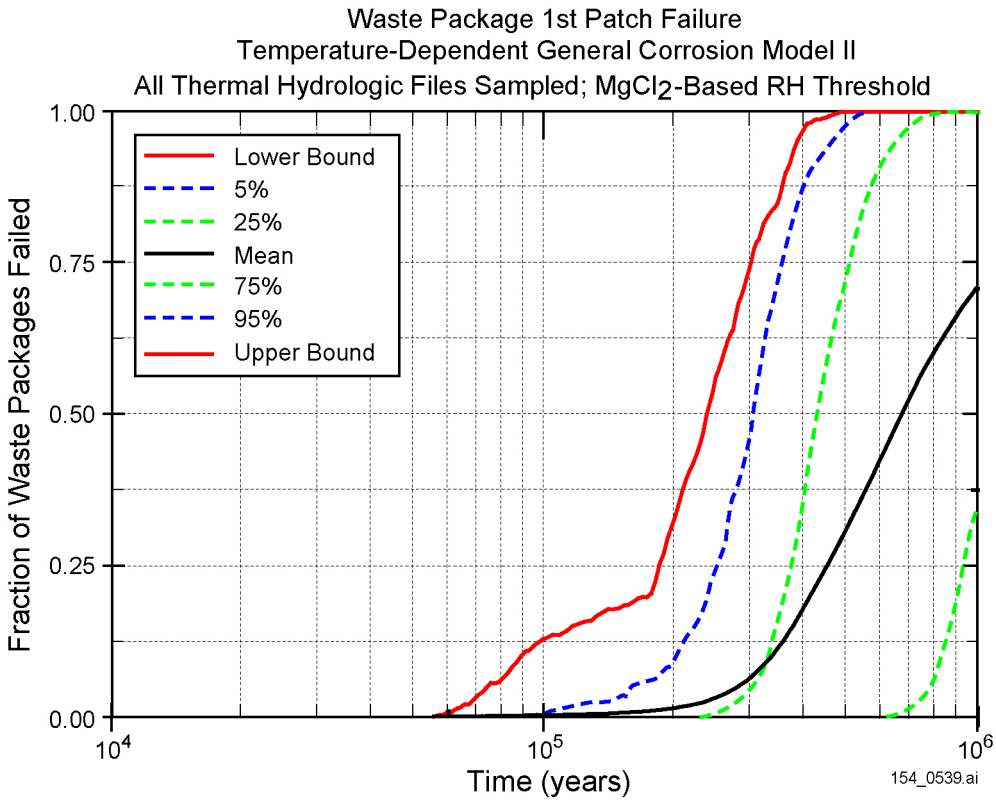

154_0539.ai

Source: Mon 2001 [DIRS 155202].

NOTE: Waste package first patch breach profile with time incorporating the temperature-dependent Alloy 22 general corrosion model II and using a critical relative humidity function based on $MgCl_2$ deliquescence points. Shown are the upper bound, mean, and 95th, 75th and 25th percentile confidence intervals of the failure (first breach) profile of waste packages with time. The analysis assumes 100 percent uncertainty in the general corrosion rates for the Alloy 22 waste package outer barrier. The relative humidity and temperature histories of the waste packages and drip shields included in the analysis are sampled from the temperature and relative humidity histories for the entire repository.

Figure 7.3.5-10 Waste Package First Patch Breach Profile with Time Incorporating the Temperature-Dependent Alloy 22 General Corrosion Model II

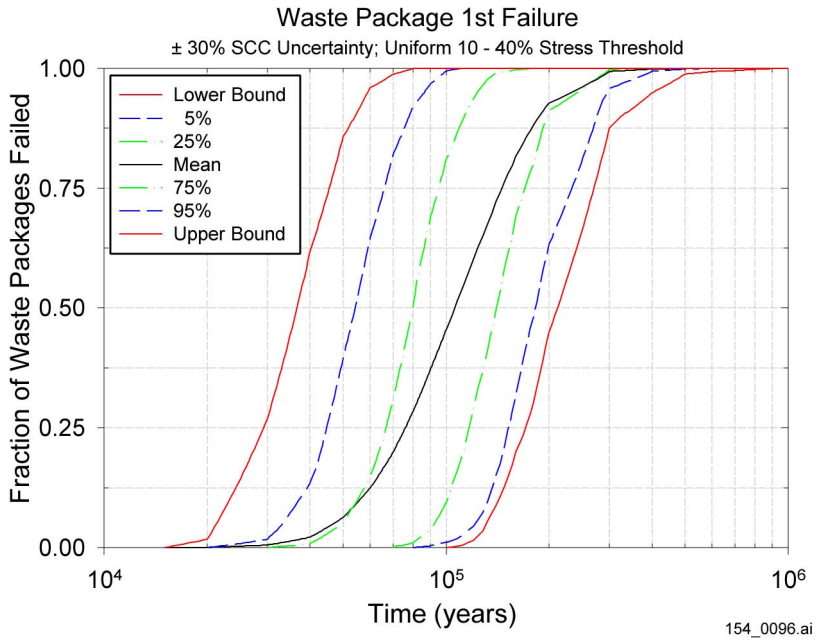

154_0096.ai

Source: Mon 2001 [DIRS 154872].

NOTE: Shown in the figure are the upper and lower bounds, mean, and 95th, 75th, 25th and 5th percentile confidence intervals of the first breach (failure) profile of waste packages with time. SCC = stress corrosion cracking.

Figure 7.4-1. Waste Package Failure over Time for the Baseline WAPDEG Model

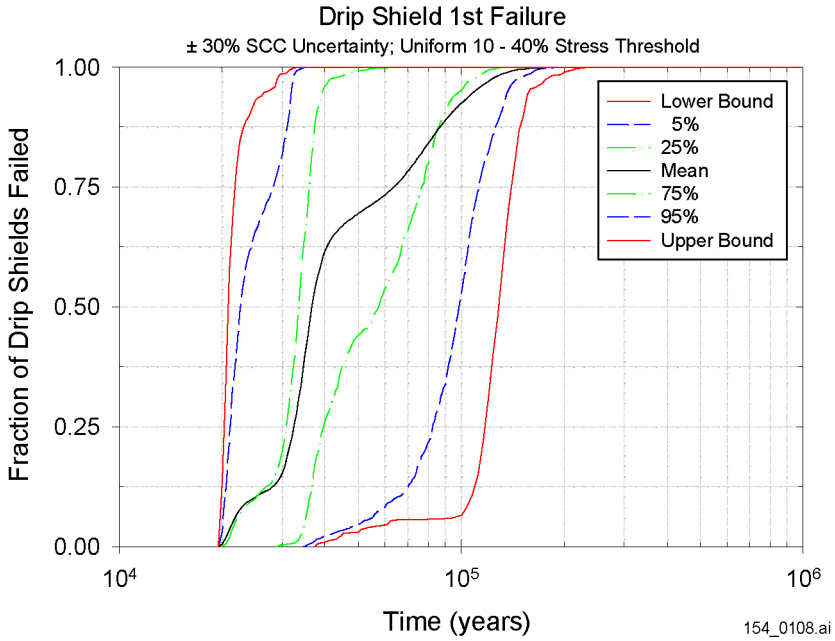

154_0108.ai

Source: Mon 2001 [DIRS 154872].

NOTE: Shown in the figure are the upper and lower bounds, mean, and 95th, 75th, 25th and 5th percentile confidence intervals of the first breach (failure) profile of drip shields with time. SSC = stress corrosion cracking.

Figure 7.4-2. Drip Shield Failure over Time for the Baseline WAPDEG Model

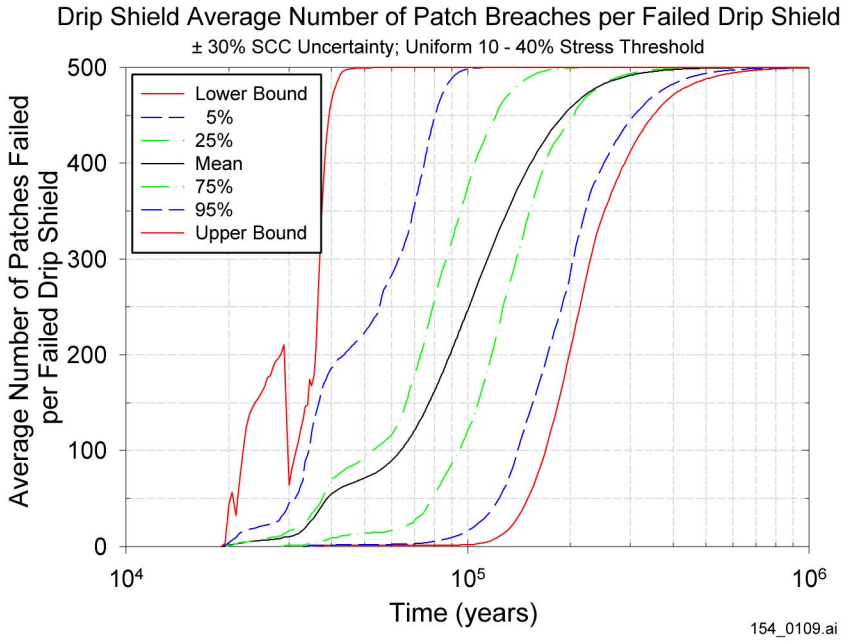

154_0109.ai

Source: Mon 2001 [DIRS 154872].

NOTE: Shown in the figure are the upper and lower bounds, mean, and 95th, 75th, 25th and 5th percentile confidence intervals of the average number of drip shield patch breaches per failed drip shield with time. SSC = stress corrosion cracking.

Figure 7.4-3. Average Number of Drip Shield Patch Breaches per Failed Drip Shield for the Baseline WAPDEG Model

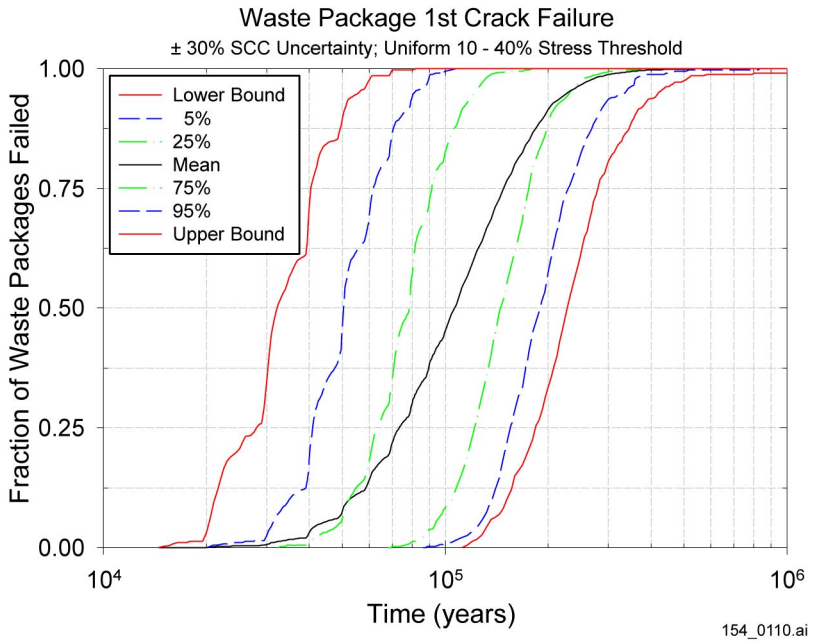

154_0110.ai

Source: Mon 2001 [DIRS 154872].

NOTE: Shown in the figure are the upper and lower bounds, mean, and 95th, 75th, 25th and 5th percentile confidence intervals of the first crack failure of waste packages with time. SSC = stress corrosion cracking.

Figure 7.4-4. Waste Package First Crack Failure for the Baseline WAPDEG Model

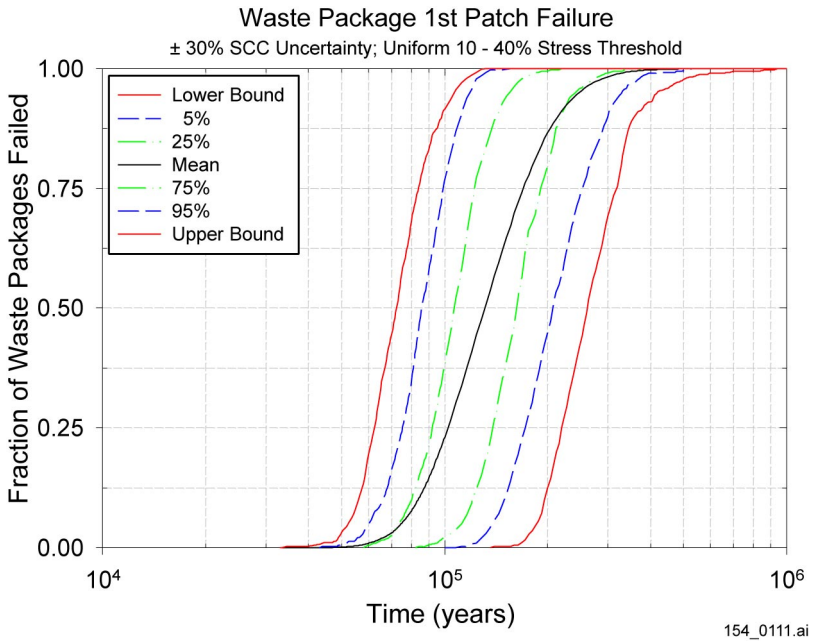

154_0111.ai

Source: Mon 2001 [DIRS 154872].

NOTE: Shown in the figure are the upper and lower bounds, mean, and 95th, 75th, 25th and 5th percentile confidence intervals of the first patch failure of waste packages with time. SSC = stress corrosion cracking.

Figure 7.4-5. Waste Package First Patch Failure for the Baseline WAPDEG Model

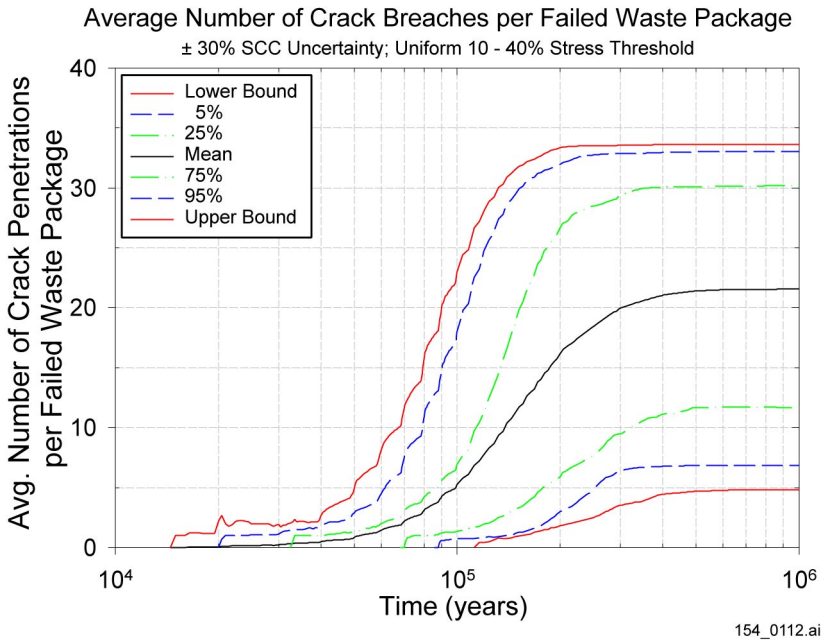

154_0112.ai

Source: Mon 2001 [DIRS 154872].

NOTE: Shown in the figure are the upper and lower bounds, mean, and 95th, 75th, 25th and 5th percentile confidence intervals of the average number of crack breaches per failed waste package with time. SSC = stress corrosion cracking.

Figure 7.4-6. Average Number of Crack Breaches per Failed Waste Package for the Baseline WAPDEG Model

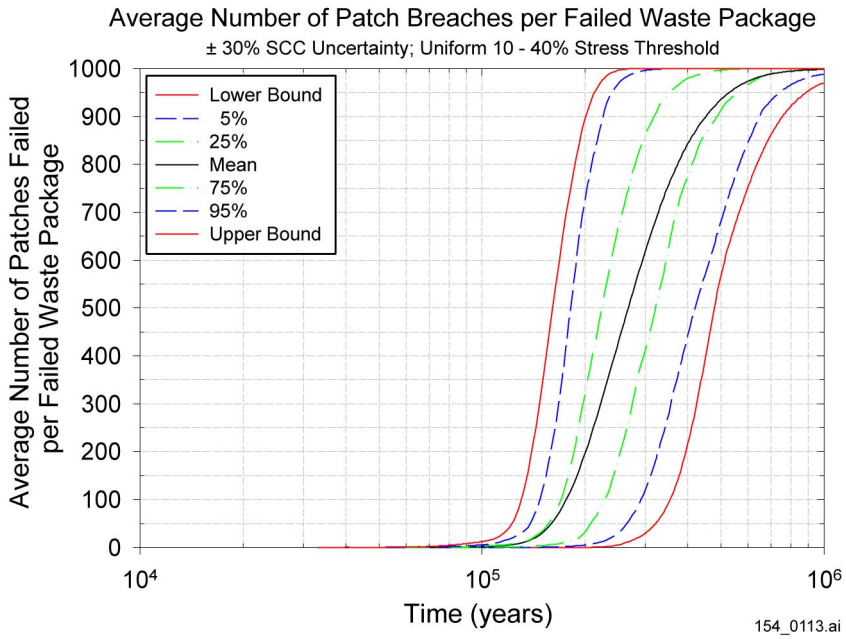

154_0113.ai

Source: Mon 2001 [DIRS 154872].

NOTE: Shown in the figure are the upper and lower bounds, mean, and 95th, 75th, 25th and 5th percentile confidence intervals of the average number of patch breaches per failed waste package with time. SSC = stress corrosion cracking.

Figure 7.4-7. Average Number of Patch Breaches per Failed Waste Package for the Baseline WAPDEG Model

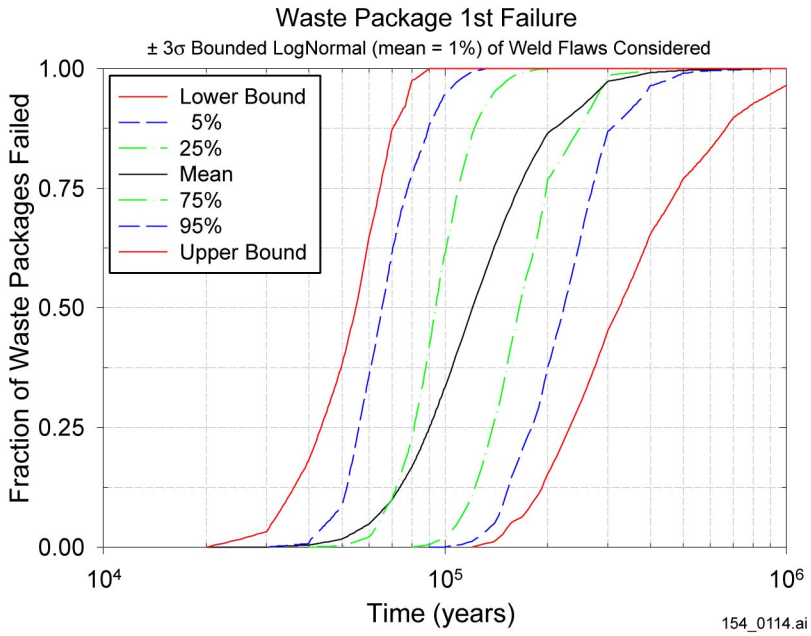

154_0114.ai

Source: Mon 2001 [DIRS 154872].

NOTE: Shown in the figure are the upper and lower bounds, mean, and 95th, 75th, 25th and 5th percentile confidence intervals of the first breach (failure) profile of waste packages with time. The fraction of weld flaws capable of propagation is sampled from a log-normal distribution with a mean of 0.01 and bounded by +3 standard deviations at 0.5 and –3 standard deviations at 0.0002.

Figure 7.4-8. Waste Package Failure with Time Incorporating the Updated Uncertainty for Weld Flaw Orientation

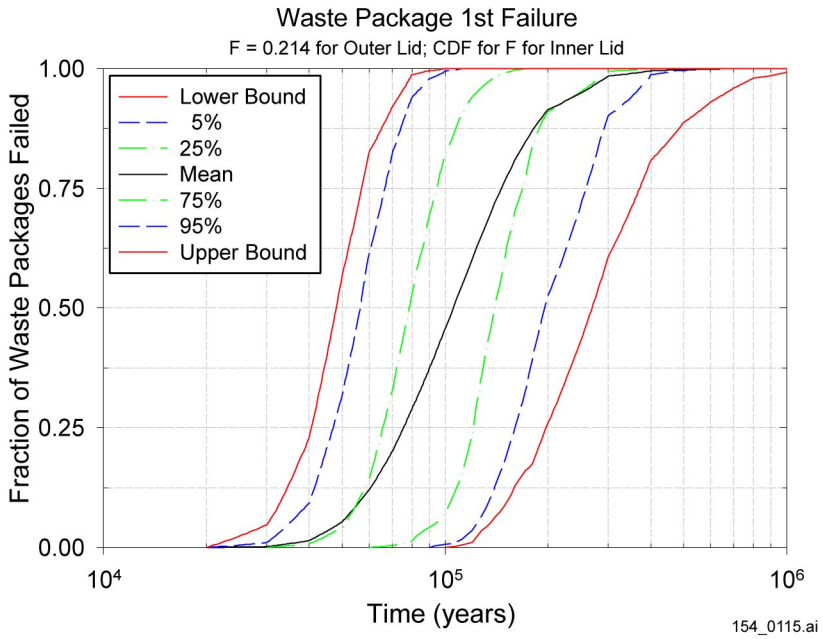

154_0115.ai

Source: Mon 2001 [DIRS 154872].

NOTE: Shown in the figure are the upper and lower bounds, mean, and 95th, 75th, 25th and 5th percentile confidence intervals of the first breach (failure) profile of waste packages with time.

Figure 7.4-9. Waste Package Failure with Time Incorporating the Updated Stress Uncertainty Bounds for the Outer and Inner Closure-Lids of the Waste Package Outer Barrier

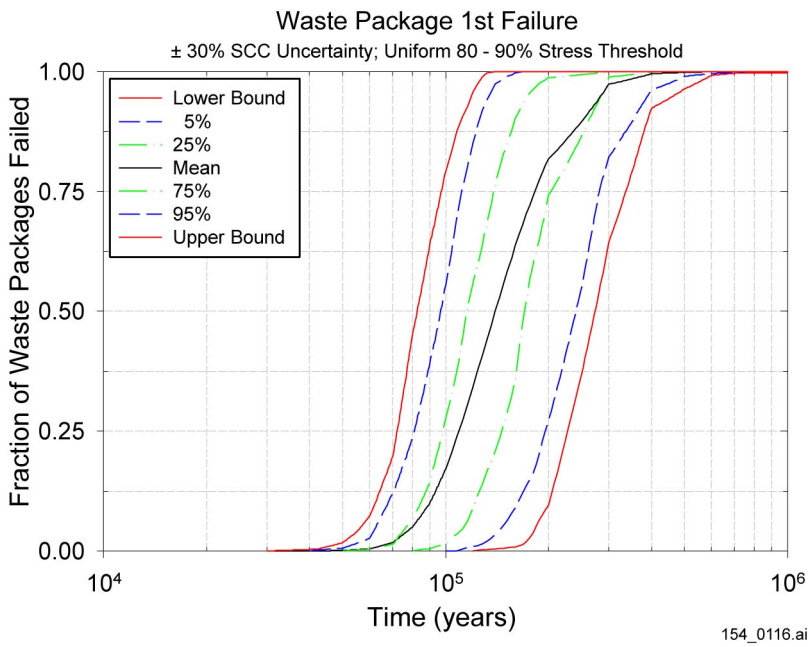

154_0116.ai

Source: Mon 2001 [DIRS 154872].

NOTE: Shown in the figure are the upper and lower bounds, mean, and 95th, 75th, 25th and 5th percentile confidence intervals of the first breach (failure) profile of waste packages with time.

Figure 7.4-10. Waste Package Failure with Time Incorporating the Updated Stress Threshold Uncertainty for Crack Initiation by Stress Corrosion Cracking

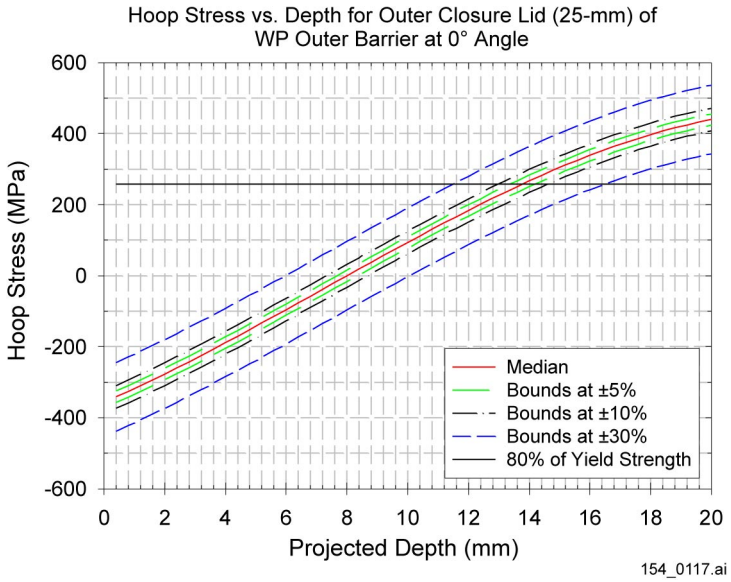

154_0117.ai

Source: DTN: MO0010MWDSUP04.010 [DIRS 152884].

NOTE: Shown in the figure is hoop stress as a function of depth in the Alloy 22 outer closure-lid weld region (25-mm thick) using uncertainty bounds at ±5, 10, and 30 percent of the yield strength, along with the lower bound of the threshold stress (80 percent of the yield strength).

Figure 7.4-11. Hoop Stress versus Depth for Outer Closure-Lid Weld Region of Waste package Outer Barrier

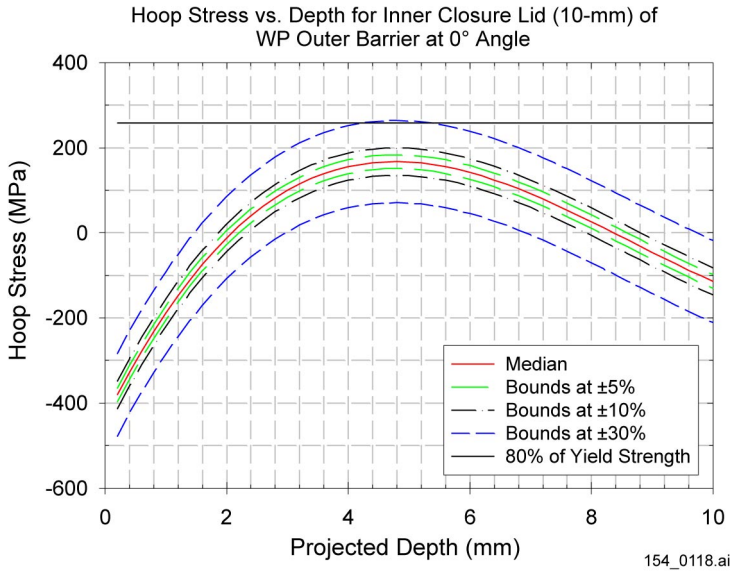

154_0118.ai

Source: DTN: MO0010MWDSUP04.010 [DIRS 152884].

NOTE: Shown in the figure is hoop stress as a function of depth in the Alloy 22 inner closure lid weld region (10-mm thick) using uncertainty bounds at ±5, 10, and 30 percent of the yield strength, along with the lower bound of the threshold stress (80 percent of the yield strength).

Figure 7.4-12. Hoop Stress versus Depth for Inner Closure-Lid Weld Region of Waste Package Outer Barrier for Crack Initiation by Stress Corrosion Cracking

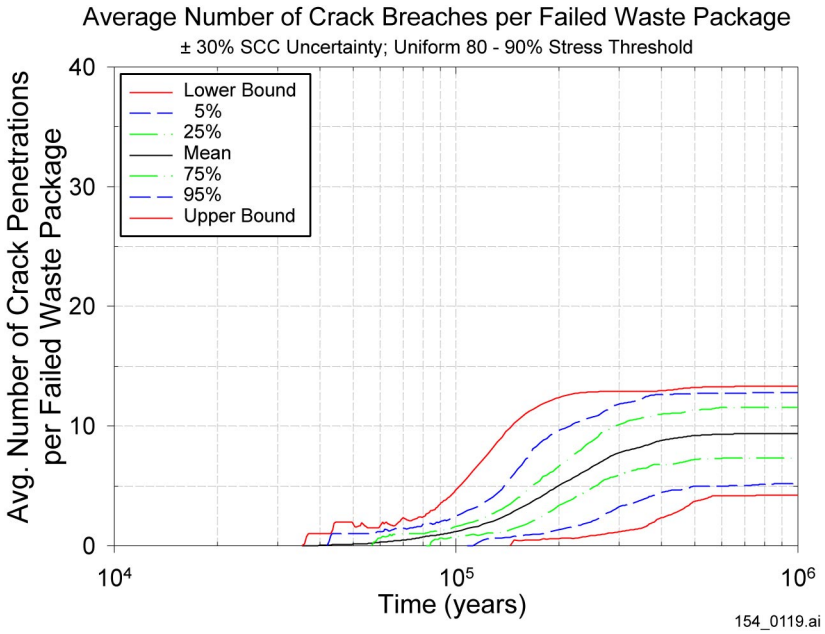

154_0119.ai

Source: Mon 2001 [DIRS 154872].

NOTE: Shown in the figure are the upper and lower bounds, mean, and 95th, 75th, 25th and 5th percentile confidence intervals of the average number of crack breaches per failed waste package with time.

Figure 7.4-13. Average Number of Crack Breaches per Failed Waste Package with Time Incorporating the Updated Stress Threshold Uncertainty for Crack Initiation by Stress Corrosion Cracking

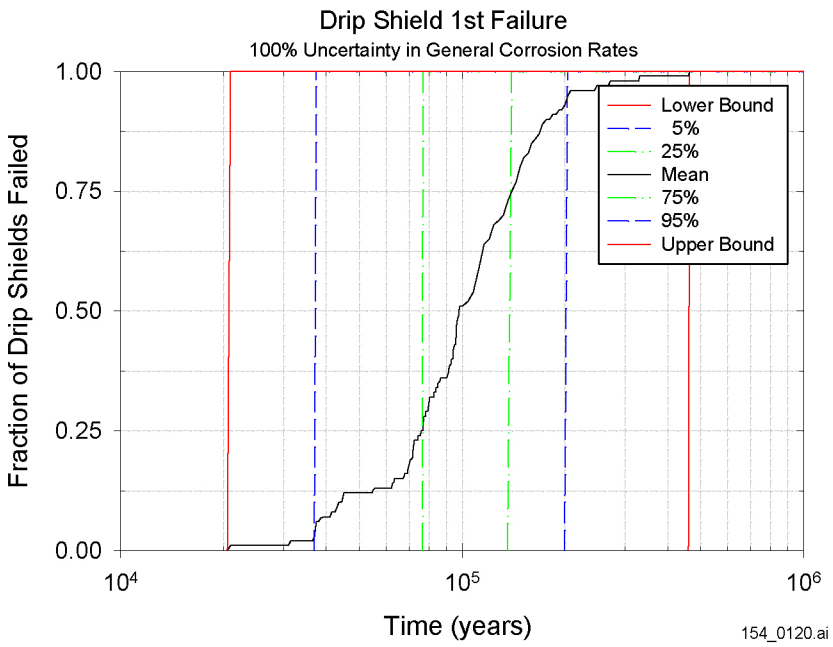

154_0120.ai

Source: Mon 2001 [DIRS 154872].

NOTE: Shown in the figure are the upper and lower bounds, mean, and 95th, 75th, 25th and 5th percentile confidence intervals of the first breach (failure) profile of drip shields with time. The analysis assumes 100 percent uncertainty in the general corrosion rates for the Titanium Grade 7 drip shield.

Figure 7.4-14. Drip Shield Failure with Time Assuming 100 Percent Uncertainty in the General Corrosion Rates

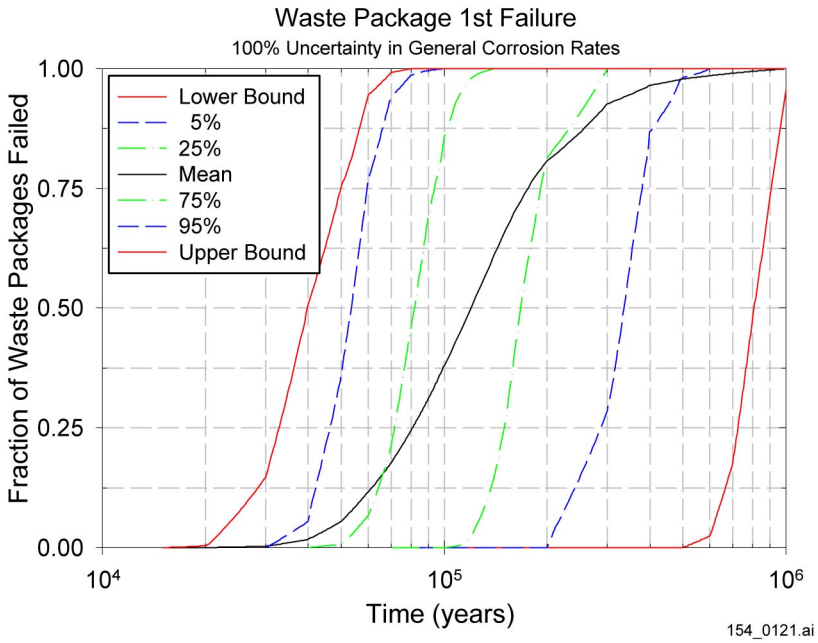

154_0121.ai

Source: Mon 2001 [DIRS 154872].

NOTE: Shown in the figure are the upper and lower bounds, mean, and 95th, 75th, 25th and 5th percentile confidence intervals of the first breach (failure) profile of waste packages with time. The analysis assumes 100 percent uncertainty in the general corrosion rates for the Alloy 22 waste package outer barrier.

Figure 7.4-15. Waste Package First Failure with Time Assuming 100 Percent Uncertainty in the General Corrosion Rates

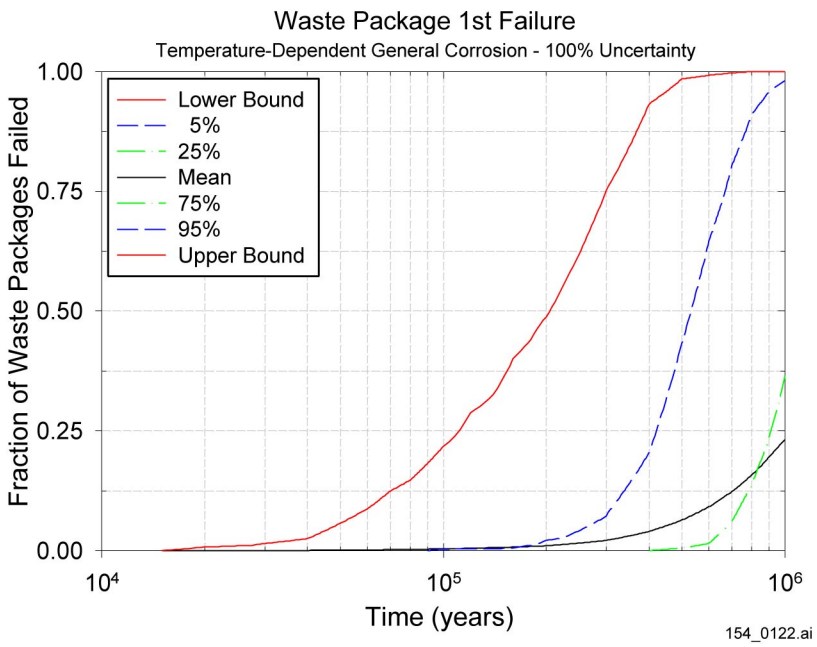

154_0122.ai

Source: Mon 2001 [DIRS 154872].

NOTE: Shown in the figure are the upper and lower bounds, mean, and 95th, 75th, 25th and 5th percentile confidence intervals of the first breach (failure) profile of waste packages with time. The analysis assumes 100 percent uncertainty in the general corrosion rates for the Alloy 22 waste package outer barrier.

Figure 7.4-16. Waste Package Failure with Time Incorporating the Temperature-Dependent Alloy 22 General Corrosion Model I

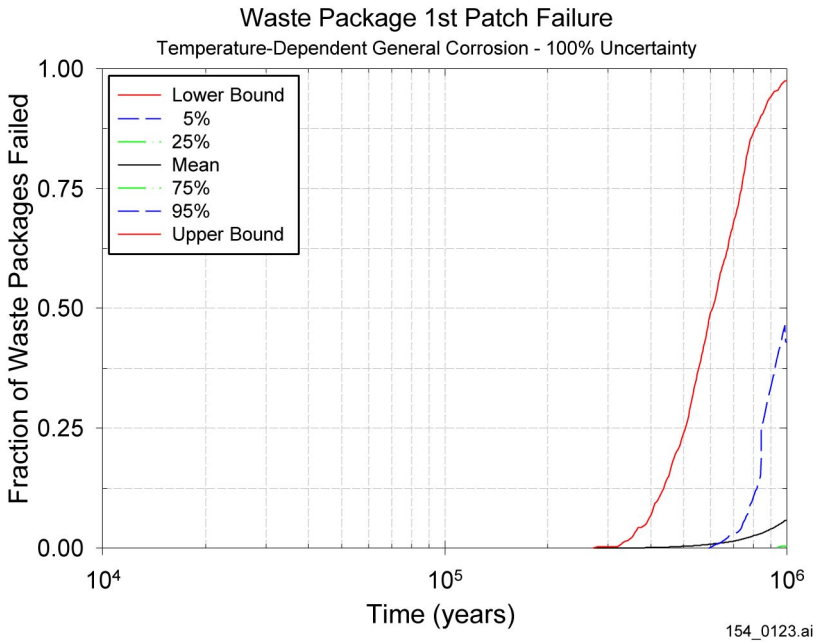

154_0123.ai

Source: Mon 2001 [DIRS 154872].

NOTE: Shown in the figure are the upper and lower bounds, mean, and 95th, 75th, 25th and 5th percentile confidence intervals of the first patch breach profile of waste packages with time. The analysis assumes 100 percent uncertainty in the general corrosion rates for the Alloy 22 waste package outer barrier.

Figure 7.4-17. Waste Package First Patch Failure for the Update Case Incorporating the Temperature-Dependent Alloy 22 General Corrosion Model II

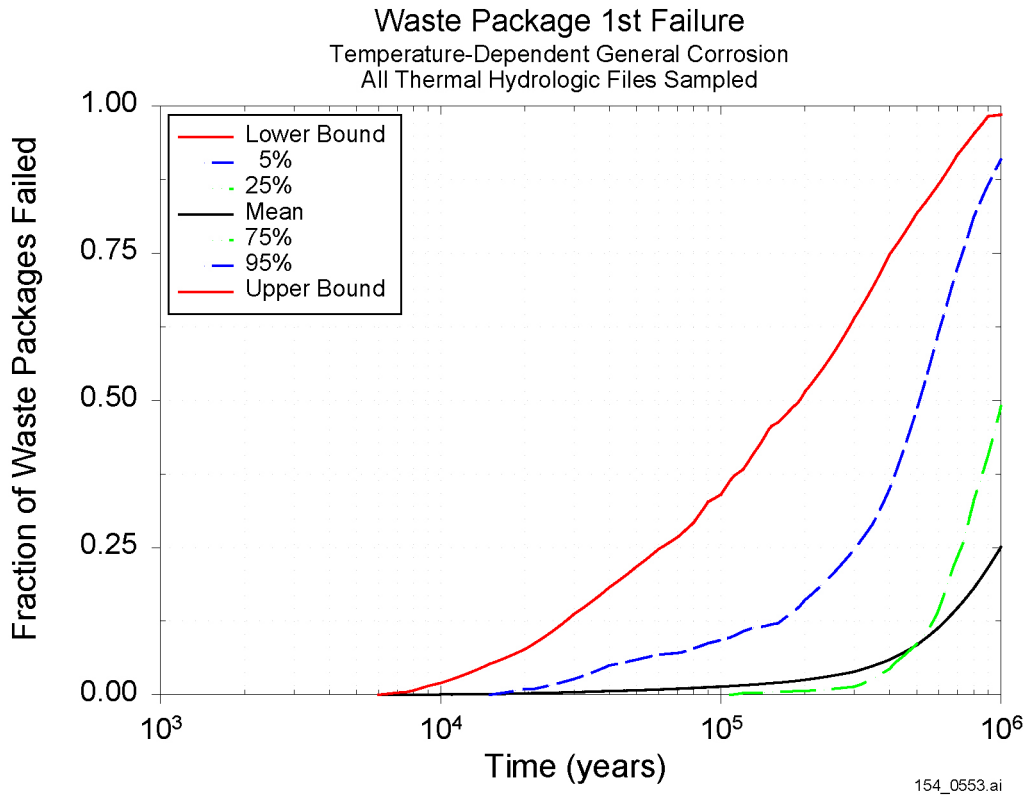

154_0553.ai

Source: Mon 2001 [DIRS 154872].

NOTE: Shown in the figure are the upper and lower bounds, mean, and 95th, 75th, 25th and 5th percentile confidence intervals of the first breach profile of waste packages with time. The analysis assumes 100 percent uncertainty in the general corrosion rates for the Alloy 22 waste package outer barrier. The relative humidity and temperature histories of the waste packages and drip shields included in the analysis are sampled from the temperature and relative humidity histories over the entire repository.

Figure 7.4-18. Waste Package Failure Profile with Time Incorporating the Temperature-Dependent Alloy 22 General Corrosion Model I

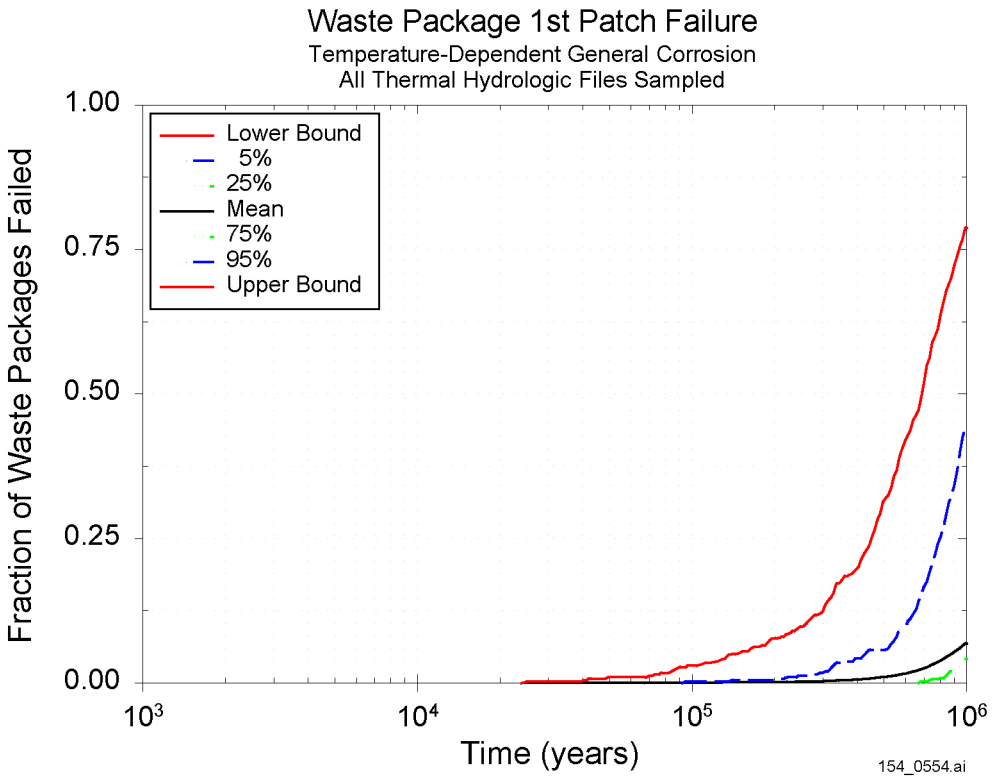

154_0554.ai

Source: Mon 2001 [DIRS 154872].

NOTE: Shown in the figure are the upper and lower bounds, mean, and 95th, 75th, 25th and 5th percentile confidence intervals of the first patch breach profile of waste packages with time. The analysis assumes 100 percent uncertainty in the general corrosion rates for the Alloy 22 waste package outer barrier. The relative humidity and temperature histories of the waste packages and drip shields included in the analysis are sampled from the temperature and relative humidity histories over the entire repository.

Figure 7.4-19. Waste Package First Patch Breach Profile with Time Incorporating the Temperature-Dependent Alloy 22 General Corrosion Model I

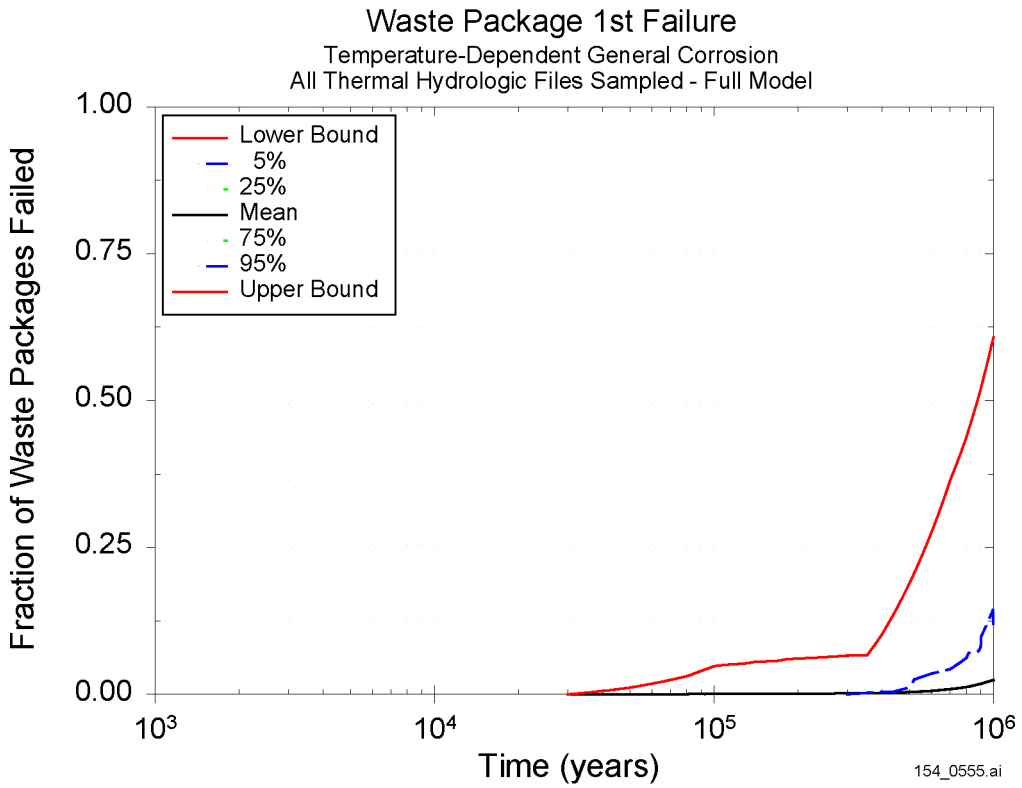

154_0555.ai

Source: Mon 2001 [DIRS 154872].

NOTE: Shown in the figure are the upper and lower bounds, mean, and 95th, 75th, 25th and 5th percentile confidence intervals of the first breach profile of waste packages with time.

Figure 7.4-20. Waste Package Failure Profile with Time for the Integrated Model I

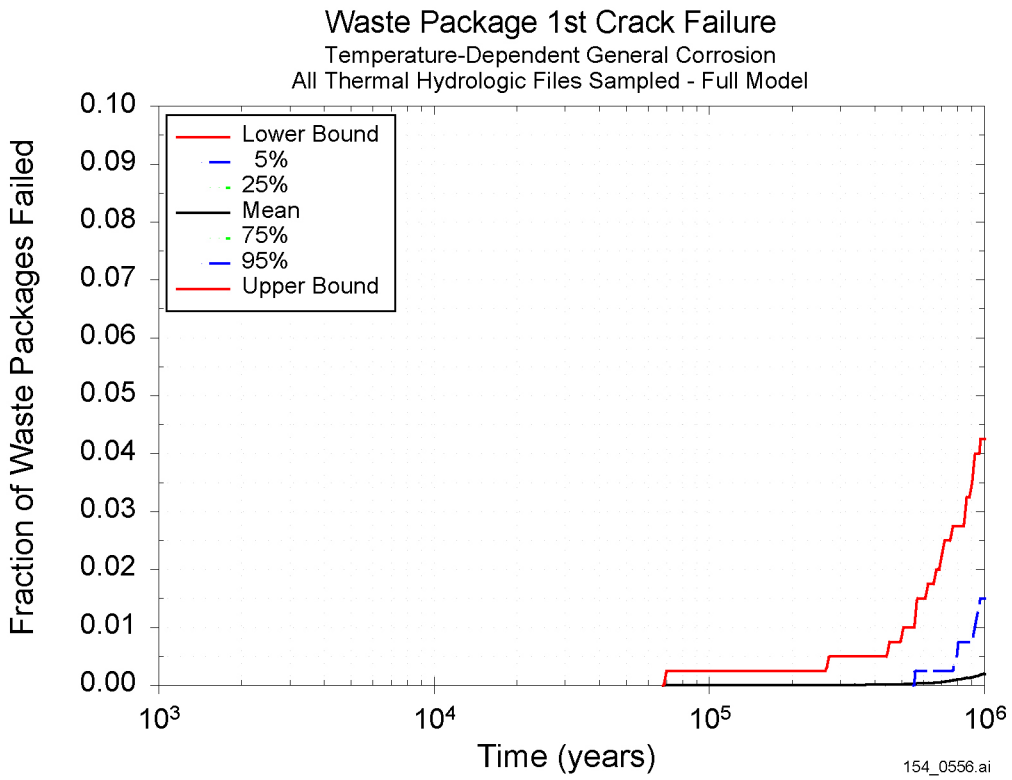

154_0556.ai

Source: Mon 2001 [DIRS 154872].

NOTE: Shown in the figure are the upper and lower bounds, mean, and 95th, 75th, 25th and 5th percentile confidence intervals of the first crack breach profile of waste packages with time.

Figure 7.4-21. Waste Packages First Crack Breach Profile with Time for the Integrated Model I

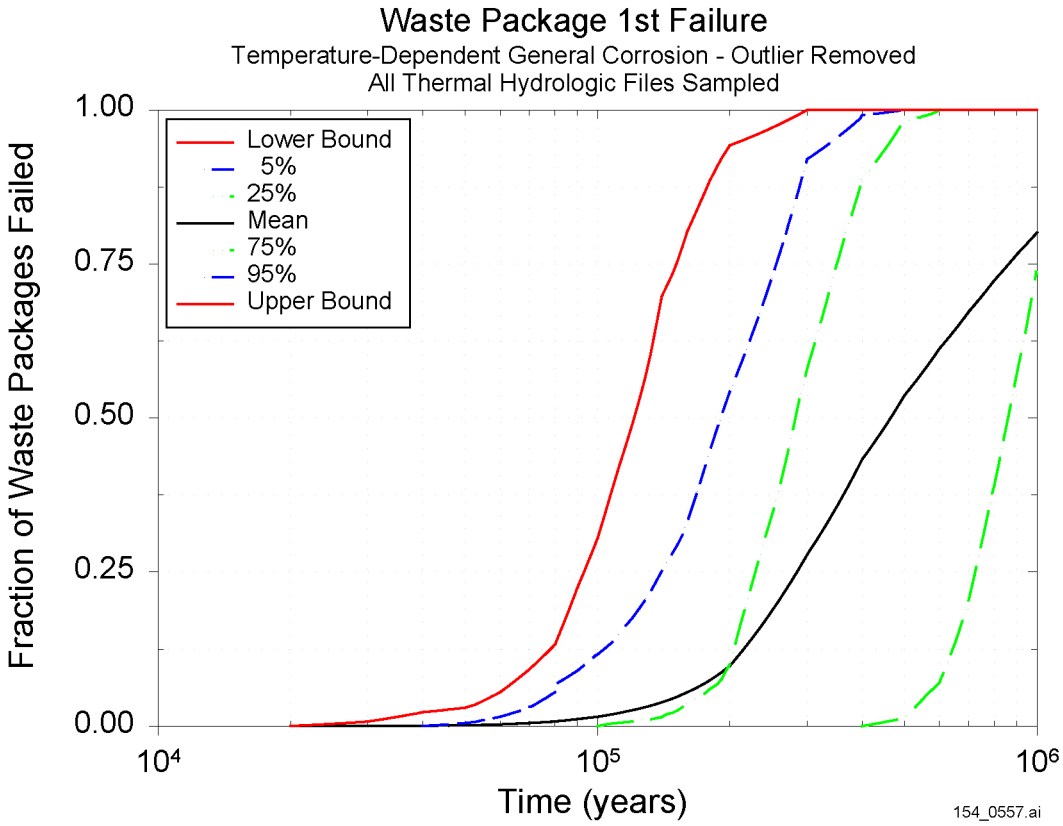

154_0557.ai

Source: Mon 2001 [DIRS 154872].

NOTE: Shown in the figure are the upper and lower bounds, mean, and 95th, 75th, and 25th percentile confidence intervals of the first breach profile of waste packages with time. The analysis assumes 100 percent uncertainty in the general corrosion rates for the Alloy 22 waste package outer barrier. The relative humidity and temperature histories of the waste packages and drip shields included in the analysis are sampled from the temperature and relative humidity histories over the entire repository.

Figure 7.4-22. Waste Package Failure Profile with Time Incorporating the Temperature-Dependent Alloy 22 General Corrosion Model II

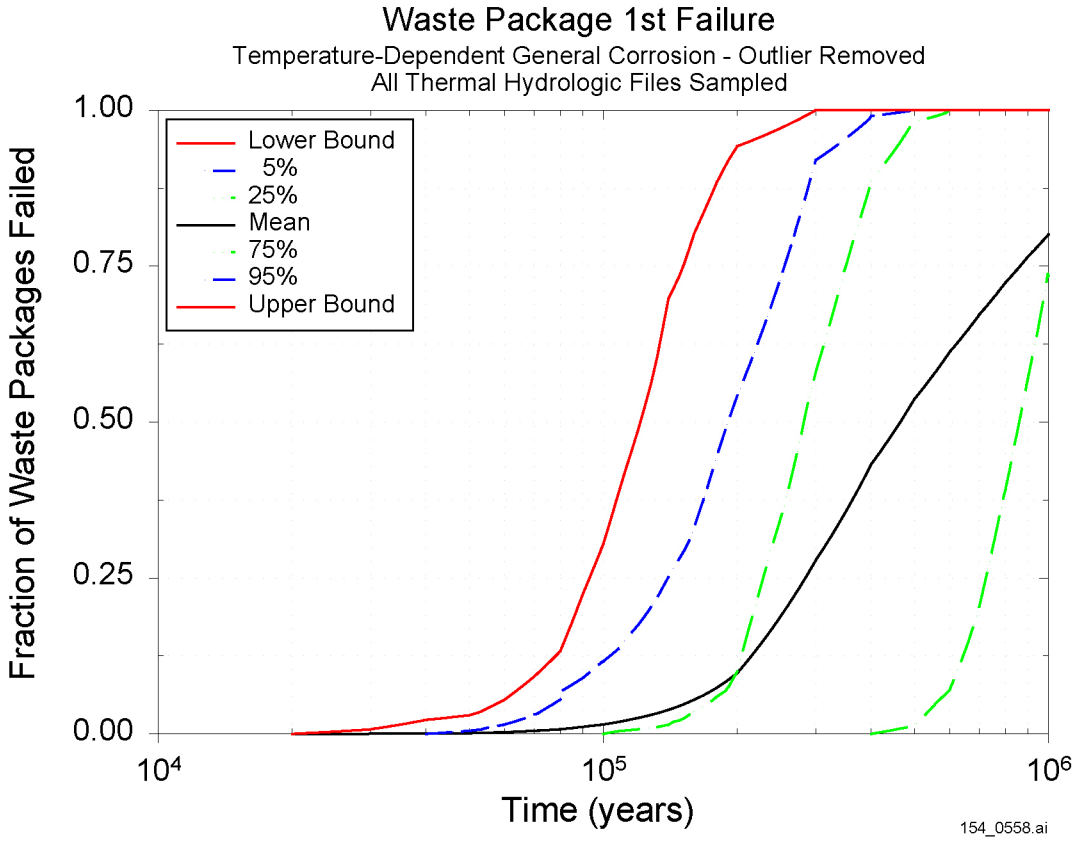

154_0558.ai

Source: Mon 2001 [DIRS 154872].

NOTE: Shown in the figure are the upper and lower bounds, mean, and 95th, 75th and 25th percentile confidence intervals of the first patch breach profile of waste packages with time. The analysis assumes 100 percent uncertainty in the general corrosion rates for the Alloy 22 waste package outer barrier. The relative humidity and temperature histories of the waste packages and drip shields included in the analysis are sampled from the temperature and relative humidity histories over the entire repository.

Figure 7.4-23. Waste Package First Patch Breach Profile with Time Incorporating the Temperature-Dependent Alloy 22 General Corrosion Model II

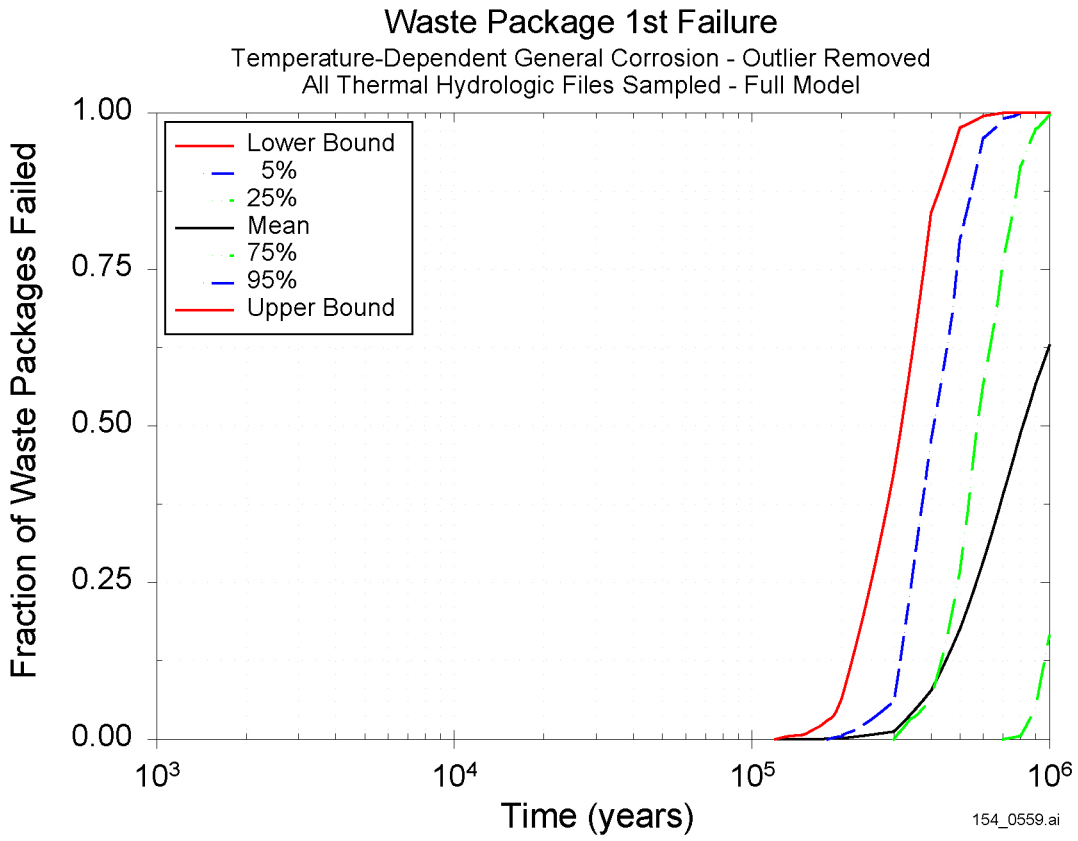

154_0559.ai

Source: Mon 2001 [DIRS 154872].

NOTE: Shown in the figure are the upper and lower bounds, mean, and 95th, 75th and 25th percentile confidence intervals of the first breach profile of waste packages with time.

Figure 7.4-24. Waste Package Failure Profile with Time for the Integrated Model II

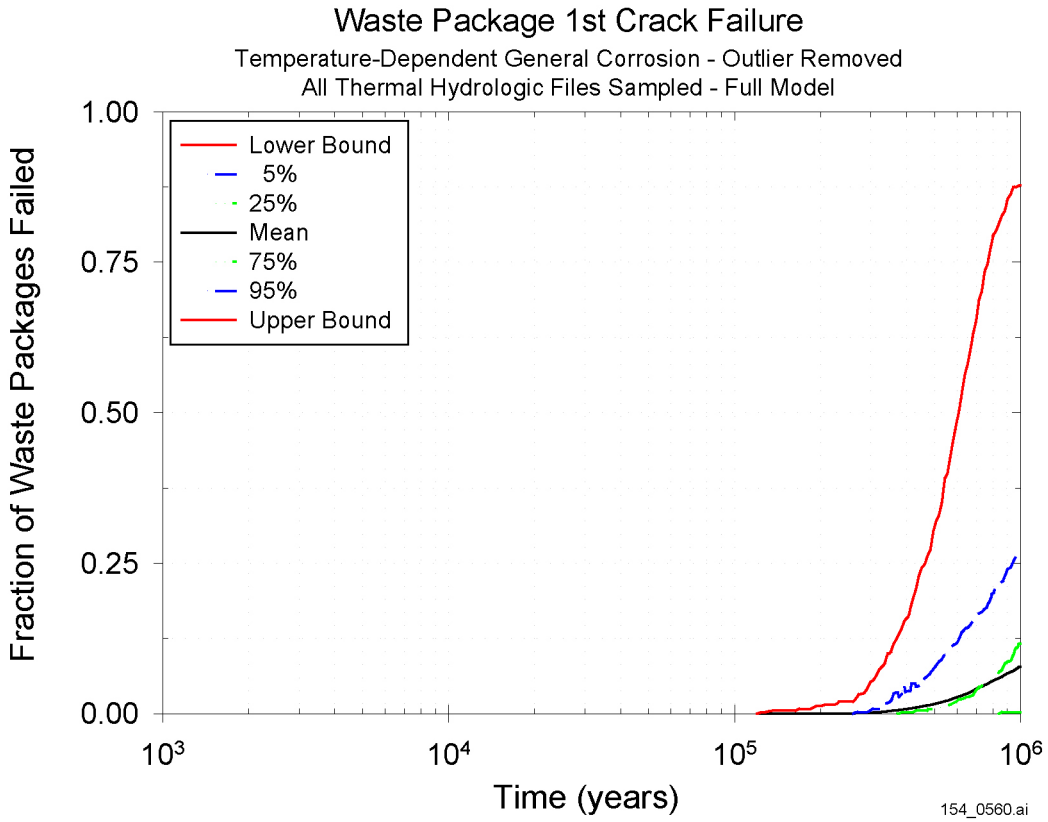

154_0560.ai

Source: Mon 2001 [DIRS 154872].

NOTE: Shown in the figure are the upper and lower bounds, mean, and 95th, 75th and 25th percentile confidence intervals of the first crack breach profile of waste packages with time.

Figure 7.4-25. Waste Packages First Crack Breach Profile with Time for the Integrated Model II

INTENTIONALLY LEFT BLANK

8 Water Diversion Performance of the Engineered Barrier System

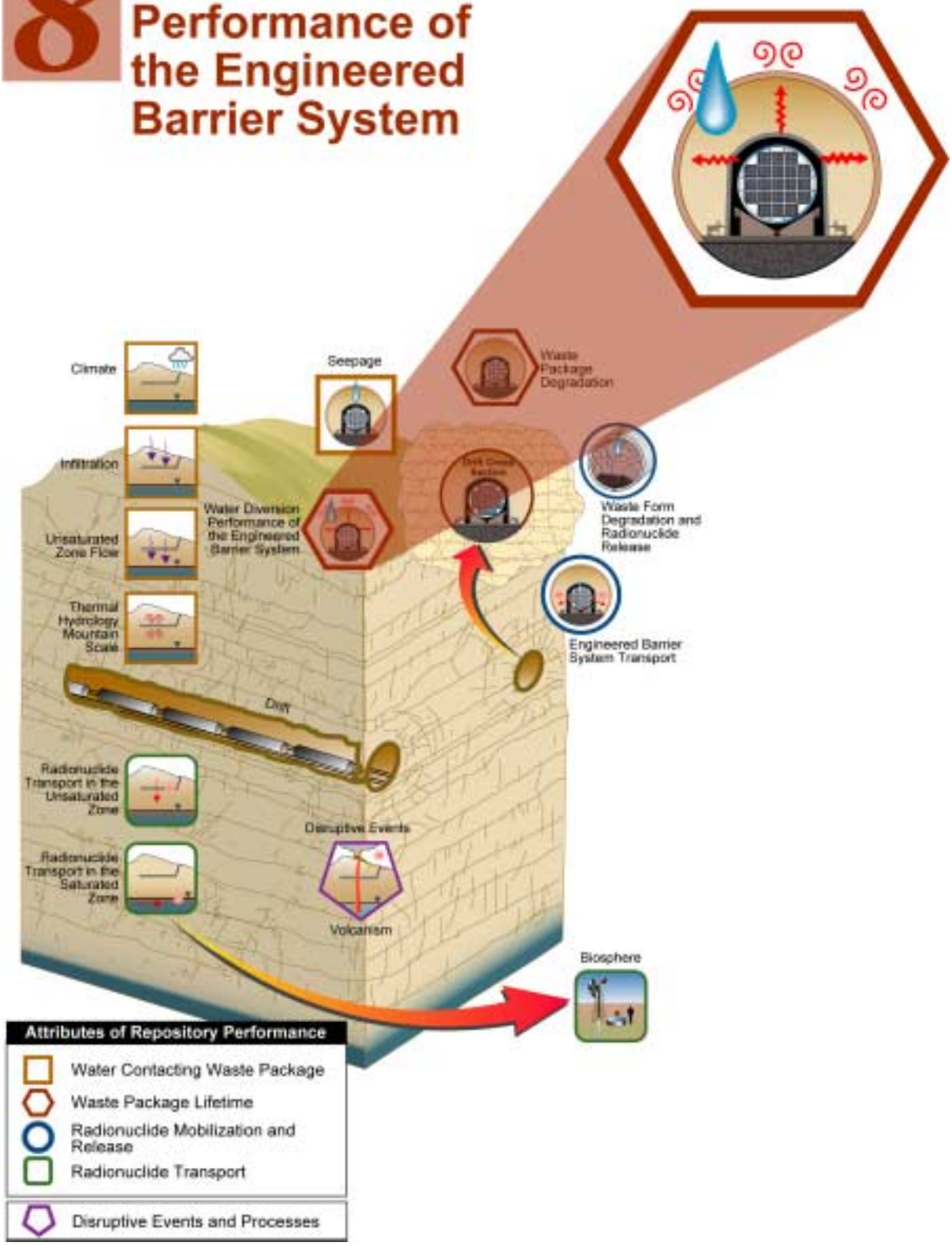

8. WATER DIVERSION PERFORMANCE

8.1 INTRODUCTION

Section 8 describes the new information developed to produce a more realistic model for water diversion (principally by the drip shield) through the engineered barrier system (EBS). More specifically, this information is designed to quantify uncertainties and reduce conservatisms in the EBS water diversion for the *Total System Performance Assessment for the Site Recommendation* (TSPA-SR) (CRWMS M&O 2000 [DIRS 153246]). The new information provides supplemental models or analysis in the following areas: (1) drip shield fluxes, (2) evaporation of seepage from the drip shield, (3) invert evaporation/condensation inside the drip shield, (4) waste package fluxes, and (5) bathtub flow through the waste package. Table 8-1 summarizes the rationale for the supplemental models and analyses in these five areas and identifies the specific section that documents the new information.

Evaporation of Seepage Contacting the Drip Shield (8.3.1)–The evolution of waste package heat has the potential to evaporate a portion of in-drift seepage that might contact the drip shield. The model provides an estimate of the fraction of this heat needed to evaporate seepage as it contacts the drip shield. Drip shield evaporation depends on a number of parameters: waste package heat evolution, forced air ventilation of the preclosure period, natural ventilation during the postclosure period, and drip shield surface conditions. The fraction of heat is treated as a random variable with potentially more evaporation taking place in the higher-temperature operating mode. The TSPA model was based upon a flow splitting algorithm that included flux into breaches and away from breaches in the drip shield (CRWMS M&O 2000 [DIRS 153246] Section 3.6.2.1). No credit is taken for potential evaporation at the surface of the drip shield. Consideration of this process potentially reduces the amount of seepage available for transport through the EBS. Alternative thermal operating modes are addressed by assuming two different temperature and relative humidity distributions for the higher- and lower-temperature operating modes. The impact on the amount of seepage available for transport over the range of thermal operating modes can be inferred from the time histories of time-dependent fluxes through the EBS (drip shield, waste package, and invert).

Model for Drip Shield Condensation (8.3.2)–This model quantifies the condensate flux on the underside of the drip shield due to evaporation and addresses what fraction will fall on the waste package. It was developed for the original EBS flow abstraction, but was not included in subsequent calculations. This activity is only meant to supplement the rationale for screening out this process due to low consequence. Alternative thermal operating modes will not affect the conceptual model for condensation on the underside of the drip shield and waste package.

Flux through the Drip Shield and Waste Package (8.3.3)–The waste package degradation model (i.e., the WAPDEG V4.0 code) provides for predictions of the type, number, and timing of breaches in the drip shield and waste package. This information is used by the EBS water diversion abstraction to define the time-dependent fluxes that flow through (or are diverted around) the drip shield and the waste package. In this model, droplets fall randomly on a drip shield, and the model accounts for a random fraction of water that flows over the drip shield but is captured by breaches. The abstraction implemented in the TSPA-SR (CRWMS M&O 2000

Table 8-1. Summary of Supplemental Models and Analyses

Key Attributes of System	Process Model (Section of S&ER)	Topic of Supplemental Scientific Model or Analysis	Reason For Supplemental Scientific Model or Analysis			Performance Assessment Treatment of Supplemental Scientific Model or Analysis[a]		
			Unquantified Uncertainty Analysis	Update in Scientific Information	Lower-Temperature Operating Mode Analysis	Section of Volume 1	TSPA Sensitivity Analysis	Included in Supplemental TSPA Model
Long-Lived Waste Package and Drip Shield	In-Drift Moisture Distribution (4.2.5)	Condensation under drip shields	X			8.3.2	X	
		Evaporation of seepage	X		X	8.3.1	X	X
		Effect of breached drip shields or waste package on seepage	X		X	8.3.3	X	X
		Waste package release flow geometry (flow-through, bathtub)	X			8.3.4	X	

NOTE: S&ER = *Yucca Mountain Science and Engineering Report* ([DOE 2001 [DIRS 153849]).

[a] Performance assessment treatment of supplemental scientific model or analysis discussed in SSPA Volume 2 (McNeish 2001 [DIRS 155023]).

[DIRS 153246], Section 3.6.3.1) conservatively considered all of the seepage entering the drift as falling on the crown of the drip shield and that all fluid that drips onto the drip shield or waste package occurs at the same axial location as the breach. The analyses are not intended to address alternative thermal operating modes, but rather to quantify conservatism in the TSPA-SR (CRWMS M&O 2000 [DIRS 153246]).

Model for Bathtub Flow Through the Waste Package (8.3.4)–An alternative conceptual model to the flow-through geometry is the bathtub geometry, which allows seepage to collect in the waste package before being released to the EBS. This effect will be most important during the first 20,000 years. At longer durations (100,000 years or greater), the presence of multiple penetrations for multiple groups of waste packages makes a flow-through geometry the likely long-term configuration. This model provides estimates of the time delays for the bathtub versus the flow-through model and an approach to quantify the uncertainty and sensitivity of total system performance assessment (TSPA) results to the bathtub versus the flow-through conceptual model. Alternative thermal operating modes will not affect the conceptual model for flow through the waste package.

The EBS is designed to function with the natural barriers at the site to minimize water contact with waste packages and waste forms. The components that will perform this function include the drip shield, the waste package, the waste package pallet, the invert (consisting of a steel support structure with crushed rock ballast), and the steel ground support. Another aspect of EBS performance is to moderate the transport of released radionuclides from breached waste packages to the host rock at the drift floor. This will be accomplished for the case of a breached waste package under an intact drip shield using a diffusion barrier concept. For the case of a breached drip shield, transport will be moderated through partial performance by reducing the amount of water that contacts the waste package. Finally, free drainage from the drifts is important for EBS performance. Sufficient drainage capacity will prevent partial inundation of waste packages or their supports, promote diffusion barrier performance of the invert, and prevent saturated flow conditions that could lead to faster transport for released radionuclides through the EBS and the host rock.

After the waste packages are emplaced, radioactive decay of the waste will heat the drifts. This heating process may evaporate some (or all) of the groundwater near the drifts, thereby perturbing the natural flow pattern for percolation of water through the mountain. As the drifts cool and the natural flow pattern is reestablished, some of the water percolating through the mountain may seep into the drifts and contact some of the drip shields. Any water dripped onto intact drip shields is considered to be diverted to the invert, except that which is evaporated directly. Over time, the drip shields and waste packages are expected to degrade. Once this occurs water can contact the waste form, resulting in the mobilization and transport of radionuclides through the EBS. This water may be flowing or dripping slowly through the EBS. Alternatively, this water may form a continuous film of stationary liquid. Water, as a stationary film or a flowing liquid, must be present for mobilization of radionuclides in the waste form and their transport through the invert and into the unsaturated zone (UZ).

The EBS flow abstraction model implemented for this study differs from the original model in the following respects.

Evaporation of Seepage Contacting the Drip Shield–Waste packages emit substantial quantities of heat for a few thousand years after emplacement. This model allows a fraction of this heat to evaporate seepage as it contacts the drip shield. The fraction of heat is treated as a random variable, with potentially more evaporation taking place in the higher-temperature operating mode.

Flux through the Drip Shield and Waste Package–The type, number, and timing of breaches in the drip shield and waste package are predicted by the *WAPDEG Analysis of Waste Package and Drip Shield Degradation* V4.0 model (CRWMS M&O 2000 [DIRS 151566]). This information is used by the EBS flow abstraction to define the time-dependent fluxes that flow through (or are diverted around) the drip shield and the waste package. In this model, droplets fall randomly on a drip shield, and the model accounts for the fact that a fraction of the water that flows over the drip shield may be captured by breaches.

Model for Drip Shield Condensation–This model was developed for the original flow abstraction, but not included in subsequent calculations. It is implemented in this study. As discussed in Section 8.2, the basis for the conclusion is the low evaporation rates from the invert, which would be the principal source of water for drip shield condensation.

Bathtub Model for the Waste Package–This model allows liquid to accumulate in waste packages. This bathtub effect can occur when there are corrosion patches on the drip shield and the top surface of the waste package, but no penetrations on the bottom surface of the waste package. Water is eventually released from such a waste package when a breach forms on the bottom half.

The EBS flow abstraction model implemented in the TSPA-SR model (CRWMS M&O 2000 [DIRS 153246]) is described next. Each of the submodels summarized above is described in subsequent sections.

8.2 REVIEW OF TOTAL SYSTEM PERFORMANCE ASSESSMENT-SITE RECOMMENDATION TREATMENT

The source of inflow to the EBS is the seepage flux into the drift that results from the downward infiltration of fluid through the existing fracture system at Yucca Mountain. The seepage flux is conceptualized to fall vertically downward onto the drip shield from discrete fractures above the roof of the drift, as represented in *Abstraction of Drift Seepage* (CRWMS M&O 2001 [DIRS 154291]) for EBS flow and transport.

The seepage flows through the EBS along eight pathways, as shown in Figure 8.2-1. These pathways are:

1. Seepage flux entering the drift–This is the liquid flow into the EBS.

2. Flow through the drip shield–Liquid flux through the drip shield begins once patches form due to general corrosion. Patches are defined from the results of the WAPDEG V4.0 model as void areas penetrating through the drip shield. The number of patches through the drip shield is calculated by the WAPDEG V4.0 model (CRWMS M&O 2000 [DIRS 151566], Section 6.5.1) independently of the EBS flow

abstraction. The nominal size of a patch is fixed for the WAPDEG V4.0 calculations for a generic waste package (CRWMS M&O 2001 [DIRS 153940], Section 4, Table 1). It is currently defined to be 7.21×10^4 mm^2. The liquid flux through any patches in the drip shield is proportional to the seepage flux entering the drift multiplied by the ratio of the axial length of all patches in the drip shield to the total axial length of the drip shield.

3. Diversion around the drip shield–The portion of the flux that does not flow through the drip shield is modeled as bypassing the invert and flow directly into the UZ. This approach is consistent with a pseudo-steady flow because the sum of the fluid volume entering the drip shield (Pathway 2) and the fluid volume diverted around the drip shield (Pathway 3) must equal the fluid volume entering the EBS (Pathway 1) for a steady-state system. Diversion directly to the UZ is also reasonable because diverted flow does not contact the waste form and is not contaminated with radionuclides. It is, therefore, ignored by the EBS transport abstraction.

4. Flow through the waste package–The fluid flow through the waste package is based on the presence of patches due to general corrosion. The number of patches through the waste package is calculated by the WAPDEG V4.0 model independently of the EBS flow abstraction. The nominal size of a patch is fixed for the WAPDEG V4.0 calculations; it is currently defined to be 2.346×10^4 mm^2 (CRWMS M&O 2000 [DIRS 153940], Section 4, Table 1). The area of each stress corrosion crack, 4.08×10^{-6} m^2 (CRWMS M&O 2000 [DIRS 153940], p. 51), is estimated from gap width calculations in the *EBS Radionuclide Transport Abstraction* (CRWMS M&O 2000 [DIRS 153940], Section 6.3.1.2.1) based upon residual stresses in the welded lids of the waste package in *Stress Corrosion Cracking of the Drip Shield, the Waste Package Outer Barrier, and the Stainless Steel Structural Material* (CRWMS M&O 2000 [DIRS 151564], Figure 13). This area corresponds to a hole with an elliptical cross section that is 1.6 inches long by 0.005 inches wide (CRWMS M&O 2000 [DIRS 153940], Section 6.3.1.2.1). The liquid flux through any patches in the waste package is proportional to the seepage flux falling on the waste package multiplied by the ratio of the axial length of all patches in the waste package to the total axial length of the waste package. The seepage flux falling on the waste package is equal to the liquid flux through the drip shield plus a condensation flux for unanticipated conditions in which condensation would form under the drip shield.

5. Flow diversion around the waste package–The portion of the flux that does not flow through the drip shield and into the waste package is modeled as bypassing the waste form and flow directly to the invert.

6. Evaporation from the invert condensation underneath the drip shield–The magnitude of the evaporative flux from the invert is based on the thermal-hydrologic abstraction (CRWMS M&O 2001 [DIRS 154594]). If the drip shield is cooler than the invert, then all the evaporative flux is modeled as dripping on the waste package. If the drip shield is hotter than the invert, then no evaporative condensation flux drips on the waste package. The magnitude of the evaporative flux and the temperatures of the drip shield and invert are precalculated and abstracted to provide runtime input data

for the EBS model in the TSPA-SR (CRWMS M&O 2000 [DIRS 153246], Section 3.6.2.1). The rationale for this approach is explained in the *EBS Radionuclide Transport Abstraction* (CRWMS M&O 2000 [DIRS 153940], Section 6.3.3). Analysis results from the *Water Distribution and Removal Model* (CRWMS M&O 2001 [DIRS 152016], Section 6.4) show that condensation is not likely to occur before 10,000 years. At times after 10,000 years, the evaporation rates in the invert are insignificant, less than 0.013 m^3/year/m-drift (CRWMS M&O 2001 [DIRS 154594], Section 6.4.6).

7. Flow from the waste package to the invert–All flux from the waste package flows to the invert, independent of breach location on the waste package. The presence of the emplacement pallet is ignored, and the waste package is modeled as lying on the invert so that a continuous liquid pathway for diffusive transport exists at all times.

8. Flow through the invert into the UZ–All fluid and mass flux into the invert is immediately released into the UZ, consistent with the quasi-static assumption for flow through the EBS.

These pathways are time-dependent because of thermal effects and corrosion. At early times, when the waste package internal temperature is above the boiling point of water in the higher-temperature operating mode, the spent nuclear fuel (SNF) will remain dry and advective transport is impossible. At later times, corrosive processes will create time-dependent breaches in the drip shield and waste package. Breaches in both the drip shield and the waste package must exist before advective flow can transport radionuclides out of the waste package. These pathways are also location-dependent. For example, all pathways will have zero advective flux in the non-dripping areas of the repository.

The most important element of the EBS flow abstraction is the flow-splitting algorithm, which determines the fluid volume that flows through the drip shield or waste package and the remainder that flows around the drip shield or waste package. This algorithm assumes that the liquid flux through any patches or pits that penetrate the drip shield or waste package is proportional to the ratio of the total length of all penetrating patches or pits in the axial direction to the total axial length of the drip shield or waste package. This algorithm is equivalent to assuming that a patch or pit will collect all fluid that drips or flows onto the drip shield or waste package at the same axial location as the patches or pits. It assumes that drips on the right-hand side of a drip shield or waste package would contribute to the flow through a patch or pit on the left-hand side. This is not physically possible because the droplets cannot flow uphill, against the direction of gravity.

Inputs to the flow abstraction are taken primarily from other elements of the TSPA. These inputs include:

- The flux of fluid into the EBS, as defined by the seepage flow abstraction (CRWMS M&O 2001 [DIRS 154291], Section 6.5; CRWMS M&O 2000 [DIRS 123916], Section 6.3)

- The temperature, relative humidity, saturation, and evaporative flux from the invert, as defined by the abstraction of thermal hydraulic calculations (CRWMS M&O 2001 [DIRS 154594], Section 6.3)

- The timing, size, number, and location (upper or lower surface) of breaches in the drip shield and waste package, as defined by results from WAPDEG V4.0 analyses (CRWMS M&O 2000 [DIRS 151566]).

Outputs from the flow abstraction include the time-dependent fluxes through the drip shield, waste package, and invert. These fluxes are used by the EBS transport abstraction to determine the mass of radionuclides released to the UZ.

The EBS flow abstraction for the TSPA-SR (CRWMS M&O 2000 [DIRS 153246]) is based on a reasonable approach that attempts to bound the average response of the EBS. It is based on typical flow processes, such as the advective flow of liquid water through the EBS and the potential for evaporation from the invert and condensation of water vapor on the underside of the drip shield. The use of reasonable bounds was employed because of potentially large uncertainties in the response of a very complex engineered system over long periods of time. Following are the noteworthy conservatisms in the flow abstraction.

Seepage Through the Drip Shield Is Assumed to Always Fall on a Waste Package–The current potential repository design has a small axial gap between adjacent waste packages. It is possible that the seepage through the drip shield between adjacent waste packages will fall directly to the invert, avoiding the waste package entirely. Also, it is possible that flow that occurs through the drip shield outside the waste package footprint would fall directly to the invert and avoid the waste package. These possibilities are conservatively ignored. Both these are minor conservatisms when the spacing between adjacent waste packages and the gap width between the waste package and the drip shield are small compared to the length of the waste package.

Seepage Is Assumed to Wet the Drip Shield and Waste Package Randomly–The pathways for seepage into the drifts are fractures or fracture sets. As a result, seepage will vary spatially and temporally over the waste packages. Therefore, the response of groups of waste packages is represented as averages for performance assessment. In addition, breaches are considered to be located so that it will collect all fluid that drips onto the drip shield or waste package at the same axial location as the breach. This representation conservatively ignores the fact that fluid dripping onto the lower portion of the drip shield or waste package will not flow through a breach high on the drip shield or waste package. It also conservatively ignores the fact that seepage on the left half of a drip shield or waste package cannot flow through a breach on the right half. Breach location is, therefore, conservative by a factor of approximately two for the calculation of fluid flows into the drip shield and waste package.

Release of Radionuclides Through Advective Transport Is Independent of the Location of Breaches on the Waste Package–Advective transport out of the waste package is based on a flow-through model that is independent of the location of penetrations through the drip shield or waste package. This means that advective transport will occur even if a waste package has only

one penetration, or if it has one or more penetrations on its upper surface and none on its lower surface.

Evaporation Within and on the Waste Package Is Ignored–Diffusive transport will cease if the heat from the waste form can evaporate any thin liquid films on the waste form. Advective transport will cease if the heat from the waste form can evaporate the small seepage flux onto and into the waste package. The potential for evaporation to eliminate radionuclide transport is conservatively ignored in the EBS abstractions. This is a minor conservatism for diffusive releases from the waste package. As discussed in Section 7.2.2, the best estimate of the thermal aging model, based on available data, indicates that thermal aging of Alloy 22 base metal would not progress to a significant level in the first 10,000 years (CRWMS M&O 2000 [DIRS 147639], Section 6.2). The earliest breach of any waste package occurs after 10,000 years, and the mean waste package lifetime is tens of thousands of years (CRWMS M&O 2000 [DIRS 153246], p. xviii).

Each of the new submodels developed for this study is described in the following sections. Evaporation of seepage is presented in Section 8.3.1. Section 8.3.2 presents the drip shield condensation model. New waste package and drip shield flux models are presented in Section 8.3.3. A bathtub waste package flow model is presented in Section 8.3.4.

8.3 UNCERTAINTY ANALYSES

8.3.1 Evaporation of Seepage

8.3.1.1 Goal of the Model

In this model, the source of inflow to the EBS is the seepage flux into the drift that results from the downward infiltration of fluid through the existing fracture system at Yucca Mountain. The seepage flux is conceptualized to flow from discrete fractures above the roof of the drift, falling vertically downward onto the drip shield and waste package. A significant portion of the seepage that contacts the drip shield may evaporate, thus reducing the amount of seepage ultimately available for transport. The goal of this model is to calculate the amount of seepage flux that evaporates as a function of time and reduce the amount of liquid seepage moving through the EBS accordingly.

8.3.1.2 Identification of Unquantified Uncertainties in Total System Performance Assessment-Site Recommendation

The potential for evaporation to reduce seepage is conservatively ignored in the EBS abstractions. In the nominal scenario, the earliest breach of any waste package occurs after 10,000 years (CRWMS M&O 2000 [DIRS 147639], Section 6.2). The mean waste package lifetime is tens of thousands of years (CRWMS M&O 2000 [DIRS 153246], p. xviii). Evaporation will be most significant when in-drift temperatures are elevated after repository closure, and would affect mass transport only modestly. However, in the unlikely event that waste packages or drip shield might degrade due to juvenile failures, evaporation has the benefit of providing defense-in-depth. For this reason, evaporation effects on seepage were added to the TSPA abstraction models developed in Volume 2 (McNeish 2001 [DIRS 155023], Sections 3.2.6 and 4.2.6).

The effectiveness of evaporation on decreasing the seepage flow available for advective transport is uncertain, primarily because of representational model uncertainty. Heat from the waste package is transferred to the drip shield, then to the drift wall, by conduction, convection, and thermal radiation. The portion of this heat flux that goes to evaporating seepage is uncertain with respect to location and timing.

8.3.1.3 Model for Evaporation of Seepage

The approach taken to account for the potential evaporation rate of the incoming water at the top of the drip shield after emplacement is based on the evaporation model presented in the *Abstraction of NFE Drift Thermodynamic Environment and Percolation Flux* (CRWMS M&O 2001 [DIRS 154594], Section 6.3.10).

The evaporation rate at the top of the drip shield is bounded by the amount of heat available to vaporize water on the upper portion of the drip shield. This heat flow rate into the upper portion of the drip shield is used to determine the maximum volumetric flow rate of incoming seepage water that can be completely vaporized at this location.

The evaporation rate is computed according to the following steps. An energy balance is performed on the upper surface of the drip shield. The energy balance relates the heat input at this location to the maximum amount of incoming water that can be completely vaporized by the heat flow. Also, it relates to the effect of evaporative cooling for liquid that would fall directly on the drip shield, as discussed in Section 8.3.2.3. The energy balance is (CRWMS M&O 2001 [DIRS 154594], Section 6.3.10, Equation 4):

$$q_{ds} = \rho_l Q_{EVAP} h_{fg} \qquad \text{(Eq. 8-1)}$$

where

q_{ds} = heat input to the drip shield [W]
ρ_l = density of the incoming water [kg/m^3]
Q_{EVAP} = drip shield evaporation which equals the maximum rate that water can be vaporized by the heat at this location [m^3/s]
h_{fg} = latent heat of vaporization [J/kg].

The seepage rate into the drift is considered to be non-episodic, and the seepage is modeled as falling randomly on the upper surface of the drip shield. In the energy balance equation, the incoming water reaches the top of the drip shield at the vaporization temperature of the drip shield, which neglects heating by radiation, convection, or convection of liquid water (typically small compared to latent heat exchange).

The heat input at the drip shield, q_{ds}, can be rewritten in terms of the waste package heat output. The representative heat flow (by thermal radiation) from the top waste package to the underside of the top portion of the drip shield is some fraction χ, nominally one-half of the total waste package heat generation rate (q_{wp}). Thermal radiation is the dominant mode of heat transfer in a no-backfill emplacement drift. Implementing this and rearranging the energy balance equation,

the maximum evaporation rate is (CRWMS M&O 2001 [DIRS 154594], Section 6.3.10, Equation 5):

$$Q_{EVAP} = \frac{\chi q_{wp}}{\rho_l h_{fg}} \quad \text{(Eq. 8-2)}$$

The waste package heat generation rate, q_{wp}, is evaluated for an average commercial SNF waste package (Figure 8.3.1-1). The non-commercial waste package heat output is based on DOE high-level radioactive waste (Figure 8.3.1-2). Implementation of an average waste package heat generation rate implies that the waste packages are close enough together that the radiant heat exchange and the (axial) heat flux through the drip shield is uniform.

The energy balance equation can be evaluated using temperature-dependent or constant (evaluated at an appropriate average temperature) fluid properties. To reduce the complexity of the model, constant fluid properties are used at an average incoming fluid temperature of 60ºC. Calculations show that this is reasonable, with a negligible difference between evaporation rates obtained with constant and temperature-dependent properties (CRWMS M&O 2001 [DIRS 154594], Section 6.3.10).

8.3.1.4 Implementation of Seepage Evaporation Model

The actual fraction of total heat flux emitted that is available for evaporating seepage is uncertain because of several factors. Heat flux is variable over the length of a waste package and drip shield, with the center of the waste package and drip shield likely being hotter than the edges. This variability is influenced by waste package spacing, with closely spaced waste packages tending to have less variation in heating from the center to the edges. Drips are modeled as falling randomly on the drip shield. If drips fall on a portion of the drip shield where the heat flux is low, such as near the ends of a waste package, the effective rate of evaporation will be lower compared to drips falling on a higher heat flux region, such as near the center of the package. In addition, evaporation effectiveness may be reduced if all the seepage is concentrated in a single stream, as opposed to several randomly spaced smaller drips, since smaller drips require less heat flux for evaporation. In addition, smaller drips will tend to experience more evaporation because they fall from the drift wall to the drip shield, thus reducing the seepage that actually impinges on the drip shield. To account for these uncertainties, the expression for evaporation rate is modified by introducing a random number from zero to one, f_{evap}. This parameter determines the fraction of potential evaporation that may occur. Using this parameter, the effective evaporation rate per waste package is determined using an approach similar to the drip shield evaporation (CRWMS M&O 2001 [DIRS 154594], Equation 5):

$$Q_{EVAP} = \frac{\left(1/2\right) q_{wp}}{\rho_l h_{fg}} f_{evap} \quad \text{(Eq. 8-3)}$$

In the present treatment, f_{evap} is a random number that ranges from 0 to 1 in the higher-temperature operating mode (1.45 kW/m) and from 0 to 0.8 in the lower-temperature operating mode (1.12 kW/m). These heat loadings are presented in Table 2-1. The latter upper bound is considered to be equal to the ratio of the linear thermal loading, that is, 1.12/1.45, or approximately 0.8.

The net amount of seepage that is potentially available for sheet flow across the drip shield is given by the difference between the seepage flow onto the drip shield minus the seepage evaporated, as discussed in Section 8.3.3.3.1. This net amount of sheet flow not evaporated (Q_{SFNE}) is given by:

$$Q_{SFNE} = Q_{SFNE} - Q_{EVAP} \quad \text{(Eq. 8-4)}$$

where Q_{SF} is the sheet flow of water onto the top part of the drip shield [in m^3/yr] as determined by the drip shield flux model. Note that Q_{SFNE} may range from zero to a value of Q_{SF}. In the latter case, all water that flows onto the drip shield evaporates**.**

8.3.2 Drip Shield Condensation Model

8.3.2.1 Goal of Model

The drip shield condensation model is used to quantify the amount of condensate that may form on the underside of the drip shield and fall on the waste package.

8.3.2.2 Identification of Unquantified Uncertainties in Total System Performance Assessment-Site Recommendation

As noted in Section 8.2 (Item 6), the formation of condensate on the underside of the drip shield due to evaporation is not included because analyses indicated that the effect of this process on repository performance would be insignificant.

If condensate forms on the underside of a drip shield, it will form during the cooling period. For condensate to form underneath the drip shield, the partial vapor pressure at the invert interface underneath the drip shield must be greater than the saturation vapor pressure at the drip shield. Thermal hydrology results show the potential for this condition to occur at times later than 1,000 years (CRWMS M&O 2001 [DIRS 152016], Section 6.4). Two key uncertainties in the process of drip shield condensation are: (1) how much water condenses on the drip shield (if condensation occurs) for the given thermal-hydrologic environment, and (2) what fraction of this condensate will fall on the waste package rather than flow downward along the sides of the drip shield. These uncertainties are addressed together by considering that the rate of condensation is proportional to the rate of evaporation from the invert where the proportionality constant, denoted f_c, is a random number between 0 and 1. This is written as:

$$q_{cond} = E_{invert} f_c \quad \text{(Eq. 8-5)}$$

where E_{invert} (m^3/yr/m-drift) is the evaporation rate in the invert as provided by the results in the *Abstraction of NFE Drift Thermodynamic Environment and Percolation Flux* (CRWMS M&O 2001 [DIRS 154594], Section 6.3.10). This flux value, q_{cond}, is converted to a condensate flow rate underneath the drip shield Q_{CWP} using:

$$Q_{CWP} = q_{cond} L_{WP} \quad \text{(Eq. 8-6)}$$

where L_{WP} is the length of the waste package, equal to 5.17 m for commercial SNF (e.g., a 21-PWR waste package) and 3.59 m for high-level waste (HLW) (e.g., a 5-DHLW/DOE SNF Short waste package) (BSC 2001 [DIRS 154461], Item 3, Table 9).

8.3.2.3 Implementation of the Drip Shield Condensation Model

A conceptual model for drip shield condensation based on a simple node network has been developed that provides qualitative information for the formation of drip shield condensation. Figure 8.3.2.3-1 presents a conceptual model for EBS sensible and latent heat flow paths and drip shield condensation. The conceptual model treats the waste package, the drip shield, the invert, the air spaces between the waste package and the drip shield, and between the drip shield and the drift wall. It considers the latent heat exchange from evaporation off of the invert and potential film condensation underneath the drip shield.

The decay heat produced by the waste package during the postclosure period is the principal driver for EBS processes within the drift. The flow of heat from the waste package into the surrounding environment creates temperature differences, which result in thermal gradients for heat transfer by convection and radiation and liquid and vapor transport.

Heat is transferred from the waste package to the drip shield above and the invert below by thermal radiation and convection. These same mechanisms transfer heat from the drip shield to the drift wall. Conduction and mass transport carry the heat from the invert and drift wall into the surrounding rock.

8.3.2.3.1 Sensible Heat Transfer Within the Annulus

The following discusses methods used to estimate the heat transfer for radiation, convection, and conduction within the EBS. Radiative heat transfer can be modeled for gray bodies through modification of the Stefan-Boltzmann equation between two surfaces, such as concentric cylinders (Incropera and DeWitt 1996 [DIRS 107784], p. 739) that account for geometry above and below the drip shield.

The nature of the thermal radiation varies with temperature and relative humidity. The degree to which the gas participates in the radiative heat transport varies as a function of the water vapor density. At low water vapor pressures, the water vapor is relatively transparent and intersurface radiation heat transport (waste package to drip shield, drip shield to drift wall) dominates. As the water vapor density increases, the water begins to participate; a portion of the energy radiated from the hot surface is absorbed by the water vapor, which radiates to the cold surface. The net effect is to diminish the relative contribution of thermal radiation to the intersurface heat transport (Siegel and Howell 1992 [DIRS 100687], pp. 572 to 573).

Several convection cells (Figure 8.3.2.3.1-2) that are symmetrical about the vertical mid-plane characterize the free convective heat transfer in the annular space between long, horizontal concentric cylinders (Incropera and DeWitt 1996 [DIRS 107784], p. 512). If the inner test cell or waste package is heated to a temperature T_{WP} and the drip shield is cooled to a temperature T_{DS}, fluid ascends and descends along the inner and outer cylinders, respectively (Incropera and DeWitt 1996 [DIRS 107784], p. 512). The effective thermal conductivity is the value that a stationary fluid should have to transfer the equivalent amount of heat as the moving fluid, the

effective thermal conductivity is a function of the Prandlt and Raleigh numbers (Incropera and DeWitt 1996 [DIRS 107784], pp. 512 and 509).

The nature of the convective pattern varies with the temperature difference between the bounding surfaces. Just after incipient gas motion, large roll cells form in the gas. Thermal and viscous boundary layer thicknesses are on the same order as the cavity dimensions, making the temperature of the gas dependent on its location in the cavity. Rising gases above the heat source (inner cavity: waste package; outer cavity: top of drip shield) are hotter than descending gases (inner cavity: drip shield sides; outer cavity: drift walls).

As the driving temperature differences increase, laminar flow instabilities form above the waste package and the top of the drip shield. The large roll cells begin to divide into smaller cells. These processes begin to homogenize the gas temperatures within the roll cells.

When the temperature differences are sufficiently large, the large-scale roll cell structure becomes completely transient. Cell breakdown and oscillation combine to make the bulk of the gas nearly isothermal. Under these conditions, the local heat transfer between a bounding surface and the gas is a function of the local conditions: local wall temperature, wall inclination, and gas temperature.

The velocities associated with the large-scale roll cells will increase with an increasing temperature difference in the region above the base of the waste package. However, between the waste package and the invert, the temperature gradient favors fluid stability for heating from above. Only the cooling from the drip shield walls would drive any large-scale roll cells. This should cause a small amount of counterflow in the region below the waste package.

The invert is composed of crushed tuff and has a thermal conductivity less than that of the surrounding rock because of its higher porosity and predominantly air-filled voids, as presented in the *Water Distribution and Removal Model* (CRWMS M&O 2001 [DIRS 152016], Table 4-5 and Attachment XIV.1). The various analyses show that the invert is at a somewhat higher temperature than the wall. If the invert were a perfect thermal insulator, the top surface would have the same temperature as the adjacent air. If the gas within the drip shield is nearly isothermal and drip shield cooling is sufficiently strong due to latent heat transfer (evaporative cooling), the invert surface temperature might exceed the temperature at the top of the drip shield. Although this scenario is very unlikely, as discussed below, the temperature difference is one of the requirements for condensation under the drip shield.

8.3.2.3.2 Invert Evaporation

Water vapor and heat are carried away from the immediate vicinity of the invert surface by the turbulent bulk flow of parcels of air containing quantities of heat and vapor. These parcels are carried upward in a chaotic manner, exchanging their contents with other parcels, which, in turn, are carried away from the surface. The net result is a transport of heat and water vapor between two heights: the invert surface and some height within the annulus. This turbulent flux is proportional to the vapor concentration or temperature difference (Jury et al. 1991 [DIRS 102010], p. 173). The difference in vapor pressure between the invert surface and the annulus is called the saturation pressure deficit. The heat transfer coefficient, h_H, and the water

vapor transfer coefficient, h_v, are considered to be equal according to the similarity hypothesis, which is reasonably accurate under most conditions at the surface (Jury et al. 1991 [DIRS 102010], p. 172). During the transient drying of the invert, control of the evaporation can pass from the temperature-humidity conditions of the annulus to the soil resistance of the invert. Also, vapor pressure lowering can be effected by osmolality. The rate of evaporation from a wet, bare soil surface is limited by internal conditions within the annulus. In contrast, water loss from a soil with a dry surface layer is regulated primarily by soil water resistances that limit the rate at which water moves upward to the evaporating surface, as described by the Penman Equation (Jury et al. 1991 [DIRS 102010], p. 153). In this latter case, the water evaporation rate will likely be less than the maximum potential loss dictated by the conditions within the annulus through the use of the Penman Equation.

Note that in the conceptual model described above, an upward latent heat flux from the surface (as governed by the Penman Equation) occurs outside the footprint of the waste package, and would result in latent heat exchange to the annulus. Heat transfer directly below the waste package represents heating from above. Vertical heat transfer in this zone would be conduction dominated with little convective enhancement. As the driving temperature difference increases, the fraction of heat that moves downward through the invert decreases.

8.3.2.3.3 Film Condensation Underneath the Drip Shield

According to Incropera and DeWitt (1996 [DIRS 107784], p. 568), latent heat transfer by drop-wise condensation is an order of magnitude larger than that for film condensation. Therefore, if condensation occurs, it would occur initially by film condensation. As discussed below, the basis for this is that film condensation is an effective latent heat transfer mechanism relative to evaporation from the invert.

Condensation will occur on the inner surface of the drip shield if the drip shield temperature, T_{DS}, is less than the saturation temperature, T_{sat}, which is set to equal to the annulus temperature, T_{AN}. In modeling the heat transfer due to condensation, the drip shield can be approximated as a cylindrical surface. Incropera and DeWitt (1996 [DIRS 107784], pp. 560 to 568) present solutions for film based upon Newton's Law of Cooling. The rate of condensation below the drip shield equals the rate of evaporation from the invert outside the waste package footprint.

According to the nonlinear relation for heat transfer by radiation and convection, the invert temperature is highly dependent upon the heat flux partitioning under the drip shield. Larger fractions of the heat traveling downward through the invert will produce higher invert temperatures and lower drip shield temperatures. The network model shows that smaller fractions of heat traveling vertically downward will produce lower invert temperatures and higher drip shield temperatures. Therefore, to determine if condensation under the drip shield is possible, some knowledge of the heat flux partitioning produced by the combined mechanisms of thermal radiation and gas convection, as they can be studied with the simple network model presented above, is necessary.

The EBS Pilot Scale Test #3, conducted at the Atlas Facility in North Las Vegas, Nevada, consisted of a simulated quarter-scale waste package and drip shield resting on an invert of crushed tuff. The temperature, relative humidity, and flow data (DTN: SN0003L1011398.003

[DIRS 149765]) collected from this test provides information for validating the numerical models described above that form the basis of the EBS performance assessment model.

The most significant observations from EBS Pilot Scale Test #3 (BSC 2001 [DIRS 154479], Section 5) were:

- After heater power-up, temperatures approached steady state-conditions within a period of 3 to 5 days.
- Temperature differences were observed along the waste package surface due to natural convection.
- The coolest temperatures on the drip shield were higher than the coolest parts of the invert.
- No condensation of water was observed below the drip shield.

The test observations are consistent with recorded drip shield temperatures above the waste package (BSC 2001 [DIRS 154479], Figure 35) and at the point where the drip shield rests on the invert (BSC 2001 [DIRS 154479], Figure 38). The latter data, which reflects the invert temperature, shows that for the conditions simulated in the test, relative humidities increased during dripping. In comparing the dewpoint temperatures with the drip shield temperature, at no point were the two equal.

EBS Pilot Scale Test #3 provides important information on the concept of a drip shield to effectively protect simulated waste packages from infiltrating water under heated conditions at the one-quarter scale. No drip water or condensation was seen under the drip shield or on the waste package for conditions simulated in the test. The relative humidity at the top of the test cell stayed at about 85 percent, and under the drip shield it was about 65 percent. Based on temperatures and relative humidity, the water vapor pressure appeared to be approximately the same at these locations, with slight variations as a function of temperature variations.

As noted previously, in order for condensate to form underneath the drip shield, the partial vapor pressure at the invert interface underneath the drip shield must be greater than the saturation vapor pressure at the drip shield. The vapor pressures at the drip shield and invert are reduced somewhat by the presence of dissolved salts. In addition, the vapor pressure at the invert is reduced somewhat by capillary pressure. These effects on vapor pressure are rather complex, as discussed above, and no attempt will be made to include them in the model described here.

The conceptual model presented above shows that drip condensation is not anticipated to occur because the drip shield temperature is higher than the invert temperature. A possible scenario for drip shield condensation is that seepage impinging on the top surface of the drip shield cools the drip shield sufficiently to satisfy the dewpoint temperature on the inner surface of the drip shield. However, in the pilot scale test described above, the infiltration condition evaluated was higher than 300 mm/yr (BSC 2001 [DIRS 154479], Section 2.3.1), which is much higher than the anticipated percolation rates for the repository as presented in the *Water Distribution and Removal Model* (CRWMS M&O 2001 [DIRS 152016], Section 5.1.6). Therefore, cooling of the

drip shield by evaporation off the upper surface is not expected to result in drip shield condensation.

If TSPA results show that drip shield condensate is potentially important, then a more detailed model incorporating some of the features discussed above would be warranted. In the present implementation approach, condensate on the drip shield forms if:

$$T_{DS} \leq T_{invert} \quad \text{(Eq. 8-7)}$$

where T_{DS} and T_{invert} are the temperatures of the drip shield and invert [°C], respectively. If this condition is satisfied, the condensate flux value is calculated using the flux equation in Equation 8-6.

8.3.3 Drip Shield and Waste Package Flux Models

8.3.3.1 Goal of Model

The drip shield and waste package limit the amount of water contacting the waste forms during the postclosure period. The drip shield and waste package seepage flux models are used to quantify the amount of seepage that penetrates a breached drip shield and waste package.

8.3.3.2 Identification of Unquantified Uncertainties in Total System Performance Assessment-Site Recommendation

The EBS flow abstraction conservatively modeled all of the seepage as entering the drift falls on the crown of the drip shield as discussed in detail in the *EBS Radionuclide Transport Abstraction* (CRWMS M&O 2000 [DIRS 153940], Section 5.1). For seepage to contact the drip shield, droplets must form and fall from the rock roof. Other modes of flow, such as film flow on the drift wall, are possible, and may divert some or all of the seepage influx around the wall of the opening without dripping. This latter flow mode was conservatively ignored. In addition, the drip shield and waste package seepage flux models conservatively modeled any breach as located so that it will collect all fluid that drips onto the drip shield or waste package at the same axial location as the breach (CRWMS M&O 2000 [DIRS 153940], Section 5.1). These conservatisms were implemented in part to obviate the need to explicitly account for uncertainty in flux calculations.

To provide a more reasonable and less conservative estimate of flow onto the drip shield, drips will be modeled as falling randomly on the upper surfaces of the drip shield or waste package. Therefore, the probability of a drip intercepting a breach is given by the ratio of projected breach area to upper drip shield or waste package surface area. The probability that a drip will not intercept a breach is the complement of this probability. The fraction of non-intercepting drips that ultimately penetrate the drip shield and waste package is an uncertain quantity and has been identified as an uncertainty that will be quantified.

8.3.3.3 Model for Drip Shield and Waste Package Flux

In the present treatment, seepage is modeled as comprised of drips that fall randomly on the upper surface area of the drip shield, rather than along the crown of the drip shield. If a random

drip falls onto a breach, it is modeled as penetrating the drip shield. If a drip does not fall onto a breach, a fraction of this drip may splatter or flow into a neighboring breach. The fraction of seepage that penetrates the drip shield resulting from splatter and flow is treated as uncertain. The total seepage penetrating the drip shield is therefore that fraction of the seepage that directly intercepts breaches and that fraction of the seepage that splatters or flows into breaches. After seepage penetrates the drip shield, it may be assumed to fall on the upper half of the waste package or form film flow on the underside of the drip shield. The modeling approach and considerations used for the drip shield are also used to calculate the seepage through the waste package, the difference being that the corresponding waste package breach and projected areas are used.

8.3.3.3.1 Drip Shield Flux Model

The probability (P_{FDIB}) of flow droplets impinging directly onto the breach and displacing water is given by the ratio of the projected breach area ($A_{B,DS}$) to the projected drip shield surface area (A_{DS}):

$$P_{FDIB} = \frac{A_{B,DS}}{A_{DS}} \qquad \text{(Eq. 8-8)}$$

Here, projected area refers to the area seen in a plan view of the drip shield looking downward from the crown of the emplacement drift. To simplify the present treatment, $A_{B,DS}$ is considered to be equal to the actual breach area on the upper surface of the drip shield. This is slightly conservative because the actual breach area is always greater than the projected breach area on the upper curved surface of the drip shield. The probability as evaluated above is therefore slightly higher for a random drip to intercept the breach. The complementary probability of a drip not directly intercepting a breach is given by (1 - P_{FDIB}). The lengths of the waste packages for commercial SNF and HLW are 5.17 m and 3.59 m, respectively, (BSC 2001 [DIRS 154461], Item 3, Table 9). The width of the drip shield is 2.51 m (CRWMS M&O 2000 [DIRS 153940], Table 1). The A_{DS} is equal to $2.51\ m \times 5.17\ m = 12.98\ m^2$ for commercial SNF waste packages and $2.51\ m \times 3.59\ m = 9.01\ m^2$ for HLW waste packages. Waste package length is used to calculate the areas.

The total amount of seepage penetrating a drip shield is given by the sum of the seepage flow directly into breaches (Q_{FDIB}) and sheet or splattering flow into breaches (Q_{SFIB}). The partitioning of flow, discussed below, is illustrated by the conceptual drip shield flux model in Figure 8.3.3-1 and the event tree in Figure 8.3.3-2. The following flow definitions are presented:

Q_{SEEP} = Seepage flow into the drift
Q_{DS} = Flow on the top part of the drip shield
Q_{ODS} = Flow outside the drip shield
Q_{FDIB} = Seepage flow directly into breaches
Q_{SF} = Sheet flow onto drip shield
Q_{SFNE} = Sheet flow not evaporated
Q_{EVAP} = Drip shield evaporation
Q_{SFIB} = Sheet or splattering flow into breaches
Q_{SFAB} = Sheet flow away from breaches

The following probabilities are defined:

P_{FDS} = Probability of flow directly onto the drip shield

P_{FDIB} = Probability of flow droplets impinging directly onto the breach and displacing water

P_{EVAP} = Probability of drip shield evaporation

P_{SFNE} = Probability of sheet flow not evaporated (depends on temperature and relative humidity)

P_{SFIB} = Combined probability of sheet flow into breaches and water moving through the crevices to the underside of the drip shield (depends on temperature and relative humidity)

The first level of the event tree is the flow partitioning of the in-drift seepage (Q_{SEEP}) that flows directly onto the top part of the drip shield (Q_{DS}) and that falls outside the footprint of the drip shield (Q_{ODS}) (shown by the dotted lines on Figure 8.3.3-1). Flow outside the drip shield flows directly to the invert without contacting the drip shield. The probability (P_{FDS}) can be estimated by the simple ratio of the drip shield footprint to the tunnel footprint. The second level of the event tree is that water drops could fall directly onto breaches and potentially displace droplets by impact through the drip shield. This model for flow is described in the *Water Distribution and Removal Model* (CRWMS M&O 2001 [DIRS 152016], Section 6.1.1.2). Drops falling directly on the patches (saturated and unsaturated) result in kinetic energies that convert to pressure pulses (impulsive force) that break the capillary and gravitational force equilibrium if water is present. This causes some or all of the water to be displaced out of the crevices.

The spreading from the primary and secondary drops produces a thin film of water on the drip shield that very slightly thickens away from the crest (CRWMS M&O 2001 [DIRS 152016], Section 6.1.1.2). This is defined as sheet flow on the drip shield (Q_{SF}). It is assumed that splashing and spreading cause the dripping water to be uniformly distributed on the drip shield. For sheet flow onto the drip shield (Q_{SF}), a portion of the sheet flow (Q_{EVAP}) may evaporate, as discussed previously. The evaporation rate on the drip shield depends deterministically on the temperature and relative humidity environment, which in turn would depend on variations in thermal and hydrological properties of the EBS and the surrounding media. This results in a probability P_{EVAP} and the complementary probability (P_{SFNE}) of sheet flow water that is not evaporated.

As discussed in the *Water Distribution and Removal Model* (CRWMS M&O 2001 [DIRS 152016], Section 6.1.1.2), the breaches or crevices in the drip shield can be characterized for potential for capillary suspension. Crevices of various sizes will be developed in the drip shields due to pitting and crevice corrosions (i.e., by general corrosion and stress corrosion). Crevices in the drip shield can draw water from the thin film due to capillary suction and gravitational forces. The direction of the capillary force changes from downward to upward during the filling process, as discussed in the *Water Distribution and Removal Model* (CRWMS M&O 2001 [DIRS 152016], Section 6.1.1.2, Figure 6-3), which shows that the contact angle of water in the capillary increases from less than 90° to greater than 90° to accommodate the weight increase. The capillary force acts against gravity in holding the water in place when the contact angle is greater than 90°. The maximum contact angle is reached at 180º, which corresponds to a

maximum water holding capacity. Water content in the crevices can vary from saturated to partially-saturated to not capable of holding water (CRWMS M&O 2001 [DIRS 152016], Table 6-1) as the aperture sizes increase.

Film flows over saturated crevices have little impact on water held in the crevices due to the effects of capillarity. However, film flows into the partially-saturated crevices can cause pendant drops to be formed and released on the underside of the drip shield in a discrete manner.

The above discussion highlights some of the complexities in evaluating the potential for water to be imbibed into crevices for sheet flow. These complexities can be represented by the probability P_{SFIB}, which represents the combined probability of sheet flow occurring over breaches in the drip shield above the waste package and water moving through the crevice to the underside of the drip shield.

The event tree (Figure 8.3.3-2) provides the basis for assessing the probability for flow through the drip shield from seepage flow directly into breaches (Q_{FDIB}) and for sheet flow outside the drip shield into breaches (Q_{SFIB}), respectively:

$$Q_{FDIB} = P_{FDIB} \cdot P_{FDS} \cdot Q_{SEEP}$$

$$Q_{SFIB} = P_{SFIB} \cdot P_{SFNE} \cdot (1 - P_{FDIB}) \cdot P_{FDS} \cdot Q_{SEEP} \qquad \text{(Eq. 8-9)}$$

The conceptual model for flow through the drip shield provides a qualitative illustration for assessing advection through the drip shield. While actual probabilities may be assigned conservatively through selection of probabilities, the conceptual model indicates that droplets impacting on crevices would be low-probability events with high consequence for advection; while drip shield flow into breaches may occur with a somewhat higher probability, the consequence (depending on the environment) might be low.

8.3.3.3.2 Waste Package Flux Model

The modeling approach outlined in the preceding section for the drip shield is applied directly to the waste package as shown in Figure 8.3.3-2b. The following flow definitions are presented:

Q_{CDS}	=	Condensate flow rate underneath the drip shield
Q_{WP}	=	Flow onto waste package
Q_{OWP}	=	Film flow on the inside of the drip shield or outside the waste package
Q_{WPFDIB}	=	Waste Package flow directly into breaches
Q_{WPSF}	=	Sheet flow onto waste package
Q_{WPSFNE}	=	Waste package sheet flow not evaporated
Q_{WPEVAP}	=	Waste package evaporation
Q_{WPSFIB}	=	Waste package sheet flow into breaches
Q_{WPSFAB}	=	Waste package sheet flow away from breaches

The following probabilities are defined:

P_{FOWP} = Probability of flow directly onto the waste package

P_{WPFDIB} = Probability of flow droplets impinging directly onto the waste package breach and displacing water

P_{WPSFNE} = Probability of waste package sheet flow not evaporated (depends on temperature and relative humidity)

P_{WPSFIB} = Probability of sheet flow into waste package breaches (depends on temperature and relative humidity)

Once flow has occurred through the drip shield, there is a large probability that film flow will occur on the inside surface of the drip shield without flow dropping onto the waste package. This results in a low probability of flow (P_{FOWP}) directly onto the waste package. As discussed in the results of EBS Pilot Scale Test #3 (BSC 2001 [DIRS 154479], Section 5), no drip water or condensation was observed under the drip shield or on the waste package for conditions simulated in the test. The water that had flowed through the interface of the metal strap and the drip shield, and through the interface between the drip shields, formed a thin film near the interface and flowed on the inside surface of the drip shield without contacting the waste package surface. While this observation does not apply in general to corrosion crevices and the narrow range of test conditions in the EBS Pilot Scale Test #3, it nevertheless shows that water flows are anticipated to dominantly form thin films.

The event tree presented for the waste package flux model indicates a very similar approach to the partitioning of waste package flow for the given temperature and RH environment. The total amount of seepage entering the waste package by advection is therefore respectively:

$$Q_{WP} = P_{WPFDIB}\, P_{FOWP} \cdot (Q_{FDIB} + Q_{SFIB} + Q_{CDS})$$

$$Q_{WPSFIB} = P_{WPSFIB} \cdot P_{WPSFNE} \cdot (1 - P_{WPFDIB}) \cdot P_{FOWP} \cdot (Q_{FDIB} + Q_{SFIB} + Q_{CDS}) \quad \text{(Eq. 8-10)}$$

As in the case of the drip shield model, probability of flow droplets impinging directly on the waste package breaches and displacing water is given by:

$$P_{WPFDIB} = \frac{A_{B,WP}}{A_{WP}} \quad \text{(Eq. 8-11)}$$

where $A_{B,WP}$ is the total breach area on the upper half of the waste package and A_{WP} is the projected area of the upper half of the waste package. As before, the probability of occurrence, f_{WP}, is assigned as a random number between zero and one. A_{WP} is equal to 8.07 m^2 and 7.29 m^2 for commercial SNF and HLW packages, respectively (length and diameter dimensions are taken from BSC 2001 [DIRS 154461], Item 3, Table 9).

8.3.3.4 Implementation of Drip Shield and Waste Package Seepage Flux Models

The implementation of the drip shield model and waste package flux models require estimates of the various probabilities for flow. As noted previously, several of the probabilities can be

estimated by geometric factors, while others require more complex technical analysis. For some of the factors, conservative assumptions are made regarding probabilities in the absence of technical analysis or test data. Figure 8.3.3-3 presents information on geometric factors used in the drip shield model.

As discussed in the previous section, the probability of flow directly onto the drip shield (P_{FDS}) can be estimated by the simple ratio of the drip shield footprint to the tunnel footprint, or by the ratio of the projected width of the drip shield (D) to the tunnel diameter (D_T). The probability of flow droplets impinging directly onto breaches and displacing water (P_{FDIB}) is assigned by the ratio of the breached area of the drip shield ($A_{B,DS}$) to the projected area of the drip shield (A_{DS}) as is presented in Equation 8-8.

The probability of sheet flow into breaches (P_{SFIB}) can in part be estimated by noting that sheet flow could occur from the crown of the drift shield to the sides of the drip shield. If a characteristic length (L) is calculated based upon the square of the breached area of the drip shield ($\sqrt{A_{B,DS}}$), then an estimate of P_{SFIB} would be the product of L and D/2 divided by the area of the drip shield (A_{DS}). To account for the fact that in-drift seepage drips on the drip shield below the location of the crevice, the P_{SFIB} can be multiplied by a random number (f_{DS}) varying from zero to 1.

The *Water Diversion Model* (CRWMS M&O 2000 [DIRS 131108], Section 6.2.4) provides an analysis of the occurrence and flow of water through capillary tubes or parallel crevices. As the drip shield becomes wetter, a fraction of the voids will be filled with water and become available for flow. The tendency for water to be drawn in through the drip shield depends on the moisture potential on the inside surface of the drip shield. The moisture potential, in turn, depends on the relative humidity (RH) and absolute temperature (T) on the inside surface of the drip shield. At equilibrium, the water vapor potential equals the liquid water potential (Jury et al. 1991 [DIRS 102010], p. 60). Since the vapor and liquid phases are at about the same elevation, the relative humidity can be expressed as (Jury et al. 1991 [DIRS 102010], p. 60):

$$RH = exp\left(\frac{M_w \psi}{\rho_w R T}\right) \qquad \text{(Eq. 8-12)}$$

$$\psi = \frac{\rho_w R T}{M_w} ln(RH) \qquad \text{(Eq. 8-13)}$$

where

ψ = Moisture potential (bar)
ρ_w = Mass density of water (kg/m^3)
T = Temperature (K)
M_w = Molecular weight of water (0.018 kg/ mole)
R = Universal Gas Constant (8.314 Joule/(mole-K))
RH = Relative Humidity.

Figure 8.3.3-4 presents a plot of the relationship of the moisture potential (ψ) to relative humidity from the equation above. The moisture potential (ψ) is a strong function of relative

humidity (Equation 8-13), or the ratio of the vapor pressure (P_v) on the inside of the drip shield to the saturated vapor pressure (P_{vsat}) at absolute temperature (T).

The *Water Diversion Model* (CRWMS M&O 2000 [DIRS 131108], Section 6.2.4) requires information on the flow geometry of the breaches in the drip shield to provide a flow analysis. However, at present the WAPDEG V4.0 model (CRWMS M&O 2000 [DIRS 151566], Section 6.5.1) only predicts the occurrence of patches ($A_{B,DS}$), and no information exists on the flow geometry or distribution of crevice sizes for a deteriorating drip shield that could be applied to assessing the modification to probability. However, the analysis presented above suggests that the occurrence of flow is a strong nonlinear function of moisture potential or relative humidity. With this in mind, the modification probability for sheet flow into breaches (P_{SFIB}) can in part be conservatively assigned as the ratio of vapor pressure to the saturated vapor pressure or the relative humidity. The modification to probability P_{SFIB} would be near one for a relative humidity of 100 percent, reflecting the potential retention and flow of water in crevices. At a lower relative humidity, such as 50 percent, the percentage of crevices retaining flow water would certainly be less than 50 percent, and a 50 percent relative humidity would tend to overestimate the probability for sheet flow into breaches.

The discussion above shows there will be a strong tendency for flow to occur in films on the inside surface of the drip shield, which would lower the probability P_{FOWP}. However, for large crevices in an environment of 100 percent saturation, there is a far higher probability for water to form droplets through crevices in the drip shield. A conservative approach to evaluating flow would be again to assign the probability P_{FOWP} on the basis of the relative humidity, which would tend to overestimate P_{FOWP} on the basis of the technical analysis presented above.

The same principles for assigning probabilities for the drip shield flux model apply to assigning probabilities for the waste package flux model. Since the waste package would have different temperature and RH environments, the overall probability for waste package flow would be lower.

8.3.4 Bathtub versus Flow Through Waste Package Model

8.3.4.1 Goal of Model

The EBS flow abstraction model initiates advective flow through a waste package as soon as a single general corrosion patch forms anywhere on its surface (assuming that the drip shield already has failed and that the package is located in a region with seepage). There is no long-term buildup and retention of liquid within the waste package. There is also no significant resistance to flow through the waste form. This approach maximizes the immediate release and mobilization of radionuclides into the local groundwater environment, and is referred to as the flow-through geometry.

The approach is physically unrealistic because advective flow cannot occur through a single patch on the waste package when considering the bathtub effect. Also, water would be stored for some residence time on the waste package. The degree of conservatism in the approach will depend, in part, on the time delay between the first patch and the next patch that forms a continuous flow pathway through the waste package. In general, the onset of advective flow

through a waste package will be delayed until there is at least one patch on both the upper and lower surfaces of the waste package. This delay time was (conservatively) ignored in the TSPA-SR (CRWMS M&O 2000 [DIRS 153246], Section 3.6.1.1).

An alternative conceptual model to the flow-through geometry is the "bathtub" geometry. The bathtub geometry allows seepage to collect within the waste package before being released to the EBS when a patch forms in the lower half of the waste package. In theory, the patch failure scenario for a bathtub geometry could result in the sudden release of a large pulse of radionuclides. The bathtub effect will be most important during the first 20,000 years after repository closure (CRWMS M&O 2000 [DIRS 153940], Section 6.6). Patches are not anticipated, as discussed in Section 8.3.4.3. In this situation, there may be penetrations through the top of the waste package while the bottom surface remains intact, leading to retention of liquid water. At longer durations, such as 100,000 years or more, the presence of multiple penetrations for multiple groups of waste packages makes a flow-through geometry the likelier long-term configuration.

The goal of this model is twofold: (1) provide estimates of the time delays for the bathtub versus the flow-through model for the waste package, and (2) provide an approach to quantify the uncertainty and sensitivity of TSPA results to the bathtub versus flow-through conceptual model.

Alternative thermal operating modes will not affect the conceptual model for flow through the waste package.

8.3.4.2 Identification of Unquantified Uncertainties in Total System Performance Assessment-Site Recommendation

Prior to the TSPA-SR calculations (CRWMS M&O 2000 [DIRS 153246]), the response of the bathtub geometry was evaluated for a primary case and for three secondary cases (CRWMS M&O 2000 [DIRS 153940], Sections 6.6.1 and 6.6.2). The primary case includes consideration of two types of radionuclide release mechanisms: dissolution rate-limited and solubility-limited. The results for the primary case are based on a closed form analytic solution with constant values of inflow rate, dissolution rate, and solubility. The three secondary cases consider a step change in inflow rate (such as would occur from a climatic change), a change in groundwater chemistry, and a step change in flow geometry (such as would occur if a patch suddenly failed beneath the waterline). The basic geometry and flow pattern for the bathtub geometry is shown in Figure 8.3.4-1.

The general conclusion from the comparison of the flow-through and bathtub geometries is that the bathtub model often introduces a time delay in the release of radionuclides in comparison to the flow-through model (CRWMS M&O 2000 [DIRS 153940], Section 6.6.3). The flow-through model is therefore conservative in relation to the bathtub geometry for these cases. However, the flow-through model is not clearly conservative in all cases. For example, a pulse (additional mass) of radionuclides is released from a bathtub geometry if a (second) patch opens instantaneously beneath the water line. In this case, the flow-through model is not clearly conservative.

The uncertainty in radionuclide release due to the use of a flow-through versus bathtub geometry for the waste package was not quantified for the TSPA-SR (CRWMS M&O 2000 [DIRS 153246]). Several factors led to this decision: (1) the flow-through model is conservative for early arrival of radionuclides, (2) sorption in the unsaturated and saturated zones will tend to smooth out any discrete pulse released by the bathtub geometry, and (3) the repository is represented as 30 groups of waste packages, so a single bathtub failure for one group is averaged out by the response of the other groups. However, the concerns about the potential nonconservatism of the pulse release from the bathtub geometry make it advantageous to consider this alternative conceptual model for releases from the waste package.

8.3.4.3 Quantification of Previously Unquantified Uncertainty

The WAPDEG V4.0 model (CRWMS M&O 2000 [DIRS 151566]) provide detailed information about the growth of patches, pits, and stress corrosion cracks on the surface of the drip shield and waste package. The WAPDEG V4.0 model is appropriate because it encompasses the full variability in waste package response due to corrosion rates, package-to-package variability, and environmental factors.

WAPDEG V4.0 output includes the time of first failure for patches, pits, and stress corrosion cracks in the drip shield and on the upper and lower surfaces of the waste package. This information is ideal for estimating the delay in release from a waste package if a bathtub geometry forms. For example, if the upper surface of the waste package fails before the lower surface, then fluid will collect in the waste package until a patch forms on the lower surface. Similarly, there is no bathtub delay time if the lower surface of the waste package fails before (Case 2001 [DIRS 155053], p. 1) the upper surface.

This analysis focuses on the formation of patches for two reasons. First, pits are not anticipated to form in the drip shield and waste package for the in-drift environment. Second, advective flow through stress corrosion cracks is expected to be negligible because their small size and the presence of a meniscus or corrosion products in the cracks will reduce the advective flux through cracks to insignificant levels compared to a patch. Patches are then the main advective pathway through the waste package.

Patch location on the waste package will influence the magnitude of any pulse release of radionuclides caused by a sudden failure in the lower surface. For example, a patch that forms at the bottom of the waste package will tend to maximize the pulse released by the bathtub effect. On the other hand, a patch high on the side of the waste package is unlikely to release a pulse, but will merely delay releases until the waste package fills to its level and begins to overflow.

In the following analysis, the patch location is considered to be at the crown for a top patch and at the bottom for a patch on the lower surface of the waste package. This approach provides a reasonable estimate of the variability in delay times for the bathtub versus flow-through models. It also is most relevant to the case for a pulse release that was identified as potentially nonconservative for the flow-through model. WAPDEG V4.0 output data (Case 2001 [DIRS 155053], p. 2) identify patches on the upper and lower surface, but do not provide information on their azimuthal location.

Output data (Case 2001 [DIRS 155053], p. 2) from a WAPDEG V4.0 calculation for 100 realizations have been analyzed to determine potential delays from a bathtub geometry. Each realization considers 400 waste packages, each of which provides a different time delay for the bathtub effect in the waste package. Analysis of the frequency and magnitude of the bathtub delay time in the 400 realizations is useful because: (1) it provides quantitative estimates of the time delays for the bathtub versus the flow-through model for the waste package, and (2) the WAPDEG V4.0 output provides distributions that can be sampled to determine the sensitivity of TSPA results to the bathtub versus flow-through models.

WAPDEG V4.0 output (Case 2001 [DIRS 155053], p. 2) includes the times for first failure of the top of the drip shield, of the top and bottom of the outer barrier of the waste package, and of the top and bottom of the inner barrier of the waste package. Since the outer barrier always fails before the inner barrier, its presence is ignored here. The following definitions provide the delay time for the bathtub effect:

$$T_{accum} \equiv Max(t_{fail,DS}, t_{fail,topWP})$$
$$T_{flow-thru} \equiv Max(t_{fail,DS}, t_{fail,topWP}, t_{fail,bottomWP}) \quad \text{(Eq. 8-14)}$$
$$T_{delay} \equiv T_{flow-thru} - T_{accum}$$

where

T_{accum} = time when fluid begins to accumulate in the waste package
$T_{flow\text{-}thru}$ = time when a flow-through geometry first forms
T_{delay} = the bathtub delay time
$t_{fail,\ DS}$ = time of first failure of the drip shield
$t_{fail,\ top\ WP}$ = time of first failure of the top surface of the waste package
$t_{fail,\ bottom\ WP}$ = time of first failure of the bottom surface of the waste package.

The first definition states that a continuous pathway through the top surfaces of all barriers is required for seepage to accumulate within the waste package. The second definition states that flow-through cannot begin until failures in both the top and bottom surfaces of the waste package are present. The third equation defines the time delay between when water starts to accumulate and when an advective flow can occur through the waste package. This is the time delay due to the bathtub effect.

Figure 8.3.4-2 presents the delay times from a single WAPDEG V4.0 realization as a cumulative distribution function (CDF). The maximum bathtub delay time is 60,400 years (Case 2001 [DIRS 155053], p. 3). About half of the bathtub delay times are zero because failure of the top or bottom surfaces of the waste package is equally likely on the surfaces of the waste package. In this situation, the bottom of the inner barrier fails before the top of the inner pseudo-barrier in approximately half the realizations, so there is no bathtub effect for these cases.

Figure 8.3.4-3 presents the delay times from 100 WAPDEG V4.0 realizations as CDFs. Each function is based on the results for 400 waste packages for each realization. Note the large variability in the results, indicative of the large variability in corrosion rates and package-to-package variability for the corrosion models in the WAPDEG V4.0 model (CRWMS

M&O 2000 [DIRS 151566], Section 6.5.1). Although many realizations have zero bathtub delay times in 50 percent of the waste packages, there is one outlier with zero bathtub delay in approximately 90 percent of the waste packages. This realization probably has very slow corrosion rates for the drip shield in comparison to the waste package, so patches have already formed on the underside of the waste package by the time the drip shield fails. Note that the maximum delay time is over 200,000 years.

These results provide for a broad range of uncertainty. The WAPDEG V4.0 model provides an efficient analysis with multiple realizations to obtain mean values and variance. It also provides a CDF that can be used directly in the TSPA model to determine the appropriate bathtub delay time.

8.4 SUMMARY AND ABSTRACTION PROVIDED TO TOTAL SYSTEM PERFORMANCE ASSESSMENT

The preceding sections outline the submodels and uncertainties that should be quantified in further uncertainty analyses of water flow in the EBS. Where possible, reasonable ranges and/or distributions of uncertain TSPA input parameters are provided.

The following recommendations are made. The waste package heat rate that contributes to evaporation off the drip shield should be set to a fraction χ (nominally one-half), as governed by Equation 8-2. The drip shield condensation model states the principle that condensation can only occur if the invert temperature exceeds the drip shield temperature. The results of EBS Pilot Scale Test #3 suggest that the invert temperature did not exceed the drip shield temperature for the simulated test conditions. Other arguments presented in Section 8.3.2.3.3 support the recommendation that drip shield condensation not be included.

The following list summarizes the assignment of probabilities for the drip shield and waste package flux models:

- Assign the probability of flow directly onto the drip shield (P_{FDS}) by the simple geometric ratio of the drip shield footprint to the tunnel footprint, or by the ratio of the projected width of the drip shield (D) to the tunnel diameter (D_T).

- Assign the probability of flow droplets impinging directly into breaches and displacing water (P_{FDIB}) by the ratio of the breached area of the drip shield ($A_{B,DS}$) to the projected area of the drip shield (A_{DS}) (Equation 8-8).

- Assign the probability for sheet flow into breaches (P_{SFIB}) on the top of the drip shield over the waste packages based on the square root of the breached area of the drip shield multiplied by half the drip shield width in plan (D) and divided by the area of the drip shield (A_{DS}). To account for the fact that in-drift seepage drips on the drip shield below the location of the crevice, the probability P_{SFIB} can be multiplied by a random f_{DS} between zero and one. It should be noted that there is uncertainty in the assignment of this probability, and that it could alternatively be assigned as the ratio of the breached area to the area of the drip shield.

- Assign a modification to the probability for sheet flow into breaches (P_{SFIB}) to account for retention of water in breaches. The modification to the probability is based upon the relative humidity that would result in no flow reduction at 100 percent relative humidity and some reduction at lower relative humidities.

- Assign the probability for flow onto the waste package (P_{FOWP}) on the basis of the relative humidity inside the drip shield. At high relative humidities, the probability is one to reflect the potential for pendant water to fall on the drip shield. At lower relative humidities, flow is much more likely to be dominated by film flow on the inside surface of the drip shield.

- Assign the flow onto the waste package using a similar approach to that of the drip shield for sheet flow and flow through the waste package using the waste package flow geometry.

It is recommended that the bathtub release model not be used because the flow-through model is conservative for the reasons cited in Section 8.3.4.2.

INTENTIONALLY LEFT BLANK

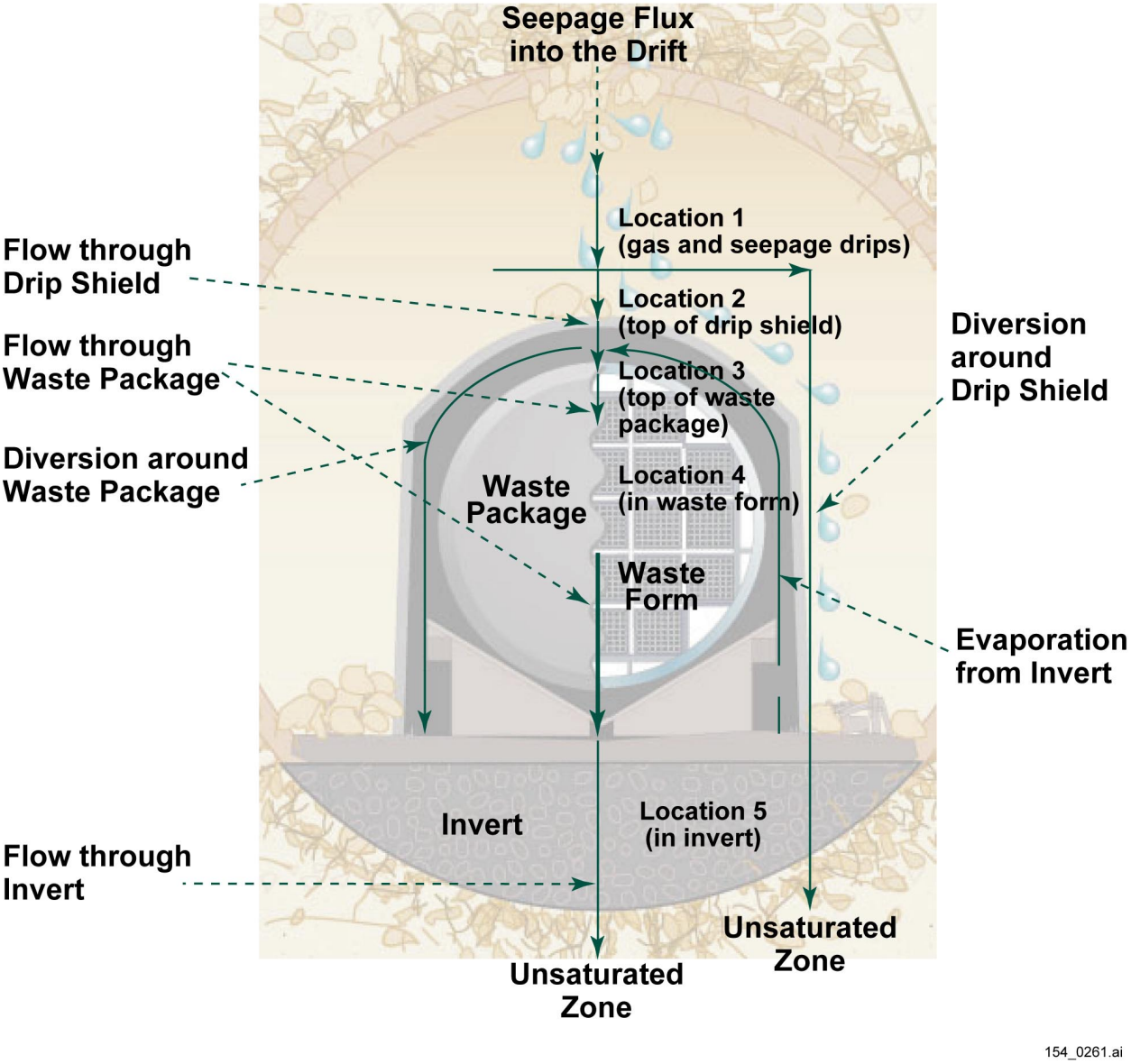

154_0261.ai

Figure 8.2-1. Schematic Diagram of Engineered Barrier System Flow Pathways

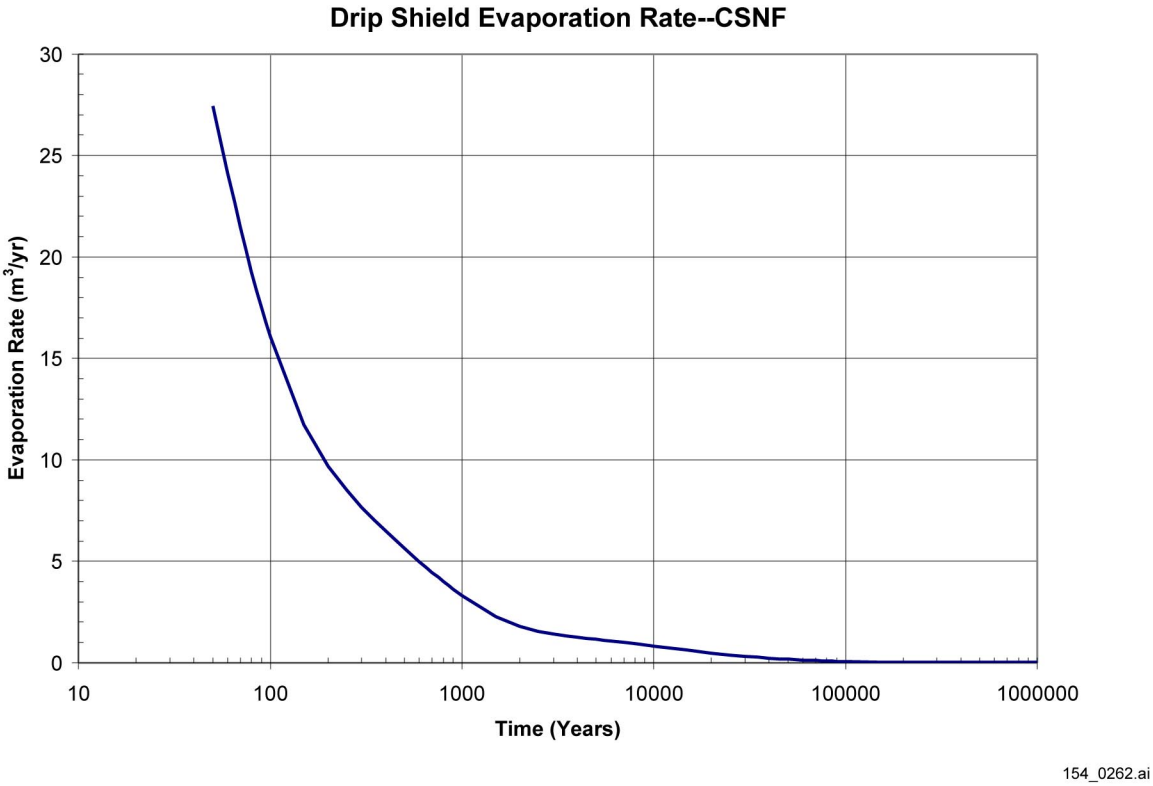

154_0262.ai

Source: CRWMS M&O 2001 [DIRS 154594], Figure 53.

Figure 8.3.1-1. Average High Level Radioactive Waste Drip Shield Evaporation Rate

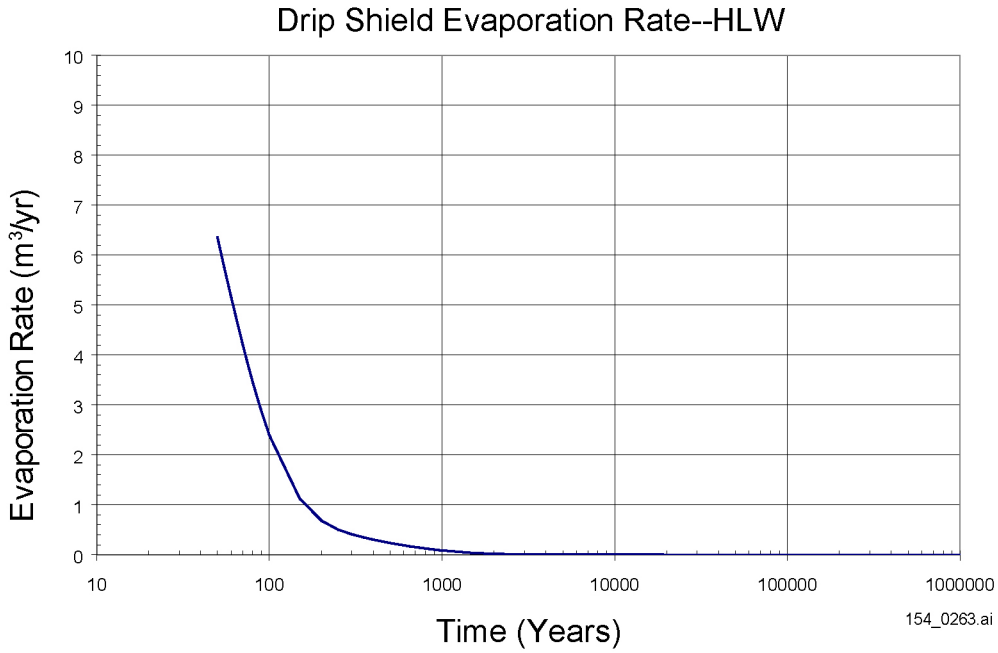

154_0263.ai

Source: CRWMS M&O 2001 [DIRS 154594], Figure 54.

Figure 8.3.1-2. Average Non-Commercial Drip Shield Evaporation Rate

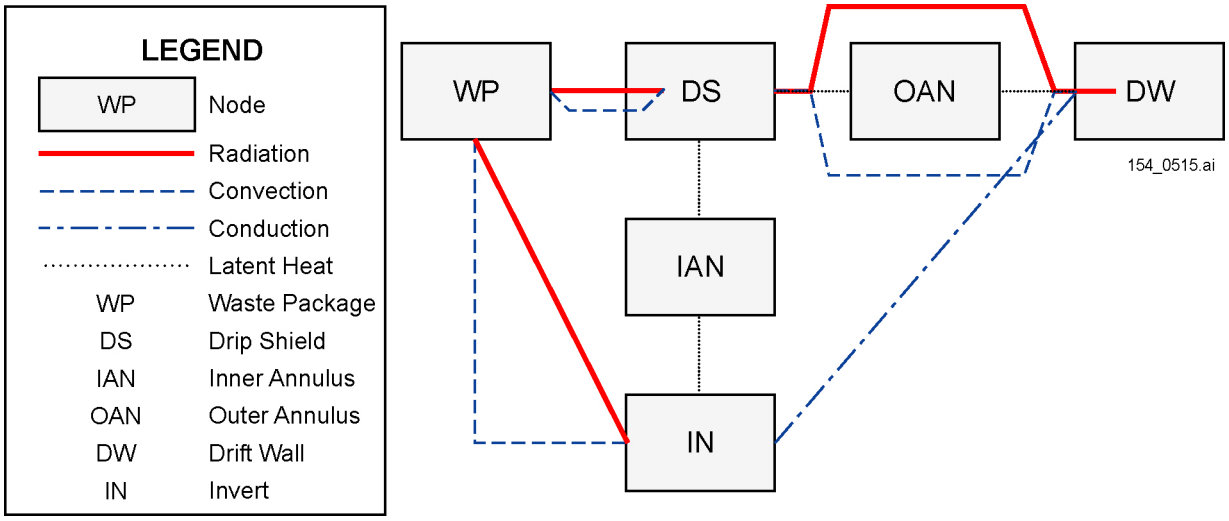

154_0515.ai

Figure 8.3.2.3-1. Conceptual Model for EBS Sensible and Latent Heat Flow Paths and Drip Shield Condensation

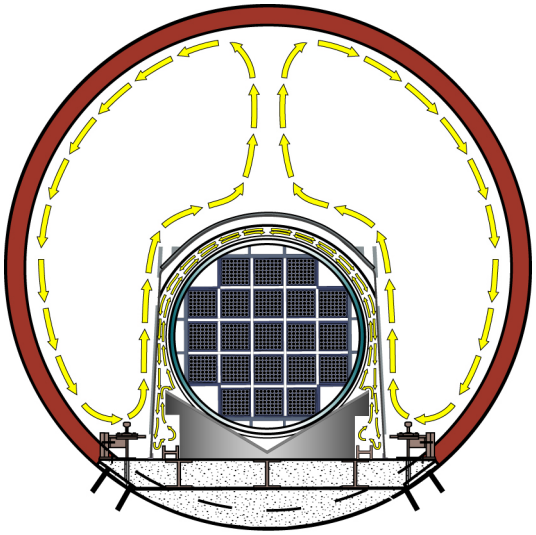

154_0516.ai

Figure 8.3.2.3.1-1. Main Convection Cells within the EBS

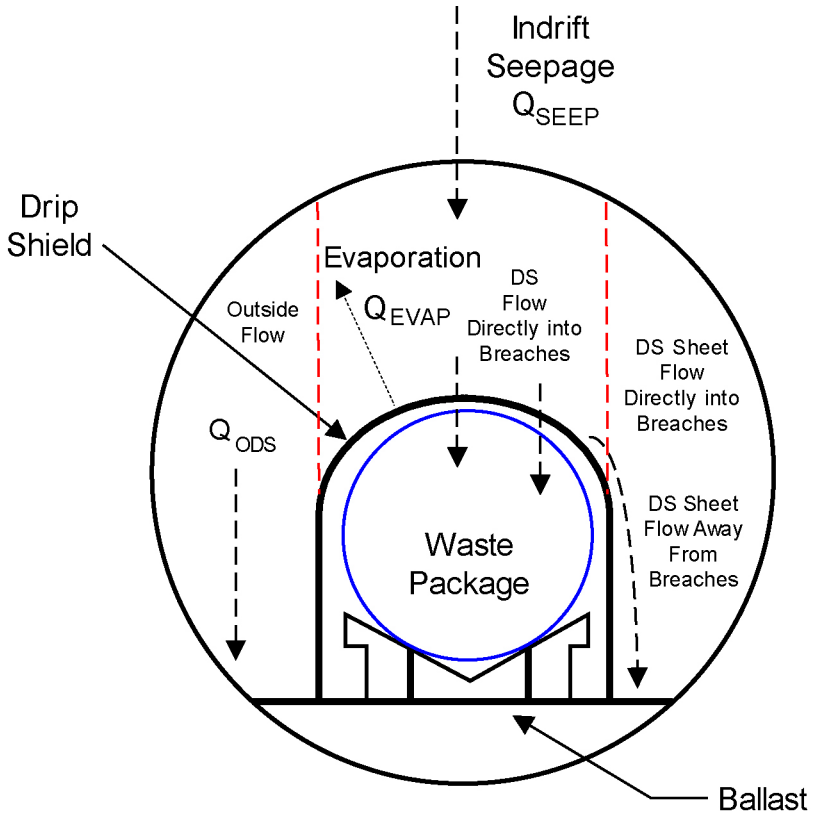

$$Q_{EVAP} = \frac{\left(\frac{1}{2}\right) q_{wp}}{\rho_l h_{fg}} f_{evap}$$

Eq. 8.3

154_0453.ai

154_0453.ai

Figure 8.3.3-1. Conceptual Drip Shield Flux Model

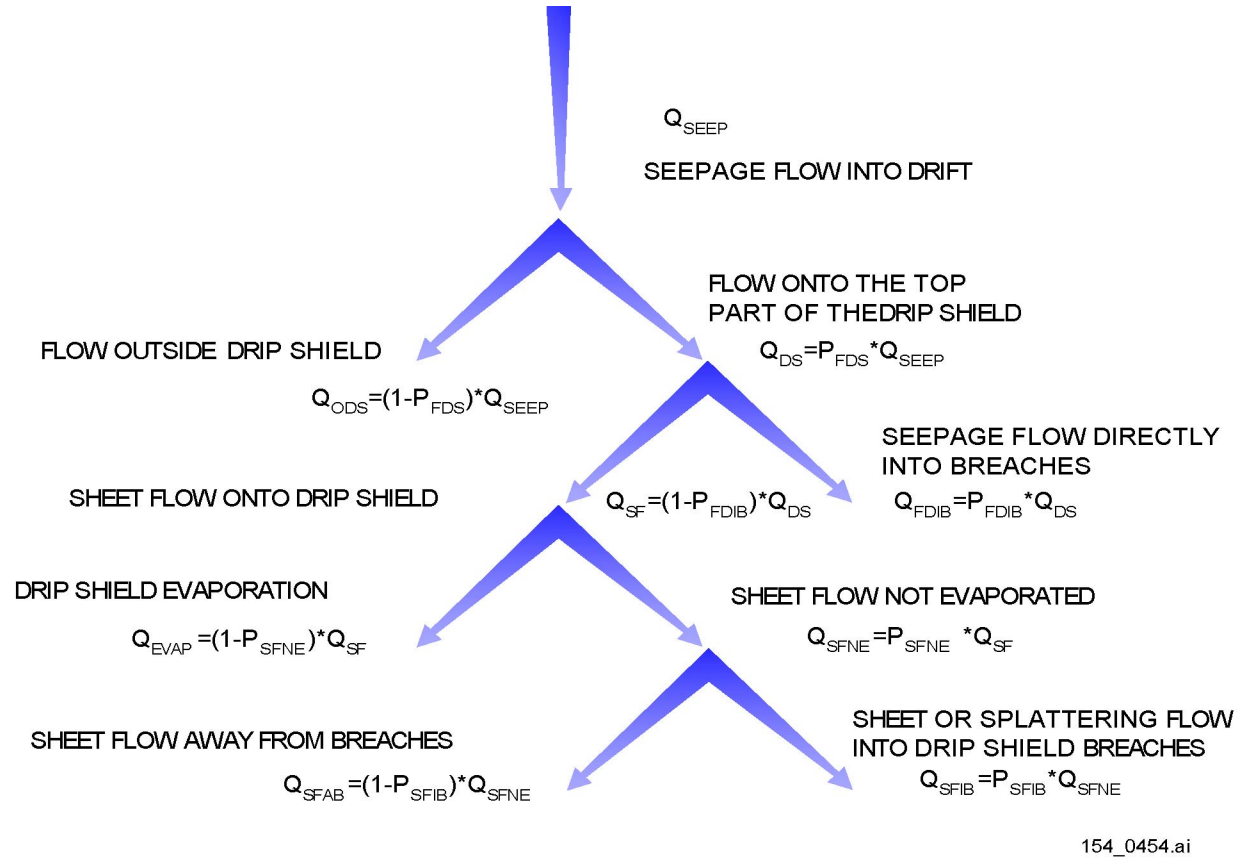

154_0454.ai

Figure 8.3.3-2. Event Tree for the Drip Shield Flux Model

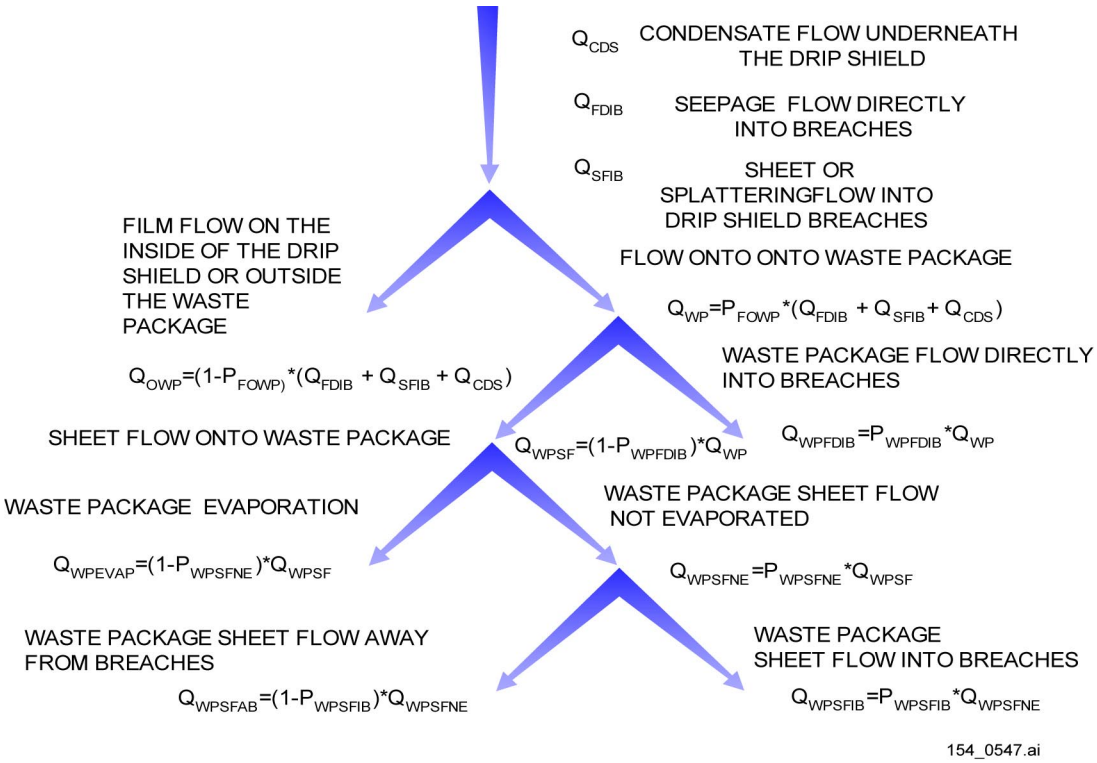

154_0547.ai

Figure 8.3.3-2b Event Tree for the Waste Package Flux Model

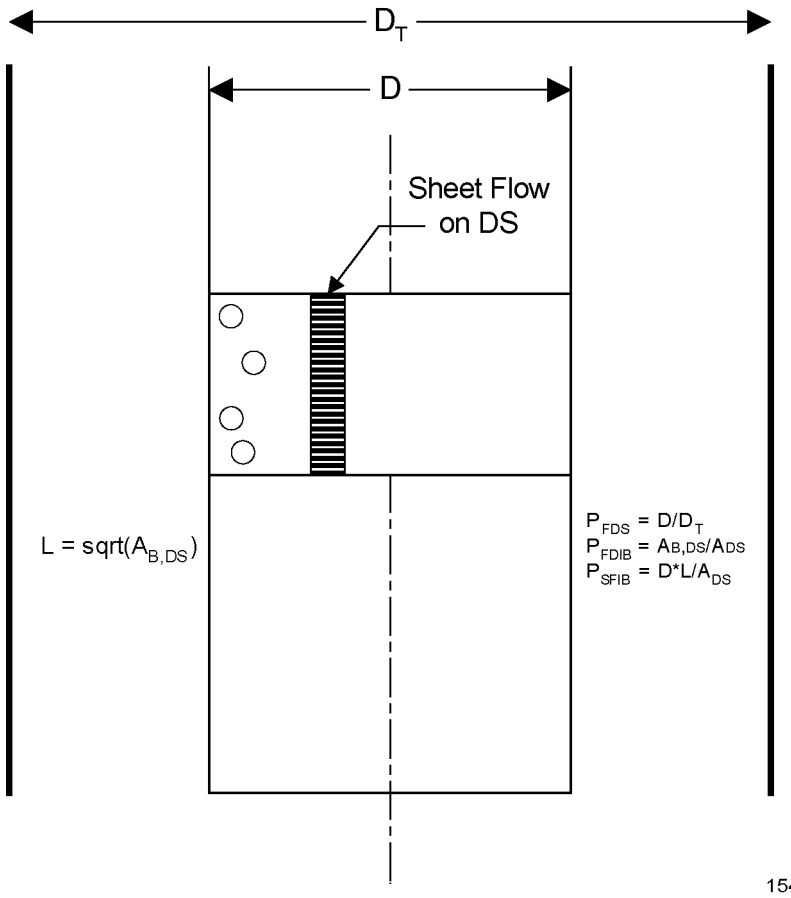

154_0455.ai

Figure 8.3.3-3. Geometric Factors in the Assignment of Probabilities

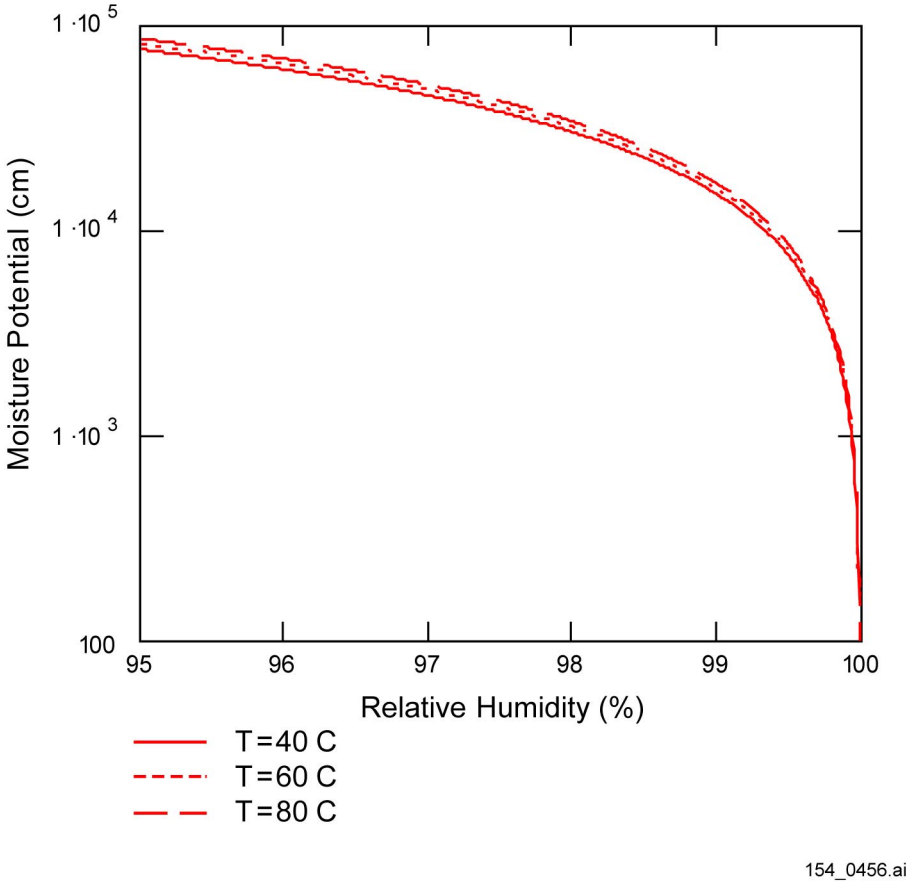

154_0456.ai

Source: CRWMS M&O 2000 [DIRS 131108], Figure 13.

Figure 8.3.3-4. Relationship of Moisture Potential to Relative Humidity

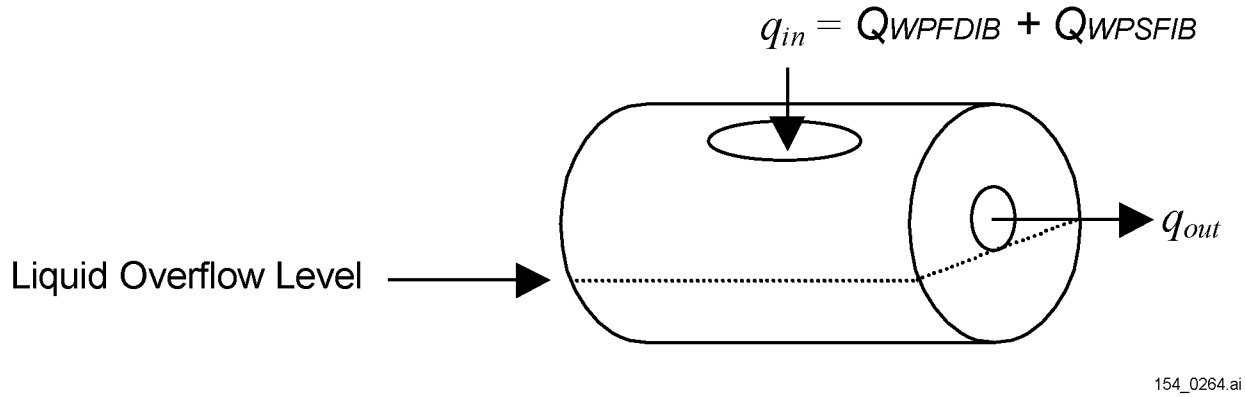

154_0264.ai

Note: See Section 8.3.3.3.2 for Waste Package Fluxes.

Figure 8.3.4-1. Schematic of the Bathtub Geometry for the Waste Package

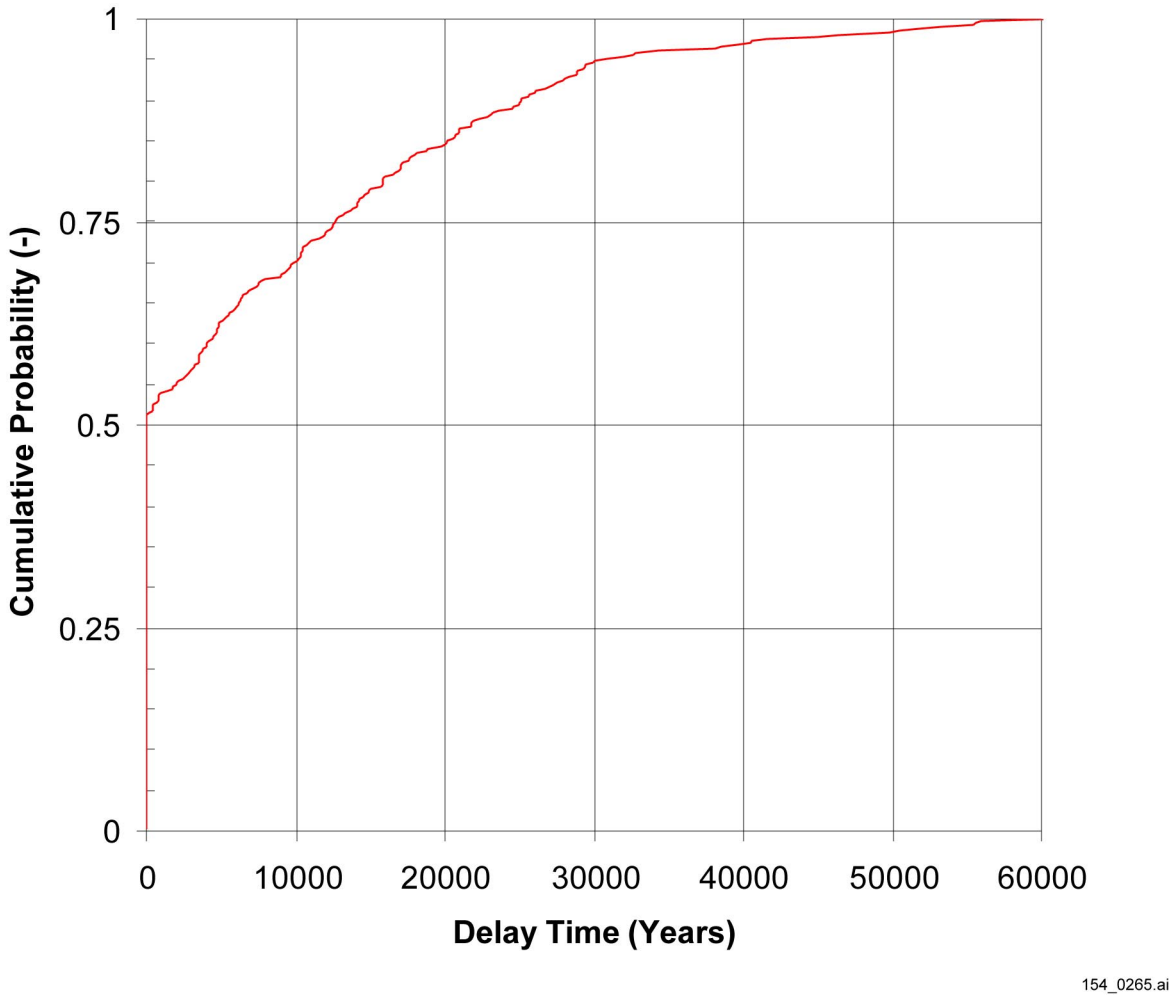

154_0265.ai

Source: Case 2001 [DIRS 155053], Figure 1.

Figure 8.3.4-2. Cumulative Distribution Function for the Bathtub Delay Time for a Single WAPDEG Realization with 400 Packages

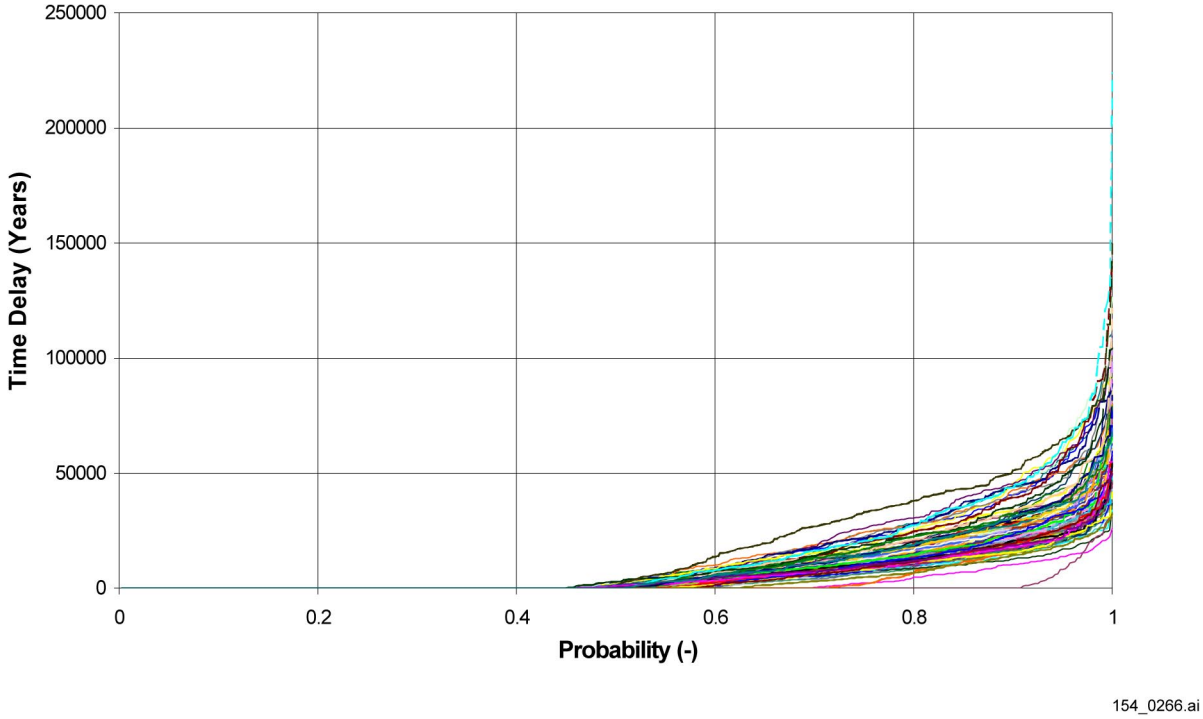

154_0266.ai

Source: Case 2001 [DIRS 155053], Figure 2.

Figure 8.3.4-3. Cumulative Distribution Function for the Bathtub Delay Time for 100 WAPDEG Realizations. Each Curve is Based on the Results for 400 Waste Packages

INTENTIONALLY LEFT BLANK

9 Waste Form Degradation and Radionuclide Release

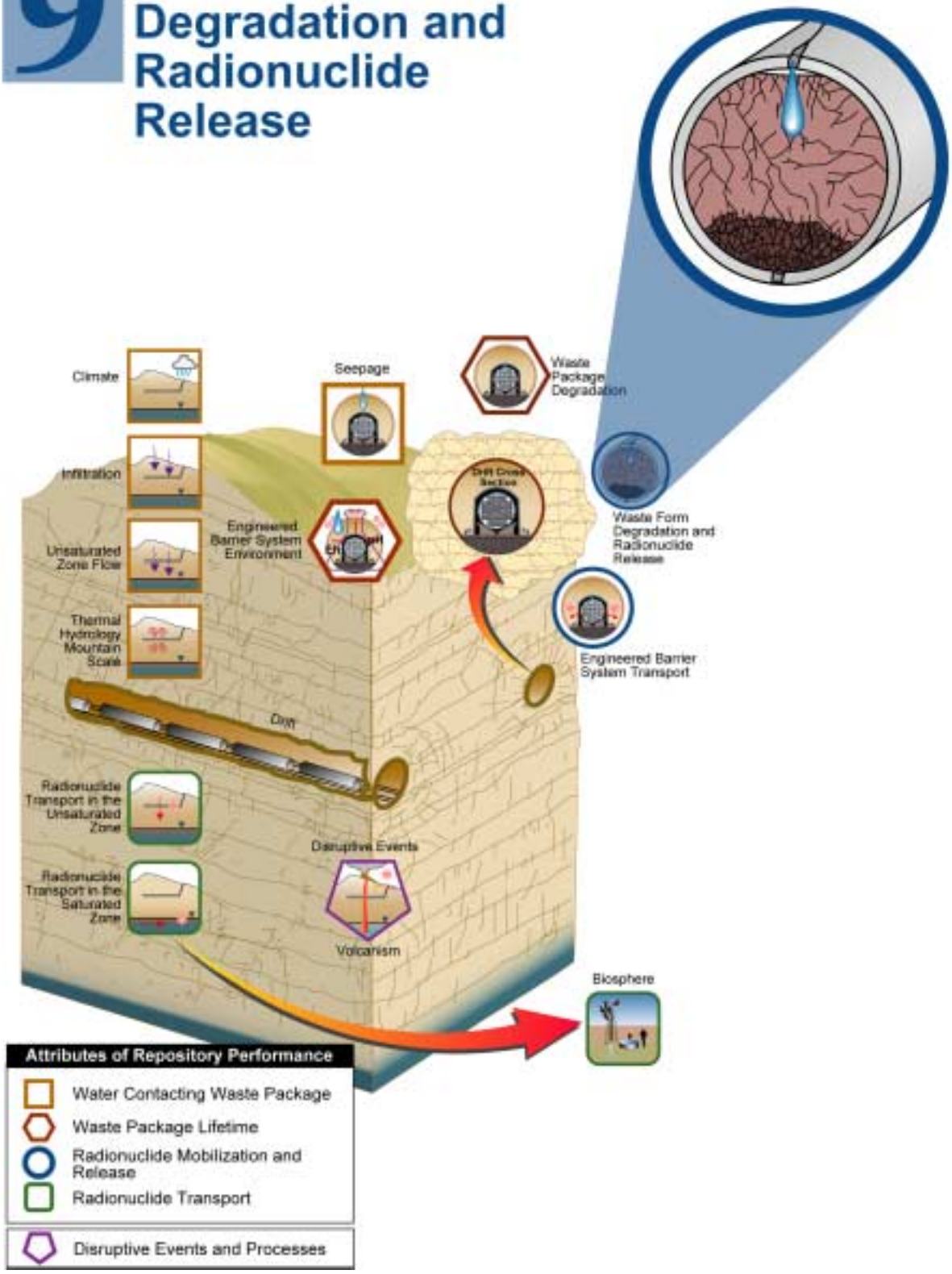

9. WASTE FORM DEGRADATION AND RADIONUCLIDE RELEASE

9.1 INTRODUCTION AND CONCEPTUAL BASIS

The function of the waste form degradation model is to determine three outputs over time: dissolved radionuclide concentration, reversible colloidal radionuclide concentration, and irreversible colloidal radionuclide concentration. To do this, the model synthesizes eight major modeling/analysis efforts: radioisotope inventory, in-package chemistry, commercial spent nuclear fuel (SNF) degradation, commercial SNF cladding degradation, U.S. Department of Energy (DOE) SNF degradation, high-level radioactive waste (HLW) degradation, radioisotope dissolved concentration (solubility), and radioisotope colloidal concentration, as summarized in the *Yucca Mountain Science and Engineering Report* (S&ER) (DOE 2001 [DIRS 153849], Section 4.2.6). The radionuclides most important to human dose were identified and quantified per waste package design for inclusion in a total system performance assessment (TSPA) (DOE 2001 [DIRS 153849], Section 4.2.6.4.1). Reaction-path modeling of the breached waste form environment was used to assess the long-term evolution of in-package chemistry using as input water flux into the waste package; degradation of the steel, aluminum, DOE and commercial SNF, and HLW inside the package; and a chemical thermodynamics database (DOE 2001 [DIRS 153849], Section 4.2.6.3.2). Water chemistry parameters such as hydrogen ion concentration, total carbonate concentration, ionic strength, fluoride, and chloride concentrations are estimated for subsequent use in models used to predict commercial SNF cladding and matrix degradation, HLW degradation, radionuclide solubility, and colloid availability and stability.

The waste form models implemented in *Total System Performance Assessment for the Site Recommendation* (TSPA-SR) (CRWMS M&O 2000 [DIRS 153246]) were in most cases conservative models that bounded significant uncertainties. Table 9-1 shows the five waste form models that were chosen for further analysis because they were most likely to affect system performance. The waste form models implemented in this study differ from the TSPA-SR model in the following respects:

- **In-Package Chemistry** (Section 9.3.1)–The effects of HLW glass degradation rate and steel degradation rate on in-package chemistry were evaluated because sensitivity studies showed that degradation rates of in-package steels and glass have an impact on pH-time trajectories, which in turn can influence actinide solubilities. Lower degradation rates were investigated to quantify uncertainties associated with the conservative assignment of glass and steel degradation rates used in the TSPA-SR (CRWMS M&O 2000 [DIRS 153246]). Revised pH-time trajectories for commercial SNF and codisposal packages provided the basis for new TSPA runs and sensitivity analyses. As shown in Table 9-1, the distributions were based, in part, on updated scientific information, but this work was not prompted by thermal operating mode issues. The in-package chemistry model was developed when early waste package failures were screened out based on low probability (DOE 2001 [DIRS 153849], Section 4.2.4.3.1).

Table 9-1. Summary of Supplemental Models and Analyses

Key Attributes of System	Process Model (Section of S&ER)	Topic of Supplemental Scientific Model or Analysis	Reason For Supplemental Scientific Model or Analysis			Section of Volume 1	Performance Assessment Treatment of Supplemental Scientific Model or Analysis[a]	
			Unquantified Uncertainty Analysis	Update in Scientific Information	Lower-Temperature Operating Mode Analysis		TSPA Sensitivity Analysis	Included in Supplemental TSPA Model
Limited Release of Radionuclides from the Engineered Barriers	In-Package Environments (4.2.6)	Effect of HLW glass degradation rate and steel degradation rate on in-package chemistry	X	X		9.3.1	X	X
	Cladding Degradation and Performance (4.2.6)	Effect of initial perforations, creep rupture, stress corrosion cracking, localized corrosion, seismic failure, rock overburden failure, and unzipping velocity on cladding degradation	X	X		9.3.3	X	X
	DHLW Degradation and Performance (4.2.6)	HLW glass degradation rates	X	X		9.3.1		
	Dissolved Radionuclide Concentrations (4.2.6)	Solubility of neptunium, thorium, plutonium, and technetium	X	X		9.3.2	X	X
	Colloid-Associated Radionuclide Concentrations (4.2.6)	Colloid mass concentrations	X			9.3.4	X	

NOTE: S&ER = *Yucca Mountain Science and Engineering Report* (DOE 2001 [DIRS 153849]).

[a] Performance assessment treatment of supplemental scientific model or analysis discussed in SSPA Volume 2 (McNeish 2001 [DIRS 155023]).

Waste packages started failing between 10,000 and 100,000 years (DOE 2001 [DIRS 153849], Figure 4-92) when the chemical system was well into the extended cool-down period with a representative temperature of 50ºC (DOE 2001 [DIRS 153849], Table 4-17). Because the in-package chemistry model presumed waste package breach after any thermal pulse had passed (BSC 2001 [DIRS 153724], Section 1), it was insensitive to front-end thermal conditions.

- **Dissolved Concentrations** (Section 9.3.2)–The dissolved concentrations of thorium, neptunium, plutonium, and technetium are evaluated because sensitivity studies in support of TSPA-SR (CRWMS M&O 2000 [DIRS 153246]) show these elements to have the largest effect on dose. As shown in Table 9-1, the distributions are based, in part, on updated scientific information. Differing alternative thermal operating modes do not affect the models for these elements.

- **Cladding** (Section 9.3.3)–Cladding degradation is evaluated because sensitivity studies in support of TSPA-SR (CRWMS M&O 2000 [DIRS 153246]) showed several uncertain cladding degradation parameters as important to peak dose. As shown in Table 9-1, the distributions are based, in part, on updated scientific information, but were not prompted by the consideration of a cooler thermal-operating mode. The behavior of the cladding within the repository is not expected to differ significantly between a low and high temperature-operating mode as long as a cladding temperature of 350°C is not exceeded (CRWMS M&O 2001 [DIRS 151662], Section 6.2.4 and Figure 14). Waste package temperature is treated as an independent variable in the creep cladding degradation abstraction (CRWMS M&O 2001 [DIRS 151662], Section 6.2.4, Table 8) and the intrinsic dissolution part of the unzipping rate abstraction (CRWMS M&O 2001 [DIRS 151662], Section 6.6.2)). This abstraction is applicable for a hot (backfill) design such as that considered in the total system performance assessment for the viability assessment (TSPA-VA) (CRWMS M&O 1998 [DIRS 100362], Figure 6-10), the TSPA-SR higher-temperature design, and any future cool repository design. Alternative thermal operating modes do not affect the waste form model as parameterized for the TSPA-SR or for this evaluation.

- **Colloids** (Section 9.3.4)–The effect of colloids is evaluated because of the significant uncertainties within the model. Thermal effects are being evaluated, but are expected to be overwhelmed by other uncertainties within the system.

The assessments made in the following sections are based upon a series of documented program scientific analyses and calculations, as well as assumptions, expert judgement, and best estimates. The purpose of their collection is to provide a means for establishing the sensitivity of system performance to various chemical and physical inputs describing waste form behavior.

9.2 REVIEW OF SCIENCE AND ENGINEERING REPORT TREATMENT

Conservatisms and bounding analyses are used in the TSPA-SR (CRWMS M&O 2000 [DIRS 153246]) to address a number of uncertainties that were unquantified. Some of the latter are prompted by simplified conceptual models for waste form degradation processes, while others reflect uncertainty in the ranges of inputs to reasonably well-agreed-upon models. In each

case, the intention has been to err on the side of maximizing radionuclide transport in the calculation.

9.3 UNCERTAINTY ANALYSES

Efforts to address unquantified uncertainties have focussed on several areas: the in-package chemistry model (BSC 2001 [DIRS 153724]) and abstraction (BSC 2001 [DIRS 154620]), which are used to estimate in-package chemical conditions over the life of the potential repository and over a range of bounding conditions; the dissolved concentration abstraction (CRWMS M&O 2001 [DIRS 154286]), which develops functions describing dissolved radionuclide concentrations as a function of in-package fluid compositions; the glass degradation model (CRWMS M&O 2001 [DIRS 153846]), which provides a glass degradation rate law that is used as input in the in-package chemistry calculation; the cladding model (CRWMS M&O 2001 [DIRS 151662]), which provides estimates describing the persistence of cladding protection in waste forms containing commercial SNF; and the waste form colloid model (CRWMS M&O 2001 [DIRS 153933]), which develops a method for estimating fluxes of colloidally-transported radionuclides.

The waste form models were developed when early waste package failures were screened out based on low probability (DOE 2001 [DIRS 153849], Section 4.2.4.3.1). Further analysis, however, indicated that improper heat treatment of waste packages could result in failure of up to two waste packages with the failure assumed to be at the time of closure (see Section 7.3.6). These early failures have implications on degradation processes within the waste packages and require re-evaluation for the in-package chemistry model, the cladding degradation model, and the screening of criticality. The scenario after early breach indicates that the materials within the waste package will be exposed to hot air, with humidity increasing and temperature decreasing with time (Figures 5.2-4 and 5.2-5). The waste package model predicts the drip shield will prevent ground water from dripping onto the waste package during the regulatory 10,000-year period (Figure 7.4-2). Consequently, only humid air or condensed water will enter the package during the regulatory period.

The temperature dependence of the most important thermodynamic data used in the in-package chemistry model is being evaluated for future use of the model for early waste package failures. Other inputs such as f_{CO2} and water vapor influx rates are being considered. For the cladding degradation model, early waste package failures require the re-evaluation of the rate of possible dry or humid unzipping. However, changes in these models to cover the early waste package failures may not significantly change the dose in the regulatory period because of the limited transport in this scenario. Continued functioning of the drip shield prevents advective releases, and breach at the waste package welds limits diffusive releases.

Criticality during the regulatory period was screened out when early failures were screened out. Even in the unlikely event of early waste package failures the conditions required for criticality are not likely. The failure mode postulated for early failures (e.g., cracks in the closure weld) is not sufficient for criticality to occur. Criticality would require the occurrence of additional low-probability events including the transport of a sufficient quantity of water through a waste package to cause the removal of criticality controlling material to form a critical configuration. Water transport into a waste package during the regulatory period is expected to be limited by

the nature of the failure (i.e., small cracks through the closure weld on the side of a package are not conducive to water flow through a package), by the presence of a drip shield (DOE 2001 [DIRS 153849], p. 4-219), and by the evaporation of water entering the package due to the decay heat of the waste (CRWMS M&O 2000 [DIRS 149626]). Criticality evaluations for various waste forms will be conducted prior to license application to confirm that the repository system will meet the criticality probability criterion of less than 1×10^{-4} per year for the entire repository for the regulatory period.

The models presented in the remainder of Section 9 were developed for scenarios where the waste packages breach after the thermal pulse. The use of these models for waste packages with early failures has not been validated. However, given the large uncertainty in many of these models, the use of these models for sensitivity studies is reasonable.

9.3.1 In-Package Chemistry

Unquantified uncertainties in the in-package chemistry model include uncertainties in the model inputs: degradation rates, masses and surface areas of waste form components, and the composition of the incoming fluid. Unquantified conceptual model uncertainties are also associated with the use of the mixing model, which ignores small-scale heterogeneities of fluid flow and water contact with the various in-package components. The discussions below focus on the quantification of the numerical uncertainty associated with model inputs.

9.3.1.1 Goal of Model

The goal of the in-package chemistry model is to identify the range of major element fluid compositions (pH, Eh, alkalinity, and ionic strength) likely to exist inside the waste package once drift fluids come into contact with breached waste forms. The transport rates of species in and out of the package and the reaction rates of materials within the package will control these important chemical parameters. Detailed modeling of this coupled system with reactive transport codes has not been attempted in part due to the large uncertainty in the transport properties of the degrading waste package and its contents. Random sampling of the important chemistry parameters can give parameter combinations that are impossible to achieve within the waste package based on mass balance constraints. Based on these considerations, the in-package chemistry model was built using a reaction path model and conservative carbon dioxide and oxygen concentrations. This type of model can predict a wide range of chemistries depending on the input parameters, but these chemistries are constrained by mass balance considerations, and the output can be used to provide insight into the processes controlling the chemistry. In-package fluid compositions are predicted using the reaction path model EQ6 V7.2bLV that estimates the reaction of in-package solids (steel and fuel elements) with incoming fluids over time. This mixing cell calculation assumes continual equilibration with ambient carbon dioxide and oxygen. The nature and abundance of waste form solids are determined from project design calculations. The rates at which the solids dissolve are derived from a number of supporting analysis model reports (AMRs).

The primary output of the in-package chemistry model is a series of pH-time trajectories for two waste types (commercial versus codisposal) and inflow boundary conditions. In general, equilibrium between fluids and secondary, uranium-bearing minerals is predicted for long

periods of time in commercial spent fuel packages. Eh is conservatively assumed to be oxidizing and fixed by equilibrium with atmospheric levels of free oxygen. Similarly, carbonate alkalinity levels are conservatively assumed to be controlled by equilibrium with atmospheric carbon dioxide. Output pH-time trajectories are abstracted as input for TSPA. Ultimately, these abstractions are used by TSPA to calculate the dissolved radionuclide concentration limits for a number of important radionuclides.

9.3.1.2 Identification of Unquantified Uncertainties in Total System Performance Assessment-Site Recommendation

The inputs that have significant uncertainty for the in-package chemistry model include: incoming water composition, incoming water rate, and the component surface areas and reaction rates. The latter includes the exposed surface area of spent fuel under breached cladding. The uncertainty in fluid flow rates and exposed spent fuel surface area are handled explicitly by using a range of inputs and defining the output as a function of these input parameters. The S&ER (DOE 2001 [DIRS 153849]) models also used two corrosion rates for each of the major components, a high rate and a more likely rate 10 times lower (CRWMS M&O 2000 [DIRS 111880]).

The importance of incoming fluid composition was tested in a series of calculations (BSC 2001 [DIRS 153724], Section 4.1.2), using J-13 well water, evaporated J-13 well water, and an output composition from the Near Field Environment Process Model Report (CRWMS M&O 2000 [DIRS 146589], Table 3-5). The results of the sensitivity studies indicated that the chemical composition of the influent water did not impact the pH-time trajectories. Hence, J-13 well-water composition was used for subsequent analyses.

Critical unquantified uncertainties that remain in the in-package chemistry calculation include those associated with: steel and glass degradation rates, oxygen fugacity, and in-package sorption. New information (BSC 2001 [DIRS 154840]) developed since completion of the S&ER (DOE 2001 [DIRS 153849]) models includes a series of sensitivity studies to assess the impact of varying the individual dissolution rates of the various waste form components. This effort was prompted in part by the aforementioned observation of trajectory sensitivity to rates and the geochemical evolution of waters associated with localized environments inside the waste form. Also, a more thorough examination of in-package sorption has been performed (Section 10.3.4).

The S&ER (DOE 2001 [DIRS 153849]) in-package chemistry model presumes waste package breach after any thermal pulse has passed (BSC 2001 [DIRS 153724], Section 1). It is, therefore, insensitive to front-end thermal conditions, and there is no need for an explicit consideration of initial thermal configuration impacts on model outputs.

9.3.1.3 Quantification of Previously Unquantified Uncertainty

A number of solids are expected to degrade after contacted by fluids that enter breached waste packages. The most important solids are 316 stainless steel, A516 steel, 304 steel, HLW glass, commercial SNF, borated 316 stainless steel, and aluminum alloy. Degradation of these solids will alter the chemical composition of in-package fluids. The effect on pH depends on the

chemical composition of the particular solid, its mass, and its rate of dissolution. Dissolution of steels tends to cause pH to decrease; the magnitude of the decreases depends on the composition and degradation rate of the particular steel. Glass degradation causes increases in pH. Generally, one degradation process tends to dominate over individual time spans. Ultimately, influx of J-13 water causes in-package fluid to have a pH greater than 7. A secondary control over pH is the presence of degradation products (in particular, iron hydroxides from steel corrosion), which, when present, can buffer pH.

9.3.1.3.1 High-Level Waste Glass Degradation

The HLW degradation component developed for TSPA-SR (CRWMS M&O 2000 [DIRS 153246]) uses bounds on parameters of a phenomenological model to develop a simplified (Arrhenius-type) rate equation of degradation that is dependent only upon pH and temperature. Conservative estimates of the model parameters are based upon experimental data for the degradation of borosilicate glass (CRWMS M&O 2000 [DIRS 143420], Section 6.2).

Glass and mineral degradation rates tend to decrease with time (e.g., White et al. 1996 [DIRS 154473]). A more realistic treatment of glass degradation would implicitly account for the possibility of much lower rates. Therefore, for the purposes of sensitivity assessment, an uncertainty multiplier ranging from zero to one was used in the glass degradation model (BSC 2001 [DIRS 154840], Section 6.3). A lower end of zero corresponds to the case where formation of passivating alteration products completely halts dissolution. Rates may also drop with time because of dissolution of active surface sites and decreases in reactive surface area (e.g., White and Brantley 1995 [DIRS 154492]). The triangular distribution with a peak of 10^{-4} allows evaluation of the expected range of dissolution and is consistent with engineering judgement that the peak value is more likely than the bounds.

9.3.1.3.2 Steel Degradation Rates

The steel degradation rates used in the TSPA-SR in-package chemistry calculations were chosen to be high and, therefore, conservative, as discussed in *Effect of Waste Package Materials Surface Area and High-Level Waste Glass Reaction Rate on In-Package Chemistry* (BSC 2001 [DIRS 154840]). A more realistic range in rate equations for each steel type would be anchored at the low end by a value of zero and at the high end by the values used in *In-Package Chemistry for Waste Forms* (BSC 2001 [DIRS 153724]). The mechanistic explanation for the low end is the common observation of metallic components becoming coated by passivating oxide or hydroxide layers that might potentially halt corrosion by inhibiting the transport of reactants to, or products from, the metal interface (e.g., ASM International 1987 [DIRS 103753]). The long-term persistence of such iron oxides as magnetite at Yucca Mountain lends some credence to the picture of steel passivation. Moreover, the long-term persistence of such natural analogue metallic objects as josephinite, iron-nickel meteorites, and various iron artifacts suggest at least qualitatively that the values used in performance assessment are indeed high and consequently conservative. A series of scoping calculations were performed (see section that follows) to assess the impact of lower steel degradation rates on in-package chemistry.

9.3.1.3.3 Impact of Glass and Steel Degradation Unquantified Uncertainties on In-package pH

EQ6 calculations have been done to assess the impact of the degradation rate uncertainties on in-package chemistry, in particular on in-package pH (CRWMS M&O 2000 [DIRS 111880]; BSC 2001 [DIRS 153724]; BSC 2001 [DIRS 154840]). These calculations provide insight into the importance of input parameter uncertainty and the effect of heterogeneous flow and reaction inside the waste form on effluent chemistry. Since the S&ER (DOE 2001 [DIRS 153849]), two sets of calculations have been performed. The first set of calculations were performed to update the chemistry model with a new glass degradation model and focused on lower fluid flow rates (BSC 2001 [DIRS 153724]). The second set was performed to further explore the sensitivity of the pH on individual degradation rates (BSC 2001 [DIRS 154840]). The most important input parameters used in the three cases (S&ER, updated expected, and sensitivity cases) are summarized in Table 9-2. Details of other varied input parameters may be found elsewhere (BSC 2001 [DIRS 153724]; BSC 2001 [DIRS 154840]). Because the glass degradation functions are V-shaped with pH (DOE 2001 [DIRS 153849], Figure 4-104), they are evaluated here at pH = 2 and pH = 7 for comparison. For the sensitivity calculations, the effective dissolution rates (rate multiplied by surface area) of the metal components were lowered by an order of magnitude or the component was removed from the calculation. The rates for the glass were decreased by two, and four orders of magnitude, or the glass was removed.

The 10,000-year pH-trajectories calculated for the S&ER case are shown in DOE (2001 [DIRS 153849], Figures 4-100 and 4-101). The million-year pH-trajectories of the updated expected case and the sensitivity case are shown in Figures 9-1 through 9-4. The model results for the commercial spent fuel package for the S&ER and the updated expected cases (Figure 9-1) were abstracted for TSPA as sets of response surfaces of pH as a function of water flux, fuel exposure and steel corrosion rates. The pH ranges covered by these response surfaces are summarized in Tables 9-3 and 9-4. The model results for the codisposal package (Figure 9-2) showed little dependence on flow rate or DOE SNF fuel types. Consequently, these results were abstracted as ranges only for each time period (Figure 9-2, Table 9-5). Because the sensitivity cases included unphysical scenarios where components were removed, these abstractions were also only provided as uncertainty ranges (Table 9-5).

The abstraction of in-package pH has been considerably refined since the S&ER (DOE 2001 [DIRS 153849]) model. In particular, pH values have been abstracted into four time periods instead of the original two. The goal of the abstractions is to simplify the observed pH histories into a format that is compatible for implementation in TSPA while honoring the fundamental trends observed in the pH histories. The time discretization was chosen based on the analyst judgement of the magnitude of change in pH. For example, if all of the modeled scenarios were reaching low pH values over a specific time period, followed by a trend of increasing pH, a time division was inserted at that point of change. The pH criteria chosen for each time period are shown in the last column in Tables 9-4 and 9-5. These criteria were chosen based on whether all of the pH-time histories were trending toward minimum or maximum pH values during a particular time interval. Although this method only provides a coarse discretization of the pH-time history, it still honors the overall observed pH trends in the data.

The commercial spent fuel package results (Figure 9-1) show two pH lows, in the early time (about 1 to 50 years), and again in the period between about 10,000 to 200,000 years, that bracket a period of near neutral pH. These pH lows can be attributed to dissolution of carbon steel for the early time and 316 stainless steels for the latter. The carbon steel contains a small amount of sulfur, which is calculated to oxidize to sulfuric acid and drive the pH down. The 316 stainless steels contain a significant amount of chromium and molybdenum, which are calculated to liberate protons upon oxidation/hydrolysis. The period of neutral pH is facilitated primarily by the buffering by $Fe(OH)_3(s)$, which precipitated during dissolution of the carbon steel.

As in the commercial spent fuel packages, the carbon steel in the codisposal packages is calculated to drive the pH down at early times (Figure 9-2). After the carbon steel has been depleted, the pH steadily increases as high-level waste glass tends to dominate the effluent chemistry with release of several alkalinity generating species (e.g., sodium, potassium, phosphate, and borate).

The two sensitivity cases that have the most discernible impact are zero dissolution of A516 steel (Figure 9-3) and zero degradation of glass (Figure 9-4). In both cases, the minimum in-package pH tends to drop to between pH = 2 and pH = 3. For the first case, the pH drop occurs because in the absence of A516 dissolution, there is little accumulation of ferric hydroxides, which tend to buffer the in-package pH. For the zero glass degradation case, the pH drop occurs because the acid consumption, which would otherwise occur with glass degradation, cannot counter the acidity production that occurs from steel degradation. These two unlikely cases increase the abstracted uncertainty range from the updated expected case model to the sensitivity model.

9.3.1.4 Other Lines of Evidence to Support Models

Analogs (natural and other) were used to assess more realistic ranges for degradation rates for the steels and glasses (see Sections 9.3.1.3.2 and 9.3.1.3.1). As discussed in Section 7.3.2.4.2, steel analogs show remarkable phase stability.

Section 9.3.2.3 provides a qualitative discussion of pH trajectories observed in Argonne National Laboratory (ANL), spent nuclear fuel (SNF), and HLW tests, which are consistent with the first years of the much longer term pH ranges predicted by the in-package chemistry model.

9.3.2 Dissolved Concentrations

The goal of the dissolved concentration component is to predict concentrations of radioisotopes of interest as a function of fluid composition inside the waste form. Specifically, the solubilities of radionuclides that might affect dose were considered. The sources of information include EQ3/6 V7.2b simulations of in-package chemistry for three categories of radionuclides (CRWMS M&O 2001 [DIRS 154286], Section 6). Three radioisotope solubilities were abstracted as a function of in-package chemistry (neptunium, uranium, and americium), and three radionuclide solubilities (actinium, curium, and samarium) were set equal to that of americium. Four additional radioisotope solubilities were defined by probability distributions (plutonium, lead, protactinium, and nickel). The solubilities of the remaining screened-in radioisotopes were set at bounding values.

9.3.2.1 Identification of Unquantified Uncertainties

The radionuclides considered most important to dose and which are conservatively modeled in TSPA-SR (CRWMS M&O 2000 [DIRS 153246]) are thorium, neptunium, plutonium, and technetium. Uncertainties in the dissolved levels of these radioelements are associated with uncertainties in the thermodynamic data, in the assumed in-package oxygen fugacity (which has a profound effect on the solubilities of some radionuclides (Chen 2001 [DIRS 155247]), and in the identity of the concentration-limiting solid. Solubility calculations used to estimate dissolved concentration limits depend on assumed system boundary conditions (e.g., pH, carbon dioxide, and oxygen fugacity), a known set of chemical species, and reasonably precise thermodynamic relations describing equilibrium between them all. There are uncertainties associated with each of these quantities and with the assumption of thermodynamic equilibrium itself. The primary species identity uncertainty is mainly associated with the choice of what is to be the solubility-limiting solid phase. In the dissolved concentration AMR (CRWMS M&O 2001 [DIRS 154286]), the most soluble oxyhydroxide was conservatively assumed to control dissolved concentrations, and atmospheric oxygen levels were conservatively assumed to prevail. Over time though, soluble, hydrated minerals tend to dehydrate and become more crystalline and less soluble (CRWMS M&O 2001 [DIRS 154286], Section 6.5.2). Moreover, pooling of water, oxygen consumption by steel degradation, or the passivation of otherwise oxidizable surfaces by degradation products would tend to lead to local reduced zones inside the waste package. The unquantified uncertainty effort consequently focussed on these concentration-decreasing effects for the radionuclides of most concern to dose.

9.3.2.2 Quantification of Previously Unquantified Uncertainties

The accumulated unquantified uncertainties in dissolved radionuclide concentrations were constrained by setting the upper limit of dissolved levels to either the value set by the most soluble hydroxide phase in equilibrium with atmospheric levels of oxygen and ambient levels of carbon dioxide (10^{-3} bar) or, where no such phase exists, by inventory limits. The lower dissolved concentration limit was calculated by setting oxygen fugacities 40 log-units lower and letting dissolved levels of a particular radionuclide be set by the most stable solid phase(s) and calculating equilibrium concentrations from about $pH = 3$ to about $pH = 10$ (Chen 2001 [DIRS 155247]). The lower oxygen fugacity was chosen for the purposes of sensitivity studies to assess radionuclide solubilities that might be observed in natural waters under reducing conditions. Work focussed on thorium, technetium, and plutonium.

9.3.2.2.1 Thorium

The *Summary of Dissolved Concentration Limits* AMR (CRWMS M&O 2001 [DIRS 154286]) does not provide a thorium solubility range because of uncertainties in the nature and extent of thorium-carbonate complexation (Chen 2001 [DIRS 155247]). Instead, a fixed solubility of 10^{-5} mol/L (2.3 mg/L) was used in TSPA-SR (CRWMS M&O 2000 [DIRS 153246]).

Two thorium-carbonate species, $Th(CO_3)_5^{6-}$ and $Th(OH)_3CO_3^-$, were added to data0.ymp.R0, the qualified thermodynamic database (DTN: MO0009THRMODYN.001 [DIRS 152576]). Using this database and the EQ3NR software code from the EQ3/6 V7.2b code suite, thorium solubility in J-13-derived water was calculated (Chen 2001 [DIRS 155247]). The calculation assumes

$ThO_{2(am)}$ is the solubility-controlling mineral. The environmental conditions for the calculations are pH ranges from 3.4 to 9.8, $\log f_{CO2}$ ranges from -5.0 to -1.5, $\log f_{O2} = -0.7$, and temperature is 25ºC. The results have a maximum of 7.19×10^{-4} mol/kg (1.65×10^{2} mg/L) and a minimum of 2.74×10^{-9} mol/kg (6.3×10^{4} mg/L), with a geometric mean of 6.30×10^{-7} mol/kg (1.45×10^{-1} mg/L), which is about two orders of magnitude lower than the TSPA-SR (CRWMS M&O 2000 [DIRS 153246]) value of 1.0×10^{-5} mol/kg [2.3 mg/L]).

Because actinides tend to form many types of carbonate complexes (e.g., Langmuir 1997 [DIRS 100051]), it is possible that more thorium-carbonates will be reported. Less soluble, more stable thorium-bearing phases may form (Chen 2001 [DIRS 155247]) and limit the dissolved thorium concentrations to lower values. To establish the lower range of possible thorium concentrations, EQ6 calculations were done in which the most stable thorium-bearing phase (among the thorium phases given in the thermodynamic database) was considered (CO_2 fugacity was fixed at 10^{-3} bars). The results are plotted in Figure 9-5 along with the thorium solubility controlled by $ThO_{2(am)}$. The two solubility curves have similar shapes, and the most stable phase (thorianite) yields thorium solubility 4 to 6 orders of magnitude lower than that given by $ThO_{2(am)}$ (Figure 9-5). For pH less than 6, the difference is about 4 orders of magnitude, while for pH greater than 6, the difference is about 5.5 orders of magnitude.

The $ThO_{2(am)}$ curve (for $\log f_{CO2} = -3.0$) can be represented by Equation 9-1 (Chen 2001 [DIRS 155247]). Equation 9-1 describes predicted thorium concentrations (mg/L) as a function of solution composition and was derived by fitting individual EQ3NR predictions of dissolved thorium concentrations. Although the latter are calculated output, the thermodynamic parameters that are used in the individual calculations were derived largely from experimental measurements. Nevertheless, the model parameters (e.g., numerical coefficients and exponents) and their precision do not imply any specific mechanistic basis or particular level of process understanding. The expressions are not valid outside of the range of fluid compositions from which the model was derived. Note lastly that the same approach is applied subsequently for other radionuclides.

$$\log[\mathrm{Th}] = 11891 - 2781.5\mathrm{pH} + 354.02\mathrm{pH}^2 - 23.309\mathrm{pH}^3 + 0.62247\mathrm{pH}^4 - 26221/\mathrm{pH} + 23348/\mathrm{pH}^2 \quad \text{(Eq. 9-1)}$$

where [Th] is thorium solubility in mg/L. The uncertainty in thorium solubility associated with the controlling phase is accounted for based on the above equation. Specifically, moving this curve down 2 orders of magnitude gives the mean of thorium solubility (mg/L), with a term of plus-or-minus 2.0 to cover the ranges. That is (Chen 2001 [DIRS 155247]):

$$\log[\mathrm{Th}] = 11889 \pm 2 - 2781.5\mathrm{pH} + 354.02\mathrm{pH}^2 - 23.309\mathrm{pH}^3 + 0.62247\mathrm{pH}^4 - 26221/\mathrm{pH} + 23348/\mathrm{pH}^2 \quad \text{(Eq. 9-2)}$$

Equation 9-2 predicts thorium concentrations [Th] at high and low pHs to be higher than is physically realistic. Dissolved thorium levels will be limited by the absolute availability of solvating water molecules. An upper bound of 1 mol/L (2.3×10^{5} mg/L) is thus applied in addition to Equation 9-2. The upper bound for uranium, neptunium, and plutonium solubility is for the same reasons set at 1 mol/L (see below).

9.3.2.2.2 Technetium

Under oxidizing conditions, technetium is highly soluble (e.g., Langmuir 1997 [DIRS 100051]). Therefore, technetium levels are unlikely to be controlled by the formation of a technetium-containing solid. For TSPA-SR (CRWMS M&O 2000 [DIRS 153246]), technetium solubility is set to 1.0 mol/L (9.9×10^4 mg/L), which will allow the waste inventory to control its release. However, under reducing conditions ($\log f_{O2}$ = -40.7 bar), EQ6 calculations show that TcO_2 could precipitate and limit technetium solubility (Chen 2001 [DIRS 155247]). Over the pH range from 4.75 to 9.5, technetium solubility varies from 5.59×10^{-6} to 4.13×10^{-1} mol/kg (5.53×10^{-1} to 4.09×10^4 mg/L). A log-triangular distribution for technetium is proposed based on the judgement that oxidizing conditions are more likely than reducing conditions. The lower end of the distribution is, therefore, the minimum value of technetium calculated above: log [Tc (mg/L)] = -0.254, where [Tc] is the concentration of technetium. The distribution has a peak equal to its higher end (i.e., log [Tc] = (mg/L)] = 5).

9.3.2.2.3 Neptunium

For TSPA-SR (CRWMS M&O 2000 [DIRS 153246]), neptunium solubility was evaluated with the conventional solubility evaluation approach and Np_2O_5 was assumed as the solubility-controlling mineral (CRWMS M&O 2001 [DIRS 154286], Section 6.4.2). However, Np_2O_5 has not been identified in spent fuel dissolution experiments, nor have other neptunium pure phases been identified (CRWMS M&O 2000 [DIRS 146677], Section 6.7.2). Moreover, neptunium concentrations measured in spent fuel experiments are several orders of magnitude lower than the neptunium concentrations predicted by Np_2O_5 solubility model (CRWMS M&O 2001 [DIRS 154286], Figure 2). Neptunium release from spent nuclear fuel may not be controlled by dissolution of Np_2O_5 or other neptunium pure phases but by a different mechanism. Based on analyses of the crystal-chemical properties of the uranium-oxygen bond, neptunium-oxygen bond, and plutonium-oxygen bond, Burns et al. (1997 [DIRS 100389]) predicted that the substitutions $Pu^{6+} \leftrightarrow U^{6+}$ and (Np^{5+}, Pu^{5+}) $\leftrightarrow U^{6+}$ are likely to occur in most U^{6+} structures. Later, Buck et al. (1998 [DIRS 100388]) confirmed the prediction by transmission electron microscopy analyses of the corrosion products of spent fuel drip-tests. In that study, neptunium was found to be incorporated into dehydrated schoepite (Buck et al. 1998 [DIRS 100388]). However, the mechanism(s) for neptunium retention in spent fuel dissolution experiments were not firmly established. Retention of neptunium in the ANL drip experiments may be explained (CRWMS M&O 2000 [DIRS 146677], Section 6.7.2) by one or more of several factors, including:

- Incomplete oxidation of Np(IV) in the fuel to Np(V) under the experimental conditions in the ANL drip tests
- Coprecipitation of neptunium in U(VI) compounds
- Sorption of neptunium onto solid corrosion products or components of the fuel holder in the test vessel (or both)
- Ion exchange of neptunium species with cations in existing minerals (e.g., NpO_2^+ replacing Na^+ in Na-boltwoodite).

Pending clearer identification of the mechanism(s) responsible for neptunium release from spent fuel, an empirical neptunium solubility model, which is documented in a calculation (Chen 2001 [DIRS 155247]), has been developed for the sensitivity studies. The model defines a concentrating factor F_c to describe the solution ratios of neptunium to uranium compared to the ratios in spent fuel with which it is in contact:

$$F_c = \frac{(Np/U)_{solu}}{(Np/U)_{fuel}} \quad \text{(Eq. 9-3)}$$

which rearranges to:

$$[Np] = F_c (Np/U)_{fuel} [U] \quad \text{(Eq. 9-4)}$$

where Np is neptunium and U is uranium. Equation 9-4 links dissolved neptunium levels to dissolved uranium levels and the measured ratio of neptunium to uranium in the fuel, through a concentrating factor, F_c, determined from spent fuel dissolution experiments. Figure 9-6 shows F_c from the ANL drip tests (Chen 2001 [DIRS 155247], Figure 4) as a function of time. The solid lines are tests with ATM-103 fuel while the dashed lines are tests for ATM-106 fuel. Two significant features can be observed. First, in those four tests, F_c of neptunium fluctuates around 1.0; the geometric mean of F_c is about 1.0. Secondly, in the tests conducted to date, the highest F_c occurs in the first sample, and then F_c decreases and reaches the lowest value within 2 years. In other words, large transient variations in F_c occur primarily in the first 2 years and dampen with time.

Figure 9-6 shows that F_c of neptunium fluctuates around 1.0 and appears to dampen to 1.0 as time increases. The fact that F_c of neptunium fluctuates around 1.0 suggests that neptunium and uranium enter water congruently. This has been observed elsewhere, for example in Pacific Northwest National Laboratory Series 2 and Series 3 steady-state tests results (CRWMS M&O 1997 [DIRS 100348]), and in experiments conducted by the Spanish Nuclear Waste Program (Bruno et al. 1998 [DIRS 101565]). Incorporation of neptunium into uranyl minerals is the simplest explanation for this relation.

Using only long-term data (longer than 2 years) from the four drip tests (28 data points) (Chen 2001 [DIRS 155247]) suggests that F_c can be approximated using a normal distribution of $\log(F_c)$ with a mean of 0 and a standard deviation of 0.5. The ratio of neptunium/uranium in the fuel can be calculated from the average waste inventory (BSC 2001 [DIRS 154841], Table 34). After adjusting for decay of americium-241, $(\text{neptunium/uranium})_{\text{fuel}} = 0.00194$. Using schoepite as the uranium solubility-controlling mineral, uranium solubility (in mg/L) is represented as a function of pH, temperature, and fugacity of CO_2 (Chen 2001 [DIRS 155247]):

$$\log [U] = 7.9946 - 2.6963*pH + 0.42918*pH^2 - 1.6286*\log f_{CO2} + 9.5352e\text{-}3*T + 0.41613*pH*\log f_{CO2} - 5.1148e\text{-}3*pH*T - 2.1621e\text{-}3*\log f_{CO2}*T \quad \text{(Eq. 9-5)}$$

Combining values of F_c, (neptunium/uranium)$_{fuel}$, and the solubility of uranium, [U], the abstracted neptunium solubility for the sensitivity studies was calculated, letting log F_c have a normal distribution with a mean of 0 and a standard deviation of 0.5:

$$\log [Np] = 5.2806 - 2.6963*pH + 0.42918*pH^2 - 1.6286*\log f_{CO2} + 9.5352e\text{-}3*T + 0.41613*pH*\log f_{CO2} - 5.1148e\text{-}3\ pH*T - 2.1621e\text{-}3*\log f_{CO2}*T + \log F_c \quad \text{(Eq. 9-6)}$$

where [Np] is the neptunium solubility in mg/L.

Figure 9-6b compares abstracted neptunium solubility models with EQ3/6 calculation output and experimental data. The TSPA-SR abstraction (CRWMS M&O 2000 [DIRS 153246], Table 3.5-8) is shown as a solid pink line over the black crosses showing the EQ3/6 calculated values for the solubility of Np_2O_5 (CRWMS M&O 2000 [DIRS 143569], Table 14, third column, with units converted). This model was only valid for the pH range plotted. Revision 1 of this analysis (CRWMS M&O 2001 [DIRS 154286], Table 14) calculated the Np_2O_5 solubility over a larger pH range shown by the black circles. The sensitivity model presented in Equation 9-6 including plus and minus three standard deviations is plotted as red lines. These lines fall over the black squares showing the ANL experimental data from the spent fuel drip tests. Because this model is concave upward outside the range of data, and it includes a cap on the largest concentrations possible, it is valid for use at any pH within the TSPA sensitivity studies. The mean of the sensitivity model is up to four orders of magnitude lower than the TSPA-SR model at acid pHs, and the uncertainty has been increased by three orders of magnitude.

9.3.2.2.4 Plutonium

Despite numerous studies of plutonium solubility, the stabilities of many plutonium-containing solids remain poorly known. The most studied are PuO_2 and $PuO_2{\cdot}2H_2O_{(am)}$ (or equivalently $Pu(OH)_{4(am)}$, where am stands for amorphous). Solids precipitated from over-saturation experiments (CRWMS M&O 2001 [DIRS 154629], Section 6.1) have a dark green color, which is characteristic of Pu(IV) solid phases. X-ray diffraction data match the data reported for PuO_2. However, the diffuse and broad X-ray diffraction peaks suggest poor crystalline structures. Nonetheless, precipitates at higher temperatures (90ºC) have a sharper X-ray pattern than solids precipitated at lower temperatures. Therefore, the solubility-controlling minerals in these laboratory experiments are believed to be plutonium hydroxides and/or plutonium colloids, aging towards $PuO_2{\cdot}xH_2O$ (CRWMS M&O 2001 [DIRS 154629], Section 6.1). The value of X should vary from 2 to zero. For X = 2, it is $Pu(OH)_{4(am)}$, the amorphous end member. For X = 0, it is PuO_2(c) (where c refers to crystalline), the crystalline end member. Rai and Ryan (1982 [DIRS 112060]) reported that in 1,300 days, $^{238}PuO_2$(c) was found to convert to a less crystalline form of PuO_2, denoted as $PuO_{2(lc)}$, (where lc refers to less crystalline) due to α-decay of plutonium isotopes. That means the crystal structure of $PuO_{2(c)}$ may be damaged by α-decay and a less crystalline form of PuO_2 would control plutonium solubility. Because the thermodynamic properties of the less crystalline PuO_2 forms are unknown, it is not possible to use it as the solubility-controlling phase in plutonium solubility calculations. To be conservative, for the TSPA-SR (CRWMS M&O 2000 [DIRS 153246]), $PuO_2{\cdot}2H_2O_{(am)}$ was selected as the controlling solid for plutonium.

More realistic calculations of plutonium solubility require consideration of more crystalline, less hydrated plutonium solids and lower oxygen fugacities. Rai and Ryan (1982 [DIRS 112060]) observed that plutonium hydroxide gradually converted to anhydrous crystalline material; therefore, over geological time, plutonium hydroxides are expected to convert to $PuO_{2(c)}$. The calculation (Chen 2001 [DIRS 155247]) is conducted for J-13 derived water, and other environmental conditions considered are: pH from 5.0 to 9.8; log f_{CO2} from –5.0 to –1.5; log f_{O2} = -0.7; and temperature is at 25ºC. The results have a maximum of 3.6×10^{-2} mol/kg (8.6×10^{3} mg/L) and a minimum of 5.48×10^{-6} mol/kg (1.31 mg/L) with a geometric mean of 6.27×10^{-4} mol/kg (1.5×10^{2} mg/L). The results for log f_{CO2} = –3.0 are the top line with black circles plotted in Figure 9-7, and can be represented as function of pH:

$$\log[Pu] = 26.952 - 7.0629 \times pH + 0.49436 \times pH^2 \qquad \text{(Eq. 9-7)}$$

where [Pu] is plutonium solubility in mg/L. The solubility of $PuO_{2(c)}$, shown in Figure 9-7 has a similar pH-dependence to $PuO_2 \cdot 2H_2O_{(am)}$ but is 2 to 3 orders of magnitude lower.

Also shown in Figure 9-7 are plutonium solubilities estimated under reduced conditions (log f_{O2} = -40.7) for conditions where $PuO_{2(c)}$ (red squares) or $PuO_{2(am)}$ (green circles) controls solubility. Under these reduced conditions, plutonium solubilities are less dependent on pH and drop by six orders of magnitude.

Data from degradation of commercial spent nuclear fuel are also shown in Figure 9-7. The plutonium concentrations measured at ANL and PNNL overlap the values calculated under reducing conditions. These results suggest that in a potential repository at Yucca Mountain, plutonium concentration from spent fuel dissolution will be close to 1.0E-5 mg/L.

For the sensitivity studies, the uncertainties in plutonium solubility associated with the controlling phase and redox conditions are modeled with an equation similar to Equation 9-7, but with an uncertainty term (ε):

$$\log[Pu\ (mg/L)] = 20.952 - 7.0629 \times pH + 0.49436 \times pH^2 + \varepsilon \qquad \text{(Eq. 9-8)}$$

where ε is a random variable with a normal distribution, a mean of 0, and a standard deviation of 2. Figure 9-7b shows the abstraction for the sensitivity studies with plus or minus three standard deviations plotted on top of the data and calculations used in development of the abstraction. This range covers all of the experimental data, the theoretical concentrations from the amorphous solid in air, the crystalline material at log $f_{O2\ (atm.)}$ of –40.7, and honors the pH dependence in air. Because this model is concave upward outside the range of data, and it includes a cap on the largest concentrations possible, it is valid for use at any pH within the TSPA sensitivity studies. This abstraction has a lower mean and a wider range than the log-uniform distribution ($10^{-4.62}$ to $10^{+1.68}$ mg/L) used in the TSPA-SR (CRWMS M&O 2000 [DIRS 153246], Table 3.5-8) shown by the bar on the left side of Figure 9-7b.

9.3.2.2.5 Upper Bound Concentrations

Application of the dissolved concentration expressions for plutonium, uranium, neptunium and thorium beyond the pH regions in which they were calculated (typically between pH = 4 and

pH = 9) generally leads to the prediction of physically unattainable results. For this reason the dissolved concentration limits for these elements are capped at 1 mol/kg bound. The physical justification for the bounding value is illustrated using the case of plutonium levels being set by equilibrium with $PuO_2 \cdot 2H_2O$. Dilute water with a molecular weight of about 18 g/mole and a density of about 1 g/cm^3 (Lide 1991 [DIRS 131202], p. 6-10) contains about 55 moles of water in a liter (110 moles of hydrogen atoms, 55 moles of oxygen atoms). If every oxygen atom in solution were associated with a dissolved plutonium ion, there would be 27.5 moles of plutonium (neglecting changes in the specific volume of water). However at pH = 9 and above, plutonium forms a soluble carbonate species and each plutonium tends to be associated with 11 oxygen atoms, in which case the limiting plutonium concentration would be 5 mol/kg. Even 5 mol/kg is too high because water molecules will associate with other salts dissolved in the water as well. Consequently, substantially fewer water molecules will be available for association with dissolved plutonium. The limited supply of water in concentrated mixed solutions sets a physical upper bound approximated as 1 mol/kg (239,000 mg/L) for dissolved plutonium. A similar analogy was applied to bound the upper limit for dissolved levels of uranium (238,000 mg/L), thorium (230,000 mg/L), and neptunium (237,000 mg/L).

9.3.2.2.6 In-Package Sorption

At present, TSPA-SR (CRWMS M&O 2000 [DIRS 153246]) conservatively takes no account of sorption inside breached waste packages or along the transport pathway to the invert, allowing pure or mixed phase solubility to control the concentration of radionuclides leaving the package. In reality, plutonium, and to a lesser extent neptunium, sorb strongly and irreversibly to most minerals and in particular to iron hydroxides (Lu et al. 2000 [DIRS 154422]), the primary degradation product predicted to occur in waste packages. Irreversible sorption refers to the fraction of the initially sorbed contaminant that becomes embedded or buried in the host surface and no longer available for subsequent desorption followed by aqueous transport. K_ds describe radionuclide transport in only limited situations. Their present-day use is primarily a numerical convenience. Dozens of technical articles, presentations, and books have accumulated over the past half century pointing to the extreme association of bomb-pulse fallout with particle surfaces and the resulting sharp attenuation of plutonium transport in soil profiles (e.g., Brady et al. 1999 [DIRS 154421], Appendix E and F; Bunzl et al. 1995 [DIRS 154468]; Coughtrey et al. 1986 [DIRS 154494]; Coughtrey et al. 1983 [DIRS 132164]). These observations (i.e., fallout data, hazardous waste sites, and laboratory experiments) suggest that plutonium (and to a lesser extent neptunium) will sorb strongly to solid surfaces, and they will do so irreversibly (i.e., not by a K_d-type model), possibly never leaving the waste package and invert, except as colloids.

Pertechnetate, which is usually assumed to have a K_d of zero and is therefore estimated to contribute significantly to dose, may sorb on copper oxides, the most likely alteration product of copper rails beneath the waste package. Conservative neglect of in-package sorption in general, and irreversible sorption of plutonium and neptunium in particular, may dwarf all other conservatisms in waste form. For the sensitivity studies, in-package sorption was added as an additional control of radionuclide concentrations. Further discussion is presented in Section 10.

9.3.2.3 Other Lines of Evidence to Support Models

As noted in Section 9.3.1.4, SNF and HLW tests done at ANL constitute another line of evidence to support the model (CRWMS M&O 2000 [DIRS 131861]). The range of leachate chemistries observed in laboratory studies of aqueous corrosion of unirradiated UO_2 and commercial spent UO_2 fuel (commercial SNF) provides confidence that the potential water chemistries that are modeled to develop in breached waste packages are realistic. Such corrosion studies conducted at ANL are of two types: drip tests and batch tests. The drip tests are dynamic flow-through studies in which the solids being studied are exposed to periodic injections of tuff-equilibrated J-13 well water (EJ-13) at a flux low enough to allow precipitation of solid corrosion products (secondary phases). The batch studies expose crushed solids with relatively high surface areas (UO_2 and SNF) to small volumes of EJ-13 water. While the experimental conditions do not exactly match those modeled in the in-package chemistry calculation, the reactions affecting major element fluid compositions are the same in both, as are the broad trends observed.

A plot of dissolved uranium as a function of pH from the ANL drip and batch tests on unirradiated UO_2 and commercial SNF is displayed in Figure 9-8. Also shown in Figure 9-8 are thermodynamic stability fields for some U(VI) silicates and predominance fields for aqueous U(VI) species. Dissolved uranium and pH measured in the leachates fall within the range suggesting that uranium solids may play an important role in controlling uranium concentrations (and possibly pH), qualitatively similar to what is observed in the in-package chemistry calculations. Figure 9-8 illustrates the wide range of dissolved uranium concentrations and pH values that have been observed in the ANL drip and batch tests. Total dissolved uranium spans a range of more than six orders of magnitude, and pH values span a range of more than four log units.

9.3.2.3.1 Pure and Mixed-Phase Concentration Control

Neptunium–The potential influence that solid uranium(VI) corrosion products may have on dissolved radionuclide concentrations is currently under study. Microscopic examinations of radionuclide-bearing corrosion products taken from the ANL unsaturated drip and vapor tests on commercial SNF have shown that U(VI) solids may incorporate certain radioelements into their structures under the experimental conditions. Perhaps most notable among these discoveries is the identification of neptunium in the uranyl oxyhydroxide "dehydrated schoepite" that formed on commercial SNF that had reacted in humid air at 90ºC. To date, neptunium-bearing dehydrated schoepite has not been identified from any drip tests with spent fuel; however, dissolved uranium and neptunium concentrations appear to be correlated in the ANL drip experiments (Figure 9-9). This correlation has been suggested as indicating that neptunium-bearing U(VI) corrosion products help limit the concentration of dissolved neptunium in leachates from the ANL drip tests.

Technetium–Technetium is released at a nearly constant rate in the ANL high drip-rate tests, consistent with the hypothesis that technetium is not solubility-limited in those tests. Analyses of solid corrosion products indicate that technetium is not incorporated into U(VI) solids in significant amounts. Electron energy loss spectra of the uranyl silicate, β-uranophane, formed in one ANL high drip-rate tests, reveal only a trace amount of technetium in this U(VI) compound; however, technetium was close to the detection limit for electron energy loss spectra (Finn

et al. 1998 [DIRS 100392], p. 9), and uranophane is not believed to significantly limit the release of technetium in the ANL drip tests.

Plutonium–The cumulative release behavior of plutonium in the ANL drip tests, like those of the actinides uranium, neptunium, and americium, exhibits early rapid release followed by substantial slowing after approximately 1.5 years of reaction. This behavior is consistent with plutonium release being limited by saturation with a plutonium-bearing solid. Transmission electron microscope examinations have identified plutonium-rich amorphous solids on the surfaces of reacted fuel grains in the ANL tests, and these may explain plutonium release behavior in the drip tests. Over long times (100,000 years) plutonium may display geochemical behavior similar to that of thorium in natural waters and may precipitate in minerals analogous to naturally occurring thorium minerals.

9.3.3 Cladding

Since the 1950s, most commercial SNF has been clad in 600 to 900 μm of zircaloy, a zirconium alloy. This material was selected for reactor use because it is corrosion-resistant and has attractive neutronic properties. The cladding was not considered as a barrier to the release of radionuclides in early TSPAs. However, information has accumulated in the literature indicating that cladding plays a major role in delaying the release of radionuclides to the environment.

9.3.3.1 Goal of Model

Clad degradation modeling is currently used as the basis for extending the period of wet storage, for licensing dry storage facilities, and for licensing shipping cask for commercial SNF by the Nuclear Regulatory Commission (NRC). The zircaloy cladding is not an engineered barrier of the Yucca Mountain disposal system but rather is an existing characteristic of the commercial SNF that is important to determining the rate of release of radionuclides once the waste package has breached. For TSPA-VA (CRWMS M&O 1998 [DIRS 100362], Section 6.3.1.1), several cladding degradation modes were combined into a time-varying function to evaluate failure.

The commercial SNF cladding degradation component is potentially important in reducing the peak dose because it restricts the amount of commercial spent fuel that is exposed to water and available for dissolution. Inventories of the two most important commercial SNF radionuclides in the nominal scenario, technetium-99 and neptunium-237, represent over 86 percent and 95 percent of the total inventory of these nuclides in the repository, respectively. Hence, the commercial SNF cladding degradation component can directly influence the peak dose by reducing the release of rate of these two radionuclides. The goal of the commercial SNF cladding degradation component is to determine the quantity of commercial SNF matrix that is exposed and, thereby, ready for radionuclides to dissolve into any available water.

9.3.3.2 Identification of Unquantified Uncertainties in Total System Performance Assessment for Site Recommendation

For TSPA-SR (CRWMS M&O 2000 [DIRS 153246]), two steps of cladding degradation were included, perforation and unzipping. The perforation of the cladding was modeled to occur because the cladding:

- Is damaged (initial perforations) before being received at the potential repository (during reactor operation and storage, dry storage, or transportation periods)
- Experiences creep rupture or stress corrosion cracking (SCC) during dry storage or initial disposal in the repository
- Experiences localized corrosion over time
- Experiences mechanical damage because of shaking from earthquakes or crushed by rock overburden.

Once perforated, the cladding may split along the axis (unzip) because the underlying uranium dioxide oxidizes further to uranium minerals that take up much more volume.

Some aspects of cladding perforation were evaluated using available data and therefore were realistic in TSPA-SR (CRWMS M&O 2000 [DIRS 153246]). However, many aspects of cladding perforation and unzipping were simply bounded.

The cladding degradation component of the model samples six parameters for the TSPA-SR (CRWMS M&O 2000 [DIRS 153246]). These parameters are represented by mathematical distributions covering the expected range of values of the parameter. The parameters used are:

- The number of rods initially perforated in a commercial SNF waste package
- The fraction of cladding perforated because of creep rupture and stress corrosion cracking
- The uncertainty in localized corrosion rate
- Uncertainty in mechanical damage (seismic). Rock overburden failures have been added for sensitivity calculations since the TSPA-SR model
- The uncertainty of the commercial SNF degradation rate
- The uncertainty in the unzipping velocity of the cladding, which represents the uncertainty in the surface area of the commercial SNF matrix inside the cladding that is available for degradation.

In TSPA-SR (CRWMS M&O 2000 [DIRS 153246], Section 3.5.4), the parameters that show importance in determining uncertainty in the dose in the first 100,000 years are those associated with initial cladding perforation and the unzipping velocity of the cladding. This is because in

this model the only cladding perforated is that initially perforated (i.e., as received) in that time period. However, between 100,000 years and 1,000,000 years, localized corrosion and mechanical damage perforation of the cladding become important. Predictions past the regulatory period are needed to address peak dose issues for the Environmental Impact Statement. During this period, uncertainties in two parameters show up as important: the order of magnitude uncertainty in the commercial SNF degradation rate and the two orders of magnitude uncertainty in the unzipping rate (i.e., active surface area).

Waste package temperature is treated as an independent variable in the cladding model and the lower temperature design does not affect the model.

9.3.3.3 Quantification of Previously Unquantified Uncertainty

Table 9-6 lists the primary uncertainties that were considered in TSPA-SR (CRWMS M&O 2000 [DIRS 153246], Section 3.5.4) and subsequently.

9.3.3.3.1 Initial Cladding Perforation

The TSPA-SR (CRWMS M&O 2000 [DIRS 153246]) uncertainty on the percentage of cladding initially perforated is a triangular distribution with a mode of 0.0948 percent and range between 0.0155 percent and 1.285 percent. This upper range was determined by assuming that around any rod, the four closest were also damaged. The lower range was determined by assuming the distribution was symmetrical. The assumption that the upper limit is a factor of four is conservative since this represents all of the surrounding rods. A triangular distribution is proposed based on engineering judgement that the most likely percentage of perforated clad is well known and more likely than the upper and lower bounds. No refinement of this uncertainty is considered at this time.

9.3.3.3.2 Creep and Stress Corrosion Cracking Perforation

The TSPA-SR (CRWMS M&O 2000 [DIRS 153246]) repository design is cool enough that little or no creep rupture or stress corrosion cracking perforation are expected in the potential repository. The conservative creep model used in TSPA-SR, however, predicted failures during dry storage. This model used an unirradiated creep correlation for irradiated cladding and a lower-limit failure criteria of 0.4 percent creep strain. The percent failure range was defined as a triangular distribution, with a mode of 2.44 percent and mean of 7.5 percent and a range between 1.05 percent and 19.4 percent. A revised calculation (CRWMS M&O 2001 [DIRS 151662], Section 6.2) used an irradiated cladding creep correlation and the NRC recommended lower limit creep failure criteria of 1 percent creep strain (NRC n.d. [DIRS 147797]). This revised calculation does not predict creep failures during vacuum drying, dry storage, or in the repository with lower waste package temperatures. It does predict an upper limit of 0.47 percent of the rods failing from SCC. Based on these new calculations, a more realistic range between 0 percent and 0.5 percent with a uniform distribution was chosen for the sensitivity calculations (CRWMS M&O 2001 [DIRS 151662], Section 6.2.5).

9.3.3.3.3 Localized Corrosion Perforation

The conditions necessary for localized corrosion of zircaloy are not predicted to occur in the in-package bulk solutions but have not been ruled out for localized and/or non-equilibrium effects such as microbially induced corrosion, galvanic coupling, radiolysis, or extreme concentration by evaporation. Because the probability of damage from any of these mechanisms is difficult to quantify, a simplified model was utilized for TSPA-SR (CRWMS M&O 2000 [DIRS 153246]). This model assumes the amount of localized corrosion of the cladding is proportional to the amount of water that seeps into the waste package because most of these effects require seepage. A log-uniform distribution from 0.0041 to 0.41 percent localized failure per m^3 water seeping into the waste package was used. Although this model is generally conservative, it does not predict perforation from localized corrosion in packages that do not have water seeping into them. Thus, for about 87 percent of the waste packages (CRWMS M&O 2000 [DIRS 153246], Section 4.1.2), the intact cladding (i.e., cladding not initially damaged in the reactor or during dry storage) will not perforate until mechanically damaged.

To test the sensitivity of the peak dose on the localized corrosion model, the range of this simple model was lowered about an order of magnitude with greater probability in the low range (Table 9-7). In addition, a minimum failure rate of about 10^{-9} of the rods/year was added for the packages without seepage.

9.3.3.3.4 Seismic Failures

For modeling perforation by shaking during earthquakes, TSPA-SR (CRWMS M&O 2000 [DIRS 153246]) used a bounding model, which perforated all cladding whenever large ground motion (frequency less than 1.1×10^{-6} per year) was sampled to occur. To test the sensitivity of TSPA to this parameter, the complementary cumulative distribution function for the frequency of seismic cladding failure (Table 9-8) was used.

9.3.3.3.5 Rock Overburden Failures

In TSPA-SR (CRWMS M&O 2000 [DIRS 153246]) calculations, the cladding was protected from rock falls or rock overburden by the drip shield and waste package during the regulatory time period of 10,000 years. For the sensitivity calculations, damage to cladding from rock fall or rock overburden was added for the period when the waste package no longer protects the cladding. After severe degradation of the drip shield and waste package, the static load of the overburden resting on the cladding within areas of the waste package that have structurally failed, have been conservatively modeled and calculated to breach (CRWMS M&O 1999 [DIRS 136105], Section 5.3). In the sensitivity model, the cladding perforation from rock overburden starts to occur when 50 percent of the modeled waste package surface area has been corroded through by generalized corrosion. The fraction of breached cladding increases linearly with the fraction of the waste package that is corroded until all cladding is breached when the entire waste package has been corroded by general corrosion.

9.3.3.3.6 Cladding Unzipping

In TSPA-VA (CRWMS M&O 1998 [DIRS 108000]), most of the radionuclide inventory in a rod was assumed available for dissolution once the cladding on a rod was perforated. For TSPA-SR

(CRWMS M&O 2000 [DIRS 153246]), only the fast release fraction (gap inventory and initial fuel dissolution) is modeled to be available at initial perforation. The remaining inventory is made available only as the cladding splits open, thus representing a more realistic approach. A simple model based on swelling of the fuel was developed, which predicted the splitting rate to be 40 times the intrinsic dissolution velocity (uncertainty is triangular shape 1, 40, and 240 times).

For the sensitivity calculations, the distribution of the unzipping velocity has been reevaluated and summarized (CRWMS M&O (2001 [DIRS 151662], Section 6.6.1; see also Table 9-9). The lower limit is set at the intrinsic dissolution velocity (velocity multiplier = 1). This is equivalent to the fuel being dissolved at the intrinsic dissolution velocity at the face of the pellets and propagate axially along the fuel rod. The upper range, 15,000 times the intrinsic dissolution velocity, is introduced to represent axial splitting of the cladding in an anoxic environment. This type of unzipping has occurred in an ANL fuel dissolution test with clad fuel (Cunnane 2001 [DIRS 154818]). It is occasionally observed in boiling water reactors (BWRs) (Edsinger 2000 [DIRS 154433]; Lysell et al. 2000 [DIRS 154432]) and is associated with oxygen starvation and the collection of hydrides in the cladding leading to a type of delayed hydride cracking. This type of unzipping is quick, exposing the pellets in tens of days. Armijo (1994 [DIRS 154411], p. 411), reports that axial splitting occurs in 22 percent of the 48 failed BWR rods that he studied. For the sensitivity model, it is assumed that oxygen starved conditions, similar to BWR conditions, are generated in all waste packages for a short time. A probability of 22 percent is assumed for all the failed rods to unzip quickly. When this occurs, the pellets are available to dissolve using a surface area for irradiated pellets developed by Barner (1985 [DIRS 109194], Table 4.6, p. 4.16). Bare fuel has an equivalent wet unzipping velocity multiplier of 15,000.

9.3.3.3.7 Thermal Operating Mode

The behavior of the cladding within the repository is not expected to differ significantly between a low and high temperature-operating mode as long as the cladding temperature limit of 350°C is not exceeded. The revised *Clad Degradation - Summary and Abstraction* AMR (CRWMS M&O 2000 [DIRS 147210], Section 6.2.4 and Figure 14) shows that with the cladding below 350°C, cladding failure is not expected. There are some secondary temperature effect included in the abstraction. The waste form dissolution rate is weakly temperature dependent and is included in the cladding unzipping calculation. This feedback only occurs after water ingression into the waste package. The waste package temperature is treated as an independent variable in the cladding degradation abstraction (CRWMS M&O 2000 [DIRS 147210], Attachment I). This abstraction is applicable for a hot (backfill) design such as that considered in TSPA-VA (CRWMS M&O 1998 [DIRS 108004]), the TSPA-SR (CRWMS M&O 2000 [DIRS 153246]) warm design, and any future cool repository design.

9.3.3.4 Other Lines of Evidence to Support Model

The direct and indirect evidence that supports the various features of the DOE cladding degradation model can be found in the extensive experimental literature on zircaloy and zirconium. Earlier studies (Ahn et al. 1999 [DIRS 135894]; Henningson 1998 [DIRS 112089]; Manaktala 1993 [DIRS 101719]; Pescatore et al. 1990 [DIRS 101230]; Rothman 1984 [DIRS 100417]) evaluated cladding degradation under repository conditions. Others

(Cunningham et al. 1987 [DIRS 101591]; Einziger and Kohli 1984 [DIRS 101605]; Peehs 1998 [DIRS 109219]) evaluated fuel performance under dry storage conditions similar to early repository conditions. As part of the development of U.S. Environmental Protection Agency environmental standards, S. Cohen & Associates (1999 [DIRS 135910]) did a detailed study of cladding degradation, before receipt at, and emplacement in, a potential repository. Sanders et al. (1992 [DIRS 102072]) reviewed the condition of cladding after reactor operation and reviewed the potential of damage from external mechanical loading. Experiments (Wilson 1985 [DIRS 102147]; Wilson 1987 [DIRS 102150]; Wilson 1990 [DIRS 100793]) also measured the releases of radionuclides from damaged cladding under possible repository conditions. The latest TSPA by the Electrical Power Research Institute (EPRI 2000 [DIRS 154149]) included cladding degradation. Other sources address specific degradation mechanisms. An International Atomic Energy Agency report (IAEA 1998 [DIRS 150560]) summarizes work on water side corrosion and gives 538 references and a bibliography of 45 books. Cox (1990 [DIRS 152954]) summarizes the pellet-clad work (235 references). Cox (1990 [DIRS 152778]) also summarizes the stress corrosion cracking work (106 references).

9.3.4 Colloids

9.3.4.1 Goal of Model

The goal of the colloid model is to quantify the impacts of uncertainties in the behavior of colloids generated from the degradation of HLW glass, commercial SNF, and DOE SNF, as well as colloid-facilitated transport of radionuclides from the waste package. It is anticipated that colloids will also be mobilized as a result of corrosion of waste package components, in addition to the degradation of HLW and SNF waste forms. The abundance of colloids within the breached waste package will depend on the extent of waste form alteration and the nature of the alteration products formed.

Colloid abundance and stability also depend on many environmental factors, including the ionic strength, pH, cation concentrations, colloid content of groundwater entering the waste package from the drift, presence of fulvic and humic acids, and microbe fragments (CRWMS M&O 2001 [DIRS 153933], Section 1.0). Suspended colloids may subsequently flocculate and settle by gravity, be chemically or mechanically filtered, or dissolve. If environmental factors change, colloids may be peptized; colloid-sized particles may precipitate; or other natural processes may occur. In addition, colloids may sorb readily at the interfaces between air and water in rocks and engineered barriers and, depending upon the degree of saturation of the porous medium as well as its configuration, may be retarded, immobilized or transported (CRWMS M&O 2001 [DIRS 153933], Section 6.1.5). These issues are of concern within the engineered barrier system in the drift and in the near- and far-fields (CRWMS M&O 2001 [DIRS 153933], Section 6.1.5). They are relevant as well to transport within the waste package. The colloid source term is defined here as the total of those radionuclides associated with colloids that: are mobilized at the surface of the waste form, are transported within the waste package to the waste package wall, leave the waste package at a breach (or breaches) in the waste package wall, and enter the drift. The present discussion is restricted to the in-package portion of the potential repository system.

9.3.4.2 Identification of Unquantified Uncertainties Total System Performance Assessment for Site Recommendation

To begin with, large-scale uncertainties burden the collective understanding of colloidal fate and transport. For the colloidal radioisotope concentration component, the conceptualization used YMP-relevant experimental results from YMP-specific work and from the published literature as summarized in *Waste Form Colloid-Associated Concentrations Limits: Abstraction and Summary* (CRWMS M&O 2001 [DIRS 153933], Section 6.1). The conceptualization identified the availability and the stability of three categories of colloids: existing colloids in the groundwater, colloids generated during degradation of the waste form, and colloids generated during degradation of the waste package. A number of unquantified uncertainties were identified in the TSPA-SR (CRWMS M&O 2000 [DIRS 153246]) and subsequently. They can be roughly grouped as pertaining to: amounts of colloids available, nature and extent of sorption to colloids, and colloid retardation. Generally, in TSPA-SR, uncertainties were addressed by following bounding approaches and choosing conservative inputs and/or conceptual models. A number of uncertainties, bounding assumptions, and conservatisms are outlined below.

9.3.4.2.1 DOE Spent Nuclear Fuel Degradation Colloids

The potential for colloid-facilitated migration of radionuclides derived from the degradation of metallic uranium fuel is not considered in the current colloid model and will be addressed by ongoing laboratory experiments. Preliminary unpublished results from the experimental degradation of metallic uranium fuels indicate that the fuel degrades rapidly, to generate fine particles, some of them colloidal in size (CRWMS M&O 2001 [DIRS 153933], p. 33, Section 6.1.1.1).

9.3.4.2.2 Commercial Spent Nuclear Fuel Degradation Colloids

The uncertainty associated with the potential contribution of irreversibly attached radionuclides on colloids generated from commercial SNF degradation will be addressed by ongoing laboratory experiments. The only existing data on irreversibly attached plutonium concentrations are from those generated from the degradation of defense high level waste (HLW) glass (CRWMS M&O 2001 [DIRS 154071], Table 4); data from commercial SNF have been inconclusive because insufficient numbers of colloids have been collected from degradation experiments (CRWMS M&O 2001 [DIRS 154071], pp. 31 to 36).

9.3.4.2.3 Air-Water Adhesion

Colloids adhere strongly to the interface between air and water, such as thin films and bubbles (CRWMS M&O 2001 [DIRS 153933], Section 6.1.5). The analysis of this important process is site specific (i.e., must be tailored specifically to the system under investigation) and can be quite complex. Leaving colloid sorption onto the air-water interface out of the colloid model is likely conservative. Adhesion to a fixed interface (e.g., as part of a water film on a component in the waste package) would serve to immobilize the colloid as long as the interface remained intact. Adhesion to the surface of a freely suspended bubble, on the other hand, would enable the colloid to be transported with the bubble, although the relatively large size of the bubble may

cause it to become filtered out at constrictive passageways. Air-water interface adhesion of colloids is neglected in the present model.

9.3.4.2.4 Waste Package Retardation

Colloid retardation in the waste package is ignored. The development of defensible parameters describing retardation of colloids in the waste package is challenging because of uncertainty in the detailed nature of flow paths and pore structures. Changing ratios of divalent to monovalent cations along this initial flow path might also cause destabilization of colloids (e.g., Stumm and Morgan 1996 [DIRS 125332]).

9.3.4.2.5 Microbes

Microbial effects have been ignored. These effects might include: organic coatings on mineral colloids, which would tend to sorb radionuclides as well as destabilize the colloid suspension and cause the colloids to agglomerate, and development of colloids comprised of monocellular microbes and fragments, which could sorb and transport radionuclides and/or agglomerate and immobilize radionuclides (CRWMS M&O 2001 [DIRS 153933], Section 6.1.8). Thus, either of two competing processes, one that encourages colloid mobilization, another that encourages colloid agglomeration and flocculation, may prevail. It is uncertain which process would dominate at a particular location or point in time within the repository. Microbial effects are discussed at greater length in Section 10.

9.3.4.2.6 Temperature

Thermal effects on colloidal transport are largely unknown, but colloid stability is generally expected to decrease with increasing temperature. Actinide and metal sorption onto metal hydroxides colloids tends to increase with temperature paralleling temperature-dependent increases in metal hydroxide anionic surface charge (Machesky 1990 [DIRS 145046]). K_ds of uranium, neptunium, plutonium, and americium on hematite, montmorillonite, and silica increase roughly one order of magnitude as temperature increases from 20º to 80ºC in J-13 well water for 10-day runs (Lu et al. 2000 [DIRS 154422]).

9.3.4.2.7 Mineralogy

In TSPA-SR (CRWMS M&O 2000 [DIRS 153246]), the properties of groundwater colloids flowing into the drift are assumed to be bounded by smectite. Other colloids may be present, including silica, zeolites, feldspars, iron-(hydr)oxides, etc. Smectite has a higher affinity for radionuclides than many of these other minerals, and, therefore, this assumption may overestimate colloidal uptake of radionuclides and be conservative. Information on colloid mineralogy collected from YMP-area wells may justify use of a mixture of mineralogies including less sorptive minerals (e.g., silica). A preliminary review of data presented in Lu et al. (2000 [DIRS 154422]) suggests that while K_d values for plutonium and americium sorption are generally higher for montmorillonite than silica, the difference is less than one order of magnitude. For TSPA, it is critical that enough different colloids are modeled to capture the overall behavior of the system. The waste form and waste package degradation product colloids, and the uncertainty associated with their parameters (formation, abundance, and sorption), might outweigh any uncertainty in the groundwater colloid parameters.

9.3.4.2.8 Steel Degradation Colloids

Degradation of waste packages will generate large quantities of iron hydroxides that may collectively constitute the most significant source of colloids in the system. Although the nature and reactivity of these colloids is discussed in greater detail in Section 10, a number of the implications of waste form colloidal export will be touched on below.

9.3.4.2.9 Consideration of Radionuclides Other than Plutonium and Americium

In the current waste form degradation model americium is assumed to behave similarly to plutonium (i.e., may be incorporated into a colloid as irreversibly attached). The quantities of plutonium and americium irreversibly attached to colloids are determined at each time step in TSPA by the radionuclide inventory remaining at each time step (CRWMS M&O 2001 [DIRS 153933], p. 51).

In the current colloid model, plutonium and americium are treated as irreversibly attached to waste form colloids. These two radionuclides were considered potentially the most significant sparingly soluble radionuclides that could readily become irreversibly attached to colloids and subsequently be transported from the waste package. In addition to plutonium and americium, two other radionuclides, protactinium and thorium, are considered for reversible attachment to waste form colloids and subsequent transport. The fractions of release from colloids associated with other dose-important radionuclides are considered insignificant relative to their dissolved concentrations.

9.3.4.3 Quantification of Previously Unquantified Uncertainty

9.3.4.3.1 Combined Groundwater and Corrosion Colloid Concentrations

Limited data exist for concentrations of iron-(hydr)oxide colloids in natural systems. At the Morro de Ferro natural analogue site (Poços de Caldas, Brazil) concentrations of iron-hydroxide [$Fe(OH)_3$] colloids were measured in deep groundwaters adjacent to an iron-rich rock body (CRWMS M&O 2000 [DIRS 150707], Section 3.8.2.3.1). The measured concentration, 0.25 mg/L, is similar to concentrations of other inorganic colloids found in natural waters at other deep sites (CRWMS M&O 2000 [DIRS 150707], Section 3.8.2.3.1). The upper end of the range used, 1.0 mg/L, imparts a four-fold conservatism relative to the concentration observed at the analogue site.

There are more abundant measurements of groundwater colloid concentrations than there are of corrosion colloid concentrations. Consequently uniform distributions were ascribed to a combined population of groundwater and corrosion colloids for two different ionic strength ranges. Reasonable ranges for this combined reversible colloid population are log uniform distributions between 10^{-6} and 10^{-1} mg/L (for ionic strength less than or equal to 0.05) and 10^{-9} and 10^{-3} mg/L (for ionic strength greater than 0.05 M).

9.3.4.3.2 Plutonium Irreversibly Associated with Waste Form Colloids

Reasonable distributions for plutonium irreversibly associated with waste form colloids are log-uniform distributions between 10^{-11} and 10^{-6} mol/L (for ionic strength less than or equal

to 0.05 M) and 10^{-14} and 10^{-8} mol/L (for ionic strength greater than 0.05 M). The upper range is roughly centered on the bounding concentration of 8×10^{-8} mol/L defined in CRWMS M&O (2001 [DIRS 153933], Figures 7 and 13). The minimum value is approximately four orders of magnitude lower. The maximum value of the distribution, 10^{-4}, is approximately three orders of magnitude greater. Similarly, the lower range is centered on the minimum concentration measured experimentally, 10^{-11} mol/L (CRWMS M&O 2001 [DIRS 154071], Table 4, p. 20). The minimum and maximum values of the higher ionic strength range are then plus-or-minus 3 orders of magnitude from 10^{-11} mol/L.

9.3.4.3.3 Colloid Sorption of Plutonium and Americium

A recent review of the data presented in *Waste Form Colloid-Associated Concentrations Limits: Abstraction and Summary* (CRWMS M&O 2001 [DIRS 153933], Attachment XVI) and in Lu et al. (2000 [DIRS 154422]) corroborates the currently used K_d values for plutonium and americium sorption (10^4 and 10^5 ml/g respectively) for sorption onto montmorillonite (proxy colloid mineral for waste form and groundwater colloids). In contrast, a preliminary review of the Lu et al. (2000 [DIRS 154422]) data suggest that the currently used K_d values for iron-(hydr)oxides (proxy colloid mineral for steel corrosion colloids) may be underestimated by as much as one to two orders of magnitude. One factor that may contribute to overly conservative K_d values is that materials used in the Lu et al. (2000 [DIRS 154422]) experiments probably optimize measurements of sorption, because they provided fresh, clean surfaces for actinide attachment, which would not likely be the case in the potential repository environment. Furthermore, the studies considered did not evaluate the impact of other solutes (including less critical radioisotopes) regarding competition for radionuclide uptake (the exception is the Lu et al. (2000 [DIRS 154422]) sorption determinations for a range of ionic strengths; only the monovalent cation Na^+ was used in the solutions). These accumulated uncertainties are reflected in the recommended log-normal distribution of the K_d describing plutonium and americium sorption, namely a mean of 10^5 ml/g with a geometric standard deviation of plus-or-minus 2 log units.

9.4 SUMMARY AND PARAMETERS PROVIDED TO TOTAL SYSTEM PERFORMANCE ASSESSMENT FOR SENSITIVITY CALCULATIONS

The preceding sections outline the quantification of waste form model uncertainty since the TSPA-SR (CRWMS M&O 2000 [DIRS 153246]). Some of the sections (e.g., in-package sorption and colloidal transport) are treated in greater detail in Section 10. Complementary information is provided here to emphasize the integration among the sub-components. The new waste form models and parameters provided to TSPA for the sensitivity calculations are summarized here.

9.4.1 In-Package Chemistry

Two new in-package chemistry models were developed for TSPA: an updated expected case and a sensitivity case. The updated expected model has been implemented in TSPA for the supplemental studies, but the sensitivity model is presented for insight only. For the commercial SNF packages, the pH-time trajectories are abstracted using response surfaces for four time periods (BSC 2001 [DIRS 154620]) and are summarized in Section 9.3.1.3.3. The pH-time

trajectories for the codisposal packages were abstracted into four ranges (Table 9-5, first two columns). These models cover pH ranges similar to the TSPA-SR models, but provide better time discretization.

9.4.2 Dissolved Concentrations

New solubility models were provided for thorium (Equation 9-2), neptunium (Equation 9-6), plutonium (Equation 9-8), and technetium (a log-triangular distribution from 0.56 to a peak of 10^5 mg/L). In all four cases, the mean solubility was lower, and the distribution was larger, than in the TSPA-SR.

9.4.3 Cladding

Changes in the cladding models are discussed in Section 9.3.3.3 and summarized in Table 9-6. The most important changes are the lowering of initial failures due to creep during dry storage and the addition of late time rock load breaching.

9.4.4 Colloids

The colloid model was simplified, and the uncertainty ranges were expanded in the supplemental studies (see Section 9.3.4.3). The groundwater and corrosion product colloids were combined to provide a single colloid type with reversible radionuclide attachment. Over 5 orders of magnitude of uncertainty were added to the concentration of this colloid type. The new ranges were log-uniform distributions between 10^{-6} and 10^{-1} mg/L (for ionic strength less than or equal to 0.05 M) and 10^{-9} and 10^{-3} mg/L (for ionic strength greater than 0.05 M). Instead of using separate K_ds for each radionuclide, a single K_d for reversible sorption of plutonium, americium, protactinium, and thorium was defined. This K_d was chosen in the high range from the earlier modeling but with a broader uncertainty range. A log-normal distribution with a geometric mean of 10^5 ml/g and a geometric standard deviation of 2 log units was chosen.

Approximately 5 orders of magnitude of uncertainty were added to the modeled concentration of irreversibly attached plutonium. The new ranges were log-uniform distribution between 10^{-11} and 10^{-6} mol/ L (for ionic strength less than or equal to 0.05 M) and 10^{-14} and 10^{-8} mol/L (for ionic strength greater than 0.05 M). The concentration of irreversibly attached americium was calculated in proportion to its inventory relative to plutonium.

Table 9-2. Important Input Parameters for the Impact of Glass and Steel Degradation Unquantified Uncertainties on In-package pH Calculations

Model	Parameter	High	Medium	Low	None
Science and Engineering[a]					
	A516 rate (μm/yr)	72		7	
	flow rate (L/yr)	150	15	1.5	
	fuel exposed	0.99	0.8	0.01	
	glass rate (pH=2) (μm/yr)	36		3.6	
	glass rate (pH=7) (μm/yr)	0.007		0.0007	
Updated Expected Case[b]					
	A516 rate (μm/yr)	72		7	
	flow rate (L/yr)	15	1.5	0.15	
	fuel exposed		0.1	0.01	
	glass rate (pH=2) (μm/yr)	0.5			
	glass rate (pH=7) (μm/yr)	0.007			
Sensitivity[c]					
	A516 rate (μm/yr)	72		7[d]	0
	flow rate (L/yr)			0.15	
	fuel exposed			0.01	
	glass rate (pH=2) (μm/yr)	5.00E-01	5.00E-03	5.00E-05	0
	glass rate (pH=7) (μm/yr)	7.00E-03	7.00E-05	7.00E-07	0

Source: [a] CRWMS M&O 2000 [DIRS 111880], Table 1 and p. 17 with units converted.
[b] BSC 2001 [DIRS 153724], Table 2 and p. 20 with units converted.
[c] BSC 2001 [DIRS 154840], Tables 1, 2, and 3 with units converted.
[d] Effective rate decreased by decreasing surface area.

NOTE: Glass and metal dissolution units were converted from mol/cm^2·s to μm/yr by multiplying by the defined molecular weight of 100 g/mol, dividing by the density (A516 = 7.86 g/cm^3; glass = 2.85 g/cm^3), and multiplying by 10^4 μm/cm, and 3.1558×10^7 seconds/year.

Table 9-3. Total System Performance Assessment Model Results for pH Ranges

Total System Performance Assessment Model		
Time Period (years)	**Process Model Range for CSNF**	**Process Model Range for Codisposal**
0-1,000	3.4-5.5 (minimum pH) (a)	4.8-6.4 (minimum) (c)
1,000 – 1,000,000	5.7-7.3 (average pH) (b)	8.1-10.0 (maximum) (d)

Source: CRWMS M&O 2000 [DIRS 129287], (a) Tables 2 and 3, (b) 4 and 5, (c) 7 and 9, and (d) 10 and 11.

Table 9-4. Model Results for Commercial Spent Fuel Package pH Ranges

New CSNF Package Models			
Time Period (years)	**Updated Expected Case Process Model[a]**	**Sensitivity Abstraction[b]**	**pH Criteria**
0-200	3.9-6.7	4.4-6.7	Minimum
200 - 10,000	6.0-7.3	4.3-7.5	Average
10,000 - 300,000	3.9-6.6	2.8-6.8	Minimum
300,000 - 1,000,000	6.1-6.7	6.0-6.8	Stabilized

Sources: [a] BSC 2001 [DIRS 154620], Tables 3 to 9.
[b] BSC 2001 [DIRS 154840], Table 6.

NOTE: Uncertainty of +/- 1 pH unit added to these ranges.

Table 9-5. Model Results for Codisposal Fuel Package pH Ranges

New Codisposal Package Models			
Time Period (years)	**Updated Expected Case Abstraction**	**Sensitivity Abstraction**	**pH Criteria**
0-300	3.3-3.6	2.6-4.5	Minimum
300 - 10,000	5.6-7.7	3-7.4	Average
10,000 - 400,000	9.1-10.0	4.7-10	Maximum
400,000 - 1,000,000	8.8-10.0	6.5-8.9	Stabilized

Source: BSC 2001 [DIRS 154840], Tables 8 and 9.

NOTE: Uncertainty of +/- 1 pH unit added to these ranges.

Table 9-6. Primary Cladding Uncertainties Considered

Description	Parameter	Parameter Distribution in TSPA-SR[a]	Parameter Distribution in Unquantified Uncertainty Analysis[b]
Percentage of cladding with initial perforation.	Initial_Rod_Failure fraction	Triangular (0.0155%, 0.0948%, 1.285%)	Triangular (0.0155%, 0.0948%, 1.285%)
Percent of cladding perforated due to creep rupture and stress corrosion cracking.	Creep_Used	Triangular (1.05%, 2.44%, 19.4%)	Uniform (0.0 to 0.5%)
Uncertainty in the localized corrosion rate.	% rods/m^3 water	0.041%/m^3, uncertainty multiplier, Log-uniform (0.1, 10)	Specified CCDF (range 5×10^{-4}% to 5×10^{-2}%, minimum rate added)
Uncertainty in the CSNF intrinsic dissolution rate multiplier (10^{Uncert_a0}).	Uncert_a0	Uniform (-1, 1)	Uniform (-1, 1)
Seismic failure.	Frequency	1.1 E-6 /yr, no uncertainty range	Specified CCDF (range 4.9×10^{-6} to 2.7×10^{-12}).
Rock overburden failure.	Fraction f(pf, waste package patch fraction)	Not included	0, pf < 50% 2 x (pf-50), pf >= 50%
Uncertainty in unzipping velocity multiplier.	Unzip_uncert	Triangular (1, 40, 240)	Specified CCDF (range 1.0 to 15,000).

Sources: [a] CRWMS M&O 2000 [DIRS 153246], Sections 3.5.3.2 and 3.5.4.2.
[b] CRWMS M&O 2001 [DIRS 151662] and this work.

NOTE: CCDF = complementary cumulative distribution function.

Table 9-7. Complementary Cumulative Distribution Function for Fraction of Rods Failed per m^3 of Seepage

Complementary Cumulative Distribution Function	Percent of Rods Failed per m^3
1.00	5 E-4
0.50	5 E-4
0.00	5 E-2

Table 9-8. Complementary Cumulative Distribution Function for Frequency of Seismic Cladding Failure

Complementary Cumulative Distribution Function	Frequency (/yr)
1.00	4.90 E-06
0.95	4.90 E-06
0.85	1.10 E-06
0.50	6.40 E-08
0.15	6.20 E-10
0.05	2.70 E-12
0.00	2.70 E-12

Table 9-9. Complementary Cumulative Distribution Function for Unzipping Velocity Multiplier

Complementary Cumulative Distribution Function	Velocity Multiplier
1.00	1
0.90	1
0.50	9
0.25	18
0.23	180
0.22	15,000
0.00	15,000

Source: CRWMS M&O 2001 [DIRS 151662], Section 6.6.1 and Section 9.3.3.3.6 of this document.

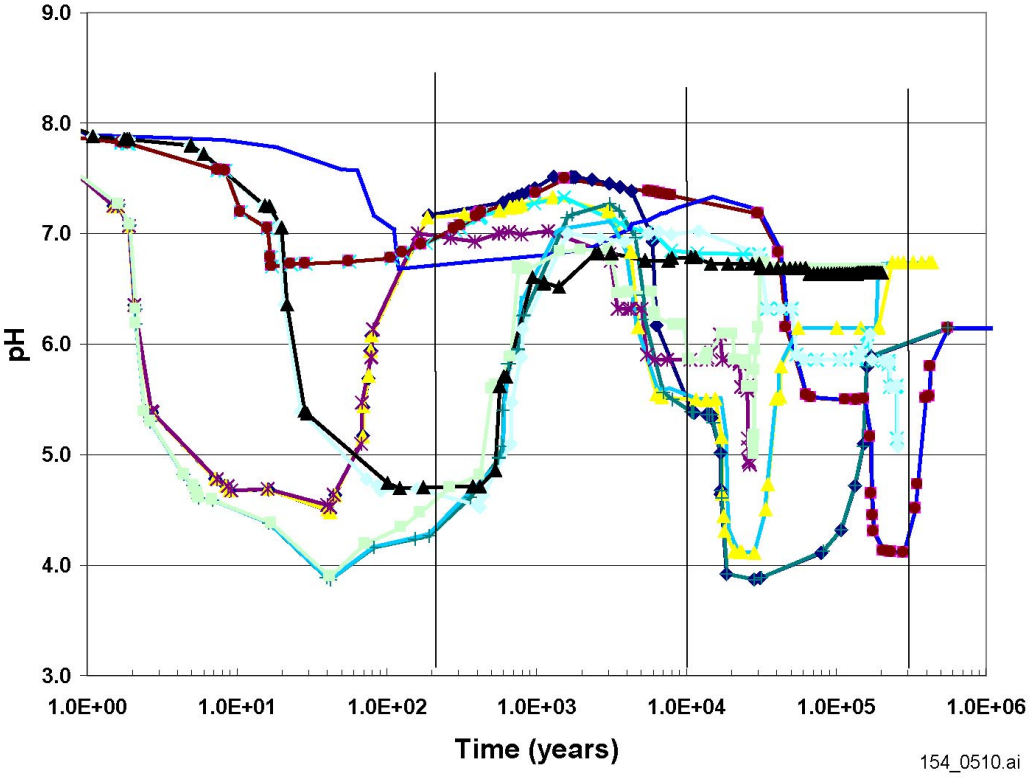

154_0510.ai

Source: BSC 2001 [DIRS 154620], Figure 1.

NOTE: Updated base-case model pH-time trajectories for commercial spent nuclear fuel packages. Lines represent trajectories calculated over a range of water fluxes (15-0.15 L per waste package per year), clad exposures (1-10 percent) and steel degradation rates (BSC 2001 [DIRS 154620]).

Figure 9-1. Updated Expected Case Model pH-Time Trajectories for Commercial Spent Nuclear Fuel Packages

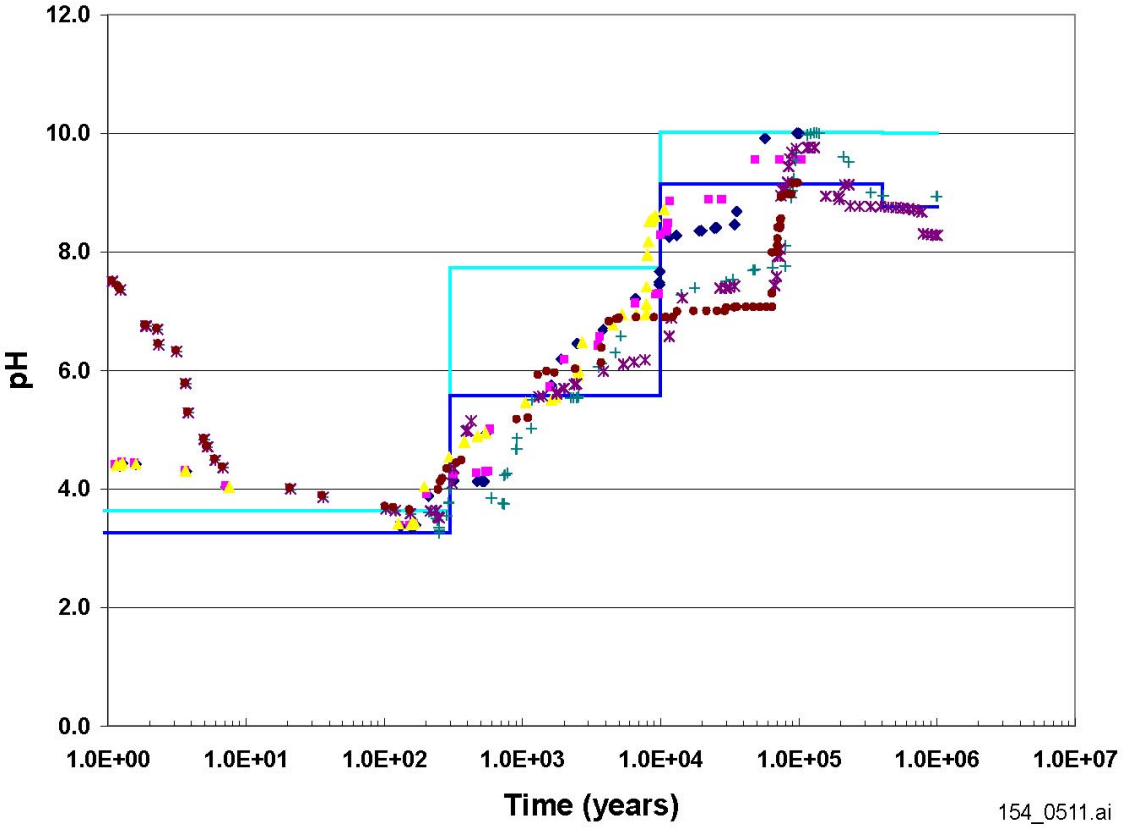

154_0511.ai

Source: BSC 2001 [DIRS 154840], Figure 13.

NOTE: Updated base-case model pH-time trajectories for codisposal packages. Points represent Fast Flux Test Facility and Fermi waste package trajectories calculated over a range of water fluxes (15-0.15 L per waste package per year). The lines represent model abstractions of the minimum, maximum, and average pH ranges (BSC 2001 [DIRS 154620]).

Figure 9-2. Updated Expected Case Model pH-Time Trajectories for Codisposal Packages

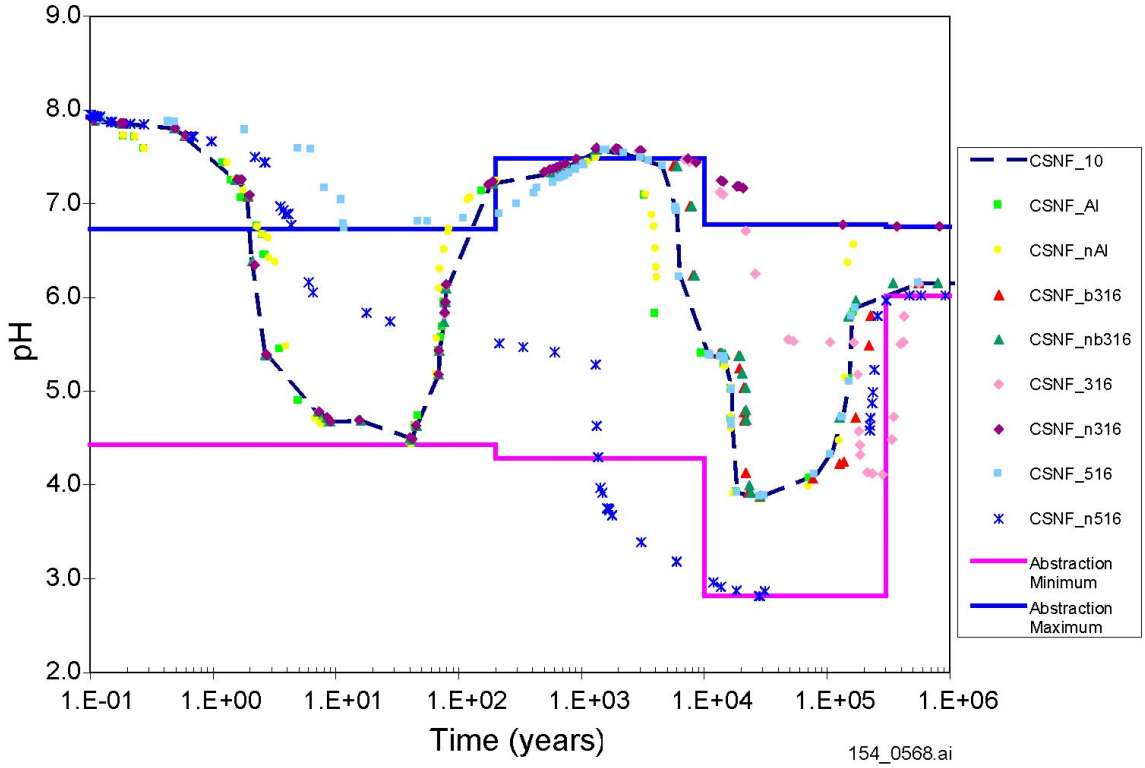

154_0568.ai

Source: BSC 2001 [DIRS 154840], Figure 6.

NOTE: CSNF = Commercial Spent Nuclear Fuel.

Figure 9-3. Sensitivity Model pH-Time Trajectories for Commercial Spent Nuclear Fuel Packages

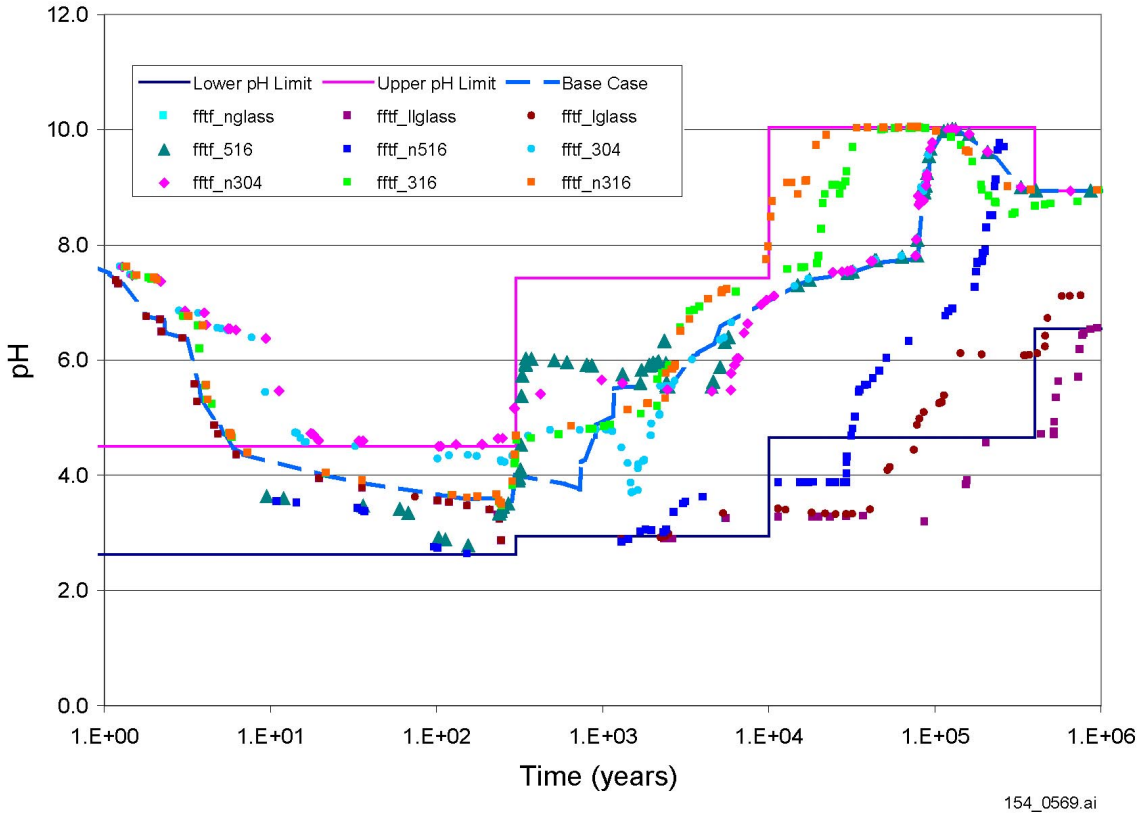

154_0569.ai

Source: BSC 2001 [DIRS 154840], Figure 12.

Figure 9-4. Sensitivity Model pH-Time Trajectories for Codisposal Packages

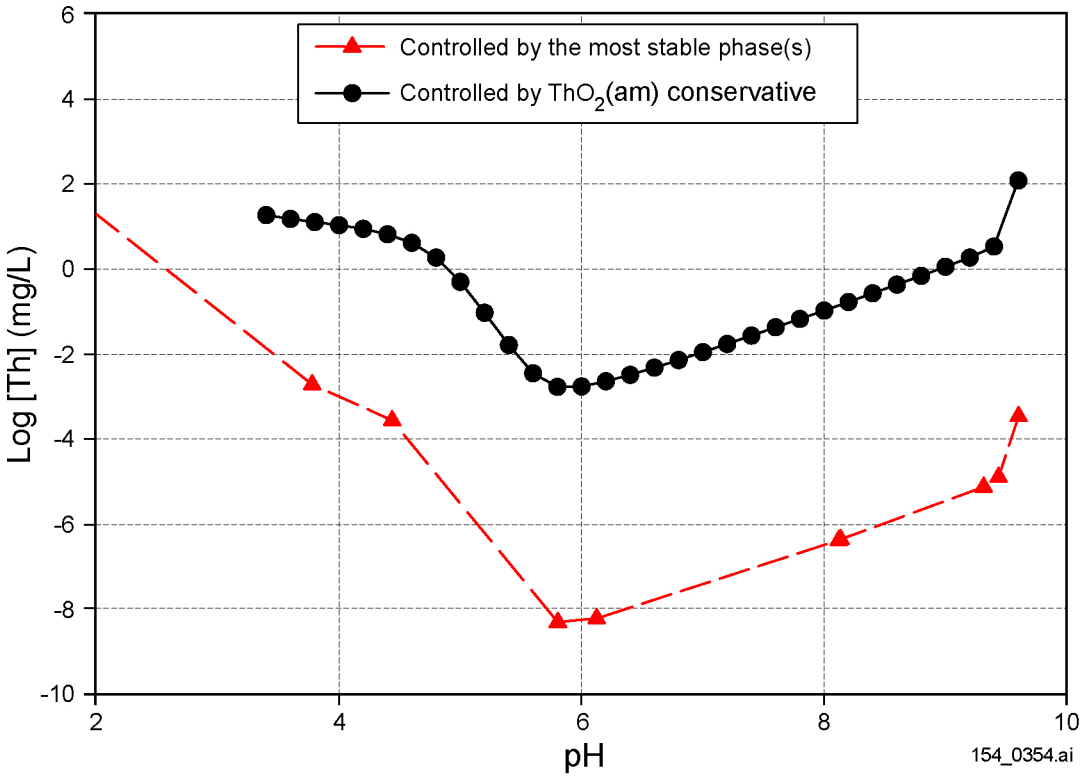

154_0354.ai

Source: Chen 2001 [DIRS 155247], Figure 8.

NOTE: The most stable phase (thorianite) yields thorium solubility 4 to 6 orders of magnitude lower than that for $ThO_{2(am)}$.

Figure 9-5. Thorium Solubility versus pH with Different Controlling Minerals

(a)

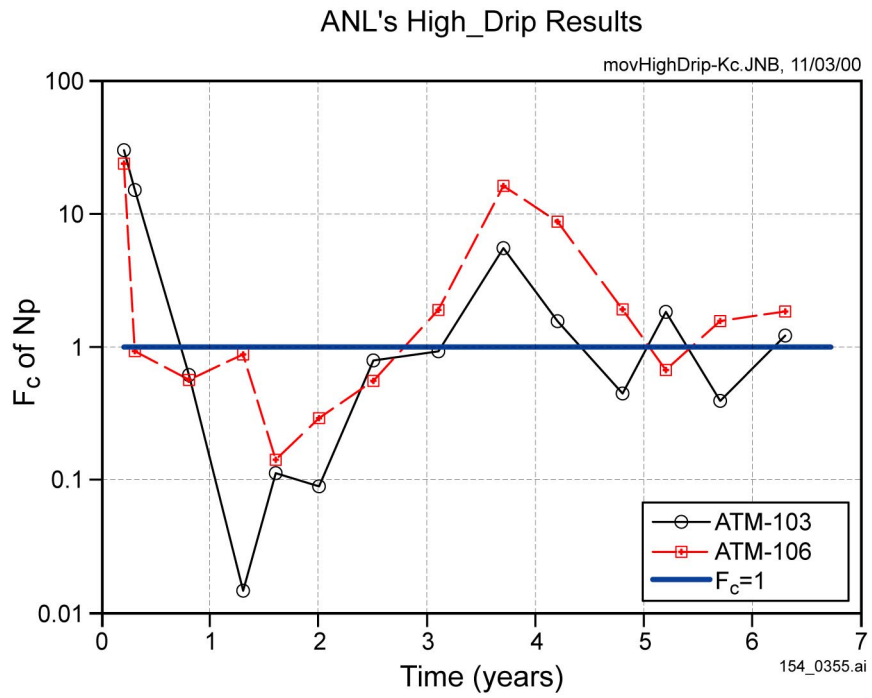

(b)

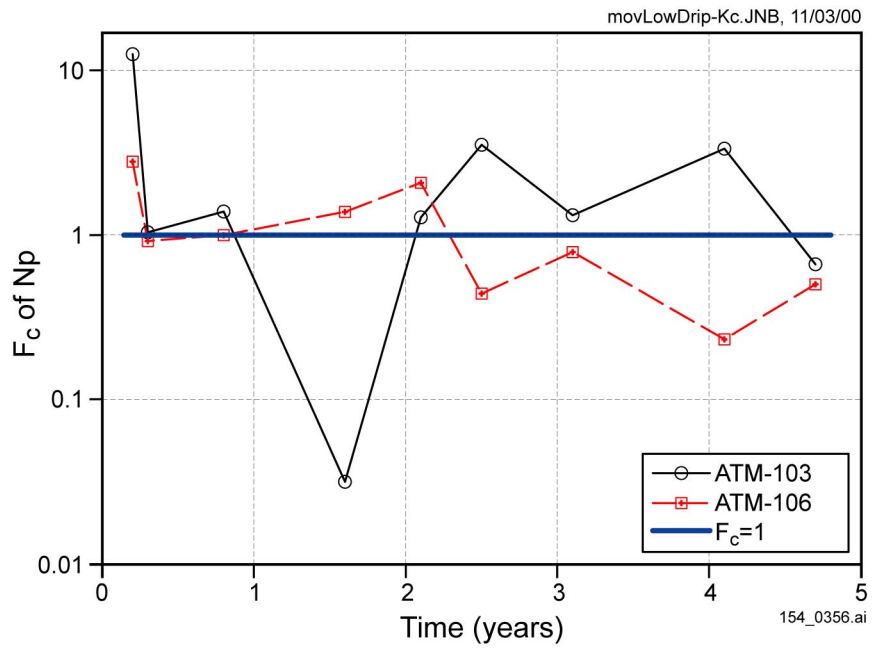

154_0355.ai / 154_0356.ai

Source: Chen 2001 [DIRS 155247], Figure 4.

NOTE: Argonne National Laboratory (ANL) (a) high-drip and (b) low-drip tests. The concentrating factor (F_c) of neptunium (Np) fluctuates around 1.0 and appears to dampen to 1.0 as time increases.
ATM = approved testing material

Figure 9-6. Concentrating Factors of Neptunium in Drip Tests

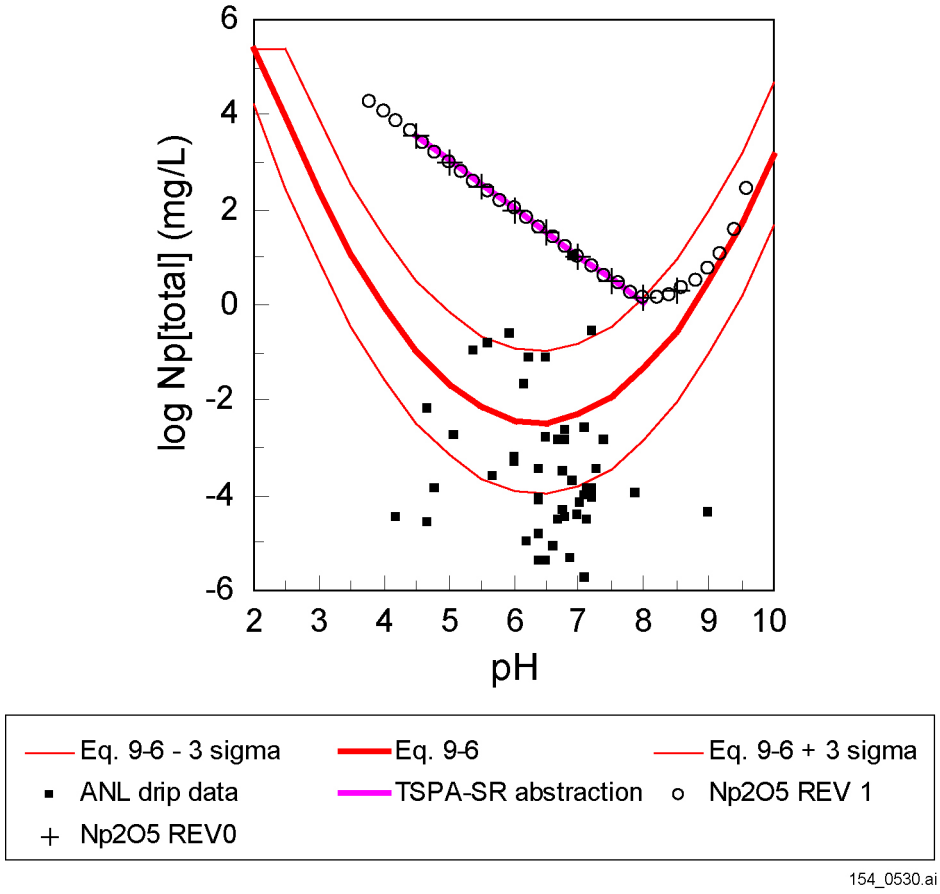

154_0530.ai

Source: Chen 2001 [DIRS 155247], Figure 6.

Figure 9-6b. Neptunium Dissolved Concentration Limit Models and Data

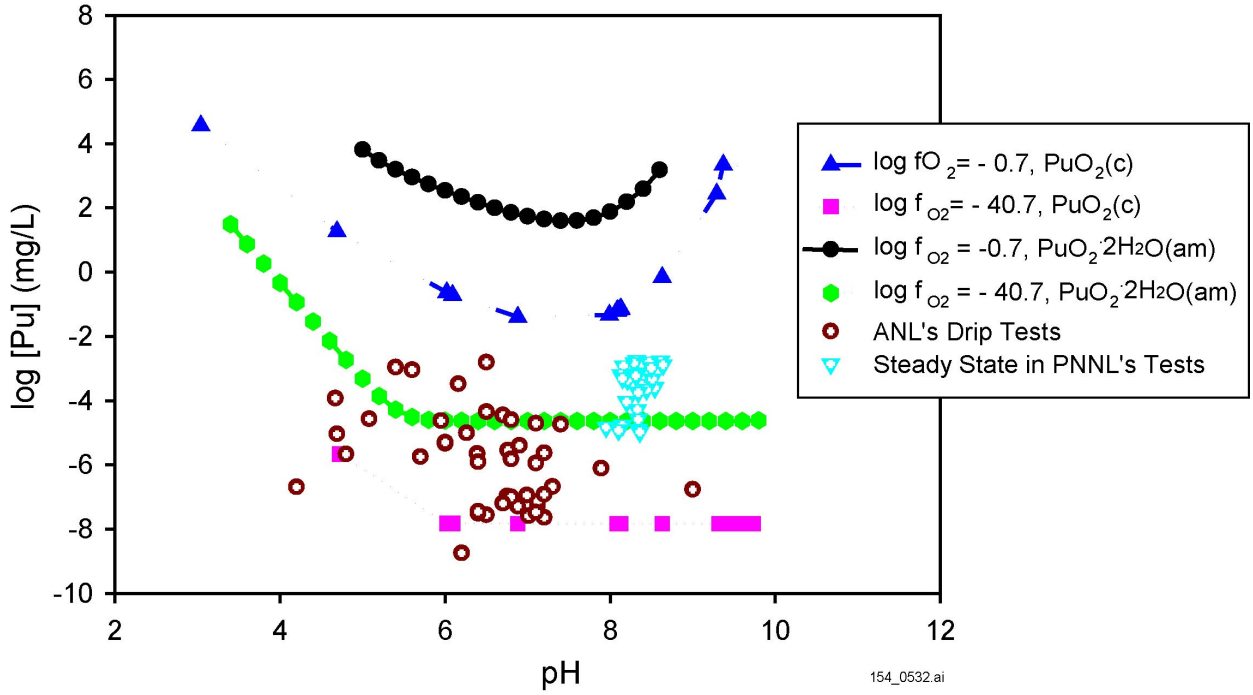

154_0532.ai

Source: Chen 2001 [DIRS 155247], Figure 10.

NOTE: ANL = Argonne National Laboratory; PNNL = Pacific Northwest National Laboratory.

Figure 9-7. Plutonium Dissolved Concentration Limit Estimations and Data

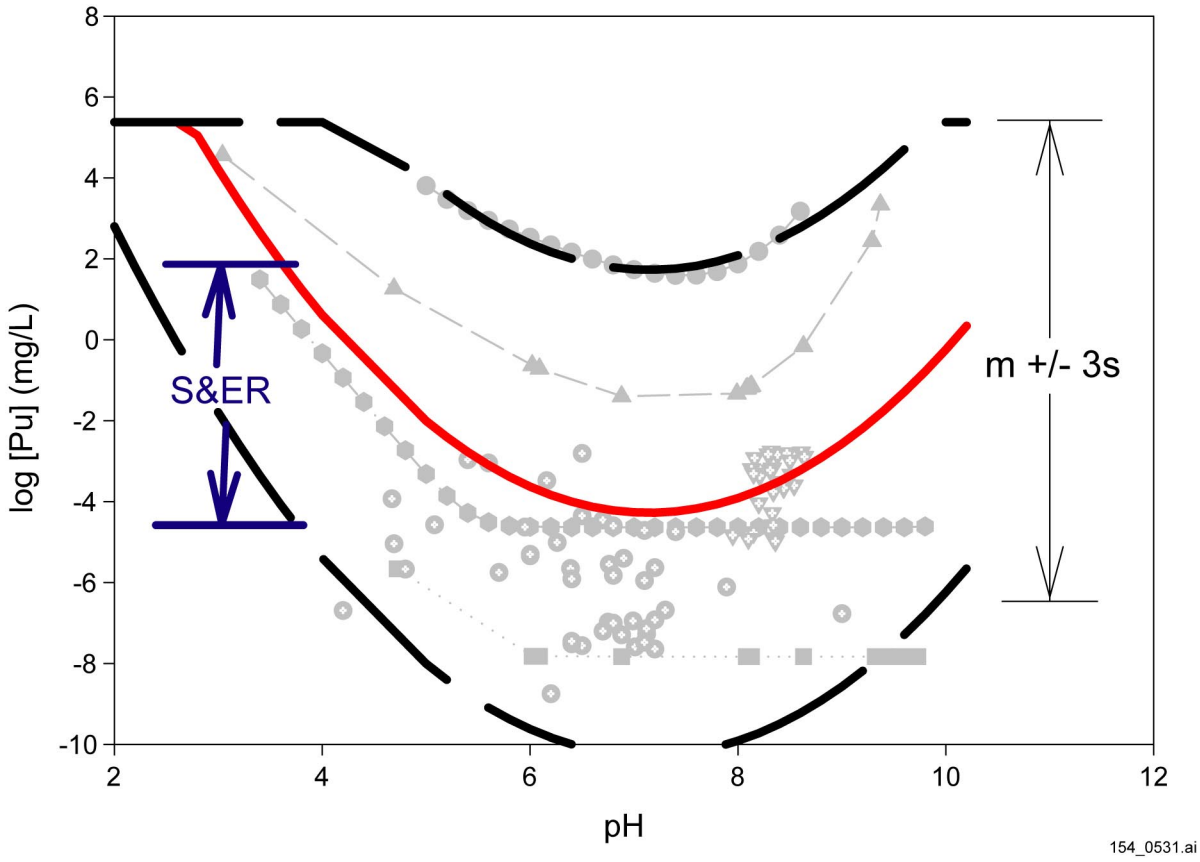

154_0531.ai

Source: Chen 2001 [DIRS 155247], Figure 11.

NOTE: S&ER = *Yucca Mountain Science and Engineering Report* (DOE 2001 [DIRS 153849]).

Figure 9-7b. Plutonium Dissolved Concentration Limit Abstraction and Data

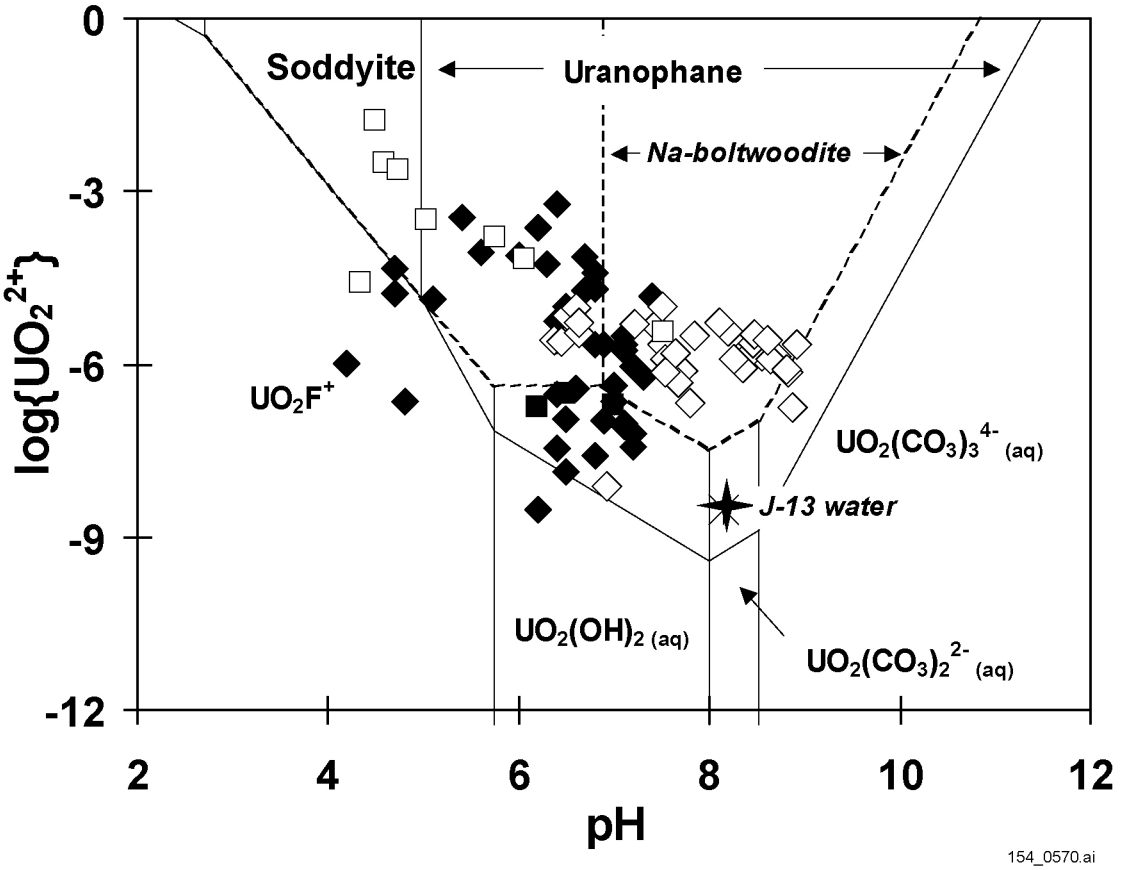

154_0570.ai

NOTE: Data from Argonne National Laboratory dip and batch studies of spent nuclear fuel and UO_2 corrosion (CRWMS M&O 2000 [DIRS 131861]). Black diamonds: commercial spent nuclear fuel drip tests; black squares: commercial spent nuclear fuel batch tests; hollow diamonds: UO_2 drip tests; hollow squares: UO_2 batch tests. Also shown are thermodynamic stability fields for uranium(VI) solids and predominance fields for aqueous uranium (VI) species in equilibrium with Well J-13-like water chemistries over a range of pH values (Finn et al. 1998 [DIRS 100392], Figure 61).

Figure 9-8. Experimentally Measured pH and Dissolved Uranium of Leachates

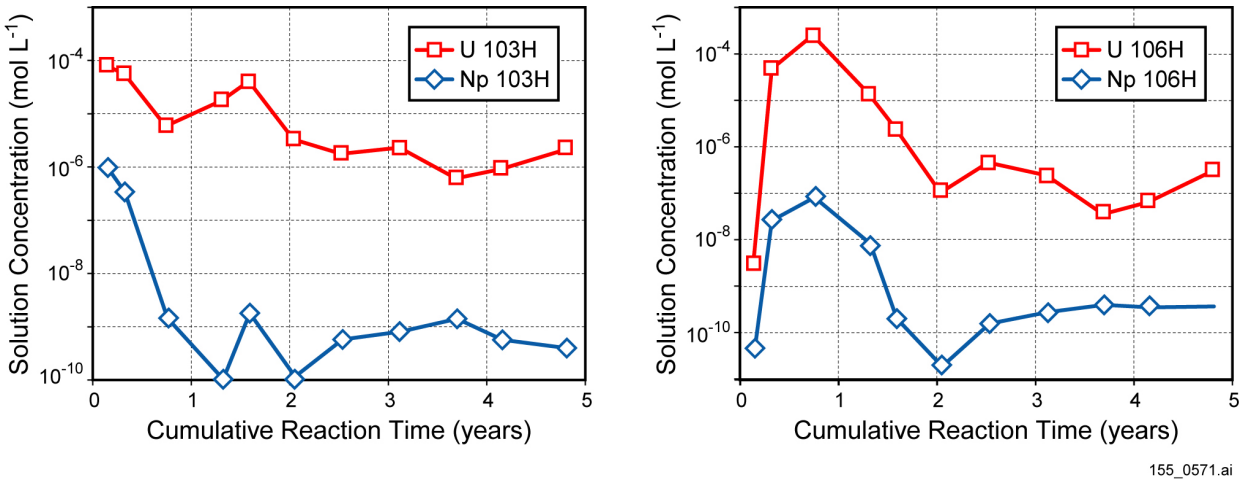

155_0571.ai

Source: BSC 2001 [DIRS 154844], Figure A4.

NOTE: Data on neptunium (Np) and uranium (U) leachates from Argonne National Laboratory high drip-rate tests on commercial spent nuclear fuel. Left panel = ATM-103; right panel = ATM-106.
ATM = approved testing material.

Figure 9-9. Temporal Variations in the Molar Concentrations of Neptunium and Uranium

INTENTIONALLY LEFT BLANK

10 Engineered Barrier System Transport

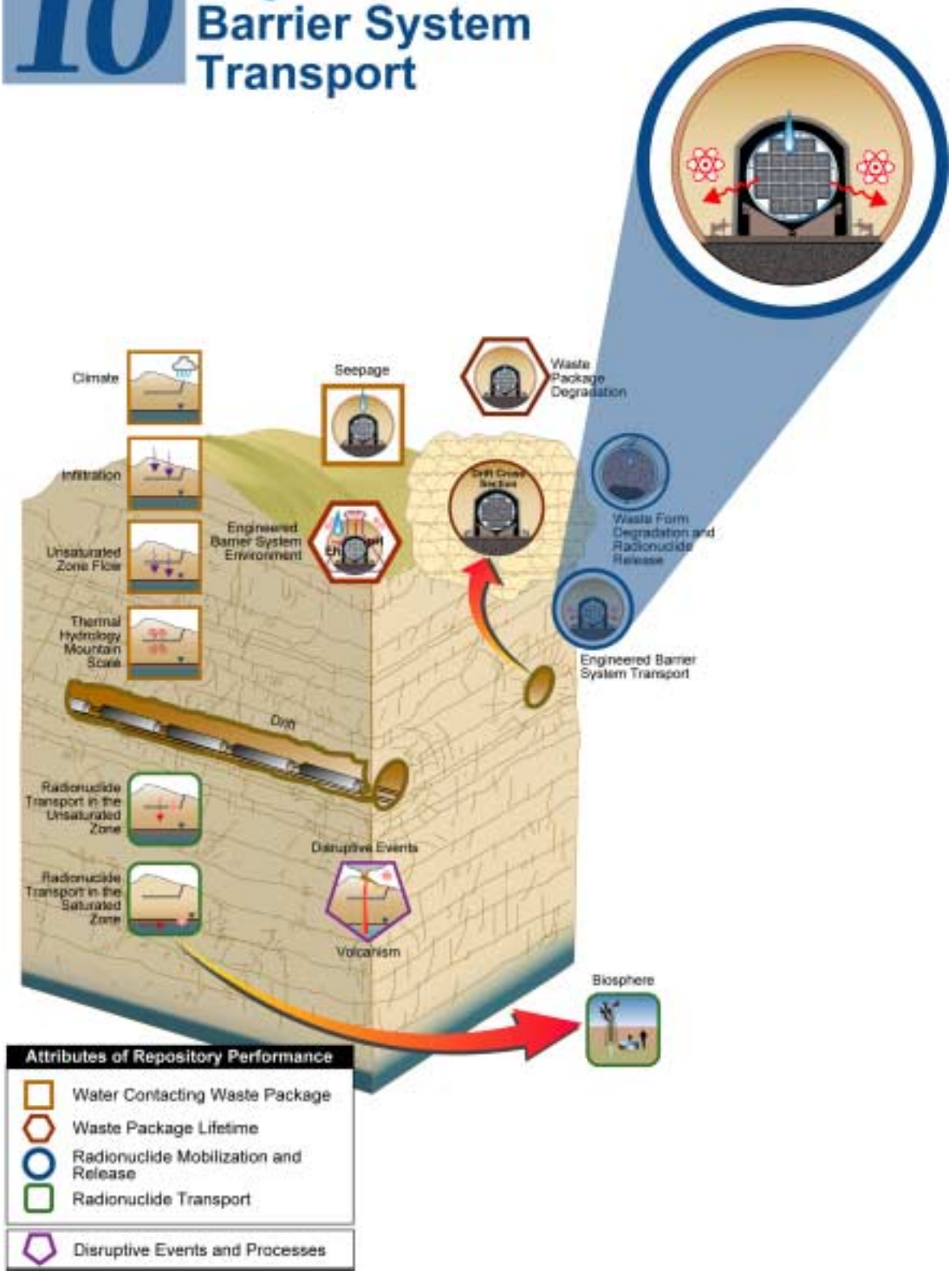

10. ENGINEERED BARRIER SYSTEM TRANSPORT

Section 10 describes the new information developed to produce a more realistic model for transport of radionuclides through the engineered barrier system (EBS). More specifically, this new information is designed to quantify uncertainties and reduce conservatisms in the EBS radionuclide transport abstraction for the *Total System Performance Assessment for the Site Recommendation* (TSPA-SR) (CRWMS M&O 2000 [DIRS 153246]). The new information provides supplemental models or analysis in six areas: (1) diffusive transport within the waste package, (2) transport from the waste package to the invert, (3) diffusive transport through the invert, (4) sorption of dissolved radionuclides, (5) transport via colloids, and (6) transport via microbes. Table 10-1 summarizes the rationale for the supplemental models and analyses in these six areas and identifies the specific section that documents the new information.

Diffusion in the waste package, diffusion from the waste package to the invert, sorption of dissolved radionuclides, and microbial sorption and transport are based on new conceptual models for transport through the EBS. While these new conceptual models provide a more realistic simulation of the transport process, they also include parameters that represent the uncertainties in long-term EBS performance. Diffusion through the invert and colloidal transport of radionuclides primarily involve better definition of the unquantified uncertainties in the previous TSPA-SR models (CRWMS M&O 2000 [DIRS 153246]).

Transport processes in the EBS have no impact on alternative thermal operating modes for the repository. However, the thermal operating mode does influence transport through the EBS, both directly and indirectly. A direct influence exists because the diffusion coefficient is a function of the temperature. The indirect influences exist because the diffusion coefficient is a function of liquid saturation and the adsorption of water vapor on surfaces is a function of the relative humidity. The time-dependent values for liquid saturation and relative humidity are both functions of the thermal operating mode.

Finally, multiple lines of evidence are provided for sorption, colloidal transport, and microbial transport. The supporting evidence for sorption is based on laboratory column tests, which are similar to the downward migration of radionuclides through materials representing the waste form and invert. The supporting evidence for colloidal transport is based on numerous investigations of colloid stability and transport properties; common principles have been employed in the development of this model. The supporting evidence for microbial transport of radionuclides is based on a substantial experimental basis documenting radionuclide uptake by microbes and their subsequent movement as colloidal particles in unsaturated environments.

10.1 INTRODUCTION AND CONCEPTUAL MODEL

The waste form is the source of all radionuclides in the EBS. Radionuclides can be transported downward from breached waste packages, through the invert, and into the unsaturated zone. Transport can occur through advection, in which radionuclides are carried along by a fluid when there is fluid flow through the waste package and invert. Transport can also occur by diffusion, whereby radionuclides migrate from a zone of high concentration to a region of lesser concentration. Both advective and diffusive transport can occur simultaneously when there is a fluid flux through the waste package and invert. Diffusion can occur in the absence of an

Table 10-1. Summary of Supplemental Models and Analyses

Key Attributes of System	Process Model (Section of S&ER)	Topic of Supplemental Scientific Model or Analysis	Reason For Supplemental Scientific Model or Analysis			Section of Volume 1	Performance Assessment Treatment of Supplemental Scientific Model or Analysis[a]	
			Unquantified Uncertainty Analysis	Update in Scientific Information	Lower-Temperature Operating Mode Analysis		TSPA Sensitivity Analysis	Included in Supplemental TSPA Model
Limited Release of Radionuclides from the Engineered Barriers	EBS (Invert) Degradation and Transport (4.2.6, 4.2.7)	Diffusion inside waste package	X	X		10.3.1	X	X
		Transport pathway from inside waste package to invert	X	X		10.3.2		
		Sorption inside waste package	X	X		10.3.4	X	X
		Sorption in invert	X	X		10.3.4	X	X
		Diffusion through invert	X			10.3.3	X	X
		Colloid stability in the invert	X			10.3.5		
		Microbial transport of colloids	X	X		10.3.6		

NOTE: S&ER = Yucca Mountain Science and Engineering Report (DOE 2001 [DIRS 153849]).

[a] Performance assessment treatment of supplemental scientific model or analysis discussed in SSPA Volume 2 (McNeish 2001 [DIRS 155023]).

advective liquid flux if there is a continuous liquid pathway, possibly in the form of thin films, on the waste form, the waste package, the invert, and solid surfaces. Note that gaseous transport of volatile radionuclides has been screened out of the nominal scenario for the total system performance assessment (TSPA) because of low consequence (CRWMS M&O 2000 [DIRS 150806], FEP 3.2.10.00.00).

Advective and diffusive transport in the engineered barrier system may occur through unsaturated porous media or liquid films. The invert, with a granular backfill material, is conceptualized to behave as an unsaturated porous medium. It will have both advective and diffusive transport in those regions of the repository where in-drift seepage or imbibition from the host rock create an advective flux through the invert. Liquid films can exist on EBS components, even in repository regions without seepage, because water vapor will adsorb onto surfaces with corrosion products. Transport through very thin liquid films will be primarily by diffusion through corrosion products because the advective velocity is negligible. Thicker liquid films may have large advective fluxes within which advection is the dominant transport mechanism.

A one-dimensional transport model has been used to represent advection and diffusion in the EBS. This approach is appropriate because (1) the major transport path is downward, from the waste package to the invert to the unsaturated zone, and (2) lateral pressure and saturation gradients directly beneath the waste package are anticipated to be minor, so a one-dimensional model should maximize releases to the unsaturated zone. Further, because the advective travel time through the invert is anticipated to be very fast in comparison to the travel times through the unsaturated and saturated zones, dispersivity is neglected in the transport model for the EBS.

Radionuclides are transported in two physical forms: as dissolved chemical species and as colloidal particles. Dissolved and colloidal radionuclides will diffuse through thin films of water and stress corrosion cracks in the waste package lids. They may also migrate by advection through larger patches formed by general corrosion. Migration through the invert may be by diffusion, advection, or both.

Colloid-facilitated transport of radionuclides is important for certain radionuclides that have limited solubility (as dissolved species) but strong affinity for colloidal-size particles that are mobile in water. Two general classifications of colloids can be defined. First, abiotic colloids are small particulates, with a typical size range of 10^{-3} to 10^{-6} mm (Freeze and Cherry 1979 [DIRS 101173], p. 127), that can physically or chemically bind with ions in an aqueous environment. They often occur naturally in the geologic environment because clay minerals and some geochemical weathering products of rocks are of colloidal size and can persist in aqueous solutions for long periods of time. Three types of abiotic colloids are expected in the EBS: (1) waste form colloids, (2) colloids produced from corrosion of repository materials, and (3) natural colloids in the partially saturated media and groundwater at the repository horizon. Second, microbes also behave similarly to colloids and can be considered biotic colloids. Radionuclides in waste form colloids may be irreversibly embedded or reversibly attached by chemical sorption. Radionuclides in corrosion-product and groundwater colloids are likely to be reversibly attached, although sorption of metal ions to iron-(hydr)oxide colloids can be quite strong.

10.1.1 Alternative Conceptual Models

Several alternative conceptual models for transport were considered but, because they are improbable or not supported by available data, were not incorporated in the TSPA-SR (CRWMS M&O 2000 [DIRS 153246]) conceptual model for EBS transport. These models are described in the following paragraphs.

It is possible that ponding could occur in the emplacement drifts due to clogging in the invert or in the host rock that drains the invert. Drainage pathways could become clogged with fine materials from geochemical alteration of EBS materials, dust from long-term ventilation of the drifts, fines from rockfalls, or precipitates of uranium compounds derived from the waste form. Possible consequences include an increased rate of radionuclide transport to and through the unsaturated zone. For example, radionuclides might be transported laterally along the drift to a major fault or fracture zone where rapid drainage through the host rock could occur. In this situation, transport through the unsaturated zone could occur faster than if the drainage was more uniform. However, the fracture permeability and drainage capacity of the host rock is large enough that ponding is sufficiently unlikely (CRWMS M&O 2000 [DIRS 133329], Section 6.6) and has not been included in the EBS flow abstraction for the TSPA-SR (CRWMS M&O 2000 [DIRS 153246], Section 3.6.2.1).

It is possible that radionuclides can be sorbed by steel corrosion products, and that episodes of increased fluid flux could cause temporarily increased rates of radionuclide release. However, the increased flux would cause dilution downstream, which would tend to mitigate the effect on dose rate in the biosphere.

It is possible that precipitates and salts could accumulate in the invert during the thermal period. Any change in invert porosity could alter the invert transport properties. However, the salts would be readily dissolved when water returned during cooldown, leaving the less soluble precipitates (mainly of silica and calcite) at later times, when waste package failure is most likely to occur. These precipitates would occupy only a portion of the available porosity (CRWMS M&O 2000 [DIRS 133329], Section 6.1). Consequently, the effect on transport properties of the invert ballast material from precipitation in the interparticle porosity would be limited. If water entering the drift is imbibed into the intraparticle porosity and evaporates there, the relative changes from precipitation may be greater; however, the effects on invert hydrologic properties and transport properties have not been evaluated.

10.2 REVIEW OF TOTAL SYSTEM PERFORMANCE ASSESSMENT-SITE RECOMMENDATION TREATMENT

Over tens of thousands of years, the drip shields and waste packages will gradually degrade, leading to the mobilization and transport of radionuclides through the EBS. The primary transport medium through the engineered barriers is (liquid) water. Flowing water or a continuous film of water is necessary for radionuclide transport out of the waste package to the invert and through the invert into the unsaturated zone.

Once a waste package is breached, water may enter the package as water vapor or as drips. This water will come into contact with the metal cladding of commercial spent nuclear fuel rods or

with the stainless steel canister surrounding vitrified high-level waste. If the metal cladding that encases the spent nuclear fuel pellets is also breached, radionuclides may dissolve in the water and be transported out of the waste package. Similarly, if the stainless steel canister surrounding the vitrified waste form is breached, the glass and its associated radionuclides may dissolve and be mobilized for transport out of the waste package. Figure 10.2-1 illustrates this transport process for patches formed by general corrosion of the drip shield and waste package. As shown in this figure, the patches provide a path for dripping water to enter the top of the waste package, contact the waste form, mobilize radionuclides, and carry these radionuclides out the bottom of the waste package through the invert and into the unsaturated zone. Patches are large areas on the surface of the waste package that form due to general corrosion. The timing and size of patches are predicted by waste package degradation models, independent of the EBS flow and transport abstractions.

The dissolved concentration of each mobilized radionuclide cannot exceed the radionuclide solubility limit unless colloids are present. Colloids are important for transport because they can increase the mobilized concentration of radionuclides. Colloids can also increase the transport velocity of radionuclides, although this will be a minor effect over the short distances in the EBS.

Radionuclides that are mobilized as dissolved species or as colloidal particles may be transported by advection or diffusion. Both advection and diffusion are important for transport through patches produced by general corrosion of the waste package. Advective transport is anticipated to be the main transport mechanism through patches if there is a significant dripping flux through the waste package, while diffusive transport through patches will be important in the dry areas of the repository. In the TSPA-SR (CRWMS M&O 2000 [DIRS 153246], p. 3-134), a one-dimensional advection-diffusion transport model combines both of these mechanisms. Diffusive transport is anticipated to be the dominant mechanism through stress corrosion cracks because their small size and associated capillary forces resist an advective flux.

Once outside the package, radionuclides will be transported through the invert by diffusion if fluid velocities are sufficiently small, or by diffusion and advection if fluid velocities are large.

Microbial transport and sorption were not included in the EBS transport abstraction for the TSPA-SR model (CRWMS M&O 2000 [DIRS 153246], Section 3.6.2.2).

10.2.1 Transport Abstraction

The waste form is the source of all radionuclides in the EBS. After a breach of the waste package, radionuclides can be transported downward through the invert and into the unsaturated zone (UZ), as shown in Figure 10.2-1. Advective and diffusive transport can occur through patches formed by general corrosion of the waste package, as discussed above. Transport can also occur by diffusion through stress corrosion cracks. The transport abstraction conservatively assumes that diffusion begins immediately after stress corrosion cracks form, regardless of whether conditions are consistent with the existence of a continuous liquid pathway.

Colloid-facilitated transport of radionuclides is included as an additional source term. Radionuclides are transported from the waste package either as dissolved species or bound to colloids. The total concentration for certain radionuclides, particularly plutonium and

americium, can be increased well above the solubility limit by colloidal transport. There are three types of colloids in the engineered barrier system: (1) waste form colloids, (2) iron-(hydr)oxide colloids, and (3) groundwater colloids. The waste form colloids may have irreversibly attached (embedded) or reversibly attached (sorbed) radionuclides. The iron-(hydr)oxide and groundwater colloids have only reversibly attached radionuclides.

The diffusion coefficient for dissolved species in the invert is based on the self-diffusivity of water as an upper bound. Each radionuclide complex could be assigned a unique value for its free water diffusion coefficient. The complexity of the time-dependent chemistry in the waste package makes this a challenging task, so a simpler approach has been incorporated into the TSPA-SR (CRWMS M&O 2000 [DIRS 153246], p. 3-138). The value of the free water diffusion coefficient for all radionuclides is set equal to the self-diffusivity of water at 25°C. This is a reasonable and conservative approximation because the self-diffusivity of water has been shown to be a bounding value for all radionuclides of interest (CRWMS M&O 2000 [DIRS 153940], Section 6.4.1) in the TSPA-SR.

The value of the free water diffusion coefficient must be corrected for the presence of a porous medium in the invert. The functional dependence of these corrections is given in the *EBS Radionuclide Transport Abstraction* (CRWMS M&O 2000 [DIRS 153940], Section 6.4.1):

$$D = D_0 s^{1.849} \phi^{1.3} f(T)$$

where

- D = the time-dependent diffusion coefficient
- D_0 = the self-diffusivity of water at 25°C
- s = the time-dependent liquid saturation in the invert
- ϕ = the (constant) porosity of the invert
- $f(T)$ = the correction for invert temperature, T.

Finally, the diffusion coefficient for radionuclides bound to colloids is given by the diffusion coefficient for the dissolved species divided by 100:

$$D_{colloid} = D/100 = (0.01) D_0 s^{1.849} \phi^{1.3} f(T)$$

The rationale for the factor of 100 reduction is based on an approximation of the ratio of the ionic radii of a dissolved species to that of a colloid (CRWMS M&O 2000 [DIRS 125156], Section 6.17).

Diffusive transport calculations through the invert also require boundary conditions on the top and bottom of the invert. The boundary condition on the top of the invert is simply the radionuclide concentration within the waste package. The boundary condition on the bottom of the invert, at the boundary with the UZ, is a zero concentration (swept away) boundary condition. The zero concentration boundary condition is implemented by defining a flow cell with a small volume of water but a very high advective outflow, effectively sweeping all radionuclides away from the lower boundary. This is a reasonable approximation when advective fluxes in the host rock are large enough to sweep radionuclides away from the invert,

diluting the local concentrations below it. This can be a conservative assumption if the advective fluxes in the host rock are small, so that seepage into the drift is negligible and the dominant transport mechanism is diffusion. In this case, the radionuclide concentrations in the host rock directly beneath the invert may be large enough to substantially reduce diffusive transport through the invert. This conservatism has not been quantified in the present studies because quantifying the uncertainties in sorption and in-package diffusion were expected to be more important for EBS performance.

Corrosion products from the waste package and spent nuclear fuel have the potential to strongly sorb actinides. Sorption on corrosion products will be beneficial to performance because this process can retain radionuclides in the EBS and delay their release to the UZ. The potential advantages of retardation were conservatively ignored in the transport abstraction.

10.2.2 Conservatisms and Uncertainties in the Transport Abstraction

The transport abstraction described above is based on a reasonable approach that bounds the transport and release of radionuclides to the UZ. The use of reasonable bounds is appropriate because of potentially large uncertainties in the response of a very complex engineered system over long periods of time. Following are the noteworthy conservatisms and uncertainties in the TSPA-SR (CRWMS M&O 2000 [DIRS 153246]) abstractions:

Diffusion from the Waste Package Is Maximized–The abstraction has a number of assumptions that maximize diffusive releases:

1. All mobilized radionuclides are immediately available to diffuse through any breaches in the waste package. For example, the potential delay associated with in-package diffusion between fuel rods and a stress corrosion crack is conservatively neglected in the transport abstraction.

2. Stress corrosion cracks and the invert are covered with a thin film of liquid that supports diffusive transport at all times. The thermal effect from evaporation drying out selected elements of the system, such as the emplacement pallet or surface of the waste package, is conservatively ignored.

3. The waste package is assumed to be in contact with the invert, providing a short, continuous pathway for diffusion from the waste package to the invert. The potential delay associated with diffusion through the longer pathway along the outer surfaces of the waste package and emplacement pallet is (conservatively) ignored.

The result of these assumptions is that radionuclides will be released by diffusion through a patch or a stress corrosion crack, even when the drip shield is intact and there is no advective flux into the waste package. The thermal effect referred to in Item 2 may have tremendous benefit for defense-in-depth and degraded barrier sensitivity studies, such as a waste package juvenile failure scenario.

The Diffusion Coefficient Is Based on a Bounding Abstraction–The free water diffusion coefficient for all radionuclides is based on the self-diffusivity of water at 25°C. This approach provides a bounding value for the free water diffusivity of all radionuclide species relevant to the

TSPA. The self-diffusivity of water is conservative (larger) than the radionuclide-specific values by a factor of 1 to 3.8, depending on the ionic charge (see Section 10.3.3.3.2). This assumption therefore enhances diffusive transport by a factor of 1 to 3.8. In addition, the correction for porosity of the invert is conservative by about 40 percent.

Sorption Is Ignored in the Waste Package and Invert–Reversible sorption is known to be an important process for contaminant transport when iron corrosion products are present in a system, as will occur in the waste package and invert (see Section 10.3.4). Irreversible sorption is known to be an important process for transport of plutonium, thorium, and neptunium (see Section 10.3.4.3.3.4). The transport abstraction (conservatively) ignores retardation in the EBS.

The next section provides model abstractions to quantify the uncertainty and conservatism associated with diffusion inside the waste package, transport along the outer surface of the waste package and the emplacement pallet, the bounding abstraction for the diffusion coefficient in the invert, sorption of dissolved species, colloidal-mediated transport, and the effects of microbial populations on the transport process.

10.3 UNCERTAINTY ANALYSES

The conservatisms and uncertainties in the TSPA-SR transport abstraction (CRWMS M&O 2000 [DIRS 153246], Section 3.6.3.1) are quantified in this section. The relationships between the conservatisms in Section 10.2.1 and the uncertainty analyses in this section are described below.

Diffusion from the Waste Package–The conservative or bounding assumptions for the TSPA-SR diffusive transport abstraction (CRWMS M&O 2000 [DIRS 153246], p. 3-141) abstraction have been analyzed in three steps: diffusion in the waste package (see Section 10.3.1), diffusion from the waste package to the invert (see Section 10.3.2), and diffusion through the invert (see Section 10.3.3).

Diffusion Coefficient–The conservatisms in the calculation of the free water diffusion coefficient and the diffusion coefficient in unsaturated granular media are quantified in Section 10.3.3.

Sorption–The potential for sorption of radionuclides in the EBS is evaluated in Section 10.3.4, and ranges of partition coefficients for seven radionuclides are provided in that section.

Colloidal/Microbial Transport–Although not identified as a conservatism in the TSPA-SR abstraction (CRWMS M&O 2000 [DIRS 153246], Section 3.6.3.1), the potential uncertainties in radionuclide transport via colloids and microbes are discussed in Sections 10.3.5 and 10.3.6.

10.3.1 Diffusion in the Waste Package

10.3.1.1 Goal of the Model

The goal of this model is to quantify the impact of in-package diffusion on radionuclide transport through the waste package. Transport within the waste package can occur through advective or diffusive mechanisms. Advective transport occurs when a radionuclide, either as a dissolved species in an aqueous solution or attached to a colloidal particle, moves with a flowing fluid.

Diffusive transport occurs when a radionuclide, either as a dissolved species in aqueous solution or attached to a colloidal particle, moves from a region of high concentration to a region of lower concentration in a stagnant film or body of water. Both advective and diffusive transport will occur for those waste packages exposed to a dripping environment in the repository. Only diffusive transport is anticipated to occur in those waste packages in the dry (non-seeping) regions of the repository. Since approximately 87 percent of the waste packages are in a dry region of the repository (CRWMS M&O 2000 [DIRS 153246], pp. 4-5), in-package diffusion is an important process for release of radionuclides from the waste package. This section provides a model to quantify the impact of in-package diffusion on repository performance.

10.3.1.2 Identification of Unquantified Uncertainties in Total System Performance Assessment-Site Recommendation

Dripping from seeps is not expected to occur in about 87 percent of the potential repository at Yucca Mountain (CRWMS M&O 2000 [DIRS 153246], pp. 4-5). In this situation, advective transport of radionuclides within waste packages will be negligible for the bulk of the repository. However, diffusive transport is still possible through the thin film of adsorbed water that will cover all surfaces exposed to the humid air in the repository drifts. The objective of this analysis is to develop an abstraction for calculating the diffusive releases from waste packages where no drips or other advective releases occur.

The current TSPA-SR transport model for the waste package (CRWMS M&O 2000 [DIRS 153246], p. 3-141) conservatively assumes that all radionuclides released by the waste form are immediately available to diffuse through any breaches in the package. In other words, the potential delay between release of radionuclides from the pellets in a commercial spent nuclear fuel (SNF) fuel rod and their arrival at the surface of the waste package is ignored. Similarly, the potential delay between the release of radionuclides at the surface of a vitrified form and their arrival at the surface of the waste package is ignored. This approach is equivalent to assuming instantaneous in-package diffusion, which is a conservative approach.

Alternative thermal operating modes will affect the in-package diffusion model in two ways. First, the diffusion coefficient for in-package corrosion products is a direct function of temperature (CRWMS M&O 2000 [DIRS 153940], p. 62). Second, the thermal operating mode will indirectly affect the thickness of in-package water films and the saturation of in-package corrosion products because these quantities are functions of the thermally-dependent relative humidity in the repository, as discussed in Sections 10.3.1.3.2 and 10.3.1.3.5.

10.3.1.3 Quantification of Previously Unquantified Uncertainty

The focus in this section is on diffusive releases from commercial SNF waste packages in non-dripping regions of the repository. A diffusive release model for U.S. Department of Energy (DOE) high-level radioactive waste packages is not being implemented for the TSPA-SR sensitivity studies because the glass dissolution process may result in advective releases from the waste package if the relative humidity is high enough (see Section 10.3.1.3.1.1).

10.3.1.3.1 Conceptual Model for the Commercial SNF In-Package Environment

Fuel rods are expected to be extremely robust because the Zircaloy cladding around the fuel pellets is highly corrosion-resistant; at 100°C, the cladding will remain intact for at least 100,000 years (CRWMS M&O 2000 [DIRS 136058], p. 48) barring damage from rockfalls. However, some fuel rods may be damaged while in use or during handling and shipping to the repository. A number of mechanisms cause fuel rod failure inside a reactor core, including damage from debris striking the rods, manufacturing defects, radiation-enhanced corrosion resulting in splitting of the rods, pitting corrosion, and chafing where the rods contact the assembly spacer grids. Because estimated failure rates of fuel rods due to corrosion are essentially zero after emplacement in the potential repository, the TSPA-SR model (CRWMS M&O 2000 [DIRS 153246], p. 3-112) assumed that the cladding will fail in a certain fraction of the fuel rods over specified periods of time. These failed rods will release radionuclides through diffusion once a continuous film of liquid water is present on the internal components of the waste package.

Baskets and guides support fuel rod assemblies inside a waste package for commercial SNF. These support components are fabricated from carbon steel and will begin to corrode once a waste package is breached. Corrosion begins when the relative humidity becomes great enough to produce aqueous conditions on the surface. A threshold value of 70 percent has been estimated (CRWMS M&O 2000 [DIRS 151951], Assumption 5.3.9, p. 45), although the presence of deliquescent salts can result in aqueous conditions at lower values of relative humidity. As the support components become thinner due to corrosion, they will weaken and eventually allow fuel rod assemblies to fall to the bottom of the waste package.

Corrosion of the internal support components will increase the surface area for adsorption of water and increase the area for diffusive transport, resulting in greater diffusive releases from the waste package. The fuel rods could also be bent if sections of the support components fail sooner than other parts. This could result in enhanced rod failure rates, with a greater mass of radionuclides available to diffuse out of a waste package.

The waste package inner liner, made of Stainless Steel Type 316NG, has a very long lifetime as computed from known general corrosion rates. However, the potential performance credit of the stainless steel layer was not included in the nominal TSPA-SR analysis (CRWMS M&O 2000 [DIRS 146427], p. 32). As with the baskets and other waste form components (except for the fuel rods), the degradation of the inner liner will provide additional surface area for adsorption of water and additional cross-sectional area for diffusion of radionuclides through the water film.

10.3.1.3.1.1 Conceptual Model for U.S. Department of Energy High-Level Radioactive Waste In-Package Environment

When glass is exposed to humid air, water molecules will adsorb onto specific sites on the glass surface (primarily silanol and alkali metal). The amount of water that adsorbs on the glass will depend on the relative humidity of the air, the temperature of the glass surface, and the hygroscopicity of the glass surface. The adsorption isotherm for water on a reference waste glass made with Savannah River Laboratory 165 frit has been measured at about 23°C (Ebert et al. 1991 [DIRS 111028], p. 134, Figure 1b). The measured isotherm for Savannah River

Laboratory 165U glass was fit using the following equation (CRWMS M&O 2001 [DIRS 153846], p. 35):

$$\theta = \left[\frac{-3.2}{ln(RH)} \right]^{1/1.5} \quad \text{(Eq. 10-1)}$$

where θ is the number of layers of water adsorbed and RH is the relative humidity. The first layer forms at a relative humidity of only a few percent. This corresponds to adsorption at the primary sites. Subsequent layers form as water vapor bonds with adsorbed water to form beads of water on the glass surface. At relative humidities above about 80 percent (CRWMS M&O 2001 [DIRS 153846], pp. 35), a sufficient amount of water has condensed to coalesce into a thin film covering the entire surface.

The DOE high-level radioactive waste, in the form of glass logs, will eventually degrade completely from the reactions at the outer surface. Once glass degradation has begun, a film of water will exist on the outer surface of the glass logs. This coating will provide a pathway for radionuclides to diffuse through breaches in the waste package.

The film of water may also be thick enough to result in advective flow within the waste package. The rate of degradation of the glass is provided by the glass degradation model (CRWMS M&O 2001 [DIRS 153846], pp. 39 to 40). The concentrated solutions containing dissolved glass are hygroscopic, and will continue to absorb water and further degrade the glass. In this situation, the thickness of the water film can be related to the degradation rate, but the water film thickness may not increase; rather, once a certain thickness is reached, it will drain off the glass and either pool in the bottom of the waste package or flow out of breaches in the waste package into the invert. The rate of flow will be equal to the rate of condensation, which in turn will be proportional to the rate of degradation, with fresh condensation offsetting the dissolution and concentration of glass degradation products.

Thus, two transport mechanisms may be occurring simultaneously—diffusion and advection—even when there is no dripping or other flow of liquid water into a waste package (i.e., when water vapor diffuses into a waste package and adsorbs or condenses on the waste package internals). The TSPA-SR model ignores the beneficial effects from a partly saturated and degraded waste form on in-package transport (CRWMS M&O 2000 [DIRS 153246], p. 3-141) for all types of waste packages. Considering the lack of information on adsorption of water vapor into films containing dissolved glass, this approach seems to be reasonable for the codisposal waste packages that contain vitrified glass waste forms. An in-package diffusion model for DOE high-level radioactive waste has therefore not been implemented in the sensitivity studies.

10.3.1.3.2 Adsorption of Water Vapor

All surfaces exposed to water vapor will adsorb water. The amount of adsorbed water vapor depends principally on the nature of the material and the relative humidity. In many cases, the first layer of water adsorbed is chemically bound to the surface and is difficult to remove except at high temperatures, considerably higher than will exist in the repository. Subsequent layers are

less tightly bound, being attracted simply by van der Waals forces to lower water layers. The first few layers of water often form an ice-like structure with little mobility. As the relative humidity approaches 100 percent, the outer layers of water begin to behave more like bulk liquid; at 100 percent relative humidity, bulk condensation of water occurs, forming a liquid phase.

Except for inert metals such as gold and platinum, most metals form an oxide surface layer when exposed to oxygen or water. In the case of Alloy 22, stainless steel, Zircaloy, and aluminum—metals found in the waste package or waste form—the surface oxide layer is passivating. Oxygen diffuses very slowly through the oxide layer, protecting the metal underneath. Thus, all metals in a waste package contain a surface oxide layer on which water adsorption takes place.

Adsorption isotherms define the amount of water adsorbed as a function of relative humidity or relative pressure, provided sufficient time is allowed for equilibrium to take place. Extensive measurements have been made for a few substances, such as iron oxide and titanium oxide, but adsorption isotherms are only available for a few materials. Isotherms for metal oxides found in waste packages have been measured for NiO, Fe_2O_3, and ZrO_2. Isotherms for other major components of stainless steel, such as Cr_2O_3 and Mo_2O_3, are not readily available in the open literature. However, the oxides of iron, nickel, and zirconium make up the bulk of oxides in a package and are representative of in-package materials. Figure 10.3.1-1 presents the adsorption isotherms for Fe_2O_3, NiO, and ZrO_2, each of which is discussed in the following sections.

10.3.1.3.2.1 Iron Oxide Isotherm

The adsorption isotherm of α-Fe_2O_3, a form of hematite, has been extensively measured and reported in the literature (McCafferty and Zettlemoyer 1970 [DIRS 154382]; Jurinak 1964 [DIRS 154381]). These measurements are directly relevant to the repository because (1) hematite should be the predominant form of iron oxide in a degrading waste package (YMP 1998 [DIRS 104441]), and (2) hematite should comprise the bulk of the corrosion products in the waste package. The second point follows because steel accounts for most of the mass in a waste package and iron is the major component of both carbon steel and stainless steel.

Although it is not the most recent measurement of water vapor adsorption on hematite, Jurinak (1964 [DIRS 154381], p. 486) provides a functional relationship for the coverage (i.e., number of monolayers of water adsorbed) as a function of relative humidity based on the Frenkel-Halsey-Hill (FHH) equation for multilayer adsorption:

$$\log_{10} P/P_0 = -\frac{1.1}{(V/V_m)^{2.45}}$$

where

P = partial pressure of water [Pa]
P_0 = vapor pressure of water [Pa]
V = volume of water vapor adsorbed at reference conditions [m^3]
V_m = volume of adsorbed water vapor that provides a one-monolayer coverage on the surface [m^3].

The ratio of water vapor partial pressure to vapor pressure is the relative humidity (*RH*). The ratio of V to V_m is the number of monolayers of water (i.e., the number of layers of individual water molecules) adsorbed on the surface, assuming complete and uniform coverage. Letting $\theta_a = V / V_m$ and $RH = P / P_0$, Jurinak's correlation may be written in general terms with parameters *k* and *s*:

$$\ln(RH) = -\frac{k}{\theta_a^s \log_{10} e}$$

or

$$\theta_a = \left(\frac{k}{\log_{10} e} \right)^{\frac{1}{s}} \left[-\ln(RH) \right]^{-1/s}$$

With $k = 1.1$ and $s = 2.45$:

$$\ln(RH) = -2.5328 \theta_a^{-2.45}$$

or

$$\theta_a = 1.461296 \left[-\ln(RH) \right]^{-0.40816} \qquad \text{(Eq. 10-2)}$$

This isotherm is plotted in Figure 10.3.1-2 with the data of McCafferty and Zettlemoyer (1970 [DIRS 154382]) for comparison.

The average thickness of a monolayer of water can be computed from the cross-sectional area of a water molecule. Although Jurinak (1964 [DIRS 154381], p. 480) assumes an area of 10.8 $Å^2$ per molecule, an area of 10.6 $Å^2$ seems to be more commonly used (McCafferty and Zettlemoyer 1970 [DIRS 154382], p. 454); Holmes et al. 1974 [DIRS 154379], p. 368), while Gregg and Sing (1982 [DIRS 153010], p. 264) indicate that 10.5 $Å^2$ per molecule represents a "close-packed" monolayer. Using 10.6 $Å^2$ per molecule and a water density at 25°C of 997.0449 kg/m^3 (Weast 1985 [DIRS 111561], p. F-4), the thickness of a water monolayer, t_f, is:

$$t_f = \frac{18.01528 \times 10^{-3} \ \frac{\text{kg}}{\text{mol}}}{\left(10.6 \times 10^{-20} \ \frac{\text{m}^2}{\text{molec}} \right) \left(997.0449 \ \frac{\text{kg}}{\text{m}^3} \right) \left(6.0221367 \times 10^{23} \ \frac{\text{molec}}{\text{mol}} \right)} \qquad \text{(Eq. 10-3)}$$

$$= 2.83 \times 10^{-10} \text{ m.}$$

At 50°C, the density of water is 988.0363 kg/m^3 (Weast 1985 [DIRS 111561], p. F-5) and the adsorbed water monolayer thickness is 2.85×10^{-10} m, which shows that the monolayer thickness is not highly sensitive to temperature.

10.3.1.3.2.2 NiO Isotherm

Pure nickel reacts spontaneously with oxygen in air to form a NiO film that is 16Å to 32Å thick after 3 to 48 hours (Lee 1994 [DIRS 154380], p. 56). The NiO(s) film is highly insulating and coherent. The NiO(s) film is highly insulating and coherent. It retains its identity as a chemical species when in contact with water vapor or bulk water.

Lee (1994 [DIRS 154380], pp. 276 to 277) found that an oxide layer forms on the nickel surface in N_2/H_2O, but no further oxidation occurs. Oxide grows on nickel with relative humidity in the air and water at a constant temperature. The amount of water adsorbed on nickel is not affected by the thickness of nickel oxide (Lee 1994 [DIRS 154380], p. 251). Multilayer and capillary condensation occur as the relative humidity increases. At 25°C, the amount of water adsorbed on nickel at RH = 80 percent is about 2.10×10^{-7} g/cm^2 (Lee 1994 [DIRS 154380], Figure 4.48). Using a monolayer coverage of 3.1033×10^{-8} g/cm^2 (Lee 1994 [DIRS 154380], p. 173) and a surface roughness factor of 4 (Lee 1994 [DIRS 154380], p. 231), the mass gain data in g/cm^2 from Lee (1994 [DIRS 154380], Figure 4.48) are converted to monolayer coverage by dividing by $(3.1033 \times 10^{-8})(4) = 1.24132 \times 10^{-7}$. These results (Lee 1994 [DIRS 154380], Figure 4.48) are for N_2 carrier gas, rather than for air; however, the amount of water adsorbed from air appears to be slightly less than from N_2 (Lee 1994 [DIRS 154380], Figures 4.49 and 4.50), so using these data should be conservative in terms of overestimating the amount of water available for diffusion of radionuclides. The data of Lee (1994 [DIRS 154380]) at 25°C, converted from g/cm^2 mass gain to monolayers of water by dividing by 1.24132×10^{-7}, are shown in Figure 10.3.1-3.

The NiO film is very thin, and the adsorption isotherm for NiO results in a film thickness that is less than the film thickness for iron oxide at all values of relative humidity, as shown in Table 10.3.1-1. The iron oxide isotherm has therefore been used to estimate film thickness for the corroded waste package internal components because it is conservative relative to the adsorption isotherm for NiO.

10.3.1.3.2.3 ZrO_2 Isotherm

The adsorption isotherm for water vapor on ZrO_2 at 25°C (Holmes et al. 1974 [DIRS 154379], p. 367, Figure 3) is shown in Figure 10.3.1-4. Measurements by Holmes et al. (1974 [DIRS 154379]) during adsorption-desorption cycling revealed that the sample irreversibly adsorbed 4.8 mg water/g sample, which compares favorably with the estimated chemisorption capacity of 5.7 mg/g. In the initial outgassing of the sample, the weight loss between 25°C and 500°C was equivalent to about 2.3 monolayers of chemisorbed water. The monolayer capacities are equivalent to specific surface areas of about 14 to 15 m^2/g, based on 10.6 Å^2 per adsorbed water molecule. Nitrogen and argon adsorption data on the water-covered zirconium oxide surface gave specific surface areas of 18.6 m^2/g for nitrogen and 17.8 m^2/g for argon. This difference emphasizes the specificity involved in water adsorption on oxide surfaces and the accompanying uncertainty in specific surface areas estimated from such data. Using 14.5 m^2/g for specific surface area, the amount adsorbed per monolayer of water is:

$$\frac{\left(14.5\,\frac{\mathrm{m}^2}{\mathrm{g\ ZrO_2}}\right)\left(18.0153\times10^{3}\,\frac{\mathrm{mg\ H_2O}}{\mathrm{mol}}\right)}{\left(10.6\times10^{-20}\,\frac{\mathrm{m}^2}{\mathrm{molecule}}\right)\left(6.0221367\times10^{23}\,\frac{\mathrm{molecule}}{\mathrm{mol}}\right)} = 4.092\,\frac{\mathrm{mg\ H_2O}}{\mathrm{g\ ZrO_2}}/\mathrm{monolayer}$$

The data for the adsorption of water onto ZrO_2 are presented graphically in Holmes et al. (1974 [DIRS 154379], Figure 3). For easier use, these data have been fit to the commonly-used FHH multilayer adsorption isotherm equation (Lee 1994 [DIRS 154380], p. 96). The FHH isotherm is attractive for its simple mathematical form and its applicability to multilayer adsorption, which is observed for water vapor on ZrO_2:

$$\ln RH = -\frac{k}{\theta_a^s}$$

or equivalently,

$$\theta_a = \left(\frac{-k}{\ln RH}\right)^{1/s}$$

which relates the number of monolayers of water, θ_a, to the relative humidity, RH. The parameter k and exponent s are obtained by a linear least squares fit of data read from Holmes et al. (1974 [DIRS 154379], Figure 3). The FHH equation can be linearized in terms of k and s by taking the log of both sides of the equation:

$$-\ln[-\ln(RH)] = s\ln(\theta_a) - \ln(k)\,.$$

This equation is for a straight line:

$$Y = sX - \ln k$$

where

$$Y = -\ln[-\ln(RH)]$$
$$X = \ln(\theta_a)$$

Table 10.3.1-2 presents the least squares analysis of the transformed data performed using Microsoft® Excel 97. The Add Trendline capability was used for the linear regression, resulting in the relationship:

$$Y = 1.8318X - 1.8976$$

where s is the slope (1.8318) and -ln k = -1.8976 is the intercept, so k = 6.67. The coefficient of determination for the linear regression is R^2=0.984.

Thus, the data from Holmes et al. (1974 [DIRS 154379], Figure 3) as fit to an FHH multilayer adsorption isotherm correlation become:

$$\theta_a = \left(\frac{-6.67}{\ln RH} \right)^{1/1.8318}$$

The predicted relative humidity is based upon a least squares fit linear regression analysis. The slope s = 1.8318, and the intercept ln(k) = -1.8976.

10.3.1.3.2.4 Behavior of Thin Water Films

Water at solid surfaces varies in nature from a highly structured form on hydrophilic substrates to a loose, entropic form on more hydrophobic substrates possessing hydrophilic sites (Lee 1994 [DIRS 154380], p. 74). The adsorption of water on solids depends on the capacity of the surface to orient the water dipoles, usually with the proton outward. Near polar surfaces of solids such as metal and oxides, the source of orientation of water molecules at the interface could be either hydrogen bonding or dipole-dipole interactions, depending on the chemical nature of the solid. Depending on the dissimilarity between the ordered (dipole-dipole), induced structure near the interface and the bulk structure, various thicknesses of the ordered layers are possible (Lee 1994 [DIRS 154380], p. 75).

The structure of liquid water is considered to consist of unbonded molecules and of molecules hydrogen-bonded in clusters that have a mean size of about 90 molecules at 0°C (Lee 1994 [DIRS 154380], p. 79). At hydrophilic surfaces, such as oxides, the structure of water resembles that of ice (McCafferty and Zettlemoyer 1971 [DIRS 154378], p. 239). This behavior is attributed to the existence of a monolayer in which the adsorbed water is held rigidly to the solid surface at fixed sites. The first layer is localized by double hydrogen bonding of a single water molecule to two surface hydroxyls. This highly constrained first layer relaxes in the next layers, where the water molecules start to possess a rotational degree of freedom, being singly hydrogen-bonded. The second layer becomes more ordered when hydrogen bonds to a third layer, and so on, until the ordering effect of the surface is overcome and bulk liquid layers form farther from the surface. On a hydrophobic surface, such as silica, different behavior is observed. When half of the surface hydroxyls on silica are occupied by water, the water starts to agglomerate into clusters instead of adsorbing uniformly over the surface.

Layers of water adsorbed on an oxide surface can promote lateral ion movement, which sets up localized electrochemical cells due to inhomogeneities in the underlying metal (Lee 1994 [DIRS 154380], p. 141). Such cells promote pitting corrosion. Surface water dipoles may act to shield oxygen ions from an internal field that promotes ion movement. On the other hand, the gel-like structure of a metal-(hydr)oxide may not support the charge separation that normally accounts for the field-driven process. Instead, ion movement may take place under the influence of a concentration gradient. The first layers of adsorbed water often do not contain ions from the solid (Lee 1994 [DIRS 154380], p. 73). This suggests that multiple water layers are needed in order for solid species (such as radionuclides) to dissolve and diffuse.

10.3.1.3.3 Specific Surface Areas of Component Materials

Most studies of the nature of adsorbed water at solid surfaces have been done with solid powders whose specific surface area is at least 5 m^2/g. Such high interfacial areas are required for sufficient sensitivity in the measurements of adsorbed mass using routine gravimetric techniques. However, the use of surface areas of 10 to 20 m^2/g typical of the samples used in adsorption studies for Fe_2O_3, NiO, and ZrO_2 should be conservative in the sense that predicted quantities of adsorbed water will be larger than might be realistically expected, resulting in an overestimation of the amount of radionuclides released by purely diffusive mechanisms.

Table 10.3.1-3 lists the specific areas of waste form component oxides. Jurinak (1964 [DIRS 154381], p. 480) measured surface area of Fe_2O_3 by nitrogen adsorption ranging from 9.60 to 9.70 m^2/g, whereas water adsorption surface areas ranged from 6.52 to 9.10 m^2/g. It was concluded that about one-third of the Fe_2O_3 is covered with chemisorbed water which, unless removed by activation (i.e., heating to at least 425°C), blocks water adsorption sites on the surface. Jurinak (1964 [DIRS 154381]) assumed a cross-sectional area of 10.8 $Å^2$ for water. McCafferty and Zettlemoyer (1970 [DIRS 154382], p. 453) report a single value of 10 m^2/g for "nominal argon surface area" and assume a cross-sectional area of the water molecule of 10.6 $Å^2$. For comparison, Gregg and Sing (1982 [DIRS 153010], p. 188) report surface area measurements of a material identified only as "iron oxide" by mercury porosimetry and by nitrogen adsorption; these respective values are shown in Table 10.3.1-3.

For ZrO_2, Holmes et al. (1974 [DIRS 154379], pp. 367 to 368) measured specific surface areas after outgassing at 500°C of 23.7 m^2/g by nitrogen adsorption and of 23.9 m^2/g by argon adsorption. Monolayer capacities for water were equivalent to specific surface areas of about 14 to 15 m^2/g based on 10.6 $Å^2$ per adsorbed water molecule; the average value of 14.5 m^2/g is shown in Table 10.3.1-3. Nitrogen and argon adsorption data on the water-covered ZrO_2 surface gave specific surface areas of 18.6 m^2/g for nitrogen and 17.8 m^2/g for argon. "This difference emphasizes the specificity involved in water adsorption on oxide surfaces and the accompanying uncertainty in specific surface areas estimated from such data" (Holmes et al. 1974 [DIRS 154379], p. 368).

10.3.1.3.3.1 Interior Surface Area for Commercial Spent Nuclear Fuel Waste Package

The internal surface area of an as-emplaced waste package (i.e., in an undegraded state) containing commercial SNF can be approximated if the dimensions and numbers of fuel rods, baskets, side guides, and other support components are known. Since the surface area will increase by orders of magnitudes as the waste package components degrade, the initial surface area is useful only as a limiting value, but one that can be estimated fairly accurately (unlike the surface area of corrosion products). Typical measurements for a 21-PWR waste package are given in Table 10.3.1-4. The surface areas of fuel assembly spacer grids and end connections are ignored. The total internal surface area of a 21-PWR waste package as emplaced is approximately 1,023 m^2. The surface area of basket components is computed as shown in Table 10.3.1-4 (footnote a) by dividing the total mass of each component by the density of the material (which gives the volume of material), then dividing by the thickness of the component. This results in the area of component material as though it were a plate, ignoring the area of

edges. To account for both sides of the component being exposed to air and able to adsorb water, the area is multiplied by two.

The calculation shown in Table 10.3.1-4 assumes that all the fuel rods are intact. The surface area of intact fuel rods accounts for about 62 percent of the total surface area. It is estimated that an average of 2.2 fuel rods per assembly in a 21-PWR waste package have failed by the time they are emplaced (CRWMS M&O 2000 [DIRS 151659], p. 53), during reactor operation, in dry storage, or due to damage in transportation. Fuel rods that are estimated to have failed cladding may also be susceptible to cladding unzipping and fuel dissolution when the waste package fails. The interior surface of failed rods, as well as the fuel pellets themselves, may adsorb water. The inside cladding surface of these rods will increase the total surface area only slightly. SNF pellets are generally highly fractured and can contribute more significantly to the surface area available for adsorption when a waste package is first breached.

The calculation of pore volume and porosity for a commercial SNF waste package is summarized in Table 10.3.1-5. The porosity of an average 21-PWR waste package is 4.9724/7.6047 = 0.6539. In the TSPA-SR sensitivity analyses, the impact on waste package porosity and surface area from volume changes resulting from oxide formation is ignored.

In *Total System Performance Assessment - 1995: An Evaluation of the Potential Yucca Mountain Repository* (CRWMS M&O 1995 [DIRS 100198], Section 5.6.1), the presence of cladding was conservatively ignored. The surface area of the SNF was taken to be 39.6 cm^2/g (CRWMS M&O 1998 [DIRS 102839], p. 18). The total surface area of the fuel, which was all fully exposed, was computed as 96,200 cm^2/kg water, with the assumption that the entire void space of the waste package was filled with J-13 well water (CRWMS M&O 1998 [DIRS 102839], p. 27). Using the pore volume of a 21-PWR waste package of 4.9724 m^3 (as calculated in Table 10.3.1-5) and a density of J-13 well water assumed to be 1,000 kg/m^3 (CRWMS M&O 1998 [DIRS 102839], p. 6, Assumption 3.2), the surface area of the SNF is:

$$SA_{fuel} = \left(96200 \frac{\text{cm}^2}{\text{kg water}}\right)\left(1000 \frac{\text{kg}}{\text{m}^3}\right)\left(4.9724\ \text{m}^3\right)\left(10^{-4} \frac{\text{m}^2}{\text{cm}^2}\right) = 47834.5\ \text{m}^2$$

The initial surface area of fuel baskets and other internal waste package structures remains the same as in Table 10.3.1-4. However, the calculation of SNF surface area (CRWMS M&O 1998 [DIRS 102839], pp. 18 and 27) did not include the Zircaloy cladding, so the waste package internal surface area for this calculation is 1023.201 - 636.933 + 47834.5 = 48220.8 m^2, or a factor of 47 larger than the surface area when all fuel rods are intact.

Another way to estimate the initial internal surface area of a waste package would be to assume that an average of 2.2 rods per assembly have failed at the time of emplacement (CRWMS M&O 2000 [DIRS 151659], p. 53), but that all other fuel rods are intact. In a 21-PWR waste package, the SNF in 2.2 × 21 = 46.2 fuel rods would be assumed to be fully exposed, although the cladding is still present, with the inside and outside surfaces of the 46.2 fuel rods exposed. The surface area of SNF in 46.2 rods per waste package is computed (CRWMS M&O 1998 [DIRS 102839], pp. 18 and 27) using a specific surface area of SNF of 39.6 cm^2/g and a mass of

fuel in each rod of 1.98219 kg/rod (CRWMS M&O 1998 [DIRS 100733], Attachment I, Table 1):

$$SA_{fuel} = \left(1.98219 \frac{\text{kg fuel}}{\text{rod}}\right)(46.2 \text{ rod})\left(39.6 \frac{\text{cm}^2}{\text{g}}\right)\left(10^{-4} \frac{\text{m}^2}{\text{cm}^2}\right)\left(10^{3} \frac{\text{g}}{\text{kg}}\right) = 362.646 \text{ m}^2$$

It is clear that the highly fractured SNF contributes greatly to the exposed surface area inside a waste package. Including the exposed fuel surface area of the 46.2 rods per waste package with the total obtained in Table 10.3.1-5 results in 1,385.847 m^2. The inside surface area of the 46.2 fuel rods, where the cladding thickness is 0.0225 in. = 0.05715 cm (DOE 1992 [DIRS 102588], p. 2A-30), is:

$$SA_{cladding} = \pi(0.94996 - 0.05715 \text{ cm})(384.96 \text{ cm})\left(10^{-4} \frac{\text{m}^2}{\text{cm}^2}\right)(46.2) = 4.988 \text{ m}^2$$

In this case, the total internal surface area of a 21-PWR waste package is initially 1023.214 + 362.646 + 4.988 = 1390.848 m^2. The materials making up this surface are: (1) about 26 percent SNF, composed mostly of UO_2 (about 95 mole percent [CRWMS M&O 1998 [DIRS 102839], Table 5.2.1-1, p. 23]); (2) about 46 percent ZrO_2; and (3) about 28 percent products of corrosion of various steels, mostly Fe_2O_3 and NiO.

Over time, the fraction of steel corrosion products surface area would be expected to increase greatly relative to the surface areas of SNF and ZrO_2, since the cladding is predicted to degrade and fail at an extremely slow rate. The amount of additional SNF exposed as fuel rods fail will increase at a correspondingly slow rate; however, because of the high surface area of SNF in each fuel rod, the surface area will increase in discrete amounts of about 8 m^2 (7.85 m^2 of SNF and 0.11 m^2 of inside cladding surface) as each fuel rod fails. This assumes that the entire contents of a fuel rod are accessible by water vapor diffusion when the fuel rod is breached.

In principle, the surface area inside a waste package can be computed as a function of time, if the degradation rates of the basket components and the stainless steel inner liner are known, and the failure rate of fuel rods. The calculation is complicated by the different compositions of each component of the waste package. Spatial variability in degradation rates due to variations in accessibility to water vapor further complicate the picture. For example, the fuel rod assemblies in 44-BWR waste packages are enclosed in flow tubes that provide added protection from corrosion over 21-PWR fuel rod assemblies. However, an average corrosion rate for a 21-PWR waste package should be an acceptably conservative approximation from which surface areas and quantities of adsorbed water can be computed.

The complete degradation of a waste package gives an estimated upper bound on the surface area available for adsorption. For this bounding estimate, the assumption is made that all corrodible material inside a 21-PWR waste package is iron that completely oxidizes to Fe_2O_3. The mass of each major component for three types of waste package is listed in Table 10.3.1-6. The amounts and composition of each waste package component are converted to total moles of material in Table 10.3.1-7.

Assume that the inner liner stainless steel fully corrodes, but that the Alloy 22 outer liner remains intact (except for breaches, the sizes of which are assumed to be negligible). Assume that the Zircaloy fuel claddings and assembly grid spacers do not degrade because the Zircaloy will remain uncorroded for tens of thousands of years after the steel has fully corroded. The surface area of SNF, even if fully exposed, is relatively small (47,834 m^2, as calculated above), and, as will be seen, can be ignored in this estimate.

The masses of materials differ little between the two types of waste packages for commercial SNF (21-PWR and 44-BWR), and all other types of packages comprise a much smaller fraction of the total waste in the repository. Therefore, the calculation will be done for the 21-PWR waste package as representative of all packages in the repository.

The computational procedure is as follows. Based on the elemental composition of each material (CRWMS M&O 2000 [DIRS 151561]) shown in Table 10.3.1-7, convert the mass of each material listed in Table 10.3.1-6 to moles by element. Add up the total moles, assume all moles are iron, and determine the stoichiometrically equivalent amount of Fe_2O_3 in the waste package. Using the measured surface area of Fe_2O_3, calculate the total surface area for adsorption from the basket materials and liners. This value provides an estimated upper bound for the surface area for adsorption in a completely degraded waste package. The atomic weights for conversion to moles (Weast 1985 [DIRS 111561]) are as follows:

- Iron 0.055847 kg/mol
- Molybdenum 0.09594 kg/mol
- Chromium 0.051996 kg/mol
- Nickel 0.05871 kg/mol
- Aluminum 0.0269815 kg/mol
- Oxygen 0.0159994 kg/mol.

The total amount of material in a 21-PWR waste package (treated as though it were iron) is 355,218 moles (see lower right-hand entry in Table 10.3.1-7). This iron will oxidize to 177,609 mol $Fe_2O_3 \times 0.1596922$ kg/mol = 28,363 kg Fe_2O_3. Using a specific surface area of 9.1 m^2/g for the oxide (Jurinak 1964 [DIRS 154381]; see also Table 10.3.1-3), the estimated upper bound for total surface area for adsorption in a 21-PWR waste package is $(28{,}363\ g)(9.1 \times 10^3\ m^2/kg) = 2.58 \times 10^8\ m^2$/package.

Table 10.3.1-8 summarizes the various estimates of surface area within a 21-PWR waste package.

10.3.1.3.4 Mass Balance Considerations

It is generally assumed that there is no limitation on the amount of water vapor available to adsorb onto surfaces within a waste package. However, this may be an overly conservative assumption, particularly at early times when the only breaches in a waste package are small stress corrosion cracks. Even at later times, when general corrosion patches are present, the patches are modeled as filled with corrosion products (Lee et al. 1996 [DIRS 100913], p. 5-62) that severely limit the diffusion of water vapor into the waste package. The following calculation shows that the rate of water vapor diffusion through stress corrosion cracks is

probably high enough to provide all the water that adsorbs onto internal waste package surfaces. However, there is not overwhelming excess, so the assumption of plentiful water vapor for adsorption may be conservative.

Another consideration is the rate at which water or oxygen is consumed by corrosion relative to the rate of diffusion of water vapor and oxygen into the waste package. A calculation will show that the diffusion rate is just adequate for assumed corrosion rates. Assume a diffusion distance of $\Delta x = 2$ cm (thickness of waste package outer liner). Assume that the temperature of the waste package and drift air is 50°C, the relative humidity in the drift is 90 percent, and the relative humidity is zero inside the waste package. Then the humidity is 0.082 kg water/kg dry air (Perry 1963 [DIRS 119529], Figure 15-3). Using molecular weights for water of 0.01801528 kg/mol and for air of 0.028964 kg/mol (Weast 1985 [DIRS 111561], p. F-150), the molal humidity is 4.55169 mol H_2O/34.5256 mol dry air, or 0.1165 mol H_2O/mol wet air. With an ideal gas molar density of 22,414 cm^3/mol (at 0°C and 1 atmosphere) (Weast 1985 [DIRS 111561], p. F-194), the concentration of water vapor in air at 50°C and 90 percent relative humidity is:

$$C_{wv} = \frac{\left(0.1165 \frac{\text{mol H}_2\text{O}}{\text{mol air}}\right)\left(18.01528 \frac{\text{g H}_2\text{O}}{\text{mol H}_2\text{O}}\right)}{\left(22414 \frac{\text{cm}^3}{\text{mol}}\right)\left(\frac{323.15\ \text{K}}{273.15\ \text{K}}\right)} = 7.915 \times 10^{-5} \frac{\text{g H}_2\text{O}}{\text{cm}^3\ \text{air}}$$

For the binary diffusion coefficient, the following equation is used (Bird et al. 1960 [DIRS 103524], Equation 16.3-1):

$$D_{AB} = a\left(\frac{T}{\sqrt{T_{cA}T_{cB}}}\right)^b (p_{cA}p_{cB})^{1/3}(T_{cA}T_{cB})^{5/12}\left(\frac{1}{M_A} + \frac{1}{M_B}\right)^{1/2} p^{-1}$$

where

D_{AB} is the diffusion coefficient [cm^2/s] for water (A) in air (B)
T is absolute temperature [K]
p is pressure [atm]
M is molecular weight [g/mol]
a and b for H_2O with a nonpolar gas are 3.640×10^{-4} and 2.334, respectively
subscript c refers to critical properties.

For water, T_{cA} = 374.1°C = 647.25 K, p_{cA} = 218.3 atm (Weast 1985 [DIRS 111561], p. F-64), and $M_A = 18.01528$ g/mol; for air, $T_{cB} = 132$ K, $p_{cB} = 36.4$ atm (Bird et al. 1960 [DIRS 103524], p. 744), and $M_B = 28.964$ g/mol (Weast 1985 [DIRS 111561], p. F-150). Substituting these values into the above equation:

$$D_{AB} = \left(3.640\times10^{-4}\right)\left(\frac{323.15}{\sqrt{(374.1)(132.)}}\right)^{2.334}\left[(218.3)(36.4)\right]^{1/3}\left[(374.1)(132.)\right]^{5/12}\cdot$$
$$\left(\frac{1}{18.01528}+\frac{1}{28.964}\right)^{1/2}(1.0)^{-1}$$
$$= 0.4715959\ \mathrm{cm}^2/\mathrm{s}$$

Then the rate of diffusion of water vapor is:

$$q = D_{AB}A\frac{\Delta C}{\Delta x} = D_{AB}A\frac{C_{wv}}{\Delta x}$$
$$= \left(0.472\ \frac{\mathrm{cm}^2}{\mathrm{s}}\right)A\left(\frac{7.915\times10^{-5}\ \frac{\mathrm{g}}{\mathrm{cm}^3}}{2\ \mathrm{cm}}\right)$$
$$= 1.87\times10^{-5}\,A\ (\mathrm{g/s})$$

where A is the cross-sectional area [cm^2] of stress corrosion cracks through which water vapor can diffuse. The typical cross-sectional area of a stress corrosion crack is 4.08×10^{-6} m^2 per stress corrosion crack (CRWMS M&O 2000 [DIRS 153940], p. 51), and an average of 25 stress corrosion cracks per waste package is expected (CRWMS M&O 2000 [DIRS 146427], p. 81); then $A = 1.02 \times 10^{-4}$ m^2 $= 1.02$ cm^2, and the rate of diffusion of water vapor is $q = 1.907 \times 10^{-5}$ g/s = 33.40 mol H_2O/yr.

When stress corrosion cracks first appear, water vapor that diffuses through will probably be consumed by corrosion of the most reactive materials within a waste package, namely the A 516 carbon steel that makes up the baskets. These steel components will have a median lifetime of 168 years (CRWMS M&O 2000 [DIRS 151561], Table 32). From Table 10.3.1-6, the total mass of A 516 steel in a 21-PWR waste package is 5,723.68 kg, or 102,489 mol Fe (see Table 10.3.1-7). The consumption rate of iron is then 102489 mol/168 yr = 610 mol Fe/yr. Assuming a stoichiometry of 3 mol H_2O/2 mol Fe (to form Fe_2O_3), corrosion of A 516 carbon steel consumes 915 mol H_2O/yr, which is a factor of 27 greater than the rate of diffusion of water vapor through stress corrosion cracks.

If the corrosion rate is limited by the rate of diffusion of water vapor, then the lifetime of the carbon steel components will be considerably greater than 168 years. The diffusion rate of 33.40 mol H_2O/yr will allow 22.27 mol Fe/yr to corrode, thereby requiring 102,489 mol Fe/(22.27 mol Fe/yr) = 4,602 years for all A 516 steel components to degrade fully once stress corrosion cracks appear.

This assumes that the stress corrosion cracks remain fully open and are not plugged with corrosion products, and that water is not consumed by any other corrosion process or evaporation. If water is preferentially consumed by corrosion reactions, none will be available to adsorb onto surfaces to form a thin film through which radionuclides can diffuse. Thus, the carbon steel will act as a water getter as long as water vapor diffusion into a waste package is limited by stress corrosion cracks and precludes releases of radionuclides.

Since dry air oxidation can also proceed once stress corrosion cracks appear, the rate of oxygen diffusion through cracks should also be considered. Using the appropriate parameters for oxygen (A) diffusing in air—T_{cA} = 154.58 K, p_{cA} = 5.043 MPa = 49.77 atm (Weast 1985 [DIRS 111561], p. F-62), and $M_A = 31.9988$ g/mol—it follows that:

$$D_{AB} = \left(3.640\times10^{-4}\right)\left(\frac{323.15}{\sqrt{(154.58)(132.)}}\right)^{2.334}\left[(49.7)(36.4)\right]^{1/3}\left[(154.58)(132.)\right]^{5/12}\cdot$$
$$\left(\frac{1}{31.9988}+\frac{1}{28.964}\right)^{1/2}(1.0)^{-1}$$
$$= 0.477721\,\text{cm}^2/\text{s}.$$

Assume the oxygen concentration in air in a drift outside a waste package is the same as in the atmosphere: 20.946 volume-percent (Weast 1985 [DIRS 111561], p. F-156) or 0.20946 mol O_2/mol air. With 22414 cm^3/mol, the O_2 concentration is $C_{O_2} = 9.34505\times10^{-6}$ mol O_2/cm^3 air at 0°C, or 7.89912×10^{-6} mol O_2/cm^3 at 50°C. Inside a waste package, assume the oxygen concentration is essentially zero. For 25 stress corrosion cracks with a total cross-sectional area of 1.02 cm^2, the rate of diffusion of oxygen is:

$$q = D_{AB}A\frac{\Delta C_{O_2}}{\Delta x}$$
$$= \left(0.477721\,\frac{\text{cm}^2}{\text{s}}\right)(1.02\,\text{cm}^2)\left(\frac{9.34505\times10^{-6}\,\frac{\text{mol}}{\text{cm}^3}}{2\,\text{cm}}\right)\left(3.1556926\times10^{7}\,\text{s/yr}\right)$$
$$= \left(2.2768\times10^{-6}\,\text{mol/s}\right)\left(3.1556926\times10^{7}\,\text{s/yr}\right)$$
$$= 71.849\,\text{mol}\,O_2/\text{yr}$$

With corrosion stoichiometry of 3 moles of O_2/4 mol Fe to produce Fe_2O_3, the rate of corrosion allowed by diffusion of oxygen through stress corrosion cracks is (71.849)(4/3) = 95.8 mol Fe/yr. Again, the corrosion rate is limited by diffusion through stress corrosion cracks and the lifetime of A 516 carbon steel components in the waste package will be 102489/95.8 = 1,070 yr.

If both water vapor and oxygen can diffuse simultaneously through the stress corrosion cracks without hindering each other, then the total diffusion-limited corrosion rate would be the sum of the diffusion rates of water vapor and oxygen, 95.8 + 33.4 = 129.2 mol Fe/yr. At this rate, the

A 516 carbon steel in a 21-PWR waste package would consume H_2O and O_2 as fast as they diffuse into a waste package for 102,489/129.2 = 793 years after stress corrosion cracks appear. On the other hand, if corrosion of the Stainless Steel Type 316NG inner liner is also accounted for, then consumption of water by corrosion could preclude adsorption of water and diffusion of radionuclides for a much longer period of time.

In view of the assumptions and uncertainties in corrosion rates and stress corrosion crack behavior in this simple model of gas diffusion and corrosion of steel waste package components, it can only be stated that the rates of diffusion of oxygen and water vapor into a waste package are comparable to their rate of consumption by corrosion of A 516 steel. Calculations show that corrosion of A 516 steel may consume all water vapor that diffuses into a waste package for several thousands of years following a breach by stress corrosion cracks. In this situation, the assumption that sufficient water vapor is available for thin water films to adsorb onto all surfaces inside a waste package is fairly conservative. Even in a humid drift environment, the assumption that radionuclides can diffuse out of a waste package via the hypothetical water films is conservative, since the water film may not exist as long as stress corrosion cracks are the only breaches in a waste package. Of course, once general corrosion patches penetrate both the inner and outer layers of the waste package, diffusion of H_2O or O_2 through the openings will no longer limit corrosion rates or adsorption of water. But the first patches often appear much later than the first stress corrosion cracks in the current corrosion models, so the capability of corrosion to limit formation of a diffusive pathway is important.

These calculations suggest that a more accurate mass balance for water and oxygen inside a waste package could greatly reduce predicted releases of radionuclides to the invert, and thus to the accessible environment. Releases could be delayed for several thousand years compared with current estimates as the corrosion of fuel baskets and inner liner components scavenges water and oxygen that diffuse through small stress corrosion cracks. Formation of a diffusive pathway may then be delayed until corrosion of iron-based materials is largely completed. This possibility has not been included in the TSPA-SR sensitivity analyses.

10.3.1.3.5 Cross-Sectional Areas and Effective Diffusivity

10.3.1.3.5.1 Cross-Sectional Area for the Waste Package

The rate of diffusion of radionuclides, q [kg/s], from a waste package to the exterior is given by:

$$q = D_s A \frac{\partial C}{\partial x}$$

where

D_s = the effective diffusion coefficient [m^2/s]
A = the cross-sectional area of the diffusive pathway [m^2]
C = the concentration of the radionuclide [kg/m^3]
x = the length of the path [m].

The amount of water vapor that adsorbs on a surface has been determined. This provides the thickness of the water film. To calculate the cross-sectional area of the pathway, the width of the water film is also needed. Because of the difficulty in characterizing the waste, not only initially but especially as it degrades, this width (and consequently, the cross-sectional area) is very difficult to calculate. The length of the diffusive path is also highly variable because the radionuclide sources may develop at random locations within a waste package and the path length will depend on the geometry of the film connecting the source to a breach. Finally, the effective diffusion coefficient itself depends on the complex interactions of source term composition, water chemistry, porosity, water saturation, and tortuosity, none of which can be characterized in a deterministic fashion. Thus, each term in the above equation—D_s, A, and Δx—needs to be sampled, and a reasonable range and distribution for each has to be determined. All three terms are interrelated through the geometry assumed for the waste package interior, and all are effectively a function of relative humidity and time.

In the simplest model, a single fuel rod has failed in one location, a point source, and an adsorbed water film covers the fuel rod and provides direct connection to a breach. In this case, the cross-sectional area for diffusion is that of the film uniformly covering the cylindrical fuel rod. The thickness of the film is obtained from the adsorption isotherm of water vapor adsorbed on ZrO_2 at the known relative humidity. Thus,

$$A = \frac{\pi}{4}\left[\left(D_0 + t_f\right)^2 - D_0^2\right]$$
$$= \frac{\pi t_f}{4}\left(2D_0 + t_f\right),$$

where D_0 is the diameter of the fuel rod [m] and t_f is the adsorbed water film thickness [m]. A reasonable value for the diffusion coefficient would be the bulk water coefficient, as given in the *EBS Radionuclide Transport Abstraction* (CRWMS M&O 2000 [DIRS 153940], pp. 58 to 60). In this simple case, the minimum path length, Δx, would be the shortest distance along a solid surface from a fuel rod to the exterior of a waste package. This minimum length is 7 cm, which is the combined thickness of the two waste package liners. In this instance, the fuel rod would have to have intimate contact with the waste package inner liner at an insignificant distance from the source for the value of A to remain consistent. The maximum value for Δx would be the length of a fuel rod plus the maximum distance from a fuel rod to the exterior (approximately the diameter of a waste package), for a total of 3.85 m + 1.56 m = 5.41 m (using a waste package outer diameter of 1.56 m [CRWMS M&O 2000 [DIRS 144128]], Attachment I, Sketch SK-0175]). A uniform distribution is reasonable for Δx in this case.

At a relative humidity of 95 percent (used as an example throughout this section), the adsorbed water film on ZrO_2 is 56 monolayers thick, as shown in Figure 10.3.1-4, based on data from Holmes et al. (1974 [DIRS 154379], Figure 3). From Equation 10-3, the thickness of a water monolayer is $t_f = 2.83 \times 10^{-10}$ m, so the cross-sectional area on a 0.94996-cm diameter fuel rod is:

$$\begin{aligned} A &= \pi\left(2.83\times10^{-10}\text{ m}\right)\left[2\left(0.94996\times10^{-2}\text{ m}\right)+2.83\times10^{-10}\text{ m}\right]/4 \\ &= 4.22\times10^{-12}\text{ m}^2 \\ &= 4.22\times10^{-6}\text{ mm}^2 \end{aligned}$$

This is a very small area through which radionuclides will diffuse, and releases from a single failed rod should be insignificantly small. However, if the average 2.2 rods per assembly, or 46.2 rods per waste package, have failed initially, then the total cross-sectional area of adsorbed water films on fuel rods for a waste package is 1.95×10^{-4} mm^2, which is still very small but not insignificant.

Another approach to determining the cross-sectional area is to ignore the dispersion of water over all surfaces within a waste package. Assume that all the water adsorbed on surfaces is collected into a tube, connecting the source to the exterior surface. As shown in Table 10.3.1-4, the total initial surface area in a waste package is 1,023.2 m^2, neglecting any exposed SNF in failed fuel rods. Most of the surfaces are oxidized steel, so it is appropriate to use the Fe_2O_3 adsorption isotherm. From Figure 10.3.1-2 or Equation 10-2, at an example 95 percent relative humidity, the amount of water adsorbed is 4.91 monolayers. Using a monolayer thickness of 2.83×10^{-10} m, the water film is 1.39×10^{-9} m thick. The total volume of adsorbed water is then (1023.2 m^2)(1.39×10^{-9} m) = 1.42×10^{-6} m^3. If the length of the diffusion pathway is the total inside length of a waste package (4.775 m), then the cross-sectional area for diffusion is (1.42×10^{-6} m^3)/(4.775 m) = 2.97×10^{-7} m^2 = 0.30 mm^2, equivalent to a square about 0.5 mm on a side. This is a relatively large area for diffusion, considering that diffusion will take place for thousands of years. Since porosity, saturation, and tortuosity have been neglected, this is an extremely conservative estimate for cross-sectional area.

To carry this estimate further, consider the initial surface area when (1) an average of 46.2 fuel rods per waste package have failed initially, and (2) cladding is neglected. The surface area for adsorption is 1,390.835 m^2 and 48,220.8 m^2, respectively, for these two cases. For a diffusive path the length of the inside of a waste package, the cross-sectional areas are 4.05×10^{-7} m^2 = 0.405 mm^2 = (0.636 mm)^2 and 1.40×10^{-5} m^2 = 14.0 mm^2 = (3.75 mm)^2, respectively. Again, these are relatively large diffusive areas, considering the time over which diffusion will occur. These are also extremely conservative estimates.

At the other extreme in time and waste package condition, consider the cross-sectional area available when the interior of a waste package is fully degraded, at least to the extent that all iron-containing basket and inner liner components have completely corroded. The Alloy 22 outer layer should still be largely intact at this point; a number of general corrosion patches will have penetrated the waste package, but it will still provide some overall structural support. By this time, a large number of fuel rods will have failed by pitting or unzipping, but the Zircaloy

spacer grids will provide enough support to hold assemblies together and support assemblies collapsed on top of them. Interspersed throughout the assemblies are porous corrosion products. In this scenario, the source is dispersed throughout the waste package interior. Diffusion will occur through the porous medium in which all surfaces are coated with the thin film of adsorbed water.

The cross-sectional area can be conservatively estimated for this degraded state. The fully degraded surface area is derived in Section 10.3.1.3.3.1 and summarized in Table 10.3.1-8 to be 2.58×10^8 m^2. At an example 95 percent relative humidity, the film thickness is 1.39×10^{-9} m, so the diffusion area over a path the length of a waste package is $0.075\ \text{m}^2 = (0.27\ \text{m})^2$. Although this estimate is exceedingly conservative, the magnitude is clearly large enough to conclude that there will be essentially no resistance to diffusion inside a fully degraded waste package.

A more realistic estimate must take into account the saturation and porosity of the corrosion products. For homogeneous porous media such as soils, the diffusion coefficient is modified by a tortuosity factor to account for the increased path length and decreased cross-sectional area of the diffusing solute in an unsaturated porous medium. In the absence of an advective flux and negligible vapor phase transport, one-dimensional transient diffusion is given by:

$$\frac{\partial C}{\partial t} = D_s \frac{\partial^2 C}{\partial x^2}$$

where the diffusion coefficient D_s [m^2/s] is defined as (CRWMS M&O 2000 [DIRS 150793], p. 29):

$$D_s = \frac{D_e}{\theta} = \frac{D_e}{\phi S_e}$$

Here, D_e [m^2/s] is the effective dispersion-diffusion coefficient, θ is the volumetric moisture content, ϕ is the porosity, and S_e is the effective water saturation. With no advective flux, D_e is equal to the solute diffusion coefficient, D_{sl}, which in turn is a function of the binary diffusion coefficient in water, D_{wl}, and of the liquid tortuosity factor, $\xi(\theta)$:

$$D_e = D_{sl} = \xi(\theta) D_{wl}$$

Various correlations have been proposed for $\xi(\theta)$; the *EBS Radionuclide Transport Model* (CRWMS M&O 2000 [DIRS 150793], pp. 30 to 31) compares a Modified Millington Quirk correlation with Archie's Law (CRWMS M&O 2000 [DIRS 153940], p. 60) for application to diffusion in the invert, which is composed of a granular material. These correlations are:

$$\xi(\theta) = \theta^{10/3} \phi^{-2} \qquad \text{Modified Millington Quirk}$$

$$\xi(\theta) = \theta^{2} \phi^{-0.7} \qquad \text{Archie's Law}$$

Thus, the diffusion coefficient using each of these correlations would be:

$$\left.\begin{aligned} D_s &= \frac{D_e}{\theta} = \frac{\xi(\theta) D_{wl}}{\theta} \\ &= \theta^{7/3} \phi^{-2} D_{wl} \\ &= \theta^{10/3} \phi^{-3} S_e^{-1} D_{wl} \\ &= \phi^{1/3} S_e^{7/3} D_{wl} \end{aligned}\right\} \quad \text{Modified Millington Quirk}$$

$$\left.\begin{aligned} D_s &= \frac{D_e}{\theta} = \frac{\xi(\theta) D_{wl}}{\theta} \\ &= \theta^{2} \phi^{-0.7} D_{wl} \\ &= \theta^{3} \phi^{-1.7} S_e^{-1} D_{wl} \\ &= \phi^{1.3} S_e^{2} D_{wl} \end{aligned}\right\} \quad \text{Archie's Law}$$

The exponents in Archie's law are typical values, and will vary for different materials (Bear 1988 [DIRS 101379], p. 116). The typical values (1.3 and 2) are used throughout this section to estimate in-package diffusion coefficients.

Conca and Wright (1992 [DIRS 100436]) performed measurements for the diffusion coefficient of unsaturated soil, gravel, bentonite, rock, and crushed tuff from Yucca Mountain over a broad range of water contents (DTN: MO9810SPA00026.000 [DIRS 137076]). These data have been used to analyze the dependence of diffusion coefficient on volumetric moisture content, θ, for a variety of granular materials, as explained in Section 10.3.3.3.1. The resulting equation for diffusivity as a function of porosity and saturation (Equation 10-14), with the notation changed to that of this section, is:

$$D_s = \phi^{1.849} S_e^{\,1.849} D_{wl} \qquad \text{(Eq. 10-4)}$$

Equation 10-4 is consistent with Archie's law, except that the exponents are based on a statistical fit to experimental data for a variety of granular materials.

Either the Modified Millington Quirk or Archie's Law might be appropriate in the later stages of waste package degradation, since the package would be nearly filled with porous corrosion products. Equation 10-4 has been selected for the TSPA sensitivity calculations because it is based on measured data for granular materials and is consistent with the calculation of the diffusion coefficient for the invert, as discussed in Section 10.3.3.3.1. No experimental data exist for the degraded waste package materials, so it cannot be determined which of these (or some other correlation) is correct.

The self-diffusion coefficient for water is used as a bounding value for the binary diffusion coefficient in water, D_{wl}, as discussed in Section 10.3.3 (CRWMS M&O 2000 [DIRS 153940], p. 58).

The effective water saturation, S_e, is obtained from adsorption isotherms as a function of relative humidity. Assume that the corrosion products are Fe_2O_3. The water saturation is given by:

$$S_e = \frac{V_w\left(\frac{s_{WP}}{s_{N_2}}\right)}{V_{WP}}$$

where

V_w is the volume of water adsorbed [m^3 H_2O/g Fe_2O_3]
V_{WP} is the pore volume of a waste package [m^3 pore volume]
s_{WP} is the surface area of a waste package [m^2]
s_{N_2} is the surface area of the porous degraded waste form [m^2/g Fe_2O_3], typically obtained by BET nitrogen adsorption measurements.

Since V_w is normalized to the surface area of Fe_2O_3, it must be multiplied by $\left(s_{WP}/s_{N_2}\right)$ to obtain the volume of water in an entire waste package. V_w/s_{N_2} is the volume of water adsorbed per unit surface area, which is multiplied by the total surface area of the waste package to get the volume of water adsorbed in the entire waste package; it is divided by the pore volume of the waste package to obtain the saturation. V_w/s_{N_2} is obtained from an FHH multilayer adsorption isotherm model (Jurinak 1964 [DIRS 154381], p. 486), shown in Section 10.3.1.3.2.1, that gives the fractional surface coverage, or number of monolayers θ_a covering a surface:

$$\theta_a = \frac{V_w}{V_m} = \frac{m_w}{m_m} = \left(\frac{-1.1}{\log_{10} RH}\right)^{\frac{1}{2.45}}$$

where

V_m is the volume of adsorbed water vapor that provides a one monolayer coverage on the surface [m^3]
m_w is the mass adsorbed per unit mass of adsorbent [kg H_2O/kg Fe_2O_3]
m_m is the mass of one monolayer of adsorbate per unit mass of adsorbent [kg H_2O/kg Fe_2O_3].

The mass of a monolayer is obtained from the cross-sectional area of a water molecule, A_w=10.6 $Å^2 = 10.6 \times 10^{-20}$ m^2/molecule (see discussion preceding Equation 10-3 in Section 10.3.1.3.2.1). An upper bound for the specific surface area of Fe_2O_3, s_{N_2}, is 9.1 m^2/g (Jurinak 1964 [DIRS 154381], Table I; see also Table 10.3.1-3), as deduced from BET N_2 adsorption measurements. The molecular weight of water is M_w= 18.01528 $\times$ 10^{-3} kg H_2O/mol.

Avogadro's number is $N_A = 6.0221367\times10^{23}$ molecule/mol; then the specific mass of a monolayer coverage on Fe_2O_3 is:

$$
\begin{aligned}
m_m &= \frac{s_{N_2} M_w}{A_w N_A} \\
&= \frac{\left(9.1 \frac{\mathrm{m}^2}{\mathrm{g\ Fe_2O_3}}\right)\left(18.01528\times10^{-3}\ \frac{\mathrm{kg\ H_2O}}{\mathrm{mol}}\right)}{\left(10.6\times10^{-20}\ \frac{\mathrm{m}^2}{\mathrm{molecule}}\right)\left(6.0221367\times10^{23}\ \frac{\mathrm{molecule}}{\mathrm{mol}}\right)} \\
&= 2.56818\times10^{-6}\ \frac{\mathrm{kg\ H_2O}}{\mathrm{g\ Fe_2O_3}} \\
&\approx 2.57\ \frac{\mathrm{mg\ H_2O}}{\mathrm{g\ Fe_2O_3}}
\end{aligned}
$$

Assume that bulk liquid properties apply to the adsorbed water, in particular that the density of adsorbed water is equal to that of liquid water. Then

$$m_w = \rho_w V_w$$

and

$$m_m = \rho_w V_m$$

Combining these expressions with the definition of θ_a,

$$
\begin{aligned}
m_w &= m_m \theta_a \\
&= \frac{s_{N2} M_w}{A_w N_A}\theta_a \\
&= \rho_w V_w
\end{aligned}
$$

Then the quantity $\left(V_w / s_{N_2}\right)$ needed for the saturation is:

$$
\begin{aligned}
\frac{V_w}{s_{N_2}} &= \frac{M_w}{\rho_w A_w N_A}\theta_a \\
&= \frac{M_w}{\rho_w A_w N_A}\left(\frac{-1.1}{\log_{10} RH}\right)^{\frac{1}{2.45}}.
\end{aligned}
$$

Inserting this expression into S_e gives the effective water saturation of the entire waste package:

$$S_e = \frac{V_w}{s_{N_2}} \frac{s_{WP}}{V_{WP}} = \frac{s_{WP}}{V_{WP}} \frac{M_w}{\rho_w A_w N_A} \left(\frac{-1.1}{\log_{10} RH} \right)^{\frac{1}{2.45}} \quad \text{(Eq. 10-5)}$$

The parameters used in this expression include the surface area and void volume of the waste package. As summarized in Table 10.3.1-8, estimates of the surface area can vary over five orders of magnitude. The initial void volume, as shown in Table 10.3.1-5, is 4.9724 m^3. This volume will decrease somewhat as corrosion products form, since the oxides occupy greater volume than the metals from which they are formed. However, the change depends on time and extent of corrosion, so for simplicity the initial void volume will be used. To give some idea of the effect of water saturation on surface area, some values of saturation are listed in Table 10.3.1-9 for various relative humidity values. The value used for the density of water is 988.0363 kg/m^3 at 50°C. The surface areas used are those summarized in Table 10.3.1-8 for different degradation states of the waste package. It is clear that the saturation can change enormously between the initial condition when the surface area is on the order of 1,000 m^2 to the time when the steel components are fully degraded.

Inserting S_e into the expression for the diffusion coefficient, and using water density at 50°C and the initial waste package porosity of 0.6539 (Section 10.3.1.3.3.1),

$$D_s = \phi^{1.3} S_e^2 D_{wl} = \phi^{1.3} \left(\frac{s_{WP}}{V_{WP}} \frac{M_w}{\rho_w A_w N_A} \right)^2 \theta_a^2 D_{wl}$$

$$= (0.6539)^{1.3} \left[\frac{s_{WP} \left(18.01528 \times 10^{-3} \frac{\text{kg H}_2\text{O}}{\text{mol}} \right)}{\left(4.9724\ \text{m}^3 \right) \left(988.0363 \frac{\text{kg H}_2\text{O}}{\text{m}^3} \right) \left(10.6 \times 10^{-20} \frac{\text{m}^2}{\text{molec.}} \right) \left(6.0221367 \times 10^{23} \frac{\text{molec.}}{\text{mol}} \right)} \right]^2 \theta_a^2 D_{wl}$$

$$D_s = 1.89957263654 \times 10^{-21} s_{WP}^2 \left(\frac{-1.1}{\log_{10} RH} \right)^{\frac{2}{2.45}} D_{wl} = 2.05326900807 \times 10^{-21} s_{WP}^2 \left(-\log_{10} RH \right)^{-0.816326530612} D_{wl}$$

For consistency with other uses of adsorption models, use natural logarithms instead of base 10 logs, using the relation

$$-\log_{10} RH = -\log_{10} \left(e^{\ln RH} \right) = -\ln RH \log_{10} e$$

Then the final expression for the diffusion coefficient is:

$$D_s = 4.05631924941 \times 10^{-21} s_{WP}^2 \left(-\ln RH\right)^{-0.816326530612} D_{wl} \qquad \text{(Eq. 10-6)}$$

Table 10.3.1-10 lists some values for D/D_{wl} for surface areas from Table 10.3.1-8 over a range of relative humidity values, showing the range of factors that impact the diffusion coefficient.

The difficulty in specifying the diffusion coefficient lies in determining at what point a correlation such as Archie's Law is valid and what type of correlation would be more appropriate at an intermediate degraded state. The approach used here is to compute diffusive fluxes using both a correlation for diffusion through porous media and a calculation for diffusion along failed fuel rods, then compare the results to determine which calculation is more appropriate or conservative.

If radionuclide sources (i.e., failed fuel rods) are distributed more or less uniformly throughout a waste package, then the source can be thought of as residing at the inside surface of the waste package, particularly if the inside of the package is largely degraded. In this case, the diffusive path is very short: the distance through the breach in the corrosion-resistant outer layer. The cross-sectional area for diffusion is the area of the water film covering the material that fills the corrosion patch. If the corrosion patch is mostly empty space, then diffusion must occur through a much smaller area around the perimeter of the breach. This situation will occur if the corroded Alloy 22 falls away, leaving a gaping hole where the breach occurs. In any event, the size of the breach, rather than the diffusive path area inside the waste package, will be the limiting factor for diffusion out of a waste package.

10.3.1.3.5.2 Diffusion Through General Corrosion Patches

Lee et al. (1996 [DIRS 100913]) developed a model for steady-state and "quasi-transient" diffusive releases from waste packages into the invert. In this model, perforations in the package are assumed to be cylindrical in shape. The diffusion path consists of the approach to the opening of the perforation from the waste form side; the path through the cylindrical portion of the perforation, which is filled with corrosion products; and the path through the exit disk separating the perforation from the invert. The waste is assumed to be distributed uniformly inside the waste container. The package is approximated by an equivalent spherical configuration, and the underlying invert is represented by a spherical shell surrounding the package.

The model of Lee et al. (1996 [DIRS 100913]) is suitable for the late stages of package degradation, when the waste form has become a mass of porous corrosion products. Although Lee et al. (1996 [DIRS 100913]) assumed the packages failed by pitting corrosion, which is no longer expected to occur (CRWMS M&O 2000 [DIRS 147648], p. 27), this model should be equally applicable to failure by patches from general corrosion.

The assumption of Lee et al. (1996 [DIRS 100913]) that the waste (i.e., the radionuclide source) is uniformly distributed inside the waste package restricts the applicability of the model to late times. The object of the present in-package diffusion model is to provide more realism at earlier and intermediate times, when the waste cannot yet be considered a uniform porous medium. On

the other hand, as discussed above, the fundamental assumption that diffusive releases are controlled by diffusion through breaches that are filled with porous corrosion products may be valid over much of the waste package lifetime, including early times, when stress corrosion cracks are the first breaches to appear. Lee et al. (1996 [DIRS 100913], p. 5-67) assume that the porosity of the perforations is $\phi_{cp} = 0.4$ and the percent volumetric water content is $\Phi = 10$ percent (i.e., $\Phi = 10$), so the water saturation in the perforations is a constant $S = \Phi/(100\phi_{cp}) = 0.25$. They compute a diffusion coefficient, D [cm^2/s] (Lee et al. 1996 [DIRS 100913], p. 5-67), for the porous corrosion products filling the perforations based on data from Conca and Wright (1990 [DIRS 101582]; 1992 [DIRS 100436]):

$$\log_{10} D = -8.255(\pm 0.0499) + 1.898(\pm 0.0464)\log_{10} \Phi \qquad \text{(Eq. 10-7)}$$

where the numbers in parentheses are one standard deviation. For $\Phi = 10$ percent, $D = 4.4 \times 10^{-7}$ cm^2/s for comparison, they assume that the diffusion coefficient inside the waste package is 10^{-5} cm^2/s (Lee et al. 1996 [DIRS 100913], p. 5-67). As a further comparison, the self-diffusion coefficient for water is 2.299×10^{-5} cm^2/s (CRWMS M&O 2000 [DIRS 153940], p. 58), and for many actinides the diffusion coefficient in water is roughly 5×10^{-6} cm^2/s (CRWMS M&O 2000 [DIRS 153940], Table 7). The value for D given by Equation 10-7 accounts for porosity and saturation, and so is comparable to the value for D_s given by Equation 10-6. If the self-diffusion coefficient for water is used for D_{wl}, then Equation 10-7 gives $D/D_{wl} = 1.91 \times 10^{-2}$. This is greater than the largest value in Table 10.3.1-10, indicating that the Lee et al. (1996 [DIRS 100913]) model for D represents very high relative humidity and very high surface area if adsorption is the sole mechanism for water appearing in the corrosion products. If no advection takes place, the assumption of a saturation of 0.25 is excessive. Using the lower saturations obtained from adsorption isotherms brings the diffusion coefficient from Equation 10-7 into closer agreement with the values in Table 10.3.1-10. For example, if $S = 10^{-5}$, then Equation 10-7 would give $D/D_{wl} = 9 \times 10^{-11}$. A more detailed calculation can be done to estimate the surface area of corrosion patches, the amount of water adsorbed at various relative humidity values, the resulting water saturation of the patches, and obtain a diffusion coefficient using Equation 10-6 or Equation 10-7.

10.3.1.3.5.3 Cross-Sectional Areas of General Corrosion Patches

The nominal area of a general corrosion patch is fixed in the current waste package degradation model (i.e., WAPDEG V4.0) at 2.346×10^4 mm^2, based on the equivalent area of 1,000 nodes on the surface of the package (CRWMS M&O 2000 [DIRS 153940], p. 37). If the patch exists through the Alloy 22 layer, which is 2 cm thick, the volume of the patch is 4.692×10^{-4} m^3. If the porosity, ϕ_{cp}, is 0.4, as used by Lee et al. (1996 [DIRS 100913]), the solids volume is 2.8152×10^{-4} m^3. Using a density for Fe_2O_3 of $\rho_{Fe_2O_3} = 5{,}240$ kg/m^3 (Weast 1985 [DIRS 111561], p. B-104), the mass of corrosion products filling the corrosion patch is 1.475 kg. The surface area of Fe_2O_3 in the patch, with a specific surface area of $\bar{s}_{Fe_2O_3} = 9.1 \times 10^3$ m^2/kg, is 1.342×10^4 m^2. The water saturation within the corrosion patch, $S_{e,cp}$, can be obtained as a function of RH using Equation 10-5, where V_{WP} and s_{WP} are replaced by V_{cp}, the total volume of

the corrosion patch (not the pore volume), and s_{cp}, the surface area of the patch (instead of the entire package). Since the surface area of corrosion products is:

$$\begin{aligned} s_{cp} &= m_{cp}\bar{s}_{Fe_2O_3} \\ &= \rho_{Fe_2O_3} V_{cp}\left(1-\phi_{cp}\right)\bar{s}_{Fe_2O_3} \end{aligned}$$

where m_{cp} is the mass of corrosion products [kg], the ratio of surface area to volume of the corrosion patch can be expressed as:

$$\frac{s_{cp}}{V_{cp}} = \rho_{Fe_2O_3}\bar{s}_{Fe_2O_3}\left(1-\phi_{cp}\right),$$

and the effective saturation of the patch is given by:

$$\begin{aligned} S_{e,cp} &= \frac{s_{cp}}{V_{cp}}\frac{M_w}{\rho_w A_w N_A}\left(\frac{-1.1}{\log_{10} RH}\right)^{\frac{1}{2.45}} \\ &= \frac{\rho_{Fe_2O_3}\bar{s}_{Fe_2O_3}\left(1-\phi_{cp}\right)M_w}{\rho_w A_w N_A}\theta_a \\ &= 1.19419\times 10^{-2}\left(-\ln RH\right)^{-1/2.45} \end{aligned} \qquad \text{(Eq. 10-8)}$$

The equivalent of Equation 10-6, which gives the effective diffusion coefficient based on Archie's Law, can similarly be obtained for the patch:

$$\begin{aligned} D_s &= \phi_{cp}^{1.3} S_{e,cp}^2 D_{wl} \\ &= (0.4)^{1.3}\left[1.19419\times 10^{-2}\left(-\ln RH\right)^{-1/2.45}\right]^2 D_{wl} \\ &= 4.33337\times 10^{-5}\left(-\ln RH\right)^{-0.816326530612} D_{wl} \end{aligned} \qquad \text{(Eq. 10-9)}$$

Alternatively, the diffusion coefficient can be obtained using Equation 10-7, in which

$$\Phi = 100 S_{e,cp}\phi_{cp} = 0.477676\left(-\ln RH\right)^{-0.40816}$$

then

$$\begin{aligned} \log_{10} D &= -8.255 + 1.898\log_{10}\Phi \\ &= -8.255 + 1.898\left[-0.320866 - 0.40816\log_{10}\left(-\ln RH\right)\right] \\ &= -8.864 - 0.775\log_{10}\left(-\ln RH\right) \end{aligned} \qquad \text{(Eq. 10-10)}$$

For example, at RH = 95 percent, and using $D_{wl} = 2.299\times 10^{-9}$ m^2/s, self-diffusion coefficient for water (CRWMS M&O 2000 [DIRS 153940], p. 10), the effective diffusion coefficient for the patch using Archie's Law (Equation 10-9) is $D_s = 1.13\times 10^{-12}$ m^2/s, and using Equation 10-10,

$D = 1.37 \times 10^{-8}$ m^2/s. For comparison with earlier estimates, such as Table 10.3.1-10 or Section 10.3.1.3.5.2, $D_s / D_{wl} = 4.90 \times 10^{-4}$ and 5.95 for these respective cases.

10.3.1.3.5.4 Cross-Sectional Areas of Stress Corrosion Cracks

When stress corrosion cracks first appear and are the only breaches in the package, the steel components will be largely intact and the surface area and cross-sectional areas of internal components will control diffusive releases. The total area of stress corrosion crack openings (assuming a mean of 25 stress corrosion cracks per waste package) is 1.02 cm^2, as shown above. Since even the very conservative estimate of initial cross-sectional area for diffusion within a package is 2.97×10^{-7} m^2 = 2.97×10^{-3} cm^2, it is the adsorbed water film inside the package that controls diffusive releases. This viewpoint is appropriate when corrosion products fill the stress corrosion cracks, as they eventually will, and radionuclides diffuse through these products.

If the stress corrosion crack is not filled with corrosion products, diffusion can still occur through an adsorbed water film on the sides of the stress corrosion cracks. In this case, the cross-sectional area through the stress corrosion cracks is computed from the perimeter of the stress corrosion crack and the film thickness. The *EBS Radionuclide Transport Abstraction* (CRWMS M&O 2000 [DIRS 153940], p. 51) gives a maximum crack length of 4 cm. Although a stress corrosion crack is theoretically ellipsoidal in shape, it is so narrow that the perimeter is approximately twice the length, or 8 cm. With 25 stress corrosion cracks/package, the total width of the diffusive path is 200 cm. The water film thickness, assuming adsorption on Fe_2O_3 at RH = 95 percent, as an example, is 1.39×10^{-9} m (4.91 monolayers of thickness $t_f = 2.83 \times 10^{-10}$ m), so the cross-sectional area for diffusion on the sides of stress corrosion cracks is 2.78×10^{-5} cm^2, or a factor of 100 less than the high estimate for cross-sectional area inside the waste package. While it is not unreasonable for the actual diffusive area inside the waste package to be at least two orders of magnitude less than the conservative estimate, the area for diffusion along the walls of the stress corrosion cracks is at least as small as the diffusive area in the interior of the waste package, and may in fact be the controlling dimension. If the stress corrosion cracks are filled with corrosion products, then the area inside the waste package is more likely to be controlling, as discussed in the preceding paragraph.

Expressions for the effective saturation and diffusion coefficient based on Archie's Law in a stress corrosion crack are identical to those obtained above for general corrosion patches, as long as the same porous material properties are assumed. In Equation 10-8 (effective saturation), the ratio of the surface area to the volume of patches, s_{cp} / V_{cp}, is independent of the dimensions of the penetration, since $s_{cp} / V_{cp} = \bar{s}_{Fe_2O_3} \rho_{Fe_2O_3} \left(1 - \phi_{cp}\right)$, where $\bar{s}_{Fe_2O_3}$ is the specific surface area of Fe_2O_3 [m^2/kg], whose density is $\rho_{Fe_2O_3}$ [kg/m^3], and porosity is ϕ_{cp}. Hence, the effective saturation and diffusion coefficient will be identical if the same porous material properties are valid.

10.3.1.3.6 Diffusive Path Length

For stress corrosion cracks, the diffusion path length may be as long as the waste package or longer, depending on the tortuosity. It may also be only a few centimeters, the shortest distance

from a fuel rod through a stress corrosion crack to the exterior of a waste package. The distance for corrosion patches will generally be shorter, since by then the waste package should be filled with porous corrosion products through which a more direct path will exist from failed fuel rods to the exterior. This is the key assumption of the Lee et al. (1996 [DIRS 100913]) model: that the interior of a waste package is a uniformly mixed source and the invert is contiguous to the exterior of the waste package.

When a package is first breached and the interior components have not yet degraded (except for the few initially failed fuel rods), a range of path lengths can be estimated with some certainty. As the steel components inside a package corrode, the diffusion path will likely become more tortuous on a microscopic scale, but more direct on a larger scale. The uncertainty in related parameters—porosity, saturation, cross-sectional area—will be so great that range and uncertainty in path length become relatively unimportant.

10.3.1.3.7 Comparison of Diffusive Release Estimates

In Table 10.3.1-11, the cross-sectional diffusion areas are summarized for the conditions described above. In addition, the quantity $D_s A / \Delta x = q / \Delta C$ is computed to provide a consistent comparison among the different states and conditions for a waste package. Based on these results, the highest releases are predicted to occur when all the adsorbed water is consolidated into a single bulk water pathway in a package with fully degraded internal components. However, this result is based on the most extreme degradation state and on the most conservative approach to calculating diffusive releases from a waste package. More realistic estimates for this quantity range from 10^{-15} to 10^{-11} m^3/s.

10.3.1.3.8 Implementation of In-Package Diffusion Model

This section summarizes the general approach, major assumptions, main steps in the computational algorithm, and the stochastic parameters for the in-package diffusion model for TSPA-SR sensitivity studies. The mathematical equations for the in-package diffusion model are described in Section 10.4.1.

10.3.1.3.8.1 General Approach

The general approach for the 21-PWR and 44-BWR waste packages is to consider three limiting pathways for diffusion: (1) along failed fuel rods; (2) through porous corrosion products inside the waste package; and (3) through porous corrosion products filling breaches (either stress corrosion cracks or general corrosion patches) in the outer layer of the waste package. Starting from the time when a package is first breached, the extent of degradation is determined. This gives the amount of corrosion products present inside a package and the size of penetrations, and allows water saturations and effective diffusion coefficients to be computed. The diffusive flux for releases by way of failed fuel rods and through corrosion products within the package is calculated, and the larger of these two is selected. Next, the diffusion rate through breaches in the package is computed. Since these two diffusion rates are in series, the smaller rate controls the overall diffusive release, so the smaller of the in-package diffusion rate and the breach diffusion rate is selected as the diffusive release.

10.3.1.3.8.2 Assumptions and Algorithms

The major assumptions for the in-package diffusion model are:

- This analysis applies when the seepage or dripping flux into the drifts is zero. This model also applies when the seepage flux is less than the rate of evaporation from the drip shield and waste package.

- The TSPA-SR model for transport in the waste package (CRWMS M&O 2000 [DIRS 153246], Section 3.6.1.2) will be used for those waste packages exposed to seepage because advective flow and transport through the waste package is anticipated to dominate diffusion in the seeping regions of the repository.

- This analysis applies to commercial SNF waste packages. Releases from DOE high-level radioactive waste packages should be calculated using the TSPA-SR models (CRWMS M&O 2000 [DIRS 153246], Section 3.6.1.2).

- There are no diffusive releases from any waste package until a breach occurs.

- Archie's Law is used to calculate the diffusion coefficient for unsaturated porous media. The exponents for porosity and saturation are based on experimental data for granular materials (see Section 10.3.1.3.5.1).

The major steps in the computational algorithm for in-package diffusion of commercial SNF waste packages are:

1. Determine the extent of degradation of the iron-based internal components of the waste package and the resulting surface area available for adsorption of water vapor. The extent of degradation is estimated from the lifetime of the internal components. More specifically, the effective surface area for adsorption is interpolated between the initial surface area and the fully degraded surface area as a function of the component lifetimes and the current simulation time.

2. Using the adsorption isotherm for Fe_2O_3, and assuming that the waste package void volume remains constant at 4.97 m^3 (Table 10.3.1-5), compute the amount of water vapor adsorbed (number of monolayers and film thickness) and the water saturation in the package.

3. Compute the effective diffusion coefficient for steel corrosion products, using Archie's Law and the water saturation obtained in Step 2. Calculate the total cross-sectional area of the corrosion products, depending on the main direction (axial or radial) for diffusion. Use axial diffusion if only stress corrosion cracks are present in the waste package; use radial diffusion once a patch forms.

4. Compute the amount of water adsorbed using the adsorption isotherm for ZrO_2, calculate the cross-sectional area for diffusion (not of the oxide layer) on the failed fuel rods, assuming axial diffusion, and assume that the effective diffusion coefficient is equal to the diffusion coefficient of radionuclides in water.

5. Calculate the diffusion rates through the steel corrosion products and along failed fuel rods. Use the larger of these two quantities as the in-package diffusion rate through the waste package. These two pathways are in parallel, so the larger rate will dominate diffusive transport.

6. Using the adsorption isotherm for Fe_2O_3, compute the amount of water vapor adsorbed (number of monolayers and film thickness) and the water saturation in breaches in the waste package. Compute the effective diffusion coefficient, using Archie's Law and the water saturation obtained in Step 6. Obtain the total area of all breaches (stress corrosion cracks and patches) in the waste package. Calculate the diffusion rate through patches. This approach assumes that all breaches are filled with Fe_2O_3 corrosion products.

7. Compare the diffusion rates for in-package diffusion (Step 6) and diffusion through breaches (Step 7), and select the smaller quantity as the rate of diffusion out of the waste package. These two pathways are sequential, so the smaller rate will limit diffusive transport.

The only sampled parameters that are not already used in another model are the diffusion path length, the corrosion rate of steel components, and the surface area factor for the waste package. The sampled parameters and their distributions are summarized in Table 10.3.1-12.

10.3.2 Diffusion from the Waste Package to the Invert

10.3.2.1 Goal of Model

The goal of this model is to quantify the impact of radionuclide transport on the outer surface of the waste package and on the emplacement pallet. Transport between the waste package and invert can occur through advective or diffusive mechanisms. Advective transport occurs when a radionuclide moves with a flowing fluid, such as droplets or films, on the surface of the waste package and emplacement pallet. Diffusive transport occurs when a radionuclide moves from a region of high concentration to a region of lower concentration on the surface of the waste package. Advective and diffusive transport will occur for those waste packages exposed to a dripping environment in the repository. Diffusive transport may be the primary transport mechanism in the dry regions of the repository. Because 87 percent of the waste packages are not expected to be subject to dripping seepage at ambient conditions (CRWMS M&O 2000 [DIRS 153246], p. 4-5), diffusion is an important process for release of radionuclides from the waste package to the invert. This section provides a model to evaluate the potential impact of these transport processes on repository performance.

10.3.2.2 Identification of Unquantified Uncertainties in Total System Performance Assessment-Site Recommendation

In 87 percent of the potential repository in Yucca Mountain, dripping from seeps is not expected to occur. In these no-drip regions, diffusive transport is always possible, with diffusion of radionuclides occurring through a thin film of adsorbed water that will cover all surfaces exposed to the humid air in the repository drifts. Advective transport is also possible if the thin films become thick enough to advect under gravity. The objective of this analysis is to develop an

abstraction for calculating radionuclide transport between the waste package and invert in the regions of the repository without seepage.

The TSPA-SR transport model for the waste package (CRWMS M&O 2000 [DIRS 153246], p. 3-141) conservatively assumes that the waste package is always in contact with the invert. In other words, the diffusive path length is essentially zero between the waste package and the invert because the emplacement pallet is assumed to have failed. This is a conservative assumption because the emplacement pallet support members are fabricated from Alloy 22 (CRWMS M&O 2000 [DIRS 150953], Section 2.3.3), a corrosion-resistant material, and because the design specification for the pallet and invert requires that they maintain the horizontal position of the waste package for 10,000 years (CRWMS M&O 2000 [DIRS 150953], Section 1.2.1.21).

Alternative thermal operating modes could affect the model for transport between the waste package and the invert in two ways. First, as discussed in Section 10.3.3.2, solute diffusion coefficients vary as a direct function of temperature. Second, as discussed in Section 5.3.1.4, the time-history of relative humidity in the drifts differs according to the thermal operating mode. Relative humidity affects the thickness of water films (Section 10.3.2.3) and the saturation of corrosion products (Section 10.3.1.3.2).

10.3.2.3 Quantification of Previously Unquantified Uncertainty

10.3.2.3.1 Water Films and Their Relevance to Transport

Water films can act as a medium for diffusive or advective transport of radionuclides, particularly on the outer surfaces of the waste package and pallet. Both mechanisms will occur simultaneously, but if diffusion predominates, radionuclide transport will be slow and the so-called “diffusive barrier” will contribute to waste isolation. The following discussion develops an estimate for the value of relative humidity at which advection on vertical or sloping surfaces could overwhelm diffusion and eliminate the diffusive barrier on the waste package/pallet surfaces.

Evidence for solute transport in water films is provided by the laboratory tracer testing of Tokunaga et al. (2000 [DIRS 152914]), which was conducted at a relative humidity greater than 99.9 percent. In addition, dye tracer migration in films has been observed in the niche studies conducted in the Exploratory Studies Facility (Wang et al. 1998 [DIRS 154423], Section 2).

Films will accumulate on solid surfaces because of adsorption and long-range ordering and because of capillarity on rough surfaces with dust or other granular material. Film thickness will increase with relative humidity in the drift environment because the films will be in moisture potential equilibrium with the gas phase (except where dripping seepage forms thicker films). Thinner films may form if they are not in full equilibrium with water vapor, as may occur with moving films.

Film thickness greater than 0.1 μm is known to occur on rock or prepared glass surfaces only at values of relative humidity approaching 100 percent. Such conditions will not occur during preclosure ventilation or early in the postclosure period because the relative humidity will be too

low. But relative humidity may approach 100 percent after cooldown begins, particularly in cooler regions of the emplacement areas, where there may be localized condensing-humidity conditions.

The following discussion pertains to the potential for advective movement of a water film without regard to water composition. Gradients in total water potential, including the effects of chemical gradients, could also drive the movement of films, as described by Landau and Lifschitz (1959 [DIRS 155006], pp. 241 to 244).

10.3.2.3.2 Film Thickness Relationships

Film thickness depends on the composite effect from different types of forces acting near the solid-liquid interface and the liquid-vapor interface. These forces can alter the liquid density, the liquid composition, and the orientation (ordering) of the liquid molecules. The combined effects from the solid-liquid and liquid-vapor interfaces determine the free energy of the film, so the energy depends on film thickness.

Long-range forces include double-layer effects and van der Waals forces, which can affect film behavior for thicknesses up to approximately 1 micron (de Gennes 1985 [DIRS 154424]). The relative contribution from each type of force depends on the nature of the solid and liquid materials. For thicker films, in the approximate range of 0.1 to 1 micron, capillarity becomes increasingly important, depending on the scale of surface roughness (Philip 1977 [DIRS 152255]). The important point is that the transition from surface-dominated to capillary-dominated behavior occurs in the same range of film thickness as the transition from relatively immobile to mobile film flow characteristics. This transition range corresponds to a relative humidity of approximately 98 to 99 percent, which is likely to occur in the repository during cooldown.

Measured data and predictive relationships for film thickness selected from the scientific literature are plotted in Figure 10.3.2-1. The various results from the literature that are shown in this figure are plotted against the variable log(1-RH) to show the important relative humidity range above 99 percent. Measurements for aqueous films contacting air are taken from Tokunaga and Wan (1997 [DIRS 139195], Figure 7) and Tokunaga et al. (2000 [DIRS 152914], Figure 6), for Bishop tuff and roughened glass, respectively. These data are plotted directly from the sources, with conversion of values on the abscissas from matric head to log(1-RH).

The predictive relationship from Philip (1977 [DIRS 152255], p. 5074) (power-law expression for film potential, F, versus film thickness, ν) is also plotted in Figure 10.3.2-1. This relation is reported to be consistent with limited available published data for films on wetting surfaces (Philip 1977 [DIRS 152255], pp. 5072 to 5074). The Hamaker equation (Middleman 1995 [DIRS 144046], Equation 9.2-2) is also plotted for comparison; this equation is typically applied for wetting, nonpolar liquids (such as lubricant films) on metal surfaces and is not strictly applicable to water-wetting surfaces. Water films are more complex because of the possibility of interfering double-layer effects from the solid-liquid and liquid-vapor interfaces and hydrogen bonding at the solid surface (Middleman 1995 [DIRS 144046], p. 242).

Figure 10.3.2-1 indicates that film thickness decreases rapidly with lower relative humidity and that surface roughness tends to increase the apparent average film thickness, but the contribution of roughness to the supporting data for the predictive relationships is unknown. Thus, the measured data (and the predictive relationships) may tend to indicate greater film thickness for the same relative humidity.

10.3.2.3.3 Film Transmissivity and Flow Velocity

Tokunaga et al. (2000 [DIRS 152914]) developed estimates for film transmissivity that represent the average volumetric flow rate under a unit potential gradient (i.e., gravity). Transmissivity, T, is defined as a function of film thickness, h, as:

$$T(h) = D(h)\frac{dh}{dF} \qquad \text{(Eq. 10-11)}$$

where D is the diffusivity and dh/dF is the derivative of film thickness with moisture potential. This equation corresponds to Equation 1 from Tokunaga et al. (2000 [DIRS 152914]), with a change of notation to conform to Philip (1977 [DIRS 152255]). Diffusivity D was measured directly on prepared samples using transient methods from unsaturated zone hydrology (Tokunaga et al. 2000 [DIRS 152914], pp. 1739 to 1741). The film thickness potential relationship was measured directly using a gravimetric method.

The transmissivity can be used to estimate the average film velocity (averaged through the film thickness), $\bar{v}$, on a vertical surface under the impetus of gravity (Tokunaga et al. 2000 [DIRS 152914], p. 1744):

$$\bar{v} = \frac{T(h)}{h} \qquad \text{(Eq. 10-12)}$$

The resulting plot of average film velocity for roughened glass over the range of film thickness investigated by Tokunaga et al. (2000 [DIRS 152914], Figure 10) is presented in Figure 10.3.2-2. Another approach to estimating average velocity is based on application of the Navier-Stokes equations to one-dimensional flow of a Newtonian fluid (Tokunaga and Wan 1997 [DIRS 139195], Equation 1). This approach is also plotted on Figure 10.3.2-2 for comparison, and shows that the average velocity can be much greater if viscous dissipation (from long-range ordering) and surface roughness effects are neglected.

10.3.2.3.4 Application of Film Flow Concepts to Performance Assessment

The available information for film behavior can be used to estimate how environmental conditions in the emplacement drifts can affect the transport of radionuclides released from the waste packages. More specifically, thin film behavior can be used to determine whether transport on the external surfaces of the waste package and pallet becomes advection-dominated at high humidity such that releases to the invert would not be diffusion-limited.

In the following discussion, the term “potential” refers to the additive sum of hydrostatic pressure, capillary, osmotic, and adsorptive potential components. The potential in thin films of

dilute water on smooth surfaces is dominated by the adsorptive potential, but the importance of the capillary potential increases as film thickness or surface roughness increases. The relative humidity of a gas phase contacting a water film is assumed to be at equilibrium to the potential, because each of the potential components affects the chemical activity of water. The literature data are based on tests that vary only matric potential, but the conversion to relative humidity for discussion purposes is still valid.

Recent laboratory work on roughened glass surfaces has extended the reported range of potential for direct measurement of average film thickness down to approximately –50 kPa (Tokunaga et al. 2000 [DIRS 152914]), p. 1743 and Figure 6), corresponding to an equilibrium relative humidity of approximately 99.99 percent (condensing humidity) at 25°C, according to the Kelvin equation (Atkins 1990 [DIRS 111464], p. 148, Equation 13b). At this equilibrium relative humidity, the measured film thickness was 0.75 μm (Tokunaga et al. 2000 [DIRS 152914], p. 1743), corresponding to an average vertical film flow velocity of approximately 1 cm/yr (Tokunaga et al. 2000 [DIRS 152914], Figure 10). Further reduction in velocity can be expected at a lower relative humidity because of the strong relative humidity dependence observed in these tests, and because viscous dissipation intensifies for thinner films. As film thickness approaches 0.1 μm, long-range forces promote molecular ordering of the liquid and greater viscous resistance to flow (de Gennes 1985 [DIRS 154424], p. 857). The effect of increased viscous dissipation decreases the film transmissivity and average film flow velocity (i.e., in response to gravity). As the film thickness approaches 0.01 μm, viscous dissipation can be "very strong" (de Gennes 1985 [DIRS 154424], p. 853).

Glass is water-wetted, as are tuffaceous minerals (Tokunaga and Wan 1997 [DIRS 139195]) and metal-oxides (de Gennes 1985 [DIRS 154424], p. 830). Wetting properties of common soda glass are similar to rock dust and the corrosion products that will exist on the surfaces of waste packages and emplacement pallets. The porous surface texture of roughened glass reported by Tokunaga et al. (2000 [DIRS 152914], p. 1740) represents a scale of roughness that is likely to be present on the machined surfaces of the waste package and pallet, along with roughness at other scales. Roughness at larger scales could contribute to increased average film transmissivity when conditions are sufficiently humid (see discussion of heterogeneity effects below). Roughness at smaller scales could accumulate liquid water at lower values of moisture potential (more negative), but this would be associated with smaller values of film transmissivity because of the thinner films that exist at those potentials. Consequently, the results for roughened glass are considered to be suitable for approximating the minimum relative humidity for which film mobility could become important in the EBS.

The results of Tokunaga et al. (2000 [DIRS 152914]) were limited to a moisture potential of approximately –50 kPa, but other estimates of film thickness at drier conditions are available, as discussed above. The Philip (1977 [DIRS 152255]) model predicts thicker films than Tokunaga et al. (2000 [DIRS 152914]). These estimates support an inference that the equilibrium film thickness on the waste package and pallet at more negative moisture potential (lower relative humidity) will be very small.

From the Navier-Stokes solution for film flow (Tokunaga and Wan 1997 [DIRS 139195], Equation 1), the average film velocity on a vertical surface is less than 1 cm/yr for a film thickness less than 0.01 μm (Figure 10.3.2-2). In fact, the average thickness is probably much

less than the value predicted by the Philip model, which does not explicitly account for the effects of surface roughness and long-range molecular interactions that increase when water films become very thin. Similarly, the average film velocity is probably much less than that calculated using the Navier-Stokes solution; for example, the Tokunaga et al. (2000 [DIRS 152914]) results show that this approach greatly overestimates film mobility for roughened glass (Figure 10.3.2-2).

10.3.2.3.5 Uncertainties and Limitations

Solutes affect the activity of water in solution and may change the free energy of a thin film. Ionic solutes tend to shorten the length scale for electrostatic interactions, which would affect the free energy for thin films (e.g., less than 1 μm, where adsorption becomes much more important, as discussed previously). Surface tension (against vapor) for aqueous solutions of common salts increases with concentration, but is relatively insensitive (Weast and Astle 1981 [DIRS 100833], p. F-34). By analogy, film behavior may also be relatively insensitive to the effect of solutes. The associated uncertainty in the average velocity of film flow is probably less than that associated with surface roughness heterogeneity.

This discussion is limited to film flow on wettable surfaces, which is generally applicable to metal-oxide surfaces in the EBS. However, there is a possibility that metallic surfaces in the EBS could have nonwetting characteristics, which would tend to decrease film thickness and mobility, but could also induce the formation of droplets. If droplets were in moisture equilibrium with the gas phase, their sizes could range from a few microns to a few millimeters in the relative humidity range of 99 to 99.99 percent or greater. The transport characteristics of such droplets are not addressed here.

Effects of surface heterogeneity produce channeling of flow, as observed by Tokunaga et al. (2000 [DIRS 152914], p. 1743 and Figure 5) in comparing transient film movement on roughened plate glass versus glass cast of a natural fracture surface. The macroscopic average film flow velocity may be increased because movement of thicker films in channels is less hindered by viscous dissipation. Fluid film thickness in channels may be increased by capillarity, depending on the scale of surface roughness. Capillarity was probably important in the results presented by Tokunaga et al. (2000 [DIRS 152914], p. 1740) because the surface exhibited roughness at scales similar to the average film thickness, and because the relative humidity was sufficiently high that the potential equilibrium capillary radius-of-curvature for the film surface was of the same order as the scale of surface roughness.

The Philip approach for estimating film free energy (corresponding to matrix potential) is empirical, based on selection of a functional form to represent available measured data (Philip 1977 [DIRS 152255], Equation 33). The approach would suggest that film free energy increases with absolute temperature (Philip 1977 [DIRS 152255], Equation 34), such that a thicker, more mobile film would form in equilibrium with a given value of relative humidity. However, the surface tension of pure water against air (Weast and Astle 1981 [DIRS 100833], p. F-36), and thus the energy associated with this interface, decreases with increasing temperature. This appears to be inconsistent based on an analogy between liquid-vapor and solid-liquid interactions, and is not supported by empirical data. Thus, the approach is

appropriate for estimating film behavior at ambient temperatures, but not at temperatures that differ markedly from 25°C.

10.3.2.3.6 Application to Total System Performance Assessment

The results in Figures 10.3.2-1 and 10.3.2-2 provide a basis for a rough estimate of the maximum relative humidity required for diffusion to dominate transport between the waste package and the invert in the non-seeping areas of the repository. Assuming that the advective travel time on the surfaces of the waste package and pallet must be more than 10,000 years for diffusion to dominate transport, then the advective velocity must be less than 10^{-4} m/yr (1 m/10,000 yr = 10^{-4} m/yr) for a characteristic length scale of 1 m between the waste package and invert. Figure 10.3.2-2 shows that the film thickness must be less than 0.001 μm for the advective velocity to be less than 10^{-4} m/yr, based on the Navier-Stokes equation. The corresponding limit on relative humidity is given in Figure 10.3.2-1 as 90 percent for the Phillip model. (The Hamaker equation is ignored here because water is a polar molecule.) In other words, the relative humidity must be less than 90 percent for the film thickness to be small enough that advective transport will take 10,000 years or more on the surface of the waste package and emplacement pallet.

An alternative (less conservative) approach is to use the Tokunaga data in Figure 10.3.2-2 instead of the Navier-Stokes equation. In this case, the film thickness must be less than 1 μm and the upper limit on relative humidity becomes 99.99 percent (Figure 10.3.2-1). Clearly, the range of response for relative humidity is quite large, varying from 90 percent to more than 99.99 percent.

At the low extreme, the relative humidity in the repository is expected to rise above 90 percent during the long cooldown period. This means that advective transport must be considered on the waste package and pallet if the Phillip model is valid. At the high extreme, the relative humidity may never reach 99.99 percent in the general repository and advective transport can be ignored, except perhaps near cooler waste packages or cooler regions of the repository. In this situation, the significance of advective transport will depend on the detailed three-dimensional thermal-hydrologic response of the repository for the emplaced waste packages.

The baseline model for transport between the waste package and the invert will be used until additional information is available on thin film flow and until TSPA-SR sensitivity results are analyzed to determine the impacts from the other models introduced in this section. A detailed advective-diffusive transport model between the waste form and the invert may be implemented when (1) three-dimensional predictions of relative humidity and waste package temperature are available to the required level of detail, (2) the effects of surface roughness and heterogeneity for the repository system can be quantified, and (3) the maximum value of relative humidity that will prevent advective transport within the repository system can be determined.

10.3.3 Diffusion Through the Invert

10.3.3.1 Goal of Model

The goal of this model is to quantify the impact of the uncertainty in the diffusion coefficient on radionuclide transport through the invert. The diffusion coefficient abstraction for the TSPA-SR (CRWMS M&O 2000 [DIRS 153246], pp. 3-138 to 3-139) already includes the effects of invert porosity, invert saturation, invert temperature, and the uncertainty in experimental measurements of the diffusivity of granular materials. The analysis for this model will eliminate a conservatism in the dependence of diffusivity on porosity, quantify the conservatism in using the self-diffusivity of water as a bounding value for all radionuclides of interest for the TSPA-SR, and evaluate the uncertainty in using a volume-averaged saturation for the invert rather than a more detailed saturation gradient for diffusive transport.

10.3.3.2 Identification of Unquantified Uncertainties in Total System Performance Assessment-Site Recommendation

The current model represents the diffusion coefficient in the waste package and invert as a function of porosity, saturation, and temperature (CRWMS M&O 2000 [DIRS 153940], Section 6.4.1). The TSPA-SR abstraction for diffusion coefficient is as follows:

- The self-diffusivity of water is a bounding value for the free water diffusivity of all radionuclides at 25°C.

- The free water diffusion coefficient is corrected for the porosity and (liquid) saturation of the invert as a porous medium. The correction for porosity and saturation is conservatively represented, based on Archie's law and experimental data for granular media.

- The diffusion coefficient for a partly saturated medium is corrected for the temperature of the invert.

- The effects of concentrated solutions are neglected in the TSPA-SR. The rationale for this choice (CRWMS M&O 2000 [DIRS 153940], Section 6.4.1.4) is that the maximum correction to diffusivity for a highly concentrated solution of potassium iodide is an increase of 27 percent. This increase is on the same order as the bounding approximation inherent in using the self-diffusion coefficient of water for all radionuclides, so it is neglected in the TSPA-SR.

Two of the conservatisms/uncertainties associated with this model have been quantified in previous work (CRWMS M&O 2000 [DIRS 153940]). These features are the uncertainty of the diffusivity of an unsaturated, porous medium and the use of a bounding value for free water diffusivity for all radionuclides. These conservatisms are discussed in Sections 10.3.3.3.1 and 10.3.3.3.2, respectively.

A third uncertainty relates to the use of a uniform saturation for the invert, based on the volume-averaged saturation from the NUFT multiscale model (CRWMS M&O 2000

[DIRS 139610]). An alternate approach, using a more detailed computational grid to evaluate the saturation gradient within the invert and its potential effect on diffusive transport, has been evaluated to quantify this uncertainty. These computational results are discussed in Section 10.3.3.3.3.

Alternative thermal operating modes will affect the diffusion coefficient directly, because of its functional dependence on invert temperature, and indirectly, because of its functional dependence on invert saturation.

10.3.3.3 Quantification of Previously Unquantified Uncertainty

10.3.3.3.1 Uncertainty for Unsaturated Porous Media

Conca and Wright (1992 [DIRS 100436]) measured the diffusion coefficient of unsaturated soil, gravel, bentonite, rock, and crushed tuff from Yucca Mountain over a broad range of water contents (DTN: MO9810SPA00026.000 [DIRS 137076]). These measured data have been used to analyze the dependence of the diffusion coefficient on volumetric moisture content for a variety of granular materials (CRWMS M&O 2000 [DIRS 150418], p. 3-138). Figure 10.3.3-1 presents a summary of the diffusivity data for various granular media and for volumetric moisture content between 0.5 percent and 40 percent.

A statistical analysis (CRWMS M&O 2000 [DIRS 150418], pp. 21 to 25) produced an excellent fit to the diffusivity data using a power law dependence on moisture content in the range of 1.5 percent to 66.3 percent. The statistical fit to the diffusion coefficient, D, is based on a linearizing transformation to the variables X and Y, defined as:

$$Y = \log(D / D_0)$$
$$X = \log(\theta) - 2$$

where

- D = the diffusion coefficient
- D_0 = free water diffusivity
- θ = volumetric moisture content (CRWMS M&O 2000 [DIRS 150418], Equation 31).

The slope of the X-Y relationship is evaluated to be 1.849 (CRWMS M&O 2000 [DIRS 150418], Equation 37), leading to the following linear equation for Y as a function of X:

$$Y = (1.849)X$$
$$\log\left(\frac{D}{D_0}\right) = (1.849)(\log(\theta) - 2) \qquad \text{(Eq. 10-13)}$$

In this equation, θ, the volumetric moisture content, is defined as $\theta = 100\phi s$, where ϕ is porosity and s is the liquid saturation of the porous medium. Both ϕ and s are nondimensional, with values between 0 and 1. Substituting the definition of θ into the linear fit and exponentiating both sides as powers of 10 results in:

$$D = D_0 \phi^{1.849} s^{1.849} \quad \text{(Eq. 10-14)}$$

A slightly different representation of the diffusion coefficient was used in the TSPA-SR (CRWMS M&O 2000 [DIRS 153246], p. 3-138):

$$D = D_0 \phi^{1.3} s^{1.849} \quad \text{(Eq. 10-15)}$$

This equation has the same exponent for saturation as the statistical fit, but the exponent for porosity is set equal to the cementation factor for unconsolidated sand (CRWMS M&O 2000 [DIRS 150418], Section 4.1.2, p. 7). The rationale for using Equation 10-15 in the TSPA-SR (CRWMS M&O 2000 [DIRS 153246]), rather than the direct statistical fit (Equation 10-14), is that the statistical analysis is based on a single parameter—the volumetric moisture content—and does not treat porosity as an independent variable. In reality, the porosity of the various granular materials varies. Given this situation, it seemed appropriate to use the slightly more conservative representation in Equation 10-15. For example, the diffusion coefficient is 46 percent greater for a porosity of 50 percent with the TSPA-SR representation, assuming the same value for liquid saturation.

Given the robustness of the data set, which includes crushed tuff (Figure 10.3.3-1), and the accuracy of the statistical fit over a broad range of moisture contents, it is appropriate to use the (full) statistical fit for the TSPA-SR sensitivity studies, thereby eliminating the 40 percent conservatism from using an exponent for porosity based on unconsolidated sand.

The statistical fit for the diffusion coefficient has uncertainty because of the scatter of data points in Figure 10.3.3-1. This uncertainty approximates a normal distribution for the residuals in log-log space (CRWMS M&O 2000 [DIRS 150418], Figure 4). This normal distribution has a mean value of 0.0 and a standard deviation of 0.223 (CRWMS M&O 2000 [DIRS 150418], Equation 38). The uncertainty can be incorporated into the statistical fit as an additional factor on the (full) statistical fit.

$$D = D_0 \phi^{1.849} s^{1.849} 10^{ND(a=0,\sigma=0.223)} \quad \text{(Eq. 10-16)}$$

where ND represents a normal distribution with a mean, a, of 0 and a standard deviation, σ, of 0.223. ND is in the exponent because the residuals are calculated in the log-log space of the statistical fit.

Figure 10.3.3-2 presents the statistical fit (solid line) and the upper and lower bounds (dashed lines) at two standard deviations above and below the fit. The dashed lines encompass almost all the data points, as would be expected because ± 2 standard deviations includes 97.7 percent of the area under a normal distribution. The above equation therefore accurately represents the uncertainty in the diffusivity data for the TSPA calculations.

The normal distribution was sampled for each realization of the TSPA-SR calculations (CRWMS M&O 2000 [DIRS 153246]), thereby incorporating the uncertainty of the experimental data into the diffusivity. A similar procedure should also be used for the final TSPA-SR calculations.

10.3.3.3.2 Uncertainty in the Self-Diffusivity of Water as an Upper Bound

The self-diffusion coefficient for water, 2.299×10^{-5} cm^2/s at 25°C, provides a conservative bound for the diffusion of ionic and neutral inorganic and organometal species that may be released from a waste package (CRWMS M&O 2000 [DIRS 153940], Section 6.4.1.1). This assertion is based on the following:

- A survey of compiled diffusion coefficients at 25ºC shows that simple cation and anion species (excluding the proton and hydroxyl species, which are not appropriate analogues for diffusing radionuclide species) have diffusion coefficients smaller than that of water.

- The self-diffusion coefficient for water at 90ºC is larger than compiled diffusion coefficients for simple inorganic species at 100ºC.

- Diffusion coefficients for simple lanthanide and actinide cations are much smaller than the self-diffusion coefficient of water, and are expected to be even smaller for their hydroxyl and carbonate complexes.

An alternative approach is to use four diffusion coefficients to provide a more realistic model. One coefficient could be used for each charge (monovalent, divalent, and trivalent species) and one for the hydroxyl and carbonate complexes of the actinides and lanthanides. At 25ºC, the monovalent, divalent, and trivalent species have ranges of diffusion coefficients, as shown in Figure 10.3.3-3 (CRWMS M&O 2000 [DIRS 153940], Figure 5). The free water diffusivity is shown as the dashed line on this figure. The conservatism for the monovalent, divalent, and trivalent species is indicated by the size of the vertical "gap" between the data points and the dashed line; it varies between factors of 1.07 and 2.6 for monovalent species, between factors of 2.1 to 3.8 for divalent species, and by a factor of 3.8 for the trivalent species.

Given the potential variability of the in-drift chemical environment, it is not feasible to characterize the various radionuclide complexes that may exist in the invert. The current approach, using the self-diffusivity of water as an upper bound for the free water diffusivity of all radionuclides relevant to the TSPA, will be maintained in the TSPA-SR (CRWMS M&O 2000 [DIRS 153246], p. 3-138). This approach is conservative by a factor between 1 and 3.8 for the monovalent, divalent, and trivalent species in the invert.

10.3.3.3.3 Uncertainty in the Average Saturation for the Invert

The TSPA-SR analyses (CRWMS M&O 2000 [DIRS 153246], p. 3-134) use the saturation in the invert, as defined by the abstraction of thermal-hydraulic calculations, to determine the diffusivity in the invert. If a substantial saturation gradient exists in the invert, then the calculation of diffusivity from the volume-averaged saturation may be overly conservative. For example, it is possible that the liquid saturation at the top of the invert could be substantially lower than its average value if capillarity cannot draw liquid upward throughout the invert. In

this situation, the diffusion coefficient will be substantially smaller at the top of the invert, providing a barrier to diffusive transport. This decrease can be calculated for an example 50 percent reduction in liquid saturation as follows:

$$\frac{D_{top}}{D_{vol-avg}} \propto \left(\frac{s_{top}}{s_{vol-avg}} \right)^{1.849} \propto \left(\frac{0.5}{1} \right)^{1.849} = 0.28 \qquad \text{(Eq. 10-17)}$$

where the subscripts *top* and *vol-avg* indicate the parameter values at the top surface or volume-averaged throughout the invert. A similar calculation for an order of magnitude decrease in saturation shows that the diffusion coefficient decreases by a factor of 70 (i.e., $(0.1)^{1.849} = 0.014 = 1/70$). Clearly, the value of the diffusion coefficient is sensitive to the liquid saturation along the transport pathway in the invert.

A new analysis was performed with the NUFT, RADPRO, and XTOOL computer codes to evaluate the saturation gradient in the invert. Qualified software for this analysis is:

- NUFT 3.0s for modeling fully coupled, unsaturated-saturated flow of multiple phases and multiple components under non-isothermal conditions
- RADPRO 3.22 for defining radiation connectivity within the drift
- XTOOL 10.1, which is a postprocessor for NUFT output.

The new analysis is based on the same inputs, assumptions, and qualified software used in *In-Drift Thermal-Hydrological-Chemical Model* (CRWMS M&O 2000 [DIRS 131150]) for an equivalent continuum model, with the following exceptions:

- Backfill is not present in the space between the drip shield and the drift wall because the design basis for the TSPA-SR is a repository without backfill (CRWMS M&O 2001 [DIRS 153681], p. 2-18).
- An effective thermal conductivity of 0.40 W/m/K is used for air between the drip shield and the drift wall. This value in the outer annulus is a result of model calibration and validation.
- An approximately-round shape for the waste package and a letter-box shape (a rounded top and vertical sides) for the drip shield are included in the model.
- The air gap below the drip shield extends through the space between the waste package and the invert (i.e., the waste package is not in contact with the invert).
- Simulation time is 0 to 10,000 years. This duration allows the liquid saturation in the invert to approach an approximately steady-state value.
- A lower-temperature operating mode is based on the thermal loading for the latest design (BSC 2001 [DIRS 154461]).

- The grid for the simulation (Figure 10.3.3-4) is finer than that used for typical calculations with the multiscale thermal-hydrologic model (CRWMS M&O 2000 [DIRS 139610], Figure 6-3). This finer grid provides more resolution in the invert.

Figures 10.3.3-5 and 10.3.3-6 depict the liquid saturation in the EBS and in the invert at 10,000 years, respectively. The NUFT calculation predicts constant saturation in the invert underneath the drip shield, demonstrating that the saturation beneath the waste package, in the transport pathway for radionuclides through the invert, is essentially constant (uniform). In this case, the use of a volume-averaged saturation for the invert provides acceptable accuracy for calculating the effect of saturation on the diffusion coefficient.

10.3.4 Sorption of Dissolved Radionuclides

10.3.4.1 Goal of Model

The goal of this model is to quantify the impact of sorption processes on radionuclide transport through the EBS. Transport through the EBS is a function of the adsorption and desorption of radionuclides on the materials in the waste package and invert. Adsorption describes the uptake of a radionuclide by a solid surface when in contact with a radionuclide-laden aqueous solution. This uptake typically occurs when a bond is formed by surface sites that have a chemical affinity for the radionuclide. Progressive inflow of fluids with low radionuclide concentrations would thermodynamically favor desorption of the original population of sorbed radionuclides back into solution. The fully reversible sorption and desorption of radionuclides is often described by a linear isotherm, using a partition coefficient (K_d).

Irreversible sorption refers to the tendency in natural systems for desorption to be incomplete. In other words, the amount of sorbed contaminant available for desorption in natural systems is typically less than the total sorbed mass due to chemical and physical processes occurring at or beneath the mineral surface. Sorption processes will be referred to as adsorption if the process occurs on the surface or absorption if the process occurs beneath the surface.

This section defines a conceptual model for transport through the degraded EBS, including appropriate ranges of K_d values for americium, iodine, neptunium, plutonium, technetium, thorium, and uranium, and the defensibility of irreversible sorption for these radionuclides.

10.3.4.2 Identification of Unquantified Uncertainties in Total System Performance Assessment-Site Recommendation

The current TSPA-SR transport model for the EBS assumes no sorption or retardation of dissolved species of radionuclides (CRWMS M&O 2000 [DIRS 153246], p. 3-134). This assumption is very conservative for several reasons:

- A large mass of iron-(hydr)oxides, including species such as hematite, will be generated through corrosion of mild steel and stainless steels within the waste package and invert. The iron-(hydr)oxides are known to be excellent sorbers of many radionuclide species (Table 10.3.4-1).

- Some sorbed radionuclides, such as plutonium, appear not to desorb in many geologic environments (Section 10.3.4.3.3.4). In effect, the sorption process appears partly irreversible and a substantial percentage of sorbed radionuclides would appear to be permanently attached to the corrosion products in the EBS. But it is difficult to quantify irreversibility because the time scale for laboratory experiments or field observations is much shorter than repository time scales. In this situation, the short-term data may provide misleading information about long-term irreversibility. The net effect of irreversible sorption on EBS transport will depend on two competing effects: (1) irreversible sorption on the in-drift materials will decrease releases from the EBS, and (2) irreversible sorption to stable colloidal particles will increase transport through the EBS.

- Copper is present along the top of the invert as an electrical conductor. Two corrosion products produced by the alteration of elemental copper can strongly sorb iodine and technetium species (Table 10.3.4-1), an important feature for decreasing releases of two elements that generally have minimal sorption in oxidizing environments.

Partition coefficients are typically measured for groundwaters and substrates at ambient or near ambient temperatures. There is little or no experimental data for partition coefficients at the elevated temperatures that may occur in the EBS with either the repository design and operating mode described in the *Yucca Mountain Science and Engineering Report* (DOE 2001 [DIRS 153849]) or an alternative thermal operating mode. In this situation, the available data for partition coefficients have been used to define the ranges of K_d values for TSPA analyses, but it is not possible to distinguish alternative thermal operating modes in this model.

10.3.4.3 Quantification of Previously Unquantified Uncertainty

10.3.4.3.1 Conceptual Model for the In-Drift Environment

The mild steel and stainless steel in the waste package and invert (Table 10.3.4-2) are expected to degrade to iron-(hydr)oxides more rapidly than the corrosion-resistant materials in the EBS (e.g., Alloy 22 and titanium). The time sequence for corrosion of iron-based components in the EBS is:

- Mild steel in the invert (support beams, cap plate, and gantry rails) will begin to degrade after closure of the potential repository because the invert is directly exposed to the relative humidity and temperature environment within the drifts. Corrosion begins when the relative humidity becomes great enough to produce aqueous conditions on the surface. A threshold value of 70 percent has been estimated (CRWMS M&O 2000 [DIRS 151951], Assumption 5.3.9, p. 45), although the presence of deliquescent salts can result in aqueous conditions at lower values of relative humidity.

  The steel and copper are in the top portion of the invert. More specifically, the longitudinal and transverse support beams are in the top half of the invert, based on *Committed Materials in Repository Drifts* (BSC 2001 [DIRS 154441], Figure 3). The transverse support beams are spaced at about 5-ft intervals, so the corrosion products from the beam will not always be directly beneath the emplacement pallet or stress

corrosion cracks. Below these beams, the invert is filled to depth with a granular ballast that does not contain any steel.

- Stainless steel rods in the emplacement pallet will corrode more slowly than mild steel (see footnote to Table 10.3.4-2). Again, the rods are directly exposed to the in-drift temperature and relative humidity after closure. The rods in the emplacement pallet are located directly beneath the waste package, in the anticipated flow path from the waste package.

- Mild steel (i.e., A 516 and borated steels) inside the waste package can begin to degrade after stress corrosion cracks form in the waste package. The earliest cracks form approximately 10,000 years after closure of the potential repository in the current TSPA-SR model (CRWMS M&O 2000 [DIRS 153246], p. F3-61, Figure 3.4-19 middle plot). Water vapor can enter the waste package once a crack forms, and this vapor will be adsorbed on the steel surfaces, providing an environment for corrosion within the waste package.

- Stainless steel inside the waste package can also corrode, albeit more slowly than mild steel, after a stress corrosion crack forms in the lid weld.

All mild steel components in the invert and emplacement pallet will degrade to iron-(hydr)oxides by the time the first stress corrosion cracks form at 10,000 years. In other words, iron-(hydr)oxides will be present in the invert before any radionuclides are transported from the waste package. After stress corrosion cracks form, the mild steel internals in the waste package will also degrade relatively rapidly, adding more iron-(hydr)oxides to the in-package environment. Most iron-based in-package materials will degrade to corrosion products by 25,000 years (Table 10.3.4-2), relatively early in the waste package lifetime.

The degradation products from corrosion of iron, aluminum, and copper-based materials in the waste package will include hydrous metal oxides and clays from degradation of high-level radioactive waste glass. These corrosion products are assumed to form a residue that is similar to a highly iron-rich soil or sediment in terms of its bulk chemical properties for determining appropriate ranges of K_d. The degradation products from the corrosion of iron, aluminum, and copper-based materials in the invert will include iron-(hydr)oxides and minerals from the granular backfill. The iron-(hydr)oxides are assumed to dominate the sorptive properties of the invert corrosion products for determining appropriate ranges of K_d, although the aluminum oxides and manganese oxides are also highly sorptive. These corrosion products occur in the top portion of the invert because all steel and copper is located in the top half of the invert (BSC 2001 [DIRS 154441], Figure 3).

The in-package degradation products are envisioned to be composed of unconsolidated particulates and larger agglomerations of clays, iron-(hydr)oxides, and other mineral assemblages that first slump to the bottom of the waste package and eventually collect on the top of the invert (floor of the drift) after the waste package and emplacement pallet fail. The invert degradation products are initially located near the top of the invert, but may move into the mass of granular backfill during seismic events. Any seepage through the waste package is expected to flow through this sludge of corrosion products because the invert corrosion products form

before any radionuclides can be released from the waste package and are in the flow path (i.e., at the bottom of the waste package and the top of the invert).

The sludge of corrosion products is reasonably described as a single porosity medium, given the granularity of the corrosion products and the randomness of the slumping process. Rapid flow paths with no sorption, as in the discrete fractures of a dual porosity medium, are not anticipated to occur in this unconsolidated sludge. The conceptual model for this uncertainty analysis assumes that the radionuclides have access to the mass of corrosion products. An alternative conceptual model, with corrosion products that form a contiguous mass that has a low permeability and tight pore structure, would limit access to the full sorptive capacity of the corrosion products. Similarly, if the transverse or longitudinal beams in the invert are outside the transport pathway, their efficiency as a sorber will be limited. These limitations are implicitly acknowledged in the selection of broad distributions with small minimum values for the partition coefficients (Table 10.4.4-1).

The initial sorption of radionuclides on the corrosion products is assumed to be described by a linear isotherm (i.e., a K_d). Descriptions of sorption based on a K_d are approximate because this approach is empirical, with little if any information about underlying mechanisms, and is therefore not easily extendable to different chemical environments and physical substrates (sorptive media). The use of a linear isotherm is also approximate because it does not predict saturation of the sorption sites with sorbed species that may include natural components of the groundwater. The mass of iron-(hydr)oxides from waste package corrosion is large (Table 10.3.4-3), so each waste package provides many sites for sorption. For these reasons, the K_d approach is at best an order of magnitude measure of contaminant uptake in geologic environments (Davis and Kent 1990 [DIRS 143280]).

The use of K_d to represent the subsequent release of radionuclides into fresh recharge (i.e., the desorption process) is often inconsistent with observations in geologic media. Typically, contaminants become more closely attached to a mineral surface after sorption, either adsorbed at high energy sites on the surface or absorbed through overcoating and buried due to other mineral surface reactions. The net result is that only a fraction of the original sorbed population remains available at the surface and able to react with adjacent solutions or be accessed by microorganisms. A K_d approach, on the other hand, assumes that all sorbed radionuclides are able to desorb from the substrate.

As an example, recent reviews of field and laboratory measurements indicate that the fraction of sorbed plutonium that is available for desorption rarely exceeds 1 percent (Brady et al. 1999 [DIRS 154421]; Davis and Kent 1990 [DIRS 143280]). Recognition of the strong role of irreversible sorption is implicit in models for watershed transport (Graf 1994 [DIRS 154419]) that focus solely on particulate transport. In these cases, desorption is ignored because it is rarely seen to occur with plutonium. However, as noted previously, the time scales for these observations are much shorter than the regulatory time period for repository performance (10,000 years), so the fraction of plutonium that is irreversibly sorbed in TSPA calculations has a substantial uncertainty.

10.3.4.3.2 Representation in the Total System Performance Assessment Model

The EBS should be represented as two sets of cells for the TSPA calculations. The in-package environment should be represented as a single cell. This mixing cell would include the mass of in-package corrosion products and the partition coefficients for these corrosion products. The invert should be represented by multiple cells. The cell or cells that represent the top one-third to one-half of the invert should include the mass of corrosion products in the invert and use the partition coefficients for these corrosion products. Any additional cells in the invert can represent granular backfill without corrosion products. This is a reasonable approach because most steel in the invert is in the top portion of the invert. The K_ds for the invert cells without corrosion products can be based on the partition coefficients for tuff in the unsaturated zone (CRWMS M&O 2001 [DIRS 154024]).

Irreversible sorption prevails to some extent in the natural environment for most radionuclides of interest to TSPA, as discussed above. In effect, the assumption of fully reversible sorption for radionuclides like plutonium and thorium may be conservative, although the degree of conservatism over repository time scales is difficult to evaluate. TSPA-SR calculations will be performed with a linear isotherm, which is conservative. Future TSPA calculations could be performed with irreversible sorption if a suitable implementation can be determined.

10.3.4.3.3 Sorption Parameters

This section presents and analyzes appropriate sorption parameters for the EBS. First, the mass of corrosion products (sorbers) is calculated for the potential repository design. Second, the available values for K_d are used to estimate the distributions of partition coefficients for the oxidizing in-drift environment in the waste package and invert. Third, an alternative method based on the concept of tolerance interval is used to estimate the ranges of values for K_d. The tolerance interval approach is appropriate when there is a limited sample set, as is often the case with K_d measurements. Finally, the available data on irreversible sorption of metals that are relevant to EBS transport are presented.

10.3.4.3.3.1 Mass of Corrosion Products

The mass of sorbing material in the waste package has been estimated using data from *In-Drift Microbial Communities* (CRWMS M&O 2000 [DIRS 151561], Attachment III). The mass of sorbing material in the waste package is based on the iron contents of Stainless Steel Type 304L, Stainless Steel Type 316L, Stainless Steel Type 316NG, A 516 carbon steel, Neutronit A 978, and the masses of these alloys in the four waste package types. The mass of corrosion products, assumed to be Fe_2O_3, is then calculated based on the ratio of molecular weight for iron (as Fe_2) to that for Fe_2O_3 (Table 10.3.4-3).

The mass of sorbing material in the invert has been estimated using the data from *In-Drift Microbial Communities* (CRWMS M&O 2000 [DIRS 151561], Attachment II). The iron content of the steel invert and the gantry rails is included in this calculation. The iron in the steel set ground support, the rock bolts, and the welded wire fabric steel has been ignored, even though the corrosion products from these components may fall on the invert. The contribution from the rail fittings is ignored because it is a small fraction (about 8 percent) of the contribution from the

gantry rails. The mass of corrosion products is again estimated by assuming that iron converts to Fe_2O_3 during the corrosion process. In lithophysal and nonlithophysal areas, the mass of iron (703 kg/m) converts to 1,004 kg/m of Fe_2O_3.

Finally, the amount of elemental copper in the drift is given by the nominal weight of the solid copper conductor bar rail, 1.73 kg/m, plus the copper in the communication cable, which is 50 percent by weight of the total cable weight of 0.79 kg/m (BSC 2001 [DIRS 154441], Assumptions 3.1.7, 3.1.9, and 3.2.1.3). The total weight of elemental copper per meter of drift is then (1.73 + (0.5)(0.79)) or a total of 2.13 kg/m. These values are based on the nominal mass of elemental copper, rather than the upper bound values, for conservatism. The mass of elemental copper is not explicitly represented in the TSPA model, but its presence when oxidized is important because of its role as a sorber for iodine and technetium.

The mass of copper is significant relative to that for iodine and technetium. Using a waste package length of 5.165 m for the commercial spent nuclear fuel waste package (BSC 2001 [DIRS 154441], Table III-1), there is 11.0 kg per commercial spent nuclear fuel waste package of elemental copper in the invert. This value (11.0 kg) can be compared to approximately 7.68 kg of technetium-99 and 1.80 kg of iodine-129 per commercial spent nuclear fuel waste package. Thus, there is more elemental copper than iodine or technetium using a mass or molar basis. Similarly, the 5-DHLW/DOE SNF Short waste package has a length of 3.59 m (BSC 2001 [DIRS 154441], Table III-3), implying that there is 7.63 kg of elemental copper per 5-DHLW/DOE SNF Short waste package in the invert. This mass is greater than the approximately 0.115 to 0.729 kg of technetium-99 or the 0.0251 to 0.0480 kg of iodine-129 in the codisposal waste packages (DTN: SN0009T0810599.014 [DIRS 152980]).

10.3.4.3.3.2 Partition Coefficient Values for Corrosion Products

As discussed previously, the use of a linear isotherm is an empirical, order-of-magnitude description of mineral surface processes because it is not based on underlying physical or chemical mechanisms. In essence, a K_d value is valid only for the specific substrate and chemical conditions under which it is measured. More defensible models of contaminant uptake by mineral surfaces require a more comprehensive mechanistic understanding of the chemical reactions involved (Davis et al. 1998 [DIRS 154436]). In lieu of a more involved mechanistic treatment based on surface complexation that includes a provision for irreversible sorption, K_ds can provide a first-order picture of the sorption process, using generic ranges based on soils and iron-(hydr)oxides. The rationale for this approach is described below.

The pH of waste package fluids (CRWMS M&O 2000 [DIRS 153246], Tables 3.3-7 through 3.3-9) is expected to fall within the range observed in soils and groundwaters (pH values between 4 and 10). Although the composition of in-package fluids will vary with time due to degradation of the waste package components (primarily steels, Zircaloy cladding, spent nuclear fuel, and waste glass), major element characteristics (such as alkalinity and system redox state) will likely be controlled by equilibrium with atmospheric carbon dioxide and free oxygen. The primary reactive components in the degraded waste package environment are likely to be iron hydroxides, the same mineral phases that tend to dominate trace element sorption in soils. Oxides of copper are also expected to be present. The only major element species that will be

present in waste package fluids, but that tend to be scarcer in natural soils and groundwaters, are those containing uranium.

The trace element composition of waste package fluids will differ due to the presence of metal components and various radiogenic isotopes. On the other hand, the waste package and invert environments are expected to contain greater volumes of iron hydroxides than all but the most iron-rich soils. Consequently, sorption calculations using ranges of K_ds measured on iron-containing soils or iron hydroxides probably provide a reasonable measure of sorption inside the waste package and invert.

Partition coefficients often vary by at least an order of magnitude. Each range of K_d represents the compilation of many experimental measurements with wide variations in soil composition, contaminant level, soil solution composition, and method of measurement.

Partition coefficients values for a linear, reversible isotherm can be interpreted physically (Stumm 1992 [DIRS 141778], Section 4.12). For example, a contaminant with a K_d of 1,000 ml/g will move at one ten-thousandth the rate of the carrier fluid for a rock porosity of 20 percent and a rock density of 2,000 kg/m^3. A contaminant with a K_d of 1 ml/g will move at one-eleventh the velocity of the carrier fluid, and a contaminant with a K_d of 0 moves at the velocity of the fluid, both for the same values of rock porosity and rock density. These effective transport velocities provide an estimate of the delay for first breakthrough of the contaminant; after the sorption sites are completely saturated, changes in mass flow rate will be delayed only by the fluid travel time through the system.

The K_d ranges for iodine and technetium require additional discussion. Balsley et al. (1998 [DIRS 154439], pp. 125 to 141) experimentally identified and classified potential sorbant backfills for the anions I^- and TcO_4^-. Under the oxidizing conditions that are conservatively assumed to prevail in the EBS, iodine and technetium will exist as the anions I^- and TcO_4^-. Balsley et al. (1998 [DIRS 154439], p. 126) report that neither I^- or TcO_4^- form insoluble salts or sorb appreciably to common soil minerals. Consequently, the sorption coefficients for these radionuclides are generally assumed to be very low (Brady et al. 1999 [DIRS 154421], Appendix E). For near-neutral pH, which is typical of unsaturated or alkaline soils, hydrotalcites and copper oxides are efficient sorbers (Balsley et al. 1998 [DIRS 154439], p. 140). It is then reasonable to assume nonzero K_ds for technetium and iodine because copper oxides are expected to be present in the invert.

Median values and ranges for K_d for americium, iodine, neptunium, plutonium, technetium, thorium, and uranium on typical soils or corrosion products, or under oxidizing conditions, from a variety of sources are summarized in Table 10.3.4-1. The detailed reference citations, including table and page numbers as appropriate, are identified in Table 10.3.4-1 but are not repeated in the text to enhance readability. Because the sources provide broad ranges of K_ds for a variety of materials and because the in-drift chemical environment will vary with time, a reasonable but conservative approach has been used to define the ranges of partition coefficients.

The range of values for the americium partition coefficient is based on a uniform distribution with a minimum of 85 ml/g and a maximum of 5,000 ml/g. This distribution is based on the minimum value from Onishi et al. (1981 [DIRS 154420]) and the maximum value in

Unsaturated Zone and Saturated Zone Transport Properties (U0100) (CRWMS M&O 2001 [DIRS 154024]). It is a subset of the range in Onishi et al. (1981 [DIRS 154420]), and it is more conservative than the ranges in the Electrical Power Research Institute (EPRI) (2000 [DIRS 154149]), *Unsaturated Zone and Saturated Zone Transport Properties (U0100)* (CRWMS M&O 2001 [DIRS 154024]), and Sheppard and Thibault (1990 [DIRS 109991]) for loam. Values at the extreme low end of the range for sand (Sheppard and Thibault 1990 [DIRS 109991]) were ignored because the other data for iron oxides and oxidizing environments are generally greater than the minimum value for sand.

The range of values for the iodine partition coefficient is based on a uniform distribution with a minimum of 0 and a maximum of 10 ml/g. This distribution is based on the minimum or best estimate value from EPRI (2000 [DIRS 154149]) and the median value from Onishi et al. (1981 [DIRS 154420]). It is a subset of the range in Onishi et al. (1981 [DIRS 154420]) and more conservative than the ranges for sand and loam from Sheppard and Thibault (1990 [DIRS 109991]). This maximum value (10 ml/g) is also much less than the range of values for sorption on copper oxide and copper sulfide determined by Balsley et al. (1998 [DIRS 154439]). The upper limit of 1 ml/g in EPRI (2000 [DIRS 154149]) was ignored because of data from the other sources.

The range of values for the neptunium partition coefficient is based on a uniform distribution with a minimum of 0.1 and a maximum of 79 ml/g. This distribution is consistent with the minimum value from EPRI (2000 [DIRS 154149]) and the maximum value for loam from Sheppard and Thibault (1990 [DIRS 109991]). It is more conservative than all the ranges in Table 10.3.4-1.

The range of values for the plutonium partition coefficient is based on a uniform distribution with a minimum of 100 ml/g and a maximum of 5,000 ml/g. This distribution is based on the minimum value of 100 ml/g from Onishi et al. (1981 [DIRS 154420]) and the maximum value of 5,000 ml/g from *Unsaturated Zone and Saturated Zone Transport Properties (U0100)* (CRWMS M&O 2001 [DIRS 154024]). Larger maximum values are defined in the other three references (Table 10.3.4-1), but these are ignored for conservatism. The values at the extreme low end of the range for sand (Sheppard and Thibault 1990 [DIRS 109991]) were ignored because other data for iron oxides and oxidizing environments are generally greater than the minimum value for sand.

The range of values for the technetium partition coefficient is based on a uniform distribution with a minimum of 0 ml/g and a maximum of 5 ml/g. This distribution is based on the possibility of zero sorption under extreme oxidizing conditions and the median value from Onishi et al. (1981 [DIRS 154420]). This range is consistent with the measurements by Bird and Schwartz (1997 [DIRS 154488]), and it is a conservative subset of the ranges in Onishi et al. (1981 [DIRS 154420]), EPRI (2000 [DIRS 154149]), and Sheppard and Thibault (1990 [DIRS 109991]) for sand. The maximum value (5 ml/g) is less than the range of values (30 to 60 ml/g) for sorption on copper oxide and copper sulfide determined by Balsley et al. (1998 [DIRS 154439]). The upper limit of 0.4 ml/g, in Sheppard and Thibault (1990 [DIRS 109991]) for loam, was ignored because of data from the other sources.

The range of values for the thorium partition coefficient is based on a uniform distribution with a minimum of 1,000 ml/g and a maximum of 5,000 ml/g. This distribution is based on the smallest value in three sources (1,000 ml/g; Table 10.3.4-1) and the maximum value of 5,000 ml/g from *Unsaturated Zone and Saturated Zone Transport Properties (U0100)* (CRWMS M&O 2001 [DIRS 154024]). This range is a conservative subset of the ranges in Onishi et al. (1981 [DIRS 154420]), EPRI (2000 [DIRS 154149]), and *Unsaturated Zone and Saturated Zone Transport Properties (U0100)* (CRWMS M&O 2001 [DIRS 154024]). EPRI (2000 [DIRS 154149]) and Onishi et al. (1981 [DIRS 154420]) provide greater maximum values that are ignored for conservatism. The values at the extreme low end of the range for sand (Sheppard and Thibault 1990 [DIRS 109991]) were ignored because the other data for iron oxides and oxidizing environments are generally greater than the minimum value for sand.

The range of values for the uranium partition coefficient is based on a uniform distribution with a minimum of 0.2 ml/g and a maximum of 1,000 ml/g. This distribution is based on the minimum value from Sheppard and Thibault (1990 [DIRS 109991]) for loam and the maximum value of 1,000 ml/g from *Unsaturated Zone and Saturated Zone Transport Properties (U0100)* (CRWMS M&O 2001 [DIRS 154024]) and Onishi et al. (1981 [DIRS 154420]). This range is a conservative subset of all the ranges in Table 10.3.4-1, except for the minimum value for sand (Sheppard and Thibault 1990 [DIRS 109991]). The values at the extreme low end of the range for sand (Sheppard and Thibault 1990 [DIRS 109991]) were ignored because the other data for iron oxides and oxidizing environments are generally greater than the minimum value for sand. EPRI (2000 [DIRS 154149]) provides a higher maximum value (10,000 ml/g), which was ignored for conservatism.

10.3.4.3.3.3 Partition Coefficients Based on Small Sample Sizes

An alternative approach to estimating the appropriate ranges of values for partition coefficients is based on the concept of tolerance intervals. Tolerance intervals provide a statistical estimate of parameter ranges at a given confidence level from a small data set. In other words, the tolerance interval provides an estimate of the uncertainty inherent in a finite set of data. As a reminder, there are many conceptual uncertainties associated with linear isotherms and K_ds, as discussed in Section 10.3.4.3.1. The tolerance interval approach does not represent these uncertainties for sorption behavior; rather, the goal here is to quantify the uncertainty represented by the ranges of K_d data reported in the literature. The use of this technique is illustrated here with the partition coefficients compiled by Sheppard and Thibault (1990 [DIRS 109991]).

Sheppard and Thibault (1990 [DIRS 109991], Tables A-1 to A-4) present data on the mean and standard deviation of the natural logarithm of the partition coefficient for individual elements for sands, loams, clays, and organic soils. This information includes the number of measurements. Sheppard and Thibault (1990 [DIRS 109991], p. 472) also cite previous work in which the partition coefficients are lognormally distributed. Finally, Sheppard and Thibault (1990 [DIRS 109991], p. 472) calculated the geometric mean and the geometric standard deviation for each element by soil texture for the mineral and organic soils.

The uncertainty analysis for this data set evaluates the tolerance interval to define an appropriate range of values. The tolerance interval is appropriate in estimating the range of variability of the underlying population (ASME PTC 19.1-1998, *Test Uncertainty, Instruments and Apparatus*

[DIRS 153195]). Standard ASME PTC 19.1-1998 ([DIRS 153195], Appendix A) provides a procedure for calculating the tolerance interval that contains a specific proportion of the population. The procedure to assess the tolerance interval for a partition coefficient at the 95 percent confidence level is:

1. $C_{T,95}$ is the factor for the tolerance interval to contain at 95 percent of the population, based on the number of samples. Obtain $C_{T,95}$ from ASME PTC 19.1-1998 ([DIRS 153195], p. 84, first column of Table A.1), which is reproduced in *Rock Mass Thermal Properties* (BSC 2001 [DIRS 155008], Attachment VIII).

2. Calculate the tolerance interval based upon the mean and standard deviation of the partition coefficient, based on the samples presented in Sheppard and Thibault (1990 [DIRS 109991], Table A-1). The confidence tolerance interval on the partition coefficient is calculated as:

$$\bar{k} \pm c_{T,95}(n) \cdot s_k$$

   where $\bar{k}$ and s_k represent the mean value and standard deviation for the natural logarithm of values for the partition coefficient of each element for sand, and *n* is the sample size.

3. The tolerance values can be used to construct the log-uniform distribution, or they can be compared to the lognormal distribution for the mean and standard deviation presented by Sheppard and Thibault (1990 [DIRS 109991]) for each element.

This method can be extended to calculate the tolerance interval on the basis of the combined data for sand, loam, and clay (Sheppard and Thibault 1990 [DIRS 109991], Tables A-1 to A-3). These tables present the number of samples, along with the mean and standard deviation of the natural logarithm of the partition coefficient, for measurements of sand, loam, and clay, respectively. The weighted mean value for the combined data set is given by Hahn and Shapiro (1967 [DIRS 146529], p. 38, Equation 2-31):

$$\mu \log = \frac{fs * \mu \log s + fl * \mu \log l + fc * \mu \log c}{n}$$

where

fs	=	number of measurements for sand
fl	=	number of measurements for loam
fc	=	number of measurements for clay
n	=	total number of measurements
µlog	=	mean of the natural logarithm for the combined data set
µlogs	=	mean of the natural logarithm for the sand data
µlogl	=	mean of the natural logarithm for the loam data
µlogc	=	mean of the natural logarithm for the clay data.

The standard deviation of the natural logarithm of the partition coefficient for the combined data is derived from the basic definition for standard deviation (Hahn and Shapiro 1967 [DIRS 146529], p. 48, Equation 2-51c):

$$s^2 = \frac{\sum_{i=1}^{n} (x_i - \bar{x})^2}{n-1}$$

Define a deviation value, x_D, such that the following relationship is satisfied:

$$n \cdot (x_D - \bar{x})^2 \equiv \sum_{i=1}^{n} (x_i - \bar{x})^2$$

The summation on the right-hand size of this equation can be replaced using the above definition of the standard deviation, *s*:

$$\begin{aligned} n \cdot (x_D - \bar{x})^2 &\equiv \sum_{i=1}^{n} (x_i - \bar{x})^2 \\ &= s^2 \cdot (n-1) \end{aligned}$$

Applying this definition to each of the samples for sand, loam, and clay and solving for the deviation values yields:

$$x_{Ds} = \sqrt{\sigma \log s^2 \cdot \frac{(fs-1)}{fs}} + \mu \log s$$

$$x_{Dl} = \sqrt{\sigma \log l^2 \cdot \frac{(fl-1)}{fl}} + \mu \log l$$

$$x_{Dc} = \sqrt{\sigma \log c^2 \cdot \frac{(fc-1)}{fc}} + \mu \log c$$

where the subscripts Ds, Dl, and Dc denote sand, loam, and clay, respectively. The standard deviation for the combined sample can then be calculated by applying the basic definition for standard deviation:

$$\sigma log = \sqrt{\frac{(fs \cdot (x_{Ds} - \mu log)^2 + fl \cdot (x_{Dl} - \mu log)^2 + fc \cdot (x_{Dc} - \mu log)^2)}{n-1}}$$

For the radionuclides listed in Table 10.3.4-1, the results of these calculations are presented in Table 10.3.4-4. The values in Table 10.3.4-4 account for small sample population effects in that the tolerance interval factor is a function of the number of measurements and the desired confidence level. The results show that:

- The tolerance intervals for the partition coefficients of americium and thorium are quite large, ranging from minimum values on the order of 10 ml/g up to maximum values on the order of 1 million ml/g.

- The tolerance intervals for the partition coefficients for iodine, neptunium, and technetium are relatively low, ranging from a minimum value on the order of 0.01 ml/g to maximum values of 6.2 ml/g for technetium, 300 ml/g for iodine, and 2,900 ml/g for neptunium.

- The tolerance interval for the partition coefficient of plutonium is intermediate between these extremes, with a range of 13 to 94,000 ml/g. The tolerance interval for the partition coefficient of uranium is also an intermediate case, with a very low minimum value (0.012 ml/g) and a maximum value of 230,000 ml/g.

Figures 10.3.4-1 through 10.3.4-7 present the results in Table 10.3.4-4 for log-uniform distributions based on the tolerance interval limits and for lognormal distributions based on the mean value and standard deviation for these data sets. The two types of distributions are essentially equivalent, considering the large variability in partition coefficients and the uncertainty in definition of the chemical environment and substrates in the waste package and invert.

The variability represented by Figures 10.3.4-1 through 10.3.4-7 and by Table 10.3.4-4 is limited to the parameter uncertainty in the selected range of literature data. This variability is a statistical measure of uncertainty, rather than an addressing of the conceptual uncertainties with the use of K_ds and a linear isotherm.

10.3.4.3.3.4 Irreversible Fractions for Desorption

Irreversible uptake can be the dominant control over contaminant transport in soils. Evidence for soil sequestering of bomb-pulse plutonium and americium and of uranium, iodine, technetium, cesium, and strontium from ore processing and reactor operations has been extensively documented in the literature (Coughtrey et al. 1983 [DIRS 132164]).

Estimates of the mean fraction of irreversible sorption for various radionuclides on soil, derived from Brady et al. (1999 [DIRS 154421], Appendix F), are presented in Table 10.3.4-5. The value of the irreversible fraction for the EBS is likely to differ from that for soils and will depend on the material that the specific radionuclide encounters, the speciation of the radionuclide, and other factors in the material and chemical environment. The important conclusion from Table 10.3.4-5 is that irreversible sorption is an important process for many radionuclides that potentially contribute to dose. A corollary to this conclusion is that the current reversible transport models are conservative if the corrosion products in the waste package and invert behave like soils in the natural environment.

10.3.4.4 Other Lines of Evidence

The EBS elements through which radionuclides can migrate are conceptually similar to a laboratory column test, where radionuclides are introduced at the top of the column and migrate downward through materials representing the waste form and invert. This similarity is relevant for many laboratory tests of radionuclide transport properties.

Advective Transport–Laboratory testing of radionuclide migration downward through a crushed tuff column was performed with several radionuclides (neptunium-237, plutonium-239, tritium, and pertechnetate) in two groundwaters with different chemical compositions (Triay et al. 1997 [DIRS 100422], Section V.A). The purpose of the tests was mainly to compare column transport characteristics with radionuclide sorption parameters from batch sorption tests. The tests, therefore, provided analogous information on advective transport modified by sorption in crushed tuff. The transport model in the invert is analogous to these laboratory tests, which demonstrate that sorption can be effective in crushed tuff.

Diffusive Transport–A different series of tests was performed to gather information on the diffusive uptake of radionuclides by intact samples of tuff (Triay et al. 1997 [DIRS 100422], Section VI). It was observed that certain radionuclides could diffuse through minute water-filled pores depending on porosity, heterogeneity of the pore structure, and sorptive retardation. The tests show that diffusion through the intact tuff is a slow process for the typical time scales of these experiments, particularly for radionuclides with strong sorption, such as the actinides. In highly unsaturated conditions, diffusive transport is very slow, again providing corroborating evidence for sorption in crushed tuff.

10.3.5 Colloidal Transport of Radionuclides

10.3.5.1 Goal of Model

The goal of this model is to quantify the impacts of uncertainties in the behavior of colloids generated from the degradation of high-level radioactive waste glass, commercial spent nuclear fuel, and DOE spent nuclear fuel, as well as colloid-facilitated transport properties of radionuclides in the engineered barrier system. It is anticipated that colloids will also be mobilized as a result of the corrosion of waste package and in-drift components, in addition to the waste forms. The abundance of colloids will depend on the extent of waste form alteration and the alteration products formed.

Colloid abundance and stability also depend on many environmental factors, including ionic strength, pH, cation concentrations, colloid content of groundwater entering the drift, presence of fulvic and humic acids, and microbe fragments. Suspended colloids may subsequently flocculate and settle by gravity, be chemically or mechanically filtered, or dissolve. If environmental factors change, colloids may be peptized; colloid-sized particles may precipitate; or other natural processes may occur. In addition, colloids may sorb readily at the interfaces between air and water in rocks and engineered barriers and, depending upon the degree of saturation of the porous medium as well as its configuration, may be retarded, even immobilized or transported. These issues are relevant to transport of radionuclides by colloids, a primary concern within the waste package, within the EBS, and in the near- and far-fields.

10.3.5.2 Identification of Unquantified Uncertainties in Total System Performance Assessment-Site Recommendation

The current TSPA-SR model for generation and transport properties of colloids resulting from waste form degradation (CRWMS M&O 2000 [DIRS 153246], Section 3.5.6 and p. 3-138 to 3-139) generally uses a bounding approach for incorporating relevant source data, and it uses conservative assumptions where the available data were thought to be limited (CRWMS M&O 2001 [DIRS 153933]; CRWMS M&O 2000 [DIRS 129280]). This approach has given rise to uncertainties, the most significant of which are summarized in Table 10.3.5-1.

10.3.5.2.1 Colloid Generation

Potential Contribution of Irreversibly Attached Radionuclides on Colloids Generated from Commercial Spent Nuclear Fuel Degradation–This is a significant uncertainty and may be addressed as results are evaluated from ongoing laboratory experiments. Irreversibly attached radionuclides, as currently used in the analysis, refers to those radionuclides that are bound within the colloid, either within the crystal structure or in a separate phase embedded in the colloid. The only existing data on irreversibly attached plutonium content from degradation of waste are for high-level radioactive waste glass (CRWMS M&O 2001 [DIRS 154071], Table 4); data from degradation of commercial spent nuclear fuel were inconclusive because few colloids could be collected for analysis (CRWMS M&O 2001 [DIRS 154071], pp. 31 to 36).

This operational definition of irreversible (see above paragraph) has been adopted for abstraction. The term is also used in the scientific literature in reference to surface complexation of a metal, including radionuclides, to strong sites, which may be irreversible under certain conditions or over certain time frames. This form of attachment may be reversed by a change in chemical conditions, such as a lowering of pH ["(acidification)"], chelation, or ion exchange. It should be emphasized that such attachment of metals and radionuclides to colloidal or fixed substrates may in fact be reversible without a change in conditions over very long times.

Quantities of Colloids Generated from Corrosion of Steel–This uncertainty is considered significant. Iron-(hydr)oxides will form from the corrosion of steel components within the repository, including the waste package and in-drift structural components. There are few data on quantities of iron-(hydr)oxide colloids that may be generated from steel corrosion under given aqueous chemical conditions. This is potentially significant because it has been determined that plutonium and americium have a strong affinity with iron-(hydr)oxide minerals, so radionuclides bound to such colloids have the potential to be transported considerable distances.

The evolution of steel degradation products is also uncertain. There is a natural tendency for progression to the higher oxides, which are more thermodynamically stable. Accordingly, ferrihydrite tends to alter to goethite, which tends to alter to hematite over time. As this happens, the degree of crystallinity increases and the size of the domains probably increase. With time, the colloids that are formed initially will tend to crystallize and agglomerate. This would have the effect of reducing the number of available colloids over time, but at the same time would provide relatively immobile substrates for sorption or other attachment of dissolved radionuclides. This uncertainty has therefore been incorporated into the colloidal transport

abstraction for the TSPA-SR sensitivity studies. Corrosion colloids are discussed further in Sections 10.3.5.3 and 10.3.4.

Potential Contribution of Colloids from U.S. Department of Energy Spent Nuclear Fuel Degradation–This uncertainty could be significant, and may be addressed as results are evaluated from ongoing laboratory experiments. Preliminary unpublished results from the experimental degradation of metallic uranium fuel indicate that the fuel degrades rapidly and produces fine particulates, including particulates of colloid size (CRWMS M&O 2001 [DIRS 153933], p. 33). The potential for colloid-facilitated migration of radionuclides derived from the degradation of metallic uranium fuel is not considered in the current colloid model.

10.3.5.2.2 Colloid Stability, Concentration, and Transport Properties

Dependence of Colloid Stability and Concentration on Temperature–This uncertainty may be significant; however, temperature effects on colloid stability, concentration, and transport properties are largely unknown. Ionic strength and pH in the waste package are calculated in the TSPA, as are colloid stability and concentration dependence on ionic strength and pH (CRWMS M&O 2001 [DIRS 153933]; CRWMS M&O 2000 [DIRS 129280]). Therefore, colloid stability and concentration response to changing chemical conditions resulting from changing temperature is incorporated into current TSPA methodology. Uncertainties would combine the uncertainties incorporated into the colloid versus. Ionic strength and pH relationships described in the waste form colloid analysis model report [DIRS 125156] and the uncertainties incorporated into the in-package calculation of ionic strength and pH. In any case, colloid stability is generally expected to decrease with increasing temperature. Actinide and metal sorption onto metal hydroxide colloids tends to increase with temperature, paralleling temperature-dependent increases in metal hydroxide anionic surface charge (Machesky 1990 [DIRS 145046]).

Smectite as a Proxy for Groundwater Colloids–This uncertainty is probably not significant, and has not been included in the TSPA-SR sensitivity studies. In the model, all groundwater colloids flowing into the in-drift materials are assumed to be smectite (CRWMS M&O 2001 [DIRS 153933], p. 56; CRWMS M&O 2000 [DIRS 129280], p. 22). However, other colloids may be present, including silica, zeolites, feldspars, and iron-(hydr)oxides. Experimental results suggest that smectite has a somewhat higher affinity for radionuclides than many of these other mineral colloids (iron-(hydr)oxides being exceptions; Lu et al. 2000 [DIRS 154422]), and therefore the assumption that all groundwater colloids are smectite may be overly conservative. Information on colloid mineralogy collected from wells in the Yucca Mountain area may provide justification to use a mixture of mineralogies, including less sorptive minerals (e.g., silica). A preliminary review of data presented in Lu et al. (2000 [DIRS 154422]) suggests that while K_d values for plutonium and americium sorption are generally higher on montmorillonite than on silica, the difference is less than one order of magnitude. Determination of the degree to which K_d values for various types of colloids differ would require a significant effort for TSPA. If the differences were not large, then incorporating additional K_d values specific to each colloid mineral type into the model would complicate the calculation without adding demonstrably to the quality of the result. Note as well that explicit consideration of degradation product colloids and the uncertainty associated with them would probably tend to outweigh any uncertainty in the groundwater colloid term.

Flow Rate Within the Waste Package–The significance of this uncertainty is probably low. The colloid model currently incorporates the assumption that colloids, incrementally "generated" at each TSPA calculation time step, leave a failed waste container and enter the drift (specifically the invert) (CRWMS M&O 2001 [DIRS 153933], pp. 20, 66, and 67). This approach is conservative, bounding, and simplifies the model. An alternative approach would be to use the calculation of flow rate within the waste package to provide a more realistic (and lower) estimate of colloid transport rate within and out of the container. The conservative, simplifying approach has been retained for the TSPA-SR sensitivity studies because the uncertainty probably is low.

Entrainment of colloidal particles within the waste package, possibly caused by flow transients, chemical gradients, or surface tension gradients, may serve to mobilize and concentrate colloids within the waste package. The potential effects of entrainment on colloid concentration have not been considered in the TSPA-SR sensitivity studies.

Colloid Sorption onto the Air-Water Interface–This uncertainty may be moderately significant. Colloids are considered to adhere strongly to the interface between air and water of thin films, bubbles, etc. (Wan and Wilson 1994 [DIRS 114430]). The analysis of this important process is site-specific (i.e., it must be tailored specifically to the system under investigation) and can be quite complex. Leaving colloid sorption onto the air-water interface out of the colloid model is likely conservative. Adhesion to a fixed interface (e.g., as part of a water film on a component in the waste package) would serve to immobilize the colloid as long as the interface remained intact. Adhesion to the surface of a freely suspended bubble, on the other hand, would enable the colloid to be transported with the bubble, although the relatively large size of the bubble may cause it to become filtered out at constrictive passageways. Colloid sorption onto the air-water interface is not considered in the current model.

Potential Effects on the Total Colloid Population of Organic Material, Including Introduced Organics and Microbes–The effects of organic materials are potentially significant and may include:

- Organic coatings on mineral colloids, which would tend to sorb radionuclides as well as destabilize the colloid suspension and cause the colloids to agglomerate (CRWMS M&O 2001 [DIRS 153933], Attachment VI, pp. VI-1 and VI-2).

- Development of colloids comprised of monocellular microbes and fragments, which could sorb and transport radionuclides or agglomerate and immobilize radionuclides (CRWMS M&O 2001 [DIRS 153933], Attachment VI, pp. VI-1 and VI-2).

Thus two competing processes, one that encourages colloid mobilization and another that encourages colloid agglomeration and flocculation, may prevail. It is uncertain which process would dominate at a particular location or point in time within the repository. Organic and particularly microbial effects are discussed at length in Section 10.3.6.

10.3.5.2.3 Radionuclide Attachment and Concentration

The model currently considers attachment of radionuclides to colloids either irreversible or reversible. As noted previously, "irreversibly attached radionuclides are those bound within the

colloid, either within the crystal structure or in a separate phase embedded in the colloid (CRWMS M&O 2001 [DIRS 153933], pp. 18, 25 to 33, 51, 52, and 59 to 62). Reversibly attached radionuclides are those attached to colloids by the sum of processes referred to as sorption. The distribution of a radionuclide between the aqueous solution and the colloid is described by its K_d.

Wide Range of Distribution Coefficients Used to Describe Sorption of Radionuclides on Colloids–This uncertainty is significant, as K_d is a sensitive parameter incorporated into several TSPA calculation sets. Results of laboratory investigations and literature review to determine or estimate K_ds for radionuclides onto relevant materials has yielded ranges of K_ds as great as six orders of magnitude (CRWMS M&O 2001 [DIRS 153933], pp. 12 to 16, 44 to 46, and Attachment XVI.1.1.2; Lu et al. 2000 [DIRS 154422]).

Better-Justified Upper-Bound Maximum Concentration of Plutonium Irreversibly Attached to Colloids–This uncertainty may or may not be significant. The dependence of irreversibly attached plutonium content from the degradation of high-level radioactive waste glass on ionic strength was derived by closely bounding a representative subset of the data produced in the glass degradation experiments at Argonne National Laboratory (CRWMS M&O 2001 [DIRS 153933], pp. 38 and 39).

Consideration of Radionuclides Other than Plutonium and Americium–This uncertainty is low to moderately significant. Abundant data exist only for plutonium from waste degradation experiments (CRWMS M&O 2001 [DIRS 154071], Table 4, p. 19). In the current waste form degradation model, americium is assumed to behave similarly to plutonium (i.e., it may be incorporated into a colloid as irreversibly attached). The quantities of both plutonium and americium irreversibly attached to colloids are determined at each time step in the TSPA-SR by the radionuclide inventory remaining at each time step (CRWMS M&O 2001 [DIRS 153933], p. 51).

In the current colloid model, plutonium and americium are treated as irreversibly attached to waste form colloids. These two radionuclides were considered potentially the most significant sparingly soluble radionuclides that could readily become irreversibly attached to colloids and subsequently be transported from the waste package. In addition to plutonium and americium, two other radionuclides, protactinium and thorium, are considered for reversible attachment to waste form colloids and subsequent transport. The fractions of release from colloids associated with other dose-important radionuclides are considered insignificant relative to their dissolved concentrations.

10.3.5.3 Quantification of Previously Unquantified Uncertainty

This section discusses alternative distributions for certain of the parameters discussed above. These parameters and the alternative distributions are summarized in Table 10.3.5-2.

Combined Groundwater and Corrosion Colloid Concentrations–Limited data exist for concentrations of iron-(hydr)oxide colloids in natural systems. At the Morro de Ferro natural analogue site (Poços de Caldas, Brazil), concentrations of iron-(hydr)oxide [$Fe(OH)_3$] colloids were measured in deep groundwaters adjacent to an iron-rich rock body (CRWMS M&O 2000

[DIRS 150707], pp. 3-72 to 3-81). The measured concentration, 0.25 mg/L, is similar to concentrations of other inorganic colloids found in natural waters at other deep sites. The upper end of the range, 1.0 mg/L, imparts a fourfold conservatism relative to the concentration observed at the analogue site. The proposed distribution is triangular, with a peak at 0.25 mg/L and endpoints at 10^{-3} and 1.0 mg/L. This type of distribution was selected because the data set is small. Reasonable numbers were available for peak and extreme values, so a triangular distribution was appropriate.

Given the limited data on corrosion colloid concentrations, as well as the somewhat more abundant data on groundwater colloid concentrations, uniform distributions were chosen for uncertainty analysis for a combined population of groundwater and corrosion colloids. Suitably wide concentration ranges were evaluated for two different ranges of aqueous ionic strength. Reasonable ranges for this combined colloid population, to which radionuclides may reversibly attach, are log-uniform distributions between 10^{-6} and 10^{-1} mg/L (for ionic strength $\leq$ 0.05M) and 10^{-9} and 10^{-3} mg/L (for ionic strength > 0.05M). Differences in affinities for aqueous metals, including radionuclides, were accommodated by assumptions regarding sorption distribution coefficient (K_d) values and distributions (see below).

Range of Plutonium Concentration Irreversibly Attached to Waste Form Colloids–Reasonable distributions for plutonium irreversibly associated with waste form colloids are log-uniform distributions between 10^{-11} and 10^{-6} mol/L (for ionic strength less than 0.05M) and 10^{-14} and 10^{-8} mol/L (for ionic strength greater than 0.05M). These distributions were selected to capture the potential uncertainty about and sensitivity to irreversible plutonium sorption in the present study in a way that tests the entire ranges of values uniformly (i.e., without weighting the values about a mean). The upper range is (approximately) centered on the bounding concentration of 8×10^{-8} mol/L defined in *Waste Form Colloid-Associated Concentrations Limits: Abstraction and Summary* (CRWMS M&O 2001 [DIRS 153933], Figures 7 and 13). The minimum value of the distribution (10^{-11}), is approximately four orders of magnitude lower than 8×10^{-8}, and the maximum value of the distribution (10^{-4}), is approximately three orders of magnitude greater. Similarly, the lower range is centered on the minimum concentration measured experimentally, 10^{-11} mol/L (CRWMS M&O 2001 [DIRS 154071], Table 4, p. 20). The minimum and maximum values of this range are then ±3 orders of magnitude from 10^{-11} mol/L.

Sorption of Plutonium and Americium onto Colloids–A careful review of the data presented in *Waste Form Colloid-Associated Concentrations Limits: Abstraction and Summary* (CRWMS M&O (2001 [DIRS 153933], Attachment XVI) and Lu et al. (2000 [DIRS 154422]) suggests that the currently used K_d values for plutonium and americium (10^4 and 10^5 ml/g, respectively; CRWMS M&O 2001 [DIRS 153933], Table 1) are reasonable for sorption onto montmorillonite, (a proxy colloid mineral for both waste form and groundwater colloids. However, a preliminary review of the Lu et al. (2000 [DIRS 154422]) data suggests that the currently used K_d values for iron-(hydr)oxides (a proxy colloid mineral for steel corrosion colloids) may be underestimated by as much as one to two orders of magnitude. Considering the large mass of iron-(hydr)oxides that may be present in the EBS and the uncertainty in the state of degraded materials with time, it is reasonable to use the same distribution for K_ds that describe the sorption of plutonium and americium onto colloids. The alternative distribution is a lognormal distribution with a mean

value of 10^5 ml/g and a standard deviation of two orders of magnitude. Lognormal distributions are useful for distributions in which mean values have been reasonably well determined, but in this case there is considerable variability. Therefore, a large geometric standard deviation was applied (100) so that sampled values would tend to cluster about the mean, but also span a very large range of possibilities in the TSPA iterative calculations.

10.3.5.4 Other Lines of Evidence

Numerous investigations of colloid characteristics, behavior, and transport properties have been published that relate to colloid stability and transport in the environment and the ability of colloids to facilitate the transport of radionuclides and non-radioactive-metals. Common principles have been employed in the development of this model.

Colloid Stability–A colloidal dispersion must be stable for the duration of transport and must carry significant amounts of radionuclides for radionuclide-bearing colloids to affect repository performance. Transport times can range from days to years for advective transport out of a breached waste package, and up to many thousands of years for retarded transport to the accessible environment. Thus, some relatively unstable colloids generated in the waste form may persist long enough to be transported through the EBS, but not long enough to reach the accessible environment. More stable colloids, however, can remain suspended for years and travel great distances.

Colloid Analogues–There is field evidence of colloid-facilitated transport of radionuclides. Buddemeier and Hunt (1988 [DIRS 100712], p. 536) found plutonium and americium more than 30 m below a low-level waste site in unsaturated tuff after approximately 30 years of operation. In a test at the Nevada Test Site, the isotope ratio of plutonium-240 to plutonium-239 in groundwater showed that plutonium had been transported more than 1.3 km over a 30-year period, although plutonium is assumed strongly sorbed at the Nevada Test Site and assumed to be immobile (Kersting et al. 1999 [DIRS 103282]). Plutonium is often found attached to colloids in water samples from the Nevada Test Site. In the Pahute Mesa drainage, Buddemeier and Hunt (1988 [DIRS 100712], p. 537) found colloid concentrations of 0.8 mg/L to 6.9 mg/L for particles greater than 30 nm in size.

Treated liquid wastes containing traces of plutonium and americium have been released into Mortandad Canyon at Los Alamos National Laboratory (Triay et al. 1997 [DIRS 100422], Section V.D., p. 172). The shallow alluvium at that location is composed of sandy to silty clays formed from weathering of volcanic rocks. Detectable amounts of plutonium and americium have been observed in monitoring wells up to 3.4-km (2.1-miles) downgradient from the discharge point. Sorption studies predicted that movement of plutonium and americium would be restricted to a few meters. This suggests that plutonium and americium are strongly associated with colloids that can be mobile for large distances (Triay et al. 1997 [DIRS 100422], Section V.D., p. 172).

Although colloid-facilitated plutonium transport in a qualitative sense has been "observed" in the field, the phenomenon has not been studied to the extent that other contaminants have been studied. For this reason, the model relies heavily on experiments in which conditions anticipated in the repository were simulated (to the extent possible). Accordingly, one

non-radionuclide-related natural analogue, Morro de Ferro (CRWMS M&O 2000 [DIRS 150707], pp. 3-72 to 3-81), was directly used in this model, in lieu of experimental data, to estimate concentrations of iron-(hydr)oxide colloids resulting from corrosion of steel components in the EBS.

10.3.6 Microbial Sorption and Transport

10.3.6.1 Goal of Model

The goal of this model is to quantify the impact of potential microbial communities on sorption of radionuclides to microbes and the ability of microbes to be transported as colloids through the EBS. The transport of microbes through the EBS is a function of the uptake of dissolved radionuclides onto the cell walls and the subsequent mobility of microbes through the waste package and invert.

Adsorption of radionuclides to microbes occurs in one of two ways. First, radionuclides can be adsorbed when a microbe is exposed to a radionuclide-laden aqueous solution. This uptake typically occurs when a bond is formed by surface sites on the microbial wall that have a chemical affinity for the radionuclide. This mechanism is a common one because it provides a means of protection for the cells against the toxic effects of the dissolved metals. Once a metal (or radionuclide) is adsorbed or precipitated onto the cell wall, its toxicity to microbes is greatly reduced. Second, microbes will create intracellular traps and precipitate crystalline metal deposits within the cell wall. This is also done to protect the cell against toxicity.

Sorption of uranium and plutonium onto microbes has been documented (Hersman 1997 [DIRS 100763]; Suzuki and Banfield 1999 [DIRS 154445]), and an extrapolation of uranium data for thorium and plutonium has been proposed (Macaskie 1991 [DIRS 154446]). Therefore, as a minimum, these three radionuclides must be considered for accumulation in and transport on microbial cells.

Once an individual microbe has sorbed the available radionuclides within or on its cell walls, the radionuclides become subject to the transport regime imposed on the microbe by the EBS. As discussed in Section 10.1.1, water saturation and the availability of an air-water interface within an unsaturated porous media can be related to the time-dependent saturation of the invert. Liquid saturation is a key parameter for determining whether the partition between radionuclides that adsorb onto microbes is retained within the invert and radionuclides will be available for additional "colloidal" transport into the UZ via microbes.

10.3.6.2 Identification of Unquantified Uncertainties in Total System Performance Assessment-Site Recommendation

The TSPA-SR (CRWMS M&O 2000 [DIRS 153246], Section 3.6) model does not account for the potential for microbial sorption or for transport of microbes as colloids. However, the *In-Drift Microbial Communities* model (CRWMS M&O 2000 [DIRS 151561], Section 6.6.5.2) reports that there is a potential for microbial colloids and gives a bounding value for the numbers of organisms per milliliter of flux ($1.16 \times 10^{+12}$) that could leave the EBS. This is a rather large number of potential "colloids" and could become a significant source of dose at the accessible environment, especially in light of the uncertainty work that is associated with sorption in the

EBS, as discussed in Section 10.3.4. Microbial transport, when coupled with irreversible sorption onto corrosion products, could yield significant decreases in noncolloidal releases from the EBS.

10.3.6.3 Quantification of Previously Unquantified Uncertainty

10.3.6.3.1 Conceptual Model for Microbial Sorption and Transport

As *In-Drift Microbial Communities* (CRWMS M&O 2000 [DIRS 151561]) describes, several factors influence the growth and abundance of microbes. These are primarily water availability (as a function of temperature and relative humidity), nutrient, and energy availability. In all other instances, including the ranges of pH and salinity expected in the drift, there are no physical limits to microbial growth. Microbes differ from traditional colloids in that they are able to facilitate several processes that will allow them to coexist with colloidal particles. First, microbes can agglomerate irreversibly onto existing colloids; they can also adsorb colloids onto their surfaces. These processes are joined with the ability that microbes have to make changes in their immediate environment, where gradients exist in and around themselves. Thus, microbes can establish a great diversity that would otherwise not occur in such close proximity (Hersman 1997 [DIRS 100763]). Biological processes that contribute to the mobility of microbes mainly revolve around the characteristics of the cell surface. The cell surface is prone to adhere to surfaces. The size and shape of microbes influence their ability to move, as do sedimentation, motility, and chemotaxis. These issues are discussed in some detail in Mills (1997 [DIRS 100800]). Mills also points out that in unsaturated media, gas-water interfaces may be the most important factor in controlling the movement of bacteria.

The conclusions presented in *In-Drift Microbial Communities* (CRWMS M&O 2000 [DIRS 151561]) indicate that microbial communities of some size will be present in the EBS. Associated with these communities will be opportunities to sorb and transport radionuclides. This is based on the observed capabilities of microbes to sorb and transport radionuclides, as well as the size of the microbial community that could be supported within the EBS.

10.3.6.3.1.1 Radionuclide Uptake

In a detailed discussion, Suzuki and Banfield (1999 [DIRS 154445]) report mechanisms for accumulation of radionuclides on microbes. Two types of mechanisms are discussed. One is the metabolism-dependent precipitation of uranium. This mechanism depends on changes in redox states due to the metabolic processes that microbes use to grow and subdivide. It is a complex process that depends on complex geochemical models. Suzuki and Banfield (1999 [DIRS 154445], p. 402) also report that this mechanism is small compared to the metabolism-independent uptake (or adsorption) of uranium. Therefore, only the largest effect (metabolism-independent uptake) will be quantified because the completeness gained by including both mechanisms would result in only small changes to the TSPA.

Metabolism-independent uptake (or adsorption) of uranium is modeled using a data set compiled from 25 separate literature sources for microbial uranium accumulation by microorganisms (bacteria, fungi, algae, and lichens) reported in Suzuki and Banfield (1999 [DIRS 154445], Table 2). The data set was pared down to represent only the uranium uptake by 45 species of

bacteria and fungi over a range of "optimum" pH values (i.e., pH values of 1 to 7), as shown in Figure 10.3.6-1. These data can be used to represent the uptake of uranium by potential microbial communities in the repository. Because uranium has many similarities to other actinides in terms of chemical properties, it has been demonstrated that it is possible to extrapolate data for microbial uranium accumulations to other actinides (Macaskie 1991 [DIRS 154446], pp. 42 to 55). Because U^{+4} is similar to Th^{+4} and Pu^{+4}, it can be assumed that the data in Figure 10.3.6-1 can be used as a surrogate for data on the uptake of thorium and plutonium.

10.3.6.3.1.2 Transport

As discussed in Section 10.1.1, data from laboratory column tests from Jewett et al. (1999 [DIRS 154325], Table 2) and Wan et al. (1994 [DIRS 154367]) show a strong dependence of microbial transport on the level of water saturation in the porous media (Figure 10.3.6-2). The retention of microbes in the EBS can then be linked directly to saturation levels in the invert, assuming that the analogue data are sufficient for quantifying uncertainty and that the granular invert backfill is similar to a packed sand column.

The advective transport of microbes out of the EBS can be limited by the findings of Jewett et al. (1999 [DIRS 154325]) and Wan et al. (1994 [DIRS 154367]) above a liquid saturation level of 44 percent. However, below this level, no specific control can be devised. Therefore, an assumption can be made that saturations at or below 44 percent will be able to move 5 percent of the microbes (at 44 percent saturation, 95 percent of the microbes are retained). This assumption is likely to be conservative because microbial movement will be progressively more limited as saturation decreases. Other evidence that may partially support this assumption is the work reported on the Large Block Test (Chen et al. 1999 [DIRS 154447]), which shows that bacterial transport could occur during heating, where one would expect the initial saturation levels in the fractures and matrix to decrease because of the thermal movement of water. Chen et al. (1999 [DIRS 154447]) also report that some of the bacterial tracers used to conduct the transport test had migrated to the collection points. This information indicates that some level of microbial transport occurs under these conditions.

10.3.6.3.2 Representation of a Total System Performance Assessment Model for Microbial Sorption and Transport

The representation of this model in the TSPA can be accomplished in the following manner. First, a source term for microbial biomass must be generated each time step (see Section 10.3.6.3.2.1). Second, the sorption of uranium and plutonium onto that biomass must be calculated. The uptake of uranium and plutonium is discussed in Section 10.3.6.3.2.2. Finally, the fraction of microbes that will be retained in the invert versus the fraction that will be released as colloids from the EBS must be determined (see Section 10.3.6.3.2.3).

10.3.6.3.2.1 Microbial Source Term

The source term for microbes through time is abstracted from the results of the in-drift microbial communities model (CRWMS M&O 2000 [DIRS 151561]; DTN: MO0010MWDMIN38.031 [DIRS 154299]). The values used were the cumulative growth curves through time for each of

the commercial spent nuclear fuel waste package (21-PWR) modeling runs (Cases 1 to 5 and 7) and the high-level radioactive waste package modeling runs (Cases 15 to 19 and 21) that included biomass growth from waste package failure and waste form degradation. These results were plotted in SigmaPlot 4.0 and regressed using third- and fourth-order linear regression of a log/log plot to best fit the data (Figures 10.3.6-3 and 10.3.6-4). Based on the regression analysis, the following equations represent the microbial source terms for the commercial spent nuclear fuel and high-level radioactive waste glass, respectively. The cumulative microbes produced (*CMP*) is measured in units of grams (dry weight) per meter of waste package, and *T* is time in years.

$$\log CMP_{csnf} = -5.7846 + 7.5541 (\log t) - 2.0501 (\log t)^2 + 0.1891 (\log t)^3$$

$$\log CMP_{hlw} = 1.4824 + 0.4394 (\log t) + 0.4545 (\log t)^2 - 0.1887 (\log t)^3 + 0.0207 (\log t)^4$$

The predicted biomass available for radionuclide uptake in any given year, *t*, is determined by taking *CMP* calculated at time *t* and subtracting from it the value for *CMP* at time *t*-1.

10.3.6.3.2.2 Radionuclide Uptake

The data for uranium uptake are taken from Suzuki and Banfield (1999 [DIRS 154445], Table 2). These values, which represent uranium uptake for 45 species of bacteria and fungi, were averaged, and the results are shown in Table 10.3.6-1.

The average, or mean, value in Table 10.3.6-1 (162.88 mg U/gm) is smaller than the midpoint of the minimum and maximum values (330 mg U/gm). In this situation, a normal distribution with the mean and standard deviation given in Table 10.3.6-1 is biased away from the maximum values. The distribution of uptake for TSPA purposes should therefore be a triangular distribution with a range between 45.2 and 615 mg U/gm and a median value of 111.33 mg U/gm to capture the observed range of data and provide the median value as the most likely uptake. As discussed above, plutonium and thorium are also expected to sorb onto microbes. Since there are no specific data for uptake of these two elements, the distribution for uranium uptake will also be used for plutonium and thorium. In addition, because the abundance of these two radionuclides is smaller than that of uranium, a second modeling assumption will be that plutonium and thorium are sorbed in proportion to the ratios of their dissolved concentrations with respect to uranium prior to uptake.

10.3.6.3.2.3 Transport of Microbes in the Invert

A regression of data found in Jewett et al. (1999 [DIRS 154325], Table 2, p. 85) will govern the release of microbes from the invert when saturation levels in the invert are equal to or greater than 0.45. This regression fit, which is validated by data from Wan et al. (1994 [DIRS 154367], Figure 9), is shown in Figure 10.3.6-2. The regression equation is:

$$\text{Fraction of Microbial Mass Retained in Invert} = 1.3256 + (\text{Invert Saturation})(-0.8417)$$

This equation is valid over the range of invert saturation from 0.45 to 1.0. For matrix saturation levels below 0.45, there are no data available. However, as discussed above, a conservative assumption would be that, below a saturation of 0.45, 5 percent of the microbes are transported

as colloids for any given time step, since this is the value bounded by the data from Jewett et al. (1999 [DIRS 154325], Table 2, p. 85; see also Figure 10.3.6-1). The remaining 95 percent of the microbes would no longer be able to participate in transport. This would remove 95 percent of the uranium, plutonium, and thorium sorbed to microbes from being able to contribute to overall dose.

10.3.6.4 Other Lines of Evidence to Support Model

The information compiled by Suzuki and Banfield (1999 [DIRS 154445]) and Hersman (1997 [DIRS 100763]) indicate that there is a substantial experimental basis documenting radionuclide uptake by microbes and their subsequent movement as colloidal particles in unsaturated environments.

10.4 SUMMARY AND PARAMETERS PROVIDED TO TOTAL SYSTEM PERFORMANCE ASSESSMENT

This section defines the computational algorithms for TSPA-SR sensitivity studies related to transport through the EBS. It is structured to parallel the six subsections in Section 10.3, summarizing the conceptual and mathematical models for diffusion in the waste package, transport from the waste package to the invert, diffusion through the invert, sorption of dissolved radionuclides, colloidal transport, and microbial sorption and transport. The emphasis in this section is on definition of the algorithms for TSPA; detailed technical discussions and references can be found in the corresponding portions of Section 10.3.

10.4.1 Diffusion in the Waste Package

The general approach for the commercial SNF (21-PWR and 44-BWR) waste packages is to consider three limiting pathways for diffusion: along failed fuel rods, through porous corrosion products inside the package, and through porous corrosion products filling breaches (either stress corrosion cracks or general corrosion patches) in the outer layer of the waste package. Starting from the time when a package is first breached, the extent of degradation is determined. This parameter is the basis for estimating the amount of corrosion product present inside a package and the size of penetrations, and allows the water saturation and effective diffusion coefficient to be computed. The diffusive flux for releases along failed fuel rods and through corrosion products within the package is calculated, and the larger of these two is selected. Next, the diffusion rate through breaches in the package is computed. The smaller of the in-package diffusion rate and the breach diffusion rate is selected as the net diffusive release. This is a reasonable approach because the net diffusive release from the waste package is limited by the smaller of the in-package diffusion rate and the breach diffusion rate. In other words, these pathways are sequential, so the smallest diffusion rate will be the controlling parameter. Within the waste package, however, radionuclides will diffuse along the fastest independent pathway that is available.

Figure 10.4.1-1 is a flow chart that summarizes the computational algorithms for the in-package diffusion model. The elements in Figure 10.4.1-1 have been identified with the letters that correspond to the major steps in the computational algorithm. These elements also include the section number where the equation or parameter is discussed in Section 10.3.1. The major steps in the flow chart are:

- Figure 10.4.1-1, Item A. Determine the extent of degradation of the iron-based internal components of the waste package and the resulting surface area available for adsorption of water vapor. This is a two-step process. First, the extent of degradation is computed from the estimated lifetime of the internal components. Second, the effective surface area for adsorption is interpolated between the initial surface area and the fully degraded surface area as a function of the component lifetimes and the current simulation time.

  First Step—Assume the iron-based internal components have a lifetime equal to that of the waste package inner layer, which is 50-mm thick. The cylindrical wall of each commercial SNF waste package has an inner layer made of stainless steel and an outer layer made of Alloy 22. Compute the lifetime by dividing the inner layer thickness by the corrosion rate. Assume that one-third of the iron-based internal components are carbon steel and two-thirds are stainless steel. Each type of steel corrodes at a different rate, determined by sampling its rate distribution. The lifetime of carbon steel is then given by:

$$t_{f1} = \frac{50\,\text{mm}}{r_1} = \frac{5\,\text{x}\,10^4}{r_1}$$

  where r_1 is the sampled value for the corrosion rate of carbon steel [μm/yr]. Similarly, the lifetime of stainless steel is given by:

$$t_{f2} = \frac{50\,\text{mm}}{r_2} = \frac{5\,\text{x}\,10^4}{r_2}$$

  where r_2 is the sampled value for the corrosion rate of stainless steel [μm/yr].

  Second Step—One-third of the total initial surface of the internal components is assigned to carbon steel components and two-thirds are assigned to stainless steel components, similar to the assumption for the first step. The initial surface areas are then (1/3)(1390.8 m^2) = 463.6 m^2 for carbon steel and (2/3)(1390.8 m^2) = 927.2 m^2 for stainless steel, where 1,390.8 m^2 is the total initial surface area for all waste package internal components (see Section 10.3.1.3.3.1). Similarly, the fully degraded surface areas are (1/3)(2.58×10^8 m^2) = 0.86×10^8 m^2 for carbon steel and (2/3)(2.58×10^8 m^2) = 1.72×10^8 m^2 for stainless steel, where 2.58×10^8 m^2 is the total degraded surface area for all waste package internal components (see Section 10.3.1.3.3.1). Then at the current simulation time, t, the surface areas of the carbon and stainless steel components are computed as a linear interpolation over the lifetimes of the iron-based components:

$$A_1 = 463.6 + (0.86\times10^8 - 463.6)\frac{t - t_0}{t_{f1}}, \quad for\, t_0 < t < t_0 + t_{f1}$$
$$= 0.86\times10^8, \quad for\, t > t_0 + t_{f1}$$
$$A_2 = 927.2 + (1.72\times10^8 - 927.2)\frac{t - t_0}{t_{f2}}, \quad for\, t_0 < t < t_0 + t_{f2}$$
$$= 1.72\times10^8, \quad for\, t > t_0 + t_{f2}$$

where A_1 is the surface area of the carbon steel components, A_2 is the surface area of the stainless steel components, and t_0 is the time of first breach of the waste package. The total surface area within the waste package is then $(A_1 + A_2)$. The surface area available for adsorption of water vapor, s_{WP}, is then calculated as the product of this total surface area and the sampled waste package surface area factor, f_{WPs}, that accounts for the uncertainty in the estimates of the surface area of corrosion products.

- Figure 10.4.1-1, Item B. Using the adsorption isotherm for Fe_2O_3 and assuming that the package void volume remains constant at 4.97 m^3 (Table 10.3.1-5), compute the amount of water vapor adsorbed (number of monolayers and film thickness) and the water saturation in the package as follows:

$$S_e = \frac{V_w}{s_{N_2}}\frac{s_{WP}}{V_{WP}}$$
$$= \frac{s_{WP}}{V_{cp}}\frac{M_w}{\rho_w A_w N_A}\left(\frac{-1.1}{\log_{10} RH}\right)^{\frac{1}{2.45}}$$

Symbols are defined in Sections 10.3.1.3.5.1 and 10.3.1.3.2.1.

- Figure 10.4.1-1, Items C1 and C2. Compute the effective diffusion coefficient for steel corrosion product, D_s, using Archie's Law with a fixed porosity of 0.6539 and the water saturation obtained from Item B (Item C1). Calculate $D_s A_s$, where A_s (Item C2) is the total cross-sectional area of the medium, depending on which direction diffusion is taking place. The predominant direction for diffusion will be axial (toward each end of the waste package) when only stress corrosion cracks are present; A_s should then be the cross-sectional area of a waste package. Once general corrosion patches appear in the cylindrical sides of the waste package, radial diffusion to the sides of the waste package will dominate, so A_s should then be the inside surface of the Alloy 22 layer. Both of these estimates for A_s represent upper bounds. A lower bound would be the actual area of the breaches. Depending on the direction of diffusion, sample the diffusion path length, Δx_s, uniformly from 2 cm (Alloy 22 thickness) to 4.775 m (inside length of a 21-PWR waste package) if only stress corrosion cracks are present; otherwise, sample Δx_s uniformly from 2 cm to 0.712 m (half the inside diameter of a 21-PWR waste package) when patches are present (Item C2).

- Figure 10.4.1-1, Items D1 and D2. With minimal degradation (i.e., spaces between rods are mostly free of corrosion products), diffusion occurs along failed fuel rods. Use the adsorption isotherm for ZrO_2 to obtain the thickness of the adsorbed water film on the surface of fuel rods. Compute the cross-sectional area, A_f, for diffusion along rods (see Section 10.3.1.3.5.1); multiply by number of failed rods, N_{ffr}; then multiply this product by D_{wl}, the diffusion coefficient of radionuclides in water (using the same values used to calculate radionuclide transport in the invert) to determine $D_{wl} A_f N_{ffr}$. Sample the diffusion path length, Δx_f, uniformly from 2 cm (Alloy 22 thickness) to 4.775 m (inside length of a 21-PWR).

- Figure 10.4.1-1, Items E1, E2, and E3. Calculate the diffusion rates, $q_s = D_s A_s \Delta C / \Delta x_s$ and $q_f = D_{wl} A_f N_{ffr} \Delta C / \Delta x_f$, for diffusion in-package through porous corrosion products and for diffusion along failed fuel rods, respectively (Items E1 and E2). The concentration of radionuclides inside the package is at the solubility limit (or the concentration provided by a source term model), and the concentration outside the package can either be conservatively assumed as zero or can be the concentration in the invert, if it is available. Use the larger of the two as the in-package diffusion rate through the waste package interior (Item E3):

$$q_{ip} = \max\left(q_s, q_f\right)$$

- Figure 10.4.1-1, Item F. Obtain the total area, A_b, of all breaches in the waste package outer barrier by summing the areas of all stress corrosion cracks and general corrosion patches. Assume all penetrations are filled with corrosion products with a porosity of 40 percent. Assume corrosion products are Fe_2O_3, and calculate the water saturation at the given *RH* using:

$$S_{e,cp} = 1.19419 \times 10^{-2} \left(-\ln RH\right)^{-1/2.45}$$

Use Archie's Law to get the effective diffusion coefficient for diffusion through penetrations (Equation 10-9 in Section 10.3.1.3.5.3 where the exponents on porosity and saturation are those obtained by Conca and Wright [1992 [DIRS 100436]], as discussed in Section 10.3.1.3.5.1):

$$D_s = \phi_{cp}^{1.849} S_{e,cp}^{1.8492} D_{wl}$$

Multiply the effective diffusion coefficient by the total area of all patches to evaluate the $D_{s,cp} A_b$ term in the diffusion rate expression. Sample the path length, Δx_b, uniformly from 2 cm (Alloy 22 thickness) to 7 cm (total thickness of inner and outer walls of waste package). Calculate the diffusion rate through breaches:

$$q_{cp} = D_{s,cp} A_b \Delta C / \Delta x_{cp}$$

- Figure 10.4.1-1, Item G. Compare the diffusion rates for in-package diffusion and diffusion through breaches, and select the smaller as the rate of diffusion out of the waste package:

$$q = \min\left(q_{ip}, q_b\right)$$

The only sampled parameters that are not already used in another model are the diffusion path length (Δx), the corrosion rate of steel components (r_1 and r_2), and the surface area factor for the waste package (f_{WPs}). The sampled parameters for the model are summarized in Table 10.3.1-12.

10.4.2 Transport from the Waste Package to the Invert

The baseline model for transport between the waste package and the invert will be used until additional information is available on thin film flow and until TSPA-SR sensitivity results are analyzed to determine the impacts from the other models introduced in this section. A detailed advective-diffusive transport model between the waste package and the invert may be implemented when (1) three-dimensional predictions of relative humidity and waste package temperature are available to the required level of detail, (2) the effects of surface roughness and heterogeneity for the repository system can be quantified, and (3) the maximum value of relative humidity that will prevent advective transport within the repository system can be determined.

10.4.3 Diffusion Through the Invert

The abstraction for the diffusion coefficient in the invert is as follows:

- The self-diffusivity of water is a bounding value for the free water diffusivity of all radionuclides at 25°C. The value for the self-diffusivity of water, D_0, is 2.299×10^{-5} cm^2/s. This approach is conservative by a factor of between 1 and 3.8, as explained in Section 10.3.3.3.2. This approach is unchanged from the TSPA-SR (CRWMS M&O 2000 [DIRS 153246]).

- The free water diffusion coefficient is corrected for the porosity and (liquid) saturation of the invert as a porous medium. The diffusivity, D, is calculated as:

$$D = D_0 \phi^{1.849} s^{1.849} 10^{ND(a=0,\sigma=0.223)}$$

where

D_0 is the free water diffusion coefficient
ϕ is the porosity
s is the (liquid) saturation.

ND represents a normal distribution with a mean (a) of 0 and a standard deviation (σ) of 0.223. Note that the exponent of the porosity has changed from the TSPA-SR (CRWMS M&O 2000 [DIRS 153246]). See Section 10.3.3.3.1 for additional details.

- The temperature correction for the diffusion coefficient is unchanged from the TSPA-SR (CRWMS M&O 2000 [DIRS 153246]).

- Detailed calculations with NUFT demonstrate that the use of a volume-averaged saturation for the invert is an appropriate abstraction. No changes are required from the TSPA-SR with regard to liquid saturation in the invert.

10.4.4 Sorption of Dissolved Radionuclides

Two approaches have been used to estimate ranges of partition coefficients in the EBS. The first approach uses median values and ranges for partition coefficients (K_ds) for americium, iodine, neptunium, plutonium, technetium, thorium, and uranium on typical soils and corrosion products, or under oxidizing conditions from a variety of sources. The results of this approach are summarized in Table 10.3.4-1 and described in more detail in Section 10.3.4.3.3.2.

An alternate approach to estimating the appropriate ranges of values for partition coefficients is based on the concept of tolerance interval. Tolerance intervals provide a statistical estimate of parameter ranges at a given confidence level from a small data set. In other words, the tolerance interval provides an estimate of the uncertainty inherent in a finite set of data, but it does not represent the conceptual uncertainties associated with linear isotherms and K_ds. The resulting tolerance intervals for a 95 percent confidence level for partition coefficients on sand, loam, and clay are presented in Table 10.3.4-4 and discussed in more detail in Section 10.3.4.3.3.3.

The final recommendations for partition coefficients and distribution type are presented in Table 10.4.4-1. At the low end, each range is based on the minimum value from the tolerance interval because it provides a 95 percent level of confidence. At the high end, each range is based on the maximum value for the corrosion products because the tolerance interval often has values that appear unusually high. All distributions are log uniform because K_d data is often observed to be logarithmically distributed, because a log distribution maintains uniformity of sampling in each decade, and because little is known about the distribution of K_d values throughout a given range.

Finally, the mass of iron-based corrosion products in the waste package is presented in Table 10.3.4-3. The mass of iron-based corrosion products in the invert is 1,004 kg/m of Fe_2O_3 in both the lithophysal and nonlithophysal areas of the repository.

10.4.5 Colloidal Transport of Radionuclides

The baseline model for colloidal transport of radionuclides will be used until additional information is available on colloidal concentrations and transport properties in the EBS and until the results from TSPA-SR sensitivity results are analyzed to determine the impacts on performance from the other models introduced in this section.

Combined Groundwater and Corrosion Colloid Concentrations–Reasonable ranges for this combined colloid population, to which radionuclides may reversibly attach, are log uniform distributions between 10^{-6} and 10^{-1} mg/L (for ionic strength less than or equal to 0.05) and 10^{-9} and 10^{-3} mg/L for (ionic strength greater than 0.05). Differences in affinities for aqueous metals,

including radionuclides, were accommodated by assumptions regarding sorption distribution coefficient (K_d) values and distributions.

Range of Plutonium Concentration Irreversibly Attached to Waste Form Colloids–Reasonable distributions for plutonium irreversibly associated with waste form colloids are log uniform distributions between 10^{-11} and 10^{-6} mg/L for ionic strength less than or equal to 0.05 and between 10^{-14} and 10^{-8} mg/L for ionic strength greater than 0.05.

Sorption of Plutonium and Americium onto Colloids–It is reasonable to use the same distribution for K_ds that describe the sorption of plutonium and americium onto colloids. The recommended distribution for this study is a lognormal distribution with a mean value of 10^5 mg/L and a standard deviation of two orders of magnitude.

10.4.6 Microbial Sorption and Transport

Microbial sorption and transport is not represented in the TSPA-SR model. This baseline (i.e., no microbial sorption and transport of radionuclides) will be used until additional information is available on microbial abundance and transport properties in the EBS and until the results from TSPA-SR sensitivity results are analyzed to determine the impacts on performance from the other models introduced in this section.

Source Term–The following equations represent the microbial source terms for commercial SNF and high-level radioactive waste glass, respectively. The cumulative microbes produced (*CMP*) are:

$$\text{Log } CMP_{csnf} = -5.7846 + 7.5541 (\log t) - 2.0501 (\log t)^2 + 0.1891 (\log t)^3$$

$$\log CMP_{hlw} = 1.4824 + 0.4394 (\log t) + 0.4545 (\log t)^2 - 0.1887 (\log t)^3 + 0.0207 (\log t)^4$$

where *CMP* is in units of grams (dry weight) per meter of waste package and t is time in years (see Section 10.3.6.3.2.1). The predicted biomass available for radionuclide uptake in any given year, t, is determined by taking *CMP* calculated at time t and subtracting from it the value for *CMP* at time t -1.

Radionuclide Uptake–The uptake of uranium for TSPA sensitivity studies (McNeish 2001 [DIRS 155023]) will be a triangular distribution ranging between 45.2 and 615 mg uranium/gm and with a median value of 111.33 mg uranium/gm (Section 10.3.6.3.2.2). Plutonium and thorium are also expected to sorb onto microbes. Because there are no specific data for uptake of these two elements, the sampled value from the distribution for uranium uptake will be scaled down for the relative abundances of plutonium and thorium. That is, it will be assumed that plutonium and thorium sorb onto microbes in proportion to the ratios of their dissolved concentrations with respect to uranium prior to uptake.

Transport of Microbes in the Invert–For invert saturation levels equal to or greater than 0.45, the fraction of microbial mass retained in the invert will be represented through a regression fit to experimental data:

Fraction of Microbial Mass Retained in Invert = 1.3256 + (Invert Saturation)(-0.8417)

No data are available for matrix saturation levels below 0.45. However, a conservative assumption will be to transport 5 percent of the microbes as colloids for any given time step because this is the value bounded by the experimental data (Section 10.3.6.3.2.3).

Table 10.3.1-1. Comparison of the Adsorption of Water on Various Metals

Element	RH for Monolayer Coverage (%)			H_2O Adsorbed at 80% RH and 25°C in N_2/H_2O (g/cm^2)
	25°C	45°C	90°C	
Gold	10	25	24	4.6×10^{-7}
Copper	10	10	40	3.1×10^{-7}
Nickel	35	20	20[a]	6.2066×10^{-8}
Iron	40	23	16[a]	2.48×10^{-7}

Source: Lee 1994 [DIRS 154380], Chapter 5.

NOTE: [a] The values for nickel and iron at 90°C were measured at 85°C.

Table 10.3.1-2. Least Squares Analysis of Adsorption of Water on ZrO_2

RH	Adsorption ZrO_2 (mg/g)	No. of Monolayers (θ_a)	Y=-ln(-ln(RH))	X = ln(θ_a)	Prediction of Y	Predicted RH
0.010	5.54	1.354	-1.527	0.303	-1.343	0.02
0.050	6.92	1.691	-1.097	0.525	-0.935	0.08
0.100	7.76	1.896	-0.834	0.640	-0.725	0.13
0.150	8.53	2.085	-0.640	0.735	-0.552	0.18
0.200	9.12	2.229	-0.476	0.801	-0.429	0.22
0.300	10.40	2.542	-0.186	0.933	-0.189	0.30
0.400	11.52	2.815	0.087	1.035	-0.002	0.37
0.500	12.80	3.128	0.367	1.140	0.191	0.44
0.600	14.56	3.558	0.672	1.269	0.427	0.52
0.658	16.00	3.910	0.871	1.364	0.600	0.58
0.700	17.81	4.352	1.031	1.471	0.797	0.64
0.784	24.00	5.865	1.413	1.769	1.343	0.77
0.840	32.00	7.820	1.747	2.057	1.870	0.86
0.880	40.00	9.775	2.057	2.280	2.279	0.90
0.917	48.00	11.730	2.446	2.462	2.613	0.93
0.947	56.00	13.685	2.910	2.616	2.895	0.95

Source: Holmes et al. 1974 [DIRS 154379], p. 367.

Table 10.3.1-3. Specific Surface Area of Oxide Samples Reported in Literature

Material	Specific Surface Area (m^2/g)	Reference
α-Fe_2O_3	9.10	Jurinak 1964 [DIRS 154381], p. 480
α-Fe_2O_3	10	McCafferty and Zettlemoyer 1970 [DIRS 154382], p. 453
"Iron oxide"	13.3 – 14.3	Gregg and Sing 1982 [DIRS 153010], Table 3.17
ZrO_2	14.5	Holmes et al. 1974 [DIRS 154379], p. 368 (avg. of range listed)

Table 10.3.1-4. Characteristics of a 21-PWR Waste Package

Component	Dimensions	Qty. in WP	Total Surface Area (m^2)	Mass (kg)	Density (kg/m^3)
Fuel Rods [e]	0.94996 cm OD; 384.96 cm length; 0.11488698 m^2/rod	5544	636.933	–	–
Basket A-Sideguide	10 mm thickness	32	22.013 [a]	27	7850 [b]
Basket B-Sideguide	10 mm thickness	16	14.675 [a]	36	7850 [b]
Basket A-Stiffener	10 mm thickness	64	1.174 [a]	0.72	7850 [b]
Basket B-Stiffener	10 mm thickness	32	1.223 [a]	1.5	7850 [b]
Basket C-Stiffener	10 mm thickness	32	1.875 [a]	2.3	7850 [b]
Basket Corner Guide	10 mm thickness	16	17.121 [a]	42	7850 [b]
Basket A-Plate	7 mm thickness	8	25.037 [a]	85	7760 [c]
Basket B-Plate	7 mm thickness	8	25.037 [a]	85	7760 [c]
Basket C-Plate	7 mm thickness	16	25.920 [a]	44	7760 [c]
Basket D-Plate	5 mm thickness	8	24.889 [a]	21	2700 [d]
Basket E-Plate	5 mm thickness	8	24.889 [a]	21	2700 [d]
Basket Tube [f]	4.575 m length; 22.64 cm width; 5 mm thickness	21	177.854	–	7850 [b]
Inner Shell	1.424 m ID; 4.775 m length	1	21.362	–	–
Inner Lid	1.430 m diameter	2	3.212	–	–
Total	–	–	1023.214	–	–

NOTES: [a] Surface Area = $2mN/(\rho\Delta x)$; m = mass (kg); N = quantity; ρ = density (kg/m^3); Δx = thickness (m); "2" accounts for 2 sides of a plate; edges ignored; WP = waste package.

[b] CRWMS M&O (1999 [DIRS 102933], p.10; Material: SA-516 K02700).

[c] CRWMS M&O (1999 [DIRS 102933], p.39; Material: Neutronit A 978).

[d] CRWMS M&O (1999 [DIRS 102933], p.56; Material: A96061).

[e] CRWMS M&O (1998 [DIRS 100733], Attachment I, Table 1); 264 rods/assembly.

[f] Square cross section; width listed is inside dimension; ends ignored.

Basket dimensions, quantities, mass, and material from CRWMS M&O 2000 [DIRS 144128], Attachment I, Sketch SK-0175.

W1717WL chosen as average assembly.

Table 10.3.1-5. Porosity Calculation for a 21-PWR Waste Package (Density, Mass, and Sources Listed in Table 10.3.1-4)

Component	Mass each (kg)	Quantity in WP	Total Volume (m^3)
Fuel Rods	(272.845 cm^3/rod)	5544	1.5127
Basket A-Sideguide	27	32	0.1101
Basket B-Sideguide	36	16	0.0734
Basket A-Stiffener	0.72	64	0.0060
Basket B-Stiffener	1.5	32	0.0061
Basket C-Stiffener	2.3	32	0.0094
Basket Corner Guide	42	16	0.0856
Basket A-Plate	85	8	0.0876
Basket B-Plate	85	8	0.0876
Basket C-Plate	44	16	0.0907
Basket D-Plate	21	8	0.0622
Basket E-Plate	21	8	0.0622
Basket Tube	164	21	0.4387
Total Solids Volume	–	–	2.6323
Inner WP Volume	1.424 m ID; 4.775 m length	1	7.6047
Total Void Volume	–	–	4.9724

NOTE: WP = waste package.

Table 10.3.1-6. Masses and Materials for the Three Types of Waste Packages That Will Comprise the Bulk of Waste in the Repository

Material	21-PWR Mass (kg)	44-BWR Mass (kg)	5-DHLW Mass (kg)
Alloy C-22	6663	6812	8260
Stainless Steel Type 316NG	11249	11531	11296
A 516 carbon steel	5723.68	7245	3805
Neutronit A 978	2064	2152	-
Stainless Steel Type 304L	-	-	2500
Aluminum 6061	336	336	-
Commercial SNF [a]	172.6	182.1	-
Zircaloy	2244 [b]	2063 [c]	-
DOE High-Level Waste Glass	-	-	8410[d]

Source: CRWMS M&O 2000 [DIRS 151561], Tables III-1 to III-4.

NOTES: [a] Includes only the mass of elements C, N, P, S, Mn, and Fe; does *not* include masses of U, UO_2 or Zr (CRWMS M&O 1998 [DIRS 100737], pp. I-2 and III-2).

[b] Based on 5544 fuel rods; 0.94996 cm (0.374 in.) outer diameter; 0.05715 cm (0.0225 in.) cladding thickness; 384.9624 cm (151.560 in.) length (DOE 1992 [DIRS 102588], p. 2A-30). Includes only the cladding. Density of Zircaloy 4 = 6560 kg/m^3 (CRWMS M&O 1999 [DIRS 102933], p. 44). The calculation is as follows:

$$
\begin{aligned}
m &= \pi\left\{D_o^2 - (D_o - 2t_{clad})^2\right\}L\rho N/4 \\
&= \left(\frac{\pi}{4}\right)\left\{(0.94996\ \text{cm})^2 - [(0.94996\ \text{cm}) - 2(0.05715\ \text{cm})]^2\right\}\cdot \\
&\quad (3849624\ \text{cm/rod})(6560\ \text{kg/m}^3)(5544\ \text{rods})(10^{-6}\ \text{m}^3/\text{cm}^3) \\
&= (61.70828\ \text{cm}^3/\text{rod})(5544\ \text{rods/WP})(6560\ \text{kg/m}^3)(10^{-6}\ \text{m}^3/\text{cm}^3) \\
&= (0.3421107\ \text{m}^3/\text{WP})(6560\ \text{kg/m}^3) \\
&= 2244.25\ \text{kg/WP}
\end{aligned}
$$

[c] GE BWR/4-6 8×8 Assembly (DOE 1992 [DIRS 102588], p. 2A-20); 63 fuel rods/assembly; 2772 rods total; 1.25222 cm (0.493 in.) outer diameter; 365.76 cm (144 in.) length; 0.08636 cm (0.034 in.) cladding thickness; Zircaloy 2 density: 6550 kg/m3 (CRWMS M&O 1999 [DIRS 102933], p. 41). The calculation is as follows:

$$
\begin{aligned}
m &= \left(\frac{\pi}{4}\right)\left\{(1.25222\ \text{cm})^2 - [(1.25222\ \text{cm}) - 2(0.08636\ \text{cm})]^2\right\}\cdot \\
&\quad (365.76\ \text{cm})(6550\ \text{kg/m}^3)(2722\ \text{rods/WP}) \\
&= (0.31491492\ \text{m}^3/\text{WP})(6550\ \text{kg/m}^3) \\
&= 2062.7\ \text{kg/WP}
\end{aligned}
$$

[d] CRWMS M&O 2000 [DIRS 151561], p. IV-4.

Table 10.3.1-7. Elemental Composition of Each Waste Package Material

	316NG Stainless Steel		A516 Steel		Neutronit A978		Aluminum 6061		Commercial SNF		Total
	Wt %	mol	Wt %	Mol	Wt %	mol	Wt %	mol	Wt %	mol	mol
Fe	61.8	124481	97.9	100336	66.7	24651	0.7	42	95.7	2958	252468
Mo	3.0	3518	0.0	0	0.0	0	0.0	0	0.0	0	3518
Cr	18.0	38942	0.0	0	18.5	7344	0.4	26	0.0	0	46311
Ni	14.0	26824	0.0	0	13.0	4570	0.0	0	0.0	0	31407
Al	0.0	0	0.0	0	0.0	0	96.0	11955	0.0	0	11955
Other	3.2	6446	2.1	2153	1.8	665	2.9	174	4.3	133	9571
Total	100.0	200211	100.0	102489	100.0	37230	100.0	12197	100.0	3091	355218

Source: CRWMS M&O 2000 [DIRS 151561], pp. III-4 to III-6, IV-3.

NOTE: Treat "other" as iron.

Table 10.3.1-8. Surface Area Available for Adsorption of Water Inside a 21-PWR Waste Package

Condition	Surface Area (m^2)	Comments
Initial emplacement	1023.2	Surfaces of intact fuel rods, basket components
Initial emplacement	1390.8	Includes area of SNF in 2.2 failed rods per assembly
Initial emplacement	48220.8	Includes area of SNF in all 5,544 fuel rods, but excludes surface area of fuel rod cladding
Fully degraded steel	2.58×10^{8}	Stainless steel inner liner and all basket components converted to moles of iron that is fully oxidized to Fe_2O_3

NOTE: Information based on calculations presented in Section 10.3.1.3.3.1.

Table 10.3.1-9. Effective Water Saturation in Waste Package Resulting from Adsorption of Water Vapor

WP Surface Area ($m^{2)}$	RH = 80%	RH = 90%	RH = 95%	RH = 99%
1023.2	1.584×10^{-7}	2.152×10^{-7}	2.887×10^{-7}	5.615×10^{-7}
1390.8	2.153×10^{-7}	2.925×10^{-7}	3.924×10^{-7}	7.633×10^{-7}
48220.8	7.466×10^{-6}	1.014×10^{-5}	1.361×10^{-5}	2.646×10^{-5}
2.58×10^{8}	3.995×10^{-2}	5.426×10^{-2}	7.280×10^{-2}	1.416×10^{-1}

NOTE: WP = waste package. Information based on Equation 10-5 and surface areas presented in Table 10.3.1-8.

Table 10.3.1-10. Values of Diffusion Coefficient Normalized to the Diffusion Coefficient in Water for Various Waste Package Surface Areas and Relative Humidities

Relative Humidity	D_s / D_{wl}			
	S_{WP} =1023.2 m^2	S_{WP} =1390.8 m^2	S_{WP} =48220.8 m^2	S_{WP} =2.58×108 m^2
0.1	2.15×10^{-15}	3.97×10^{-15}	4.77×10^{-12}	1.37×10^{-04}
0.2	2.88×10^{-15}	5.32×10^{-15}	6.40×10^{-12}	1.83×10^{-04}
0.3	3.65×10^{-15}	6.74×10^{-15}	8.11×10^{-12}	2.32×10^{-04}
0.4	4.56×10^{-15}	8.43×10^{-15}	1.01×10^{-11}	2.90×10^{-04}
0.5	5.73×10^{-15}	1.06×10^{-14}	1.27×10^{-11}	$3.64\times10^{-0}4$
0.6	7.35×10^{-15}	1.36×10^{-14}	1.63×10^{-11}	4.67×10^{-04}
0.7	9.85×10^{-15}	1.82×10^{-14}	2.19×10^{-11}	6.26×10^{-04}
0.8	1.45×10^{-14}	2.67×10^{-14}	3.21×10^{-11}	9.19×10^{-04}
0.9	2.67×10^{-14}	4.93×10^{-14}	5.92×10^{-11}	1.70×10^{-03}
0.95	4.80×10^{-14}	8.86×10^{-14}	1.07×10^{-10}	3.05×10^{-03}
0.99	1.82×10^{-13}	3.35×10^{-13}	4.03×10^{-10}	1.15×10^{-02}

Table 10.3.1-11. Summary of Cross-Sectional Areas for Diffusion for Various Configurations at a Relative Humidity of 95 Percent

Component/ Configuration	Diffusive Path	Path Length (m)	Cross-Sect. Area (mm^2)	Diffusion Coefficient [a] (m^2/s)	$\frac{D_s A}{\Delta x}$ (m^3/s)
Single fuel rod	Axially along fuel rod, ½ WP length	2.388	4.22×10^{-6}	2.299×10^{-9}	4.06×10^{-21}
46.2 fuel rods/WP	Axially along fuel rod, ½ WP length	2.388	1.09	2.299×10^{-9}	1.05×10^{-15}
Initial WP surface consolidated	Axially through full length of WP	4.775	0.297	2.299×10^{-9}	1.43×10^{-16}
Initial WP surface consolidated; 46.2 failed fuel rods	Axially through full length of WP	4.775	0.405	2.299×10^{-9}	1.95×10^{-16}
Initial WP surface consolidated; no cladding	Axially through full length of WP	4.775	14.0	2.299×10^{-9}	6.74×10^{-15}
Initial WP surface as porous medium	Axially through ½ length of WP	2.388	1.593×10^{6} [c]	2.04×10^{-22} [d]	1.36×10^{-22}
SCCs (filled with porous corrosion products)	Axially through SCCs in lids	0.135 [b]	102.	1.126×10^{-12}	8.50×10^{-16}
Fully degraded WP surface consolidated	Axially through ½ length of WP	2.388	7.5×10^{4}	2.299×10^{-9}	7.22×10^{-11}

Table 10.3.1-11. Summary of Cross-Sectional Areas for Diffusion for Various Configurations at a Relative Humidity of 95 Percent (Continued)

Component/ Configuration	Diffusive Path	Path Length (m)	Cross-Sect. Area (mm^2)	Diffusion Coefficient [a] (m^2/s)	$\frac{D_s A}{\Delta x}$ (m^3/s)
Fully degraded WP; porous medium	Axially through ½ length of WP	2.388	1.593×10^{6} [c]	1.80×10^{-12}	1.20×10^{-12}
Corrosion patch (1)	Radially outward through patch in Alloy 22	0.02	2.346×10^{4}	1.126×10^{-12}	1.32×10^{-12}
Corrosion patch (10)	Radially outward through patches in Alloy 22 layer	0.02	2.346×10^{5}	1.126×10^{-12}	1.32×10^{-11}
DHLW surface consolidated	Axially through ½ length of WP	2.388	0.932 [e]	2.299×10^{-9}	8.96×10^{-16}

NOTES: [a] Self-diffusion coefficient of water is used except for porous media in waste packages and in corrosion patches, which use effective diffusion coefficients.

[b] For 21-PWR; thickness of inner lid and closure lid plus the air gap between lids (CRWMS M&O 2000 [DIRS 153940], p. 65).

[c] WP cross section; inner diameter = 1.424 m (see Table 10.3.1-4).

[d] D_s / D_{wl} = 8.86×10^{-14} (for initial surface area = 1,390.8 m^2/waste package, as in Table 10.3.1-10).

[e] From adsorption isotherm (Equation 10-1), 15.73 monolayers adsorbed at a relative humidity of 0.95. Thickness of each monolayer of water is 2.83×10^{-10} m from Equation 10-3. From CRWMS M&O (2001 [DIRS 153846], p. 45, Table 6), the mean surface area of each of 5 glass logs in a DHLW package is 100 m^2, or 500 m^2/waste package. Then area = (15.73 monolayers) (2.83×10^{-10} m/monolayer) (500 m^2/package)/(2.388 m) = 9.32×10^{-7} m^2.

WP = waste package.

Table 10.3.1-12. Parameters to be Sampled for In-Package Diffusion Model

Parameter		Range	Distribution	Comments
Path length (m)	1	0.02 – 4.775	Uniform	Applicable range depends on controlling diffusion pathway: 1. In-package along fuel rods 2. In-package axially through porous corrosion products (only breaches are stress corrosion cracks) 3. In-package radially through porous corrosion products (general corrosion patches present) 4. Through breaches.
	2	0.02 – 4.775	Uniform	
	3	0.02 – 0.712	Uniform	
	4	0.02 – 0.07	Uniform	
Steel corrosion rate (μm/yr)	1	23.5 – 95.34	Normal; median = 59.42	First range and distribution applies to 1/3 of total mass of steel; second applies to 2/3 of total mass, in approx. proportion to mass of mild steel and stainless steel in waste package (see Table 10.3.1-7). Ranges and median values from CRWMS M&0 2001 [DIRS 153846], Tables 26 & 29
	2	0.0879 – 45.5	Log uniform	
Waste package surface area factor, f_{WPs}		0.01 to 100	Log triangular; most likely value = 1.0	Multiplies surface computed from extent of degradation

Table 10.3.4-1. Summary of Partition Coefficient Ranges on Corrosion Products, Sand, and Loam

Element	Substrate or Conditions	Median or Best Estimate (ml/g)	Range (ml/g)	Source/Comments
Americium	Sand	1,900	8.2 to 300,000	Sheppard and Thibault 1990 [DIRS 109991], Table 3
	Loam	9,600	400 to 48,309	
	Iron (hydr)oxides	10,000	1,000 to 20,000	EPRI 2000 [DIRS 154149], Table 6-9
	Oxidizing[a]	5,000	85 to 40,000	Onishi et al. 1981 [DIRS 154420], Table 8.96
	Iron oxide	–	1,000 to 5,000	CRWMS M&O 2001 [DIRS 154024], Table 2a
Iodine	Sand	1	0.04 to 81	Sheppard and Thibault 1990 [DIRS 109991], Table 3
	Loam	5	0.1 to 43	
	Iron (hydr)oxides	0	0 to 1	EPRI 2000 [DIRS 154149], Table 6-9. Maximum value based on IO_3^- on magnetite and goethite.
	Oxidizing[a]	10	0 to 75	Onishi et al. 1981 [DIRS 154420], Table 8.96
	Copper oxide and copper sulfide	–	58 to 1,375	Balsley et al. 1998 [DIRS 154439], Table 1, p. 135

Table 10.3.4-1. Summary of Partition Coefficient Ranges on Corrosion Products, Sand, and Loam (Continued)

Element	Substrate or Conditions	Median or Best Estimate (ml/g)	Range (ml/g)	Source/Comments
Neptunium	Sand	5	0.5 to 390	Sheppard and Thibault 1990 [DIRS 109991], Table 3
	Loam	25	1.3 to 79	
	Iron (hydr)oxides	1	0.1 to 1,000	EPRI 2000 [DIRS 154149], Table 6-9. Values reduced by about 2 orders of magnitude because uranium species will dominate sorption sites
	Oxidizing[a]	10	0.2 to 127	Onishi et al. 1981 [DIRS 154420], Table 8.96
	Iron oxide	–	500 to 1,000	CRWMS M&O 2001 [DIRS 154024], Table 2a
Plutonium	Sand	550	27 to 36,000	Sheppard and Thibault 1990 [DIRS 109991], Table 3
	Loam	1,200	100 to 5,933	
	Iron (hydr)oxides	10,000	1,000 to 20,000	EPRI 2000 [DIRS 154149], Table 6-9
	Oxidizing[a]	50,000	100 to 100,000	Onishi et al. 1981 [DIRS 154420], Table 8.96
	Iron oxide	–	1,000 to 5,000	CRWMS M&O 2001 [DIRS 154024], Table 2a
Technetium	Sand	0.1	0.01 to 16	Sheppard and Thibault 1990 [DIRS 109991], Table 3
	Loam	0.1	0.01 to 0.4	
	Iron (hydr)oxides	0	0 to 1,000	EPRI 2000 [DIRS 154149], Table 6-9. Maximum value assumes reduction of technetium on iron oxide surface
	Oxidizing*	5	0 to 100	Onishi et al. 1981 [DIRS 154420], Table 8.96
	Copper oxide and copper sulfide	–	31 to 67	Balsley et al. 1998 [DIRS 154439], Table 2, p. 139
	Sediment Sand Clayey silt and sand	4.3 (Oxic) 13.7(Anoxic) 0.2 (Oxic) (Anoxic) (Oxic) 0.5 (Anoxic)	Not provided	Bird and Schwartz 1997 [DIRS 154488]. Sediment-water ratio is 1 percent; sand-water and clayey silt/sand-water ratios are 10 percent
Thorium	Sand	3,200	207 to 150,000	Sheppard and Thibault 1990 [DIRS 109991], Table 3
	Loam	3,300	No Data	
	Iron (hydr)oxides	10,000	1,000 to 20,000	EPRI 2000 [DIRS 154149], Table 6-9
	Oxidizing[a]	10,000	10^3 to 10^6	Onishi et al. 1981 [DIRS 154420], Table 8.96
	Iron oxide	–	1,000 to 5,000	CRWMS M&O 2001 [DIRS 154024], Table 2a
Uranium	Sand	35	0.03 to 2,200	Sheppard and Thibault 1990 [DIRS 109991], Table 3
	Loam	15	0.2 to 4,500	

Table 10.3.4-1. Summary of Partition Coefficient Ranges on Corrosion Products, Sand, and Loam (Continued)

Element	Substrate or Conditions	Median or Best Estimate (ml/g)	Range (ml/g)	Source/Comments
Uranium (continued)	Iron (hydr)oxides	1,000	50 to 10,000	EPRI 2000 [DIRS 154149], Table 6-9
	Oxidizing[a]	50	16 to 1000	Onishi et al. 1981 [DIRS 154420], Table 8.96
	Iron oxide	–	100 to 1000	CRWMS M&O 2001 [DIRS 154024], Table 2a

NOTE: [a]Data encompass values in fresh water and seawater, with an emphasis on oxidizing conditions. Values shown are the minimums of the fresh or seawater cases for these elements.

Table 10.3.4-2. Expected Material Lifetimes of Invert, Pallet, and Waste Package Components in the Drift

Component	Material	Thickness (mm)	Lifetime[a] (yrs)	Source for Components, Materials, and Thickness
Invert and Pallet Components				
Transverse support beam	Mild carbon steel	14.61	246	BSC 2001 [DIRS 154441], Table 1 for the W 12 x 53 beam and Section 5.1.10
Gantry rail	Mild carbon steel	31.75	534	BSC 2001 [DIRS 154441], Table 1 for the crane rail and Section 5.1.5
Waste Package Components				
WP inner barrier	316NG stainless steel	50	25000	CRWMS M&O 2000 [DIRS 151561], Table 24
Basket guide	A 516 carbon steel	10	168	CRWMS M&O 2000 [DIRS 151561], Table 24
Basket plate	Neutronit A 978	7	175	CRWMS M&O 2000 [DIRS 151561], Table 24

NOTE: [a]Lifetime is calculated as thickness divided by median corrosion rate. The median corrosion rates are 0.05942 mm/yr for mild carbon steel, 0.002 mm/yr for Stainless Steel Type 316L, and 0.04 mm/yr for borated stainless steel similar to Neutronit A 978 (CRWMS M&O 2000 [DIRS 151561], Tables 29, 26, and 30, respectively). Lifetimes for components fabricated from Alloy 22 or titanium are not shown because they are longer than for steel components and because iron-(hydr)oxides are the main sorbers of interest. WP = waste package.

Table 10.3.4-3. Calculated Mass of Sorbing Material in the Waste Package

Waste Package Type	Mass of Iron (kg/WP)	Mass of Fe_2O_3 (kg/WP)
21-PWR	13,932	19,904
44-BWR	15,655	22,364
5-DHLW	12,333	17,619
Naval SNF	10,758	15,369

Source: Schreiner 2001 [DIRS 155038], Item 3.

NOTE: WP = waste package; SNF = spent nuclear fuel.

Table 10.3.4-4. Summary of Tolerance Interval Calculations for Sand, Loam, and Clay Data Sets

Element	Number of Data Points	ln(Mean)	ln(SD)	Mean K_d (ml/g)	K_d Range (ml/g)	Tolerance Interval Factor	Tolerance Interval (ml/gm)
Americium	60	2.2	2.21	4400	82 to 400,000	2.33	25 to 770,000
Iodine	63	0.86	2.1	2.4	0.04 to 81	2.37	0.02 to 300
Neptunium	31	2.2	1.7	10.8	0.4 to 575	2.54	0.039 to 2,900
Plutonium	78	1.9	1.7	1100	24 to 190,000	2.28	13 to 94,000
Technetium	33	1.5	1.8	0.16	0.01 to 16	2.51	0.004 to 6.2
Thorium	16	2.2	2.1	3600	24 to 160,000	2.91	6.8 to 1,900,000
Uranium	39	3.4	3.2	53	0.03 to 390,000	2.45	0.012 to 230,000

Source: Schreiner 2001 [DIRS 155038], Items 1, 5, 6, 8, 9, 10, and 11.

Table 10.3.4-5. Fraction of Contaminant Metal Irreversibly Sorbed

Element	Fraction Irreversibly Sorbed
Americium	0.6
Iodine	0.9
Plutonium	0.99
Technetium	0.1
Thorium	0.99
Uranium	0.1

Source: Brady et al. 1999 [DIRS 154421], Table 3.4.

Table 10.3.5-1. Summary of Uncertainties Considered for Engineered Barrier System Colloids

Uncertainty	Estimated Significance	Considered in TSPA-SR[a]
Potential contribution of irreversibly attached radionuclides on colloids generated from commercial spent fuel	High	No
Quantities of colloids generated from corrosion of steel	High	Yes
Potential contribution of colloids from degradation of metallic fuel	Potentially high	No
Colloid stability and concentration dependence on temperature	Unknown	No
Suitability of smectite as proxy for all groundwater colloids	Low	Yes
Flow rate within the waste package	Low	No
Colloid sorption onto the air-water interface	Potentially moderate	No
Potential effects on the total colloid population of organic material, including introduced organics and microbes	Potentially high	Partially
Wide range of distribution coefficients (K_ds) used to describe sorption of radionuclides on colloids	High	Yes
Better-justified upper-bound maximum concentration of plutonium irreversibly attached to colloids	Unknown	Yes
Consideration of radionuclides other than plutonium and americium	Low to moderate	No

NOTE: [a] CRWMS M&O 2000 [DIRS 153246], Section 3.5.6.

Table 10.3.5-2. Summary of Recommended Parameter Changes for Total System Performance Assessment

Parameter	TSPA-SR[a] Parameter Values			New Recommendations for TSPA		
	Value	Range	Distribution	Value	Range	Distribution
Combined corrosion and groundwater colloids	Determined by function	Corrosion: 10^{-3} mg/L to 1 mg/L Groundwater: 3×10^{-6} to 3×10^{-2} mg/L	–	Sampled	3×10^{-6} to 10^{-1} mg/L for I $\leq$ 0.05M; 10^{-9} to 10^{-3} mg/L for I > 0.05M	Log uniform
Range of irreversibly attached plutonium concentration on waste form colloids	Determined by function	8×10^{-8} mol/L to 1×10^{-11} mol/L	–	Sampled	10^{-11} to 10^{-6} mol/L for I $\leq$ 0.05M; 10^{-14} to 10^{-8} mol/L for I > 0.05M	Log uniform
K_ds of plutonium and americium on colloids	Pu: 10^4 ml/g Am: 10^5 ml/g	–	Log-normal $\sigma = 10$	Sampled with geometric mean values of 10^5 ml/g for Pu and Am	–	Log-normal with geometric standard deviation $\sigma = 100$

NOTE: [a] CRWMS M&O 2000 [DIRS 153246], Section 3.5.6. I = ionic strength.

Table 10.3.6-1. Distribution of Uranium Uptake for Microbial Transport

Statistical Parameter	mg Uranium/gm Dry Cell Weight
Average (mean)	162.88
Median	111.33
Standard deviation	133.05
Minimum value	45.2
Maximum value	615

Source: Jolley 2001 [DIRS 154823].

Table 10.4.4-1. Recommended Ranges and Distribution Type for the Partition Coefficients (K_ds) of Dissolved Radionuclides

Element	K_d Range for Corrosion Products (ml/g)	K_d Range from Tolerance Interval (ml/g)	Recommended K_d Range (ml/g)	Recommended Distribution Type
Americium	85 to 5,000	25 to 770,000	25 to 5,000	Log uniform
Iodine	0 to 10	0.02 to 300	0.02 to 10	Log uniform
Neptunium	0.1 to 79	0.039 to 2,900	0.039 to 79	Log uniform
Plutonium	100 to 5,000	13 to 94,000	13 to 5,000	Log uniform
Technetium	0 to 5	0.004 to 6.2	0.004 to 5	Log uniform
Thorium	1,000 to 5,000	6.8 to 1,900,000	6.8 to 5,000	Log uniform
Uranium	0.2 to 1,000	0.012 to 230,000	0.012 to 1,000	Log uniform

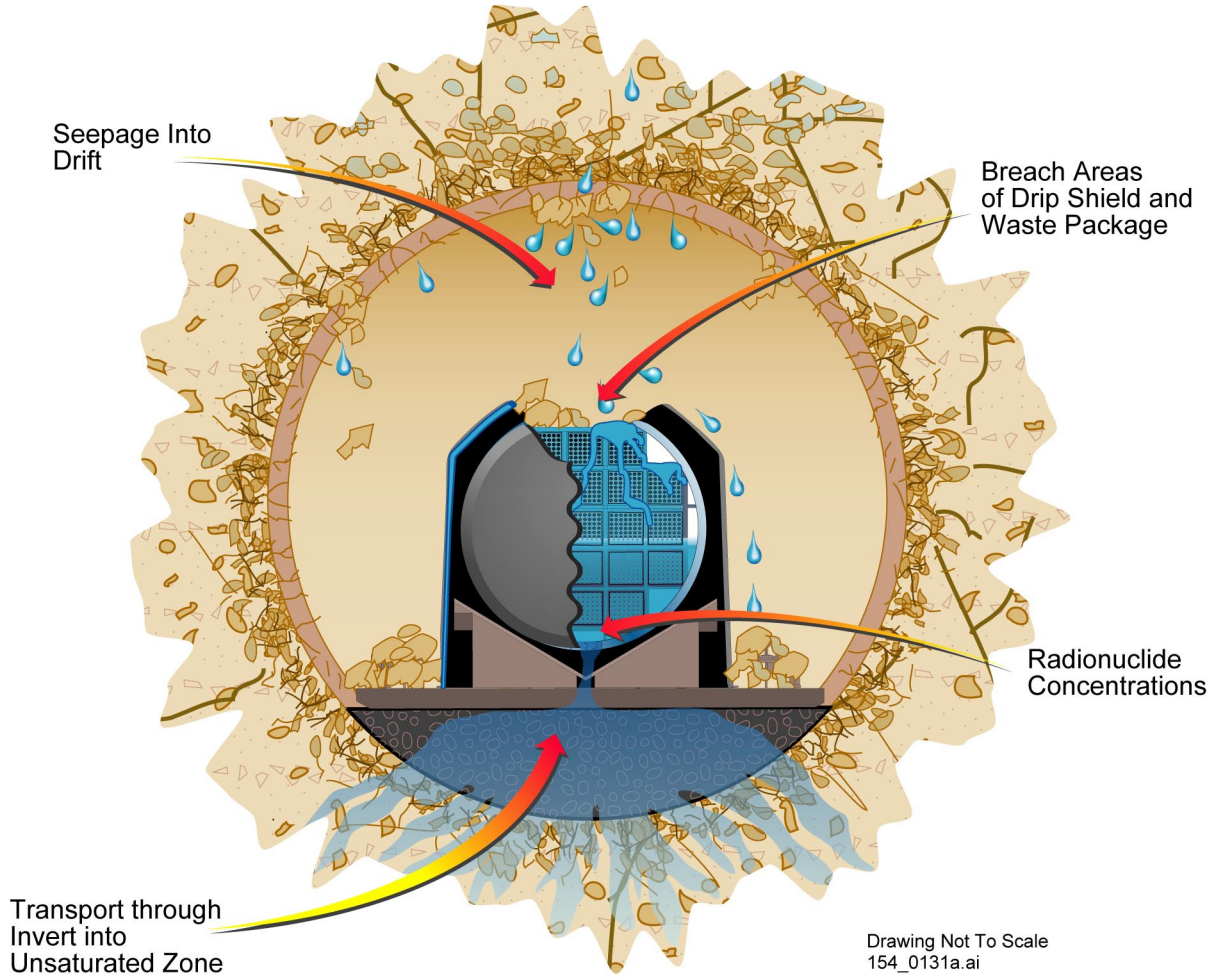

154_0131a.ai

Figure 10.2-1. Conceptualization of an Emplacement Drift after the Drip Shield and Waste Package are Breached and Radionuclides can Transport through the Engineered Barrier System

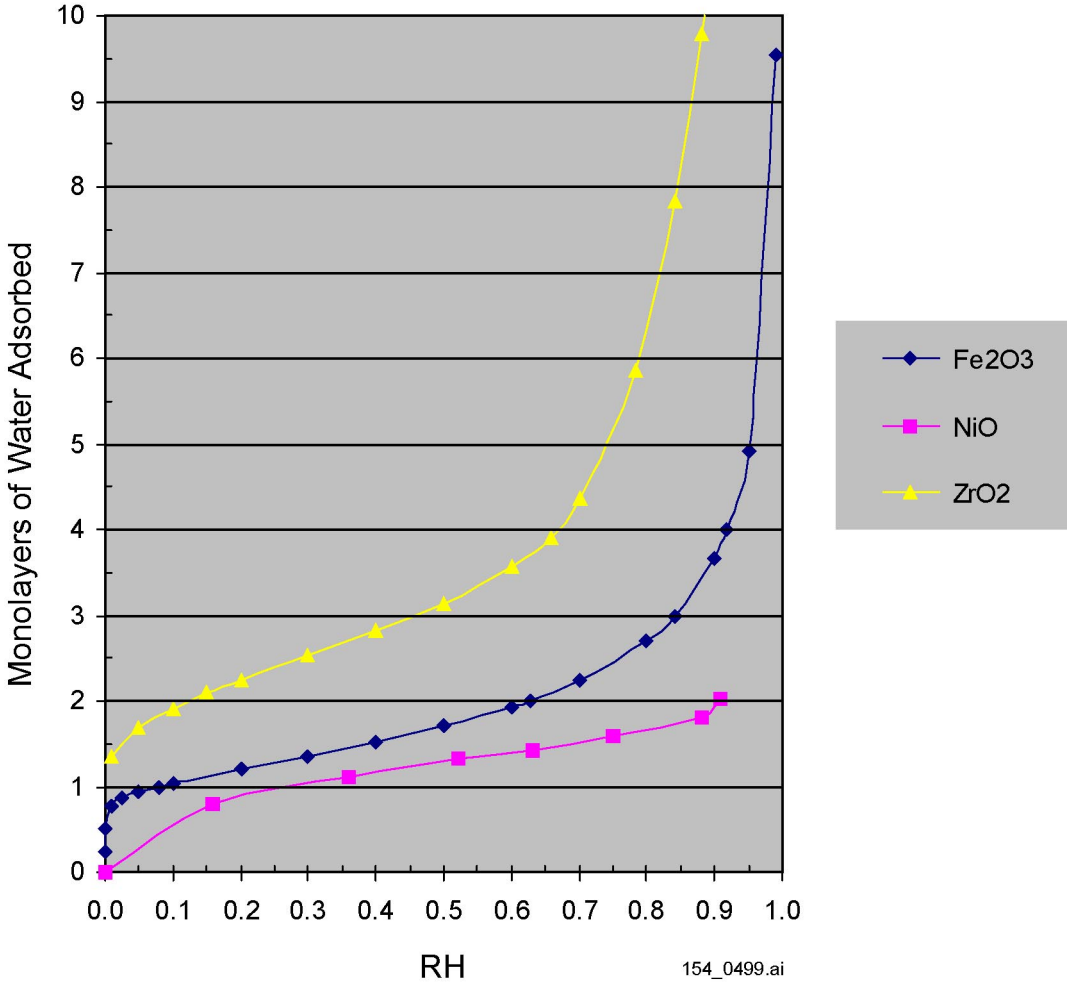

154_0499.ai

Source: Jurinak 1964 [DIRS 154381]; Lee 1994 [DIRS 154380]; Holmes et al. 1974 [DIRS 154379].

Figure 10.3.1-1. Comparison of Adsorption Isotherms for Water Vapor on Fe_2O_3, NiO, and $Zr0_2$

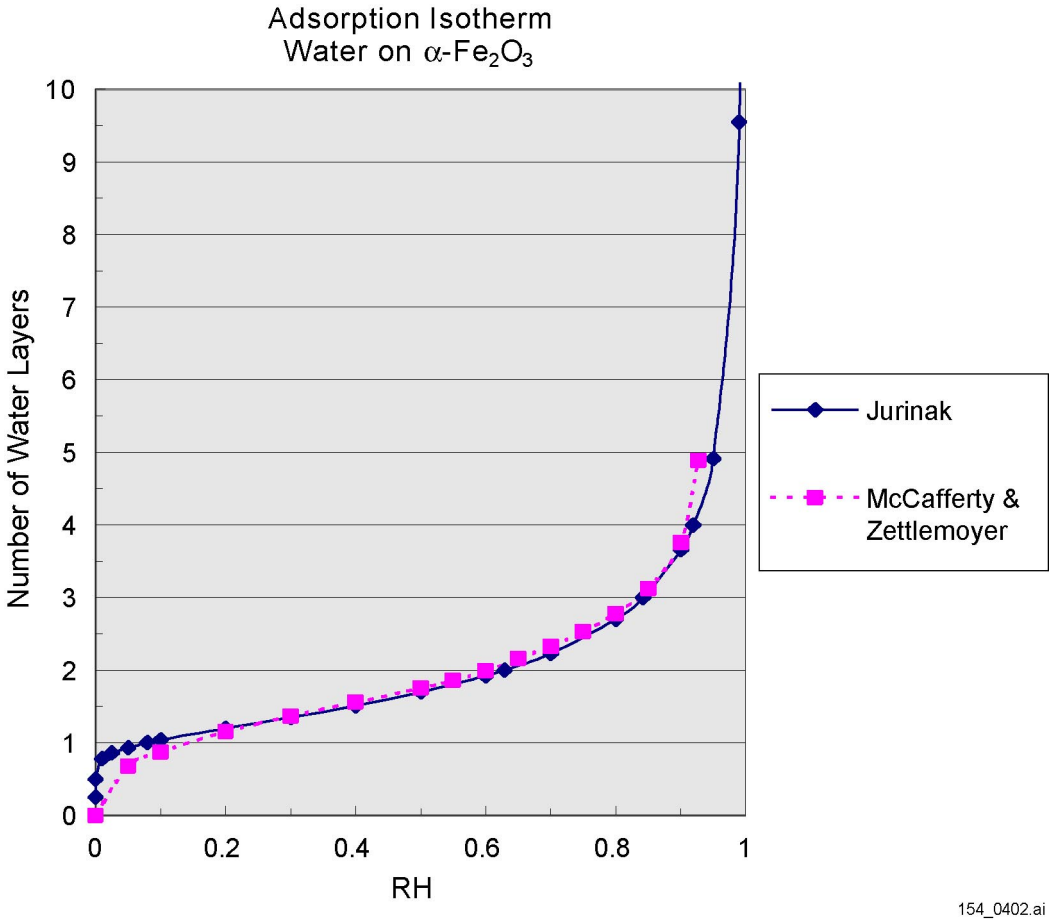

154_0402.ai

Source: Jurinak curve: Jurinak 1964 [DIRS 154381]; McCafferty and Zettlemoyer curve: McCafferty and Zettlemoyer 1970 [DIRS 154378].

Figure 10.3.1-2. Adsorption Isotherm for Water Vapor on α-Fe_2O_3

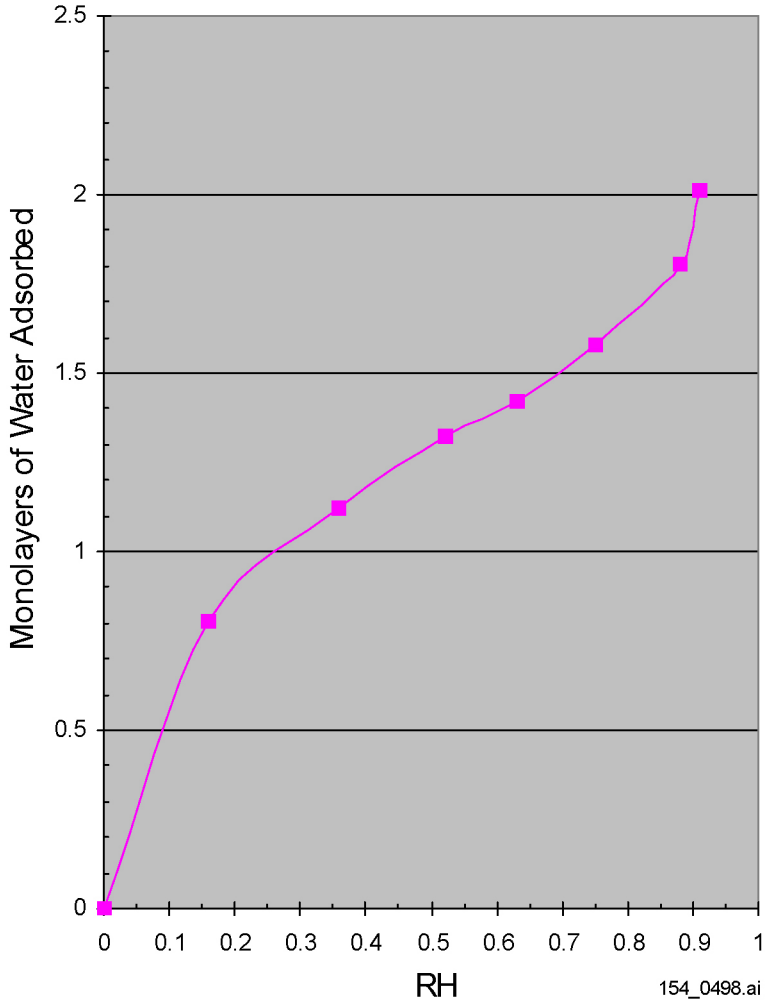

154_0498.ai

Source: Lee 1994 [DIRS 154380].

NOTE: RH = relative humidity.

Figure 10.3.1-3. Adsorption Isotherm for Water on Nickel

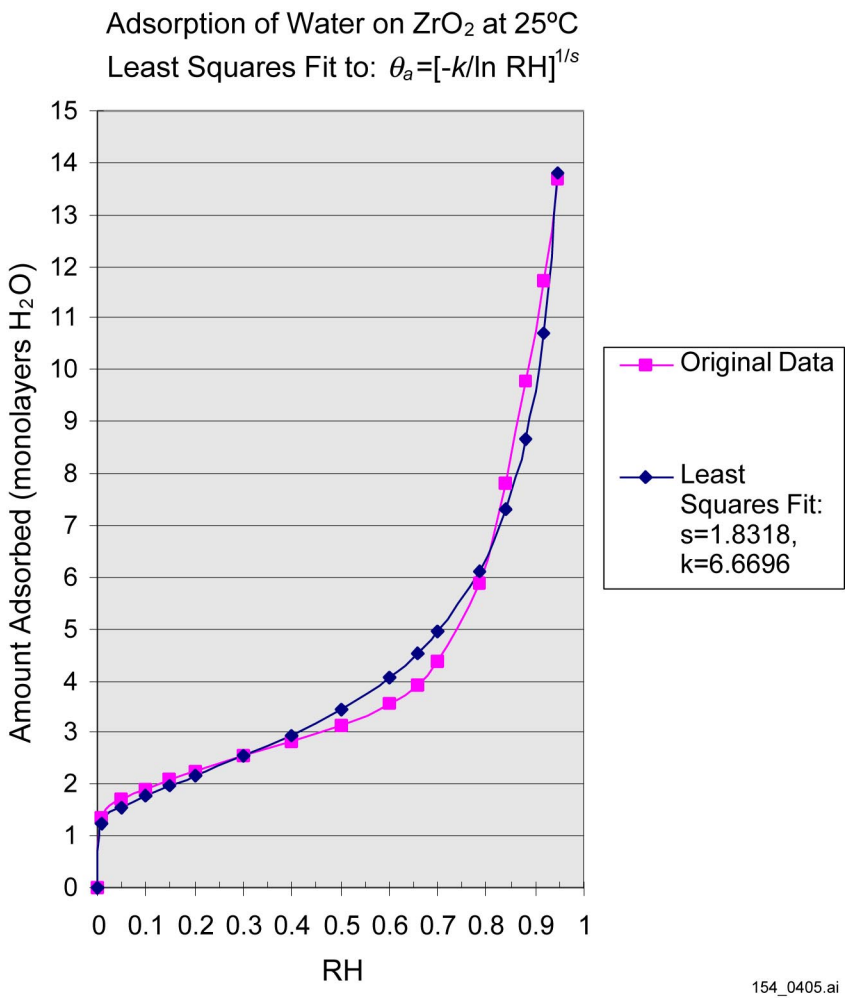

154_0405.ai

Source: Holmes et al. 1974 [DIRS 154379].

NOTE: $R^2 = 0.98$.

Figure 10.3.1-4. Regression Fit to Adsorption Isotherm Data for Water Vapor on ZrO_2

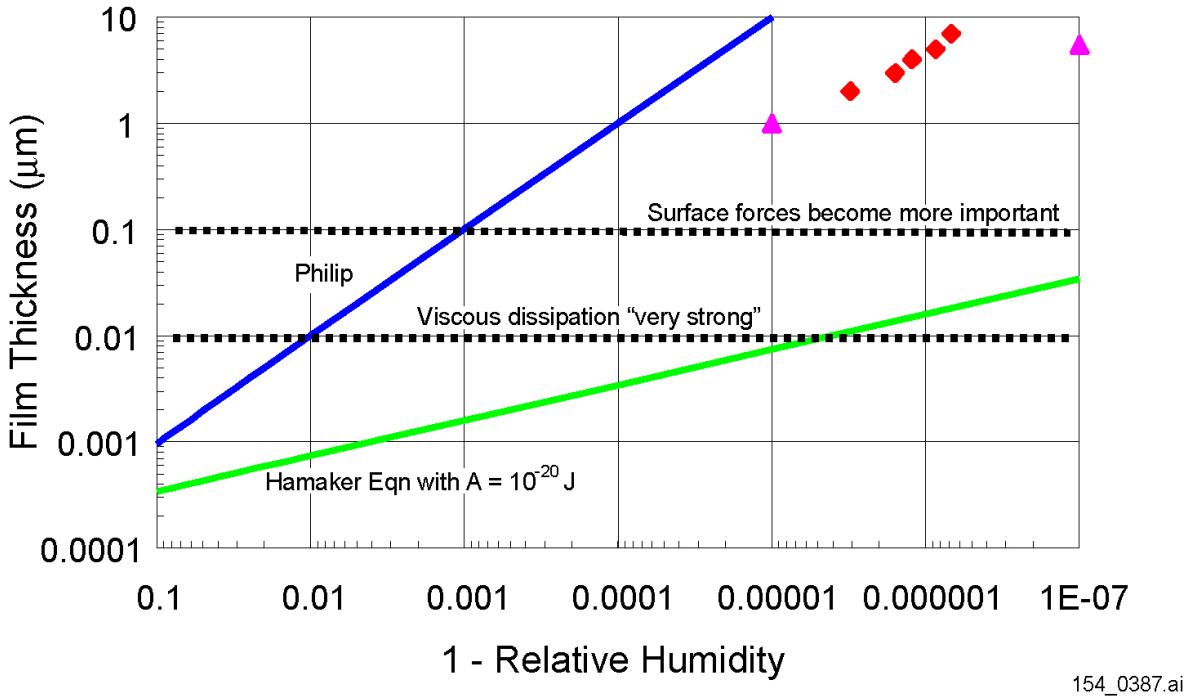

154_0387.ai

Source: Tokunaga and Wan 1997 [DIRS 139195]; Tokunaga et al. 2000 [DIRS 152914]; Philip 1977 [DIRS 152255].

NOTE: Literature data from Tokunaga and Wan (1997 [DIRS 139195]) for Bishop Tuff representing the range from Tokunaga et al. (2000 [DIRS 152914]) for rough glass.

Figure 10.3.2-1. Film Thickness Data and Predictive Relationships from the Literature

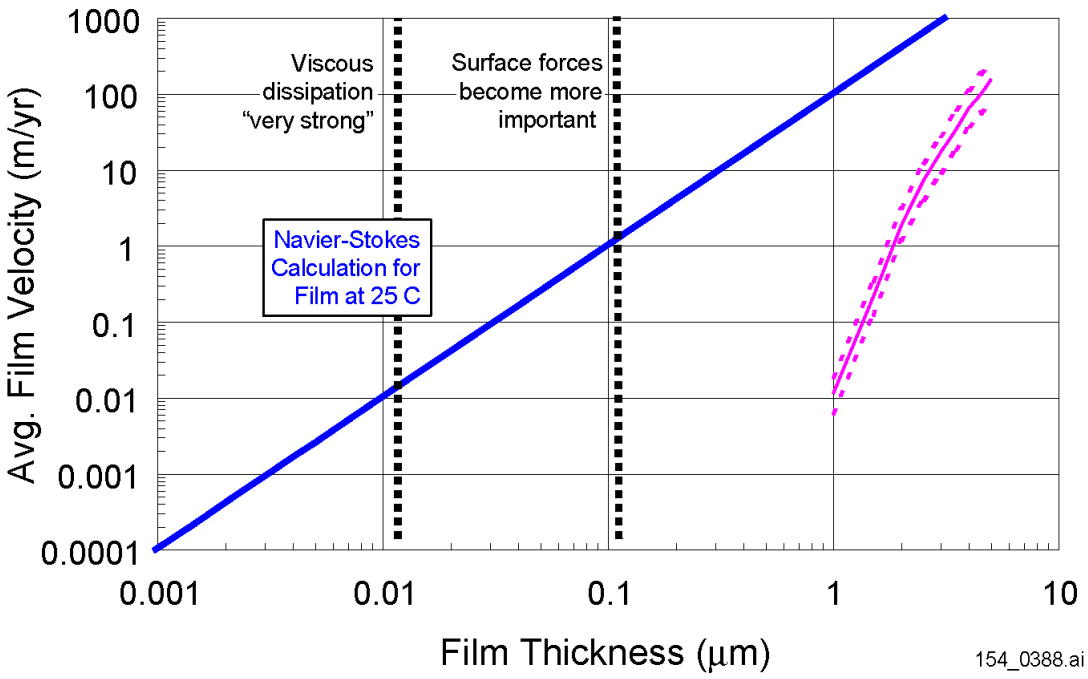

154_0388.ai

Source: Fluid velocity and uncertainty from Tokunaga et al. (2000 [DIRS 152914], Figure 10).

NOTE: Comparison of fluid velocity and uncertainty results with the one-dimensional Navier-Stokes calculation for a Newtonian fluid.

Figure 10.3.2-2. Average Film Flow Velocity versus Film Thickness

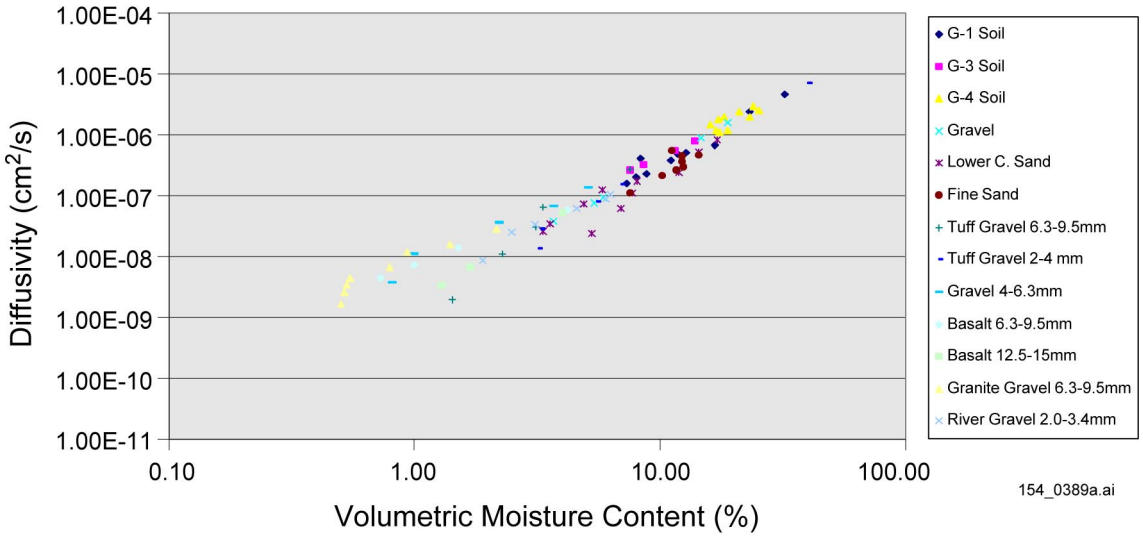

154_0389a.ai

Source: Conca and Wright 1992 [DIRS 100436]; DTN: MO9810SPA00026.000 [DIRS 137076].

NOTE: Moisture content in the range of 0.5 percent to 40 percent.

Figure 10.3.3-1. Measured Diffusivity for Various Granular Media as a Function of Volumetric Moisture Content

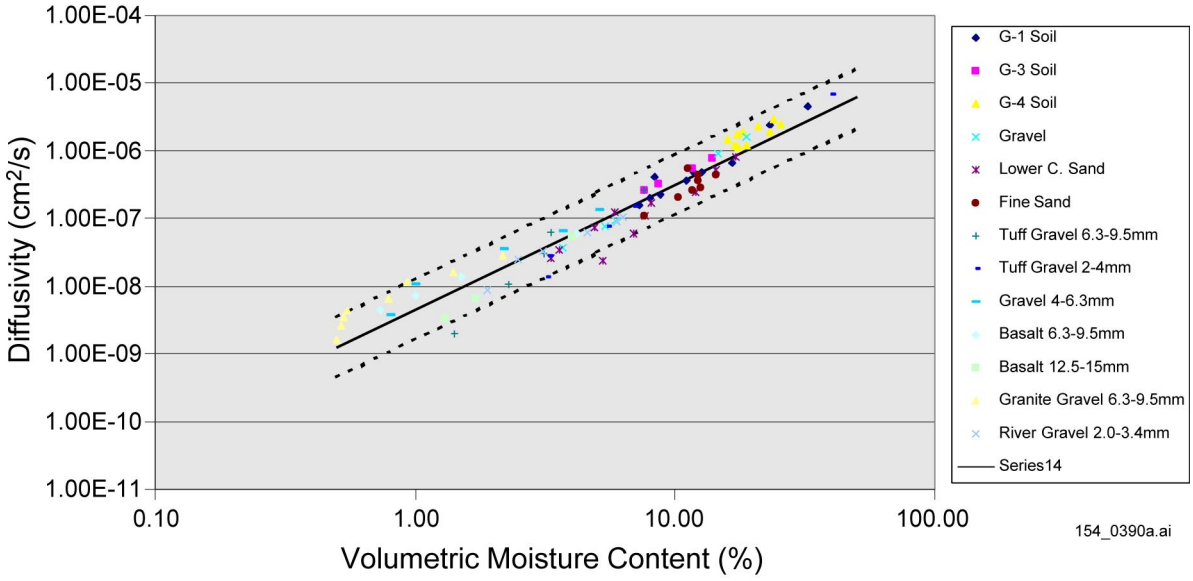

154_0390a.ai

Source: Schreiner 2001 [DIRS 155038], Item 2.

NOTE: The dashed lines correspond to two standard deviations above and below the statistical fit to the data. This uncertainty was included in the TSPA-SR (CRWMS M&O 2000 [DIRS 153246]).

Figure 10.3.3-2. Uncertainty in the Statistical Fit for the Diffusion Coefficient

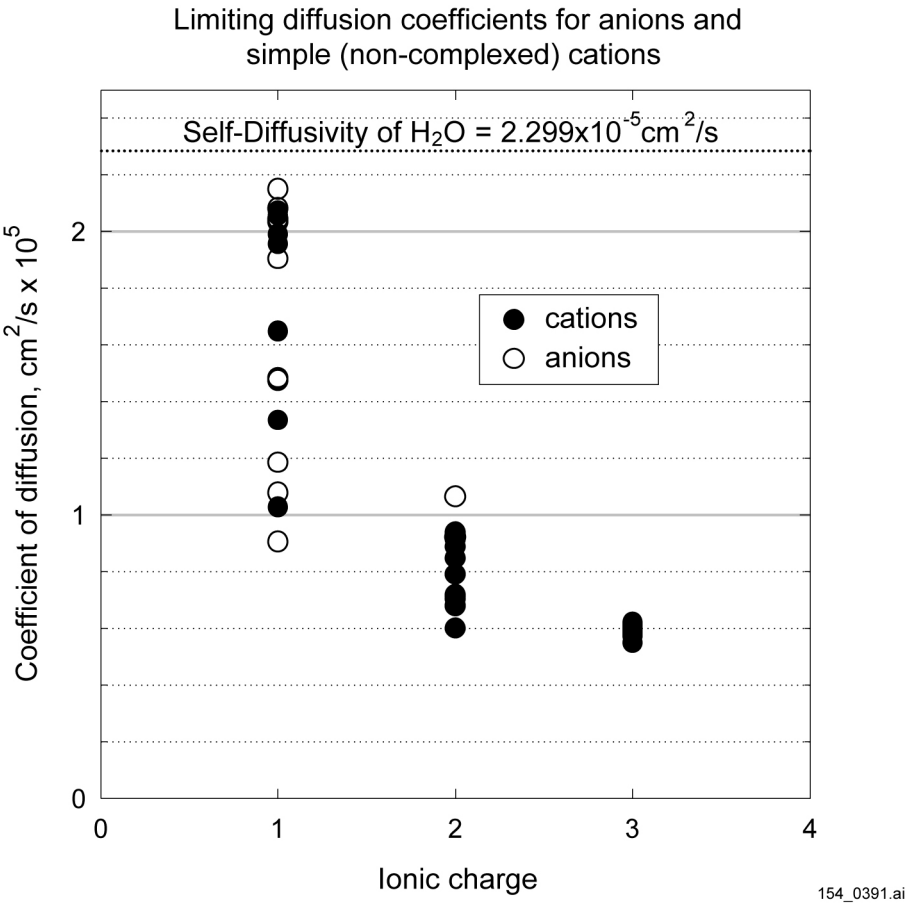

154_0391.ai

Source: CRWMS M&O 2000 [DIRS 153940], Section 6.4.1.1.

Figure 10.3.3-3. Limiting Diffusion Coefficients for Anions and Simple (Non-Complexed) Cations

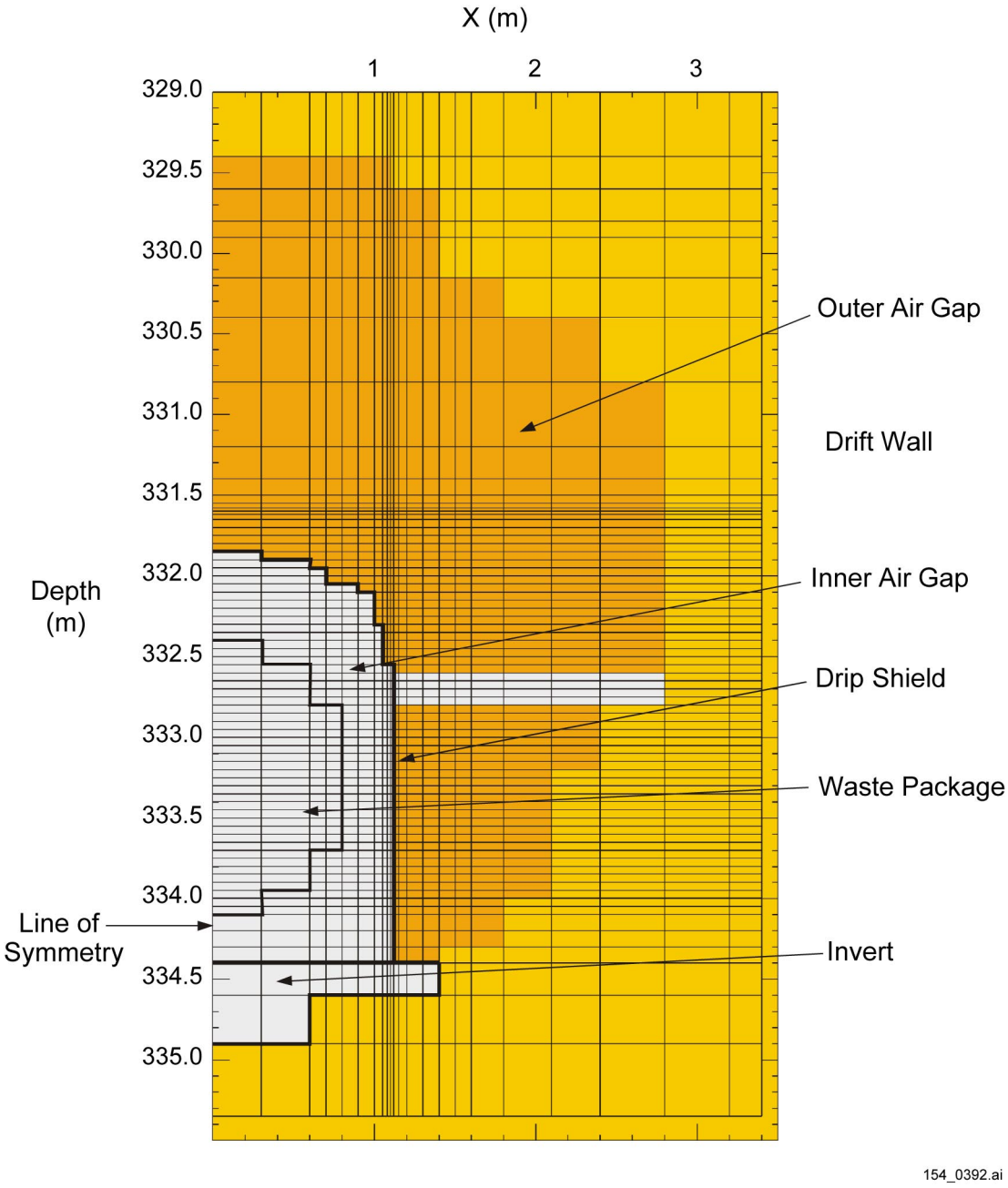

154_0392.ai

Source: Schreiner 2001 [DIRS 155038], Item 7.

Figure 10.3.3-4. Grid for NUFT Calculation of Invert Saturation

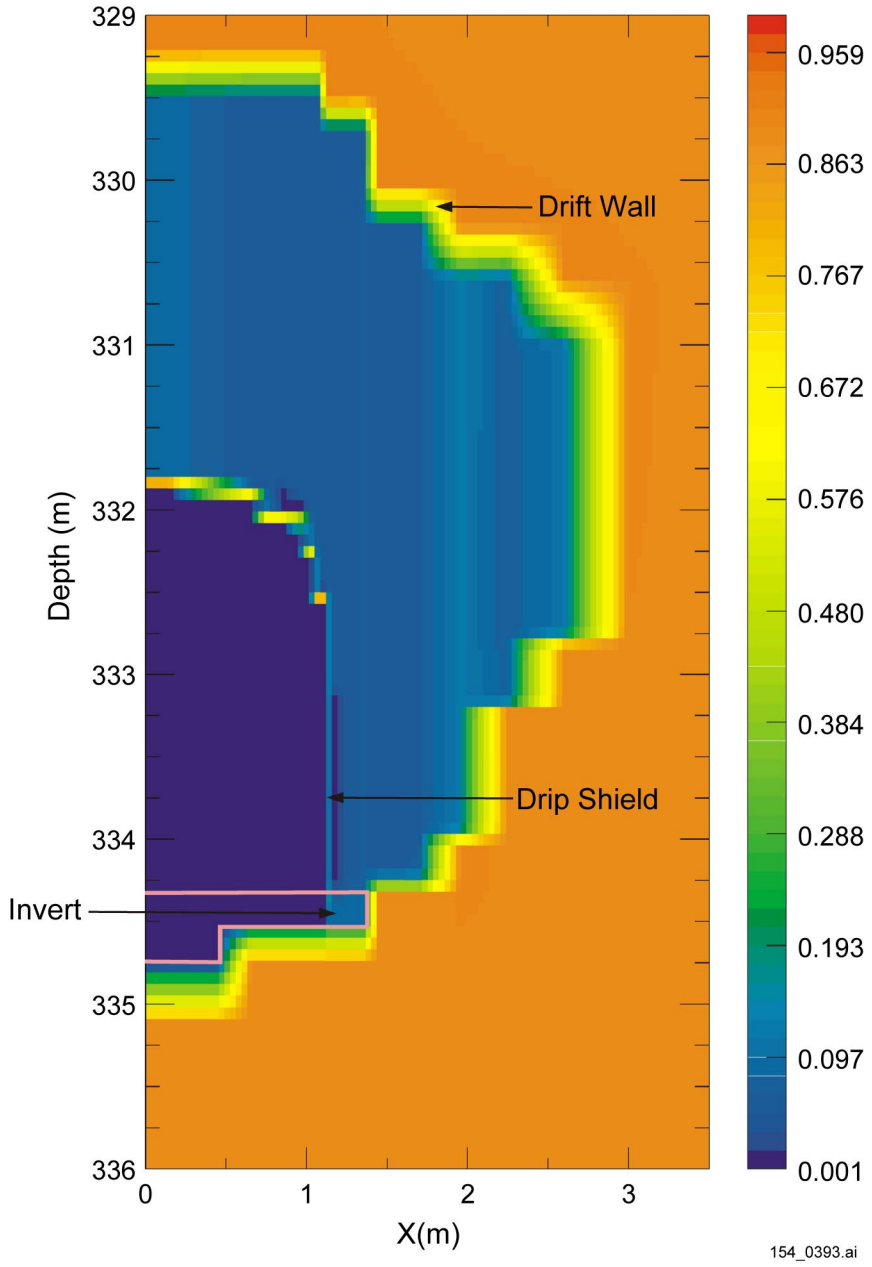

154_0393.ai

Source: Schreiner 2001 [DIRS 155038], Item 7.

NOTE: Infiltration rate of 35 mm/yr.

Figure 10.3.3-5. Liquid Saturation in the Engineered Barrier System at 10,000 Years

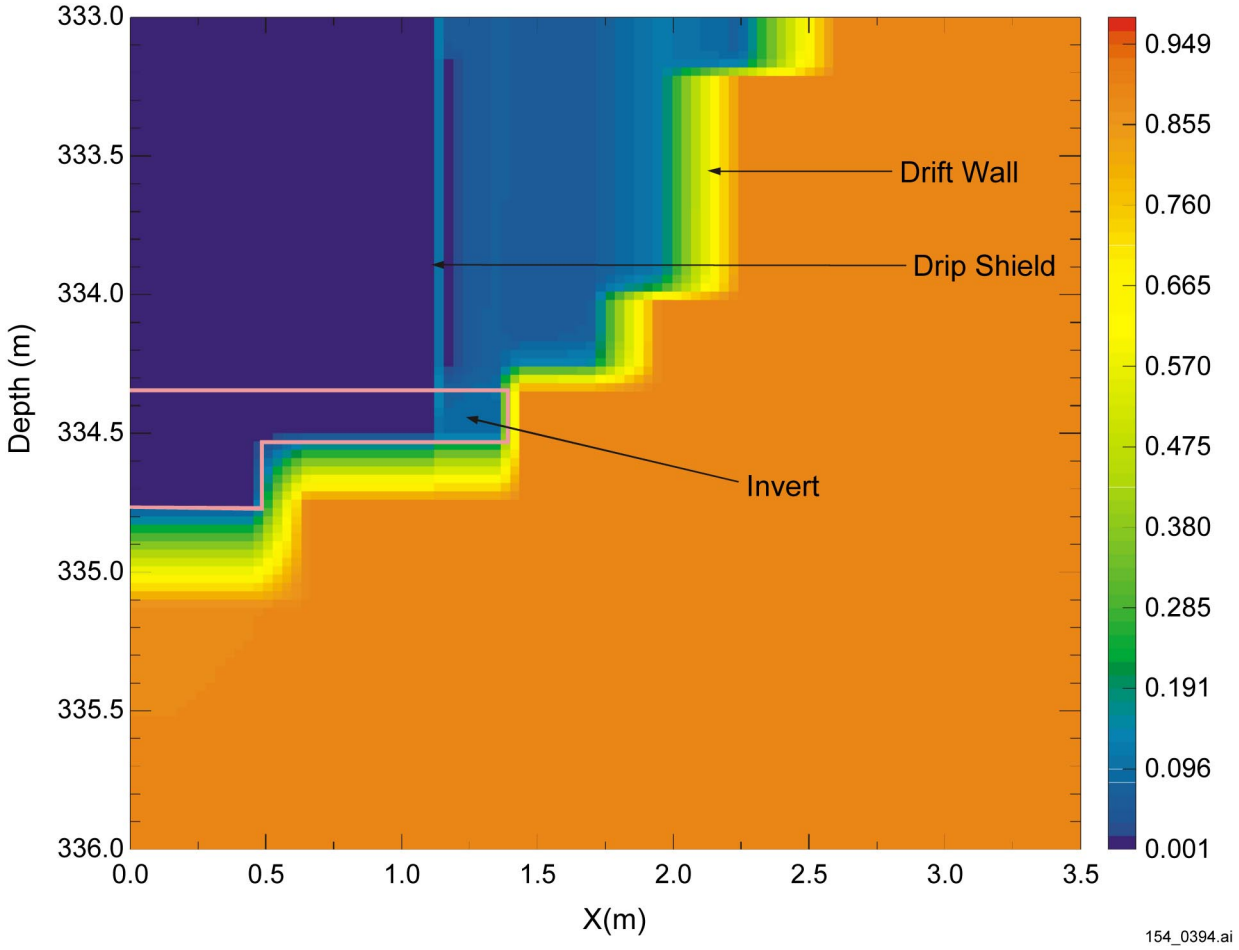

154_0394.ai

Source: Schreiner 2001 [DIRS 155038], Item 7.

NOTE: Infiltration rate of 35 mm/yr.

Figure 10.3.3-6. Liquid Saturation in the Invert at 10,000 Years

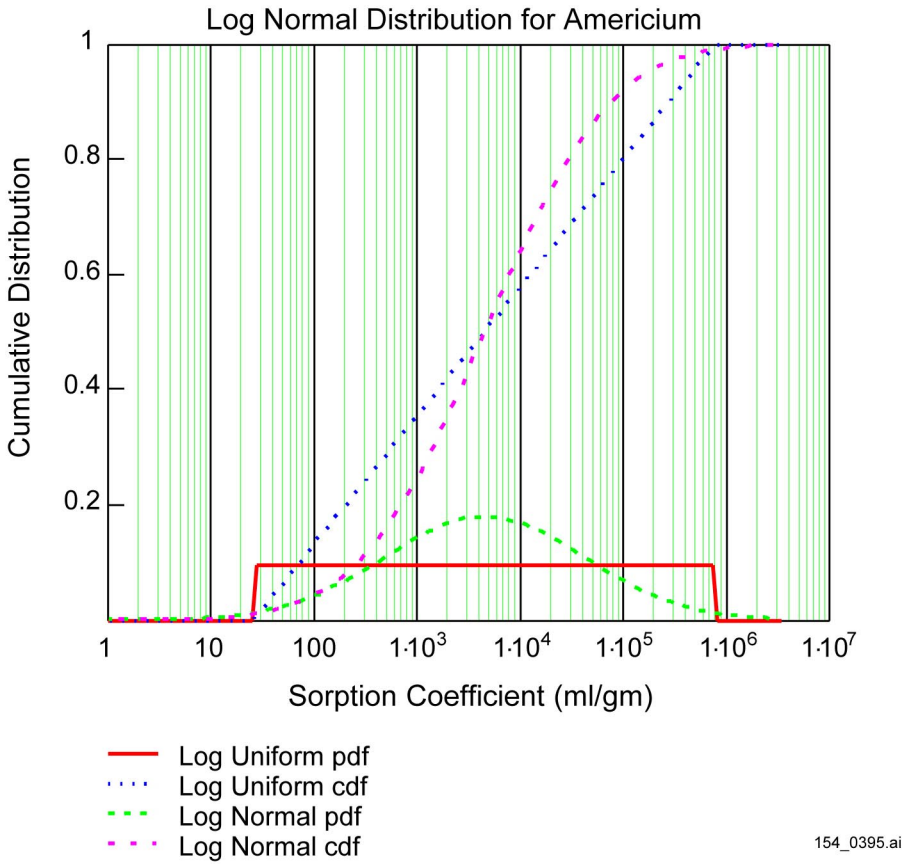

154_0395.ai

Source: Sheppard and Thibault 1990 [DIRS 109991].

NOTE: Comparison based on the tolerance interval for the 95 percent confidence level with the combined sand, loam, and clay data sets.

Figure 10.3.4-1. Comparison of Log-Normal and Log-Uniform Distributions for the Partition Coefficient of Americium

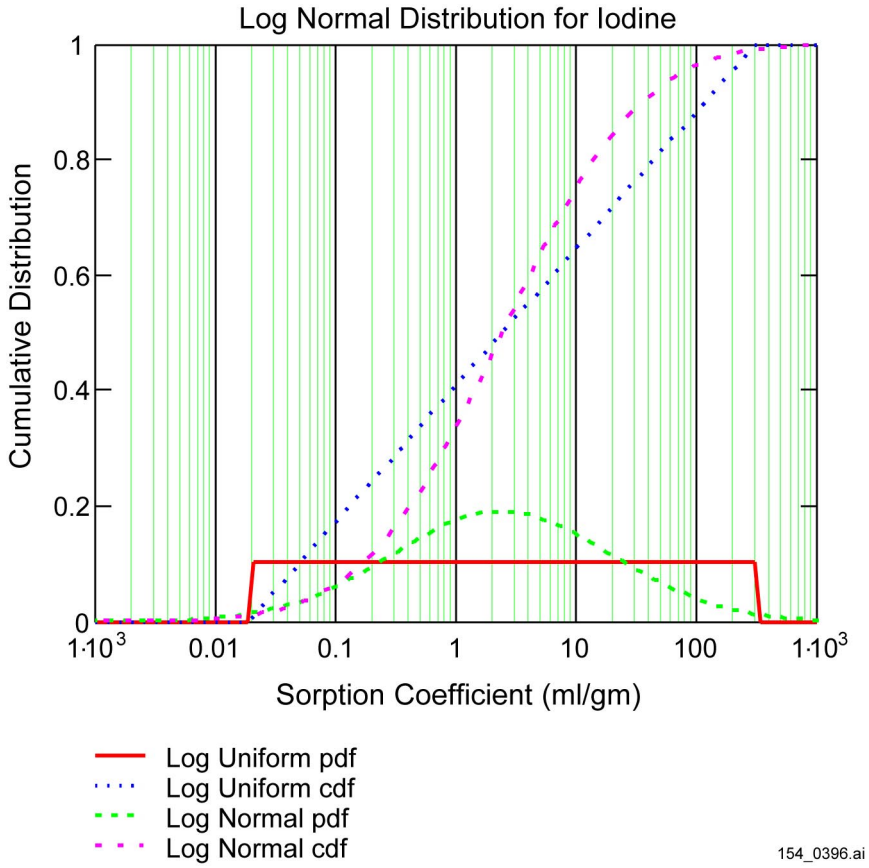

154_0396.ai

Source: Sheppard and Thibault 1990 [DIRS 109991].

NOTE: Comparison based on the tolerance interval for the 95 percent confidence level with the combined sand, loam, and clay data sets.

Figure 10.3.4-2. Comparison of Lognormal and Log Uniform Distributions for the Partition Coefficient of Iodine

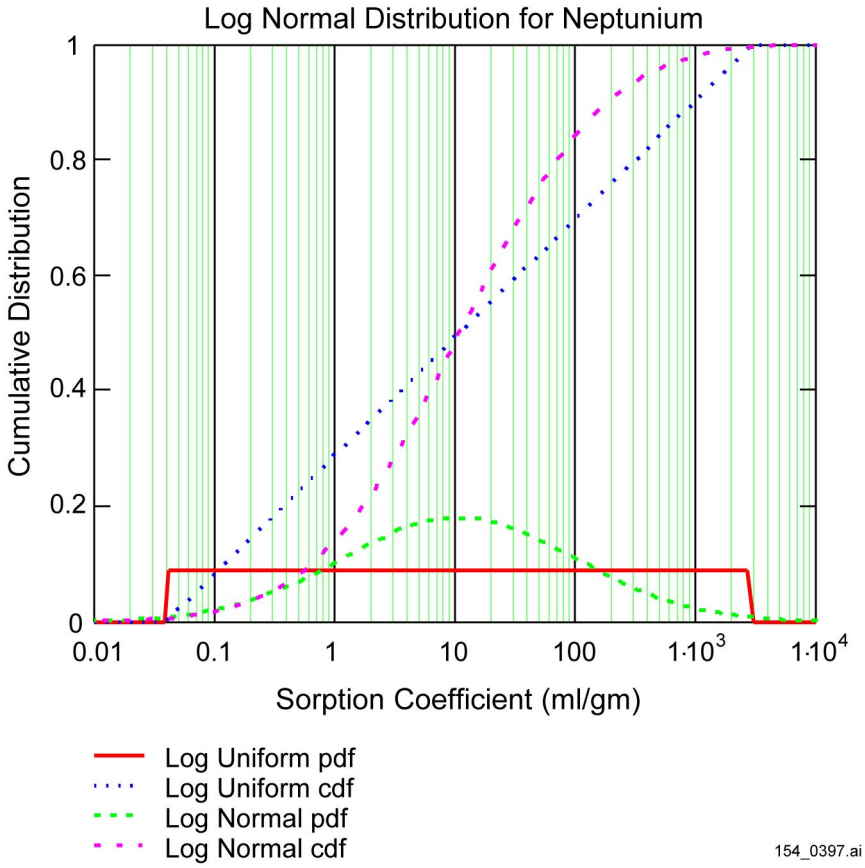

154_0397.ai

Source: Sheppard and Thibault 1990 [DIRS 109991].

NOTE: Comparison based on the tolerance interval for the 95 percent confidence level with the combined sand, loam, and clay data sets.

Figure 10.3.4-3. Comparison of Lognormal and Log Uniform Distributions for the Partition Coefficient of Neptunium

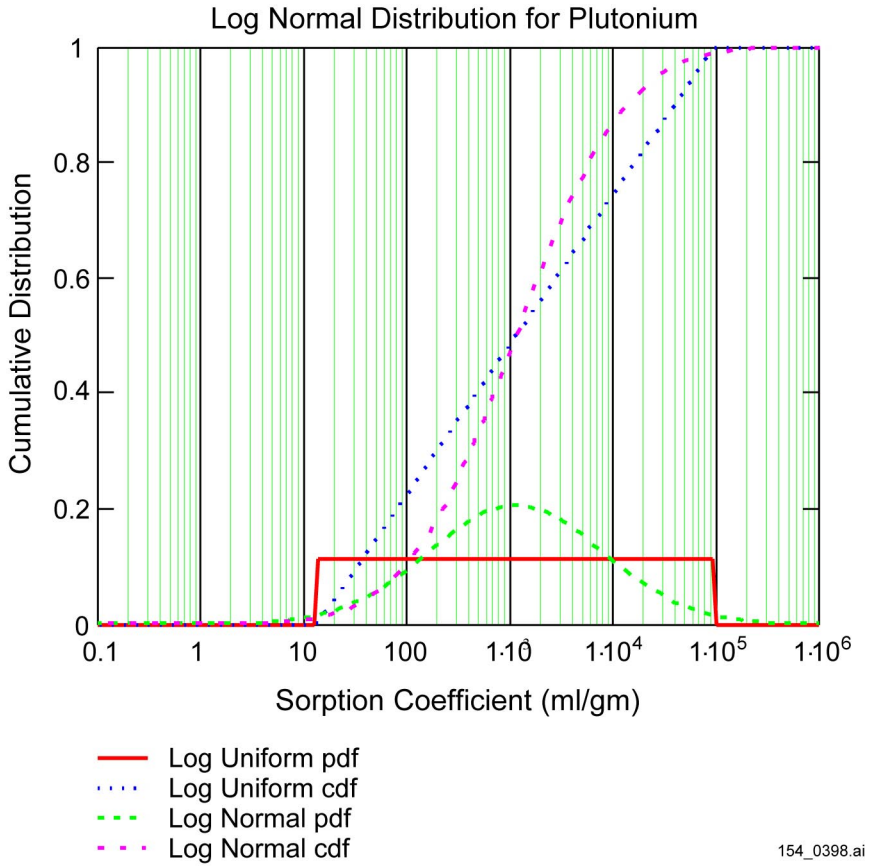

154_0398.ai

Source: Sheppard and Thibault 1990 [DIRS 109991].

NOTE: Comparison based on the tolerance interval for the 95 percent confidence level with the combined sand, loam, and clay data sets.

Figure 10.3.4-4. Comparison of Lognormal and Log Uniform Distributions for the Partition Coefficient of Plutonium

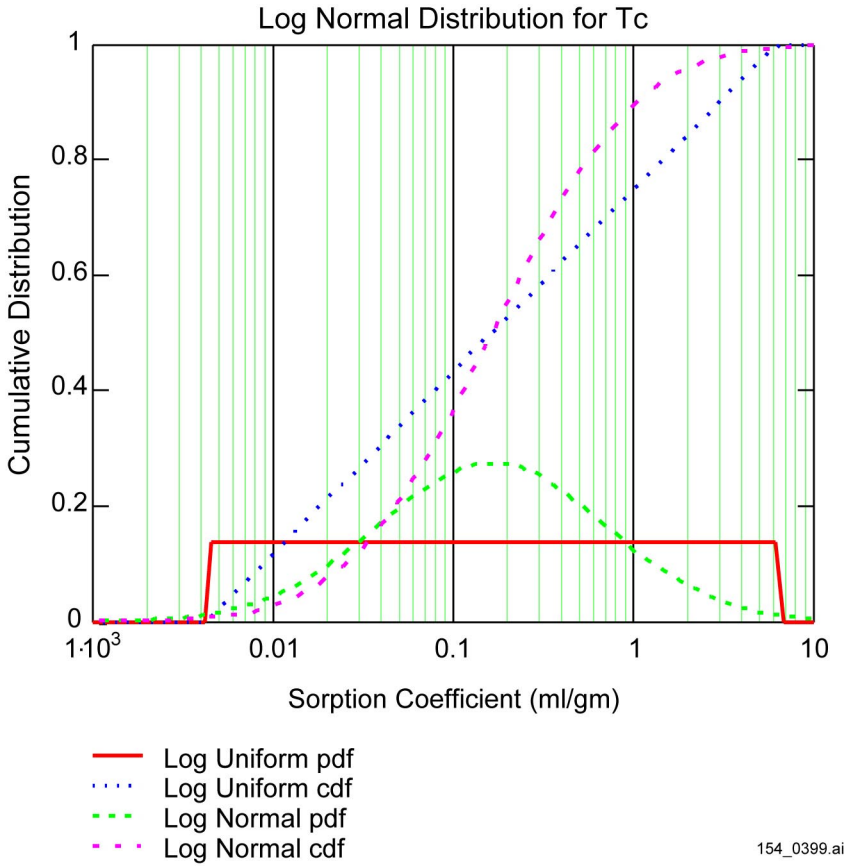

154_0399.ai

Source: Sheppard and Thibault 1990 [DIRS 109991].

NOTE: Comparison based on the tolerance interval for the 95 percent confidence level with the combined sand, loam, and clay data sets.

Figure 10.3.4-5. Comparison of Lognormal and Log Uniform Distributions for the Partition Coefficient of Technetium

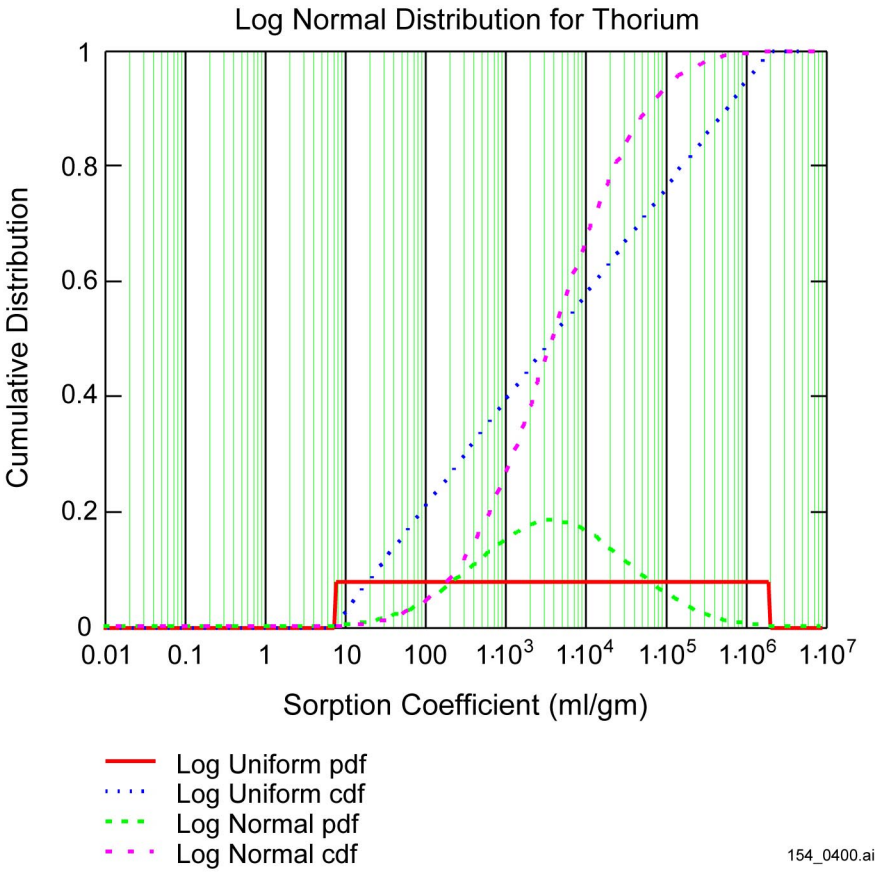

154_0400.ai

Source: Sheppard and Thibault 1990 [DIRS 109991].

NOTE: Comparison based on the tolerance interval for the 95 percent confidence level with the combined sand, loam, and clay data sets.

Figure 10.3.4-6. Comparison of Lognormal and Log Uniform Distributions for the Partition Coefficient of Thorium

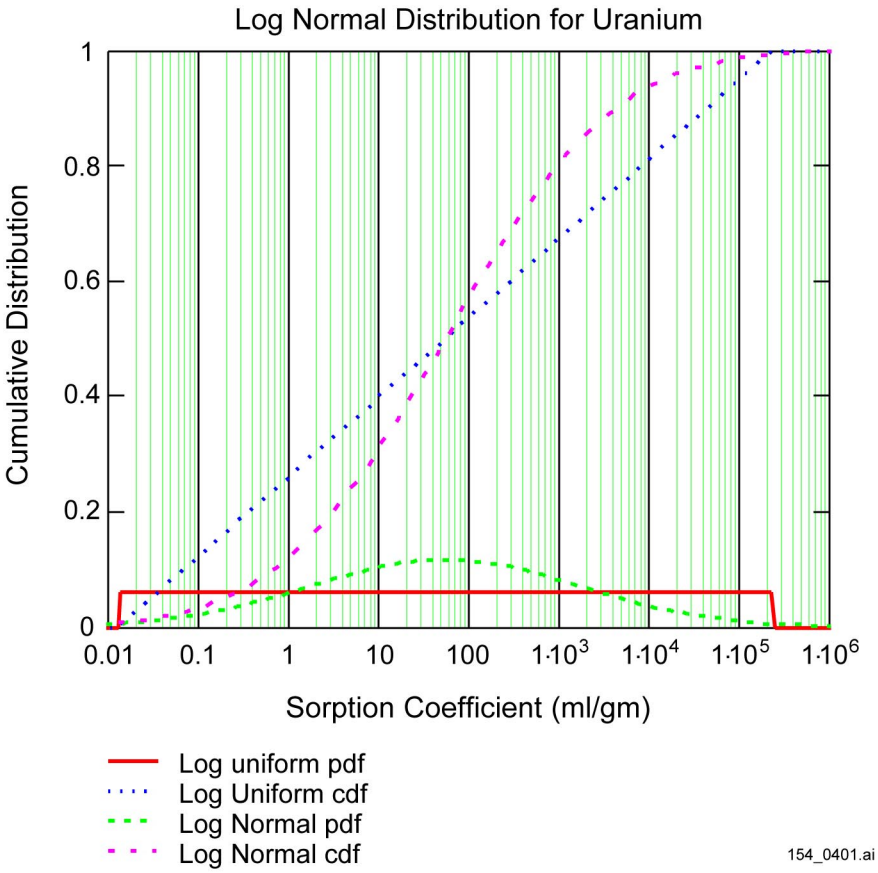

154_0401.ai

Source: Sheppard and Thibault 1990 [DIRS 109991].

NOTE: Comparison based on the tolerance interval for the 95 percent confidence level with the combined sand, loam, and clay data sets.

Figure 10.3.4-7. Comparison of Lognormal and Log Uniform Distributions for the Partition Coefficient of Uranium

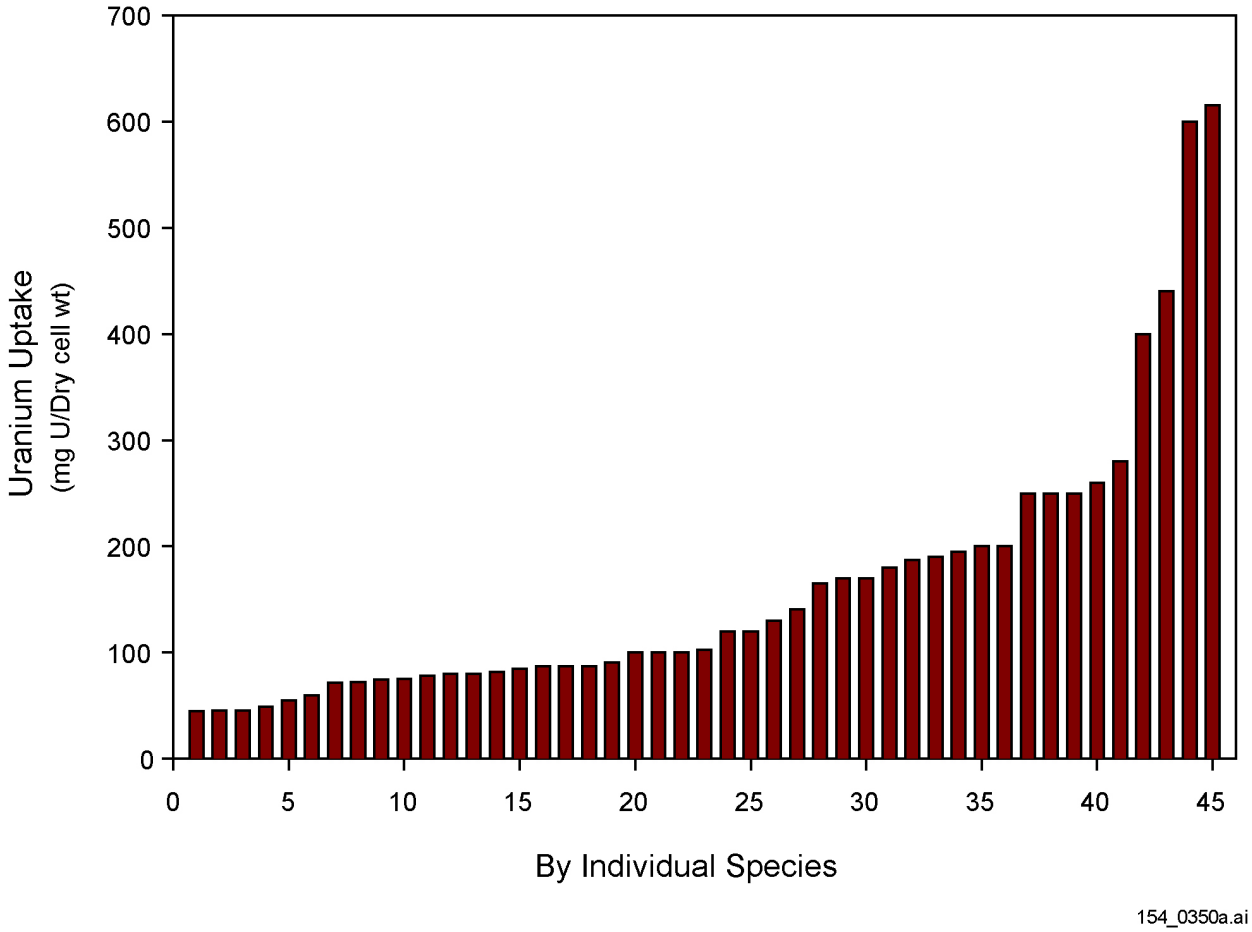

154_0350a.ai

Source: Suzuki and Banfield 1999 [DIRS 154445].

Figure 10.3.6-1. Uranium Uptake for 45 Species of Bacteria and Fungus

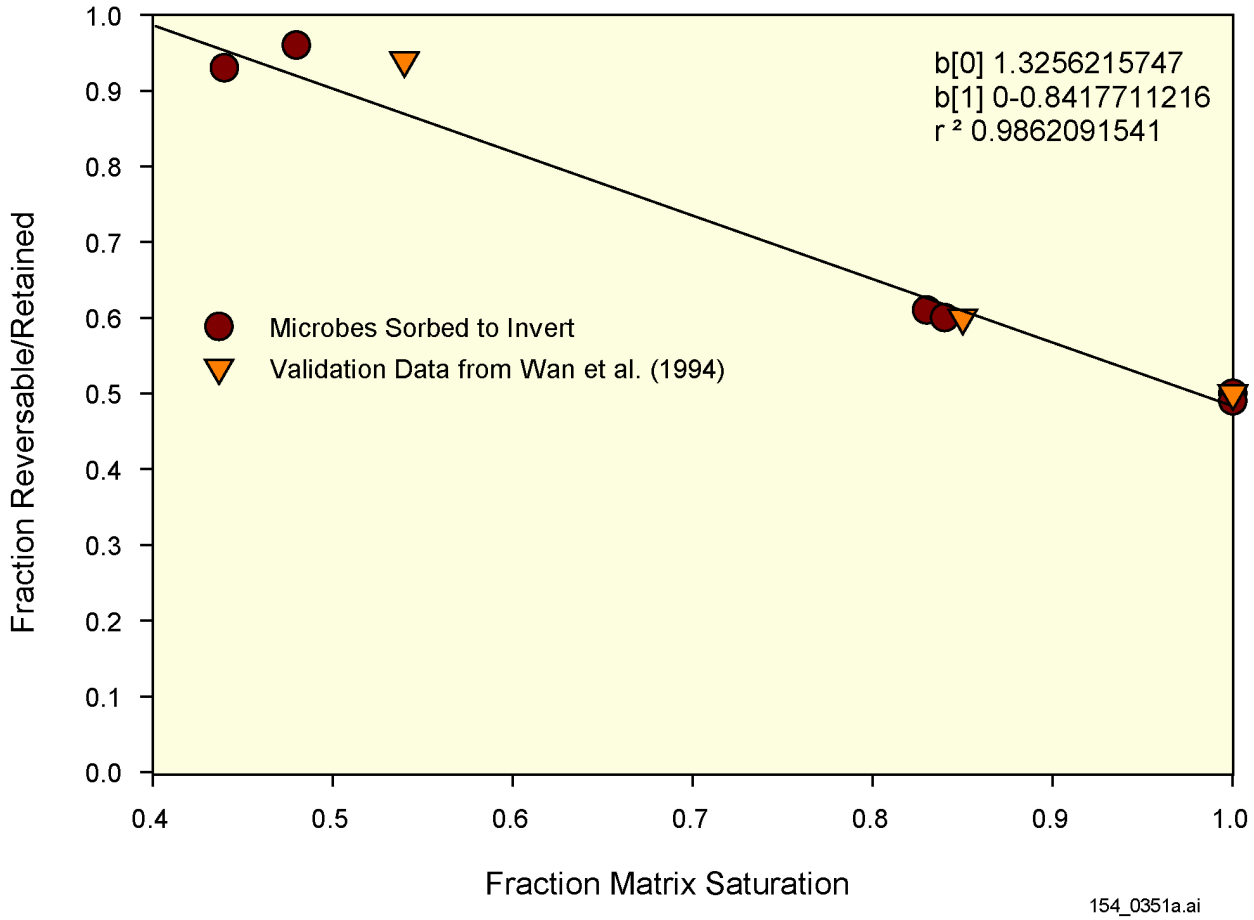

154_0351a.ai

Source: Regression data from Jewett et al. 1999 [DIRS 154325]; validation data from Wan et al. 1994 [DIRS 154367].

Figure 10.3.6-2. Retention of Microbes on Air-Water Interfaces in Unsaturated Sand Column Experiments

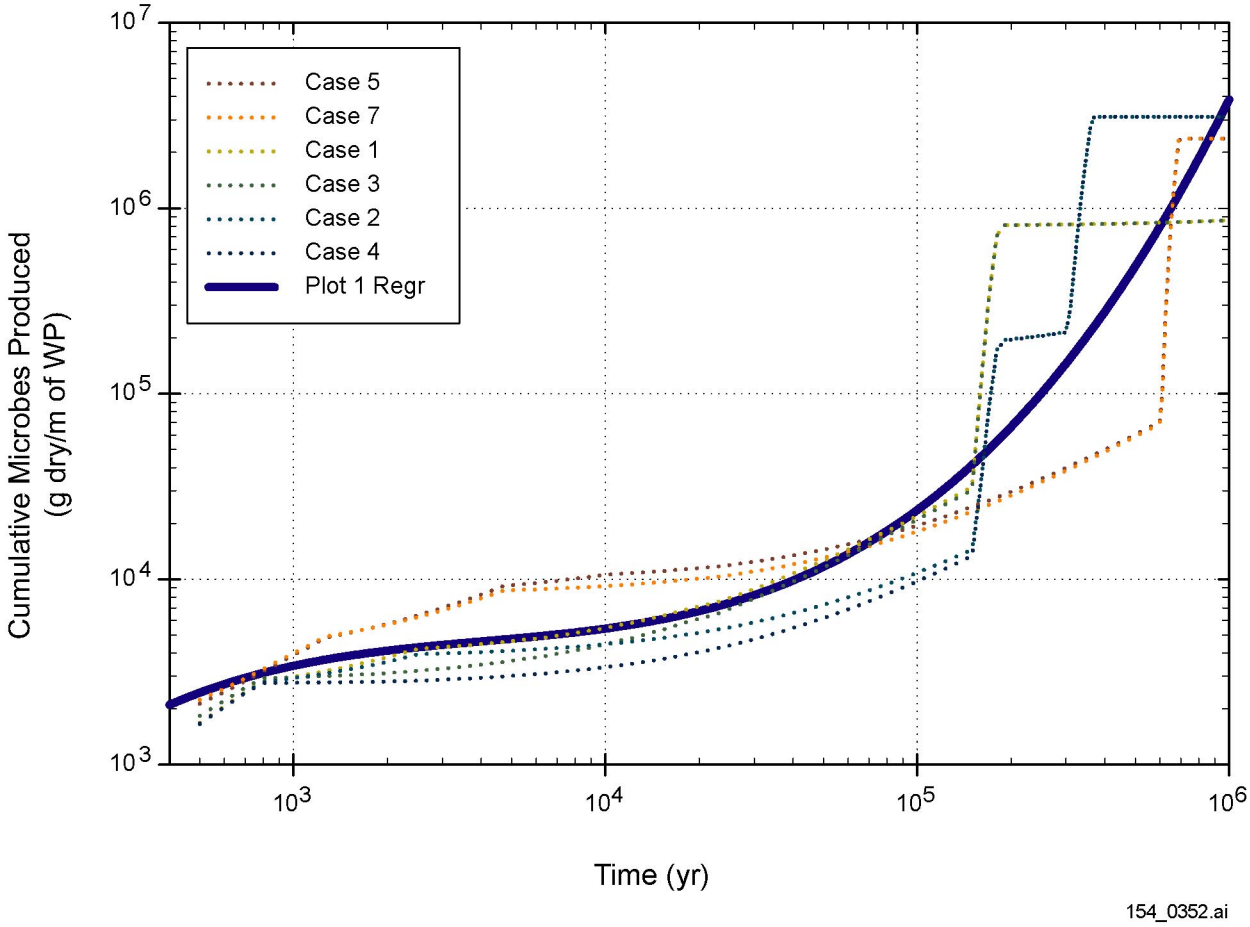

154_0352.ai

Source: Microbial growth data from CRWMS M&O 2000 [DIRS 151561]; microbial growth data documented in DTN: MO0010MWDMIN38.031 [DIRS 154299].

Figure 10.3.6-3. Third-Order Linear Regression Fit of Cumulative Microbial Growth Data for Modeling Runs Containing Commercial Spent Nuclear Fuel Waste Packages

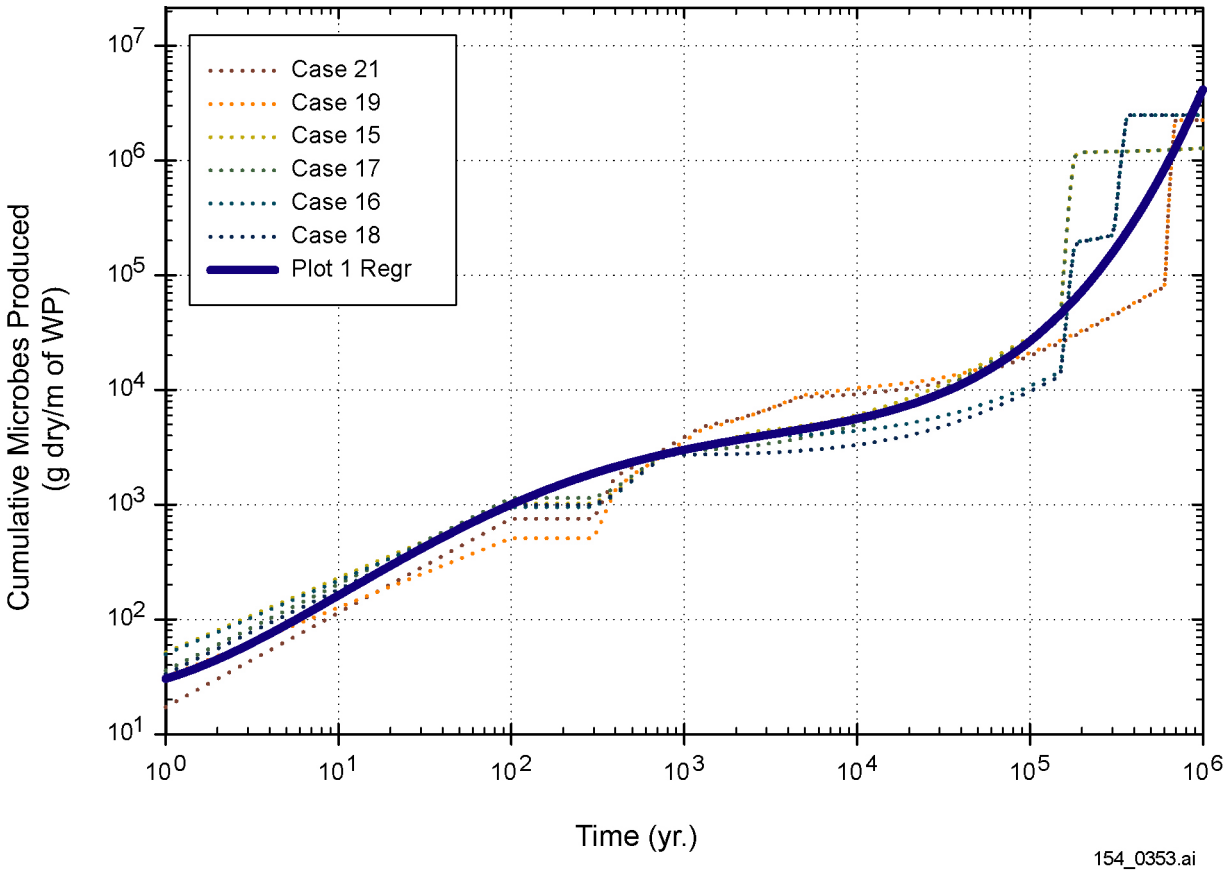

154_0353.ai

Source: Microbial growth data from CRWMS M&O 2000 [DIRS 151561]; microbial growth data documented in DTN: MO0010MWDMIN38.031 [DIRS 154299].

Figure 10.3.6-4. Fourth-Order Linear Regression Fit of Cumulative Microbial Growth Data for Modeling Runs Containing High-Level Waste Packages

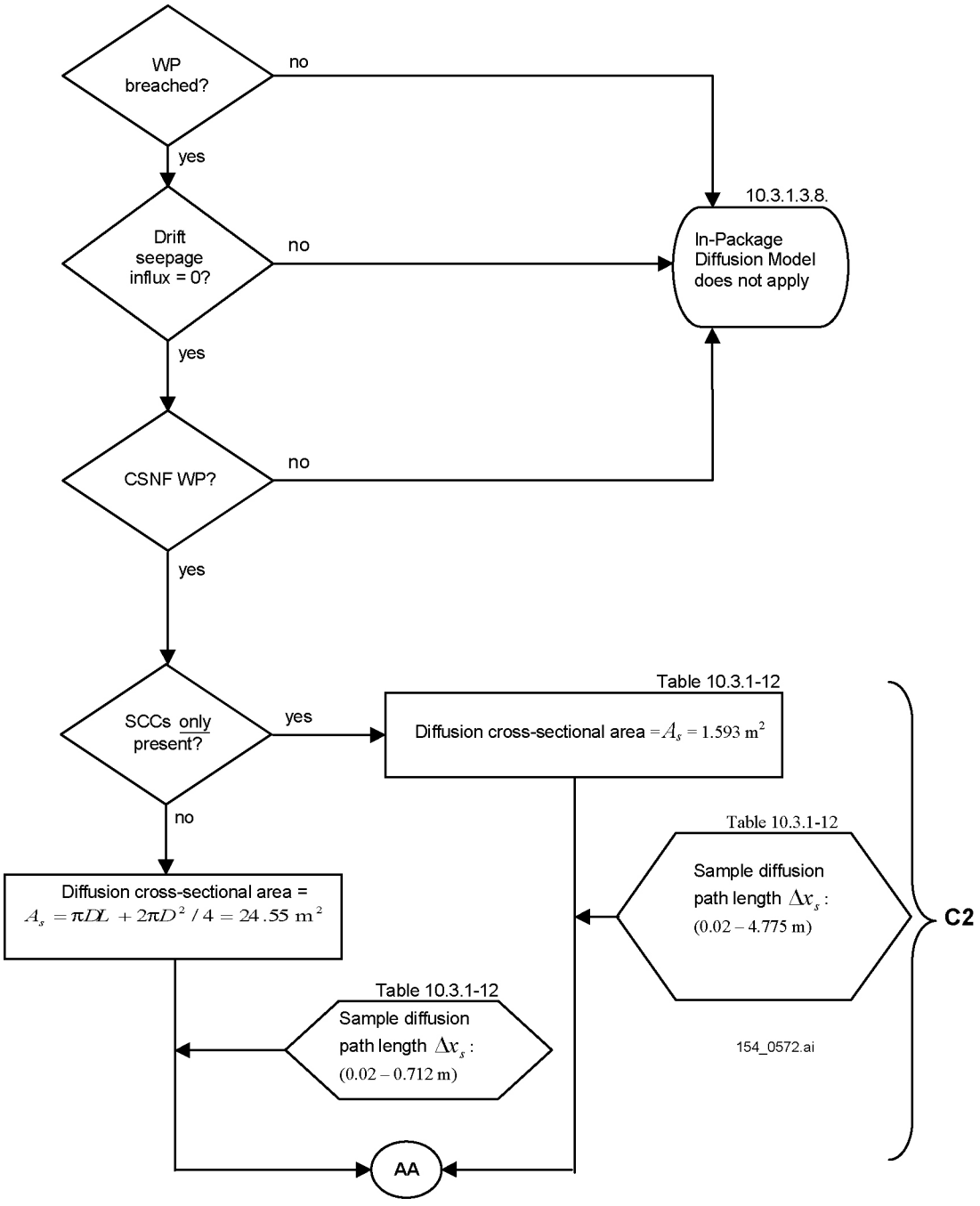

154_0572.ai

NOTE: WP = waste package; SCC = stress corrosion cracks; CSNF = commercial spent nuclear fuel; OD = outer diameter; RH = relative humidity.

Figure 10.4.1-1. Flowchart for In-Package Diffusion Model

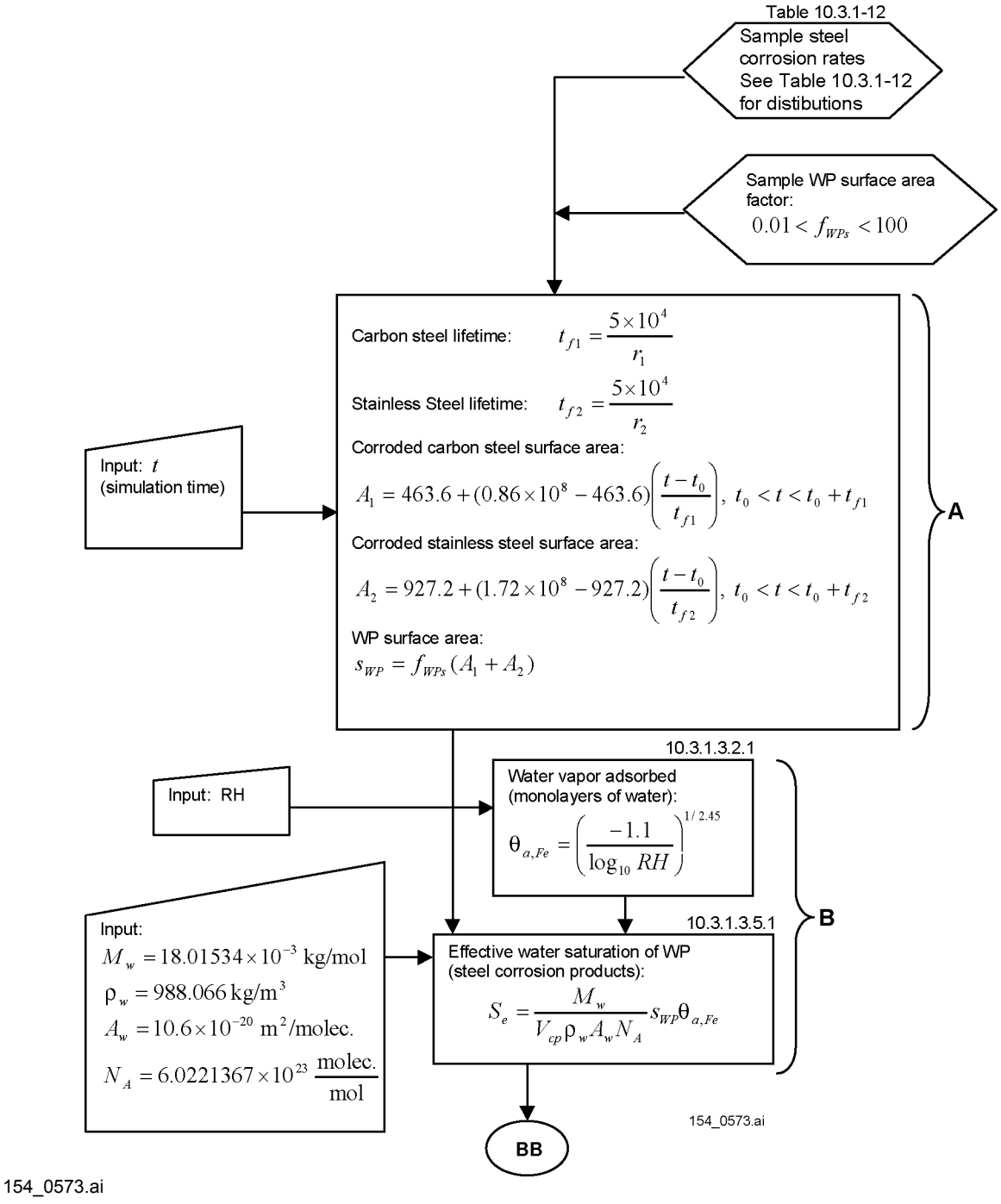

Figure 10.4.1-1. Flowchart for In-Package Diffusion Model (Continued)

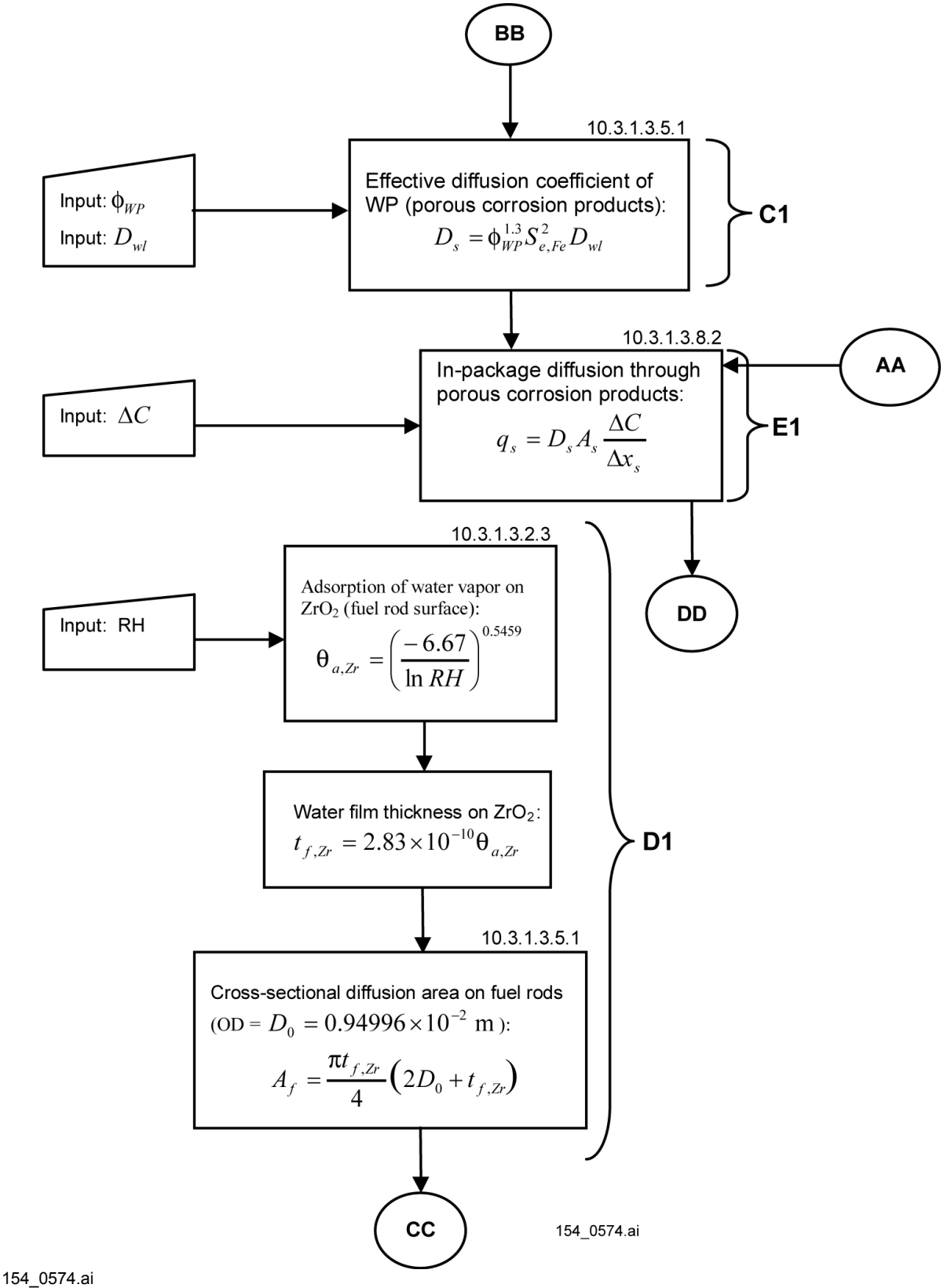

154_0574.ai

Figure 10.4.1-1. Flowchart for In-Package Diffusion Model (Continued)

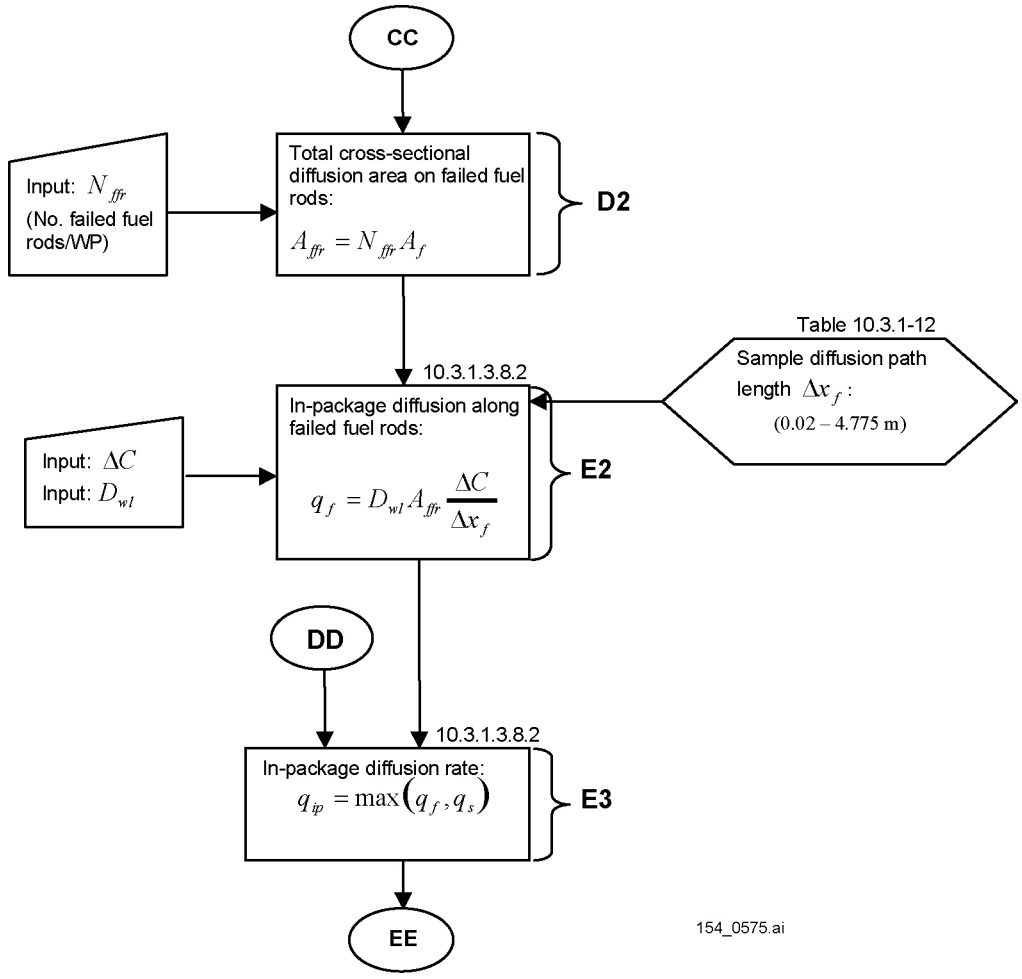

154_0575.ai

Figure 10.4.1-1. Flowchart for In-Package Diffusion Model (Continued)

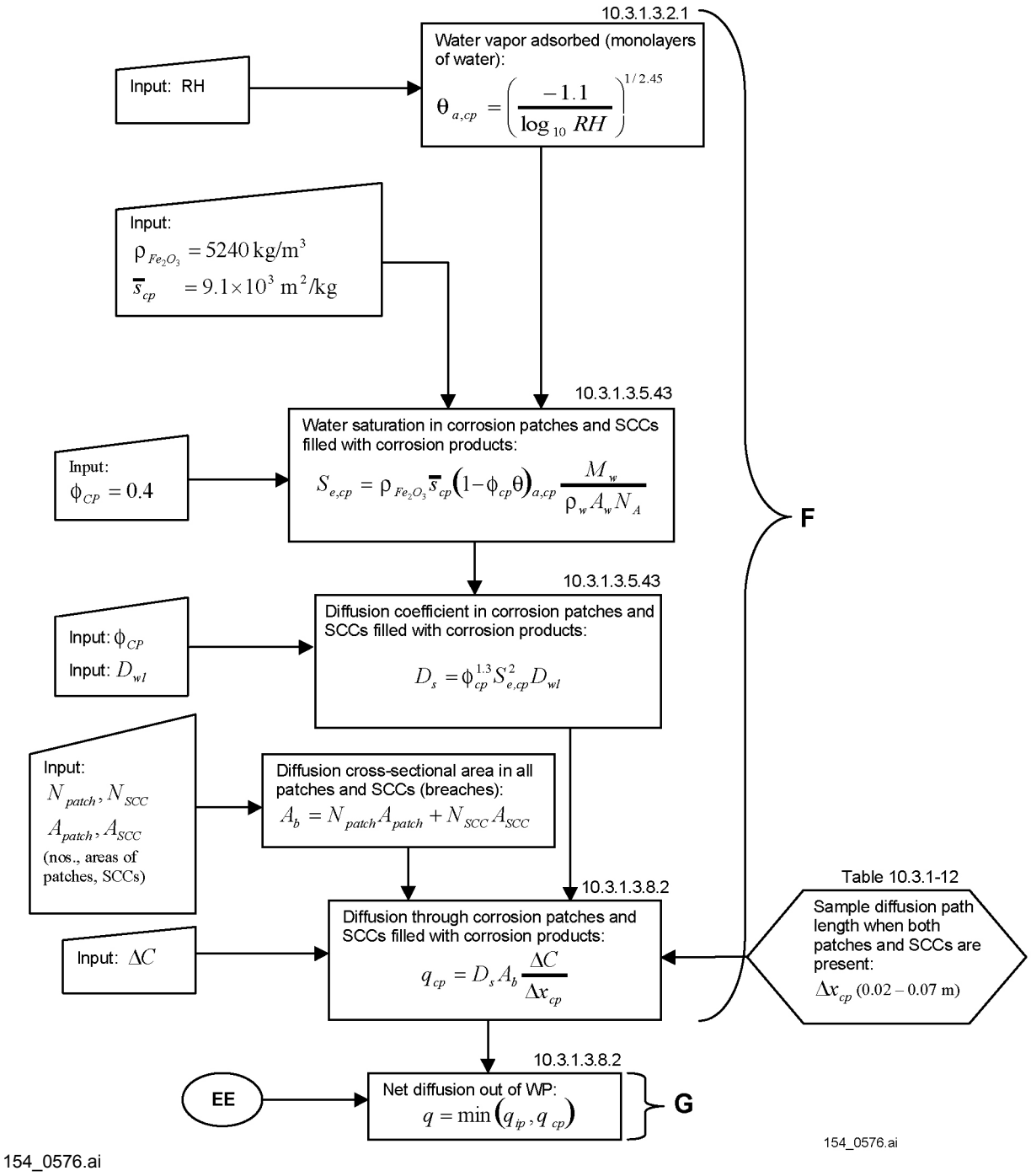

Figure 10.4.1-1. Flowchart for In-Package Diffusion Model (Continued)

INTENTIONALLY LEFT BLANK

11 Radionuclide Transport in the Unsaturated Zone

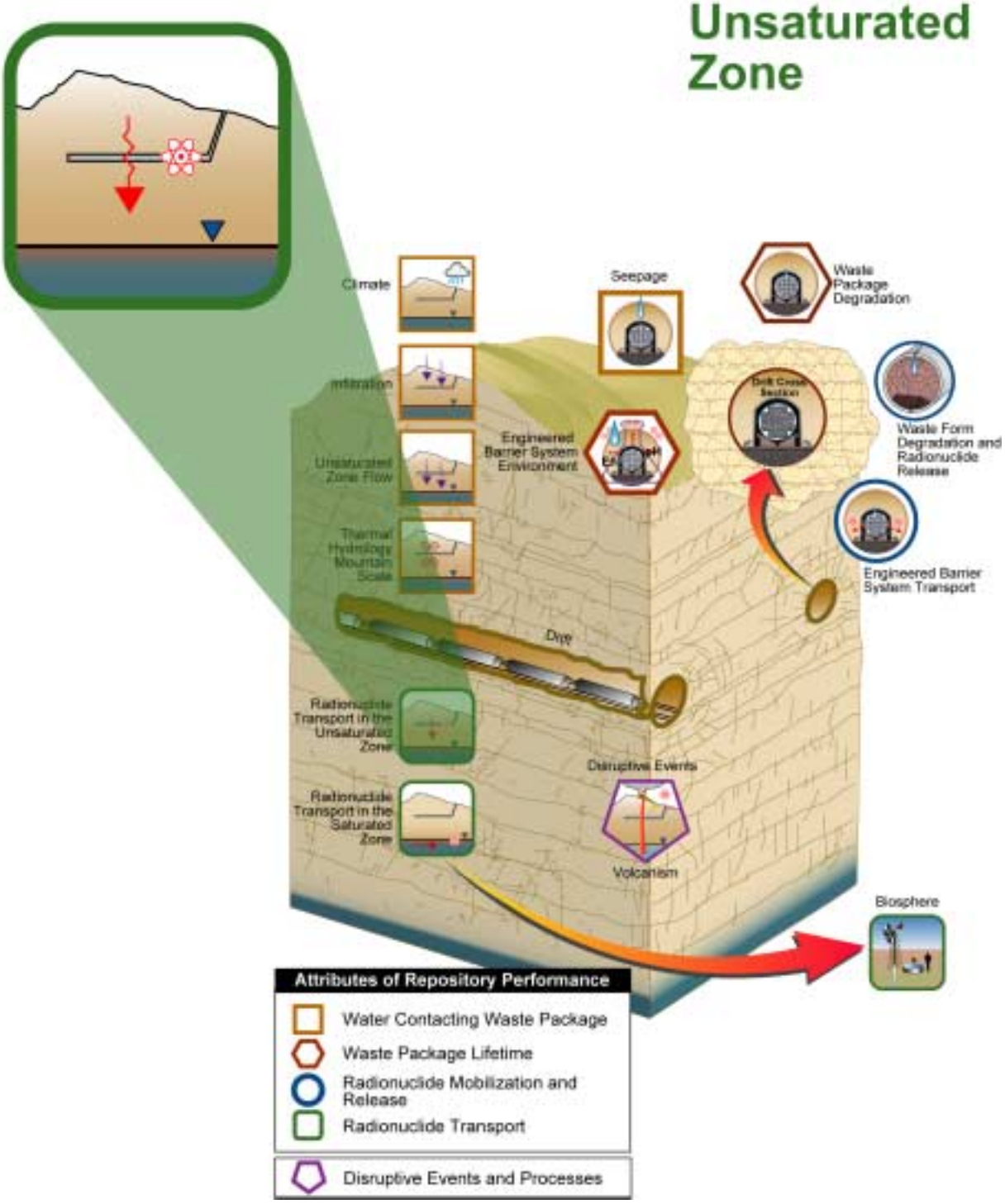

11. RADIONUCLIDE TRANSPORT IN THE UNSATURATED ZONE

11.1 INTRODUCTION

This section describes process model results, related uncertainties, and total system performance assessment (TSPA) model abstractions concerning radionuclide transport between the potential repository and the water table. The following analysis model reports provide documentation associated with this subject:

- *UZ Flow Models and Submodels* (CRWMS M&O 2000 [DIRS 122797]) provides three-dimensional site-scale transport results for technetium and neptunium using different flow models and climate scenarios

- *Radionuclide Transport Models under Ambient Conditions* (CRWMS M&O 2000 [DIRS 144331]) describes the basis for process transport models and transport sensitivity results for two and three-dimensional site-scale models, including colloid-facilitated radionuclide transport

- *Analysis of Base-Case Particle Tracking Results of the Base-Case Flow Fields (ID: U0160)* (CRWMS M&O 2000 [DIRS 134732]) describes sensitivity studies using the TSPA transport model for the three-dimensional site-scale transport problem, including comparisons between the TSPA transport model and a process transport model

- *Analysis Comparing Advective-Dispersive Transport Solution to Particle Tracking* (CRWMS M&O 2000 [DIRS 141389]) provides comparisons of the particle-tracking transport models and a direct-solution process model for transport in a one-dimensional system

- *Fault Displacement Effects on Transport in the Unsaturated Zone* (CRWMS M&O 2000 [DIRS 151953]) describes sensitivity studies concerning the effects of variations in fracture characteristics on transport

- *Particle Tracking Model and Abstraction of Transport Processes* (CRWMS M&O 2000 [DIRS 141418])–describes the TSPA model for unsaturated zone (UZ) transport

- *UZ Colloid Transport Model* (CRWMS M&O 2000 [DIRS 122799]) presents process-model results for colloid-facilitated radionuclide transport

- *Unsaturated Zone Flow and Transport Model Process Model Report* (CRWMS M&O 2000 [DIRS 151940]) provides a summary of all UZ processes and TSPA abstractions, including UZ transport.

Radionuclides released from the engineered barrier system (EBS) would enter the natural environment in the UZ. The primary mechanism by which radionuclides can migrate through the UZ is aqueous transport (CRWMS M&O 2000 [DIRS 151940], Section 3.3.11). Water carrying radionuclides is expected to generally move downwards, with some component of lateral motion caused by flow diversion around low-permeability horizons (e.g., where perched

water flows into fault zones) (CRWMS M&O 2000 [DIRS 151940], Figure 3.7-8b). Diffusion, sorption, dispersion, decay, and colloid interactions are additional processes that influence general advective radionuclide movement.

UZ transport modeling follows the general concepts used for development of the UZ flow model (CRWMS M&O 2000 [DIRS 151940], Section 3.7). Transport in fractured rock is approximated by a dual continuum model in which solute transport can occur in both the fracture continuum and the matrix continuum, with dynamic exchange between these continua through advective and diffusive transport. The transport models for radionuclide movement to the water table use the same grid as the site-scale UZ flow model. Radionuclide sorption is modeled using an infinite-capacity linear equilibrium model.

Colloid-facilitated radionuclide transport is modeled using a combination of two modes of interaction between aqueous radionuclides and radionuclides associated with colloids (CRWMS M&O 2000 [DIRS 151940], Sections 3.11.7 and 3.11.13). Radionuclides can either sorb to colloids following a linear sorption model (termed the reversible colloid-facilitated radionuclide transport model), or they can be permanently bound to the colloid (termed the irreversible colloid-facilitated radionuclide transport model). In the TSPA transport model (CRWMS M&O 2000 [DIRS 151940], Section 3.11.13), colloid filtration was limited to physical straining at tuff layer interfaces. Process model calculations for transport treated colloid filtration as a linear kinetic process. Dispersion was included using a standard Fickian representation. Radioactive decay, including chain decay, was included in the models.

11.2 TREATMENT OF UNSATURATED ZONE TRANSPORT ISSUES

This section identifies the set of five model refinements that have been evaluated for modeling radionuclide transport through the UZ from the potential repository to the water table. Subsequent subsections describe the methods used to perform these evaluations and the implications the model refinements have for modeling radionuclide transport to support TSPA evaluations of potential repository system performance. These sections represent new work and extensions of existing work. Table 11-1 identifies the primary reason for development of each section and indicates which of these analyses have been included in TSPA calculations.

11.2.1 Transport in the Drift Shadow

Process Description–The hydrologic conditions beneath waste emplacement drifts are affected by the diversion of seepage around the drift. This diversion of seepage results in a zone of reduced water saturations and flow beneath waste emplacement drifts.

An important aspect of radionuclide transport in the vicinity of the drift is how radionuclides enter the rock. Radionuclides can enter the rock from waste emplacement drifts as a result of diffusive transport or a combination of advection and diffusion. If seepage into the drift is substantial, the radionuclides will be advected out of the drift, predominantly into the rock fractures. If seepage into the drift is sufficiently small, radionuclides will either advect or diffuse, predominantly into the rock matrix. Diffusive releases of radionuclides from the drift will predominantly enter the rock matrix because its water content is considerably larger than the water content of the fractures, providing a greater cross section for diffusion. Initiating transport

Table 11-1. Summary of Supplemental Models and Analyses

Key Attributes of System	Process Model (Section of S&ER)	Topic of Supplemental Scientific Model or Analysis	Reason For Supplemental Scientific Model or Analysis			Section of Volume 1	Performance Assessment Treatment of Supplemental Scientific Model or Analysis[a]	
			Unquantified Uncertainty Analysis	Update in Scientific Information	Lower-Temperature Operating Mode Analysis		TSPA Sensitivity Analysis	Included in Supplemental TSPA Model
Delay and Dilution of Radionuclide Concentrations by the Natural Barriers	Unsaturated Zone Radionuclide Transport (Advective Pathways; Retardation; Dispersion; Dilution) (4.2.8)	Effect of drift shadow zone - advection/diffusion splitting	X		X	11.3.1	X	X
		Effect of drift shadow zone – concentration boundary condition on EBS release rates	X			11.3.1		
		Effect of matrix diffusion	X			11.3.2 11.3.3		
		3-D transport			X	11.3.2		
		Effect of coupled Thermo-Hydrologic, Thermo-Hydro-Chemical, and Thermo-Hydro-Mechanical processes on transport		X	X	11.3.5		

NOTE: S&ER = *Yucca Mountain Science and Engineering Report* (DOE 2001 [DIRS 153849]).

[a] Performance assessment treatment of supplemental scientific model or analysis discussed in SSPA Volume 2 (McNeish 2001 [DIRS 155023]).

in the rock matrix, rather than the fractures, can substantially reduce the rate of radionuclide movement away from the drift. This is caused primarily by the limited contact between the fractures and the matrix, which is consistent (see Section 11.3.1.7) with the calibration of the UZ flow model and geochemical observations. The result is long residence times in the slow-flowing matrix. Furthermore, the reduction in water saturation in the fractures beneath the drift enhances the retention of radionuclides in the matrix.

Current Modeling Approach and Uncertainties–Transport calculations for the analysis model reports listed in Section 11.1 were based on the release of radionuclides from the EBS into fracture flow, undisturbed by the presence of the waste emplacement drift, as calculated using the site-scale UZ flow model. Any effects of the drift shadow on transport were not considered. In the current approach, the shadow zone is considered directly in the process model calculations. Radionuclide releases are modeled from the emplacement drift to the rock matrix and fractures according to the physical processes that govern radionuclide movement. The effects of reduced water saturations and flow rates beneath the emplacement drift are considered in process model calculations for radionuclide transport away from the drifts. Uncertainties concerning seepage diversion, which leads to the drift shadow, are discussed in Section 4. Uncertainties in fracture-matrix interaction are estimated through calibration of hydrologic properties (CRWMS M&O 2000 [DIRS 144426]) using a range of infiltration rates.

11.2.2 Matrix Block Discretization Effects

Process Description–Dual-permeability models of UZ radionuclide transport in fractured rock commonly use a single matrix gridblock associated with each fracture gridblock. The single-matrix grid model must approximate radionuclide concentration gradients leading to diffusion between the fractures and the matrix in terms of a single matrix concentration. In reality, a continuous range of concentrations in the matrix will result from radionuclide concentration differences between the fractures and the matrix. This continuous range of concentrations can be more accurately captured using multiple-matrix gridblocks associated with each fracture grid.

Current Modeling Approach and Uncertainties–A comparison of transport calculations using a single-matrix grid model and a multiple-matrix grid model (see Section 11.3.2) shows that the leading edge of a radionuclide breakthrough curve will arrive significantly earlier using the single-matrix grid model. Transport at later times in the breakthrough are not appreciably affected by the single-matrix grid approximation. Thus, the results indicate that a single-matrix grid model is a conservative predictor of radionuclide transport behavior. More refined approaches to evaluating radionuclide transport include multiple-matrix gridblock models for both flow and transport, models for transport but not for flow, and alternative calculation schemes, such as particle tracking methods (see Section 11.2.3).

Transport calculations for performance assessment are performed using a different calculation scheme (see the discussion of FEHM V2.10 in Sections 11.2.3 and 11.3.3) that avoids the spatial discretization problem discussed here. However, the TSPA transport calculation method introduces other approximations that generally underestimate fracture-matrix interaction due to diffusion. Because of the difficulties in implementing a uniformly accurate transport calculation

method in the TSPA, a precise evaluation of the significance of the differences in these methods to overall repository performance has yet to be determined.

11.2.3 Calculation Methods for Radionuclide Transport

Process Description–Calculation schemes for radionuclide transport include particle tracking methods and direct numerical solutions of the conservation equations. The different schemes can result in different model predictions, particularly because of differences in the approaches used for matrix diffusion.

Current Modeling Approach and Uncertainties–This section describes results from three different simulation methods for UZ transport: FEHM V2.10, DCPT V1.0, and T2R3D V1.4. All three methods use the same dual-permeability grid consisting of overlapped meshes that represent fracture and matrix continua. FEHM V2.10 uses a node-based particle tracking approach with simplifying assumptions for fracture-matrix diffusive exchange. It is the only transport calculation method used in the *Total System Performance Assessment for the Site Recommendation* (TSPA-SR) (CRWMS M&O 2000 [DIRS 153246], Section 3.7.2) and in the current analyses. DCPT V1.0 uses a random walk particle tracking method that more directly implements the dual-permeability conceptual model. T2R3D V1.4 uses an integrated finite difference method to solve the conservation equations for a dual-permeability system. Although the three simulation methods tested agree for certain problems, differences between the FEHM V2.10 particle tracking method used for the TSPA and for the process-level models were found for transport calculations involving dual-permeability systems. These differences are attributable to simplifying assumptions used in the FEHM V2.10 particle tracking algorithm that provide a more efficient calculation scheme for capturing concentration gradients in the matrix (see Section 11.3.3.3). Improvements in DCPT V1.0 also provide a more accurate representation of matrix concentration gradients for fracture-matrix diffusive exchange than the baseline version.

11.2.4 Effects of Potential Repository Footprint on Three-Dimensional Transport

Process Description–Radionuclide transport in the UZ between the potential repository and the water table depends on the location, size, and shape of the potential repository (i.e., the repository footprint). This results from the unpredictable, location-specific geologic and hydrologic variability present in a natural system. These variabilities include hydrogeologic and mineralogical characteristics, hydrogeologic unit thicknesses, faulting, and surface infiltration.

Current Modeling Approach and Uncertainties–Sensitivity calculations were performed (see Section 11.3.4) to investigate the changes in radionuclide transport behavior that would result if the baseline repository footprint were extended to the south. The investigation found that radionuclide transport in the extended footprint was slower than in the baseline potential repository block, although the differences were not large (e.g., mean breakthrough times differ by less than a factor of two). Uncertainties with regard to footprint effects on radionuclide transport are primarily caused by uncertainties in the footprint itself (i.e., the potential repository design) and in the geologic characterization of regions that lie outside the baseline footprint. This uncertainty is treated by using a range of flow models. A statistical characterization is made of flow focusing as it could occur in the Topopah Spring welded hydrogeologic unit (i.e., the potential repository horizon). Also, a series of perched water conceptual models were

constructed for variable characteristics of the Calico Hills nonwelded hydrogeologic unit (e.g., degree of fracturing and zeolite content) to evaluate the potential for perched water table buildup underneath the potential repository.

11.2.5 Effects of Thermally-Driven Coupled Processes

Process Description–Thermal energy from the potential repository will induce thermal-hydrologic (TH) and thermal-hydrologic-mechanical (THM) couplings that affect flow, as well as thermal-hydrologic-chemical (THC) couplings that affect flow and geochemical conditions. All of these coupled processes affect the conditions for radionuclide transport. Because the heat source is located in the emplacement drifts, the effects of these coupled processes tend to be more pronounced in the vicinity of the drifts. The TH flow coupling is primarily caused by vaporization/condensation phenomena that result in redistribution of water and changes in flow patterns. The THM coupling affects flow behavior through changes in hydrologic characteristics resulting from induced mechanical strain in the rock. The THC coupling can cause changes to hydrologic properties through precipitation and dissolution of minerals, as well as aqueous and mineralogical changes that can affect radionuclide sorption and colloid behavior.

Current Modeling Approach and Uncertainties–Process model evaluations concerning TH effects on mountain-scale flow indicate that effects on radionuclide transport should be minimal (see Section 11.3.5). However, the dryout in the vicinity of the emplacement drift may result in significant delays in radionuclide transport in the higher-temperature operating mode. The effects of THM coupled processes on radionuclide transport were found to cause relatively small changes in hydrologic properties; hence, the effects on flow and transport should be minimal (see Section 11.3.5). Similarly, THC coupled processes were found to cause relatively small changes in hydrologic properties and, therefore, should not have much effect on radionuclide transport (see Section 11.3.5). Geochemical changes have not been fully analyzed; however, the results to date indicate only minimal effects on radionuclide transport. Uncertainties regarding coupled processes include thermal operating modes, modification of hydrologic properties resulting from precipitation/dissolution and mechanical effects, and formation-specific thermal dependency for radionuclide diffusion and sorption characteristics. These uncertainties have been treated by investigating a range of thermal operating modes, performing sensitivity studies on hydrologic properties, and collecting thermodynamic and chemical kinetic data.

11.3 INTRODUCTION TO UNCERTAINTY ANALYSIS

11.3.1 Transport in the Drift Shadow Zone

11.3.1.1 Introduction

Flow in the UZ tends to be diverted by an opening such as an emplacement drift. The underlying reason for the diversion of unsaturated flow around a drift is that capillary forces in the rock prevent water entry into the drift unless the capillary pressure in the rock decreases sufficiently for gravity forces to overcome the capillary barrier (Philip et al. 1989 [DIRS 105743]).

However, water tends to drain laterally around the drift, due to capillary and gravity forces, as saturations rise at the drift boundary. Thus, flow tends to be deflected around the cavity.

The degree to which percolation flux is deflected by the presence of the drift is the subject of Section 4. The absence of downward flow beneath the drift results in a shadow zone of reduced water flux and water saturation. Moving downward, away from the drift, the shadow zone asymptotically re-equilibrates to the undisturbed flow conditions due to capillary forces. This section discusses the consequences of the shadow zone relative to radionuclide transport behavior, not including the effects of repository heat.

11.3.1.1.1 Drift Shadow with Zero Seepage

The phenomenon of flow diversion around a cavity was investigated for a nonspecific homogeneous porous medium by Philip et al. (1989 [DIRS 105743]). The key feature of this phenomenon with respect to the transport of dissolved or colloidal material from the drift is that flow velocities in a zone beneath the drift are reduced relative to the undisturbed flow velocities away from the drift. In particular, the flow velocity at the base of the drift is exactly zero. The zone beneath the drift was also found to have lower water saturation than the undisturbed zone. This region of reduced flow velocity and water saturation beneath the drift is known as the drift shadow (Philip et al. 1989 [DIRS 105743]).

For a quasi-linear representation of the hydrogeologic properties, Philip et al. (1989 [DIRS 105743], p. 18) found that the extent of the drift shadow is a function of a characteristic sorptive length scale and the drift radius. Capillary pressure, expressed in units of length, is proportional to the logarithm of relative permeability in the quasi-linear flow formulation. The sorptive length scale is two times the constant of proportionality in this relationship. The quasi-linear model is a special case in which the logarithm of the effective water permeability is linearly proportional to the capillary pressure. The shape of the drift shadow is governed by the ratio of the drift radius to the sorptive length scale. The ratio of the drift radius to the sorptive length scale is a measure of the relative importance of gravitational forces compared with the capillary forces that define flow patterns around the drift. Philip showed that the drift shadow becomes more elongated (relative to coordinates scaled by the drift radius) as the dimensionless ratio increases (i.e., the gravitational gradient becomes more dominant). Diagrams showing contours of equal flow velocity are given in Philip et al. (1989 [DIRS 105743]). Outside the shadow, near the edge of the drift, a zone of enhanced flow occurs where the diverted flow from the top of the drift is focused.

The results of Philip et al. (1989 [DIRS 105743]) may be used as independent corroboration for the expected behavior in fractured, porous rock using the dual-permeability concept of a fracture continuum and a matrix continuum (see Section 3). Because this work was for a single continuum, this evaluation requires the approximation that, in the vicinity of the drift, the flow behavior in the fracture and matrix continua can be treated as flow in two independent and noninteracting continua. Although this is not exactly correct, interaction between the two continua is weak, as evidenced by the necessity to severely reduce fracture-matrix interaction area in the UZ flow model (CRWMS M&O 2000 [DIRS 141187], Section 6.1.3; Liu et al. 1998 [DIRS 105729]). Furthermore, additional analyses presented here that allow for interacting fracture-matrix continua verify this concept. The expected behavior of fractured rock can be

represented by this approximation in conjunction with the results from Philip et al. (1989 [DIRS 105743]) for a gravity-dominated flow system (e.g., the fracture continuum) and a capillary-dominated flow system (e.g., the matrix continuum). The reduction in flow below the drift is much more severe for the fracture continuum than for the matrix continuum. Furthermore, the very low water content of the fracture continuum below the drift, due to very low saturation and porosity (as compared with the matrix continuum), means that the vast majority of the water in the rock immediately below the drift will be in the rock matrix. This results in diffusive radionuclide releases from a waste emplacement drift into the rock, which will preferentially go into the rock matrix.

11.3.1.1.2 Drift Shadow with Nonzero Seepage

Although seepage into a drift can occur if the flow rate is sufficiently large, in many cases the drifts are expected to deflect all of the percolation flux (CRWMS M&O 2000 [DIRS 153314]). Previous calculations for the base case (CRWMS M&O 2000 [DIRS 153246], Section 4.1.2) predict that 87 percent of the drifts will not receive seepage over the first 100,000 years. The analysis given below does not extend to the case for drifts with seepage, and the effects of the drift shadow in these cases are less certain. Even drifts that receive seepage will divert some of the percolation flux, which will result in some reduction in the percolation rate immediately below the drift. However, uncertainty exists with respect to the distribution of flux coming out of the drift into rock fractures versus rock matrix. As discussed in Section 11.3.1.5.3, initiating transport in the matrix versus the fractures has a large (several orders of magnitude) effect on transport time; however, the overall significance on performance has yet to be determined.

11.3.1.1.3 The Role of Fracture/Matrix Interaction

As stated previously, the fracture and matrix continua appear to be only weakly connected. This observation is based on information from the UZ flow model calibration (CRWMS M&O 2000 [DIRS 141187], Section 6.1.3) and from geochemical comparisons of perched water (water from the fracture continuum) and matrix pore water (BSC 2001 [DIRS 154874], Section 7.5). The UZ flow model requires severely reduced fracture-matrix interaction areas for calibration against field measurements of water saturation and potential (CRWMS M&O 2000 [DIRS 144426]). Perched water and matrix pore waters are found to be significantly different in composition, indicating a lack of geochemical equilibrium between the fracture and matrix continua. Although the hydrologic and geochemical evidence indicates that the fracture and matrix continua are only weakly coupled, quantitative estimates of parameters reflecting this aspect of the fractured rock system are uncertain. Furthermore, this aspect of the system has a large impact on radionuclide transport in the drift shadow and further from the drifts. However, the overall significance on performance has yet to be determined.

11.3.1.2 Goal of the Models

The goal of the drift shadow model is to incorporate the effects of the drift shadow on radionuclide releases from the EBS and the subsequent transport of radionuclides in the flow field disturbed by the presence of the emplacement drift. This goal is achieved through the following analyses:

- Process model evaluation of the flow field below the drifts with zero seepage
- Process model evaluation of radionuclide release transport from drifts with zero seepage
- Model abstraction to be used in the Volume 2 TSPA (McNeish 2001 [DIRS 155023]) for the radionuclide concentration boundary condition at the edge of the drift if no seepage occurs
- Model abstraction to be used in the Volume 2 TSPA (McNeish 2001 [DIRS 155023]) for radionuclide transport in the drift shadow.

11.3.1.3 Discussion of Total System Performance Assessment-Site Recommendation Results

Although detailed process model calculations relating to drift seepage were performed and model abstractions developed and used in the TSPA-SR (CRWMS M&O 2000 [DIRS 153246]), the results did not include any discussion of drift shadow effects. The TSPA-SR computed seepage into the drifts, and as stated previously, TSPA-SR calculations for the base case (CRWMS M&O 2000 [DIRS 153246], Section 4.1.2) predict that 87 percent of the drifts will not receive seepage over the first 100,000 years. Furthermore, releases during the first 40,000 years are dominated by diffusion. In terms of releases from the drift, the radionuclides were assumed to be instantaneously transported from the drift. The result was a zero-concentration boundary condition at the drift wall. This condition was used for diffusive radionuclide releases from the EBS, where diffusion occurs between the radionuclide source and the drift wall. A zero-concentration boundary condition at the drift wall for the EBS diffusion model is the most conservative boundary condition that could be implemented because zero concentration gives the highest possible diffusive flux. Furthermore, all radionuclide releases into the rock were released to the fracture continuum. The flow in the fracture and matrix continua (for radionuclide transport) was assumed to be undisturbed by the presence of the drifts.

The abstractions used in the TSPA-SR (CRWMS M&O 2000 [DIRS 153246]) resulted in large, rapid, diffusive releases of radionuclides into fractures immediately below the emplacement drifts. This approach clearly overestimates the ability of radionuclides to move from the drifts into fractures immediately below for those cases without drift seepage, resulting in conservative dose estimates.

11.3.1.4 Model Developments Since the Total System Performance Assessment-Site Recommendation

The drift shadow model (CRWMS M&O 2000 [DIRS 122894]) is conceptually similar to the drift seepage process model used to support the TSPA-SR, but extends the analysis to the zone

beneath the drift. The computer codes iTOUGH2 V4.0, iTOUGH2 V4.4, and TOUGH2 V1.11, MEOS9nT V1.0 were used for this evaluation. The iTOUGH2 V4.0 code can be used for either forward calculations (as performed with TOUGH2 V1.11 MEOS9nT V1.0) or inverse calculations involving parameter estimation. In this analysis, iTOUGH2 V4.0 was used only for forward model calculations.

11.3.1.4.1 Model Grid and Hydrologic Property Sets

The calculations reported here are for a two-dimensional, homogeneous, dual-permeability model of an emplacement drift. Figure 11.3.1-1 shows the grid employed in the calculations. The area around the 5-m diameter drift uses a refined grid of 0.2 m by 0.2 m. Farther from the drift, the grid coarsens to roughly 2 m by 2 m. The property set for the tsw35 hydrogeologic unit (CRWMS M&O 2000 [DIRS 144426], Table 13), which corresponds to the lower lithophysal unit of the Topopah Spring Tuff, is used in the flow calculations. The mountain-scale property sets were used because the drift shadow extends well beyond the length scale of measurements used to define the drift-scale property sets. However, the appropriate scale of properties to be used should be considered an uncertainty in the calculation. The question of property sets is not considered to be a major uncertainty because the drift-scale and mountain-scale property sets differ primarily in their fracture permeabilities. Although the drift-scale property sets have fracture permeabilities that are roughly one order of magnitude less than the mountain-scale property sets, the effects on water flow and aqueous transport are expected to be small because for both property sets, the capacity for gravity flow in the fracture continuum is orders of magnitude greater than the existing water flow rates.

11.3.1.4.2 Boundary Conditions

The flow model requires the specification of boundary conditions. As Figure 11.3.1-1 shows, the model uses a no-flow symmetry condition along the centerline of the drift. Similarly, the far lateral boundary is also a no-flow symmetry condition reflecting the periodic, 81-m drift spacing. Flow is introduced at the top boundary at a prescribed flow rate. For the dual continuum model calculations, flow rates are prescribed separately for the fracture and matrix continua. This is necessary to develop a flow field compatible with results from the mountain-scale UZ flow model. The bottom boundary condition is simply free gravity drainage.

Guidance on how to distribute the flow into the fractures and matrix is available from model predictions given in *UZ Flow Models and Submodels* (CRWMS M&O 2000 [DIRS 122797], Section 6.6), in which the fractures in the potential repository were found to carry between 84 and 97 percent of the total flow. These percentages represent the average distribution of flow for average infiltration rates over the UZ flow model that vary from about 5 mm/yr to 33 mm/yr (CRWMS M&O 2000 [DIRS 122797], Section 6.6). The computed variations in flow rate are a function not only of the total flow rate, but also of other conditions, such as the characteristics of infiltration at the ground surface. Therefore, in the calculations that follow, the fraction of flow introduced to the fracture continuum at the top of the model is investigated for a range of values. Putting more of the flow in the fractures is conservative because matrix water content will be reduced and fracture water content will be increased. This tends to allow more releases from the drift to enter the fractures, and also results in a larger fracture/matrix contact area through the active fracture model. This area is a function of the effective water saturation of the fracture

continuum. However, it is not conservative with respect to matrix advection rates, as discussed in Section 11.3.1.5. For higher percolation rates, the percentage is adjusted to allow for more flow in the matrix than found at the lower percolation rates, short of saturating the matrix.

The center of the drift is 17.5 m below the top of the model domain, and the drift has a radius of 2.5 m. Hydrologic properties are assigned to the drift such that the capillary pressure is zero for all values of water saturation and the relative permeability is zero over nearly the entire saturation range (until water saturations exceed 0.9999999). Relative permeability is the ratio of permeability at partial saturation to permeability at full saturation.

11.3.1.4.3 Transport Parameters

Transport calculations require the specification of matrix diffusion and sorption parameters. These parameters have been chosen to be the expected values used in the TSPA-SR base case (CRWMS M&O 2000 [DIRS 153246], Tables 3.7-1 and 3.7-2). The drift shadow transport calculations presented here consider nonsorbing technetium and moderately sorbing neptunium. The transport of these radionuclides is calculated without including the effects of radioactive decay. The active fracture model, which specifies fracture-matrix area and other relevant parameters for fracture-matrix interaction, is also used for defining the corresponding properties needed to compute advective and diffusive exchange between fractures and the matrix.

11.3.1.5 Results of Analysis

11.3.1.5.1 Consistency with the Philip Analytical Model

Two calculations were performed for the problem of flow around a drift using a single continuum to compare the results of the Philip et al. (1989 [DIRS 105743]) analytical model with the results of iTOUGH2 V4.4. This comparison provides confirmation that the specific implementation of iTOUGH2 V4.4 for flow around a drift is suitable. The analytical model uses the Gardner relationship (Bear 1988 [DIRS 101379], p. 492), in which relative permeability is an exponential function of capillary pressure. The Gardner relative permeability model is not available in iTOUGH2 V4.0, but is included in iTOUGH2 V4.4, which was used for these comparison calculations only. The iTOUGH2 V4.4 calculations used the van Genuchten capillary-pressure relationship and base permeability parameters from the tsw35 property set (CRWMS M&O 2000 [DIRS 144426], Table 13). Comparisons were made for two values of the dimensionless parameter, s, in the Gardner model. A value of s equal to 0.25 is representative of the matrix continuum, where capillarity dominates gravity. A value of 8 for s corresponds to gravity-dominated flow, as expected in the fracture continuum (Philip et al. 1989 [DIRS 105743]). The comparisons were performed using a percolation rate of 10 mm/yr for the gravity-dominated system (i.e., the fracture continuum) and 0.32 mm/yr for the capillary-dominated system (i.e., the matrix continuum). These are the most representative values of s for the tsw35 fracture continuum and matrix continuum in the calculations presented in Philip et al. (1989 [DIRS 105743]).

Figures 11.3.1-2a and 11.3.1-2b compare vertical flow velocity contours for iTOUGH2 V4.4 and the analytical Philip solution using capillary coefficients of 8 and 0.25, respectively. Some discrepancies between the solutions are found farther from the drift, where grid discretization

effects contribute to discrepancies. Overall, iTOUGH2 V4.4 reproduces the analytical model results with sufficient precision, given the magnitude of other uncertainties about flow and transport in performance assessment.

11.3.1.5.2 Flow Field Results

Unsaturated flow calculations were performed for a dual continuum model using the tsw35 (lower lithophysal unit) property set (CRWMS M&O 2000 [DIRS 144426], Table 13) and the unsaturated flow code iTOUGH2 V4.0. The current repository design locates about 70 percent of the emplacement drifts in this unit (DOE 2001 [DIRS 153849], Section 2.3.4.1.3). The assumed total percolation flux is 10 mm/yr, with 97 percent introduced to the fracture continuum and 3 percent to the matrix continuum at the upper boundary of the model. Fracture-matrix interaction is described by the active fracture model. Flow calculations for tsw35 are shown in Figures 11.3.1-3 to 11.3.1-6. Figures 11.3.1-3 and 11.3.1-4 show the flow velocity and water saturation, respectively, for the fracture continuum. Figures 11.3.1-5 and 11.3.1-6 show the flow velocity and water saturation, respectively, for the matrix continuum.

The results are qualitatively similar to those found for a single continuum using the Gardner relative permeability model. In particular, the drift shadow is seen to be long and narrow for gravity-dominated fracture flow, resulting in a substantial decrease in fracture flow below the drift and for several drift diameters below the drift. For example, the flow rate within about three drift diameters, on the drift centerline below the emplacement drift, is less than 50 percent of the undisturbed flow rate. The matrix, on the other hand, has a much shorter drift shadow. The flow rate in the matrix is less than 50 percent of the undisturbed flow rate within approximately 0.2 drift diameters on the centerline below the bottom of the drift.

An important aspect of the drift shadow flow field is its effect on water saturation. The fracture flow field shows a large decrease in fracture water saturation. For the 10-mm/yr case with a 0.3-mm/yr rate in the matrix, the fracture water saturation drops 35 percent. This reduction in fracture water saturation is even larger in terms of effective water saturation, S_e, defined as:

$$S_e = \frac{S_f - S_{fr}}{1 - S_{fr}} \qquad \text{(Eq. 11.3.1-1)}$$

where S_f is the fracture water saturation and S_{fr} ($S_{fr} = 0.01$) is the residual fracture water saturation (CRWMS M&O 2000 [DIRS 145771]; DTN: LB997141233129.001 [DIRS 104055]). The effective water saturation in the fractures drops to about 15 percent of its undisturbed value. The drop in water saturation is significant with respect to diffusion from the emplacement drift and rock matrix to the fracture continuum and from the fracture continuum to the rock matrix. For diffusive exchange between the fracture and matrix continua, the active fracture model area reduction factor is $S_e^{1+\gamma}$, where S_e is the effective fracture water saturation and the active fracture model parameter, γ, is 0.41. This reduction factor ranges from about 9×10^{-4} to 6×10^{-5} in the undisturbed zone and immediately below the drift. These reduction factors can be deduced from the formula for effective fracture water saturation and the plot of fracture water saturation provided (Figure 11.3.1-4b). Conversely, for the matrix, the reductions in water saturation are relatively small, ranging from 0.83 below the drift to 0.85 in the undisturbed zone. Because of

the low values of flow and water saturation in the drift shadow immediately below the drift, transport from the drift is dominated by diffusive releases to the rock matrix and very restricted diffusion from the rock matrix to the fractures.

11.3.1.5.3 Transport in the Drift Shadow

Transport calculations were run for a dual-permeability flow and transport system using TOUGH2 V1.11 module MEOS9nT V1.0. The transport calculations were performed using the same cross-sectional model grid shown in Figure 11.3.1-1 in the tsw35. These calculations were performed for technetium and neptunium, but without radioactive decay. For each radionuclide, 1 kg was released from two drift cells connected to all the fracture and matrix cells in contact with the drift within 1 m of the drift centerline.

An important process for transport modeling is molecular diffusion in both the matrix and the fractures. Diffusion in TOUGH2 V1.11, MEOS9nT V1.0 is set through specification of the free water diffusion coefficient, roughly 1.6×10^{-9} m^2/s for strong electrolytes (Weast 1972 [DIRS 127163]), and the tortuosity. The values of matrix diffusion used here are the same values implemented for performance assessment (CRWMS M&O 2001 [DIRS 154024], Section 6.6.3). The value for technetium is 3.2×10^{-11} m^2/s, and the value for neptunium is 1.6×10^{-10} m^2/s. For the fracture continuum, tortuosity is taken to be equal to the water content of the fractures. Much lower values of tortuosity are implied by measured data (CRWMS M&O 1997 [DIRS 100401], Section VI). Diffusion in the fracture continuum is important primarily for diffusive releases from the drift to the rock. Immediately below the drift, the tortuosity is 1.3×10^{-4}, using a value of 0.011 for fracture porosity (CRWMS M&O 2000 [DIRS 145771]) and a saturation of 0.012, as seen in Figure 11.3.1-4b.

Breakthrough curves for transport to the bottom of the model (45 m below the bottom of the emplacement drift, as seen in Figure 11.3.1-1) are shown for technetium and neptunium in Figures 11.3.1-7a and 11.3.1-7b, respectively. These figures compare the technetium and neptunium transport results for a percolation rate of 10 mm/yr for two matrix percolation cases that bracket the expected ranges, from a low percolation rate of 0.3 mm/yr to a high percolation rate of 1.6 mm/yr (CRWMS M&O 2000 [DIRS 122797], Section 6.6.3). Because of the diffusive release of radionuclides from the drift to the rock matrix and the restricted fracture-matrix diffusion in the active fracture model, radionuclides are transported primarily in the matrix. The transport is dominated by advection if the 0.5 fraction arrives at the bottom of the model at the time expected for transport due to matrix advection. For the case of technetium, a 0.3 mm/yr percolation rate in the matrix, and a water content of about 0.11, the travel time for pure matrix advection is about 6,200 years, or a $\log_{10}$ value of 3.8. For the 1.6-mm/yr matrix percolation rate, the travel time for pure matrix advection is about 3,500 years, or a $\log_{10}$ time of 3.5. In this case, the travel time of the 0.5 cumulative breakthrough fraction is close to the travel time for pure matrix advection. The long tail leading up to the main breakthrough is caused by diffusive release of the radionuclides from the matrix to the fractures. Diffusive release from the matrix to the fractures dominates transport for the 0.3-mm/yr case. The plot also shows reference results using direct release to undisturbed flow in the fractures, as in the TSPA-SR transport model (CRWMS M&O 2000 [DIRS 153246], Section 3.7.2). The TSPA transport model uses the FEHM V2.10 particle tracking method for transport calculations, which was not used in this analysis. The vast difference in transport (more than three orders of

magnitude) results directly from the difference between transport through fractures and transport through the matrix. Fracture-matrix exchange is not large for either calculation, resulting in extremely rapid transport of releases to the fracture continuum compared with releases to the matrix continuum.

A comparison of the two matrix-percolation cases for neptunium transport is shown in Figure 11.3.1-7b. Neptunium transport differs from technetium transport because of sorption (K_d = 0.3 ml/g for neptunium, 0 for technetium [CRWMS M&O 2000 [DIRS 143665], Table 3.7-1]) and a matrix diffusion coefficient that is 5 times larger (1.6×10^{-10} m^2/s for neptunium versus 3.2×10^{-11} m^2/s for technetium (CRWMS M&O 2000 [DIRS 143665], Table 3.7-2). Although the higher matrix diffusion rate will cause earlier release to the fractures from the matrix, sorption helps retain neptunium in the matrix; in addition, transport through the matrix is slowed by sorption. The net effect is slower transport for neptunium than for technetium.

Transport calculations were also carried out for a percolation flux of 100 mm/yr to investigate sensitivity to percolation rate. The results of these transport calculations are shown in Figures 11.3.1-8a and 11.3.1-8b. Higher overall percolation rates result in more rapid release of radionuclides to the fractures, represented by the gently rising portion of the breakthrough curve. This is primarily a result of higher fracture water saturations and a larger fracture-matrix contact area, as computed with the active fracture model. However, the breakthrough times for the 0.5 breakthrough fractions are still dominated by matrix advection in the higher matrix percolation rate case. This can be roughly deduced by comparing the time for breakthrough of the 0.5 fraction with the time for matrix advection from the drift to the bottom of the model. The range of matrix percolation rates is more difficult to define for future climates. To address this uncertainty, a lower matrix percolation rate of 0.3 mm/yr was used. The upper percolation flux rate was taken to be 3 mm/yr and resulted in a matrix water saturation in excess of 0.99 in the undisturbed flow region.

11.3.1.5.4 Effects of the Drift Shadow on Colloid-Facilitated Radionuclide Transport

Although colloid transport is not quantitatively evaluated here, the drift shadow will have a significant impact on colloid-facilitated radionuclide transport. Because of their large size, colloids can only diffuse slowly. Furthermore, only very small colloids will be able to diffuse into the rock matrix because of size exclusion effects. Colloid diffusion in the fractures will be further restricted by the low water saturations in the drift shadow. Using a fracture tortuosity of 1.3×10^{-4} (see above), the colloid diffusion coefficient in the fractures will vary from about 10^{-16} m^2/s to 10^{-14} m^2/s for a range of colloids from 450 nm to 6 nm in diameter, respectively (CRWMS M&O 2000 [DIRS 144331], Table 6.18). Colloids will therefore tend to be trapped, to a large extent, in the emplacement drift by the drift shadow effects.

11.3.1.6 Abstraction for Total System Performance Assessment

In previous TSPA calculations (CRWMS M&O 2000 [DIRS 153246]), contaminant flux from the near-field/EBS simulated by GoldSim V6.04.007 was introduced into the fracture domain of the FEHM V2.10 UZ particle tracking model (CRWMS M&O 2000 [DIRS 153246]). The results presented in Section 11.3.1.5 indicate that a significant portion of the contaminant flux from the EBS may enter the rock matrix rather than fractures. This occurs because, in the

absence of seepage, releases from the EBS are diffusive and will enter the rock matrix and fractures roughly in proportion to the water content of the two continua. The water content of the rock matrix is on the order of 0.1, whereas the fractures have water content on the order of 10^{-4}. Therefore, nearly all of the EBS releases will go into the matrix. The FEHM V2.10 particle tracking routine was modified to account for this partitioning of contaminant flux into the fracture and matrix domains (CRWMS M&O 2000 [DIRS 141418]). The basic idea is that the mass advected through the EBS cells via seepage is released into the fracture nodes, and the mass diffused through the EBS cells is released into the matrix nodes.

11.3.1.6.1 Abstraction for Transport in the Drift Shadow

FEHM V2.10 interfaces with GoldSim V6.04.007 through collector cells that provide the contaminant flux leaving the EBS. There are five collector cells, which correspond to each infiltration bin. The five separate infiltration bins are based on the multiscale thermal-hydrologic model (CRWMS M&O 2000 [DIRS 153246], Section 3.7.2). Specifically, the model is based on the percolation flux derived from the multiscale model nodes that are 5 m above the drift crown. The advective and diffusive mass from the EBS is combined into a GoldSim V6.04.007 collector cell, then passed to FEHM V2.10 as a boundary condition. GoldSim V6.04.007 also passes an advection-diffusion flow fraction for each of the cells that represents the ratio of the advective and diffusive mass fluxes entering the collector cell. The flow fraction is used to calculate the proportion of mass entering the fracture and matrix domains. Masses from each of the collector cells are then sent to the corresponding spatial location in the FEHM V2.10 model. The FEHM V2.10 particle tracking routine partitions particles between the fracture and matrix nodes, using the flow fractions such that advective releases from the drift are passed to fracture nodes in the transport calculation and diffusive releases from the drift are passed to matrix nodes.

FEHM V2.10 does not allow radionuclides that have entered the matrix to diffuse to the fractures. Therefore, radionuclides that enter the matrix must either advect from the matrix to the fractures or travel through the matrix to the water table. This should be recognized as a nonconservative feature of TSPA calculations that incorporate the drift shadow abstraction. However, this implementation of the drift shadow provides an estimate of the potential range of results between the TSPA base case (CRWMS M&O 2000 [DIRS 153246]), which does not account for the drift shadow, and a TSPA that includes the drift shadow effect.

11.3.1.6.2 Abstraction for the Engineered Barrier System Boundary Condition

A radionuclide concentration boundary condition at the drift wall may be established based on continuity of radionuclide concentration and flux exiting the drift and entering the rock. This model abstraction is developed for the situation in which radionuclide flux is entirely diffusive in the EBS invert and advective in the rock matrix. Neglecting diffusion in the rock matrix, in combination with the assumption that advective velocities in the rock matrix are at undisturbed levels, should be acceptable (i.e., conservative) as long as the drift shadow keeps the radionuclides moving in the matrix for a few meters. The transport results in Section 11.3.1.5 support the idea that most radionuclides will transport away from the drift in the matrix for at least a few meters before entering fractures.

EBS diffusion is modeled as a one-dimensional steady-state diffusion through two different domains, the waste package and the invert (CRWMS M&O 2000 [DIRS 153246], Table 3.6-1). For steady-state diffusion in the waste package and invert:

$$\frac{d^2 c_{wf}}{dx^2} = 0 \quad \text{and} \quad \frac{d^2 c_{in}}{dx^2} = 0 \qquad \text{(Eq. 11.3.1-2)}$$

where c_{wf} is the concentration in the waste form domain and c_{in} is the concentration in the invert domain. The general solutions to these two equations are (Crank 1975 [DIRS 122990], p. 44):

$$c_{wf}(x) = F_{11}x + F_{12} \text{ and } c_{in}(x) = F_{21}x + F_{22} \qquad \text{(Eq. 11.3.1-3)}$$

where F_{ij} are the integration constants. The boundary conditions consist of the source concentration condition and continuity of concentration and flux across the boundaries:

$$\begin{aligned} & c_{wf}(0) = c_s \\ & c_{wf}(L_{wf}) = c_{in}(L_{wf}) \\ & -\phi_{wf} S_{wf} D_{wf}(S_{wf}) \frac{dc_{wf}}{dx}(L_{wf}) = -\phi_{in} S_{in} D_{in}(S_{in}) \frac{dc_{in}}{dx}(L_{wf}) \\ & -\phi_{in} S_{in} D_{in}(S_{in}) \frac{dc_{in}}{dx}(L_{wf} + L_{in}) = v_D c_{in}(L_{wf} + L_{in}) \end{aligned} \qquad \text{(Eq. 11.3.1-4)}$$

where

ϕ_{wf} and ϕ_{in} = porosities of the waste form and invert

S_{wf} and S_{in} = water saturations of the waste form and invert

$D_{wf}(S_{wf})$ and $D_{in}(S_{in})$ = effective diffusion coefficients for the waste form and invert

L_{wf} and L_{in} = diffusion path lengths in the waste form and invert

v_D = specific discharge in the rock matrix.

The interface areas between the waste form and invert and between the invert and the rock matrix are equal. The effective diffusion coefficients may be functions of water saturation, but the water saturations must be spatially uniform within each domain.

Solving these equations for F_{ij} and evaluating $c_{in}(L_{wf}+L_{in})$ (the concentration at the invert–rock matrix boundary) gives:

$$c_{in}(L_{wf} + L_{in}) = \frac{c_s}{1 + Pe_{wf} + Pe_{in}} \qquad \text{(Eq. 11.3.1-5)}$$

where the waste form and invert Peclet numbers are, respectively:

$$Pe_{wf} = \frac{v_D L_{wf}}{\phi_{wf} S_{wf} D_{wf}(S_{wf})}$$

and (Eq. 11.3.1-6)

$$Pe_{in} = \frac{v_D L_{in}}{\phi_{in} S_{in} D_{in}(S_{in})}$$

This model results in concentrations at the drift boundary that are greater than zero. The boundary concentration may be large (relative to the source concentration) for regions where the waste form and invert Peclet numbers are small.

11.3.1.7 Multiple Lines of Evidence

Evidence for fracture/matrix disequilibrium is available from field and laboratory tests (CRWMS M&O 2000 [DIRS 141187], Section 6.1.3; Liu et al. 1998 [DIRS 105729]; BSC 2001 [DIRS 154874], Section 7.5). Hydrologic measurements of matrix water potential and saturation, combined with model results, lead to the conclusion that the products of the effective interface permeability, the geometric interface area, and the driving force for fracture-matrix flow (i.e., the capillary pressure differential between fractures and the matrix) must be reduced to match field measurements (CRWMS M&O 2000 [DIRS 144426]; Liu et al. 1998 [DIRS 105729]). Although the effects of these factors are difficult to distinguish based on hydrologic observations alone, geochemical observations of matrix water composition and fracture water composition from perched water zones suggest that the fractures and matrix are not in geochemical equilibrium (BSC 2001 [DIRS 154874], Section 7.5). The only way to achieve the observed level of disequilibrium without invoking special characteristics for fractures or the matrix that are inconsistent with existing data and conceptual models is to have a severely reduced fracture-matrix contact area.

11.3.1.8 Summary of Remaining Uncertainties

The main areas of uncertainty concern the aspects of the flow and transport problem in the vicinity of the emplacement drift that have a large influence on the calculated behavior. These aspects are related primarily to fracture-matrix interaction for diffusive exchange between fractures and the matrix. The reduction in fracture-matrix interface area in the flow and transport models is supported by a combination of hydrologic and geochemical observations (Section 11.3.1.7).

The reduction in fracture-matrix interaction area in the flow model is represented through the active fracture model (CRWMS M&O 2000 [DIRS 141187], Section 6.4.5; Liu et al. 1998 [DIRS 105729]), which must be calibrated to field data to determine an empirical parameter introduced by the model. However, there is an additional effective reduction in fracture-matrix interaction because of the weighting scheme used for fracture-matrix flow calculations. Fracture-matrix flow uses upstream weighting of the relative permeability combined with downstream weighting of the saturated permeability to define the interface permeability. Typically, flow is from fracture to matrix because of the disequilibrium of capillary pressures.

Therefore, fracture to matrix flow is computed using the matrix saturated permeability and the fracture relative permeability. Given the extremely low saturations characteristic of flow in the fractures, the fracture relative permeability is typically orders of magnitude lower than the matrix relative permeability. The effective permeability of the matrix controls imbibition from fractures to the matrix; hence, the true interface permeability is biased to be lower by the ratio of the fracture relative permeability to the matrix relative permeability. This is equivalent to a fracture-matrix area reduction factor. Because the flow model is calibrated to field data, explicit recognition of this reduction factor is not critical to the flow model. However, it is important to recognize this factor when determining the area reduction factor to be used for matrix diffusion. This reduction factor is not accounted for with respect to matrix diffusion in the current drift shadow transport model. The neglect of this effect is conservative for radionuclides that initially enter the matrix because neglecting this factor gives a larger fracture/matrix interface area, leading to more fracture/matrix diffusion, shorter retention of radionuclides in the matrix and, therefore, shorter transport times. Clearly, for radionuclides that initially enter the fractures, the opposite is true and transport is more rapid. However, because the model results in most of the radionuclides initially entering the matrix, the overall effect of neglecting the additional reduction in the fracture/matrix interface area is conservative.

The variation in transport behavior investigated as a function of total percolation rate, as well as the distribution of percolation between fractures and the matrix, represents another element of uncertainty. In this case, the combination of the climate and infiltration uncertainty coupled with site-scale flow model uncertainty can capture the main aspects of this element for the drift shadow transport problem.

Additional uncertainties include drift seepage and parameter uncertainty and variability (heterogeneity). The treatment of the drift shadow for the TSPA calculations in this report captures some aspects of parameter uncertainty directly and conservatively treats the effects of drift seepage. However, the overall significance on performance remains to be determined. The input parameters for flow and transport are uncertain: the propagation of uncertainties through transport models could demonstrate the significance for these uncertainties on performance assessment. The main uncertainties for the drift shadow transport model are summarized in Table 11.3.1-1. Because of this approach, it is likely that a more realistic incorporation of seepage processes, and further development of the process models evaluating the effects of drift seepage, would result in TSPA model calculations that have lower radionuclide releases than those in the TSPA-SR (CRWMS M&O 2000 [DIRS 153246]).

11.3.1.9 Summary and Conclusions

The effects of the drift shadow have a dramatic impact on radionuclide transport times in a limited region below the waste emplacement drifts. The transport times for technetium in the drift shadow model are roughly three to four orders of magnitude longer than transport times over the same domain when computed using the transport assumptions from the TSPA-SR transport model (CRWMS M&O 2000 [DIRS 153246], Section 3.7.2). It is important to recognize that the breakthrough curves presented here are for a boundary 45 m below the potential repository, whereas the water table is an average of about 300 m below the potential repository (DOE 2001 [DIRS 153849], Section 4.3.3.1). The main portions of the radionuclide transport breakthrough curves are dominated by matrix advection for the higher matrix

percolation cases. The simulation results show that for these cases, most of the radionuclide mass still remains in the matrix at breakthrough. Therefore, the effects of the drift shadow model on transport extend beyond the zone of reduced flow beneath the waste emplacement drift and, in some cases, beyond the existing model boundary. The effect of the drift shadow transport model on breakthrough curves at the water table has not been investigated. For radionuclide releases from drifts without seepage, the results presented in this section indicate that transport times to the water table will be thousands to tens of thousands of years. The drift shadow analysis presented is a preliminary and exploratory investigation of flow and transport processes not previously included in process models or TSPA analyses of Yucca Mountain. Further justification in terms of additional analyses and field or laboratory experiments are needed prior to incorporating the complete drift shadow flow and transport analysis into the TSPA baseline.

11.3.2 Matrix Block Discretization and Its Effects on Unsaturated Zone Flow and Transport Simulations

In this section, the effects of matrix block discretization schemes on UZ flow and transport simulations are evaluated.

11.3.2.1 Introduction

Within the context of the continuum approach for modeling flow and transport in unsaturated fractured rock, a numerical gridblock generally includes a fracture block and a matrix block. Depending on the matrix block discretization scheme used for a numerical simulation, the matrix block can be treated as a single matrix gridblock or subdivided into a number of matrix gridblocks. Each matrix gridblock generally corresponds to a matrix continuum.

Because fractures and the matrix have different hydraulic properties, flow and transport between them significantly affects the overall flow and transport behavior in the UZ. Consequently, the accuracy with which flow and transport between them is calculated, which is largely determined by the matrix block discretization scheme, is a critical issue for simulating overall flow and transport processes and for assessing the performance of the potential repository.

As discussed in *Conceptual and Numerical Models for UZ Flow and Transport* (CRWMS M&O 2000 [DIRS 141187], Section 6.4), a dual-permeability model (DKM) has been used as the baseline approach for modeling UZ flow and transport processes. This approach was based on considerations regarding flow and transport behavior in the UZ, the scale of the problem, data availability, and computational feasibility (CRWMS M&O 2000 [DIRS 141187], Section 6.4.2).

Because the matrix is orders of magnitude less permeable than the fracture network, very steep gradients (sharp fronts) may develop in the matrix near fractures. In the DKM, the matrix is treated as a single continuum. As a result, capillary pressure gradients (which drive imbibition) and concentration gradients (which drive diffusion) cannot be fully described. Use of the DKM, therefore, may introduce uncertainty into simulations of UZ flow and transport. To evaluate the effect of the uncertainty, this section compares DKM simulation results to results obtained using the multiple interacting continua (MINC) discretization scheme, which was devised specifically to eliminate this source of uncertainty by using multiple matrix blocks per fracture block (Pruess and Narasimhan 1985 [DIRS 101707], pp. 14 to 16).

11.3.2.2 Goals of the Modeling Study

This modeling study evaluates the DKM for UZ flow and transport and associated uncertainties. Specifically, the goals of this study are:

1. Compare simulation results for UZ flow and transport obtained using the DKM with simulation results obtained using MINC, a more accurate matrix block discretization scheme.

2. Make recommendations for improving the current matrix discretization scheme (DKM) based on the simulation results presented in this study (Bodvarsson 2001 [DIRS 154669], Attachment 7, pp. 129 to 141).

11.3.2.3 Matrix Block Discretization

Typical schemes for matrix discretization include the effective continuum model (Pruess et al. 1990 [DIRS 100819]), the dual porosity model (Warren and Root 1963 [DIRS 100611]), the DKM (Doughty 1999 [DIRS 135997], pp. 74 to 79), and the MINC scheme (Pruess and Narasimhan 1985 [DIRS 101707], pp. 14 to 16). A diagram of these schemes for a one-dimensional column of gridblocks is illustrated in Figure 11.3.2-1.

In the effective continuum model (Figure 11.3.2-1a), liquid saturation is partitioned into the matrix and fractures in accordance with the principle of thermodynamic equilibrium, which requires equal capillary pressure in the matrix and fracture components of a gridblock. This is equivalent to assuming that flow and transport between fractures and the matrix occurs instantaneously; thus, fractures and the matrix are combined as a single continuum in a numerical simulation.

In the dual porosity model (Figure 11.3.2-1b), each gridblock includes a fracture gridblock and a matrix gridblock. Unlike the effective continuum model, the fracture and matrix gridblocks need not be in thermodynamic equilibrium. In this approach, flow and transport occurs between fractures and the matrix, but is ignored between matrix gridblocks. The DKM (Figure 11.3.2-1c) is the same as the dual-porosity model, except that it allows for global flow and transport between matrix blocks. The DKM is valid when the capillary pressure and concentration gradients near fracture-matrix interfaces are not steep.

The schemes mentioned above can give poor solutions for flow and transport involving steep fronts near fracture-matrix interfaces in unsaturated fractured rock. This happens because of the thermodynamic equilibrium assumption (in the effective continuum model) or the use of one matrix gridblock (in the other two schemes) (Doughty 1999 [DIRS 135997], pp. 74 to 79). To solve this problem, Pruess and Narasimhan (1985 [DIRS 101707], pp. 14 to 16) proposed the MINC scheme (Figure 11.3.2-1d), which is similar to the DKM except that the matrix is further subdivided into several continua, each at a different distance from the fracture-matrix interface. Thus, the MINC scheme is able to more accurately resolve sharp gradients near the fracture-matrix interfaces.

Although the MINC is known to be the most accurate of these schemes (CRWMS M&O 2000 [DIRS 141187], Section 6.4), it needs more computational effort because several matrix

gridblocks are involved for each fracture block. For this reason, the DKM has been used as the baseline approach in the UZ flow and transport models. As discussed below, a comparison of the simulation results from the DKM and MINC models indicates that the MINC results are relatively conservative. A more detailed discussion of the usefulness and limitations of the matrix block discretization schemes is given in *Conceptual and Numerical Models for UZ Flow and Transport* (CRWMS M&O 2000 [DIRS 141187]).

11.3.2.4 Modeling Approaches

To evaluate the accuracy of the DKM in modeling flow and transport in the UZ, simulation results obtained from the DKM were compared with those obtained from a MINC model. In the MINC model, a fracture network is conceptualized as two perpendicular sets of vertical fractures and the matrix is divided into five matrix gridblocks (continua) (Figure 11.3.2-2). Ratios of the distances (i.e., from interfaces between matrix continua to the fracture-matrix interface) to the corresponding fracture spacing are set at 0.004, 0.032, 0.108, and 0.256, respectively. Fine discretization is used near the fracture-matrix interface, and relatively coarse discretization is used for matrix blocks away from the interface. This is because steep gradients generally occur near the interface, as previously discussed. All the matrix continua are globally connected in the vertical direction. In nonvertical directions, only the first (outermost) matrix continuum is globally connected, while the connection parameters (e.g., node distance and interface area) are the same as those in the DKM for the same fracture configuration. All the matrix continua in Figure 11.3.2-2 have identical hydraulic properties.

Because MINC simulations are computationally intensive, a site-scale, two-dimensional cross section was used for all the simulations in this study (Figures 11.3.2-3 and 11.3.2-4). This cross section was selected because it does not contain the vitric Calico Hills Formation, where fracture-matrix interaction is not important. Fracture flow is a major flow mechanism below the potential repository, and matrix diffusion is expected to be a significant mechanism for radionuclide transport between fractures and the matrix below the potential repository (CRWMS M&O 2000 [DIRS 141187], Sections 6.1.2 and 6.2.2). Simulation results were compared for the DKM and the MINC matrix block discretization schemes. The initial conditions, boundary conditions, and rock properties (discussed below) are identical in both simulations.

The top model boundary for the two-dimensional vertical cross-sectional model domain coincides with the bedrock surface of the mountain. Net infiltration at the surface of the mountain is applied to the top boundary. The present-day infiltration map (DTN: GS000308311221.005 [DIRS 147613]) and the calibrated, base case UZ property set (DTN: LB997141233129.001 [DIRS 104055]) determined from one-dimensional inverse modeling studies were used in this study. The bottom boundary is located at the water table. The left and right boundaries are no-flow boundaries in the horizontal direction. Steady-state flow fields were simulated with the EOS9 module of TOUGH2 V1.4. Transport runs were carried out by the T2R3D V1.4 code. The active fracture model documented in *Conceptual and Numerical Models for UZ Flow and Transport* (CRWMS M&O 2000 [DIRS 141187], Section 6.4.5) was used for describing flow and transport in fractures.

In the tracer-transport simulations, a conservative (nonadsorbing) component is transported from the potential repository to the water table under steady-state flow conditions. At time zero, tracer

concentration is zero everywhere in the matrix, and a predetermined tracer concentration is applied to water in the fractures in the potential repository host rock. The simulation results for tracer transport are represented by the cumulative mass of tracer arriving at the water table over time, normalized by the total initial mass introduced at the potential repository. Hydrodynamic dispersion has no significant effect on solute transport through the unsaturated fracture-matrix system, as discussed in *UZ Flow Models and Submodels* (CRWMS M&O 2000 [DIRS 122797], Section 6.8.1), and was therefore ignored in this study. Two molecular diffusion coefficients, 0 and 3.2×10^{-11} m^2/s, were used in the simulations for all model layers. The latter value is the average matrix molecular diffusion coefficient for TcO_4^- reported in *Unsaturated Zone and Saturated Zone Transport Properties (U0100)* (CRWMS M&O 2001 [DIRS 154024], Table 16).

11.3.2.5 Results of Analysis

Figures 11.3.2-5 and 11.3.2-6 compare simulated results obtained with the DKM (solid line) and the MINC (circles), respectively, for the two columns (a14 and a23) from the two-dimensional cross section (Figure 11.3.2-4). The simulated matrix saturations are in good agreement with the two schemes of matrix block discretization under steady-state flow conditions, indicating that the whole matrix block can be treated as a single continuum (as used in the DKM). This is further supported by an observation that for a given MINC gridblock, the five matrix continua have almost identical water saturations and potentials (Figure 11.3.2-7). In other words, all five matrix continua of the MINC are in hydraulic equilibrium, consistent with the assumption used in the DKM. This is not surprising because the matrix has small van Genuchten α (i.e., strong capillarity), and flow between different matrix continua is determined purely by capillary forces. The gravity term is not involved in a connection between matrix continua for a given matrix block (Figure 11.3.2-2).

Figures 11.3.2-5 and 11.3.2-6 compare simulated distributions of water flux in fractures for the two columns from the two discretization schemes. While the DKM and the MINC agree fairly well, the DKM overestimates fracture flux (i.e., liquid flux in the fractures) in the PTn unit compared to the MINC. This is because a steep gradient of capillary pressure exists near the fracture-matrix interface, despite the uniform capillary pressure distribution that occurs within a matrix block (e.g., Figure 11.3.2-7). In a DKM, the connection distance between nodes corresponding to the fracture and matrix gridblocks is set to one-eighth (0.125) of the fracture spacing for a fracture network given in Figure 11.3.2-2 (Warren and Root 1963 [DIRS 100611]; Pruess 1983 [DIRS 100605], Table 1). This value is considerably larger than the connection distance between the fracture gridblock and the matrix gridblock corresponding to Matrix Continuum #1 in the MINC (Figure 11.3.2-7). Because the calculated water flux from fractures to matrix varies inversely with this connection distance, the DKM underestimates the flux from fractures to the matrix and overestimates the fracture flux.

While the DKM and the MINC yield similar fracture-flux distributions in the TSw unit, the DKM overestimates fracture fluxes in the CHn and CFu units (Figures 11.3.2-5 and 11.3.2-6) compared to the MINC. Compared with the TSw unit, these units have relatively small fracture permeabilities and large effective fracture-matrix interface areas, as indicated by small values of the active fracture parameter (γ) (DTN: LB997141233129.001 [DIRS 104055]). A combination of these factors and the fine discretization of the matrix block results in a larger flux from fractures to the matrix, and consequently a smaller fracture flux, for the MINC scheme than for

the DKM. The differences in fracture flux result from these factors, not from lateral flow, because the total simulated water fluxes at the water table (for both columns), including contributions from the matrix and fractures, are similar for the DKM and the MINC.

Figure 11.3.2-8 shows simulated tracer transport results with and without molecular diffusion ($D_m = 3.2 \times 10^{-11}$ m^2/s and $D_m = 0$). The use of $D_m = 0$ allows for investigation of pure advection effects. In this case (Figure 11.3.2-8a), the DKM and the MINC give similar breakthrough times (less than 10 years) but different values for the tracer cumulative flux. This results from the differences in fracture fluxes in the CHn and CFu units, as discussed above. In the DKM, the majority of tracer mass is transported through fractures from the potential repository (within TSw) to the water table, as implied by the relatively uniform fracture-flux distributions within the TSw unit and below (Figures 11.3.2-5 and 11.3.2-6). In contrast, a relatively small portion of the tracer mass is transported through the fractures to the water table in the MINC scheme.

Comparisons between simulated transport results for the two molecular diffusion coefficients further confirm the importance of the matrix diffusion indicated by the Alcove 1 test and modeling study discussed in *UZ Flow Models and Submodels* (CRWMS M&O 2000 [DIRS 122797], Section 6.8.1). The DKM and MINC schemes produce significantly different breakthrough curves in simulations using the different molecular diffusion coefficients. The comparisons also suggest the necessity to accurately consider the solute-concentration gradient near the fracture-matrix interface. For example, similar breakthrough times are simulated for both matrix-block discretization schemes using $D_m = 0$, but significantly different breakthrough times are simulated using $D_m = 3.2 \times 10^{-11}$ m^2/s. This results mainly from using different discretization schemes. Matrix diffusion is underestimated by the DKM at the early time for radionuclide transport, when there is a large concentration gradient near the fracture-matrix interface. Because the MINC scheme is expected to provide more accurate results, it is likely that the DKM underestimates the breakthrough time (i.e., it predicts earlier breakthrough) for radionuclide transport from the potential repository to the water table.

11.3.2.6 Abstraction for Total System Performance Assessment

As stated in Section 11.3.2.2, the modeling study is devoted to evaluating the DKM for modeling UZ flow and transport in general. The results indicate that the DKM conservatively predicts shorter breakthrough times than the MINC. The simulation results from this study are not directly used for TSPA abstraction; nevertheless, the results imply that it may be important to improve fracture-matrix interaction as modeled with a single matrix grid method. As discussed in Section 11.3.3, the comparisons between simulation results indicate that the effects of matrix diffusion in reducing the initial breakthrough time is not as significant in three dimensions as it seems to be in one dimension. However, the relatively significant impact found here for a two-dimensional system, and possibly more significant effects for the MINC solution, suggest that these effects could also be important for transport in the three-dimensional site-scale model.

11.3.2.7 Multiple Lines of Evidence

The simulation results indicate that the DKM might overestimate fracture flow in the nonwelded units (see comparisons between simulation results for the PTn in Figures 11.3.2-5 and 11.3.2-6). This is consistent with experimental observations from the Busted Butte site (CRWMS

M&O 2000 [DIRS 152773], Section 6.8.9). For the vitric part of the Calico Hills Formation, the current UZ model predicts that about 20 percent of the liquid water occurs in fractures (CRWMS M&O 2000 [DIRS 151940], Figure 3.6.9). In Phase 1A testing at Busted Butte, tracer was injected from a point in the vitric part of the Calico Hills formation. The observed tracer plume clearly indicates that flow and transport occurs only in the matrix of the vitric Calico Hills formation. During Phase 1B testing, in which liquid was injected immediately adjacent to a fracture, water imbibed quickly into the surrounding matrix. Details of these tests can be found in *Unsaturated Zone and Saturated Zone Transport Properties (U0100)* (CRWMS M&O 2001 [DIRS 154024], Section 6.8.9).

Observations at a number of analogue sites generally support the concept that radionuclides transported from fractures to the matrix are distributed near fracture-matrix interfaces (CRWMS M&O 2000 [DIRS 151945], Sections 13.4 and 13.6). Therefore, steep concentration gradients exist near fracture-matrix interfaces. At the Nopal I site in Peña Blanca, Mexico, and the Poços de Caldas site in Brazil, uranium has been transported small distances (almost completely along fractures) and sorbed onto ferric oxides and calcites (CRWMS M&O 2000 [DIRS 151945], Sections 13.4 and 13.6). Matrix diffusion appears to have been inconsequential at Nopal I, with evidence of uranium generally extending only a few centimeters away from the fracture-matrix interface (CRWMS M&O 2000 [DIRS 151945], Section 13.4). While advective transport along fractures has been identified as an important transport mechanism in the analogue sites, matrix diffusion is an important mechanism attributed to the loss of lead in uraninites at Oklo and Cigar Lake (Janeczek and Ewing 1992 [DIRS 125262]).

11.3.2.8 Summary of Remaining Uncertainties

The focus of this modeling study is the evaluation of the DKM, the matrix discretization scheme currently used in the UZ flow and transport model, and the associated uncertainties in modeling flow and transport in UZ. It was found that the DKM can overestimate liquid flow in fractures within nonwelded units and underestimate matrix diffusion for radionuclide transport from the potential repository to the water table at the early time, when there is a large concentration gradient near the fracture-matrix interface. These uncertainties can be eliminated by using numerical schemes that account for steep gradients near fracture-matrix interfaces (see Section 11.3.2.9).

Table 11.3.2-1 summarizes the key uncertainties related to the calculation of flow and transport between fractures and the matrix. This evaluation is based on a conceptual model that the continuum approach can be used for adequately modeling UZ flow and transport. All the uncertainties associated with using the continuum approach to model UZ flow and transport still exist. The reason for using the continuum approach for the UZ flow and transport model is documented in *Conceptual and Numerical Models for UZ Flow and Transport* (CRWMS M&O 2000 [DIRS 141187], Section 6.4).

The upstream weighting scheme was used to determine flow and transport between fractures and the matrix; that is, the relative permeability in fractures was used as the relative permeability for the connection between fractures and the matrix. Because the relative permeability for the fracture continuum is defined for flow along the fracture-matrix interface, rather than flow between fractures and the matrix, using the relative permeability for the matrix is expected to be

more appropriate for flow between fractures and the matrix. While this issue was partially accounted for in the estimation of effective parameters for flow during model calibration, its effects on overall flow and transport behavior in the UZ remain uncertain.

In this study, properties determined from a one-dimensional model calibration were used. Hence, perched water below the potential repository was not considered. While additional consideration of perched water may result in different flow and transport behavior, the evaluation results are expected to remain qualitatively unchanged. This is because the mechanisms governing flow and transport between fractures and the matrix are the same for both cases (i.e., with and without perched water).

11.3.2.9 Conclusions and Recommendations

The MINC simulation results show that under steady-state flow conditions, the matrix continua within a given gridblock have almost identical water saturations and potentials, indicating that the matrix can be treated as a single continuum. Thus, the dual-permeability concept is valid for modeling steady-state flow processes in the Yucca Mountain UZ.

Comparisons between simulation results indicate that the current dual-permeability approach overestimates fracture fluxes in some units, resulting in too large a connection distance between the fracture and matrix gridblocks. This is consistent with the noted discrepancy between the previously simulated fracture fluxes in the vitric Calico Hills Formation and those implied from the tracer-test results at the Busted Butte site (CRWMS M&O 2001 [DIRS 154024], Section 6.8.9). It is recommended that a reduced connection distance be used in generating the DKM grids for future flow simulations. The exact value of this reduced distance remains to be determined.

Simulation results demonstrate the importance of accurately representing the concentration gradients near fracture-matrix interfaces in simulating the overall radionuclide transport processes in the UZ. Because the DKM underestimates matrix diffusion during early time periods, it is likely that this model provides conservative estimates of the breakthrough time for radionuclide transport from the potential repository to the water table. This issue can be resolved using one of the following three approaches:

- Use the MINC for flow and transport in the site-scale UZ model. This approach is computationally intensive.

- Take advantage of the finding that the DKM is valid for modeling steady-state flow processes if the reduced connection distance is used. In this case, flow fields are simulated with the DKM and then mapped into a MINC grid. Radionuclide transport is simulated for the MINC grid using the computationally efficient T2R3D V1.4 code, which solves only the solute-transport equation. However, further investigations are needed to determine the reduced connection distance in this approach.

- Improve the existing particle trackers so they can handle sharp concentration gradients for a DKM grid and the corresponding flow fields. Section 11.3.3 contains a detailed discussion of current particle trackers and their capabilities.

11.3.3 A Comparison of Radionuclide Transport Calculation Methods

11.3.3.1 Introduction

This section summarizes the comparison of three transport modeling codes used in predicting radionuclide transport from the potential repository to the water table at Yucca Mountain and the discussions of the unquantified and quantified uncertainties in modeling using these three codes. Because of the differences of the modeling approaches used, the predictions of radionuclide transport for the same case may not be consistent among the codes. Therefore, a comparison study is necessary to assess the uncertainties and the suitability of each code as a modeling tool for predicting radionuclide transport in the Yucca Mountain UZ. In particular, FEHM V2.10 was used in TSPA, DCPT (Dual Continuum Particle Tracker) V1.0 was used in *Analysis of Base-Case Particle-Tracking Results of the Base-Case Flow Fields (ID: U0160)* (CRWMS M&O 2000 [DIRS 134732]) and *Analysis Comparison Advective-Dispersive Transport Solution to Particle Tracking* (CRWMS M&O 2000 [DIRS 141389]), and T2R3D V1.4 was used in *Analysis Comparison Advective-Dispersive Transport Solution to Particle Tracking* (CRWMS M&O 2000 [DIRS 141389]) and *Unsaturated Zone Flow and Transport Model Process Model Report* (CRWMS M&O 2000 [DIRS 151940]). Uncertainties in conceptual models and code implementations are presented in *Analysis Comparison Advective-Dispersive Transport Solution to Particle Tracking* (CRWMS M&O 2000 [DIRS 141389]) and *Particle Tracking Model and Abstraction of Transport Processes* (CRWMS M&O 2000 [DIRS 141418]) and summarized in Section 11.3.3.8.

Modeling three-dimensional chemical transport in unsaturated, heterogeneous, and fractured porous media such as the Yucca Mountain UZ is a challenging task, in terms of both the scientific basis and the required computational resources. The models developed using the three codes (FEHM V2.10, DCPT V1.0, and T2R3D V2.10) are based on the same dual-permeability grid formulation, with the same steady-state flow field calculated using TOUGH2 V1.4. The dual-permeability grid provides one mesh for the fractures and a second mesh for the matrix. Because each mesh occupies the entire spatial domain for a given problem, the fractures and matrix can be thought of as overlapping continua in the spatial domain. In the dual continuum approach, flow and transport in fractured porous media are conceptualized as two spatially overlapping and interactive subprocesses. Global flow and transport can take place in both fracture and matrix continua, while mass transfer between the two continua can occur locally in each grid cell. The major advantage of the dual continuum model is its capability to capture the major features of flow and transport in fractured porous rock with a minimum of computational resources. In terms of the transport calculation method, T2R3D V1.4 is based on the integral finite difference method of solving the advection-dispersion equations, FEHM V2.10 uses the node-based particle tracking method, and DCPT V1.0 uses the random-walk particle tracking method. In this comparison study, simulations were done in which all parameters (i.e., grid, flow field, and transport parameters) were exactly the same; the only difference was in the transport calculation methods used.

Uncertainties about the effect of the flow field on transport results from the dual continuum approach are presented in Section 11.3.2.8. The simulations produced by the three transport calculation methods are examined in the following sections.

11.3.3.2 Goal of Code Comparison for Modeling Unsaturated Zone Transport

The goal of the T2R3D V1.4, FEHM V2.10, and DCPT V1.0 is to predict the transport of radionuclides from the potential repository to the water table at Yucca Mountain. The goals of the code comparison were:

- Evaluate the advantages and disadvantages of the three transport simulators relative to each other
- Identify the conceptual and implementation uncertainties in the three transport simulators
- Evaluate the suitability of the three transport simulators with respect to the Yucca Mountain site.

11.3.3.3 Discussion of Total System Performance Assessment-Site Recommendation Results

A dual continuum approach with steady-state water flow was used for all three transport simulators, using the same dual-permeability grid and steady-state flow field calculated using TOUGH2 V1.4. This approach was considered appropriate because:

- The dual continuum model is capable of capturing the major features of flow and transport in fractured porous rock with a minimum of computational resources (Pan et al. 2001 [DIRS 154916], Section 3).
- Detailed prediction of transport at the discrete fracture level is not necessary for the intended use of the transport models in terms of predicting the breakthrough of radionuclides at the water table.
- A steady-state water flow field is a reasonable approximation of flow beneath the potential repository at Yucca Mountain because the long-term flow regime is approximately at a steady state under ambient condition. For comparison of different transport simulation codes, a steady-state water flow field makes the comparison simpler and allows a focus on the transport aspects.

All three simulators agree well with the analytical solutions for a dual porosity transport system approximated as a dual continuum model in which water flows only in the fractures (CRWMS M&O 2000 [DIRS 141389], Section 6.4.1; CRWMS M&O 2000 [DIRS 141418], Section 6.3.1. T2R3D V1.4 and DCPT V1.0 agree well in predicting breakthrough curves at the water table (CRWMS M&O 2000 [DIRS 141389], Sections 6.4.3 and 6.4.4) for the case of dual-permeability transport systems, which is likely to be the situation within the Yucca Mountain UZ (CRWMS M&O 2000 [DIRS 151940]). T2R3D V1.4 requires more computation time than DCPT V1.0, especially for the site-scale three-dimensional model (CRWMS M&O 2000 [DIRS 141389], Section 6.4.4). FEHM V2.10 can predict either faster or slower breakthrough of radionuclides at the water table than the other transport simulation codes, depending on the specific case (CRWMS M&O 2000 [DIRS 141418], Section 6.3). The

conceptual models and their implementations, as well as advantages and disadvantages, are described in:

- FEHM V2.10
- DCPT V1.0
- T2R3D V1.4.

Differences in the results found for FEHM V2.10 compared with T2R3D V1.4 and DCPT V1.0 are a result of the difference in implementing the diffusion process between fractures and the matrix.

T2R3D V1.4 directly simulates the mass flux between the fracture and matrix continua and uses a finite-difference approximation to calculate the concentration gradient at the fracture-matrix interface. However, after the radionuclides are released into the fractures, the concentration gradient at the fracture-matrix interface is sharper near the front of a plume than farther back in the plume. But the finite-difference approximation of the concentration gradient at the fracture-matrix interface used in T2R3D V1.4 does not distinguish this difference; instead, it uses a fixed node distance and the average concentration in the matrix block to calculate the concentration gradient through the fracture-matrix interface. Such average values account for the average behavior of the fracture-matrix mass exchange, but the small-scale features of the concentration gradient are missed.

In DCPT V1.0, the mass exchange between the fractures and the matrix is simulated as a random switch process between two continua controlled by the particle transfer probabilities. This model is based on analogies between the particle transfer probabilities (either from fracture to matrix or vice versa) and the mass flux through the fracture-matrix interface with respect to the mass amount in each continuum. The approach is similar to the residence time/transfer function method used in the particle tracking algorithm of FEHM V2.10. The difference is that DCPT V1.0 calculates the probability of a particle leaving the current continuum after a given duration, while FEHM V2.10 calculates the probability of how much time a particle will spend in the given cell. Although continuum switching of particles is statistically independent of each particle, the calculation of the particle transfer probabilities requires parameters describing the fracture-matrix system that are based on an approximation of the concentration gradient at the fracture-matrix interface. In this regard, the concentration gradient at the interface will decrease as the particles further diffuse into the matrix with time. DCPT V1.0 does not consider this dynamic feature, and uses the same approximation of the concentration gradient at the interface as T2R3D V1.4 to derive the solution of the particle transfer probability. Thus, it has the same problem as T2R3D V1.4 with a dual-permeability grid. The transport calculation results found for these codes are in good agreement (CRWMS M&O 2000 [DIRS 141389], Sections 6.4.3 and 6.4.4).

FEHM V2.10 uses the residence time/transfer function approach for tracking particles, which calculates the probability of the residence time for a particle in a cell (as well as the probability of which adjacent cell the particle will enter after staying in the current cell). This approach is based on analogies between the cumulative probability distribution function of the residence time and the relative concentration as a function of time for a cell with a given flow path length to account for diffusion and dispersion. In FEHM V2.10, particles can move between nodes only

via advection. A residence time of a particle in a cell is first calculated as the ratio of the fluid mass in the cell over the sum of the outlet mass flow rates from the cell. The residence time is then used as a scaling factor to calculate a new residence time from a dimensionless residence time to account for the diffusion and dispersion processes between nodes in the same continuum. The dimensionless residence time is determined randomly, based on a cumulative probability distribution function of the residence time that is equivalent to a one-dimensional analytical solution of the advection-dispersion equation for the cell with a step-input.

A similar approach is used to determine the modified residence time that accounts for the effects of the fracture-matrix diffusion process for the particles in the fracture continuum. The cumulative probability distribution function used in this step is based on an analytical solution of a dual porosity system (i.e., where there is no water flow through the matrix or the fracture-matrix interface). The reason for this two-step modification approach in FEHM V2.10 is to provide a more rapid calculation method that avoids the discretization errors associated with large matrix grid cells. Note that the residence time from the first modification step (accounting for diffusion and dispersion in the same continuum) is a random value, but it will be used to characterize the fracture-matrix transport system (i.e., the ratio of travel length along a fracture over the pore water velocity in the fracture) in the second modification step (accounting for diffusion between fracture and matrix). This implies that there are different fracture-matrix transport systems for particles entering the same cell.

How the introduction of randomness into the fracture-matrix transport system affects the overall simulation of the transport is not theoretically clear. However, numerical experiments show that this effect may lead FEHM V2.10 to underestimate the residence time added by diffusion into the matrix of particles traveling in the fractures. For particles in the matrix continuum, the same fracture-matrix diffusion process is neglected in FEHM V2.10. In principle, the fracture-matrix diffusion process should increase the residence time for the particles traveling in the fracture continuum and decrease the residence time for the particles traveling in the matrix continuum. This process becomes critical when the pore water velocity in the fracture continuum is higher than that in the matrix continuum. (Velocities in the fractures are typically larger than those in the matrix by several orders of magnitude.)

The uncertainties of these three simulators and their possible effects on transport modeling in terms of the repository performance evaluation are summarized as follows:

- The finite-difference approximation used in T2R3D V1.4 may be subject to discretization errors for cases with large matrix blocks and a small diffusion coefficient, especially in the early periods. Its inability to capture the small-scale concentration gradient at the fracture-matrix interface leads it to underestimate the fracture-matrix diffusion flux in early periods and to overestimate an early breakthrough, provided that the mass is released directly into fractures and the pore water velocity in the fractures is much faster than that in the matrix. Therefore, with a dual continuum grid, it tends to be a conservative predictor (i.e., it predicts early breakthrough).

- DCPT V1.0 shares this problem with T2R3D V1.4 and tends to be a conservative predictor.

- Neglecting the effect of the fracture-matrix diffusion process on the residence time of the particles in the matrix continuum will lead FEHM V2.10 to overestimate the travel time of the particles in the matrix continuum because the pore water velocity in the fracture continuum is usually much greater than that in the matrix continuum. This effect would cause the FEHM V2.10 to become an optimistic predictor (i.e., it would predict late breakthrough).

- Assuming zero pore water velocity in the matrix continuum (dual porosity model) in deriving the second cumulative probability distribution function for particles in fractures will also lead FEHM V2.10 to overestimate the residence time of the particles in the fracture continuum. This effect would also cause FEHM V2.10 to become an optimistic predictor.

- The effects of water flow through the fracture-matrix interface and the randomizing of the parameters on the calculation of the second cumulative probability distribution function for particles in the fracture continuum are not clear. However, numerical experiments show that these effects might cause FEHM V2.10 to have a much shorter delay time for particles in the fracture continuum. In some cases, such an effect can be of greater magnitude than the previous two effects and lead FEHM V2.10 to become a conservative predictor, as was found for three-dimensional site-scale model transport calculations (CRWMS M&O 2000 [DIRS 134732], Section 6.2.5).

- The analysis presented here is based on the existing baseline UZ flow model. Uncertainty in the flow model, particularly with respect to flowing fracture spacing, may affect the results of the transport comparison.

11.3.3.4 Model Developments since the Total System Performance Assessment-Site Recommendation

To solve the problem associated with the large matrix block in a dual-permeability grid, a new method to calculate the fracture-matrix particle transfer probability has been developed to capture the small-scale features of the fracture-matrix diffusion process (Bodvarsson 2001 [DIRS 154669], Attachment 8).

A MINC grid could be used to further split the matrix gridblock into multiple connected subblocks (see Section 11.3.2) and capture the small-scale concentration gradient at the fracture-matrix interface. However, the MINC approach has the following disadvantages:

- It is computationally intensive because it usually requires 5 to 10 times the grid size for the same problem.

- It is conceptually difficult to represent the global water flow in the matrix continuum (i.e., to connect the subblocks between neighboring matrix cells in a MINC grid with global water flow existing in both the fractures and the matrix). It is also practically difficult to validate such representations.

As discussed in Section 11.3.3.3, the approach used in FEHM V2.10 introduces additional uncertainties to the transport model. It yields undesired features in terms of modeling radionuclide transport in a fractured porous medium in which water flow occurs in both fractures and the matrix, as well as through the fracture-matrix interface (i.e., case-dependency as a conservative or optimistic predictor).

Capturing the small-scale features of the concentration gradient at the fracture-matrix interface with the dual continuum model remains a difficult challenge. To solve this problem, a refined model of fracture-matrix mass transfer within the framework of the dual-continuum random walk particle method was developed and incorporated into DCPT V2.0. Unlike DCPT V1.0, the new version defines the fracture-matrix particle transfer probability as a function of the active range. The active range is defined for each individual pulse (a group of particles that enter the domain at the same time) such that the probability of finding a particle of that pulse outside of the range is practically zero. That is, all particles of that pulse will be confined to this spatial range over a time step. An analytical solution is derived for the active range as a function of the particle age (the time since the particle was released into the media) based on diffusion into the matrix. DCPT V2.0 is able to capture the small-scale features of the concentration gradient at the fracture-matrix interface without having to add additional subblocks for the matrix (as with the MINC approach).

Details of Model Development–The fracture-matrix mass transfer is simulated by tracking the particles transferred between the fractures and the matrix, which is governed by the particle transfer probability. Equivalent to the finite-difference approximation for calculation of the mass transfer rate between the fractures and the matrix, the particle transfer probability from Continuum 1 to Continuum 2 can be determined as (Pan et al. 2001 [DIRS 154916], Section 3.5):

$$P_{12} = \frac{F_{12}}{F_{\text{out}} + F_{12}}[1 - \exp(-\Delta t / T_c)] \qquad \text{(Eq. 11.3.3-1)}$$

where F_{12} is a parameter that describes the strength of the water flow from Continuum 1 to Continuum 2 and the diffusion process through the interface between two continua. It is defined as follows ($Q_{12} = q_{\text{fm}} A_{12}$):

$$F_{12} = \max(Q_{12}, 0) + \frac{D_{12} A_{12}}{S_{12}} \qquad \text{(Eq. 11.3.3-2)}$$

where the effective dispersion coefficient at the fracture-matrix interface is $D_{12} = D_{\text{fm}} \theta_{\text{m}}$, the fracture-matrix interface area is A_{12}, the characteristic distance of the fracture-matrix system is S_{12}, and θ_{m} is volumetric water content in the matrix. F_{out} is a parameter that is the sum of the total water outflow from the cell to adjacent cells and the strength of the dispersion process through their interfaces through Continuum 1. The strength of the dispersion process can be calculated like the second term of Equation 11.3.3-2, but for each interface with the adjacent cells in the same continuum instead of the fracture-matrix interface. T_c is the characteristic time of Continuum 1 and is defined as a function of the water body volume in the cell (V_0), the retardation factor (R), F_{12}, and F_{out} (of Continuum 1):

$$T_c = \frac{V_0 \, R}{F_{12} + F_{\text{out}}} \qquad \text{(Eq. 11.3.3-3)}$$

Equation 11.3.3-1 shows that the particle transfer probability is a function of the time step Δt, but not t itself. In other words, the particle transfer process is assumed to be a stationary random process (i.e., the probability density function is independent of time). This is because the concentration gradient at the fracture-matrix interface can be represented as the difference of the average concentrations in the fractures and the matrix divided by the node spacing (a fixed characteristic distance). In terms of particle walking, this is equivalent to assuming that the particles in a given pulse will have the same range to walk within the matrix over time. However, this is not a proper assumption at early times when a plume has just entered the domain. Physically, a pulse only has limited influence at early times; significant time will be needed for the pulse to have its full range of influence, especially for cases with larger fracture spacing. As depicted in Figure 11.3.3-1 (lower part), the probability density function of the particle becomes wider and flatter with increasing time (t_3 is greater than t_2 and t_2 is greater than t_1). To catch this dynamic feature, the particle transfer probability defined in Equation 11.3.3-1 with Equation 11.3.3-2 and Equation 11.3.3-3 has to be modified by introducing a new concept: the active range. The active range is defined for each pulse such that the probability of finding a particle of the pulse outside of the range is practically zero; that is, all particles are confined to this spatial range over a time step. This leads to the replacement of the characteristic distance S_{12} and the water body volume V_0 in Equations 11.3.3-2 and 11.3.3-3 with the effective distance $S_{12}(t)$ and the effective volume $V_0(t)$, both of which are related to the active range. For parallel fracture systems, they can be defined as:

$$S_{12}(t) = S_{12} \frac{B^*(t)}{B} \qquad \text{(Eq. 11.3.3-4)}$$

and

$$V_0(t) = V_0 \frac{B^*(t)}{B} \qquad \text{(Eq. 11.3.3-5)}$$

where $B^*(t)$ is the active range within the matrix at time t. B is defined such that $2B$ is the fracture spacing. The effective volume for the fractures is assumed to be constant because the fracture aperture is usually so small that the active range can quickly reach its full capacity.

To get a scheme for estimating the active range $B^*(t)$, consider the transport in a system of parallel-plate fractures separated by porous rock (Figure 11.3.3-2). By the superposition principle, only the one-dimensional governing equation (in fracture-matrix dimension) is needed to derive the active range (temporarily ignoring advection):

$$\frac{\partial}{\partial t}[RC] = \frac{\partial}{\partial s}\left(D_{12} \frac{\partial C}{\partial s} \right) \qquad \text{(Eq. 11.3.3-6)}$$

where s is the distance into the matrix. With sources (and ignoring the fracture aperture $2b$ because b is much smaller than B):

$$C(s,0) = M_s\ \delta(s - 2iB) \qquad \text{(Eq. 11.3.3-7)}$$

where $\delta(s - 2iB)$ is a Dirac delta function whose value is zero everywhere except for an infinite value at point zero, which makes initial concentrations nonzero at the fractures only. The term M_s is a scaling factor that makes the concentration, C, in the final solution become a dimensionless variable within a range between 0 and 1. The i is the index of the fracture (from 0 to infinite). The solution to Equation 11.3.3-6, subject to Equation 11.3.3-7, can be expressed as (for $s \geq 0$ and using symmetry):

$$C(s,t) = \frac{2M_s}{(4\pi D_{12}\, t/R)^{1/2}} \sum_{i=0}^{\infty} \exp\left(-\frac{(s - 2iB)^2}{4D_{12}\, t/R}\right) \qquad \text{(Eq. 11.3.3-8)}$$

For very small time,

$$C(s,t) \approx \frac{2M_s}{(4\pi D_{12}\, t/R)^{1/2}} \exp\left(-\frac{s^2}{4D_{12}\, t/R}\right) \qquad \text{(Eq. 11.3.3-9)}$$

The concentration in Equation 11.3.3-9 can be interpreted as the probability of finding a particle (initially at $s = 0$) at location s and time t. Therefore, the probability a particle will be located in the active range $[0, B^*]$ is:

$$P(0 \leq s \leq B^*) = \text{erf}\left(\frac{B^*}{\sqrt{4D_{12}\, t/R}}\right) \qquad \text{(Eq. 11.3.3-10)}$$

Equation 11.3.3-10 implies that B^* should be proportional to the square root of t. By definition, a B^* should be selected such that $P(0 \leq s \leq B^*)$ is close to 1. An adequate active range for short time can be expressed as (Bodvarsson 2001 [DIRS 154669], Attachment 8, p. 140):

$$B^*(t) = \min\left(4\ \sqrt{4D_{12}\, t/R},\ B\right) \qquad \text{(Eq. 11.3.3-11)}$$

The corresponding $P(0 \leq s \leq B^*)$ is about 1×10^{-7} and B is half of the fracture spacing, which is the maximum active range by definition.

For a longer time, B^* approaches B, and the other terms in Equation 11.3.3-8 cannot be ignored. There is no simple solution like Equation 11.3.3-9 for that case. However, because the purpose is to get a proper $B^*(t)$, it can be assumed that the relative effects of the other terms in Equation 11.3.3-8 on the active range are equal to their relative contributions to concentration. In other words, the active range can be modified as follows:

$$B^*(t) = \min\left(4\ \sqrt{4D_{12}\, t/R}\, W(t),\ B\right) \qquad \text{(Eq. 11.3.3-12)}$$

The weighting function $W(t)$ is obtained as the ratio of the two-term solution over the one-term solution as defined in Equation 11.3.3-8 at a given B^*, and can be approximated as:

$$W(t) \approx 1 + \frac{1}{1 + \frac{B(B - B^*)}{D_{12}\, t/R}} \qquad \text{(Eq. 11.3.3-13)}$$

The reason for taking only two terms in calculating the weighting function is because further terms are insignificant for typical values of B.

A similar approach can be used to incorporate the effects of fracture-matrix water flow on the active range. In a dual continuum model, the total water flow rate through the interface ($s = 0$) and at $s = B$ (where Q is zero) is known. One can take a linear interpolation and get the final scheme for the active range as:

$$B^*(t) = \min\left(4\sqrt{4\, D_{12}\, t/R}\, W(t) + \frac{Q_{12}\, t}{A_{12}} \left(1 - \frac{B^*}{B} \right), B \right) \qquad \text{(Eq. 11.3.3-14)}$$

Note that the time, t, used in the above equations is for a single pulse. Multiple initial values of time (i.e., $t = 0$) have to be defined for cases with multiple pulses. In other words, for the same pair of fracture and matrix cells at the same simulation time, the particle transfer probability may be different for different individual particles. The implementation in DCPT V2.0 tracks the age of each particle, which is defined as the time elapsed since the particle was released into the domain. Thus, the particle transfer probability is a function of the age of the particle.

The above derivation of the active range is valid only for particles initially released in the fractures. The active ranges for particles released into the matrix would be different, and depend on how far from the interface they are initially located, which is not known in practice. It is assumed that all particles initially released into the matrix are uniformly distributed within the matrix, and thus the active range will always be B. A parameter called "initial status" is assigned to each particle to distinguished which continuum it is released into initially (at $t_p = 0$).

11.3.3.5 Results of Analysis

Verification with Analytical Solutions (Parallel Fractures)–An analytical solution for solute transport in fractured porous media with parallel fractures (Figure 11.3.3-2) was derived by Sudicky and Frind (1982 [DIRS 105043]). This solution is based on the assumption that solute transport between fractures and the matrix occurs through matrix diffusion in the horizontal direction only, and that matrix advection and diffusion in the vertical direction can be ignored. Table 11.3.3-1 shows the relevant parameters for the two test cases. In particular, the two different fracture spacings of 1 m and 10 m were used for Case 1 and 2, respectively.

Figure 11.3.3-3 shows the results for Case 1. Breakthrough curves produced by DCPT V1.0 and DCPT V2.0 agree well with the analytical solution. DCPT V1.0 slightly overestimates the concentration at early times for the smaller fracture spacing (1 m) case. However, DCPT V1.0 seriously overestimates the breakthrough at early times for Case 2, which has a larger fracture

spacing (10 m) (Figure 11.3.3-4). In particular, DCPT V1.0 estimates that more than 60 percent of solutes would have leached out of the system in about 0.1 yr if a plume had been injected into the top of the column. This error obviously is too large to be acceptable for predicting radionuclide transport at Yucca Mountain. Note that DCPT V1.0 agrees well with the analytical solution at much later times (i.e., after about 100,000 years), which clearly indicates that the finite-difference approximation is accurate only for later times. DCPT V2.0 agrees with the analytical solution for both cases because it catches the dynamic nature of the fracture-matrix mass transfer process (Figures 11.3.3-3 and 11.3.3-4). The dynamic concentration gradient between fractures and matrix depends on fracture spacing. At early times (up to 5,000 years), the analytical solutions for Case 1 and Case 2 shown in Figure 11.3.3-5 are almost identical. Therefore, the fracture spacing has little effect on the breakthrough during early periods of time.

Results for Transport in the Unsaturated Zone–UZ transport calculations for the site-scale model with the present-day mean infiltration map and perched water table model #1 (CRWMS M&O 2000 [DIRS 151940], Section 3.7) were used to assess the impact of different models of fracture-matrix mass transfer on overall simulated radionuclide transport behavior. Figure 11.3.3-6 shows the cumulative breakthrough curves of two radionuclides (technetium and neptunium) at the water table, as predicted by DCPT V1.0 and DCPT V2.0, respectively. DCPT V1.0 overestimates the early breakthrough for both radionuclides compared to DCPT V2.0. Technetium breaks through about 30 times faster than neptunium because it is not retarded by adsorption.

11.3.3.6 Abstraction for Total System Performance Assessment

DCPT V2.0 may be used for TSPA UZ transport calculations as an alternative particle tracking code to FEHM V2.10. DCPT has been modified to enable its use with GoldSim, the TSPA code. All connections between GoldSim V6.04.007 and DCPT V2.0 are analogous to those between GoldSim V6.04.007 and FEHM V2.10 in the TSPA-SR model (CRWMS M&O 2000 [DIRS 143665]). However, DCPT V2.0 was not used for SSPA Volume 2 calculations (McNeish 2001 [DIRS 155023]) because a version of GoldSim linked with DCPT V2.0 was not available when the TSPA calculations were performed.

11.3.3.7 Multiple Lines of Evidence

Because this section deals solely with the comparison of different software codes used in predicting radionuclide transport, multiple lines of evidence are not directly applicable.

11.3.3.8 Summary of Remaining Uncertainties

Several uncertainties concerning the suitability of the different codes for TSPA transport calculations are discussed below. Also, related uncertainties are identified in Section 11.3.2.8. The key uncertainty issues are summarized in Table 11.3.3-2.

Uncertainties Caused by Grid Discretization Effects–The current numerical model as described in Section 11.3.3.3 uses coarse grids (up to 60 m vertically and up to 200 m laterally) because of limitations on computational resources. Although numerical mixing/dispersion is not a serious problem for transport simulation in the Yucca Mountain UZ (as shown in numerical experiments reported in *Analysis Comparing Advective-Dispersive Transport Solution to*

Particle Tracking [CRWMS M&O 2000 [DIRS 141389]), any transport calculation method using a coarse grid may lack the resolution to capture the spatial variability of the flow field and transport properties. With respect to the flow solution, a coarse grid will cause TOUGH2 V1.4 to underestimate capillary effects where critical layers are thin. This will result in uncertainties in the flow-field and transport pathways for radionuclides. In a complex and heterogeneous media such as the UZ, the effects on radionuclide travel time could be very large. It is possible to reduce the uncertainty in predictions by developing numerical models of flow and transport with higher spatial resolution. Calculation of detailed flow fields for the UZ may require a supercomputer to run the TOUGH2 V1.4 code with parallel computing techniques. Considerable effort is also required to develop particle trackers that can efficiently simulate transport with large grids.

The uncertainties resulting from the grid discretization effect of matrix blocks with respect to diffusion through the fracture-matrix interface are discussed in Section 11.3.2.

Uncertainties Resulting from Limited Theoretical and Experimental Results to Support Dual Continuum Transport Calculation Methods in Fractured Porous Media–No analytical solution is currently available for transport in unsaturated, fractured porous media with global water flow occurring in both fracture and matrix continua. As a result, the transport code has been validated against analytical solutions for transport in fractured porous media assuming that water flow occurs in the fractures only (Section 11.3.3.5). Applicable field or experimental data are limited. Well-controlled experiments of transport in unsaturated, fractured porous rock would provide opportunities to verify the numerical model and further explore the nature of the fracture-matrix mass transfer process. An example of a well-controlled experiment would be a laboratory experiment of tracer with a 1-m^3 block of rock containing fractures. This type of experiment is important for building an accurate numerical model because many aspects of the fracture-matrix interaction process are still poorly understood. Many numerical experiments show that the fracture-matrix mass transfer is a critical process that controls how fast radionuclides migrate to the water table. An example of one such experiment is presented in *Analysis Comparing Advective-Dispersive Transport Solution to Particle Tracking* (CRWMS M&O 2000 [DIRS 141389], Section 6.4.3).

11.3.3.9 Summary and Conclusions

For transport in fractured porous media with water flow occurring in both continua, T2R3D V1.4 (with a dual continuum grid) or DCPT V1.0 may be a conservative predictor of radionuclide breakthrough at the Yucca Mountain water table, especially at early times. By using a residence time/transfer function approach based on analytical solutions for a simpler system, the FEHM V2.10 particle tracking algorithm does not have the discretization problem associated with large matrix blocks in a dual continuum grid. But it can be a conservative or optimistic predictor compared with T2R3D V1 or DCPT V1.0, depending on the particular case or portion of the breakthrough because of the uncertainties introduced in the implementing the fracture-matrix diffusion processes. In site-scale transport simulations performed so far (CRWMS M&O 2000 [DIRS 134732], Section 6.2.5), FEHM V2.10 is found to be generally conservative relative to DCPT V1.0. However, the implementation of the fracture-matrix diffusion processes for problems with water flow in both continua is complicated. By using the new method for calculating fracture-matrix particle transfer probability, DCPT V2.0 does not

have the problems associated with the larger matrix block in a dual-permeability grid that T2R3D V1.4 and DCPT V1.0 do. It also does not have the uncertainties of FEHM V2.10.

Of the codes evaluated, DCPT V2.0 is the most suitable simulator for such a system, considering numerical accuracy, efficiency issues, and the current understanding of transport processes in fractured porous media. T2R3D V1.4 with a MINC grid can be an alternative, but with the associated cost of poorer numerical efficiency and more complicated validation requirements.

11.3.4 Effects of Change in Potential Repository Footprint on Three-Dimensional Transport Simulation

This section summarizes the results of modeling three-dimensional radionuclide transport (TOUGH2 V1.4) with the new southern extended flow model domain. The extended domain, additional hydrogeologic settings, and flow modeling results are provided in Section 3.3.4. The new UZ transport model examines the extended potential repository design for a lower-temperature operating mode (BSC 2001 [DIRS 154548]) with the southern and northern blocks (Figure 3.3.4-7). The objective of this section is to investigate the effects of the lower-temperature operating mode on radionuclide transport under ambient flow conditions. The simulations were conducted using a conservative radionuclide and a reactive radionuclide released from the extended potential repository and transported to the water table.

11.3.4.1 Introduction

The *Unsaturated Zone Flow and Transport Model Process Model Report* (CRWMS M&O 2000 [DIRS 151940]) presents a summary of models used to simulate flow and transport processes in the Yucca Mountain UZ in support of the TSPA-SR (CRWMS M&O 2000 [DIRS 153246]). The evaluation of radionuclide transport from the potential repository horizon to the groundwater in the saturated zone is critical to assessing the performance of the potential repository. The transport modeling efforts use the flow processes of the UZ flow model as a framework for the transport of aqueous and colloidal radionuclide species. Modeled mechanisms include transport inside and between fracture and matrix continua by advective and/or diffusive processes, as well as sorption in the matrix. Results of previous three-dimensional modeling (BSC 2001 [DIRS 144331]; CRWMS M&O 2000 [DIRS 122797]) were used to identify major transport mechanisms, breakthrough times through different hydrogeologic units, effects of major hydrogeologic features (faults and perched water), and transport characteristics (sorption and matrix diffusion).

As documented in the *Unsaturated Zone Flow and Transport Model Process Model Report* (CRWMS M&O 2000 [DIRS 151940]), the transport model evaluates a suite of factors that control potential radionuclide transport to determine their effects on radionuclide breakthrough times and concentrations at the groundwater table (CRWMS M&O 2000 [DIRS 151940], Section 3.11.1.1). More than 70 three-dimensional radionuclide transport simulations (CRWMS M&O 2000 [DIRS 151940], Section 3.11; CRWMS M&O 2000 [DIRS 122797], Section 6.7; CRWMS M&O 2000 [DIRS 144331], Sections 6.10 to 6.17) were conducted to obtain insight into the various impacts of infiltration rates, perched water conceptual models, faults, retardation, matrix diffusion, and colloidal effects on tracer and radionuclide migration through the UZ.

Modeling uncertainties are attributed primarily to the large variability in the flow and transport properties over the spatial and temporal scales that have been identified during site characterization and modeling studies. Other uncertainties are model parameters for sorption (K_d) coefficients in different tuffs and matrix diffusion coefficients.

11.3.4.2 Goals of the Model

The fundamental goals of the UZ transport model are to:

- Integrate the available geochemical and isotopic data from the UZ system into a single comprehensive model
- Develop an understanding of tracer and radionuclide transport mechanisms and identify controlling processes and factors
- Estimate groundwater travel and radionuclide transport times from the potential repository to the water table and breakthrough curves and collection areas at the water table under ambient hydrologic, thermal, and geochemical conditions, as well as predict system response to future climate conditions.

11.3.4.3 Discussion of Total System Performance Assessment-Site Recommendation Results

More than 40 three-dimensional modeling studies on groundwater travel times and tracer or radionuclide transport using more than 20 three-dimensional flow fields are documented in *UZ Flow Models and Submodels* (CRWMS M&O 2000 [DIRS 122797], Section 6.7). Simulation results for conservative and reactive tracers/radionuclides were used to obtain insights into groundwater travel times and radionuclide transport from the repository to the water table.

Another 30 three-dimensional radionuclide transport simulations were conducted in support of *Radionuclide Transport Models under Ambient Conditions* (CRWMS M&O 2000 [DIRS 144331], Sections 6.10 through 6.17). Technetium-99, neptunium-237, and plutonium-239 were investigated, as well as the important members in the decay chains of neptunium-237 and plutonium-239. Transport simulations of four colloids of different sizes were also documented (CRWMS M&O 2000 [DIRS 144331], Sections 6.16 to 6.17). The report examined the influence of three climatic scenarios, as well as perched water models and fault treatment, on radionuclide transport.

The model results present a quantitative evaluation of the effects of different perched water conceptual models, faults, infiltration rates, sorption, and matrix diffusion on radionuclide transport processes. In particular, the simulations indicate that faults and fractures are the main pathway of transport because they channel flow along their orientation and limit lateral transport across their orientation. In the simulations, diffusion from the fractures into the matrix is the main mechanism retarding the transport of nonsorbing radionuclides.

Figure 11.3.4-1 correlates average infiltration rates and tracer transport times at 50 percent mass breakthrough at the water table from the 42 three-dimensional tracer transport simulations,

including 9 climatic scenarios and different perched water conceptual models. The correlations presented in Figure 11.3.4-1 indicate that:

- Radionuclide transport times decrease with increasing average surface infiltration (net water recharge) rate over the model domain. When an average infiltration rate increases from 5 to 35 mm/yr, average groundwater travel (50 percent breakthrough) times decrease by one to two orders of magnitude.

- Nonsorbing radionuclides (e.g., neptunium-237) migrate one to two orders of magnitude faster than sorbing radionuclides when traveling from the repository to the water table under the same infiltration conditions.

- Perched water conceptual models may also have a large effect on groundwater travel and transport times, but the overall impact on tracer breakthrough times at the water table is small compared to the effects of infiltration and sorption.

11.3.4.4 Model Development since Total System Performance Assessment-Site Recommendation

A new three-dimensional UZ flow model (see Section 3.3.4) has been developed to evaluate the performance of a potential expanded repository design (BSC 2001 [DIRS 154548]). The new model domain is enlarged to include a southern expansion area (i.e., a potential second southern repository block) (Figure 3.3.4-7). This extended UZ flow model was used to conduct transport studies of technetium-99 and neptunium-237 (Bodvarsson 2001 [DIRS 154669], Attachment 13, pp. 26 to 27).

11.3.4.5 Discussion and Comparison of New Flow Fields to Previous Results

This section summarizes results from the simulations of tracer and radionuclide transport using the new three-dimensional flow field for an extended southern model domain. These simulations represent transport processes for radionuclides from the potential repository to the water table given the current perched water conceptual model, mean infiltration scenarios, and steady-state ambient flow conditions described in Section 3.3.4.5.2.

In the modeling studies, a tracer or radionuclide is treated as a conservative (nonsorbing) or reactive (sorbing) component transported through the UZ. In both cases, the hydrodynamic dispersion effect through the fracture-matrix system is ignored. A constant molecular diffusion coefficient of 3.2×10^{-11} m^2/s is used for matrix diffusion for the conservative component technetium-99, and a coefficient of 1.6×10^{-10} m^2/s is used for the reactive component of neptunium-237 (CRWMS M&O 2001 [DIRS 154024], Section 6.6.3). In the case of a reactive (sorbing) tracer several K_d values, ranging from 1 to 3 ml/g, are selected to approximate those for neptunium-237 transport (CRWMS M&O 2001 [DIRS 154024], Table 2a). For a conservative tracer, K_d is set to zero. All transport simulations were run to 1 million years using a steady-state flow field generated by the new three-dimensional flow model and constant source concentration conditions at the repository fracture nodes. A total of six simulations were conducted for technetium and neptunium (neglecting radioactive decay) released from the entire potential

repository, including the southern extension and the northern potential repository model domain used in the TSPA-SR (CRWMS M&O 2000 [DIRS 148384], Section 6.3.1.3).

Tracer transport times from the potential repository to the water table can be analyzed using a cumulative or fractional breakthrough curve (Figure 11.3.4-2). The fractional mass breakthrough in these figures is defined as the cumulative mass of tracers or radionuclides (normalized by the total initial mass of the component at the potential repository blocks) predicted to arrive at the water table over the entire bottom model boundary as a function of time. In Figure 11.3.4-2, solid- or dashed-line curves represent simulation results for conservative (technetium) and reactive (neptunium) tracers released from the fractured repository blocks in the new model grid and the TSPA grid. The symbols represent tracer results released from the southern and northern potential repository blocks using the new grid.

Figure 11.3.4-2 shows release scenarios grouped into sorbing and nonsorbing. The grid refinement in the new transport model produces longer or improved tracer transport times when compared with the TSPA results shown in Figure 11.3.4-2. Sorbing and nonsorbing tracer releases from the southern potential repository block are significantly longer because the southern block is situated over an area with lower average infiltration rates and a longer travel distance to the water table. Overall, the simulations of tracer transport in the extended potential repository domain give similar, but somewhat slower, breakthrough times than the TSPA-SR flow fields shown in Figure 11.3.4-2.

11.3.4.6 Field-Scale Model Validation Studies at Busted Butte

UZ tracer tests are being conducted at Busted Butte to determine solute and colloid movement through tuff horizons that underlie the potential repository location at Yucca Mountain. The Busted Butte test block consists of three stratigraphic units. Two of these are part of the Topopah Spring Tuff, which is subdivided into an upper moderately welded vitric tuff (Tptpv2) and a lower vitric and nonwelded tuff (Tptpv1); the third is the underlying vitric and nonwelded tuff of the Calico Hills Formation (Tac). The boundary between the Topopah Spring welded hydrostratigraphic unit (TSw) and the Calico Hills nonwelded vitric hydrostratigraphic unit in the UZ flow and transport model is defined as being between units Tptpv2 and Tptpv1 (CRWMS M&O 2000 [DIRS 151940], Table 3.2-2).

Test Phase 1A was designed to provide information regarding flow and transport in the Calico Hills hydrogeologic unit and an understanding of the influence of permeability contrasts on fluid movement. Phase 1B was designed to provide data on fracture flow and transport in the welded Topopah Spring hydrogeologic unit (CRWMS M&O 2001 [DIRS 154024]). Phase 2 (Dixon 2001 [DIRS 155048], p.1) was designed to test the larger-scale behavior of the two units, including:

- Validation of scaling assumptions at various scales
- Validation of laboratory determined sorption for field-scale tests
- Colloid migration behavior.

In October 2000, Phase 2 injection was terminated. Overcore samples were collected and a mineback is currently in progress (Dixon 2001 [DIRS 155048], p. 3).

Detailed numerical models have been developed for both Phase 1B and Phase 2. Computational grids have been generated and updated based on all available physical data. The increasing grid accuracy and complexity is used to address the question of how the quantity of site-specific data improves the ability of the model to predict flow and transport (Dixon 2001 [DIRS 155048]).

11.3.4.6.1 Phase 2 Test Results: Comparison of Model with Field Data

All modeling is being done using FEHM V2.10. The current grid has almost 2 million elements and reflects the most current information about fault and stratigraphic contacts in the test block. This grid accurately represents the injection and collection boreholes. Grid resolution ranges from 0.0625 m near features to 1 m. Hydrogeologic parameters are taken from measurements at Busted Butte, as available. These include porosity, hydraulic conductivity, van Genuchten parameters for relative permeability, and sorption coefficients. Simulations assume homogeneity within units.

Initial simulation results show very good agreement with bromide breakthrough data (Dixon 2001 [DIRS 155048], p. 9, Figure 5). The actual injection rate appears to be 10 to 20 percent lower than the original rate. The observation that the quality of fit uniformly decreases with change in injection rate suggests the possibility that the laboratory-measured hydrogeologic parameters do not accurately reflect the field behavior. For example, if reported laboratory conductivities are lower than the effective field conductivities, the model would underpredict breakthrough. These issues are currently being tested.

Sensitivity analyses of the various parameters have been run to attempt to best fit the experimental tracer data. In general, simulations tend to underpredict concentration at early times and overpredict at late times.

11.3.4.6.2 Phase 2 Test Results: Validation of Scaling Assumptions

In Phase 2, collection holes were placed at different distances from the injection holes to assess the influence of travel distance. Differing travel distances also provide a range of scales for studying transport, from tens of centimeters to meters.

The effect of travel distance on tracer transport in the hydrogeologic Calico Hills unit is demonstrated by tracer breakthrough (Dixon 2001 [DIRS 155048], pp. 10 to 11). Breakthrough times at the different distances scale approximately linearly with travel distance. The observed linearly increasing travel times suggest that at the scale of tens to hundreds of centimeters, the hydrogeologic response of the unit is relatively homogeneous.

The major uncertainty in capturing the tracer response in the Phase 2 simulations seems to be the representativeness of using the hydraulic properties obtained from small core samples to model field-scale flow and transport. The qualitatively good fit of the breakthrough curves for each borehole suggests that heterogeneity plays a less significant role. The problem is how to scale up the core data to represent the processes occurring at the Busted Butte test site or to collect data at the appropriate scale for site-scale models. Currently, an inverse modeling approach is being applied to best fit the test data to determine if it is possible to use inverse modeling results to test current approaches to upscaling (Dixon 2001 [DIRS 155048], p. 11).

11.3.4.6.3 Phase 2 Test Results: Effects of Sorption

The influence of sorption/retardation has been analyzed by comparing breakthrough curves for bromide versus lithium at various boreholes. This analysis indicates that, as expected, lithium breakthrough is retarded with respect to bromide (Dixon 2001 [DIRS 155048], p. 12). Laboratory sorption measurements calculate lithium K_d values between 0.4 and 1.1 ml. All other reactive tracers used have significantly higher K_d values and were not expected to break through at any of the boreholes within the injection time frame. Analyses of rock samples from overcoring and mineback, initiated in December 2000, should provide travel distances and concentrations for other reactive tracers. The computational model predicts nickel (K_d of 48 in Tptpv1, 430 in Tptpv2) will have moved only 6.25 cm from the upper injection holes over the period of the Phase 2 experiment. Model predictions will be compared to rock analyses as they become available.

11.3.4.6.4 Phase 2 Test Results: Colloid Transport

Field experiments at Busted Butte included the injection of latex microspheres to examine colloid transport in the field (Dixon 2001 [DIRS 155048], p. 12). Analysis of the collection pads for the microspheres was inconclusive as to whether colloids were being transported in the experiment. As a result, a series of laboratory-based column experiments was used to determine the likelihood of colloid transport at Busted Butte.

Core samples 5 cm in length from all three stratigraphic units were used in the experiments (Dixon 2001 [DIRS 155048], p. 13). The initial experiments used synthetic Busted Butte water with the field concentrations of LiBr and latex microspheres (190-nm and 55-nm diameter). Results showed that the breakthrough of microspheres was affected by ionic strength. In general, as the ionic strength of a solution increases, the double layer around particulates decreases, which can lead to coagulation and flocculation of particulates in solution. The synthetic Busted Butte water (0.01 M ionic strength) has a higher divalent cation concentration than observed in the J-13 well water or local groundwater, which affects the stability of the microspheres. In addition, there was not a supply of lower ionic strength water mixing with the tracer solution in the Busted Butte experiment. The combination of these two factors is one of the reasons breakthrough of the microspheres was not observed in the field experiment. Samples collected during overcoring of injection locations will be examined to qualitatively determine if any migration of the microspheres occurred away from the injection location.

Experiments were conducted to detect breakthrough of the microspheres through saturated Tac core samples as a function of ionic strength (Dixon 2001 [DIRS 155048], p. 13, Figure 8). The breakthrough curve at 0.01 M LiBr shows that the peak of the microsphere breakthrough occurs after tracer injection is stopped and 1.5 pore volume of water has been put through the column. This is not observed in the breakthrough curves of the other two experiments (0 and 0.0005 M LiBr), in which the peak of the microsphere breakthrough occurs when the injection is switched to a water flush. The late breakthrough for the 0.01 M solution suggests that colloids are aggregated due to the high ionic strength during the injection and are not transported. When the column is switched to the water flush, the ionic strength is reduced and some of the aggregated colloids are able to break apart and be transported through the column.

This set of experimental results illustrates two points. First, under saturated conditions, colloid transport is possible under steady-state conditions. This serves as an upper bound for modeling unsaturated colloid transport. The results indicate that some of the colloids are retained, but a significant percentage is transported. Second, localized chemistry is an important factor for colloid transport.

The effects of water saturation, pH changes, and divalent cation concentrations on the stability and transport of colloids remain an area of uncertainty in the modeling.

11.3.4.7 Abstraction for Total System Performance Assessment

The work reported in this section is devoted to evaluating process model sensitivities and uncertainties. Consequently, simulation results from this study are not used to support any abstraction model that directly supports the TSPA. The results found here indicate that the process model and associated model abstractions used to represent potential repository footprint effects on three-dimensional transport effects are representative (or conservative) with respect to the TSPA-SR baseline (CRWMS M&O 2000 [DIRS 153246]). Therefore, any future changes in model abstractions for this component will not diminish the performance represented in the total system performance baseline.

11.3.4.8 Multiple Lines of Evidence

This section presents information from ongoing and past analogue studies that provide indications of the rate of transport in unsaturated media over decades and millennia and the efficacy of sorbing minerals in retarding radionuclides.

11.3.4.8.1 Peña Blanca

Preliminary results from fiscal year 2000 uranium isotope studies at the Nopal I uranium deposit at Peña Blanca, Mexico, appear to indicate low actinide mobility in unsaturated siliceous tuffs under semiarid, oxidizing conditions. Uranium-thorium age data from fracture-filling minerals indicate that the primary transport of uranium away from the Nopal I deposit along fractures occurred more than 300,000 years ago (CRWMS M&O 2000 [DIRS 141407], Section 6.5.2.1.4.2). The radium-226/thorium-230 activity ratios indicate redistribution of radium within the last 5,000 years as a result of secondary fluid events. Therefore, the data demonstrate stability over 100,000-year time scales for uranium (uranium-235 and uranium-238), thorium, and protactinium in fracture-filling materials. In an analogous sense, this stability should extend to transuranics and the rare earth elements. The high mobility of radium can be considered analogous to transport of strontium and cesium because of a similar ionic radius. Because of similarities between Peña Blanca and Yucca Mountain in hydrogeologic setting, mineralogy, and term, the tuffs at Yucca Mountain should have similar retentive properties to impede oxidized uranium mobility.

In 2000, water samples were collected from the adit, a small borehole, and a neighboring well at Peña Blanca. Stable isotope data and semi-quantitative uranium concentration data were obtained for these samples.

Table 11.3.4-1 indicates that the stable isotope data for samples AS-5 and AS-6 (from a drill hole into a perched water horizon and from a well) have significantly lower values than the other samples. They fall on the global meteoric water line (Craig 1961 [DIRS 104753]) and probably represent the average composition for the precipitation at the site. The other samples were all collected from the adit. The isotopic signature of sample AS-1 lies on the global meteoric water line, but probably does not represent a rainwater sample, since it is relatively high for meteoric water at this latitude. The other three samples all fall significantly to the left of the global meteoric water line and may represent atmospheric water vapor that has diffused into the adit and condensed in the cooler, underground environment, followed by some period of evaporation in the collection bottles. The uranium data shown in Table 11.3.4-1 indicate a rapid decrease in uranium concentration with distance from the ore body, which is closest to sample AS-1.

Pickett and Murphy (1999 [DIRS 110009]) obtained uranium and thorium measurements for waters near the Peña Blanca uranium deposit. They analyzed three types of samples: perched water trapped in an old borehole at the +10 level (the same location as AS-5), seep water from an old adit about 8 m below the surface, and groundwater in the carbonate aquifer from a sample collection point about 1.3 km southeast of the deposit. Uranium concentrations range from 7.1×10^{-10} mol/L (0.13 dpm/L) for groundwater to a range of 8.3×10^{-10} to 37.2×10^{-10} mol/L (0.15 to 0.66 dpm/L) for seep water and a range of 2.0×10^{-8} to 2.4×10^{-8} mol/L (3.6 to 4.3 dpm/L) for perched water. Thorium concentrations range from 6.1×10^{-13} mol/L (3.5×10^{-5} dpm/L) for groundwater to a range of 1.9×10^{-12} to 5.3×10^{-12} mol/L (1.1×10^{-4} to 3.0×10^{-4} dpm/L) for seep water and a range of 6.7×10^{-10} to 11.6×10^{-10} mol/L (0.038 to 0.066 dpm/L) for perched water. Pickett and Murphy (1999 [DIRS 110009]) interpreted the results in terms of mineral solubility. They found that uranium in the perched water is close to the solubility for haiweeite (a calcium uranyl silicate mineral), whereas in other waters it is undersaturated with respect to uranium minerals. However, in all the waters thorium is supersaturated with respect to thorianite, and is likely present in colloidal form (less than 0.2 μm). The occurrence of undersaturation for uranium and supersaturation for thorium indicates that radionuclide transport in the UZ may be controlled by kinetic factors, such as rock dissolution and colloid formation, which complicate interpretations based on thermodynamic (solubility) considerations.

The uranium-series modeling described in Ku et al. (1992 [DIRS 109939]) provides a means to characterize the kinetically controlled radionuclide transport at Peña Blanca. Figure 11.3.4-3a plots uranium-234/uranium-238 versus 1/uranium-238 from the Pickett and Murphy (1999 [DIRS 110009]) data. The positive linear correlation shown by the plot is expected for samples from the UZ. The one sample from the carbonate aquifer in the saturated zone shows a much lower uranium-234/uranium-238 concentration, perhaps due to a prolonged interaction with old calcites in the aquifer, which allows uranium exchange between rock and solution and masks the alpha recoil-induced uranium-234 enrichment in the water. Using this model, the uranium-234 alpha-recoil rate into fluids is estimated to be 9 dpm/L/yr at Peña Blanca, versus dissolution rates of 8.3 dpm/L/yr for uranium-238 and uranium-234. The model also allows determination of fluid transit time in the UZ. As shown in Figure 11.3.4-3b, uranium-238 increases linearly with increasing transit time, while uranium-234/uranium-238 decreases. The transit time for the seep water infiltrated into the Level +00 adit 8 m below surface is estimated to be 6 to 29 days, and that for the perched water at 10.7-m depth in an old borehole is 0.4 to 0.5 years. The large values of transit time for the perched water may reflect the long residence time of water in the borehole.

It should be noted that although the water transit time in the UZ is short, significant dissolution of uranium from fractured rocks does occur in a low-water flux, high-uranium concentration setting near the Nopal I uranium deposit. This can be seen from the uranium data in Table 11.3.4-1, which indicates a rapid decrease in uranium concentration with distance from the ore body, which is closest to sample AS-1.

11.3.4.8.2 Little Movement of Metals in the Unsaturated Zone–Akrotiri, Santorini

The Akrotiri archeological site on the island of Santorini, Greece, provided conditions for the study of trace element transport in a setting similar to Yucca Mountain in its silicic volcanic rocks, dry climate, and oxidizing, hydrologically unsaturated subsurface conditions (Murphy et al. 1998 [DIRS 126105]). About 3,600 years ago, in 1645 B.C., the Minoan eruption buried settlements under 30 m of volcanic sediment (Murphy et al. 1998 [DIRS 126105]). Evidence for a plume of copper, tin, and lead was indicated through selective leaching of packed earth and bedrock samples collected directly beneath the site, where bronze and lead artifacts were excavated from a depth of 1.5 to 2 m. Field data indicated that little of the bronze material had been transported away from its primary location. Original textures and patterns were preserved in fine detail, even on artifacts that were apparently crushed by compacting volcanic ash. The total amount of copper predicted to have been removed from the artifacts is approximately 38 cm^3, roughly three orders of magnitude smaller than the volume of the artifacts (Murphy et al. 1998 [DIRS 126105], p. 273). Neither copper nor lead was detected below a depth of 45 cm from their sources, providing a rough estimate of migration over several thousand years.

11.3.4.8.3 Importance of Clays in Sorbing Radionuclides–Oklo and Cigar Lake

Oklo, Gabon, and Cigar Lake, Canada, are localities that host uranium deposits in saturated, reducing environments. In their entirety, attributes of both sites differ significantly from conditions that could be expected at Yucca Mountain (e.g., CRWMS 2000 [DIRS 151945], Section 13). However, at Oklo, which is situated in near-surface Lower Proterozoic metasediments, and Cigar Lake, located in deep Precambrian granite, clay haloes that surround the ore deposits are effective in retarding the migration of uranium away from the source. This suggests that clays found in altered vitrophyre and fracture fillings at Yucca Mountain will also be effective in retarding the migration of actinides.

11.3.4.8.4 Fast Paths, Perched Water, and Lateral Transport–Idaho National Engineering and Environmental Laboratory

Long-range subsurface transport near the subsurface disposal area of the radioactive waste management complex at the Idaho National Engineering and Environmental Laboratory (INEEL) was investigated in a tracer test in 1999 (Nimmo et al. 2001 [DIRS 154458]). A conservative tracer was applied in infiltration ponds 1.3 km away from the subsurface disposal area. The subsurface at INEEL consists of thick layers of fractured basalts interbedded with thinner layers of coarse- to fine-grained sediments. The unsaturated zone above the Snake River Plain aquifer is 200 m thick.

Samples were collected for tracer analysis from 24 wells within 3 km of the infiltration ponds for several months. Tracer was detected in 1 of 13 sampled aquifer wells 0.2 km away from the nearest spreading area and in 8 of 11 perched water wells completed within the uppermost 70 m of the UZ from 0.2 to 1.3 km away. One of these wells is directly under the subsurface disposal area. The results indicate that percolation from the infiltration ponds can reach the water table in less than nine days, an average rate of at least 22 m/day, and that water from this source can move horizontally in the UZ at an average rate of at least 14 m a day (Nimmo et al. 2001 [DIRS 154458], p. 82).

At least under ponded infiltration, the interbeds and dense basalt layers do not prevent rapid, high-volume vertical flow through fractured basalt. However, some impediments to flow are sufficient to cause substantial perching and horizontal diversion of flow. The fact that this horizontal flow moves quickly over considerable distances suggests that there must also be layers of high horizontal permeability in the zone of perching above the impeding layers. All of the UZ detections were east of the infiltration ponds, the direction in which the interbeds tilt with a slope of 0.004. Transport along such a slope at the observed rates is plausible through extensive horizontal fractures or rubbly layers if they are nearly saturated. A combination of a low-permeability layer directly overlain by such a fractured or rubbly layer might cause the observed detections. Such geologic configurations would have to extend continuously over large distances to allow the observed fast, long-range transport. This situation may be common at the INEEL site and might be significant for long-range contaminant transport at sites such as Yucca Mountain, where the UZ is composed predominantly of fractured rock.

11.3.4.8.5 Radioisotope Migration Experiments Under Unsaturated Conditions: Results From an Experiment at a Scale of 30 cm.

Radionuclide migration experiments under unsaturated conditions have been completed by Atomic Energy of Canada Limited (AECL) on a scale of 30 cm in a block of non-welded tuff (Vandergraaf et al. 2001 [DIRS 155042]). This block was obtained from the Busted Butte UZ facility in the Calico Hills Formation. The results, obtained from elution profiles, showed that, relative to an ideal conservative tracer, tritiated water, transport of technetium (injected as an anionic TcO_4^- species) was approximately 15 percent faster, but that neptunium (injected as the neptunyl ion NpO_2^+) was retarded by a factor of approximately 3. Triay et al. (1996 [DIRS 101024], Appendix A) conducted column experiments with crushed tuff and found neptunium breakthrough curves indicating retardation coefficients always greater than 1 and ranging up to approximately 4, depending on rock type. The AECL findings fall within this range.

Retardation of sodium-22, cobalt-60, and cesium-137 by the geological material was higher than for neptunium. Post-experiment radiometric analysis of the tuff, which is currently underway, shows that the order of retardation is sodium-22 < cesium-137 < cobalt-60. This agrees qualitatively with the experimentally determined static batch sorption coefficients for these radioisotopes.

Radionuclide experiments under unsaturated and saturated conditions at a scale of 1 m in blocks of tuff from the Busted Butte UZ facility are currently underway.

11.3.4.9 Summary of Remaining Uncertainties

Table 11.3.4-2 summarizes the key uncertainties related to mountain-scale UZ radionuclide transport. These uncertainties are applicable to the baseline potential repository and to the potential extension of the repository to the south. The major differences for the southern extension are greater uncertainty in the stratigraphic and structural features, rock properties, and hydrologic conditions (such as perched water) caused by the paucity of site characterization information in this region. The uncertainties associated with flow and transport properties in the southern area, which are currently estimated by extrapolation of the baseline model, need to be studied further.

11.3.4.10 Summary and Conclusions

The effects of a potential southern extension to the baseline potential repository block on radionuclide transport in the UZ were investigated by conducting a sensitivity analysis with TOUGH2 V1.4. The results indicate that radionuclide transport between the potential repository emplacement horizon and the water table in the southern extension is slightly slower than in the baseline potential repository block. The magnitude of the other effects on radionuclide transport resulting from a southern extension of the potential repository block is insignificant.

11.3.5 Effects of Thermally-Driven Coupled Processes on Radionuclide Transport in the Unsaturated Zone

11.3.5.1 Introduction

In the previous sections, various aspects of radionuclide transport under ambient conditions were discussed. In this section, the effects of thermally driven coupled processes on radionuclide transport are considered, including TH, THC, and THM effects. Because radionuclide transport in the UZ starts at the bottom of the emplacement drifts, only flow and transport from this point to the water table is of concern. The hydrogeologic units that the radionuclides may encounter are the TSw, the CHnv (vitric and zeolitic), and a limited area of the Prow Pass unit.

This section focuses primarily on a qualitative discussion of TH, THC, and THM effects on radionuclide transport using models already described in Sections 3 and 4. TH effects are evaluated using the mountain-scale TH model described in Section 3.3.5 and the TH seepage submodel of the mountain-scale model described in Section 4.3.5.3. Results from the mountain-scale THC model described in Section 3.3.6 are used to discuss potential THC effects on radionuclide transport. Finally, results from the drift-scale continuum THM model described in Section 4.3.7 are used to infer THM effects on transport. The uncertainties associated with all of these models are described in detail in the individual sections already mentioned.

11.3.5.2 Goal of Models

The goals of the models used in this section were to evaluate the potential effects of thermally driven coupled processes on radionuclide transport. Of particular importance is the drying out of the fracture and matrix continuum in the shadow zone, an issue of much importance for repository performance. For an explanation of the shadow zone concept, refer to Section 11.3.1.

11.3.5.3 Discussion of Total System Performance Assessment-Site Recommendation Results

All effects of TH, THC, and THM coupled processes were excluded from the TSPA-SR (CRWMS M&O 2000 [DIRS 153246]) on the basis of low consequence. The screening arguments for exclusion of these coupled processes are presented in *Features, Events and Processes in UZ Flow and Transport* (BSC 2001 [DIRS 154826]). The screening arguments are based on process model analyses and qualitative reasoning.

TH coupled processes were investigated for mountain-scale UZ flow (CRWMS M&O 2000 [DIRS 144454]). The processes were found to have minimal effect on flow beneath the potential repository, indicating that only small increases in liquid flux due to TH effects should be expected below the potential repository. These findings were used as a basis for excluding the effects of TH processes on radionuclide transport.

THC coupled processes were investigated using process modeling at the drift scale in *Drift-Scale Coupled Processes (DST and THC Seepage) Models* (CRWMS M&O 2000 [DIRS 142022]; BSC 2001 [DIRS 154677]). This study found coupled THC processes have little effect on hydrogeologic properties in the vicinity of the emplacement drifts. Although some significant changes in aqueous and gas-phase compositions were predicted near the drift (see Section 6.3.1.3), most of these changes were found to dissipate within the modeled time period (100,000 years); others were found to be unrelated to the thermal perturbation (see Section 6.3.1.4). Because these interactions were studied at the emplacement drift boundaries, where thermal-chemical interactions are expected to be more severe, it was concluded that the effects of thermal-chemical interactions along the pathways of aqueous radionuclides in the UZ will be small and of limited duration. Therefore, coupled THC effects on radionuclide transport were excluded from the TSPA-SR (CRWMS M&O 2000 [DIRS 153246]).

THM coupled processes were not directly analyzed using process models. Instead, a sensitivity study was conducted that evaluated the effects of a range of fracture properties (resulting from changes in fracture aperture) in terms of radionuclide transport behavior (CRWMS M&O 2000 [DIRS 151953]). The study concluded that transport behavior is relatively insensitive to large variations in fracture aperture over the entire UZ domain and virtually insensitive to localized variations in fracture aperture. Therefore, the effects of THM coupled processes on radionuclide transport were excluded from the TSPA-SR (CRWMS M&O 2000 [DIRS 153246]).

11.3.5.4 Model Development since Total System Performance Assessment-Site Recommendation

11.3.5.4.1 Thermal-Hydrologic Models

The mountain-scale TH model presented in Section 3.3.5 evaluates the large-scale global effects of heat on UZ flow and transport; submodels are used to evaluate smaller-scale effects of heat, such as that on seepage (See Section 4.3.5). Of particular interest is how much the UZ flow below the drift is affected by heat and how this affects the radionuclide transport behavior of the system. The three-dimensional mountain-scale model computes transient changes in UZ flow as affected by heat and climate change. Figures 3.3.5-8 through 3.3.5-11 show, respectively, the

liquid flux versus elevation for a typical location through an emplacement drift for (a) a higher-temperature case for thermal properties, without and with lithophysal cavities, and (b) a lower-temperature case for thermal properties, without and with lithophysal cavities. The drift is located at an elevation of approximately 1,100 m, as evidenced by the large liquid flux at this location for the higher-temperature case, caused by large capillary suction in the dryout zone (Figures 3.3.5-8) through 3.3.5-11. Boiling processes, climate change, and the effects of the shadow zone below the drift complicate the analysis of liquid fluxes below the drift. At 600 years, climate change is assumed to occur (see Section 3.3.1.3), with a subsequent increase in precipitation and infiltration; this is reflected in higher long-term liquid fluxes below the drift at late times (2,000 years) after other complications, such as liquid boiling, are over. The effects of boiling and shadow zone can be seen clearly in Figure 3.3.5-8 for the case of a higher-temperature operating mode. However, the main implication of Figures 3.3.5-8 through 3.3.5-11 is that the UZ flow does not drastically change with changes in heat for either the higher- or lower-temperature cases. Although boiling changes UZ flow slightly for some 1,000 years, especially in the higher-temperature case, the main lasting effect results from the climate change at 600 years (USGS 2000 [DIRS 136368]). Thus, it can be concluded that the global large-scale TH effects on UZ transport below the drifts are probably negligible.

In terms of more localized effects of heat on transport, the drying out of the shadow zone due to heat and the subsequent impact on transport through this zone must be evaluated. Of particular importance is whether fractures and the rock matrix totally dry out near the bottom of the drift, because this would result in total containment until either continuum starts to rewet. The reason is that diffusion of radionuclides from the EBS at the bottom of the drift to the rock cannot occur without liquid water being present in the rock, either in the matrix or the fractures. An exception to this is radionuclide releases in the gaseous phase, which are believed to be small and are therefore neglected in the TSPA-SR. A second important consideration is that of partial or total dryout of the fracture or matrix continuum, since this will affect the relative rate of diffusion into one continuum with respect to the other.

The submodel of the TH mountain-scale model, used to evaluate TH effects on seepage in Section 4.3.5, provides the results necessary to evaluate the effects of heat on dryout in the shadow zone for the higher- and lower-temperature cases. Figures 11.3.5-1 and 11.3.5-2 show the saturation distributions at various times for the higher-temperature case and the fracture and matrix continuum, respectively. These figures show complete dryout below the drift for both the fracture and matrix continua owing to boiling. The dryout zone expands with time below the drift and reaches a maximum thickness of some 70 m after about 1,000 years (Figure 11.3.5-3). After that, the dryout zone starts to contract; it disappears after approximately 2,500 to 3,000 years. During this entire period, there can be no radionuclide transport from the drift because of the total lack of liquid water for advective or diffusive transport.

In the case of the lower-temperature operating mode, only the fractures dry out below the drift because the heat source is not sufficient to boil a significant amount of the water residing in the matrix. Figure 11.3.5-4 shows the saturation distribution within the fractures for different times in the lower-temperature case. The figure shows that dryout in fractures will occur beneath the drifts for at least 2,000 years, during which time radionuclide releases can only occur into the matrix blocks below the drifts. This is not expected to improve repository performance significantly, since most of the radionuclides are expected to diffuse primarily into the matrix

under ambient conditions because the matrix has a much higher liquid saturation (moisture content) than the fractures, as discussed in Section 11.3.1. The impact of changing water and gas chemistry on radionuclide transport is being evaluated as part of a study on the effect of alkaline plumes on the UZ below the potential repository drifts.

11.3.5.4.2 Thermal-Hydrologic-Chemical Models

Several model improvements were made to the THC seepage models (BSC 2001 [DIRS 154677]; see also Section 6.3.1.4), limiting the uncertainty of results compared to the predictions in *Drift-Scale Coupled Processes (DST and THC Seepage) Models* (CRWMS M&O 2000 [DIRS 142022]). Although there were still some important changes in aqueous and gas-phase compositions predicted near the drift, most of these changes were found to dissipate within 10,000 years, and no significant long-lasting THC effects were predicted around the drift.

A mountain-scale THC model is described in Section 3.3.6, which also discusses the results of this model regarding global UZ flow issues. These same results can be used to evaluate the potential effects of THC processes on UZ transport. The conclusions from Section 3.3.6 are that THC processes, primarily dissolution and precipitation processes, have only minor effects on UZ flow because a change in permeability of less than an order of magnitude is smaller than the natural variability of several orders of magnitude. Some enhanced THC processes result from gas convection and increased condensation near the edges of the repository, but these are confined mostly to areas near and above the potential repository. Therefore, the long-term liquid fluxes of liquid and transport below the potential repository in the UZ were not affected significantly by gas convection. The mountain-scale THC model shows some dissolution in the zeolitic rocks in the CHnv, which results in some relatively small enhancement in porosity (less than 10 percent) and permeability (less than an order of magnitude). These enhancements may lead to higher water flow through the matrix of these zeolitic units, resulting in an increased sorption of radionuclides that will enhance performance. Consequently, it is concluded that THC processes will not affect transport in the UZ more than natural variability in hydrologic properties. The possibility for an alkaline plume from the EBS to affect transport has not been evaluated in this report, but this work is currently in progress.

11.3.5.4.3 Thermal-Hydrologic-Mechanical Models

The development of a mountain-scale THM model is described in Section 3.3.7, and that of a drift-scale model in Section 4.3.7. The results from both models can be used to qualitatively discuss potential THM effects on radionuclide transport from the near field to the water table. The results from these models indicate that a change in permeability of only 10 percent to 40 percent will occur in the lower lithophysal unit because of THM effects (Figures 4.3.7-15 and 4.3.7-16). Permeability changes from THM effects in units underlying the lower lithophysal units are of the same order (Table 3.3.7-2). These are relatively small changes, so it is expected that THM effects will have a minor influence on localized flow close to drifts and global UZ flow patterns. Hence, THM effects on transport will be negligible.

11.3.5.5 Abstraction for Total System Performance Assessment

The work reported in this section is devoted to evaluating process model sensitivities and uncertainties. Consequently, simulation results from this study are not used to support any abstraction model that directly supports the TSPA. The results described in this section indicate that the process model and associated model abstractions used to represent this component in the TSPA-SR (CRWMS M&O 2000 [DIRS 153246]) are representative (or conservative) with respect to the effects of this component on total system performance. Therefore, any future changes in model abstractions for this component will not diminish the performance represented in the TSPA-SR.

11.3.5.6 Multiple Lines of Evidence

Multiple lines of evidence are provided for the thermally-driven coupled processes in Sections 3.3.5 through 3.3.7 and Sections 4.3.5 through 4.3.7.

11.3.5.7 Summary of Remaining Uncertainties

Two categories and several key uncertainty issues related to modeling the effects of thermally driven coupled processes on radionuclide transport in the UZ are summarized in Table 11.3.5-1.

11.3.5.8 Summary and Conclusions

This section evaluates the effects of thermally driven coupled processes on radionuclide transport in the UZ. TH effects on the shadow zone may have considerable beneficial effects on transport. For the higher-temperature case, model calculations show that both the rock matrix and fractures immediately below the drifts will remain totally dry because of boiling for 2,500 to 3,000 years. As a result, there can be no radionuclide release from the EBS into the UZ except for radionuclides that are transported in the gas phase (such as carbon-14). For the lower-temperature case, the fracture network below the drifts is estimated to remain dry for about 2,000 years, but the liquid saturation of the rock matrix will remain near initial ambient values. As a result, radionuclides from the UZ could only migrate from the drift invert into the adjacent rock matrix in the UZ. The effects of THC and THM processes on radionuclide transport are therefore found to be negligible for the limited studies conducted.

INTENTIONALLY LEFT BLANK

Table 11.3.1-1. Summary of Uncertainty Issues Related to the Drift Shadow Transport Model

Category	Uncertainty Issue	Treatment of Uncertainty Issue	Affected Goals
Conceptual Uncertainties	Area reduction factor versus capillary equilibrium	Based on hydrologic and geochemical evidence (Section 11.3.1.7) Implemented through active fracture model (Section 11.3.1.1.1) Confirmed through calibration for hydrologic model and field transport testing (Section 11.3.1.1.3) Alternative conceptual models examined and rejected (Liu et al. 1998 [DIRS 105729])	Development of general understanding of transport process and basis for transport prediction models
	Effective area reduction in flow model	Effective area reduction in flow model due to flow weighting scheme used for fracture-matrix flow (Section 11.3.1.8) Not used in current drift shadow transport model for area reduction in matrix diffusion. Use of this factor would result in even greater isolation of fractures and matrix (Section 11.3.1.8)	Development of general understanding of transport process and basis for transport prediction models
	Significance of drift seepage.	Current process model calculations only performed for drifts without seepage (Section 11.3.1.1.1) Conservatively accounted for in PA model through assignment of advective releases from waste emplacement drift to fractures (Section 11.3.1.6)	Transport in the drift shadow under more widely varying flow conditions
	Representation of matrix diffusion in transport models	Current model abstraction for TSPA may underestimate matrix diffusion for fracture to matrix transfers (Section 11.3.2)	Development of general understanding of transport process and basis for transport prediction models
Parameter and Data Uncertainties	Total percolation rate and fracture-matrix flow distribution	Variations in total percolation rate included in PA model through the UZ site-scale flow model for various climate/infiltration scenarios (Section 11.3.1.8) Variations in fracture-matrix flow distribution included in PA model through site-scale flow model (Section 11.3.1.8)	Transport in the drift shadow under more widely varying flow conditions
	Formation-specific parameters	Flow parameters calibrated to site-specific measurements of water saturation and capillary pressure, with uncertainty developed in accordance with calibration under uncertain infiltration rates (Section 11.3.1.1.3) Transport parameters and parameter uncertainty developed from measurements using site-specific materials (CRWMS M&O 2001 [DIRS 154024])	Determination of flow and transport formation parameters
	Heterogeneity	Captured in drift seepage analyses (CRWMS M&O 2000 [DIRS 153314])	Distribution of flow and transport parameters
	Uncertainty propagation	Uncertainty accounted for in part through drift seepage uncertainty analysis (CRWMS M&O 2001 [DIRS 154291])	Distribution of inputs for TSPA calculation (CRWMS M&O 2001 [DIRS 154291])

Table 11.3.2-1. Summary of Key Uncertainty Issues Related to Calculating Flow and Transport between Fractures and the Matrix

Category	Uncertainty Issue	Treatment of Uncertainty Issues	Affected Goals
Conceptual uncertainty	Appropriateness of the continuum approach	Based on flow and transport behavior in the UZ, scale of the problem, data availability, and computational feasibility (CRWMS M&O 2000 [DIRS 122797], Section 6.4.2) Supported by modeling study of Alcove 1 tests (CRWMS M&O 2000 [DIRS 122797], Section 6.8.1)	Development of UZ flow and transport
	Appropriateness of active fracture model	Based on unsaturated flow theory and experimental observation regarding fingering flow (CRWMS M&O 2000 [DIRS 141187], Section 6.4.5) Consistent with field observations in the UZ (Liu et al. 1998 [DIRS 105729]) Supported by modeling study of Alcove 1 tests (CRWMS M&O 2000 [DIRS 122797], Section 6.8.1)	Description of flow in fractures and fracture-matrix interaction
Uncertainty related to numerical approaches	Appropriateness of matrix block discretization (DKM vs. MINC)	Demonstrate the inadequacy of the DKM in handling sharp gradients near fracture-matrix interfaces (Section 11.3.2.5) Make recommendations to resolve this issue (Section 11.3.2.9)	Model prediction of UZ flow and transport
	Appropriateness of upstream weighting scheme for the fracture-matrix connection	Partially accounted for through the model calibration against field observations in the *Calibrated Properties Model* (CRWMS M&O 2000 [DIRS 144426]) Needs further investigation	Calibration of UZ rock properties and model prediction of UZ flow and transport
Parameter uncertainty	Appropriateness of parameters used in the modeling study reported in this section	Used properties without considering perched water Used calibrated, base case, mountain-scale parameter set	Quantitative comparison between simulation results obtained with the DKM and the MINC in this study

Table 11.3.3-1. Parameters Used for the Transport Problem in a Parallel Fracture System

Parameter	Value
Molecular diffusion coefficient	2.5×10^{-11} m^2 /s
Fracture spacing	1.0 m (Case 1) or 10.0 m (Case 2)
Retardation factor	30
Velocity in fracture	1.1574×10^{-5} m/s
Grid spacing	0.5 m
Matrix volume per cell	0.25 m^3 (Case 1) or 25.0 m^3 (Case 2)
Fracture volume per cell	0.5×10^{-5}
Fracture-matrix interface area	0.5 m^2
Domain length	36.75 m

Source: TerBerg 2001 [DIRS 155033].

Table 11.3.3-2. Summary of Key Uncertainty Issues

Category	Uncertainty Issue	Treatment of Uncertainty Issues	Affected Goals
Uncertainty related to numerical approach	Grid discretization - grid coarseness affects data resolution (i.e., an increase in grid coarseness will result in a decrease in resolution)	Partially accounted for through the model calibration against field observations in the *Calibrated Properties Model* (CRWMS M&O 2000 [DIRS 144426]) and comparisons with field measurements of tracer transport	Model prediction of UZ flow and transport
Conceptual model and model implementation uncertainty	Limited theoretical and experimental results to support dual continuum transport calculation methods in fractured porous media	Used dual–porosity model results for validation. Partially accounted for through the model calibration against field observations in the *Calibrated Properties Model* (CRWMS M&O 2000 [DIRS 144426]) and comparisons with field measurements of tracer transport	Quantitative comparison between simulation results obtained with FEHM V2.0, T2R3D V1.4, DCPT V1.0, and DCPT V2.0 in this study

Table 11.3.4-1. Stable Uranium and Stable Isotope Data from Peña Blanca

Sample	Uranium (mol/L)	delta-D (‰)	delta-Oxygen-18 (‰)	Notes
AS-1	2.8E-7	-11	-2.5	12 m from adit entrance on +00 level
AS-2	1.6E-7	-7	-3.4	15 m from adit entrance
AS-3	1.8E-8	-7	-3.6	23 m from adit entrance
AS-4	1.3E-8	-1	-2.8	8.5 m into north part of adit
AS-5	2.7E-8	-64	-9.3	Perched water from borehole at +10 level
AS-6	2.5E-8	-61	-8.7	Abandoned mining camp supply well

Source: Bodvarsson 2001 [DIRS 154669], Attachment 1, pp. 86 to 87.

NOTE: Water samples collected February 25, 2000.

Table 11.3.4-2. Summary of Key Uncertainty Issues

Category	Uncertainty Issue	Treatment of Uncertainty Issues	Affected Goals
Flow distributions and pathways	Uncertainty related to how large-scale flow variability and fracture-matrix flow exchange affect transport	Active fracture model accounts for fracture-matrix interface factors that affect flow and advective transport A range of flow models have been used to account for large-scale variability in flow fields and transport pathways, including perched water models and flow focusing into faults	Model prediction of UZ transport
Sorption coefficients	Large uncertainty ranges in K_d	Parameter ranges have been developed from laboratory experiments and scientific literature data for sorption	Model prediction of UZ transport
Matrix diffusion coefficients	Effects of fracture-matrix interface characteristics on matrix diffusion	Active fracture model accounts for fracture-matrix interface factors that affect flow and advective transport. These factors also affect matrix diffusion and are incorporated into transport calculations in terms of the active fracture model Parameter ranges have been developed from laboratory experiments on matrix diffusion	Model prediction of UZ transport

Table 11.3.5-1. Summary of Uncertainty Issues Related to the Effects of Thermally-Driven Coupled Processes on Transport in the Unsaturated Zone

Category	Uncertainty Issue	Treatment of Uncertainty Issue	Affected Goals
Conceptual uncertainties	Area reduction factor versus capillary equilibrium	Based on unsaturated flow theory, experimental observation regarding fingering flow (CRWMS M&O 2000 [DIRS 141187], Section 6.4.5), and field geochemical evidence (CRWMS M&O 2001 [DIRS 154426]) Supported by field observations from the UZ (Liu et al. 1998 [DIRS 105729]) Supported by modeling study of Alcove 1 tests (CRWMS M&O 2000 [DIRS 122797], Section 6.8.1)	Description of fracture-matrix interaction underneath the repository; development of basis for numerical transport models
Parameter and data uncertainties	Thermal operating modes	Sensitivity studies for range of environments representing both higher- and lower-temperature operating modes	Values of transport parameters near waste emplacement drifts; thermodynamic and kinetic databases and boundary conditions used in TH/THC/THM models
	Modification of porosity and permeability by chemical precipitation and dissolution	Sensitivity analyses performed in drift scale thermal tests with the DST THC model (CRWMS M&O 2001 [DIRS 154426]). Effects on mountain-scale radionuclide transport are expected to be small	Rates of advective transport; relative significance of fracture-matrix interaction
	Formation-specific radionuclide transport parameters and their thermal dependence	Transport parameters developed from laboratory measurements using site-specific materials and field tracer tests under ambient and thermal-loaded conditions Thermodynamic and kinetic databases were derived from various sources including YMP studies and other scientific literature. Sensitivity analyses were performed on thermodynamic and kinetic data (CRWMS M&O 2001 [DIRS 154426]) Radionuclides have not been explicitly simulated in the THC models yet; however, transport behavior of radionuclides may be inferred from the results presented in this section and Section 11.3.4. Diffusion and distribution coefficient ranges have been developed from laboratory experiments and scientific literature. Additional analyses on their thermal dependency would reduce uncertainty.	Determination of rates of radionuclide chemical reactions and transport through the UZ to the water table
	Heterogeneity	Captured in drift seepage analyses (Section 4.3); however, effects on mountain-scale radionuclide transport require further analyses	Spatial distribution of transport parameters

INTENTIONALLY LEFT BLANK

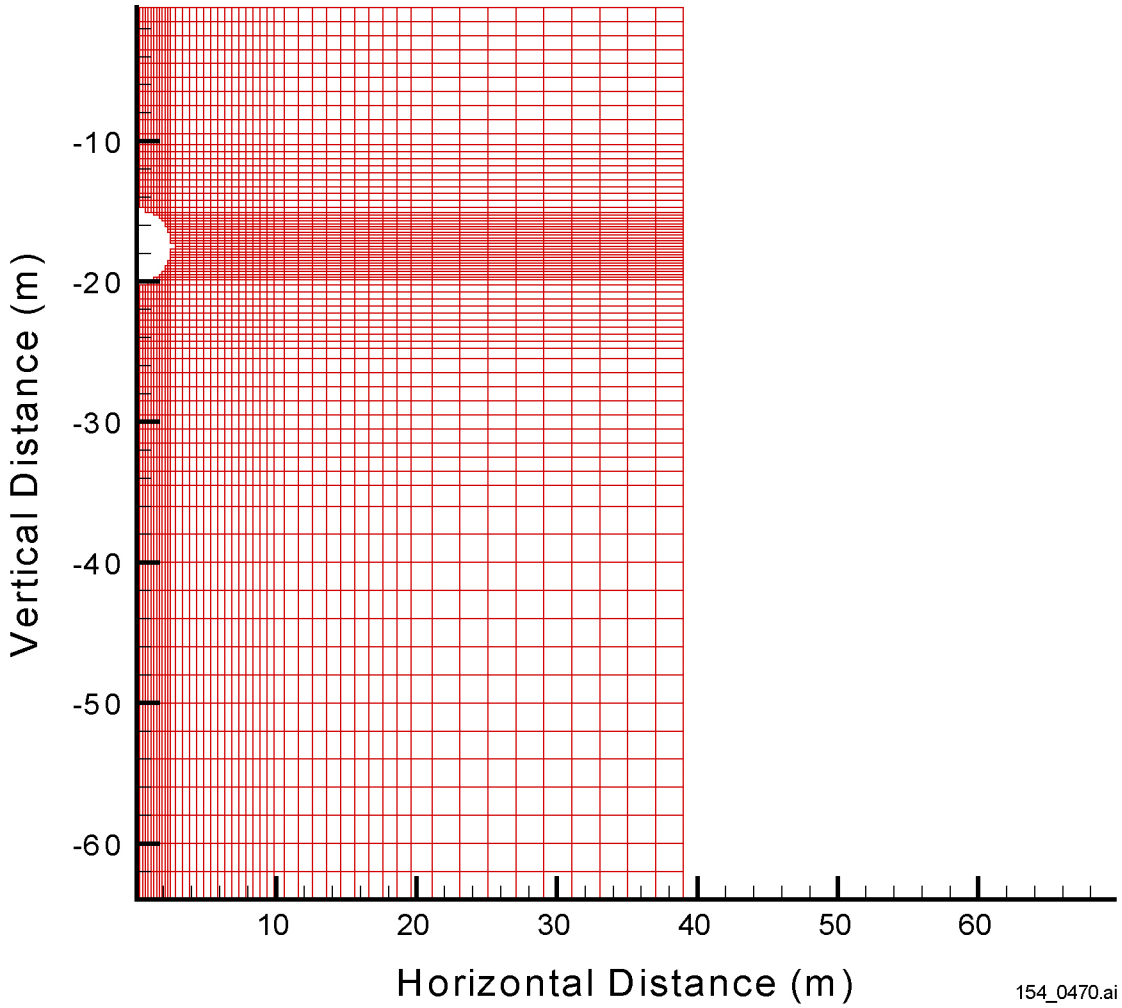

154_0470.ai

Source: Houseworth 2001 [DIRS 155144], p. 19.

NOTE: The water table is an average of 300 m below the potential repository horizon.

Figure 11.3.1-1. Model Grid with Waste Emplacement Drift used for Dual-Permeability Model

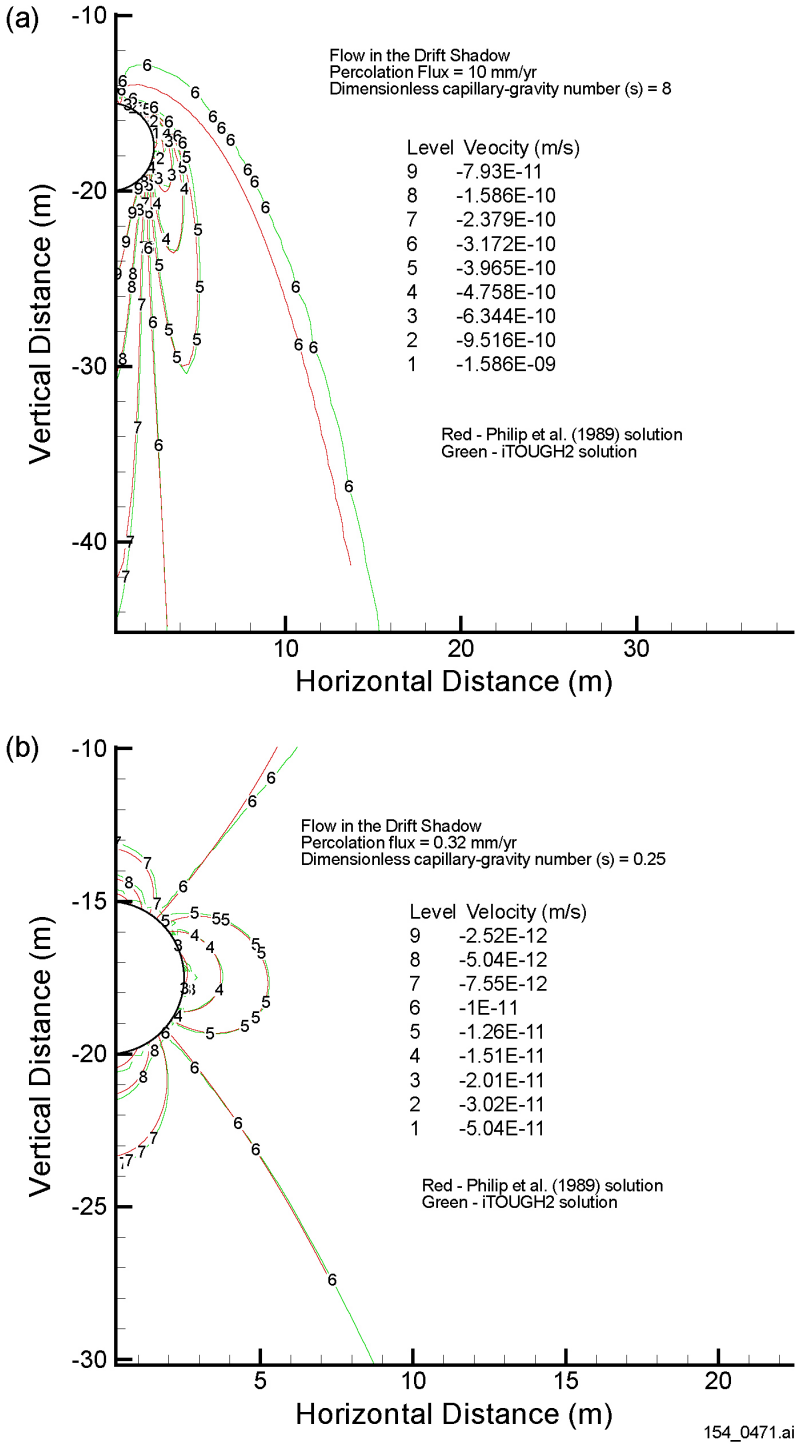

154_0471.ai

Source: Houseworth 2001 [DIRS 155144], pp. 7 to 13.

NOTE: Contours from iTOUGH2 and the analytical Philip solution for (a) percolation flux of 10 mm/yr and capillary coefficient of 8.0, and (b) percolation flux of 0.32 mm/yr and capillary coefficient of 0.25. Negative vertical flow velocities indicates downward flow.

Figure 11.3.1-2. Vertical Flow Velocity Contours for Flow in Drift Shadow

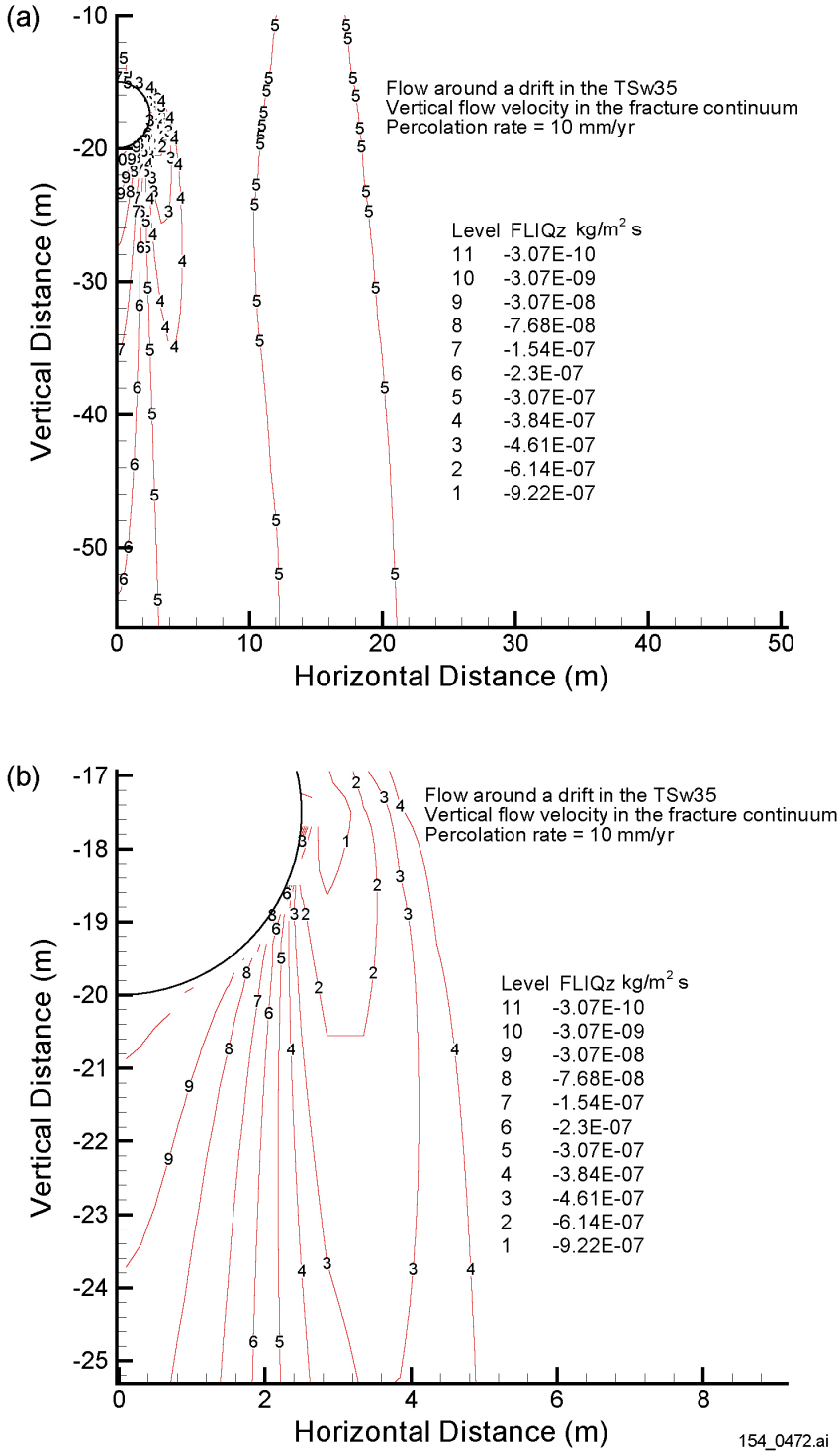

154_0472.ai

Source: Houseworth 2001 [DIRS 155144], pp. 14 to 19.

NOTE: Flow around a drift in the tsw35 fracture continuum at a percolation rate of 10 mm/yr (a) over a large area, and (b) detail near the base of the emplacement drift.

Figure 11.3.1-3. Vertical Flow Velocity Contours for Flow around a Drift in the tsw35 Fracture Continuum

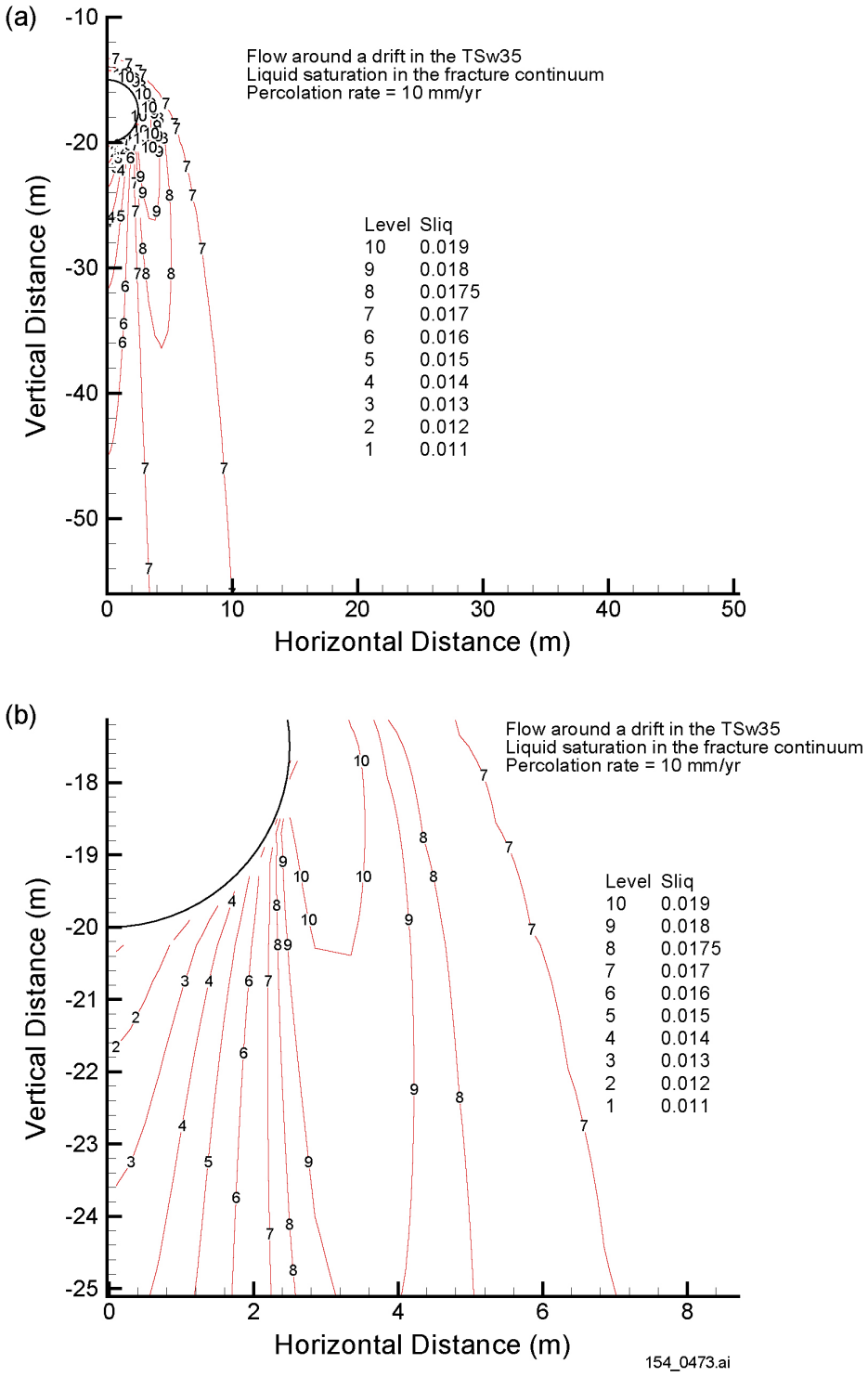

154_0473.ai

Source: Houseworth 2001 [DIRS 155144], pp. 14 to 19.

NOTE: Flow around a drift in the tsw35 at a percolation rate of 10 mm/yr (a) over a large area, and (b) detail near the base of the emplacement drift. Residual saturation is 0.01.

Figure 11.3.1-4. Water Saturation Contours for Flow around a Drift in the tsw35 Fracture Continuum

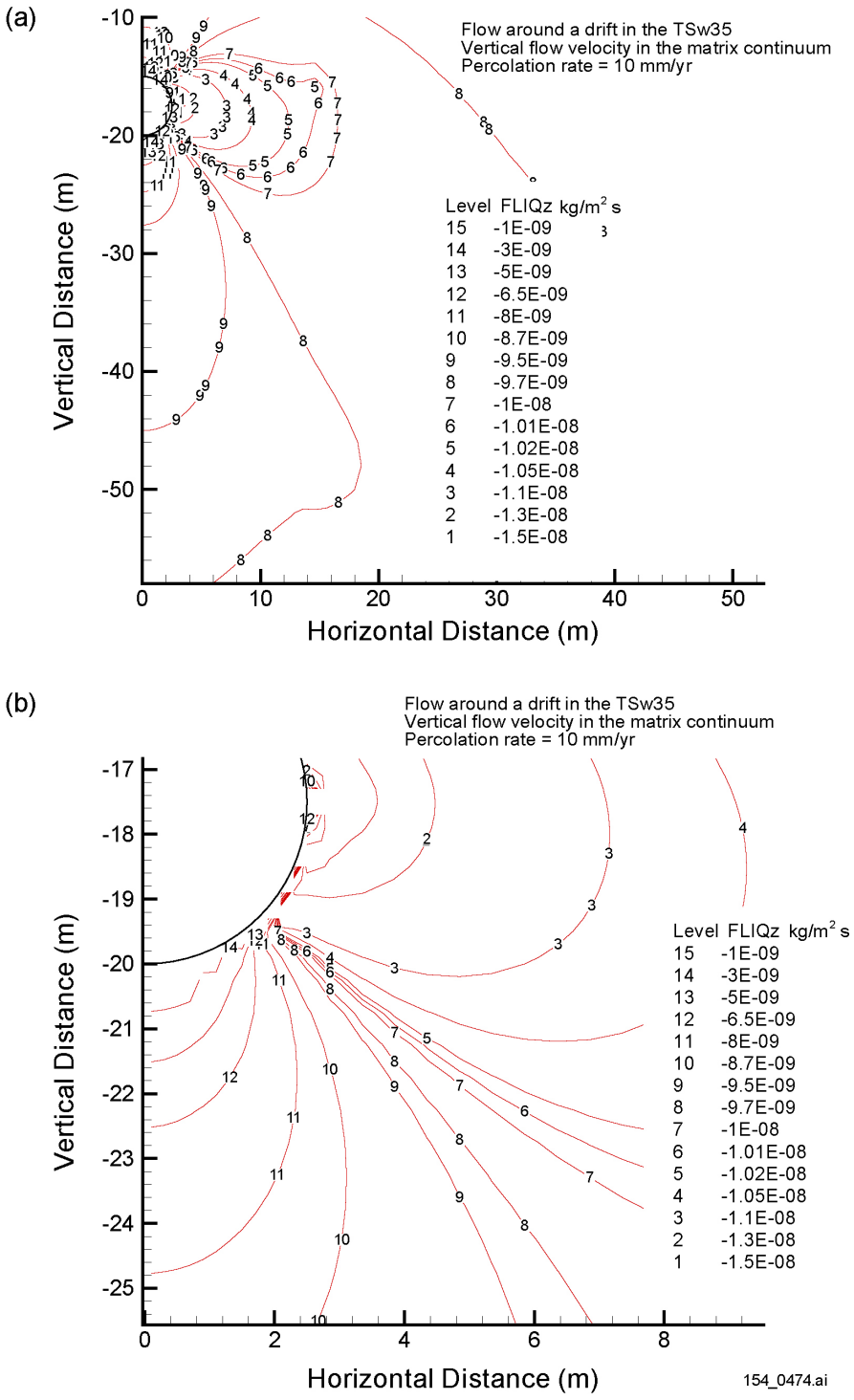

154_0474.ai

Source: Houseworth 2001 [DIRS 155144], pp. 14 to 19.

NOTE: Flow around a drift in the tsw35 at a percolation rate of 10 mm/yr (a) over a large area, and (b) detail near the base of the emplacement drift.

Figure 11.3.1-5. Vertical Flow Velocity Contours for Flow around a Drift in the tsw35 Matrix Continuum

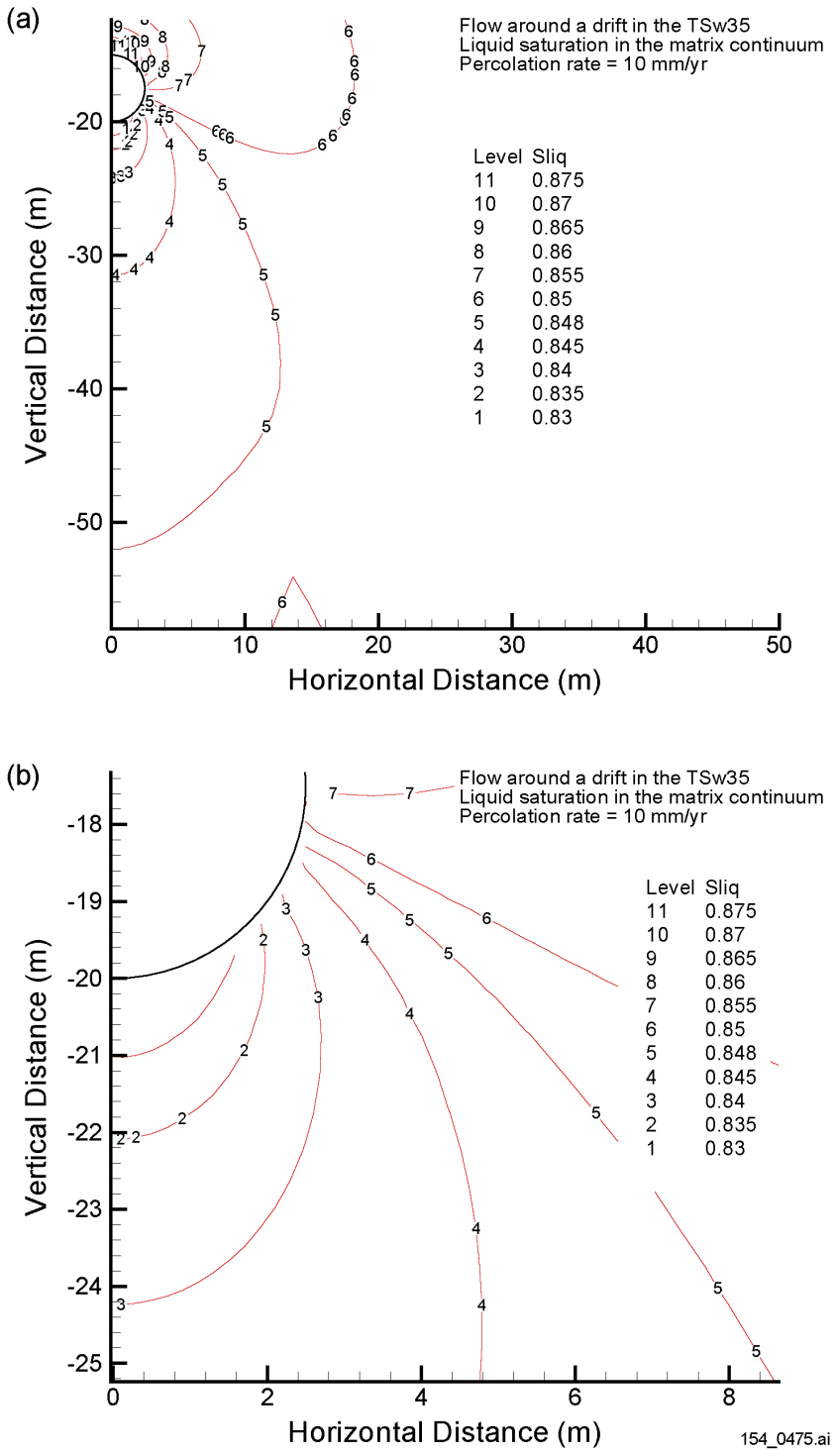

154_0475.ai

Source: Houseworth 2001 [DIRS 155144], pp. 14 to 19.

NOTE: Flow around a drift in the tsw35 at a percolation rate of 10 mm/yr (a) over a large area, and (b) detail near the base of the emplacement drift.

Figure 11.3.1-6. Water Saturation Contours for Flow around a Drift in the tsw35 Matrix Continuum

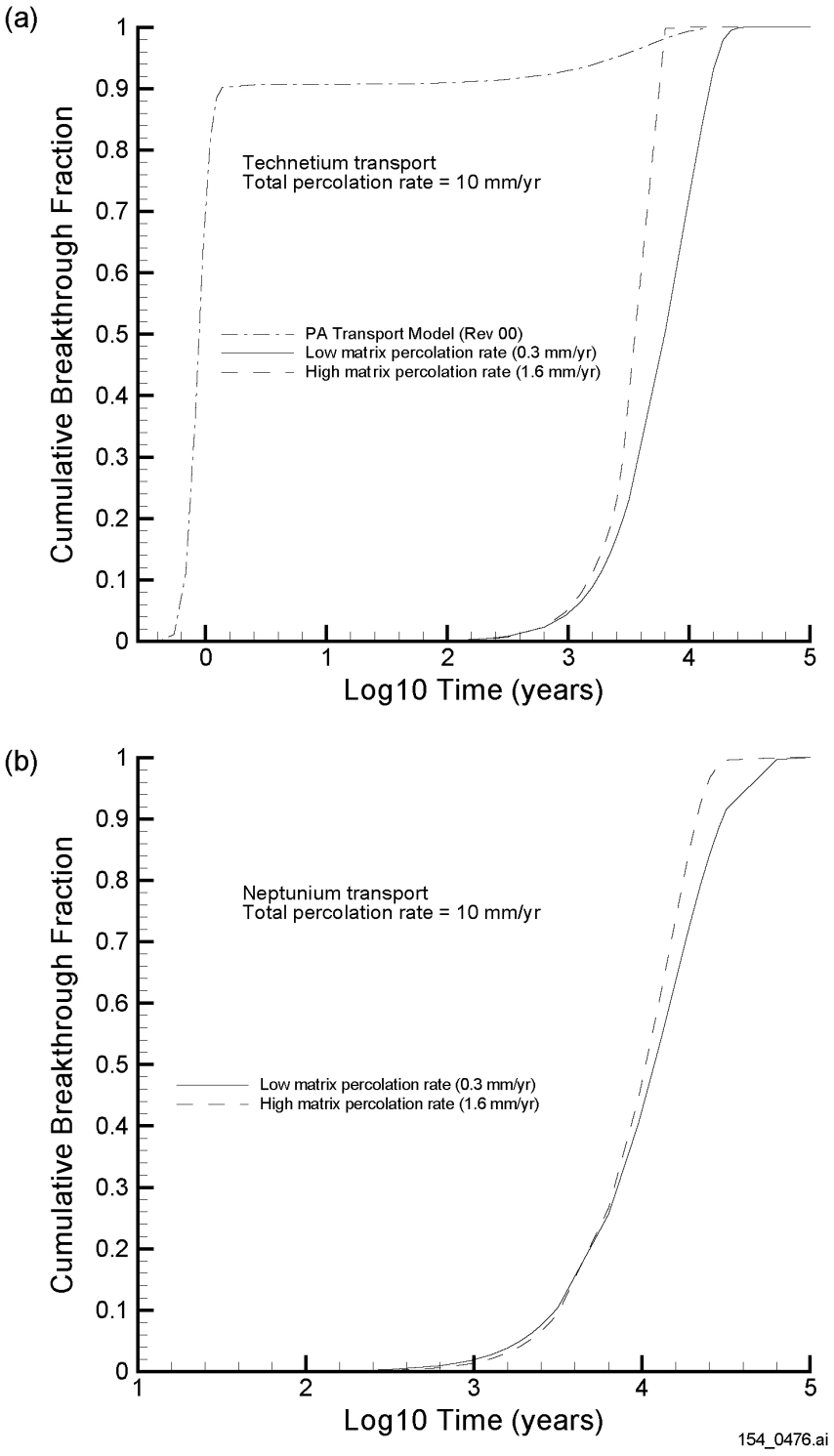

154_0476.ai

Source: Houseworth 2001 [DIRS 155144], pp. 19 to 23.

NOTE: Breakthrough is 45 m below the potential waste emplacement drift.

Figure 11.3.1-7. Technetium (a) and Neptunium (b) Transport with a Total Percolation Rate of 10 mm/yr

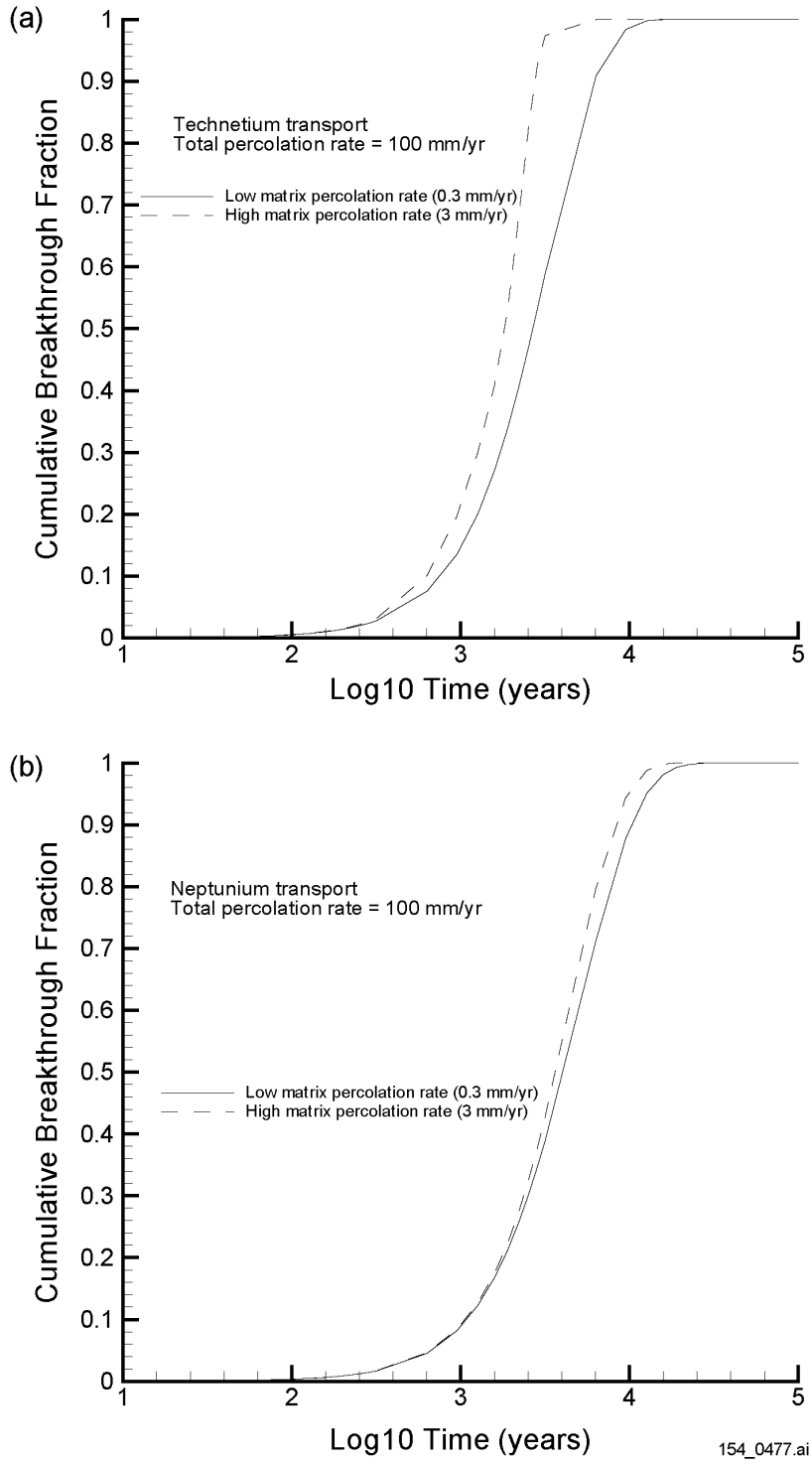

154_0477.ai

Source: Houseworth 2001 [DIRS 155144], pp. 19 to 23.

NOTE: Breakthrough is 45 m below the potential waste emplacement drift.

Figure 11.3.1-8. Technetium (a) and Neptunium (b) Transport with a Total Percolation Rate of 100 mm/yr

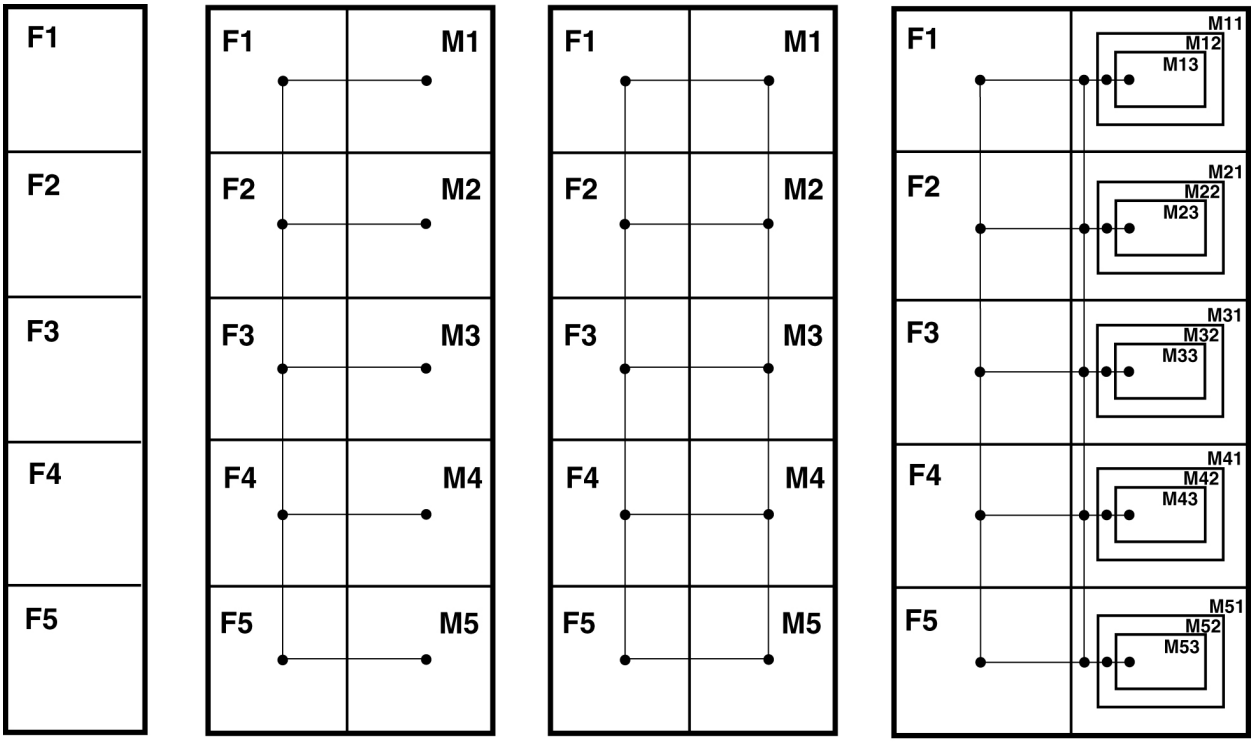

154_0029.ai

Source: Doughty 1999 [DIRS 135997], Figure 2.

NOTE: (a) Effective continuum model, (b) dual porosity model, (c) dual permeability model, and (d) multiple interacting continua model with three matrix continua (i.e., gridblocks). "F" refers to effective continuum model gridblocks in (a) and fracture gridblocks in (b), (c) and (d). "M" refers to matrix gridblocks.

Figure 11.3.2-1. Schematic Diagram of a One-Dimensional Column of Gridblocks and Four Models of Flow

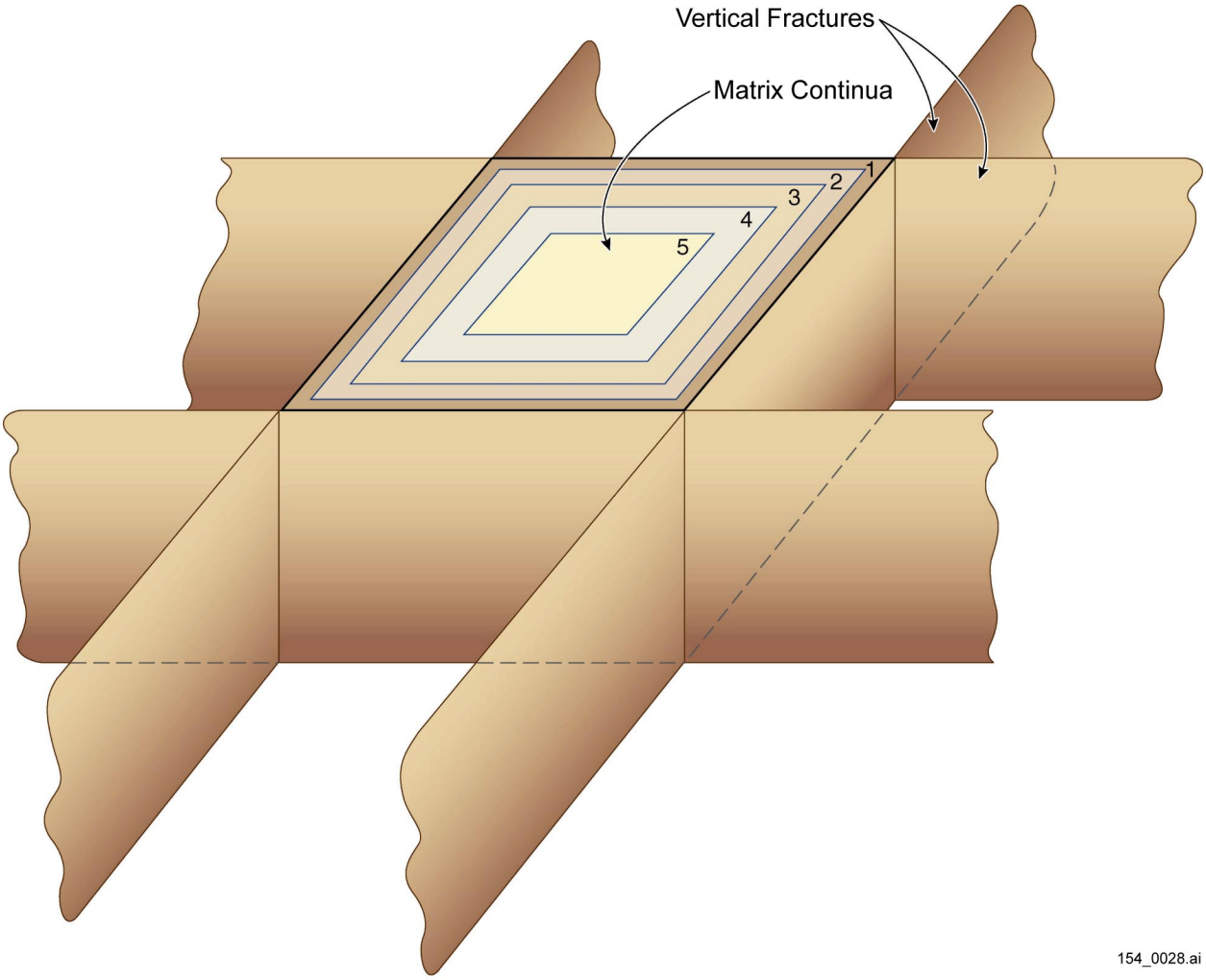

154_0028.ai

Source: CRWMS M&O 2000 [DIRS 141187], Section 6.4.

Figure 11.3.2-2. Matrix Discretization for the Multiple Interacting Continua Model Scheme

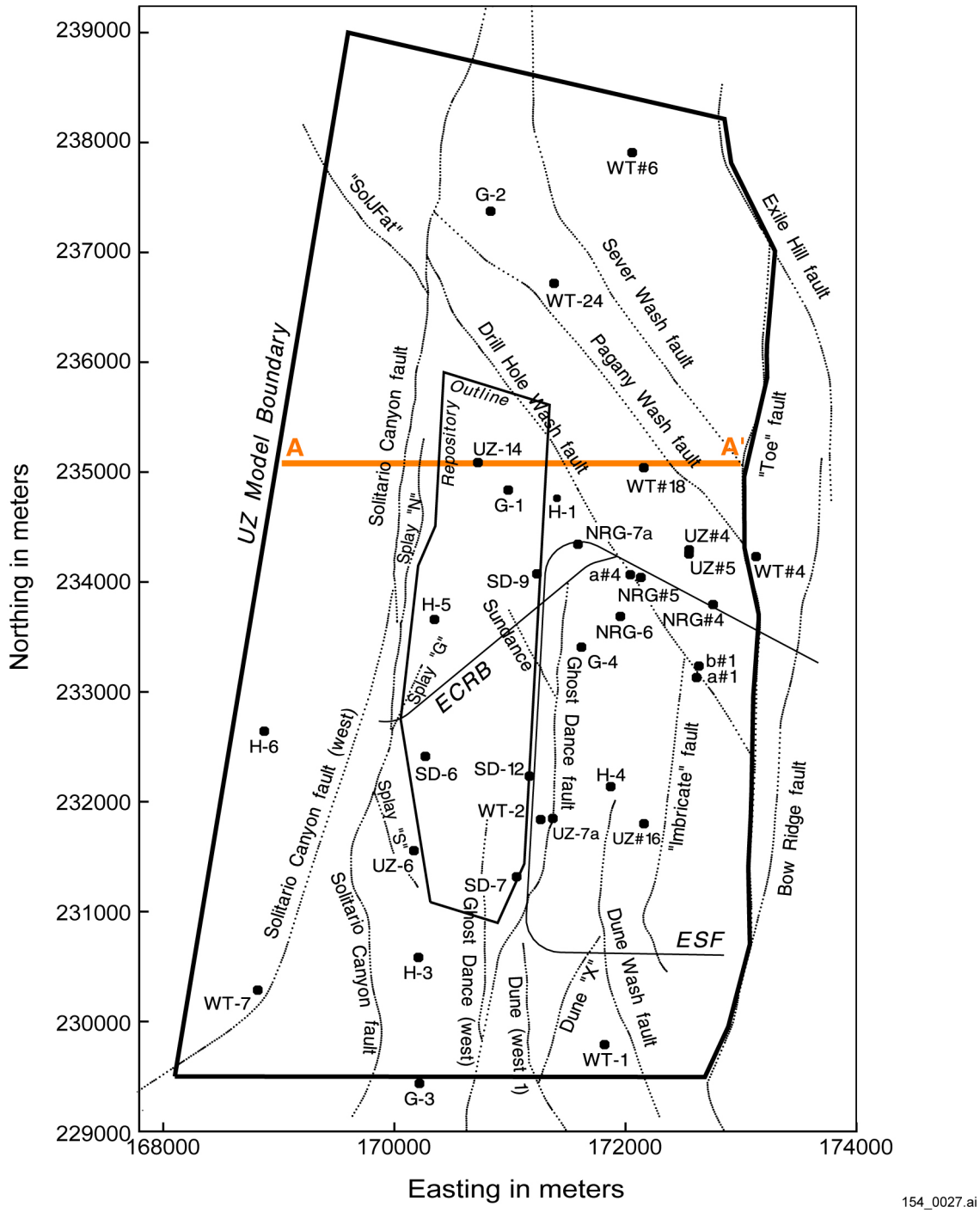

154_0027.ai

154_0027.ai

Source: CRWMS M&O 2000 [DIRS 141187], Figure 1.

NOTE: The East-West cross section (A-A') was used in numerical simulations.

Figure 11.3.2-3. Plan View of the Unsaturated Zone Model Domain and the East-West Cross Section

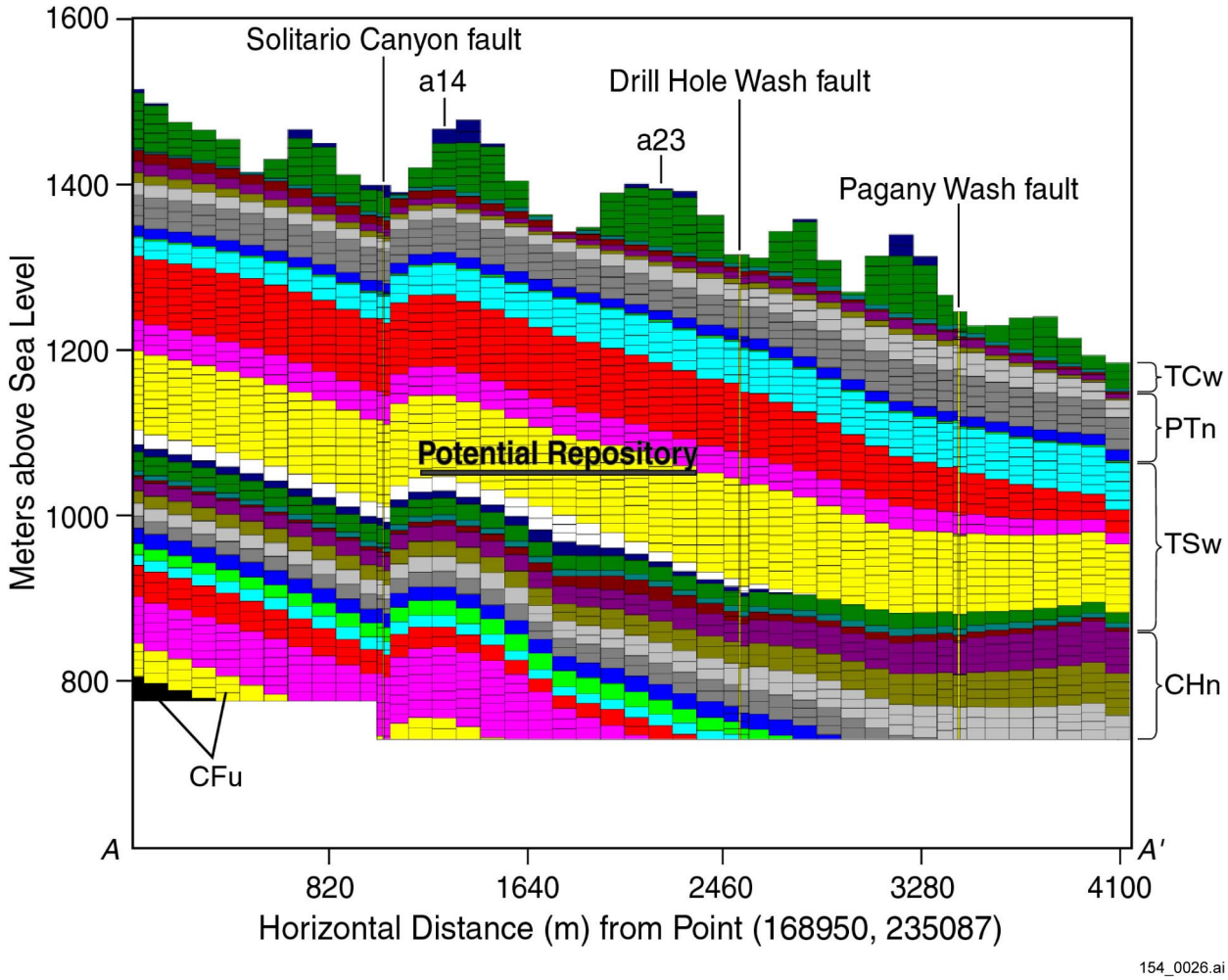

154_0026.ai

Source: TerBerg 2001 [DIRS 155111].

Figure 11.3.2-4. Two-Dimensional Numerical Grids for the East West (A-A') Cross Section

(a)

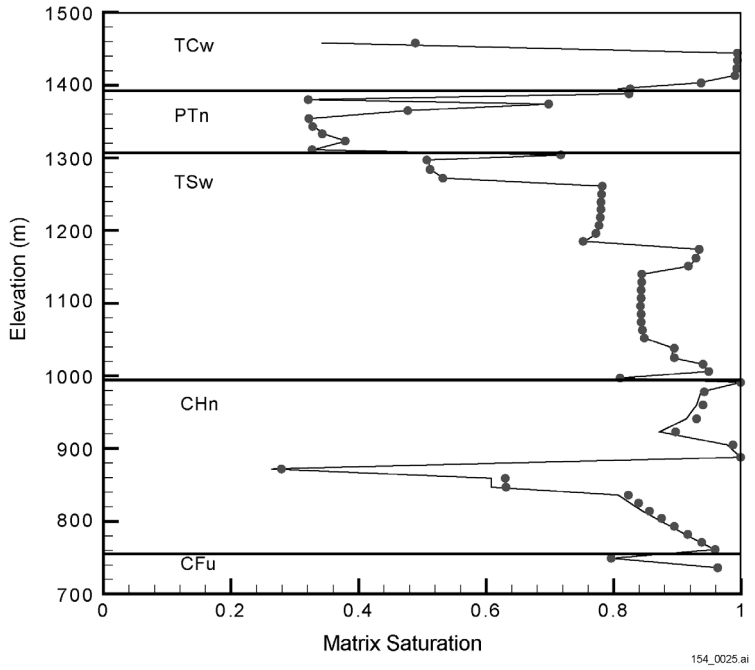

(b)

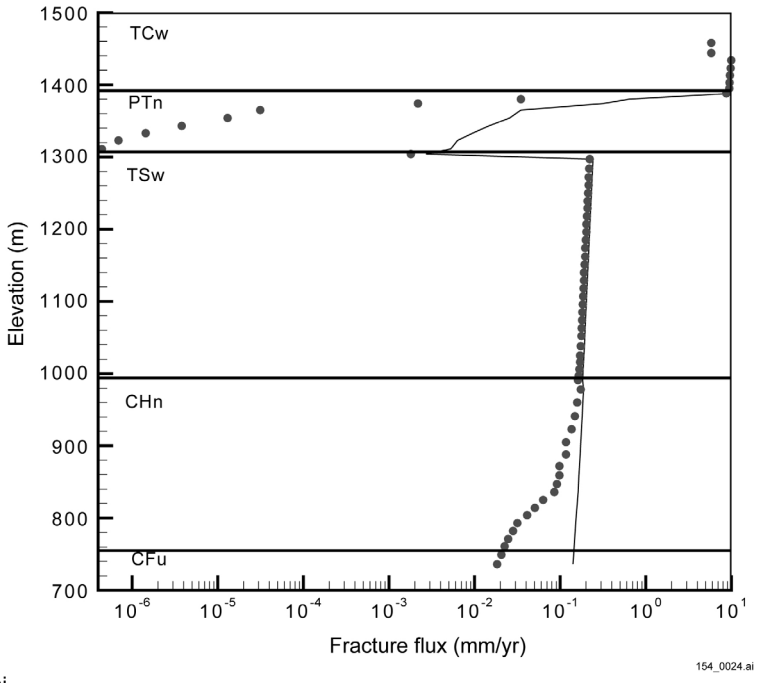

154_0025.ai / 154_0024.ai

Source: TerBerg 2001 [DIRS 155111].

NOTE: Dual permeability model (solid line); multiple interacting continua model (circles).

Figure 11.3.2-5. Comparison of (a) Saturation and (b) Fracture-Flux Output from Two Simulation Models for Vertical Column a14

(a)

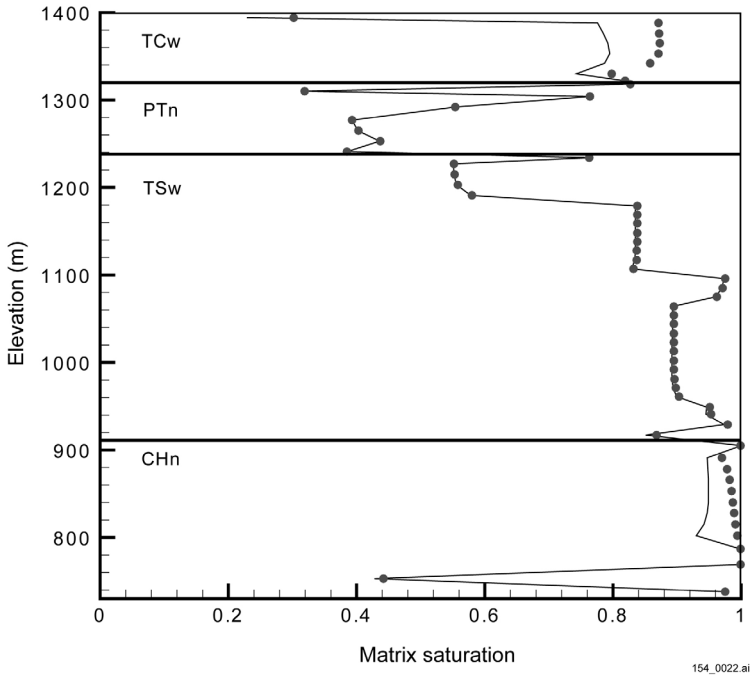

(b)

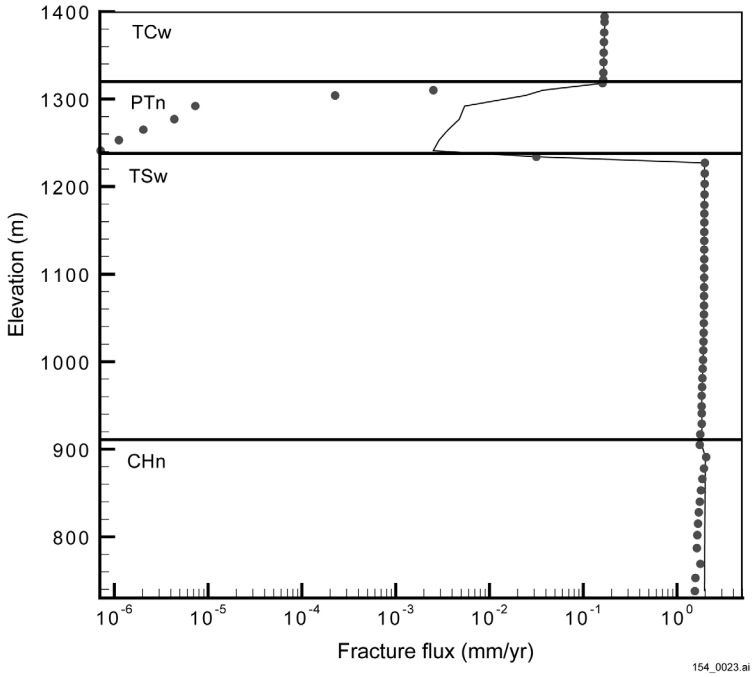

154_0022.ai / 154_0023.ai

Source: TerBerg 2001 [DIRS 155111].

NOTE: Dual permeability model (solid line); multiple interacting continua model (circles).

Figure 11.3.2-6. Comparison of (a) Matrix-Saturation and (b) Fracture-Flux Output from Two Simulation Models for Vertical Column a23

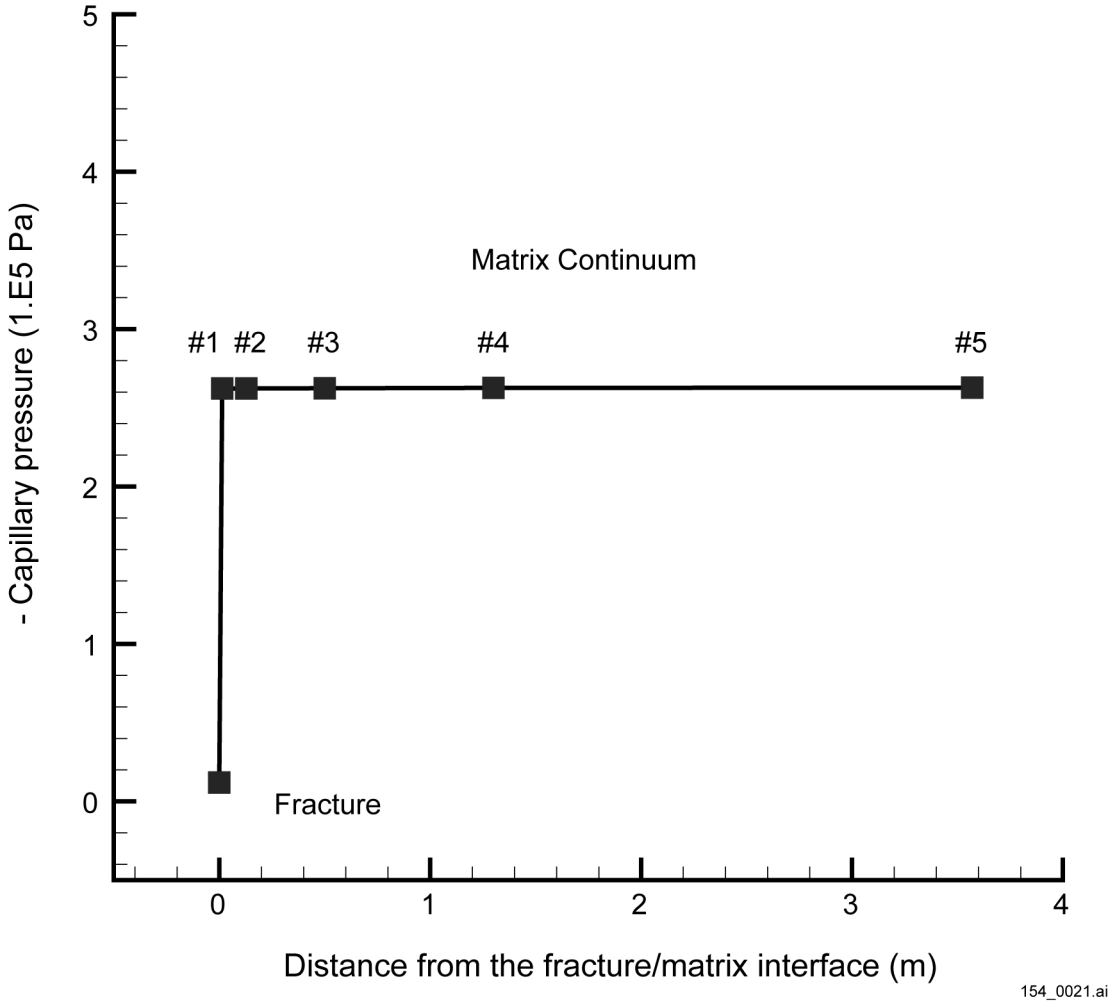

154_0021.ai

Source: TerBerg 2001 [DIRS 155111].

NOTE: Data for column a14 and a matrix block are located at an elevation of 923 m.

Figure 11.3.2-7. Distribution of Capillary Pressures Within a Matrix Block

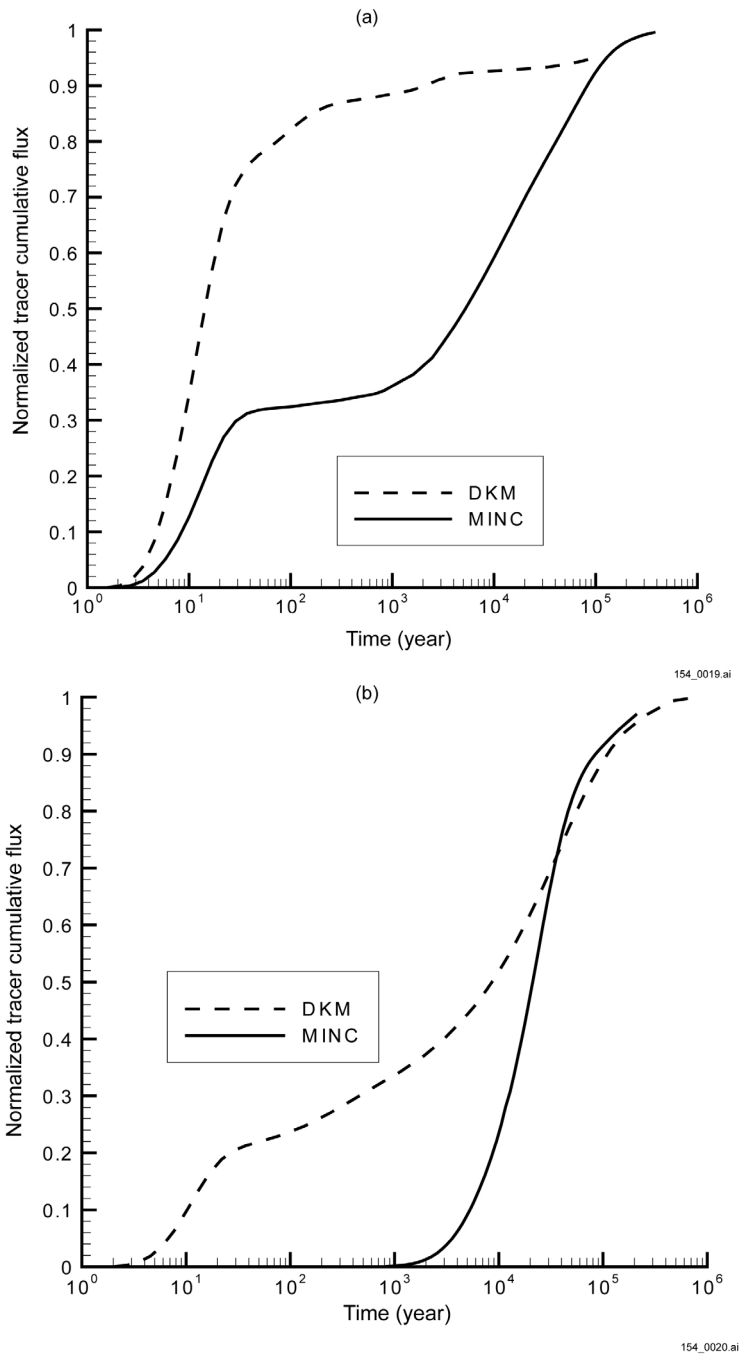

154_0019.ai / 154_0020.ai

Source: TerBerg 2001 [DIRS 155111].

NOTE: Dual permeability model (DKM); multiple interacting continua model (MINC). Model run with molecular diffusion coefficient set at (a) 3.2 x 10^{-11} m^2/s and (b) 0 m^2/s.

Figure 11.3.2-8. Normalized Tracer Cumulative Flux at Water Table as a Function of Time

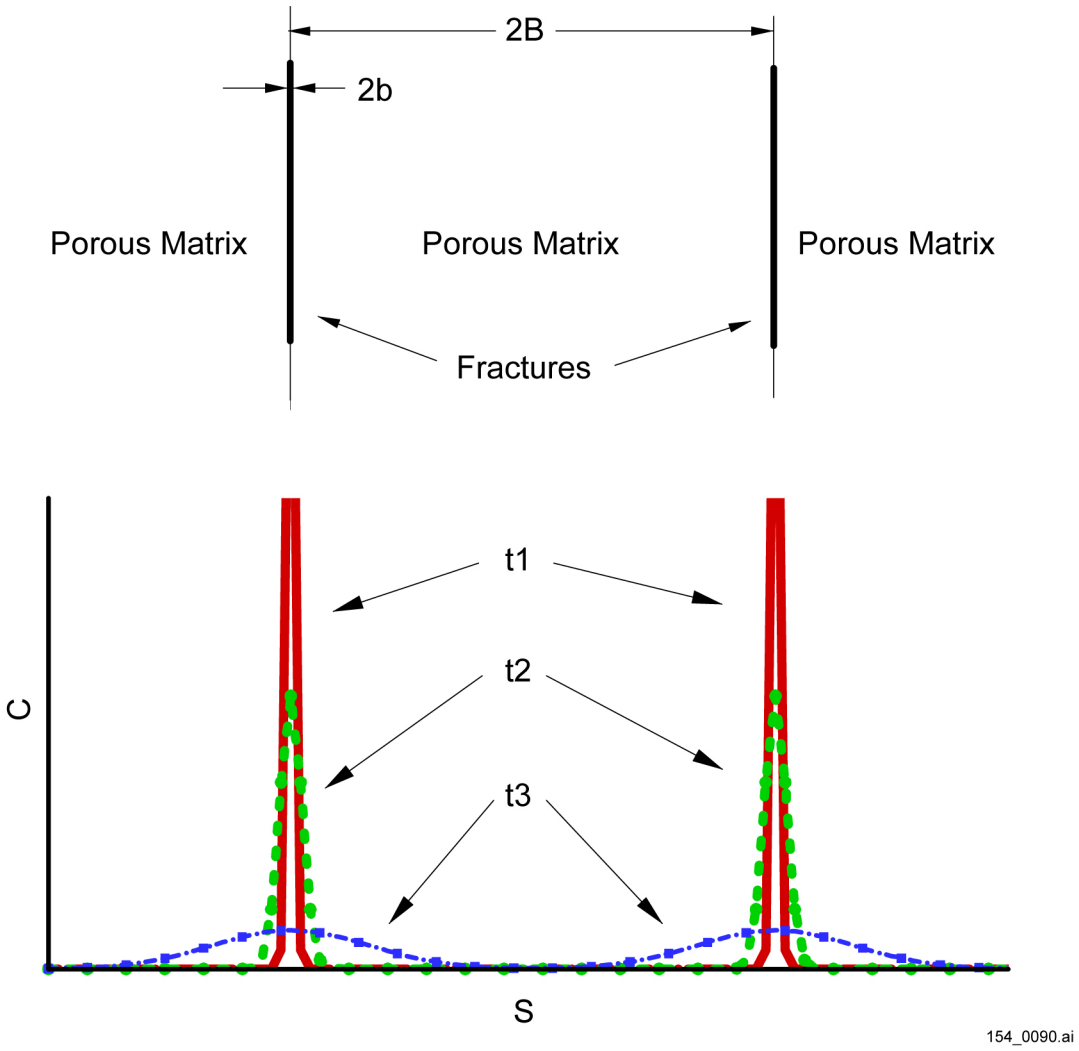

154_0090.ai

Source: TerBerg 2001 [DIRS 155033].

NOTE: C can be interpreted as the probability density function of the particles t3>t2>t1. S = distance, B = fracture spacing, and b = fracture aperture.

Figure 11.3.3-1. Schematic of the Propagation of a Pulse in Fracture-Matrix System with Time

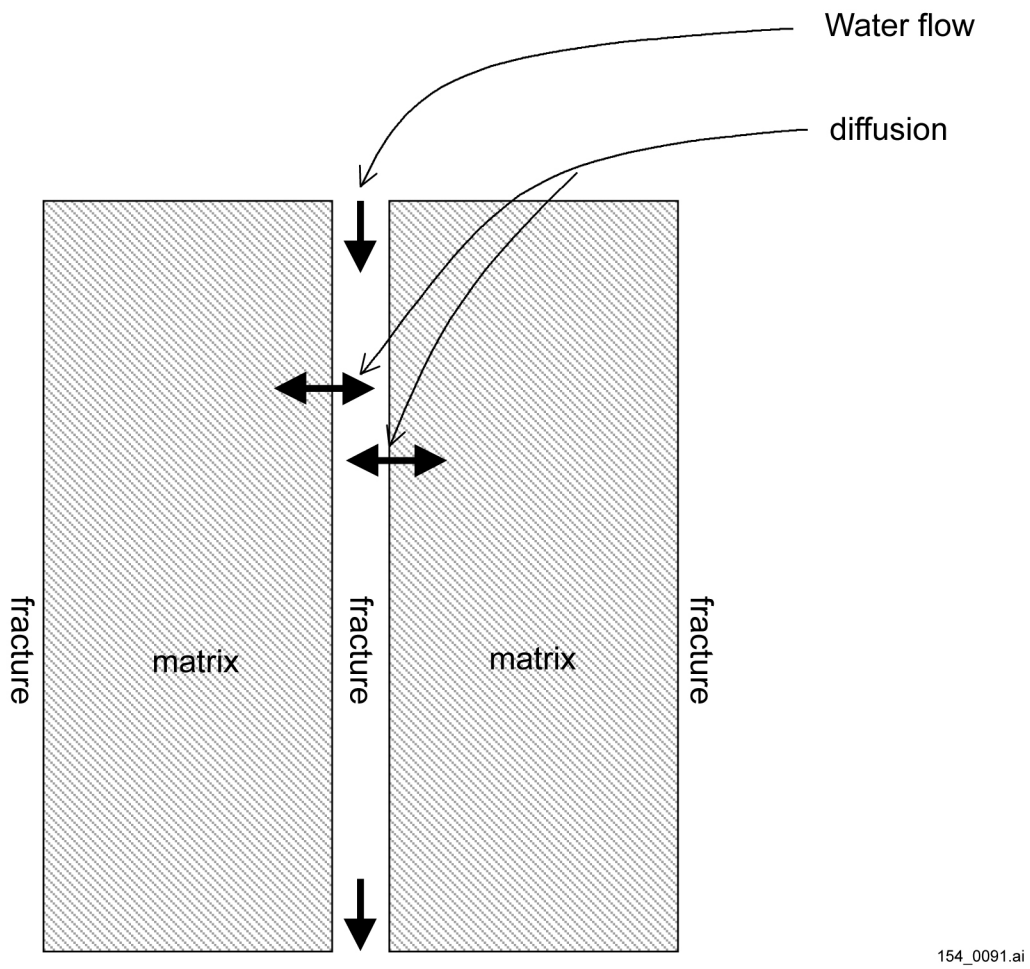

154_0091.ai

Source: TerBerg 2001 [DIRS 155033].

Figure 11.3.3-2. Schematic of a Parallel Fracture System without Water Flow between the Fractures and the Matrix

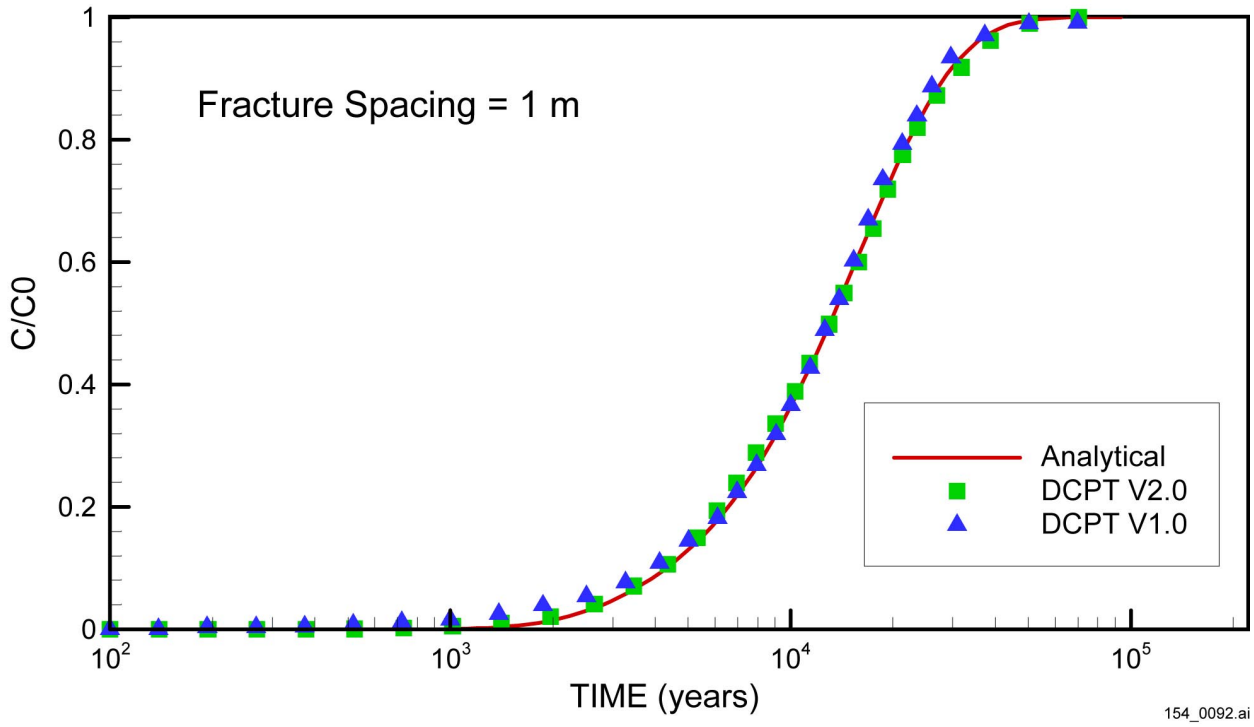

154_0092.ai

Source: TerBerg 2001 [DIRS 155033].

NOTE: The current model uses DCPT v1.0; DCPT v2.0 is a more-refined version. C is the concentration of tracer, and CO in the concentration at inlet.

Figure 11.3.3-3. Predicted Breakthrough of the Current Model, a More-Refined Model, and the Analytical Solution using 1 m Fracture Spacing

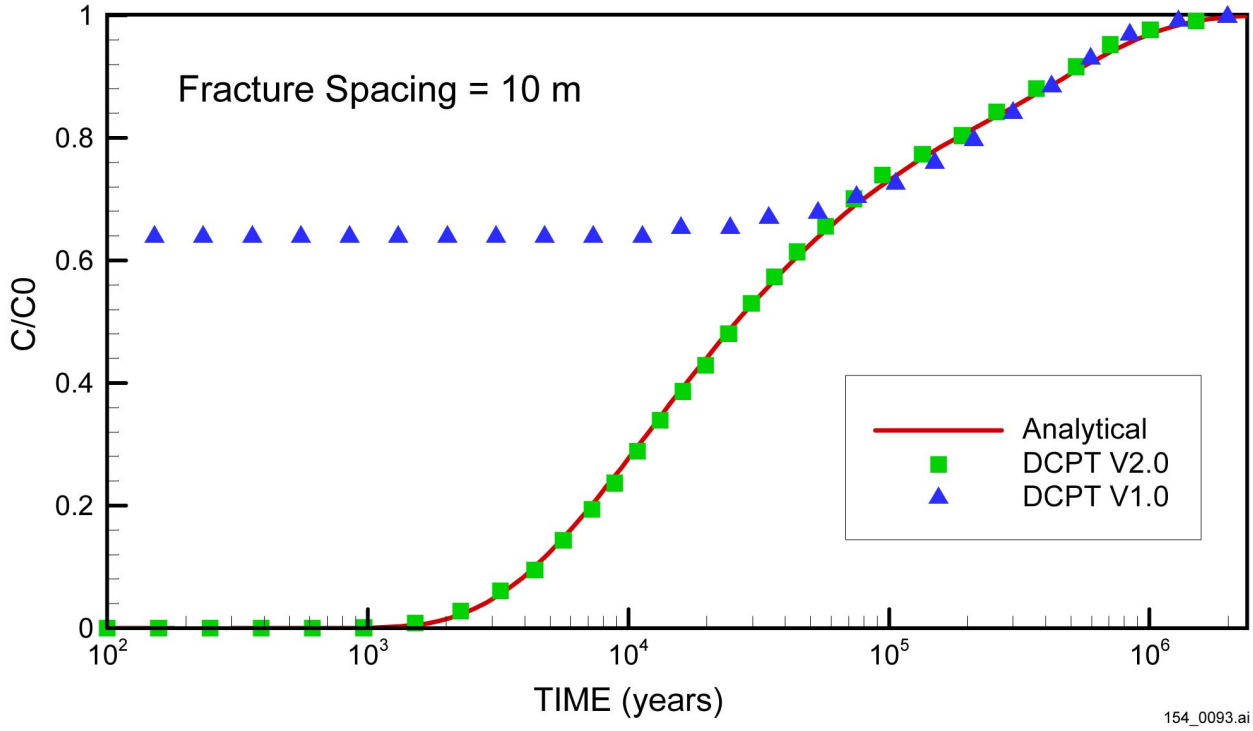

154_0093.ai

Source: TerBerg 2001 [DIRS 155033].

NOTE: The current model uses DCPT v1.0; DCPT v2.0 is a more-refined version. C is the concentration of tracer, and CO is the concentration at inlet.

Figure 11.3.3-4. Predicted Breakthrough by the Current Model, a More-Refined Model, and the Analytical Solution using 10 m Fracture Spacing

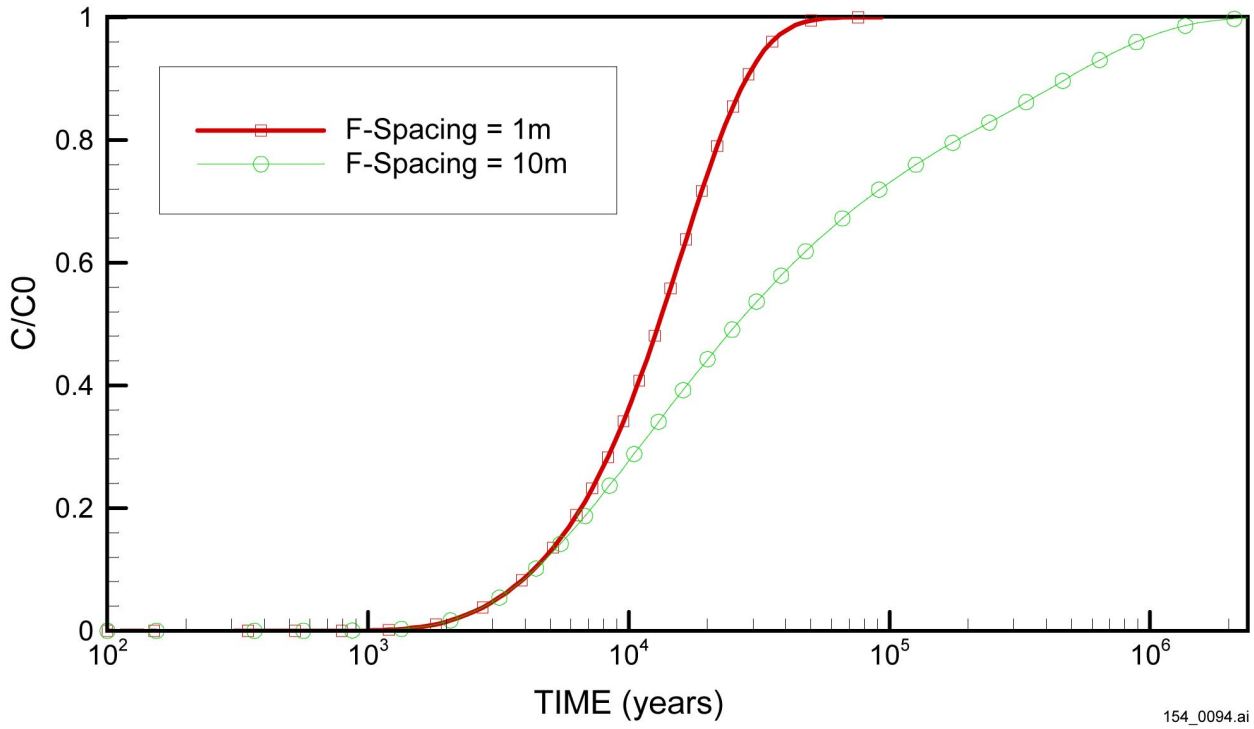

154_0094.ai

Source: TerBerg 2001 [DIRS 155033].

NOTE: C is the concentration of tracer, and CO is the concentration at inlet.

Figure 11.3.3-5. Effect of Fracture Spacing on Breakthrough as a Function of Time

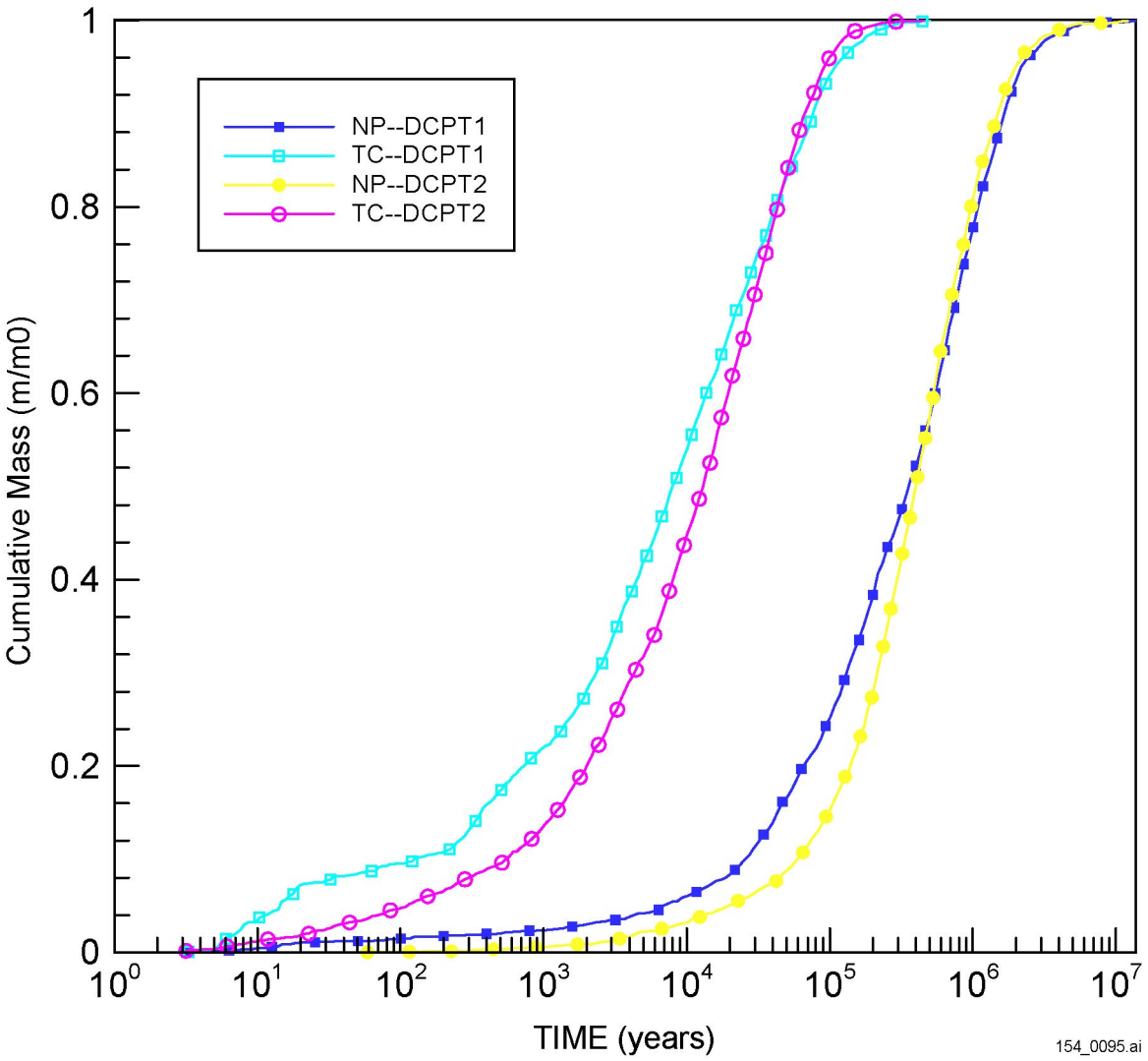

154_0095.ai

Source: TerBerg 2001 [DIRS 155033].

NOTE: The current model uses DCPT v1.0; DCPT v2.0 is a more-refined version. The base case is TSPA-SR (CRWMS M&O 2000 [DIRS 153246] with present-day mean infiltration. NP = neptunium, TC = technetium.

Figure 11.3.3-6. Predicted Cumulative Breakthrough Curves for the Base Case of the Unsaturated Zone Transport System, the Current Model, and the More-Refined Model

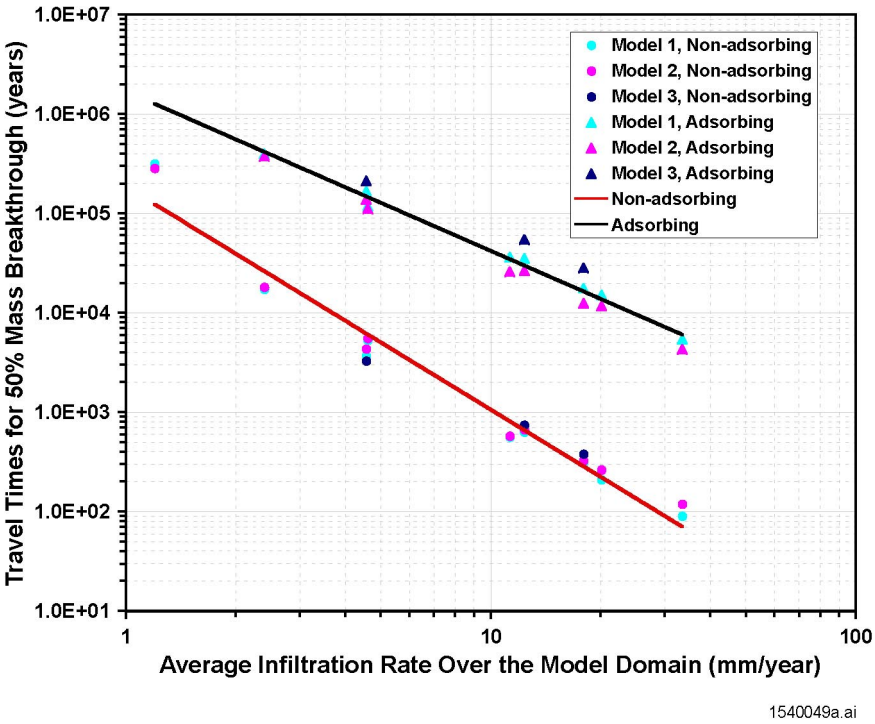

154_0049a.ai

Source: CRWMS M&O 2000 [DIRS 122797], Figure 6-57, Tables 6-29, 6-30, and 6-31.

NOTE: Transport times at 50 percent mass breakthrough for 42 simulation scenarios (model 1, 2, and 3 denote three types of perched water models).

Figure 11.3.4-1. Correlations of Average Infiltration Rates and Groundwater Travel or Tracer Transport Times

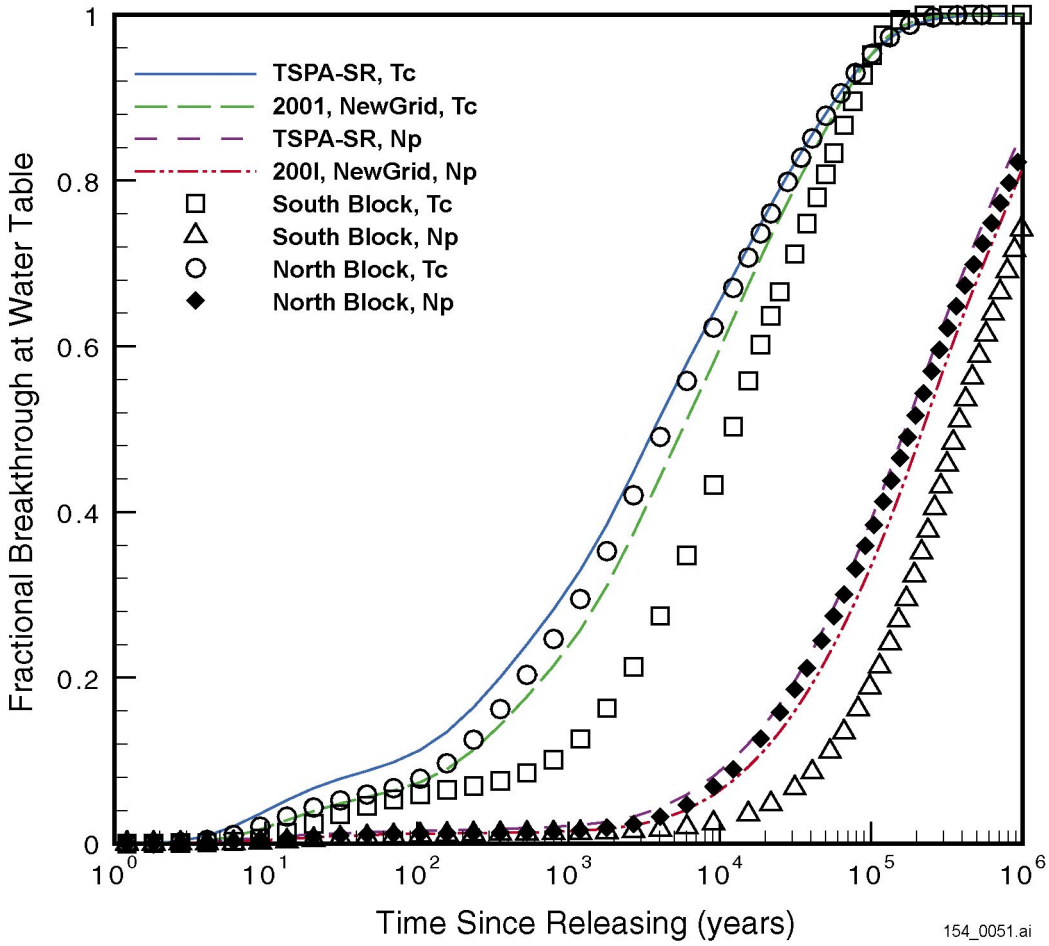

154_0051.ai

Source: Bodvarsson 2001 [DIRS 154669], Attachment 13, p. 27.

NOTE: TSPA-SR refers to results presented in CRWMS M&O (2000 [DIRS 153246]). TSPA-SR data were taken from CRWMS M&O (2000 [DIRS 122797], Section 6.7.3). Other data are from TerBerg (2001 [DIRS 155032]. Time since releasing from the potential repository using the new unsaturated zone flow field and TSPA-SR flow field for different releasing scenarios.

Figure 11.3.4-2. Simulated Breakthrough Curves of Cumulative Tracer and Radionuclide Mass Arriving at the Water Table

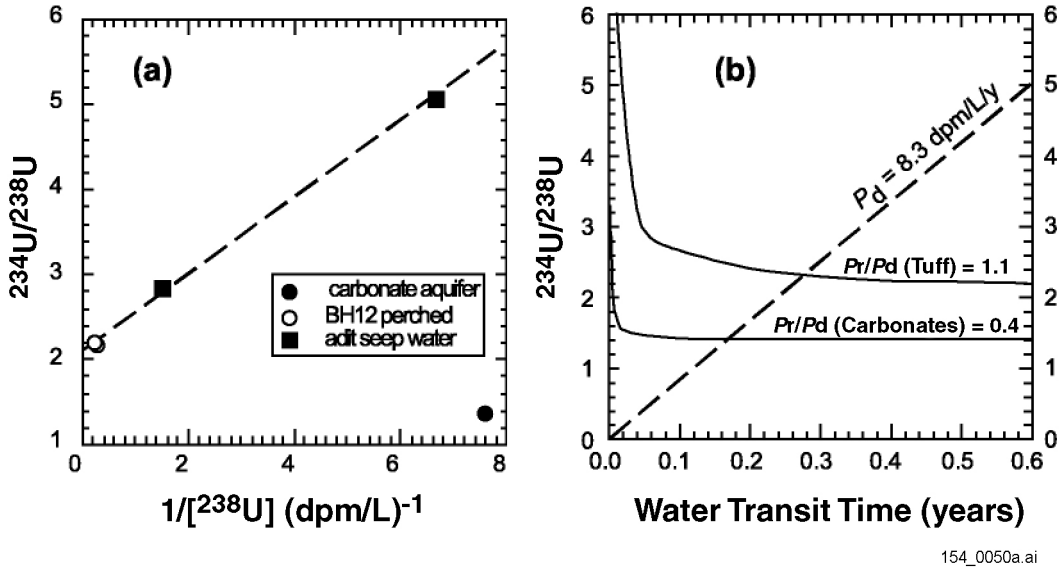

154_0050a.ai

Source: Pickett and Murphy 1999 [DIRS 110009], Figure 5) for (a); (b) derived from (a) as discussed below.

NOTE: Dashed line shows a positive linear correlation for waters sampled from the unsaturated zone. P is the supply rate of the dissolved nuclide through rock dissolution (P_d) and alpha recoil (P_r). The slope and intercept obtained through linear regression in (a) were used to derive P_d and P_r. shown in (b) (b) uranium-234/uranium-238 (solid lines), and uranium-238 activity (dashed line) as a function of water transit time in the unsaturated zone, showing a rapid decrease of uranium-234/uranium-238 to a relatively constant level within a couple of weeks after the water enters the unsaturated zone. To account for the low uranium-234/uranium-238 ratio of 1.39 in the carbonate-aquifer as shown in (a), the P_r/P_d ratio would be about 0.4, a ratio about three times smaller than that of unsaturated zone.

Figure 11.3.4-3. Uranium Activity Ratios in Peña Blanca Waters

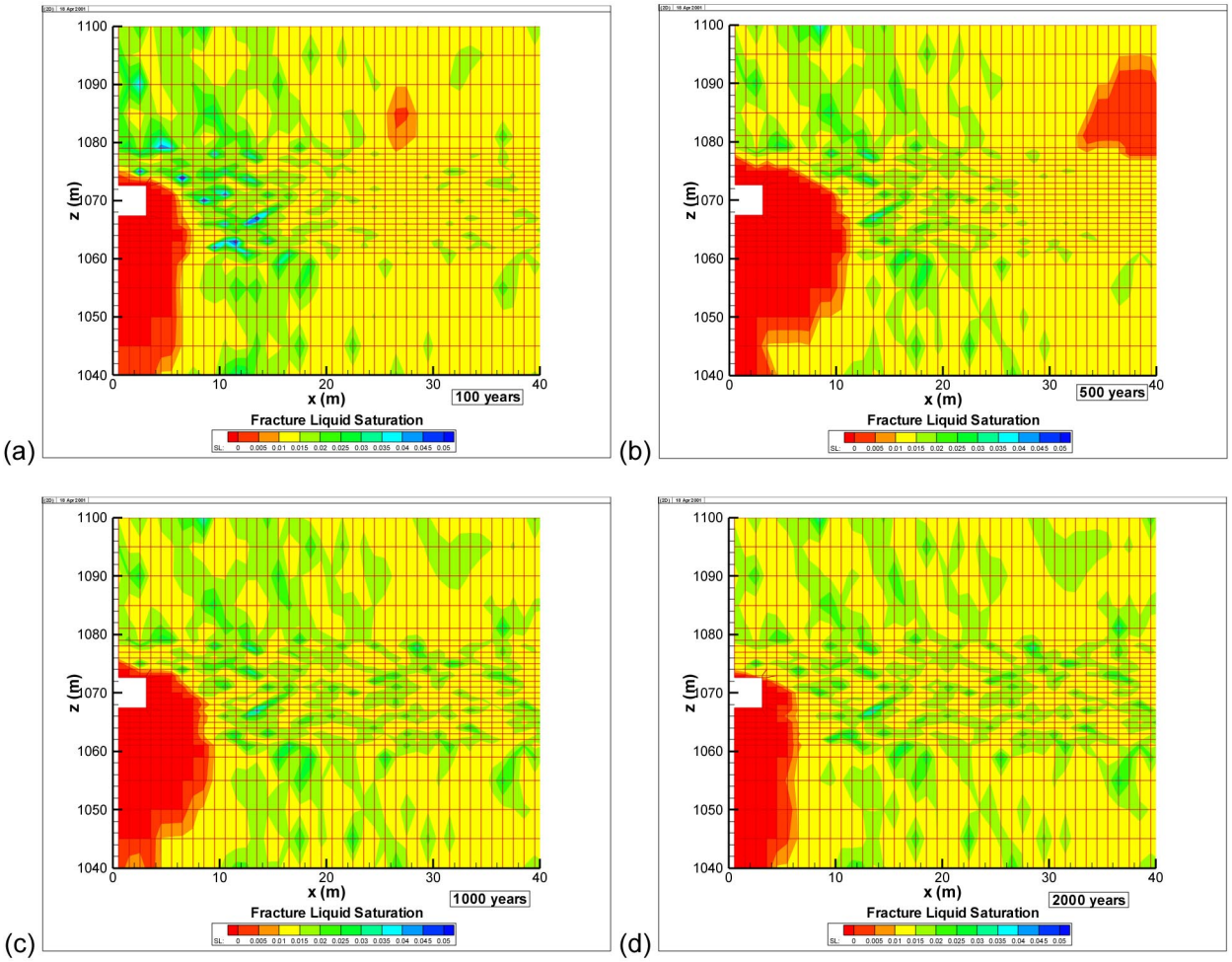

154_0258.ai

Source: Derived from data presented in Bodvarsson (2001 [DIRS 154669], Attachment 17, pp. 56 and 62).

NOTE: Four cases depict liquid saturation at (a) 100 years, (b) 500 years, (c) 1,000 years, and (d) 2,000 years.

Figure 11.3.5-1. Liquid Saturation Distributions in the Fracture Continuum for the Higher-Temperature Case

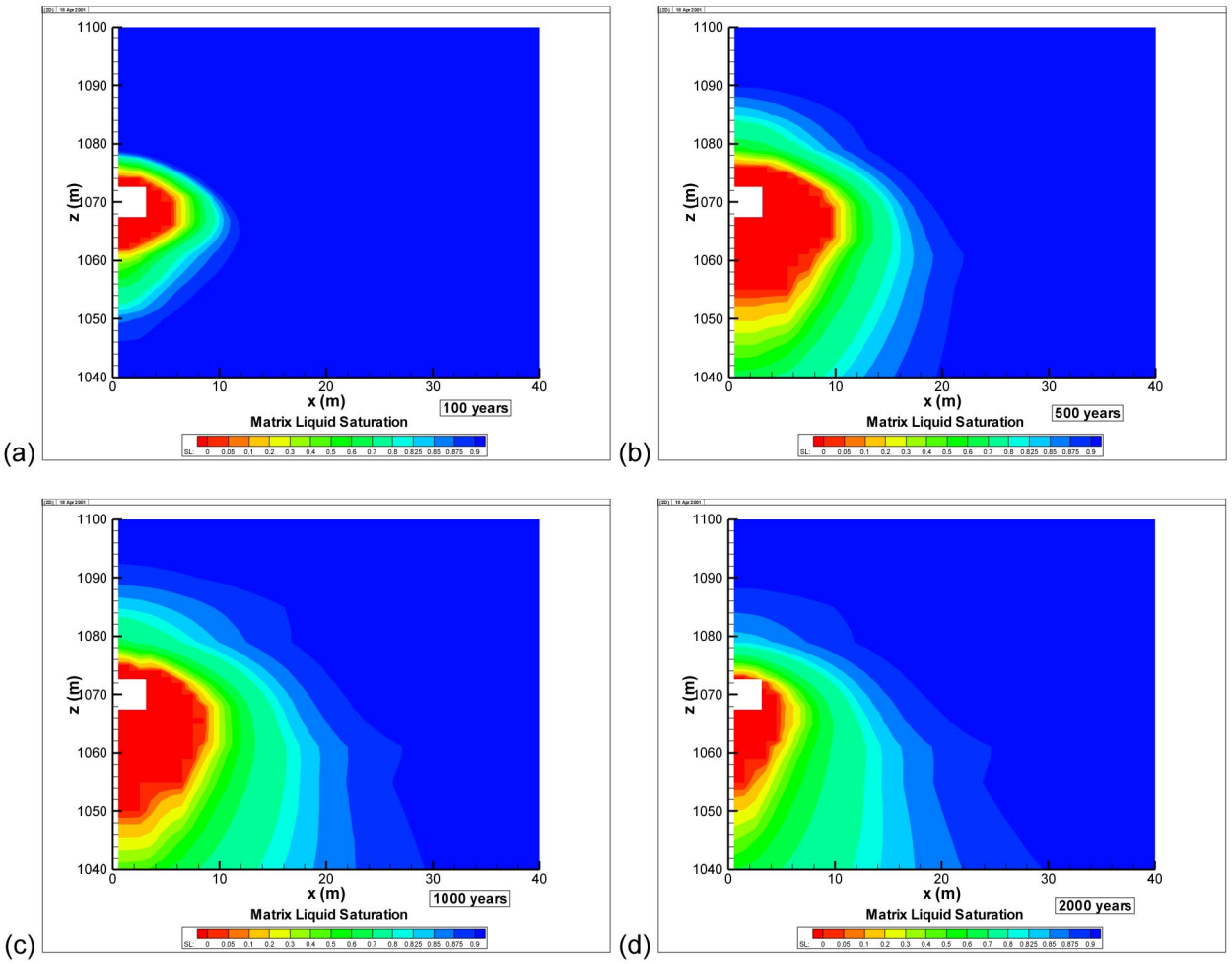

154_0257.ai

Source: Derived from data presented in Bodvarsson (2001 [DIRS 154669], Attachment 17, pp. 56 and 61).

NOTE: Four cases depict liquid saturation at (a) 100 years, (b) 500 years, (c) 1,000 years, and (d) 2,000 years.

Figure 11.3.5-2. Liquid Saturation Distributions in the Matrix Continuum for the Higher-Temperature Case

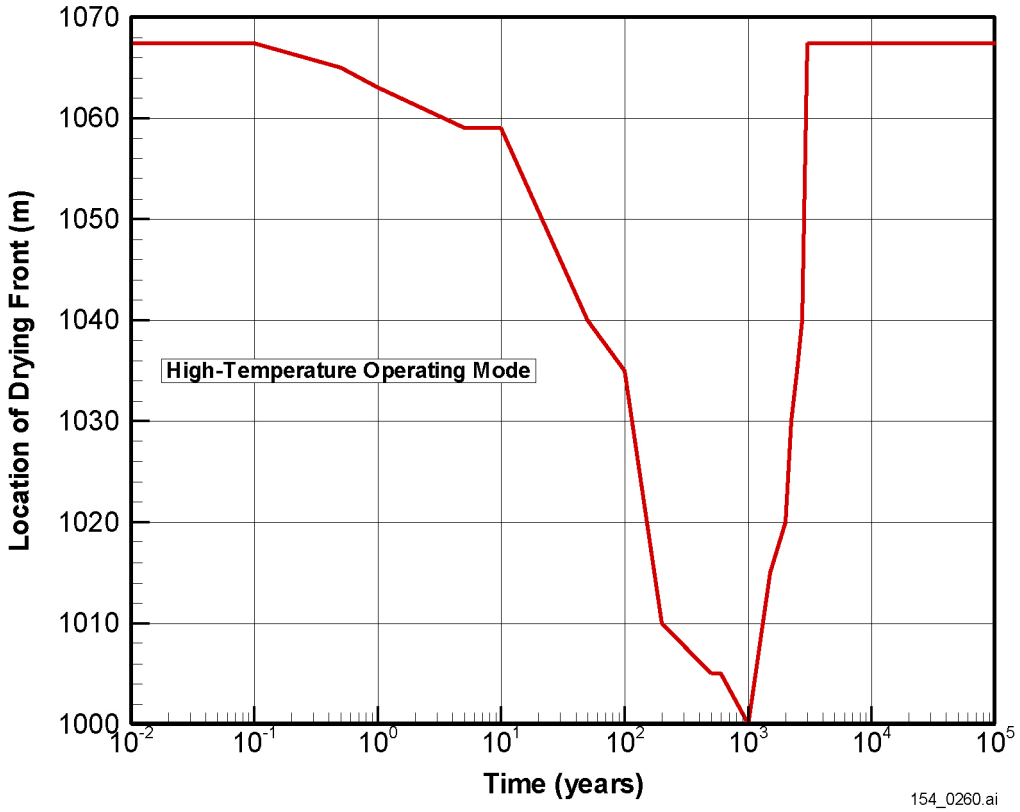

154_0260.ai

Source: Bodvarsson 2001 [DIRS 154669], Attachment 17, p. 77.

Figure 11.3.5-3. Changes in the Depth of the Dryout Zone over Time for the Higher-Temperature Case

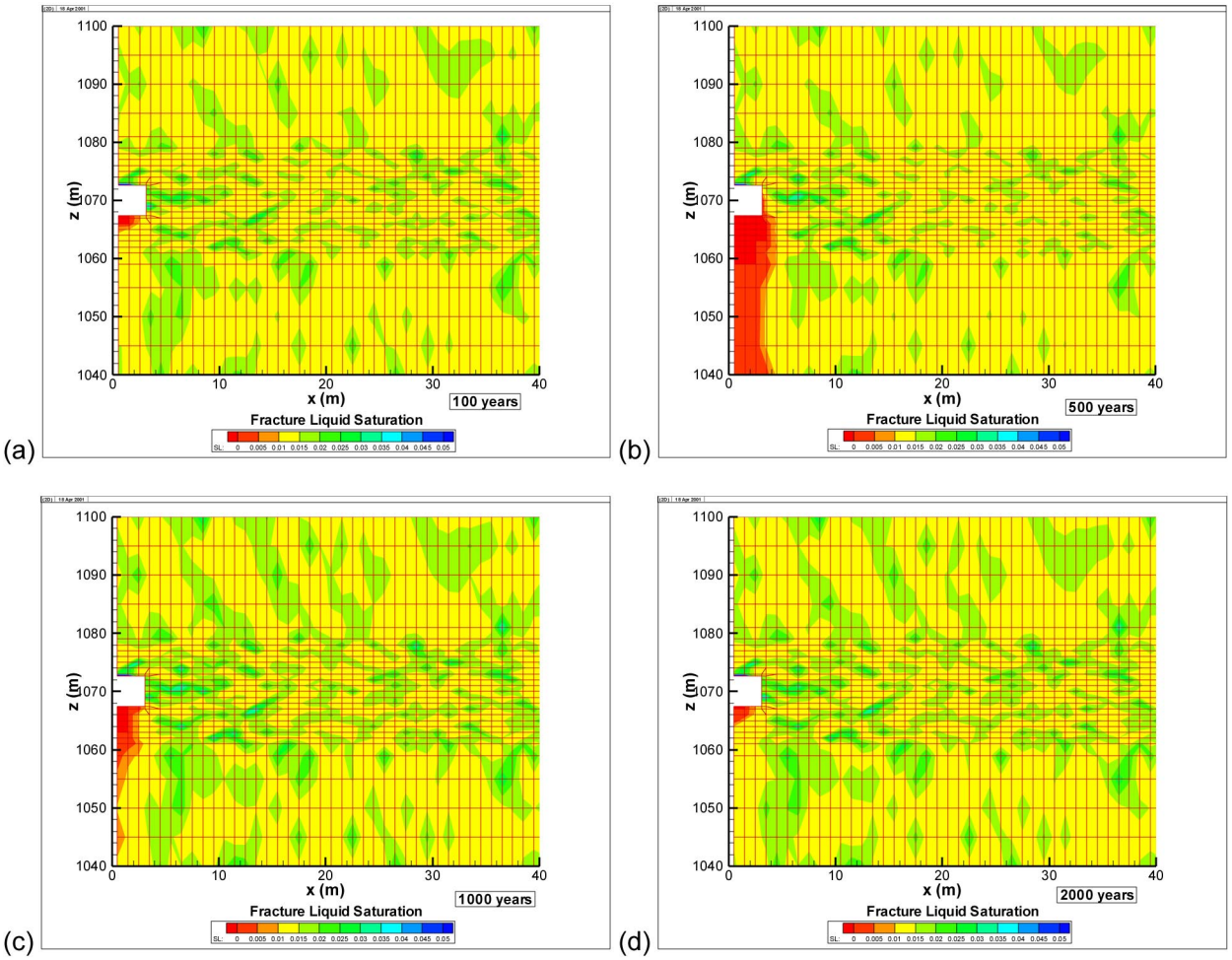

154_0259.ai

Source: Derived from data presented in Bodvarsson (2001 [DIRS 154669], Attachment 17, pp. 69 and 71).

NOTE: Four cases depict liquid saturation at (a) 100 yrs, (b) 500 yrs, (c) 1,000 yrs, and (d) 2,000 yrs.

Figure 11.3.5-4. Liquid Saturation Distributions in the Fracture Continuum for the Lower-Temperature Case

INTENTIONALLY LEFT BLANK

12 Radionuclide Transport in the Saturated Zone

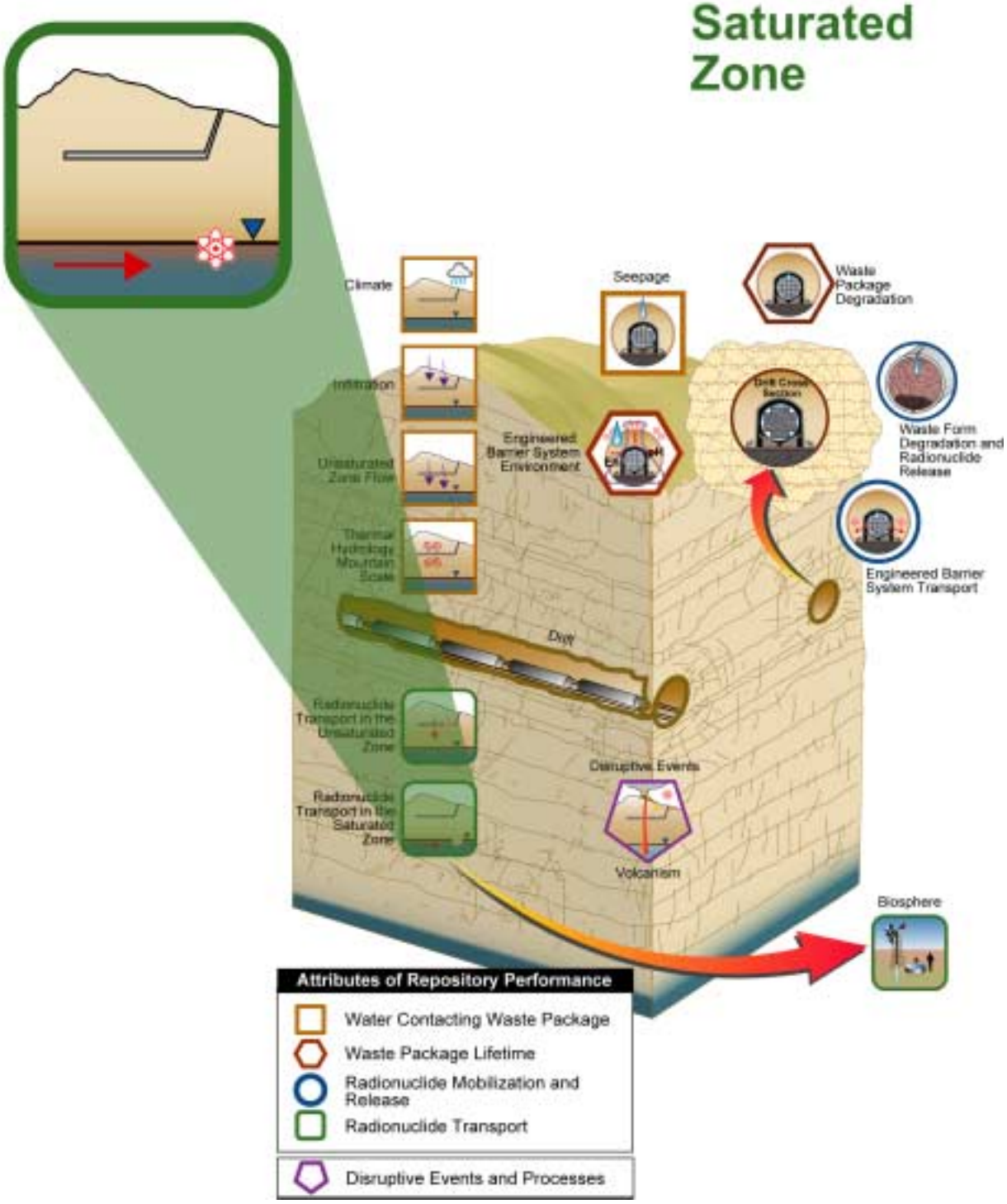

12. RADIONUCLIDE TRANSPORT IN THE SATURATED ZONE

The objective of this section is to evaluate the effect of saturated zone (SZ) information collected since the completion of the *Total System Performance Assessment for the Site Recommendation* (TSPA-SR) (CRWMS M&O 2000 [DIRS 153246]). The new information includes new data, revisions of numerical models, sensitivity analyses, and evaluation of multiple lines of evidence to increase confidence in models used to simulate flow and transport processes. A summary of the supplemental models and new analyses is given in Table 12-1.

12.1 INTRODUCTION

The *Saturated Zone Flow and Transport Process Model Report* (SZ PMR) (CRWMS M&O 2000 [DIRS 153168]) provides details of SZ data and modeling that have been conducted in support of the TSPA-SR (CRWMS M&O 2000 [DIRS 153246]). Characterizing and understanding the flow and transport of radionuclides through the SZ is important in assessing the overall strategy for safely storing radioactive materials at the potential Yucca Mountain repository. If radioactive materials in the potential repository escaped from breached waste packages, they would have to migrate approximately 300 m downward through the unsaturated zone (UZ) to reach the water table and then travel horizontally for approximately 20 km to reach the accessible environment. The nature of the rocks encountered by these radioactive particles along the 20-km flow paths in the SZ, and the time it takes for the particles to travel through the SZ, greatly affects the amount and nature of any materials that might be released to the accessible environment. Thus, the SZ reduces the potential for release through the processes of naturally attenuating radionuclide concentrations and delaying the arrival of radionuclides to the accessible environment.

The water table (i.e., the top of the SZ) under the potential repository occurs in volcanic rocks of the Tertiary Crater Flat Group in a hydrostratigraphic unit referred to as the lower volcanic aquifer. The lower volcanic aquifer is composed of three lithologic units: the Tram, Bullfrog, and Prow Pass Tuffs. After infiltrating water reaches the water table, it joins with groundwater in the lower volcanic aquifer and flows away from the potential repository area in a southeasterly direction, remaining in rocks of the Crater Flat Group. The matrix permeability of the unfractured tuffs in the Crater Flat Group is low; consequently, most of the groundwater flow in these rocks occurs in fractures.

The volcanic rocks are about 2,000 m thick beneath the potential repository, but they thin to the south and interfinger with Tertiary and Quaternary sediments. Along the flow path, at a distance somewhere between 10 and 20 km from the potential repository, groundwater close to the water table enters the valley-fill alluvium and then flows in the alluvium (Figure 12.1-1). The exact location of the transition zone from the volcanic aquifer to the alluvium is uncertain. Section 12.3.1.2.2 discusses new data related to the transition zone. Flow in the alluvium is thought to occur through pores between grains rather than in fractures. Because the effective porosity of alluvium is larger than the effective porosity of fractured rocks, the velocity of transport is expected to be slower in the alluvium.

Table 12-1. Summary of Supplemental Models and Analyses

Key Attributes of System	Process Model (Section of S&ER)	Topic of Supplemental Scientific Model or Analysis	Reason For Supplemental Scientific Model or Analysis			Section of Volume 1	Performance Assessment Treatment of Supplemental Scientific Model or Analysis[a]	
			Unquantified Uncertainty Analysis	Update in Scientific Information	Lower-Temperature Operating Mode Analysis		TSPA Sensitivity Analysis	Included in Supplemental TSPA Model
Delay and Dilution of Radionuclide Concentrations by the Natural Barriers	Saturated Zone Radionuclide Flow and Transport (4.2.9)	Groundwater specific discharge	X	X		12.3.1	X	
		Effective diffusion coefficient in volcanic tuffs	X			12.3.2	X	
		Flowing interval spacing				12.3.2	X	
		Flowing interval (fracture) porosity	X			12.3.2	X	
		Effective porosity in the alluvium	X			12.3.2	X	
		Correlation of the effective diffusion coefficient with matrix porosity	X			12.3.2	X	
		Bulk density of the alluvium	X	X		12.3.2	X	X
		Retardation for radionuclides irreversibly sorbed on colloids in the alluvium	X	X		12.3.2	X	
		No matrix diffusion in volcanic tuffs case				12.5.2	X	
		Presence or absence of alluvium				12.5.2	X	
		Sorption coefficient in alluvium for I, Tc	X	X		12.3.2	X	X
		Sorption coefficient in alluvium for Np, U	X	X		12.3.2	X	
		Sorption coefficient for Np in volcanic tuffs	X			12.3.2	X	
		Kc model for groundwater colloid concentrations Pu, Am		X		12.5.2	X	
		Enhanced matrix diffusion in volcanic tuffs				12.5.2	X	
		Effective longitudinal dispersivity	X	X		12.3.2	X	
		New dispersion tensor		X		12.3.2		
		Flexible design			X	12.3.2		
		Different conceptual models of the large hydraulic gradient and their effects on the flow path and specific discharge		X		12.3.1		
		Hydraulic head and map of potentiometric surface		X		12.3.1		

NOTE: S&ER = *Yucca Mountain Science and Engineering Report* (DOE 2001 [DIRS 153849]).

[a] Performance assessment treatment of supplemental scientific model or analysis discussed in SSPA Volume 2 (McNeish 2001 [DIRS 155023]).

Important physical processes relevant to radionuclide transport in the SZ are advection, dispersion, sorption of radionuclides, matrix diffusion in fractured media, colloid-facilitated transport, and radioactive decay and ingrowth (CRWMS M&O 2000 [DIRS 153168]). The following list provides brief definitions of these terms and describes how they relate to the conceptual model of site-scale SZ flow and transport:

- Advection is the process by which solutes (dissolved substances) are transported by the motion of naturally flowing groundwater.

- Dispersion is the spreading and dilution of solutes transported in groundwater that results from mixing due to variations in fluid flow. These variations in flow are caused by heterogeneities in the subsurface materials through which the flow occurs at a variety of scales, ranging from the pore scale to the scale of the thickness of an individual stratum and to the length of structural features (such as faults).

- Sorption is a general term to describe the binding of a solute onto a material (e.g., mineral grains in the matrix of the tuffs, minerals making up the particles of the alluvium, or colloids). Sorption in the rock matrix and the alluvium retards transport, whereas sorption on colloids can facilitate transport.

- Matrix diffusion is the movement of solutes from groundwater flowing in fractures into the relatively stagnant pore water of the rock matrix and is caused by differences in concentration. When a molecule enters the matrix, its velocity effectively goes to zero until Brownian motion carries it back into a fracture. The result is a delay of the arrival of the solute at a downgradient location from what would be predicted if the solute had remained in the fracture. Thus, matrix diffusion is a transport process that tends to retard the migration of radionuclides through the fractures in the moderately to densely welded tuffs of the SZ. This effect can be further enhanced by sorption of a dissolved radionuclide onto the matrix material once it enters the matrix by diffusion.

- Colloids are tiny particles (i.e., clay minerals, metal oxides, viruses, bacteria, and organic macromolecules) that range in size from 1 to 10,000 nm. These particles can be transported as suspended solids in the groundwater flow. Dissolved radionuclides can bind to colloids and be transported with them.

- Ingrowth is the production over time of radionuclides as decay products of other radionuclides. A particular radionuclide will decay into other radionuclides in a certain amount of time, depending on its half-life. This process is simulated with a one-dimensional model used to track radionuclide decay and radionuclide ingrowth so they are accounted for in the modeling predictions.

This section describes new information developed since completion of the initial analysis model reports (AMRs), process model reports (PMRs), the TSPA-SR (CRWMS M&O 2000 [DIRS 153246]), and the *Yucca Mountain Science and Engineering Report* (DOE 2001 [DIRS 153849]). The new information includes:

- New data and analyses to quantify previously unquantified uncertainties and to establish new uncertainty ranges.
- New data, and new technical work at the process-model level.
- Multiple lines of evidence, including natural analogues, hydrochemical and isotopic analyses, and other lines of evidence. The multiple lines of evidence are used to independently support the identification of processes affecting flow and transport, the numerical modeling of the processes, and the modeling predictions.

Much of the new information reported in Section 12 comes from sensitivity analyses. The objectives of these sensitivity analyses include, but are not limited to, examination of previously unquantified uncertainty, scoping calculations, and additional conceptual models. It is anticipated that many of the scoping calculations and sensitivity analyses will not be carried forward to future baseline project documents. Consequently, a fully-documented basis for the assumptions used in these calculations and analyses has not been developed.

Several types of new data and information have been obtained as part of the Nye County Early Warning Drilling Program (NC-EWDP). Under this program, the Nye County Nuclear Waste Repository Project Office, the U.S. Geological Survey (USGS), and the Yucca Mountain Site Characterization Office jointly collect data to characterize the saturated zone down gradient of Yucca Mountain. New measurements of hydraulic head were obtained as described in Section 12.3.1.2. These include new measurements in the NC-EWDP Phase II wells and updated water levels for Phase I wells. Lithologic descriptions and stratigraphic correlations have been completed for the Phase I and Phase II wells. Measurements of sorption coefficients in laboratory batch tests have confirmed that iodine-129 and technetium-99 are essentially nonsorbing in the alluvium under oxidizing conditions. New data from column and batch experiments have been used to define the K_d estimate for neptunium-237. Preliminary results indicate significant filtration of colloids at the Alluvium Testing Complex (ATC). In modeling, a preliminary analysis of the ATC single-well tracer test data has corroborated a continuum porous-media conceptual model for the alluvium hydrogeologic units (Section 12.3.1.2). A complete discussion of new data for flow and transport since the TSPA-SR (CRWMS M&O 2000 [DIRS 153246]) is presented in Sections 12.3.1.2 and 12.3.2.2, respectively.

Uncertainty in flow and transport modeling arises from a number of sources, including the conceptual model of the processes affecting groundwater flow and transport, water-level measurements, simplification of the model geometry, simplification of the boundary conditions, the values of permeability assigned to hydrogeologic units, and simplification of the parameters and geometry of matrix diffusion, dispersion, and sorption models. These various types of uncertainty are accounted for explicitly in the TSPA-SR site-scale SZ flow and transport model through key parameters and conceptual models. Key uncertain SZ parameters are represented stochastically as input to the site-scale SZ model. Examples of some of the important parameters

that are considered stochastically are the specific discharge under Yucca Mountain, the northern and western boundaries of the alluvium, the flowing interval spacing and porosity, sorption coefficients, and dispersivities. Horizontal anisotropy is included as an alternate conceptual flow model by considering an isotropic and an anisotropic case.

An unquantified uncertainty analysis of the site-scale SZ flow and transport model was performed based on results of the TSPA-SR (CRWMS M&O 2000 [DIRS 153246]). The unquantified uncertainty analysis consisted of multiple (100) simulations of radionuclide transport with the site-scale SZ model in which all changes resulting from the unquantified uncertainty analysis were included, as discussed in Section 12.5.1. The resulting SZ radionuclide breakthrough curves for the unquantified uncertainty case are supplied to the total system performance assessment (TSPA) simulator for the SSPA Volume 2 (McNeish 2001 [DIRS 155023]) calculations of simulated dose rates. In general, identification of unquantified uncertainty for the site-scale SZ flow and transport model consisted of re-evaluation of previously quantified uncertainty with focus on the parameters that were most important to performance. Sections 12.3.1.4 and 12.3.2.4 provide the basis for the parameters that were re-evaluated as part of the unquantified uncertainty analysis. A sensitivity analysis based on the TSPA-SR was performed to evaluate the relative importance of the stochastically varied parameters. The results indicated that the median travel time of a conservative species was most sensitive to variations in the groundwater specific discharge beneath Yucca Mountain, with the sorption coefficients, extent of the flow path in the alluvium, and parameters associated with diffusion of solutes into the rock matrix being of secondary importance (Kuzio et al. 2000 [DIRS 154928]) in the TSPA-SR. The groundwater specific discharge parameter was re-evaluated and is discussed in Sections 12.3.1.4.

Parameters affecting transport that were reevaluated as part of the unquantified uncertainty analysis included:

- Distribution of sorption coefficients for neptunium in volcanic rock and alluvium (Sections 12.3.2.4.1 and 12.3.2.4.2)
- Sorption coefficient for Uranium in alluvium (Section 12.3.2.4.3)
- Bulk density of the alluvium (Section 12.3.2.4.4)
- Retardation of radionuclides irreversibly sorbed onto colloids (Section 12.3.2.4.5)
- Distribution of the effective matrix diffusion coefficients and its correlation with the matrix porosity in volcanic rock (Section 12.3.2.4.6)
- Effective porosity of the alluvium (Section 12.3.2.4.7)
- Flowing interval (fracture) porosity in the volcanic rock (Section 12.3.2.4.8).

The bulk density in the alluvium was the only parameter that was a constant value in the TSPA-SR, and as a result of the unquantified uncertainty analyses, it was changed from a constant to a stochastic variable.

Various sensitivity analyses were conducted with the site-scale SZ flow and transport model in support of the SSPA Volume 2 calculations (McNeish 2001 [DIRS 155023]), as discussed in Section 12.5.2. The sensitivity analyses resulted in SZ radionuclide breakthrough curves that are being supplied to the TSPA simulator for the calculation of simulated dose rates in the SSPA Volume 2 (McNeish 2001 [DIRS 155023]). These analyses are performed to evaluate the sensitivity of the SSPA Volume 2 model results (McNeish 2001 [DIRS 155023]) to different parameters. Results of these sensitivity analyses are presented as histograms of times of median breakthrough curves in Section 12.5.2. The analyses investigate the effect of no matrix diffusion in the volcanic units, enhanced matrix diffusion in the volcanic units, a minimum length of alluvium in the flow path, and increased uncertainty in the reversible colloid model. The results of the sensitivity analyses in the SSPA Volume 2 calculations are discussed in more detail in McNeish (2001 [DIRS 155023], Section 3.2.10).

Additionally, sensitivity analyses and new technical work at the process-model level are described in Sections 12.3.1.3 and 12.3.2.3. These analyses are not carried forward to the SSPA Volume 2 calculations (McNeish 2001 [DIRS 155023]). The analyses include discussion of different conceptual models of the large hydraulic gradient, alternative conceptualizations of the Solitario Canyon fault, flexible repository design, new dispersion tensor, effective longitudinal dispersivity in the site-scale SZ flow and transport model, and matrix diffusion sensitivity analyses.

Section 12.4 describes the multiple lines of evidence in support of flow and transport parameter estimation and modeling at Yucca Mountain. The following areas are discussed: evidence for flow paths based on groundwater hydrochemical and isotopic data, uranium mill tailing analogues, preliminary tracer testing results in the alluvial testing complex, Electric Power Research Institute flow and transport modeling, and data transport studies on blocks of intact tuff. The primary goal of this portion of the work is to develop additional confidence in the models and parameters used for the TSPA.

12.2 REVIEW OF TOTAL SYSTEM PERFORMANCE ASSESSMENT-SITE RECOMMENDATION TREATMENT OF RADIONUCLIDE FLOW AND TRANSPORT IN THE SATURATED ZONE

The objective of the SZ flow and transport modeling effort is to provide breakthrough curves for individual radionuclides for input to performance assessment calculations. A breakthrough curve is the variation with time of the mass flux of an individual radionuclide at a distance of 20 km from the potential repository. Developing this input to performance assessment calculations has three steps: (1) hydrogeologic characterization, (2) generation of the site-scale calibrated flow field, and (3) abstraction of SZ flow and radionuclide transport modeling for performance assessment analyses. The first step provides the conceptual basis for developing numerical models used in the second and third steps. The calibrated flow field generated by the second step is used in radionuclide transport calculations performed during the third (abstraction) step.

Section 12.2 provides a summary of the process used to develop SZ input to the TSPA-SR (CRWMS M&O 2000 [DIRS 153246]). A more detailed discussion of this process is presented in the SZ PMR (CRWMS M&O 2000 [DIRS 153168], Section 3.6). An important aspect of this process is that it is periodically updated to include revised interpretations of hydrogeologic data,

new results from field and laboratory experiments, model developments, and quantification of uncertainty. A discussion of changes in these areas since the TSPA-SR is provided in Section 12.3.

12.2.1 Hydrogeologic Characterization

A large amount of information about the regional-scale hydrogeology has been learned from activities of the Yucca Mountain Site Characterization Project and from numerous hydrogeologic studies conducted in the vicinity of the Nevada Test Site (NTS). Specifically, sufficient information is available to describe the stratigraphy, structure, and hydraulic properties of rocks in this region, the recharge and discharge regions, and the groundwater flow paths.

As part of an ongoing effort, the USGS is conducting regional-scale simulations of groundwater flow in a hydrologic basin known as the Death Valley regional groundwater flow system. This model region includes the SZ flow paths from the repository to their discharge areas. This modeling effort, including data synthesis, geologic interpretation, and analysis of model results, provides an essential contribution to understanding of the hydrogeology in the vicinity of Yucca Mountain.

A detailed description of what is known about the hydrogeology of the Yucca Mountain region is contained in the SZ PMR (CRWMS M&O 2000 [DIRS 153168], Section 3.2). The following three paragraphs are abstracted from that document.

Natural recharge to the SZ is from precipitation that infiltrates at the land surface and percolates through the unsaturated zone. Recharge occurs primarily in mountainous areas where relatively large amounts of snow and rainfall occur. Areas of recharge include Yucca Mountain and other regions of higher elevation to the north and northeast. Natural discharge from the Death Valley flow system is from evapotranspiration and springs at low elevations, mainly in Death Valley, Ash Meadows, and Franklin Lake Playa. Groundwater flows from regions of recharge to regions of discharge. Flow paths in the SZ at the regional scale are inferred from a large number of measurements of water levels in boreholes and numerical modeling (D'Agnese et al. 1997 [DIRS 100131]). Taken together, information about recharge, discharge, and measured water levels provides a sound understanding of groundwater flow paths in the SZ in the vicinity of Yucca Mountain.

As groundwater moves from recharge to discharge areas, flow rates and paths depend largely on the hydraulic properties of the rocks and materials along the flow paths. Geologic studies provide a sufficient understanding to identify the important rock types and their spatial distribution. The rock types that play the largest role in regional hydrogeology are Paleozoic carbonates, Quaternary-Tertiary volcanic rocks, and Quaternary-Tertiary sediments and volcanic tuffs that fill structural depressions (referred to as valley-fill material in portions of this report). The valley fill is primarily alluvium. Relatively shallow flow occurs in the volcanic rocks and valley fill; deeper flow occurs in the regionally extensive carbonate aquifer. Along the inferred shallow flow path in the SZ from Yucca Mountain, groundwater flow occurs in volcanic rocks near the potential repository site and in younger valley-fill deposits at greater distances from the potential repository.

The permeability of the volcanic rocks in the vicinity of Yucca Mountain typically is increased by the presence of fractures. An extensive suite of field observations, interpretations of borehole logs, hydrologic tests in boreholes, lab-scale tests, and field tracer tests confirmed that fractures enhance groundwater flow in the volcanic rocks. However, flow in the alluvium occurs through the primary porosity (intergranular porosity) of these sediments.

12.2.2 Site-Scale Calibrated Flow Field

The purpose of the site-scale SZ flow and transport model is to provide a calibrated flow field as input to the step of abstracting SZ flow and radionuclide transport modeling for TSPA analyses. The flow field is three-dimensional and steady-state, and it assumes horizontally isotropic permeability within units and present-day climatic conditions. A detailed description of how this flow field was calculated is provided in the *Calibration of the Site-Scale Saturated Zone Flow Model* report (CRWMS M&O 2000 [DIRS 139582], Section 6). A brief summary is presented here.

A governing equation for mass conservation for flow described by Darcy's Law is solved numerically using the control-volume finite element method. The FEHM code (V2.00) is used to calculate a steady-state flow field. Zyvoloski et al. (1997 [DIRS 110491]) provide a description of the theoretical basis and capabilities of the code. The footprint of the site-scale SZ flow and transport model is a 30- by 45-km rectangle shown in Figure 12.2-1. The water table forms the upper surface of the model. The base of the model is a surface approximately 3,000 m below the water table. A structured grid of orthogonal hexahedral elements is used to discretize the model domain. Horizontal grid spacing is uniform (500 m), and vertical spacing ranges from 10 m near the water table to 550 m at depth.

Various aspects of the hydrogeology within the domain of the site-scale flow and transport model are being investigated as part of ongoing characterization of the region surrounding Yucca Mountain. These include the hydrostratigraphic framework, estimates of recharge rates, position of the water table, rates of groundwater flow at the model boundaries as provided by the USGS regional-scale flow model, and estimates of rock permeability. The site-scale flow and transport model used for input to the TSPA-SR used the most up-to-date information available to represent these aspects of hydrogeology, as described below.

Position of the Water Table–The position of the water table is shown in Figure 12.2-2. As noted above, this interpretation of the water table is used to define the upper surface of the site-scale flow and transport model. Also, the elevation of the water table along the model boundaries is applied as a constant-head boundary condition on the sides of the model. This interpretation of the water-level data assumes that several of the water levels measured north of Yucca Mountain represent the regional potentiometric surface rather than the top of zones of perched water. Consequently, this interpretation maximizes the gradient of the potentiometric surface north of Yucca Mountain. This region of steep gradient is referred to as the large hydraulic gradient. Analysis and interpretation of water-level data are discussed in detail in USGS (2001 [DIRS 154625], Section 6).

Hydrogeologic Framework Model–The geometry of regions with uniform permeability within the model domain is based on geometric modeling of the hydrostratigraphy and geologic

structure of the area. The result is referred to as the hydrogeologic framework model. The version of the hydrogeologic framework model used to support the TSPA-SR is documented in USGS (2000 [DIRS 146835], Section 6).

Treatment of Discrete Faults–One way in which alternative conceptual models are considered in the site-scale model is by representing faults that are believed to be hydrologically important as discrete features. Using this approach, various assumptions about the permeability, and anisotropy in permeability, of the individual faults can be tested. The fault properties assumed to calculate the calibrated flow field for the TSPA-SR are summarized in CRWMS M&O (2000 [DIRS 139582], Table 6).

Permeability Features Related to the Large Hydraulic Gradient–Some adjustments to the permeability distribution are required to better simulate the water levels that define the upgradient portions of the large hydraulic gradient. For the calculations used to generate input to the TSPA-SR, a planar east-west trending zone of low permeability (CRWMS M&O 2000 [DIRS 139582], Table 6) was positioned into the model domain to better match the observed water-level elevations. Alternative adjustments to the permeability distribution to better simulate the large hydraulic gradient are discussed in Section 12.3.1.3.

Recharge Estimates–Recharge is applied as a specified flux on the upper surface of the site-scale model. There are three components of the recharge distribution assumed for the site-scale model: distributed recharge used for the 1997 version of the USGS regional-scale model (D'Agnese et al. 1997 [DIRS 100131]), recharge calculated as the flux at the base of the UZ site-scale model, and focused recharge along Fortymile Wash. A detailed discussion of the assumed distribution of recharge is provided in CRWMS M&O (1999 [DIRS 130979], Section 6.1.1).

Calibration is the process by which values of important model parameters are estimated and optimized to produce the best fit of model output to observed data. For the site-scale flow and transport model, permeability values were optimized to minimize the sum of the squared differences between observed hydraulic conditions and those simulated by the site-scale SZ flow and transport model. Hydraulic conditions included water levels (hydraulic heads) at selected locations and lateral fluxes at selected model boundaries. The specific water levels and boundary fluxes are referred to as calibration targets. Water levels used as calibration targets are documented in USGS (2001 [DIRS 154625], Table I-1), and boundary fluxes used are documented in CRWMS M&O (1999 [DIRS 130979], Section 7.2).

Additional confidence in the results of the site-scale flow and transport model was obtained by comparing estimated to measured permeabilities and calculated flow paths to flow paths inferred from water chemistry data (CRWMS M&O 2000 [DIRS 139582], Section 6.7.8 and 6.7.6, respectively).

12.2.3 Abstraction of Saturated Zone Flow and Radionuclide Transport Modeling for Total System Performance Assessment Analyses

It is desirable to integrate detailed process-level modeling into performance assessment analyses to incorporate site-specific information about the system represented by the process-level model.

This may be accomplished by explicitly coupling the process-level computational model into the performance assessment simulator or by abstracting the process-level model results for incorporation into the performance assessment analyses. An abstraction approach was used to integrate SZ flow and transport modeling into TSPA-SR analyses primarily because of the size and complexity of the site-scale SZ flow and transport model. In addition, an abstraction approach that largely captures the information that is provided by the site-scale SZ flow and transport model about system behavior is possible. Details and results of the abstraction process, as applied to TSPA-SR, are provided in the *Input and Results of the Base Case Saturated Zone Flow and Transport Model for TSPA* report (CRWMS M&O 2000 [DIRS 139440], Section 6) and in the SZ PMR (CRWMS M&O 2000 [DIRS 153168], Section 3.7).

The site-scale SZ flow and transport model results are abstracted by performing radionuclide transport simulations that assume a constant, normalized radionuclide mass flux at the "upstream" end of the SZ. The resulting radionuclide mass breakthrough curves at the "downstream" end of the SZ basically contain all of the information about the model behavior for those source and receptor locations, assuming steady groundwater flow. Breakthrough curves for eight species or classes of species (CRWMS M&O 2000 [DIRS 139440], Section 6.3) are obtained for 100 stochastic realizations of the SZ system (the nominal case) and for one additional case using the median values for all stochastic parameters.

These results are obtained by running the site-scale SZ flow and transport model for each stochastic realization and saving the results for later use by the TSPA simulator. Radionuclide transport is simulated directly for those radionuclides that are not the product of radioactive decay and ingrowth using the FEHM V2.10 software code streamline particle-tracking algorithm. Radioactive ingrowth is the generation of radionuclide mass from the decay of a parent radionuclide.

Stochastic parameters are used to quantify uncertainty in radionuclide transport characteristics of the SZ system. Key parameters include those that describe sorption coefficients for sorbing radionuclides, flowing interval spacing, porosity, matrix porosity in fractured volcanic units, effective porosity in alluvial units, dispersivity, and effective diffusion coefficient. Parameter distributions and rationale are provided in CRWMS M&O (2000 [DIRS 147972]) and CRWMS M&O (2000 [DIRS 154927]). Additional data and inferences regarding colloid-facilitated transport of radionuclides are used (CRWMS M&O 2000 [DIRS 154927]) in the site-scale SZ flow and transport model to simulate this process (CRWMS M&O 2000 [DIRS 129286]; CRWMS M&O 2000 [DIRS 147972]). For the TSPA-SR, the stochastic parameters were sampled to generate the 100 random realizations of the SZ system.

In addition to the relatively high degree of uncertainty in the radionuclide transport characteristics of the SZ system, there is uncertainty in the groundwater flow in the system. Uncertainties exist in the SZ groundwater flux and in the direction of groundwater flow downgradient from the potential repository. To evaluate the uncertainty in groundwater flux, three discrete cases were examined. These consist of the mean case (corresponding to the mean flux of the calibrated site-scale SZ flow and transport model), the low case (mean flux times 0.1), and the high case (mean flux times 10). The flux multipliers and the corresponding probabilities for these cases are quantified based on the uncertainty distribution for specific discharge in the volcanic aquifer from the SZ expert elicitation (CRWMS M&O 1998 [DIRS 100353], p. 3-20).

The analysis is provided in CRWMS M&O (2000 [DIRS 139440], Section 6.2.5). Uncertainty in the direction of groundwater flow along the flow path from the potential repository is incorporated as alternative groundwater flow fields with and without horizontal anisotropy in permeability (CRWMS M&O 2000 [DIRS 147972]). The result of considering both types of uncertainty is six alternative groundwater flow fields (three flux cases times two anisotropy cases).

12.3 ACCOUNT FOR UNCERTAINTIES AND VARIABILITIES IN PARAMETER VALUES

This section provides supplemental information to the TSPA-SR (CRWMS M&O 2000 [DIRS 153246]) and reflects the current understanding of the flow of groundwater and transport of radionuclides through groundwater from beneath the potential repository to the accessible environment at the point of compliance per proposed NRC regulation 10 CFR Part 63 (64 FR 8640, Section 63.115(b) [DIRS 101680].

This section is subdivided into two subsections:

- Flow modeling and associated data and analyses (Section 12.3.1)
- Transport modeling and associated data and analyses (Section 12.3.2).

12.3.1 Groundwater Flow Modeling

This section covers new water-level, hydrostratigraphy, hydrochemistry, and testing data acquired in cooperation with Nye County; analyses using the flow model; and sensitivity analyses on the specific discharge and other flow parameters that affect the specific discharge.

12.3.1.1 Introduction and Goal of the Site-Scale Saturated Zone Flow Model

The purpose of the site-scale SZ flow model is to provide a calibrated flow field that is to be used for calculating radionuclide transport in the SZ. The same calibrated flow field was used for TSPA-SR and SSPA calculations. However, the site-scale model is in the process of being updated to include pertinent geologic and hydrologic information that has become available since the TSPA-SR (CRWMS M&O 2000 [DIRS 153246]) was published. An overview of this information is provided in Section 12.3.1.2. Also section 12.3.1.3 includes a discussion of developments in the numerical model and a model analysis that has been completed since the TSPA-SR was published. Revisions to the site-scale SZ flow model, discussed in Section 12.3.1.3, were not used in SSPA calculations. Unquantified uncertainty addressed in the SSPA Volume 2 (McNeish 2001 [DIRS 155023]) that pertains to the site-scale SZ flow and transport model is discussed in Section 12.3.1.4.

12.3.1.2 New Data and Analysis

The site-scale SZ flow model is being updated to include new data and geologic interpretations. New data and interpretations might require changes in the geometry of hydrostratigraphic units within the model domain, permeability values assigned to hydrostratigraphic units, hydraulic head values used as calibration targets, and boundary fluxes used as calibration targets. New

data and interpretations also help constrain conceptual models and, in some cases, are independent information that build confidence in the current model.

The new data and analysis described in this section will help future versions of the site-scale SZ flow and transport model to represent actual flow conditions in the vicinity of Yucca Mountain more accurately. The new information is not expected to result in significant changes at the TSPA level (CRWMS M&O 2000 [DIRS 139440]).

12.3.1.2.1 Hydraulic Head Data and Potentiometric Surface Map

New measurements of hydraulic head have been obtained as part of the Nye County cooperative program. These include new measurements in the NC-EWDP Phase II wells and updated water levels for Phase I wells (Figure 12.3.1.2-1). These new measurements will be used in calibrating future versions of the site-scale SZ flow model.

A revised potentiometric surface map covering the area of the site-scale SZ flow model (Figure 12.3.1.2.2) is being developed for use in future versions of the site-scale SZ flow model. This map will include data for well USW WT-24 and new data from the Nye County wells. In addition, the new map will present an alternative concept for water levels north of Yucca Mountain in the "large hydraulic gradient area." This concept assumes that water levels reported for wells USW G-2 and UE-25 WT#6 represent perched conditions and are not representative of regional potentiometric levels. Water levels at well USW WT-24, which are significantly lower than those reported for USW G-2 and UE-25 WT#6, are believed to represent the regional potentiometric level. These wells are located within several km of Yucca Mountain. Wells USW G-2 and UE-25 WT#6 are located 3 to 4 km north-northeast of Yucca Mountain. Well USW WT-24 is located about 1 km east of the crest of Yucca Mountain. The impact of this alternative conceptual model is that the large hydraulic gradient, although still present north of Yucca Mountain, is slightly more than half of the previously reported gradient. Tucci and Burkhardt (1995 [DIRS 101060], p. 9) report a value of 0.11 m/m for the large hydraulic gradient area; the gradient based on the revised potentiometric surface map ranges from 0.06 to 0.07 m/m.

Water-level measurements in the recently drilled NC-EWDP-2DB well also add information about differences in hydraulic head between the volcanic rocks and the underlying Paleozoic carbonate rocks. Previous to the drilling of NC-EWDP-2DB, there was only one other measurement of hydraulic head in the carbonate rocks at UE-25 p#1 within the domain of the site-scale SZ flow and transport model. Head measurements in that borehole, located about 4 km east of Yucca Mountain, indicated that the head in the carbonate rocks is about 20 m higher than the head in the overlying volcanic rocks (Craig and Johnson 1984 [DIRS 101039], p. 12). This difference in head is of interest because higher heads in the carbonate unit along flow pathways from the potential repository would prevent a contaminant plume from entering the regional-scale carbonate aquifer.

Water-level measurements in NC-EWDP-2DB, representing the head in the Paleozoic carbonate, indicate that the head in the carbonate rocks is about 714 m above mean sea level (NWPRO 1999 [DIRS 119607]). The head in the overlying volcanic rocks in a borehole drilled at the same site, NC-EWDP-2D, is about 706 m (NWPRO 1999 [DIRS 119607]). Therefore, the new data from

NC-EWDP-2DB support the concept that the head in the Paleozoic carbonates is higher than the head in the volcanic rocks, where flow from the potential repository is expected to occur.

The new and updated water levels for the Nye County wells will not significantly change the potentiometric surface contours south of Yucca Mountain from the contours presented in *Water-Level Data Analysis for the Saturated Zone Site-Scale Flow and Transport Model* (USGS 2001 [DIRS 154625], Section 6). These data will further constrain a moderate to steep hydraulic gradient (0.01 to 0.05 m/m) that roughly parallels U.S. Highway 95 south of Crater Flat and refine the shape of the contours in the Lathrop Wells area. The shape of the contours in the vicinity of Yucca Mountain will not change significantly.

Recent water-level measurements at the Nye County boreholes located at the northern edge of the Amargosa Desert also provide some insight into how the groundwater flow system might respond to future changes in climate. Water levels in these boreholes, located at the Lathrop Wells diatomite deposit (boreholes NC-EWDP-1S (MO0004NC99WL1S.000 [DIRS 149258]) and NC-EWDP-1D (MO0004NC99WL1D.000 [DIRS 149257])) and along Crater Flat Wash (borehole NC-EWDP-9S (MO0004NC99WL9S.000 [DIRS 149263])), show that the regional water table is at an altitude of about 800 m. These data show that 17 to 30 m of water table rise would be sufficient to reach the land surface at these sites.

12.3.1.2.2 Stratigraphy of Nye County Early Warning Drilling Program Boreholes

Lithologic descriptions and stratigraphic correlations have been completed for the Phase I and Phase II boreholes drilled under the NC-EWDP. Alluvium, tuffs, tuffaceous sedimentary rocks, and the Paleozoic rocks that comprise part of the lower carbonate aquifer have been identified. The subsurface geologic data are being compiled, together with surface-based geophysical and geologic-mapping results, to prepare (1) a generally east-west cross section aligned approximately along U.S. Highway 95, near the downgradient boundary of the site-scale SZ flow and transport model, and (2) a north-south cross section generally parallel to Fortymile Wash.

The location where flow paths from the potential repository pass from volcanic rock to alluvium is a specific stratigraphic issue that some of the new data address. Information from boreholes NC-EWDP-2D and NC-EWDP-19D1 is relevant because of the location of these wells along the inferred SZ flow path from Yucca Mountain. Data from borehole NC-EWDP-2D, located approximately 19 km from the potential repository, indicate greater than 800 ft of saturated alluvium beginning at the water table (DTN: GS000808314211.005 [DIRS 154685]; DTN: MO0004NC99WL2D.000 [DIRS 149259]). Data from borehole NC-EWDP-19D1, located approximately 18 km from the repository, show greater than 400 ft of saturated alluvium underlain by a significant section of volcanic rocks (DTN: MO0007NYE02565.024 [DIRS 154686]; Black 2000 [DIRS 154704]).

These observations indicate that groundwater flow in the SZ originating from Yucca Mountain includes flow through a portion of the porous alluvium in the area near the 20-km compliance boundary. Information from borehole NC-EWDP-19D1 is somewhat ambiguous with regard to the groundwater flow path in the alluvium because it has not been established whether greater groundwater flow would be expected in the alluvium or in the underlying volcanic unit. Further to the north of boreholes NC-EWDP-19D1, the question of whether the flow path encounters

alluvium or volcanic rocks is generally open to geologic and hydrologic interpretation. Additional drilling in this area by the Nye County drilling program will further reduce the uncertainty associated with this question. In the meantime, uncertainty about the length of the flow path through the alluvium is included in numerical simulations (CRWMS M&O 2000 [DIRS 139440], Section 6) of site-scale SZ flow and transport for the TSPA-SR.

The cross sections and associated geologic interpretations will be adapted as refinements of the hydrogeologic framework for the site-scale SZ flow and transport model are developed.

12.3.1.2.3 New Regional Flow Model

The steady-state version of the new USGS Death Valley regional flow system model is nearing completion. Stakeholders include the National Park Service, the U.S. Fish and Wildlife Service, and state and county offices in Nevada and California. Some modifications to the hydrogeologic framework and hydrologic parameters are being made as additional data are compiled and in response to calibration results. The importance of structural features, particularly faults, to groundwater flow in this region is emphasized in a new hydrostructural map. These and other geologic data are being processed for application in the next modeling phase, which is the development of a transient model.

The new regional-scale model will provide estimates of groundwater flux along the lateral boundaries of the site-scale SZ flow and transport model. It is anticipated that these new flux estimates will be used as calibration targets in future revisions of the site-scale SZ flow and transport model. Development of the regional-scale model grid and representation of hydrogeologic and hydrologic parameters are being coordinated with the site-scale SZ flow and transport model to assure compatibility at the boundaries of the site-scale model.

12.3.1.2.4 Alluvial Testing Complex

From July 2000 through November 2000, pumping tests were conducted in borehole NC-EWDP-19D1 at the ATC, and data from these tests are being evaluated. There are four screened intervals in the alluvium at this borehole; tests that pump from the four screened intervals combined, as well as from each interval individually, have been performed. These tests will provide estimates of the permeability of the alluvium at this site, including the degree to which the alluvium is heterogeneous and anisotropic with respect to permeability. Information from these tests will be used to update the conceptual understanding of the hydraulic behavior of the alluvium and to constrain the values of permeability of alluvium used in the site-scale flow model. Tracer tests are also being performed at the ATC to estimate transport properties of the alluvium (i.e., effective porosity, dispersivity, and the degree of dual-porosity behavior). Implications of the new information about transport properties are discussed in Sections 12.3.2.2 and 12.3.2.4. Isotopic data are discussed in Section 12.4.

12.3.1.3 New Model Development and Analysis Since Completion of the Total System Performance Assessment-Site Recommendation

This section discusses new model development and new analysis performed since the completion of the TSPA-SR (CRWMS M&O 2000 [DIRS 153246]). One result of the new analysis, as described in Section 12.3.1.3.1, is that different conceptual models of the origin of the large hydraulic gradient north of Yucca Mountain can result in flow paths away from the potential repository that are noticeably different from the flow paths predicted by the flow model used for the TSPA-SR. However, all flow paths are mainly in the same units, i.e., the Bullfrog Tuff and the alluvial units, regardless of the model. The net result of the newer flow paths is a relatively shorter traverse through the alluvial units compared to the paths for the original model.

12.3.1.3.1 Different Conceptual Models of the Large Hydraulic Gradient and Their Effect on the Flow Path and Specific Discharge

An area of large hydraulic gradient north of the potential high-level radioactive waste repository at Yucca Mountain has been inferred from hydraulic head measurements. This area has been a source of controversy and discussion for many years, and the cause of the gradient is unknown. An east-west trending strip with low permeability was incorporated into the SZ site-scale flow model to simulate this steep gradient in the flow field used for the TSPA-SR (CRWMS M&O 2000 [DIRS 153246]). The actual presence of such a feature has not been confirmed by field investigations. Consequently, investigation of additional conceptual models concerning the origin of the large hydraulic gradient has been initiated since the completion of the TSPA-SR.

Two additional conceptual models have been investigated to date. The first of these attributes the apparent large hydraulic gradient to the occurrence of low-permeability hydrothermally altered rock north of Yucca Mountain (DTN: LA0105GZ12213S.002 [DIRS 154888]). The second new conceptual model, in addition to incorporating the hypothesized hydrothermally altered rock north of Yucca Mountain, also attributes hydraulic importance to the faults in the northwest-southeast trending washes in northern Yucca Mountain. The sensitivity of the estimated groundwater flow paths and specific discharge to each of the conceptual models of the large hydraulic gradient has been investigated by recalibrating the numerical model to fit conditions appropriate to each conceptual model, and the input and output files for computer calculations have been recorded (DTN: LA0105GZ12213S.001 [DIRS 154887]).

Subregions within the model domain in which a geologic process is thought to have altered hydraulic properties are referred to as features in constructing and calibrating the site-scale SZ flow and transport model. The new conceptualizations of the large hydraulic gradient reduce the number of features used north of Yucca Mountain (Figure 12.3.1.3-1). To incorporate the area of extensive hydrothermal alteration in the Claim Canyon Caldera north of Yucca Mountain, the hydrogeologic units have been divided into distinct northern and southern calibration zones. Because the northern zones are represented by additional independent calibration parameters, these zones replace the complex feature set in the northern part of the original model. The two newer models differ from each other only by the inclusion of a zone that represents the northwest-southeast trending fault zone north of Yucca Mountain (Figure 12.3.1.3-1, Feature 2).

In general, the simulations of the newer conceptual models better match observations in the low-gradient region southeast of Yucca Mountain than the previous conceptual model. This is important because flow paths leaving the repository pass through this region. However, inclusion of the additional northwest-southeast trending fault zone in the second of the newer conceptual models does not seem to help the calibration.

The flow paths resulting from the simulation of the original and newer conceptual models are shown in Figures 12.3.1.3-2, 12.3.1.3-3, and 12.3.1.3-4. Although the flow paths predicted by the simulation of the newer conceptual models are similar, they differ from the flow paths predicted by simulations of the original conceptual model. The original model produces flow paths that trend in a southeasterly direction from the potential repository site (Figure 12.3.1.3-2). This result is consistent with the inferred geochemical pathlines (CRWMS M&O 2000 [DIRS 139582], Figure 9). The newer models produce pathlines leaving the potential repository that are more southerly in direction than those of the original model (Figures 12.3.1.3-3 and 12.3.1.3-4). Groundwater travels mainly in the same units, the Bullfrog Tuff and the alluvial units, regardless of the model. The net result of the newer flow paths is a relatively shorter traverse through the alluvial units compared to the paths for the original model. The more southeasterly component of the original model is due to the east-west barrier feature that is not present in the newer models. This feature acts as a dam to keep the head elevated in the north and blocks water from the north, thus allowing water from Crater Flat to enter the repository area. The newer models lack this feature and allow the water to flow directly south. This analysis demonstrates that the flow path from the repository can be sensitive to the conceptual model of the large hydraulic gradient.

12.3.1.3.2 Alternative Conceptualizations of the Solitario Canyon Fault

The parameterization of the Solitario Canyon fault is an important part of the site-scale SZ flow and transport model because it can potentially control flow from Crater Flat to Fortymile Wash. This flow, in turn, is important in determining the amount of alluvial material that groundwater flowing from beneath the potential repository region passes through en route to the accessible environment. Investigations of alternative treatments of the Solitario Canyon fault have been recently initiated. Input and output files for these computer calculations can be found in DTN: LA0105GZ12213S.004 ([DIRS 154993]). One aspect of this fault that has been investigated is its effective depth. This fault is included as a discrete feature in the site-scale SZ flow and transport model. Simulations performed for the TSPA-SR included this fault as a feature that extended from the bottom of the model to the top of the water table. The fault is modeled as an anisotropic feature with larger permeability along the plane of the fault than across it. It is possible that this treatment of anisotropy is inappropriate where it cuts the carbonate aquifer deep in the model domain. Consequently, an alternative treatment was simulated in which the fault extends from the water table only to the top of the carbonate aquifer. This simulation produced essentially the same result as the original site-scale SZ flow and transport model with the deeper fault zone, but the calibrated permeability for the fault was approximately 25 percent lower than the original.

12.3.1.4 Quantification of Groundwater Specific Discharge Uncertainty

This section summarizes unquantified uncertainty for the site-scale SZ flow model based on the TSPA-SR (CRWMS M&O 2000 [DIRS 153246]). Uncertainty in flow modeling arises from a number of sources, including the conceptual model of the processes affecting groundwater flow, water-level measurements, simplification of the model geometry, simplification of the boundary conditions, and the values of permeability assigned to hydrogeologic units. These types of uncertainty are accounted for explicitly through key parameters and conceptual models in the site-scale SZ flow and transport model for the updated TSPA-SR. Key SZ input parameters that are uncertain are represented stochastically in the site-scale SZ flow and transport model, and parameter distributions are based on site data, laboratory data, literature data, and expert elicitation. The *Uncertainty Distribution for Stochastic Parameters Report* (CRWMS M&O 2000 [DIRS 147972], Section 6) documents the uncertainties quantified for input to the site-scale SZ flow and transport model for the updated TSPA-SR.

A review was conducted on how uncertainty was treated in the site-scale SZ flow and transport model. The probability distribution for the parameter specific discharge was reevaluated as part of the unquantified uncertainty analysis. This parameter is important because the results of TSPA calculations are sensitive to it at long time periods (i.e., hundreds of thousands of years). Uncertainty in specific discharge was reevaluated because the previous range of values for this parameter is thought to be too large to represent what is reasonably known. Specifically, the principal investigators developing the site-scale SZ flow and transport model concluded that the range for specific discharge used for the TSPA-SR is overly conservative; in particular, the maximum value of the parameter range is unreasonably large.

In the TSPA-SR, specific discharge in the site-scale SZ flow and transport model is represented as three discrete cases: high, medium, and low (CRWMS M&O 2000 [DIRS 139440], Section 6.2.5.1). The medium value was obtained from the calibration effort described in the *Calibration of the Site-Scale Saturated Zone Flow Model* report (CRWMS M&O 2000 [DIRS 139582], Section 6). The low- and high-value cases were calculated by scaling values of flux, recharge, and permeability by the same amount. Calibration is preserved by this scaling process because of the linearity of the numerical model. The value for the low case was one-tenth of the value for the medium case, and the value for the high case was 10 times that of the medium case. This range of values was based primarily on the SZ expert elicitation (CRWMS M&O 2000 [DIRS 147972], Section 6.1; CRWMS M&O 1998 [DIRS 100353], p. 3-20). In sensitivity studies performed as part of the SZ unquantified uncertainty analysis, the range of specific discharge was reduced such that the low- and high-value cases were one-third and three times the medium value, respectively.

Four lines of reasoning are presented in the following paragraphs to support decreasing the range of values used for specific discharge. Specific discharge is the product of rock permeability and hydraulic gradient, and the hydraulic gradient is sufficiently characterized that most of the uncertainty in specific discharge is due to uncertainty in permeability. Consequently, the following lines of reasoning are posed in terms of rock permeability. For comparison, the value of permeability used for the Bullfrog Tuff for the medium case is $15.7 \times 10^{-12}\ m^2$ (CRWMS M&O 2000 [DIRS 139582], Table 16). The values used for the SZ unquantified uncertainty

analysis for the low- and high value cases are 5.2×10^{-12} m^2 and 47.1×10^{-12} m^2, respectively, based on analysis discussed in Section 12.3.1.4.1.

First, the 95 percent confidence interval on mean permeability, calculated from cross-hole tests in the Bullfrog Tuff at the C-wells Complex, has endpoints that are approximately one-third (5.6×10^{-12} m^2) and three times (33.6×10^{-12} m^2) the geometric mean (13.7×10^{-12} m^2) of the interval (CRWMS M&O 2000 [DIRS 139582], Table 9). The mean value, in turn, is close to the nominal calibration value of permeability for the Bullfrog Tuff (15.4×10^{-12} m^2) that was obtained for the site-scale SZ flow and transport model (CRWMS M&O 2000 [DIRS 139582], Table 8). Permeability of the Bullfrog Tuff is important for all reasonable scenarios because it is the highest permeability path for fluid leaving the repository before entering the alluvium (DTN: LA0105G2122135.001 [DIRS 154887]; DTN: LA0105G2122135.002 [DIRS 154888]; DTN: LA0105G2122135.003 [DIRS 154889]).

Second, the value for Bullfrog Tuff permeability used in the model represents the combined values of Bullfrog Tuff permeability where it is far from faults and where it is near faults that are not represented explicitly in the model. The larger values of permeability, measured in the vicinity of known faults, are thought to represent only the latter (near faults) portion of the Bullfrog Tuff. Permeability values representing the averaged Bullfrog Tuff should not exceed values representing the faulted portions. The fact that the values of permeability for the Bullfrog Tuff used for the high specific discharge case in the unquantified uncertainty analysis are close to the upper end of the range measured in the vicinity of known faults is in agreement with this line of reasoning. The values of permeability thought to represent faulted regions were calculated from saturated tests at the C-wells Complex near the Midway Valley fault (54.0×10^{-12} m^2) (Geldon et al. 1998 [DIRS 129721], Figure 3) and from air-injection tests in the UZ adjacent to the Ghost Dance fault (14.6×10^{-12} m^2) (LeCain et al. 2000 [DIRS 144612]). Applicability of air-injection tests of the Ghost Dance fault is discussed in Section 12.3.1.4.1.

Third, single-hole hydraulic tests in the vicinity of Yucca Mountain provide an estimate of the average permeability of volcanic tuffs in unfaulted regions. Using reasoning similar to that presented in the previous paragraph, a value representing the average of faulted and unfaulted regions should be larger than the value for unfaulted regions. The largest value from single-hole tests of the Bullfrog Tuff is 1.7×10^{-12} m^2 (CRWMS M&O 2000 [DIRS 139582], Table 9). This value is smaller than the value used for the low specific discharge case for the unquantified uncertainty analysis. The argument that scale effects do not cause single-hole tests to underestimate the permeability of unfaulted regions is presented in Section 12.3.1.4.1.

Fourth, calibrations of the site-scale SZ flow and transport model that are constrained by all available information about SZ flow in the vicinity of Yucca Mountain, and that consider alternative conceptual models, can only be done for a range of specific discharge values similar to those used in the unquantified uncertainty analysis.

12.3.1.4.1 Evaluation of Permeability Data

Uncertainty in specific discharge is due mainly to uncertainty in permeability. This section discusses permeability data for the volcanic rocks at Yucca Mountain and elsewhere, and it applies these data to calculations of specific discharge. Two main points are made. First, the

maximum permeability values that have been estimated from air-injection tests near the Ghost Dance fault provide an additional estimate of the permeability of faulted tuffs (14.6×10^{-12} m^2) (LeCain et al. 2000 [DIRS 144612], Table 13). Second, the expected values of permeability for unfaulted tuffs are provided by the geometric means calculated from single-hole tests. These values (CRWMS M&O 2000 [DIRS 139582] Table 9) are one to several orders of magnitude less than the values estimated for faulted tuffs.

12.3.1.4.1.1 Evaluation of Permeability in Faulted Regions

Fractured welded tuffs and relatively unfractured nonwelded tuffs occur above and below the water table. Permeabilities measured in the UZ at Yucca Mountain using air may, therefore, have some relevance to the permeability values of similar rocks located below the water table. In the UZ, air-injection tests have been conducted from surface-based boreholes in welded and nonwelded tuffs (LeCain 1997 [DIRS 100153]), and from test alcoves in and adjacent to the Ghost Dance fault zone in the densely welded Topopah Spring Tuff (LeCain et al. 2000 [DIRS 144612]). At Yucca Mountain, no water-injection tests were done in these intervals to compare with the results of the air-injection tests. However, some understanding of the probable relation between permeabilities estimated from air- and water-injection tests at Yucca Mountain can be reached based on tests in non- to partially-welded tuff at the Apache Leap experimental site near Globe, Arizona, where borehole air- and water-injection tests were made at ambient moisture conditions in the same depth intervals (Rasmussen et al. 1993 [DIRS 154688]). The relationship of permeability values estimated using these two methods at Apache Leap suggests that permeability values calculated from air-injection tests in the UZ at Yucca Mountain could provide good approximations to water-permeability values, particularly in the densely welded tuff. It is therefore assumed that air-injection values provide good estimates of water-injection values in Section 12.3.1.4 where an average of the air-injection permeability values (14.6×10^{-12} m^2) is said to represent faulted regions.

Cross-hole air-injection tests conducted in and adjacent to the Ghost Dance fault resulted in geometric mean permeability values of 4.1×10^{-12} m^2 for the hanging wall of the fault, 14.6×10^{-12} m^2 for the main fault zone (defined by a zone of significantly higher fracture density), and 7.8×10^{-12} m^2 for the footwall (LeCain et al. 2000 [DIRS 144612], Table 13). These permeabilities were higher than the permeabilities measured elsewhere in the same units from the surface-based boreholes, and 2 to 10 times higher than the permeabilities estimated for the Ghost Dance fault and adjacent rock from single-hole tests conducted from an exploratory borehole drilled before alcove excavation (LeCain et al. 2000 [DIRS 144612], p. 26).

12.3.1.4.1.2 Scale Effects

In addition to actual variations in permeability, the scale of measurement may influence the permeability value determined by a test. This effect is most often observed when the results of permeability tests conducted on cores that do not incorporate fractures are compared to the results of tests conducted in boreholes that contain fractured intervals. At Yucca Mountain, the relatively high permeabilities estimated from cross-hole tests compared to single-hole tests in the same rock unit have also been attributed to the effects of scale (Geldon 1996 [DIRS 100396], p. 69). According to this interpretation, the cause of the permeability increase in the cross-hole tests is attributed to the greater likelihood of including relatively rare but highly transmissive and

continuous features in the larger rock volume sampled by the cross-hole tests. However, recent work by Vesselinov et al. (2001 [DIRS 154706]) at the Apache Leap test site demonstrated that permeabilities determined from multiple single-well air-injection tests and simultaneous numerical inversion of multiple cross-hole air-injection tests provide comparable estimates of the mean permeability of the test volume. However, when the cross-hole tests were analyzed individually using an approach equivalent to type-curve analyses that requires the assumption of a uniform permeability field and a particular flow geometry (spherical), the resulting mean permeability estimated for the test volume was several orders of magnitude higher than the mean permeability estimated from the single-hole analyses or from more detailed simultaneous numerical inversion of the cross-hole tests. The simultaneous numerical inversion of the cross-hole tests resulted in a larger variance in permeabilities than was estimated from the multiple single-hole tests, which is a result that may have been caused by rounding errors associated with the numerical inversion. The conclusions of this work relevant to the present analysis are that the mean permeabilities would not be a function of test methodology (single-hole or cross-hole analyses) except for the inability of standard cross-hole type-curve methods to account for heterogeneity and departures of the actual flow field from the assumed flow geometry. Therefore, single-hole permeabilities reflect the true permeabilities of the hydrogeologic units in unfaulted areas and can be used to represent the hydrogeologic-unit permeabilities in numerical models, provided the effects of faults are accounted for in some manner.

12.3.2 Transport Modeling

This section covers the site-scale SZ transport model and the introduction of new data, new model development, and new analyses since the completion of the TSPA-SR (CRWMS M&O 2000 [DIRS 153246]). New data, new analyses and new model development, with the exception of that described in Sections 12.3.2.3.3 and 12.3.2.4, are not included in the Volume 2 analyses. The new data and analyses described in this section will facilitate the development of a more representative future versions of the SZ site-scale transport model. This section also discusses quantification of previously unquantified uncertainties for the site-scale SZ transport model and is included in the analyses presented in Volume 2 (McNeish 2001 [DIRS 155023]).

12.3.2.1 Introduction and Goal of Model

Predicting the migration of radionuclides through the SZ to proposed compliance boundaries is important for assessing the overall containment strategy for safely storing radioactive materials at the potential Yucca Mountain repository. The SZ is an important barrier for delaying the movement of radionuclides and potentially reducing the concentrations via the process of retardation. Radionuclides that escape the engineered barrier and near-field environment and migrate to the water table must still travel some 20 km in the aquifer. Only then, as water is being pumped from the aquifer and used for irrigation or domestic consumption, will the radionuclides present a health and safety issue.

12.3.2.1.1 Purpose of the Model

The purpose of the site-scale SZ transport model (CRWMS M&O 2000 [DIRS 151948]), which is used to perform the SZ simulations for the TSPA-SR (CRWMS M&O 2000 [DIRS 153246]),

is to predict the spatial and temporal distribution of any radionuclides that may reach the water table beneath the potential repository. Because fluid flow is the means of transport through the SZ, the site-scale SZ flow model is the basis for the transport model in terms of the potential directions and transport velocities. The transport model builds on the flow model by incorporating mechanisms specific to the migration of contaminants. These mechanisms include:

- Advection (governed solely by the flow model and the effective porosity)
- Dispersion of radionuclides during transport
- Radionuclide sorption on the solid surfaces in the aquifer
- Diffusion from the flowing fractures in the volcanic tuffs into the relatively stagnant fluid in the rock matrix
- Transport through the alluvium
- Colloid-facilitated transport
- Capture at pumping wells.

Using accepted hydrologic principles and data available from the site, the major transport processes listed above were incorporated into a particle-tracking-based transport model that predicts the velocity (migration rate and direction) of radionuclide migration under present and presumed future climatic conditions. Transport data from a variety of sources are used to constrain the model. At the field scale, tracer test results in the fractured volcanic tuffs and preliminary data from the alluvium are used to justify the conceptual models used for transport in these two media. At the laboratory scale, batch and column sorption and diffusion data are cited to define the parameters for the models. Although a large amount of site-specific data exists, there is still uncertainty in the conceptual models and in the parameters used in the models.

A major goal in developing the site-scale transport model was to capture the uncertainties in the model and how they influence the uncertainty in the transport predictions. This goal requires that the model be run for a large variety of transport parameters. Therefore, a computationally efficient model was developed that incorporates the key elements of the conceptual model in a manner that allows multiple simulations to be performed rapidly. The particle-tracking methods developed are suitable for this purpose, and the sensitivity analyses performed often used multiple realizations to characterize the uncertainties.

12.3.2.1.2 Identification of Unquantified Uncertainty from the Total System Performance Assessment for the Site Recommendation

This section summarizes the identification of unquantified uncertainty for the SZ transport model based on the TSPA-SR (CRWMS M&O 2000 [DIRS 153246]). Uncertainty in transport modeling arises from a number of sources including, but not limited to, the conceptual model, assumptions regarding matrix diffusion processes, implementation of colloid-facilitated

transport, assumptions regarding sorption of radionuclides, and the extent the flow path encounters volcanic hydrogeologic units compared to alluvial hydrogeological units. These various types of uncertainties are accounted for explicitly in the site-scale SZ transport model through key parameters and conceptual models as described in the SZ PMR (CRWMS M&O 2000 [DIRS 153168], Sections 3.6 and 3.7). The uncertainty in key SZ parameters are represented stochastically as input to the site-scale SZ model. Parameter distributions are based on a combination of site data, laboratory data, literature data, and expert elicitation. The AMR, *Uncertainty Distribution for Stochastic Parameters* (CRWMS M&O 2000 [DIRS 147972], Table 15), documents the uncertainties quantified for input to the SZ -scale model for TSPA-SR.

In general, identification of unquantified uncertainty for the site-scale SZ transport model consisted of re-evaluation of previously quantified uncertainty with focus on the parameters that were most important to performance of the SZ as a barrier to radionuclide migration. One exception is the bulk density parameter. The value of this parameter was constant in the TSPA-SR analysis (CRWMS M&O 2000 [DIRS 153246]; CRWMS M&O 2000 [DIRS 147972], Section 6.9), but it is treated stochastically in the unquantified uncertainty analysis. New data (Section 12.3.2.2) were used to develop a probability distribution for bulk density (Section 12.3.2.4). For other parameters, distributions were changed from those used for the TSPA-SR based on incorporation of new data and the reevaluation of probability distributions. The technical basis for the reevaluation of the uncertainty quantification is described in Section 12.3.2.4. Table 12.3.2.1.1-1 summarizes the results of the SZ transport unquantified uncertainty analysis.

12.3.2.2 New Data and Analyses Since Completion of Models in the Total System Performance Assessment for the Site Recommendation

The following new information has been obtained since completion of the TSPA-SR (CRWMS M&O 2000 [DIRS 153246]), the SZ PMR (CRWMS M&O 2000 [DIRS 153168]), and their supporting AMRs.

12.3.2.2.1 Bulk Density and Porosity

The average alluvium dry bulk density is 1.91 g/cm^3 based on saturated bulk density estimated from a borehole gravimetry survey in well NC-EWDP-19D1 (Black 2000 [DIRS 154704], p. 18). The corresponding average bulk porosity was calculated to be about 0.24 from the saturated bulk density, the average grain density of 2.52 g/cm^3 (USGS n.d. [DIRS 154495], pp. 3 to 4), and Equation 12.3-5. Point estimates of alluvium dry bulk density computed using the porosity, a grain density of 2.52 g/cm^3, and Equation 12.3-6 ranged from about 1.79 to 2.05 g/cm^3, and point estimates of bulk porosity ranged from 0.185 to 0.291 g/cm^3 from computations using the dry bulk density, the grain density, and Equation 12.3-5.

12.3.2.2.2 Sorption Measurement

Further analysis of batch sorption data of technetium-99 and iodine-129 (as TcO_4^- and I^-) onto alluvium samples, as well as recent technetium-99 and iodine-129 column test results, indicate that sorption distribution (K_d) values for technetium-99 and iodine-129 sorbing onto the alluvium

are zero under oxidizing (ambient) conditions (Reimus 2001 [DIRS 154994], Filename "Tc and I Alluvium Sorption").

New results from two column experiments for K_d values for neptunium-237 in the alluvium have been performed in which the effective K_d values of neptunium-237 were significantly lower than values measured in batch sorption experiments with the same material used to pack the columns as discussed in Section 12.3.2.4.2 (Reimus 2001 [DIRS 154994], Filename "Np Alluvium Sorption"). The differences between the column and batch experiments are explained in Section 12.3.2.4.2.2.

12.3.2.2.3 Conceptualization of Matrix Diffusion in the Alluvium

Preliminary single-well tracer test data at well NC-EWDP-19D1 support the use of a single-porosity flow and transport conceptual model in the alluvium. The normalized concentration responses of conservative tracers with different diffusion coefficients were identical in the tests (Reimus 2001 [DIRS 155251], Filename "ATC Tracers – 1st Test," "ATC Tracers – 2nd Test," and "ATC Tracers – 3rd Test"), indicating little or no diffusion of tracers from flowing water to stagnant water (secondary porosity) in the flow system.

12.3.2.2.4 Matrix Diffusion in the Volcanic Tuffs

Laboratory data from diffusion-cell experiments are being used to establish a correlation between matrix diffusion coefficients and matrix porosities in volcanic rocks. This correlation has been used to adjust effective matrix diffusion coefficients as a function of matrix porosity in transport simulations as described in Section 12.3.2.4.6. That is, for a given sampled value of the effective matrix diffusion coefficient, the value is adjusted upward or downward depending on the sampled value of the matrix porosity.

12.3.2.2.5 Colloid Transport in the Alluvium

Alluvium grain size distributions from well NC-EWDP-19P (Reimus 2001 [DIRS 154994], Filename "EWDP 19P Grain Sizes"), which was drilled using an air-hammer method that preserved smaller and larger grain sizes much better than rotary drilling methods, were used to refine estimates of colloid filtration rate constants in the alluvium.

Preliminary estimates of colloid detachment rate constants in the alluvium have been obtained from microsphere responses in single-well tracer tests at well NC-EWDP-19D1 (Reimus 2001 [DIRS 155251], ATC Detachment 040101). These detachment rate constants fall within the range of detachment rate constants assumed in the colloid retardation factor analysis (see Section 12.3.2.4.5).

Measurements of natural colloid concentrations in the alluvium (Nye County wells) have been consistently higher than those in the volcanics (DTN: LA0002SK831352.002 [DIRS 149194]; DTN: LA0002SK831352.001 [DIRS 149232], Filename "19D1 Colloid Concentrations"). In the lower alluvium intervals at well NC-EWDP-19D1, colloid concentrations are almost three orders of magnitude higher than in water from Well J-13 (Reimus 2001 [DIRS 154994]). The highest colloid concentrations could decrease the travel times of radionuclides that are reversibly sorbed to those colloids by a factor of 3 or 4 relative to colloid concentrations in Well J-13 water

(assuming equilibrium sorption of radionuclides to colloids and the alluvium grains). Parameter uncertainty distributions in SZ transport simulations effectively capture this potential decrease in travel times (CRWMS M&O 2000 [DIRS 147972], Figure 6), although future performance assessments will account for the greater colloid concentrations more explicitly.

12.3.2.3 New Model and Analysis Development Since Completion of the Total System Performance Assessment for the Site Recommendation

This section discusses new model development and new analysis performed since the completion of the TSPA-SR (CRWMS M&O 2000 [DIRS 153246]), the SZ PMR (CRWMS M&O 2000 [DIRS 153168]), and their supporting AMRs. New development and analysis covered in this section include analyses to support the flexible thermal design, a new dispersion tensor, effective dispersivity in the site-scale SZ model, and studies investigating the influence of matrix diffusion.

12.3.2.3.1 Flexible Design

The impact of a lower-temperature repository design for the potential repository on the site-scale SZ flow and transport model is expected to be minor because the pathways in the SZ are separated by a significant distance from the waste canisters. In the SZ PMR, it is demonstrated that the influence of heat on the SZ flow system is minor (CRWMS M&O 2000 [DIRS 153168], p. 3-94). Lower areal heat loads that may arise due to the flexible repository design approach will make this assumption even more appropriate, as the temperatures at the top of the SZ will be perturbed less than was the case in the initial revision of the SZ PMR (CRWMS M&O 2000 [DIRS 153168]). Therefore, heat effects of a lower-temperature repository design do not need to be analyzed. However, because the flexible design approach may require that waste be emplaced over a larger area, radionuclides may reach the water table over a wider area. Other techniques for reducing the temperature, such as surface aging and ventilation, are not considered here because they are expected to have even lower thermal impact on the SZ system than the designs studied to date. Typically, to examine plume size and potential flow paths from the repository to the point of compliance, particles are released from an area derived by projecting the footprint of the repository on the water table. For this sensitivity analysis, a similar analysis was performed with a larger repository footprint to determine if the results change significantly from the past simulations (radionuclides released were simulated to occur from the larger footprint). This analysis does not simulate actual release rates of radionuclides; simply the pathlines predicted for radionuclides initiated beneath the larger footprint.

Figure 12.3.2.3-1 illustrates the preliminary layout for a lower-temperature repository design that would accommodate 70,000 metric tons of heavy metal. This layout, which is preliminary in nature, was obtained from BSC (2001 [DIRS 154548], Section I, p. 2, Figure 1). To determine the particle release locations for this analysis, a software routine (add_repo_nodes.f V1.0) was used to interpolate between the western and eastern ends of each emplacement drift (the values reproduced in Table 12.3.2.3-1). The program linearly interpolates between the coordinate locations of the ends of the drift at a prescribed length spacing along the drift. To maintain an integer number of points along each drift and to include the end points, the actual spacing between points along the drift is typically larger than the input value. The code writes out the coordinates of each point with options to either interpolate to obtain the repository-level

elevation or to write out a user-defined value. For this study, an elevation of 719 m is written for all points because a series of points just below the water table are required as the starting locations in the particle-tracking simulation. The easting and northing coordinates are approximately converted from the given coordinate system (Nevada State Plane meters) to the Universal Transverse Mercator (UTM) geographic coordinate system used for the site-scale SZ model. To do this, the software routine add_repo_nodes.f V1.0 performs a simple linear transformation after using the U.S. Army Corps of Engineers code CORPSCON V5.11.08 to obtain the UTM coordinates for a single translation point in the northern end of the repository. A hand check of the linear transformation method for a point in the far southern point of the repository (farthest from the translation point) revealed that this method produced coordinate locations within about 20 m of the more accurate CORPSCON code. This error is well within the accuracy required to locate approximately the potential repository footprint in the SZ model.

Figure 12.3.2.3-2 shows the locations of the particle tracking points computed using FEHM V2.11 in the new analysis compared to the distribution of points for the original potential repository. The latter was used in previous SZ pathline studies of the SZ PMR (CRWMS M&O 2000 [DIRS 153168]). This footprint is similar to that used in the thermal analysis (Figure 2.3.4-2, Case 3). The lower-temperature, expanded repository design extends farther north, but the primary difference is the extension into a second lobe to the south. To examine the influence of this design on the results, a comparison of pathlines issuing from the previous and lower-temperature repository point distributions was performed. Pathlines are generated using the base-case SZ flow field assuming no dispersion or sorption, and the results are examined visually and in the form of breakthrough curves at the 20-km point of compliance. The results of the particle-tracking pathway analysis for the two designs are compared with the pathlines for the original repository in Figure 12.3.2.3-3a and the pathlines for the lower-temperature repository in Figure 12.3.2.3-3b. Figure 12.3.2.3-3c shows only those pathlines issuing from the southern lobe of the lower-temperature repository. The overall outline of the pathlines for Figures 12.3.2.3-3a and 12.3.2.3-3b are quite similar, suggesting that the flow paths from the lower-temperature repository footprint are quite similar to those from the earlier repository design. This result is due to the predominantly southerly flow paths issuing from nearly all locations in the repository: release locations farther south than previously assumed follow essentially those same southerly flow lines. This conclusion is confirmed in Figure 12.3.2.3-3c, which illustrates that the new pathways follow the same tracks as those from the original repository.

The final analysis is a comparison of the transport times from the repository to the 20-km point of compliance. To compare the original and lower-temperature repository design, breakthrough curves were generated for conservative particles (such as carbon-14) released from each repository footprint, assuming no diffusion or dispersion. Thus, the distribution of transport times is due only to the location of the release and the differences in flow velocities as a function of starting location. Figure 12.3.2.3-4 shows that the two repository designs yield similar breakthrough curves.

Thus, the direction of the flow paths and the transport times are all similar for the lower-temperature repository design. Therefore, the impact on radionuclide transport in the SZ is minor. It should be noted that this conclusion relates only to the performance assuming the base case model and assuming the repository footprint currently envisioned. If a future design specifies waste emplacement in another location, the analysis would need to be repeated.

Furthermore, the potential for additional site characterization, depending on the design, is perhaps more important than the performance assuming the current model. For example, waste emplaced to the west of the Solitario Canyon fault would involve portions of the SZ that are relatively less well characterized. Also, any new data that changes our current understanding of flow through the fractured volcanic tuffs, either in the unsaturated or saturated zone, might create the need to reevaluate these results. For the current designs, further characterization in that location is a relatively low priority because of the lack of sensitivity demonstrated in Figure 12.3.2.3-4. Future designs will have to be assessed with respect to the impact on site characterization needs and schedule in addition to predicted performance.

12.3.2.3.2 New Dispersion Tensor

In the *Saturated Zone Transport Methodology and Transport Component Integration* report (CRWMS M&O 2000 [DIRS 146962], Section 6), a methodology based on particle tracking was developed to simulate transport through the SZ with dispersion incorporated using a random-walk method. For the transport analyses resulting in breakthrough curves at the 20-km point of compliance, the dispersion tensor proposed by Burnett and Frind (1987 [DIRS 130526], pp. 695 to 705) was used to characterize the nature of radionuclide spreading away from the flow streamlines. This tensor, proposed as a simplified form suitable for axisymmetric media, involves the use of three independent parameters, the longitudinal dispersivity α_L, the transverse horizontal dispersivity α^H_T, and the transverse vertical dispersivity α^V_T. This form is generalized from the typical form used for isotropic media to account for the different transverse dispersivities observed in the horizontal and vertical directions of natural stratified media with flow along the bedding plane (e.g., Zheng and Bennett 1995 [DIRS 154702], Section 2.2.4, Equations 2-34 to 2-39).

In simulation models such as the site-scale SZ flow and transport model, this form of the dispersion tensor has drawbacks that make the computation of radionuclide transport difficult for large dispersivity values. Because the longitudinal dispersivity is not a function of either horizontal or vertical direction, the random-walk distance of a particle temporarily traveling vertically is, on average, just as large as for horizontal transport. The grid aspect ratio for the SZ is such that the vertical random walk can result in attempts to jump several grid cells in each random walk unless very small particle time steps are taken. However, there is no experimental basis for applying the same longitudinal dispersivities in the horizontal and vertical directions, and it can be argued that one could expect different dispersivities in the direction of flow depending on these directions. Therefore, a modified form of the Burnett and Frind (1987 [DIRS 130526]) tensor was developed and implemented in FEHM V2.11. This form includes separate longitudinal dispersivities in the horizontal and vertical directions, α^H_L and α^V_L, respectively, to go along with the transverse dispersivity terms α^H_T and α^V_T. This tensor, which we call the modified Burnett and Frind tensor, results in different expressions for the random-walk displacement matrix but reduces to the Burnett and Frind (1987 [DIRS 130526]) form when $\alpha^H_L = \alpha^V_L$.

In this analysis, the breakthrough curves at the 20-km point of compliance for the two tensors are compared. A conservative (carbon-14) and a weakly sorbing radionuclide (neptunium-237) are examined for point releases from source region 1, using the expected values of all dispersion and sorption parameters. To differentiate between the processes of dispersion and matrix diffusion,

this analysis also assumes no matrix diffusion. Figure 12.3.2.3-5 shows the breakthrough curve comparisons. The modified tensor yields a virtually identical breakthrough curve to the original Burnett and Frind tensor for the early and middle portions of the curve, deviating significantly only in the tail. This conclusion is true for carbon-14 and neptunium-237, probably because the flow is primarily horizontal in the site-scale SZ model so that, in most locations, the longitudinal dispersion is identical in the two cases. Therefore, either tensor could be used in the sensitivity analyses and breakthrough curves generated for use in the TSPA.

12.3.2.3.3 Effective Longitudinal Dispersivity in the Site-Scale Saturated Zone Flow and Transport Model

Longitudinal dispersivity for radionuclide transport simulations in the site-scale SZ flow and transport model is specified as a transport parameter (e.g., CRWMS M&O 2000 [DIRS 153168], pp. 3-151). The dispersion process is simulated by the random-walk displacement algorithm on the local scale for each time step in the transport simulation. In addition, the spatial distribution of hydrogeologic units of contrasting permeability within the site-scale SZ flow and transport model imparts additional dispersion to the simulated transport of particles as the flow paths diverge during transport. The effective longitudinal dispersivity simulated by the site-scale SZ model may be significantly larger than the desired specified value due to the additive effects of these two processes.

The effective longitudinal dispersivity in the site-scale SZ flow and transport model is analyzed for a range of values of specified longitudinal dispersivity to evaluate this effect. A point source that is beneath the repository and is located 23.7 km from the 20-km regulatory boundary is used for the analysis. No sorption or matrix diffusion is included in the simulations. Effective longitudinal dispersivity is estimated using the relationship from Kreft and Zuber (1978 [DIRS 107306], Equations 2-34 to 2-39):

$$\alpha_L = \frac{L}{2}\left(\frac{\sigma_t}{m_t}\right)^2 \qquad \text{(Eq. 12.3.2.3-1)}$$

where

α_L = effective longitudinal dispersivity
L = the flow path length
σ_t = the standard deviation in transport time
m_t = the mean transport time

The standard deviation of the dispersivity is estimated from the particle mass breakthrough curve at the 20-km regulatory boundary by taking the difference in time between the arrival of 0.159 fraction of the mass (minus one standard deviation) and the arrival of 0.841 fraction of the mass (plus one standard deviation) and dividing by 2. The mean transport time is estimated using the arrival time of 0.500 fraction of the mass.

The results of the effective longitudinal dispersivity analysis are shown in Figure 12.3.2.3-6 with the plotted open circles. The effective simulated longitudinal dispersivity is consistently about

one order of magnitude higher (bold dashed line) than the specified longitudinal dispersivity when the latter value is less than 1,000 m. These results indicate that the heterogeneous distribution of permeability in the site-scale SZ model in the region along the flow path from repository to the 20-km regulatory boundary is contributing approximately one order of magnitude of dispersivity relative to the specified value. When the specified longitudinal dispersivity is above 1,000 m, the excess longitudinal dispersivity appears to be even greater. However, these large values of longitudinal dispersivity are significantly greater than the geometric mean value of 100 m derived from the uncertainty distribution for this parameter (CRWMS M&O 2000 [DIRS 147972], p. 50).

Based on these results, the value of specified longitudinal dispersivity used in the site-scale SZ flow and transport model for the SSPA abstraction simulations (McNeish 2001 [DIRS 155023]) will be adjusted to yield the appropriate value of effective simulated longitudinal dispersivity. This is accomplished by scaling the specified longitudinal dispersivity down by one order of magnitude in the input files for each realization.

12.3.2.3.4 Matrix Diffusion Sensitivity Analyses

The original conceptual model used in the SZ transport calculations to date consists of individual flowing fractures that transmit fluid and radionuclides as illustrated in Figure 12.3.2.3-7. The surrounding rock matrix contains immobile water, but radionuclides can diffuse into and out of the rock matrix and sorb within the rock matrix. Therefore, radionuclide mass is attenuated with respect to the transport velocities within the fractures. In this section, a variety of model assumptions were explored regarding the process of matrix diffusion, ranging from no diffusion to systems in which matrix diffusion is pervasive within isolated zones of highly fractured tuff. These simulations are presented to provide perspective on the importance of matrix diffusion within the range of uncertainty currently present for this process.

The abstracted model implemented for matrix diffusion is shown in the Figure 12.3.2.3-7. It consists of equally spaced fractures (spacing = $2B$), each carrying fluid at the same velocity. The FEHM particle tracking model employs an analytical solution of Sudicky and Frind (1982 [DIRS 105043]) to impart delays to each particle traveling within the fractured volcanic tuffs so that the diffusion-delayed transport time distribution predicted by the analytical solution is obtained. The fracture aperture ($2b$) represents the mean distance across the fracture, which in reality is a rough-walled discontinuity of variable aperture. The bulk porosity of the medium is, through geometric considerations, b/B. This porosity is to be distinguished from the matrix porosity, which corresponds only to the porosity in the medium surrounding each flowing fracture.

The fracture spacing parameter is obtained from the analysis of field investigations identifying the distance between flowing fractures in boreholes at the site (DTN: SN9907T0571599.001 [DIRS 122261]). This parameter, combined with estimates of the fracture porosity (CRWMS M&O 2000 [DIRS 147972], p. 62), allows the mean fracture to be calculated.

Unfortunately, borehole logs and other data cannot be used to distinguish between single fractures and fracture zones. It is possible that a flowing interval actually represents a zone of fractures rather than an individual fracture. Therefore, an alternate conceptual model that cannot

be ruled out is one in which the flowing intervals depicted as single fractures of aperture $2b$ are actually fractured zones of enhanced permeability through which water and radionuclides transport.

To implement such a model, it is possible to use the same mathematical representation as was employed by Sudicky and Frind (1982 [DIRS 105043]), and therefore, the impact of this conceptualization can be examined using the existing particle tracking model by modifying only the parameterization. To do so, the flowing interval spacing was held constant at a mean value of 21 m (CRWMS M&O 2000 [DIRS 154927], p. 13), while adjusting the fracture porosity and, hence, aperture. The fracture porosity in such a medium is a relatively unconstrained parameter that has been sampled over a wide range. For systems with fracture zones rather than individual fractures, it would seem that the fracture porosity could be larger than assumed in previous calculations, perhaps as large as 1 percent. Keeping $2B = 21$ m, the computed aperture for a fracture porosity of 0.01 would be 0.21 m. Referring to Figure 12.3.2.3-7, fracture aperture is computed using simple geometric considerations such that fracture porosity = b/B. This seemingly large aperture value actually represents all of the pore space within the highly fractured zone, that is, the fracture volume and the intrinsic porosity within the intact rock contained in the fractured zone. By assuming that the concentration profile is constant across this zone, which could perhaps be a meter or two in breadth, a void volume equivalent to an aperture of 21 cm is not unreasonable. This parameter should be thought of as a convenience for setting the spacing and fracture porosity as it no longer has the meaning of an aperture when the model is used to represent a flowing network of fracture zones.

The other element of this alternate description of the fracture transport system is the likelihood of sorption within the fractured zones. As opposed to the individual fracture treatment, in which sorption on the faces of fractures is difficult to justify, the alternate model consists of a porous medium within the fracture zones, and retardation due to sorption is easy to justify. In the matrix diffusion model, this sorption is input as a retardation factor within the fracture zone. To set the retardation factors within the fracture zones, it is assumed that the porosity is essentially that of the intact matrix rock and that the same sorption coefficient K_d applies within the fracture zone. Then, the normal relationship between the sorption coefficient and the retardation factor R_f is assumed to apply:

$$R_f = 1 + \rho_b K_d/\theta \qquad \text{(Eq. 12.3.2.3-2)}$$

where

ρ_b = dry bulk density, including pores
θ = porosity

Two sets of simulations were performed using FEHM V2.11 to examine the impact of this alternate conceptual model. The first considers transport of a conservative species such as carbon-14 to the 20-km boundary. All base case parameters are chosen except the fracture porosity, which is set to 0.01 to capture the effect of transport through fracture zones (spaced 21 m apart) rather than through individual fractures. Figure 12.3.2.3-8 compares the breakthrough curves for a release location in region 1 of the saturated-zone footprint. Also shown in this comparison is the same simulation with no matrix diffusion. The adoption of the

concept of fracture zones results in slightly longer breakthrough times to the 20-km point of compliance compared to the case of individual flowing fractures. Both of these simulations exhibit slight delays of arrival compared to the no-diffusion case, implying that the matrix diffusion process is providing a relatively small improvement to the SZ subsystem performance for conservative radionuclides. The reason for the relatively minor impact in this study is that transport times in the alluvium for the expected case provide several hundred years of transport time delay for all cases, so for matrix diffusion to be important, the amount of delay must approach or exceed this value. With respect to the comparison of the two diffusion conceptual models, there is a tradeoff between the larger fracture porosity, which yields longer transport times within the fracture zones, and the impact of matrix diffusion. The absolute rate of mass diffusion away from the fracture zones are the same as for individual fractures, but the impact is less for fracture zones, which have a large "reservoir" of water containing radionuclide. Thus, the front is not significantly delayed by the presence of the same absolute rate of mass diffusion.

To examine sorption within the fracture zones, neptunium-237 was selected due to its importance in overall radionuclide dose calculations and its propensity to sorb weakly to the rock. This model used the same fracture porosity of 0.01 but included retardation factors within the fractured volcanic tuffs as given by Equation 12.3.2.3-2. A unique value of R_f within each rock type was calculated assuming an average rock bulk density of 2,000 kg/m^3 and the local value of matrix porosity, defined on a node-by-node basis in the site-scale SZ model. Although bulk density and porosity are probably correlated, this approximation will have only a minor affect on the results compared to the inherent uncertainty of the parameters, and therefore, the approximation is valid. The neptunium-237 curves in Figure 12.3.2.3-8 show a minor impact of the type of conceptual model selected, and in fact, the no-diffusion case yields a similar performance as well.

As demonstrated by this sensitivity study, the incorporation of the concept of fracture zones results in little or no improvement in the performance of the SZ as a barrier to radionuclide transport for the expected case. For the purposes of this document, it is concluded that the conceptual model used for the majority of the analyses, namely flow through individual fractures, is bounding in that it provides a lower bound for the transport times through the fractured volcanic tuffs when compared to fracture zone models. However, rather than negating the importance of matrix diffusion as a transport process, this result indicates that other transport barriers within the SZ subsystem can mask the importance of matrix diffusion. In particular, in the expected case, transport through the alluvium adds significant transport time at the end of the pathway to the point of compliance. If this barrier does not perform as currently thought, either because the transport pathways miss the alluvium or because the transport conceptual model for the alluvium is not valid, then matrix diffusion, and differences in the alternate models, would become more important. Therefore, the issue of which matrix diffusion model is appropriate is important despite the apparent lack of sensitivity for the nominal case.

12.3.2.4 Quantification of Previously Unquantified Uncertainty

This section discusses various uncertainty analyses related to transport modeling in the saturated zone. Sections 12.3.2.4.1 and 12.3.2.4.2 deal with sorption of neptunium on volcanic units and in the alluvium, respectively. Section 12.3.2.4.3 deals with sorption of uranium in the alluvium as well as correlation of the sorption coefficients for neptunium and uranium. Section 12.3.2.4.4

treats the bulk density of the alluvium. Section 12.3.2.4.5 discusses irreversible colloidal sorption in the alluvium. Section 12.3.2.4.6 deals with diffusion in the matrix of volcanic tuffs. Section 12.3.2.4.7 handles effective porosity in the alluvium. Finally, Section 12.3.2.4.8 discusses flowing interval porosity (fracture porosity).

12.3.2.4.1 Sorption-Coefficient Distributions for Neptunium in the Volcanic Units

Sorption of neptunium in volcanic units is an important process that contributes to the performance of the SZ as a barrier to radionuclide migration. Neptunium sorption coefficients are important for the nominal scenario results in the TSPA-SR (CRWMS M&O 2000 [DIRS 153246], Section 5.1.2). The sorption coefficient is used to compute retardation as follows Freeze and Cherry (1979 [DIRS 101173], p. 404):

$$R = 1 + \frac{\rho_b}{\theta} K_d \qquad \text{(Eq. 12.3-3)}$$

where

ρ_b = the dry bulk density of the matrix (mass/length^3)
θ = the matrix porosity (dimensionless)
R = the retardation factor in the matrix (dimensionless)
K_d = the sorption coefficient for the matrix (length^3/mass)

12.3.2.4.1.1 Treatment in the Total System Performance Assessment-Site Recommendation

For the TSPA-SR (CRWMS M&O 2000 [DIRS 153246]), the sorption-coefficient probability distribution for neptunium in the matrix was a beta distribution with a mean of 0.5 ml/g, a standard deviation of 0.5, a lower bound of 0, and an upper bound of 2.0 ml/g (CRWMS M&O 2000 [DIRS 147972], p. 62; DTN: LA0003AM831341.001 [DIRS 148751]). Four sorption-coefficient distributions per radionuclide are provided, which are defined as: iron oxides, vitric tuff, devitrified tuff, and zeolitic tuff. The sorption-coefficient distributions used in the SZ site-scale transport calculations correspond to a rock type of vitric tuff, which has the lowest mean value (a conservative approach) that can result in rapid transport through the SZ.

12.3.2.4.1.2 Development of a More Representative Probability Distribution

The main change implemented regarding the neptunium sorption-coefficient probability distribution in the volcanic units for the unquantified uncertainty analysis is that the sorption behavior of zeolitic tuffs is incorporated into the neptunium transport calculation. Because vitric tuffs tend to have the lowest affinity for neptunium (i.e., smallest sorption coefficients) of the three major tuffs (devitrified, vitric, and zeolitic), the use of sorption coefficients for vitric tuffs to represent all three tuff types puts an overly conservative bias on the TSPA-SR transport calculations (CRWMS M&O 2000 [DIRS 147972], Section 6.10). Inclusion of zeolitic tuff sorption coefficients in the transport calculations will result in more representative model simulations and reduce modeling uncertainties.

The integrated site model (V3.1) (CRWMS M&O 2000 [DIRS 146988]) was used to derive the volume of rock (by percent) that is zeolitic within the boundaries of the site-scale SZ flow and transport model and from the water table to 300 m below the water table (Table 12.3.2.4-1) (Kuzio 2001 [DIRS 155004], Filename "Table 12.3.2.4-1.doc"). Rock samples used to derive the neptunium sorption-coefficient distributions typically contained 50 to 60 percent zeolite (CRWMS M&O 2001 [DIRS 154024], Section 6.4.4.1.4.2). However, experiments with pure zeolite yielded lower sorption coefficients than natural rock samples containing 50 to 60 percent zeolite (CRWMS M&O 2001 [DIRS 154024], Section 6.4.4.1.4.2). Therefore, some phase other than zeolite also sorbed neptunium in these samples. To compensate for the sorption by this other phase, it is assumed that a rock must have at least 30 percent zeolite to qualify as a zeolitic tuff. Based on Table 12.3.2.4-1, the volume of zeolitic tuff within the total saturated rock volume with 30 percent or more zeolite is approximately 33 percent. This value is used in the sampling of the neptunium sorption-coefficient probability distributions. That is, the neptunium sorption-coefficient probability distribution for zeolitic tuffs was sampled for 33 percent of the simulations, and the neptunium sorption-coefficient probability distribution for vitric tuffs was sampled for 66 percent of the simulations. The zeolitic probability distribution that was sampled 33 percent of the time is a beta distribution with a mean of 1.0 ml/g, a standard deviation of 0.25, a lower bound of 0, and an upper bound of 5.0 ml/g (DTN: LA0003AM831341.001 [DIRS 148751]).

12.3.2.4.1.3 Summary of the Technical Basis for Uncertainty Analysis

In summary, the probability distribution used for the neptunium sorption coefficient in the matrix was changed from a probability distribution based on a vitric rock type to a probability distribution that is more representative of the rock types that the flow path will encounter. For a given set of realizations (that is, simulations with Monte Carlo sampling) the new probability distribution is determined by sampling the vitric distribution 66 percent of the time and the zeolitic distribution 33 percent of the time.

12.3.2.4.2 Sorption-Coefficient Distributions for Neptunium in the Alluvium

Sorption of neptunium in alluvial material is an important process that contributes to the performance of the SZ as a barrier to radionuclide migration. Neptunium sorption coefficients are important for the nominal scenario results in the TSPA-SR (CRWMS M&O 2000 [DIRS 153246], Section 5.1.2). In general, alluvium has a greater potential for retardation than the tuff matrix (the sorption coefficients are typically larger) due to factors such as mineralogy, reaction kinetics, and water chemistry (CRWMS M&O 2001 [DIRS 154024], Section 6.4.5.2). In addition, sorption in the alluvium is a relatively certain process in that it occurs independent of other processes. By contrast, matrix diffusion must occur in the volcanic units for sorption to become active. No such dependence exists for sorption in the alluvium. Retardation in the alluvium is computed from the sorption coefficient of neptunium using Equation 12.3-3.

12.3.2.4.2.1 Treatment in the Total System Performance Assessment-Site Recommendation

For the TSPA-SR (CRWMS M&O 2000 [DIRS 153246]), the sorption coefficient for neptunium in the alluvium was represented as a beta distribution with a mean of 18.2, a standard deviation

of 18.8, a lower bound of 0, and an upper bound of 100 (CRWMS M&O 2000 [DIRS 147972], p. 63) The source for this parameter (DTN: LA0003AM831341.001 [DIRS 148751]) was developed from preliminary laboratory batch sorption tests using alluvial material from the site (DTN: LA0003JC831341.001 [DIRS 147176]).

12.3.2.4.2.2 Development of a More Representative Probability Distribution

The probability distribution for the neptunium sorption coefficient in alluvium has been modified on the basis of newly acquired laboratory results. These results include batch sorption experiments and column experiments using alluvium samples and water from a well in the alluvium.

The neptunium K_d values (ml/g) were measured in batch sorption tests using alluvium obtained from NC-EWDP boreholes 2D, 3S, and 9SX and samples that were dry sieved to the 75- to 500-micron size range (Reimus 2001 [DIRS 154994], Filename "Np Alluvium Sorption"; DTN: LA0003JC831341.001 [DIRS 147176]). The water for the experiments was from borehole NC-EWDP-3S. Figure 12.3.2.4-1 shows these neptunium batch-sorption K_d values (ml/g). The sorption coefficients obtained for the NC-EWDP-3S borehole samples tended to be at the high end of the range, possibly because Eh conditions in this borehole were more reducing than in the other boreholes. The NC-EWDP-3S data were not used in constructing the final probability distribution function because these data could represent conditions that may not be representative of the dominant flow paths to the accessible environment. The distribution without the NC-EWDP-3S data is shown in Figure 12.3.2.4-1 with diamonds. The mean of the experimental results is 29 ml/g, and the median is 16 ml/g.

The neptunium K_d value obtained in two column experiments was about 0.5 ml/g, which is lower than any of the batch measurements (Reimus 2001 [DIRS 154994], Filename "Np Alluvium Sorption"). The material used to pack the columns had a batch K_d value of about 6 ml/g. The differences in the batch and column results likely reflect the kinetics of the neptunium sorption reactions or rate limitations imposed by mass-transfer processes (e.g., diffusion of neptunium between flowing water and sorbing mineral phases). If the columns were run at slower flow rates, the retardation factors obtained would likely increase in value.

With this new information, a cumulative distribution function (CDF) for neptunium K_d values was derived (Kuzio 2001 [DIRS 155004]) that gives considerable weight to the column experiments to provide conservatism (Figure 12.3.2.4-2). This distribution uses the result of the column experiment that ranges from 0.0 to 0.5 ml/g 33 percent of the time. The remainder of the distribution is derived (Reimus 2001 [DIRS 154994], Filename "Np Alluvium Sorption") from the batch sorption measurements in Figure 12.3.2.4-1 with a range of K_d values from 0.5 to 10 ml/g 47 percent of the time and from 10 and 95 ml/g 20 percent of the time.

12.3.2.4.2.3 Summary of the Technical Basis for Uncertainty Analysis

In summary, the probability distribution used for the unquantified uncertainty analysis was changed from a probability distribution based on laboratory batch experiments to one that represents batch and column laboratory experiments. The distribution function gives

considerable weight to the column experiments, which gives more weight to the lower sorption-coefficient values.

12.3.2.4.3 Sorption-Coefficient Distributions for Uranium in the Alluvium and Correlation of the Sorption Coefficients for Neptunium and Uranium in the Alluvium

Sorption of radionuclides in alluvial material is an important process that contributes to the performance of the SZ as a barrier to uranium migration. As for the case of neptunium, alluvium has a greater potential for retardation than the tuff matrix (the sorption coefficients are typically larger) (CRWMS M&O 2001 [DIRS 154024], Section 6.4.5.2) due to factors such as mineralogy, reaction kinetics, and water chemistry. In addition, sorption in the alluvium is a relatively certain process in that it occurs independently of other processes. By contrast, matrix diffusion must occur in the volcanic units for sorption to become active. No such dependence exists for sorption in the alluvium. Retardation in the alluvium is computed from the sorption coefficient using Equation 12.3-3.

12.3.2.4.3.1 Treatment in the Total System Performance Assessment-Site Recommendation

For the TSPA-SR (CRWMS M&O 2000 [DIRS 153246]), the sorption coefficient for uranium in the alluvium was represented as a uniform distribution with a lower bound of 0 and an upper bound of 8 (CRWMS M&O 2000 [DIRS 147972], p. 63).

12.3.2.4.3.2 Development of a More Representative Probability Distribution

Although sorption-coefficient data for uranium have not been obtained on alluvium samples taken from potential flow paths, an alternative approach for the derivation of sorption-coefficient data was developed in the absence of experimental data. The approach is based on the recognition that uranium and neptunium have similarly small affinities for sorption onto the tuffs within Yucca Mountain (CRWMS M&O 2001 [DIRS 154024], Sections 6.4.4.1.4.2 and 6.4.4.1.4.4). This observation likely reflects the fact that, under oxidizing conditions, these elements form oxycations (uranyl and neptunyl ions, respectively), which have similar sorption mechanisms. On this basis, the sorption-coefficient probability distribution for neptunium in alluvium is taken to also represent the sorption-coefficient probability distribution of uranium in alluvium.

This approach for the derivation of uranium sorption-coefficient probability distributions in alluvium does not reduce the uncertainty in the calculated transport rates for uranium in alluvium in terms of reducing the range of possible error in the calculated rates. However, as discussed below, it does provide conservative estimates of the transport rates for uranium in alluvium. In this sense, it reduces the likelihood that the calculated uranium transport rates are larger than they will be in the natural environment.

A comparison of sorption coefficients for uranium and neptunium obtained for volcanic tuffs indicates that the uranium sorption coefficients are consistently larger in value than the sorption coefficients for neptunium obtained for similar rock samples under similar conditions (Well J-13

water and oxidizing conditions). Data supporting this conclusion are presented in Table 12.3.2.4-2.

12.3.2.4.3.3 Summary of the Technical Basis for Uncertainty Analysis

On this basis, in the absence of experimental data on uranium sorption coefficients in alluvium, the sorption-coefficient probability distribution for neptunium in the alluvium is taken to also represent the sorption-coefficient probability distribution for uranium in the alluvium.

This use of the neptunium sorption-coefficient probability distribution in alluvium for that of the uranium distribution underestimates the uranium transport rates in alluvium because the sorption coefficients for uranium are generally higher in volcanic tuffs than the corresponding ones for neptunium (Table 12.3.2.4-2). The sampling of uranium and neptunium should be identical for a given realization (Monte Carlo simulation result); therefore, the probability distributions for uranium and neptunium have a one-to-one correlation. If they were not correlated, different values would result from sampling identical distributions.

12.3.2.4.4 Bulk Density of the Alluvium

The dry bulk density of the alluvium is important in the computation of the retardation of sorbing radionuclides. The dry bulk density is related to the matrix retardation coefficient through Equation 12.3-4 (Freeze and Cherry 1979 [DIRS 101173], p. 404), which for alluvium, is:

$$R' = 1 + \frac{\rho_b}{\theta} K_m \qquad \text{(Eq. 12.3-4)}$$

where

R' = the retardation factor in the alluvium (dimensionless)
ρ_b = the dry bulk density of the alluvium (mass/length^3)
θ = the porosity of the alluvium (dimensionless)
K_m = the distribution coefficient in the alluvium (length^3/mass)

As can be seen from the equation, the retardation coefficient is linearly dependent on the dry bulk density.

12.3.2.4.4.1 Treatment in the Total System Performance Assessment-Site Recommendation

For the TSPA-SR (CRWMS M&O 2000 [DIRS 153246]), the dry bulk density was considered to be a constant and set to 1.27 g/cm^3 (CRWMS M&O 2000 [DIRS 147972], Section 6.9). The basis for this parameter value is a set of tests performed on four five-foot alluvial intervals from each of the NC-EWDP boreholes 2D, 9S, and 3S at depths of 395 to 415 feet, 145 to 165 feet, and 60 to 80 feet, respectively (DTN: LA0002JC831341.001 [DIRS 147081]). The range of the dry bulk density values in laboratory columns packed with alluvium from these wells was 1.2 to 1.3 g/cm^3. The data are presented in *Unsaturated Zone and Saturated Zone*

Transport Properties (U0100) (CRWMS M&O 2001 [DIRS 154024], p. 86) with a note stating that densities were measured in the laboratory and do not represent in-situ conditions.

12.3.2.4.4.2 Development of a More Representative Model

The values used in the TSPA-SR (CRWMS M&O 2000 [DIRS 153246]) were low compared to dry bulk densities measured in alluvium at Frenchman Flat and the NTS near Yucca Mountain (Howard 1985 [DIRS 153266], Table 3, p. 81, and Table A-1, p. 38). Similarly, a comparison to the range of dry bulk densities of alluvial material in general (Manger 1963 [DIRS 154474], pp. E41 to E42) led to the conclusion that the values used in the TSPA-SR were likely an underestimate of the true bulk density.

Borehole gravimeter surveys were conducted by EDCON Incorporated (Black 2000 [DIRS 154704], pp. 2 to 18) at well NC-EWDP-19D1 directly south of Yucca Mountain on U.S. Highway 95. A total of 36 values of saturated bulk density were estimated based on the geophysical milligal measurements taken from this well (Black 2000 [DIRS 154704], p. 18). Seventeen measurements were taken from a depth corresponding to the inferred depth of the flow path through the alluvium near Yucca Mountain (401.5 to 776 feet). The wet bulk density computed from gravimeter measurements is presented in Table 12.3.2.4-3 as well as the porosity and dry bulk density computed from Freeze and Cherry (1979 [DIRS 101173], p. 337) and Black (2000 [DIRS 154704], p. 18):

$$\theta = \frac{\rho_{sat} - \rho_{grain}}{\rho_{w} - \rho_{grain}} \qquad \text{(Eq. 12.3-5)}$$

$$\rho_{b} = \rho_{grain}(1 - \theta) \qquad \text{(Eq. 12.3-6)}$$

where

θ = porosity (dimensionless)
ρ_b = dry bulk density in g/cm^3
ρ_{sat} = saturated bulk density in g/cm^3
ρ_{grain} = the average grain density for these samples (2.52 g/cm^3)
ρ_w = the density of water (1.0 g/cm^3)

The mean dry bulk density for this set of measurements was 1.91 g/cm^3. This value is close to dry bulk density values previously measured at Frenchman Flat and the NTS in similar rock at similar depth, and it is the value used as the mean in the unquantified uncertainty simulations. The computed standard deviation for these measurements is 0.080 g/cm^3.

The average grain density was computed to be 2.52 g/cm^3 from alluvial samples from other boreholes in the vicinity of Yucca Mountain (USGS n.d. [DIRS 154495], pp. 3 to 4). The grain density varied little (2.49 to 2.55 g/cm^3), and so the average was used in the computation of the porosity and dry bulk density. A normal distribution was selected to characterize the uncertainty in the dry bulk density based on frequency plots of that parameter.

12.3.2.4.4.3 Summary of the Technical Basis for Uncertainty Analysis

To summarize, the value for dry bulk density in the alluvium is changed from a constant value of 1.27 g/cm^3 to a stochastic variable that more properly characterizes uncertainty at Yucca Mountain for the unquantified uncertainty computations. The new dry stochastic bulk density is chosen from a normal distribution. The mean dry bulk density, 1.91 g/cm^3, and standard deviation, 0.080 g/cm^3, as well as the distribution form are based on new data taken at well NC-EWDP-19D1. Figure 12.3.2.4-3 gives the distribution of 100 realizations of dry bulk density for the alluvium; the normal distribution was used to characterize the dry bulk density. This distribution was found to give a reasonable fit to the data taken at the NC-EWDP-19D1 well, also shown in Figure 12.3.2.4-3.

12.3.2.4.5 Retardation of Radionuclides Irreversibly Sorbed on Colloids in the Alluvium

Radionuclides that sorb strongly to solid geologic materials are generally considered to be immobile. However, colloid-facilitated transport is the one mechanism that can result in enhanced mobility of these radionuclides (discussed below). For the TSPA-SR (CRWMS M&O 2000 [DIRS 153246]), two conceptual models of colloid-facilitated transport of radionuclides were implemented: the first conceptual model involves radionuclides that are irreversibly or permanently (in the time frame of groundwater transport) sorbed onto colloids; the second deals with radionuclides that are reversibly or temporarily attached to colloids.

This section discusses the retardation of radionuclides irreversibly sorbed on colloids in the alluvium. The available data for colloid filtration are reduced in a manner that provides estimates of the colloid retardation factor. However, the particle tracking code component of FEHM V2.10 calls for a K_d value as input for porous continua such as the alluvium. Therefore, in the site-scale SZ flow and transport model, the estimated colloid retardation factors for the alluvium units are converted to a value of effective sorption coefficient according to a rearranged form of Equation 12.3-3 (Freeze and Cherry 1979 [DIRS 101173], p. 404):

$$K_d^{eff} = \frac{(R_f - 1)\phi_{eff}}{\rho_b} \qquad \text{(Eq. 12.3-7)}$$

where

K_d^{eff} = the effective K_d
R_f = the retardation factor for irreversible colloids
θ_{eff} = effective porosity
ρ_b = bulk density

The units are the same ones as in Equation 12.3-3.

12.3.2.4.5.1 Summary of the Treatment in the Total System Performance Assessment-Site Recommendation

The development in the TSPA-SR (CRWMS M&O 2000 [DIRS 153246]) of the CDF for the retardation factor of radionuclides that are irreversibly sorbed to colloids in the alluvium is described in the *Saturated Zone Colloid-Facilitated Transport* report (CRWMS M&0 2000

[DIRS 129286], Figure 8). This AMR provides a theoretical approach based, in part, on field tests at other alluvial aquifers. At the time of that report, the Yucca Mountain alluvium had not been characterized. The CDF was obtained using the following equation for the retardation factor *R*:

$$R = 1 + \frac{\rho_a}{\theta}\frac{k_f}{k_r} \qquad \text{(Eq. 12.3-8)}$$

where

ρ_a = the density of the alluvial material in g/cm^3
θ = the alluvium porosity
k_f = the rate of colloid attachment onto the immobile material in 1/hr
k_r = the detachment rate in g/cm^3-hr

The attachment rate k_f is further defined as (Harvey and Garabedian 1991 [DIRS 109256], Equation 2):

$$k_f = v\frac{3}{2}\frac{(1-\theta)}{d}\alpha\eta \qquad \text{(Eq. 12.3-9)}$$

where

v = the fluid velocity
d = the diameter of the porous media grains
α = the collision efficiency factor
η = the single-collector efficiency

The single-collector efficiency η can be estimated from:

$$\eta = \eta_D + \eta_I + \eta_G = 0.9\left[\frac{kT}{\mu d_p dv}\right]^{2/3} + 1.5(d_p/d)^2 + \frac{(\rho_p - \rho)g d_p^{\,2}}{18\mu v} \qquad \text{(Eq. 12.3-10)}$$

where

η_D = the colloid collector collision caused by Brownian motion
η_I = the colloid collector collision caused by interception
η_G = the colloid collector collision caused by settling
k = the Boltzmann constant
T = the solute temperature (absolute temperature)
μ = the fluid viscosity
d_p = the colloid diameter
d = the diameter of the porous media grains
ρ = the fluid density
ρ_p = the colloid density
g = acceleration due to gravity

For Equations 12.3-8 through 12.3-10, the following parameters were held constant: k (1.38×10^{-16} erg/K), T (25°C), μ (0.01 g/cm-sec), ρ (1.0 g/cm^3), ρ_p (2.6 g/cm^3), ρ_a (1.27 g/cm^3), and g (980 cm/sec^2). Parameters that were varied and their assumed distributions are listed in Table 12.3.2.4-4. Each of the parameter distributions in that table were randomly sampled using the GoldSim V6.04.007 software package, and the resulting parameters were used in Equations 12.3-8 through 12.3-10 to obtain an estimate of the colloid retardation factor, R. A CDF was then constructed from 10,000 such realizations of R.

12.3.2.4.5.2 Development of a More Representative Probability Distribution

The revised CDF for the retardation factor of radionuclides that are irreversibly sorbed to colloids in the alluvium was generated using the same equations and procedure as the CDF in the TSPA-SR (CRWMS M&O 2000 [DIRS 153246]). However, the alluvium grain size distribution was modified to reflect actual grain size data from well NC-EWDP-19P and from other locations at the NTS. Additionally, the grain size distribution was weighted by the permeability associated with the different grain sizes, as calculated using the Carman-Kozeny equation (Dagan 1989 [DIRS 147409], p. 104). Thus, given equal volumes of large and small grain sizes, colloids were more likely to encounter larger grains because significantly more flow is conducted through larger grains.

The procedure for obtaining the grain size distribution used in the generation of the revised retardation factor CDF was:

1. Fifty-one alluvium grain size (diameter) distribution data sets from the NTS were fitted assuming a lognormal distribution. The sampling locations included multiple intervals/locations within boreholes u-3bl-d2, u-3bh, and u-3bh-c2 in Yucca Flat (Bechtel Nevada 1998 [DIRS 149177], Table I-1; McKeown 1992 [DIRS 102330], Appendix 1), and trenches near the current location of the Exploratory Studies Facility (ESF) north portal and well NC-EWDP-19P (Reimus 2001 [DIRS 154994], Filename "EWDP 19P Grain Sizes").

2. Discrete and Gaussian CDFs of the means and standard deviations of the 51 lognormal distributions were obtained by fitting the data.

3. The discrete distributions obtained in Step 2 were randomly sampled and the resulting means and standard deviations were used to generate artificial grain size distributions assuming a lognormal distribution. Effective diameters (d_{eff}) of these distributions were obtained by calculating the surface area to volume ratio (A/V) for the entire distribution and then calculating the effective diameter from $d_{eff} = 6V/A$ (which applies to spherical particles).

4. An unweighted CDF was obtained for effective diameters by repeating Step 3 many times.

5. For each effective diameter in the unweighted CDF, a relative permeability, k, was calculated using the Carman-Kozeny equation (Dagan 1989 [DIRS 147409], p. 104):

$$k = \frac{\theta^3}{180\,(1-\theta^2)}\,d_{\text{eff}}^2 \qquad \text{(Eq. 12.3-11)}$$

6. The contribution of each bin in the unweighted CDF to the overall permeability was determined by multiplying the permeability associated with that bin by the probability of that bin. These products were then summed over all bins, and the probability of a colloid experiencing an effective diameter associated with a given bin was assumed to be the product for that bin divided by the sum of the products for all bins. In effect, this procedure made the effective diameter probabilities proportional to the volumetric flow rates through the different bins. Thus, a new CDF of effective diameters with probabilities weighted by volumetric flow rates was created.

7. The weighted CDF from Step 6 was randomly sampled instead of the original uniform distribution of grain diameters in Table 12.3.2.4-4 to obtain a new CDF of colloid retardation factors.

The new and original CDFs for retardation factors of radionuclides irreversibly sorbed to colloids are plotted in Figure 12.3.2.4-4. It is apparent that the new CDF results in lower retardation factors than the original one used in the TSPA-SR (CRWMS M&O 2000 [DIRS 147972], Figure 6).

12.3.2.4.5.3 Summary of the Technical Basis for Uncertainty Analysis

The new CDF for retardation factors of radionuclides irreversibly sorbed to colloids assumes that most water flow, and therefore colloid migration in the alluvium, will occur in high-permeability regions, which should have larger grain sizes than lower-permeability regions. In sampling the CDF, it is implicitly assumed that colloids will experience the same sampled grain size distribution (effective diameter) throughout the entire alluvium. In reality, individual flow streamlines may experience a variety of grain size distributions through the alluvium. The assumption of a single distribution effectively implies a layered system or the existence of continuous channels of interconnected material of similar grain sizes. Although this assumption has not been proven or tested, any distribution of grain sizes that are linked in series will tend to have a permeability and, presumably, a colloid retardation coefficient that is dominated by the lowest permeability and grain size.

The alluvium bulk density assumed in generating the new CDF of retardation factors was 1.27 g/cm^3; the same value that was assumed in the generation of the original CDF, despite the fact that the bulk density was modified based on the borehole gravimeter data from NC-EWDP-19D1 (see Section 12.3.2.4.4). The new value of bulk density will be incorporated into future calculations of the retardation factor CDF. The use of the old bulk density value yields retardation factors that are about 35 percent lower than values calculated using the new bulk density.

Other assumptions associated with the generation of the colloid retardation factor CDF are described in *Saturated Zone Colloid-Facilitated Transport* (CRWMS M&O 2000 [DIRS 129286], pp. 12 to 14).

12.3.2.4.6 Effective Diffusion Coefficient and Correlation

Matrix diffusion is a key retardation process in the volcanic tuffs. For non-sorbing radionuclides, diffusion into the stagnant fluid in the tuff matrix reduces travel times. For sorbing radionuclides, matrix diffusion also provides the mechanism for contact of the radionuclides with the rock matrix which is a necessary precondition for sorptive retardation.

Section 12.3.2.3.4 describes a modest sensitivity of the model results to uncertainty in the matrix diffusion model. However, these simulations all assumed significant transport pathways through the porous alluvium. The matrix diffusion process is anticipated to be most important in providing an additional transport barrier in the event that the transport times provided by the alluvium are not realized.

12.3.2.4.6.1 Treatment in the Total System Performance Assessment-Site Recommendation

In the TSPA-SR calculations, effective radionuclide diffusion coefficients in volcanic matrices were randomly sampled from a log-uniform distribution having values ranging from 10^{-10} to 10^{-13} m^2/sec (CRWMS M&O 2000 [DIRS 147972], p. 62). The basis for this parameter, for the radionuclides of interest, included an analysis of the ionic radius, charge, and most importantly, the differences in tortuosity. Fracture apertures and matrix porosity also influence matrix diffusion of radionuclides. The former is effectively determined in the preprocessor for the site-scale SZ flow and transport model (CRWMS M&O 2000 [DIRS 139440], Section 6.2.1.3) by the fracture porosity divided by the flowing interval spacing, both of which are randomly sampled from distributions (log uniform with bounds of 10^{-1} to 10^{-5} for fracture porosity and lognormal with a geometric mean of approximately 20 m and a $\log_{10}$ standard deviation of 0.43 for flowing interval spacing). The matrix porosity is a constant value for a given TSPA realization, based on the stratigraphic unit(s) in which the SZ transport is assumed to occur. In the TSPA-SR (CRWMS M&O 2000 [DIRS 153246]), there was no correlation between the sampled matrix diffusion coefficients and the matrix porosities.

12.3.2.4.6.2 Development of a More Representative Probability Distribution

Changes made in the treatment of radionuclide matrix diffusion for the SSPA unquantified uncertainties (McNeish 2001 [DIRS 155023]) calculations include the following:

- The distribution for radionuclide effective matrix diffusion coefficients was modified from log uniform to log triangular probability distribution. The upper and lower bounds are still 10^{-10} and 10^{-13} m^2/sec, but the most probable value is 3.2×10^{-11} m^2/sec. The basis for this is to put more emphasis on the mean value compared to sampling a uniform distribution that results in sampling equally all values in the distribution. The effect of this change is that larger and smaller effective diffusion coefficients are less probable.

- The distribution for fracture porosity in the volcanics was modified from log uniform to log triangular. The upper and lower bounds are still 10^{-1} and 10^{-5}, but the most probable value is now 10^{-3}. The basis for this is to put more emphasis on the mean value compared to sampling a uniform distribution that results in sampling equally all values in the distribution.

- Sampled matrix diffusion coefficients are now correlated with matrix porosities using a relationship developed from laboratory diffusion-cell experiments in which anion diffusion coefficients through tuff matrices from various stratigraphic units from the C-wells Complex (Reimus 2001 [DIRS 154994]) and from Pahute Mesa at the NTS (Reimus et al. 1999 [DIRS 154689], pp. 27 to 29; Reimus 2001 [DIRS 154994], Filename "Diffusion Cell Data") were measured. For a given sampled value of the effective matrix diffusion coefficient, the value is adjusted upward or downward, depending on the sampled value of the matrix porosity relative to the average volcanic matrix porosity from laboratory studies, by a value of 0.15 (CRWMS M&O 2000 [DIRS 147972], Section 6.5). The laboratory-derived relationship between matrix diffusion coefficients and matrix porosity is shown in Figure 12.3.2.4-5.

12.3.2.4.6.3 Summary of the Technical Basis for Uncertainty Analysis

To determine whether the probability distributions described above result in realistic treatment of radionuclide matrix diffusion in volcanic rocks, the distributions of mass transfer coefficients obtained from 300 realizations of the SZ flow and transport model with laboratory- and field-derived mass transfer coefficients were compared, as described in the following sections.

The mass transfer coefficient (MTC) is defined as (Robinson 2001 [DIRS 155060]):

$$\frac{\theta}{b}\sqrt{D_{\mathrm{m}}} \quad (\mathrm{sec}^{-1/2}) \qquad \text{Eq. 12.3-12}$$

where

θ = matrix porosity
b = the fracture half-aperture (m)
D_{m} = the matrix diffusion coefficient ($\mathrm{m}^2/\mathrm{sec}$)

Figure 12.3.2.4-6 shows mass transfer coefficients (for halides) as a function of tracer residence time derived from laboratory transport experiments conducted using fractured cores from the C-wells or Pahute Mesa (NTS) and field transport experiments conducted either at the C-wells or Pahute Mesa. The MTCs span a range of almost 4 orders of magnitude of mean tracer residence time, with an apparent trend of decreasing MTC as time scale increases. For comparison, Figure 12.3.2.4-7 shows the distribution of MTCs from 300 realizations of the SZ flow and transport model for the modified uncertainty distributions for diffusion coefficient and fracture porosity described here**.** It is apparent that the distribution of simulated MTCs spans the experimental range with the lower end of the distribution extending to significantly lower values than the experimental range. This result is considered acceptable because the experimental data

suggest a potential decrease in MTC as time scales extend beyond the experimental range to values relevant for performance assessment.

12.3.2.4.7 Effective Porosity in the Alluvium

The effective porosity in the alluvium is an important parameter controlling transport times through the alluvium. For a given groundwater flux, the travel time of a conservative radionuclide is directly proportional to the effective porosity. In addition, for sorbing radionuclides, Equation 12.3-3 shows that the retardation factor is inversely influenced by the porosity.

12.3.2.4.7.1 Treatment in the Total System Performance Assessment-Site Recommendation

For the TSPA-SR (CRWMS 2000 [DIRS 153246]), effective porosity in the alluvium was a truncated normal distribution with a mean of 0.18, a standard deviation of 0.051, a lower bound of 0, and an upper bound of 0.35 (CRWMS M&O 2000 [DIRS 147972], Section 6.3). The basis for this parameter was Bedinger et al. (1989 [DIRS 129676], p. A18, Table 1). There were no site data for effective porosity in the alluvium at the time of the TSPA-SR. Bedinger et al. (1989 [DIRS 129676]) includes a study of hydraulic characteristics of alluvium within the Southwest Basin and Range Province. This study appears relevant to the local basin fill conditions and provides values for effective porosity as a stochastic parameter.

12.3.2.4.7.2 Development of More Representative Probability Distribution

The mean alluvium flow effective porosity was decreased from 0.18 to 0.15, based primarily on the preliminary results of single-well, isolated interval hydraulic tests at well NC-EWDP-19D1. These results, to date, have indicated that there are negligible hydraulic responses in well screens above and below any isolated screened interval that has been pumped in the alluvium (Kuzio 2001 [DIRS 155004], Filename "transducer data.xls"). That is, the pressure transducers above and below the packers used to isolate the pumped intervals have not responded significantly during pumping. These results suggest that there may be considerable vertical anisotropy in hydraulic conductivity in the alluvium, possibly due to subhorizontal layering of varying degrees of grain coarseness and/or cementation.

12.3.2.4.7.3 Summary of the Technical Basis for Uncertainty Analysis

In summary, the probability distribution used for effective porosity in the alluvium changed from a probability distribution based primarily on Bedinger et al. (1989 [DIRS 129676]) to a probability distribution that is more representative of preliminary results from single-well, isolated-interval hydraulic tests at well NC-EWDP-19D1. The distribution used for the SSPA Volume 2 (McNeish 2001 [DIRS 155023]) calculation was changed from a truncated normal distribution with a mean of 0.18, a standard deviation of 0.051, a lower bound of 0, and an upper bound of 0.35, to a normal distribution with a mean of 0.15, a standard deviation of 0.051, a lower bound of 0, and an upper bound of 0.30. The rational for changing the upper bound from 0.35 to 0.30 is Table 12.3.2.4-3, which indicates a maximum total porosity of approximately 0.30.

12.3.2.4.8 Flowing Interval (Fracture) Porosity

Fracture porosity is defined as the proportion of effective porosity of fractures in which fluid flow and advective solute transport occur. At Yucca Mountain, rather than attempt to define the porosity of individual fractures, a flowing interval is defined as the region in which significant groundwater flow occurs at a well. The fracture porosity then characterizes these flowing intervals rather than individual fractures. The advantage to this means of defining fracture porosity is that in-situ well data may be used to characterize the parameter. Fracture porosity is considered a key parameter in the matrix diffusion process.

12.3.2.4.8.1 Treatment in the Total System Performance Assessment-Site Recommendation

For the TSPA-SR (CRWMS M&O 2000 [DIRS 153246]), the flowing interval (fracture) porosity probability distribution was a uniform distribution with an upper bound of $\log_{10}$ of -1.0 and a lower bound of $\log_{10}$ of -5.0 (CRWMS M&O 2000 [DIRS 147972], p. 39). The basis for this parameter were estimates of fracture porosity in intact cores of volcanic rock and the results of pumping tests and tracer tests in the Bullfrog Tuff at the C-wells Complex (CRWMS M&O 2000 [DIRS 129286]).

12.3.2.4.8.2 Development of More Representative Probability Distribution

The probability distribution for the flowing interval porosity has been modified on the basis of two new sources of information about flowing interval porosity. These are tests in unsaturated tuff in the ESF and the results of tracer tests in saturated tuffs at the C-wells Complex.

Fracture porosity has been estimated in unsaturated volcanic tuff in the ESF for the middle nonlithophysal welded tuff (UZ model layer tsw34) by two methods.

The first method is the gas tracer test. The assumptions used in obtaining the fracture porosity from gas tracer tests are that the diffusion of gas into the rock matrix is negligible compared to the flow through the fractures, that the fracture network is well connected, and that the geometry of the network is known.

This calculation of fracture porosity is documented in the *Analysis of Hydrologic Properties Data* AMR (CRWMS M&O 2000 [DIRS 145771], p. 42). The estimated values of fracture porosity range from 0.006 to 0.02.

For the second method, water was pumped into intervals of boreholes UL, UM, and UR with tracers to identify the travel time to a nearby niche. Based on the water seepage rate and the water release fluxes for the intervals, a seepage threshold flux was determined. From this flux and the arrival time, the average volumetric water content may be estimated from the *Analysis of Hydrologic Properties Data* AMR (CRWMS M&O 2000 [DIRS 145771], Equation 34, p. 58). The volumetric water content approximates the fracture porosity under near saturated conditions. The assumptions are that the liquid flow is downward and steady, and the medium is porous and isotropic (it is assumed that the fractured rock behaves as an equivalent porous medium); that flow is infinite, and flow in the upstream direction is spatially uniform; that an exponential relation exists between the unsaturated hydraulic conductivity and the moisture potential; and

that near saturated conditions exist (under these conditions, the water content is a good approximation of the fracture porosity) (Philip et al. 1989 [DIRS 105743], pp. 16 to 23).

From the tests documented in the *Analysis of Hydrologic Properties Data* AMR (CRWMS M&O 2000 [DIRS 145771], p. 60) the estimated water content values were 0.0242, 0.0124, and 0.0024. These values cover a range similar to the gas-tracer test method.

Fracture porosity has also been estimated using the residence time of conservative tracers during cross-hole tracer tests at the C-wells Complex (Robinson 2001 [DIRS 155060]). This method assumes that the mean tracer arrival time is equal to the time required to drain a homogenous, fractured cylinder of rock with a radius equal to the distance between the pumping well and the tracer-injection well. A large range in estimated fracture porosity for the saturated Bullfrog Tuff resulted from this method because the tracers were interpreted to have traveled along two paths with different travel times. The path with the longer travel time resulted in a larger estimate of fracture porosity. The resulting lower and upper bounds of fracture porosity were 0.0037 and 0.12, respectively (Robinson 2001 [DIRS 155060]). Cross-hole tracer testing in a second interval at the C-wells Complex (the Prow Pass Tuff) resulted in fracture porosity estimates ranging from 0.0027 to 0.0062 (Robinson 2001 [DIRS 155060]).

12.3.2.4.8.3 Summary of the Technical Basis for Uncertainty Analysis

The new data from the ESF and the C-wells tracer tests provide estimates of flowing interval porosity that fall in the upper half of the distribution used for this parameter in the TSPA-SR (CRWMS M&O 2000 [DIRS 153246]). For the SSPA Volume 2 (McNeish 2001 [DIRS 155023]) calculations, a new log-triangular distribution with a lower bound of –5.0, a most-likely value of –3.0, and an upper bound of –1.0 was selected for this parameter. This distribution places more weight at the mid-point of the distribution range compared to the TSPA-SR (CRWMS M&O 2000 [DIRS 153246]; CRWMS M&O 2000 [DIRS 147972], Table 15) uniform distribution that results in equal probabilities for the given range. This midpoint value of –3.0 is representative of the smallest values of fracture porosity estimated from the new data from the ESF and all previous field tests.

12.4 MULTIPLE LINES OF EVIDENCE

This section discusses multiple lines of evidence and confidence-building activities that are independent of TSPA.

Groundwater hydrochemical data were interpreted to estimate flow paths in the vicinity of Yucca Mountain (Section 12.4.1). These estimated flow paths are consistent with flow paths predicted by the site-scale SZ flow model.

Ongoing cleanup efforts at 24 inactive uranium ore processing sites will continue to provide independent information about dispersion and retardation of radionuclides in the subsurface (Section 12.4.2). Studies, to date, provide some information about the transport of uranium that is relevant to Yucca Mountain. First, some fraction of the total uranium inventory of mill tailings appears to be transported as a nonsorbing to weakly sorbing contaminant. Second, the TSPA-SR treatment of uranium as weakly sorbing in the model calculations is supported (CRWMS M&O 2000 [DIRS 153246]). However, the TSPA-SR assumes oxidizing conditions.

More strongly retarding conditions will be appropriate in future performance assessment calculations if new data support the existence of reducing conditions along the flow paths away from Yucca Mountain.

Preliminary results from single-well tracer testing at the ATC are available (Section 12.4.3). These tests are being performed in wells drilled by Nye County as part of their Early Warning Drilling Program. The preliminary results for dissolved tracers suggest diffusion into stagnant or slowly moving groundwater is not an important process in retarding transport of dissolved species in the alluvial materials. This conclusion supports the single-porosity model currently used by the TSPA-SR for transport in alluvium (CRWMS M&O 2000 [DIRS 153246]). Transport of colloids was also investigated in the ATC tests. Preliminary analysis of the behavior of synthetic microspheres indicates that colloids attach to mineral surfaces in the alluvium. This attachment is, however, reversible. These results support the conceptual model used as the basis of the TSPA-SR colloid transport model in alluvium, that is, a model in which colloids attach and detach from mineral surfaces.

The Electric Power Research Institute (EPRI) performed independent modeling of flow and transport in the SZ (Section 12.4.4). The EPRI analysis supports the TSPA-SR conceptualization (CRWMS M&O 2000 [DIRS 153246]) that diffusion of solutes into the matrix of fractured tuffs can slow transport of radionuclides away from the repository. In addition, EPRI concurs that use of flowing intervals is a reasonable conceptualization of SZ conditions. However, EPRI argues that the implementation of dual-porosity transport in the TSPA-SR model is overly conservative in that the assumed distance between fractures is too large.

Preliminary results from the testing of transport behavior of selected radionuclides and compounds on a trial block of intact tuff from the Busted Butte Unsaturated Zone Facility (located near Yucca Mountain) are available and employed to corroborate values used in the transport modeling predictions and performance assessment calculations (Section 12.4.5). The preliminary results indicate that they are consistent with the performance assessment calculations. This statement will be further quantified after the full block test of the Busted Butte Tuff has been completed and a larger fraction of the injected neptunium recovered.

Analogue sites provide data on the transport of uranium, in some cases, over millions of years (Section 12.4.6). Although the geology and geochemistry at many of these sites differ from that at Yucca Mountain, they provide data that may be used to calibrate computer codes, and their analysis can yield a picture of the flow and transport of uranium under various conditions. The sites studied range from ore bodies, such as the Alligator Rivers site in Australia, Poços de Caldas in Brazil, the Oklo site in Gabon, and the Cigar Lake site, to U.S. Department of Energy (DOE) facilities, such as the Idaho National Engineering and Environmental Laboratory (INEEL) site and the NTS.

Measurement of chloride concentrations and uranium isotope activity ratios in groundwater in the Yucca Mountain region serve as a self-analogue study of the site (Section 12.4.7). Such data test the reasonableness of the flow path and travel time computed by the TSPA-SR flow and transport model (CRWMS M&O 2000 [DIRS 153246]).

The Center for Nuclear Waste Regulatory Analysis (CNWRA) completed a flow and transport calculation of radionuclides to assist the U.S. Nuclear Regulatory Commission (NRC) in evaluating the potential repository at Yucca Mountain (see Section 12.4.8). The processes simulated are similar to those included in the TSPA SZ model.

12.4.1 Evidence for Flow Paths Based on Groundwater Hydrochemical and Isotopic Data

Groundwater hydrochemical and isotopic data have been examined to provide estimates of groundwater flow directions in the Yucca Mountain area (CRWMS M&O 2001 [DIRS 154795], Sections 6.5.2.1 and 6.5.2.2, Figure 17). In that analysis, similarities and, more importantly, differences in the concentrations of a number of geochemical and isotopic species were used to identify compositionally distinct waters and trace their movement downgradient. The analysis assumed that the species of interest (i.e., oxygen-18, deuterium, chlorine, SO_4, calcium, and sodium) were sufficiently conservative (species that travel at the speed of the groundwater) that any changes in the species along a flow path were minor compared to differences between adjacent flow paths; thus, relative rather than absolute conservatism of individual species is assumed in the analysis. Maps of the hydraulic head gradient constrained the direction of possible flow paths insofar as groundwater is known not to flow upgradient. However, the flow paths traced from groundwater chemical and isotopic data were allowed to be arbitrarily oblique to the hydraulic gradient to allow for the possible effects of anisotropy in permeability due to preferred north-south fault orientations in the Yucca Mountain area. One important aspect of the flow path analysis is that, under the assumption of two-dimensional steady-state groundwater flow, flow paths do not cross in map view. Therefore, after some flow paths are drawn, the locations of subsequent flow paths are constrained by the existing flow paths.

Other limitations of the two-dimensional flow path analysis discussed in *Geochemical and Isotopic Constraints on Groundwater Flow Directions, Mixing, and Recharge at Yucca Mountain, Nevada* (CRWMS M&O 2001 [DIRS 154795]) pertained to possible bias imparted to the inferred flow directions as a result of compositional changes caused by aquifer mixing or recharge. Compositional changes resulting from these three-dimensional processes would cause the flow paths to be artificially diverted around areas where these effects are important. Groundwater at Yucca Mountain itself may include a large component of local recharge, based on the unique uranium-234/uranium-238 activity ratio of Yucca Mountain perched water and underlying groundwater (CRWMS M&O 2001 [DIRS 154795], Section 6.5.3). Thus, Yucca Mountain itself may be one area where upgradient groundwater is artificially diverted around Yucca Mountain in the analysis.

The groundwater flow paths determined from the analysis of groundwater hydrochemical and isotopic data are shown superimposed on a map of groundwater chloride concentrations in Figure 12.4-1. The red pathline (Path #6) in the figure shows a flow path leading from the potential repository area at Yucca Mountain. This pathline traces the movement of groundwater with chloride concentrations less than 6 mg/L found near the Ghost Dance fault southeastward along Dune Wash and then southwestward to well NC-EWDP-2D along the west side of Fortymile Wash. South of Dune Wash, groundwater west of this pathline has higher chloride and sulfate concentrations than groundwater along the pathline; groundwater east of this pathline has oxygen-18 and deuterium compositions that associate the groundwater with Fortymile Wash (CRWMS M&O 2001 [DIRS 154795], Figures 5, 6, 12, 13, and 26). These same chemical and

isotopic relations, and the previously drawn pathlines (Paths #2 and #5), constrain the position of the pathline (Path #6) southward toward the southern boundary of the site model area.

Due to the different starting positions of particles used to trace groundwater flow paths from the potential repository area in the site-scale model, there is some dispersion in the simulated particle pathlines (CRWMS M&O 2000 [DIRS 139582], Figure 7; see also Figure 12.4-2). Particles entering the groundwater in the northern part of the repository area tend to have a stronger eastward component in their trajectory than particles originating in the southern part of the repository area. Overall, however, there is good agreement between the average trend of pathlines from the repository predicted by the site-scale model and the pathline estimated from the groundwater hydrochemical and isotopic data.

12.4.2 Uranium Mill Tailing Analogues

The Uranium Mill Tailings Remedial Action (UMTRA) Project was authorized by Congress in 1978 to clean up 24 inactive uranium ore processing sites. These sites had been operated during the 1950s through the 1970s to produce uranium for defense and other purposes (DOE 1982 [DIRS 154691]; DOE 1996 [DIRS 154693]). The 24 sites are located mainly in the western United States, but also include two sites in Pennsylvania and one in Texas. Many of the sites are located in the Rocky Mountain states of Colorado (8 sites), Utah (3 sites), Wyoming (2 sites), and New Mexico (2 sites). Sites are also located in Arizona (2 sites), Oregon (1 site), Idaho (1 site), and North Dakota (2 sites). Most of the sites consisted of a uranium processing mill with associated tailings piles and other processing waste streams. The tailings piles were generally initiated on bare soil without intervening barriers. The size of the tailings piles at different sites varied greatly, depending on the volume of uranium ore processed at the site. Sites such as Grand Junction, Rifle, and Naturita in Colorado had large tailings piles, whereas piles at sites in other states were generally smaller. The time of operation also varied. The Old Rifle site started as early as 1924, whereas the sites in North Dakota were only operated in the early 1960s. Most of the sites began operation in the mid- to late-1950s and ended operations in the early 1960s to early 1970s. During the 1980s and 1990s, the tailings piles located at the 24 sites were either capped in place or removed to another location and encapsulated. Therefore, most of the tailings piles were sources of contaminants for, at most, 30 to 40 years. Since 1991, the UMTRA Ground Water Project has been monitoring and developing remediation strategies for the contaminant plumes in the ground at the various sites.

The ores processed at the various locations contained other elements besides uranium, such as vanadium, arsenic, selenium, manganese, molybdenum, barium, and other trace metals. In addition, chemicals used in processing the ore also ended up in the tailings piles. Important among these were sulfate, nitrate, ammonium, and hydrogen ions (i.e., acid solutions). Because the tailings piles were not covered, infiltrating rain and snow have leached constituents from the tailings and subsequently percolated into the subsoils beneath the tailings. Studies of the fate and transport of these constituents in the subsurface is the aspect of the UMTRA Project that is of the greatest interest to the DOE. The DOE is particularly interested in the dispersion characteristics of the plumes and in the retardation behavior of constituents such as uranium that also occur in nuclear waste to be emplaced in a repository.

Although some monitoring has been performed at all the UMTRA sites, selected sites have been monitored more extensively than others. This approach largely reflects the perceived risks associated with the various sites. Those sites where the volumes of ore processed were small and/or where the subsurface geology inhibited transport, monitoring was less extensive. At most of the sites, contaminants related to uranium processing are confined to shallow alluvial aquifers and have not penetrated into the bedrock below the sites. For example, at the site in Gunnison, Colorado, the uranium plume is restricted in depth to the Quaternary alluvium deposited by Tomichi Creek. Further, the areal shape of the plume shows only limited lateral dispersion over most of the length (approximately 1 mile) of the plume (DOE 1994 [DIRS 154692], Figure 3.12). Sulfate was also a major site-related contaminant. This constituent is generally thought to behave conservatively (i.e., is not retarded) in oxidizing groundwaters. The fact that the uranium plume is similar in shape and extent to the sulfate plume indicates at least some of the uranium is also transported with little or no retardation at this site (DOE 1994 [DIRS 154692], Figure 3.11).

At Rifle and Naturita, Colorado, extensive monitoring programs have been conducted to characterize more fully the extent of contaminant transport in the subsurface. Some of the results of these monitoring programs have been made public while the work in progress remains to be published. For the Rifle site, the final observational work plan for the UMTRA Project at New Rifle Site (DOE 1999 [DIRS 154687]) contains extensive detail on the hydrology, hydrogeology, and hydrochemistry of the site. The two volumes of this report also contain the results of transport modeling studies. They form the basis for the discussion presented below. For the Naturita site, the published information is more limited, but several important studies on uranium sorption behavior are in progress at the USGS in Menlo Park, California. Summaries of the results available for these two sites will be discussed below.

The Rifle site is located along the Colorado River approximately 90 miles east of Grand Junction, Colorado. The site actually consists of two separate sites known as Old Rifle and New Rifle. The New Rifle site has been studied in the greatest detail and is, for this reason, the subject of this summary. The site is located within the broad alluvial floodplain of the Colorado River with most of the original site on a strip of land within 0.5 miles of the river. The site is underlain by alluvial sediments deposited by the Colorado River. These, in turn, are underlain by sedimentary rocks of the Eocene Wasatch Formation. Monitoring has shown that contaminants originating from the site are found only in the alluvial sediments.

Monitoring at the New Rifle site has shown that the site-related constituents most prevalent in the alluvial aquifer include ammonia, calcium, nitrate, molybdenum, and uranium. Of these constituents, uranium and molybdenum are of interest to the DOE. Molybdenum is of interest because its chemistry is similar to technetium. Although the molybdenum plume (DOE 1999 [DIRS 154687], Figure 5-31) does not extend as far downgradient as the plume for a conservative constituent such as nitrate (DOE 1999 [DIRS 154687], Figure 5-32), this fact most likely reflects differences in source-term concentrations combined with analytical detection limits. The results of batch sorption coefficient determinations (DOE 1999 [DIRS 154687], Table 4-6) suggest that molybdenum retardation would be minimal in the alluvial aquifer.

Measured uranium concentrations at the New Rifle site are above the regulatory limit of 0.044 mg/L up to 3 miles downgradient from the site (DOE 1999 [DIRS 154687], Figure 5-36).

This distribution is similar to the downgradient extent of the plume observed for the conservative constituent nitrate (DOE 1999 [DIRS 154687], Figure 5-32). The similar lengths of the nitrate and uranium plumes suggest that at least some of the uranium is transported as a conservative constituent. Batch sorption coefficient measurements for uranium using alluvial materials and local groundwaters show a range of coefficients from –0.3 to 1.4 ml/g (DOE 1999 [DIRS 154687], Table 4-6). The conclusion that could be drawn from these data is that some fraction of the uranium emanating from the site follows pathways associated with little or no retardation potential. Transport calculations suggest that natural flushing of the aquifer will reduce the uranium concentrations in the alluvial aquifer beneath the site to below the 0.044 mg/L regulatory limit in 40 years.

The Naturita site along the Dolores River in western Colorado is in a hydrogeologic setting similar to the Rifle site. The contaminants associated with uranium ore processing are confined to groundwater in an alluvial aquifer (DOE 1994 [DIRS 154692]). The details of the uranium and other contaminant plumes are also similar to the New Rifle site. Of particular interest to the DOE is the on-going work pursued by the U.S. Geological Survey (J. Davis, USGS, Menlo Park, CA). The objective of the USGS work is to characterize the controls on contaminant transport behavior, particularly of uranium and vanadium. The work to date has included hydrogeologic characterization and modeling, contaminant concentration monitoring, hydrochemical characterization, in-situ leaching studies, and laboratory studies of the sorption behavior of uranium. A main goal of the present laboratory effort is to develop a surface complexation model of uranium adsorption onto natural aquifer materials. The data obtained to date suggest pH and alkalinity have by far the greatest impact on uranium sorption behavior. The sorption model that provides the best fit to the experimental data is the generalized composite model that was developed by Davis et al. (1998 [DIRS 154436]). This result will be of use to the Yucca Mountain Site Characterization Project in modeling the sorption behavior of uranium in the part of the flow path that is in alluvium.

The overall conclusion from this brief summary of the uranium mill tailings analogues is that, in these systems, some fraction of the total uranium inventory appears to transport as a nonsorbing to weakly sorbing contaminant. Although the hydrogeologic settings of these plumes are different than those expected downgradient from Yucca Mountain, several features of the geochemistry of these systems are pertinent to Yucca Mountain: redox state, pH, and alkalinity. The low pH and high alkalinity of the mill tailings systems tend to minimize the retardation of uranium. The redox state of these systems is variable. Where the redox conditions are not oxidizing, uranium is moderately retarded if alkalinity and pH are in the range found in Yucca Mountain groundwaters. To the extent that the transport pathways from Yucca Mountain to the compliance boundaries are oxidizing, the mill tailings results support the treatment of uranium as weakly sorbing in the model calculations. More strongly retarding conditions might be expected for flow paths traveling through reducing portions of the aquifer. If flow models and field data eventually lead to this result, it will be used in the transport calculations. Until then, the sorption coefficients used in the transport models are conservative and supported by these field analogues.

12.4.3 Preliminary Tracer Testing Results in the Alluvial Testing Complex

Tracer testing is ongoing in the wells of the ATC drilled by Nye County as part of their Early Warning Drilling Program. The goals of the tracer testing are to confirm the transport

conceptual models used in the site-scale SZ model for dissolved radionuclides and colloids and to obtain field-scale parameters for use in transport model simulations. This suite of tests will augment the testing carried out in the C-wells Complex (CRWMS M&O 2000 [DIRS 153168], Section 3.1.3.2.1), which examined transport through the fractured volcanic tuffs. The ATC tracer tests will play a similar role for transport in the alluvium and a combination of single-well and multiple-well tracer experiments are planned. Because interwell tests are more suitable for deriving field-scale transport parameters, fulfilling this goal of the testing program awaits the drilling and completion of new wells that are paired with existing wells. To date, single-well tests have been carried out, and a preliminary interpretation of the results has been performed. These tests are more appropriate for discriminating between conceptual models. Therefore, this section qualitatively describes the preliminary results in the context of the conceptual model.

In a single-well test, known masses/concentrations of tracers are injected into the test interval, followed by a large volume of tracer-free chase water that pushes the tracers away from the injection borehole (minimizing the influence of wellbore effects on the tracer responses). The tracer and chase water injection is followed by an optional rest period during which there is no injection or pumping so that the tracers are free to drift with the prevailing groundwater flow and diffuse into stagnant water (nonadvective porosity) in the flow system. After the rest period, well pumping is initiated and samples are collected and analyzed for tracers. Figure 12.4-3 is a plot of tracers versus volume extracted from single-well tracer testing in NC-EWDP-19D1. The tracer response curves were collected during three sets of tracer injections into the uppermost screened interval in the well (a 20-ft interval ranging from approximately 50 to 70 ft below the water table): (1) injection of 2,6-DFBA and iodide, followed by a 2-day rest period before pumping; (2) injection of 2,4-DFBA, chloride, and 640-nm diameter microspheres, followed immediately by pumping (no rest period); and (3) injection of PFBA and bromide, followed by a 30-day rest period before pumping.

Tracer solution and chase water volumes were approximately the same in all three tests. The first and third tests both featured flow interruptions. The responses in all three tests indicate little diffusion into nonflowing porosity (solutes with different diffusion coefficients essentially overlap each other). This result is qualitatively different than transport in the fractured volcanic tuff, for which a matrix diffusion model was determined to be more appropriate.

With respect to colloid transport, the microspheres in the second test (zero rest period) exhibited the most rapid recovery rates in the first samples produced, after which they were recovered at a much lower rate than the dissolved tracers. These results are consistent with the spheres being reversibly filtered very near the wellbore during injection. In addition, the overall microsphere recovery is relatively low compared to the solutes, indicating considerable filtration. Figure 12.4-4 is a plot of total microsphere recovery as a function of volume pumped (the sum of the second and third tests. Note the breaks in slope upon resumption of pumping at the start of the third test and after the flow interruption in the third test. These effects, though masked somewhat when presented as fractional recoveries instead of concentrations, represent significant increases in microsphere concentrations and suggest that flow transients are quite effective in mobilizing a small fraction of the microspheres. This result is consistent with the filtration model used to characterize colloid transport in the alluvium.

In summary, the initial results of the alluvial tracer-testing program, though preliminary, support the single-porosity model for transport of dissolved species in the alluvium, which is in contrast to the dual-porosity model that best explains solute transport in fractured tuffs. In addition, microsphere data are consistent with the filtration model used to simulate colloid transport in the alluvium in the site-scale SZ model.

The first and third tests both featured flow interruptions, which served as additional diagnostic tools for investigating diffusion into stagnant water in the flow system. A significant increase in tracer concentrations upon resumption of pumping would indicate such diffusion, provided the interruption is conducted during the tailing portion of the tracer responses.

The two tracers with different diffusion coefficients used in each of the three single-well tests (iodide and 2,6-DFBA in Test 1, chloride and 2,4-DFBA in Test 2, and bromide and PFBA in Test 3) had essentially identical responses (Figure 12.4-3). There was also little change in the tracer concentrations after flow interruptions. These results are both consistent with little diffusion into nonflowing porosity in the alluvium, and they suggest that a continuum flow and transport model without diffusive mass transfer between flowing and stagnant water (i.e., a single-porosity model) is appropriate for the alluvium. This result is qualitatively different than transport in the fractured volcanic tuff, for which a matrix diffusion model was determined to be more appropriate. The differences in the tracer response curves for different rest periods (Figure 12.4-3) are almost certainly due to varying amounts of drift with the natural gradient. These different responses will be analyzed in an attempt to obtain estimates of drift velocity in the test interval.

With respect to colloid transport, the microspheres in the second test (zero rest period) exhibited the most rapid recovery rates in the first samples produced (Figure 12.4-3), after which they were recovered at a much lower rate than the dissolved tracers. These results are consistent with the spheres being reversibly filtered very near the wellbore during injection. In addition, the overall microsphere recovery is relatively low compared to the solutes, indicating considerable filtration. Figure 12.4-4 is a plot of microsphere normalized concentrations as a function of time (encompassing both the second and third tests). Note the increases in concentrations upon resumption of pumping at the start of the third test and after the flow interruption in the third test. These effects suggest that flow transients are quite effective in mobilizing a small fraction of the microspheres. This result is consistent with the filtration model used to characterize colloid transport in the alluvium.

In summary, the initial results of the alluvial tracer-testing program, though preliminary, support the single-porosity model for transport of dissolved species in the alluvium, which is in contrast to the dual-porosity model that best explains solute transport in fractured tuffs. In addition, microsphere data are consistent with the filtration model used to simulate colloid transport in the alluvium in the site-scale SZ model.

12.4.4 Electric Power Research Institute Flow and Transport Modeling

The EPRI performed flow and transport modeling in both the UZ and SZ (EPRI 2000 [DIRS 154149]). The EPRI SZ flow and transport model incorporates three-dimensional, steady-state flow and transient mass transport in a dual-porosity media. This model represents

only the portion of the SZ close to a contaminant plume. The rectangular domain is 22 km long, 8.5 km wide, and has a vertical thickness of 200 m. Rock stratigraphy is represented in an idealized way. In the EPRI base case, the upstream 18 km of the domain is volcanic rock, and the downstream 4 km of the domain is assumed to be alluvium. The footprint of the repository is represented as a $2{,}500 \times 700$-m rectangular region on the upper surface of the domain. It is located 2 km from the upstream boundary of the model domain. The TSPA-SR model, in contrast, includes a much larger region of the SZ and a more detailed representation of actual geologic complexity (CRWMS M&O 2000 [DIRS 147972], Section 6.6). The results of these two models, therefore, can only be compared in a qualitative sense.

The most significant conceptual difference between the EPRI and TSPA-SR models is treatment of dual-porosity transport in fractured tuff. In the TSPA-SR model, a flowing interval is represented by a single fracture at the center of the interval (CRWMS M&O 2000 [DIRS 154927], p. 7). Diffusion can occur into a single matrix block between each pair of flowing intervals. In the EPRI model, a flowing interval is treated as a region in which multiple fractures exist and solutes diffuse into smaller blocks between the individual fractures. Mass transfer by diffusion into smaller blocks is faster because there is more surface area of the matrix exposed to fractures. With other factors being equal, the EPRI model predicts slower transport of radionuclides toward the accessible environment in fractured tuff than the TSPA-SR model. EPRI (2000 [DIRS 154149], p. 7-26) argues that the implementation of dual-porosity transport in the TSPA-SR model is overly conservative.

The EPRI analysis supports the TSPA-SR conceptualization that diffusion of solutes into the matrix of fractured tuffs can slow transport of radionuclides away from the repository. In addition, EPRI concurs that use of flowing intervals is a reasonable conceptualization of SZ conditions. The main issue is whether or not the use of smaller matrix block sizes in TSPA-SR models can be supported by the available data. To date, the DOE is of the opinion that the data are not sufficient to support the use of smaller block sizes.

12.4.5 Transport Studies on Blocks of Intact Tuff

The transport behavior of selected radionuclides and compounds (tritium, technetium-95m, neptunium-237, cobalt-60, cesium-137, sodium-fluorescein) is being studied in the laboratory using blocks of intact tuff mined from the Busted Butte Unsaturated Zone Facility. The transport behavior of these radionuclides is being studied under both unsaturated and saturated conditions. Initial results for unsaturated flow conditions have been obtained on a trial block (Vandergraaf et al. n.d. [DIRS 154948]). The results indicate that technetium-95m and sodium-fluorescein elute from the block slightly ahead of tritium. Because tritium moves at the rate of the water, this result indicates technetium-95m and sodium-fluorescein are preferentially eluted probably due to exclusion from small pores (e.g., anion exclusion). The total recovery of tritium, technetium-95m, and sodium-fluorescein was in the range of 70 percent to 80 percent. Batch sorption experiments with crushed tuff show slightly negative sorption coefficients confirming the exclusion behavior (DTN: LA0103TV12213U.001 [DIRS 154929]).

The first breakthrough of neptunium was retarded relative to tritium indicating neptunium had sorbed onto the rock matrix. A retardation factor of 3.2 was calculated from the early elution data. However, the fraction of neptunium that was recovered represented only 0.1 percent of the

total neptunium injected into the block. After the initial breakthrough, the neptunium concentration in the eluted water decreased as additional water was eluted from the block. This result indicates that the 0.1 percent fraction represents an early breakthrough fraction and that most of the neptunium was more strongly retarded. Batch sorption experiments on crushed tuff material and simulated Busted Butte water gave sorption coefficients in the range of 0.43 to 1.09 ml/g (DTN: LA0103TV12213U.001 [DIRS 154929]). Assuming a bulk density of 2.0 g/cm^3 and a porosity of 0.35 (for example, CRWMS M&O 2001 [DIRS 154024], Sections 6.8.7.2 and 6.8.7.3, Table 38), these sorption coefficients equate to retardation factors of 3.5 to 7.2. The fact that the bottom end of this range exceeds the measured retardation factor (3.2) is consistent with the fact that only a small fraction of the neptunium was recovered in the block tests. That is, the calculated retardation factors would predict later breakthrough than was observed. However, the observed breakthrough curve was not of the (simple) type that would be expected from a simple retardation calculation. The greater complexity of the observed breakthrough curve explains the lower retardation factor (3.2) observed in the block test.

The range of neptunium sorption coefficient values measured in the batch tests with Busted Butte materials falls within the probability distribution function for neptunium sorption coefficient (0 to 6 ml/g with an expected value of 1.0 ml/g) in vitric tuff as used in performance assessment calculations (CRWMS M&O 2001 [DIRS 154024], Tables 2a and 2b). Thus, the data obtained on the trial block test are consistent with the performance assessment calculations. This statement will be further quantified once the full block test has been completed and a larger fraction of the injected neptunium recovered.

12.4.6 Analogue Studies

Analogue sites such as the Alligator Rivers site in Australia, Poços de Caldas in Brazil, the Oklo site in Gabon, and the Cigar Lake site provide data on the transport of uranium; in some cases, over millions of years. Although the geology and geochemistry at these sites differ from that at Yucca Mountain, they provide data that may be used to calibrate computer codes, and their analysis can give us a picture of the flow and transport of uranium under various conditions. In Sections 12.4.6.1 and 12.4.6.2, a summary of the geohydrological and geochemistry are given for the Alligator Rivers and Poços de Caldas sites. A summary of the Jove-Colon comparison of the transport of uranium at these sites along with that of the Oklo and Cigar Lake sites is given in Section 12.4.6.3. This study notes that uranium often does not migrate a significant distance from the source due to sorption, even over extended time spans. The analogue site data given by the INEEL site in Section 12.4.6.4 and the Beasley et al. (1998 [DIRS 102430]) study at INEEL provides a degree of confirmation of the conservative or retarding nature of a number of the same radionuclides as would be present in a Yucca Mountain repository (e.g., chlorine-36, technetium-99, uranium-236, iodine-129, and neptunium-237). Underground nuclear test data taken at the NTS (see Section 12.4.6.5) provide valuable information about radionuclide transport of chlorine-36, krypton-85, ruthenium-106, plutonium-240, plutonium-239, and iodine-129 through volcanic tuffs and alluvium. These data are important because the geology and the chemistry at the NTS are similar to that at Yucca Mountain.

12.4.6.1 Alligator Rivers, Australia

The Koongarra secondary enriched-uranium deposit is found in the Alligator Rivers region of the Northern Territory of Australia. The Koongarra ore body lies in two distinct parts separated by a barren zone. The two parts are composed of uraninite- and pitchblende-bearing veins within a zone of steeply dipping, sheared quartz-chlorite schists and a fault that brings the ore body in contact with the Kombolgie sandstone (Airey 1986 [DIRS 127680], Figure 4.15). The primary ore at depth is being leached by groundwater to form a secondary uranium mineralization (Isobe et al. 1992 [DIRS 113260], p. 175) that extends from the ground surface to the base of the weathered zone at about 30 m.

Weathering of the quartz-chlorite schist produces different mineral assemblages according to degree of alteration. The migration behavior of nuclides at each depth is thought to be related to the chlorite alteration mineral assemblage (Ohnuki et al. 1990 [DIRS 126172], p. 607). The zone of lowest uranium concentration corresponds to the chlorite-rich zone, that of intermediate uranium concentration to the vermiculate-rich zone, and that of greatest uranium concentration to the kaolinite-rich zone. Although kaolinite is not being considered in the present Yucca Mountain waste package design, it is considered in the design of many high-level nuclear waste sites. The data provided at the Koongarra site could serve as a means of estimating the sorbing effects of kaolinite over a long period of time and might be used to calibrate geochemistry codes.

As a result of the weathering front, a dispersion fan has developed in the weathering zone where uranium has been mobilized. Secondary minerals are found as far as 50 m downstream from the ore body with detectable concentrations of uranium-series nuclides for about 300 m downstream in the dispersion fan. The age of the dispersion fan has been estimated from 0.5 to 3.0 Ma (Golian and Lever 1992 [DIRS 134175], p. ix).

Isobe et al. (1992 [DIRS 113260]) describe uranium redistribution associated with weathering. Uranium activity closely follows oxidation fronts in the slightly weathered zone and advances most readily along cracks and fissures in which percolation of oxidizing groundwater is most enhanced. Significant flow occurs as fracture flow rather than as porous media flow. Uranium distribution in the most strongly weathered rocks depends only on the mineralogy present and is not controlled by the presence of fissures, as is the case for the more moderately weathered rocks. In the dispersion fan, processes that control the amount of radionuclides that are removed from the groundwater include equilibrium sorption, chemical incorporation into iron oxides, uranium minerals or other crystalline phases, and recoil transfer of daughter products caused by alpha-particle decay (Golian and Lever 1992 [DIRS 134175], p. viii). The fact that the uranium distribution depends only on the mineralogy in strongly weathered (fractured) rocks has implications for the Yucca Mountain conceptual model, which assumes the volcanic tuff is sufficiently fractured to act as an equivalent porous medium for radionuclide transport. Data from the less-weathered rocks, where the uranium concentration in fissures differs from that of the "matrix," is important in establishing the amount of fissuring necessary for the equivalent porous media model to be valid.

Groundwaters are slightly acidic to neutral in pH, oxidizing, relatively dilute, with the major ion chemistry dominated by magnesium and bicarbonate. Waters from the weathered zone are undersaturated with respect to a number of uranium-bearing minerals, consistent with the idea

that the present groundwaters may be dissolving and dispersing the uranium in the phosphate zone of the deposit (Sverjensky et al. 1992 [DIRS 134225], p. 40).

Colloids in groundwater samples taken from drill holes were dominated by iron-rich particles, and uranium was only found in iron-rich species (Ivanovich et al. 1987 [DIRS 125227], pp. 300 to 309). Low colloid concentrations (about 10^6 particles/L or less) and the absence of radionuclides in colloids outside the center of the ore body indicated that colloidal transport of radionuclides is minor at Koongarra (Payne et al. 1992 [DIRS 124812], p. 481). Understanding the absence of radionuclide transport in colloids outside the ore body may have implications for colloid transport at Yucca Mountain. Also, the data provided by the Koongarra site is useful because it is a well-studied site and represents transport carried out over an extremely long time period.

12.4.6.2 Poços de Caldas, Brazil

The Poços de Caldas caldera is a ring structure composed of Cretaceous phonolites, carbonatites, and nepheline syenites (Schorscher and Shea 1991 [DIRS 127147]; Miller et al. 1994 [DIRS 126089]). Two major hydrothermal events that affected the caldera led to widespread argillization (alteration to clay minerals) and zeolite formation. During the first event, local magmatic brecciation occurred in association with intense hydrothermal potassium- and sulfur-rich alteration (Schorscher and Shea 1991 [DIRS 127147], p. 25). A second hydrothermal event is believed responsible for formation of the numerous ore bodies within the caldera complex about 76 Ma (Schorscher and Shea 1991 [DIRS 127147], p. 28).

The Osamu Utsumi open-pit mine is a disseminated, low-grade uranium ore body with subsidiary thorium, zirconium, and REE (rare-earth element, or lanthanide) enrichment and a sharp, well-developed redox front. Morro do Ferro, in contrast, is a thorium and REE ore body with subsidiary uranium. The Morro do Ferro hill has been deeply weathered, so that the hill is now composed of gibbsite, kaolinite, and illite, with additional veins of magnetite and manganese hydroxides. The thorium-REE ore occurs as elongated mineralized lenses that extend down the hill slope. Thorium and REE mineralization is very enriched, with up to 3 weight % ThO_2 and up to 20 weight % total REE in some soils and weathered rocks (Waber 1991 [DIRS 126924], p. 120).

Groundwaters in the Poços de Caldas area typically have low concentrations (less than 1 mg/L) of colloids (Miekeley et al. 1989 [DIRS 126083]; Miekeley et al. 1991 [DIRS 127199], p. i). Most of the colloids are composed of iron and organic species. Only minor amounts of uranium are associated with colloids, but greater amounts of thorium and REEs are transported in the colloidal fraction. The suspended particle concentration is 5 to 10 times greater at Morro do Ferro than at Osamu Utsumi, but there appears to be very little thorium transport at Morro do Ferro, either by colloids or true solution. Amorphous phases in suspension or as mineral coatings are the principal reactive surfaces for many trace elements in solution. The presence of amorphous phases tends to reduce the concentration and mobility of trace elements in solution (Chapman et al. 1991 [DIRS 100423], p. 129). Radionuclide and other trace-element transport by colloidal material in deep groundwaters does not play a significant role in the geochemical processes of weathering, dissolution, and erosion of these ore deposits. This observation is

attributed to filtration of particulate material, which seems to be efficient, even in the highly fractured and porous rocks of the Poços de Caldas plateau (Smellie et al. 1989 [DIRS 126636]).

Microbial activity is important for the oxidation of pyrite and may be responsible for the mobilization and reprecipitation of uraninite at the redox front (West et al. 1989 [DIRS 100834]). This mechanism could explain the observation that the redox front is moving faster than would be expected simply on the basis of dissolved oxygen concentration. Flow channeling in fractures and solute transport in the rock matrix are the key controls of the shape and movement of the redox fronts at Poços de Caldas. The front movement appears to be very slow, and solute transport over the front is dominated by diffusion. The front plays a significant role in retarding a wide spectrum of trace elements.

Colloidal transport of uranium was shown to be minimal at Koongarra and Poços de Caldas, where filtration of colloids appears to be effective. The filtration of colloids that have the potential of carrying radionuclides by the highly fractured and porous rocks at this site has important implications in Yucca Mountain colloid transport in the saturated zone because an increase in colloid filtration will result in a reduction of radionuclides reaching the site boundary.

12.4.6.3 Comparison Study

A comparison study was made of plumes from uranium ore bodies and contaminated sites to identify characteristics of uranium plume movement (Jove-Colon et al. 2001 [DIRS 154444], p. 1). The study included uranium mines and natural analogue sites (Koongarra, Oklo, Poços de Caldas, and Cigar Lake) as well as Title I and Title II UMTRA plumes. Despite the uncertainties and variability of the magnitude of the original contaminant source, geologic setting, and hydrologic regime of the sites, as well as age of the plumes and availability of time-series data, the plume dataset provides a relatively consistent picture of uranium plume behavior. Specifically, the uranium plumes appeared to have stopped spreading rapidly within a few years; they exceed approximately 2 km in length only in special cases where in situ leaching has been carried out, and they exhibit very similar uranium chemistry between sites (Jove-Colon et al. 2001 [DIRS 154444], p. 1).

Although the hydrologic conductivity, K_d values, and original contaminant source masses for the various sites varied by orders of magnitude, plume trajectories seemed to cluster and to suggest that the combined effects of dispersion and chemical reaction are sufficient to arrest most uranium plumes before they move more than roughly a kilometer from their source (Jove-Colon et al. 2001 [DIRS 154444], p. 24). The natural life cycle of a uranium plume appears to involve an initial movement away from a source region that takes place within a few years and does not exceed 2 km, followed by a geologically long period of immobile quiescence. Natural plumes from ores that have been weathered and subjected to periodic meteoric inputs for long periods of time do not migrate appreciably beyond their known natural barriers, even during mining. Similarly, the UMTRA sites do not show a significant dispersion of contaminants beyond the limits of the contaminated area, even though these sources are not as deeply buried and are in more porous strata than those found in the natural analogue and uranium mining sites. The plume length and the uranium concentration in monitoring wells remain relatively constant or change insignificantly for periods of time approaching 15 years in many cases. It appears that sorption, dilution, and precipitation are sufficiently effective sinks to limit the advance of

artificial uranium plumes in the short term (years to decades). In long-term situations of thousands to millions of years, weathering processes and secondary precipitation of oxidized uranyl phases appears to limit advance of natural plumes.

Jove-Colon et al. (2001 [DIRS 154444], p. 259) concluded that source-term removal alone can limit plume advance, assuming no change in the geochemical state of the uranium near the source, such as the introduction of chelating agents and/or a deleterious shift in redox conditions. Only two of the few plumes examined for the Title II sites exceed plume lengths of more than 2.5 km (Jove-Colon et al. 2001 [DIRS 154444], p. 29). Title II sites may produce longer plumes than Title I sites because the source term is still in place; however, with the two exceptions, the rest fell well within the plume-length distribution range (less than 2 km) obtained for both UMTRA Title I and Title II sites (Jove-Colon et al. 2001 [DIRS 154444], p. 29). Geochemical factors favor uranium transport over transport of many other cationic metals and radionuclides, such as lead, cadmium, strontium-90, or cesium-137, because uranium is a relatively weak sorber and because the fraction of uranium that sorbs irreversibly in soils is relatively small. For these reasons a plume advance for most other cationic metals and radionuclides should be substantially less than the 2 km observed for uranium.

12.4.6.4 Retardation at Idaho National Engineering and Environmental Laboratory

From 1952 until 1984, low-level radioactive waste was discharged from the Idaho Chemical Processing Plant (ICPP) by means of an injection well and seepage ponds. Over time, a suite of radionuclides has been measured in the Snake River Plain (SRP) aquifer, including tritium, chlorine-36, strontium-90, cesium-137, iodine-129, and plutonium isotopes. Beasley et al. (1998 [DIRS 102430]) reported the first measurement of the long-lived radionuclides technetium-99, uranium-236, and neptunium-237 in the aquifer and their downgradient concentration changes during water transport through fractured basalt. Their study showed that chlorine-36 and technetium-99 behave conservatively during transport whereas iodine-129, uranium-236, and neptunium-237 were retarded.

The calculated residence time of water in the SRP aquifer is 55 to 82 years, although water travel times within different parts of the aquifer, from recharge to discharge points, are estimated between 12 and 350 years (Beasley et al. 1998 [DIRS 102430], p. 3876). Groundwater flow is from the northeast to the southwest, and depth to groundwater varies from about 60 m at the northern site boundary to about 275 m at the southern site boundary. Beasley et al. (1998 [DIRS 102430], p. 3876) report that the average hydraulic gradient across the INEEL is about 2 m/km, and water travel times between the ICPP and the southern site boundary have been estimated at 2 m/day.

Over a period of four years, monitoring wells at INEEL were sampled for radionuclide measurements. Activity concentrations were measured for chlorine-36, technetium-99, uranium-236, iodine-129, and neptunium-237. To determine the relative mobility of these radionuclides, individual radionuclide activities in wells near the ICPP were normalized to those at a distance. The close correspondence in the decrease of chlorine-36 and technetium-99 concentrations with distance from the ICPP suggests that technetium-99, like chlorine-36, behaves conservatively in the fractured basalt and that observed concentration decreases occur only as a result of dilution or dispersion (Beasley et al. 1998 [DIRS 102430], p. 3880).

Iodine-129 is attenuated, and neptunium-237 and uranium-236 are even more attenuated. However, the authors point out that even though the absolute amounts of radioactivity most likely varied over time, the ratios of radionuclides in the discharges probably were consistent in order not to affect the composition of radioactivity in the waste streams.

Although the initial conditions and geologic medium are different at INEEL than at Yucca Mountain, the Beasley et al. (1998 [DIRS 102430]) study at INEEL provides a degree of confirmation of the conservative or retarding nature of a number of the same radionuclides as would be present in a Yucca Mountain repository (e.g., chlorine-36, technetium-99, uranium-236, iodine-129, and neptunium-237). In particular, the INEEL site appears to be much closer in terms of geology to Yucca Mountain than the Koongarra, Oklo, and Poços de Caldas.

12.4.6.5 Colloids at Nevada Test Site

Data taken at the NTS from underground nuclear tests provide valuable information about transport through volcanic tuffs and alluvium. These data are important because the geology and the chemistry at NTS are similar to that at Yucca Mountain due to its proximity. An important consideration in the evaluation of these tests is the distance that radionuclides may transport immediately after the event.

Data from a field experiment initiated in 1974 at the Cambric site have provided direct information on the transport rates of radionuclides through saturated alluvium (Hoffman and Daniels 1981 [DIRS 125168]). The field study began with the completion of a satellite well 91 m from the Cambric cavity, followed by drilling of a reentry well into the cavity itself. Both solid and liquid samples were taken from the reentry well to determine the distribution of radionuclides between the solid material and the groundwater. Water was then pumped from the satellite well to induce an artificial gradient sufficient to draw water from the Cambric cavity through the surrounding rocks.

Approximately two years after pumping began, significant amounts of tritiated water were found in water from the satellite well, signaling the arrival of water from the Cambric cavity region. After almost six years of pumping, the tritium concentration in the pumped water reached a maximum (Hoffman et al. 1977 [DIRS 125087], p. 52). By the end of September 1984, about 60 percent of the initial tritium inventory had been pumped out through the satellite well.

Other radionuclides were also measured in water from the satellite well, including chlorine-36, krypton-85, ruthenium-106, and iodine-129. Strontium-90 and cesium-137 were not detected in the pumped water during the 10-year experiment (Thompson 1986 [DIRS 126796], p. 3). The chlorine-36 pulse and the iodine-129 pulse preceded the tritium pulse. Krypton was correlated with tritium but more strongly sorbed onto alluvium than tritium. Ruthenium-106 was detected in well RNM-2S water and was unretarded in the alluvium (Thompson 1986 [DIRS 126796], p. 3).

The Cheshire event took place in 1976 (Buddemeier and Hunt 1988 [DIRS 100712], p. 537). Detonation occurred at a depth of 1,167 m, approximately 544 m below the water table, in fractured rhyolitic lavas of Paiute Mesa. Water was obtained from two wells, one inside the Cheshire experimental site and the other 300 m away. Tritium, krypton, strontium, cesium,

antimony, cobalt, cerium, and europium were detected in the pumped water. All of the cobalt, cerium, and europium were associated with colloids in samples from both locations. The authors maintained that the presence of colloidal radionuclides outside the cavity indicates radionuclide transport as colloids.

The Benham test was detonated in 1968 at a depth of 1402 m below the water table. In a recent field test, plutonium was measured in groundwater at the NTS ER-20-5 wells at a maximum activity concentration of 0.63 pCi/L (Kersting et al. 1999 [DIRS 103282], p. 57). The ratio of plutonium-240/plutonium-239 indicates that the plutonium originated at the site of the nuclear test Benham, which is a distance of 1.3 km from the wells. The minimum distance for plutonium migration at the NTS is therefore 1.3 km in 28 years. The plutonium detected was associated with colloidal material consisting mainly of clays, zeolites, and silica (Kersting et al. 1999 [DIRS 103282], p. 2). It is not likely that the plutonium was transported by prompt injection or that its soluble fraction migrated along fast flow paths. Colloidal transport is a possible mechanism for plutonium migration because colloidal transport of radionuclides was observed at the Cheshire site. Possible colloid transport of plutonium at the NTS has important implications to Yucca Mountain due to the similar geology at this site.

12.4.7 Yucca Mountain Self-Analogue Using Uranium Isotopes

The flow model for the saturated zone predicts that radionuclides that reach the saturated zone would have a travel time of at least 3,600 years before they could reach the accessible environment, which is defined as being 20 km from the potential repository (CRWMS M&O 2000 [DIRS 153168], Sections 3.6 and 3.7). The model is based on a site conceptual model and discretization with model hydrologic parameters chosen to be consistent with measured hydrologic data. Chemical and isotopic data for groundwater in the Yucca Mountain area can be used to test the reasonableness of the flow path and travel time computed by the TSPA-SR flow and transport model (CRWMS M&O 2000 [DIRS 153246]). As such, the chemical and isotopic data serve as a sort of self-analogue.

Figure 12.4-5 shows a map of the chloride concentrations. The contours, which denote waters of similar composition, clearly show a flow path from north of Yucca Mountain to the Amargosa Desert south of Yucca Mountain, a flow path that is in agreement with that derived from TSPA-SR flow and transport modeling and hydrologic head data (CRWMS M&O 2000 [DIRS 153246]). Within this general flow path, the TSPA-SR flow modeling suggests a short flow eastward from beneath Yucca Mountain towards Fortymile Wash with continued flow to the south. Any radionuclides that reached the saturated zone beneath the potential repository would be expected to follow this flow path.

Naturally occurring radioactive isotopes of uranium can be used to examine what has happened over thousands of years to radioactive atoms that have passed through the unsaturated zone and reached the saturated zone beneath the mountain. There are three radioactive isotopes of uranium. Of interest for this analogue are uranium-238, which has a half-life of 4.468×10^9 years, and one of its daughter products (uranium-234), which has a half-life of 2.446×10^9 years. When the amount of uranium-234 being produced by the decay of uranium-238 is equal to the amount lost by the decay of uranium-234, the two isotopes are in secular equilibrium and, by definition, have an activity ratio of 1.0. The activity ratio for uranium-234/uranium-238 is

generally near 1.0 for most geologic materials, but certain nuclear-chemical processes can cause uranium-234 to become enriched or depleted relative to its parent. This outcome has been documented to occur for groundwater in many arid regions where there is a small volume of water moving through a large volume of rock.

At Yucca Mountain, the uranium dissolved in water has an extremely anomalous activity ratio within the unsaturated zone. Analyses of perched water from two wells within the unsaturated zone yield uranium-234/uranium-238 activity ratios greater than 7.0 (CRWMS M&O 2001 [DIRS 154795], Figure 18). As this water eventually reaches the saturated zone, these anomalous ratios provide a natural analogue to the escape of radioactive materials from a potential repository.

Figure 12.4-6 shows a map of activity ratios for uranium-234/uranium-238 in water from the saturated zone. As expected, the water directly beneath Yucca Mountain has anomalously large activity ratios that have been acquired by the slow percolation of waters from the unsaturated zone above. These anomalous ratios are noted again in well J-13 on the edge of Fortymile Wash, as predicted by the SZ flow model. Although the data do not appear to form a distinct plume southward down gradient of the mountain as would be expected from the flow model, elevated values of the activity ratio (as compared to surrounding area) may be observed in most wells along Fortymile Wash and south of Yucca Mountain along the predicted flow path. Values for uranium-234/uranium-238 are somewhat elevated in well J-12 about 5 km south of J-13 and also on the edge of Fortymile Wash. The anomaly becomes more subdued about 1 km further south in well JF-3. The uranium-234/uranium-238 values decrease to essentially background level in well NC-EWDP-2D within Fortymile Wash about 20 km south of Yucca Mountain.

The lack of a distinct plume could be due to some chemical causes, but it is likely due to mixing with recharge along Fortymile Wash as well as inflow from waters to the east and north of Yucca Mountain. Flow and transport modeling, assuming a high activity source at Yucca Mountain, may help yield understanding of the data. A chemical consideration would be the possible dissolution of uranium from minerals in the aquifer as the water moves south, thereby diluting the signal of the natural radioactive tracer. However, uranium concentrations in groundwater beneath and south of Yucca Mountain are fairly similar, and therefore, a swamping of the signal by dissolved uranium seems unlikely.

Another consideration is the unique hydrology of Yucca Mountain that may create a nearly stagnant pocket of water there. The anomalous uranium activity ratios occur south of the large hydraulic gradient. It may be that a large proportion of the flow from the north is diverted to the east and west of Yucca Mountain or to the carbonate aquifer beneath Yucca Mountain such that there is a small pocket of very slowly moving water beneath the potential repository with only minor flow towards Fortymile Wash.

In summary, the chemical and isotopic data for chloride concentrations confirm the general flow paths of the saturated-zone flow model. The uranium-234/uranium-238 activity ratio data appear to indicate a south to southeast movement of the water beneath Yucca Mountain and, in addition, suggest a significant dilution or dispersion during flow. These data provide an independent confirmation of the flow path direction of the TSPA-SR (CRWMS M&O 2000 [DIRS 153246])

model and, in the future, may help to provide confirming evidence of inflow and recharge in the Yucca Mountain area.

12.4.8 U.S. Nuclear Regulatory Commission Flow and Transport Studies

The CNWRA supports the NRC role of evaluating the potential repository at Yucca Mountain by developing a set of computer codes to simulate the behavior of the repository. The CNWRA calculates transport of radionuclides along one-dimensional streamtubes in the saturated zone (NRC 2001 [DIRS 154949]). The processes simulated by the NRC model include advective transport through tuff and alluvial aquifers, longitudinal dispersion, chemical sorption and retardation in the alluvium and matrix of the tuff, and diffusion of radionuclides from fractures into the matrix of the tuff. The streamtubes are abstracted from results of a detailed two-dimensional flow model. This model provides an opportunity to check results of the SZ site-scale flow and transport model because it is based on the same data set of rock properties and hydraulic head measurements, and because it simulates a similar suite of transport processes.

12.5 SENSITIVITY ANALYSIS

Section 12.5.1 describes the unquantified uncertainty analysis conducted with the site-scale SZ flow and transport model. These analyses were performed to evaluate the sensitivity of the TSPA-SR supplemental analysis (McNeish 2001 [DIRS 155023]) to changes in parameters as a result of the unquantified uncertainty analysis in the model. Section 12.5.2 discusses several additional sensitivity analyses conducted to evaluate the sensitivity of model results to specific critical features or processes in the site-scale SZ model. The FEHM computer code (V2.10) was used to perform transport calculations for all of the analyses discussed in Section 12.5. Additionally, the GoldSim (V6.04.007) computer code was used to sample the parameter distributions for the transport calculations for all of the analyses discussed in Section 12.5. Calculated breakthrough curves are documented in Kuzio (2001 [DIRS 154912], Filename "archive_sspa_v1_data"). The analyses are based on a model that is appropriately conservative for TSPA sensitivity analyses and is not intended to represent expected radionuclide breakthrough or groundwater transport time for the SZ portion of the Yucca Mountain flow system.

12.5.1 Unquantified Uncertainty Sensitivity Analysis for Supplemental Science and Performance Analyses

This section describes the unquantified uncertainty analysis conducted to evaluate the sensitivity of the TSPA-SR supplemental analysis (McNeish 2001 [DIRS 155023]) results to changes in parameters as a result of the unquantified uncertainty analysis in the site-scale SZ model. The unquantified uncertainty analysis consisted of multiple (100) simulations of radionuclide transport with the site-scale SZ model in which all changes resulting from the unquantified uncertainty analysis were included. The resulting SZ radionuclide breakthrough curves for the unquantified uncertainty case are supplied to the TSPA simulator for the Volume 2 calculation of simulated dose rates. The results of the unquantified uncertainty sensitivity analysis from the model are discussed in Section 3 of Volume 2.

The simulated radionuclide breakthrough curves from the unquantified uncertainty analysis (Kuzio 2001 [DIRS 154912], Filename "archive_sspa_v1_data/uu") have shorter transport times for long time periods and longer transport times for early time periods than the TSPA-SR supplemental analysis (McNeish 2001 [DIRS 155023]). As an example, the histograms of times of median breakthrough for neptunium are compared to the unquantified uncertainty case and the TSPA-SR supplemental analysis (Figure 12.5.1-1). Visual comparison of the upper histogram for the TSPA-SR supplemental analysis and the lower histogram for the unquantified uncertainty case shows a reduction in the width of the histogram transport times. The unquantified uncertainty analysis includes changes to many parameters, as indicated in Table 12.5.1-1. Some of the changes to the parameters result in a reduction in transport times; other changes could result in an increase in transport time. The overall uncertainty in the times of median breakthrough, as represented by the reduced width of the histograms, represents primarily the uncertainty associated with the parameter groundwater specific discharge.

12.5.2 Additional Sensitivity Analyses for Supplemental Science and Performance Assessment

Several other sensitivity analyses are conducted with the site-scale SZ flow and transport model (Sections 12.5.2 and 12.5.3) in addition to the unquantified uncertainties analysis. These system analyses were performed to evaluate the sensitivity of the TSPA-SR supplemental analysis results (McNeish 2001 [DIRS 155023]) to specific critical features or processes in the site-scale SZ model. Each sensitivity analysis consisted of multiple (100) simulations of radionuclide transport with the site-scale SZ model in which all stochastic parameters were varied, as in the original model, with the exception of the parameter controlling the process or feature being evaluated. The resulting suite of SZ radionuclide breakthrough curves for each sensitivity case was supplied to the TSPA for the Volume 2 calculation of simulated dose rates (Kuzio 2001 [DIRS 154912], Filename "archive_sspa_v1_data"). Results of the sensitivity analyses from the model are discussed in Section 3 of Volume 2.

12.5.2.1 No Matrix Diffusion in Volcanic Units

Diffusion of radionuclides into the matrix of volcanic units of the SZ is potentially significant to transport in groundwater because of the higher porosity in the matrix and because of the sorptive capacity of the matrix for some radionuclides. Both of these effects tend to delay the migration of radionuclides relative to transport solely in the fractures of the system. The sensitivity case in which no matrix diffusion occurs represents a bounding analysis with respect to the matrix diffusion process.

The sensitivity analysis for no matrix diffusion is implemented in the site-scale SZ flow and transport model by reducing the value of the effective matrix diffusion coefficient by 10 orders of magnitude in all realizations (Kuzio 2001 [DIRS 154912], Filename "archive_sspa_v1_data/high_diff"). This large reduction in the matrix diffusion coefficient effectively renders the simulated radionuclide mass delay to matrix diffusion insignificant. Other stochastic parameters for the SZ have the same values used for the sensitivity analysis as the TSPA-SR supplemental analysis (McNeish 2001 [DIRS 155023]).

The simulated radionuclide breakthrough curves from the no matrix diffusion analysis have somewhat shorter transport times than the breakthrough curves from the TSPA-SR supplemental analysis (McNeish 2001 [DIRS 155023]) on a realization-by-realization basis. The differences in the transport time between the no matrix diffusion case and the TSPA-SR supplemental analysis are greater for those radionuclides that experience significant sorption in the volcanic matrix (Kuzio 2001 [DIRS 154912], Filename "archive_sspa_v1_data/no_diff"). As an example, the histograms of times of median breakthrough (i.e., the time at the midpoint of the breakthrough curve) for uranium are compared for the no matrix diffusion case and the TSPA-SR supplemental analysis in Figure 12.5.2-1. Uranium is used in this example because it experiences moderate sorption in the volcanic rock matrix for most realizations of the TSPA-SR supplemental analysis case, and therefore it should show discernible differences for the no matrix diffusion case. The upper histogram shows the results for the TSPA-SR supplemental analysis case, and the lower histogram shows the results for the no matrix diffusion case. As expected, the distribution of times of median breakthrough for the no matrix diffusion case is shifted toward shorter transport times, with 61 of the realizations having times of median breakthrough less than 10,000 years for the no diffusion case and 54 of the realizations having times of median breakthrough less than 10,000 years for the TSPA-SR supplemental analysis case. However, the overall uncertainty in the times of median breakthrough, as represented by the width of the histograms, is larger than the shift in times of median breakthrough from the TSPA-SR supplemental analysis case to the no matrix diffusion case.

12.5.2.2 Enhanced Matrix Diffusion in Volcanic Units

Another sensitivity analysis is defined for the case in which the effects of matrix diffusion in the volcanic units of the SZ are greatly enhanced. The enhanced matrix diffusion case represents a bounding analysis at the opposite extreme from the no matrix diffusion case. For this case, most of the rock matrix in the volcanic units is available for radionuclide storage and sorption in the transport process in most of the realizations. The sensitivity analysis for the enhanced matrix diffusion case is implemented by reducing the flowing interval spacing by two orders of magnitude for all realizations. This approach reduces the geometric mean of the flowing interval spacing from about 20 to 0.2 m, which is a relatively small distance for matrix diffusion (CRWMS M&O 2000 [DIRS 154927], Section 7). Other stochastic parameters for the SZ have the same values for the sensitivity analysis as the TSPA-SR supplemental analysis (McNeish 2001 [DIRS 155023]).

The simulated radionuclide breakthrough curves from the enhanced matrix diffusion analysis have longer transport times than for the TSPA-SR supplemental analysis (Kuzio 2001 [DIRS 154912], Filename "archive_sspa_v1_data/high_diff"; McNeish 2001 [DIRS 155023]). As an example, the histograms of times of median breakthrough for neptunium are compared for the enhanced matrix diffusion case and the TSPA-SR supplemental analysis case in Figure 12.5.2-2. Neptunium is used in this example because it experiences a small amount of sorption in the volcanic rock matrix for most realizations of the TSPA-SR supplemental analysis and because neptunium-237 is a major contributor to dose in the TSPA analyses. Visual comparison of the upper histogram for the TSPA-SR supplemental analysis and the lower histogram for the enhanced matrix diffusion case shows the generally longer transport times for the enhanced matrix diffusion case, as expected. In the enhanced diffusion case, 25 of the times of median breakthrough are less than 10,000 years, whereas in the TSPA-SR supplemental

analysis, 40 of the times of median breakthrough for neptunium are less than 10,000 years. As in the no matrix diffusion case, the overall uncertainty in the times of median breakthrough, as represented by the width of the histograms, is much larger than the shift in times of median breakthrough from the TSPA-SR supplemental analysis to the enhanced-diffusion case.

12.5.2.3 Minimum Length of Alluvium in the Flow Path

The length of the flow pathway from the repository in the alluvium of the SZ could be significant to radionuclide migration rates because of the relatively high effective porosity in the alluvium and because of the potentially higher sorptive capacity of the alluvium relative to the volcanic rocks, particularly for neptunium. Both of these factors result in longer transport times for radionuclides through the SZ system. The objective of the minimum alluvium analysis is to examine the impact of uncertainty in the location along the flow path from the repository at which groundwater flow transitions from fractured volcanic units to the alluvium in a bounding manner. In addition, the minimum alluvium analysis indirectly examines the potential consequences of an alternative flow path farther to the west of Fortymile Wash that remains in the volcanic units approximately to the location of U.S. Highway 95 (see Figure 12.3.1.3-3 for the location of the predicted flow path from the repository). This sensitivity analysis is bounding in the sense that flow path length in the alluvium is reduced to the minimum reasonable value, based on current geologic data. However, it is not absolutely bounding because it still includes approximately 1 to 2 km of alluvium at the end of the flow path near the 20-km point of compliance as defined per proposed NRC regulation 10 CFR Part 63 (64 FR 8640, Section 63.115(b) [DIRS 101680]).

The minimum-alluvium sensitivity analysis is implemented in the site-scale SZ flow and transport model by reducing the extent of the alluvium uncertainty zone to zero. This reduction has the effect of leaving the default volcanic hydrogeologic units and their associated transport properties in the flow path from the repository up to the approximate location of U.S. Highway 95 (Figure 12.3.1.2-1).

The simulated breakthrough curves for the minimum alluvium case have shorter transport times than those for the TSPA-SR supplemental analysis, as expected (Kuzio 2001 [DIRS 154912], Filename “archive_sspa_v1_data/no_alluv”; McNeish 2001 [DIRS 155023]). Example results for neptunium transport with the site-scale SZ model are shown in Figure 12.5.2-3. The upper histogram shows the distribution of times of median breakthrough for neptunium in the TSPA-SR supplemental analysis, and the lower histogram shows the transport times for the minimum alluvium sensitivity study. The times of median breakthrough are somewhat lower for the minimum alluvium case, with 56 realizations having times of median breakthrough less than 10,000 years, compared to 40 realizations for the TSPA-SR supplemental analysis. As for the no matrix diffusion case, the overall uncertainty in the times of median breakthrough, as represented by the width of the histograms, is larger than the shift in times of median breakthrough from the TSPA-SR supplemental analysis to the minimum alluvium case.

12.5.2.4 Increased Uncertainty in the Reversible Colloid (K_c) Model

The model of colloid-facilitated transport used in the TSPA for radionuclides that are reversibly attached to colloids is implemented within several components of the repository engineered and natural systems. Considerable uncertainty exists in the parameters associated with this model. An integrated re-analysis of uncertainty associated with the parameterization of this model was conducted for all components of the repository system as a sensitivity study for Volume 2 (McNeish 2001 [DIRS 155023]).

The sensitivity analysis for the SZ consists of simulation of radionuclide breakthrough curves for the two classes of radionuclides associated with the reversible colloid model: strongly sorbing radionuclides (americium and thorium) and moderately sorbing radionuclides (strontium, plutonium, cesium, and protactinium) (Kuzio 2001 [DIRS 154912]), Filename "archive_sspa_vl_data/alt_colloids"). These simulations are implemented in the site-scale SZ flow and transport model using resampled values for the K_c parameter and for the K_d of strongly sorbing radionuclides. The values for the K_c parameter used in this analysis are based on sampling of uncertainty distributions for the K_d of americium onto colloids and for the concentration of colloids in the groundwater, as explained in Volume 2 (McNeish 2001 [DIRS 155023], Section 3). The uncertainty distribution for K_d of strongly sorbing radionuclides onto the alluvium material is changed to beta distribution with greater statistical mass near the expected value of 50 ml/g (McNeish 2001 [DIRS 155023], Section 3). Other stochastic parameters for the SZ have the same values for the sensitivity analysis as the TSPA-SR supplemental analysis (McNeish 2001 [DIRS 155023]). Also, the SZ breakthrough curves for other radionuclides are identical to those from the TSPA-SR supplemental analysis case.

The results of the sensitivity analysis for the increased uncertainty in the reversible-colloid model are shown in Figure 12.5.2-4. The upper histogram shows the distribution of times of median breakthrough for the TSPA-SR supplemental analysis case (McNeish 2001 [DIRS 155023]), and the lower histogram shows similar results for the case of increased uncertainty in the K_c model. As illustrated in Figure 12.5.2-4, the case of increased uncertainty in colloid-facilitated transport results in somewhat longer transport times compared to the TSPA-SR supplemental analysis case. There are 13 realizations of times of median breakthrough less than 10,000 years for this case and 16 realizations of transport times less than 10,000 years for the TSPA-SR supplemental analysis case (Kuzio 2001 [DIRS 154912], Filename "archive_sspa_vl_data/alt_colloids"). The distribution of values for the K_c parameter in the case of increased uncertainty in colloid-facilitated transport is significantly broader than in the TSPA-SR supplemental analysis case, containing several values of K_c greater than 1.0 in the 100 realizations. Higher values of K_c result in shorter transport times through the SZ system. The narrower distribution of values for the K_d onto the aquifer medium of the strongly sorbing radionuclides used in the case of increased uncertainty in colloid-facilitated transport tends to reduce the variability in simulated transport times in an opposing fashion.

12.5.3 Evaluation of Boundary to the Accessible Environment

The recently issued EPA regulation, 40 CFR 197.12 (66 FR 32074 [DIRS 155216]), specifies the controlled area boundary as follows:

> Controlled area means:
>
> (1) the surface area, identified by passive institutional controls, that encompasses no more than 300 square kilometers. It must not extend farther:
>
> (a) south than 36º 40' 13.6661" north latitude, in the predominant direction of ground water flow; and
>
> (b) than five kilometers form the repository footprint in any other direction; and
>
> (2) the subsurface underlying the surface area.

The boundary is defined at the point above the highest concentration of radionuclides in the simulated plume of contamination where the plume crosses the southernmost boundary of the controlled area (at a latitude of 36º 40' 13.6661" North) and reaches the accessible environment. This southern boundary is approximately 18 km (11 mi), compared to the original distance of approximately 20 km (12 mi) used in the saturated zone transport modeling for TSPA-SR. To evaluate compliance with the EPA regulation, additional SZ breakthrough curves were calculated for neptunium-237 and carbon-14 to simulate radionuclide transport from the water table beneath the potential repository to a defined downgradient location using the revised definition of the accessible environment. The maximum southerly extent of the controlled area corresponds to a distance of approximately 18 km from the potential higher-temperature operating mode repository.

A sensitivity analysis was performed (using 100 realizations of the site-scale SZ flow and transport model) to compare simulated breakthrough curves at 20-km and 18-km from the site (Kuzio 2001 [DIRS 155244], Appendix 2 and 3). Other stochastic parameters for the SZ simulations use the same values as was used in the breakthrough curves for the SSPA supplemental analysis (McNeish 2001 [DIRS 155023]).

The simulated radionuclide breakthrough curves at 18 km have somewhat shorter transport times (Kuzio 2001 [DIRS 155244], Appendix 2 and 3) than those at 20 km as presented in SSPA supplemental analysis (McNeish 2001 [DIRS 155023]) on a realization-by-realization basis. As examples, the histograms of times of median breakthrough (i.e., the times at the midpoints of the breakthrough curves) for neptunium (a sorbing radionuclide) and carbon (a nonsorbing radionuclide, which acts as a surrogate for other non-retarding radionuclides such as technetium-99 and iodine-129) have been simulated and compared for the 18 km and 20 km distances (Figures 12.5.3-2 and 12.5.3-3). These radionuclides were chosen because they are representative of the solutes that would be most rapidly transported (i.e., nonsorbing carbon-14) or are among the largest contributors to peak dose (i.e., neptunium-237) (CRWMS M&O 2000 [153246]) Page F4-19, Figure 4.1-19a) and together they bound the range of solute transport.

For the neptunium times of median breakthrough at 20 km, 42 of the times of median breakthrough are less than 10,000 years; while at 18 km, 53 times of median breakthrough are less than 10,000 years. For the carbon at 20 km, 19 of the times of median breakthrough are less than 100 years; while at 18 km, 28 times of median breakthrough are less than 100 years. The somewhat shorter times of median breakthrough for carbon are primarily a result of a reduction in the flow path length. The shorter times of median breakthrough for neptunium can be attributed to a reduction in the flow path length and a reduction in the amount of sorption that could occur because the flow path length in alluvium has been reduced. As noted in Section 12.5, the analyses are based on a model that is appropriately conservative for TSPA sensitivity analyses and is not intended to represent expected radionuclide breakthrough or groundwater transport time for the SZ portion of the Yucca Mountain flow system.

Table 12.3.2.1.1-1. Identification and Treatment of Unquantified Uncertainties Based on the Total System Performance Assessment-Site Recommendation

Identification of Unquantified Uncertainties	TSPA-SR Treatment of Uncertainties	Reevaluation of the Quantified Uncertainties
Bulk Density	Constant value of 1.270 kg/m^3, based on a limited data set	Defined as a probability distribution based on site data. Normal distribution E(x): 1910 kg/m^3, SD: 80
Sorption coefficient for neptunium in the alluvium	CDF based on a preliminary data set	Redefined CDF based on complete data set
Sorption coefficient for technetium and iodine in the alluvium	Probability distribution based on a preliminary data set	Final data sets did not show sorption occurring for oxidizing conditions
Sorption coefficient for uranium in the Alluvium	Uniform distribution LB: 0 mL/g; UB: 8.0 mL/g	Redefined to be the same as the CDF for neptunium in the alluvium
Correlation of sorption coefficient in the alluvium for uranium and neptunium	Not correlated	Correlated neptunium and uranium one to one
Fracture porosity	Uniform distribution: Log_{10}(LB): -5.0; Log_{10}(UB): -1.0	Redefined the shape of the probability distribution. Triangular: Log_{10}(LB): -5.0; Log_{10}(UB): -1.0, Most likely value Log_{10}: -3.0
Effective diffusion coefficient	Uniform distribution: Log_{10}(LB): -13.0 m^2/s; Log_{10}(UB): -10.0 m^2/s	Redefined the shape of the probability distribution. Triangular: Log_{10}(LB): -13.0; Log_{10}(UB): -10.0, most likely value Log_{10}: -10.5 (m^2/s)
Effective porosity in the alluvium	Normal distribution, E(x) = 0.18, SD: 0.051; upper bound 0.35	Shifted the E(x) to 0.15 and truncated the upper end at 0.3
Correlation of matrix porosity and effective diffusion coefficient	Not correlated	Matrix porosity was correlated to the effective diffusion coefficient
Neptunium sorption coefficient in the volcanic units	Probability distribution was based on the vitric rock type. Beta distribution: E(x): 0.5 mL/g; SD: 0.5, and LB: 0.0 mL/g, UB: 2.0 mL/g	Sampled the vitric neptunium sorption coefficient 66% of the time and sampled the zeolitic neptunium sorption coefficient distribution 33% of the time
Retardation factor for irreversible colloids in the alluvium	Site grain size data was not available	New probability distribution derived from new grain size data

Source: Information in columns 1 and 2 are from the *Uncertainty Distribution for Stochastic Parameters* report (CRWMS M&O 2000 [DIRS 147972], Section 7, Table 15).

NOTE: UB = Upper bound; LB = Lower bound; E(x) = mean; SD = standard deviation; CDF = cumulative distribution function. Identification and treatment of unquantified uncertainties is based on the TSPA-SR (CRWMS M&O 2000 [DIRS 153246]).

Table 12.3.2.3-1. Bounding Nevada State Plane Coordinates for the Emplacement Area for the Potential Lower-Temperature Operating Mode Repository Footprint

Drift Number	East Side of Emplacement Drift			West Side of Emplacement Drift		
	Northing (m)	Easting (m)	Elevation (m)	Northing (m)	Easting (m)	Elevation (m)
PC1	236,606.073	171,378.875	1,032.437	236,391.550	170,718.641	1,032.437
1	236,521.040	171,379.292	1,033.659	236,292.756	170,676.706	1,033.659
2	236,434.396	171,374.751	1,034.831	236,193.962	170,634.770	1,034.831
3	236,347.752	171,370.210	1,036.002	236,095.168	170,592.834	1,036.002
4	236,261.109	171,365.669	1,037.173	235,996.374	170,550.899	1,037.173
5	236,174.465	171,361.129	1,038.345	235,897.579	170,508.963	1,038.345
6	236,087.821	171,356.588	1,039.516	235,798.785	170,467.027	1,039.516
7	236,001.177	171,352.047	1,040.687	235,699.991	170,425.092	1,040.687
8	235,914.533	171,347.506	1,041.858	235,601.197	170,383.156	1,041.858
9	235,827.889	171,342.965	1,043.030	235,502.403	170,341.221	1,043.030
10	235,741.245	171,338.424	1,044.201	235,403.608	170,299.285	1,044.201
11	235,654.601	171,333.884	1,045.372	235,304.814	170,257.349	1,045.372
12	235,567.957	171,329.343	1,046.544	235,206.020	170,215.414	1,046.544
13	235,481.314	171,324.802	1,047.715	235,102.137	170,157.816	1,047.715
14	235,394.670	171,320.261	1,048.886	235,005.154	170,121.454	1,048.886
15	235,308.026	171,315.720	1,050.058	234,918.510	170,116.913	1,050.058
16	235,221.382	171,311.180	1,051.229	234,831.866	170,112.372	1,051.229
17	235,134.738	171,306.639	1,052.400	234,745.222	170,107.831	1,052.400
18	235,048.094	171,302.098	1,053.571	234,658.578	170,103.290	1,053.571
19	234,961.450	171,297.557	1,054.743	234,571.935	170,098.749	1,054.743
20	234,874.806	171,293.016	1,055.914	234,485.291	170,094.209	1,055.914
21	234,788.163	171,288.475	1,057.085	234,398.647	170,089.668	1,057.085
22	234,701.519	171,283.935	1,058.257	234,312.003	170,085.127	1,058.257
23	234,614.875	171,279.394	1,059.428	234,225.359	170,080.586	1,059.428
24	234,528.231	171,274.853	1,060.599	234,138.715	170,076.045	1,060.599
25	234,441.587	171,270.312	1,061.770	234,052.071	170,071.505	1,061.770
26	234,354.943	171,265.771	1,062.942	233,965.427	170,066.964	1,062.942
27	234,268.299	171,261.231	1,064.113	233,878.784	170,062.423	1,064.113
28	234,181.655	171,256.690	1,065.284	233,792.140	170,057.882	1,065.284

Table 12.3.2.3-1. Bounding Nevada State Plane Coordinates for the Emplacement Area for the Potential Lower-Temperature Operating Mode Repository Footprint (Continued)

Drift Number	East Side of Emplacement Drift			West Side of Emplacement Drift		
	Northing (m)	Easting (m)	Elevation (m)	Northing (m)	Easting (m)	Elevation (m)
29	234,095.012	171,252.149	1,066.456	233,705.496	170,053.341	1,066.456
30	234,008.368	171,247.608	1,067.627	233,618.852	170,048.801	1,067.627
31	233,921.724	171,243.067	1,068.798	233,532.208	170,044.260	1,068.798
32	233,835.080	171,238.527	1,069.969	233,445.564	170,039.719	1,069.969
33	233,748.436	171,233.986	1,071.141	233,358.817	170,034.860	1,071.141
34	233,661.792	171,229.445	1,072.312	233,276.916	170,044.916	1,072.312
35	233,575.148	171,224.904	1,073.483	233,195.015	170,054.972	1,073.483
36	233,488.504	171,220.363	1,074.655	233,113.114	170,065.029	1,074.655
37	233,401.861	171,215.822	1,075.826	233,031.213	170,075.085	1,075.826
38	233,315.217	171,211.282	1,076.997	232,949.312	170,085.141	1,076.997
39	233,228.573	171,206.741	1,078.169	232,867.411	170,095.197	1,078.169
40	233,141.929	171,202.200	1,079.340	232,785.510	170,105.253	1,079.340
41	233,055.285	171,197.659	1,080.511	232,703.609	170,115.309	1,080.511
42	232,968.641	171,193.118	1,081.682	232,621.708	170,125.366	1,081.682
43	232,881.997	171,188.578	1,082.854	232,539.807	170,135.422	1,082.854
44	232,795.353	171,184.037	1,084.025	232,457.906	170,145.478	1,084.025
45	232,708.710	171,179.496	1,085.196	232,376.005	170,155.534	1,085.196
46	232,622.066	171,174.955	1,086.368	232,294.104	170,165.590	1,086.368
47	232,535.422	171,170.414	1,087.539	232,212.203	170,175.647	1,087.539
48	232,448.778	171,165.874	1,088.710	232,130.301	170,185.703	1,088.710
49	232,362.134	171,161.333	1,089.881	232,048.400	170,195.759	1,089.881
50	232,275.490	171,156.792	1,091.053	231,966.499	170,205.815	1,091.053
51	232,188.846	171,152.251	1,092.224	231,884.598	170,215.871	1,092.224
52	232,102.202	171,147.710	1,093.395	231,802.697	170,225.927	1,093.395
53	232,015.558	171,143.169	1,094.567	231,720.796	170,235.984	1,094.567
54	231,928.915	171,138.629	1,095.738	231,638.895	170,246.040	1,095.738
55	231,842.271	171,134.088	1,096.909	231,556.994	170,256.096	1,096.909
56	231,755.627	171,129.547	1,098.081	231,475.093	170,266.152	1,098.081

Table 12.3.2.3-1. Bounding Nevada State Plane Coordinates for the Emplacement Area for the Potential Lower-Temperature Operating Mode Repository Footprint (Continued)

Drift Number	East Side of Emplacement Drift			West Side of Emplacement Drift		
	Northing (m)	Easting (m)	Elevation (m)	Northing (m)	Easting (m)	Elevation (m)
57	231,668.983	171,125.006	1,099.252	231,393.192	170,276.208	1,099.252
58	231,582.339	171,120.465	1,100.423	231,311.291	170,286.265	1,100.423
59	231,495.695	171,115.925	1,101.594	231,229.390	170,296.321	1,101.594
60	231,409.051	171,111.384	1,102.766	231,147.489	170,306.377	1,102.766
61	231,322.407	171,106.843	1,103.937	231,065.588	170,316.433	1,103.937
62	231,228.794	171,080.845	1,105.126	230,983.689	170,326.489	1,105.126
63	231,129.221	171,036.512	1,106.128	230,901.788	170,336.545	1,106.128
64	231,029.648	170,992.179	1,107.130	230,819.887	170,346.601	1,107.130
65	230,161.806	170,680.331	1,112.032	230,059.664	170,365.970	1,112.032
66	230,075.660	170,677.322	1,112.463	229,973.518	170,362.962	1,112.463
67	229,989.514	170,674.314	1,112.894	229,887.373	170,359.954	1,112.894
68	229,903.957	170,673.116	1,113.279	229,801.227	170,356.946	1,113.279
69	229,823.182	170,686.637	1,113.667	229,715.081	170,353.937	1,113.667
70	229,746.888	170,713.951	1,114.115	229,628.935	170,350.929	1,114.115
71	229,671.164	170,743.018	1,114.549	229,543.716	170,350.774	1,114.549
72	229,595.440	170,772.086	1,115.001	229,454.670	170,338.840	1,115.001
73	229,519.716	170,801.154	1,115.479	229,361.994	170,315.734	1,115.479
74	229,443.993	170,830.221	1,115.957	229,269.318	170,292.627	1,115.957
75	229,368.269	170,859.289	1,116.434	229,176.641	170,269.520	1,116.434
76	229,292.545	170,888.357	1,116.912	229,083.965	170,246.413	1,116.912
77	229,216.821	170,917.424	1,117.389	228,991.289	170,223.306	1,117.389
78	229,141.098	170,946.492	1,117.275	228,898.612	170,200.200	1,117.275
79	229,065.285	170,975.285	1,116.251	228,804.965	170,174.104	1,116.251
80	228,986.633	170,995.342	1,115.190	228,721.372	170,178.952	1,115.190
81	228,907.407	171,013.632	1,114.059	228,646.270	170,209.934	1,114.059
82	228,828.182	171,031.923	1,112.851	228,573.648	170,248.548	1,112.851
83	228,748.957	171,050.214	1,111.535	228,501.026	170,287.162	1,111.535
84	228,669.731	171,068.504	1,110.219	228,428.404	170,325.776	1,110.219

Table 12.3.2.3-1. Bounding Nevada State Plane Coordinates for the Emplacement Area for the Potential Lower-Temperature Operating Mode Repository Footprint (Continued)

Drift Number	East Side of Emplacement Drift			West Side of Emplacement Drift		
	Northing (m)	Easting (m)	Elevation (m)	Northing (m)	Easting (m)	Elevation (m)
85	228,590.506	171,086.795	1,108.903	228,355.782	170,364.389	1,108.903
87	228,432.055	171,123.376	1,106.271	228,210.538	170,441.617	1,106.271
88	228,352.829	171,141.667	1,104.955	228,137.916	170,480.231	1,104.955
89	228,273.604	171,159.957	1,103.663	228,065.294	170,518.845	1,103.663
90	228,194.378	171,178.248	1,102.370	227,992.672	170,557.459	1,102.370
91	228,115.153	171,196.539	1,101.078	227,920.050	170,596.072	1,101.078

Source: BSC 2001 [DIRS 154548], Table 1.

Table 12.3.2.4-1. Zeolitic Rock Volume

Zeolitic Percentage	Percentage of Rock Mass Volume with the Zeolitic Percentage or Greater
5	38.4
10	38.2
20	34.9
30	32.1
40	25.4
50	16.2
60	2.2
70	0.07

Source: Kuzio 2001 [DIRS 155004], Filename "Table 12.3.2.4-1.doc".

Table 12.3.2.4-2. Comparison of Sorption Coefficients for Uranium and Neptunium

Solid Phase	pH	Uranium K_d (ml/g)	Neptunium K_d (ml/g)
G4-268 Devitrified Tuff	7	0.2	0.007
	8.5	0.7	(-0.04)[a]
GU3-1405 Vitric tuff	7	(-0.5)[a]	0.2
	8.5	0.6	0.3
G4-1510 Zeolitic Tuff	7	16[b]	3
	8.5	8[b]	1.5

Sources: Data for samples G4-268 and GU3-1405 are from Triay et al. (1997 [DIRS 100422], Table 15).
Data for sample G4-1510 are from CRWMS M&O (2001 [DIRS 154024], Section 6.4.4.1.4.2).

NOTES: [a]Negative values most likely reflect analytical artifacts. The magnitude of the negative value provides an indication of the analytical error associated with this type of analysis.

[b]These K_d values are for solution concentrations less than 1 mg/L.

Table 12.3.2.4-3. Measured Saturated Density, Computed Porosity, and Computed Dry Bulk Density for Depths from 402 to 776 Feet Below the Surface at the Nye County EWDP-19D1 Well

Sample Dept (ft)	Drift-Corrected Saturated Bulk Density, ρ_{sat} (g/cm^3)	Computed Porosity, θ	Computed Dry Bulk Density, ρ_b (g/cm^3)
402	2.231	0.190	2.04
422	2.156	0.239	1.92
442	2.180	0.224	1.96
485	2.163	0.235	1.93
505	2.174	0.228	1.95
525	2.214	0.201	2.01
569.95	2.148	0.245	1.90
589.9	2.142	0.249	1.89
610	2.105	0.273	1.83
630	2.079	0.290	1.79
649.95	2.077	0.291	1.79
669.95	2.133	0.255	1.88
690	2.121	0.262	1.86
715.95	2.158	0.238	1.92
736	2.143	0.248	1.90
756	2.105	0.273	1.83
776	2.239	0.185	2.05

Source: Black 2000 [DIRS 154704], p.18.

Table 12.3.2.4-4. Parameters for Retardation Factor Calculations and Uncertainty Range Distributions

Parameter	Min	Max	Distribution
Grain size (d) (cm) [a]	0.02	0.11	Uniform
Colloid Size (d_p) (cm) [b]	6.0E-07	4.5E-05	Uniform
Alpha (α) [c]	.005	.025	Uniform
Porosity (θ) [d]	0 (min limit)	1 (max limit)	Truncated Normal (mean = 0.18, σ = 0.055)
Flux (q) (m/yr) [e]	0.2	20	Discrete (0.2, 24%; 2.0, 52%; 20.0, 24%)
Detachment Rate (k_r) (g/ml-hr) [f]	1.0E-05	3.33	Log-Uniform

Sources: [a] Marshall et al. 1996 [DIRS 144573], Figure 1.2, p. 4; Bechtel Nevada 1998 [DIRS 149177], Table I-1; Bechtel Nevada 1998 [DIRS 149178].

[b] CRWMS M&O 2000 [DIRS 122799], p. 24.

[c] Harvey and Garabedian 1991 [DIRS 109256], pp. 178 to 185.

[d] CRWMS M&O 2000 [DIRS 147972], Section 6.3 (effective porosity of the alluvium).

[e] CRWMS M&O 2000 [DIRS 139440], Section 6.2.5.1 and Section 6.5.1 (flux was approximated from this information).

[f] Bales et al. 1997 [DIRS 144535], Table 3, parameter K2 and CRWMS M&O 2000 [DIRS 129286], Table 6.

Table 12.5.1-1. Identification and Treatment of Unquantified Uncertainties Based on the Total System Performance Assessment-Site Recommendation

Identification of Unquantified Uncertainties	TSPA-SR Treatment of Uncertainties	Reevaluation of the Quantified Uncertainties
Bulk density	Constant value of 1.27 g/cm^3, based on a limited data set	Defined as a probability distribution based on site data. Normal distribution E(x): 1.91 g/cm^3, SD: 0.08
Sorption coefficient for neptunium in the alluvium	CDF based on a preliminary data set	Redefined CDF based on complete data set
Sorption coefficient for technetium and iodine in the alluvium	Probability distribution based on a preliminary data set	Final data sets did not show sorption occurring for oxidizing conditions
Sorption coefficient for uranium in the Alluvium	Uniform distribution LB: 0; UB: 8.0 (ml/g)	Redefined to be the same as the CDF for neptunium in the alluvium
Correlation of sorption coefficient in the alluvium for uranium and neptunium	Not correlated	Correlated neptunium and uranium 1:1
Fracture porosity	Uniform distribution: Log_{10}(LB): -5.0; Log_{10}(UB): -1.0	Redefined the shape of the probability distribution. Triangular: Log_{10}(LB): -5.0; Log_{10}(UB): -1.0, Most likely value Log_{10}: -3.0
Effective diffusion coefficient	Uniform distribution: Log_{10}(LB): -13.0 m^2/s; Log_{10}(UB): -10.0 (m^2/s)	Redefined the shape of the probability distribution. Triangular: Log_{10}(LB): -13.0; Log_{10}(UB): -10.0, most likely value Log_{10}: -10.5 (m^2/s)
Effective porosity in the alluvium	Normal distribution, E(x) = 0.18, SD: 0.051; upper bound 0.35	Shifted the E(x) to 0.15 and truncated the upper end at 0.3
Correlation of matrix porosity and effective diffusion coefficient	Not correlated	Matrix porosity was correlated to the effective diffusion coefficient
Retardation factor for irreversible colloids in the alluvium	Site grain size data was not available	New probability distribution derived from new grain size data
Neptunium sorption coefficient in the volcanic units	Probability distribution was based on the vitric rock type. Beta distribution: E(x): 0.5; SD: 0.5 and LB: 0.0, UB: 2.0 ml/g	Sampled the vitric neptunium sorption coefficient 66% of the time and sampled the zeolitic neptunium sorption coefficient distribution 33% of the time
Groundwater specific discharge	Probability distribution based on SZ Expert Elicitation. Three discrete cases considered (low: 0.06, medium: 0.6, high: 6.0 m/yr	Three discrete cases adjusted to (low: 0.2, medium: 0.6, high 1.8 m/yr)

Source: Information in Columns 1 and 2 is from the *Uncertainty Distribution for Stochastic Parameters* report (CRWMS M&O 2000 [DIRS 147972], Section 7, Table 15).

NOTES: CDF = cumulative distribution function; E(x) = expected value; UB = upper bound; LB = lower bound; SD = standard deviation. Identification and treatment of unquantified uncertainties is based on the TSPA-SR (CRWMS M&O 2000 [DIRS 153246]).

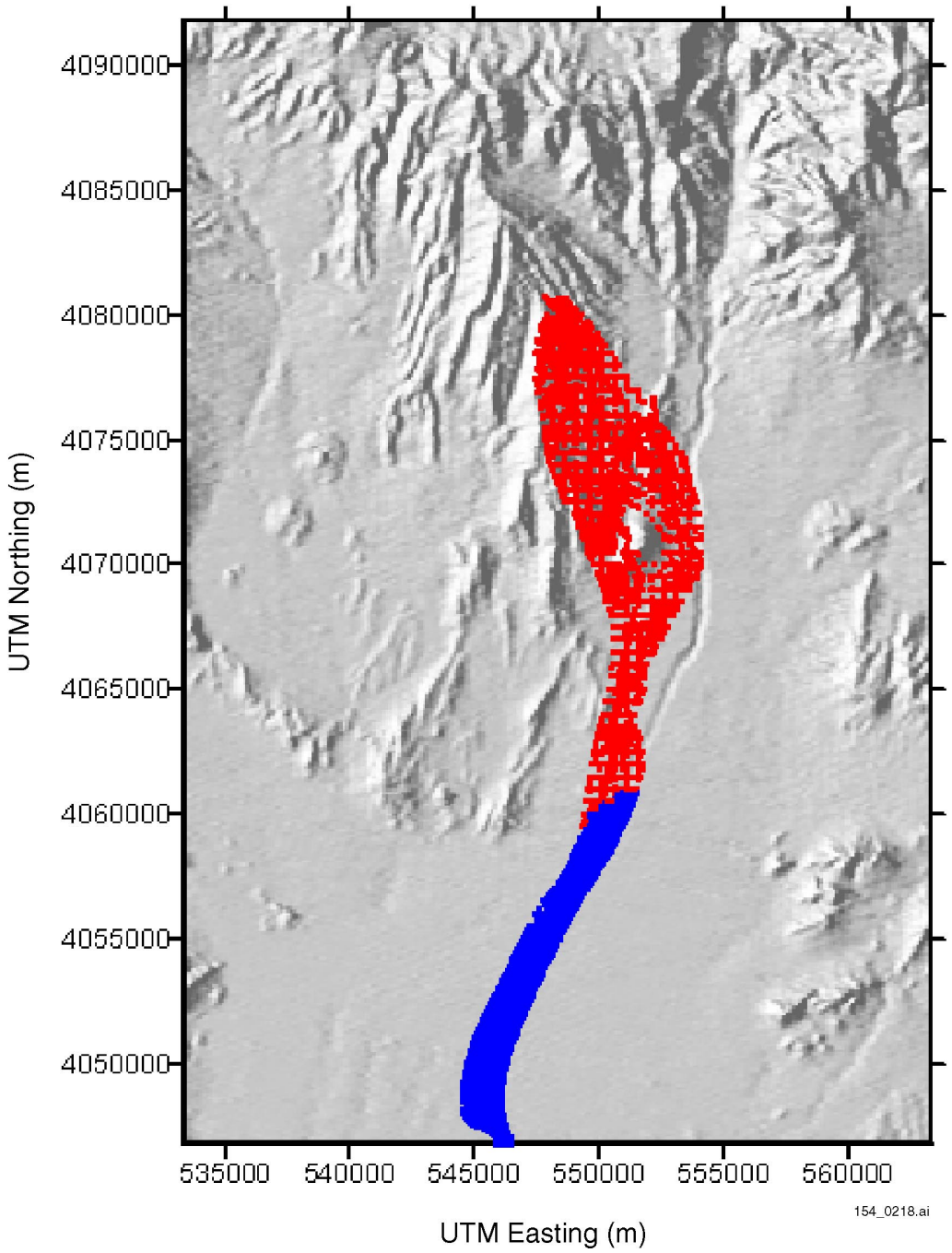

154_0218.ai

Source: Adapted from DOE 2001 [DIRS 153849], Figure 4-129.

NOTE: The potential repository is located in the upper central part of the figure. Released particles move from the upper central area in the figure to the bottom. The red portion of the illustration indicates flow (particle positions) through fractured volcanic tuff, and the blue portion indicates flow through alluvium (modeled as a porous medium). The spatial pattern in the volcanic tuff reflects the numerical algorithm that illustrates particle positions at grid boundaries or at the end of a time step. The location of the contact of tuff and alluvium is uncertain and is treated stochastically, and it is shown here at the expected-value location.

Figure 12.1-1. Flow Paths Predicted by the Site-Scale Saturated Zone Flow and Transport Model

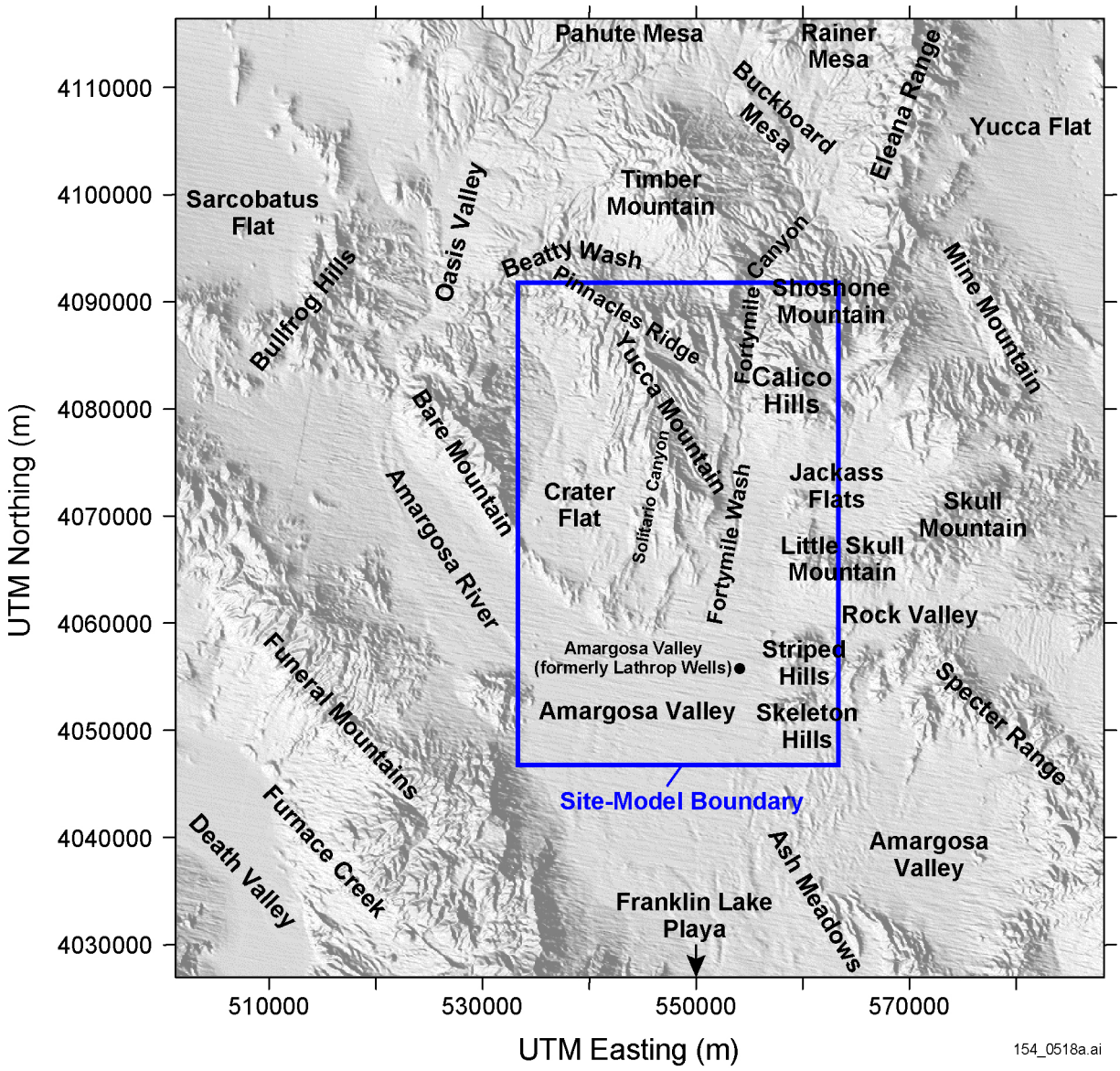

154_0518a.ai

Source: CRWMS M&O 2000 [DIRS 139582], p. 24.

Figure 12.2-1. Boundary of the Numerical Model for the Site-Scale Saturated Zone Flow and Transport Model

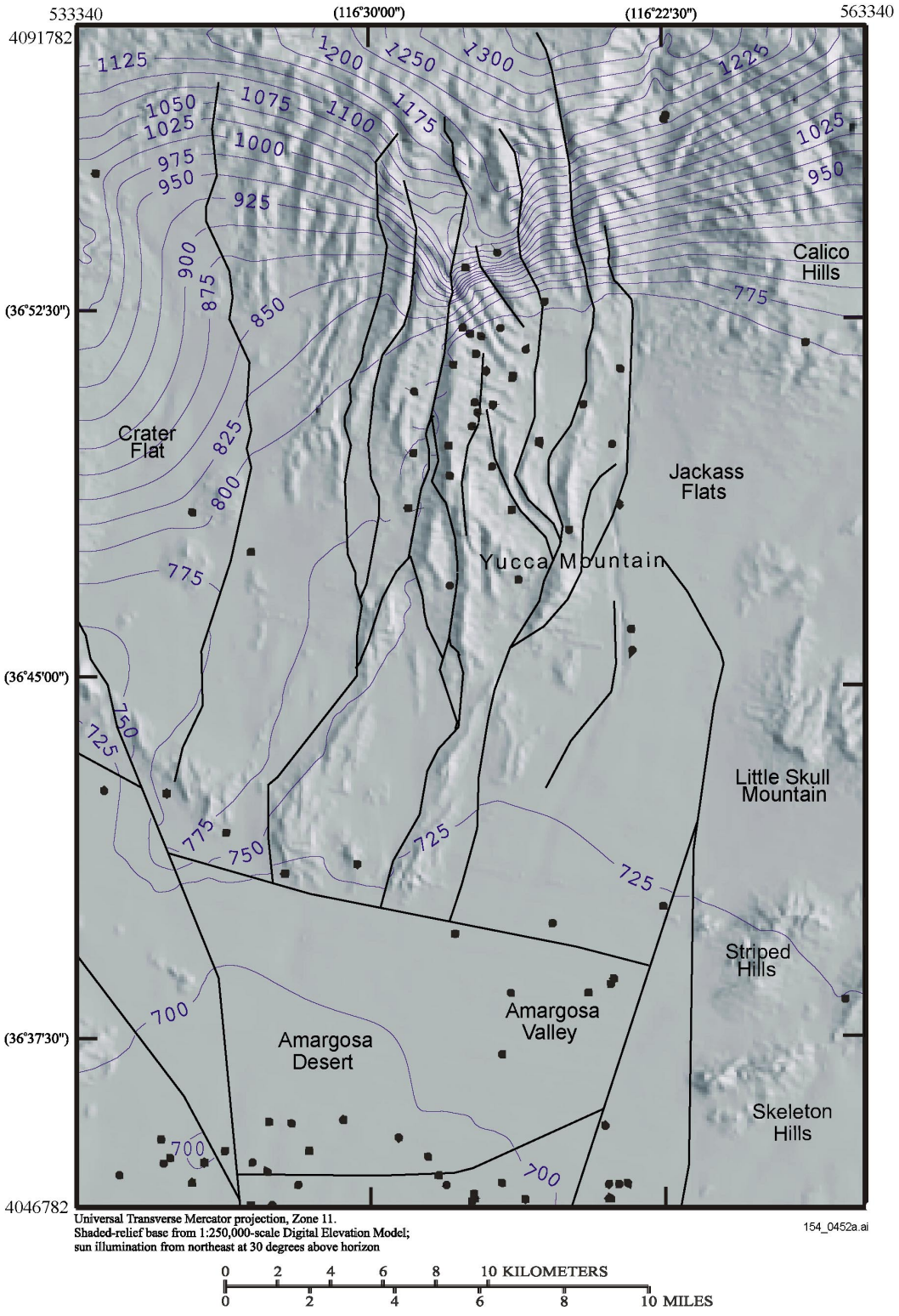

154_0452a.ai

Source: Adapted from USGS 2001 [DIRS 154625], Figure 1-2.

Figure 12.2-2. Borehole Locations, Water-Level Altitudes, Potentiometric Surface Contours, and Location of Tertiary Faults in the Site-Scale Saturated Zone Model Area

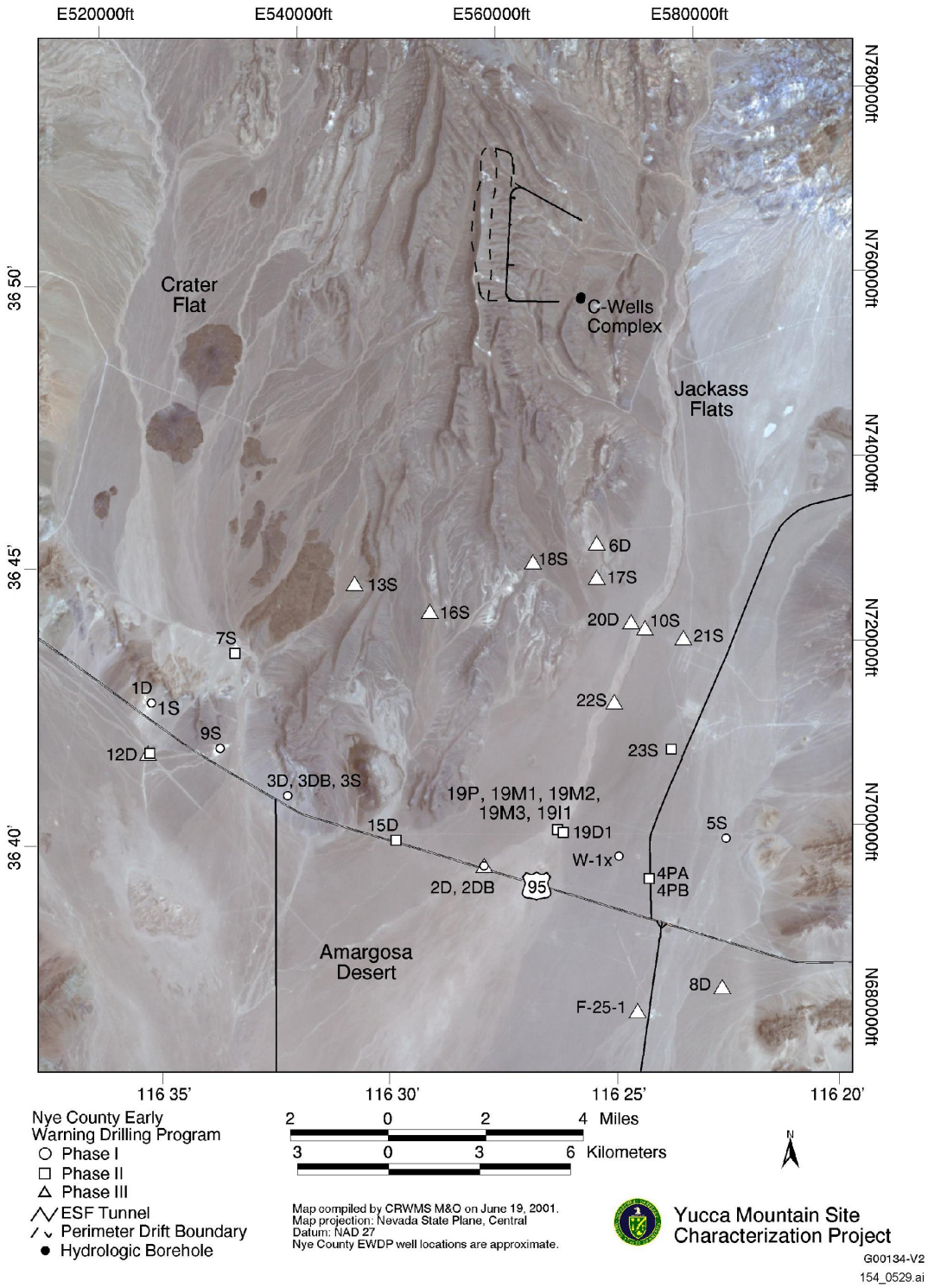

154_0529.ai

Source: CRWMS M&O 2000 [DIRS 153168], Figure 2-3.

NOTE: Borehole NC-EWDP-9SX is located adjacent to Borehole NC-EWDP-9S.

Figure 12.3.1.2-1. Locations of Nye County Early Warning Drilling Program Wells

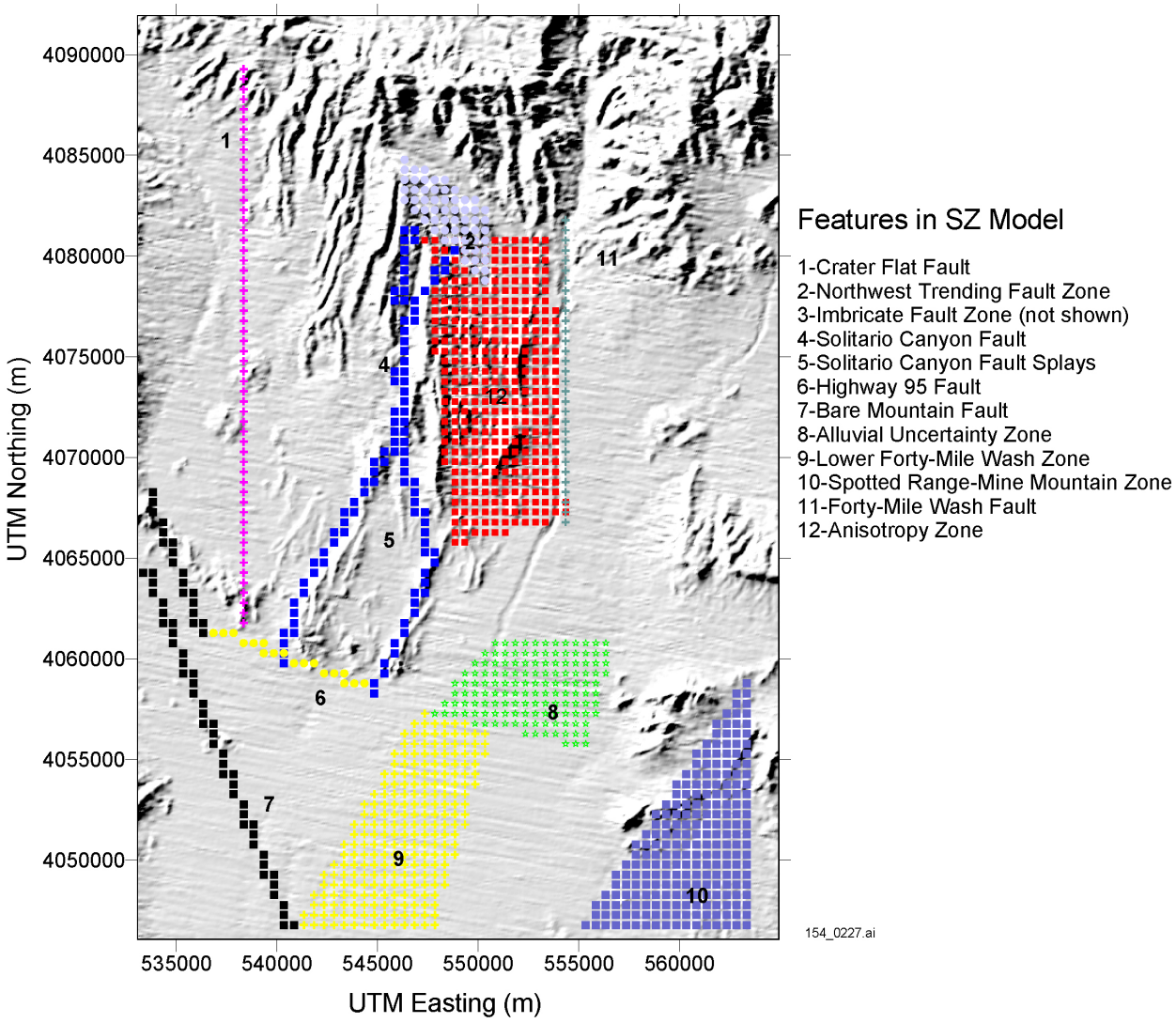

154_0227.ai

Source: DTN: LA0105GZ12213S.001 [DIRS 154887]; DTN: LA0105GZ12213S.002 [DIRS 154888]; DTN: LA0105GZ12213S.003 [DIRS 154889].

NOTE: The east-west barrier of the original model is not included in this newer model.

Figure 12.3.1.3-1. Features in the Newer Saturated Zone Model

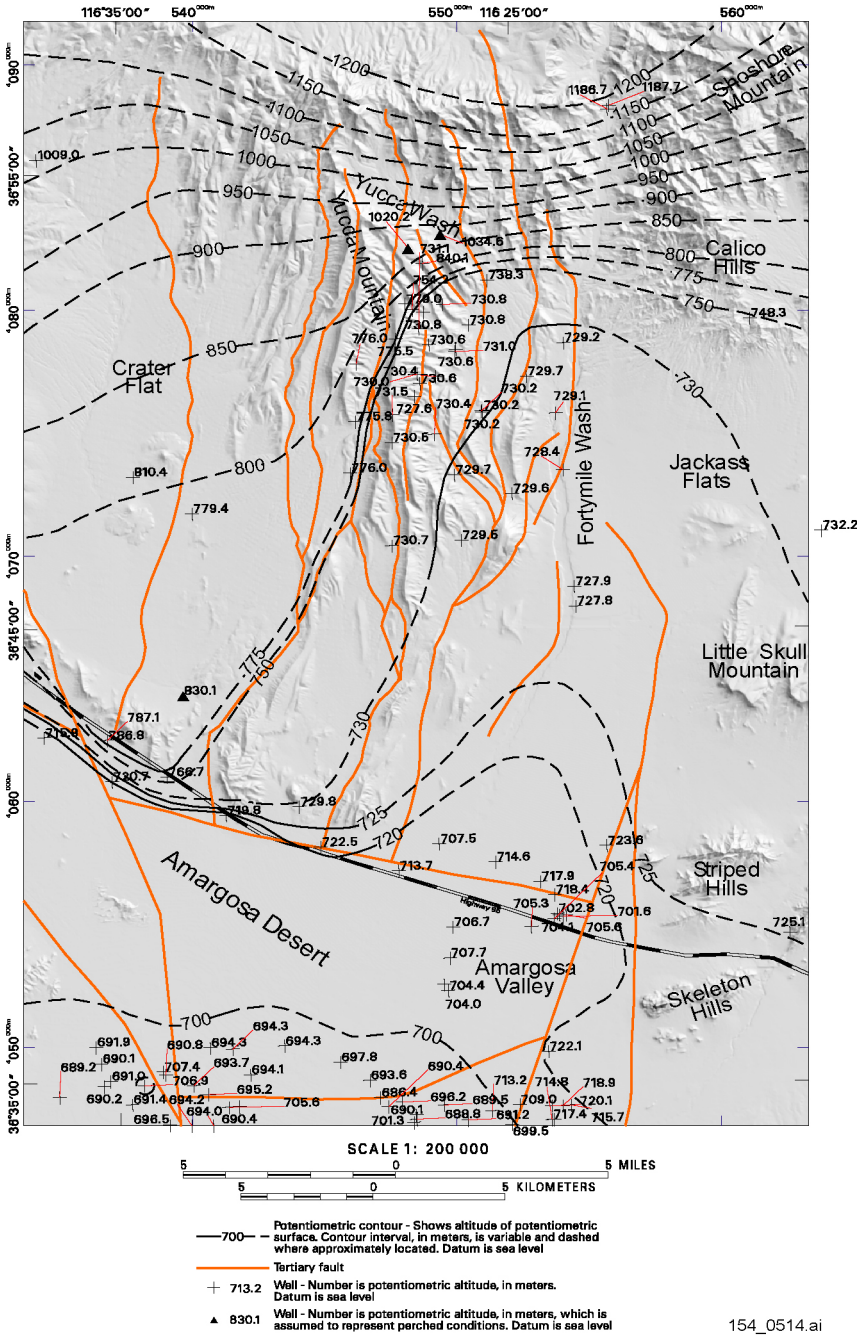

154_0514.ai

Source: BSC 2001 [DIRS 155312].

NOTE: The potentiometric surface map was developed assuming perched conditions north of Yucca Mountain.

Figure 12.3.1.2-2. Potentiometric Surface Map in the Saturated Zone Site-Scale Model Area

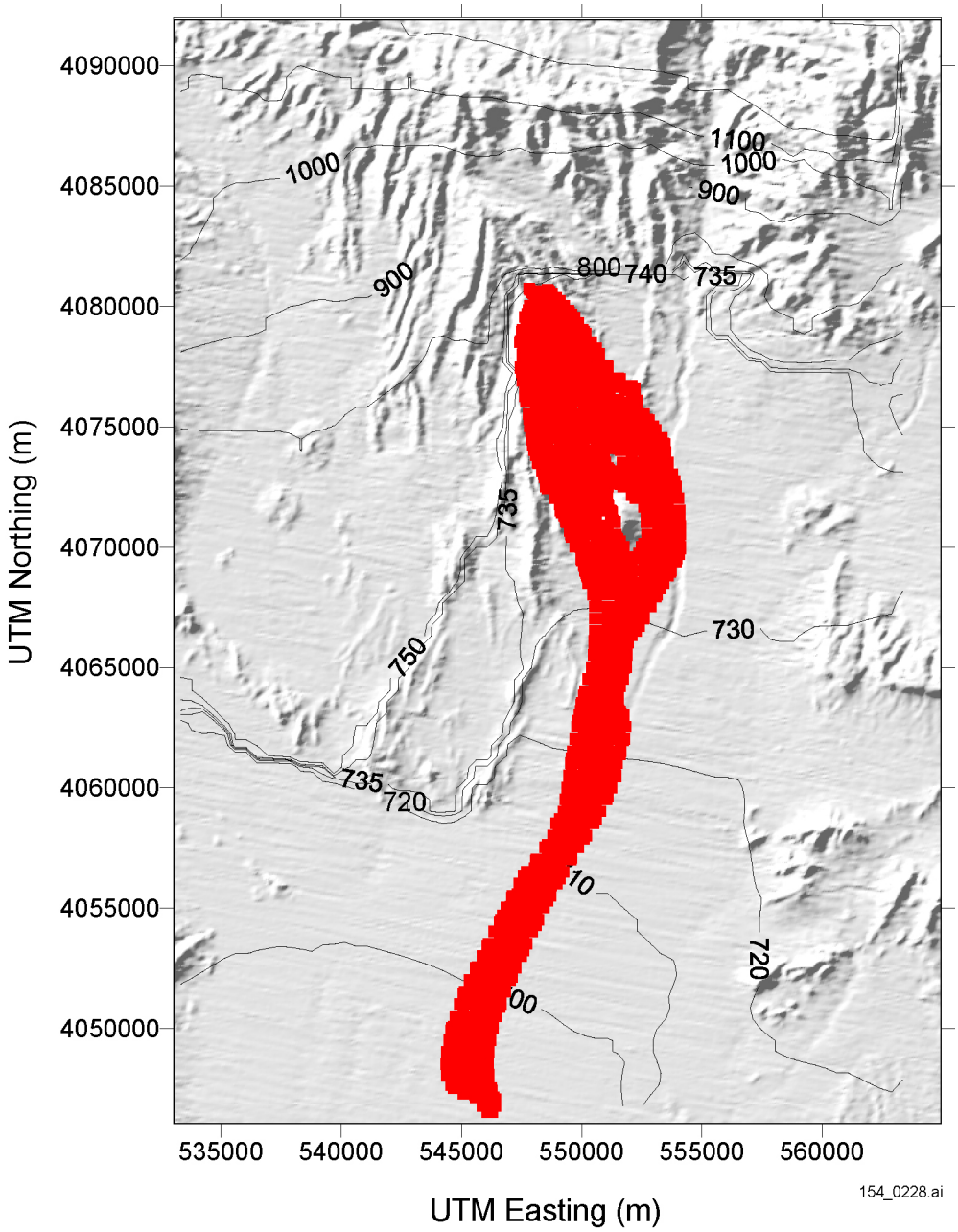

154_0228.ai

Source: Adapted from CRWMS M&O 2000 [DIRS 139582], Figure 8.

NOTE: All features in the original site-scale model, including the east-west barrier, are represented in this simulation.

Figure 12.3.1.3-2. Flow Paths Simulated with the Original Site-Scale Saturated Zone Flow and Transport Model

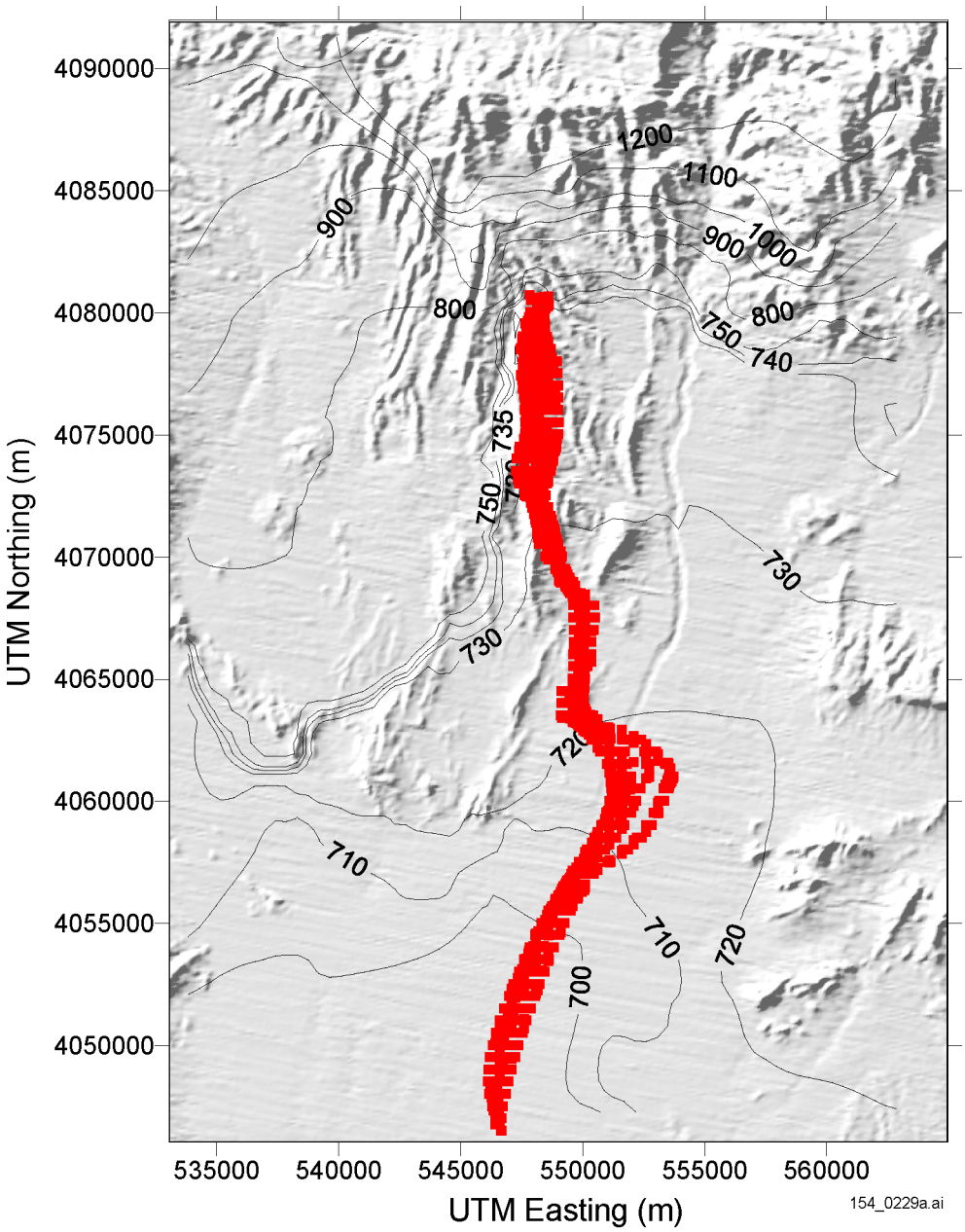

154_0229.ai

Source: DTN: LA0105GZ12213S.002 [DIRS 154888].

NOTE: All features in Figure 12.3.1.3-1, except the northwest trending fault zone (Feature 2), are represented in this simulation.

Figure 12.3.1.3-3. Flow Paths Simulated with the New Saturated Zone Model (Excluding the Northwest Trending Fault Zone)

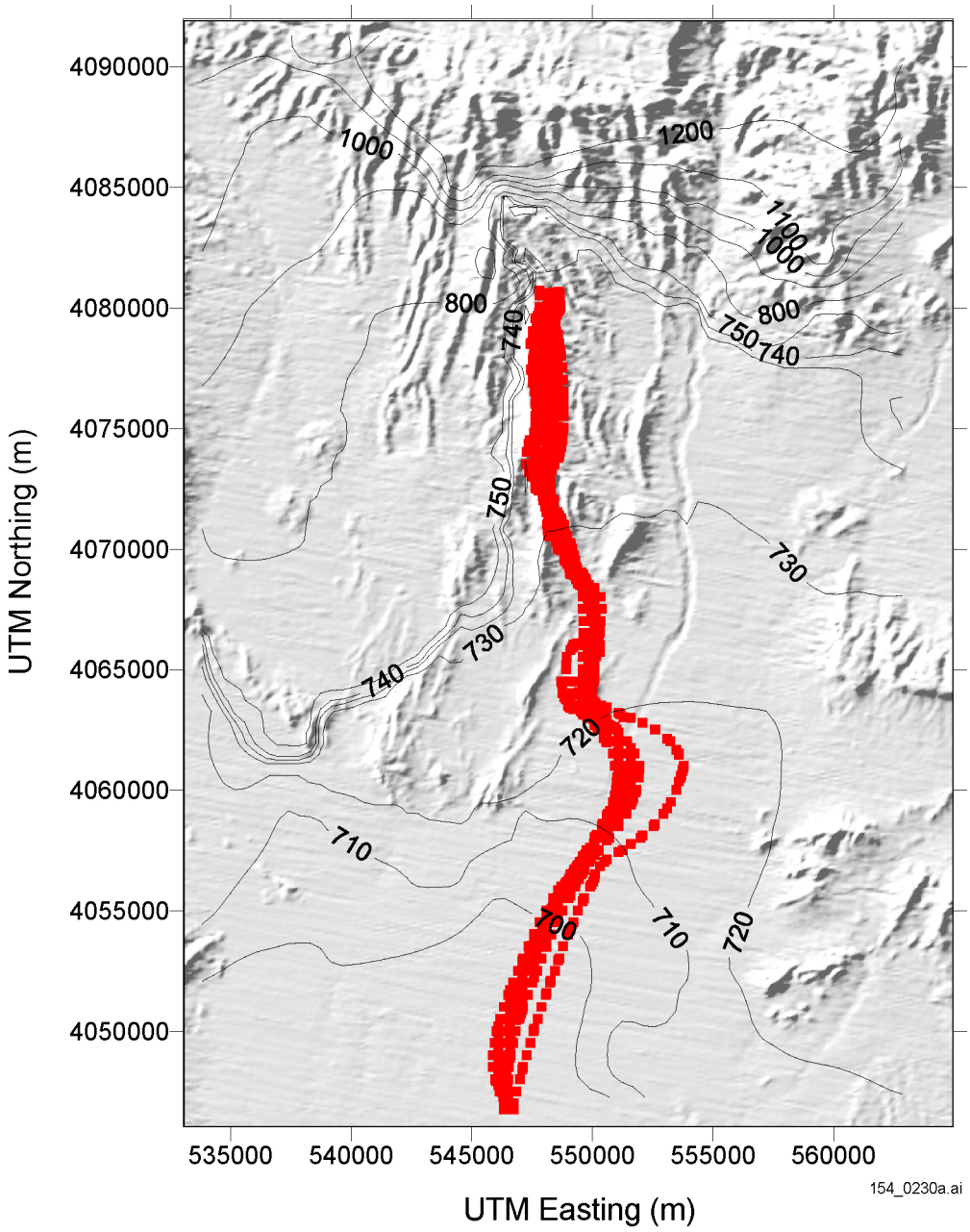

154_0230a.ai

Source: DTN: LA0105GZ12213S.001 [DIRS 154887].

NOTE: All features in Figure 12.3.1.3-1, including the northwest trending fault zone (Feature 2), are represented in this simulation.

Figure 12.3.1.3-4. Flow Paths Simulated with the New Saturated Zone Model (Including the Northwest Trending Fault Zone)

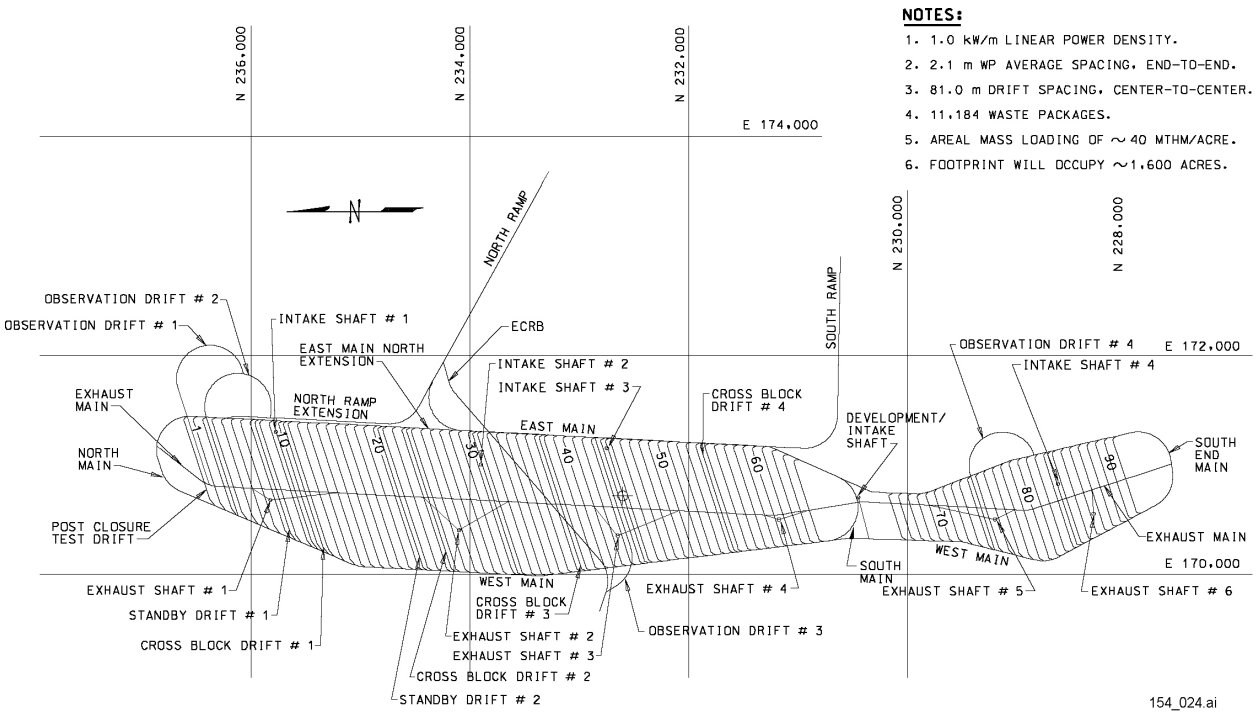

154_024.ai

Source: BSC 2001 [DIRS 154548], Section I, Figure 1, p. 1.

NOTE: MTHM = metric tons of heavy metal.

Figure 12.3.2.3-1. Preliminary 70,000 MTHM Layout for the Lower-Temperature Operating Mode

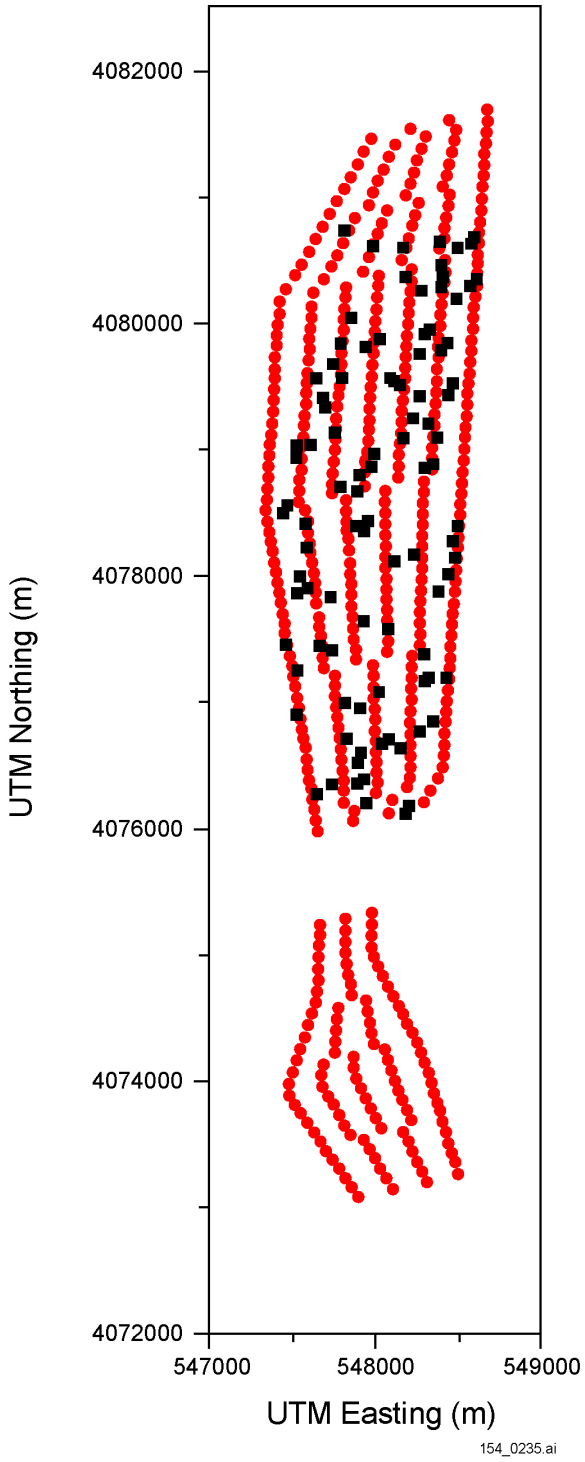

154_0235.ai

Source: Robinson 2001 [DIRS 154995], Filename “original_points.txt” and “out.pts250”.

NOTE: Original potential repository footprint (black squares) and the increased footprint (red circles) associated with the flexible design.

Figure 12.3.2.3-2. Locations of Particle Tracking Points Associated with Differing Potential Repository Footprints

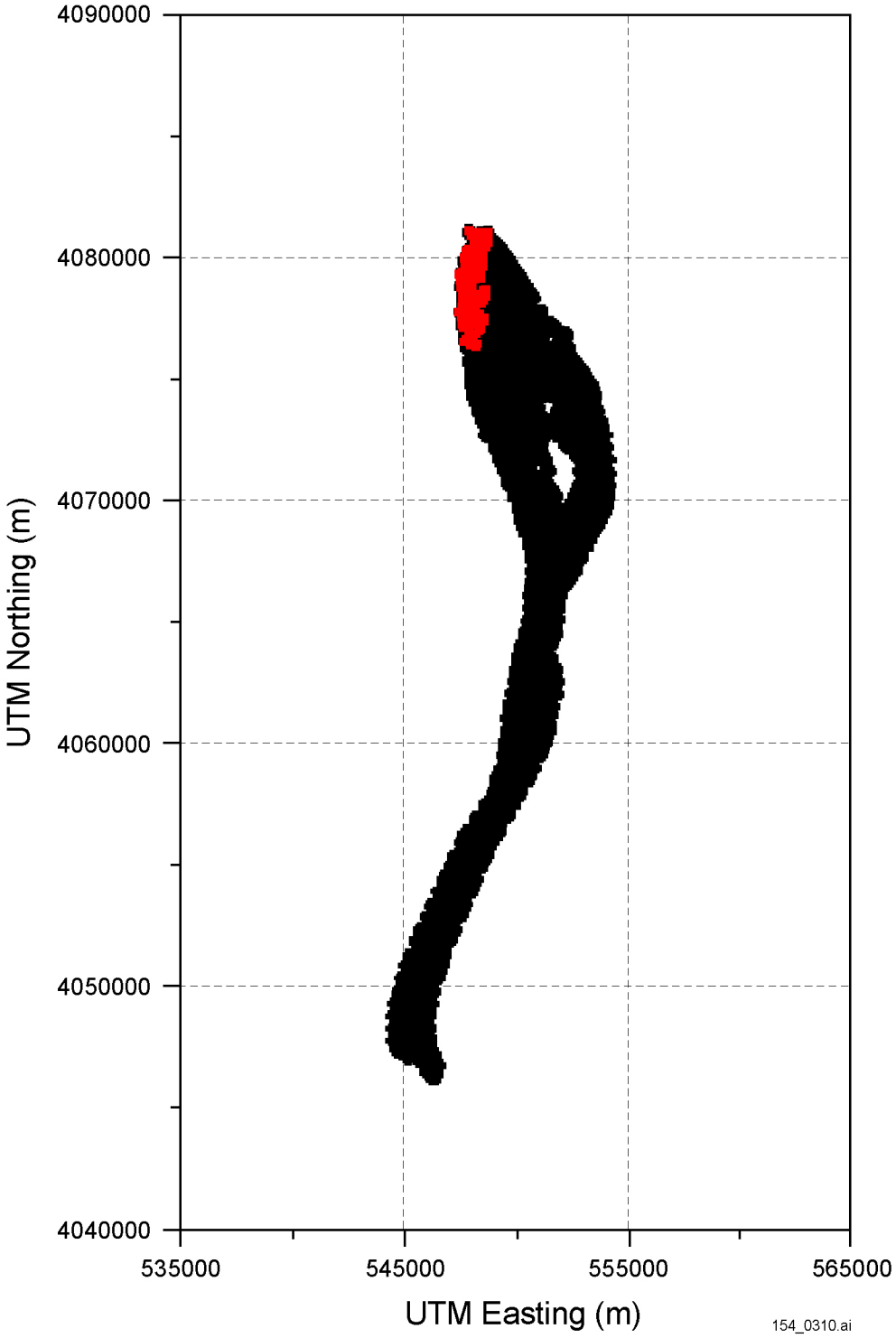

154_0310.ai

Source: Robinson 2001 [DIRS 154995], Filename “02_calib.sptr2.sr”.

Figure 12.3.2.3-3a. Plan View of Particle Pathlines the Higher-Temperature Operating Mode for the Potential Repository

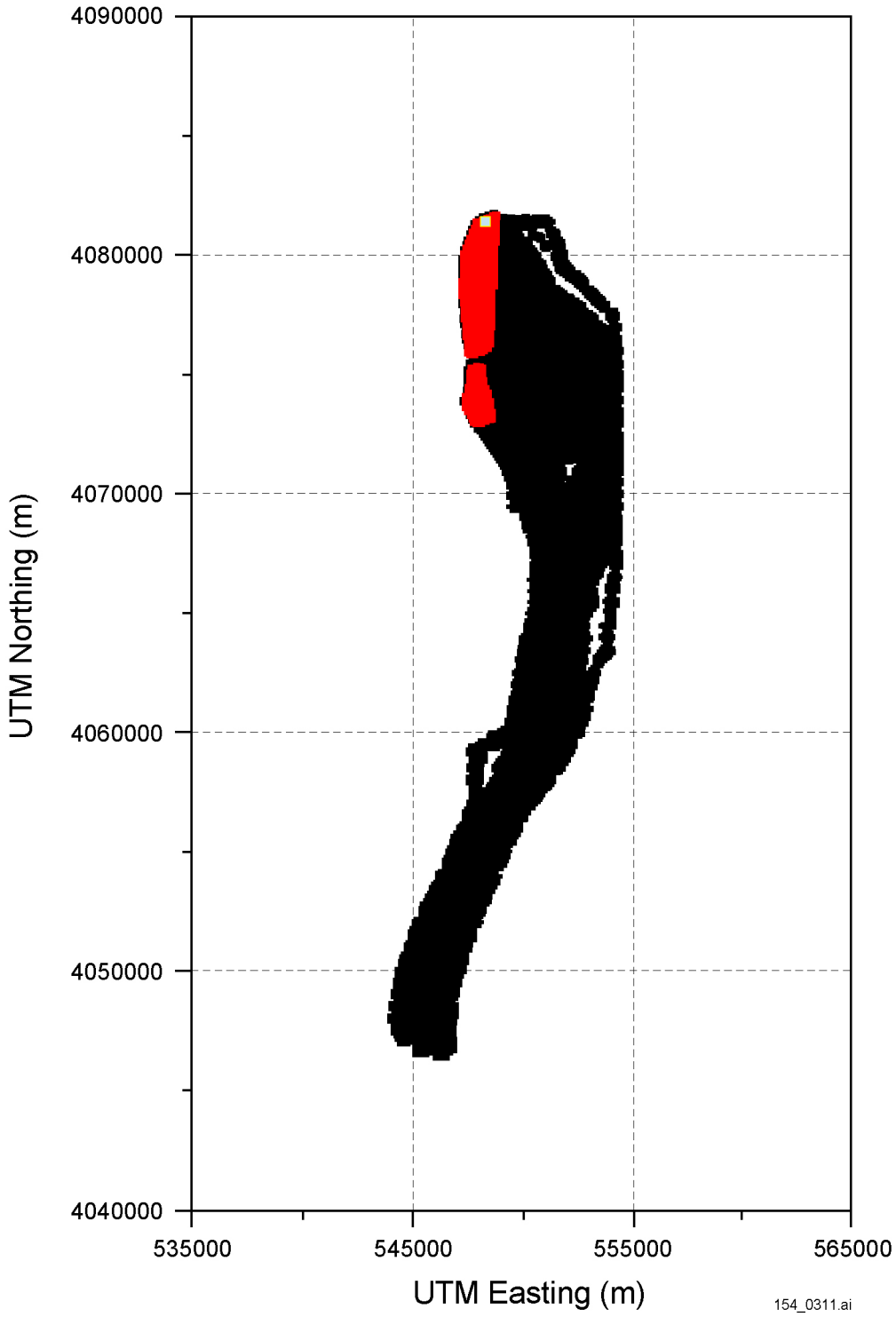

154_0311.ai

Source: Robinson 2001 [DIRS 154995], Filename "02_calib.sptra2.enlarged".

Figure 12.3.2.3-3b. Plan View of Particle Pathlines from the Potential Repository with Pathlines from an Increased Repository Footprint

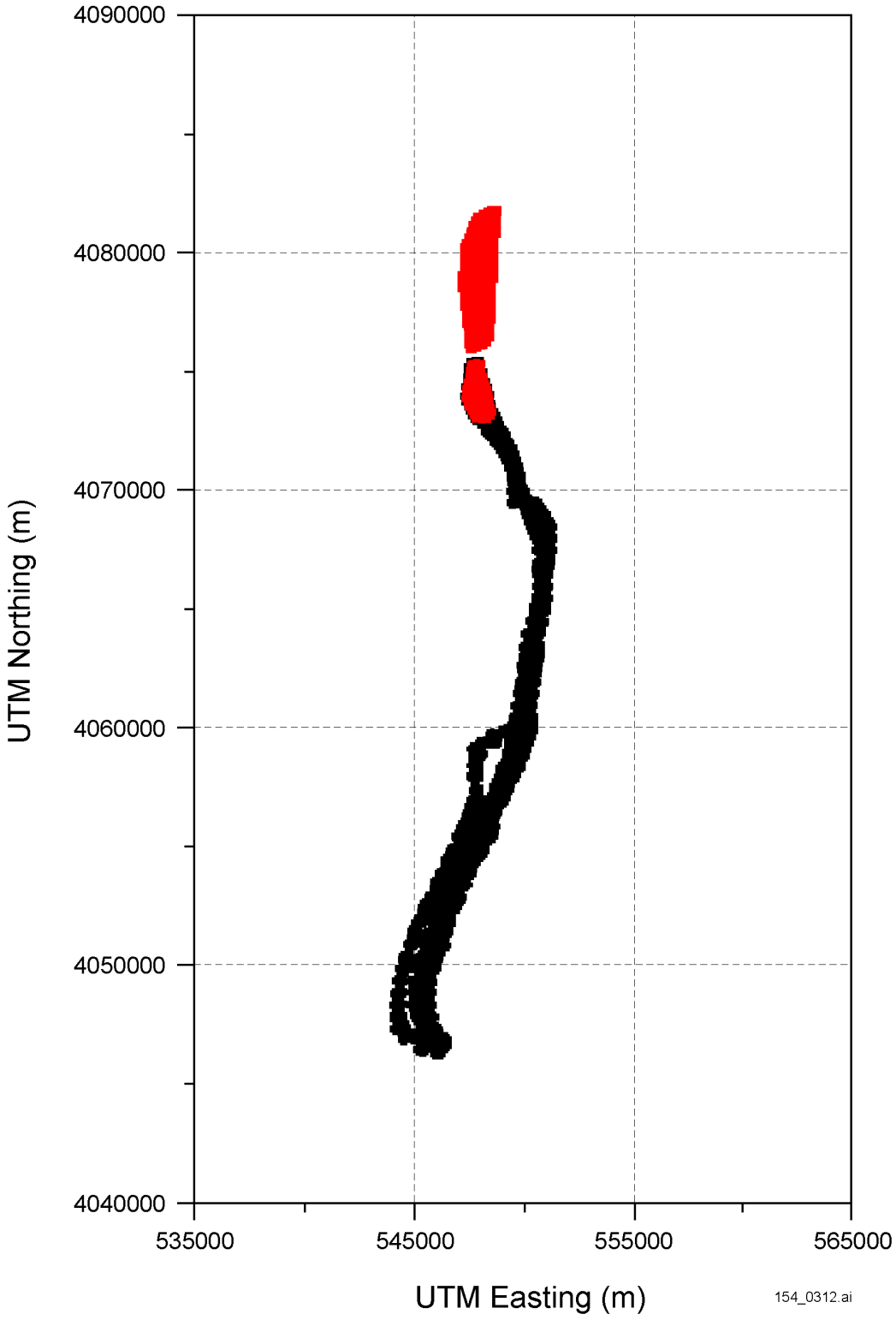

154_0312.ai

Source: Robinson 2001 [DIRS 154995], Filename "02_calib.sptr2".

Figure 12.3.2.3-3c. Plan View of Particle Pathlines from the Potential Repository with Pathlines from the Southern Lobe of an Increased Repository Footprint

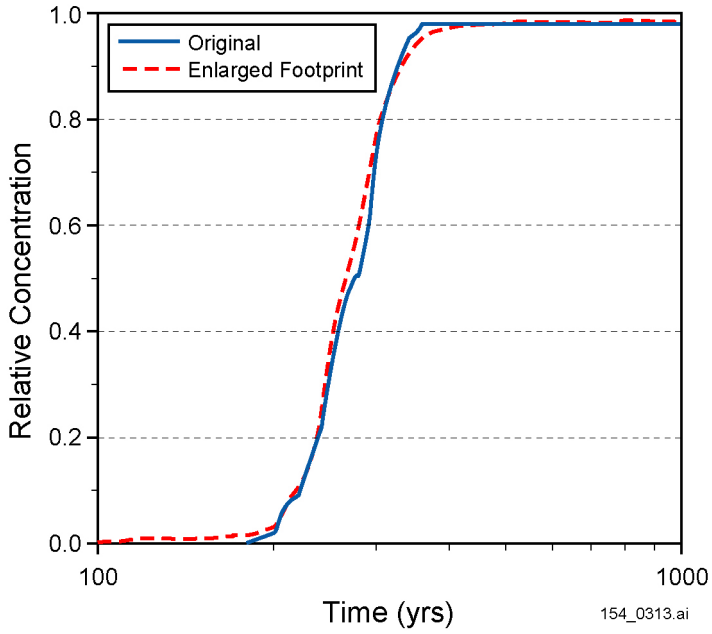

154_0313.ai

Source: Robinson 2001 [DIRS 154995], Filename “fig4.txt”.

NOTE: Data for the original potential repository footprint and the increased footprint associated with the flexible design are shown. The model was run using expected values for all parameters and no diffusion. The model used to generate the breakthrough curves is reasonably conservative for TSPA analyses, and furthermore, the resulting times only represent travel in the saturated zone portion of the system. Consequently, the results should not be used to evaluate the expected breakthrough of radionuclides or groundwater travel time at the point of compliance.

Figure 12.3.2.3-4. Breakthrough Curves to the 20-km Compliance Boundary for the Case of No Matrix Diffusion and Distributed Release Over the Entire Potential Repository Footprint

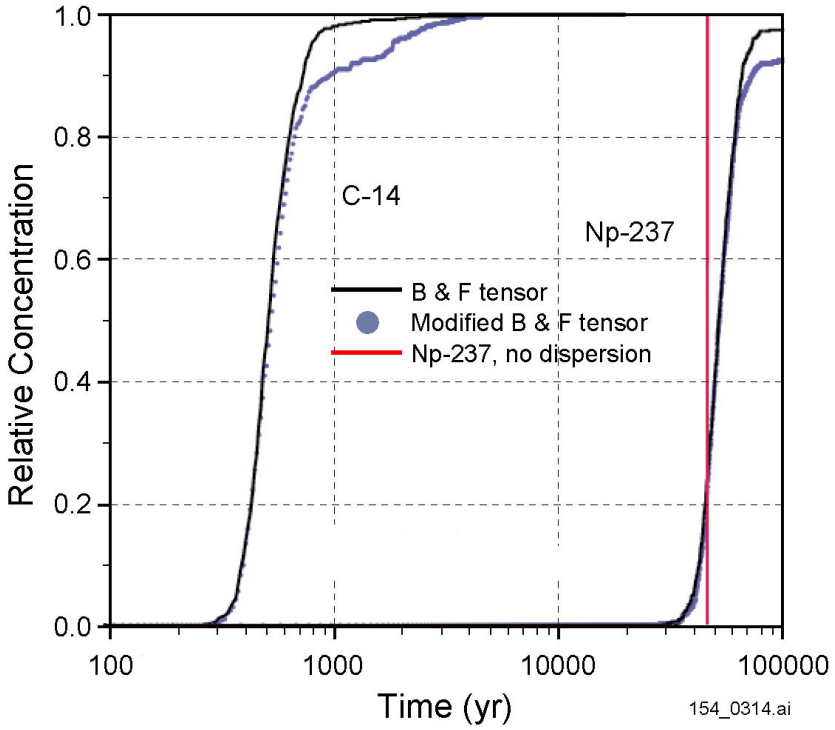

154_0314.ai

Source: Robinson 2001 [DIRS 154995], Filename “fig5c-14.txt” and “fig5np-237.txt”.

NOTE: Black curves use the Burnett and Frind (1987 [DIRS 130526]) tensor; blue points use the modified Burnett and Frind tensor. C-14 = carbon-14; Np-237 = neptunium-237. The model was run using expected values for all parameters and no matrix diffusion. The model used to generate the breakthrough curves is reasonably conservative for TSPA analyses, and furthermore, the resulting times only represent travel in the saturated zone portion of the system. Consequently, the results should not be used to evaluate the expected breakthrough of radionuclides or groundwater travel time at the point of compliance.

Figure 12.3.2.3-5. Breakthrough Curves at the 20-km Point of Compliance Using Two Dispersion Coefficient Tensors and Two Radionuclides

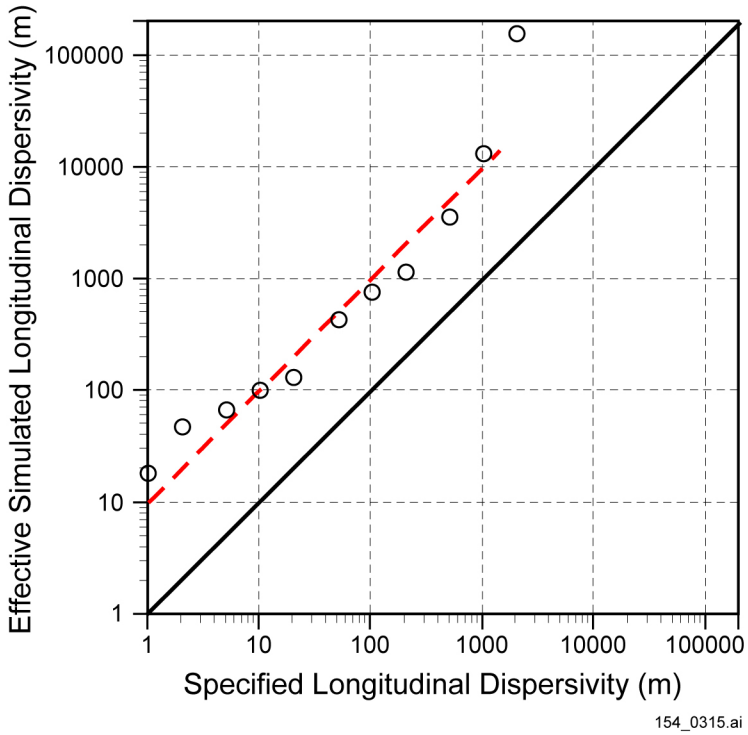

154_0315.ai

Source: Kuzio 2001 [DIRS 154912].

NOTE: Data from the site-scale saturated zone flow and transport model. Open circles are the results of the effective longitudinal dispersivity analysis. The bold line is the specified longitudinal dispersivity.

Figure 12.3.2.3-6. Effective Simulated Longitudinal Dispersivity Versus Specified Longitudinal Dispersivity

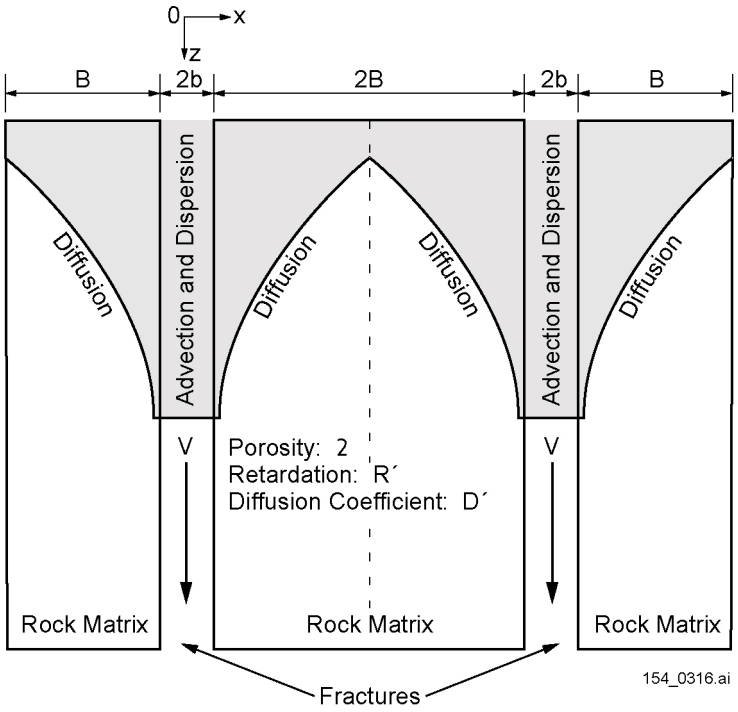

154_0316.ai

Figure 12.3.2.3-7. Schematic Diagram of the Matrix Diffusion Model

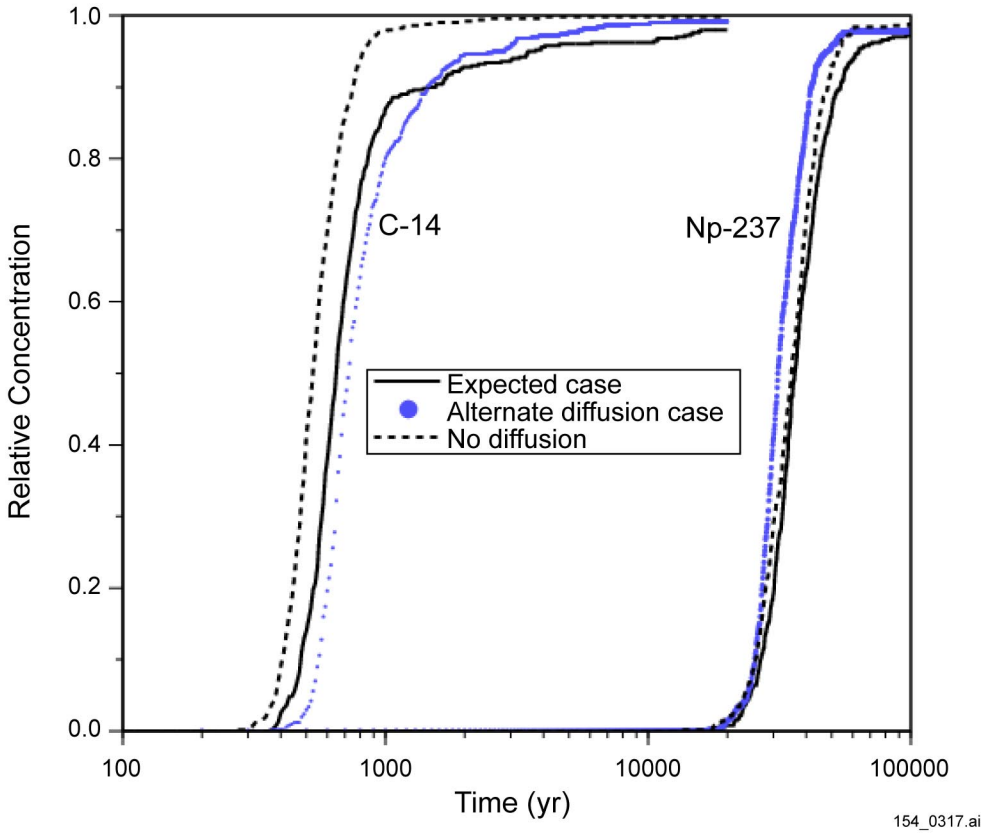

154_0317.ai

Source: Robinson 2001 [DIRS 154995], Filenames “fig8c-14.txt” and “fig8np-237.txt”.

NOTE: C-14 = carbon-14; Np-237 = neptunium-237. The model used to generate the breakthrough curves is reasonably conservative for TSPA analyses, and furthermore, the resulting times only represent travel in the saturated zone portion of the system. Consequently, the results should not be used to evaluate the expected breakthrough of radionuclides or groundwater travel time at the point of compliance.

Figure 12.3.2.3-8. Matrix Diffusion Models for Carbon-14 (Conservative) and Neptunium-237 (Weakly Sorbing) Radionuclides

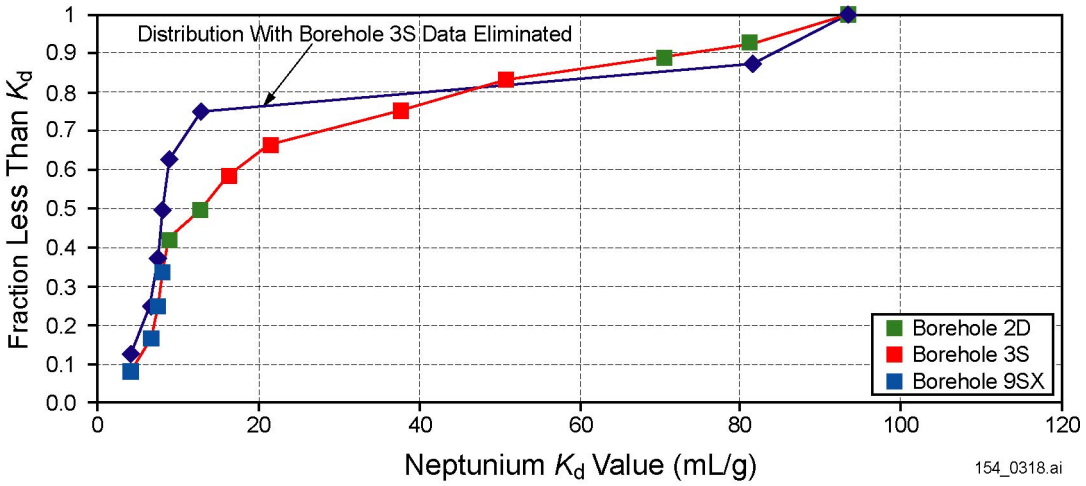

154_0318.ai

Source: Reimus 2001 [DIRS 154994], File "Neptunium Alluvium Sorption"; DTN: LA0003JC831341.001 [DIRS 147176].

NOTE: Alluvium samples for these sorption tests were obtained from NC-EWDP boreholes 2D, 3S, and 9SX. The red curve includes all data cited in the legend, and the blue curve includes all data cited in the legend except for the 3S data.

Figure 12.3.2.4-1. Neptunium Sorption Coefficients results from Batch Sorption Tests

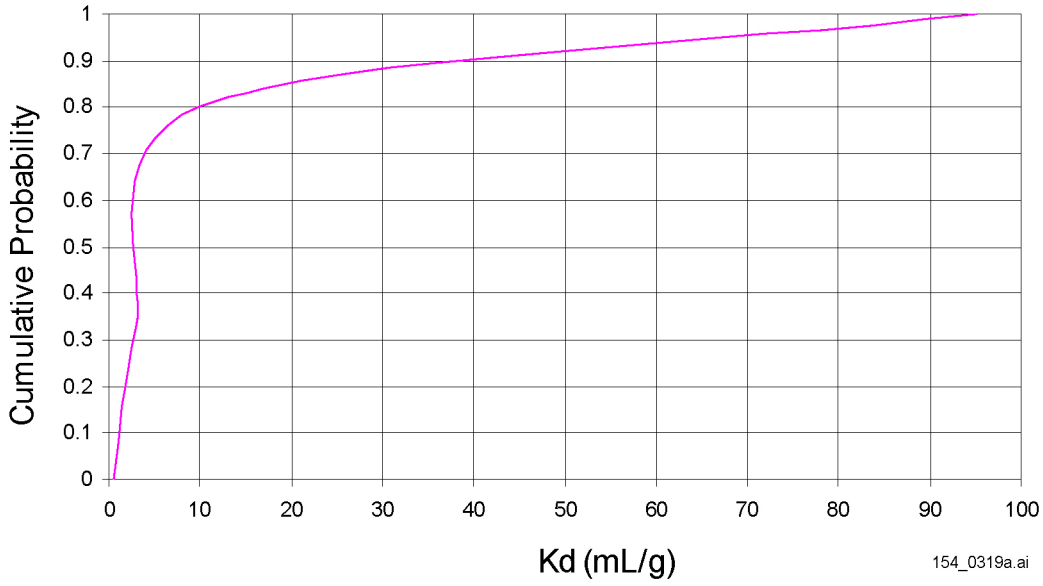

154_0319a.ai

Source: Kuzio 2001 [DIRS 154912], Filename “archive_sspa_v1_data/Np_cdf_uu”.

Figure 12.3.2.4-2. Cumulative Distribution Function for Neptunium Sorption Coefficients (K_ds) used for Unquantified Uncertainty Calculations

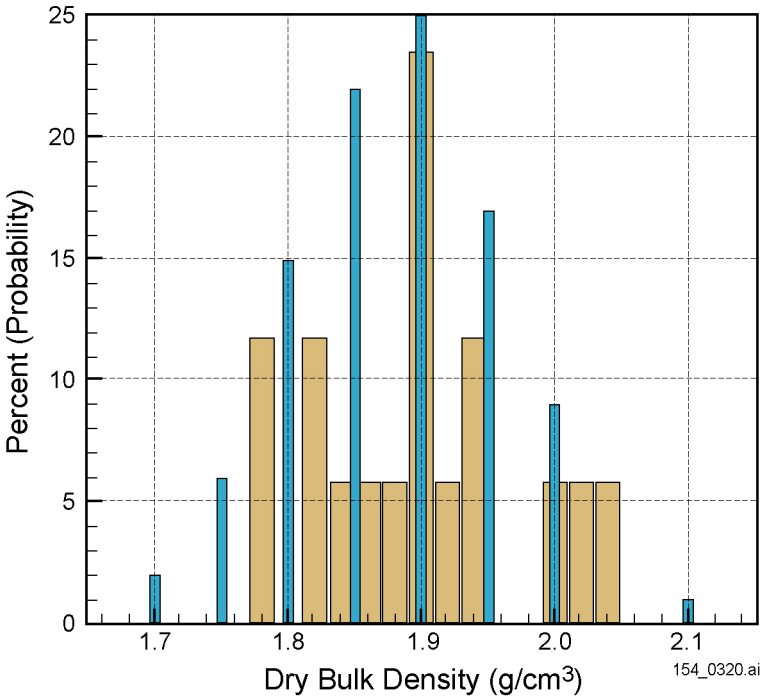

154_0320.ai

Source: Computed from saturated bulk densities presented by Black (2000 [DIRS 154704], p. 18).

NOTE: Thick bars represent measured data; thin bars represent data used in TSPA-SR supplemental analysis (McNeish 2001 [DIRS 155023]). The bars are located at the midpoint of the histogram interval.

Figure 12.3.2.4-3. Distribution of Simulated and Measured Dry Bulk Density for Alluvium

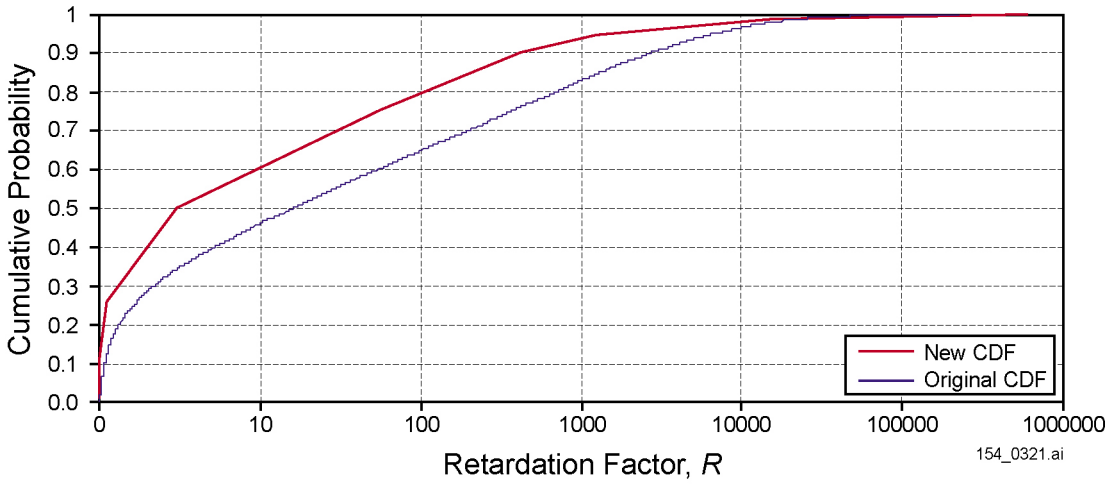

154_0321.ai

Source: Original CDF: CRWMS M&O 2000 [DIRS 129286], Figure 10, Curve B. New CDF: Kuzio 2001 [DIRS 155004], Filename "Grain_Size_Calcs_Submit", 5th Worksheet.

Figure 12.3.2.4-4. Original and new Cumulative Probability Density Functions for the Retardation Factor of Radionuclides Irreversibly-Sorbed to Colloids in the Alluvium.

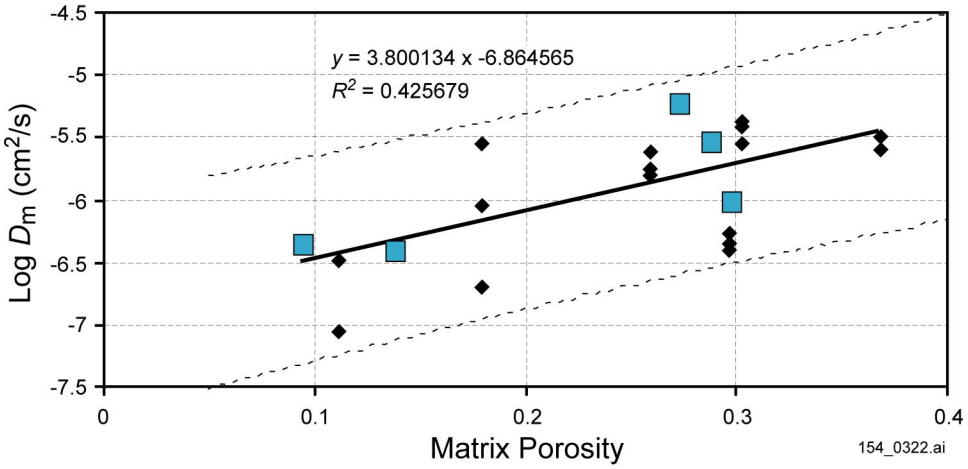

154_0322.ai

Source: Reimus 2001 [DIRS 154994], Filename "diffusion cell data for C-wells data"; C-wells data: DTN: LA9909PR831231.005 [DIRS 129624] (these data are non-Q because non-Q software was used to obtain diffusion coefficients from experimental data). Pahute Mesa data: Reimus et al. (1999 [DIRS 154689], p. 24, Table 2-2).

NOTE: D_m = matrix diffusion coefficient. Results of laboratory diffusion-cell experiments for bromide from C-wells cores (squares) and iodide from borehole ER-20-6 #1 on Pahute Mesa at the NTS (diamonds). Solid line is the best linear regression fit to all the data; dashed lines are 95 percent confidence intervals.

Figure 12.3.2.4-5. Matrix Diffusion Coefficients as a Function of Matrix Porosity

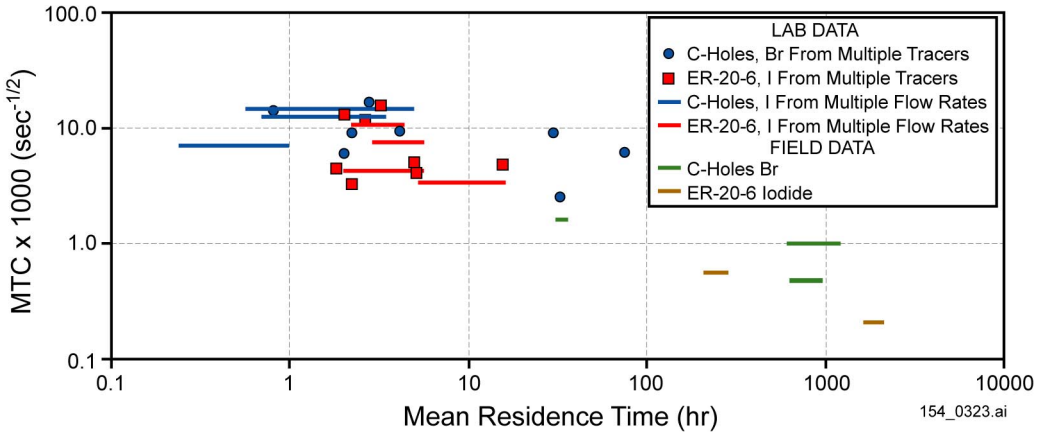

154_0323.ai

Source: Lab data for borehole ER-20-6 is from Reimus et al. 1999 [DIRS 154689], pp. 27 to 29, Tables 3-2 to 3-8; Reimus 2001 [DIRS 154994], Filename "Diffusion MTCs-Volcanics". Field data for borehole ER-20-6 is from Reimus and Haga 1999 [DIRS 154705], p.19. DTN: LA9909PR831231.003 [DIRS 140107]. DTN: LA9909PR831231.005 [DIRS 129624]. (C-wells data only).

NOTE: MTC = mass transfer coefficient. C-Holes refers to the C-wells Complex. Results from laboratory and field transport experiments in fractured volcanic rocks at the Nevada Test Site.

Figure 12.3.2.4-6. Matrix Diffusion Mass Transfer Coefficients as a Function of Mean Tracer Residence Time

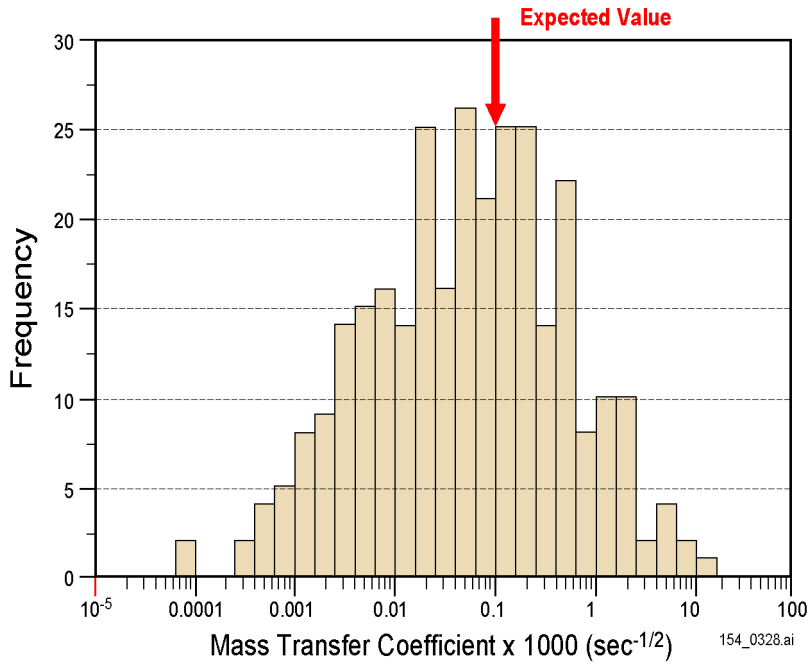

154_0328.ai

Source: Kuzio 2001 [DIRS 154912], Filename "archive_sspa_v1_data/mass_transfer_coeff/mass_transfer_coeff_300_fp_dc.xls".

NOTE: Data from 300 realizations of the site-scale SZ flow and transport model for TSPA.

Figure 12.3.2.4-7. Histogram of Mass Transfer Coefficient Values

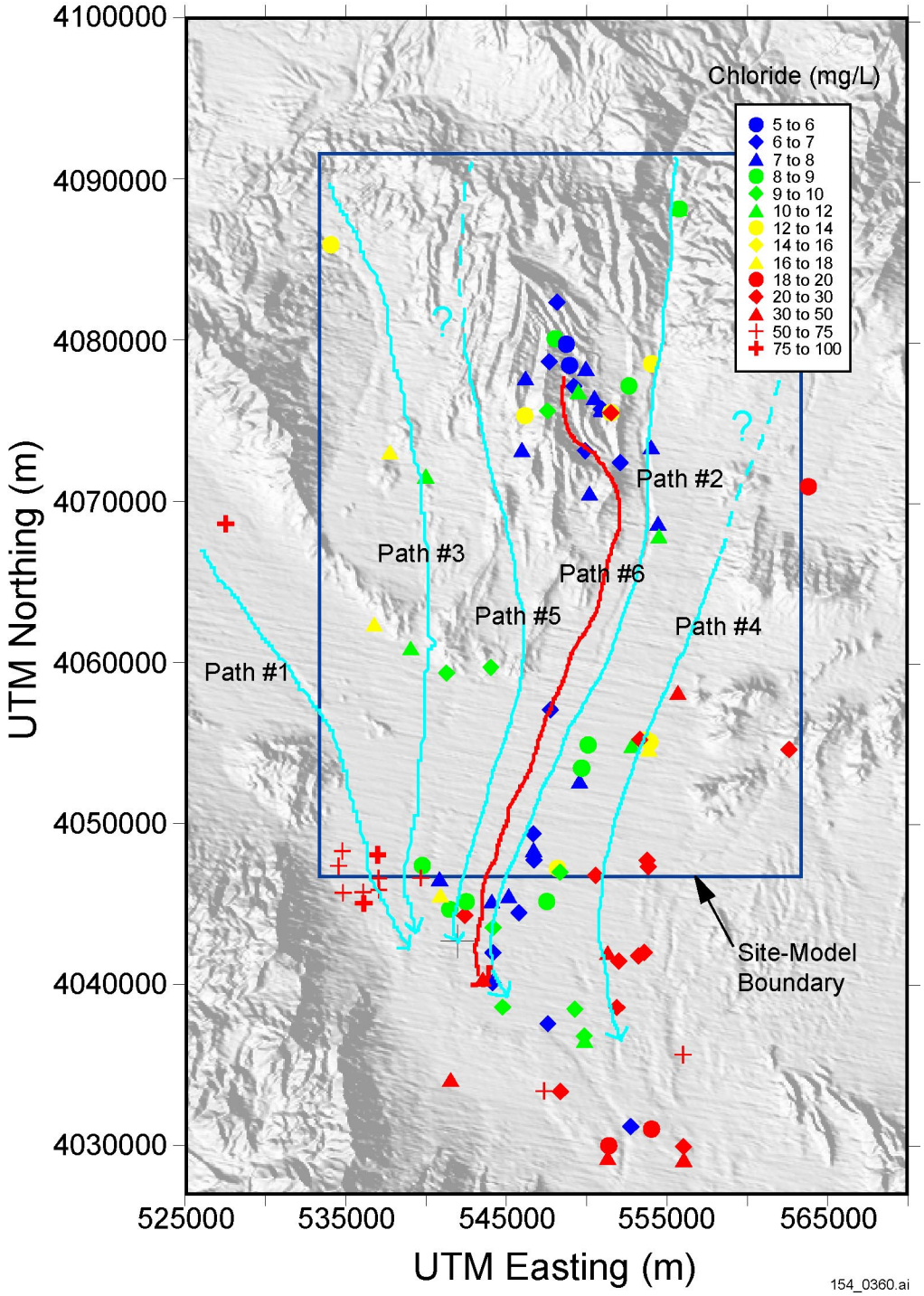

154_0360.ai

Source: Adapted from CRWMS M&O 2001 [DIRS 154795], Figure 17.

Figure 12.4-1. Groundwater Flow Paths Determined from Hydrochemical and Isotopic Data

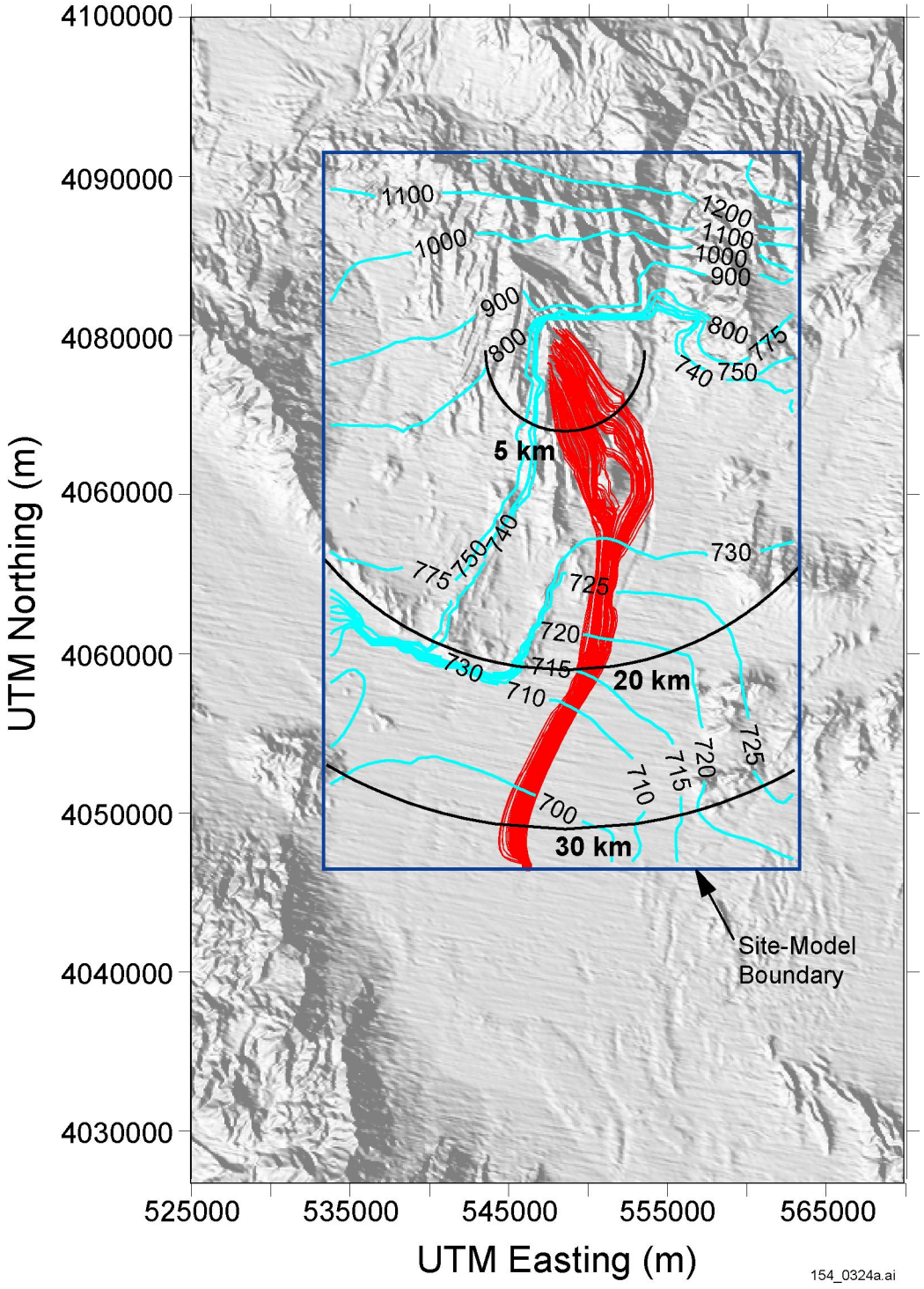

154_0324a.ai

Source: Adapted from CRWMS M&O 2000 [DIRS 139582], Figure 87.

NOTE: Blue lines are hydraulic head contours (m); red lines are the particle pathlines.

Figure 12.4-2. Groundwater Flow Paths Determined from Simulated Particle Pathlines

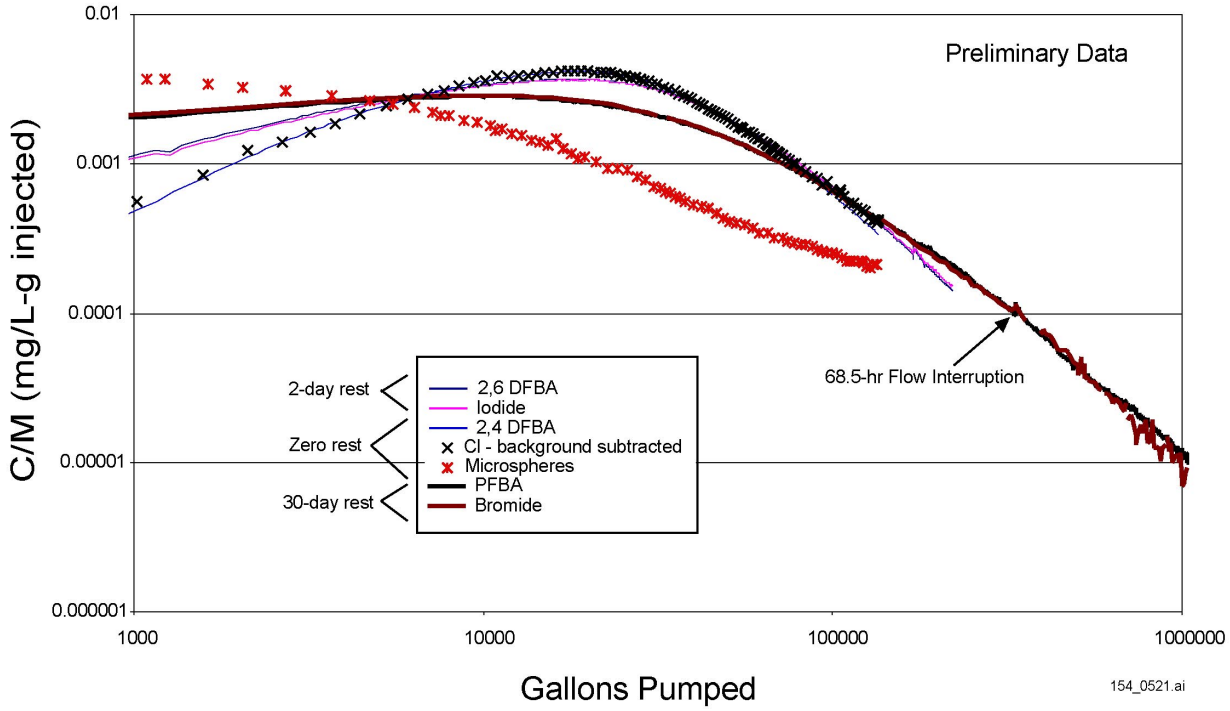

154_0521.ai

Source: Reimus 2001 [DIRS 155251], Filename "ATC Tracers – 1st Test", "ATC Tracers – 2nd Test", and "ATC Tracers – 3rd Test".

NOTE: The vertical axis is normalized concentration, which is concentration divided by injection mass. Tracers injected in earlier tests continued to be recovered in subsequent tests, but only the responses obtained prior to the injection of additional tracers are shown here.

Figure 12.4-3. Normalized Tracer Concentration Versus Gallons Pumped in Three Single-Well Tracer Tests Conducted in the Uppermost Screened Interval of Well NC-EWDP-19D1

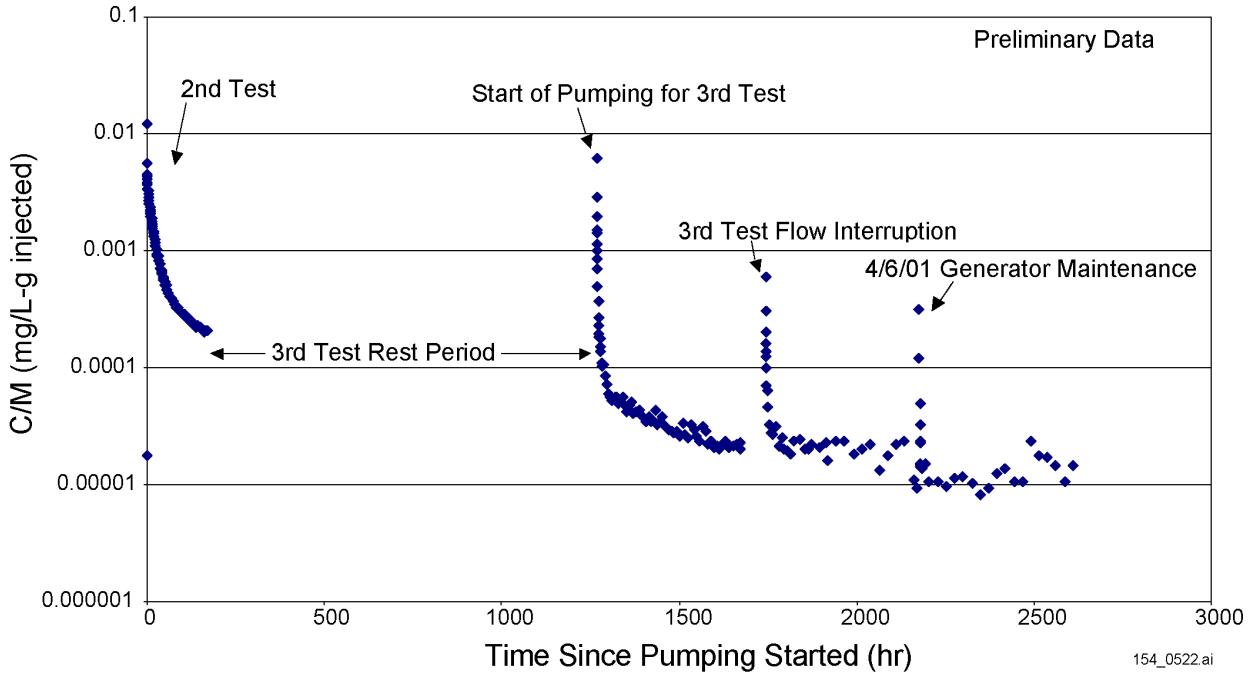

154_0522.ai

Source: Reimus 2001 [DIRS 155251], Filename "ATC Tracers – 2nd Test" and "ATC Tracers – 3rd Test".

NOTE: The vertical axis is normalized concentration, which is concentration divided by injection mass. Microspheres were injected only in the second test. However, the concentrations increased dramatically for a short time each time the pump was restarted after a shutdown.

Figure 12.4-4. Normalized Microsphere Concentrations Versus Time During the Second and Third Single-Well Tests in the Uppermost Screened Interval in Well NC-EWDP-19D1.

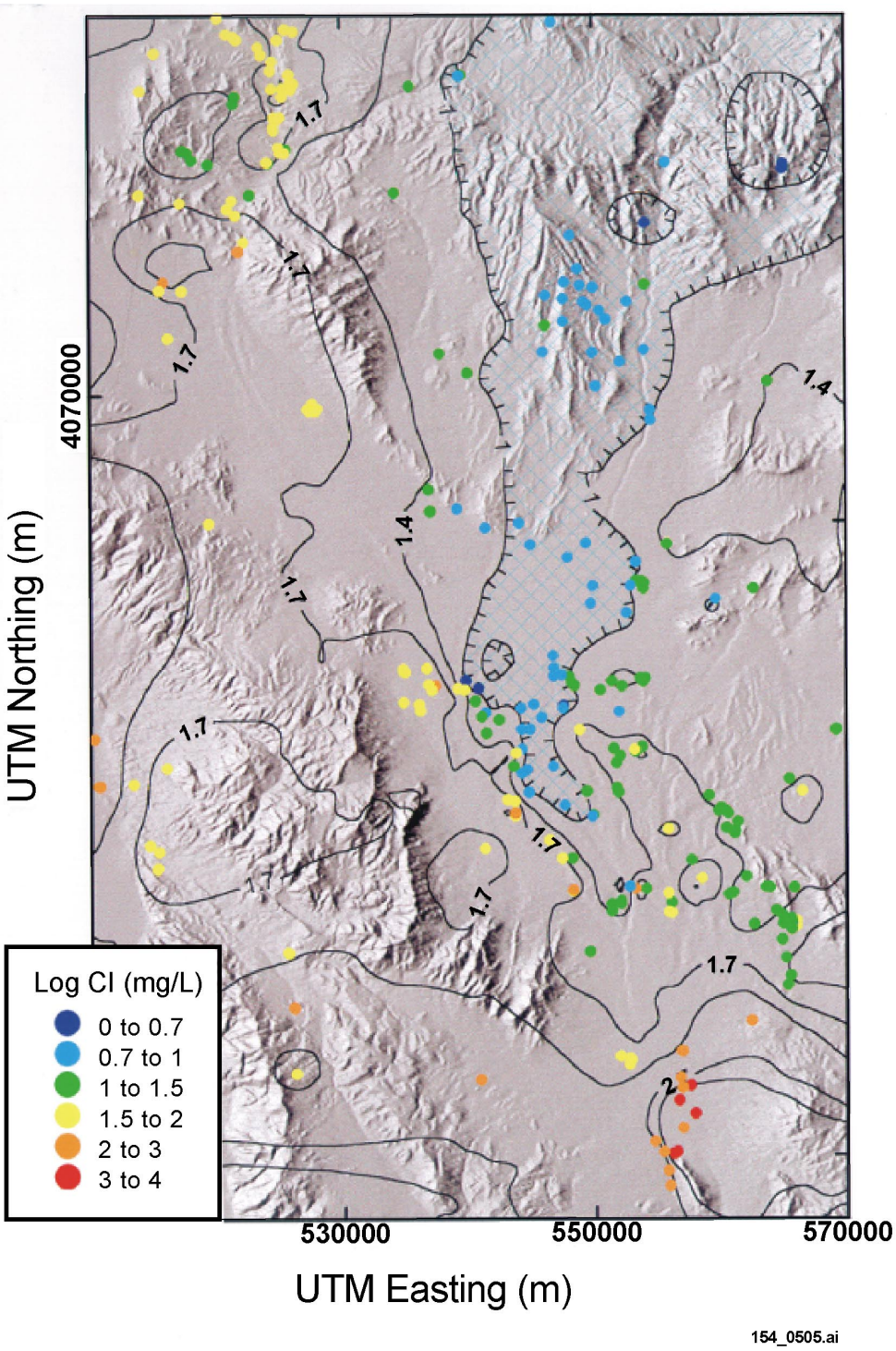

154_0505.ai

Source: Adapted from CRWMS M&O 2001 [DIRS 154795], Figure 5.

NOTE: Contours denote waters of similar composition.

Figure 12.4-5. Chloride Concentration in Groundwater

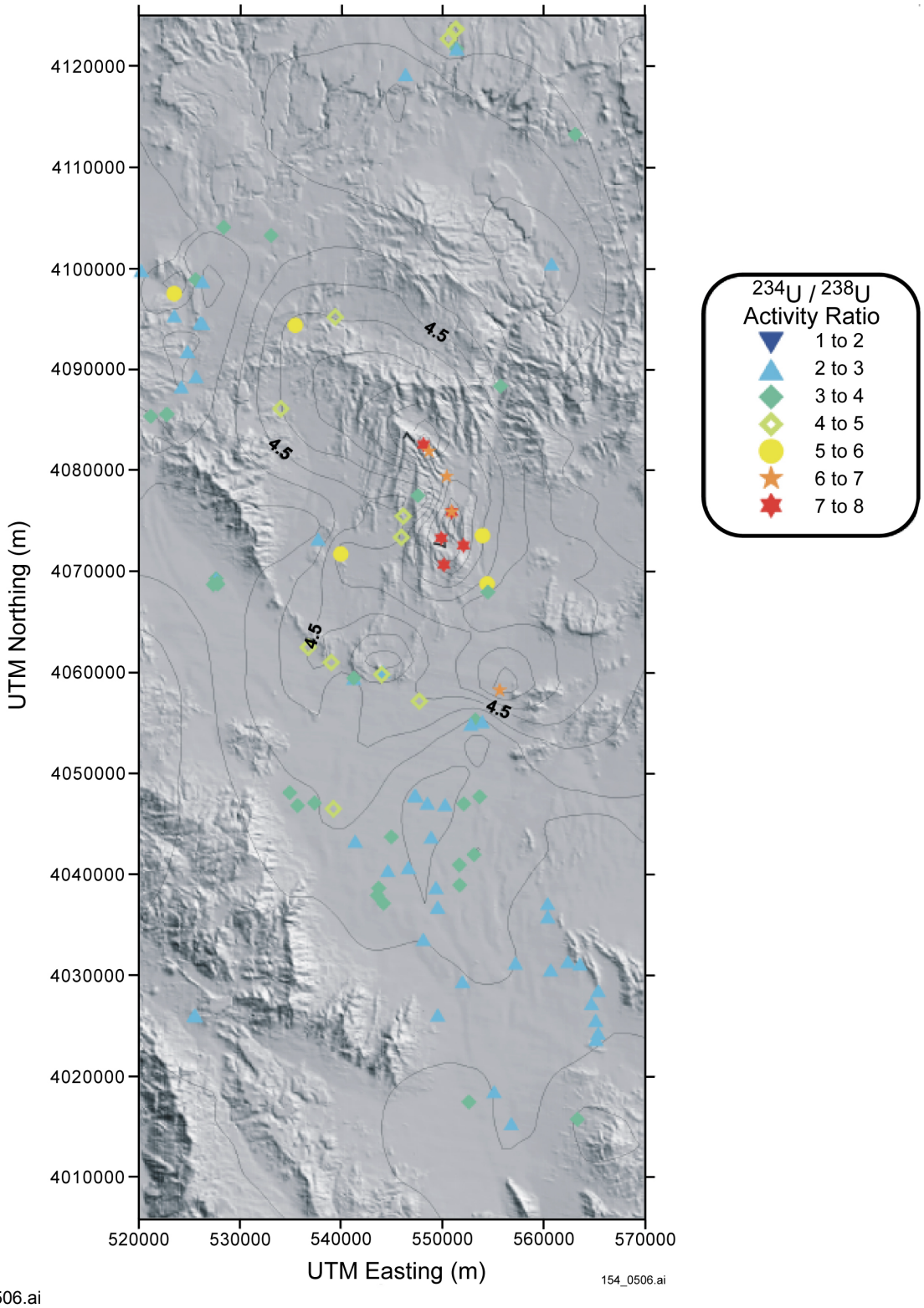

154_0506.ai

Source: Adapted from CRWMS M&O 2001 [DIRS 154795], Figure 18.

NOTE: Contours denote waters of similar composition.

Figure 12.4-6. Uranium Activity Ratios in Saturated Zone Waters

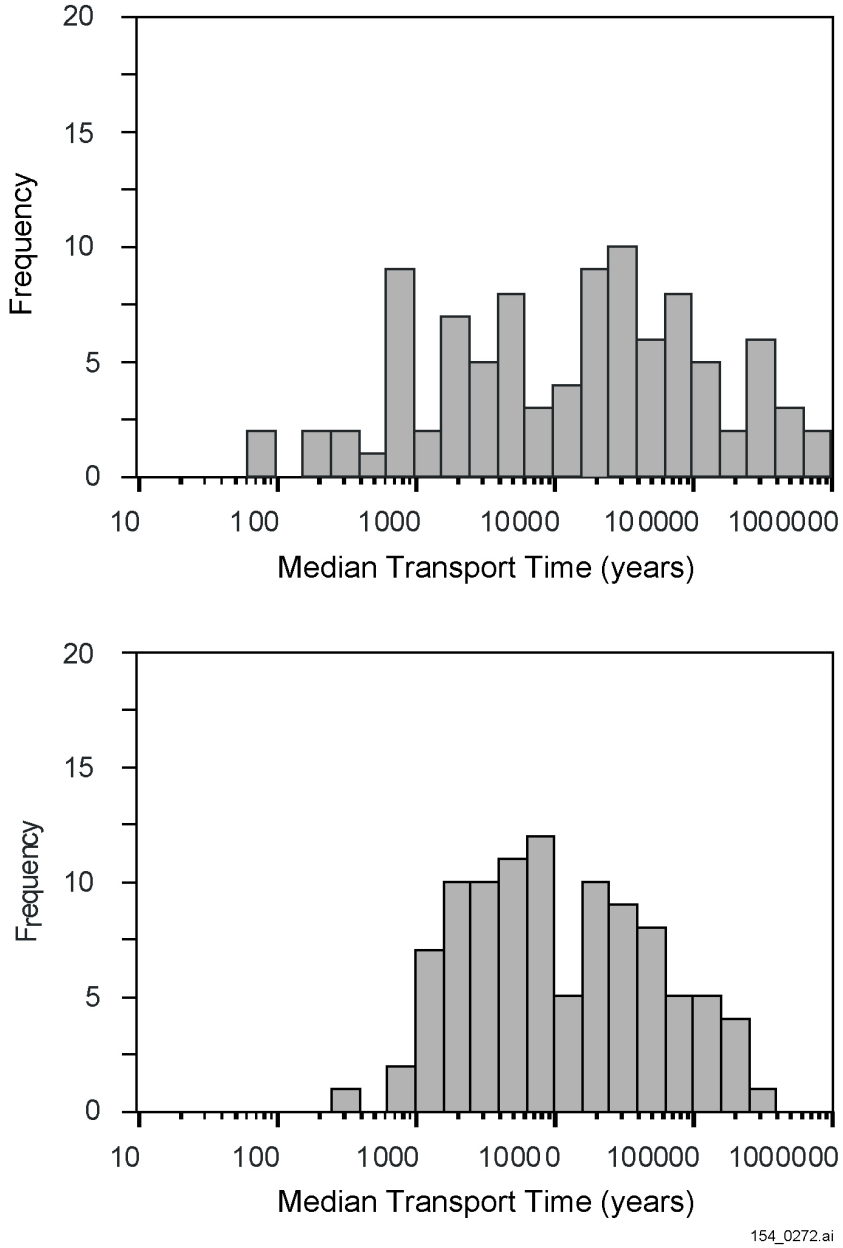

154_0272.ai

Source: Kuzio 2001 [DIRS 154912], Filenames “archive_sspa_v1_data/uu/btc_medians_Np_01.dat” and “archive_sspa_v1_data/nominal_case/btc_medians_Np_01.dat”.

NOTE: Results of the supplemental science and performance analysis (upper) (McNeish 2001 [DIRS 155023]) and unquantified uncertainty (lower) cases based on 100 realizations of the site-scale saturated zone flow and transport model. The model used to generate the breakthrough curves is reasonably conservative for TSPA analyses, and furthermore, the resulting times only represent travel in the saturated zone portion of the system. Consequently, the results should not be used to evaluate the expected breakthrough of radionuclides or groundwater travel time at the point of compliance.

Figure 12.5.1-1. Simulated Median Transport Times of Neptunium for the Supplemental Science and Performance Analysis and the Unquantified Uncertainty Cases

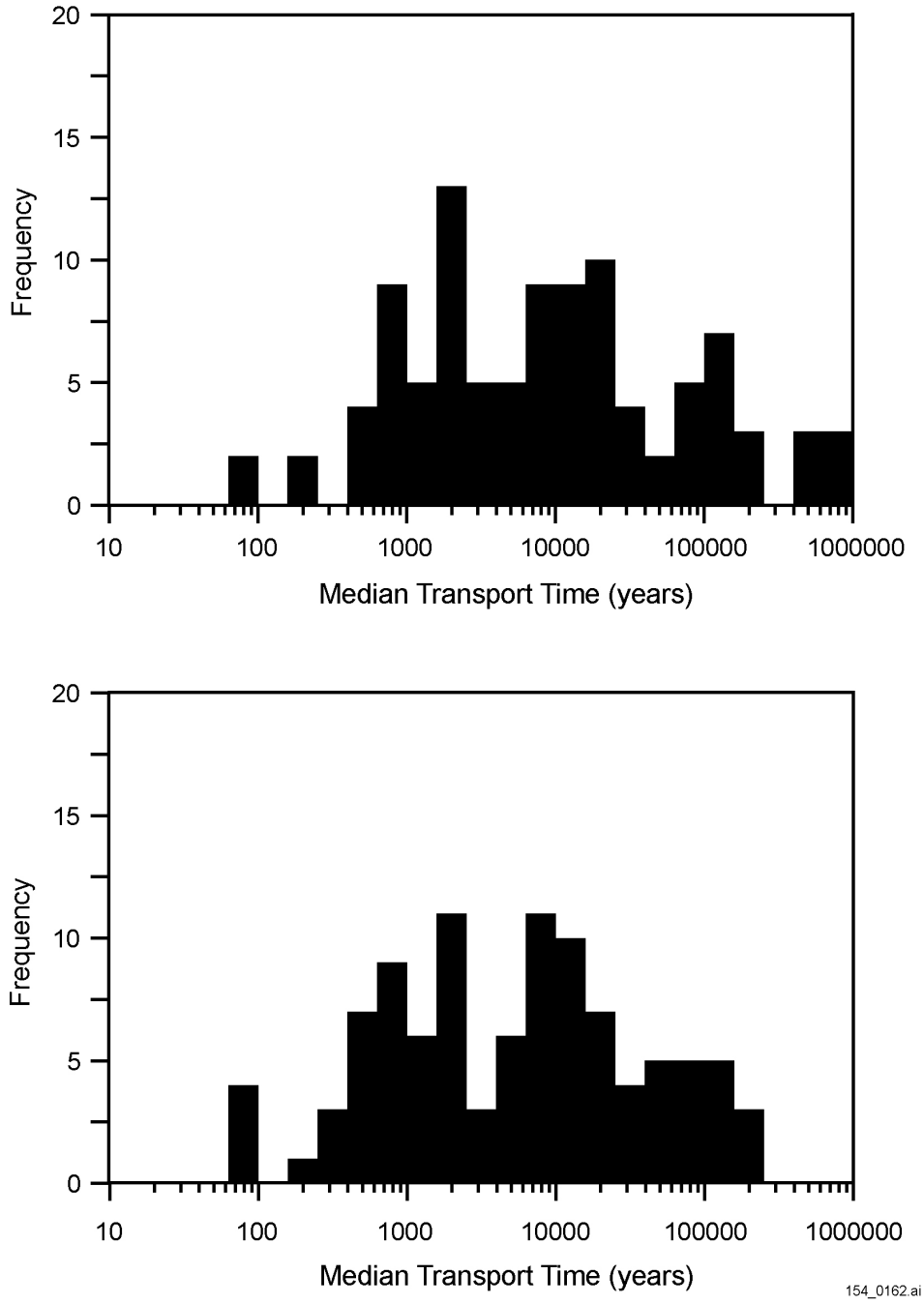

Source: Kuzio 2001 [DIRS 154912] Filename "archive_sspa_v1_data/no_diff/btc_medians_U_01.dat" and "archive_sspa_v1_data/nominal_case/btc_medians_U_01.dat".

NOTE: Histograms for 100 realizations of the supplemental science and performance analysis (upper) (McNeish 2001[DIRS 155023]) and no-matrix-diffusion (lower) cases from the site-scale saturated zone flow and transport model. The model used to generate the breakthrough curves is reasonably conservative for TSPA analyses, and further, the resulting times only represent travel in the saturated zone portion of the system. Consequently, the results should not be used to evaluate the expected breakthrough of radionuclides at the point of compliance.

Figure 12.5.2-1. Simulated Median Transport Times of Uranium for the Supplemental Science and Performance Analysis and the No-Matrix-Diffusion Cases

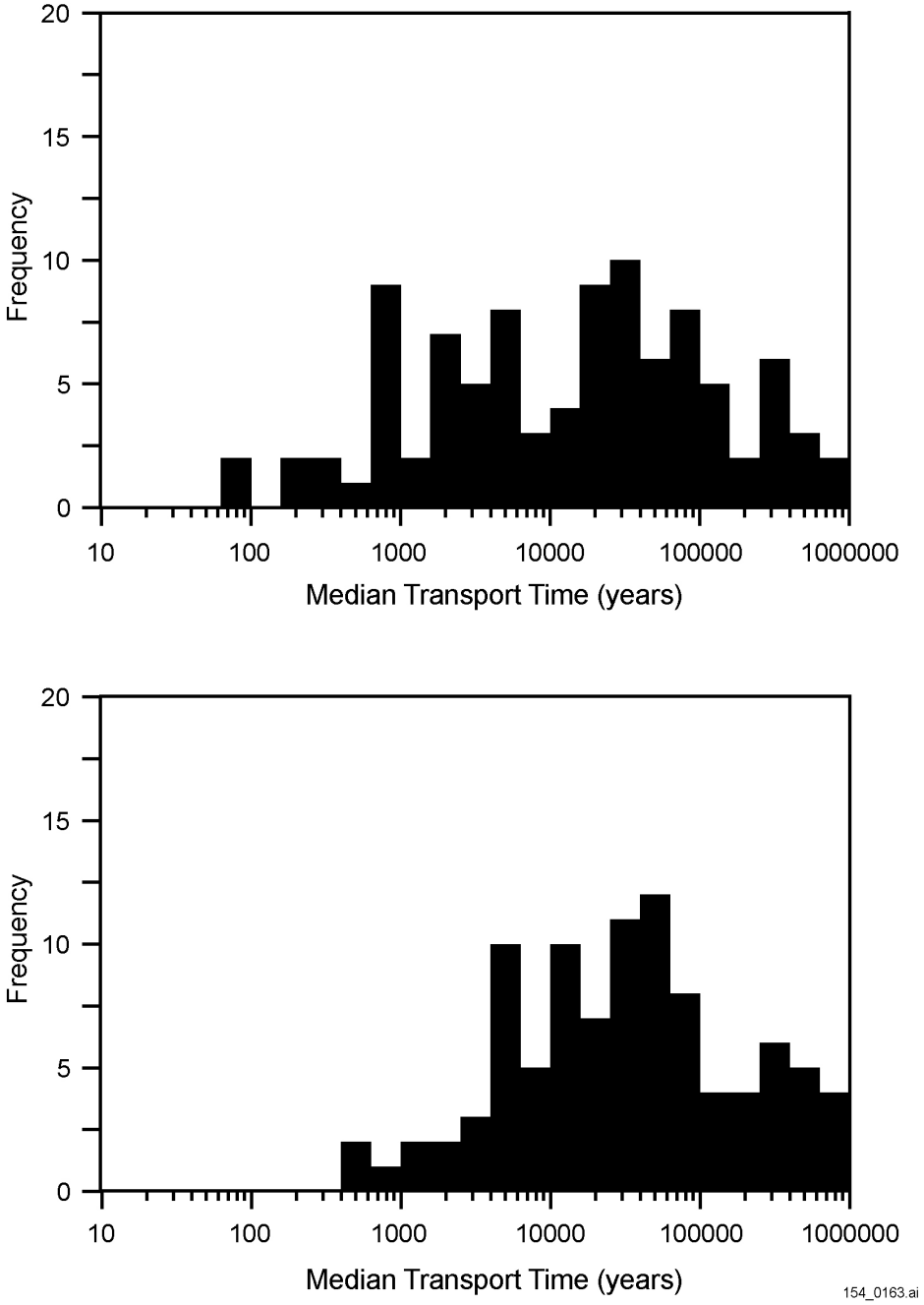

154_0163.ai

Source: Kuzio 2001 [DIRS 154912], Filename "archive_sspa_v1_data/high_diff/btc_medians_Np_01.dat" and "archive_sspa_v1_data/nominal_case/btc_medians_Np_01.data".

NOTE: Histograms for 100 realizations of the supplemental science and performance analysis (upper) (McNeish 2001 [DIRS 155023]) and enhanced-matrix-diffusion (lower) cases from the site-scale saturated zone flow and transport model. The model used to generate the breakthrough curves is reasonably conservative for TSPA analyses, and further, the resulting times only represent travel in the saturated zone portion of the system. Consequently, the results should not be used to evaluate the expected breakthrough of radionuclides at the point of compliance.

Figure 12.5.2-2. Simulated Median Transport Times of Neptunium for the Supplemental Science and Performance Analysis and Enhanced Matrix Diffusion Cases

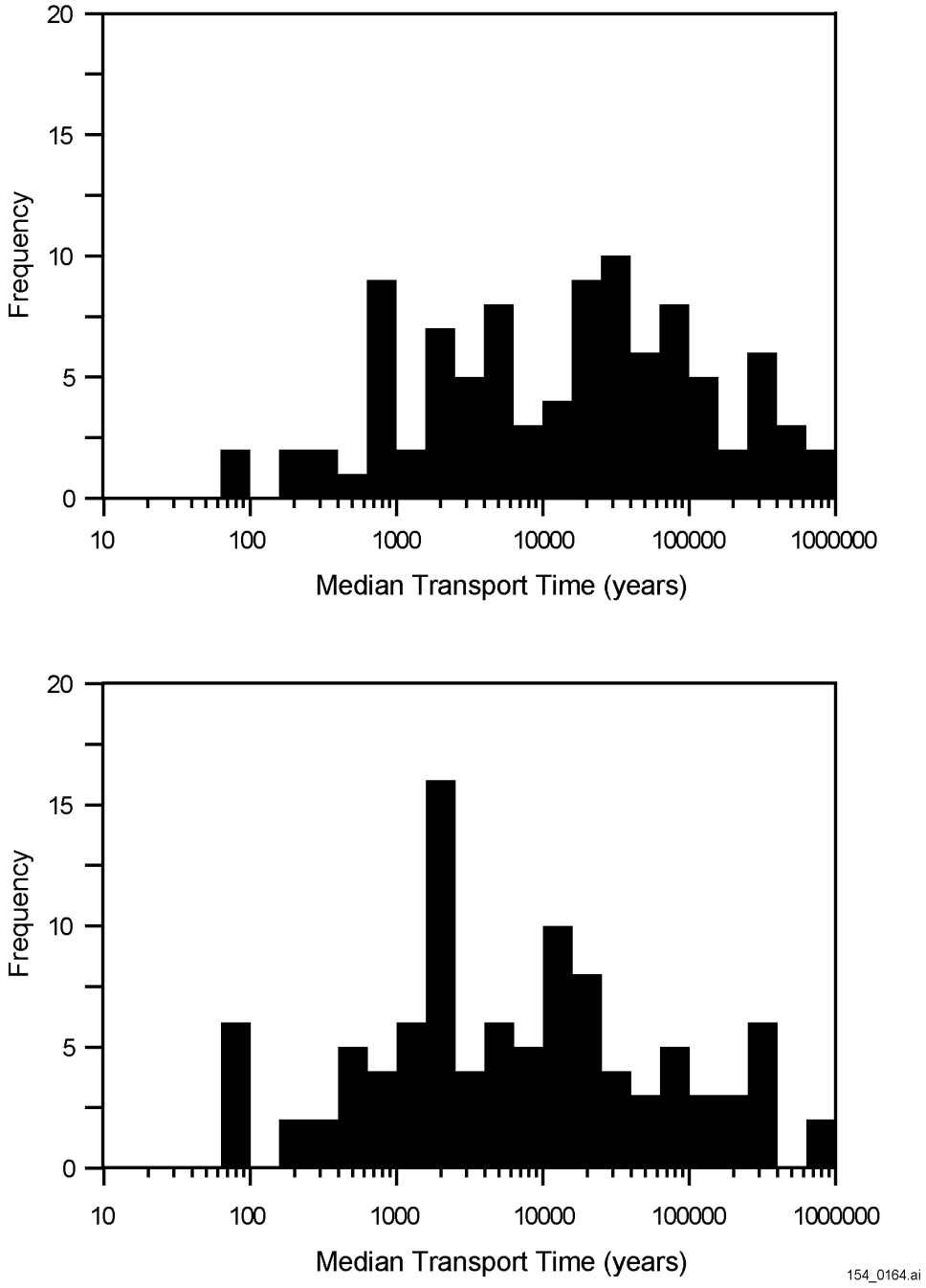

154_0164.ai

Source: Kuzio 2001 [DIRS 154912] Filename "archive_sspa_v1_data/no_alluv/btc_medians_Np_01.dat" and "archive_sspa_v1_data/nominal_case/btc_medians_Np_01.dat".

NOTE: Histograms for 100 realizations of the supplemental science and performance analysis (upper) (McNeish 2001 [DIRS 155023]) and minimum-alluvium (lower) cases from the site-scale saturated zone flow and transport model. The model used to generate the breakthrough curves is reasonably conservative for TSPA analyses, and further, the resulting times only represent travel in the saturated zone portion of the system. Consequently, the results should not be used to evaluate the expected breakthrough of radionuclides at the point of compliance.

Figure 12.5.2-3. Simulated Median Transport Times of Neptunium for the Supplemental Science and Performance Analysis and the Minimum Alluvium Cases

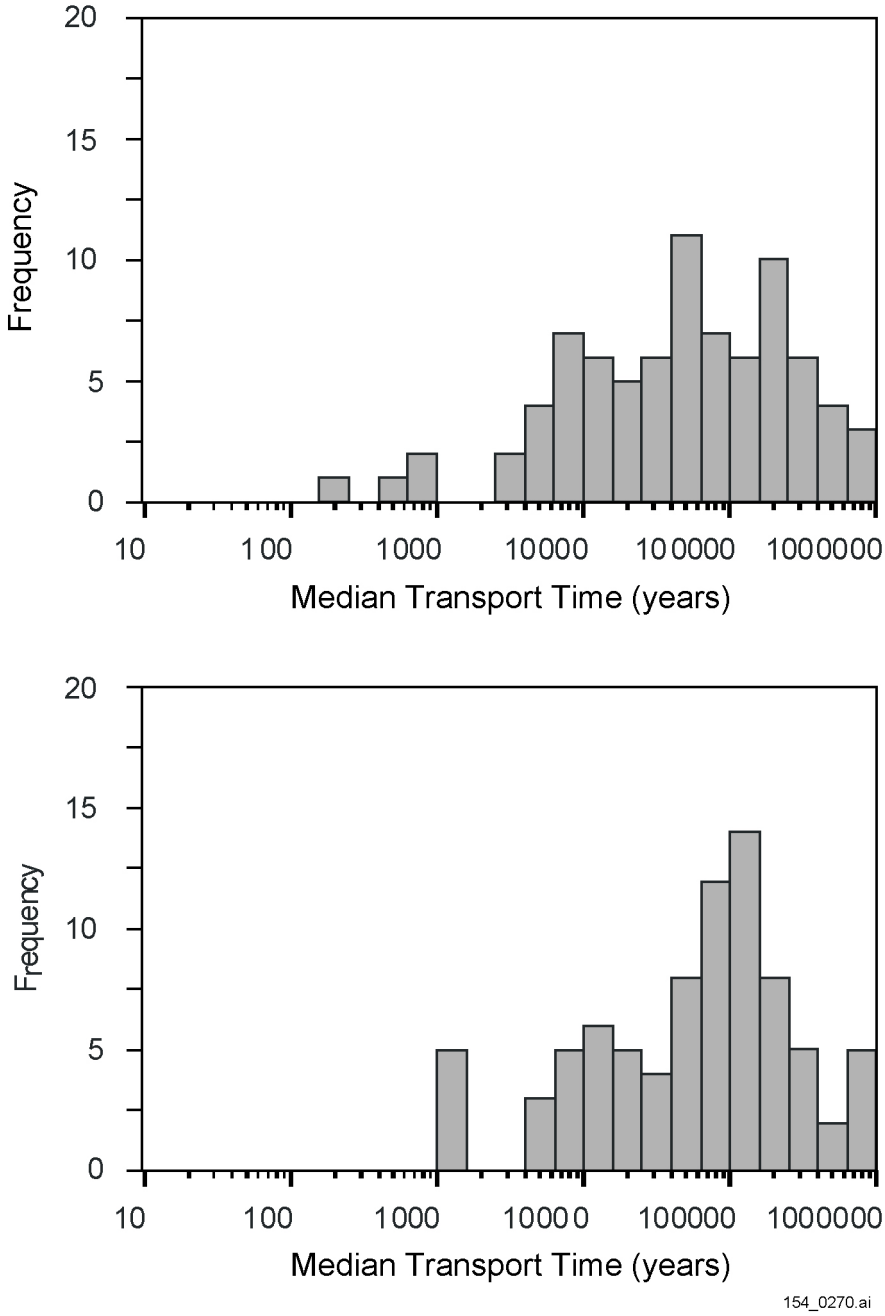

154_0270.ai

Source: Kuzio 2001 [DIRS 154912] Filename "archive_sspa_v1_data/alt-colloids/btc_medians_kc_01.dat" and archive_sspa_v1_data/nominal_case/btc_medians_kc_01.dat".

NOTE: Histograms for 100 realizations of the supplemental science and performance analysis (upper) (McNeish 2001 [DIRS 155023]) and increased uncertainty in colloid-facilitated transport (lower) cases from the site-scale saturated zone flow and transport model. The model used to generate the breakthrough curves is reasonably conservative for TSPA analyses, and further, the resulting times only represent travel in the saturated zone portion of the system. Consequently, the results should not be used to evaluate the expected breakthrough of radionuclides at the point of compliance.

Figure 12.5.2-4. Simulated Median Transport Times of Plutonium Reversibly Sorbed onto Colloids (K_c Model)

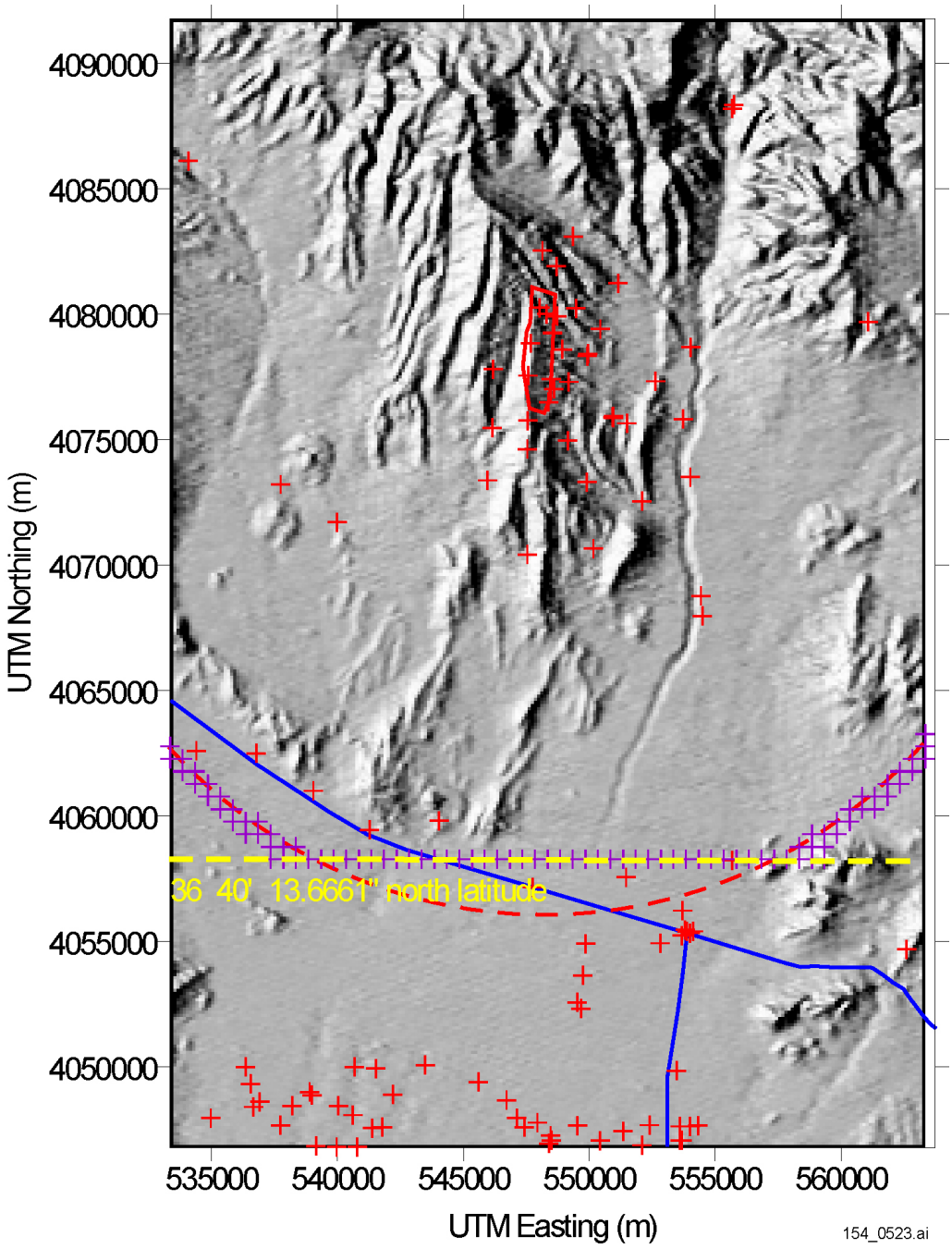

154_0523.ai

Source: Kuzio 2001 [DIRS 155244], Appendix 1.

NOTE: The yellow dashed line represents the southernmost boundary between the controlled area and accessible environment (36° 40' 13.6661" North latitude as per EPA 40 CFR 197.12 (66 FR 32074 [DIRS 155216])). The red dashed line represents the 20-km fence used in TSPA-SR to evaluate compliance with proposed EPA and NRC regulations. The purple crosses represent the intersection of the new southernmost boundary with the 20-km fence used in TSPA-SR evaluations. The red crosses are well locations, and the blue lines represent Highway 95 and Highway 373.

Figure 12.5.3-1 Southernmost Boundary of the Controlled Area and the Accessible Environment

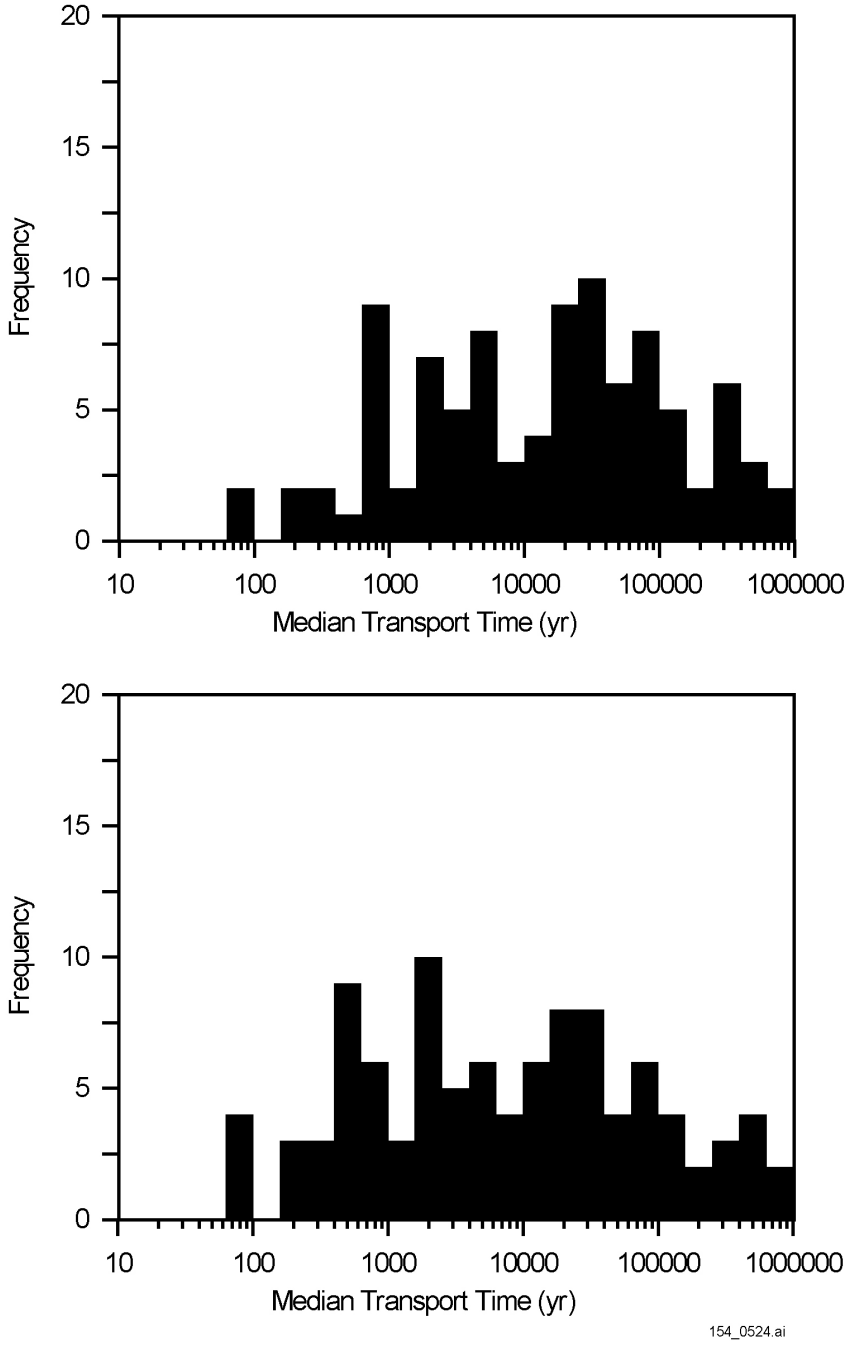

154_0524.ai

Source: Kuzio 2001 [DIRS 155244], Appendix 2.

Note: Upper panel is histogram for breakthrough 20 km from the potential repository, and lower panel is histogram for 18 km. The model used to generate the breakthrough curves is reasonably conservative for TSPA analyses, and furthermore, the resulting times only represent travel in the saturated zone portion of the system. Consequently, the results should not be used to evaluate the expected breakthrough of radionuclides or groundwater travel time at the point of compliance.

Figure 12.5.3-2. Frequency of Breakthrough for Simulated Median Transport Times of Neptunium-237

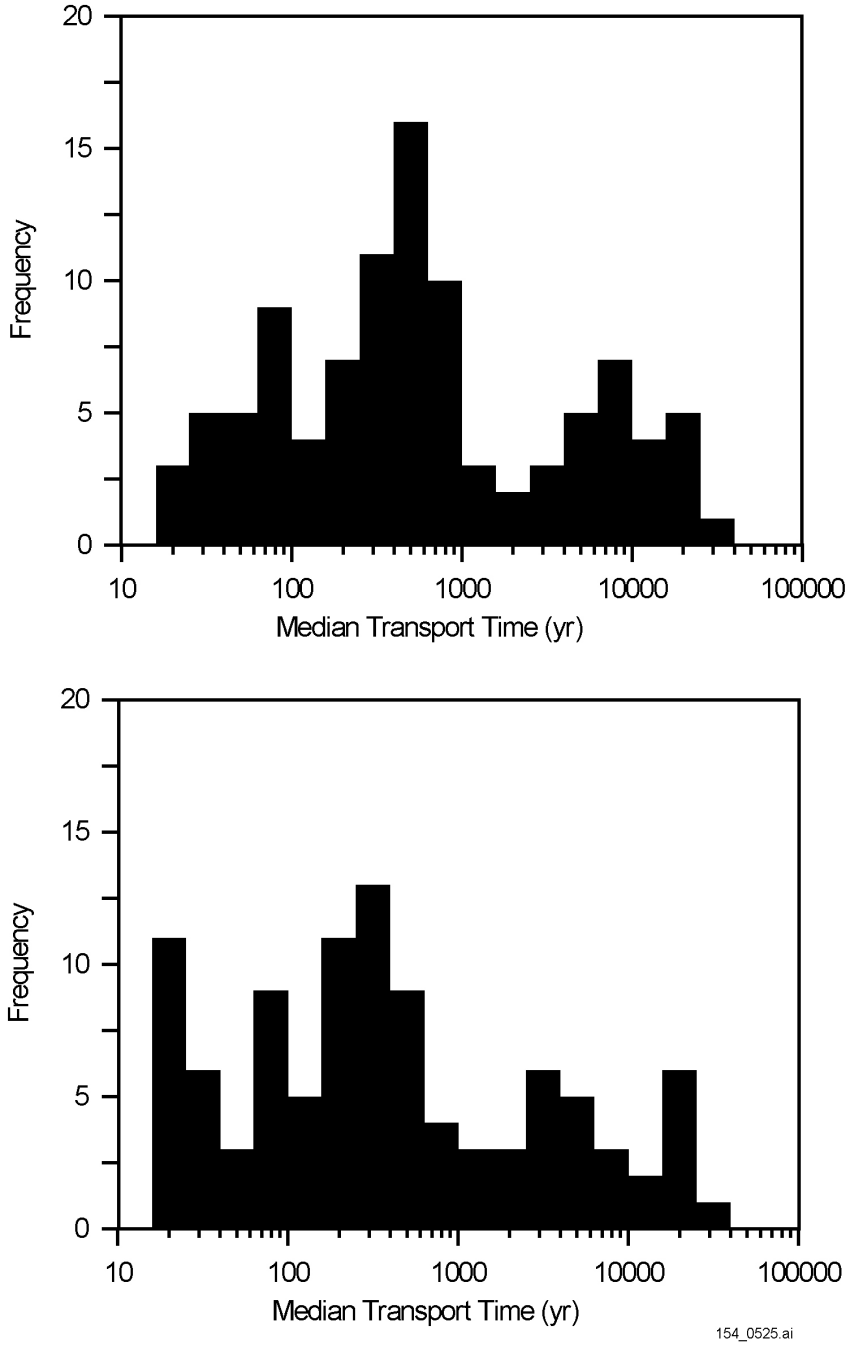

154_0525.ai

Source: Kuzio 2001 [DIRS 155244], Appendix 3.

Note: Upper panel is histogram for breakthrough 20 km from the potential repository, and lower panel is histogram for 18 km. The model used to generate the breakthrough curves is reasonably conservative for TSPA analyses, and furthermore, the resulting times only represent travel in the saturated zone portion of the system. Consequently, the results should not be used to evaluate the expected breakthrough of radionuclides or groundwater travel time at the point of compliance.

Figure 12.5.3-3. Frequency of Breakthrough for Simulated Median Transport Times of Carbon-14

INTENTIONALLY LEFT BLANK

13 Biosphere

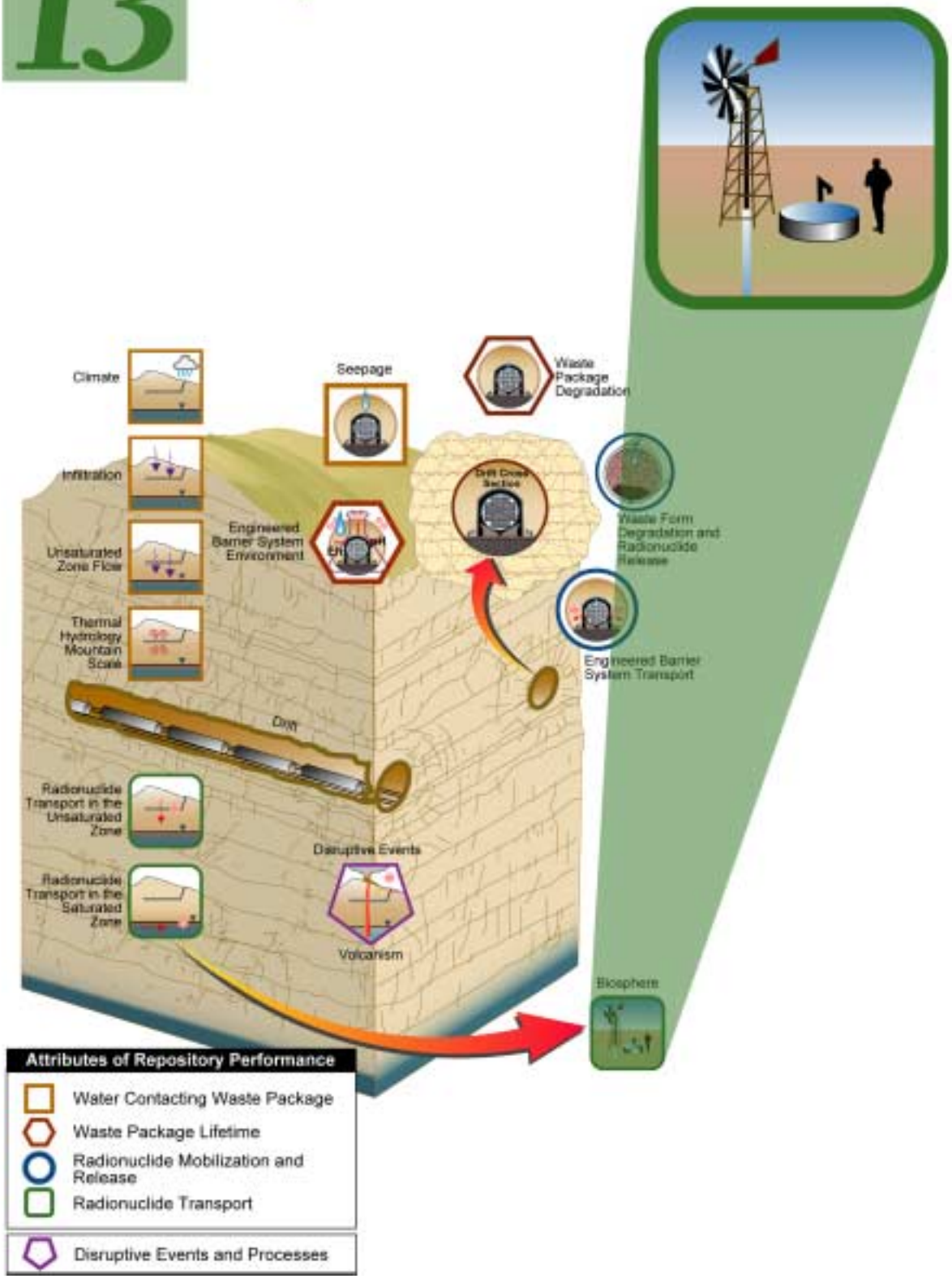

13. BIOSPHERE

13.1 INTRODUCTION AND CONCEPTUAL BASIS

The biosphere is comprised of those parts of the crust of the earth, the waters, and the atmosphere that support life. As opposed to this understanding of the biosphere as a global feature, the Yucca Mountain reference biosphere is limited in spatial extent, that at a minimum should include all biosphere-related features, events, and processes (FEPs) applicable to the Yucca Mountain region. The biosphere conceptual model applies to the Yucca Mountain reference biosphere. If radionuclides from the potential repository find their way to the reference biosphere, there is a possibility that humans, as well as other living entities, will be exposed to radiation in addition to the natural radiation background. The biosphere analyses provide the means of evaluating radiation exposure to humans from radioactive material that might be released to the limited Yucca Mountain biosphere. The biosphere model includes both the characteristics of the receptor of interest (such as lifestyles, including dietary and activity habits) and the characteristics of the environment around these potentially exposed people that are important to assessing their radiation exposure.

The reference biosphere is a component of the repository system. Because of the location of the receptor (proposed 10 CFR 63.115(b) [64 FR 8640 [DIRS 101680]]), the reference biosphere is sufficiently distant from the engineered barriers component of the potential repository that there are no direct interactions between these two system components. Thus, the thermal operating conditions within the repository have no effect on the biosphere model or the dose prediction capability. This section, therefore, addresses new data and previously unquantified uncertainties that apply irrespective of the thermal design of the potential repository.

The starting point for developing a biosphere model was to define the reference biosphere. Once the reference biosphere was defined, the subsequent step in developing a biosphere model was to identify the appropriate routes for introducing the radionuclides into the biosphere. Two potential mechanisms for radionuclide release into the biosphere were identified (CRWMS M&O 2000 [DIRS 153246], pp. xiv to xv and Figures ES-8 and ES-9). The first arises from pumping of contaminated groundwater to support the needs of a hypothetical farming community at a specified location (proposed 10 CFR 63.115 [64 FR 8640 [DIRS 101680]]). This release is characteristic of the nominal, human intrusion, and igneous intrusion groundwater transport scenarios. The second release mechanism is through the action of a volcanic eruption that entrains and disperses the radionuclides in the waste with the ensuing ash fall. The biosphere modeling is thus performed for two types of human exposure scenarios, one associated with groundwater release (usage of contaminated groundwater), the other associated with ash fall (deposition of contaminated volcanic ash on the ground surface).

During the development of the biosphere model, biosphere-related FEPs were identified. The intent was to capture all aspects of the biosphere model that can affect human exposure using the primary FEPs. The subsequent screening process evaluated the significance of each FEP and identified those that could be associated with nontrivial exposures. These FEPs were then modeled in more detail and included in the biosphere model.

The implementing computer code for the biosphere model was GENII-S V.1.4.8.5, which was developed for the Waste Isolation Pilot Plant in New Mexico. The approach adopted to support the *Total System Performance Assessment for the Site Recommendation* (TSPA-SR) (CRWMS M&O 2000 [DIRS 153246]) was to use GENII-S V.1.4.8.5 for each radionuclide of interest (CRWMS M&O 2000 [DIRS 136383], Section 3.9) to develop an annual dose prediction for unit concentration of that radionuclide in groundwater and ash. These values of annual dose for unit concentrations are known as biosphere dose conversion factors (BDCFs). This approach allowed the TSPA-SR to generate doses once radionuclide concentrations at the source of contamination had been calculated. A number of input parameters to the code were represented by distributions of values to reflect inherent uncertainty. The GENII-S V.1.4.8.5 code can accept such input distributions for many (but not all) parameters, and in turn generates the associated BDCF distribution for use in a total system performance assessment (TSPA). Once generated and abstracted, these BDCF distributions are provided to analysts for use in stochastic dose determinations.

The approach outlined above was used to support both the TSPA-SR (CRWMS M&O 2000 [DIRS 153246]) and the TSPA presented in Volume 2 (McNeish 2001 [DIRS 155023]). To supplement the TSPA-SR, some additional uncertainties associated with the biosphere model have been identified and quantified. Estimates of the impacts of uncertainties not previously considered on BDCFs and dose predictions have been generated. Additional analyses have been conducted to provide a demonstration of the robustness of the approach.

Since the TSPA-SR (CRWMS M&O 2000 [DIRS 153246]) was conducted, some analysis model reports (AMRs) supporting the biosphere effort have been updated. In addition, some new analyses have been conducted (Wu 2001 [DIRS 154892]; Wu 2001 [DIRS 154893]; Wu 2001 [DIRS 154894]; Tappen 2001 [DIRS 154890]) to provide more information on previously unquantified uncertainties. The first part of Section 13.2 provides a review of the AMRs developed to support the TSPA-SR evaluation. The section also identifies new work in the updated AMRs that supports the TSPA presented in Volume 2 (McNeish 2001 [DIRS 155023]). Unquantified uncertainties in the biosphere model are presented and discussed in Section 13.2.2. Section 13.2.3 presents a comparison of biosphere modeling efforts adopted by this and other programs. The similarity of constituent models and data is used to describe multiple lines of evidence in the biosphere model and provide confidence in the approach described in this report.

The main intent of the new biosphere analyses was to assess model uncertainties and sensitivities that had not been previously addressed. Section 13.3 presents the results of these efforts. Several areas of uncertainty are discussed and summarized in Table 13.1-1. The table also shows updates in scientific information.

The first of the analyses presented in Section 13.3 looks at the sensitivity of the dose calculation to the definition of the receptor of interest. The second provides some insight into the ramifications of performing a dose calculation using International Commission on Radiological Protection (ICRP) 72 (ICRP 1996 [DIRS 152446]) methodology rather than that specified in ICRP 30 (ICRP 1979 [DIRS 110386]; ICRP 1980 [DIRS 110351]; ICRP 1981 [DIRS 110352]). Both analyses were intended to provide confidence in the approaches used in TSPA-SR calculations and demonstrate robustness in that approach. They are followed by two uncertainty assessments of the inability of GENII-S V.1.4.8.5 to represent some processes stochastically.

Table 13-1. Summary of Supplemental Models and Analyses

Key Attributes of System	Process Model (Section of S&ER)	Topic of Supplemental Scientific Model or Analysis	Reason For Supplemental Scientific Model or Analysis			Section of Volume 1	Performance Assessment Treatment of Supplemental Scientific Model or Analysis[a]	
			Unquantified Uncertainty Analysis	Update in Scientific Information	Lower-Temperature Operating Mode Analysis		TSPA Sensitivity Analysis	Included in Supplemental TSPA Model
Delay and Dilution of Radionuclide Concentrations by the Natural Barriers	Biosphere (4.2.10)	Receptor of interest	X			13.3.1		
		Comparison of dose assessment methods	X			13.3.2		
		Radionuclide removal from soil by leaching	X			13.3.3		
		Uncertainties not captured by GENII-S	X			13.3.4		
		Influence of climate change on groundwater usage and BDCFs	X			13.3.5 13.3.7		
		BDCFs for groundwater and igneous releases		X		13.3.6 13.3.8 13.4	X	X

NOTE: S&ER = Yucca Mountain Science and Engineering Report (DOE 2001 [DIRS 153849]).

[a] Performance assessment treatment of supplemental scientific model or analysis discussed in SSPA Volume 2 (McNeish 2001 [DIRS 155023]).

The first evaluates the effect on BDCFs arising from the uncertainty in the partition coefficient through its impact on the leaching coefficient. The second investigation builds on the previous one and considers additional BDCF uncertainty from some parameters defining the leafy vegetable pathway. In Section 13.3.5, possible changes in annual water usage estimates for the proposed farming community are assessed for the present and future climate using the predicted irrigation requirements of alfalfa. The next section presents a reevaluation of the inhalation exposure pathway that reduces some uncertainty in the BDCF values. Section 13.3.7 evaluates the effect of the predicted climate change on the BDCF values. The final section presents BDCF data for two radionuclides (selenium-79 in both release cases and neptunium-237 in the disruptive scenario) that have not been previously considered as important dose contributors in TSPA-SR calculations (CRWMS M&O 2000 [DIRS 153246]).

Section 13 ends with a summary discussion of the work performed and the data provided on BDCFs for exposure scenarios and annual groundwater usage to support the TSPA analysis documented in Volume 2 (McNeish 2001 [DIRS 155023]).

The International Atomic Energy Agency (IAEA) recently completed an international peer review of the DOE's biosphere modeling work (IAEA 2001 [DIRS 155188]). The final report was not available in time to consider it in this update of work supporting the SR, but will be taken under consideration for subsequent phases of repository performance evaluations, if the site is recommended and designated. The IAEA review resulted in 37 specific suggestions for further work on improving the bases, and extending the application, of the modeling of the biosphere. The review will be followed up with a response and with a work plan to implement the suggestions that are most appropriate given the specific regulatory and national context of the Yucca Mountain project.

13.2 REVIEW OF TOTAL SYSTEM PERFORMANCE ASSESSMENT-SITE RECOMMENDATION TREATMENT AND UPDATES

Section 13.2.1 reviews the approach described in biosphere documents supporting the TSPA-SR (CRWMS M&O 2000 [DIRS 153246]) and changes that are incorporated into the TSPA described in Volume 2 (McNeish 2001 [DIRS 155023]). Section 13.2.2 discusses unquantified uncertainties in the biosphere model, and Section 13.2.3 describes multiple lines of evidence supporting the results of that model.

13.2.1 Relationship of Biosphere Model Tasks

Development of the biosphere model and BDCF outputs included several categories of tasks. One of them was to develop the data necessary to define the reference biosphere and the receptor of interest. The selection of radionuclides for which BDCFs were required is provided in *Inventory Abstraction* (CRWMS M&O 2000 [DIRS 150561], Section 7.1). Another function involved performing BDCF calculations using GENII-S V.1.4.8.5 for the two exposure scenarios under consideration. In addition, pathway and sensitivity analyses were performed. Finally, data generated by GENII-S V.1.4.8.5 were further processed to provide abstractions for using the BDCFs in a TSPA. These tasks were conducted initially during the 1999 to 2000 year to support the TSPA analysis summarized in the *Yucca Mountain Science and Engineering Report* (DOE 2001 [DIRS 153849]), as described in a series of biosphere AMRs and in the *Biosphere*

Process Model Report (CRWMS M&O 2000 [DIRS 151615]). Many of those AMRs have since been updated to include contributions to the resolutions of key technical issues (NRC 2000 [DIRS 149372]), incorporation of recent data, more comprehensive documentation of biosphere tasks, and corrections to the initial versions of the documents. The following sections briefly describe how those tasks were conducted in the biosphere AMRs and changes that have been made to support the TSPA analysis presented in Volume 2 (McNeish 2001 [DIRS 155023]).

13.2.1.1 Evaluation of the Applicability of Biosphere-Related Features, Events, and Processes

Total System Performance Assessment-Site Recommendation Treatment–In the *Evaluation of the Applicability of Biosphere-Related Features, Events, and Processes (FEP*) (CRWMS M&O 2000 [DIRS 142844]), which supported the TSPA-SR (CRWMS M&O 2000 [DIRS 153246]), a screening analysis of FEPs that were potentially biosphere-related was performed. This analysis was based on U.S. Department of Energy (DOE) guidance (Dyer 1999 [DIRS 105655]) and limited to those FEPs considered relevant given current conditions. The analysis indicated that 22 of the primary FEPs in the Yucca Mountain Site Characterization Project (YMP) database (CRWMS M&O 1999 [DIRS 142970]) were applicable to Yucca Mountain. However, because of the specificity of the guidance, climatic evolution and surficial processes were not considered to be relevant.

Updated Treatment–The update of the FEPs evaluation (BSC 2001 [DIRS 153921]) applied the DOE guidance (Dyer 1999 [DIRS 105655]) and proposed 10 CFR Part 63 (64 FR 8640 [DIRS 101680]) to a reevaluation of the biosphere-related FEPs in an updated YMP database (CRWMS M&O 2000 [DIRS 150806]). Consideration of proposed 10 CFR Part 63 resulted in an increase in the number of relevant primary FEPs, which now include climatic evolution and surface processes. Twenty-five primary FEPs were determined as applicable, in part or total, to the biosphere analyses. The effects of the added FEPs and their associated uncertainty were addressed in the *Nominal Performance Biosphere Dose Conversion Factor Analysis* (CRWMS M&O 2001 [DIRS 152539]) and *Evaluate Soil/Radionuclide Removal by Erosion and Leaching* (CRWMS M&O 2001 [DIRS 152517]).

13.2.1.2 Identification of the Receptor of Interest

Total System Performance Assessment-Site Recommendation Treatment–The *Identification of the Critical Group (Consumption of Locally Produced Food and Tap Water)* (CRWMS M&O 2000 [DIRS 143940]) documented one of the analyses that developed input parameters for GENII-S V.1.4.8.5. This report identified a receptor of interest for the TSPA-SR analyses (CRWMS M&O 2000 [DIRS 153246]) as the average member of the critical group (proposed 10 CFR 63.115(b) [64 FR 8640 [DIRS 101680]]). The receptor was defined using attributes of the potential behaviors and characteristics of the population surrounding Yucca Mountain. Characteristics examined included the consumption of locally produced food and tap water, as identified in a food consumption survey (DOE 1997 [DIRS 100332]); lifestyle characteristics, including employment and recreation; type of housing; and land uses that would lead to the highest potential exposures. Employment behaviors were based on data from the U.S. Census Bureau (1999 [DIRS 135344]), and an assumption of outdoor recreation was based on data from a national U.S. Environmental Protection Agency (EPA) survey (EPA 1997 [DIRS 116135]).

The report identified a receptor that would be expected to exhibit the attributes of a residential farming group who raise and consume some of their own food and obtain all their drinking and irrigation water from a contaminated groundwater supply. This group would be expected to spend a considerable amount of time outdoors on contaminated land, including agricultural or construction employment and outdoor recreational activities, such as gardening. Members of this group would be expected to live in mobile or manufactured housing and have a land use characteristic associated with irrigated land.

Updated Treatment–An update (CRWMS M&O 2001 [DIRS 153342]) further examined the potential behaviors and characteristics of the population surrounding Yucca Mountain. Relative behavioral factors for unit concentrations were developed for four key radionuclides: technetium-99, iodine-129, neptunium-237, and plutonium-239 (CRWMS M&O 2001 [DIRS 153342], Section 6.2). These factors represent annual dose per unit activity concentration of a radionuclide in groundwater as the result of a predefined behavior. The relative behavioral factors provide a tool for evaluating relative exposures to the receptor groups. These factors were summed across combinations of behaviors to identify a receptor group that exhibits those behaviors and characteristics that will result in the highest expected annual doses. The analysis showed that for the groundwater release exposure scenario, diet was the most significant contributor to potential exposure, contributing over 99 percent of the total for technetium-99, iodine-129, and neptunium-237 and approximately 90 percent of the total for plutonium-239. Consideration of alternative receptors and analysis of changes in predicted annual dose caused by varying the characteristics of the receptor are discussed in Section 13.3.1.

13.2.1.3 Groundwater Usage by the Proposed Farming Community

Total System Performance Assessment-Site Recommendation Treatment–Consistent with proposed 10 CFR Part 63 (64 FR 8640 [DIRS 101680]), the approach used in the TSPA-SR analysis (CRWMS M&O 2000 [DIRS 153246], Section 3.9) conservatively assumed that all radionuclides reaching the location of the receptor, approximately 20 km south of the potential repository, were captured by the water used by a hypothetical farming community of approximately 100 people living on 15 to 25 farms.

Annual water usage in the Amargosa Valley area (State of Nevada 1997 [DIRS 110951]) was examined to derive water usage and statistical uncertainty for an average farm. Once this information was known, it was a straightforward step to generate a sampling algorithm for the TSPA to provide a statistically meaningful annual consumption for the hypothetical farming community.

Updated Treatment–This analysis was not updated. However, the effect of climate change on the predicted distribution of water usage by the hypothetical farming community was evaluated, as described in Section 13.3.5.

13.2.1.4 Input Parameter Values for External and Inhalation Radiation Exposure Analysis

Total System Performance Assessment-Site Recommendation Treatment–Estimates of inhalation exposure time, mass loading, and chronic breathing rate were developed to provide

GENII-S V.1.4.8.5 input for the inhalation pathway. In the initial version of *Input Parameter Values for External and Inhalation Radiation Exposure Analysis* (CRWMS M&O 1999 [DIRS 110602]), a distribution of inhalation exposure time was developed based on time spent indoors and outdoors in the contaminated area by Amargosa Valley residents who commute to distant areas to work (minimum exposure) and farmers and others who work outdoors in the area (maximum exposure). Mass loading (i.e., mass of suspended particles per volume of air) was calculated based on measurements of suspended air particles less than 10 μm (PM_{10}) taken at Yucca Mountain between 1992 and 1997. A typical volume of air breathed per day by an average adult male was selected as the chronic breathing rate.

To provide GENII-S V.1.4.8.5 input for the external exposure pathway, estimates of soil exposure time, home irrigation rate, and home irrigation duration were developed. The distribution of soil exposure time was based on the time commuters and outdoor workers spend outdoors in the contaminated area. A distribution of home irrigation rate was calculated based on the irrigation requirements of bermuda grass (minimum) and tall fescue (maximum) in Amargosa Valley. A value for year-round home irrigation duration was selected based on the watering requirements of those turf grasses. A change to the initial report (CRWMS M&O 2000 [DIRS 149880], Section 6.5) introduced minor modifications that included changed irrigation rates for residential lawns.

Updated Treatment–In the updated report (CRWMS M&O 2000 [DIRS 152438], Section 6), the following changes were made:

- Distributions for the duration of external exposure and soil exposure were developed to better match employment scenarios for potential receptor groups in a farming community.

- New distributions of mass loading were selected based on measurements of total suspended particles in farming communities and, separately, for the conditions following volcanic eruptions.

- Additional distributions of home irrigation rate and duration were calculated based on a change from the present-day climate to a glacial-transition climate.

See Section 13.3.6 for a description of changes in the inhalation exposure parameters.

13.2.1.5 Identification of Ingestion Exposure Parameters

Total System Performance Assessment-Site Recommendation Treatment–*Identification of Ingestion Exposure Parameters* (CRWMS M&O 2000 [DIRS 133719]) describes the selection and justification of the values for the ingestion exposure pathway parameters used by GENII-S V.1.4.8.5. In this report, 13 ingestion exposure parameters (some of them divided into multiple food type categories) were developed. The estimates were based on the current climate in the Yucca Mountain region.

Updated Treatment–*Identification of Ingestion Exposure Parameters* (CRWMS M&O 2000 [DIRS 133719]) was not revised. However, selected ingestion exposure parameters applicable to

the cooler and wetter glacial-transition climate were developed to support BDCF calculations for the evolved climate. Additionally, the values of some parameters for the current climate were revised. These calculations are documented in the *Nominal Performance Biosphere Dose Conversion Factor Analysis* (CRWMS M&O 2001 [DIRS 152539], Section 6.5.2 and Attachment III).

13.2.1.6 Environmental Transport Parameter Analysis

Total System Performance Assessment-Site Recommendation Treatment–The purpose of the *Environmental Transport Parameters Analysis* (CRWMS M&O 1999 [DIRS 110520]) was to develop or select values for environmental transport parameters, which include over 50 values required by GENII-S V.1.4.8.5. The code's default parameters were evaluated for adequacy by comparing them with the values in the scientific literature. The parameter value selections were justified and documented.

Updated Treatment–One change was made (CRWMS M&O 2001 [DIRS 152434]) to include additional input parameters for biosphere dose modeling. A set of new crop resuspension factors was developed based on a high mass loading after a volcanic eruption. A new value for the crop resuspension factor for the arid agricultural area was developed for the groundwater release exposure scenario. This was done because the previously developed resuspension factor was derived from Yucca Mountain site data, and it was found to be lower than the typical value in arid agricultural areas.

13.2.1.7 Transfer Coefficient Analysis

Total System Performance Assessment-Site Recommendation Treatment–*Transfer Coefficient Analysis* (CRWMS M&O 1999 [DIRS 110523]) describes the selection of values for transfer coefficients, including soil-to-plant transfer factors for four crop categories, animal feed transfer coefficients for four animal products, and bioaccumulation factors for freshwater fish. Because these parameters are element-specific, seventeen elements were included in the initial report. Distributions for two scaling factors were also considered. These distributions attempted to quantify the uncertainties in deterministic values used for each of the soil-to-plant and animal uptake coefficients. To perform the analysis, parameter values were collected from a search of the scientific literature. Typically, about ten references were considered for each parameter.

Updated Treatment–After the initial report was issued, two changes were made. The first (CRWMS M&O 2000 [DIRS 149879]) was made to clarify selection criteria, correct a few previously selected values, and make editorial modifications. The second (CRWMS M&O 2000 [DIRS 152435]) added lead, bismuth, and polonium to the analysis. This change was made to accommodate the modified list of radionuclides of interest based on the source term inventory.

13.2.1.8 Dose Conversion Factor Analysis: Evaluation of GENII-S Dose Assessment Methods

Total System Performance Assessment-Site Recommendation Treatment–The dose assessment component of GENII-S V.1.4.8.5, the code used to implement the biosphere model, was evaluated (CRWMS M&O 1999 [DIRS 110635]) to ensure that the calculated doses were consistent with doses calculated using other radiation dose assessment methods currently

accepted by the scientific and engineering community. For internal exposure, doses calculated by GENII-S V.1.4.8.5 were compared with doses calculated using published values of dose conversion factors. It was recommended that GENII-S V.1.4.8.5 internal dose assessment be conducted with no modifications to the code's auxiliary files containing dose conversion factors for internal exposure. For external exposure, GENII-S V.1.4.8.5 dose coefficients were replaced with more recently published dose coefficient values from Federal Guidance Report No. 12 (Eckerman and Ryman 1993 [DIRS 107684]).

Updated Treatment–This report has not been updated. However, an additional evaluation of dose assessment methods was conducted, as described in Section 13.3.2.

13.2.1.9 Evaluation of Soil and Radionuclide Removal by Erosion and Leaching

Total System Performance Assessment-Site Recommendation Treatment–The effort described in *Evaluate Soil/Radionuclide Removal by Erosion and Leaching* (CRWMS M&O 2000 [DIRS 136281]) focused on the removal of radionuclides from soil by leaching and erosion, including wind and water removal. An appropriate leaching coefficient was derived for each elemental contaminant by using the overwatering term (estimated in a separate analysis), the partition coefficient, and the soil model employed in GENII-S V.1.4.8.5. Assuming accepted agricultural methods, the analysis also derived estimates of annual soil removal rates for the soil types present in the Amargosa Valley region.

Updated Treatment–The updated report (CRWMS M&O 2001 [DIRS 152517]) addressed the impact of possible climate change on the parameters derived from the initial analysis. The findings were that a cooler and wetter climate would not change the annual rate of soil removal as long as current cultivation practices continue. The analysis of climate effects on leaching rate showed that the leaching rate of radionuclides from the top 15-cm surface layer could vary as a function of changes in the annual overwatering rate. Such a change could result from modifications in irrigation practices under different climatic regimes. Climate change had no effect on leaching rate because an overwatering rate of 15 cm/yr was assumed in all analyses to account for the removal of salts.

13.2.1.10 Biosphere Dose Conversion Factors for the Groundwater Release Exposure Scenario

Total System Performance Assessment-Site Recommendation Treatment–The objective of *Non-Disruptive Event Biosphere Dose Conversion Factors* (CRWMS M&O 2000 [DIRS 136285]) was to develop the BDCFs for the nominal postclosure performance assessment. The analysis used input data from the reports listed in Section 13.2.1.2 and Sections 13.2.1.4 through 13.2.1.9. Radionuclide-specific BDCFs were calculated for sixteen radionuclides: carbon-14, technetium-99, iodine-129, actinium-227, thorium-229, uranium-232, uranium-233, uranium-234, uranium-236, uranium-238, neptunium-237, plutonium-238, plutonium-239, plutonium-240, americium-241, and americium-243. The selection of these radionuclides is discussed in CRWMS M&O (2000 [DIRS 136285], Section 4.2.2). The analysis included stochastic runs, which were performed to propagate the defined uncertainties of input parameters to the output BDCFs. The BDCFs were subsequently used in the TSPA-SR

(CRWMS M&O 2000 [DIRS 153246]) to determine the expected annual dose from the potential repository.

Biosphere Dose Conversion Factors for Reasonably Maximally Exposed Individual and Average Member of Critical Group (CRWMS M&O 2000 [DIRS 144700]) documented the development of BDCFs for seven additional radionuclides identified in Section 5 as: strontium-90, cesium-137, lead-210, radium-226, protactinium-231, thorium-230, and plutonium-242. This brought the total number of radionuclides investigated to 23. After the initial BDCFs were developed (CRWMS M&O 2000 [DIRS 136285]), these radionuclides were identified as being potentially significant for evaluating the radiological impact of the potential repository for up to 1 million years after permanent closure. BDCFs were also calculated for the reasonably maximally exposed individual prescribed in EPA regulations.

Updated Treatment–The updated analysis (CRWMS M&O 2001 [DIRS 152539]) developed BDCFs for all TSPA scenarios resulting in groundwater release. The analysis:

- Used revised input parameters
- Incorporated an analysis of climate change effects on the BDCFs for the groundwater release scenario
- Added pathway and limited uncertainty analyses
- Appended the list of radionuclides to include those that may be important for up to 1 million years after permanent closure of the potential repository
- Changed the document title to better describe the document purpose and contents
- Added the biosphere model validation.

The title of the report was changed to *Nominal Performance Biosphere Dose Conversion Factor Analysis* (CRWMS M&O 2001 [DIRS 152539]). The updated analysis used revised input data where available (see list of input reports above).

13.2.1.11 Sensitivity Analysis for the Groundwater Release Biosphere Dose Conversion Factors

Total System Performance Assessment-Site Recommendation Treatment–The *Non-Disruptive Event Biosphere Dose Conversion Factor Sensitivity Analysis* (CRWMS M&O 2000 [DIRS 144692]) determined the sensitivity of the nominal performance BDCFs, which were developed in *Non-disruptive Event Biosphere Dose Conversion Factors* (CRWMS M&O 2000 [DIRS 136285]), to variations in the input parameters and documented the results of an exposure pathway analysis. These analyses provided insights regarding the parameters and exposure pathways that have the greatest impact on the BDCFs.

Updated Treatment–The report has not been updated. However, an updated pathway analysis for the groundwater release BDCFs was conducted in the *Nominal Performance Biosphere Dose Conversion Factor Analysis* (CRWMS M&O 2001 [DIRS 152539]; see also Section 13.2.1.10).

13.2.1.12 Distribution Fitting to the Stochastic Biosphere Dose Conversion Factors for the Groundwater Release Exposure Scenario

Total System Performance Assessment-Site Recommendation Treatment–The activity documented in *Distribution Fitting to the Stochastic BDCF Data* (CRWMS M&O 2000 [DIRS 144055]) was conducted to derive statistical distributions of the BDCFs. The individual realizations (130 for this approach) for each GENII-S V.1.4.8.5 run were analyzed to ascertain which of several distributions were acceptable for representing the data. The distributions included normal, lognormal, shifted lognormal, and others. The chi-square test was used to determine acceptability of fitting.

Radionuclides that exhibited a change in mean BDCF value of less than 15 percent over the periods of continuing irrigation considered were represented by the distribution derived from the longest period of irrigation. In cases where the change in BDCF mean value was larger than 15 percent over the period of irrigation, the data were further analyzed to incorporate the effect of soil erosion.

Updated Treatment–The updated report (CRWMS M&O 2001 [DIRS 153207]) documented distribution fitting to the updated BDCFs for the groundwater release exposure scenario. The approach to distribution fitting was identical to that presented above. For this iteration, 150 individual model realizations were generated per each GENII-S V.1.4.8.5 run. This increase in sample size improved the treatment of statistical uncertainty inherent in the process.

In the case of carbon-14, none of the distributions considered were deemed to be acceptable; therefore, an empirical distribution was used in the TSPA. The empirical distribution was specified in terms of percentiles at five-percent intervals.

13.2.1.13 Abstraction of Biosphere Dose Conversion Factor Distributions for Irrigation Periods

Total System Performance Assessment-Site Recommendation Treatment–In cases where radionuclide buildup in soils was found to be potentially significant (see Section 13.2.1.12), the BDCF data (see Section 13.2.1.10) were subjected to additional analysis, as documented in *Abstraction of BDCF Distributions for Irrigation Periods* (CRWMS M&O 2000 [DIRS 144054], Section 6). The mean value of the fitted data for each radionuclide was shown to be in the form of an asymptotic exponential function, as expected from the model used by the GENII-S V.1.4.8.5 code for radionuclide loss from decay, leaching, and harvesting. The exponential factor was then modified to include the additional loss mechanism of soil removal, with a characteristic time of 250 years. The overall effect was to reduce the asymptotic (long-term) BDCF value by some degree. For radionuclides with a short buildup time compared to 250 years, the change in BDCF was insignificant. However, in cases where the predicted radionuclide buildup was long compared to 250 years, the effect was significant. In all cases, the long-term, and therefore conservative, values of BDCFs were used in the TSPA. This conservative approach eliminated the need to define and justify a representative distribution for the number of years that various plots of land associated with the hypothetical community had been subject to continuing (or sporadic) irrigation and production.

Updated Treatment–In the updated report (CRWMS M&O 2001 [DIRS 153206]), the revised BDCF data were used (see Section 13.2.1.10). Otherwise, the methods were the same as those used for the TSPA-SR treatment.

13.2.1.14 Volcanic Eruption Biosphere Dose Conversion Factor Analysis

Total System Performance Assessment-Site Recommendation Treatment–The second exposure scenario considered in biosphere modeling concerned the conditions of human exposure following a volcanic eruption through the repository. BDCFs for a volcanic eruption were documented in the *Disruptive Event Biosphere Dose Conversion Factor Analysis* (CRWMS M&O 2000 [DIRS 143378]). The initial exposure scenario considered only a thin layer of contaminated ash deposition, although the scenario was subsequently modified to include an event that resulted in thicker deposits of ash. The analysis used input data from the reports listed in Section 13.2.1.2 and Sections 13.2.1.4 through 13.2.1.9. Radionuclide-specific BDCFs for volcanic eruptions were calculated for twelve radionuclides: strontium-90, cesium-137, actinium-227, thorium-229, protactinium-231, uranium-232, uranium-233, plutonium-238, plutonium-239, plutonium-240, americium-241, and americium-243. The analysis included stochastic runs, which were performed to propagate the defined uncertainties of input parameters to the output BDCFs. As the result of the exposure scenario change, these BDCFs were not used in the TSPA-SR to calculate the annual doses for a volcanic eruption. Instead, a new set of BDCFs was developed (see below) that corresponded to the eruption conditions predicted by the TSPA-SR analyses.

Scoping Calculation for Volcanic Eruption Biosphere Dose Conversion Factors (CRWMS M&O 2000 [DIRS 152632]) documents the development of updated sets of volcanic eruption BDCFs, which were subsequently used in the TSPA-SR. Compared to the previous approach (CRWMS M&O 2000 [DIRS 143378]), the following changes were made:

- The list of radionuclides was expanded to include those important in assessing repository performance during the 10,000-year compliance period and those that may be important to repository performance for up to 1 million years.
- Three exposure scenarios based on three phases during and after volcanic eruption were considered.
- BDCFs were calculated for two thicknesses of contaminated ash: 1 cm and 15 cm.

Updated Treatment–The update to the *Disruptive Event Biosphere Dose Conversion Factor Analysis* (CRWMS M&O 2001 [DIRS 152536]):

- Incorporated the revised exposure scenarios
- Used revised input parameters
- Added pathway and limited uncertainty analyses

- Appended the list of radionuclides to include those that may be important for up to 1 million years after permanent closure of the potential repository

- Added a biosphere model validation.

13.2.1.15 Sensitivity Analysis for the Volcanic Eruption Biosphere Dose Conversion Factors

Total System Performance Assessment-Site Recommendation Treatment–The *Disruptive Event Biosphere Dose Conversion Factor Sensitivity Analysis* (CRWMS M&O 2000 [DIRS 149736]) determined the sensitivity of the volcanic eruption BDCFs, which were developed in *Disruptive Event Biosphere Dose Conversion Factor Analysis* (CRWMS M&O 2000 [DIRS 143378]), to variations in input parameters. The report also documented the results of the exposure pathway analysis. These analyses provided insights regarding the parameters and exposure pathways that have the greatest impact on the BDCFs.

Updated Treatment–This report has not been updated. However, an updated pathway analysis was conducted for the *Disruptive Event Biosphere Dose Conversion Factor Analysis* (CRWMS M&O 2001 [DIRS 152536]; see also Section 13.2.1.12).

13.2.2 Identification of Unquantified Uncertainties in the Biosphere Model

In any numerical modeling activity, such as TSPA or its constituent models, there are numerous sources of uncertainty. In a deterministic model, where all parameters are defined by fixed values, the uncertainties (or errors) are of a systematic nature: uncertainties in the input parameter(s) or modeling approach produce a result that is biased. In the case of a stochastic model (such as GENII-S V.1.4.8.5), where some input parameters are sampled from justifiable distributions, the effects of parameter uncertainties can be propagated through to the desired result. After many evaluations have been made using randomly selected input values, the collection of individual results is a distribution. This section discusses uncertainties in the conceptual model, the mathematical model, and input parameters, as well as the uncertainties between BDCFs for various radionuclides. GENII-S V.1.4.8.5 is used in the stochastic mode to evaluate the effect of parameter uncertainties. The numerical modeling uncertainties are assumed to be insignificant when compared to other uncertainties, since the GENII-S code (including V.1.4.8.5) has gained acceptance within the radiation community (CRWMS M&O 2000 [DIRS 151615], Sections 3.2.1.1 and 3.2.1.3).

BDCF data generated for the TSPA have included parametric uncertainty. To put this assessed uncertainty of the BDCFs into perspective, the results of GENII-S V1.4.8.5 using data presented later in this section can be used. For instance, the groundwater release BDCF distributions for selenium-79 are presented in Table 13.3-22. The median BDCF value for the 6^{th} irrigation period is 1.28×10^{-5} rem per pCi/L. The 5 percent and 95 percent points are approximately a factor of 2.8 below and above the median. Thus, the uncertainty in BDCFs from currently estimated parametric uncertainty covers a range of about a factor of eight. If any other uncertainty produces a much smaller additional variation, the effect can safely be ignored.

13.2.2.1 Conceptual Model Uncertainty

FEPs Screening–The biosphere conceptual model describes the human exposure pathways associated with the FEPs that were screened and found to be applicable to the biosphere model. Although uncertainty associated with the screening decisions (i.e., decisions to include or exclude selected FEPs and associated exposure pathways in the model) was not mathematically evaluated, there should be little additional uncertainty because potentially significant FEPs were included in the conceptual model.

Conceptual Models of Radionuclide Transport–The conceptual model of radionuclide transport in the biosphere (i.e., between the environmental media) is based on the selection of participating media (e.g., groundwater, soil, air, fauna, flora) and the FEPs that cause the transport of radionuclides between them. The behavior of radionuclides in the biosphere may, in principle, be complex because of the variety of participating media and transport processes; however, it is neither possible nor necessary to engage such complexity to construct a conceptual model of radionuclide transport. Simplified compartment models are used by modelers in codes such as GENII-S V.1.4.8.5. Such models are inevitably a simplified representation of actual radionuclide migration in the biosphere, and uncertainty is an inherent part of such representation. Uncertainties associated with the model representation of environmental radionuclide transport have not been quantified. However, the model used by GENII-S V.1.4.8.5 compares favorably with alternative models (see Section 13.2.3). Additional uncertainties are likely to be minor relative to the overall range of uncertainty in the BDCFs.

Conceptual Models of the Receptor of Interest–Human exposure was evaluated for the hypothetical receptor. To quantify radiation exposure from interactions with contaminated environmental media, the attributes and behavioral characteristics of the receptor that may influence the degree of radiation exposure have to be determined. An example of a behavioral characteristic is employment outdoors, and a corresponding attribute is the amount of time spent at outdoor locations. Another behavioral characteristic potentially leading to radiation exposure is consumption of locally produced food. Attributes of this behavior include consumption rates of various locally produced food types. Although the receptor is defined in proposed 10 CFR 63 (64 FR 8640 [DIRS 101680]) and 40 CFR 197 (64 FR 46976 [DIRS 105065]), there is no unequivocal way of defining the appropriate characteristics and attributes. Therefore, selection of characteristics and attributes of the receptor involves uncertainty. This is a concern for both of the human exposure scenarios under consideration and their corresponding parameters (e.g., consumption rates for locally produced food and water). The sensitivity of BDCF results to variations in the definition of the receptor is discussed in Section 13.3.1.

13.2.2.2 Mathematical Model Uncertainty

Overall Uncertainty of the Mathematical Model–The mathematical model of radionuclide transport and human exposure in the biosphere is based on the model used by GENII-S V.1.4.8.5. This code was selected as the implementing software for the biosphere assessment, except for the treatment of radionuclide removal by soil erosion and the groundwater usage analysis. The overall uncertainty associated with this mathematical model has not been quantified. Many individual model components contribute to the overall uncertainty, as

described in this section. The multiple lines of evidence presented in Section 13.2.3 indicate that mathematical uncertainties contribute little additional uncertainty.

Exposure Pathways Not Included in GENII-S V.1.4.8.5–The mathematical model is based on a specific choice of the environmental media and radionuclide transport processes—which, together, make up the human exposure pathways—that are believed to be the most important for total radiation exposure. However, there is always a possibility that all pathways will not be included in a given mathematical model. For example, among the GENII-S V.1.4.8.5 ingestion pathways, only one kind of meat (beef) is included; organs, such as beef or chicken livers, are not. Other pathways that are not modeled in GENII-S V.1.4.8.5 include soil ingestion by grazing animals and inhalation by animals. The impact of these omissions on model uncertainty was not mathematically evaluated. Since potentially significant FEPs were included in the conceptual model, little additional uncertainty should be introduced.

Treatment of Environmental Transport within the Mathematical Model–Radionuclide transport between the environmental media via transport processes contributing to the human exposure pathways is represented in the mathematical model as a series of pathway submodels. Each of these submodels represents a simplified way to describe and quantify complex radionuclide behavior in the environment. This particular approach to radionuclide pathway transport modeling is subject to uncertainty because of the simplification of the process when represented by a mathematical model and the representation of the interfaces between the modeled processes. These uncertainties were not evaluated. Given the acceptance of GENII-S V.1.4.8.5, additional uncertainties are assumed to be inconsequential and, therefore, are likely to be minor relative to the overall range of uncertainty in the BDCFs.

General Categorization of Input Parameters–Many of the input parameters used in GENII-S V.1.4.8.5 are composed of several contributing data points: their values are selected by grouping available data for a given parameter. For example, transfer factors for leafy vegetables were derived using transfer coefficients for individual crops, such as lettuce, cabbage, and spinach. The available data for the same crops would also be used to calculate other parameters for leafy vegetables, such as irrigation rate, growing time, and irrigation time. Some uncertainties are associated with this method of grouping data points to arrive at the values of composite parameters. The parameters associated with these pathways were represented by distributions to approximate these uncertainties.

Limitations on Correlations Between Sampled Parameters–The mathematical model (and implementing computer code) does not allow the user to specify the correlation between pairs of parameters belonging to different groups of inputs defined by distributions. For example, the correlation between mass loading (inhalation and external exposure) and the resuspension factor (ingestion) cannot be defined in GENII-S V.1.4.8.5.

Each food transfer coefficient group (crops and animal products) uses the same transfer coefficient scaling factor for all coefficients in the group. Although such treatment provides a way of correlating transfer coefficients between members of the group, it introduces additional uncertainty, which was not quantified.

Fixed Parameter Values–GENII-S V.1.4.8.5 has the capability to represent some model parameters by probability distribution functions or fixed values. However, many parameters can only be represented by fixed values (e.g., leaching rate, time duration of previous irrigation, weathering rate for the removal of contamination from foliage). In this case, software limitations prevent the user from factoring uncertainty associated with some parameters into the model. Uncertainty resulting from an inability to select a range of parameter values for certain parameters was not quantified. Limited studies presented in Sections 13.3.3 and 13.3.4 evaluated the additional uncertainty introduced by this limitation. They concluded that the uncertainty in the three parameters under consideration was estimated to impact BDCFs by ±50 percent in the cases of iodine-129, neptunium-237, and plutonium-239 and by up to 400 percent in the case of technetium-99.

13.2.2.3 Model Parameter Uncertainty

Use of Literature Data Instead of Site-Specific Data–The development of a fully site-specific biosphere model at Yucca Mountain is not possible because of the limited availability of site-specific data. Wherever possible, the modeling effort used site-specific and regional information. Information from scientific literature was selected with care when site-specific or regional information was not available. The magnitude of uncertainty resulting from the use of information from literature in lieu of site-specific or regional data was not evaluated. However, the range over which the parameters were distributed was considered sufficient to capture these uncertainties.

Selection of Fixed Parameter Values–Many parameters are used in performing BDCF calculations. GENII-S V.1.4.8.5 can represent some of the model parameters by their probability density function. However, not every input parameter that could be represented this way was. In general, distributions were used for parameters with a large amount of uncertainty or a major influence on the final BDCFs; otherwise, fixed values were used. Representing less important parameters as fixed values reduced the computational burden on the software and allowed an increase in the maximum possible number of model realizations, improving the statistical representation of the outcome. Since fixed values were used in place of distributions for pathways making relatively minor contributions, this omission likely added little additional uncertainty to the calculation of the BDCFs.

Parameter Ranges for Probability Distributions–In many instances, probability distributions were based on temporal and spatial variations in the data rather than on uncertainty. This was the case for the consumption rates of locally produced food, for many of the ingestion exposure parameters (e.g., rates and durations), and for the growing times of various crops. The range of variations examined in selecting these parameters was intended to be large enough to account for uncertainty in site-specific conditions. However, the contribution of uncertainty to these distributions was not evaluated.

User-Defined Correlations Between Parameters–Parameters represented by their probability density functions were assumed to vary independently, except for transfer factors representing plant-to-soil and animal food to animal product transfers. Therefore, the covariance among parameters for BDCF calculations was not included in the biosphere model. In general, the effect of neglecting covariances is to imprecisely estimate confidence intervals on the BDCFs.

In other words, if the correlation among input parameters is positive, the uncertainty in the BDCFs will be underestimated, while if the correlation is negative, the uncertainty will be overestimated. This uncertainty was not quantified.

Statistical Error in Data–Statistical errors in the data were not quantified, yet they may constitute an additional source of uncertainty. For example, uncertainties in the consumption rates of locally produced food due to the sampling procedure were not determined. In addition, the selection of a smaller population subgroup from the larger sample, which was done to identify the receptor, leads to an increase in standard error. This uncertainty was not evaluated. Because variability in the consumption habits of the receptor was large, additional sampling uncertainty likely was of little consequence.

13.2.2.4 Uncertainty in the Model Results

Correlations Between the Results–The impact of possible correlations between the BDCFs for individual radionuclides (e.g., the BDCFs for various isotopes may be correlated) is a concern for their use in the TSPA. The uncertainty depends on the predicted radionuclide concentration and could not be evaluated in this report. Such correlations may have an impact on the uncertainty in the expected annual dose calculated in the TSPA model.

Uncertainty Associated with Model Abstraction–Using statistical distributions to abstract the BDCFs generated by the biosphere model was shown to provide a reasonable and statistically acceptable representation (CRWMS M&O 2001 [DIRS 153207]; CRWMS M&O 2001 [DIRS 153206]). However, because a limited number of model realizations could be generated (130 realizations in the initial analysis and 150 in the update), there is an intrinsic sampling uncertainty in the overall modeling result. The uncertainty in the mean value of a given set of BDCF data is small compared to the distribution width, so it was ignored. This is achieved by calculating the uncertainty in the mean value from the standard deviation, as reported in *Distribution Fitting to the Stochastic BDCF Data* (CRWMS M&O 2000 [DIRS 144055]).

13.2.3 Multiple Lines of Evidence in the Biosphere Model

This section summarizes the evidence that supports the validity of the approach adopted in modeling the biosphere. The approach taken was to compare the YMP biosphere modeling details with work performed and published by peers.

13.2.3.1 Biosphere Conceptual and Mathematical Model

The YMP biosphere model is based on the GENII-S V.1.4.8.5 code, which was developed and used for the Waste Isolation Pilot Plant performance assessment as part of the application for a certificate of compliance from the EPA (Leigh et al. 1993 [DIRS 100464], Abstract). The code was also used by the Center for Nuclear Waste Regulatory Analyses in support of a performance assessment for the potential repository at Yucca Mountain (LaPlante and Poor 1997 [DIRS 101079]).

A preliminary comparison was conducted between the model used for the groundwater release exposure scenario for the potential repository at Yucca Mountain and the International Atomic Energy Agency (IAEA) biosphere model developed by the BIOMASS program

(BIOMASS 2000 [DIRS 154522], Example Reference Biosphere 2A). The assessment context for the biosphere model gives background information and the requirements of the performance assessment. Several aspects of the assessment context were compared for the YMP model for groundwater release and the BIOMASS Example Reference Biosphere 2A model (Table 13.2-1). The comparison indicated that the two models are very similar. Many aspects are identical, while others are equivalent. Using the same or equivalent aspects of the assessment context, an overall comparison of the pathways and methodologies used in the two biosphere models was conducted, as shown in Table 13.2-2. Each pathway included in the models was compared. Most pathways are considered in both models using the same or similar methods, although some pathways are considered in only one of the models. However, the model comparisons indicated that the pathways not included in the YMP model were of lesser significance when compared with other pathways for the groundwater release model. Documentation for the BIOMASS program (BIOMASS 2000 [DIRS 154522], Section 8), indicates that some pathways, such as water immersion and aerosol inhalation, are much less important than other pathways, such as drinking water and crop consumption.

13.2.3.2 Biosphere Input Parameters

Several methods were used to develop input parameters for the YMP biosphere model (CRWMS M&O 2000 [DIRS 151615]). Using site-specific information was the first priority for developing input parameters. Site-specific information included Yucca Mountain site field measurements (such as meteorological data), a regional food consumption survey of such items as food consumption rates, and firsthand observations in Amargosa Valley of behaviors such as well water usage. The quality of site-specific information depends on data collection methods. Furthermore, site-specific information may be subject to temporal variations and, therefore, reflect the conditions at the time of measurement. Other regional and national demographic data, such as mass loading for agricultural area, were also used in the development of some environmental parameters and human behavior attributes.

If site-specific data were not available, parameter values were obtained from the literature. Literature information includes scientific articles in reviewed journals, published technical reports, and internationally accepted generic databases. The reliability of the derived values depends on many factors, including the uncertainties in the source data, decisions regarding the applicability of the data for conditions other than the original ones, and the ability to define distributions and ranges of parameters. When literature information was used for the YMP biosphere model, input data were chosen to best reflect the local conditions (such as environmental transport parameters). This method of selecting parameter values (CRWMS M&O 2000 [DIRS 152435]; CRWMS M&O 2000 [DIRS 152438]; CRWMS M&O 2001 [DIRS 152517]; CRWMS M&O 2001 [DIRS 152434]) incorporated an aspect of multiple lines of evidence because it considered a significant portion of current scientific knowledge reported by others.

13.3 UNCERTAINTY, SENSITIVITY, AND NEW ANALYSES

The previous two sections identified multiple areas in the biosphere that are potentially subject to uncertainty. Each of these uncertainties propagates through the biosphere calculation, where their combined effects are incorporated into a distribution for each radionuclide identified as

important to dose and for defined release/exposure scenarios. This section describes only those analyses conducted since the development of the TSPA-SR (CRWMS M&O 2000 [DIRS 153246]). These additional analyses were conducted to help the DOE better understand the uncertainties and sensitivities inherent in the biosphere model or to provide new or updated analyses of the biosphere. The following paragraphs briefly introduce each analysis and identify the rationale for the work performed.

The first analysis provides information on the sensitivity of predicted annual doses to the modeling of the receptor of interest. In draft regulations, both regulatory agencies—the U.S. Nuclear Regulatory Commission (NRC) in proposed 10 CFR 63.115(b)(2) (64 FR 8640 [DIRS 101680]) and the EPA in proposed 40 CFR 197.21(b) (64 FR 46976 [DIRS 105065])—identify their receptor of interest for evaluation of annual doses from potential repository releases. The detailed implementation of the receptor of interest within the computer code is subject to uncertainty, so the sensitivity of annual dose to the details of the receptor definition is evaluated and discussed.

Annual dose limits evaluated by the biosphere effort to support the TSPA-SR (CRWMS M&O 2000 [DIRS 153246]) are based on the definition of the total effective dose equivalent (TEDE) in 10 CFR 20.1003. A sensitivity study investigated the changes in the BDCFs for four important radionuclides that would be expected if the more recent International Commission on Radiological Protection recommendations (ICRP 1991 [DIRS 101836]) were used.

Three uncertainty analyses follow the sensitivity study. The first investigates the previously unquantified uncertainty of partition coefficients on BDCFs. The uncertainty in a given partition coefficient for an element affects its leaching coefficient. Uncertainty in this parameter causes variation in the degree of radionuclide buildup in soil from prolonged irrigation and has a direct effect on BDCFs. The second analysis focuses on the four dominant radionuclides, and investigates the effect of uncertainty on several ingestion pathway parameters that GENII-S V.1.4.8.5 can only accept as fixed inputs. The remaining uncertainty analysis develops a sampling algorithm to predict the annual rate of water usage by the proposed farming community in a future cooler and wetter climate.

Section 13.3 closes with the details of three new analyses, each generating new data. The first of these investigated the parameters associated with inhalation. In particular, the estimates of the mass loading of particulate matter in the atmosphere were revised, along with inhalation exposure time and breathing rate. The revised mass loading values were used in both the groundwater release scenario and the volcanic eruption scenario. These new data were used to generate revised BDCFs.

The second new analysis involved the generation of BDCFs for the predicted cooler and wetter climate over the 10,000-year compliance period. This new data was generated to evaluate the sensitivity of the BDCFs to expected climate change.

The final analysis supported dose calculations for two radionuclides that had not been previously identified as of concern to dose calculations, selenium-79 and neptunium-237. BDCFs were generated for both release scenarios for selenium and for the extrusive scenario for neptunium.

13.3.1 Receptor of Interest

Inherent in the reference biosphere for the potential repository at Yucca Mountain is the representation of the population expected to be at risk. The model represents the potentially exposed population as a hypothetical individual, referred to as the receptor of interest or simply the receptor. Biosphere pathway analyses were performed for a receptor called the average member of the critical group, as defined in proposed 10 CFR Part 63 (64 FR 8640 [DIRS 101680]). An alternative receptor is the reasonably maximally exposed individual, defined in 40 CFR Part 197 (66 FR 32074 [DIRS 155216]). The parameters to define both receptors are based on the behaviors and characteristics of the Amargosa Valley population.

The task of identifying a receptor of interest for the performance assessment had three objectives. The first was to define the population at risk, consisting of the hypothetical groups of exposed individuals and the corresponding characteristics of their expected behavior. The second was to develop estimates of the parameters or attributes for the expected behaviors that are required to evaluate the magnitude of radiation exposure of the group members. The final objective was to choose a receptor or a critical receptor group that is representative of the individuals in the population at risk expected to receive the highest annual doses.

Although the representation of the receptor is based on proposed regulations (see Section 13.3.1.1), the actual realization of the requirements pertaining to the receptor includes many sources of uncertainty. The effect of some of these uncertainties on the outcome of biosphere modeling is evaluated in this section. One question posed was: How sensitive is the modeling outcome to the selection of the attributes of behaviors and characteristics for the receptor? To address this subject, five different farming receptor groups were analyzed, each represented by different values of behavioral attributes.

13.3.1.1 Existing Guidance and Requirements

The representation of the expected population at risk was based on proposed NRC (64 FR 8640 [DIRS 101680]) and EPA (64 FR 46976 [DIRS 105065]) regulations. In the proposed NRC regulations, the exposed population is represented by the average member of the critical group (proposed 10 CFR 63.113(c), 64 FR 8640 [DIRS 101680]). The critical group selected based on the proposed regulations and guidance should be a group of people whose location and habits are characteristic of those individuals that are expected to receive the highest annual doses from the potential release of radionuclides. Specific requirements for assessment of the critical group are as follows (proposed 10 CFR 63.115(b), 64 FR 8640 [DIRS 101680]):

1) The critical group shall reside within a farming community located approximately 20 km south from the underground facility (in the general location of U.S. Route 95 and Nevada Route 373, near Lathrop Wells, Nevada).

2) The behaviors and characteristics of the farming community shall be consistent with current conditions of the region surrounding the Yucca Mountain site. Changes over time in the behaviors and characteristics of the critical group including, but not necessarily limited to, land use, lifestyle, diet, human physiology, or metabolics; shall not be considered.

3) The critical group resides within a farming community consisting of approximately 100 individuals, and exhibits behaviors or characteristics that will result in the highest expected annual doses.

4) The behaviors and characteristics of the average member of the critical group shall be based on the mean value of the critical group's variability range. The mean value shall not be unduly biased based on the extreme habits of a few individuals.

5) The average member of the critical group shall be an adult. Metabolic and physiological considerations shall be consistent with present knowledge of adults.

To select a critical group, individuals likely to be at the highest risk from among the potentially exposed population must be specified. In the process, assumptions are made about diet, nature of human activities, lifestyles, and exposure pathways that affect the level of radiation exposure. The proposed EPA regulations used the reasonably maximally exposed individual (RMEI) to represent the exposed population (proposed 40 CFR 197.20, 64 FR 46976 [DIRS 105065]).

On June 13, 2001, the Environmental Protection Agency (EPA) issued the final rule 40 CFR Part 197 (66 FR 32074 [DIRS 155216]) to establish "public health and safety standards for radioactive material stored or disposed of in the potential repository at Yucca Mountain." The EPA final rule requires the DOE to calculate the annual dose to a reasonably maximally exposed individual (RMEI) as a result of nominal, disruptive, and stylized human intrusion scenarios projected to occur during the 10,000-year compliance period. The calculated annual dose to the RMEI is to demonstrate whether there is reasonable expectation that the individual protection standard is satisfied.

To demonstrate compliance with the EPA individual protection standard, a hypothetical receptor must be defined. 40 CFR 197.21 [DIRS 155216] sets the following criteria for defining the hypothetical receptor, called the reasonably maximally exposed individual:

> The reasonably maximally exposed individual is a hypothetical person who meets the following criteria:
>
> a) Lives in the accessible environment above the highest concentration of radionuclides in the plume of contamination;
>
> b) Has a diet and living style representative of the people who now reside in the Town of Amargosa Valley, Nevada. The DOE must use projections based upon surveys of the people residing in the Town of Amargosa Valley, Nevada, to determine their current diets and living styles and use the mean values of these factors in the assessments conducted for 40 CFR 197.20 and 197.25; and
>
> c) Drinks 2 liters of water per day from wells drilled into the groundwater at the location specified in (a).

By specifying a series of requirements and assumptions about the reasonably maximally exposed individual and the average member of the critical group, the EPA (66 FR 32074 [DIRS 155216], p. 32090) and the NRC (64 FR 8640 [DIRS 101680], p. 8645) establish a reasonably

conservative basis for protection of the individuals expected to be at risk from a potential repository at Yucca Mountain. The concepts used are consistent with the proposed NRC rule and the EPA rule.

The location of the point of compliance is a basic part of the total system performance assessment scenarios. However, location is not included for calculating the biosphere dose conversion factors for the receptor. The exact location of the receptor, whether in the accessible environment (just beyond controlled area southern boundary at approximately 18 km) as specified by EPA (40 CFR 197.21(a) (66 FR 32074 [DIRS 155216]), or in the general location of U.S. Route 95 and Nevada Route 373, near Lathrop Wells, Nevada (at approximately 20 km) as specified by NRC (proposed 10 CFR 63.115(b)(1) 64 FR 8640, [DIRS 101680]), is not a factor in defining the characteristics of the receptor for biosphere modeling because the characteristics of the receptor, as specified by both NRC and EPA, are based on the population residing in the region surrounding the Yucca Mountain site.

The RMEI is similar in many aspects to the average member of the critical group. Both receptors are composite individuals. Also, the use of site-specific dietary and lifestyle characteristics are analogous for the proposed NRC (proposed 10 CFR 63.115(b)(2) (64 FR 8640 [DIRS 101680]) and EPA (40 CFR 197.21(b) (66 FR 32074 [DIRS 155216]) regulations.

Drinking water consumption for the average member of the critical group and for the RMEI is also consistent. The average member of the critical group is estimated to drink an average of 2.1 L (0.54 gal) of water per day from wells drilled into the groundwater, which is comparable with the RMEI's defined water consumption of 2 L (0.53 gal) per day.

Further discussion of these two receptors in the context of the sensitivity analysis is provided in Sections 13.3.1.3 and 13.3.1.8. Given these sensitivity and uncertainty considerations for receptor concepts, the current receptor (average member of the critical group) is similar to the reasonably maximally exposed individual defined by the EPA (40 CFR 197.21, 66 FR 32074 [DIRS 155216]).

13.3.1.2 Development of the Receptor of Interest

As noted previously, the average member of the critical group was chosen as the receptor of interest for the TSPA-SR (CRWMS M&O 2000 [DIRS 153246]) analyses. Identification of the receptor was an iterative process. The first step was to identify screening groups based on the framework of criteria identified in the proposed NRC and EPA regulations. Data regarding behaviors and characteristics of the population in the vicinity of Yucca Mountain were used to characterize screening groups and identify a preliminary receptor. This group exhibited behaviors and characteristics that would result in expected annual doses among the highest in the potentially exposed population. Finally, the analysis examined additional lifestyle and land use data to refine the characterization of the receptor. The results of this analysis are documented in *Identification of the Critical Group (Consumption of Locally Produced Food and Tap Water)* (CRWMS M&O 2001 [DIRS 153342]).

The critical group was selected as the one with the highest exposure of all the potentially exposed groups identified using attributes of the potential behaviors and characteristics of the

population in Amargosa Valley (CRWMS M&O 2000 [DIRS 143940]; CRWMS M&O 2001 [DIRS 153342]). The behaviors and characteristics identified were based upon U.S. Census Bureau data (U.S. Census Bureau 1999 [DIRS 135344]), the *Exposure Factors Handbook* (EPA 1997 [DIRS 103038]; EPA 1997 [DIRS 152549]; EPA 1997 [DIRS 116135]), and a 1997 food consumption survey conducted in the Yucca Mountain region (DOE 1997 [DIRS 100332]). The selected receptor was represented by a farmer who worked 40-60 hours per week outdoors in the contaminated area, recreated a considerable number of hours (over two hours per day) outdoors in the contaminated area, lived in a mobile home or trailer, had a food garden, and consumed locally produced food and well water.

The average member of the critical group, as used in the TSPA analyses, is defined as a composite individual, similar to the definition of the RMEI. The characteristics of both the RMEI and the average member of the critical group are defined from consideration of a range of conditions, typical of the local environment and the local population, that affect exposures. The development of the specifications for the critical group in the context of the potential repository at Yucca Mountain is based on the principles of ICRP, as discussed in the supplementary information to the proposed 10 CFR Part 63 (64 FR 8640 [DIRS 101680], p. 8645). The critical group used in the TSPA analyses, similar to the RMEI, is located directly above the path of the contamination plume, where the exposures are expected to be the highest.

As noted previously, the receptor selection is not unequivocal. The outcome of the process of modeling the receptor of interest depends on many factors, assumptions, and circumstances that contribute to the overall uncertainty associated with the final selection. This section describes how sensitive the resulting annual dose is to the uncertainties in the definition of the receptor. The effects of several factors were evaluated, including:

- Attributes of behaviors and characteristics of the critical group
- Critical group size
- Temporal changes of exposure conditions
- Selection of exposure scenario
- Critical group composition.

13.3.1.3 Effect of Behavioral Attributes

The selected receptor can be described by the set of attributes for behaviors and characteristics used as input parameters in GENII-S V.1.4.8.5 to calculate the BDCFs. These attributes allow quantification of the expected level of exposure of the receptor to radionuclides in the environment. The following characteristics and their corresponding attributes were considered:

- Employment and recreation, which are characterized by the attributes of inhalation exposure time; soil (external) exposure time; and inadvertent soil ingestion rate

- Diet, which is characterized by consumption rates of water and the following locally produced food types: leafy vegetables, other (root) vegetables, fruit, grain, meat (beef and pork), poultry, milk, eggs, and fish.

The attributes of inhalation and soil exposure times are indices of human exposure to airborne and soil contamination, respectively. Both quantities reflect time activity budgets and the associated exposure levels, outdoors and indoors, for the population at risk. Dietary attributes (consumption rates) apply to only that portion of the diet that is derived from local sources.

To explore the effect of choosing a specific set of attributes to characterize a receptor, several alternative receptors characterized by different sets of attributes were analyzed. The analysis focused on the dietary attributes and developed several possible sets of consumption rate values. The alternative receptors included, a receptor based on average food consumption rates for the U.S. population, a receptor based on the food consumption rates recommended for the license termination dose assessment (Kennedy and Strenge 1992 [DIRS 103776]), and three receptors based on the consumption rates of locally produced food for the Amargosa Valley population, as explained in Section 13.3.1.3.3. The first two of the alternative receptors were based on the assumption that 100 percent of the receptor's diet is locally produced, although the food consumption survey (DOE 1997 [DIRS 100332]) did not identify such a dietary pattern among the population in the vicinity of Yucca Mountain. Because it was determined that the receptor of interest was represented by a farmer, the behavioral characteristics of employment, with their associated attributes of inhalation and soil exposure times, were not modified. The analysis employed pathway factors calculated using GENII-S V.1.4.8.5 as described in Section 13.3.1.3.1.

The current receptor in the biosphere model was based on characteristics of the population of the Yucca Mountain region, such as employment, recreation, land use, and diet. Although the employment attributes, including the amount of time spent outdoors, were characteristic of farmers, the dietary attributes were not specific to farmers. They were derived from the results of the food consumption survey, irrespective of the actual employment of the respondents. It was then assumed that the dietary attributes of the receptor coincided with the consumption rates of those members of the Amargosa Valley population who consumed locally produced food and water and had a garden.

13.3.1.3.1 Calculation of Pathway Factors

Radionuclide-specific pathway factors were calculated using a method similar to the one used to calculate BDCFs for the groundwater release exposure scenario (CRWMS M&O 2001 [DIRS 152539], Section 6.7). Pathway factors were calculated for the condition of assumed radionuclide equilibrium concentrations in soil. Radionuclide concentration in soil is important because the magnitude of exposure from a number of exposure pathways depends on this value.

Pathway factors represent annual dose per unit pathway exposure per unit radionuclide concentration in groundwater. The significance of pathway factors is that they represent radionuclide transport in the biosphere for a specific pathway and can be used, as multipliers, to calculate the annual dose for any level of pathway exposure. For example, pathway factors for ingestion of leafy vegetables represent the annual dose resulting from an annual consumption of 1 kg of leafy vegetables grown using contaminated irrigation water with a radionuclide concentration of 1 pCi/L. The summary of pathway factors can be found in Table 13.3-1 (Wu 2001 [DIRS 154894], Table 2).

The annual dose to an individual from a specific radionuclide can be calculated using pathway factors, radionuclide concentration in groundwater, and the actual level of pathway exposure with the following formula:

$$Annual\ Dose\left[rem\right] = PF\left[\frac{\frac{rem}{kg,\ L,\ or\ hr}}{\frac{pCi}{L}}\right] \times PE\left[kg,\ L,\ or\ hr\right] \times C_w\left[\frac{pCi}{L}\right] \quad \text{(Eq. 13-1)}$$

where:

PF = pathway factor
PE = annual pathway exposure
C_w = radionuclide concentration in groundwater.

13.3.1.3.2 Individual Annual Doses for the Farming Group Based on the Amargosa Valley Population

Several assumptions were made in selecting the receptor for Yucca Mountain. Since there was not enough information to accurately integrate attributes of behavioral characteristics for the critical group comprised of farmers, the values of the attributes were developed such that the result would be a conservative value at the high end of the range of annual doses for the exposed population. For example, inhalation and external exposure times were calculated assuming that the person spent a substantial part of the day outdoors. The dietary characteristics were typical of a subset of the Amargosa Valley population, specifically those individuals who consumed locally produced food and had a garden. Individuals who had a garden were determined to consume higher quantities of locally produced crops.

To assess the expected range of individual annual doses to a hypothetical group composed of farmers based on the dietary attributes of the Amargosa Valley population, and to evaluate the sensitivity of the group selection to the values of dietary attributes, the annual doses to individuals in a group composed of farmers were evaluated. The individual annual doses were based on the whole set of the consumption survey responses for the Amargosa Valley population. Annual doses presented in this section are estimates generated only for comparisons (sensitivity studies) and were not directly used in the performance assessment process.

The individual annual doses were determined by combining pathway factors with estimates of the consumption rates of locally produced food and water for individual members of the Amargosa Valley population (DOE 1997 [DIRS 100332]). The food consumption survey was conducted in 1997 to collect socioeconomic information for biosphere modeling. For this purpose, dietary and lifestyle data were collected on adults residing within a 50-mile grid centered on Yucca Mountain. It was estimated that nearly 13,000 adults resided in the total study area at the time of the survey, with about 900 of them in Amargosa Valley, comprising approximately 450 households (DOE 1997 [DIRS 100332], p. vi). The total survey sample consisted of 1,079 responses, with an Amargosa Valley sample of 195. Not all responses from

Amargosa Valley were used in this sensitivity analysis; incomplete responses were deleted from the set. Overall, 37 responses were excluded from consideration.

The food consumption survey determined the consumption frequencies of locally produced food and the consumption rates of water. To estimate individual consumption rates, consumption frequencies were multiplied by the contingent average daily intakes (CADI) for these food groups (DOE 1997 [DIRS 100332], Section 3.6). Since the CADIs represent average values, the individual consumption rates calculated using the survey results do not correspond to the actual consumption rates of the surveyed individuals. Instead, they represent the annual consumption of locally produced food for a hypothetical individual characterized by an average contingency diet and the consumption frequency characteristic of the individuals participating in the survey. (Average contingent intakes, unlike per capita intakes, are calculated for consumers only.) The consequence of this approach is that, although the mean values of consumption rates are represented correctly using the survey results (provided the sample is large enough), the variability of individual consumption rates in the population is not captured. In other words, there is more uncertainty in the distribution of individual consumption rates than indicated by the survey results. Water consumption rates were based on the actual amount of water consumed by individuals surveyed.

Individual annual doses to a hypothetical group of farmers characterized by the estimated values of the individual consumption rates for the Amargosa Valley population were calculated using the mean values of radionuclide concentrations in groundwater at 25,000 years after repository closure predicted in the TSPA-SR (CRWMS M&O 2000 [DIRS 153246]), the pathway factors described in the previous section, and the individual exposure pathway levels for the hypothetical group of farmers (Wu 2001 [DIRS 154894], Section 3.6). The distribution of the annual doses is shown in Figure 13.3-1. The histogram shows that the annual doses for the majority of the individuals are in the low and moderate range of the distribution. Only a few individuals would receive the annual doses in the upper range of the distribution.

The reason for selecting 25,000 years, as opposed to the compliance period of 10,000 years, to evaluate annual doses for the groundwater release scenario results from the expected repository performance predicted by the TSPA-SR (CRWMS M&O 2000 [DIRS 153246], Section 4.3.2). When the performance of the potential repository is evaluated, the probability-weighted consequences for the nominal scenario and the two igneous disruption scenarios are added together. Because there are no predicted nominal waste package failures during the 10,000-year compliance period, the nominal scenario contributes nothing to the combined annual dose from the repository; the combined annual dose comes from igneous disruption alone. The combined annual dose is dominated by the nominal annual dose only at later times because of the larger number of nominal waste package failures (CRWMS M&O 2000 [DIRS 153246], Section 4.3.2). The 25,000-year point in time was also selected for the TSPA-SR calculation (CRWMS M&O 2000 [DIRS 153246], Figure 4.1-6).

13.3.1.3.3 Comparison of the Current Receptor with Alternative Receptors

To evaluate the sensitivity of the biosphere model to the selection of the receptor, annual doses to the receptor as used in the TSPA-SR (CRWMS M&O 2000 [DIRS 153246]) were compared with annual doses to alternative receptors. The receptors were assumed to be characterized by a

specific set of dietary attributes (food consumption rates), but otherwise have the characteristics of the current receptor. The analysis was focused on the dietary attributes because ingestion of locally produced food and tap water was by far a dominant exposure pathway (CRWMS M&O 2001 [DIRS 152539]) in the groundwater release exposure scenario.

The consumption rates for the current receptor were based on the group of 77 individuals who eat locally produced food and have a garden. These individuals were selected from the 195 survey responses for the Amargosa Valley residents. The consumption rates for the alternative receptors were based on the responses of 158 individuals because 37 incomplete responses were excluded from the set, as described in the previous section. In addition, consumption of leafy vegetables was adjusted to reflect the re-classification of consumption of tomatoes from the leafy vegetables group to the fruit group. This resulted in the decreased consumption of leafy vegetables and increased consumption of fruit.

Table 13.3-2 summarizes annual exposure levels for the current receptor and the alternative receptors (Wu 2001 [DIRS 154894], Table 3; Wu 2001 [DIRS 155203], Table 1). The annual consumption rates for the current receptor listed in Table 13.3-2 correspond to those used for both the TSPA-SR analyses (CRWMS M&O 2000 [DIRS 153246]) and the analyses presented in Volume 2 (McNeish 2001 [DIRS 155023]). Other potential receptors were developed based on published consumption rates and the food consumption survey results. For the alternative receptors, labeled U.S. Average Receptor and NUREG/CR-5512 Receptor (Kennedy and Strenge 1992 [DIRS 103776]), 100 percent of the food and water are assumed to be locally produced. This assumption is inconsistent with the findings of the food consumption survey (DOE 1997 [DIRS 100332]), which did not identify any individuals whose entire diet would come from local sources. Nevertheless, these alternative receptors were included to provide bounding values for the analysis.

The consumption rates for the U.S. Average Receptor were derived from the *Exposure Factors Handbook* (EPA 1997 [DIRS 103038]; EPA 1997 [DIRS 152549]) and correspond to the recommended average values for the U.S. population. NUREG/CR-5512 (Kennedy and Strenge 1992 [DIRS 103776]) provides guidance for the dose assessment from exposures to residual radioactive contamination after decommissioning of nuclear facilities. The report identifies the limiting exposure scenarios and provides methods of exposure pathway analysis for critical groups at decommissioned facilities. The report provides numerical values for a wide spectrum of model parameters that may be used in generic screening scenarios. The recommended consumption parameters from NUREG/CR-5512 (Kennedy and Strange 1992 [DIRS 103776], Table 6.23) are listed in Table 13.3-2. Note that the fraction of diet from gardens, recommended for license termination dose assessment, is 0.25 (Kennedy and Strange 1992 [DIRS 103776], Table 6.23), which would decrease the consumption rates of locally produced food by a factor of 4 compared with the values listed in Table 13.3-2.

Table 13.3-2 includes three alternative receptors whose consumption rates were based on the dietary attributes of the Amargosa Valley population: these receptors are labeled in Table 13.3-2 as the Alternative Amargosa Valley Receptors 1, 2, and 3. The annual consumption rates for the Alternative Amargosa Valley Receptor 1 were constructed using the 95th percentile of the estimated locally produced food consumption rates for the Amargosa Valley population (based on 158 individual survey responses) and a daily water consumption of 2 L. The Alternative

Amargosa Valley Receptor 2 is an average member of a group selected using the top 5 percent of annual doses at 25,000 years and 100,000 years.

The decision for selecting the group that receives the top 5 percent of annual doses was influenced by recommendations from the BIOMASS program sponsored by the International Atomic Energy Agency (BIOMASS 1999 [DIRS 154523]). These recommendations concern the determination of critical and other hypothetical exposed groups for analyses of solid radioactive waste disposal. The report states that, as far as the consumption of specific dietary items is concerned, it is often assumed that, provided the sampled population is sufficiently large, the top 5 percent of a distribution may be taken as representative of a high consumer group (BIOMASS 1999 [DIRS 154523], Executive Summary).

The results of the food consumption survey conducted in the Yucca Mountain region indicated that the consumption rates of the local population were highly inhomogeneous. In other words, people who consumed high fractions of a specific food type from local sources usually did not consume much locally grown food of other types. To select a subset of the Amargosa Valley population that would potentially be exposed to the highest annual doses, individuals who received the top 5 percent of the annual dose at 25,000 years were selected (9 individuals). Because the annual doses are time-dependent, this group was combined with individuals whose potential annual doses at 100,000 years were the in the top 5 percent. This group also consisted of 9 different individuals, only one of whom also belonged to the first group; therefore, the final group consisted of 17 individuals. Consideration of the upper 5 percent of annual doses at 250,000 years did not produce any individuals other than those already included in the 25,000-and 100,000-year set. By composing an alternative group of the individuals whose exposures would be among the highest at different times, the group selection becomes independent of the time after repository closure. In other words, the average member of the group receives relatively high exposures regardless of the time after closure when the exposure took place. The consumption rates (consumption exposure levels) for the average member of this alternative farming group (Alternative Amargosa Valley Receptor 2) are listed in Table 13.3-2.

The Alternative Amargosa Valley Receptor 3 was based on the estimated average locally produced food consumption rates for the Amargosa Valley population and a daily water consumption of 2 L. Dietary attributes of this receptor meet the definition of the RMEI in the proposed 40 CFR 197.21(b) and (c) (64 FR 46976 [DIRS 105065]) in contrast with the definition of the RMEI, living style of this receptor does not represent the average lifestyle of people residing in Amargosa Valley, but rather is characteristic of a person who spends a large portion of the day outdoors. This difference is insignificant for the groundwater release exposure scenario because consumption of locally produced food and water is the key contributor to the potential annual dose (CRWMS M&O 2001 [DIRS 152539], Table 15). (For the volcanic eruption scenario, the Alternative Amargosa Valley Receptor 3 is more conservative than the RMEI because of the greater inhalation exposure that results from more time spent outdoors breathing air containing higher concentrations of resuspended contaminated ash particles.)

To test the sensitivity of the annual doses to the receptor's diet, the average annual doses were calculated for all receptors listed in Table 13.3-2 for 25,000 years and 100,000 years after closure (Wu 2001 [DIRS 154894], Section 3.7; Wu 2001 [DIRS 155203], Section 2). The results in

terms of pathway and total annual doses are summarized in Tables 13.3-3 and 13.3-4 for 25,000 years and 100,000 years, respectively (Wu 2001 [DIRS 154894], Section 3.7; Wu 2001 [DIRS 155203], Section 2). It should be emphasized that these are estimated annual doses produced only for comparison and were not used in the TSPA-SR analyses (CRWMS M&O 2000 [DIRS 153246]).

At 25,000 years, annual doses calculated for the receptor based on the NUREG/CR-5512 (Kennedy and Strenge 1992 [DIRS 103776]) consumption rates are the highest annual doses for all receptors considered. However, aquatic food consumption rate is the dominant pathway for this receptor because of the extremely high consumption rate of fish assumed for the screening scenario, exceeding the 99th percentile of U.S. freshwater fish consumption. If the aquatic food ingestion annual dose is disregarded, then the ratio between the highest annual dose (U.S. Average Receptor) and the annual dose to the current receptor is 4. At 100,000 years, the ratio between the highest annual dose and the annual dose to the current receptor is less than 2. Annual doses are the lowest for the Alternative Amargosa Valley Receptor 3, whose dietary attributes are consistent with those of the RMEI (proposed 40 CFR 197.21(b) and (c) [64 FR 46976 [DIRS 105065]]).

13.3.1.4 Effect of Critical Group Size

The annual dose to the average member of the exposed group depends on the critical group size. This concept is demonstrated in Figure 13.3-2, which shows the relationship between the annual dose to the average member of the hypothetical group of 158 farmers at 25,000 years and the number of members in the group (Wu 2001 [DIRS 154894], Section 3.8).

The data presented in Figure 13.3-2 were obtained by arranging the 25,000-year annual doses to the hypothetical farming group based on the Amargosa Valley population in descending order, then calculating the average annual dose for the increasing number of individuals in the group. As the group count increases, the average annual dose decreases because of the inclusion of lower annual doses in the average. The curve decreases more steeply when the number of group members is less than 20, then flattens out as the most probable values for annual dose are included. For the exposed group considered in this sensitivity assessment, the average annual dose may vary by up to a factor of 5, depending on the size of the group.

13.3.1.5 Effect of Temporal Changes of Exposure Conditions

The annual doses to the receptor of interest, depend on the number of circumstances and parameters that may change with time. One of the changing conditions of human exposure includes varying radionuclide concentrations at the source of contamination, such as groundwater. This effect has been apparent in the process of selecting one of the alternative receptors, described in Section 13.3.1.3. Based on the dietary characteristics of the Amargosa Valley population, the group of the most exposed individuals at 25,000 years was different than the group of the most exposed individuals at 100,000 years because of the different composition of radionuclide contaminants in groundwater.

As shown in the TSPA-SR (CRWMS M&O 2000 [DIRS 153246], Figures 4.1-6 and 4.1-19b), different radionuclides are dominant, from the perspective of their contribution to the total

annual dose to the receptor, at different times. Therefore, the contribution of exposure pathways to annual dose also varies with time.

Radionuclide buildup in soil is another example of the temporal evolution of exposure conditions. Some pathways, such as consumption of contaminated groundwater, do not depend on the concentration of radionuclides in the soil. However, many exposure pathways, such as inhalation exposure, external exposure, and some processes considered for the ingestion pathway (e.g., root uptake of radionuclides from soil), depend on the concentration of radionuclides in the soil. Therefore, consideration of radionuclide buildup in the soil may influence the process of selecting the receptor of interest.

The effect of climate change on receptor selection is yet another aspect of extrapolating into the future. It is conceivable that, if climate conditions change and the weather becomes wetter and cooler, the receptor may adapt its behavior in response to these changing environmental conditions. The types of crops grown, agricultural practices and parameters (e.g., the amount of water used for irrigation), crop growing seasons, and crop yields may also change. This effect was partly evaluated by considering selected agricultural parameters typical of Spokane, Washington, which was selected as an analogue of the evolved climate for up to 10,000 years (CRWMS M&O 2001 [DIRS 152539], Section 6.4). These parameters were used to calculate the BDCFs for the evolved climate (see Section 13.4.2).

13.3.1.6 Effect of the Exposure Scenario

A TSPA was conducted for the nominal scenario and two disruptive scenarios. As noted in Section 13.3.1.3.2, the probability-weighted consequences for both these types of scenarios are added together to evaluate the performance of the potential repository. At early times (before about 40,000 years), igneous disruption doses dominate the scenario combination. However, during later times (after about 40,000 years), the combined dose is dominated by the nominal dose (CRWMS M&O 2000 [DIRS 153246], Section 4.3.2).

The biosphere model for the nominal scenario used the groundwater release exposure scenario (see Section 13.1). The same exposure scenario is also used for the human intrusion and igneous intrusion groundwater transport scenarios. In the disruptive scenarios, the assessment is focused on a volcanic eruption (extrusive igneous event). The corresponding biosphere model uses the exposure scenario associated with the deposition of contaminated volcanic ash on the ground. The pathway analyses for the BDCFs for the two respective exposure scenarios (CRWMS M&O 2001 [DIRS 152539], Section 6.7; CRWMS M&O 2001 [DIRS 152536], Section 6.6) showed substantial differences between pathway compositions. In the groundwater release exposure scenario, the majority of the annual dose was contributed by drinking water and leafy vegetable consumption. In contrast, the dominant pathway for the volcanic eruption exposure scenario was inhalation of airborne, contaminated ash and soil. Thus, a unique receptor representative of the population most at risk cannot be defined *a priori*. The actual receptor is time- and scenario-dependent and requires a knowledge of TSPA results.

The consequence of such pathway contributions to the BDCFs, and thus the annual dose, is such that for a population exposed to high concentrations of airborne contaminants, the receptor could be determined based primarily on the inhalation exposure. The selection criteria associated with

dietary habits, which were used to identify the receptor for the groundwater release exposure scenario, are of limited importance for the postulated volcanic eruption scenario. However, the condition that the receptor spends a considerable amount of time working outdoors, although not critical for identification of the receptor in the groundwater release scenario, is sufficient to substantiate the selection of the same receptor for an assessment of the consequences of a volcanic eruption.

Other conceivable exposure scenarios include the exposure conditions of a subsistence farmer receptor. The consideration of the subsistence farmer receptor is based on the assumption that subsistence farmers make a (reasonable) maximum use of local environmental resources. For example, exclusive reliance on local water supplies for all uses—including agricultural purposes—will tend to enhance radiological exposures compared with situations where more diverse sources are exploited. The deliberate recycling of materials and nutrients would also be expected to enhance the accumulation of radionuclides in environmental media, maximizing radiation exposure. Thus, such farmers might be expected to have the highest exposure risk (BIOMASS 1999 [DIRS 154523], Section 3.2.1).

It is not immediately evident, however, that such a group necessarily provides a fully sufficient basis for ensuring consistency of protection with that afforded by today's radiation protection practices, or that it would always be associated with the highest potential risks. Furthermore, there is little information available concerning biosphere systems and human behavior relating to true subsistence farming methods, compared with typical practices presently adopted. In this document, "true subsistence farming" refers to farming in which only local resources are available to the farmer. This would preclude the use of modern farming practices that make use of many imported resources (e.g., factory-produced equipment, fuel, and fertilizers). True subsistence farming would involve, for example, the use of farm animals for plowing or composting as the sole source of fertilizer (BIOMASS 1999 [DIRS 154523], Section 3.2.1).

13.3.1.7 Effect of the Critical Group Composition

Consideration of the age composition of the critical group could also affect selection. Non-adults are not considered appropriate for the analysis of long-term repository performance (ICRP 2000 [DIRS 152447]), Section 4.2). Considering the time scale of the assessment, it could be assumed that radioactive contamination of the biosphere from repository releases is likely to remain constant over periods considerably longer than the human life span. It is then reasonable to calculate the annual dose averaged over the lifetime of individuals, which means that it is not necessary to calculate doses to different age groups. This average can be adequately represented by the annual dose to an adult (ICRP 2000 [DIRS 152447]).

13.3.1.8 Conclusions

The definition of the receptor is a source of uncertainty. The process was shown to be complex because the relative concentrations of radionuclides affect the receptor selection. Therefore, any attempt to define the receptor before the TSPA concentration results are known is uncertain.

Evaluation of the sensitivity of the biosphere modeling results to the definition of the receptor of interest involved calculations of estimated annual doses. This dose assessment was conducted

for sensitivity studies only and the resulting dose estimates were not used in the performance assessment process. Also, the dose assessment method (see Sections 13.3.1.3.1 and 13.3.1.3.2) was different from the one used in the TSPA.

Among the receptors whose dietary characteristics were based on the Amargosa Valley population, the estimated annual doses at 25,000 years for Alternative Amargosa Valley Receptors 1 and 2 (3.0×10^{-5} rem, and 3.1×10^{-5} rem, respectively) are higher than those for the current receptor (1.5×10^{-5} rem) by a factor of about 2, while the annual dose to the Alternative Amargosa Valley Receptor 3 (1.1×10^{-5} rem) is lower than that for the current receptor by about 27 percent. This difference can be put into perspective by considering that the stochastic BDCFs, where some quantifiable uncertainties are considered, are distributed about their mean values by a factor of about three.

As noted in Section 13.3.1.3.3, the Alternative Amargosa Valley Receptor 3 was consistent with the definition of the RMEI in the proposed 40 CFR Part 197 (64 FR 46976 [DIRS 105065]) and the final rule (66 FR 32074 [DIRS 155216]) with regard to the dietary characteristics (it was based on the average consumption rates of locally produced food and water for the Amargosa Valley population). Because of the lifestyle characteristics, such as employment associated with greater than the average potential for exposure outdoors, this alternative receptor would be more at risk than the RMEI, which is characterized by the average lifestyle characteristics (proposed 40 CFR 197.21(b), 64 FR 46976 [DIRS 105065]; 40 CFR 197.21(b), 66 FR 32074 [DIRS 155216]). The exposure to the Alternative Amargosa Valley Receptor 3 is therefore a conservative estimate of the exposure to the RMEI, as defined by the EPA. Based on the analysis for the Alternative Amargosa Valley Receptor 3, the estimated annual dose to the RMEI for the groundwater contamination exposure scenario at 25,000 years, would be lower than that for the current receptor (the average member of the critical group) by less than about 30 percent.

Given sensitivity and uncertainty consideration for the receptors based on the Amargosa Valley population, the exposures to average member of the critical group and the RMEI are consistent. Both of these receptors are considered to be composite individuals representing a group located in small area above the contaminated plume, and have comparable dietary characteristics, both with respect to the drinking water as well as the locally produced food. These similarities result in the expected exposures from the potential repository being comparable for these two receptors.

For a receptor approximating a subsistence farmer, where all food consumed is locally grown, the highest predicted annual dose at 25,000 years is 8.7×10^{-5} rem. However, even for this extreme receptor, the predicted annual dose is less than six times that predicted for the current receptor at 25,000 years and less than two times that predicted for the current receptor at 100,000 years. This factor should provide an upper limit on the uncertainty associated with using the current receptor of interest. However, for this value to be approached, several inhabitants would have to be identified whose entire food intake was all locally grown. While this has a probability of occurring, the survey data was not able to identify a single individual who approached such extreme eating habits. The likelihood of several such individuals being present in Amargosa Valley without a single example being observed is low.

By considering the individual annual doses for the people most at risk in the survey and forming the average of the highest individual annual doses, the variation of average annual dose with population size can be observed. As Figure 13.3-2 shows, the average annual dose is predicted to change by about a factor of two as the number of critical group members goes from one to about twenty. This approach to generating the critical group increases the mean annual dose by a factor of about three for a group consisting of about ten people.

By evaluating several alternative methods of defining the receptor, it appears likely that the annual dose uncertainty from the definition of the current receptor is approximately bounded by a factor of three to that used in the TSPA-SR (CRWMS M&O 2000 [DIRS 153246]) and in the analysis presented in Volume 2 (McNeish 2001 [DIRS 155023]).

13.3.2 Comparison of Dose Assessment Methods

13.3.2.1 Introduction

Under 10 CFR Part 20 [DIRS 104787] and proposed 10 CFR Part 63 (64 FR 8640 [DIRS 101680]), the annual dose received by an individual as a result of radionuclide intake (ingestion and inhalation) and the external exposure to radioactive materials in a given year is referred to as the TEDE.

As defined by the NRC in 10 CFR 20.1003 [DIRS 104787], the TEDE is "the sum of the deep-dose equivalent (for external exposure) and the committed effective dose equivalent (for internal exposure)." The committed effective dose equivalent (CEDE) is defined by the NRC in 10 CFR 20.1003 [DIRS 104787] as the "sum of the products of the weighting factors applicable to each of the body organs or tissues that are irradiated and the committed dose equivalent to those organs or tissues."

The EPA rule (40 CFR 197.2 [DIRS 155216]) introduced the following definitions: "*Annual committed effective dose equivalent* means the effective dose equivalent received by an individual in one year from radiation sources external to the individual plus the committed effective dose equivalent," and the "*Committed effective dose equivalent* means the effective dose equivalent received over a period of time (e.g., 30 years), as determined by NRC, by an individual from radionuclides internal to the individual following a one-year intake of those radionuclides." Annual CEDE, as defined by the EPA, is equivalent to the TEDE resulting from one-year exposure.

The organ/tissue weighting factors used in the definition of CEDE were recommended by ICRP 30 (ICRP 1979 [DIRS 110386]; ICRP 1980 [DIRS 110351]; ICRP 1981 [DIRS 110352]). These weighting factors are used by the EPA to calculate the exposure-to-dose conversion factors for inhalation and ingestion presented in Federal Guidance Report No. 11 (Eckerman et al. 1988 [DIRS 101069]). The exposure-to-dose conversion factor, more commonly referred to as a dose conversion factor (DCF), is one of the fundamental representations of a dosimetric model used in assessing potential radiation dose. Specifically, the DCF allows an exposure to a radionuclide to be converted to a dose.

After the incorporation of ICRP 30 methodology and associated weighting factors into various U.S. regulations, the ICRP introduced a new set of dose conversion factors in ICRP 72

(ICRP 1996 [DIRS 152446]). This set was based on updated biokinetic data and models and the revised method for computing radiation doses presented in ICRP 60 (ICRP 1991 [DIRS 101836]). In ICRP 60, a new dosimetric quantity—the effective dose—was introduced. To date, the revised ICRP dosimetric method and the new DCFs have not been incorporated into U.S. regulations.

13.3.2.2 Purpose of the Comparison

Because of the difference between the two dosimetric methods, a comparison was conducted to evaluate the impact of the revised methodology on previously calculated BDCFs (Tappen 2001 [DIRS 154890]). The analysis was also meant to determine the magnitude of changes the new dosimetry might have on calculations of annual dose, as well as improve confidence in the analysis results. The comparison estimates the potential impact on BDCFs if the revised ICRP method were incorporated into U.S. regulations.

The previously developed BDCFs were calculated using dosimetric models based on the conceptual approach recommended in ICRP 26 (ICRP 1977 [DIRS 101075]) and the dosimetric methods outlined in ICRP 30 (ICRP 1979 [DIRS 110386]; ICRP 1980 [DIRS 110351]; ICRP 1981 [DIRS 110352]). This method uses a set of tissue/organ weighting factors that reflect the organs' relative contribution to the total health detriment (risk) when the entire body is uniformly irradiated. These factors are based on the data and biokinetic models available at the time ICRP 30 was issued.

13.3.2.3 Development of Assessment

ICRP 72 (ICRP 1996 [DIRS 152446]) introduced a new set of dose conversion factors based on a revised method for computing radiation dose presented in ICRP 60 (ICRP 1991 [DIRS 101836]). The method introduced a new dosimetric quantity, the effective dose.

The effective dose considers an expanded list of tissues/organs, updated biokinetic data and models, and revised tissue/organ weighting factors. In computing the revised weighting factors, the ICRP made two fundamental changes. First, the application of the weighting factor was changed from consideration of absorbed dose at a point in the organ to consideration of absorbed dose averaged over the total organ (ICRP 1991 [DIRS 101836], p. 5). Second, the concept of detriment (risk) was expanded (ICRP 1991 [DIRS 101836], p. 13). Under this concept, detriment considers the risk of both fatal and nonfatal cancers, hereditary defects over all future generations, and the relative loss of life expectancy given the occurrence of a fatal cancer or severe genetic disorder (ICRP 1991 [DIRS 101836], p. 23). A comparison of the tissue/organ weighting factors used in the two dosimetric methods is presented in Table 13.3-5.

For the purpose of quantifying the magnitude of the potential impact of the revised ICRP dosimetric method (ICRP 1996 [DIRS 152446]) on previously calculated BDCFs, the BDCFs for two exposure scenarios were evaluated. These were (1) the mean BDCFs for the first irrigation period of the groundwater release scenario for the current climate (CRWMS M&O 2001 [DIRS 152539], Table 9), and (2) the mean BDCF for the volcanic eruption, transition phase, assuming a 1-cm ash layer and annual average mass loading (CRWMS M&O 2001 [DIRS 152536], Table 11).

In order to accomplish this, it was necessary to first calculate pathway-specific BDCFs for each radionuclide of interest. This was done by multiplying the previously calculated radionuclide-specific mean BDCF by the percent pathway contribution for each of the three primary pathways (CRWMS M&O 2001 [DIRS 152539], Table 15; CRWMS M&O 2001 [DIRS 152536], Table 16). Pathway-specific BDCFs were calculated for each pathway that contributed 1 percent or more to the total radionuclide-specific BDCF. Each of the pathway-specific BDCFs was then multiplied by the ratio of the ICRP 72 DCF (ICRP 1996 [DIRS 152446]) to the GENII-S V.1.4.8.5 DCF for that pathway. For each radionuclide, these pathway BDCFs were then added to obtain the BDCF for all pathways. This is what the modified BDCF would be for each radionuclide if the ICRP 72 DCFs were used.

13.3.2.4 Results of the Assessment

The results of this assessment are presented in Tables 13.3-6 and 13.3-7. It is important to note that the modified BDCFs were developed to quantify the impact of an alternative ICRP methodology and provide confidence to stakeholders, not to support any evaluation of regulatory compliance. The measure of the impact of the revised methodology is the BDCF ratio, which is the ratio of the modified BDCF for a radionuclide divided by the original mean BDCF for that radionuclide.

To assess the potential impact of the alternative dosimetric method, the effect of the method on each BDCF for the principal dose-contributing radionuclides in the nominal and disruptive scenarios was examined. In the nominal scenario out to 100,000 years, the TSPA-SR analysis identified four radionuclides—technetium-99, iodine-129, neptunium-237, and plutonium-239—as the primary contributors to annual dose (CRWMS M&O 2000 [DIRS 153246], Section 4.1). As shown in Table 13.3-6, the application of the alternative method increases the BDCF for iodine-129 by a factor of approximately 1.6 and the BDCF for technetium-99 by about 10 percent, while the BDCFs for neptunium-237 and plutonium-239 show decreases by factors of approximately 13 and 4, respectively. The annual dose associated with each of these radionuclides would show a similar change.

In the disruptive scenario, americium-241, plutonium-240, plutonium-239, and plutonium-239 are identified as the major contributors to annual dose during the first 2,000 years (CRWMS M&O 2000 [DIRS 153246]). Strontium-90 is identified as a significant contributor during the extremely early stage of the scenario, but rapidly decreases due to radioactive decay. Comparison of the modified BDCFs for these radionuclides with the BDCFs previously calculated for the volcanic eruption indicates that the annual dose associated with these radionuclides would decrease. The annual dose attributable to americium-241 would decrease by approximately 22 percent, while the annual dose associated with each of the plutonium isotopes would remain essentially unchanged (a decrease of only 3 percent). The BDCF for strontium-90 shows a decrease of approximately 12 percent.

After approximately 2,000 years, the annual dose from igneous activity would be dominated by radionuclides associated with groundwater releases from waste packages damaged by igneous intrusion (CRWMS M&O 2000 [DIRS 153246], Section 4.2.2). The impact of the revised ICRP methodology on the BDCF developed for this time period would be consistent with that described for the nominal scenario.

If the ICRP 72 DCF were used instead of the ICRP 30 DCFs, the nominal scenario doses would be slightly higher at the time when iodine-129 and technetium-99 are the dominant radionuclides (by less than a factor of 1.6). However, when neptunium-237 and plutonium-239 become dominant at the later time, the total annual dose would be several times lower if the ICRP 72 DCFs were used.

13.3.3 Uncertainties Associated with Radionuclide Removal from Soil by Leaching

13.3.3.1 Introduction

The GENII-S V.1.4.8.5 code considers radionuclide accumulation in and depletion from the surface soil in which crops are rooted. In the case of the groundwater release scenario, irrigation provides the source for accumulation. The removal mechanisms (Napier et al. 1988 [DIRS 100953], Section 4.6.2) are radioactive decay (the code contains half-life data that are used to derive the loss rate), crop uptake (the code calculates the rate of removal from the user-specified crops), and leaching. In the case of leaching, the user can specify fixed leaching coefficients for those elements under consideration. As discussed below, the leaching coefficient is derived from the partition coefficient of the element. The partition coefficient is subject to a degree of uncertainty, thereby implying that the leaching coefficient should be modeled as a range of values rather than a fixed value. This analysis assesses the effect of this uncertainty in partition coefficients on BDCF values. This section briefly reviews the leaching submodel and the data developed to support the calculation of BDCFs as a function of irrigation period. These data were discussed, developed, and reported in *Evaluate Soil/Radionuclide Removal by Erosion and Leaching* (CRWMS M&O 2001 [DIRS 152517]).

13.3.3.2 Soil Leaching Model and Data

The leaching coefficient used by the GENII-S V.1.4.8.5 code is derived from the leaching model developed by Baes and Sharp (1983 [DIRS 109606]). This model was used to calculate leaching coefficients for radionuclide elements introduced to the soil through surface irrigation with contaminated groundwater. The Baes and Sharp (1983 [DIRS 109606], Equation 13-2) relationship is considered to be an appropriate and defensible model to calculate soil leaching coefficients for the TSPA-SR (CRWMS M&O 2001 [DIRS 152517], Section 6.2):

$$\lambda = \frac{P + I - E}{D \times \theta \times (1.0 + \rho / \theta \times \mathrm{K_d})} \qquad \text{(Eq. 13-2)}$$

where:

λ = the leaching coefficient (1/yr)

P, I, and E = the annual precipitation, irrigation, and evapotranspiration rates, respectively ($P + I - E$ = 15 cm/yr) (CRWMS M&O 2001 [DIRS 152517], Section 6.2)

D = depth of surface soil (the default value is 15 cm) (CRWMS M&O 2001 [DIRS 152434], Table 14)

θ = the volumetric water content of soil (the assumed value is 0.217 ml/cm^3 or cm^3/cm^3)

ρ = surface soil bulk density (225 kg/m^3) (CRWMS M&O 2001 [DIRS 152434], Table 14)

K_d = the surface soil solid/liquid partition coefficient for a specific radionuclide (isotope-independent) and soil type (L/kg or cm^3/g).

The only parameter that depends on the contamination species is the partition coefficient; the others are soil and irrigation parameters. *Evaluate Soil/Radionuclide Removal by Erosion and Leaching* (CRWMS M&O 2001 [DIRS 152517]), from which the leaching coefficients were derived, uses the same values for *(P + I - E)*, *D*, and ρ that were used as inputs to the GENII-S V.1.4.8.5 code. Each of these values is subject to uncertainty. However, as these inputs are also used in GENII-S V.1.4.8.5, this stand-alone uncertainty assessment cannot evaluate the total effect on BDCF uncertainty. As discussed below, the uncertainty in the K_d values can be an order of magnitude or more. The values for K_d and θ were obtained from scientific publications. Although both values are subject to some degree of uncertainty, they were both used as single-valued deterministic inputs to the GENII-S V.1.4.8.5 code. This was not done by choice, but because the GENII-S V.1.4.8.5 code cannot accept the leaching factor parameter (λ) as a distribution that reflects its inherent uncertainty.

It should be apparent that the leaching process, which is driven by irrigation, is not a continuous process, but only occurs during and immediately after irrigation. At times of overwatering, performed to flush out any accumulated salts in the soil from previous irrigation, the upper layer of soil requires a high water content to allow downward transport to occur. Thus, at times when leaching is occurring, the moisture content of the soil has to be high and the value used for volumetric water content, θ, is likely to be subject to a relatively small uncertainty. However, the values of K_d are subject to large potential uncertainty (International Atomic Energy Agency 1994 [DIRS 100458], pp. 30 to 31). Because of the inability of GENII-S V.1.4.8.5 to accept a distribution for leaching, this source of uncertainty has not been previously addressed.

Uncertainty in Current Model—As reported in *Evaluate Soil/Radionuclide Removal by Erosion and Leaching* (CRWMS M&O 2001 [DIRS 152517], Section 6.2), published information on radionuclide-specific K_d measurements for soils in the Amargosa Valley does not exist. Therefore, there is a degree of uncertainty in how the K_d values used in the analysis (CRWMS M&O 2001 [DIRS 152517], Table 4) would differ from the values that would be obtained from actual experimental analysis on the Amargosa Valley soils considered. The data source used for the K_d values also provides an estimate of the range of values for each element. Using the values given in Table 13.3-8 as values used, lower limit and upper limit, in Equation 13-2, the respective leaching coefficient can be determined. Taking the inverse of the leaching coefficient provides an estimate of the characteristic time for the buildup of radionuclides in soil if only leaching is considered. The actual buildup time can be calculated by formulating a total removal rate that is the sum of the removal rates from all processes. In GENII-S V.1.4.8.5, the individual removal processes are leaching, radioactive decay, and harvest removal. The values for each of these parameters appropriate for Amargosa Valley soils, along with the radionuclides identified as the major total annual dose contributors (CRWMS M&O 2000 [DIRS 153246], Figure 4.1-6),

are shown in Table 13.3-8. The K_d values were obtained from *Evaluate Soil/Radionuclide Removal by Erosion and Leaching* (CRWMS M&O 2001 [DIRS 152517], Table 4), and the limiting K_d values were obtained from *Handbook of Parameter Values for the Prediction of Radionuclide Transfer in Temperate Environments* (International Atomic Energy Agency 1994 [DIRS 100458], pp. 30 to 31).

In assessing the impact on BDCFs of values of K_d sampled from over the suggested range, two cases have to be considered. The first arises when the value of K_d is below the value used in the calculations for existing BDCFs; the second occurs when the sampled value is above the value used.

If the correct K_d is lower than the value used, the leaching coefficient is increased and results in less radionuclide buildup in soil. Thus, BDCFs can only be decreased. However, for the BDCFs for the groundwater release scenario (CRWMS M&O 2001 [DIRS 153207], Table 3), a significant effect was only seen in the case of plutonium-239. Even in this case, the buildup only amounted to 50 percent. If the actual K_d values are lower than the K_d values used and shown in Table 13.3-8, the result is a small reduction in BDCFs and predicted annual doses.

The effect on BDCFs when the correct K_d is higher than the value used in calculations is more complex. In the case of plutonium, where the buildup is predicted to take many thousands of years (comparable to the values for characteristic removal time for leaching shown in Table 13.3-8), it can be shown (CRWMS M&O 2001 [DIRS 153206], Section 6.2.3) that contamination removal by other processes, such as soil removal by erosion, with its characteristic removal time of 250 years (CRWMS M&O 2001 [DIRS 153206], Section 6.2.2), will dominate the loss process. As the loss process is dominated by soil erosion, there will be no significant change in the BDCF values already used in TSPA calculations for which erosion was considered (CRWMS M&O 2001 [DIRS 153206]). However, for the other dominant radionuclides in the TSPA, further calculations had to be conducted. The results of these calculations for the 6th irrigation period are given in Table 13.3-9. This is the most conservative irrigation period of those calculated, where five-sixths of the buildup has been completed when considering leaching and radioactive decay.

13.3.3.3 Conclusions on the Effect of Partition Coefficient Uncertainty on Biosphere Dose Conversion Factors

For iodine-129 and neptunium-237, a large change in the assumed leaching coefficient (which is more than two orders of magnitude; see Table 13.3-8) results in a BDCF change of a few tens of percent even after long periods of continual irrigation. The underlying reason for this effect is that the transfer coefficient from soil to plant, in which the soil reservoir would play a part, is not a significant pathway for these elements. The dominant mechanism for these radionuclides to contaminate crops is through leaf absorption from contact with irrigation water.

In the case of technetium-99, the soil reservoir plays a more important role because the root uptake by vegetables is significant. Thus, in this case the net result is an increase of about a factor of five in the mean BDCF value. If the actual site-specific K_d for technetium-99 is higher than the value used to generate the revised BDCFs, there could be some underestimation of annual dose. To obtain an estimate for the net effect of the uncertainty in partition coefficients, a

simple average can be generated by assuming equal probabilities of K_d being (1) around the present value used, (2) significantly below the value used, or (3) significantly above the value used (i.e., about the values used to generate the data in Table 13.3-9). If this sampling were done for the TSPA, the impact would be to increase the estimated average annual dose from technetium-99 by about a factor of 2.3 over the annual dose estimated from the BDCFs discussed in Section 13.2. The distribution width (i.e., the standard deviation) of the BDCFs would be increased once the uncertainty in K_d had been taken into account, thereby reflecting the increased total uncertainty. A similar weighting approach to the BDCFs for iodine-129, neptunium-237, and plutonium-239 estimates changes in the mean BDCF values of about 10 percent.

13.3.4 Uncertainties from Fixed Parameter Values

GENII-S V.1.4.8.5 has the capability to represent many input parameters as distributions and thereby incorporate uncertainty into the calculation of BDCF distributions. However, some parameters can only be represented by single values (Leigh et al. 1993 [DIRS 100464], Section 5.8). These fixed value parameters are known to be subject to potential uncertainty, but the construction of the code does not allow this uncertainty to be incorporated and propagated through to the distribution of BDCFs. This section evaluates the magnitude of one group of parameters and their uncertainties in the second most important ingestion pathway, leafy vegetables. For this assessment, attention was focused on the four radionuclides shown in the TSPA (CRWMS M&O 2000 [DIRS 153246], Table 4.1-6) to be the most significant contributors to annual dose: technetium-99, iodine-129, neptunium-237, and plutonium-239.

To identify the pathways of importance, a deterministic GENII-S V.1.4.8.5 run was conducted for each of the four important radionuclides in the groundwater release scenario. These calculations, reported in Wu (2001 [DIRS 154892]), were conducted using best estimate parameter values, with leaching and soil erosion included, and a sufficiently long period of previous irrigation such that BDCF equilibrium had been achieved. For each of the four radionuclides, the contribution of the significant pathways to BDCF values was determined (Table 13.3-10).

The drinking water pathway is dominant, but the leafy vegetable pathway is the second most important contributor to BDCFs for the groundwater release scenario. These two pathways together contribute more than 80 percent of the BDCF for all four radionuclides (Table 13.3-10). The only input parameter required to calculate the dose from drinking water is the quantity of water ingested. For leafy vegetables, several parameters must be defined. Any unquantified uncertainties in those parameters could propagate through the calculation and impact the BDCF values. To demonstrate the impact of these uncertainties, consider the case where the drinking water dose is known and the leafy vegetable contribution is allowed to vary. If the parameters used in the calculation of the leafy vegetable contribution were changed such that they caused this pathway to give a zero contribution to the BDCF value, there would be about a 25 percent change in the BDCFs. If the leafy vegetable input parameters were changed such that this pathway contribution were doubled, there would only be about a 25 percent increase in BDCFs. A similar elementary assessment can show that the uncertainties in other, smaller contribution pathways will have less impact on BDCF uncertainty for the same magnitude of pathway uncertainty. Because the vegetable (leafy and other) pathway was the second most significant

contributor to the BDCF value for each of the four radionuclides, attention was directed to the uncertainties associated with this pathway.

Three of the GENII-S V.1.4.8.5 input parameters in the vegetable pathway are subject to large uncertainty, but these parameters can only be represented in GENII-S V.1.4.8.5 by fixed values. These parameters are:

A. The weathering half-life (removal of radionuclides from plant foliage by weathering)

B. The translocation factor (the fraction of contamination that is incorporated in the edible portion of the plant from its surfaces) for leafy vegetables

C. The leaching coefficient of radionuclides from soils by irrigation.

From literature surveys, the estimate for the weathering half-life value was justified to be 14 days (CRWMS M&O 2001 [DIRS 152434], Section 6.6). For this study, the values that were considered as lower and upper limits were 5 days and 56 days (CRWMS M&O 2001 [DIRS 152434], Table 10). The translocation factor, which was assigned a value of unity to generate the BDCFs for the *Yucca Mountain Science and Engineering Report* (DOE 2001 [DIRS 153849]), was estimated to have a range of variability between 0.1 and 1.0 (CRWMS M&O 2001 [DIRS 152434], Table 11). It should be noted that both parameters have a range of uncertainty that spans an order of magnitude.

The leaching coefficient, a function of the partition coefficient (K_d) (Equation 13-2), was determined from the expected variability of the K_d values (the values used in this evaluation are those presented in Table 13.3-8). These values depended on the element considered. For technetium-99, the range of leaching coefficients (from low to high) was a factor of 35; for plutonium-239, the range was a factor of almost 900. The range for the other two elements fell in between: iodine-129 had a range factor of 540, and neptunium-237 had a range factor of 420. For plutonium-239, using the lower limit of the leaching coefficient, the time required for continuous irrigation (in the absence of soil loss) to approach equilibrium is approximately 25,000 years. The approach used to calculate the period of radionuclide buildup in soils from a knowledge of the leaching coefficient and other rates of removal of radionuclides is discussed in *Abstraction of BDCF Distributions for Irrigation Periods* (CRWMS M&O 2001 [DIRS 153206], Sections 6.1 and 6.2). The other radionuclides require only a few hundred years of irrigation to reach the same degree of buildup in soil. Because of the long time needed for the plutonium buildup, the data for 25,000 years was disregarded because soil loss would dominate the process, causing much less radionuclide buildup (CRWMS M&O 2001 [DIRS 153206], Sections 6.2.2 and 6.5).

GENII-S V.1.4.8.5 was run using various combinations of the three parametric values discussed above. All other parameter values and distributions were the same as those used to generate the data for the TSPA-SR (CRWMS M&O 2000 [DIRS 153246]), as noted in the *Nominal Performance Biosphere Dose Conversion Factor Analysis* (CRWMS M&O 2001 [DIRS 152539], Section 6). Table 13.3-11 shows the mean BDCF value used in the *Yucca Mountain Science and Engineering Report* (DOE 2001 [DIRS 153849]) and the minimum and

maximum mean BDCF values for the input parameter combinations taken from the extremes of the ranges.

The BDCF values provided to the TSPA-SR (CRWMS M&O 2000 [DIRS 153246]) correspond to the data shown in the row labeled "Long Irrigation" "Nominal" in Table 13.3-11 (CRWMS M&O 2001 [DIRS 153206], Section 7; CRWMS M&O 2001 [DIRS 153207], Section 7). The variations in the parameter values discussed above could increase the BDCF values to those shown in the row labeled "Long Irrigation" "Maximum." The parameter variations could also cause the BDCFs to be as low as the values shown in the row labeled "Zero Irrigation" "Minimum." These extreme values can be used with data in the row labeled "Long Irrigation" "Nominal" to derive multiplying factors for converting a groundwater release BDCF to an extreme value due to uncertainties (Table 13.3-12).

In conclusion, the large estimated uncertainty in each of three parameters that cannot be represented in GENII-S V.1.4.8.5 as distributions are estimated to impact BDCFs by approximately ±50 percent for iodine-129, neptunium-237, and plutonium-239. In the case of technetium-99, the BDCF uncertainty is larger and varies over the range of -20 percent to +400 percent. The large BDCF increase for technetium-99 is attributed to the more significant root uptake by vegetables after the radionuclide has accumulated in soil (see Section 13.3.3.3). It should be noted that the change in mean BDCF values is a result of the uncertainties in three input parameters, two with a range of a factor of 10 and one with a range greater than 30.

If these additional uncertainties have to be incorporated into an annual dose calculation, a simple algorithm can be used. The approach is based on the BDCF abstractions (CRWMS M&O 2001 [DIRS 153206], Section 7; CRWMS M&O 2001 [DIRS 153207], Section 7) and the uncertainty range defined in Table 13.3-12. Sample the most recent BDCF values (CRWMS M&O 2001 [DIRS 153206], Section 7; CRWMS M&O 2001 [DIRS 153207], Section 7) from the distribution (x). Then sample a random number triangularly distributed with the mode at unity and the lower and upper limits in Table 13.3-12 (z). For the modified BDCF in which the additional uncertainty is to be approximately incorporated, use the product ($x \times z$) to generate the BDCF value to use in calculating the annual dose for that radionuclide.

In this approach, the true but unknown distribution of the multiplying factor is assumed to be approximated by a triangular distribution, since this distribution provides some of the statistical requisites. The distribution mode is at unity (i.e., the most likely value corresponds to the value generated by using the expected values of each parameter). The distribution density function monotonically decreases as a sample is further from the mode, and the distribution is limited to the range defined by the lower and upper limits.

13.3.5 Uncertainty in Annual Groundwater Usage

13.3.5.1 Introduction

The annual water used for dose calculations is based on annual well withdrawal (CRWMS M&O 2000 [DIRS 144056]). For a sustainable year-round alfalfa yield, the state assumed water usage is below that estimated from the evapotranspiration requirements of alfalfa. One goal of this new analysis is to assess the impact of actual (and increased) alfalfa irrigation requirements

on annual groundwater usage and the attendant decrease in radionuclide concentration and annual dose. A second goal is to estimate the possible impact of a reduced watering rate for a future cooler and wetter climate on anticipated annual groundwater usage. In this evolved climate, the radionuclide concentrations will increase and so will the predicted annual dose.

To avoid speculation regarding the relative locations of the wells used by the hypothetical farming community and the groundwater radionuclide contamination plume, the NRC allowed a bounding approach be taken. This approach says:

> "The concentration of radionuclides in the water, … can be determined by dividing the annual release of radionuclides to the location of the farming community by the annual water demands of the farming community" (preamble to proposed 10 CFR Part 63 [64 FR 8640 (DIRS 101680), p. 8646]).

The annual water demands of the community (between 15 and 25 farms) were determined by using data published by the state of Nevada on water usage in Amargosa Valley (CRWMS M&O 2000 [DIRS 144056]). Analyzing data for agricultural usage (i.e., disregarding commercial, municipal, and mining usage) allows a statistical distribution of annual water usage per farm to be derived for the present assembly of farms. These data are then used to derive the anticipated distribution of water usage for the required community, documented in *Groundwater Usage by the Proposed Farming Community* (CRWMS M&O 2000 [DIRS 144056]). Domestic water usage is only a small perturbation on total agricultural usage and can be conservatively ignored.

In this approach, the most probable annual water usage (mode) by the community is 1,938 acre-feet per year. The lower and upper bounds on the usage distribution are 887 acre-feet per year and 3,367 acre-feet per year, respectively. The 1997 annual withdrawal for Amargosa Valley was 13,900 acre-feet. Thus, the predicted rate of water use by the proposed community is significantly below 1997 usage (CRWMS M&O 2000 [DIRS 144056], Table 12).

The values for groundwater usage are based on an irrigation rate for alfalfa of 5 acre-feet per year per acre. This crop-specific irrigation rate can be determined by referring to *Groundwater Usage by the Proposed Farming Community* (CRWMS M&O 2000 [DIRS 144056], Attachment II) and identifying in the "remarks" column those rows for which alfalfa is identified as the crop (i.e., 32, 38, 42, and 60). For each of these alfalfa entries, the annual groundwater usage can be determined by the entry in the column labeled "used." The column labeled "acres irr or use" provides the area in acres that receives the irrigation. For example, in row 32, H. Watson (column "owner of record") is identified as growing alfalfa on a land area of 172.90 acres (column "acres irr") and using an annual groundwater consumption of 864.50 acre-feet (column "used"). From these values, the annual irrigation rate per acre used by the owner of record can be determined by dividing the total volume of water used (864.50 acre-feet) by the crop area (172.9 acres). This gives an annual groundwater usage of 5 acre-feet per year. Similar calculations on other rows where the remarks column shows alfalfa to be the crop result in the same annual irrigation rate per acre of alfalfa.

13.3.5.2 Discussion of Groundwater Usage Findings

The water usage for the proposed farming community used in the TSPA calculations (CRWMS M&O 2000 [DIRS 153246]) from which radionuclide concentration in groundwater is derived is described by the following sampling algorithm (CRWMS M&O 2000 [DIRS 144056]):

1. Select a random number, R, distributed uniformly over the interval -1 to 1.

2. Determine the stochastic sample of the annual water usage, A, by forming A = mean + R × uncertainty, where mean = 96.92 acre-ft/yr and uncertainty = 37.77 acre-ft/yr.

3. Select a random number, S, distributed uniformly over the interval 15 to 25 (the number of farms specified).

4. Determine the annual water usage by multiplying A and S.

The values used in this algorithm are based on alfalfa growers using 5 acre-feet per year per acre. If the actual irrigation usage were to change to a new value, then the result from the algorithm would change by the ratio of the new value to the old value. The approach given here assesses the validity of the estimated annual alfalfa irrigation rate of 5 acre-feet per year per acre (as explained in Section 13.3.5.1) to determine agricultural water usage in the Amargosa Valley for the present and future climate. These data are then used to derive scale factors to permit reasonable estimates of annual water for use in dilution calculations for both extreme climate conditions.

The *Nominal Performance Biosphere Dose Conversion Factor Analysis* (CRWMS M&O 2001 [DIRS 152539], Attachment 3) provides a relationship to derive irrigation requirements. The irrigation rate necessary for a crop is the sum of the crop's annual evapotranspiration and the deep percolation requirement (to prevent yield loss from salts building up in the soil) minus the annual precipitation rate. Table 13.3-13 gives estimates of these parameters for alfalfa for the present and future climate, as calculated in the *Nominal Performance Biosphere Dose Conversion Factor Analysis*.

The value of 60 inches per year estimated in Section 13.3.5.1 appears to be a low estimate to sustain a commercial alfalfa operation under present climatic conditions. In the projected cooler and wetter climate (Spokane was taken to be a present-day surrogate for the future climate), the alfalfa irrigation requirement is biased in the opposite direction. In this case, the estimated value for today's irrigation rate would overestimate future irrigation requirements. These differences in irrigation values will, for the present climate, increase dilution and decrease annual dose, but they will lead to decreased dilution with increased annual dose estimates in cooler and wetter times.

In conclusion, there is a systematic bias between the irrigation requirements of alfalfa and the pumping rate used to estimate the annual water usage of the proposed farming community. The implication of this bias for the present and future climates has been quantified. Specifically, for the present climatic conditions in the Amargosa Valley, the algorithm presented above underestimates water usage by a factor of 1.58. In the future, at times when the climate is wetter and cooler, the same algorithm provides an estimate of water usage that has to be reduced by

multiplying by a factor of 0.70. For a given annual dose calculation based on the water usage sampled by using the algorithm, this uncertainty leads to an annual dose reduction for the present climate by a factor of 0.63. For the projected wetter and cooler future climatic conditions, the annual dose would be increased by a factor of 1.44.

13.3.6 Inhalation Exposure Pathway

Inhalation of resuspended particulate matter is one of the exposure pathways considered for both the groundwater release exposure scenario and the exposure scenario associated with volcanic eruption. In the groundwater release scenario, inhalation is a minor contributor to BDCFs for the case of no prior irrigation (CRWMS M&O 2001 [DIRS 152539], Table 15). However, inhalation may become an important contributor for some radionuclides (e.g., isotopes of thorium) after prolonged prior irrigation with contaminated water, which results in radionuclide buildup in soil (CRWMS M&O 2001 [DIRS 152539], Section 6.5.4.2).

Inhalation of resuspended particles is the dominant contributor to BDCFs in the exposure scenarios used to evaluate the consequences of a volcanic eruption. For most of the radionuclides and volcanic eruption scenarios evaluated, this pathway accounts for more than 90 percent of the BDCFs during, immediately following, and for several years after the event (CRWMS M&O 2001 [DIRS 152536], Section 6.6). Therefore, understanding and reducing uncertainty in the parameter values used to model this pathway is important for reducing uncertainty in the biosphere model used for the volcanic eruption exposure scenario (CRWMS M&O 2000 [DIRS 149736], Section 6.3.2). This section describes the analyses conducted to revise the parameter values for inhalation exposure and reduce their uncertainty. All assumptions and inputs for this analysis are identified in *Input Parameter Values for External and Inhalation Radiation Exposure Analysis* (CRWMS M&O 2000 [DIRS 152438]).

The atmospheric mass loading of contaminated ash particles is a result of resuspension and transport of the particles from the extended ash-fall region. The predicted mass loading was used to develop inhalation exposure. However, in developing the BDCFs the biosphere model did not consider the long-term effects of accumulation (from weathering processes) of contaminated ash in the vicinity of the proposed farming community. The removal and accumulation of contamination from the extrusive volcanic event is discussed in Section 14.3.6.7.

The inhalation pathway component of the biosphere model determines the contribution to BDCFs of inhaling contaminated ash during the ash fall or resuspended, contaminated dust or ash after the event. The GENII-S V.1.4.8.5 code requires three parameter values for that calculation:

1. Mass loading: mass of suspended particles per volume of air. This parameter is used to calculate the concentration of radionuclides in the air resulting from suspended contaminated ash or soil particles.

2. Inhalation exposure time: the amount of time a person inhales contaminated, suspended dust or ash.

3. Chronic breathing rate: the volume of air inhaled by a person per unit of time. This parameter is used to calculate the activity of suspended particles that are inhaled.

13.3.6.1 Inhalation Exposure Model Updates

The revision of inhalation exposure parameters was conducted because the mass loading values for the volcanic eruption scenario needed to account for much higher ash depths predicted by the modified model for an extrusive volcanic event. In addition, the revision had to consider mass loading conditions and associated uncertainties for farming communities and better reflect the annual dose resulting from inhalation of various-size particles (CRWMS M&O 2000 [DIRS 152438], Section 6.1; CRWMS M&O 2001 [DIRS 152536], Section 5.2). Also, refinement of the characteristics of the receptor resulted in a reevaluation of inhalation exposure time to consider behaviors and associated uncertainties of a group of farmers (CRWMS M&O 2000 [DIRS 152438], Section 6). The value for chronic breathing rate was not modified because it adequately addressed the proposed NRC requirements and would not be influenced by a volcanic event (CRWMS M&O 2000 [DIRS 152438], Section 6.3).

Mass Loading–To account for conditions specific to the groundwater release and volcanic eruption scenarios, separate distributions of mass loading were developed for each scenario. In addition, these distributions of mass loading were based on concentrations of total suspended particles (TSP) rather than small particles (i.e., PM_{10}), which is a more conservative approach.

Concentrations of TSP were used in developing revised mass loading distributions to account for inhalation of particles larger than 10 μm. This approach was considered conservative. The predicted distribution of the average size of ash particles resulting from a volcanic eruption at Yucca Mountain is log-triangular with a minimum of 10 μm, a mode of 100 μm, and a maximum of 1,000 μm (CRWMS M&O 2000 [DIRS 142657], Section 6.5.1). Thus, only a small fraction of particles (the smallest predicted average ash sizes have a very low probability of occurrence) would be available for resuspension. This distribution was based in part on measurements of particle size distributions from the Cerro Negro eruption, which was a violent Strombolian eruption. This is the type anticipated at Yucca Mountain in the unlikely event that an eruption occurs (CRWMS M&O 2000 [DIRS 142657], Section 6.5.1).

To calculate annual doses from inhalation, DCFs are used to convert predicted radionuclide intake by inhalation into predicted dose. DCFs for inhalation of suspended particles depend on particle size, represented by the activity median aerodynamic diameter. Although the size of resuspended particles ranges over several orders of magnitude, the GENII-S V.1.4.8.5 code can accommodate only one set of coefficients in converting radionuclide intake by inhalation to doses. Most commonly used DCFs for inhalation apply to particulates whose diameter is distributed lognormally with an activity median aerodynamic diameter of 1 μm (Eckerman et al. 1988 [DIRS 101069]). Such conversion factors are also built into GENII-S V.1.4.8.5. Applicability of these coefficients for a wider size range of particles that could become resuspended in the air was evaluated using methods described in ICRP 30 (ICRP 1979 [DIRS 110386]; CRWMS M&O 2001 [DIRS 152536], Section 5.2).

It was concluded that DCFs for particles with an activity median aerodynamic diameter of 1 μm adequately represent particle sizes expected to be deposited on the ground by volcanic eruption. Since the expected distribution contains a significant fraction of large particles, application of DCFs for 1 μm particles led, in most cases, to overestimates of the resulting dose (CRWMS M&O 2001 [DIRS 152536], Section 5.2).

To determine TSP concentrations for the groundwater release scenario, average annual outdoor distributions of PM_{10} from analogue arid farming communities were multiplied by the ratio of TSP to PM_{10} at Yucca Mountain to develop a distribution of mass loading representative of the reference biosphere farming community (CRWMS M&O 2000 [DIRS 152438], Section 6.1.1). Because no measurements of air quality have been made at the farming area in Amargosa Valley, analogue measurements from arid, rural, agricultural sites elsewhere in the United States were selected. The measurements selected were very high compared to those taken at Yucca Mountain and elsewhere in the United States: the average of the measurements was greater than 96 percent of over 10,000 other PM_{10} values reported for the United States between 1994 and 1999, and the maximum was greater than 99.7 percent of the other measurements. The selected PM_{10} measurements were multiplied by a factor of 2.5 to convert to TSP. That factor was based on 1,276 simultaneous measurements of PM_{10} and TSP taken at Yucca Mountain. The resulting mass loading distribution is normally distributed, with an average of 105 $\mu g/m^3$. This value is more than an order of magnitude larger than the one selected in *Input Parameter Values for External and Inhalation Radiation Exposure Analysis* (CRWMS M&O 2000 [DIRS 149880], Section 6.1). Because this distribution is based on analogue data from very dusty, arid farming communities, it likely bounds any uncertainties in future environmental conditions and farming practices in the reference biosphere.

Two distributions of mass loading were developed for the volcanic eruption scenario (CRWMS M&O 2000 [DIRS 152438], Section 6.1.2). The first is applicable to deep ash deposits, and describes changes in annual average mass loading through a 10-year transition period. The transition period is characterized by an increased concentration of airborne particulates compared with pre-eruption conditions. This distribution was developed to bound uncertainties in mass loading for extreme ash depths, the characteristic of a volcanic eruption likely to have the greatest influence on mass loading. The second distribution describes the relationship between ash depth and transition-period (i.e., 10-year) average mass loads, and is intended to account for uncertainties in mass loading caused by variations over all predicted ash depths.

Four assumptions were made to account for uncertainties in ash depth and other characteristics of a volcanic event, such as concentration of suspended particulates in air (CRWMS M&O 2000 [DIRS 152438], Section 5.1). First, an average annual particulate concentration of 1,000 $\mu g/m^3$ (PM_{10}) was assumed for the first year following a volcanic eruption. This annual level is high compared to most short-term concentrations of PM_{10} measured during farming and other activities following volcanic eruptions. Because exposure to much lower concentrations of particulate matter are known to cause health effects, it is likely that people would take precautions to avoid long-term exposure to concentrations as high or higher than 1,000 $\mu g/m^3$. This first-year annual average is therefore valid for even the largest ash depths predicted. Second, it was assumed that the concentration of ash particles decreases exponentially after an eruption. This assumption was based on mathematical functions commonly used in resuspension models and is more conservative (i.e., would result in a higher BDCF) than other functions that have been used to predict changes in resuspension of radionuclides. Third, the concentration of resuspended particles was assumed to decrease to background levels within ten years of a volcanic eruption. This rate of decrease results in a transition period that is more than an order of magnitude longer than the one measured after the Mount St. Helens eruption (CRWMS M&O 2000 [DIRS 152438], Section 5.1.3). Fourth, based on measurements of resuspended

particulate concentrations during agricultural work following the Mount St. Helens eruption, a ratio of TSP to PM_{10} of 3.0 was assumed.

Based on these assumptions, mass loading concentrations experienced at the maximum ash depths were predicted to decrease exponentially, from an annual average of 3,000 $\mu g/m^3$ the first year following an eruption to 105 $\mu g/m^3$ within 10 years. The average value representing this 10-year period is 864 $\mu g/m^3$. This distribution is intended to represent the 10-year period following an eruption that deposits a large amount of ash at the location of the receptor population.

The distribution of transition-period mass loading concentrations applicable to all ash depths is predicted to be exponential, with a maximum of 864 $\mu g/m^3$ (the average of the distribution for maximum ash depth). Predicted low values of ash depths are so small (10^{-5} to 10^{-2} cm) that they will cause no detectable change in mass loading; therefore, the minimum value for this distribution is the same as the average mass loading for a farming community (105 $\mu g/m^3$). This distribution is intended for modeling the effects of ash depths and for sampling mass loading values that cover the range of all predicted depths.

Inhalation Exposure Time–The distribution of inhalation exposure time in *Input Parameter Values for External and Inhalation Radiation Exposure Analysis* (CRWMS M&O 2000 [DIRS 149880], Section 6.2) was based on the entire population of working adults in Amargosa Valley; therefore, an additional distribution was developed to represent behaviors of farmers and other outdoor workers (CRWMS M&O 2000 [DIRS 152438], Section 6.2.2). Because no adequate survey of the activity budgets of farmers has been conducted, and because of uncertainties in the recreational habits and other behaviors of Amargosa Valley farmers, this new distribution was intended to bound the likely inhalation exposure time of a group of farmers. The lower bound (5,794 hours/year) was based on the time-activity budget of a salaried farm or construction worker who works outdoors 40 hours per week, recreates outdoors, and resides in the contaminated area. This value is more than 60 percent higher than the lower bound for the distribution of Amargosa Valley residents. The upper bound (6,354 hours/year) was based on the time-activity budget of a farmer who spends 60 hours per week outdoors, recreates outdoors, and resides in the contaminated area. The values of inhalation exposure time include inhalation exposure time outdoors and indoors. The inhalation exposure time indoors is equal to 50 percent of the time spent indoors because it is assumed that the particulate concentration indoors is half of that outdoors. The upper bound is very conservative (i.e., will result in a high BDCF) because it is based on the assumption that a farmer would work outdoors year-round for a large number of hours and then spend more than two hours per day recreating outdoors. It is not reduced to account for time spent repairing equipment indoors, conducting business away from the farm, illnesses, vacations, or other weekday activities that would occur indoors or away from the farming community. Also, this bounding value is higher than the values from two other recent Yucca Mountain biosphere or performance assessment analyses. Thus, this distribution adequately bounds uncertainties in the behavior of farmers in Amargosa Valley.

13.3.6.2 Conclusions

Modification of the parameter values for mass loading and inhalation exposure time resulted in inhalation becoming the dominant pathway for the volcanic eruption scenario, accounting for

86 to 99 percent of the BDCFs for the transition phase for 13 of 17 radionuclides evaluated (CRWMS M&O 2001 [DIRS 152536], Section 6.6). This change was due primarily to the increase in mass loading values. Because the revised distribution of mass loading bounds uncertainties in ash depth and conservatively incorporates the whole range of particle sizes available for resuspension, the resulting BDCFs account for the most important uncertainties of this scenario.

Changing the values of mass loading and inhalation exposure time used in the analysis of the groundwater release scenario had little impact on BDCFs for no prior irrigation. Inhalation contributed 0.013 percent of the BDCFs for the most sensitive radionuclides (thorium-229 and uranium-232) when the original parameter values were used (CRWMS M&O 2000 [DIRS 144692], Section 6.3.3) and less than 0.3 percent when the revised values were used (CRWMS M&O 2001 [DIRS 152539], Table 15). The importance of the inhalation pathway increases significantly with the duration of prior irrigation for some radionuclides that show the effect of radionuclide buildup in soil. Therefore, using modified inhalation exposure parameter values provides a better bound on uncertainties associated with the inhalation exposure pathway of the biosphere model.

13.3.7 Impacts of Climate Change on Biosphere Dose Conversion Factors

As discussed in more detail below, it is predicted that precipitation and average temperature in southern Nevada will change over time (see Section 3.3.1). Any analysis of potential repository performance has to consider the impact of such climatic changes. The effect of such changes on the expected annual dose for the defined receptor has to be evaluated consistently to allow a complete analysis to be performed. This section reports the development of BDCFs for the predicted climatic change.

The climate of central and southern Nevada is basically arid, but the degree of aridity varies in space (mostly by elevation) and in time (seasonally and annually). Hence, the area is occasionally called “semiarid.” However, the term “arid” should be used for general descriptions of the regional climate at Yucca Mountain (CRWMS M&O 2000 [DIRS 151945]). Geologic media provide a historical record of the types and periodicity of climate change in the Yucca Mountain region. The past-to-future climate analogue forecasts that the modern-day climate at Yucca Mountain should persist from 400 to 600 years, followed by a warmer and much wetter monsoon climate for 900 to 1,400 years and a cooler and wetter glacial-transition climate for 8,000 to 8,700 years (CRWMS M&O 2000 [DIRS 151945], p. 6.5-3). The analysis performed to estimate climatic variables for the next 10,000 years (USGS 2000 [DIRS 136368]) identified representative meteorological stations selected to represent future climates. The stations selected provided an upper and lower climate bound for each future climate. The forecasted future climate states, analogue sites (USGS 2000 [DIRS 136368], Table 2), and corresponding average long-term meteorological parameters are listed in Table 13.3-14 (CRWMS M&O 2001 [DIRS 152539]).

Conditions representative of a glacial-transition climate were selected to represent evolved climatic conditions at Yucca Mountain and evaluate the impact of climate change on BDCFs. A glacial-transition climate was selected because it is predicted to occur for most of the next 10,000 years (CRWMS M&O 2000 [DIRS 151945], p. 6.5-3). Also, the conditions at the

Spokane, Washington, analogue station differ the most from the current conditions in the Yucca Mountain region. In Spokane, the average maximum temperature is the lowest and the amount of overall precipitation (including snow) is the greatest from among the selected analogue sites. Therefore, this site was chosen to represent future climate conditions for the biosphere analysis.

The method used to calculate the BDCFs for the two climate conditions was the same, but selected input parameters representative of the two climates under consideration had to be developed. A preliminary evaluation is documented in the *Nominal Performance Biosphere Dose Conversion Factor Analysis* (CRWMS M&O 2001 [DIRS 152539]). It was assumed that the receptor remained unchanged, which was consistent with proposed 10 CFR 63.115(b) (64 FR 8640 [DIRS 101680]).

13.3.7.1 Development of Input Parameters

To evaluate the change in BDCFs due to climate evolution, the impact of the cooler and wetter climate on all parameters was examined. It was determined that many ingestion exposure parameters, such as crop growing time, irrigation time, and irrigation rate, were affected by climate change. Crop irrigation requirements differ between the Spokane climate and the Amargosa Valley climate. In Amargosa Valley, irrigation is needed year-round, although the irrigation rate is lower during the winter season. In Spokane, no irrigation is necessary in winter because precipitation exceeds evapotranspiration (CRWMS M&O 2001 [DIRS 152539], Appendix III). In addition, few crops grow during that period of time in Spokane.

For the preliminary evaluation, only limited input parameters were redeveloped for the evolved climate, as documented in the *Nominal Performance Biosphere Dose Conversion Factor Analysis* (CRWMS M&O 2001 [DIRS 152539], Appendix III). Some conclusions of that analysis are:

- Crop growing times in Spokane are longer than those in Amargosa Valley due to cooler weather, except for winter wheat, which was assumed not to grow during winter months in Spokane.

- Most crop irrigation times in Spokane are longer than in Amargosa Valley, except for alfalfa and wheat, which do not grow in winter in Spokane.

- Irrigation rates in Spokane are 20 to 60 percent lower than in Amargosa Valley, except for leafy vegetables, which have comparable irrigation rates. This is because the growing requirements of leafy vegetables, especially as related to temperature, are similar for both areas, which results from different planting seasons for leafy vegetables.

- Crop yields in both areas are the same, except for alfalfa, a multiharvesting crop, which has a shorter growing season in Spokane.

13.3.7.2 Biosphere Dose Conversion Factor Results

BDCFs for both climate conditions were calculated using statistical simulations consisting of 150 individual model realizations for each radionuclide. Twenty-four radionuclides were evaluated. In addition, radionuclide buildup in soil was modeled by considering six different

irrigation periods. These irrigation time models allow the calculation of BDCFs that include radionuclide buildup in soil irrigated with contaminated water.

The BDCF results for the current climate, the evolved climate, and irrigation periods 1 and 6 are listed in Table 13.3-15. To evaluate the degree of radionuclide buildup in soil, the buildup factors were calculated for each radionuclide. The buildup factor is a ratio of the mean value of period 6 (longest) to period 1 (no prior irrigation).

BDCFs for the evolved climate tend to increase with the duration of prior irrigation, similar to the BDCFs for the current climate. However, the amount of increase for the evolved climate is less than that for the current climate for every radionuclide. Leaching coefficients were not reevaluated for the evolved climate (i.e., the same set was used as the one for the current climate). Therefore, the 6th irrigation period was the same for both climate conditions.

Out of the 24 radionuclides analyzed, 11 do not show significant radionuclide buildup in soil (less than 15 percent) and their BDCFs remain relatively unchanged as the irrigation duration lengthens. The remaining 13 radionuclides show various degrees of buildup, up to the maximum buildup factor value of 39.8 for thorium-230. As in the current climate case, radionuclides showing the greatest degree of buildup need very long periods of continuous irrigation, on the order of thousands of years, to reach an equilibrium activity concentration in soil.

The BDCFs for the evolved climate are up to 10 percent lower than the BDCFs for the current climate, mainly because of the decreased irrigation rate. The difference is greater for the sixth irrigation period. The BDCFs for the evolved climate may be up to about 44 percent lower than the BDCFs for the current climate. The difference is the greatest for such radionuclides as isotopes of thorium, which build up slowly in soil.

13.3.7.3 Pathway Analysis for the Evolved Climate

The pathway analysis for the evolved climate was intended to find the relative change for each pathway compared with the current climate. It was assumed that the climate change does not affect drinking water consumption, a dominant pathway, because the same receptor was considered for both climates. Therefore, the overall BDCF decrease comes from the decrease of other pathway BDCFs. This results in an even greater contribution of the water consumption pathway BDCFs to the evolved climate BDCFs.

To analyze the combined effect of prior irrigation and climate change on the BDCFs, a graph was constructed that shows pathway BDCF ratios for plutonium-239 for the 1st and 6th irrigation periods in the evolved and current climates (Figure 13.3-3). This radionuclide exhibits a moderate degree of buildup, and it was identified as one of the key radionuclides in the TSPA-SR analysis (CRWMS M&O 2000 [DIRS 153246]). The ratios of pathway BDCFs for the evolved and current climate are less than one except in the water consumption and fish consumption pathways, which do not depend on radionuclide concentration in soil.

13.3.7.4 Conclusions

The anticipated future wetter climatic conditions are predicted to systematically reduce BDCF values from the values for the current climate. The reduction is predicted to be a maximum of a

factor of two, with the majority of radionuclides showing a reduction of 20 percent or less. Only the current climate BDCFs were used in the TSPA analyses. The BDCFs for the evolved climate were not used because the current BDCFs were conservative.

13.3.8 Biosphere Dose Conversion Factors for Selenium-79 and Neptunium-237

13.3.8.1 Introduction

Since the generation of the TSPA-SR data (CRWMS M&O 2000 [DIRS 153246]), the parameters defining the reference biosphere and the receptor of interest have been reevaluated. These revised inputs were used to generate the updated BDCFs used in the analyses presented in Volume 2 (McNeish 2001 [DIRS 155023]). Both analyses are discussed in Section 13.2. These data are provided in Section 13.4 and are not discussed further in this section.

The BDCFs for the suite of radionuclides originally defined as being of potential importance for annual dose calculations in the TSPA-SR (CRWMS M&O 2000 [DIRS 153246]) have been developed and documented in *Nominal Performance Biosphere Dose Conversion Factor Analysis* (CRWMS M&O 2001 [DIRS 152539]) and *Disruptive Event Biosphere Dose Conversion Factor Analysis* (CRWMS M&O 2001 [DIRS 152536]). Since this work was completed, neptunium-237 has been identified as a potential contributor to annual dose not only for the nominal scenario, as previously considered, but also for the disruptive scenario (CRWMS M&O 2000 [DIRS 150561], Section 7). Therefore, BDCFs for neptunium-237 were developed for the volcanic eruption exposure scenario. Because BDCFs for neptunium-237 had been generated for the groundwater release exposure scenario, the input data had already been selected and justified. The inputs and assumptions were the same ones used for generating the BDCFs for the other radionuclides, as reported in *Nominal Performance Biosphere Dose Conversion Factor Analysis* (CRWMS M&O 2001 [DIRS 152539]) and *Disruptive Event Biosphere Dose Conversion Factor Analysis* (CRWMS M&O 2001 [DIRS 152536]). In the case of selenium-79, Wu (2001 [DIRS 154893]) presents supporting documentation for the radionuclide-dependent parameters.

Discussions with independent review bodies, the IAEA, and the Electrical Power Research Institute indicated that selenium-79 may be a significant contributor to annual dose (Smith et al. 1996 [DIRS 101085], Section 5). Although selenium-79 was not identified as a significant contributor to annual dose in the TSPA-SR (CRWMS M&O 2000 [DIRS 153246]; CRWMS M&O 2000 [DIRS 150561], Section 7), it was considered prudent to provide the TSPA with the capability to include this radionuclide in the total annual dose calculations, if necessary. BDCFs for selenium-79 were developed for both scenarios. Because selenium-79 had not been previously considered, element-specific GENII-S V.1.4.8.5 input parameter values had to be developed. These data are presented below.

The objective of this new analysis was to provide the TSPA with the capability to evaluate the contributions from neptunium-237 and selenium-79 to the total annual dose for both scenarios.

13.3.8.2 Model Input Development

GENII-S V.1.4.8.5 was used to generate the required BDCF data. This code requires many parameters that quantify the transport of radionuclides through the multiple pathways that

contribute to annual dose. The values for parameters that were not radionuclide-specific were the same ones used for the generation of the revised BDCFs in *Nominal Performance Biosphere Dose Conversion Factor Analysis* (CRWMS M&O 2001 [DIRS 152539]) and *Disruptive Event Biosphere Dose Conversion Factor Analysis* (CRWMS M&O 2001 [DIRS 152536]).

In the case of selenium-79, which had not been previously considered in TSPA calculations, required data were derived from published sources. The approach to parameter selection and the data sources investigated were the same as those cited in the AMR supporting previous iterations.

13.3.8.2.1 Parameter Selection

The following parameters were evaluated and selected:

- Soil-to-plant transfer factors
- Animal feed-to-animal product transfer coefficients
- Bioaccumulation factors
- Leaching coefficients, removal constant, and prior irrigation period
- External dose coefficients for air submersion and exposure to contaminated soil
- Inhalation and ingestion dose conversion factors.

A summary of transfer factors, transfer coefficients, and bioaccumulation factors is listed in Table 13.3-16. The data selection was based on the same method used in *Transfer Coefficient Analysis* (CRWMS M&O 2000 [DIRS 152435]).

13.3.8.2.2 Parameters for Radionuclide Buildup in Soil

The leaching coefficient for selenium-79 was developed and documented in *Evaluate Soil/Radionuclide Removal by Erosion and Leaching* (CRWMS M&O 2001 [DIRS 152517], Section 6.2). In order to evaluate the radionuclide buildup in soil, the BDCFs were calculated for six periods of prior irrigation. (The period of prior irrigation represents the number of years that the land has been irrigated with contaminated water before the exposure occurs.) The calculation method was documented in Section 6.3.2 of the *Nominal Performance Biosphere Dose Conversion Factor Analysis* (CRWMS M&O 2001 [DIRS 152539]). The results are shown in Table 13.3-17.

13.3.8.2.3 External Dose Coefficients

Federal Guidance Report No. 12 (Eckerman and Ryman 1993 [DIRS 107684]) was used as a source of dose coefficients for exposure to soil contaminated with selenium-79 to a depth of 15 cm and 1 cm. The same method as the one used previously and documented in the *Nominal Performance Biosphere Dose Conversion Factor Analysis* (CRWMS M&O 2001 [DIRS 152539]) was used to develop input parameters for external exposure. The dose coefficients developed are listed in Table 13.3-18.

13.3.8.2.4 Inhalation and Ingestion Dose Conversion Factors

A GENII-S V.1.4.8.5 DOSINC.DAT file containing the inhalation and ingestion DCFs for the worst-case solubility, which was updated in 1993 (Rittmann 1993 [DIRS 107744]), was used for the BDCF calculations. The DOSINC.DAT is the binary file and contains detailed organ DCFs. A comparison of DCFs was made between GENII-S V.1.4.8.5 and Federal Guidance Report No. 11 (Eckerman et al. 1988 [DIRS 101069]) for some radionuclides and documented in *Dose Conversion Factor Analysis: Evaluation of GENII-S Dose Assessment Methods* (CRWMS M&O 1999 [DIRS 110635]). It was recommended that the GENII-S V.1.4.8.5 internal dose assessment be conducted with no modifications to the DOSINC.DAT file.

13.3.8.3 Results

The BDCFs for selenium-79 and neptunium-237 for the groundwater release scenario were developed using the methods documented in the *Nominal Performance Biosphere Dose Conversion Factor Analysis* (CRWMS M&O 2001 [DIRS 152539]). The BDCFs for selenium-79 for the volcanic eruption exposure scenarios were developed using the methods documented in the *Disruptive Event Biosphere Dose Conversion Factor Analysis* (CRWMS M&O 2001 [DIRS 152536]).

For the volcanic eruption BDCF data, the TSPA-SR (CRWMS M&O 2000 [DIRS 153246]) was provided with an abstraction in the form of a table of percentiles, as it was done previously (CRWMS M&O 2001 [DIRS 152536]). These data are presented in Tables 13.3-19 and 13.3-20, respectively, for selenium-79 and neptunium-237. In the case of the groundwater release exposure scenario, Table 13.3-21 gives a summary of the output data for selenium-79 showing the mean values of BDCFs and their standard deviation for the six irrigation periods.

The abstraction approach (CRWMS M&O 2001 [DIRS 153206]), as done in previous iterations for the current climate, was to attempt to determine a distribution that could be statistically justified as an acceptable representation of the stochastic GENII-S V.1.4.8.5 data. The distributions tested were the normal, the lognormal, and the shifted lognormal. None of these distributions provided an acceptable representation of the BDCF data. Therefore, the percentile table approach to abstraction was used. The data are shown in Table 13.3-22.

The mathematical model for the radionuclide buildup process in soils was developed previously (CRWMS M&O 2001 [DIRS 153206], Section 6.1). It was shown that the time dependency of the buildup process is governed by an expression of $e^{-t/a}$. In this expression, t is time and a is a characteristic time defining the rate of the process that depends on the radionuclide. The inverse of a is the rate of loss of the radionuclide from the soil because of leaching, radioactive decay, and harvesting. For selenium-79, the value of a is about 80 years (this value is an inverse of the removal constant by leaching, shown in Table 13.3-17). Since this period is less than the characteristic time for erosion, 250 years (CRWMS M&O 2001 [DIRS 153206], Section 6.2.2), the effects of erosion on the BDCF values would be small, and were therefore not estimated. This approach is conservative and requires no further justification. The data for 146 years of irrigation were used to represent the BDCF for selenium-79 at all times. At this time, the buildup factor for the mean BDCF values was calculated to be 1.27. The asymptotic buildup factor (after an infinite period of irrigation) was estimated to be 32 percent. Therefore, the use of

period 6 (146 years) data to represent the BDCF for selenium-79 could be underestimating the actual mean value by 4 percent or overestimating it by 27 percent. The magnitude of this error estimate can be put into perspective by realizing that the standard deviation of the BDCF distribution for period 6 (146 years of irrigation) arising from input parameter uncertainty is about 60 percent of the mean value.

All BDCF data were updated and documented in AMRs. The new abstractions (CRWMS M&O 2001 [DIRS 153207]; CRWMS M&O 2001 [DIRS 153206]) were developed under the quality assurance program and are in the Technical Database Management System, ready for use in a TSPA. The data discussed above for neptunium-237 and selenium-79 are documented in Wu (2001 [DIRS 154893]).

13.4 SUMMARY AND PARAMETERS PROVIDED TO TOTAL SYSTEM PERFORMANCE ASSESSMENT

This section provides a summary of the work performed and the data generated in the biosphere area to support the TSPA analyses presented in Volume 2 (McNeish 2001 [DIRS 155023]). This work was primarily documented in revisions of the AMRs listed in Section 13.2.1. Most of the supporting documents were updated to reflect improvements in modeling and a more comprehensive data assessment. These changes were propagated through the BDCF calculation process to produce new inputs for use in the TSPA. The biosphere inputs to the TSPA were in the form of BDCF abstractions and BDCF percentile tables. These parameters enable calculations of expected annual doses from predicted radionuclide concentrations at the source of contamination.

13.4.1 Biosphere Dose Conversion Factors for the Groundwater Release Exposure Scenario

The BDCFs for the groundwater release exposure scenario were developed in the *Nominal Performance Biosphere Dose Conversion Factor Analysis* (CRWMS M&O 2001 [DIRS 152539]). Calculations of BDCFs were performed in a series of individual runs consisting of 150 model realizations for the 24 radionuclides under consideration: carbon-14, nickel-63, strontium-90, technetium-99, iodine-129, cesium-137, lead-210, radium-226, actinium-227, thorium-229, thorium-230, protactinium-231, uranium-232, uranium-233, uranium-234, uranium-236, uranium-238, neptunium-237, plutonium-238, plutonium-239, plutonium-240, plutonium-242, americium-241, and americium-243 (CRWMS M&O 2000 [DIRS 136383], Sections 7.1 and 7.2). This selection included 16 radionuclides identified as important in the nominal scenario during the compliance period of up to 10,000 years, 3 additional radionuclides considered for human intrusion, and 5 radionuclides used in estimating potential dose beyond the compliance period of 10,000 years to the expected time of peak dose or 1 million years. In addition, BDCFs for selenium-79 were calculated after revision of the *Nominal Performance Biosphere Dose Conversion Factor Analysis* (CRWMS M&O 2001 [DIRS 152539]), as described in Section 13.3.8.

In the groundwater release scenario, BDCFs are expressed in terms of TEDE from annual exposure (i.e., annual dose) per unit of activity concentration per radionuclide in groundwater, which is consistent with proposed 10 CFR 63.2 (64 FR 8640 [DIRS 101680]). The annual dose

denotes the dose from one year of exposure (i.e., the sum of the committed dose from annual radionuclide intake by ingestion and inhalation, and the annual exposure to external sources). Although credited to one year of exposure, the annual dose includes the dose that would be received during the 50 years following the intake (ingestion and inhalation) of radionuclides. Therefore, it is inappropriate to equate the annual dose with the dose per year or the dose rate, which is the dose received during one year. The annual dose is expressed in units of rem, while the dose rate would be expressed in units of rem/yr.

BDCFs are measured per unit of activity concentration of a specific radionuclide in groundwater, and units typically are given as rem/(pCi/L). Similarly, the BDCF units for volcanic eruption are rem/(pCi/m^2). This approach is consistent with proposed regulations that express the performance objective (10 CFR 63.113 [64 FR 8640 (DIRS 101680)]) and the individual protection standard (40 CFR 197.20 [64 FR 46976 (DIRS 105065)]) in units of mrem.

13.4.1.1 Biosphere Dose Conversion Factors for the Current Climate

Radionuclide-specific BDCFs were developed for both the current climate and the representation near the upper bound of the glacial-transition climate (CRWMS M&O 2001 [DIRS 152539]). Each set included considerations of radionuclide buildup in soil due to previous irrigation. Probabilistic analysis was used to develop BDCF values based on the revised values of input parameters. To support the preliminary analysis of the BDCFs for an evolved climate, several parameter values characteristic of the cooler and wetter climate were developed. The analysis was augmented with pathway and uncertainty studies.

The outcome of the BDCF statistical calculation consisted of 150 results of individual model realizations for each radionuclide for every irrigation period, which was sufficient to obtain statistically valid results. The corresponding means and standard deviations are listed in Table 13.4-1 for the first and the sixth irrigation period. BDCFs for selenium-79 calculated after revision of the *Nominal Performance Biosphere Dose Conversion Factor Analysis* (CRWMS M&O 2001 [DIRS 152539]) can be found in Tables 13.3-21 and 13.3-22 of this document. The ratio of BDCFs for these two periods allows a determination of the degree of radionuclide buildup in soil, represented by the buildup factor. The buildup factor is a ratio of the mean value of period 6 (longest) to period 1 (no prior irrigation). Buildup factors are also listed in Table 13.4-1. For those radionuclides whose buildup factor was greater than 1.15, BDCFs were also calculated for the remaining irrigation periods (i.e., periods 2 through 5).

The analysis of model results indicates that for 10 radionuclides, the BDCFs increase relatively insignificantly with prior irrigation time (i.e., the buildup factor is less than 1.15). Among these radionuclides were technetium-99, iodine-129, and neptunium-237, which were considered among the key radionuclides in the TSPA-SR analysis (CRWMS M&O 2000 [DIRS 153246], Figure 4.1-6). The buildup factor for the remaining 14 radionuclides ranged from 1.17 for uranium-238 to 65.6 for thorium-230. However, some radionuclides with a buildup factor greater than 1.15 were associated with thousands of years of continuous irrigation before the equilibrium for radionuclide concentrations in soil is achieved. In addition, radionuclide removal by soil erosion has not been factored in because this mechanism was addressed in the abstraction phase of biosphere modeling.

13.4.1.2 Biosphere Dose Conversion Factor Abstraction

The statistical sampling approach adopted for generating the BDCFs allows the uncertainties in the input parameters to be incorporated into the BDCF predictions. The uncertainties in many of the input parameters defining both the reference biosphere and the processes therein, as well as the receptor, were represented by distributions. These parametric distributions were subsequently sampled within GENII-S V.1.4.8.5 to arrive at stochastic BDCFs representing the reference biosphere and the receptor.

The abstraction method used to provide the stochastic BDCFs to the TSPA-SR model (CRWMS M&O 2000 [DIRS 153246]) and to enable the effects of soil erosion to be taken into account was the approximation of statistical distributions. With the exception of a single radionuclide (carbon-14, which is discussed later in this section), three distributions provided acceptable abstractions of all BDCFs: normal, lognormal, and shifted lognormal distributions.

Of all the radionuclides considered in the distribution fitting exercise, carbon-14 was the only one for which an acceptable distribution not found. Carbon-14 did not show any significant buildup in BDCF due to protracted irrigation. In this case, an empirical distribution for the BDCFs was provided to the TSPA in the form of a table giving the cumulative distribution function in terms of the percentile values (defined at each fifth percentile starting at 0 percent, the minimum BDCF value generated by GENII-S V.1.4.8.5). These empirical data for carbon-14 are shown in Table 13.4-2.

For those radionuclides where soil buildup effects produced an increase in the mean BDCF value of less than 15 percent, the distributions used in the TSPA assessment were the abstractions for period 6. The distribution and associated parameters used in the TSPA are given in Table 13.4-3.

Some of the radionuclides have BDCFs that were significantly influenced by radionuclide buildup in soil. Examples are americium-243, thorium-229, and uranium-232, none of which had been significant contributors to the annual dose in previous TSPA evaluations (see Section 13.1.1). In addition, for thorium-229 and americium-243, the period needed for buildup to approach the maximum level was thousands of years. For such extended periods, it could be considered speculative but conservative to assume continuous farming activity on a single plot of irrigated land. In addition, the calculations did not include radionuclide removal by soil erosion. The time constant for erosion loss was estimated to be 250 years (CRWMS M&O 2001 [DIRS 153206], Section 6.2.2). Therefore, for radionuclides where a predicted buildup period without soil erosion was several hundred years or more, the buildup was limited by erosion. Table 13.4-4 gives buildup factors for some representative radionuclides with and without consideration of soil erosion.

To avoid introducing speculation by having to define an appropriate period for the prior irrigation (or to develop a model to allow a justifiable distribution for this period to be sampled), the same approach was used as that for radionuclides with a small buildup factor. The BDCF distributions provided to the TSPA were those with asymptotic buildup factors derived with the inclusion of erosion.

The recommended distributions and geometric parameters for the TSPA-SR (CRWMS M&O 2000 [DIRS 153246]) for those radionuclides that show a small degree of buildup are presented in Table 13.4-3. Statistical distributions for these radionuclides are given for the maximum period of previous irrigation (period 6). For the 14 radionuclides with a significant (i.e., greater than 15 percent) buildup, statistical distributions of BDCFs were determined after incorporation of the soil loss effect. The recommended BDCF distributions and parameters for these radionuclides are summarized in Tables 13.4-5 to 13.4-7 for radionuclides having a normal distribution, a lognormal distribution, and a shifted lognormal distribution, respectively (CRWMS M&O 2001 [DIRS 153206], Tables 8 and 9). The values cited in the references were adjusted for the scale factor.

13.4.1.3 Modeling Output for the Evolved Climate

To evaluate the effect of future climate variations on biosphere, BDCFs were developed for the climatic conditions corresponding to the upper bound of the glacial-transition climate (CRWMS M&O 2001 [DIRS 152539], Section 6.5.5), as described in Section 13.3.7. Also, following the same calculation technique as the one used for the current climate, BDCFs were calculated in a series of GENII-S V.1.4.8.5 simulations for each of the 24 radionuclides. Each simulation resulted in 150 model realizations.

The outcome of the BDCF statistical calculation for the evolved climate also consisted of 150 results of individual model realizations for each radionuclide for all or selected irrigation periods, depending on the value of buildup factor. The corresponding means and standard deviations for the evolved climate are listed in Table 13.4-8 for the 1st and the 6th irrigation period. The summary of the BDCFs for selenium-79 for the evolved climate calculated after revision of the *Nominal Performance Biosphere Dose Conversion Factor Analysis* (CRWMS M&O 2001 [DIRS 152539]) can be found in Table 13.3-21. To evaluate the degree of radionuclide buildup in soil, the buildup factors were calculated for each radionuclide (Table 13.4-8). For those radionuclides whose buildup factor was greater than 1.15, BDCFs were also calculated for the remaining irrigation periods (i.e., periods 2 through 5). The modeling results for the evolved climate and a comparison with the BDCFs for the current climate are discussed in Section 13.3.7.

13.4.1.4 Results of Pathway Analysis

Results of the pathway analysis are documented in *Nominal Performance Biosphere Dose Conversion Factor Analysis* (CRWMS M&O 2001 [DIRS 152539], Section 6.7). This section summarizes the findings.

For all radionuclides except carbon-14 and cesium-137, consumption of drinking water was the dominant pathway, accounting for 55 to 69 percent of the BDCF, depending on the radionuclide. Leafy vegetable consumption ranked second, contributing from 23 to 27 percent, depending on the radionuclide. Together, consumption of drinking water and leafy vegetables accounted for 82 to 96 percent of the BDCF values for radionuclides. The remaining consumption pathways accounted for up to a few percent of the BDCFs. Inhalation and external exposure pathways were not significant, and neither of them contributed more than a few tenths of a percent for all radionuclides except cesium-137 (7.7 percent) and radium-226 (2.5 percent). For carbon-14,

consumption of fish was by far the most important pathway (93 percent of the BDCF). Pathway contributions to BDCFs for cesium-137 include 23 percent from consumption of drinking water, 12 percent from leafy vegetables, 12 percent from meat, 36 percent from fish, and 8 percent from external exposure.

Contribution of the specific pathways to the BDCFs was affected by radionuclide buildup in soil because some pathways depend on radionuclide concentrations in soil. Among the pathways unaffected by radionuclide buildup in soil was consumption of drinking water, which was the major pathway for most radionuclides. Also, the contribution to BDCFs from consumption of fish and that fraction of the BDCF that results from activity deposition on a plant's surfaces from irrigation water were unrelated to radionuclide concentration in soil.

For many radionuclides for which the effect of radionuclide buildup in soil was insignificant, such as technetium-99, iodine-129, and neptunium-237, pathway contributions to BDCFs remain virtually unchanged regardless of the previous irrigation practices. This, however, was not the case for radionuclides whose levels in soil increase significantly with prolonged irrigation.

The effect of radionuclide buildup in soil on pathway contributions to the BDCFs was evaluated for selected radionuclides whose BDCFs increase with the duration of prior irrigation. This analysis was carried out assuming a constant level of activity concentration in water for the entire length of time needed to obtain steady-state conditions of radionuclide concentrations in soil (thousands of years for some radionuclides). In addition, other removal mechanisms, such as soil removal by erosion, were not factored in because they were considered in the abstraction process. The addition of soil removal from erosion would considerably shorten the time needed to obtain an equilibrium radionuclide concentration in soil and make the analysis of the BDCFs for very long periods of prior irrigation (such as those for thorium-230) irrelevant.

The graph shown in Figure 13.4-1 shows percentage pathway contributions to BDCF for plutonium-239 at different periods of prior irrigation. Contributions to BDCF from consumption of all crop types and contributions from consumption of all animal products were portrayed as their respective category. Plutonium-239 was a radionuclide that shows a moderate degree of radionuclide buildup in soil. The graph shows the decreasing importance of the water consumption pathway with irrigation time and the growing inhalation and soil ingestion components.

13.4.2 Groundwater Withdrawal by the Farming Community

The annual groundwater usage by the proposed community has not been reevaluated. The predicted distribution for groundwater usage by the farming community was given in Section 13.4.1.2. However, the average groundwater withdrawal by the farming community was reviewed, as described in Section 13.3.5, for consistency between the irrigation rate of 5 acre-feet per year per acre estimated by the state of Nevada and irrigation levels based on area-specific evapotranspiration values. The result of this assessment was a simple scalar multiplier for the present-day climate or the glacial-transition climate. Water usage was estimated to increase by a factor of 1.58 in the present-day climate, while usage was predicted to be reduced by a factor of 0.63 in the cooler and wetter future glacial-transition climate.

13.4.3 Biosphere Dose Conversion Factors for the Volcanic Eruption Exposure Scenarios

BDCFs that apply to the direct release of radionuclides from the potential repository as a result of volcanic eruption are described in the *Disruptive Event Biosphere Dose Conversion Factor Analysis* (CRWMS M&O 2001 [DIRS 152536], Section 6.5). BDCF calculations were done for seventeen radionuclides: strontium-90, cesium-137, lead-210, radium-226, actinium-227, thorium-229, thorium-230, protactinium-231, uranium-232, uranium-233, uranium-234, plutonium-238, plutonium-239, plutonium-240, plutonium-242, americium-241, and americium-243. The selection included radionuclides that may be significant dose contributors during the compliance period of up to 10,000 years, as well as radionuclides of importance for up to 1 million years after closure of the potential repository. In addition, BDCFs for selenium-79 and neptunium-237 were calculated after revision of the *Disruptive Event Biosphere Dose Conversion Factor Analysis* (CRWMS M&O 2001 [DIRS 152536]), as described in Section 13.3.8.

From the perspective of BDCF calculation for volcanic eruption, three different human exposure scenarios were specified for different phases during and following volcanic eruption: (1) eruption, (2) transition, and (3) steady-state (CRWMS M&O 2001 [DIRS 152536], Section 6.3.1). The eruption phase refers to the conditions during the volcanic eruption. Because of the expected high concentration of particulates in air during this phase, inhalation of airborne, contaminated ash particles was the only primary pathway considered in the calculation.

The transition phase is characterized by resuspension of volcanic ash deposited on the ground during the eruption phase. The contaminated ash is thus available for inhalation. Resuspended ash, if deposited on plant surfaces, may cause contamination on crops used for human consumption and animal feed. Contamination of crops may also occur through the root uptake of radioactivity in the soil. Contaminated animal feed results in contamination of animal products such as milk, meat, and eggs. It was postulated that contaminated ash was not mixed into the soil below the ash layer for the duration of the entire transition phase. This was a conservative approach that maximized inhalation of resuspended particles but did not affect other pathways, such as root uptake. Concentration of resuspended particles in air during the transition phase was assumed to decrease exponentially until it reached pre-eruption conditions (CRWMS M&O 2000 [DIRS 152438], Section 5.1.2). The process of reduction of initially high dust concentrations in air was assumed to take up to 10 years (CRWMS M&O 2000 [DIRS 152438], Section 5.1.3). When the biosphere system returns to pre-eruption dust levels, the third and steady-state phase begins. This phase is characterized by the same levels of suspended particulates in the air as those used for the development of the groundwater release BDCFs. In the steady-state phase, radioactivity previously deposited on the ground from a volcanic eruption was assumed to be uniformly mixed into a 15-cm layer of topsoil, regardless of the initial thickness of the ash deposit.

13.4.3.1 Dose Factors for the Eruption Phase

For the eruption phase, dose factors were developed rather than BDCFs. Dose factors represent the TEDE resulting from a one-day intake of radionuclides (called here a daily dose, by analogy with the annual dose) by inhalation of air containing unit activity concentration of a radionuclide under consideration (1 pCi/m^3). It was assumed that inhalation exposure time was equal to

6,073.5 hours per year (CRWMS M&O 2000 [DIRS 152438], Section 6.2.2), which includes time spent outdoors and half of the time spent indoors in that area, as described in Section 13.3.3.2.2. Such inhalation exposure time resulted in an inhalation exposure factor of 0.693, calculated by dividing 6073.5 hours of inhalation exposure time per year by the total number of hours per year (8,760 hours). Inhalation exposure time and, subsequently, the inhalation exposure factor do not reflect actual time spent outdoors. Rather, they are scaling factors that include inhalation exposure both outdoors and indoors.

Dose factors for the eruption phase were developed using DCFs for inhalation from Federal Guidance Report No. 11 (Eckerman et al. 1988 [DIRS 101069], Table 2.1). When more than one DCF was given for a particular radionuclide, the most conservative was used. Dose factors are listed in Table 13.4-9. Eruption-phase dose factors for selenium-79 and neptunium-237, calculated after revision of the *Disruptive Event Biosphere Dose Conversion Factor Analysis* (CRWMS M&O 2001 [DIRS 152536]), can be found in Tables 13.3-19 and 13.3-20, respectively.

The use of dose factors to calculate daily dose for the eruption phase is (CRWMS M&O 2001 [DIRS 152536], Equation 5):

$$Dose\,(rem) = S\left(\frac{g}{m^3}\right) \times C_{ash}\left(\frac{pCi}{g}\right) \times DF\left(\frac{rem\ m^3}{pCi}\right) \qquad \text{(Eq. 13-3)}$$

where:

S = average daily mass concentration of particulates in air (i.e., TSP), $\frac{g}{m^3}$

C_{ash} = activity concentration of radionuclide in ash, $\frac{pCi}{g}$.

13.4.3.2 Biosphere Dose Conversion Factors for the Transition and Steady-State Phases

Volcanic eruption BDCFs were developed for the transition and steady-state phases. The most important parameter distinguishing these two phases was mass loading, a GENII-S V.1.4.8.5 parameter that quantifies mass concentration of suspended particulates in air. In the steady-state phase, the distribution of mass loading was assumed to be the same as the distribution used for the groundwater source of contamination. (The steady-state phase begins when the mass loading returns to pre-eruption conditions.) In calculations of transition-phase BDCFs, two distributions of mass loading were considered. Detailed descriptions of these distributions are documented in *Input Parameter Values for External and Inhalation Radiation Exposure Analysis* (CRWMS M&O 2000 [DIRS 152438], Section 6.1.2). The first was a distribution of possible annual average values of mass loading following the deposition of a deep ash layer at the location of the receptor. This distribution describes changes in average annual mass loading conditions during one 10-year transition period, and was intended to bound uncertainties in mass loading due to variation in ash depth. The second was a distribution of transition-period (10-year) average

values of mass loading that correspond to differences in predicted ash depth at the location of the receptor.

Another parameter important in the biosphere modeling for the volcanic eruption was the thickness of ash layer at the location of interest. The thickness of the ash layer that could be deposited 20 km from the potential repository was uncertain (CRWMS M&O 2000 [DIRS 153246], Section 3.10.5.1). The median eruptive event was predicted to produce an ash layer less than 1 cm thick 20 km downwind. The minimum ash layer calculated for the midpoint of the plume at 20 km was less than 0.1 mm, corresponding to a relatively small eruption that produces only a dusting of ash at that distance. The maximum ash layer was 36 cm, corresponding to a large eruption that produces a major ash fall covering a large area (CRWMS M&O 2000 [DIRS 153246], Section 3.10.5.1).

Because of the wide range of ash thicknesses, transition-phase BDCFs were developed for two different thicknesses of ash: 1 cm, representing the more likely conditions, and 15 cm, representing thicker ash deposits. The thicker ash layer was chosen to be 15 cm because this thickness corresponds to the depth of surface soil constituting the plant growing zone (it was assumed that 100 percent of a plant's roots were in the surface soil layer) (CRWMS M&O 2001 [DIRS 152434], Sections 6.4.1 and 6.4.4), which is one of the input parameters in GENII-S V.1.4.8.5. Greater thicknesses do not have a significant effect on the calculation outcome because it was assumed that plant roots do not extend past 15 cm in depth. The BDCFs for the steady-state phase use the 15-cm thickness for the ash or soil layer.

Taking into consideration the possible combinations of mass loading and ash thicknesses, the following sets of BDCFs were developed:

- Transition-phase, 1 cm ash layer and annual average mass loading
- Transition-phase, 1 cm ash layer and 10-year average mass loading
- Transition-phase, 15 cm ash layer and annual average mass loading
- Transition-phase, 15 cm ash layer and 10-year average mass loading
- Steady-state phase.

BDCFs were calculated in a series of GENII-S V.1.4.8.5 simulations for each of the 17 radionuclides. Each simulation resulted in 150 model realizations. These results were converted into discrete cumulative probability distributions, which were used in the TSPA with other input parameters to evaluate expected annual doses following a volcanic eruption.

Table 13.4-10 gives the summary of the BDCF calculations for the volcanic eruption. The table includes the means, standard deviations, minimums, and maximums for the BDCFs. The BDCFs for selenium-79 and neptunium-237, calculated after revision of the *Disruptive Event Biosphere Dose Conversion Factor Analysis* (CRWMS M&O 2001 [DIRS 152536]), can be found in Tables 13.3-19 and 13.3-20, respectively. For most radionuclides, BDCFs differ between the scenarios under consideration. The highest BDCFs were for the transition phase, 1-cm ash layer and the annual average mass loading. This set of BDCFs can be compared with the transition-phase BDCFs for a 15-cm ash layer and annual average mass loading. The reason for the difference is that in the 1-cm contaminated ash layer, radionuclides are concentrated in the upper soil. Therefore, the activity concentration in air from resuspended contaminated material

is higher than that for the 15-cm layer of ash, where the same radioactivity is diluted in 15 times more material; thus, the resuspended particles would contain less radioactivity. This effect can be observed predominantly for those radionuclides whose BDCF contribution from the inhalation pathway was significant, such as isotopes of plutonium, thorium, uranium, and americium. For radionuclides whose BDCFs do not depend on the inhalation pathway, such as strontium-90, the difference was less significant (CRWMS M&O 2001 [DIRS 152536], Section 6.5.4).

The two sets of transition phase BDCFs for 10-year average mass loading showed a similar relationship: the values for a 1-cm ash layer were higher than those for the 15-cm ash layer for radionuclides with a significant contribution from the inhalation pathway. Overall, BDCFs developed using 10-year average mass loading were lower than those developed using annual average mass loading. This is because annual average mass loading conditions include the high mass loading values characteristic of the initial period of the transition phase, when the concentration of particulates in air is high. BDCFs developed using annual average mass loading apply to the annual average condition for any time during the eruption phase. BDCFs developed using 10-year averages do not include extreme dustiness conditions because the mass loading values they use are integrated over the entire transition phase (CRWMS M&O 2001 [DIRS 152536], Section 6.5.4).

13.4.3.3 Volcanic Eruption Biosphere Dose Conversion Factor Abstraction

In the case of volcanic dispersion of radionuclides, the same mechanisms for radionuclide loss from soil that are included in GENII-S V.1.4.8.5 were considered, that is, leaching, harvest removal, and radioactive decay (Napier et al. 1988 [DIRS 100953], Section 4.6.2). In this case, the losses were only considered during a single year of agricultural land use (the receptor uptake period). In contrast to the approach used for the groundwater release exposure scenario, no attempt was made to address the effect of leaching losses due to prolonged irrigation and precipitation over many years. This approach is conservative because it assumes no continual radionuclide removal from the root zone of plants by leaching, harvesting, or decay. An issue resolution status report on volcanic activity (NRC 1999 [DIRS 151592]) recommended that the consequence of the eruptive event be evaluated in a probabilistic manner by calculating the expected (i.e., probability-weighted) dose from events assumed to occur in each of the preceding years. The additional loss mechanisms over the intervening years could be used to justifiably reduce the expected annual dose from such an event.

13.4.3.4 Pathway Analysis

BDCF values include contributions from various radiological exposure pathways in the biosphere. The evaluation of the degree to which different pathways contribute to BDCFs was the subject of an independent assessment. To determine the contributions from different exposure pathways to BDCF values, a single GENII-S V.1.4.8.5 deterministic assessment was performed for each radionuclide and for each of five cases (CRWMS M&O 2001 [DIRS 152536], Section 6.5).

For most radionuclides (except strontium-90, cesium-137, lead-210, and radium-226), inhalation of resuspended particulates was a dominant pathway for all four cases for the transition phase,

accounting for over 90 percent of the BDCFs. Inadvertent soil ingestion ranked second, contributing less than 7 percent to the BDCFs. Together, inhalation and inadvertent soil ingestion accounted for over 99 percent of most transition-phase BDCF values for these radionuclides. Consumption of leafy vegetables was usually the third-ranking pathway, but its contribution was normally less than one percent. Pathway contributions to the transition-phase BDCFs for strontium-90, cesium-137, lead-210, and radium-226 were different. Consumption of vegetables was a dominating pathway for strontium-90, external exposure ranks first for cesium-137, and pathway contributions for lead-210 and radium-226 were more evenly balanced among inhalation and crop consumption.

Pathway contributions for the remaining four cases showed a similar pattern for the transition phase, 1-cm ash layer, and annual average mass loading. For most of the radionuclides, the inhalation pathway tends to dominate the overall exposure, with the remaining pathways contributing only to a small degree. The contribution of other pathways, especially the inadvertent soil ingestion pathway, was most significant in the steady-state phase. Pathway contributions to the BDCFs for strontium-90, cesium-137, lead-210, and radium-226 remained more diversified than those for the heavier radionuclides.

In the steady-state phase, inhalation was still a dominant pathway for most radionuclides other than strontium-90, cesium-137, lead-210, and radium-226. However, the percentage contribution to the BDCFs was less than that in the transition phase. Vegetable consumption pathways dominate for strontium-90, lead-210, and radium-226, while the BDCF for cesium-137 was due almost entirely to external exposure.

INTENTIONALLY LEFT BLANK

Table 13.2-1. Comparison of the Assessment Context for the Yucca Mountain Project and BIOMASS Biosphere Models

	YMP Assessment Context	BIOMASS Assessment Context	Comparison
Assessment Endpoint	Biosphere dose conversion factor based on total effective dose equivalent (TEDE)	Annual individual effective dose (ED)	Equivalent YMP – TEDE from ICRP 30[a]; BIOMASS – ED from ICRP 72[b] (see Section 13.3.2)
Assessment Philosophy	Contaminant transport pathways based on reasonable conservative values; human exposure pathways based on cautious approach	Equivalent except with respect the critical group definition	Equivalent Both models consider the reasonable values of input parameters for the critical group
Repository Type	Deep repository for long-lived solid radioactive waste	Deep repository for long-lived solid radioactive waste	Same
Site Context	Amargosa valley, groundwater usage and limited climate change	Generic inland repository, with aquifer at accessible depth, no biosphere change	Equivalent YMP – Site-specific BIOMASS – generic
Geosphere/ Biosphere Interface	Groundwater from wells for drinking, agriculture and domestic use	Well intruding into aquifer plume with abstraction at a rate consistent with domestic and agricultural use	Same
Source Term	Constant unit concentration for each radionuclide	Constant unit concentration for each radionuclide	Same
Societal Assumptions	Farming community, with vegetable garden and animal farms and fisheries	Agricultural community, adopting modern practices for cultivation and animal husbandry	Equivalent Similar ingestion pathways for the locally produced food
Time Frame	10,000 years, up to 1 million years	Up to 1 million years	Same

NOTES: [a] ICRP 1979 [DIRS 110386]; ICRP 1980 [DIRS 110351]; ICRP 1981 [DIRS 110352].
[b] ICRP 1996 [DIRS 152446].

Table 13.2-2. Comparison of the Pathways and Methodologies Used in the Yucca Mountain Project Groundwater Release and BIOMASS Biosphere Models

Pathways		YMP Model Groundwater Release	BIOMASS ERB 2A[a]	Notes
External Exposure	Contaminated soil	X	X	Same method
	Water immersion	---	X	---
Inhalation Dose	Air dust	X	X	Same method
	Aerosols/spray	---	X	---
Ingestion Dose	Soil	X	X	Same method
	Drinking water	X	X	Same method
	Leafy vegetables	X	X	Same method for root uptake, different for leaf deposition
	Root vegetables	X	X	
	Fruit	X	---	---
	Grain	X	X	Same method for root uptake, different for leaf deposition
	Fresh feed for cows	X	X	
	Stored feed for poultry	X	---	---
	Meat	X	X	Same for feed and water, no soil and inhalation in YMP model
	Milk	X	X	
	Offal	---	X	---
	Poultry	X	---	---
	Eggs	X	---	---
	Fish	X	---	---
Total Dose		X	X	---

NOTES: × = included in model.

[a] Example Reference Biosphere 2A.

Table 13.3-1. Pathway Factors

Nuclide	Water	Leafy Veg	Other Veg	Fruit	Grain	Meat	Poultry	Milk	Eggs	Fish	Soil Ing.	External	Inhale
C-14	2.1E-09	3.0E-08	4.0E-08	2.6E-08	1.0E-07	6.7E-08	1.1E-07	1.9E-08	8.7E-08	1.0E-04	0.0E+00	0.0E+00	0.0E+00
Tc-99	2.2E-09	5.6E-08	1.4E-08	3.7E-09	1.2E-08	9.1E-10	1.1E-10	6.4E-08	1.1E-08	4.5E-08	6.7E-09	4.1E-14	2.6E-15
I-129	2.5E-07	4.8E-06	6.9E-07	3.3E-07	1.1E-06	3.8E-06	6.4E-09	3.1E-06	1.1E-06	1.0E-05	3.5E-06	1.9E-11	2.1E-13
Pb-210	5.4E-06	9.4E-05	1.5E-05	7.8E-06	2.5E-05	5.5E-06	3.8E-07	2.0E-06	7.4E-06	1.6E-03	1.3E-03	1.4E-10	4.0E-10
Ra-226	9.8E-07	3.8E-05	1.8E-05	7.4E-06	2.6E-05	6.1E-06	2.6E-07	4.7E-06	3.9E-06	4.9E-05	9.7E-03	1.4E-06	3.9E-09
Ac-227	1.4E-05	2.7E-04	4.1E-05	1.7E-05	5.6E-05	8.2E-07	7.9E-08	4.8E-07	3.8E-08	3.6E-04	3.1E-03	4.4E-08	1.6E-07
Th-229	3.5E-06	7.5E-05	1.1E-05	5.0E-06	1.5E-05	4.9E-07	2.6E-08	7.9E-07	9.8E-09	3.5E-04	7.4E-03	3.0E-07	4.2E-07
Th-230	5.4E-07	1.3E-05	3.1E-06	1.3E-06	4.4E-06	4.3E-07	2.5E-08	3.3E-07	3.9E-07	5.3E-05	2.0E-03	1.4E-07	6.4E-08
Pa-231	1.1E-05	2.2E-04	3.2E-05	1.5E-05	5.1E-05	4.2E-07	6.6E-08	5.8E-07	3.2E-08	1.2E-04	4.1E-02	3.2E-07	1.3E-06
U-233	2.9E-07	5.8E-06	1.0E-06	3.9E-07	1.2E-06	2.0E-07	5.1E-07	2.2E-07	4.2E-07	2.9E-06	1.2E-04	6.5E-10	5.7E-09
U-234	2.8E-07	5.7E-06	1.0E-06	3.9E-07	1.2E-06	1.9E-07	5.0E-07	2.1E-07	4.1E-07	2.9E-06	1.0E-04	1.5E-11	4.8E-09
U-236	2.7E-07	5.4E-06	9.6E-07	3.7E-07	1.1E-06	1.8E-07	4.7E-07	2.0E-07	3.9E-07	2.7E-06	9.7E-05	8.3E-12	4.6E-09
U-238	2.6E-07	5.1E-06	9.7E-07	3.6E-07	1.1E-06	1.8E-07	4.5E-07	2.0E-07	3.7E-07	2.6E-06	9.7E-05	4.4E-09	4.4E-09
Np-237	5.2E-06	1.0E-04	1.5E-05	7.1E-06	2.1E-05	1.2E-05	2.9E-08	3.3E-08	1.5E-08	1.6E-04	3.1E-04	6.5E-09	3.7E-09
Pu-238	3.2E-06	6.1E-05	9.0E-06	3.9E-06	1.2E-05	7.0E-08	1.8E-08	4.2E-09	3.5E-08	9.5E-05	2.1E-03	1.0E-11	2.5E-08
Pu-239	3.6E-06	7.0E-05	1.0E-05	4.5E-06	1.4E-05	7.8E-08	2.0E-08	4.8E-09	3.9E-08	1.1E-04	5.6E-03	5.0E-11	6.8E-08
Pu-240	3.6E-06	7.0E-05	1.0E-05	4.5E-06	1.4E-05	7.8E-08	1.9E-08	4.8E-09	3.9E-08	1.1E-04	5.5E-03	2.5E-11	6.8E-08
Pu-242	3.3E-06	6.5E-05	9.2E-06	4.2E-06	1.3E-05	7.2E-08	1.8E-08	4.5E-09	3.7E-08	9.8E-05	5.4E-03	2.2E-11	6.5E-08
Am-241	3.6E-06	7.2E-05	1.0E-05	4.6E-06	1.5E-05	1.6E-07	3.0E-08	8.7E-09	2.0E-08	1.1E-04	5.0E-03	6.5E-09	6.1E-08
Am-243	3.6E-06	7.2E-05	1.1E-05	4.6E-06	1.5E-05	1.6E-07	3.1E-08	8.8E-09	2.0E-08	1.1E-04	6.8E-03	1.7E-07	8.1E-08

Source: Wu 2001 [DIRS 154894], Table 2.

NOTE: Units are rem/(pCi/L) per kg, L, or hr.

Table 13.3-2. Annual Pathway Exposure Levels for the Current Receptor and Alternative Receptors

Exposure Pathway	Annual Pathway Exposure Levels					
	Current Receptor [a]	U.S. Average Receptor [a]	NUREG/ CR-5512 Receptor [a]	Alternative Amargosa Valley Receptor 1 [a]	Alternative Amargosa Valley Receptor 2 [a]	Alternative Amargosa Valley Receptor 3 [b]
Water (L/yr)	753	511	730	730	1118	730
Leafy vegetables (kg/yr)	15	28	11	24	11	4
Root/other vegetables (kg/yr)	8	85	51	21	8	5
Fruit (kg/yr)	16	89	46	53	24	13
Grain (kg/yr)	0	108	69	0	0	0
Meat (kg/yr)	3	29	59	18	8	3
Poultry (kg/yr)	1	16	9	3	0	0
Milk (L/yr)	4	131	100	30	38	5
Eggs (kg/yr)	7	8	10	25	11	6
Fish (Freshwater) (kg/yr)	0	2	10	2	2	0
Soil (kg/yr)	0.0183	0.0183	0.0183	0.0183	0.0183	0.0183
External Exposure (hr/yr)	3387	3387	3387	3387	3387	3387
Inhalation Exposure (hr/yr)	6074	6073.5	6074	6074	6074	6074

Sources: [a] Wu 2001 [DIRS 154894] Table 3.
[b] Wu 2001 [DIRS 155203] Table 1.

NOTE: Consumption rates were rounded to the nearest kilogram or liter.

Table 13.3-3. Average Annual Doses to the Current Receptor and to Alternative Receptors at 25,000 Years Postclosure

Exposure Pathway	Total Annual Dose (rem)					
	Current Receptor [a]	U.S. Average Receptor [a]	NUREG/ CR-5512 Receptor [a]	Alternative Amargosa Valley Receptor 1 [a]	Alternative Amargosa Valley Receptor 2 [a]	Alternative Amargosa Valley Receptor 3 [b]
Water	7.4E-06	5.0E-06	7.2E-06	7.2E-06	1.1E-05	7.2E-06
Crop Ingestion	4.1E-06	1.8E-05	9.4E-06	7.2E-06	3.3E-06	1.3E-06
Animal Products Ingestion	1.4E-06	3.0E-05	2.5E-05	8.5E-06	9.0E-06	1.5E-06
Aquatic Food Ingestion	2.1E-06	9.0E-06	4.5E-05	6.8E-06	7.4E-06	1.2E-06
Total Ingestion	5.4E-06	4.8E-05	3.4E-05	1.6E-05	1.2E-05	2.8E-06
Inhalation	2.5E-08	2.5E-08	2.5E-08	2.5E-08	2.5E-08	2.5E-08
External Exposure	3.2E-09	3.2E-09	3.2E-09	3.2E-09	3.2E-09	3.2E-09
Total	1.5E-05	6.2E-05	8.7E-05	3.0E-05	3.1E-05	1.1E-05

Sources: [a] Wu 2001 [DIRS 154894], Table 4.
[b] Wu 2001 [DIRS 155203] Table 2.

Table 13.3-4. Average Annual Doses to the Current Receptor and to Alternative Receptors at 100,000 Years Postclosure

Exposure Pathway	Total Annual Dose (rem)					
	Current Receptor [a]	U.S. Average Receptor [a]	NUREG/ CR-5512 Receptor [a]	Alternative Amargosa Valley Receptor 1 [a]	Alternative Amargosa Valley Receptor 2 [a]	Alternative Amargosa Valley Receptor 3 [b]
Water	3.8E-02	2.6E-02	3.7E-02	3.7E-02	5.6E-02	3.7E-02
Crop Ingestion	1.8E-02	6.9E-02	3.6E-02	3.1E-02	1.4E-02	5.5E-03
Animal Products Ingestion	4.0E-04	6.3E-03	7.8E-03	2.5E-03	1.8E-03	4.1E-04
Aquatic Food Ingestion	7.3E-04	3.1E-03	1.5E-02	2.3E-03	2.5E-03	4.2E-04
Total Ingestion	1.8E-02	7.5E-02	4.4E-02	3.3E-02	1.6E-02	5.9E-03
Inhalation	2.1E-03	2.1E-03	2.1E-03	2.1E-03	2.1E-03	2.1E-03
External Exposure	3.8E-04	3.8E-04	3.8E-04	3.8E-04	3.8E-04	3.8E-04
Total	5.9E-02	1.1E-01	9.9E-02	7.5E-02	7.8E-02	4.6E-02

Sources: [a] Wu 2001 [DIRS 154894], Table 5.
[b] Wu 2001 [DIRS 155203] Table 3.

Table 13.3-5. Comparison of International Commission on Radiological Protection Tissue Weighting Factors

Tissue/Organ	Weighting Factor ICRP 26	Weighting Factor ICRP 60
Gonads	0.25	0.20
Bone marrow (red)	0.12	0.12
Colon	N/A	0.12
Lung	0.12	0.12
Stomach	N/A	0.12
Bladder	N/A	0.05
Breast	0.15	0.05
Liver	N/A	0.05
Esophagus	N/A	0.05
Thyroid	0.03	0.05
Skin	N/A	0.01
Bone Surface	0.03	0.01
Remainder	0.30	0.05

Sources: ICRP 1977 [DIRS 101075]; ICRP 1991 [DIRS 101836].

Table 13.3-6. Comparison of Biosphere Dose Conversion Factors for the Groundwater Release Scenario

Radionuclide	Previously Developed Mean BDCF	Modified Mean BDCF	BDCF Ratio
Carbon-14	5.2E-05	5.2E-05	1.0E+00
Nickel-63	7.2E-07	7.2E-07	1.0E+00
Strontium-90	1.6E-04	1.3E-04	8.5E-01
Technetium-99	3.3E-06	3.6E-06	1.1E+00
Iodine-129	3.1E-04	5.0E-04	1.6E+00
Cesium-137	1.3E-04	1.3E-04	1.0E+00
Lead-210	6.7E-03	3.1E-03	4.6E-01
Radium-226	1.1E-03	1.2E-03	1.1E+00
Actinium-227	1.5E-02	4.4E-03	2.9E-01
Thorium-229	4.0E-03	2.1E-03	5.1E-01
Thorium-230	6.1E-04	8.4E-04	1.4E+00
Protactinium-231	1.2E-02	2.8E-03	2.4E-01
Uranium-232	1.5E-03	1.4E-03	9.4E-01
Uranium-233	3.2E-04	2.1E-04	6.5E-01
Uranium-234	3.1E-04	2.0E-04	6.4E-01
Uranium-236	3.0E-04	1.9E-04	6.4E-01
Uranium-238	2.9E-04	1.8E-04	6.4E-01
Neptunium-237	5.8E-06	4.5E-07	7.8E-02
Plutonium-238	3.5E-03	9.2E-04	2.6E-01
Plutonium-239	3.9E-03	1.0E-03	2.6E-01
Plutonium-240	3.9E-03	1.0E-03	2.6E-01
Plutonium-242	3.6E-03	9.6E-04	2.7E-01
Americium-241	4.0E-03	8.1E-04	2.0E-01
Americium-243	4.0E-03	8.1E-04	2.0E-01

Source: Tappen 2001 [DIRS 154890], Table 1.

Table 13.3-7. Comparison of Biosphere Dose Conversion Factors for the Volcanic Eruption Scenario (Transition Phase, 1-cm Ash Layer, Annual Average Mass Loading)

Radionuclide	Previously Developed Mean BDCF	Modified Mean BDCF	BDCF Ratio
Strontium-90	9.0E-09	8.0E-09	8.8E-01
Cesium-137	1.9E-09	1.8E-09	9.5E-01
Lead-210	1.9E-08	1.5E-08	7.5E-01
Radium-226	5.9E-09	1.7E-08	2.9E+00
Actinium-227	2.3E-06	6.9E-07	3.1E-01
Thorium-229	7.2E-07	3.0E-07	4.1E-01
Thorium-230	1.1E-07	1.2E-07	1.2E+00
Protactinium-231	4.5E-07	1.8E-07	3.9E-01
Uranium-232	2.3E-07	4.8E-08	2.1E-01
Uranium-233	4.6E-08	1.2E-08	2.7E-01
Uranium-234	4.5E-08	1.2E-08	2.7E-01
Plutonium-238	1.4E-07	1.3E-07	9.7E-01
Plutonium-239	1.5E-07	1.5E-07	9.7E-01
Plutonium-240	1.5E-07	1.5E-07	9.7E-01
Plutonium-242	1.4E-07	1.4E-07	9.7E-01
Americium-241	1.5E-07	1.2E-07	7.8E-01
Americium-243	1.5E-07	1.2E-07	7.8E-01

Source: Tappen 2001 [DIRS 154890], Table 2.

Table 13.3-8. Parameters Used to Characterize the Leaching Process for Sandy Soils

Element	Parameter	Parameter value for a given K_d		
Technetium		K_d Value Used 0.1 L/kg	Lower K_d Limit 0.0037 L/kg	Upper K_d Limit 5 L/kg
	Leaching coefficient (1/yr)[a]	2.77E+00	4.57E+00	1.32E-01
	Characteristic removal time for leaching (yr)	3.67E-01	2.19E-01	7.58E+00
Iodine		K_d Value Used 1 L/kg	Lower K_d Limit 0.013 L/kg	Upper K_d Limit 85 L/kg
	Leaching coefficient (1/yr)[a]	5.92E-01	4.30E+00	7.96E-03
	Characteristic removal time for leaching (yr)	1.72E+00	2.33E-01	1.26E+02
Neptunium		K_d Value Used 5 L/kg	Lower K_d Limit 0.14 L/kg	Upper K_d Limit 120 L/kg
	Leaching coefficient (1/yr)[a]	1.32E-01	2.38E+00	5.64E-03
	Characteristic removal time for leaching (yr)	7.58E+00	4.20E-01	1.77E+02
Plutonium		K_d Value Used 550 L/kg	Lower K_d Limit 18 L/kg	Upper K_d Limit 16,000 L/kg
	Leaching coefficient (1/yr)[a]	1.23E-03	3.74E-02	4.24E-05
	Characteristic removal time for leaching (yr)	8.13E+02	2.67E+01	2.36E+04

Source: Wu 2001 [DIRS 154892], Table 2.

NOTE: [a] Calculated from Equation 13-2.

Table 13.3-9. Impact of Leaching Factor Changes on Biosphere Dose Conversion Factor Mean Values

Radionuclide	Leaching Coefficient 1/yr [a]	Mean BDCF rem/(pCi/L)[b]	Fractional Increase in BDCF [c]
Technetium-99	2.77	3.39E-6	4.9
	0.132	1.67E-5	
Iodine-129	0.592	3.1E-4	1.4
	0.00796	4.4E-4	
Neptunium-237	0.132	5.84E-3	1.3
	0.00564	7.84E-3	

Source: Wu 2001 [DIRS 154892].

NOTES: [a] Wu 2001 [DIRS 154892], Table 2.
[b] Wu 2001 [DIRS 154892], Tables 5, 6, and 7.
[c] Ratio of high to low Mean BDCF values.

Table 13.3-10. Pathway Contribution (Percent) to Biosphere Dose Conversion Factors

Pathway	Radionuclide			
	Technetium-99	Iodine-129	Neptunium-237	Plutonium-239
Drinking water	55.3	61.1	67.9	68.4
Leafy vegetables	27.9	23.6	26.2	26.3
Other vegetables	3.5	1.8	2.0	2.0
Other pathways	13.3	13.5	3.9	3.3

Source: CRWMS M&O 2001 [DIRS 152539], Table 15.

Table 13.3-11. Mean Biosphere Dose Conversion Factor Values (rem/(pCi/L))

Irrigation Period	BDCF Values	Radionuclide			
		Technetium-99	Iodine-129	Neptunium-237	Plutonium-239
Zero Irrigation	Nominal	3.34E-06	3.10E-04	5.76E-03	3.88E-03
	Minimum	2.75E-06	2.10E-04	4.12E-03	2.79E-03
	Maximum	4.63E-06	4.70E-04	8.01E-03	5.38E-03
Long Irrigation	Nominal	3.39E-06	3.11E-04	5.84E-03	5.78E-03
	Minimum	2.80E-06	2.40E-04	4.47E-03	3.94E-03
	Maximum	1.67E-05	4.70E-04	8.09E-03	7.28E-03

Source: Wu 2001 [DIRS 154892], Tables 5, 6, 7, and 8.

Table 13.3-12. Lower and Upper Limit of the Multiplying Factor to be Applied to Groundwater Release Biosphere Dose Conversion Factors to Reflect Additional Uncertainty in Input Parameter Uncertainty

Limit of Multiplying Factor	Radionuclide			
	Technetium-99	Iodine-129	Neptunium-237	Plutonium-239
Lower	0.81	0.68	0.71	0.48
Upper	4.93	1.52	1.39	1.26

Source: Calculated using values from Table 13.3-11.

Table 13.3-13. Parameters Forming a Basis for Alfalfa Irrigation for the Present and Future Climate

Parameter	Value Present Climate [a] (in/yr)	Value Future Climate [b] (in/yr)
Annual evapotranspiration	92.7	43.3
Precipitation during growing season	4.0	7.5
Deep percolation	6.0	6.0
Annual irrigation [c]	95	42

NOTES: [a] CRWMS M&O 2001 [DIRS 152539], Table III-1 and Section III.2.3.
[b] CRWMS M&O 2001 [DIRS 152539], Table III-6 and Section III.2.3.
[c] Annual irrigation was rounded to the nearest inch.

Table 13.3-14. Annual Average Meteorological Parameters for Potential Future Climate States at Yucca Mountain and the Analogue Sites for the Climate Change Analysis

Climate State	Representative Meteorological Stations	Max Temperature (°F)	Min Temperature (°F)	Snowfall (inches)	Precipitation (inches)
Monsoon Climate Average Upper Bound	Nogales 6N, Arizona Hobbs, New Mexico	79.4 76.5	42.7 47.8	0.45 5.18	17.55 16.44
Monsoon Climate Average Lower Bound	Yucca Mountain site and regional meteorological stations (e.g., Amargosa Farms)	81.9	48.3	0.10	4.48
Glacial Transition Climate Average Upper Bound	Spokane, Washington Rosalia, Washington St. John, Washington	58.1 58.1 60.9	38.1 36.1 35.8	42.14 24.34 25.78	16.15 18.10 17.06
Glacial Transition Climate Average Lower Bound	Beowawe, Nevada Delta, Utah	65.0 65.4	30.8 34.8	14.39 25.15	8.64 7.79
Modern Interglacial Climate	Yucca Mountain site and regional meteorological stations (e.g., Amargosa Farms)	81.9	48.3	0.10	4.48

Source: CRWMS M&O 2001 [DIRS 152539], Table 4.

Table 13.3-15. Comparison of the Biosphere Dose Conversion Factors (rem per pCi/L) and Buildup Factors for the Current and Evolved Climate[a]

Radionuclide	1st Irrigation Period			6th Irrigation Period			Buildup Factor[b]	
	BDCF for Current Climate	BDCF for Evolved Climate	Evolved/ Current BDCF Ratio	BDCF for Current Climate	BDCF for Evolved Climate	Evolved/ Current BDCF Ratio	Current Climate	Evolved Climate
C-14	5.19E-05	5.11E-05	0.99	5.19E-05	5.11E-05	0.99	1.00	1.00
Ni-63	7.22E-07	6.60E-07	0.91	1.16E-06	9.72E-07	0.84	1.61	1.47
Sr-90	1.55E-04	1.41E-04	0.91	2.57E-04	2.23E-04	0.87	1.66	1.58
Tc-99	3.34E-06	3.00E-06	0.90	3.39E-06	2.99E-06	0.88	1.01	1.00
I-129	3.10E-04	2.81E-04	0.91	3.11E-04	2.82E-04	0.91	1.00	1.00
Cs-137	1.26E-04	1.13E-04	0.90	4.54E-04	2.81E-04	0.62	3.60	2.49
Pb-210	6.67E-03	6.24E-03	0.94	6.86E-03	6.38E-03	0.93	1.03	1.02
Ra-226	1.10E-03	1.01E-03	0.92	1.81E-02	1.08E-02	0.60	16.5	10.7
Ac-227	1.54E-02	1.43E-02	0.93	1.64E-02	1.49E-02	0.91	1.06	1.04
Th-229	4.01E-03	3.74E-03	0.93	4.91E-02	2.71E-02	0.55	12.2	7.25
Th-230	6.05E-04	5.66E-04	0.94	3.97E-02	2.25E-02	0.57	65.6	39.8
Pa-231	1.15E-02	1.07E-02	0.93	4.55E-02	2.84E-02	0.62	3.96	2.65
U-232	1.45E-03	1.34E-03	0.92	2.34E-03	1.80E-03	0.77	1.61	1.34
U-233	3.19E-04	2.96E-04	0.93	3.62E-04	3.19E-04	0.88	1.13	1.08
U-234	3.13E-04	2.90E-04	0.93	3.52E-04	3.12E-04	0.89	1.12	1.08
U-236	2.97E-04	2.75E-04	0.93	3.33E-04	2.95E-04	0.89	1.12	1.07
U-238	2.86E-04	2.65E-04	0.93	3.36E-04	2.92E-04	0.87	1.17	1.10
Np-237	5.76E-03	5.37E-03	0.93	5.84E-03	5.42E-03	0.93	1.01	1.01
Pu-238	3.50E-03	3.27E-03	0.93	3.73E-03	3.38E-03	0.91	1.07	1.03
Pu-239	3.88E-03	3.63E-03	0.94	5.78E-03	4.59E-03	0.79	1.49	1.26
Pu-240	3.88E-03	3.62E-03	0.93	5.66E-03	4.53E-03	0.80	1.46	1.25
Pu-242	3.61E-03	3.37E-03	0.93	5.41E-03	4.29E-03	0.79	1.50	1.27
Am-241	3.96E-03	3.69E-03	0.93	5.28E-03	4.39E-03	0.83	1.33	1.19
Am-243	3.95E-03	3.69E-03	0.93	1.44E-02	9.05E-03	0.63	3.65	2.45

NOTES: [a] CRWMS M&O 2001 [DIRS 152539], Tables 9, 12, and 14.
[b] Ratio of mean BDCF for 6th irrigation period to mean BDCF for 1st (no prior irrigation) period.

Table 13.3-16. Recommended Transfer Parameter Values for Selenium

Soil-to-Plant Transfer Factors				Animal Feed Transfer Coefficients				Bioaccumulation Factor for Fish (L/kg)
Leafy Vegetables	Root Vegetables	Fruit	Grain	Beef (d/kg)	Poultry (d/kg)	Milk (d/L)	Eggs (d/kg)	
2.5E-02	2.5E-02	2.5E-02	2.5E-02	1.5E-02	9.0E+00	4.0E-03	9.3E+00	1.7E+02

Source: Wu 2001 [DIRS 154893], Table 10.

Table 13.3-17. Removal Constants and Prior Irrigation Time Periods for Selenium-79

Removal constant, 1/y			Prior Irrigation Periods, y[a]					
Radioactive Decay[b]	Leaching[c]	Effective[d]	1	2	3	4	5	6
1.07E-05	1.23E-2	1.23E-02	0	15	33	56	89	146

Source: Wu 2001 [DIRS 154893], Table 11.

NOTES: [a] Prior irrigation periods were calculated using CRWMS M&O 2001 [DIRS 152539], Equation 2.
[b] Rittmann 1993 [DIRS 107744], p. 2-5; removal constant for radioactive decay = (ln 2)/(half-life).
[c] CRWMS M&O 2001 [DIRS 152517], Section 6.2.
[d] Effective removal constant = sum of radioactive decay and leaching removal constants.

Table 13.3-18. Dose Coefficients for Exposure to Soil Contaminated with Selenium-79

Contamination Depth	Dose Coefficient	
	Sv/s per Bq/m^3 [a]	Sv/y per Bq/m^3 [b]
15 cm	9.96E-23	3.14E-15
1 cm	5.77E-23	1.82E-15

NOTES: [a] Source: Wu 2001 [DIRS 154893], Table 12.
[b] (Sv/s per Bq/m^3) $\times$ (3.15×10^7 s/y) = Sv/y per Bq/m^3.

Table 13.3-19. Selenium-79 Biosphere Dose Conversion Factors for the Three Volcanic Eruption Exposure Scenarios

	Dose Factor for Eruption Phase (rem/(pCi/m^3))	BDCFs for Transition Phase (rem/(pCi/m^2))				BDCFs for Steady-State Phase (rem/(pCi/m^2))
		1-cm Ash Layer, Annual Average Mass Loading	1-cm Ash Layer, 10-year Average Mass Loading	15-cm Ash Layer, Annual Average Mass Loading	15-cm Ash Layer, 10-year Average Mass Loading	
Mean	1.56E-07	4.93E-11	4.37E-11	3.10E-11	3.07E-11	3.05E-11
STD	---	5.97E-11	5.78E-11	5.67E-11	5.67E-11	5.67E-11
Min.	---	1.15E-11	1.12E-11	8.78E-13	8.56E-13	8.20E-13
5%	---	1.25E-11	1.19E-11	1.54E-12	1.39E-12	1.34E-12
10%	---	1.54E-11	1.37E-11	2.16E-12	1.99E-12	1.91E-12
15%	---	1.72E-11	1.50E-11	3.23E-12	2.89E-12	2.77E-12
20%	---	1.92E-11	1.66E-11	4.86E-12	4.59E-12	4.47E-12
25%	---	2.09E-11	1.78E-11	6.29E-12	5.94E-12	5.66E-12
30%	---	2.18E-11	1.97E-11	7.52E-12	7.19E-12	7.08E-12
35%	---	2.51E-11	2.08E-11	8.47E-12	7.95E-12	7.90E-12
40%	---	2.62E-11	2.16E-11	9.10E-12	8.69E-12	8.52E-12
45%	---	2.81E-11	2.29E-11	1.11E-11	1.03E-11	1.01E-11
50%	---	3.04E-11	2.55E-11	1.24E-11	1.18E-11	1.14E-11
55%	---	3.35E-11	2.94E-11	1.49E-11	1.46E-11	1.44E-11
60%	---	3.70E-11	3.07E-11	1.82E-11	1.80E-11	1.77E-11
65%	---	4.29E-11	3.44E-11	2.07E-11	2.03E-11	2.03E-11
70%	---	4.78E-11	3.99E-11	2.69E-11	2.68E-11	2.67E-11
75%	---	5.24E-11	4.76E-11	3.59E-11	3.58E-11	3.57E-11
80%	---	6.37E-11	5.69E-11	4.34E-11	4.30E-11	4.29E-11
85%	---	7.43E-11	7.16E-11	5.77E-11	5.75E-11	5.74E-11
90%	---	1.31E-10	1.18E-10	1.05E-10	1.04E-10	1.04E-10
95%	---	2.41E-10	2.38E-10	2.24E-10	2.24E-10	2.24E-10
Max.	---	5.26E-10	5.16E-10	4.96E-10	4.96E-10	4.96E-10

Source: Wu 2001 [DIRS 154893], Table 14.

Table 13.3-20. Neptunium-237 Biosphere Dose Conversion Factors for the Three Volcanic Eruption Exposure Scenarios

	Dose Factor for Eruption Phase (rem/(pCi/m^3))	BDCFs for Transition Phase (rem/(pCi/m^2))				BDCFs for Steady-State Phase (rem/(pCi/m^2))
		1-cm Ash Layer, Annual Average Mass Loading	1-cm Ash Layer, 10-year Average Mass Loading	15-cm Ash Layer, Annual Average Mass Loading	15-cm Ash Layer, 10-year Average Mass Loading	
Mean	8.61E-03	2.28E-07	1.03E-07	2.16E-08	1.32E-08	9.01E-09
STD	---	1.91E-07	5.33E-08	1.83E-08	1.44E-08	1.42E-08
Min.	---	3.50E-08	3.44E-08	2.75E-09	2.61E-09	1.77E-09
5%	---	3.76E-08	3.60E-08	3.15E-09	2.86E-09	2.07E-09
10%	---	4.45E-08	3.97E-08	4.38E-09	3.78E-09	2.53E-09
15%	---	5.42E-08	4.53E-08	5.21E-09	4.52E-09	2.73E-09
20%	---	6.19E-08	4.88E-08	6.58E-09	5.12E-09	2.95E-09
25%	---	7.34E-08	5.65E-08	7.98E-09	6.10E-09	3.22E-09
30%	---	8.13E-08	6.05E-08	9.55E-09	7.08E-09	3.53E-09
35%	---	1.04E-07	6.78E-08	1.10E-08	7.68E-09	3.85E-09
40%	---	1.12E-07	7.43E-08	1.23E-08	8.01E-09	4.14E-09
45%	---	1.31E-07	8.01E-08	1.43E-08	8.73E-09	4.48E-09
50%	---	1.58E-07	8.97E-08	1.58E-08	9.74E-09	4.94E-09
55%	---	1.88E-07	1.00E-07	1.94E-08	1.09E-08	5.35E-09
60%	---	2.21E-07	1.15E-07	2.09E-08	1.22E-08	5.81E-09
65%	---	2.57E-07	1.27E-07	2.53E-08	1.31E-08	6.34E-09
70%	---	3.00E-07	1.33E-07	2.85E-08	1.41E-08	7.58E-09
75%	---	3.59E-07	1.50E-07	3.13E-08	1.54E-08	8.87E-09
80%	---	4.15E-07	1.60E-07	3.59E-08	1.66E-08	1.13E-08
85%	---	5.02E-07	1.78E-07	4.28E-08	1.83E-08	1.28E-08
90%	---	5.95E-07	2.00E-07	5.03E-08	2.80E-08	2.19E-08
95%	---	7.12E-07	2.14E-07	6.20E-08	5.79E-08	5.48E-08
Max.	---	7.85E-07	2.22E-07	1.15E-07	1.13E-07	1.11E-07

Source: Wu 2001 [DIRS 154893], Table 15.

Table 13.3-21. Biosphere Dose Conversion Factors for Selenium-79, Groundwater Release Scenario, for the Current Climate and the Evolved Climate

	BDCFs for the Current Climate (rem/(pCi/L))		BDCFs for the Evolved Climate (rem/(pCi/L))	
Irrigation Period	Mean	STD	Mean	STD
1	1.18E-5	6.64E-6	1.05E-5	5.78E-6
2	1.24E-5	6.90E-6	1.08E-5	5.86E-5
3	1.31E-5	7.33E-6	1.12E-5	6.00E-6
4	1.37E-5	7.85E-6	1.16E-5	6.20E-6
5	1.43E-5	8.52E-6	1.20E-5	6.44E-6
6	1.50E-5	9.23E-6	1.24E-5	6.77E-6

Source: Wu 2001 [DIRS 154893], Table 13.

Table 13.3-22. Biosphere Dose Conversion Factors for Selenium-79, Groundwater Release Scenario, for the Current Climate

Irrigation Period	1	2	3	4	5	6
Time (yr)	0	15	33	56	89	146
Percentile	**Biosphere Dose Conversion Factor (rem/(pCi/L))**					
0%	1.84E-06	2.03E-06	2.03E-06	2.21E-06	2.24E-06	2.27E-06
5%	3.78E-06	3.92E-06	3.92E-06	4.14E-06	4.24E-06	4.40E-06
10%	4.63E-06	4.89E-06	4.89E-06	5.34E-06	5.47E-06	5.71E-06
15%	5.14E-06	5.71E-06	5.71E-06	6.22E-06	6.48E-06	6.88E-06
20%	6.20E-06	6.58E-06	6.58E-06	7.19E-06	7.37E-06	7.47E-06
25%	6.97E-06	7.63E-06	7.63E-06	8.36E-06	8.42E-06	8.76E-06
30%	7.77E-06	8.35E-06	8.35E-06	9.30E-06	9.53E-06	9.87E-06
35%	8.48E-06	9.12E-06	9.12E-06	1.03E-05	1.07E-05	1.12E-05
40%	9.54E-06	1.01E-05	1.01E-05	1.12E-05	1.18E-05	1.21E-05
45%	1.02E-05	1.10E-05	1.10E-05	1.18E-05	1.22E-05	1.24E-05
50%	1.10E-05	1.14E-05	1.14E-05	1.20E-05	1.26E-05	1.28E-05
55%	1.16E-05	1.19E-05	1.19E-05	1.28E-05	1.33E-05	1.39E-05
60%	1.23E-05	1.27E-05	1.27E-05	1.35E-05	1.43E-05	1.50E-05
65%	1.34E-05	1.42E-05	1.42E-05	1.49E-05	1.50E-05	1.56E-05
70%	1.42E-05	1.48E-05	1.48E-05	1.57E-05	1.62E-05	1.64E-05
75%	1.47E-05	1.54E-05	1.54E-05	1.64E-05	1.69E-05	1.75E-05
80%	1.54E-05	1.62E-05	1.62E-05	1.92E-05	1.98E-05	2.01E-05
85%	1.63E-05	1.82E-05	1.82E-05	2.15E-05	2.19E-05	2.29E-05
90%	1.96E-05	2.09E-05	2.09E-05	2.32E-05	2.49E-05	2.59E-05
95%	2.38E-05	2.41E-05	2.41E-05	2.93E-05	3.14E-05	3.36E-05
100%	3.76E-05	4.27E-05	4.27E-05	5.37E-05	5.96E-05	6.47E-05

Source: Results from GENII-S statistical runs documented in files listed in Attachment I.1 of Wu 2001 [DIRS 154893].

Table 13.4-1. Summary of the Biosphere Dose Conversion Factors for the Groundwater Release Scenario for the Current Climate and the Corresponding Buildup Factors

	BDCF, 1st Irrigation period (rem/(pCi/L))		BDCF, 6th Irrigation Period (rem/(pCi/L))			
Radionuclide	**Mean**	**Standard Deviation**	**Duration of Irrigation Period, yr**	**Mean**	**Standard Deviation**	**Buildup Factor [a]**
Carbon-14	5.19E-5	1.40E-4	14	5.19E-5	1.40E-4	1.00
Nickel-63	7.22E-7	4.20E-7	208	1.16E-6	1.04E-6	1.61
Strontium-90	1.55E-4	8.21E-5	26	2.57E-4	2.57E-4	1.66
Technetium-99	3.34E-6	2.26E-6	5	3.39E-6	2.34E-6	1.01
Iodine-129	3.10E-4	1.62E-4	5	3.11E-4	1.62E-4	1.00
Cesium-137	1.26E-4	1.47E-4	71	4.54E-4	1.72E-4	3.60
Lead-210	6.67E-3	4.02E-3	53	6.86E-3	4.08E-3	1.03
Radium-226	1.10E-3	5.61E-4	1005	1.81E-2	8.36E-3	16.5
Actinium-227	1.54E-2	8.07E-3	54	1.64E-2	8.09E-3	1.06
Thorium-229	4.01E-3	2.14E-3	5848	4.91E-2	1.13E-2	12.2

Table 13.4-1. Summary of the Biosphere Dose Conversion Factors for the Groundwater Release Scenario for the Current Climate and the Corresponding Buildup Factors (Continued)

Radionuclide	BDCF, 1st Irrigation period (rem/(pCi/L))		BDCF, 6th Irrigation Period (rem/(pCi/L))			Buildup Factor [a]
	Mean	Standard Deviation	Duration of Irrigation Period, yr	Mean	Standard Deviation	
Thorium-230	6.05E-4	3.23E-4	8108	3.97E-2	1.64E-2	65.6
Protactinium-231	1.15E-2	6.05E-3	1432	4.55E-2	1.10E-2	3.96
Uranium-232	1.45E-3	7.49E-4	62	2.34E-3	7.87E-4	1.61
Uranium-233	3.19E-4	1.66E-4	93	3.62E-4	1.68E-4	1.13
Uranium-234	3.13E-4	1.63E-4	93	3.52E-4	1.65E-4	1.12
Uranium-236	2.97E-4	1.54E-4	93	3.33E-4	1.56E-4	1.12
Uranium-238	2.86E-4	1.49E-4	93	3.36E-4	1.51E-4	1.17
Neptunium-237	5.76E-3	3.02E-3	14	5.84E-3	3.04E-3	1.01
Plutonium-238	3.50E-3	1.84E-3	196	3.73E-3	1.84E-3	1.07
Plutonium-239	3.88E-3	2.04E-3	1423	5.78E-3	2.14E-3	1.49
Plutonium-240	3.88E-3	2.04E-3	1341	5.66E-3	2.12E-3	1.46
Plutonium-242	3.61E-3	1.90E-3	1455	5.41E-3	1.99E-3	1.50
Americium-241	3.96E-3	2.08E-3	915	5.28E-3	2.16E-3	1.33
Americium-243	3.95E-3	2.08E-3	3983	1.44E-2	3.19E-3	3.65

Source: CRWMS M&O 2001 [DIRS 152539], Table 9.

NOTE: [a] Ratio of mean BDCF for 6th irrigation period to mean BDCF for 1st (no prior irrigation) period.

Table 13.4-2. The Biosphere Dose Conversion Factor Distribution for Carbon-14 Given as an Empirical Percentile Table

Percentile	BDCF (rem/(pCi/L))	Percentile	BDCF (rem/(pCi/L))
0%	6.73E-07	55%	5.14E-06
5%	1.58E-06	60%	5.66E-06
10%	2.14E-06	65%	6.03E-06
15%	2.49E-06	70%	7.40E-06
20%	2.89E-06	75%	1.14E-05
25%	3.22E-06	80%	2.56E-05
30%	3.53E-06	85%	5.47E-05
35%	3.83E-06	90%	1.30E-04
40%	4.30E-06	95%	3.36E-04
45%	4.60E-06	100%	8.12E-04
50%	4.93E-06	---	---

Source: CRWMS M&O 2001 [DIRS 153207], Table 10.

Table 13.4-3. Distributions and Parameters for Abstracted Biosphere Dose Conversion Factors for those Radionuclides Exhibiting Less than a 15 Percent Build-Up Due to Continuing Irrigation

Radionuclide	Distribution			
	Normal		Log-normal	
	Arithmetic Mean (rem/(pCi/L))	Arithmetic SD (rem/(pCi/L))	Geometric Mean (rem/(pCi/L))	Geometric SD (dimensionless)
Actinium-227	1.58E-02	8.34E-03	---	---
Iodine-129	3.03E-04	1.61E-04	---	---
Neptunium-237	5.68E-03	3.14E-03	---	---
Lead-210	---	---	5.84E-03	1.76E+00
Plutonium-238	3.59E-03	1.90E-03	---	---
Technetium-99	---	---	2.84E-06	1.84E+00
Uranium-233	3.53E-04	1.74E-04	---	---
Uranium-234	3.42E-04	1.70E-04	---	---
Uranium-236	3.25E-04	1.61E-04	---	---

Source: CRWMS M&O 2001 [DIRS 153207], Table 9.

NOTE: SD = Standard Deviation.

Table 13.4-4. Asymptotic Buildup Factors for Those Radionuclides Showing Significant Buildup Before and After the Inclusion of the Soil Erosion Mechanism

Radionuclide	Asymptotic Buildup Factor with Leaching No Erosion	Asymptotic Buildup Factors with One Dominant Removal Mechanism (Leaching or Erosion)
Americium-241	1.4	1.2
Americium-243	4.6	1.4
Cesium-137	5.9	5.6
Nickel-63	1.4	1.4
Protactinium-231	5.0	2.2
Plutonium-239	1.6	1.2
Plutonium-240	1.6	1.2
Plutonium-242	1.6	1.2
Radium-226	20.2	8.9
Strontium-90	1.5	1.5
Thorium-229	15.7	2.1
Thorium-230	NM (>60)	3.9
Uranium-232	3.2	3.2
Uranium-238	1.2	1.2

Source: CRWMS M&O 2001 [DIRS 153206], Table 7.

NOTES: NM = Not meaningful.

For thorium-230, the concentration increase of decay products into the soil did not permit the actual asymptotic value of buildup to be accurately determined. The buildup factor was, however, greater than 60. When erosion was considered with its characteristic removal time of 250 years, decay product in-growth was of no consequence.

Table 13.4-5. Recommended Biosphere Dose Conversion Factor Parameters for the Radionuclides Having a Normal Distribution for the Groundwater Release Scenario and the Current Climate

Radionuclide	Normal Distribution	
	Arithmetic Mean (rem/(pCi/L))	Arithmetic Standard Deviation (rem/(pCi/L))
Americium-241	4.40E-03	2.16E-03
Plutonium-239	4.47E-03	2.13E-03
Plutonium-240	4.45E-03	2.13E-03
Plutonium-242	4.16E-03	1.98E-03
Thorium-230	2.26E-03	6.37E-04
Uranium-232	4.63E-03	9.41E-04
Uranium-238	3.38E-04	1.56E-04

Source: CRWMS M&O 2001 [DIRS 153206], Table 8.

Table 13.4-6. Recommended Biosphere Dose Conversion Factor Parameters for the Radionuclides Having a Log-normal Distribution for the Groundwater Release Scenario and the Current Climate

Radionuclide	Log-normal Distribution	
	Geometric Mean (rem/(pCi/L))	Geometric Standard Deviation (dimensionless)
Americium-243	4.81E-03	1.59E+00
Radium-226	3.22E-02	7.87E-01
Strontium-90	2.27E-04	2.08E+00
Thorium-229	6.24E-03	1.54E+00

Source: CRWMS M&O 2001 [DIRS 153206], Table 9.

Table 13.4-7. Recommended Biosphere Dose Conversion Factor Parameters for the Radionuclides Having a Shifted Log-normal Distribution for the Groundwater Release Scenario and the Current Climate

Radionuclide	Shifted Log-normal Distribution		
	Geometric Mean (rem/(pCi/L))	Geometric Standard Deviation (dimensionless)	Shift (rem/(pCi/L))
Cesium-137	1.39E-04	1.53E+00	3.32E-04
Nickel-63	2.57E-06	1.18E+00	-1.21E-06
Protactinium-231	5.30E-02	1.14E+00	-3.02E-02

Source: CRWMS M&O 2001 [DIRS 153206], Table 9.

Table 13.4-8. Summary of Biosphere Dose Conversion Factors for the Groundwater Release Scenario for the Evolved Climate and their Corresponding Buildup Factors

Radionuclide	BDCF, 1st Irrigation Period (rem/(pCi/L))		BDCF, 6th Irrigation Period (rem/(pCi/L))			Buildup Factor [a]
	Mean	Standard Deviation	Time, y	Mean	Standard Deviation	
^{14}C	5.11E-5	1.41E-4	14	5.11E-5	1.41E-4	1.00
^{63}Ni	6.60E-7	3.67E-7	208	9.72E-7	7.63E-7	1.47
^{90}Sr	1.41E-4	7.36E-5	26	2.23E-4	2.15E-4	1.58
^{99}Tc	3.00E-6	1.89E-6	5	2.99E-6	1.95E-6	1.00
^{129}I	2.81E-4	1.46E-4	5	2.82E-4	1.46E-4	1.00
^{137}Cs	1.13E-4	1.43E-4	71	2.81E-4	1.52E-4	2.49
^{210}Pb	6.24E-3	3.84E-3	53	6.38E-3	3.87E-3	1.02
^{226}Ra	1.01E-3	5.23E-4	1005	1.08E-2	6.88E-3	10.7
^{227}Ac	1.43E-2	7.55E-3	54	1.49E-2	7.56E-3	1.04
^{229}Th	3.74E-3	2.01E-3	5848	2.71E-2	6.57E-3	7.25
^{230}Th	5.66E-4	3.03E-4	8108	2.25E-2	1.35E-2	39.8
^{231}Pa	1.07E-2	5.66E-3	1432	2.84E-2	7.69E-3	2.65
^{232}U	1.34E-3	6.99E-4	62	1.80E-3	7.11E-4	1.34
^{233}U	2.96E-4	1.55E-4	93	3.19E-4	1.55E-4	1.08
^{234}U	2.90E-4	1.52E-4	93	3.12E-4	1.52E-4	1.08
^{236}U	2.75E-4	1.44E-4	93	2.95E-4	1.44E-4	1.07
^{238}U	2.65E-4	1.39E-4	93	2.92E-4	1.39E-4	1.10
^{237}Np	5.37E-3	2.82E-3	14	5.42E-3	2.82E-3	1.01
^{238}Pu	3.27E-3	1.72E-3	196	3.38E-3	1.72E-3	1.03
^{239}Pu	3.63E-3	1.91E-3	1423	4.59E-3	1.94E-3	1.26
^{240}Pu	3.62E-3	1.91E-3	1341	4.53E-3	1.93E-3	1.25
^{242}Pu	3.37E-3	1.78E-3	1455	4.29E-3	1.80E-3	1.27
^{241}Am	3.69E-3	1.95E-3	915	4.39E-3	1.98E-3	1.19
^{243}Am	3.69E-3	1.94E-3	3983	9.05E-3	2.38E-3	2.45

Source: CRWMS M&O 2001 [DIRS 152539], Table 12.

NOTE: [a] Ratio of mean BDCF for 6th irrigation period to mean BDCF for 1st (no prior irrigation) period.

Table 13.4-9. Dose Factors for the Eruption Phase

Radionuclide	Dose Factors rem-m^3/pCi
Strontium-90	3.82E-06
Cesium-137	5.09E-07
Lead-210	2.17E-04
Radium-226	1.37E-04
Actinium-227	1.07E-01
Thorium-229	3.42E-02
Thorium-230	5.19E-03
Protactinium-231	2.05E-02
Uranium-232	1.05E-02
Uranium-233	2.16E-03
Uranium-234	2.11E-03
Plutonium-238	6.25E-03
Plutonium-239	6.84E-03
Plutonium-240	6.84E-03
Plutonium-242	6.55E-03
Americium-241	7.08E-03
Americium-243	7.02E-03

Source: CRWMS M&O 2001 [DIRS 152536], Table 5.

Table 13.4-10. Volcanic Eruption Biosphere Dose Conversion Factors (rem/(pCi/m^2))

	90Sr	137Cs	210Pb	226Ra	227Ac	229Th	230Th	231Pa	232U	233U	234U	238Pu	239Pu	240Pu	242Pu	241Am	243Am
Transition Phase, 1-cm Ash Layer, Annual Average Mass Loading																	
Mean	9.01E-09	1.86E-09	1.93E-08	5.86E-09	2.27E-06	7.20E-07	1.08E-07	4.50E-07	2.27E-07	4.58E-08	4.51E-08	1.36E-07	1.51E-07	1.51E-07	1.41E-07	1.54E-07	1.54E-07
STD	2.03E-08	2.43E-09	1.28E-08	3.92E-09	2.02E-06	6.42E-07	9.65E-08	3.89E-07	2.02E-07	4.06E-08	4.00E-08	1.18E-07	1.31E-07	1.31E-07	1.22E-07	1.33E-07	1.33E-07
Min.	2.30E-10	1.01E-09	7.73E-09	1.67E-09	3.00E-07	9.43E-08	1.42E-08	6.79E-08	3.06E-08	6.21E-09	6.11E-09	2.06E-08	2.28E-08	2.28E-08	2.12E-08	2.33E-08	2.33E-08
Max.	1.85E-07	2.79E-08	9.55E-08	2.31E-08	8.10E-06	2.57E-06	3.87E-07	1.59E-06	8.09E-07	1.63E-07	1.61E-07	4.81E-07	5.34E-07	5.33E-07	4.97E-07	5.44E-07	5.43E-07
Transition Phase, 1-cm Ash Layer, 10-year Average Mass Loading																	
Mean	8.92E-09	1.82E-09	1.52E-08	4.01E-09	9.57E-07	3.03E-07	4.56E-08	1.95E-07	9.61E-08	1.94E-08	1.91E-08	5.92E-08	6.56E-08	6.55E-08	6.11E-08	6.70E-08	6.69E-08
STD	2.03E-08	2.39E-09	1.17E-08	3.13E-09	5.53E-07	1.76E-07	2.64E-08	1.06E-07	5.52E-08	1.11E-08	1.10E-08	3.23E-08	3.58E-08	3.58E-08	3.34E-08	3.65E-08	3.64E-08
Min.	2.24E-10	1.01E-09	7.53E-09	1.62E-09	3.00E-07	9.43E-08	1.41E-08	6.77E-08	3.02E-08	6.13E-09	6.03E-09	2.05E-08	2.27E-08	2.27E-08	2.12E-08	2.32E-08	2.32E-08
Max.	1.85E-07	2.75E-08	9.21E-08	2.17E-08	2.24E-06	7.12E-07	1.07E-07	4.47E-07	2.24E-07	4.52E-08	4.45E-08	1.36E-07	1.50E-07	1.50E-07	1.40E-07	1.53E-07	1.53E-07
Transition Phase, 15-cm Ash Layer, Annual Average Mass Loading																	
Mean	8.71E-09	5.81E-09	6.71E-09	1.86E-09	1.52E-07	4.87E-08	7.24E-09	3.07E-08	1.57E-08	3.19E-09	3.13E-09	9.13E-09	1.01E-08	1.01E-08	9.43E-09	1.05E-08	1.06E-08
STD	2.02E-08	2.45E-09	1.13E-08	3.06E-09	1.34E-07	4.26E-08	6.40E-09	2.57E-08	1.33E-08	2.69E-09	2.65E-09	7.82E-09	8.67E-09	8.66E-09	8.08E-09	8.82E-09	8.80E-09
Min.	7.17E-11	4.33E-09	5.77E-10	1.85E-10	2.03E-08	6.86E-09	9.55E-10	4.94E-09	2.09E-09	4.25E-10	4.17E-10	1.40E-09	1.55E-09	1.55E-09	1.45E-09	1.67E-09	1.80E-09
Max.	1.83E-07	3.17E-08	8.23E-08	1.98E-08	5.20E-07	1.66E-07	2.48E-08	1.02E-07	5.20E-08	1.05E-08	1.03E-08	3.09E-08	3.43E-08	3.42E-08	3.19E-08	3.50E-08	3.51E-08
Transition Phase, 15-cm Ash Layer, 10-year Average Mass Loading																	
Mean	8.70E-09	5.81E-09	6.44E-09	1.74E-09	6.44E-08	2.09E-08	3.06E-09	1.37E-08	6.97E-09	1.42E-09	1.40E-09	3.98E-09	4.41E-09	4.40E-09	4.11E-09	4.68E-09	4.83E-09
STD	2.02E-08	2.45E-09	1.13E-08	3.06E-09	3.66E-08	1.17E-08	1.75E-09	7.07E-09	3.81E-09	7.75E-10	7.63E-10	2.14E-09	2.37E-09	2.37E-09	2.21E-09	2.42E-09	2.42E-09
Min.	7.17E-11	4.33E-09	5.63E-10	1.80E-10	2.00E-08	6.76E-09	9.48E-10	4.81E-09	2.02E-09	4.12E-10	4.04E-10	1.37E-09	1.52E-09	1.51E-09	1.41E-09	1.62E-09	1.76E-09
Max.	1.83E-07	3.17E-08	8.23E-08	1.98E-08	1.50E-07	4.80E-08	7.13E-09	3.01E-08	1.52E-08	3.12E-09	3.06E-09	9.04E-09	1.00E-08	1.00E-08	9.34E-09	1.03E-08	1.05E-08
Steady-State Phase																	
Mean	8.70E-09	5.81E-09	6.30E-09	1.68E-09	2.03E-08	6.84E-09	9.53E-10	5.18E-09	2.56E-09	5.33E-10	5.23E-10	1.38E-09	1.53E-09	1.53E-09	1.42E-09	1.75E-09	1.90E-09
STD	2.02E-08	2.45E-09	1.13E-08	3.06E-09	4.05E-09	1.25E-09	1.88E-10	1.17E-09	1.35E-09	2.97E-10	2.91E-10	2.35E-10	2.60E-10	2.60E-10	2.43E-10	4.02E-10	4.02E-10
Min.	7.02E-11	4.33E-09	5.28E-10	1.67E-10	1.09E-08	3.86E-09	5.04E-10	3.15E-09	1.21E-09	2.49E-10	2.44E-10	8.40E-10	9.32E-10	9.31E-10	8.68E-10	1.07E-09	1.23E-09
Max.	1.83E-07	3.17E-08	8.22E-08	1.98E-08	3.02E-08	1.01E-08	1.43E-09	1.10E-08	1.24E-08	2.70E-09	2.65E-09	1.98E-09	2.20E-09	2.19E-09	2.04E-09	3.98E-09	4.15E-09

Source: CRWMS M&O 2001 [DIRS 152536], Tables 11 to 15.

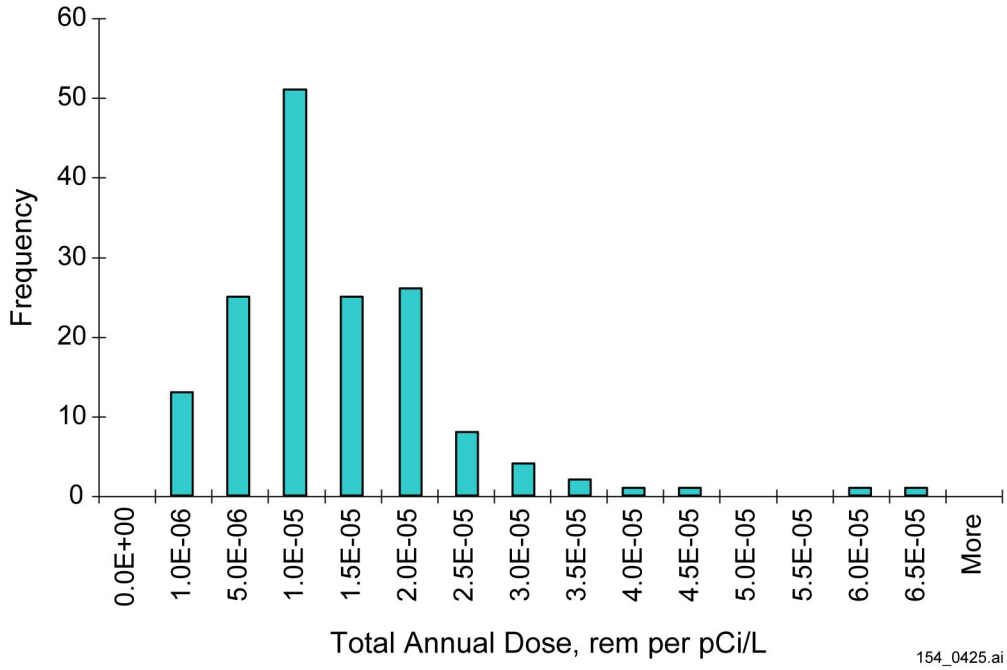

154_0425.ai

Source: Wu 2001 [DIRS 154894], Figure 1.

Figure 13.3-1. Distribution of Annual Doses at 25,000 years for a Hypothetical Group of Farmers Based on Amargosa Valley Population

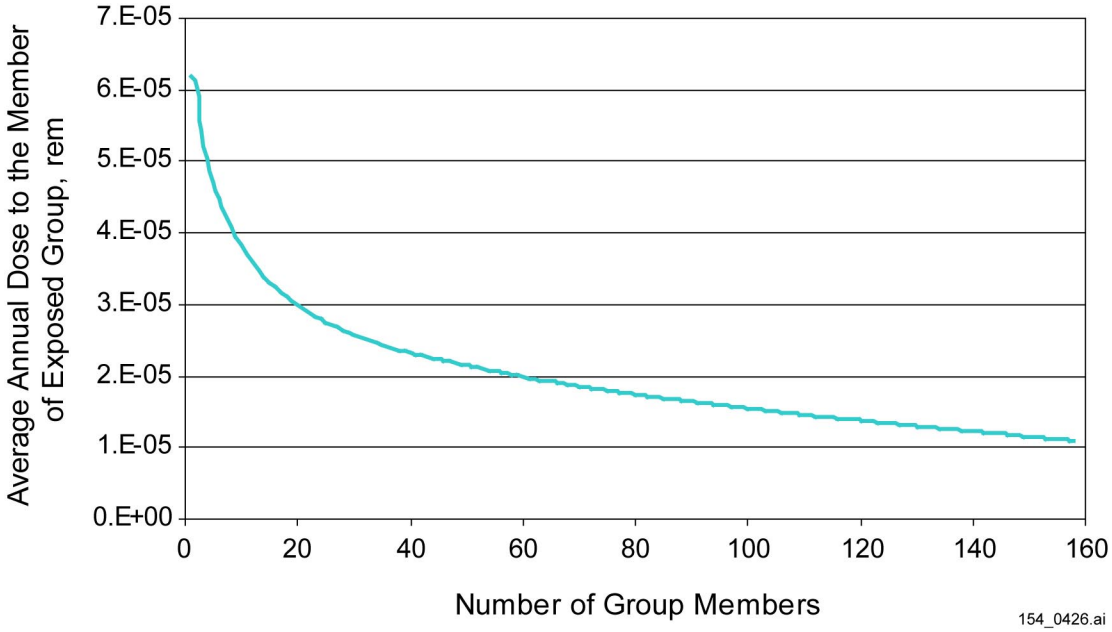

154_0426.ai

Source: Wu 2001 [DIRS 154894], Figure 2.

Figure 13.3-2. Dependence of the Average Annual Dose to the Members of the Exposed Group at 25,000 years on the Group Size

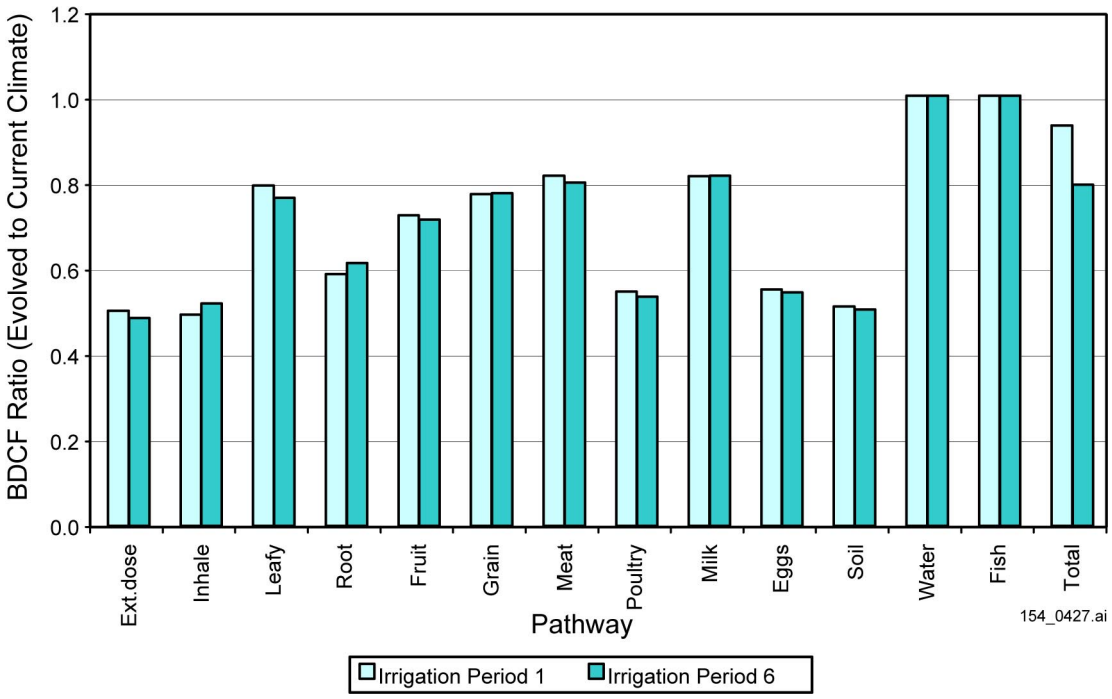

154_0427.ai

Source: CRWMS M&O 2000 [DIRS 152539], Figure 11.

Figure 13.3-3. Pathway Biosphere Dose Conversion Factor Ratios for Plutonium-239 for Groundwater Release of Evolved and Current Climates

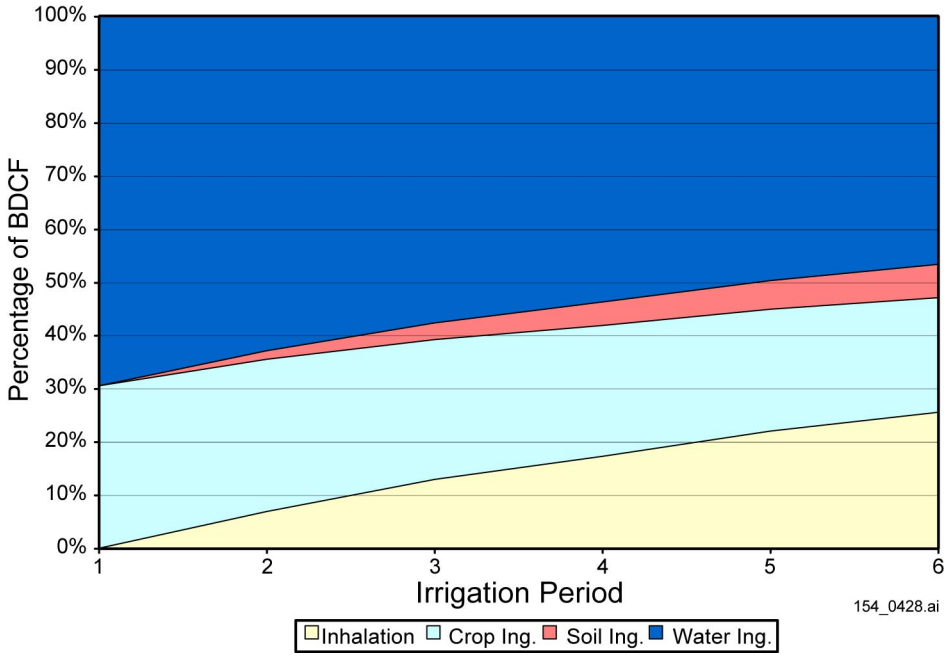

154_0428.ai

Source: CRWMS M&O 2001 [DIRS 152539], Figure 7.

Figure 13.4-1. Contributions of Major Exposure Pathways to Biosphere Dose Conversion Factors for Plutonium-239 for Groundwater Release at Different Irrigation Periods

14 Disruptive Events

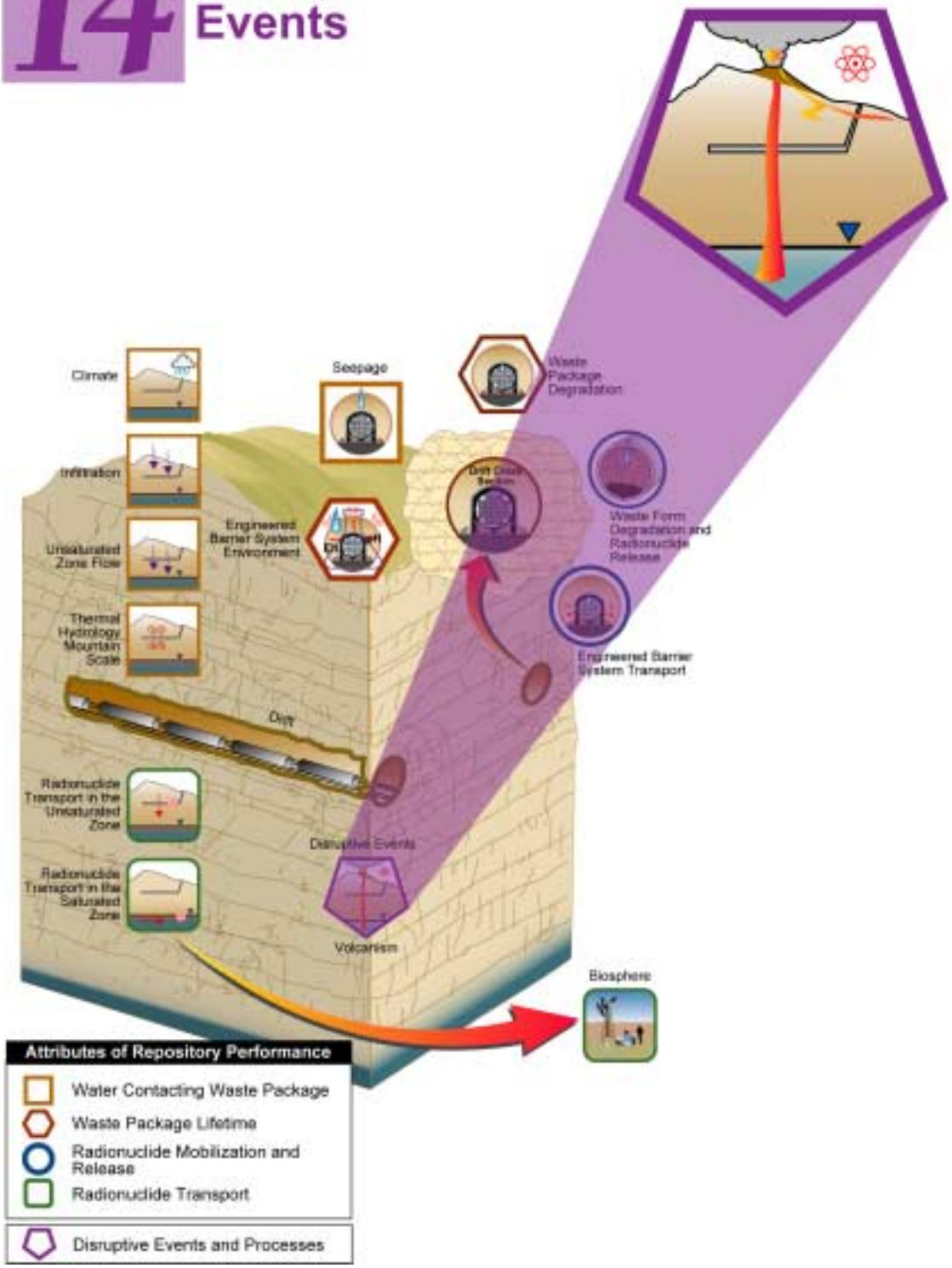

14. VOLCANIC AND SEISMIC DISRUPTIVE EVENTS

The *Yucca Mountain Science and Engineering Report* (S&ER) identifies disruptive conditions that were considered in evaluating the performance of a potential repository at Yucca Mountain (DOE 2001 [DIRS 153849], Section 4.3.2). These conditions (e.g., igneous activity, seismic activity, and human intrusion) are extremely unlikely to occur, but could, if they were to happen, significantly reduce the capability of a repository to isolate waste. In addition, a fourth disruptive condition, nuclear criticality, was considered but determined not to have a significant impact on repository performance (DOE 2001 [DIRS 153849], Section 4.3.3.2).

This section supplements the information on disruptive events presented in the S&ER for the conditions of igneous activity and seismic activity. It presents a discussion of how uncertainties were addressed for disruptive events and the impacts of considering a range of thermal operating modes. It describes new data and provides additional lines of evidence that increase confidence in existing analyses.

14.1 INTRODUCTION

Proposed 10 CFR 963.17(b) (64 FR 67054 [DIRS 124754]) identifies four disruptive processes and events for consideration in evaluating the total system performance of a geologic repository at Yucca Mountain: (1) volcanism, (2) seismic events, (3) nuclear criticality, and (4) inadvertent human intrusion. This section addresses the first two of these. A qualitative discussion of criticality is found in the *Total System Performance Assessment for the Site Recommendation* (TSPA-SR) (CRWMS M&O 2000 [DIRS 153246], Section 4.5.6). Inadvertent human intrusion is analyzed separately from the probabilistic total system performance assessment (TSPA) analysis. Proposed 10 CFR 963.16(a)(2) describes human intrusion as a stylized event that is assigned prescribed conditions. Analysis of human intrusion is contained in Section 4.4 of the TSPA-SR.

Analysis of volcanism includes both intrusive and extrusive igneous activity. The geologic aspect of intrusive igneous activity that is of primary interest is the development of dikes that may interact with the potential repository's emplacement drifts. For extrusive (eruptive) activity, the geologic aspect of primary interest is the development of a conduit (or conduits) that may interact with the emplacement drifts in the potential repository and feed a volcano on the surface. Such a volcano may incorporate waste into an erupting plume of volcanic ash.

Analysis of seismic events focuses on the vibratory ground motion and fault displacement associated with earthquakes. Of interest are the consequences of these effects on emplacement drift stability, rockfall, and shaking or shearing of components of the natural or engineered barrier systems.

Since completion of the S&ER (DOE 2001 [DIRS 153849]), additional analyses of disruptive events have been carried out to better characterize uncertainties, to incorporate new information, and to examine analysis sensitivities (Table 14-1). Sensitivities examined include those associated with a range of thermal operating modes.

Table 14-1. Summary of Supplemental Models and Analyses

Key Attributes of System	Process Model (Section of S&ER)	Topic of Supplemental Scientific Model or Analysis	Reason For Supplemental Scientific Model or Analysis			Section of Volume 1	Performance Assessment Treatment of Supplemental Scientific Model or Analysis[a]	
			Unquantified Uncertainty Analysis	Update in Scientific Information	Lower-Temperature Operating Mode Analysis		TSPA Sensitivity Analysis	Included in Supplemental TSPA Model
Low Mean Annual Dose Considering Potentially Disruptive Events	Volcanism/ Igneous Activity (4.3.2)	Probability of dike intersection of repository for the operating mode described in S&ER		X		14.3.3.1		X
		Scaling factors to evaluate impacts of repository design changes			X	14.3.3.2		
		Contribution to release of Zones 1 and 2		X		14.3.3.3	X	
		Sensitivity to waste particle size distribution		X		14.3.3.4	X	
		New wind speed data		X		14.3.3.5	X	X
		Explanation of method for handling ash/waste particle size and density		X		14.3.3.6		
		Volcanism inputs for Supplemental TSPA Model		X		14.3.3.7		X
		New aeromagnetic data		X		14.3.3.8		

NOTE: S&ER = *Yucca Mountain Science and Engineering Report* (DOE 2001 [DIRS 153849]).

[a] Performance assessment treatment of supplemental scientific model or analysis discussed in SSPA Volume 2 (McNeish 2001 [DIRS 155023]).

14.1.1 Repository Operating Mode Alternatives and Disruptive Events Analyses

For disruptive events analyses, the two key aspects of the operating mode are the layout of emplacement drifts, including the location and overall extent of the repository footprint, and whether backfill of emplacement drifts is included. The layout and footprint affect the calculation of the annual probability that an igneous dike will intersect an emplacement drift. They also influence calculation of the number of volcanic conduits that might develop through a repository and analysis of the number of waste packages that might be damaged. Inclusion or exclusion of backfill from an operating mode affects the analysis of magma interactions with emplacement drifts and the evaluation of the effects of seismically induced rockfall.

To place in context some of the new analyses of igneous disruptive events discussed in later sections of this report, it is useful to summarize the operating mode alternatives that have been considered. Three alternatives have been examined in disruptive events analyses to support consideration of a site recommendation:

1. Enhanced Design Alternative (EDA) II higher-temperature operating mode (CRWMS M&O 1999 [DIRS 150421], Item 1; CRWMS M&O 1999 [DIRS 107292], Figure 5.9, Tables 6.2 and 6.3, Section 7.1)

2. *Yucca Mountain Science and Engineering Report* higher-temperature operating mode (DOE 2001 [DIRS 153849]; CRWMS M&O 2000 [DIRS 146021], Sections 4.2.1.5 and 6.3.1, Figure 11, Table 28)

3. Lower-temperature operating mode (e.g., BSC 2001 [DIRS 154548]).

All of these alternatives are designed to store 70,000 metric tons of heavy metal (MTHM), but they have different layouts and footprints (Figure 14.1-1). The EDA II operating mode includes backfill in the emplacement drifts, while the operating mode described in the S&ER does not. The lower-temperature operating mode also does not include backfill in emplacement drifts. Table 14.1-2 summarizes some attributes of the layouts for different thermal operating modes.

Igneous disruptive events analyses to support TSPA-SR are based on the operating mode addressed in the *Yucca Mountain Science and Engineering Report*. Earlier analyses for the TSPA model (CRWMS M&O 2000 [DIRS 143665], Section 3.10) were carried out for the EDA II higher-temperature operating mode alternative. In this report, an analysis is presented for a lower-temperature operating mode (Section 14.3.3.2) to examine the sensitivity of the annual probability of igneous dike intersection to changes in operating mode.

14.1.2 Section Organization

First, the treatment of disruptive events in the S&ER (DOE 2001 [DIRS 153849]) is summarized (Section 14.2). Then the disruptive condition of volcanism is addressed (Section 14.3). The treatment of uncertainties for volcanism is discussed (Section 14.3.1) and new analyses are described (Section 14.3.3). Because all applicable lines of evidence were used in developing the analysis of volcanism, no additional lines of evidence are available to support the model. Section 14.3.2 explains that continuing analysis of the lines of evidence already gathered (i.e., analogues) focuses on clarifying the applicability of portions of the analogue where the

entire analogue is not applicable. The disruptive condition of seismic events is addressed in Section 14.4. Treatment of uncertainties is discussed in Section 14.4.1, and an additional line of evidence pertaining to vibratory ground motion is presented in Section 14.4.2. No new work has been carried out in the area of seismic events.

14.2 PREVIOUS TREATMENT OF DISRUPTIVE EVENTS

In evaluating the postclosure performance of a potential repository at Yucca Mountain, disruptive events were considered in developing scenarios of the most plausible evolution of the geologic system and the occurrence of unlikely adverse conditions (DOE 2001 [DIRS 153849], Section 4.3.2). The specific disruptive conditions considered were inadvertent human intrusion, volcanism, and seismic events. For the condition of human intrusion, a stylized scenario was considered in a separate TSPA calculation (CRWMS M&O 2000 [DIRS 153246], Section 4.4) to provide a basis for judging the resilience of the repository system to this type of disruptive event. This approach is prescribed in proposed 10 CFR Part 963 (64 FR 67054 [DIRS 124754], Section 963.16(a)(2)).

For the conditions of volcanism and seismic events, an evaluation of features, events, and processes (FEPs) was carried out (CRWMS M&O 2000 [DIRS 151553]) using the probability and consequence criteria in proposed 10 CFR Part 963 (64 FR 67054 [DIRS 124754], Sections 963.16(b)(4) and 963.16(b)(5), respectively) to determine whether they should be included in the TSPA. Based on this evaluation, igneous disruptive scenarios (i.e., volcanic eruption and igneous intrusion groundwater transport) were developed and vibratory ground motion damage to commercial spent nuclear fuel (SNF) rod cladding was incorporated into the nominal scenario (CRWMS M&O 2000 [DIRS 153246]).

Key documents supporting the S&ER (DOE 2001 [DIRS 153849]) and TSPA-SR (CRWMS M&O 2000 [DIRS 153246]) include the *Disruptive Events Process Model Report* (CRWMS M&O 2000 [DIRS 151968]), eight analysis model reports (AMRs), and two calculations. These documents are listed in Table 14.2-1.

Two of the disruptive events AMRs summarize the results of expert elicitation projects that provided the technical basis for assessing hazards related to volcanism and seismic events (CRWMS M&O 2000 [DIRS 151551]; CRWMS M&O 2000 [DIRS 142321]). The two documents produced by these projects were the *Probabilistic Volcanic Hazard Analysis for Yucca Mountain, Nevada* (referred to as the PVHA for both the document and the study) (CRWMS M&O 1996 [DIRS 100116]) and the *Probabilistic Seismic Hazard Analyses for Fault Displacement and Vibratory Ground Motion at Yucca Mountain, Nevada* (referred to as the probabilistic seismic hazard analysis (PSHA) for the document and the study) (Wong and Stepp 1998 [DIRS 103731]). The PVHA expert elicitation project produced estimates of the annual probability of a volcanic event (dike intrusion) intersecting the repository. The PSHA produced estimates of the annual probability of exceedance of specified levels of vibratory ground motion and fault displacement associated with seismic events. Both analyses include in their results the associated uncertainty. Figure 14.2-1 shows the location of post-Miocene volcanoes in the Yucca Mountain region, and Figures 14.2-2a and 14.2-2b show the location of known or suspected significant faults in the region.

14.2.1 Volcanism

Two disruptive event scenarios for igneous activity are described in the S&ER (DOE 2001 [DIRS 153849], Section 4.4.3): a volcanic eruption scenario and an igneous intrusion groundwater transport scenario. The volcanic eruption scenario (CRWMS M&O 2000 [DIRS 153246], Section 3.10) assumes that an igneous dike or dike swarm rises through the crust of the earth and intersects one or more drifts in the potential repository. Along this dike, one or more eruptive conduits form within the repository footprint, producing a volcano at the surface. (It is also possible that no conduits will form within the repository footprint.) Waste packages in the path of the conduit are damaged to the extent that they provide no further protection for the waste, and the waste is available to be entrained in the eruption. Volcanic ash with waste particles attached to it is erupted and then transported by wind, with the wind direction fixed to the south toward the critical group (see proposed 10 CFR 63.115(b) [64 FR 8640 [DIRS 101680]] for a description of the critical group). Ash settles out of the plume as it is transported downwind, resulting in an ash layer on the land surface. The receptor (average member of the critical group) receives a radiation dose from various pathways associated with the contaminated ash (Section 13.2).

The igneous intrusion groundwater transport scenario describes the possible effects of a basaltic dike that intersects a section of the potential repository and partially or completely engulfs some waste packages in magma (CRWMS M&O 2000 [DIRS 153246], Section 3.10). Waste packages near the point of intersection are damaged such that they provide no further protection for the waste (Zone 1); packages farther down the intersected drifts are damaged, but still provide some protection for the waste (Zone 2). Radionuclides are then released from waste packages damaged by the intrusion and become available for transport in groundwater. Because analogue studies indicate that hydrothermal circulation and alteration is limited to the region in the immediate vicinity of intrusive dikes (Valentine et al. 1998 [DIRS 119132], Section IV.C), groundwater flow and radionuclide transport in this disruptive scenario are represented using models from the nominal scenario.

14.2.2 Seismic Events

In addition to evidence of Quaternary volcanism, the Yucca Mountain region is also characterized by faults (Figure 14.2-2), some of which have experienced repeated displacements in the Quaternary Period (CRWMS M&O 2000 [DIRS 151945], Section 12.3). Thus, consequences of seismic events have also been analyzed for possible impacts to the performance of a potential repository (DOE 2001 [DIRS 153849], Section 4.3.2.2). These analyses considered the potential effects of fault displacement on emplacement drifts and on engineered barriers in the drifts (CRWMS M&O 2000 [DIRS 151954]), potential fault displacement effects on radionuclide transport through the unsaturated zone at the mountain scale (CRWMS M&O 2000 [DIRS 151953]), potential rockfall resulting from vibratory ground motion (CRWMS M&O 2000 [DIRS 151635]), and the effects of vibratory ground motion on engineered barriers (CRWMS M&O 2000 [DIRS 154694]). The results of these analyses and calculations led to the conclusion that seismic-related FEPs, with the exception of damage to cladding, could be screened out of the TSPA-SR (CRWMS M&O 2000 [DIRS 151553], Table 4). Seismically induced damage to cladding is included within the nominal scenario in the TSPA-SR (CRWMS M&O 2000 [DIRS 153246]).

14.3 VOLCANISM

This section focuses on three topics for the disruptive condition of volcanism. First, it discusses the treatment of uncertainty in volcanism analyses. Second, it describes the lines of evidence used to develop and evaluate conceptual models of igneous activity in the Yucca Mountain region. It points out that because of the low rate of occurrence of volcanoes in the Yucca Mountain region during the Quaternary Period, there is little site-specific evidence to support characterization of potential igneous activity and eruptive processes at Yucca Mountain. Thus, analogue data are relied on extensively. Third, new work to address aspects of volcanism is presented.

14.3.1 Treatment of Uncertainty for Volcanism

Discussion of the treatment of uncertainty associated with the impact of volcanism on dose to the critical group presented in this section covers several areas. There is uncertainty in the probability of a volcanic event occurring and the probability that it will affect the potential repository. For volcanism, this source of uncertainty was analyzed in an expert elicitation (CRWMS M&O 1996 [DIRS 100116]). There is uncertainty in parameters and the value ranges of the parameters that together characterize volcanism scenarios. This uncertainty is usually represented by development of parameter distributions (CRWMS M&O 2000 [DIRS 151560], Section 6). For consequence analysis, there is uncertainty in the response of engineered barrier elements to the impacts of either intrusive or eruptive volcanism. To support disruptive events analysis, documents have been developed by engineering groups that discuss this aspect of the problem, (e.g., CRWMS M&O 1999 [DIRS 121300]). Process model reports provide a high-level summary of these analyses and calculations (CRWMS M&O 2000 [DIRS 150707]; CRWMS M&O 2000 [DIRS 151804]). The discussion of sensitivities associated with a range of repository layouts is deferred to Section 14.3.3.2.1, in which the impact of various repository thermal operating modes on probability and consequence is analyzed. The discussion that follows focuses on uncertainty related to conceptualizing volcanism scenarios and the parameters associated with those scenarios, beginning with the uncertainties to be considered in probability analyses.

The process model for volcanic hazard was developed through an expert elicitation project, (CRWMS M&O 1996 [DIRS 100116]). To ensure appropriate quantification of scientific uncertainty in the hazard analysis, the U.S. Department of Energy identified ten experts to evaluate data, volcanic processes, and features. The product of the expert elicitation (PVHA) was a quantitative assessment of the probability of a basaltic dike intersecting the potential repository and discussion of the uncertainty associated with that assessment, reflecting a diversity and range of alternative scientific interpretations. A probability distribution of the annual frequency of intersection of the repository footprint by a dike was computed for each of the ten experts' interpretations (CRWMS M&O 1996 [DIRS 100116], Figure 4-31); these distributions typically spanned approximately 2 orders of magnitude. The ten experts' results were aggregated to form a quantitative assessment of the probability of a basaltic dike intersecting the potential repository. Specifically, the hazard is a probability distribution for the annual frequency of intersection of a basaltic dike with the repository footprint. The PVHA fully documents the treatment of uncertainty in all aspects of the assessment. A summary of the

PVHA process is contained in the *Disruptive Events Process Model Report* (CRWMS M&O 2000 [DIRS 151968], Section 2.1.2).

The PVHA probability distribution for volcanic hazard defined a volcanic disruption as the intersection of the potential repository by a dike. Based on the PVHA results, the report *Characterize Framework for Igneous Activity at Yucca Mountain, Nevada* (CRWMS M&O 2000 [DIRS 151551]) calculated the probability of an eruption intersecting the repository, conditional on dike intersection. That report quantifies the uncertainty by using clearly documented inputs, such as the number of eruptive centers per volcanic event (based on the PVHA), to develop a probability distribution for the annual frequency of a volcanic event that produces one or more eruptive centers (conduits) within the repository. The calculation considers a model that allows conduit formation anywhere along a dike and one stating that conduits will preferentially form within intersected drifts (CRWMS M&O 2000 [DIRS 151551], Section 6.3.2). This aspect of the distribution calculation quantifies the uncertainty between two different conceptual models for conduit formation.

Volcanic processes are characterized largely from field observation and expert interpretation, so they necessarily contain some degree of uncertainty. In most cases, distributions and point values representing volcanic processes are based on documented data sources from analogue volcanic systems, some in the Yucca Mountain region. The report *Characterize Eruptive Processes at Yucca Mountain, Nevada* (CRWMS M&O 2000 [DIRS 142657]) examines analogues, discusses various attributes of the eruptive process, and gives a range of values for parameters that characterize the eruptive process. The report provides magma characteristics, including temperature, chemistry, and volatile (including water) content, that support analysis of the interaction of the magma with repository elements, as well as contribute to characterization of the eruption. The report uses analogue sources to characterize the expected geometry of the volcanic intrusion through conduit diameter, dike width, and number of dikes to be expected. Eruption duration and erupted particle size are also provided. The uncertainties for all of the preceding parameters and others developed by the report were quantified.

The TSPA-SR contains the results of sensitivity analyses that examined the effects of several parameters, including fixed wind direction, wind speed, removal of contaminated soil by erosion, volume of material erupted, and number of waste packages damaged by volcanic eruption and intrusion (CRWMS M&O 2000 [DIRS 153246], Section 5.2.9). An analysis showing sensitivity to an alternative model for the probability of igneous activity was also performed. This analysis fixed the annual probability of dike intrusion at 10^{-7} (CRWMS M&O 2000 [DIRS 153246], Section 5.2.9.1).

14.3.1.1 Treatment of Uncertainty in the Igneous Intrusion Groundwater Transport Model

The igneous intrusion groundwater transport model estimates the amount of waste that could be exposed by disruption of waste packages from exposure directly to magma from a dike or from shock wave pressure, pyroclastics, and heat from the dike intrusion. In this model, waste is picked up by groundwater that has percolated in after the magma has cooled. Movement of the groundwater and any dissolved waste is modeled using the unsaturated zone (UZ) and the saturated zone (SZ) flow and transport models (CRWMS M&O 2000 [DIRS 153246],

Sections 3.7, 3.8 and 3.10). The igneous intrusion groundwater transport model has several components: magma and dike characteristics, assumptions regarding the interaction of the magmatic dike with the drift and drift elements, assumptions regarding the behavior of waste packages and other engineered barrier system (EBS) elements exposed to the magmatic environment, and flow and transport of waste released using the UZ and SZ models. Disruptive events analyses provide distributions for parameters used by the first two components of the model (CRWMS M&O 2000 [DIRS 151551]; CRWMS M&O 2000 [DIRS 142657]). For the components listed, the parameters most significant to the model were those related to dike geometry (i.e., dike width, number of dikes in a swarm, and dike spacing in a swarm) and those related to dike-drift interaction (i.e., the number of waste packages contacted directly by magma from a dike and the down-drift effects of magma-repository interactions). These parameters are most important in determining the number of waste packages hit, and, therefore, the amount of waste potentially made available for transport.

Uncertainty about magma and dike properties (the first component of the igneous intrusion groundwater transport model) was quantified using analogue data, as discussed in Section 14.3.1. *Characterize Eruptive Processes at Yucca Mountain, Nevada* contains the results of these analyses (CRWMS M&O 2000 [DIRS 142657], Section 7). The analyses considered the possibility that a new volcano would be accompanied by emplacement of more than one dike, which is known as a "dike swarm." Uncertainties such as the number of dikes in a swarm were handled by developing a distribution (CRWMS M&O 2000 [DIRS 142657], Section 6.1). The geologic basis (observations of eroded volcanic centers in the Yucca Mountain region) for this distribution is described in *Characterize Eruptive Processes at Yucca Mountain, Nevada* (CRWMS M&O 2000 [DIRS 142657]).

Uncertainty associated with parameters for the second component of the model (i.e., interaction of the magmatic dike, the drift, and drift elements) was addressed with bounding assumptions because data from tests or analogues are lacking. These parameters and bounding assumptions are described in *Dike Propagation Near Drifts* (CRWMS M&O 2000 [DIRS 151552]), which describes the theoretical interaction of the dike with the host rock surrounding the repository; the potential effects of the higher-pressure dike intrusion reacting with the lower-pressure emplacement drift, and the effect those interactions could have on waste packages not in direct contact with magma; and the interaction of the magma flow with the drift, drip shields, and waste packages. The report uses inputs for magma characteristics (CRWMS M&O 2000 [DIRS 142657]), the behavior of waste packages under extreme heat (CRWMS M&O 1999 [DIRS 121300]), and assumptions supported by representative data distributions.

The treatment of uncertainty for the third component (behavior of waste packages in the magmatic environment) of the igneous intrusion groundwater transport model was also addressed by using a bounding assumption. There is limited information on the behavior of waste packages, drip shields, and other drift elements in a magmatic environment. Therefore, it was assumed that the waste packages in direct contact with the magma are damaged to the extent that they provide no further protection for the waste. In addition, it was assumed that all waste packages in the drifts crossed by a dike, but not in direct contact with the magma, suffer some damage that impacts their ability to contain waste. Shock wave pressure, pyroclastics, and heat from the dike intrusion were assumed to cause the damage. A range of openings in endcap welds sampled from a distribution was used to characterize the damage in this zone. The minimum

opening is a small hole and the maximum is a hole the size of the entire endcap. Therefore, the possible range of endcap damage was bounded by the most extreme end member for this type of damage (e.g., the entire endcap is compromised) (CRWMS M&O 2000 [DIRS 151560], Section 6.2).

The fourth component of the model (flow and transport of waste released) used the UZ and SZ flow and transport models, and therefore had the uncertainties associated with the UZ and SZ flow and transport models (see Sections 3, 11, and 12). A sensitivity analysis in the TSPA-SR (CRWMS M&O 2000 [DIRS 153246], Section 5.2.9.7) shows that performance is only moderately sensitive to the total number of packages that are damaged by intrusion, with peak dose increasing by less than a factor of two.

14.3.1.2 Treatment of Uncertainty in the Volcanic Eruption Model

The volcanic eruption release model assumptions about the number of waste packages exposed to potential damage by eruption are based on a combination of the geometry and characteristics of volcanic dikes and conduits. In addition, a modeling code (ASHPLUME V1.4LV-dll) was implemented as part of the TSPA model (CRWMS M&O 2000 [DIRS 151560]) to capture the nature of the eruptive column and waste dispersal. Therefore, for the volcanic eruption release model, key parameters with significant impacts on performance assessment include volcanic conduit diameter, number of eruptive centers (conduits) on a dike, eruption volume, and wind direction and speed.

Uncertainty in conduit diameter is quantified by the development of a distribution for this parameter on the basis of analogue information in *Characterize Eruptive Processes at Yucca Mountain, Nevada* (CRWMS M&O 2000 [DIRS 142657], Section 6.1). Uncertainties in this parameter are related mainly to a limited amount of published data on conduit diameters for volcanoes having volume, composition, and eruptive mechanisms similar to those in the Yucca Mountain region. The number of conduits on a dike is calculated assuming that any dike reaching shallow crustal levels, such as the level of the repository, will result in the formation of one or more conduits feeding a volcano or volcanoes. All, some, or none of these conduits may form within the repository. The possibility of multiple volcanoes forming along the length of a dike is included to reflect the presence of chains of volcanoes within the Quaternary geologic record of the Yucca Mountain region. Although it is not clear that the volcanoes that make up an individual chain all erupted from the same dike and erupted contemporaneously, that possibility cannot be ruled out. The variation in the number of volcanic centers along a dike is based on the interpretations of PVHA experts and other considerations, as described in *Characterize Framework for Igneous Activity at Yucca Mountain, Nevada* (CRWMS M&O 2000 [DIRS 151551]). Because conduits form on dikes, uncertainties associated with dikes affect conduit location. Uncertainty in dike location was quantified by the PVHA project (CRWMS M&O 1996 [DIRS 100116]), while uncertainties associated with the number of conduits on a dike and conduit location along dikes is quantified in *Characterize Framework for Igneous Activity at Yucca Mountain, Nevada* (CRWMS M&O 2000 [DIRS 151551]).

The response of EBS elements to the eruptive conduit environment is treated by making an assumption. The characteristics of magma erupting through a conduit (e.g., temperature, chemistry, and abrasive properties), combined with the duration of eruption, support the

assumption that any waste packages directly contacted by the conduit are degraded. It is assumed that they are degraded to the extent that they would provide no further protection for the waste (CRWMS M&O 2000 [DIRS 142657], Sections 6.1, 6.2, and 6.3). There are no data available to support a different assumption.

Sensitivity of overall performance to uncertainty about the diameter of eruptive conduits, their location, and the number of eruptive conduits within the repository is described in the TSPA-SR (CRWMS M&O 2000 [DIRS 153246], Section 5.2.9.6, Figure 5.2-22). Performance is moderately sensitive to the total number of packages damaged as a result of conduit parameters, and peak dose may be increased by a factor of 1.5.

The ASHPLUME code and its application to the volcanic eruption release model are discussed in detail in *Igneous Consequence Modeling for the TSPA-SR* (CRWMS M&O 2000 [DIRS 151560], Sections 5.4 and 6.1) and in the TSPA-SR (CRWMS M&O 2000 [DIRS 153246], Sections 3.10 and 4.2). The volume of ash erupted is a key input parameter to the model used in the ASHPLUME code to calculate eruption power and eruptive column height. The range for this parameter expected in the Yucca Mountain area is defined in *Characterize Framework for Igneous Activity at Yucca Mountain, Nevada* (CRWMS M&O 2000 [DIRS 151551], Section 6.2 and Table 4). The U.S. Nuclear Regulatory Commission (NRC) issue resolution status report for igneous activity (Reamer 1999 [DIRS 119693], p. 129) defines an eruptive volume range with a higher maximum end member. *Igneous Consequence Modeling for the TSPA-SR* captures both of these ranges in defining the range for use in the ASHPLUME code by using the NRC maximum value for the upper end member of the range.

The TSPA-SR (CRWMS M&O 2000 [DIRS 153246]) documented a sensitivity analysis for the volume of material erupted and reported that the total annual dose rate is insensitive to the range of values selected for erupted volume. The model runs used the 5^{th} and 95^{th} percentile of the distribution (CRWMS M&O 2000 [DIRS 153246], Section 5.2.9.5). In ASHPLUME, the total erupted volume determines the column height and energy of the event; therefore, the dose calculation was shown to be insensitive to uncertainty regarding these parameters as well.

The wind speed used by ASHPLUME for ash dispersal modeling is related to erupted volume. Erupted volume is used to calculate the eruptive column height, and wind speed varies with eruptive column height. Wind speed, paired with direction, is a parameter with a distribution derived from site data (CRWMS M&O 2000 [DIRS 151560], Section 6.1.2.2.1). In the TSPA-SR model (CRWMS M&O 2000 [DIRS 153246]), the erupted volume used as input for ASHPLUME (V1.4LV-dll) results in a calculated eruptive column height that exceeds the maximum height for wind speed obtained from site data (CRWMS M&O 2000 [DIRS 151560], Section 6.1.2.2.1). Because wind speeds tend to increase with height, the wind speed used with larger erupted volumes may be underestimated in the TSPA-SR. Therefore, new data were examined and used as the basis of a sensitivity study described in the next paragraph.

To assess the sensitivity of the TSPA-SR model (CRWMS M&O 2000 [DIRS 153246]) to the wind speed distribution, a sensitivity analysis has been performed using a different wind speed distribution derived from data taken at the Desert Rock airstrip (NOAA n.d. [DIRS 154435]). These data were taken at elevations that would cover the ASHPLUME (V1.4LV-dll)-calculated eruption column height. Details of this new wind distribution are given in Section 14.3.3.5.

A comparison of the TSPA model doses (DOE 2001 [DIRS 153849]) to doses obtained using the Desert Rock wind speed distribution is provided in Volume 2 (McNeish 2001 [DIRS 155023], Section 3). The new wind speed distribution better captures the uncertainty in wind speed by providing data points from heights as high as or higher than the maximum column heights calculated by ASHPLUME (V1.4LV-dll).

14.3.1.3 Treatment of Uncertainty in Other Volcanism Analyses

The geologic conceptual model for volcanism was developed in *Characterize Framework for Igneous Activity at Yucca Mountain, Nevada* (CRWMS M&O 2000 [DIRS 151551]) and *Characterize Eruptive Processes at Yucca Mountain, Nevada* (CRWMS M&O 2000 [DIRS 142657]). The conceptual model assumes that if a dike intrusion rises in the crust of the earth to the elevation of the potential repository, the dike will continue propagating upward to the surface of the earth and a conduit will form, feeding a volcano. In all versions of a TSPA conducted to date, when the number of waste packages hit is calculated for the igneous intrusion groundwater release model there is no subtraction of waste packages to account for those that were calculated as being impacted by the volcanic eruption release model. The same applies when the number of waste packages hit by a conduit is calculated for the volcanic eruption release model. The number of waste packages available to be impacted is assumed to be the total number in the repository. This assumption represents conservatism in modeling releases caused by volcanism.

14.3.2 Lines of Evidence Supporting the Volcanism Conceptual Model

For many of the models developed to describe processes operating at Yucca Mountain, there exist multiple lines of evidence that are relevant. The models are developed on the basis of some of the lines of evidence, while other lines provide corroborative information or additional confidence in the results of the model. For volcanism, however, additional lines of evidence are not available because all available data have been used in developing the model.

The rate of Quaternary volcanism in the Yucca Mountain region is low. Thus, there exist few site data from which to characterize potential future igneous activity. To define parameter values and ranges for igneous models at Yucca Mountain, therefore, observations of analogous volcanoes in other regions of the world are used. It is for this reason that other, independent lines of evidence are unavailable to support volcanism models. Continuing analysis of the information already gathered will focus on clarifying the applicability of portions of the analogues where the entire analogue is not applicable.

14.3.3 New Work for Volcanism Analysis

This section contains discussions of new work that supplements the information presented in the S&ER (DOE 2001 [DIRS 153849]). The new work described was performed for several purposes. One analysis is documented in *Characterize Framework for Igneous Activity at Yucca Mountain, Nevada* (CRWMS M&O 2000 [DIRS 151551]) and provides the results of a new analysis of the probability of dike intrusion performed for the higher-temperature operating mode described in the S&ER (DOE 2001 [DIRS 153849], Section 14.3.3.1). New work was performed to address the impacts of considering a range of thermal operating modes

(Section 14.3.3.2). Other analyses were performed to elucidate the relative releases from different damage zones associated with the igneous intrusion groundwater transport scenario (Section 14.3.3.3), to examine the sensitivity to dose of waste particle size distribution (Section 14.3.3.4), and to characterize a new wind speed distribution for use in the volcanic eruption scenario (Section 14.3.3.5). The discussion in Section 14.3.3.6 is presented to clarify how the ASHPLUME code treats the density of waste entrained in ash in the eruptive plume for the volcanic eruption scenario. Other volcanic input values revised since completion of the analyses supporting the S&ER, and used in the TSPA are described in Volume 2 (McNeish 2001 [DIRS 155023]), and in Section 14.3.3.7. Evaluation of new aeromagnetic data and its potential impact on the probability that an igneous dike will intersect a repository is addressed in Section 14.3.3.8.

14.3.3.1 Recalculate Probability of Dike Intrusion for the Operating Mode Addressed in the S&ER

This section contains a summary of the results of *Characterize Framework for Igneous Activity at Yucca Mountain, Nevada* (CRWMS M&O 2000 [DIRS 151551]), which were not represented in the S&ER (DOE 2001 [DIRS 153849]). The results described were used as input to the TSPA supplemental model presented in Volume 2 (McNeish 2001 [DIRS 155023]).

The PVHA produced a probability distribution for volcanic hazard that only addressed the intrusive portion of a volcanic event (CRWMS M&O 1996 [DIRS 100116], Section 3.1.1). *Characterize Framework for Igneous Activity at Yucca Mountain, Nevada* (CRWMS M&O 2000 [DIRS 151551]) calculates the probability of a conduit or conduits forming on a dike, conditional on dike intersection. This probability calculation supports the volcanic eruption scenario. *Characterize Framework for Igneous Activity at Yucca Mountain,* recalculates the dike intersection probability for two potential repository operating modes: (1) the EDA II higher-temperature operating mode, Figure 14.1-1a (CRWMS M&O 1999 [DIRS 107292]); and (2) the higher-temperature operating mode described in the S&ER (DOE 2001 [DIRS 153849]), Figure 14.1-1b (CRWMS M&O 2000 [DIRS 146021]). The report documents probability distributions for the annual frequency of intersection of the potential repository footprint by a dike for the primary block and for the primary and contingency blocks combined. It also documents distributions for length (inside of repository) and azimuth of an intersecting dike and for the number of eruptive centers (conduits) within the potential repository footprint.

In *Characterize Framework for Igneous Activity at Yucca Mountain, Nevada* (CRWMS M&O 2000 [DIRS 151551]), the output probabilities for the length and orientation of dikes intersecting the repository footprint of the S&ER (DOE 2001 [DIRS 153849]) operating mode alternative reflect a changed geographic location for the repository footprint from the EDA II operating mode alternative. The new input probabilities reported (CRWMS M&O 2000 [DIRS 151551], Section 7.1, Tables 13 and 13a) differ slightly from the results reported in the initial report (CRWMS M&O 2000 [DIRS 141044]), although the typical difference is only a small percentage. For example, the mean frequency of intersection for the combined primary and contingency blocks in the initial report was 1.55×10^{-8}/yr, rounded to a value of 1.6×10^{-8}/yr. The mean frequency of intersection in the updated report is 1.62×10^{-8}/yr, rounded to a value of 1.6×10^{-8}/yr.

This update (CRWMS M&O 2000 [DIRS 151551], Section 6.5.2.2) uses a distribution for average spacing of eruptive centers (conduits) to calculate the number of eruptive centers within the repository footprint. This change from the single point estimate used in the initial report (CRWMS M&O 2000 [DIRS 141044]) results in an increase in the total number of eruptive centers. In the initial report, the highest number of eruptive centers within the repository was five. In the updated report, the maximum possible number of eruptive centers is twelve for the primary block and thirteen for the primary and contingency blocks combined.

The change in repository footprint and inclusion of additional uncertainty in the conceptual model of conduit formation also result in an increase to 0.77 in the probability that at least one conduit will form within the repository footprint. In TSPA-SR (CRWMS M&O 2000 [DIRS 153246]), a probability value of 0.36 was used.

These results were incorporated into the igneous inputs provided to Volume 2 (McNeish 2001 [DIRS 155023]) for the TSPA supplemental model.

14.3.3.2 Scaling Factors to Evaluate the Impact of Repository Footprint and Layout Changes on Total System Performance Assessment Model Results

Evaluation of the effects of igneous activity depends in part on the footprint of the potential repository, the layout of drifts, and the size and spacing of waste packages in the drifts. These attributes vary for different repository operating mode temperatures. Lower-temperature operating modes generally have larger footprints and greater spacing between waste packages, drifts, or both.

In general, the larger the repository footprint, the higher the probability that an igneous dike will intersect it. Based on the spatial distribution of volcanic sources defined in the PVHA, extension of the repository footprint to the north or south would likely have a greater impact on the probability of intersection than an extension of the footprint to the east (assuming an equal increase in footprint area). The geographic position of the footprint relative to the volcanic sources also affects the probability of intersection.

However, while the probability of intersection may increase for lower-temperature operating modes, the number of waste packages affected per drift by an intersecting igneous dike decreases because fewer waste packages are located in each drift. The net result of these competing effects (i.e., higher probability of intersection, fewer waste packages per intersected drift) depends on the specific footprint and layout being considered. In the following sections, approximate scaling factors are examined for lower-temperature operating modes based on simplifying approaches. The analysis is presented as supplemental information to support decision-makers and does not contribute to analyses in Volume 2 (McNeish 2001 [DIRS 155023]).

This section presents a new analysis that allows an approximation of the effect on the probability of a dike intrusion when footprint size and location, drift spacing, or waste package spacing are varied (Section 14.3.3.2.2). It provides a similar approximation of the effect on the number of waste packages damaged (and therefore, the consequences of waste release) for the two volcanism scenarios: volcanic eruption (Section 14.3.3.2.3) and igneous intrusion groundwater transport (Section 14.3.3.2.4). A discussion of the repository thermal operating mode parameters

that are most important to the probability and consequences of volcanism introduces the analysis (Section 14.3.3.2.1). Changes in these parameters translate to changes in the impact of volcanism. These thermal operating mode parameters, or combinations of them, are referred to as scaling factors in the analysis that is presented. The results of the analysis of the release associated with volcanism for an operating mode with these factors specified (e.g., a storage capacity of 70,000 MTHM, no backfill, higher-temperature operating mode (CRWMS M&O 2000 [DIRS 146021]) has been determined (CRWMS M&O 2000 [DIRS 153246], Sections 4.2 and 4.3). Therefore, the proportional, or scaled, response of the release can be approximated by assessment of the effects of proportional changes in these thermal operating mode parameters.

14.3.3.2.1 Repository Thermal Operating Mode Parameters Important to Releases Associated with Volcanism

Various repository thermal operating mode parameters, singly and in combination, influence the impact of volcanism on repository performance. Changes in these parameters can result in changes in the release from waste packages damaged by volcanism, and therefore, impact calculations of dose to the critical group. Repository thermal operating mode parameters critical to the evaluation of volcanism effects on repository performance include:

- Repository footprint (location, length, and width)
- Total repository area and total number of waste packages
- Combined waste package length and waste package spacing
- Drift spacing
- Number of emplacement drifts.

The external geometry of the system, or repository footprint (i.e., location, length, and width), and total repository area are closely related in their effect on the probability and consequences associated with the volcanism scenarios. Dike intrusions (or dike swarms) are narrow, linear features that would encounter the emplacement drifts of a potential repository at an angle (DOE 2001 [DIRS 153849], Figure 4-160). The magma source generating them has a greater likelihood of arising in certain locations in relation to the repository location (CRWMS M&O 2000 [DIRS 151551], Section 6.4.2). The probability and consequence of a dike intrusion arise from the geometric relationships between the dikes as they fan out from their point of origin and the repository location and shape. Changes in these geometric relationships result in changes to the probability. The consequences of dike intersection are affected by the internal geometry of the system.

The internal geometry of the potential repository (i.e., drift spacing, number of waste packages, and spacing of waste packages) similarly affects the manner in which dikes will encounter drifts and waste packages. Therefore, if the geometry of the system varies, the number of waste packages damaged will vary, which will impact the release that affects dose to the critical group. There is some difference in the manner in which varied geometries impact releases for the two volcanism scenarios, as discussed in Sections 14.3.3.2.3 and 14.3.3.2.4.

The following discussion will illustrate the effect of uncertainty in these parameters. The discussion will begin by illustrating potential variability in factors necessary to achieve higher- and lower-temperature operating modes and discussing their potential impact on waste release. The latter part of the discussion will present a new analysis of a method to approximate releases when comparing potential thermal operating modes (Section 14.3.3.2.2 through Section 14.3.3.2.4).

Table 14.1-2 summarizes the variation of key thermal operating mode parameters for all of the alternatives to be discussed in this section. Figure 14.1-1 illustrates three alternatives that will be mentioned. The EDA II operating mode includes backfill and results in a relatively higher-temperature repository approach (Figure 14.1-1a) (CRWMS M&O 1999 [DIRS 107292]). Figure 14.1-1b is for the operating mode described in the S&ER (DOE 2001 [DIRS 153849]) that was also considered under the higher-temperature repository approach (CRWMS M&O 2000 [DIRS 146021], Section 6.3, Figure 11). Figure 14.1-1c is for one hypothetical layout for a lower-temperature repository operating mode (BSC 2001 [DIRS 154548], Item 1). While the hypothetical lower-temperature operating mode scenarios have been considered by the Yucca Mountain Site Characterization Project, they are used in this section only as a set of assumed scenarios to assist in this discussion.

All of the operating modes considered are to store 70,000 MTHM, but they have different layouts and footprints (Figure 14.1-1). The higher-temperature repository operating modes generally have a smaller footprint, whereas the lower-temperature repository operating modes such as Scenario 1 in Table 14.1-2, generally have larger footprints that represent extensions of higher-temperature footprints. The northern segment of the diagram in Figure 14.1-1c (drifts 1 through 58) is identical to the footprint and repository area for the thermal operating mode described in the S&ER (DOE 2001 [DIRS 153849]), as shown in Figure 14.1-1b. The southern segment of the diagram represents the extended footprint and repository area associated with an alternative thermal operating mode concept.

The total repository area parameter of the thermal operating mode impacts:

- Annual frequency of dike intersection of the repository footprint
- Conditional probabilities associated with dike length/azimuth angle pairs intersecting with, and contained within, the repository footprint
- Conditional probabilities associated with the number of eruptive centers (conduits) occurring on a dike within the repository footprint.

The probabilities are discussed in *Characterize Framework for Igneous Activity at Yucca Mountain, Nevada* (CRWMS M&O 2000 [DIRS 151551]) for the operating mode described in the S&ER (DOE 2001 [DIRS 153849]) and the EDA II higher-temperature operating mode alternatives.

For the hypothetical lower-temperature operating mode shown in Figure 14.1-1c (BSC 2001 [DIRS 154548], Item 1), the repository footprint has an approximate north-south length of 8,700 m and an area of 1,600 acres. These values represent an increase in the north-south length

of approximately 70 percent and an increase in area of approximately 30 percent as compared to the alternative described in the S&ER (DOE 2001 [DIRS 153849]), shown in Figure 14.1-1b. As a first approximation, it is assumed that the relationship between the frequency of dike intersection with the repository footprint (identified above) and the repository north-south length is linear. The impact of this assumption is discussed further in Section 14.3.3.2.2.

The thermal operating mode parameters of waste package length, waste package spacing, and drift spacing impact the calculation of the number of waste packages contained within the diameter of a conduit in the volcanic eruption scenario (CRWMS M&O 2000 [DIRS 153097], Section 5.2). This calculation assumes two placements of a conduit to calculate the maximum number of waste packages contained within the diameter of a conduit (CRWMS M&O 2000 [DIRS 153097], Section 5.2). The first placement assumes that the conduit is centered on a drift. For this placement, the sum of waste package length and waste package spacing divided by conduit diameter equals the number of waste packages contained within the diameter of a conduit. The second placement assumes that the conduit is centered on a pillar. For this placement, when the conduit diameter is larger than the drift spacing, the conduit will hit two drifts (the maximum number of drifts that can be intersected by a single conduit). Based on the geometric relationship between a circular conduit and parallel drifts (CRWMS M&O 2000 [DIRS 153097], Section 5.2 and Figure I-3c), this placement may result in a larger number of waste packages contained within the conduit diameter.

Table 14.3.3.2-1 summarizes the calculated maximum number of waste packages contained within the diameter of a conduit for the thermal operating mode described in the S&ER (DOE 2001 [DIRS 153849]) and the six hypothetical alternatives listed in Table 14.1-2. The range of conduit diameters corresponds to the range used to calculate the cumulative distribution function (CDF) for the number of waste packages hit per conduit diameter, as reported in *Igneous Consequence Modeling for the TSPA-SR* (CRWMS M&O 2000 [DIRS 151560], Figure 3 and Attachment I). Review of Table 14.3.3.2-1 indicates that the maximum number of waste packages contained within a conduit diameter ranges from a high of 51 for the thermal operating mode described in the S&ER (DOE 2001 [DIRS 153849]) and Scenarios 2 and 6 to a low of 23 for Scenario 4. As a first approximation, it is assumed that there is a linear relationship between the combined length of an individual waste package and waste package spacing and the number of waste packages contained within a conduit diameter for a given drift spacing.

The analysis in the S&ER (DOE 2001 [DIRS 153849], Section 2.3]) is based on a higher-temperature operating mode (CRWMS M&O 2000 [DIRS 146021], Section 6.3). Figure 14.1-1b is a schematic diagram of the repository footprint for this operating mode. The impact of varying thermal operating mode parameters on the results reported in the S&ER is evaluated in Sections 14.3.3.2.2 through 14.3.3.2.4 using, scaling factors. The scaling factors identified in these sections are used to provide a qualitative estimate of the impact of repository thermal operating mode alternatives.

14.3.3.2.2 Scaling Factors for Probabilities

The probabilities associated with dike intersection of the repository include consideration of:

- The frequency of dike intersection with the repository
- The conditional probability distribution associated with dike length/azimuth angle pairs that occur within the repository footprint
- The conditional probability distribution for number of eruptive centers (conduits) that occur on a dike within the repository footprint.

The thermal operating mode parameters that impact these probabilities are the location and size of the repository footprint. Two alternative thermal operating modes are compared in this discussion: the one described in the S&ER (DOE 2001 [DIRS 153849]) and one alternative hypothetical layout for a lower-temperature operating mode (Scenario 1 in Table 14.1-2) (BSC 2001 [DIRS 154548], Item 1).

Figure 14.1-1c is a schematic diagram of one alternative hypothetical 70,000 MTHM layout for a lower-temperature operating mode repository concept. The northern segment of this footprint (drifts 1 through 58) is similar to the footprint and repository area for the thermal operating mode described in the S&ER (DOE 2001 [DIRS 153849]), as shown in Figure 14.1-1b. The southern segment of the diagram represents the extended footprint and repository area associated with an alternative lower-temperature concept. This extended footprint adds approximately 3,300 m to the length and 475 acres to the area. These values represent an increase in length of approximately 70 percent and an increase in area of approximately 30 percent compared to the thermal operating mode described in the S&ER (DOE 2001 [DIRS 153849]).

The annual frequency of intersection of the repository footprint by a dike is most sensitive to a change in length of the repository layout; it is less sensitive to a change in area. The relationship between annual frequency of intersection and repository length is not linear, but it was assumed to be linear for a first approximation. Using this assumption, the increased length of the alternative layout for a lower-temperature operating mode (BSC 2001 [DIRS 154548], Item 1) would result in an increase in the annual frequency of intersection of approximately 70 percent as compared to the annual frequency of intersection for the thermal operating mode described in the S&ER (DOE 2001 [DIRS 153849], Section 4.4.3). Using this scaling factor, the mean annual frequency of intersection of 1.6×10^{-8} (DOE 2001 [DIRS 153849], Section 4.4.3) may increase for the Scenario 1 hypothetical lower-temperature operating mode (BSC 2001 [DIRS 154548], Item 1) to a qualitatively estimated mean annual frequency of intersection of 2.72×10^{-8}.

The conditional probability distribution of dike intersection lengths within the alternative layout (BSC 2001 [DIRS 154548], Item 1) and the frequency of at least one eruptive center (conduit) within the elongated footprint associated with this alternative layout would both change. The dike intersection lengths would be skewed to longer lengths because of the longer repository length. The tail of the distribution would extend to higher intersection lengths, up to the full length of the alternative layout. The frequency that at least one eruptive center would occur

within the repository would probably increase somewhat. Quantifying the change in the conditional probability distribution of dike intersection and the frequency of at least one eruptive center (conduit) occurring within the repository footprint would require a new analysis using the repository footprint for the alternative layout. Finally, it is not clear how an elongated repository footprint would impact the conditional probability distribution of azimuths for an intersecting dike without running a new analysis, but the change would probably be insignificant.

The mean frequency of at least one eruptive center (conduit) within the elongated footprint associated with the alternative layout (BSC 2001 [DIRS 154548], Item 1) is assumed to scale proportionally with an increase in the annual frequency of intersection; therefore it would increase approximately 70 percent. Using this assumption, the increased length of the hypothetical lower-temperature operating mode (BSC 2001 [DIRS 154548], Item 1) would result in the same mean conditional probability (conditioned on the probability that a dike intersects the repository) of at least one conduit (eruptive center) intersecting the repository footprint. The probability is approximately 77 percent (DOE 2001 [DIRS 153849], Section 4.3.2.1.2).

For the thermal operating mode reported in the S&ER (DOE 2001 [DIRS 153849], Section 4.3.2.1.2), the estimate of the number of conduits (eruptive centers) was based on the relative weighting of a number of different distribution models (CRWMS M&O 2000 [DIRS 151551], Section 6.5.2.2) that yielded a maximum of 13 conduits. Using this approach, it is estimated that the maximum number of conduits for the alternative layout for a lower-temperature repository operating mode (BSC 2001 [DIRS 154548], Item 1), which is approximately 3,300 m longer than the one described in the S&ER (DOE 2001 [DIRS 153849]), would be approximately 21.

14.3.3.2.3 Scaling Factors for Releases from Waste Packages Hit in the Volcanic Eruption Scenario

The key repository thermal operating mode parameters that impact the number of waste packages hit in the volcanic eruption scenario include the repository footprint (location, length, and width), drift spacing, and the combined length of the waste package and waste package spacing.

For the hypothetical repository lower-temperature operating mode scenarios identified in Table 14.1-2 with a drift spacing of 81 m, the scaling factor is equal to the average combined waste package length and waste package spacing for the thermal operating mode described in the S&ER (DOE 2001 [DIRS 153849]) (approximately 5 m) (CRWMS M&O 2000 [DIRS 146021]) divided by the combined waste package length and waste package spacing for an alternative operating mode (Table 14.1-2, Scenarios 1, 2, 4, 5, and 6). This scaling factor is multiplied by the volcanic eruption release reported in the S&ER (DOE 2001 [DIRS 153849], Section 4.4.3.3). For example the scaling factor for Scenario 1 is 0.71 (5 m divided by 7 m). Using this scaling factor, the probability-weighted mean total effective dose equivalent reported in the S&ER as 0.004 mrem/yr roughly 300 years after repository closure would be reduced to approximately 0.003 mrem/yr for the Scenario 1 hypothetical lower-temperature operating mode. For repository thermal operating modes with a drift spacing other than 81 m (e.g., Scenario 3, which has a drift spacing of 120 m), a simple scaling factor cannot be applied to estimate waste package releases for alternative operating modes.

14.3.3.2.4 Scaling Factor for Releases from Waste Packages Hit in the Igneous Intrusion Groundwater Transport Scenario

Conceptually, an approximation of igneous intrusion groundwater transport releases from alternative thermal operating modes could be estimated by multiplying the releases reported in the S&ER by a scaling factor equal to the waste package density (number of waste packages per acre of repository area) for the thermal operating mode described in the S&ER (DOE 2001 [DIRS 153849]) divided by the waste package density in the alternative. However, significant revisions to key disruptive events AMRs and calculations were accomplished after the S&ER was finalized. Because of the cumulative impact of these revisions, a simple scaling factor cannot be applied to estimate the approximate magnitude of the release for alternative thermal operating modes.

14.3.3.3 Contribution to Release of Zones 1 and 2 in the Igneous Intrusion Groundwater Transport Model

The new work presented in this section was performed to reduce uncertainty in the impacts of releases from different damage zones associated with the igneous intrusion groundwater transport scenario. Information on the contribution to waste release from different damage zones will support focusing analyses on those areas where uncertainty exists and may be reduced by further analysis. The analysis in this section supports a sensitivity analysis in Volume 2 (McNeish 2001 [DIRS 155023]).

The initial version of *Igneous Consequence Modeling for the TSPA-SR* addressed igneous intrusion groundwater transport consequence modeling for a repository thermal operating mode that included backfill (CRWMS M&O 2000 [DIRS 139563]). An update of this report addresses igneous consequence modeling for an operating mode with no backfill (CRWMS M&O 2000 [DIRS 151560]). The effect that a dike (or dikes) intersecting emplacement drifts has on waste package damage in the igneous intrusion groundwater transport scenario varies with proximity to the dike (CRWMS M&O 2000 [DIRS 151552]). Waste package damage in Zone 1 consists of the area immediately around the dike/drift intersection. Waste package behavior in Zone 1 for the backfill and no-backfill operating modes is bounded by the conservative assumption that three packages on either side of the dike, plus a minimum of one package in the path of the dike (seven total packages minimum, depending on dike width), are sufficiently damaged that they provide no further protection for the waste. For multiple dikes in an event (dike swarm), there are seven waste packages damaged in Zone 1 for each dike.

In an update to *Dike Propagation Near Drifts* (CRWMS M&O 2000 [DIRS 151552]), a Zone 2 region is introduced for the no-backfill thermal operating mode described in the S&ER (DOE 2001 [DIRS 153849]). Zone 2 is defined as the portion of an emplacement drift that has been crossed by a dike and is not included in Zone 1. In the absence of backfill, the waste packages in these drifts are directly exposed to a shock wave and pyroclastic flow resulting from the dike encountering the relatively lower pressure in the repository. Pressure in the emplacement drifts would likely have to rise to lithostatic before the dike could continue to propagate upward. The combination of high temperature (1,040° to 1,170°C) and high pressure (approaching the magmatic lithostatic pressure of 7.5 Mpa at the repository depth) would likely be sufficient to cause some degree of failure of the waste packages in Zone 2. The degree of

failure is uncertain, and damage is likely to range from moderate to extensive. In the TSPA-SR model for the repository without backfill (CRWMS M&O 2000 [DIRS 153246]), all Zone 2 packages in all drifts intersected by a dike are assumed to be breached with a hole of uncertain cross-sectional area, and all drip shields and cladding in the intersected drifts are assumed to be destroyed to the extent that they provide no further protection for the waste. Endcap failure is used as a surrogate for all types of Zone 2 damage related to dike/waste package interaction.

The area of the hole created by endcap weld failure represents the cross-sectional area of a crack that might open in a failed weld before gas flow into the failed waste package equalizes internal and external pressures, halting the propagation of the crack. In *Igneous Consequence Modeling for the TSPA-SR* (CRWMS M&O 2000 [DIRS 151560], Section 6.2), a lognormal distribution is developed to represent the uncertainty in the cross-sectional area of holes in failed endcaps. The minimum value of area in the distribution is 1 cm^2 and the maximum area is 1.9×10^4 cm^2, which is an approximation of the full cross-sectional area of a representative endcap with a radius of 77 cm. The mean value of the distribution is 10 cm^2.

Log-normal distributions are selected when the uncertain distribution of values within a population is reasonably believed to be characterized by a normal distribution of logarithms. The distribution is often used when the range of the population spans several orders of magnitude and the mean value is expected to fall relatively closer to the lower bound. Using a normal or uniform distribution for such parameters (rather than a lognormal) would yield a distribution with a mean value that is orders of magnitude above the lower end of the range. In the case of the endcap weld failures, relatively small aperture failures are considered most likely because they would be sufficient to allow gas pressure to equilibrate quickly between the inside and outside of the package. Larger apertures could not be ruled out, so the log-normal distribution was chosen with a relatively small mean values and a low-probability tail that includes the full cross-sectional area of the endcap as the upper bound.

In addition to the degree of waste package failure in Zone 2, the number of packages damaged in Zone 1 and Zone 2 is represented in the TSPA-SR model (CRWMS M&O 2000 [DIRS 153246]) with stochastic data elements. The CDFs for the number of waste packages intersected are discussed in *Number of Waste Packages Hit by Igneous Intrusion* (CRWMS M&O 2000 [DIRS 153097]). The CDFs for the number of packages hit in Zones 1 and 2 take into account dike orientation, length, width, and the number of dikes in a swarm. Two CDFs are used, one for the number of packages in Zone 1 only and one for the number of packages in the combination of Zones 1 and 2. These CDFs were sampled within the TSPA-SR model to determine how many packages are intersected by the igneous intrusion. The methodology for sampling these CDFs is to first sample from Zone 1 only, then sample from the combined Zones 1 and 2 CDFs. The number of packages affected in Zone 2 is simply the number of packages intersected in the combined Zones 1 and 2 CDF minus the number of packages intersected in Zone 1.

The base case no-backfill igneous intrusion groundwater transport scenario described in the TSPA-SR (CRWMS M&O 2000 [DIRS 153246]) included both Zones 1 and 2 in the dose calculation. To assess the relative importance of Zones 1 and 2 to the dose to the critical group, a TSPA analysis is described in Volume 2 (McNeish 2001 [DIRS 155023], Section 3) that only considers the damage to waste packages in Zone 1. The results of this additional Zone 1 only

case in terms of the mean annual dose rate to the critical group are compared to results from the base case to show the relative contributions of Zone 1 and Zone 2 to releases in the igneous intrusion groundwater transport scenario (McNeish 2001 [DIRS 155023], Section 3).

14.3.3.4 Total System Performance Assessment - Site Recommendation Sensitivity to Waste Particle Size Distribution

The new work reported in this section was performed to evaluate uncertainty in the effect on dose to the critical group from waste particle size distribution. This parameter is associated with the volcanic eruption scenario (CRWMS M&O 2000 [DIRS 151560], Section 6.1 and Table 4). The analysis presented in this section supports a sensitivity analysis in Volume 2 (McNeish 2001 [DIRS 155023], Section 3).

The ASHPLUME code (V1.4LV-dll) calculates the areal density of both volcanic ash and spent nuclear fuel in grams per square centimeter on the surface of the earth as a function of relative location from the volcanic vent. For each parameter realization by the TSPA model (all versions), the ASHPLUME code is executed to determine the SNF areal density at the critical location. For each execution of ASHPLUME, the code makes two internal passes: one for calculation of ash deposition, and one for calculation of fuel deposition. The same mathematical model is used for both calculations. In the pass for the fuel deposition calculation, the code simply modifies the ash particle density to account for the incorporation of a fuel particle and determines what fraction of the combined particle mass consists of fuel. An "incorporation ratio" is used to calculate a "fuel fraction," or the ratio of fuel mass to ash mass. For example, an incorporation ratio of 0.3 would mean that a waste particle one-half the diameter of an ash particle could be incorporated into the ash particle. A detailed description of the mathematical model for the ash and fuel deposition calculation is available in Jarzemba et al. (1997 [DIRS 100987]). The combined ash/waste particle density treatment is further clarified in Section 14.3.3.6.

Within the ASHPLUME code, waste particles are treated as varying in size, with the variation in particle size following a log-triangular distribution (Jarzemba et al. 1997 [DIRS 100987], Section 2.2). The particle size distribution is defined by specifying the minimum, mode, and maximum diameter of the fuel particle size distribution. These three parameters are important in determining the ground-level waste density calculated by ASHPLUME because, along with the incorporation ratio, they are used to determine the total mass of fuel contained in waste packages intersected by the volcanic event that is actually entrained in the ash column and transported downwind. In addition, because of the effect of waste particle mass in altering the density of ash particles, the waste particle size distribution will also affect the dispersion calculation within ASHPLUME.

In *Igneous Consequence Modeling for the TSPA-SR* (CRWMS M&O 2000 [DIRS 151560], Section 6.1.2.1.12), the minimum, mode, and maximum diameter for waste fuel particle size were specified as 0.0001, 0.002, and 0.05 cm, respectively. *Miscellaneous Waste-Form FEPs* (CRWMS M&O 2001 [DIRS 153938], Attachment I) notes that waste forms may have different particle diameters in the eruptive environment, depending both on the initial type of the waste (commercial SNF or high-level radioactive glass waste) and the degree and type of alteration of the waste. This uncertainty in waste particle size distribution was examined by conducting a

series of sensitivity runs, which are described in Volume 2 (McNeish 2001 [DIRS 155023], Section 3) with the TSPA model using several different values for the minimum, mode, and maximum waste particle sizes that define the log-triangular distribution. For the sensitivity analysis, the minimum waste particle size was reduced by a factor of one-half and the maximum waste particle size was increased by a factor of two. The mode value for the log-triangular particle size distribution was varied between 0.0002 and 0.02 cm, or a range of one-tenth to ten times the base case mode value. The results of this sensitivity analysis are discussed in Volume 2 (McNeish 2001 [DIRS 155023], Section 3.3.1) in terms of the mean dose rate history to the critical group compared to the TSPA-SR (DOE 2001 [DIRS 153849]) igneous disruption scenario. Table 14.3.3.4-1 shows the assumed minimum, mode, and maximum values of particle sizes used in the sensitivity analysis. The TSPA-SR values are also shown in the table for comparison.

14.3.3.5 New Wind Speed Data for Various Heights of Eruption

The new work reported in this section was performed to evaluate uncertainty in the effect on dose to the critical group from wind speed affecting various heights in an ash column during an eruption. This parameter is associated with the volcanic eruption scenario (CRWMS M&O 2000 [DIRS 151560], Section 6.1 and Table 4).

The TSPA-SR (CRWMS M&O 2000 [DIRS 153246]) analysis using ASHPLUME (V1.4LV-dll) employed a distribution for wind speed that was developed in *Igneous Consequence Modeling for the TSPA-SR* (CRWMS M&O 2000 [DIRS 151560]). Wind speed, paired with direction, is a parameter with a distribution derived from site data taken at altitudes from approximately 1.5 to 5 km above sea level (CRWMS M&O 2000 [DIRS 151560], Section 6.1.2.2.1). Because it is possible for violent strombolian volcanic eruptions of the type possible in the Yucca Mountain region to produce ash plumes higher than 5 km, the distribution of wind speed was reexamined to include wind speeds taken at higher altitudes than those used in the TSPA-SR (CRWMS M&O 2000 [DIRS 153246]). This section documents the development of a new wind speed parameter distribution based on data taken from the Desert Rock Airstrip (NOAA n.d. [DIRS 154435]) between 1978 and 1995. The new distribution for wind speed was used with the TSPA in a sensitivity modeling run that is documented in Volume 2 (McNeish 2001 [DIRS 155023], Section 3).

Wind speed is treated as a stochastic data element within the TSPA model. It is sampled for each realization of the model and passed to the ASHPLUME (V1.4LV-dll) code. The ASHPLUME (V1.4LV-dll) code uses the wind speed information in the calculation of the areal concentration of ash and waste downwind from a potential volcanic eruption through the repository. The wind speed distribution used in the TSPA model is important in determining the ground-level waste concentration, and, therefore, dose to the critical group (proposed 10 CFR 63.115(b) (64 FR 8640 [DIRS 101680])), at the critical location 20 km south of the potential repository.

Igneous Consequence Modeling for the TSPA-SR (CRWMS M&O 2000 [DIRS 151560]) provides a wind speed distribution based on data reported by Quiring (1968 [DIRS 119317]) for the Yucca Mountain region for a seven-year period (1957 to 1964). All wind speed data obtained from different times of the year, different elevations, and different wind directions were

considered together to yield an overall wind speed distribution for the Yucca Mountain region. The data were obtained from elevations of approximately 1,500 to 5,000 m above sea level. The wind speed distribution provided in *Igneous Consequence Modeling for the TSPA-SR* (CRWMS M&O 2000 [DIRS 151560], Section 6.1.2.2.1; DTN: SN0010T0502900.003 [DIRS 154654]) varies between 0.0 and 2,366 cm/s, with a median value of approximately 650 cm/s. This wind speed distribution was used for the TSPA-SR (CRWMS M&O 2000 [DIRS 153246]).

Wind speed is generally a function of height; however, the ASHPLUME code considers wind speed constant with height for each realization. The code also considers the maximum ash column height to be a function of the eruption magnitude, with ash/waste particles diffusing out of the column along the entire height. In order to better understand the sensitivity of the TSPA-SR dose calculations (CRWMS M&O 2000 [DIRS 153246]) to this limitation of the ASHPLUME code, a different wind speed distribution reflecting generally higher wind speeds was used in an analysis described in Volume 2 (McNeish 2001 [DIRS 155023], Section 3) and results compared to the base case dose calculation.

For the analysis in Volume 2 (McNeish 2001 [DIRS 155023], Section 3), wind speed data taken from the Desert Rock Airstrip (NOAA n.d. [DIRS 154435]) between 1978 and 1995 were used to develop the new wind speed distribution, using the same methodology described in *Igneous Consequence Modeling for the TSPA-SR* (CRWMS M&O 2000 [DIRS 151560], Section 6.1.2.2.1). Desert Rock 300 millibar wind speed data (taken from an average height of 9,434 m from all wind directions) were combined to create the new distribution. The data were grouped into 2 knot (102.86 cm/s) wind speed intervals in an Excel 97 spreadsheet, and a CDF was developed based on the number of wind speed occurrences within each interval. This new wind speed CDF is shown in Figure 14.3.3.5-1, and the data points are listed in Table 14.3.3.5-1. This wind speed CDF includes wind speeds up to 5,683 cm/s, which is approximately 2.4 times faster than the maximum wind speed given in *Igneous Consequence Modeling for the TSPA-SR* (CRWMS M&O 2000 [DIRS 151560], Section 6.1.2.2.1). The median value for the new distribution is 1,033 cm/s, or approximately 1.6 times faster than in *Igneous Consequence Modeling for the TSPA-SR*. As in the initial TSPA-SR (CRWMS M&O 2000 [DIRS 143665]) calculations, wind direction for this TSPA model calculation was considered to be toward due south (i.e., directly toward the critical group). The assumption of a wind direction toward due south places the critical group on the centerline of the ash plume, where ash thickness is greatest.

The results of the TSPA model run with the new wind speed CDF are presented in Volume 2 (McNeish 2001 [DIRS 155023], Section 3). Results are compared to the initial TSPA-SR calculation (CRWMS M&O 2000 [DIRS 143665]) in terms of the average annual dose rate to the critical group.

14.3.3.6 ASHPLUME Combined Ash and Waste Particle Density Treatment

The discussion in this section is presented for clarification of the issue of how the ASHPLUME code (all versions) treats the density of waste entrained in ash in the eruptive plume for the volcanic eruption scenario. This discussion does not contribute to the analysis in Volume 2 (McNeish 2001 [DIRS 155023]).

Ash particle density is an important parameter within the mathematical model because of its effect on the calculation of the terminal velocity of a particle as it settles in the atmosphere (Jarzemba et. al. 1997 [DIRS 100987]). The particle terminal velocity affects the settling time, and therefore the degree of dispersion that occurs as the particle settles back to earth after an eruption. Because the density of waste is, in general, different from the density of ash, the density of an ash particle will change when it is combined with a waste particle. The correct treatment of this density change in the combined ash and waste particles is necessary if the terminal velocity calculation is to be accurate. The report on *Igneous Consequence Modeling for the TSPA-SR* (CRWMS M&O 2000 [DIRS 139563]) indicates that the ash density does not change after the incorporation of a waste particle. This erroneous indication was corrected in an update to the report (CRWMS M&O 2000 [DIRS 151560], Section 6.1.1).

Igneous Consequence Modeling for the TSPA-SR (CRWMS M&O 2000 [DIRS 151560], Section 6.1.1) provides a description of how the ASHPLUME code (all versions) uses relative particle sizes when determining how waste mass is to be distributed among ash mass. Waste mass is not divided equally among the ash particles. The input parameter "incorporation ratio" is used to calculate a "fuel fraction," which is the ratio of waste fuel mass to ash mass (Jarzemba et al. 1997 [DIRS 100987], Equation 2-8). The fuel fraction calculation prescribes that a waste particle can only be incorporated into an ash particle of a certain size or larger. Thus, larger ash particles will carry more waste mass and smaller ash particles will carry less waste mass, or maybe even none at all.

The particle terminal velocity, V_0, is calculated according to Jarzemba et al. (1997 [DIRS 100987], Equation 2-3). The particle density ("psi" sub p) used in that equation is modified by the ASHPLUME code to account for fuel mass when making the combined-particle dispersion calculation. The combined-particle density is adjusted by the statement (ashden = ashden × [1 + fuel fraction]) in the ASHPLUME code. In this statement, "ashden" represents the ash particle density and "fuel fraction" represents the mass fraction of fuel in the combined particle. This calculation is located in Function ASHDEN.

The update to *Igneous Consequence Modeling for the TSPA-SR* (CRWMS M&O 2000 [DIRS 151560]) represents a change only in the discussion of particle density; it does not represent a change in the ASHPLUME code. The ASHPLUME code was not modified in regard to the particle density calculation. ASHPLUME V1.0, V1.3, and V1.4LV-dll all implement the particle density adjustment correctly.

14.3.3.7 Volcanism Inputs Supporting Total System Performance Assessment Analysis

In addition to the new work described in Section 14, other new work not included in the S&ER (DOE 2001 [DIRS 153849] is contained in updates of disruptive events analysis model reports and calculations. For the TSPA reported in Volume 2 (McNeish 2001 [DIRS 155023]), volcanism inputs were taken from *Igneous Consequence Modeling for the TSPA-SR* (CRWMS M&O 2000 [DIRS 151560]), with the exception of the wind speed distribution. The distribution for wind speed is from Section 14.3.3.5 above. These inputs are summarized in Tables 14.3.3.7-1 and 14.3.3.7-2. While some of these inputs are unchanged from those used for the TSPA-SR (CRWMS M&O 2000 [DIRS 153246]), others have been updated. An asterisk in

the "Distribution or Value" column of the tables indicates inputs that have been updated since the TSPA-SR.

14.3.3.8 Potential Impact of New Aeromagnetic Data on Probability of Dike Intrusion

Since completion of the *Probabilistic Volcanic Hazard Analysis for Yucca Mountain, Nevada* (CRWMS M&O 1996 [DIRS 100116]), the USGS has gathered new aeromagnetic data for the Amargosa Valley/Crater Flat/Yucca Mountain region (Blakely et al. 2000 [DIRS 151881]). These data are being assessed to evaluate the likelihood that magnetic anomalies identified in the survey represent buried volcanoes and, if so, provide information on their properties. These results will then be evaluated within the framework of the PVHA to determine whether additional steps are needed to quantify possible changes in the calculated probability of a dike intersection of the potential repository footprint.

The PVHA experts allowed for the presence of undetected volcanoes in the Yucca Mountain region by assigning a "hidden event" factor (typically 1.1 to 1.5) that was used to increase observed volcano counts, which included buried volcanoes that had been inferred at the time of the PVHA.

It is probable that the presence of any newly identified igneous features would not significantly impact the PVHA results because they would be accounted for by the hidden event factor. However, assessing the impact of the new aeromagnetic survey data will depend on the outcome of a full analysis of these data. Aeromagnetic anomalies, tentatively identified to date, are within or very near the volcano source zones identified by the PVHA experts, which suggests that the spatial distribution of volcanoes in the region would not significantly change.

14.4 SEISMIC EVENTS: TREATMENT OF UNCERTAINTIES, MULTIPLE LINES OF EVIDENCE, AND NEW WORK

Seismic events during the postclosure period have been evaluated to determine their potential to disrupt a geologic repository at Yucca Mountain. To assess this potential, a PSHA was carried out to determine the probability of future fault displacement and vibratory ground motion. The seismic hazard, which is the basis for analyses of the seismic response of the repository system, is based on evaluations of tectonic processes and models developed by an expert elicitation process (Wong and Stepp 1998 [DIRS 103731]). This work is summarized in *Characterize Framework for Seismicity and Structural Deformation at Yucca Mountain, Nevada* (CRWMS M&O 2000 [DIRS 142321]).

Separate analyses were performed to evaluate the effects of seismic events on natural and engineered barrier systems. Except for damage to commercial SNF cladding, earthquake-initiated events were screened out of the TSPA-SR (CRWMS M&O 2000 [DIRS 153246]) on the basis of low probability or low consequence to dose (CRWMS M&O 2000 [DIRS 151553], Section 6.2).

In the sections that follow, treatment of uncertainty in seismic analyses is summarized and an additional line of evidence pertaining to ground motion hazard at Yucca Mountain is presented. No new work has been carried out to address the disruptive condition of seismic events.

14.4.1 Treatment of Uncertainties

Probabilistic Seismic Hazard Analysis–In the PSHA, uncertainties associated with the probabilistic seismic hazard model were addressed explicitly by employing an expert elicitation process (Wong and Stepp 1998 [DIRS 103731]; CRWMS M&O 2000 [DIRS 142321]). Two types of uncertainty were considered and documented (Wong and Stepp 1998 [DIRS 103731], Sections 7.1.1 and 8.1.3; CRWMS M&O 2000 [DIRS 142321], Sections 6.5.2 and 6.6.2):

1. Aleatory uncertainty, which represents the randomness inherent in the natural phenomena of earthquake generation and seismic wave propagation

2. Epistemic uncertainty, which derives from incomplete scientific knowledge of earthquake generation and ground motion propagation processes and the limited data available for use in selecting between alternative conceptual models and interpretations.

Epistemic uncertainty was documented by having multiple experts evaluate alternative interpretations. This information was captured for the probabilistic seismic hazard computation through the use of a logic tree approach in which the branches of the logic tree represent alternative interpretations. Each expert defined branches of the logic tree, then assigned weights to alternative branches depending on the assessment of the degree to which the available data supported that alternative. These multiple interpretations were propagated through the analysis, resulting in a suite of hazard curves and associated weights.

Aleatory uncertainty is captured in the hazard computation by integrating over all variables of the seismic hazard model and is included in each hazard curve. The complete suite of weighted hazard curves from all the experts was then summarized by mean and median curves and 5^{th}, 15^{th}, 85^{th}, and 95^{th} fractile curves. The mean and median curves reflect the central tendency of the hazard analysis, while the separation of the fractile curves reflects the epistemic uncertainty.

At low annual frequencies of exceedance—lower than about 10^{-6}—the hazard uncertainty distribution is increasingly skewed, causing the mean hazard curve to diverge from the median curve. For example, at a 10^{-6} annual frequency of exceedance, the mean peak horizontal ground acceleration is approximately equivalent to the 85^{th} fractile value (DTN: MO0004MWDRIFM3.002 [DIRS 149092]). For an annual frequency of exceedance of 10^{-8}, the mean peak horizontal ground acceleration has likely exceeded the 90^{th} fractile. The increased skewness results from a broadening of the uncertainty distribution at the higher ground motion levels as some of the alternative input parameter sets begin to produce nearly zero hazard. As a result, at low annual frequencies of exceedance, the extreme upper tails of the uncertainty drive the mean hazard.

This result of the extreme skewing in the uncertainty distribution must be appropriately considered in using the hazard curves for regulatory decision-making. When the annual exceedance frequency of interest is in the range of 10^{-5} to 10^{-6} or higher, the mean hazard is generally consistent with physically realizable values. For annual exceedance frequencies below 10^{-6}, however, the mean seismic hazard for Yucca Mountain is increasingly inconsistent with physically realizable ground motion and fault displacement values. At low annual frequencies of

exceedance, the median hazard is considered to represent more appropriately the central tendency of the hazard uncertainty for the purpose of FEPs screening. Further discussion of this issue is found in *Features, Events, and Processes: Disruptive Events* (CRWMS M&O 2000 [DIRS 151553], Section 5, Assumption 5.5).

Effects of Fault Displacement on Emplacement Drifts–*Effects of Fault Displacement on Emplacement Drifts* (CRWMS M&O 2000 [DIRS 151954]) was carried out to examine the stresses and rock movement induced on an emplacement drift by nearby fault displacement associated with an earthquake. Uncertainties in the amount of fault displacement and the spatial relationship between the fault and a drift were addressed by analyzing ranges of values.

Fault displacement values ranging from 0.1 to 100 cm were considered (CRWMS M&O 2000 [DIRS 151954], Section 5.13). The upper portion of this range is on the same order of magnitude as the largest displacements observed from paleoseismic studies of the Solitario Canyon fault (120 to 130 cm) and exceeds those for the Bow Ridge fault (CRWMS M&O 2000 [DIRS 151945], Table 12.3-8b). The Solitario Canyon and Bow Ridge faults are the largest in the immediate vicinity of the potential waste emplacement area. Median values of fault displacement hazard for sites within the potential waste emplacement area are less than 100 cm (DTN: MO0004MWDRIFM3.002 [DIRS 149092]).

Other uncertainties in the analysis are type of faulting, rock mass quality in the vicinity of an emplacement drift, and distance from a fault to an emplacement drift. Uncertainty in type of faulting is addressed by considering both normal and strike-slip faulting cases (CRWMS M&O 2000 [DIRS 151954], Section 6). Uncertainty in rock mass quality is included in the analysis by considering two cases that bound the possible range (RMQ = 1 and RMQ = 5). Finally, the analysis looks at the effects of faulting over a range of distances (0 to 100 m) from the fault (CRWMS M&O 2000 [DIRS 151954], Section 6).

Fault Displacement Effects on Transport in the Unsaturated Zone–In *Fault Displacement Effects on Transport in the Unsaturated Zone* (CRWMS M&O 2000 [DIRS 151953]), uncertainties in defining the effects of faulting on the hydraulic properties of fractures is addressed using a bounding approach. Rather than trying to model the changes for a specific earthquake, values are selected to encompass those changes that would be caused by expected fault displacements. Thus, cases were evaluated in which fracture aperture was increased by a factor of 10 and decreased by a factor of 0.2 (or 0.5 for a wetter climate) (CRWMS M&O 2000 [DIRS 151953], Section 6.2.1.5).

In addition, two bounding cases were considered for the spatial distribution of changes to fracture hydraulic properties. In one case, only properties for fractures in fault zones were altered. In the other case, fracture properties were changed throughout the UZ model domain (CRWMS M&O 2000 [DIRS 151953], Section 6.2.1).

14.4.2 Multiple Lines of Evidence: Implications for Vibratory Ground Motion from Studies of Precarious Rocks at Yucca Mountain

There are some lines of evidence that provide additional confidence that seismic hazard and related effects have been appropriately considered. The existence of precariously balanced rocks

in the Yucca Mountain region puts some constraints on the level of vibratory ground motion experienced at the site over the past several tens of thousands of years.

Preliminary information on precariously balanced rocks was available to ground motion experts during the PSHA. At that time, however, they did not consider the information in developing their interpretations because of limited knowledge on the duration and frequency of ground motion needed to topple rocks, possible shadow zone effects, and a lack of information on rocks that had been toppled (Wong and Stepp 1998 [DIRS 103731], p. 5-19). Since the PSHA, additional work has been carried out to better understand the implications of precariously balanced rocks.

Precariously balanced rocks provide evidence that past levels of strong vibratory ground motion have been insufficient to topple them. In areas where strong ground motions are known to have occurred historically, precarious rocks are not observed. For example, based on reconnaissance field surveys in southern California, Brune (1996 [DIRS 154300], p. 43) concluded that no precarious rocks are found within 15 km of zones of high-energy release of historic large earthquakes. Laboratory physical modeling, numerical modeling, and field tests provide confidence that rough estimates of the accelerations required to topple precarious rocks can be made without extensive controlled testing (Brune 2000 [DIRS 154301], p. 1107; Anooshehpoor and Brune 2000 [DIRS 154302], pp. 2 to 4). Brune and Whitney (2000 [DIRS 154573], p. 18) noted that numerous precarious rocks exist along Solitario Canyon and argued that accelerations at Yucca Mountain have not exceeded about 0.3 g at the surface during the past 75,000 to 80,000 years. This inference is consistent with information indicating that the last significant surface offset on the Solitario Canyon fault occurred 15,000 to 30,000 years ago (CRWMS M&O 2000 [DIRS 151945], Table 12.3-8b). Vibratory ground motions at the depth of potential waste emplacement would be less than those at the surface.

Precarious rocks have also been used to test ground motion attenuation relations. Brune (2000 [DIRS 154301], p. 1107) notes that, in contrast to observations in the vicinity of strike-slip faults, precarious and semi-precarious rocks are found nearly to the fault trace on the footwall side of normal faults in Nevada and California. Comparison of estimated toppling accelerations with accelerations predicted by a ground motion attenuation relation based largely on data for strike-slip earthquakes suggests that the attenuation relation may be conservative. The attenuation relation overestimates accelerations on the footwall of normal faults at near distances (Brune 2000 [DIRS 154301], Figure 2). This result is consistent with results from dynamic foam rubber models of strike-slip and normal faulting earthquakes (Brune and Anooshehpoor 1999 [DIRS 154303]). That is, the models indicate that ground motions near the fault trace are less for normal faulting earthquakes than for strike-slip earthquakes. The implication of this observation is that seismic hazard estimates using ground motion attenuation curves based largely on data from strike-slip earthquakes, such as were evaluated in the PSHA, may result in conservative values of hazard for sites such as Yucca Mountain, where normal faulting dominates.

14.4.3 Analyses to Evaluate Seismic Events and Their Effects

No new seismic analyses have been carried out since the completion of the S&ER (DOE 2001 [DIRS 153849]). If the site is recommended, additional analyses will be carried out to support a TSPA for the license application. These analyses would address any enhancements of the

repository thermal operating modes and finalize or provide additional confidence in current seismic-related FEPs evaluations.

14.5 SUMMARY OF DISRUPTIVE EVENTS ANALYSES AND PARAMETERS PROVIDED TO TOTAL SYSTEM PERFORMANCE ASSESSMENT

Changes to disruptive events analyses since completion of the work described in the S&ER (DOE 2001 [DIRS 153849]) have included updates to analysis model reports and calculations, as well as additional analyses presented for the first time in Section 14.3.3. Three of these additional analyses provide supplemental information, but are not used in the TSPA sensitivity runs or in the TSPA described in Volume 2 (McNeish 2001 [DIRS 155023]). The analysis described in Section 14.3.3.2 was conducted only to provide an understanding of how changes in repository layouts to achieve lower-temperature operating modes would affect disruptive events analyses. The analysis presented in Section 14.3.3.6 simply clarifies how one aspect of the ASHPLUME code works. Section 14.3.3.8 addresses consideration of new aeromagnetic data in the Yucca Mountain region. The other analyses described in Section 14.3.3 support TSPA analyses described in Volume 2 (McNeish 2001 [DIRS 155023]) as follows:

- Analysis of the probability of intersection of a dike or conduit with a potential repository having a 70,000 MTHM storage capacity and using no backfill in emplacement drifts is used as an input in the supplemental TSPA (Section 14.3.3.1).

- Analysis of the contribution to release of waste packages damaged in Zones 1 and 2 in an igneous intrusion groundwater release model (Section 14.3.3.3) supports a TSPA sensitivity analysis.

- A range of waste particles sizes was developed (Section 14.3.3.4) to support a sensitivity analysis of waste particle size distributions.

- A new distribution of wind speeds was selected (Section 14.3.3.5) and is used in a sensitivity analysis of wind speed and as an input in the TSPA of disruptive events.

- Some volcanism input values contained in analysis model reports and calculations were updated (Section 14.3.3.7) and are used as inputs in the TSPA, as summarized in Tables 14.3.3.7-1 and 14.3.3.7-2.

INTENTIONALLY LEFT BLANK

Table 14.1-2. Repository Features and Hypothetical Operating Modes that Produce a Range of Temperatures

Feature	EDA-II Higher-Temperature Operating Mode[a]	Higher-Temperature Operating Mode Addressed in the S&ER[b]	Example Operating Mode Parameters for 70,000 MTHM Inventory For Lower Temperature Repository					
			Example 1: Lower Waste Package Temperature through Extended Ventilation and Increase in Emplacement Area			Example 2: Lower Waste Package Temperature through Increased Emplacement Area and Limited Period of Forced Ventilation		Example 3: Lower Drift Wall Temperature and Relative Humidity through Natural Ventilation
			Scenario 1	Scenario 2	Scenario 3	Scenario 4	Scenario 5	Scenario 6
Number of waste packages	10,039	11,184	~11,000	~16,000	~11,000	~11,000	~11,000	~11,000
Waste package spacing (m)	0.1	0.1	2	0.1	0.1	6	2	0.1
Approximate waste package length (m)	5.1	4.9	~5	~5	~5	~5	~5	~5
Drift center-to-drift center spacing (m)	81	81	81	81	120	81	81	81
Total emplacement drift length (km)	54	56	80	80	60	130	80	60
Required emplacement area (acres)	1,050	1,125	~1,600	~1,600	~1,700	~2,500	~1,600	~1,100
Backfilled	Yes	No	No	No	No	No	No	No

Sources: [a] CRWMS M&O 1999 [DIRS 150421], Item 1; CRWMS M&O 1999 [DIRS 107292], Section 7.1, Tables 6.2 and 6.3; [b] CRWMS M&O 2000 [DIRS 146021], Sections 4.2.1.5 and 6.3.1, Table 28.

NOTE: The example operating mode parameters for a 70,000 MTHM inventory for a lower-temperature repository are assumed. They are used only for sensitivity analyses and do not need to be verified.

Table 14.2-1. Key Documents Supporting the Analysis of Disruptive Processes and Events

Document	Document Identifier Number
Disruptive Events Process Model Report (CRWMS M&O 2000 [DIRS 151968])	TDR-NBS-MD-000002
Features, Events, and Processes: Disruptive Events (CRWMS M&O 2000 [DIRS 151553])	ANL-WIS-MD-000005
Characterize Framework for Igneous Activity at Yucca Mountain, Nevada (CRWMS M&O 2000 [DIRS 151551])	ANL-MGR-GS-000001
Characterize Eruptive Processes at Yucca Mountain, Nevada (CRWMS M&O 2000 [DIRS 142657])	ANL-MGR-GS-000002
Dike Propagation Near Drifts (CRWMS M&O 2000 [DIRS 151552])	ANL-WIS-MD-000015
Igneous Consequence Modeling for TSPA-SR (CRWMS M&O 2000 [DIRS 151560])	ANL-WIS-MD-000017
Characterize Framework for Seismicity and Structural Deformation at Yucca Mountain, Nevada (CRWMS M&O 2000 [DIRS 142321])	ANL-CRW-GS-000003
Fault Displacement Effects on Transport in the Unsaturated Zone (CRWMS M&O 2000 [DIRS 151953])	ANL-NBS-HS-000020
Effects of Fault Displacement on Emplacement Drifts (CRWMS M&O 2000 [DIRS 151954])	ANL-EBS-GE-000004
Number of Waste Packages Hit by Igneous Intrusion (CRWMS M&O 2000 [DIRS 153097])	CAL-WIS-PA-000001
Comparison of ASHPLUME Model Results to Representative Tephra Fall Deposits (CRWMS M&O 2000 [DIRS 152998])	CAL-WIS-MD-000011

Table 14.3.3.2-1. Summary of the Number of Waste Packages Contained within a Conduit Diameter for the Operating Modes Presented in Table 14.1-2

Conduit Diameter (m)	Number of Waste Packages Contained Within a Conduit Diameter			
	Scenarios 2 and 6	Scenarios 1 and 5	Scenario 4	Scenario 3
4.5	1	1	1	1
10	2	2	1	2
15	3	3	2	3
20	4	3	2	4
25	5	4	3	5
30	6	5	3	6
35	7	5	4	7
40	8	6	4	8
45	9	7	5	9
50	10	8	5	10
55	11	8	5	11
60	12	9	6	12
65	13	10	6	13
70	14	10	7	14
75	15	11	7	15
80	16	12	8	16
85	17	13	8	17

Table 14.3.3.2-1. Summary of the Number of Waste Packages Contained within a Conduit Diameter for the Operating Modes Presented in Table 14.1-2 (Continued)

Conduit Diameter (m)	Number of Waste Packages Contained Within a Conduit Diameter			
	Scenarios 2 and 6	Scenarios 1 and 5	Scenario 4	Scenario 3
90	18	13	9	18
95	20	15	10	19
100	24	17	11	20
105	27	20	13	21
110	30	22	14	22
115	33	24	15	23
120	36	26	17	24
125	38	28	18	25
130	41	30	19	26
135	43	31	20	27
140	46	33	21	29
145	48	35	22	33
150	51	37	23	36

Source: BSC 2001 [DIRS 154933].

Table 14.3.3.4-1. Waste Particle Sizes Used in Total System Performance Assessment and in the Sensitivity Analysis for Volume 2 Using New Distributions

	Minimum (cm)	Mode (cm)	Maximum (cm)
Base case	0.0001	0.002	0.05
Assumed values	0.00005	0.0002	0.005
	0.00005	0.002	0.1
	0.00005	0.02	0.05
	0.0001	0.0002	0.1
	0.0001	0.0002	0.005
	0.0001	0.02	0.1
	0.0001	0.02	0.05

Sources: DOE 2001 [DIRS 153849]; McNeish 2001 [DIRS 155023].

Table 14.3.3.5-1. Desert Rock Wind Speed Cumulative Probability Distribution

Wind Speed (cm/s)	Cumulative Probability
0.00	0.0000
25.72	0.0003
128.58	0.0113
231.44	0.0365
334.30	0.0761
437.16	0.1241
540.02	0.1823
642.88	0.2474
745.74	0.3183
848.60	0.3814
951.46	0.4442
1054.32	0.5143
1157.18	0.5763
1260.04	0.6305
1362.90	0.6864
1465.76	0.7357
1568.62	0.7798
1671.48	0.8217
1774.34	0.8504
1877.20	0.8771
1980.06	0.9016
2082.92	0.9250
2185.78	0.9422
2288.64	0.9566
2391.50	0.9667
2494.36	0.9754
2597.22	0.9827
2700.08	0.9874
2802.94	0.9915
2905.80	0.9931
3008.66	0.9951
3111.52	0.9966
3214.38	0.9980
3317.24	0.9987
3471.53	0.9992
3677.25	0.9994
3934.40	0.9997
4705.85	0.9998
5683.02	1.0000

Source: Statham 2001 [DIRS 154932].

NOTE: Data obtained from an average height of 9,434 m.

Table 14.3.3.7-1. Volcanic Eruption Event Input Parameters for Total System Performance Assessment Supplemental Model

Input Parameter	Input Parameter Format	Distribution or Value
ASHPLUME – min grid location on x-axis	Point Value	0
ASHPLUME – max grid location on x-axis	Point Value	0
ASHPLUME – min grid location on y-axis	Point Value	-20
ASHPLUME – max grid location on y-axis	Point Value	0
ASHPLUME – # of grid locations on x-axis	Point Value	1
ASHPLUME – # of grid locations on y-axis	Point Value	1
ASHPLUME – max particle diameter for transport	Point Value	10 cm
ASHPLUME – min height of eruption column	Point Value	1 m
ASHPLUME – threshold limit on ash accumulation	Point Value	1e-10
ASHPLUME – run type: deterministic or stochastic	Point Value	deterministic
ASHPLUME – option to save particle size info at dose point	Point Value	Not saved
ASHPLUME – particle shape factor	Point Value	0.5
ASHPLUME – air density	Point Value	0.001117 g/cm^3
ASHPLUME – air viscosity	Point Value	0.0001758 g/m-s
ASHPLUME – constant [C] relating to eddy diffusivity and particle fall time	Point Value	400 cm^2 /sec$^{5/2}$
ASHPLUME – incorporation ratio	Point Value	0.3
ASHPLUME – ash settled density	Point Value	1.0 g/cm^3
ASHPLUME – ash particle densities at min/max particle sizes	Point Value	2.08 g/cm^3 (for 0.001 cm ash particle) 1.04 g/cm^3 (for 1.0 cm ash particle)
ASHPLUME – ash min/max log-diameter particle sizes for densities	Point Value	-3 (density 2.08 g/cm^3) 0 (density 1.04 g/cm^3)
ASHPLUME – waste particle diameter: minimum mode maximum	 Point Value Point Value Point Value	 0.0001 cm; 0.002 cm; and 0.05 cm
ASHPLUME – event eruptive volume	CDF	0.002 km^3 – 0.44 km^3
ASHPLUME – mean ash particle diameter	CDF	0.001 cm – 0.1 cm
ASHPLUME – mean ash particle diameter standard deviation	CDF	1 – 3 phi units (phi unit is defined to be the negative logarithm in base 2 of the particle diameter in millimeters)
ASHPLUME – event power	CDF	1.0e09 W – 6.31e13 W
ASHPLUME – ash dispersion controlling constant	CDF	0.01 – 0.5
ASHPLUME – conduit diameter	CDF	4.5 m – 150 m [a]
ASHPLUME – initial eruption velocity	CDF	633 cm/sec – 22,294 cm/sec [a]
ASHPLUME – wind speed	CDF	0 cm/sec – 5,683 cm/sec [a]
ASHPLUME – wind direction	Point Value	-90^o (toward due south)

Table 14.3.3.7-1. Volcanic Eruption Event Input Parameters for Total System Performance Assessment Supplemental Model (Continued)

Input Parameter	Input Parameter Format	Distribution or Value
Number of packages hit per conduit (volcanic eruption)	CDF	1 – 51 [a]
Number of conduits intersecting waste packages	PDF	1 – 13 [a]
Probability of > 0 conduits occurring within the repository	Point value	.77 [a]
Percent of hit packages that fail	Point value	100%
Event probability (frequency that an igneous event intersects the repository footprint)	CDF	1.380E-11 to 4.28E-07 [a]

Source: CRWMS M&O 2000 [DIRS 151560], Sections 6.1.2, 6.1.3, and Attachment I.

NOTES: [a] Information updated from analyses reported in the S&ER (DOE 2001 [DIRS 153849]).
All references to ASHPLUME in this table refer to Version 1.4LV-dll.
PDF = probability density function.

Table 14.3.3.7-2. Igneous Intrusion Groundwater Transport Event Input Parameters for Total System Performance Assessment Supplemental Model

Input Parameter	Input Parameter Format	Distribution or Value
Event probability (frequency that an igneous event intersects the repository footprint)	CDF	1.380e-11 – 4.283e-07 [a]
Number of Zone 1 packages intersected (igneous intrusion)	CDF	98 – 1,785 [a]
Number of combined Zone 1 and 2 packages intersected (igneous intrusion)	CDF	0 – 11,184 [a]
Damage to packages in Zone 1	Point value	100%
Damage to packages In Zone 2	Truncated log-normal distribution	Minimum - 1.0 cm^2 Mean - 10 cm^2 Maximum - 1.9E4 cm^2 (size of hole created by end cap weld failure) Standard deviation = 1

Source: CRWMS M&O 2000 [DIRS 151560], Sections 6.1.2, 6.1.3, and Attachment I.

NOTE: [a] Information updated from analyses reported in the S&ER (DOE 2001 [DIRS 153849]).

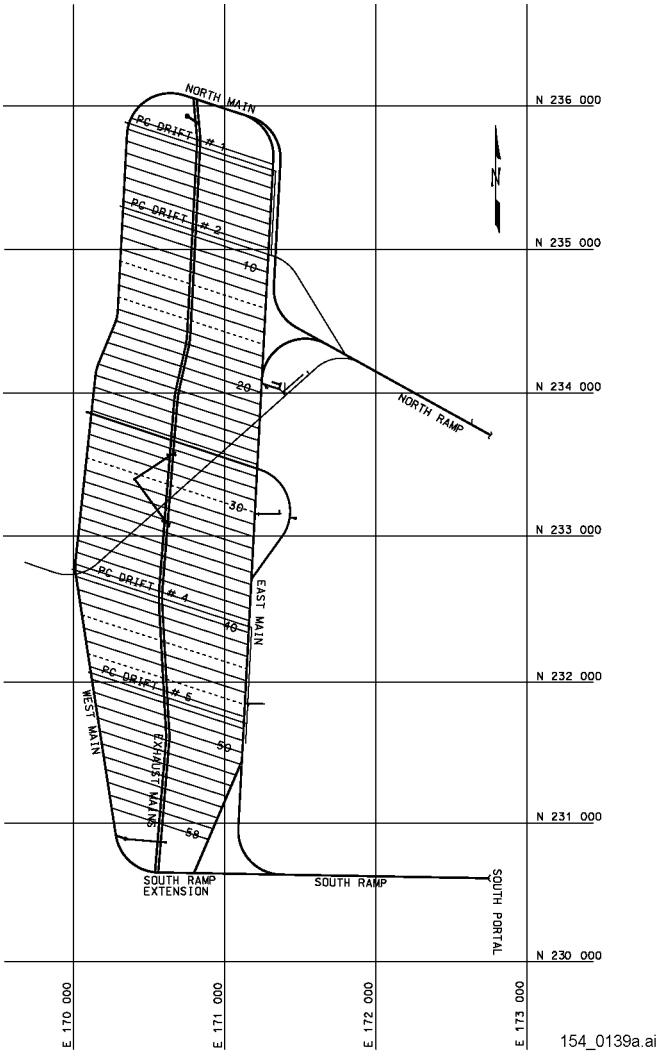

154_0139a.ai

Source: CRWMS M&O 1999 [DIRS 107292].

NOTE: PC Drift = Performance confirmation drift. Dimensions and coordinates are in m. Northing and easting values are from the Nevada State Plane Coordinate System, NAD 27.

Figure 14.1-1a. Repository Layout Used in Disruptive Events Analyses: Enhanced Design Alternative II Higher-Temperature Operating Mode

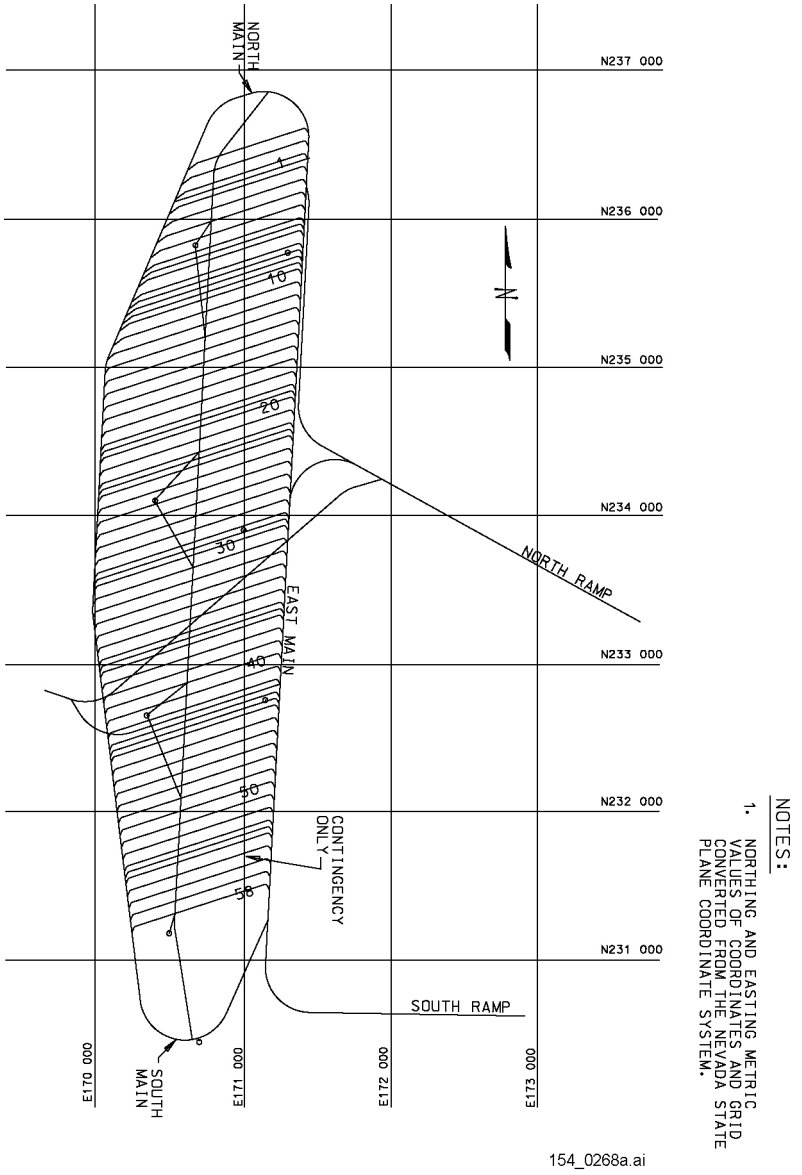

154_0268a.ai

Source: CRWMS M&O 2000 [DIRS 146021].

NOTE: Dimensions and coordinates are in m. Northing and easting values are from the Nevada State Plane Coordinate System, NAD 27. *Yucca Mountain Science and Engineering Report* (DOE 2001 [DIRS 153849]).

Figure 14.1-1b. Repository Layout Used in Disruptive Events Analyses: Higher-Temperature Operating Mode Addressed in the Yucca Mountain Science and Engineering Report

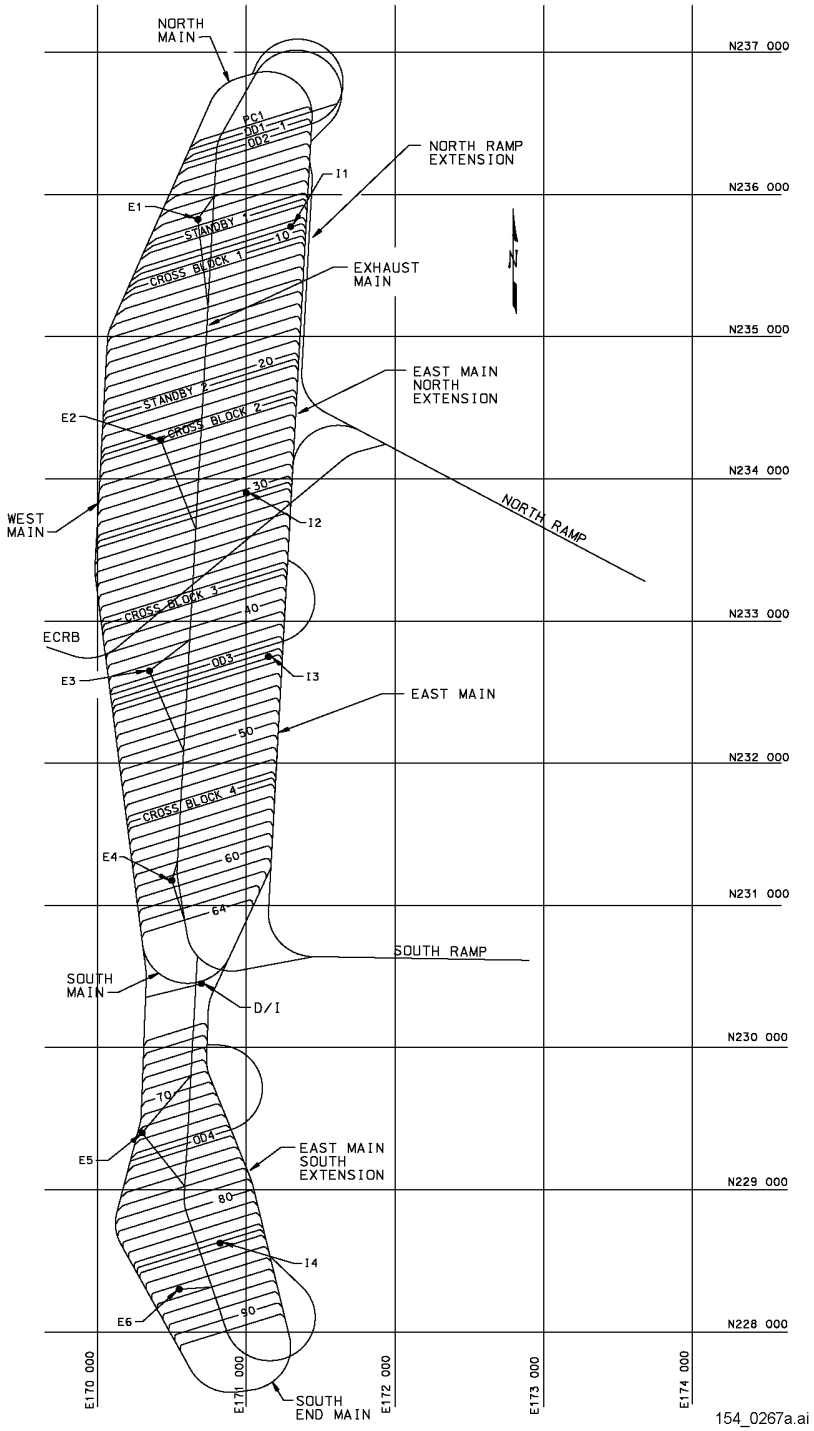

154_0267a.ai

Source: BSC 2001 [DIRS 154548].

NOTES: This repository layout relates to Scenario 1 in Table 14.1-2. Dimensions and coordinates are in m. Northing and easting values are from the Nevada State Plane Coordinate System, NAD 27. PC = Performance confirmation drift. OD = Observation drift. I1 = Intake shaft. E1 = Exhaust shaft. D/I = Development/Intake shaft. ECRB = Enhanced Characterization of the Repository Block.

Figure 14.1-1c. Repository Layout Used in Disruptive Events Analyses: Lower-Temperature Operating Mode

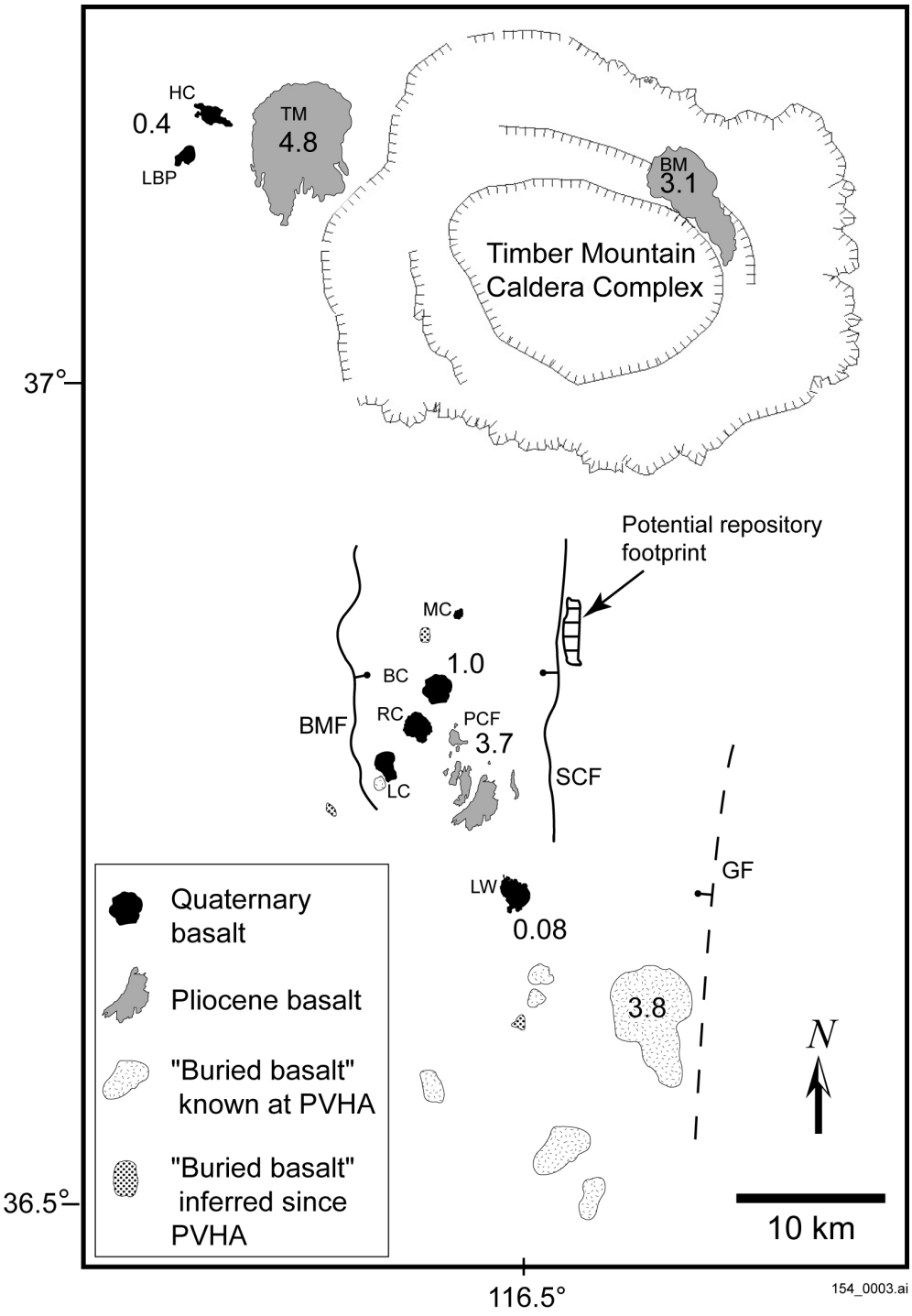

154_0003.ai

Source: CRWMS M&O 2000 [DIRS 151551], Figure 3.

NOTES: Post-Miocene ages are less than 5.3 my. Clusters are shown where multiple volcanoes have indistinguishable ages. Numbers by each volcano indicate approximate age in millions of years. BC = Black Cone; BM = Buckboard Mesa; BMF = Bare Mountain Fault; GF = Gravity Fault; HC = Hidden Cone; LBP = Little Black Peak; LC = Little Cones; LW = Lathrop Wells; MC = Makani Cone; PCF = Pliocene Crater Flat; RC = Red Cone; SCF = Solitario Canyon Fault; TM = Thirsty Mesa; PVHA = Probabilistic Volcanic Hazard Analysis.

Figure 14.2-1. Location and Age of Post-Miocene Volcanoes in the Yucca Mountain Region

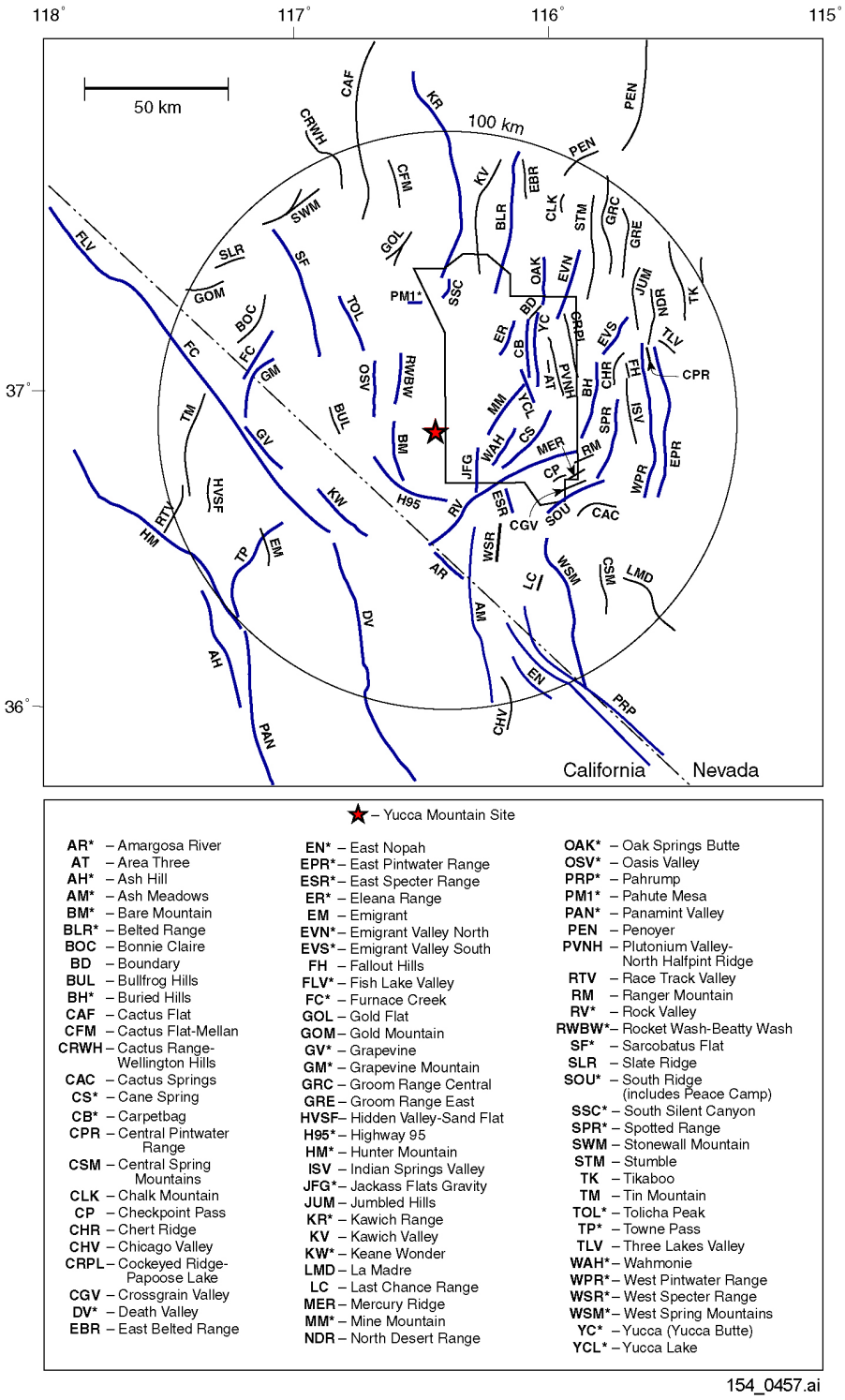

154_0457.ai

Source: Modified from CRWMS M&O 2000 [DIRS 142321].

NOTE: Faults included in the PSHA (Wong and Stepp 1998 [DIRS 103731]) are shown as bold lines on the map and asterisks in the legend.

Figure 14.2-2a. Known or Suspected Quaternary Faults and Potentially Important Local Faults within 100 km of Yucca Mountain

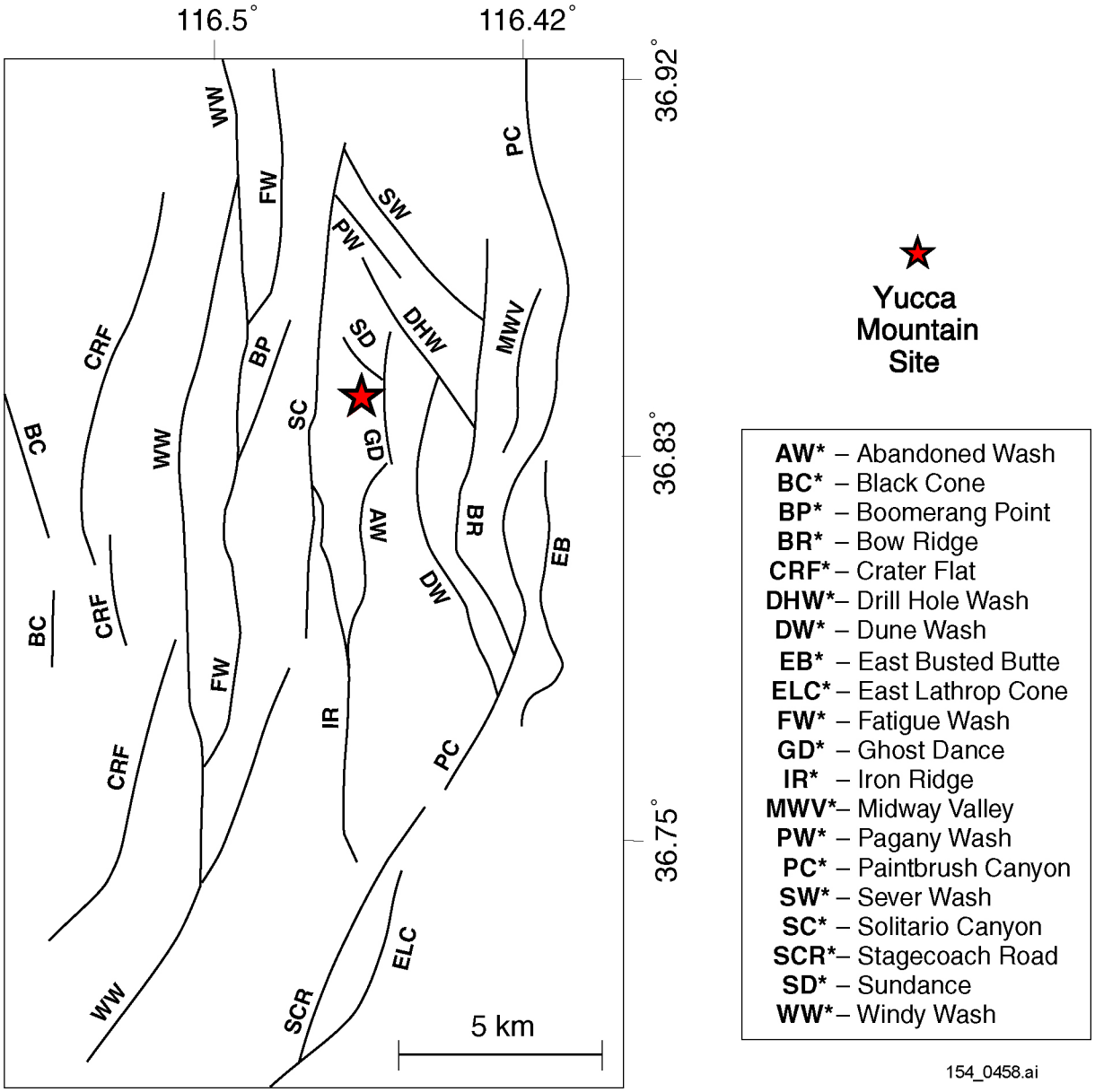

154_0458.ai

Source: CRWMS M&O 2000 [DIRS 142321].

NOTE: These faults are included in the PSHA (Wong and Stepp 1998 [DIRS 103731]).

Figure 14.2-2b. Known or Suspected Quaternary Faults and Potentially Important Local Faults in the Vicinity of the Yucca Mountain Site

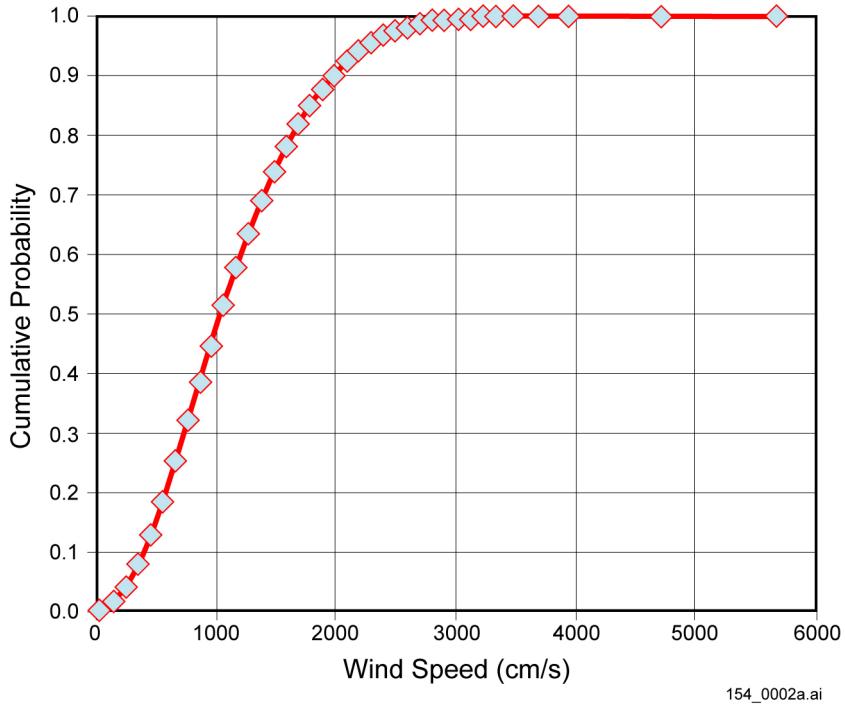

154_0002a.ai

Source: Statham 2001 [DIRS 154932].

NOTES: Data points listed in Table 14.3.3.5-1. Average height = 9,434 m.

Figure 14.3.3.5-1. Desert Rock Airstrip Wind Speed Cumulative Probability Distribution

INTENTIONALLY LEFT BLANK

15 Summary

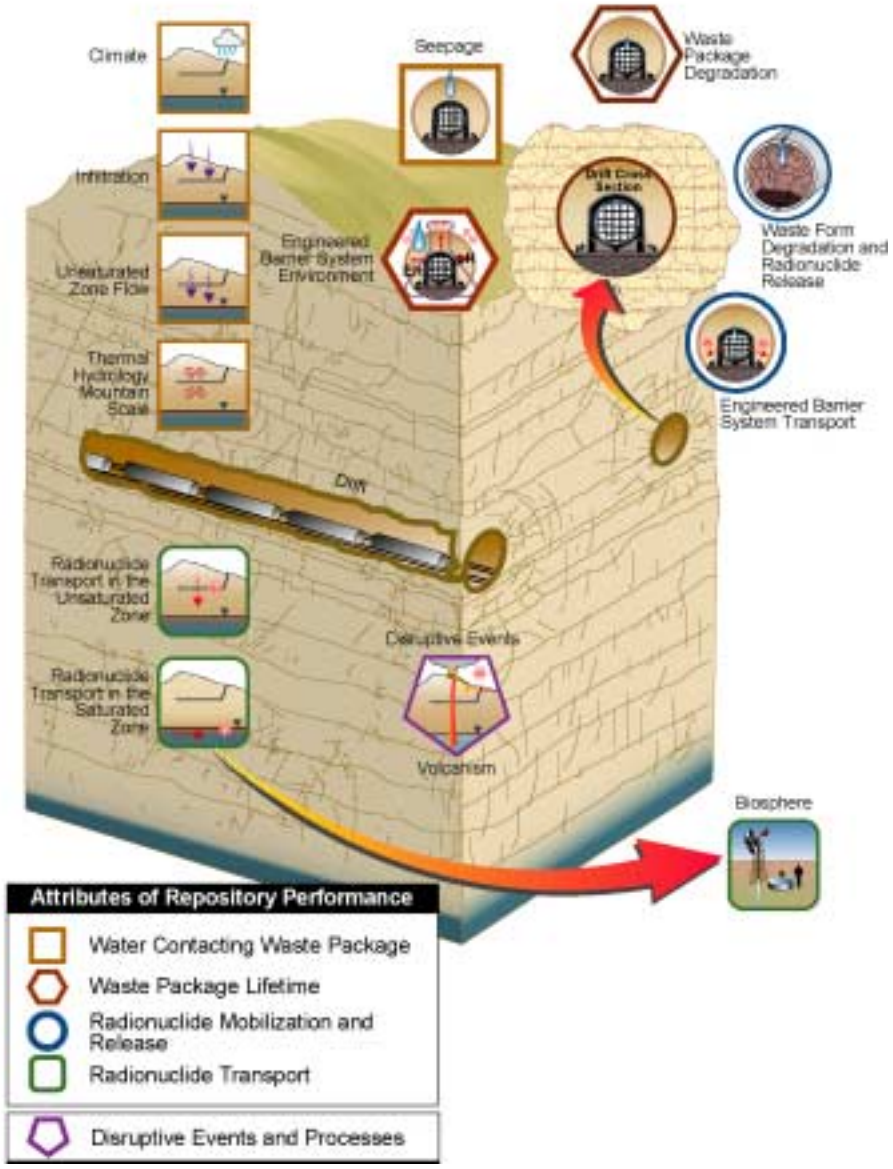
Climate
Infiltration
Unsaturated Zone Flow
Thermal Hydrology Mountain Scale
Seepage
Engineered Barrier System Environment
Waste Package Degradation
Drift Cross Section
Waste Form Degradation and Radionuclide Release
Engineered Barrier System Transport
Drift
Radionuclide Transport in the Unsaturated Zone
Radionuclide Transport in the Saturated Zone
Disruptive Events
Volcanism
Biosphere
Attributes of Repository Performance
Water Contacting Waste Package
Waste Package Lifetime
Radionuclide Mobilization and Release
Radionuclide Transport
Disruptive Events and Processes

15. SUMMARY AND CONCLUSIONS

The *FY01 Supplemental Science and Performance Analysis, Volume 1: Scientific Bases And Analyses* Report (SSPA) describes new information developed since completion of the *Yucca Mountain Science and Engineering Report* (S&ER) (DOE 2001 [DIRS 153849]), and its key references, the *Total System Performance Assessment for the Site Recommendation* (TSPA-SR) (CRWMS M&O 2000 [DIRS 153246]), and the Analysis and Model Reports and Process Model Reports cited therein. Volume 1 describes the new technical work at the process model level. The *FY01 Supplemental Science and Performance Analysis, Volume 2: Performance Analyses* (McNeish 2001 [DIRS 155023]) describes analyses conducted to gain insight into the implications of the new technical work on the performance of the potential repository.

The analyses described in this report were performed to address uncertainties that were acknowledged in the S&ER (DOE 2001 [DIRS 153849]). As described in Section 4.1 of the S&ER (DOE 2001 [DIRS 153849]), the DOE approach to accommodating uncertainty includes a quantitative analysis of performance, supplemented by several additional measures designed to independently provide confidence that the quantitative models are defensible. The additional measures include the selection of a site and design of a repository system that provides defense in depth and a margin of safety compared to requirements, insights obtained from natural and man-made analogues, and a commitment to a long term performance confirmation, management and monitoring program.

Although the S&ER (DOE 2001 [DIRS 153849]) and its key references include substantial discussions of uncertainty, the DOE determined that additional work to augment the characterization and treatment of uncertainty was warranted. Therefore, several types of analyses were identified and performed to supplement the treatment of uncertainty in support of the consideration of a possible site recommendation. The supplemental information can be divided into three areas:

- **Unquantified Uncertainties Analysis**–Some of the uncertainties that were not quantified in the TSPA-SR (CRWMS M&O 2000 [DIRS 153246]) have been quantified. Newly quantified uncertainties include updates to parameter bounds, conceptual models, assumptions, and in some cases, statistically biased or skewed distributions on input parameters. The primary goals of this portion of the effort were to provide insight into the importance of the unquantified uncertainties and the degree of conservatism in the overall assessment of the performance of the potential repository presented in TSPA-SR (CRWMS M&O 2000 [DIRS 153246]).

- **Updates in Scientific Information**–New information has been developed for the process models supporting the total system performance assessment (TSPA). This work includes new experimental results, new conceptual models, new analysis approaches, and the results of continued research efforts. It also includes identification and discussion of multiple lines of evidence that have been used directly to support modeling or indirectly to develop confidence in modeling results. The primary goals of this portion of the work were to provide insights into the impact of the new scientific results and improved models (i.e., updated since completion of the S&ER (DOE 2001

[DIRS 153849])) and to develop additional confidence in the models and parameters used for TSPA.

- **Lower-Temperature Operating Mode Analysis**–The effects of a range of thermal operating modes (including lower operating temperatures in the potential repository) on projected system performance have been evaluated. Different thermal modes are compared with the design and operating mode described in the S&ER (DOE 2001 [DIRS 153849]). The primary goals of evaluating a range of thermal operating modes were to provide insights into the effect of thermal parameters on predicted repository performance, including uncertainty of those predictions, and to increase confidence in the predicted repository performance over a range of thermal conditions.

The SSPA provides information that can be used to assess the robustness of the analyses and results presented in the S&ER (DOE 2001 [DIRS 153849]). It also provides a technical basis for a preliminary evaluation of some of the advantages and disadvantages of alternative thermal operating modes for the potential repository. The new analyses described in Sections 3 through 14 of this volume are organized and presented by key system attributes and by process models, as they are defined in the S&ER (DOE 2001 [DIRS 153849], Table 4-3). Table 1-1 in Section 1 (Introduction) of this report shows the supplemental models and analyses that were performed for the SSPA, and the rationale for the analyses. The updated models and sensitivity analyses that were incorporated in the supplemental total system performance assessment models are described in Volume 2 (McNeish 2001 [DIRS 155023]) are identified in Table 1-1.

General Conclusions–The analyses described in the SSPA have enhanced the DOE understanding of the uncertainties inherent in assessments of the potential future performance of a Yucca Mountain repository. The quantification of uncertainties has improved the understanding of conservative and potentially non-conservative assumptions contained in the process models described in the S&ER (DOE 2001 [DIRS 153849]) and its references. Depending on the process model, reductions in uncertainties can be obtained from either the lower-temperature operating mode (LTOM) or the higher-temperature operating mode (HTOM). The preliminary evaluation of thermal operating modes indicates that post-closure effects on performance can be evaluated by selecting appropriate initial conditions for the models. The analysis of waste package degradation indicates that performance models should consider the thermal dependence and the local chemical environment that control corrosion mechanisms and rates. The expanded consideration of multiple lines of evidence throughout the SSPA is a useful exercise that has improved understanding by the DOE of processes important to repository performance, independent of the results of the quantitative TSPA.

Preliminary Comparison of Lower- and Higher-Temperature Operating Modes–The preliminary evaluations presented in the SSPA indicate that the process models used for the TSPAs for Yucca Mountain are appropriate for analyzing the LTOM and HTOM. The results of the analyses suggest that the differences between thermal operating modes are significant only for the first few thousand years after emplacement, because the thermal differences are negligible after the initial thermal pulse. This fact largely accounts for the similarity in postclosure performance results. Process model results indicate that natural processes (e.g., unsaturated zone flow above the repository, seepage into drifts, and flow and transport in the unsaturated and saturated zones below the repository) are not significantly influenced over the long term by the

thermal operating mode. Evaluation of coupled thermal-hydrologic-chemical-mechanical processes demonstrates that LTOMs have lesser (and less complex) effects on the processes operating in the thermally perturbed region near emplacement drifts, but also shows that the effects are generally small, and relatively short-lived, for higher-temperature modes. Process models representing the performance of the engineered barrier system components are sensitive to the physical (temperature and relative humidity) and chemical environment in the repository. However, the analyses also suggest that the relatively short duration of conditions in which drip shield or waste package corrosion may be possible is unlikely to result in significant degradation of performance. The analysis of varying operating modes indicates that a variety of design/operating mode parameters and configurations can be used to manage the thermal environment.

15.1 KEY ATTRIBUTE: LIMITED WATER ENTERING EMPLACEMENT DRIFTS

The processes that control the amount of water available to enter emplacement drifts in the potential repository are described in Sections 3 (Unsaturated Zone Flow) and 4 (Seepage) of the SSPA. Since the completion of the S&ER (DOE 2001 [DIRS 153849]), a variety of improvements to the unsaturated zone and seepage flow models have been made, and additional analyses have been undertaken to assess the possible effect of LTOMs on the uncertainties associated with the models. In particular, the LTOM analyses have addressed the coupled thermal-hydrologic-chemical-mechanical processes that influence the flow of water and the potential transport of radionuclides in the thermally affected region near emplacement drifts.

The results of the SSPA analyses generally indicate that the effects of the improved models on performance results are small, or that the assumptions used in the S&ER (DOE 2001 [DIRS 153849]) and the TSPA-SR (CRWMS M&O 2000 [DIRS 153246]) were conservative. In most cases, the effects of the improved models are less than the variability and/or uncertainty that was incorporated into the TSPA-SR (CRWMS M&O 2000 [DIRS 153246]). Similarly, the evaluations presented in the SSPA confirm that thermal effects on coupled hydrologic, chemical and mechanical processes on performance is less for LTOMs than for HTOMs. However, the differences between the HTOM and LTOM appear to be small for all of the processes analyzed.

The discussions that follow provide a brief synopsis of the SSPA results for each of the topics addressed:

Post-10,000-Year Climate Model–A post-10,000-year climate model has been developed for inclusion in supplemental TSPA analyses. The model of climate over the next 1,000,000 years incorporates alternating climate stages including intermediate, monsoon, interglacial, and three distinct full glacial stages. Each stage has been defined by a range of mean annual precipitation rates and temperatures. Full-glacial stages encompass about 21 percent of the next 1,000,000 years. Based on paleoecological and paleoclimatic records and analogue site data, the climate is expected to be cyclical within 400,000-year periods and the climate changes are assumed to relate to earth orbital precession and eccentricity parameters. The effect of the variable climate has been incorporated in the TSPA results presented in Volume 2 (McNeish 2001 [DIRS 155023]). Although the range of potential climates is broadly represented, uncertainties remain with respect to the timing, duration, and nature of climate changes over the next 1,000,000 years. Tectonic changes and other climate forcing functions

(such as the rain shadow effect caused by uplift of the Sierra Nevada Mountains) have remained relatively constant during the past 1 million years and are expected to remain so for the next 500,000 years, but may impact future climate at the 1 million year time scale.

Infiltration Rates for the Post-10,000-Year Climate Model–The predictions of future climate, precipitation, and resulting infiltration rates show that as climate changes from interglacial (modern) to monsoon, to intermediate (glacial-transition) to glacial, the mean precipitation and infiltration rates also increase. Updated estimates of net infiltration for 10,000 years to 1,000,000 years in the future have been developed based on the precipitation rates and temperatures predicted for each future climate state. Relatively high net infiltration rates occur generally in the northern portion of the site at high elevations and along ridges where fractured bedrock is exposed. The uncertainty in net infiltration from imperfect knowledge of input parameters has been quantified for the intermediate (glacial-transition) climate, the dominant climate in the next 1,000,000 years. These results are included in the performance assessment analyses described in Volume 2 (McNeish 2001 [DIRS 155023]).

Flow in the Non-Welded Paintbrush Tuff (PTn)–Additional analyses of flow in the PTn have been developed to test simulation models by comparing their results to available data and revising the models where appropriate. These analyses included the use of chloride data to evaluate the distribution of net infiltration with isotropic permeability within the PTn; the use of a detailed two-dimensional model of the PTn to evaluate the importance of lateral flow due to capillary barrier diversion within the unit; and analyses developed to resolve the difference between the net infiltration distribution above the PTn and the calibrated net infiltration distribution below the PTn. The high matrix porosity and low fracture frequency in the tilted, non-welded PTn can effectively damp out episodic infiltration pulses and divert percolating water to the intercepting faults and fault zones. The evaluations also suggest that lateral flow within the PTn hydrogeologic unit may lead to a relatively uniform percolation distribution below the PTn. The relatively uniform percolation (which is consistent with observations and the chloride data) may reduce the variability and associated uncertainties in assessments of unsaturated zone waste-isolation capacities.

Three-Dimensional Flow Fields–New three-dimensional flow fields have been developed to support analyses of an expanded repository layout including a southern repository extension, further analyses of a steep hydraulic gradient near the northern end of the repository footprint, variable thickness of PTn and fault property uncertainty. Uncertainties in boundary conditions (especially the infiltration rates and distributions) and in rock properties contribute to uncertainties in the three-dimensional flow fields. Sensitivity and bounding studies were used to identify and quantify uncertainties. Unsaturated zone model results have been compared with data and evaluated to test the sensitivity of the model to processes, parameters, alternative conceptual models, and other numerical approaches. These evaluations indicate that the unsaturated zone model incorporates site characteristics and important processes in a manner that is consistent with observations and test results, providing confidence in the unsaturated zone flow model.

Effects of Lithophysal Porosities–The effects of lithophysal porosities on thermal properties were analyzed and indicate that the lithophysal cavities reduce the effective thermal conductivity and the thermal capacity of the matrix continuum in the upper-lithophysal (tsw33) and

lower-lithophysal (tsw35) hydrogeologic units. For the same thermal load, explicitly accounting for the effects of lithophysal cavities leads to an increase in temperature caused by heat released over the same period. These updated properties have been incorporated in performance assessment analyses described in Volume 2 (McNeish 2001 [DIRS 155023]).

Mountain-Scale Thermal-Hydrologic Effects–The mountain-scale thermal-hydrologic models provide analyses of temporal and spatial variability in the unsaturated zone conditions under thermal loads. The S&ER (DOE 2001 [DIRS 153849]) describes an operating mode with an initial thermal load of 72.7 kW/acre (1.45 kW/m of drift), and a forced ventilation period of 50 years, during which 70 percent of the decay heat was assumed to be removed. To lower the drift wall temperature below the boiling point, a lower areal thermal load (57 kW/acre or 1.13 kW/m of drift), longer forced-ventilation period (300 years), and higher heat-removal efficiency (80 percent) are evaluated. Induced temperature changes have effects at drift walls, within the pillars, at perched water bodies, at the water table, and throughout the unsaturated zone system. The coupled thermal-hydrologic processes can change the extent of two-phase and dryout zones around the drifts, induce large liquid and gas flux in the near- and far-field environments, redistribute the moisture, and affect the drainage potential through the pillars. Thermal conductivity and heat capacity of the rock mass are modified to account for the lithophysal porosity in the tuff matrix properties. For the lower-temperature cases, the thermal-hydrologic models predict little change in unsaturated zone liquid flux except in the immediate vicinity of the potential repository drift. Because boiling conditions do not occur, and the fractures are not completely dry, the mountain-scale thermal-hydrologic model predicts reduced (but nonzero) flow crossing the repository horizon throughout the thermal-loading period (about 2,000 years). Uncertainties in the unsaturated zone flow system model contribute to uncertainties in the mountain-scale thermal-hydrologic processes.

Mountain-Scale Thermal-Hydrologic-Chemical Effects–The mountain-scale thermal-hydrologic-chemical model has been updated and used to evaluate how coupled thermal-hydrologic-chemical processes may affect rock properties and flow and transport processes at the mountain or potential repository scale. The updated model incorporates new thermodynamic and kinetic parameters, calibrated against drift-scale heater tests, and water chemistry data from matrix pore water collected near the ongoing drift-scale test. Temperature dependent processes such as condensation and dryout/boiling have been analyzed, as have the effects of elevated temperatures on reaction rates and the thermodynamic stabilities of minerals. The updated analyses have also considered the effect on pH, mineral-water reactions, and reaction rates caused by the release of carbon dioxide out of water and transport in the gas phase via advection and diffusion. Uncertainties in flow processes (including gas convection, liquid flow focusing, and diversion) and data have been studied. Data uncertainties analyzed include thermodynamic and kinetic data of vitric and zeolitic tuffs, precipitating mineral assemblages, effective mineral-water reactive areas in heterogeneous unsaturated fracture rocks, fracture and lithophysal hydrologic properties, and distributions of water and gas chemistry in the unsaturated zone and in the infiltrating water. Sensitivity studies were conducted to understand the impact of thermal-hydrologic-chemical processes on mineral changes during thermal periods in the zeolitic CHn, on matrix porosity reduction in the TSw, on enhanced precipitation at the edges of the potential repository block with gas convection, and on many other thermal-hydrologic-chemical effects. These analyses indicate that the effect of thermal-hydrologic-chemical processes such as mineral precipitation and dissolution on hydrologic properties and percolation flux are not

significant compared to the changes in flow processes and rates caused by the thermal-hydrologic effects described above. The overall range in chemistry is comparable to that observed in previous analyses. The ranges in pH of about 7 to 9 are strongly linked to changes in gas-phase carbon dioxide concentrations. In the center of the repository, pH tends to be higher (and carbon dioxide lower) than near the edges of the repository.

Mountain-Scale Thermal-Hydrologic-Mechanical Effects–A new coupled thermal-hydrologic-mechanical model was developed to calculate the impact of thermal-hydrologic-mechanical processes on flow at the mountain scale. The mechanical behavior of porous and fractured media responds to changes in temperature, in effective stress, and in strain, resulting in permeability, porosity, and flow-field changes. The model results indicate that mountain-scale changes to hydrologic properties are moderate. Nevertheless, uncertainties in the thermal-hydrologic-mechanical model contribute to uncertainties in the thermal-hydrologic model, and further work is ongoing to build confidence in the models.

Effect of Flow-Focussing on Seepage–Analyses were conducted to investigate flow-focussing within the heterogeneous permeability field and the effects of episodic infiltration. The studies used a stochastic fracture continuum model to evaluate flow focusing through fractures from the bottom of the PTn to the potential repository horizon. These studies were carried out using a 100-m wide and 150-m deep two-dimensional cross section covering the upper five TSw hydrogeological units at Yucca Mountain. Heterogeneous fracture permeability distributions were generated using a stochastic approach conditioned on field-measured air-permeability data. The studies considered various percolation fluxes, correlation lengths, and uniform and nonuniform percolation-flux boundary conditions. The results provide a quantitative analysis of flow focusing. All simulation results indicate that the flow focusing factor is likely to be much smaller than the value used in previous TSPA calculations (CRWMS M&O 2000 [DIRS 153246]); therefore, the TSPA calculations are conservative with respect to flow focusing issues, since they use a flow focusing factor that may be an order of magnitude higher than that suggested by the new studies. In addition, the sensitivity analyses indicate that frequency distributions of normalized flux are insensitive to the magnitudes or spatial distributions of percolation fluxes specified on the upper boundary or to the spatial correlation structure of the permeability fields within the unsaturated zone.

Effects of Drift Degradation and Rock Bolts on Seepage–Drift degradation and the impact of rock bolts were investigated in order to quantify uncertainty in seepage rates associated with those processes. The studies indicate that there is no significant enhancement of seepage caused by intact or degraded rock bolts, and that rock bolts may be neglected as a seepage-enhancement factor for performance assessment. The studies also indicate that seepage enhancement due to drift degradation processes is relatively small (on the order of 0 to 5 percent).

Thermal-Hydrologic Effects on Seepage–Thermal effects on seepage were examined through a modeling study that assessed model uncertainties regarding grid resolution and heterogeneity. The study also examines the impact of lithophysal cavities on thermal properties, the potential for liquid water to penetrate superheated region, causing episodic seepage events, and the development of a vaporization barrier. Moreover, percolation flux was calculated for a range of thermal operating modes.

The updated model considered thermal expansion as well as dissolution and precipitation of minerals that could lead to changes in fracture aperture and fracture coatings, potentially affecting the unsaturated hydrogeologic properties, fracture-matrix interaction, and the flow of liquid water or water vapor near drifts. Conceptual and parametric uncertainties in the model have been examined through extensive sensitivity analyses. These studies suggest that the simplifying assumptions contained in the seepage abstraction for performance assessments are conservative (i.e., they yield seepage estimates that are higher than the process model results).

Thermal-Hydrologic-Chemical Effects on Seepage–Thermal-hydrologic-chemical processes may impact seepage through thermally induced changes in unsaturated hydrogeologic properties. Additional validation studies were performed, enhancing the confidence into the thermal-hydrologic-chemical modeling approach. Sensitivity analyses were performed, examining different in-drift designs, different, heterogeneous host rock units, different systems of components and minerals, different kinetic models for mineral-water interactions, different permeability-porosity relations during precipitation and dissolution, and changed thermodynamic data and initial conditions. All these studies helped reduce conceptual uncertainties in the thermal-hydrologic-chemical models. Additional studies of coupled processes were performed for an extended range of temperatures, covering various thermal operating modes. The evaluations indicate that thermal-hydrologic-chemical effects on flow are small compared to the ambient variability around emplacement drifts for the HTOMs, and even smaller for the LTOM.

Thermal-Hydrologic-Mechanical Effects on Seepage–In support of the TSPA-SR (CRWMS M&O 2000 [DIRS 153246]), a distinct-element analysis was performed to examine thermal-mechanical effects of drift excavation and repository heat on hydrogeological properties. This analysis has now been revised and extended to provide a more robust estimate of thermal-mechanical effects in fracture permeability. The evaluations indicate that thermal-hydrologic-mechanical effects on flow properties are small compared to the ambient variability around emplacement drifts for the HTOMs, and even smaller for the LTOM. In addition, a fully coupled thermal-hydrologic-mechanical continuum model was developed and calibrated against air-permeability data from three niches and the Drift Scale Heater Test area. The successful calibration increased confidence in the conceptual model and reduced uncertainties in the subsequent prediction runs, which included two thermal operating modes.

15.2 KEY ATTRIBUTE: LONG-LIVED WASTE PACKAGE AND DRIP SHIELD

The processes affecting the life span of the drip shield and waste package in a potential repository are described in Sections 5 through 8 of this volume of the SSPA. Important processes include the water diversion performance of the engineered barriers, the distribution of moisture within the drifts, and drip shield and waste package degradation performance, which are a function of the physical (temperature and relative humidity) and chemical environment within the drifts. The SSPA describes a variety of analyses undertaken primarily to quantify some of the uncertainties in the analyses described in the S&ER (DOE 2001 [DIRS 153849]), and to assess the impact of a LTOM. In general, although the uncertainties are significant, the results of the analyses suggest that the representations of processes included in the TSPA-SR (CRWMS M&O 2000 [DIRS 153246]) and the S&ER (DOE 2001 [DIRS 153849]) are conservative.

The effects of numerous processes and properties on water movement, in-drift physical and chemical environment, and drip shield and waste package performance were addressed through extensive sensitivity and uncertainty analyses presented in the SSPA. These evaluations indicate that models of the physical environment in the drifts (e.g., temperature and relative humidity) are sensitive to the thermal properties of the rock mass, especially lithophysal porosity, and to some of the operating mode variables that can be used to manage the thermal environment, such as the efficiency of ventilation in removing heat. Differences between alternative thermal models have been examined.

Corrosion and degradation rates for drip shields and waste packages are also sensitive to the chemical environment in the drifts, which can be affected by the composition of dust in the underground environment, as well as the chemical composition of seepage waters that may contact the engineered barriers. The evolution of water chemistry as fluids evaporate in the drift also affects the potential for degradation.

A model for early failures of waste packages has been developed and included in the TSPA-SR (CRWMS M&O 2000 [DIRS 153246]). This non-mechanistic model is based on a scenario in which improper heat treatment leads to the early failure of a small fraction of waste packages. In contrast, the inclusion of temperature dependence in degradation models has a significant positive effect on long-term assessments of waste package performance. Reduced corrosion rates associated with declining temperatures after the first few thousand years may result in increased package lifetimes, and improved performance compared to the models used for the TSPA-SR (CRWMS M&O 2000 [DIRS 153246]).

Overall, the analyses indicate little difference between LTOMs and HTOMs for waste package performance. The reason for the similarity is that few packages fail during the first few thousand years in either case. Waste packages emplaced in a LTOM repository would not experience physical (temperature, relative humidity) or chemical conditions favorable for corrosion. Waste packages emplaced in a HTOM may experience physical conditions in which crevice corrosion could occur for up to a few thousand years, but the aggressive chemical conditions necessary for crevice corrosion are not likely to occur.

Multiscale Thermal-Hydrologic Model, Including Effects of Rock Dryout–The multiscale thermal-hydrologic model was updated to incorporate improved representations of the thermal processes affecting flow in and near emplacement drifts, and to assess the effect of LTOMs on repository performance. Temperature-humidity conditions on typical pressurized water reactor waste package surfaces were analyzed for the HTOM and LTOM cases. All geographic locations (edge, corner, and center) were included for the two operating modes. Temperature-humidity conditions progress over time, ending at ambient conditions of about 25ºC and 100 percent relative humidity. The LTOM results in lower relative humidity for any given temperature, or lower-temperature for any given relative humidity for most locations. The range of temperature-humidity conditions over time was compared to the environmental conditions in which Alloy-22 may be susceptible to initiation of crevice corrosion. As defined in the SSPA, this region of susceptibility is more conservative than that defined within the *License Application Design Selection Report* (CRWMS M&O 1999 [DIRS 103955], Figures 5-18, 5-32 and 6-1). Based on the deliquescence point of sodium nitrate, and the conservative assumption that stress corrosion cracking can occur in an environment which would sustain a stable water film, the

region of susceptibility is defined by a lower temperature of between 85ºC and 90ºC and by relative humidity of 20 to 70 percent (determined by which salts may be present on the waste package surface). LTOM waste packages are nearly always at temperatures below the window of crevice corrosion susceptibility. In contrast, the HTOM waste package corrosion analyses must include evaluation of crevice corrosion for at least 3,000 years after emplacement when the temperatures drop to below 80ºC.

Sensitivity to Thermal Property Sets, and Effect of In-Drift Convection on Temperatures, Humidities, Invert Saturations, and Evaporation Rates–Analyses were conducted using submodels of the multiscale thermal-hydrologic model to consider the sensitivity to operational parameters and to the uncertainty and variability of properties of the natural and engineered systems. These analyses considered the HTOM and the LTOM. The focus was on the effects of heat-driven coupled-processes on in-drift thermal-hydrologic conditions. The environmental conditions considered include temperature and relative humidity at the waste packages and drip shield, and saturation at the drift wall and in the invert.

Peak temperatures at the drip shield and waste package were most sensitive to ventilation parameters and to thermal conductivity used in the models. The uncertainty in host rock thermal conductivity had the most significant effect. The drift wall and drip shield peak temperatures had a range of 85 and 20°C (for the HTOM and LTOM) resulting from a thermal conductivity range of 1.13-2.01 W/m•K (saturated) and 0.54-1.54 W/m•K (dry). The key factor determining the spatial variability of thermal conductivity is the variability of lithophysal porosity. The range of drift wall and drip shield temperatures was about 100 and 25°C (for the HTOM and LTOM) when a range of 0 to 25 percent of lithophysal porosity was used. The increase in temperature was due to the additional effect of porosity on heat capacity, in addition to the effect on thermal conductivity.

The second most significant factors were those related to ventilation. There was a range of about 60°C (for the HTOM and LTOM) in pre-closure peak drip shield temperatures resulting from using constant versus time-dependent ventilation efficiency. A 14° and 7°C postclosure drip shield temperature range (for the HTOM and LTOM, respectively), resulted from a 20 percent variation in ventilation efficiency (heat removal). For the LTOM, it was concluded that a 44-year variability in ventilation duration from one part of the repository to another would have only a minor effect on postclosure temperatures.

The important uncertainties resulting from using two-dimensional analyses were also quantified. The detailed three-dimensional analyses of in-drift thermal-hydrologic effects calculated 26° and 8°C ranges (for the HTOM and LTOM, respectively) in postclosure peak temperatures from the hottest to the coolest waste packages.

The ventilation efficiency was calculated using two independent models, and compared to the quarter-scale tests. The models, which used a wide range of convective heat transfer coefficients, bracketed the measured results. The influence of water entering the drift and evaporating into the dry ventilation air was not significant on overall ventilation efficiency, and had only a minor effect on ventilation air humidity.

A number of other parameters were investigated, including the effect of lithophysal porosity on gas storage, seepage effects on in-drift humidity, imbibition hysteresis, buoyant gas-phase convection in the rock, thermal-hydrologic-chemical and thermal-hydrologic-mechanical processes, host rock permeability, invert conductivity, and treatment of thermal radiation and natural convection in the drift. These parameters had only small effects on the magnitude of in-drift temperatures. However, the invert conductivity and the sophistication of natural convection models were found to influence which part of the Engineered Barrier System are cooler than others, with potential influence on formation of condensate which could be the source for corrosion or transport.

Finally, multiple approaches to achieving LTOM temperatures were evaluated. Derating pressurized water reactor waste packages was the most effective method of reducing peak temperatures, followed by waste package spacing and finally, drift spacing (for line-loaded drifts). However, the range of temperatures among these methods was small (within 7°C); therefore, other factors may determine the selection of a design/operating mode for the license application.

Composition of Water and Gas Entering Drift–Thermal-hydrologic-chemical seepage models were used to predict the composition of waters and gases that could enter potential waste emplacement drifts. Modeled thermal-hydrologic-chemical processes are complex, and the number and variability of model input parameters are large. For this reason, a rigorous quantification of model uncertainty is not achievable, and thermal-hydrologic-chemical modeling work performed to date has concentrated on limiting and qualitatively assessing uncertainty. Uncertainties affecting the predicted composition of fluids that could enter drifts were evaluated. These were related primarily to infiltration rates, thermodynamic and kinetic data, pore water and infiltration-water compositions, boundary carbon dioxide partial pressures, potential repository thermal operating modes, and potential repository host rock units. Input thermodynamic and kinetic data were identified as some of the main model uncertainties. These uncertainties can be minimized by model validation and calibration against field and experimental data. In such case, the uncertainty in initial and infiltration water compositions input into the thermal-hydrologic-chemical seepage models may overwhelm other model uncertainties. Relative to the variability in possible model input water compositions, predicted water compositions were not very sensitive to the investigated ranges of boundary carbon dioxide partial pressures, repository host rock units, or infiltration rates. The largest predicted effect of thermal loading on water compositions was decarbonation through volatilization of carbon dioxide. This is a common heating effect observed in natural geothermal systems. However, carbon dioxide concentrations in fractures around the drift are not predicted to reach high values (typically less than 4,000 ppmv). Higher-temperatures increase the variability of predicted concentrations at the drift wall, relative to lower temperatures. However, heating effects are predicted to be relatively short-lived. As temperatures decrease and return to ambient values (within 100,000 years), the predicted water compositions at the drift crown return to ambient values. At large liquid saturations around the drift (which would be most favorable to water-rock interaction and potential seepage into the drift), no extreme pH or salinity values were predicted.

Evolution of In-Drift Water Chemistry–The in-drift chemical environment was evaluated for uncertainty while attempting to provide more consistency between process model outputs

supporting the TSPA analyses. Three submodels are used in the uncertainty analyses: the precipitates/salts model, the microbial communities model, and the in-drift (applied in the invert) water mixing model. All three of the submodels integrate geochemical inputs (e.g., water fluxes and chemical compositions) in a more consistent manner than prior calculations while supporting the TSPA.

- **Precipitates/Salts Model**–This model extends a model of brine concentration to combinations of chemical concentration and composition for which few calculations have been effective in the past. This allows quantitative prediction within validation criteria of the kind of solutions or salt precipitates that are available for metallic corrosion and geochemical interaction in the drift. Model validation has demonstrated that given accurate inputs for starting water and gas compositions, the precipitates/salts model will likely provide results that are within a factor of two for chloride concentrations and ionic strength and within a pH unit for pH predictions.

- **Microbial Communities Model**–This model provides bounding estimates through time of the numbers of potential microbes that could grow in the repository drift, while evaluating uncertainty from: drift temperature, relative humidity, water chemical concentrations, gas fugacities, and the percolation flux through time. Current model output indicates few significant changes compared to TSP SR (CRWMS M&O 2000 [DIRS 153246]), because of the conservative assumptions formerly employed.

- **In-Drift Water Mixing Model**–This model is designed to mix three different chemical solutions with differing water fluxes (crown, invert, and waste package) to determine the mixed solution pH, and ionic strength. At the same time, the in-drift water mixing model is used to evaluate the uncertainty from the percentage of fluid leaked from waste packages that mixes with other water sources in the invert. Such analyses indicate waste package leaking must be hundreds of times greater than presently calculated at the 50,000 year time step in the TSPA to produce mixed acidic waters which can enhance transport of radionuclides. These three submodels are used to determine the chemical conditions, over thousands of years up to a million years, that are used for the calculation of radionuclide releases from the Engineered Barrier System.

Thermal-Hydrologic-Chemical Model Comparison to Plug Flow Reactor and Fracture Plugging Experiment–Thermal-hydrologic-chemical simulations of a plug-flow reactor tuff dissolution experiment were performed. Using the same thermodynamic and kinetic data, as well as the same rock mineralogy and geochemical components as those used in the thermal-hydrologic-chemical seepage models, these simulations yield relatively good agreement between measured and predicted water compositions. Although the length of the modeled experiment (two months) is likely too short to fully assess the uncertainty of the thermal-hydrologic-chemical seepage model over thousands of years, this work improved the confidence in the thermal-hydrologic-chemical seepage models and their input thermodynamic and kinetic data.

Effects of Fracture Size and Spacing on Drift Degradation–The uncertainties associated with the extent of fracture planes and the spacing of subhorizontal joints in the rockfall model have been analyzed. The quantification of these uncertainties provides additional confidence that the model for rockfall can adequately predict the size ranges and quantities of rock that may fall into

emplacement drifts. The sensitivity analyses for the rockfall model presented in this report confirm the appropriateness of the analysis parameter selection in the *Drift Degradation Analysis* (CRWMS M&O 2000 [DIRS 151635]). These sensitivity analysis results indicate no impact to the repository subsystems potentially affected by rockfall.

Evaporation of Seepage Contacting the Drip Shield–The heat contained in the waste package has the potential to evaporate a portion of in-drift seepage that might contact the drip shield. An updated model provides an estimate of the fraction of this heat needed to evaporate seepage as it contacts the drip shield. Drip shield evaporation depends on a number of parameters: waste package heat evolution, forced air ventilation of the preclosure period, natural ventilation during the postclosure period, and drip shield surface conditions. More evaporation will occur in the HTOM. The updated process model is based upon a flow splitting algorithm that included flux into breaches and away from breaches in the drip shield. No credit is taken for potential evaporation at the surface of the drip shield. Consideration of this process potentially reduces the amount of seepage available for transport through the Engineered Barrier System. Alternative thermal operating modes are addressed by assuming two different temperature and relative humidity distributions for the HTOMs and LTOMs. The impact on the amount of seepage available for transport over the range of thermal operating modes can be inferred from the time histories of time-dependent fluxes through the Engineered Barrier System (drip shield, waste package, and invert).

Condensation Under Drip Shields–This updated model quantifies the condensate flux on the underside of the drip shield due to evaporation and addresses what fraction will fall on the waste package. The model was developed for the original Engineered Barrier System flow abstraction, but was not included in subsequent calculations. This activity is only meant to supplement the rationale for screening out this process due to low consequence. Alternative thermal operating modes do not affect the conceptual model for condensation on the underside of the drip shield and waste package.

Effect of Breached Drip Shields or Waste Packages–The waste package degradation model provides for predictions of the type, number, and timing of breaches in the drip shield and waste package. This information is used by the Engineered Barrier System water diversion abstraction to define the time-dependent fluxes that flow through (or are diverted around) the drip shield and the waste package. In this model, droplets fall randomly onto a drip shield, and the model accounts for a random fraction of water that flows over the drip shield but is captured by breaches. The abstraction implemented in the TSPA-SR (CRWMS M&O 2000 [DIRS 153246], Section 3.6.3.1) conservatively considered all of the seepage entering the drift as falling on the crown of the drip shield and that all fluid that drips onto the drip shield or waste package occurs at the same axial location as the breach. This analysis did not address alternative thermal operating modes, but was used to quantify conservatism in the TSPA-SR (CRWMS M&O 2000 [DIRS 153246]).

Waste Package Release Flow Geometry (Bathtub, Flow-through)–An alternative conceptual model to the flow-through geometry is the bathtub geometry, which allows seepage to collect in the waste package before being released to the Engineered Barrier System. This effect will be most important during the first 20,000 years. At longer durations (100,000 years or greater), the presence of multiple penetrations for multiple groups of waste packages makes a flow-through

geometry the likely long-term configuration. This model provides estimates of the time delays for the bathtub versus the flow-through model and an approach to quantify the uncertainty and sensitivity of TSPA results to the bathtub versus the flow-through conceptual model. Alternative thermal operating modes will not affect the conceptual model for flow through the waste package.

Environment on Waste Package and Drip Shield Surfaces–Previous analyses of the possible environments on the surfaces of the waste package and drip shield focused on carbonate-based dilute waters. These waters, when concentrated by evaporation, result in high pH brines. More recent analyses have included non-carbonate based dilute waters. These are similar to the pore waters in the host rock and, when evaporatively concentrated, evolve into near-neutral pH brines with dissolved calcium and magnesium ions. The presence of these cations in aqueous solution could result in the formation of calcium and magnesium chloride salt solutions that are stable at low relative humidities. However, calcium and magnesium ions in the solution would decrease significantly during evaporation by the formation of insoluble precipitates. Thus, large quantities of seepage water would need to be evaporatively concentrated in order to form an aggressive environment. Therefore, development of calcium or magnesium chloride salt solution on the waste package and drip shield surfaces will be limited under expected repository conditions. New analyses also included assessments of the effect of potentially deleterious minor constituents, such as lead. The measured concentrations of lead in the waters at Yucca Mountain are very low. In addition, a review of data in the literature shows that sorption of lead to the surface of minerals such as smectite and calcite will limit the amount of lead in solution. Evaporative concentration of Yucca Mountain waters has shown that lead is likely removed from the solution as lead-containing mineral precipitates, and, therefore, the amount of lead available in solution is expected to be insignificant.

Aging and Phase Stability–Aging and phase stability of Alloy 22 was reevaluated using new data and analyses. These analyses confirm the prior conclusion that aging of the Alloy 22 waste package outer barrier will not pose a problem. Since this conclusion is based on limited data, alternative lines of evidence were evaluated, including mechanical property changes due to aging, natural analogues, and theoretical modeling. All of these corroborate the conclusion that for the estimated peak waste package temperatures of 200°C or lower, aging effects such as long-range ordering or grain boundary and bulk precipitation of secondary phases will not affect waste package performance.

Stress Corrosion Cracking–In the case of stress corrosion cracking of the Alloy 22 barrier, new analyses were conducted to quantify the uncertain parameters and remove conservatisms in the previous analyses. Based on new data, literature reviews, and analyses, models of the residual stress uncertainty, the threshold stress for stress corrosion cracking initiation, and the orientation of manufacturing flaws were revised. In addition, the analyses included an evaluation of the effects of temperature on stress corrosion cracking, which showed that there is currently no basis for establishing a temperature threshold for stress corrosion cracking. Some of the new data evaluated included stress corrosion cracking test data on Alloy 22 in solutions containing lead. The data show that under very aggressive (unrealistic) conditions (pH of 0.53, 250°C, and 1,300 ppm lead), Alloy 22 may fail because of stress corrosion cracking. However, tests under conditions relevant to Yucca Mountain (1 weight-percent lead in mixed-ion solutions at a pH

of 2.7 and 76°C) show no stress corrosion cracking failures. Overall, the technical bases for the stress corrosion crack model were improved with the new data and analyses.

Long-Term Passive Film Stability of Alloy 22–In TSPA-SR (CRWMS M&O 2000 [DIRS 153246]), data from relatively short-term tests (two years of exposure) were used to estimate the general corrosion rate of Alloy 22. Extrapolation of two-year data to predict performance over thousands of years was based on the assumption that the passive film on the surface would remain stable over a long period. To reduce the uncertainties associated with this assumption, a comprehensive testing and analysis program has been initiated. A mechanistic conceptual model for predicting the behavior of the passive film has been developed, and this conceptual model, along with associated model parameters, is being implemented into the passive film stability model. Preliminary calculations have been performed using values for model parameters that are based on stainless steels in nuclear power plant piping. A testing program is underway to provide data relevant to Alloy 22 for the conditions expected in the potential repository. When completed, the passive film stability model will be incorporated into the integrated waste package degradation model to analyze the effects of long-term passive film stability on waste package performance. The current model indicates that the passive film on Alloy 22 would remain stable under the exposure conditions expected in the potential repository. Data from ongoing testing programs and detailed mechanistic modeling will provide useful information to determine the long-term stability of the passive film under repository-relevant exposure conditions.

General Corrosion of Alloy 22–Previous analyses of Alloy 22 general corrosion were based on data from weight-loss measurements on samples exposed for approximately two years. Because of the low corrosion rates in the material, the data showed significant uncertainties that are due mostly to measurement uncertainty. As a result, the data showed no discernible effects of temperature, environment, or exposure times on corrosion rates. New analyses based on new electrochemical data have been conducted to evaluate the effects of temperature on the Alloy 22 general corrosion rate. While the correlation developed is based on limited data over a small temperature range, the model provides a basis for evaluating waste package performance over ranges of time and location in the potential repository. The updated model indicates that inclusion of temperature dependence in the process models for waste package degradation will result in decreased corrosion rates, and longer waste package lifetimes, than previous analyses. The increased lifetimes are reflected in the performance analyses described in Volume 2 (McNeish 2001 [DIRS 155023]).

Early Waste Package Failure: Improper Heat Treatment–For the TSPA-SR (CRWMS M&O 2000 [DIRS 153246]) model, an extensive literature review was conducted to identify scenarios or conditions that could lead to early failure of waste packages. Mechanisms that could lead to early failure, except for weld flaws in the closure weld area, were considered but not included in the TSPA-SR model. This exclusion was based on the low probability of the individual mechanisms and the planned use of administrative controls to further reduce the likelihood of early failure mechanisms. In reevaluating the potential for early failure mechanisms and their potential consequences for the SSPA, a more conservative approach was adopted. This approach resulted in the inclusion of an improper heat treatment event which conservatively results in the subsequent failure of the waste packages in the supplemental total system performance analyses described in Volume 2 (McNeish 2001 [DIRS 155023]). This

non-mechanistic model results in the early failure of a small fraction of the waste packages. To ensure that the potential consequence of early waste package failures is treated conservatively, it is included in the nominal scenario for the performance assessment, not as a sensitivity analysis. The analysis results show that the probability of having at least one waste package improperly heat-treated in the potential repository is 20.2 percent, and the probability of having two waste packages affected is 2.6 percent. Assuming a total of 100 realizations for the waste package degradation analysis model, those probabilities provide that about 77 out of 100 realizations would have no waste packages affected by improper heat treatment. Out of 100 realizations, about 23 realizations would have at least one waste package affected.

15.3 KEY ATTRIBUTE: LIMITED RELEASE OF RADIONUCLIDES FROM THE ENGINEERED BARRIERS

The processes that influence the potential dissolution and transport of radionuclides that could occur after a waste package is breached are described in Sections 9 and 10 of the SSPA. As described in the S&ER (DOE 2001 [DIRS 153849]), the key processes affecting performance include the degradation of spent fuel cladding, and commercial and DOE high-level radioactive waste glass, which depend on the chemical environment inside the waste package. After the spent fuel or high-level radioactive waste glass is degraded, the processes controlling repository performance include the dissolution or colloid associated suspension of radionuclides, and the potential transport of radionuclides through the package and the engineered barrier system.

In the SSPA, analyses of uncertainties in transport processes within the Engineered Barrier System were performed to provide insight into the uncertainties recognized in the S&ER (DOE 2001 [DIRS 153849]). In general, these analyses indicate that uncertainty in the relevant processes either did not significantly affect performance (e.g., high-level radioactive waste glass dissolution rates, cladding degradation) or that the assumptions used in the TSPA-SR (CRWMS M&O 2000 [DIRS 153246]) were conservative (e.g., radionuclide solubilities). In addition, several improved process model representations (e.g., neptunium solubility, diffusion inside the waste package) were developed and implemented in the TSPA described in Volume 2 (McNeish 2001 [DIRS 155023]). These updated models replaced conservative representations in the TSPA-SR (CRWMS M&O 2000 [DIRS 153246]), generally resulting in delays in releases of radionuclides from the Engineered Barrier System.

Lower-temperature operating modes do not have a significant effect on glass degradation rates, radionuclide solubilities, diffusion or other transport processes within the engineered barriers. These processes only occur after waste packages are breached, which is generally at a time when the thermal differences between operating modes are negligible.

Effect of High-Level Waste Glass and Steel Degradation Rate on In-Package Chemistry– The effect of uncertainties in high-level waste and steel degradation rates on in-package chemistry was evaluated in a series of sensitivity studies wherein a wide range of waste form component degradation rates were used as input into reaction-path calculations. This allowed better quantification of the limits of fluid compositions likely to prevail in breached waste packages. Changing the input reaction rates has the effect of altering the assumed proportion of waste form components with which incoming fluids might react. Consequently, this approach allows an assessment of the effects of heterogeneous inflow contact with waste form materials on

in-package chemistry and the effect of uncertainties in the input degradation rates on in-package chemistry. Reaction-path outputs suggest only minor deviations from earlier predictions of in-package chemistry bounds. One exception is the case of zero dissolution of A516 steel wherein the minimum in-package pH tends to drop down to between pH 2 and 3, which increases the abstracted uncertainty range.

Effect of Creep Rupture, Localized Corrosion, Seismic Failure, Rock Overburden Failure, and Unzipping Velocity on Cladding Degradation–An improved irradiated cladding creep correlation and failure criteria were developed. The localized corrosion model was improved to include corrosion in damp waste packages (no dripping) and a less conservative cumulative complementary distribution function. A sensitivity study showed little effect from a more precise seismic frequency curve for cladding damage. The effect of cladding failure from a rock overburden after waste package degradation has been added.

U.S. Department of Energy High-Level Radioactive Waste Degradation Rates–The effect of variable DOE high-level radioactive waste degradation on in-package chemistry was assessed in a series of reaction-path calculations that used as input a spectrum of different DOE high-level radioactive waste degradation rates. Degradation of DOE high-level radioactive waste might occur at different rates due, for example, to the buildup of reaction-limiting secondary mineral phases at the glass-solution interface. Calculations indicated that DOE high-level radioactive waste rates lower than the values presently used result in a pH range in the in-package fluids that is substantially less alkaline. This pH-lowering works against radionuclide transport in some cases (i.e., when pH is lowered from 10 to 9), but more favorable in others (e.g., if pH is lowered from 4 to 3). The latter scenario has been used to expand the abstracted uncertainty range in in-package pH. New, more detailed abstractions of pH-time trajectories were developed for commercial spent nuclear fuel and codisposal waste forms.

Solubility of Neptunium, Thorium, Uranium, Plutonium, and Technetium–The solubilities of thorium, plutonium, and technetium were more closely examined using a much wider variety of in-package scenarios than the conservative bounding case considered in the TSPA-SR (CRWMS M&O 2000 [DIRS 153246]). The latter assumed uniformly oxidizing conditions and that amorphous, hydrated oxide minerals controlled the dissolved levels of thorium and plutonium as opposed to the more crystalline phases that might form over longer periods of time. Pooling of water and degradation of metallic in-package components might cause lower oxygen fugacities to prevail, thus stabilizing reduced forms of plutonium and technetium. Moreover, long periods of reaction might favor the conversion of soluble oxide minerals to thermodynamically stable, but less soluble, oxides. Sensitivity tests showed that the presence of less soluble oxides and lower oxygen fugacities lead to predictions of much lower dissolved concentrations of thorium, plutonium, and technetium.

A new model of neptunium release from fuel was calibrated using solid solution analysis and neptunium concentrations derived from ongoing fuel degradation tests at Argonne National Laboratory and Pacific Northwest National Laboratory.

Colloid Mass Concentrations–Unquantified uncertainties in the waste form colloid model were examined to more closely model colloidal uptake of radionuclides. The number of corrosion product colloids were combined with the groundwater colloid abundance and their sum assigned

an uncertainty distribution. The mean value was based on deep groundwater analyses. A log normal distribution of radionuclide sorption K_ds was then developed. A probability distribution was likewise developed to describe irreversible sorption of plutonium on waste form colloids.

Diffusion Inside Waste Package–The current TSPA-SR (CRWMS M&O 2000 [DIRS 153246]) transport model for the waste package conservatively assumes that all radionuclides released by the waste form are immediately available to diffuse through any breaches in the package. This approach is equivalent to assuming instantaneous in-package diffusion. A new model for diffusion inside the waste package was developed that incorporates information on the adsorption of water vapor on iron-(hydr)oxides, on Zircaloy oxides, and on nickel oxide, which are anticipated to exist in the waste package once corrosive processes begin after the package is breached. The model calculates diffusion rates through the films of water adsorbed onto corrosion products. The general approach for commercial spent nuclear fuel waste packages is to consider three limiting pathways for diffusion: along failed fuel rods, through porous corrosion products inside the package, and through porous corrosion products filling breaches (either stress corrosion cracks or general corrosion patches) in the outer layer of the waste package. The diffusive flux for releases along failed fuel rods and through corrosion products within the package is calculated, and the larger of these two is selected (radionuclides will diffuse along the fastest independent pathway that is available). Next, the diffusion rate through breaches in the package is computed. The smaller of the in-package diffusion rate and the breach diffusion rate is selected as the net diffusive release. This is reasonable because these pathways are sequential so the smallest diffusion rate will be the controlling parameter.

The model quantifies the impact of in-package diffusion on radionuclide transport for commercial spent nuclear fuel waste packages in a non-dripping environment.

Transport Pathway From Inside Waste Package to Invert–A detailed advective-diffusive transport model between the waste form and the invert has not been incorporated in performance assessment analyses. This approach is reasonable because three-dimensional predictions of relative humidity and waste package temperature are not currently available to the required level of detail, the effects of surface roughness and heterogeneity may be significant but have not been studied in detail, and there is a wide range in the maximum value of relative humidity that will prevent advective transport. Additional research on thin film flow is ongoing, and sensitivity results will be evaluated to determine the impacts from the other models introduced in this section.

Sorption Inside the Waste Package–Two approaches have been used to estimate ranges of partition coefficients in the engineered barrier system. The first approach utilizes median values and ranges for partition coefficients (K_ds) for americium, iodine, neptunium, plutonium, technetium, thorium, and uranium on typical soils and corrosion products, or under oxidizing conditions from a variety of sources. The second approach to estimating the appropriate ranges of values for partition coefficients is based on the concept of tolerance interval. Tolerance intervals provide a statistical estimate of parameter ranges at a given confidence level from a small data set. The final recommendations for partition coefficients and distribution type are based on a merging of these two approaches. At the low end, each range is based on the minimum value from the tolerance interval because it provides a 95 percent level of confidence using data for sand, loam and clays. At the high end, each range is based on the maximum value

for the corrosion products because the tolerance interval often has values that appear unusually high.

Sorption Inside the Invert–The approach for sorption inside the invert is identical to that for sorption inside the waste package, as discussed above.

Diffusion Through the Invert–The diffusion coefficient abstraction for the TSPA-SR (CRWMS M&O 2000 [DIRS 153246]) includes the effects of invert porosity, invert saturation, invert temperature, and the uncertainty in the experimental measurements for the diffusivity of granular materials. Analyses were conducted to evaluate conservatism in the dependence of diffusivity on porosity, to quantify conservatism in using the self-diffusivity of water as a bounding value for all radionuclides of interest for TSPA, and to evaluate uncertainty in using a volume averaged saturation for the invert versus a more detailed saturation gradient for diffusive transport. The formulation for the dependence of diffusivity on porosity for the TSPA-SR sensitivity studies reduces the diffusion coefficient by 32 percent in comparison to the value used in the TSPA-SR (CRWMS M&O 2000 [DIRS 153246]) at a porosity of 50 percent. The conservatism in using the self-diffusivity of water as a bounding value for the diffusion coefficient is a factor of 1.07 to 3.8, and is a function of the valence of the species. The uncertainty in using the volume-averaged saturation for the invert is very small because the invert saturation state beneath the waste package is almost uniform from the top of the invert to the bottom of the drift.

Colloid Stability in the Invert–The goal of this analysis is to quantify the impacts of uncertainties in the behavior of colloids generated from the degradation of high-level radioactive waste glass, commercial spent nuclear fuel, and DOE spent nuclear fuel, as well as colloid-facilitated transport properties of radionuclides in the engineered barrier system. The current TSPA-SR (CRWMS M&O 2000 [DIRS 153246]) model for generation and transport properties of colloids resulting from waste form degradation generally uses a bounding approach for incorporating relevant source data, and it uses conservative assumptions where the available data were thought to be limited. Uncertainties have been quantified for the combined concentrations of groundwater and corrosion colloids, for plutonium irreversibly attached to waste form colloids, and for the reversible sorption of plutonium and americium on waste form and groundwater colloids. The uncertainties in the combined concentrations of groundwater and corrosion colloids have been characterized for a low and a high range of ionic strength. Distributions for plutonium irreversibly associated with waste form colloids were selected to capture the potential uncertainty for and sensitivity to irreversible plutonium sorption in the present study, in a way that tests the entire ranges of values uniformly. Finally, a preliminary review suggested that the currently used K_d values for iron-(hydr)oxides (proxy colloid mineral for steel corrosion colloids) may be underestimated by as much as one to two orders of magnitude. Considering the large mass of iron-(hydr)oxides that may be present in the engineered barrier, it is reasonable to use the same distribution for K_ds that describe the sorption of plutonium and americium onto colloids. The recommended distribution for this study is a log normal distribution with a mean value of 10^5 mg/L and a standard deviation of two orders of magnitude.

Microbial Transport of Colloids–The goal of this model is to quantify the impact of potential microbial communities on sorption of radionuclides to microbes and the ability of microbes to be transported as colloids through the engineered barrier system. The transport of microbes through

the engineered barrier system is a function of the uptake of dissolved radionuclides onto the cell walls and the subsequent mobility of microbes through the waste package and invert. The representation of uncertainty for the microbial transport model is based on the distribution for uptake of uranium and plutonium on microbes. The uptake of uranium for sensitivity studies will be a triangular distribution with a range between 45.2 and 615 mg uranium/gm and with a median value of 111.33 mg uranium/gm. Plutonium and thorium are also expected to sorb onto microbes. Because there are no specific data for uptake of these two elements, the sampled value from the distribution for uranium uptake will be scaled to the relative abundances of plutonium and thorium versus that of uranium.

15.4 KEY ATTRIBUTE: DELAY AND DILUTION OF RADIONUCLIDE CONCENTRATIONS BY THE NATURAL BARRIERS

Sections 11 (Unsaturated Zone Radionuclide Transport), 12 (Saturated Zone Radionuclide Transport) and 13 (Biosphere) of the SSPA describe the processes that contribute to delaying and reducing the concentrations of any radionuclides that may be released from the potential repository. Important transport processes acting in the natural barriers beneath Yucca Mountain include the effects of a drift shadow (a zone of reduced water saturation below emplacement drifts) in the unsaturated zone, and matrix diffusion and sorption in both the unsaturated and saturated zones.

In the SSPA, a series of evaluations was performed to assess the sensitivity of flow and transport calculations to uncertainties in flow processes, and to variability and uncertainty in hydrologic properties in volcanic rocks and alluvium. Improved models were developed that describe the colloidal transport of radionuclides, and the potential for sorption of radionuclides in alluvium. In most cases, the uncertainty analyses and the improved models indicate that the simplified models used in the TSPA-SR (CRWMS M&O 2000 [DIRS 153246]) are conservative, and that the unsaturated and saturated zones are likely to delay and reduce radionuclide concentrations more than previous analyses indicated. In one case (sorption coefficient for iodine and technetium in alluvium), the parameter values used in the TSPA-SR (CRWMS M&O 2000 [DIRS 153246]) were judged to be non-conservative based on recent information, so the saturated zone transport model was revised accordingly.

Analysis of the possible effects of LTOMs on radionuclides transport away from the potential repository indicates that thermal effects on transport properties and processes are likely to be small and not significantly affect performance.

Effect of Drift Shadow Zone–The hydrologic conditions beneath waste emplacement drifts are affected by the diversion of seepage around the drift. This diversion of seepage results in a zone of reduced water saturations and flow beneath waste emplacement drifts. An important aspect of radionuclide transport near the drift is how radionuclides enter the rock. Radionuclides can enter the rock from waste emplacement drifts as a result of diffusive transport or a combination of advection and diffusion. If seepage into the drift is substantial, the radionuclides will be advected out of the drift predominantly into the rock fractures. If seepage into the drift is sufficiently small, radionuclides will either advect or diffuse predominantly into the rock matrix. Diffusive releases of radionuclides from the drift will predominantly enter the rock matrix because its water content is considerably larger than the water content of the fractures, providing

a greater cross section for diffusion. Initiating transport in the rock matrix, rather than the fractures, can substantially reduce the rate of radionuclide movement away from the drift. This is primarily caused by the limited contact between the fractures and the matrix, which is consistent with calibration of the unsaturated zone flow model and geochemical observations. The result is long residence times in the slow-flowing matrix. Furthermore, the reduction in water saturation in the fractures beneath the drift enhances the retention of radionuclides in the matrix. An approximate representation of the drift shadow is included in TSPA by defining the release domain according to the Engineered Barrier System-to-rock transport mechanism. Diffusive releases from the Engineered Barrier System enter the rock matrix and advective releases enter the rock fractures. Other aspects of the drift shadow, in particular the reduced saturations and flow velocities in this zone, are not included in the present TSPA implementation.

Matrix Block Discretization Effects–Dual-permeability models of unsaturated zone radionuclide transport in fractured rock commonly use a single matrix gridblock associated with each fracture gridblock. The single-matrix-grid model must approximate radionuclide concentration gradients leading to diffusion between the fractures and matrix in terms of a single matrix concentration. In reality, a continuous range of concentrations in the matrix will result from radionuclide concentration differences between the fractures and matrix. This continuous range of concentrations can be more accurately captured using multiple-matrix gridblocks associated with each fracture grid. A comparison of transport calculations using a single-matrix grid model and a multiple-matrix grid model shows that the leading edge of a radionuclide breakthrough curve will arrive significantly earlier using the single-matrix grid model. Transport at later times in the breakthrough are not appreciably affected by the single-matrix grid approximation. Thus, the results indicate that a single-matrix grid model is a conservative predictor for radionuclide transport behavior. More refined approaches to evaluating radionuclide transport include multiple-matrix gridblock models for flow and transport, for transport but not for flow, and alternative calculation schemes such as particle tracking methods.

Calculation Methods for Radionuclide Transport–Calculation schemes for radionuclide transport include particle-tracking methods and direct numerical solution of the conservation equations. The different schemes can result in different model predictions, particularly due to the differences in the approaches used for matrix diffusion. Simulation results from three different simulation methods for unsaturated zone transport are described. All three methods use the same dual-permeability grid, consisting of overlapped meshes that represent fracture and matrix continua. Although the three simulation methods tested agree for certain problems, differences between the particle-tracking method used for TSPA-SR and the process-level models were found for transport calculations involving dual-permeability systems. These differences are attributable to simplifying assumptions used in the TSPA-SR particle-tracking algorithm that provide a more efficient calculation scheme for capturing concentration gradients in the matrix. Improvements in an alternative particle tracking method is found to also provide a more accurate representation of matrix concentration gradients for fracture-matrix diffusive exchange than the baseline version, while avoiding some of the assumptions used in the TSPA-SR algorithm.

Effects of Potential Repository Footprint on Three-Dimensional Transport–Radionuclide transport in the unsaturated zone between the potential repository and the water table is

dependent on the location, size, and shape of the potential repository (i.e., the repository footprint). This results from the unpredictable location-specific geologic and hydrologic variability present in a natural system. Sensitivity calculations were performed to investigate the changes in radionuclide-transport behavior from the potential repository to the water table if the baseline potential repository footprint should be extended to the south. The results of the investigation found that radionuclide transport in the extended footprint were slower than in the baseline potential repository block, although the differences were not large (e.g., mean breakthrough times differ by less than a factor of 2). Uncertainties with regard to footprint effects on radionuclide transport are primarily caused by uncertainties in the footprint itself (i.e., the potential repository design) and in the geologic characterization for regions that lie outside the baseline footprint. This uncertainty is treated by using a range of flow models.

Effects of Thermally-Driven Coupled Processes–Thermal energy from the potential repository will induce thermal-hydrologic and thermal-hydrologic-mechanical couplings that affect flow, and thermal-hydrologic-chemical couplings that affect flow as well as geochemical conditions. All of these processes affect the conditions for radionuclide transport. Because the heat source is located in the waste emplacement drifts, the effects of these coupled processes tend to be more pronounced near the waste emplacement drifts. The thermal-hydrologic flow coupling is primarily caused by vaporization/condensation phenomena that result in redistribution of water and changes in flow patterns. The thermal-hydrologic-mechanical coupling affects flow behavior through changes in hydrologic characteristics resulting from induced mechanical strain in the rock. The thermal-hydrologic-chemical coupling can cause changes to hydrologic properties through precipitation/dissolution of minerals, as well as aqueous and mineralogical changes that can affect radionuclide sorption and colloid behavior. Process-model evaluations concerning thermal-hydrologic effects on mountain-scale flow indicated that effects on radionuclide transport should be minimal. However, the dryout near the waste emplacement drift may result in significant delays in radionuclide transport for the high-temperature case. The effects of thermal-hydrologic-mechanical coupled processes on radionuclide transport were found to cause only relatively small changes in hydrologic properties; hence the effects on flow and transport should be minimal. Similarly, thermal-hydrologic-chemical coupled processes were found to cause only relatively small changes in hydrologic properties and, therefore, should not have much effect on radionuclide transport.

Groundwater Specific Discharge Uncertainty–In the TSPA-SR (CRWMS M&O 2000 [DIRS 153246]), specific discharge in the site-scale saturated zone flow and transport model is represented as three discrete cases: high, medium, and low. The value for the low case was one-tenth of the value for the medium case, and the value for the high case was 10 times that of the medium case (0.6 m/yr). In sensitivity studies performed as part of the saturated zone unquantified uncertainty analysis, the range of specific discharge was reduced such that the low- and high-value cases were one-third and three times the medium value, respectively.

Effective Diffusion Coefficient in Volcanic Tuffs–The probability distribution for radionuclide effective diffusion coefficients was modified from log uniform to log-triangular probability distribution. The upper and lower bounds are still the same as in TSPA-SR (CRWMS M&O 2000 [DIRS 153246]), 10^{-10} and 10^{-13} m²/s, respectively, but the most probable value is 3.2×10^{-11} m²/s. The basis for this was to put more emphasis on the mean value compared to sampling a uniform distribution that results in sampling equally all values in the distribution.

The effect of this change is that larger and smaller effective diffusion coefficients are less probable.

Flowing Interval (Fracture) Porosity, Enhanced Matrix Diffusion Case–The probability distribution for flowing interval porosity was modified from a log-uniform to a log-triangular distribution with a lower bound of –5.0, a most-likely value of –3.0, and an upper bound of –1.0 (the same upper and lower bounds as the TSPA-SR). This distribution places more weight at the mid-point of the distribution range compared to the TSPA-SR (CRWMS M&O 2000 [DIRS 153246]) uniform distribution, which results in equal probabilities for the given range.

Effective Porosity in the Alluvium–The probability distribution used for effective porosity in the alluvium was modified to a probability distribution that is more representative of preliminary results from single-well, isolated-interval hydraulic tests at well NC-EWDP-19D1. The distribution used for the SSPA Volume 2 (McNeish 2001 [DIRS 155023]) calculation was changed from a truncated normal distribution with a mean of 0.18, a standard deviation of 0.051, a lower bound of 0, and an upper bound of 0.35, to a normal distribution with a mean of 0.15, a standard deviation of 0.051, a lower bound of 0, and an upper bound of 0.30.

Correlation of the Effective Diffusion Coefficient with Matrix Porosity–Sampled matrix diffusion coefficients were correlated with matrix porosities using a relationship developed from laboratory diffusion-cell experiments. These experiments measured anion diffusion coefficients through tuff matrices from various stratigraphic units from the C-wells Complex and from Pahute Mesa at the Nevada Test Site.

Bulk Density of the Alluvium–New average dry bulk density values were estimated based on a saturated bulk density and porosity measurements from a borehole gravimetry survey in well NC-EWDP-19D1. Based on the new data this parameter was represented stochastically for the unquantified uncertainty analysis. The value for dry bulk density in the alluvium is changed from a constant value of 1.27 g/cm^3 to a stochastic variable that is more representative of uncertainty for dry bulk density at Yucca Mountain. The new dry stochastic bulk density is based on data from well NC-EWDP-19D1 and is represented by a normal distribution with a mean of, 1.91 g/cm^3, and standard deviation, 0.080 g/cm^3.

Retardation for Radionuclides Irreversibly Sorbed on Colloids in the Alluvium–Alluvium grain size distributions from well NC-EWDP-19P and from other locations at the Nevada Test Site were used to refine estimates of colloid filtration rate constants in the alluvium. This well was drilled using an air-hammer method that preserved smaller and larger grain sizes much better than rotary drilling methods. The revised cumulative distribution function for the retardation factor of radionuclides that are irreversibly sorbed to colloids in the alluvium was generated using the same equations and procedure as the cumulative distribution function in the TSPA-SR (CRWMS M&O 2000 [DIRS 153246]).

Presence or Absence of Alluvium–This sensitivity analysis is bounding in the sense that flow path length in the alluvium is reduced to the minimum reasonable value, based on current geologic data. However, it is not absolutely bounding because it still includes approximately 1 to 2 km of alluvium at the end of the flow path near the 20-km point of compliance.

The minimum-alluvium sensitivity analysis is implemented in the site-scale saturated zone flow and transport model by reducing the extent of the alluvium uncertainty zone to zero.

Sorption Coefficient in Alluvium for Iodine and Technetium–Further analysis of batch sorption data of technetium-99 and iodine-129 (as TcO_4^- and I^-) onto alluvium samples, as well as recent technetium-99 and iodine-129 column test results, indicate that sorption distribution (K_d) values for technetium-99 and iodine-129 sorbing onto the alluvium are zero under oxidizing (ambient) conditions. Therefore, sorption coefficients in the alluvium for iodine and technetium were considered to be zero in the saturated zone transport model.

Sorption Coefficient in Alluvium for Neptunium and Uranium–New results from two column experiments for K_d values for neptunium-237 in the alluvium have been performed in which the effective K_d values of neptunium-237 were significantly lower than values measured in batch sorption experiments with the same material used to pack the columns. Therefore, the probability distribution for neptunium sorption coefficient in the alluvium was changed from a probability distribution based on laboratory batch experiments to one that represents batch and column laboratory experiments. The distribution function gives considerable weight to the column experiments, which weights the lower sorption-coefficient values. Based on the absence of experimental data on uranium sorption coefficients in alluvium, the probability distribution for uranium is represented as the sorption-coefficient probability distribution for neptunium in the alluvium.

Sorption Coefficient for Neptunium in Volcanic Tuffs–The probability distribution used for the neptunium sorption coefficient in the matrix was changed from a probability distribution based on a vitric rock type to a probability distribution that is more representative of the rock types that the flow path will encounter. For a given set of realizations (i.e., simulations with Monte Carlo sampling) the new probability distribution is determined by sampling the vitric distribution approximately 67 percent of the time and the zeolitic distribution 33 percent of the time.

K_c (Reversible Colloids) Model for Groundwater Colloid Concentrations–The sensitivity analysis for the saturated zone consists of simulation of radionuclide breakthrough curves for the two classes of radionuclides associated with the reversible colloid model: strongly sorbing radionuclides (plutonium, americium, and thorium) and moderately sorbing radionuclides (strontium, cesium, and protactinium). These simulations are implemented in the site-scale saturated zone flow and transport model using resampled values for the K_c parameter and for the K_d of strongly sorbing radionuclides. The values for the K_c parameter used in this analysis are based on sampling of uncertainty distributions for the K_d of americium onto colloids and for the concentration of colloids in the groundwater, as explained in Volume 2 (McNeish 2001 [DIRS 155023], Section 3). The uncertainty distribution for K_d of strongly sorbing radionuclides onto the alluvium material is changed to beta distribution with greater statistical mass near the expected value of 50 ml/g (McNeish 2001 [DIRS 155023], Section 3). Other stochastic parameters for the saturated zone have the same values for the sensitivity analysis as the SSPA Volume 2 (McNeish 2001 [DIRS 155023]) supplemental analysis.

Enhanced Matrix Diffusion–For this case, most of the rock matrix in the volcanic units is available for radionuclide storage and sorption in the transport process in most of the

realizations. The sensitivity analysis for the enhanced-matrix-diffusion case is implemented by reducing the flowing interval spacing by two orders of magnitude for all realizations. This approach reduces the geometric mean of the flowing interval spacing from about 20 to 0.2 m, which is a relatively small distance for matrix diffusion. Other stochastic parameters for the saturated zone have the same values for the sensitivity analysis as the SSPA Volume 2 (McNeish 2001 [DIRS 155023]) supplemental analysis.

No Matrix Diffusion–The sensitivity analysis for no matrix diffusion is implemented in the site-scale saturated zone flow and transport model by reducing the value of the effective matrix diffusion coefficient by ten orders of magnitude in all realizations. This large reduction in the matrix diffusion coefficient effectively renders the simulated radionuclide mass delay to matrix diffusion insignificant. Other stochastic parameters for the saturated zone have the same values for the sensitivity analysis as the SSPA Volume 2 (McNeish 2001 [DIRS 155023]) supplemental analysis.

Biosphere Uncertainty Analyses for Groundwater and Igneous Releases–Because of the location of the receptor, the reference biosphere is sufficiently distant from the engineered barriers component of the potential repository that there are no direct interactions between these two system components. Thus, the thermal operating conditions within the repository have no effect on the reference biosphere or the dose predictions. Therefore, the new biosphere analyses only address the effect of new data and of previously unquantified uncertainties. Biosphere dose conversion factors (BDCFs) were developed based on revised input for all the radionuclides in TSPA-SR (CRWMS M&O 2000 [DIRS 153246]) plus selenium-79 and neptunium-237. These BDCF data were generated for the radionuclides released into the biosphere with contaminated groundwater and contaminated volcanic ash. The robustness of the biosphere approach was investigated by performing sensitivity studies on the impact on both BDCFs and annual dose of the definition of the human receptor and alternative dose assessment methodologies as recommended by the International Commission on Radiological Protection. The uncertainties in BDCFs for important radionuclides were quantified for several parameters that had previously been considered fixed and not subject to uncertainty. Examples of such uncertainties are leaching factors, weathering factor for removal of contamination from plant leaves, and translocation factors. In addition, the change in BDCF values and annual groundwater usage due to projected climate change was assessed.

15.5 KEY ATTRIBUTE: LOW MEAN ANNUAL DOSE CONSIDERING POTENTIALLY DISRUPTIVE EVENTS

Section 14 of the SSPA describes analyses completed to incorporate new information about the potential for disruptive events at Yucca Mountain, and to assess the effect of LTOMs on the probability that disruptive events could affect the performance of a potential repository. The possible changes in the footprint of the repository associated with alternative operating modes could slightly change probability calculations that depend on the spatial extent of the repository.

In addition to the analyses related to the configuration of the repository, the DOE has developed improved models that describe the possible consequences of volcanic eruptions. In general, the

changes to the probability estimates and the process models for disruptive events at Yucca Mountain are small and do not significantly affect repository performance.

Probability of Dike Intrusion–Additional analyses have been conducted to evaluate the probability distribution for dike intrusion for the repository footprint described in the S&ER (DOE 2001 [DIRS 153849]). The evaluations were carried out for operating modes both with and without backfill. The effort characterized the probability distribution for the annual frequency of dike intersection with the potential repository footprint for the primary block and for the primary and contingency block combined. Other distributions required to evaluate the consequences of the event were derived. These parameters include the length and orientation of the dike intersection with respect to the repository and the number of conduits (or eruptive centers) with the footprint of the potential repository.

Scaling Factors to Evaluate Impacts of Alternative Operating Modes–The degree of interaction between a dike and the waste entombed in the potential repository is dependent upon the configuration of the facility. The degree of interaction is dictated by such factors as footprint area, footprint location, drift spacing, and waste package spacing. This effort derived scaling factors to allow an approximate but rapid evaluation of the effect that alternative operating modes and repository configurations could have on the probability and consequences of volcanic events.

Calculation of Contribution of Releases from Zones 1 and 2–In the igneous intrusion scenario, damage to waste packages in drifts intersected by an igneous dike is divided into two zones. In Zone 1, damage is extensive and the waste package provides no further protection to the waste. In Zone 2, waste packages are also damaged, but still provide some protection. In the TSPA-SR (CRWMS M&O 2000 [DIRS 153246]), Zones 1 and 2 were treated jointly. For the uncertainty study, the relative contributions to dose from Zone 1 and Zone 2 were determined. Results are reported in SSPA Volume 2 (McNeish 2001 [DIRS 155023]). Because backfill would minimize magma transport along any intersected drift, Zone 2 phenomenology only applies to the non-backfill case. This study allowed a more complete understanding of the total system performance assessment results for the intrusive groundwater release scenario.

Sensitivity to Waste Particle Size Distribution–Particle size distribution of the ash from a volcanic event plays a dominant role in determining the characteristic of the atmospheric transport of the ash. The waste particle size distribution and their interaction with the ash particles during the event play a potentially significant role in determining the dose consequence of that event. The volcanic predictive capability (ASHPLUME V1.4LV-dll) that is run in TSPA-SR was provided with a set of reasonable particle (ash and waste) size distribution to enable a sensitivity study to be conducted. The results of this study are presented and discussed in Volume 2 (McNeish 2001 [DIRS 155023]).

New Wind Speed Data for Various Heights of Eruption–The transport of ash during an eruption, with any entrained contaminants, is a function of many factors such as eruption characteristics and atmospheric conditions. In TSPA-SR (CRWMS M&O 2000 [DIRS 153246]) a simple atmospheric model was used that assumed the wind velocity (speed and direction) was a constant and independent of altitude. The wind speed cumulative distribution function was based on data gathered at altitudes of approximately 1,500 to 5,000 m above sea level. Because

of the potential for an eruptive plume of ash to extend higher than 5,000 m into the atmosphere, a new cumulative distribution function for wind speed was developed based on an alternative data set. These data were acquired from an average height of 9,434 m and are consistent with possible plume heights for the Yucca Mountain region. The maximum and median of the new distribution function are approximately twice those used in the TSPA-SR (CRWMS M&O 2000 [DIRS 153246]) and form the basis for a sensitivity analysis in SSPA Volume 2 (McNeish 2001 [DIRS 155023]).

Method for Handling Ash/Waste Particle Density–Ash particle density is an important parameter in the code used to model the dispersion of waste-contaminated volcanic ash in the TSPA-SR (CRWMS M&O 2000 [DIRS 153246]). Density affects the calculation of the terminal velocity of a particle as it settles in the atmosphere. In the code, ash particle density is appropriately modified when an ash particle is combined with a waste particle.

Volcanism Inputs for Supplemental TSPA Model–Updated information consistent with the current understanding of the probability and consequences of disruptive events has been incorporated in the analyses described in Volume 2 (McNeish 2001 [DIRS 155023]).

Potential Impact of New Aeromagnetic Data on Probability of Dike Intrusion–The U.S. Geological Survey has gathered new aeromagnetic data for the Amargosa Valley/Crater Flat/Yucca Mountain region. These data are being assessed to evaluate the likelihood that magnetic anomalies identified in the survey represent buried volcanoes and, if so, provide information on their properties. These results will then be evaluated to determine whether additional steps are needed. It is probable that the presence of any newly identified igneous features would not significantly impact performance assessment results because they would be accounted for by the uncertainties already included in the model. However, assessing the impact of the new aeromagnetic survey data will depend on the outcome of a full analysis of these data.

16 References

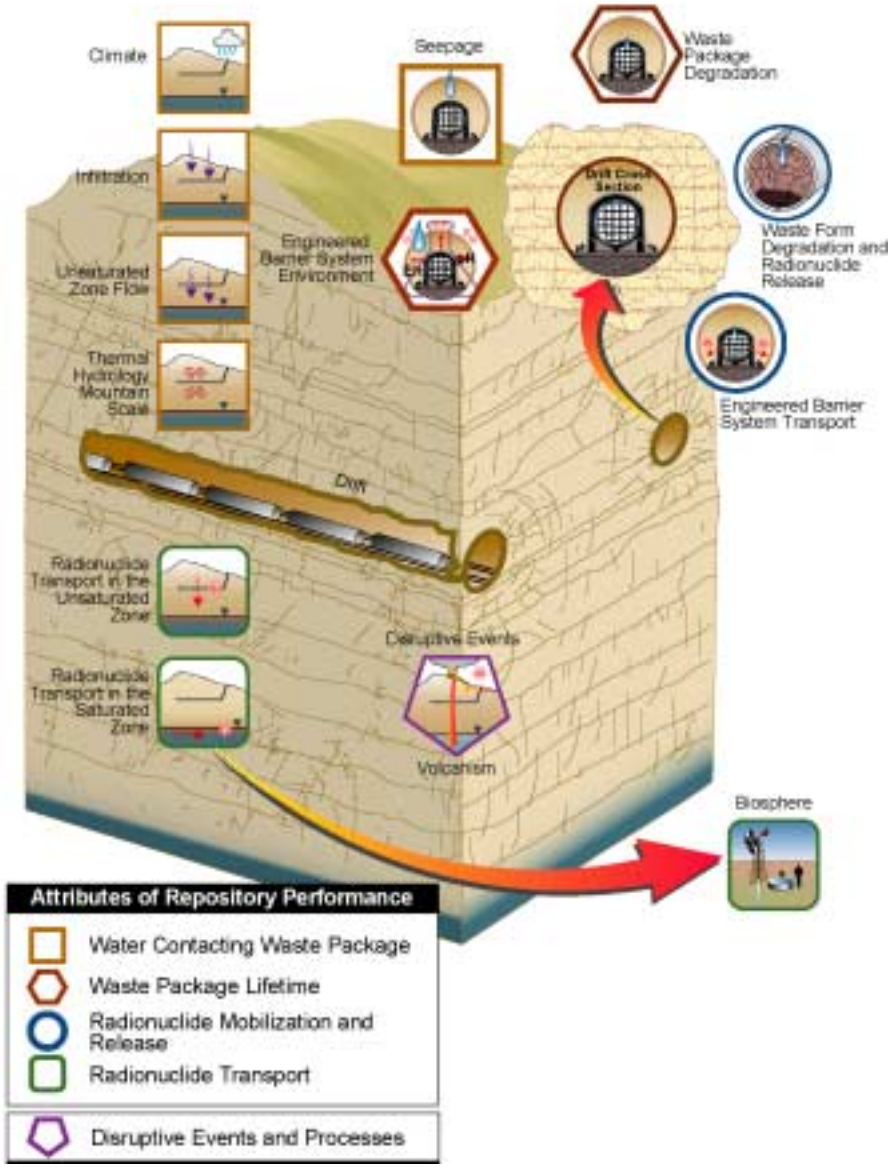

16. REFERENCES

NOTE: The following references are sorted in numerical order using a unique YMP identifier.

16.1 DOCUMENTS CITED

100006 Bish, D.L. and Aronson, J.L. 1993. "Paleogeothermal and Paleohydrologic Conditions in Silicic Tuff from Yucca Mountain, Nevada." *Clays and Clay Minerals, 41,* (2), 148-161. Long Island City, New York: Pergamon Press. TIC: 224613.

100051 Langmuir, D. 1997. *Aqueous Environmental Geochemistry.* Upper Saddle River, New Jersey: Prentice Hall. TIC: 237107.

100058 Matyskiela, W. 1997. "Silica Redistribution and Hydrologic Changes in Heated Fractured Tuff." *Geology, 25,* (12), 1115-1118. Boulder, Colorado: Geological Society of America. TIC: 236809.

100105 Bruton, C.J. 1995. *Testing EQ3/6 and GEMBOCHS Using Fluid-Mineral Equilibria in the Wairakei Geothermal System.* Letter Report MOL206. Livermore, California: Lawrence Livermore National Laboratory. ACC: MOL.19960409.0131.

100116 CRWMS M&O 1996. *Probabilistic Volcanic Hazard Analysis for Yucca Mountain, Nevada.* BA0000000-01717-2200-00082 REV 0. Las Vegas, Nevada: CRWMS M&O. ACC: MOL.19971201.0221.

100123 Hardin, E.L. 1998. *Near-Field/Altered-Zone Models Report.* UCRL-ID-129179. Livermore, California: Lawrence Livermore National Laboratory. ACC: MOL.19980630.0560.

100131 D'Agnese, F.A.; Faunt, C.C.; Turner, A.K.; and Hill, M.C. 1997. *Hydrogeologic Evaluation and Numerical Simulation of the Death Valley Regional Ground-Water Flow System, Nevada and California.* Water-Resources Investigations Report 96-4300. Denver, Colorado: U.S. Geological Survey. ACC: MOL.19980306.0253.

100145 Fabryka-Martin, J.T.; Wolfsberg, A.V.; Dixon, P.R.; Levy, S.S.; Musgrave, J.A.; and Turin, H.J. 1997. *Summary Report of Chlorine-36 Studies: Sampling, Analysis, and Simulation of Chlorine-36 in the Exploratory Studies Facility.* LA-13352-MS. Los Alamos, New Mexico: Los Alamos National Laboratory. ACC: MOL.19980812.0254.

100153 LeCain, G.D. 1997. *Air-Injection Testing in Vertical Boreholes in Welded and Nonwelded Tuff, Yucca Mountain, Nevada.* Water-Resources Investigations Report 96-4262. Denver, Colorado: U.S. Geological Survey. ACC: MOL.19980310.0148.

100161 Montazer, P. and Wilson, W.E. 1984. *Conceptual Hydrologic Model of Flow in the Unsaturated Zone, Yucca Mountain, Nevada.* Water-Resources Investigations Report 84-4345. Lakewood, Colorado: U.S. Geological Survey. ACC: NNA.19890327.0051.

100178 Rousseau, J.P.; Loskot, C.L.; Thamir, F.; and Lu, N. 1997. *Results of Borehole Monitoring in the Unsaturated Zone Within the Main Drift Area of the Exploratory Studies Facility, Yucca Mountain, Nevada.* Milestone SPH22M3. Denver, Colorado: U.S. Geological Survey. ACC: MOL.19970626.0351.

100186 Tsang, C-F.; Birkholzer, J.; Li, G.; and Tsang, Y. 1997. *Drift Scale Modeling: Progress in Studies of Seepage into a Drift.* Milestone SP331CM4. Berkeley, California: Lawrence Berkeley National Laboratory. ACC: MOL.19971204.0420.

100194 Yang, I.C.; Rattray, G.W.; and Yu, P. 1996. *Interpretation of Chemical and Isotopic Data from Boreholes in the Unsaturated Zone at Yucca Mountain, Nevada.* Water-Resources Investigations Report 96-4058. Denver, Colorado: U.S. Geological Survey. ACC: MOL.19980528.0216.

100198 CRWMS M&O 1995. *Total System Performance Assessment - 1995: An Evaluation of the Potential Yucca Mountain Repository.* B00000000-01717-2200-00136 REV 01. Las Vegas, Nevada: CRWMS M&O. ACC: MOL.19960724.0188.

100245 CRWMS M&O 1997. *Repository Subsurface Layout Configuration Analysis.* BCA000000-01717-0200-00008 REV 00. Las Vegas, Nevada: CRWMS M&O. ACC: MOL.19971201.0879.

100289 McCright, R.D. 1998. *Corrosion Data and Modeling Update for Viability Assessment.* Volume 3 of *Engineered Materials Characterization Report.* UCRL-ID-119564, Rev. 1.1. Livermore, California: Lawrence Livermore National Laboratory. ACC: MOL.19981222.0137.

100332 DOE (U.S. Department of Energy) 1997. *The 1997 "Biosphere" Food Consumption Survey Summary Findings and Technical Documentation.* Las Vegas, Nevada: U.S. Department of Energy, Office of Civilian Radioactive Waste Management. ACC: MOL.19981021.0301.

100348 CRWMS M&O 1998. *Constraints on Solubility-Limited Neptunium Concentrations for Use in Performance Assessment Analyses.* B00000000-01717-2200-00191 REV 00. Las Vegas, Nevada: CRWMS M&O. ACC: MOL.19980213.0484.

100353 CRWMS M&O 1998. *Saturated Zone Flow and Transport Expert Elicitation Project.* Deliverable SL5X4AM3. Las Vegas, Nevada: CRWMS M&O. ACC: MOL.19980825.0008.

100358 CRWMS M&O 1998. "Near-Field Geochemical Environment." Chapter 4 of *Total System Performance Assessment-Viability Assessment (TSPA-VA) Analyses Technical Basis Document.* B00000000-01717-4301-00004 REV 01. Las Vegas, Nevada: CRWMS M&O. ACC: MOL.19981008.0004.

100362 CRWMS M&O 1998. "Waste Form Degradation, Radionuclide Mobilization, and Transport Through the Engineered Barrier System." Chapter 6 of *Total System Performance Assessment-Viability Assessment (TSPA-VA) Analyses Technical Basis Document.* B00000000-01717-4301-00006 REV 01. Las Vegas, Nevada: CRWMS M&O. ACC: MOL.19981008.0006.

100388 Buck, E.C.; Finch, R.J.; Finn, P.A.; and Bates, J.K. 1998. "Retention of Neptunium in Uranyl Alteration Phases Formed During Spent Fuel Corrosion." *Scientific Basis for Nuclear Waste Management XXI, Symposium held September 28-October 3, 1997, Davos, Switzerland.* McKinley, I.G. and McCombie, C., eds. *506,* 87-94. Warrendale, Pennsylvania: Materials Research Society. TIC: 240702.

100389 Burns, P.C.; Ewing, R.C.; and Miller, M.L. 1997. "Incorporation Mechanisms of Actinide Elements into the Structures of U{superscript 6+} Phases Formed During the Oxidation of Spent Nuclear Fuel." *Journal of Nuclear Materials, 245,* ([1]), 1-9. Amsterdam, The Netherlands: North-Holland. TIC: 235501.

100392 Finn, P.A.; Wronkiewicz, D.J.; Finch, R.J.; Hoh, J.C.; Mertz, C.; Emery, J.W.; Buck, E.C.; Fortner, J.; Wolf, S.F.; Neimark, L.A.; and Bates, J.K. 1998. *Yucca Mountain Project — Argonne National Laboratory, Annual Progress Report, FY 1997 for Activity WP1221 Unsaturated Drip Condition Testing of Spent Fuel and Unsaturated Dissolution Tests of Glass.* ANL-98/12. Argonne, Illinois: Argonne National Laboratory. ACC: MOL.19980818.0230.

100396 Geldon, A.L. 1996. *Results and Interpretation of Preliminary Aquifer Tests in Boreholes UE-25c #1, UE-25c #2, and UE-25c #3, Yucca Mountain, Nye County, Nevada.* Water-Resources Investigations Report 94-4177. Denver, Colorado: U.S. Geological Survey. ACC: MOL.19980724.0389.

100401 CRWMS M&O 1997. *Summary Report Geochemistry/Transport Laboratory Tests.* Deliverable SP23QM3. Las Vegas, Nevada: CRWMS M&O. ACC: MOL.19980122.0053.

100417 Rothman, A.J. 1984. *Potential Corrosion and Degradation Mechanisms of Zircaloy Cladding on Spent Nuclear Fuel in a Tuff Repository.* UCID-20172. Livermore, California: Lawrence Livermore National Laboratory. ACC: NNA.19870903.0039.

100422 Triay, I.R.; Meijer, A.; Conca, J.L.; Kung, K.S.; Rundberg, R.S.; Strietelmeier, B.A.; and Tait, C.D. 1997. *Summary and Synthesis Report on Radionuclide Retardation for the Yucca Mountain Site Characterization Project.* Eckhardt, R.C., ed. LA-13262-MS. Los Alamos, New Mexico: Los Alamos National Laboratory. ACC: MOL.19971210.0177.

100423 Chapman, N.A.; McKinley, I.G.; Shea, M.E.; and Smellie, J.A.T. 1991. *The Pocos de Caldas Project: Summary and Implications for Radioactive Waste Management.* SKB Technical Report 90-24. Stockholm, Sweden: Swedish Nuclear Fuel and Management Company. TIC: 205593.

100436 Conca, J.L. and Wright, J. 1992. "Diffusion and Flow in Gravel, Soil, and Whole Rock." *Applied Hydrogeology, 1,* 5-24. Hanover, Germany: Verlag Heinz Heise GmbH. TIC: 224081.

100458 International Atomic Energy Agency 1994. *Handbook of Parameter Values for the Prediction of Radionuclide Transfer in Temperate Environments.* Technical Report Series No. 364. Vienna, Austria: International Atomic Energy Agency. TIC: 232035.

100464 Leigh, C.D.; Thompson, B.M.; Campbell, J.E.; Longsine, D.E.; Kennedy, R.A.; and Napier, B.A. 1993. *User's Guide for GENII-S: A Code for Statistical and Deterministic Simulations of Radiation Doses to Humans from Radionuclides in the Environment.* SAND91-0561. Albuquerque, New Mexico: Sandia National Laboratories. TIC: 231133.

100534 Hardin, E.L. and Chesnut, D.A. 1997. *Synthesis Report on Thermally Driven Coupled Processes.* Milestone SPL8BM4. Livermore, California: Lawrence Livermore National Laboratory. ACC: MOL.19980113.0395.

100550 DOE (U.S. Department of Energy) 1998. *Total System Performance Assessment.* Volume 3 of *Viability Assessment of a Repository at Yucca Mountain.* DOE/RW-0508. Washington, D.C.: U.S. Department of Energy, Office of Civilian Radioactive Waste Management. ACC: MOL.19981007.0030.

100567 Deutsch, C.V. and Journel, A.G. 1992. *GSLIB Geostatistical Software Library and User's Guide.* New York, New York: Oxford University Press. TIC: 224174.

100588 Leverett, M.C. 1941. "Capillary Behavior in Porous Solids." *AIME Transactions, Petroleum Development and Technology, Tulsa Meeting, October 1940. 142,* 152-169. New York, New York: American Institute of Mining and Metallurgical Engineers. TIC: 240680.

100589 Lichty, R.W. and McKinley, P.W. 1995. *Estimates of Ground-Water Recharge Rates for Two Small Basins in Central Nevada.* Water-Resources Investigations Report 94-4104. Denver, Colorado: U.S. Geological Survey. ACC: MOL.19960924.0524.

100605 Pruess, K. 1983. *GMINC - A Mesh Generator for Flow Simulations in Fractured Reservoirs.* LBL-15227. Berkeley, California: Lawrence Berkeley Laboratory. ACC: NNA.19910307.0134.

100610 van Genuchten, M.T. 1980. "A Closed-Form Equation for Predicting the Hydraulic Conductivity of Unsaturated Soils." *Soil Science Society of America Journal, 44,* (5), 892-898. Madison, Wisconsin: Soil Science Society of America. TIC: 217327.

100611 Warren, J.E. and Root, P.J. 1963. "The Behavior of Naturally Fractured Reservoirs." *Society of Petroleum Engineers Journal, 3,* (3), 245-255. Dallas, Texas: Society of Petroleum Engineers. TIC: 233671.

100623 Incropera, F.P. and DeWitt, D.P. 1985. *Introduction to Heat Transfer.* New York, New York: John Wiley & Sons. TIC: 224038.

100640 Nitao, J.J. 1997. *Distribution of Post-Emplacement Seepage into the Repository Drifts with Parametric Variation of Intrinsic Properties [and] Models and Bounds for Post-Emplacement Seepage into the Repository.* Deliverables SPLC2M4 and SPLC3M4. Livermore, California: Lawrence Livermore National Laboratory. ACC: MOL.19980107.0401.

100641 Nitao, J.J. 1997. *Models for the Distribution of Percolation at the Repository Level and Seepage into Drifts Under Pre-Emplacement Conditions.* Deliverable SPLB2M4. Livermore, California: Lawrence Livermore National Laboratory. ACC: MOL.20000728.0489.

100642 Rautman, C.A. and Engstrom, D.A. 1996. *Geology of the USW SD-12 Drill Hole Yucca Mountain, Nevada.* SAND96-1368. Albuquerque, New Mexico: Sandia National Laboratories. ACC: MOL.19970613.0101.

100644 Sass, J.H.; Lachenbruch, A.H.; Dudley, W.W., Jr.; Priest, S.S.; and Munroe, R.J. 1988. *Temperature, Thermal Conductivity, and Heat Flow Near Yucca Mountain, Nevada: Some Tectonic and Hydrologic Implications.* Open-File Report 87-649. [Denver, Colorado]: U.S. Geological Survey. TIC: 203195.

100670 Engstrom, D.A. and Rautman, C.A. 1996. *Geology of the USW SD-9 Drill Hole, Yucca Mountain, Nevada.* SAND96-2030. Albuquerque, New Mexico: Sandia National Laboratories. ACC: MOL.19970508.0288.

100676 Flint, L.E.; Flint, A.L.; Rautman, C.A.; and Istok, J.D. 1996. *Physical and Hydrologic Properties of Rock Outcrop Samples at Yucca Mountain, Nevada.* Open-File Report 95-280. Denver, Colorado: U.S. Geological Survey. ACC: MOL.19970224.0225.

100687 Siegel, R. and Howell, J.R. 1992. *Thermal Radiation Heat Transfer.* 3rd Edition. Washington, D.C.: Taylor & Francis. TIC: 236759.

100712 Buddemeier, R.W. and Hunt, J.R. 1988. "Transport of Colloidal Contaminants in Groundwater: Radionuclide Migration at the Nevada Test Site." *Applied Geochemistry, 3,* 535-548. Oxford, England: Pergamon Press. TIC: 224116.

100722 Dean, J.A. 1992. *Lange's Handbook of Chemistry.* 14th Edition. New York, New York: McGraw-Hill. TIC: 240690.

100733 CRWMS M&O 1998. *AREST-CT Parameter Input: Calculation of Spent Fuel Volume Fraction, Porosity, and Radius.* B00000000-01717-0210-00025 REV 01. Las Vegas, Nevada: CRWMS M&O. ACC: MOL.19981030.0236.

100737 CRWMS M&O 1998. *MING Parameter Input: Waste Package Design Compositional Information.* B00000000-01717-0200-00168 REV 00. Las Vegas, Nevada: CRWMS M&O. ACC: MOL.19980904.0547.

100743 Eugster, H.P. and Hardie, L.A. 1978. "Saline Lakes." Chapter 8 of *Lakes,Chemistry, Geology, Physics.* Lerman, A., ed. New York, New York: Springer-Verlag. TIC: 240782.

100763 Hersman, L.E. 1997. "Subsurface Microbiology: Effects on the Transport of Radioactive Wastes in the Vadose Zone." Chapter 16 of *The Microbiology of the Terrestrial Deep Subsurface.* Amy, P.S. and Haldeman, D.L., eds. Boca Raton, Florida: CRC Lewis Publishers. TIC: 232570.

100792 Wilder, D.G., ed. 1996. *Volume II: Near-Field and Altered-Zone Environment Report.* UCRL-LR-124998. [Livermore, California]: Lawrence Livermore National Laboratory. ACC: MOL.19961212.0121; MOL.19961212.0122.

100793 Wilson, C.N. 1990. *Results from NNWSI Series 3 Spent Fuel Dissolution Tests.* PNL-7170. Richland, Washington: Pacific Northwest Laboratory. ACC: NNA.19900329.0142.

100800 Mills, A.L. 1997. "Movement of Bacteria in the Subsurface." Chapter 13 of *The Microbiology of the Terrestrial Deep Subsurface.* Amy, P.S. and Haldeman, D.L., eds. Boca Raton, Florida: CRC Lewis Publishers. TIC: 232570.

100814 Harrar, J.E.; Carley, J.F.; Isherwood, W.F.; and Raber, E. 1990. *Report of the Committee to Review the Use of J-13 Well Water in Nevada Nuclear Waste Storage Investigations.* UCID-21867. Livermore, California: Lawrence Livermore National Laboratory. ACC: NNA.19910131.0274.

100819 Pruess, K.; Wang, J.S.Y.; and Tsang, Y.W. 1990. "On Thermohydrologic Conditions Near High-Level Nuclear Wastes Emplaced in Partially Saturated Fractured Tuff, 2. Effective Continuum Approximation." *Water Resources Research, 26,* (6), 1249-1261. [Washington, D.C.]: American Geophysical Union. TIC: 224854.

100829 Stumm, W. and Morgan, J.J. 1981. *Aquatic Chemistry – An Introduction Emphasizing Chemical Equilibria in Natural Waters.* New York, New York: John Wiley & Sons. TIC: 208448.

100833 Weast, R.C. and Astle, M.J., eds. 1981. *CRC Handbook of Chemistry and Physics: A Ready Reference Book of Chemical and Physical Data.* 62nd Edition. Boca Raton, Florida: CRC Press. TIC: 240722.

100834 West, J.M.; McKinley, I.G.; and Vialta, A. 1989. "The Influence of Microbial Activity on the Movement of Uranium at Osamu Utsumi Mine, Pocos de Caldas, Brazil." *Scientific Basis for Nuclear Waste Management XII, Symposium held October 10-13, 1988, Berlin, Germany.* Lutze, W. and Ewing, R.C., eds. *127,* 771-777. Pittsburgh, Pennsylvania: Materials Research Society. TIC: 203660.

100859 Gdowski, G.E. 1991. *Survey of Degradation Modes of Four Nickel-Chromium-Molybdenum Alloys.* UCRL-ID-108330. Livermore, California: Lawrence Livermore National Laboratory. ACC: NNA.19910521.0010.

100896 Haynes International. 1997. Hastelloy C-22 Alloy. Kokomo, Indiana: Haynes International. TIC: 238121.

100913 Lee, J.H.; Chambre, P.L.; and Andrews, R.W. 1996. "Mathematical Models for Diffusive Mass Transfer from Waste Package Container with Multiple Perforations." *Proceedings of the 1996 International Conference on Deep Geological Disposal of Radioactive Waste, September 16-19, 1996, Winnipeg, Manitoba, Canada.* Pages 5-61–5-72. Toronto, Ontario, Canada: Canadian Nuclear Society. TIC: 233923.

100953 Napier, B.A.; Peloquin, R.A.; Strenge, D.L.; and Ramsdell, J.V. 1988. *Conceptual Representation.* Volume 1 of *GENII - The Hanford Environmental Radiation Dosimetry Software System.* PNL-6584. Richland, Washington: Pacific Northwest Laboratory. TIC: 206898.

100987 Jarzemba, M.S.; LaPlante, P.A.; and Poor, K.J. 1997. *ASHPLUME Version 1.0—A Code for Contaminated Ash Dispersal and Deposition, Technical Description and User's Guide.* CNWRA 97-004, Rev. 1. San Antonio, Texas: Center for Nuclear Waste Regulatory Analyses. TIC: 239303.

101008 Rautman, C.A. and Engstrom, D.A. 1996. *Geology of the USW SD-7 Drill Hole Yucca Mountain, Nevada.* SAND96-1474. Albuquerque, New Mexico: Sandia National Laboratories. ACC: MOL.19971218.0442.

101024 Triay, I.R.; Furlano, A.C.; Weaver, S.C.; Chipera, S.J.; and Bish, D.L. 1996. *Comparison of Neptunium Sorption Results Using Batch and Column Techniques.* LA-12958-MS. Los Alamos, New Mexico: Los Alamos National Laboratory. ACC: MOL.19980924.0049.

101027 Stock, J.M.; Healy, J.H.; Hickman, S.H.; and Zoback, M.D. 1985. "Hydraulic Fracturing Stress Measurements at Yucca Mountain, Nevada, and Relationship to the Regional Stress Field." *Journal of Geophysical Research, 90,* (B10), 8691-8706. Washington, D.C.: American Geophysical Union. TIC: 219009.

101039 Craig, R.W. and Johnson, K.A. 1984. *Geohydrologic Data for Test Well UE-25p#1, Yucca Mountain Area, Nye County, Nevada.* Open-File Report 84-450. Denver, Colorado: U.S. Geological Survey. ACC: NNA.19870406.0256.

101053 Perfect, D.L.; Faunt, C.C.; Steinkampf, W.C.; and Turner, A.K. 1995. *Hydrochemical Data Base for the Death Valley Region, California and Nevada.* Open-File Report 94-305. Denver, Colorado: U.S. Geological Survey. ACC: MOL.19940718.0001.

101060 Tucci, P. and Burkhardt, D.J. 1995. *Potentiometric-Surface Map, 1993, Yucca Mountain and Vicinity, Nevada.* Water-Resources Investigations Report 95-4149. Denver, Colorado: U.S. Geological Survey. ACC: MOL.19960924.0517.

101069 Eckerman, K.F.; Wolbarst, A.B.; and Richardson, A.C.B. 1988. *Limiting Values of Radionuclide Intake and Air Concentration and Dose Conversion Factors for Inhalation, Submersion, and Ingestion.* EPA 520/1-88-020. Federal Guidance Report No. 11. Washington, D.C.: U.S. Environmental Protection Agency. TIC: 203350.

101075 ICRP (International Commission on Radiological Protection) 1977. *Recommendations of the International Commission on Radiological Protection. Annals of the ICRP.* Sowby, F.D., ed. ICRP Publication 26. New York, New York: Pergamon Press. TIC: 221568.

101079 LaPlante, P.A. and Poor, K. 1997. *Information and Analyses to Support Selection of Critical Groups and Reference Biospheres for Yucca Mountain Exposure Scenarios.* CNWRA 97-009. San Antonio, Texas: Center for Nuclear Waste Regulatory Analyses. TIC: 236454.

101085 Smith, G.M.; Watkins, B.M.; Little, R.H.; Jones, H.M.; and Mortimer, A.M. 1996. *Biosphere Modeling and Dose Assessment for Yucca Mountain.* EPRI TR-107190. Palo Alto, California: Electric Power Research Institute. TIC: 231592.

101173 Freeze, R.A. and Cherry, J.A. 1979. *Groundwater.* Englewood Cliffs, New Jersey: Prentice-Hall. TIC: 217571.

101230 Pescatore, C.; Cowgill, M.G.; and Sullivan, T.M. 1990. *Zircaloy Cladding Performance Under Spent Fuel Disposal Conditions, Progress Report May 1 - October 31, 1989.* BNL 52235. Upton, New York: Brookhaven National Laboratory. ACC: NNA.19900710.0055.

101246 Higgins, J.D.; Burger, P.A.; and Yang, I.C. 1997. *The One-Dimensional Compression Method for Extraction of Pore Water from Unsaturated Tuff and Effects on Pore-Water Chemistry.* Water-Resources Investigations Report 96-4281. Denver, Colorado: U.S. Geological Survey. ACC: MOL.19980219.0818.

101303 Tucci, P.; Goemaat, R.L.; and Burkhardt, D.J. 1996. *Water Levels in the Yucca Mountain Area, Nevada, 1993.* Open-File Report 95-159. Denver, Colorado: U.S. Geological Survey. ACC: MOL.19961118.0104.

101323 Carey, J.W.; Chipera, S.J.; Vaniman, D.T.; Bish, D.L.; Viswanathan, H.S.; and Carter-Krogh, K. 1997. *Three-Dimensional Mineralogic Model of Yucca Mountain, Nevada, Rev. 1.* Deliverable SP344BM4. Draft R1. Los Alamos, New Mexico: Los Alamos National Laboratory. ACC: MOL.19971117.0110.

101326 Carlos, B.A.; Chipera, S.J.; and Bish, D.L. 1995. *Distribution and Chemistry of Fracture-Lining Minerals at Yucca Mountain, Nevada.* LA-12977-MS. Los Alamos, New Mexico: Los Alamos National Laboratory. ACC: MOL.19960306.0564.

101367 Albin, A.L.; Singleton, W.L.; Moyer, T.C.; Lee, A.C.; Lung, R.C.; Eatman, G.L.W.; and Barr, D.L. 1997. *Geology of the Main Drift - Station 28+00 to 55+00, Exploratory Studies Facility, Yucca Mountain Project, Yucca Mountain, Nevada.* Milestone SPG42AM3. Denver, Colorado: Bureau of Reclamation and U.S. Geological Survey. ACC: MOL.19970625.0096.

101379 Bear, J. 1988. *Dynamics of Fluids in Porous Media.* New York, New York: Dover Publications. TIC: 217568.

101441 Yang, I.C.; Yu, P.; Rattray, G.W.; Ferarese, J.S.; and Ryan, J.N. 1998. *Hydrochemical Investigations in Characterizing the Unsaturated Zone at Yucca Mountain, Nevada.* Water-Resources Investigations Report 98-4132. Denver, Colorado: U.S. Geological Survey. ACC: MOL.19981012.0790.

101480 Steefel, C.I. and Lasaga, A.C. 1994. "A Coupled Model for Transport of Multiple Chemical Species and Kinetic Precipitation/Dissolution Reactions with Application to Reactive Flow in Single Phase Hydrothermal Systems." *American Journal of Science, 294,* (5), 529-592. New Haven, Connecticut: Kline Geology Laboratory, Yale University. TIC: 235372.

101540 CRWMS M&O 1997. *Single Heater Test Status Report.* BAB000000-01717-5700-00002 REV 01. Las Vegas, Nevada: CRWMS M&O. ACC: MOL.19980416.0696.

101565 Bruno, J.; Cera, E.; Eklund, U.-B.; Eriksen, T.E.; and Grive, M. 1998. *Some Preliminary Modeling Results of Long Term Radiolytic Mass Balance Experiments.* Presentation at the Spent Fuel Workshop 1998, Las Vegas, Nevada, May 18-20, 1998. [Barcelona, Spain]: Quantisci. TIC: 240716.

101582 Conca, J.L. and Wright, J. 1990. "Diffusion Coefficients in Gravel Under Unsaturated Conditions." *Water Resources Research, 26,* (5), 1055-1066. Washington, D.C.: American Geophysical Union. TIC: 237421.

101591 Cunningham, M.E.; Simonen, E.P.; Allemann, R.T.; Levy, I.S.; Hazelton, R.F.; and Gilbert, E.R. 1987. *Control of Degradation of Spent LWR Fuel During Dry Storage in an Inert Atmosphere.* PNL-6364. Richland, Washington: Pacific Northwest Laboratory. ACC: HQO.19941222.0016.

101605 Einziger, R.E. and Kohli, R. 1984. "Low-Temperature Rupture Behavior of Zircaloy-Clad Pressurized Water Reactor Spent Fuel Rods Under Dry Storage Conditions." *Nuclear Technology, 67,* (1), 107-123. Hinsdale, Illinois: American Nuclear Society. TIC: 216868.

101656 Anderson, R.E.; Hanks, T.C.; Reilly, T.E.; Weeks, E.P.; and Winograd, I.J. 1998. *Viability Assessment of a Repository at Yucca Mountain, A Report to the Director, U.S. Geological Survey, November 25, 1998.* [Reston, Virginia: U.S. Geological Survey]. ACC: HQO.19990205.0013.

101707 Pruess, K. and Narasimhan, T.N. 1985. "A Practical Method for Modeling Fluid and Heat Flow in Fractured Porous Media." *Society of Petroleum Engineers Journal, 25,* (1), 14-26. Dallas, Texas: Society of Petroleum Engineers. TIC: 221917.

101719 Manaktala, H.K. 1993. *Characteristics of Spent Nuclear Fuel and Cladding Relevant to High-Level Waste Source Term.* CNWRA 93-006. San Antonio, Texas: Center for Nuclear Waste Regulatory Analyses. TIC: 208034.

101779 DOE (U.S. Department of Energy) 1998. *Viability Assessment of a Repository at Yucca Mountain.* DOE/RW-0508. Overview and five volumes. Washington, D.C.: U.S. Department of Energy, Office of Civilian Radioactive Waste Management. ACC: MOL.19981007.0027; MOL.19981007.0028; MOL.19981007.0029; MOL.19981007.0030; MOL.19981007.0031; MOL.19981007.0032.

101836 ICRP (International Commission on Radiological Protection) 1991. "1990 Recommendations of the International Commission on Radiological Protection." Volume 21, No. 1-3 of *Annals of the ICRP.* ICRP Publication 60. New York, New York: Pergamon Press. TIC: 235864.

102010 Jury, W.A.; Gardner, W.R.; and Gardner, W.H. 1991. *Soil Physics.* 5th Edition. New York, New York: John Wiley & Sons. TIC: 241000.

102072 Sanders, T.L.; Seager, K.D.; Rashid, Y.R.; Barrett, P.R.; Malinauskas, A.P.; Einziger, R.E.; Jordan, H.; Duffey, T.A.; Sutherland, S.H.; and Reardon, P.C. 1992. *A Method for Determining the Spent-Fuel Contribution to Transport Cask Containment Requirements.* SAND90-2406. Albuquerque, New Mexico: Sandia National Laboratories. TIC: 232162.

102097 Rousseau, J.P.; Kwicklis, E.M.; and Gillies, D.C., eds. 1999. *Hydrogeology of the Unsaturated Zone, North Ramp Area of the Exploratory Studies Facility, Yucca Mountain, Nevada.* Water-Resources Investigations Report 98-4050. Denver, Colorado: U.S. Geological Survey. ACC: MOL.19990419.0335.

102111 CRWMS M&O 1999. *Preliminary Results from the Key Block Analysis.* Design Input Transmittal SEI-SSR-99088.T. Las Vegas, Nevada: CRWMS M&O. ACC: MOL.19990217.0213.

102147 Wilson, C.N. 1985. *Results from NNWSI Series 1 Spent Fuel Leach Tests.* HEDL-TME 84-30. Richland, Washington: Hanford Engineering Development Laboratory. ACC: HQS.19880517.2579.

102150 Wilson, C.N. 1987. *Results from Cycles 1 and 2 of NNWSI Series 2 Spent Fuel Dissolution Tests.* HEDL-TME 85-22. Richland, Washington: Hanford Engineering Development Laboratory. ACC: HQS.19880517.2581.

102330 McKeown, M. 1992. *Soil and Rock Geotechnical Investigations Field and Laboratory Studies, North Ramp Surface Facility Exploratory Studies Facility, Yucca Mountain Project, Nevada.* Technical Memorandum 3610-92-35. Denver, Colorado: U.S. Department of Interior, Bureau of Reclamation. ACC: NNA.19930607.0020.

102430 Beasley, T.M.; Dixon, P.R.; and Mann, L.J. 1998. "99Tc, 236U, and 237Np in the Snake River Plain Aquifer at the Idaho National Engineering and Environmental Laboratory, Idaho Falls, Idaho." *Environmental Science & Technology, 32,* (24), 3875-3881. Easton, Pennsylvania: American Chemical Society. TIC: 243863.

102588 DOE (U.S. Department of Energy) 1992. *Characteristics of Potential Repository Wastes.* DOE/RW-0184-R1. Four volumes. Washington, D.C.: U.S. Department of Energy, Office of Civilian Radioactive Waste Management. ACC: HQO.19920827.0001; HQO.19920827.0002; HQO.19920827.0003; HQO.19920827.0004.

102839 CRWMS M&O 1998. *EQ6 Calculations for Chemical Degradation of PWR LEU and PWR MOX Spent Fuel Waste Packages.* BBA000000-01717-0210-00009 REV 00. Las Vegas, Nevada: CRWMS M&O. ACC: MOL.19980701.0483.

102933 CRWMS M&O 1999. *Waste Package Materials Properties.* BBA000000-01717-0210-00017 REV 00. Las Vegas, Nevada: CRWMS M&O. ACC: MOL.19990407.0172.

103038 EPA (U.S. Environmental Protection Agency) 1997. "General Factors." Volume 1 of *Exposure Factors Handbook.* EPA/600/P-95/002Fa. Washington, D.C.: U.S. Environmental Protection Agency. TIC: 241060.

103282 Kersting, A.B.; Efurd, D.W.; Finnegan, D.L.; Rokop, D.J.; Smith, D.K.; and Thompson, J.L. 1999. "Migration of Plutonium in Ground Water at the Nevada Test Site." *Nature, 397,* ([6714]), 56-59. [London, England: Macmillan Journals]. TIC: 243597.

103524 Bird, R.B.; Stewart, W.E.; and Lightfoot, E.N. 1960. *Transport Phenomena.* New York, New York: John Wiley & Sons. TIC: 208957.

103731 Wong, I.G. and Stepp, C. 1998. *Probabilistic Seismic Hazard Analyses for Fault Displacement and Vibratory Ground Motion at Yucca Mountain, Nevada.* Milestone SP32IM3, September 23, 1998. Three volumes. Oakland, California: U.S. Geological Survey. ACC: MOL.19981207.0393.

103753 ASM International 1987. *Corrosion.* Volume 13 of *Metals Handbook.* 9th Edition. Metals Park, Ohio: ASM International. TIC: 209807.

103776 Kennedy, W.E. and Strenge, D.L. 1992. *Technical Basis for Translating Contamination Levels to Annual Total Effective Dose Equivalent.* Volume 1 of *Residual Radioactive Contamination from Decommissioning.* NUREG/CR-5512. Washington, D.C.: U.S. Nuclear Regulatory Commission. TIC: 234470.

103955 CRWMS M&O 1999. *License Application Design Selection Report.* B00000000-01717-4600-00123 REV 01. Las Vegas, Nevada: CRWMS M&O. ACC: MOL.19990528.0303.

104247 Wilkins, D.R. and Heath, C.A. 1999. "Direction to Transition to Enhanced Design Alternative II." Letter from D.R. Wilkins (CRWMS M&O) and C.A. Heath (CRWMS M&O) to Distribution, June 15, 1999, LV.NS.JLY.06/99-026, with enclosures, "Strategy for Baselining EDA II Requirements" and "Guidelines for Implementation of EDA II." ACC: MOL.19990622.0126; MOL.19990622.0127; MOL.19990622.0128.

104366 Wang, J.S.Y. and Elsworth, D. 1999. "Permeability Changes Induced by Excavation in Fractured Tuff." *Rock Mechanics for Industry, Proceedings of the 37th U.S. Rock Mechanics Symposium, Vail, Colorado, USA, 6-9 June 1999.* Amadei, B.; Kranz, R.L.; Scott, G.A.; and Smeallie, P.H., eds. *2,* 751-757. Brookfield, Vermont: A.A. Balkema. TIC: 245246.

104441 YMP (Yucca Mountain Site Characterization Project) 1998. *Disposal Criticality Analysis Methodology Topical Report.* YMP/TR-004Q, Rev. 0. Las Vegas, Nevada: Yucca Mountain Site Characterization Office. ACC: MOL.19990210.0236.

104753 Craig, H. 1961. "Isotopic Variations in Meteoric Waters." *Science, 133,* 1702-1703. Washington, D.C.: American Association for the Advancement of Science. TIC: 236943.

104945 Greenspan, L. 1977. "Humidity Fixed Points of Binary Saturated Aqueous Solutions." *Journal of Research of the National Bureau of Standards, 81A,* (1), 89-96. Washington, D.C.: U.S. Department of Commerce. TIC: 241138.

104966 Cieslak, M.J.; Headley, T.J.; and Romig, A.D., Jr. 1986. "The Welding Metallurgy of Hastelloy Alloys C-4, C-22, and C-276." *Metallurgical Transactions A, 17A,* (11), 2035-2047. Warrendale, Pennsylvania: Metallurgical Society of AIME. TIC: 233952.

105043 Sudicky, E.A. and Frind, E.O. 1982. "Contaminant Transport in Fractured Porous Media: Analytical Solutions for a System of Parallel Fractures." *Water Resources Research, 18,* (6), 1634-1642. Washington, D.C.: American Geophysical Union. TIC: 217475.

105113 Sedriks, A.J. 1996. *Corrosion of Stainless Steels.* 2nd Edition. New York, New York: John Wiley & Sons. TIC: 245121.

105157 Buscheck, T.A.; Nitao, J.J.; and Saterlie, S.F. 1994. "Evaluation of Thermo-Hydrological Performance in Support of the Thermal Loading Systems Study." *High Level Radioactive Waste Management, Proceedings of the Fifth Annual International Conference, Las Vegas, Nevada, May 22-26, 1994. 2,* 592-610. La Grange Park, Illinois: American Nuclear Society. TIC: 210984.

105230 CRWMS M&O 1998. *Repository Subsurface Waste Emplacement and Thermal Management Strategy.* B00000000-01717-0200-00173 REV 00. Las Vegas, Nevada: CRWMS M&O. ACC: MOL.19980918.0084.

105655 Dyer, J.R. 1999. "Revised Interim Guidance Pending Issuance of New U.S. Nuclear Regulatory Commission (NRC) Regulations (Revision 01, July 22, 1999), for Yucca Mountain, Nevada." Letter from J.R. Dyer (DOE/YMSCO) to D.R. Wilkins (CRWMS M&O), September 3, 1999, OL&RC:SB-1714, with enclosure, "Interim Guidance Pending Issuance of New NRC Regulations for Yucca Mountain (Revision 01)." ACC: MOL.19990910.0079.

105729 Liu, H.H.; Doughty, C.; and Bodvarsson, G.S. 1998. "An Active Fracture Model for Unsaturated Flow and Transport in Fractured Rocks." *Water Resources Research, 34,* (10), 2633-2646. Washington, D.C.: American Geophysical Union. TIC: 243012.

105743 Philip, J.R.; Knight, J.H.; and Waechter, R.T. 1989. "Unsaturated Seepage and Subterranean Holes: Conspectus, and Exclusion Problem for Circular Cylindrical Cavities." *Water Resources Research, 25,* (1), 16-28. Washington, D.C.: American Geophysical Union. TIC: 239117.

106146 Wang, J.S.Y.; Trautz, R.C.; Cook, P.J.; Finsterle, S.; James, A.L.; and Birkholzer, J. 1999. "Field Tests and Model Analyses of Seepage into Drift." *Journal of Contaminant Hydrology, 38,* (1-3), 323-347. New York, New York: Elsevier. TIC: 244160.

106316 Keith, T.E.C.; White, D.E.; and Beeson, M.H. 1978. *Hydrothermal Alteration and Self-Sealing in Y-7 and Y-8 Drill Holes in Northern Part of Upper Geyser Basin, Yellowstone National Park, Wyoming.* Geological Survey Professional Paper 1054-A. Washington, D.C.: U.S. Government Printing Office. TIC: 219043.

106794 CRWMS M&O 1999. *Post Closure Open-Loop Natural Ventilation.* BCAD00000-01717-0210-00002 REV 00. Las Vegas, Nevada: CRWMS M&O. ACC: MOL.19990806.0069.

107292 CRWMS M&O 1999. *License Application Design Selection Report.* B00000000-01717-4600-00123 REV 01 ICN 01. Las Vegas, Nevada: CRWMS M&O. ACC: MOL.19990908.0319.

107306 Kreft, A. and Zuber, A. 1978. "On the Physical Meaning of the Dispersion Equation and Its Solutions for Different Initial and Boundary Conditions." *Chemical Engineering Science, 33,* (11), 1471-1480. New York, New York: Pergamon Press. TIC: 245365.

107676 Agarwal, D.C. and Herda, W.R. 1997. "The 'C' Family of Ni-Cr-Mo Alloys' Partnership with the Chemical Process Industry: The Last 70 Years." *Materials and Corrosion (Wekstoffe und Korrosion), 48,* 542-548. Weinheim, Germany: VCH Verlagsgesellschaft mbH. TIC: 245611.

107684 Eckerman, K.F. and Ryman, J.C. 1993. *External Exposure to Radionuclides in Air, Water, and Soil, Exposure-to-Dose Coefficients for General Application, Based on the 1987 Federal Radiation Protection Guidance.* EPA 402-R-93-081. Federal Guidance Report No. 12. Washington, D.C.: U.S. Environmental Protection Agency, Office of Radiation and Indoor Air. TIC: 225472.

107722 CRWMS M&O 1998. *Waste Package Phase II Closure Methods Report.* BBA000000-01717-5705-00016 REV 00. Las Vegas, Nevada: CRWMS M&O. ACC: MOL.19981208.0099.

107744 Rittmann, P.D. 1993. *Verification Tests for the July 1993 Revision to the GENII Radionuclide and Dose Increment Libraries.* WHC-SD-WM-TI-596. Richland, Washington: Westinghouse Hanford Company. TIC: 233965.

107784 Incropera, F.P. and DeWitt, D.P. 1996. *Introduction to Heat Transfer.* 3rd Edition. New York, New York: John Wiley & Sons. TIC: 241057.

107792 Heubner, U.L.; Altpeter, E.; Rockel, M.B.; and Wallis, E. 1989. "Electrochemical Behavior and Its Relation to Composition and Sensitization of NiCrMo Alloys in ASTM G-28 Solution." *Corrosion , 45,* (3), 249-259. Houston, Texas: National Association of Corrosion Engineers. TIC: 240169.

108000 CRWMS M&O 1998. *Total System Performance Assessment-Viability Assessment (TSPA-VA) Analyses Technical Basis Document.* Las Vegas, Nevada: CRWMS M&O. ACC: MOL.19981008.0001; MOL.19981008.0002; MOL.19981008.0003; MOL.19981008.0004; MOL.19981008.0005; MOL.19981008.0006; MOL.19981008.0007; MOL.19981008.0008; MOL.19981008.0009; MOL.19981008.0010; MOL.19981008.0011.

108004 CRWMS M&O 1998. *Total System Performance Assessment - Viability Assessment Base Case.* B00000000-01717-0210-00011 REV 01. Las Vegas, Nevada: CRWMS M&O. ACC: MOL.19981202.0279.

108839 Wang, J.S.Y.; Cook, N.G.W.; Wollenberg, H.A.; Carnahan, C.L.; Javandel, I.; and Tsang, C.F. 1993. "Geohydrologic Data and Models of Rainier Mesa and Their Implications to Yucca Mountain." *High Level Radioactive Waste Management, Proceedings of the Fourth Annual International Conference, Las Vegas, Nevada, April 26-30, 1993. 1,* 675-681. La Grange Park, Illinois: American Nuclear Society. TIC: 208542.

109194 Barner, J.O. 1985. *Characterization of LWR Spent Fuel MCC-Approved Testing Material–ATM-101.* PNL-5109, Rev. 1. Richland, Washington: Pacific Northwest Laboratory. TIC: 240883.

109219 Peehs, M. 1998. *Assessment of Dry Storage Performance of Spent LWR Fuel Assemblies with Increasing Burn-Up.* Erlangen, Germany: Bereich Energieerzeugung. TIC: 245171.

109256 Harvey, R.W. and Garabedian, S.P. 1991. "Use of Colloid Filtration Theory in Modeling Movement of Bacteria Through a Contaminated Sandy Aquifer." *Environmental Science and Technology, 25,* (1), 178-185. Washington, D.C.: American Chemical Society. TIC: 245733.

109450 Petit, J.R.; Jouzel, J.; Raynaud, D.; Barkov, N.I.; Barnola, J.-M.; Basile, I.; Bender, M.; Chappellaz, J.; Davis, M.; Delaygue, G.; Delmotte, M.; Kotlyakov, V.M.; Legrand, M.; Lipenkov, V.Y.; Lorius, C.; Pepin, L.; Ritz, C.; Saltzman, E.; and Stievenard, M. 1999. "Climate and Atmospheric History of the Past 420,000 Years from the Vostok Ice Core, Antarctica." *Nature, 399,* (6735), 429-436. London, England: Macmillan Magazines. TIC: 245695.

109454 Reheis, M. 1999. "Highest Pluvial-Lake Shorelines and Pleistocene Climate of the Western Great Basin." *Quaternary Research, 52,* (2), 196-205. San Diego, California: Academic Press. TIC: 245885.

109464 Thompson, R.S.; Anderson, K.H.; and Bartlein, P.J. 1999. *Atlas of Relations Between Climatic Parameters and Distributions of Important Trees and Shrubs in North America—Hardwoods.* Professional Paper 1650-B. Denver, Colorado: U.S. Geological Survey. TIC: 245910.

109606 Baes, C.F., III and Sharp, R.D. 1983. "A Proposal for Estimation of Soil Leaching and Leaching Constants for Use in Assessment Models." *Journal of Environmental Quality, 12,* (1), 17-28. Madison, Wisconsin: American Society of Agronomy. TIC: 245676.

109736 Wang, J.S.Y. 1991. "Fracture Flow and Matrix Flow in the Unsaturated Zone at Yucca Mountain and at Rainier Mesa." Appendix B of *A Review of Rainier Mesa Tunnel and Borehole Data and Their Possible Implications to Yucca Mountain Site Study Plans.* LBL-32068. Berkeley, California: Lawrence Berkeley Laboratory. ACC: NNA.19920506.0020.

109901 Bruton, C.J.; Glassley, W.E.; and Bourcier, W.L. 1993. "Testing Geochemical Modeling Codes Using New Zealand Hydrothermal Systems." *Proceedings of the Topical Meeting on Site Characterization and Model Validation, FOCUS '93, September 26-29, 1993, Las Vegas, Nevada.* Pages 240-245. La Grange Park, Illinois: American Nuclear Society. TIC: 102245.

109923 Glassley, W.E. and Christenson, B.W. 1992. "Water-Rock Interaction in New Zealand Hydrothermal Systems: Comparison of Some Simulated and Observed Geochemical Processes." *High Level Radioactive Waste Management, Proceedings of the Third International Conference, Las Vegas, Nevada, April 12-16, 1992. 1,* 352-356. La Grange Park, Illinois: American Nuclear Society. TIC: 204231.

109939 Ku, T.-L.; Luo, S.; Leslie, B.W.; and Hammond, D.E. 1992. "Decay-Series Disequilibria Applied to the Study of Rock-Water Interaction and Geothermal Systems." Chapter 18 of *Uranium-Series Disequilibrium: Applications to Earth, Marine, and Environmental Sciences.* Invanovich, M. and Harmon, R.S.; eds. 2nd Edition. New York, New York: Oxford University Press. TIC: 234680.

109991 Sheppard, M.I. and Thibault, D.H. 1990. "Default Soil Solid/Liquid Partition Coefficients, Kds, for Four Major Soil Types: A Compendium." *Health Physics, 59,* (4), 471-482. New York, New York: Pergamon. TIC: 245952.

110009 Pickett, D.A. and Murphy, W.M. 1999. "Unsaturated Zone Waters from the Nopal I Natural Analog, Chihuahua, Mexico - Implications for Radionuclide Mobility at Yucca Mountain." *Scientific Basis for Nuclear Waste Management XXII, Symposium held November 30-December 4, 1998, Boston, Massachusetts.* Wronkiewicz, D.J. and Lee, J.H., eds. *556,* 809-816. Warrendale, Pennsylvania: Materials Research Society. TIC: 246426.

110071 WoldeGabriel, G.; Keating, G.N.; and Valentine, G.A. 1999. "Effects of Shallow Basaltic Intrusion into Pyroclastic Deposits, Grants Ridge, New Mexico, USA." *Journal of Volcanology and Geothermal Research, 92,* ([3]), 389-411. [New York, New York]: Elsevier Science B.V. TIC: 246037.

110351 ICRP (International Commission on Radiological Protection) 1980. *Limits for Intakes of Radionuclides by Workers.* Volume 4, No. 3/4 of *Annals of the ICRP.* Sowby, F.D., ed. ICRP Publication 30 Part 2. New York, New York: Pergamon Press. TIC: 4941.

110352 ICRP (International Commission on Radiological Protection) 1981. *Limits for Intakes of Radionuclides by Workers.* Volume 6, No. 2/3 of *Annals of the ICRP.* Sowby, F.D., ed. ICRP Publication 30 Part 3, Including Addendum to Parts 1 and 2. New York, New York: Pergamon Press. TIC: 4943.

110386 ICRP (International Commission on Radiological Protection) 1979. *Limits for Intakes of Radionuclides by Workers.* Volume 2, No. 3/4 of *Annals of the ICRP.* Sowby, F.D., ed. ICRP Publication 30 Part 1. New York, New York: Pergamon Press. TIC: 4939.

110491 Zyvoloski, G.A.; Robinson, B.A.; Dash, Z.V.; and Trease, L.L. 1997. *Summary of the Models and Methods for the FEHM Application—A Finite-Element Heat- and Mass-Transfer Code.* LA-13307-MS. [Los Alamos, New Mexico]: Los Alamos National Laboratory. TIC: 235587.

110520 CRWMS M&O 1999. *Environmental Transport Parameters Analysis.* ANL-MGR-MD-000007 REV 00. Las Vegas, Nevada: CRWMS M&O. ACC: MOL.19991115.0238.

110523 CRWMS M&O 1999. *Transfer Coefficient Analysis.* ANL-MGR-MD-000008 REV 00. Las Vegas, Nevada: CRWMS M&O. ACC: MOL.19991115.0237.

110602 CRWMS M&O 1999. *Input Parameter Values for External and Inhalation Radiation Exposure Analysis.* ANL-MGR-MD-000001 REV 00. Las Vegas, Nevada: CRWMS M&O. ACC: MOL.19990923.0235.

110635 CRWMS M&O 1999. *Dose Conversion Factor Analysis: Evaluation of GENII-S Dose Assessment Methods.* ANL-MGR-MD-000002 REV 00. Las Vegas, Nevada: CRWMS M&O. ACC: MOL.19991207.0215.

110951 State of Nevada 1997. *Ground Water Pumpage Inventory Amargosa Valley, No. 230 1997.* Carson City, Nevada: State of Nevada, Department of Conservation and Natural Resources. ACC: MOL.19990329.0141.

111028 Ebert, W.L.; Hoburg, R.F.; and Bates, J.K. 1991. "The Sorption of Water on Obsidian and a Nuclear Waste Glass." *Physics and Chemistry of Glasses, 32,* (4), 133-137. Sheffield, England: Society of Glass Technology. TIC: 246078.

111464 Atkins, P.W. 1990. *Physical Chemistry.* 4th Edition. New York, New York: W.H. Freeman and Company. TIC: 245483.

111561 Weast, R.C., ed. 1985. *CRC Handbook of Chemistry and Physics.* 66th Edition. Boca Raton, Florida: CRC Press. TIC: 216054.

111880 CRWMS M&O 2000. *Summary of In-Package Chemistry for Waste Forms.* ANL-EBS-MD-000050 REV 00. Las Vegas, Nevada: CRWMS M&O. ACC: MOL.20000217.0217.

111961 Bulmer, M.G. 1979. *Principles of Statistics.* 3rd Edition. New York, New York: Dover. TIC: 245835.

112060 Rai, D. and Ryan, J.L. 1982. "Crystallinity and Solubility of Pu(IV) Oxide and Hydrous Oxide in Aged Aqueous Suspensions." *Radiochimica Acta, 30,* 213-216. München, Germany: R. Oldenbourg Verlag. TIC: 219107.

112089 Henningson, P.J. 1998. *Cladding Integrity Under Long Term Disposal.* 51-1267509-00. Lynchburg, Virginia: Framatome Technologies. ACC: MOL.19990310.0103.

112115 Evans, M.; Hastings, N.; and Peacock, B. 1993. *Statistical Distributions.* 2nd Edition. New York, New York: John Wiley & Sons. TIC: 246114.

112178 Shoesmith, D.W. and King, F. 1998. *The Effects of Gamma Radiation on the Corrosion of Candidate Materials for the Fabrication of Nuclear Waste Packages.* AECL-11999. Pinawa, Manitoba, Canada: Atomic Energy of Canada Limited. ACC: MOL.19990311.0212.

112757 Lawrence Berkeley National Laboratory 1999. *Software Code: ITOUGH2 V3.2_drift.* V3.2_drift. SUN. 10055-3.2_DRIFT-00.

113260 Isobe, H.; Murakami, T.; and Ewing, R.C. 1992. "Alteration of Uranium Minerals in the Koongarra Deposit, Australia: Unweathered Zone." *Journal of Nuclear Materials, 190,* 174-187. Amsterdam, The Netherlands: Elsevier Science Publishers. TIC: 246371.

113942 Lawrence Berkeley National Laboratory 1999. *Software Code: T2R3D V1.4.* V1.4. SUN, DEC / ALPHA. 10006-1.4-00.

113943 LBNL 1999. *Software Code: TOUGH2* . V1.11 MEOS9nTV1.0. MAC, SUN, DEC/Alpha, PC. 10065-1.11MEOS9NTV1.0-00.

114109 Incropera, F.P. and DeWitt, D.P. 1985. *Fundamentals of Heat and Mass Transfer.* New York, New York: John Wiley & Sons. TIC: 208420.

114277 CRWMS M&O 2000. *Development of Numerical Grids for UZ Flow and Transport Modeling.* ANL-NBS-HS-000015 REV 00. Las Vegas, Nevada: CRWMS M&O. ACC: MOL.19990721.0517.

114430 Wan, J. and Wilson, J.L. 1994. "Colloid Transport in Unsaturated Porous Media." *Water Resources Research, 30,* (4), 857-864. Washington, D.C.: American Geophysical Union. TIC: 222359.

116135 EPA (U.S. Environmental Protection Agency) 1997. "Activity Factors." Volume 3 of *Exposure Factors Handbook.* EPA/600/P-95/002Fc. Washington, D.C.: U.S. Environmental Protection Agency. TIC: 241062.

117033 Bruton, C.J.; Glassley, W.E.; and Meike, A. 1995. *Geothermal Areas as Analogues to Chemical Processes in the Near-Field and Altered Zone of the Potential Yucca Mountain, Nevada Repository.* UCRL-ID-119842. Livermore, California: Lawrence Livermore National Laboratory. ACC: MOV.19980504.0002.

117076 Sandia National Laboratories 1998. *Software Code: GENII-S V1.4.8.5* . V1.4.8.5. 30034 V1.4.8.5.

117112 Pruess, K.; Faybishenko, B.; and Bodvarsson, G.S. 1999. "Alternative Concepts and Approaches for Modeling Flow and Transport in Thick Unsaturated Zones of Fractured Rocks." *Journal of Contaminant Hydrology, 38,* (1-3), 281-322. New York, New York: Elsevier. TIC: 244160.

117127 Sonnenthal, E.L. and Bodvarsson, G.S. 1999. "Constraints on the Hydrology of the Unsaturated Zone at Yucca Mountain, NV from Three-Dimensional Models of Chloride and Strontium Geochemistry." *Journal of Contaminant Hydrology, 38,* (1-3), 107-156. New York, New York: Elsevier. TIC: 244160.

117161 Wu, Y-S.; Haukwa, C.; and Bodvarsson, G.S. 1999. "A Site-Scale Model for Fluid and Heat Flow in the Unsaturated Zone of Yucca Mountain, Nevada." *Journal of Contaminant Hydrology, 38,* (1-3), 185-215. New York, New York: Elsevier. TIC: 244160.

117820 Stockman, H.; Krumhansl, J.; Ho, C.; and McConnell, V. 1994. *The Valles Natural Analogue Project.* NUREG/CR-6221. Washington, D.C.: U.S. Nuclear Regulatory Commission. TIC: 246123.

119132 Valentine, G.A.; WoldeGabriel, G.; Rosenberg, N.D.; Carter Krogh, K.E.; Crowe, B.M.; Stauffer, P.; Auer, L.H.; Gable, C.W.; Golf, F.; Warren, R.; and Perry, F.V. 1998. "Physical Processes of Magmatism and Effects on the Potential Repository: Synthesis of Technical Work through Fiscal Year 1995." Chapter 5 of *Volcanism Studies: Final Report for the Yucca Mountain Project.* Perry, F.V.; Crowe, B.M.; Valentine, G.A.; and Bowker, L.M., eds. LA-13478. Los Alamos, New Mexico: Los Alamos National Laboratory. TIC: 246726.

119317 Quiring, R.F. 1968. *Climatological Data Nevada Test Site and Nuclear Rocket Development Station.* ESSA Research Laboratories Technical Memorandum - ARL 7. Las Vegas, Nevada: U.S. Department of Commerce, Environmental Science Services Administration Research Laboratories. ACC: NNA.19870406.0047.

119392 Brooks, R.H. and Corey, A.T. 1966. "Properties of Porous Media Affecting Fluid Flow." *Journal of the American Society of Civil Engineers, Irrigation and Drainage Division, 92,* (IR2), 61-89. New York, New York: American Society of Civil Engineers. TIC: 216867.

119404 Brekke, T.L.; Cording, E.J.; Daemen, J.; Hart, R.D.; Hudson, J.A.; Kaiser, P.K.; and Pelizza, S. 1999. *Panel Report on the Drift Stability Workshop, Las Vegas, Nevada, December 9-11, 1998.* Las Vegas, Nevada: Management and Technical Support Services. ACC: MOL.19990331.0102.

119412 CRWMS M&O 2000. *Seepage Calibration Model and Seepage Testing Data.* MDL-NBS-HS-000004 REV 00. Las Vegas, Nevada: CRWMS M&O. ACC: MOL.19990721.0521.

119529 Perry, R.H., ed. 1963. *Chemical Engineers' Handbook.* 4th Edition. New York, New York: McGraw-Hill. TIC: 237828.

119544 Roy, A.K.; Fleming, D.L.; and Lum, B.Y. 1998. "Stress Corrosion Cracking of Fe-Ni-Cr-Mo, Ni-Cr-Mo and Ti Alloys in 90°C Acidic Brine." *Corrosion 98, [Proceedings, San Diego, California, March 22-27, 1998].* Paper No. 157. Pages 1-6. Houston, Texas: NACE International. TIC: 242765.

119607 NWRPO (Nuclear Waste Repository Project Office) 1999. *Nye County Early Warning Drilling Program Phase I - FY 1999 Data Package.* Pahrump, Nevada: Nye County Nuclear Waste Repository Project Office. ACC: MOL.19991101.0001.

119693 Reamer, C.W. 1999. "Issue Resolution Status Report (Key Technical Issue: Igneous Activity, Revision 2)." Letter from C.W. Reamer (NRC) to Dr. S. Brocoum (DOE/YMSCO), July 16, 1999, with enclosure. ACC: MOL.19990810.0639.

120498 Thomas, J.G.N. 1994. "The Mechanism of Corrosion Prevention by Inhibitors." Volume 2, Chapter 17.3 of *Corrosion: Corrosion Control.* Shreir, L.L.; Jarman, R.A.; and Burstein, G.T., eds. 3rd Edition. Woburn, Massachusetts: Butterworth-Heinemann. TIC: 244694.

120903 CRWMS M&O 2000. *Ventilation Model.* ANL-EBS-MD-000030 REV 00. Las Vegas, Nevada: CRWMS M&O. ACC: MOL.20000107.0330.

121006 Lichtner, P.C.; Keating, G.; and Carey, B. 1999. *A Natural Analogue for Thermal-Hydrological-Chemical Coupled Processes at the Proposed Nuclear Waste Repository at Yucca Mountain, Nevada.* LA-13610-MS. Los Alamos, New Mexico: Los Alamos National Laboratory. TIC: 246032.

121082 Biot, M.A. 1941. "General Theory of Three-Dimensional Consolidation." *Journal of Applied Physics, 12,* 155-164. [New York, New York: American Institute of Physics]. TIC: 220089.

121169 Buscheck, T.A. and Nitao, J.J. 1991. *Nonequilibrium Fracture-Matrix Flow During Episodic Infiltration Events in Yucca Mountain.* [Livermore, California]: Lawrence Livermore National Laboratory. ACC: NNA.19920131.0220.

121300 CRWMS M&O 1999. *Waste Package Behavior in Magma.* CAL-EBS-ME-000002 REV 00. Las Vegas, Nevada: CRWMS M&O. ACC: MOL.19991022.0201.

122125 Kracek, F.C. 1928. "P-T-X Relations for Systems of Two or More Components and Containing Two or More Phases (L-V, LI-LII-V, and S-L-V Systems)." *International Critical Tables of Numerical Data, Physics, Chemistry and Technology.* 1st Edition. Washburn, E.W., ed. Volume 3. Pages 351-385. New York, New York: McGraw-Hill Book Company. TIC: 243268.

122797 CRWMS M&O 2000. *UZ Flow Models and Submodels.* MDL-NBS-HS-000006 REV 00. Las Vegas, Nevada: CRWMS M&O. ACC: MOL.19990721.0527.

122799 CRWMS M&O 2000. *UZ Colloid Transport Model.* ANL-NBS-HS-000028 REV 00. Las Vegas, Nevada: CRWMS M&O. ACC: MOL.20000822.0005.

122894 CRWMS M&O 2000. *Seepage Model for PA Including Drift Collapse.* MDL-NBS-HS-000002 REV 00. Las Vegas, Nevada: CRWMS M&O. ACC: MOL.19990721.0525.

122990 Crank, J. 1975. *The Mathematics of Diffusion.* 2nd Edition. Oxford, United Kingdom: Oxford University Press. TIC: 9662.

123261 Ho, C.K. and Wilson, M.L. 1998. "Calculation of Discrete Fracture Flow Paths in Dual-Continuum Models." *High-Level Radioactive Waste Management, Proceedings of the Eighth International Conference, Las Vegas, Nevada, May 11-14, 1998.* Pages 375-377. La Grange Park, Illinois: American Nuclear Society. TIC: 237082.

123650 USGS (U.S. Geological Survey) 2000. *Simulation of Net Infiltration for Modern and Potential Future Climates.* ANL-NBS-HS-000032 REV 00. Denver, Colorado: U.S. Geological Survey. ACC: MOL.20000801.0004.

123761 Tsang, C-F.; Li, G.; Birkholzer, J.; and Tsang, Y. 1997. *Drift Scale Abstraction: Additional Results on Seepage into Drifts and Model Testing Against Niche Liquid Release Test.* Internal Report. Berkeley, California: Lawrence Berkeley National Laboratory. ACC: MOL.19980506.0008.

123916 CRWMS M&O 2000. *Abstraction of Drift-Scale Coupled Processes.* ANL-NBS-HS-000029 REV 00. Las Vegas, Nevada: CRWMS M&O. ACC: MOL.20000525.0371.

124152 Goodwin, B.W.; McConnell, D.B.; Andres, T.H.; Hajas, W.C.; LeNeveu, D.M.; Melnyk, T.W.; Sherman, G.R.; Stephens, M.E.; Szekely, J.G.; Bera, P.C.; Cosgrove, C.M.; Dougan, K.D.; Keeling, S.B.; Kitson, C.I.; Kummen, B.C.; Oliver, S.E.; Witzke, K.; Wojciechowski, L.; and Wikjord, A.G. 1994. *The Disposal of Canada's Nuclear Fuel Waste: Postclosure Assessment of a Reference System.* AECL-10717. Pinawa, Manitoba, Canada: Whiteshell Laboratories. TIC: 212480.

124275 Carroll, S.; Mroczek, E.; Alai, M.; and Ebert, M. 1998. "Amorphous Silica Precipitation (60 to 120°C): Comparison of Laboratory and Field Rates." *Geochimica et Cosmochimica Acta, 62,* (8), 1379-1396. New York, New York: Elsevier Science. TIC: 243029.

124293 Klein, C. and Hurlbut, C.S. 1999. *Manual of Mineralogy.* 21st Edition, Revised. New York, New York: John Wiley & Sons. TIC: 246258.

124812 Payne, T.E.; Edis, R.; and Seo, T. 1992. "Radionuclide Transport by Groundwater Colloids at the Koongarra Uranium Deposit." *Scientific Basis for Nuclear Waste Management XV, Symposium held November 4-7, 1991, Strasbourg, France.* Sombret, C.G., ed. *257,* 481-488. Pittsburgh, Pennsylvania: Materials Research Society. TIC: 204618.

125087 Hoffman, D.C.; Stone, R.; and Dudley, W.W., Jr. 1977. *Radioactivity in the Underground Environment of the Cambric Nuclear Explosion at the Nevada Test Site.* LA-6877-MS. Los Alamos, New Mexico: Los Alamos Scientific Laboratory. ACC: HQS.19880517.1989.

125130 CRWMS M&O 1999. *In Drift Corrosion Products.* ANL-EBS-MD-000041 REV 00. Las Vegas, Nevada: CRWMS M&O. ACC: MOL.20000106.0438.

125156 CRWMS M&O 2000. *Waste Form Colloid-Associated Concentrations Limits: Abstraction and Summary.* ANL-WIS-MD-000012 REV 00. Las Vegas, Nevada: CRWMS M&O. ACC: MOL.20000525.0397.

125168 Hoffman, D.C. and Daniels, W.R. 1981. *Assessment of the Potential for Radionuclide Migration from a Nuclear Explosion Cavity.* LA-UR-81-3181. Los Alamos, New Mexico: Los Alamos National Laboratory. TIC: 204725.

125227 Ivanovich, M.; Duerden, P.; Payne, T.; Nightingale, T.; Longworth, G.; Wilkins, M.A.; Edghill, R.B.; Cockayne, D.J.; and Davey, B.G. 1987. "Natural Analogue Study of the Distribution of Uranium Series Radionuclides Between the Colloid and Solute Phases in the Hydrogeological System of the Koongarra Uranium Deposit N.T., Australia." *Natural Analogues in Radioactive Waste Disposal, Proceedings, Symposium held in Brussels, Belgium, 28-30 April 1987.* Come, B. and Chapman, N.A., eds. EUR 11037 EN. Pages 300-313. Norwell, Massachusetts: Graham & Trotman. TIC: 247254.

125262 Janeczek, J. and Ewing, R.C. 1992. "Dissolution and Alteration of Uraninite Under Reducing Conditions." *Journal of Nuclear Materials, 190,* 157-173. Amsterdam, The Netherlands: Elsevier Science. TIC: 247465.

125291 Johnson, A.B., Jr. and Francis, B. 1980. *Durability of Metals from Archaeological Objects, Metal Meteorites, and Native Metals.* PNL-3198. Richland, Washington: Pacific Northwest Laboratory. TIC: 229619.

125332 Stumm, W. and Morgan, J.J. 1996. *Aquatic Chemistry: Chemical Equilibria and Rates in Natural Waters.* 3rd Edition. New York, New York: John Wiley & Sons. TIC: 246296.

125338 Rosenberg, N.D.; Knauss, K.G.; and Dibley, M.J. 1999. *Evaporation of J13 Water: Laboratory Experiments and Geochemical Modeling.* UCRL-ID-134852. Livermore, California: Lawrence Livermore National Laboratory. TIC: 246322.

125339 Rosenberg, N.D.; Knauss, K.G.; and Dibley, M.J. 1999. *Evaporation of Topopah Spring Tuff Pore Water.* UCRL-ID-135765. [Livermore, California]: Lawrence Livermore National Laboratory. TIC: 246231.

126083 Miekeley, N.; Jesus, H.C.; Silveira, C.L.P.; and Kuechler, I.L. 1989. "Colloid Investigations in the 'Pocos de Caldas' Natural Analogue Project." *Scientific Basis for Nuclear Waste Management XII, Symposium held October 10-13, 1988, Berlin, Germany.* Lutze, W. and Ewing, R.C., eds. *127,* 831-842. Pittsburgh, Pennsylvania: Materials Research Society. TIC: 203660.

126089 Miller, W.; Alexander, R.; Chapman, N.; McKinley, I.; and Smellie, J. 1994. *Natural Analogue Studies in the Geological Disposal of Radioactive Wastes.* Studies in Environmental Science 57. New York, New York: Elsevier. TIC: 101822.

126105 Murphy, W.M.; Pearcy, E.C.; Green, R.T.; Prikryl, J.D.; Mohanty, S.; Leslie, B.W.; and Nedungadi, A. 1998. "A Test of Long-Term, Predictive, Geochemical Transport Modeling at the Akrotiri Archaeological Site." *Journal of Contaminant Hydrology, 29,* 245-279. New York, New York: Elsevier. TIC: 247211.

126172 Ohnuki, T.; Murakami, T.; Sekine, K.; Yanase, N.; Isobe, H.; and Kobayashi, Y. 1990. "Migration Behavior of Uranium Series Nuclides in Altered Quartz-Chlorite Schist." *Scientific Basis for Nuclear Waste Management XIII, Symposium held November 27-30, 1989, Boston, Massachusetts.* Oversby, V.M. and Brown, P.W., eds. *176,* 607-614. Pittsburgh, Pennsylvania: Materials Research Society. TIC: 203658.

126475 CRWMS M&O 1999. *TBV-332/TBD-325 Resolution Analysis: Geotechnical Rock Properties.* B00000000-01717-5705-00134 REV 00. Las Vegas, Nevada: CRWMS M&O. ACC: MOL.19991005.0235.

126636 Smellie, J.; Chapman, N.; McKinley, I.; Penna Franca, E.; and Shea, M. 1989. "Testing Safety Assessment Models Using Natural Analogues in High Natural-Series Groundwaters. The Second Year of the Pocos de Caldas Project." *Scientific Basis for Nuclear Waste Management XII, Symposium held October 10-13, 1988, Berlin, Germany.* Lutze, W. and Ewing, R.C., eds. *127,* 863-870. Pittsburgh, Pennsylvania: Materials Research Society. TIC: 203660.

126796 Thompson, J.L., ed. 1986. *Laboratory and Field Studies Related to the Radionuclide Migration Project, October 1, 1984—September 30, 1985.* LA-10644-PR. Los Alamos, New Mexico: Los Alamos National Laboratory. TIC: 246828.

126924 Waber, N. 1991. *Mineralogy, Petrology and Geochemistry of the Pocos de Caldas Analogue Study Sites, Minas Gerais, Brazil. II. Morro do Ferro.* SKB Technical Report 90-12. Stockholm, Sweden: Swedish Nuclear Fuel and Waste Management Company. TIC: 206350.

127012 Neymark, L.A. and Paces, J.B. 2000. "Consequences of Slow Growth for 230Th/U Dating of Quaternary Opals, Yucca Mountain, NV, USA." *Chemical Geology, 164,* 143-160. Amsterdam, The Netherlands: Elsevier Science. TIC: 246316.

127147 Schorscher, H.D. and Shea, M.E. 1991. *The Regional Geology, Mineralogy and Geochemistry of the Pocos de Caldas Alkaline Caldera Complex, Minas Gerais, Brazil.* SKB Technical Report 90-10. Stockholm, Sweden: Swedish Nuclear Fuel and Waste Management Company. TIC: 206335.

127163 Weast, R.C., ed. 1972. *CRC Handbook of Chemistry and Physics.* 53rd Edition. Cleveland, Ohio: Chemical Rubber Company. TIC: 219220.

127199 Miekeley, N.; Coutinho de Jesus, H.; Porto da Silveira, C.L.; and Degueldre, C. 1991. *Chemical and Physical Characterisation of Suspended Particles and Colloids in Waters from the Osamu Utsumi Mine and Morro do Ferro Analogue Study Sites, Pocos de Caldas, Brazil.* SKB Technical Report 90-18. Stockholm, Sweden: Swedish Nuclear Fuel and Waste Management Company. TIC: 206355.

127275 CRWMS M&O 1999. *Software Code: EQ6, Version 7.2bLV*. V7.2bLV. 10075-7.2bLV-00.

127382 Smith, R.M. and Martell, A.E. 1976. *Inorganic Complexes.* Volume 4 of *Critical Stability Constants.* New York, New York: Plenum Press. TIC: 224070.

127680 Airey, P.L. 1986. "Radionuclide Migration Around Uranium Ore Bodies in the Alligator Rivers Region of the Northern Territory of Australia — Analogue of Radioactive Waste Repositories — A Review." *Chemical Geology, 55,* (3/4), 255-268. Amsterdam, The Netherlands: Elsevier. TIC: 246691.

127768 Chapman, N.A.; McKinley, I.G.; and Smellie, J.A.T. 1984. *The Potential of Natural Analogues in Assessing Systems for Deep Disposal of High-Level Radioactive Waste.* KBS Technical Report 84-16. Stockholm, Sweden: Swedish Nuclear Fuel and Waste Management Company. TIC: 205295.

127906 LLNL (Lawrence Livermore National Laboratory) 1999. *Software Code: NUFT V3.0s.* . V3.0s. 10088-3.0s-00.

128009 Hartman, H.L. 1982. *Mine Ventilation and Air Conditioning.* Mutmansky, J.M. and Wang, Y.J., eds. 2nd Edition. New York, New York: John Wiley & Sons. TIC: 210152.

129261 CRWMS M&O 1999. *Single Heater Test Final Report.* BAB000000-01717-5700-00005 REV 00 ICN 1. Las Vegas, Nevada: CRWMS M&O. ACC: MOL.20000103.0634.

129278 CRWMS M&O 2000. *In-Drift Gas Flux and Composition.* ANL-EBS-MD-000040 REV 00. Las Vegas, Nevada: CRWMS M&O. ACC: MOL.20000523.0154.

129280 CRWMS M&O 2000. *In-Drift Colloids and Concentration.* ANL-EBS-MD-000042 REV 00. Las Vegas, Nevada: CRWMS M&O. ACC: MOL.20000509.0242.

129281 CRWMS M&O 2000. *Seepage/Cement Interactions.* ANL-EBS-MD-000043 REV 00. Las Vegas, Nevada: CRWMS M&O. ACC: MOL.20000317.0262.

129283 CRWMS M&O 2000. *Seepage/Invert Interactions.* ANL-EBS-MD-000044 REV 00. Las Vegas, Nevada: CRWMS M&O. ACC: MOL.20000523.0156.

129286 CRWMS M&O 2000. *Saturated Zone Colloid-Facilitated Transport.* ANL-NBS-HS-000031 REV 00. Las Vegas, Nevada: CRWMS M&O. ACC: MOL.20000609.0266.

129287 CRWMS M&O 2000. *In-Package Chemistry Abstraction.* ANL-EBS-MD-000037 REV 00. Las Vegas, Nevada: CRWMS M&O. ACC: MOL.20000418.0818.

129667 Lee, M.Y. and Haimson, B.C. 1999. "Initial Stress Measurements in the Exploratory Studies Facility Yucca Mountain, Nevada." *Rock Mechanics for Industry, Proceedings of the 37th U.S. Rock Mechanics Symposium, Vail, Colorado, USA, 6-9 June 1999.* Amadei, B.; Kranz, R.L.; Scott, G.A.; and Smeallie, P.H., eds. *2,* 743-750. Brookfield, Vermont: A.A. Balkema. TIC: 245246.

129676 Bedinger, M.S.; Sargent, K.A.; Langer, W.H.; Sherman, F.B.; Reed, J.E.; and Brad, B.T. 1989. *Studies of Geology and Hydrology in the Basin and Range Province, Southwestern United States, for Isolation of High-Level Radioactive Waste—Basis of Characterization and Evaluation.* Professional Paper 1370-A. Denver, Colorado: U.S. Geological Survey. ACC: NNA.19910524.0125.

129721 Geldon, A.L.; Umari, A.M.A.; Earle, J.D.; Fahy, M.F.; Gemmell, J.M.; and Darnell, J. 1998. *Analysis of a Multiple-Well Interference Test in Miocene Tuffaceous Rocks at the C-Hole Complex, May-June 1995, Yucca Mountain, Nye County, Nevada.* Water-Resources Investigations Report 97-4166. Denver, Colorado: U.S. Geological Survey. TIC: 236724.

130084 Kuehn, T.H. and Goldstein, R.J. 1978. "An Experimental Study of Natural Convection Heat Transfer in Concentric and Eccentric Horizontal Cylindrical Annuli." *Journal of Heat Transfer, 100,* 635-640. New York, New York: American Society of Mechanical Engineers. TIC: 244433.

130526 Burnett, R.D. and Frind, E.O. 1987. "Simulation of Contaminant Transport in Three Dimensions 2. Dimensionality Effects." *Water Resources Research, 23,* (4), 695-705. Washington, D.C.: American Geophysical Union. TIC: 246359.

130561 Buscheck, T.A. and Nitao, J.J. [1994]. *The Impact of Buoyant, Gas-Phase Flow and Heterogeneity on Thermo-Hydrological Behavior at Yucca Mountain.* [UCRL-JC-115351]. Livermore, California: Lawrence Livermore National Laboratory. ACC: NNA.19940524.0012.

130979 CRWMS M&O 1999. *Recharge and Lateral Groundwater Flow Boundary Conditions for the Saturated Zone Site-Scale Flow and Transport Model.* ANL-NBS-MD-000010 REV 00. Las Vegas, Nevada: CRWMS M&O. ACC: MOL.19991118.0188.

131108 CRWMS M&O 2000. *Water Diversion Model.* ANL-EBS-MD-000028 REV 00. Las Vegas, Nevada: CRWMS M&O. ACC: MOL.20000107.0329.

131150 CRWMS M&O 2000. *In-Drift Thermal-Hydrological-Chemical Model.* ANL-EBS-MD-000026 REV 00. Las Vegas, Nevada: CRWMS M&O. ACC: MOL.20000113.0488.

131202 Lide, D.R., ed. 1991. *CRC Handbook of Chemistry and Physics.* 72nd Edition. Boca Raton, Florida: CRC Press. TIC: 3595.

131816 Daily, W.; Lin, W.; and Buscheck, T. 1987. "Hydrological Properties of Topopah Spring Tuff: Laboratory Measurements." *Journal of Geophysical Research, 92,* (B8), 7854-7864. Washington, D.C.: American Geophysical Union. TIC: 226512.

131861 CRWMS M&O 2000. *Commercial Spent Nuclear Fuel Degradation in Unsaturated Drip Tests.* Input Transmittal WP-WP-99432.T. Las Vegas, Nevada: CRWMS M&O. ACC: MOL.20000107.0209.

132164 Coughtrey, P.J.; Jackson, D.; and Thorne, M.C. 1983. *Radionuclide Distribution and Transport in Terrestrial and Aquatic Ecosystems, A Critical Review of Data.* Five of six volumes. Rotterdam, The Netherlands: A.A. Balkema. TIC: 240299.

132447 Los Alamos National Laboratory 2000. *Software Code: FEHM* . V2.10. SUN Ultra Sparc, PC. 10086-2.10-00.

132448 LBNL 1999. *Software Code: DCPT.* V1.0. PC. 10078-1.0-00.

133329 CRWMS M&O 2000. *Water Distribution and Removal Model.* ANL-EBS-MD-000032 REV 00. Las Vegas, Nevada: CRWMS M&O. ACC: MOL.20000504.0303.

133378 ASM International 1987. *Corrosion.* Volume 13 of *ASM Handbook.* Formerly 9th Edition, Metals Handbook. [Materials Park, Ohio]: ASM International. TIC: 240704.

133719 CRWMS M&O 2000. *Identification of Ingestion Exposure Parameters.* ANL-MGR-MD-000006 REV 00. Las Vegas, Nevada: CRWMS M&O. ACC: MOL.20000216.0104.

134136 Lawrence Berkeley National Laboratory 1999. *Software Code: GSLIB V1.0 Module SISIM V1.203.* V1.0. Sun, PC. 10001-1.0MSISIMV1.203-00.

134141 Lawrence Berkeley National Laboratory 1999. *Software Code: EXT.* V1.0. Sun. 10047-1.0-00.

134175 Golian, C. and Lever, D.A. 1992. "Radionuclide Transport." Volume 14 of *Alligator Rivers Analogue Project.* DOE/HMIP/RR/92/084. Menai, New South Wales, Australia: Australian Nuclear Science and Technology Organisation. TIC: 235988.

134225 Sverjensky, D.; Bennett, D.G.; and Read, D. 1992. *Geochemical Modelling of Secondary Uranium Ore Formation.* Volume 11 of *Alligator Rivers Analogue Project.* DOE/HMIP/RR/92/081. Menai, Australia: Australian Nuclear Science and Technology Organisation. TIC: 235986.

134666 Keenan, J.H.; Keyes, F.G.; Hill, P.G.; and Moore, J.G. 1969. *Steam Tables, Thermodynamic Properties of Water Including Vapor, Liquid, and Solid Phases (English Units).* New York, New York: John Wiley & Sons. TIC: 246766.

134732 CRWMS M&O 2000. *Analysis of Base-Case Particle Tracking Results of the Base-Case Flow Fields (ID: U0160).* ANL-NBS-HS-000024 REV 00. Las Vegas, Nevada: CRWMS M&O. ACC: MOL.20000207.0690.

135344 U.S. Census Bureau 1999. "1990 US Census Data, Database: C90STF3A, Summary Level: State--County--County Subdivision, Amargosa Valley Division: FIPS.STATE=32, FIPS.COUNTY90=023, FIPS.COUSUB=94028." Washington, D.C.: U.S. Census Bureau. Accessed November 12, 1999. TIC: 245829. http://venus.census.gov/cdrom/lookup

135894 Ahn, T.M.; Cragnolino, G.A.; Chan, K.S.; and Sridhar, N. 1999. "Scientific Bases for Cladding Credit as a Barrier to Radionuclide Release at the Proposed Yucca Mountain Repository." *Scientific Basis for Nuclear Waste Management XXII, Symposium held November 30-December 4, 1998, Boston, Massachusetts.* Wronkiewicz, D.J. and Lee, J.H., eds. *556,* 525-533. Warrendale, Pennsylvania: Materials Research Society. TIC: 246426.

135910 S. Cohen & Associates 1999. *Effectiveness of Fuel Rod Cladding as an Engineered Barrier in the Yucca Mountain Repository.* McLean, Virginia: S. Cohen & Associates. TIC: 246541.

135997 Doughty, C. 1999. "Investigation of Conceptual and Numerical Approaches for Evaluating Moisture, Gas, Chemical, and Heat Transport in Fractured Unsaturated Rock." *Journal of Contaminant Hydrology, 38,* (1-3), 69-106. New York, New York: Elsevier. TIC: 244160.

136058 CRWMS M&O 2000. *Clad Degradation–Local Corrosion of Zirconium and Its Alloys Under Repository Conditions.* ANL-EBS-MD-000012 REV 00. Las Vegas, Nevada: CRWMS M&O. ACC: MOL.20000405.0479.

136060 CRWMS M&O 2000. *CSNF Waste Form Degradation: Summary Abstraction.* ANL-EBS-MD-000015 REV 00. Las Vegas, Nevada: CRWMS M&O. ACC: MOL.20000121.0161.

136105 CRWMS M&O 1999. *Breakage of Commercial Spent Nuclear Fuel Cladding by Mechanical Loading.* CAL-EBS-MD-000001 REV 00. Las Vegas, Nevada: CRWMS M&O. ACC: MOL.19991213.0237.

136281 CRWMS M&O 2000. *Evaluate Soil/Radionuclide Removal by Erosion and Leaching.* ANL-NBS-MD-000009 REV 00. Las Vegas, Nevada: CRWMS M&O. ACC: MOL.20000310.0057.

136285 CRWMS M&O 2000. *Non-Disruptive Event Biosphere Dose Conversion Factors.* ANL-MGR-MD-000009 REV 00. Las Vegas, Nevada: CRWMS M&O. ACC: MOL.20000307.0383.

136368 USGS (U.S. Geological Survey) 2000. *Future Climate Analysis.* ANL-NBS-GS-000008 REV 00. Denver, Colorado: U.S. Geological Survey. ACC: MOL.20000629.0907.

136383 CRWMS M&O 2000. *Inventory Abstraction.* ANL-WIS-MD-000006 REV 00. Las Vegas, Nevada: CRWMS M&O. ACC: MOL.20000414.0643.

136384 Bodvarsson, G.S.; Pruess, K.; Haukwa, C.; and Ojiambo, S. B. 1990. "Evaluation of Reservoir Model Predictions for Olkaria East Geothermal Field, Kenya." *Geothermics, 19,* (5), 399-414. Oxford, United Kingdom: Pergamon. TIC: 246739.

136391 Bodvarsson, G.S.; Pruess, K.; Stefansson, V.; Bjornsson, S.; and Ojiambo, S.B. 1987. "East Olkaria Geothermal Field, Kenya, 1. History Match with Production and Pressure Decline Data." *Journal of Geophysical Research, 92,* (B1), 521-539. [Washington, D.C.]: American Geophysical Union. TIC: 236629.

136393 Bodvarsson, G.S.; Pruess, K.; Stefansson, V.; Bjornsson, S.; and Ojiambo, S.B. 1987. "East Olkaria Geothermal Field, Kenya, 2. Predictions of Well Performance and Reservoir Depletion." *Journal of Geophysical Research, 92,* (B1), 541-554. [Washington, D.C.]: American Geophysical Union. TIC: 246738.

137136 Bodvarsson, G.S.; Pruess, K.; Stefansson, V.; and Eliasson, E.T. 1984. "The Krafla Geothermal Field, Iceland, 2. The Natural State of the System." *Water Resources Research, 20,* (11), 1531-1544. Washington, D.C.: American Geophysical Union. TIC: 246734.

137139 Bodvarsson, G.S.; Pruess, K.; Stefansson, V.; and Eliasson, E.T. 1984. "The Krafla Geothermal Field, Iceland: 3. The Generating Capacity of the Field." *Water Resources Research, 20,* (11), 1545-1559. Washington, D.C.: American Geophysical Union. TIC: 246737.

137409 O'Sullivan, M. J.; Barnett, B. G.; and Razali, M. Y. 1990. "Numerical Simulation of the Kamojang Geothermal Field, Indonesia." *1990 International Symposium on Geothermal Energy, Transactions, Geothermal Resources Council, 1990 Annual Meeting, 20-24 August, 1990, Kailua-Kona, Hawaii.* Volume 14, Part II. Pages 1317-1324. Davis, California: Geothermal Resources Council. TIC: 246942.

137923 Menzies, A.J.; Granados, E.E.; Sanyal, S.K.; Merida-I, L.; and Caicedo-A, A. 1991. "Numerical Modeling of the Initial State and Matching of Well Test Data from the Zunil Geothermal Field, Guatemala." *Proceedings, Sixteenth Workshop, Geothermal Reservoir Engineering, January 23-25, 1991, Stanford, California.* Workshop Report SGP-TR-134. Pages 193-201. Stanford, California: Stanford University. TIC: 246832.

138273 Zimmerman, R.M.; Schuch, R.L.; Mason, D.S.; Wilson, M.L.; Hall, M.E.; Board, M.P.; Bellman, R.P.; and Blanford, M.L. 1996. *Final Report: G-Tunnel Heated Block Experiment.* SAND84-2620. Albuquerque, New Mexico: Sandia National Laboratories. ACC: MOL.19961217.0085.

138603 Bodvarsson, G.S.; Bjornsson, S.; Gunnarsson, A.; Gunnlaugsson, E.; Sigurdsson, O.; Stefansson, V.; and Steingrimsson, B. 1988. "A Summary of Modeling Studies of the Nesjavellir Geothermal Field, Iceland." *Proceedings, Thirteenth Workshop, Geothermal Reservoir Engineering, January 19-21, 1998, Stanford, California.* Workshop Report SGP-TR-113. Pages 83-91. Stanford, California: Stanford University. TIC: 246824.

138618 Bodvarsson, G.S.; Gislason, G.; Gunnlaugsson, E.; Sigurdsson, O.; Stefansson, V.; and Steingrimsson, B. 1993. "Accuracy of Reservoir Predictions for the Nesjavellir Geothermal Field, Iceland." *Proceedings, Eighteenth Workshop, Geothermal Reservoir Engineering, Stanford, California, January 26-28, 1993.* Ramey, H.J., Jr.; Horne, R.N.; Kruger, P.; Miller, F.G.; Brigham, W.E.; and Cook, J.W., eds. Workshop Report SGP-TR-145. Pages 273-278. Stanford, California: Stanford University. TIC: 246821.

138860 CRWMS M&O 2000. *Geologic Framework Model (GFM3.1).* MDL-NBS-GS-000002 REV 00 ICN 01. Las Vegas, Nevada: CRWMS M&O. ACC: MOL.20000121.0115.

138960 CRWMS M&O 2000. *Mineralogical Model (MM3.0).* MDL-NBS-GS-000003 REV 00 ICN 01. Las Vegas, Nevada: CRWMS M&O. ACC: MOL.20000120.0477.

139195 Tokunaga, T.K. and Wan, J. 1997. "Water Film Flow Along Fracture Surfaces of Porous Rock." *Water Resources Research, 33,* (6), 1287-1295. Washington, D.C.: American Geophysical Union. TIC: 242739.

139422 USGS 2000. *Software Code: INFIL.* V2.0. 10307-2.0-00. URN-0349.

139440 CRWMS M&O 2000. *Input and Results of the Base Case Saturated Zone Flow and Transport Model for TSPA.* ANL-NBS-HS-000030 REV 00. Las Vegas, Nevada: CRWMS M&O. ACC: MOL.20000526.0330.

139563 CRWMS M&O 2000. *Igneous Consequence Modeling for the TSPA-SR.* ANL-WIS-MD-000017 REV 00. Las Vegas, Nevada: CRWMS M&O. ACC: MOL.20000501.0225.

139582 CRWMS M&O 2000. *Calibration of the Site-Scale Saturated Zone Flow Model.* MDL-NBS-HS-000011 REV 00. Las Vegas, Nevada: CRWMS M&O. ACC: MOL.20000825.0122.

139610 CRWMS M&O 2000. *Multiscale Thermohydrologic Model.* ANL-EBS-MD-000049 REV 00. Las Vegas, Nevada: CRWMS M&O. ACC: MOL.20000609.0267.

139918 Lawrence Berkeley National Laboratory 9/16/99. *Software Code: iTOUGH2.* V4.0. SUN, DEC. 10003-4.0-00.

140641 Phillips, O.M. 1991. *Flow and Reactions in Permeable Rocks.* New York, New York: Cambridge University Press. TIC: 236237.

140907 Buscheck, T.A. and Nitao, J.J. 1993. "Modeling Hydrothermal Flow in Variably Saturated, Fractured, Welded Tuff During the Prototype Engineered Barrier System Field Test of the Yucca Mountain Project." *Proceedings of Workshop V: Flow and Transport Through Unsaturated Fractured Rock—Related to High-Level Radioactive Waste Disposal, Tucson, Arizona, January 7-10, 1991.* Evans, D.D. and Nicholson, T.J., eds. NUREG/CP-0040. Pages 147-152. Washington, D.C.: U.S. Nuclear Regulatory Commission. TIC: 207128.

141044 CRWMS M&O 2000. *Characterize Framework for Igneous Activity at Yucca Mountain, Nevada (T0015).* ANL-MGR-GS-000001 REV 00. Las Vegas, Nevada: CRWMS M&O. ACC: MOL.20000720.0541.

141187 CRWMS M&O 2000. *Conceptual and Numerical Models for UZ Flow and Transport.* MDL-NBS-HS-000005 REV 00. Las Vegas, Nevada: CRWMS M&O. ACC: MOL.19990721.0526.

141389 CRWMS M&O 2000. *Analysis Comparing Advective-Dispersive Transport Solution to Particle Tracking.* ANL-NBS-HS-000001 REV 00. Las Vegas, Nevada: CRWMS M&O. ACC: MOL.19990721.0518.

141400 CRWMS M&O 2000. *In Situ Field Testing of Processes.* ANL-NBS-HS-000005 REV 00. Las Vegas, Nevada: CRWMS M&O. ACC: MOL.20000504.0304.

141407 CRWMS M&O 2000. *Natural Analogs for the Unsaturated Zone.* ANL-NBS-HS-000007 REV 00. Las Vegas, Nevada: CRWMS M&O. ACC: MOL.19990721.0524.

141418 CRWMS M&O 2000. *Particle Tracking Model and Abstraction of Transport Processes.* ANL-NBS-HS-000026 REV 00. Las Vegas, Nevada: CRWMS M&O. ACC: MOL.20000502.0237.

141580 Nicholl, M.J.; Glass, R.J.; and Wheatcraft, S.W. 1994. "Gravity-Driven Infiltration Instability in Initially Dry Nonhorizontal Fractures." *Water Resources Research, 30,* (9), 2533-2546. Washington, D.C.: American Geophysical Union. TIC: 243493.

141615 ASM International 1990. *Properties and Selection: Nonferrous Alloys and Special-Purpose Materials.* Volume 2 of *ASM Metals Handbook.* Materials Park, Ohio: American Society for Metals. TIC: 241059.

141778 Stumm, W. 1992. *Chemistry of the Solid-Water Interface, Processes at the Mineral-Water and Particle-Water Interface in Natural Systems.* New York, New York: John Wiley & Sons. TIC: 237213.

142004 CRWMS M&O 2000. *Abstraction of Drift Seepage.* ANL-NBS-MD-000005 REV 00. Las Vegas, Nevada: CRWMS M&O. ACC: MOL.20000322.0671.

142022 CRWMS M&O 2000. *Drift-Scale Coupled Processes (DST and THC Seepage) Models.* MDL-NBS-HS-000001 REV 00. Las Vegas, Nevada: CRWMS M&O. ACC: MOL.19990721.0523.

142166 Moore, D.E.; Morrow, C.A.; and Byerlee, J.D. 1986. "High-Temperature Permeability and Groundwater Chemistry of Some Nevada Test Site Tuffs." *Journal of Geophysical Research, 91,* (B2), 2163-2171. Washington, D.C.: American Geophysical Union. TIC: 226311.

142169 Morrow, C.; Lockner, D.; Moore, D.; and Byerlee, J. 1981. "Permeability of Granite in a Temperature Gradient." *Journal of Geophysical Research, 86,* (B4), 3002-3008. Washington, D.C.: American Geophysical Union. TIC: 220001.

142190 Rimstidt, J.D.; Newcomb, W.D.; and Shettel, D.L., Jr. 1989. "A Vertical Thermal Gradient Experiment to Simulate Conditions in Vapor Dominated Geothermal Systems, Epithermal Gold Deposits, and High Level Radioactive Repositories in Unsaturated Media." *[Proceedings of the 6th International Symposium on Water-Rock Interaction, WRI-6, Malvern, United Kingdom, 3-8 August 1989]*. Miles, D.L., ed. Pages 585-588. Rotterdam, The Netherlands: A.A. Balkema. TIC: 241868.

142321 CRWMS M&O 2000. *Characterize Framework for Seismicity and Structural Deformation at Yucca Mountain, Nevada.* ANL-CRW-GS-000003 REV 00. Las Vegas, Nevada: CRWMS M&O. ACC: MOL.20000510.0175.

142657 CRWMS M&O 2000. *Characterize Eruptive Processes at Yucca Mountain, Nevada.* ANL-MGR-GS-000002 REV 00. Las Vegas, Nevada: CRWMS M&O. ACC: MOL.20000517.0259.

142736 CRWMS M&O 2000. *Invert Effective Thermal Conductivity Calculation.* CAL-WIS-TH-000004 REV 00. Las Vegas, Nevada: CRWMS M&O. ACC: MOL.20000317.0593.

142844 CRWMS M&O 2000. *Evaluation of the Applicability of Biosphere-Related Features, Events, and Processes (FEP).* ANL-MGR-MD-000011 REV 00. Las Vegas, Nevada: CRWMS M&O. ACC: MOL.20000420.0075.

142970 CRWMS M&O 1999. *YMP FEP Database Rev. 00C.* Las Vegas, Nevada: CRWMS M&O. ACC: MOL.19991214.0518; MOL.19991214.0519.

143244 CRWMS M&O 2000. *Analysis of Infiltration Uncertainty.* ANL-NBS-HS-000027 REV 00. Las Vegas, Nevada: CRWMS M&O. ACC: MOL.20000525.0377.

143280 Davis, J.A. and Kent, D.B. 1990. "Surface Complexation Modeling in Aqueous Geochemistry." Chapter 5 of *Mineral-Water Interface Geochemistry.* Hochella, M.F., Jr. and White, A.F., eds. Reviews in Mineralogy Volume 23. Washington, D.C.: Mineral Society of America. TIC: 224085.

143378 CRWMS M&O 2000. *Disruptive Event Biosphere Dose Conversion Factor Analysis.* ANL-MGR-MD-000003 REV 00. Las Vegas, Nevada: CRWMS M&O. ACC: MOL.20000303.0216.

143420 CRWMS M&O 2000. *Defense High Level Waste Glass Degradation.* ANL-EBS-MD-000016 REV 00. Las Vegas, Nevada: CRWMS M&O. ACC: MOL.20000329.1183.

143569 CRWMS M&O 2000. *Summary of Dissolved Concentration Limits.* ANL-WIS-MD-000010 REV 00. Las Vegas, Nevada: CRWMS M&O. ACC: MOL.20000525.0372.

143665 CRWMS M&O 2000. *Total System Performance Assessment for the Site Recommendation.* TDR-WIS-PA-000001 REV 00. Las Vegas, Nevada: CRWMS M&O. ACC: MOL.20001005.0282.

143940 CRWMS M&O 2000. *Identification of the Critical Group (Consumption of Locally Produced Food and Tap Water).* ANL-MGR-MD-000005 REV 00. Las Vegas, Nevada: CRWMS M&O. ACC: MOL.20000224.0399.

144046 Middleman, S. 1995. *Modeling Axisymmetric Flows, Dynamics of Films, Jets, and Drops.* San Diego, California: Academic Press. TIC: 246835.

144054 CRWMS M&O 2000. *Abstraction of BDCF Distributions for Irrigation Periods.* ANL-NBS-MD-000007 REV 00. Las Vegas, Nevada: CRWMS M&O. ACC: MOL.20000517.0257.

144055 CRWMS M&O 2000. *Distribution Fitting to the Stochastic BDCF Data.* ANL-NBS-MD-000008 REV 00. Las Vegas, Nevada: CRWMS M&O. ACC: MOL.20000517.0258; MOL.20000601.0753.

144056 CRWMS M&O 2000. *Groundwater Usage by the Proposed Farming Community.* ANL-NBS-MD-000006 REV 00. Las Vegas, Nevada: CRWMS M&O. ACC: MOL.20000407.0785.

144128 CRWMS M&O 2000. *Design Analysis for UCF Waste Packages.* ANL-UDC-MD-000001 REV 00. Las Vegas, Nevada: CRWMS M&O. ACC: MOL.20000526.0336.

144229 CRWMS M&O 2000. *General Corrosion and Localized Corrosion of Waste Package Outer Barrier.* ANL-EBS-MD-000003 REV 00. Las Vegas, Nevada: CRWMS M&O. ACC: MOL.20000202.0172.

144331 CRWMS M&O 2000. *Radionuclide Transport Models Under Ambient Conditions.* MDL-NBS-HS-000008 REV 00. Las Vegas, Nevada: CRWMS M&O. ACC: MOL.19990721.0529.

144397 Bodvarsson, G.S.; Benson, S.M.; Sigurdsson, O.; Stefansson, V.; and Eliasson, E.T. 1984. "The Krafla Geothermal Field, Iceland, 1. Analysis of Well Test Data." *Water Resources Research, 20,* (11), 1515-1530. Washington, D.C.: American Geophysical Union. TIC: 247406.

144410 Bullivant, D.P. and O'Sullivan, M.J. 1998. "Inverse Modelling of the Wairakei Geothermal Field." *Proceedings of the TOUGH Workshop '98, Berkeley, California, May 4-6, 1998.* Preuss, K., ed. LBNL-41995. Pages 53-58. Berkeley, California: Lawrence Berkeley National Laboratory. TIC: 247159.

144426 CRWMS M&O 2000. *Calibrated Properties Model.* MDL-NBS-HS-000003 REV 00. Las Vegas, Nevada: CRWMS M&O. ACC: MOL.19990721.0520.

144454 CRWMS M&O 2000. *Mountain-Scale Coupled Processes (TH) Models.* MDL-NBS-HS-000007 REV 00. Las Vegas, Nevada: CRWMS M&O. ACC: MOL.19990721.0528.

144461 Davis, O.K. 1990. "Caves as Sources of Biotic Remains in Arid Western North America." *Palaeogeography, Palaeoclimatology, Palaeoecology, 76,* (3/4), 331-348. Amsterdam, The Netherlands: Elsevier Science Publishers B.V. TIC: 247413.

144612 LeCain, G.D.; Anna, L.O.; and Fahy, M.F. 2000. *Results from Geothermal Logging, Air and Core-Water Chemistry Sampling, Air-Injection Testing, and Tracer Testing in the Northern Ghost Dance Fault, Yucca Mountain, Nevada, November 1996 to August 1998.* Water-Resources Investigations Report 99-4210. Denver, Colorado: U.S. Geological Survey. TIC: 247708.

144692 CRWMS M&O 2000. *Non-Disruptive Event Biosphere Dose Conversion Factor Sensitivity Analysis.* ANL-MGR-MD-000010 REV 00. Las Vegas, Nevada: CRWMS M&O. ACC: MOL.20000420.0074.

144700 CRWMS M&O 2000. *Biosphere Dose Conversion Factors for Reasonably Maximally Exposed Individual and Average Member of Critical Group.* CAL-MGR-MD-000002 REV 00. Las Vegas, Nevada: CRWMS M&O. ACC: MOL.20000306.0251.

144730 Bilinski, H. and Schindler, P. 1982. "Solubility and Equilibrium Constants of Lead in Carbonate Solutions (25°C, I = 0.3 mol dm[-3])." *Geochimica et Cosmochimica Acta, 46,* 921-928. New York, New York: Pergamon Press . TIC: 247074.

144971 CRWMS M&O 2000. *General Corrosion and Localized Corrosion of the Drip Shield.* ANL-EBS-MD-000004 REV 00. Las Vegas, Nevada: CRWMS M&O. ACC: MOL.20000329.1185.

144986 CRWMS M&O 2000. *Analysis of Geochemical Data for the Unsaturated Zone.* ANL-NBS-HS-000017 REV 00. Las Vegas, Nevada: CRWMS M&O. ACC: MOL.20000725.0453.

145046 Machesky, M.L. 1990. "Influence of Temperature on Ion Adsorption by Hydrous Metal Oxides." *Chemical Modeling of Aqueous Systems II, Los Angeles, California, September 25-30, 1988.* Melchior, D.C. and Bassett, R.L., eds. ACS Symposium Series 416. Pages 282-292. Washington, D.C.: American Chemical Society. TIC: 241139.

145103 ASME (American Society of Mechanical Engineers) 1998. *1998 ASME Boiler and Pressure Vessel Code.* 1998 Edition with 1999 and 2000 Addenda. New York, New York: American Society of Mechanical Engineers. TIC: 247429.

145225 CRWMS M&O 1998. *Software Code: MING V1.0* . V1.0. 30018 V1.0.

145625 Zimmerman, R.M.; Blanford, M.L.; Holland, J.F.; Schuch, R.L.; and Barrett, W.H. 1986. *Final Report, G-Tunnel Small-Diameter Heater Experiments.* SAND84-2621. Albuquerque, New Mexico: Sandia National Laboratories. ACC: HQS.19880517.2365.

145631 Buesch, D.C.; Spengler, R.W.; Nelson, P.H.; Vaniman, D.T.; Chipera, S.J.; and Bish, D.L. 1995. "Geometry of the Vitric-Zeolitic Transition in Tuffs and the Relation to Fault Zones at Yucca Mountain, Nevada." *International Union of Geodesy and Geophysics, XXI General Assembly, July 2-14, 1995,* A426. Boulder, Colorado: Geological Society of America. TIC: 237709.

145636 Kneafsey, T.J. and Pruess, K. 1998. "Laboratory Experiments on Heat-Driven Two-Phase Flows in Natural and Artificial Rock Fractures." *Water Resources Research, 34,* (12), 3349-3367. Washington, D.C.: American Geophysical Union. TIC: 247468.

145771 CRWMS M&O 2000. *Analysis of Hydrologic Properties Data.* ANL-NBS-HS-000002 REV 00. Las Vegas, Nevada: CRWMS M&O. ACC: MOL.19990721.0519.

145806 Villar, E.; Bonet, A.; Diaz-Caneja, B.; Fernandez, P.L.; Gutierrez, I.; Quindos, L.S.; Solana, J.R.; and Soto, J. 1985. "Natural Evolution of Percolation Water in Altamira Cave." *Cave Science, 12,* (1), 21-24. Bridgwater, United Kingdom: British Cave Research Association. TIC: 247713.

146021 CRWMS M&O 2000. *Site Recommendation Subsurface Layout.* ANL-SFS-MG-000001 REV 00. Las Vegas, Nevada: CRWMS M&O. ACC: MOL.20000908.0276.

146022 CRWMS M&O 2000. *Ground Control for Emplacement Drifts for SR.* ANL-EBS-GE-000002 REV 00. Las Vegas, Nevada: CRWMS M&O. ACC: MOL.20000414.0875.

146427 CRWMS M&O 2000. *WAPDEG Analysis of Waste Package and Drip Shield Degradation.* ANL-EBS-PA-000001 REV 00. Las Vegas, Nevada: CRWMS M&O. ACC: MOL.20000526.0332.

146496 Lawrence Berkeley National Laboratory 1/14/2000. *Software Code: TOUGH2 V1.4.* V1.4. Sun Workstation and DEC/ALPHA. 10007-1.4-01.

146529 Hahn, G.J. and Shapiro, S.S. 1967. *Statistical Models in Engineering.* New York, New York: John Wiley & Sons. TIC: 247729.

146589 CRWMS M&O 2000. *Near Field Environment Process Model Report.* TDR-NBS-MD-000001 REV 00. Las Vegas, Nevada: CRWMS M&O. ACC: MOL.20000421.0034.

146609 Lawrence Berkeley National Laboratory 9/16/1999. *Software Code: GSLIB V2.0 MSISIMV2.0.* V2.0. Sun and PC. STN: 10098-2.0MSISIMV2.0-00.

146677 CRWMS M&O 2000. *Secondary Uranium-Phase Paragenesis and Incorporation of Radionuclides into Secondary Phases.* ANL-EBS-MD-000019 REV 00. Las Vegas, Nevada: CRWMS M&O. ACC: MOL.20000414.0644.

146835 USGS (U.S. Geological Survey) 2000. *Hydrogeologic Framework Model for the Saturated-Zone Site-Scale Flow and Transport Model.* ANL-NBS-HS-000033 REV 00. Denver, Colorado: U.S. Geological Survey. ACC: MOL.20000802.0010.

146910 Rebak, R.B.; Koon, N.E.; Dillman, J.R.; Crook, P.; and Summers, T.S.E. 2000. "Influence of Aging on Microstructure, Mechanical Properties, and Corrosion Resistance of a Ni-22Cr-13Mo-3W Alloy." *Corrosion 2000, [Proceedings, Orlando, Florida, 26-31 March 2000]*. Paper 00181. Pages 1-16. Houston, Texas: NACE International. TIC: 247157.

146915 Summers, T.S.E.; Wall, M.A.; Kumar, M.; Matthews, S.J.; and Rebak, R.B. 1999. "Phase Stability and Mechanical Properties of C-22 Alloy Aged in the Temperature Range 590 to 760°C for 16,000 Hours." *Scientific Basis for Nuclear Waste Management XXII, Symposium held November 30-December 4, 1998, Boston, Massachusetts.* Wronkiewicz, D.J. and Lee, J.H., eds. *556,* 919-926. Warrendale, Pennsylvania: Materials Research Society. TIC: 246426.

146962 CRWMS M&O 2000. *Saturated Zone Transport Methodology and Transport Component Integration.* MDL-NBS-HS-000010 REV 00. Las Vegas, Nevada: CRWMS M&O. ACC: MOL.20000824.0513.

146971 LANL (Los Alamos National Laboratory) 1999. *Software Code: FEHM V2.00.* V2.00. SUN Ultra Sparc. 10031-2.00-00.

146988 CRWMS M&O 2000. *Integrated Site Model Process Model Report.* TDR-NBS-GS-000002 REV 00 ICN 01. Las Vegas, Nevada: CRWMS M&O. ACC: MOL.20000121.0116.

147025 Lawrence Berkeley National Laboratory 03/09/2000. *Software Routine: get_a_layer_v0.f V1.0.* V1.0. Sun workstation w/Unix OS. 10221-1.0-00.

147031 Lawrence Berkeley National Laboratory 03/09/2000. *Software Routine: hsource_v0.f V1.0.* V1.0. Sun workstation w/Unix OS. 10225-1.0-00.

147210 CRWMS M&O 2000. *Clad Degradation – Summary and Abstraction.* ANL-WIS-MD-000007 REV 00. Las Vegas, Nevada: CRWMS M&O. ACC: MOL.20000602.0055.

147359 CRWMS M&O 2000. *Analysis of Mechanisms for Early Waste Package Failure.* ANL-EBS-MD-000023 REV 01. Las Vegas, Nevada: CRWMS M&O. ACC: MOL.20000223.0878.

147403 Nitao, J.J.; Buscheck, T.A.; and Chesnut, D.A. 1993. "Implications of Episodic Nonequilibrium Fracture-Matrix Flow on Repository Performance." *Nuclear Technology, 104,* (3), 385-402. La Grange Park, Illinois: American Nuclear Society. TIC: 226953.

147409 Dagan, G. 1989. *Flow and Transport in Porous Formations.* New York, New York: Springer-Verlag. TIC: 234219.

147480 Drever, J.I. 1997. "Evaporation and Saline Waters." Chapter 15 of *The Geochemistry of Natural Waters: Surface and Groundwater Environments.* 3rd Edition. Upper Saddle River, New Jersey: Prentice Hall. TIC: 246732.

147531 Cohon, J.L. 1999. Comments on the Process for Selecting the Repository Design. Letter from J.L. Cohon (NWTRB) to L.H. Barrett (DOE/OCRWM), July 9, 1999. ACC: MOL.20000412.0786.

147574 Lawrence Livermore National Laboratory 1999. *Software routine: YMESH V1.53.* V1.53. Sun SPARC, UNIX OS. 10172-1.53-00.

147639 CRWMS M&O 2000. *Aging and Phase Stability of Waste Package Outer Barrier.* ANL-EBS-MD-000002 REV 00. Las Vegas, Nevada: CRWMS M&O. ACC: MOL.20000410.0407.

147648 CRWMS M&O 2000. *Abstraction of Models for Pitting and Crevice Corrosion of Drip Shield and Waste Package Outer Barrier.* ANL-EBS-PA-000003 REV 00. Las Vegas, Nevada: CRWMS M&O. ACC: MOL.20000526.0327.

147797 NRC (U.S. Nuclear Regulatory Commission) n.d. "ISG-11 - Storage of High Burnup Spent Fuel." Interim Staff Guidance - 11. Washington, D.C.: U.S. Nuclear Regulatory Commission. Accessed March 21, 2000. TIC: 247227. http://www.nrc.gov/OPA/reports/isg11.htm

147972 CRWMS M&O 2000. *Uncertainty Distribution for Stochastic Parameters.* ANL-NBS-MD-000011 REV 00. Las Vegas, Nevada: CRWMS M&O. ACC: MOL.20000526.0328.

148375 CRWMS M&O 2000. *Stress Corrosion Cracking of the Drip Shield, the Waste Package Outer Barrier, and the Stainless Steel Structural Material.* ANL-EBS-MD-000005 REV 00. Las Vegas, Nevada: CRWMS M&O. ACC: MOL.20000504.0312.

148384 CRWMS M&O 2000. *Total System Performance Assessment (TSPA) Model for Site Recommendation.* MDL-WIS-PA-000002 REV 00. Las Vegas, Nevada: CRWMS M&O. ACC: MOL.20001226.0003.

148463 CRWMS M&O 1999. *Final Report Total System Performance Assessment Peer Review Panel.* Las Vegas, Nevada: CRWMS M&O. ACC: MOL.19990528.0155.

148612 Savino, J.M.; Smith, K.D.; Biasi, G.; Sullivan, T.; and Cline, M. 1999. "Earthquake Ground Motion Effects on Underground Structures/Tunnels." *Eos, Transactions (Supplement), 80,* (17), S10. Washington, D.C.: American Geophysical Union. TIC: 247757.

148637 Lawrence Livermore National Laboratory 2000. *Software routine: RADPRO V3.22.* V3.22. Sun Ultra10. 10204-3.22-00.

148638 Lawrence Livermore National Laboratory 2000. *Software routine: XTOOL V10.1.* V10.1. Sun Ultra10. 10208-10.1-00.

148713 CRWMS M&O 2000. *Repository Safety Strategy: Plan to Prepare the Safety Case to Support Yucca Mountain Site Recommendation and Licensing Considerations.* TDR-WIS-RL-000001 REV 04. Three volumes. Las Vegas, Nevada: CRWMS M&O. ACC: MOL.20001003.0112.

148905 Tsang, Y.W.; Apps, J.; Birkholzer, J.T.; Freifeld, B.; Hu, M.Q.; Peterson, J.; Sonnenthal, E.; and Spycher, N. 1999. *Single Heater Test Borehole Perspective.* LBNL-42537. Berkeley, California: Lawrence Berkeley National Laboratory. ACC: MOL.20000331.0665.

149040 CRWMS M&O 2000. *Calculation of Permeability Change Due to Coupled Thermal-Hydrological-Mechanical Effects.* CAL-NBS-MD-000002 REV 00. Las Vegas, Nevada: CRWMS M&O. ACC: MOL.20000711.0192.

149177 Bechtel Nevada 1998. *Data Interpretations.* Volume 1 of *Hydrogeologic Characterization of the Unsaturated Zone at the Area 3 Radioactive Waste Management Site.* DOE/NV/11718-210. Las Vegas, Nevada: Bechtel Nevada. TIC: 247707.

149372 NRC (U.S. Nuclear Regulatory Commission) 2000. *Issue Resolution Status Report Key Technical Issue: Total System Performance Assessment and Integration.* Rev. 2. Washington, D.C.: U.S. Nuclear Regulatory Commission. TIC: 247614.

149540 DOE (U.S. Department of Energy) 2000. *Quality Assurance Requirements and Description.* DOE/RW-0333P, Rev. 10. Washington, D.C.: U.S. Department of Energy, Office of Civilian Radioactive Waste Management. ACC: MOL.20000427.0422.

149574 CRWMS M&O 2000. *Rock Fall on Drip Shield.* CAL-EDS-ME-000001 REV 00. Las Vegas, Nevada: CRWMS M&O. ACC: MOL.20000509.0276.

149626 CRWMS M&O 2000. *Water Pooling-Evaporation in a Waste Package.* CAL-EBS-NU-000009 REV 00. Las Vegas, Nevada: CRWMS M&O. ACC: MOL.20000424.0698.

149733 YMP (Yucca Mountain Site Characterization Project) 2000. *Q-List.* YMP/90-55Q, Rev. 6. Las Vegas, Nevada: Yucca Mountain Site Characterization Office. ACC: MOL.20000510.0177.

149736 CRWMS M&O 2000. *Disruptive Event Biosphere Dose Conversion Factor Sensitivity Analysis.* ANL-MGR-MD-000004 REV 00. Las Vegas, Nevada: CRWMS M&O. ACC: MOL.20000418.0826.

149850 Mongano, G.S.; Singleton, W.L.; Moyer, T.C.; Beason, S.C.; Eatman, G.L.W.; Albin, A.L.; and Lung, R.C. 1999. *Geology of the ECRB Cross Drift - Exploratory Studies Facility, Yucca Mountain Project, Yucca Mountain, Nevada.* [Deliverable SPG42GM3]. Denver, Colorado: U.S. Geological Survey. ACC: MOL.20000324.0614.

149862 CRWMS M&O 2000. *Multiscale Thermohydrologic Model.* ANL-EBS-MD-000049 REV 00 ICN 01. Las Vegas, Nevada: CRWMS M&O. ACC: MOL.20001208.0062.

149879 CRWMS M&O 2000. *Transfer Coefficient Analysis.* ANL-MGR-MD-000008 REV 00 ICN 1. Las Vegas, Nevada: CRWMS M&O. ACC: MOL.20000413.0692.

149880 CRWMS M&O 2000. *Input Parameter Values for External and Inhalation Radiation Exposure Analysis.* ANL-MGR-MD-000001 REV 00 ICN 1. Las Vegas, Nevada: CRWMS M&O. ACC: MOL.20000501.0228.

149953 Shcherbinskii, V.G. and Myakishev, V.M. 1970. "Statistical Distribution of Welding Defects with Respect to Azimuth." *Translated from Defektoskopiya, No. 4,* 143-144. New York, New York: Plenum Publishing. TIC: 247890.

149956 Erbing Falkland, M.L. 2000. "Duplex Stainless Steels." Chapter 38 of *Uhlig's Corrosion Handbook.* Revie, R.W., ed. 2nd Edition. New York, New York: John Wiley & Sons. TIC: 248360.

149968 Pasupathi, V. 2000. "Documentation of Literature on Residual Stress Measurements." Interoffice correspondence from V. Pasupathi (CRWMS M&O) to G.M. Gordon, May 19, 2000, LV.WP.VP.05/00-070, with enclosures. ACC: MOL.20000522.0146.

149991 CRWMS M&O 2000. *Software Code: DRKBA.* V 3.3. PC. 10071-3.3-00.

150043 Hardin, E.L. and Chesnut, D.A. 1997. *Synthesis Report on Thermally Driven Coupled Processes.* UCRL-ID-128495. Livermore, California: Lawrence Livermore National Laboratory. TIC: 234838.

150092 Nelson, P.H.; Rachiele, R.; Remer, J.S.; and Carlsson, H. 1981. *Water Inflow into Boreholes During the Stripa Heater Experiments.* LBL-12574. Berkeley, California: Lawrence Berkeley Laboratory. TIC: 228851.

150202 CRWMS M&O 2000. *Longevity of Emplacement Drift Ground Support Materials.* ANL-EBS-GE-000003 REV 01. Las Vegas, Nevada: CRWMS M&O. ACC: MOL.20000414.0874.

150418 CRWMS M&O 2000. *Invert Diffusion Properties Model.* ANL-EBS-MD-000031 REV 01. Las Vegas, Nevada: CRWMS M&O. ACC: MOL.20000912.0208.

150421 CRWMS M&O 1999. *Layout of Repository Drifts for Site Recommendation Design, Including Information on Those Which Are Anticipated to Contain Emplaced Waste.* Input Transmittal NEP-EBS-99332.T. Las Vegas, Nevada: CRWMS M&O. ACC: MOL.20000131.0184; MOL.19990901.0312; MOL.19990901.0311.

150512 Itasca Consulting Group, Inc. 1998. *3DEC V2.0.* V2.0. STN:10025-2.0-00.

150560 IAEA (International Atomic Energy Agency) 1998. *Waterside Corrosion of Zirconium Alloys in Nuclear Power Plants.* IAEA-TECDOC-996. Vienna, Austria: International Atomic Energy Agency. TIC: 248234.

150561 CRWMS M&O 2000. *Inventory Abstraction.* ANL-WIS-MD-000006 REV 00 ICN 01. Las Vegas, Nevada: CRWMS M&O. ACC: MOL.20001130.0002.

150707 CRWMS M&O 2000. *Waste Form Degradation Process Model Report.* TDR-WIS-MD-000001 REV 00 ICN 01. Las Vegas, Nevada: CRWMS M&O. ACC: MOL.20000713.0362.

150793 CRWMS M&O 2000. *EBS Radionuclide Transport Model.* ANL-EBS-MD-000034 REV 00 ICN 01. Las Vegas, Nevada: CRWMS M&O. ACC: MOL.20000727.0091.

150806 CRWMS M&O 2000. *The Development of Information Catalogued in REV00 of the YMP FEP Database.* TDR-WIS-MD-000003 REV 00. Las Vegas, Nevada: CRWMS M&O. ACC: MOL.20000705.0098.

150953 CRWMS M&O 2000. *Emplacement Drift System Description Document.* SDD-EDS-SE-000001 REV 01. Las Vegas, Nevada: CRWMS M&O. ACC: MOL.20000803.0348.

151014 CRWMS M&O 2000. *Tabulated In-Drift Geometric and Thermal Properties Used in Drift-Scale Models for TSPA-SR.* CAL-EBS-HS-000002 REV 00. Las Vegas, Nevada: CRWMS M&O. ACC: MOL.20000718.0219.

151018 Marshall, B.D.; Neymark, L.A.; Paces, J.B.; Peterman, Z.E.; and Whelan, J.F. 2000. "Seepage Flux Conceptualized from Secondary Calcite in Lithophysal Cavities in the Topopah Spring Tuff, Yucca Mountain, Nevada." *SME Annual Meeting, February 28-March 1, 2000, Salt Lake City, Utah.* Preprint 00-12. [Littleton, Colorado]: Society for Mining, Metallurgy, and Exploration. TIC: 248608.

151052 Morel, F.M.M. and Hering, J.G. 1993. *Principles and Applications of Aquatic Chemistry.* New York, New York: John Wiley & Sons. TIC: 248465.

151202 Golder Associates 2000. *Software Code: GoldSim.* 6.04.007. 10344-6.04.007-00.

151467 CRWMS M&O 2000. *Subsurface Facility System Description Document.* SDD-SFS-SE-000001 REV 01. Las Vegas, Nevada: CRWMS M&O. ACC: MOL.20000807.0078.

151549 CRWMS M&O 2000. *Abstraction of Models of Stress Corrosion Cracking of Drip Shield and Waste Package Outer Barrier and Hydrogen Induced Corrosion of Drip Shield.* ANL-EBS-PA-000004 REV 00 ICN 01. Las Vegas, Nevada: CRWMS M&O. ACC: MOL.20001213.0065.

151551 CRWMS M&O 2000. *Characterize Framework for Igneous Activity at Yucca Mountain, Nevada.* ANL-MGR-GS-000001 REV 00 ICN 01. Las Vegas, Nevada: CRWMS M&O. ACC: MOL.20001221.0001.

151552 CRWMS M&O 2000. *Dike Propagation Near Drifts.* ANL-WIS-MD-000015 REV 00 ICN 1. Las Vegas, Nevada: CRWMS M&O. ACC: MOL.20001213.0061.

151553 CRWMS M&O 2000. *Features, Events, and Processes: Disruptive Events.* ANL-WIS-MD-000005 REV 00 ICN 1. Las Vegas, Nevada: CRWMS M&O. ACC: MOL.20001218.0007.

151554 CRWMS M&O 2000. *Drift Degradation Analysis.* ANL-EBS-MD-000027 REV 00 ICN 01. Las Vegas, Nevada: CRWMS M&O. ACC: MOL.20001103.0004.

151559 CRWMS M&O 2000. *Hydrogen Induced Cracking of Drip Shield.* ANL-EBS-MD-000006 REV 00 ICN 01. Las Vegas, Nevada: CRWMS M&O. ACC: MOL.20001025.0100.

151560 CRWMS M&O 2000. *Igneous Consequence Modeling for the TSPA-SR.* ANL-WIS-MD-000017 REV 00 ICN 01. Las Vegas, Nevada: CRWMS M&O. ACC: MOL.20001204.0022.

151561 CRWMS M&O 2000. *In-Drift Microbial Communities.* ANL-EBS-MD-000038 REV 00 ICN 01. Las Vegas, Nevada: CRWMS M&O. ACC: MOL.20001213.0066.

151563 CRWMS M&O 2000. *Physical and Chemical Environmental Abstraction Model.* ANL-EBS-MD-000046 REV 00 ICN 01. Las Vegas, Nevada: CRWMS M&O. ACC: MOL.20001204.0023.

151564 CRWMS M&O 2000. *Stress Corrosion Cracking of the Drip Shield, the Waste Package Outer Barrier, and the Stainless Steel Structural Material.* ANL-EBS-MD-000005 REV 00 ICN 01. Las Vegas, Nevada: CRWMS M&O. ACC: MOL.20001102.0340.

151566 CRWMS M&O 2000. *WAPDEG Analysis of Waste Package and Drip Shield Degradation.* ANL-EBS-PA-000001 REV 00 ICN 01. Las Vegas, Nevada: CRWMS M&O. ACC: MOL.20001208.0063.

151568 CRWMS M&O 2000. *Environment on the Surfaces of the Drip Shield and Waste Package Outer Barrier.* ANL-EBS-MD-000001 REV 00 ICN 01. Las Vegas, Nevada: CRWMS M&O. ACC: MOL.20001219.0080.

151592 NRC (U.S. Nuclear Regulatory Commission) 1999. "Issue Resolution Status Report Key Technical Issue: Igneous Activity." Rev. 2. [Washington, D.C.]: U.S. Nuclear Regulatory Commission. Accessed September 18, 2000. TIC: 247987. http://www.nrc.gov/NMSS/DWM/ia-rev2.htm

151615 CRWMS M&O 2000. *Biosphere Process Model Report.* TDR-MGR-MD-000002 REV 00 ICN 01. Las Vegas, Nevada: CRWMS M&O. ACC: MOL.20000620.0341.

151635 CRWMS M&O 2000. *Drift Degradation Analysis.* ANL-EBS-MD-000027 REV 01. Las Vegas, Nevada: CRWMS M&O. ACC: MOL.20001206.0006.

151659 CRWMS M&O 2000. *Initial Cladding Condition.* ANL-EBS-MD-000048 REV 00 ICN 01. Las Vegas, Nevada: CRWMS M&O. ACC: MOL.20001002.0145.

151662 CRWMS M&O 2001. *Clad Degradation – Summary and Abstraction.* ANL-WIS-MD-000007 REV 00 ICN 01. Las Vegas, Nevada: CRWMS M&O. ACC: MOL.20010214.0229.

151804 CRWMS M&O 2000. *Engineered Barrier System Degradation, Flow, and Transport Process Model Report.* TDR-EBS-MD-000006 REV 00 ICN 01. Las Vegas, Nevada: CRWMS M&O. ACC: MOL.20000724.0479.

151817 Pratt, H.R.; Hustrulid, W.A.; and Stephenson, D.E. 1978. *Earthquake Damage to Underground Facilities.* DP-1513. Aiken, South Carolina: E.I. du Pont de Nemours and Company, Savannah River Laboratory. TIC: 210276.

151821 Wang, J-M. 1985. "The Distribution of Earthquake Damage to Underground Facilities During the 1976 Tang-Shan Earthquake." *Earthquake Spectra, 1,* (4), 741-757. [Berkeley, California]: Earthquake Engineering Research Institute. TIC: 226272.

151825 CRWMS M&O 2000. *Draft of AMR "Multiscale Thermohydrologic Model" (ANL-EBS-MD-000049).* Input Transmittal 00176.Ta. Las Vegas, Nevada: CRWMS M&O. ACC: MOL.20000911.0290.

151875 Finsterle, S. 2000. "Using the Continuum Approach to Model Unsaturated Flow in Fractured Rock." *Water Resources Research, 36,* (8), 2055-2066. [Washington, D.C.]: American Geophysical Union. TIC: 248769.

151881 Blakely, R.J.; Langenheim, V.E.; Ponce, D.A.; and Dixon, G.L. 2000. *Aeromagnetic Survey of the Amargosa Desert, Nevada and California: A Tool for Understanding Near-Surface Geology and Hydrology.* Open-File Report 00-188. [Denver, Colorado]: U.S. Geological Survey. TIC: 248767.

151940 CRWMS M&O 2000. *Unsaturated Zone Flow and Transport Model Process Model Report.* TDR-NBS-HS-000002 REV 00 ICN 02. Las Vegas, Nevada: CRWMS M&O. ACC: MOL.20000831.0280.

151945 CRWMS M&O 2000. *Yucca Mountain Site Description.* TDR-CRW-GS-000001 REV 01 ICN 01. Las Vegas, Nevada: CRWMS M&O. ACC: MOL.20001003.0111.

151948 CRWMS M&O 2000. *Saturated Zone Flow and Transport Process Model Report.* TDR-NBS-HS-000001 REV 00 ICN 01. Las Vegas, Nevada: CRWMS M&O. ACC: MOL.20000821.0359.

151951 CRWMS M&O 2000. *Engineered Barrier System: Physical and Chemical Environment Model.* ANL-EBS-MD-000033 REV 01. Las Vegas, Nevada: CRWMS M&O. ACC: MOL.20001228.0081.

151953 CRWMS M&O 2000. *Fault Displacement Effects on Transport in the Unsaturated Zone.* ANL-NBS-HS-000020 REV 01. Las Vegas, Nevada: CRWMS M&O. ACC: MOL.20001002.0154.

151954 CRWMS M&O 2000. *Effects of Fault Displacement on Emplacement Drifts.* ANL-EBS-GE-000004 REV 00 ICN 01. Las Vegas, Nevada: CRWMS M&O. ACC: MOL.20000504.0297.

151957 Stuckless, J.S. 2000. *Archaeological Analogues for Assessing the Long-Term Performance of a Mined Geologic Repository for High-Level Radioactive Waste.* Open-File Report 00-181. Denver, Colorado: U.S. Geological Survey. TIC: 248774.

151964 CRWMS M&O 2000. *Thermal Tests Thermal-Hydrological Analyses/Model Report.* ANL-NBS-TH-000001 REV 00 ICN 01. Las Vegas, Nevada: CRWMS M&O. ACC: MOL.20010109.0004.

151967 CRWMS M&O 2000. *Reference Design Description for a Geologic Repository.* TDR-MGR-SE-000008 REV 03. Las Vegas, Nevada: CRWMS M&O. ACC: MOL.20000821.0355.

151968 CRWMS M&O 2000. *Disruptive Events Process Model Report.* TDR-NBS-MD-000002 REV 00 ICN 02. Las Vegas, Nevada: CRWMS M&O. ACC: MOL.20001220.0047.

152005 Phillips, O.M. 1996. "Infiltration of a Liquid Finger Down a Fracture into Superheated Rock." *Water Resources Research, 32,* (6), 1665-1670. [Washington, D.C.]: American Geophysical Union. TIC: 239025.

152016 CRWMS M&O 2001. *Water Distribution and Removal Model.* ANL-EBS-MD-000032 REV 01. Las Vegas, Nevada: CRWMS M&O. ACC: MOL.20010214.0031.

152097 CRWMS M&O 2000. *Analysis of Mechanisms for Early Waste Package Failure.* ANL-EBS-MD-000023 REV 02. Las Vegas, Nevada: CRWMS M&O. ACC: MOL.20001011.0196.

152104 CRWMS M&O 2000. *Waste Package Operations Fabrication Process Report.* TDR-EBS-ND-000003 REV 01. Las Vegas, Nevada: CRWMS M&O. ACC: MOL.20000927.0002.

152146 CRWMS M&O 2000. *Operating a Below-Boiling Repository: Demonstration of Concept.* TDR-WIS-SE-000001 REV 00. Las Vegas, Nevada: CRWMS M&O. ACC: MOL.20001005.0010.

152249 Chauvet, J-M.; Deschamps, E.B.; and Hillaire, C. 1996. *Dawn of Art: The Chauvet Cave.* New York, New York: Harry N. Abrams, Publishers. TIC: 248775.

152255 Philip, J.R. 1977. "Unitary Approach to Capillary Condensation and Adsorption." *The Journal of Chemical Physics, 66,* (11), 5069-5075. New York, New York: American Institute of Physics. TIC: 249050.

152269 CRWMS M&O 2000. *Natural Ventilation Study: Demonstration of Concept.* TDR-SVS-SE-000001 REV 00. Las Vegas, Nevada: CRWMS M&O. ACC: MOL.20001201.0103.

152286 CRWMS M&O 2000. *Fracture Geometry Analysis for the Stratigraphic Units of the Repository Host Horizon.* ANL-EBS-GE-000006 REV 00. Las Vegas, Nevada: CRWMS M&O. ACC: MOL.20000918.0286.

152354 Cragnolino, G.A.; Dunn, D.S.; Brossia, C.S.; Jain, V.; and Chan, K.S. 1999. *Assessment of Performance Issues Related to Alternate Engineered Barrier System Materials and Design Options.* CNWRA 99-003. San Antonio, Texas: Center for Nuclear Waste Regulatory Analyses. TIC: 248875.

152434 CRWMS M&O 2001. *Environmental Transport Parameter Analysis.* ANL-MGR-MD-000007 REV 00 ICN 01. Las Vegas, Nevada: CRWMS M&O. ACC: MOL.20010208.0001.

152435 CRWMS M&O 2000. *Transfer Coefficient Analysis.* ANL-MGR-MD-000008 REV 00 ICN 02. Las Vegas, Nevada: CRWMS M&O. ACC: MOL.20001016.0005.

152438 CRWMS M&O 2000. *Input Parameter Values for External and Inhalation Radiation Exposure Analysis.* ANL-MGR-MD-000001 REV 01 ICN 00. Las Vegas, Nevada: CRWMS M&O. ACC: MOL.20001122.0005.

152446 ICRP (International Commission on Radiological Protection) 1996. *Age-Dependent Doses to Members of the Public from Intake of Radionuclides: Part 5 Compilation of Ingestion and Inhalation Dose Coefficients.* Volume 26, No. 1 of *Annals of the ICRP*. Smith, H., ed. ICRP Publication 72. New York, New York: Pergamon Press. TIC: 235870.

152447 ICRP (International Commission on Radiological Protection) 2000. *Radiation Protection Recommendations as Applied to the Disposal of Long-lived Solid Radioactive Waste.* Volume 28, No. 4 of *Annals of the ICRP*. Valentin, J., ed. ICRP Publication 81. New York, New York: Pergamon Press. TIC: 249031.

152496 CRWMS M&O 2000. *GVP Software Routine Report.* SDN: 10341-SRR-1.02-00. Las Vegas, Nevada: CRWMS M&O. ACC: MOL.20000908.0038.

152499 CRWMS M&O 2000. *SCCD Software Routine Report.* SDN: 10343-SRR-2.01-00. Las Vegas, Nevada: CRWMS M&O. ACC: MOL.20010205.0113.

152517 CRWMS M&O 2001. *Evaluate Soil/Radionuclide Removal by Erosion and Leaching.* ANL-NBS-MD-000009 REV 00 ICN 01. Las Vegas, Nevada: CRWMS M&O. ACC: MOL.20010214.0032.

152536 CRWMS M&O 2001. *Disruptive Event Biosphere Dose Conversion Factor Analysis.* ANL-MGR-MD-000003 REV 01. Las Vegas, Nevada: CRWMS M&O. ACC: MOL.20010125.0233.

152539 CRWMS M&O 2001. *Nominal Performance Biosphere Dose Conversion Factor Analysis.* ANL-MGR-MD-000009 REV 01. Las Vegas, Nevada: CRWMS M&O. ACC: MOL.20010123.0123.

152542 CRWMS M&O 2000. *Calculation of General Corrosion Rate of Drip Shield and Waste Package Outer Barrier to Support WAPDEG Analysis.* CAL-EBS-PA-000002 REV 01. Las Vegas, Nevada: CRWMS M&O. ACC: MOL.20001024.0075.

152549 EPA (U.S. Environmental Protection Agency) 1997. *Food Ingestion Factors.* Volume II of *Exposure Factors Handbook.* EPA/600/P-95/002Fb. Washington, D.C.: U.S. Environmental Protection Agency. TIC: 241061.

152575 CRWMS M&O 2000. *Data Qualification Report for Thermodynamic Data File, Data0.ympR0 for Geochemical Code, EQ3/6.* TDR-EBS-MD-000012 REV 00. Las Vegas, Nevada: CRWMS M&O. ACC: MOL.20001016.0004.

152576 MO0009THRMODYN.001. Input Transmittal for Thermodynamic Data Input Files for Geochemical Calculations. Submittal date: 09/20/2000.

152614 Dynamic Graphics 1998. *Software Code: EARTHVISION.* 5.1. Silicon Graphics Indigo R4000. 10174-5.1-00.

152624 CRWMS M&O 2000. *Software Routine: CWD* . V1.0. 10363-1.0-00.

152632 CRWMS M&O 2000. *Scoping Calculation for Volcanic Eruption Biosphere Dose Conversion Factors.* CAL-MGR-MD-000003 REV 00. Las Vegas, Nevada: CRWMS M&O. ACC: MOL.20000809.0358.

152663 Keith, T.E.C. and Muffler, L.J.P. 1978. "Minerals Produced During Cooling and Hydrothermal Alteration of Ash Flow Tuff from Yellowstone Drill Hole Y-5." *Journal of Volcanology and Geothermal Research, 3,* 373-402. Amsterdam, The Netherlands: Elsevier. TIC: 219077.

152753 CRWMS M&O 2000. *Waste Package FY-00 Closure Methods Report.* TDR-EBS-ND-000005 REV 00. Las Vegas, Nevada: CRWMS M&O. ACC: MOL.20001002.0149.

152766 Rosenberg, N.D.; Gdowski, G.E.; and Knauss, K.G. 2000. *Evaporative Chemical Evolution of Natural Waters at Yucca Mountain, Nevada.* UCRL-JC-137818. Livermore, California: Lawrence Livermore National Laboratory. ACC: MOL.20000427.0039.

152773 CRWMS M&O 2000. *Unsaturated Zone and Saturated Zone Transport Properties (U0100).* ANL-NBS-HS-000019 REV 00. Las Vegas, Nevada: CRWMS M&O. ACC: MOL.20000829.0006.

152778 Cox, B. 1990. "Environmentally-Induced Cracking of Zirconium Alloys – A Review." *Journal of Nuclear Materials, 170,* 1-23. [Amsterdam, The Netherlands]: North-Holland. TIC: 234774.

152788 CRWMS M&O 2000. *Software Code: ANSYS.* V5.2SGI. Unix. 30013 V5.2SGI.

152816 Lawrence Berkeley National Laboratory 10/17/2000. *Software Routine: CutDrift.* V1.0. SUN w/Unix OS. STN: 10375-1.0-00.

152823 Lawrence Berkeley National Laboratory 10/17/2000. *Software Routine: AddBound.* V1.0. SUN w/Unix OS. STN: 10357-1.0-00.

152824 Lawrence Berkeley National Laboratory 10/17/2000. *Software Routine: MoveMesh.* V1.0. SUN w/Unix OS. STN: 10358-1.0-00.

152826 Lawrence Berkeley National Laboratory 10/17/2000. *Software Routine: Perm2Mesh.* V1.0. SUN w/Unix OS. STN: 10359-1.0-00.

152828 Lawrence Berkeley National Laboratory 2000. *Software Routine: CutNiche.* V1.3. SUN w/Solaris OS. 10402-1.3-00.

152871 Lawrence Berkeley National Laboratory 2001. *Software Routine: Meshbd.f.* V1.0. SUN. 10467-1.0-00.

152872 Lawrence Berkeley National Laboratory 2001. *Software Routine: mininipresf.f.* V1.0. SUN. 10470-1.0-00.

152880 Lawrence Berkeley National Laboratory 03/06/2000. *Software Routine: minrefine3df.f.* V1.0. SUN. 10472-1.0-00.

152914 Tokunaga, T.K.; Wan, J.; and Sutton, S.R. 2000. "Transient Film Flow on Rough Fracture Surfaces." *Water Resources Research, 36,* (7), 1737-1746. [Washington, D.C.]: American Geophysical Union. TIC: 249028.

152954 Cox, B. 1990. "Pellet-Clad Interaction (PCI) Failures of Zirconium Alloy Fuel Cladding - A Review." *Journal of Nuclear Materials, 172,* 249-292. [Amsterdam, The Netherlands]: Elsevier Science Publishers B.V. TIC: 248990.

152998 CRWMS M&O 2000. *Comparison of ASHPLUME Model Results to Representative Tephra Fall Deposits.* CAL-WIS-MD-000011 REV 00. Las Vegas, Nevada: CRWMS M&O. ACC: MOL.20001204.0032.

153010 Gregg, S.J. and Sing, K.S.W. 1982. *Adsorption, Surface Area and Porosity.* 2nd Edition. San Diego, California: Academic Press. TIC: 249076.

153038 CRWMS M&O 2000. *Documentation of Million-Year TSPA.* Input Transmittal 00393.T. Las Vegas, Nevada: CRWMS M&O. ACC: MOL.20001110.0057; MOL.20001120.0173.

153045 CRWMS M&O 2001. *Seepage Calibration Model and Seepage Testing Data.* MDL-NBS-HS-000004 REV 01. Las Vegas, Nevada: CRWMS M&O. ACC: MOL.20010122.0093.

153097 CRWMS M&O 2000. *Number of Waste Packages Hit by Igneous Intrusion.* CAL-WIS-PA-000001 REV 01. Las Vegas, Nevada: CRWMS M&O. ACC: MOL.20001220.0041.

153101 LBNL (Lawrence Berkeley National Laboratory) 2000. *Software Code: TOUGHREACT.* V2.3. SUN and DEC w/Unix OS. STN: 10396-2.3-00. URN-0730

153104 CRWMS M&O 2000. *Abstraction of Flow Fields for TSPA.* ANL-NBS-HS-000023 REV 00 ICN 01. Las Vegas, Nevada: CRWMS M&O. ACC: MOL.20001208.0060.

153165 Hadley, G.R. 1986. "Thermal Conductivity of Packed Metal Powders." *International Journal of Heat and Mass Transfer, 29,* (6), 909-920. [New York, New York]: Pergamon Journals. TIC: 249320.

153166 Kunii, D. and Smith, J.M. 1960. "Heat Transfer Characteristics of Porous Rocks." *American Institute of Chemical Engineers Journal, 6,* (1), 71-78. [New York, New York: American Institute of Chemical Engineers]. TIC: 249321.

153168 CRWMS M&O 2000. *Saturated Zone Flow and Transport Process Model Report.* TDR-NBS-HS-000001 REV 00 ICN 02. Las Vegas, Nevada: CRWMS M&O. ACC: MOL.20001102.0067.

153193 Cline, K.M. 2000. "Transmittal of MTS Report of Conservatism in Process Models and TSPA." Letter from K.M. Cline (MTS) to S. Brocoum (DOE/YMSCO), October 12, 2000, LV.MTS.KMC.10/00-218, with attachment. ACC: MOL.20001113.0311.

153206 CRWMS M&O 2001. *Abstraction of BDCF Distributions for Irrigation Periods.* ANL-NBS-MD-000007 REV 00 ICN 01. Las Vegas, Nevada: CRWMS M&O. ACC: MOL.20010201.0027.

153207 CRWMS M&O 2001. *Distribution Fitting to the Stochastic BDCF Data.* ANL-NBS-MD-000008 REV 00 ICN 01. Las Vegas, Nevada: CRWMS M&O. ACC: MOL.20010221.0148.

153217 LBNL (Lawrence Berkeley National Laboratory) 08/29/1999. *Software Code: SOLVEQ/CHILLER.* V1.0. PC w/Windows OS. STN: 10057-1.0-00.

153219 LBNL (Lawrence Berkeley National Laboratory) 09/21/1999. *Software Code: TOUGHREACT.* V2.2. DEC and SUN w/Unix OS. STN: 10154-2.2-00.

153246 CRWMS M&O 2000. *Total System Performance Assessment for the Site Recommendation.* TDR-WIS-PA-000001 REV 00 ICN 01. Las Vegas, Nevada: CRWMS M&O. ACC: MOL.20001220.0045.

153265 CRWMS M&O 2001. *In-Drift Precipitates/Salts Analysis.* ANL-EBS-MD-000045 REV 00 ICN 02. Las Vegas, Nevada: CRWMS M&O. ACC: MOL.20010220.0008.

153266 Howard, N.W. 1985. *Variation in Properties of Nuclear Test Areas and Media at the Nevada Test Site.* UCRL-53721. Livermore, California: Lawrence Livermore National Laboratory. TIC: 229690.

153282 Howard, C.L.; Finley, R.L.; Johnston, R.L.; Taylor, R.S.; George, J.T.; Lowry, W.E.; and Mason, N.G. 2001. *Engineered Barrier System—Pilot Scale Test #3, Heated Drip Shield Test Results.* TDR-EBS-SE-000001 REV 00. Las Vegas, Nevada: Bechtel SAIC Company. ACC: MOL.20010529.0330.

153314 CRWMS M&O 2000. *Seepage Model for PA Including Drift Collapse.* MDL-NBS-HS-000002 REV 01. Las Vegas, Nevada: CRWMS M&O. ACC: MOL.20010221.0147.

153342 CRWMS M&O 2001. *Identification of the Critical Group (Consumption of Locally Produced Food and Tap Water).* ANL-MGR-MD-000005 REV 01 ICN 00. Las Vegas, Nevada: CRWMS M&O. ACC: MOL.20010119.0109.

153363 CRWMS M&O 2000. *Near Field Environment Process Model Report.* TDR-NBS-MD-000001 REV 00 ICN 03. Las Vegas, Nevada: CRWMS M&O. ACC: MOL.20001121.0041.

153410 CRWMS M&O 2001. *Effective Thermal Conductivity for Drift-Scale Models Used in TSPA-SR.* CAL-EBS-HS-000001 REV 00. Las Vegas, Nevada: CRWMS M&O. ACC: MOL.20010301.0252.

153471 LBNL (Lawrence Berkeley National Laboratory) 2000. *Software Routine: bot_sum.f.* V1.0. SUN AND DEC. 10349-1.0-00.

153681 CRWMS M&O 2001. *Monitored Geologic Repository Project Description Document.* TDR-MGR-SE-000004 REV 02 ICN 01. Las Vegas, Nevada: CRWMS M&O. ACC: MOL.20010212.0296.

153724 BSC (Bechtel SAIC Company) 2001. *In-Package Chemistry for Waste Forms.* ANL-EBS-MD-000056 REV 00. Las Vegas, Nevada: Bechtel SAIC Company. ACC: MOL.20010322.0490.

153752 BSC (Bechtel SAIC Company) 2001. *Dose Rate Calculation for the 21-PWR UCF Waste Package.* CAL-UDC-NU-000002 REV 01. Las Vegas, Nevada: Bechtel SAIC Company. Submit to RPC URN-0860.

153802 CRWMS M&O 2000. *Waste Package Degradation Process Model Report.* TDR-WIS-MD-000002 REV 00 ICN 02. Las Vegas, Nevada: CRWMS M&O. ACC: MOL.20001228.0229.

153846 CRWMS M&O 2001. *Defense High Level Waste Glass Degradation.* ANL-EBS-MD-000016 REV 00 ICN 01. Las Vegas, Nevada: CRWMS M&O. ACC: MOL.20010130.0004.

153848 MO0004RIB00035.001. Rock Thermal Expansion. Submittal date: 04/07/2000.

153849 DOE (U.S. Department of Energy) 2001. *Yucca Mountain Science and Engineering Report.* DOE/RW-0539. [Washington, D.C.]: U.S. Department of Energy, Office of Civilian Radioactive Waste Management. ACC: MOL.20010524.0272.

153921 BSC (Bechtel SAIC Company) 2001. *Evaluation of the Applicability of Biosphere-Related Features, Events, and Processes (FEP).* ANL-MGR-MD-000011 REV 01. Las Vegas, Nevada: Bechtel SAIC Company. ACC: MOL.20010226.0003.

153933 CRWMS M&O 2001. *Waste Form Colloid-Associated Concentrations Limits: Abstraction and Summary.* ANL-WIS-MD-000012 REV 00 ICN 01. Las Vegas, Nevada: CRWMS M&O. ACC: MOL.20010130.0002.

153937 CRWMS M&O 2001. *FEPs Screening of Processes and Issues in Drip Shield and Waste Package Degradation.* ANL-EBS-PA-000002 REV 01. Las Vegas, Nevada: CRWMS M&O. ACC: MOL.20010216.0004.

153938 CRWMS M&O 2001. *Miscellaneous Waste-Form FEPs.* ANL-WIS-MD-000009 REV 00 ICN 01. Las Vegas, Nevada: CRWMS M&O. ACC: MOL.20010216.0006.

153940 CRWMS M&O 2000. *EBS Radionuclide Transport Abstraction.* ANL-WIS-PA-000001 REV 00 ICN 02. Las Vegas, Nevada: CRWMS M&O. ACC: MOL.20001204.0029.

153964 CRWMS M&O 1999. *Software Code: EQ3/6.* V7.2b. UCRL-MA-110662 (LSCR198).

153995 CRWMS M&O 2001. *Precipitates/Salts Model Results for THC Abstraction.* CAL-EBS-PA-000008 REV 00 ICN 01. Las Vegas, Nevada: CRWMS M&O. ACC: MOL.20010125.0231.

154024 CRWMS M&O 2001. *Unsaturated Zone and Saturated Zone Transport Properties (U0100).* ANL-NBS-HS-000019 REV 00 ICN 1. Las Vegas, Nevada: CRWMS M&O. ACC: MOL.20010201.0026.

154071 CRWMS M&O 2001. *Colloid-Associated Radionuclide Concentration Limits: ANL.* ANL-EBS-MD-000020 REV 00 ICN 01. Las Vegas, Nevada: CRWMS M&O. ACC: MOL.20010216.0003.

154149 EPRI (Electric Power Research Institute) 2000. *Evaluation of the Candidate High-Level Radioactive Waste Repository at Yucca Mountain Using Total System Performance Assessment, Phase 5.* 1000802. Palo Alto, California: Electric Power Research Institute. TIC: 249555.

154176 CRWMS M&O 2000. *Subsurface Radon Calculations.* CAL-SSM-NU-000003 REV 00. Las Vegas, Nevada: CRWMS M&O. ACC: MOL.20001220.0016.

154286 CRWMS M&O 2001. *Summary of Dissolved Concentration Limits.* ANL-WIS-MD-000010 REV 01. Las Vegas, Nevada: CRWMS M&O. ACC: MOL.20010223.0061.

154291 CRWMS M&O 2001. *Abstraction of Drift Seepage.* ANL-NBS-MD-000005 REV 01. Las Vegas, Nevada: CRWMS M&O. ACC: MOL.20010309.0019.

154293 Knight, J.H.; Philip, J.R.; and Waechter, R.T. 1989. "The Seepage Exclusion Problem for Spherical Cavities." *Water Resources Research, 25,* (1), 29-37. [Washington, D.C.]: American Geophysical Union. TIC: 240851.

154295 Buecher, R.H. 1999. "Microclimate Study of Kartchner Caverns, Arizona." *Journal of Cave and Karst Studies, 61,* (2), 108-120. Huntsville, Alabama: National Speleological Society. TIC: 249657.

154296 Jagnow, D.H. 1999. "Geology of Kartchner Caverns State Park, Arizona." *Journal of Cave and Karst Studies, 61,* (2), 49-58. Huntsville, Alabama: National Speleological Society. TIC: 249658.

154297 Weeks, K.R. 1998. "Valley of the Kings." *National Geographic, 194,* (3), 2-33. Washington, D.C.: National Geographic Society. TIC: 249629.

154300 Brune, J.N. 1996. "Precariously Balanced Rocks and Ground-Motion Maps for Southern California." *Bulletin of the Seismological Society of America, 86,* (1A), 43-54. [Stanford, California]: Seismological Society of America. TIC: 249711.

154301 Brune, J.N. 2000. "Precarious Rock Evidence for Low Ground Shaking on the Footwall of Major Normal Faults." *Bulletin of the Seismological Society of America, 90,* (4), 1107-1112. El Cerrito, California: Seismological Society of America. TIC: 249712.

154302 Anooshehpoor, A. and Brune, J.N. [2000]. *Annual Report, Precarious Rock Methodology for Seismic Hazard.* Reno, Nevada: University of Nevada, Reno. ACC: MOL.20000824.0562.

154303 Brune, J.N. and Anooshehpoor, A. 1999. "Dynamic Geometrical Effects on Strong Ground Motion in a Normal Fault Model." *Journal of Geophysical Research, 104,* (B1), 809-815. Washington, D.C.: American Geophysical Union. TIC: 249707.

154320 Rogers, K.L.; Repenning, C.A.; Luiszer, F.G.; and Benson, R.D. 2000. "Geologic History, Stratigraphy, and Paleontology of SAM Cave, North-Central New Mexico." *New Mexico Geology, 22,* (4), 89-100. Socorro, New Mexico: New Mexico Bureau of Mines and Mineral Resources. TIC: 249818.

154321 Lawrence Berkeley National Laboratory 2001. *Software Routine: AssignRock.* V1.0. SUN w/Solaris OS. STN: 10465-1.0-00.

154322 Lawrence Berkeley National Laboratory 03/31/2001. *Software Code: TOUGH2.* V1.5. SUN and DEC-Alpha w/Unix OS. STN: 10007-1.5-00. URN-0845.

154325 Jewett, D.G.; Logan, B.E.; Arnold, R.G.; and Bales, R.C. 1999. "Transport of Pseudomonas Fluorescens Strain P17 Through Quartz Sand Columns as a Function of Water Content." *Journal of Contaminant Hydrology, 36,* ([1-2]), 73-89. New York, New York: Elsevier. TIC: 249653.

154337 Lawrence Berkeley National Laboratory 1999. *Software Code: ITOUGH2.* V3.2. SUN OS. STN: 10054-3.2-00.

154341 Lawrence Berkeley National Laboratory 03/31/2001. *Software Code: Wingridder.* V1.1. PC w/MS Windows. STN: 10024-1.1-00. URN-0846.

154342 Lawrence Berkeley National Laboratory 03/31/2001. *Software Code: DCPT.* V2.0. PC w/MS Windows. STN: 10078-2.0-00. URN-0847.

154343 Lawrence Berkeley National Laboratory 2001. *Software Routine: MINCgridv1.f.* V1.0. DEC-Alpha w/Unix OS. STN: 10469-1.0-00.

154344 Lawrence Berkeley National Laboratory 2001. *Software Routine: RoutineRick1.* V1.0. SUN w/Unix OS. STN: 10474-1.0-00.

154345 Lawrence Berkeley National Laboratory 2001. *Software Routine: vf_con.for.* V1.0. PC w/Windows. STN: 10466-1.0-00.

154346 Lawrence Berkeley National Laboratory 2001. *Software Routine: parallelf.java.* V1.0. PC w/Windows. STN: 10457-1.0-00.

154347 Lawrence Berkeley National Laboratory 2001. *Software Routine: mddf.f.* V2.0. SUN w/Solaris OS. STN: 10456-2.0-00.

154349 Lawrence Berkeley National Laboratory 2001. *Software Routine: mk_generGL.f.* V1.0. SUN w/Solaris OS. STN: 10476-1.0-00.

154367 Wan, J.; Wilson, J.L.; and Kieft, T.L. 1994. "Influence of the Gas-Water Interface on Transport of Microorganisms through Unsaturated Porous Media." *Applied and Environmental Microbiology, 60,* (2), 509-516. Washington, D.C.: American Society for Microbiology. TIC: 249543.

154378 McCafferty, E. and Zettlemoyer, A.C. 1971. "Adsorption of Water Vapour on Alpha-Fe2O3." *Discussions of the Faraday Society, 52,* 239-263. [London, England: Gurney and Jackson]. TIC: 249665.

154379 Holmes, H.F.; Fuller, E.L., Jr.; and Beh, R.A. 1974. "Adsorption of Argon, Nitrogen, and Water Vapor on Zirconium Oxide." *Journal of Colloid and Interface Science, 47,* (2), 365-371. [New York, New York]: Academic Press. TIC: 249666.

154380 Lee, S. 1994. *Report to TRW on Contract No. DX 1456KP2L, Adsorption Studies of Water on Gold, Copper, Nickel and Iron Using the Quartz-Crystal Microbalance Technique.* [Minneapolis, Minnesota]: University of Minnesota. ACC: NNA.19940428.0129.

154381 Jurinak, J.J. 1964. "Interaction of Water with Iron and Titanium Oxide Surfaces: Goethite, Hematite, and Anatase." *Journal of Colloid Science, 19,* 477-487. [New York, New York: Academic Press]. TIC: 249667.

154382 McCafferty, E. and Zettlemoyer, A.C. 1970. "Entropy of Adsorption and the Mobility of Water Vapor on Alpha-Fe2O3." *Journal of Colloid and Interface Science, 34,* (3), 452-460. [New York, New York: Academic Press]. TIC: 249668.

154411 Armijo, J.S. 1994. "Performance of Failed BWR Fuel." *Proceedings of the 1994 International Topical Meeting on Light Water Reactor Fuel Performance, West Palm Beach, Florida, April 17-21, 1994.* 410-422. La Grange Park, Illinois: American Nuclear Society. TIC: 243043.

154412 Paces, J.B.; Whelan, J.F.; Peterman, Z.E.; Marshall, B.D.; and Neymark, L.A. 2000. "Formation of Calcite and Silica from Percolation in a Hydrologically Unsaturated Setting, Yucca Mountain, Nevada." *Abstracts with Programs - Geological Society of America, 32,* (7), A-259. Boulder, Colorado: Geological Society of America. TIC: 249113.

154415 Marshall, B.D. and Whelan, J.F. 2000. "Isotope Geochemistry of Calcite Coatings and the Thermal History of the Unsaturated Zone at Yucca Mountain, Nevada." *Abstracts with Programs - Geological Society of America, 32,* (7), A-259. Boulder, Colorado: Geological Society of America. TIC: 249113.

154419 Graf, W.L. 1994. *Plutonium and the Rio Grande, Environmental Change and Contamination in the Nuclear Age.* New York, New York: Oxford University Press. TIC: 249730.

154420 Onishi, Y.; Serne, R.J.; Arnold, E.M.; Cowan, C.E.; and Thompson, F.L. 1981. *Critical Review: Radionuclide Transport, Sediment Transport, and Water Quality Mathematical Modeling; and Radionuclide Adsorption/Desorption Mechanisms.* NUREG/CR-1322. Washington, D.C.: U.S. Nuclear Regulatory Commission. TIC: 249732.

154421 Brady, P.V.; Spalding, B.P.; Krupka, K.M.; Waters, R.D.; Zhang, P.; Borns, D.J.; and Brady, W.D. 1999. *Site Screening and Technical Guidance for Monitored Natural Attenuation at DOE Sites.* SAND99-0464. Albuquerque, New Mexico: Sandia National Laboratories. TIC: 249720.

154422 Lu, N.; Conca, J.; Parker, G.R.; Leonard, P.A.; Moore, B.; Strietelmeier, B.; and Triay, I.R. 2000. *Adsorption of Actinides Onto Colloids as a Function of Time, Temperature, Ionic Strength, and Colloid Concentration, Waste Form Colloids Report for Yucca Mountain Program (Colloid Data Summary from 1999 to 2000 Research).* LA-UR-00-5121. Los Alamos, New Mexico: Los Alamos National Laboratory. TIC: 249708.

154423 Wang, J.S.Y.; Trautz, R.C.; Cook, P.J.; and Salve, R. 1998. *Drift Seepage Test and Niche Moisture Study: Phase 1 Report on Flux Threshold Determination, Air Permeability Distribution, and Water Potential Measurement.* Milestone SPC315M4. Berkeley, California: Lawrence Berkeley National Laboratory. ACC: MOL.19980806.0713.

154424 de Gennes, P.G. 1985. "Wetting: Statics and Dynamics." *Reviews of Modern Physics, 57,* (3, Part 1), 827-863. New York, New York: American Physical Society. TIC: 249713.

154426 CRWMS M&O 2001. *Drift-Scale Coupled Processes (DST and THC Seepage) Models.* MDL-NBS-HS-000001 REV 01. Las Vegas, Nevada: CRWMS M&O. ACC: MOL.20010314.0003.

154432 Lysell, G.; Grigoriev, V.; and Efsing, P. 2000. "Axial Splits in Failed BWR Fuel Rods." *Proceedings, International Topical Meeting on Light Water Reactor Fuel Performance, April 10-13, 2000, Park City, Utah, U.S.A.* La Grange Park, Illinois: American Nuclear Society. TIC: 248973.

154433 Edsinger, K. 2000. "A Review of Fuel Degradation in BWRs." *Proceedings, International Topical Meeting on Light Water Reactor Fuel Performance, April 10-13, 2000, Park City, Utah, U.S.A.* La Grange Park, Illinois: American Nuclear Society. TIC: 248973.

154435 NOAA (National Oceanic and Atmospheric Administration) n.d. *Upper Air Data: Desert Rock, Nevada, 1978-1995.* Reno, Nevada: National Oceanic and Atmospheric Administration, Western Regional Climate Center. TIC: 249335.

154436 Davis, J.A.; Coston, J.A.; Kent, D.B.; and Fuller, C.C. 1998. "Application of the Surface Complexation Concept to Complex Mineral Assemblages." *Environmental Science and Technology, 32,* (19), 2820-2828. Washington, D.C.: American Chemical Society. TIC: 249656.

154439 Balsley, S.D.; Brady, P.V.; Krumhansl, J.L.; and Anderson, H.L. 1998. "Anion Scavengers for Low-Level Radioactive Waste Repository Backfills." *Journal of Soil Contamination, 7,* (2), 125-141. [Boca Raton, Florida: Lewis Publishers]. TIC: 249779.

154441 BSC (Bechtel SAIC Company) 2001. *Committed Materials in Repository Drifts.* CAL-GCS-GE-000002 REV 00. Las Vegas, Nevada: Bechtel SAIC Company. ACC: MOL.20010412.0157.

154444 Jove-Colon, C.F.; Brady, P.V.; Siegel, M.D.; and Lindgren, E.R. 2001. "Historical Case Analysis of Uranium Plume Migration." *Soil and Sediment Contamination, 10,* 71-115. Amhearst, Massachusetts: Association for Environmental Health and Sciences. On Order Library Tracking Number-249777.

154445 Suzuki, Y. and Banfield, J.F. 1999. "Geomicrobiology of Uranium." Chapter 8 of *Uranium: Mineralogy, Geochemistry and the Environment.* Burns, P.C. and Finch, R., eds. Reviews in Mineralogy Volume 38. Washington, D.C.: Mineralogical Society of America. TIC: 247121.

154446 Macaskie, L.E. 1991. "The Application of Biotechnology to the Treatment of Wastes Produced from the Nuclear Fuel Cycle: Biodegradation and Bioaccumulation as a Means of Treating Radionuclide-Containing Streams." *Critical Reviews in Biotechnology, 11,* (1), 41-112. [Boca Raton, Florida]: CRC Press. TIC: 249386.

154447 Chen, C.-I.; Meike A.; Chuu Y.-J.; Sawvel, A.; and Lin, W. 1999. "Investigation of Bacterial Transport in the Large-Block Test, A Thermally Perturbed Block of Topopah Spring Tuff." *Scientific Basis for Nuclear Waste Management XXII, Symposium held November 30-December 4, 1998, Boston, Massachusetts.* Wronkiewicz, D.J. and Lee, J.H., eds. *556,* 1151-1158. Warrendale, Pennsylvania: Materials Research Society. TIC: 246426.

154451 Chrenko, R.M. 1980. "Residual Stress Measurements on Type 304 Stainless Steel Welded Pipes." Paper No. 21 of *Proceedings: Seminar on Countermeasures for Pipe Cracking in BWRs.* EPRI WS-79-174. Palo Alto, California: Electric Power Research Institute. TIC: 249915.

154452 Nicot, J-P. 2001. "Transmittal of 'Plugging of Stress Corrosion Cracks by Precipitates', CAL-EBS-MD-0000017 [CAL-EBS-MD-000017], REV. 00A." Memorandum from J-P. Nicot (BSC) to RPC = 2, May 29, 2001, PROJ.05/01.061, with enclosure. ACC: MOL.20010529.0184.

154453 Kolts, J. 1986. "Heat Treatment and Environmental Embrittlement of High-Performance Alloys." *Corrosion '86. Paper No. 407.* Houston, Texas: National Association of Corrosion Engineers. Library Tracking Number-249604.

154454 EPRI (Electric Power Research Institute) 1983. *Induction Heating Stress Improvement.* EPRI NP-3375. Palo Alto, California: Electric Power Research Institute. TIC: 249914.

154455 Roy, A.K.; Estill, J.C.; Gordon, S.R.; and Logoteta, L.F. 1999. *Stress Corrosion Cracking of Ni-Base and Ti Alloys Under Controlled Potential.* UCRL-JC-132511. Livermore, California: Lawrence Livermore National Laboratory. ACC: MOL.19990610.0040.

154456 Shack, W.J. and Ellingson, W.A. 1980. "Measured Residual Stresses in Type 304 Stainless Steel Piping Butt Weldments." Paper No. 22 of *Proceedings: Seminar on Countermeasures for Pipe Cracking in BWRs, Volume 2.* EPRI WS-79-174. Palo Alto, California: Electric Power Research Institute. TIC: 249915.

154457 Speidel, M.O. 1981. "Stress Corrosion Cracking of Stainless Steels in NaCl Solutions." *Metallurgical Transactions A, 12A,* (5), 779-789. Warrendale, Pennsylvania: Metallurgical Society of American Institute of Mining, Metallurgical, and Petroleum Engineers. TIC: 245394.

154458 Nimmo, J.R.; Perkins, K.S.; Rose, P.E.; Rousseau, J.P.; Orr, B.R.; Twining, B.V. 2001. "Kilometer-Scale Rapid Flow in a Fractured-Basalt Unsaturated Zone at the Idaho National Engineering and Environmental Laboratory." *Proceedings of Fractured Rock 2001, Toronto, Ontario, Canada, March 26-28, 2001.* Toronto, Ontario: U.S. Department of Energy, EPA. Copyright Requested Library Tracking Number-249689.

154459 Phillips, O.M. 1994. "Liquid Infiltration Through the Boiling-Point Isotherm in a Desiccating Fractured Rock Matrix." *High Level Radioactive Waste Management, Proceedings of the Fifth Annual International Conference, Las Vegas, Nevada, May 22-26, 1994. 4,* 2189-2196. La Grange Park, Illinois: American Nuclear Society. TIC: 210984.

154460 Kneafsey, T.J.; Apps, J.A.; and Sonnenthal, E.L. 2001. "Tuff Dissolution and Precipitation in a Boiling, Unsaturated Fracture." *"BACK TO THE FUTURE - Managing the Back End of the Nuclear Fuel Cycle to Create a More Secure Energy Future," Proceedings of the 9th International High-Level Radioactive Waste Management Conference (IHLRWM), Las Vegas, Nevada, April 29 - May 3, 2001.* La Grange Park, Illinois: American Nuclear Society. TIC: 247873.

154461 BSC (Bechtel SAIC Company) 2001. *Design Input for the Engineered Barrier System Environment and Barriers.* Input Transmittal 00422.Ta. Las Vegas, Nevada: Bechtel SAIC Company. ACC: MOL.20010405.0196.

154462 Andresen, P.L.; Young, L.M.; and Emigh, P.W. 2000. *Stress Corrosion Crack Initiation & Growth Measurements in Environments Relevant to High Level Nuclear Waste Packages.* [Schenectady, New York]: General Electric Corporate Research & Development Center. ACC: MOL.20001208.0089.

154463 Haynes International. 1998. Hastelloy C-2000 Alloy. H-2111. Kokomo, Indiana: Haynes International. TIC: 249630.

154468 Bunzl, K.; Flessa, H.; Kracke, W.; and Schimmack, W. 1995. "Association of Fallout 239+240Pu and 241Am with Various Soil Components in Successive Layers of a Grassland Soil." *Environmental Science & Technology, 29,* (10), 2513-2518. Washington, D.C.: American Chemical Society. TIC: 234160.

154473 White, A.F.; Blum, A.E.; Schulz, M.S.; Bullen, T.D.; Harden, J.W.; and Peterson, M.L. 1996. "Chemical Weathering Rates of a Soil Chronosequence on Granitic Alluvium: I. Quantification of Mineralogical and Surface Area Changes and Calculation or Primary Silicate Reaction Rates." *Geochimica et Cosmochimica Acta, 60,* (14), 2533-2550. New York, New York: Pergamon Press. TIC: 249749.

154474 Manger, G.E. 1963. *Porosity and Bulk Density of Sedimentary Rocks*. Geological Survey Bulletin 1144-E. Washington, D.C.: U.S. Government Printing Office. TIC: 249699.

154479 BSC (Bechtel SAIC Company) 2001. *Engineered Barrier System - Pilot Scale Test #3, Heated Drip Shield Test Results (TDR-EBS-SE-000001).* Input Transmittal 00445.T. Las Vegas, Nevada: Bechtel SAIC Company. ACC: MOL.20010406.0009.

154481 Dunn, D.S.; Pan, Y-M.; and Cragnolino, G.A. 1999. *Effects of Environmental Factors on the Aqueous Corrosion of High-Level Radioactive Waste Containers—Experimental Results and Models.* CNWRA 99-004. San Antonio, Texas: Center for Nuclear Waste Regulatory Analyses. TIC: 246615.

154486 Nitao, J.J. and Glassley, W.E. 1999. "Modeled Near-Field Environment Porosity Modification Due to Coupled Thermohydrologic and Geochemical Processes." *Scientific Basis for Nuclear Waste Management XXII, Symposium held November 30-December 4, 1998, Boston, Massachusetts.* Wronkiewicz, D.J. and Lee, J.H., eds. *556,* 705-711. Warrendale, Pennsylvania: Materials Research Society. TIC: 246426.

154488 Bird, G.A. and Schwartz, W.J. 1997. "Partition Coefficients (Kd Values) for Tc in Shield Lake Sediments Under Oxidizing and Reducing Conditions." *Water Research, 31,* (7), 1673-1678. New York, New York: Pergamon Press. TIC: 249771.

154492 White, A.F. and Brantley, S.L., eds. 1995. *Chemical Weathering Rates of Silicate Minerals.* Reviews in Mineralogy Volume 31. Washington, D.C.: Mineralogical Society of America. TIC: 222496.

154494 Coughtrey, P.J.; Jackson, D.; Jones, C.H.; Kane, P.; and Thorne, M.C. 1986. *Radionuclide Distribution and Transport in Terrestrial and Aquatic Ecosystems, A Critical Review of Data.* Volume six. Rotterdam, The Netherlands: A.A. Balkema. On Order Library Tracking Number-240299

154495 USGS (U.S. Geological Survey) n.d. Bulk Density. [Denver, Colorado: U.S. Geological Survey]. ACC: NNA.19940406.0076.

154496 Barkatt, A. and Gorman, J.A. 2000. *Tests to Explore Specific Aspects of the Corrosion Resistance of C-22.* Presentation to the Nuclear Waste Technical Review Board on August 1, 2000, Carson City, Nevada. [Washington, D.C.]: Catholic University of America. TIC: 249714.

154501 Stevens, P.R. 1977. *A Review of the Effects of Earthquakes on Underground Mines.* Open-File Report 77-313. Reston, Virginia: U.S. Geological Survey. TIC: 211779.

154503 Dobson, P.; Hulen, J.; Kneafsey, T.J.; and Simmons, A. 2001. "Permeability at Yellowstone: A Natural Analog for Yucca Mountain Processes." *"BACK TO THE FUTURE - Managing the Back End of the Nuclear Fuel Cycle to Create a More Secure Energy Future," Proceedings of the 9th International High-Level Radioactive Waste Management Conference (IHLRWM), Las Vegas, Nevada, April 29 - May 3, 2001.* La Grange Park, Illinois: American Nuclear Society. TIC: 247873.

154504 Carpenter, D.W. and Chung, D.H. 1986. *Effects of Earthquakes on Underground Facilities: Literature Review and Discussion.* NUREG/CR-4609. Washington, D.C.: U.S. Nuclear Regulatory Commission. TIC: 203428.

154505 Sharma, S. and Judd, W.R. 1991. "Underground Opening Damage from Earthquakes." *Engineering Geology, 30,* (3/4), 263-276. Amsterdam, [The Netherlands]: Elsevier. TIC: 226268.

154510 Baker, E.A. 1988. "Long-Term Corrosion Behavior of Materials in the Marine Atmosphere." *Degradation of Metals in the Atmosphere, [Proceedings of the Symposium on Corrosion of Metals, Philadelphia, PA, 12-13 May 1986].* Dean, S.W. and Lee, T.T., eds. ASTM STP 965. 125-144. Philadelphia, Pennsylvania: American Society for Testing and Materials. TIC: 224019.

154511 Dunn, D.S.; Brossia, C.S.; and Pensado, O. 2001. "Long-Term Dissolution Behavior of Alloy 22: Experiments and Modeling." *Corrosion 2001.* Paper 01125. Houston, Texas: National Association of Corrosion Engineers. TIC: 208528.

154513 Scully, J.R.; Ilevbare, G.; and Marks, C. 2001. *Passivity and Passive Corrosion of Alloys 625 and 22, January 31, 2001 Progress Report.* Charlottesville, Virginia: University of Virgina. On Order Library Tracking Number-248056.

154522 BIOMASS (Biosphere Modelling and Assessment) 2000. *Example Reference Biosphere 2A: Agricultural Well, Constant Biosphere.* Draft TECDOC. BIOMASS/T1/WD08. Vienna, Austria: International Atomic Energy Agency, Division of Radiation and Waste Safety. TIC: 249456.

154523 BIOMASS (Biosphere Modelling and Assessment) 1999. *Guidance on the Definition of Critical and Other Hypothetical Exposed Groups for Solid Radioactive Waste Dispsoal [Disposal]*. Draft TECDOC. BIOMASS/T1/WD03. Vienna, Austria: International Atomic Energy Agency, Division of Radiation and Waste Safety. TIC: 249451.

154524 Sturchio, N.C.; Keith, T.E.C.; and Muehlenbachs, K. 1990. "Oxygen and Carbon Isotope Ratios of Hydrothermal Minerals from Yellowstone Drill Cores." *Journal of Volcanology and Geothermal Research, 40,* 23-37. Amsterdam, The Netherlands: Elsevier. TIC: 249710.

154525 Sturchio, N.C.; Binz, C.M.; and Lewis, C.H., III 1987. "Thorium-Uranium Disequilibrium in a Geothermal Discharge Zone at Yellowstone." *Geochimica et Cosmochimica Acta, 51,* (7), 2025-2034. New York, New York: Pergamon Press. TIC: 249702.

154527 Fournier, R.O.; Pisto, L.M.; Howell, B.B.; and Hutchinson, R.A. 1993. "Taming a Wild Geothermal Research Well in Yellowstone National Park." *Geothermal Resources Council Transactions, 17,* 33-36. Davis, California: Geothermal Resources Council. TIC: 249701.

154529 Sturchio, N.C.; Bohlke, J.K.; and Binz, C.M. 1989. "Radium-Thorium Disequilibrium and Zeolite-Water Ion Exchange in a Yellowstone Hydrothermal Environment." *Geochimica et Cosmochimica Acta, 53,* 1025-1034. [New York, New York]: Pergamon Press. TIC: 249703.

154530 White, D.E.; Fournier, R.O.; Muffler, L.J.P.; and Truesdell, A.H. 1975. *Physical Results of Research Drilling in Thermal Areas of Yellowstone National Park, Wyoming.* Geological Survey Professional Paper 892. Washington, D.C.: U.S. Government Printing Office. TIC: 235251.

154531 Grindley, G.W. and Browne, P.R.L. 1976. "Structural and Hydrological Factors Controlling the Permeabilities of Some Hot-Water Geothermal Fields." *Development and Use of Geothermal Resources, Proceedings of the Second United Nations Symposium, San Francisco, California, May 20-29, 1975. Volume 1,* Washington, D.C.: U.S. Government Printing Office. On Order Library Tracking Number-249789

154535 Jolley, D.M. 1997. "A Climatic Model for Potential CO2 Gas Abundance in the Unsaturated Zone of Yucca Mountain, Nevada." *Abstracts with Programs - Geological Society of America, 29,* (6), A-328. Boulder, Colorado: Geological Society of America. TIC: 236901.

154537 BSC (Bechtel SAIC Company) 2001. *Rockfall Sensitivity Calculations.* Input Transmittal 00453.T. Las Vegas, Nevada: Bechtel SAIC Company. ACC: MOL.20010416.0090.

154547 Dobson, P.; Hulen, J.; Kneafsey, T.J.; and Simmons, A. 2001. "The Role of Lithology and Alteration on Permeability and Fluid Flow in the Yellowstone Geothermal System, Wyoming." *Proceedings, Twenty-Sixth Workshop, Geothermal Reservoir Engineering, January 29-31, 2001.* Workshop Report SGP-TR-168. Pages xx. Stanford, California: Stanford University. On Order Library Tracking Number-249825

154548 BSC (Bechtel SAIC Company) 2001. *Design Input for the Engineered Barrier System Environment and Barriers.* Input Transmittal 00422.T. Las Vegas, Nevada: Bechtel SAIC Company. ACC: MOL.20010410.0256.

154554 BSC (Bechtel SAIC Company) 2001. *Lower-Temperature Subsurface Layout and Ventilation Concepts.* ANL-WER-MD-000002 REV 00. Las Vegas, Nevada: Bechtel SAIC Company. Submit to RPC URN-0871

154564 BSC (Bechtel SAIC Company) 2001. *Net Infiltration Modeling Results for Post - 10K Climate Scenarios.* Input Transmittal 00316.T. Las Vegas, Nevada: Bechtel SAIC Company. ACC: MOL.20010322.0427.

154567 O'Sullivan, M.J.; Bullivant, D.P.; Follows, S.E.; and Mannington, W.I. 1998. "Modelling of the Wairakei - Tauhara Geothermal System." *Proceedings of the TOUGH Workshop '98, Berkeley, California, May 4-6, 1998.* Pruess, K., ed. LBNL-41995. Pages 1-6. Berkeley, California: Lawrence Berkeley National Laboratory. TIC: 247159.

154568 Antunez, E.U.; Menzies, A.J.; and Sanyal, S.K. 1991. "Simulating a Challenging Water Dominated Geothermal System: The Cerro Prieto Field, Baja California, Mexico." *Proceedings, Sixteenth Workshop on Geothermal Reservoir Engineering, Stanford, California, January 23-25, 1991.* Workshop Report SGP-TR-134. Pages 183-191. Stanford, California: Stanford University. TIC: 246832.

154569 Pham, M.; Menzies, A.J.; Sanyal, S.K.; Lima, E.; Shimada, K.; Juarez, J.; and Cuevas, A. 1996. "Numerical Modeling of the High-Temperature Geothermal System of Amatitlan, Guatemala." *Geothermal Resources Council Transactions, 20,* 833-838. Davis, California: Geothermal Resources Council. TIC: 249728.

154570 Paulsson, B.N.P.; King, M.S.; and Rachiele, R. 1980. *Ultrasonic and Acoustic Emission Results from the Stripa Heater Experiments.* Parts 1 & 2. LBL-10975. Berkeley, California: Lawrence Berkeley National Laboratory. TIC: 211547.

154571 Tulinius, H. and Sigurdsson, O. 1989. "Two-Dimensional Simulation of the Krafla-Hvitholar Geothermal Field, Iceland." *Proceedings, Fourteenth Workshop on Geothermal Reservoir Engineering, Stanford, California, January 24-26, 1989.* Workshop Report SGP-TR-122. Pages 87-93. Stanford, California: Stanford University. TIC: 249225.

154573 Brune, J.N. and Whitney, J.W. 2000. "Precarious Rocks and Seismic Shaking at Yucca Mountain, Nevada." Chapter M of *Geologic and Geophysical Characterization Studies of Yucca Mountain, Nevada, A Potential High-Level Radioactive-Waste Repository.* Whitney, J.W. and Keefer, W.R., eds. Version 1.0. DDS-058. Denver, Colorado: U.S. Geological Survey. TIC: 249438.

154574 Bodvarsson, G.S.; Bjornsson, S.; Gunnarsson, A.; Gunnlaugsson, E.; Sigurdsson, O.; Stefansson, V.; and Steingrimsson, B. 1990. "The Nesjavellir Geothermal Field, Iceland, Part 1. Field Characteristics and Development of a Three-Dimensional Numerical Model." *Geothermal Science and Technology, 2,* (3), 189-228. New York, New York: Gordon and Breach Science Publishers. TIC: 249715.

154575 Bodvarsson, G.S.; Bjornsson, S.; Gunnarsson, A.; Gunnlaugsson, E.; Sigurdsson, O.; Stefansson, V.; and Steingrimsson, B. 1991. "The Nesjavellir Geothermal Field, Iceland, 2. Evaluation of the Generating Capacity of the System." *Geothermal Science and Technology, 2,* (4), 229-261. New York, New York: Gordon and Breach Science Publishers. TIC: 249716.

154585 CRWMS M&O [1999]. *Thermal Test Progress Report #2.* BABEAF000-01717-5700-00001 REV 00. Las Vegas, Nevada: CRWMS M&O. ACC: MOL.19991104.0270.

154587 Rutqvist, J.; Borgesson, L.; Chijimatsu, M.; Kobayashi, A.; Jing, L.; Nguyen, T.S.; Noorishad, J.; and Tsang, C.-F. 2001. "Thermohydromechanics of Partially Saturated Geological Media: Governing Equations and Formulation of Four Finite Element Models." *International Journal of Rock Mechanics and Mining Sciences, 38,* (1), 105-127. Oxford, United Kingdom: Elsevier. TIC: 249744.

154594 CRWMS M&O 2001. *Abstraction of NFE Drift Thermodynamic Environment and Percolation Flux.* ANL-EBS-HS-000003 REV 00 ICN 02. Las Vegas, Nevada: CRWMS M&O. ACC: MOL.20010221.0160.

154599 Cho, M.; Liou, J.G.; and Bird, D.K. 1988. "Prograde Phase Relations in the State 2-14 Well Metasandstones, Salton Sea Geothermal Field, California." *Journal of Geophysical Research, 93,* (B11), 13,081-13,103. Washington, D.C.: American Geophysical Union. TIC: 249734.

154600 Hulen, J.B. and Lutz, S.J. 1999. "Altered Volcanic Rocks as Hydrologic Seals on the Geothermal System of Medicine Lake Volcano, California." *Geothermal Resources Council Bulletin, 28,* (7), 217-222. Davis, California: Geothermal Resources Council. TIC: 249735.

154601 Bird, D.K. and Elders, W.A. 1976. "Hydrothermal Alteration and Mass Transfer in the Discharge Portion of the Dunes Geothermal Sysytem, Imperial Valley of California, USA." *Development and Use of Geothermal Resources, Proceedings of the Second United Nations Symposium, San Francisco, California, May 20-29, 1975. 1,* 285-295. Washington, District of Columbia: U.S. Government Printing Office. On Order Library Tracking Number-249829

154602 Elders, W.A. 1982. "Determination of Fracture History in Geothermal Reservoirs Through Study of Minerals." *Fractures in Geothermal Reservoirs.* Special Report No. 12. Pages 62-66. Davis, California: Geothermal Resources Council. TIC: 249737.

154606 Bjornsson, G. and Bodvarsson, G. 1990. "A Survey of Geothermal Reservoir Properties." *Geothermics, 19,* (1), 17-27. [New York, New York]: Pergamon Press. TIC: 249741.

154608 Birkholzer, J.T. and Tsang, Y.W. 2000. "Modeling the Thermal-Hydrologic Processes in a Large-Scale Underground Heater Test in Partially Saturated Fractured Tuff." *Water Resources Research, 36,* (6), 1431-1447. Washington, D.C.: American Geophysical Union. TIC: 248278.

154613 Yang, I.C. 2001. *Percolation Flux and Transport Velocity in the Unsaturated Zone, Yucca Mountain, Nevada.* Preprint. [Denver, Colorado: U.S. Geological Survey]. TIC: 249766.

154614 Fournier, R.O. 1983. "Self-Sealing and Brecciation Resulting from Quartz Deposition within Hydrothermal Systems." *Water-Rock Interaction, Proceedings from the Fourth International Symposium, August 29 - September 3, 1983, Misasa, Japan.* 137-140. Rotterdam, The Netherlands: A.A. Balkema. Copyright Requested Library Tracking Number-249755.

154615 Apps, J.A. 1995. "Natural Geochemical Analogues of the Near Field of High-Level Nuclear Waste Repositories." *Proceedings of the Workshop on the Role of Natural Analogs in Geologic Disposal of High-Level Nuclear Waste, held in San Antonio, Texas, July 22-25, 1991.* Kovach, L.A. and Murphy, W.M., eds. NUREG/CP-0147. Pages 75-99. Washington, D.C.: U.S. Nuclear Regulatory Commission. TIC: 225202.

154620 BSC (Bechtel SAIC Company) 2001. *In-Package Chemistry Abstraction.* ANL-EBS-MD-000037 REV 01. Las Vegas, Nevada: Bechtel SAIC Company. ACC: MOL.20010315.0053.

154621 Mroczek, E.K. 1994. *Review of Silica Deposition Rates at Ohaaki, Rotokawa and Wairakei Geothermal Fields and Comparison of Observed Rates with Predicted Deposition Rates Calculated using Three Different Kinetic Deposition Models.* Client Report 722305.15. Taupo, New Zealand: Institute of Geological & Nuclear Sciences. On Order Library Tracking Number-249770.

154622 BSC (Bechtel SAIC Company) 2001. *Geologic Framework Model Analysis Model Report.* MDL-NBS-GS-000002 REV 00 ICN 02. Las Vegas, Nevada: Bechtel SAIC Company. ACC: MOL.20010313.0505.

154625 USGS (U.S. Geological Survey) 2001. *Water-Level Data Analysis for the Saturated Zone Site-Scale Flow and Transport Model.* ANL-NBS-HS-000034 REV 00 ICN 01. Denver, Colorado: U.S. Geological Survey. ACC: MOL.20010405.0211.

154629 CRWMS M&O 2001. *Pure Phase Solubility Limits - LANL.* ANL-EBS-MD-000017 REV 00 ICN 01. Las Vegas, Nevada: CRWMS M&O. ACC: MOL.20010126.0005.

154630 Moore, D.E.; Lockner, D.A.; and Byerlee, J.D. 1994. "Reduction of Permeability in Granite at Elevated Temperatures." *Science, 265,* ([5178]), 1558-1561. Washington, D.C.: American Association for the Advancement of Science. TIC: 249760.

154631 Moore, D.E.; Morrow, C.A.; and Byerlee, J.D. 1983. "Chemical Reactions Accompanying Fluid Flow Through Granite Held in a Temperature Gradient." *Geochimica et Cosmochimica Acta, 47,* 445-453. [New York, New York]: Pergamon Press. TIC: 249761.

154632 Elders, W.A. 1987. "A Natural Analogue for Near-Field Behaviour in a High Level Radioactive Waste Repository in Salt: The Salton Sea Geothermal Field, California, USA." *Natural Analogues in Radioactive Waste Disposal, Proceedings, Symposium held in Brussels, Belgium, 28-30 April 1987.* Come, B. and Chapman, N.A., eds. EUR 11037 EN. Pages 342-353. Norwell, Massachusetts: Graham & Trotman. TIC: 247254.

154633 Hutcheon, I. 1984. "A Review of Artificial Diagenesis During Thermally Enhanced Recovery." *Clastic Diagenesis.* McDonald, D.A. and Surdam, R.C., eds. AAPG Memoir 37. 413-429. Tulsa, Oklahoma: American Association of Petroleum Geologists. TIC: 249756.

154634 Sedimentology Research Group 1981. "The Effects of In Situ Steam Injection on Cold Lake Oil Sands." *Bulletin of Canadian Petroleum Geology, 29,* (4), 447-478. Calgary, Alberta, Canada: Canadian Society of Petroleum Geologists. TIC: 249763.

154635 Zhou, Z.; Dudley, J.S.; Wiwchar, B; and Gunter, W.D. 1999. "The Potential of Permeability Damage During Thermal Recovery of Cold Lake Bitumen." *Journal of Canadian Petroleum Technology, 38,* (9), 55-60. Montreal, Canada: Canadian Institute of Mining, Metallurgy & Petroleum. Copyright Requested Library Tracking Number-249767.

154637 Lefebvre, R. and Hutcheon, I. 1986. "Mineral Reactions in Quartzose Rocks During Thermal Recovery of Heavy Oil, Lloydminster, Saskatchewan, Canada." *Applied Geochemistry, 1,* 395-405. New York, New York: Pergamon Journals. TIC: 249759.

154638 Hutcheon, I. and Abercrombie, H.J. 1990. "Fluid-Rock Interactions in Thermal Recovery of Bitumen, Tucker Lake Pilot, Cold Lake, Alberta." *Prediction of Reservoir Quality Through Chemical Modeling.* Meshri, I.D. and Ortoleva, P.J., eds. AAPG Memoir 49. 161-170. Tulsa, Oklahoma: American Association of Petroleum Geologists. TIC: 249757.

154639 Kirk, J.S.; Bird, G.W.; and Longstaffe, F.J. 1987. "Laboratory Study of the Effects of Steam-Condensate Flooding in the Clearwater Formation: High Temperature Flow Experiments." *Bulletin of Canadian Petroleum Geology, 35,* (1), 34-47. Calgary, Alberta, Canada: Canadian Society of Petroleum Geologists. TIC: 249758.

154640 Boon, J.A.; Hamilton, T.; Holloway, L.; and Wiwchar, B. 1983. "Reaction Between Rock Matrix and Injected Fluids in Cold Lake Oil Sands—Potential for Formation Damage." *Journal of Canadian Petroleum Technology, 22,* (3-4), 55-66. Montreal, Canada: Canadian Institute of Mining and Metallurgy. TIC: 249754.

154641 Chigira, M. and Watanabe, M. 1992. "Experimental Approach to the Self-Sealing of Rock-Water Systems." *Water-Rock Interaction, Proceedings of the 7th International Symposium on Water-Rock Interaction–WRI-7, Park City, Utah, 13-18 July 1992.* Kharaka, Y.K. and Maest, A.S., eds. *2,* 1397-1400. Brookfield, Vermont: A.A. Balkema. TIC: 208527.

154642 Gunter, W.D.; Wiwchar, B.; Holloway, L.; and Perkins, E.H. 1992. "Silica Geothermometers for Use in Predicting Temperatures in Alberta Oil Sand Reservoirs During Steam-Assisted Thermal Recovery." *Water-Rock Interaction, Proceedings of the 7th International Symposium on Water-Rock Interaction–WRI-7, Park City, Utah, 13-18 July 1992.* Kharaka, Y.K. and Maest, A.S., eds. *2,* 1451-1454. Brookfield, Vermont: A.A. Balkema. TIC: 208527.

154643 Boon, J.A. [1978]. "Fluid-Rock Interactions During Steam Injection." *[The Oil Sands of Canada-Venezuela, 1977.* Redford, D.A. and Winestock, A.G., eds. CIM Special Volume 17]. 133-138. [Montreal, Canada: Canadian Institute of Mining and Metallurgy]. TIC: 249753.

154644 Schiffman, P.; Bird, D.K.; and Elders, W.A. 1985. "Hydrothermal Mineralogy of Calcareous Sandstones from the Colorado River Delta in the Cerro Prieto Geothermal System, Baja California, Mexico." *Mineralogical Magazine, 49,* (3), 435-449. London, England: Mineralogical Society of Great Britain. TIC: 249764.

154645 Wells, J.T. and Ghiorso, M.S. 1991. "Coupled Fluid Flow and Reaction in Mid-Ocean Ridge Hydrothermal Systems: The Behavior of Silica." *Geochimica et Cosmochimica Acta, 55,* (9), 2467-2481. New York, New York: Pergamon Press. TIC: 249765.

154647 Butler, J.N. 1982. *Carbon Dioxide Equilibria and Their Applications.* Reading, Massachusetts: Addison-Wesley Publishing Company. TIC: 222594.

154663 Grindley, G.W. 1965. *The Geology, Structure, and Exploitation of the Wairakei Geothermal Field, Taupo New Zealand.* New Zealand Geological Survey Bulletin 75. Wellington, New Zealand: Department of Scientific and Industrial Research. Copyright Requested Library Tracking Number-249790.

154667 Andrews, K. 1999. Copyright Clearance Request and Release for Joy Mining Machinery Documents for Fan Curves. Letter from K. Andrews (CRWMS M&O) to D. Johnston (Joy Technologies), June 16, 1999, with attachment. ACC: MOL.20010425.0004

154669 Bodvarsson, G.S. 2001. "Scientific Notebooks Referenced in FY01 Supplemental Science and Performance Analyses, Volume 1: Scientific Bases and Analyses, DI: TDR-MGR-MD-000007 REV 00." Interoffice correspondence from G.S. Bodvarsson (BSC) to File, May 31, 2001, with attachments. ACC: MOL.20010531.0079.

154671 CRWMS M&O 2001. *Software Code: ANSYS.* V5.6.2. IRIX 6.5. 10145-5.6.2-00.

154672 Chan, T.; Binnall, E.; Nelson, P.; Stolzman, R.; Wan, O.; Weaver, C.; Ang, K.; Braley, J.; and McEvoy, M. 1980. *Thermal and Thermomechanical Data from In Situ Heater Experiments at Stripa, Sweden.* LBL-11477. Berkeley, California: Lawrence Berkeley Laboratory. TIC: 211543.

154674 USGS (U.S. Geological Survey) 2001. *Simulation of Net Infiltration for Modern and Potential Future Climates.* ANL-NBS-HS-000032 REV 00 ICN 01. Denver, Colorado: U.S. Geological Survey. ACC: MOL.20010405.0002.

154677 BSC (Bechtel SAIC Company) 2001. *Drift-Scale Coupled Processes (DST and THC Seepage) Models.* MDL-NBS-HS-000001 REV 01 ICN 01. Las Vegas, Nevada: Bechtel SAIC Company. ACC: MOL.20010418.0010.

154687 DOE (U.S. Department of Energy) 1999. *Final Site Observational Work Plan for the UMTRA Project New Rifle Site.* GJO-99-112-TAR, Rev. 1. Grand Junction, Colorado: U.S. Department of Energy, Grand Junction Office. TIC: 249902.

154688 Rasmussen, T.C.; Evans, D.D.; Sheets, P.J.; and Blanford, J.H. 1993. "Permeability of Apache Leap Tuff: Borehole and Core Measurements Using Water and Air." *Water Resources Research, 29,* (7), 1997-2006. [Washington, D.C.]: American Geophysical Union. TIC: 245278.

154689 Reimus, P.W.; Haga, M.J.; Humphrey, A.R.; Anghel, I.; Counce, D.; and Callahan, T.J. 1999. *Laboratory Experiments to Support Interpretation of the BULLION Forced-Gradient Experiment: Update Report. Underground Test Area (UGTA) Project Report.* Los Alamos, New Mexico: Los Alamos National Laboratory. On Order Library Tracking Number-249903

154691 Albrethsen, H., Jr. and McGinley, F.E. 1982. *Summary History of Domestic Uranium Procurement Under U.S. Atomic Energy Commission Contracts.* GJBX-220(82). Grand Junction, Colorado: Bendix Field Engineering. TIC: 233199.

154692 DOE (U.S. Department of Energy) 1994. *Final Remedial Action Plan and Site Design for Stabilization of Inactive Uranium Mill Tailings Site at Gunnison, Colorado.* Albuquerque, New Mexico: U.S. Department of Energy, UMTRA Project Office. On Order Library Tracking Number-250151

154693 DOE (U.S. Department of Energy) 1996. *Final Programmatic Environmental Impact Statement for the Uranium Mill Tailings Remedial Action Ground Water Project.* DOE/EIS-0198. Two volumes. Grand Junction, Colorado: U.S. Department of Energy, Grand Junction Project Office. TIC: 249817.

154694 CRWMS M&O 2000. *Input Transmittal for Seismic Evaluations of Waste Packages and Emplacement Pallets.* Input Transmittal 00230.Ta. Las Vegas, Nevada: CRWMS M&O. ACC: MOL.20000808.0079.

154702 Zheng, C. and Bennett, G.D. 1995. *Applied Contaminant Transport Modeling, Theory and Practice.* New York, New York: Van Nostrand Reinhold. TIC: 249865.

154704 EDCON 2000. *Report for the Borehole Gravity Survey in the NC-EWDP-19D Well in Nye County, Nevada on Behalf of TRW Corp.* EDCON Job# 00011. Denver, Colorado: EDCON, Inc. TIC: 249823.

154705 Reimus, P.W. and Haga, M.J. 1999. *Analysis of Tracer Responses in the BULLION Forced-Gradient Experiment at Pahute Mesa, Nevada.* LA-13615-MS. Los Alamos, New Mexico: Los Alamos National Laboratory. TIC: 249826.

154706 Vesselinov, V.V.; Illman, W.A.; Hyun, Y.; Neuman, S.P.; Di Federico, V.; and Tartakovsky, D.M. 2001. "Observation and Analysis of a Pronounced Permeability and Porosity Scale-Effect in Unsaturated Fractured Tuff." *Fractured Rock.* Toronto, Canada: xxxx. On Order Library Tracking Number-249909.

154707 Raghavan, M.; Mueller, R.R.; Vaughn, G.A.; and Floreen, S. 1984. "Determination of Isothermal Sections of Nickel Rich Portion of Ni-Cr-Mo System by Analytical Electron Microscopy." *Metallurgical Transactions A, 15A,* ([5]), 783-792. [Warrendale, Pennsylvania: Metallurgical Society of American Institute of Mining, Metallurgical, and Petroleum Engineers]. TIC: 240057.

154714 Anderko, A.; McKenzie, P.; and Young, R.D. 2001. "Computation of Rates of General Corrosion Using Electrochemical and Thermodynamic Models." *Corrosion, 57,* (3), 202-213. Houston, Texas: National Association of Corrosion Engineers. TIC: 233120.

154715 Bojinov, M.; Fabricius, G.; Laitinen, T.; Makela, K.; Saario, T.; and Sundholm, G. 2001. "Influence of Molybdenum on the Conduction Mechanism in Passive Films on Iron–Chromium Alloys in Sulfuric Acid Solution." *Electrochimica Acta, 46,* ([9]), 1339-1358. New York, New York: Pergamon. TIC: 249796.

154716 Botto, R.I. and Morrison, G.H. 1976. "Josephinite: A Unique Nickel-Iron." *American Journal of Science, 276,* (3), 241-274. New Haven, Connecticut: Kline Geology Laboratory, Yale University. TIC: 249797.

154717 Liu, C-T. and Lindsay, W.T., Jr. 1972. "Thermodynamics of Sodium Chloride Solutions at High Temperatures." *Journal of Solution Chemistry, 1,* 45-69. New York, New York: Plenum Publishing. On Order Library Tracking Number-249798.

154718 Lorang, G.; Jallerat, N.; Quang, K.V.; and Langeron, J.-P. 1990. "AES Depth Profiling of Passive Overlayers Formed on Nickel Alloys." *Surface and Interface Analysis, 16,* 325-330. [New York, New York]: John Wiley & Sons. TIC: 249830.

154719 Macdonald, D.D. 1992. "Viability of Hydrogen Water Chemistry for Protecting In-Vessel Components of Boiling Water Reactors." *Corrosion, 48,* (3), 194-205. Houston, Texas: National Association of Corrosion Engineers. TIC: 249803.

154720 Macdonald, D.D. 1992. "The Point Defect Model for the Passive State." *Journal of the Electrochemical Society, 139,* (12), 3434-3449. Manchester, New Hampshire: Electrochemical Society. TIC: 249804.

154721 Macdonald, D.D. 1999. "Passivity–the Key to Our Metals-Based Civilization." *Pure and Applied Chemistry, 71,* (6), 951-978. Oxford, England: Blackwell Scientific Publishers. TIC: 249795.

154724 Paces, J.B. and Whelan, J.F. 2001. "Water-Table Fluctuations in the Amargosa Desert, Nye County, Nevada." *"BACK TO THE FUTURE - Managing the Back End of the Nuclear Fuel Cycle to Create a More Secure Energy Future," Proceedings of the 9th International High-Level Radioactive Waste Management Conference (IHLRWM), Las Vegas, Nevada, April 29 - May 3, 2001.* La Grange Park, Illinois: American Nuclear Society. TIC: 247873.

154735 Macdonald, D.D.; Liu, C.; Urquidi-Macdonald, M.; Stickford, G.H.; Hindin, B.; Agrawal, A.K.; and Krist, K. 1994. "Prediction and Measurement of Pitting Damage Functions for Condensing Heat Exchangers." *Corrosion, 50,* (10), 761-780. Houston, Texas: National Association of Corrosion Engineers.

154736 Macdonald, D.D. 2001. *Model for Predicting Corrosion Potential and Uniform Corrosion Rate on HLNW Containers.* Interim Progress Report. State College, Pennsylvania: Digby D. Macdonald. ACC: MOL.20010504.0595.

154738 Marcus, P. and Maurice, V. 2000. "Passivity of Metals and Alloys." Chapter 3 of *Corrosion and Environmental Degradation Vol. I.* Schutze, M., Volume Editor. Materials Science and Technology, A Comprehensive Treatment. New York, New York: Wiley-VCH. TIC: 249831.

154739 Naumov, G.B.; Ryzhenko, B.N.; and Khodakovsky, I.L. 1974. *Handbook of Thermodynamic Data.* USGS-WRD-74-001. Menlo Park, California: U.S. Geological Survey. TIC: 229402.

154741 Urquidi, M. and Macdonald, D.D. 1985. "Solute-Vacancy Interaction Model and the Effect of Minor Alloying Elements on the Initiation of Pitting Corrosion." *Journal of the Electrochemical Society, 132,* (3), 555-558. [New York, New York]: Electrochemical Society. TIC: 249843.

154742 Zhang, L. and Macdonald, D.D. 1998. "Segregation of Alloying Elements in Passive Systems—II. Numerical Simulation." *Electrochimica Acta, 43,* (18), 2673-2685. [New York, New York]: Pergamon Press. TIC: 249846.

154743 Zhang, L. and Macdonald, D.D. 1998. "Segregation of Alloying Elements in Passive Systems—I. XPS Studies on the Ni–W System." *Electrochimica Acta, 43,* (18), 2661-2671. [New York, New York]: Pergamon Press. TIC: 249845.

154744 Carroll, S.; Esser, B.; Randall, S.; O'Day, P.; Bono, A.; and Luther, G.W., III. 1999. *Geochemical Characterization of Seaplane Lagoon Sediments, Alameda Naval Air Station.* UCRL-ID-135193. Livermore, California: Lawrence Livermore National Laboratory. TIC: 249746.

154746 Krishnarao, J.S.R. 1964. "Native Nickel-Iron Alloy, Its Mode of Occurrence, Distribution and Origin." *Economic Geology, 59,* (3), 443-448. Lancaster, Pennsylvania: Economic Geology Publishing. TIC: 249850.

154748 CRWMS M&O 2000. *Software Code: ASHPLUME.* V1.4LV-dll. STN. 10022-1.4LV-dll-00.

154749 Dick, H.J.B. 1974. "Terrestrial Nickel-Iron from the Josephine Peridotite, Its Geologic Occurrence, Associations, and Origin." *Earth and Planetary Science Letters, 24,* 291-298. Amsterdam, The Netherlands: North-Holland Publishing. On Order Library Tracking Number-249849.

154750 Göpel, C.; Manhès, G.; and Allègre, C.J. 1990. "U-Pb Isotope Systematics in Josephinites and Associated Rocks." *Earth and Planetary Science Letters, 97,* (1/2), 18-28. Amsterdam, The Netherlands: Elsevier. TIC: 249851.

154762 Jolley, D. 2001. "Delivery of Drift Scale THC Abstraction Results and the Resulting Precipitates Salts Analysis Look Up Tables for the SSPA Volume 1 Report." Memorandum from D. Jolley (BSC) to D. Sevougian, May 3, 2001, PROJ.05/01.010, with enclosure. ACC: MOL.20010510.0518.

154771 DOE (U.S. Department of Energy) 2001. *Reference Design Description for a Geologic Repository.* TDR-MGR-SE-000008 REV 03 ICN 2. [Las Vegas, Nevada]: U.S. Department of Energy, Office of Civilian Radioactive Waste Management. ACC: MOL.20010206.0156.

154773 Whelan, J.F.; Roedder, E.; and Paces, J.B. 2001. "Evidence for an Unsaturated-Zone Origin of Secondary Minerals in Yucca Mountain, Neveda." *"BACK TO THE FUTURE - Managing the Back End of the Nuclear Fuel Cycle to Create a More Secure Energy Future," Proceedings of the 9th International High-Level Radioactive Waste Management Conference (IHLRWM), Las Vegas, Nevada, April 29 - May 3, 2001.* La Grange Park, Illinois: American Nuclear Society. TIC: 247873.

154777 Webb, S.W. and Hickox, C.E., Jr. 2001. "Assessment of the Equivalent Permeability Relationship for Open Space Natural Convection." *"BACK TO THE FUTURE - Managing the Back End of the Nuclear Fuel Cycle to Create a More Secure Energy Future," Proceedings of the 9th International High-Level Radioactive Waste Management Conference (IHLRWM), Las Vegas, Nevada, April 29 - May 3, 2001.* La Grange Park, Illinois: American Nuclear Society. TIC: 247873.

154783 LBNL (Lawrence Berkeley National Laboratory) 2001. *Software Code: FLAC3D.* V2.0. PC. STN: 10502-2.0-00. URN-0848.

154784 LBNL (Lawrence Berkeley National Laboratory) 2001. *Software Code: iTOUGH2.* V4.4. SUN UltraSparc. STN: 10003-4.4-00. URN-0849.

154785 LBNL (Lawrence Berkeley National Laboratory) 2001. *Software Code: Wingridder.* V2.0. PC. STN: 10024-2.0-00. URN-0850.

154787 LBNL (Lawrence Berkeley National Laboratory) 2001. *Software Routine: 2kgrid8.for.* V1.0. SUN UltraSparc, DEC-Alpha, PC. STN: 10503-1.0-00. URN-0851

154788 LBNL (Lawrence Berkeley National Laboratory) 2001. *Software Routine: CalBT.for.* V1.0. PC. STN: 10504-1.0-00. URN-0852.

154791 LBNL (Lawrence Berkeley National Laboratory) 2001. *Software Routine: Delb.dat.* V1.0. PC. STN: 10507-1.0-00. URN-0853.

154792 LBNL (Lawrence Berkeley National Laboratory) 2001. *Software Routine: Gpzones.dat.* V1.0. PC. STN: 10509-1.0-00. URN-0854.

154793 LBNL (Lawrence Berkeley National Laboratory) 2001. *Software Code: infil2grid.* V1.7. SUN UltraSparc, DEC-Alpha, PC. 10077-1.7-00. URN-0861.

154794 LBNL (Lawrence Berkeley National Laboratory) 2001. *Software Routine: tin.dat.* V1.0. PC. STN: 10512-1.0-00. URN-0855.

154795 CRWMS M&O 2001. *Geochemical and Isotopic Constraints on Groundwater Flow Directions, Mixing, and Recharge at Yucca Mountain, Nevada.* ANL-NBS-HS-000021 REV 00 ICN 1. Las Vegas, Nevada: CRWMS M&O. ACC: MOL.20010123.0120.

154818 Cunnane, J.C. 2001. ANL Waste Form Task Progress Report for November and December 2000. Letter from J.C. Cunnane (ANL) to Dr. C. Stockman (SNL), January 24, 2001. ACC: MOL.20010508.0127.

154820 Smailos, E.; Schwarzkopf, W.; Köster, R.; Fiehn, B.; and Halm, G. 1990. *Corrosion Testing of Selected Packaging Materials for Disposal of High-Level Waste Glass in Rock Salt Formations.* KFK 4723. [Karlsruhe, Germany]: Kernforschungszentrum Karlsruhe GmbH. TIC: 215124.

154823 Jolley, D. 2001. "Delivery of Electronic Files for the Microbial Sorption & Transport Work Reported in the SSPA Volume I Report." Memorandum from D. Jolley (BSC) to M. Gross, May 3, 2001, PROJ.05/01.009, with enclosure. ACC: MOL.20010510.0519.

154826 BSC (Bechtel SAIC Company) 2001. *Features, Events, and Processes in UZ Flow and Transport.* ANL-NBS-MD-000001 REV 01. Las Vegas, Nevada: Bechtel SAIC Company. ACC: MOL.20010423.0321.

154837 GSA (Geological Society of America) 2000. *Summit 2000, Abstracts with Programs.* Boulder, Colorado: Geological Society of America. TIC: 249113.

154840 BSC (Bechtel SAIC Company) 2001. *Effect of Waste Package Materials Surface Area and High-Level Waste Glass Reaction Rate on In-Package Chemistry.* Input Transmittal 00474.T. Las Vegas, Nevada: Bechtel SAIC Company. ACC: MOL.20010529.0190.

154841 BSC (Bechtel SAIC Company) 2001. *Inventory Abstraction.* ANL-WIS-MD-000006 REV 00 ICN 02. Las Vegas, Nevada: Bechtel SAIC Company. ACC: MOL.20010416.0088.

154842 Metcalf, R. 2001. "Delivery of In-Drift ANC/pH Model Results and Validation for the SSPA Volume 1 Report." Memorandum from R. Metcalf (BSC) to B. MacKinnon and D. Jolley, May 15, 2001, PROJ.05/01.032, with enclosure. ACC: MOL.20010516.0246.

154843 NADP/NTN (National Atmospheric Deposition Program/National Trends Network 2001. *National Atmospheric Deposition Program/NTN Anuual/Seasonal Depositions, Seasonal Data for Site: NV00 (Red Rock Canyon), From January 22, 1985 - October 3, 2000.* Champaign, Illinois: National Atmospheric Deposition Program Office, Illinois State Water Survey. TIC: 249981.

154844 BSC (Bechtel SAIC Company) 2001. *Secondary Uranium-Phase Paragenesis and Incorporation of Radionuclides into Secondary Phases.* ANL-EBS-MD-000019 REV 00 ICN 01. Las Vegas, Nevada: Bechtel SAIC Company. Submit to RPC URN-0840.

154845 Lieser, K.H. and Ament, A. 1993. "Radiochemical Investigation of the Partition and Sorption of Lead in Groundwater/Sediment Systems." *Radiochimica Acta, 60,* (2/3), 153-158. München, Germany: R. Oldenbourg Verlag. TIC: 249835.

154847 Rickard, D.T. and Nriagu, J.O. 1978. "Aqueous Environmental Chemistry of Lead." Chapter 8 of *The Biogeochemistry of Lead in the Environment, Part A.* [Topics in Environmental Health]. Nriagu, [J.O.], ed. Pages 219-284. [New York, New York: Elsevier]. On Order Library Tracking Number-248543.

154849 Ferri, D.; Grenthe, I.; Hietanen, S.; and Salvatore, F. 1987. "Studies on Metal Carbonate Equilibria.18. Lead(II) Carbonate Complexes in Alkaline Solutions." *Acta Chemica Scandinavica. Series A: Physical and Inorganic Chemistry, A41,* 349-354. [Copenhagen, Denmark: Munksgaard]. TIC: 249841.

154850 Siantar, D.P. and Fripiat, J.J. 1995. "Lead Retention and Complexation in a Magnesium Smectite (Hectorite)." *Journal of Colloid and Interface Science, 169,* (2), 400-407. Orlando, Florida: Academic Press. TIC: 249847.

154851 Nagy, N.M. and Konya, J. 1998. "Ion-Exchange Processes of Lead and Cobalt Ions on the Surface of Calcium-Montmorillonite in the Presence of Complex-Forming Agents I. The Effect of EDTA on the Sorption of Lead and Cobalt Ions on Calcium-Montmorillonite." *Colloids and Surfaces A: Physicochemical and Engineering Aspects, 137,* ([1-3]), 231-242. [New York, New York]: Elsevier. TIC: 249837.

154852 Roy, W.R.; Krapac, I.G.; and Steele, J.D. 1993. "Soil Processes and Chemical Transport, Sorption of Cadmium and Lead by Clays from Municipal Incinerator Ash–Water Suspensions." *Journal of Environmental Quality, 22,* 537-543. [Madison, Wisconsin: American Society of Agronomy]. TIC: 249842.

154853 Wang, Z. and Stumm, W. 1987. "Heavy Metal Complexation by Surfaces and Humic Acids: A Brief Discourse on Assessment by Acidimetric Titration." *Netherlands Journal of Agricultural Science, 35,* 231-240. [Wageningen, The Netherlands: Koninklijk Genootschap voor Landbouwwetenschap]. TIC: 249855.

154854 Summers, T.S.E.; Rebak, R.B.; and Seeley, R.R. 2000. *Influence of Thermal Aging on the Mechanical and Corrosion Properties of C-22 Alloy Welds.* UCRL-JC-137727. Livermore, California: Lawrence Livermore National Laboratory. ACC: MOL.20010517.0257.

154855 BSC (Bechtel SAIC Company) 2001. *Thermal Hydrology EBS Design Sensitivity Analysis.* CAL-EBS-HS-000003 REV 00 ICN 01. Las Vegas, Nevada: Bechtel SAIC Company. ACC: MOL.20010525.0080.

154862 Rosenberg, N.D.; Gdowski, G.E.; and Knauss, K.G. 2001. "Evaporative Chemical Evolution of Natural Waters at Yucca Mountain, Nevada." *Applied Geochemistry, 16,* (9-10), 1231-1240. New York, New York: Pergamon. TIC: 249879.

154863 CRWMS M&O 2000. *Rock Properties Model Analysis Model Report.* MDL-NBS-GS-000004 REV 00 ICN 02. Las Vegas, Nevada: CRWMS M&O. ACC: MOL.20010216.0001.

154864 BSC (Bechtel SAIC Company) 2001. *Bases for the Supplemental Science and Performance Analyses (SSPA) Vol 1 Calculations.* Input Transmittal 00455.T. Las Vegas, Nevada: Bechtel SAIC Company. ACC: MOL.20010522.0196.

154867 Ellenwood, F.O. and Mackey, C.O. 1962. *Thermodynamic Charts.* Second Edition. New York, New York: John Wiley and Sons. On Order Library Tracking Number-249904.

154871 Lee, J.H. 2001. "Effect of Temperature on Passive Current Density of Alloy 22 Under Potentiostatic Control for Use in SSPA Volume 1 Report." Memorandum from J.H. Lee (BSC) to RPC = 1, May 17, 2001, PROJ.05/01.040. ACC: MOL.20010517.0255.

154872 Mon, K. 2001. "WAPDEG Simulations for Section 7.4 of the SSPA Report." Memorandum from K. Mon (BSC) to P. Pasupathi, May 15, 2001, PROJ.05/01.042, with enclosure. ACC: MOL.20010517.0256.

154873 BSC (Bechtel SAIC Company) 2001. *Climate Scenarios for 10,000-1,000,000 Years - for Infiltration Modeling in UZ PMR and the SSPA Vol. 1 Summary Reports.* Input Transmittal 00465.T. Las Vegas, Nevada: Bechtel SAIC Company. ACC: MOL.20010530.0157.

154874 BSC (Bechtel SAIC Company) 2001. *Analysis of Geochemical Data for the Unsaturated Zone.* ANL-NBS-HS-000017 REV 00 ICN 01. Las Vegas, Nevada: Bechtel SAIC Company. ACC: MOL.20010405.0013.

154881 Karmazin, L. 1982. "Lattice Parameter Studies of Structure Changes of Ni–Cr Alloys in the Region of Ni2-Cr." *Materials Science and Engineering, 54,* 247-256. Amsterdam, The Netherlands: Elsevier. TIC: 249655.

154890 Tappen, J.J. 2001. "Delivery of Comparison of Dose Assessment Methods for the SSPA Volume 1 Report." Memorandum from J.J. Tappen (BSC) to RPC = 70, May 17, 2001, PROJ.05/01.046, with enclosures. ACC: MOL.20010522.0159.

154891 Lee, J.H. 2001. "Effect of Temperature, pH and Electrolyte Ratio on Passive Current Density of Alloy 22 Under Potentiostatic Control for Use in SSPA Volume 1 Report." Memorandum from J.H. Lee (BSC) to RPC = 2, May 17, 2001, PROJ.05/01.047. ACC: MOL.20010518.0146.

154892 Wu, D.W. 2001. "Delivery of Uncertainty Evaluation for Fixed GENII-S Input Parameters for the SSPA Volume 1 Report." Memorandum from D.W. Wu (BSC) to RPC = 25, May 17, 2001, PROJ.05/01.044, with enclosures. ACC: MOL.20010518.0149.

154893 Wu, D.W. 2001. "Delivery of Se-79 and Np-237 BDCFs for the SSPA Volume 1 Report." Memorandum from D.W. Wu (BSC) to RPC = 29, May 17, 2001, PROJ.05/01.043, with enclosures. ACC: MOL.20010518.0147.

154894 Wu, D.W. 2001. "Delivery of Development of Human Receptor of Interest for the SSPA Volume 1 Report." Memorandum from D.W. Wu (BSC) to RPC = 26, May 17, 2001, PROJ.05/01.045, with enclosures. ACC: MOL.20010518.0148.

154912 Kuzio, S. 2001. "Data Cited in Volume 1 of the SSPA." Memorandum from S. Kuzio (SNL) to Yucca Mountain Records Processing Center, May 17, 2001, with enclosure. ACC: MOL.20010522.0160.

154916 Pan, L.; Liu, H.H.; Cushey, M.; and Bodvarsson, G.S. 2001. *New Particle Tracker for Modeling Transport in Dual-Continuum Media Users Manual.* LBNL-42958. Berkeley, California: Lawrence Berkeley National Laboratory. On Order Library Tracking Number-249895.

154918 Wu, Y-S.; Zhang, W.; Pan, L.; Hinds, J.; and Bodvarsson, G.S. 2000. *Capillary Barriers in Unsaturated Fractured Rocks of Yucca Mountain, Nevada.* LBNL-46876. Berkeley, California: Lawrence Berkeley National Laboratory. TIC: 249912.

154921 BSC 2001. *Software Code: MkTable.* V1.00. PC. 10505-1.00-00.

154922 Dobson, P. 2001. Evaluation of Local Altered Hydraulic Characteristics and the Effects of Near Field Thermal and Chemical Alterations. Scientific Notebook YMP-LBNL-DSM-ELS-PD-1. ACC: MOL.20010104.0286; MOL.20010209.0167.

154924 Danko, G.; Bahrami, D.; and Adu-Acheampong, A. 2001. "Ventilation Analysis of a Cold Conceptual Repository Using MULTIFLUX with NUFT." *"BACK TO THE FUTURE - Managing the Back End of the Nuclear Fuel Cycle to Create a More Secure Energy Future," Proceedings of the 9th International High-Level Radioactive Waste Management Conference (IHLRWM), April 29 - May 3, 2001, Las Vegas, Nevada.* La Grange Park, Illinois: American Nuclear Society. TIC: 247873.

154927 CRWMS M&O 2000. *Probability Distribution for Flowing Interval Spacing.* ANL-NBS-MD-000003 REV 00 ICN 01. Las Vegas, Nevada: CRWMS M&O. ACC: MOL.20001204.0034.

154928 Kuzio, S.P.; Arnold, B.W.; and Gauthier, J.H. [2000]. *Parameter Sensitivity in the Saturated Zone Site-Scale Model for Performance Assessment at Yucca Mountain.* SAND 2000-1599A. Albuquerque, New Mexico: Sandia National Laboratories. ACC: MOL.20000824.0642.

154932 Statham, W.H. 2001. *Desert Rock Wind Computation - 2 Winzipped Files.* Las Vegas, Nevada: Bechtel SAIC Company. ACC: MOL.20010517.0417.

154933 BSC (Bechtel SAIC Company) 2001. *Records Package for Documenting the Calculation Procedure for Determining the Number of Waste Packages Contained in an Area Circumscribed by a Conduit Diameter Used in the SSPA Volume I Section 14.3.3, Table 14.3.3-1.* Las Vegas, Nevada: Bechtel SAIC Company. ACC: MOL.20010515.0241.

154934 Turchi, P.E.A. 2001. "Delivery of Property Diagram (Phase Fraction Versus Temperature) of Alloy 22 at Its Nominal Composition." Memorandum from P.E.A. Turchi (BSC) to RPC = 3, May 21, 2001, PROJ.05/01.051, with enclosure. ACC: MOL.20010522.0158.

154935 Pasupathi, V. 2001. "Results of Slow Strain Rate Tests (SSRT) and Electrochemical Studies Performed at the Lawrence Livermore National Laboratory (LLNL) Using Specimens of Alloy 22 for Use in SSPA Volume 1 Report." Memorandum from V. Pasupathi (BSC) to RPC = 2, May 22, 2001, PROJ.05/01.050. ACC: MOL.20010522.0157.

154936 Pasupathi, V. 2001. "Results of Constant Load Uniaxial Tension Tests Performed at the Lawrence Livermore National Laboratory (LLNL) Using Specimens of Alloy 22, Ti Gr 7, and Types 304 and 316 NG Stainless Steels for Use in SSPA Volume 1 Report." Memorandum from V. Pasupathi (BSC) to RPC = 3, May 21, 2001, PROJ.05/01.049. ACC: MOL.20010522.0156.

154943 BSC (Bechtel SAIC Company) 2001. *Update to Waste Package DBE Rockfall Analysis.* Input Transmittal 00459.T. Las Vegas, Nevada: Bechtel SAIC Company. ACC: MOL.20010524.0105.

154948 Hyer, D. 2001. Request for Assignment of an Accession Number for a Document Being Used in the SSPA, Volume 1, Section 12. Letter from D. Hyer (LANL) to K. Quinnell (BSC), May 23, 2001, EES-9-05-23-264, with enclosure. ACC: MOL.20010601.0257; MOL.20010522.0215.

154949 Mohanty, S. and McCartin, T. 2001. *Conceptual Models and Data.* Volume 1 of *NRC Sensitivity and Uncertainty Analyses for a Proposed HLW Repository at Yucca Mountain, Nevada, Using TPA 3.1.* NUREG-1668. Washington, D.C.: U.S. Nuclear Regulatory Commission. TIC: 249896.

154951 CRWMS M&O 2001. *Repository Safety Strategy: Plan to Prepare the Safety Case to Support Yucca Mountain Site Recommendation and Licensing Considerations.* TDR-WIS-RL-000001 REV 04 ICN 01. Las Vegas, Nevada: CRWMS M&O. ACC: MOL.20010329.0825.

154985 BSC (Bechtel SAIC Company) 2001. *Three-Dimensional Heterogeneous LDTH Model from MSTH Rev 00/ICN02A.* Input Transmittal 00468.T. Las Vegas, Nevada: Bechtel SAIC Company. ACC: MOL.20010524.0107.

154988 Carpenter, C.E., Jr. and Lund, A.L. 1999. "BWR Internals Cracking Issues." *Corrosion 99.* Paper No. 438. Pages 1-7. Houston, Texas: NACE International. TIC: 249986.

154989 Shoemaker, D.P. and Shoemaker, C.B. 1988. "Icosahedral Coordination in Metallic Crystals." Chapter 1 of *Introduction to Quasicrystals.* Jaric, M.V., ed. Aperiodicity and Order Volume 1. San Diego, California: Academic Press. TIC: 245244.

154994 Reimus, P. 2001. "Delivery of Data Files on CD, Title: Reimus, P.W. 2001. Data Files for the SSPA, Volume 1, Section 12.3.2 and Subsections and Section 12.4.3. Submittal date: 05/21/01." Letter from P. Reimus (LANL) to M. Lee (BSC), May 23, 2001, EES-9-05-23-263, with enclosures ACC: MOL.20010525.0085.

154995 Robinson, B. 2001. "Delivery of Data Files on CD, Title: Robinson, B.A. 2001. Data Files for the SSPA, Volume 1, Section 12.3.2.3. Submittal Date: 05/19/01." Letter from B. Robinson (LANL) to M. Lee (BSC), May 23, 2001, EES-9-05-23-262, with enclosures. ACC: MOL.20010525.0084.

155004 Kuzio, S. 2001. "Data Cited in Volume 1 of the SSPA, Title: Data for Parameters Associated with Unquantified Uncertainty Analysis in the Saturated Zone." Memorandum from S. Kuzio (SNL) to Yucca Mountain Records Processing Center, May 24, 2001, with enclosure. ACC: MOL.20010525.0150.

155005 Blair, S. 2001. "Submittal of Draft Copy of ANL-NBS-HS-000037 Rev00C, Coupled Thermal Hydrologic Mechanical Effects on Permeability Analysis and Models Report." Memorandum from S. Blair (BSC) to File, May 25, 2001, LLYMP0105066, with attachment. ACC: MOL.20010530.0238.

155006 Landau, L.D. and Lifshitz, E.M. 1982. *Fluid Mechanics.* Volume 6 of *Course of Theoretical Physics.* 1st Edition. New York, New York: Pergamon Press. TIC: 249911.

155007 BSC (Bechtel SAIC Company) 2001. *Three-Dimensional Heterogeneous LDTH Model from MSTH Rev 00/ICN 02A.* Input Transmittal 00471.T. Las Vegas, Nevada: Bechtel SAIC Company. ACC: MOL.20010529.0191.

155008 BSC (Bechtel SAIC Company) 2001. *Thermal Conductivity Properties for the Tptpll and Tptpul.* Input Transmittal 00472.Ta. Las Vegas, Nevada: Bechtel SAIC Company. Submit to RPC URN-0881.

155010 BSC (Bechtel SAIC Company) 2001. *Lower-Temperature Subsurface Facility and Ventilation Concepts Analysis (Review Copy).* Input Transmittal 00469.T. Las Vegas, Nevada: Bechtel SAIC Company. ACC: MOL.20010529.0186.

155011 BSC (Bechtel SAIC Company) 2001. *Thermal Management Analysis for Low Temperature Design (Check Copy).* Input Transmittal 00470.T. Las Vegas, Nevada: Bechtel SAIC Company. ACC: MOL.20010529.0187.

155012 Buscheck, T.A. 2001. "Delivery of Input & Output Files for Sensitivity Calculations in the SSPA Volume 1 Report, Chapter 5." Memorandum from T.A. Buscheck (BSC) to J.A. Blink, June 25, 2001, PROJ.06/01.065, with enclosures. ACC: MOL.20010625.0388.

155014 Casale, I.B. 1967. "Boiling Temperatures of Mg Cl Solutions - Their Application in Stress Corrosion Studies." *Corrosion, 23,* (10), 314-317. [Houston, Texas]: National Association of Corrosion Engineers. TIC: 240226.

155016 Freedman, Y.E.; Magaritz, M.; Long, G.L.; and Ronen, D. 1994. "Interaction of Metals with Mineral Surfaces in a Natural Groundwater Environment." *Chemical Geology, 116,* (1-2), 111-121. Amsterdam, The Netherlands: Elsevier. TIC: 249834.

155017 Summers, T. 2001. "Micrograph of Josephinite." Memo from T. Summers to RPC = 1, May 27, 2001. ACC: MOL.20010529.0183.

155018 Summers, T. 2001. "Delivery of Extrapolation of Weld Stability Kinetics to Repository Relevant Temperatures Figure." Memo from T. Summers to RPC = 4, May 27, 2001, with enclosure. ACC: MOL.20010529.0181.

155019 Summers, T. 2001. "Delivery of Extrapolation of LRO Kinetics to Repository Relevant Temperatures Figure." Memo from T. Summers to RPC = 3, May 27, 2001, with enclosure. ACC: MOL.20010529.0182.

155023 McNeish, J. 2001. "Preliminary REV 00A Version of FY01 Supplemental Science and Performance Analyses, Volume 2: Performance Analyses, TDR-MGR-PA-000001." Memorandum from J. McNeish (BSC) to RPC = 4, May 29, 2001, PROJ.05/01.063, with enclosure. ACC: MOL.20010529.0377.

155024 BSC (Bechtel SAIC Company) 2001. *ANSYS/FLOTRAN Results for 2-D Natural Convective Cooling.* Input Transmittal 00460.T. Las Vegas, Nevada: Bechtel SAIC Company. ACC: MOL.20010510.0232.

155025 BSC (Bechtel SAIC Company) 2001. *Ventilation Model.* Input Transmittal 00473.T. Las Vegas, Nevada: Bechtel SAIC Company. ACC: MOL.20010529.0188.

155032 TerBerg, R. 2001. "Data Submittal Supporting Section 4.3.4 of SSPA, Vol. 1: Scientific Bases and Analyses (TDR-MGR-MD-000007)." Memorandum from R. TerBerg (LBNL) to Records Processing Center, May 23, 2001, with attachments. ACC: MOL.20010530.0233.

155033 TerBerg, R. 2001. "Data Submittal Supporting Section 11.3.3 of SSPA, Vol. 1: Scientific Bases and Analyses (TDR-MGR-MD-000007)." Memorandum from R. TerBerg (LBNL) to Records Processing Center, May 23, 2001, with attachments. ACC: MOL.20010530.0235.

155034 Bullard, B. 2001. "Section 7.3.5 of the SSPA Report, Figures and Tables." Memorandum from B. Bullard (BSC) to P. Pasupathi, May 30, 2001, PROJ.05/01.069, with enclosure. ACC: MOL.20010530.0590.

155035 Bullard, B. 2001. "Section 7.3.3 Table 2, Fig. 1 & 2 of the SSPA Report." Memorandum from B. Bullard (BSC) to P. Pasupathi, May 30, 2001, PROJ.05/01.070, with enclosure. ACC: MOL.20010530.0589.

155036 Bullard, B. 2001. "Section 7.3.6 of the SSPA Report, Table 7.3.6-1." Memorandum from B. Bullard (BSC) to P. Pasupathi, May 30, 2001, PROJ.05/01.071, with enclosure. ACC: MOL.20010530.0588.

155038 Schreiner, R. 2001. "Delivery of Calculations of Tolerance Intervals for Several Raionuclides [Radionuclides] for the SSPA Volume 1 Report." Memorandum from R. Schreiner (BSC) to RPC, May 22, 2001, PROJ.05/01.052, with enclosure. ACC: MOL.20010531.0065.

155041 Mariner, P. 2001. "Informal Calculation Regarding Precipitates/Salts Model Sensitivity Analyses in Support of SSPA Volume 1." Memorandum from P. Mariner (BSC) to B. MacKinnon, May 30, 2001, PROJ.05/01.075, with enclosure. ACC: MOL.20010531.0029.

155042 Vandergraaf, T.T.; Drew, D.J.; Ticknor, K.V.; and Seddon, W.A. 2001. "Radionuclide Migration in Tuff Under Unsaturated Conditions." *"BACK TO THE FUTURE - Managing the Back End of the Nuclear Fuel Cycle to Create a More Secure Energy Future," Proceedings of the 9th International High-Level Radioactive Waste Management Conference (IHLRWM), Las Vegas, Nevada, April 29 - May 3, 2001.* La Grange Park, Illinois: American Nuclear Society. TIC: 247873.

155048 Dixon, P.R. 2001. "Submittal of Preliminary Report on Field Investigtions [Investigations] of Unsaturated Zone Transport at Busted Butte." Memorandum from P.R. Dixon (LANL) to File, May 31, 2001, EES-13-05-01-266, with attachment. ACC: MOL.20010604.0140.

155051 BSC (Bechtel SAIC Company) 2001. *Technical Work Plan for Unsaturated Zone (UZ) Flow and Transport Process Model Report.* TWP-NBS-HS-000001 REV 01. Las Vegas, Nevada: Bechtel SAIC Company. ACC: MOL.20010404.0007.

155053 Case, J.B. 2001. "WAPDEG and Analysis of Bathtub Delays Using the WAPDEG Output Data." Memorandum from J.B. Case to Record Processing Center, May 30, 2001, PROJ.05/01.068, with enclosures. ACC: MOL.20010531.0066.

155055 BSC (Bechtel SAIC Company) 2001. *Technical Work Plan for FY01 Supplemental Science and Performance Analyses: Volume 1 – Scientific Bases and Analyses, Volume 2 – Performance Analyses.* TWP-MGR-MD-000014 REV 01. Las Vegas, Nevada: Bechtel SAIC Company. ACC: MOL.20010601.0152.

155057 Niemi, A. and Bodvarsson, G.S. 1988. "Preliminary Capillary Hysteresis Simulations in Fractured Rocks, Yucca Mountain, Nevada." *Journal of Contaminant Hydrology, 3,* 277-291. [Amsterdam, The Netherlands]: Elsevier. TIC: 222596.

155058 Ozment, K. 1999. "Journey to the Copper Age." *National Geographic, 195,* (4), 72-79. Washington, D.C.: National Geographic Society. TIC: 249913.

155060 Robinson, B. 2001. "Transmittal of C-Holes Update Report: Reinterpretation of the Reactive Tracer Test in the Bullfrog Tuff and Results of Laboratory Testing." Memorandum from B. Robinson (BSC) to RPC=2, June 1, 2001, PROJ.06/01.001, with enclosure. ACC: MOL.20010601.0102.

155075 Francis, N.D. 2001. "Documentation of Parameter Development and Sensitivity Studies for In-Drift Parameters Reported in the SSPA Volume 1 Report." Memorandum from N.D. Francis (SNL) to RPC, May 22, 2001, with attachment. ACC: MOL.20010601.0217.

155076 Reed, A.W. 2001. "Documentation of Sensitivity Studies for Invert Thermal Conductivity Reported in the SSPA Volume 1 Report." Memorandum from A.W. Reed (SNL) to RPC, May 22, 2001, with attachment. ACC: MOL.20010601.0218.

155081 LANL 2001. *Software Code: add_repo_nodes.f.* V1.0. 10548-1.0-00. URN-0862

155082 LANL 2001. *Software Code: CORPSCON.* V5.11.08. 10547-5.11.08-00. URN-0863

155083 LLNL 2001. *Software Code: DICTRA.* V20. 10391-20-00. URN-0864.

155084 LANL 2001. *Software Code: FEHM.* V2.11. 10086-2.11-00. URN-0865.

155085 LLNL 2001. *Software Code: Image Pro Plus.* V4.1. 10422-4.1-00. URN-0866.

155087 BSC 2001. *Software Code: MULTIFLUX.* V1.0. 10485-1.0-00. URN-0868.

155088 LLNL 2001. *Software Code: THERMO-CALC.* VM. 10170-M-00. URN-0869.

155102 TerBerg, R. 2001. "Data Submittal Supporting Section 4.3.3 of SSPA, Vol. 1: Scientific Bases and Analyses (TDR-MGR-MD-000007)." Memorandum from R. TerBerg (LBNL) to Records Processing Center, May 23, 2001, with attachment. ACC: MOL.20010530.0230.

155107 BSC (Bechtel SAIC Company) 2001. *Design Input for the Engineered Barrier System Environment and Barriers.* Input Transmittal 00422.Tb. Las Vegas, Nevada: Bechtel SAIC Company. ACC: MOL.20010518.0144.

155111 TerBerg, R. 2001. "Data Submittal Supporting Section 11.3.2 of SSPA, Vol. 1: Scientific Bases and Analyses (TDR-MGR-MD-000007)." Memorandum from R. TerBerg (LBNL) to Records Processing Center, May 23, 2001, with attachments. ACC: MOL.20010530.0234.

155128 Jurani, R. 2001. "Ventilation Test for Repository Subsurface Design." Memorandum from R. Jurani (BSC) to Records Processing Center (RPC) = 9, June 4, 2001, PROJ.06/01.003, with enclosure. ACC: MOL.20010604.0205.

155132 Howard, C. 2001. Preclosure Ventilation Test – 1/4-Scale. Scientific Notebook SN-SNL-SCI-020-V1. ACC: MOL.20010529.0267.

155144 Houseworth, J. 2001. "Scientific Notebook Referenced in FY01 Supplemental Science and Performance Analyses, Volume 1: Scientific Bases and Analyses, DI: TDR-MGR-MD-000007 REV 00." Interoffice correspondence from J. Houseworth (BSC) to File, June 5, 2001, with attachment. ACC: MOL.20010606.0224.

155166 BSC (Bechtel SAIC Company) 2000. *Software: WAPDEG.* V4.0. PC. 10000-4.0-00.

155186 Lloyd, A.C.; Shoesmith, D.W.; McIntyre, N.S.; and Noël, J.J. 2001. "Investigating the Localized Corrosion Properties of Ni-Cr-Mo Alloys for Their Use in Nuclear Waste Disposal Systems." *Stainless Steel World, 13,* (4), 29-33. [Zutphen, The Netherlands]: KCI Publishing B.V. TIC: 249982.

155188 IAEA (International Atomic Energy Agency) 2001. *An International Peer Review of the Biosphere Modelling Programme of the US Department of Energy's Yucca Mountain Site Characterization Project, Report of the IAEA International Review Team.* Vienna, Austria: International Atomic Energy Agency. TIC: 250092.

155189 Los Alamos National Laboratory 2001. *FIDAP.* 8.0. 10549-8.0-00. URN-0873.

155190 Los Alamos National Laboratory 2001. *Software Code: FLUENT.* V5.5. 10550-5.5-00. URN-0874.

155201 BSC (Bechtel SAIC Company) 2000. *Software: MVIEW.* V2.20. HP, SUN, SGI, DEC. 10072-2.20-00.

155202 Mon, K. 2001. "Additional Figures for Section 7.3.5 of the SSPA Report." Memorandum from K. Mon (BSC) to P. Pasupathi (BSC), June 15, 2001, PROJ.06/01.032, with enclosure. ACC: MOL.20010615.0184.

155203 Wu, D.W. 2001. "Delivery of Development of Supplementary Receptor for the SSPA Volume 1 Report." Memorandum from D.W. Wu (BSC) to RPC, June 14, 2001, PROJ.06/01.030 with enclosures. ACC: MOL.20010615.0185.

155232 IADC (International Association of Drilling Contractors) 1992. *Drilling Manual.* 11th Edition. [Houston, Texas]: International Association of Drilling Contractors. TIC: 232344.

155233 Bourgoyne, A.T., Jr.; Millheim, K.K.; Chenevert, M.E.; and Young, F.S., Jr. 1986. "Rotary Drilling Bits." Chapter 5 of *Applied Drilling Engineering.* SPE Textbook Series Volume 2. Richardson, Texas: Society of Petroleum Engineers. TIC: 250085.

155234 Warren, T.M. 1987. "Penetration-Rate Performance of Roller-Cone Bits." *DRILLING.* SPE Reprint Series No. 22. Pages 182-191. Richardson, Texas: Society of Petroleum Engineers. TIC: 250084.

155241 Lee, J.H. 2001. "Median Lead Concentration in Groundwater Samples Cited in Section 7.3.1.3.4 of the SSPA Report Vol. 1." Memorandum from J.H. Lee (BSC) to P. Pasupathi, June 20, 2001, Proj.06/01.049, with enclosure. ACC: MOL.20010621.0155.

155244 Kuzio, S. 2001. "Data Cited in Volume 1 of the SSPA for Section 12.5.3." Memorandum from S. Kuzio (SNL) to Yucca Mountain Records Processing Center, June 21, 2001, with enclosure. ACC: MOL.20010621.0626.

155246 BSC (Bechtel SAIC Company) 2001. *ANSYS Calculations in Support of Natural Ventilation Parametric Study for SR.* CAL-SVS-HV-000003 REV 00 ICN 01. Las Vegas, Nevada: Bechtel SAIC Company. ACC: MOL.20010613.0250.

155247 Chen, Y. 2001. "Delivery of Draft of CAL-WIS-MD-000012 for the SSPA Volume 1 Report." Memorandum from Y. Chen (BSC) to RPC, June 22, 2001, PROJ.06/01.054, with enclosure. ACC: MOL.20010622.0222.

155251 Reimus, P. 2001. "Delivery of Data Files on CD, TITLE: Reimus, P. W. 2001. Data Files for Modified Figures in REV 00F of the SSPA, Volume 1, Section 12.4.3. Submittal date: 06/19/01." Letter from P. Reimus (LANL) to M. Lee (BSC), June 19, 2001, EES-9-06-19-270, with enclosures. ACC: MOL.20010625.0199.

155308 Dunn, S. 2001. "Delivery of 2nd Natural Convection Modeling for the Low Energy (0.12 kw/m) Input Phase I Case Files Used." Memorandum from S. Dunn (BSC) to J.A. Blink, June 27, 2001, PROJ.06/01.069, with enclosures. ACC: MOL.20010627.0188.

155309 Blair, S. 2001. "Delivery of Input and Output Files of 3 DEC LBT Simulations for the SSPA Volume 1 Report, Chapter 5." Memorandum from S. Blair (BSC) to J.A. Blink, June 27, 2001, PROJ.06/01.066, with enclosure. ACC: MOL.20010627.0187.

155312 BSC (Bechtel SAIC Company) 2001. *Input Transmittal Potentiometric Map.* Input Transmittal 00467.T. Las Vegas, Nevada: Bechtel SAIC Company. URN-0880.

155321 Francis, N; Itamura, M. 2001. TH ABSTRACTION RESULTS FOR THE LTOM AND HTOM DESIGN OPTIONS Sandia National Laboratories Memorandum. URN-0884.

155324 LLNL (Lawrence Livermore National Laboratory) 2001. *Software Routine: MSTHAC.* Version 6.4.2. 10419-6.4.2-00. URN-0885.

155327 Hoxie, D. 2001. "Analogue for Leakage of Radionuclides from a Potential Repository at Yucca Mountain." E-mail from D. Hoxie to A. Eddebbarh (CRWMS M&O), June 29, 2001, with attachment. ACC: MOL.20010629.0079.

155328 CRWMS M&O 2001. *Pretest Predictions for Ventilation Tests.* CAL-EBS-MD-000013 REV 00. Las Vegas, Nevada: CRWMS M&O. ACC: MOL.20010205.0014.

155449 Buscheck, T.A. 2001. "Delivery of Input and Output Files MSTHAC V.6.4.2 and the DDT Models Used in the SSPA Volume 1, ICN 01, Chapter 5 Report Superceding Previous Submission." Memorandum from T.A. Buscheck (BSC) to J.A. Blink, July 17, 2001, PROJ.07/01.007, with enclosures. URN-0919

155457 Leem, J. 2001. "Delivery of Thermal-Hydrology Sensitivity Calculations for Pre-Closure Ventilation Efficiency and Ventilation Duration for the SSPA Volume 1 Report Memorandum from J. Leem (BSC) to J. Blink, July 17, 2001, PROJ.07/01.029, with enclosure. URN-0918

16.2 CODES, STANDARDS, REGULATIONS, AND PROCEDURES

101680 64 FR 8640. Disposal of High-Level Radioactive Wastes in a Proposed Geologic Repository at Yucca Mountain, Nevada. Proposed rule 10 CFR Part 63. Readily available.

104787 10 CFR 20. Energy: Standards for Protection Against Radiation. Readily available.

105065 64 FR 46976. Environmental Radiation Protection Standards for Yucca Mountain, Nevada. Proposed rule 40 CFR Part 197. Readily available.

124754 64 FR 67054. Office of Civilian Radioactive Waste Management; General Guidelines for the Recommendation of Sites for Nuclear Waste Repositories; Yucca Mountain Site Suitability Guidelines. Proposed rule 10 CFR Part 963. Readily available.

153195 ASME PTC 19.1-1998. *Test Uncertainty, Instruments and Apparatus.* New York, New York: American Society of Mechanical Engineers. TIC: 249327.

153202 AP-SV.1Q, Rev. 0, ICN 2. *Control of the Electronic Management of Information.* Washington, D.C.: U.S. Department of Energy, Office of Civilian Radioactive Waste Management. ACC: MOL.20000831.0065.

154517 AP-3.10Q, Rev. 2, ICN 4. *Analyses and Models.* Washington, D.C.: U.S. Department of Energy, Office of Civilian Radioactive Waste Management. ACC: MOL.20010405.0009.

154534 AP-2.21Q, Rev. 1, ICN 0, BSCN 001. *Quality Determinations and Planning for Scientific, Engineering, and Regulatory Compliance Activities.* Washington, D.C.: U.S. Department of Energy, Office of Civilian Radioactive Waste Management. ACC: MOL.20010212.0018.

154712 ASTM G 28-97. 2000. *Standard Test Methods of Detecting Susceptibility to Intergranular Corrosion in Wrought, Nickel-Rich, Chromium-Bearing Alloys.* West Conshohocken, Pennsylvania: American Society for Testing and Materials. TIC: 249897.

154886 AP-SI.1Q, Rev. 3, ICN 1. *Software Management.* Washington, D.C.: U.S. Department of Energy, Office of Civilian Radioactive Waste Management. ACC: MOL.20010515.0126.

155009 66 FR 23013. Office of Civilian Radioactive Waste Management; Yucca Mountain Science and Engineering Report; Site Recommendation Consideration and Request for Comment. Readily available.

155216 66 FR 32074. 40 CFR Part 197, Public Health and Environmental Radiation Protection Standards for Yucca Mountain, NV; Final Rule. Readily available.

155318 ASM (American Society for Metals) 1997. *Metals Handbook.* 10th printing. Metals Park, Ohio: American Society for Metals. On Order Library Tracking Number-250192.

16.3 SOURCE DATA

103769 MO9901MWDGFM31.000. Geologic Framework Model. Submittal date: 01/06/1999.

104055 LB997141233129.001. Calibrated Basecase Infiltration 1-D Parameter Set for the UZ Flow and Transport Model, FY99. Submittal date: 07/21/1999.

105821 LB980901233124.001. Pneumatic Pressure and Air Permeability Data from Niches 3107 and 4788 in the ESF from Chapter 2 of Report SP33PBM4: Fracture Flow and Seepage Testing in the ESF, FY98. Submittal date: 09/14/1998.

105855 LB980901233124.004. Pneumatic Pressure and Air Permeability Data from Alcove 6 in the ESF. Submittal date: 09/14/1998.

106089 SNT05071897001.012. Source Data for Base Case Thermal Property Data for TSPA-VA (Total System Performance Assessment-Viability Assessment) (VA Supporting Data). Submittal date: 05/25/1999.

106748 GS980808312242.014. Physical Properties of Borehole Core Samples and Water Potential Measurements Using the Filter Paper Technique for Borehole Samples from USW SD-6. Submittal date: 08/11/1998.

106785 LB990701233129.001. 3-D UZ Model Grids for Calculation of Flow Fields for PA for AMR U0000, "Development of Numerical Grids for UZ Flow and Transport Modeling". Submittal date: 09/24/1999.

106787 LB990501233129.001. Fracture Properties for the UZ Model Grids and Uncalibrated Fracture and Matrix Properties for the UZ Model Layers for AMR U0090, "Analysis of Hydrologic Properties Data". Submittal date: 08/25/1999.

107293 GS961108312261.006. Gas Chemistry, ESF Alcoves 2 and 3, 11/95 - 4/96; Water Chemistry, Alcove 2 (Tritium), Alcove 3, and ESF Tunnel; and Pneumatic Pressure Response from Boreholes in Exploratory Studies Facility Alcoves 2 and 3, 10/95 - 5/96. Submittal date: 11/12/1996.

109966 MO9901RIB00044.000. Reference Information Base Data Item - Hydrologic Characteristics: Unsaturated Zone Flow Characteristics. Submittal date: 01/06/1999.

110226 LB990861233129.001. Drift Scale Calibrated 1-D Property Set, FY99. Submittal date: 08/06/1999.

110828 LB980912332245.001. Air Injection Data from Niche 3107 of the ESF. Submittal date: 09/30/1998.

111485 SN9907T0872799.001. Heat Decay Data and Repository Footprint for Thermal-Hydrologic and Conduction-Only Models for TSPA-SR (Total System Performance Assessment-Site Recommendation). Submittal date: 07/27/1999.

113495 LA9908JC831321.001. Mineralogic Model "MM3.0" Version 3.0. Submittal date: 08/16/1999.

113584 GS960708312132.002. Porosity, Water Content, Mineralogy and Other Data Derived from Geophysical Logs and Cores for 26 Boreholes. Submittal date: 07/09/1996.

122261 SN9907T0571599.001. Probability Distribution of Flowing Interval Spacing. Submittal date: 07/15/1999.

122733 LA9909JF831222.010. Chloride, Bromide, Sulfate, and Chlorine-36 Analyses of ESF Porewaters. Submittal date: 09/29/1999.

122736 LA9909JF831222.012. Chloride, Bromide, and Sulfate Analyses of Porewater Extracted from ESF Niche 3566 (Niche #1) and ESF 3650 (Niche #2) Drillcore. Submittal date: 09/29/1999.

122757 LB990801233129.003. TSPA Grid Flow Simulations for AMR U0050, "UZ Flow Models and Submodels" (Flow Field #3). Submittal date: 11/29/1999.

128157 LB991215123142.001. CO2 Analysis of Gas Samples Collected from the Drift Scale Test. Submittal date: 02/17/2000.

129624 LA9909PR831231.005. Interpretations of Tracer Data - Modeling Data. Submittal date: 09/02/1999.

137076 MO9810SPA00026.000. Diffusion Coefficient Model for TSPA-VA. Submittal date: 10/29/1998.

140107 LA9909PR831231.003. Interpretations of Bullfrog Reactive Tracer Test Data - Modeling Data. Submittal date: 09/02/1999.

142884 LL000114004242.090. TSPA-SR Mean Calculations. Submittal date: 01/28/2000.

144922 LL990702804244.100. Borehole and Pore Water Data. Submittal date: 07/13/1999.

145533 GS930408312271.014. Analysis of CO2 Concentration of Syringe Samples Taken During USW UZ-1 Borehole Gas Sampling, May, 1989, thru Jan., 1991. Submittal date: 03/30/1993.

145598 LA9909JF831222.004. Chloride, Bromide, and Sulfate Analyses of Busted Butte and Cross Drift Tunnel Porewaters in FY99. Submittal date: 09/29/1999.

146231 LA9909JF831222.006. Cation Analyses of ESF, Cross Drift and Busted Butte Porewaters in FY99. Submittal date: 09/29/1999.

146816 GS000100001221.001. EarthInfo, Inc. Western US Meteorologic Station Weather Data - NCDC Summary of Day (West 1) and NCDC Summary of Day (West 2). Submittal date: 01/25/2000.

146877 GS990908314224.009. Detailed Line Survey Data for Horizontal and Vertical Traverses, ECRB. Submittal date: 09/16/1999.

146878 LB002181233124.001. Air Permeability and Pneumatic Pressure Data Collected Between October 27, 1999 through November 7, 1999 from Niche 5 (ECRB Niche 1620) of the ESF. Submittal date: 02/18/2000.

147022 GS000399991221.002. Rainfall/Runoff/Run-on 1999 Simulations. Submittal date: 03/10/2000.

147081 LA0002JC831341.001. Depth Intervals and Bulk Densities of Alluviums. Submittal date: 03/08/2000.

147176 LA0003JC831341.001. Adsorption of NP-237 in Three Types of Alluvium as a Function of Time and Stratigraphic Position. Submittal date: 03/09/2000.

147334 LB991121233129.002. Calibrated Parameters for the Present-Day, Mean Infiltration Scenario, Used for Simulations with Perched Water Conceptual Model #2 for the Mean Infiltration Scenarios of the Present-Day, Monsoon and Glacial Transition Climates. Submittal date: 03/11/2000.

147607 MO0003SEPDRDDA.000. Results from Drift Degradation Analysis. Submittal date: 03/08/2000.

147613 GS000308311221.005. Net Infiltration Modeling Results for 3 Climate Scenarios for FY99. Submittal date: 03/01/2000.

148295 MO0003RIB00079.000. Rock Mechanical Properties. Submittal date: 03/30/2000.

148524 MO9911SEPGRP34.000. Geotechnical Rock Properties. Submittal date: 11/10/1999.

148596 MO9912SPAPAI29.002. PA Initial Abstraction of THC Model Chemical Boundary Conditions. Submittal date: 01/11/2000.

148751 LA0003AM831341.001. Probability Distributions for Sorption Coefficients (Kd's). Submittal date: 03/29/2000.

148850 MO0003RIB00071.000. Physical and Chemical Characteristics of Alloy 22. Submittal date: 03/13/2000.

149092 MO0004MWDRIFM3.002. Results of the Yucca Mountain Probabilistic Seismic Hazard Analysis (PSHA). Submittal date: 04/14/2000.

149194 LA0002SK831352.002. Total Colloidal Particles Concentration and Size Distribution in Groundwaters Around Yucca Mountain. Submittal date: 02/25/2000.

149232 LA0002SK831352.001. Total Colloidal Particles Concentration and Size Distribution in Groundwaters from the Nye County Early Warning Drilling Program. Submittal date: 02/24/2000.

149257 MO0004NC99WL1D.000. Water Level Measurements in Boreholes, NC-EWDP-1D, NC-EWDP-1D Shallow, & NC-EWDP-1D Deep, Nye County Early Warning Drilling Program. Submittal date: 04/19/2000.

149258 MO0004NC99WL1S.000. Water Level Measurements in Borehole, NC-EWDP-1S, Nye County Early Warning Drilling Program. Submittal date: 04/18/2000.

149259 MO0004NC99WL2D.000. Water Level Measurements in Borehole, NC-EWDP-2D, Nye County Early Warning Drilling Program. Submittal date: 04/18/2000.

149263 MO0004NC99WL9S.000. Water Level Measurements in Borehole, NC-EWDP-9S, Nye County Early Warning Drilling Program. Submittal date: 04/19/2000.

149765 SN0003L1011398.003. Engineered Barrier System (EBS) Testing Program - Pilot-Scale Testing: 1/4 Scale Engineering Demonstration Testing, Canister #3. Submittal date: 03/03/2000.

150798 LL000509112312.003. TSPA-SR Multiscale TH Results (E0120) Mean Calculations Using Drift Scale Property Set. Submittal date: 05/18/2000.

150930 MO0005PORWATER.000. Perm-Sample Pore Water Data. Submittal date: 05/04/2000.

151029 MO0006J13WTRCM.000. Recommended Mean Values of Major Constituents in J-13 Well Water. Submittal date: 06/07/2000.

151514 SN0005T0581699.005. Geometric Means and Standard Deviations for Fracture Aperture Distributions for Unsaturated Zone (UZ) Transport in TSPA-SR. Submittal date: 05/24/2000.

151812 MO0008SPATHS03.001. Thermal-Hydrological Sensitivity Calculations for Various Ventilation Times, Lineal Heat Loading, and Infiltration Rates in Support of the Report CAL-EBS-HS-000003. Submittal date: 08/24/2000. Submit to RPC URN-0657.

152545 SN0007T0872799.014. Abstraction of Thermal Hydrologic (TH) Data for TSPA-SR for the No Backfill Repository Design. Submittal date: 07/05/2000.

152884 MO0010MWDSUP04.010. Supporting Data for Abstraction of Models of Stress Corrosion Cracking of Drip Shield and Waste Package Outer Barrier and Hydrogen Induced Corrosion of Drip Shield. ANL-EBS-PA-000004 REV 00 ICN 01. Submittal date: 10/25/2000.

152926 MO0003RIB00073.000. Physical and Chemical Characteristics of TI Grades 7 and 16. Submittal date: 03/13/2000.

152980 SN0009T0810599.014. Updated Average Radionuclide Activities for Commercial Spent Nuclear Fuel (CSNF) and Co-Disposal Waste Packages for Total System Performance Assessment-Site Recommendation (TSPA-SR) and Final Environmental Impact Statement (TSPA-FEIS). Submittal date: 09/20/2000.

153044 MO0003RIB00076.000. Physical and Chemical Characteristics of Type 316N Grade. Submittal date: 03/14/2000.

153155 LB0011AIRKTEST.001. Air Permeability Testing in Niches 3566 and 3650. Submittal date: 11/08/2000.

153380 LB0011THCDISSX.001. Summary of Results from TPTPMN Tuff Dissolution Experiment. Submittal date: 12/07/2000.

153393 LB0010SCMREV01.002. Developed Data from Seepage Calibration Modeling AMR U0080. Submittal date: 11/29/2000.

153470 LB0011DSTFRAC1.001. Drift-Scale Properties Update: 1. Updated Drift-Scale Properties. This is Input Data for AMR U0110 (MDL-NBS-HS-000001 REV01). Submittal date: 12/06/2000.

153570 LB0011SMDCREV1.002. Seepage Model for PA Including Drift Collapse: 2. Tables of Seepage Percentages AMR U0075 (MDL-NBS-HS-000002 REV01). Submittal date: 12/07/2000. Submit to RPC URN-0794.

153574 LB0011SMDCREV1.001. Seepage Model for PA Including Drift Collapse: 1. Model Input/Output Files AMR U0075 (MDL-NBS-HS-000002 REV01). Submittal date: 12/07/2000. Submit to RPC URN-0877.

153677 GS981008312272.004. Analysis for Chemical Composition of Pore Water from Boreholes USW UZ-7A, USW WT-24, USW SD-6, USW SD-7, and USW SD-12 During FY 1997 and 1998. Submittal date: 10/28/1998.

153688 SN0012T0511599.003. Results from Abstraction of Drift Seepage, Rev. 01. Submittal date: 12/20/2000.

154012 MO0102SPAFRA01.002. Fracture Intensity for External Actinide Accumulation. Submittal date: 02/20/2001. Submit to RPC URN-0883.

154048 MO0010RDDAAMRR.002. Results from Drift Degradation Analysis. Submittal date: 10/17/2000.

154087 MO0007RIB00077.000. In Situ Rock Conditions. Submittal date: 07/18/2000.

154299 MO0010MWDMIN38.031. MING V1.0 Calculations for the In Drift Microbial Communities Model. Submittal date: 10/10/2000.

154577 LB0101THCPRCPX.001. Summary of Results from TPTPMN Tuff Precipitation Experiment. Submittal date: 02/13/2001.

154578 LB0011THCDISSM.002. Comparison Modeling for TPTPMN Tuff Dissolution Experiment: 2. Output Data for AMR U0110 REV01. Submittal date: 12/07/2000.

154586 LB0012AIRKTEST.001. Niche 5 Air K Testing 3/23/00-4/3/00. Submittal date: 12/21/2000.

154636 MO0001MWDEQ346.007. EQ3/6 Input/Output Files for THC Abstraction In-Drift Precipitates/Salts Analysis. Submittal date: 01/31/2000.

154654 SN0010T0502900.003. Igneous Consequence Data for Total System Performance Assessment-Site Recommendation (TSPA-SR) Revised to Support No-Backfill Design Change. Submittal date: 10/30/2000.

154656 LB0101DSTTHCR1.001. Pore Water Composition and CO2 Partial Pressure Input to Thermal-Hydrological-Chemical (THC) Simulations: Table 3 of AMR N0120/U0110 Rev01, "Drift-Scale Coupled Processes (Drift-Scale Test and THC Seepage) Models". Submittal date: 01/26/2001.

154664 LL010109723123.011. Input and Output Files Supporting Coupled Thermal-Hydrologic-Mechanical Effects on Permeability Analysis and Model Report. Submittal date: 04/18/2001.

154685 GS000808314211.005. Interpretations of the Lithostratigraphy in Boreholes NC-EWDP-01DX, NC-EWDP-02D, NC-EWDP-03D, and NC-EWDP-09SX, Nye County Early Warning Drilling Program Phase I, FY 99. Submittal date: 08/14/2000.

154686 MO0007NYE02565.024. Cuttings Sample Log for Borehole NC-EWDP-19D. Submittal date: 07/11/2000. Submit to RPC URN-0859.

154713 SN0104T0511599.004. Developed Data for Analysis of Asperity-Induced Episodic Infiltration into Superheated Rock. Submittal date: 04/24/2001.

154759 LB0011DSTTHCR1.001. Tables Showing Geochemical and Drift-Scale Seepage Model Data Which are Presented in AMR U0110/N0120, "Drift-Scale Coupled Processes (DST and THC Seepage) Models REV01". Submittal date: 12/19/2000.

154760 LA0002JF12213U.001. Chemistry Data for Porewater Extracted from Drillcore from Surface-Based Boreholes USW NRG-6, USW NRG-7A, USW UZ-7A, USW UZ-14, UE-25 UZ#16, USW UZ-N55, USW SD-6, USW SD-7, USW SD-9, USW SD-12, and USW WT-24. Submittal date: 02/15/2000.

154868 LB0102DSTHCLTD.001. Drift Scale THC Seepage Model - Low Temperature Design: 1. Summary Spreadsheets. Submittal date: 02/28/2001.

154887 LA0105GZ12213S.001. SZ Flow Model with No East-West Barrier with NW Trending Fault Zone. Submittal date: 05/11/2001. Submit to RPC URN-0837.

154888 LA0105GZ12213S.002. SZ Flow Model with No East-West Barrier. Submittal date: 05/11/2001. Submit to RPC URN-0838.

154889 LA0105GZ12213S.003. SZ Flow Model with No East-West Barrier with Anisotropic Permeability. Submittal date: 05/11/2001. Submit to RPC URN-0839.

154929 LA0103TV12213U.001. Static Batch Sorption Coefficients and Retardation Coefficients. Submittal date: 03/30/2001. Submit to RPC URN-0836.

154993 LA0105GZ12213S.004. SZ Flow Model with Shallow Solitario Canyon Fault. Submittal date: 05/24/2001. Submit to RPC URN-0876.

154998 GS010508311221.001. Mean Annual Air Temperature Used for Simulation of Infiltration for Modern Climate Scenario. Submittal date: 05/25/2000.

155252 Pasupathi, P. 2001. "Cyclic Polarization Results Using Calcium Chloride Solutions." Memorandum from P. Pasupathi (BSC) to J. Lee, June 14, 2001, PROJ.06/01.031, with enclosure. ACC: MOL.20010613.0374.

155255 SN0106F3409100.003. Preclosure Ventilation Test: 1/4-Scale, Including Data from Cases 1 through 6 (with Results from 10/5/2000 through 12/22/00). Submittal date: 06/04/2001. Submit to RPC URN-0875.

INTENTIONALLY LEFT BLANK

APPENDIX A
HUMAN INTRUSION SCENARIO

APPENDIX A
HUMAN INTRUSION SCENARIO

Introduction–The EPA standard in 40 CFR 197.25 (66 FR 32074 [DIRS 155216]) requires that the DOE determine when a human intrusion could occur based upon the earliest time that current technology and practices could lead to waste package penetration without the driller noticing. The EPA standard also establishes different dose standards, based on the earliest time (i.e. at or before 10,000 years after disposal or occurs more than 10,000 years after disposal) that a complete waste package penetration is projected to occur unnoticed. The proposed NRC rule states that, rather than speculating on the nature and probability of future intrusion, it is more useful to assess how resilient the geologic repository would be against a postulated intrusion (64 FR 8640 [DIRS 101680], p. 8675) and requires an assessment of repository performance based on a postulated human intrusion occurring 100 years after permanent closure. The DOE included in proposed 10 CFR 963.16 (64 FR 67054 [DIRS 124754]) the requirement for a performance assessment of stylized human intrusion into the repository as defined by NRC regulations (64 FR 67054 [DIRS 124754], p. 67079). The stylized human intrusion scenario takes the form of a drilling event that results in a single, nearly vertical borehole that penetrates a waste package, extends to the saturated zone, and is not adequately sealed (64 FR 8640 [DIRS 101680], p. 8677). To evaluate the likelihood of compliance with these requirements, the DOE evaluated two stylized human intrusion scenarios in the TSPA-SR (CRWMS M&O 2000 [DIRS 153246]). Figure 4.4-12 of the TSPA-SR shows a comparison of the mean human intrusion annualized dose curve from an intrusion at 100 and 10,000 years.

The purpose of this appendix is to provide a preliminary analysis of whether a driller would likely notice, based on current technology and practices, the complete penetration of a waste package at or before 10,000 years or more than 10,000 years after disposal.

Regulatory Basis–The EPA standard published in 40 CFR 197.25 (66 FR 32074 [DIRS 155216]) requires that the DOE determine when a human intrusion could occur based upon the earliest time that current technology and practices could lead to waste package penetration without the drillers noticing that the waste package had been penetrated.

Proposed NRC rule 10 CFR 63 (64 FR 8640 [DIRS 101680]) includes requirements that the DOE potential repository design must still perform as intended if an assumed, stylized intrusion occurs (64 FR 8640 [DIRS 101680], p. 8651). The NRC has proposed that DOE use current practices for resource exploration to establish properties (e.g., diameter of the borehole, drilling rate, composition of drilling fluids) for the intrusion scenario. The proposed rule requires an assessment of the ability of the geologic repository to limit radiological exposures in the event of limited human intrusion into the engineered barrier system. Compliance is to be demonstrated through a separate performance assessment that meets the requirements specified at proposed 10 CFR 63.114 (64 FR 8640 [DIRS 101680]) and uses the reference biosphere and critical group specified at proposed 10 CFR 63.115 (64 FR 8640 [DIRS 101680]). The assessment has to assume that the human intrusion occurs 100 years after permanent closure and takes the form of a drilling event that results in a single, nearly vertical borehole that penetrates a waste package, extends to the saturated zone, and is not adequately sealed. (64 FR 8640 [DIRS 101680], p. 8677).

The DOE has also included, in proposed 10 CFR 963.16 (64 FR 67054 [DIRS 124754]), a requirement to determine postclosure suitability based on TSPA analyses of repository performance in cases with and without a stylized human intrusion event (64 FR 67054 [DIRS 124754], p. 67073). The requirements for this second TSPA include the assumptions for a stylized human intrusion into the repository, as defined by NRC regulations (64 FR 67054 [DIRS 124754], p. 67079).

Performance Assessment Background–The considerations used in the TSPA-SR (CRWMS M&O 2000 [DIRS 153246] Section 4.4) for a stylized human intrusion into the repository are summarized in Table 4.4-1 of the TSPA-SR. The stylized human intrusion was assumed to occur 100 years following permanent closure. TSPA-SR Figure 4.4-11 shows 300 simulated annualized dose histories along with some statistical measures of the annualized dose distribution. The peak mean human intrusion annualized dose during the first 10,000 years after potential repository closure is approximately 0.008 mrem/yr., occurring at approximately 1,000 years. No annualized dose for any of the 300 realizations exceeds 0.5 mrem/yr over the first 10,000 years. TSPA-SR Figure 4.4-12 shows a comparison of the mean human intrusion annualized dose curve from an intrusion at 10,000 years with the mean annualized dose curve from the base case intrusion at 100 years. For the intrusion at 10,000 years, there were no annualized doses prior to 10,000 years and the peak mean annualized dose over 100,000 years is less than that for the base case intrusion at 100 years. At 100,000 years, the mean annualized dose is nearly identical to the mean annualized dose from the base case, and is approximately 0.004 mrem/yr. (CRWMS M&O 2000 [DIRS 153246], Section 4.4)

The results of the TSPA-SR drip shield and waste package studies indicate long lifetimes for these components (CRWMS M&O 2000 [DIRS 153246], Section 3.4), with the first drip shield failures occurring after about 20,000 years. The first failures of the waste package outer material, Alloy 22, by general corrosion occur after approximately 30,000 years (this general corrosion duration does not consider the 5 cm of stainless steel beneath the Alloy 22). While general corrosion occurs gradually over time up to the time of failure, the oxidation process is a surface phenomenon, and the underlying metal retains its integrity and resistance to drilling. Although TSPA-SR results show failures at early time, these failures are the result of localized corrosion and are not associated with degradation of the overall structural integrity of the waste package, and the resistance to drilling is maintained.

Waste Package Penetration by Drilling–There are a number of operational parameters that would indicate to a driller that down-hole conditions had changed and merit additional investigation and possibly a bit run (the removal of the bit from the hole for review and grading). A factor of two change in the rate of penetration or torque would be sufficient to indicate a change in drilling conditions and prompt additional investigations leading to the recognition that the driller had inadvertently drilled into a metallic material (i.e., drip shield or waste package).

The following discussion presents several lines of evidence relevant to estimating the time when a human intrusion could occur based upon the earliest time that current technology and practices could lead to waste package penetration without a driller noticing waste package penetration as being after the 10,000 year regulatory period.

The initial selection of bit type is typically made on the basis of what is known about the formation characteristics. The terms usually used by drilling engineers to describe the formation characteristics are drillability and abrasiveness. The drillability of the formation is a measure of how easy the rock formation is to drill. It is inversely related to the compressive strength of the rock, although other factors are also important. The abrasiveness of the formation is a measure of how rapidly the cutting surface of a bit will wear when drilling the formation. Although there are some exceptions, the abrasiveness tends to increase as the drillability decreases (Bourgoyne et al. 1986 [DIRS 155233]).

The bases for these discussions are typical practices used in drilling water wells in southwestern United States. The International Association of Drilling Contractors (IADC 1992 [DIRS 155232]) has developed a classification chart for selection of roller bits. Using this classification chart, roller bits with characteristics of 7-1 or 7-2 (hard semi-abrasive and abrasive formations) would be selected for drilling through the welded geologic units at Yucca Mountain, based on geo-mechanical properties. The 7-1 roller drill bits utilize 80 to 90 degree short chisel tungsten-carbide inserts, whereas the 7-2 roller drill bits utilize 60 to 70 degree short projectile tungsten-carbide inserts. Roller bits are typically used in drilling water wells due to their low cost and wide range of operational flexibility. Polycrystalline diamond cutter and diamond cutter drag bits typically are not used in water well drilling because of the high costs of these drill bits. Direct circulation hammer drills are sometimes used to drill brittle competent rock such as welded volcanic tuff, but they typically are inefficient in unconsolidated alluvium or incompetent rock formations. This limitation reduces the use of these drills in typical water well drilling. However, the discussions provided herein would be generally applicable to roller or hammer bits.

Uniaxial compressive strengths for the major geologic units at Yucca Mountain were determined using confined compression tests (Table A-1). Static Young's Modulus values were computed from stress-strain data obtained from unconfined compression tests. The intact rock unconfined compressive strength and elastic modulus by rock unit are given in Table A-1.

Based on the design described in the *Yucca Mountain Science and Engineering Report* (DOE 2001 [DIRS 153849]), Titanium grades 7 and 24 are candidate materials for drip shield fabrication and Alloy 22 and 316 nuclear grade stainless steel are candidate materials for waste package fabrication (DOE 2001 [DIRS 153849] Sections 2.4.4 and 3). Physical and chemical properties for these materials have been determined, and the tensile strength and modulus of elasticity for candidate drip shield and waste package materials are shown in Table A-2.

There have been a number of studies conducted to correlate operational parameters to rate of penetration of the drill bit. Many of these studies indicate that the rate of penetration is inversely proportional to the square of the compressive strength of the material being drilled, all other factors being equal (Bourgoyne et al. 1986 [DIRS 155233]; Warren 1987 [DIRS 155234]). This would indicate that a change of approximately 1.4 in the compressive strength of the material would be adequate to produce the factor of two change in the rate of penetration necessary for recognition by a driller.

Roller bits are designed to take advantage of brittle failure of the rock matrix to crush, break, and remove rock in an efficient manner. The volume of rock that is newly fractured by a tooth depends on the geometry, rock properties, and tooth penetration depth below the rock surface. The force applied to the tooth for a particular situation determines the tooth penetration depth. The bit tooth always penetrates into the rock until the resistant force offered back by the rock equals the force applied to the tooth. The tooth penetrates until the shear stress on the tooth caused by the weight on the bit is balanced by the shear strength of the rock. The rock may also become more ductile so that a greater tooth penetration is required to cause sufficient strain for chipping to occur (Warren 1987 [DIRS 155234]). As a load is applied to a bit tooth, the pressure beneath the tooth increases until it exceeds the crushing strength of the rock and a wedge of finely powered rock then is formed beneath the tooth. As the force of the tooth increases, the material in the wedge compresses and exerts high lateral forces on the solid rock surrounding the wedge until the shear stress exceeds the shear strength of the solid rock and the rock fractures. These fractures propagate along a maximum shear surface. As the force of the tooth increases above the threshold value, subsequent fracturing occurs in the region above the initial fracture, forming a zone of broken rock. The bit tooth moves forward until it reaches the bottom of the crater, and the process repeats (Bourgoyne et al. 1986 [DIRS 155233]).

The failure mechanisms between brittle rock and ductile steel differ significantly. The ductility of a material, usually measured as the percent reduction in area or elongation that occurs during a tensile test, can provide indications on how a material will fail. Ductile materials, with a minimum elongation in tensile testing, will not fail in service through brittle fracture (ASM 1997 [DIRS 155318]).

Selection of a bit for drilling involves knowledge of the characteristics of the rock. As indicated in Tables A-1 and A-2, there are differences between the tensile strengths and ductility of the geologic units at Yucca Mountain and the candidate materials for the drip shield and waste package. Because the materials used in the drip shield and waste packages have high compressive strengths and high ductility, the tooth of a roller bit cannot penetrate enough to cause sufficient strain for chipping to occur, resulting in a tearing action with associated high torque values. Bits designed for drilling rock would not be efficient for drilling through metal; boring in metals typically utilizes a milling technique. Milling produces a different failure mechanism than brittle failure that roller bits and hammer bits typically produce.

Bit operating conditions–Bit operating conditions (i.e., bit weight and rotary speed) affect the rate of penetration and the vibrations felt on the drill rig. The bit operating conditions affect and are affected by the rounded geometry of the emplacement drift, drip shield, and waste package, and size, orientation, and location of where the drilling assembly enters the emplacement drift and contacts the drip shield and waste package.

The loss of circulation of the drill and the sudden drop in weight when the drill bit breaks through the top of the emplacement drift would provide indications that conditions had changed. However, the lithophysal and fractured nature of certain of the Topopah Spring Tuff rock units could provide similar indications. Bit stabilization would be reduced as a result of the free space provided by the size of the emplacement drift (5.5 m) and the space between the crown of the emplacement drift and the drip shield and waste package if the drifts remain stable. A key block analysis has been performed to provide an indication of ground stability and the level of ground

support necessary to keep repository openings stable during the operational period. This analysis indicates a block volume of approximately 0.1 cubic meters, at a 75 percent cumulative frequency of occurrence, would fall into the emplacement drifts should the drifts collapse (CRWMS M&O 1999 [DIRS 102111]). These relatively small rocks would tend to move or shift under small loads and the uneven loading on the drill bit would increase the lateral deviation forces by a phenomenon called preferential chip formation (Bourgoyne et al. 1986 [DIRS 155233]). As such, even if the drifts collapse the character of the rubble would be insufficient to stabilize the drill string. Severe wobbling bit action results as the bit is rotated if the drill collars or stabilizers above the bit are not held in a concentric position in the borehole.

The drilling assembly would have to contact the relatively small areas that make up the apex of the drip shield or waste package, where the surfaces are essentially perpendicular to the drill bit in order to have any possibility of penetrating these barriers. Lateral deviation forces increase with relatively small changes in the contact angle between the bit and the drilled material (Bourgoyne et al. 1986 [DIRS 155233]). Only the apex of the drip shield or waste package provides a perpendicular plane for which drip shield and waste package geometry would not increase the lateral deviation forces. If the drilling assembly contacted any location other than the relatively small areas that make up the apex of the drip shield or waste package, the combination of the large lateral deviation forces, the relatively small drill bit diameter and high rotational speeds, the lack of drill bit insert penetration and uneven loading on the bit (preferential chip formation), the high compressive strengths of the material used in the drip shield and waste package, and the lack of drilling assembly stability would likely cause the drill bit to slip off of the drip shield or waste package. Any penetration of the waste package or instability would be accompanied by a noticeable increase in drill string torque and reduced rate of penetration as the bit teeth contacted the metal. This increased torque would exacerbate the instability and increase the likelihood of the bit sliding past the metal. The chatter (vibration) resulting from the assembly bouncing on the top or side of these barriers would likely cause the drilling operator to change parameters in an attempt to smooth out operations.

Conclusion–The information presented in this appendix addresses the issue of when a human intrusion could occur based upon the earliest time that current technology and practices could lead to waste package penetration without the driller noticing waste package penetration. Conclusions based on information presented in this appendix suggest that a human intrusion event, if it were to occur, would not happen in the timeframe of regulatory compliance. The time to general corrosion failure of waste packages is approximately 30,000 years. Before this time, the presence of steel will be recognizable to the drillers, generally through loss of rate of penetration. This conclusion is conservative, because it is based on comparisons related to strength of the rock and steel and does not consider the 5 cm of stainless steel underneath the outer material of Alloy 22. The ductility of the metals makes them nearly impenetrable by techniques used in drilling rock, and the milling techniques needed to bore steel are not used in rock drilling, unless required for fishing operations or other specialized applications.

The elevation of the mountain and the resultant greater depth to water, especially when compared to shallower wells that would be required to the south of the mountain, make exploration unlikely. However, the regulations specify consideration of a human intrusion event. The TSPA-SR (CRWMS M&O 2000 [DIRS 153246]) considered a stylized event occurring at 100 years, as specified in the proposed NRC regulation 10 CFR Part 63 (64 FR 8640 [DIRS 101680]). The TSPA-SR also examined the mean human intrusion annualized dose from an intrusion at 10,000 years. Both of these evaluations show that performance is within the regulatory limits.

Table A-1. Uniaxial Compressive Strength and Young's Moduli by Rock Unit

Rock Unit		Uniaxial Compressive Strength Mean [MPa]/Range	Elastic (Young's Modulus) Mean [GPa]
Tiva Canyon (welded)		127.5/36.0 to 230.9	29.4
Paintbrush Tuff (non-welded)		6.4/1.3 to 19.3	2.5
Topopah Springs (welded 1)		58.2/26.7 to 65.2	20.4
Topopah Springs (welded 2)		167.9/103.8 to 187.5	33.0
Proposed Repository Unit	Tptpmn	187.5	32.9
Proposed Repository Unit	Tptpll	103.8	27.5
	Tptpln	144.4	35.5
Topopah Springs (welded 3)		16.4/16.4	37.4
Calico Hills (non-welded)		23.2/20.5 to 24.6	5.6

Source: DTN: MO0003RIB00079.000 [DIRS 148295].

Table A-2. Candidate Material Properties for Drip Shield and Waste Package Fabrication

Engineered Barrier Material	Use	Tensile Strength [MPa]	Modulus of Elasticity [GPa]
Titanium Grade 7[a]	Drip Shield	345	106.9
Titanium Grade 24	Drip Shield	895[d]	113.8[e]
Alloy 22[b]	Waste Package	802	206
Type 316 Nuclear Grade Stainless Steel[c]	Waste Package	550	196

Source: [a] DTN: MO0003RIB00073.000 [DIRS 152926].
[b] DTN: MO0003RIB00071.000 [DIRS 148850].
[c] DTN: MO0003RIB00076.000 [DIRS 153044].
[d] Tensile Strength for Titanium Grade 24 (ASM International 1990 [DIRS 141615]).
[e] Modulus of Elasticity for Titanium Grade 24 (ASME 1998 [DIRS 145103]).

NOTE: Candidate materials based on the design described in the Yucca Mountain Science and Engineering Report (DOE 2001 [DIRS 153849], Sections 3.4 and 2.4.4).

INTENTIONALLY LEFT BLANK